

# Diagnostics of hollow cathode arc plasma source by optical emission spectroscopy

X. Zhong<sup>1</sup>, and A. Lunk<sup>2</sup>

<sup>1</sup> Department of Physics, Shanghai Jiao Tong University, 200030, Shanghai, China

<sup>2</sup> Institute of Plasma Research, University of Stuttgart, D-70569 Stuttgart, Germany

**Abstract** In this paper it will be presented that results of investigations on the properties of hollow cathode arc (HCA) as a source of atomic nitrogen measured by optical emission spectroscopy. The experiment was performed at constant argon flow ( $Q_{Ar} = 40$  sccm) and variable discharge current ( $10\text{ A} < I_D < 90\text{ A}$ ). The nitrogen as well as the helium flow was changed. The pressure inside the chamber corresponds to  $2 \times 10^{-3}$  mbar working in Ar and increases adding  $N_2$  and He correspondingly. The intensity of  $N_2^-$ ,  $N_2^+$ ,  $N^-$ ,  $N^+$ -lines, Ar- and  $Ar^+$ - as well as He- lines were measured in dependence on gas flow and discharge current. It was found that at constant current ( $I_D = 40\text{ A}$ ) the ratio of intensity of  $Ar^+/Ar$ -lines ( $I_{410}/I_{463}$ ) increases by the factor of 2 with adding a small amount of nitrogen to pure argon (from  $Q_{N_2} = 0$  to  $Q_{N_2} = 2$  sccm) and becomes saturated as nitrogen flow increases. Also the intensity ratio  $N^+/N_2^-$  lines ( $I_{463}/I_{337}$ ) becomes saturated at  $Q_{N_2} > 2$  sccm. With the increase of helium flow at constant nitrogen flow the intensity ratio  $N^+/N_2^-$  lines ( $I_{463}/I_{337}$ ) remains nearly constant, which indicates that the charge transfer collision between helium ion and nitrogen can be neglected in our experiments. Changing the current in the saturation mode intensity ratio of  $Ar^+/Ar$ -lines ( $I_{410}/I_{463}$ ) as well as of  $N^+/N_2^-$  lines ( $I_{463}/I_{337}$ ) increases with increasing current by the factor of about 20 for  $Ar^+/Ar$  and factor of about 17 at  $N^+/N_2$  in the region of  $10\text{ A} \leq I_D \leq 90\text{ A}$ . At a current of  $I_D = 50\text{ A}$  or so, the relative maxima of the intensities of different species lines were found. The experimental results will be discussed in terms of dissociation and ionisation of plasmas species.

## Reference

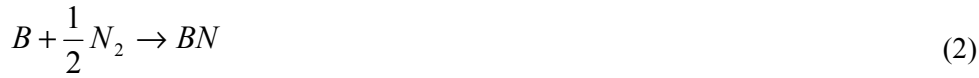
1. Lunk, et al, *Spectroscopic in situ diagnostics of boron nitride film growth in plasma-enhanced deposition*, Applied Physics A Materials Science & Processing, 72, 2001.
2. Jian Ye, Dissertation: *Depositin of Cubic Boron Nitride Thin Films by Radio Frequency Bias Sputtering*, University Kaiserslautern D386
3. G. Rohrbach, et al, *Characterization of plasma conditions in a hollow cathode arc evaporation device*, Surface coating and technology, 123, 2000
4. S. Kagge, et al, *Probe diagnostics of anisotropic plasma in a hollow cathode arc*, J. Appl. Phys. 70 (1), 1991.
5. A. R. Striganov, *Tables of Spectral lines of Neutral and Ionized Atoms*, IFI / Plenum Newyork-washington, 1968
6. Lofthus, et al, *The spectrum of Molecular Nitrogen*, J. Phys. Chem. Ref. Data., Bol. 6, No. 1, 1977
7. G. Herzberg, et al, *Molecular spectra and molecular structure I. spectra of diatomic molecules*, Robert E. Krieger Publishing Company, Malabar, Florida, 1989
8. P. Prigent, et al, *Selective population of some N triplet states in a low-pressure pulsed He/ $N_2$  plasma*, J. Phys. B: At, Mol. Phys. 20, 1987

## 1. Introduction

c-BN is very promising material as a hard protective coatings for cutting tools especially in the situations where the utilization of diamond is limited. Besides its favorable combination of mechanical and chemical properties, c-BN has the second highest thermal conductivity. Thus, it is very attractive as heat sink for electronic devices. In addition, cubic boron nitride is a potential electronic material for fabricating high-temperature, high-frequency semiconductive devices and ultraviolet optoelectronic devices for the future since it has the widest bandgap among IV and III-V group materials and, moreover, the incorporation of both p- and n-type shallow dopant impurities have been achieved [1-4].

In the last decade, many group have successfully grown c-BN using various techniques including ion beam assisted deposition, r.f. sputtering, ion plating, laser ablation, plasma enhanced deposition. In our group, plasma enhanced deposition of c-BN film was performed using the hollow cathode arc as plasma source. During the deposition of c-BN film, the following two processes are always included, and the process (1) is

more effective and important, i.e. the atomic nitrogen plays an important role in the deposition of c-BN film, which is directly related to the characteristics of the plasma source.



The present work is focused on the possibility of the application of the hollow cathode arc as a source of atomic nitrogen for deposition of c-BN film by optical emission spectroscopy. With this motivation, we had investigated the variation of spectra of different nitrogen and argon species-lines with several discharging parameters of hollow cathode arc. In this paper, the experimental setup and the experimental parameters are described in sec. 2, the experimental results are illustrated and analyzed in sec. 3, and in set. 4 the conclusions are given.

## 2. Experiments

The experimental setup used here is shown in Fig. 1. The plasma is generated by hollow cathode discharge. The light emitted from plasma is reflected by mirror 1 and mirror 2 to a lens with focal length of 20 cm, which focuses the light on the slit of a grating spectrometer (BM 100) coupled to a photomultiplier (PMT). Through an A/D convertor, the signal from PMT are analyzed and recorded in computer, which is also used

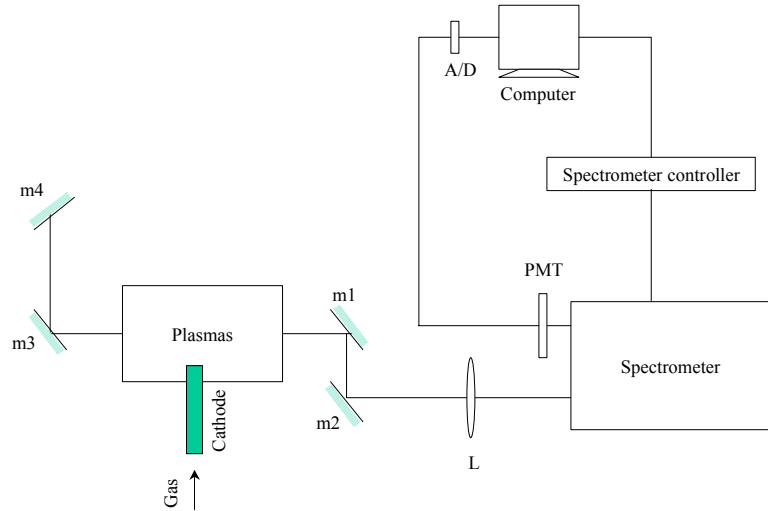


Fig. 1 The diagram the experimental setup

to control the spectrometer controller (BM 693). The slit of spectrometer is 50  $\mu\text{m}$ , the scanning velocity is 0.5 nm/s, each data recorded on the computer corresponds to an average over 1000 shots. In our experiments, the plasma was detected at a distance of 0.5 cm from the cathode orifice. At standard condition, the discharge current of cathode was kept constant at 40 A, the pressure inside the chamber corresponds to  $2 \times 10^{-3}$  mbar working in the argon with flux of 40 sccm and increases correspondingly with the addition of nitrogen and helium. The intensity of  $N_2^-$ ,  $N_2^+$ ,  $N^-$ ,  $N^+$  lines, Ar- and  $Ar^+$  as well as He- lines were measured in dependence on gas flow and discharge current. The lines and corresponding transitions of the plasmas species discussed in this paper is shown in Tab.1 [5-7].

Tab. 1 lines and corresponding transitions of plasmas species

Species	Lines	Transitions
$N^+$	463.0 nm	$(3p^3P - 3s^3P)$
$N_2$	337.1 nm	$C^3\Pi_u(v=0) \rightarrow B^3\Pi_g(v=0)$
$Ar^+$	410.4 nm	$(5s^4P - 4p^4D)$
Ar	462.8 nm	$(5p^2[5/2] - 4s^2[1/2])$



### 3. Results and discussion

#### 3.1 Influence of nitrogen flow

Fig. 2 shows the behavior of atomic nitrogen ion in the Ar / N<sub>2</sub> plasma as a function of nitrogen flow, where the emission intensities of atomic nitrogen N<sup>+</sup> at 463.0 nm and molecular nitrogen N<sub>2</sub><sup>+</sup> at 337.1 nm together with the ratio of them are displayed. As the nitrogen flow increases, the emission intensities of N<sup>+</sup> at 463.0 nm increase linearly, while its relative intensity with molecular nitrogen N<sub>2</sub><sup>+</sup> at 337.1 nm remains constant. In general, the degree of dissociation and ionization of a gas molecule depends on the residence time of the gas in the plasma, which is calculated by the equation  $t = PV/Q$ , where  $t$  is the gas residence time,  $P$  the gas pressure,  $V$  the chamber volume, and  $Q$  the gas flow rate. More dissociation and ionization occurs for longer residence times in the plasma because of the many collisions between gas molecules and high-energy electrons, vice versa. In our experiments, the gas pressure increase with the increase of nitrogen flow, the gas residence time in the chamber keeps nearly unchanged, and therefore results in the relative constant dissociation and ionization rate. So, it can be concluded that dissociation as well as ionization processes of molecular N<sub>2</sub> do not depend on nitrogen flow rate.

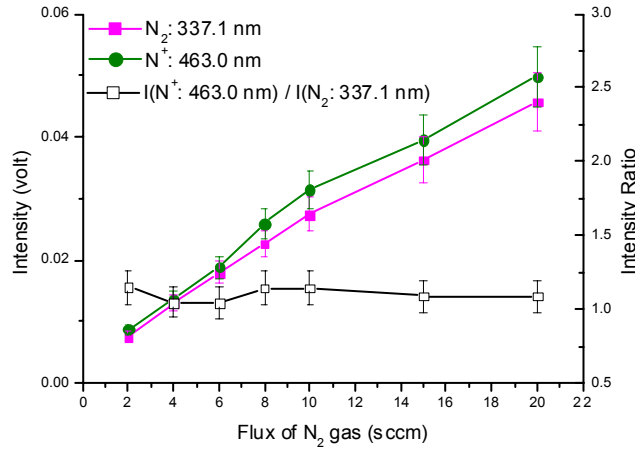


Fig. 2 Influence of nitrogen flow on the atomic nitrogen ion

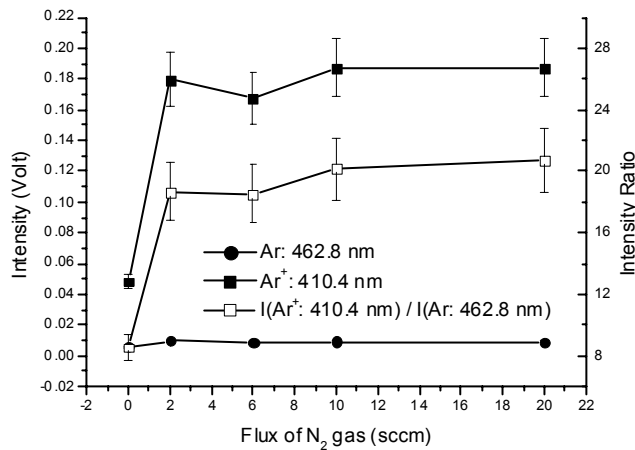


Fig. 3 Influence of nitrogen flow on atomic argon ion

Fig. 3 shows the behavior of atomic argon ion as a function of nitrogen flow where the emission intensity of atomic argon Ar at 462.8 nm and atomic argon ion at 410.4 nm are given, and the ratio of between them are applied to investigate the dependence of the ionization and excitation process of argon on the nitrogen flow. It can be noted that the relative intensity of atomic argon ion at 410.4 nm with that of atomic argon at 462.8

nm increases by a factor of about 2 with 2 sccm nitrogen addition. The result can be explained as that a small amount of nitrogen will favor the excitation and the ionization of argon due to charge exchange collision between argon and nitrogen. Similar to the dependence of atomic nitrogen ion on nitrogen flow shown in fig. 2, the flow of nitrogen gas above 2 sccm has no much effect on the ionization of the argon.

### 3.2 Influence of Helium flow

In high-current helium-molecular-gas mixture plasmas, the concentrations of ionic  $\text{He}^+$  states are often large enough to induce dissociation and ionization of the molecules by charge transfer collision as shown in the relation (3), of which the effectiveness had been demonstrated by P. Prigent and B. Dureuil in ref. 8.

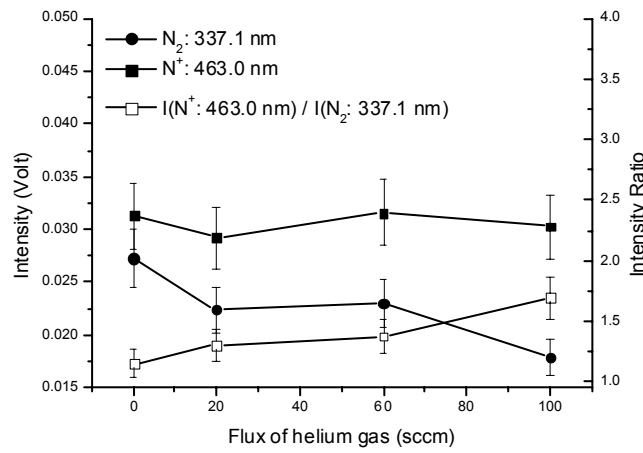
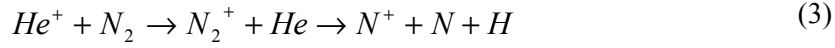


Fig. 4 Influence of helium flow on the atomic nitrogen ion

In our experiment, the influence of helium flow on the atomic nitrogen ion is shown in Fig.4 at standard condition and with the nitrogen flux of 10 sccm, where emission intensities of atomic nitrogen ion at 463 nm and molecular nitrogen at 337.1 nm as well as their ratio are displayed. As the increase of helium flow, the emission intensity of molecular nitrogen decreases, this decrease may be due to the dilution effect, while the emission intensity of atomic nitrogen ion keeps nearly unchanged, and the ratio of the emission intensity of atomic nitrogen ion and that of molecular nitrogen is increased by a factor of 1.5 with 100 sccm helium addition. Comparing the results in ref.8, in our case, the effect of helium on atomic nitrogen ion is so small that means the charger transfer collision between atomic helium ion and molecular nitrogen could be neglected.

### 3.3 Influence of cathode current

Fig. 5 shows the dependence of the atomic nitrogen ion in the plasma source on the cathode current. With cathode current increasing, the emission intensity of the atomic nitrogen ion  $\text{N}_2^+$  at 463 nm increases up to cathode current 40 A, decreases above cathode current 60 A, at a current of  $I_D = 50$  A or so, the relative maxima of the emission intensity are found. And the emission intensity of  $\text{N}_2^+$  with respect to that of  $\text{N}_2$  is increased by a factor of about 17 with cathode increasing from 10 A to 90 A.

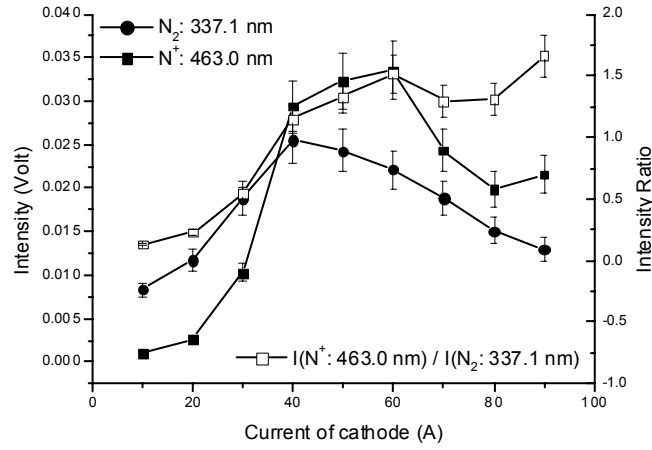


Fig. 5 The influence of cathode current on atomic nitrogen ion

Similar results can be also seen in the fig. 6, in which the emission intensities of atomic argon at 462.8 nm and atomic argon ion at 410.4 nm are shown and the intensity ratio between them is increased by a factor of about 20. The increase of intensity ratio in Fig. 5 and Fig. 6 should be due to the increases in electron density and average energy of electrons with the cathode current. The dependence of emission intensity on the cathode current could be explained as below.

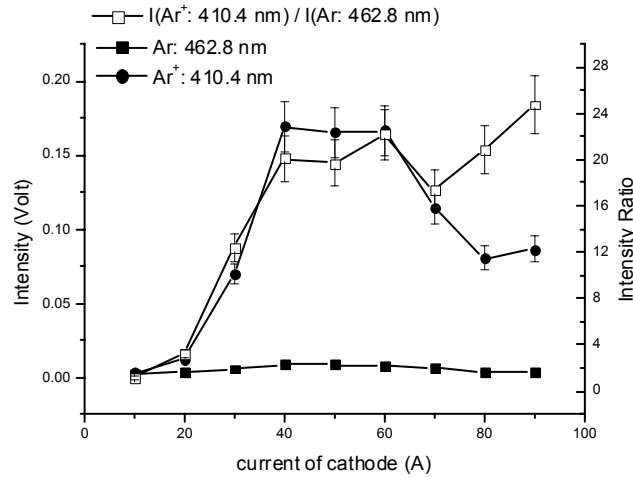


Fig. 6 The influence of cathode current on the atomic argon ion

For electrons, there are two kinds of collisions, one is electron-species collision, and the other is electron-electron collision. The electron-species collision is the main process that excites, ionizes and dissociates different species in the plasma. The electron-electron collision can be neglected at the low current, while shows much probability at high current. The increase of the cathode current will make the average energy of electrons in plasma increase as shown in fig. 5 and fig. 6, and which will further result in that the collisions between electrons and between electrons and species happen frequently. At low current, more species are excited, ionized and dissociated with the increase of current due to the more frequent electron-species collisions. At high current, the electron-electron collision should be taken account of, which compete with the process of electron-species collision, and result in the less active species as shown in fig. 5 and fig. 6

#### **4. Conclusions**

We report here our work on investigating the optical emission spectra of hollow cathode arc plasma source at different experimental condition, which can be summarized as below. The ionization of argon is benefited from a small amount of nitrogen gas (up to 2 sccm), which is possibly due to the charge exchange process between atomic argon and molecular nitrogen. The dissociation and ionization of molecular nitrogen into atomic nitrogen and the ionization of atomic argon are independent of nitrogen flow above 2 sccm. In our case, the charge transfer collision between atomic helium ion and molecular nitrogen could be neglected. With cathode current increasing, the electron density and average temperature increase. And due to the electron-electron collisions at the higher current, the emission intensity of the different species-lines in the plasma source decreases with the current increasing.

#### **Acknowledgement**

Thank Mr. Ulrich, Mr. Mahle, Mr. Shakhatre, Mr. Gross, Mr. Vinogradov, Mr. Fateev, and Mr. Xie for helpful discussion and kindly cooperation. Thank the government of Baden-Württemberg for the support of the exchange project.

# **Influence of the gas mixture (argon/neon) on electron density and temperature in a IPVD reactor**

S.Gurlui \*\*, L.De Poucques\*, O.Leroy\*, C.Boisse-Laporte\*, M.Touzeau\*.

\*\* *Al I Cuza University, Faculty of Physics, Dept. of Optics and Spectr., B-dul Carol I, nr 11, Iasi, Romania*

\* *Laboratoire de Physique des Gaz et des Plasmas, Bât.210, Université Paris-Sud, 91405 Orsay Cedex, France*

## **Abstract:**

To monitor both plasma parameters and atomic species from a d.c. magnetron discharge assisted by two additional microwave discharges, different methods of diagnostic such as electrical Langmuir probes (emissive and cylindrical) and optical methods (emission and absorption) have been used. Optical diagnostic is performed on a direction perpendicular to the magnetron-substrate axis, where as electrical diagnostic are made on the axis of the system. The influence of the argon/neon gas mixture on electron density and temperature created by the microwave discharges is presented.

## **1. Introduction:**

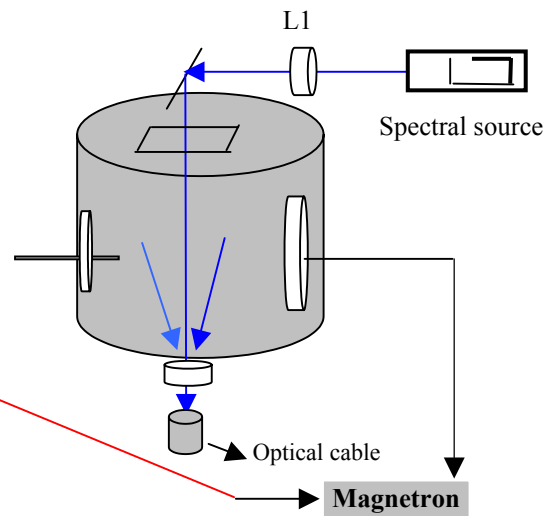
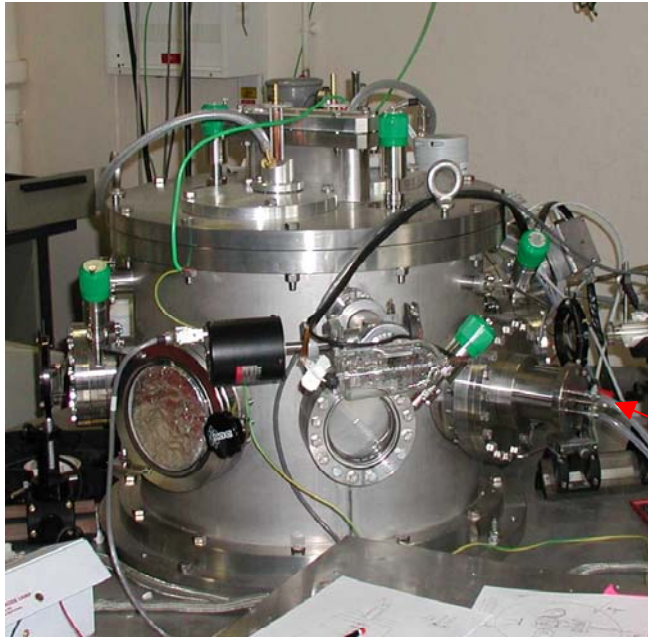
Among different methods of industrial thin layer deposition, the ionised physical vapour deposition is one of main interest [1]. Increase of the deposition efficiency and quality of the thin layer mainly requires an increase of the ionisation degree of the metallic atoms sputtered by the target of a magnetron discharge.

Recently, a new method consisting of a d.c. magnetron discharge assisted by two additional microwave discharges has been proposed [2,4]. This microwave discharge is created by coaxial systems ('antennas') placed between the magnetron and the substrate, on both sides of the vapour sputtering flow. Each antenna is covered with a metallic protective shield in order to avoid metal deposition on it. The d.c. magnetron discharge and the microwave discharge are respectively supplied by a 1.5 kW dc generator and two 1.2 kW 2,45 GHz generators. The discharge is made in argon/neon mixtures in the 2-10 Pa range of pressure using a titanium target. The electron temperature  $T_e$ , plasma potential  $V_p$  and electron density  $n_e$  along the axis of the system have been determined as a function of the distance from the magnetron, for different gas pressures, microwave powers and argon-neon mixtures.

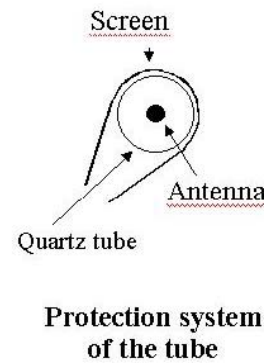
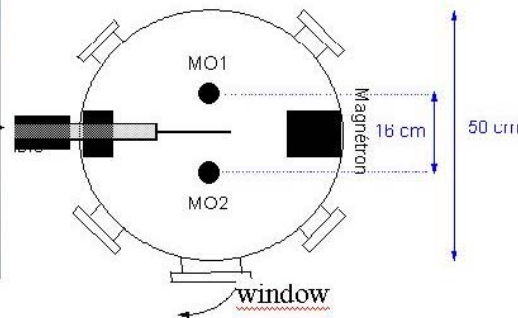
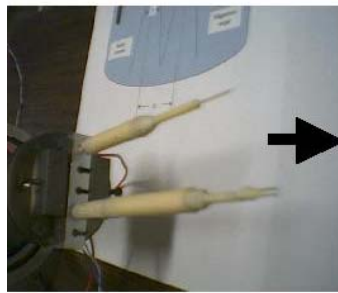
## **2. Experimental set-up**

### **□ The plasma reactor**

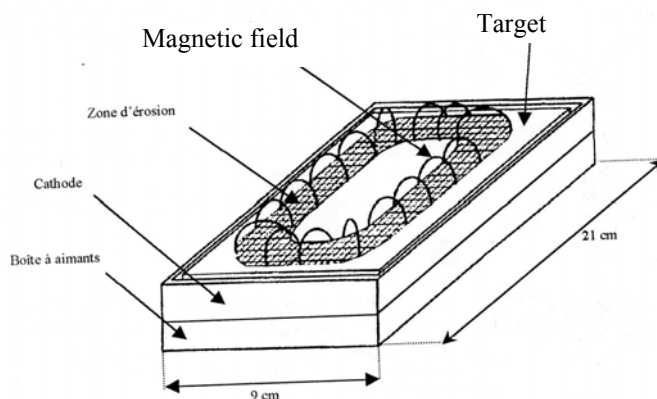
The scheme of the plasma reactor is given in **Figure 1**. The device permits the using of the electric diagnostic methods (Langmuir and emissive probes) and of spectral emission and absorption methods, respectively. The optic measurements (**Figure 2**) are made on a direction perpendicular to the magnetron axis and the electric ones are made on the magnetron axis. Two microwave antennas have been used. These are perpendicular to the magnetron axis and they each are placed at 8 cm from it. The distance from the magnetron to the antennas' plane is of 10 cm and it can move to 20 cm. The chamber has 10 openings necessary for the magnetron, pump, electrical and spectral diagnostic, etc. The pumping is ensured by a turbomolecular pump of 500 l/s. The device can operate between 0.7-50 Pa at a gas flow of 5-200 sccm. The working gases are argon, neon and argon-neon mixtures (Ar:Ne-1/9 ; 2/8 ; 3/7 ; ... ;8/2 ;9/1). For reducing the metallic deposition on the quartz tubes, these have been covered with special geometrical shields . The cathode magnetron is powered by a generator of 1,5 kw and each microwave system is powered by a generator of 2,45 GHz. Here we show the obtained results for the titanium target for different Ar-Ne mixtures.



**Figure 2** Optical arrangement for emission and absorption diagnostic methods



**Figure 1.** The scheme of the plasma reactor and of the microwave system for the metallic vapours ionisation.



**Figure 3.** The cathode magnetron

#### □ The magnetron cathode

The magnetron cathode (**Figure 3**) is a rectangular one of 21 cm in length and 9 cm in width. The target is made of titanium. The magnetic field is ensured by a system of permanent magnets. The magnetron cathode is powered by a generator of 1,5 kw, the current intensity reaching 3A. The voltage varies according to the experimental conditions between 230-300 V.

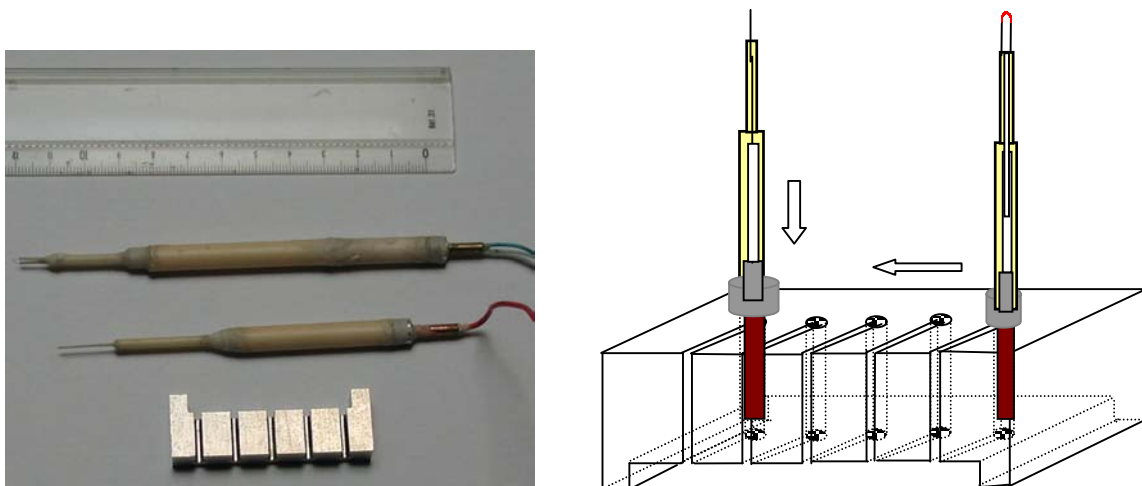
#### □ The coaxial microwave system

Each antenna is powered in the lower part by a generator of 2,45 GHz and 1,2 kw. The microwaves are directed towards the antenna through a wave-guide. In **Figure 1** there are presented the two antennas with a ray of 5 mm. The antennas are surrounded by a quartz tube with the inner ray  $r_{int}=13$  mm and the outer ray  $r_{ext}=15$  mm and between the tube and the antennas the air at atmosphere pressure has been used for cooling

the antennas. The microwaves that propagate along the antenna axis create dense plasma around the quartz tubes. The waves went upwards as a plasma mode. Reaching one end of the antenna, these reflect and propagate in the opposite way. The metallic vapors resulted from the pulverization of the magnetron target can deposit in the all regions inside the reactor and also on the quartz tubes. The metallic deposits reflect the microwaves and disturb the plasma modes. The effect of the disturbance consists in the fact that the power of the microwave radiation will not be completely absorbed by the plasma. For limiting these depositions special shields have been built (**Figure 1**).

#### ❑ **Langmuir and emissive probes**

The electric diagnostic is done by the axis of the magnetron (perpendicular to the surface of the magnetron). For the two probes a special system was designed (**Figure 4**). The Langmuir probes characteristics are recorded in different experimental conditions: the power of the microwave generator, gas pressure, the nature of the gas (He, Ne or mixture He-Ne).



**Figure 4** Probes and guiding system

The Langmuir probe is made of tungsten and it has 6 mm in length and 0.1-0.2 mm in diameter. In **Figure 4** there is also shown an emissive probe used for measuring the plasma potential with high precision ( $\sim 0.1V$ ) [3]. The probe characteristics have been recorded using an electronic system called SOFIE, too. Using a typical software (Tishy) -designed by Pavel Kudrna, Department of Electronics and Vacuum Physics, Faculty of Mathematics and Physics, Charles University-, there have been obtained: electronic density, electronic temperature and potential of plasma at different distances from the magnetron surface.

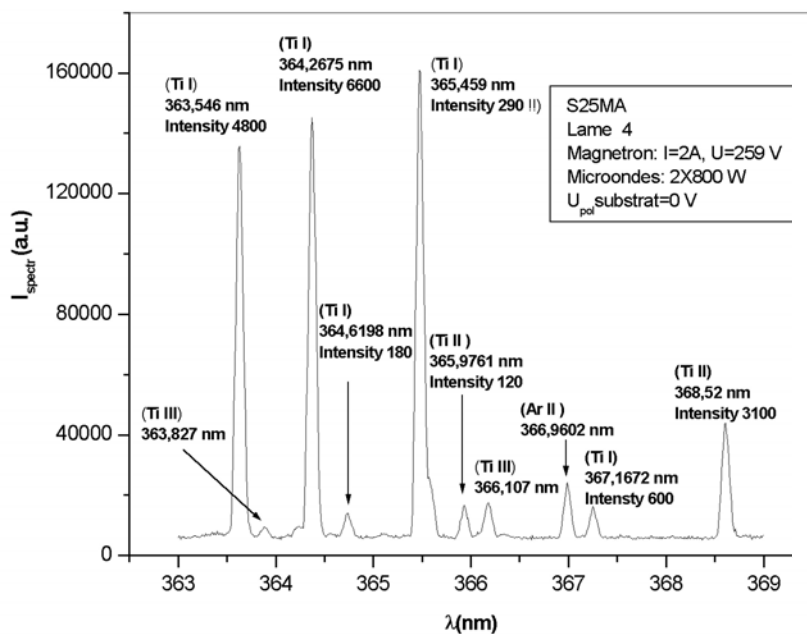
#### ❑ **Emission and absorption spectroscopy**

For the study of the atomic and molecular species in the reaction, especially in the film deposited region, absorption and emission spectral methods have been used.

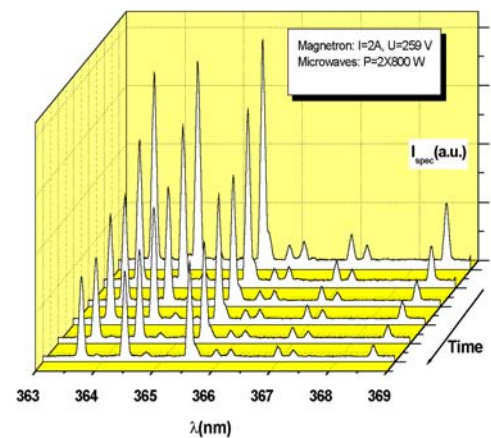
### **Experimental results**

#### ❑ **Spectral investigations**

The emission spectra of the atomic and ionic species for different powers of the microwave generator, pressures of the working gas have been recorded. These spectra are presented in **Figures 5-7**



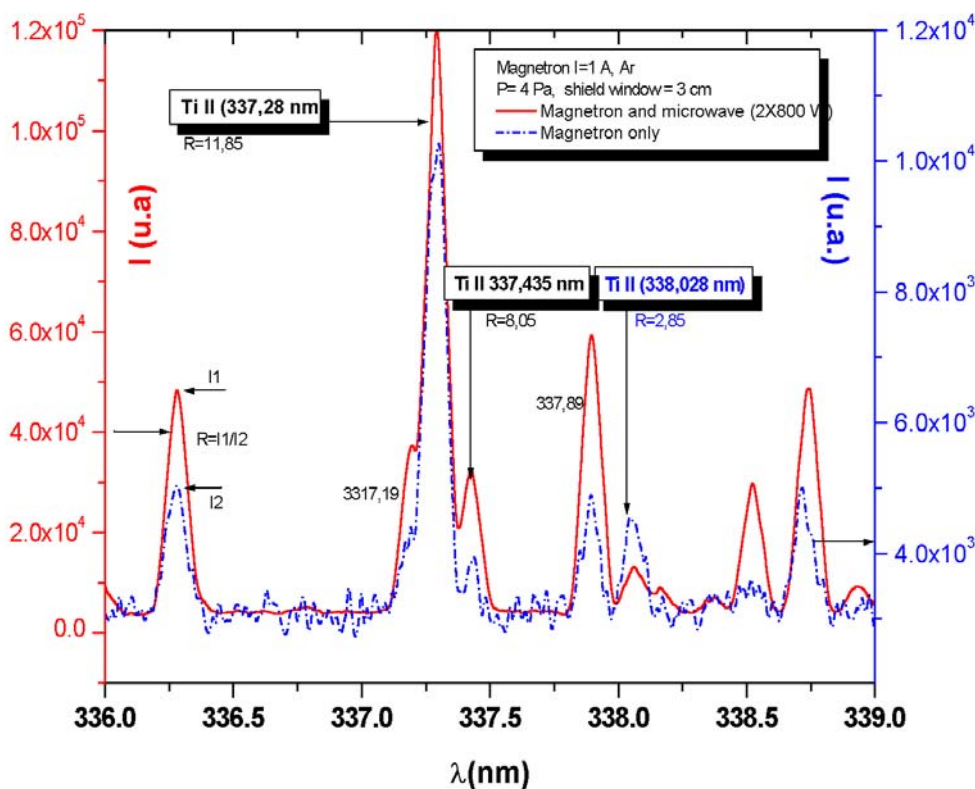
**Figure 5.** The emission spectra recorded when the magnetron discharge was assisted by a microwave discharge



**Figure 6.** Emission spectra recorded at different times during a process.

Different ionic and atomic titanium lines and one ion line have been identified in the spectral range 363-369 nm (**Figure 5**). The intensity of the spectral lines decreases with time because of the metallic depositions on

the quartz tube walls of the microwave discharge. This effect is shown in **Figure 6**. In **Figure 7** two emission spectra are given and correspond to the situation when the microwave radiation has been used and the other when microwave radiation has not been used. We can observe a significant increasing of the titanium ions emission by using the microwave discharge

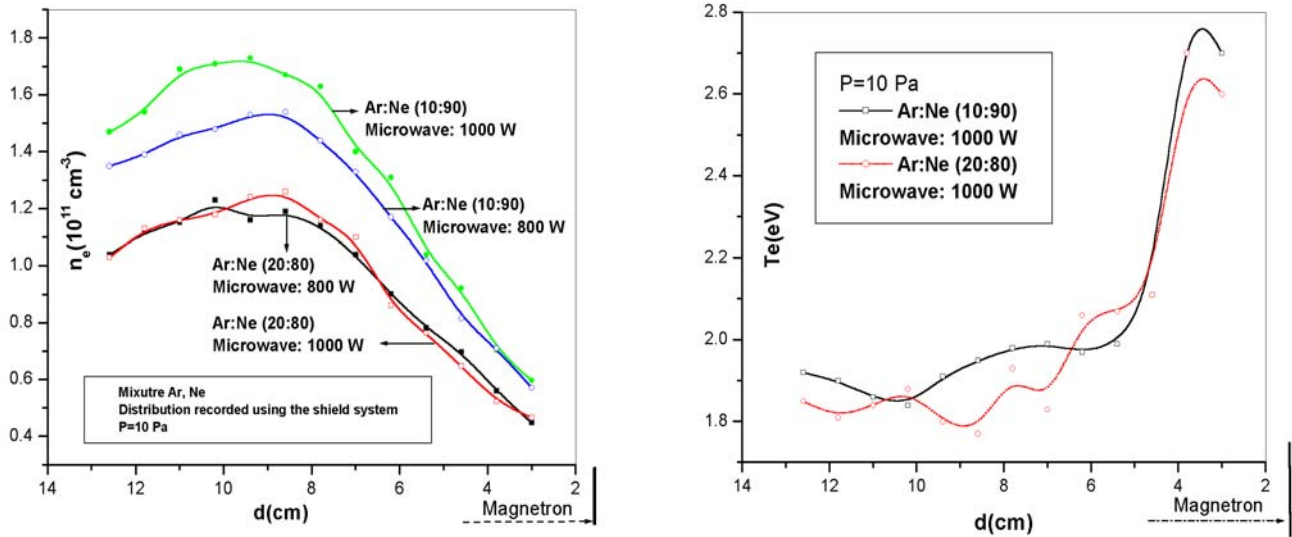


**Figure 7.** Atomic and ionic spectral distribution recorded with and without microwave discharge

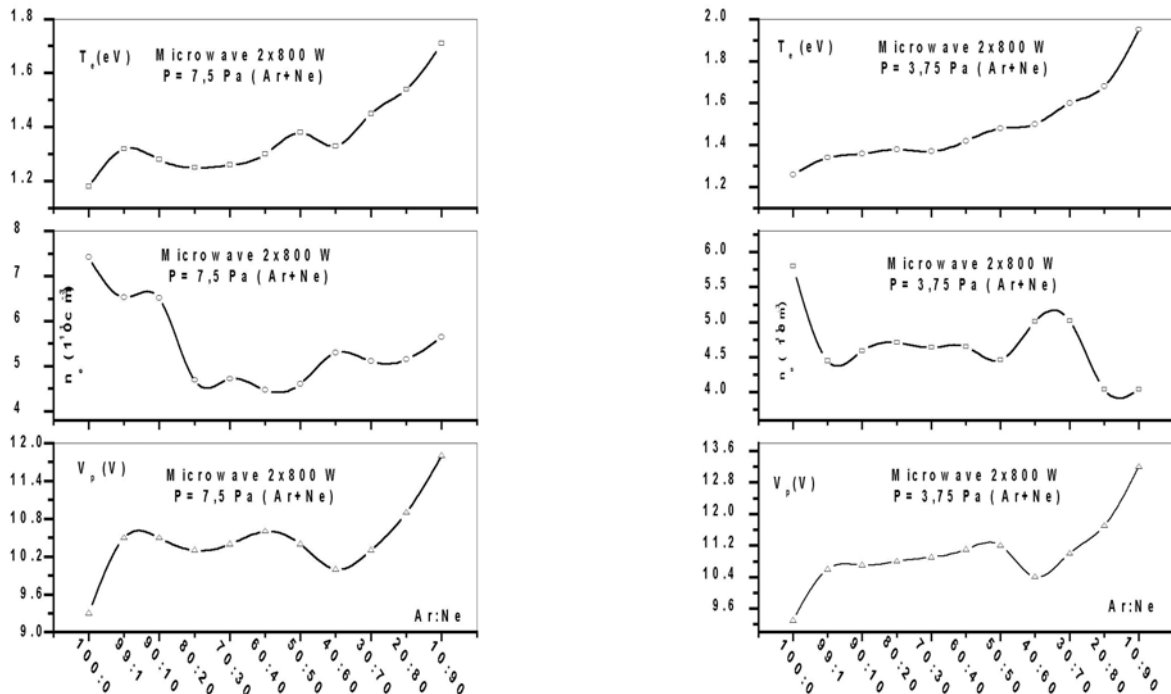


## □ Measurements of the plasma parameters using a Langmuir probe

The Langmuir probe characteristics are recorded and the following parameters: electronic density, plasma potential, electronic temperature and electronic distribution function by energy,  $f(E)$  have been obtained (Figures 8-10).



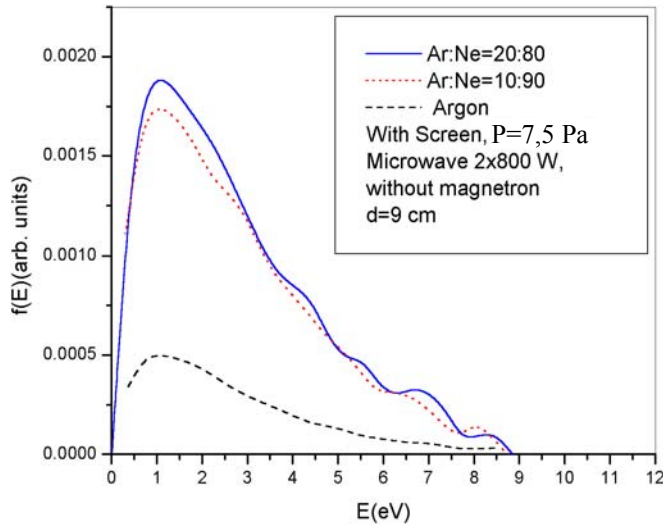
**Figure 8** Profiles of the electronic density and the electronic temperature with shield and without



**Figures 9.** Profiles of the electronic densities, temperature and plasma potential recorded at 9 cm from the magnetron using mixtures argon and neon.

These measurements show that:

- The maximum of the electronic density is obtained on the magnetron axis at approx. 9 cm of the magnetron, at the location of the shields apertures and it depends on the pressure and on the nature of the gas.
- The electron temperature is maximum for the mixture Ar-Ne (10: 90) at 10 Pa.



**Figure.10** The electronic energy distribution function for argon, neon or mixture argon-neon.

➤ The electronic density and the electronic temperature are still high if we use a mixture as following: Ar (10-20%) and Ne (80-90%) at 10 Pa pressure and the microwave generator power is between 800 and 1000W. The electronic energy distribution function was obtained from the probe characteristics using the relation:

$$f(\varepsilon) \propto \sqrt{V} \frac{d^2 I_{probe}}{dV^2},$$

where V is the potential measured versus plasma potential  $V_p$ . Figure 10, the EEDF function obtained on the magnetron axis, at 9 cm from magnetron, is given for different Ar-Ne mixture.

As we can see from this figure the introduction of neon enhances the concentration and the electronic temperature.

### 3. Conclusions

The main conclusions are the following:

- ❑ The spatial distribution of the electron temperature (from 1 to 3eV) is constant along a large region of the plasma except near the magnetron, where the temperature increases.
- ❑ The spatial distributions both for electron density (in the order of  $10^{11}$  to  $10^{12}$  cm<sup>-3</sup>) and plasma potential (about 10 V) exhibit a maximum near the microwave antenna.
- ❑ The presence of the shield around the microwave antenna increases the value of  $T_e$  by an order of 1.5 to 2 but reduces the values of  $n_e$  by an order of 5 to 8.
- ❑ In the argon/neon mixture, from pure argon to pure neon,  $T_e$  increases (typically from 1 to 2 eV at 4 Pa) but  $n_e$  may decrease (from 5 to  $1.5 \cdot 10^{11}$  cm<sup>-3</sup> at 4 Pa and 2x400Watt of microwave power)

### 4. References:

- [1] S.M.Rossnagel, J. Vac. Sci. Technol. B 16, 2585 (1998)
- [2] C.Boisse-Laporte, O.Leroy, L.de Poucques, B.Agius, J.Bretagne, M.C.Hugon, L.Teulé-Gay, M.Touzeau, submitted in a special issue of Surface and Coatings Technology, PSE 2002.
- [3] J.W.Bradley, S.Thompson and Y.Aranda Gonzalvo, Measurement of the plasma potential in a magnetron discharge, Plasma Sources SCI. Technol., 10 (2001) 490-501.
- [4] Microwave Discharges: Fundamentals and Applications, Edited by C. Boisse-Laporte and J. Marec, EDP Sciences Les Ulis France, Journal de Physique IV, vol 8, Pr7, 1998.

# REACTIVE PLASMA SPRAYING : IN-FLIGHT NITRIDATION OF ALUMINIUM AND TITANIUM ALLOY

A. DENOIRJEAN, A. GRIMAUD, F. RALETZ, P. LEFORT, J. JARRIGE, P. FAUCHAIS

SPCTS UMR CNRS 6638 – 123 Avenue Albert Thomas – 87060 Limoges CEDEX - France

## Abstract

The reactive plasma spraying of both titanium aluminium vanadium (Ti-6wt%Al-4 wt%V) alloy and aluminium particles have been performed in a nitrogen direct current (d.c.) plasma jet flowing in a nitrogen atmosphere ( $1.05 \cdot 10^5$  Pa) in a controlled atmosphere chamber. The nitridation of the Ti-6Al-4V alloy occurs through the molten phase and particles collected in flight at a stand off distance of 100 mm are composed of substiochiometric TiN grains surrounded by a  $Ti_wAl_xV_yO_z$  cement. Most of the reaction occurs by convective effect within the particles during their flight in the plasma core. With aluminium the gas phase reaction with the recondensation of the AlN at the surface of the particles is observed only at the extremity of the plasma plume where temperature are lower than 3000K.

## 1. Introduction

Reactive plasma spraying is a possible route to produce coatings containing nitrides resulting on the one hand from the in-flight reaction of metal particles with a nitrogen plasma or a plasma jet where the surrounding pure nitrogen atmosphere has been pumped and / or on the other hand from the nitridation of the successive passes during the coating formation. Such coatings or particles nitridation in flight have been achieved by d.c. or RF plasma [1-11].

The goal of this work is to determine how nitridation is achieved during direct current plasma spraying of metals with nitrogen in the plasma forming gases. Two materials has been chosen : a titanium alloy where nitridation occurs preferentially through the liquid phase [12] and aluminium where nitridation is mainly through the gas phase.

## 2. Experiment

### Nitridation apparatus

The nitridation apparatus is composed of a plasma torch in which the metallic powder is injected externally by a 2 mm internal diameter injector, located inside a controlled atmosphere chamber (see Figure 1) in such a way the mean particle trajectory makes an angle of  $3.5^\circ$  with the torch axis.

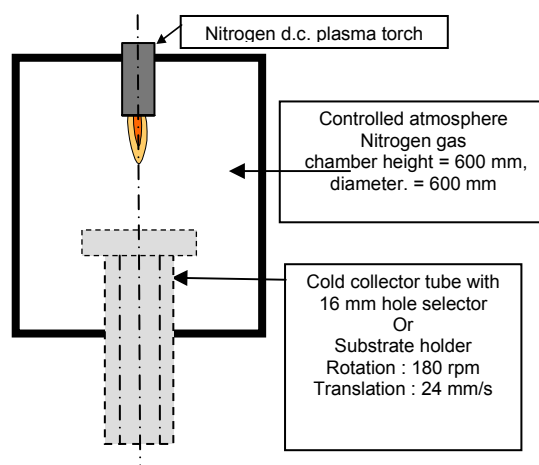


Figure 1 : Nitridation apparatus

The nitrided particles are collected in a powder collector, with an inlet hole water cooled and protected by a nitrogen jet blown orthogonally to its axis. The distance torch-collector can be modified by moving the torch or the collector up and down along the chamber axis.

First, the chamber is placed under primary vacuum ( $10^{-4}$  Pa), and then industrial nitrogen (provided by L'Air Liquide S.A.) is introduced at a pressure slightly higher than atmospheric pressure in order to prevent air entry. The torch, which has been designed at the laboratory [13], also works with nitrogen of the same quality. Experimental conditions of spraying are presented in Table 1.

Table 1 : Experimental conditions

Plasma gas characteristics	Flow rate : 40 slm Forming gas : N <sub>2</sub>
Torch characteristics	Internal diameter : 7 mm (nozzle) Arc current : 500 A / 80 V
Chamber atmosphere	P <sub>N<sub>2</sub></sub> = 1.03 10 <sup>5</sup> Pa
Powder characteristics	Microspheres Ti-6Al-4V (22 < Ø < 45 µm) Aluminium (10 < Ø < 160 µm)
Injection of powder	External injection Gas flow rate : 5 slm Ø injector : 2 mm (internal) Localization : 7.5 mm from the torch axis 3 mm downstream of the nozzle exit

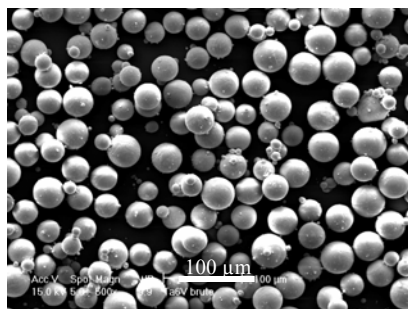
#### Starting powders

The powders have been supplied by Starck company for the aluminium and by Pyrogenesis Inc. (Montreal - CANADA) for the Ti-6Al-4V alloy. Their grain size is specified in Table 1.

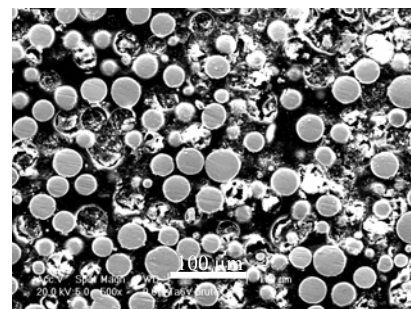
Ti-6Al-4V is a diphase alloy, with the  $\alpha$ Ti phase (compact hexagonal structure) and the  $\beta$ Ti phase (cubic centred structure). Its composition has been controlled with a Casting micro-probe on grain cross-sections and Table 2 shows that it was close to the nominal values, but one can also see that a non negligible quantity of oxygen was present, probably dissolved in the  $\alpha$ Ti phase. The good sphericity of the grains is illustrated by the SEM micrograph of Figure 1a, while Figure 1b shows that there was no porosity visible inside. The grain size appeared as being rather homogeneous with a mean diameter of 30 µm and with a few small particles below 10 µm.

Table 2 : Mean measured chemical composition of the Ti-6Al-4V microspheres.

Average value	Ti	Al	V	O	N
Atomic %	82.3	9.5	3.7	4.1	0.17
Weight %	89.4	5.8	4.8	1.5	0.05



a)



b)

Figure 2 : Micrograph of Ti-6Al-4V microspheres : a) general view ; b) after inclusion in a resin and cutting.

Aluminium powder is an atomised powder with a particle mean size of 80  $\mu\text{m}$  and a size distribution between 160 and 10  $\mu\text{m}$ . Its X ray Diffraction (XRD) only reveals pure aluminium phase which means that the oxide content, as classical, is non crystallised and in low quantity (probably below 1 vol%).

#### Characterisation of the nitrided powders

The sprayed particles or splat are observed by scanning electron microscopy (SEM Philips XL30 with an acceleration voltage of 15 to 20 kV). The powders are analysed by XRD (Diffractometer D5000 Kristalloflex with a Cu anti-cathode equipped with a back monochromator). The lattice parameter of the titanium nitride has been calculated with the help of the software U-fit (Diffract Socabim) while its composition was determined with the Castaing microprobe (EPMA) CAMECA SX 50 of IFREMER (Brest, France) using the lines  $K_{\alpha}$  of Titanium, Vanadium, Aluminium, Nitrogen and Oxygen (analysing crystals respectively PET, LIF, TAP, PC1 and PC1). The precision is about 0.5 % for all metallic elements and 1 % for nitrogen and oxygen.

### **3. Results and discussion**

#### Titanium alloy particles

Measurements performed in air (to simplify the experiment) with a DPV 2000 [14] for particles in the 20-35  $\mu\text{m}$  range (which are by far statistically the most numerous), and collected at a distance  $z = 100$  mm from the nozzle exit have shown that their mean velocity was  $250 \pm 8$  m/s and their mean temperature was  $3200 \pm 320$  K. This result proves that the particles of alloy are liquid during their flight inside the plasma jet, and even that a certain vaporization is not to be excluded (vaporisation of titanium, the most refractory of the three metals, occurs at a.3530 K). These temperatures are close the melting one of TiN (3223 K), so that the nitride formed is perhaps itself more or less liquid. Of course, concerning aluminium, the boiling temperature of which being of 2740 K only, an important evaporation can be expected. As far as the treatment conditions allows to assert that a.95wt% of the grains have really travelled in the plasma jet core, it is clear that the alloy has reacted following a liquid / gas reaction.

Figure 3 shows that the spherical shape of the particles have not been modified by the treatment, with perhaps a slight decreasing of the mean diameter of the microspheres .

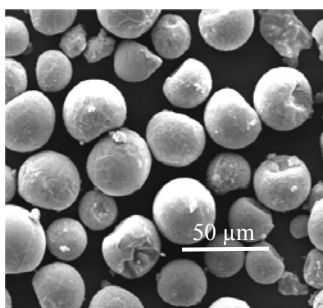


Figure 3 : Morphology of the nitrided microspheres.

The main visual difference before and after treatment is that the surface of some grains are fissured, such as a sort of shell have enveloped the grains, and have been sometimes broken, as illustrated on the SEM micrograph of Figure 4. The origin of these cracks can be linked to their collision with the wall of the collector or between themselves or due to a thermal shock when the grains were quenched inside the collecting tube (the cooling rate is estimated to be about  $10^5$  K/s [16]).

The composition of the grains has entirely change since XRD spectra do not longer identify the initial alloy, but mainly the cubic phase  $\delta\text{TiN}$  with peaks shifted to larger angles, which reveals an important substoechiometry, consistent with a lattice parameter calculated is  $a_0 = 0.4217$  nm, markedly smaller than that of stoichiometric titanium nitride ( $a_0 = 0.4242$  nm [17]). A second phase, corresponding to peaks by far weaker and very broad, is identified as the ternary alloy  $\text{Al}_3\text{Ti}_{0.66}\text{V}_{0.33}$  (JCPDS file 43-1159).

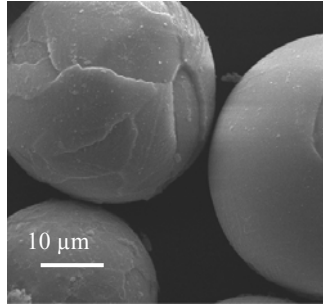


Figure 4: Examples of surface flaws after nitridation.

The composition of a particle (imbedded it in a resin for polishing) has been determined by EPMA. The microanalysis presented on the Figure 5 presents the elementary content of the five elements Ti, Al, V, N and O analysed along a straight line close to its diameter. Their atomic percentages exhibit very important spatial fluctuations which period is about 4  $\mu\text{m}$  : from 61 to 71 at% for Ti, 14 to 36 at% for N, 2 to 7 at% for V, 0 to 8 at% for O and 0 to 3 at% for Al. This has to be considered as a consequence of the treatment because the initial composition of the alloy was very uniform. Moreover, it can be noticed that when the vanadium content is the highest, those of the aluminium and oxygen are also the highest while the nitrogen content is the lowest. A similar effect has already been observed after nitridation of Ti-6Al-6V in a classical furnace, where the formation of titanium nitride expels vanadium and aluminium [18].

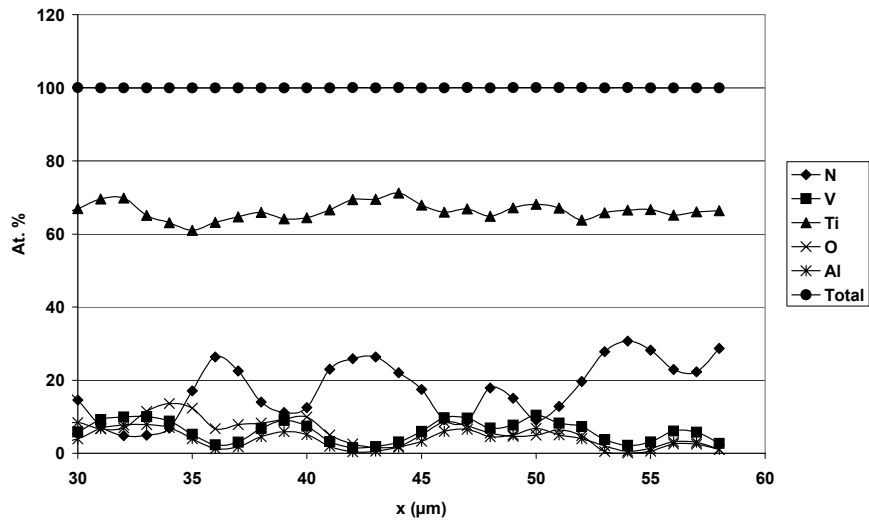


Figure 5 : Fluctuation of the elementary composition inside a particle after nitridation.

A careful observation of the cross section of a nitrided microsphere presented on Figure 6 allows to distinguish, inside the particles, small grains (3 to 4  $\mu\text{m}$  large) distinct from each other but very coherent between themselves. In these small grains, EPMA identifies quasi-exclusively titanium and nitrogen. They are quite similar to those observed by Suzuki et al [5] using SEM with backscattered electrons.

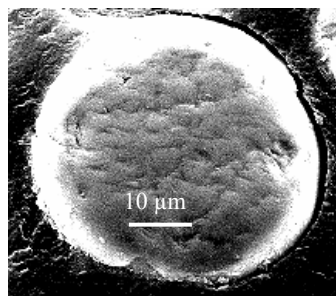


Figure 6 : Cross-section of a particle showing small individualized grains inside

In order to explain these results, it must be considered that the liquid which is nitrified inside the plasma jet rapidly reaches a very low viscosity, and it is certainly crossed by important convective movements. Nitrogen reacts rather with titanium than with the other metals because titanium nitride is the most stable nitride liable to be formed. So, while germs of titanium nitride appear at the external gas / liquid interface, fresh alloy is continuously renewed at the droplet surface, and as fast as the germs are formed, they are entrained within the droplets as well as, probably, dissolved nitrogen. When fresh aluminum arrives at the surface, it is oxidized by traces of oxygen existing in the chamber as well as by the oxygen trapped within the starting particles and entrained at the particle surface by the convection (aluminum is the most oxidizable of the three metals). At the considered temperatures, the stable aluminum oxide is  $Al_2O_3$  (gas) which is entrained as vapor, as shown by spectroscopic measurements [19], thus Al acts as an oxygen getter.

The TiN germs entrained inside the droplets, grow thanks to the nitrogen dissolved in the liquid Ti. When the particles leave the plasma jet, the convective movement within the droplets does not any more exist, but the growth of solid substoichiometric titanium nitride grains keeps going. During that time, the liquid phase becomes richer and richer in aluminum and vanadium, and also in residual oxygen. It forms by this way the secondary phase well identified by XRD, but probably with a more complex real composition than  $Al_3Ti_{0.66}V_{0.33}$ , which can be written  $Ti_wAl_xV_yO_z$ . (This can justify the broadening of the diffraction peaks). After cooling, this metallic phase plays the role of a cement between the substoichiometric titanium nitride small grains, making the particles particularly solid.

During the last ms before cooling, the droplets go on reacting, in surface, so forming the TiN shell seen in Figure 4 and which is sometimes broken in the collector.

#### Aluminium particles

Contrary to what happens with Ti-6Al-4V particles, the aluminium particles collected in flight as well as their cross sections show no evidence of AlN formation. This is confirmed by the XRD analysis of this powder showing only tiny AlN peaks among huge Al peaks. Within the plasma jet core and the first centimeters of its plume the temperature is too high. When AlN is formed by the reaction between Al vapour and nitrogen atoms in the boundary layer around the in-flight particles, it is destroyed as soon as it diffuses towards the hot gases. Thus AlN can only be formed at the extremity of the plasma which explains its low quantity. In order to confirm that most of the reaction occurs in gas phase at temperature below 2400 K splats have been collected on stainless steel (316 L) smooth substrates ( $R_a < 0.05 \mu m$ ) preheated at different temperatures by the plasma jet plume at 100 mm downstream of the nozzle exit. As long as substrates are maintained below about 600 °C (see figure 6) nothing happens and splats are only made of aluminium. Over 600 °C some sort of needles start to show up and their quantity increases with the mean substrate temperature. It is believed that the Al vapour reacts with the nitrogen close to the substrate at temperature around 2000 K and the solid AlN needles formed recondense on the splat. Such a phenomenon has already been observed when heating Al in a crucible by a d.c. plasma jet : a solid of AlN made of needles grow against the plasma jet outside of the crucible.

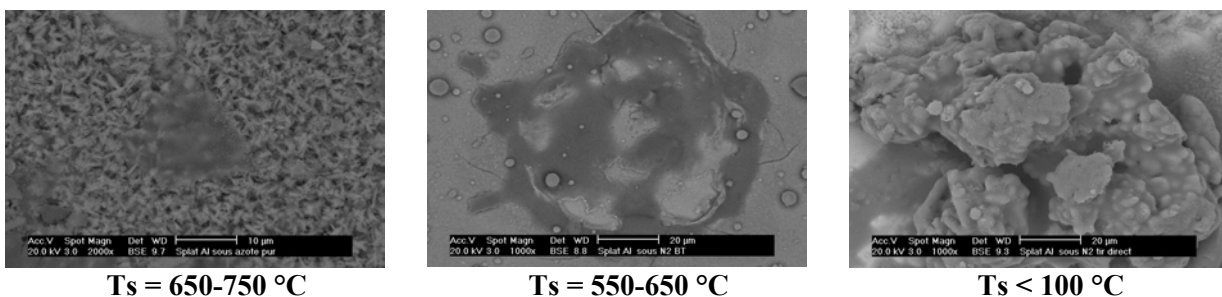


Figure 7 : Splat morphology for aluminium powder sprayed at different surface temperature for the substrate

## Conclusions

Titanium alloy (Ti-6Al-4V) and aluminium particles d.c. plasma sprayed in a nitrogen plasma flowing in a controlled atmosphere chamber filled with nitrogen at  $1.03 \cdot 10^5$  Pa behave quite differently. With the titanium alloy the nitridation reaction occurs between the nitrogen plasma and the molten alloy mainly during the particle flight within the plasma jet core. A convective effect is induced within the fully molten particles by the plasma jet ( $Re > 20$  and ratio of plasma to particle dynamic viscosities higher than 50) thus creating substoichiometric TiN grains (a few  $\mu\text{m}$  in diameter) inside a  $\text{Ti}_w\text{Al}_x\text{V}_y\text{O}_z$  cement. The oxygen comes from that already present within the raw powder, the low purity of the plasma forming gases and the chamber leakages. With the aluminium particles the reaction occurs between nitrogen atoms and aluminium vapors. AlN can recondense onto the particles only when the surrounding gas temperature is below 2000 K i.e. at the extremity of the plasma plume. This is confirmed by collecting splats at a distance of 100 mm from the injection point inside the torch : AlN needles are observed only on splats collected on substrates preheated at least over 600 °C which corresponds to temperature in the 200 – 300 K in the boundary layer close to the substrate.

## Acknowledgements to Stéphane Valette

### References

- [1] Y. Tsunekawa, M. Hiromura and Okuniga, J. of Thermal Spray Technology 2 (1) (2000) 83
- [2] A. Ohmori, Y.C. Zhang and Y. Arata, in Thermal Spray : Research and Applications (ed.)
- [3] T.F. Bernecki (pub.) ASM int. Materials Park OH, USA (1991) 605-610
- [4] A. Ohmori, S. Hirano and K. Kamada, J. of Thermal Spray Technology 2 (2) (1993) 137-144
- [5] M. Suzuki, S. Sodeoka, T. Inoue, K. Ueno and T. Valente, in Proc. of Int. Thermal Spray Conference 2002 Essen G. (ed.), Lugscheider E. (pub.), DVS, Germany (2002) 605-620
- [6] P.V. Ananthapadmanabhan, Patrick R. Taylor, Wenxian Zhu, Journal of Alloys and Compounds, 287, (1999), 126-129
- [7] Seung-Min Oh, Dong-Wha Park, Thin solid Films, 316, (1998) 189-194
- [8] Lidong Zhao, Erich Lugscheider, Wear, 253 (2002), 1214-1218
- [9] L.H. Cao, K.A. Khor, L. Fu, F. Boey, Journal of Materials Processing Technology, 89-90, (1999), 392-398
- [10] T. Bacci, L. Bertamini, F. Ferrari, F.P. Galliano, E. Galvanetto, Materials Science and Engineering, A283, (2000), 189-195
- [11] Yasuhiro Hoshiyama, Hidekazu Miyake, Kenji Murakami, Hideo Nakajima, Materials Science and Engineering, A333, (2002), 92-97
- [12] A. Denoirjean, P. Lefort, P. Fauchais, to be published.
- [13] O. Lagnoux, A. Denoirjean, A. Grimaud, V. Gourlaouen, P. Fauchais, Proceedings of the 14 th International Plasma Chemistry Conference, (ed.) M. Harabovsky, M. Konrad, V. Kopecky (pub.) Institute of Physics, Ac. of Sciences, Prague, Cz, 2 (1999) 2057-2062
- [14] C. Moreau, P. Gougeon, M. Lamontagne, V. Lecasse, G. Vaudreuil, P. Cielo, in Thermal Spray Industrial Application, (ed.) C.C. Berndt, S. Sampath, (pub.) ASM International Materials Park Ohio, USA, (1994), 431-436
- [15] Ph. Roumilhac, J.F. Coudert and P. Fauchais, in Plasma Processing and Synthesis of Materials (ed.) D. Apelian and J. Szekely (pub.) MRS Pittsburg, USA 190 (1990) 227-238
- [16] G. Espie, P. Fauchais, B. Hannoyer, J.C. Labbe, A. Vardelle, Proceeding of the 14 th International Plasma Chemistry Conference, (ed.) M. Harabovsky, M. Konrad, V. Kopecky (pub.) Institute of Physics, Ac. of Sciences, Prague, Cz, 2 (1999) 2025-2030
- [17] W. Wong-Ng, H. Mc Murdie, B. Paretkin, C. Hubbard and A. Dragoo, NBS, Gaithersburg, MD, ICDD Grant-in-Aid, 1987.
- [18] C. Ponticaud, A. Guillou, P. Lefort, Phys. Chem. Chem. Phys. 2 (2000) 1709-1715
- [19] M. Vardelle, A. Vardelle, P. Fauchais, C. Trassy, Rev. Int. Hautes Tempér et Réfract., 25 (1989), 121 - 127



# **New advances in analysis methods for thin hard coatings**

Grégory Favaro, Richard A J Soden, Liliana Buform

*CSM Instruments SA, Rue de la Gare 4, CH-2034 Peseux, SWITZERLAND*

## **Abstract**

Thin films and coatings are becoming more and more evident and finding function in many different industrial applications. In order to simulate (and if possible extend) the service life of a particular system and to improve efficiency, it is important to characterize the material properties within the system. The value of any instrument is based on the reproducibility of fidelity of those measurements made, independent of human operation. A variety of different instruments, techniques and methods are here presented for the principal characterization of the surface mechanical properties for various ranges: Nano Scratch, Nano Hardness and Tribometer instrumentation.

## **Hard Coatings**

While combining the voluminal properties of basic material, the substrate, and the properties of surface conferred to this surface by the hard coating, the thin layers bring financially viable solutions to problems as varied as the increase in the lifespan of cutting tools, the amelioration of the systems resistance to wear, corrosion or damage at high temperatures, in conjunction with improvements in the friction behavior, etc..

The properties of films deposited for example on a metal device can be very different from that of the substrate to address specific usage of this film substrate combination. Consequently, the techniques of material deposition and are constantly being developed and improved. The various processes of development of thin films have all of them the constraints related to their principle end use. The choice of deposition process must take in to account the conditions of use such as, for example, a threshold temperature not to exceeded to avoid any modification of structure, composition, texture of the substrate and even of the dimensional variations.

The carachterisation methods for the surface mechanical properties of hard coatings must evolve with the developments in both the coating applications and the coating deposition processes[1]. We will present here three differrent instruments for indentation, scratch testing and tribometry, with a resume of their principle and application for hard coatings.

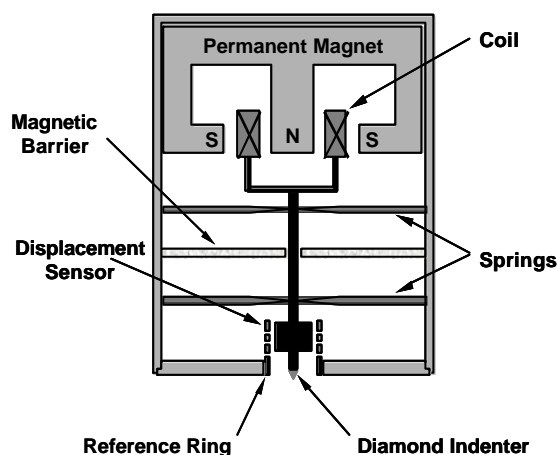
## **Hardness testing by instrumented indentation**

Hardness, the resistance of a material against deformation, is measured on a number of differing scales. Analogous to the temperature ranges Centigrade and Fahrenheit, the differing hardness scales (Vickers, Rockwell, Martens, etc.) offer differing values for the same test surface based on the test procedures and methods of each scale. It is important to remember that although several differing scales are used currently, due either to historical use or the accuracy of specific material properties that can be obtained, one should not confuse one scale with another.

Instrumented hardness testing is achieved by pressing an indenter, usually a diamond, of known geometry into the test surface. During this indentation, penetration depth and applied load are monitored both during the insertion and withdrawal of the indenter. Using such a method, material hardness, elastic modulus, strain-hardening exponent, fracture toughness and viscoelastic behaviors of the surface can all be characterized [2, 3, 4].

The importance of using an instrumented indentation technique over traditional methods is that much greater when characterizing the properties of thin films. To avoid the influence of the substrate on the measurements taken, one must take into consideration the interface stress field. As such penetration depths for the indentation should be kept below 10% of the overall film thickness, as a rule of thumb. With such low penetration depths, the uncertainties in the optical observation of the residual imprint, associated with traditional hardness measurement, lead to very high errors in the hardness values obtained[5]. These errors can be reduced by instrumented indentation, where accurately measuring the penetration depth and normal forces.

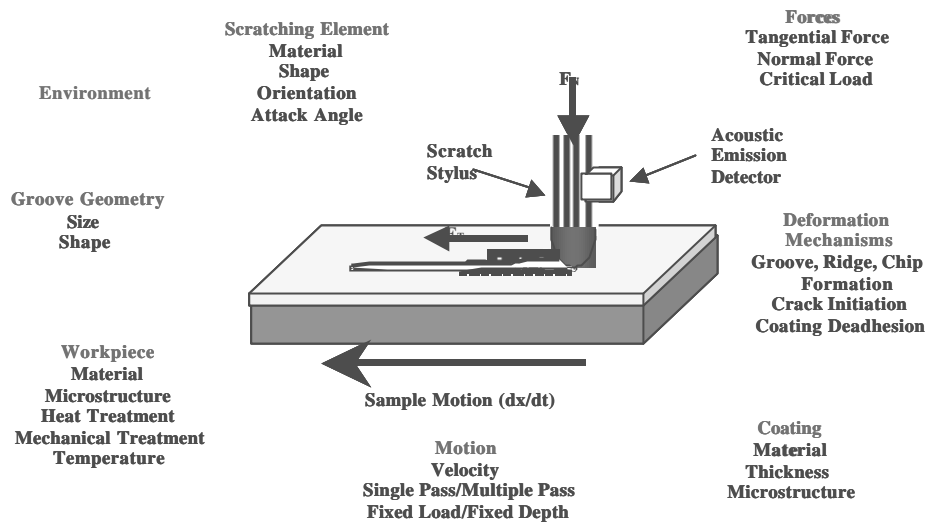
The Nano Hardness Tester used in these experiments was conceived specifically to address such applications, where low forces and high accuracy of displacement and applied load are required. Figure 1 shows a schematic of the head arrangement. The diamond indenter is pushed through the magnetic repulsion of the coil as a current is passed through it. The displacement of the indenter is measured with respect to the surface, through the reference ring and depth sensor arrangement that allows this system to minimize the compliance in the system to the few millimeters of material between the indenter tip and the sensor arrangement. With this system a maximum force of 300 mN and a depth of 500  $\mu\text{m}$  can be achieved with resolutions of 1  $\mu\text{N}$  and 0.04 nm (over a range of 20  $\mu\text{m}$ ).



**Figure 1. Nano Hardness Test head**

### **Scratch Testing**

Scratch testing is a versatile tool to evaluate the adherence, stress and strain between a coating and a substrate as a diamond stylus is passed over the surface with some normal load applied[5]. The mechanical response can be measured by simultaneously recording friction transients, acoustic emissions and changes in surface morphology whilst this scratch on the test surface is applied. The principle of the method and the characteristic elements involved in the scratch process are shown in Figure 2.



**Figure 2. The test principle and main elements involved in the scratch process**

Examples of fields where this technology can be readily demonstrated include the thin DLC overcoats used in the magnetic hard disk industry and varnish clearcoats used in the automobile industry, etc.

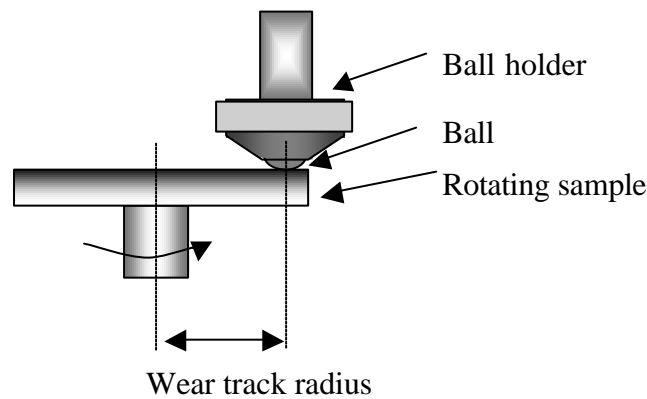
The Nano Scratch Tester (NST) is designed to exploit the normal force range from 10 mN to 1 N, this being achieved by using three interchangeable cantilevers of varying stiffness to apply the required load range. The tip is mounted on the cantilever and deflection is measured by a Linear Voltage Differential Transformer (LVDT).

Owing to the small size of the scratched path, it is not always easy to distinguish interesting features under a conventional optical microscope, due to lack of resolution. One solution is to profile the scratched area with a stylus profilometer, but in certain cases this can significantly damage the sample. The NST incorporates a standard optical microscope, but has the additional option of an integrated scanning force microscope (SFM) objective. This permits high resolution imaging of a scratched area and quantitative measurement of lateral and depth dimensions. In addition, surface morphology can be investigated before scratching.

### **Tribometry**

Tribometry the study of friction, wear and lubrication, relates the interaction of two surfaces that are interact through a sliding motion.

A flat or a sphere shaped indenter is loaded on to the test sample with a precisely known force. The indenter, (a pin or a ball), is mounted on a stiff lever, designed as a frictionless force transducer. As the disk is rotated, resulting frictional forces acting between the pin and the disk are measured by very small deflections of the lever using an LVDT sensor. Wear coefficients for both the pin and sample are calculated from the volume of material lost during a specific friction run.(figure 3) This simple method facilitates the determination and study of friction and wear behavior of almost every solid state material combination, with varying time, contact pressure, velocity, temperature, humidity, lubrication, etc.



**Figure 3. Tribometer Pin-on-Disk principle**

With point radius of curvatures of tens of nanometres, the atomic force or scanning probe microscope has been used with great success, in the investigation of the mechanical properties such as wear, lubrication and friction of surfaces at an atomic scale. Research has brought results and great interest in the field of semiconductors, where such measurement has been used to investigate and develop materials for hard disk drives and has proved invaluable in the development of Micro Electro Mechanical Systems (MEMS), from fundamental issues such as the tribological properties of bulk materials, modified surface chemistry, to thin films, lubrication, diamond like coatings, the effectiveness of micro scale bearing forms and even down to the Nanomechanics of the Microsystems themselves[6-8].

The tip of the calibrated cantilever in the Nanotribometer, and therefore the flat/pin/sphere in this arrangement, has freedom of mobility in both vertical and horizontal directions. The flat/pin/sphere is loaded onto the test sample with a precisely known force using piezo-actuation. The friction coefficient is determined during the test by measuring the deflection of this elastic arm in both horizontal and vertical planes with two high precision displacement sensors. These sensors not only allow the measurement of the imposed horizontal frictional force that is produced as the sample is moved under the cantilever, but also allows the system to fix the normal load and through a feedback loop, and the piezo-actuation, maintain this load independent of any surface irregularities. Wear coefficient for the pin and disk materials are calculated from the volume of material lost during the test. Furthermore, the control of the test parameters such as speed, frequency, contact pressure, time and the environmental parameters (temperature, humidity and lubricant) allows one to closely reproduce the real life conditions of a practical wear situation. This arrangement offers a low load range down to  $50\mu\text{N}$  with a resolution of  $1\mu\text{N}$ .

### **Experimental Arrangement**

Three samples were used in these experiments. These were all high speed steel substrates coated by PECVD with DLC coatings of 200nm,  $1\mu\text{m}$  and  $2\mu\text{m}$  thickness respectively.

Hardness tests were carried out with the CSM Nano Hardness Tester (NHT). Using a Berkovich indenter, normal loads were applied of 1mN, 3mN, 10mN, 30mN and 100mN.

Scratch testing was carried out using the CSM Nano Scratch instrument (NST). Two standard Rockwell indenters, radius  $2\mu\text{m}$  and  $5\mu\text{m}$  were used, with a constant sliding speed of 6mm/min for a length of 6mm. An increasing load was normally applied of 0.05mN to 80mN to the  $2\mu\text{m}$  indenter, 0.5mN to 300mN for the  $5\mu\text{m}$  indenter over the duration of the scratch.

Tribometry test were carried out using the CSM Nano Tribometer (NTR). A 2mm diameter ball of 100Cr6 (AISI E 52100 Steel) was fixed to the tip of the calibrated two-axis cantilever. The samples were placed on the rotating table of the Nanotribometer arrangement. Between tests both the sample surfaces and the fixed ball were cleaned with ethanol. The tests were performed with normal loads of 1mN, 50mN, 300mN and 1000mN and constant linear velocity of  $4.2 \text{ mms}^{-1}$ .

## Results

### Hardness Tests

Figure 4 shows the instrumented hardness values and the maximum penetration depth as a function of normal load for each of the three DLC coated samples. The average hardness for such a coating is in the range of 20000 GPa. It can be seen that for low loads where the penetration depths are low, the hardness measurements are representative for this kind of film. As the normal load is augmented, the resulting hardness measurements are increasingly influenced by the underlying substrate, for which the approximative hardness is in the range of 10 000GPa. For the 200nm thickness film the reduction in hardness values associated with the increased load is already seen with the first load at 1mN.

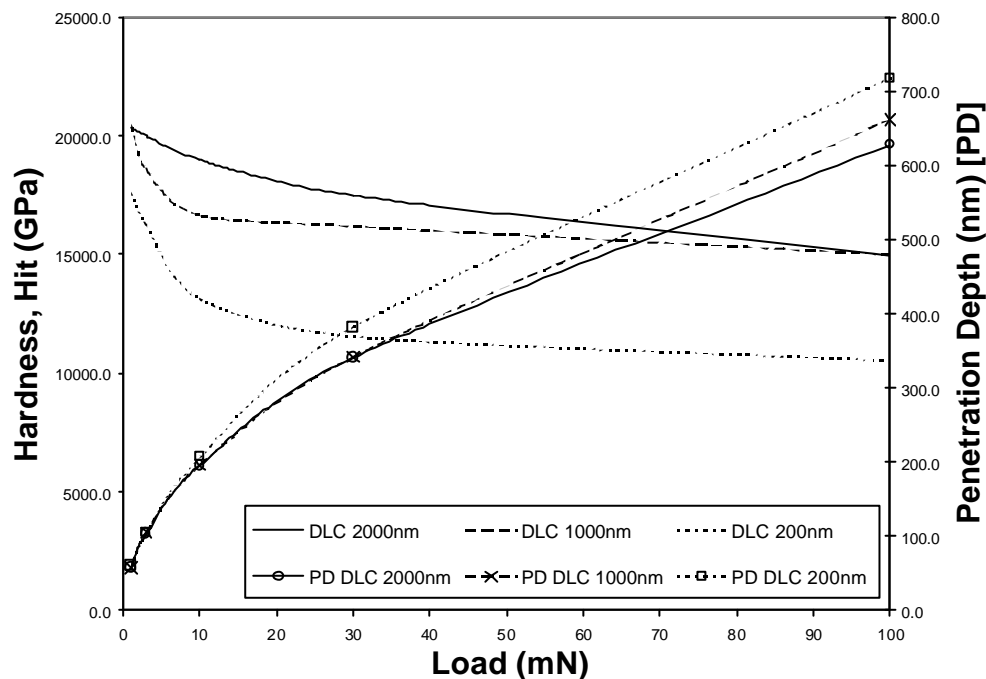


Figure 4. Penetration depth and Instrumented hardness as a function of applied normal load

Figure 5, shows the hardness values obtained as a function of the percentage of the coating layer penetration. At 1mN the indenter has already penetrated at least 30% of the 200nm DLC coating thickness and the resulting hardness value falls between that of the coating and that of the substrate. This figure demonstrates the importance of minimising the indentation depth, and thus minimising normal loads, for the characterisation of thin films. For the thicker films, the lower normal loads produce indentation depths that fall within the first 10% of the coating thickness. The resulting hardness measurements at these loads are a closer representation of those of the DLC film. Similarly for measurement of the elastic

modulus of these film, figure 5 demonstrates the same tendency for the values to approach those of the substrate with increased indentation depth.

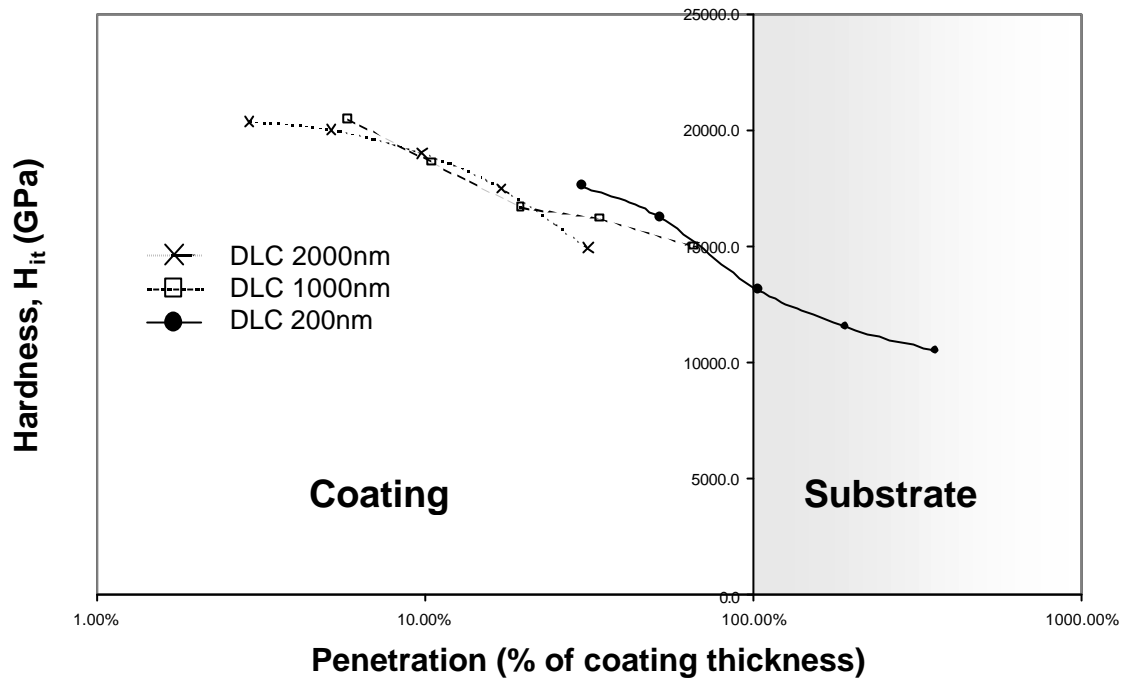


Figure 5. Instrumented hardness as a function of penetration depth

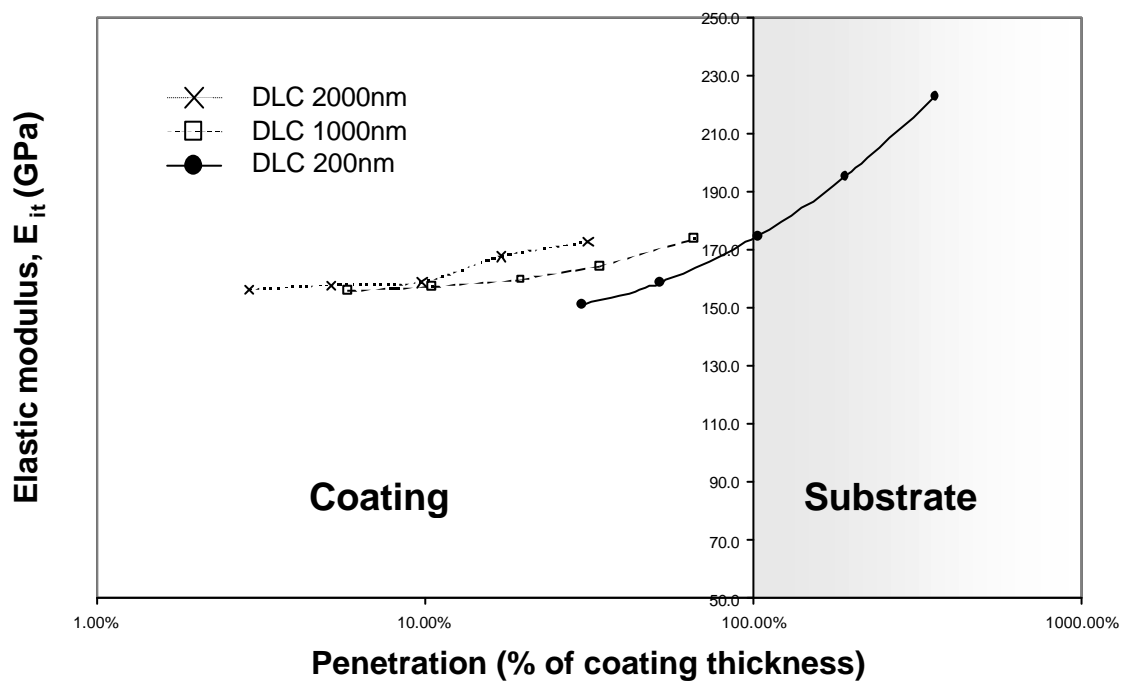
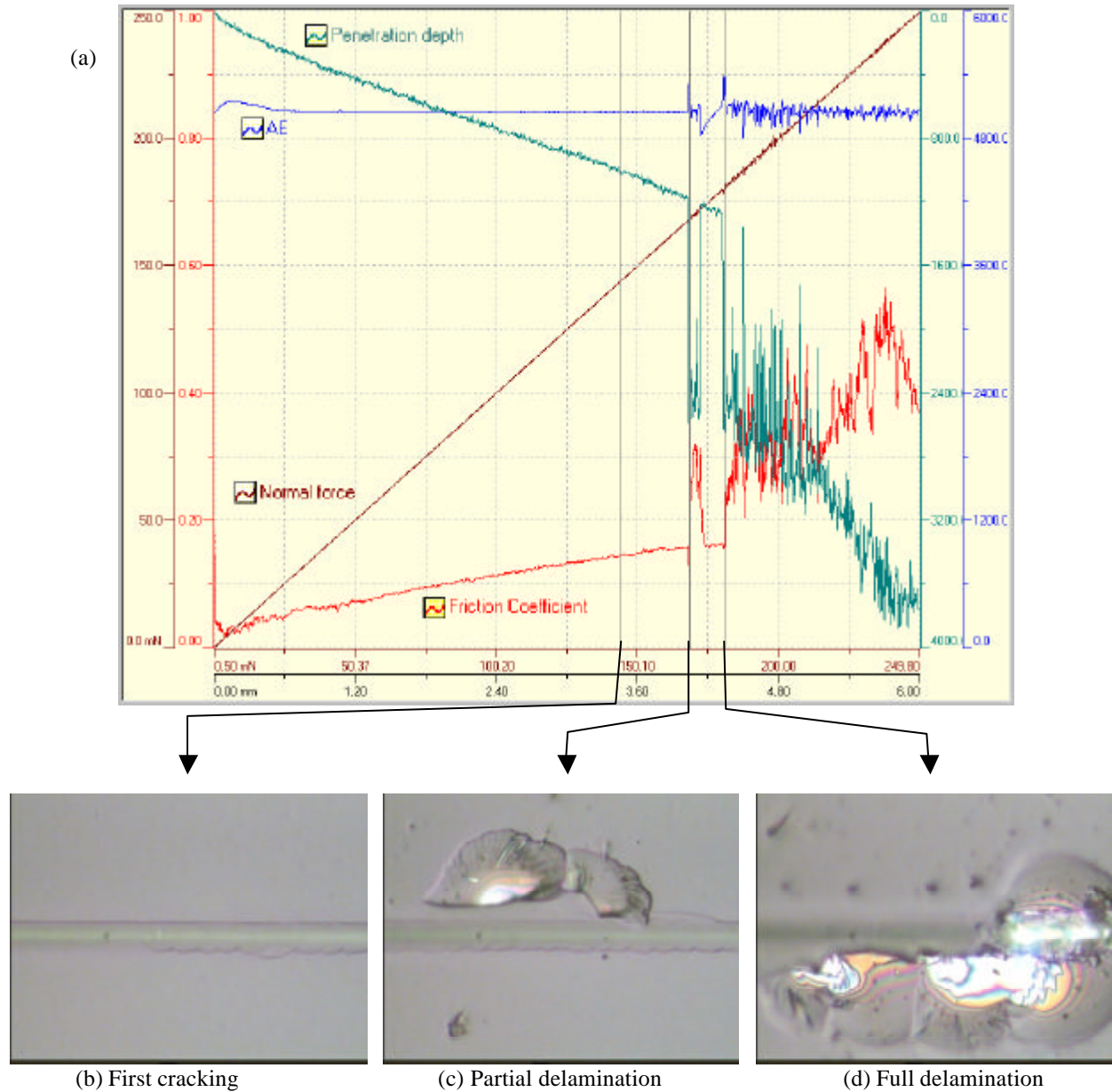


Figure 6. Instrumented Elastic modulus as a function of penetration depth

## Scratch Testing

A typical scratch test result containing penetration depth, acoustic emission (AE) and friction coefficient as the increasing normal force, is shown in figure 7. The combination of numerical data and optical observation gives details of the surface behaviour under critical conditions.



**Figure 7. Scratch test results and visualisation of surfaces failures**

This instrument (NST) allows one to identify critical loads along the scratch length that are associated with changes in frictional forces, acoustic emissions and physical changes in surface profile, along with optical identification of failures; cracking, delamination, chipping, etc. From this information it is possible to obtain quantitative information concerning the DLC protective coatings performance. It was observed (table 1) that the first partial delamination for the DLC film with 200nm thickness appears only after 23μm at the

beginning of the scratch then for the other samples after 72 $\mu$ m respectively 75 $\mu$ m. Probably this is due to the difference of chemical and physical properties between coating and substrates. The high internal stress levels in the films, combined with the ensuing lattice mismatch when DLC is applied to different substrates including stainless steel substrate, commonly leads a certain adhesion. If there are no abrupt changes in composition, the stress is introduced into the film gradually. For the first sample, probably a mixture of tetrahedral ( $sp^3$ ) and trigonal ( $sp^2$ ) bonding constituents of carbon enrichment the interface between stainless steel substrate and DLC coating and gives more fragility to the surface of the sample[1].

Tip Radius	Failure	First cracking	Part. delamination	Full delamination
2 $\mu$ m	DLC 2000nm	54	76	-
	DLC 1000nm	53	72	77
	DLC 200nm	-	23	25
5 $\mu$ m	DLC 2000nm	146	186	-
	DLC 1000nm	147	163	182
	DLC 200nm	-	37	54

**Table 1. Critical loads of scratch tests on DLC coated samples**

### Nano Tribometry

Similarly to the hardness results obtained, the influence of the substrate on the overall friction characteristics increases with increasing load. At low loads, any deformation in the system of substrate, coating and sliding steel ball remains in an elastic regime. As the normal load is increased we observe an augmentation in the friction coefficient (Table 2).

Applied Force				
Samples	1mN	50mN	300mN	1000mN
DLC 2000nm	0.12	0.12	0.13	0.14
DLC 1000nm	0.12	0.13	0.14	0.17
DLC 200nm	0.11	0.13	0.19	0.28

**Table 2. Friction Coefficients of tribological tests on DLC coatings**

### Conclusion

The advantages provided by a number of different instruments, techniques and methods have been presented for the principal characterization of the surface mechanical properties for various ranges: Nano Hardness, Nano scratch and Tribometer instrumentation. We have regarded as an example, the comportment of DLC coatings of different thickness, in both elastic and plastic deformation regimes and the influence of the substrate on those results.



Using Nano Hardness techniques the importance of low normal loads during indentation has been demonstrated, where one wishes to characterize the coating without the influence of the underlying substrate. The current development of Pico Hardness instrumentation is driven by this demand for measurement where film thicknesses are a few hundred nanometers.

Nano Scratch tests provided quantitative information concerning the internal stresses and failure modes by simultaneously recording friction transients, acoustic emissions and changes in surface morphology whilst this scratch on the test surface is applied.

Tribometer experiments present the characteristics of the samples with respect to friction and wear. DLC coatings are commonly used as wear protective layers for high precision components. The increase in friction coefficients, associated with higher normal loads, indicate plastic deformation of the surface that can be an indicative of system wear.

The complimentary mechanical information given by the instruments, Nano Hardness Tester, Nano Scratch Tester, Nano Tribometer, offer information on the coating-substrate system, that can be used in development of deposition techniques, lifetime prediction of components and new film technologies.

## References

- [1] J. Robertson, *Mater. Sci. Eng. R* 37 (2002) 129
- [2] M.F. Doerner, and W.D. Nix, "A method for interpreting the data from depth sensing indentation instruments", *J. Mater. Res.*, 1, (1986), 601-609
- [3] W.C. Oliver, G.M. Pharr, "An improved technique for determining hardness and elastic modulus using load and displacement sensing indentation experiments", *J. Mat. Res.*, 7(6), June 1992, 1564-1583
- [4] ISO/DIS Standard 14577-1, ISO/DIS 14577-2
- [5] A.C. Fischer-Cripps, *Nanoindentation*, Springer Mechanical Engineering Series, 2002.
- [6] R. Consiglio, N. X. Randall, B. Bellaton and J. von Stebut, *Thin Solid Films* 332 (1998) 151-156
- [7] M. Scherge, S.I. Ahmed, O. Mollenhauer, F. Spiller, , *Technisches Messen*, 67 7-8, (2000) 324 – 327
- [8] H. Liu, S.I.-U. Ahmed, M. Scherge, *Thin Solid Films*, 381 (2001) 135 – 142.
- [9] I.M. Hutchings, *Tribology: Friction and Wear of Engineering Materials*, Butterworth-Heinemann, Fifth ed. 2001

## Contact Information

CSM Instruments SA, Galileo Center, Rue de la Gare 4, 2034 Peseux, Switzerland. Tel : 0041 32 557 56 00. Fax : 0041 32 557 56 10. <mailto:gregory.favaro@csm-instruments.com>

# **Splat formation on different oxide iron – relation with the adhesion of the alumina coating**

S. Valette, A. Denoirjean, P. Lefort, P. Fauchais

*Science des Procédés Céramique et de Traitement de Surface, University of Limoges, UMR CNRS 6638; FRANCE*

To improve the adhesion of alumina coatings on low carbon steel, it is necessary to develop an oxide layer with a controlled thickness and chemistry at its surface. During the last 3 years of our work, oxide layers production under controlled atmosphere and pressure in a furnace have been well defined, and the adhesion of these layers before and after plasma preheating characterized. It appears that it is the lower oxidation state for iron oxide which has the most important influence to improve the adhesion of the coating. The growth of the wüstite oxide layer on a smooth ( $R_a \sim 0.05 \mu\text{m}$ ) surface is characterized by a prismatic crystal microstructure with an average roughness around  $1 \mu\text{m}$  and a good adhesion. The other oxide layer types have a lower roughness and a poor adhesion.

In this paper two main studies are developed. The first one consists, for the Wüstite layer, to study the influence of the thickness of the oxide layer on the adhesion of the coating. The second one is aimed to determine for the adhesion mechanism the part of the influence of the chemistry in comparison to that due to mechanical adhesion related to the roughness of the oxidized surface. The splat formation is analyzed by AFM and SEM, the coating adhesion is measured by the adhesion test ASTM C273. The three types of oxide layer ( $\text{FeO}$ ,  $\text{Fe}_3\text{O}_4$ ,  $\text{Fe}_2\text{O}_3$ ) produced by furnace preoxidation before plasma spraying are tested and the oxide layers are coated with alumina without polishing and after polishing on SIC paper grade 4000 to obtained the same range of roughness. The influence of the substrate preheating is also considered.

# KINETIC MODEL of DEPOSITION for FILM PRODUCTION by PLASMA CHEMICAL METHOD

B.F.Gordiets<sup>2</sup>, J.L.Andujar<sup>1</sup> and E.Bertran<sup>1</sup>

<sup>1</sup> *Departament de Física Aplicada i Òptica, Universitat de Barcelona,  
Av.Diagonal 647, 08028, Barcelona, Spain*

<sup>2</sup> *Lebedev Physical Institute of Russian Academy of Sciences, Moscow*

## Abstract

A kinetic model is proposed to describe the production by plasma-enhanced chemical vapour deposition of a thin film containing two components, A and B. The deposition and erosion rates, surface and volume densities of A and B components are calculated as a function of probabilities for the elementary processes of gas(plasma)-surface interactions.

## 1. Introduction.

Much research effort has recently been directed to the use of plasma-enhanced chemical vapour deposition (PECVD) to produce thin-films which consist of one or two chemical components (for example, Si, C, SiC). Many of the characteristics of thin films have been identified experimentally, and their dependence on various parameters (gas composition, pressure, temperature, discharge current, power, ion energy and substrate) has been established. Theoretical models have also been presented (see, for example, [1-8]). Such models are usually specific and describe particular experiments and situations.

A series of experiments on thin-film production have been carried out and the characteristics of these films have been investigated experimentally at the Department of Applied Physics and Optics of Barcelona University [9-12].

Here we present a general kinetic model of binary deposition which includes the probabilities and rate coefficients for the elementary processes of gas (plasma)-surface interactions, and which can be used for calculations of the macro characteristics of thin-film production by PECVD. The model also provides qualitative and quantitative interpretation of experiments done at Barcelona University.

## 2. The simple kinetic model for deposition and its equations.

We study the production of thin films that contain two chemical components: A and B. We assume that one component has two or more dangling chemical bonds and the other component – three or more dangling bonds. We also assume that the film production is due to "flaky" (layer-on-layer) deposition and that every layer of film can have components A and B. The chemical bonds A-A, A-B, B-B are formed between A and B.

We calculate the surface densities  $N_n^A$  and  $N_n^B$  of A and B components respectively in the *open* layer with number " $n$ ". The term "open" is used to mean that the layer is in contact with the gas phase. Numbering begins with the substrate, for which  $n=0$ . The master balance equations for  $N_n^A$  and  $N_n^B$  ( $n \geq 1$ ) are:

$$\frac{dN_n^A}{dt} = -(P_n^{AA} + P_n^{AB})N_n^A + P_{n-1}^{AA}N_{n-1}^A + P_{n-1}^{BA}N_{n-1}^B \quad (a)$$

$$\frac{dN_n^B}{dt} = -(P_n^{BB} + P_n^{BA})N_n^B + P_{n-1}^{BB}N_{n-1}^B + P_{n-1}^{AB}N_{n-1}^A \quad (b) \quad (1)$$

Here  $t$  is time and  $P_n^{ij}$  are the probabilities (in  $s^{-1}$ ) to cover component " $i$ " in layer " $n$ " by component " $j$ " in layer " $n+1$ ". As a result, the deposited component " $j$ " appears on the open layer " $n+1$ ".

It is important to note that the gas phase components A and B are not usually "pure" atoms of A or B. They can be gas phase molecular radicals or ions which contain A or B atom (ion) and have been provided by plasma chemical gas phase reactions. The new surface chemical bond is usually created by collisions of these radicals with surface A or B atoms.

Thus, we have described the deposition in a discrete form using the discrete master equations (1). However, the continuous analogy of Eqs.(1) will be used to obtain the analytical solution of our task. For this, we decompose the values  $P_{n+\Delta n}^{ij} N_{n+\Delta n}^i$  in Taylor series:

$$P_{n+\Delta n}^{ij} N_{n+\Delta n}^i \approx P_n^{ij} N_n^i + \frac{\partial(P_n^{ij} N_n^i)}{\partial n} \Delta n + \dots; \quad \Delta n = \pm 1; \quad i=A,B; \quad j=A,B \quad (2)$$

Inserting (2) in (1), we obtain the equations in the partial derivatives:

$$\frac{\partial N_n^A}{\partial t} = -\frac{\partial(P_n^{AA} N_n^A)}{\partial n} - \frac{\partial(P_n^{BA} N_n^B)}{\partial n} - P_n^{AB} N_n^A + P_n^{BA} N_n^B \quad (a)$$

$$\frac{\partial N_n^B}{\partial t} = -\frac{\partial(P_n^{BB} N_n^B)}{\partial n} - \frac{\partial(P_n^{AB} N_n^A)}{\partial n} + P_n^{AB} N_n^A - P_n^{BA} N_n^B \quad (b) \quad (3)$$

If we assume that

$$P_n^{ij} = P^{ij} \quad i=A,B; \quad j=A,B, \quad (4)$$

the analytical solution of Eqs.(3) can be obtained:

$$N_n^A(t) = C_1 N_0^0 \exp\left\{-\left(P_{dep} t - n + 1\right)\right\} \left[\exp\left\{-(\gamma - 1)(P_{dep} t - n + 1)\right\} - 1\right] \quad \text{for } n - 1 \leq P_{dep} t \quad (a)$$

$$N_n^A(t) = 0 \quad \text{for } n - 1 > P_{dep} t \quad (b) \quad (5)$$

$$N_n^B(t) = C N_n^A(t), \quad (c)$$

where  $C_1$  is the normalisation factor;  $\gamma = P_0 / P_{dep}$  and  $P_{dep}$  is the probability of deposition (in  $s^{-1}$ ):

$$P_{dep} = \frac{P^{AA} + P^{AB} + P^{BB} C + P^{BA} C}{1 + C} \quad (6)$$

$C$  is constant. Here  $P_0 = P_0^A + P_0^B$ ;  $P_0^A$  and  $P_0^B$  are the probabilities (in  $sec^{-1}$ ) for chemical absorption of A and B species by substrate;  $N_0^0$  is the initial surface density (in  $cm^{-2}$ ) of substrate sites (non occupied at  $t=0$ ). It is assumed that the probabilities  $P_0^A$ ,  $P_0^B$ ,  $P^{AA}$ ,  $P^{AB}$ ,  $P^{BA}$ ,  $P^{BB}$  are independent of time.

Equation (5) gives the number  $n_b$  for boundary layer of film, which increases during the deposition:

$$n_b = P_{dep} t + 1 \approx P_{dep} t \quad (7)$$

The deposition rate  $J_{dep}$  and the thickness  $L_{film}$  of the film are

$$J_{dep} = l P_{dep}; \quad L_{film} = l P_{dep} \tau_{dep}, \quad (8)$$

where  $\tau_{dep}$  is the total deposition time;  $l$  is the thickness of one layer. It is the parameter of task.

The coefficient  $C$  in (6) depends on probabilities  $P^{ij}$  ( $i=A,B; j=A,B$ ). To calculate it, we sum (1a) and (1b) from  $n=1$  to  $n_b$ . We obtain (using (5c))

$$\frac{dN_{surf}^A}{dt} = N_{surf}^A (C P^{BA} - P^{AB}), \quad \frac{dN_{surf}^B}{dt} = N_{surf}^B \left( \frac{1}{C} P^{AB} - P^{BA} \right) \quad (9)$$

where  $N_{surf}^A = \sum_{n=1}^{n_b} N_n^A$ ,  $N_{surf}^B = \sum_{n=1}^{n_b} N_n^B$  are the total densities of A and B species on all the *open* layers, that is on the film surface. Further, we will investigate the quasi stationary conditions, when

$\frac{dN_{surf}^A}{dt} \approx 0$ ;  $\frac{dN_{surf}^B}{dt} \approx 0$ . In this case, from (9) and if  $N_{surf}^A + N_{surf}^B = N_0^0$ :

$$C = \frac{P^{AB}}{P^{BA}} = \frac{\Theta^B}{\Theta^A}; \quad \Theta^A = \frac{P^{BA}}{P^{BA} + P^{AB}}; \quad \Theta^B = \frac{P^{AB}}{P^{BA} + P^{AB}}; \quad \Theta^A + \Theta^B = 1 \quad (10)$$

The values  $\Theta^A$  and  $\Theta^B$  are the surface covering species A and B, respectively, which are the relative surface densities. Besides deposition rate (8) and relative surface densities (10), the relative volume densities  $V^A$  and  $V^B$  of species A and B can also be calculated. We have:

$$V^A = \frac{P^{AA}\Theta^A + P^{BA}\Theta^B}{P_{dep}} \quad (11)$$

$$V^B = \frac{P^{AB}\Theta^A + P^{BB}\Theta^B}{P_{dep}} \quad (12)$$

It interesting to note that the relative surface densities (10) are different from the volume densities  $V^A$ ,  $V^B$  and determined only by the probabilities  $P^{AB}$ ,  $P^{BA}$  (unlike  $V^A$ ,  $V^B$ , which also depend on  $P^{AA}$ ,  $P^{BB}$ ). The reason is that the surface densities are determined by the densities on *all open* layers and volume densities are determined by densities inside the film (that, is by the densities of the closed layer).

### 3. The generalization of model.

The simplest case of binary deposition and thin-film production have been investigated in Sec.2. The real situation can be more complex.

*First*, the part of the surface of growing film can be occupied by "passive" species M (molecules), which do not form chemical bonds with A or B species. Indeed, physical (but not chemical) absorption of species M can take place.

*Second*, the film surface can be bombarded by energetic particles (usually ions), which causes the desorption of M species and breaks the bonds A-A, A-B, B-B on the upper film layers. These actions are, respectively, the cleaning of film surface and film erosion.

Let us now consider these effects. Let  $M_A$  and  $M_B$  be the "passive" species that may cover our "active" surface species A and B respectively. In the framework of our "flaky" model for deposition, the following parts  $(dN_n^A/dt)_{M,D}$ ,  $(dN_n^B/dt)_{M,D}$  must be added to the right side of Eqs. (1a), (1b):

$$\begin{aligned} \left( \frac{dN_n^A}{dt} \right)_{M,D} &= P^{MA} N_{n+1}^{M_A} - P^{AM} N_n^A + D_{n+1}^{MA} N_{n+1}^{M_A} - (D_n^{AA} + D_n^{AB}) N_n^A + D_{n+1}^{AA} N_{n+1}^A + D_{n+1}^{BA} N_{n+1}^B \quad (a) \\ \left( \frac{dN_n^B}{dt} \right)_{M,D} &= P^{MB} N_{n+1}^{M_B} - P^{BM} N_n^B + D_{n+1}^{MB} N_{n+1}^{M_B} - (D_n^{BB} + D_n^{BA}) N_n^B + D_{n+1}^{BB} N_{n+1}^B + D_{n+1}^{AB} N_{n+1}^A \quad (b) \end{aligned} \quad (13)$$

Beside this, the new equations can be written for the surface densities  $N_n^{M_A}$  and  $N_n^{M_B}$  of "passive" components  $M_A$  and  $M_B$ :

$$\frac{dN_n^{M_A}}{dt} = P^{AM} N_{n-1}^A - P^{MA} N_n^{M_A} - D_n^{MA} N_n^{M_A} \quad (a)$$

$$\frac{dN_n^{M_B}}{dt} = P^{BM} N_{n-1}^B - P^{MB} N_n^{M_B} - D_n^{MB} N_n^{M_B} \quad (b) \quad (14)$$

Here  $P^{AM}$ ,  $P^{BM}$  and  $P^{MA}$ ,  $P^{MB}$  are respectively the probabilities (in  $s^{-1}$ ) for physical absorption and desorption (usually spontaneous) of "passive" components  $M_A$  and  $M_B$  on film surface covered by "active" sites A and B. The values  $D_n^{MA}$  and  $D_n^{MB}$  are the probabilities (in  $s^{-1}$ ) for desorption of  $M_A$  and  $M_B$  due to collisions with energetic bombarding particles (ions). Finally,  $D_n^{ij}$  are the probabilities (in  $s^{-1}$ ) of the chemical bonds breaking.

To solve Eqs.(1) with additional parts (13) and Eqs.(14) we have used the approximation (2) and obtained the coupled system of equations in the partial derivatives. Note that only the "transitions" between neighbouring layers are taken into account in (13), (14) for simplicity (that is  $\Delta n = \pm 1$  in (2) and (13), (14)). The energetic ions can penetrate inside film and break more than one chemical bond, that is, the transitions can be for  $|\Delta n| > 1$ . However, this effect can be taken into account if we insert in equations (14) the parts  $D_{n+\Delta n}^{ij} N_{n+\Delta n}^i$  with  $\Delta n \geq 2$  and use for description of such parts the decomposition (2) with

$\Delta n \geq 2$  for receiving of equations in partial derivatives. It can see that this case corresponds to an increase of probabilities  $D^{ij}$  in 2; 3 ... and so on times.

The solution of these equations gives:

The deposition rate  $J_{dep}$  :

$$J_{dep} = lP_{dep}^{(1)} \quad (15)$$

Here, the probability of deposition  $P_{dep}^{(1)}$  (instead of  $P_{dep}$ , see (6)) is

$$P_{dep}^{(1)} = (P^{AA} - D^{AA} + P^{AB} - D^{AB})\Theta^A + (P^{BB} - D^{BB} + P^{BA} - D^{BA})\Theta^B \quad (16)$$

The surface coverings for species A, B,  $M_A$ ,  $M_B$  here are the following

$$\Theta^B = \frac{P^{AB} + D^{AB}}{P^{BA} + D^{BA}}\Theta^A; \quad \Theta^{M_A} = \frac{P^{AM}}{P^{MA} + D^{MA}}\Theta^A; \quad \Theta^{M_B} = \frac{P^{BM}}{P^{MB} + D^{MB}}\Theta^B \quad (17)$$

$$\Theta^A + \Theta^B + \Theta^{M_A} + \Theta^{M_B} = 1 \quad (18)$$

Some peculiarity exists for probabilities  $D^{ij}$ . They depend not only on energy and flux of bombarding ions but also on probabilities of  $R_{ij}$  opening (after breaking the chemical bond  $i-j$  and one particle  $i$  escaping) the species  $j$  on the lower layer. The values  $D^{ij}$  can be presented as

$$D^{ij} = D_0^{ij} R^{ij} \quad i=A,B; j=A,B \quad (19)$$

where  $D_0^{ij}$  (in  $\text{sec}^{-1}$ ) depends on energy and flux of bombarding ions and type of chemical bond  $i-j$ . The dimensionless probabilities  $R^{ij}$  are

$$R^{AA} = V^A; \quad R^{AB} = V^B \quad (20)$$

$$R^{BB} = V^B; \quad R^{BA} = V^A \quad (21)$$

Thus, we have in the common case eight non linear equations (17), (18), (20), (21) to obtain eight values  $\Theta^A$ ,  $\Theta^B$ ,  $\Theta^{M_A}$ ,  $\Theta^{M_B}$ ,  $R^{AA}$ ,  $R^{AB}$ ,  $R^{BA}$ ,  $R^{BB}$  as a functions of probabilities  $P^{ij}$ ,  $D_0^{ij}$ ,  $P^{AM}$ ,  $P^{BM}$ ,  $P^{MA}$ ,  $P^{MB}$ ,  $D_0^{MA}$ ,  $D_0^{MB}$ . After solution of these equations, the problem will be solved. The deposition rate can be calculated from (15), (16) and the relative volume densities  $V^A$ ,  $V^B$  are following

$$V^A = \frac{(P^{AA} - D^{AA} - D^{AB})\Theta^A + P^{BA}\Theta^B}{P_{dep}^{(1)}}; \quad (22)$$

$$V^B = \frac{(P^{BB} - D^{BB} - D^{BA})\Theta^B + P^{AB}\Theta^A}{P_{dep}^{(1)}} \quad (23)$$

Note, that besides the calculation of deposition rate and the other characteristics of the thin film, the sputter-erosion rate of prepared film can be determined for the case when the bombardment of film by the energetic particles (ions) takes place. The sputter-erosion rate  $J_{eros}$  can be calculated from the Eqs.(15)-(18) without the probabilities  $P^{ij}$ ,  $P^{AM}$ ,  $P^{BM}$ ,  $P^{MA}$ ,  $P^{MB}$ :

$$J_{eros} = -l[(D_{eros}^{AA} + D_{eros}^{AB})\Theta^A + (D_{eros}^{BB} + D_{eros}^{BA})\Theta^B] \quad (24)$$

The surface coverings for species A, B here are following

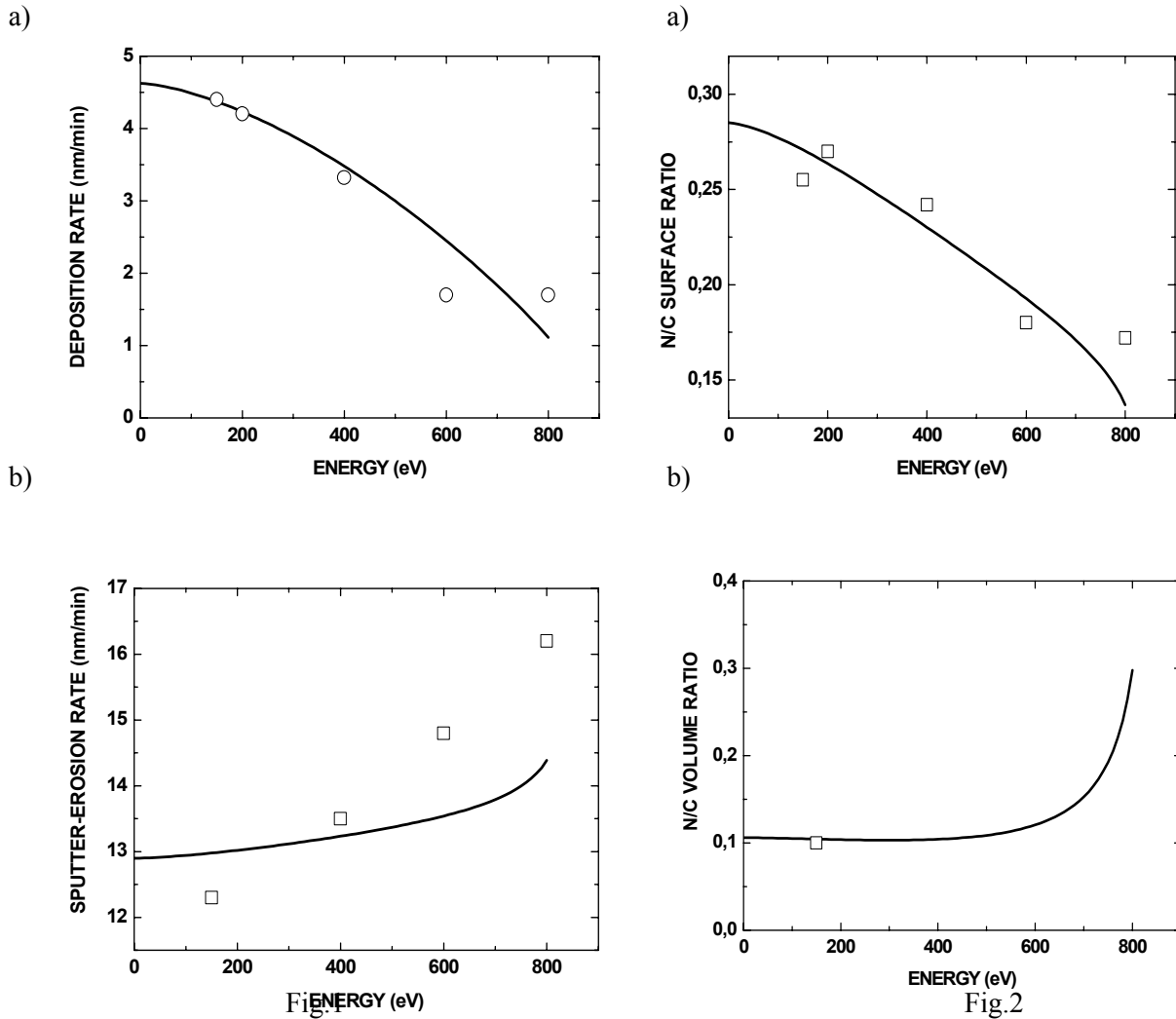
$$\Theta^B = \frac{D_{eros}^{AB}}{D_{eros}^{BA}}\Theta^A; \quad \Theta^A + \Theta^B = 1; \quad D_{eros}^{ij} = D_{0eros}^{ij} R_{film}^{ij} \quad (25)$$

The sign "-" on the right hand side (24) means that the film thickness decreases due to erosion. The values  $D_{0eros}^{ij}$  in (24), (25) depend on the flux and energy of ions bombarding the film and causing erosion.

However, the values  $R_{film}^{ij}$  depend on the history of film production, that is on all probabilities  $P^{ij}$ ,  $D_0^{ij}$ ,  $P^{AM}$ ,  $P^{BM}$ ,  $P^{MA}$ ,  $P^{MB}$ ,  $D_0^{MA}$ ,  $D_0^{MB}$  during the deposition.

#### 4. The comparison with experiment.

Here we compare some calculations in the framework of the model with the experimental results [12]. In [12], the amorphous carbon nitride thin-film (a-CN) was prepared in a hybrid plasma-based deposition process that allows independent control of nitrogen ion bombardment, by combining r.f.-magnetron sputtering of a graphite target with simultaneous nitrogen-ion-beam assistance from a capacitively coupled r.f. ion source. The films were deposited on silicon substrates at 0.3 Pa of total pressure, using Ar and N<sub>2</sub> gas flows of 3 and 1 sccm, respectively. The energy of bombarding nitrogen ions was increased from 140 to 800 eV. The deposition rate and relative densities of C and N species on surface and inside of films were measured. Beside this, the sputter-erosion rate of prepared a-CN films due to bombardment by 12 kV Ar<sup>+</sup> ion beam was also measured. The experimental results and calculations of the model are given in Figs. 1, 2.



**Fig.1** - Experimental [12] (white squares) and model calculation (lines) of deposition rate (a) and sputter-erosion rate by 500 nA 12 kV Ar<sup>+</sup> ion beam of CN film (b) as a function of nitrogen ion beam energy during deposition.

**Fig.2** - Experimental [12] (white squares) and present model calculation (lines) of nitrogen to carbon surface (a) and volume (b) atomic ratio as a function of nitrogen ion beam energy during deposition.

Figs 1 and 2 show satisfactory agreement between theory and experiment. Of course, to obtain this agreement, probabilities  $P^{ij}$ ,  $D_0^{ij}$ ,  $D_{0ers}^{ij}$  were chosen. It was assumed that the film surface is cleaned during

the deposition and erosion (that the probabilities  $P^{AM}$ ,  $P^{BM}$ ,  $P^{MA}$ ,  $P^{MB}$  are equal to zero and  $\Theta^A + \Theta^B = 1$ ). This assumption is justified because the cleaning of film surface by energetic ions takes place during deposition and erosion. The agreement with the experiment was obtained for the following values of probabilities  $P^{NN} = 0$ ;  $P^{NC} = 0.2 \text{ sec}^{-1}$ ;  $P^{CN} = 0.285 P^{NC}$ ;  $P^{CC} = 2.4 P^{NC}$ ;  $D_0^{NC} = D_0^{CN} = 0.28(E/1000)^{1.5} \text{ sec}^{-1}$ ;  $D_0^{CC} = 2 D_0^{CN}$ ;  $D_0^{NN} = D_{0eros}^{NN} = 0$ ;  $D_{0eros}^{NC} = D_{0eros}^{CN} = 0.7 \text{ sec}^{-1}$ ;  $D_{0eros}^{CC} = 2 D_{0eros}^{CN}$ .

We also assumed the thickness of one layer to be 0.17 nm. The ion energy  $E$  here is in eV. The power 1.5 in the energy dependencies  $(E/1000)^{1.5}$  for probabilities  $D_0^{ij}$  gives a good agreement for calculated and measured dependencies on  $E$  for deposition rate and surface relative densities of N and C atoms (see Fig.1a, 2a). The value  $(E/1000)^{1.5}$  is proportional to ion energy flux at the film surface.

Note that above given comparison experiment and model calculations is rough and has limitation because the above obtained formulas describe the deposition of components which everyone has two and more dangling chemical bonds. The situation is different for case C-N thin film because atom N has only one dangling bond. The kinetic model of binary deposition with such type component will be developed in the future.

## 5. Conclusion.

The kinetic model for thin-film production by the deposition of two components A and B allows calculation of the film macro characteristics which can be measured: deposition and erosion rates, relative densities of A and B components on the surface and in the volume of film. The model takes into consideration the various processes of gas (plasma)-surface interaction. The kinetic model contains the probabilities for elementary actions of these processes of gas(plasma)-surface interaction. The probabilities depend on energies and fluxes of different gas phase components at the film surface as well as on film (substrate) temperature, sticking coefficients and probabilities of breaking chemical or physical bonds on the film surface. These sticking coefficients and probabilities can be determined from the comparison of the model with the measurements of film characteristics and calculated (or measured) gas phase densities of different molecules, radicals, ions and so on. This is a task for future investigations.

## Acknowledgement

This work was partially supported by a PIV 2001 grant of Catalonia Government and the CICYT of Spain (projects MAT 1999-0569-C02-01 and MAT 2002-04263-C04).

## References

1. M.J.McCaughy and M.J.Kushner (1989) J.Appl.Phys. v.65, p.186.
2. D.S.Dandy and M.E.Coltrin (1995) J.Mater.Res., v.10, 1993.
3. E.A.Haupfear, E.C.Olson and L.D.Schmidt(1994) J.Electrochem.Soc., v. 141, p.1943.
4. H.M.Liu and D.S.Dandy (1996) J.Electrochem.Soc., v. 143, p.1104.
5. M.Ibncharaa, M.Jaouen, J.Delafond and L.Pranevicius (1997) Surf.Coating Techn., v. 92, p.1.
6. E.Meeks, R.L.Larson, P.Heo, et al. (1998) J.Vac.Sci.Technol. v.A 16, p.544.
7. Min Tae Kim (1999) Thin Solid Film, v.347, p.99.
8. P.Barathieu, B.Caussat, E.Shield, D.Jaume and J.P.Couderc (1999) J. de Physique, v.9, p.173.
9. J.L Andujar, E.Bertran,A.Canillas, C.Roch and J.L.Morenza (1991) J.Vac.Sci.Technol. v.A 9, p.2216.
10. E.Bertran, J.L.Andujar, A.Canillas, C.Roch, J.Serra and G.Sardin (1991) Thin Solid Film, v.205, p.140.
11. J.I. Andujar, E.Bertran and M.C.Polo (1998) J.Vac.Sci.Technol. v.A 16, p.578.
12. J.L.Andujar, F.J.Pino, M.C.Polo and E.Bertran (2001) Diam.Relat.Mater., v.10, p.1175.



# Thermionic Vacuum Arc – a new technique for high purity carbon film deposition

G. Musa<sup>1</sup>, I. Mustata<sup>1</sup>, M. Blideran<sup>1</sup>, V. Ciupina<sup>2</sup>, R. Vladoiu<sup>2</sup>, G. Prodan<sup>2</sup>, E. Vasile<sup>2</sup>,  
H. Ehrich<sup>3</sup>

<sup>1</sup>*National Institute for Physics of Laser, Plasma and Radiation, Bucharest-Magurele, Romania*

<sup>2</sup>*Department of Physics, “ Ovidius University “, Constanta, Romania*

<sup>3</sup>*Department of Physics, University of Essen, Essen, Germany*

## Abstract

New equipment for the technology of thin film deposition using thermoionic vacuum arc with carbon anode is presented. The carbon film is bombarded during its deposition by energetic carbon ions with established value of directed energy. High purity, hydrogen free and nanostructured layers are obtained the characteristic size of structures being in the order of few nanometers.

## 1. Introduction

One of the most promising thin film layers are those obtained by DLC (diamond like carbon) coating as a result of plasma-chemical processing of hydrocarbons (like methane). Usually the obtained thin films have a content of hydrogen.

Recently, hydrogen free thin layers of DLC are studied expecting better quality of such films. . Amorphous carbon (a-C) films that contain a significant fraction of sp<sup>3</sup> bonding, gives diamond like carbon (DLC) structures with valuable properties like high mechanical hardness, low friction, increased chemical inertness. Depending on the used technology, it is possible to obtain hydrogenated or hydrogen free DLC films. Plasma chemical reactors using hydrocarbons as main gas, generates hydrogenated DLC films. Due to the technological difficulties, hydrogen free DLC films have been less investigated carbon arc in vacuum is one of the common technology to obtain hydrogen free DLC. Unfortunately, droplets are present in the deposited films. In order to avoid this difficulty, filtered arc or mass spectrometry separated carbon ions deposition is used. Unfortunately, in this case the efficiency of film deposition is quite low.

The aim of this paper is to present a new, very promising technology, with a broad area of application and especially suitable for high quality carbon thin film deposition in high vacuum conditions. This technology has been used successfully for various metal or oxide thin film deposition. This new equipment generates a pure, gas-free metal vapor plasma containing ions with a directed energy. Advantages of this system are underlined extended applications possibilities of this new technology for increase of the microhardness of the pieces, decrease of the friction of moving pieces, change of the chemical reactivity of the pieces (corrosion resistant components) an also will be used for the development of nanostructures materials are given.

The most adequate application is related to nanostructured carbon film deposition. Indeed, the carbon anode is easily transformed into vapors due to electron beam bombardment, the purity of the deposited film is ensured by high vacuum condition and the compactness and smoothness due to the film growing under the high energy ion bombardment during deposition.

## 2. Experimental

Thermionic Vacuum Arc can be ignited in vacuum (or UHV) between a heated cathode surrounded by an electron focusing Whenelt cylinder and an anode (tungsten crucible) containing the material to be deposited. Due to the electron bombardment of the anode by the accelerated thermo-electrons from the grounded cathode towards the anode (which is at high voltage), anode material first melts and afterwards starts to evaporate ensuring a steady state concentration of the evaporated atoms in the cathode – anode space. At further increase of the applied high voltage, a bright discharge is established inside of the vacuumated vessel in the vapors of the anode material.

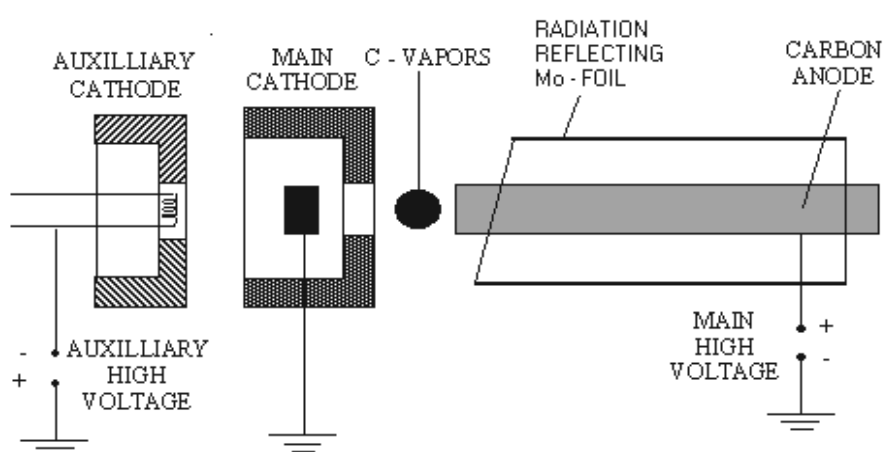
Because this system can heat at elevated temperature any material, it is one of the most adequate technology for carbon evaporation. In this case instead of crucible containing the material to be evaporated is used directly a carbon rod. Moreover, the discharge can be ignited in high vacuum condition, ensuring high purity and deposition of hydrogen free carbon layer.

This new type of arc offers the unique opportunity to generate energetic ions, with a controlled value of the directed energy, which are bombarding the condensing thin film on the substrate. The ions are just those (the substrate bombarding ions are generated just from the atoms of the depositing material, no gas being present in the vacuum chamber during the process) of the depositing atoms on substrate.

In figure 1 it is schematically shown the TVA electrodes arrangement with indirectly heated cathode (by electron bombardment) in order to increase the cathode life-time which was reacting with carbon vapor generating tungsten carbide and diminishing the cathode life time.

Also, in order to reduce heat-losses from the anode by radiation, molybdenum cylindrical reflector was mounted at anode.

The following parameters are fully controlling the TVA: arc current  $I_{arc}$ , cathode thermoelectronic emission current, controlled by the heated cathode temperature  $T_c$ , interelectrode distance  $d$ , angle  $\phi$  between an imaginary perpendicular line on the anode and the axis of the heated cathode.



**Fig. 1.** Schematic view of the electrodes arrangement for carbon plasma generation (indirectly heated cathode)

In table I are given the working parameters of thermionic vacuum arc for a number of deposition experiments of carbon films using small cathode carbon rod distance (a few mm):

Table I

Rod diameter (mm)	Auxiliary discharge		Main discharge		Voltage drop over discharge space (V)
	Voltage (kV)	Current (A)	Voltage applied (kV)	Arc current (A)	
4	2	0.2	1.7	1.8-2	400
3	2	0.2	2	2.5-3	240

(Deposition duration few minutes up to 5 minutes)

The thickness of the deposited carbon films on Si wafers of the order of 100-200 nm.

During the arc running and C thin film deposition, the anode was continuously rotating with 6 rotation/minute and also the cathode-anode distance was adjusted each time when the arc current was decreasing more than 10%. This way, a continuous working of the TVA was ensured. Since the cathode of TVA is at earth potential and vacuum vessel also, it results that the plasma has a potential accelerating ions towards against the vacuum vessel wall. This potential is roughly equal with the cathode potential fall (see Fig.2).

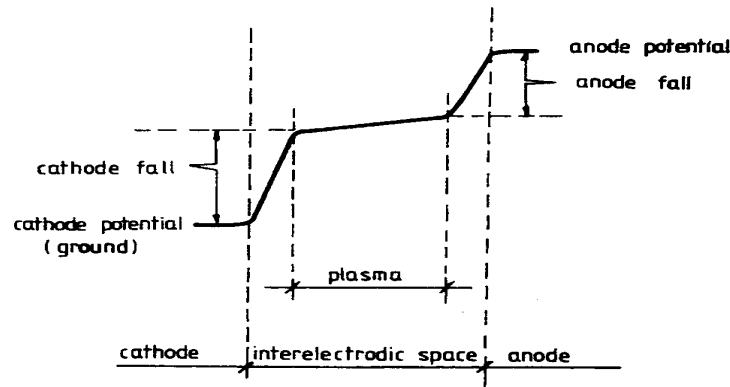
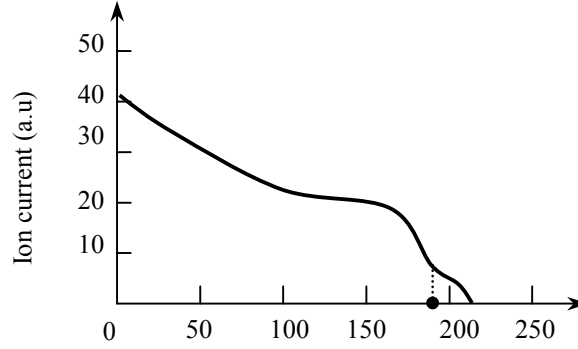


Fig. 2. Potential distribution in the cathode – anode space

In these circumstances, besides the evaporated neutral atoms, on the sample are also incident energetic ions. So, the thin film is growing under the bombardment of ions of the material to be deposited. This is a major advantage in obtaining high purity thin films because the discharge is ignited in vacuum and the film is bombarded during its growing with own atoms which are ionized. We measured, using a special retarding potential analyzer, the energy of ions in a TVA discharge, an experimental curve being given as example in fig.3.

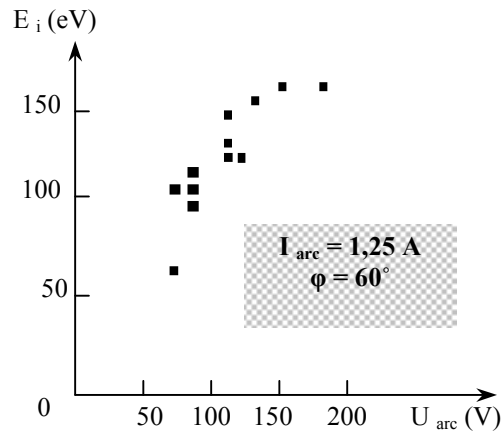
The ions have a random energy superposed on a much higher directed energy towards the wall. Directed energy of ions can achieve values of the order of 250 V. Our measurements on the potential distribution inside the vacuum vessel during TVA discharge have proved a continuous plasma source decrease of this potential from the value of the potential of the to the ground potential of the vacuum vessel wall. It results that the ion energy is directly related to the potential difference between vacuum vessel potential and plasma potential i.e., cathode potential fall.



**Fig. 3:** Energy distribution of ions in TVA metal vapor plasma Ion energy (eV)

The ions have a random energy superposed on a much higher directed energy towards the wall. Directed energy of ions can achieve values of the order of 250 V. Our measurements on the potential distribution inside the vacuum vessel during TVA discharge have proved a continuous decrease of this potential from the value of the potential of the plasma source to the ground potential of the vacuum vessel wall. It results that the ion energy is directly related to the potential difference between vacuum vessel potential and plasma potential i.e., cathode potential fall. As a result, the ion energy of the TVA plasma can be straightforward controlled and established at needed value even during arc running. For this, it is enough to control the given cathode potential fall.

We were able to establish the means to control the ion energy at a constant maintained TVA arc current. For example, a cathode fall increase is obtained using one of the below changes of TVA parameters: (1) decrease of the cathode temperature, (2) increase of angle  $\varphi$ , (3) increase of the interelectrode distance  $d$ . In figure 4 is presented the dependence of the copper ions for a thermoionic vacuum arc discharge in respect with the arc current for two values of the angle  $\varphi$ . Strong dependence of the ion energy on these parameters can be seen.



**Fig. 4.** Correlation of measured maximum ion energies and the arc voltage drop  $U_{arc}$  where  $\varphi$  defines the angle between the imaginary line perpendicular to the anode and the axis of the cathode.

An empirical relation can be established between the cathode potential fall and the TVA arc voltage drop, the relation between these two parameters being a linear one. In most of the cases, the ratio between these two potentials is roughly 1/2 - 1/3. In Fig. 4 is given the correlation between experimentally measured values of the energy of ions and the arc voltage drop. These data were taken for a TVA discharge with an arc current of 1.25 A and for a value of the parameter  $\phi=80^\circ$ . A steadily increase of the energy of ions with the value of the arc voltage drop can be observed. Consequently, the continuously measured value of the arc voltage drop can be used as a directly information on the value of the ion energy.

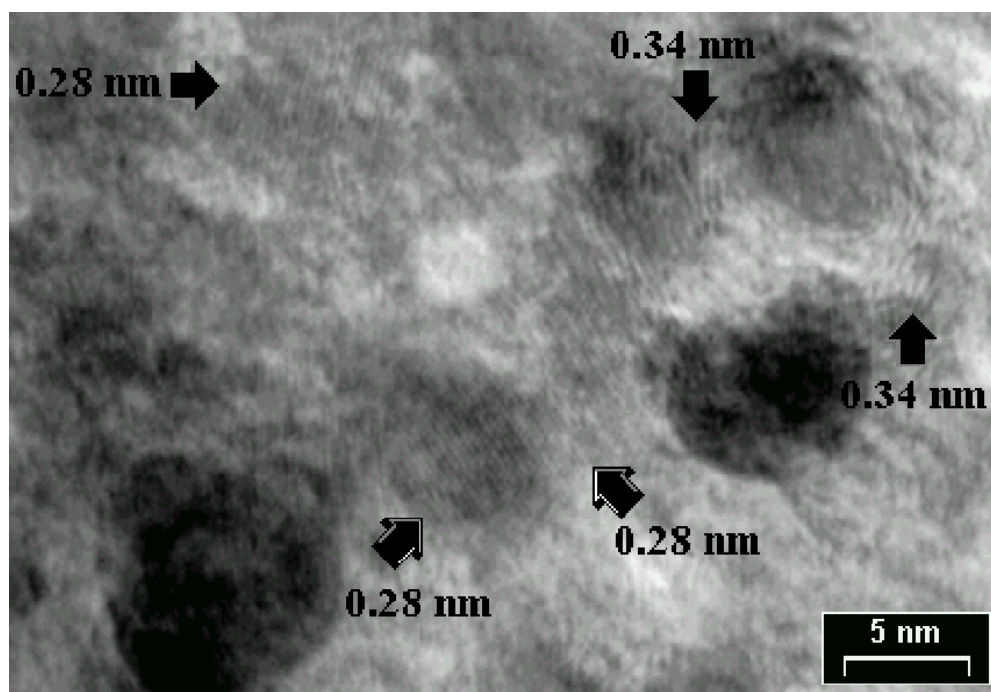
We shall now underline our main obtained results in using TVA technology for thin film deposition: SEM analysis of the deposited thin films have shown no droplets (droplets free deposition) and presented a compact structure of the fractured film.

### 3. Results and Discussions

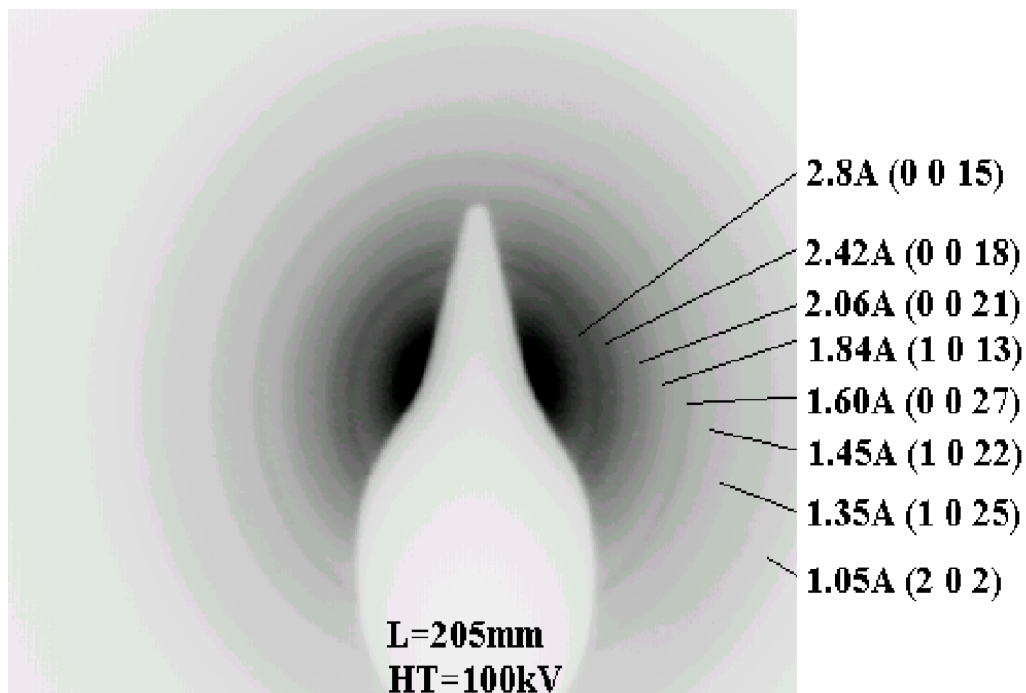
Taking into consideration the peculiarities of the carbon film deposition, we consider that TVA is one of the most adequate technologies for this field of applications. Indeed, due to the ensured high purity of the deposition process (in vacuum vessel only carbon being introduced besides refractory metals used as electrodes), completely hydrogen free carbon film can be obtained. In the same time, TVA technology ensures high value for the energy spent to heat carbon which needs temperatures higher than 4000K. Because of vacuum conditions and high sublimation temperature of the carbon, the main energy losses are practically only by radiation. Taking into account these advantages, we used TVA for carbon evaporation and deposition.

The deposited C films were studied using TEM electronic microscopy with a magnification of 1.4 M and a resolution of 1.4 Å. The samples of deposited carbon films (deposited on NaCl or KCl monocrystals, solved in water before TEM examination) show nanostructure films.

Fig. 5 shows the contrast fringes given by complex crystalline particles included in amorphous film. Particles are embedded in film with graphite zone that cover particles. The size of the particles is about 3-11 nm in diameter.



**Fig. 5.** High-resolution TEM image of the film deposited using TVA



**Fig. 6.** Electron-diffraction pattern

Rhomboedral structure with lattice parameters:  $a = 0.25221 \text{ nm}$ ,  $c = 4.3245 \text{ nm}$  (ASTM pattern: 79-1473) of diamond/carbon has been obtained from electron diffraction pattern as it is shown in Fig. 6.

#### 4. Conclusions

We can conclude that Thermoionic Vacuum Arc (TVA) can be used successfully for hydrogen free carbon film deposition, ensuring good qualities and high purity. Nanostructured carbon films with low value of the roughness can be obtained quite easily. Further developments will be related mainly to the improvement of the TVA stability at the transition from electron bombardment heating of carbon rod to the TVA arc plasma ignition and running. In this paper we present first results on characteristics of DLC film obtained using TVA

#### 5. References

- [1]. S. Ainsenberg, F. Kimock; Materials Sci. Forum, **52& 53**, Trans Tech. Switzerland , 1-40 (1990).
- [2]. J. Robertson; Diamond and related materials, **2** , 984 – 989 (1993).
- [3]. G. Musa, H. Ehrich, M. Mausbach; Journal of Vacuum Science and Technology, **A12** 2887-2895, (1994).
- [4]. G. Musa, H. Ehrich, J. Schuhmann; IEEE Transactions of Plasma Science, **25**, 386-391, (1997).
- [5]. H. Ehrich, J. Schuhmann, G. Musa, A. Popescu, I. Mustata; Thin Solid Films, **333**, nr. 1-2, 95-102, (1998).
- [6]. H. Ehrich, G. Musa, A. Popescu, I. Mustata, A. Salabas, M. Cretu, G. F. Leu; Thin Solid films, **332**, 1-4 (1998).
- [7]. H. Ehrich, J. Schuhmann, G. Musa, A. Popescu, I. Mustata; Thin Solid Films **333**, 95–102, (1998).

# GLIDING DISCHARGE CFCs DECOMPOSITION IN REDUCING CONDITIONS

Teresa Opalińska, Anna Opalska

*Industrial Chemistry Research Institute, ul. Rydygiera 8, 01-792 Warsaw, Poland*

Well known methods of halogene derivatives of methane and ethane (Freons) destruction consist of the combustion of them in a temperature above 2000K. The high temperature is necessary to prevent synthesis of dangerous compounds like dioxins and furans during the process. This temperature is obtained either in a oxygen-hydrogen flame or in a stream of equilibrium plasma generated in a plasma torch. In both cases, the process of Freons combustion is conducted in the presence of water vapor. The obtained final product contains, besides carbon dioxide, hydrogen chloride and hydrogen fluoride instead of chlorine and fluorine. The temperature is the main parameter deciding the degree of decomposition of Freons.

The authors showed the results of Freons combustion in non-equilibrium conditions of gliding discharge in the earlier studies. It was found that some additionally Freons which differed from the substrate were formed in the process. A limitation of Freons forming can be found when carrying out the process in reducing conditions instead an oxidizing one.

In this study the process of decomposition of difluoro-dichloromethane and difluoro-chloromethane mixture (Freon R12 and R22) in non-equilibrium conditions of gliding discharge is obtained in the presence of hydrogen.

The objective of the study was to find the influence of hydrogen concentration on the decomposition degree of Freons and the composition of final products of the process.

The main element of the used apparatus was a reactor which was working on the principle of gliding discharge. The mixture of Freons, hydrogen and argon was introduced into the reactor. A total flow rate of gas mixture (1.63 m<sup>3</sup>/h) and the Freons concentration in it (1.5 vol.%) were constant in experiments. After the absorption of hydrogen chloride and hydrogen fluoride the composition of off-gases was determined using a gas chromatography method.

It was found that aliphatic hydrocarbons (acetylene, methane, ethane and ethane), the hydrogen chloride, hydrogen fluoride and soot were main products of the process. A freon R13 (CClF<sub>3</sub>) was the undesirable by-product.

An increase of hydrogen concentration in the mixture of reagents caused:

- an increase of decomposition degree of Freons from 72,1 % to 92.9 %,
- a decrease of formation degree of CClF<sub>3</sub> to 0.6 %,
- a decomposition of acetylene which was formed in the process into soot and
- an increase of energetic yield of the process.

The process of Freons decomposition of gliding discharge in reducing conditions is much effective than the one in oxidizing conditions

# Emission Characteristics of Xenon Dielectric Barrier Discharge Fluorescent Lamps

Hideki Motomura, Masafumi Jinno and Masaharu Aono

*Department of Electrical and Electronic Engineering, Ehime University, Matsuyama, Japan*

## Abstract

The Characteristics of xenon vacuum ultraviolet (VUV) emissions generated by a pulsed discharge were observed as a fundamental research on mercury-free fluorescent lamps. All lamps were operated by pulsed dielectric barrier discharge (DBD). As the pulsed width decreased, higher intensity of VUV emissions is obtained, and luminance and efficacy increase. As the pulse frequency increases, intensity of VUV emissions increases, however the radiative output per one pulse period decreases and efficacy decreases.

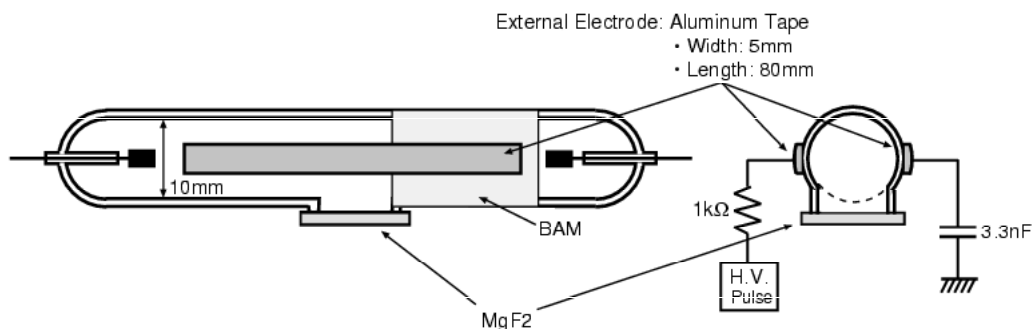
## 1. Introduction

In the field of light sources, mercury discharge fluorescent lamps has been used for general lighting. However, mercury causes environmental issues therefore lamp manufacturers are now trying to develop new lamps as less mercury or non-mercury light sources. Xenon is suitable as substitution for mercury because it is environmental-friendly and the emission characteristics are not influenced by ambient temperature. Many researches on low-pressure xenon discharge and its vacuum ultra-violet emission (VUV, 147nm and 172nm) have been done[1-5], however, as long as we know, none of high intensity low-pressure xenon discharge lamps have been developed for general lighting.

In this research we measured VUV characteristics, phosphor emission characteristics and infrared emission characteristics of pulsed pure xenon dielectric barrier discharge (DBD) fluorescent lamps as a fundamental research for development of xenon fluorescent discharge lamps. These results are expected to be useful for understanding discharge phenomena and are helpful for modelling.

## 2. Experimental Setup

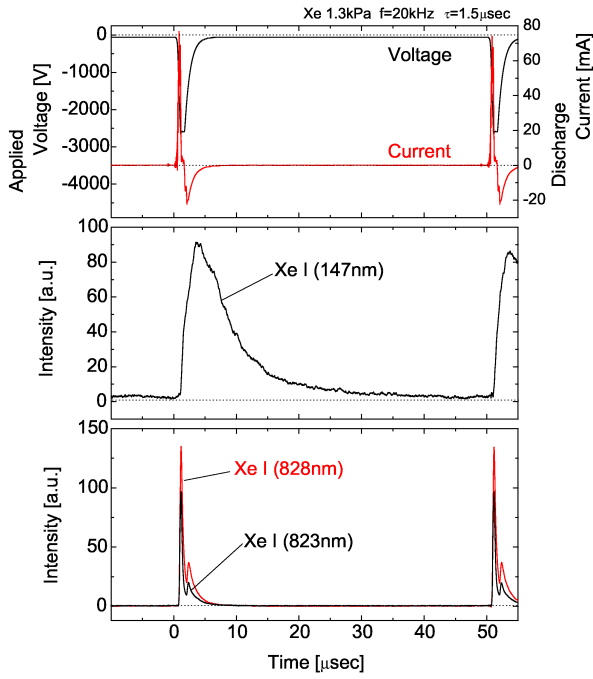
The schematics of the lamps which were used for this research is shown in Fig.1. Xenon is introduced with two different pressures of 1.3kPa and 10.7kPa. The inner diameter of these lamps is 10mm. They have  $\text{MgF}_2$  window for VUV measurements. Aluminium tapes are set on the external wall of each lamp as external electrodes and their width are 5mm. The half part in the axial direction of inner wall of each lamp is coated with blue phosphor (BAM). The luminance of phosphor-coated part was measured by luminance meter (TOPCOM BM-7).



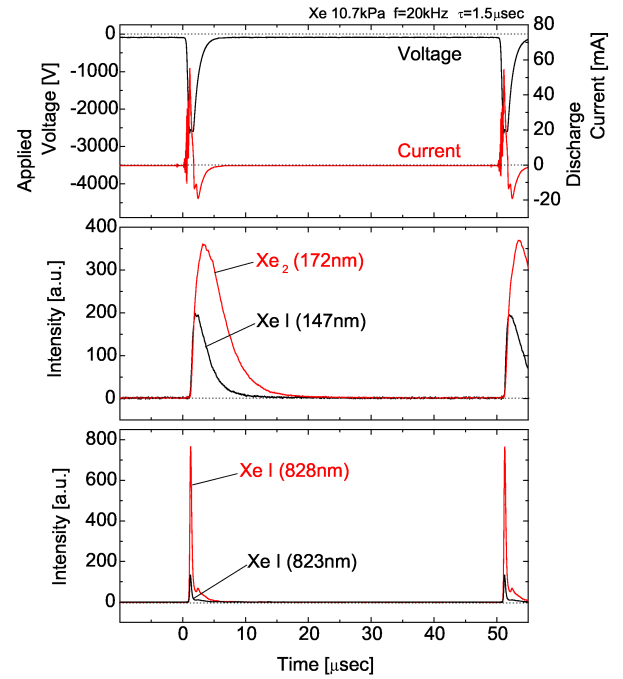
**Fig 1. The Lamp with External Electrodes**

The pulsed circuit was used for operating the lamps. The pulse voltage is generated by switching MOS-FET connected to a capacitor which is charged by a DC power supply. The pulse frequency and pulse width were controlled by a pulse signal to the gate of the FET from digital pulse generator (Stanford Research DG-535). A negative pulse is applied to the lamp by this pulse circuit, and the maximum voltage of this system is 5.0kV. As shown in Fig.1 a small capacitor (3.3nF) was placed between the anode and the earth in order to measure the input power to the lamp by measuring the accumulated charge to this capacitor[6]. The VUV emissions were introduced into the VUV monochromator through the  $\text{MgF}_2$

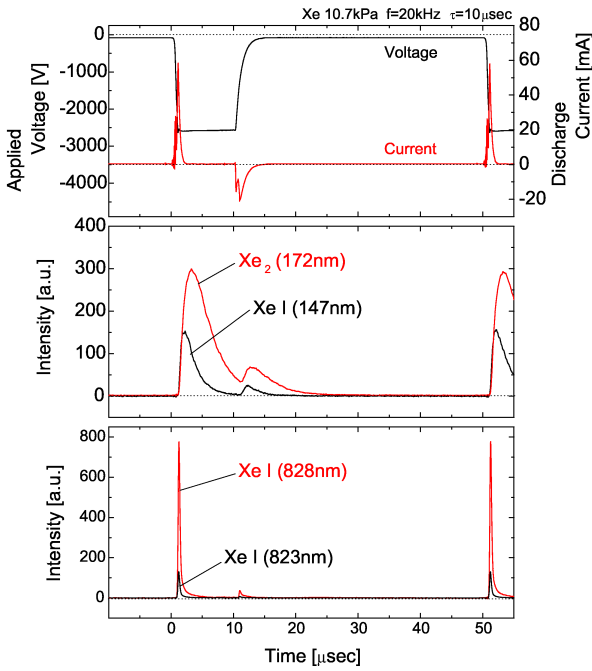




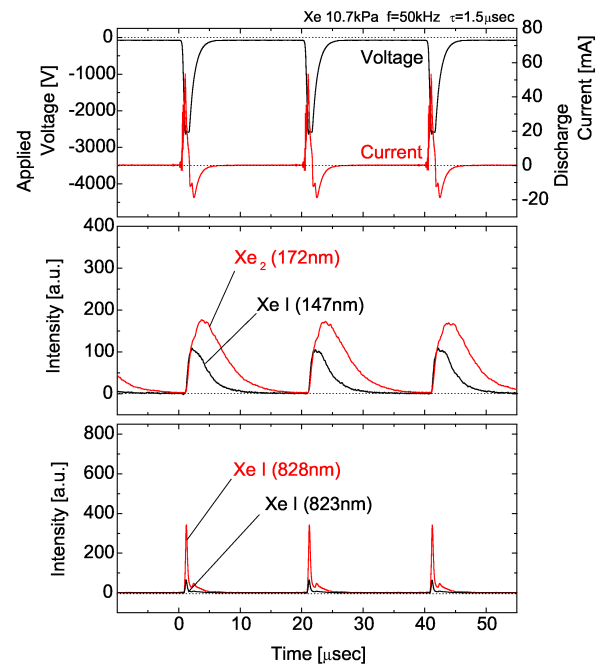
**Fig. 2** Traces of VUV and IR Emissions of **Xenon** (Pressure 1.3kPa, Frequency 20kHz, Pulse Width 1.5 $\mu$ s)



**Fig. 3** Traces of VUV and IR Emissions of **Xenon** (Pressure 10.7kPa, Frequency 20kHz, Pulse Width 1.5 $\mu$ s)



**Fig. 4** Traces of VUV and IR Emissions of **Xenon** (Pressure 10.7kPa, Frequency 20kHz, Pulse Width 10 $\mu$ s)



**Fig. 5** Traces of VUV and IR Emissions of **Xenon** (Pressure 10.7kPa, Frequency 50kHz, Pulse Width 1.5 $\mu$ s)

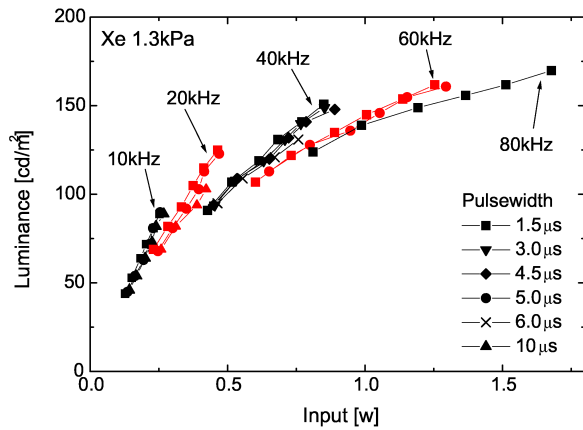
window on each lamp which was set in the vacuum chamber in which the pressure was less than  $5.0 \times 10^{-5}$  Pa. The IR emissions (828nm and 823nm) were measured by a visible-near IR monochromator. The traces of current, voltage and emissions were observed and recorded by a digital oscilloscope.

### 3. Experimental Results

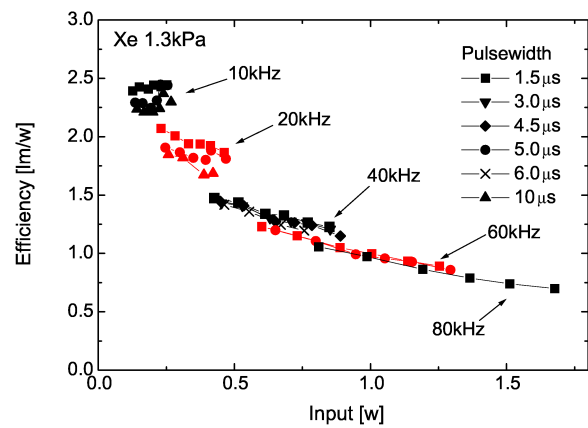
#### 3.1. Traces of Current, Voltage and Emissions

The discharge driven by external electrodes is named as dielectric barrier discharge (DBD). When this type of discharge is driven by a pulsed voltage, generally traces of both emissions and current have two

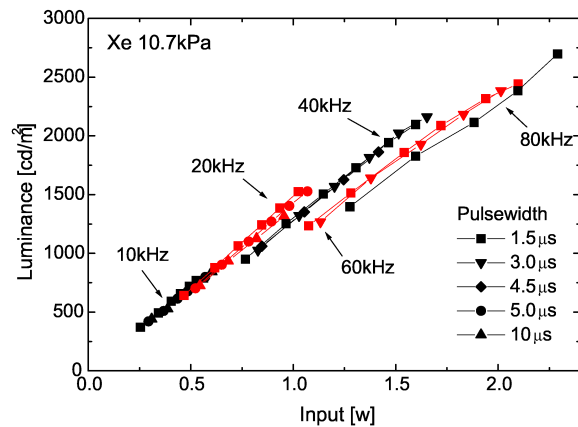
peaks in one pulse. The first peak is observed during the discharge just after the rising of the voltage, and the current flows in the forward direction of the applied voltage. As the current flows, electrical charges accumulate on the inner walls of the glass tube. Electrons accumulate on the inner wall of anode side and ions accumulate on the inner wall of cathode side. These accumulated charges forms inner electric field opposite to the external electric field applied by the pulsed circuit. As the inner electric field increases the total electric field in the lamp decreases and when it becomes lower than the discharge voltage, the discharge stops. Then the pulsed voltage stops and reversal discharge starts by the accumulated electric charges on the inner walls. This second reversal discharge generates the second peaks of current. Not all time second peak of emission is observed. It depends on the condition such as frequency, pulse width etc.



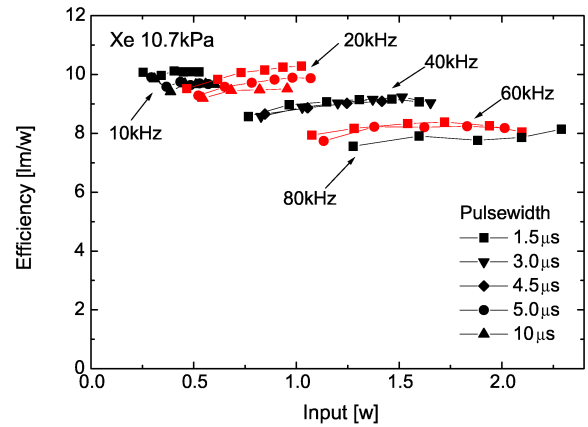
**Fig. 6 Luminance versus Input Power**  
(Pressure 1.3kPa)



**Fig. 7 Efficacy versus Input Power**  
(Pressure 1.3kPa)



**Fig. 8 Luminance versus Input Power**  
(Pressure 10.7kPa)



**Fig. 9 Luminance versus Input Power**  
(Pressure 10.7kPa)

### 3.2. VUV and IR Emissions

The traces of current, voltage and VUV (147nm and 172nm) and IR (823nm and 828nm) emissions are shown in Figs.2 and 3 by the pulsed operation at the pulse frequency of 20kHz, the pulse width of 1.5μs and the voltage of 2.5kV. Fig.2 is the result with the pressure of xenon of 1.3kPa, and Fig.3 is that of 10.7kPa. The xenon excimer's emission at 172nm is not observed at the xenon pressure of 1.3kPa. The decay time constants of the emission of 147nm are 6.1μs at 1.3kPa and 2.2μs at 10.7kPa. The decay time constant of 172nm excimer's emission at 10.7kPa is 3.1μs and this decay is slower than that of 147nm resonance atomic emission.

Fig.4 shows the traces of VUV and IR emissions at the pulse width of 10μs, the pulse frequency of 20kHz and the xenon pressure of 10.7kPa. In the case of 10μs pulse width, the second peaks of 147nm and 172nm emissions are observed as shown in Fig. 4 though they are not observed in the case of 1.5μs pulse width as shown in Fig.3. At the operation with the 10μs pulse width, the maximum intensity of the first peaks of VUV emissions and the maximum intensity of IR emissions decrease comparing with the case of 1.5μs.

The traces of VUV and IR emissions at the pulse frequency of 50kHz, the pulse width of 1.5μs, and the xenon pressure of 10.7kPa are shown in Fig. 5. In this case (50kHz), the IR emissions become weaker than the other cases shown in Figs. 2-4. This shows that the IR emission decreases as the pulse frequency increases.

### 3.3. Luminance

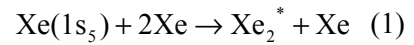
Figs. 6 and 7 show the luminance and the efficacy versus the input power at the xenon pressures of 1.3kPa. In both Fig. 6 and Fig. 7, the frequency, applied voltage and pulse width were varied from 10kHz to 80kHz, from 2.5kV to 5.0kV and from 1.5μs to 10μs respectively. At a constant input power, the luminance and the efficacy increase as the frequency decreases. These two figures show that as the pulse frequency increases, the input power increases. However, the increase of the luminance shows salutation and the efficacy decreases. At a constant power and frequency, the luminance and the efficacy increase as the pulse width becomes shorter. Moreover at a constant frequency and input power, as the pulse width becomes shorter, the luminance and efficacy increase. At a constant frequency with constant pulse width, as the input power increase, the efficacy decreases.

Figs. 8 and 9 show the luminance and the efficacy versus the input power at the xenon pressures of 10.7kPa. In both Fig. 8 and Fig. 9, the frequency, the applied voltage and the pulse width were varied from 10kHz to 80kHz, from 2.5kV to 5.0kV and from 1.5μs to 10μs respectively. At the constant power, the luminance and the efficacy increase as the frequency decreases or as the pulse width becomes shorter. This is same behaviour as the case of the xenon pressure of 1.3kPa. On the contrary the efficacy is independent of frequency. Higher luminance is obtained as the input power increases with constant frequency and pulse width. The luminance and the efficacy are improved comparing with them at 1.3kPa.

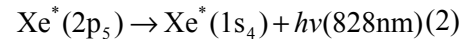
## 4. Discussion

### 4.1 Influence of Xe Pressure on the Emission Characteristics

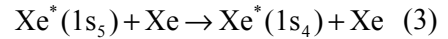
In Fig. 10, a simplified Grotrian energy level diagram of Xe atom and Xe dimer is shown. The xenon excimer, which radiates 172nm VUV emission, is mainly generated by the following process.



At 1.3kPa, the pressure is so low and this three-body collision process does not happen so frequently. This is the reason why 172nm VUV emission is not observed at 1.3kPa. The following process generates xenon resonance atoms ( $1s_4$ ) and radiate the IR emission of 828nm.



The following process also generates xenon resonance atoms ( $1s_4$ ) by quenching collision between xenon atom and xenon metastable atom [7,8].



It seems that at low pressure the main process which generates xenon resonance atom ( $1s_4$ ) during the off period of voltage is quenching process shown as (3) because Fig. 2 shows that though the 147nm resonance radiation lasts long after discharge finishes, the IR radiation of 828nm finishes right after the cut off

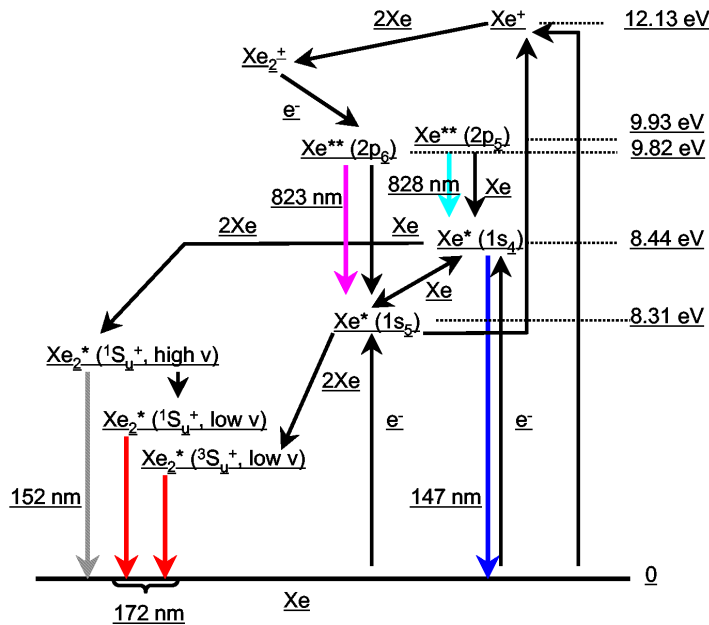


Fig. 10 Energy Levels of Xenon Atom and Molecule

of voltage pulse and the life time of the resonance atom ( $1s_4$ ) is so short as 3.7ns [9]. If the process (2) was main process then the 828nm radiation should appear during the off period of the voltage.

As the xenon pressure increases, the three-body collision shown as (1) increases and becomes main processes comparing with the two-body quenching process shown as (3). As the xenon pressure increases

the collision frequency increases and metastable atoms are consumed rapidly. Then the decays of 147nm and 172nm VUV radiation become faster.

We measured temporal behaviour of number density of excited xenon atoms of  $1s_4$  and  $1s_5$  at the pressure of 1.3kPa, frequency of 20kHz and pulse width of 1.5 $\mu$ s by IR-Laser Absorption Spectroscopy [10]. This measurement shows that at 1.3kPa metastable atoms which were generated during discharge and just after a discharge stay long and about 20% of the peak still exist at the time when the next discharge starts. This is because in a low pressure as 1.3kPa both processes (1) and (3) does not happen so much and VUV emission decreases. Finally as shown in Fig.7, the efficacy becomes lower at 1.3kPa than at 10.7kPa.

#### 4.2 Influence of Pulse Frequency and Width on the Emission Characteristics

Figs. 3 and 4 show that as the pulse width becomes shorter, the luminance and efficacy increase because the first peak of VUV emission radiating during the voltage pulse is applied and the second peak of that radiating just after the voltage pulse is cut superposes. A short pulse reduces the power consumption. This is the reason why the efficacy is improved with short pulse operation.

As the pulse frequency increases, the number of residual ions and electrons increases because of the length of non-discharge period. These increases in the number of residual ions and electrons reduce the electron temperature during a discharge. Then the excitations to higher levels decrease. This is quite understandable from the results shown in Figs. 4 and 5 where the IR emissions become weak at high pulse frequency. As shown in Figs. 4 and 5, VUV emission becomes weak as the pulse frequency increases. These results, i.e. decrease in number of higher excited atoms and weaker emission of IR and VUV at higher frequency operation, lead us to the following conclusion that the excited atoms at resonance level ( $1s_4$ ) are mainly generated by the transition from the upper level ( $1s_5$ ), which is shown as the process (1).

#### 5. Conclusion

The emission characteristics of xenon dielectric barrier discharge fluorescent lamps were observed under pulsed operation. At the xenon pressure of 10.7kPa, the VUV radiation of xenon excimer at 172nm is observed and luminance and efficacy of the lamps increase more than the case at 1.3kPa. As the pulse width becomes shorter, both VUV emissions at 147nm and 172nm increase, hence, the luminance and efficacy also increase. As the pulse frequency increases, the input power increases, however, the intensity of VUV emissions during one cycle decreases and the efficacy decreases. Finally these results show how to increase the luminance and efficacy, i.e., the short pulse gives both higher luminance and efficacy. The future work is to find best frequency at which xenon DBD fluorescent lamps achieve higher luminance and efficacy simultaneously.

#### Acknowledgement

The authors would like to thank Mr. Hisayoshi Kurokawa, a technician at Ehime University, for his great contribution to prepare so many special lamps for this research. This research would not have done without his remarkable skills making fluorescent lamps. Messer. Yoshihisa Ikeda, Hirofumi Kashima contributed to this research through their master and bachelor theses at Ehime University. The phosphor was a gift from Nichia Chemical Co. Ltd. and the authors would like to thank this company for its help.

#### References

- [1] M. Aono, H. Kurokawa, M. Jinno: *Proc. 8th Int. Symp. Science & Technology of Light Sources*, Greifswald (1998) 272.
- [2] M. Jinno, H. Kurokawa, M. Aono: *Jpn. J. Appl. Phys.* **38** (1999) 4613
- [3] J.-Y. Zhang, I. W. Boyd : *J. Appl. Phys.* **84** (1998) 1174.
- [4] R. H. Stark, A. El-Habachi, W. Shi, K. H. Schenbach : *Proc. 8th Int. Symp. Science & Technology of Light Sources*, Greifswald, 1998, p.244.
- [5] F. Adler, S. Muller : *Proc. XXIV ICPIG*, Warsaw, **4**, (1999) 73
- [6] T. Tomida, A. Iwato, M. Tanaka : *Trans. IEE Japan*, **118-A** (1998) 537 [in Japanese]
- [7] T. Tamida, S J Sanders, M. Tanaka : *Jpn. J. Appl. Phys.* **39** (2000) 583
- [8] Y. Sakai, M. A. Bratescu, M. Ohkubo, M. Miclea, M. Osiac, G. Musa : *Proc. XXIV ICPIG*, Warsaw, **4** (1999) 45
- [9] R Payling, P L Larkins : *Optical Emission Lines of the Elements*, John Wiley & Sons (1999)
- [10] H. Motomura, M. Jinno and M. Aono : *Proc. 2002 Joint Conf. ACED & Korea-Japan Symposium on Electrical Discharge and High Voltage Engineering*, Seoul (2002) B-205

# Entrainment of Ambient air into H<sub>2</sub>O/Ar Arc Plasma Jet

T.Kavka, M. Hrabovsky, M. Konrad, V. Kopecky, V. Sember, O. Chumak

*Institute of Plasma Physics, Prague, Czech Republic*

## Abstract

Entrainment of ambient air and development of plasma flow properties along the jet were studied for thermal plasma jet generated by hybrid plasma torch with water-argon stabilization of arc. Two main diagnostic methods, enthalpy probe and emission spectroscopy, were used. Effect of mass flow rate of plasma at the nozzle exit was studied. An increase of mass flow rate results in reduction of power loss from the jet, increase of mass and heat fluxes and prolongation of the jet core.

## Introduction

Atmospheric pressure thermal plasma jets are utilized in various plasma processing applications like plasma spraying or waste treatment. Plasma temperature, velocity and composition as well as stability and structure of flow field within the jet are strongly influenced by interaction of flowing plasma with ambient air. Production of turbulence and entrainment of cold gas into plasma jet are most important consequences of this interaction [1]. Although these phenomena strongly influence properties of plasma jet and its performance characteristics in plasma processing, there is still lack of knowledge about effect of plasma properties and jet characteristics on this process.

Plasma flow velocity and ratio of plasma density to the cold gas density are two principle factors that control process of interaction of plasma jet with surrounding gas [2,3]. In this paper we studied a development of properties of the jet in interaction with air for plasma jet generated in hybrid argon/water torch [4] that is characterized by extremely high velocity and low plasma density at the torch exit. In this torch plasma flow density and mass flow rate can be changed with minimum changes of heat flux within the jet. Previous study of properties of plasma jet generated by hybrid torch showed strong entrainment of ambient air into the jet [5]. This paper presents study of effect of arc current and gas flow rate on development of jet properties and gas entrainment into flowing plasma.

## 2. Experimental Setup

Plasma jet was generated by plasma torch with water-argon stabilization of arc (Fig. 1) [3]. Argon flow rate was varied in the range 12-27,5 slpm. The changes in gas flow rate had only little effect on arc power and plasma temperature due to large difference in values of enthalpy of H<sub>2</sub>O and argon plasma. Plasma torch was moved in horizontal and vertical directions allowing radial scanning of plasma jet on different distances from the exit nozzle.

Several diagnostics techniques have been employed. Temperature and composition of plasma jet close to the exit nozzle were measured by means of emission spectroscopy. The electron number density was obtained from Stark broadened H<sub>β</sub> line independently of the assumption of LTE. The temperature was calculated from the ratio of various argon atomic and ionic lines assuming Saha equilibrium. In colder parts, where there were no ionic lines detected, the temperature was estimated from the approximate LTE composition and measured electron number density. The plasma composition was determined from ratios of emission coefficients of argon, oxygen and hydrogen atomic lines using LTE equations. Then a new estimate of LTE values of temperature was obtained and the calculation of composition repeated, if necessary.

Profiles of temperature, velocity and composition in downstream parts of the jet were performed using the enthalpy probe system Tekna (Tekna Plasma Systems, Sherbrooke) connected with quadruple mass spectrometer Balzers. Enthalpy probe is a double-walled water-cooled probe with sample line. The inner

diameter of the probe used is 1.27 mm (ENT-476). Plasma temperature is evaluated from enthalpy, which is measured by calorimetric method. Plasma velocity is obtained from measurement of difference between stagnation and atmospheric pressures assuming incompressibility of plasma flow.

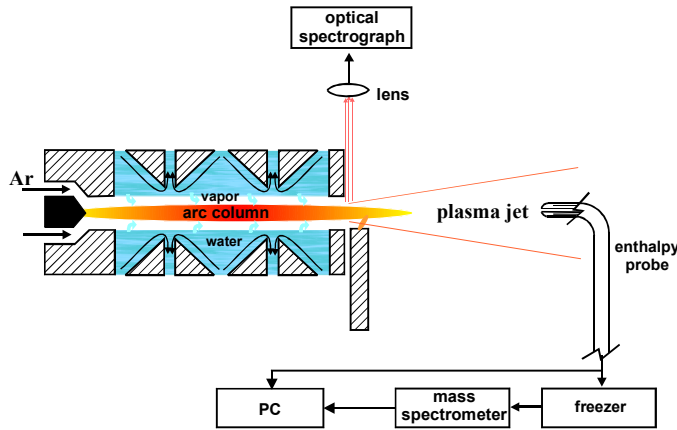


Fig. 1. Schematic diagram of hybrid plasma torch and experimental arrangement

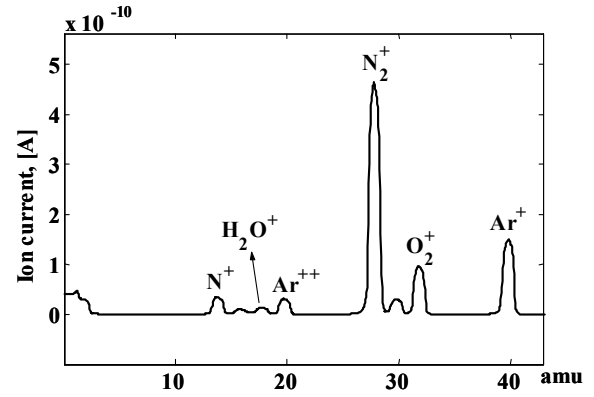


Fig. 2. Typical spectrum of plasma jet components obtained from mass spectrometric measurement

The content of hydrogen and oxygen in the jet could not be measured directly as after recombination in the probe water condenses in the enthalpy probe system. Freezer was used to prevent influx of water inside main components of Tekna system. Thus, spectrum corresponding to mixture of argon with air was obtained with only minor peak of water (Fig. 2). Real composition and properties of plasma were then evaluated from measured data using the assumption that ratio of plasma gases (argon and steam) at measured point is the same as spectroscopically determined ratio at the nozzle exit. De-mixing of components of plasma along the jet is thus neglected. Ratio of plasma to entrained air was then determined from ratio of content of argon to nitrogen.

The shape of luminous jet core was evaluated from the images obtained by short-shutter camera Sensicam Computer Optics.

### 3. Results and discussion

Profiles of plasma temperature and composition at the nozzle exit shown in Fig. 3 and Fig. 4 were evaluated from spectroscopic measurements. It can be seen from the Fig. 3 that effect of argon flow rate on plasma temperature is insignificant. This is in agreement with our previous measurements of properties of hybrid

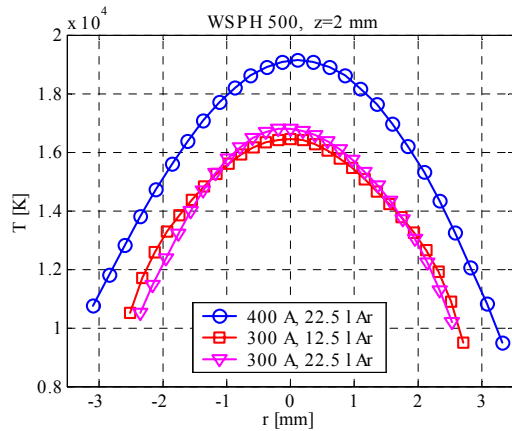


Fig. 3. Profiles of plasma temperature at the position 2 mm downstream of the torch exit for various argon flow rates for arc currents 300 A and 400 A.

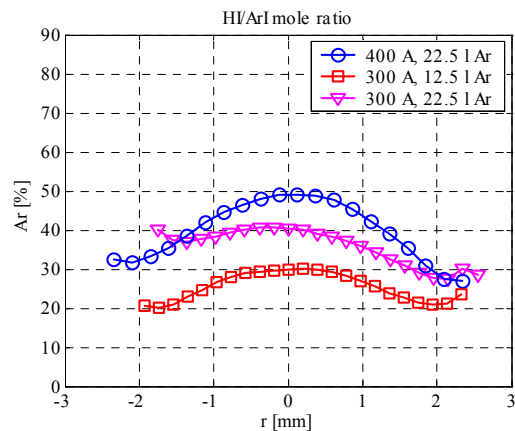


Fig. 4. Profiles of ratio of argon to steam at the position 2 mm downstream of the torch exit for various argon flow rates for arc currents 300 A and 400 A.

plasma torch [1]. As argon has very low enthalpy compared to enthalpy of steam plasma, addition of argon into water-stabilized part has little effect on power balance of the arc and on heat flux in the jet. This is illustrated in Fig. 5 where power balance of the torch is shown in dependence on flow rate of argon. The input power and power loss changed only insignificantly with changes of argon flow rate. Profiles of ratio of argon to steam in plasma at the torch exit are presented in Fig. 4. The curves were determined from ratio of lines of hydrogen and argon ions assuming LTE. We suppose in the following evaluation of measurements with enthalpy probe that this ratio is constant along the jet.

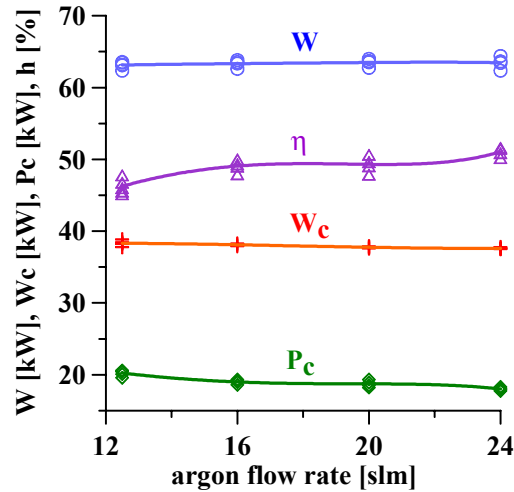


Fig. 5. Effect of flow rate of argon on balance of power of hybrid plasma torch for arc current 300 A. W – total power input, Wc – power input into water stabilized arc channel, Pc – power loss, η - efficiency

Profiles of concentration of argon in the jet evaluated from enthalpy probe measurements are shown in Fig. 6. It can be seen how due to air entrainment into the jet argon concentration decreases with increasing distance from the torch exit and the argon profiles are smoothed down. Decrease of concentration of plasma gas components at the centerline position is shown in Fig. 7. Close to the nozzle exit, where composition was determined by spectroscopic measurements, no evidence of air was found. At the positions farther from the exit nozzle decrease of plasma fraction due to air entrainment is substantial. Rapid decrease of plasma fraction up to 60 mm is slowed down at longer distances. This change can correspond to the change of character of the jet flow from transitional to fully turbulent. The observed decrease of plasma fraction was accompanied by decrease of plasma temperature and velocity.

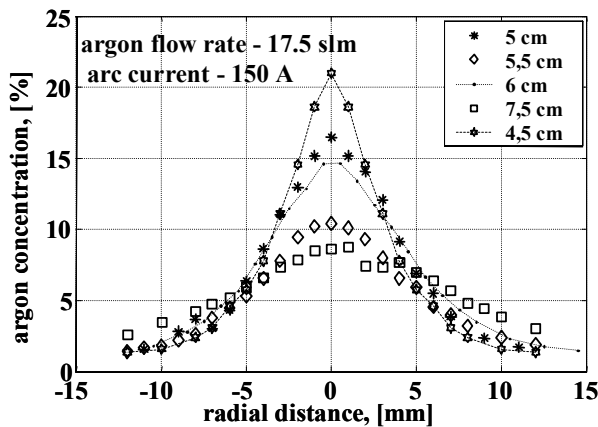


Fig. 6. Argon concentration profiles for various distances from the torch exit

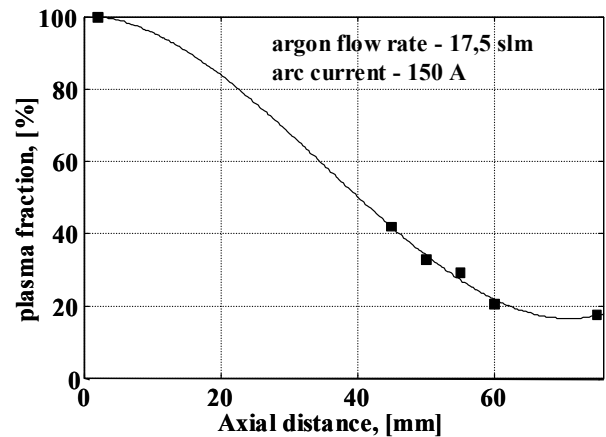


Fig. 7. Development of plasma fraction along the centerline of the plasma jet

The decrease of heat flux density along the jet is illustrated in Fig. 8 where profiles for arc current 300 A and argon flow rate 12.5 slm are shown. At the distances between 150 mm and 120 mm heat flux at the jet centerline decreases more than two times.

In the following an effect of argon flow rate on jet properties is studied. Increase of argon flow rate, which leads to an increase of plasma mass flux, results in an increase of flow velocity and slight decrease of plasma temperature (Fig. 9). Effect of argon flow rate on profiles of heat and mass fluxes and velocity is illustrated in Figs. 10, 11 and 12. All fluxes are increased due to rise of argon flow rate and the jet spread is higher. The luminous jet core is prolonged as can be seen in Fig. 13 where images recorded by short-shutter camera for two flow rates of argon are shown.

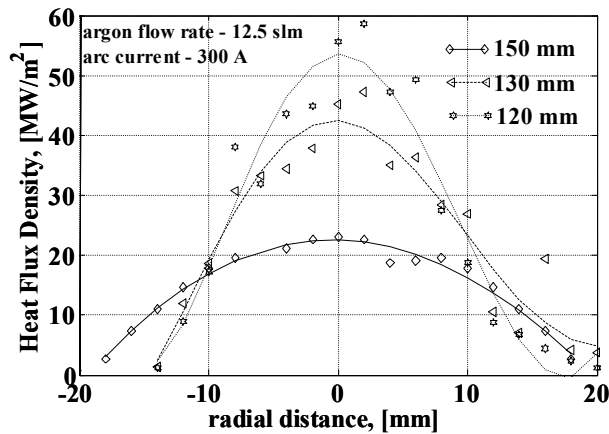


Fig. 8. Profiles of heat flux density at various distances from the nozzle exit.

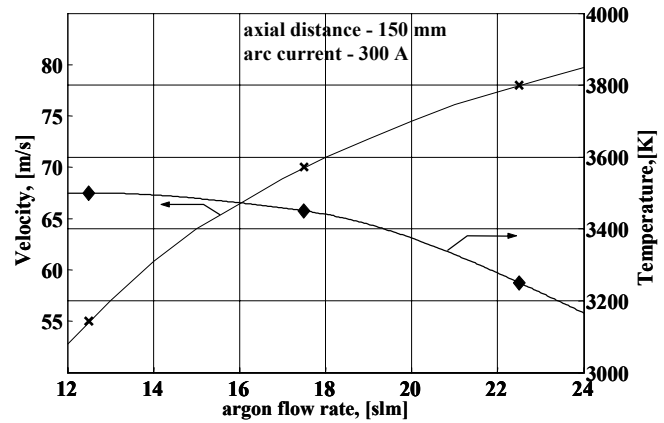


Fig. 9. Dependence of centreline velocity and temperature on argon flow rate

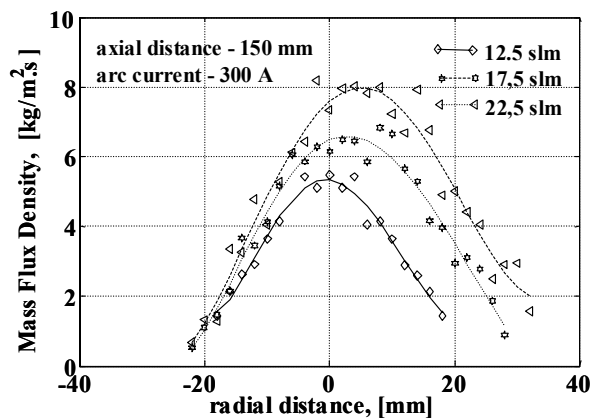


Fig. 10. Profiles of mass flux density at various flow rates of argon

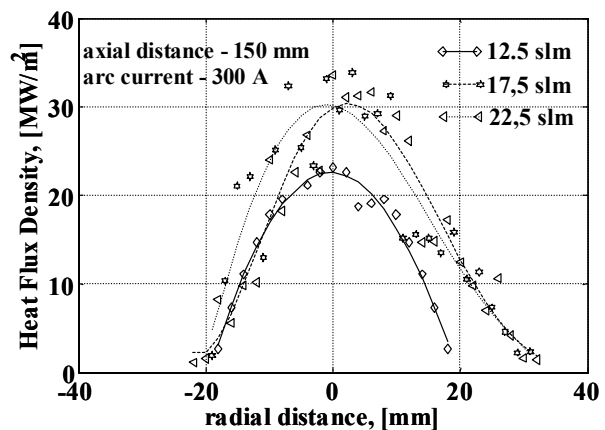


Fig. 11. Profiles of heat flux density at various flow rates of argon

Effect of flow rate of argon on shape of the jet is illustrated in Fig. 13. Jet core photographed by short shutter camera with exposure time  $3 \mu\text{s}$  was prolonged due to increase of argon flow rate, the spread angle of the jet evaluated from profiles of mass flux density was increased. As can be seen from Figs. 10 – 13 the increase of plasma mass flow rate from the torch leads to increase of velocity and mass and heat fluxes and jet dimensions. It is surprising especially for the case of heat flux, as total heat flux at the nozzle exit changes insignificantly when argon flow rate is changed (Fig. 5). Thus increase of plasma mass flow rate results in lowering of heat loss mechanisms in the jet. This may be related to the reduction of intensity of turbulence production and entrainment of cold gas as these phenomena are strongly dependent on ratio of



density of plasma to ambient gas density. Increase of content of argon in argon-steam plasma leads to substantial increase of plasma density while plasma enthalpy change is not so significant as argon enthalpy is very low compared to enthalpy of oxygen-hydrogen plasma.

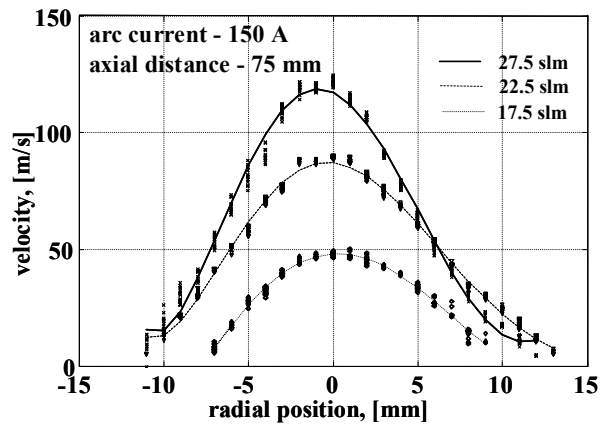


Fig. 12. Profiles of velocity at various flow rates of argon

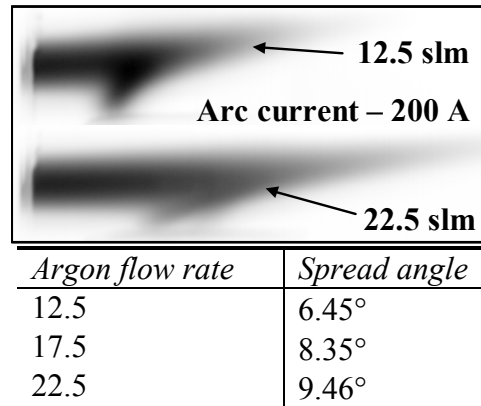


Fig. 13. Images of luminous jet core recorded by short shutter camera and spread angles of the jet for various flow rates of argon

## Conclusions

Entrainment of ambient air and development of plasma flow properties along the jet were studied for thermal plasma jet generated by hybrid plasma torch with water-argon stabilization of arc. Enthalpy probe and emission spectroscopy were used for determination of plasma composition, temperature and velocity and the jet was photographed by short-shutter camera. Effect of mass flow rate of plasma at the nozzle exit was studied. An increase of mass flow rate resulted in reduction of power loss from the jet, increase of mass and heat fluxes and prolongation of the jet core.

## Acknowledgement

The authors gratefully acknowledge the support of this work by the Grant Agency of the Czech Republic under the project No. 202/01/1563.

## References

- [1] E.Pfender, J.Fincke, and R.Spores, Plasma Chem. Plasma Process. 11, 529 (1991)
- [2] G.L.Brown, A.Roshko, J. Fluid Mech. 64, 775 (1974)
- [3] R.Spores, E.Pfender, Proc. Of the National Thermal Spray Conf., Cincinnati, 85 (1988)
- [4] V.B. Brezina, M. Hrabovsky, M.Konrad, V.Kopecky and V.Sember, Proc. Of 15<sup>th</sup> Int.Symp. on Plasma Chemistry (ed. A.Bouchoule et al.), Vol.III, 9-13 July 2001, Orleans, 1021
- [5] T.Kavka, M.Hrabovsky, Czech. J. Phys. 52 (2002), D637-642

# Investigation of Surface Reactions During Organic Low-*k* Film Etching by FT-IR Ellipsometry

Hideki Motomura<sup>1</sup>, Tatsuru Shirafuji<sup>2</sup>, Toshihiro Nakamura<sup>3</sup> and Kunihide Tachibana<sup>4</sup>

<sup>1</sup> Department of Electrical and Electronic Engineering, Ehime University, Matsuyama, Japan

<sup>2</sup> International Innovation Center, Kyoto University, Kyoto, Japan

<sup>3</sup> Venture Business Laboratory, Kyoto University, Kyoto, Japan

<sup>4</sup> Department of Electronic Science and Engineering, Kyoto University, Kyoto, Japan

## Abstract

Surface reactions on SiLK film during N<sub>2</sub>/H<sub>2</sub> ICP plasma etching was investigated in terms of FT-IR ellipsometry. By etching SiLK film in N<sub>2</sub>/H<sub>2</sub> plasma with bias voltage, absorption peak attributed to C-N bond formed on SiLK film appeared. On the other hand, when only N<sub>2</sub> or H<sub>2</sub> gas was employed, this peak did not appear. It is thought that H radicals impinging to SiLK surface make dangling bonds, and then N radicals or N<sup>+</sup> ions adsorbed to the site and form C-N bonds.

## 1. Introduction

The decrease in the design rule of ultralarge-scale integrated circuits below sub-micron level causes difficulty in fabrication with conventional materials [1]. For example, if silicon oxide and aluminum is used in the interconnection stack with small design rule, the resistance-capacitance time delay is not negligible compared to the switching time delay in each transistor. Thus it is proposed to make interconnection stack with low resistance and capacitance by copper and low dielectric (low *k*) constant materials. Recently, various low-*k* materials for interlayer have been developed. One of the most promising candidates is to use organic polymer materials, such as SiLK<sup>TM</sup> (Dow Chemical) and FLARE<sup>TM</sup> (Honeywell).

In order to integrate copper wiring and low-*k* interlayer process with a damascene-structure, it is indispensable to develop a low-*k* film etching technology without reactive ion etching (RIE) lag, bowing profile, microtrenching and hard-mask shrinkage. To suppress these problems and to realize an anisotropic etching process with under sub-micron design rule, it is important to investigate surface reactions and to clarify mechanisms of plasma-surface interactions during low-*k* film etching.

## 2. Experimental Setup

We employed a technique combining an FT-IR and an ellipsometry (FT-IR phase modulated spectroscopic ellipsometry: FT-IR PMSE) [2, 3] for high sensitivity observation of chemical bonds formed on SiLK surface during etching. With this method, optical density of deposited material is given by,

$$D = -\ln\left(\frac{\rho}{\rho_{\text{sub}}}\right) = -\ln\left(\frac{\tan \Psi}{\tan \Psi_{\text{sub}}}\right) - i(\Delta - \Delta_{\text{sub}}), \quad (1)$$

where  $\rho$  represents reflectance ratio between that for p- and s-polarized IR,

$$\rho = \frac{r_p}{r_s} \equiv \tan \Psi \exp(i\Delta), \quad (2)$$

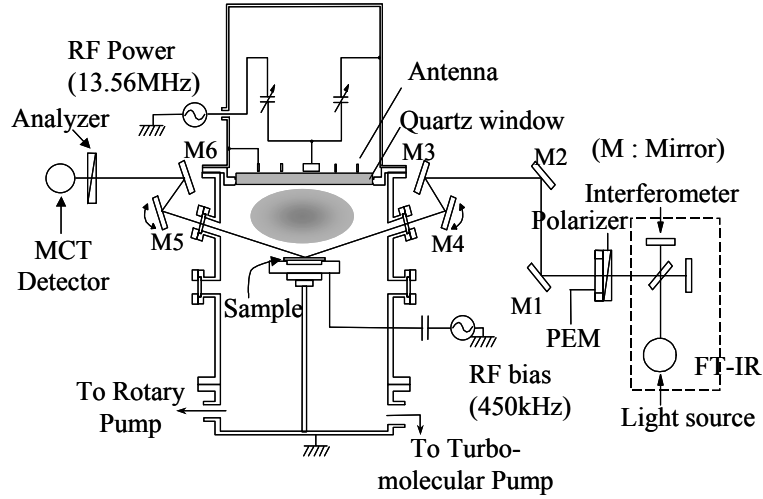


Fig. 1. A schematic illustration of our experimental setup.

and suffix ‘sub’ represents data for substrate without deposited film. The reflectance  $r_p$  and  $r_s$  are functions of thickness and dielectric function of the film and substrate. Since the vibration modes of chemical bonds in film have oscillation frequency in IR range, it becomes possible to observe film thickness and chemical bonds included in the film by measuring optical density in IR range.

A schematic illustration of our experimental setup is shown in Fig. 1. The ICP source and the arrangement for the FT-IR PMSE measurement are identical to those used in previous work [4]. A flat spiral type antenna of 160 mm in outer diameter with 2 turns was powered by an rf (13.56 MHz) generator. The antenna was located on a quartz window of 25 mm in thickness. The chamber was 260 mm in inner diameter

and 400 mm in height, which was evacuated by a turbomolecular pump (180 l/s) backed by a mechanical pump. Substrates were placed on a holder located 115 mm below the quartz window. The wafer holder was connected to another rf (450 kHz) power supply through an insulating disc in order to supply a self-bias voltage to the substrate. FT-IR PMSE measurement system consists of commercial FT-IR spectrometer (JEOL, Winspec-100), a photo-elastic modulator (PEM), a polarizer, an analyzer, and a Mercury-Cadmium-Telluride (MCT) detector. In this measurement, the IR beam coming out from the spectrometer was led to the detector via mirrors M1 to M6. Three signals obtained at frequencies of DC,  $f$  and  $2f$  for the PEM frequency of  $f$  were used to deduce the optical density [3].

Etching was carried out for 30 s using  $N_2/H_2$  gases. Typical experimental conditions were used and given as follows: rf power of 300 W, pressure of 10 mTorr and total flow rate of the feed gas of 20 sccm. Blank

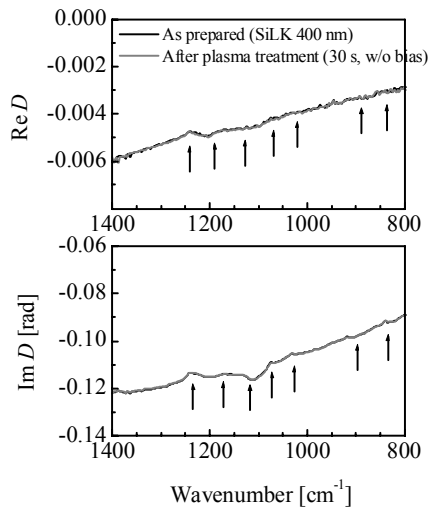


Fig. 2. The real and imaginary part of optical density spectra for 400-nm SiLK film coated on Si substrate (black line). The spectra taken after 30-s plasma treatment without bias voltage application are also shown as gray line; the feed gases were  $N_2$  (19 sccm) and  $H_2$  (1 sccm).

(not patterned) wafers with SiLK films of 400-nm or 200-nm thick on silicon substrates were prepared by spin-coating procedure.

### 3. Results and Discussion

Figure 2 shows real and imaginary parts of optical density spectra for 400-nm SiLK film coated on Si substrate (black line). The spectra taken after 30-s plasma treatment without bias voltage application are also shown as gray line; the feed gases were  $N_2$  (19 sccm) and  $H_2$  (1 sccm). Both  $Re D$  and  $Im D$  spectra shifted and tilted its baselines according to the amount of phase shift when the IR went through SiLK film: entering to the SiLK surface, reflected on boundary between Si substrate and SiLK film, and exiting from SiLK surface. Several peaks attributed to chemical bond groups included in SiLK film appeared, which were indicated by arrows in Fig. 2. Moreover, it should be noted that there was no obvious difference between the spectra taken before and after plasma treatment. It shows that etching of SiLK film did not occur and no bond groups did not generated on the surface by plasma treatment under this condition.

Figure 3 shows real and imaginary parts of optical density spectra for SiLK film coated on Si substrate before and after etching under several bias conditions. The SiLK film thickness was 200 nm before etching. The conditions of feed gas and plasma treatment time were identical to that of experiment of Fig. 2. The baseline of  $Re D$  and  $Im D$  spectra shifted upward as the bias voltage was increased. This shows that the SiLK film was etched by applying bias voltage and the etching rate increased by increasing the bias voltage. The etching rate of SiLK film calculated from the amount of baseline shift of  $Im D$  spectra was shown in Fig. 4 as a function of bias voltage. The etching rate saturated at higher bias voltage, on the other hand, that increased linearly to bias voltage less than the absolute value of 120 V. In comparison with the spectra taken under no bias condition, there is obvious difference at  $1115\text{ cm}^{-1}$  in the  $Re D$  spectra; an absorption peak

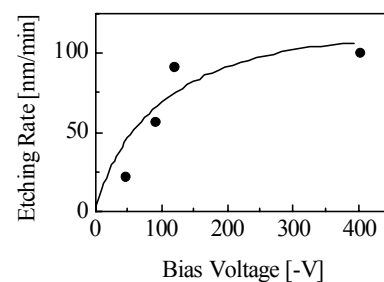
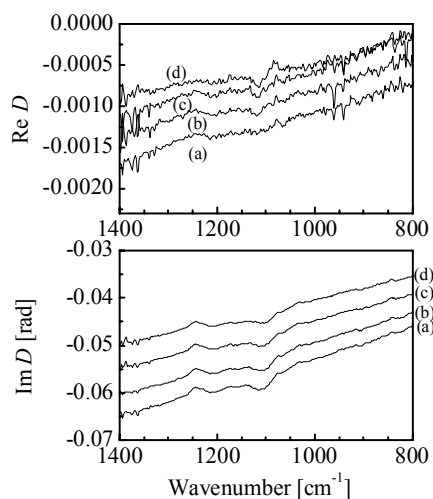


Fig. 4. The etching rate of SiLK film as a function of bias voltage. This was calculated from the amount of baseline shift of  $Im D$  spectra.

Fig. 3. The real and imaginary parts of optical density spectra for SiLK film coated on Si substrate before (a) and after etching under several bias conditions ((b):  $-45\text{ V}$ , (c):  $-90\text{ V}$  and (d):  $-120\text{ V}$ ). The feed gases were  $N_2$  (19 sccm) and  $H_2$  (1 sccm).

appeared in  $\text{Re } D$  spectra when bias voltage was applied. On the other hand, although it is difficult to identify the appearance of the peak in  $\text{Im } D$  spectra because of existing a peak according to bond group in SiLK film centered at  $1100 \text{ cm}^{-1}$ , a little change of the form of this peak at  $1115 \text{ cm}^{-1}$  occurred by increasing the bias voltage. Nagai *et al.* found that N radicals and  $\text{N}_2^+$  ions would form CN compound on the bottom of pattern during patterned organic low- $k$  material (FLARE<sup>TM</sup>) etching [5]. Morikawa *et al.* found that the behavior of  $\text{N}^+$ ,  $\text{N}_2^+$  and  $\text{N}_2\text{H}^+$  ions are related to the anisotropic etching and formation of sidewall passivation layers in  $\text{N}_2/\text{H}_2$  and  $\text{N}_2/\text{NH}_3$  plasmas from the experiments using quadruple mass spectrometer [6]. It can be assigned that this peak is attributed to the bond group including C-N bond. This result shows that SiLK etching in  $\text{N}_2/\text{H}_2$  plasma involves some chemical reactions and formation of C-N bonds on the surface with the assistance of ion bombardment.

We carried out etching by varying a ratio of  $\text{H}_2$  to  $\text{N}_2$  in the feed gas. The flow rate of the feed gas was kept at 20 sccm. The bias voltage was fixed at  $-400 \text{ V}$ . Real and imaginary parts of optical density spectra for SiLK film coated on Si substrate measured before and after etching are shown in Fig. 5. The etching rate as a function of the ratio of  $\text{H}_2$  to feed gas is also shown in Fig. 6. The absorption peak at  $1115 \text{ cm}^{-1}$  in the  $\text{Re } D$  spectra attributed to bond group including C-N bonds appeared under  $\text{N}_2$  and  $\text{H}_2$  mixing condition, as indicated by a circle in Fig. 5, whereas that did not appeared when etching was carried out by only  $\text{N}_2$  or  $\text{H}_2$  plasma. Moreover, the etching rates by  $\text{N}_2/\text{H}_2$  mixed gas plasma were higher than that by  $\text{N}_2$  or  $\text{H}_2$  plasma. It is believed that H radical play an important role in isotropic etching of organic low- $k$  materials, while N radical cannot etch without ion bombardments [5]. Therefore, it is thought that the mechanism of formation of bond group including C-N bond is as follows. First, H radicals impinging to SiLK surface make dangling bonds, and then N radicals or  $\text{N}^+$  ions adsorbed to the site and form C-N bonds. Analysis of gas phase reactions by measuring radicals and ions impinging to surface or desorbed molecules are necessary for

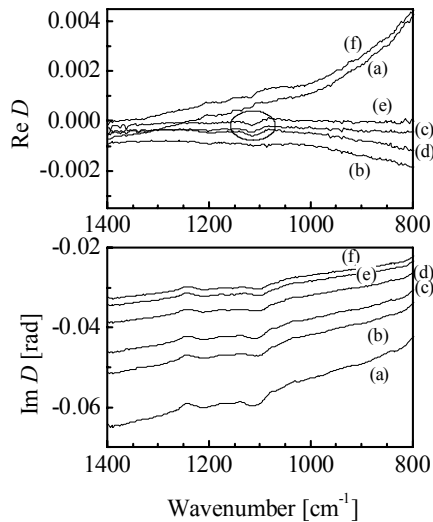


Fig. 5. The real and imaginary parts of optical density spectra for SiLK film coated on Si substrate before (a) and after etching under several  $\text{H}_2$  ratio conditions ((b): 0 %, (c): 30 %, (d): 50 %, (e): 70 % and (f): 100 %). The total flow rate was kept at 20 sccm. The bias voltage was  $-400 \text{ V}$ .

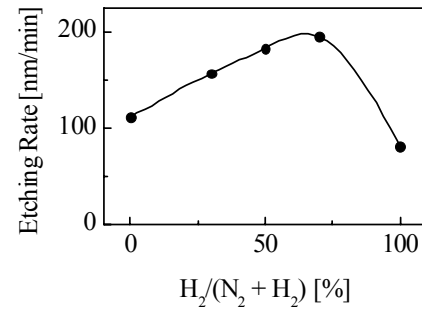


Fig. 6. The etching rate of SiLK film as a function of ration of  $\text{H}_2$  to the feed gas. This was calculated from the amount of baseline shift of  $\text{Im } D$  spectra.

understanding how the formed bond groups affect the etching characteristics. Investigation of gas phase reactions by measuring desorbed molecules in terms of FT-IR absorption spectroscopy is now under progress.

#### 4. Conclusions

Investigation of surface reactions during organic low-*k* film (SiLK) etching was carried out in terms of FT-IR ellipsometry. Under non-bias condition, etching did not occur and no chemical bonds were formed on the surface. When bias voltage was applied, etching occurred and absorption peak was observed at 1115 cm<sup>-1</sup>, which is attributed to bond group including C-N bond, in N<sub>2</sub>/H<sub>2</sub> plasma, on the other hand, when only N<sub>2</sub> or H<sub>2</sub> gas was employed, this peak did not appear. It is thought that the mechanism of formation of bond group including C-N bond is as follows; first, H radicals impinging to SiLK surface make dangling bonds, and then N radicals or N<sup>+</sup> ions adsorbed to the site and form C-N bonds. From now on, analysis of gas phase reactions by measuring radicals and ions impinging to surface or desorbed molecules are necessary for understanding how the formed bond groups affect the etching characteristics.

#### Acknowledgements

One of the authors, Hideki Motomura, would like to thank Prof. Masaharu Aono in Ehime University for useful discussion. This work was supported partially by NEDO (New Energy and Industry Developments Organization) through ASET (Association of Super-Advanced Electronics Technologies).

#### References

- [1] M. Fukuma: Oyo Buturi, **71**, 946 (2002) [in Japanese]
- [2] A. Canillas, E. Pascual and B. Drévillon: Rev. Sci. Instrum. **65**, 2153 (1993)
- [3] K. Tachibana, T. Shirafuji and S. Muraishi: Jpn. J. Appl. Phys. **35**, 3652 (1996)
- [4] H. Motomura, S. Imai and K. Tachibana: Thin Solid Films **390**, 134 (2001)
- [5] Hisao Nagai, Seigou Takashima, Mineo Hiramatsu, Masaru Hori and Toshio Goto: J. Appl. Phys., **91**, 2615 (2002)
- [6] Y. Morikawa, S. Yasunami, W. Chen, T. Hayashi and T. Uchida: J. Vac. Sci. Technol. A **19**, 1747 (2001)

# Application of a DBD reactor for the partial oxidation of methane to synthesis gas in the presence of a nickel catalyst

B. Pietruszka, K. Anklam, M. Heintze.

*Institute of Low Temperature Plasma Physics (INP)-Greifswald,  
Friedrich-Ludwig-Jahn-Strasse 19, 17489 Greifswald, Germany*

## Abstract

The combination of a dielectric barrier discharge and an  $\alpha$ -alumina supported nickel catalyst for the combined steam-oxygen reforming of methane to synthesis gas ( $H_2$  and CO) was investigated. Both the reagent conversion and the product distribution were found to be affected by the presence of Ni catalyst in the plasma zone. The energy requirement for syngas production was lowered by the presence of the catalyst to about 25% of the value obtained with the discharge alone.

## 1. Introduction

Recently, plasma processes have been widely used in the field of energy and environmentally safe technologies, like removing  $NO_x$  [1] and greenhouse gases ( $CH_4$  and  $CO_2$ ) [2]. Particularly atmospheric pressure non-equilibrium plasmas obtained in dielectric barrier discharges (DBD) are often involved in this research [3]. The DBD may be operated with dielectric material, i.e. a ceramic foam (also pellets or grains) in the discharge zone, so that the plasma is also sustained in the foam structure [4] which can support the catalyst in plasma-catalytic investigations. The other advantage of a DBD relevant for technological applications is the possibility to operate it reliably in different gas mixtures and in a wide range of flow rates. The successful application of the DBD for plasma-chemical reactions depends on the efficiency of generating reactive states of atoms and molecules. In comparison to catalytic processes, plasma processes are often less selective and a possible way obtain the desired products could be the combination of plasma and catalysis by incorporating a catalyst in the discharge zone.

Conversion of natural gas (NG) to synthesis gas ( $H_2$  and CO) is mainly done by steam reforming of methane (STM:  $CH_4 + H_2O \rightleftharpoons CO + 3H_2$ ,  $\Delta H^\circ = 206$  kJ/mol) or partial oxidation of methane (POM:  $CH_4 + \frac{1}{2}O_2 \rightleftharpoons CO + 2H_2$ ,  $\Delta H^\circ = -36$  kJ/mol). The recent developments in fuel cell technology and a potential demand for hydrogen as an alternative fuel forced the scientific activity towards investigating new ways of hydrogen production. Currently, hydrogen is mainly obtained in the STM process ( $H_2:CO = 3:1$ ), however, this process is highly endothermic and energy-cost expensive. The POM process, slightly exothermic seems to be much favourable, however using pure oxygen is still uneconomical and air leads to nitrogen dilution of the products. Also the  $H_2:CO$  ratio of 2:1 is lower than for STM. As reported by Maiya et al. [5], the POM process combined with water gas shift reaction (WGSR:  $CO + H_2O \rightleftharpoons CO_2 + H_2$ ,  $\Delta H^\circ = -41$  kJ/mol), realised in a separate reactor can maximise  $H_2$  production.

An alternative method to thermal processes, non-thermal plasmas are investigated in combination with catalysis. As presented by Kogelschatz et al. [6,7] and Kraus [4,8], the dielectric barrier discharge can be effectively used for exciting of species in a  $CH_4 - CO_2$  plasma. Kappes et al. [9] applied a DBD for steam reforming of hydrocarbons. Recently, we have investigated the partial oxidation of methane to synthesis gas in a DBD reactor up to 400°C under atmospheric pressure [10-12]. It was observed that plasma significantly promotes the catalytic reaction in comparison to the process only over a catalyst, especially at lower temperatures.

## 2. Experimental

The DBD reactor [10] consists of two coaxial quartz tubes with a 1.5 mm discharge gap, where the catalyst is placed. The length of the discharge zone is 10 cm giving a reaction volume of approximately 7 cm<sup>3</sup>. The inner electrode (high voltage) is formed by a thin metal coating inside the inner tube. Around the outer tube a metal heating band is wound, which serves also as the grounded electrode. To operate the discharge an AC high voltage (frequency: 27.8 kHz) was applied with a maximum of 10 kV rms. The discharge power was calculated from the time-averaged product of discharge voltage and current. Up to 50 W of plasma power was used in the current experiments. The reactor temperature was measured at the outside tube of the reactor by a thermocouple.

A commercial Ni catalyst (Süd-Chemie G90B), with a specific surface area of 6 m<sup>2</sup>/g, grains size 0.71 - 1.0 mm, containing about 10% of Ni, initially oxidised to NiO was used. The catalyst was first calcinated in air and reduced in a mixture of 6.6% H<sub>2</sub> in Ar before plasma-catalytic measurements.

Plasma-catalytic measurements were carried out using 2 g of catalyst, filling about 1/3 of the discharge volume. The tests were conducted at temperatures up to 400°C using air as oxidant. A small amount of argon (6.6% vol.) was added to the input gas to monitor the total volume flow rate at the reactor outlet and the volume variations during the reaction. The gas mixture at flow rates from 170 to 510 sccm (CH<sub>4</sub>:Air:Ar = 5:10:2) was saturated with steam in a bubbler heated to 40°C ( $p_{\text{H}_2\text{O}} = 7.38 \times 10^3 \text{ Pa}$ ) giving the final reagents composition CH<sub>4</sub>:O<sub>2</sub>:H<sub>2</sub>O = 2.8:1:0.7. Product analysis was done on-line, using non-dispersive infrared spectrometry (NDIR), mass spectrometry (MS) and gas chromatography (GC/FID).

### 3. Results

#### 3.1 Conversion and product distribution

In the present investigation, methane conversion was only observed during plasma operation. The main products analysed were CO, CO<sub>2</sub>, H<sub>2</sub>O, and H<sub>2</sub>. Only at 500°C the Ni-catalyst alone was active and the plasma had then only little effect on the conversion and product distribution

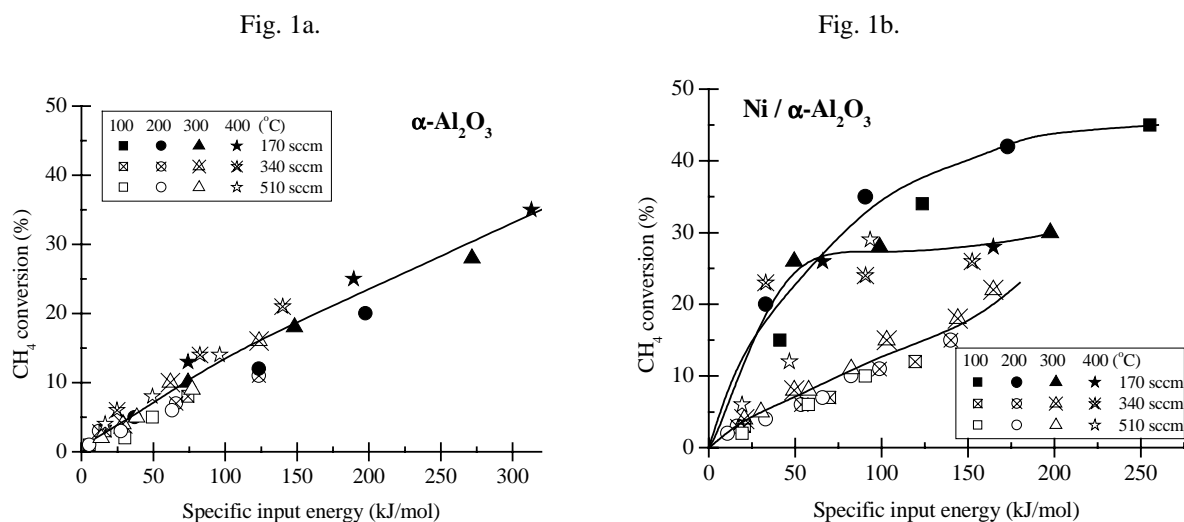


Fig. 1: Methane conversion versus specific input energy at different temperatures (100 – 400°C) and total flow rates (170 sccm – 510 sccm) over 2 g of  $\alpha\text{-Al}_2\text{O}_3$  (Fig. 1a) and  $\text{Ni}/\alpha\text{-Al}_2\text{O}_3$  (Fig. 1b) in the discharge zone.

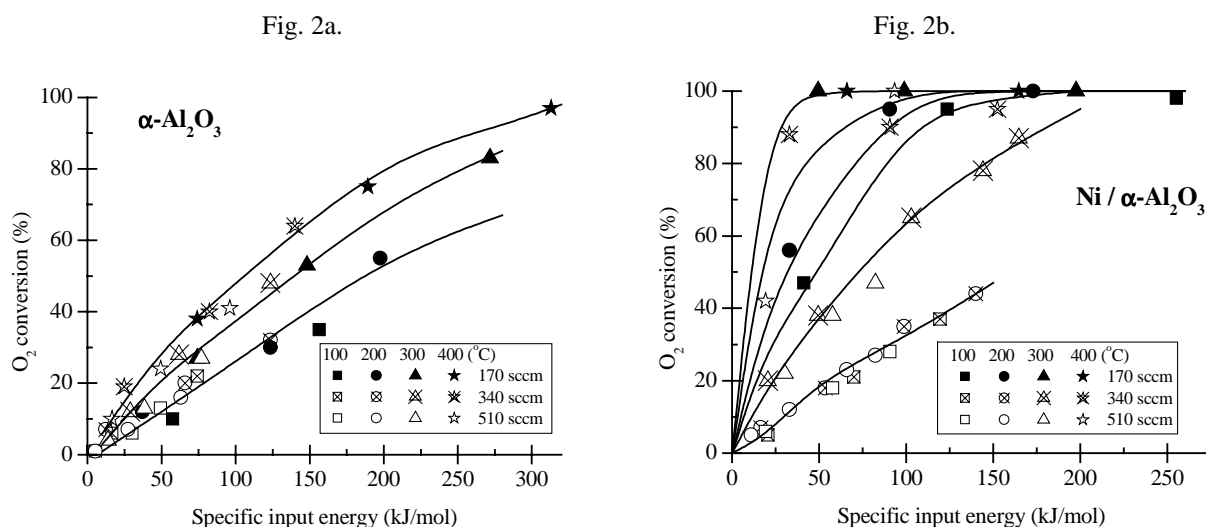


Fig. 2: Oxygen conversion versus specific input energy at different temperatures (100 – 400°C) and total flow rates (170 sccm – 510 sccm) over 2 g of  $\alpha\text{-Al}_2\text{O}_3$  (Fig. 2a) and  $\text{Ni}/\alpha\text{-Al}_2\text{O}_3$  (Fig. 2b) in the discharge zone.



Traces of methanol and  $C_2$  hydrocarbons, amounting to less than 0.1%, were detected as by-products. Fig. 1 shows the methane conversion versus the specific energy input and in Fig. 2 the oxygen conversion is presented in the same conditions as for Fig. 1.

The amount of water in the product stream after the reaction was always higher than the amount initially added to the reagent mixture, resulting in a net production of water despite possible dissociation in the plasma. The calculated selectivity to  $H_2O$  is based on this net production. The specific input energy (SIE) was calculated as the discharge energy dissipated in 1 mole of the reagent gas mixture ( $CH_4 + O_2 + N_2 + Ar + H_2O$ ).

The methane conversion over  $\alpha-Al_2O_3$ , shown in Fig. 1a, is independent of temperature and reagent flow rates and increases linearly with the specific input energy. Over the  $Ni/\alpha-Al_2O_3$  catalyst the  $CH_4$  conversion (Fig. 1b) depends on the SIE in the same way as over only  $\alpha-Al_2O_3$  for temperatures  $\leq 300^\circ C$  and total flows  $\geq 340$  sccm. At 170 sccm for 100 -  $400^\circ C$  and at  $400^\circ C$  for 170 - 510 sccm, the conversion is much higher than over only  $\alpha-Al_2O_3$ . The highest methane conversion was obtained at the flow rate of 170 sccm.

The oxygen conversion over only  $\alpha-Al_2O_3$  (Fig. 2a) was found to increase slightly with temperature for a given SIE, unlike the methane conversion (see Fig. 1a).

Fig. 3a.

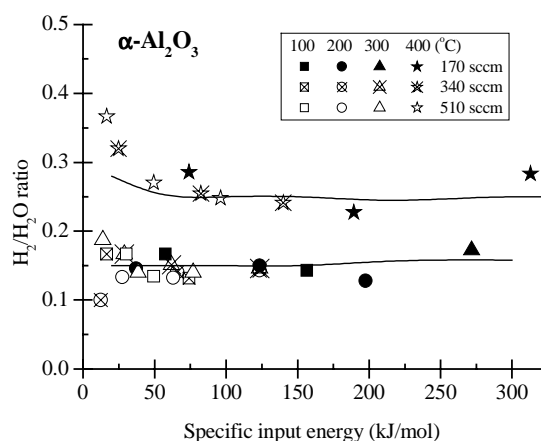


Fig. 3b.

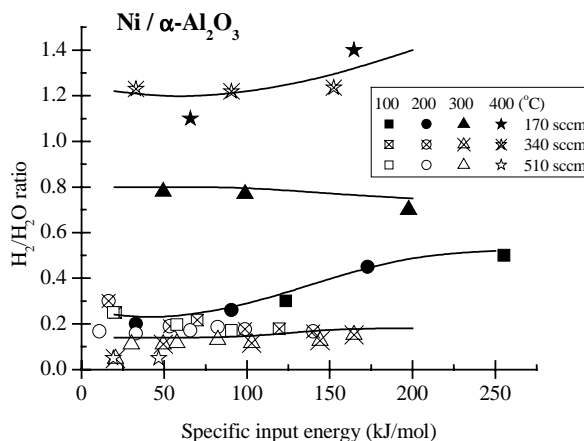


Fig. 3: Hydrogen-to-water ratio versus specific input energy at different temperatures (100 –  $400^\circ C$ ) and total flow rates (170 sccm – 510 sccm) over 2 g of  $\alpha-Al_2O_3$  (Fig. 3a) and  $Ni/\alpha-Al_2O_3$  (Fig. 3b) in the discharge zone.

Fig. 4a.

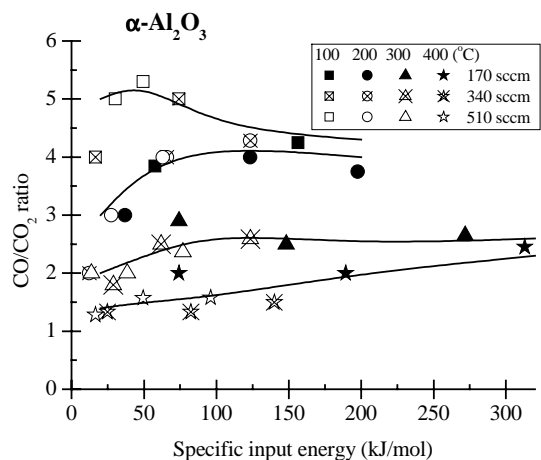


Fig. 4b.

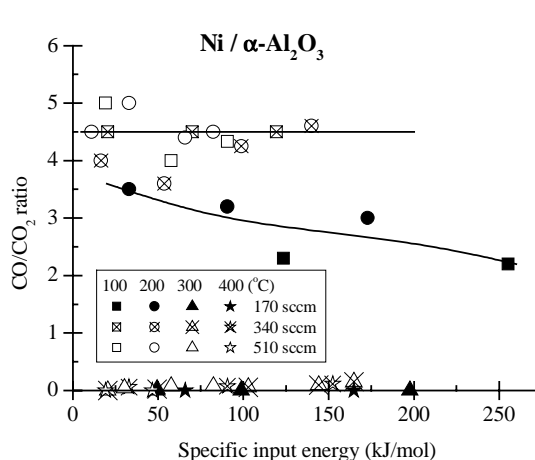


Fig. 4: Carbon monoxide-to-carbon dioxide ratio versus specific input energy at different temperatures (100 –  $400^\circ C$ ) and total flow rates (170 sccm – 510 sccm) over 2 g of  $\alpha-Al_2O_3$  (Fig. 4a) and  $Ni/\alpha-Al_2O_3$  (Fig. 4b) in the discharge zone.

Over the Ni/ $\alpha$ -Al<sub>2</sub>O<sub>3</sub> catalyst the oxygen conversion is greatly enhanced as compared to the pure  $\alpha$ -Al<sub>2</sub>O<sub>3</sub>, for the conditions where an enhanced methane conversion was observed (Fig. 1b). Over  $\alpha$ -Al<sub>2</sub>O<sub>3</sub> nearly complete oxygen conversion (97%) was only obtained at the highest temperature and the lowest flow rate investigated, whereas over the Ni/ $\alpha$ -Al<sub>2</sub>O<sub>3</sub> catalyst total oxygen consumption was observed for a much wider set of experimental parameters.

In Fig. 3 the H<sub>2</sub>/H<sub>2</sub>O ratio and in Fig. 4 the CO/CO<sub>2</sub> ratio versus the SIE over  $\alpha$ -Al<sub>2</sub>O<sub>3</sub> and Ni/ $\alpha$ -Al<sub>2</sub>O<sub>3</sub> are presented. The product distribution is fairly independent of the SIE. Over  $\alpha$ -Al<sub>2</sub>O<sub>3</sub> the H<sub>2</sub> to H<sub>2</sub>O ratio is constant up to 300°C (Fig. 3a) and slightly higher at 400°C. The fraction of CO decreases with increasing temperature over  $\alpha$ -Al<sub>2</sub>O<sub>3</sub> (Fig. 4a), together with the increase in oxygen conversion (see Fig. 2a). Higher temperature apparently causes the oxidation of CO to CO<sub>2</sub> without affecting methane conversion (Fig. 1a). Over the nickel catalyst, not only the temperature determines the product selectivity, but also the reagent flow rate. For the lowest flow rate of 170 sccm, a significant influence of temperature on the catalyst-discharge interactions is observed. At lower temperatures, between 100 and 200°C, mainly CO and H<sub>2</sub>O are formed (Fig. 3b and 4b), as it was also observed over  $\alpha$ -Al<sub>2</sub>O<sub>3</sub>. Starting from 300°C almost no CO is formed and an increase in hydrogen production is observed. The nickel catalyst is active in the presence of the discharge, shifting the product distribution from CO and H<sub>2</sub>O to CO<sub>2</sub> and H<sub>2</sub>.

### 3.2. Efficiency of CO and H<sub>2</sub> formation

In Fig. 5a and Fig. 5b the energy required for CO and H<sub>2</sub> formation versus specific input energy over  $\alpha$ -Al<sub>2</sub>O<sub>3</sub> and Ni/ $\alpha$ -Al<sub>2</sub>O<sub>3</sub> are presented. The efficiency of syngas production is the inverse of the plasma energy needed per molecule of CO and H<sub>2</sub> formed.

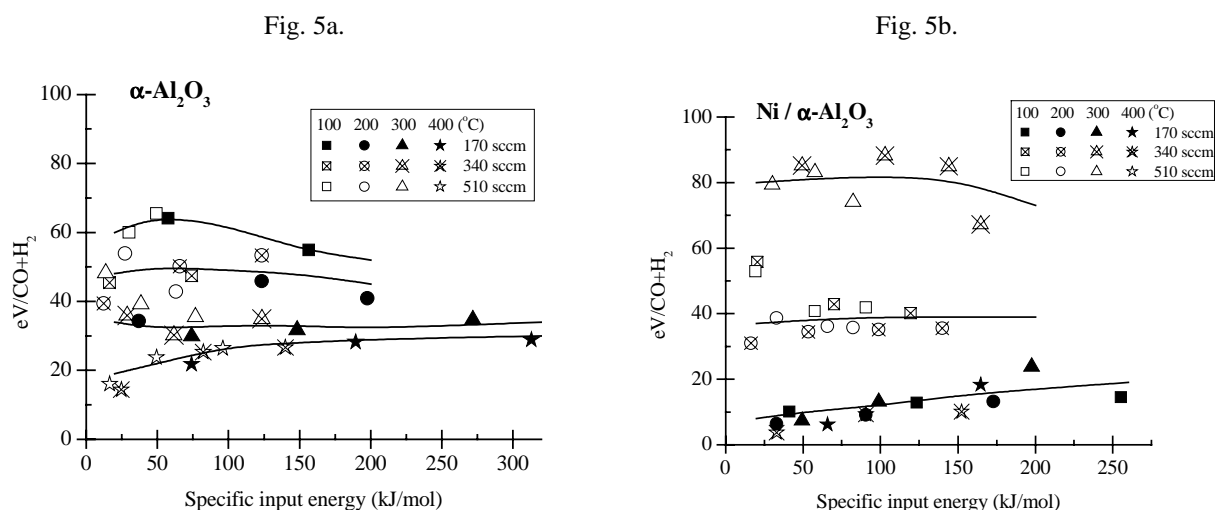


Fig. 5: Energy requirement per molecule of CO and H<sub>2</sub> produced versus specific input energy at different temperatures (100 – 400°C) and total flow rates (170 sccm – 510 sccm) over 2 g of  $\alpha$ -Al<sub>2</sub>O<sub>3</sub> (Fig. 5a) and Ni/ $\alpha$ -Al<sub>2</sub>O<sub>3</sub> (Fig. 5b) in the discharge zone.

The efficiency of syngas production in the plasma over  $\alpha$ -Al<sub>2</sub>O<sub>3</sub> depends at lower values of the SIE mainly on the reactor temperature (Fig. 5a). With increasing SIE the temperature dependence becomes less pronounced. Above 300 kJ/mol the efficiency will most likely reach a value about 30-35 eV per molecule of produced CO and H<sub>2</sub>, independent of temperature. A similar tendency was observed for the CO/CO<sub>2</sub> ratio. Although it might be expected, the higher H<sub>2</sub> formation at 400°C (Fig. 3a) has only little influence on the total efficiency of CO and H<sub>2</sub> formation.

Over the Ni/ $\alpha$ -Al<sub>2</sub>O<sub>3</sub> catalyst the efficiency depends much more on the temperature and flow rates. For the lowest flow rate (170 sccm) and over the entire temperature range investigated, as well as at 400°C for all values of total gas flow rate, the highest efficiency (lowest energy requirement) are achieved at low SIE. The energy requirement increases from less than 10 to about 20 eV/molecule H<sub>2</sub> or CO when increasing the SIE from about 30 to 250 kJ/mol. These values are significantly lower than those obtained over  $\alpha$ -Al<sub>2</sub>O<sub>3</sub>. For the

higher flow rates (340 and 510 sccm) and temperatures between 100 and 300°C, the energy requirement for syngas production is much higher, ranging from about 40 to 80 eV/molecule.

To explain such fluctuation of the efficiency values versus temperature and reagent flow rates we must consider the methane conversion and the product distribution. Over the Ni/ $\alpha$ -Al<sub>2</sub>O<sub>3</sub> catalyst the methane conversion, as well as hydrogen production, are enhanced at low flow rates (Fig. 3b). At higher flow rates (340 or 510 sccm) the H<sub>2</sub>/H<sub>2</sub>O ratio (Fig. 3b) is still low up to 300°C, however CO is only produced in significant amounts up to 200°C, resulting in the maximum in energy requirement for syngas production at 300°C.

#### 4. Discussion

In the combined oxygen-steam reforming of methane over a nickel catalyst in the temperature range between 100 and 400°C methane conversion was observed only in the presence of the plasma. In this respect, the POM without steam addition over the same Ni-catalyst showed different results: at temperatures  $\geq 300^\circ\text{C}$  methane conversion was observed [11] in the absence of the discharge. However, at lower temperatures the combination of the plasma and the catalyst did not enhance the methane conversion as compared to the discharge over only Al<sub>2</sub>O<sub>3</sub>, the Ni only catalysed CO oxidation at temperatures  $\geq 300^\circ\text{C}$ .

This different behaviour indicates that the steam addition plays a significant role in activating the catalyst at lower temperatures. It could possibly be connected to the adsorption of water below 300°C, which was also observed by temperature programmed desorption (TPD). However, the reaction is relatively slow, only at the lowest flow rate the contact time is high enough. Adding more catalyst in the present reactor was not helpful, because different zones of oxidation states are formed in the catalyst and also coke formation near the reactor outlet was observed.

In the oxygen-steam reforming also CO oxidation is observed over the Ni-catalyst at  $T \geq 300^\circ\text{C}$ . However, since the oxygen conversion reaches 100%, the hydrogen yield is much enhanced as compared to POM due to a suppressed hydrogen combustion.

Water was always produced by methane oxidation rather than consumed in steam reforming under the present conditions. To verify this assumption, some measurements were carried out under the same experimental conditions only without oxygen addition. It was found that the methane conversion did not exceed 8% and the conversion of water remained below the detection limit. Similar results were reported by Kappes et al. [9], about 6% conversion for methane and 1% for steam.

#### 5. Conclusions

In the combined oxygen-steam reforming of methane to synthesis gas in a DBD water did not react with methane. Over the catalyst support ( $\alpha$ -Al<sub>2</sub>O<sub>3</sub>) the methane conversion is only determined by the specific input energy. However, the Ni/ $\alpha$ -Al<sub>2</sub>O<sub>3</sub> catalyst is active towards methane and oxygen conversion even at very low temperatures (100°C) in the presence of water, provided the contact time is not too short. The energy requirement for syngas production is considerably less than for POM without addition of water. Values down to 7 eV/molecule of H<sub>2</sub> + CO were achieved. CO oxidation to CO<sub>2</sub> on the partially oxidised Ni surface at  $T \geq 300^\circ\text{C}$  is observed as in POM, however due to total oxygen conversion the loss of hydrogen through oxidation is suppressed.

#### Acknowledgements.

This research was supported by the E.U. (contract number ICA2-CT-2000-10004)

#### References

- [1] K.Yan, S.Kanazawa, T.Ohkubo and Y.Nomoto, Plasma Chem. Plasma Processing **19**, 421 (1999)
- [2] L.M.Zhou, B.Xue, U.Kogelschatz and B.Eliasson, Energy and Fuels **12**, 1191 (1998)
- [3] B.Eliasson, W.Egli and U. Kogelschatz, Pure & Appl. Chem. **66**, 1275 (1994).
- [4] M.Kraus, B.Eliasson, U.Kogelschatz and A.Wokaum, Phys. Chem. Chem. Phys. **3**, 294 (2001).
- [5] P.S. Maiya, T.J. Anderson, R.L. Mieville, J.T. Dusek, J.J. Picciolo, U.Balachandran, Appl. Catal. A, **169**, 65 (2000)
- [6] U.Kogelschatz, B.Eliasson, W.Egli, J. Phys. IV, **7 (C4)**, 47 (1997).

- [7] U.Kogelschatz, M.Kraus, Proc. 4th Int. Conf. on Greenhouse Gas Control Tech., 30.08-02.09. Interlaken, Switzerland 1998
- [8] M.Kraus, PhD thesis, Swiss Federal Institute of Technology, Zurich, 2001.
- [9] T.Kappes, W.Schiene, T.Hammer, Proc. VIII Sym. High-Pressure Low Temp. Plasma Chem. (HAKONE 8<sup>th</sup>), Tartu, Estonia, p. 196. (2002)
- [10] B.Pietruszka and M.Heintze, Proc. VIII Sym. High-Pressure Low Temp. Plasma Chem. (HAKONE 8<sup>th</sup>) Tartu, Estonia, p.166 (2002)
- [11] M.Heintze, B.Pietruszka, submitted to Catal. Today.
- [12] B. Pietruszka, K. Anklam, M. Heintze, Proc. XXXV Polish Catalytic Symposium, 2-4 April Krakow, Poland 2003 (ISBN 83-907325-6-4)

# Modelling of Transport Processes in Electric Arcs Between Vaporizing Electrodes

V. A. Zhovtyansky<sup>1</sup>, V. M. Patriyuk<sup>1</sup> and A. B. Murphy<sup>2</sup>

<sup>1</sup> Radiophysics Department, Taras Shevchenko Kyiv National University, 01033, Kyiv, Ukraine

<sup>2</sup> CSIRO Telecommunications and Industrial Physics, P.O. Box 218, Lindfield NSW 2070, Australia

## Abstract

The diffusion of vapour derived from vaporizing electrodes is investigated for low erosion rates. In the case of low temperatures, the problem is solved analytically for free-burning and wall-stabilized electric arcs, and the influence of thermal diffusion is examined. For a wider temperature range, the problem is solved by numerical simulation.

## 1. Introduction

The majority of modern high-technology plasma applications, such as welding, plasma spraying of protective coatings, thermochemical production of low-reactivity fuels, and modern switching devices, take place in a gas mixture, where one of the gases is, as a rule, an electrode vapour. An electric arc between vaporizing electrodes as a source of high-density plasma is another example of such applications. The material that is vaporized due to the current enters the gap between the electrodes. Since the metal vapour atoms have low ionization energy in comparison with atoms of the ambient gas (usually noble gases or air), ionization of the metal vapour contributes substantially to the electron density. As a result, the metal vapour plays a key role in the heat, mass and charge transfer processes in the plasma. Thus, the basic electric arc parameters are largely determined by the vaporized electrode material. The electrode vapour concentration usually doesn't exceed 1–10%, so diffusive transport should dominate [1,2]. This mode is considered in the present paper.

## 2. Diffusion of metal electrode erosion products in an electric arc

We consider an electric arc between vaporizing electrodes at atmospheric pressure in one-dimension. The radial distribution of the vaporizing material in the arc is determined from the continuity equation:

$$\frac{1}{r} \frac{d}{dr} (r J_A) = w_A, \quad (1)$$

where index  $A$  corresponds to metal vapour, and the mass production rate of metal per unit volume  $w_A$  is approximated by either a step function or a Gaussian distribution:

$$w_A = \begin{cases} w_0, & r \leq r_a \\ 0, & r > r_a \end{cases}, \quad w_A = k_w w_0 \cdot \exp(-r^2/r_a^2), \quad (2a,b)$$

where  $r_a$  is the arc channel radius. The correction factor  $k_w = \{1 - \exp[-(r_w/r_a)^2]\}^{-1}$  ( $r_w$  is the radius of adsorbing quasi-wall) is included so that the metal flux into the arc area from both electrodes,

$$\int_0^{r_w} w_A(r) \cdot 2\pi r dr, \text{ is the same whether expression (2a) or (2b) is used to determine } w_A(r). \text{ When } r_w/r_a \rightarrow \infty,$$

$k_w \rightarrow 1$  exponentially, and for  $r_w/r_a > 2$  the value of  $k_w = 1$  with satisfactory accuracy. In both cases,  $w_0 = 2G/(\pi r_a^2 L)$ , where  $G$  is the erosion rate and  $L$  is the electrode separation. This reflects the fact that the erosion product flow from both electrodes ( $2G$ ) fills the volume of the arc channel ( $\pi r_a^2 L$ ). The distribution of copper along the electric arc is considered to be homogeneous, because the rate of copper transport is determined by the diffusion coefficient, which is larger within the arc channel due to the high temperature.

We apply the approach derived in [3] to calculate the metal diffusion flux in a  $q$ -species gas mixture. Let  $i = 1$  denotes electrons,  $i = 1, \dots, p$  are species of gas  $A$  (metal vapour), and  $i = p + 1, \dots, q$  are species of gas  $B$  (ambient gas). In this approach, the  $\frac{1}{2} q(q-1)$  multi-component ordinary diffusion coefficients  $D_{ij}$  and the  $(q-1)$  thermal diffusion coefficients were replaced by one combined ordinary diffusion coefficient  $\overline{D_{AB}^x}$  and one combined thermal diffusion coefficient  $\overline{D_{AB}^T}$ . The expression for the diffusive mass flux then becomes

$$\overline{J_A} = -\left(n^2/\rho\right) \overline{m_A m_B} \overline{D_{AB}^x} \cdot d\overline{x_A}/dr - \overline{D_{AB}^T} \cdot d\ln T/dr, \quad (3)$$

which describes the diffusion of all metal components with respect to all ambient gas components. Here  $n$  and  $\rho$  are the mass and number density of mixture, respectively,  $T$  is the temperature, and

$$\overline{m_A} = \sum_{i=2}^p (m_i x_i + m_i Z_i x_i) / \sum_{i=2}^p x_i, \quad \overline{m_B} = \sum_{i=p+1}^q (m_i x_i + m_i Z_i x_i) / \sum_{i=p+1}^q x_i, \quad \overline{x_A} = \sum_{i=2}^p (1 + Z_i) x_i, \quad (4a,b,c)$$

are respectively the average masses of the species of gases  $A$  and  $B$ , and the mole fraction of gas  $A$ . Here  $m_i$ ,  $x_i = n_i/n$ ,  $n_i$  and  $Z_i$  are respectively the mass, mole fraction, number density and charge number of the  $i$ -th species. The coefficients  $\overline{D_{AB}^x}$  and  $\overline{D_{AB}^T}$  are given by:

$$\overline{D_{AB}^x} = \frac{1}{\overline{m_B}} \sum_{i=2}^p s_i \sum_{j=1}^q m_j D_{ij} \frac{\partial x_i}{\partial x_B}, \quad \overline{D_{AB}^T} = -\frac{n^2 \overline{m_A}}{\rho} \sum_{i=2}^p s_i \sum_{j=1}^q m_j D_{ij}^T \frac{\partial x_i}{\partial T} \quad (5a,b)$$

Here the stoichiometric coefficients are given by

$$s_i = b_i \sum_{i=2}^p x_i / \sum_{i=2}^p b_i x_i, \quad (6)$$

where  $b_i$  is the number of atoms in a molecule of species  $i$ : thus  $b_i = 2$  for a diatomic molecule or ion, and  $b_i = 1$  for an atom or monatomic ion.

In the usual case of low values of electrode vapour fraction in the arc plasma, the expressions  $\rho \sim 1/T$  and  $\overline{m_A} = m_A$  are correct to sufficient accuracy. As a result, the expression for the mass flux (3) simplifies to

$$\overline{J_A} = -\rho \overline{D_{AB}^x} \cdot d\overline{c_A}/dr - \overline{D_{AB}^T} \cdot d \ln T/dr, \quad (7)$$

Here  $\overline{c_A}$  is the sum of mass fraction of copper components

$$\overline{c_A} = \sum_{i=2}^p (1 + Z_i) c_i, \quad (8)$$

where  $c_i = \rho_i/\rho$  and  $\rho_i$  are the mass fraction and density of  $i$ -th species, respectively.

The flux in the form (7) is analogous to the flux of one of the two components in a binary mixture. It is often used in simplified treatments of diffusion processes in multi-component mixtures, where either a binary diffusion coefficient, a diffusion coefficient related to the viscosity, or a quasi-binary diffusion coefficient is used in the place of  $\overline{D_{AB}^x}$ . The adequacy of such approximations was analysed in [4]. It was shown in particular that such approximations lead to false values of the flux at temperatures for which ionization is significant. We therefore used the expression for combined ordinary diffusion coefficient in (8).

The system of equations (1), (2), (7) is closed by the equation of state

$$p_a/(k_B T) = n \quad (9)$$

and the boundary conditions

$$d\overline{c_A}/dr|_{r=0} = 0, \quad \overline{c_A}|_{r=r_w} = 0. \quad (10a, b)$$

In the case of the wall-stabilized arc,  $r = r_w$  in boundary condition (10b) refers to the wall radius, and in the case of the free-burning arc to the quasi-wall radius. The concept of the adsorbing quasi-wall arises because of the mathematical model chosen – the equations are solved in a one-dimensional cylindrical coordinate system. For some  $R > r_a$  on the periphery of the electric arc, only metal atoms and ambient gas, with density  $\rho_A$  and  $\rho_B$  respectively, exist. Diffusion of metal atoms in the atmosphere of ambient gas is then described by the binary diffusion coefficient  $D_{AB} = \text{const}$  at constant temperature. We may then write the following expression for the metal diffusion flux density  $J_r^{Me}$  through a cylindrical surface of radius  $r$  and unit length:

$$J_r^{Me} = -2\pi r D_{AB} \cdot d\rho_A/dr = \text{const}. \quad (11)$$

As a result of single integration from  $R$  to  $r > R$ , we obtain:

$$J_r^{Me} = 2\pi D_{AB} \cdot [\rho_A(R) - \rho_A(r)] / \ln(r/R). \quad (12)$$

If  $r \rightarrow \infty$ , this flux decreases to the zero logarithmically and therefore cannot provide transfer of copper vapour. The concept of an adsorbing quasi-wall is not applicable in two-dimensional geometry. Further, for  $r \sim L/2$  in a free-burning electric arc, the geometry becomes spherical in character [5].

Equation (1) with boundary condition (10a) can be integrated once, taking into account the expressions for  $w_A$  in the form of (2a,b), with the respective results:

$$\overline{J_A^{step}} = \begin{cases} (r_a w_0/2) \cdot (r/r_a), & r \leq r_a \\ (r_a w_0/2) \cdot (r/r_a)^{-1}, & r > r_a \end{cases}, \quad \overline{J_A^{Gauss}} = k_w \frac{r_a w_0}{2} \frac{1 - \exp[-(r/r_a)^2]}{r/r_a}. \quad (13a,b)$$

### 3. Diffusion coefficients and their analytical approximation

We consider a mixture in which copper is the metal and nitrogen the ambient gas. In *fig. 1*, the values of the combined ordinary diffusion coefficient and combined thermal diffusion coefficient, calculated according to (5a,b), are shown. The collision integrals used to calculate the multi-component diffusion coefficients are given in [4] and [6]. It is evident that for low temperatures (up to 7000 K),  $\overline{D_{Cu,N}^x}$  is practically independent of the copper concentration, and can be approximated by a simple power dependence of the form

$$\overline{D_{Cu,N}^x} = D_0 (T/T_0)^{n_D}, \quad (14)$$

where  $D_0$ ,  $T_0$ ,  $n_D$  are constants. An example of such a calculation is shown by full curve *A* in *fig. 1a* for  $n_D = 2$ ,  $T_0 = 6700$  K and  $D_0 = 45$  cm<sup>2</sup>/s. Similar behaviour is found for a nitrogen-argon mixture [3].

If the temperature of the arc plasma between the copper electrodes is greater than 7000 K [7], the combined ordinary diffusion coefficient has a complicated dependence on both the temperature and the copper content. For  $\overline{c_{Cu}} < 10$  % in the interval 300 – 12000 K, we can approximate the dependence with satisfactory accuracy by the following analytic expression:

$$\overline{D_{Cu,N}^x}(T, \overline{c_{Cu}}) = \frac{2}{1 + \exp(0.18/T)} \frac{C_1 (\overline{c_{Cu}})^{1/2} T^{1/2}}{[T - C_2 (\overline{c_{Cu}})^2] + C_3 (\overline{c_{Cu}})}, \quad (15)$$

with the temperature  $T$  in eV, where

$$\begin{aligned} C_1 (\overline{c_{Cu}}) &= 2.41 + 3.01 \cdot \overline{c_{Cu}} - 167 \cdot (\overline{c_{Cu}})^2 + 2240 \cdot (\overline{c_{Cu}})^3, \\ C_2 (\overline{c_{Cu}}) &= 0.60 + 3.51 \cdot \overline{c_{Cu}} - 55.0 \cdot (\overline{c_{Cu}})^2 + 310 \cdot (\overline{c_{Cu}})^3, \\ C_3 (\overline{c_{Cu}}) &= 0.054 + 1.60 \cdot \overline{c_{Cu}} - 30.1 \cdot (\overline{c_{Cu}})^2 + 161 \cdot (\overline{c_{Cu}})^3. \end{aligned} \quad (16)$$

In *fig. 1a* this approximation is shown by the broken curves.

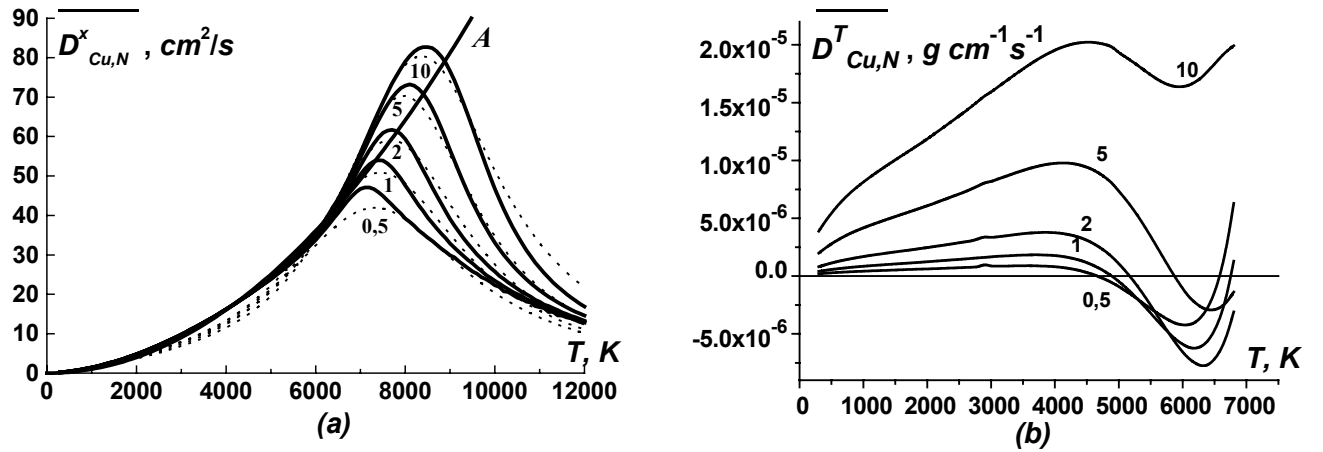


Figure 1. Temperature dependence of the combined ordinary (a) and thermal (b) diffusion coefficients (full curves) and approximations (broken curve on *fig.a*). Numbers near the curves denote copper mass fraction in percent. Curve *A* on *fig.a* shows the approximation of the combined ordinary diffusion coefficient for low temperatures by the power dependence with the power  $n_D = 2$ .

In contrast to  $\overline{D_{Cu-N}^x}$ , which has a strong dependence on the temperature and a very weak dependence on the copper content for relatively low temperatures, the combined thermal diffusion coefficient has a strong dependence on the copper content and a weaker dependence on the temperature. In paper [3] this was also shown for the example of an argon-nitrogen mixture. In *fig. 1b*  $\overline{D_{Cu-N}^T}$  is shown for 300 K <  $T$  < 7000 K. For this temperature interval, it can be approximated by a linear dependence on the copper mass fraction:

$$\overline{D_{Cu-N}^T} = D_0^T \overline{c_{Cu}}, \quad (17)$$

with  $D_0^T = 1.63 \cdot 10^{-4}$  g/(cm·s).

## 4. Results and discussion

### 4.1. Diffusion processes at low temperatures (up to 7000 K)

In this section, we neglect thermal diffusion. Its influence on the metal vapour content distribution will be discussed in Sec. 4.3. For the Gaussian radial temperature profile typical of free-burning arcs

$$T(r_n) = T_0 \exp(-ar_n^2), \quad (18)$$

where  $T_0$  is the temperature at the arc centre and  $r_n = r/r_a$ , the solution of (13a) together with (7), (9), (10b), (14) is:

$$\overline{x_{Cu}}(r_n) = \begin{cases} p[\text{Ei}(\beta(r_w)_n^2) - \text{Ei}(\beta) + \exp(\beta)/\beta - \exp(\beta r_n^2)/\beta], & r_n \leq 1 \\ p[\text{Ei}(\beta(r_w)_n^2) - \text{Ei}(\beta r_n^2)], & 1 < r_n \leq (r_w)_n \end{cases}, \quad (19)$$

where  $(r_w)_n = r_w/r_a$ ,  $\text{Ei}(x)$  is the Cauchy principal value integral [8],  $\beta = \alpha(n_D - 1)$ ,  $p = Gk_B T_0 / (2\pi L p_a D_0 m_{Cu})$ .

If the combined ordinary diffusion coefficient is approximated with satisfactory accuracy by the dependence (14), where  $n_D = 2$  (see *fig. 1*, curve *A*), the equation (13b) can be solved analytically for all areas at once, which gives the following result:

$$\overline{x_{Cu}}(r_n) = k_w p \left\{ \text{Ei}[1, (r_w)_n^2 (1 - \alpha)] - \text{Ei}[1, r_n^2 (1 - \alpha)] + \text{Ei}(\alpha(r_w)_n^2) - \text{Ei}(\alpha r_n^2) \right\}. \quad (20)$$

For a wall-stabilized electric arc, in which the product of erosion of the electrodes is deposited on the surface of the wall, it is possible to find the solution of equation (13) based on the double-layer quasi-channel model of the arc [9]. We write the temperature dependence of the thermal conductivity as  $\lambda(T) = \lambda_w (T/T_w)^{n_\lambda}$ , where  $\lambda_w$ ,  $n_\lambda$  are constants of approximation and  $T_w = 300 \text{ K}$  is the wall temperature, obtaining

$$T(r_n) = \begin{cases} T_0 (1 - Ar_n^2)^{1/(n_\lambda + 1)}, & r_n \leq 1 \\ T_0 [B \ln((r_w)_n / r_n) + C]^{1/(n_\lambda + 1)}, & 1 < r_n \leq (r_w)_n \end{cases}, \quad (21)$$

where

$$A = 1 - (T_1/T_0)^{n_\lambda + 1}, \quad B = 2(T_0^{n_\lambda + 1} - T_1^{n_\lambda + 1})(T_1^{n_\lambda + 1} - T_w^{n_\lambda + 1}) / (T_0 T_1)^{n_\lambda + 1}, \quad C = (T_w/T_0)^{n_\lambda + 1}, \quad (22)$$

$$D = \frac{2p}{B\xi} \left[ (B \ln((r_w)_n) + C)^\xi - C^\xi \right] - \frac{p}{A\xi} (1 - A)^\xi, \quad T_1 = T(r_n = 1).$$

We also specify  $w_0$  in the form of a “step”, as in equation (2a). The solution is:

$$\overline{x_{Cu}}(r_n) = \begin{cases} D + (p/\xi A) \cdot (1 - Ar_n^2)^\xi, & r_n \leq 1 \\ \frac{2p}{\xi B} \left\{ [B \ln((r_w)_n / r_n) + C]^\xi - C^\xi \right\}, & 1 < r_n \leq (r_w)_n \end{cases}, \quad (23)$$

where  $\xi = (n_\lambda - n_D + 2)/(n_\lambda + 1)$ .

*Fig. 2* shows examples of calculations. The parabolic approximation for the dependence of  $\overline{D_{Cu-N}^x}$  on temperature (14) was used. The value  $n_\lambda = 5/2$  was assumed for the exponent in the temperature dependence of the thermal conductivity. The measured temperature profile reported in [10] for  $L = 0.8 \text{ cm}$  and  $I = 3.5 \text{ A}$  was approximated by a Gaussian profile (18) with parameters  $T_0 = 6700 \text{ K}$  and  $\alpha = 0.4$ . The erosion rate for a current  $3.5 \text{ A}$  was taken to be, in accordance with [11], equal to  $56 \mu\text{g/s}$  (in calculating this value, the mean duration of the arc was assumed to be  $100 \text{ ms}$ ).

From the results presented in *fig. 2*, it is possible to conclude the following. The somewhat larger values of copper mole fraction  $\overline{x_{Cu}}$  obtained for the “step” distribution of the copper production rate  $w_{Cu}$  (curve 1), compared with those obtained for the Gaussian distribution of  $w_{Cu}$  (curve 1a), are explained by the greater localization of the copper production in the arc channel in the first case. Yet the calculated concentration of the electrode vapour in the arc depends to only a small extent on the distribution of the copper production rate near the electrode.

The results of calculations of copper concentration for different temperature profiles (*fig. 2b*) show significant, but mainly small, differences. In [12] the spatial distribution of the self-absorption of the  $510.5 \text{ nm}$  spectral line in a free-burning arc between copper electrodes was investigated by laser diagnostic methods. According to the results obtained, the copper concentration profile represented by curve 2 in *fig. 2b* is more suitable than the others. This suggests that the temperature profile represented by curve 2 in *fig. 2a* is



more realistic than the widely-used Gaussian profile [13], and shows that it is necessary to choose the temperature profile at the periphery of arc very carefully.

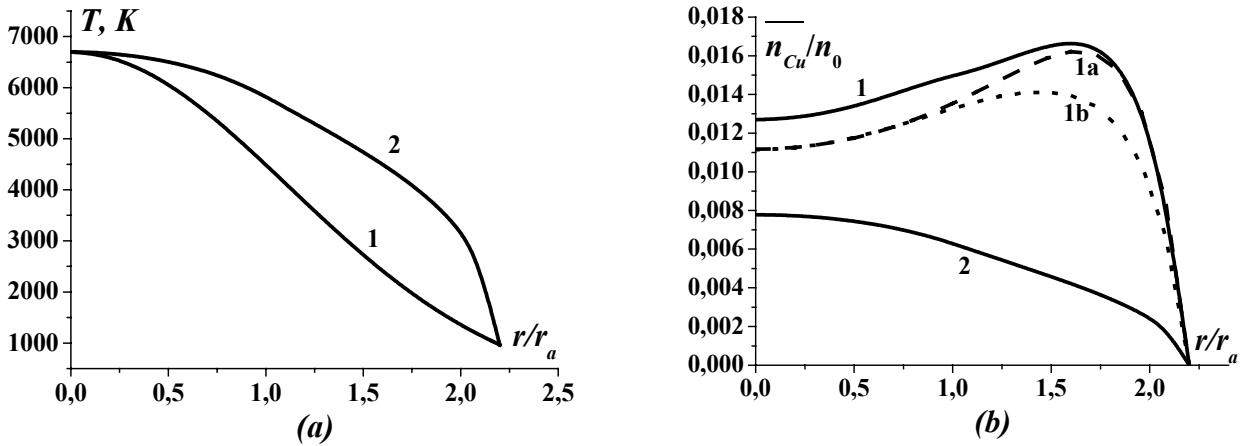


Figure 2. Radial normalized temperature profiles  $T(r_n)/T_0$  (a) and copper concentration  $\overline{n_{Cu}}/\overline{n_0} = \overline{x_{Cu}}/(T/T_0)$  ( $n_0 = p_a/[k_B T_0]$ ,  $p_a$  – atmospheric pressure) (b) for a Gaussian temperature distribution (curves 1, 1a, 1b) and for the temperature profile obtained from a self-consistent solution of the thermal conductivity equation (curve 2). (1) – Solution for a step distribution of  $w_{Cu}$  and  $n_D = 2$  (1a) – solution for Gaussian distribution of  $w_{Cu}$  and  $n_D = 2$ , (1b) – solution of differential equation (14b) together with the combined ordinary diffusion coefficient in the form of (16).  $(r_w)_n = 2.2$ .

#### 4.2. Diffusion processes for wide temperature interval (up to 12 000 K)

For determining copper vapour distribution over a wide temperature range, equation (13b) together with boundary condition (10b) was solved numerically for the specified Gaussian temperature profile  $T(r_n)$ :

$$T(r_n) = (T_0 - T_w) \exp(-\alpha r_n^2) + T_w, \quad (24)$$

For  $I = 30$  A the erosion rate equals  $216.7 \mu\text{g/s}$  [11]. The results of calculations for three positions of the adsorbing wall are presented in *fig. 3*. If  $(r_w)_n > 2$ , the copper mass fraction becomes greater than the 10% limit assumed in this paper. For the calculations, the following values of parameters were used:  $L = 0.8$  cm,  $T_0 = 8500$  K and  $\alpha = 0.6$  [7]. The corresponding solutions obtained with parabolic temperature dependence of the combined ordinary diffusion coefficient are shown by the broken curve on *fig. 3*. While these provide an estimate of the copper content in the arc plasma at low temperature, they give incorrect values for high temperatures because the diffusion coefficients are overestimated (*fig. 1a*).

It is possible to conclude from results presented that as the distance from the arc to the adsorbing wall increases, then the maximum copper concentration on the periphery of the vapour diffusion region increases. This is due to the lower value of the combined ordinary diffusion coefficient at low temperatures, and because of the fact that the density of gas increases with decreasing temperature at constant pressure. No significant increase in the copper vapour mole fraction is observed as the distance from the arc axis increases. This is contrary to the interpretation of the experimental results presented in reference [14]. These results, as was remarked in [15], can be explained in terms of the non-equilibrium state of the plasma at the arc periphery due to the influence of resonance radiation transfer.

Curve 1b on *fig. 2b* shows the solution of equation (13b) with the diffusion coefficient in the form of equation (15) for the same parameters. The small differences between the curves 1a and 1b arise because of deviations from the parabolic dependence in the approximation of the combined ordinary diffusion coefficient at low temperatures.

#### 4.3. The influence of thermal diffusion on diffusion processes at low temperatures

Thermal diffusion may influence the copper vapour content distribution in an electric arc in a region of relatively high temperatures and large temperature gradients. The system of equations (7), (10b), (13b), (14) and (17) was solved numerically for the two types of temperature profiles considered, determined by equations (18) and (21). The results of calculations show that demixing processes cause a flux of the heavier chemical element (copper) to regions at lower temperature for both temperature profiles (*fig. 4*). In the case of the wall-stabilized arc, the large temperature gradient at the arc periphery (curve 2 in *fig. 2a*) does not lead to a significant decrease in the copper concentration (curves 2, 2' in *fig. 4*). This is because the large gradient is compensated by the fact

that the coefficient  $\overline{D_{Cu,N}^T}$  in this region is small, due to its proportionality to  $c_{Cu}$  (17). In the case of the free-burning arc, thermal diffusion has an effect in the arc's central areas, because the temperature gradient is maximum here ( $T = T_{max}$  when  $r/r_a = (2\alpha)^{-1/2}$ ) (curve 1 on fig. 2a) and the values of coefficient  $\overline{D_{Cu,N}^T}$  are larger than in the case of the wall-stabilized arc. Comparison of the two different arc regimes shows that the copper concentration is larger at all radii ( $r = 0 - r_w$ ) in the free-burning arc. This is because temperatures in the free-burning arc are everywhere lower, so that the coefficient  $\overline{D_{Cu,N}^x} \sim T^2$  is smaller.

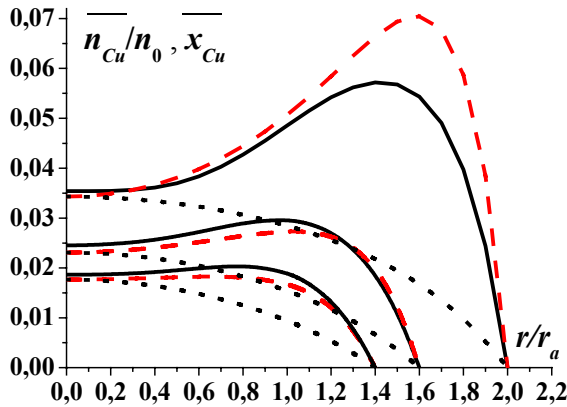


Figure 3.

Radial profiles of normalized concentration  $\overline{n_{Cu}}/\overline{n_0}$  (full curves) and copper mole fraction  $\overline{x_{Cu}}$  (dotted curves) for a Gaussian temperature distribution and for various positions of the adsorbing wall. Corresponding values of  $\overline{n_{Cu}}/\overline{n_0}$  calculated with a parabolic temperature dependence of the combined ordinary diffusion coefficient are shown by broken curves.

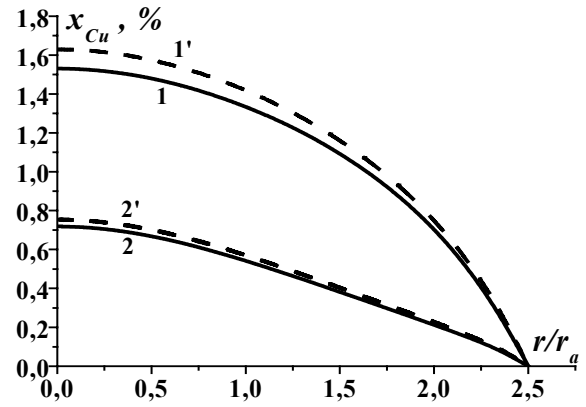


Figure 4.

Radial profiles of the temperature (a) and copper mole fraction (b) typical for free-burning (curves 1,1') and wall-stabilized (curves 2,2') arcs. Broken curves (1',2') show solutions obtained without including thermal diffusion.  $r_w/r_a = 2.5$ .

## 5. Conclusion

Using papers [1-4] as starting points, we have solved the problem of determining the electrode vapour distribution in free-burning and wall-stabilized electric arcs using the combined diffusion coefficient formulation to treat diffusion. We have shown that the calculated concentration of the electrode vapour in the arc depends strongly on the temperature profile that is assumed, and to a much smaller extent on the distribution of the copper production rate near the electrode. The influence of thermal diffusion on the copper vapour content for free-burning and wall-stabilized arcs was investigated. In both cases, the copper vapour concentration in the arc region decreased, although in the case of the wall-stabilized arc the change was found to be small.

## References

1. Zhovtyansky V.A., Patriyuk V.M., *Ukrainian Phys. J.* **47**, 338 (2002) [in Ukrainian].
2. Zhovtyansky V.A., Murphy A.B., Patriyuk V.M., *Indust. Heat Eng.* **25**, 5 (2003) [in Russian].
3. Murphy A.B., *Phys. Rev. E* **48**, 3594 (1993).
4. Murphy A.B., *J. Phys. D: Appl. Phys.* **29**, 1922 (1996).
5. Zhovtyansky V.A., Patriyuk V.M., *Ukrainian Phys. J.* **45**, 1059 (2000) [in Ukrainian].
6. Murphy A.B., *Plasma. Chem. Plasma Process.* **14**, 451 (1994).
7. Babich I.L., Veklich V.A., Zhovtyansky V.A., Cheredarchuk A.I., *J. Eng. Phys. Thermophys.* **71**, 127 (1998).
8. Korn G.A., Korn T.M. *Mathematical Handbook*, (Moscow, 1973). – p.730-732 [in Russian].
9. *Physics and technics of a low-temperature plasma*, ed. Dresvin S.V. (Moscow, 1972). p.219-228 [in Russian].
10. Babich I.L., Veklich A.N., Zhovtyansky V.A., *Cont. Papers SPIG-19* (Zlatibor, Yugoslavia), 517 (1995).
11. Cobine J.P., Vanderslice T.A., *IEEE Trans. Commun. Electron.* № 66, 240 (1963).
12. Babich I.L., Veklich V.A., Zhovtyansky V.A., *J. Appl. Spectr.* (translated from Russian). **51**, 1028 (1989).
13. Paton B.E., Gvozdetzky B.S., Dudko D.A., *Microplasmous Welding* (Kyiv, 1979). – p.248 [in Russian].
14. Rahal A.M., Rahhaoui B., Vacquie S., *J. Phys. D: Appl. Phys.* **17**, 1807 (1984).
15. Babich I.L., Cheredarchuk A.I., Veklich A.N., Zhovtyansky V.A., *Proc. ISPC-12* (Minneapolis, USA), **4**, 1861 (1995).

# **On line measurements of particles velocity in plasma and study of residence time. Incidence of particle shape**

S. Darwiche, M. Benmansour, E. Francke, D. Morvan, J. Amouroux.

*ENSCP / UPMC, Laboratoire de Génie des Procédés Plasmas et Traitement de Surface. (LGPPTS)  
11 Rue P. et M. Curie, 75231 Paris Cedex . France.*

Plasma processes are frequently applied to material treatment and purification. Residence time and shape of grains of powder material treated are governing treatment conditions and its efficiency. The metallurgical grade silicon powder is obtained by grinding then sieving it to calibrate it in size. The irregular shape of fragments resulting from grinding must be previously filtered by screen to reduce the distribution. Residence time is tightly correlated with momentum transfer ability.

We investigate possible distributions in size of particles, to be as close as possible to physical characteristics observed on grains of powder before their injection. Considering various shapes of particles such as spherical, cylindrical or irregular cubic fragments, we choose finally a normal distribution, of elongated irregular cubic fragments centered in mass at 366 ng and with  $\sigma = 120$  ng. For three particles size range of this distribution (small, medium, and large one ) momentum transfer is significantly different.

The choice of a specific particle trajectory in the plasma is a key of understanding the various forces acting on grains. As we were able to take a lot of just treated particles on the ring around central melt material, and as they keep their shape imprinted in flight even after impacting on substrate, we considered a particular trajectory arriving on the substrate at 12 mm from the axial point, after a 30 cm trajectory.

The step of the study is the characterization of main parameter governing the treatment as: concentration on path-lines, velocity along trajectories from injection  $Z = 0$  cm  $V_{\text{Part.}} = 6 \text{ ms}^{-1}$ , down to  $Z = 30$  cm when impacting on the substrate with  $V_{\text{Part.}} = 18 \text{ ms}^{-1}$ . Then it is possible to calculate acceleration of particles, heat transfer, deceleration, and particles characteristics for various state liquid droplets, or solid particles.

These experimental measurements in flight provide data which allow to compare the particle velocity data  $V_{\text{Part.}}$  measured on one hand between  $10 \text{ ms}^{-1}$  up to  $25 \text{ ms}^{-1}$ , with the gas velocity calculated between  $V_G = 72 \text{ ms}^{-1}$  pushing particles, and  $V_G = 5 \text{ ms}^{-1}$  at  $Z = 30$  cm pulling them before impacting. Crossing those two approaches, we calculate viscosity forces dragging particles along trajectory, and evaluate the residence time with validation, in each zone of trajectory. In that conditions the residence time of particles is between 9 and 12 ms.

The complementary approaches calculated data and measured one, confirm one another, and allow to predict important characteristics such as of residence time of particles in plasma, rich path-lines trajectories, acceleration, impacting, and so on.

# On line measurement of particules size and Silicon vapor concentration in plasma gas , due to evaporation phenomena.

M. Benmansour, S. Darwiche, R. Kerboussa, E. Francke, D. Morvan, J. Amouroux.

\*S. Dresvin

ENSCP / UPMC, *Laboratoire de Génie des Procédés Plasmas et Traitement de Surface. (LGPPTS)*

11 Rue P. et M. Curie, 75231 Paris Cedex . France.

\* St. Petersburg State Technical University, Polytechnicheskaya Str. 29, 195251 St. Petersburg. RUSSIE

## Abstract

Plasma processes techniques are studied in this presentation, to combine purification and deposition processes. As we demonstrated in previous studies, main part of thermal and chemical treatment of silicon material, occurs very early when grains are injected in thermal plasma: between  $Z=0$  cm and  $Z=10$  cm. In this area, the temperature of plasma is high ( 7000 K to 9000 K ), and light emitted by plasma is maximum when passing inductive coils in this new designed torch.

## I. Introduction

As previous studies of silicon material treatment demonstrated [1],[2],[3] mainly occurs just when powder grains pass the injector, for  $Z$  position between 3 and 10 cm. To investigate properly this initial part of particles trajectory, and measure accurate data for particles concentration, velocity and diameter of liquefied particles using PDA device inside the new torch, we had to resolve previously three main hard physical conditions: high magnetic field, high plasma temperature, intense optical radiation of plasma. The challenge of this study is to focus our measurements in this important region.

## II. Experimental set-up and results.

### II. 1 Development of a new plasma torch for treatment of silicon particles.

#### a- New geometry design torch

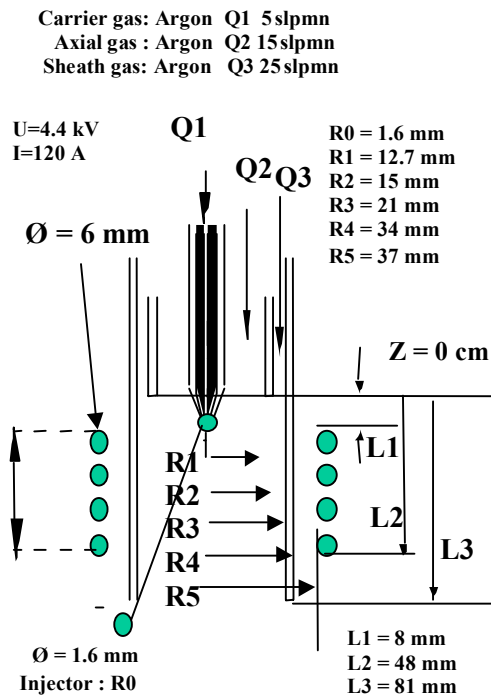
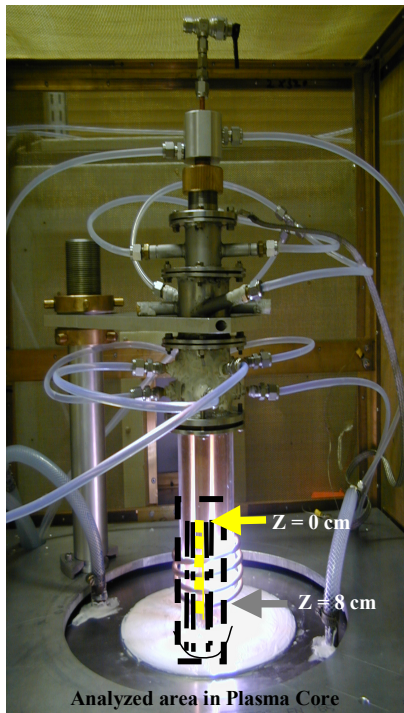


Figure 1 : New plasma design torch,

Standard characteristics and geometry 's torch.

The new plasma torch is placed on the top of a water cooled vessel as shown on figure 1. The plasma is operating at atmospheric pressure, and is composed of three different flows: Q1, Q2, Q3 of argon controlled by flows meters. On the other hand the silicon particles are injected with the argon carrier gas Q1 through the axial nozzle injector. The powder injection rate is controlled and adjusted independently to the carrier gas flow rate between  $0.1 \text{ g.min}^{-1}$  and  $0.25 \text{ g.min}^{-1}$ . As shown figure 1, the new design of torch allows to measure in flight particles behavior, close to the injector, as we have free optical access to particles on trajectory through a single glass cylindrical envelop. It's possible then to undertake measurements even near the injector in extreme physical conditions ( magnetic field, intense light, high temperature). If we satisfy all proper reserves required to reduce those constraints, then it is possible to undertake the expected measurements, passing between two figures the incident pair of laser beams and collecting the emitted bursts between another pair of fingers.

#### **b- Numerically calculated data of plasma flow**

Calculation of the model is based on Navier Stokes equations including mass, motion and energy conservations. In addition, we take into account the Maxwell equations for the electromagnetic field inducted. The geometry considered for the torch, the boundary conditions and the standard rates of flows are exactly those of our R.F. Thermal plasma. The field of plasma temperature  $T_G$  obtained, indicates a high temperature range (9000 K ) located at inductive coil level. On the axis, the injection of axial gas (  $Q_1$  ) decreases the plasma temperature down to ( 3000 K- 4000 K ) [ 4 ] and [5].

The field of plasma velocity  $V_G$  reported shows then a rise of velocity up to  $72 \text{ m.s}^{-1}$  on the axis when passing the injector, and a regular decrease along trajectory.

The mass flow field  $\psi$  (  $\text{kg.s}^{-1}$  ) shows that the maximum of flow is concentrated close to the wall. On the opposite, near the axis where the temperature is higher, the mass-flow decrease down to  $10^{-8} \text{ kg.s}^{-1}$ . To analyse the treatment of particles along first centimeters of their trajectory, from the injector down stream to the substrate, we start our analyze right on the axis of plasma flow:  $Z = 2 \text{ cm}$ ,  $r = 0$ , ( fig. 1).

## **II. 2 Distribution size of particles.**

The silicon material is grounded to powder in a mortar and screened through various sieves, and we inject those with calibrated size range:  $+53\mu\text{m}$ ,  $-63\mu\text{m}$ .

### **Normal distribution of number of particles versus their mass : $\mathcal{N}(366 \text{ ng}, 120 \text{ ng})$**

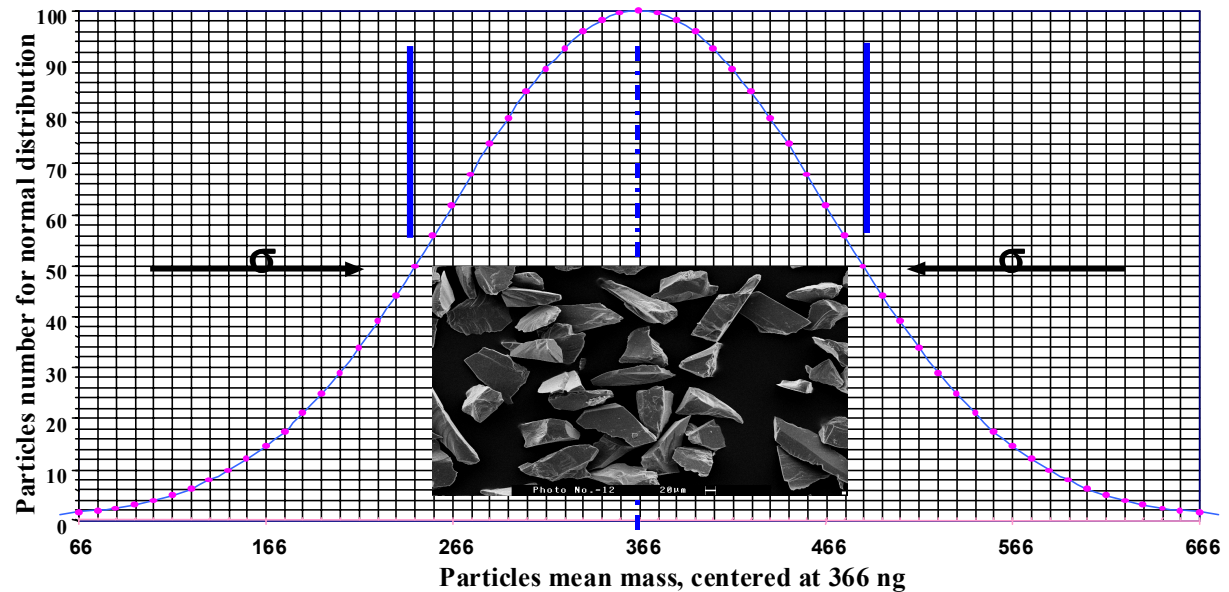


Figure 2 : Particle size distribution.



As shown figure 2, their shapes are very different, so the fragments cannot be classified versus their shape, we chose then a normal distribution of their mass. We evaluate the mean mass by weighing and counting a large number of particles (more than 2000), and we found  $m_0 \approx 366$  ng. The observation of many SEM Micrography leads us to chose  $\sigma = 120$  ng. So we assume a normal distribution kind  $N(m_0, \sigma)$ , centred on  $m_0 = 366$  ng with  $\sigma = 120$  ng. We calculate the equivalent diameter of spherical particles:  $D_{Part.} = 38\mu m$  for the smaller one ( $m_{min} = 66$  ng), and  $D_{Part.} = 81\mu m$  for the larger one ( $m_{max} = 666$  ng), and  $D_{Part.} = 66.9\mu m$  for the medium ( $m_{mean} = 366$  ng).

### II. 3 On line measurement of velocities and diameter of particles in high brightness glare

- PDA equipment adapted to new Torch
- Precision of collecting angle

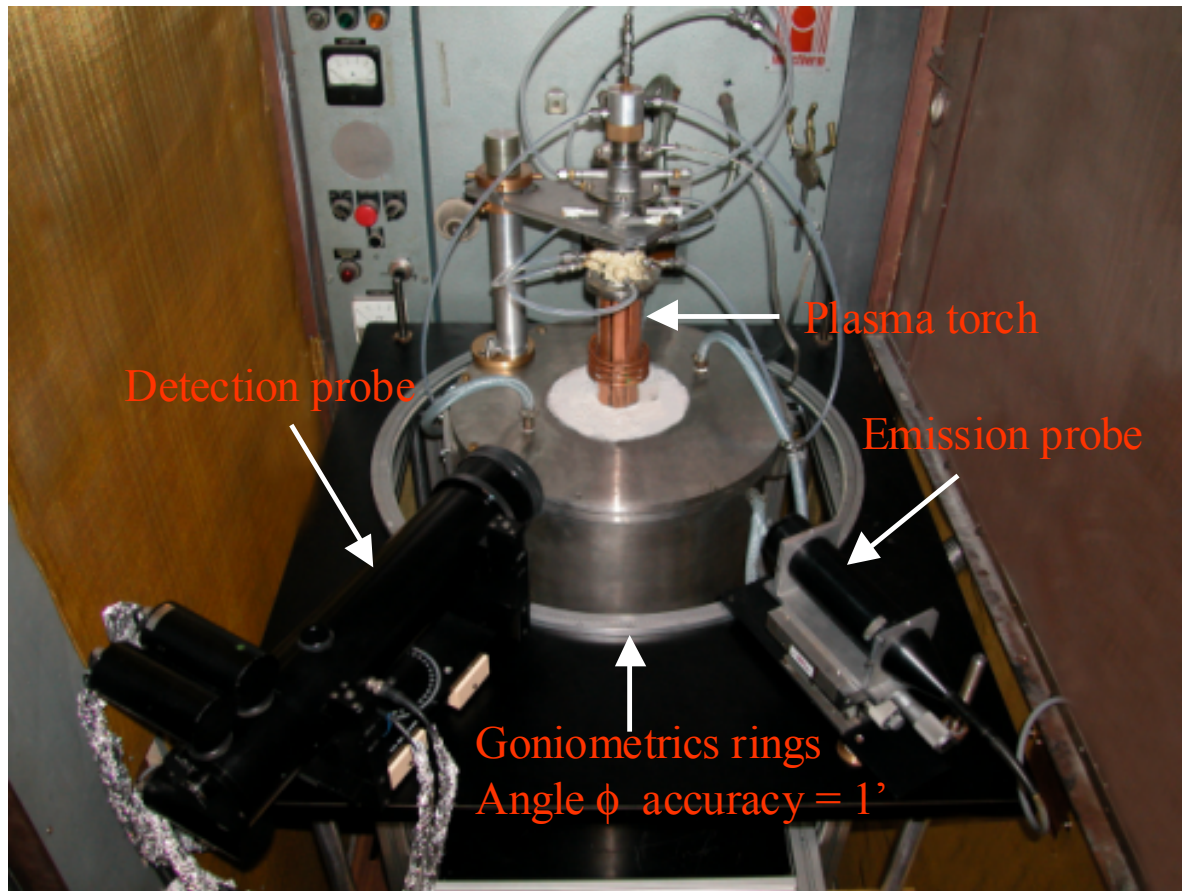


Figure 3 : View of experimental set-up, -goniometrics rings.

The Ar\* laser source is 300 mW power, and we used  $\lambda = 514.5$  nm wavelength. The optical transmitter separates the laser beam in two coherent sources  $S_1$  and  $S_2$ , and one of it is "Bragged" at 40MHz. The two beams emitted by  $S_1$  and  $S_2$  secondary sources of the optical probe cross one another at 35 cm in analyse volume.

Due to optical properties of silicon material ( $n = 4.39$ ;  $k = 0.273$ ), we chose to operate with scattering order  $P = 0$  ( pure reflection ), with a collecting angle  $\phi = 119.5^\circ$ , where are arranged large optical accesses through the water-cooled chamber vessel.

Around the torch an optical table was installed with a pair of goniometric rings, allowing only coaxial rotations of optical probes. This axis is common with torch (figure 3). Fixed in this configuration it was possible to appreciate collecting angle  $\phi$  with a precision of  $1^\circ$ .

First results: data inside plasma, in axial position, just passing the injector, and discussion.

Obviously we have to face a strong hindrance to collect the bursts -by the brightness light emitted by plasma in this area, as it masks the signal scattered by particles, and -by magnetic field RF pulsed by inductive coil.. Nevertheless we obtained interesting histogram with a sharp peak for velocity acquired on a great number of particles attempted, with a mean value  $V_{\text{Part.}} = 14.2 \text{ m/s}$ , as reported figure 4. More over , we obtained also good histograms for particles diameter, with sharp peak centred at  $D_{\text{Part.}} = 192 \text{ }\mu\text{m}$ , reported figure 4. This value is impossible, as particles initially introduced were calibrated size between 53 and 63  $\mu\text{m}$ , we assumed then that it was an artefact due to the intensity of magnetic field of inductive coil . In next experiments we reinforced Faraday cage namely around the 3 photomultipliers, and those histograms disappeared . That confirmed the valid measurement as we supposed.

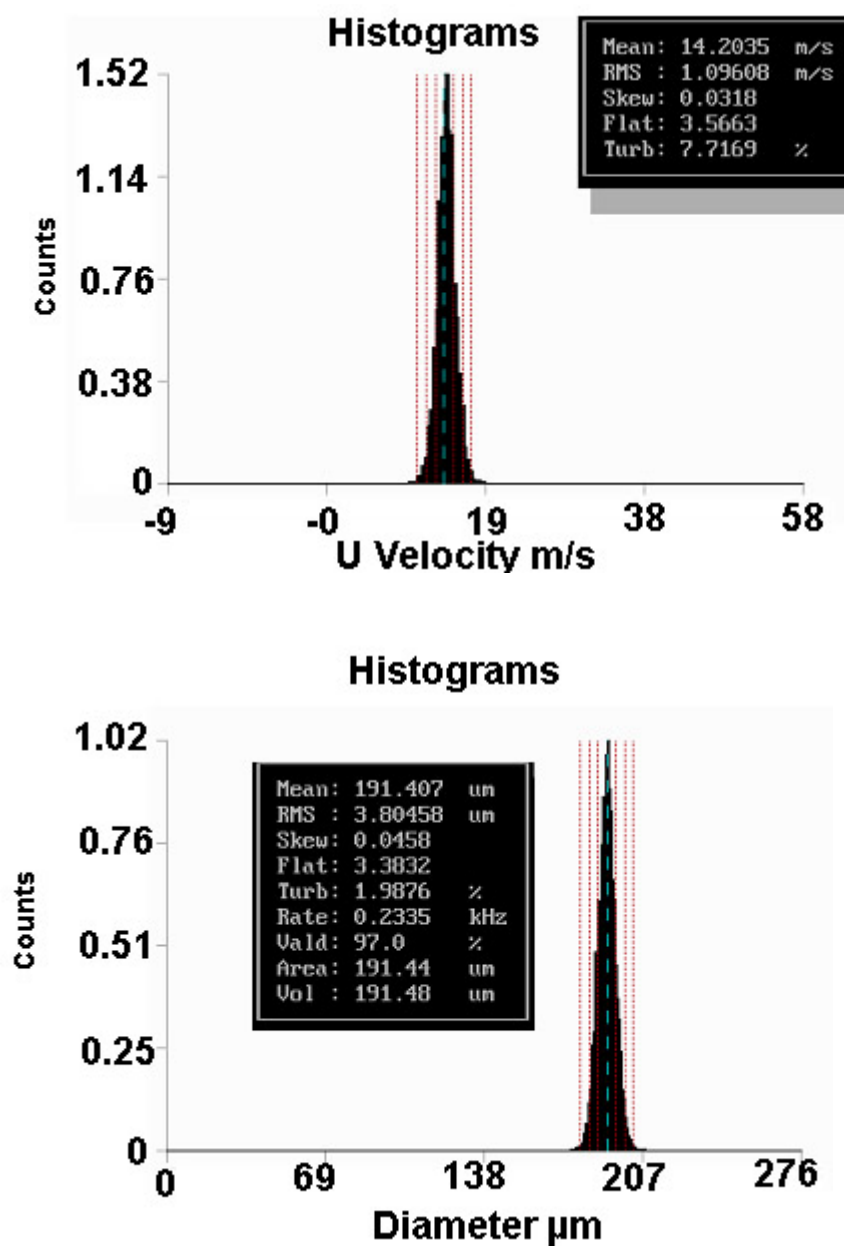


Figure 4 : Histograms of particles diameter and velocity.  $D_{\text{Part.}} = 192 \text{ }\mu\text{m}$ ,  $V_{\text{mean}} = 14.2 \text{ m/s}$ .

## II. 4- New experimental set –up to reduce drastically electromagnetic field and optical disturbs in measurements. New results and discussion

We interposed shelters then to reduce plasma emission with conical shape, and reduce the plasma brightness with those screen and interferential filters.

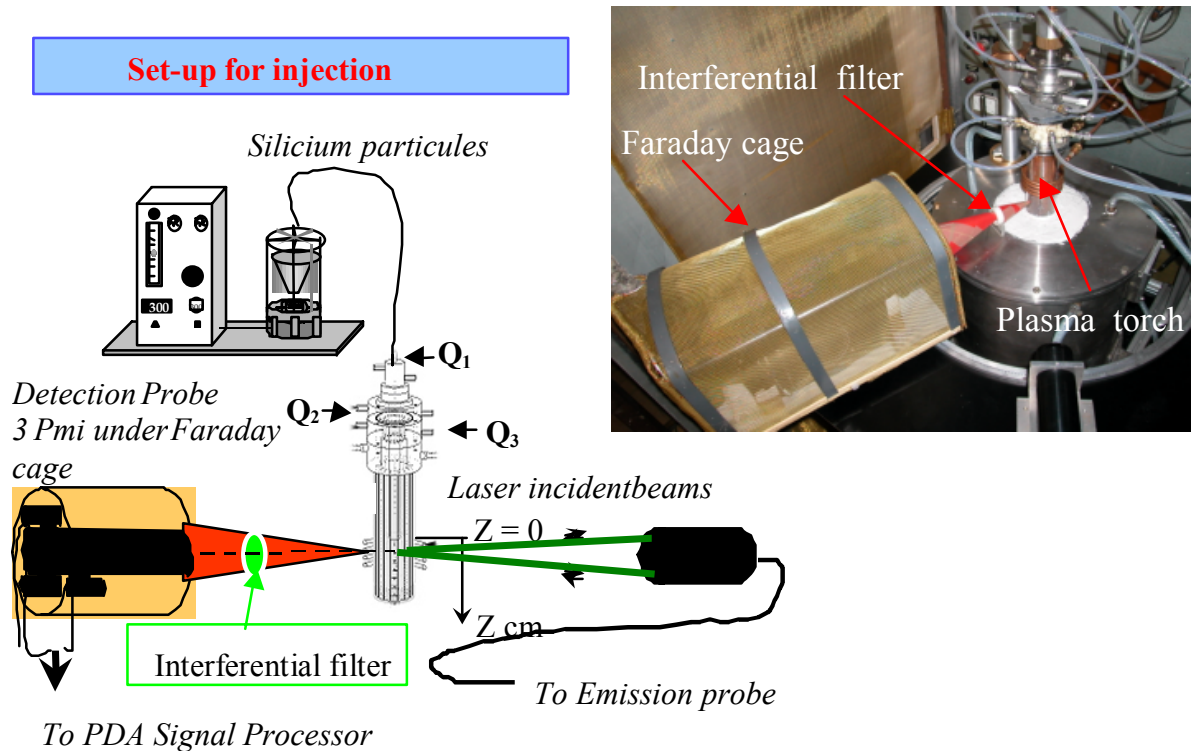
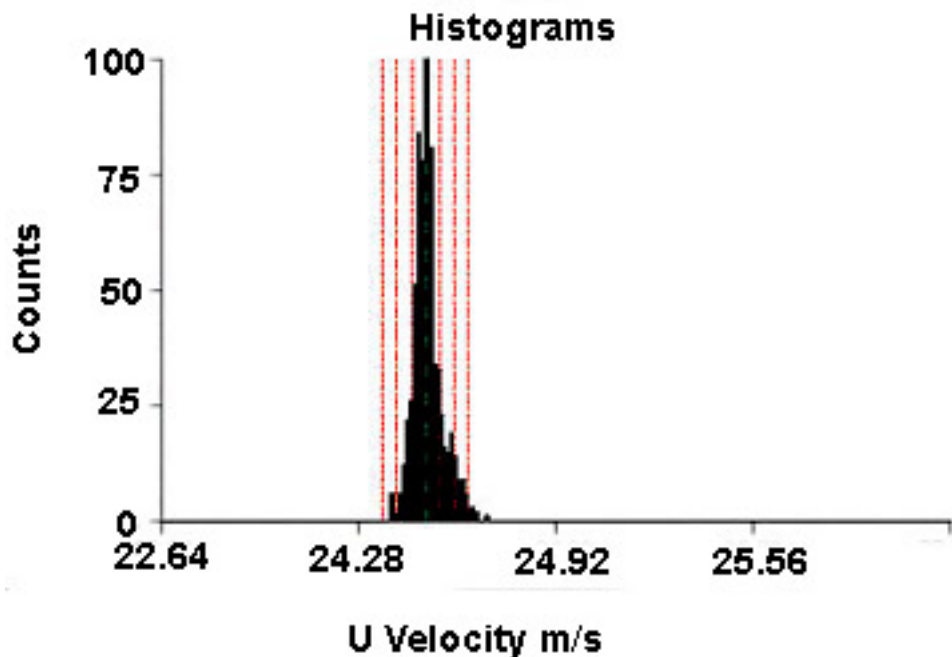


Figure 5 : View of optical and magnetic field additive protection.

## II. 4- New experimental set –up. New results

We obtained interesting histograms for velocity and diameter of particles, acquired with a great number of attempted particles, mean value of particles velocity is 24 m/s. We obtained as well histogram of Diameter which looked like background noise, and a mean value  $D_{part} = 104 \mu m$ . so roughly in the middle of the scale, presented figure 6. This histogram confirms that collecting optical probe was well focalized, and the particles are not melted yet.

We evidenced then, that the only solution is to increase laser source.





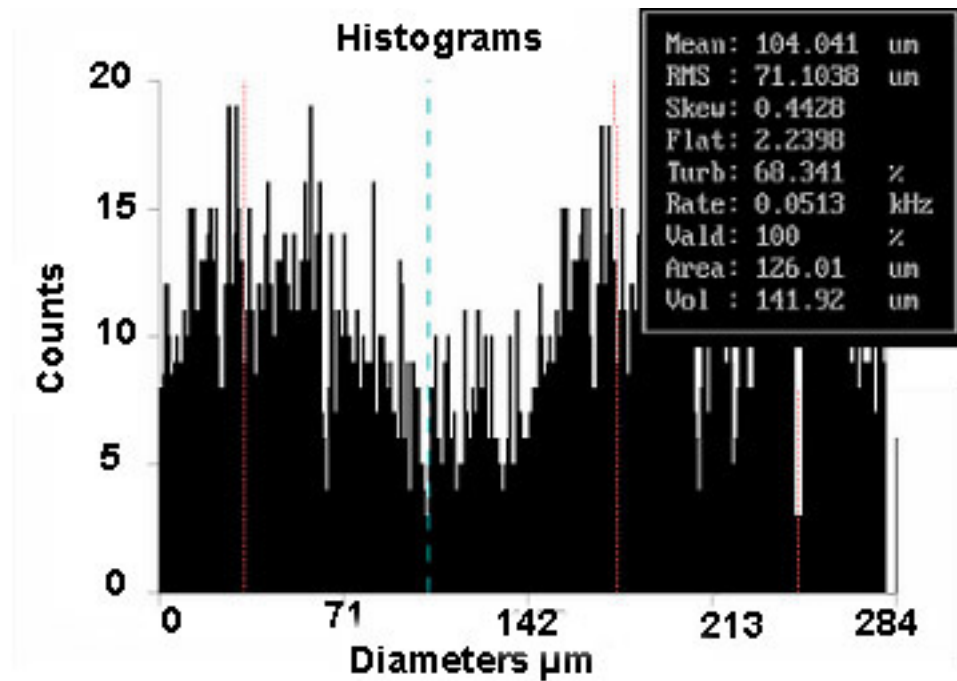


Figure 6 : Histograms of particles diameter and velocity.  $D_{\text{part}} = 104 \mu\text{m}$ ,  $V_{\text{mean}} = 24 \text{ m/s}$ .

### Conclusions

First results reported in this paper are very promising, proving that we have good efficiency of PDA equipment adapted to efficiency of measurements, despite so difficult physical conditions occurring in plasma core, during first centimeter just passing injector. A watchful attention is request to interpret every measured data.

They evidence, by reliable histograms reported, - the good focalization of detecting probe on analyze volume, - the good protection against magnetic field, - good protection against glare plasma brightness. They prove again that entering particules as misshapen fragments are not melted immediately.

Our perspective now is a new technological step by increasing laser source power (  $\times 15$  ), we are installing now a new strong source of 3 W for 5145 wavelength, and we expect then to observe burst scattering more intense in comparison plasma brightness.

### References

- [1]- J.R. Finck, W.D. Swank, C.L. Jeffery  
Appl. Phys. Letter, Vol **49**, n°23. (1986)
- [2]- D. Morvan, F. Krayem, S.F. Miraläi, J. Amouroux.  
Proc. 14 th E.C. Photovoltaic Solar energy Conference Barcelona, Vol **11**, pp 1513-1516 (1997)
- [3]- M. Vardelle, A. Vardelle, P. Fauchais.  
Journal of Thermal Spray Thechnology, Vol **2**, n°2 pp19-91 (1993)
- [4]- D. Morvan, F. Krayem, M. Benmansour, E. Francke, J. Amouroux.  
Proc. 16 th European Photovoltaic Solar Energy Conference. Glasgow. U.K. (2000)
- [5]- E. Francke, M. Benmansour, D. Morvan, J. Amouroux  
Proc. 15 th ISCP, Orleans, Vol **III** , pp 1063-1068 (2001)

# A simple theoretical model for the electrical discharge machining process

L.I. Sharakhovsky<sup>§</sup>, A. Marotta and A.M. Essiptchouk<sup>§</sup>

*Instituto de Física “Gleb Wataghin”, Universidade Estadual de Campinas, Unicamp, 13083-970,  
Campinas, São Paulo, Brazil*

*<sup>§</sup>Permanent address: The Luikov Heat & Mass Transfer Institute, P. Brovki street, 15, 220072,  
Minsk, Republic of Belarus*

## Abstract

The simple erosion model developed for Electric Arc Heaters [1,2] is modified to the calculations of the material removal rate during Electrical Discharge Machining. New model is obtained by reduction one-dimensional “point heat source model” [3] to the equivalent one-dimensional planar thermal source model. Approximated analytical relationships are derived and validated via comparisons with the different author’s experimental data. A good agreement of model with the experiments is obtained.

## 1. Introduction

The basic mechanism of the Electrical Discharge Machining (EDM), a process used in industry for cutting and shaping a wide variety of solid materials, is still under discussion. Different gas discharge processes, conduction and breakdown in liquids and the theory of underwater explosions were proposed (see [1-3] and references therein). However, the main conclusion was that heat conduction and melting are the dominant processes for workpiece removal rate. In this report, a new EDM cathode erosion model is proposed and compared to different author’s experimental results [3-6]. The model approach is based on the one successfully applied to electrode erosion in Electric Arc Heaters (EAHs) [7,8] and some special regimes of EDM (see [9-11]).

In [1] there was assumed a “point heat source model” with infinite current density, which is unrealistic from the physical point of view. As it was shown in [9,11], assuming a finite cathode spot current density, a simple EDM cathode erosion model was proposed and compared to experimental results in [1] for the diesinker machine experiments. In [9,11], the optimum discharge pulse duration was chosen to obtain maximum workpiece removal rate. For these experiments, with selected pulse duration, authors [11] have shown that the effective enthalpy is approximately the same for all presented regimes. This corresponds to the concept of constant effective enthalpy for a given material, assumed in [7,8,10]. However, for regimes with arbitrary chosen parameters this model is unsuitable, as a more complete analysis of a larger sample of experimental data shows. The reasons for this are the following: the step-wise model does not consider the influence to the erosion of the pause between the subsequent pulses, although this influence in EDM is very substantial; in the step-wise model, the discharge spot current density is assumed constant, independently on current and time.

As for the first consideration, this occurs because the discharge in EDM has a tendency to be tied to one and the same point, although it moves during the same pulse, as shown in [12,13]. Thus, the local temperature beneath the discharge spot is different from the mean workpiece temperature and this difference depends on the pulse interval  $\tau_{pa}$  as well as the pulse duration  $\tau_{pu}$ .

As for the second consideration, a constant current density corresponds to the conditions in the EAH. However, this assumption does not allow to explain the strong increase in the specific erosion with current, which occurs in EDM. Actually, in the planar one-dimensional model with constant heat flux density (due to constant current density  $q = jU$ ), the regime of electrode cooling under the spot after pulse is identical for any current and depends only on  $\tau_{pa}$  and  $\tau_{pu}$ . In that case the specific erosion (per 1 Coulomb) ought to be constant for any current if  $\tau_{pu}$  and  $\tau_{pa}$  are constants too. At the same time experiments with conditions  $\tau_{pu} = const$  and  $\tau_{pa} = const$ , but changing in current ( $I = var$ ) reveals strong dependence of the specific erosion and workpiece removal rate (in  $m^3s^{-1}$ ) on current. In EAHs the temperature of the electrode grows with increasing current, because it is heated not only by the spot, but also by convection and plasma radiation. This results in strong increase in the erosion. In EDM all these factors are absent, however, the increase in erosion nevertheless occurs.

The “point heat source model”, proposed in [3], allows take into account change both in the local material temperature and in the current density. In this model the heat flux is supplied through an infinitesimal point that represents discharge spot. Thus, the isotherms have spherical symmetry and heat-flux density on the isotherm is a function of current and radius. Model allows calculate a radius  $R$  of the isotherm that corresponds to melting temperature  $T_f$  from the equation [3]:

$$T = T_f = T_0 + \left( \frac{UI}{2\pi\lambda R} \right) \operatorname{erfc} \left( \frac{R}{2\sqrt{a\tau_{pu}}} \right) \quad (1)$$

Here  $U$  – thermal volt-equivalent of discharge, V;  $I$  – current, A. So,  $UI$  is the heat flux entered discharge spot;  $\tau_{pu}$  is pulse duration;  $T_0$ ,  $T_f$  is the workpiece initial temperature (before the pulse) and fusion temperature, respectively. The equation (1) determines the motion of the boundary of melting.

As shown in [3], the erosion experimental value is different from the volume of molten metal calculated in accordance with “point heat source” model, nevertheless the ratio between a molten and withdrawn amount of metal depends on current and pulse duration. It is interesting and important for us, that if we assume, that this withdrawn metal carries amount of heat spent to it’s heating to temperature of melting, we obtain approximately constant enthalpy of erosion for all regimes presented. Even more, the same enthalpy of erosion (approximately  $4.5 \text{ MJkg}^{-1}$ ) are obtained using planar step-wise model in [11], where heat spent to erosion calculated using another assumption – change of boundary conditions on the surface after onset of fusion. This can evidence about similarity of both approaches and possibility to reduce one model to another.

Unfortunately, the “point heat source” model does not permit to use concept of effective enthalpy of erosion directly, as it was done in planar step-wise model. The effective enthalpy of erosion  $h_{ef}$  was obtained there under assumption of stationary position of melting isotherm, arranged on the electrode surface in accordance with the first kind boundary conditions [14]. This assumption strongly simplify the problem through replacing the heat of fusion by a change in the kind of boundary conditions, as it was done in [1,9,10] and it completely justify itself in the arc heaters. However, the problem of calculation of the real motion of the melted boundary (Stephan’s problem) is very complex even at prescribed constant heat-flux density [15]. Therefore in order to obtain simple analytical theoretical and empirical relationships for the calculation of erosion in EDM, in this work we will seek the possibility to join one-dimensional planar step-wise model ([1,11]) with the one-dimensional “point heat source” model ([3]).

## 2. Assumptions for reduced model

In order to take account variable character of current density and the surface temperature in EDM we will consider the following assumptions:

- Initial radius of the plasma at discharge is very small, so that it is possible to use the point model of thermal source;
- Initial erosion, which appears with the asymptotic approximation of a radius of source to zero, can be disregarded;
- Thermal volt-equivalent of the discharge, which is equal to the relation of the energy, which enters the cathode, to the current, can be taken as constant and independent on the current;
- For the defining of a radius of isotherm of melting it is possible to disregard the heat of fusion and to consider heat expenditures only for material heating to the fusion point;
- For each radius  $R$  of the molten hemispherical volume, formed to the end of the discharge, it is possible to find equivalent radius  $r$  of the surface heat source, for which the effective enthalpy of the material ablation  $h_{ef}$ , (according to one-dimensional planar model), is function only the properties of material and does not depend on the operational parameters of EDM.

Assumptions 1-4 are substantiated and validated experimentally in [3]. The new and most cardinal assumption 5 has to be validated experimentally in the present work.

## 3. Approach to model construction

As it was shown in [11], planar one-dimensional model with the neglect of residual preheating from the previous pulse gives for the special regimes of EDMing, presented in [3], good agreement between theory and experiment and the linear dependence of material removal rate  $V$  (in  $\text{m}^3\text{s}^{-1}$ ) in function of dimensional group  $UW_s I \bar{\tau} \rho^{-1}$ :

$$V = \frac{UW_s I \bar{\tau}}{\rho h_{ef}} \quad (2)$$

In this dimension group along with current  $I$ , volt-equivalent  $U$  and erosion effective enthalpy  $h_{ef}$  enters the relative duration of discharge pulse  $\bar{\tau}$ , defined as

$$\bar{\tau} = \frac{\tau_{pu}}{\tau_{pu} + \tau_{pa}} \quad (3)$$

and non-dimensional energy of erosion  $W_s$ :

$$W_s = \frac{2}{\pi} \left( \tan^{-1} \sqrt{\frac{1-f_s}{f_s}} - \sqrt{f_s(1-f_s)} \right) \quad (4)$$

that is a function of non-dimensional fusion parameter  $f_s$ :

$$f_s = \frac{\pi}{4a\tau_{pu}} \left[ \frac{(T_f - T)\lambda}{j_e U} \right]^2 \quad (5)$$

However, to take into account the influence of the pause time, it is necessary to give proper weight of the local residual preheating of the workpiece surface from the previous pulse. The pulse time  $\tau_{pu}$  and current  $I$  determine penetration depth of the molten boundary and establish initial temperature field before pause in vicinity of discharge spot. For the distant points the workpiece temperature  $T_0=300$  K remains invariable. On the other hand, the degree of the temperature relaxation and, consequently, the surface temperature on the onset of the next discharge depends on the pause time  $\tau_{pa}$  and current  $I$ .

From the known residual temperature  $T$  on the hemi-spherical surface of the eroded cavern before the next pulse we can find such compensating current density  $j_e$ , which would keep constant the value of nondimensional fusion parameter  $f_s$ , calculated accordingly eq. (5), for the  $T$  calculated. Applying this approach for each experimental point of the special regimes in [11] (taken from [3]), where we have obtained good agreement between step-wise model and experiment under the assumption of the constant surface temperature  $T=T_0=300$  K, we can obtain new variable current density  $j_e$  for these experiments, depending on the residual temperature. Thus, new compensating (or effective) current density  $j_e$  makes it possible to find radius  $r$  of equivalent surface thermal source:

$$r = \sqrt{I/(\pi j_e)} \quad (6)$$

For the planar approximation we have to take this variable radius  $r$  since it is the function of the pulse time, current and residual temperature. Further, if the obtained for these experiments relationship for  $j_e$  has general nature, then it will be correct for another regimes of EDMing. This must be validated experimentally. The thermo-physical properties of steel for these calculations of experiments from [3] we have taken accordingly [3], namely:  $\lambda = 56.1 \text{ Wm}^{-1}\text{K}^{-1}$ ,  $C_p = 575 \text{ Jkg}^{-1}\text{K}^{-1}$ ,  $\rho = 7545 \text{ kgm}^{-3}$ ,  $T_f = 1808 \text{ K}$ .

Now we seek residual temperature on radius  $R = f(\tau_{pu})$  from the previous pulse. Since discharge is not actually motionless, but according to [13], it moves, we will consider heating only from one previous discharge, which simplifies problem. Residual temperature we find from the numerical solution of differential equation [1]

$$\frac{1}{a} \frac{\partial T}{\partial \tau} = \frac{\partial^2 T}{\partial R^2} + \frac{2}{R} \frac{\partial T}{\partial R} \quad (7)$$

under boundary and initial conditions

$$T(\tau_{pu}, R) = T_f \quad (8)$$

according to eq. (1) for  $T=T_f$ . Substituting calculated according to eqs. (7), (8) the value  $T$  into the eq. (5) for  $f_s$  for each experimental point, from the condition of conservation of  $f_s$  we find new, effective value of current density  $j_e$  for planar heat source. Corresponding values of  $r$  obtained by eq. (6) can be expressed simply in function of  $R$ :

$$r = 0.3R_0^{0.82} \quad (9)$$

Analytical relationships are more convenient for the practical applications. Therefore, the obtained numerical solutions were approximated by function of the nondimensional criteria of Fo (Fourier number) and Po (Pomerantsev number). For our case, Fourier number characterizes the time of cooling during pause:

$$Fo = \frac{a\tau_{pa}}{R_0^2} \quad (10)$$

while Pomerantsev number – characterizes the heat flux introduced to workpiece during heating [14]:

$$Po = \frac{UI}{\lambda R_0 T_f} \quad (11)$$

To obtain analytical relation we introduced a nondimensional residual temperature  $\bar{T}$ , defined as

$$\bar{T} = \frac{T - T_0}{T_f - T_0} \quad (12)$$

Thus, using numerical calculations within the range of  $\bar{T} = 0.025 \div 0.9$ ,  $Fo = 4.6 \times 10^{-4} \div 23.0$ ,  $Po = 6.3 \div 570$  the following expression for the  $\bar{T}$  was obtained:

$$\bar{T} = \alpha\beta + \text{erf}[(0.061 - 1.81\alpha)\beta] + \gamma \quad (13)$$

Here

$$\alpha = 1.129 \exp(2.107 - 1.076Po) + 5.77 \times 10^{-3} \ln Po - 1.66 \times 10^{-6} Po - 0.115 \quad (14)$$

$$\beta = \ln\left(\frac{1}{4Fo}\right) - 0.604 \ln Po + 3.607 \exp(-0.1427Po) + 0.187 \quad (15)$$

$$\gamma = 0.467 - 0.659 \exp(-3.362 - 0.038Po) + 8.625 \times 10^{-8} Po^2 \quad (16)$$

Expressed in variables  $Fo$  and  $Po$ , the nondimensional temperature  $\bar{T}$  is a function of current, thermal volt-equivalent, duration of pulse and pause, and also of thermo-physical parameters of the material of cathode (melting point, thermal conductivity and thermal diffusivity).

#### 4. Comparison to experimental data

The different authors experimental data was used to check relationship (13). The volumetric material removal rate (presented in [3], [6]-[8]) was obtained for different and arbitrary operational regimes and for five different grades of steel with different thermophysical properties. These experimental data and calculations are presented in Figures 1 and 2.

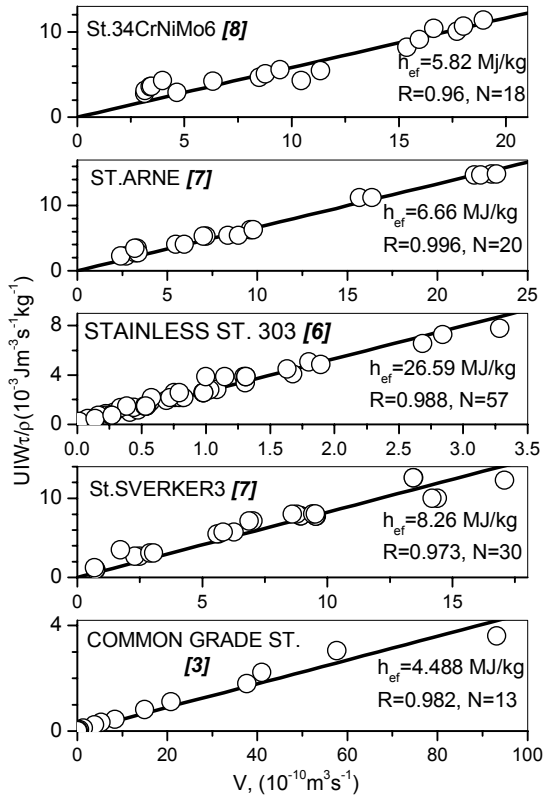


Figure 1. Dimensional group  $UWI\tau\rho^{-1}$  versus workpiece removal rate  $V$  for different grade of steels.

Data [3] are related with common grade steel. Authors [6] give the results of experiments on EDMing of the stainless steel 303 over wide range of regimes. Among them the material removal rate  $V$  in function of current  $I$  under constant duration of pulse  $\tau_{pu}$  and pause  $\tau_{pa}$ , and also in function of time of pulse  $\tau_{pu}$  under  $I = \text{const}$ ,  $\tau_{pa} = \text{const}$ , and, moreover, with constant operational parameters  $(I, \tau_{pu}, \tau_{pa})$ , but different tool (anode) material. The thermophysical properties of steel 303 we took according to [16]:  $\lambda = 14.6 \text{ Wm}^{-1}\text{K}^{-1}$ ,  $a = 3.728 \times 10^{-6} \text{ m}^2\text{s}^{-1}$  and  $T_f = 1672 \text{ K}$  from [17].

In [7] authors give the results of the cathode EDMing for two grades of steels: ARNE and SVERKER3 with arbitrary variation of operational parameters over wide range. Thermophysical properties of these steels we took according to [18]: for ARNE:  $\lambda = 32 \text{ Wm}^{-1}\text{K}^{-1}$ ,  $a = 8.92 \times 10^{-6} \text{ m}^2\text{s}^{-1}$ ,  $T_f = 1808 \text{ K}$  and for SVERKER3:  $\lambda = 20.5 \text{ Wm}^{-1}\text{K}^{-1}$ ,  $a = 5.788 \times 10^{-6} \text{ m}^2\text{s}^{-1}$ ,  $T_f = 1808 \text{ K}$ .

The thermophysical properties of the steel 34CrNiMo6 we have taken according to the producer

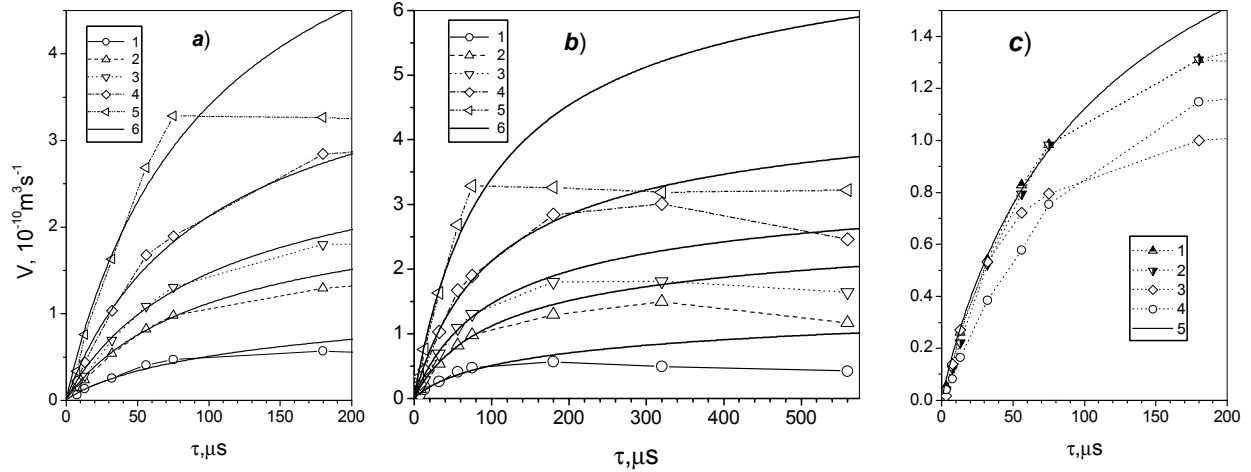


Fig. 2. Workpiece (steel 303, [6]) removal rate  $V$  with varied on-times and currents at constant off-time of  $100 \mu s$ . a) - range  $0-200 \mu s$ ; b) - range  $0-600 \mu s$ . 1 – current 8.3 A; 2 – 14.8 A; 3 – 18.3 A; 4 – 24.8 A; 5 – 37.1 A. c) different anode materials at current 14.8 A. 1,2 – zirconium diboride/copper composite material; 3 – graphite; 4 – copper. Theoretical line (with no symbols) is calculated accordingly to the present model for corresponding experimental points labelled with lines and symbols.

data [19]:  $\lambda = 37.7 \text{ Wm}^{-1}\text{K}^{-1}$ ,  $a = 1.044 \times 10^{-5} \text{ m}^2\text{s}^{-1}$ ,  $T_f = 1808 \text{ K}$  and  $\rho = 7850 \text{ kgm}^{-3}$ .

Figure 1 shows the dependence of the dimension group  $UWI\bar{\tau}\rho^{-1}$ , calculated according to eqs. (1)-(5), (13) on the experimental material removal rate  $V$  for each steel mentioned above. For calculations the thermal volt-equivalent  $U$  was assumed constant  $U=4.575\text{V}$ , accordingly [3]. An effective current density  $j_e$  in  $f$  (see eq. (5)) was calculated by formula (6) using the effective radius of the discharge spot  $r$ , calculated by (1) and (9). The nondimensional residual temperature  $\bar{T}$  was calculated according to the formulae (12), (13). It is evident from Figure 1, that dimension group  $UWI\bar{\tau}\rho^{-1}$  and material removal rate  $V$  has clear linear dependence with high correlation coefficients  $R$  (from 0.97 to 0.99). This result confirms the validity of the model of the material ablation with constant effective enthalpy  $h_{ef}$ , which depends only on the thermo-physical properties of material but does not depend on operational parameters of EDM.

From Figure 1 it is possible to determine the effective enthalpy of erosion for the materials under study by using eq. (2). Thus we obtain: for common grade steel [3] –  $h_{ef}=4.49 \text{ MJkg}^{-1}$ , for steel ARNE [7] –  $h_{ef}=6.66 \text{ MJkg}^{-1}$ , for steel SVERKER3 [7] –  $h_{ef}=8.26 \text{ MJkg}^{-1}$ , for stainless steel 303 [6] –  $h_{ef}=26.6 \text{ MJkg}^{-1}$ , and for steel 34CrNiMo6 [8] –  $h_{ef}=5.82 \text{ MJkg}^{-1}$ .

According to [6], the normal range of the on-time (time of pulse) used in most industries is from 10 to  $180 \mu s$ . Therefore, the Figure 1 presents the results of processing experiments in the range of the pulse duration up to  $200 \mu s$ , as typical applied in the industry. The on-time influence on the efficiency of production, i.e. on material removal rate  $V$ , is shown in the Figure 2.

Whereas Figure 2a presents the dependence of the cathode erosion [6] on the pulse time (up to  $200 \mu s$  also) and current taken as parameter, Figure 2b shows the same experiments in the range of the pulse duration up to  $600 \mu s$ . In addition, there we give the comparison of these experimental results with the calculations according to the formulae (1)-(5), (12), (13). The effective enthalpy of erosion was taken as  $h_{ef}=4.49 \text{ MJkg}^{-1}$ , for common grade steel results (see Figure 1). A good agreement of the model with the experiment is evident for  $\tau_{pu} < 200 \mu s$ , while for the large pulse duration the measured values of erosion lower than calculated. Accordingly [6], this can be explained by contamination of inter-electrode gap by the eroded material and it's deposition on the cathode.

Figure 2c presents volumetric removal rate  $V$  versus discharge time  $\tau_{pu}$  for anodes from different materials. One can see, the best agreement between theory and experiment is observed for the short pulse duration. The separation grows with the pulse time  $\tau_{pu}$ . For more stable anodes the workpiece removal rate is higher and  $V$  is nearer to the calculated.

It is possible to assume that the anode material influence on the erosion rate is explained, to the most extent, by effect of the contamination level of the gap. Besides, the material of the anode, just as dielectric, can have an effect also on thermal volt-equivalent  $U$ , but this influence appeared to be less.

## 5. Conclusion

The modified step-wise model of erosion of cold electrodes in the unsteady arc spots is proposed and adapted to the conditions for electrical discharge machining. Model is based on the unification of the basic assumptions of two different one-dimensional thermal models of the electrode erosion: planar one-dimensional step-wise model [1,2,11] and the “point heat source model” [3]. This make it possible to use for EDM, just as for the electrodes of arc heaters a concept of the effective enthalpy of the erosion, obtained by replacing the real physical processes in the moving phase border to a simple change in the kind of boundary conditions on the virtual stationary surface. For the practical application the fundamental statements of model are approximated in the dimensionless parameters of  $Fo = a\tau_{pa} / R^2$  and  $Po = UI / (\lambda T_f R)$  that took account all parameters of process - current, the discharge time and pause, the thermal volt-equivalent of discharge and thermophysical properties of material.

Comparison of the model with the experimental results of different authors on different grade of steels shows the high correlation coefficient (0.97-0.99). This result confirms the basic concept of model, i.e. assumption of constancy of the effective enthalpy for each material as the characteristics of its erosional durability during EDMing. For different grades of steel the effective enthalpies of erosion are obtained within the limits from 4.5 (common grade steel) to 26.6 MJkg<sup>-1</sup> (stainless steel 303).

## Acknowledgments

We thank Mr. A. A. B. do Prado for his technical assistance in this work. We acknowledge the financial support of CNPq, FAPESP and FINEP of Brazil.

**Nomenclature.**  $T, T_0, T_f$  – temperature, initial temperature, fusion temperature, respectively, K;  $U$  – thermal volt-equivalent, V;  $I$  – current, A;  $\lambda, a, C_p$ , - thermal conductivity, thermal diffusivity and specific heat, Js<sup>-1</sup>m<sup>-1</sup>K<sup>-1</sup>, m<sup>2</sup>s<sup>-1</sup> and Jkg<sup>-1</sup>K<sup>-1</sup>, respectively;  $R_0, r$  – radius of isotherm of fusion, radius of equivalent planar heat source, respectively, m;  $\tau$  - time, s;  $\tau_{pu}, \tau_{pa}$  - pulse and pause time, respectively, s;  $\bar{\tau}$  - non-dimensional pulse time;  $V$  - volumetric material removal rate, m<sup>3</sup>s<sup>-1</sup>;  $W_s$  non-dimensional erosion energy for step-wise model;  $f_s$ —non-dimensional fusion parameter for step-wise model;  $\rho$  - mass density, kgm<sup>-3</sup>;  $h_{ef}$  – effective enthalpy of ablation of material, Jkg<sup>-1</sup>;  $j, j_e$  – current density and effective current density, respectively, Am<sup>-2</sup>;  $Fo$  – Fourier number;  $Po$  – Pomerantsev number;

## References

- [1] A. Marotta, L. I. Sharakhovsky, A. M. Essiptchouk – JEPTER, **76**, 2 (2003)
- [2] A. Marotta, L.I. Sharakhovsky and A. M. Essiptchouk – Annals of the New York Academy of Sciences, **891**, (1999).
- [3] D.D. DiBitonto, P.T. Eubank, M.R. Patel and M.A. Barrufet – J. Appl. Phys., **66**, 9, (1989).
- [4] M.R. Patel, M.A. Barrufet and P.T. Eubank – J. Appl. Phys., **66**, 9, (1989).
- [5] P.T. Eubank, M.R. Patel, M.A. Barrufet and B. Bozkurt – J. Appl. Phys., **73**, 11, (1993).
- [6] S. Norasetthekul, P.T. Eubank, B. Stucker, W.L. Bradley and B. Bozkurt – J. Materials Science, **34**, 6, (1999).
- [7] H. Cornelissen, R. Snoeys and J.P. Kruth – Annals of the CIRP, **27/1**, (1978).
- [8] H.E. de Bruyn - Annals of CIPR. **31/1** (1982).
- [9] A. Marotta, L. I. Sharakhovsky – J. of Phys. D: Appl. Phys., **29**, (1996).
- [10] A. Marotta, L. I. Sharakhovsky – IEEE Transactions on Plasma Science, **25**, 5, (1997).
- [11] L. I. Sharakhovsky, A. Marotta, and A. M. Essiptchouk – JEPTER **76**, 2, (2003)
- [12] M. Kunieda, H. Kojima – Annals of the CIRP, **39/1**, (1990).
- [13] M. Kunieda, H. Xia and N. Nishivaki – Annals of the CIRP, **41/1**, (1992).
- [14] A.V. Luikov – Analytical heat diffusion theory, Academic Press, New York and London, (1968).
- [15] B. Gellert and W. Egli – J. of Phys. D: Appl. Phys., **21**, (1988).
- [16] <http://www.sz-metal.si/products/steels/PK11S.htm>

- [17] Y.S. Touloukian, R.W. Powell, C.Y. Ho, P.G. Klemens – Thermophysical properties of matter, Vol.1, Thermal conductivity Metallic Elements and Alloys, IFI/Plenum, New-York-Washington, 1970, p.1174.
- [18] [www.uddeholm.com](http://www.uddeholm.com).
- [19] [19] [www.sz-metal.si/products/steels/VCNMO150.htm](http://www.sz-metal.si/products/steels/VCNMO150.htm).



# Heat transfer and structure of plasma flows in three-jet arc reactors

L. Krasovskaya<sup>1</sup>, M. Britch<sup>2</sup>

<sup>1</sup> *Department of Physical Chemistry, Belorussian State Technological University, Minsk, Belarus*

<sup>2</sup> *Heat and Mass Transfer Institute, National Academy of Sciences, Minsk, Belarus*

The three-dimensional model of plasma jet mixing is developed and used to numerically investigate the gasdynamic and thermal structure of plasma flows in three-jet mixing chambers of several types and in cylindrical reactors with such chambers. It is found that cylindrical mixing chambers with the base diameters ranging from 5 to 10 cm and the anode nozzle diameters of plasma torches of 1–2 cm provide for the intensive mixing of jets and for the formation of fairly uniform temperature and velocity fields in the channels of plasma reactors. The gasdynamic features of the mixing of plasma jets in conical chambers are revealed; in particular, the possibility is demonstrated of the emergence of return flows at the outlet from conical chambers with the base diameter of 10 cm and apex angles of 120°, 90°, and 60°. The calculations are compared with spectral data for radial temperature distribution of the plasma flows.

The influence of cold air insufflation (for transport of dispersed raw materials) into the reactors is analysed.

# Investigation of Anode Attachment in dc Arc Plasma Spraying Torch with External Anode

O. Chumak, M. Hrabovský, V. Kopecký

*Institute of Plasma Physics, Academy of Sciences of CR, Praha, Czech Republic*

## **Abstract.**

Behavior of anode attachment region in a restrike mode in dc arc plasma spraying torch is investigated. Effect of arc current and plasma flow rate on position of anode attachment and arc voltage fluctuations is studied and processes that control the position are discussed. Simple model of process of restrike is formulated.

## **1. Introduction**

Anode processes play an important role in dc arc plasma torches as they substantially influence plasma properties and flow characteristics of generated plasma jet. The anode jet, produced close to the electrode surface due to interaction of arc current with its self-magnetic field, causes deflection and flow instability in the main plasma jet [1, 2]. Position of an anode root at the anode surface, which is in common torch design parallel to the arc column axis, determines arc voltage and thus arc power [3]. The position and behavior of anode arc attachment are controlled by a complex of mechanisms that has not been still fully understood.

Usually the arc attachment in dc arc torches is in so called restrike mode that is characterized by periodical movement of arc root in stream-wise direction followed by ignition of new arc root in an upstream position accompanied with sudden decrease of arc voltage and shortening of the arc [4]. This phenomenon causes fluctuations of arc voltage and power as position of arc root determines arc voltage. Downstream movement of arc root is caused by gas dynamic drag acting on arc attachment in gas flow in the arc fringes and due to action of self-magnetic field on current loop in anode region. The mechanism of sudden restrike in an upstream position is less understood and usually it is referred as breakdown, although available voltage difference is too small to cause classical breakdown. Nevertheless, the phenomenon of a restrike is of utmost importance as this is the mechanism that determines arc root position and consequently arc power and plasma temperature. It postulated in [5] that arc root position is determined from balance of gas-dynamic drag force and magnetic body force. Steenbeck's minimum principle was used in [6] for determination of arc root position.

In this paper we investigate behavior of anode attachment region in a restrike mode in dc arc plasma spraying torch with hybrid argon-water arc stabilization [7]. The torch is equipped with external rotating disc anode and thus direct observation of anode attachment region and its interaction with plasma jet is possible. As active surface of anode is parallel to the jet axis and movement of anode surface due to rotation is slow compared with movement of anode attachment along the surface, the conditions in the anode region are similar to the situation in common gas torches with nozzle anodes. The results thus can contribute to better understanding of processes that control restrike behavior of anode region of dc arc torches.

## **2. Experimental setup**

The experiments were performed with hybrid water/argon plasma torch [7]. In the hybrid torch argon plasma generated in short cathode arc chamber enters the second chamber with water stabilization. Here water evaporates and argon/oxygen/hydrogen plasma is produced. The torch is equipped with external disc anode. The arrangement of anode region can be seen in Fig. 1.

The anode region of the arc downstream of the nozzle exit was photographed using fast shutter camera SensiCam PCO Computer Optics with minimum exposure time 100 ns. Arc voltage and the potential difference between exit nozzle and the anode were measured using high resistance dividers with the frequency range up to 100 MHz. The anode attachment position and extent of its movement along the electrode surface was determined from many repeated shots of anode region. An example of image of plasma jet with anode attachment is shown in Fig. 1.

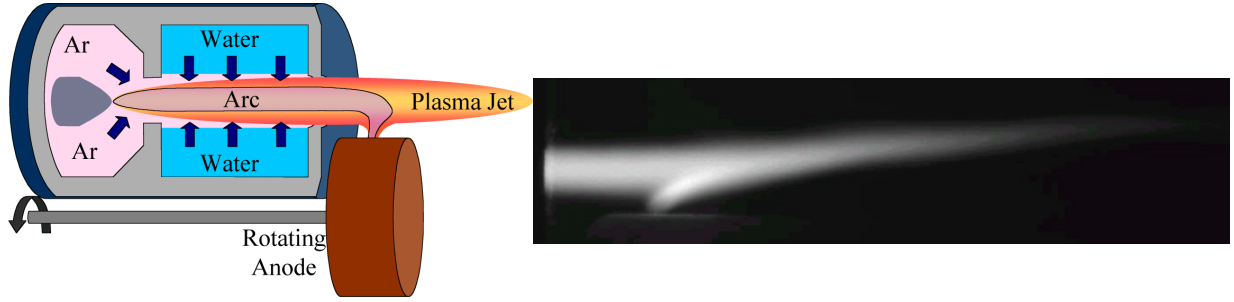


Fig. 1. Schematics of plasma torch and image of the jet with anode attachment.  
Arc current  $I = 400$  A, argon flow rate  $F_{Ar} = 17.5$  slm, exposure time  $t = 3$   $\mu$ s.

### 3. Experimental results

The shape of the jet in the anode region can be seen from the shape of isophotic lines in Fig. 2 that were evaluated from the image of the jet. The image was taken at the moment of decay of an old anode attachment and formation of a new one at the position about 6 mm upstream. It can be seen that the jet contours are parallel to anode surface upstream of arc attachment position and thus the depth of sheath of colder gas between conducting jet core and the electrode surface is almost constant along the electrode surface.

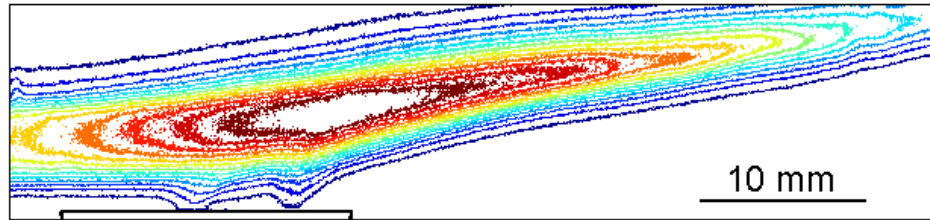


Fig 2. Lines of the same intensity evaluated from the image of the jet in restrike moment. Arc current  $I = 400$  A, argon flow rate  $F_{Ar} = 8.5$  slm, exposure time  $t = 700$  ns.

A number of repeated camera records were taken for various arc currents and argon flow rates. Examples of statistical distribution of positions of anode attachment are shown in Fig. 3.

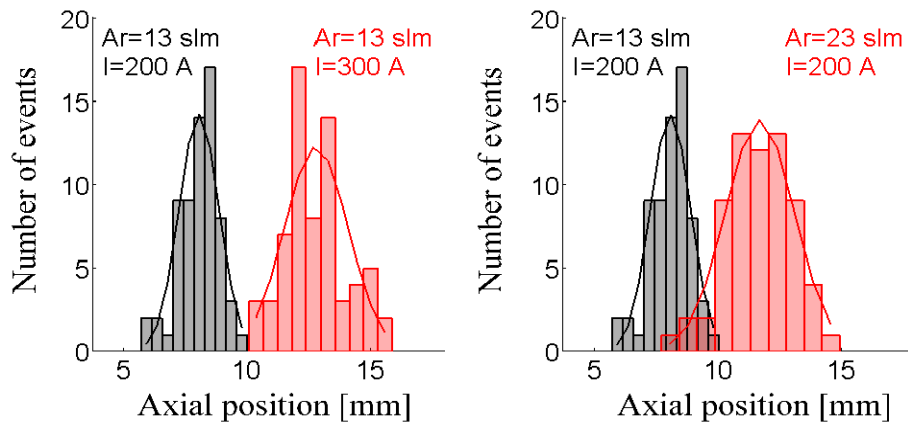


Fig. 3. Statistical distribution of anode attachment position for two arc currents and two flow rates of argon.

Effect of arc current and effect of plasma mass flow rate were studied. Changes of arc current result not only in changes of arc power but also mass flow rate in the jet was changed due to change of evaporation rate of water in the arc chamber [7]. As argon has very low enthalpy compared to steam, changes of argon flow rate had minor effect on arc power. Thus the effect of plasma mass flow rate could be separately studied by changing argon flow rate. An increase of current as well as an increase of gas flow rate resulted in shift of

anode attachment in the stream-wise direction and increase of extent of anode attachment movement. This can be seen in Fig. 4 where mean position of anode attachment and mean quadratic deviation of position are plotted in dependence on arc current for various gas flow rates. Effects of current and gas flow rate are stronger for lower arc currents while for higher currents the mean position of attachment and its scatter is almost constant. This is probably related to the fact that for lower currents the sheath between the arc jet and anode is thicker and anode attachment is thus longer and it is more sensitive to changes of gas flow in the sheath.

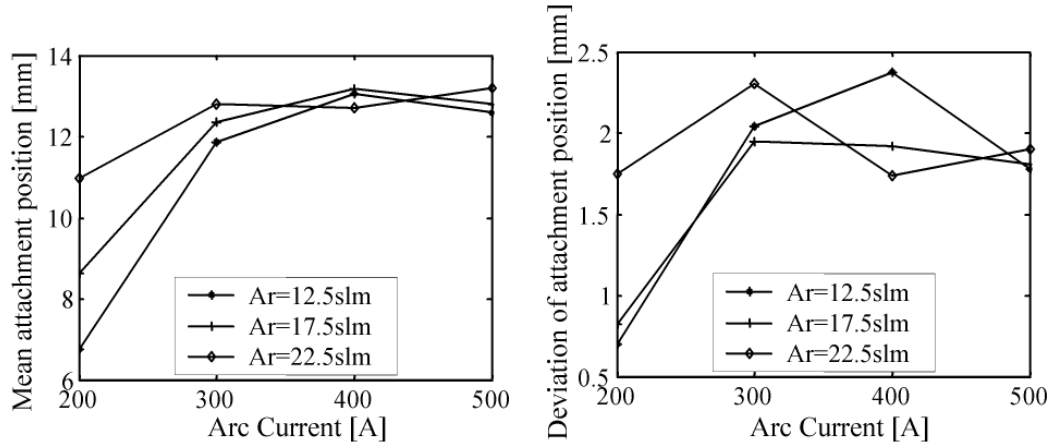


Fig. 4. Dependence of mean position of anode attachment and mean quadratic deviation on arc current and argon flow rate.

The relation between an observed anode attachment behavior and an arc voltage saw tooth fluctuations was investigated.

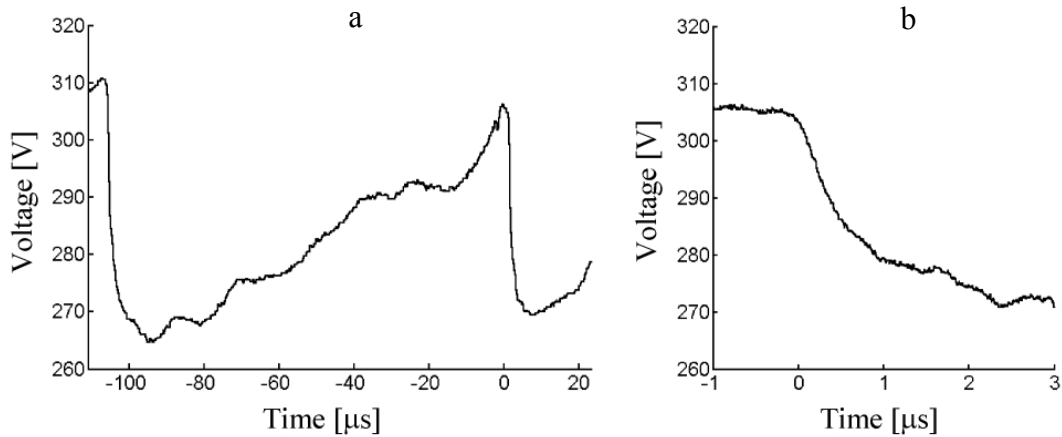


Fig. 5. Arc voltage curve between two restrikes (a) and changes of voltage during a restrike (b).

Arc voltage steadily increases during stream-wise motion of anode attachment. At some moment a restrike in an upstream position occurs and new arc attachment starts its stream-wise movement again (Fig. 5). The curve of arc voltage drop during the restrike is determined by mechanism of the restrike and formation of new anode attachment. The amplitude of saw-tooth fluctuations of arc voltage is related to the extent of arc root movement and to electric field intensity in the arc jet. Histogram of amplitudes of voltage fluctuations for two argon flow rates is in Fig. 6. An increase of argon flow resulted in slight decrease of voltage drop amplitude and to higher scatter of values. The effect of argon flow rate on rate of rise of arc voltage between restrikes is shown in Fig. 7. The rate of rise of voltage increases with increasing flow rate of plasma as velocity of motion of anode attachment is increased, while the amplitude  $\Delta U$  is changed only slightly. This is seen also in Fig. 8 where  $\Delta U$  is plotted in dependence on arc current for two values of argon flow rate and for

two distances of anode surface from the jet axis (Fig. 1). Amplitude  $\Delta U$  is reduced due to reduction of the distance and decreases with increasing current. Frequency of restrikes increases with increasing arc current especially for lower distance of anode surface from the plasma jet.

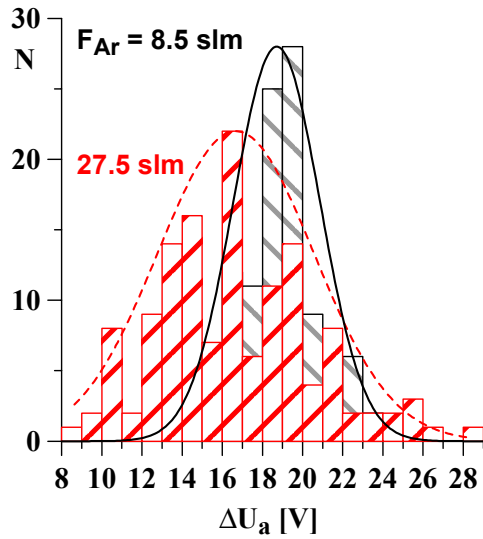


Fig. 6. Statistical distribution of amplitude of arc voltage saw-tooth fluctuations for two values of argon flow rate. Arc current  $I = 400$  A.

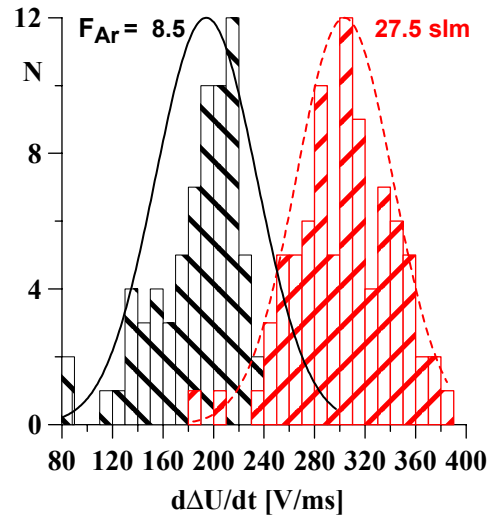


Fig. 7. Histogram of values of rate of rise of arc voltage between restrikes for two values of argon flow rate. Arc current  $I = 400$  A.

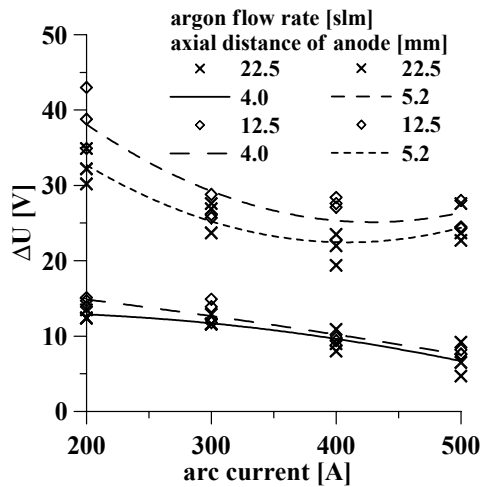


Fig. 8. Dependence of amplitude of saw-tooth fluctuations of arc voltage on arc current for two argon flow rates and two distances between anode surface and jet axis.

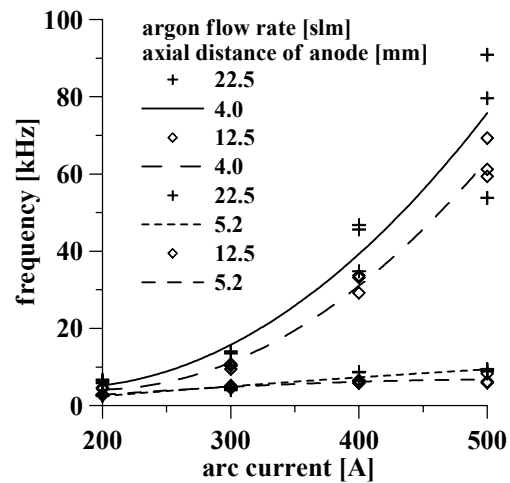


Fig. 9. Dependence of frequency of voltage fluctuations on arc current for two argon flow rates and two distances between anode surface and jet axis.

#### 4. Analysis of phenomena decisive for anode attachment position

Mechanisms that determine position of anode attachment have not yet been fully understood. In [5] the arc root position is explained by balance between gas-dynamic drag force and magnetic body force that is induced in the S shaped current-carrying column. In [6] position of steady non-moving attachment is calculated from Steenbeck's minimum principle. We believe that in a restrike mode the position as well as the range of movement of anode attachment is determined by processes that control formation of new attachment by restrike.

Following mechanisms of the restrike are considered. Diffuse current flows between arc jet and anode surface through the layer of colder gas due to potential difference between the jet and anode. The gas is pumped into the layer due to plasma flow and it is here heated and partially ionized due to heat transfer from the highly conducting jet core by heat conduction, radiation and turbulent mixing. Especially ultraviolet radiation from the high temperature arc core is strongly absorbed in the colder gas due to photo-ionization and photo-dissociation. Additional energy comes from Joule heating due to passage of diffuse currents. As gas temperature in the layer and thus electric conductivity  $\sigma$  rises in the stream-wise direction while electric field in the sheath  $E_s$  decreases, in some point a maximum of  $\sigma E_s^2$  can exist. If in this position the Joule heating term reaches some critical value for which heat input is higher than power loss, temperature in this point and thus conductivity and consequently Joule heating rapidly rise which leads to so called thermal breakdown with rapid increase of plasma conductivity and formation of new constricted conducting channel which takes over arc current.

We now estimate position of maximum  $\sigma E_s^2$  in the region behind moving anode attachment from a simple 1D model. Electric field intensity in the layer can be approximated by relation  $E_s = DU/d$ , where  $DU$  is potential difference between arc column and the anode surface and  $d$  is layer depth.  $DU$  is increasing in the counter-stream-wise direction from the point of anode spot,  $d$  is considered as constant. As electric field intensity in the arc column  $E_c$  can be assumed constant we can write the potential difference between arc column and anode at position  $x$  as  $DU = E_c \cdot (x_A - x) + U_A$ , where  $x_A$  is position of anode attachment and  $U_A$  potential drop on anode attachment. Electric field intensity in the layer is then given by equation

$$E_s = \frac{U_A + E_c(x_A - x)}{d} \quad (1)$$

If existence of LTE is assumed an electric conductivity  $\sigma$  of gas in the layer is determined by the temperature of gas. The temperature is determined by heating of cold gas flowing along the jet by the heat transferred to the layer from the arc jet. Energy balance at this layer can be then written as

$$\rho v \frac{dh}{dx} = Q \quad (2)$$

where  $x$  is coordinate in the direction of arc axis (Fig. 1),  $\rho$  is density,  $v$  flow velocity and  $h$  enthalpy of gas,  $Q$  is power input. As arc columns in axial flows are characterized by very low changes of arc properties along the column, we will assume that  $Q$  is independent of  $x$ . We will suppose that also mass flux density  $\rho v$  is constant within the layer and solution of (2) has then simple form  $h = h_0 + (Q/\rho v)x$ . Relation between gas enthalpy and electric conductivity is defined by the gas composition. We will approximate this relation by power function  $\sigma = k_\sigma h^n$  and we can derive an equation for dependence of electric conductivity in the sheath  $\sigma$  on axial coordinate  $x$ . Joule term in position  $x$  is then equal to

$$\sigma E_s^2 = k_\sigma \left( \frac{Q}{\rho v} x \right)^n \left( \frac{U_A + E_c(x_A - x)}{d} \right)^2 \quad (3)$$

where we put  $h = 0$  for  $x = 0$ . We can find value of coordinate  $x$  corresponding to maximum of  $\sigma E_s^2$  for given position of anode attachment  $x_A$ . Position of maximum is then given by the equation

$$x_m = \frac{n}{n+2} \left( \frac{U_A}{E_c} + x_A \right) \quad (4)$$

The position  $x_m$  moves as  $x_A$  is increased during arc attachment movement. At the same time the value of  $(\sigma E_s^2)_m$  at this position is increased. Restrike occurs in the moment when this value reaches critical value for development of thermal breakdown. The position of the restrike is according to (3) and (4) determined by heat flux  $Q$  and mass flux density  $\rho v$ , material coefficients  $k_\sigma$  and  $n$ , depth of the sheath  $d$ , electric field intensity in the arc column  $E_c$  and voltage drop on arc attachment  $U_A$ . Due to many simplifications the equations can be used for qualitative estimations of effects of various quantities rather than for exact calculations.

## 5. Discussion and conclusions

Anode attachment position is determined by dynamic balance between Joule heating and power loss at the layer of partially ionized gas between plasma arc column and electrode surface. Electric conductivity of the gas in the layer together with its depth and potential difference between arc column and electrode surface are decisive factors for initiation of a restrike. Increase of plasma mass flow rate leads to an increase of gas flow in the layer and thus to decrease of Joule heating. Position of the restrike then moves in the stream-wise direction. As in hybrid torch increase of current leads to the increase of plasma flow rate, position of the anode attachment moves also downstream. These effects are more distinct for lower currents and higher distances of anode from the jet when the depth of the layer of the cold gas is larger.

The work was supported by the Grant Agency of the Czech Republic under the project number 202/01/1563.

## References

- [1] Hrabovsky M., Konrad M., Kopecky V., Hlina J., Benes J., Vesely E., Motion of anode attachment and fluctuations of plasma jet in dc arc plasma torch, *J. of High. Temp. Material Processes* **1** (1997), 167 - 178
- [2] Hrabovsky M., Konrad M., Kopecky V., Sember V., Effect of Anode Attachment on Flow Structure of Plasma Jet Generated in Water Stabilized Torch, *Annals New York Academy of Sciences* **891**, Heat and Mass transfer under Plasma Conditions, 1999, 98-105.
- [3] Brillhac, J.F. et al. 1995. Study of dynamic and static behavior of dc vortex plasma torches: Part I: Button type cathode. *Plasma Chem. and Plasma Process.* **15**: 231-277.
- [4] Wutzke S.A., Pfender E., Eckert E.R.G., *AIAA J.* **6**, 1474 (1968).
- [5] Russ S., Pfender E., Heberlein J., Anode arc attachment control using boundary layer bleed holes *Proc. of Nat. Thermal Spray Conf.*, 1993, Anaheim, 97 – 103.
- [6] S. Paik, P.C. Huang, J. Heberlein, E. Pfender, Determination of the arc-root position in a dc plasma torch, *Plasma Chem. Pl. Process.* **13** (1993), 379 – 397.
- [7] V. Brezina, M. Hrabovsky, M. Konrad, V. Kopecky and V. Sember, *Proc. of 15<sup>th</sup> Int. Symp. on Plasma Chemistry* (ed. A. Bouchoule et al.), Vol. III, 9-13 July 2001, Orleans, 1021 – 1026.

# In-situ measurement system for correlating splat morphology and solidification process under plasma spraying conditions

K. Shinoda, R. Takenoshita, Y. Kojima and T. Yoshida

*Department of Materials Engineering, Graduate School of Engineering, The University of Tokyo  
7-3-1 Hongo, Bunkyo-Ku, Tokyo 113-8656, Japan*

*Corresponding author: K. Shinoda, shinoda@plasma.t.u-tokyo.ac.jp  
Tel/Fax: +81-3-5841-7099*

## Abstract

We developed an in-situ measurement system for precise 1:1 correlation between splat morphology and temperature history of molten particle with sampling the impinging events successively under plasma spraying conditions. In order to verify the effectiveness of the system, the deformation and solidification process of yttria-stabilized zirconia powder sprayed by hybrid plasma was measured successively at a transversing moving substrate heated up to 700 K by a radiation plate. The temperature was measured by 700 and 1000 nm emissions from a droplet, and the droplet size was evaluated ex-situ precisely based on the three dimensional morphology of the splat. The system is capable to sample about 10 single particles successively within 10 second, and correlate precisely the relations among the physical parameters of each droplet, deformation-solidification process, and splat morphology.

## 1. Introduction

Application fields of thermal plasma spraying are now expanding to next generation coating technology, which demands even nano-level-designed microstructures [1], and thus needs new approaches/principles based on the fundamental phenomena in spraying process. However, a large distribution in the state of impacting particles, in terms of size, velocity and temperature, hinders explicit understanding of the solidification process during plasma spraying. Recently, outstanding numerical simulations relating the deformation and solidification process of sprayed particles have been developed rapidly [2]. Unfortunately, however, most simulations have to assume the thermal contact resistance between the splat and the substrate as a fitting parameter, although it cannot be applied simply in such cases that the temperature gap exceeds 2000K. In this regards, it is clear that a complementary approach between in-situ measurement and numerical simulation is needed to understand the key process in spraying, and experimental approaches have been highly anticipated at this stage. There are only few papers relating the measurements of deposition process [3-5], despite many excellent papers have been published for the last decade regarding the measurements of an in-flight process [6]. In addition, the correlation between the splat morphology and the measurement results is not always sufficient in their systems. Therefore, in this research, we developed an in-situ measurement system that can measure a single particle behavior successively on the temperature-controlled substrate in an airtight chamber and derived the relationship between the splat morphology and the various spraying parameters.

## 2. Experimental

The newly developed in-situ measurement system is schematically shown in Fig. 1. The system consists mainly of a hybrid plasma spraying system, a single particle collection apparatus, two sets of emission detectors and a data storage apparatus. The hybrid plasma spraying system consisted of an rf power supply of 4MHz-60kW, a dc power supply of 10kW, a dc-rf hybrid plasma torch and an air-tight chamber. This can measure the deformation and solidification process under a wide variety of conditions such as: 1) YSZ powder size range up to 100  $\mu\text{m}$ , 2) particle velocity ranging from 20 to 70 m/s, and 3) airtight atmosphere in wide pressure range. The schematic view of a cross section of the single particle collection part is shown in Fig. 2. Essentially, two apertures made of boron nitride (BN) were used to regulate the number of particles so that only a few particles can reach to the substrate within a second. The diameters of the first (upper side) and the second (lower side) were 1.5 mm and 500  $\mu\text{m}$ , and the distances of them from the substrate were 30 mm and 7 mm, respectively. The first was set to limit the number of in-flight particles not to clog the second orifice. A collimator of the slit of 600  $\mu\text{m}$  in height and of 800  $\mu\text{m}$  in width was set just under the second aperture to measure in-flight particle. Second orifice diameter is smaller than the slit width of collimator so that the collimator can detect all the particles that pass through the second orifice. In addition, the substrate holder was designed to be movable horizontally with a speed up to 1 mm/s in order to avoid overlapping of the splats. The first aperture served as also a radiation-heating device of the substrate. It was heated up to



2000 K by plasma flame and consequently has the capability to heat the substrate up to 400 °C. Figure 3 shows an example of the temperature increase at the quartz substrate as a function of time after opening a shutter. The temperature measured by a thermocouple, increased gradually up to 300 °C, and kept constant in that case. Just only 10 seconds would be enough to collect 10 particles on the substrate. Therefore, the temperature variation during the 10 s experiment was expected to be within a few K and negligible, even if the experiment was conducted before the temperature reached the steady state. The temperature – time curve shown in Fig. 3 suggests the usefulness of the heating device to control the substrate temperature.

We used two optical systems to detect the thermal emission from a particle. One was connected to the preceding collimator, and used to measure the surface temperature and velocity of the in-flight particle just before impinging, which was developed by Sakuta et al. [6]. We selected 500 nm and 700 nm wavelengths for the temperature measurement. Detected signal itself works as a trigger for the record of a sequence measurements for the event of particle flattening. The emission condenser consisted of two optical lenses with the focal lengths of 40 mm and 70 mm. This condenser focused at an angle of 20 degree on the substrate where the particle impinged and its viewing field on the substrate was an ellipse of 1.7 mm x 5 mm. The detected light was divided into reflection and transmission beams by a beam splitter, which were filtered by 10 nm-width narrow band-pass filters of 700 nm and 1000 nm, respectively. All the photomultipliers used here were Hamamatsu-made R1104 for 500 nm, R2228 for 700 nm for in-flight particle measurement, R943-02 for 700 nm, and R3310-02 for 1000nm for impinging. The digital oscilloscope, Sony Tektronix TDS-754D, has four channel monitors with an 8-bit vertical resolution, namely, a maximum time resolution of 1 ns/sample, and can memorize 50,000 address/channel. It has also important function that can share one buffer during one experiment, which enables to collect single particles continuously. The data collected by the digital oscilloscope were sent to PC via GP-IB, and was analyzed on PC. Regarding the estimation of the droplet size, we used ex-situ method to calculate it from the volume of the deposited splat, because the in-situ measurement has the difficulties to know precise size. Three-dimensional laser microscope, KEYENCE VK-8500, was used to measure the volume, and also used to evaluate the morphology of the splat.

Table 1 shows the spraying conditions. 8YSZ powder (fused and crushed powder, size distribution was ranging from 63 to 88  $\mu\text{m}$ ) was sprayed by 8%  $\text{H}_2$ -Ar atmospheric hybrid plasma. Powder feeding rate was adjusted below 0.6 g/min to limit the number of the impinging particles onto the moving substrate. By

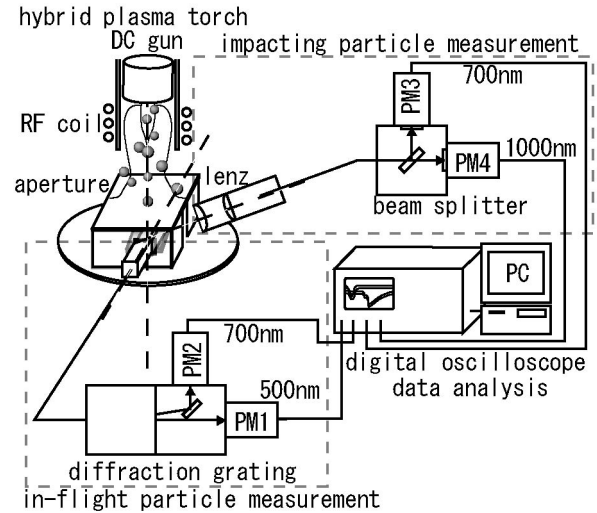


Fig. 1 Schematic diagram of the in-situ measurement system, which consists of five different parts; dc-rf hybrid plasma torch, single particle collection part, in-flight particle measurement system, impacting particle measurement system, and data analysis facility.

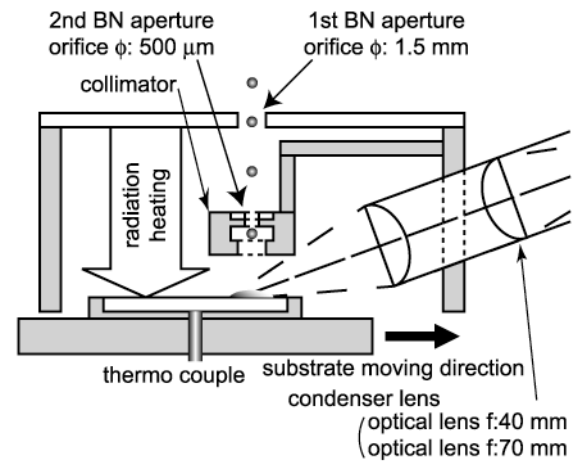


Fig. 2 Single particle collection part

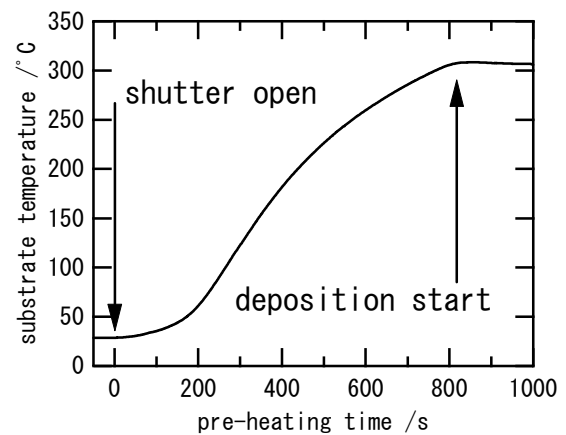


Fig. 3 Substrate temperature history

this condition, overlapping of the splats was avoided. The quartz substrate was 20 mm x 10 mm x 0.7 mm, and its surface roughness was 0.04  $\mu\text{m}$ . The substrate temperature was set about 300  $^{\circ}\text{C}$  to get disk-shaped splat [7].

### 3. Results

Figure 4 (a) shows the splats sprayed intermittently in a line on the substrate moving in the direction of the arrow shown in the figure. The emission signals obtained during the spraying are shown in Fig. 4 (b). There can be seen eight splats and eight pairs of 700/1000 emissions in Fig. 4 (a) and (b), respectively, and the intensity of each pair of emissions are approximately proportional to the size of each splat in the order of deposited. Therefore, the each splat was corresponding 1:1 to the emission signals as numbered in Fig. 4.

One example of the waveforms obtained by the two optical systems is shown in Fig. 5. The particle velocity just before impacting was measured to be 43 m/s. The surface temperature of the in-flight particle was about 3500 K and the initial surface temperature of the impacting particle was about 3300 K. The deformation time was 79.2  $\mu\text{s}$  that is defined here as a period until when the intensity of 700/1000 nm emissions reached its maximum. In this case, neither obvious plateau nor recalescence was observed in the temperature history calculated from 700/1000 nm emissions.

The flattening degrees for the eight splats are plotted against the in-flight particle velocity in Fig. 6. Numbers shown beside the open circles corresponds to the numbers shown in Fig. 4. The size of the inner solid circles and the outer open circles indicate the diameter of the droplet and of the deposited splats, respectively. The gray scale shown within the inner solid circles indicates the surface temperatures of the impinging particles. Although the flattening degree slightly increased with the increase of the velocity for this range from 31 to 68 m/s, most of the splats showed perfect disk shapes with the flattening degrees above 3.

### 4. Discussion

#### 4.1 The accuracy of the measurement

As stated above, we successfully performed the sampling of 10 single-splats that were intermittently deposited in a queue on the substrate within 10 seconds. The data obtained with these experiments would be very useful for the statistic evaluation of the fundamental process of the particle impinging. Although the size and velocity estimation was conducted very precisely, the accuracy of the temperature measurements

Table. 1 experimental condition

Parameters	Settings
DC Ar gas flow rate /slm	10
DC current /A	400
RF tangential Ar gas flow rate /slm	10
RF radial Ar gas flow rate /slm	30
RF radial hydrogen gas flow rate /slm	5
RF input /kW	50
Powder carrier gas flow rate /slm	2
Powder feeding rate / g/min	0.6
Stand-off distance /cm	8

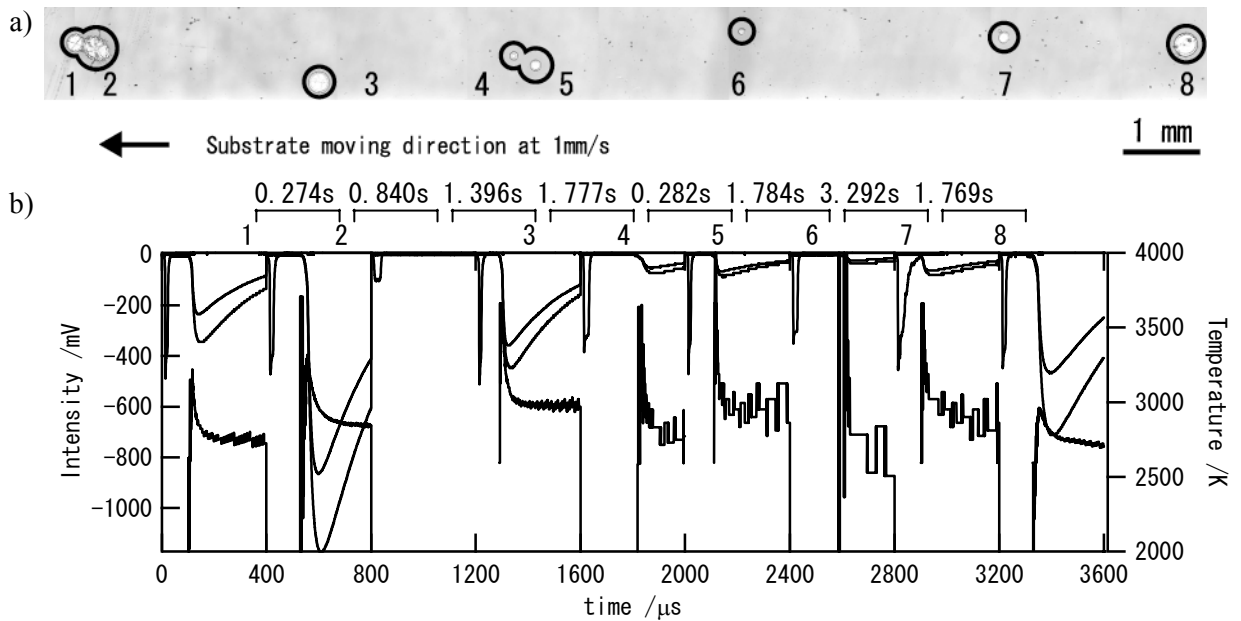


Fig. 4 a) Picture of laser microscope of the collected YSZ splats on the quartz substrate.  
b) Thermal emissions obtained during the spraying corresponding 1:1 to the splats shown in a).

will have to be improved. Especially, background noise was significant for the initial temperature estimation because of the small emission intensity and of the relatively low digital resolution of the oscilloscope for this small emission range. Some of the radiation from the heated BN plate of the first aperture finally reached the surface of the substrate after reflecting some times on the inside wall of the box. Black-painting inside of the box and covering the focused part were effective for reducing the emission, although the small noise was still observed.

#### 4.2 Super-cooling effect

As mentioned above, the flattening degrees of the splats sprayed by hybrid plasma were greater than 3.0, although their sprayed velocities were relatively small as compared to that of dc plasma spraying. This fact suggests that if the particles are fully melted, the velocity is not always the governing factor for desirable plasma spraying. Among the eight splats, the No.8 droplet should be noted for its low impacting temperature of 2520K. Accordingly, within the measurements uncertainty, it may safely be said that there existed under-cooled droplets in the sprayed particles. This finding is the most interesting to be investigated in the future, since no one has measured such undercooled droplets under spraying conditions. But, further investigation on the solidification structure of splats should be needed to confirm this.

#### 4.3 Viscosity estimation

As the first step of the complementary approach between the measurements and the simulation, the viscosity of YSZ at melting temperature was suggested to be around 0.025 Pa.s.

### 5. Conclusion

Although we performed successfully the sequence sampling of the 10 splats within 10 seconds and confirmed the effectiveness of our approach to investigate the deformation and solidification phenomena, there are many items to be improved for increasing the accuracy of the measurements.

The following items must be improved:

1. Reduction of the radiation from the surroundings at the measuring spot.
2. The configuration of the emission condenser, especially, the increase of an angle of elevation from 20 degree to higher.
3. Increase the temperature range to be measured, especially, the lowest limit to be less than 2000K.

#### Acknowledgement

The present research is supported in part by a Grant for 21st Century COE Program 'Human-Friendly Materials based on Chemistry' from the Ministry of Education, Culture, Sports, Science, and Technology of Japan.

#### References

- [1] T. Yoshida – *Materia Japan* (2001) 322-325.
- [2] J. Mostaghimi, et al. – *Surf. Coat. Technol.*, **163-164** (2003) 1-11.
- [3] C. Moreau, et al. – *Meas. Sci. Technol.*, **1** (1990) 807-814.
- [4] M. Vardelle, et al. – *Meas. Sci. Technol.*, **5** (1994) 205-212.
- [5] P. Gougeon and C. Moreau – *J. Thermal Spray Technol.*, **10**, 1 (2001) 76-82.
- [6] T. Sakuta and M. I. Boulos – *Rev. of Sci. Instrum.*, **59** (1988) 285.
- [7] K. Shinoda, P. Han, and T. Yoshida – 15<sup>th</sup> International Symposium on Plasma Chemistry (2001).

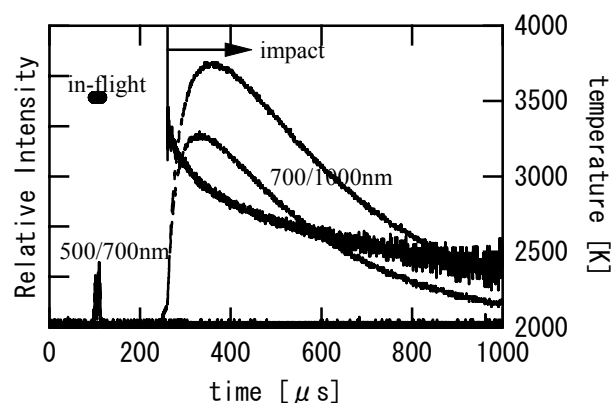


Fig. 5 Example waveforms obtained by two temperature measurement systems

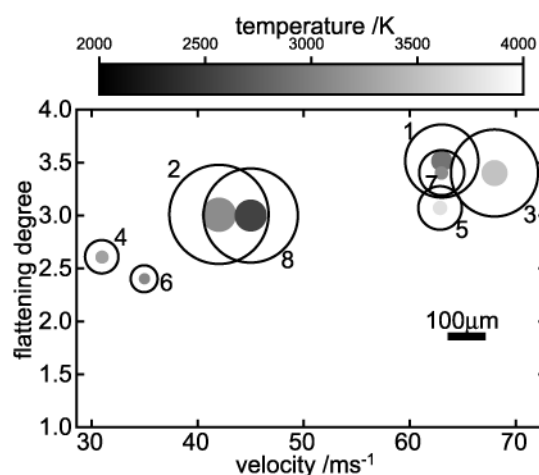


Fig. 6 Correspondence between the velocity, the size, and the substrate temperature of the impacting particles and the flattening degree

# Mechanisms of electronic conduction in metal/semiconducting cBN/insulating tBN junction diodes

K. Nose and T. Yoshida

*Department of Materials Engineering, Faculty of Engineering, The University of Tokyo,  
7-3-1 hongo, Bunkyo-ku, Tokyo 113-8656 Japan*

## Abstract

Cubic boron nitride (cBN) thin films were deposited under low ion energy (below 100eV) condition by heating the substrate up to 1023K. Current-voltage (I-V) characteristics of these cBN/tBN/n-Si layered structures were measured at temperatures from room temperature to 570 K. Rectification properties of n-Si/p-cBN heterojunction were observed even at 570K. Activation energies for carrier conduction decreased drastically with increasing the forward bias, although they were constant (0.48eV) for the negative bias.

## 1. Introduction

cBN has superior properties such as wide bandgap and high thermal conductivity. These basic properties are desirable for electronic and electro-optical devices that operate at high temperature and high power [1]. In addition, cBN is easier to be doped as both n-[2] and p-[3] types compared to diamond. Recently, some results have been reported about elemental devices in the form of thin film [4,5]. However, cBN films inevitably contain spontaneously-grown initial turbostratic BN (tBN) layer [6,7], and the purities of the cBN phase are not always high. Due to the low purity of cubic phase, the intervened tBN layer, and the defects caused by energetic species, the ideal performances of cBN thin film devices are not achieved until now.

In the formation of cubic phase in thin film, it is essential to bombard ions to the growing surface [8]. Residual stresses [9,10], dislocations, antisites, and vacancies caused by impinged high-energy ions have much effect to the carrier density and its mobility in semiconductors. Films deposited under the low ion energy condition have less damage than that deposited under higher energy conditions. In this work, by increasing substrate temperature we synthesized cBN thin films under low ion energy conditions. As a study of high temperature device application, electrical measurements were performed at up to 570K for those films. Particularly, we focused to rectification properties observed in the I-V characteristics of the n-Si/intrinsic p-cBN layered structure. The carrier transport mechanism through films was analysed with respect to the activation energy at the barrier emerged in the junctions.

## 2. Experimental

cBN thin films were deposited by the phase-regulated diode RF bias sputtering [11]. The schematic diagram of the apparatus was shown in Fig.1. Base pressure of the main chamber was maintained below  $2 \times 10^{-8}$  Torr. A 50mm diameter pBN (pyrolytic boron nitride: unidirectionally grown hBN by CVD method, Shin-etsu Chemical Co., Ltd.) was used as a target. The substrate can be heated up to 1100 K by a radiational heater. In this apparatus, the substrate RF power induces acceleration of  $\text{Ar}^+$  ions to the substrate surface. Both cubic and  $sp^2$ -bonded BN phases can be selectively grown by controlling the substrate dc bias (Vdc,s).

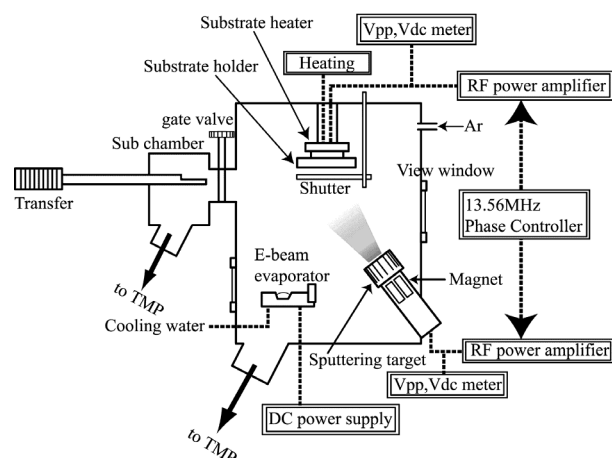


Fig1: Schematic of the phase-regulated RF bias sputtering chamber. Phase controller synchronizes the phase of the target and substrate RF.

Table1 : Deposition parameters.

Base pressure (Torr)	$2 \times 10^{-8}$
Gas flow rate (sccm)	Ar 10
Deposition pressure (Torr)	10
Substrate Vdc (V)	0~100
Target power (W/mm $\phi$ )	200/50
Deposition temperature (K)	R.T.~1100

Other deposition parameters are summarized in Table 1. After the deposition of films, aluminum and nickel dot electrodes were fabricated using a simple shadow mask. The diameter of the electrodes was 1mm. To make ohmic back contacts to the silicon substrates, aluminum was deposited after mechanical scratching. I-V characteristics were measured at temperatures from room temperature to 570 K using a semiconductor parameter analyser (Hewlett Packard 4156B).

### 3. Results

#### 3.1 Deposition

In Fig.2, IR absorptions of both hexagonal and cubic phases are plotted against deposition temperature. They were measured in 100 $\mu$ m square areas in the centre of substrates. The value of  $V_{dc,s}$  was kept at -60V at all temperatures. There can be seen a clear temperature threshold at approximately 840K for the concentration of hexagonal phase. In addition, the appearances of the deposited films were heavily dependent on the deposition temperatures. They were categorized to two patterns, A and B, as shown in the insets in Fig.2. The concentration of cubic phase is high in the gray zones. Single and double concentric flower patterns were formed above and below the threshold, respectively.

Figure 3 shows the correlation between the IR absorption peak position of  $sp^3$  bonded B-N stretching and the deposition bias voltages. Compressive stress in the cubic layer decreased by decreasing the energy of impinging ions. The smallest energy for high concentration cubic phases was 55eV, corresponding to  $V_{dc,s} = -20V$ , at 970K. The average thickness of the initial layer was estimated to be 18nm at that case.

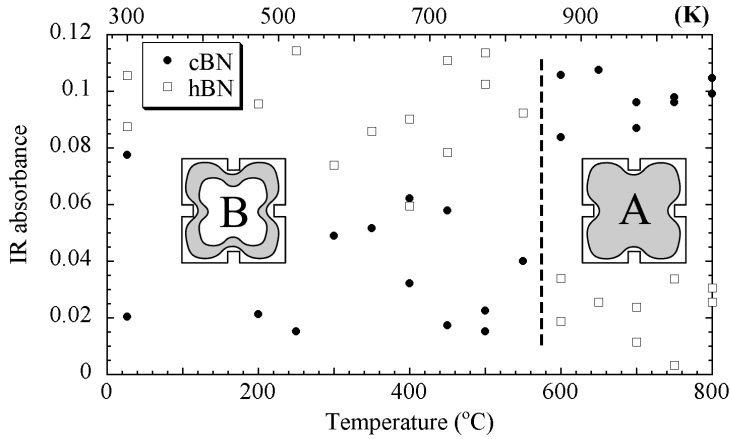


Fig.2: Temperature dependence of growth modes. Insets (A and B) show the typical appearances of the films deposited at the temperature range.

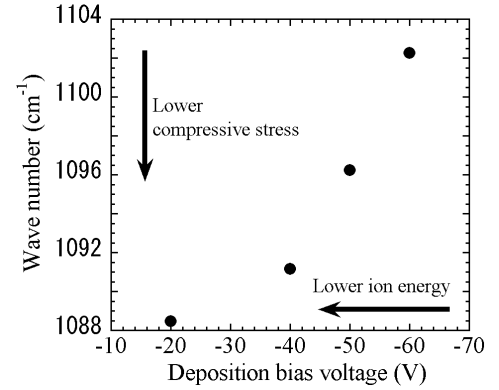


Fig.3: Dependence of cBN peak shifts on the deposition bias voltages. The deposition temperature was 970K.

#### 3.2 Electronic measurements

I-V measurements were performed in a cBN(92nm)/tBN(26nm) film at temperatures from room temperature to 570K. There were no clear differences in the I-V characteristics between nickel and aluminum top electrodes. Typical p-n diode properties were observed in the temperature region. Rectification ratios at room temperature were in the range of 1 to  $4 \times 10^4$  for 16 electrodes fabricated on the specimen. The ratio was approximately  $1 \times 10^1$  at 550K, though they decreased by increasing the temperature. Ideal factors for forward currents were calculated to be 2.3 at 290K and 2.1 at 570K, respectively[12].

Figure 4 shows Arrhenius plots of the I-V characteristics in the temperature. In both positive and negative bias region,  $\ln(I)$  increase linearly against  $1/T$ . The estimated activation energies for carrier conduction are plotted against the voltages in Fig. 5. It can be seen that the barrier height was diminished for forward biasing. On the other hand, the height of the backward barrier was maintained constant for negative bias.

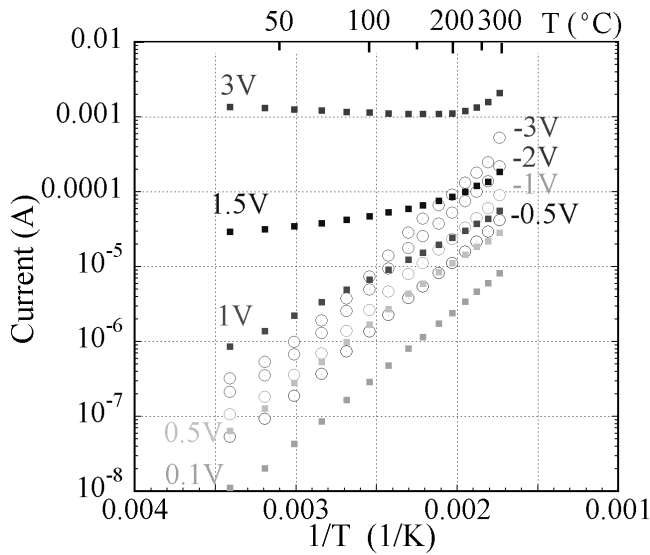


Fig.4: Arrhenius plots of the I-V characteristics. The gradients for the forward currents drastically decreased with increasing the applied voltages. Although they are constant for negative bias,

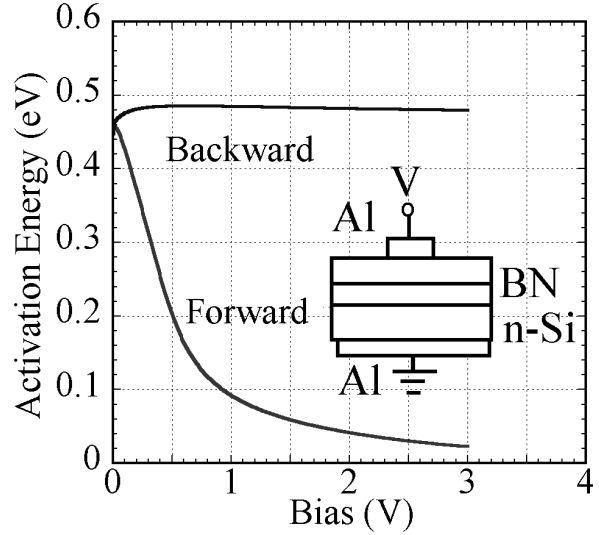


Fig.5: The change of the activation energy against the forward and backward bias.

## 4. Discussions

### 4.1 Deposition

As shown in Fig.2, a clear threshold was found at approximately 840K for cBN growth in the centre of the substrate. In the case of deposition at lower than 840K, purities of cubic phase were high only in the limited area near the metal substrate cover. It is natural to conclude that the metal cover, of which conductivity is much higher than that of the substrate, affects the impinging ion conditions. On the other hand, cubic growth in the wide centre area corresponds to the growth under the condition with less effect of the cover. It is well known that the flux and the energy of impinging ions and the substrate temperature are critical for nucleation and growth of cubic phase. Generally, cBN can be synthesized under the “milder” deposition condition, i.e. smaller flux and lower energy of impinging ion under conditions, in the higher temperature condition. Temperature thresholds of cubic growth were accepted to be approximately 400K for various techniques. The observed high temperature threshold for cBN growth is an evidence that the energy of 95eV, i.e.  $V_{dc,s} = -60V$  for  $Ar^+$ , was much smaller than the optimum for low temperature depositions. Figure 3 shows the clear decrease of residual compressive stress in the cubic phase by decreasing the ion energy. The minimum ion energy for high purity cubic phase growth was 55eV for 970K, corresponds to the condition  $V_{dc,s} = -20V$ . It was much lower than the value for the deposition under 840 K, where  $V_{dc,s} = -60V$  was needed at least.

### 4.2 Electric measurements

Figure 4 shows that currents were limited by thermionic excitations. In the region of forwardly bias for the heterojunction, the barrier height decreased drastically against the applied voltages. And the barrier that limits the backward currents was kept at constant height against the bias. An ideal band diagram of the n-Si/p-(tBN/cBN) layered structure was shown in Fig. 6. The relation between the actual applied voltages ( $V_{Si}$  for n-type doped Si region and  $V_{BN}$  for p-type doped cBN region) to both p- and n- type layers in heterojunction diodes is given by  $N_{D,Si}\epsilon_{Si}(V_{b,Si} - V_{Si}) = N_{A,BN}\epsilon_{BN}(V_{b,BN} - V_{BN})$  [13]. Here,  $N_{D,Si}$  and  $N_{A,BN}$  are carrier densities in both layers.  $V_{b,Si}$  and  $V_{b,BN}$  are the built-in voltages in both regions.

For the heterojunction made by high doped n-Si and low doped p-BN,  $N_{A,BN}\epsilon_{BN}/N_{D,Si}\epsilon_{Si}$  must be much smaller than unity. In consequence, we can conclude most of the applied voltages were actually applied to the BN layers. This assumption is supported by the result that shows a drastically drop of barrier height for forwardly bias, lowering the barrier for holes that are transported by thermionic emission to silicon. On the other hand, the backward bias only causes an increase of the

barrier height, and has no effects on the backward currents. Although the origin of small backward currents was not identified yet, the rectification observed in those films can be explained by this change of the barrier height for both bias conditions. From these discussions, it was suggested that heavier doping of tBN and cBN layer and decreasing the thickness of narrower band gap tBN layer were desirable for greater rectifications at high temperatures. In addition, it is important to try BN homojunctions by controlling dopant profiles.

## 5. Conclusion

High temperature deposition of cubic boron nitride thin films was performed successfully by phase regulated RF bias sputtering. The temperature threshold for the deposition of high purity cBN under low ion energy condition was approximately 870K. It was clearly observed that residual stresses in cubic layer decreased by decreasing the impinging ion energy.

Reproducible rectifications by n-Si/p-BN heterojunction [14] were observed. The rectification ratio reached  $4 \times 10^4$  at room temperature. An energy band diagram and a calculation of the actual bias voltages in the p-n heterojunction diode explained the conduction through layers. It was suggested that wider band gap semiconductor/BN heterojunction, and BN homojunction diodes were desirable for rectification devices at high temperature.

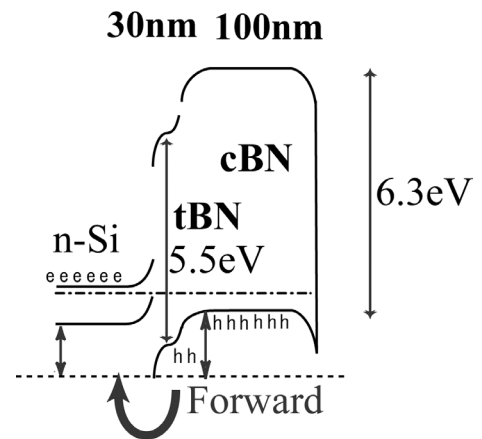


Fig6: Energy band diagram for the ideal n-Si/p-tBN/p-cBN junction structure. The big arrow shows the direction of forward currents by holes in BN layers.

## 6. Acknowledgements

This work was financially supported by a Grant-in-Aid for Scientific Research A Grant No. 13355028, The Ministry of Education, Culture, Sports, Science and Technology.

## References

- [1] S. Noor Mohammad-Solid-State Electron. **46** 203 (2002)
- [2] T. Taniguchi, T. Teraji, S. Koizumi, K. Watanabe and S. Yamaoka- Jpn. J. Appl. Phys. **41** L109 (2002)
- [3] H. Tomokage, N. Nomura, T. Taniguchi, T. Ando-Diamond & Relat. Materials **9** 606 (2000)
- [4] X.W. Zang, Y.J. Zou, H. Yan, B. Wang, G.H. Chen and S.P. Wong-Materials Lett. **45** 111 (2000)
- [5] K.J. Liao, W.L. Wang and C.Y. Kong-Surface & Coating Technol. **141** 216 (2001)
- [6] T. Yoshida-Diamond Films and Technol. **7** No.2 87 (1997)
- [7] T.E. Mousang and J.E. Lowther-Physical Review B **66** 014112 (2002)
- [8] P.B. Mirkarimi, K.F. McCarty, D.L. Medlin -Materials Science and Engineering. **R21**, 47-100 (1997)
- [9] G. Reisse, S. Weissmantel, D. Rost- Diamond and Relat. Materials **11** 1276 (2002)
- [10] C. Fits, A. Kolitsch, and W. Möller-Appl. Phys. Lett. **80** 55 (2002)
- [11] O. Tsuda, Y. Yamada, T. Fujii, and T. Yoshida-J. Vac. Sci. & Technol. A **13** No.6 2843 (1995)
- [12] D.K. Schroder- *Semiconductor Material and Device Characterization 2<sup>nd</sup> ed.*: Wiley, New York p170 (1998):
- [13] S.M. Sze-*Physics of Semiconductor Devices 2<sup>nd</sup> ed.*: Wiley, New York, p122 (1981)
- [14] S. Kerdiles, A. Berthelot, R. Rizk and L. Pichon: Appl. Phys. Lett. **80** 3772 (2002)

# Growth of crystalline Si thin films at ultra-fast deposition rate via hybrid thermal plasma CVD

M. Kambara, T. Chiba, Y. Hamai, K. Eguchi and T. Yoshida

*Department of Materials Science and Engineering, University of Tokyo,  
7-3-1, Hongo, Bunkyo-Ku, Tokyo 113-8656 Japan*

## Abstract

Thermal plasma chemical vapour deposition (TP-CVD) has been successfully applied to produce microcrystalline silicon thin films as an intrinsic layer for the photovoltaic solar cells. Photosensitivity of around  $10^3$  has been achieved in the films produced at a deposition rate greater than 20 nm/s. Despite relatively low substrate temperature, the Raman spectroscopy suggested the presence of the crystalline phase and less defects introduced in the film. In addition, a distinct agglomeration of nano-sized grains was observed uniformly in the film exhibiting high photosensitivity, which might attribute to an enhancement of the optoelectric properties.

## 1. Introduction

Thermal plasma technique has been established as an essential technology for coatings of the structural materials. Owing to its high energy densities, thermal plasma chemical vapour deposition (TP-CVD) has also successfully demonstrated its potential to produce high dense microcrystalline silicon films at ultra-fast deposition rates, i.e. nearly three orders of magnitude greater than the values achievable with the conventional CVD techniques [1]. This is a promising indication of an effective technique for solar cell technology development, which currently seeks for cost- and performance- effective production techniques without impairing the optoelectronic properties.

Conventionally, low pressure plasma chemical vapor deposition (LPP-CVD) has been used to produce amorphous silicon and several new techniques have been attempted for crystalline Si thin film production. However, for most of the methods, due primarily to low process pressure, the deposition process is characterized via surface reaction probabilities of radicals and thus the deposition rates are typically around 1 nm/s. Unlike LPP-CVD, TP-CVD achieves much higher gas temperatures and therefore extremely high supersaturation. This infers that clusters of either silicon atoms or radicals or both are highly likely generated just before impinging onto the substrate, which can contribute to an ultra-fast growth of the films. Besides, this rapid growth of crystalline silicon could be of the 3D nucleation mode of hot clusters which requires significantly larger driving force than that for migration of clusters into possible kinks on the crystal surface. Formation of these clusters affect the nucleation events itself and subsequent microstructural evolution. In other words, TP-CVD process may possess possibilities to attain novel microstructures with enhanced optoelectric properties, which can not be realized by other conventional CVD methods. An ex-situ experiment using microtrench has already revealed an existence of clusters with around 1nm in size. Several physical models have also found an essential role of clustering in the entire TP-CVD process at the boundary layer between plasma and substrate [2]. However, the crystals grown at higher deposition rates in general carry more defects, which behave as recombination centers for the light induced carriers and hence degrades the properties. It is therefore important to understand the relationship between growth rate and quality of the films with respect to the optoelectric properties.

In this work, we performed an investigation on the silicon thin films produced by RF TP-CVD technique. The microstructural evolutions are compared with the film quality, which are measured by Raman spectroscopy, X-ray diffraction and solar-simulator, and discussed from a viewpoint of feasibility of the TP-CVD method for photovoltaic silicon thin film production.

## 2. Experimental

The thermal plasma CVD system with hybrid dc and rf plasma generators has been used in this study and the detailed specifications can be found in elsewhere [1]. This system has already demonstrated its high potential to



achieve remarkably high deposition rate as mentioned in the introduction section. The silicon thin films produced by this system, however, have been suffered from undetermined problems in attaining optoelectronic properties. This is presumably due to pronounced influence of surface oxidation on the overall properties of thinner films. In this work, therefore, we prolonged the deposition time by employing the rf generator to create plasma. In addition, a stationary and running-water-cooled copper substrate holder was used instead of hBN turn table to hold a  $\text{SiO}_2$  glass substrate. A 1mm hole was made at the center of substrate for monitoring the temperature of the substrate, which is heated by a direct exposure to the plasma flame (Fig.1). R-type thermocouple was mounted from the bottom of the substrate and placed to appear the tip of the thermocouple partly from the substrate surface. Prior to deposition, the reactor chamber was evacuated by turbo molecular pump (TMP) up to  $10^{-5}$  Torr to sweep out the possible contamination sources. Argon gas was then injected, along with He shielding gas, to the chamber at a rate of 5 slm and a plasma was generated at a power of 15 kW-5MHz. The chamber pressure at this point reached 6 Torr and was maintained throughout the plasma deposition. A 3% silane ( $\text{SiH}_4$ ) diluted with  $\text{H}_2$  gas was subsequently introduced into the plasma from the center of the rf coils at a rate of 2 slm. Deposition was carried out for 25 minutes.

The films so produced were examined by optical microscope, scanning electron microscopy (SEM), X-ray diffraction (XRD) analysis, Raman spectroscopy, to identify the microstructural characteristics. The optoelectric properties of the films were evaluated solar simulator by coplanar transport mode.

### 3. Results and discussion

Figure 2 shows the variations of the thickness of the films and its resultant photosensitivity, the ratio of photoconductivity and dark conductivity, as a function of the substrate temperature. It should be noted that the photosensitivity increases with decreasing the substrate temperature and reaches as high as  $10^3$  at around  $133^\circ\text{C}$ . Another important finding is that the film has grown thicker than  $30\text{ }\mu\text{m}$  during the total deposition time of 25 minutes. The deposition rate is thus estimated to be  $20\text{ nm/sec}$ , which is slower by two orders of magnitude than the maximum achievable speed by this TPCVD system [1] but is roughly two times faster than the top deposition speed attained for amorphous Si thin films [3]. To the best of our knowledge, the photosensitivity of  $10^3$  achieved in the present work is comparable to the maximum values reported for the microcrystalline silicon thin films [4], although it is still quite a low value compared with that for amorphous based Si thin film, which typically reaches up to  $10^6$  [5,6]. Yet, this is the first and direct evidence of a remarkably fast production rate at low production temperature for photovoltaic silicon thin films via TPCVD.

Figure 2 also shows that the photosensitivity decreases with increasing the substrate temperature whereas the film thickness seems not to be sensitive to the temperature. This suggests that the condition at the boundary between plasma and substrate could be altered and subsequently the formation mechanism of the silicon films are affected. In order to identify the microstructural characteristics responsible for this variation in the photosensitivity, the films were analyzed by XRD and Raman

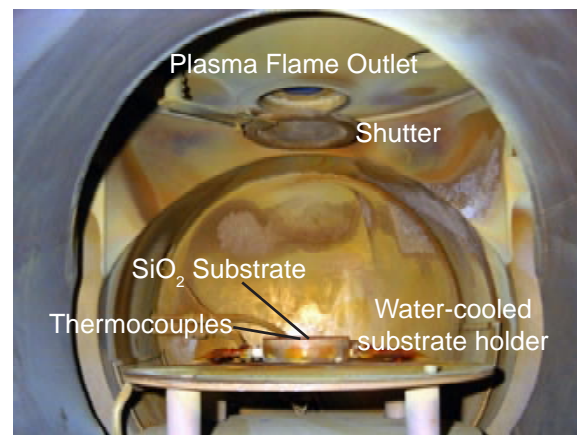


Fig.1 View inside the reaction chamber.

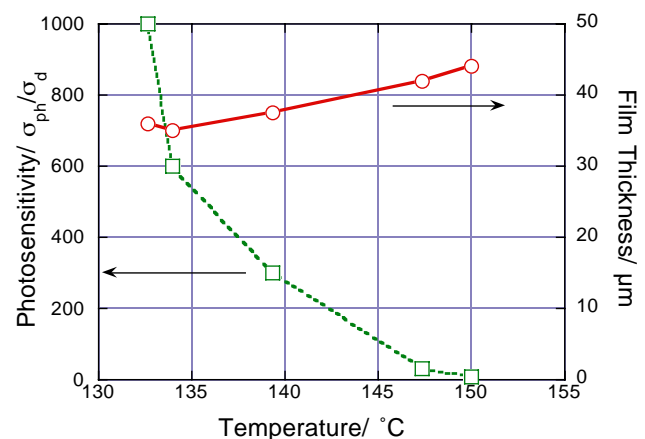


Fig.2 Temperature dependence of the film thickness and photosensitivity.

spectroscopy as a function of the temperature. (The substrate temperature is obviously sensitive to its position in the substrate, i.e. the extent of the thermocouple tip area exposed directly to the plasma flame. Nevertheless, the temperature variation was within the temperature range of 5°C at a fixed position of the substrate surface.)

Figure 3 exhibits the variation of the XRD patterns for the films deposited at different temperatures. It can be seen that one relatively large broadening of the peaks is present at around 28°, where the diffraction from Si(111) appears for the crystalline Si. Despite the different substrate temperatures, no significant change in the X-ray peak patterns was observed. This may indicate that the microstructure consists of either amorphous or very fine crystalline particles or the mixture of both, irrespective of the temperature.

Raman spectra were then measured for these films as summarized in Fig.4. It shows the frequency at the maximum peak in the Raman spectrum and its full-width-half-maxima as a function of the substrate temperature. Although no clear dependence in XRD patterns on temperature was observed, all of the Raman shifts are found between 495 and 515 cm<sup>-1</sup> and show a general trend of decrease towards the low frequency with increase in temperature. The shape of the maximum Raman peak was found to be almost symmetry and no significant increase in the intensity at the bottom of the peak at the high frequency region, indicating less probability of the existence of the amorphous phase in all the films. Therefore, taking account of the XRD results, very fine crystalline phases are at least present in the films containing less amorphous phase [6]. Furthermore, it is evident that the Raman FWHM, associated with the defects involved in the film, increases with temperature. This fact further underlines the importance of the boundary between either crystalline/amorphous or crystalline grains for high optoelectric properties. In other words, within the microstructure of the films, both the fraction of the crystalline phase and the size and spatial distribution of very fine crystalline grains change with temperature and are essentially responsible for an enhancement of the photosensitivity.

An apparent difference in the microstructure was observed in the SEM images for the films produced at different substrate temperatures, i.e. different photosensitivities. Figure 5 compares the cross sections of the films (a) which exhibits negligibly-small amount of photosensitivity and of the film (b) showing high photosensitivity of 10<sup>3</sup>. In the case of the film (a) deposited at higher temperature, only the line defects in the growth direction are observed clearly in the film with rather plain microstructure. However, no distinct grains are observed anywhere within the film at this magnitude of image. Considering the results of Raman spectroscopy, the possible microstructure formation would be that fine nano-sized crystalline grains are distributed individually and uniformly within the amorphous matrix from the beginning of the film growth. In contrast, in the film (b) which shows high photosensitivity, there can be seen the white-contrasted grains distributed rather uniformly from the bottom to the top of the film. These white colored phases are less than 300 nm in size and further found to consist of much smaller grains. Dark conductivity of the latter was evaluated to be in the range of 10<sup>-10</sup> to 10<sup>-11</sup> (Ω<sup>-1</sup>cm<sup>-1</sup>), which is lower by roughly five orders of magnitude than the typical values reported for crystalline Si [4]. This is another indication of an increased number of grain boundaries as scattering sites for thermally equilibrium

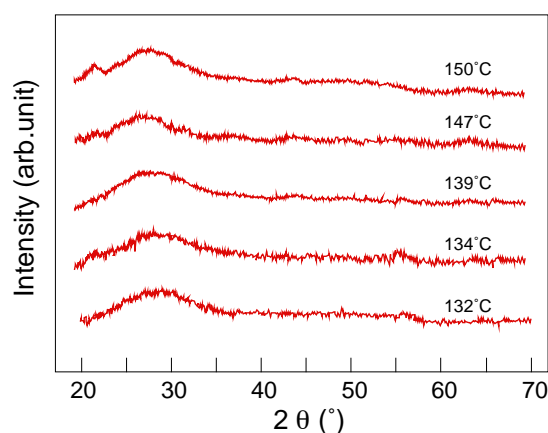


Fig.3 Variation of X-ray diffraction patterns with substrate temperature.

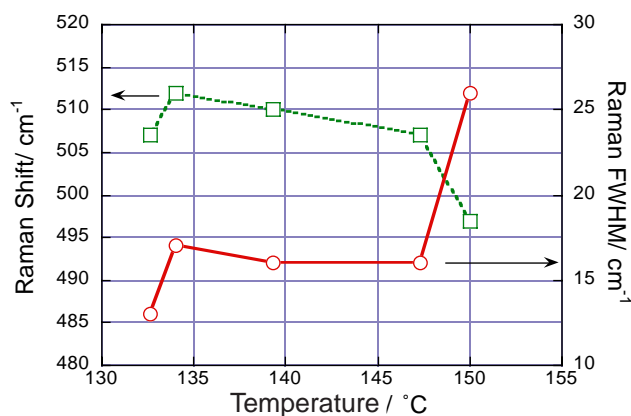


Fig.4 Substrate temperature dependence of the Raman shift and FWHM.

carriers. Given the high photosensitivity, however, they are not active recombination centers for the light induced carriers.

Similar microstructure has been observed in the microcrystalline Si thin films produced by dc plasma CVD at rather high pressure of 150 Pa, although no correlation with the optoelectric properties was reported [7]. This fact may imply that formation of the present grain agglomeration is associated with large temperature gradient above the substrate which is attained by high pressure plasma processing. Another type of agglomeration, distributed in the different manner from the present result, has also been observed by the conventional PECVD processing [8]. In this microstructure, the aggregates generate much larger grain boundaries, which is considered to cause the potential drop in the band gap. In other words, the boundaries between the smaller grains within the aggregates is not necessarily the primary barrier to reduce the carrier transport. Detailed TEM observation will be required to identify the characteristics and formation mechanism of the boundaries between the neighboring aggregates and also between the individual nano-sized grains within them. Yet, the aggregation of nano grains observed in the present work could have an essential role in attaining high optoelectric properties.

#### 4. Conclusion

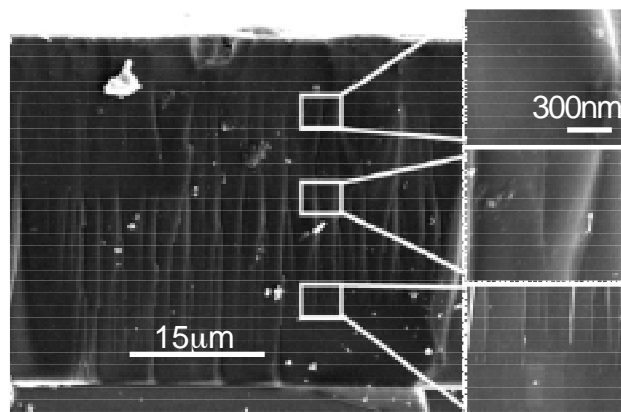
We have successfully produced microcrystalline Si thin films with high photosensitivity of  $10^3$  at the deposition rate faster than 20 nm/s. These figures prove the high potential of TPCVD as an effective technique for photovoltaic solar cell production. Uniform distribution of distinct aggregates of nano sized grains was evident in this film, which might be responsible for an enhancement of photosensitivity. The high deposition rate and photosensitivity will be enhanced further if the formation of this microstructure is to be well understood.

#### Acknowledgements

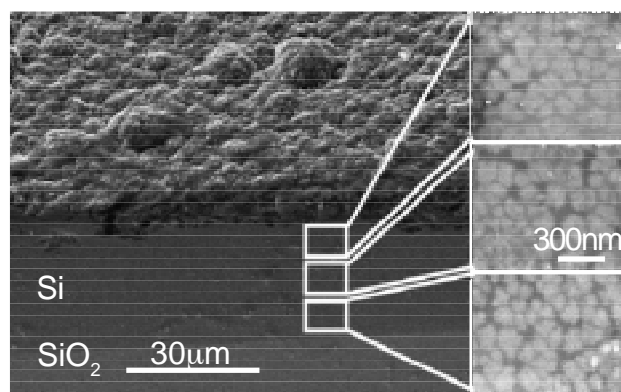
This work was supported by a Grant for 21st Century COE Program "Human-Friendly Materials based on Chemistry" from the Ministry of Education, Culture, Sports, Science and Technology, Japan.

#### References

- [1] Y. K. Chae, H. Ohno, K. Eguchi, T. Yoshida, J. Appl. Phys., **89**, 8311 (2001).
- [2] P. Han, T. Yoshida, J. Appl. Phys., **91**, 1814 (2002).
- [3] W. M. M. Kessels, R. J. Severens, A. H. M. Smets, B. A. Korevaar, G. J. Adriaenssens, D. C. Schram, M. C. M. van de Sanden, J. Appl. Phys., **89**, 2404 (2001).
- [4] J. P. Conde, V. Schotten, S. Arekat, P. Brogueira, R. Sousa, V. Chu, Jpn. J. Appl. Phys., **36** [1A], 38 (1997).
- [5] C. Das and S. Ray, Thin Solid Films, **403-404**, 81 (2002).
- [6] S. Veprek, F. A. Sarott, Z. Iqbal, Phys. Rev. B, **36**, 3344 (1987).
- [7] D. Franz, F. Grangeon, T. Delachaux, A.A. Howling, Ch. Hollenstein, J. Karner, Thin Solid Films, **383**, 11 (2001).
- [8] J. Kocka, H. Stuchlikova, J. Stuchlik, B. Rezek, T. Mates, V. Screck, P. Fojtik, I. Pelant, A. Fejfar, J. Non cryst. Solid, **299-302**, 355 (2002).



(a) Photosensitivity: 10



(b) Photosensitivity: 1000

Fig.5 SEM images of the film deposited at different substrate temperature; (a) 150 and (b) 133°C.

# ***In situ* mass and energy measurement of chemical species responsible for cBN growth by ICP-CVD**

H. S. Yang and T. Yoshida,

*Department of Materials Engineering, School of Engineering, The University of Tokyo,  
Hongo 7-3-1, Bunkyo-ku, Tokyo 113-8656, Japan.*

## **Abstract**

The mass and energy of chemical species in plasma are crucial for understanding the cubic boron nitride growth mechanism and controlling cubic boron nitride growth. In this study, the plasma condition for cubic boron nitride growth in low-pressure inductively coupled plasma-enhanced chemical vapor deposition process was analyzed by Quadrupole mass spectrometer with ion energy analyzer. Diborane gas was revealed to be totally ionized in plasma when the plasma power was higher than 2 kW. The main products were  $B^+$  ion with a small amount of  $BH^+$ ,  $BH_2^+$  and  $B_2H_X^+$  ( $X = 1-5$ ).  $N_2$  in plasma was partially ionized and the ionization yield increased with introduction of Ar gas into the system, resulting in the formation of cubic boron nitride. Neutral atoms of nitrogen and hydrogen were not detected under the deposition conditions. The existence of neutral  $N_2$  molecules inhibits the cBN growth, indicating a surface rather than a subsurface growth of cubic boron nitride in vapor phase deposition.

## **1. Introduction**

Cubic boron nitride (cBN) thin films have attracted extensive researcher's interests due to their excellent physical and chemical properties. Low-pressure inductively coupled plasma-enhanced chemical vapor deposition (ICP-CVD) is one of the most successful deposition techniques in cBN thin film preparation [1-3]. However, even in CVD process, ion bombardment has been considered to play a key role in the cBN formation, as is used in PVD techniques for cBN growth [4-6]. In the conventional plasma conditions, the ionization yield is less than 1%. Therefore, besides the ion bombardment, interaction between the film surface and neutral species may also play a significant role in cBN growth.

In the present study, the plasma condition for cBN growth was measured *in situ* by quadrupole mass spectrometer with ion energy analyzer (QMS-IEA) in ICP-CVD system. The ionization condition of each gas, including  $N_2$ , Ar, and  $B_2H_6$  were systematically investigated. The roles of ions and neutral species for cBN growth were presented and discussed.

## **2. Experimental details**

Cubic boron nitride thin films were deposited on (111)-oriented Si wafers by ICP-CVD using a Time-Dependent Biasing Technique (TDBT) [1, 2]. The 13.56 MHz RF excitation is coupled into the plasma with a three-turn coil around a water-cooled quartz tube 50 mm in diameter. Plasma was generated inside a 38-mm-diameter pyrolytic BN tube placed inside the quartz tube to avoid contamination from the quartz tube.  $N_2$ ,  $H_2$ , and Ar gases were fed into the reactor chamber from the top of the plasma source, while the boron source, diborane, was introduced through a water-cooled copper probe into the plasma. The plasma was generated at 1 mTorr with an input power adjusting from 2 to 7 kW. The deposited cBN films were characterized using a Fourier transform infrared spectrometer (JASCO FT/IR-700) with transmission mode and an analysis area of  $200 \times 200 \mu m^2$  at normal incidence.

The differentially pumped QMS-IEA (Hiden Analytical Limited EQP 3.1 spectrometer) was mounted in the substrate holder. It consists of an ion extractor with a  $100 \mu m$  aperture followed by a  $45^\circ$ -sector field electrostatic energy analyzer matched to a triple section quadrupole mass filter and a pulse-counting electron multiplier. The spectrometer design provides a high dynamic range for plasma ion and neutral measurements. The probe housing is pumped by a turbomolecular pump (Varian-70) to give a typical working pressure in the manifold of the order of  $10^{-7}$  Torr. In neutral species measurements, the impact electron energy was set at 70 eV and emission current was set at 500  $\mu A$  in order to obtain strong signals. In appearance potential spectroscopy measurements, the electron energy was scanned from 10 to 40 eV with an energy step of 0.1 eV at an emission current of 100  $\mu A$ . In ions measurements, the emission current was set at 100  $\mu A$ , and ion fluxes were obtained by integrating the ion energy distribution curves.

### 3. Results and discussions

#### a. Mass spectra without plasma

Figure 1 shows the mass spectrum measured with the same gas flows under the optimal deposition condition but without plasma. In addition to the two strongest peaks due to Ar (20, 36 and 40 amu), with 70 eV energy electrons impact, the  $B_2H_6$  molecules dissociated into  $B^+$  and  $B_xH_y^+$  ( $X=1-2$ ,  $Y=1-5$ ). The intensities of  $B_2H_y$  were much stronger than those of  $BH_y$ . In addition, the peaks of  $H_2O$  (16, 17 and 18 amu) and  $CO_2$  (44 amu) were also detected, revealing the presence of water and  $CO_2$  in the chamber. The amount of water can be reduced effectively by baking the chamber and substrate holder or by  $H_2$  plasma pre-treatment. Table 1 shows the measured appearance potential data of the species detected in this study. After the electron energy was calibrated with the appearance potentials of Ar (15.8 eV) and He (24.5 eV), the measured data of water,  $H_2$ , and  $N_2$  were in good agreement with the data reported. The appearance potentials for  $B_xH_y$  were also found to be ranging from approximately 11.6 to 19.3 eV, which is in agreement with previous reports [7].

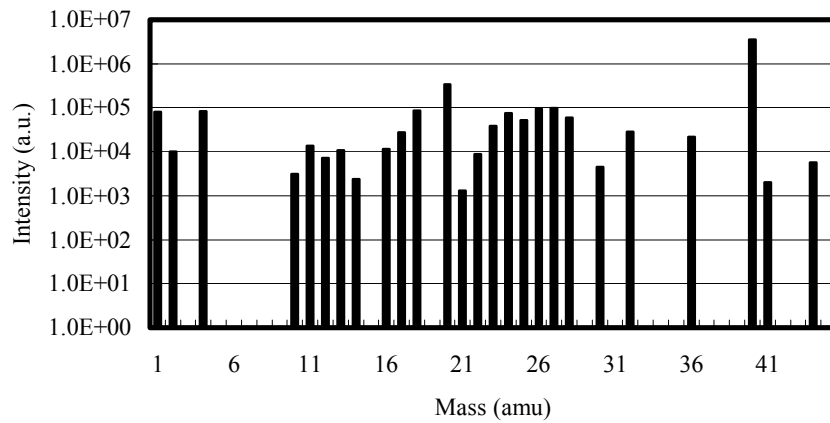


Figure 1. Mass spectrum measured in the same gas flows as those under optimal deposition condition but without plasma (19 sccm Ar + 0.7 sccm  $N_2$  + 7 sccm  $B_2H_6$  diluted in He with pressure of 1.0 mTorr).

Table 1. The appearance potential of species measured in this study and data from reference [7].

Appearance potential (eV)	This study	Reference [7]	Gases under 1 mTorr
Ar	15.8	15.8	Pure Ar
$N_2$	15.7	15.6	Ar + $N_2$
$H_2O$	12.9	12.6	Pure Ar
N	24.3	24.3	Ar + $N_2$
He	24.5	24.5	Ar + He + $B_2H_6$
B in $B_2H_6$	19.2	18.4	Ar + He + $B_2H_6$
BH in $B_2H_6$	16.6	16.4	Ar + He + $B_2H_6$
$BH_2$ in $B_2H_6$	15.1	15.5	Ar + He + $B_2H_6$
$BH_3$ in $B_2H_6$	16.3	14.9	Ar + He + $B_2H_6$
$B_2H$ in $B_2H_6$	14.2	No data	Ar + He + $B_2H_6$
$B_2H_2$ in $B_2H_6$	13.2	14.0	Ar + He + $B_2H_6$
$B_2H_3$ in $B_2H_6$	11.8	1.3	Ar + He + $B_2H_6$
$B_2H_4$ in $B_2H_6$	11.6	12.4	Ar + He + $B_2H_6$
$B_2H_5$ in $B_2H_6$	11.6	12.0	Ar + He + $B_2H_6$
$B_2H_6$ in $B_2H_6$	13.0	No data	Ar + He + $B_2H_6$

#### b. Ar/ $N_2$ plasma

Figure 2 illustrates the ion fluxes in pure Ar plasma and pure  $N_2$  plasma. The ion flux increased with the plasma power, indicating the increase in the ionization yield. The total ion flux in pure Ar plasma almost equaled to that in pure  $N_2$  plasma under the same plasma conditions. This tendency was contrary to Fritsche's

result of RF magnetron Ar/N<sub>2</sub> plasma under low plasma power, which indicated that the ion flux in pure N<sub>2</sub> plasma is considerably lower than that in pure Ar plasma under the same conditions [8]. The flux of N<sup>+</sup> ion increased rapidly when the plasma power increased up to 5 kW, suggesting the change of plasma from glow discharge to ICP [9], while no such tendency was observed in pure Ar plasma during the plasma power being adjusted between 2 to 7 kW.

Figure 3 illustrates the ion flux change in 7 kW Ar plasma with the increase in N<sub>2</sub> flow rate. When the N<sub>2</sub> gas percentage increased from 2% to 18%, the total ion flux was almost kept constant. However, the sum of N<sup>+</sup> + N<sub>2</sub><sup>+</sup> ion flux only increased from  $3.0 \times 10^7$  to  $7.5 \times 10^7$ . In this study, assuming the total ionization yield to be 1% in 7-kW-power plasma (a typical ionization yield in ICP), the ionization yield of N<sub>2</sub> decreased from approximately 15 to 4.5% as the N<sub>2</sub> percentage increased from 2 to 18%. In other words, the neutral N<sub>2</sub> concentration increased from 1.7 to 17.2%, which indicated that the ionization yield of N<sub>2</sub> decreased dramatically with the increase of N<sub>2</sub> gas percentage, although the total ion fluxes of N<sup>+</sup> and N<sub>2</sub><sup>+</sup> increased slightly.

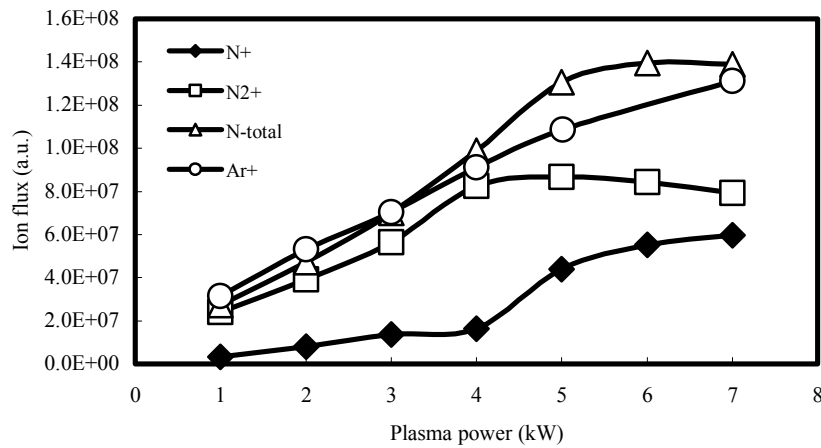


Figure 2. Ion fluxes in pure Ar and pure N<sub>2</sub> plasma at different plasma powers. Plasma working pressure during QMS-IEA measurement was 1.0 mTorr. “N-total” was the sum of flux of N<sub>2</sub><sup>+</sup> and N<sup>+</sup> in pure N<sub>2</sub> plasma.

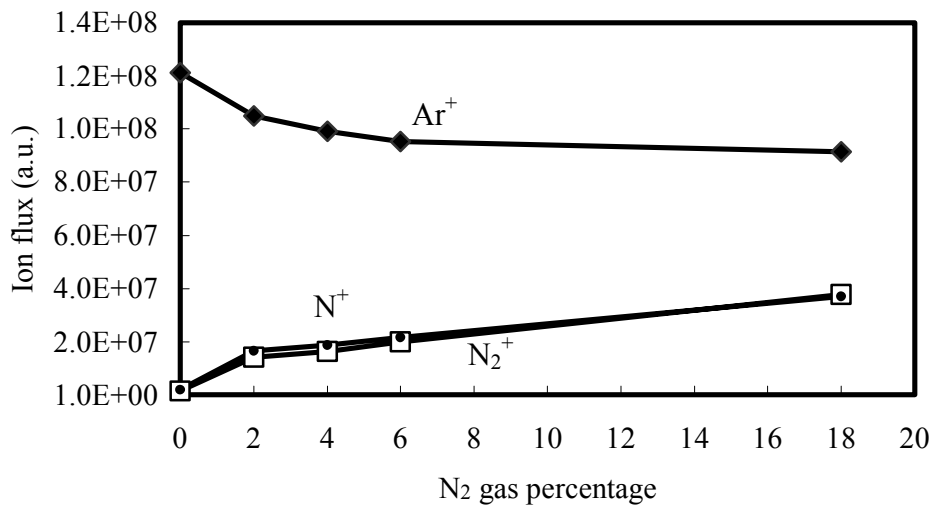


Figure 3. Ion fluxes at different Ar percentages in the 7 kW plasma. Working pressure was 1.0 mTorr.

### c. Neutral species and ions under deposition conditions

Figure 4 shows the appearance potential profiles of atomic hydrogen in pure H<sub>2</sub> plasma under the deposition condition. In pure H<sub>2</sub> plasma, large atomic H flux was detected. However, no atomic H was detected in deposition condition (B<sub>2</sub>H<sub>6</sub> was used as B source), which suggested that all the H<sub>2</sub> and H species decomposed from B<sub>2</sub>H<sub>6</sub> were ionized. Moreover, atomic N also cannot be detected under deposition

condition and in pure N<sub>2</sub> plasma, indicating a low fraction of neutral nitrogen atoms even the plasma power reached 7 kW. Fig. 5 shows the neutral species mass spectrum under deposition condition. Besides the strong peaks of Ar (20, and 40 amu), traces of O<sub>2</sub> (32 amu), H, H<sub>2</sub>, CO<sub>2</sub> (12 and 44 amu), N<sub>2</sub> (14 and 28 amu), H<sub>2</sub>O (16, 17 and 18 amu) were detected. However no neutral species of B<sub>x</sub>H<sub>y</sub> was detected, which indicated that all the B<sub>x</sub>H<sub>y</sub> species were ionized in plasma. Further measurements showed that 2 kW plasma power is enough for total ionization of B<sub>2</sub>H<sub>6</sub>. Therefore, the main neutral species under deposition condition were N<sub>2</sub>, He and Ar.

Figure 6 shows the ion species under deposition conditions. BH<sub>x</sub><sup>+</sup>, particularly B<sup>+</sup> ions, were the main products of diborane ionization, revealed that all the boron sources in plasma existed as ions but not radicals. The peaks of ion energy distribution of Ar<sup>+</sup>, N<sub>2</sub><sup>+</sup> and B<sub>x</sub>H<sub>y</sub><sup>+</sup> were at the same position of approximately 60 eV. All the ion energy distributions showed single narrow peaks with full-width at half-maximum (FWHM) of approximately 7 eV, suggesting no collision occurred in the plasma sheath under 1 mTorr pressure. However, the ion energy of N<sup>+</sup> was approximately 10 eV higher than that of N<sub>2</sub><sup>+</sup> and Ar<sup>+</sup>. Moreover, the fluxes of H<sup>+</sup> and H<sub>2</sub><sup>+</sup> are as strong as that of Ar<sup>+</sup>, and stronger than those of N<sub>2</sub><sup>+</sup> and N<sup>+</sup>, which again proved that diborane was ionized into B<sub>x</sub>H<sub>y</sub><sup>+</sup> and H<sup>+</sup>, H<sub>2</sub><sup>+</sup>. The energy of H<sup>+</sup> and H<sub>2</sub><sup>+</sup> was approximately 25 to 40 eV higher than that of other ions; also the peaks were wider than that of other ions.

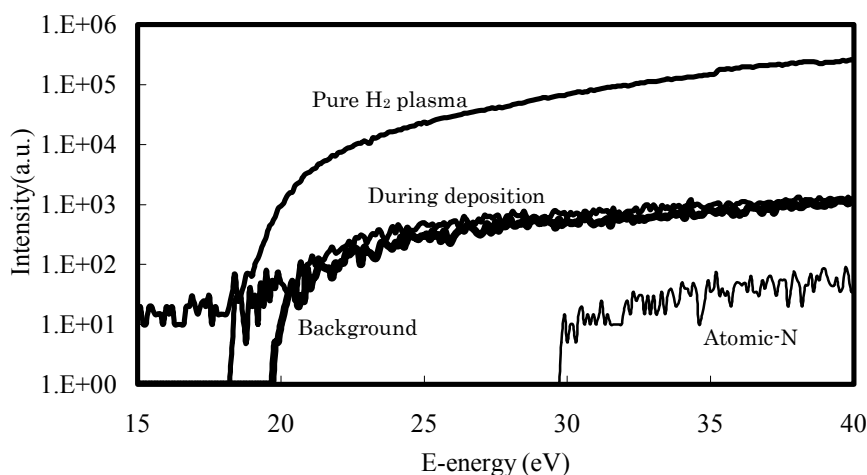


Figure 4. The appearance mass spectra of hydrogen atom under pure H<sub>2</sub> plasma and deposition condition with 7 kW plasma power. For comparison, the background measured under chamber pressure of  $4 \times 10^{-6}$  mTorr was also measured. “Atomic-N” was the atomic N appearance mass spectrum under deposition condition. The appearance potential was before calibration.

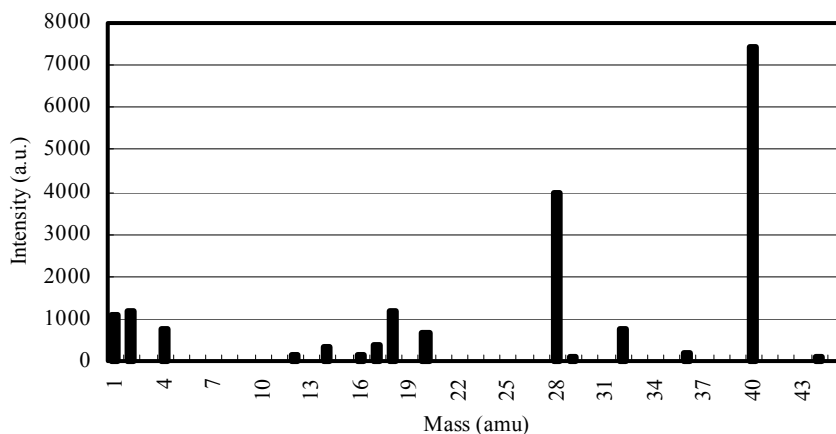


Figure 5. The neutral species under cBN film deposition condition. The gases flow rates were 19 sccm Ar, 0.7 sccm N<sub>2</sub> and 7 sccm B<sub>2</sub>H<sub>6</sub> diluted with He, respectively. Working pressure was 1.0 mTorr. The emission current was set at 100  $\mu$ A in this measurement.

Figure 7 shows the IR absorbance of cBN films prepared under different  $N_2$  concentration. It was obvious that the cBN concentration decreased with the increase in  $N_2$  content. When no Ar gas was introduced into the deposition system, no cubic phase was detected in any of our experiments with systematic change of the plasma power and substrate bias. High-quality cBN films can be prepared only when the  $N_2$  concentration was less than 11%. While in 96% Ar +  $N_2$  plasma, cBN films with more than 98% (volume%) cubic phase were prepared [2]. As has been discussed in Ar/ $N_2$  plasma system, the neutral  $N_2$  molecule flux increased drastically with the increase in  $N_2$  flowrate. Therefore, the existence of neutral  $N_2$  induced the  $sp^2$ -bonded BN growth. The introduction of Ar reduced the  $N_2$  molecule flux.

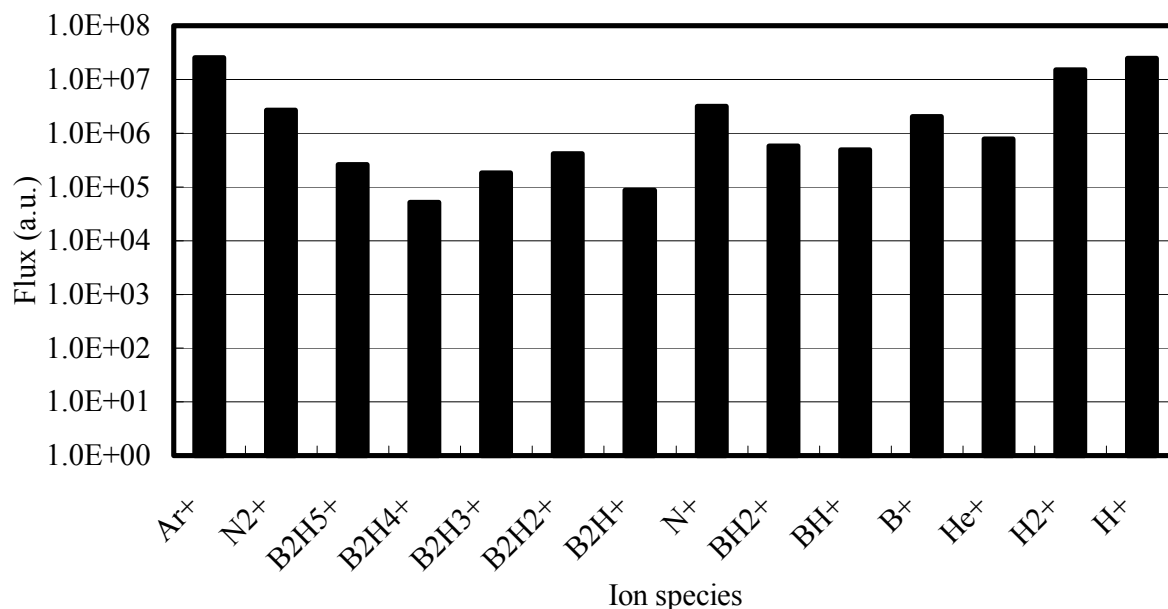


Figure 6. Ion species under cBN film deposition condition. The gases flow rates were 19 sccm Ar, 0.7 sccm  $N_2$  and 7 sccm  $B_2H_6$  diluted with He, respectively. Working pressure was 1.0 mTorr.

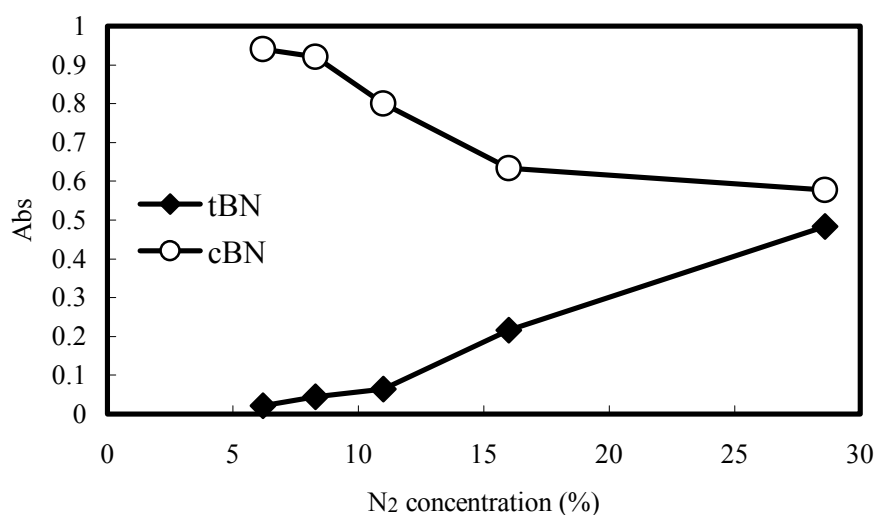


Figure 7. FTIR absorption of cBN films prepared at different  $N_2$  concentration [ $N_2/(N_2+Ar)$ ]. Films were deposited using TDBT from  $-150$  V to  $-20$  V in 7kW plasma power, and gas flow rates of  $N_2$  and  $B_2H_6$  diluted with He were 1 and 10 sccm, respectively.

The existence of  $H_2^+$  or  $H^+$  seems no harmful for cBN growth. As was shown in Fig. 6, the flux of  $H_2^+$  and  $H^+$  was similar as that of  $Ar^+$ , and even larger than the flux of  $N_2^+$  or  $N^+$ ; however, high quality cBN films



still can be prepared. But the existence of neutral H atoms or H<sub>2</sub> molecules in the deposition system was found to inhibit cBN growth. In the present study, the cubic phase content was reduced with the introduction of H<sub>2</sub>, and almost no cBN can be deposited when approximately 10% of H<sub>2</sub> was introduced into the deposition system. The fact that neutral H atoms, H<sub>2</sub> and N<sub>2</sub> molecules inhibited the cBN growth suggested that cBN nucleates and grows at the film surface [10]. To reduce the neutral H atoms, H<sub>2</sub> and N<sub>2</sub> molecules is one of the keys to control cBN growth in vapor phase deposition.

#### 4. Conclusions

QMS-IEA was used to analyze the plasma condition of ICP-CVD cBN thin film growth. N<sub>2</sub> in plasma was only partly ionized, and the ionization yield of N<sub>2</sub> increased with the decrease of N<sub>2</sub> volume percentage in the deposition system. The energy of bombardment ions was approximately 60 V. Diborane was totally ionized in plasma when the plasma power was higher than 2 kW. The main products were B<sup>+</sup> ion, and small amounts of BH<sup>+</sup>, BH<sub>2</sub><sup>+</sup> and B<sub>2</sub>H<sub>x</sub><sup>+</sup>. Hydrogen decomposed from diborane was also totally ionized to H<sup>+</sup> and H<sub>2</sub><sup>+</sup> with ion energy approximately 25 to 40 eV higher than those of other ions. No atomic neutral nitrogen or hydrogen was detected under deposition conditions. Introducing Ar into plasma system can successfully reduce the flux of N<sub>2</sub> molecules, and enhance the cBN growth.

#### Acknowledgments

The present research was financially supported by a grant-in-Aid for Scientific Research (A) (Grant No. 13355028), and partly supported by a Grant for 21<sup>st</sup> Century COE Program "Human-Friendly Materials based on Chemistry" from the Ministry of Education, Culture, Sports, Science and Technology, Japan. H. S. Yang acknowledges the financial assistance from Marubun Research Promotion Foundation, Japan.

#### Reference

- [1] H. S. Yang, C. Iwamoto, T. Yoshida, J. Appl. Phys. **91**, 6695 (2002).
- [2] H. S. Yang, C. Iwamoto, T. Yoshida, Thin Solid films **407**, 67 (2002).
- [3] C. Iwamoto, H.S. Yang, T. Yoshida, Diamond Relat. Mater. **11**, 1854 (2002).
- [4] Y. Yamada, Y. Tatebayashi, O. Tsuda and T. Yoshida, Thin Solid films **259**, 137 (1997).
- [5] D. J. Kester, R. Messier, J. Appl. Phys. **72**, 504 (1992).
- [6] D. R. McKenzie, W. D. McFall, W. G. Sainty, C. A. Collins, Diamond Relat. Mater. **2**, 970 (1993).
- [7] J. H. Wilson, H. A. Jr. McGee, J. Chem. Phys. **46**, 1444 (1967).
- [8] B. Fritsche, T. Chevolleau, J. Kourtev, A. Kolitsch, W. Moller, Vacuum **69**, 139 (2003).
- [9] T. Ichiki, T. Yoshida, Jpn. J. Appl. Phys. **33**, 4385 (1994).
- [10] T. Yoshida, Diamond Relat. Mater. **5**, 501 (1996).

# Twin hybrid plasma spraying of thermal barrier coatings

H.Huang, K.Eguchi, T.Yoshida

*Department of Materials Engineering, The University of Tokyo  
Hongo 7-3-1, Bunkyo-ku, Tokyo 113-8656, Japan*

## Abstract

We developed a novel 300kW Twin Hybrid Plasma Spraying System for thermal barrier coatings. The two high power hybrid plasma torches, together with a rotatable substrate holder, enabled deposition of  $\text{ZrO}_2\text{-}8\text{wt}\%\text{Y}_2\text{O}_3$  (8YSZ) composite coatings by utilizing each torch for thermal plasma PVD and powder spraying. Dense coating over  $300\mu\text{m}$  was sprayed on large Inconel substrates ( $50\text{mm}\times 50\text{mm}$ ) at  $900^\circ\text{C}$  without peeling off. Peculiar structure consisted of powder-sprayed splats and vapor-grown fine columns, layer by layer, was successfully deposited for the first time, at rates over  $150\mu\text{m}/\text{min}$ .

## 1. Introduction

In the field of thermal barrier coating (TBC) technology, two main processing methods have been adopted for decades. One is vapor deposition, which includes EB-PVD (Electron-Beam Physical Vapor Deposition), PE-CVD (Plasma Enhanced Chemical Vapor Deposition), LCVD (Laser Chemical Vapor Deposition), etc. The other is molten particle deposition, typically, APS (Atmospheric Plasma Spraying). TBCs made by the former method are characterized by columnar microstructures while splats structures are common in those deposited by APS. Due to this structural difference, the thermal and mechanical properties of such TBCs vary remarkably, as summarized in Table 1 [2-4].

Table.1 Properties of TBCs at room temperature

Property/characteristic	EB-PVD	PE-CVD	LCVD	APS
Thermal conductivity (W/mK)	1.5~1.9		2	0.8~1.1
Surface roughness ( $\mu\text{m}$ )	1			10
Adhesive strength (MPa)	400			20~40
Young's modulus (GPa)	90			200
Growth rate ( $\mu\text{m}/\text{h}$ )	200~300	250	600	10000
Production cost	high	high	high	low

The vapor deposited TBCs have the following merits: 1) Excellent strain tolerance; 2) Excellent surface finish; 3) Good erosion resistance; 4) Relative long lifetime. However, these merits are at the expense of rather high thermal conductivity and high production cost [4-7]. On the other hand, molten particle deposited TBCs demonstrate: 1) The lowest thermal conductivity; 2) High processing efficiency and low cost, but not so durable [8]. It seems that each of these two methods has its own unique strong points and shortcomings. Therefore, a new process which is able to combine all the merits would be of high interest. This research aims to develop novel composite TBCs with ultra low thermal conductivity, high strain tolerance and good affordability by a newly established high power twin hybrid plasma spraying system, which combines vapor deposition and powder spray processing together.

## 2. Thermal barrier structure design

According to the theory of thermal conductivity [3,9,10], layered TBC is widely accepted as an effective structure to increase both phonon and photon scattering. At temperature over  $1200^\circ\text{C}$ , YSZ based TBCs was significantly transparent to thermal radiation at wavelength between  $0.3\sim 5\mu\text{m}$  [11]. Therefore, a quarter wavelength filter for YSZ TBC

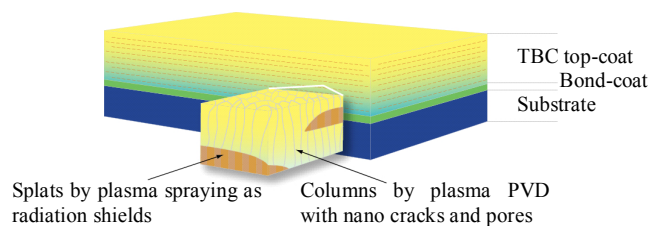


Fig.1 Model of composite thermal barrier coating, which will be prepared only by the combination of thermal plasma PVD and spraying

(between  $\lambda/4$  and  $\lambda$ ) could be achieved if the layer periodicity is between 0.2~2 $\mu\text{m}$ , which will increase the photon scattering significantly.

We designed such a layered TBC system based on the combination of vapor deposited columnar structure and sprayed splats, as shown in figure 1. In the top coat, columnar YSZ grains grow on the surface of splats layer by layer. And a dense sprayed layer near the bond-coat is preferred in order to improve oxidation resistance of the TBC system.

### 3. Apparatus and experimental procedure

Figure 2 (a) illustrates the schematic diagram of the novel system developed in this study. Two hybrid plasma torches, each of which is capable for plasma PVD, CVD or spraying, are positioned in a water-cooled deposition chamber. A rotatable substrate holder enables alternate exposure of substrates to the two plasma flame, and thus allows cyclic deposition by PVD, CVD and spraying, if different processes are assigned to the two hybrid torches. Each of the two torches has its own DC power supply, RF power supply and gas feeding system. And the whole system also consists of a water cooling system, a twin powder feeder and vacuum system.

Figure 2 (b) shows the detailed hybrid plasma torch used here. The specifications of this twin hybrid plasma spraying system are listed in table 2.

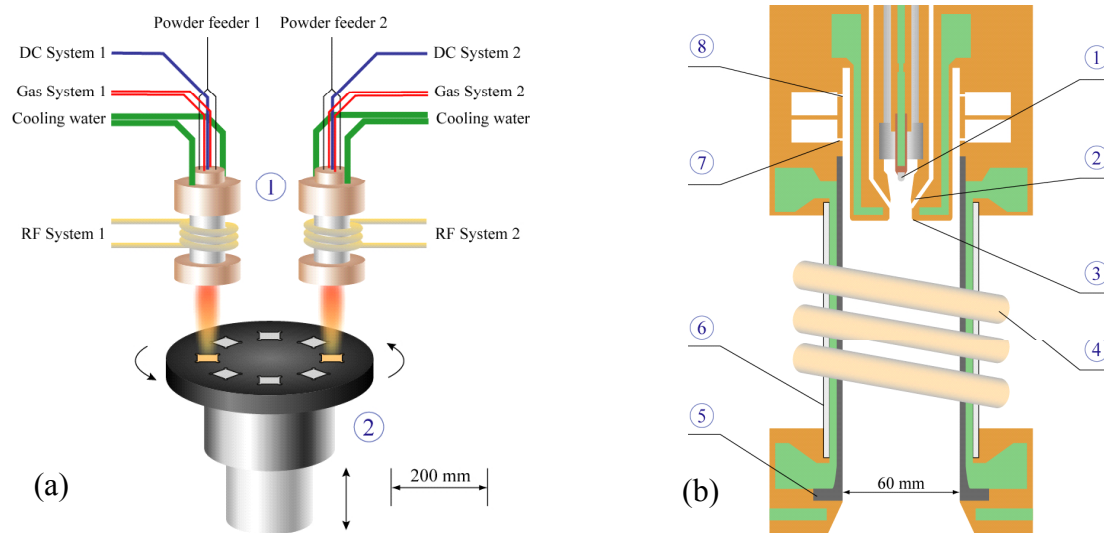


Fig.2 (a): Schematic diagram of twin hybrid plasma system. (①two hybrid plasma torches, ②rotatable substrate holder)  
(b): Detailed hybrid plasma torch. (①DC cathode; ②powder feeding nozzle; ③DC anode; ④RF coil; ⑤Si<sub>3</sub>N<sub>4</sub> tube; ⑥quartz tube; ⑦&⑧gas injection nozzles)

Table 2. Specifications of the twin hybrid plasma spraying system

Power input:	DC Power: 15kW×2; RF Power: 150kW×2
Torch:	Water cooled: 80L/min Inner tube: Si <sub>3</sub> N <sub>4</sub> , H=150mm, D <sub>inner</sub> =60mmØ Outer tube: Quartz, H=130mm, D <sub>outer</sub> =80mmØ RF coil: copper tube, 3-turns, 14mmØ, D <sub>inside</sub> =84mmØ, H≈55mm
Plasma gas flow rate:	Pure O <sub>2</sub> : 100~300 SLM Ar+H <sub>2</sub> : 80+40 SLM (at 100kW)
Vacuum system:	Mechanical booster pump: 1200L/s Water circulation pump: 2500L/s×2
Substrate holder:	SiC coated graphite, 410mmØ Rotating speed: ~200rpm

SUS304 stainless steels of 50mm×50mm×5mm and Inconel768 of 50mm×50mm×4.5mm were mainly used as substrates. Pretreatments such as sand blasting were not performed to the substrates. Commercial NiCoCrAlY powder (Starck 415.6, 44~125 $\mu\text{m}$ , Germany) was firstly sprayed on the substrates as a bond-coat, then two kinds of 8YSZ powders (Starck 825.0, sieved, 5~12 $\mu\text{m}$ , Germany and mechanically crushed

and sieved 8YSZ, 63~88 $\mu$ m) were deposited to form TBC top-coat by thermal plasma PVD and powder spraying when the substrate was heated up to prescribed temperature. The back-side temperature of the substrate was measured by a thermocouple. The estimated temperature gradient in the substrate is around 50K/mm, and a great temperature difference of about 250K would exist when 5mm-thickness substrates were used. Typical experimental conditions are listed in table 3. The microstructures of the prepared coatings were analyzed by field-emission scanning electron microscope (Hitachi, FE-SEM S4200).

Table 3. Typical experimental conditions

- 
- |  |  |
|--|--|
| (1) Gas flow rate (SLM):               | DC arc jet = 10; Ar radial sheath = 140; Ar tangential sheath = 30; H2 radial sheath = 30; Carrier = 4 |
| (2) Powder injection rate = 4~20 g/min |  |
| (3) RF plate power output = 100 KW     |  |
| (4) DC power supply = 8 KW             |  |
| (5) Chamber pressure = 300~500 Torr    |  |
- 

#### 4. Preliminary results

Figure 3 shows a as-sprayed sample. The top-coat with thickness around 300 $\mu$ m covered the whole substrate surface (50mm $\times$ 50mm) without peeling off. The white parts on both sides were under clasps used to fix the substrates. The color of the as sprayed coating was grey, indicating a slight reduction by Ar-H2 plasma.

Figure 4 (a) is the FE-SEM micrograph of polished cross section, showing a dense structure without clear boundaries between the splats. The interface between top-coat and bond-coat was clean and free of cracks. Continuous growth of YSZ grains between splats was observed in unpolished cross section, as shown in Fig.4 (b), which proved strong adhesion at the splats interfaces.

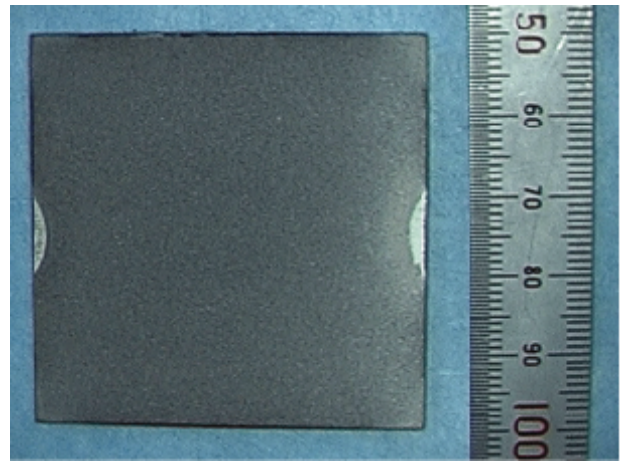
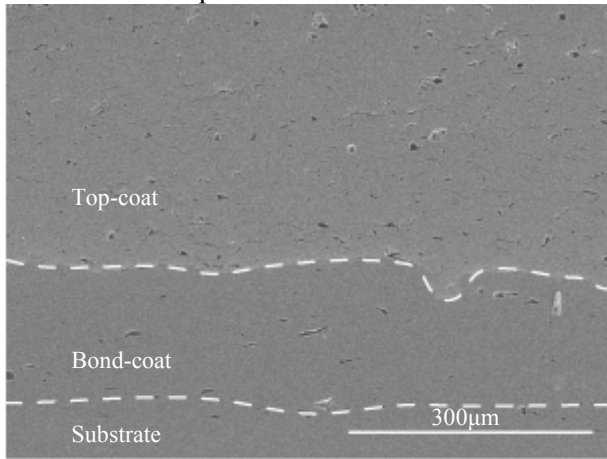
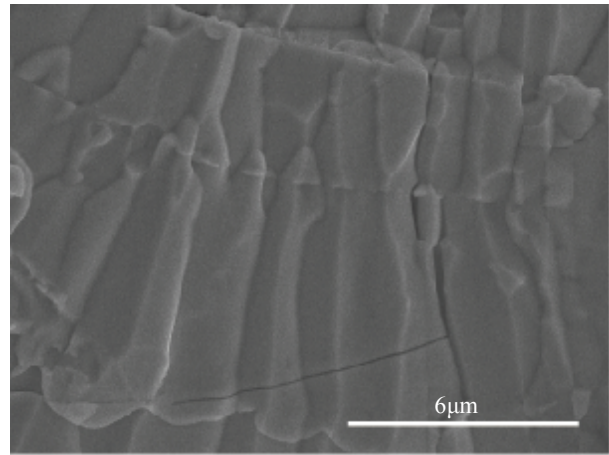


Fig.3 Photos of as sprayed sample



(a)



(b)

Fig.4 FE-SEM micrographs of sprayed TBC for (a) polished cross section; (b) unpolished microstructure

Figure 5 is the FE-SEM micrograph of the cross section of a peculiar layered structure deposited by both thermal plasma PVD and powder spraying. The layer periodicity was around 2 $\mu$ m, which was in the range to act as a quarter wavelength filter, as mentioned above. The height of the columnar structures between two splats was 100~200nm, note that these grew in just one turn between the substrate rotated in and out the plasma flame, which was only about 0.04 second. This means the growth rate exceeding 150 $\mu$ m/min was achieved, which was 30 times faster than that of ordinary EB-PVD. This is because in thermal plasma PVD, the vapor of YSZ is mainly directed to the substrate by the plasma flame, while in

other vapor depositions, such as EB-PVD, the vapor disperses in the whole chamber. The diameter of the vapor grown columns was 100~200nm.

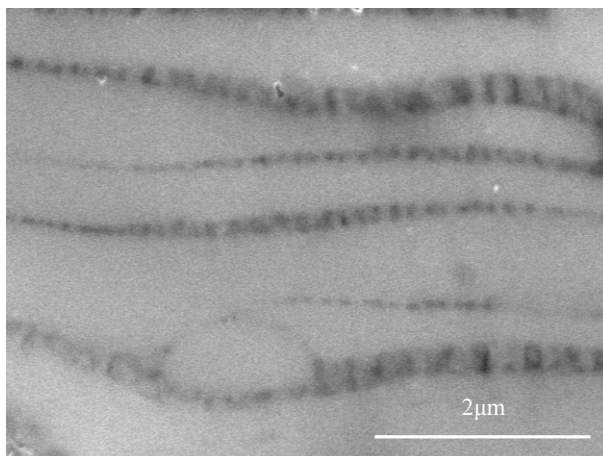


Fig.5 Layered structure of thermal plasma PVD-Spraying

## 5. Summary

Good morphological properties were found for TBCs deposited by twin hybrid plasma spraying system. High speed depositions of a dense sprayed layer together with layered structure consisted of powder-sprayed splats and vapor-grown columns are attractive for novel TBCs. Other properties relevant to this type of application are currently being investigated, such as thermal properties and lifetime in cyclic high-temperature conditions.

## Acknowledgement

The present research has been financed by the Japan Society for Promotion of Science and is supported in part by a Grant for 21st Century COE Program “Human-Friendly Materials based on Chemistry” from the Ministry of Education, Culture, Sports, and Technology of Japan.

## References

- [1] T. Yoshida, T. Tani, H. Nishimura, K. Akashi – J. Appl. Phys. **54**, 640 (1983)
- [2] N.P. Padture, M. Gell, E.H. Jordan – Science. **296**, 280 (2002).
- [3] J.R. Nicholls, K.J. Lawson, A. Johnstone, D.S. Rickerby – Surf. Coat. Technol. **151-152**, 383 (2002).
- [4] B. Preauchat, S. Drawin – Surf. Coat. Technol. **146-147**, 94 (2001).
- [5] T.E. Strangman, J.L. Shienle – J. Eng. Gas Turbines Power, **112**.
- [6] T.E. Strangman – Thin. Solid. Films **127**, 93 (1985).
- [7] M. Peters, K. Fritscher, G. Staniek, W.A. Kaysser, U. Schultz – Materialwissen. Werkstofftech. **28**, 357 (1997).
- [8] R.L. Jones – Metallurgical and Ceramic Coatings, K.H. Stern, Ed. (Chapman and Hall, London, 1996), p.194.
- [9] P.G. Klemens – R.P. Tye (Ed.), Thermal Conductivity of Solids, 1, Academic Press, London, 1969.
- [10] J.E. Parrott, A.D. Stuckes – Thermal Conductivity in Solids, Pion Limited, 1975.
- [11] J.R. Nicholls, K.J. Laswon, D.S. Rickerby, P. Morrel – NATO Workshop on Thermal Barrier Coatings, Aalborg, Denmark, AGARD-R-823, 1998.

# Influence of Plasma Jet atmosphere on the In-flight Chemical Reactivity of Sprayed Particles

A.A. Syed, A. Denoirjean, P. Denoirjean, J.C. Labbe, P. Fauchais

*SPCTS-UMR-CNRS 6638, Université de Limoges, Limoges, France*

## Abstract

Engulfment of surrounding atmosphere by the plasma jet can have pronounced effects on the in-flight particle chemical reactions. Current work is an attempt on establishing better understanding towards a correlation between in-flight particles reactivity and the plasma jet atmosphere composition.

316L stainless steel Techphy (-63+50  $\mu\text{m}$ ) particles were initially air plasma sprayed (APS) using a dc plasma gun (PTF4 type) and were quenched in-flight in an argon atmosphere. Collected particles exhibited oxide nodules within them and a surface oxide layer.

The powder was later sprayed in a controlled atmosphere chamber varying  $p_{\text{O}_2} / p_{\text{N}_2}$  or  $p_{\text{O}_2} / p_x$  where  $x$  was altered by varying  $\text{N}_2$  and Ar content around the plasma jet environment. Amount of oxygen in collected particles was found to be a linear function of  $\text{O}_2$  content in the plasma jet atmosphere whereas oxide nodules followed a parabolic relationship. Given a similar volume percentage of  $\text{O}_2$  in the plasma jet atmosphere, particles with higher oxygen content were collected in an Ar rich surrounding. Oxide nodules surface area was, however, remained unchanged.

## 1. Introduction

At anode nozzle exit at dc plasma torches, thermal plasma jets of high velocities of order 600 to 2000  $\text{ms}^{-1}$  and temperatures ranging from 8000 to 14000 K enter into a cold and static atmosphere. The velocity difference between plasma jets and its atmosphere results in turbulent shear at plasma boundary generating ring vortices which are pulled down along the plasma flow [1]. Adjacent vortex rings coalesce forming larger vortices where entanglement and then engulfment of cold eddies into the jet occur [2]. Besides engulfment of cold eddies at plasma boundary, entrainment of surrounding atmosphere also occurs due to fluctuations of plasma arc root [3]. Plasma jet velocity and viscosity as well as the composition of plasma forming gases influence the quantity of entrained atmosphere [4, 5]. Viscosity and temperature differences between plasma jet and engulfed atmosphere restrict mixing of the eddies which are retained towards the outer plasma boundary in first 5 to 8 mm downstream. Rapid heating of entrained species by plasma facilitates their mixing and transport towards the plasma core [6]. Plasma thermo-physical properties and mass flux can be modified to a large extent by varying quantity and composition of gas or mixture of gases entrained by the jet [7].

When spraying reactive particles, in most cases heated over their melting temperatures, fast chemical reactions may occur if the surrounding atmosphere of the plasma jet is composed of reactive gaseous species such as oxygen. This has been an area of much concern for metallic [8, 9] and carbide particles spraying [10, 11]. Controlling in-flight oxidation and decarburization, often resulting in non-equilibrium secondary phases in the deposits, has been of prime interest. In some cases these secondary phases may lead to a deterioration of corrosion [12] and wear properties [13]. For other applications, however, better results were obtained for oxidized metallic coatings where oxide phase had shown improved wear resistance [14, 15], compressive behavior [16], wetting and adhesion [17], etc. In-flight decarburization of chromium carbide resulting in  $\text{Cr}_7\text{C}_3$  precipitation in  $\text{Cr}_3\text{C}_2$  is vital for enhanced wear resistance of these deposits [18].

Another area where researchers have been focusing on in-flight particle reactivity is Reactive Plasma Spraying (RPS) [19, 20]. Results regarding nitride and carbide deposits through RPS or other reactive techniques were presented in several studies where nitrogen or methane rich atmospheres were mostly exploited [21, 22]. All these studies, though improved our understanding of complex in-flight particle behavior, remained restricted to a lower percentage of secondary phase not exceeding 8 wt%.

The present study was performed to better understand possible influences of plasma jet surrounding environment on the mechanisms and kinetics of particle reactivity.



## 2. Experimental Technique

Sprayed material was a gas atomized 316L austenitic stainless steel powder produced commercially named as grade TY316L ( $-63+50\text{ }\mu\text{m}$ ) from Techphy Group H.T.M., France (Figure 1). Chemical compositions of the powder is given in Table 1.

Powder was, Initially, air plasma sprayed (APS) using a PTF4 type dc plasma gun. Plasma spray parameters are listed in Table 2. Sprayed particles were collected in a cylindrical collector where they are quenched by Argon jets limiting hot gases penetration into the collector. A pneumatic water cooled double disk system was disposed at the top of the collector. Complete description of the setup used for powder collection in APS was described elsewhere [23].

A modified setup was, later, fabricated to collect particles after spraying in controlled atmosphere. A schematic of the setup is shown in Figure 2. Argon atmosphere was generated in cylindrical collector after vacuuming the chamber along with the collector to 1.33 kPa. The chamber was, then, filled with required gas or gases mixture. A gas mixing system consisting of mixing compartment and pressure gages was installed at atmosphere gas inlet to inject precise gas composition in the plasma jet atmosphere.

Table 1: Starting 316L Techphy powder composition.

Cr	Ni	Mo	Mn	Si	C	Fe
19	11	2.4	1.2	0.4	0.01	Bal

Table 2: Plasma Spray Parameters

Voltage (V)	61
Current Intensity (A)	550
Thermal Efficiency (%)	56
Ar flow rate (slm)	45
(g/min)	80.4
H <sub>2</sub> flow rate (slm)	15
(g/min)	3.4
Anode Diameter (mm)	7
Distance of Powder injector (mm)	+3
Powder carrier gas	Ar
Carrier gas flow rate (slm)	6.5
Powder mass flux (kg/h)	1.5
Spray Distance (mm)	100

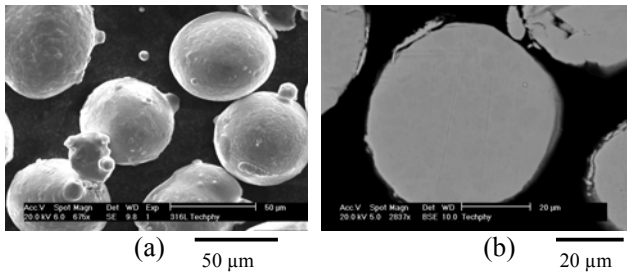


Figure 1: Starting Techphy particles surface (a) and cross section (b).

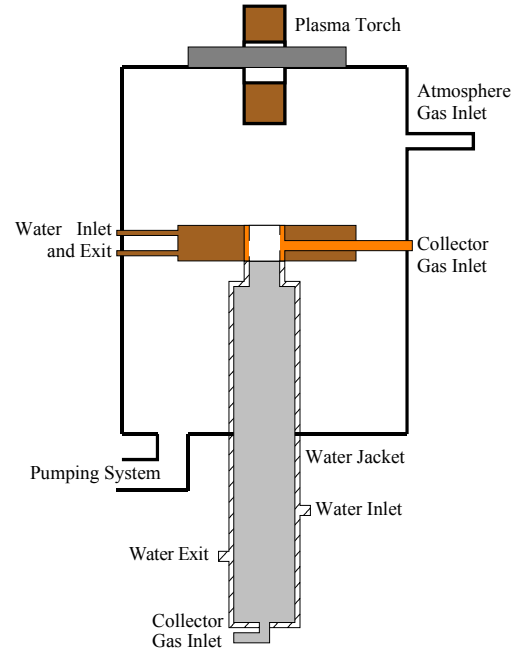


Figure 2: Controlled atmosphere spray setup.

Table 3: Plasma jet Atmosphere Composition.

Batch Ref	Atmosphere Gases Composition %Vol		
	O <sub>2</sub>	N <sub>2</sub>	Ar
CN1.	0	100	0
CN2.	5	95	0
CN3.	10	90	0
CN4.	15	85	0
CN5.	20	80	0
CNA6.	10	40	50
CNA7.	10	0	90

During spraying the chamber pressure was maintained at 0.1 MPa while introducing continuously atmosphere gas at a rate of 60 slm. Primarily, the influence of oxygen content in the surrounding atmosphere of the jet on the reactivity of metal particles was studied. Subsequently, the effect of surrounding gases other than oxygen was examined. Table 3 enlists details of atmospheres created in the plasma jet surroundings. Global oxygen content in starting and collected particles was determined using an ‘extractive fusion’ technique (LECO, USA). 5 samples, each weighing 2 g, for every batch were tested. Scanning electron microscopy was utilized for micrographs which were, later, used for statistical measurements of oxide nodules. The data were collected after treating 60 particles for each batch. Elemental analysis was performed using EDS.

### 3. Results and Discussion

#### *Air Plasma Spraying:*

0.03 wt% oxygen was detected in starting powder since low amount of oxides may form during powder manufacturing. The oxide was considered to be accumulated on particles surface as a thin layer since no oxides were observed within particles as it can be seen in for starting Techphy powders (Figure 1).

In collected Techphy particles, after spraying in ambient atmosphere, the outer layer was composed of two different regions: a fine grained cap forming towards one end of the particle and a coarser grained layer covering the rest of the particle (Figure 3a). EDS analysis of the coarse layer (Figure 3d) revealed a composition closer to that of base metal (Figure 3b) though a weak oxygen peak was detected. EDS of cap area, on the other hand, indicated high chromium and oxygen content along with low Fe and negligible Ni concentration (Figure 3e). This difference in the microstructure and composition can be due to possible difference in the type of oxide or difference in the formation mechanism. In the cross section of collected particles (Figure 3c), three distinct zones were observed;

1. brighter matrix of metal (ref Figure 3b for EDS),
  2. more or less spherical darker nodules (ref Figure 3e for EDS),
  3. oxide cap and thin layer covering the rest of the Techphy particle (ref Figure 3g for EDS).
- As nodules and cap were composed of oxygen and chromium rich phase with Fe and Si as secondary elements, a complex or mixed oxides can be predicted.

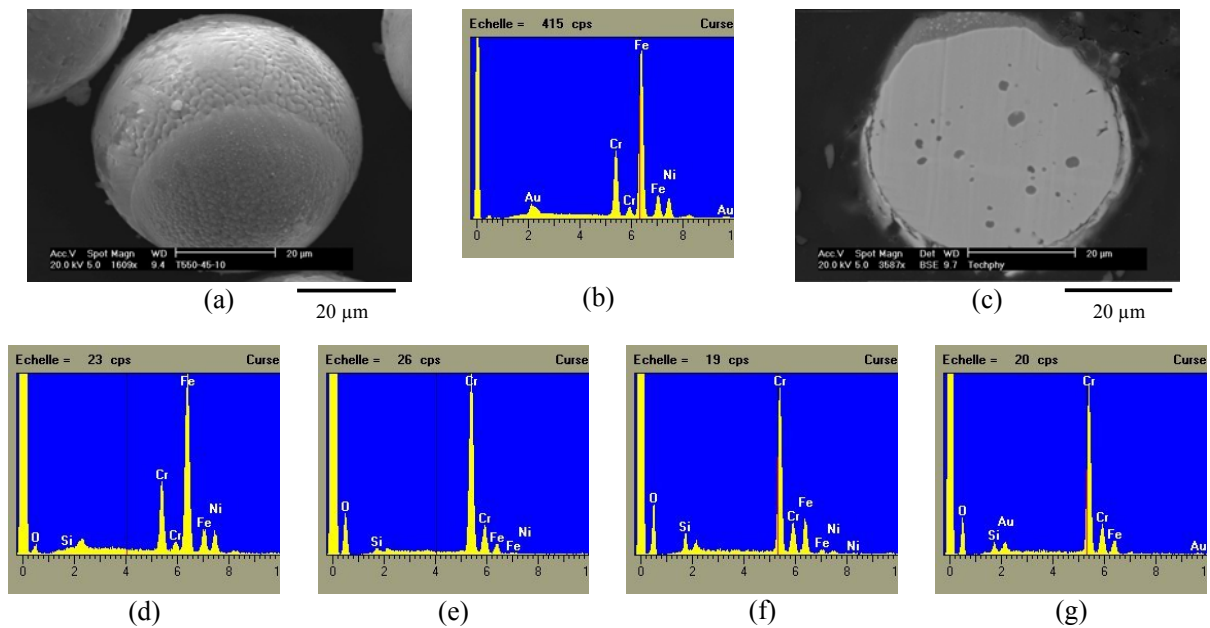


Figure 3: Collected oxidized particles surface (a) and cross section (c). EDS analysis of Base metal (b), Coarse grained (d) and Oxide cap on the Techphy surface (e), oxide nodule (h) and oxide cap (i) in particle cross section.



Nodule and cap formation mechanisms, their detailed elemental and phase analysis in air plasma sprayed particles, accompanied with other results to elaborate the proposed explanation, were discussed by the authors in previous articles [9, 23], where it was shown that convective movement within the liquid particle during first 50 mm downstream may occur if plasma-particle kinematic viscosity ratio ( $\nu_{\text{plasma}}/\nu_{\text{particle}}$ ) is greater than 50 and particle Reynolds's number (Re) is superior to 20. This convection introduces mass transfer from particle surface to its interior entraining surface oxide and resulting in oxide nodules. Convective movement ceases after 50 mm as  $\nu_{\text{plasma}}/\nu_{\text{particle}}$  drops rapidly and classical surface oxidation dominates. The surface oxide may segregate toward the particle tail in an oxide cap if metal and oxide phases of the particle are maintained in liquid form at high particle Re values.

#### *Controlled Atmosphere Plasma Spraying*

Figure 4 presents micrographs of collected particles after spraying under different  $\text{O}_2\text{-N}_2$  environments around plasma jet. A considerable reduction in entrained oxide nodules was observed as oxygen partial pressure in the plasma jet surrounding was reduced. Particles sprayed in “less oxidizing” conditions exhibited surface effects indicating convective movements as shown in Figure 4f. Surface oxide, in other samples, that forms once the convective movements ceases, masked such surface effects.

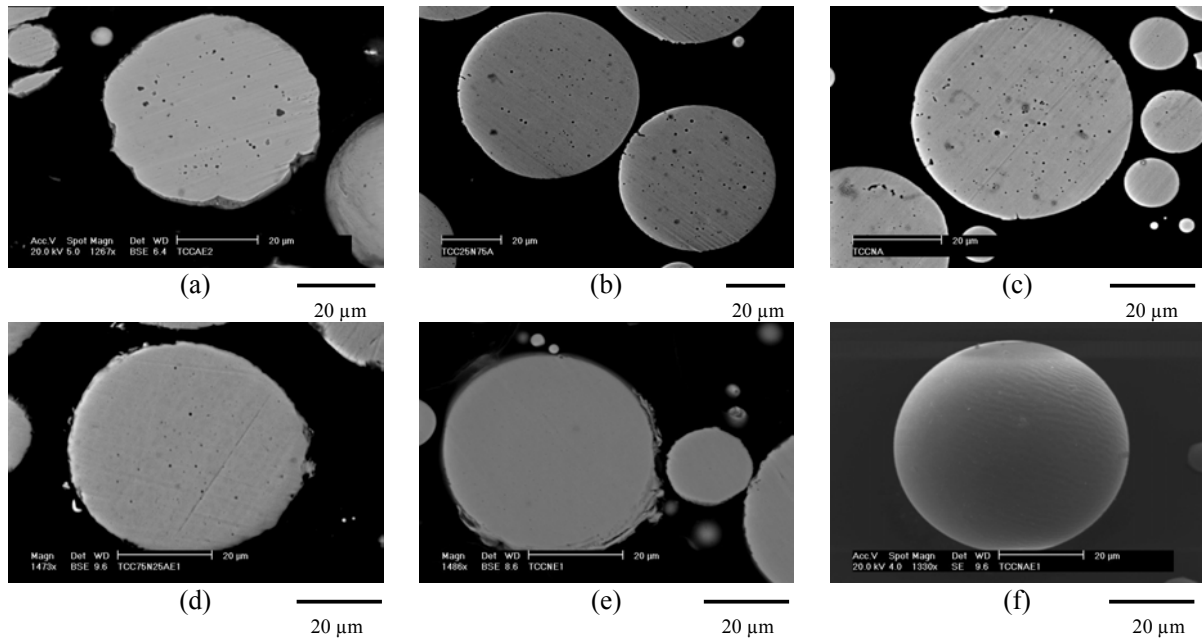


Figure 4: Collected particles sprayed in different  $\text{O}_2\text{-N}_2$  surrounding environments of plasma jet. CN5 (a), CN4 (b), CN3 (c), CN2 (d), CN1 (e). Surface of one of the particles exhibiting convective waves at the surface (f). See Table 3 for the definition of CNi.

These observations were quantified using LECO technique and image analysis treatment of collected particles to give global oxygen amount and convective oxide content in all batches. The results are summarized in Figure 5. In collected particles oxide nodules exhibited a parabolic evolution whereas total oxygen amount was close to a linear function of oxygen partial pressure in plasma jet atmosphere within the studied range. Hackett and Settles [24], while studying oxidation of Fe, deposited by HVOF, also established a linear relationship between  $\text{O}_2$  in entrained atmosphere of HVOF and mass fraction of oxygen in Fe deposits.

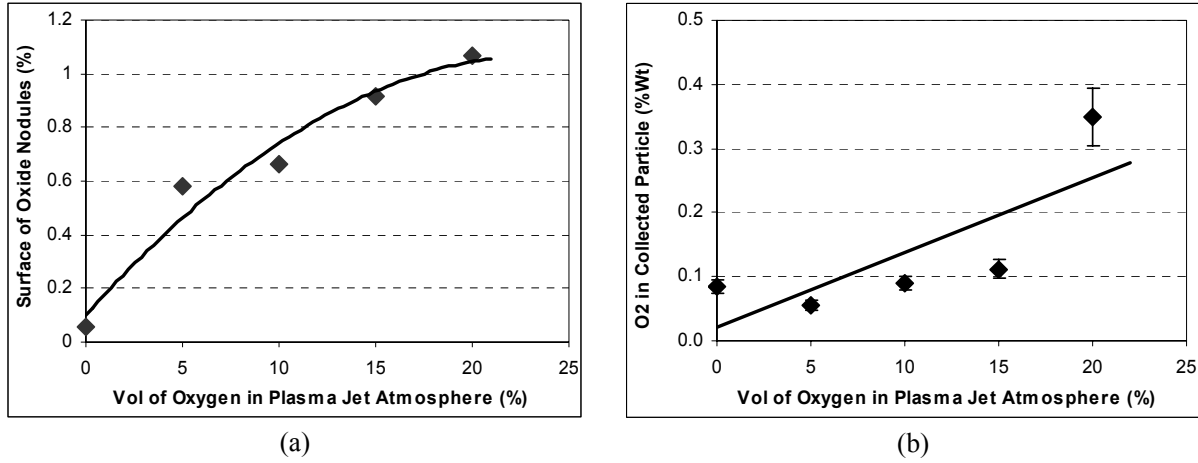


Figure 5: Surface area of oxide nodules (a) and O<sub>2</sub> weight (b) variation in collected particles with O<sub>2</sub> content in plasma jet surrounding atmosphere.

In another series of experimentations, influence of secondary gases besides O<sub>2</sub> on the particle in-flight reactivity was studied. For that purpose,  $p_{O_2} / p_X$  (X being the secondary gas or gases mixture) was kept at a constant value of 0.11, whereas secondary gas composition was altered to have Ar or N<sub>2</sub> or a mixture of both gases in the surrounding of the plasma jet. Cross sections of collected particles from each batch are shown in Figure 6 and the measurements of oxide nodules surface area and total oxygen mass percentages are illustrated in Figure 7. Interestingly, the mass fraction of oxygen in collected powder increases with an increase in Ar partial pressure or decrease in N<sub>2</sub> partial pressure in the plasma jet atmosphere whereas no significant variation in oxide nodules surface area was established.

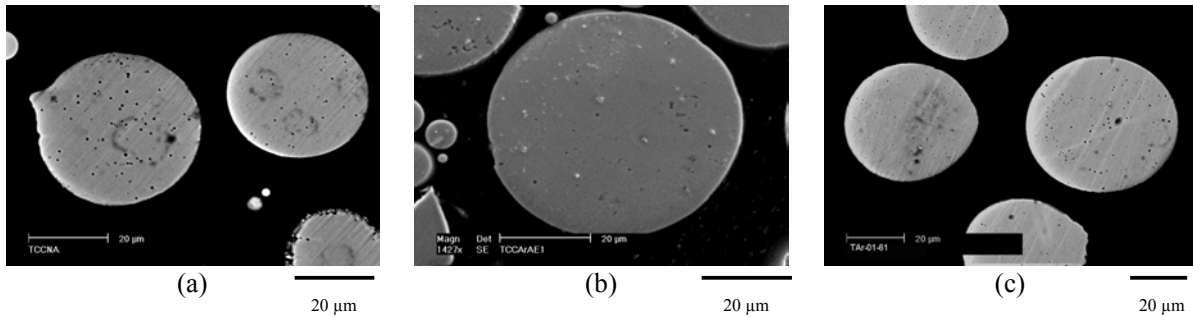


Figure 6: Particles collected after spraying in different O<sub>2</sub>-N<sub>2</sub>-Ar atmospheres around plasma jet. CN3 (a), CNA6 (b), CNA7 (c). See Table 3 for the definition of sample references.

Leylaverigne et al [25] developed mathematical model to study the influence of pure Ar or N<sub>2</sub> atmospheres around plasma jet on its properties and that of developed coatings. According to authors, the plasma jet, in Ar atmosphere, undergoes a gradual decrease in temperature and velocity. On the other hand, in N<sub>2</sub> atmosphere, though the deceleration of plasma jet is almost similar to that in Ar atmosphere, a steep temperature decay occurs between 15 and 20 mm downstream from nozzle exit. The decay rate stabilizes later and approaches to that of plasma jet in Ar atmosphere. A higher initial diffusion of atmosphere towards plasma jet axis was also reported in N<sub>2</sub> environment. The entrained gases mass flux in both conditions were, however, found to converge to equivalent values after 60 mm stand off distance.

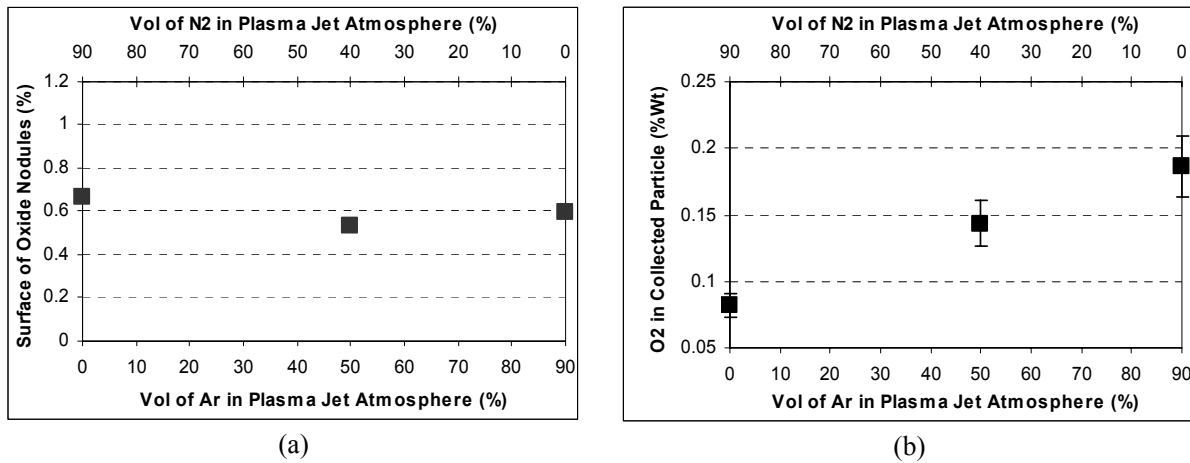


Figure 7: Surface area of oxide nodules (a) and O<sub>2</sub> weight (b) in particles collected after varying Ar and N<sub>2</sub> content in plasma jet surrounding atmosphere while keeping O<sub>2</sub> vol% at 10.

Particles sprayed in Ar surrounded plasma jet would have similar behavior to those sprayed in N<sub>2</sub> atmosphere till 15 mm downstream of nozzle exit. As the N<sub>2</sub> surrounding plasma experiences a rapid temperature drop, Re and kinematic viscosities of plasma and particles decrease, though still high enough for convective movements within the particles [ $v_{\text{plasma}}/v_{\text{particle}} > 50$ ;  $Re_{\text{particle}} > 20$ ]. Lower convective movements were compensated by higher O<sub>2</sub> flux and thus the particles had almost same amount of oxide nodules. After 50 mm, O<sub>2</sub> flux is almost identical in both conditions but the temperature of Ar surrounded plasma is superior to N<sub>2</sub> surrounded one that can lead to higher total oxygen and oxide content in particles sprayed under former condition.

#### 4. Conclusion

In-flight reactivity, particularly oxidation, of stainless steel particles was studied as a function of plasma jet surrounding atmosphere. Collected 316L stainless steel (-63+50  $\mu\text{m}$ ) particles after APS exhibited oxide nodules within them and surface oxide layer. The surface oxide layer was distinguishable into a segregated cap, forming major surface oxide mass, and a thin layer covering the whole particle.

The powder was, then, sprayed in a controlled atmosphere chamber varying  $p_{\text{O}_2}/p_{\text{N}_2}$  in the plasma jet surroundings between 0 and 0.25. It was found that oxygen content in collected particles increases linearly with  $p_{\text{O}_2}$  whereas a parabolic relationship was established between oxide nodules surface area and  $p_{\text{O}_2}$ .

Moreover, influence of secondary gases forming plasma jet atmosphere on particle in-flight reactivity was studied keeping surrounding  $p_{\text{O}_2}/p_{\text{X}}$  at 0.11 while modifying composition of X species by altering N<sub>2</sub> and Ar content. Particles with slightly higher oxygen content were collected in Ar rich surrounding whereas no distinct difference in oxide nodules surface area was measured. This is due to hotter plasma plumes obtained in argon atmosphere.

#### 5. References

- [1] M. Hrabovsky, M. Konrad, V. Kopecky, in Progress in Plasma Processing of Materials, (ed.) P. Fauchais, (pub.) Begell House, USA, 1999, 293-298.
- [2] E. Pfender, J. Fincke, R. Spoores, 11 (4), 1991, 529-543.
- [3] O. Lagnoux, J.F. Coudert, K. Wittman, P. Fauchais, in Thermal Spray: Surface Engineering via Applied research, (ed.) C. C. Berndt, (pub.) ASM International, 2000, 71-77.
- [4] A. Denoirjean, O. Langnoux, P. Fauchais, V. Sember, in Thermal Spray: Meeting the Challenges of 21<sup>st</sup> Century, (ed.) C. Coddet, (pub.) ASM International, 1998, 809-814.
- [5] V. Gourlaouen, F. Remy, J.M. Leger, J. Sattonnet, in Thermal Spray: Meeting the Challenges of 21<sup>st</sup> Century, (ed.) C. Coddet, (pub.) ASM International, 1998, 797-801.

- [6] O. Lagnoux, Ph. D. Thesis, Université de Limoges, France, 1999, (in French).
- [7] C.M. Hackett, G.S. Settles, "Turbulent mixing of the HVOF thermal spray and coating oxidation", in Thermal Spray Industrial Applications, (ed.) C.C. Berndt and S. Sampath, (pub.) ASM International, 1992, 611-618.
- [8] R.A. Neiser, M.F. Smith, R.C. Dykhuizen; J. Thermal Spray Technology; 7 (4); 1998; 537-545.
- [9] A. A. Syed, P. Denoirjean, A. Denoirjean, J. C. Labbe, P. Fauchais, B. Hannoyer, in EMRS G-TPP7 Thermal Plasma Processes symposium, Strasbourg, France, June 2002.
- [10] R.B. Heimann, Key Engineering Materials, 122-124, 1996, 399-442.
- [11] L.M. Berger, P. Vuoristo, T. Mäntylä, W. Gruner, in Thermal Spray: Meeting the Challenges of 21<sup>st</sup> Century, (ed.) C. Coddet, (pub.) ASM International, 1998, 75-82.
- [12] P. Siitonen, T. Kinoshita, P.O. Kettunen, in Thermal Spray Industrial Applications, (ed.) C. C. Berndt and S. Sampath, (pub.) ASM international, 1994, 105-110.
- [13] R. Nieminen, P. Vuoristo, K. Niemi, T. Mantyla, G. Barbezat, Wear 212, 1997, 66-77.
- [14] S.E. Hartfield-Wunsch, S.C. Tung; in Thermal Spray Industrial Applications; (ed.) C.C. Berndt and S. Sampath; (pub.) ASM international; 1994; 19-24.
- [15] B. Hwang, S. Lee, J. Ahn, Material Science & Engineering A, 335, 2002, 268-280.
- [16] K. Vollenk, V. Novak, J. Dubsky, P. Chraska, K. Neufuss; Materials Science & Engineering A; 234-236; 1997; 493-496.
- [17] G. Espie; Ph. D. Thesis; Université de Limoges, France; 2000, (in French).
- [18] U. Menne, A. Mohr, M. Bammer, C. Verpoort, K. Ebert, R. Baumann, in Proc. TS'93, Thermal Spray Conference, Aachen (D), March 1993, 277-284.
- [19] R.W. Smith, Powder Metallurgy International, 25 (1), 1993, 9-16.
- [20] P. Fauchais, A. Vardelle, A. Denoirjean, Surface & Coating technology, 97, 1997, 66-78.
- [21] L. Zhao, E. Lugscheider, Wear, 9238, 2002, 1-5.
- [22] N. Sakoda, M. Hida, Y. Sakakibara, T. Tajiri, in International Thermal Spray Conference: Tagung and Conference Proceeding, (ed.) E. Lugscheider, (pub.) ASM International, 2002, 1042-1046.
- [23] A.A. Syed, A. Denoirjean, P. Denoirjean, J.C. Labbe, P. Fauchais, accepted in International Thermal Spray Conference (ITSC), 2003.
- [24] C.M. Hackett, G.S. Settles, in Proc. 8<sup>th</sup> National Thermal Spray Conference, Houston, Texas, September 1995, 21-29.
- [25] M. Leylaverigne, B. Dussoubs, A. Vardelle, N. Goubot, J. Thermal Spray Technology, 7 (4), 1998, 527-536.

# Diagnostics of stable and transient species in pulsed rf plasmas containing fluorocarbons

M. Geigl, O. Gabriel, K. Li and J. Meichsner

*Institute of Physics, Ernst Moritz Arndt University of Greifswald, Greifswald, Germany*

Fluorocarbon plasmas demonstrate a dual character: such plasmas can be used for etching processes and for film deposition. The prevailing process is determined by plasma properties, mainly by plasma composition which in turn depends on the process conditions (discharge type, gas composition, pressure, etc.). The understanding of the elementary processes and reaction kinetics provides control of the plasma-technological process. The main purpose of the presented study is the diagnostics of transient (e.g.  $\text{CF}_x$ -radicals,  $x = 1-3$ ) as well as stable species (e.g.  $\text{CF}_4$ ,  $\text{C}_2\text{F}_6$ ) in fluorocarbon plasmas of pulsed capacitively coupled RF discharges (13.56 MHz).

The following field of the process parameters was chosen for plasma creation:  $\text{CF}_4$ -,  $\text{C}_2\text{F}_6$ - and  $\text{C}_3\text{F}_8$ - $\text{H}_2$  gas mixtures in the pressure range from 10 to 100 Pa and gas flows from 1 to 10 sccm. The pulse frequency was varied between 1 and 100 Hz with different duty cycles.

To connect the gas phase chemistry with the properties of deposited films the time dependence of the absolute concentration of molecular species in the gas phase has been measured by means of Infrared Tuneable Diode Laser Absorption Spectroscopy (IR-TDLAS) with a time resolution up to 300  $\mu\text{s}$ . Appearance Potential Mass Spectrometry (APMS) and electron Attachment Mass Spectrometry (EAMS) have been used to find out the time dependence of the concentrations of radicals (e.g.  $\text{CF}_2$ ,  $\text{C}_2\text{F}_5$ ) and high weight molecules (up to  $\text{C}_4\text{F}_8$ ). The growth rate of the films was derived from measurements with an *in-situ* ellipsometer and the optical properties of the films were examined with a spectral ellipsometer (300 - 800 nm).

The figures 1 and 2 below show the influence of the pulsed mode of the RF discharge on the gas phase and film growth.

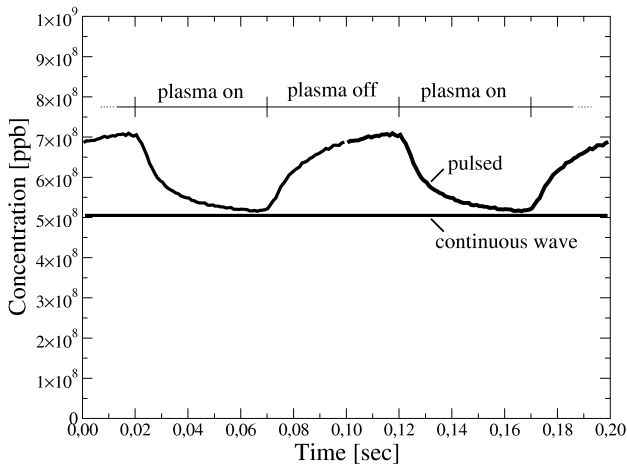


Figure 1: Modulation of the  $\text{CF}_4$  fragmentation in the pulsed mode (10 W, 50 Pa, 5 sccm  $\text{CF}_4$ , 10 Hz)

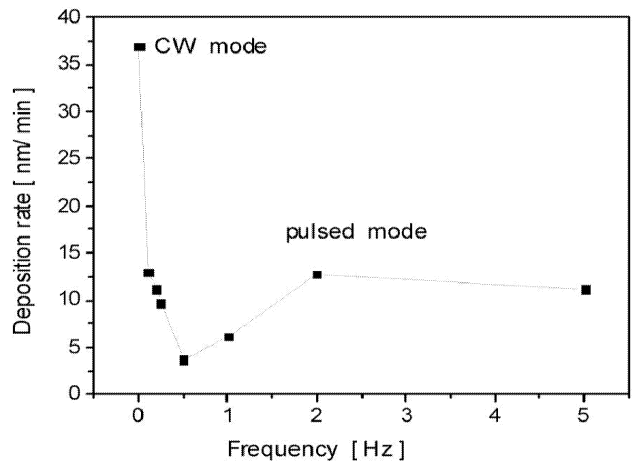


Figure 2: Dependence of film deposition rate on pulse frequency (100 W, 100 Pa, 10 sccm  $\text{CF}_4$ , 10 sccm  $\text{H}_2$ , duty cycle 50%)

We acknowledge generous support by the Deutsche Forschungsgemeinschaft through the Sonderforschungsbereich 198 and by the BMBF through project 13N8051.

# Influence of temperature gradients on spatial density distribution of atomic oxygen in an rf-discharge

S. Peters, A. Mengel, M. Geigl, O. Gabriel, B. Krames, K. Li, and J. Meichsner

*Institute of Physics, Ernst Moritz Arndt University of Greifswald, Greifswald, Germany*

Within the widespread field of applied surface processing the atomic oxygen is responsible for many plasma surface reactions like oxidation or the etching of polymer films. Therefore investigations on spatial density distributions provide a good approach for enhanced knowledge of plasma surface interactions. To determine spatial distributions of O atoms in an asymmetric capacitively coupled oxygen rf-discharge two-photon laser induced fluorescence spectroscopy (TALIF) is used. With a reference measurement at a spectrally close two-photon resonance of xenon the data are calibrated [1]. Due to the uncooled electrode system a temperature gradient of the atomic and molecular oxygen distribution is estimated, which influence the absolute amounts of the O atom density. For two

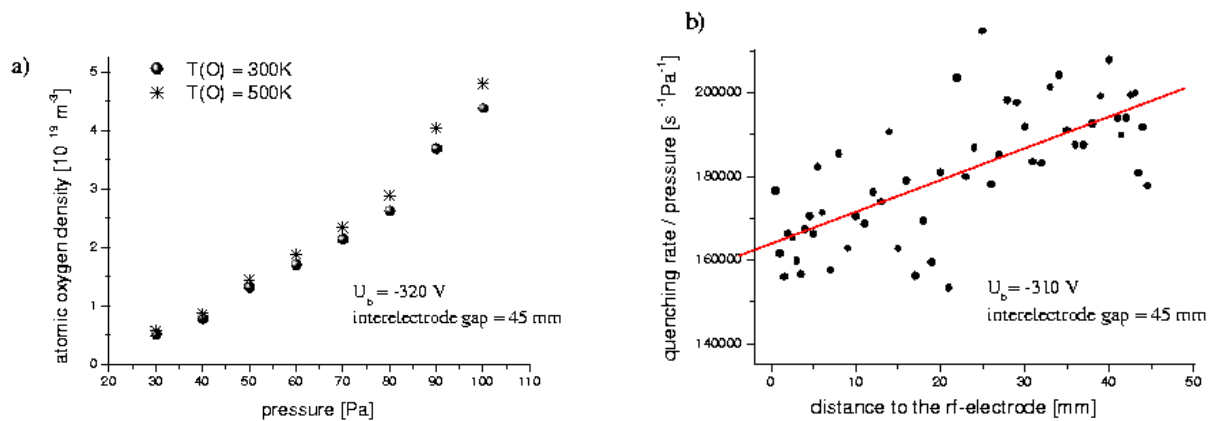


Figure 1: a) Pressure dependence of O atoms calculated for two different temperatures of the atomic oxygen. b) Axial distribution of the quenching rate.

different temperatures figure 1a) shows the pressure dependence of the atomic oxygen, measured in the middle of the discharge. Using the fine structure levels of the ground state, the temperature of the atomic oxygen can be estimated. This measurements yielded a Boltzmann distribution with a temperature difference of 100–150 K, between the middle of the discharge and the region near to the grounded electrode. Contradictorily results are found close to the rf-electrode, therefore further investigations have to be done. Measuring the decay rate of the fluorescence as a function of pressure, quenching losses, had to be determined, which are necessary for the calibration. Figure 1b) show an axial distribution of the quenching rate divided by pressure. The apparently increase can be explained by an axial temperature gradient of the  $\text{O}_2$ -molecules, to be the prominent species depleting the excited state of the atomic oxygen. The atmospheric  $\text{O}_2$ -band was utilised to measure the rotational temperature of the  $\text{O}_2$ -molecules, which is found to  $370 \pm 20 \text{ K}$  comparable to Barucki [2] inside the plasma bulk (pressure  $p = 50 \text{ Pa}$ , selfbias voltage  $U_b = -320 \text{ V}$ ). This leads to a quenching coefficient of  $(9.24 \pm 0.5) \times 10^{-10} \text{ cm}^3 \text{ s}^{-1}$  and a lifetime of 36 ns, which is in good agreement with Niemi et al.[3]. The spatial temperature profiles of molecular and atomic oxygen, as well as radial distributions of the quenching rate will be presented.

(Acknowledgement to the Deutsche Forschungsgemeinschaft through SFB 198)

## References

- [1] A. Goehlich et al., J. Chem. Phys. **108**, 9362 (1998).
- [2] K. Barucki, diploma-thesis, Chemnitz University of Technology,(1996).
- [3] K. Niemi, J. Phys.D: Appl. Phys.**34**, 2330 (2001).

# Time-resolved temperature measurements in a turbulent argon plasma jet

G. Gregori<sup>1</sup>, U. Kortshagen, E. Pfender, J. Heberlein

*Department of Mechanical Engineering, University of Minnesota, Minneapolis, MN 55455*

<sup>1</sup> *Present address: Lawrence Livermore National Laboratory, L-399 P.O. Box 808, Livermore, CA 94551*

## Abstract

In this paper we present an experimental characterization of the temperature behavior along the axis of a turbulent argon plasma jet. Absolute intensity emission spectroscopy and Thomson laser scattering are used to obtain time-resolved electron temperature and electron density measurements at different positions along the jet axis. Both techniques yield similar results showing that temperature fluctuations in the potential core of the jet are intense even close to the nozzle exit. At the same time, we observe a large displacement of the entire jet column downstream of the nozzle exit. This suggests that anode arc root attachment instabilities inside the nozzle are the main driving mechanisms of jet instabilities under these conditions.

## Introduction

It is well known that atmospheric plasma jets exhibit several instability mechanisms. One class of such instabilities is referred to as arc attachment instabilities, since they correlate with the movement of the arc-root attachment inside the anode nozzle<sup>1</sup>. Arc instabilities are traced by fluctuations in the arc voltage.

During typical torch operation, the anode attachment is pushed downstream on the anode wall by the carrier gas flow, resulting in a progressive lengthening of the arc. This process will continue until the potential difference between the anode and the arc column favors the formation of a new breakdown channel at a closer location from the cathode<sup>2</sup>. As the anode-arc attachment moves on the nozzle walls, “bubbles” of hot plasma gas embedded in cold surrounding gas are continuously ejected, thus generating a quite non homogeneous jet at the nozzle exit<sup>3</sup>. Eventually, arc instability will trigger the formation of fluid-dynamic instabilities, such as Kelvin-Helmholtz or Rayleigh-Taylor instabilities, as the jet exits from the nozzle and expands in the surrounding medium. We have then a strong entrainment of ambient gas into the plume, leading to the rapid formation of a turbulent velocity profile<sup>4</sup>. The transition to fully turbulent flow is driven by shear motion at the surface of the jet that feeds the formation of vortices. Such vortices move downstream, while increasing in size, and initiate the mixing between the ambient and the plasma gas. These vortices are convected downstream until they dissipate in the fully turbulent regime.

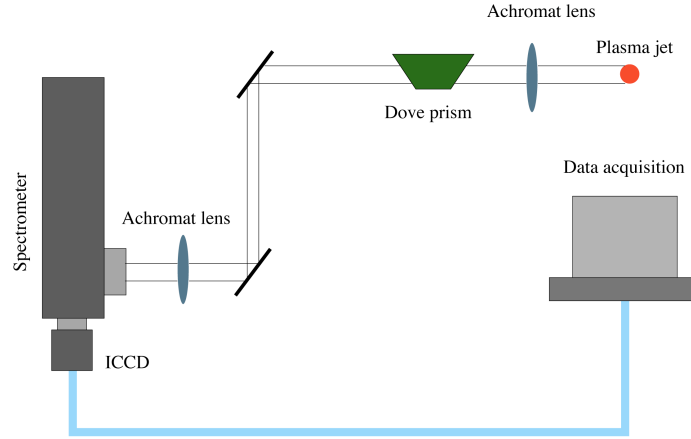
The aforementioned effects contribute to a large-scale rapid change of the plasma properties inside any *Eulerian* control volume in the jet. Thus, quantities such as temperature and density of the ions and the electrons as well as neutral gas particles, cannot be simply described by time-averaged values, but their full time dependence needs to be known if, for example, reliable and reproducible industrial applications of these type of plasma jets are required.

In this paper we are mainly interested in the temperature characterization along the jet axis. We have performed a series of time-integrated and time-resolved absolute line-intensity emission spectroscopy measurements. Such measurements provide both averaged and instantaneous temperatures, that indeed reveal a highly variable jet morphology even very close to the nozzle exit. Comparison with Thomson scattering measurements taken on the same plasma jet<sup>5</sup> show that temperature values that we obtain from laser scattering are comparable with the ones derived from emission spectroscopy, suggesting even larger fluctuations with time of the local values.

## Experimental setup for spectroscopic measurements

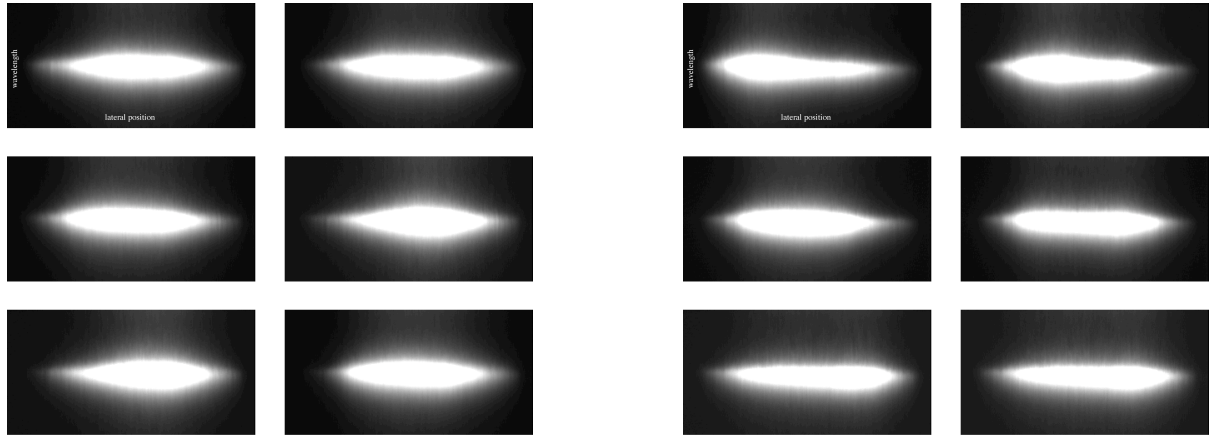
The experimental setup for line intensity measurements is shown in Fig 1. The integrated argon emission line at  $\lambda=750.4$  nm across the transverse (or lateral) dimension of the jet is focused on the 100  $\mu$ m slit width of a 1 m Czerny-Turner monochromator equipped with a 140x120 mm<sup>2</sup>, 1800 groove/mm holographic grating. The line profile is then measured with a 2-D intensified charge-coupled device (ICCD) gated array detector. Since the monochromator slit is aligned vertically (parallel to the jet axis), a Dove prism is used to rotate the image by 90°. A 600 A dc torch operating at atmospheric pressure with an argon flow rate of 35.0 l/min has

been used to generate the jet. Lateral scans of the jet have been taken at 3.0 mm and 11.0 mm downstream the nozzle exit, respectively. Each scan was obtained by gating the ICCD for 50 ns. At each axial location we have taken 100 single images with a repetition rate of 5 Hz. Absolute values of the line intensity have been obtained using a tungsten calibration lamp.



**Figure 1:** Experimental setup for spectroscopic measurements.

A sequence of 6 consecutive frames recorded on the CCD array at 3.0 mm and 11.0 mm downstream is shown Fig 2. It is evident that there is a strong asymmetry of the lateral profiles at 11.0 mm downstream, as well as a rapid change in shape from one image to another. On the other hand, this effect is much less pronounced at 3.0 mm from the nozzle exit.



**Figure 2:** CCD images of the argon  $\lambda=750.4$  nm emission line at 3.0 mm (left) and 11.0 mm (right) downstream from the nozzle exit. Each image is collected with 50 ns exposure time and with 5 Hz repetition rate.

Together with the emission line signal from the jet, the arc voltage has been monitored. A typical voltage spectrum is reported in Fig 3. The arc voltage shows a broad frequency peak at  $f_v \sim 3-5$  kHz while the mean voltage is at 30.6 V. Arc-root fluctuations produce changes in the plasma properties that are advected downstream, thus  $f_v$  is also the frequency at which fluctuations of the temperature along the jet axis are most likely to occur. Since our spectroscopic measurements are taken at a much lower sampling rate, they are unable to provide accurate spectral analysis of the jet behavior. On the other hand, they are only intended as an indication of the level of the temperature fluctuations.

### Spectroscopic results

From the lateral intensity profiles  $I_i(y)$  it is possible to derive the local spectral intensity  $I(r)$  under the assumption of a radially symmetric source using the Abel inversion technique<sup>6</sup>. This is a quite strict assumption, and it only holds if the jet light is integrated over a time  $t > 1/f_v \sim 0.25$  ms. At shorter exposures,



the jet is not symmetric and in order to still use Abel inversion, two radially symmetric profiles are then artificially generated from one experimental profile by dividing the line at the maximum intensity and then creating, for each half profile, the corresponding mirror image. The two symmetric lateral profiles thus provide an upper and lower bound for the temperature estimates. If  $I^s_l(y)$  is such a symmetrized profile, then the local intensity profile is given by<sup>6</sup>

$$I(r) = \frac{1}{\pi} \int_0^R \frac{dI^s_l(y)}{dy} \frac{dy}{\sqrt{y^2 - r^2}}, \quad (1)$$

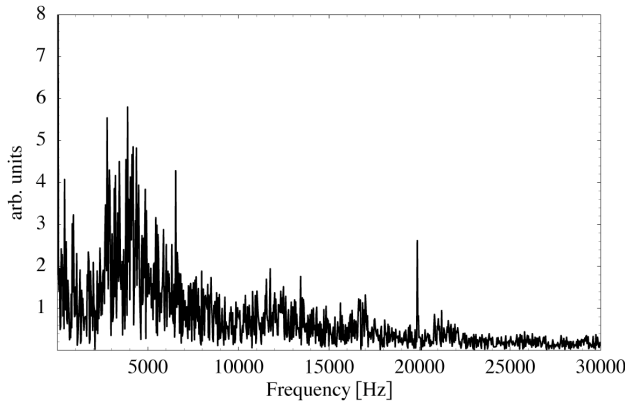
where  $R$  is the radius of the plasma jet, which is estimated to be at the location where the measured intensity drops below 5% of the maximum. To limit errors introduced by the numerical derivative in (1), the line intensity profile  $I^s_l(y)$  has been digitally smoothed through a low-pass filter to remove any high frequency noise in the data. In order to get an estimate for the temperature, the measured local intensity  $I(r)$  needs to be compared with the theoretical spectral intensity  $I_l(r)$  which is given by

$$I_l(r) = \frac{hc}{4\pi} A^u_l n_0 \frac{g_u}{Q_{Ar}} \exp\left[-\frac{E_u}{k_B T}\right], \quad (2)$$

under the assumption of complete local thermodynamic equilibrium (LTE). Here, the argon partition function is taken as

$$Q_{Ar} = 1 + 1463.0 \exp\left[-\frac{1.656 \times 10^5}{T}\right]. \quad (3)$$

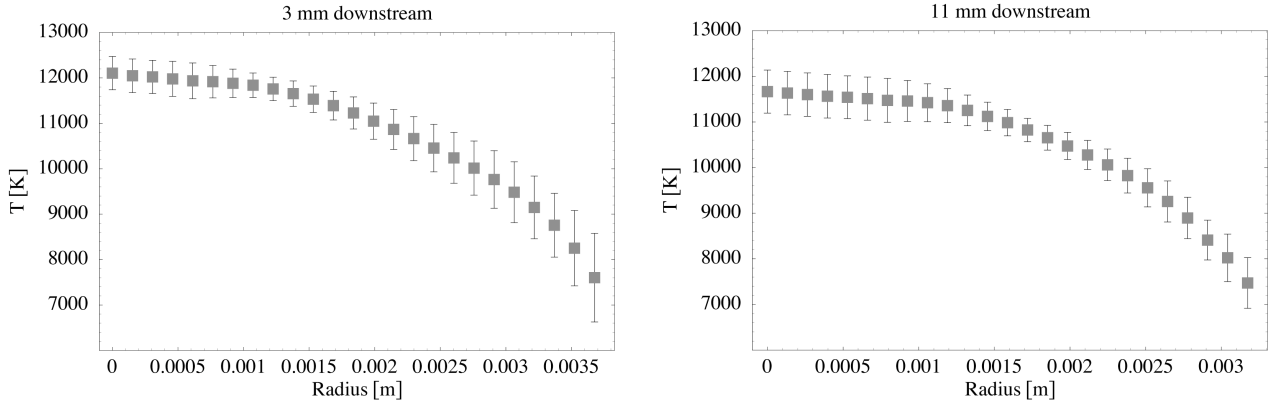
The statistical weight of the upper state is  $g_u=1$ , the transition coefficient is  $A^u_l=4.45 \times 10^7 \text{ s}^{-1}$ , and  $E_u=2.16 \times 10^{-18} \text{ J}$ . The total neutral argon density  $n_0$  is calculated from  $p=(n_0+2n_e)k_B T$ , where  $p=1 \text{ atm}$  is the gas pressure. The electron density  $n_e \sim n_i$  is then calculated using the Saha equation<sup>7</sup>.



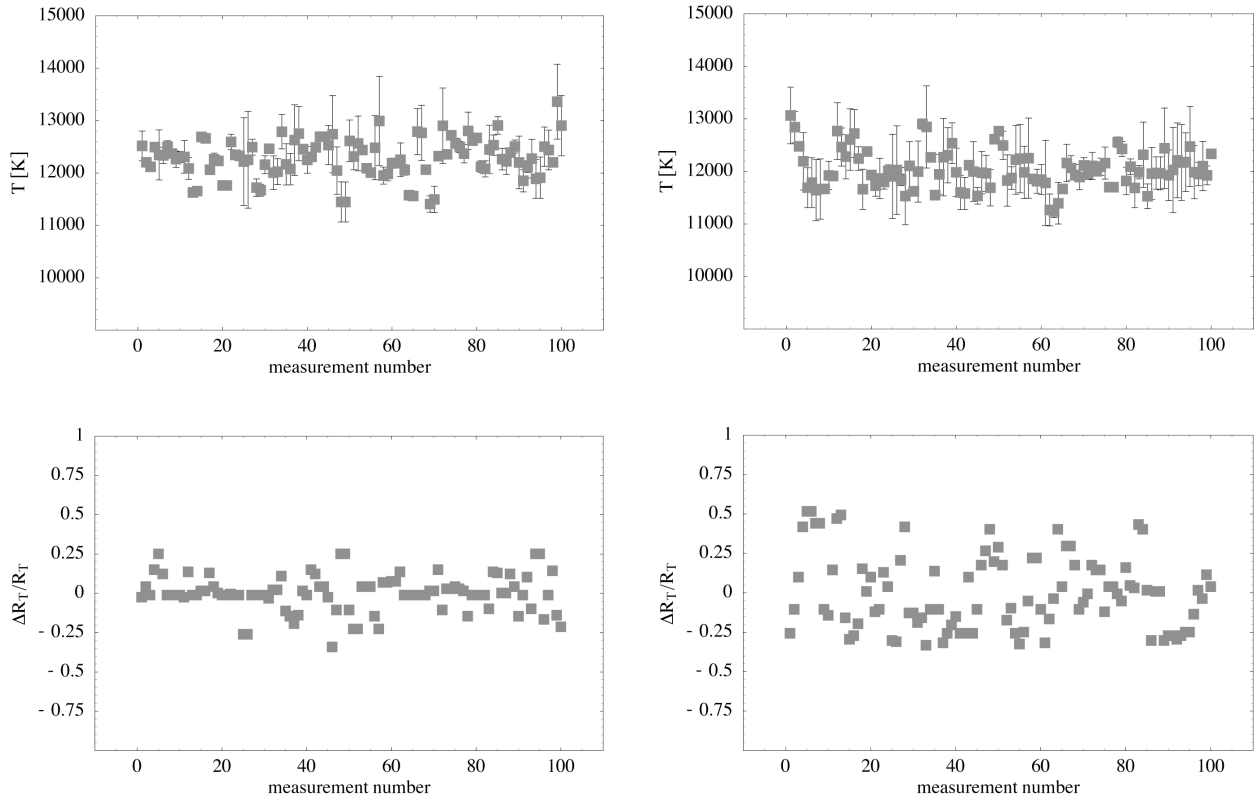
**Figure 3:** Power spectrum of the arc voltage.

Averaged temperature profiles are obtained by summing the intensities of 100 consecutive single frames, and then performing the Abel inversion on the resulting lateral profiles. The resulting radial temperature profiles at 3.0 mm and 11.0 mm downstream from the nozzle exit are shown in Fig. 4. We see that the centerline temperature is  $T \sim 12000 \text{ K}$  at 3.0 mm and  $T \sim 11500 \text{ K}$  at 11.0 mm downstream.

At each axial location, 100 different frames are recorded with the CCD camera, from which temperature values are derived. Figure 5 shows the maximum measured temperatures at 3.0 mm and 11.0 mm from the nozzle exit, respectively. The same figure also shows the variation of  $\Delta R_T(t) = R_{Tmax}(t) - R_T$ , where  $R_{Tmax}(t)$  is the position of the maximum temperature at time  $t$  with the respect to the laboratory frame and  $R_T = \langle R_{Tmax}(t) \rangle$  is its mean position over 100 consecutive samples. Larger positive values of  $\Delta R_T(t)$  at 11.0 mm downstream from the nozzle exit are associated with a shift in the position of the entire jet as a result of the preferred attachment of the arc root on the anode. It is also interesting to note that the level of temperature fluctuations is  $2\% \sim 6\%$ , almost constant along the jet axis. In addition, the mean temperature that we obtain by averaging each single exposure is  $\sim 500 \text{ K}$  higher than the average temperature derived from the accumulated intensity profile over all the 100 single exposures. This can be used as an indication of the error introduced by smoothing of the intensity profiles resulting from long-time integration of the line signal.



**Figure 4:** Radial temperature profiles obtained by averaging 100 consecutive frames.



**Figure 5: (Top)** Variation of the maximum gas temperature at 3.0 mm (left) and 11.0 mm (right) downstream from the nozzle exit. The standard deviation of the data is  $\sigma=374$  K (3.0 mm), and  $\sigma=363$  K (11.0 mm). **(Bottom)** Variation of the relative location of the maximum temperature with respect to its average position at 3.0 mm (left) and 11.0 mm (right) downstream. Standard deviation is  $\sigma=0.115$  (3.0 mm) and  $\sigma=0.237$  (11.0 mm).

### Thomson scattering measurements

We have conducted time-resolved Thomson scattering measurements on the axis of the same arc plasma jet and at the same spatial locations. The experimental apparatus has been extensively discussed elsewhere<sup>5</sup>. In this particular experiment, Thomson scattered light has been collected at  $90^\circ$  scattering angle, and, to increase signal-to-noise ratio, a Glan-Thompson polarizer filter has been positioned in front of the collection optics. Since Thomson scattering preserves polarization, the Glan-Thompson filter is used to reject unpolarized light from the plasma. The laser has been operated at maximum beam intensity,  $\sim 400$  mJ/pulse, with a waist diameter on the jet axis on the order of 2 mm. At these energy densities, inverse bremsstrahlung heating of the electrons is typically 500 K, accounting only for a few percent of the measured electron

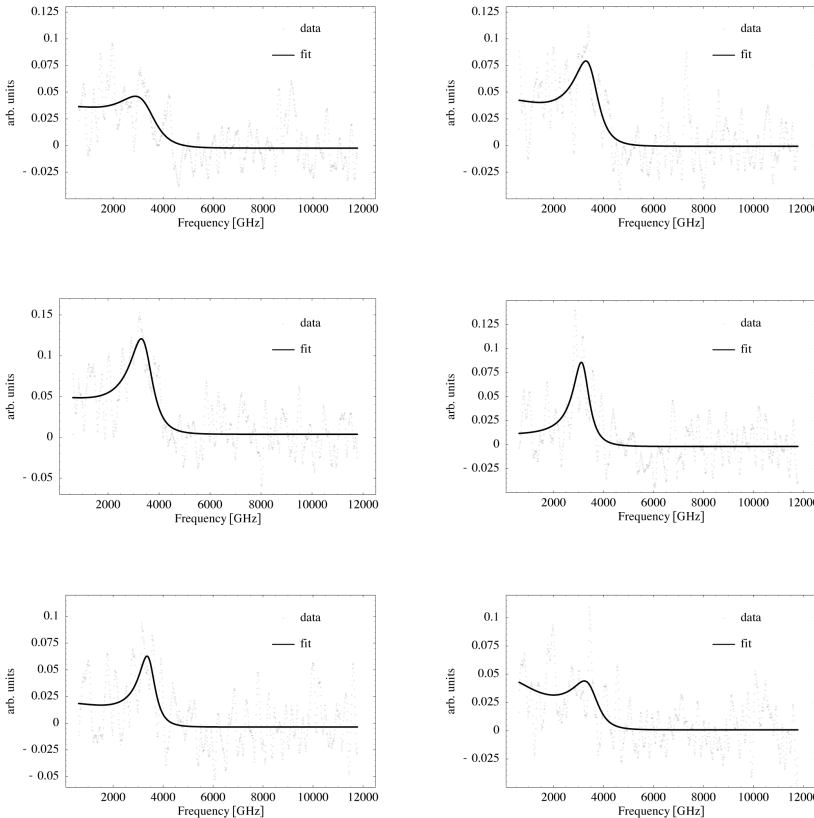
temperature. Fluctuations in the laser power were within 2.5-4.5%. Scattered light from single laser pulses, each with a duration of 10 ns, has been stored individually and then post-processed through a Savitzky-Golay smoothing filter in order to remove high frequency noise in the data.

The memory function formalism<sup>5</sup> (MFF) approach for the spectral density function has been used to derive electron density and electron temperature values from the measured light spectrum. Instrumental broadening and temperature variations in the scattering volume were not considered in this analysis. In fact, instrumental broadening is negligible under most experimental conditions, introducing errors in the measured density and temperature, which are not significant compared to other typical noise sources. Temperature variations in the scattering volume may be important. However, to correctly estimate them we would need to get simultaneous measurements at different scattering angles, which is not possible with the current experimental setup. On the other hand, at 90° scattering angle the collection volume is at its minimum size, and temperature variations are probably not too dramatic. Moreover, if we only restrain our analysis to pulse-to-pulse variations of the plasma properties, the corrections introduced by inhomogeneities in the scattering volume become less relevant since only the difference between the density and temperature values obtained from light collected in consecutive pulses is important and not their absolute values.

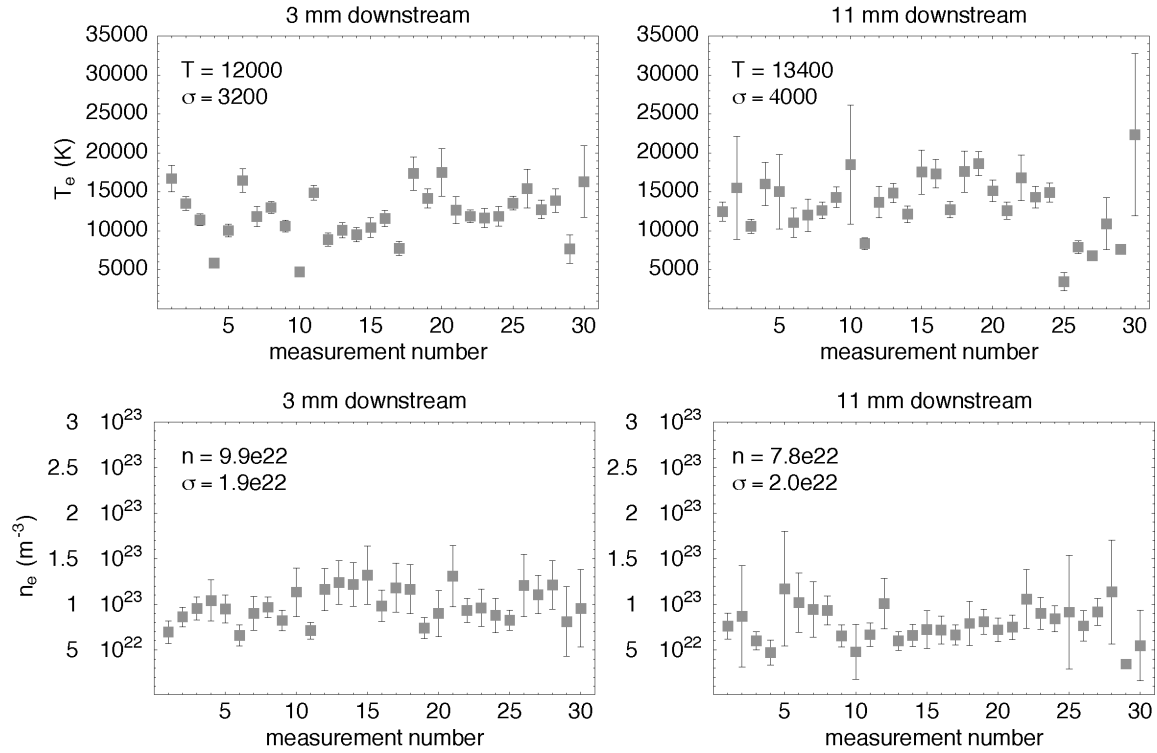
In Ref. 5 we have discussed in details the MMF approach for the case of a fully ionized ( $Z=1$ ) two-component plasma, where  $Z$  is the average charge per atom. On the other hand, for typical conditions found in plasma jets, only a certain fraction of the total number of atoms gets ionized ( $Z<1$ ). This effect can be easily included in the expression for the normalized frequency moments of the dynamic form factor, giving in the Debye-Hückel limit the result:

$$\begin{aligned}\square_0^2 &= \frac{1}{2}(kv_t)^2 + \frac{Z+1}{2}\square_p^2 \\ \square_{11}^2 &= 3(kv_t)^2 + \square_p^2\end{aligned}\quad (4)$$

where  $v_t$  is the electron thermal speed and  $\square_p$  is the plasma frequency and  $k$  the probe wavenumber. As explained in Ref. 5, the normalized moments  $\square_0$  and  $\square_{11}$  are direct observables from the experimental lineshapes. The value of the ionization state  $Z$  requires a detailed knowledge of the equation of state (EOS) of argon. Under the condition of LTE, however, average spectroscopic temperatures should agree with the electron temperatures obtained from Thomson scattering. This is indeed satisfied by setting  $Z\sim 0.7$ , and eq. (4) can be used to directly extract temperature and density values from the experimental data.



**Figure 6:** Experimental lineshapes obtained at 90° scattering angle. Each plot corresponds to the light collected from a single laser pulse. The data has been fitted using the MFF model for the spectral density function. The plasma is sampled on the jet axis, 3.0 mm downstream the nozzle exit at random intervals in time



**Figure 7:** Electron temperature (top) and electron density (bottom) fluctuations. Average values and standard deviations are indicated in the plot.

In Fig. 6 we show the experimental lineshapes obtained from sampling the jet at random time intervals. In these plots we see large variations of the measured spectrum of the scattered light, suggesting indeed very large fluctuations of the plasma properties in time. This is clear from Fig. 7. Electron temperature and electron density show large variations from sample to sample, indeed suggesting that the plasma flow consists of hot bubbles followed by cold gas. At 11.0 mm downstream the nozzle exit, fluctuations in density and temperature are even larger than at 3.0 mm downstream, probably resulting from the onset of large-scale fluid-dynamic instabilities and the entrainment of the surrounding gas in the jet core.

## Conclusions

We have shown that the potential core of turbulent plasma jets undergoes large-scale fluctuations of the entire column. These fluctuations are driven by the arc-root attachment instability inside the torch and by fluid-dynamic instability as the jet expands in the ambient medium. Time-resolved fluctuation data were obtained with both emission spectroscopy and Thomson laser scattering, showing intense variations from the average values even very close to the nozzle exit.

## Acknowledgements

This work was supported by the US Department of Energy, Basic Energy Sciences, Grant No. DE-FG02 85ER13433.

<sup>1</sup> L. Beall et al., in 15<sup>th</sup> International Thermal Spray Conference (Nice, France, 1998), p. 815.

<sup>2</sup> S.A. Wuztke, E. Pfender, and E.R.G. Eckert, AIAA Journal **6**, 1474 (1968).

<sup>3</sup> J.F. Coudert and P. Fauchais, High Temp. Materials Processes **1**, 149 (1997).

<sup>4</sup> E. Pfender, Plasma Chem. Plasma Process. **19**, 1 (1999).

<sup>5</sup> G. Gregori et al., Phys. Rev. E **65**, 046411 (2002).

<sup>6</sup> H. Griem, *Principles of Plasma Spectroscopy* (Cambridge, MA, 1964).

<sup>7</sup> M. I. Boulos, P. Fauchais, and E. Pfender, *Thermal Plasmas: Fundamentals and Applications* (Plenum, NY, 1994).

# Oxygen Radical Density Measurement using Electrically Heated Pt Thin Wire in Glow Discharge Positive Column Plasma

S. Ono, N. Haraki and S. Teii

*Department of Electrical Engineering, Musashi Institute of Technology, Tokyo, Japan*

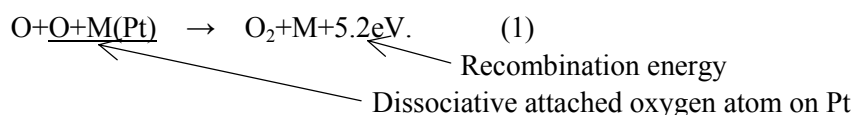
## Abstract

An experimental study of oxygen radical density measurement method using surface recombination of oxygen radicals on platinum surface has been described. The oxygen radical density measurement was achieved by electrically heating up the temperature of platinum thin wire to 800K in case of relatively low density condition. In the sphere of an experiment, it was shown that measurement of the oxygen radical density by this method is possible in  $2.8 \times 10^{13} \text{cm}^{-3}$  -  $5.0 \times 10^{15} \text{cm}^{-3}$ .

## 1. Introduction

Oxygen plasma has been used for various plasma processes. Many researchers have performed the measurement and control of oxygen radicals, because the role of oxygen radical is important in various applications. Especially in recent O radical measurement, LIF (Laser Induced fluorescence) measurement has been widely adopted, however LIF has the difficulty which needs expensive equipment. Moreover, the derivation of absolute value of O radical density needs a complicated procedure. We are advancing the investigation about the new method that can measure the O radical density using the comparatively simple system.

We had found the phenomenon of red heat of platinum thin wire immersed in oxygen nitrogen mixture gas plasma [1]. The cause of red heat of Pt wire has been explained by the recombination energy supply as follows;[3][4]



Therefore, this temperature rise of Pt wire is proportional to the oxygen radical density. Theoretical calculation of the constituent species in the  $\text{O}_2\text{-N}_2$  mixture gas plasma [2] had been done to investigate this temperature rise, and it has been understood that the oxygen radical density estimated from the temperature rise of Pt wire agreed with the numerically calculated oxygen radical density. So, this phenomenon is expected to be applicable to measure the oxygen radical density in the plasma.

When O radical density is high, thin platinum wire is easily heated up and the radical density can calculate from the supplied energy by re-combination of the O radicals. However, since there is little surface temperature rise of platinum wire when the radical density is comparatively low, surface recombination cannot occur easily and the radical density measurement becomes difficult. Therefore, it was considered to set the platinum surface temperature in 800K to which recombination reaction actively happened to facilitate the measurement of the recombination energy on the surface of platinum. This paper described that the measurement of low oxygen radical density become possible using electrically heated Pt thin wire.

## 2. Experimental method and apparatus

Pyrex glass made discharge tube, I.D=2.4cm, has been used in the experiment. Anode-cathode distance is 50cm, and these cylindrical shape electrodes are made of stainless steel. Oxygen-nitrogen mixture gas is introduced in the discharge tube at pressure of several Torr. The reason why we use oxygen-nitrogen mixture gas is controllability of the oxygen atom density. In our previous work [2], we have demonstrated the drastic oxygen atom density change by mixing of nitrogen in the oxygen plasma.

A constant current DC power supply is used for the discharge. The discharge tube is evacuated by rotary pump. The quadrupole mass spectrometer, evacuated by a turbo molecular pump, is installed with connecting through a small orifice fitted on the discharge tube wall. Moreover, two ports are provided on the discharge tube to insert the Pt wire and an electrostatic probe.

Figure 1 shows Pt thin wire probe and power supply with voltage and current monitor (TR-6143, Advantest Ltd.) which elevate Pt thin wire temperature. A direct current is passed to a platinum thin wire by TR-6143, and Pt wire temperature is set as 800K. The input electric power at this time is expressed as  $P_1$ . A set point of platinum thin-wire temperature is calculable from change of the electric resistance of a thin wire. In the plasma containing O radical, recombination of oxygen atoms arise on the platinum thin-wire surface, and excessive energy is emitted to the platinum surface. When the input electric power from a power supply required in order to keep the platinum thin wire at 800K in this situation is expressed as  $P_2$ , the energy  $P_r$  supplied by recombination is expressed as

$$P_r = P_1 - P_2 \quad (2)$$

O radical density is computed by assuming that O radical which arrived at the platinum surface by thermal motion is recombined 100%. The past research shows that this assumption is appropriate. [1]

Since this experiment was the measurement in the case of a comparatively low oxygen radical density, the Pt probe is installed in the glass tube port which connected to the discharge tube wall, and the measurement has been performed mainly in the position of outside of the discharge wall. The platinum thin wire used as a probe is 0.05mm in the diameter and 20mm in length

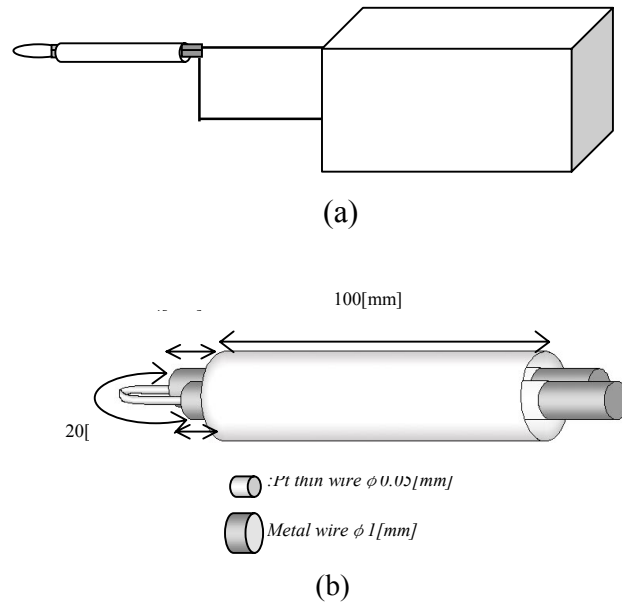


Fig.1 Pt thin wire probe and power supply.

### 3. Experimental results and discussion

Figure 2 shows nitrogen mixture ratio dependence on the supplied recombination energy to the Pt thin wire for 800K and 400K Pt wire temperature  $T_p$ . The results of the experiment at the discharge tube wall Pt probe position are shown in this figure. The numerical analysis of  $O_2$ - $N_2$  glow discharge plasma have predicted that the oxygen radical density is relatively low at 100% oxygen gas discharge condition, however the oxygen radical density increases rapidly with increasing nitrogen mixture ratio. That have been

also confirmed in our former experiments. Figure 2 shows that in case of  $T_p=400\text{K}$ , the recombination energy of oxygen radicals is extremely few amounts of energy and do not depend nitrogen mixture ratio. However in case of  $T_p=800\text{K}$ , the supplied recombination energy changes with nitrogen mixture ratio as predicted by our calculation.[2]

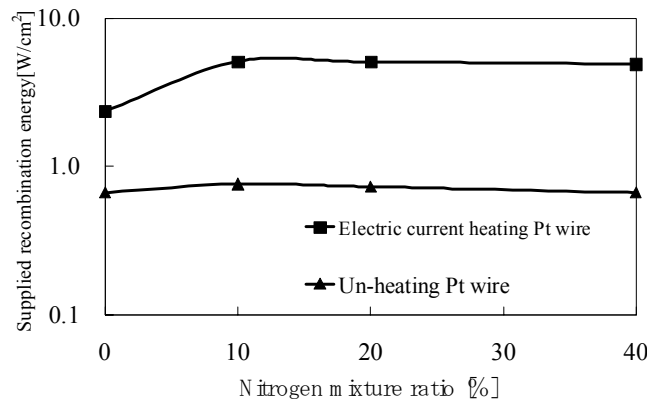


Figure 2 Nitrogen mixture ratio dependence of the supplied recombination energy on Pt wire for  $T_p=800\text{K}$  and  $T_p=400\text{K}$ . The mixture gas pressure is 0.6Torr, the gas flow rate is 60ml/min. The discharge current is 10mA

These experiments means that there is suitable temperature for oxygen radical recombination on the Pt surface. If the temperature of Pt wire set to suitable temperature, the measurement of recombination energy will become easy. The literature of beam experiment shows that the most effective temperature for recombination is around 800K. It seems that this experimental results is reflected the different Pt surface recombination efficiency for  $T_p=400\text{K}$  and 800K.

Figure 3 shows Pt wire position dependence on supplied recombination energy of oxygen radicals on Pt surface for various Pt wire temperature  $T_p$ .  $T_p$  is controlled by controlling electric current which flows the Pt wire, because  $T_p$  is determined by the energy balance of supplied energy (recombination and joule heating) and energy loss of Pt wire through metal supporter conductor etc. In fig.3, horizontal axis  $x$  means the distance from discharge tube wall position in the glass tube (15mm in diameter) which is installed to insert Pt wire probe. The experiments have been done for several different  $T_p$  to investigate the effect of wire temperature  $T_p$  on the recombination of oxygen radicals. The supplied energy to the Pt wire by the recombination of oxygen radical increases with increasing  $T_p$  as shown in fig.3. In case of  $T_p=800\text{K}$ , the supplied recombination energy to the Pt wire decreases with drawing in the glass tube which is fit up to the discharge tube wall, and that seems to reflect the change of the oxygen radical density in the glass tube. It seems that the recombination is not almost observed at  $T_p=400\text{K}$  and the oxygen radical which arrive to the Pt surface in part recombine on the Pt surface at  $T_p=600\text{K}$ . On the other hand, the supplied recombination energy at  $T_p=1000\text{K}$  shows large quantities of value in the position of relatively long distance from discharge tube axis where the oxygen radical density is essentially low. It appears that the production of the oxygen radical occurs around the high temperature Pt wire from the above experiment. Therefore it appears that Pt wire temperature  $T_p$  should not exceed the suitable temperature (probavely nealy 800K) for oxygen radical measurement in oxygen molecule mixture gas plasma.

The spatial distribution of oxygen radical density calculated from the supplied recombination energy are shown in fig.4 for the sevrsl nitrogen mixture ratios. The Pt wire temperature has been set  $T_p=800\text{K}$ , the most suitable tempetature for this experiment. The oxygen radical density decreases with increasing  $x$ , the distance from discharge tube wall position. There is little influence of the nitrogen mixture ratio to an oxygen radical density at 5% or more of nitrogen. This tendency agree with the theoretical calculation. The lowest oxygen radical density,  $2.8 \times 10^{13}\text{cm}^{-3}$ , are obserbed at  $x=15\text{mm}$  and 0% nitrogen mixture ratio in the present experiment.

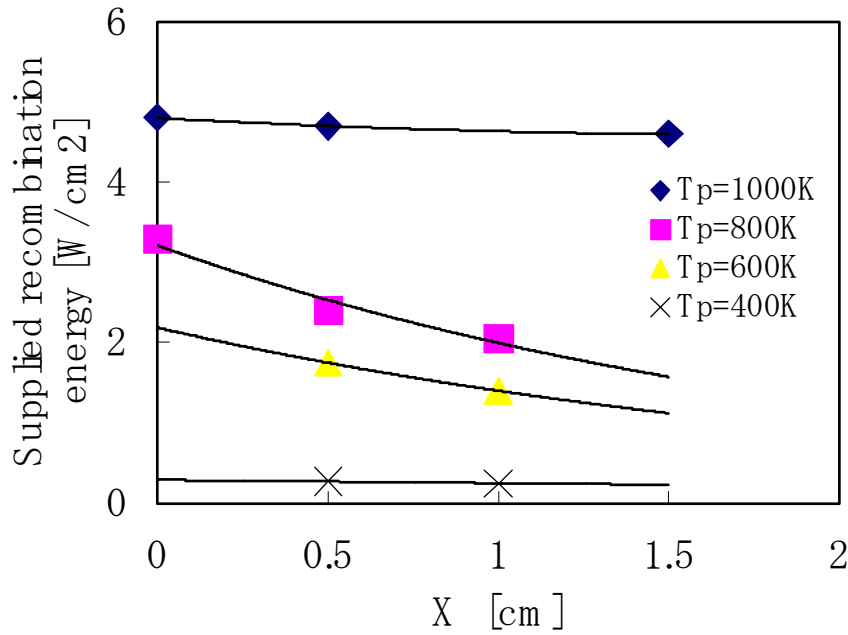


Fig.3 Spatial distribution of the supplied recombination energy on Pt wire for various  $T_p$ . Total gas pressure:0.6Torr, nitrogen mixture ratio 5%, discharge current 10mA.

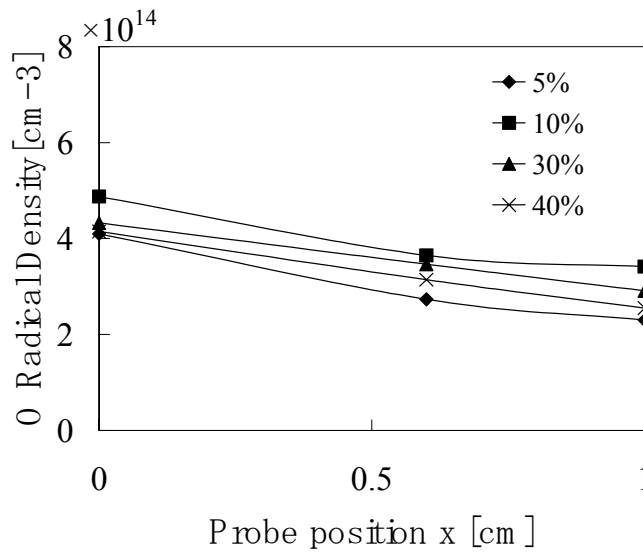


Fig.4 Spatial distribution of O radical density in the pylex glass tube which is connected to the discharge tube wall for several nitrogen mixture ratios. Total gas pressure:0.6Torr, discharge current:10mA,  $T_p$ :800K.

Table I shows that the range of measured oxygen radical density for the electrically heated Pt wire method, the present experiment, and for non-heating method, our previous experiment. The oxygen radical density measuring range of Pt wire probe which was not heated electrically was  $10^{11}$  cm<sup>-3</sup> to  $10^{13}$  cm<sup>-3</sup>, and of the electrically heated Pt wire probe was  $10^{10}$  cm<sup>-3</sup> to  $10^{13}$  cm<sup>-3</sup>. It is to be noted that this heated Pt wire probe method is able to measure the relatively low density oxygen radical density in which it was impossible to measure the



density using un-heating Pt probe. It is understood that the activated catalytic action on the platinum wire surface whose temperature is elevated by the joule heating make the oxygen radical detection easy. It is desirable for lower oxygen radical density measurement to compensate the effect of surrounding gas temperature, as it is necessary to detect small change of Pt wire temperature at low oxygen radical density. On the other hand, it is found that the selection of probe geometry whose temperature maintain below about 800K is important in relatively high oxygen radical density measurement in case of using un-heating probe, as the high temperature, above 1000K, Pt wire produce oxygen radicals by the dissociation of surrounding oxygen molecule.

#### **4. Summary**

The study of the oxygen radical density measurement had been performed using the platinum thin wire. The experimental investigation for the oxygen radical density measurement in relatively low radical density condition has been discussed in this paper. It is found that the relatively low oxygen radical density is able to measure by the Pt thin wire probe which is heated up to about 800K by the electric current. Moreover, it is also found that the Pt wire temperature of about 1000K gives rise to the serious error in the radical density measurement, as the high temperature Pt wire produces radicals by the dissociation of oxygen molecule. It is found that the suitable Pt wire temperature for this method is about 800K.

#### **Acknowledgment**

The part of this study was supported by a Grant-in-Aid for Scientific Research (C) by the Ministry of Education, Culture, Sports, Science and Technology.

#### **References**

- [1] S. Ono and S. Teii: Trans. IEE of Japan, 116-A(7), 659-660(1996)
- [2] S. Ono and S. Teii: Proc. of the 2<sup>nd</sup> Inter. Symp. on Non-Thermal Plasma Technology for Gaseous Pollution Control 142-147(1997)
- [3] G.D.W. Smith and J.S. Anderson: Faraday Trans. I, **72**, 1231 (1976)
- [4] R. Lewis and R. Gomer: Surface Sci., **12**, 157, (1968)
- [5] N. Haraki, S. Ono, S. Teii, Proc. of ESCAMPIG16, ICRP5, 131(2002)

# ON THE PECVD DEPOSITION OF TRANSPARENT CONDUCTIVE TIN OXIDE THIN FILMS DEPOSITED ON POLYMER SUBSTRATES AND THEIR ELECTROCHEMICAL STABILITY FOR NONFOULING PROPERTIES

J. Pulpytel<sup>1</sup>, M. Ghassami<sup>1</sup>, H. Cachet<sup>2</sup>, D. Festy<sup>3</sup>, F. Arefi-Khonsari<sup>1</sup>

<sup>1</sup>Laboratoire de Génie des procédés Plasmas, ENSCP-UPMC, Paris, France

<sup>2</sup>Laboratoire de Physique des Liquides et Electrochimie, UPR15-CNRS associé à l'UPMC - CP 133

<sup>3</sup>Ifremer – Centre de Brest – Service Matériaux et Structures – 29280 – Plouzané (France)

## Abstract

Transparent conductive tin oxide films have been deposited from a mixture of O<sub>2</sub>/Ar/TMT on different polymers (PMMA, PC and TPX). On PMMA, in order to obtain coatings which resist to washing with ethanol or water, an organometallic intermediate adhesive layer had to be deposited before depositing the carbon free tin oxide to decrease mechanical stress. The square resistance of the tin oxide coated polymers increases sharply upon ageing. Preliminary results by F doping of the films limits this ageing effect and give rise to much higher current densities, during electrochemical tests, necessary for biofouling properties.

## Introduction

Biofouling reduction is a major problem for underwater instrumentation, involving optical measurements or viewing. An effective window protection technique has been developed, based on seawater electrolysis at the very optical surface for producing active chlorine species (hypochlorous acid : HClO). In a practical way, this is achieved by depositing a transparent conductive tin dioxide coating [1]. Among the different TCO coatings tin oxide presents the highest stability in terms of electrochemistry [2]. On glass substrates able to support  $\approx 500^{\circ}\text{C}$  deposition temperature, spray pyrolysis technique can be used [3]. The problem is quite different when transparent polymeric substrates, like PMMA (polymethylmethacrylate), PC (polycarbonate) or TPX (polymethylpentene), are considered. This is the interest of plasma-assisted CVD techniques to allow oxide thin film deposition at ambient temperatures, without heating [4].

The first part of this paper will be devoted to the deposition of carbon free transparent tin oxide coatings on different polymer films. In order to optimise the experimental conditions to obtain carbon free tin oxide films, mass spectrometry was performed by using a calibration mixtures composed of inert gases. The latter allowed us to determine the molar fraction of the stable species produced in the discharge, such as CO & CO<sub>2</sub> namely those which witness the carbon etching of the organometallic precursor that is TMT. For this study the role of the two major parameters i.e. power and oxygen partial pressure in the reactor have been studied. The purpose of the second part was to obtain good adhesive properties of the tin oxide layers to the different polymers which resist to washing in water or ethanol. Finally the density and the mobility of the charge carriers of the deposited layers on polymers were determined by the Hall effect measurements and compared to those obtained on glass in order to define the electrical characteristics required for the antifouling properties which we are looking for, and which have been studied by Cachet et al. [1] on glass substrates coated with tin oxide layers deposited by pyrolysis. (Fig. 1)

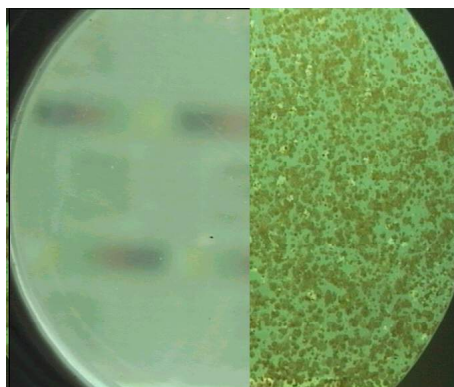


Fig. 1. Effect of electrochemical antifouling treatment of a glass window immersed in natural seawater for 5 months : unprotected surface (left); electrochemically chlorine-protected surface owing to SnO<sub>2</sub> coating (right).

## Experimental

Tin oxide thin films were deposited in a capacitively coupled RF 13.56 MHz reactor at a pressure of 15 Pa. This pressure was regulated by a butterfly valve and measured by a capacitive gauge. The gaseous mixture (O<sub>2</sub>/Ar/TMT : 66%/33%/1%) was introduced through the RF-powered shower electrode. The substrate electrode was biased by a second RF 13.56 MHz generator [4].

## Results and Discussion

In order to deposit carbon free tin oxide films plasmas of mixtures of TMT/O<sub>2</sub>/Ar were used. One of the most important parameters that allows to obtain carbon free tin oxide films is the optimisation of the gas composition. In a previous study it has been shown that depending on the gas composition in a diode reactor, the deposited films presented a wide range of conductivities. The latter was tightly correlated to the carbon content of the deposited films [5]. The respective roles of electrons and oxygen atoms in the PECVD of SiO<sub>2</sub>-like films were investigated in different installations from precursors such as TEOS (tetraethyl orthosilicate) or HMDSO (hexamethyldisiloxan). The authors agree that electrons play an important role in the decomposition of the organometallic or silicon precursor, and that oxygen atoms act as carbon and hydrogen strippers [6]. This has also been confirmed in our case i.e. as soon as a few percent of TMT is introduced in the discharge, the TMT is dissociated above 90% giving rise to carbon fragments which are oxidized by oxygen resulting in the formation of CO, CO<sub>2</sub> and H<sub>2</sub>O stable species. In order to increase the electron density and the dissociation of oxygen in our relatively low electron density capacitively coupled reactor, as compared to an ECR system [6], mixtures of Ar + O<sub>2</sub> were introduced with a very low TMT flow rate (<2%).

### Mass spectrometry

TMT which was introduced in the Ar/O<sub>2</sub> mixture goes through dissociation by electronic impact. The neutral species detected in the discharge were quantified by using a calibration mixture composed of noble gases. The plasma was analyzed by an Hiden analytical EPIC 500 mass spectrometer, with a base pressure of 6x10<sup>-6</sup> Pa in the chamber, and an operating pressure of 1x10<sup>-4</sup> Pa. During deposition of tin oxide thin films, the following neutral species CO<sub>2</sub>, CO have been quantified from the following equation,

$$S_A = n_A \cdot I_e \cdot \sigma_{A \rightarrow A^+} \cdot \alpha_{m/z} \quad (1)$$

where  $S_A$  is the measured signal (s<sup>-1</sup>),  $n_A$  is the number density in the ionizer (cm<sup>-3</sup>),  $I_e$  is the electron current in the ionizer (C.s<sup>-1</sup>),  $\sigma_{A \rightarrow A^+}$  is the ionization cross section (cm<sup>2</sup>) and  $\alpha_{m/z}$  is a coefficient that is the product of the extraction efficiency of the ion from the ionizer, the transmission efficiency of the quadrupole mass filter and the coefficient of the channeltron detector [7]. With the help of the calibration gases,  $\alpha_{m/z}$  was estimated to be around  $7 \cdot 10^{17} / m_A$ , where  $m_A$  is the mass of the ion (amu). As the neutral species are sampled through a 100 μm diam aperture, the Knudsen number was estimated to be 0.267, then the gas flow through the aperture is molecular. Since the gas flow  $\phi_A$  is proportional to  $(m_A)^{-1/2}$ , all density numbers have been corrected to represent the ratio inside the process chamber.

The variation of CO and CO<sub>2</sub> vs. power is shown in Fig. 2. One can note that measured CO and CO<sub>2</sub> molar fractions increase with the increase of the power transferred to the plasma. However, the ratio CO/CO<sub>2</sub> varies from 1.0 to 1.4. As mentioned before, since atomic oxygen and electrons play an important role in the deposition of carbon free tin oxide films, we have presented the calculated O and electron molar fractions variation with the power obtained from a model developed for our reactor in a mixture of Ar/O<sub>2</sub> [8]. For such experimental conditions the mean electronic temperature seems to remain constant with the increase of the power for the gas mixture used, and has been estimated to be equal to 2.5 eV. For a power as high as 3 W, the TMT dissociation rate is about 96%.

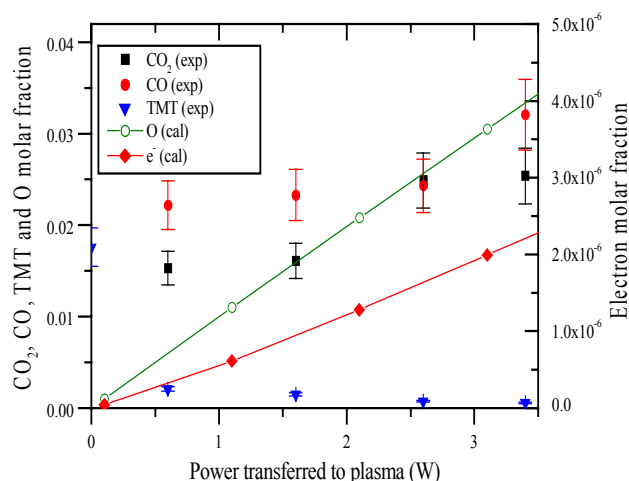


Fig. 2. Measured molar fraction of CO, CO<sub>2</sub> and TMT , as well as calculated O and electron mole fractions inside the process chamber.

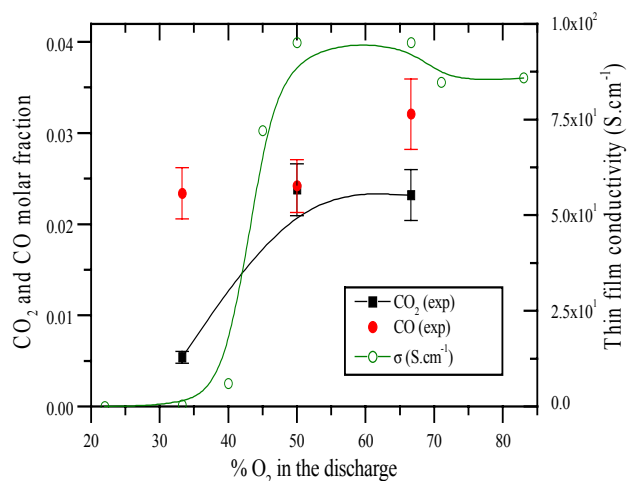
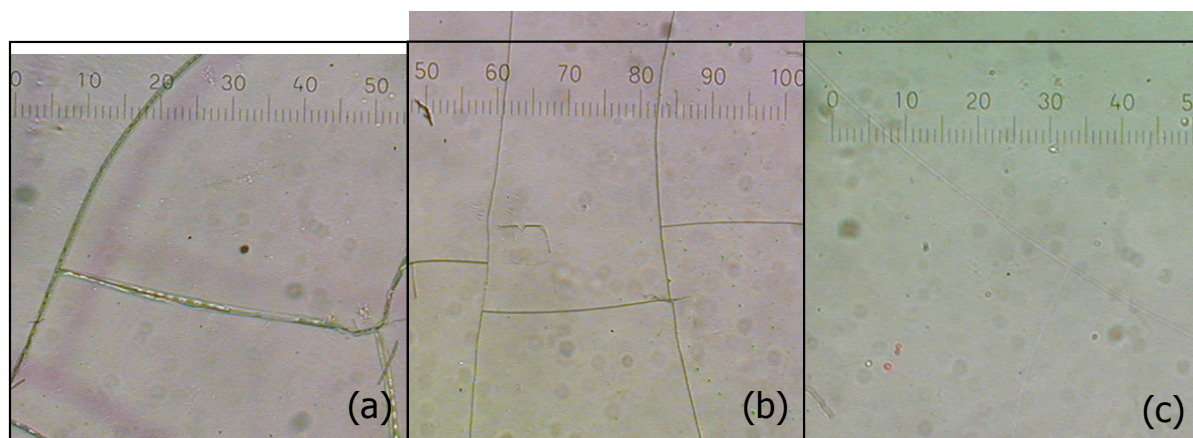


Fig. 3. Molar fractions of CO and CO<sub>2</sub>, and tin oxide thin film conductivity versus the O<sub>2</sub> percentage in the discharge. Power transferred to plasma is equal to 3.5 W.

On Fig. 3. the molar fractions of CO and CO<sub>2</sub> have been presented versus the O<sub>2</sub> percentage in the discharge. One can note that the molar fractions of CO<sub>2</sub> increases and reaches a plateau, while that of CO remains constant. The conductivity of the films obtained with different percentages of O<sub>2</sub> in the discharge has also been reported on this figure, which shows almost the same trend as the CO<sub>2</sub> molar fraction. These results confirm the fact that, in order to obtain carbon free films presenting a certain conductivity (around 100 S.cm<sup>-1</sup>), we should work with O<sub>2</sub> percentages ranging between 50% < %O<sub>2</sub> < 70%.

### Adhesion of the tin oxide films on polymers

The deposited films on PC and TPX present very good adhesive properties while those deposited on PMMA are washed easily off. PMMA is known to be a polymer which is mechanically fragile. The latter explains why the deposition of an inorganic film such as tin oxide which is also compressive directly onto an organic polymer such as PMMA peels off as soon as it is washed in ethanol. In order to solve this problem an intermediate organometallic layer was deposited from a mixture of Ar & TMT (≈ 10-20 nm thick). Then the 300-500 nm thick tin oxide layer was prepared from a mixture of 2/3 O<sub>2</sub> and 1/3 Ar with 1-2% TMT. Such prepared samples presented a much lower mechanical stress and in this way they resisted to water and ethanol washing (see Fig. 4)



**Figure 4.** Optical microscopy pictures of tin oxide coating deposited on PMMA with an intermediate adhesive layer presenting different thickness (a) 30 nm thick layer, (b) 45 nm thick layer, (c) 60 nm thick layer

The chemical composition of the deposited films has been analysed by Raman spectroscopy on a PPMA substrate, as depicted in Fig. 5. The spectrum shows an intense and broad peak at 450-750  $\text{cm}^{-1}$ , which is attributed to  $\text{SnO}_2$ . Peaks detected at 2867 and 2934  $\text{cm}^{-1}$  corresponding to  $\text{CH}_3$  and  $\text{CH}_2$  probably are due to the polymer or carbon contamination of the films.

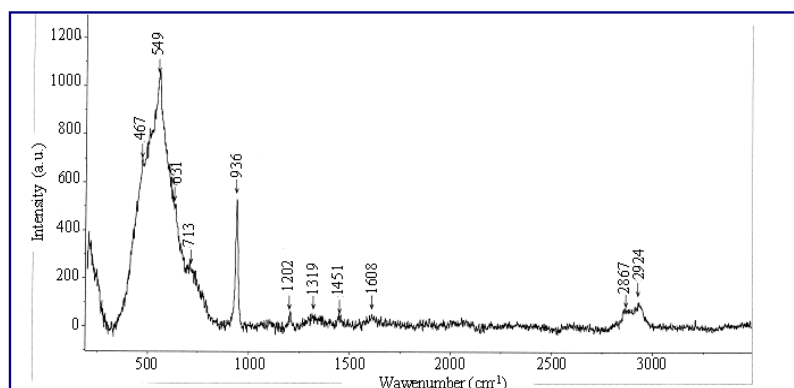


Fig. 5. Raman spectrum of a  $\text{SnO}_2$  layer PACVD taken off from its PMMA substrate.

Figure 6. shows the optical properties of tin oxide thin films PACVD-deposited on different polymer substrates (PMMA, Polycarbonate, TPX). Transparency in the visible part of spectrum is satisfying, around 80% for 250nm thick layers. At wavelengths longer than 1  $\mu\text{m}$ , absorption bands of polymer substrates are dominating.

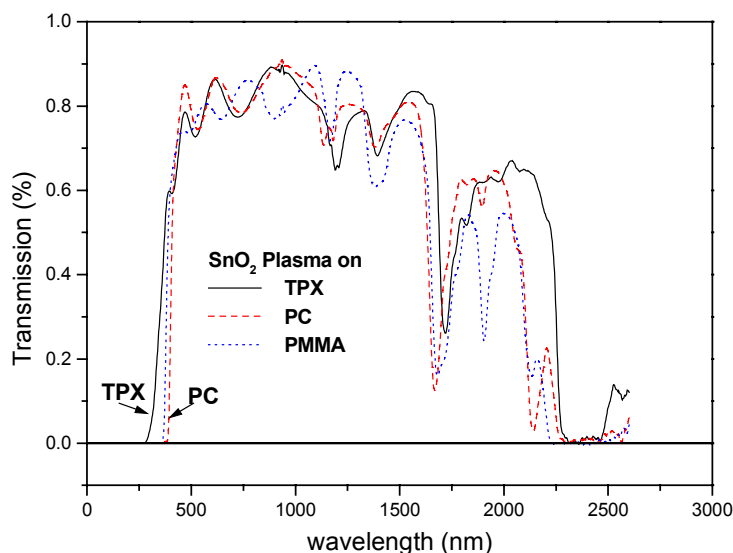


Fig. 6. Optical transmission of undoped  $\text{SnO}_2$  films deposited on different polymer substrates.

## Study of the electrical measurements and anticorrosion behaviour

Tin dioxide, even highly doped, is known to present large overpotentials for oxidation reactions, for instance oxygen evolution and halide oxidation. Such an electrochemical behaviour is due to the n-type semiconducting character of  $\text{SnO}_2$  giving rise to electron depletion at anodic potentials, with a barrier formed at the electrolyte-oxide interface. The barrier is associated with a space-charge region the width  $w_{sc}$  of which is inversely proportional to the square root of the free electron concentration  $N$ . For instance, for  $N=10^{20}\text{cm}^{-3}$ ,  $w_{sc} \approx 3\text{ nm}$ , but for  $N=10^{17}\text{cm}^{-3}$   $w_{sc}$  reaches  $\approx 100\text{ nm}$ . As electron transfer to the electrolyte can only occur by tunnelling, high doping levels are therefore needed for electrochemical applications. For oxide materials, the position of the Fermi level at the surface is fixed by the pH of the aqueous electrolyte in contact. This position is deduced from space-charge capacitance measurements and Mott-Schottky analysis. The energy distance between the Fermi level and the bottom of the conduction band depends on the bulk electron concentration. They are lined up for a  $3.10^{19}\text{ cm}^{-3}$  electron density. In seawater, with  $\text{pH}=8.2$ , the conduction band edge is located around  $-0.7\text{ V/SCE}$ , where SCE stands for the saturated calomel reference electrode

(4.75 eV below the vacuum level). It means that applying potentials in the range of +0.5 to 2.0 V/SCE leads to barrier heights from 1.2 to 2.7 V, yielding a blocking effect with respect to charge transfer. It has been shown that for highly doped SnO<sub>2</sub> films a limited corrosion process takes place as soon as OH<sup>°</sup> or Cl<sup>°</sup> radical species have been produced, *i.e.* at potentials more anodic than +1.2 V/SCE [9]. Surface modifications induced by corrosion contribute to create surface states short-circuiting the surface potential barrier allowing a more efficient electron transfer. The drawback is that such an activation mechanism for charge transfer will be inefficient when the electron concentration lies far below 10<sup>20</sup> cm<sup>-3</sup>.

Electrical properties of PACVD-deposited tin oxide thin films are gathered in Table 1, showing the dependence on the doping element and ageing time. One can note first of all that doping with oxygen vacancies or fluorine by using SF<sub>6</sub> precursor give rise to electron densities in the order of 10<sup>20</sup> cm<sup>-3</sup>, even after being aged during 2 years. Secondly, these measurements show that the ageing effect of the tin oxide films is tightly dependent on the nature of the substrate, namely glass and polycarbonate. On glass we can observe only a slight decrease of the conductivity of the films by a factor 4-5 after 3 years, as well as the electron density and charge carriers. Although the square resistance is almost the same for the freshly deposited tin oxide layers on both substrates, in the case of the polycarbonate substrate, the ageing process leads to a continuous increase of the square resistance (about 3 orders of magnitude). The latter is probably due to a diffusion of polymer chains from the amorphous substrate in the amorphous tin oxide layer. This phenomenon leads to the formation of an organometallic layer presenting a high square resistance. SIMS analysis should be performed in order to verify this hypothesis.

Substrate	Doping	Thickness (nm)	Resistivity (Ohm.cm)	Ageing time (days)	Square resistance (Ohm)	Electron density (cm <sup>-3</sup> )	Mobility (cm <sup>2</sup> V <sup>-1</sup> s <sup>-1</sup> )
polycarbonate	Oxygen vacancies	200	0.04	0	2000		
			24	15	1.2 10 <sup>6</sup>	1.9 10 <sup>17</sup>	1.4
Glass	Oxygen vacancies	500	9.5.10 <sup>-3</sup>	0	570	9.3 10 <sup>19</sup>	7.1
Glass	Oxygen vacancies	500	0.07	3 years	1400	2.3 10 <sup>19</sup>	3.9
Glass	SF <sub>6</sub>	200	0.02	3 years	2630	6.6 10 <sup>19</sup>	1.8

Table 1 : Electrical properties of PACVD-deposited SnO<sub>2</sub> films on polycarbonate and glass substrates with various dopings and ageing times.

These conditions are not favourable to a good electrochemical response, as depicted in Fig.7. As we can observe, since the resistance increase sharply after 15 days, the current density measured in seawater at potentials corresponding to chlorine and oxygen evolution is below 1 μA.cm<sup>-2</sup>, compared to a few hundreds ones for a highly F doped polycrystalline SnO<sub>2</sub> electrode currently used in the electrochemical cleaning of glass windows [1] This is due to the barrier formed associated with the considerable space charge which is developed at the electrolyte-oxide interface. The reason why the current then further decreases after a few cycles is probably due to the fact that oxygen is produced at the anode which would neutralize the oxygen vacancies. In order to have good electrochemical responses on polymers, first of all, we should deposit highly F-doped tin oxide films. This will be done by using SF<sub>6</sub> precursor or by a new precursor which is C<sub>4</sub>F<sub>8</sub>. Preliminary results obtained by doping tin oxide films by placing a Teflon disk close to the polymer substrate shows that besides the fact that the conductivity increase, the ageing process is much slower in the case of PC substrates (increase of the square resistance from 2 500 Ω to 50 300 Ω after 20 days).

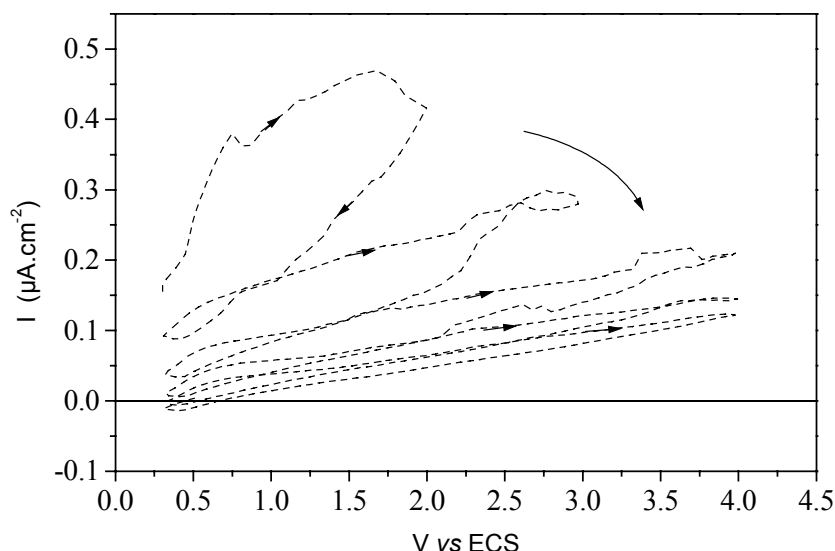


Fig . 7. Effect of anodic electrochemical cycling on undoped-SnO<sub>2</sub> on polycarbonate immersed in natural seawater;  $t_{\text{ageing}} = 15$  days; Potential scan rate : 50 mV.s<sup>-1</sup>

## Conclusion

Transparent conductive tin oxide films have been deposited from a mixture of O<sub>2</sub>/Ar/TMT on glass and polymers. Experimental conditions such as power and oxygen partial pressure in the reactor were optimised. The most conductive films were obtained for oxygen percentage in the discharge between 50% and 70%. For such mixtures quantitative mass spectrometric measurements showed also a maximum of CO<sub>2</sub> molar fraction. The first results pointed out that the adhesion of the deposited tin oxide films is closely correlated to the structure and mechanical properties of the polymer. Good adhesion properties of the tin oxide layer on polycarbonate is obtained. However in the case of PMMA, in order to obtain a good adherence between the tin oxide layer and PMMA, an organometallic intermediate adhesive layer had to be deposited from a mixture of Ar and TMT before depositing the carbon free tin oxide layer. In this case the necessary thickness of the intermediate layer was determined. Nevertheless in all cases very good optical properties were obtained.

Although one obtains the same electrical properties i.e in terms of electron density, number of charge carriers and electrical conductivity for tin oxide deposited films both on glass and polymers, the latter ages very quickly giving rise to a sharp increase of the square resistance of the films and therefore unsatisfactory electrochemical response of the deposited films. Preliminary results by F doping of the films limits this ageing effect and gives rise to much higher current densities in seawater, showing the possibility to use tin oxide coated polymers as windows for underwater instrumentation.

## References

- [1] H. Cachet, D. Festy, G. Folcher, F. Mazeas, B. Tribollet, *Matériaux et Techniques*, **7/8**, 37 (2002)
- [2] G. Folcher, H. Cachet, M. Froment, J. Bruneaux, *Thin Solid Films*, **301**, 242-248 (1997)
- [3] A. Messad, H. Cachet, M. Froment, J. Bruneaux, *J. Mater. Sci.*, **29**, 5095 (1994)
- [4] F. Arefi-Khonsari, F. Hellegouarc'h, J. Amouroux, *Journal of Vacuum Science and Technology*, **A16(4)**, 2240 (1998)
- [5] Y. Farber, F. Arefi-Khonsari, J. Amouroux, *Thin Solid Films*, **241** (1994)
- [6] A. Granier, F. Nicolazo, C. Vallée, A. Gouillet, G. Turban, B. Grolleau, *Plasma Sources Sci. Technol*, **6** (1997)
- [7] H. Singh, J. W. Coburn, D. B. Graves, *Journal Vacuum Society Technologie*, **A18(2)**, (2000)
- [8] W. Morscheidt, K. Hassouni, F. Arefi-Khonsari, J. Amouroux, accepted for publication in *Plasma Chem. and Plasma Proc.*, **23(1)** (2003)
- [9] H. Cachet, F. Zenia, M. Froment, *J. Electrochem. Soc.*, **146**, 977 (1999)

# Optimization for Arc Ash Melting Process by Numerical Simulation

H. Nishiyama<sup>1</sup>, T. Shimizu<sup>2</sup>, and T. Sato<sup>1</sup>

<sup>1</sup> Institute of Fluid Science, Tohoku University, Sendai, Japan

<sup>2</sup> Mitsubishi Heavy Industries, Ltd., Yokohama, Japan

## Abstract

For the optimization of arc ash melting process, the present study has proposed the new numerical model to consider the arc-electrodes boundary condition without assumptions and also the complex interactions between the arc and molten soil interface with phase change. The effects of arc current, inlet gas flow rate, electrode gap and cathode vertex angle on the thermofluid field and net effective process efficiency of arc-ash melting system are clarified by numerical simulation.

## 1. Introduction

Since arc has the advantages of stable and controllable heating, it has been extensively utilized as a heat source for welding, cutting, metallurgical processings and further in the waste treatment. In recent years, the needs for arc ash melting systems are increasing to reduce the ash to smaller volume, to promote the stability of ash and to reduce dioxins [1]. By using this systems, we can reduce the waste volume considerably and separate evaporated heavy metal and further seal up it into the slag with glass phase. However, there has been rising the problems about electric power consumption, electrode cost and safety for secondary hazardous matter.

Since arc ash melting process includes the complex interaction between the plasma arc and molten soil, experimental work is rather limited for determining the optimum operating condition in the arc ash melter. Then, numerical simulation is effective method to optimize the arc ash melting system [2, 3].

In the present study, numerical modelling is conducted for arc ash melting process to consider the arc-electrodes boundary conditions without assumptions and complex interaction between arc and molten soil interface with phase change. The effects of arc current, inlet flow rate, electrode gap and cathode geometry on heat transfer and fluid flow in the molten pools are numerically clarified. Finally, the net effective electric power efficiency and ash melting rate for those parameters are evaluated for optimization of arc ash melting process.

## 2. Numerical modelling

Figure 1 shows a schematic illustration of an arc ash melting system and the coordinate system. In order to derive the governing equations, the following assumptions are introduced here.

- (1) A steady, 2D axisymmetric, and laminar arc and molten pool flow are prevailed.
- (2) Argon arc is optically thin in local thermodynamic equilibrium (LTE) state.

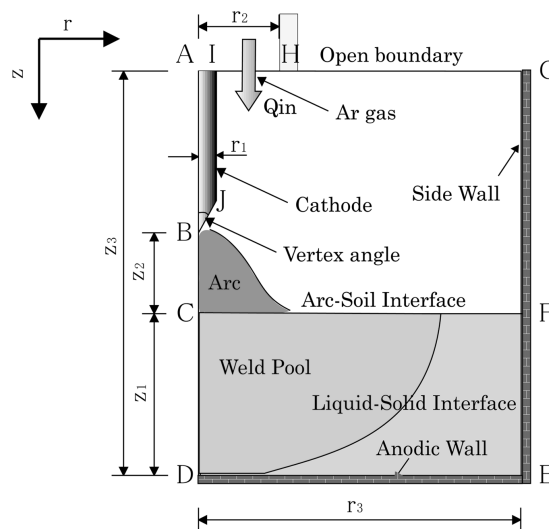


Figure 1 Schematic illustration of arc ash melting system



- (3) There are temperature dependent thermodynamic and transport properties.
- (4) Melting, evaporation and deformation on electrodes are not considered.
- (5) Evaporation, deformation, electric charge and surface tension at molten pool surface are not considered.
- (6) Radiation from cathode, reactor wall and molten pool surface are not considered.
- (7) The gravitational force, viscous dissipation and compressed work are neglected.
- (8) The induction magnetic field has an axisymmetrical and azimuthal component.

Under these assumptions, the governing equations are presented as follows:

Conservation of mass (arc, soil)

$$\frac{\partial}{\partial z}(\rho u) + \frac{1}{r} \frac{\partial}{\partial r}(r \rho v) = 0 \quad (1)$$

Conservation of momentum (arc, soil)

$$\begin{aligned} & \frac{\partial}{\partial z}(\rho u u) + \frac{1}{r} \frac{\partial}{\partial r}(r \rho u v) \\ &= -\frac{\partial p}{\partial z} + 2 \frac{\partial}{\partial z} \left( \eta_{Ar,Soil} \frac{\partial u}{\partial z} \right) + \frac{1}{r} \frac{\partial}{\partial r} \left( r \eta_{Ar,Soil} \left( \frac{\partial u}{\partial r} + \frac{\partial v}{\partial z} \right) \right) - \frac{2}{3} \frac{\partial}{\partial z} \left( \eta_{Ar,Soil} \left( \frac{\partial u}{\partial z} + \frac{1}{r} \frac{\partial(rv)}{\partial r} \right) \right) \end{aligned} \quad (2)$$

$$\begin{aligned} & + j_r B_\theta + \rho g \\ & \frac{\partial}{\partial z}(\rho v u) + \frac{1}{r} \frac{\partial}{\partial r}(r \rho v v) \\ &= -\frac{\partial p}{\partial r} + \frac{\partial}{\partial z} \left( \eta_{Ar,Soil} \left( \frac{\partial v}{\partial z} + \frac{\partial u}{\partial r} \right) \right) + \frac{2}{r} \frac{\partial}{\partial r} \left( r \eta_{Ar,Soil} \frac{\partial v}{\partial z} \right) - \frac{2}{3} \frac{\partial}{\partial r} \left( \eta_{Ar,Soil} \left( \frac{\partial u}{\partial z} + \frac{1}{r} \frac{\partial(rv)}{\partial r} \right) \right) \\ & - \eta_{Ar,Soil} \frac{2v}{r^2} - j_z B_\theta \end{aligned} \quad (3)$$

Conservation of energy

in the arc:

$$\begin{aligned} & \frac{\partial}{\partial z}(\rho h u) + \frac{1}{r} \frac{\partial}{\partial r}(r \rho h v) \\ &= \frac{\partial}{\partial z} \left( \frac{\lambda_{Ar}}{C_{p(Ar)}} \frac{\partial h}{\partial z} \right) + \frac{1}{r} \frac{\partial}{\partial r} \left( \frac{r \lambda_{Ar}}{C_{p(Ar)}} \frac{\partial h}{\partial r} \right) + \frac{j_z^2 + j_r^2}{\sigma_{Ar}} + \frac{5}{2} \frac{k_b}{e} \left( \frac{j_z}{C_{p(Ar)}} \frac{\partial h}{\partial z} + \frac{j_r}{C_{p(Ar)}} \frac{\partial h}{\partial r} \right) - Ra \end{aligned} \quad (4)$$

in the soil:

$$\frac{\partial}{\partial z}(\rho h u) + \frac{1}{r} \frac{\partial}{\partial r}(r \rho h v) = \frac{\partial}{\partial z} \left( \frac{\lambda_{Soil}}{C_{p(Soil)}} \frac{\partial h}{\partial z} \right) + \frac{1}{r} \frac{\partial}{\partial r} \left( \frac{r \lambda_{soil}}{C_{p(Soil)}} \frac{\partial h}{\partial r} \right) + \frac{j_z^2 + j_r^2}{\sigma_{soil}} \quad (5)$$

inside the cathode:

$$\frac{\partial}{\partial z} \left( \frac{\lambda_C}{C_{p(C)}} \frac{\partial h}{\partial z} \right) + \frac{1}{r} \frac{\partial}{\partial r} \left( \frac{r \lambda_C}{C_{p(C)}} \frac{\partial h}{\partial r} \right) + \frac{j_z^2 + j_r^2}{\sigma_C} = 0 \quad (6)$$

Equation of state

$$p = \rho R T \quad (7)$$

Conservation of electric current (all regions)

$$\frac{\partial}{\partial z} \left( \sigma_{Ar,C,Soil} \frac{\partial \phi}{\partial z} \right) + \frac{1}{r} \frac{\partial}{\partial r} \left( r \sigma_{Ar,C,Soil} \frac{\partial \phi}{\partial r} \right) = 0 \quad (8)$$

Ohmic equation (all regions)

$$j_z = -\sigma_{Ar,C,Soil} \frac{\partial \phi}{\partial z} \quad (9)$$

$$j_r = -\sigma_{Ar,C,Soil} \frac{\partial \phi}{\partial r} \quad (10)$$

Ampere's rule

$$\frac{1}{r} \frac{\partial}{\partial r}(r B_\theta) = \mu_0 j_z \quad (11)$$

Table 1 shows the geometry and operating conditions of arc ash melting system.

Table 1 System geometry and operating conditions

Operating pressure	$p_0 = 1.01 \times 10^5$ (Pa)
Arc current	$I = 500, 1000, 2000$ (A)
Argon flow rate	$Q_{in} = 100, 300, 500$ (l/min)
Cathode radius	$r_1 = 12$ (mm)
Nozzle radius	$r_2 = 36$ (mm)
Melter radius	$r_3 = 400$ (mm)
Electrode tip angle	$\theta = 30^\circ, 60^\circ, 180^\circ$
Soil depth	$z_1 = 200$ (mm)
Electrode gap	$z_1 + z_2 = 300, 275, 225$ (mm)
Computational axial length	$z_3 = 450$ (mm)

The boundary conditions in arc, cathode, soil regions, interface between arc and soil are given here without any assumptions on the cathode [4].

Arc and cathode region:

axis AB:	$\frac{\partial T}{\partial r} = 0$	$\frac{\partial \phi}{\partial r} = 0$	
axis BC:	$\frac{\partial T}{\partial r} = 0$	$\frac{\partial \phi}{\partial r} = 0$	$\frac{\partial u}{\partial r} = v = 0$
wall FG:	$T = 1000$ K	$\frac{\partial \phi}{\partial r} = 0$	$u = v = 0$
exit GH:	$\frac{\partial^2 T}{\partial z^2} = 0$	$\frac{\partial \phi}{\partial z} = 0$	$\frac{\partial u}{\partial z} = v = 0$
inlet HI:	$T = 300$ K	$\frac{\partial \phi}{\partial z} = 0$	$u = u_{in} \quad v = 0$
cathode root IA:	$T = 300$ K	$-\sigma_c \frac{\partial \phi}{\partial z} = j_{in}$	
cathode surface IJB:	$u = v = 0$		

Soil region:

axis CD:	$\frac{\partial T}{\partial r} = 0$	$\frac{\partial \phi}{\partial r} = 0$	$\frac{\partial u}{\partial r} = v = 0$
anode surface DE:	$T = 1000$ K	$\phi = 0$	$u = v = 0$
wall EF:	$T = 1000$ K	$\frac{\partial \phi}{\partial r} = 0$	$u = v = 0$

Interface CF:

molten state:	$-\lambda_p \frac{\partial T_p}{\partial z} = \lambda_{Soil} \frac{\partial T_{Soil}}{\partial z}$	$-\eta_p \frac{\partial v_p}{\partial z} = \eta_{Soil} \frac{\partial v_{Soil}}{\partial z}$	$u = 0$
solid state:	$-\lambda_p \frac{\partial T_p}{\partial z} = \lambda_{Soil} \frac{\partial T_{Soil}}{\partial z}$		$u = v = 0$

The criterion for phase change is given here.

solid state:	$T_{Soil} \leq T_{melt} = 1,428$ K
molten state:	$T_{Soil} > T_{melt}$

### 3. Numerical results and discussion

Figures 2 (a) (b) show the stream line, isotherm, plasma-soil interface and solid-liquid boundary in the arc melter. The input currents are 1,000 A and 2,000 A respectively, electrode gap: 300 mm, flow rate: 500 l/min and cathode vertex angle is 60°. At the operating current of 2,000 A in Fig.2 (b), the maximum

temperature increases due to the active Joule heating in the arc, and also arc impinging velocity increases due to the strong radial Lorentzian force. Then, the shear force at the molten surface and the buoyancy in the molten pool increase. Finally, since the thermal conduction to the molten surface and further Joule heating and convection heat transfer in the molten pool increase, molten soil volume also increases.

Figures 3 (a) (b) show respectively the effects of applied arc current and electrode gap on energy

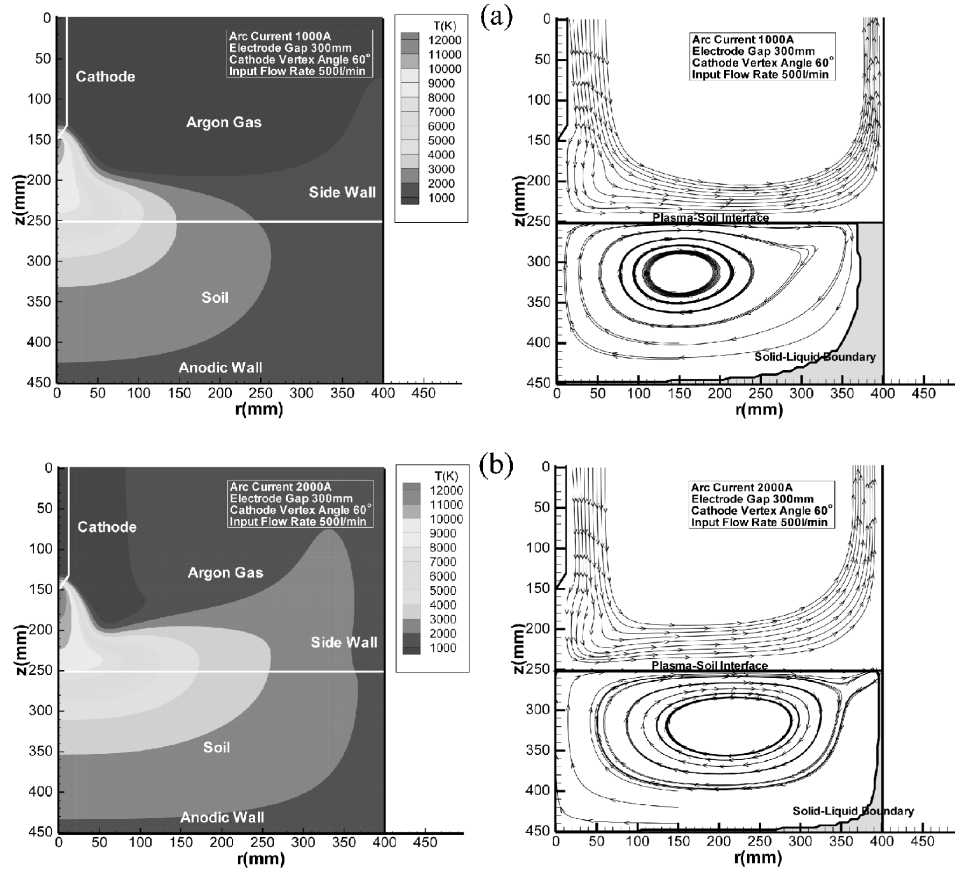


Figure 2 Effect of arc current on arc ash melting process

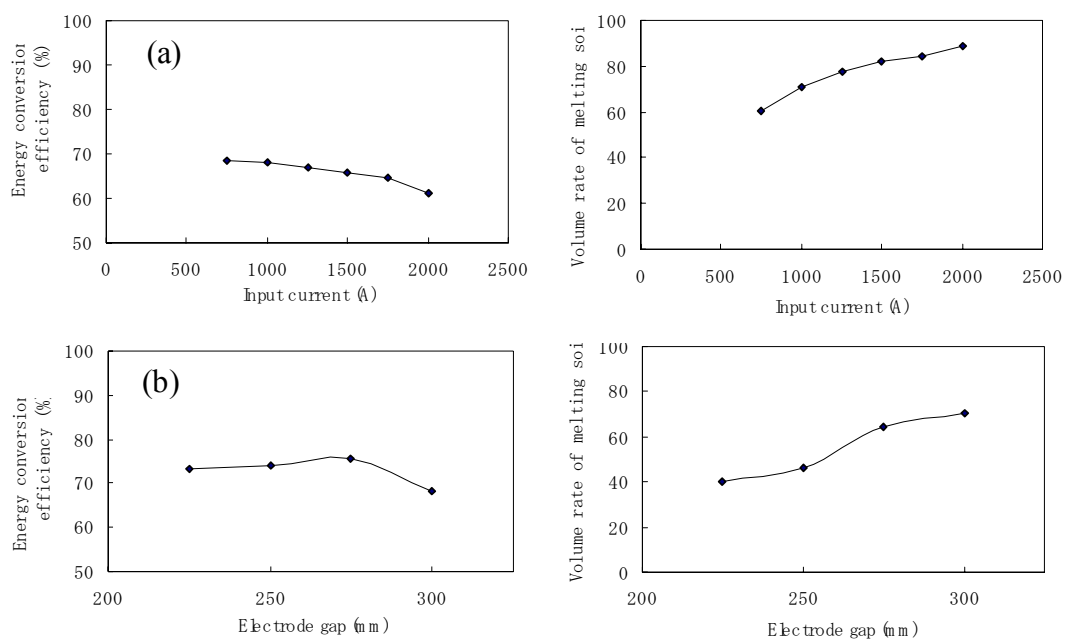


Figure 3 Arc ash melting process efficiency

conversion efficiency for melting process and volume rate of melting soil. Here, the energy conversion efficiency is defined as the ratio of the heat transfer from arc to soil plus Joule heating in the molten soil to input electric power. The volume rate of melting soil increases with the input current at first but it finally saturates. On the other hand, the energy conversion efficiency decreases gradually with the input current due to the relative saturation of Joule heating generation. When the electrode gap increases, a high temperature region spreads along the interfaces. Then, the volume rate of melting soil increases since heat conduction to the soil and convective heat transfer in the soil increase. However, the energy conversion efficiency attains a maximum around gap of 275 mm and then decreases suddenly at large electrode gap due to large heat loss from arc.

#### **4. Conclusion**

Numerical modelling is conducted for arc-ash melting system by taking the complex interactions between arc and electrode, molten soil interface into account. The results obtained here by numerical simulation are as follows:

- (1) The impinging velocity and maximum temperature increase and then the high temperature region spreads along the interface toward the side wall with increase in the input current and in the electrode gap. In this case, melting efficiency of soil increase, but the energy conversion efficiency decreases.
- (2) There exists the optimum input current for given molten soil rate to obtain maximum energy conversion efficiency. It is effective to set the electrode gap as large as possible to make the large arc volume within the stable arc generation.

#### **References**

- [1] Y. Liu, et al. - *Trans. Mater. Res. Soc. Japan.* **25**, 381 (2000).
- [2] S. Paik, G. Hawkes and H. D. Nguyen – *Plasma Chem. and Plasma Process.* **15**, 677 (1995).
- [3] I. S. Kim and A. Basu – *J. Materials Process. Tech.* **77**, 17 (1998).
- [4] H. Nishiyama, et al. – *ISIJ International*, **43** (2003), in press.

# **Application of argon and oxygen plasma in fiber-reinforce polymer composites: the influence of fiber volume fraction**

M. O. H. Cioffi<sup>1</sup>, A. L. Horovistiz<sup>2</sup>, R. O. Hein<sup>2</sup>, H. J. C. Voorwald<sup>1</sup>

<sup>1</sup>*Fatigue and Aeronautic Research Group, <sup>2</sup>LAIMat, Department of Materials and Technology, State University of São Paulo. Ariberto Pereira da Cunha, 333 CEP 12516410, Guaratinguetá/SP - Brazil*

Fibrous composites technology have been considered in projects in which weight parameter must be to take into account, specially for aeronautic applications. Fibre/matrix interface properties play an important role for mechanical behaviour of structurally composite. In the case of low energy, frequently associated to thermoplastics composites, surface treatment is necessary to promote an adequate fibre/matrix interface.

Due to the chemical inertness of poly(ethylene therephtalate) (PET) fibres, Radio Frequency plasma was utilised to improve the surface properties, energy and roughness, of fibres according to the following conditions: excitation frequency was 13.56 MHz, the power of the electrical field was 50 W, the pressure of treatment was kept at 40 Pa by a double stage mechanic pump, the mass flow controller maintained  $3.33 \times 10^{-7}$  m<sup>3</sup>/s gas flux and the treatment time varied from 5 s to 100 s. As matrix was used poly(methyl methacrylate) (PMMA) which was synthesised at 100°C and the unidirectional composites were processed in a filament winding equipment.

Tensile tests of the matrix and the composites were conducted in an INSTRON 4204 equipment. Increase in tensile strength and young modulus values was observed for composites in comparison to matrix in single form. This change was related to fibre volume fraction of PET fibres/PMMA matrix composites. Volume fraction of fibres has been measured by digital image analysis, using light microscopy under darkfield illumination.

# Asymmetry Effects in the Diagnostics and Simulation of RF Inductively Coupled Plasma Torch

V. Colombo<sup>1</sup>, G. Gao<sup>2</sup>, E. Ghedini<sup>1</sup>, J. Mostaghimi<sup>2</sup>

<sup>1</sup>*Dipartimento di Ingegneria delle Costruzioni Meccaniche, Nucleari, Aeronautiche e di Metallurgia (D.I.E.M.) and C.I.R.A.M., Università degli Studi di Bologna, Via Saragozza 8, 40123 Bologna, Italy.  
Phone: +39 (0)51 2093978 Fax: +39 (0)51 582528 e-mail: [colombo@ciram.ing.unibo.it](mailto:colombo@ciram.ing.unibo.it)*

<sup>2</sup>*Centre for Advanced Coating Technologies, Faculty of Applied Science and Engineering, University of Toronto, 40 St. George Street, Toronto, Ontario, Canada.  
Phone: +1 416 978 5604 Fax: +1 (416) 946 8252 e-mail: [mostag@mie.utoronto.ca](mailto:mostag@mie.utoronto.ca)*

## Abstract

In this paper, we examine both experimentally and numerically the effects on the plasma fields of the actual 3-D shape of the helicoidal coil of an inductively coupled plasma torch. Temperature results from numerical simulation are used to reconstruct, for some characteristic Ar-I wavelengths, side-on emission intensity profiles. Predicted profiles are then compared with the ones obtained from direct optical emission spectroscopy methods. The arising of non-symmetric behaviour of the plasma discharge is shown.

## 1. Introduction

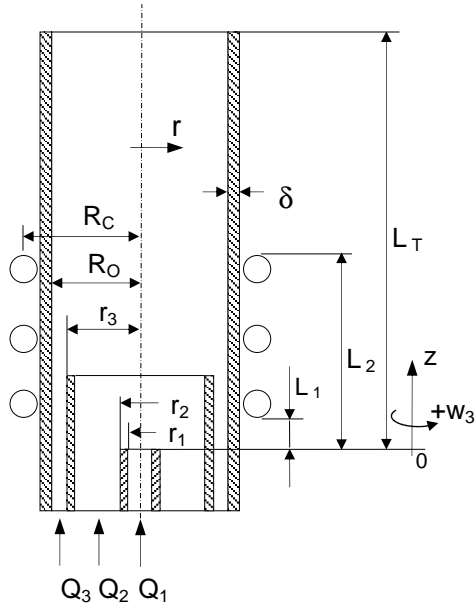
Inductively coupled plasma torches are used as a tool for producing thermal plasmas for various applications that go from spectroscopy to plasma spraying of materials [1]. Diagnostics in the core of the plasma discharge [2] is a very difficult task, so a lot of efforts have been devoted to mathematically modelling the plasma flow and heat transfer coupled with the electromagnetic field, in order to develop useful tools for the design and optimization of this kind of devices. Numerical analysis of radio frequency inductively coupled plasma normally assumes the plasma fields are two-dimensional and axisymmetric by means of the assumption that the induction coil is made up of perfectly symmetric rings. This assumption led to the development and use of 2-D electromagnetic models [2-4] and to results in which the radial Lorentz forces generated by the coil are perfectly balanced. Still in the actual torches the coil shape is not symmetric and becomes the main non-axisymmetry source for the discharge. A recently developed 3-D model [5-8] has shown that the unbalanced Lorentz forces induced by the helicoidal coil can lead to a significant deviation from the axisymmetric hypothesis of the discharge. The same trend has been also evidenced by some experimental spectroscopic measurements in which the side-on emission profiles is not exactly symmetric. In this paper, we examine both experimentally and numerically the effects on the plasma fields of the actual 3-D shape of the helicoidal coil of an Argon radio frequency inductively coupled plasma torch operating at atmospheric pressure. Temperature results from numerical simulation are used to reconstruct side-on emission intensity profiles for some characteristic Ar-I wavelengths, and then compared with the ones obtained from direct spectroscopy measurements.

## 2. Torch Geometry and Operating Conditions

Measurement and modelling are performed upon the torch schematically shown in Fig. 1 with corresponding dimensions and operating conditions summarized in Tab. 1. The torch is operated with argon at atmospheric pressure, with generator plate power of 300 W and coil current frequency of 40 MHz. We assume as first approximation that the power is equal to the power dissipated into the discharge  $P_0 = 300$  W, due to the high efficiency of the solid state RF generator. The sheath gas is injected with a swirl component  $w_3 = 20$  m/s, to improve plasma confinement. Inlet gas temperature  $T_0$  and wall external temperature  $T_{w0}$  are assumed to be 350 K. Schematic of the torch and coil used in the 3-D code is shown in Fig. 2, and reproduces the actual shape of the coil used in the experimental torch in the laboratories of the University of Toronto. Reference views for the side-on emission measurement and numerical reconstruction are shown from the top view in Fig. 3.

## 3. Spectroscopic Measurements

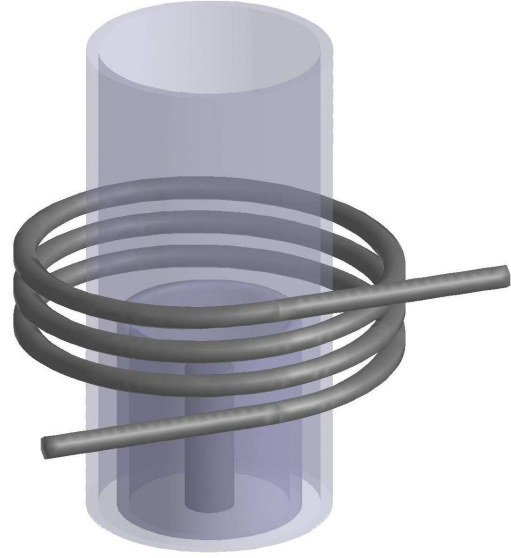
Due to the high temperature and small size of the plasma torch, it is impossible to use any intrusive technique to measure the plasma fields. The optical emission spectroscopy (OES) method was applied in our



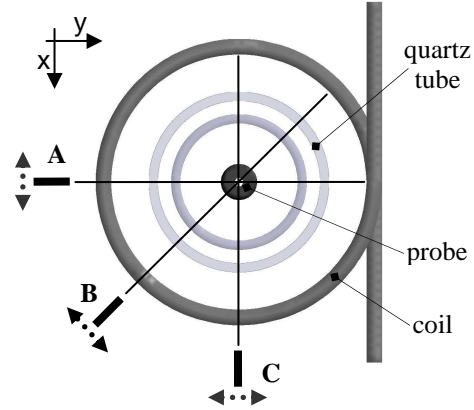
**Fig. 1** Schematic and dimensions of the plasma torch geometry.

**Tab. 1 Dimensions and operating conditions**

$r_1 = 0.5 \text{ mm}$	$R_0 = 9.0 \text{ mm}$	$L_1 = 1.0 \text{ mm}$
$r_2 = 2.0 \text{ mm}$	$R_c = 15.0 \text{ mm}$	$L_2 = 12.0 \text{ mm}$
$r_3 = 7.5 \text{ mm}$	$\delta = 1.0 \text{ mm}$	$L_T = 25.0 \text{ mm}$
$Q_1 = 0.0 \text{ L/min}$	$P_0 = 300 \text{ W}$	$f = 40 \text{ MHz}$
$Q_2 = 1.0 \text{ L/min}$	$T_{w0} = 350 \text{ K}$	$T_0 = 350 \text{ K}$
$Q_3 = 7.6 \text{ L/min}$	$p = 1 \text{ atm}$	$w_3 = 20 \text{ m/s}$



**Fig. 2** 3-D plasma torch schematic, reproducing the actual coil of the experimental torch.



**Fig. 3** Top view of the relative configuration used for side-on emission measurements and numerical reconstruction.

study to obtain the emission pattern of plasma, and consequently the plasma temperature and electron number density. The OES system includes a monochromator, a CCD detector, an Electro-optical scanner, and focusing lenses. The 0.55m monochromator (Jobin-Yvon Inc., model Triax 550) has 0.025nm Resolution with 1200 g/mm grating. The CCD detector (Jobin-Yvon Inc., model CCD 3000) with liquid nitrogen cooling apparatus was used to capture the spectrally dispersed plasma emission. A 2-D electro-optical scanner (GSI Lumonics Inc., model XY5067) was used for the sampling of optical emissions from any desired location within the plasma. The radiation of the plasma, through the scanner, focusing lenses, and optical fibre, was oriented onto the entrance slit of the spectrometer. The spectrum at certain wavelength was then output by the CCD detector. A calibrated quartz tungsten halogen (QTH) lamp from Thermo Oriel was used for the calibration of spectral intensity. Spectroscopic measurement was conducted detecting the emission line intensities of Ar-I neutral species, with the assumptions of optically thin plasma and negligible reflection and scattering effects due to the tube and coil. We have found that applying the Abel inversion to the left or right half of the side-on emission profiles, different local emission distribution profiles are obtained. The measurement shows this kind of non-axisymmetry emission exists within the coil zone, while the emission profiles are symmetric for the position far from the coil zone, where the Abel inversion can safely be applied to get the local emission coefficient. For the purpose of comparison between experimental and numerical results, the side-on emission intensity will not be processed by the Abel inversion and will be plotted as is, highlighting its non-axisymmetry. Besides, a tomographic technique is applied in order to obtain the 2-D emission field on a z-perpendicular plane inside the discharge. We measured lateral emission profiles at  $z = 15 \text{ mm}$  (just outside of the coil zone) from 7 directions placed in 180 degree sector. We

assume an axisymmetric profile as initial guess at first. Then we correct the profile by each lateral emission profile. We go through all the lateral emission profiles in one iteration cycle. When it finally comes to convergence, we will obtain 2D local emission coefficient profile, which is in agreement with all the measured lateral emission.

#### 4. 3-D Model

In order to analyze the effects of the actual coil in the behaviour of the discharge, a recently developed 3-D model [epjd] in the framework of the FLUENT<sup>®</sup> environment is used. The Maxwell equations are solved in their vector and scalar potential form, neglecting the displacement current, and taking into account the effect of the space varying electrical conductivity:

$$\nabla^2 \mathbf{A} - \mu_0 \sigma (\nabla V + \partial \mathbf{A} / \partial t) + \mu_0 \mathbf{J}^{coil} = 0 \quad (1) \quad \nabla \cdot [\sigma (\nabla V + \partial \mathbf{A} / \partial t)] = 0 \quad (2)$$

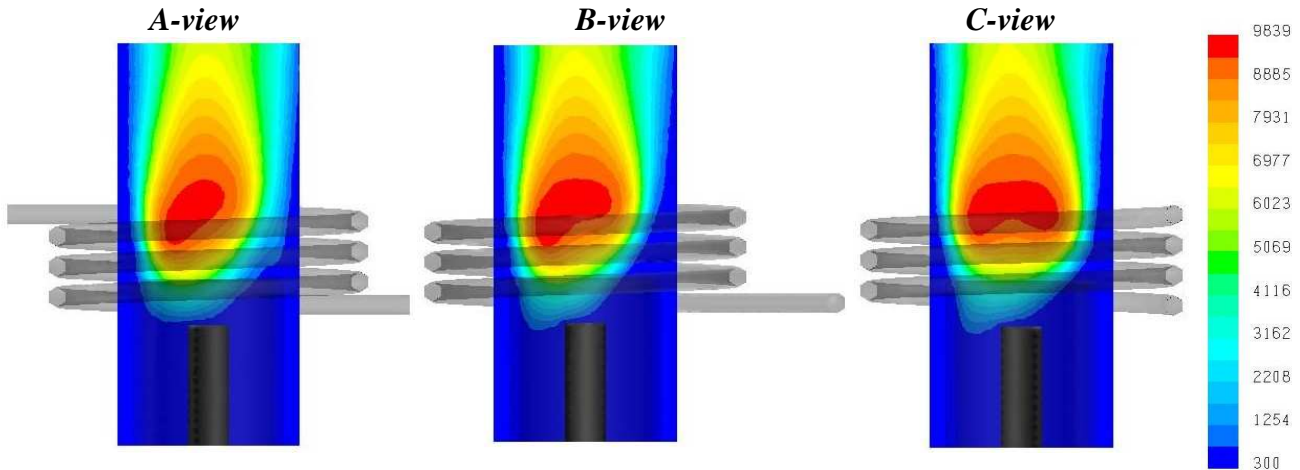
where the term  $\mathbf{J}^{coil}$  represents the current density in the coil region. The electric and magnetic fields in their classical form can be expressed through the definitions of the vector and scalar potentials:  $\mathbf{E} = -\partial \mathbf{A} / \partial t - \nabla V$ ,  $\mathbf{B} = \nabla \times \mathbf{A}$ . Boundary conditions for the electromagnetic equations are applied in the framework of the extended field model [2, 4]. A detailed description of the model can be found in [2]. Plasma calculation involves the solution of the energy and the Navier-Stokes equations and is performed under the assumption of LTE in the entire domain. Due to the high operating frequency, this assumption leads to some differences between the experimental and numerical results that will be discussed in the next paragraphs. The line emission coefficient  $\varepsilon_L$  is evaluated neglecting absorption and assuming Boltzmann distribution for the density of the neutrals in the upper level  $n_u$ , as follows:

$$\varepsilon_L(\lambda_{ul}) = \frac{1}{4\pi} \frac{hc}{\lambda_{ul}} n g_u A_{ul} \exp\left(-\frac{E_u}{kT}\right) \frac{1}{Q_{el}(T)} \quad (3)$$

where  $n$  is the density of the neutrals obtained by means of the Saha equation,  $\lambda_{ul}$  the line frequency due to a transition from an upper to a lower level,  $g_u$  the statistical weight of the upper level,  $A_{ul}$  the transition probability between levels,  $E_u$  the energy of the upper level and  $Q_{el}(T) = \sum_s g_s \exp(-E_s/kT)$  the electronic partition function.  $\varepsilon_L$  is expressed in  $\text{W/m}^3 \text{ster}$ . Data for calculations are obtained from the NIST Atomic Spectra Database for the ArI. The volumetric emission is then integrated along a path as it was seen by an ideal optic fibre, infinitely thin, neglecting light deflection due to the quartz tube, as shown in Fig. 3. The integral takes the form:

$$\varepsilon_L^{lat} = \int \varepsilon_L dl \int_{\Omega} d\Omega \delta(\Omega - \Omega_0) \quad (4)$$

where  $d\Omega$  is the differential solid angle,  $\Omega_0$  the integration direction and  $\delta$  is the Dirac function. By means of Eqs. 3 - 4 side-on emission intensity field, expressed in  $\text{W/m}^2$ , have been obtained.

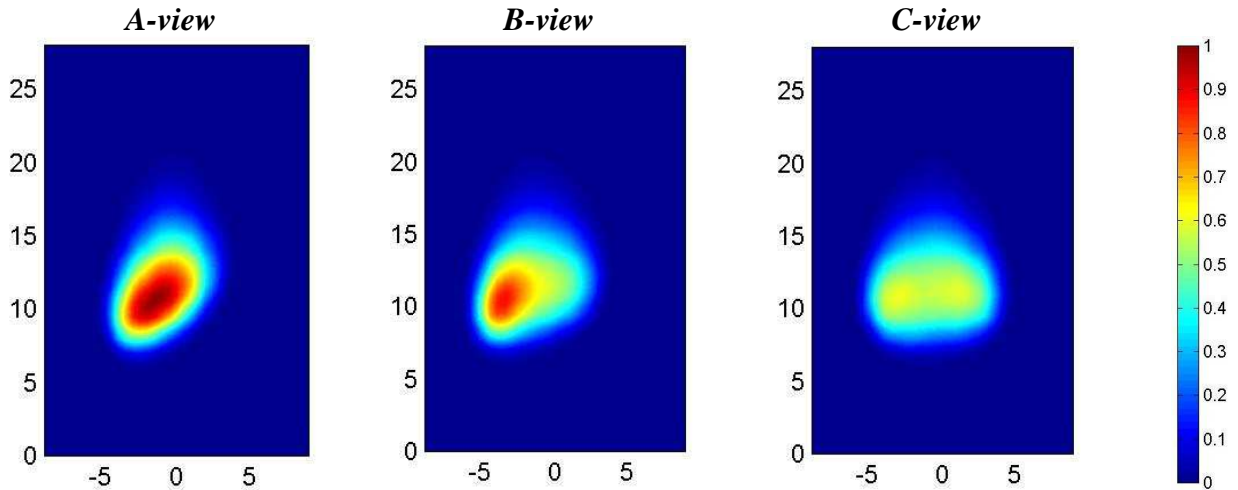


**Fig. 4** Temperature field [K] on three planes passing through the axis of the torch, for the three different views.

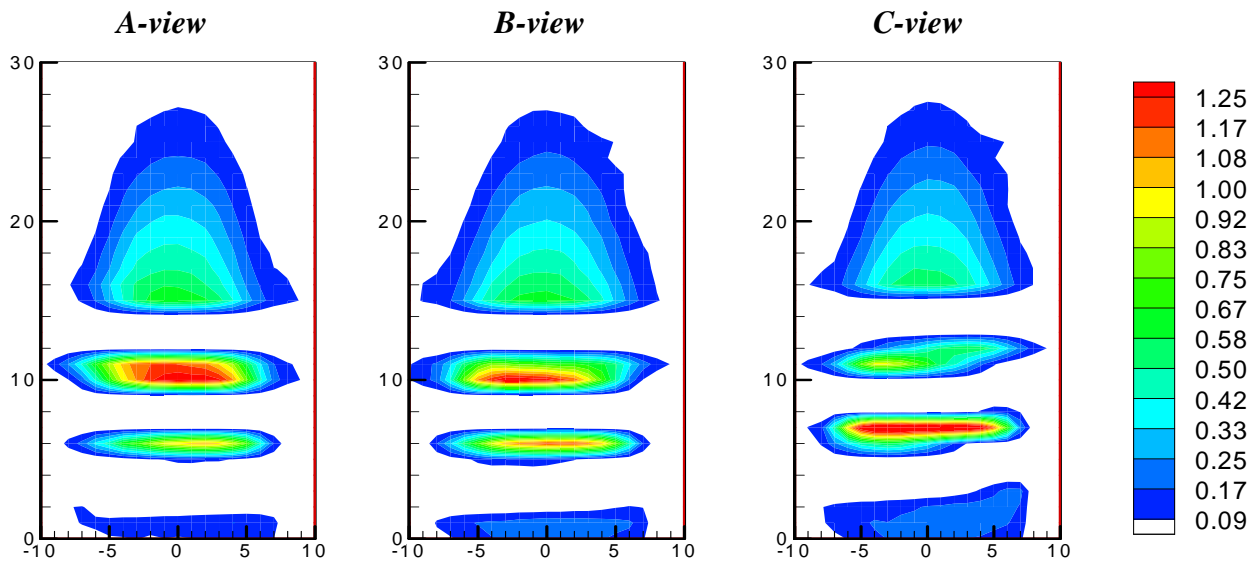


#### 4. Results and Comparisons

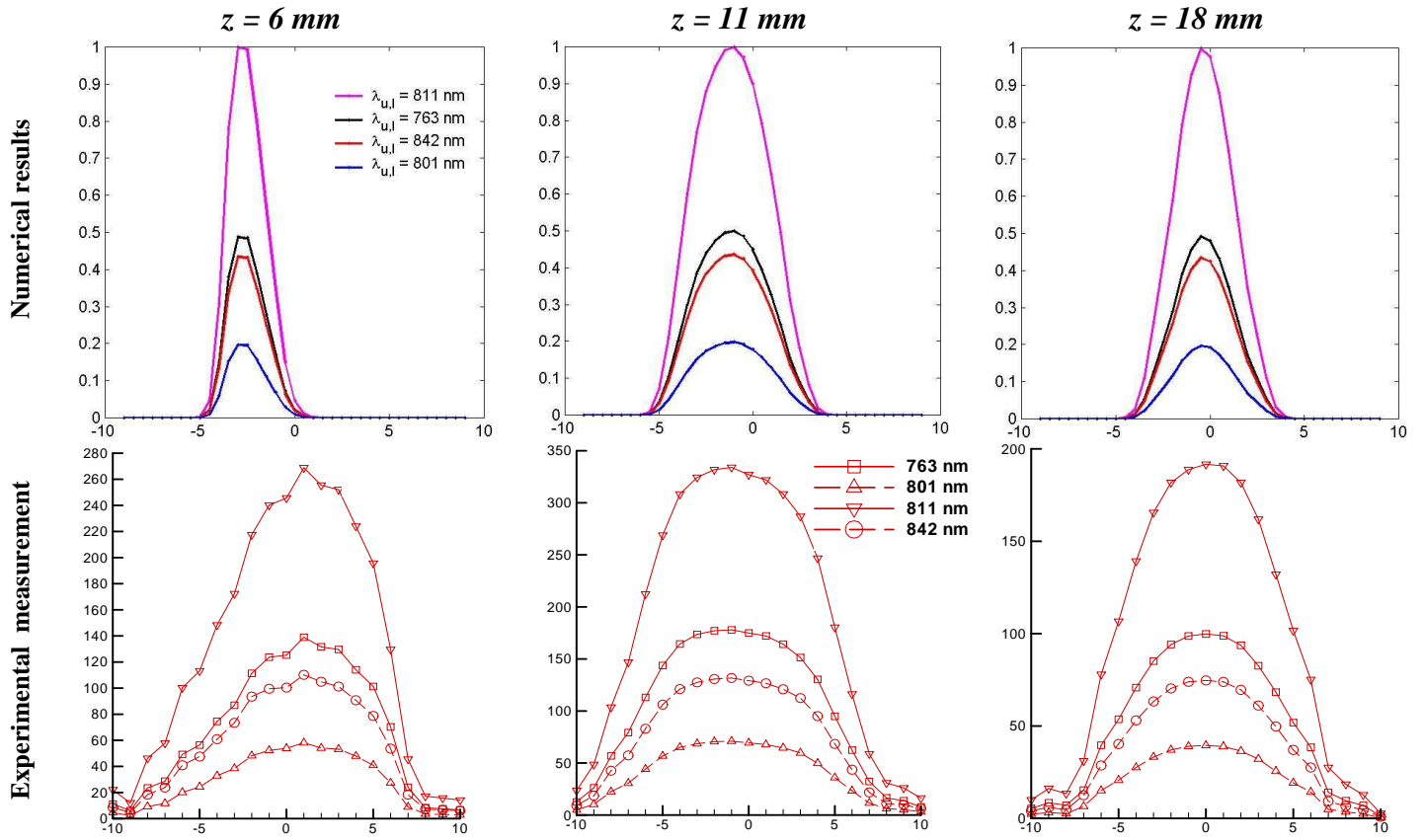
Plasma temperature field obtained by means of numerical calculation is shown in Fig. 4 for three planes passing through the axis of the torch, evidencing the predicted non-axisymmetric behaviour of the discharge. Calculated side-on emission intensity profile by means of the 3-D temperature field and using Eqs. 3 and 4, is shown in Fig. 5 for the three different views, normalized with the absolute maximum value. In Fig. 6 the corresponding experimentally measured side-on emission intensity is shown; the white regions are due to the presence of the coil turns that makes impossible to perform spectroscopic measurements at some heights. To better compare the results, in Fig. 7 and Fig. 8 the radial behaviour of the side-on emission intensity, calculated from 3-D modeling and measured, is shown for three specific torch heights and different wavelength. While for  $z = 6$  mm in Fig. 7 the calculated profiles do not agree with measurements, the results  $z = 11$  mm and  $z = 18$  mm seem to be in a qualitatively good agreement, showing the same kind of displacement for the discharge. In order to better compare the results, the abovementioned tomographic technique is applied on experimental measurements, obtaining the 2-D non-axisymmetric distribution in the plane at  $z = 15$  mm, using measured side-on emission profiles at various angles at the same height. The result is shown in Fig. 9 and compared with the calculated emission from the numerical model, with good agreement; the main differences between simulated and experimental results being mainly in the radial extension of the emitting zone, probably due to the LTE hypothesis of the model and to the presence of the cylindrical confinement tube which distorts the path of the emitted radiation [8]. Sheath gas inlet swirl velocity magnitude plays an important role in predicting the shape of the discharge; in the actual torch the



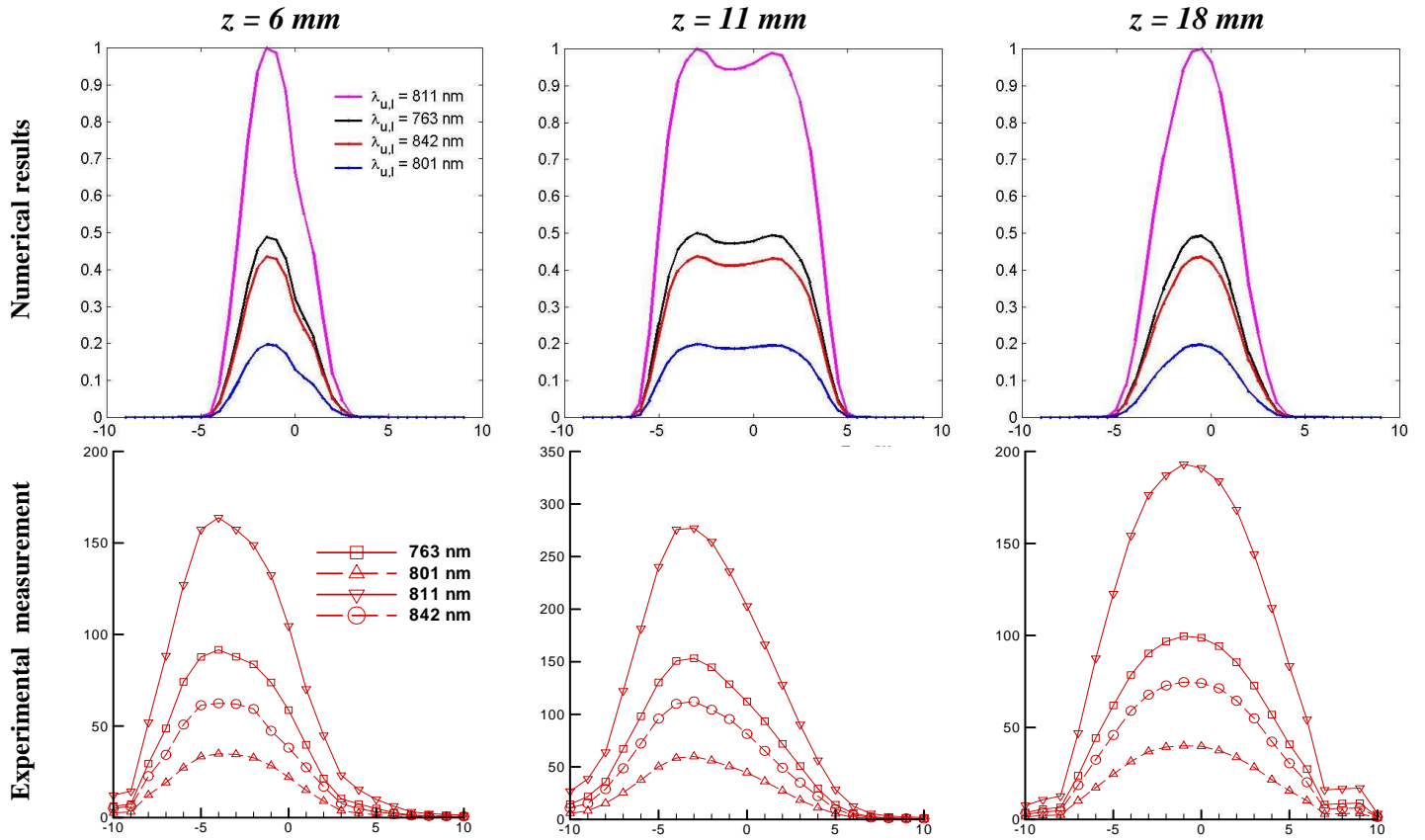
**Fig. 5** Normalized side-on emission intensity from simulation at  $\lambda_{ul} = 430.01$  nm, for the three views.



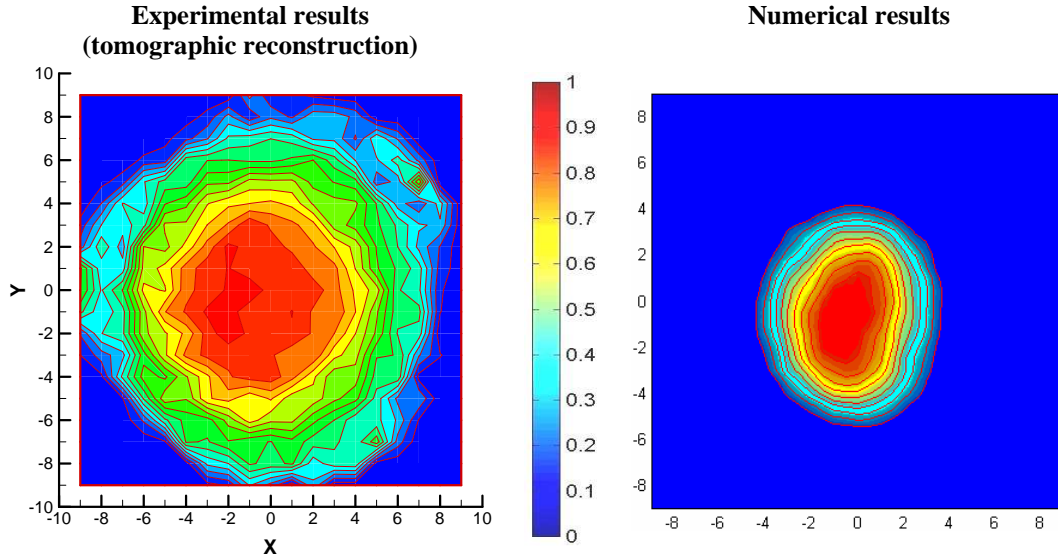
**Fig. 6** – Side-on emission intensity [ $\text{W/m}^2$ ] from measurements at  $\lambda_{ul} = 430.01$  nm, for the three views.



**Fig. 7** A-view side-on emission intensity from 3-D modelling [normalized] and measurements [ $\text{W}/\text{m}^2$ ] at various frequency values as function of the torch radius [mm];  $\lambda_{u,l} = 763.51, 801.48, 811.37$  and  $842.47 \text{ nm}$ .



**Fig. 8** C-view side-on emission intensity from 3-D modelling [normalized] and measurements [ $\text{W}/\text{m}^2$ ] at various frequency values as function of the torch radius [mm];  $\lambda_{u,l} = 763.51, 801.48, 811.37$  and  $842.47 \text{ nm}$ .



**Fig. 9** 2-D normalized non-axisymmetric distribution of line emission at  $\lambda_{u,l} = 696$  nm,  $z = 15$  mm.

sheath gas is inserted well upstream the coil region (in this reference frame  $z \sim -60$  mm), while in the model, for grid size reduction purposes, it is inserted only a few millimeters upstream the coil region ( $z \sim -12$  mm); since swirl velocity magnitude decreases significantly along  $z$ , from the gas inlet region to the coil zone, this difference in boundary conditions may be one of the reasons for differences in the numerically predicted shape of the discharge when compared with experimental measurements.

## 5. Conclusions

Measurement results and numerical calculations show that in an inductively coupled plasma torch, non-axisymmetric behaviour may arise due to the actual shape of the coil. These effects are located mainly in the coil zone, where the effects of unbalanced Lorentz forces are more noticeable, while at the torch exit the discharge seems to reach an axisymmetric state. Comparisons between measured and calculated results show a qualitatively good agreement, predicting a similar kind of displacement of the discharge. The main differences are on the radial extension of the discharge and on the absolute value of the side-on emission, due to the LTE assumption of the numerical model, since non equilibrium effects play an important role at this working generator frequency. The next steps in this research will be the developing of a two temperature 3-D model that will try to fit more tightly the physics of actual torch, in order to better predict the device behaviour.

## Acknowledgements

The authors would like to thank Prof. Leonardo Seccia and Dr. Riccardo Rossi for the use of the parallel calculation facilities at CTFD-Lab of the Faculty of Engineering in Forlì, Italy. Work performed with partial financial support from the University of Bologna Goal-Oriented project 2001-2003 and ex-60% 2001-2002 projects, from the Italian Ministry of Education, University and Scientific Research (M.I.U.R.) national project COFIN 2002 and National Group for Mathematical Physics (G.N.F.M.) of the Italian Institute of High Mathematics.

## References

- [1] M.I. Boulos, High Temp. Mater. Proc. **1**, 1 (1997)
- [2] V. Colombo, C. Panciatichi, A. Zazo, G. Cocito, L. Cognolato, IEEE Trans. Plasma Sci. **25**, 5 (1997)
- [3] J. Mostaghimi, M.I. Boulos, Plasma Chem. Plasma Process. **9**, 1 (1988)
- [4] S. Xue, P. Proulx, M.I. Boulos, J. Phys. D: Appl. Phys. **34**, 1897 (2001)
- [5] D. Bernardi, V. Colombo, E. Ghedini, A. Mentrelli, Eur. Phys. J. D **22** (2003)
- [6] D. Bernardi, V. Colombo, E. Ghedini, A. Mentrelli, *Three-Dimensional Modelling of Inductively Coupled Plasma Torches*, invited contribution, this conference
- [7] D. Bernardi, V. Colombo, E. Ghedini, A. Mentrelli, *Three-Dimensional Effects in the Modelling of ICPTs: I – Fluid-Dynamics and Electromagnetics and II - Induction Coil and Torch Geometry*, this conference
- [8] F. Cramarossa, S. De Benedictis, G. Ferraro, J. Quant. Spectrosc. Radiat. Transf. **23**, 3 (1980)

# Three-Dimensional Modelling of Inductively Coupled Plasma Torches

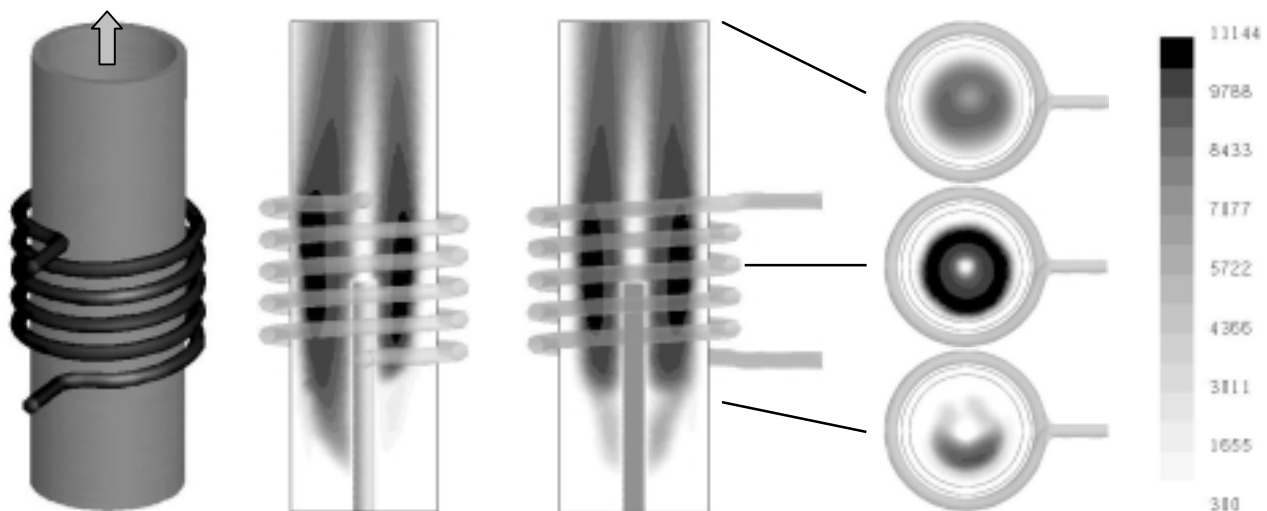
D. Bernardi, V. Colombo, E. Ghedini, A. Mentrelli

Università degli Studi di Bologna, Dipartimento di Ingegneria delle Costruzioni Meccaniche, Nucleari, Aeronautiche e di Metallurgia (D.I.E.M.) and C.I.R.A.M., Via Saragozza 8, 40123 Bologna, Italy.

Phone: +39 (0)51 2093978 - 2093986 Fax: +39 (0)51 582528 e-mail: [colombo@ciram.ing.unibo.it](mailto:colombo@ciram.ing.unibo.it)

A 3-D model for the simulation of inductively coupled plasma torches (ICPTs) working at atmospheric pressure is presented, using customized CFD commercial code FLUENT<sup>®</sup> [1-3]. The helicoidal coil is taken into account in its actual 3-D shape, showing its effects on the plasma discharge for various geometric, electric and operating conditions without axisymmetric hypotheses of simplification. Steady flow and energy equations are solved for Ar optically thin plasmas under the assumptions of LTE and laminar flow. The electromagnetic field equations are solved in their vector and scalar potential form, taking into account the charge density distribution that arises inside the plasma [3-4]. In order to evaluate the importance of various 3-D effects on calculated plasma temperature and flow fields, comparisons of our new results with the ones obtainable from 2-D models and from an improved 2-D model that includes 3-D coil effects [4] are presented. Three-dimensional results for different geometric configurations of the induction coil are presented, changing various shape parameters, such as coil axial length and number of coil turns; planar coil configurations are also presented. Optimization of torch design to avoid the formation of a hot temperature spot in the confinement tube wall due to the axial displacement of the plasma fireball is considered in the frame of the new model. Results are presented showing the effects of changing inlet gas flow rates and direction of the swirl velocity component as well as the net amount of power dissipated in the discharge. Axial particle (metallic or ceramic powders) injection in the plasma zone through a carrier gas is also taken into account, to realistically predict the experimental evidence of loss of material to the torch wall and the actual shape of the deposit zone downstream the torch exit. The effect of asymmetric secondary radial gas injection to carry particles in the plasma fireball is taken into account.

- [1] Bernardi, V. Colombo, E. Ghedini, A. Mentrelli, *Three-Dimensional Effects in the Modeling of ICPTs. I – Fluid-Dynamics and Electromagnetics and II – Induction Coil and Torch Geometry*, this conference.
- [2] Bernardi, V. Colombo, E. Ghedini, A. Mentrelli, *Three-dimensional Modelling of Inductively Coupled Plasma torches*, in press on Eur. Phys. J. D (2002).
- [3] D. Bernardi, V. Colombo, E. Ghedini, A. Mentrelli, A. Vertuan, *Fully 3D Modeling of Inductively Coupled Plasma Torches*, 55<sup>th</sup> Annual Gaseous Electronics Conference, Minneapolis, October 2002.
- [4] S. Xue, P. Proulx, M.I. Boulos, *Effect of coil angle in an inductively coupled plasma torch: a novel two-dimensional model*, in press on Plasma Chem. Plasma Process. (2003).



Plasma temperature fields [K] for the Tekna PL-50 plasma torch operated at 25kW discharge power and 3 MHz.

# Three-Dimensional Effects in the Modelling of ICPTs

## I – Fluid Dynamics and Electromagnetics

D. Bernardi, V. Colombo, E. Ghedini, A. Mentrelli

*Dipartimento di Ingegneria delle Costruzioni Meccaniche, Nucleari, Aeronautiche e di Metallurgia (D.I.E.M.) and C.I.R.A.M., Università degli Studi di Bologna, Via Saragozza 8, 40123 Bologna, Italy.*  
Phone: +39 (0)51 2093978 - 2093986 Fax: +39 (0)51 582528  
e-mail: [colombo@ciram.ing.unibo.it](mailto:colombo@ciram.ing.unibo.it) ; [davide.bernardi@mail.ing.unibo.it](mailto:davide.bernardi@mail.ing.unibo.it)

In this paper we investigate the 3-D effects of different flow operating conditions and of complete or simplified treatments of the electromagnetic field on the characteristics of the discharge in inductively coupled plasma torches working at atmospheric pressure. Results of parameterization on the net amount of power dissipated in the discharge, frequency of the RF generator, flow rate distribution of inlet gases and swirl velocity are presented, showing the impact of these parameters on the fluid-dynamic and electromagnetic behaviour of the plasma.

### 1. Introduction

Modelling is a useful tool in order to investigate the characteristics of inductively coupled plasma torch, since an accurate characterization of the physics that occur in the core of a plasma discharge by means of any diagnostics method is very to perform, especially for what concerns the flow field. Numerical modelling of this kind of devices involves the coupled solution of the fluid-dynamic, electromagnetic and energy equations. The authors have recently developed a fully 3-D model [1-4], in the framework of the FLUENT<sup>®</sup> code, to remove the axisymmetric assumption which is the fundamental hypothesis of all the previous 2-D codes [5-7], with the aim of predicting the non-axisymmetric effects induced by the actual shape of the induction coil. Apart from the increased computational effort needed by the grid complexity and the arising of the number of vector components in the governing equations, 3-D extension of the numerical model for the electromagnetic field implies that also the scalar potential must be taken into account, due to the presence of a space-varying electrical conductivity inside the plasma discharge [8]. In this paper we show the impact on the solution of using either a simplified or a complete electromagnetic model, taking into account or neglecting the scalar potential. Moreover, a parameterization on the power actually dissipated into the discharge and on the working frequency is performed. Investigations on fluid dynamics are performed by means of different distributions of inlet gas flow rate and swirl velocity magnitude and direction, in order to highlight the effect of their change on the 3-D behaviour of the discharge. Finally a comparison of results using Argon and Ar/N<sub>2</sub> plasma is performed.

### 2. Geometry and Model

Torch geometry and common operating conditions employed in the following simulations are shown in Fig. 1, with corresponding dimensions summarized in Tab. 1, referring to a Tekna PL-50 torch. Maxwell equations are solved in their vector and scalar potential formulation:

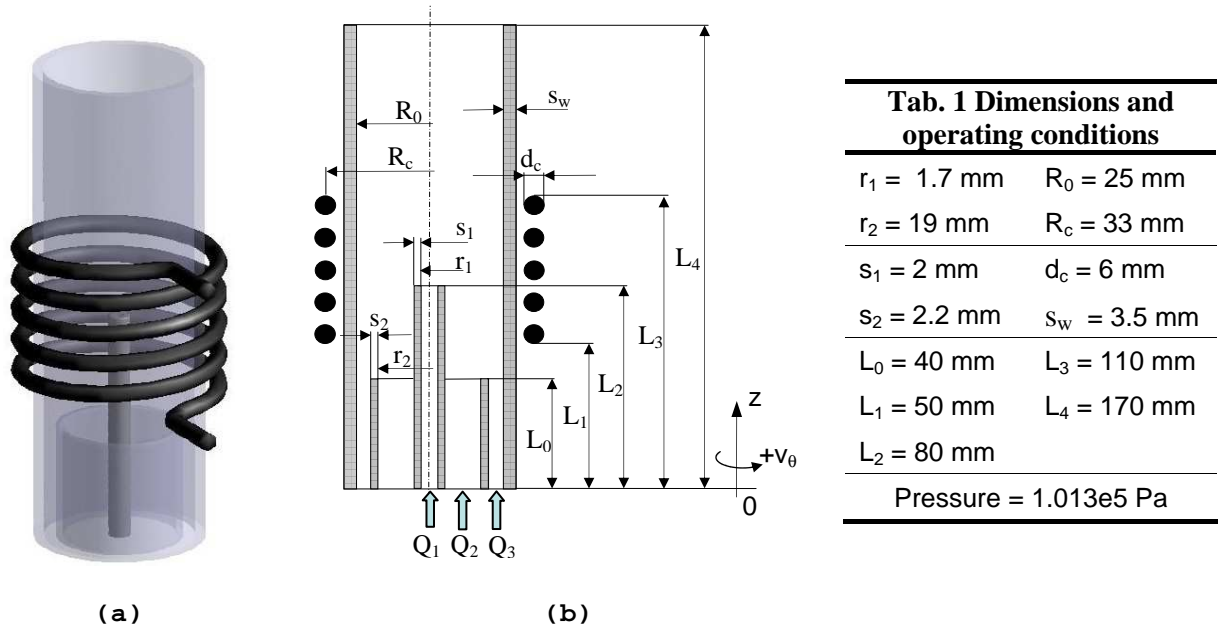
$$\nabla^2 \mathbf{A} - \mu_0 \sigma (\nabla V + \partial \mathbf{A} / \partial t) + \mu_0 \mathbf{J}^{coil} = 0 \quad (1) \quad \nabla \cdot [\sigma (\nabla V + \partial \mathbf{A} / \partial t)] = 0 \quad (2)$$

where the term  $\mathbf{J}^{coil}$  represents the current density in the coil region. The electric and magnetic fields in their classical form can be expressed through the definitions of the vector and scalar potentials:  $\mathbf{E} = -\partial \mathbf{A} / \partial t - \nabla V$ ,  $\mathbf{B} = \nabla \times \mathbf{A}$ . The simplified electromagnetic model is obtained neglecting the Eq. 2 that take into account the space-varying conductivity and the arising of a charge distribution. Vanishing boundary conditions are applied in an extended mesh outside the plasma region [6,7]. Energy and Navier-Stokes equations are solved inside the FLUENT<sup>®</sup> environment under the assumptions of an optically thin plasma in LTE condition on the entire torch domain and laminar flow for the gas.

### 3. Results

Fields representing physical quantities will be visualized for all the results on two perpendicular planes passing through the axis of the torch, whose relative position is evidenced by coil view. For each case, detailed operating conditions are summarized in the corresponding figure caption. Temperature and velocity





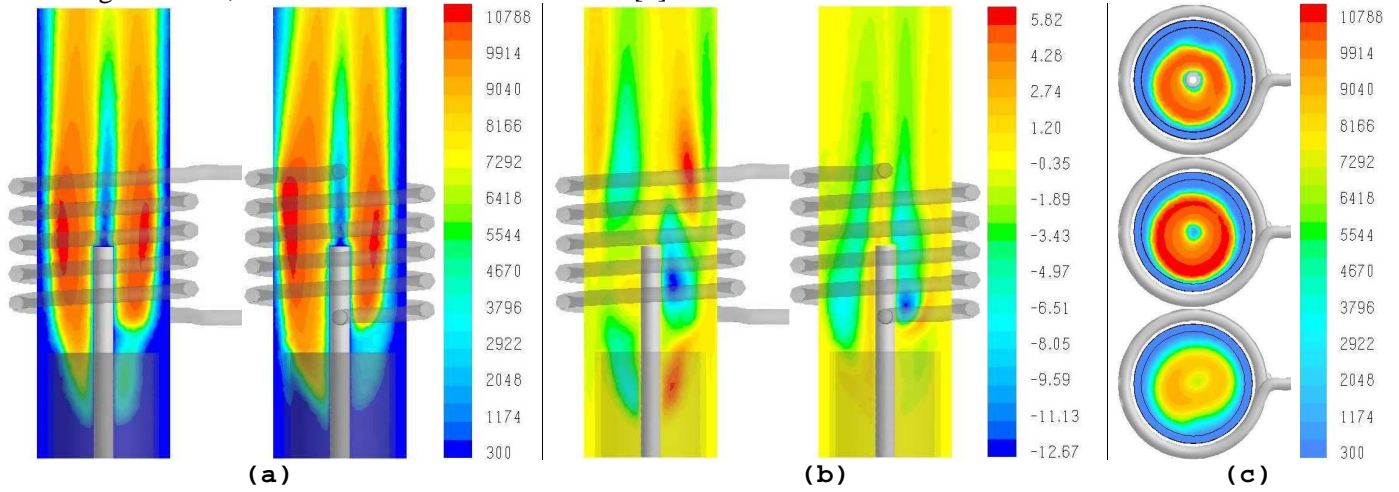
**Fig. 1** (a) 3-D schematic reproducing the actual coil and (b) dimensions of the plasma torch.

fields of an Argon operated torch with net power dissipated in the plasma  $P = 25 \text{ kW}$ , without inlet gas swirl velocity and within the simplified electromagnetic model, are shown in Fig. 2, in order to introduce a reference case to which compare the other results. The arising of the non axisymmetry due to the actual coil geometry, without any swirl confinement, leads to a temperature maximum near the quartz tube, as evidenced also by the Fig. 2c. The effects of using the complete electromagnetic model are shown in Fig. 3, for the same operating conditions of the previous case. Temperature field differences between the two cases are negligible, while the tangential velocity field obtained using the complete model reduces its magnitude with respect to the simplified one. Charge density distribution that arises due to the conductivity gradient is shown in Fig. 4, with real and imaginary component; charges are mainly located in areas corresponding to maximum values of the temperature gradient. Corresponding scalar potential fields, whose source is the charge density, are shown in Fig. 5. Temperature fields obtained introducing a swirl component  $v_{\theta s} = \pm 20 \text{ m/s}$  in the sheath gas, are shown in Fig. 6, showing that presence of a swirl component for the sheath gas induces a better confinement of the plasma discharge with respect to the previous cases, and that the maximum temperature is far from the quartz tube, avoiding the risk of melting. Fig. 6 puts also into evidence that a change in sheath gas swirl direction leads to much different results in the temperature fields at the torch exit and in the upstream region of the discharge, as a result of the complex 3-D fluid-dynamics phenomena that occur inside a plasma torch. As an alternative to the previous case, a swirl component  $v_{\theta p} = \pm 20 \text{ m/s}$  is applied to the plasma gas; corresponding results are shown in Fig. 7, showing a lower efficiency in discharge confinement with respect to the previous case. Reducing the power dissipated into the discharge, to  $P = 15 \text{ kW}$ , with a swirl component in the sheath gas  $v_{\theta s} = +10 \text{ m/s}$ , leads to results of Fig. 8 and Fig. 9, with and without carrier gas, respectively. The effect of an increase of the operating frequency from  $3 \text{ MHz}$  to  $5 \text{ MHz}$  is shown in Fig. 10. Finally Fig. 11 and Fig. 12 show the effects of using  $\text{Ar/N}_2$  (5 % by volume) instead of pure Argon on the temperature and velocity fields and in the power density distribution.

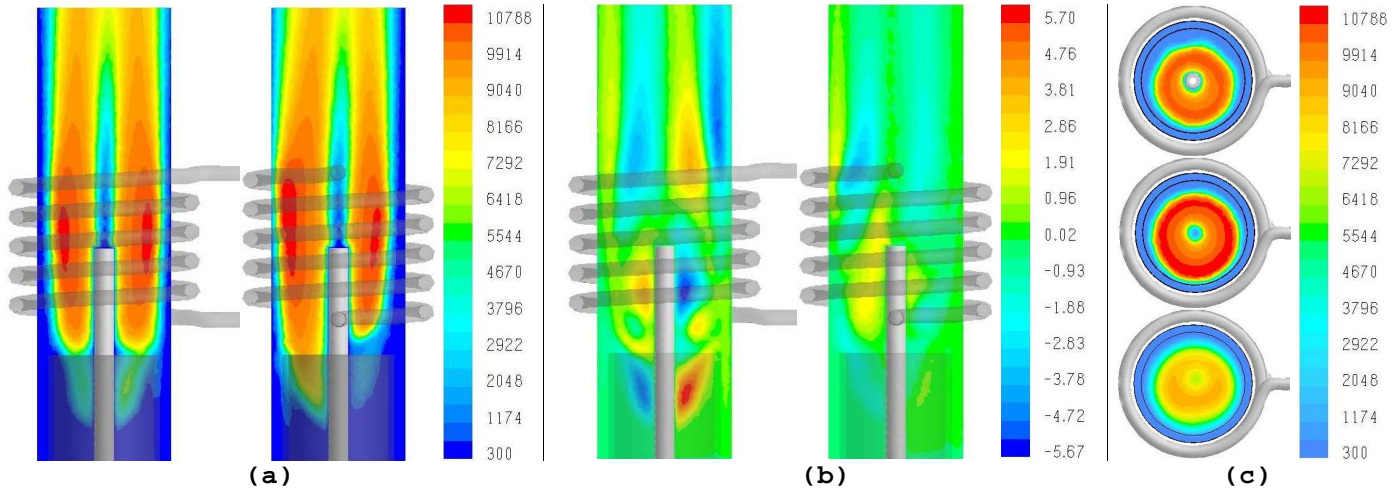
#### 4. Conclusions

Investigations performed in this work show that 3-D effects in the inductively plasma torches play an important rule in the physical characterization of the discharge. The electromagnetic equations can be solved, as a first approximation, neglecting the scalar potential, to obtain temperature results, but a full model should be used if a detailed prediction of the fluid-dynamics is needed. The complexity of the phenomena involved inside this kind of devices, especially for what concerns the fluid-dynamics, let the results be quite difficult to foresee when changing torch operating parameters. For this reason the 3-D code developed by the authors can be a useful tool in the design of inductively plasma torch. Also important as a next step in this research

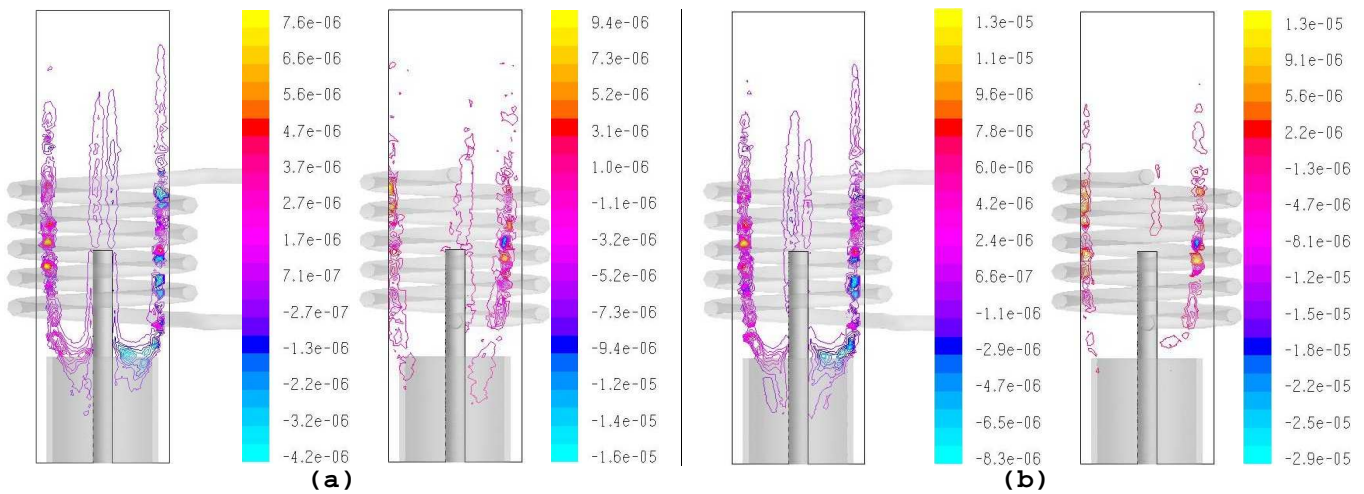
will be the comparisons between numerical and experimental results in different torch operating conditions and geometries, in order to test and tune the code [4].



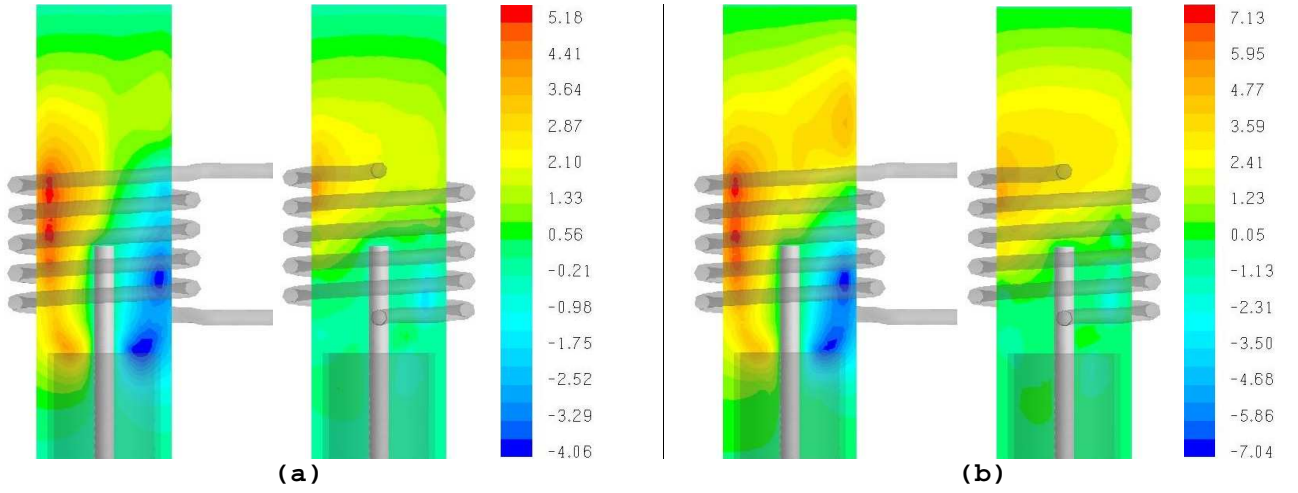
**Fig. 2**  $P = 25$  kW;  $f = 3$  MHz;  $Q_1/Q_2/Q_3 = 10/30/120$  slpm; working gas: Ar; (a) Plasma temperature [K] and (b) tangential velocity [m/s] fields, calculated using the simplified e.m. model; (c) plasma and wall temperature fields [K] on three horizontal planes located at  $z = 60, 90, 170$  mm respectively, from top to bottom.



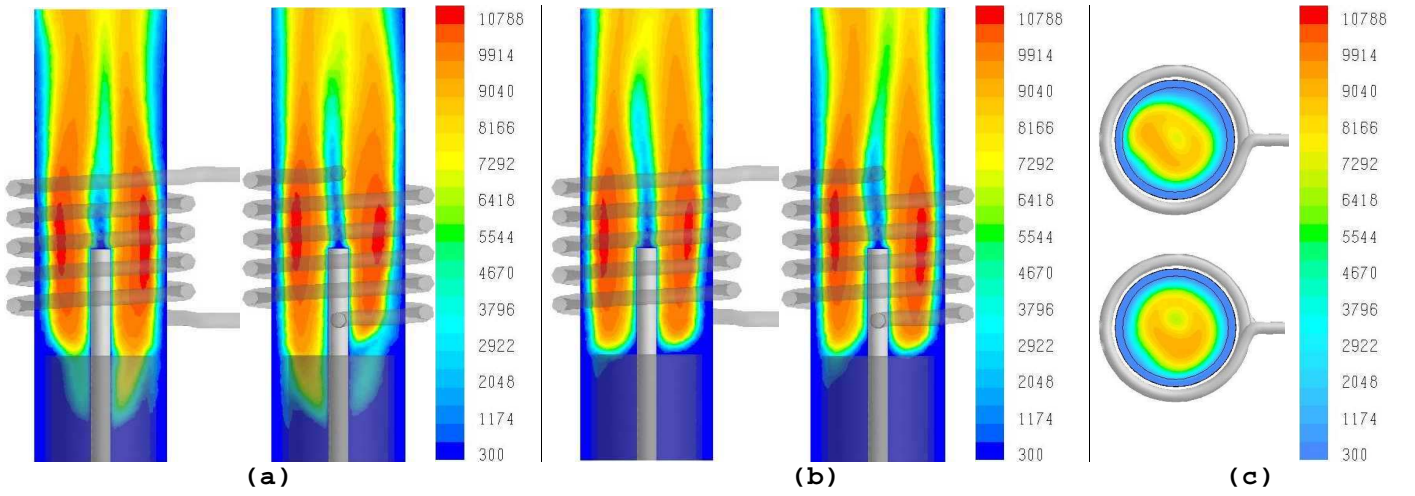
**Fig. 3**  $P = 25$  kW;  $f = 3$  MHz;  $Q_1/Q_2/Q_3 = 10/30/120$  slpm; working gas: Ar; (a) Plasma temperature [K] and (b) tangential velocity [m/s] fields, calculated using the complete e.m. model; (c) plasma and wall temperature fields [K] on three horizontal planes located at  $z = 60, 90, 170$  mm respectively, from top to bottom.



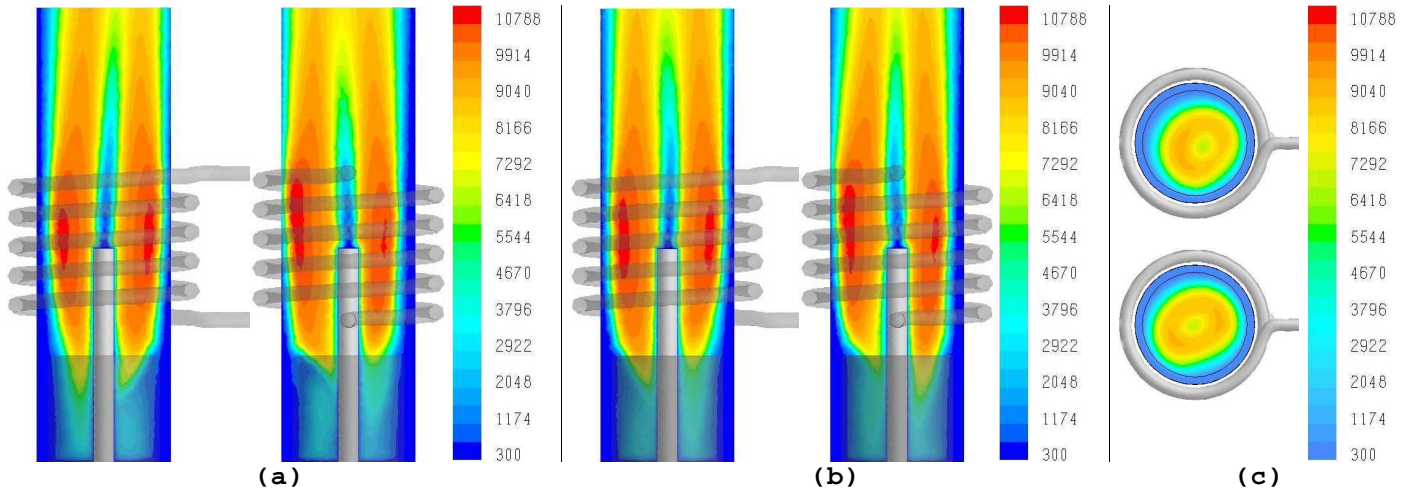
**Fig. 4** (a) Real and (b) imaginary parts of the electric charge density distribution [C/m<sup>3</sup>] in the plasma, for the case of Fig 3.



**Fig. 5** (a) Real and (b) imaginary parts of the scalar potential field [V] in the plasma, for the case of Fig. 3.

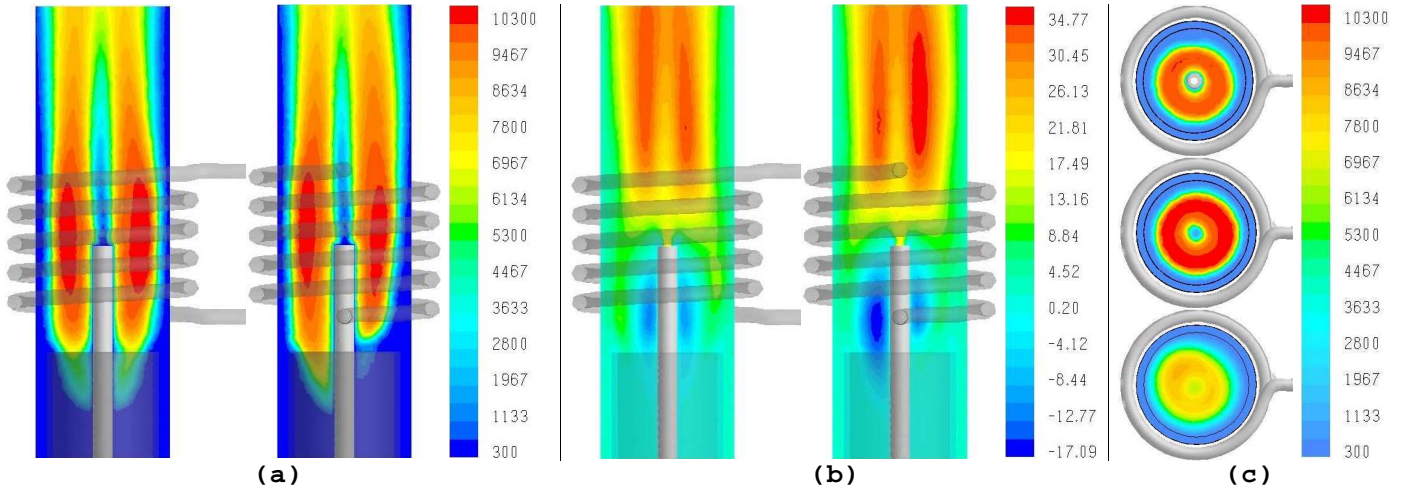


**Fig. 6** (a) Plasma temperature [K] fields, calculated using the simplified e.m. model, for the same case of Fig. 2 but with  $v_{0s} = 20$  m/s; (b) as in (a) but with  $v_{0s} = -20$  m/s; (c) plasma and wall temperature fields [K] at the torch exit for the cases (a) and (b) respectively, from top to bottom.

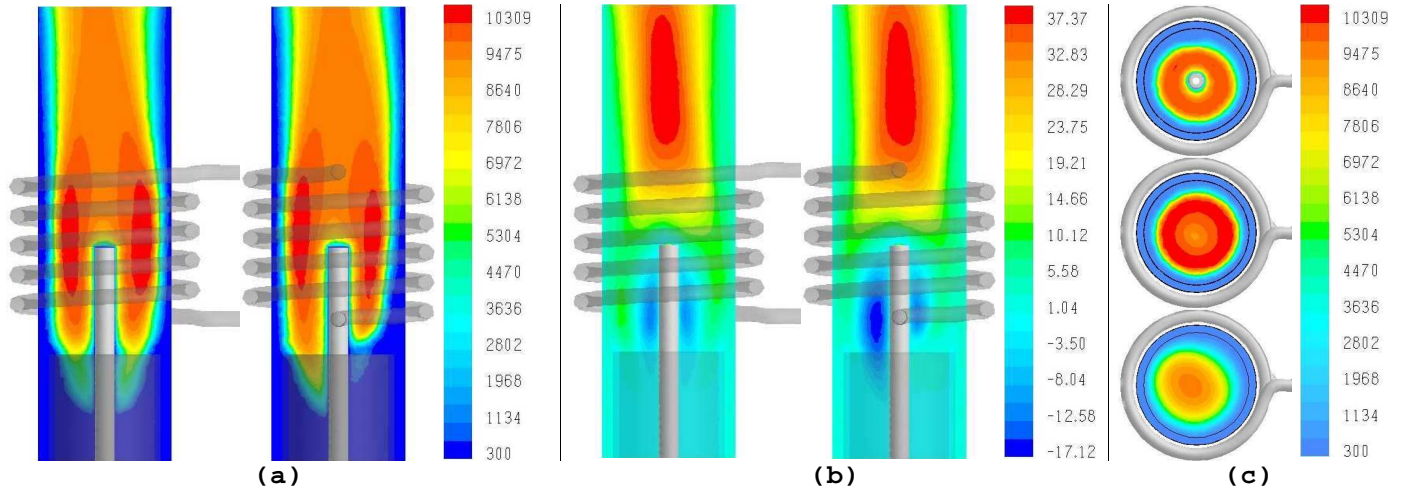


**Fig. 7** (a) Plasma temperature fields [K], calculated using the simplified e.m. model, for the same case of Fig. 2 but with  $v_{0p} = 20$  m/s; (b) as in (a) but with  $v_{0p} = -20$  m/s; (c) plasma and wall temperature fields [K] at the torch exit for the cases (a) and (b) respectively, from top to bottom.

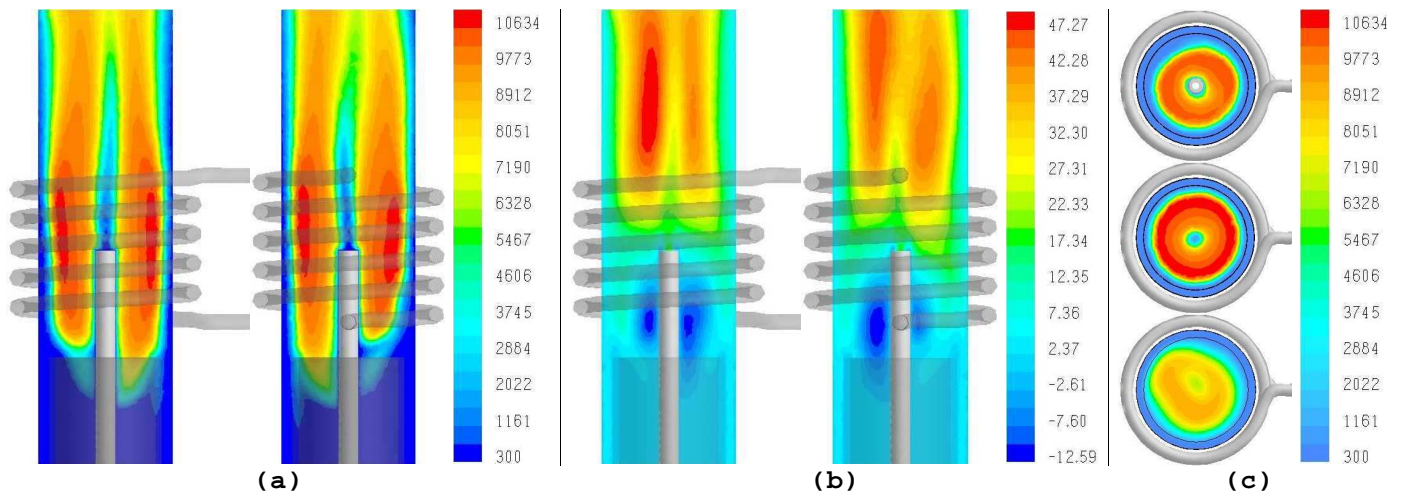




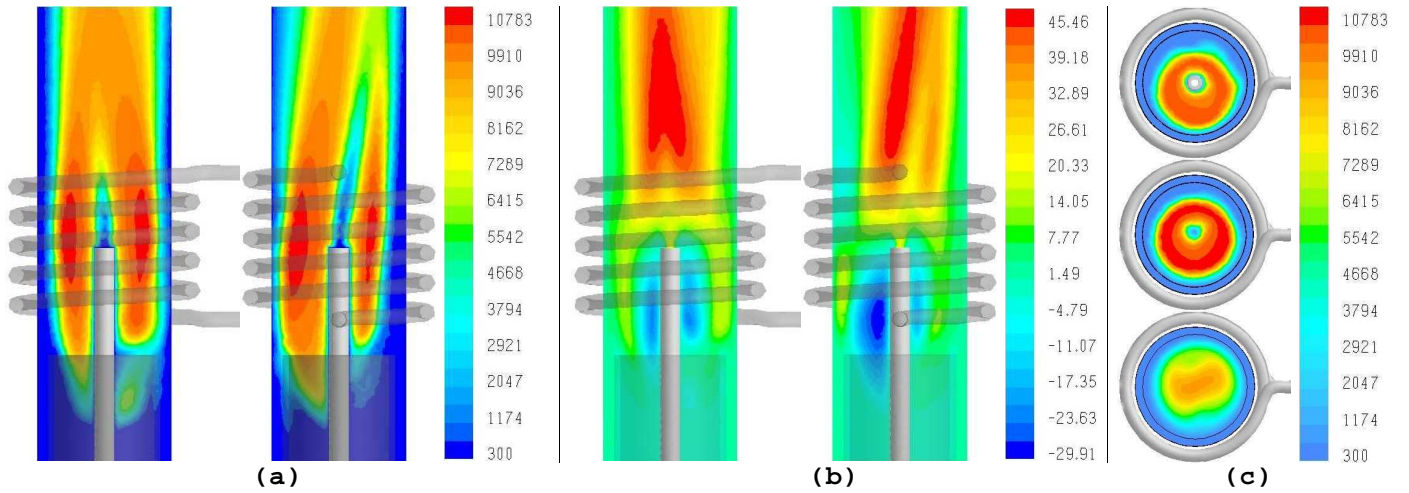
**Fig. 8**  $P = 15$  kW;  $f = 3$  MHz;  $Q_1/Q_2/Q_3 = 10/30/120$  slpm;  $v_{0s} = 10$  m/s; working gas: Ar; (a) Plasma temperature [K] and (b) axial velocity [m/s], calculated using the simplified e.m. model; (c) plasma and wall temperature fields [K] on three horizontal planes located at  $z = 60, 90, 170$  mm respectively, from top to bottom.



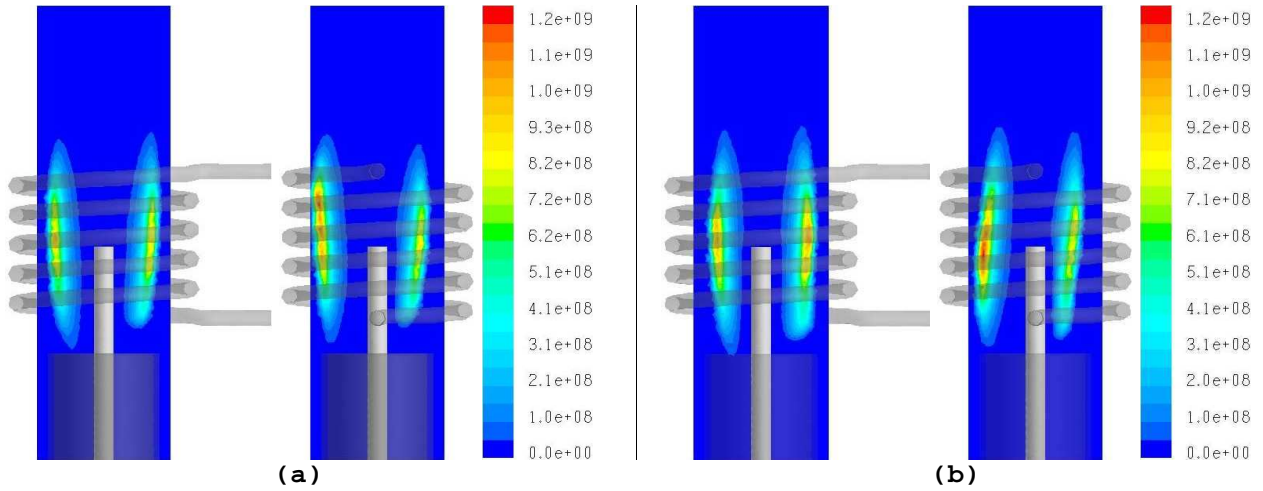
**Fig. 9**  $P = 15$  kW;  $f = 3$  MHz;  $Q_1/Q_2/Q_3 = 0/30/120$  slpm;  $v_{0s} = 10$  m/s; working gas: Ar; (a) Plasma temperature [K] and (b) axial velocity [m/s], calculated using the simplified e.m. model; (c) plasma and wall temperature fields [K] on three horizontal planes located at  $z = 60, 90, 170$  mm respectively, from top to bottom.



**Fig. 10**  $P = 25$  kW;  $f = 5$  MHz;  $Q_1/Q_2/Q_3 = 10/30/120$  slpm;  $v_{0s} = 20$  m/s; working gas: Ar; (a) Plasma temperature [K] and (b) axial velocity [m/s], calculated using the simplified e.m. model; (c) plasma and wall temperature fields [K] on three horizontal planes located at  $z = 60, 90, 170$  mm respectively, from top to bottom.



**Fig. 11**  $P = 25$  kW;  $f = 3$  MHz;  $Q_1/Q_2/Q_3 = 10/30/120$  slpm;  $v_{0s} = 0$ ;  $v_{0p} = 0$ ; working gas: Ar/N<sub>2</sub> (5% by volume); (a) Plasma temperature [K] and (b) axial velocity [m/s] fields, calculated using the simplified e.m. model; (c) plasma and wall temperature fields [K] on three horizontal planes located at  $z = 60, 90, 170$  mm respectively, from top to bottom.



**Fig. 12** Power density [W/m<sup>3</sup>] for the cases corresponding to (a) Fig. 2 (working gas: Ar) and (b) Fig. 11 (working gas: Ar/ N<sub>2</sub>, 5% by volume)

### Acknowledgements

The authors would like to thank Prof. Leonardo Seccia and Dr. Riccardo Rossi for the use of the parallel calculation facilities at CTFD-Lab of the Faculty of Engineering in Forlì, Italy. Work performed with partial financial support from the University of Bologna Goal-Oriented project 2001-2003 and ex-60% 2001-2002 projects, from the Italian Ministry of Education, University and Scientific Research (M.I.U.R.) national project COFIN 2002 and National Group for Mathematical Physics (G.N.F.M.) of the Italian Institute of High Mathematics.

### References

- [1] D. Bernardi, V. Colombo, E. Ghedini, A. Mentrelli, *Eur. Phys. J. D* **22** (2003)
- [2] D. Bernardi, V. Colombo, E. Ghedini, A. Mentrelli, *Three-Dimensional Modelling of Inductively Coupled Plasma Torches*, invited contribution for the section "Modelling in plasma chemistry", this conference
- [3] D. Bernardi, V. Colombo, E. Ghedini, A. Mentrelli, *Three-Dimensional Effects in the Modelling of ICPTs: I – Fluid-Dynamics and Electromagnetics and II - Induction Coil and Torch Geometry*, this conference
- [4] V. Colombo, G. Gao, E. Ghedini, J. Mostaghimi, *Asymmetry Effects in the Diagnostics and Simulation of RF Inductively Coupled Plasma Torch*, this conference
- [5] J. Mostaghimi, M.I. Boulos, *Plasma Chem. Plasma Process.* **9**, 1 (1988)
- [6] V. Colombo, C. Panciatichi, A. Zazo, G. Cocito, L. Cognolato, *IEEE Trans. Plasma Sci.* **25**, 5 (1997)
- [7] S. Xue, P. Proulx, M.I. Boulos, *J. Phys. D: Appl. Phys.* **34**, 1897 (2001)
- [8] D. Bernardi, V. Colombo, E. Ghedini, A. Mentrelli, *Three-Dimensional Effects in the Design of Inductively Coupled Plasma Torches*, XVI Congresso Nazionale Sulla Scienza e Tecnologia del Vuoto, Catania, Italia, 7-9 Ottobre 2002.

# Three-Dimensional Effects in the Modelling of ICPTs

## II - Induction Coil and Torch Geometry

D. Bernardi, V. Colombo, E. Ghedini, A. Mentrelli

*Università degli Studi di Bologna, Dipartimento di Ingegneria delle Costruzioni Meccaniche, Nucleari, Aeronautiche e di Metallurgia (D.I.E.M.) and C.I.R.A.M., Via Saragozza 8, 40123 Bologna, Italy.*

*Phone: +39 (0)51 2093978 - 2093986 Fax: +39 (0)51 582528*

*e-mail: [colombo@ciram.ing.unibo.it](mailto:colombo@ciram.ing.unibo.it) ; [andrea.mentrelli@mail.ing.unibo.it](mailto:andrea.mentrelli@mail.ing.unibo.it)*

### Abstract

A 3-D numerical study is performed to investigate the effects of induction coil design and torch geometry on the characteristics of argon discharges in inductively coupled plasma torches working at atmospheric pressure. Results are presented for different coil geometries including conventional helicoidal, double-stage and planar configurations. The physical behaviour of torches with elliptical cross-section is also analyzed. Additionally, the effects on plasma fields of reducing the post-coil length in a conventional torch are shown.

### 1. Introduction

Mathematical modeling represents a useful tool to predict the characteristics of the discharge in inductively coupled plasma torches (ICPTs), as the detailed diagnostics of these systems is very difficult to be carried out, in particular with regard to flow field and power distribution in the plasma. Although 2-D axisymmetric models [1-3], which have been widely employed in the past, can describe with good approximation the main physical phenomena occurring within ICPTs, 3-D approaches must be used to analyze the asymmetry effects due to the actual shape of the induction coil or to investigate torches with non conventional cross-sections. In this frame, a fully 3-D model including both a simplified and a complete treatment of the electromagnetic field has been recently developed by the authors within customized commercial code FLUENT<sup>®</sup> [4-6]. While in the first part of this work, in this same conference [7], we use such a model to evaluate the effects on the behaviour of a standard conventional torch of different flow and operating conditions, adopting either a simplified or a complete electromagnetic field approach, also on gas mixtures, in this paper the attention is focused on the impact of different coil shapes and torch geometries on the characteristics of pure argon discharges. Simulation results will be presented for conventional helicoidal, planar and double-stage coil configurations and for a torch with elliptical cross-section. Moreover, the effects of reducing the post-coil length on plasma temperature and velocity distributions are shown for the same torch geometry considered in [7].

### 2. Modelling approach

All the calculations are performed for optically thin plasmas, under the assumptions of LTE and laminar flow conditions. Plasma temperature and velocity fields are obtained by solving the 3-D version of mass, momentum and energy conservation equations, while the electromagnetic field is calculated by means of the simplified model which neglects the scalar potential due to the electric charge density distribution in the plasma. Since this assumption does not have a great impact on the solution, as shown in [5, 7], it is adopted here for the sake of simplicity. The coupled set of governing equations is solved within customized FLUENT<sup>®</sup> code, using the UDS approach [3] for the treatment of the vector potential. Typical boundary conditions for plasma temperature and velocity are applied (see [4] for more details), while vanishing boundary conditions on a grid extended also outside the torch region are used for the electromagnetic field.

### 3. Numerical results

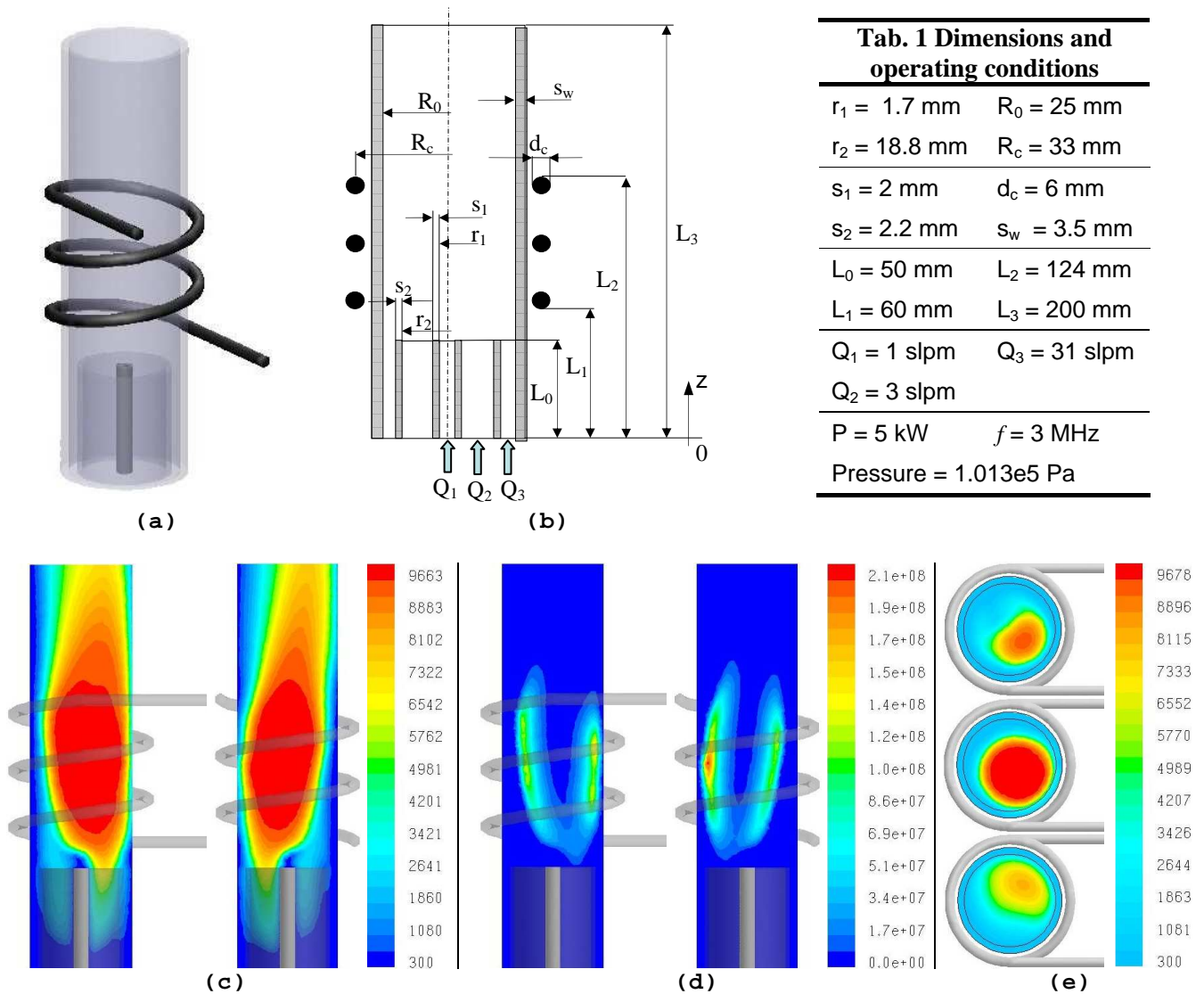
Where not specified, the presented results refer to two perpendicular planes passing through the axis of the torch, whose relative position is evidenced by coil view. In the following,  $P$  denotes the net amount of power dissipated in the discharge,  $f$  is the generator frequency,  $Q_1$ ,  $Q_2$ ,  $Q_3$  (or, alternatively,  $Q$ ) are the carrier, plasma and sheath gas flow rates, respectively, (or, alternatively, the total gas flow rate). In Fig. 1, plasma temperature and power density distributions are shown for a conventional torch with 2.5 coil turns (with inclination of  $6.60^\circ$ ): a significant displacement of the plasma fireball towards the confinement tube and the consequent formation of a hot spot on the wall appear, as a result of the strong non-axisymmetry of the coil shape. In Fig. 2, plasma temperature and power density fields, along with axial and tangential velocity



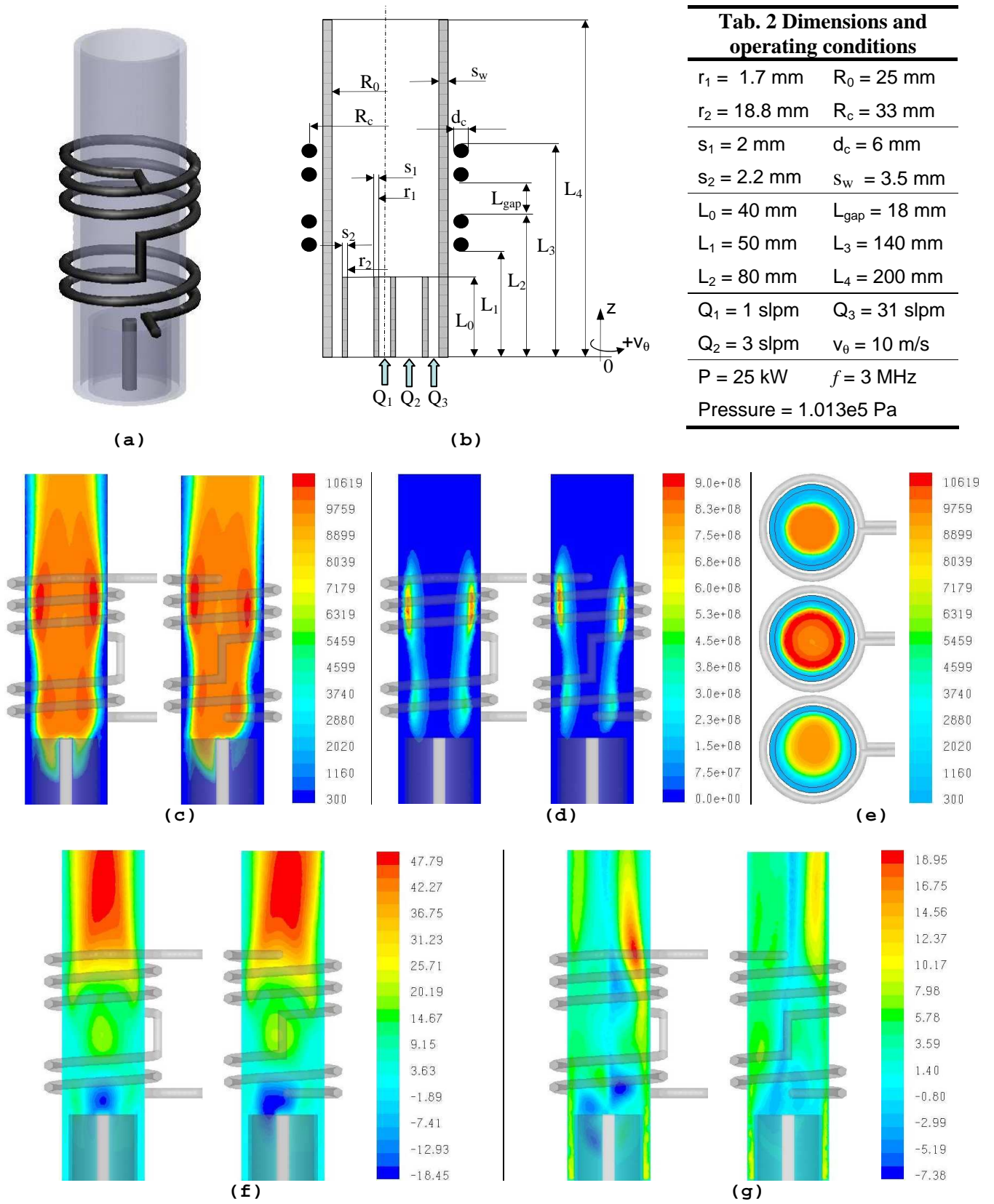
distributions, are presented for a double-stage coil configuration [8] in which a swirl velocity component,  $v_\theta$ , is introduced in the sheath gas. Fig. 2c shows that such configuration is characterized by an extended discharge volume that makes this type of torch particularly suitable for powder treatment. As evidenced in Fig. 2d, the RF power is dissipated mainly in the upper part of the coil. The effect of a planar coil geometry [8] on plasma temperature and power distributions is shown in Fig. 3. It can be observed in Fig. 3e that this kind of coil configuration significantly modifies the way power is transferred to the plasma with respect to the helicoidal shape. In Fig. 4, simulation results including plasma temperature and axial velocity fields, as well as power density distribution, are presented for a torch with elliptical cross-section. Fig. 4b, 4d and 4e clearly show that, in this case, the non-axisymmetry effects are mainly located along the short axis. Finally, in Fig. 5, plasma temperature and velocity fields are presented for the same conventional torch adopted in [7] but with a shorter post-coil.

#### 4. Conclusions

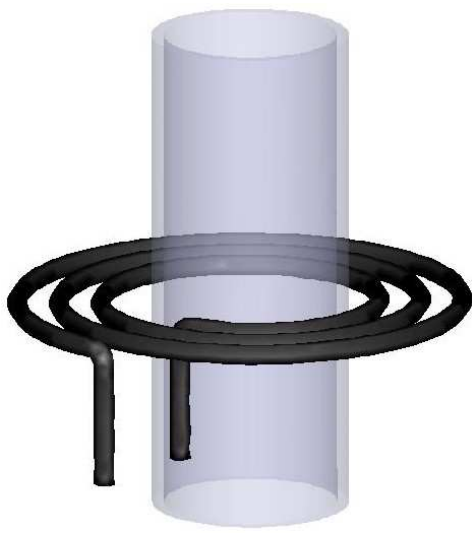
In addition to the important role played in the physical characterization of the discharge in inductively coupled plasma torches, as shown in the first part of this work, in this same conference [7], the results presented in this paper demonstrate that our 3-D model can be particularly helpful also in the design stage of such devices, in which the detailed prediction of relevant asymmetry effects especially due to non conventional coil configurations or torch geometries might be important.



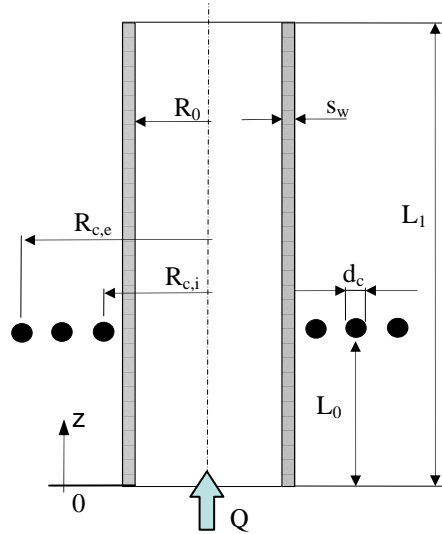
**Fig. 1** Conventional coil with 2.5 turns: (a) 3-D schematic and (b) dimensions and operating conditions of the plasma torch; (c) plasma temperature field [K]; (d) power density distribution [ $\text{W/m}^3$ ]; (e) plasma and wall temperature fields [K] on three horizontal planes located at  $z = 60, 92, 200 \text{ mm}$  respectively, from top to bottom.



**Fig. 2** Double-stage coil: (a) 3-D schematic and (b) dimensions and operating conditions of the plasma torch; (c) plasma temperature field [K]; (d) power density distribution [ $\text{W/m}^3$ ]; (e) plasma and wall temperature fields [K] on three horizontal planes located at  $z = 90, 120, 200 \text{ mm}$  respectively, from top to bottom; (f) axial and (g) tangential plasma velocity fields [m/s].

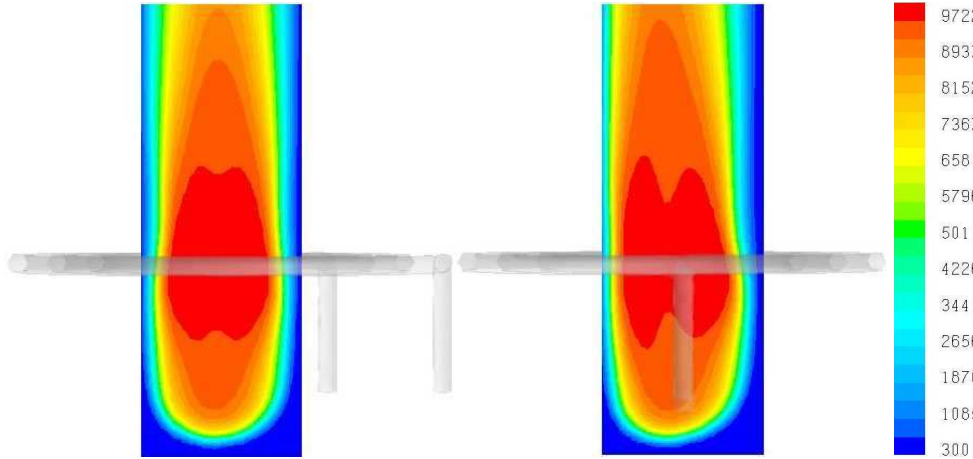


(a)

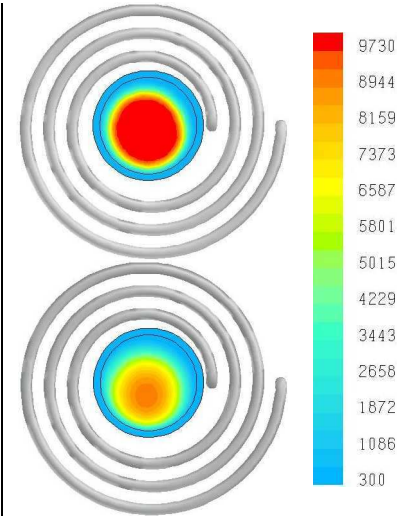


(b)

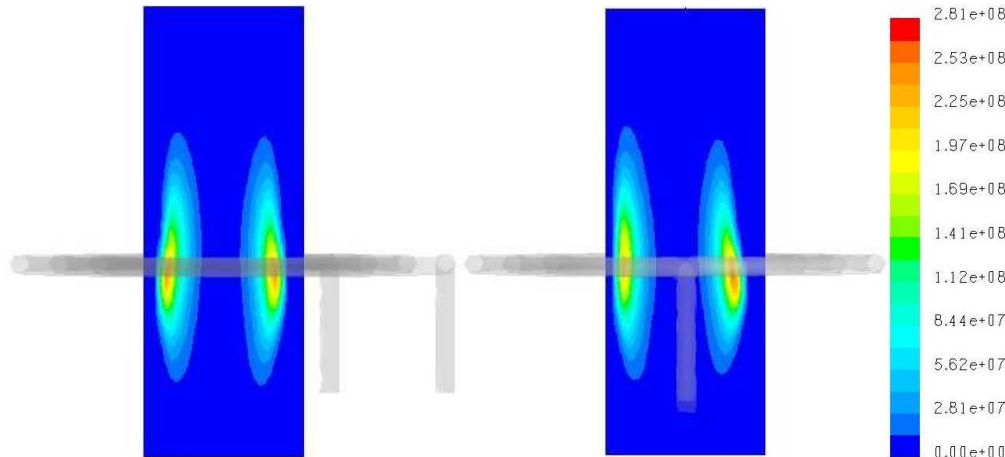
Tab. 3 Dimensions and operating conditions	
$R_0 = 25 \text{ mm}$	
$R_{c,i} = 33 \text{ mm}$	$R_{c,e} = 70 \text{ mm}$
$s_w = 3.5 \text{ mm}$	$d_c = 6 \text{ mm}$
$L_0 = 57 \text{ mm}$	$L_1 = 140 \text{ mm}$
$Q = 35 \text{ slpm}$	
$P = 5 \text{ kW}$	$f = 3 \text{ MHz}$
Pressure = $1.013 \times 10^5 \text{ Pa}$	



(c)



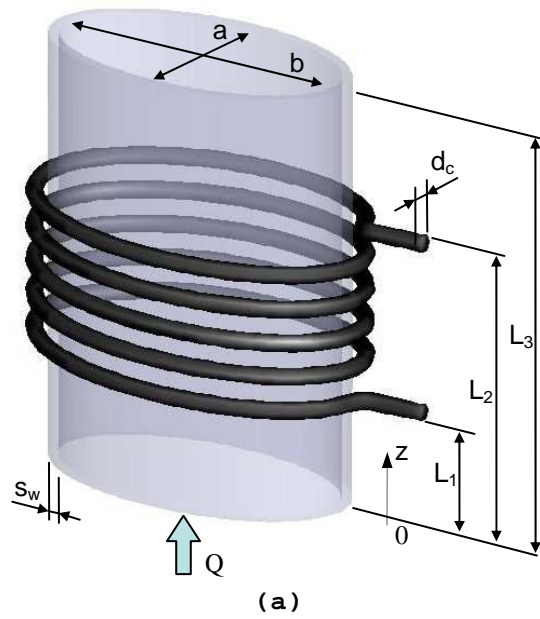
(d)



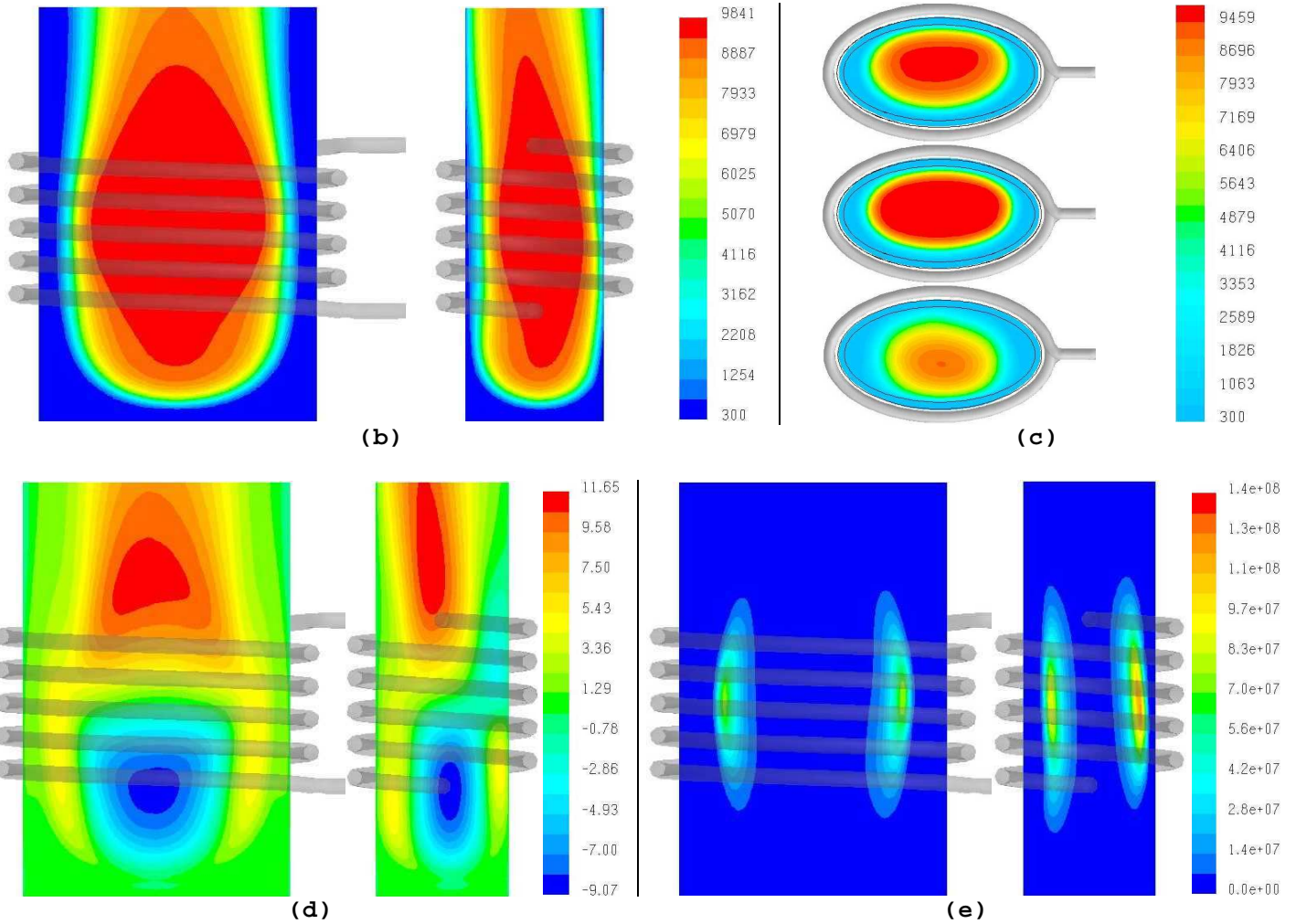
(e)

**Fig. 3** Planar coil: (a) 3-D schematic and (b) dimensions and operating conditions of the plasma torch; (c) plasma temperature field [K]; (d) plasma and wall temperature fields [K] on two horizontal planes located at  $z = 60, 140 \text{ mm}$  respectively, from top to bottom; (e) power density distribution [ $\text{W}/\text{m}^3$ ].

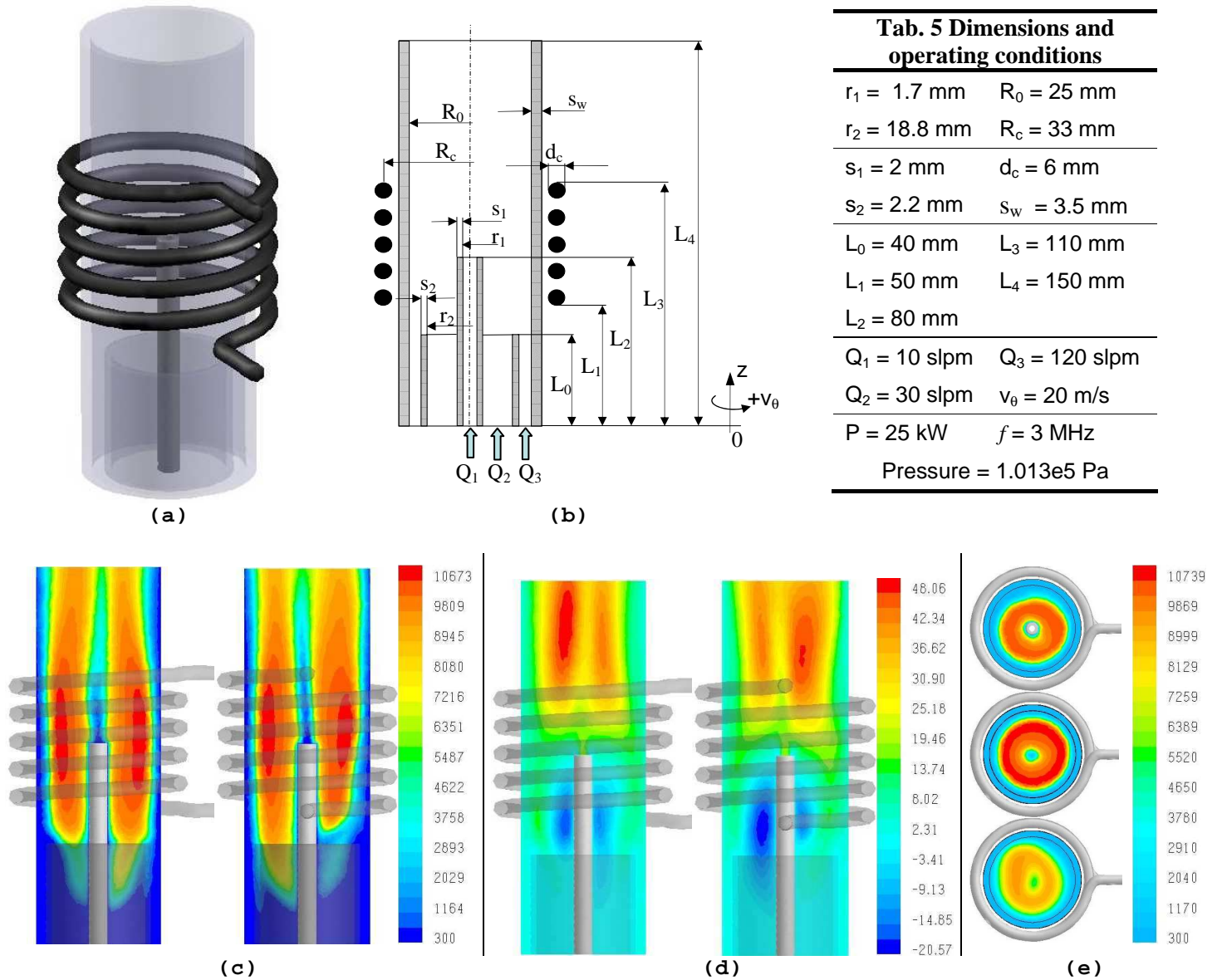




Tab. 4 Dimensions and operating conditions	
$a = 50 \text{ mm}$	$d_c = 6 \text{ mm}$
$b = 100 \text{ mm}$	$s_w = 3.5 \text{ mm}$
$L_1 = 37 \text{ mm}$	$L_3 = 150 \text{ mm}$
$L_2 = 103 \text{ mm}$	$Q = 40 \text{ slpm}$
$P = 5 \text{ kW}$	$f = 3 \text{ MHz}$
Pressure = $1.013 \times 10^5 \text{ Pa}$	



**Fig. 4** *Elliptical shaped coil*: (a) 3-D schematic, dimensions and operating conditions of the plasma torch; (b) plasma temperature field [K]; (c) plasma and wall temperature fields [K] on three horizontal planes located at  $z = 40, 70, 150 \text{ mm}$  respectively, from top to bottom; (d) axial velocity field [m/s]; (e) power density distribution [ $\text{W/m}^3$ ].



**Fig. 5** Conventional coil with 5 turns and reduced post-coil length: (a) 3-D schematic and (b) dimensions and operating conditions of the plasma torch; (c) plasma temperature field [K]; (d) axial velocity field [m/s]; (e) plasma and wall temperature fields [K] on three horizontal planes located at  $z = 50, 90, 150 \text{ mm}$  respectively, from top to bottom.

### Acknowledgements

The authors would like to thank Prof. Leonardo Seccia and Dr. Riccardo Rossi for the use of the parallel calculation facilities at CTFD-Lab of the Faculty of Engineering in Forlì, Italy. Work performed with partial financial support from the University of Bologna Goal-Oriented project 2001-2003 and ex-60% 2001-2002 projects, from the Italian Ministry of Education, University and Scientific Research (M.I.U.R.) national project COFIN 2002 and National Group for Mathematical Physics (G.N.F.M.) of the Italian Institute of High Mathematics.

### References

- [1] J. Mostaghimi, M.I. Boulos, *Plasma Chem. Plasma Process.* **9**, 1 (1988)
- [2] V. Colombo, C. Panciatichi, A. Zazo, G. Cocito, L. Cognolato, *IEEE Trans. Plasma Sci.* **25**, 5 (1997)
- [3] S. Xue, P. Proulx, M.I. Boulos, *J. Phys. D: Appl. Phys.* **34**, 1897 (2001)
- [4] D. Bernardi, V. Colombo, E. Ghedini, A. Mentrelli, *Eur. Phys. J. D* **22** (2003)
- [5] D. Bernardi, V. Colombo, E. Ghedini, A. Mentrelli, *Three-Dimensional Effects in the Design of Inductively Coupled Plasma Torches*, XVI Congresso Nazionale Sulla Scienza e Tecnologia del Vuoto, Catania, Italia, 7-9 Ottobre 2002.
- [6] D. Bernardi, V. Colombo, E. Ghedini, A. Mentrelli, *Three-Dimensional Modelling of Inductively Coupled Plasma Torches*, invited contribution for the section "Modelling in plasma chemistry", this conference
- [7] D. Bernardi, V. Colombo, E. Ghedini, A. Mentrelli, *Three-Dimensional Effects in the Modelling of ICPTs: I – Fluid-Dynamics and Electromagnetics*, this conference
- [8] J.W. McKelliget, N. El-Kaddah, *J. Appl. Phys.* **64**, 6 (1988)



# Time-Dependent 3D Modeling of Laser & Plasma Surface Heating for the Hardening of Metallic Materials

A. Mentrelli<sup>1</sup>, V. Colombo<sup>1</sup>, T. Trombetti<sup>2</sup>

<sup>1</sup> *Dipartimento di Ingegneria delle Costruzioni Meccaniche, Nucleari, Aeronautiche e di Metallurgia (D.I.E.M.) and C.I.R.A.M., Università degli Studi di Bologna, Via Saragozza 8, 40123 Bologna, Italy.*

*Phone: +39 (0)51 2093978 - 2093986 Fax: +39 (0)51 582528*

*e-mail: [andrea.mentrelli@mail.ing.unibo.it](mailto:andrea.mentrelli@mail.ing.unibo.it), [colombo@ciham.ing.unibo.it](mailto:colombo@ciham.ing.unibo.it)*

<sup>2</sup> *Dipartimento di Ingegneria delle Costruzioni Meccaniche, Nucleari, Aeronautiche e di Metallurgia (D.I.E.M.), Università degli Studi di Bologna, Viale Risorgimento 2, 40136 Bologna, Italy.*

*Phone: +39 (0)51 2093460 Fax: +39 (0)51 2093412; e-mail: [tullio.trombetti@mail.ing.unibo.it](mailto:tullio.trombetti@mail.ing.unibo.it)*

## Abstract

A numerical code for the time-dependent three-dimensional modelling of the laser surface heating for the hardening of metallic materials has been developed and a numerical investigation of the effects on thermal behaviour of the treated material of changing one or more process parameters is presented. The results are compared with those coming from the simulation of the same type of treatment with the laser beam replaced by a RF thermal plasma jet.

## 1. Introduction

High-power laser facilities are widely used in industrial processes of welding, cutting, drilling as well as for surface treatments of materials. In particular, laser sources can provide a controllable high-density energy deposition for producing small hardened zones on the surface of a treated material (laser surface hardening, LSH). A lot of factors influence the evolution of the temperature distribution in the three-dimensional workpiece as a consequence of the laser-material interaction including the power of the laser source, the absorption coefficient of the workpiece, the laser spot shape and dimensions and the thermal properties of the metal [1]. When all these working parameters are known, the thermal behaviour of the treated workpiece may be evaluated by means of analytical expressions available in the literature [2-5]. Yet, these expressions, with few exceptions [5], come from idealized models of the hardening process and assume that heat flows only in the direction perpendicular to the treated surface (one-dimensional heat flow), and that the workpiece is very large, compared to the spot size. As a consequence, they don't permit to evaluate the effects of the edges and corners of the piece, which tend to concentrate the heat flow. In addition, they assume that the thermal properties of the metal don't vary with temperature. In reality, heat diffusion is a three-dimensional phenomenon, the workpiece has often dimensions comparable with the laser spot ones and the thermal properties of the metals are not at all temperature-independent. Moreover, sometimes it is necessary to realize complex patterns of the laser spot, or to overlap hardening passes, and no analytical expression is available for the evaluation of the effects of these events on the process result. In this framework, numerical simulation is an useful tool as it permits to reduce the idealization errors that affect the analytical expressions. It becomes also feasible to consider real workpiece geometry and complex patterns of the hardening passes. Besides that, numerical simulation may also help in optimizing the process itself. In this paper we present a numerical investigation on the effects on the thermal behaviour of the treated material of changing one or more process parameters: power of the laser beam, dimensions of the laser spot, scanning speed and pattern are taken into account in the frame of a heating process that doesn't lead to material melting or evaporation. The results are then compared with those coming from simulations of the same type of treatment with the laser beam replaced by a thermal RF plasma jet.

## 2. Modelling approach

The time-dependent three-dimensional transport equation governing the energy transfer in the workpiece in the absence of material melting or evaporation, written in terms of enthalpy ( $h$ ) for a metal of density  $\rho$ , thermal conductivity  $k$  and constant-pressure specific heat  $c_p$

$$\frac{\partial(\rho h)}{\partial t} = \nabla \cdot \left( \frac{k}{c_p} \nabla h \right) \quad (1)$$

is discretized with a finite-volume technique and solved in the reference frame of the workpiece with a numerical code implemented by the Authors, in which the temperature-dependence of the thermal properties of the material (stainless steel) is suitably taken into account. In the case of surface heating treatment with a laser source, Eq. (1) is subject to boundary conditions that take into account the heat introduced in the piece by the laser beam and the cooling effect of the ambient gas (at temperature  $T_a = 300$  K) via convection, where a convection coefficient  $h_c = 2500$  W/m<sup>2</sup>K has been considered as long as an uniformly distributed power density  $q$  in the square laser spot (Fig. 1a) and an absorption coefficient of 70% of the metal surface. In the case of surface heating with a RF plasma jet (Fig. 1b), the temperature of the plasma-material interface is calculated processing the output power content of the plasma jet and its temperature distribution, coming from a numerical model previously developed by the Authors for the investigation of the behaviour of inductively coupled plasma torches [6,7].

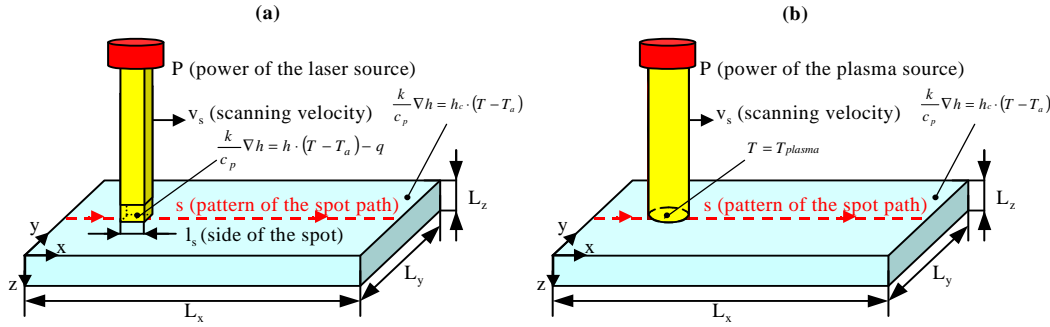


Fig. 1: Schematic of the workpiece with the laser beam (a) and with the RF plasma jet (b) with process parameters and boundary conditions.

### 3. Selected results

Numerical simulations of the laser surface heating process have been carried out for various dimensions  $L_x$ ,  $L_y$  and  $L_z$  of the slab-shaped workpiece and of the square-shaped spot (with side  $l_s$ ). Different scanning velocity of the moving spot ( $v_s$ ) and different values of the source power ( $P$ ) have been considered, as well as various patterns of the spot path.

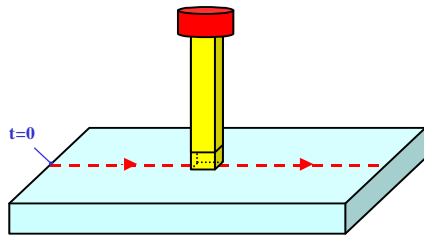


Fig. 2: Schematic of the workpiece and of the laser source moving along the  $x$ -direction with a single-pass hardening pattern.

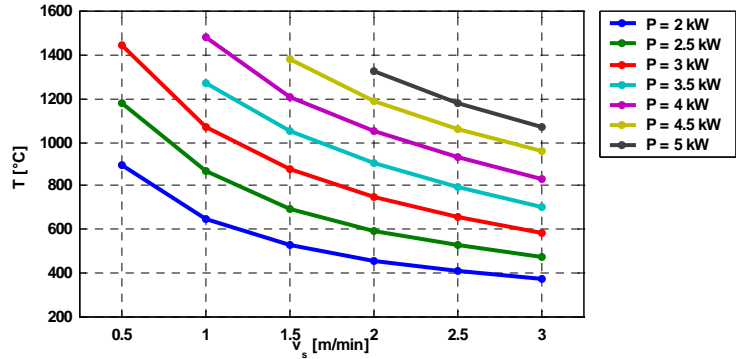


Fig. 3: Maximum temperature of the workpiece treated with a single-pass hardening pattern (see Fig.2) for different scanning velocity ( $v_s$ ) and power of the laser source ( $P$ ).

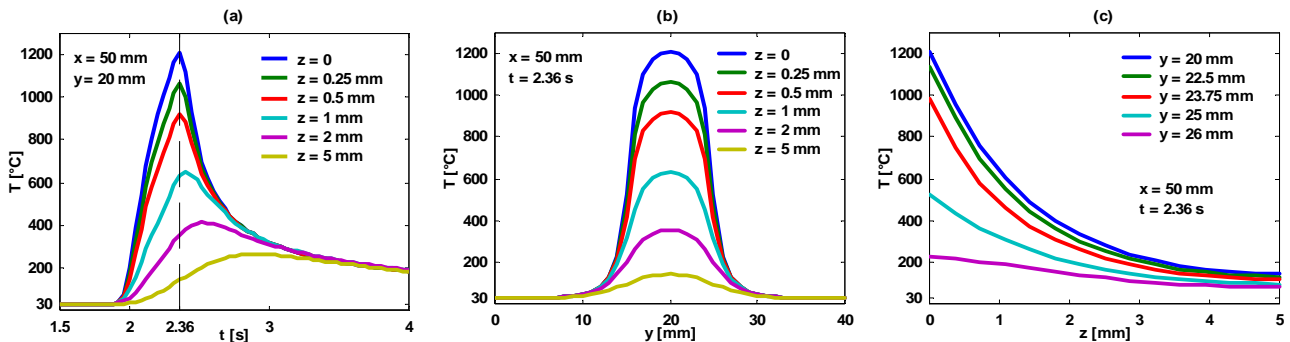


Fig. 4: Temperature evolution on the vertical axis passing through the centre of the workpiece (a) and temperature distribution (at time  $t=2.36$  s) on a vertical plane parallel to the  $y$ -axis and passing through the centre of the workpiece (b,c). Dimensions of the workpiece:  $L_x=100$  mm;  $L_y=40$  mm;  $L_z=5$  mm. Working parameters:  $P=4$  kW;  $v_s=1.5$  m/min;  $l_s=10$  mm; type of pattern: single-pass hardening pattern.

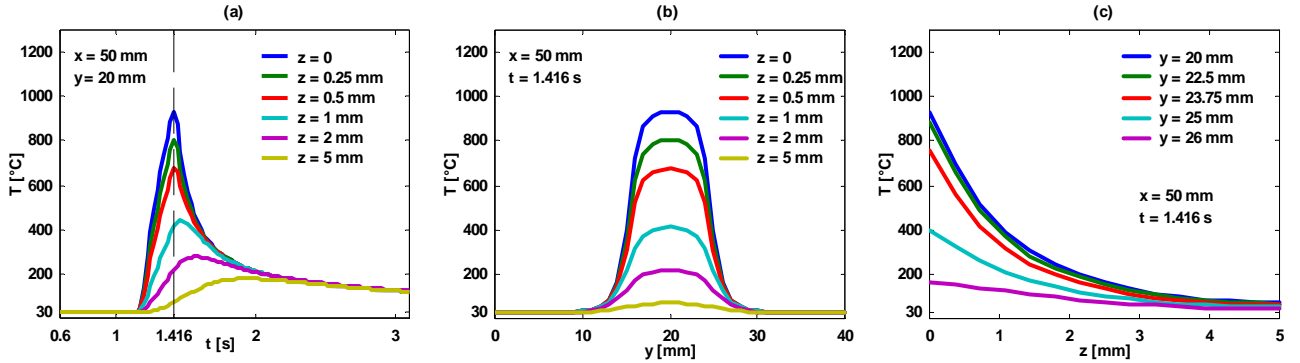


Fig. 5: Temperature evolution on the vertical axis passing through the centre of the workpiece (a) and temperature distribution (at time  $t = 1.416$  s) on a vertical plane parallel to the  $y$ -axis and passing through the centre of the workpiece (b,c). Dimensions of the workpiece:  $L_x=100$  mm;  $L_y=40$  mm;  $L_z=5$  mm. Working parameters:  $P=4$  kW;  $v_s=2.5$  m/min;  $l_s=10$  mm; type of pattern: single-pass hardening pattern.

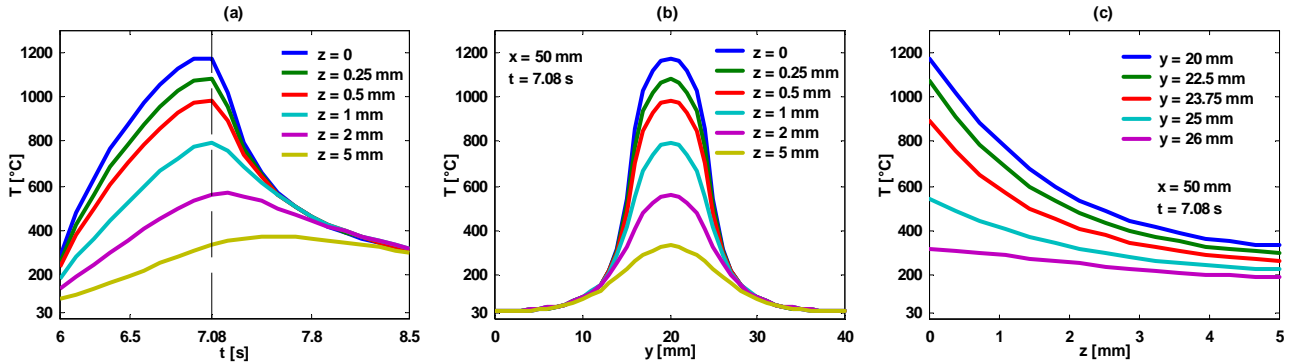


Fig. 6: Temperature evolution on the vertical axis passing through the centre of the workpiece (a) and temperature distribution (at time  $t = 7.08$  s) on a vertical plane parallel to the  $y$ -axis and passing through the centre of the workpiece (b,c). Dimensions of the workpiece:  $L_x=100$  mm;  $L_y=40$  mm;  $L_z=5$  mm. Working parameters:  $P=2.5$  kW;  $v_s=0.5$  m/min;  $l_s=10$  mm; type of pattern: single-pass hardening pattern.

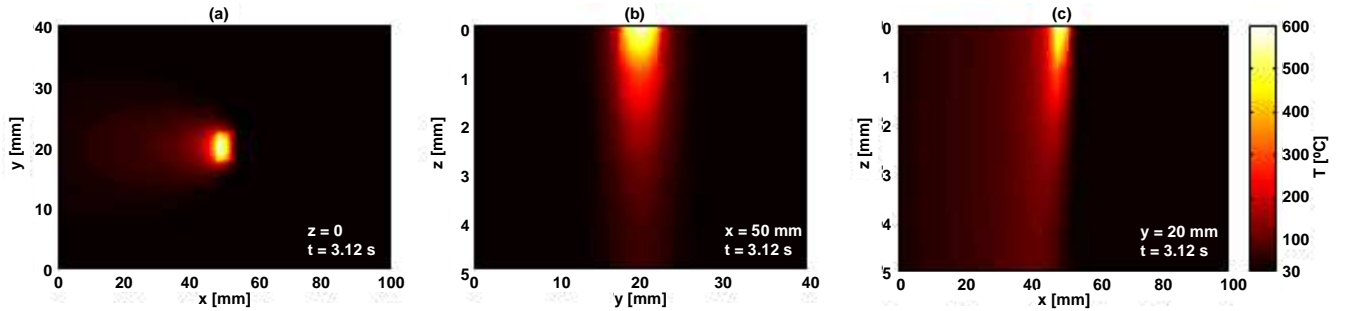


Fig. 7: Temperature distribution (at  $t=3.12$  s) on the surface of the workpiece (a) and on two planes perpendicular to the  $x$ - (b) and to the  $y$ -axis (c). Dimensions of the workpiece:  $L_x=100$  mm;  $L_y=40$  mm;  $L_z=5$  mm. Working parameters:  $P=0.75$  kW;  $v_s=1$  m/min;  $l_s=5$  mm; type of pattern: single-pass hardening pattern.

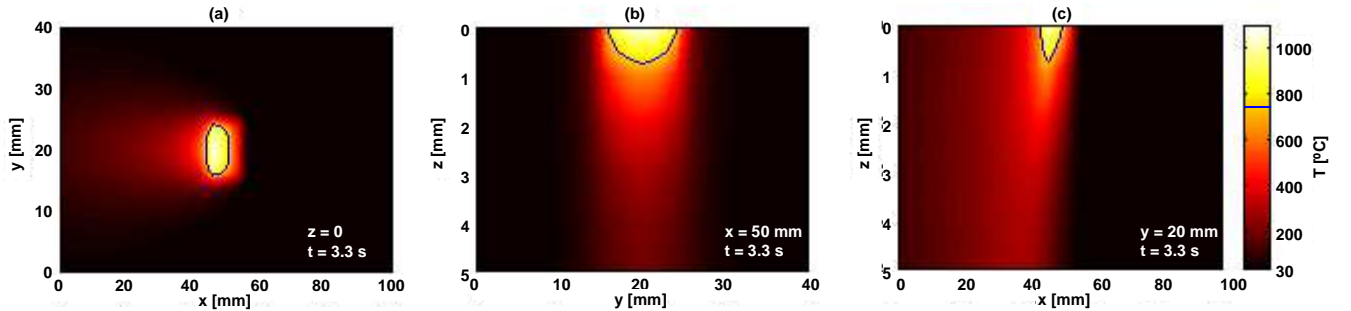


Fig. 8: Temperature distribution (at  $t=3.3$  s) on the surface of the workpiece (a) and on two planes perpendicular to the  $x$ - (b) and to the  $y$ -axis (c). Dimensions of the workpiece:  $L_x=100$  mm;  $L_y=40$  mm;  $L_z=5$  mm. Working parameters:  $P=3$  kW;  $v_s=1$  m/min;  $l_s=10$  mm; type of pattern: single-pass hardening pattern.

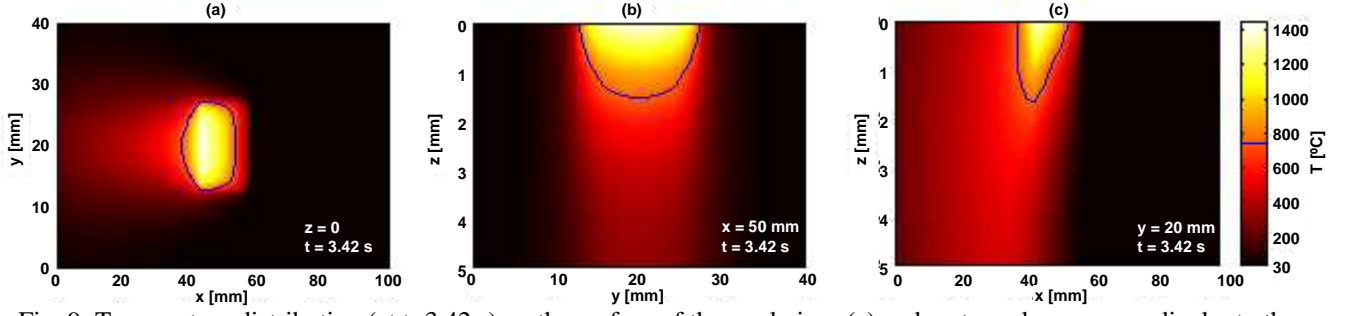


Fig. 9: Temperature distribution (at  $t=3.42$  s) on the surface of the workpiece (a) and on two planes perpendicular to the x- (b) and to the y-axis (c). Dimensions of the workpiece:  $L_x=100$  mm;  $L_y=40$  mm;  $L_z=5$  mm. Working parameters:  $P=6.75$  kW;  $v_s=1$  m/min;  $l_s=15$  mm; type of pattern: single-pass hardening pattern.

For the case of a single-pass hardening pattern (Fig. 2), an excerpt of the results of an exhaustive parameterization on  $P$  and  $v_s$  is shown in Figs. 3, 4, 5 and 6; while in Figs. 7, 8 and 9 the effects of changing the spot size on temperature distribution for fixed power density in the spot ( $3 \times 10^7$  W/m<sup>2</sup>) and workpiece dimensions are shown. The case of double-pass hardening pattern (Fig. 10), of practical interest, has been considered, in the situations of overlapping, non-overlapping and of a gap left between the two parallel tracks of the beam. Temperature distributions in the workpiece are reported in Figs. 11, 12 and 13 in a test case with, respectively, an overlapping of 2 mm, a non-overlapping and a 2 mm gap left between the parallel tracks. Complex patterns of the beam spot of industrial interest have also been studied: multiple-discontinuous passes (see Fig. 14(a)), multiple-continuous passes (Fig. 15(a)) and spiral pattern covered in both the ways (Fig. 16(a) and Fig. 17(a)) are here presented. For all these patterns the temperature of the moving centre of the spot in test cases is reported in Figs. 14(b), 15(b), 16(b) and 17(b), showing the effects on the heating process of the different trajectory and sharp discontinuities in the path of the spot. In Fig. 18 results coming from the simulation of the surface heating treatment with a RF plasma jet replacing the laser beam are presented. The surface temperature in the circular spot of the plasma jet is known from a numerical simulation of the ICPT system carried out by the Authors.

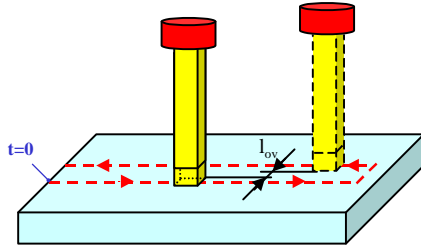


Fig. 10: Schematic of the workpiece and of the laser source moving on the workpiece surface with a double-pass hardening pattern with an overlap between the parallel tracks ( $l_{ov} > 0$ ), with a non-overlap ( $l_{ov} = 0$ ) or with a gap left between the two parallel tracks ( $l_{ov} < 0$ ).

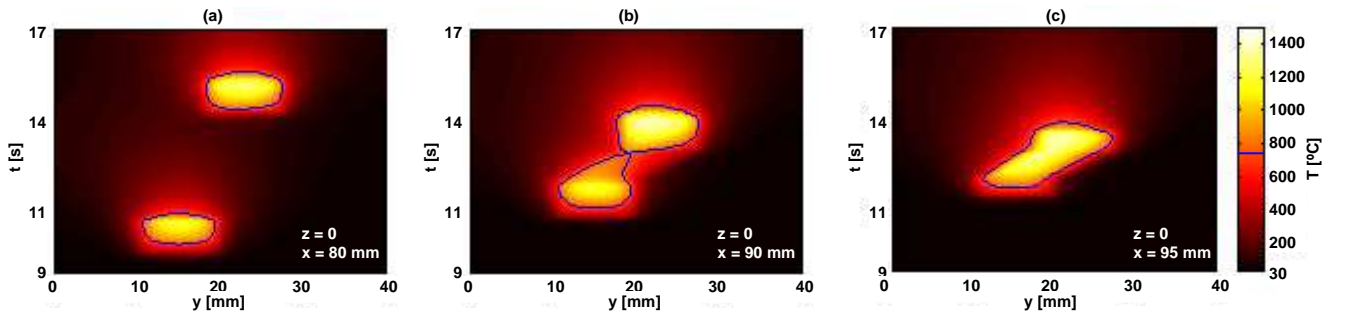


Fig. 11: Evolution of the temperature on the surface of the workpiece along the y-axis for different  $x$  positions. Dimensions of the workpiece:  $L_x=100$  mm;  $L_y=40$  mm;  $L_z=5$  mm. Working parameters:  $P=2.5$  kW;  $v_s=0.5$  m/min;  $l_s=10$  mm; type of pattern: double-pass hardening pattern with a 2 mm overlap ( $l_{ov}=2$  mm).

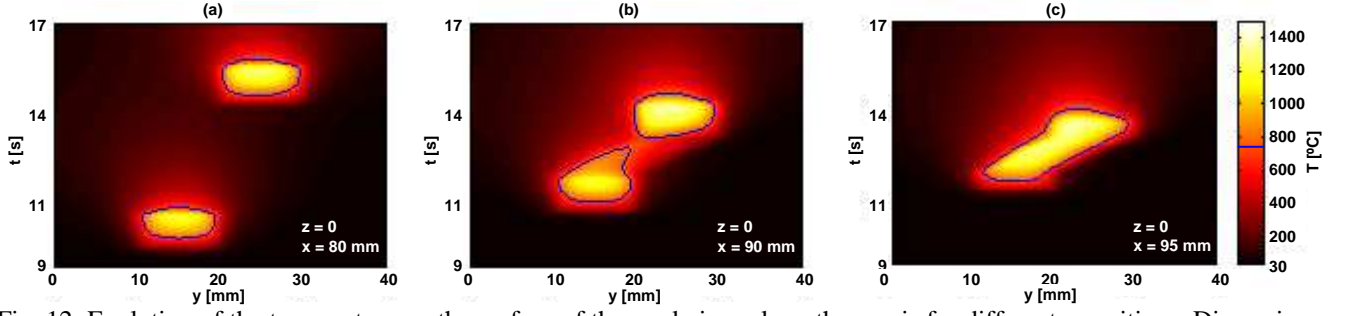


Fig. 12: Evolution of the temperature on the surface of the workpiece along the y-axis for different  $x$  positions. Dimensions of the workpiece:  $L_x=100$  mm;  $L_y=40$  mm;  $L_z=5$  mm. Working parameters:  $P=2.5$  kW;  $v_s=0.5$  m/min;  $l_s=10$  mm; type of pattern: double-pass hardening pattern with no overlap ( $l_{ov}=0$ ).

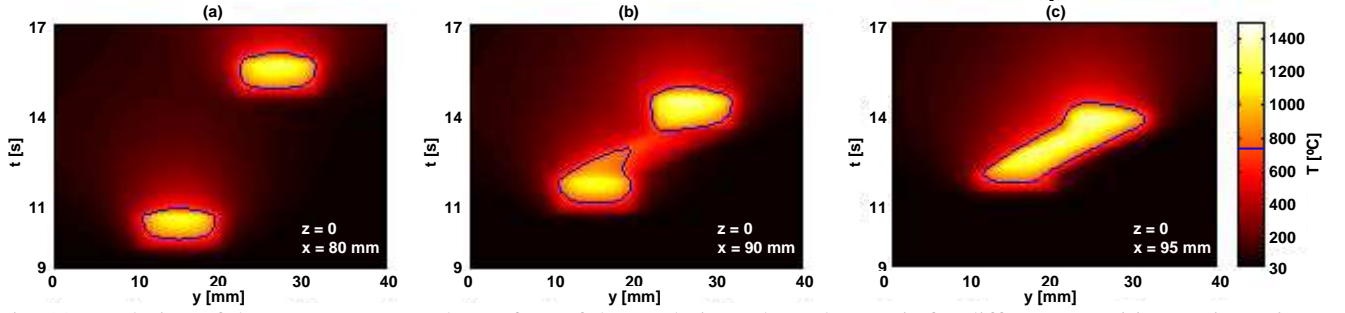


Fig. 13: Evolution of the temperature on the surface of the workpiece along the y-axis for different  $x$  positions. Dimensions of the workpiece:  $L_x=100$  mm;  $L_y=40$  mm;  $L_z=5$  mm. Working parameters:  $P=2.5$  kW;  $v_s=0.5$  m/min;  $l_s=10$  mm; type of pattern: double-pass hardening pattern with a 2 mm gap between the parallel passes ( $l_{ov}=-2$  mm).

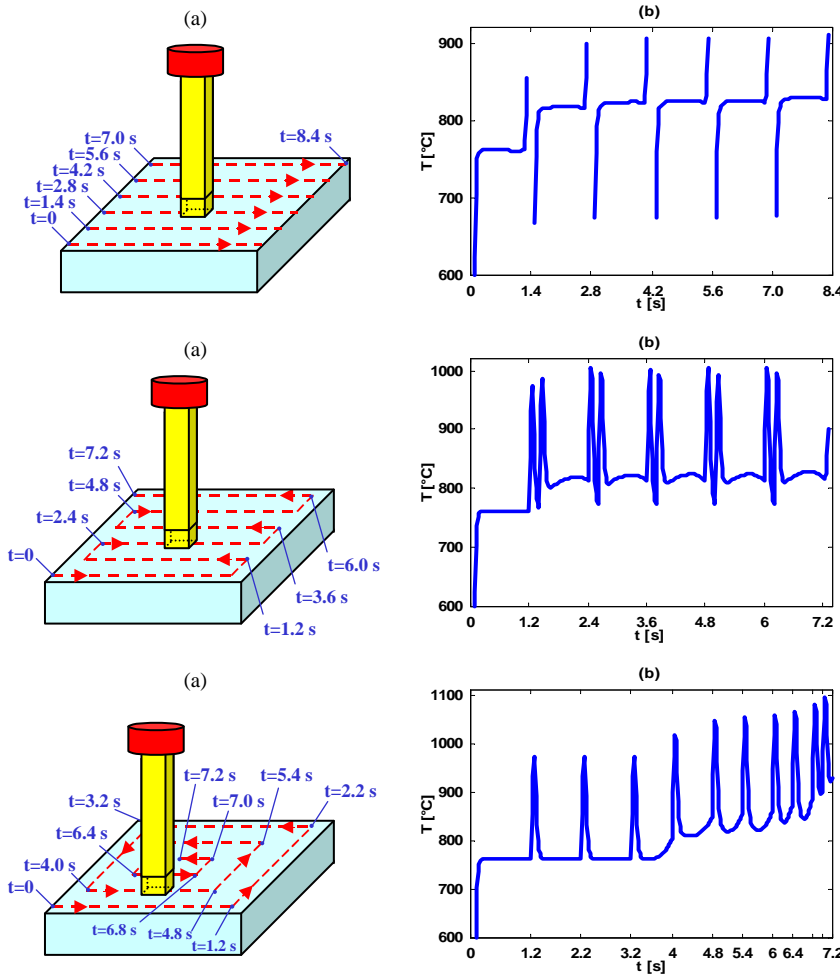


Fig. 14: Schematic of the workpiece with multiple, discontinuous hardening pattern (a) and temperature evolution of the moving centre of the spot (b). Dimensions of the workpiece:  $L_x=60$  mm;  $L_y=60$  mm;  $L_z=5$  mm. Working parameters:  $P=5$  kW;  $v_s=3$  m/min;  $l_s=10$  mm.

Fig. 15: Schematic of the workpiece with multiple, continuous hardening pattern (a) and temperature evolution of the moving centre of the spot (b). Dimensions of the workpiece:  $L_x=60$  mm;  $L_y=60$  mm;  $L_z=5$  mm. Working parameters:  $P=5$  kW;  $v_s=3$  m/min;  $l_s=10$  mm.

Fig. 16: Schematic of the workpiece with spiral hardening pattern from the periphery to the centre (a) and temperature evolution of the moving centre of the spot (b). Dimensions of the workpiece:  $L_x=60$  mm;  $L_y=60$  mm;  $L_z=5$  mm. Working parameters:  $P=5$  kW;  $v_s=3$  m/min;  $l_s=10$  mm.

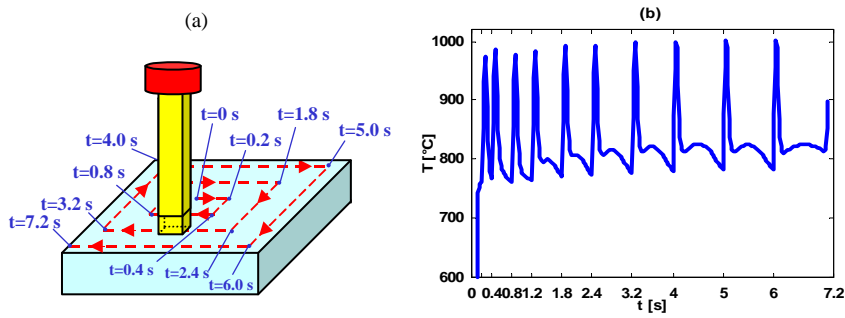


Fig. 17: Schematic of the workpiece with spiral hardening pattern from the centre to the periphery (a) and temperature evolution of the moving centre of the spot (b). Dimensions of the workpiece:  $L_x=60$  mm;  $L_y=60$  mm;  $L_z=5$  mm. Working parameters:  $P=5$  kW;  $v_s=3$  m/min;  $l_s=10$  mm.

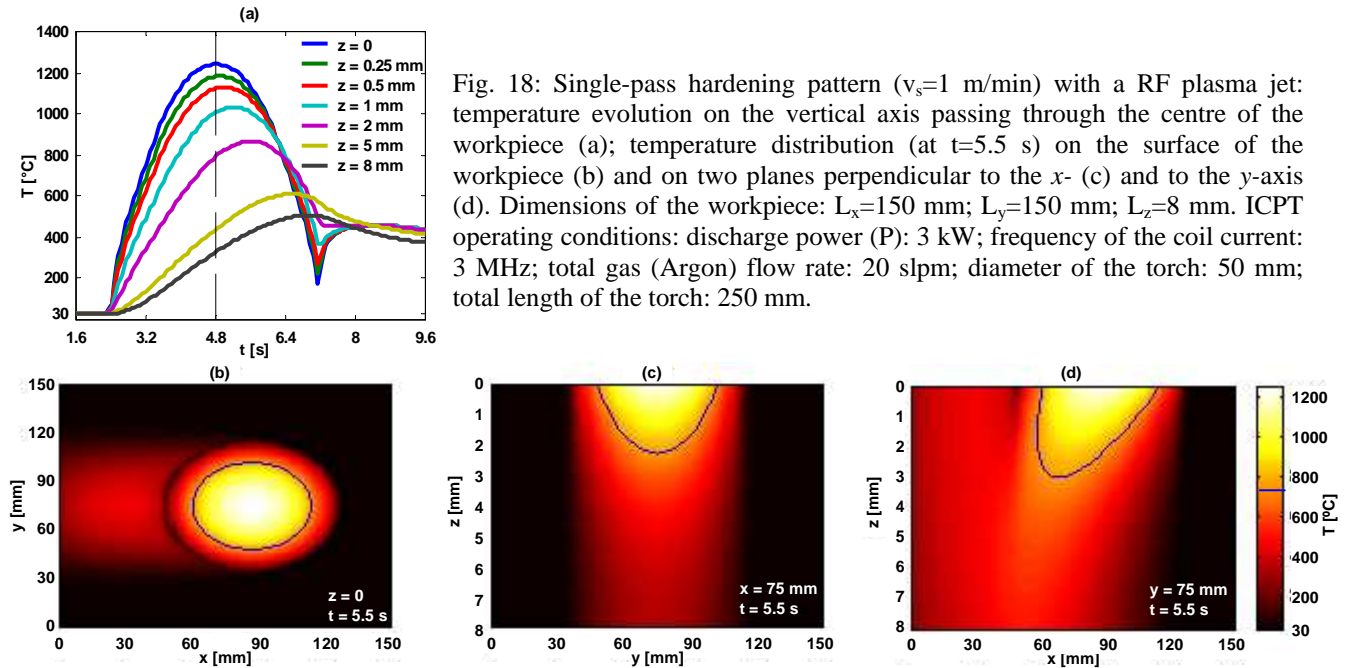


Fig. 18: Single-pass hardening pattern ( $v_s=1$  m/min) with a RF plasma jet: temperature evolution on the vertical axis passing through the centre of the workpiece (a); temperature distribution (at  $t=5.5$  s) on the surface of the workpiece (b) and on two planes perpendicular to the  $x$ - (c) and to the  $y$ -axis (d). Dimensions of the workpiece:  $L_x=150$  mm;  $L_y=150$  mm;  $L_z=8$  mm. ICPT operating conditions: discharge power ( $P$ ): 3 kW; frequency of the coil current: 3 MHz; total gas (Argon) flow rate: 20 slpm; diameter of the torch: 50 mm; total length of the torch: 250 mm.

## Acknowledgements

The Authors would like to thank Dr. Maichi Cantello and Dr. Federico Giachino at RTM in Vico Canavese (Italy) for the useful suggestions and discussions concerning laser surface hardening process and operating conditions. Work performed with partial financial support from the University of Bologna Goal-Oriented project 2001-2003 and ex-60% 2001-2002 projects, from the Italian Ministry of Education, University and Scientific Research (M.I.U.R.) national project COFIN 2002 and National Group for Mathematical Physics (G.N.F.M.) of the Italian Institute of High Mathematics.

## References

- [1] W. M. Steen, *Laser Material Processing*, Springer, London (1991).
- [2] A. Yáñez, J.C. Álvarez, A.J. López, G. Nicolás, J.A. Pérez, A. Ramil, E. Saavedra, *Modelling of temperature evolution on metals during laser hardening process*, *Applied Surface Sciences*, **186**, 611-616 (2002).
- [3] R. Brockmann, K. Dickmann, P. Geshev, K.-J. Matthes, *Calculation of temperature field in a thin moving sheet heated with laser beam*, *Int. J. Heat Mass Transfer*, **46**, 717-723 (2003).
- [4] J. Mazumder, P. S. Mohanty, A. Kar, *Mathematical modelling of laser materials processing*, *Int. J. of Materials and Product Technology*, **11**, 193-252 (1996).
- [5] A. Kar, J. Mazumder, *Three-dimensional transient thermal analysis for laser chemical vapor deposition on uniformly moving finite slabs*, *J. Appl. Physics*, **65**, 2923-2934 (1989).
- [6] D. Bernardi, V. Colombo, G.G.M. Coppa, A. D'Angola, *Simulation of the Ignition Transient in RF Inductively-Coupled Plasma Torches*, *Eur. Phys. J. D*, **14**, 337-348 (2001).
- [7] D. Bernardi, V. Colombo, E. Ghedini, A. Mentrelli, *Three-Dimensional Modelling of Inductively Coupled Plasma Torches*, *Eur. Phys. J. D*, **22**, 119-125 (2003).



# Heat transfer in under-expanded supersonic plasma jets impinging on a flat plate

S.E. Selezneva<sup>1</sup>, J. Weber<sup>2</sup>, and M.I. Boulos

*Department of Chemical Engineering, Université de Sherbrooke, Sherbrooke, Québec, Canada*

<sup>1</sup>*present address: C&MT, General Electric Global Research Center, Niskayuna, NY USA*

<sup>2</sup>*University of Stuttgart, Department of Aerospace Engineering, Stuttgart, Germany*

## Abstract

In the article, we study the heat transfer in Ar/Ar+H<sub>2</sub> plasma jets generated by inductively coupled plasma torch with two different supersonic nozzles that accelerate plasma up to the Mach numbers of M=1.5 and M=3, while the chamber pressure is maintained at 2 kPa. We study the effects of the distance between the nozzle outlet and the barrier, the nozzle configuration, the torch power and the material of the barrier on the distribution of the local heat flux along the radius of the barrier. For the case of pure argon, the results of the probe measurements are compared with the numerical simulations performed with the help of FLUENT. We show that depending on the distance between the nozzle outlet and the barrier, the structure of the flow in the impingement zone changes. If the barrier is placed within the initial supersonic region of the jet, under certain conditions we observe the formation of a stagnation bubble, which leads to the decreasing of the heat flux in the stagnation point. The success of the computer simulations in the prediction of this bubble formation depends on the way of turbulence modeling.

## 1. Introduction

Supersonic impinging plasma jets find applications in plasma processing of materials and in aerospace industry. In these applications, the knowledge about the surface heat transfer rates is of especial interest. Although some insight [1-5] has been provided into the gas dynamical properties of under-expanded cold gas jets impinging onto a barrier, the heat transfer in impinging plasma jets is still poorly understood. Previous studies [1-6] that have been conducted on the impinging flows have revealed a variety of complex and interesting flow phenomena affecting the distribution of the heat flux and pressure over the barrier surface. For instance, in any flow pattern resulting from the normal impingement of an axisymmetric supersonic jet on a flat plate, one expects that the pressure and the local heat flux profiles along the plate both should have maxima at the center point of the plate as the central shock is normal to the axis due to the symmetry. However, many cases have been reported in the literature [1-6], where the maximal pressure measured on the plate occurs off the center, and the pressure measured at the center of the plate is less than the normal shock recovery pressure. Such pressure distributions have been explained as an indication of the presence of a bubble of slowly recirculating gas in the shock layer. This bubble can have a diameter comparable with a jet diameter and its height may be large enough to force the plate shock to take a peaked shape. For practical purposes, it is important to study the nature and the conditions of the occurrence of this bubble and its effect on the heat flux in the stagnation point.

There have been reported two different classes of the situations in which bubbles occur. One is at moderate plate displacements in under-expanded jets, the other is at small plate displacements in certain under-expanded jets and nominally uniform jets. The plausible explanation to the occurrence of the bubble in the first case was proposed by Ginzburg et al [2] and Gubanova et al [3]. They both ascribe the existence of the bubble to the following mechanism. The intersection of the jet shock with the stand-off plate shock divided the flow into two regions, of which the outer has the higher total pressure. Mixing occurs along the slipline, which exists between the two flows and it is the interaction of this high-pressure shear layer with the inner-region boundary layer, which causes separation and the formation of the bubble. An explanation to the occurrence of the bubble in the second case was proposed by Kalghatgi et al [4], and they presented the evidence that the flows with bubbles can be produced by very weak shocks from nozzle walls when these shocks intersect the plate shock close to the axis and the mechanism by which the nozzle shocks produce the bubble is essentially that described by Ginzburg et al [3] and Gubanova et al [4].

Besides, the turbulent pulsations certainly play role in the formation of the bubble, as a computer modeling of this phenomena cannot be made using simplified models of turbulence such as k-ε model, for example [5]. Alvi et al [5] showed that both Spalart One-Equation Model with Rotation and Curvature Correction and Shear-Stress Transport Two-Equation Model are able to capture the significant features of the complex flow containing stagnation bubble and are in remarkably good agreement with experimental data.

In the present article we report the results of the study of the heat transfer in Ar/Ar+H<sub>2</sub> plasma jets generated by inductively coupled plasma torch with two different supersonic nozzles that accelerate plasma up to the Mach numbers of M=1.5 and M=3. In the experiments, the plasma jet flows into the expansion chamber, where the pressure is 2kPa; and impinges perpendicular onto a flat plate. We study the effects of the distance between the nozzle outlet and the barrier, the nozzle configuration, the torch power and the material of the barrier on the distribution of the local heat flux along the radius of the barrier. For the case of pure Ar the results of the probe measurements are compared with the numerical simulations performed with the help of FLUENT using the Reynolds Stress Model (RSM) of turbulence [7-9].

## 2. Experimental set-up

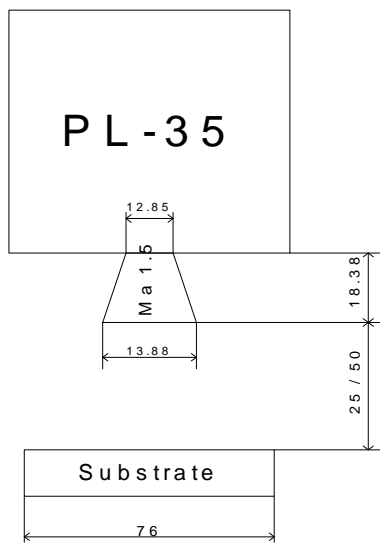


Fig.1 Schematic of experimental set-up, dimensions are in mm

In the experiments, under-expanded supersonic plasma jets are generated using inductively –coupled plasma torch with adjusted supersonic nozzle [10](Fig1). The heat flux at the stagnation point

$$q = mC_p (T_{out} - T_{in})$$

is measured with the aid of a specially designed probe. During the experiments, two parameters have to be controlled: the cooling water mass flow rate,  $m$  and the difference between outcoming and incoming water temperatures ( $T_{out} - T_{in}$ ). The probe consists of a water-cooled cylinder made of bronze with a diameter of about 7 cm, which represents a flat plate. The probe head with a diameter of 6.3mm is placed in the center of the cylinder. The supply pipes and the probe head are swathed in a heat resistant ceramics. In order to move the probe along and perpendicular to the axis of the plasma jet, the plasma torch and the vacuum pump have to be shut down and the chamber has to be ventilated. Because of the fact that the probe head has a relatively small surface area, it needs only a small amount of cooling water. The smallest possible water flow

rate of the system, is however 130 ml /min. The error of 25% is expected using this minimal mass flow rate. In the experiments, we have chosen the mass flow rate of the cooling water of about 240 ml/min in order to reduce the error of the measurement, which is evaluated to be within 15%.

The experimental conditions are summarized in Table 1.

**Table 1**

Chamber pressue, Pch, kPa	2 kPa	2kPa
Nozzle Mach number	1.5	3
Torch power	20kW	12kW
Material of probe head	stainless steel, copper	stainless steel, copper
Distance from the nozzle	2.5cm, 5 cm	2.5cm, 5cm
Gases	1. pure argon 60slpm 2. argon+4.8%hydrogen 60slpm+3slpm	1. pure argon 60slpm 2. argon+4.8%hydrogen 60slpm+3slpm



For the measurements, the TEKNA enthalpy probe system was used with the enthalpy probe replaced by the designed heat flux probe. The system was regulated via a personal computer with the appropriate software. All parameters, as for example the water mass flow rate, the water temperature difference and the heat load were displayed graphically.

The optical analysis of the plasma flow is done with the aid of a digital camera, which is directly connected to the computer. The camera takes black and white pictures, which can be colored using appropriate software. On these pictures, white and red regions represent higher radiation intensity.

### 3. Model

The computational domain used for modeling the ICP axisymmetric jet flowing from the convergent-divergent nozzles represents a cylinder of radius 7.6 cm and the length equal to the barrier displacement distance. The axial coordinate  $x=0$  corresponds to the nozzle outlet. For  $M=1.5$  nozzle, the length of the simulated chamber part is  $L_{ch}=0.025m$  and  $0.05m$ . Boundary conditions set in the present study are as follows. At the nozzle inlet the total mass flow rate  $0.00174\text{ kg/s}$  ( $60\text{slm}$ ) is given. The gas is assumed to be described by a perfect gas approximation. Reynolds Stress Model (RSM) of turbulence [7-9] is used in the calculations. The gas temperature  $6000K$  is assigned at the nozzle outlet. The turbulence intensity is assumed to be 5% at the nozzle inlet, where the flow velocity is about  $2000\text{m/s}$  ( $M=1.5$ ) and the static pressure is about  $P_{in}=0.12\text{ atm}$ . At the wall we use a constant condition for the heavy particle temperature ( $300K$ ), a zero normal derivative condition for the electron temperature and non-slip velocity boundary condition. At the chamber outlet the pressure  $P_{ch}=2\text{kPa}$  is specified. The computations start on a nonstructural grid that is very fine near the barrier surface. The calculations proceed using the second order accuracy scheme for coupled solver of Navier Stokes equations until the residuals of all the equations become less than  $10^{-4}$ .

### 4. Results and discussion

Fig.1a represents the photograph of a pure argon jet generated by ICP torch having  $20\text{kW}$  input

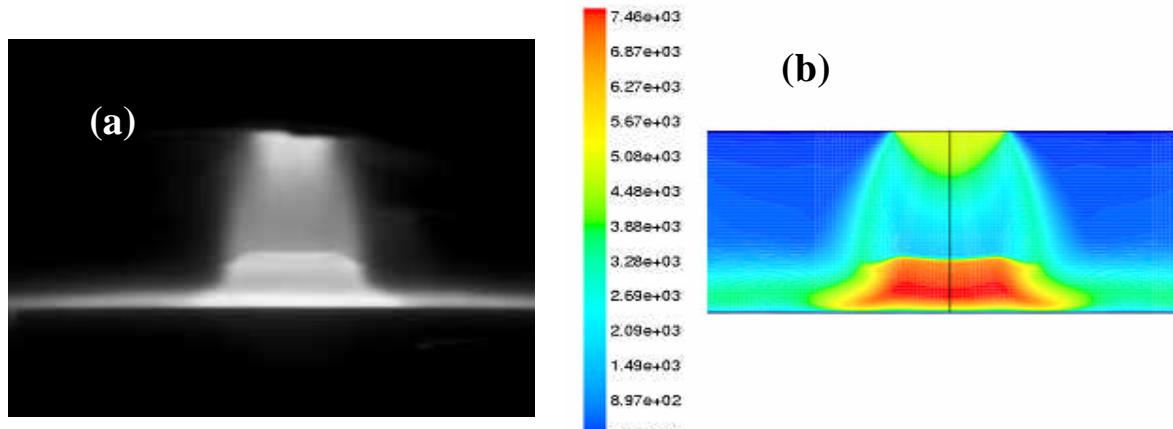


Fig.2 a) photograph, b)calculated gas temperature contours of argon impinging jet  $M=1.5$ ,  $20\text{kW}$  power,  $2.5\text{cm}$  displacement distance

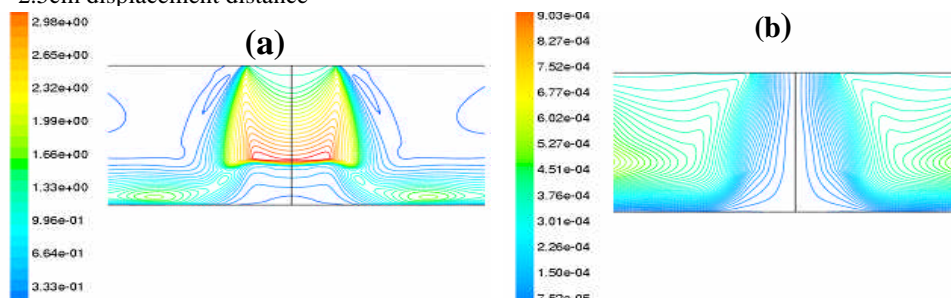


Fig.3 a) calculated Mach number contours, b)calculated stream function contours of argon impinging jet  $M=1.5$ ,  $20\text{kW}$  power,  $2.5\text{cm}$  displacement distance

power, with  $M=1.5$  supersonic nozzle. The distance from the nozzle outlet to the barrier is  $2.5\text{ cm}$ . As it can be seen from the results of free jet simulations [10], this distance corresponds to the end of

the first expansion zone of the jet. The results of the computer simulations of the impinging jet are shown in Fig. 2b and 3 for the gas temperature, Mach number and stream functions profiles correspondingly. The results confirm that the flow patten of impinging flow does not contain the stagnation bubble at this small displacement of the barrier. Instead, a normal stand-off shock wave is formed close to the barrier. The temperature rises up to 7500K in this shock wave (Fig.2b) and the local Mach number experiences a transition from 3.3 to the subsonic values (Fig.3a). Besides, the contours of stream functions do not show the presence of any recirculation zones in the impinging region (Fig.3b).

Note, that the flow pattern drastically changes when the plate is moved 5 cm downstream of the nozzle outlet. For this distance, Fig.4a represents the photograph of a pure argon jet generated by ICP torch having 20kW input power, with  $M=1.5$  supersonic nozzle. As it can be seen from the

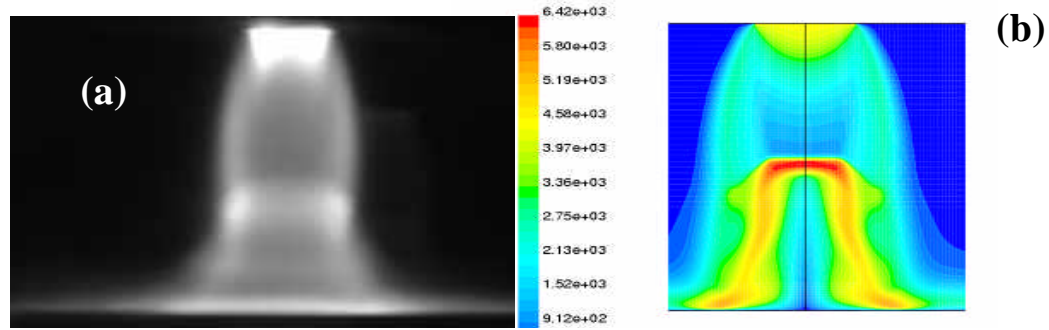


Fig.4 a) photograph, b)calculated gas temperature contours of argon impinging jet  $M=1.5$ , 20kW power, 5cm displacement distance

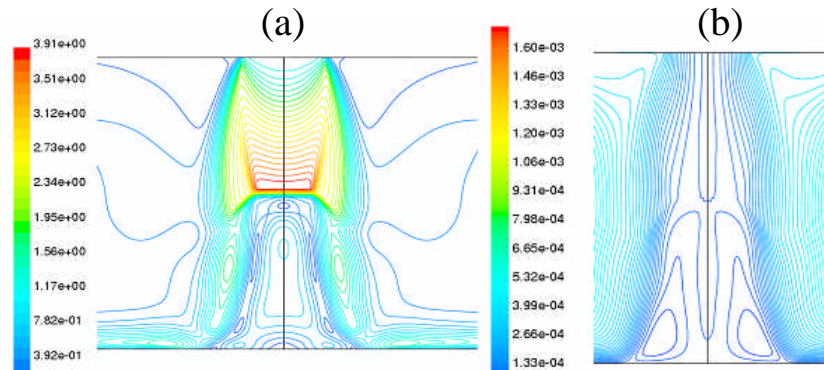


Fig.5 a) calculated Mach number contours,b)calculated stream function contours of argon impinging jet  $M=1.5$ . 20kW power. 5cm displacement distance

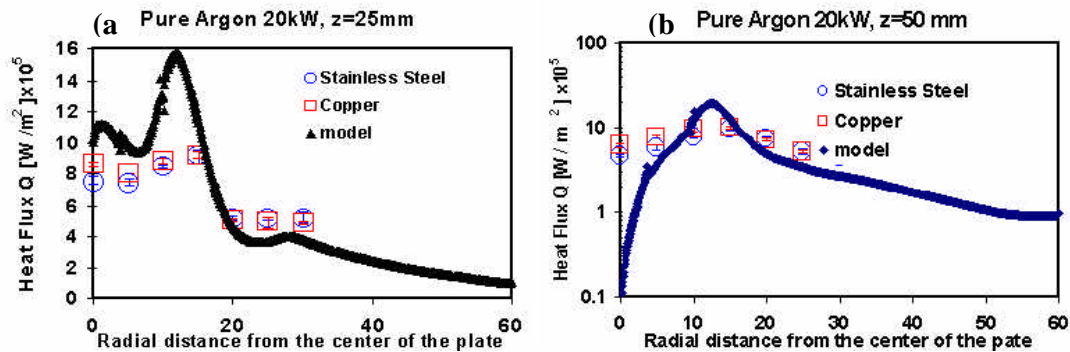


Fig.6 Local heat flux along the barrier in argon impinging jet  $M=1.5$ , 20kW power, a)2.5cm displacement distance, b) 5 cm displacement distance

results of free jet simulations [10], this distance corresponds to the end of the first compression zone of the jet and the beginning of the second expansion zone. The results of the computer simulations

of this impinging jet are shown in Fig. 4b and 5a and b for the gas temperature, Mach number and stream function profiles correspondingly. The results show that in this case a stagnation bubble is formed near the barrier, i.e. instead of a normal stand-off shock wave close to the barrier we observe a shock wave at about 3 cm from the nozzle outlet. As it follows from the simulation results the temperature rises up to 6400K in this shock wave (Fig.4b) and the local Mach number experiences a transition from 3.9 down to subsonic values (Fig.5a). Stream functions contours indicate the presence of the recirculation zones in the impinging region (Fig.5b).

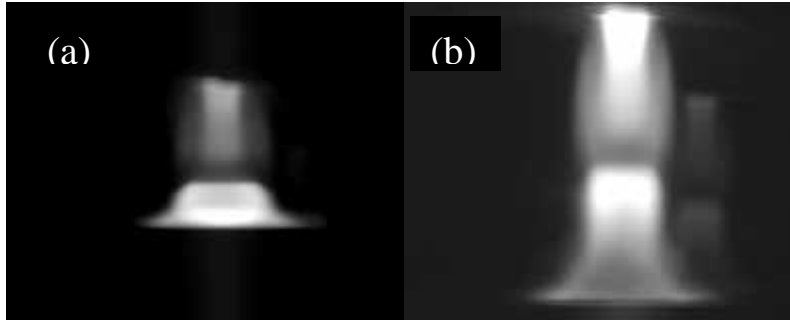


Fig.7 photograph of impinging jet of argon and hydrogen mixture,  $M=1.5$ , 20kW power, a) 2.5cm distance, b) 5 cm displacement distance of the barrier

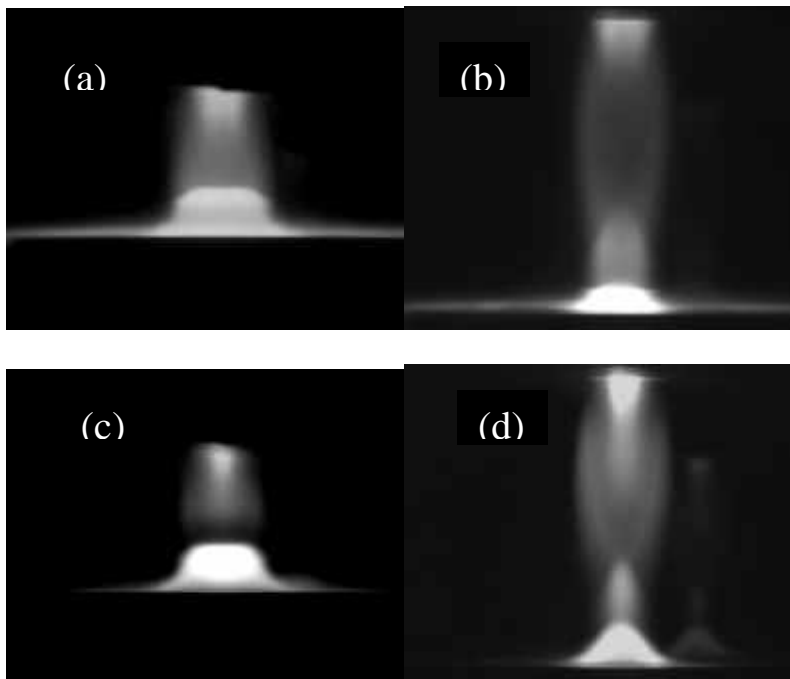


Fig.8 photograph of impinging jet,  $M=3$ , 12kW power, a) 2.5cm distance, pure argon b) 5cm, pure argon, c) 2.5cm distance, mixture of argon and hydrogen b) 5cm distance, mixture of argon and hydrogen

The effect of the stagnation bubble on the local heat flux along the plate surface is demonstrated in Fig.6 showing the radial profiles of the heat flux for 2.5 and 5 cm displacement lengths. In both cases the profiles have off-axis maxima. However, in the case of 2.5cm displacement this maximum is much less pronounced than in the case of 5 cm displacement length. This observation can be explained by the presence of the stagnation bubble when the plate is placed 5 cm downstream of the nozzle. For a mixture of argon with hydrogen, Fig.7a and 7b represent the photographs of the jets generated by ICP torch having 20kW input power, with  $M=1.5$  supersonic nozzle at 2.5 cm and 5

cm displacement of barrier respectively. We see that in principle, the flow pattern does not change much as compared to the pure argon pattern: the stagnation bubble is observed at 5 cm displacement, while this bubble is absent at 2.5 cm displacement distance. Changing the supersonic nozzle from  $M=1.5$  to  $M=3$  shape and changing the input torch power from 20 kW to 12 kW result in significant changing of the flow pattern. In that case, the stagnation bubble is absent both at 2.5 cm and 5 cm displacement distance in pure argon as well as in the mixture of argon with hydrogen (Fig. 8). At the same time, the local heat flux profile along the plate has a not very well pronounced off-axis maximum (Fig.9), and this flux is significantly larger in the case of mixture of argon and hydrogen as compared to pure argon.

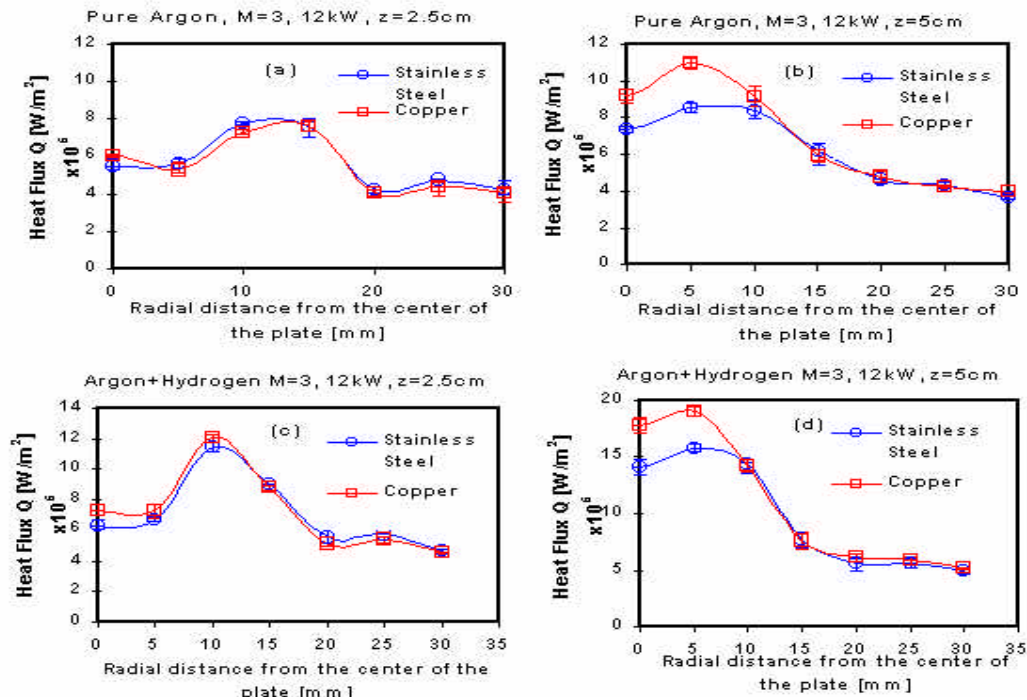


Fig.9 Local heat flux along the barrier in argon impinging jet  $M=3$ , 12kW power, a) pure argon 2.5 displacement distance, b) pure argon 5 cm displacement distance, c) mixture of argon and hydrogen 2.5 displacement distance, d) mixture of argon and hydrogen 5 cm displacement distance

## 5. Summary

In the present article we study the heat transfer in impinging plasma jets of argon and a mixture of argon and hydrogen. We show that under certain conditions a stagnation bubble is formed near the stagnation point; this bubble is a result of the interaction of the jet oblique shock with the bow shock wave formed ahead of the stagnation point. This bubble leads to the significant decreasing of the heat flux in the stagnation point, while the hydrogen admixture increases this heat flux.

## References

- [1] Donaldson C.DuP., Snedeker R.S. Journal of Fluid Mechanics, **45**, 281 (1971)
- [2] Ginzburg I.P., Semiletenko B.G., Terpigor'ev V.S., and Uskov V.N. Journal of Engineering Physics, **19**, 1081, (1973)
- [3] Gubanova O.I., Lunev V.V., Plastinina L.N. Fluid Dynamics **6**, 298 (1973)
- [4] Kalghatgi G.T. and Hunt B.L. Aeronautical Quarterly, p.169, August (1976)
- [5] Alvi F.S., Ladd J.A., Bower W.W. AIAA Journal, **40**, 4 599 (2002).
- [6] Luk'yanov, G.A. Supersonic plasma jets, Leningrad, Mashinostroenie, 269p (1985) (in Russian)
- [7] Gibson M. M. and Launder B. E. J. Fluid Mech., **86**, 491(1978)
- [8] Launder B. E. Inter. J. Heat Fluid Flow **10**(4) 282 (1989)
- [9] Launder B. E., Reece G. J. and Rodi W.J. Fluid Mech., **68** (3) 537, April (1975)
- [10] Selezneva, S.E. and Boulos, M.I. J.Appl.Phys **91**, 5 (2002)

# **Investigation on Characteristics of Plasma Produced by BDB Plasma Gun**

Zhang guang qiu; Ge yuan jing; Zhang yue fei; Chen guang liang

*Beijing institute of Printing Beijing 102600, China*

Dielectric Barrier Discharge (DBD) plasma is a special plasma kind operating at high pressure including atmospheric pressure. The behaviors of this kind of plasma have been studied in some laboratories [1.2. 3]. Someone has used it to modify the surface of materials, such as paper, plastic, textile fabric etc successfully [4.5]. However, this kind of plasma is unstable and not uniform. In 1997, a new type DBD plasma device named Induced Dielectric Barrier Discharge (IDBD) device was created in our laboratory. By using this machine, stable and uniform surface plasma can be formed at atmospheric pressure. This plasma is called IDBD plasma and has been used to treat carbon black at atmospheric pressure [6].

However, all the DBD plasma and IDBD plasma have large size. They can not be used to modify surface locally or prepare polymerized film on a special area of surface under atmospheric pressure condition which are necessary in industry.

In order to solve this problem, a DBD plasma gun was developed in our laboratory. Some experiment investigations on the dynamical characteristics and application of plasma formed by this Plasma Gun have been done. The investigated results showed that:

1. Depending on different discharge parameters, a stable plasma column with diameter of 1~3mm, spouting length of 1~5cm can be obtain at high pressure (including atmospheric pressure).
2. The macroscopic temperature of plasma column is almost room temperature.
3. This kind of plasma can be used to modify material surface locally and prepare polymerization film on a special local surface.

In this paper, the dynamical behaviors and application results of this kind of plasma will be reported in detail.

- [1] X. J. Xu et al, Physics of Gas Discharge, Fudan Publication House, (1996)
- [2] S. X. He, University Physics, Press of Chongqing University, China, (1986)
- [3] R. B. Eliasson, B. Cellert, J. Appl.phys. 68. 2026 (1990)
- [4] G. Q. Zhang et al, Plasma Science and Technology Vol.3, No.4. 877 (2002)
- [5] S. K. Khall et al, Appl Phys, 69(9) 6719-6324(1991)
- [6] Y. J. Ge et al, Proceeding of Symposium On nuclear Fusion and Plasma Application. Chengdo, China, 25 (1998)

# Study on the diameter and discharge duration of the filament in dielectric barrier discharge in Air/Argon

Zengqian Yin<sup>1</sup>, LiFang Dong<sup>1</sup>, Yafeng He<sup>1</sup>, Zhifang Chai<sup>1</sup>, Long Wang<sup>2</sup>

<sup>1</sup>*College of Physics Science & Technology, Hebei University, Baoding 071002, China*

<sup>2</sup>*Institute of Physics, Chinese Academy of Sciences, Beijing 100080, China*

## Abstract

The diameter of filament and light emission emitted from the total active region in dielectric barrier discharge in Air/Ar have been investigated by using optical method. It's found that the diameter and discharge duration of the filament decrease as the air concentration increasing, while the coherence of the discharge moments of the filaments weakens as the air concentration increasing. The experimental results have been interpreted with the theory of electron drifting.

## 1. Introduction

Dielectric barrier discharge (DBD) is typical non-equilibrium gas discharge, in which at least one of the electrodes is covered with dielectric layer. There are two regimes in DBD concluding filamentary discharge and glow-like discharge, which depend on the experimental parameters. In filamentary regime, a number of micro-discharge channels distribute in the active region, which can arrange static or drift pattern under appropriate condition.<sup>[1-4]</sup> Pattern formation is a well known phenomenon in nonlinear dissipative system and has been investigated in systems of different origins. DBD has motivated intensive applications and fundamental studies due to its unique combination of non-equilibrium and quasi-continuous behavior. In recent years, the spatio-temporal dynamics of individual filament and the dynamical interactions between filaments become an important issue of DBD as it will establish a link between microscopic conditions inside DBD filaments and macroscopic patterns in which the filaments are organized. Such a link would be of considerable interest in the field of nonlinear dynamics, and it might prove beneficial to DBD application. Many researchers attempted to measure the dynamic behavior of filaments in DBD. I.Brauer et al have reported on the interactions between solitary current density spots observed in a DBD system.<sup>[5]</sup> M. Klein et al obtained the time-resolved (in microsecond time scale) imaging of spatio-temporal patterns in one-dimensional dielectric barrier discharge.<sup>[6]</sup> In our previous works, it's found that the filaments arrangement irregular patterns can be obtained in Air<sup>[7]</sup>. While the regular patterns, such as hexagon and square patterns can be obtained in Ar.<sup>[8]</sup> The obviously different spatio-temporal behaviors have been presented, which indicate that the component of the gas is one of the important factors to depend the character of DBD. There is no report to investigate the relation between the spatio-temporal behaviors and the gas component at atmospheric pressure in the order of nanosecond. In this paper, the mixtures of air and argon at atmospheric pressure are used to discharge gas, spatio-temporal behaviors of DBD under different air concentration have been investigated by using a special setup with two water electrodes, which is favorable for both pattern formation and optical measurement. It's found that the diameter and discharge duration of the filament decrease as the air concentration increasing, while the coherence of the discharge moments of the filaments weakens as the air concentration increasing. The experimental results have been interpreted with the theory of electron drifting.

## 2. Experimental setup

The experimental device is shown in Fig.1. Two cylindrical containers with diameter of 4.67 cm filled with ordinary water are used as electrodes. The metallic rings connected with power supply are immersed in the water for conducting current. The parallel glass with thickness 1.5 mm served as dielectric end walls of the containers. The gas gap width between the dielectric layers can be adjusted with the micrometer caliper. The water is also served as coolant and transparent media for observation. The overall structure is put into a chamber, which is connected with the mechanical pump and inlet chamber. A sinusoidal ac voltage (with the frequency 10-42 kHz) is applied to the electrodes. Resistors are used to monitor the applied voltage. The light emitted from the filaments is detected by PMT (RCA7265) and recorded with an oscilloscope (Tektronix TDS3054B, 500MHz). By means of this system, the temporal behavior of light emission from filaments can be recorded. A digital camera (Canon Powershot G1) is used to take the picture of patterns.

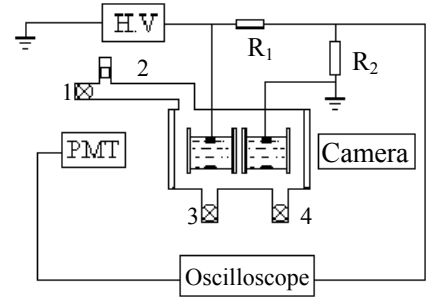


Fig.1 Experimental setup (1: gas source, 2: flowmeter, 3: manometer, 4: pump,  $R_1=200\text{M}\Omega$ ,  $R_2=1.5\text{M}\Omega$ )

## 3. Experimental results and discussion

The spatio-temporal behaviors of filaments under different conditions have been investigated. The typical results will be given in this paper. The breakdown voltage under different air concentration ( $\chi$ ) in Air/Ar is measured firstly. The experimental results are shown in Fig.2. It's found that the breakdown voltage increases as the air concentration increasing. In DBD, the discharge can maintain when the applied voltage is less than the breakdown voltage. Fig.3 gives the picture of filament pattern obtained under condition in which the applied voltage is slight less than the breakdown voltage and corresponding waveforms of the total light emission under different air concentration. The bright spots in left picture are filaments, which arranged to irregular pattern. It's found that the diameter of the filament decreases as the air concentration increasing. The waveforms of the total emission reflect the temporal aspects of the discharge. From Fig.3 one can see that the discharge burst in each half cycle of applied voltage is consist of a serious discharge pulses, the duration of each discharge pulse is about 30ns under the condition  $\chi=100$ . While the discharge burst is consist of only one pulse with the duration about 850ns under the condition  $\chi=0.001\%$ . As the air concentration  $\chi$  increasing, the number of pulses within burst increases, while the duration of pulse decreases. It's obvious that the case can be result in two factors. One is that the discharge duration of the filament decreases as  $\chi$  increasing, the other is that the coherence of the discharge moments of the filaments within the pattern weakens as  $\chi$  increasing. The detail experimental data not shown here indicate that both factors result in the case collectively.

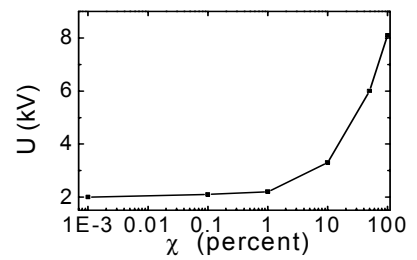


Fig.2 Breakdown voltage as a function of the air concentration in the mixtures of Air/Ar in DBD (other experimental parameters: width of gas gap  $d=1.7\text{mm}$ , frequency of applied voltage  $f=26\text{kHz}$ , gas pressure  $p=760\text{Torr}$ )

It's generally believed that the diameter of the filament as well as the duration of the filament discharge is related with the transit time of electron across the gas gap. Individual current avalanches spread as the

discharge processes across the gas gap, the drift and the diffusion tend to widen the avalanche's lateral extent. So the longer the transit time across the gap, the more the discharge will spread. Because increasing applied voltage decreases the transit time, which should also decrease the lateral extent of individual discharges, and the dimension of the filament seemingly becomes small. In a word, as the applied voltage increasing, the drift velocity of electron increases which result in decreasing the discharge duration and decreasing the lateral extent of the filament. So the diameter and the duration of the filament discharge decreases as  $\chi$  increasing due to the applied voltage increasing. In addition, the accumulated charges on dielectric surface created by the filament discharge create a field within very time when the duration is small, which against the filament breakdown in its neighboring region. So the coherence of the discharge moments of the filaments can't be realized. While the accumulation of the surface charges will last a long time when the duration of the filament discharge is big, the breakdown can take place in the neighboring region of the filament in the duration, which would be the factor to the coherence of the discharge moments.

#### 4. Conclusion

The diameter of filament and total light emission in dielectric barrier discharge in Air/Ar have been investigated by using optical method. It's found that the diameter and discharge duration of the filament decrease as the air concentration increasing, while the coherence of the discharge moments of the filaments weakens as the air concentration increasing. The experimental results have been interpreted with the theory of electron drifting.

**Acknowledgement:** This work is supported by Ministry of Education, China under Grant No. 02020 and Committee of Science and Technology, Hebei Province, China under Grant No. 01212180.

#### References

- [1] D.G.Boyers, and W.A.Tiller, Appl. Phys.Lett. **41**, (1982) 28
- [2] E.Ammelt, D.Schweng, and H.-G.Purwins, Phys.Lett.A **179**, (1993) 348
- [3] E.Ammelt, Yu.A.Astrov, and H.-G.Purwins, Phys.Rev.E **58**(6), (1998) 7109
- [4] I.Muller, C.Punset, E.Ammelt, H.-G.Purwins, and J.P.Boeuf, IEEE Trans. on Plasma Sci., **27**, (1999) 20
- [5] I.Brauer, M.Bode, E.Ammelt, and H.-G.Purwins, Phys.Rev.Lett. **84**(18), (2000) 4104
- [6] M.Klein, N.Miller, and M.Walhout, Phys. Rev. E, **64**, (2001) 026402
- [7] L.F.Dong, Z.Q.Yin, and X.Ch.Li et al, Journal of Electrostatics, **57**, (2003) 243
- [8] L.F.Dong, X.Ch.Li, and Z.Q.Yin et al, 6<sup>th</sup> APCPST, (invited talk), I-O3, Jeju, Korea, (July, 2002), Thin Solid Films (in press)

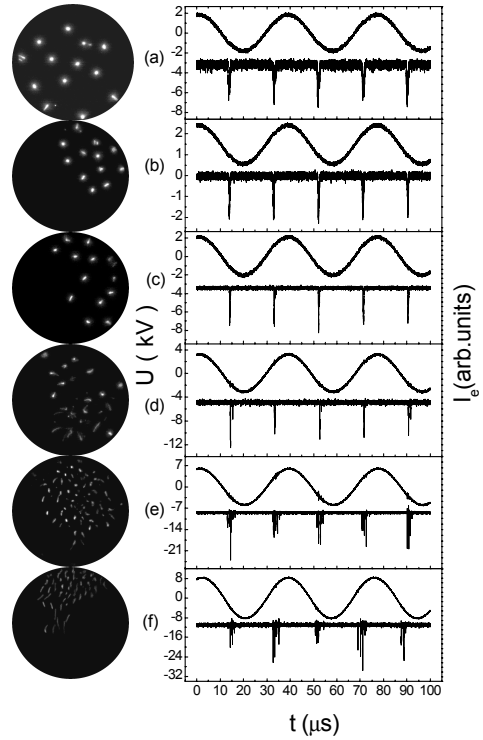


Fig.3 Filament patterns and waveforms of the total light emission varying as the air concentration: (a)  $\chi = 0.001\%$ ,  $U = 2\text{kV}$ ; (b)  $\chi = 0.1\%$ ,  $U = 2.1\text{kV}$ ; (c)  $\chi = 1\%$ ,  $U = 2.2\text{kV}$ ; (d)  $\chi = 10\%$ ,  $U = 3.3\text{kV}$ ; (e)  $\chi = 50\%$ ,  $U = 6\text{kV}$ ; (f)  $\chi = 100\%$ ,  $U = 8.1\text{kV}$ ; the other parameters: width of gas gap:  $d = 1.7\text{mm}$ ; gas pressure:  $p = 760\text{Torr}$ ; exposure time of pictures:  $25\text{ms}$



# **C<sub>4</sub>F<sub>6</sub> – 1,3 Hexafluorobutadiene – A New Etching Gas: Studies on Material Compatibility, Behavior in an Inductively Coupled Plasma and Etch Process Performance**

A. Nicoletti<sup>1</sup>, P. Srinivasan<sup>1</sup>, M. Riva<sup>1</sup>, E. Benck<sup>2</sup>, Amanda Goyette<sup>2</sup>, Yicheng Wang<sup>2</sup>  
Jong Moon Kim<sup>3</sup>, Peter Hsieh<sup>3</sup>, Amulya Athayde<sup>3</sup> and Ajey M. Joshi<sup>3</sup>

<sup>1</sup>*SolvaySolexis S.p.a., Bollate (MI) Italy*

<sup>2</sup>*National Institute of Standards and Technology, Gaithersburg, Maryland 20889-8421 USA*

<sup>3</sup>*Applied Materials, Inc., Sunnyvale, California 94086 USA*

## **Abstract**

Hexafluoro-1,3-butadiene (C<sub>4</sub>F<sub>6</sub>) is a relatively new etch gas for the manufacturing of semiconductor devices and is able to combine very high performance with a benign environmental effect. Ion energy distributions and mass resolved total ion current fluxes are reported from inductively coupled plasmas of pure C<sub>4</sub>F<sub>6</sub> and C<sub>4</sub>F<sub>6</sub>:Ar mixtures. We also report on the material compatibility of this gas, which show how this ‘exotic’ gas can be handled with standard materials. Advantages of C<sub>4</sub>F<sub>6</sub> based etch processes, such as high aspect ratio contact / via etch, high selectivity mask open, and dual damascene etch processes, developed on an Applied Materials dielectric etcher, and analyses of PFC emissions data are discussed.

## **Introduction**

Low-pressure radio frequency (rf) fluorocarbon discharges are commonly used in the manufacturing of microelectronics. Typically, saturated fluorocarbons gases such as CF<sub>4</sub> or *c*-C<sub>4</sub>F<sub>8</sub> have been used, particularly with the etching of silicon and silicon dioxide. Unfortunately, there has been a growing concern over the ecological impact of these manufacturing processes. The 100 year integrated global warming potential (GWP<sub>100</sub>) relative to CO<sub>2</sub> for many of the commonly used fluorocarbon gases (CF<sub>4</sub> 5700, *c*-C<sub>4</sub>F<sub>8</sub> 11299, and CHF<sub>3</sub> 14800)<sup>1</sup> are quite large and the concentration of these gases in the atmosphere has been consistently growing in recent years. There has been an effort to identify alternative gas chemistries that are more environmentally benign. Moreover, in the past few years, the semiconductor industry has continued its march according to Moore’s Law toward ever-shrinking device dimensions made possible by innovations in all aspects of device fabrication from novel integration schemes to film compositions, lithographic techniques, and etch processes to metallization. Also the unique field of dielectric etch has continued to increase performance requirements in terms of aspect ratio and selectivity.

An alternative etching process that uses 1,3 hexafluorobutadiene (C<sub>4</sub>F<sub>6</sub>), is available. The global warming potential of this gas is so low (GWP<sub>100</sub>=0.027)<sup>2</sup> that it is typically ignored in global warming impact calculations. An initial study by Chatterjee et al demonstrated an 80 % decrease in global warming plasma emissions from a C<sub>4</sub>F<sub>6</sub> based etching process when compared to a standard C<sub>3</sub>F<sub>8</sub> etching process<sup>3</sup>.

The process advantage of C<sub>4</sub>F<sub>6</sub> is not only related to its environmental aspects, but its etching performance is also unique. The most significant benefits of C<sub>4</sub>F<sub>6</sub> gas become evident from its demonstrated performance for a range of increasingly demanding advanced etch processes that require concomitant high selectivity to 193 nm photoresists, hardmasks, and a variety of underlayers while preserving critical dimension and profile control.

## **Section I: Ion Energy Distribution and Optical Measurements in High-Density, Inductively Coupled C<sub>4</sub>F<sub>6</sub> Discharges**

### **I. Experimental Apparatus**

The plasmas examined in this section were created in a modified inductively coupled Gaseous Electronics Conference (GEC) Reference Cell which has been previously described.<sup>4,5</sup> The plasma is created with a flat 5 turn, 100 mm diameter spiral coil separated from the plasma by a fused silica vacuum interface. An additional quartz confinement ring is attached to the coil assembly to improve the plasma stability and increase the operating range. A gap of approximately 2.54 cm exists between the lower electrode and the quartz confinement ring. The lower electrode was water cooled and grounded to the vacuum chamber. A 140

mm diameter stainless steel plate with a bare 100 mm diameter silicon wafer on top was centered on the lower electrode.

The discharge was generated by applying a 13.56 MHz voltage to the coil through a matching network. The rf power values presented in this article are the net power to the matching network driving the coil. The actual rf power dissipated in the plasma has been determined to be approximately 80% of the power listed.<sup>5</sup> The gas pressure is maintained by a variable gate valve between the pump and the GEC cell. The gas flow was maintained by mass flow controllers at 3.73  $\mu\text{mol/s}$  or 7.45  $\mu\text{mol/s}$  (5 sccm or 10 sccm). Where gas mixtures are used, the percentages reported in this paper are based on the volume fraction of the gases.

The energy analyzer/mass spectrometer was mounted on a side port with the inlet orifice grounded. The configuration of the energy analyzer/mass spectrometer has been previously described.<sup>6</sup> The ions are collected through a 10  $\mu\text{m}$  aperture located 9.5 mm above the steel plate and at a distance of 46 mm from the radial center of the reactor, 11 mm inside the inner diameter of the quartz confinement ring. The resolution of the energy analyzer {full width at half maximum (FWHM)} was 1 eV, and the uncertainty in its energy scale is estimated to be  $\pm 1$  eV. Ion intensities were corrected to account for previously measured variations in ion transmission as a function of ion mass.<sup>7</sup> After such corrections, the ion transmission is estimated to be uniform to within 20 % over the range of ion masses and ion energies studied here.

To calibrate the ion fluxes measured by the mass spectrometer, a Faraday cup with a 1.59 mm diameter aperture was mounted at the same radius and height as the mass spectrometer orifice. The dc current measured when the cup was dc biased at -20 V was divided by the area of the aperture to obtain the total ion current density. This value was then used to normalize the relative ion fluxes measured by the mass spectrometer. Uncertainties on the absolute ion flux intensities are on the order of 25 %.

## II. Results and Discussion

### Pure $\text{C}_4\text{F}_6$

Figure 1 shows the mass spectrum of the ions produced in a pure  $\text{C}_4\text{F}_6$  plasma at 1.33 Pa (10 mTorr) and 200 W.  $\text{CF}^+$  is the dominant ion, but there are significant contributions from  $\text{CF}_2^+$  and from the  $\text{SiF}_x^+/\text{COF}_x^+$  ions. This is very different from what would be expected from direct electron impact ionization of  $\text{C}_4\text{F}_6$ . The relatively low molecular weight of the plasma ions suggests a high degree of dissociation of the parent gas, and the significant proportion of ions which contain either Si or O, indicates a considerable contribution from surface reactions to the overall ion chemistry. This is very different from inductively coupled  $\text{CF}_4$  discharges which were measured in the same chamber that showed ion mass distributions which could be attributed mainly to direct electron impact of the feed gas<sup>11</sup>, but is similar to other fluorocarbon etching gases such as  $\text{C}_2\text{F}_6$  and  $\text{c-C}_4\text{F}_8$ .<sup>12</sup> It is worthwhile noting that electron attachment to  $\text{C}_4\text{F}_6$  occurs at low energies with appreciable rates<sup>13,14</sup>, and presents a likely decomposition channel which is of much lesser importance in  $\text{CF}_4$ .

The resolution of the mass spectrometer is not sufficient to distinguish between the Si and CO masses, so there remains an uncertainty to the identity of the  $\text{SiF}_x^+/\text{COF}_x^+$  ions. Etching of the fused silica window and confinement ring beneath the induction coil is probably the main source of both oxygen and silicon for the plasma. Since no bias is applied to the lower electrode, thick fluorocarbon layers form on the silicon wafer limiting it as a source of Si to the plasma. Utilizing the isotopic ratios to distinguish between CO and Si containing molecular ions produced inconsistent results. The isotopic ratios measured with the mass spectrometer indicate that the lowest mass ions (28 au) are mostly  $\text{CO}^+$  molecular ions, while the higher mass ions seem to be almost entirely  $\text{SiF}_x^+$  molecular ions.

Figure 2 shows the ion flux dependence on pressure. The overall ion flux shows a decrease with increasing pressure over the range from 0.67 Pa to 2.66 Pa (5 mTorr to 20 mTorr). This is consistent with most of the fluorocarbon gases previously studied in this plasma source, except for  $\text{C}_2\text{F}_6$ .<sup>11,12,15</sup> The total flux was significantly lower than the other fluorocarbon gases measured in the same vacuum chamber. This result is probably due in part to sampling the flux from the side of the plasma instead of through the center of the grounded lower electrode and the presence of fused silica confinement ring.  $\text{CF}^+$  remains the dominant ion over the entire pressure range, but there are strong contributions from the other molecular ions. At 0.67 Pa,  $\text{CF}_2^+$  is the second most intense ion flux while at 2.66 Pa  $\text{SiF}^+/\text{COF}^+$  and  $\text{SiF}_2^+/\text{COF}_2^+$  become the second most abundant ions.  $\text{CF}^+$  and  $\text{CF}_2^+$  show a decrease in flux with increasing pressure, while  $\text{CF}_3^+$  shows essentially no dependence. The  $\text{SiF}_x^+$  ( $x=1-3$ ) ions have a maximum flux at the intermediate pressure of

1.33 Pa. Atomic ion fluxes of  $C^+$  and  $Si^+/CO^+$  as well as  $C_2^+$  decrease rapidly with increasing pressure.  $C_3^+$ , on the other hand, increases with increasing pressure. This increase in  $C_3^+$  may be indicative of increasingly favorable conditions within the plasma for the formation of larger carbon clusters and particulates as the pressure is increased.

Figure 3 shows how the ion energy distribution (IED) of  $CF^+$  changes with pressure. The IEDs of all three pressures show the characteristic double peak distribution. The intermediate pressure, 1.33 Pa, has the greatest width. This differs from what we have observed in inductively coupled discharges generated in other fluorocarbon gases,<sup>12</sup> in which the IEDs typically broaden monotonically with increasing pressure.

#### **C<sub>4</sub>F<sub>6</sub>: Ar Mixture**

Figure 4 shows the total ion flux and flux of component ions for an inductively coupled plasma sustained in C<sub>4</sub>F<sub>6</sub>: Ar gas mixtures with a pressure of 1.33 Pa (10 mTorr) at 200 W. The total ion current demonstrates a slow decrease with increasing C<sub>4</sub>F<sub>6</sub> input concentration. This is probably due to increasing power being necessary to dissociate the molecular components. In the mixtures, the dominant ion flux was always Ar<sup>+</sup>, although it dropped proportionally with decreasing percentage of Ar. CF<sup>+</sup> had the second highest flux followed by CF<sub>2</sub><sup>+</sup>, SiF<sup>+</sup>/COF<sup>+</sup>, and SiF<sub>2</sub><sup>+</sup>/COF<sub>2</sub><sup>+</sup> which all had similar ion fluxes. Except for Ar<sup>+</sup> and C<sup>+</sup>, all the ion fluxes increased with increasing percentage of C<sub>4</sub>F<sub>6</sub>. It is interesting to note that although the fluxes of both CF<sup>+</sup> and CF<sub>2</sub><sup>+</sup> increased almost proportionally with C<sub>4</sub>F<sub>6</sub> addition from 25 % C<sub>4</sub>F<sub>6</sub> to 75 % C<sub>4</sub>F<sub>6</sub>, the fluxes of both ions showed a similar leveling off as the mixture approached 100 % C<sub>4</sub>F<sub>6</sub>, whereas the flux of CF<sub>3</sub><sup>+</sup> continued to increase in proportion to C<sub>4</sub>F<sub>6</sub> addition.

Figure 5 shows the total ion flux and the flux of component ions for an inductively coupled plasma sustained in a 50 % C<sub>4</sub>F<sub>6</sub>: 50 % Ar mixture at 200 W as a function of gas pressure. The magnitude of the total ion flux exhibits a slight downward trend over the pressure range from 0.67 Pa to 2.66 Pa (5 mTorr to 20 mTorr), similar to that observed in other fluorocarbon: argon mixtures.<sup>11,12,15</sup> The dominant ion under all conditions is Ar<sup>+</sup>, similar to the behavior of CHF<sub>3</sub>:Ar mixtures. As with the case of pure C<sub>4</sub>F<sub>6</sub>, the total ion flux was significantly lower than the other fluorocarbon gases measured in the same vacuum chamber.

Of particular interest is the differing behavior of the CF<sub>x</sub><sup>+</sup> and SiF<sub>x</sub><sup>+</sup>/COF<sub>x</sub><sup>+</sup> (x=0 to 4) ions. As with the pure C<sub>4</sub>F<sub>6</sub> discharges, there is a general shift in the ion composition from fluorocarbon ions to secondary ions, which originate from etching byproducts as the pressure is increased, again underscoring the contributions of these processes to the overall ion chemistry. The fluxes of most of the fluorocarbon ions decrease with increasing pressure with the exception of CF<sub>3</sub><sup>+</sup>, which showed a slight increase at the highest pressure. The SiF<sub>x</sub><sup>+</sup> molecular ions showed the exact opposite behavior, increasing ion flux with increasing pressure. The fluxes of atomic ions were very small and strongly decreased with increasing pressure.

For gas mixtures, the average energy of the IEDs are lower than those for the pure C<sub>4</sub>F<sub>6</sub> discharges shown in Fig. 3. For a 50 % C<sub>4</sub>F<sub>6</sub>: 50 % Ar mixture the average energies are lower by about 5 eV. In addition, the IEDs are narrower and at the lowest pressure (0.67 Pa) the dual peak IED combines into a single peak.

## **Section II: C<sub>4</sub>F<sub>6</sub>: Material Compatibility with Perfluoro Rubbers and Plastomers**

### **I. Experimental**

The compatibility tests with C<sub>4</sub>F<sub>6</sub> were carried out in a 17 L Hastelloy reactor at 50 °C for 336 h. The samples used to study the change in mechanical properties were prepared following the standards - ASTM D412 for the elastomers and ASTM D1708 for the plastomers. 11 samples of each material was prepared for these tests. 3 were exposed to the liquid phase and 3 to the vapor phase. The remaining 5 samples were used as blanks. 4 additional samples were used to determine the changes in volume and weight of the materials after exposure.

The reactor was filled with about 10.5 kg of C<sub>4</sub>F<sub>6</sub> by connecting the evacuated reactor to the gas cylinder. The reactor was heated and maintained at 50 °C by means of a resistance heater with an audible alarm at 55 °C and a cut off at 60 °C. The corresponding pressure inside the reactor was 446 kPa. After the exposure for 336 h, the reactor was cooled to the ambient temperature within 2 h and the gas discharged into an evacuated container. The samples were removed and the mechanical properties determined. The changes in weight and volume were determined within a short period of time after the completion of the tests in order to avoid excessive evaporation of the gas from the samples.

Throughout the period of tests, suitable precautions were taken during handling of  $C_4F_6$ , considering its toxic and flammable nature.

## II. Results and Discussion

The results of the compatibility tests are shown in Table I. As can be seen from the results, surprisingly, low density polyethylene (LDPE), show much better compatibility than the fluorinated and perfluorinated polymers. The compatibility with perfluoro-rubbers (Tecnoflon<sup>®</sup> PFR94) has been poor, as the one for bisphenolic-perfluoromonomers polymers (Tecnoflon<sup>®</sup> FOR435). EPDM rubbers show a better compatibility in comparison with fluoro-rubber.

### **Section III: $C_4F_6/O_2$ Based Processes for Sub-130nm Technology Nodes in Applied Materials' Dielectric Etch eMAX<sup>™</sup> Chamber**

#### I. Experimental

Hexafluoro-1,3-butadiene ( $C_4F_6$ ) based dielectric etch processes, such as high aspect ratio (HAR) contact etch and FSG Via Dual Damascene (DD) etch developed on Applied Materials' Dielectric Etch eMAX<sup>™</sup> chamber were studied. The Dielectric Etch eMAX<sup>™</sup> product is a medium density, magnetically enhanced reactive ion etch (MERIE) chamber operating at 13.56 MHz and is designed for a wide operating regime (high and low pressure, high flow conditions, high and low RF power). The enhanced liner technology successfully provides a production-worthy solution for applications ranging from nitride and oxide hardmask etch to HAR and high selectivity self-aligned contact, via, and dual damascene etch applications<sup>16, 17</sup>. Silicon wafers coated with appropriate film stacks and patterned with photoresist mask were etched in this chamber. A typical etch process exposed the patterned oxide wafer to an RF plasma generated in a mixture of  $C_4F_6$ , oxygen, and Ar as diluent optimized to deliver the desired selectivity, critical dimension (CD), and profile performance. The calibrations and quantitative measurements of emissions of gas and vapor phase species were made in accordance to the accepted industry protocol (*Equipment Environmental Characterization Guidelines; Rev. 3.0*), using a Quadrupole Mass Spectroscopy (UTI QMS analyzer) and Fourier Transform Infrared Spectroscopy (Nicolet Nexus<sup>™</sup> FTIR spectrometer with a 5 cm gas cell).

#### II. Results and Discussion

Fluorocarbon gases, such as  $CF_4$ ,  $CHF_3$ , and  $C_2F_6$  have been widely used for etching dielectric films (e.g., undoped and doped silicon dioxides and silicon nitride) while providing adequate selectivity to photoresist masks as well as underlayer materials like silicon, metal silicides, and titanium nitride through the 250 nm device generation. Progressively thinner photoresist masks, driven by resolution considerations, coupled with changes in resist materials with each new generation of photolithography technology (from 365 nm/i-line to 248 nm/KrF to 193 nm/ArF) have resulted in increased photoresist selectivity and integrity requirements. Consequently, identifying new etch gases that offer new capabilities has become imperative. Over the past few years, the Applied Materials Etch Division has developed and characterized, and patented<sup>18</sup> extensively, processes using the fluorocarbon gas hexafluoro-1,3-butadiene ( $C_4F_6$ ) for a wide range of critical etch applications and are currently implemented in production for the sub-130nm technology nodes.

Figure 6 shows the trend in photoresist selectivity with increasing intrinsic C/F ratio of fluorocarbon gases  $C_4F_8$ ,  $C_5F_8$ , and  $C_4F_6$ . The total fluorine, argon dilution, and fluorine to oxygen atomic ratio were held constant by adjusting the fluorocarbon gas flows to allow such a comparison. For example,  $C_4F_8$  and  $C_5F_8$  flows of 20 sccm would be considered equivalent to 24 sccm  $C_4F_6$  in terms of total available fluorine. Undoped oxide coated silicon wafers patterned with 180 nm via patterns (248 nm photoresist) were used for this study. The oxide and photoresist etch rates were measured by comparing SEM cross-sections of partially etched wafers with those of the pre-etch condition. The  $C_4F_6$  chemistry, consistent with the higher intrinsic C/F ratio yields higher selectivity to photoresist compared to both  $C_4F_8$  and  $C_5F_8$ . In addition, the  $C_4F_6/O_2/Ar$  combination alone yields >25:1 selectivity to silicon nitride underlayer, while a similar  $C_4F_8/O_2/Ar$  process produces the much lower selectivity of <5:1. It is well known that adding CO to  $C_4F_8$  to increase the effective C/F ratio and reducing oxygen flow is typically necessary to obtain >20:1 selectivity to silicon nitride underlayers<sup>19, 20</sup>. Addition of CO is also thought to help bind reactive free F radicals (often thought to cause selectivity degradation) into relatively stable carbonyl fluoride ( $COF_2$ ) species.

Figure 7 shows some examples of critical etch process capabilities of the eMAX<sup>TM</sup> chamber. Excellent profile and CD control with high selectivity to the silicon nitride barrier (>25:1, nitride loss <10 nm on flat and <20 nm at nitride corner) and the photoresist mask (>6-10:1), a striation-free performance with up to 20:1 aspect ratio capability, and a wide process window can be realized using C<sub>4</sub>F<sub>6</sub> based processes.

The newest addition to the evolving list of criteria for new gas evaluation arises from the concern regarding global warming phenomena. Certain commonly used fluorocarbon etchants, such as CF<sub>4</sub>, C<sub>2</sub>F<sub>6</sub>, and even c-C<sub>4</sub>F<sub>8</sub>, have been shown to have a very high global warming potential (GWP<sub>100</sub>) typically expressed as kg carbon equivalents (kgCE) per 100 years<sup>1,3</sup>. Silicon wafers coated with 1000 nm fluorinated silicon oxide (FSG oxide) over 50 nm silicon nitride and patterned with 248 nm photoresist to resolve nominally 180nm via features were etched in an eMAX<sup>TM</sup> chamber, and the effluent gases and volatile byproducts were measured. In addition to unreacted hexafluorobutadiene (C<sub>4</sub>F<sub>6</sub>) and oxygen input gases, etch byproducts tetrafluoromethane (CF<sub>4</sub>), hexafluoroethane (C<sub>2</sub>F<sub>6</sub>), perfluoroethene (C<sub>2</sub>F<sub>4</sub>), carbon monoxide (CO), carbon dioxide (CO<sub>2</sub>), fluorine (F<sub>2</sub>), silicon tetrafluoride (SiF<sub>4</sub>), hydrogen fluoride (HF), and carbonyl fluoride (COF<sub>2</sub>) were detected at the exhaust of the vacuum pump during FSG via etch process. Typical FTIR spectra, QMS time resolved spectra, and masses of various byproducts for the via etch process are shown in Figures 8, 9 and 10, respectively. The quantitative analysis and utilization efficiencies recorded during the etch process are summarized in Table II.

The breakdown efficiency of ≈94 % observed for C<sub>4</sub>F<sub>6</sub> in the medium density MERIE reactor is similar to that reported for an inductively coupled reactor in the NIST study (see above). This is consistent with the presumed relatively low ionization / dissociation energies of C<sub>4</sub>F<sub>6</sub><sup>12,13</sup> as discussed in Section I of this paper. The fluorine mass balance was closed to 88 %. The discrepancy is attributed partly to fluorocarbon polymers deposited on the chamber and wafer surfaces and partly to volatile but reactive HF that was not measured in this study.

As expected, not all C<sub>4</sub>F<sub>6</sub> is used to etch the wafer as some of it is transformed into C<sub>2</sub>F<sub>4</sub>, CF<sub>4</sub>, and C<sub>2</sub>F<sub>6</sub>. CF<sub>4</sub> and C<sub>2</sub>F<sub>6</sub> byproducts have high global warming potential when emitted into the atmosphere therefore, appropriate abatement is necessary to dispose of those PFCs. The relatively large amount of C<sub>2</sub>F<sub>4</sub> measured points indirectly to a relatively large concentration of ‘C<sub>2</sub>’ fragments, such as C<sub>2</sub>F<sub>4</sub><sup>+</sup> species, in the plasma. This needs to be corroborated by direct plasma emission measurements; however in earlier studies with c-C<sub>4</sub>F<sub>8</sub>, such species were shown to create the etch rate differential and hence the selectivity between silicon oxide and nitride films. The high selectivity (20-30:1) of oxide to nitride for C<sub>4</sub>F<sub>6</sub>/O<sub>2</sub> based processes is consistent with such a conclusion. Formation of CO, CO<sub>2</sub>, and COF<sub>2</sub> species likely results from interaction between oxygen and carbon contributed by photoresist and C<sub>4</sub>F<sub>6</sub>. As mentioned earlier, CO, in this case formed *in situ*, is thought to help reduce resist selectivity degradation by effectively binding free F radicals into COF<sub>2</sub>. From the quantitative analysis of CF<sub>4</sub> and C<sub>2</sub>F<sub>6</sub> byproducts, total emissions are calculated at a negligible 0.04 kgCE/100 years for the 1 μm FSG via etch on the eMAX<sup>TM</sup> chamber.

In addition, the C<sub>4</sub>F<sub>6</sub> based process capability has been extended successfully to the two newest additions to Applied Materials’ etch product portfolio, *viz.* to the capacitively coupled dual frequency reactor, the Dielectric Etch Enabler<sup>TM</sup> chamber for 65 nm node, and to the novel dual frequency, high productivity, twin chamber product, the Producer<sup>TM</sup> Etch. Results of this work will be presented separately in the future.

## Summary

The mass-analyzed ion flux densities have been measured for inductively coupled RF plasmas in pure C<sub>4</sub>F<sub>6</sub> and in mixtures of C<sub>4</sub>F<sub>6</sub> with Ar. The dominant ion in pure C<sub>4</sub>F<sub>6</sub> was CF<sup>+</sup> and in the C<sub>4</sub>F<sub>6</sub>: Ar mixtures it was Ar<sup>+</sup> with CF<sup>+</sup> as the most abundant fluorocarbon ion. In all cases, there were strong ion fluxes due to etching byproducts (SiF<sub>x</sub><sup>+</sup>/COF<sub>x</sub><sup>+</sup>) even though there was no bias applied to the lower electrode. The etchants ions CF<sub>x</sub><sup>+</sup> tended to exhibit trends different from the etching byproducts SiF<sub>x</sub><sup>+</sup>/COF<sub>x</sub><sup>+</sup> as plasma conditions were varied. The higher mass carbon molecular ions (C<sub>3</sub><sup>+</sup>) increased relative to the lighter carbon ions (C<sup>+</sup>, C<sub>2</sub><sup>+</sup>) as gas pressure increased and may indicate the development of plasma conditions suitable for carbon particulate growth. The ion energy distributions functions were double peaked, showing that the ions crossing a ground sheath are significantly modified by the time varying electric fields.

The superior etch selectivity performance of C<sub>4</sub>F<sub>6</sub>/O<sub>2</sub> based plasma processes for sub-130 nm critical dielectric etch applications is attributed in part to intrinsically higher carbon to fluorine (C/F) ratio. Results

of PFC emission studies for critical dielectric etch applications using hexafluoro-1,3-butadiene (C<sub>4</sub>F<sub>6</sub>) based plasmas in an Applied Materials' advanced Dielectric Etch eMAX<sup>TM</sup> chamber show high level of dissociation efficiency into species that yield high selectivity to photoresist and substrate underlayers. C<sub>4</sub>F<sub>6</sub> exhibits a negligible global warming potential, has an intrinsically higher C/F ratio, and shows a favorable plasma dissociation pattern, making it an ideal candidate for advanced dielectric etch applications.

Combined with the eMAX<sup>TM</sup> chamber, C<sub>4</sub>F<sub>6</sub> process chemistry is a technology enabler for advanced, critical dielectric etch applications, especially for technologies which require extremely high aspect ratios and the newer, more fragile and sensitive materials and photoresists to deliver higher selectivity, striation-free etch performance, and improved profile and CD control.

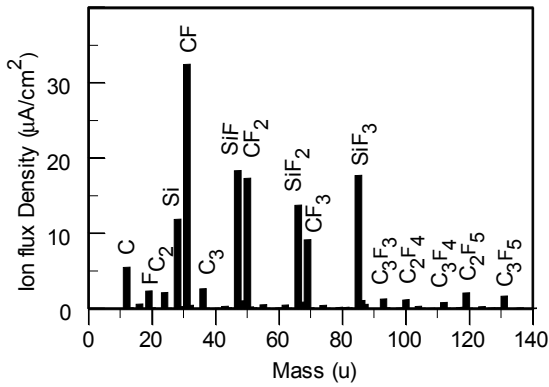
## Acknowledgments

The authors (JMK, PH, AA, AMJ) would like to thank Rafika Smati, Yelitza Maldonado, and Dustin Ho of Applied Materials Environmental Assessment Services for collecting the PFC emissions data for various processes on the eMAX<sup>TM</sup> chamber. Hexafluoro-1,3-butadiene was purchased from Solvay Solexis S.p.a. Certain commercial equipment, instruments, or materials are identified in this paper to specify adequately the experimental procedure. Such identification does not imply recommendation or endorsement by the National Institute of Standards and Technology.

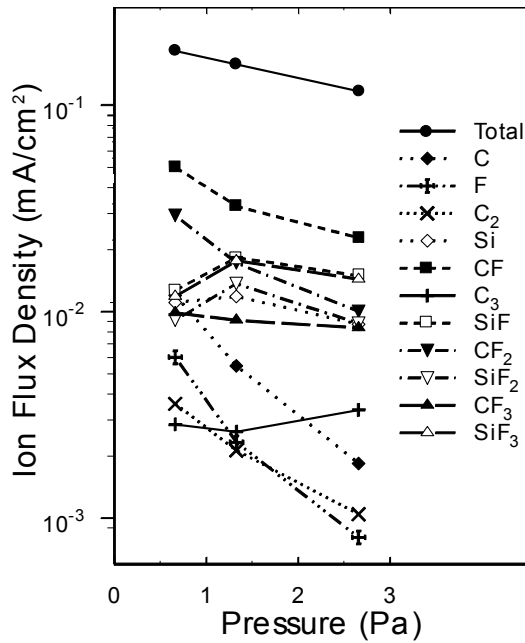
## REFERENCES

- 1 "Scientific assessment of ozone depletion: 1998," Report No. 44 (1998).
- 2 G. Acerboni, J. A. Beukes, N. R. Jensen, J. Hjorth, G. Myhre, C. J. Nielsen, and J. K. Sundet, *Atmospheric Environment* **35**, 4113-4123 (2001).
- 3 R. Chatterjee, S. Karecki, R. Reif, V. Vartanian, and T. Sparks, *J. Electrochem.Soc.* **149**, G276-G285 (2002).
- 4 P. J. Hargis, Jr., et al, *Rev. Sci. Instrum.* **65**, 140-154 (1994).
- 5 P. A. Miller, G. A. Hebner, K. E. Greenberg, P. D. Pochan, and B. P. Aragon, *J. Res. Natl. Inst. Stand. Technol.* **100**, 427-439 (1995).
- 6 M. A. Sobolewski, Y. Wang, and A. Goyette, *J. Appl. Phys.* **91**, 6303-6314 (2002).
- 7 Y. Wang and J. K. Olthoff, *J. Appl. Phys.* **85**, 6358-6365 (1999).
- 8 E. C. Benck, G. Y. Golubiatnikov, and G. T. Fraser, *JVSTA* (2002).
- 9 H. M. Pickett, R. L. Poynter, E. A. Cohen, M. L. Delitsky, J. C. Pearson, and H. S. P. Muller, *J. Quant. Spectrosc. Rad. Transfer* **60**, 883 (1998).
- 10 H. S. P. Muller, S. Thorwirth, D. A. Roth, and G. Winnewisser, *Astronomy and Astrophysics* **370**, L49-L52 (2001).
- 11 J. K. Olthoff and Y. Wang, *J. Vac. Sci. Technol. A* **17**, 1552-1555 (1999).
- 12 A. N. Goyette, Y. Wang, M. Misakian, and J. K. Olthoff, *J. Vac. Sci. Technol. A* **18**, 2785-2790 (2000).
- 13 I. Sauers, L. G. Christophorou, and J. G. Carter, *J. Chem. Phys.* **71**, 3016 (1979).
- 14 A. A. Christodoulides, L. G. Christophorou, R. Y. Pai, and C. M. Tung, *J. Chem. Phys.* **70**, 1156 (1979).
- 15 Y. Wang, M. Misakian, A. N. Goyette, and J. K. Olthoff, *J. Appl. Phys.* **88**, 5612-5617 (2000).
- 16 YS Kim, K. Doan, C. Bjorkman, A. Paterson, Z. Sui and H. Shan, *Electrochemical Society Proceedings Vol. 2002-17*, 277-289 (2002)
- 17 J. Wang, B. Pu, C. Bjorkman, T. Komatsu, JW Woo, R. Wang, H. Shan, *IEEE/SEMI Advanced Semiconductor Manufacturing Conference*, 101-105 (2001)
- 18 For example, Patents No. US 6,174,451 (2001); US 6,211,092 (2001); US 6,362,109 (2002); US 6,387,287 (2002); US 6,403,491(2002); and US 6,432,318 (2002).
- 19 W. Graf, D. Basso, F. Gautier, J. M. Martin, E. Sabouret and G. Skinner, *IEEE/SEMI Advanced Semiconductor Manufacturing Conference*, 314-319 (1998)
- 20 K. Kurihara and M. Sekine, *Plasma Source Sci. Technol.* **5**, 121 (1996).

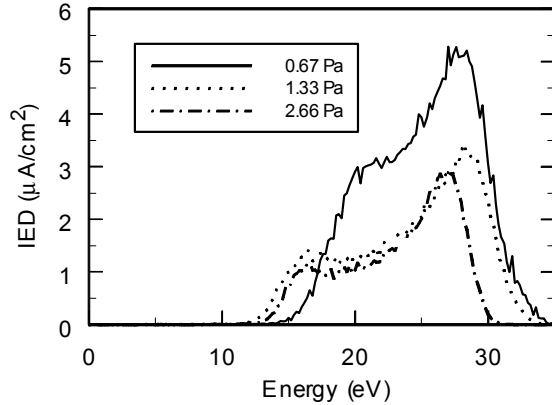
## Figures and Tables



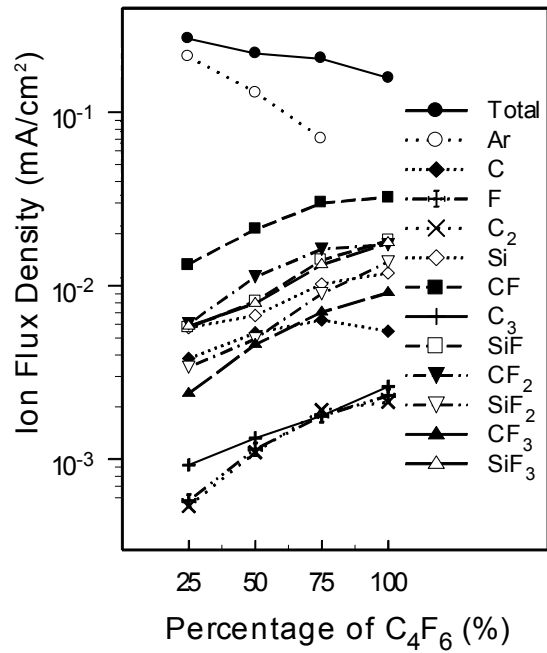
**Figure 1** - Mass spectrum of ions from the GEC cell from a 200 W, 133 Pa  $C_4F_6$  discharge.



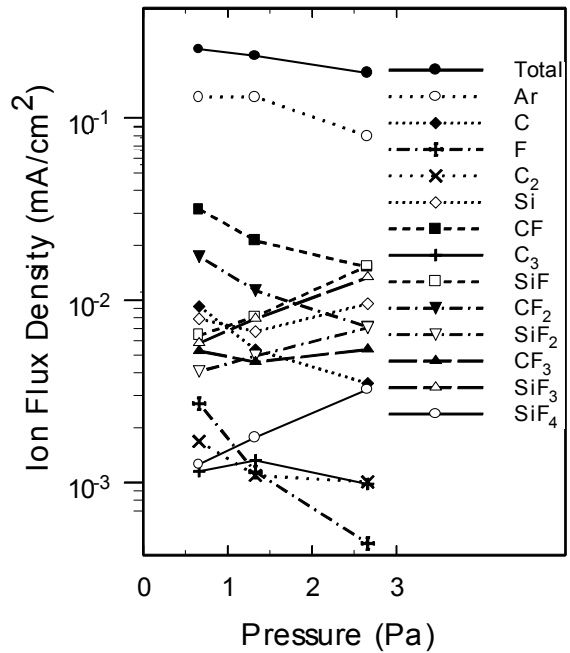
**Figure 2** - Mass analyzed ion flux measured for a 200 W,  $C_4F_6$  plasma as a function of pressure.



**Figure 3** - Ion energy distributions for  $CF^+$  ions sampled from a 200 W,  $C_4F_6$  plasma as a function of pressure.



**Figure 4** - Mass analyzed ion flux, as a function of  $C_4F_6$ :Ar mixtures for a 200 W and 1.33 Pa plasmas.



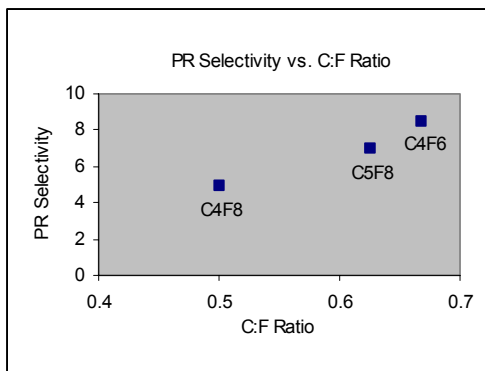
**Figure 5** - Mass analyzed ion flux, as a function of pressure for a 50 %  $C_4F_6$ :50 % Ar mixtures for a 200 W and 1.33 Pa plasmas.

**Table I: Materials Compatibility Table**

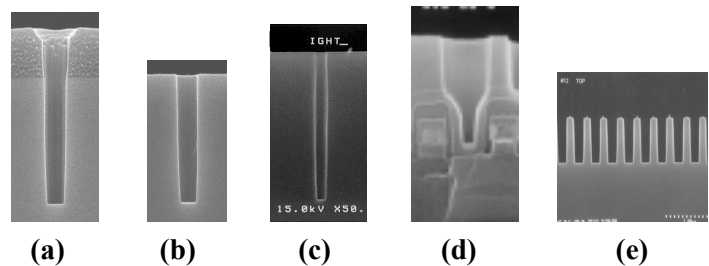
Temperature : 50 °C  
Time : 336 h

Date: 14/03/03

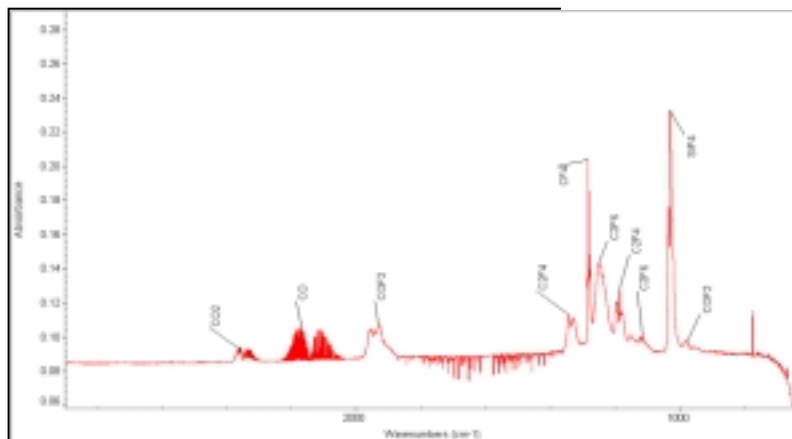
		M 100	Break S.	Break E.	Sh. A 3"	Weight	Volume
Sample:		Mpa	Mpa	%	Points		
PFR 94Liquid phase	△:	-	-75,5 %	- 52,3%	- 4 pt	28 %	40 %
EPDM Liquid phase	△:	-0,1%	-27,5 %	- 29,9%	1 pt	1 %	1 %
FOR 435 Liquid phase	△:	-9,8%	- 41,2%	-31,5 %	- 11 pt	23 %	29 %
		Modulus	Yield P.	B.S. Max	Break E.		
		Mpa	Mpa	Mpa	%		
LDPE Liquid phase	△:	-7,9%	- 0,2%	- 0,8%	8,0 %	2 %	1 %
		M 100	Break S.	Break E.	Sh. A 3"	Weight	Volume
		Mpa	Mpa	%	Points		
PFR 94Vapour phase	△:	-	- 70,1%	-42,6%	-4 pt	18 %	26 %
EDPM Vapour phase	△:	- 4,8%	- 31,9%	-30%	- 1 pt	4 %	3 %
FOR435 Vapour phase	△:	- 19,2%	- 42,2%	-27,2%	- 8 pt	18 %	23 %
		Modulus	Yield P.	B.S. Max	Break E.		
		Mpa	Mpa	Mpa	%		
LPDE Vapour phase	△:	- 4,7%	0,0%	- 11,9%	-8,1%	2 %	1 %



**Figure 6 – Effect of C/F ratio on photoresist selectivity**

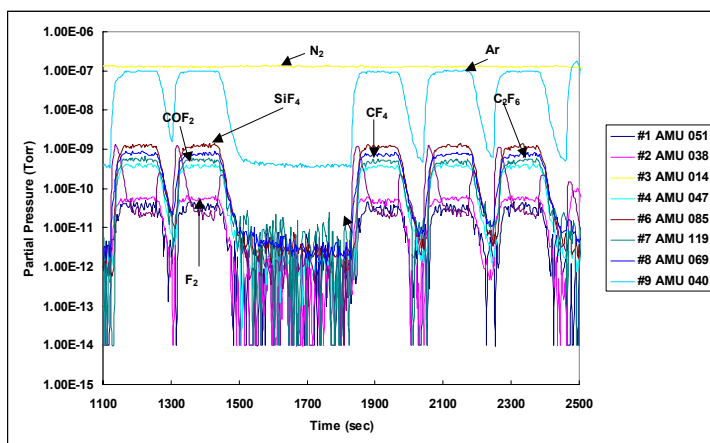


**Figure 7 – SEM cross-sections of 180nm FSG via (a) before and (b) after photoresist strip, (c) a 100nm HAR contact (patterned using 193nm photoresist, AR ~13), (d) a self-aligned contact showing high nitride corner selectivity, and (e) 180nm oxide hardmask (AR ~4.5:1), using C<sub>4</sub>F<sub>6</sub> based processes.**



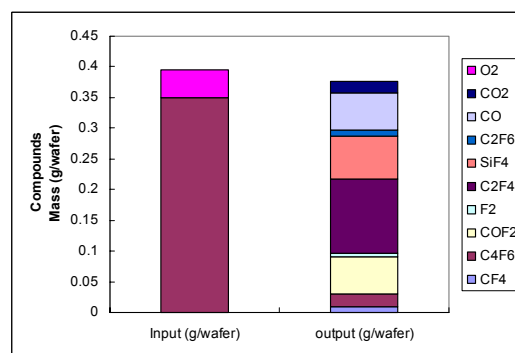
**Figure 8 – Typical FTIR spectra collected during breakdown efficiency analysis of C<sub>4</sub>F<sub>6</sub>.**





**Figure 9** – Time resolved QMS response recorded during FSG DD Via etch.

Emission Compounds	Volume (scc)	Equivalent Halide	Mass (g/wafer)	Breakdown Efficiency (%)	F Volume Closure (%)
C4F6 IN	48	288	0.35	94	88
O2 IN	32	NA	0.045		
C4F6 OUT	2.88	17.28	0.02		
CF4	1.5	6	0.01		
C2F6	1.76	10.56	0.01		
C2F4	27.78	111.12	0.12		
COF2	21.51	43.02	0.06		
F2	4.08	8.16	6.92E-03		
SiF4	14.02	56.08	0.07		
CO	47.2	NA	0.06		
CO2	7.84	NA	0.02		
Overall Emission	128.57	252.22	0.37		



**Figure 10** – Mass of products and emissions.

**Table 2:** Summary of Emission Data from FTIR and QMS Measurements for a C<sub>4</sub>F<sub>6</sub>/O<sub>2</sub>/Ar FSG DD via Etch Process in Applied Materials' Dielectric Etch eMAX™ Chamber.

# **A fast model for the thermal history of particle under plasma conditions**

Pateyron B., Delluc G., ElGanaoui M., Fauchais P.

Sciences des Procédés Céramiques et Traitements de Surface (SPCTS), CNRS UMR 6638, Faculté des Sciences, 123  
avenue Albert Thomas 87060 Limoges Cedex.

In this part the forecast of the temperature history with heat propagation of a particle within a d.c. plasma jet is studied. A very fast numerical treatment is needed to avoid a time penalization of the model. Here a rough integral method is presented allowing to compute the particle temperature field in the case of a quick change of the boundary condition with the time.

The average heat in the particle is conserved (Karman-Pohlhausen's hypothesis). The solution is searched for the geometry of a semi infinite wall of thickness  $\delta(t)$  changing with the time  $t$ . The same method allows the forecast of the melting front position  $s(t)$ . A classical change of variable gives the solution in the spherical case.

# **Surface modification by a remote atmospheric glow discharge**

Eef Temmerman\*, Christophe Leys\*, Stefan Wiedmer\* and Jo Verschuren\*\*

*\* Department of Applied Physics, Ghent University, Rozier 44, B-9000 Ghent, Belgium*

*\*\* Department of Textiles, Ghent University, Technologiepark 9, B-9000 Ghent, Belgium*

A remote atmospheric pressure glow discharge is used for treatment of fabric and polymer foils. The envisaged plasma effect is an increase in the surface energy of the treated material, leading e.g. towards a better wettability or adhesion. In order to test the efficiency of the plasma treatment, some tests are performed that quantify the wettability of the treated samples. The samples, treated here, are PET-foil (polyethylene terephthalate) and silicone. For these materials, the surface energy is derived from the contact angle of small water droplets deposited on the surface. The results show that the surface energy is increased by the treatment and the increase is proportional to the treatment time.

# Alternating Current Glow Discharges in Air at Atmospheric Pressure

Y. Yang<sup>1</sup>, J.W. Proctor<sup>1</sup>, C. P. Garner<sup>1</sup>, D.W.Hoare<sup>2</sup>, J. E. Harry<sup>2</sup>

<sup>1</sup> *Wolfson School of Mechanical and Manufacturing Engineering,*

<sup>2</sup> *Department of Electronic and Electrical Engineering,  
Loughborough University, Loughborough, Leics. LE11 3TU, United Kingdom*

## Abstract

Stable atmospheric pressure glow discharges at up to 20kHz have been demonstrated. These homogenous glow discharges were distinguished from stable diffuse glow discharge stabilised with a dielectric barrier by their waveforms. The discharges were sustained between electrodes in a pin-to-plane configuration 3 to 22mm apart in static air. An array of glow discharges using multiple electrodes formed a dense plasma layer with electron densities greater than  $10^{17} \text{ m}^{-3}$  was obtained from a single supply. The impedance in series with the pin electrodes stabilises the glow discharge, prevents the glow-to-arc-transition, and enables the multiple discharges to be operated from a common power source.

## 1. Introduction

Atmospheric pressure glow discharges (APGD) and their applications for cold plasma processes have been studied extensively since the 1980s. There has been considerable interest in finding methods for efficiently producing large volume APGD with electron densities greater than  $10^{16} \text{ m}^{-3}$  in air and at gas temperatures below 2000K [1, 2]. One example is the APGD stabilised by dielectric barriers [3, 4]. APGD are homogeneous discharges in the sense that they have the same behaviour as a low-pressure glow discharge and are not the sum of a number of filaments [4]. The dielectric barrier controlled APGD can easily be stabilised in gases such as helium, nitrogen or gas mixtures, but is difficult to achieve in air at atmospheric pressure.

Gas flow stabilised APGD in air have been demonstrated [5], in which the plasma is cooled faster than the rate of growth of instabilities in the discharge. Prevention of the onset of instabilities near the cathode region is particularly important in order to avoid the glow-to-arc-transition. One of the methods that have been used to prevent the onset of the instabilities near the cathodes is by using multiple cathodes, which are separately stabilised [6].

Direct-current micro-hollow cathode discharges (MHCD) have also been used to stabilise APGD in air. The cathodes had small holes ( $\sim 200 \mu\text{m}$ ) that served as an externally controlled electron emitter by means of a third, positively biased electrode on the anode side of the MHCD [7]. By using this kind of external source the instabilities in the cathode fall region of the discharge can be reduced.

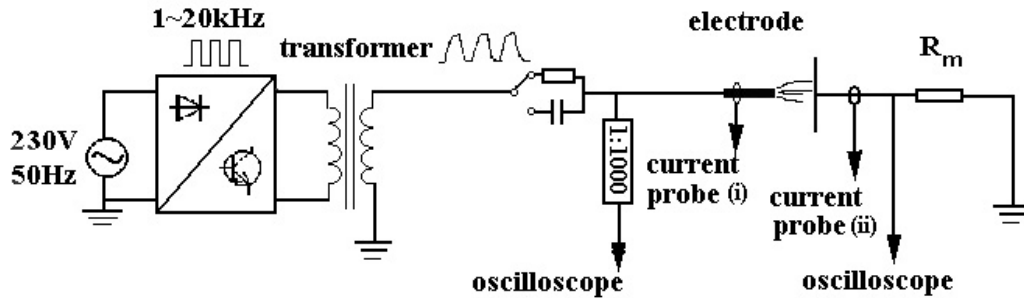
To stabilise APGD in air, the cathode area or the current cross section at the cathode should be reduced to as a small size as possible [8]. In a gas flow controlled APGD or micro-hollow cathode sustained APGD, the cathodes are composed of pins or small holes, and even in the dielectric barrier controlled APGD a mesh grid electrode is necessary [9]. The onset of bulk instabilities can also be prevented or delayed either by flowing gases or an external electron emitter.

In our previous studies [10], another type of APGD is introduced and stabilised by a ballasting resistor or capacitor. The alternating current APGD has been sustained in air at atmospheric pressure

by a 1~2kHz source [11, 12]. In this paper we show that the alternating current APGD can either be stabilised by resistors or capacitors at frequencies up to 20kHz. In addition, multiple pin glow discharges can be realised such that an array can be operated with a common power supply to produce non-equilibrium plasma with a large volume and high density.

## 2. Supply and Measurement Circuits

A diagram of the experimental arrangement is shown in Fig.1. The experiment was carried out in open air. A high voltage (1-10 kV) at a frequency between 1-20 kHz was applied between the two electrodes. The ballasting resistor  $R$  or capacitor  $C$  stabilise the glow discharge. A digital oscilloscope (500 MHz, 2 GS/s) was used to record the voltage and current signals. The current was measured by a grounded resistor in series with one electrode and with a probe with a rise time of less than 10ns. The current was measured by the current probe at the high voltage electrode or the ground electrode.



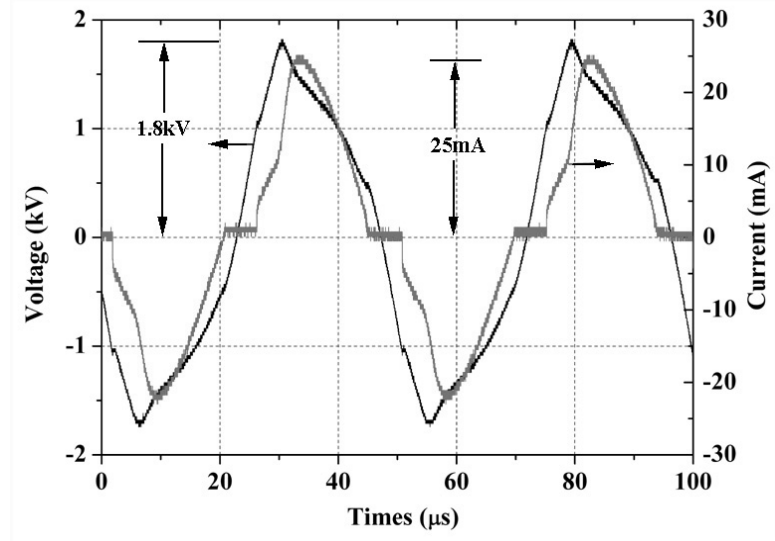
**Figure 1:** Circuit diagram

## 3. Results and Discussions

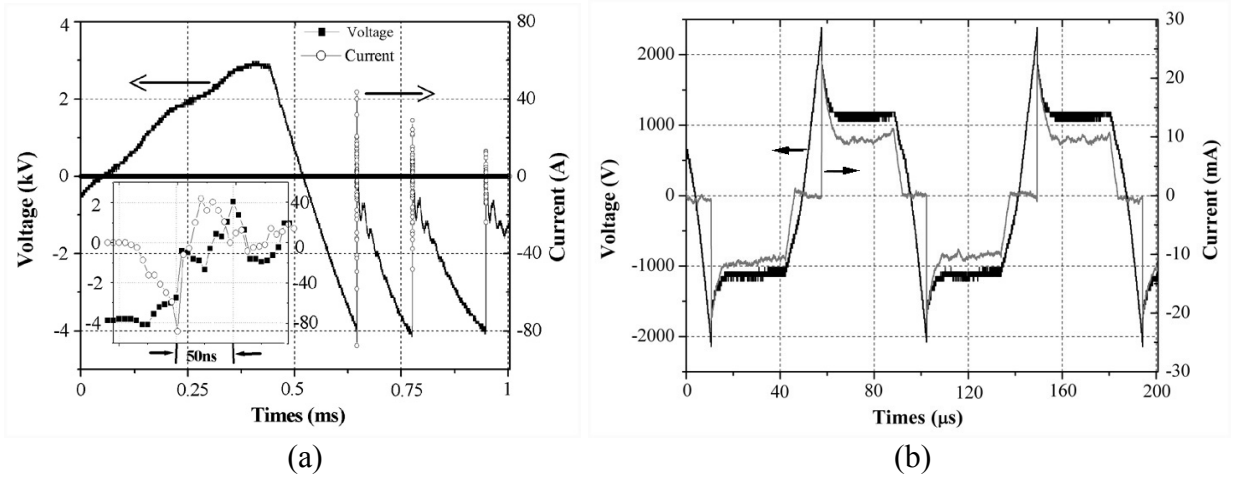
### 3.1 Electrical Characteristics

Figure 2 shows the voltage and current waveforms of the glow discharge at a frequency of 20 kHz in air at 1 bar. The discharges extend over the whole alternating-current cycle and no short rise time pulses exist, and appeared as a homogenous glow over the entire inter-electrode space. The value of the peak voltage is about 1.8kV and the peak current is about 25mA.

Figure 3(a) shows typical voltage and current waveforms of a corona discharge for comparison with Figure 2. The inset in the Figure 3(a) shows the voltage and current waveform of one pulse over 50ns. The corona discharge current is a short time pulse with a rise time of less than 50ns, reaching a peak value of more than 80A. In contrast, the current of glow discharge shows in Figure 2 is a smooth, pulse-free low current (10-25mA). The current waveforms of a glow discharges are also different from those of APGD stabilised by a dielectric barrier [4] in which the dielectric barrier stabilised APGP is a sequence of pulsed discharges, even in the diffuse mode.



**Figure 2:** Voltage and current waveforms of an alternating current glow discharge at a frequency of 20 kHz in air at 1 bar.



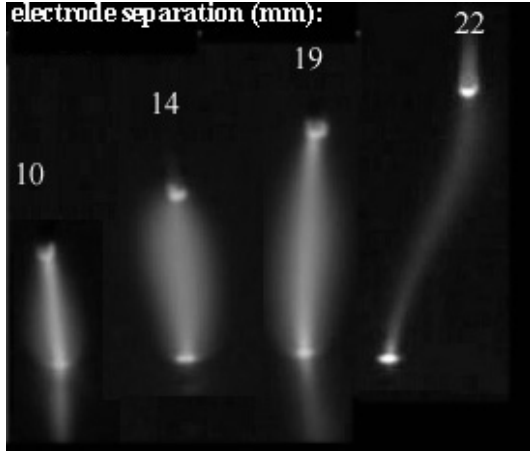
**Figure 3:** Voltage and current waveforms across the discharge corresponding to: (a) corona discharge; and (b) pseudo-glow discharge.

The glow discharge with the smooth current variations shown in Figure 2 changes to a discharge with current pulses. The transition depends on many factors such as the impedance of the ballasting resistor or capacitor (Fig.1), the distance between the electrodes, applied voltages and the surface temperature of the electrodes. We believe the surface temperature at the high voltage electrode, which can be varied by changing the applied voltages, is the most important factor. When the ballasting resistor or capacitor was absent and by adjusting the applied voltage and input power to low values that the surface temperature at the high voltage electrode was low, the plasma was normally the pulse-contained discharge. Typical waveforms of applied voltage and discharge current of these pulse-containing discharges in air at 1 bar are shown in Fig. 3(b). These discharges have features common to both filamentary and glow discharges. The current pulses are longer ( $\sim 50\mu\text{s}$ ) compared to the corona discharge of Fig. 3(a) ( $\sim 50\text{ns}$ ) and unlike the corona discharge a continuous waveform is observed. The pulse current is between 10 and 200 mA, compared with the corona discharge of Fig. 3(a) where the current pulses could reach up to 80A or more. These pulsed discharges refer to as pseudo-glow

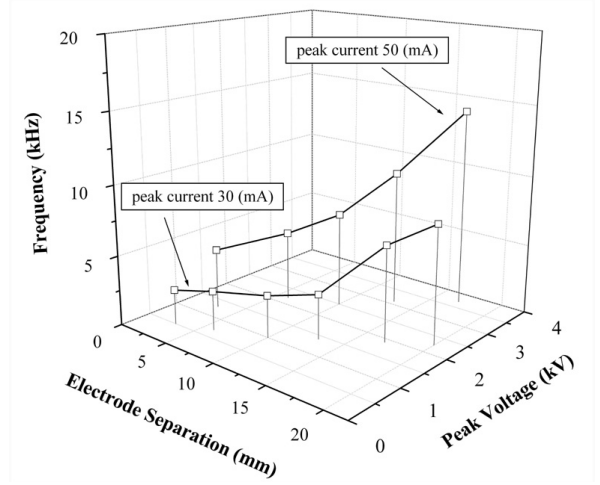
discharges have been studied in helium [13] where the discharges exhibited streamer, glow or pseudo-glow character.

### 3.2 Effect of Electrode Separation

The discharge length, in the case of a glow discharge with a peak voltage of about 3kV and 6.8W power input, extended up to 22mm as shown in Figure 4. The discharges change their shapes for the axial diameter when increase the electrode separation which is related to an increase in peak voltage. The variation of discharge voltage and frequency with electrode separations are shown in Figure 5.



**Fig.4:** Glow discharges stabilised at atmospheric pressure in air.



**Fig. 5:** Variation of discharge voltage with electrode separation and frequency.

### 3.3 Electron Density

The electron density  $n_e$  in this glow discharge can be estimated from the following equation:

$$n_e = j / (E \mu_e e) \quad (1)$$

where  $E$  is the electric field,  $j$  is the current density and  $\mu_e$  is the electron mobility. In air, at room temperature ( $T_0 \approx 300K$ ),  $\mu_e$  and pressure  $p$  have following relationship [14] :

$$(\mu_e p)_{300K} = 6.0 \times 10^4 \quad (\text{m}^2 \text{Pa/V s}) \quad (2)$$

Assuming that  $\mu_e p$  varies linearly with gas temperature  $T$ :

$$(\mu_e p)_T = \frac{T}{T_0} (\mu_e p)_{T_0} \quad (\text{m}^2 \text{Pa/V s}) \quad (3)$$

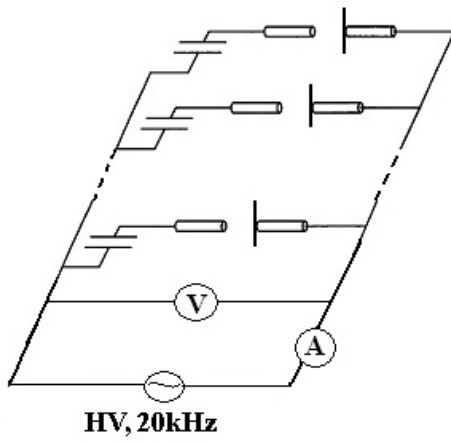
Assuming that the electric field in the discharge is given as the peak voltage divided by the electrode separation  $d$ , the peak value of voltage is about 1.8 kV,  $d \sim 10$  mm at a frequency of 20kHz, and the electric field  $E$  is  $1.8 \times 10^5$  V/m. At a peak value of current of 25 mA, the cross section of the discharge at the centre is about  $\pi \times (0.15 \times 10^{-2})^2 \approx 7.07 \times 10^{-6}$  m<sup>2</sup>, so that the current density  $j$  is about  $3.54 \times 10^5$  A/m<sup>2</sup>. Recent measurements of micro-hollow cathode sustained APGD showed that the gas temperature  $T$  in air glow discharges at currents of approximately 10mA is below 2000K [15]. For  $p = 1.0133 \times 10^5$  Pa and  $T = 2000K$ , the electron density from equations (1), (2) and (3) is about  $n_e \approx 3.1 \times 10^{17}$  m<sup>-3</sup>.

In our experiments, we used the brass electrodes as the high voltage electrode for which the melting point is 1232K. The discharge voltage and current are shown in Fig.2. The gas temperature was below

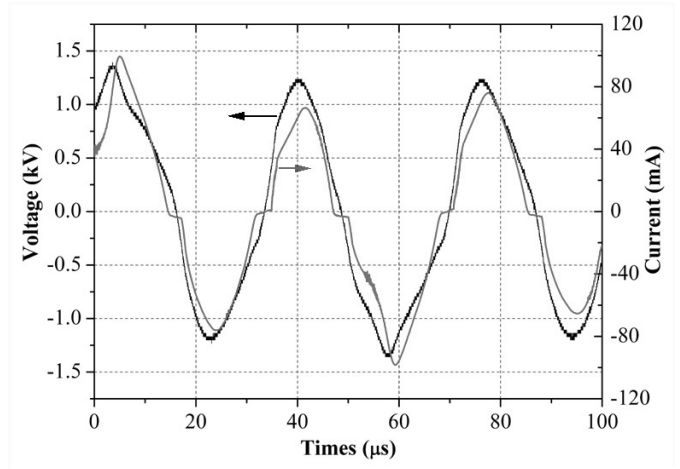
1232K otherwise the electrode would be melted at a peak current of about 25 mA. The electron density calculated by equations (1), (2) and (3) is about  $n_e \approx 5.1 \times 10^{17} \text{ m}^{-3}$  at gas temperature of 1232K.

### 3.4 Multiple Glow Discharges

It has been demonstrated that an array of glow discharges can be operated simultaneously to form a dense plasma in static air with a single ac power source. Fig. 6 shows the schematic diagram of an array of glow discharge modules sharing a common power supply and controlled by ballasting capacitors. Fig. 7 shows the waveforms of the total voltage and current of four discharges supplied by a single ac power source. The electric field  $E$  is about  $1.25 \times 10^5 \text{ V/m}$  and the current density  $j$  is about  $2.48 \times 10^5 \text{ A/m}^2$ . The electron density from equations (1), (2) and (3) is about  $n_e \approx 5 \times 10^{17} \text{ m}^{-3}$  at gas temperature of 1232K.



**Fig. 6:** Schematic diagram of an array of glow discharge modules sharing a common power source and controlled by ballasting capacitors.



**Fig. 7:** The total voltage and current waveforms of four glow discharges sharing a common power source.

The number of the glow discharges is only limited by the power of the supply. The capacitors work as stabilising circuit elements. Without them, the discharges cannot exist simultaneously when supplied by a single common source. This is because when one ignites; it tends to short out the voltage across all of the other electrode pairs connected in parallel. The capacitors also prevent the development of glow-to-arc transition.

### 4. Conclusions

Stabilisation of alternating current glow and pseudo-glow discharges has been studied in air at 1 bar using pin-to-plane or multi-pin electrode configurations at frequencies up to 20kHz. These non-equilibrium homogenous glow discharges, which can be distinguished from the stable diffuse glow discharges stabilised using a dielectric barrier, were sustained between closely spaced electrodes, but the separation could be extended to 22mm. The electron density was about  $5.1 \times 10^{17} \text{ m}^{-3}$  at a gas temperature of 1232K. An array of glow discharges using separated stabilised electrodes to form a dense plasma layer in the open air by a single ac power source with electron density greater than  $10^{17} \text{ m}^{-3}$  has been demonstrated. The resistors or capacitors in series with the pin electrodes stabilise the glow discharges. Large numbers of electrodes supplied from a single supply can be stabilised by



stabilising each discharge separately enabling electrode arrays to be increased only limited by the output of the supply. The alternating-current glow discharges may be applicable to applications such as waste-gas treatment, instantly activated reflectors and absorbers for electromagnetic radiation, surface treatment, and thin film deposition etc.

## Acknowledgment

We acknowledge the support of the UK Engineering and Physical Sciences Research Council (EPSRC).

## References

- [1] L.Yu, C.O.Laux, D.M.Packan and C.Kruger, *J. Appl. Phys.*, **91**, 2678-2686(2002).
- [2] E.E. Kunhardt, *IEEE Trans. Plasma Sci.*, **28**, 189-200(2000).
- [3] S.Okazaki, M.Kogoma, M.Uehara, and Y.Kimura, *J. Phys. D: Appl. Phys.*, **26**, 889-892(1993).
- [4] F.Massines, A.Rabehi, P.Decomps, R.B.Gadri, P.Segur, and C.Mayoux, *J. Appl. Phys.*, **83**, 2950-2957(1998).
- [5] Y.S.Akishev, A.A.Deryugin, A.P.Napartovich and N.I.Trushkin, *J. Phys. D: Appl. Phys.*, **26**, 1630-1637(1993).
- [6] J.E.Harry, and D.R.Evans, *J. Appl. Phys.*, **65**, 1363-1366(1988).
- [7] R.H.Stark and K.H.Schoenbach, *Appl. Phys. Lett.*, **74**(25), 3770-3772(1999).
- [8] A.A.Yahya and J.E.Harry, *Inter. J. Electronics*, **86**, 755 – 762(1999).
- [9] Y.Sawada, S.Ogawa, and M.Kogoma, *J. Phys. D: Appl. Phys.*, **28**, 1661-1669(1995).
- [10] J.E.Harry, R.D.Alcock and C.P.Garner, *15th International Symposium on Plasma Chemistry*, July 9-13, 2001, Orleans, France.
- [11] Y.Yang, *Ind. Eng. Chem. Res.*, **41**, 5918-5926(2002).
- [12] Y.Yang, *IEEE Trans. on plasma Sci.*, **31**(1), Feb. 2003, in press
- [13] R.Bartnikas, *J. Appl. Phys.*, **40**, 1974-1976(1969).
- [14] Y.P.Raizer, *Gas Discharge Physics*, Springer, Berlin, 1991, pp.11.
- [15] F.Leipold, R.H.Stark, A. El-Habachi and K.H.Schoenbach, *J. Phys. D: Appl. Phys.*, **33**, 2268-2273(2000).

# SIMULATION OF POSITIVE SHEATH NEAR ISOLATED SOLIDS AT LOW PRESSURE RF PLASMAS

I.Abdoullin<sup>1</sup>, L.Aboutalipova<sup>1</sup> and V.Jeltoukhine<sup>2</sup>

<sup>1</sup>Light Industries Department of Kazan State Technological University, Kazan, Russia

<sup>2</sup>Computing Mathematics Department of Kazan State University, Kazan, Russia

An isolated solid in RF plasmas like as added electrode under floating potential. Therefore, positive sheath features near the solid are defined by surface charge dynamics and interaction with quasineutral plasma around. Let us solid is a plane plate and its dimensions are much more than electron and ion free paths  $l_e$ ,  $l_i$  and Debye length  $\lambda_D$ . In this case, a mathematical model of RF plasmas near the solid at some  $l_{e,i}$  distance is described by following equations

$$\begin{aligned} -\frac{\partial}{\partial x} \left( \varepsilon \frac{\partial \varphi_{ch}}{\partial x} \right) &= \frac{e(n_i - n_e)}{\varepsilon_0} \\ \frac{\partial n_{e,i}}{\partial t} &= \frac{\partial}{\partial x} \left[ D_{e,i} \frac{\partial n_{e,i}}{\partial x} \pm e\mu_{e,i} \left( E - \frac{\partial \varphi_{ch}}{\partial x} \right) n_{e,i} \right] + \nu_i n_e \\ \frac{d\sigma_s}{dt} &= j_e - (1 + \gamma_i) j_i - j_{ae} \end{aligned}$$

Here  $x$  is the coordinate perpendicular to the surface;  $\varepsilon$ ,  $\varepsilon_0$  are relation permittivity and the electric constant,  $\varphi_{ch}$  is electrostatic potential,  $n_e$ ,  $n_i$  are electron and ion densities,  $D_{e,i}$ ,  $\mu_{e,i}$  are diffusion coefficients and mobilities,  $E(x, t) = E_a(x) \exp(i\omega t)$  is electrical intensity in quasi-neutral plasma,  $e$  is the electron charge,  $\nu_i$  is an ionisation frequency,  $\sigma_s$  is a surface charge density,  $\gamma_i$  is an ionic-electron emission coefficient,  $j_{ae}$  is an autoelectronic emission current,

$$j_{e,i} = -e \frac{D_{e,i}}{n_{e,i}} \frac{\partial n_{e,i}}{\partial x} \pm e\mu_{e,i} \left( E - \frac{\partial \varphi_{ch}}{\partial x} \right)$$

Initial and boundary conditions take into account of processes sheath-solid interaction, such as ionic-electron and cold emission.

Results of calculations show that an average ion energy  $E_i$  and ion density onto the surface  $j_i$  are achieved the following values in argon RF plasmas at  $p = 13.3 \div 133$  Pa, gas flow rate  $G = 0 \div 0.3$  g/s:

- $E_i = 10 \div 30$  eV and  $j_i = 15 \div 25$  A/m<sup>2</sup> in inductive coupled RF plasma jet at  $f = 1.76$  MHz, discharge power  $P_d = 1.0 \div 5.0$  kW, inductor draw current from 2.0 up to 6.0 A;
- $E_i = 30 \div 50$  eV and  $j_i = 3 \div 15$  A/m<sup>2</sup> in hybrid (both inductive and capacitive) coupled RF plasma jet at  $f = 1.76$  MHz, discharge power  $P_d = 0.8 \div 4.0$  kW, inductor draw current from 1.0 up to 3.0 A, added electrode voltage up to 200 V;
- $E_i = 50 \div 100$  eV,  $j_i = 0.15 \div 3.0$  A/m<sup>2</sup> in capacitive coupled RF argon plasma jet at  $f = 13.56$  MHz, discharge power  $P_d = 0.3 \div 3.5$  kW, electrode voltage from 150 up to 400 V.

# Atmospheric Pressure Alternating Current Glow Discharge – A Promising Method in Plasma Chemistry Process

Y. Yang<sup>1</sup>, J.W. Proctor<sup>1</sup>, C. P. Garner<sup>1</sup>, J. E. Harry<sup>2</sup>

<sup>1</sup> *Wolfson School of Mechanical and Manufacturing Engineering,  
Loughborough University, Loughborough, Leics. LE11 3TU, United Kingdom*

<sup>2</sup> *Department of Electronic and Electrical Engineering,  
Loughborough University, Loughborough, Leics. LE11 3TU, United Kingdom*

Atmospheric pressure alternating current glow discharge has been introduced in our previous study [1] by pin-to-plane or multi-pin configurations. In this report we now show that the operating frequency can be increased up to 20 kHz. The properties of the homogenous glow discharges are different from those of stable diffuse glow discharges using a dielectric barrier. The impedance of the resistors that in series with the pin electrodes was important to sustain the glow discharges and the transition of streamer-to-glow and pseudo-glow, but also acted as stabilise the multiple discharges. The energy input and the discharge properties of each pin glow discharges are easy to vary, and hence the control of the plasma chemistry is possible.

Our first example is the direct non-oxidative conversion of methane [2]. The glow discharge produces acetylene, ethylene and ethane in approximately equal quantities, while the pulse-contained pseudo-glow discharge is mainly selective to acetylene. The second example is CO<sub>2</sub> reforming and steam reforming of methane. With the multi-pin glow discharges the energy cost could below 120 MJ/kg of H<sub>2</sub>.

Further potential applications could be instantly activated reflectors and absorbers for electromagnetic radiation, remediation and detoxification of gaseous pollution, and surface treatment etc.

- [1] Y.Yang, Alternative current glow and pseudo-glow discharges in atmospheric pressure, *IEEE Trans. on Plasma Sci.*, Vol. 31, Feb., 2003, in press.
- [2] Y.Yang, Methane conversion and reforming by nonthermal plasma on pins, *Ind. Eng. Chem. Res.*, 41, 5918-5926(2003).

# Spectroscopic Observation of Low Pressure Plasma Deposition of Thin Silane and Siloxane Based Films

Zuzana Rašková, Hana Šormová, Iveta Havelková, František Krčma,  
Jan Vaněk, Radek Přikryl, Vladimír Čech

*Faculty of Chemistry, Brno University of Technology, Purkyňova 118, 612 00 Brno, Czech Republic,  
raskova@fch.vutbr.cz*

## Abstract

The main part of this work is focused on the identification of the spectra measured during the plasma deposition using the vinyltriethoxysilane in a continual regime and also in a pulsed regime with the varied relative pulse duration and during deposition with an amount of oxygen added in various ratios. The next part is focused on spectroscopic observation during the plasma deposition using the hexamethyldisiloxane and  $\gamma$ -metacryloxypropyltrimethoxysilane.

## Introduction

The plasma deposition of various thin films has been a subject of many studies during last years. The special focus is on the layers based on organic molecules and organo-silicone molecules. The study of the deposition process is currently at the first stage. Our experimental work focuses on the optical emission spectroscopy during the RF low-pressure discharge deposition of the organosilicone thin films. The discharge was studied in two different regimes. The first of them was continual, the other was pulsed with the relative pulse duration varied between 0.005 and 0.5 at the repeating frequency between 10 and 500 Hz. The main part of this work was focused on the identification of the spectra observed during the plasma deposition using the vinyltriethoxysilane, in the following section the focus was on spectroscopic observation during plasma deposition using the hexamethyldisiloxane and  $\gamma$ -metacryloxypropyltrimethoxysilane. Monomer structures as given in Fig.1.

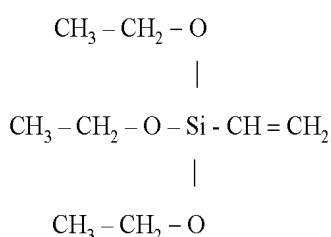


Fig. 1a: Vinyltriethoxysilane (VTEO)

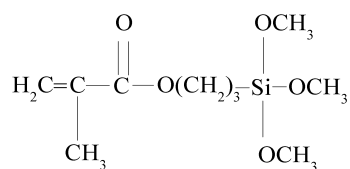


Fig. 1b:  $\gamma$ -metacryloxypropyltrimethoxysilane

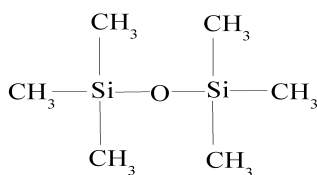


Fig. 1c: Hexamethyldisiloxane (HMDSO)

## Experimental part

A schematic diagram of the device for low-pressure plasma deposition is given in Fig. 2. As a plasma source the RF inductively coupled discharge was used. During the whole experiment gas pressure of 1-1,1 Pa was used. Argon and oxygen pipes are connected to the device. Argon is used only for purification of the reactor. The monomer is kept in the thermostat box so that the defined monomer pressure and its constant flow rate during the deposition process could be obtained. For optical emission spectra measurement a spectrometer Jobin Yvon Triax 550 with CCD detector was used.

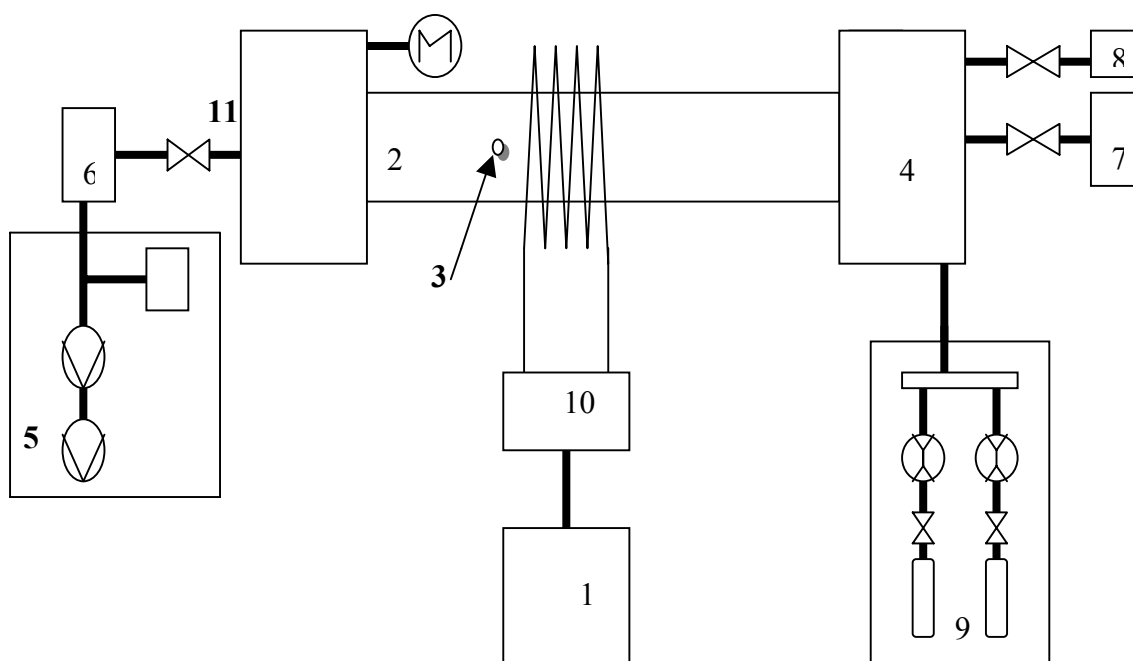


Fig.2: Scheme of the experimental device: 1-RF generator, 2-reactor, 3-point of the spectroscopic measurement, 4-supply, 5-vacuum system, 6-LN<sub>2</sub> trap, 7-monomer, 8-vacuum gauge, 9-gases (Ar, O<sub>2</sub>), 10-matching network, 11-driving force.

## Results

Initially, a small amount of nitrogen was added into the discharge to estimate the neutral gas temperature as a function of the total discharge power in the continual regime. Due to the low resolution of the nitrogen second positive spectra, our program *Simul* was applied [1]. The results show the rotational temperature of

( $400 \pm 50$ ) K, more or less independent of the total discharge power. Simultaneously the spectral system mentioned above was used for the vibrational temperature calculation.

This quantity was established at ( $2850 \pm 150$ ) K, also independent of the RF power.

The pure vinyltriethoxysilane was used in the first set of the experiments. The plasma composition was studied initially in the continual regime under the following experimental conditions: power was changed from 10 to 100 W, gas pressure was about 1 Pa, monomer flow rate 0,5 sccm. The emission of the hydrogen lines and molecular hydrogen bands was remarkably high each time. Besides, many bands with very complex structure originating from the same spectral system were observed, see Fig 3a. Some of them were identified [2] as the radiation of the  $\text{CH}_2\text{O}$  molecule. The bands of  $\text{CH}_2\text{O}$  were observed in the region from 380 to 522 nm. Some bands were observed at shorter wavelengths under 380 nm, no reference for them has been found up to now. Moreover, the CO bands (Angström system  $\text{B}^1\Sigma - \text{A}^1\Pi$  as well as much weaker Herzberg system  $\text{C}^1\Sigma - \text{A}^1\Pi$ ) were observed.

For the second part of our work the same experimental conditions were used and the pulse duration was changed from 1:1 to 1:999.

The spectrum obtained in the pulsed regime is shown in Fig 3a. It appears to be completely different from the non pulsed plasma, which was analysed as the first one. Among the bands corresponding to the  $\text{CH}_2\text{O}$  molecule could be recognised only some bands with very low intensity. On the other hand, a strong emission of the  $\text{C}_2$  Swan system ( $\text{A}^3\Pi_g - \text{X}^3\Pi_u$ ) was also observed. The intensities of both these bands are strongly dependent on the pulse duration. The hydrogen lines and molecular bands were also present in the other regime.

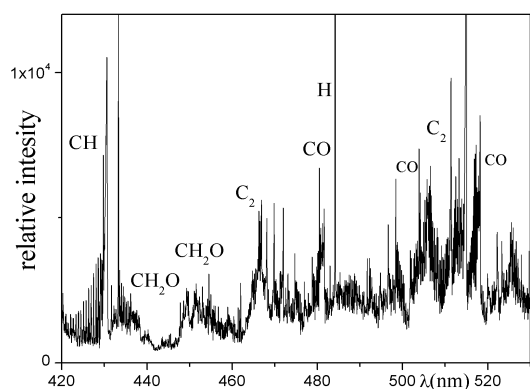


Fig. 3a: Optical emission spectrum obtained during measurement of plasma deposition using VTEO in pulsed regime (pulse duration 1:9)

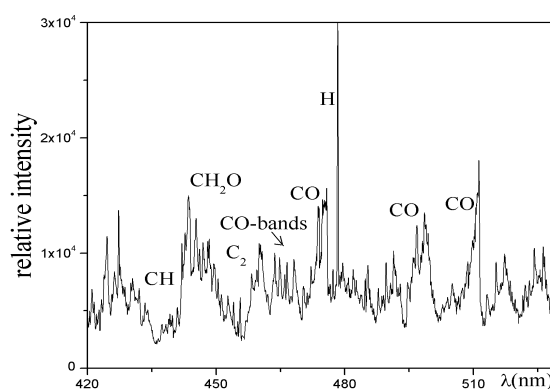


Fig.3b: Optical emission spectrum obtained during measurement of plasma deposition using VTEO in continual regime.

These results led to the idea to measure the dependence of the  $\text{C}_2$  and  $\text{CH}_2\text{O}$  band intensities as a function of the pulse duration. The results of these observations are shown in Fig. 4.

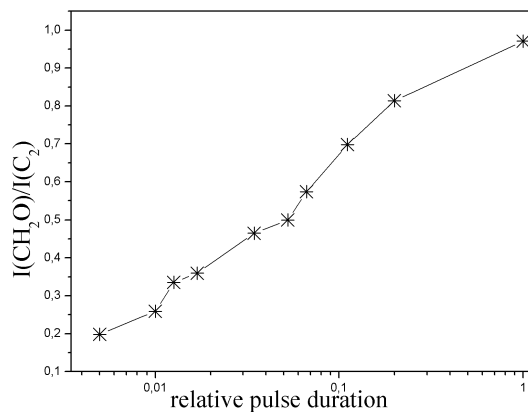


Fig. 4: Dependence of the  $\text{CH}_2\text{O}$  band intensity related to the  $\text{C}_2$  band intensity as a function of the relative pulse duration.

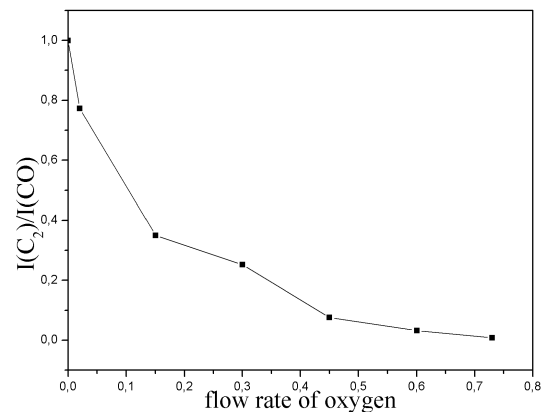


Fig. 5: Dependence of the  $\text{C}_2$  band intensity related to the  $\text{CO}$  band intensity as a function of the oxygen flow rate.

The second part of this work was focused on spectroscopic observations during the plasma deposition using the vinyltriethoxysilane monomer with various oxygen additions. This deposition was carried out in the pulsed regime (with pulses 1:9) and under the gas pressure of about 1,1 Pa. Oxygen flow rate was changed from 0,02 sccm (partial pressure of oxygen was 0,093 Pa) to 0,73 sccm.

The same spectral bands were identified during this experiment but the intensity of the spectral bands of  $\text{CO}$  was stronger. Thus, these bands can be observed in many other spectral regions than before. The  $\text{CO}$  band intensities, in accordance with our estimations, increase with the increase of oxygen addition, whereas the intensities of  $\text{CH}_2\text{O}$  and  $\text{C}_2$  spectral bands were decreasing with the increase of the amount of oxygen.

Furthermore, hexamethyldisiloxane and  $\gamma$ -metacryloxypropyltrimethoxysilane were used for plasma deposition in the continual regime and especially in the pulsed regime. Experimental conditions were the same as during the first part of the experiment. During the spectroscopic observations we have found out that lines and bands of hydrogen ( $\text{H}$ ,  $\text{H}_2$ ) and  $\text{CH}$  band (Angström system  $\text{A}^2\Delta - \text{X}^2\Pi$ ) were the most intensive ones in both regimes. In the spectra measured during the plasma deposition using hexamethyldisiloxane in pulsed regime, bands of  $\text{CO}^+$  (first negative system  $\text{B}^2\Sigma - \text{X}^2\Sigma$ ) and bands of  $\text{CO}$  in the region of 450 – 500 nm the bands appeared in considerable intensities. The ratio of the relative intensity of  $\text{CO}^+$  to total intensity of the spectrum increased with the decreasing pulse duration (Fig. 6).

When using  $\gamma$ -metacryloxypropyltrimethoxysilane for plasma deposition, besides hydrogen ( $\text{H}$ ,  $\text{H}_2$ ) and  $\text{CH}$  bands, many bands of  $\text{CO}$  (Angström system  $\text{B}^1\Sigma - \text{A}^1\Pi$  and triplet bands ( $\text{d}^3\Delta - \text{a}^3\Pi$ ) and bands of  $\text{C}_3$  ( $^1\Pi_u - ^1\Sigma_g^+$ ) were observed.

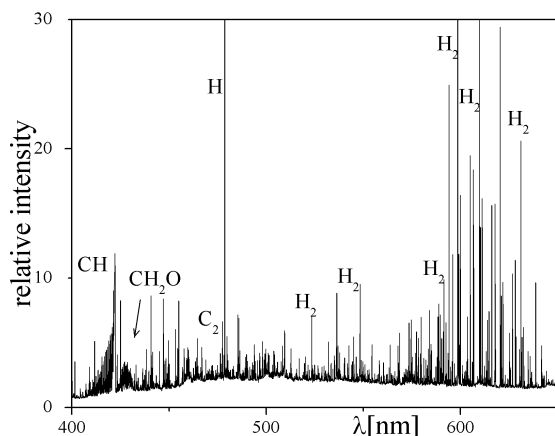


Fig.5a: Optical emission spectrum obtained during measurement of plasma deposition using HMDSO in continual regime.

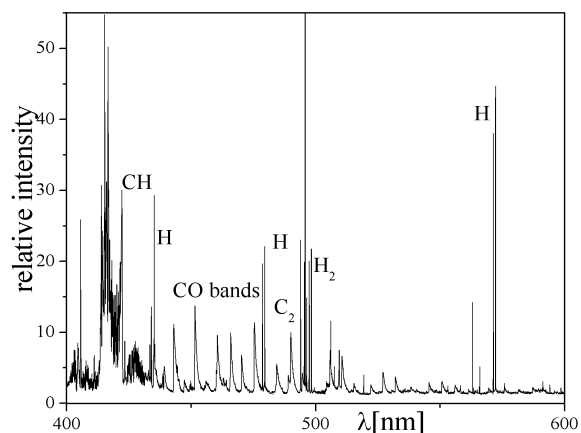


Fig.5b: Optical emission spectrum obtained during measurement of plasma deposition using HMDSO in pulsed regime.

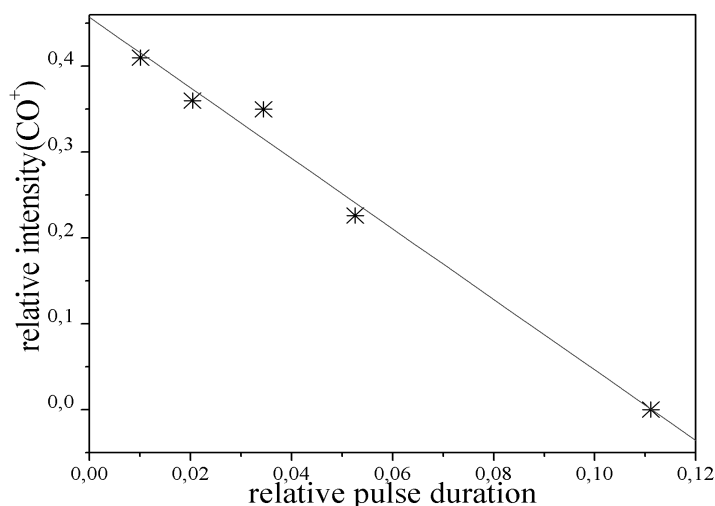


Fig.6: Dependence of the CO<sup>+</sup> band intensity as a function of relative pulse duration.

## Conclusions

In our work we studied the plasma deposition process of the organosilicone thin layers by the emission spectroscopy. A dependence of the CH<sub>2</sub>O band intensity related to C<sub>2</sub> as a function of the pulse duration shows that the character of optical spectrum approaches to the continual regime with increasing energy (increasing relative pulse duration). On the other hand, more C<sub>2</sub> bands in higher intensity appear in the spectrum with the shorter pulse duration. It is probably caused by the elimination of the vinyl group from the molecule of monomer. Intensities of the CH<sub>2</sub>O and CO bands grow much weaker with shorter pulse duration. In the case of the long pulse duration it is possible to expect the preferential elimination of the ethoxy group. From the optical emission



spectra measured during the plasma deposition using vinyltriethoxysilane with various amount of oxygen, a significant oxidation of all the components can be observed through the increase of the CO band intensity and decrease of the CH<sub>2</sub>O and C<sub>2</sub> spectral bands. Spectroscopic observations of plasma deposition using hexamethyldisiloxane show strong increase of the relative intensity of the CO bands and CO<sup>+</sup> bands in case of pulsed regime.

Oxygen could be eliminated from Si-O-Si bonds. Collisions and combination with carbon from CH<sub>3</sub> groups are probable and growth of the Si-H and CO bonds is presumable in the plasma. Due to the appearance of C<sub>2</sub> and C<sub>3</sub> bands in the emission spectrum, we can suppose also CH<sub>2</sub> and CH<sub>3</sub> or Si-CH<sub>3</sub> groups in primary state.

As for spectroscopic measurements during deposition using  $\gamma$ -metacryloxypropyltrimethoxysilane, it was found out that there was not a considerable difference between continual regime and pulsed regime. The lines of hydrogen, CH<sub>2</sub>O, C<sub>3</sub> bands and CO bands were very intensive in the spectrum.

The results obtained by the emission spectroscopy correspond with physical properties of the prepared layers [3]. The dependence of the layer properties on the plasma conditions will be a subject of further experiments as well as creating the appropriate kinetic model of the plasma processes during plasma depositions.

### Acknowledgements

This work was supported by the COST grants No. OC 527.110 and ME 597, by Research Programme of the Czech Ministry of Education No. CEZ:J07/98:1431000019, and by the Czech Ministry of Education, grant contract No. 0895/2003.

### References

- [1] Krčma F., Hajduchová H.: *Proc. 13<sup>th</sup> SAPP*, 52-53, Tále 2001
- [2] Pearse R. W. B., Gaydon A. G.: *The Identification of Molecular Spectra*, John Wiley, London 1976
- [3] Bálková R., Přikryl R., Grycová A., Vaněk J., Čech V.: *Czech. J. Phys.* **52** (2002) D807

# Experimental study of ozone synthesis in atmospheric pressure needle-to-plane gas discharge

V. Golota, B. Kadolin, V. Karas', I. Paschenko, S. Pugach and A. Yakovlev

*Department of Non-equilibrium Low-temperature Plasma Chemistry, National Science Center "Kharkov Institute of Physics and Technology", Kharkov, Ukraine*

## Abstract

The research of negative, positive coronas and also a non-stationary streamer discharge was carried out. The  $O_3$  synthesis, emission spectrums of NO and atomic oxygen O on wave length 777,1 nm were investigated experimentally. The concept of ozone synthesis in atmospheric pressure gas discharge was offered.

## 1. Introduction

Most industrial ozone generators are the classical DBD setups. However, recently, attention is also attracted to ozone generators on high-pressure needle-to-plane gas discharge.

As is well known the basic reaction of ozone synthesis is  $O_2 + O + M \rightarrow O_3 + M$ . The concentrations of  $O_2$  and M set by feeding gas composition. The main task is increasing of O generation efficiency, i.e. increasing of  $O_2$  dissociation rate.

Electron energy distribution defines the dominant dissociative processes. Thus, it is possible to attempt to adjust discharge parameters with the purpose of effective generation of atomic oxygen, and therefore synthesis of ozone, if the chain of  $O_2$  dissociation processes is known.

Non-stationary streamer discharge (SD), positive (PC) and negative (NC) coronas in the needle-to-plane electrode geometry was experimentally investigated. The analyses of peculiarities and similarity of physical processes of these discharges will allow determining the mechanism of dissociation  $O_2$ .

## 2. Experiment

The needle-to-plane electrode system was located in the hermetically sealed chamber with controlled air feeding (1 l/min). The air pressure was atmospheric. There was a possibility to apply to needle-electrode both positive and negative DC voltages. There was a quartz window in the chamber for registration of a radiation spectrum of discharge. There was no possibility to control O concentration. Therefore we observed the discharge byproducts such as  $O_3$  and NO, and also radiation of atomic oxygen O at wavelength 777,1 nm.

The type of the discharge was determined from nature of a current signal by fast current probe and oscilloscope Tektronix TDS-210.

Ozone concentration was measured at the output of the discharge chamber by absorption at wavelength 253,7 nm (cross-section -  $\sigma_{O_3}=1155 \cdot 10^{-20}$  sm<sup>2</sup>/mole) using monochromator MDR-12U and FEM-39A.

For all three type of the discharge the radiation spectrums were registered over the range of wavelengths 200 – 800 nm using monochromator MDR-12U with gitter 1200 grating grooves per mm and by FEM-39A, FEM-79A.

## 3. Results

First of all it's necessary to look into physical processes which are distinctive for each of considered types of the discharge.

**Trichel pulses mode of negative corona.** The charged particles appear only at a short distance from needle-electrode (zone of generation), where there is a strong electric field ( $\geq 115$  Td in air). In these fields the cross-section of ionization becomes larger than cross-section of attachment of conduction electrons to  $O_2$  molecules. In the rest part of the discharge channel the current is provided by ions. The current in a drift space of corona discharge is non-self-maintained discharge; the gas there is not ionized and is not excited.

The reason of the non-stationary effects (Trichel pulses) in a negative corona is explained by electronegativity of gas. In electropositive gases the Trichel pulses are not discovered. In air the conduction electrons move away from the needle in direction of decreasing electric field strength and attach to  $O_2$  molecules. The space charge of negative ions weakens an external field, ionization and current damp [1].

**Positive corona.** Stationarity of positive corona is determined by Townsend ionization only in region where  $E/N \geq 115 \text{ Td}$  ( $E$  - electric field strength,  $N$  – gas density). The conduction electrons, appeared in a zone of generation, move in direction of increasing electric field strength and processes of attachment are not effective.

It is possible to conclude that the basic difference of negative and positive coronas is the availability of large density of negative ions in the first one and practical absence of it in the second.

**Non-stationary streamer discharge.** This type of gas discharge exists only in electronegative gases. The streamer appears in zone of generation near an anode surface and propagates through a gap to the cathode due to secondary ionization processes (photoionization). According to criterion of avalanche-to-streamer transition [1, 2, 3] positively charged head of a streamer should maintain processes, at which it was formed, and provide conditions for requisite level of photoionization. Thus the processes of electron attachment practically do not take place before and inside the head of a streamer. The head of a streamer and anode are linked by the quasineutral channel, electric field strength in which is not enough for ionization. Electrons coming from a region with large electric field ( $E/N \sim 1000 \text{ Td}$  [3]) of a streamer head partially attach to the  $\text{O}_2$  molecules inside a streamer channel. The processes of attachment not only enable existence of non-stationary streamer discharge, but also, as well as in case of negative corona, cause a series of its peculiarities, such as secondary wave of ionization [4].

The analysis of results of numerous experiments and analytical investigations has allowed to draw a conclusion, that in zones of generation of positive and negative coronas, and also in the streamer head the same processes occur. The differences can be only quantitative. The basic differences for these types of discharges are outside ionization zones. It is significance of attachment processes in negative corona and non-stationary streamer discharge and practical absence of negative ions in positive corona.

**Results of the present investigation.** For all three types of discharges the voltage-current characteristics with simultaneous monitoring of  $\text{O}_3$  concentration were measured. The obtained dependences are represented at fig. 1.

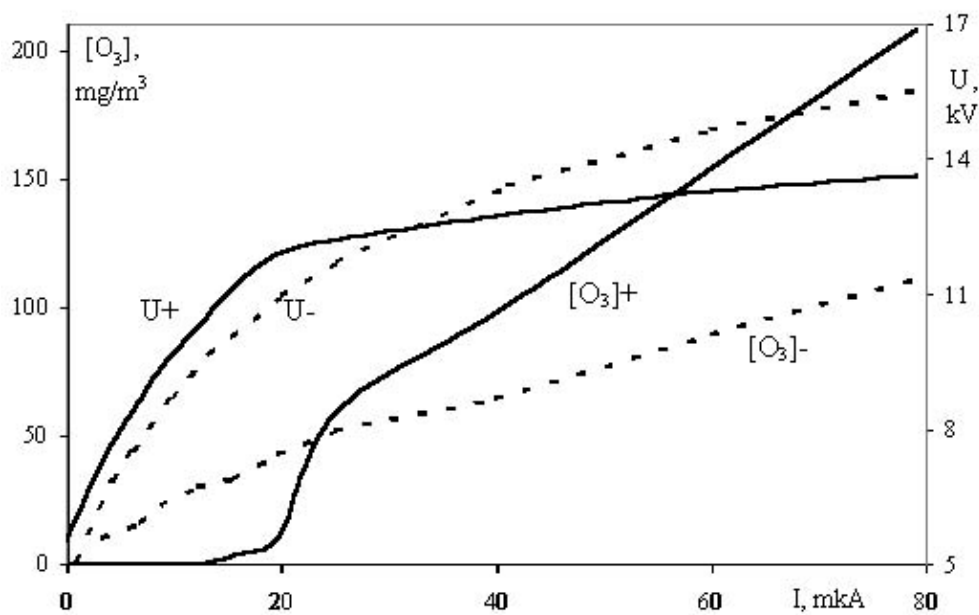


Fig. 1. V-I characteristic and  $\text{O}_3$  concentration for the positive potential on the needle. Solid lines – positive potential at the needle, dotted lines – negative potential at the needle.

It is possible to observe the abrupt change on the current-voltage characteristic. This point separates the positive corona and non-stationary streamer discharge [5].

The radiation spectrums in a wave band  $200 \div 300 \text{ nm}$  were obtained with the purpose to register the  $\gamma\text{-NO}$  band (fig. 2) for all three types of discharge.

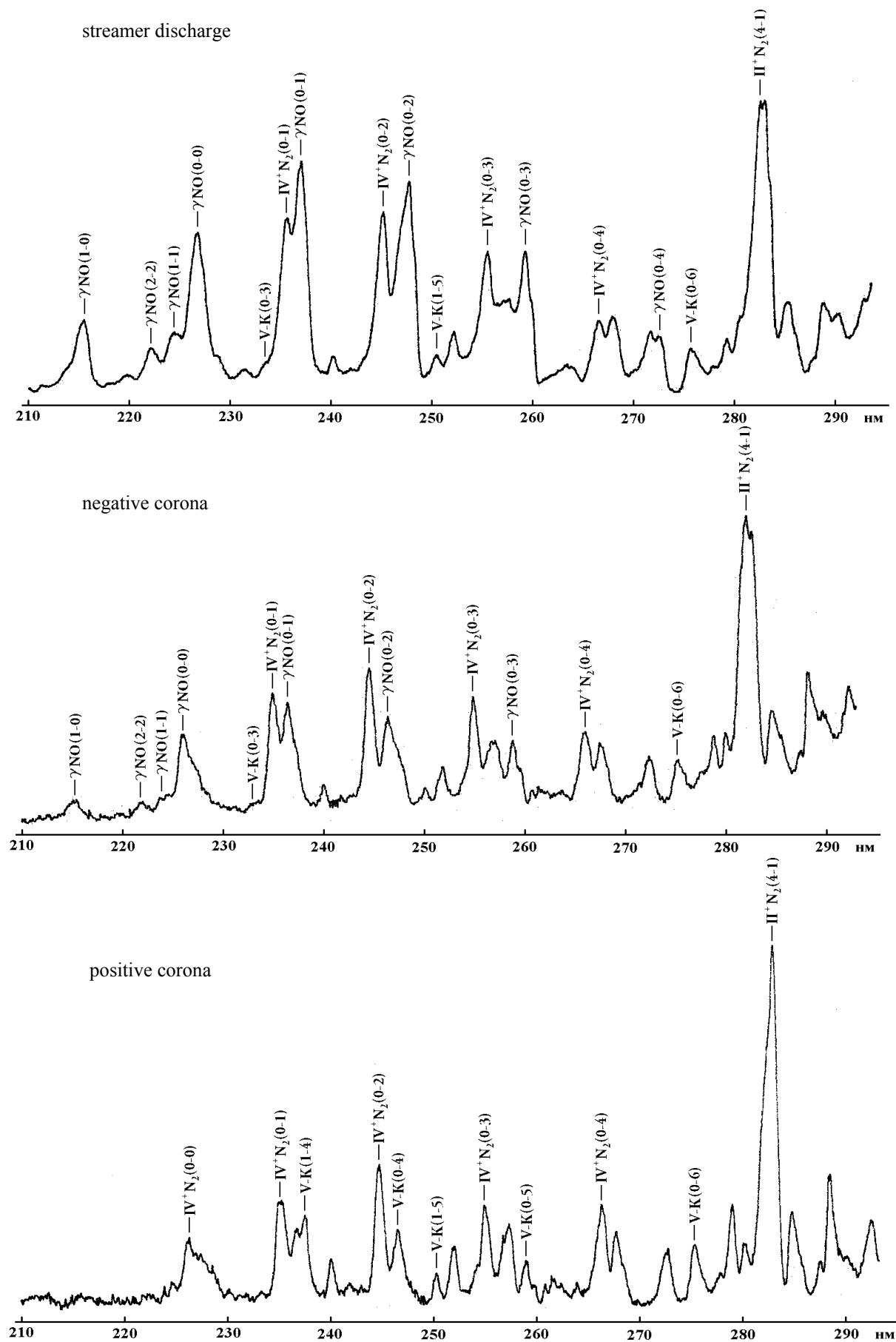


Fig. 2. Discharge radiation spectrum.

Some of the experimental and analytical results of physical processes of non-stationary streamer discharge, positive and negative coronas are presented in the table 1. Column 1 of this table is a power consumption  $w$  for ozone synthesis in SD, PC and NC normalized on power consumption of SD  $w_{sd}$ . Also, the ratios of  $\gamma$ -NO (0-1) intensity to intensity of  $IV^+ N_2$  (0-1) ( $I_{\gamma NO(0-1)}/I_{IV^+ N_2(0-1)}$ ) and O-radiation (777,1 nm) intensity to  $II^+ N_2$  (0-3) intensity  $I_{O(777.1)}/I_{II^+ N_2(0-3)}$  are presented in Columns 2 and 3 respectively. The Column 4 of the table explains the role of negative ions for SD, PC and NC.

Table 1. Experimental results.

	1	2	3	4
	$\frac{w}{w_{sd}}$	$\frac{I_{\gamma NO(0-1)}}{I_{IV^+ N_2(0-1)}}$	$\frac{I_{O(777.1)}}{I_{II^+ N_2(0-3)}}$	Negative ions
SD	1	1.32	0.2	This mode is controlled by negative ions
NC	~2	0.91	0.1	Negative ions determine pulse regime
PC	>10	≈0	0.03	Negative ions practically are absent

#### 4. Concept

Rigorous correlation between availability in discharge of negative ions, i.e. processes of attachment, with availability (or signs) of dissociative processes products may be observed (table 1). Thus, it is possible to conclude that the main channels of atomic oxygen generation are the processes from the table 2.

Table 2. The main dissociative processes.

№	Process	Threshold, eV	Ref.
1	$O_2 + e \rightarrow O^- + O$	4.2	[6]
2	$O_2 + e \rightarrow O + O + e$	5.58	[7]
3	$O_2 + e \rightarrow O + O(^1D) + e$	8.4	[8]

It is possible to draw a conclusion, that the processes of ionization and  $O_2$  dissociation are separated in time and/or in space, and the atomic oxygen density can not be more then electron density in the current channel.

So, the effective dissociative processes must be realized in two stages. In the first one the required level of ionization in the streamer channel can be reached by reduced electric field 1000 Td and more. In the second one the reduced electric field must quickly decrease to the value ~100 Td where processes from the table 2 effectively occur. The special shape of power pulse can optimize these conditions as against the DC power supply.

The present concept has allowed us to elaborate the ozone generator at non-stationary streamer discharge with following parameters:  $O_3$  concentration - 2÷5 %, power consumption - 8÷13 Wh/g $O_3$ , feeding gas – 20 %  $N_2$  + 80 %  $O_2$ .

This work was supported by Science and Technology Center in Ukraine (projects № 2144, 1069).

#### References

- [1] L. Leeb - Basic processes of electrical discharges in gases. Moscow: "Gostechteoretizdat", 1950 (in Rus.)
- [2] Yu.P. Rajzer - Gas discharge physics Moscow: "Nauka", 1987 (in Rus.)
- [3] E.M. Bazelyan, Yu.P. Rajzer – Spark discharge, MSU, 1997 (in Rus.)
- [4] R.S. Sigmond - J.Appl.Phys. 1984. V.56. N.5. P.1355.
- [5] A.A. Bruev, V.I. Golota, L.M. Zavada, B.B. Kadolin, V.I. Karas', I.A. Paschenko, S.G. Pugach - Problems of Atomic Science and Technology, 1 (2000) 50-53.
- [6] D. Rapp, P. Englander-Golden, J. Chem. Phys., 43 (1965), 1464.
- [7] K. Klopovsky, T. Rakhimova, Moscow State University, private comm. 1994.
- [8] B. Eliasson, U. Kogelschatz, Asea Brown Boveri Forschungszentrum CH-5405, Baden, KLR 86-11C, June. 1986.

# INVESTIGATIONS OF NON-STATIONARY MODES OF NEEDLE-TO-PLANE GAS DISCHARGE AND STREAMER PROPAGATION AT ATMOSPHERIC PRESSURE

V. Golota, L. Zavada, B. Kadolin, V. Karas<sup>\*</sup>, I. Paschenko, S. Pugach and A. Yakovlev

*National Science Center "Kharkov Institute of Physics and Technology",  
Akademicheskaya St. 1, Kharkov 61108, Ukraine*

## 1. Introduction

The purpose of the given work was investigation of non-stationary modes of needle-to-plane gas discharge at atmospheric pressure and streamer propagation. The instantaneous values of a current signal and optical signal from different areas of an inter-electrode gap for different oxygen-contained gas mixtures (dried air, ambient air, oxygen) were studied.

## 2. Experiment

The needle-to-plane electrode system was located in the hermetically sealed chamber (1 dm<sup>3</sup>) with controlled air feeding. The chamber pressure was equal to atmospheric. The positive DC voltage was applied to the needle electrode.

The light-tight shield with 1 mm slit, which disposed transverse to the streamer channel, covered quartz window of the chamber. This slit allowed to register a radiation from a specified area of a discharge gap.

## 3. Results

The analysis of the oscillograms of both a discharge current and optical signals has allowed to sort the non-stationary streamer discharge into two modes: first non-stationary mode - streamer do not reach the cathode (BC portion of the VAC from fig. 1) and second nonstationary mode - full locking of the gap by the streamer channel (osc. 4 and 5, fig. 2; CD portion of the VAC from fig. 1).

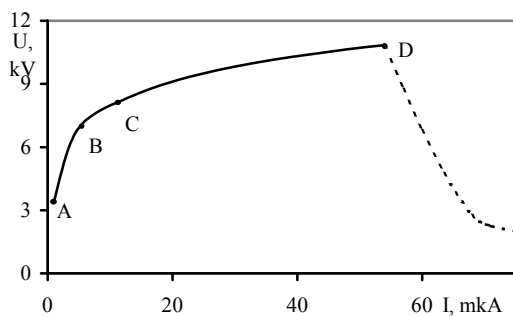


Fig. 1. The typical volt-ampere characteristic (VAC) of atmospheric pressure needle-to-plane gas discharge. AB – stationary mode (positive corona), BD – non-stationary streamer discharge, BC - streamers do not reach the cathode, CD – full locking of the gap by the streamer channel.

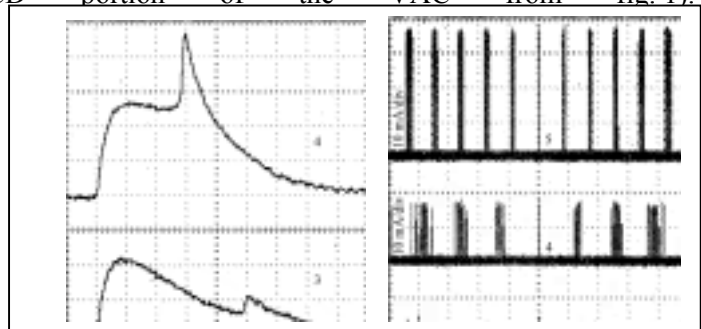


Fig.2. The typical oscillogramms of discharge current pulses in ambient air (inter-electrode gap is 11 mm)

- 3 -  $U=6.2$  kV,  $I_{av}=3.8$   $\mu$ A;
- 4 -  $U=6.4$  kV,  $I_{av}=4.2$   $\mu$ A;
- 5 -  $U=11$  kV,  $I_{av}=50$   $\mu$ A.

These two non-stationary modes of discharge are distinguished by the physical processes. In comparison with the first non-stationary mode in the second one the following features are existed: 1) the propagation of a secondary ionization wave after locking of inter-electrode gap by a streamer; 2) influence of a field emission on current dynamics and rate of streamer propagation near the cathode. Besides the discontinuous change of repetition frequency of current pulses was observed at mode crossover.

The dependence of streamer propagation rate vs. location of its head in the gap was obtained from analysis of optical signals. Near electrodes the streamer propagation rate increased, and in middle of the gap it tends to diminish. Notice that for different oxygen-contained gas mixtures (oxygen, dried and ambient air) the current pulse parameters and also dynamics of a streamer propagation were very different (e.g., streamer repetition frequency in oxygen was  $\sim 100$  kHz, while in ambient air it was  $\sim 10$  kHz).

This work was partially supported by Science and Technology Center in Ukraine (project №1069).

# Evaluation of Ceramic Spraying Process by Computational Experiment

Takehiko Sato<sup>1</sup>, Oleg P. Solonenko<sup>2</sup> and Hideya Nishiyama<sup>1</sup>

<sup>1</sup>*Institute of Fluid Science, Tohoku University, Japan*

<sup>2</sup>*Inst. Theoretical and Applied Mechanics Sib. Br., Russian Academy of Sciences, Russia*

## Abstract

A plasma spraying process from a ceramic particle injection to a coating formation was evaluated computationally by integrating a particle-laden plasma flow, splat formation and coating formation models. Since the plasma flow is unsteady, radial distributions of a particle impact temperature and the particle impinging point are obtained. The particle impact temperature is increased effectively by applying an RF electromagnetic field. Furthermore, a coating thickness distribution is strongly influenced by particle size and RF electromagnetic field.

## 1. Introduction

Plasma is regarded as a multifunctional fluid, because it has high energy density, chemical reactivity and variable transport properties. Therefore, plasma spraying has been widely utilized to produce thermal barrier coating (TBC) and chemical reactive coating. However, it has very complex particle-laden thermofluid field in extreme conditions [1, 2]. Since experimental study is difficult to obtain the optimum operating conditions, a computational experiment is supposed to be effective method for optimizing plasma spraying process. Characteristics of the particle-laden plasma flow have been investigated so far [3-8]. The deformation process of an impact molten droplet has also reported [9-15]. Then recently, a numerical simulation of plasma spraying processes from the particle injection to the coating formation has been reported [16]. A ceramic splat formation model has also been presented [17].

In the present study, the ceramic spraying process is evaluated by computational experiment. To achieve this, three numerical models are integrated. Particle velocity and temperature prior to impact on a substrate, which are the most important parameters for splat formation, are calculated by using the particle-laden plasma flow model. Splat thickness and diameter are calculated by using the ceramic splat formation model. Particle characteristics are simulated by using the particle-laden plasma flow model and substrate characteristics are given. Finally, coating thickness distributions are evaluated by the coating formation model.

## 2. Numerical Model

### 2.1 Particle-laden plasma flow model

Governing equations of a plasma flow, particle characteristics and an induction electromagnetic field are presented under the following assumptions.

(1) The DC plasma flow is treated only downstream of the arc region. (2) The plasma is a continuous, ideal gas in Local Thermodynamic Equilibrium (LTE) and is optically thin with variable thermodynamic and transport properties. (3) The flow, temperature and electromagnetic fields are two-dimensionally axisymmetric. (4) All injected particles are spheres with the same diameter, and the internal temperature is uniform because the temperature difference is 50 K at maximum when the particle diameter is smaller than 50  $\mu\text{m}$ . (5) Only drag force acts on the particles. (6) Collisions between particles are neglected due to the dilute particle-loading condition. (7) There is one-way coupling between the dispersed phase and the carrier phase. (8) The thermodynamic and transport properties of the solid particles are a function of particle temperature. (10) The nozzle and the chamber are electrically insulated. (11) The vector potential and the induction electric field have only an azimuthal component.

### Plasma flow

The Eulerian approach is adopted for the plasma flow which is governed by equations of continuity, momentum, energy and state [5, 8].

$$\left. \begin{aligned}
\frac{d\mathbf{r}}{dt} + \nabla \cdot (\mathbf{r}\mathbf{u}) &= 0 \\
\frac{\partial(\mathbf{u})}{\partial t} + \nabla \cdot (\mathbf{r}\mathbf{u}\mathbf{u}) &= -\nabla p + \nabla \cdot \mathbf{\bar{\bar{\tau}}} + \mathbf{F} \\
\frac{\partial}{\partial t} e + \nabla \cdot [(e + p)\mathbf{u}] &= \nabla \cdot (\mathbf{I}\nabla T) + \Phi_D + Q_j - Q_r \\
p &= \mathbf{r}RT
\end{aligned} \right\} \quad (1)$$

Here,  $\mathbf{F}$  is Lorentz force ( $\mathbf{j} \times \mathbf{B}$ ).  $e$ ,  $Q_j$  and  $\Phi_D$  are stagnant internal energy per unit volume, Joule heating ( $\mathbf{j} \cdot \mathbf{E}$ ) and dissipation loss, respectively.  $Q_r$  is radiation loss given by approximation curve fittings from the experimental radiation data [18].

In the equations for the plasma flow,  $\mathbf{u}$ ,  $p$ ,  $\mathbf{E}$ ,  $\mathbf{B}$ ,  $T$  and  $C_v$  represent plasma velocity, pressure, electric field intensity, magnetic flux density, plasma temperature and specific heat at constant volume, respectively.  $\mathbf{r}$ ,  $\mathbf{s}$ ,  $\mathbf{m}$  and  $\mathbf{I}$  represent density, electrical conductivity, viscosity and thermal conductivity, respectively.

#### Particle

The Lagrangian approach is adopted for the particle characteristics which are derived from the equations of motion and heat balance of a particle [5].

$$\left. \begin{aligned}
m_p \frac{d\mathbf{u}_p}{dt} &= \frac{\mathbf{p}}{8} d_p^2 \mathbf{r} C_{Df} (\mathbf{u} - \mathbf{u}_p) |\mathbf{u} - \mathbf{u}_p| \\
m_p c_p \frac{dT_p}{dt} &= \mathbf{p} d_p^2 [h_f (T_\infty - T_p) - \mathbf{e}_p \mathbf{s}_{SB} (T_p^4 - T_a^4)] (T_p < T_m \text{ and } T_m < T_p < T_b) \\
C_{Df} &= \frac{24}{Re_p} (1 + 0.15 Re_p^{0.687}) \left( \frac{\mathbf{r}_\infty \mathbf{m}_\infty}{\mathbf{r}_s \mathbf{m}_s} \right)^{-0.45} \\
h_f &= \frac{\mathbf{I}_f}{d_p} (2 + 0.6 Re_p^{1/2} Pr^{1/3}) \left( \frac{\mathbf{r}_\infty \mathbf{m}_\infty}{\mathbf{r}_s \mathbf{m}_s} \right)^{0.6} \left( \frac{C_{p\infty}}{C_{ps}} \right)^{0.38}
\end{aligned} \right\} \quad (2)$$

Here,  $C_{Df}$  and  $h_f$  are drag coefficient and heat transfer coefficient taking variable transport properties in the particle boundary layer into consideration.

The criterions of complete melting state (a) and complete evaporation state (b) of particle are as follows.

$$\left. \begin{aligned}
\int_0^t Q_n dt &\geq m_p \int_{T_0}^{T_{pm}} c_p dT + m_p L_{pm} \equiv Q_{pm} \quad (T_p \geq T_{pm}) \\
\int_0^t Q_n dt &\geq Q_{pm} + m_p \int_{T_{pm}}^{T_{bm}} c_p dT + m_p L_{pb}
\end{aligned} \right\} \quad (3)$$

In the equations for the particle motion and the heat transfer,  $m_p$ ,  $\mathbf{u}_p$ ,  $d_p$ ,  $Re_p$ ,  $c_p$ ,  $T_p$ ,  $T_{pm}$ ,  $L_{pm}$  and  $L_{pb}$  respectively represent the mass, velocity, diameter, Reynolds number, specific heat, temperature, melting point, latent heat of melting and latent heat of boiling of the particle, and  $T_a$  represents ambient temperature. The ambient temperature is given as room temperature.  $\mathbf{m}$ ,  $\mathbf{e}_p$  and  $\mathbf{s}_{SB}$  represent viscosity, particle emissivity and Stefan-Boltzmann's constant, respectively. Subscripts  $s$ ,  $\infty$  and  $f$  correspond to particle surface, bulk and film, respectively. For example, parameters  $\mathbf{m}_s$  and  $\mathbf{m}_\infty$  represent the viscosities of the plasma flow at the particle surface temperature and at the plasma temperature, respectively, the latter being unaffected by the boundary layer, around the particle. Parameters  $\mathbf{r}$ ,  $T$  and  $C_p$  are defined by the same



method as employed for  $\mathbf{m}_s$  and  $\mathbf{m}_\infty$ . The transport properties are given by approximation of multiterms as a function of temperature [19].

#### Induction electromagnetic field

The vector potential equation is derived from Maxwell's equations as follows [20]:

$$\left. \begin{aligned} \nabla^2 \mathbf{A}_c - i \mu_0 \omega \mathbf{A}_c &= 0 \\ \mathbf{E}_c &= -i \omega \mathbf{A}_c \\ \mathbf{B}_c &= \nabla \times \mathbf{A}_c \\ \omega &= 2\pi f_{RF}, \mathbf{A}(\mathbf{r}, t) = \mathbf{A}_c(\mathbf{r}) e^{i\omega t}, \mathbf{B}(\mathbf{r}, t) = \mathbf{B}_c(\mathbf{r}) e^{i\omega t}, \mathbf{E}(\mathbf{r}, t) = \mathbf{E}_c(\mathbf{r}) e^{i\omega t} \end{aligned} \right\} \quad (4)$$

In the equations for the electromagnetic field,  $\mathbf{A}$ ,  $\mathbf{E}$ ,  $\mathbf{B}$ ,  $f_{RF}$ ,  $\omega$ ,  $\mu_0$  and  $i$  represent vector potential, electric field intensity, magnetic flux density, frequency of RF coil current, angular frequency, permeability of vacuum and imaginary unit, respectively.

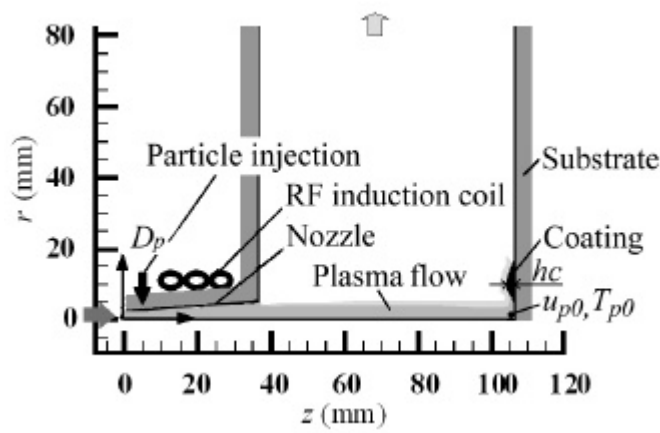


Fig. 1. Schematic illustration of a plasma spraying model

#### 2.2 Ceramic splat formation model

The ceramic splat formation process for the melted ceramic particle on the substrate is analyzed under the condition of  $T_{pm} > T_c$ ,  $T_{sm} > T_c$ . Here,  $T_c$ ,  $T_{pm}$  and  $T_{sm}$  are respectively contact temperature, melting point of the particle and melting point of the substrate. Figure 2 shows the two stages of the potential flow and viscous flow in the ceramic splat formation model [17]. Two stage flow model is proposed for ceramic splat formation process because Prandtl number of a ceramic droplet is high. When a ceramic droplet impinges on a substrate, it is deformed with potential flow in the first stage. When melting thickness in the splat becomes smaller than dynamic boundary layer thickness, the second stage starts. And the deformation takes viscous flow into consideration. The splat thickness is derived from Stefan's equations under the following assumptions. (1) Splat formation process has two steps from potential flow to viscous flow. (2) Impact particles are solidified to the disk shape. (3) Surface tension of the melted particle in the stage of its deformation is neglected. (4) Super cooling effect during solidification is neglected. (5) Impact particles contact to the substrate ideally. (6) Heat transfer to the substrate is only considered as 1-D. (7) The transport properties of particles and substrate materials depend on the phase states.

Figure 3 shows the definition of the  $h_{s1}$  and  $h_s$  which are ceramic splat thickness formed by the potential flow and final ceramic splat thickness. They are defined as follows [2, 17]:

$$\left. \begin{aligned} h_{s1} / D_p &= (c_z^2 / 2 Pe) [\sqrt{1 + 4 Pe (1 - h_n) / c_z^2} - 1] \\ h_s / D_p &= \sqrt[3]{c \sqrt{2} c_z (y_* + \bar{h}_{s1} / 3 c_z)} / \sqrt[3]{Pe \sqrt{Re}} \end{aligned} \right\} \quad (5)$$

$$\left. \begin{aligned} Pe &= D_p u_{po} / a_{pm}^{(l)}, c_z = P [\sqrt{1 + 4 Q / P^2} - 1] / 2, h_n = d_n / D_p \\ P &= \frac{\rho l_{p,p}^{(s,l)} Ku_p^{(l)} + 2(1 + a_c) K_e^{(b,p)} (J_{po} - 1)}{\sqrt{p} K_e^{(b,p)} Ku_p^{(l)}}, \end{aligned} \right\} \quad (6)$$

$$\left. \begin{aligned} Q &= \frac{2I_{p,p}^{(s,l)}(1-J_{bo})}{Ku_p^{(l)}} \cdot \left[ 1 - \frac{(1+a_c)(J_{po}-1)}{(1-J_{bo})K_e^{(b,p)}} \right] \\ J_c &= \left( \sqrt{p} I_{p,p}^{(s,l)} + c_z K_e^{(b,p)} J_{bo} \right) / \left( \sqrt{p} I_{p,p}^{(s,l)} + c_z K_e^{(b,p)} \right) \end{aligned} \right\} \quad (6)$$

Here,  $Pe$  is Peclet number,  $Fo^*$  is the dimensionless time of the splat formation,  $c_z$  is the solidification rate,  $D_p$ ,  $r_p$ ,  $u_{p0}$  and  $a_{pm}$  are respectively particle diameter, particle density at melting point, particle impact velocity and thermal diffusivity.  $Ku_p^{(l)}$  is the Stefan – Kutateladze criterion for the phase transition,  $K_e^{(b,p)}$  is the thermal activity criterion for particle and substrate materials and  $I_{p,p}^{(s,l)} = I_{pm}^{(s)} / I_{pm}^{(l)}$ . Superscripts  $l$  and  $s$ , and subscripts  $p$  and  $s$  correspond to liquid and solid, and particle and substrate, respectively.

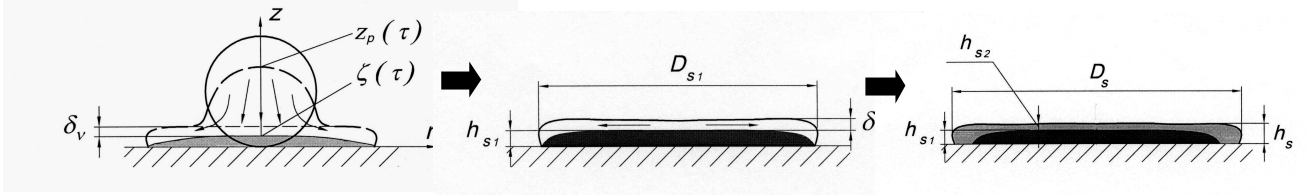


Fig.2 Stages of the potential flow and the viscous flow in the ceramic splat formation model

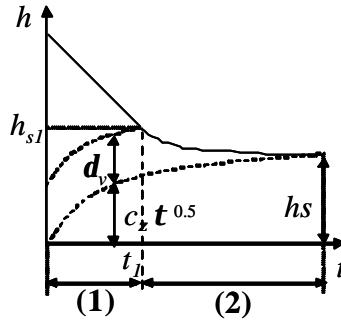


Fig. 3 Definitions of the  $h_{s1}$  and the  $h_s$ . (1) and (2) represent respectively potential flow and viscous flow.

### 2.3 Coating formation model

Coating formation takes thermal boundary layer thickness  $l_0$  on the substrate into consideration, because heat transfer from the particle to the substrate depends on the  $l_0$ . When the  $l_0$  is less than coating thickness, thermodynamic properties of substrate can be regarded as a splat material instead of substrate material. The  $l_0$  is defined as follows:

$$l_0 = \sqrt[3]{a_{pm}^{(l)} / b}, \quad b = |u_\infty| / d_n^2 \quad (7)$$

Here,  $a_{pm}^{(l)}$ ,  $u_\infty$  and  $d_n$  are respectively the thermal diffusivity of melted particle, the external flow velocity of the viscous layer and the boundary-layer thickness.

Figure 4 shows the schematic of a coating formation process. The coating is formed by superposing each splat divided by the width of 1 mm.

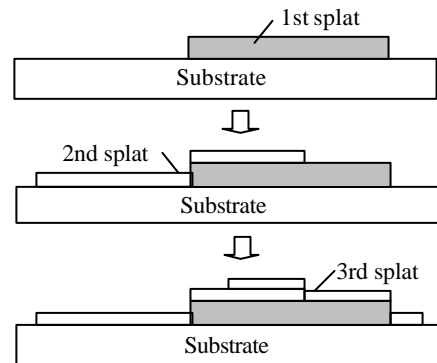


Fig. 4 Schematic of a coating formation process

### 3. Results and discussion

Figure 5 shows the radial distribution of the impact particle temperature. Particle impact temperature is increased up to 30 % by applying an RF electromagnetic field. Especially, particles located at outer region achieve boiling temperature because of its longer residence time.

Figure 6 shows the radial distribution of the splat thickness. The splat thickness is decreased by 20 % when RF electromagnetic field is applied, because the increase of the impact particle temperature causes longer solidification time and the increase of the impact particle velocity causes the increase of a splat formation velocity. On the other hand, the uniform radial distribution is observed.

Figure 7 shows the radial distribution of the coating thickness. Peak positions of coating thickness distributions depend on the particle diameter because larger particle, which has large inertia, goes into the center region. Coating thickness is also influenced by the RF electromagnetic field.

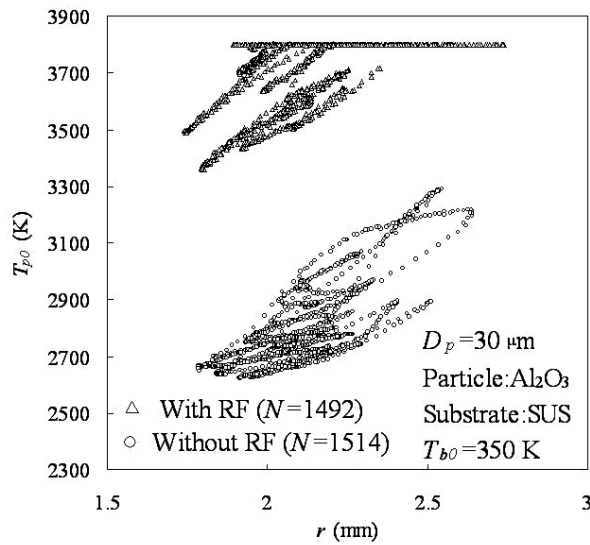


Fig. 5 Radial distribution of the particle impact temperature

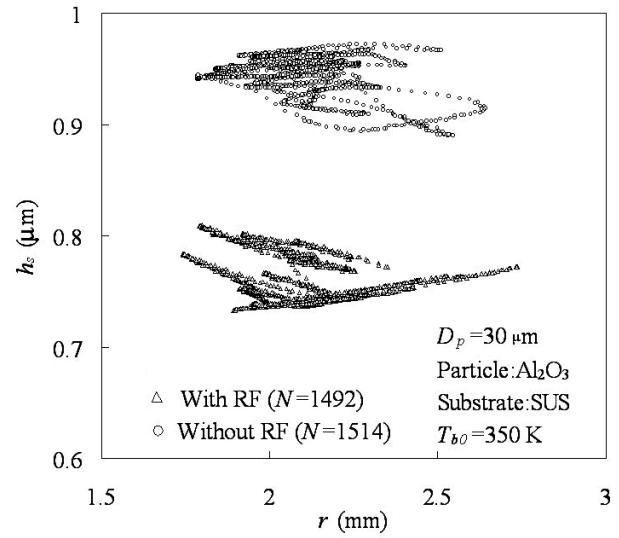


Fig. 6 Radial distribution of the splat thickness

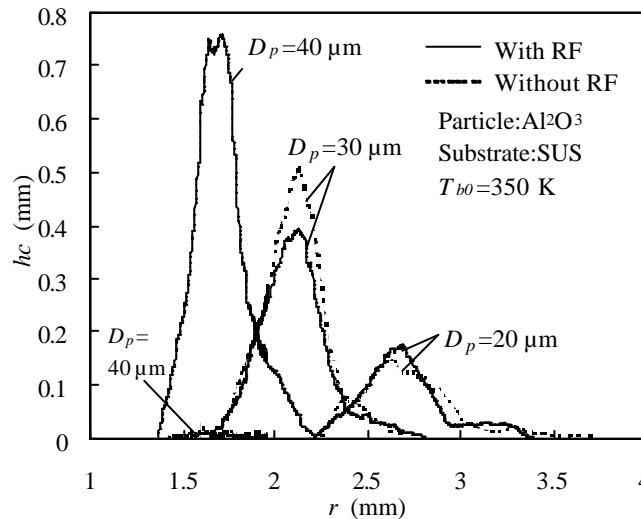


Fig. 7 Radial distribution of the coating thickness

#### 4. Conclusions

In the present study, the complete ceramic spraying process was evaluated by computational experiment to gain valuable information on the optimization for operating conditions. The results obtained here can be summarized as follows:

- (1) The radial distributions of the particle impact temperature and the particle impinging point are observed due to the unsteady effect of plasma flow.
- (2) The splat thickness is decreased by 20 % when the RF electromagnetic field is applied, because the particle impact temperature is increased effectively.
- (3) The coating thickness distribution is strongly influenced by particle size and the applied RF electromagnetic field.

#### Acknowledgements

The present study was supported by grant-in-aid for scientific research (B) from the Japan Society for Promotion of Science and was conducted by the supercomputer collaboration research 2 (No.C01MAR02) from the Institute of Fluid Science, Tohoku University, Japan.

#### References

- [1] R. B. Heimann, Plasma-Spray Coating, VCH Publishers, New York, (1996).
- [2] O. P. Solonenko, State-of-the art of Thermophysical Fundamentals of Plasma Spraying, Thermal Plasma and New Materials Technology, 2, Cambridge Interscience Press, England, (1995) 7.
- [3] E. Pfender, *Plasma Chem. Plasma Process.*, **9** (1989) 167S.
- [4] A. Vardelle, M. Vardelle and P. Fauchais, *Plasma Chem. Plasma Process.*, **2** (1982) 255.
- [5] H. Nishiyama, M. Kuzuhara, O. P. Solonenko and S. Kamiyama, *Plasma Chem. Plasma Process.*, **19** (1999) 363.
- [6] S. W. Nam, H. Nishiyama and S. Kamiyama, *JSME Int. J., Series B*, **39** (1996) 134.
- [7] E. Pfender and Y. C. Lee, *Plasma Chem. and Plasma Process.*, **5** (1985) 211.
- [8] Y. C. Lee, Y. P. Chyou and E. Pfender, *Plasma Chem. and Plasma Process.*, **5** (1985) 391.
- [9] O. P. Solonenko, A. V. Smirnov, V. A. Klimenov, V. G. Butov, Yu. F. Ivanov, *Physical Mesomechanics*, **2** (1999) 113.
- [10] Y. K. Chae, J. Mostaghimi and T. Yoshida, *Science and Technology of Advanced Materials*, **1** (2001) 147.
- [11] H. Zhang, *Int. J. Heat Mass Transfer*, **42** (1999) 2499.
- [12] Y. X. Gao, H. Fan and Z. Xiao, *Acta Materialia*, **48** (2000) 863.
- [13] J.-P. Delplanque and R. H. Rangel, *Acta Materialia*, **47** (1999) 2207.
- [14] M. Chung and R. H. Rangel, *Int. J. Heat Mass Transfer*, **44** (2001) 605.
- [15] P. Fauchais and A. Vardelle, *Int. J. Therm. Sci.*, **39** (2000) 852.
- [16] T. Sato, O. P. Solonenko and H. Nishiyama, *Thin Solid Films*, **407** (2002) 54.
- [17] O.P. Solonenko, *Physical Mesomechanics*, **4**(6) (2001) 45.
- [18] D. L. Evans and R. S. Tankin, , *Phys. Fluids*, **10**(6) (1967) 1137.
- [19] J. F. Bilodeau and A. Gleizes, , *Plasma Chem. and Plasma Process.*, **16**(4) (1997) 605.
- [20] J. Mostaghimi and M. I. Bolous, *Plasma Chem. and Plasma Process.*, **9** (1989) 25.

# Modeling a pilot-scale combustion/vitrification furnace under oxygen plasma arc transferred between twin torches

B. Barthelemy<sup>1</sup>, C. Girolid<sup>1</sup>, C. Delalandre<sup>2</sup>, B. Paya<sup>3</sup>, J.M. Baronnet<sup>4</sup>

<sup>1</sup> CEA/VALRHO/DEN/DIEC/SCDV/LPIC, BP 17171, 30207 Bagnols sur Cèze, France

<sup>2</sup> EDF/Site de Chatou/MTI/MFTT, 6 quai Watier, BP 49, 78401 Chatou cedex, France

<sup>3</sup> EDF/Site des Renardières/Arc Plasma et Induction, 77818 Moret sur Loing Cedex, France

<sup>4</sup> Laboratoire de Chimie des Plasmas / Université de Limoges, 123 avenue Albert Thomas, 87060 Limoges, France

## Abstract

This paper deals with 3D simulation of flows inside a plasma furnace devoted to combustion/vitrification of radioactive wastes, based on a molten glass bath under an electric arc transferred between two metallic electrodes. After a brief description of the experimental set-up and a short presentation of the software with hypothesis and used equations, results for glass domain are given for an example through velocity, temperature and volumic power distributions and shape of the obtained glass ingot. Then results for the arc domain are presented : isotherms map, temperature, volumic power, magnetic field and velocity distributions and so, oxygen concentration distribution for mixing of oxygen into argon ; the arc shape is compared to an arc picture and the temperature calculated distribution to the measured values.

## Introduction

Since 1990, CEA has been investigating the feasibility of combustion and vitrification of radioactive waste in a cold-wall plasma reactor, -without any refractory so the furnace is running as a cold crucible-, called SHIVA. The crucible is filled with synthetic glass in order to trap mineral radio nuclides inside the melt. Previous works have led to a reactor in which a transferred electric plasma arc is established between two aerial metallic electrodes operating in a gaseous mixture of argon and oxygen [1] [2]. Surrogate wastes (bitumen, ion exchange resins, processing wastes) have been processed in order to test and validate the pilot [3].

To improve operating parameters and to define the best zone for injection of the waste and of the recycled dusts, the knowledge of velocity, temperature and oxygen concentration spatial distributions inside the whole furnace is necessary. To achieve this objective, we have carried on modeling of the flows and the thermal transfers inside by using and adapting the computational fluid dynamics (CFD) code: ESTET.

## Experimental set-up

The furnace is a stainless steel double-wall unit cooled by pressurized water; it is 60 cm in diameter, 50 cm high with 20 cm for crucible depth, it contains up to 100 kg of glass. Anode and cathode of the cold-wall plasma combustion/vitrification melter are aerial metallic electrodes (Figure 1).

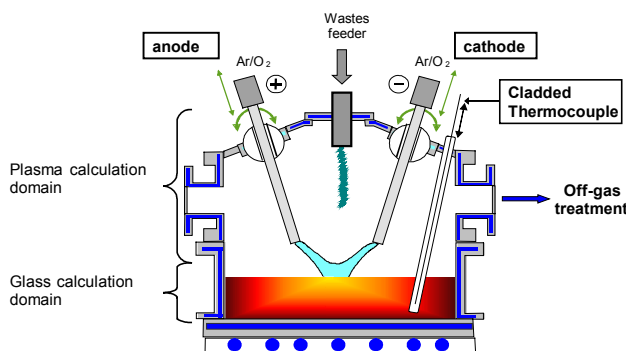


Figure 1: SHIVA furnace



Figure 2 : Details of plasma gas injection

The electric arc is struck between the two electrodes; argon is introduced along the electrodes and oxygen through sleeves around the electrodes (Figure 2); oxygen ensures the incineration of the waste and combustion of gases. An inductive heating system has been added to plasma system in order to assist the melting

and the homogenization of the glass matrix. Off-gases are sent to a suitable treatment system including two filters (granular bed filter and bags filter) and a scrubber. After waste incineration, the dusts are recovered to be recycled in the furnace and a homogeneous glass ingot is obtained.

Argon and oxygen flow-rates are respectively 40NL/min and 80 NL/min at each electrode, intensity is 200 A and voltage about 80 V. After the arc is stricken, the glass frit is progressively melted and the molten glass becomes slightly electrically conductive; then the arc is partially transferred through the melt and the voltage rises from ~80 V up to ~160 V, the glass is thus heated by Joule effect.

Heat losses in each cooling circuit are measured.

### ESTET 3.4 CFD code

Some CFD codes have been already developed to model plasma arc and(or) processes [4] [5]. We chose to use ESTET, a 3D unsteady calculation code based on a “finite volume” mesh. The software is suitable for single- or multiphase flow studies with compressible or incompressible material under laminar or turbulent flow conditions [6]. The electromagnetic terms are solved by using potential vector trick, because simulations are led in 3D [7]. The energy and electromagnetic equations are solved using a SIMPLEC algorithm; a modified algorithm with high pressure and velocity coupling is used for the momentum and mass conservation equations [8].

Velocities in the gas phase and in the glass melt differ through 5 to 7 magnitude orders so the furnace was subdivided into two calculation domains: the arc domain and the glass domain; they are modeled separately. The plasma arc is simulated by considering the plasma is asymmetric (lack of symmetrical axes), in local thermodynamic equilibrium, stable and laminar.

### Modeling of the glass domain

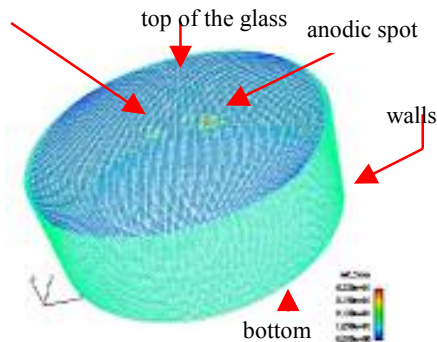


Figure 3: 3D cylindrical mesh of glass crucible

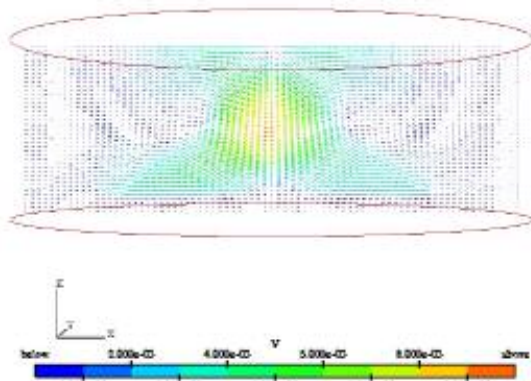


Figure 4: Velocity vectors in the glass melt ( $\text{m.s}^{-1}$ )

A 3D cylindrical grid was used to represent the experimental melter crucible (Figure 3). Moreover, to take into account the not melted thin layer of glass frit along the crucible walls and bottom, ESTET has been modified to integrate physic properties of the glass frit and to model the melting of the glass for a temperature of about  $700^{\circ}\text{C}$  (that is to say a melting temperature determined from the transition temperature  $-500^{\circ}\text{C}$  in this case -from solid to liquid glass).

The arc transfer through the glass, i.e. Joule effect, is taken into account in the simulation by supplementing the mesh with two spots representing the transferred arc contact points: the cathodic and anodic spots are initialized by a thermal flux of  $10^7 \text{ W.m}^{-2}$  and  $10^6 \text{ W.m}^{-2}$  [9] and at electrical potentials of 0 and 80 V respectively.

Figure 4 shows the evolution of melt motion in the melted glass. Two recirculation loops are generated to stabilize the flow. The maximum of the displacement velocity is obtained in the center of the crucible, and reaches about  $9 \text{ mm.s}^{-1}$ . The mean velocity in the hot zone of the crucible is about  $6.5 \text{ mm.s}^{-1}$ ; liquid glass is entrained from the top of the crucible to the bottom. In the others parts of the crucible, the results obtained with the model indicate low displacement velocities of about  $0.1 \text{ mm.s}^{-1}$ .

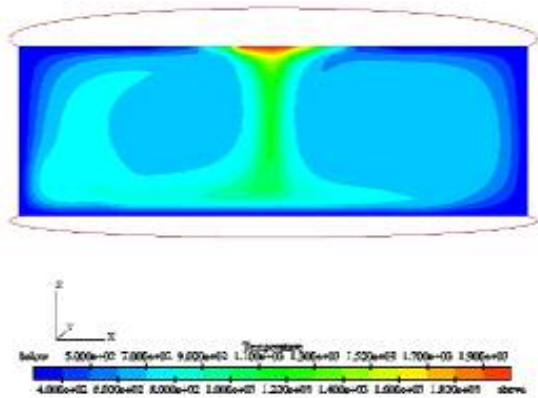


Figure 5: Temperature distribution in the glass melt (°C)

power in the glass, that is to say the Joule effect power induced in the melt by the current passage through the glass melt. The Joule effect throughput is about 0.5 kW.

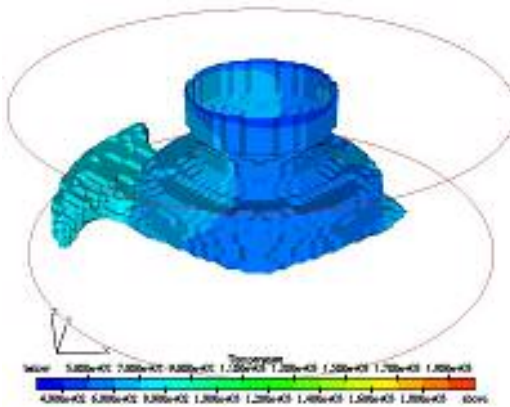


Figure 7 : 3D shape of the obtained glass ingot

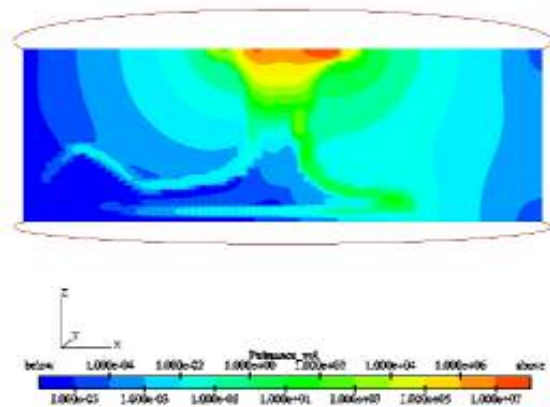


Figure 7 : Distribution of volumic power in the melt (W.m<sup>-3</sup>)

### Modeling of the arc domain: 3D simulation of the unsteady electric arcs

Electromagnetic equations were introduced into the ESTET calculation code via the vector potential, allowing a 3D simulation of the displacement of the plasma arc, which was considered as a quasi steady-state phenomenon. Various simplifications allowed us to calculate the magnetic field from the vector potential [10] [7]. This method using the vector potential to determine the magnetic field was validated by comparison with Ampere's theory in simple geometry and was successfully used to simulate thermal plasmas in SF6 [6].

Temperatures are in the range of 7 000 to 15 000 K, so radiative terms ( $10^{-7}$  W.m<sup>-3</sup>) that are overall less than Joule effect ( $10^9$  W.m<sup>-3</sup>) have been neglected [11].

Anodic and cathodic falls (about 10 to 20 V) are not taken into account for this simulation

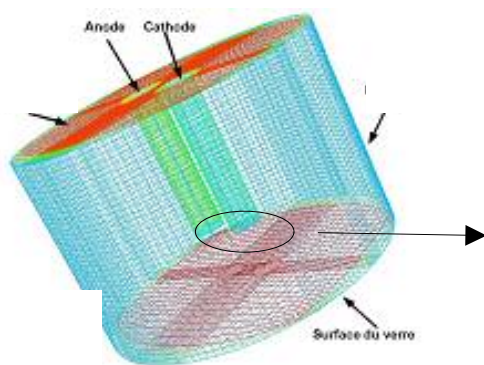


Figure 8: Plasma domain computational mesh

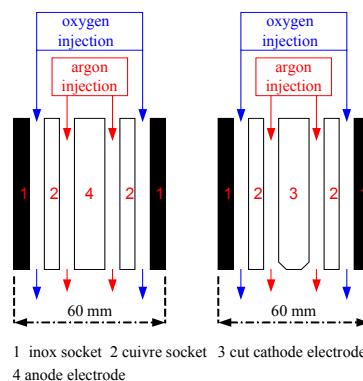


Figure 9 : Details of plasma gas injection

The arc domain was modeled on a 3D structured mesh representative of the SHIVA melter geometry integrating two parallel torches (furnace diameter = 600 mm, torch diameter = 60 mm, h = 400 mm). The mesh (Figure 8) was too coarse to allow proper integration of



the gas injection zones and especially the cathode and anode zones at zero velocity with different dimensions. This mesh is constituted by about 420 000 computational nodes.

The ignition of the electric arc is modeled by striking the arc with a hot column between the electrodes. This zone was intentionally initialized at high temperature (about 6000°C) to increase the conductivity of the gas medium and thus accelerate the inception of the arc.

The figure 10 shows the isotherms distribution between the twin torches. We have chosen the 9 000 °C isotherm to materialize the plasma arc volume. Moreover, we may observe that the maximum of temperature is reached near the cathode tip. These results are in good agreement with experimental values measured by atomic emission spectroscopy in the two plasma jets and in the coupling zone: the same temperature values at  $\pm 1500$  K and, close the cathode tip, a bulb at higher temperature than near the anode ( $\Delta T \sim 2000$  K).

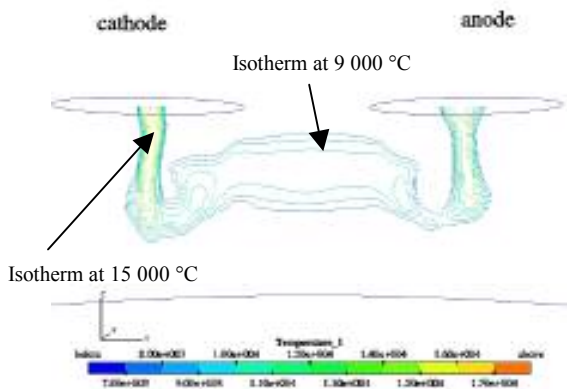


Figure 10 : Representative isotherms of the plasma (from 6 000 °C to 15 000 °C)

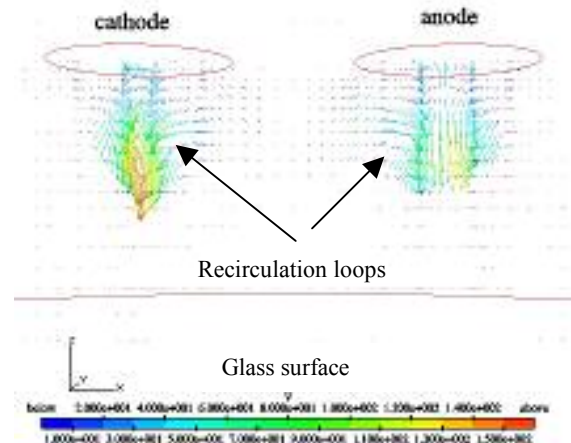


Figure 11 : Distribution of the velocity in the plasma zone

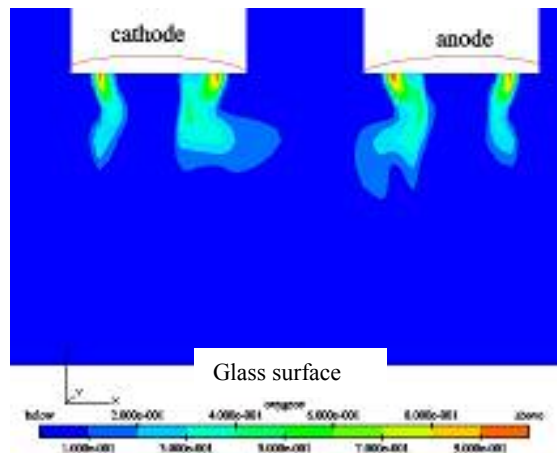


Figure 12 : Distribution (kg/kg) of oxygen plasma gas near to the electric arc

The velocity of gases (Figure 11) outside the arc is negligible but it can reach 150 m.s<sup>-1</sup> and 120 m.s<sup>-1</sup> for cathodic and anodic jets. Two recirculation loops involve mixing of plasma gases (oxygen and argon). We may observe this phenomenon on the figure 12: at this time, plasma arc is essentially constituted by argon; the mixing with oxygen is not yet completed.



Figure 13 shows electrical potential that reaches 120 V on the anode. Cathode potential is fixed at 0 V.. Moreover, the power generated by Joule effect reaches 36 kW in electrical arc. Joule effect is the principal term allowing the heating of the plasma zone (Figure 14).

The magnetic field (Figure 15) exhibits circular motion beneath the electrodes in particular; this produces a repulsion and attraction phenomenon between the two plasma jets. These one is underlined by Laplace forces, as we may see on the figure 16. The electric arc motion and its shape may be registered with a high-speed camera (Figures 17 and 18) so, showing that the magnetic field simulation may be considered as consistent with reality

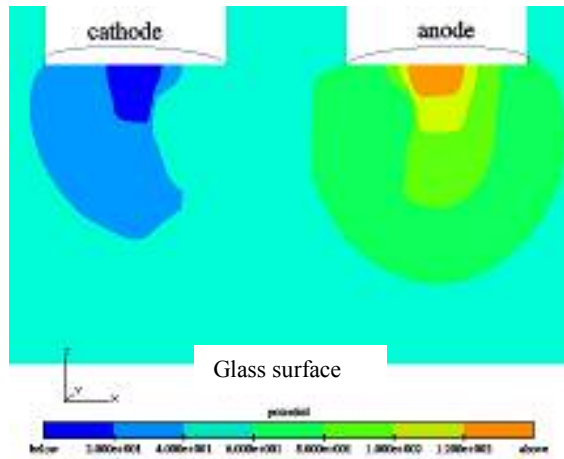


Figure 13 : Electrical potential (V)

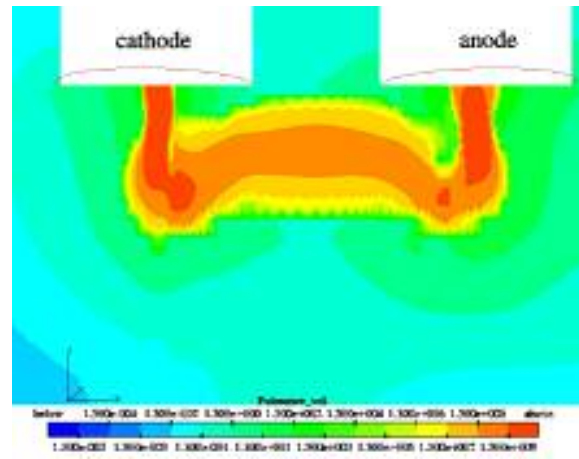


Figure 14 : Distribution of volumic power ( $\text{W.m}^{-3}$ ) due to Joule effect

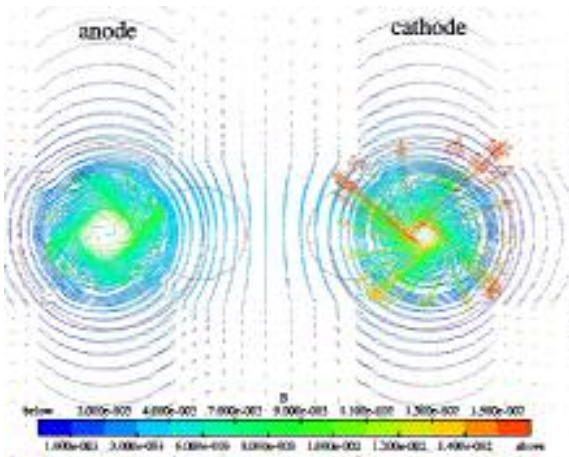


Figure 15 : Magnetic field (T) near the nozzle of the electrodes

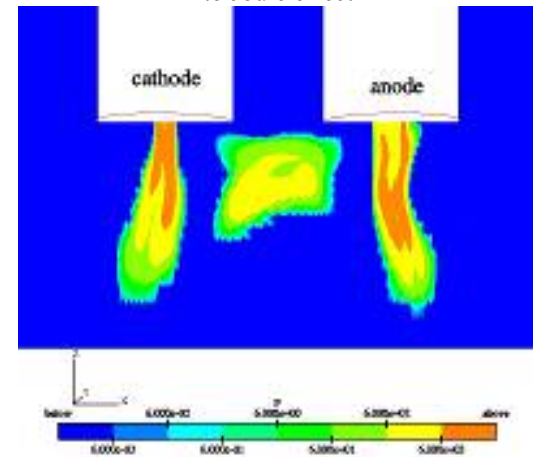


Figure 16 : Evolution of Laplace forces ( $\text{W.m}^{-3}$ )

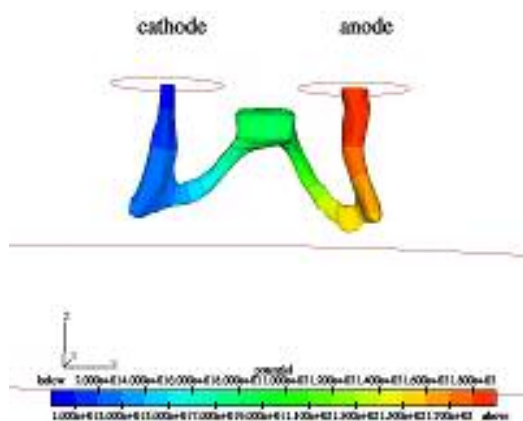


Figure 17 : 3D shape of electric arc colored by electrical potential

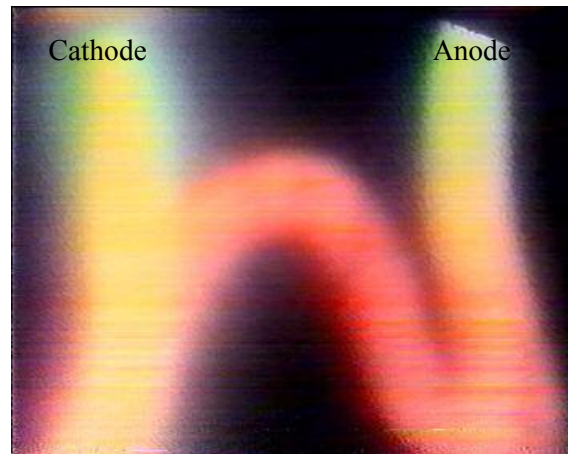


Figure 18 : High speed observation of electrical arc

## Conclusion

A 3D simulation of the glass domain allows the temperature of the glass melt to be reached according to the operating conditions and material flows in a melting cold crucible. The model allows to predict the probable quantity of melted glass but not the shape of the ingot. Moreover the new function integrated in the CFD code to take into account the thickness of the solid glass covering the crucible walls in any cold-wall melting process gives some results in good agreement with experimental ones. Nevertheless, some parameters must be better controlled to obtain a global prediction of the glass melting.

The 3D model of the electric arc provides conclusive results: electrical potential, arc shape, and temperature of the plasma are in agreement with some experimental results such as emission spectroscopy or arc observation with an high speed camera. But, the spreading of oxygen in the arc does not yet completed. To obtain a good distribution of oxygen, some simulations must be carried on.

Now the two different domains are separately simulated, so they have any interaction between theses two parts. A future work will allow us to couple glass and plasma calculation domains and then interactions between electric arc and melt will be taken into account.

## References

- [1] GIROLD C., " Incinération / vitrification de déchets radioactifs et combustion de gaz de pyrolyse en plasma d'arc", PhD thesis, Université de Limoges, (1997).
- [2] TAUPIAC J.P., "Incinération de déchets nucléaires en plasma d'arc", Ph.D. thesis, Université Paul Sabatier de Toulouse, 1993.
- [3] GIROLD C., BARTHELEMY B., CERQUEIRA N., VANDENSTEENDAM C., BARONNET J.M., "Medium level burnable radioactive waste Incineration/Vitrification under oxygen transferred arc plasma", pp. 611-616, ISPC 15, Orléans (2001).
- [4] FRETON P., Etude d'un arc de découpe par plasma d'oxygène ; modélisation – expérience, PhD thesis, Université Paul Sabatier de Toulouse, (1993).
- [5] BOUSSAGOL A., MARIAUX G., LEGROS E., VARDELLE A., NYLEN P., 3D modeling of a DC plasma jet using different commercial CFD codes, pp. 1015-1020, ISPC 15, Orléans (2001).
- [6] MATTEI J.D., THAI VAN, LAVIEVILLE J., EDF report No. HE-44/97/018B, (1997)
- [7] L. TRENTY, "Modélisation du chauffage de bains métalliques par un plasma d'arc transféré", PhD thesis, Ecole Centrale de Paris, (1997).
- [8] DELALONDRE C., BOUVIER A., CARUSO A., MECHITOUA N., SIMONIN O., VERITE J.C., "Fluid dynamic modelling of electric arcs for industrial applications", Pure and Applied Chemistry, **70**, N° 6, pp. 1163-1168, (1998).
- [9] ALEXIS J., RAMIREZ M., TRAPAGA G., JÖNSSON P., "Modeling of a DC electric arc furnace - Heat transfer from the arc", The Iron and Steel Institute of Japan, **40**, n°11, pp. 1089-1097, (2000).
- [10] DOUCE A., BOUVIER, DELALONDRE C., "Progress in Plasma Processing of Materials" 1999, Proceedings of TPP5, St Petersburg, July (1998).
- [11] A. DOUCE, "Modélisation 3D du chauffage d'un bain métallique par plasma d'arc transféré. Application à un réacteur axisymétrique", PhD Thesis, Ecole Centrale de Paris, (2000).

# Sterilization of food packaging materials by low-pressure microwave plasmas

J. Schneider<sup>1</sup>, J. Feichtinger<sup>1</sup>, J. Krüger<sup>1</sup>, P. Muranyi<sup>2</sup>, A. Schulz<sup>1</sup>,  
M. Walker<sup>1</sup>, J. Wunderlich<sup>2</sup>, and U. Schumacher<sup>1</sup>

<sup>1</sup>*Institut fuer Plasmaforschung, University of Stuttgart, Pfaffenwaldring 31, D-70569 Stuttgart, Germany*

<sup>2</sup>*Fraunhofer Institut fuer Verfahrenstechnik und Verpackung, Giggenhauser Str. 35, D-85354 Freising, Germany*

## Abstract

Low-pressure microwave plasmas are a means to efficiently sterilize materials for all kind of applications. Three different plasma sources were used to sterilize polymer substrates with contaminations between  $10^6$  and  $10^7$  test spores, showing up to five orders of magnitude in spore reduction within less than one second of plasma treatment. The article shows various sterilization kinetics, obtained from four different test spores, using flat substrates and hollow bodies, with a comparison of homogeneous vs. spot contamination.

## 1. Introduction

Dry heat, hot steam, hydrogen peroxide, and other chemicals are state of the art sterilization agents in industrial applications [1]. Many comestible goods are sensitive to residues of sterilization agents, because their smell and taste can be changed by these agents. If this sensitive comestible goods packaging consists of polymer materials, chemicals often cause difficulties when they are absorbed or adsorbed by the polymer. This disadvantage can easily be prevented by using low-pressure microwave plasmas for sterilization: no dangerous or even toxic materials are formed while treating food packaging materials with such a form of plasmas. Moreover, a spore reduction of five orders of magnitude within less than one second and more than six orders of magnitude after only a few seconds of plasma treatment can be obtained, and no after-treatment of the sterilized food packaging materials is necessary. In addition to that, this extremely short time of plasma treatment helps avoiding high thermal loads, which is essential for many thermally irrisistant polymers (see also [1], [2]).

Three different types of low-pressure microwave plasma sources were used during the sterilization experiments. The plasma sources of the Duo-Plasmaline<sup>®</sup> type produce a homogeneous linearly extended plasma, whereas the new Planartron<sup>®</sup> leads to a homogeneously extended 2-dimensional plasma area. Using the electron-cyclotron-resonance-(ECR)-coupling of the microwave to a corresponding magnetic field, a homogeneous plasma can be formed exclusively within a hollow body.

The experiments carried out with the plasma sources of the Duo-Plasmaline<sup>®</sup> type focused on the sterilization effect of UV light produced by the plasma.

Using the Planartron<sup>®</sup>, the fastest spore reduction kinetics were obtained. A comparison of flat substrates with homogeneous spore contamination and those with all spores concentrated on a tiny spot (spot contamination) nevertheless showed great differences in the timescale of spore reduction. Combining the Planartron<sup>®</sup> and the ECR-type plasma, even PET bottles could efficiently be sterilized.

## 2. Experimental details

### 2.1 Plasma Sources

#### 2.1.1 The Duo-Plasmaline<sup>®</sup> and the Plasmodul<sup>®</sup>

According to the Duo-Plasmaline<sup>®</sup> principle microwave power is fed by a coaxial waveguide to two opposite sides of a vacuum vessel (see fig. 2.1). Within the vacuum vessel, the outer coaxial waveguide is replaced by a quartz tube [3]. There is atmospheric pressure inside the quartz tube,  $p \approx 10 \dots 1000$  Pa inside the vacuum vessel. As the microwave power cannot be absorbed inside the quartz tube at atmospheric pressure because the mean free path of the electron is too short to ionize the gas particles inside the quartz tube, the microwave propagates through the quartz tube into the vacuum vessel. Unlike the conditions inside the quartz tube at atmospheric pressure, the mean free path of the electrons is long enough to ionize the gas particles inside the vacuum vessel.

Starting with low microwave power, the sphere of ionized particles is restricted to the two ends of the quartz tube. As a consequence, short plasma hoses surrounding the quartz tube appear at its both ends. Increasing

the microwave power makes the plasma hoses extend along the quartz tube until they combine. Thus the plasma surrounding the quartz tube substitutes the outer coaxial waveguide.

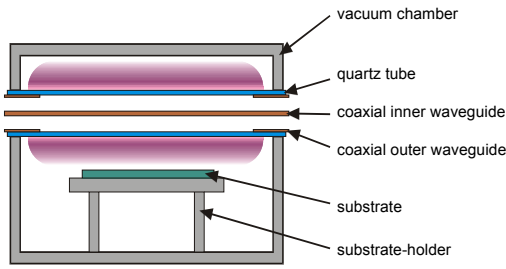


Fig. 2.1: Scheme of the Duo-Plasmaline®

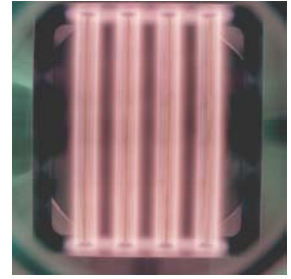
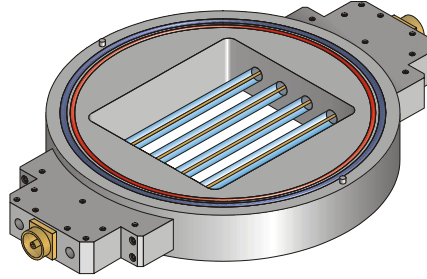


Fig. 2.2a and b: Scheme (a) of the Plasmodul® array (b)

The Duo-Plasmaline® leads to a homogeneous linearly extended plasma. To get to a homogeneous 2-dimensional plasma area, several Duo-Plasmalines® have to be arranged parallelly and equidistantly. A 18x20 cm<sup>2</sup> plasma area is obtained by having four Duo-Plasmalines® in parallel. This configuration is carried out in the Plasmodul® (see fig. 2.2a and b) [4][5].

The scalability of the Duo-Plasmaline® only depends on sufficient microwave power to generate a unified plasma around each quartz tube. The scalability was proved by constructing a 3 m Duo-Plasmaline® driven by just 2 kW of microwave power.

### 2.1.2 The Planartron®

In the Planartron®, the inner coaxial waveguide carrying the microwave is in the shape of a meander (fig. 2.3). The outer coaxial waveguide restricts the propagation of the microwave to the inside of the vacuum vessel. A quartz plate is placed on top of the Planartron®, being the interface between the low-pressure regime inside the vacuum vessel and the waveguide at atmospheric pressure. Microwaves carried by the inner coaxial waveguide can easily propagate through the quartz plate into the low-pressure regime at  $p \approx 20$  Pa. As a consequence, the Planartron® produces a homogeneous 2-dimensional plasma area directly on top of the quartz plate.

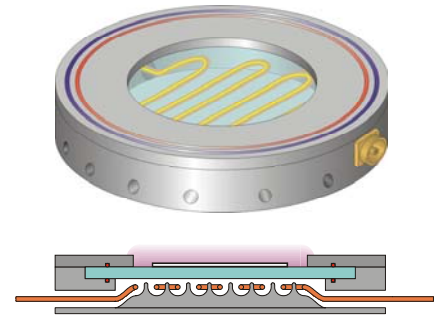


Fig. 2.3: Scheme of the Planartron®

### 2.1.3 The Electron-Cyclotron-Resonance-(ECR)-plasma

A microwave propagating into a low-pressure regime will be coupling to electrons in an existing magnetic field if the microwave frequency  $f$  corresponds to the magnetic field strength  $B$  according to the resonance condition

$$2 \cdot \pi \cdot f = \frac{e \cdot B}{m} \quad (2.1).$$

In the experiment the microwave frequency is  $f = 2.45$  GHz. This corresponds to the magnetic field strength of  $B = 0.0875$  T.

The sterilization experiments were carried out in the Planartron®. The PET bottle was placed directly on top of the quartz plate, while a Co-Sm permanent magnet with the magnetic field strength of  $B = 0.0875$  T was positioned inside the PET bottle. At a pressure of  $p \approx 4$  Pa inside the vacuum vessel as well as inside the PET bottle, the Planartron® was fed with microwave power. Having the magnet inside the bottle, there was no plasma on top of the quartz plate, but it homogeneously filled the inner of the PET bottle (see fig 2.4).



Fig. 2.4: ECR-plasma inside a PET bottle

## 2.2 Microbiological sample preparation and evaluation

All test samples were prepared at Fraunhofer Institut fuer Verfahrenstechnik und Verpackung (IVV) in Freising. They used four different test spores for contamination: *Bacillus subtilis*, *Aspergillus niger*, *Bacillus stearothermophilus*, and *Saccaromyces cerevisiae*. These test spores were chosen because of their overall robustness and their resistance to UV light and heat, respectively. The material of the test samples was polyethyleneterephthalate (PET) to be very close to food packaging materials currently in use. A PET foil of 180  $\mu\text{m}$  thickness representing food packaging foils and 0.5 l PET bottles as hollow body substrates were chosen.

A spraying technique guaranteed the homogeneous contamination of the substrates. Thus the test spores were homogeneously spread on an area of about  $7 \times 7 \text{ cm}^2$  on the flat PET foil samples, leading to the spore density of approximately  $2.0 \cdot 10^4 / \text{cm}^2$ . The spraying technique even allowed to homogeneously contaminate the 0.5 l PET bottles from bottom to bottleneck.

Some PET foil substrates were spot contaminated to see how difficult plasma sterilization would be compared to homogeneously contaminated samples. When spot contaminating the PET foil samples, a little drop carrying more than  $10^6$  spores was deposited in the middle of the sample, leaving a contaminated area of about  $0.07 \text{ cm}^2$  after having dried. This is equivalent to the spore density of approximately  $1.4 \cdot 10^7 / \text{cm}^2$ .

Immediately after the plasma treatment the PET foil substrates were stored in a bag with buffer solution, and the PET bottles were filled with this buffer solution and closed by an aseptic top. After the plasma treatment the substrates were sent back to Fraunhofer IVV to count the spores still able to form colonies. These spores are called colony forming units.

## 3. Results and discussion

### 3.1 Plasma sterilization with the Plasmodul: the role of UV light

The aim of the first experiments was to find out if there is an effect on the sterilization kinetics when different working gases are used in plasma sterilization [6]. For that reason, PET foil substrates with spore contaminations in the range of  $10^6$  to  $10^7$  were sterilized by using ordinary laboratory air, argon, and ammonia, respectively. The gas flow of each gas was 100 sccm (standard cubic centimetres per minute), leading to the pressure of  $p \approx 15 \text{ Pa}$  inside the Plasmodul<sup>®</sup>. The distance between the PET foil substrates and the array of four Duo-Plasmalines<sup>®</sup> inside the Plasmodul<sup>®</sup> was  $d = 12 \text{ cm}$ . Finally, the plasma was produced by 1200 W of microwave power.

Fig. 3.1 shows the results of these first experiments. Taking into account that the original spore contamination of the PET foil substrates sterilized in the ammonia plasma was approximately a factor of almost five higher compared to those exposed to the air plasma, the corresponding kinetics of ammonia and laboratory air are nearly comparable. In contrast, the kinetic obtained by using argon plasma doesn't present equivalent results: the spore reduction is even lower by a factor of approximately 10, and in addition to that there is a tailing to be seen for times  $t > 60 \text{ s}$ .

These results can be explained by looking at the UV spectra of the three gases at low-pressure conditions.

The ammonia plasma produces a lot of UV light because of the formation of hydrogen molecules ( $\text{H}_2$ ); the spectrum of  $\text{H}_2$  increases significantly towards smaller wavelengths in the UV region. In the spectrum of air, there are many intense NO molecule ion bands in the UV region, caused by the reaction of oxygen radicals and ions with nitrogen [7]. Compared to the spectra of ammonia and air, the share of UV light in the argon spectrum is very low.

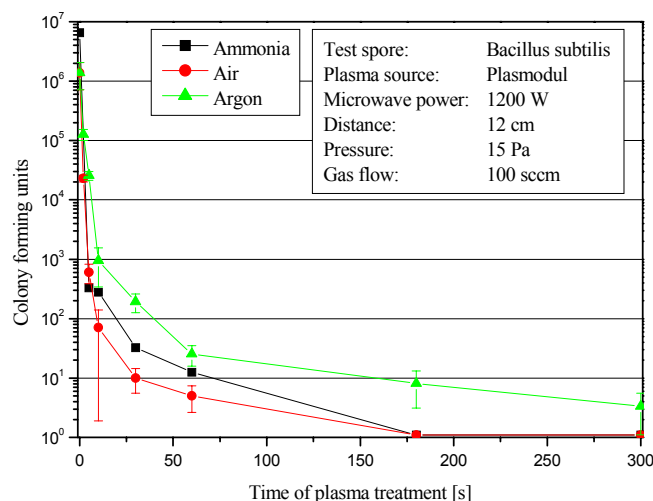


Fig. 3.1: Sterilization of *Bacillus subtilis* by various working gases



The next step was to find out what light energies in the UV region would be necessary to have significant sterilization effects. Therefore, the test spore *Aspergillus niger* was chosen. This test spore is pigmented, so that a certain protection from the effect of UV light was to be expected. The same experiments were carried out with the test spore *Bacillus subtilis*. Because of its high share of UV light in the spectrum, ammonia was chosen for the following experiments (see also [6]).

There was one important change in the experimental setup compared to the direct plasma treatment of the PET foil substrates. To separate the effects of the plasma particles from the effects of the UV light produced by the plasma, the substrates were covered with optical edge filters. These filters are marked according to the wavelength where these filters show 50 % optical transmission. At wavelengths just below, the transmission rapidly drops to zero, whereas the transmission comparably raises at higher wavelengths.

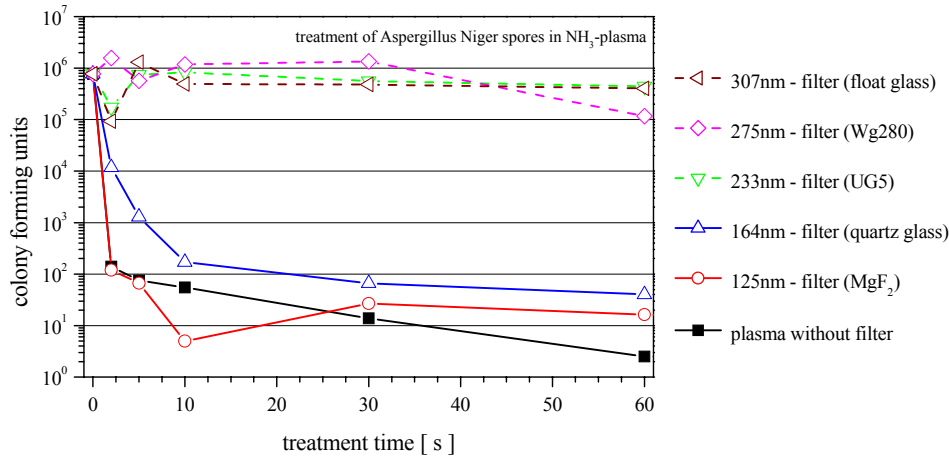


Fig. 3.2: *Aspergillus niger* sterilization kinetics obtained by covering the substrates with different optical edge filters

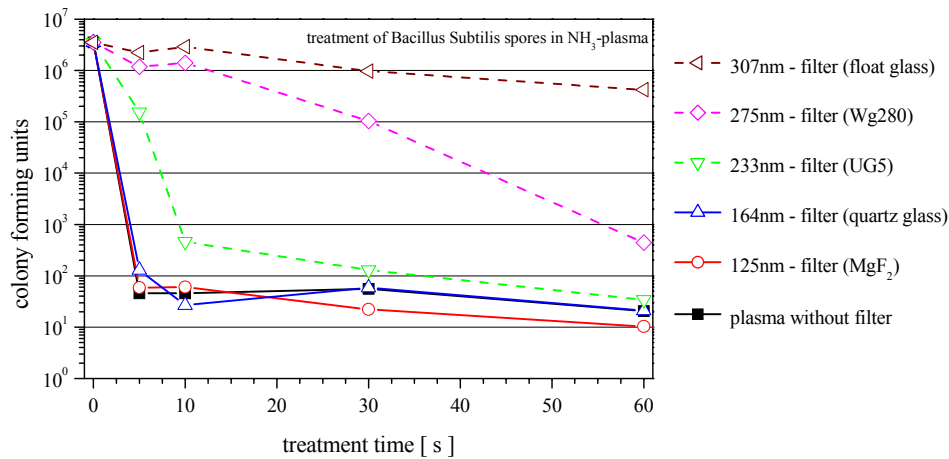


Fig. 3.3: *Bacillus subtilis* sterilization kinetics obtained by covering the substrates with different optical edge filters

Having 307 nm, 275 nm, or even 233 nm optical edge filters on the PET foil substrate with *Aspergillus niger* contamination, nearly no sterilization effect can be noted (see fig. 3.2). UV light from the plasma down to the wavelength of  $\lambda = 164$  nm shows a significant sterilization effect. Using the 125 nm optical edge filter, the spore reduction kinetic obtained by direct plasma treatment is reproduced.

Fig. 3.3 shows the resulting sterilization kinetics of *Bacillus subtilis* test spores using the same optical edge filters. In contrast to the results of *Aspergillus niger*, UV light from the plasma down to the wavelength of 275 nm already shows a significant sterilizing effect. Furthermore, the sterilization kinetic of *Bacillus subtilis* obtained by using the 164 nm optical edge filter already reproduces the results of the direct plasma treatment.

### 3.2 Plasma sterilization with the Planartron

#### 3.2.1 Sterilization of PET foils with homogeneous contamination

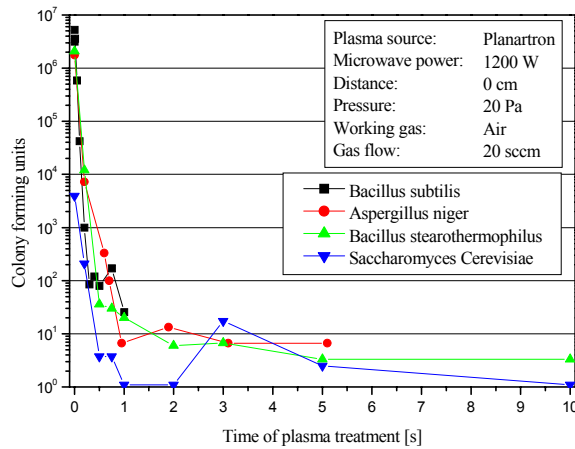


Fig. 3.4: Spore reduction kinetics of all four test spores using the Planartron®

The symbols at  $t = 0$  s represent the initial contamination of the substrates. The reference contamination of the *Saccharomyces cerevisiae* kinetic is significantly lower compared to the other kinetics despite the initial contamination between  $10^6$  and  $10^7$  spores, because only about  $4 \cdot 10^4$  colony forming spores could be found by Fraunhofer IVV on the reference samples. This could be put down to the sensitivity of the *Saccharomyces cerevisiae* spores to the transport from Fraunhofer IVV in Freising to IPF in Stuttgart and vice versa.

Regardless of the spore type, all kinetics show a reduction in colony forming units of more than five orders of magnitude within less than one second. A reduction of more than six orders of magnitude is obtained in only a few seconds.

Additional investigations were carried out to find out reasons for the tailing, i.e. why some few colony forming units could still be detected after five seconds of plasma treatment. It turned out that some spores got to the backside of the PET foil samples when spraying the spores on the samples at Fraunhofer IVV. Being in the vacuum vessel of the Planartron® directly between the quartz plate and the PET foil, the spores on the backside of the samples weren't exposed neither to plasma particles nor to UV light produced by the plasma.

#### 3.2.2 Comparison between homogeneous and spot contamination

In Fig. 3.5 two different sterilization kinetics of *Bacillus subtilis* spores are presented. The experiments underlying the sterilization kinetics were performed with the Planartron® using 20 sccm of ordinary laboratory air with the pressure of  $p \approx 20$  Pa. The microwave power was  $P = 1200$  W. The kinetic of the homogeneously contaminated PET foil samples shows a reduction in colony forming units of five orders of magnitude within less than one second (see also fig. 3.4). When having a spot contaminated sample at the same sterilization parameters, it takes about  $t = 30$  s to obtain the same spore reduction.

A reason for the long-term kinetic obtained for the spot contamination could be found in a kind of self-protection of the spores. Being a number of more than  $10^6$  spores restricted to the area of about  $0.07 \text{ cm}^2$ ,

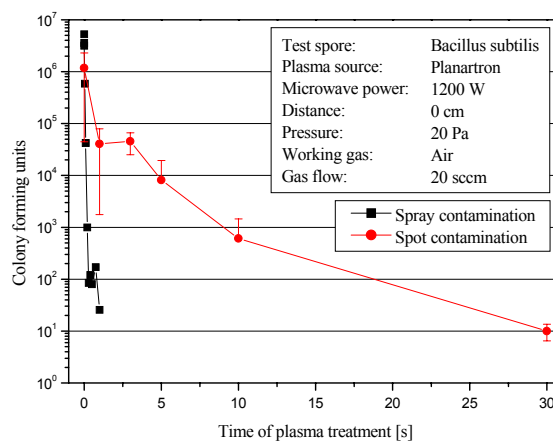


Fig. 3.5: Spore reduction kinetics of homogeneous vs. spot contamination

there are most of the spores lying on each other in several layers. It is assumed that the spores on top protect those lying underneath to a certain extent from the influence of the UV light produced in the plasma. This model for itself cannot explain why it is nonetheless possible to have a long-term sterilization effect as it can be seen in fig. 3.5. There must be an etching effect of the plasma, too, destroying the cell membranes of the spores. As a consequence, UV light as well as plasma particles can destroy the DNA and the cell membranes of the spores having been underneath, these spores then being unable to form colonies, too.

### 3.2.3 First results of hollow body sterilization

A small Co-Sm permanent magnet was positioned inside a 0.5 l PET bottle, standing directly on top of the quartz plate of the Planartron<sup>®</sup> plasma source. The entire apparatus was filled with ordinary laboratory air at the pressure of  $p \approx 4$  Pa. Only 240 W of microwave power was necessary to produce a homogeneous plasma which was restricted to the inside of the PET bottle.

According to fig. 3.6, the colony forming units were reduced by six orders of magnitude within nine seconds. By varying the parameters, e.g. looking for other suitable parameter combinations of working gas, pressure, and microwave power, it should be possible to get to higher values of microwave power, which in return would probably lead to much shorter times of plasma treatment with comparable results in spore reduction.

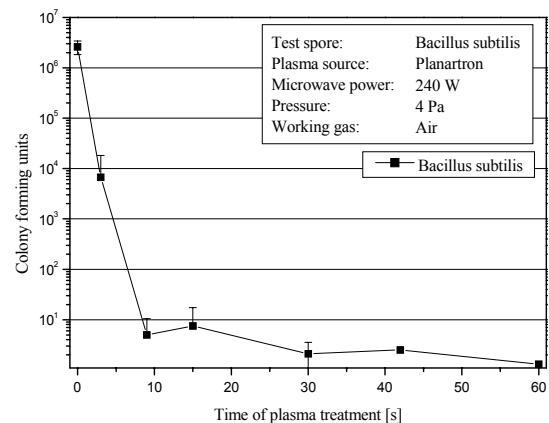


Fig. 3.6: Spore reduction kinetic of PET bottles

## 4. Conclusions

According to the experiments carried out with the Plasmodul<sup>®</sup>, the UV light produced by the plasma, especially the effect of UV wavelengths  $\lambda < 200$  nm was found to be the main spore reduction mechanism.

Comparing the spore reduction kinetics obtained by the Plasmodul<sup>®</sup> to those of the Planartron<sup>®</sup>, the Planartron<sup>®</sup> showed a significantly faster spore reduction. Using the Planartron<sup>®</sup>, all four test spores were reduced by five orders of magnitude within less than one second in case of spray contamination on flat PET foil substrates. After only a few seconds of plasma treatment, the spore reduction could be increased to six orders of magnitude.

Significantly slower spore reduction kinetics were obtained when sterilizing spot contaminated PET foil samples and spray contaminated PET bottles with the Planartron<sup>®</sup>. Nevertheless, these results show that comparable results in spore reduction with much shorter times of plasma treatment should be achievable.

In summary, low-pressure microwave plasmas are an efficient alternative to state of the art sterilization processes.

## Acknowledgements

The authors wish to thank Fraunhofer Institut fuer Verfahrenstechnik und Verpackung (IVV) in Freising for the microbiological preparation and evaluation of the test samples, and Bundesministerium fuer Bildung und Forschung (BMBF) for funding this research project under contract number 13N7603-3.

## References

- [1] M. Moisan, et al. - International Journal of Pharmaceutics **226**, 1 (2001).
- [2] J. Reece Roth, et al. - Surface and Coatings Technology **131**, 528 (2000).
- [3] German Patent, DE 19503205 C1, 02.02.1995.
- [4] M. Kaiser, et al. - Surface and Coatings Technology **116-119**, 552 (1999).
- [5] A. Schulz, et al. - Surface and Coatings Technology **142-144**, 771 (2001).
- [6] J. Feichtinger, et al. - to be published in Surface and Coatings Technology.
- [7] S. Moreau, et al. - Journal of Applied Physics **88(2)**, 1166 (2000).



# Atmospheric pressure plasma source for industrial gas phase and/or surface treatment applications

Thierry Sindzingre, Patrick Lassagne, Mathieu Thomachot

*AcXys Technologies, info@acxys.com, www.acxys.com*

## Abstract

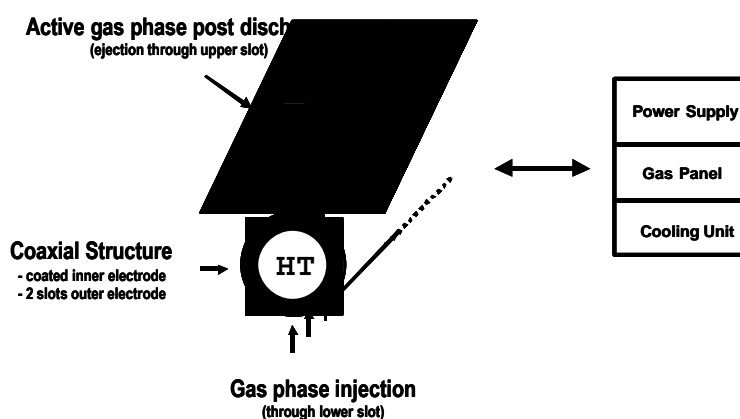
A new atmospheric and low temperature plasma technology is presented. This new technology is built for gas phase treatment or surface treatment. It produces very active atmosphere (oxidizing or reducing atmosphere). It allows thin films coating to be produced at atmospheric pressure and room temperature. Batch processes as well as in-line treatments are being developed for solving industrial issues (adhesion, cleaning,...) on different materials (plastics, metals, semiconductors,...).

## Introduction

A new plasma technology working at atmospheric pressure is being reported. Built around a compact design, this new plasma technology produces active atmosphere for chemical treatment in gas phase or for surface treatment. Industrial processes are being developed to solve critical issues such as adhesion (for adhesives, paints, varnishes, inks,...), cleaning (semiconductor, optics, metals,...) or coating/functionalizing (textiles, paper,...). This new and safe technology applies to nearly all kind of substrats, from thin to thick material foils, 3D objects, foam, profile, tubes and wires.... Batch and in-line processes are being proposed.

## Description of system

The new plasma technology is developed around an electrical discharge that works at atmospheric pressure (or around atmospheric pressure). To achieve such a discharge a coaxial electrode structure has been designed. The central electrode is covered with an dielectric coating to prevent any cathode spots that could derive in arcs. The gap between the electrodes is typically 1 mm. The outer electrode is made out of aluminium or stainless steel. Coating the outer electrode with a dielectric is also possible and it will slightly change the nature of the discharge.



Gas mixture flows through the structure crosswise. It travels in and out through two slots longitudinally opposed. Flow velocity and gas mixture are adjusted according to the process requirement. Gas consumption can be very low to insure heat up of the gas when thermal activation is needed ( $\sim 250^{\circ}\text{C}$ ) or larger to insure

the discharge reaction products to remain cold. Dwelling time is of the order of milliseconds. Various gas mixtures can be injected into the system depending on the nature of the chemical process to be achieved.

The energy fed to the discharge is delivered by a power supply through a 100 kHz quasi-alternative voltage. A high voltage cable connects the power supply to the plasma source. Cooling is added to keep the system under safe mode of operation. Up to now, plasma source from few centimeters connected to a 1,2 kW power supply up to 400 mm long device connected to a few kW power supply can be delivered. Longer systems (few meter range) could be developed for larger industrial applications.

### Nature of the discharge

The discharge itself is mainly located in the narrow gap area between the electrodes. It can only be seen by the 2 slots (injection and ejection slots). Apart from visual inspections, OES spectroscopy and electrical measurements it is difficult to make any observation.

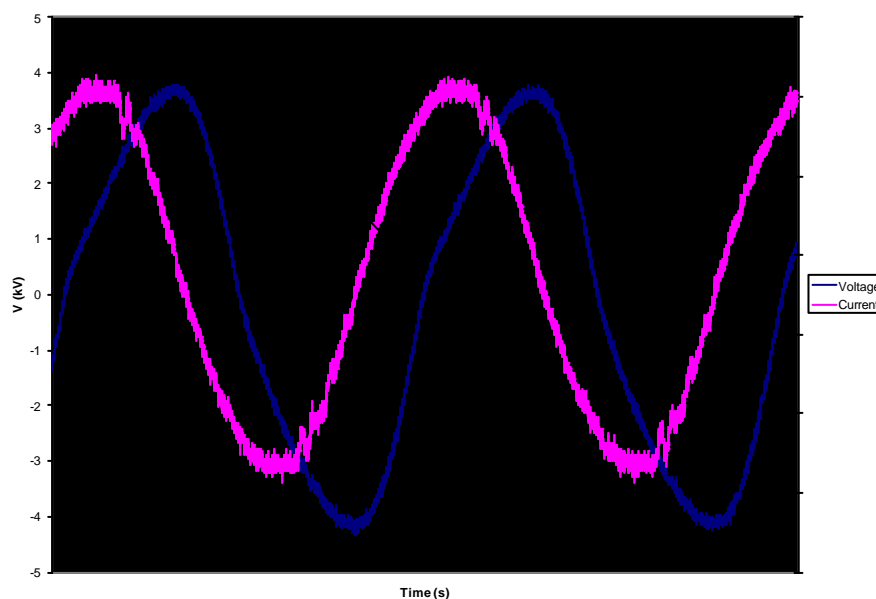
Experiments show that a minimum threshold power has to be injected into the system to obtain a discharge that spread on the whole length of the electrodes and do not remain located only at one end. This seems to indicate that such a discharge could support surface wave propagation inside the coaxial structure. Investigations will be carried on to gain in understanding on that point.

As monitored by OES analysis, the discharge looks very stable and reproducible. Working at atmospheric pressure makes start/stop procedures very fast and safe. That leads to optimum exploitation in industrial environment. A light-emission based process control will be shortly developed to follow discharge conditions.

Electrical analysis of a plasma source always leads to very useful information that may explain the behaviour of the discharge. As a plasma source is not a linear load it is difficult to obtain I(V) curve. Up to now some electrical measurements have been carried out: V(t) and I(t) at the port of the source. Spectral analysis of V(t) and I(t) shows many harmonics of fundamental frequency. A high level of noise has been monitored. No emission is visible above 30 MHz. From that observation it can be decided that only very few microsparks or streamers exist in this plasma technology under our conditions (N<sub>2</sub> mixture).

It appears that there is a strong connection between electrical characteristics and nature of the discharge. Slope changes on the voltage curves reveal discharge starting point and extinction points (see v(t) graph hereafter). Pursuing this analysis will lead to design a plasma system with a higher efficiency.

As deduced from electrical measurements, the behaviour of the discharge is more in the range of an



dielectric barrier discharge rather than in the range of a corona or a silent discharge. It can be seen as a glow discharge working at atmospheric pressure having the same structure as a glow discharges under low pressure.

### **Nature of the post discharge.**

Some gas mixtures lead to a very active post-discharge generation. This is very attractive for chemical treatment applications. Of course only long lifetime radicals and metastable species are being used. These species are flowing out of the discharge area into the post discharge zone that starts when the gas mixture flows out of the coaxial structure through the second slot. Its length along the gas flow direction can be few centimeters long ( $> 10$  cm).

In the post-discharge zone, electrons and ions are no more present in perceptible quantities, but sufficient to prevent any electrostatic charge effect. It contains principally excited species and active radicals. Their effects on surfaces is chemical. Temperature range of the post discharge extends from  $50^{\circ}\text{C}$  up to  $200^{\circ}$  or higher. External heating may be added when required.

This plasma source helps in producing active atmospheres at low temperature that can fill open tunnel enclosure for in-line surface treatment or close vessel for batch processes.

### **Typical processes**

The simplest process consist of feeding air into the plasma source (clean and water/oil free). But for many reasons  $\text{N}_2$  based mixture are preferred. Addition of doping gases produces specific atmospheres depending on final applications:

#### **Oxidizing atmosphere**

Oxygen (or moisture) is added to nitrogen in the ppm level range. Radicals like O (or OH) are produced. Such process is being evaluated to produce surface treatment of plastics in order to increase the surface wettability and adhesion of adhesives, inks, varnishes, so-gel coating,...It also applies on metals or glass materials to achieve an efficient cleaning by removing organics and hydrocarbons.

#### **Reducing atmosphere**

Addition of hydrogen in the % level range leads to the production of a highly reducing atmosphere. Very demonstrative effects are obtained on copper surface that can be de-oxidize by post discharge treatment at low temperature. Reducing atmosphere have also been tested for surface preparation before joining with adhesive. Shear tests demonstrate that reducing atmosphere can strongly promote the adhesion of adhesive other polymers surfaces, to a higher level than oxidizing atmosphere and up to cohesive failure.

#### **Other atmospheres**

Like for low pressure plasma chemistry, all kinds of mixtures are possible. Additions of gas mixture (or liquid chemicals through sprays dispersion), either in the main stream of gas before the discharge or in the post discharge zone may lead to advanced processes such functionalizing, grafting or deposition of materials.

Investigation around HMDSO and/or  $\text{SiH}_4$  injection are being conducted. Preliminary results show that  $\text{SiO}_x$  material is deposited at room temperature. It opens up the road of making hydrophobic or hydrophilic materials under easy-to-implement industrial conditions.

Dust generation and dust contamination is always an issue in material deposition process. However, working in the post discharge area may lead to longer equipment uptime before cleaning as the discharge will not be

affected by the dust generation. Moreover, simple, fast and light maintenance procedures will be proposed to solve the dust contamination issue.

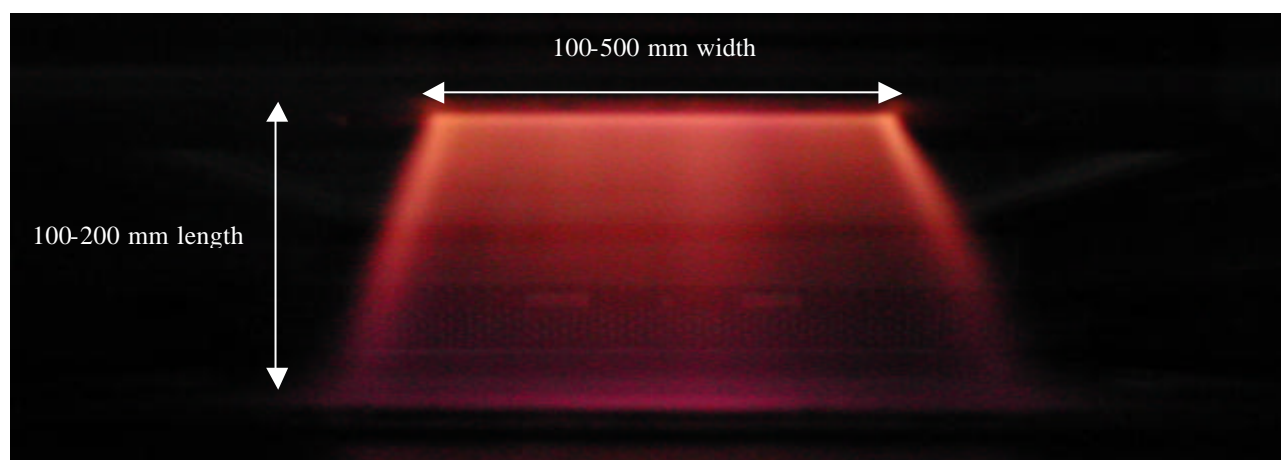
Etching with fluorine based chemistries will also be investigated in a near future.

### **A promising technology for gas phase treatment**

As very low pressure drop is needed to operate this new plasma technology around the atmospheric pressure, a very large flow rate of exhaust gas can be easily injected inside the plasma source. It makes it very attractive for abatement treatment. Different process chemistries could be developed in order to achieve complete reactions. These process chemistries may include several steps such as mixing before and/or after the gas to be treated with additional chemicals (gas, spray,...), or basic well-known chemical devices (traps, catalysts,...).

Intermediate between gas treatment and surface treatment, this technology may be used for fluidized-bed treatment of powders, small particules or small objects. Again several process steps may be combined like mixing with additional mixture (gas, spray,...) or thermal assistance (laser heating, furnace,...). Typical field of investigation for plasma fluidized-bed treatment would be for example the food industry or the design of nano-materials.

The following photograph shows the post-discharge in which chemicals could be introduced. The coaxial structure is on the top of the post-discharge and is not seen. Gas flows downwards. Typical dimensions are 100 - 500 mm width and 100 -200 mm length along the gas flow. Such dimensions would be very useful for industrial applications.



### **A promising technology for surface treatment.**

Working at atmospheric pressure opens up road to plasma technology for surface treatment in the general industry production facilities. This new technology can be set up under in-line operations or batch conditions. It may sometimes be necessary to "sweep" the surface to be treated by the active gas generated by the discharge. This can be obtain by moving the surface or the plasma source relatively to each other.

This plasma technology can fit either on existing lines with retrofit equipment or on a stand alone equipment. It can deal with lots of different material shape and aspects. It is adequate for thin or thick subtrates, wire or tubes, foam and 3 dimensionnal objects.

The following photographs shows atmospheric equipment for batch treatment and in-line treatment. These equipments are available from us for industrial applications and development works.



Atmospheric Plasma Batch equipment



Atmospheric Plasma In line equipment

Fast, easy to use, nearly maintenance free, this new technology can bring numerous benefits to users. For example, adding the new plasma source on an existing product line can enlarge the manufacturing process window and therefore lead to an increase of the production yield or of the quality level. It can be used to develop a new product that require a specific surface treatment with a high through-put under reduced cost condition in order to keep the final product attractive. Finally it can be used in substitution of other technologies for environmental reasons or to cut costs.

## Conclusion

A new plasma technology working at atmospheric pressure is now available. From nitrogen based mixture, it generates an active atmosphere well adapted for gas phase treatment and surface treatment. Simple processes (surface preparation to promote adhesion) and more sophisticated applications (hydrophilic/hydrophobic surfaces) are achievable with this atmospheric plasma technology.

Using this technology in an industrial environment can bring several benefits. Among them, higher production yield, quality improvement, solutions for a better environment, new products development or cost cutting are the most important .

## **Ion-Induced effects during thin film growth**

A. von Keudell<sup>1</sup>, C. Hopf<sup>2</sup>, M. Meier<sup>2</sup>, T. Schwarz-Selinger<sup>2</sup>, W. Jacob<sup>2</sup>

<sup>1</sup>*Arbeitsgruppe Reaktive Plasmen, Ruhr-Universität Bochum, Universitätsstr. 150, 44708 Bochum*

<sup>2</sup>*Centre for Interdisciplinary Plasma Science, Max-Planck-Institut für Plasmaphysik, EURATOM Association, Boltzmannstr. 2, 85748 Garching*

The interaction of a plasma with a solid is governed by heterogeneous surface reactions since different radicals and ions interact simultaneously with the exposed film surface. Individual surface processes for single ions or single radicals are often studied in dedicated surface science experiments. However, the simultaneous interaction of several species with the surface may lead to various synergisms or anti-synergisms. These heterogeneous surface processes are studied in detail in a dedicated beam experiment. Two examples are presented, chemical sputtering and ion-assisted film formation, which play an important role in thin film deposition or etching in any low temperature plasma process. Chemical sputtering occurs if an impinging flux of ions and neutrals leads to an enhanced erosion yield if compared to the erosion yield of ions or neutrals alone. This process is demonstrated for the sputtering of carbon materials at room temperature and at low ion energies. Ion-assisted film growth occurs if the chemisorption of neutral radicals at the film surface is mediated by the formation of surface dangling bonds by incident ions. This process is demonstrated and quantified for C:H film formation from CH<sub>3</sub>, H radical beams and an additional flux of hydrogen or noble gas ions. The implication of these results for the understanding of surface processes in low temperature plasmas is discussed.



# The Destruction of CFCs in a Non-Thermal, Atmospheric Pressure Plasma

Claire L. Ricketts, Anna E. Wallis, J. Christopher Whitehead and Kui Zhang

*Department of Chemistry, University of Manchester, Oxford Road, Manchester, M13 9PL, UK*

## Abstract

The destruction of CFC-12 ( $\text{CF}_2\text{Cl}_2$ ) has been studied in an AC, non-thermal, atmospheric pressure plasma reactor packed with barium titanate beads. Destructions as high as 43% are found for processing in nitrogen although there is an intrinsic source of oxygen in the  $\text{BaTiO}_3$  beads which plays an important role in the removal chemistry. The addition of water (< 5%) increases the destruction efficiency but the addition of molecular hydrogen brings about no enhancement. Destruction in air is about half as efficient as for  $\text{N}_2$ .

## 1. Introduction

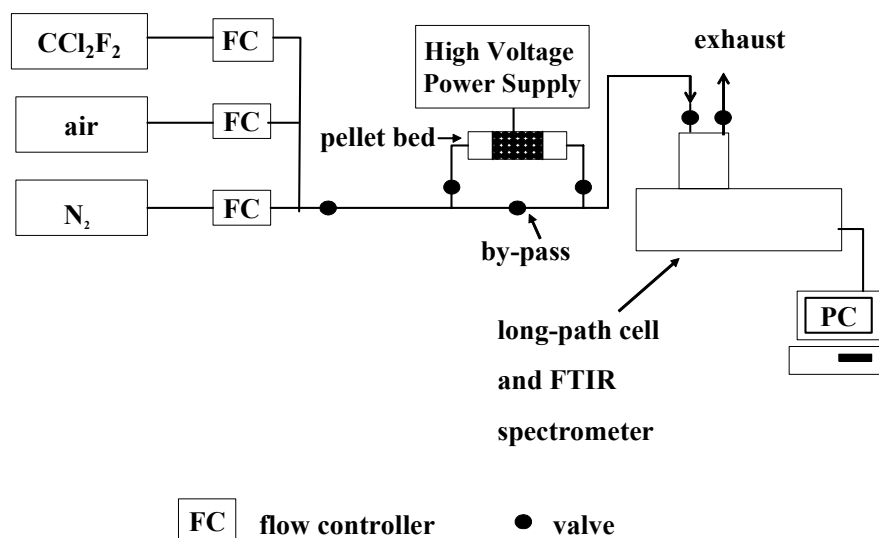
There is an urgent need to develop efficient methodologies for the destruction of CFCs to prevent the release of such ozone-depleting substances (ODS) into the atmosphere and their subsequent migration into the stratosphere. EC Regulations came into force on January 1st, 2002 requiring redundant domestic refrigerators and freezers to be recycled. Two and a half million domestic and about 500,000 commercial refrigerators are replaced in the UK every year. Studies have found the average lifespan of a fridge to be 11 years. It is particularly difficult to safely recover the ODS materials used in their construction. Between 20-25% of ODS are held as liquid refrigerant and 75-80% are contained within the rigid foam insulation. Various techniques including direct incineration, shredding and incineration, granulation with cryo-condensation or carbon absorption and subsequent high-temperature incineration of gases are used to deal with the various components. Particularly high temperature ( $\geq 1250^\circ\text{C}$ ) are needed to ensure that the halogenated ODS components are safely destroyed without the formation of dioxins. It is against this background that many groups have investigated the prospect of using thermal and non-thermal plasma methods as an energy efficient method of destroying ODS compounds, in particular CFCs.

In this paper, we report studies of the destruction by non-thermal, atmospheric pressure plasma of CFC-12, dichlorodifluoromethane ( $\text{CF}_2\text{Cl}_2$ ) in various gas streams (air and nitrogen including the addition of molecular hydrogen and water) using an AC, packed-bed plasma reactor loaded with  $\text{BaTiO}_3$  beads. Previous studies of the destruction of  $\text{CF}_2\text{Cl}_2$  by plasma at atmospheric pressure include the use of microwave plasma [1], thermal plasma torch [2,3], dielectric barrier discharge and a pulsed corona discharge[4]. A packed bed, plasma reactor similar to that used in this experiment has been employed to study the destruction of CFC-113 ( $\text{CCl}_2\text{F}-\text{CClF}_2$ ) at atmospheric pressure [5].

## 2. Experimental

The experimental arrangement is essentially that used previously [6,7] and is shown schematically in Figure 1. The plasma source is a dielectric pellet-bed reactor consisting of a glass tube of 24 mm internal diameter with two electrodes ~25 mm apart through which the gas passes. The space between the electrodes is packed with 3.5 mm diameter barium titanate beads. The diameter of the beads is chosen to allow for as large a number of beads as possible, thereby maximising the number of contact points for the formation of discharges whilst not restricting the porosity of the reactor significantly. This balances the requirements of gas flow and having as uniform a discharge as possible. An AC voltage ( $V_{\text{pk-pk}} \approx 15 \text{ kV}$ ) at a frequency between 10.25 and 13.25 kHz is applied between the electrodes. Using a digital storage oscilloscope (Tektronix TDS 3012), we record the current and voltage waveforms for the discharge by using a calibrated high voltage probe and measuring the current across a 1 k $\Omega$  resistor in the return earth path from the reactor. The average power of the discharge is then obtained by integrating the product of voltage and current as a function of time.





**Figure 1** A schematic diagram of the plasma experiment

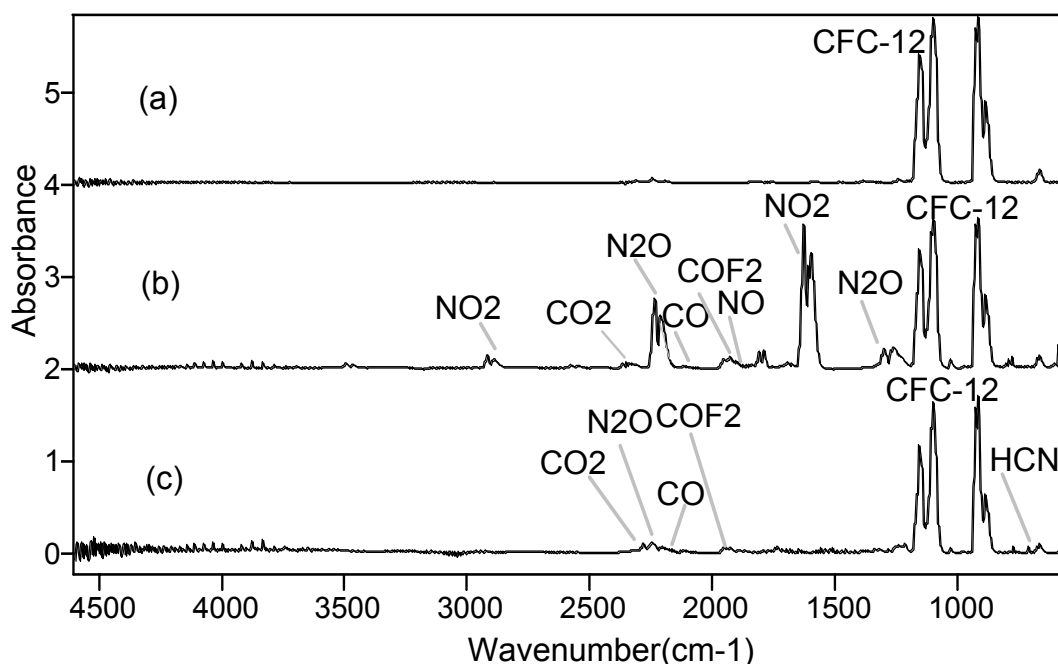
A flow ( $0.25 - 1.5 \text{ litre min}^{-1}$ ) of pure air or nitrogen at room temperature controlled by flow controllers (MKS Mass Flo) is either blended with a small flow of gaseous  $\text{CCl}_2\text{F}_2$  giving a concentration of  $\sim 30 - 500$  ppm entering the plasma reactor. Small amounts of hydrogen could be added directly to the gas stream and also water by bubbling nitrogen through liquid water to investigate the effect of these additives on the processing. The gas mixture was maintained at a pressure of  $\sim 1$  bar. For a total gas flow of  $1 \text{ litre min}^{-1}$ , the residence time in the reactor is  $0.25 \text{ s}$ . Dichlorodifluoromethane (Argo International,  $> 99\%$  purity) was used as supplied. No attempt was made to further purify or dry the gas. The end-products of the plasma processing were monitored on-line by infrared spectroscopy using a long-path gas cell ( $4.8 \text{ m}$ , Venus Series) and a Fourier Transform Infrared (FTIR) spectrometer (Shimadzu 8300) with a resolution of  $1 \text{ cm}^{-1}$ . Stainless steel, nylon and PTFE tubing, valves and fittings of  $1/4"$  external diameter were used to handle the gases as appropriate. No attempt was made to bake or otherwise condition the surfaces of the system.

### 3. Results

Figure 2 shows a comparison of the FTIR spectrum obtained for dichlorodifluoromethane without plasma processing and with plasma processing in air and nitrogen. In air, the percentage destruction ranges between 8 and 39% depending on the initial concentration and the flow rate, with the highest destruction being obtained for the lowest flow rate of  $0.25 \text{ l min}^{-1}$  and an initial  $\text{CF}_2\text{Cl}_2$  concentration of 120 ppm. The detected products for the processing in air at flow rates of  $1.0 - 1.5 \text{ litre min}^{-1}$  were CO ( $\sim 30\%$ ),  $\text{CO}_2$  ( $\sim 15\%$ ) and  $\text{COF}_2$  ( $\sim 55\%$ ) accounting for 97% of the destroyed carbon;  $\text{COF}_2$  was the only detected halogen-containing end-product and account for  $\sim 55\%$  of the removed fluorine. There was substantial production ( $\sim 300 \text{ ppm}$ ) of nitrogen oxides, principally  $\text{NO}_2$  ( $\sim 60\%$ ) and  $\text{N}_2\text{O}$  ( $\sim 30\%$ ) with the balance being NO. For the lower flow rates where the residence time in the plasma reactor is higher, significantly more of the destroyed carbon becomes CO and  $\text{CO}_2$  rather than  $\text{COF}_2$  ( $57\%$  *c.f.*  $45\%$ ) together with higher production of the oxides of nitrogen ( $\sim 500 \text{ ppm}$ ).

In nitrogen, the destructions were approximately twice as large as the corresponding values for processing in air, ranging from 13 – 43%. The major carbon containing end-products are HCN (trace), CO,  $\text{CO}_2$  and  $\text{COF}_2$  accounting for  $\sim 85\%$  of the carbon removed. No other halogen-containing end-products could be detected by FTIR. Small amounts of NO and  $\text{N}_2\text{O}$  were formed ( $\sim 25 \text{ ppm}$ ) in a ratio of 1:2. The origin of the oxygen in this system will be discussed below. Small amounts of hydrogen ( $< 2\%$ ) were added to the nitrogen carrier gas but no change was observed in the magnitude of the destruction or the identity of the

end-products. Similarly, small amounts of water (< 5%) were added to the nitrogen bringing about an increase in destruction efficiency from 20 to 30%. The identity of the products was unchanged but most of the increased destruction resulted in additional production of CO.



**Figure 2** FTIR spectra of the end-products of the plasma processing of CFC-12, dichlorodifluoromethane. (a) plasma off; (b) in air; (c) in nitrogen. Resolution is 1 cm<sup>-1</sup>.

For the experiments reported here, the power supplied to the plasma was measured as 1.08 W irrespective of the flow rate or identity of the carrier gas. In terms of reduced energy density, this ranges between 40 and 260 J litre<sup>-1</sup> corresponding to an minimum energy requirement of between 265 and 570 eV per molecule of CF<sub>2</sub>Cl<sub>2</sub> removed in nitrogen and air, respectively.

#### 4. Discussion

The primary step of the decomposition of CF<sub>2</sub>Cl<sub>2</sub> in nitrogen is either by electron impact dissociation involving dissociative electron attachment [8] followed by neutralisation of the resulting negative ion or by collision-induced dissociation with metastable triplet molecular nitrogen, N<sub>2</sub> (*A*<sup>3</sup>Σ<sub>u</sub><sup>+</sup>) which has an excitation energy of 6.23 eV. The most likely end-products for the dissociative channels are CF<sub>2</sub>Cl and Cl in either case. Wang et al. [8] have shown that the dissociative electron attachment channel



is exoergic and because the C-Cl bond in CF<sub>2</sub>Cl is much weaker than the C-F bond, the channel



will be dominant. If there is a source of atomic oxygen in the system, the rate of the direct reaction with CF<sub>2</sub>Cl<sub>2</sub> is too small to allow this route to contribute to the decomposition of CF<sub>2</sub>Cl<sub>2</sub>. However, the oxygen atoms can oxidise the CF<sub>2</sub>Cl radical into CF<sub>2</sub>



This radical can be further oxidised along with any smaller radicals such as CF and CF<sub>2</sub> to produce CO and CO<sub>2</sub>. This gives the range of carbon containing end-products that we observe in the presence of oxygen. The absence of any phosgene, COCl<sub>2</sub>, which we could not detect in our FTIR spectra (minimum sensitivity of 1 ppm) or any halocarbon products confirms the original dissociation channel and the subsequent chemistry. The fluorine that is not present as COF<sub>2</sub> is most likely to be in the form of F<sub>2</sub> (undetectable by FTIR). The total absence of any chlorine-containing end-products in our experiments confirms the postulated mechanism and suggests that Cl<sub>2</sub> (undetectable by FTIR) is the likely end-product formed by recombination of chlorine atoms or by reaction involving the intermediate ClO.

Whilst it is clear about the source of oxygen when the dissociation takes place in air, the presence of oxygen-containing end-products when the carrier gas is nitrogen seems at first glance to be surprising. However, there is evidence that BaTiO<sub>3</sub> beads in packed bed plasma reactors constitute a source of intrinsic oxygen that can be released under plasma action. Ogata *et al.* [9] have shown that lattice oxygen species in BaTiO<sub>3</sub> play an important role in the oxidation of methane and in the formation of N<sub>2</sub>O. They have shown that the N<sub>2</sub>O that is formed comes from the oxidation of molecular nitrogen with lattice oxygen species and that these species are also able to oxidise the hydrocarbon preferentially to CO. We invoke a similar explanation for the production of oxygen containing species during our plasma processing of CFC-12 in nitrogen.

The different sources of oxygen for discharges in air and nitrogen can be most clearly distinguished in the case of the yield of the oxides of nitrogen. In the air discharge, the dominant oxide of nitrogen is NO<sub>2</sub> formed by the reactions of nitrogen atoms produced in the discharge whilst in the nitrogen discharge production of N<sub>2</sub>O dominates. In an air discharge, NO is formed initially by the recombination of oxygen and nitrogen atoms and NO<sub>2</sub> is produced from NO by several routes including reaction with oxygen atoms. This production of NO<sub>x</sub> is largely independent of the mechanism that decomposes the CFC. Ogata *et al.* [9] have identified that the source of N<sub>2</sub>O is the BaTiO<sub>3</sub> lattice oxygen whereas the NO<sub>x</sub> (NO and NO<sub>2</sub>) is formed by the alternative gas-phase mechanism.

We can compare our detected end-products with those obtained in other studies. In their microwave study of 2 – 8% CF<sub>2</sub>Cl<sub>2</sub>, Jasinski *et al.* [1] found that COF<sub>2</sub>, COCl<sub>2</sub>, Cl<sub>2</sub>, CO and CO<sub>2</sub> were produced together with NO, NO<sub>2</sub> and N<sub>2</sub>O<sub>4</sub>. They achieved up to 100% destruction with microwave powers of 100 W. We agree with these findings except for the production of phosgene, COCl<sub>2</sub>, and the absence of N<sub>2</sub>O which is not surprising if we accept that its production is a function of the use of BaTiO<sub>3</sub> as discussed above. Jian *et al.* [10] studied the destruction of 2.6% CF<sub>2</sub>Cl<sub>2</sub> in air in an atmospheric pressure, dielectric barrier discharge. For residence times of greater than 30 s, they could achieve complete destruction of the CFC yielding COF<sub>2</sub>, COFCl and CF<sub>4</sub>.

We can comment on the relative efficiencies of the various gas streams used in our work. The most efficient destruction is found in nitrogen where the small trace of oxygen that is intrinsic to the barium titanate beads is effective in converting the initially formed dissociation products of CF<sub>2</sub>Cl<sub>2</sub> into stable end-products. This is enhanced by the addition of water presumably by the production of OH radicals that will accelerate the conversion of the dissociation products compared with the effect of oxygen. The addition of molecular hydrogen has no effect on the destruction probably because it is relatively unreactive compared with radicals such as oxygen atoms or OH. The reduction in destruction efficiency in air where there is a large amount of oxygen present comes from the competition for electrons in the plasma discharge between CF<sub>2</sub>Cl<sub>2</sub> and the oxygen. Reduction in the electron attachment to CF<sub>2</sub>Cl<sub>2</sub> will affect the overall amount of dissociation by this channel. The increase in atomic oxygen produced in the air discharge will have no effect on the degree of CFC dissociation as attack by O atoms on the CFC plays no part in its destruction.

In terms of energy costs, the corona studies [4] found a value of 2000 eV / molecule for the destruction of CF<sub>2</sub>Cl<sub>2</sub> in humidified air, compared with our value of 265 – 570 eV / molecule. In contrast, destruction by the microwave torch [1] is at an energy cost for the CF<sub>2</sub>Cl<sub>2</sub> destruction of 4 kW hr kg<sup>-1</sup> or 0.05 eV / molecule.

## Conclusions

The effectiveness of non-thermal, atmospheric pressure plasma processing for the destruction of CFC-12,  $\text{CF}_2\text{Cl}_2$ , has been demonstrated in gas streams of air and nitrogen. The initial destruction step for the CFC comes about by dissociative electron attachment together with collision-induced dissociation by the metastable  $\text{N}_2$  ( $A$ ) state. The subsequent chemistry depends on oxygen-containing species which either come from the plasma discharge in air or are released by plasma action on the barium titanate beads in the packed bed. Under these conditions, complete destruction would yield  $\text{CO}_2$ ,  $\text{Cl}_2$  and  $\text{F}_2$ . However, short residence times or insufficient energy means that oxidation is incomplete and the products also include  $\text{COF}_2$  and  $\text{CO}$ . An undesirable by-product of the plasma processing is the co-production of high levels of nitrogen oxides especially in the case of processing in air. We are currently investigating the hybrid technique of plasma-assisted catalysis in which the  $\text{NO}_x$  will be converted into  $\text{N}_2$  on a suitable catalyst which may also enhance the destruction of the CFC increasing the overall energy efficiency of the process.

**Acknowledgement** Support of this work by the UK Engineering and Physical Sciences Research Council is gratefully acknowledged.

## References

- [1] M Jasinski, J Mizeraczyk, Z Zakrzewski, High Temp. Mat. Proc. 6 (2002) 317.
- [2] AB Murphy, T McAllister, Appl. Phys. Lett. 73 (1998) 459.
- [3] YP Malkov, AA Davidyan, YE Filippov, MA Rotinyan, Appl. Phys. Lett. 75 (2002) 946.
- [4] RA Korzekwa, MG Grothaus, RK Hutcherson, RA Roush, R Brown, Rev.Sci.Instr. 69 (1998) 1886.
- [5] T Yamamoto, BW-L Jang, IEEE Trans. Ind. Appl. 35 (1999) 736.
- [6] C Fitzsimmons, JT Shawcross, JC Whitehead, J. Phys. D: Appl. Phys. 32 (1999) 1136.
- [7] C Fitzsimmons, F Ismail, JC Whitehead, JJ Wilman, J. Phys. Chem. A. 104 (2000) 6032.
- [8] Y Wang, LG Christophorou, JK Verbrugge, J. Chem. Phys. 109 (1998) 8304.
- [9] A Ogata, K Mizuno, S Kushiya, T Yamamoto, Plasma Chem. & Plasma Proc. 18 (1998) 363.
- [10] H Jian, S Wei-ming, L Chao-min, S Wang, H Hui-qi, J. Environ. Sci. 11 (1999) 82.

# Orietational effects induced by plasma treatment in amino acids adsorption processes on polysiloxane.

G.L. Gambino<sup>1</sup>, C. Satriano, G. Marletta

*Laboratory for Molecular Surfaces and Nanotechnology (LAMSun) - Department of Chemical Science, University of Catania, Catania, Italy*

## Abstract

The present paper deals with the study of the adsorption process of l-lysine and l-cysteine on poly(hydroxymethyl)siloxane thin films modified by oxygen plasma and aged in water or air environment. The amino acids surface coverage and orientation were correlated to the surface chemical structure and composition as well as to the surface free energy properties of plasma-modified surfaces.

## 1. Introduction

Plasma treatment of polymers is a well-established technique to change the interfacial properties—such as adhesion, friction, and biocompatibility—through the modification of surface properties of polymers such as chemical structure and composition, morphology as well as the related surface free energy [<sup>1,2</sup>]. In particular, modification by plasma of silicon-based polymers is a general way to increase their wettability properties by formation of silica-like phases [<sup>2,3</sup>]. Moreover, the stability and aging processes of plasma-treated surfaces are critical factors that can drastically influence the wettability, either through the hydrophobic recovery process, for instance by chain rearrangements or by diffusion of untreated polymer fragments through cracks in the treated layer [<sup>2</sup>], or, in the opposite case, by reactions of surface reactive species induced by plasma, such as radicals, ions, etc., with polar molecules from contacting phase, producing a very hydrophilic surface [<sup>4</sup>]. For instance, Everaert et al. found a minimal recovery of plasma-treated silicone after storage in water and negligible recovery in liquid nitrogen when compared to storage in ambient air [<sup>5</sup>].

The wettability and, in general, the surface free energy properties of surfaces have been often invoked as crucial parameters ruling the interaction of plasma-treated surfaces with biological systems, including cells, proteins and amino acids [<sup>1,2,6,7</sup>].

In this work the surface properties of a polysiloxane were modified by oxygen plasma treatment and controlled aging processes. The adsorption behavior on these surfaces of two selected amino acids, lysine and cysteine, was investigated by means of Angular-Resolved X-ray Photoelectron Spectroscopy (AR-XPS) and Surface Free Energy (SFE) measurements. These specific amino acids were chosen in order to explore the influence of different intermolecular interactions, including van der Waals forces, hydrogen bonding and coulombic interactions on substrates having very similar compositions but different surface free energy properties.

## 2. Materials and Methods

Poly(hydroxymethyl)siloxane (PHMS) thin films of (500±20) nm of thickness were deposited from a commercial solution (ACCUGLAS 512B, purchased from Allied Signal, USA) on either p-doped silicon (100) wafers by using the spin coating technique (3000 r.p.m. for 60s at room temperature). PHMS samples were modified by O<sub>2</sub>-plasma treatment using the following operative conditions: excitation frequency, 13.56 MHz; power, 100 W; pressure, 53.3 Pa; modification time, 60 seconds. The plasma-treated samples were studied both immediately after the modification (PHMSm samples) and after aging for 24Hrs respectively in laboratory atmosphere (PHMSm\_A samples) or deionized water (PHMSm\_W samples). Silicon dioxide of 520 nm of thickness, obtained by thermal growth, was considered as reference substrate.

Solutions of L-Lysine (Lys) [NH<sub>3</sub><sup>+</sup>(CH<sub>2</sub>)<sub>4</sub>CH-(NH<sub>2</sub>)COO<sup>-</sup>] and L-Cysteine (Cys) [SH-CH<sub>2</sub>-CH-(NH<sub>3</sub><sup>+</sup>)COO<sup>-</sup>] (purchased as powders from Sigma Chemical Co.) were prepared at a final concentration of 7x10<sup>-2</sup> M in Millipore water. The measured pH of amino acid solutions were close to the isoelectric pH of each amino acid, i.e., 9.5 (±0.2) and 6.5(±0.2) for Lys and Cys, respectively. The study of the adsorption processes was performed by soaking the substrates in the amino acid solutions for 1 hour, therefore rinsing with 2 ml of Millipore water and drying in air.

Plasma-modification and aging effects as well as the interaction of the various surfaces with the amino acids were investigated by means of X-Ray Photoelectron Spectroscopy (XPS) and Surface Free Energy (SFE)

measurements.

XPS analysis was performed with a Kratos HX AXIS spectrometer equipped with a dual Al/Mg anode and a hemispherical analyzer. The spectra were obtained by using Mg  $K\alpha_{1,2}$  radiation (at 1253.6 eV) in FAT mode with pass energy of 40 eV. The XPS spectra were analyzed by using an iterative least squares fitting routine based onto gaussian peaks and a linear background subtraction. In order to subtract the charging effect the C1s photoelectric peak was fixed at a binding energy (BE) value of 285.0 eV. Angular Resolved XPS (ARXPS) measurements were obtained at the take-off angles ranging from 30° to 90°, as measured with respect to sample surface.

SFE measurements were performed, in the framework of the Lifshitz - van der Waals (LW) and the short-range acid-base (AB) model [8], through the determination of static contact angle of the three following probe liquids: pure deionized water, with a surface energy of  $\gamma_w = 72.8 \text{ mJ/m}^2$ , glycerol ( $\gamma_{Gl} = 63.4 \text{ mN/m}$ ) and tricresyl phosphate (TCP) ( $\gamma_{TCP} = 40.9 \text{ mJ/m}^2$ ) [9] (Aldrich Chem. Co.) Measurements were performed at room temperature with the sessile drop method by using a Kernco instrument. Each value was obtained by averaging the results of at least 5 droplets on different zones of each sample.

## 2. Results and Discussion

### 2.1 Surface characterization of plasma-modified substrates

The change of surface properties of PHMS films after plasma treatment and the two different aging process were carefully investigated by means of ARXPS and SFE measurements.

Table 1 shows the average surface compositions for the various samples at take-off angles of 90° and 30°, which respectively correspond to sampling depths of  $\sim 98 \text{ \AA}$  and  $48 \text{ \AA}$ , as calculated by assuming an attenuation length of  $\sim 32.6 \text{ \AA}$  [10] for Si2p signal in SiO<sub>2</sub>-like phases.

**Table 1** Surface atomic percentages and O/Si ratio for untreated and the various plasma-treated PHMS as function of take-off angle.

Table1	C (at. %)		O (at. %)		Si (at. %)		O/Si	
	90°	30°	90°	30°	90°	30°	90°	30°
PHMS	29.2	35.0	43.2	40.0	26.0	25.0	1.7	1.6
PHMSm	0	4.8	75.9	73.2	24.1	22.0	3.2	3.3
PHMSm_A	6.0	5.5	69.9	72.2	24.2	22.3	2.9	3.2
PHMSm_W	5.7	6.8	71.3	71.3	23.0	22.0	3.1	3.2
SiO <sub>2</sub>	0	6.6	77.8	71.9	22.6	21.5	3.4	3.3

One can see that the original PHMS surface, having a stoichiometry of [Si<sub>1</sub>C<sub>1.1</sub>O<sub>1.7</sub>], is drastically converted by O<sub>2</sub> plasma in a SiO<sub>2</sub>-like phase. In fact, the freshly-modified samples exhibit the complete removal of the carbonaceous species from the surface and the change to a stoichiometry of [Si<sub>1</sub>O<sub>3.2</sub>], that is very similar to that found for SiO<sub>2</sub> surfaces (i.e., [Si<sub>1</sub>O<sub>3.4</sub>]). On the other hand, both PHMSm\_A and PHMSm\_W aged surfaces display a low and comparable carbon content of about 6%. Furthermore, the comparison between the Si/O ratios at the two different take-off angles reveals that the SiO<sub>2</sub>-like phases induced by plasma treatment are quite homogeneous within the sampled depths for both aging processes.

**Table 2** Static water contact angle  $\theta$  (°) and surface free energies ( $\text{mJ/m}^2$ ): total ( $\gamma^{\text{TOT}}$ ), dispersive ( $\gamma^{\text{LW}}$ ) and polar ( $\gamma^{\text{AB}}$ ) components, where  $\gamma^{\text{TOT}} = \gamma^{\text{LW}} + \gamma^{\text{AB}}$ .

	$\theta(^{\circ}) \pm \varepsilon(^{\circ})$	$\gamma^{\text{LW}}$	$\gamma^{\text{AB}}$	$\gamma^{\text{TOT}}$
PHMS	88 (±1)	25.00	0.00	25.00
PHMSm	2 (±1)	40.40	23.53	63.93
PHMSm_A	8 (±1)	37.52	22.48	60.00
PHMSm_W	15 (±1)	23.94	1.36	25.30
SiO <sub>2</sub>	38 (±1)	39.39	17.43	56.82

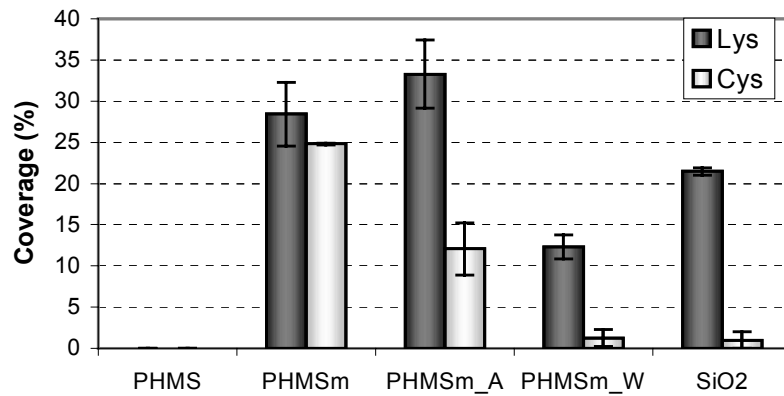
The SFE analysis of the various surfaces evidences significant changes of polar character of the surfaces induced by plasma.

In fact, as shown in Table 2, the PHMS untreated samples exhibit the highest water contact angle  $\theta$  (i.e., highly hydrophobic surfaces), the PHMSm samples are very hydrophilic surfaces (with  $\theta$  values very close to zero), and finally the aged PHMSm\_A and PHMSm\_W exhibit a mild recovery of  $\theta$  respectively to 8° and 15° values. It is to note that the larger hydrophobic recovery of water-aged surfaces with respect to the air-aged ones is probably due to the removal of water-soluble, low-molecular-weight, oxidized

material produced by plasma treatment and dissolved during storage in water [11]. This assumption is supported by the analysis of the surface free energy in terms of apolar Lifshitz van der Waals ( $\gamma^{LW}$ ) and polar Lewis acid-base ( $\gamma^{AB}$ ) components. In fact, as one see in Table 2, while the untreated PHMS exhibits a completely dispersive character, the plasma treatment induces the appearance of the polar  $\gamma^{AB}$  component. As to the aged plasma-treated surfaces, while the  $\gamma^{AB}$  term drastically decreases for PHMSm\_W to a value of  $\sim 1$  mJ/m<sup>2</sup>, for PHMSm\_A the plasma-induced polar character is kept almost unchanged with respect to the freshly-modified surfaces. As to the SiO<sub>2</sub> samples, their relatively mild hydrophilic character suggests that the termination of these surfaces does not consist of a homogeneous layer of Si-OH groups, that instead should have a contact angle of 0-5° [12].

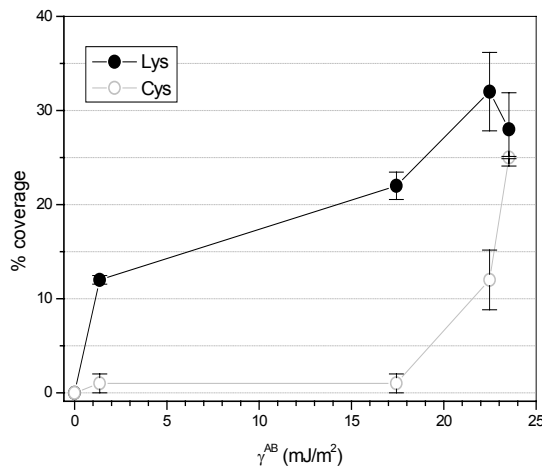
## 2.2 Amino acids- surfaces interactions

The amino acids surface coverage on the various surfaces, from XPS analysis, is reported in Fig.1 for both Lys and Cys.



**Fig. 1-** Lys and Cys average coverages on untreated PHMS, the various plasma-treated PHMS and SiO<sub>2</sub>. (Note that the error bar represents the standard deviation of the coverage calculated from the attenuation of N1s and Si2p signals, taken as XPS marker respectively for adlayer and substrate).

One see clearly that, while no adsorption is observed for both amino acids onto PHMS untreated, Lys exhibits a comparable and high coverage (about 30%) both on PHMSm and on PHMSm\_A, a significantly lower coverage on PHMSm\_W (about 12%), and the intermediate coverage of  $\sim 20\%$  on SiO<sub>2</sub> surfaces. On the other hand, the Cys exhibits for all the substrates a lower coverage than Lys. In particular, the Cys coverage on PHMSm is about twice then onto PHMSm\_A, while no significant Cys coverage was found on both PHMSm\_W and SiO<sub>2</sub> surfaces.



**Fig. 2-** Amino acid coverage vs. Lewis acid-base components of the SFE for the various substrates.

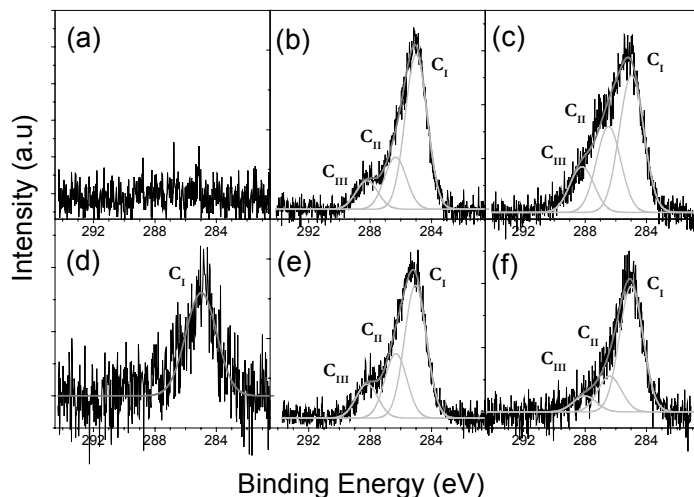
The observed different coverages for the different substrates can be related to the surface free energy properties, and in particular to the polar Lewis acid-base components.

In fact, Fig.2 shows that there is a general increase of amino acid coverage with increasing values of  $\gamma^{AB}$ , with different “threshold” values of  $\gamma^{AB}$  for each amino acid. In fact, while Lys coverage is even observed on PHMSm\_W samples surfaces, which have the very small value of  $\gamma^{AB} \sim 2$  mJ/m<sup>2</sup>, in the case of Cys a significant coverage can be observed only for surfaces PHMSm and PHMSm\_A, which have both  $\gamma^{AB}$  values higher than  $\sim 18$  mJ/m<sup>2</sup>. This finding suggests that the adsorption behavior of Cys molecules on the studied

substrates is mainly due to the polar interactions, probably electrostatic and hydrogen bonds. In the Lys adsorption process onto substrates having a very low

polar character, the observed significant coverage is probably due to the active role played by dispersive interaction forces. In fact, at variance of the small molecules of Cys, the larger hydrophobic side chains of Lys molecules may provide to this amino acid a some apolar character [13]. More insight on the chemical structure of the amino acid adlayers on the two substrates which exhibited the highest coverage, i.e., PHMSm and PHMSm\_A, were obtained from the detailed analysis of the C1s and N1s XPS peaks.

Fig. 3 shows the C1s peaks of both bare and amino acid-incubated samples for freshly plasma-treated and air aged plasma-treated surfaces.



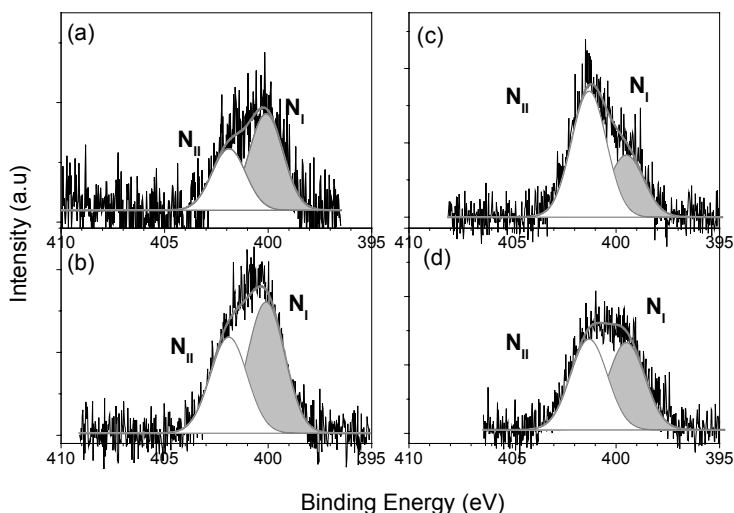
**Fig. 3-** C1s XPS peaks for: bare PHMSm (a) and incubated-PHMSm with Lys (b) and Cys (c); bare PHMSm\_A (d) and incubated-PHMSm\_A with Lys (e) and Cys (f).

As to the PHMSm surfaces, while on the bare substrate (Fig.3a) no trace of C1s peak was visible, the corresponding Lys- (Fig.3b) and Cys- (Fig.3c) incubated samples exhibited the characteristic amino acid C1s peakshape. In fact, from the peak fitting analysis, the following components were identified: C<sub>I</sub>, at 285.0±0.2 eV of binding energy (BE), assigned to C-C and C-H aliphatic bonds; C<sub>II</sub>, at 286.4±0.2 eV of BE, due to C-N and, for Cys, C-S bonds; C<sub>III</sub>, at 288.2±0.2 eV, assigned to COO<sup>-</sup> groups [14].

As to the PHMSm\_A samples, while the Lys-covered surfaces (Fig.3e) exhibit a C1s peak different to that of the corresponding not-incubated substrate (Fig.3d) and again the characteristic peakshape of the amino acid, as observed in the case of Lys on PHMSm, the Cys-incubated PHMSm\_A samples (Fig.3f), according to the lower coverage discussed above, do not display strong evidence of amino acid components.

The N1s peaks at take-off angles of 90° and 30° for PHMSm and PHMSm\_A are reported respectively in Figs. 4 and 5 for Lys- for Cys-incubated samples.

In particular, Fig. 4 shows that PHMS freshly plasma-treated surfaces exhibit similar N1s peakshapes for both take-off angles. The peakfitting evidenced two components, centered respectively at 400.1±0.2 eV (N<sub>I</sub>) and 402.1±0.2 eV (N<sub>II</sub>) of BE. These components, according to literature data [15], have been assigned



**Fig. 4 –** N1s XPS peaks of Lys-covered surfaces of: PHMSm at take off angles of 90° (a) and 30° (b); PHMSm\_A at take off angles of 90° (c) and 30° (d).



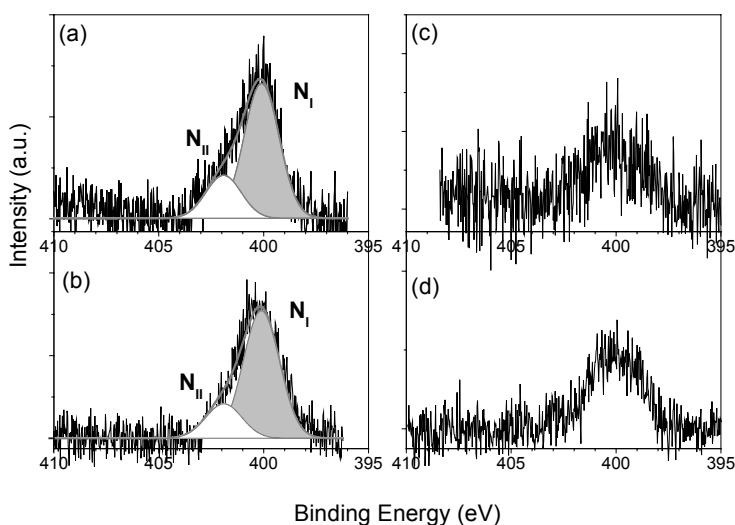
respectively to  $-\text{NH}_2$  and  $-\text{NH}_3^+$  groups H-bonded with surface  $\text{SiOH}$  and  $\text{SiOSi}$  groups ( $\text{N}_\text{I}$  component) and  $\text{NH}_3^+$  groups bonded via strong electrostatic interactions to negatively charged  $\text{SiO}^-$  groups ( $\text{N}_\text{II}$  component). One can see that the ratio  $\text{N}_\text{I}/\text{N}_\text{II}$  is of about 1.5 for both take-off angles, as consequence of the higher surface density of  $\text{SiOH}$  groups with respect to  $\text{SiO}^-$ , as expected for the  $\text{SiO}_2$ -like surfaces of PHMSm, if any in experimental conditions of basic pH (see Materials and Methods) [17].

The fact that the  $\text{N}_\text{I}/\text{N}_\text{II}$  ratio does not appreciably change for the two different sampling depths suggests that both N-containing groups (i.e.,  $\alpha$ -N and  $\epsilon$ -N) of Lys molecules are expected to interact with the surface, i.e. the adlayer is not more thick than a monolayer. Furthermore, the N/Si ratio changes from the value of 0.28 for  $90^\circ$  of take-off angle to 0.59 and 0.77, respectively for  $45^\circ$  and  $30^\circ$  of take-off angles, supporting the idea that Lys adsorbed as a homogeneous layer uniformly covering the substrate.

At variance of this, for the air aged plasma-treated PHMS surfaces the  $\text{N}_\text{I}$ s peak for the take-off angle of  $90^\circ$  (Fig. 4c) is significantly different from that one at  $30^\circ$  (Fig. 4d), and the ratio between the two components changes from  $\sim 0.5$  for  $90^\circ$  to  $\sim 1$  for  $30^\circ$  of take-off angle. Furthermore, the peak positions are significantly shifted of  $\sim 0.6$  eV towards the lower binding energies, respectively of 399.5 eV for  $\text{N}_\text{I}$  and 401.5 eV for  $\text{N}_\text{II}$ . This observation suggests that probably the interaction of amine and ammonium groups of the Lys with PHMSm\_A surfaces is not as much strong as in the case of PHMSm and in particular, that not all the N-containing groups are directly bound to the surface. Hence, in this case, probably the Lys adsorbs on the surface with island coverage consisting of aggregates of amino acid molecules within the adlayer. This consideration is supported by the N/Si ratio that does not significantly change for the examined sampling depths. In fact, the observed N/Si ratios are 0.39, 0.55 and 0.57 respectively for  $90^\circ$ ,  $45^\circ$  and  $30^\circ$  of take-off angles.

For Cys-covered samples, figure 5 shows that, while for PHMSm substrates the  $\text{N}_\text{I}$ s peak exhibits the same

$\text{N}_\text{I}$  and  $\text{N}_\text{II}$  components described above for the corresponding Lys-incubated PHMSm samples, but with very different relative ratios ( $\text{N}_\text{I}/\text{N}_\text{II} \sim 3$  instead of 1.5), the PHMSm\_A substrates have a quite symmetric peak centered around the  $\text{N}_\text{I}$  position. Furthermore, for both substrates no significant differences are evident for the two take off angles of  $90^\circ$  and  $30^\circ$ . It is to note that the very low contribution of the  $\text{N}_\text{II}$  component that, as described above, is related to  $\text{NH}_3^+$  species bonded to  $\text{SiO}^-$ , reflects the expected low relative surface density of  $\text{SiO}^-$  groups with respect to  $\text{SiOH}$ , due to the acid pH ( $\sim 6$ ) of the solution [16]. The measured N to Si ratio for the Cys-incubated surfaces is respectively of 0.2 for PHMSm and 0.1 for PHMSm\_A at take off angles of  $90^\circ$ . For decreasing sampling depths such ratios increase linearly suggesting a homogeneous coverage of a thin adlayers.



**Fig. 5-**  $\text{N}_\text{I}$ s XPS peaks of Cys-covered surfaces of: PHMSm at take off angles of  $90^\circ$  (a) and  $30^\circ$  (b); PHMSm\_A at take off angles of  $90^\circ$  (c) and  $30^\circ$  (d).

### 3. Conclusions

In this work we show that the adsorption of lysine and cysteine on polysiloxane surfaces modified by oxygen plasma strongly depends on the surface free energy properties, which change by different aging process after plasma treatment, despite the minimal changes in the chemical composition. In particular the amino acid coverage is found to be related to the plasma-induced high polar character of the surfaces, while the structure of the adlayer is in turn related to the specific functional groups both on the plasma-treated surfaces and on the amino acid molecules. In fact, while both Lys and Cys adsorb as uniform layers with strong interaction

between the amino acid N-groups and silanolic groups of the substrates, on the air aged surfaces the very small amount of adsorbed Cys is still an homogeneous layer, but Lys is found in island coverage.

### Acknowledgements

The financial supports from FIRB (RBNE01458S) and Progetto Giovani Ricercatori (Università degli Studi di Catania, 2000) are gratefully acknowledged.

### References

---

- [1] Polymer Surfaces and Interfaces; Mittal, K. L., Lee, K.W.,Eds; VSP: Utrecht, The Netherlands, 1997.
- [2] C. Satriano, S. Carnazza, S. Guglielmino, G. Marletta, Langmuir, **18**, 9469 (2002).
- [3] M. J. Owen, P. J. Smith, Polymer Surface modification: Relevance to Adhesion, K. L. Mittal (ed.) 1995, pp. 33-48.
- [4] T.R. Gengenbach, H.J. Griesser, Surf. Interface Anal. **26**, 498 (1998).
- [5] E. P.Everaert, C.H. van der Mei, H. J. Busscher, J. Adhesion Sci. Technol., 10, 4, 351 (1996).
- [6] Ch. Baquey, F. Palumbo, M.C. Porte-Durrieu, G. Legeay, A. Tressaud, R. d'Agostino Nucl. Instr. Meth.B 151, 255 (1999).
- [7] Ch. Dupont-Gillain, P.G. Rouxhet, Langmuir, **17** 7261 (2001).
- [8] R.J. Good, J.Adhes.Sci.Technol. **6**, 1269 (1992).
- [9] X Qin, W. V. Chang, , J. Adhes. Sci. Technol. **9**, 823 (1993).
- [10] S. Tanuma, C.J Powell, D.R Penn., Surf. Interface Anal. **17**, 927 (1991).
- [11] R. Foerch, G. Kill, M. J. Walzak, J. Adhesion Sci. Technol. **7**, 1077 (1993).
- [12] B. Janczuk, A. Zdziennicka, J. Mater. Sci. **29**, 3559 (1994)
- [13] Van Oss, C.J. Coll.and Surf. B: Bioninterfaces **5**, 91 (1995).
- [14] P.A. Gerin, P.B. Dengins. P.G. Rouxhet, J. Chim. Phys. **92**, 1043 (1995).
- [15] I.V Chernyshova, K.H. Rao, A.Vidyadhar, Langmuir, **16**, 8071 (2000).
- [16] Y. Duval, J. A. Mielczarski, O. S. Pokrovsky, E. Mielczarski, J. J. Ehrhardt, J. Phys. Chem. B **106**, 2937 (2002) .

***16<sup>th</sup> International Symposium on Plasma Chemistry***

***PAPER SUBMISSION FORM***

**Author Contacting Details**

Mr. ( ) Ms. ( )

*Family Name	GAMBINO		
*First Name	GRAZIA LAURA		
*Title	OTHER		
*Institute /Company	UNIVERSITY OF CATANIA		
*Address	VIALE ANDREA DORIA, 6		
*Zip Code	95125		
*City	CATANIA	*Country	ITALY
Phone	+39 095 7385075		
§E-mail	LGAMBINO@UNICT.IT		
§Fax	+39 095 336422		

**Contribution Details**

Abstract File Code	<b>ISPC- 661</b>		
*Paper Title	ORIENTATIONAL EFFECTS INDUCED BY PLASMA TREATMENT IN AMINO ACIDS ADSORPTION PROCESSES ON POLYSILOXAN		
*Presenting author	G. L. Gambino		
*Key Words	Amino acid adsorption	Polysiloxane	Plasma modification

# Plasma Diagnostics and Deposition of a-C:H in a High Density Inductively Coupled Methane Discharge

T. Mezziani, P. Colpo, G. Ceccone, and F. Rossi

*Joint Research Centre of the European Commission, Ispra, Italy*

## I Abstract

The deposition of a-C:H was investigated in a novel inductively coupled plasma source developed in our lab. The results in terms of growth rate and mechanical properties were related to the diagnostics of the plasma phase carried out by means of optical emission spectroscopy, mass spectrometry and Langmuir probe. The relative concentrations of atomic hydrogen and methyl radicals appeared to be strongly related to the growth rate of the films. In some conditions the hydrocarbon ions seem to participate in a significant manner to the DLC film growth.

## II Introduction

The attractive properties of amorphous hydrogenated carbon coatings (a-C:H) led to a high interest of the research community. Among all the different methods used for the deposition of diamondlike carbon coatings, inductively coupled plasma sources have the advantage of an independent control of the ion energy over the ion flux by applying a separate bias to the substrate.

This study deals with the deposition of amorphous hydrogenated carbon coatings with a novel inductively coupled plasma source demonstrating high plasma density and uniformity [1]. The main results of the diagnostics carried out in the plasma phase during the DLC deposition by  $CH_4$  decomposition are presented. The plasma was studied by Langmuir probe measurements, optical emission spectroscopy and by mass spectrometry, including ion detection and ion energy distribution (IED) measurements.

## III Experimental

A schematic diagram of the Magnetic Pole Enhanced ICP (MaPE-ICP) reactor [1] is shown in figure 1. The

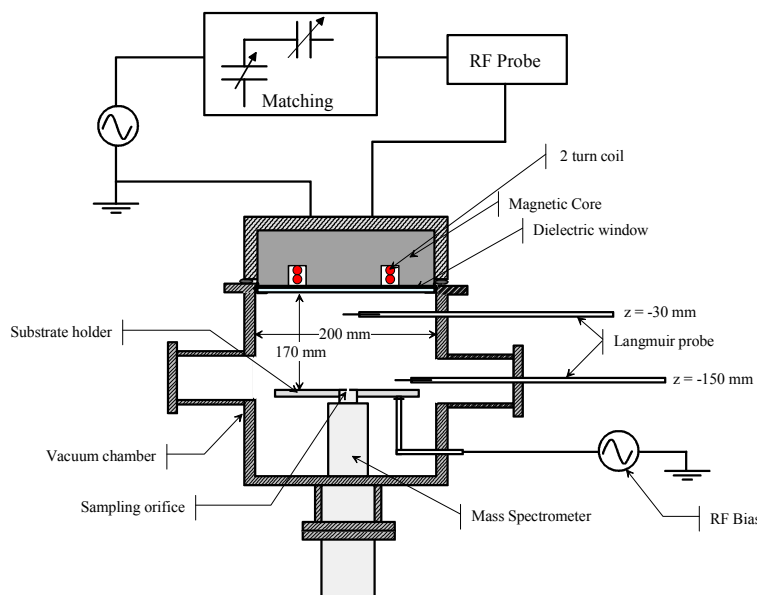


figure 1. Schematic diagram of the experimental setup

stainless steel plasma chamber has a cylindrical geometry with a 200-mm internal diameter and a 300-mm height. The 2-turn water-cooled coil is powered by a 13.56 MHz RF generator via a 'T' layout matching network composed of two driven air capacitors (Advanced Energy RFX II generator 1.25 kW, matching network AZ90). The coil antenna is embedded in a magnetic core allowing for a higher plasma density and uniformity.

The diamondlike carbon coatings are deposited through the decomposition of methane ( $CH_4$ ). The precursor gas is injected through a ring tube placed at the top of the chamber. This gas was sometimes diluted with Argon in order to study the effect of the noble gas addition on mechanical properties.

A parametric study was carried out in order to assess the effect of the different process parameters on the deposition results in terms of growth rate and mechanical properties. The coatings thickness was measured by alphastep profilometry, and their hardness and young modulus are measured by nanoindentation. The compressive stress in the films is deduced from the substrate curvature measurements as measured by laser profilometry, and their density is measured by quartz crystal microbalance. These results were related to the gas phase diagnostics as done by

Langmuir probe, mass spectrometry including ion detection and ion energy distribution measurements, and optical emission spectroscopy.

#### IV Results and Discussion

##### 1. Pressure effect:

The effect of varying the total pressure in the reactor chamber is illustrated in figure 2. As the total pressure increases, the plasma is confined near the creation region because the diffusion mechanisms are reduced. The electron density at the substrate location, i.e. 170 mm away from the dielectric window, goes then through a maximum that is measured at 20 mtorr.

The electron energy distribution function (eedf) was also measured and showed a net transition from a bi-Maxwellian distribution at low pressure to a Maxwellian, and then to a Druyvestein at higher pressure. The bi-Maxwellian distribution results from two different electron heating mechanisms [2]: ohmic and stochastic heating. Part of the low energy electrons created by inelastic collisions reach the sheath edge and may acquire energy by the stochastic heating mechanism, contributing to the “hot” population. Some of them lose energy by collisions and some are lost to the walls. When the pressure increases, the stochastic heating mechanism is reduced and the distribution gets closer to a Maxwellian distribution. At higher pressures, the loss of high energy electrons by inelastic collisions becomes important and the eedf turns into a Druyvestein.

The growth rate of diamondlike carbon in the same conditions is presented in figure 4. It passes through a maximum at 20 mtorr varying the same way as the electron density. This evolution of the growth rate can be explained by 2 main phenomena: the increase in active species concentration in the gas phase as the pressure increases, and their confinement close to the dielectric window added to the higher recombination collisions probability during their transport between the creation region and the substrate. Above 20 mtorr, the decrease observed in growth rate can thus be explained by the reduction of the active species concentration near the substrate.

##### 2. Power Effect:

As the RF power applied to the inductive coil increases, the charged particle density increases linearly, while the electron temperature is nearly constant as usually found in ICP sources. The concentration of the methyl radical and the atomic hydrogen in the gas phase are very important since they are believed to be the main species responsible for the carbon film growth [3]. The relative concentration of these species, as measured by

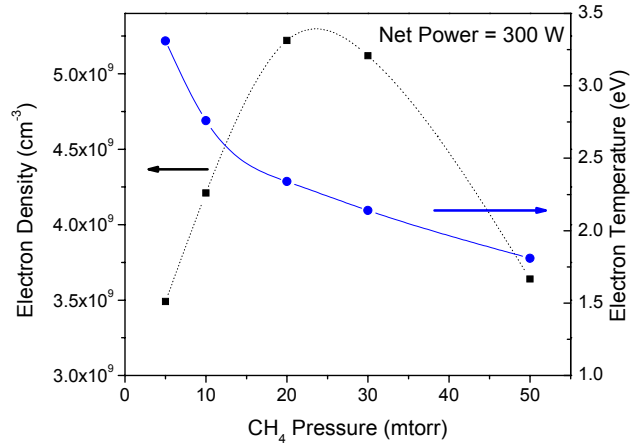


figure 2. Plasma parameters at the substrate location vs gas pressure.

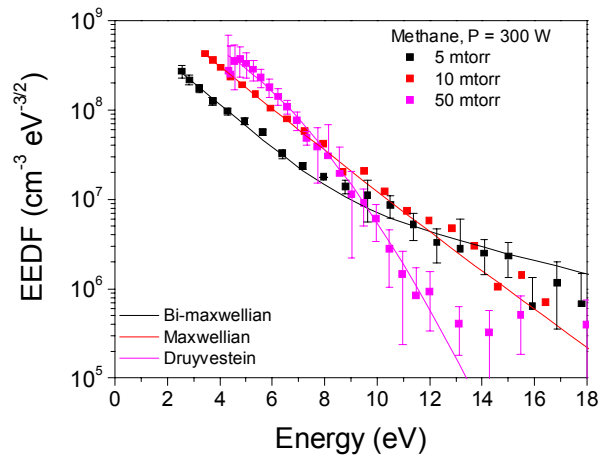


figure 3. Electron energy distribution function vs total pressure in a methane discharge (P = 300 W)

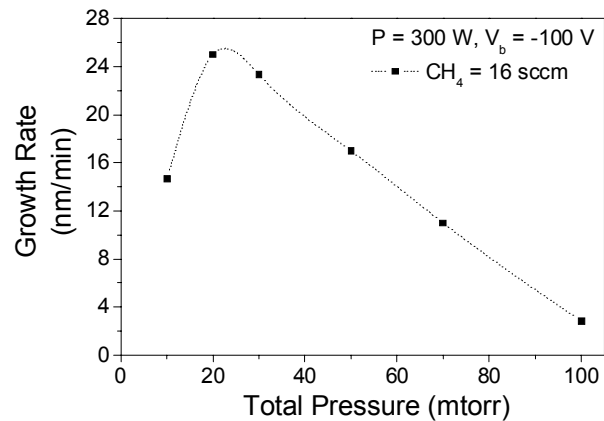


figure 4. Diamonlike carbon films growth rate vs methane pressure (P = 300 W).

appearance potential mass spectrometry, is presented in figure 5.

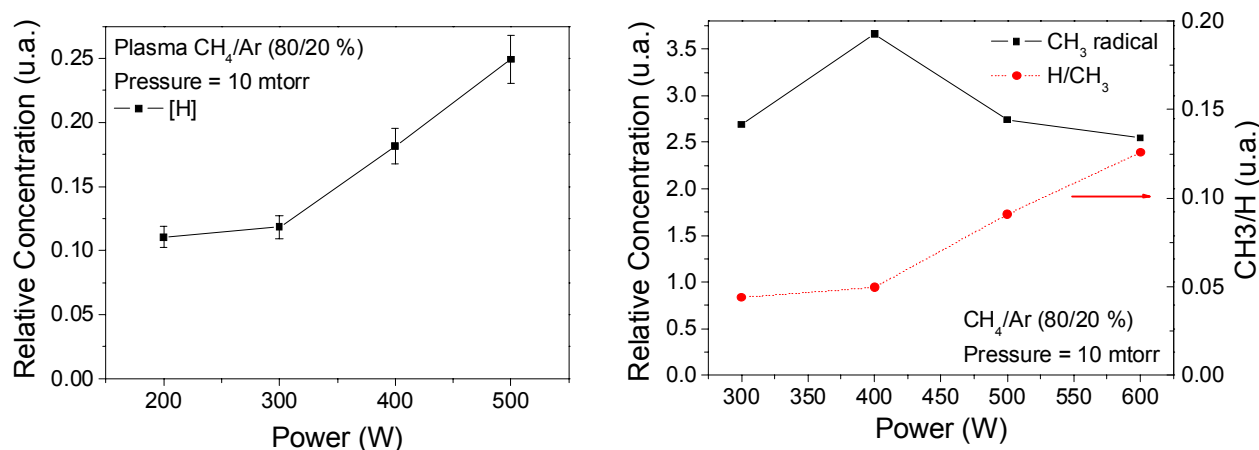


figure 5. Variation of the relative concentration of the hydrogen and methyl radicals vs RF power at 10 mtorr and for a methane/argon mixture operated at 10 mtorr.

Between 200 W and 300 W, the atomic hydrogen is created mainly through the dissociation reaction of the precursor  $CH_4$  and its concentration increases slowly. Above 300 W, a transition is observed where its concentration increases rapidly while the precursor fragmentation slows down as shown by the dissociation rate measurements. It seems that atomic hydrogen is then created from the dissociation of  $H_2$  as well as from other reaction pathways in which the discharge ions and argon metastables contribute significantly.

It is interesting to note that the methyl radical concentration passes through a maximum at 300 W (figure 5) indicating that this molecule is lost through other reactions including ionisation and dissociation at high powers.

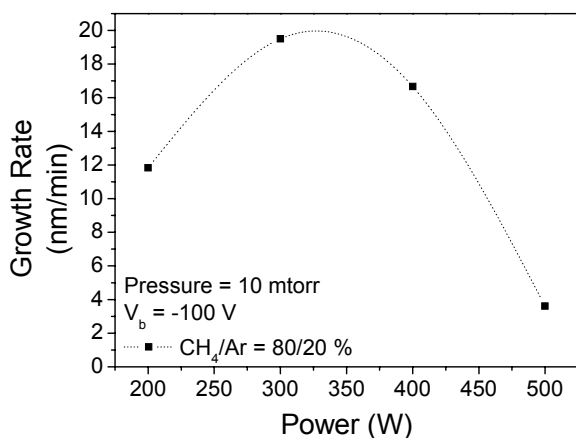


figure 6. Growth rate of the carbon films vs RF power applied to the inductive coil for a methane/argon mixture at 10 mtorr.

sources reaching about 90 % with the gas flow used in this study. It is usually observed that the diamondlike carbon growth rate is maximum for an intermediate value of the dissociation rate (between 40 and 60 %) [4,5]. This is mainly because the atomic hydrogen etches the hydrocarbon molecules on the surface and thus limits the growth rate if present in high quantity. As shown in figure 7, the growth rate increases with the total flow (i.e. with the residence time and dissociation rate decrease) while the coatings hardness seems to reach a plateau. As shown in the same figure, the stress is relatively high and varies almost the same way as hardness.

The growth rate (figure 6) increases from 200 W to 300 W because the hydrocarbon radicals and ion concentration increase while the atomic hydrogen concentration is nearly stable. From 300 W and above, the growth rate decreases significantly mostly because of the net increase of the atomic hydrogen concentration (that etches the hydrocarbon molecules on the surface) and of the substrate temperature. The mechanical properties vary the same way with in particular the coatings hardness that goes through a maximum from 300 W RF power.

### 3. Residence time :

The residence time was varied by changing the gas flow in the reactor while maintaining the total pressure constant.

The residence time influences mainly the dissociation rate and thus the composition of the plasma.

The dissociation rate is relatively high in this type of

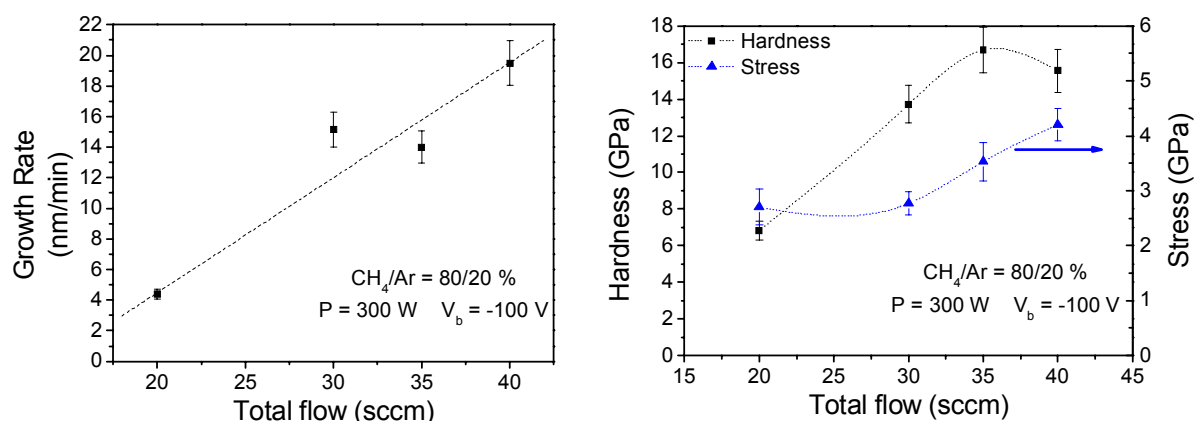


figure 7. Growth rate and mechanical properties of the amorphous carbon films deposited at 10 mtorr total pressure vs total flow rate.

#### 4. Substrate bias:

The possibility to apply an independent biasing to the substrate provides for a control of the ion bombardment energy without affecting the ion flux as was verified in this study for our reactor. All the previous results were obtained at a bias voltage of -100 V. If the substrate bias voltage is now varied, we observe a high influences the coatings properties. As shown in figure 8.b, the coatings hardness and stress goes through a maximum for  $V_b = -170\text{ V}$ . The growth rate decreases with the ion energy increase mainly because of the densification of the film, and also because of the enhancement of the surface sputtering.

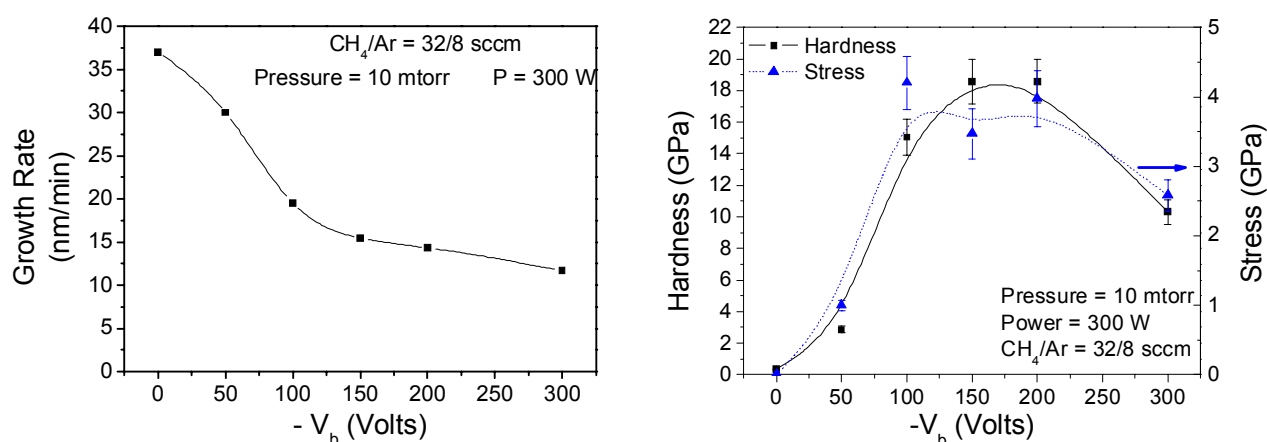


figure 8. Effect of the substrate bias voltage on (a) the films' growth rate and (b) mechanical properties at 10 mtorr pressure and for 300 W net power.

The FTIR analysis showed a transition from a polymer-like structure to a diamond-like structure of the deposited coatings as the negative substrate bias voltage increases from 0 to 200 V.

#### 5. Argon dilution:

The precursor is often diluted with a rare gas in order to modify the film structure and properties by modifying the nature and flux of the ion bombardment on the surface and especially to increase the ion flux with respect to the neutral flux bombarding the substrate. Most of the previous experiments were carried out with the dilution of the precursor gas with 20 % of argon. We now investigate the effect of the precursor dilution with argon in our reactor and the main results are presented in figure 9.

The addition of argon in the mixture while maintaining the total flow constant appears to have a net effect on the growth rate of the deposited films. The density of the films was also measured in order to determine the

cause of the deposition rate variations. Above 10% of argon in the mixture, a drop in the coatings growth rate can be observed and this decrease cannot only be explained by the densification of the film. The main cause of this decrease appears then to be related to the dilution of the precursor and thus to the decrease in the concentration of the radical species responsible for the growth of the layer. Figure 8.b shows that the hydrocarbon ions concentration increases in spite of the precursor dilution mostly because of the energy supply from the high lifetime argon metastables and ions (like  $\text{Ar}^+ [^2\text{P}_{3/2}]$ ). This seems to indicate that these ions don't contribute significantly to the growth of the carbon films.

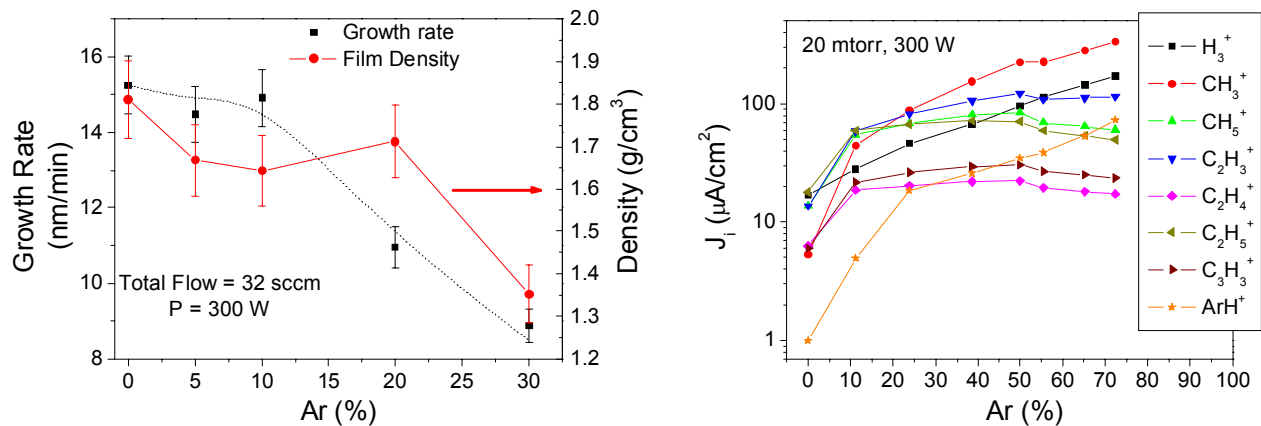


figure 9. (a) Growth rate and density of the carbon films vs argon content in the mixture. (b) Mass resolved ion current density vs argon content. P = 300 W, 20 mtorr.

The addition of argon influences also the mechanical properties of the deposited carbon coatings as shown in figure 10. It appears that the coatings' hardness decreases with the increase in argon content in the mixture. This result is consistent with the increase in the fraction of the  $sp^2$  sites as shown by Raman spectroscopy measurements.

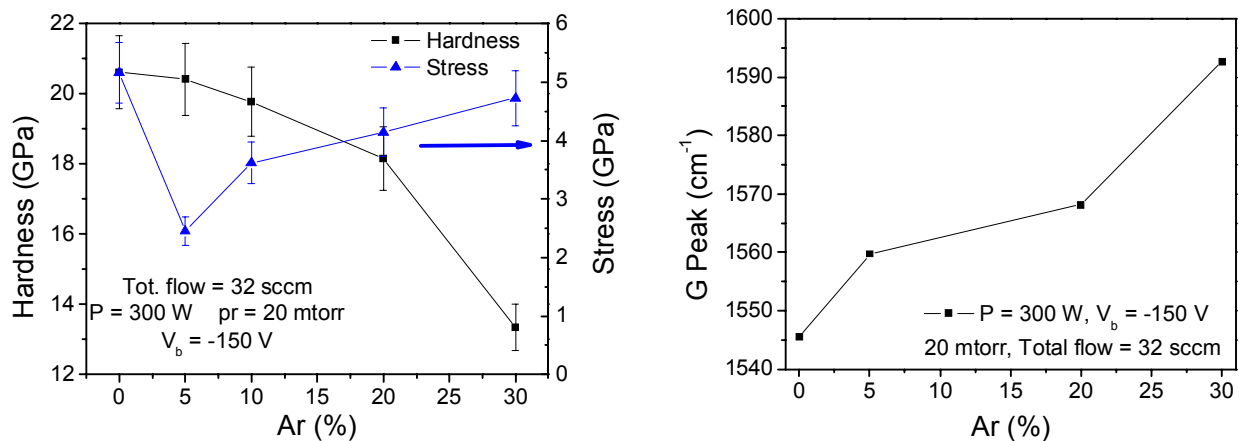


figure 10. (a) Variation of the coatings' hardness and stress and (b) Raman shift of the G peak vs argon content in the mixture.

## 6. Source-substrate distance:

In the experimental setup presented in figure 1, the distance between the source and the substrate was relatively high (170mm), which led to a non monotonous variation of the films growth rate with pressure (figure 4). The configuration of the reactor chamber has been modified by reducing this distance to 50 mm in order to take advantage from the high plasma density and high reactivity near the plasma creation region. Furthermore, this lower distance allows for a more direct control of the plasma parameters and lower losses on the walls.



Much higher values of the growth rate are obtained with this configuration. It appears that the growth rate is twice higher as the one measured before in the same process conditions. These values are further increased by a factor two when the thermal contact between the substrate and the water-cooled substrate holder is improved thanks to a thermal paste (figure 11).

The most noticeable difference in the deposition process with the previous configuration (except for a much higher growth rate that reached values  $> 150$  nm/min) appears with the dilution of the precursor with argon. Indeed, the growth rate increases until 30% Ar content although the precursor is diluted (figure 12). The variation of the atomic hydrogen concentration as measured by optical emission actinometry decreases monotonically with the Ar dilution and though this technique can not be applied rigorously to the hydrocarbonated radicals like  $CH$ , we can suppose that their concentration vary the same way. If we look at the concentration of the hydrocarbonated ions, the observed variation of the growth rate can be explained by suggesting that these ions participate in a significant manner to the growth of the carbon layers in this reactor configuration.

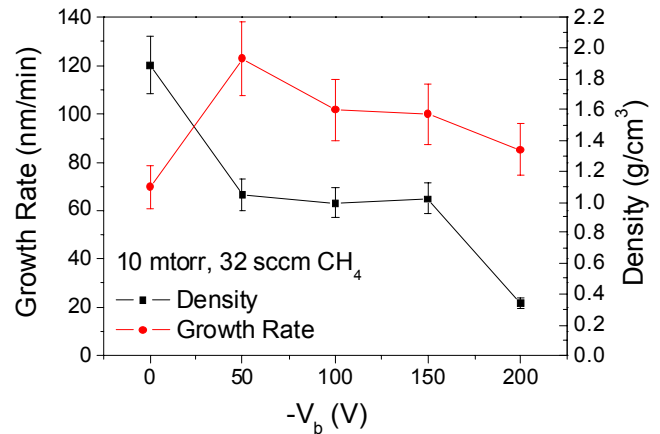


figure 11. Growth rate and density of the hydrogenated carbon coatings vs substrate bias in the second reactor configuration.

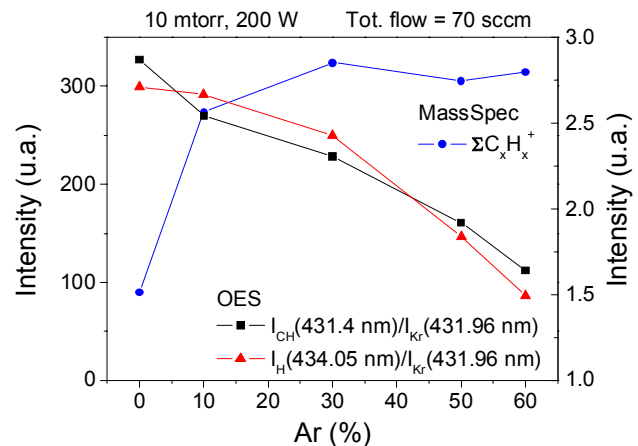
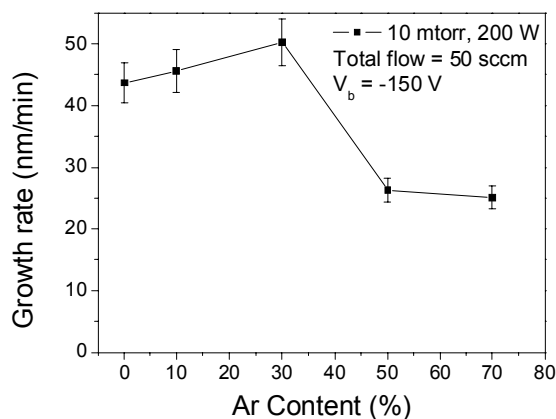


figure 12. (a) Growth rate of carbon films vs argon content in the mixture. (b) Variation of the concentration of the hydrocarbon ions as measured by mass spectrometry, and of the relative intensity of H and CH as measured by OES.

## V Conclusion

Though they appear as the main tools for dry etching, inductively coupled plasma sources can also be very interesting in PACVD. It has been shown in this study that hard ( $> 25$  GPa) amorphous hydrogenated carbon coatings could be deposited at high rates ( $> 150$  nm/min) using these types of sources. The diagnostic of the plasma phase showed that the methyl radicals and the atomic hydrogen play a major role in the deposition process. However, in some conditions, the hydrocarbonated ions present in high concentrations can participate in a significant manner to the growth of these films.

## VI References

- [1] T. Meziani, P. Colpo, F. Rossi, Plasma Sources Sci. Technol. 10 (2001) 276.
- [2] V.A. Godyak, R.B. Piejak, B.M. Alexandrovich, Plasma Sources Sci. Technol. 1 (1992) 36.
- [3] A. von Keudell, T. Schwarz-Selinger, M. Meier, W. Jacob, Appl. Phys. Lett. 76 (2000) 676.
- [4] A. Vanhulsel, J.-P. Celis, E. Dekempeneer, J. Meneve, J. Smeets, K. Vercammen, Diamond & Related Materials 8 (1999) 1193.
- [5] E. Dekempeneer, J. Smeets, J. Meneve, L. Eersels, R. Jacobs, Thin Solid Films 241 (1994) 269.

# A numerical tool for plasma spraying. Part I: modelling of plasma jet and particle behaviour.

G. Delluc, G. Mariaux, A Vardelle., P.Fauchais, B. Pateyron

Sciences des Procédés Céramiques et Traitements de Surface (SPCTS), CNRS UMR 6638  
Faculté des Sciences, 123 avenue Albert Thomas 87060 Limoges Cedex, FRANCE

## Abstract.

The current models of plasma spraying are generally complex and time-consuming, especially when they use a 3-D geometry and elliptic solvers. Therefore, these models are difficult to use as a tool to engineer specific coating properties and optimise the operating conditions of the spray systems. However, various clever numerical methods were developed in the past to simulate 2-D parabolic gas flow as laminar boundary layers or jets. For example, the *Genmix* algorithm developed by Spalding and Patankar and known as the *Bikini method* necessitates a very low-cost memory algorithm. This algorithm makes, it possible when using the right thermodynamics and transport properties of plasma gases, to predict in a fast and rather realistic way, the velocity and temperature fields of the plasma jet. The first part of this paper deals with the validation of the predictions for plasma jets obtained with the *Genmix* 2-D computational fluids dynamics code from experimental results and 3-D predictions obtained with the *ESTET* 3.4 CFD *ESTET* code

## 1. Introduction

Mathematical models of the atmospheric pressure plasma spray process have existed for almost twenty years [1-3]. Three modelling regions have to be considered [4] i.e. the electrode region, the plasma jet and its plume region where particles are injected, accelerated and heated and at last the region where the coating is generated. The first region is very difficult to model [4, 5] because of the non equilibrium phenomenon at the electrodes and the three dimensional (3D) transient behaviour of the arc connecting column to the anode. The coating generation modelling is still in its infancy even if sophisticated 3D models for a single particle flattening and cooling have been recently developed [6]. The plasma jet region modelling is probably the most developed one. The plasma flow is usually modelled by using low Reynolds k- $\epsilon$  codes to account for the laminar structure of the jet core and its turbulent one in the jet fringes and plume; the particle injection orthogonally to the jet, requires a 3D modelling [7]. In spite of a few problems which are not yet solved such as the engulfment process of the cold surrounding gas, the dispersion of the particles trajectories due to their size and velocity distributions as well as their collision between themselves and the injector wall, the particles parameters at impact are rather well modelled. It is now well recognized that these parameters: diameter, velocity and temperature control coating properties and reproducibility [8]. However the main drawbacks of the existing sophisticated codes is the computing time which is not compatible with industrial needs. That is why there is boom for simplified models able to give quickly (in few seconds) at least good trends. This is the goal of this paper.

Various clever numerical methods were developed in the past to simulate 2-D parabolic gas flows for laminar boundary layers or jets. For example, the *Genmix* algorithm developed by Spalding and Patankar [9] and known as the *Bikini method* requires a very low-cost memory and computing time. This algorithm makes it possible, when using the proper thermodynamics and transport properties of plasma gases, to predict in a fast and rather realistic way, the velocity and temperature fields of the plasma jet. The first part of this paper deals with the validation of the predictions for plasma jet velocity and temperature distributions obtained with the *Genmix* 2-D axi-symmetric computational fluid dynamics code (CFD) through their comparison with experimental results and 3-D predictions obtained with the *ESTET* 3.4 code.

## 2. Simulation of the temperature and velocity distributions of the plasma flame

The fast software *Jets&Poudres* [10] is build on the GENeral MIXing (*Genmix*) computer code, improved by using thermodynamic and transport properties closely related to the local temperature and composition. These properties are obtained from the T&TWinner data base [11].

### 2.1 Description of *Jets&poudres* plasma jet simulation

*Genmix* handles the two-dimensional, parabolic flows, i.e., those of high Reynolds and Peclet numbers, with not recirculation. "parabolic" flows are:

- steady,

- predominantly in one direction, defined as that in which the velocity vector has nowhere a negative component; and
- without recirculation or diffusion effects in that direction.

These conditions can be used as a first approximation of plasma jets, where the Reynolds and Peclet numbers, based upon the cross-stream dimension are large. Genmix embodies a self-adaptive computational grid, which enlarges or contracts to cover only the regions of interest (hence it explains the relatively small demand on computing power and its nickname, i.e., the Bikini method). The turbulence can be simulated by different models, but in the case of a plasma jet it is the classical mixing length which appears to be the simplest and the fastest.

In Jets&poudres the input data are:

- the mass flow rate  $m_0^p$  and the composition of the plasma forming gas,
- the composition of the gas atmosphere far away from the jet,
- the electric current intensity I,
- the electric power P with such previous conditions (obtained from experiments),
- the efficiency of energy transfer to the gas  $\rho_{th}$

Then the specific enthalpy  $h = \rho_{th}P / m_0^p$  is calculated from the ratio of effective power  $\rho_{th}P$  to the mass flow rate and the enthalpy temperature is obtained from the equilibrium properties at atmospheric pressure. From this temperature the specific volume of the gas is calculated and thus its mean velocity. Uniform radial profiles of temperature and velocity are assumed such as the gas enthalpy and mass flow rate at the nozzle exit are conserved. Whatever may be the profiles at the nozzle exit within a few tenth of mm the code creates its own profile independently of the starting ones.

## 2.2 Turbulence model and gas transport properties

Many models of turbulence with one, two or more equations can be solved with the Genmix code such as the k- $\epsilon$  model (two equations) or dissipation energy of Prandtl (one equation). In general all this models underestimate the surrounding atmosphere entrainment which is in fact of the engulfment type and not well represented by the classical models when the three components of the turbulent velocity are assumed to be equal. However because these models are not satisfactory even in the case of plume flows, a simple standard model of mixing length is used in Jets&poudres. In the mixing length hypothesis, each location in the flow is characterized by a value of the quantity  $l_m$  the mixing length, and the turbulent contribution to the effective viscosity,  $\mu_t$ , is then calculated from the formula :

$$\mu_t = \rho l_m^2 \left| \frac{\partial u}{\partial y} \right|$$

In common applications of the mixing-length hypothesis,  $l_m$  is taken as uniform in radial direction but variable longitudinally. It is not the case with the flows described by the Genmix builder where  $l_m$  is allowed to vary as described in /9/. To take into account of the laminar behaviour of the jet core at high temperature the mixing length  $l_m$  is smoothed by a coefficient computed as  $(300/T(x,0))^{1/n}$  where  $T(x,0)$  is the temperature along the jet axis at the distance x from the nozzle exit and n is a factor of adjustment which has been chosen equal to 9 to match the best with the experiments.

The effective viscosity used is  $\mu_{eff} = \mu_t + \mu_l$  where the three subscripts denote “effective”, “turbulent” and “laminar” respectively. For the transport properties other than viscosity, the effective ratio of Prandtl to Schmidt numbers  $\sigma$  is assumed to be constant. Further  $\Gamma_t$  may be calculated from  $\Gamma_t = \mu_t / \sigma_t$ , where  $\sigma_t$  is the turbulent Prandtl or Schmidt number assumed to be constant ( $\sigma_t = 0.85$ ) and  $\Gamma_{eff} = \Gamma_t + \Gamma_l$ . Then the appropriate expression for  $\sigma_{eff}$  becomes:

$$\sigma_{eff} = \frac{\mu_t + \mu_l}{\mu_t / \mu_l + \Gamma_l}$$

The laminar values of the transport properties are expressed at each point according to the transport properties of the plasma gas and those of the surrounding atmospheric gas using a linear rule for each concentration. The transport properties of the plasma jet and its surrounding atmosphere are accurately forecasted from T&TWinner data base [11/].

### 2. 3. Comparison of the Jets&poudres plume model with the results of Estet3.4

A plasma jet and its plume has been computed using the sophisticated code Estet3.4 [8] for a flow rate of 45/15 slm Ar-H<sub>2</sub>, a nozzle internal diameter of  $\phi = 7$  mm, an effective power of 21.5 kW (65 V, 600 A,  $\rho_{th} = 55\%$ ). The turbulence model of Estet was k- $\epsilon$  RNG and the 3D grid was 71, 88 and 71 according to the x, y, z directions. The Figures 2a, 2b, 2c compare the radial profiles of velocity, temperature and surrounding atmosphere concentration at 0.0004 m, 0.0222 m, 0.0314 m, 0.594m (thin lines) with the same computation with Jets&poudres (thick lines). It can be seen that for temperatures and velocities near the nozzle exit and far away from it the profiles are very close but at the intermediate axial distance (0.0314 m) the profiles are somewhat different. In fig. 3c it can be seen that the dilution of the plume by the surrounding atmosphere is more important in the forecast from Jets&poudres.

However it should be noted that Estet underestimates the experimental results obtained with an enthalpy probe at that distance.

Fig. 2d presents the comparison of the axial profiles for temperature and it can see that Estet code (Estet) or Jets&poudres (J) forecasts a smoother evolution of temperature than Jets&poudres with standard  $l_m$  (Jgenuine) in the intermediate axial distance from the nozzle exit. However with the modified mixing length the trend of Jets&poudres is the same as that given by Estet.

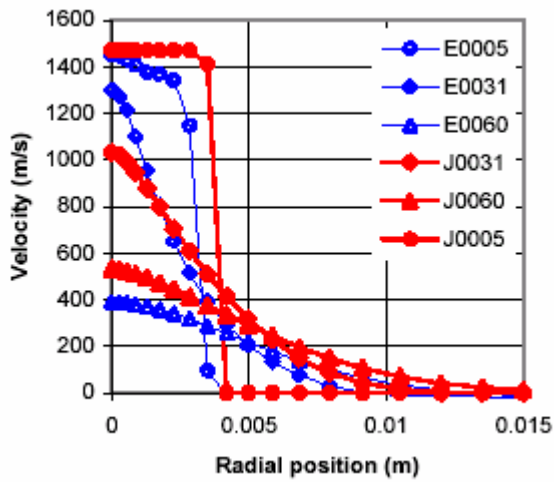


Figure 2a

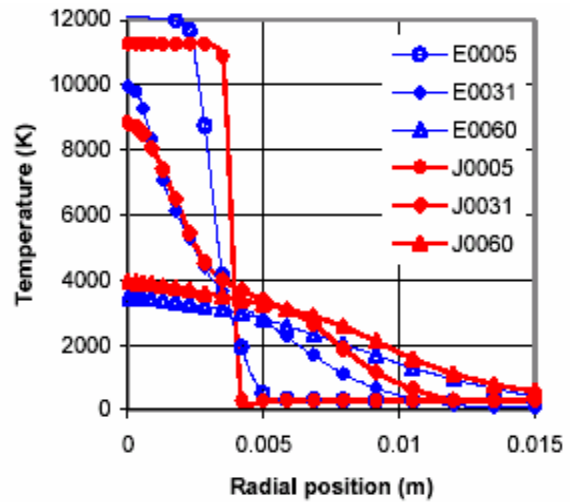


Figure 2b

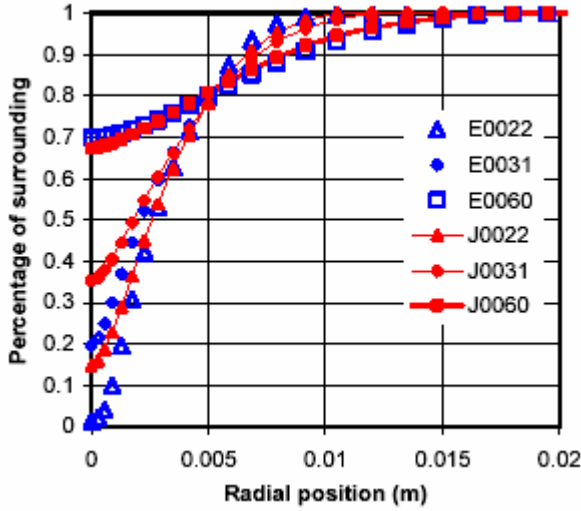


Figure 2c

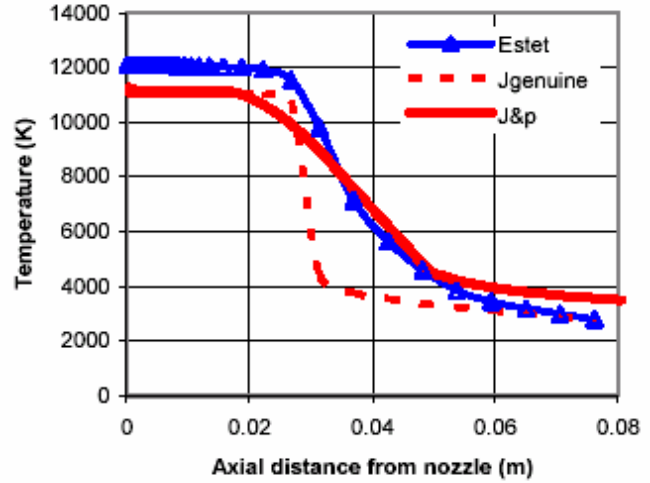


Figure 2d

Figure 2. Radial distribution of velocity (a), temperature (b) and percentage of surrounding atmosphere (c) calculated with Jets&poudres (J curves) and Estet3.4 computer code (E curves) at different distances from the nozzles exit: E0022, J0022 at 0.0022 m, E0031, J0031 at 0.0031m, E0060, J0060 at 0.0060 m, for an Ar-H<sub>2</sub> (45-15 slm, d.c. plasma jet, P= 36300 kW,  $\rho_{th} = 0.50$ , anode nozzle i.d.=0.0007 m.

(d) Comparison of the axial profile for temperature forecast by Estet code (Estet), Jets&poudres (J) and Jets&poudres with standard  $l_m$  (Jgenuine)

### 2.3 Comparison with other plasma jet plume

Jets&poudres allows to calculate many different plasma jets. In fig. 3a, 3b, 3c are presented the results of the calculations from Jets&poudres, those of the McKelliget's model [12] together with the experimental results for a Miller torch with the plasma jet flowing in air atmosphere with a plasma forming gas argon flow rate of 35.4 slm, an electric power of 7.4 kW and a thermal efficiency of 52 % and 8 mm nozzle diameter. It can be seen that the general tendency of Jets&poudres is to forecast a faster dilution in the surrounding atmosphere than the McKelliget's model. The two models frame the experimental results.

Figure 4 compares the measurements of Coudert [13] with the Jets&poudres code forecast of the axial temperature of a plasma jet for the following conditions flow rate of 81 slm Ar, 8 slm H<sub>2</sub>, I=550A, V=64V, efficiency = 58% in an surrounding atmosphere of air, nitrogen and argon respectively. It can be seen that in air atmosphere as it could expected, the temperatures are lower than in nitrogen atmosphere and that in argon atmosphere the temperatures are higher than in air or nitrogen atmosphere. The same tendencies are observed with the experimental data. However with both diatomic gases the Jets&poudres forecasts a much faster axial cooling than shown by the experimental points [14]. This is due to a faster surrounding atmosphere entrainment resulting in a fast cooling of the jet with nitrogen and oxygen dissociations.

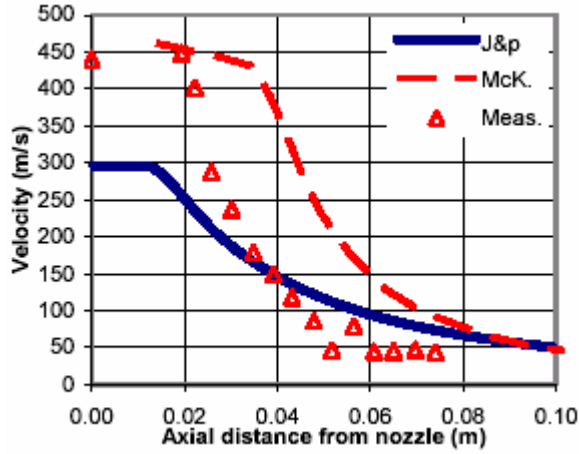


Figure 3a

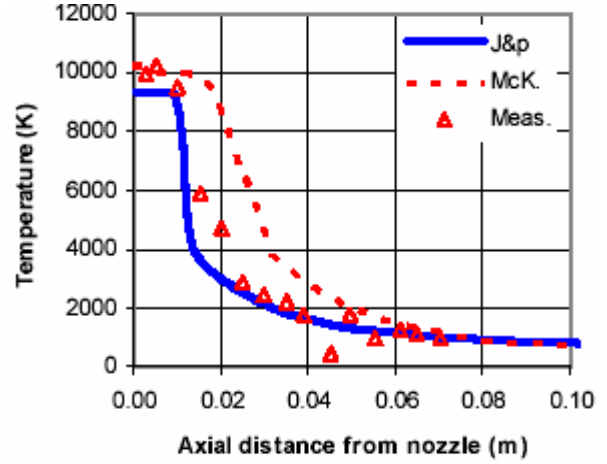


Fig 3b

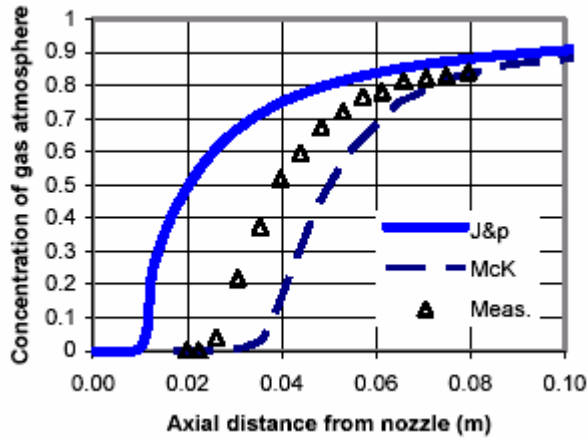


Fig 3c

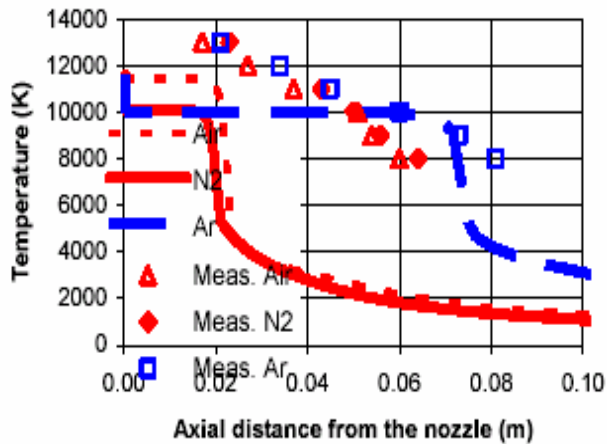


Figure 4. Jets&poudres code forecast of axial temperature Coudert [13] of a plasma jet with an Ar flow rate of 81 : H<sub>2</sub>, I = 550A, V = 64V, efficiency = 58% in surrounding nitrogen and argon.

### 3. Conclusions

Compared to the 3D Estet code or the 2D code of McKelliget et al. which are elliptical models the simplified 2D parabolic model Jets&poudres gives the same trends for temperature and velocity distributions. However as for the most sophisticated codes its weakness is the way the mixing with the surrounding atmosphere is taken into account. By using a smoothing coefficient of the mixing length the Jet&poudres code match not too badly with the experimental results. Its major advantage compared to the 3D Estet code is its computing time which is three orders of magnitude shorter. As it will be seen in next part the calculation of the heat and momentum transfers to particles in flight are very fast and compare well with experiments which is probably due to the dumping of the plasma jet properties by the particles inertia

### 4. References

- /1/ R. Westoff, G. Trapaga and J. Szekely, Met. Trans. B, 23B (1984) 683-693.
- /2/ P. Fauchais, A. Vardelle and B. Dussoubs, J. Thermal Spray Technology **10** (1) (2001) 44-66.
- /3/ P. Fauchais and A. Vardelle, IEEE on Plasma Science, **25** (6) (1997) 1258-1280.
- /4/ G. Mariaux, E. Lrgros and A. Vardelle, *Modelling of coating formation and heat flux to substrate by particles and plasma jet in plasma spraying*, accepted in ITSC 2003 proc. (pub) ASM int. Mazterials Park, OH, USA (2003) ITSC 2003.
- /5/ G. Mariaux, P. Fauchais, A. Vardelle and B. Pateyron, in Progress in plasma processing of materials, (ed. P. Fauchais, J. Amouroux (pub) Begell House, N.Y., USA (2001) 263-287.
- /6/ P. Fauchais, M. Fukumoto, A. Vardelle and M. Vardelle, *Knowledge concerning splat formation: An invited review*, J. of Thermal Spray Technology 2003.
- /7/ / M. Vardelle, A. Vardelle, P. Fauchais, K. I. Li, B. Dussoubs and N.J. Themelis, Journal of Thermal Spray Technol. **10** (2)(2001) 267-284.
- /8/ P. Fauchais and M. Vardelle, *How to improve the reliability and reproducibility of plasma sprayed coating*, accepted ITSC 2003 Proc. (Pub.) ASM int. Material Park, Oh, USA (2003).
- /9/ T&TWINner can be downloaded from <http://ttwinner.free.fr>
- /10/ Jets&Poudres can be downloaded from <http://jets.poudres.free.fr>
- /11/ S.V. Patankar & D.B. Spalding (1970) *Heat and mass transfer in boundary layers; 2nd edition*, Morgan-Grampian, London.  
See also:  
D.B. Spalding (1977), *GENMIX; a general computer program for two-dimensional parabolic phenomena*, Pergamon Press, Oxford.  
GENMIX can be downloaded from CHAM's web-site from  
<http://www.cham.co.uk/website/new/genmix/genmix.htm>
- /12/ J.W. McKelliget, G. Trapaga, E.Gutierrez-Miravete, M. Cybulski, *An integrated mathematical model of the plasma spraying process*, Thermal Spray Meeting: the challenges of the 21<sup>st</sup> century (ed. C. Coddet) ASM International USA. (1998) 335-340.
- /13/ P. Fauchais, J.F. Coudert, B. Pateyron, *La production des plasmas thermiques*, Rev. Gén. Therm. (1996) 35 543-560.
- /14/ A. Denoirjean, O. Lagnoux, P. Fauchais, V. Sember, *Oxidation control in atmospheric plasma spraying: comparison between Ar/H<sub>2</sub>/He and Ar/H<sub>2</sub>* 15th International Thermal Spray Conference, Ed C. Coddet IPSE (Pub), ASM int. Oh. (USA) 1998; 809-814

# **A numerical tool for plasma spraying. Part II: Model of statistic distribution of alumina multi particle powder.**

G. Delluc, L. Perrin, H. Ageorges, P. Fauchais, B. Pateyron

*Science des Procédés Céramiques et de Traitements de Surface (SPCTS), CNRS UMR 6638*

*Faculté des Sciences, 123 avenue Albert Thomas, 87060 Limoges Cedex, FRANCE*

## **Abstract.**

Particle statistical size distribution of an alumina powder is generated and fed (3D) with a carrier gas through an injector into the plasma jets calculated in part I. The initial velocity of each particle is randomized through a law resulting of experimental observations. Characteristic residence times of the particles from the injector to the target and characteristic times for the melting of the particles are obtained. Also size, temperature and velocity distributions of particles impacting on the target are calculated to characterize the coating deposition.

## **1. Introduction**

Plasma spray consists in realizing deposits on substrates in order to improve their surface properties. Spray materials are introduced in the form of particles (in the tens of  $\mu\text{m}$  range) in a flame or a plasma jet where they are accelerated and melted, before they flatten onto the substrate or previously deposited layers where the deposit is formed by the resulting splats layering. In order to increase the quality of deposits, many studies have been performed on the plasma spray of ceramics, cermets, metals and alloys [1, 2]. But deposit properties depends on many parameters such as those of the plasma torch (current intensity, plasma forming gases composition and flow rates, design of the torch), those of the powder (type of material, particle mean diameter, microstructure and morphology), those of the injection [3] (injector internal diameter, mass flow rate of the carrier gas, position of the injector, powder mass flow rate), the interaction plasma/particle (acceleration and heating of the particles within the plasma jet) [4], the relative movements torch/substrate, the substrate parameters (surface preheating temperature, roughness) [5] and mean coating temperature control during spraying and upon cooling. To obtain a coating with the required properties many experiments are necessary to optimize the process. The numerical forecast constitutes an interesting way for this technology to minimize the number of experiments. In that way, during the last decade numerous workers have studied the particles dynamics and their temperature histories in thermal plasmas. Many computational codes have been developed to predict the properties of the plasma jet (velocity, temperature) [6] and the particles behavior within the plasma jet (temperature, velocity, melting state) [2, 7]. According to the particle injection orthogonally to the plasma jet, the models have to be 3D. However, such codes need several hours if not several days of calculations to obtain the results of one condition. It is thus interesting to develop simplified codes with computing time in order of a few minutes in order to forecast rapidly spray conditions and help the operators to find optimum conditions.

The objective of this paper is to present a fast code *Jets&poudres* which runs on Visual Basic and needs only few seconds to few minutes to simulate the plasma spraying of a single particle and a powder respectively.

The model, its assumptions and the forecast of the behavior of a particle in the plasma jet with the *Jets&Poudres* software is presented and the results of the plasma spray of a powder of about ten thousand particles is discussed.

## **2. Jets & Poudres model for plasma spray**

The model *Jets&Poudres*, forecasts the dynamic of a single or multi particles fed in a plasma jet. This model, built in Visual Basic, allows a convivial exchange. Its aim is not to forecast a result very close to experiment but to:

- compute rapidly the parameters of the plasma spray ;
- present synthetic and explicit results;
- give the tendencies and phenomena orders of magnitude.

### **2.1 Spray material particle model.**

For the particles sprayed by a plasma jet two types of phenomena are of interest. One is the dynamic of the movement of particles with their trajectories, velocities and accelerations. The second is their thermal history, i.e., their temperature, melting or freezing, as well as the heat flux at their surface.



### 2.1.1 Dynamic of a single particle in the plasma jet

Under the assumption that the Stoke's drag is the dominant force [7] in the dynamic of the particle injected in the plasma jet, the movement equation can be written as:

$$m_p \frac{dv}{dt} = -\frac{1}{2} C_D \cdot \pi \cdot \frac{d_p^2}{4} \cdot \rho_\infty \cdot |U - v| \cdot (U - v) + F_x \quad (1)$$

where:  $C_D$  is the drag coefficient depending of the morphology of the particle and the Reynolds number;  $d_p$  is the initial diameter of the particle (m) ;  $v$  is the particle velocity ( $m.s^{-1}$ );  $U$  is the plasma velocity ( $m.s^{-1}$ );  $\rho_\infty$  is the plasma specific mass ( $kg.m^{-3}$ ) and  $\mu_\infty$  the plasma viscosity ( $kg/m.s$ ).  $C_D$  is an empirical function of

$$\text{the Reynolds' number } Re = \frac{2r\rho_\infty|U - v|}{\mu_\infty} \quad (2)$$

In this paper, according to the literature, it has been chosen [8]  $C_d = \left(\frac{24}{Re}\right) \left(1 + 0.11 \cdot Re^{0.81}\right) f_0 \quad (3)$

Where  $f_0$  is a correction factor to take into account properties gradient in the boundary layer around the

particle. In this paper  $f_0 = \left(\frac{\rho_\infty \mu_\infty}{\rho_p \mu_p}\right)^{0.45}$  as proposed by Lee et al. [8], where subscribes  $\infty$  and  $p$  respectively

indicate plasma and particle for specific mass and viscosity.

The external forces  $F_x$  are rather well represented by the thermophoresis force resulting from the very high thermal gradient in the fluid and the gravity force. The force due by the thermal gradient can be of the same order of magnitude than the gravitational acceleration [7], but here both are not considered relatively to the drag force which is three or four orders of magnitude higher. It is also assumed that the particles have no influence on plasma jet (no load effect).

### 2.1.2 Heat exchange between a single particle and the plasma jet

The heat transfer mechanisms to the particle in the plasma jet can be expressed by four successive steps [9]: the heating of the solid particle, its melting, the heating of the molten particle and its vaporization. The governing differential equations for the temperature time evolution of a spherical particle are the following:

- The heating of the solid particle

The particle temperature ( $T_p$ ), neglecting the heat propagation is calculated through the total heat energy in a

film at the particle surface. Its expression is: 
$$\frac{dT_p}{dt} = \frac{6 \cdot Q_n}{\pi \cdot d_p^3 \cdot c_p \cdot \rho_p} \quad (4)$$

where:  $Q_n$  is the energy required for heating up the particle, it is a conduction – convection heat energy ( $W/m^2$ );  $C_p$  is the mass specific heat at constant pressure of the particle depending of the material ( $J/kg.K$ ).

In this paper to take in account the steep temperature gradients within the thermal boundary layer around the

particle, the integrated thermal conductivity  $\tilde{K}(T) = \frac{1}{T_\infty - 300} \int_{300}^{T_\infty} K(\theta) d\theta \quad (5)$

is used instead of the thermal conductivity  $K(T)$ , then with the radiative cooling it comes:

$$Q_n = \pi d_p^2 \left\{ (T_\infty - 300) \tilde{K}(T_\infty) - (T_p - 300) \tilde{K}(T_p) - \varepsilon \sigma_s (T_p^4 - T_a^4) \right\} \quad (6)$$

where  $T_\infty$  is the temperature outside the boundary layer,  $T_a$  is the surrounding temperature,  $\varepsilon$  is the particle emissivity and  $\sigma_s$  the Stephan-Boltzmann constant.

- Melting of the particle at constant temperature  $T = T_F$

When  $T_p = T_F$  (melting temperature), it is assumed that the total energy from the plasma to the particle is converted into the latent heat of fusion  $\Delta H_F$ . The melting mass fraction  $X_p$  is governed by

$$\frac{dX_p}{dt} = \frac{6 \cdot Q_n}{\pi \cdot d_p^3 \cdot \Delta H_F \cdot \rho_p} \quad (7)$$

where:  $\Delta H_F$  is the latent heat of fusion ( $J/kg$ ).  $X_p$  is in the range 0 to 1. If  $X_p = 0$ , the particle is solid and if  $X_p = 1$ , it is fully melted.

- Heating of the liquid particle

Two assumptions are possible in this step: the liquid phase of the particle vaporizes or not. If the liquid phase of the particle is not vaporizing the heating of the liquid is similar to that of the solid particle (eq. 4) with the specific heat at constant pressure of the liquid. If the liquid particle vaporizes its diameter decreases

according to the following equation: 
$$\frac{d(d_p)}{dt} = \frac{6 \cdot Q'_n}{\pi \cdot d_p^3 \cdot \Delta H_{vap} \cdot \rho_p} \quad (8)$$

where:  $\Delta H_{vap}$  is the specific latent heat of particle vaporization ( $J \cdot kg^{-1}$ );  $Q'_n$  is the thermal energy lost when vaporizing the particle ( $W/m^2$ ). When  $T_p = T_b$  (boiling temperature), the assumed total energy from the plasma to the particle is converted in latent heat of vaporization. The diameter evolution of the particle is given by an equation similar the last one (eq. 8).

## 2.2 Model of the powder of the spray material

To simulate the formation of a deposit, a large quantity of particles ( $10^9 - 10^{10}$ ) has to be sprayed in the plasma jet. Unfortunately the particles in a powder have different diameters. The particle size analysis of a commercial powder shows that they have roughly a Gaussian distribution in diameter. Thus, two cases are studied to simulate a powder, either that with the distribution given by the experimental particle size analysis or that with a Gaussian distribution according to the limit central theorem with twelve shot randomly numbered.

The powder is injected by a carrier gas in the plasma jet. This phenomenon could be quickly complex, so to simplify the model the assumptions are the following: the particles have the same velocity as that of the carrier gas, they are not interacting between themselves, the carrier gas flow rate does not vary with time, the injector walls are smooth and straight, and the velocity of the carrier gas is not time dependant but depends of the injection radius. The radial profile of particle velocity at the injector exit is parabolic and given by the

following equation: 
$$v(r) = v_0 \cdot \left(1 - \left(\frac{r}{R}\right)^2\right) \quad (9)$$

where:  $r$  is the radial position of the particle at the injector exit (m);  $R$  is the internal radius of the injector (m);  $v_0$  is the maximum velocity of the carrier gas (at axis where  $r = 0$ );  $v(r)$  is the exit velocity of the particle at the radius  $r$  ( $m \cdot s^{-1}$ ). The injection velocity is adjusted to the mean size of the particles in such a way their trajectory makes an angle of  $3.5^\circ$  with the plasma jet axis.

The particle collisions between themselves and with the injector wall induce a dispersion of the particle jet at the injector exit. To integrate this phenomenon, which has been measured [2] for a  $-45+22 \mu m$  alumina particles as a cone with an angle of  $20^\circ$ , the model attributes to each particle an inclined angle of the exit injector velocity between 0 and  $20^\circ$  by firing at random a number. In order to rapidly obtain results only 32 000 particles are generated to build a sample of powder which allows the computation of the deposit height distribution.

## 3. Results and discussion

In order to validate the model, two powders,  $ZrO_2$  and  $NiCrAlY$ , are modelled and compared with the experimental results of Smith and al. [9]. The plasma spray parameters for the calculation are respectively the same as those of the two experimental tests and summarized in Fig 1, except the injection of the powder which is assumed by an external injector in both modelled powders, disposed at 6 mm from the torch exit and at 8 mm from the plasma jet axis. The argon carrier gas flow rate is 1.1 L/min for zirconia powder and 0.7 L/min for  $NiCrAlY$ , resulting in a mean velocity of the particle at the injector exit on its axis of 15m/s and 10 m/s respectively. The size distributions are in range between  $-42 +30 \mu m$  for  $ZrO_2$  powder and  $-50+40 \mu m$  for  $NiCrAlY$  which correspond to a mean diameter of 36 and 45  $\mu m$  respectively. The thermal properties and characteristics of both powders are summarized in Table 1. The boiling point of  $NiCrAlY$  is considered to be the same as that of Cr.

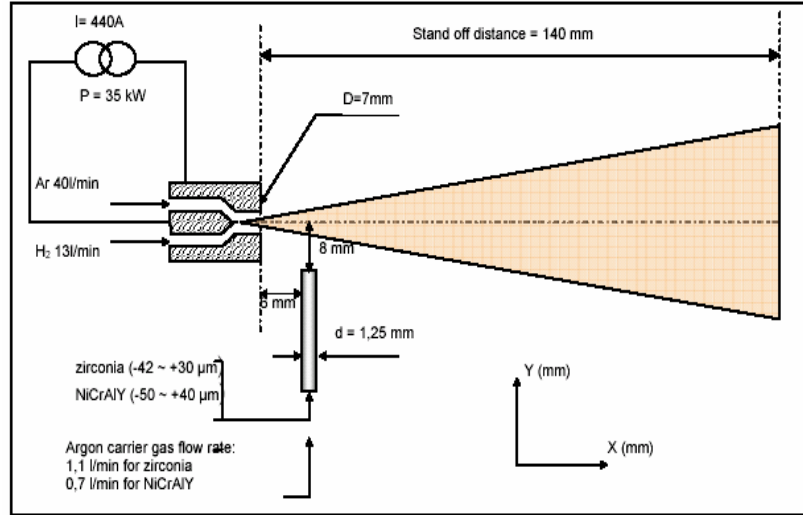


Figure 1: Plasma spraying parameters of Smith and al. [9] to study the behaviour the particles in the plasma jet

Table 1: Thermal properties and particle sizes of the modelled plasma spraying powders

Material powders	Particles size [μm]	Specific Mass [kg.m <sup>-3</sup> ]	Specific heat [J.kg <sup>-1</sup> .K <sup>-1</sup> ]	Melting point [K]	Thermal conductivity [W.m <sup>-1</sup> .K <sup>-1</sup> ]
ZrO <sub>2</sub>	-42 +30	5680	408.8	2983	1.66
NiCrAlY	-50 +40	8902	837.3	1726	91
Al <sub>2</sub> O <sub>3</sub>	-45 +10	3900	1363	2327	5

For each particle and position in the plasma jet, the software gives its temperature and velocity and computes the Sommerfeld's parameter to predict the type of impact of the droplets. In order to have simplified graphics, only one, two or three representative particles are presented.

Figures 2 and 3 show the temperature and velocity, in the plasma jet, of representative diameters of the zirconia and NiCrAlY particles respectively. As it could be expected the axial velocity of the biggest zirconia particle is lower than that of the smallest one (see Fig.2a). For both materials, the simulated velocity results are in good agreement with the Smith's experimental measurements [9] in the plasma jet.

Figure 2b does not show any temperature difference between the two sizes of particle. With the zirconia material computational results are in good correlation with the experimental ones. A difference of 10 % could be estimated between calculated and experimental temperatures, this difference is the same as the experimental error. The experimental results of the NiCrAlY temperature are higher than those calculated. It might be due to the melting temperature of NiCrAlY which has not be found in the literature and has been estimated to be the same as that of Cr, limiting the liquid temperature of NiCrAlY to the Cr boiling point temperature. For both materials, it can be noted that the melting stage at constant temperature appears at about 10 mm from the torch exit that is only 3 to 4 mm downstream of the injector. Less than 10 mm from the injector exit, the particle reaches its highest temperature (boiling temperature) and keeps it during all its flight in the plasma jet.

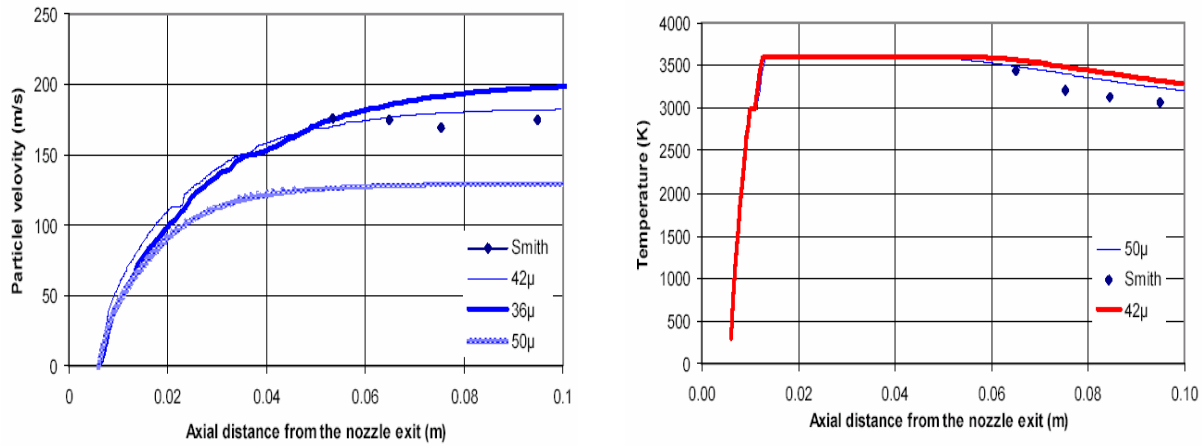


Figure 2: Modelled and measured velocity of representative diameters of zirconia particles in the plasma jet, with the plasma parameters of Smith and al. [9]. a – velocity, b- temperature

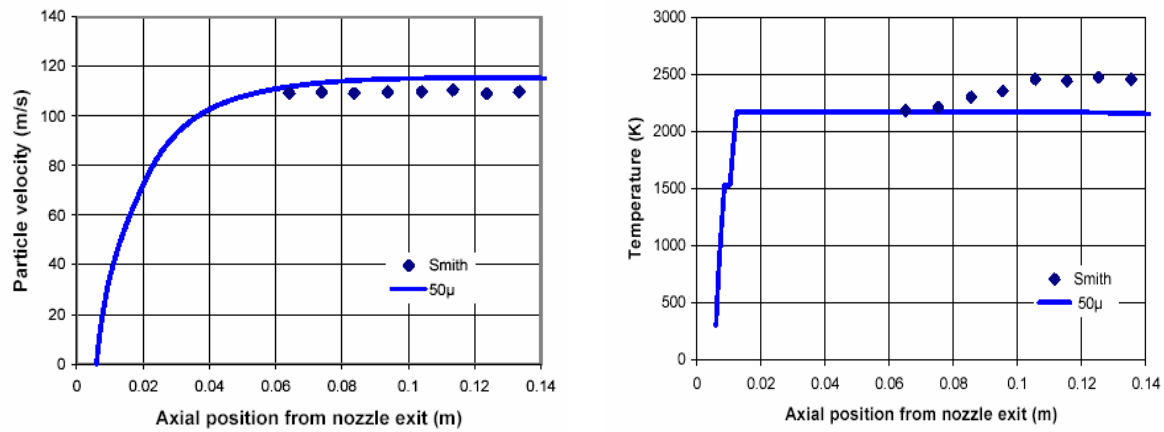


Figure 3: Modelled and measured velocity of 50μ diameter NiCrAlY particles in the plasma jet, with the plasma parameters of Smith and al. [10]. a – velocity, b- temperature

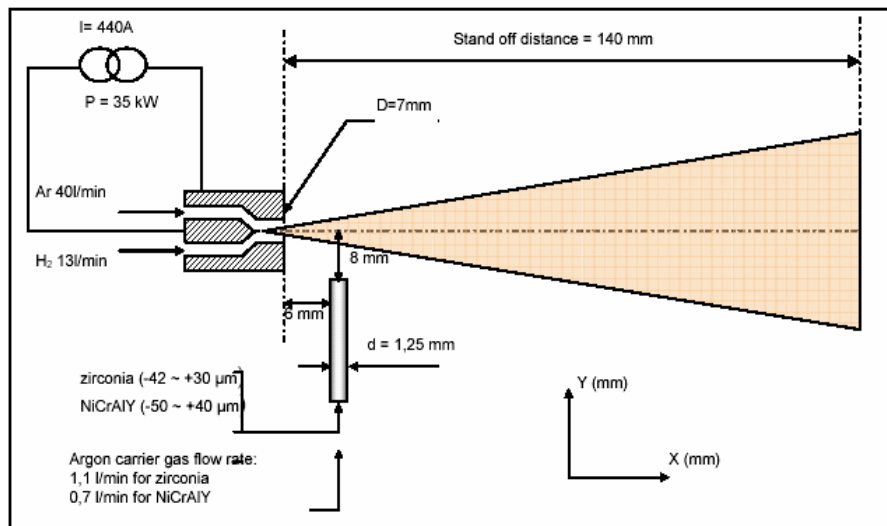


Figure 4: Plasma spraying parameters of Denoirjean and al. [11] to study the impact of droplet

To model the impact of particles on the substrate, the same experimental set up is used with the plasma spraying parameters presented in Fig. 4. The particle material studied is alumina injected with an internal injector and 6 sl/min of argon as carrier gas, resulting in a mean velocity of the particle at the injector exit of

40 m/s. To simplify the simulation unlike to the experiment, alumina is injected with an external injector [10]. The size distribution of alumina powder is in the range of 10 to 45  $\mu\text{m}$ . The simulated distribution of diameters is made according to the commercial powder size distribution.

The Figure 5 shows the simulated and measured radial profiles, of temperature and velocity of an alumina powder, in the plasma jet at 10 cm from the torch exit. For both characteristics, simulated values have the same tendency but are superior to those of experiment. The measured velocity of the particles decreases when the radial distance from the axis increases. The temperature computational profile is about 5 % superior to the experimental one. This difference which is not obvious in the behaviour of a single particle can be explained by a poor randomisation of the initial velocity fed into the plasma jet.

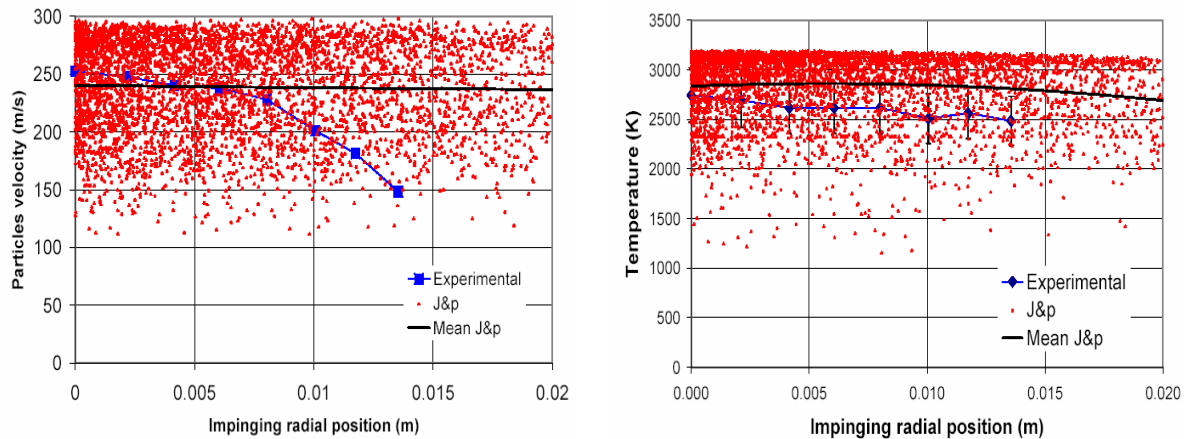


Figure 5. Radial profile of simulated and measured of a powder in the plasma jet at 100 mm from the torch nozzle exit, with the plasma parameters of Denoirjean and al. [11]. a – velocity, b- temperature

#### 4. Conclusion

Jets & Poudres software appears as a fast simulation a few minutes to forecast the dynamic of a single particle or a particles sample fed in a plasma jet. This model has been validated by comparing its results for  $\text{ZrO}_2$ ,  $\text{NiCrAlY}$  and  $\text{Al}_2\text{O}_3$  particles with those of different experiments. For single particles the agreement is good within 5%. For a powder load the code gives good trends. Of course the code has to be improved to take a better account of the particle trajectories distribution at the injector exit as well as some corrections in heat and momentum transfers to particles, especially when the latters evaporate.

#### References

- [1] P. Fauchais, A. Vardelle, B. Dussoubs, J. of Thermal Spray Technology, **10** (1) (2001), 44-66.
- [2] M. Vardelle, A. Vardelle, B. Dussoubs, P. Fauchais, T.J. Roemer, R.A. Neiser, M.F. Smith, in *Thermal Spray Meeting*, (Ed.) Coddet, Pub. ASM International Materials Park Oh, USA (1998), 887 -894
- [3] M. Vardelle, A. Vardelle, P. Fauchais, K.-I. Li, B. Dussoubs, and N.J. Themelis, J. of Thermal Spray Technology, **10** (2) (2001), 267-284.
- [4], M. Vardelle, A. Vardelle, A.C. Leger, P. Fauchais, D. Gobin, J. of Thermal Spray Technology, **4**, (1994).
- [5] C. Escure, (in French), Ph. D. thesis, 2000, University of Limoges.
- [6] B. Dussoubs, (in French), Ph. D. thesis, 1998, University of Limoges.
- [7] S. L. Soo, *Fluid Dynamics of Multiphase systems*. Blaisdell Publishing Co., New York, (1967).
- [8] Y.C. Lee, K. Hsu, E. Pfender, 5<sup>th</sup> International Symposium on Plasma Chemistry, Edinburgh, U.K. **2**, 795-801 (1981)
- [9] M.I. Boulos, P. Fauchais, E. Pfender and A. Vardelle in *Plasma spraying* (Ed) R. Suryanarayanan (Pub) World scientific, Singapore, 1993, 3-57.
- [10] W. Smith, T.J. Jewett, S. Sampath, W.D. Swank, and J.R. Fincke, in *Thermal Spray: A United Forum for Scientific and Technological Advances*, (Ed.) C.C. Berndt, (Pub.) ASM International, Materials Park, OH, (1997), 607-612.
- [11] A. Denoirjean, O. Lagnoux, P. Fauchais, V. Sember, in *Thermal Spray Meeting*, (Ed.) Coddet, Pub. ASM International Materials Park Oh, USA (1998), 809-814

# Study of the peptide adsorption on Ar and O<sub>2</sub> plasma micropatterned polymer surfaces

C. Satriano<sup>1</sup>, M. Manso<sup>2</sup>, G. Ceccone<sup>2</sup>, F. Rossi<sup>2</sup> and G. Marletta<sup>1</sup>

<sup>1</sup> *Laboratory of Molecular Surfaces and Nanotechnology - Department of Chemistry, University of Catania, Catania, Italy*

<sup>2</sup> *European Commission, Joint Research Center, Ispra (VA), Italy*

Thin films of polycaprolactone (PCL), polyethyleneglycol (PEG) and polyhydroxymethylsiloxane (PHMS) were patterned by cold microwave plasmas of both inert (Ar) and reactive gases (O<sub>2</sub>) through simple masks. The dimension of the patterns stripes and pitches were typically between 30 and 100 μm. The surface properties changes were characterized by spatially resolved X-Ray Photoelectron Spectroscopy (XPS) and Time of Flight Secondary Ion Mass Spectrometry (ToF-SIMS), for the chemical structure and composition, by Atomic Force Microscopy (AFM), for the roughness determination on the micro- and nanometer scale, by Zeta Potential (ZP) and Surface Free Energy (SFE) measurements, to estimate respectively the surface charge and dispersive/polar forces distribution and finally by the Quartz Crystal Microbalance with Dissipation monitoring (QCM-D) technique, to investigate the change of thickness and visco-elastic properties of the films.

The adsorption of RGD peptide sequences was investigated as a function of the plasma treatment parameters, including power, pressure and plasma exposure. The *in-situ* kinetics of adsorption and modeling of the viscoelastic properties of the adsorbed peptide layers were studied by using QCM-D technique, while the chemical structure and lateral distribution of the adlayers were characterized *ex situ* by Small Spot XPS, ToF-SIMS Imaging measurements and AFM.

The results showed that selective patterning of the adsorbed peptide sequences could be achieved mainly in connection with the polar to dispersive ratio of the surface free energy. In particular, the surface modification seems to affect also the morphology adlayers.

# Grafting of hyaluronic acid on plasma-treated PMMA surfaces

Z. Lipani, C. Satriano and G. Marletta

*Laboratory of Molecular Surfcaces and Nanotechnology (LAMSun), Department of Chemistry, University of Catania, Catania, Italy*

The use of polymethylmethacrylate (PMMA) is very common in the field of biomaterials for the fabrication of contact and intraocular lenses. In this work the surfaces of PMMA thin films, deposited by spin coating, were modified by irradiation techniques in order to optimize the grafting process of hyaluronic acid (HA), in order to achieve an optimal biological response to the prosthetic implants.

In particular several plasma treatments, including both inert (Ar) and active (O<sub>2</sub>, N<sub>2</sub>) gases, were performed by changing the experimental parameters of power, treatment time and aging conditions.

The characterization of the surface composition properties of PMMA films before and after the modification was carried out by means of X-Ray Photoelectron Spectroscopy (XPS), the topography changes at micro- and nanometer scale was investigated by Atomic Force Microscopy (AFM), the surface free energies (SFE) in terms of dispersive and polar acid-base components were determined by contact angle measurements, finally the Quartz Crystal Microbalance with Dissipation monitoring technique (QCM-D) was used in order to evaluate modifications of thickness and viscoelastic properties.

The efficiency of the grafting process of HA was investigated *ex-situ* by XPS and *in-situ* by QCM-D measurements. The observed results on the adsorbed HA adlayers indicated a general increase of the HA grafting with the increase of the surface free energies, in particular with the irradiation-induced change of the Lewis acid character of the surfaces.

# Low temperature plasma deposition of N Doped a-SiC:H films and annealed by pulsed electron beam.

J. Huran<sup>1</sup>, I. Hotový<sup>2</sup>, A. P. Kobzev<sup>3</sup>, N. I. Balalykin<sup>3</sup>

<sup>1</sup> Institute of Electrical Engineering, Slovak Academy of Sciences, Dúbravská cesta 9, Bratislava, 842 39, Slovakia

Phone: +421 2 54775826 2778, Fax: +421 2 54775816, E-mail: huran@savba.sk

<sup>2</sup> Faculty of Electrical Engineering and Information Technology, Slovak Technical University, Ilkovičova 3, Bratislava, 812 19, Slovakia

<sup>3</sup> Joint Institute for Nuclear Research, Dubna, 141980, Moscow Region, Russia

## Abstract

The properties of nitrogen-doped amorphous SiC films irradiated by pulse electron beams are presented. The I-V characteristics of diodes made of irradiated SiC films grown on silicon substrates were investigated. The results showed that the film conductivity increased by about two orders of magnitude as nitrogen fraction was increased from 10 at % to 14 at %. The film conductivity was enhanced by about one order of magnitude as a result of twofold increase of pulse electron beam irradiation.

## 1. Introduction

Much attention has been given to SiC, currently the most mature of the wide-bandgap ( $2.0 \text{ eV} < E_g < 7.0 \text{ eV}$ ) semiconductors, as a material well-suited for high temperature operation. High-temperature circuit operation from  $350^\circ\text{C}$  to  $500^\circ\text{C}$  is desired for use in aerospace applications (turbine engines and more electric aircraft initiative), nuclear power instrumentation, satellites, space exploration, and geothermal wells [1-2]. In addition to high-temperature applications, SiC has potential for use in high-power, high-frequency, and radiation-resistant applications [3]. Silicon carbide (SiC), aluminum nitride (AlN), gallium nitride (GaN), boron nitride (BN), diamond, and zinc selenum (ZnSe) are just some of the premier wide-bandgap semiconductors now being developed for use in the aforementioned applications. However, SiC has several advantages over other wide-bandgap semiconductors at the present time including commercial availability of substrates [4], known device processing techniques, and the ability to grow a thermal oxide for use as masks in processing, device passivation layers, and gate dielectrics. Furthermore, SiC can also be used as a thin buffer layer for the growth of diamond films on silicon substrates [5]. For example, a-Si<sub>1-x</sub>C<sub>x</sub>:H was used as a wide window material to enhance the conversion efficiency of amorphous solar cell [6]. The significance of this material follows from the fact that its electrical and optical properties can be controlled by varying the carbon, silicon and hydrogen composition of the film. Standard technologies for silicon carbide devices production as ion implantation at room temperature and subsequent thermal annealing of radiation damage at moderate temperatures cannot be adopted because the radiation damage in SiC is extremely stable. Very high temperatures are necessary for its annealing and to activate dopants [7]. One way to overcome this problem is to perform pulsed electron or ion beams.

In the present paper we report of a systematic study of the properties of nitrogen-doped amorphous SiC films irradiated by pulse electron beams. The current-voltage (I-V) characteristics of diodes made of doped and irradiated SiC films grown on silicon substrates were studied and the dependence of the electrical properties of these devices on the conditions of electron beam irradiation was investigated.

## 1. Experiment

Nitrogen-doped amorphous silicon carbide films were grown by plasma enhanced chemical vapour deposition (PE CVD) technique. All films were prepared on lightly doped n-type Si substrates (111). The films were deposited in a high frequency parallel-plate plasma reactor in which the frequency, the RF power and the substrate temperature were maintained at 13.56 MHz, 0.06 Wcm<sup>-2</sup>, and  $350^\circ\text{C}$ , respectively. Samples with different amount of N were achieved by small addition of ammonia NH<sub>3</sub> into the gas mixture of silane SiH<sub>4</sub> and methane CH<sub>4</sub> which were directly introduced into the reaction chamber. The actual amount of nitrogen in the SiC films was determined by Rutherford backscattering spectrometry (RBS). The hydrogen concentration was



determined by the elastic recoil detection (ERD) method. For this purpose the  $^4\text{He}^+$  ion beam from a Van de Graaff accelerator at JINR Dubna was applied. The energy of 2.4 MeV was chosen. The target was tilted at an angle of  $15^\circ$  with respect to the beam direction and the recoiled protons were measured in forward direction at an angle of  $30^\circ$ . The samples were irradiated in combined small pulse ion-electron source which consisted of high voltage accelerating generator, vacuum diode, vacuum and diagnostic systems.<sup>6</sup> The negative polarity of the pulse voltage of Marx-Arkad'ev high voltage generator was used for production of the electron beam. For irradiation experiments we used electron beams with a kinetic energy 160 keV and 200 keV, a pulse duration 300 ns, and a beam current 150 A/cm<sup>2</sup>. The number of pulses was altered from 10 to 20 pulses. For electrical characterization of the SiC films vertical diode structures were formed on the prepared SiC/Si samples. Circular Au dots with a diameter of 0.5 mm and a thickness of 50 nm were evaporated after the cleaning procedure of SiC surface. Al served as large area back contact to Si substrate. The I-V characteristics of devices prepared from different SiC films were measured and evaluated.

### 3. Results and discussion.

The thickness and refractive index of the SiC films were measured by a Gaertner Ellipsometer. Figure 1 shows RBS spectra of two samples RD1 and RD2 which were irradiated by electron beam with different energy, RD1 160 keV and RD2 200 keV, respectively.

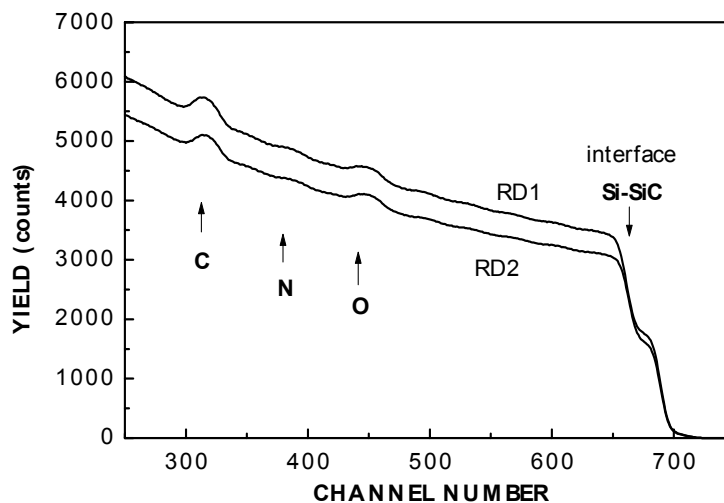


Fig. 1. The RBS spectra of as deposited hydrogenated amorphous SiC films on Si substrate irradiated by pulse electron beam, RD1(10 pulses, 160 keV), RD2 (10 pulses, 200 keV)

The channel numbers at which the steps occur correspond to those of carbon and silicon. Other steps represent oxygen and nitrogen. After modeling, we can show from calculated results that the concentrations of nitrogen and oxygen are 10 and 6 at.% respectively. The concentration of silicon and carbon were approximately the same. ERD calculated results are very interesting because the concentration of hydrogen in the layers remain nearly unaffected after irradiation by pulse electron beam. The ERD spectra are shown in Figure 2.

For technological conditions which represented by sample D2, the deposition rate was 12 nm per minute and refractive index was 2. For sample D3 the deposition rate and refractive index was practically the same. The nitrogen concentration was 10 at % in sample D2 and 14 at % in sample D3. Figure 3 shows the infrared spectra of as deposited samples D2 and D3. There is no essential difference between the spectra of the two samples with different amount of nitrogen. The films contain features typical for hydrogenated amorphous silicon carbide: the main band at  $780\text{ cm}^{-1}$  is related with the Si-C stretching modes, the C-H stretching band at around  $2900\text{ cm}^{-1}$  and the band around  $2100\text{ cm}^{-1}$  are assigned to Si-H stretching vibrations.

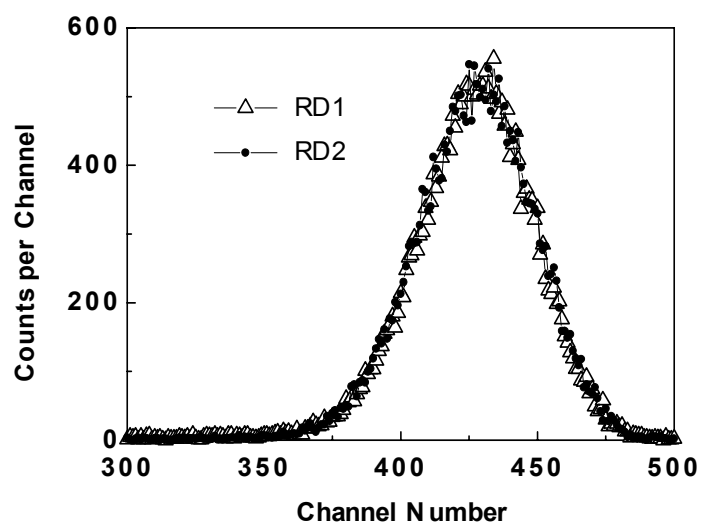


Fig. 2. The ERD spectra of recoiled hydrogen obtained with 2.4 MeV  $^4\text{He}^+$ . The concentration of hydrogen for samples RD1 and RD2 are 21, 22 at %, respectively.

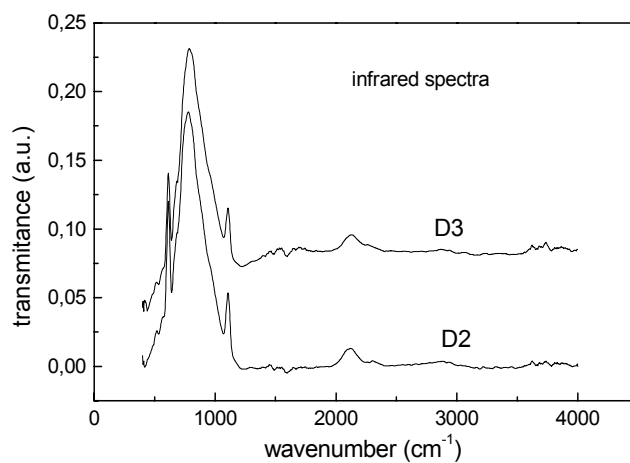


Fig. 3. IR spectra of as deposited hydrogenated amorphous SiC samples (D2 and D3 indicate the samples with different nitrogen content).

The effect of pulse electron beam irradiation was investigated by means of I-V measurements of diode structures prepared from nitrogen doped SiC films. For this purpose, four samples were studied and analyzed. The electron beam irradiation experiments were carried out as follows: samples D2 and D3 (with different nitrogen concentrations) were irradiated by 20 pulses (indicated as D2e20, D3e20) and by 10 pulses (indicated as D2e10, D3e10). Representative curves obtained from the I-V measurements of diodes are illustrated in Figure 4 and Figure 5. The I-V characteristics of diodes from samples with different nitrogen-doped SiC films are compared in Figure 4. Both samples D2 and D3 were exposed to the same pulse electron beam irradiation conditions (20 pulses). The diode currents at applied bias of 5 V were about 2 pA and 200 pA for samples D2e20 and D3e20, respectively. These results confirm the fact that samples D3e20 with higher nitrogen doping (i. e. with nitrogen content of 14 at %) exhibit about two orders of magnitude higher conductivity (i. e. lower resistivity) as compared to lightly doped samples D2e20 (with nitrogen content of 10 at %). Figure 5 shows the influence of different electron beam irradiation conditions on the I-V characteristics of diodes prepared from doped SiC films with nitrogen content of 14 at %. The samples irradiated by 10 pulses (D3e10) and by 20 pulses (D3e20) are compared. The diode currents of the sample irradiated by 10 pulses (D3e10) were about 15 pA. These results can be summarized as follows: the electrical conductivity of nitrogen doped SiC film was increased by about one order of magnitude as a result of twofold increase of pulse electron beam exposition.

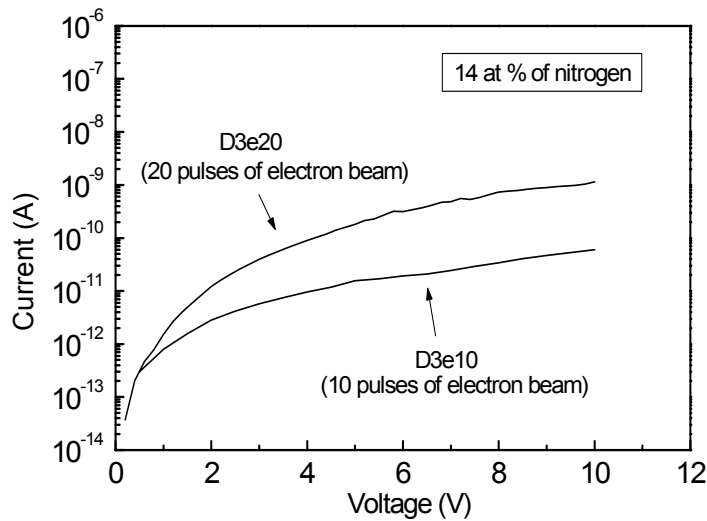


Fig. 4. I-V characteristics of diodes prepared from samples with nitrogen-doped SiC films irradiated by 20 pulses of electron beam (sample D2e20 - 10 at % of nitrogen, sample D3e20 - 14 at % of nitrogen)

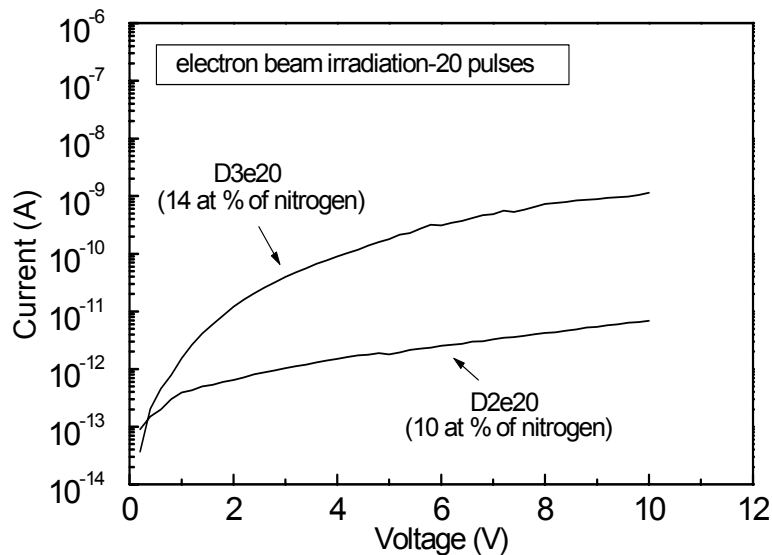


Fig. 5. Comparison of the I-V characteristics of diodes prepared from higher doped SiC film (D3) exposed to different pulse electron beam irradiation conditions (sample D3e10 is irradiated by 10 pulses, sample D3e20 is irradiated by 20 pulses).

#### 4. Conclusion

It was observed that nitrogen incorporation during deposition produces doping of amorphous SiC films but their resistivity is fairly high. Therefore the high current pulse electron beam irradiation was applied to activate the nitrogen dopants in the amorphous SiC films. The electrical conductivity was evaluated by means of I-V measurements of diodes prepared from two nitrogen-doped SiC films and the influence of different pulse electron beam irradiation conditions was investigated. It was found that with increased nitrogen doping and following activation of dopants the resistivity of the amorphous SiC films was substantially reduced.

#### Acknowledgement

The work was supported by the Slovak Grant Agency for Science through grant No. 2/1167/22.

#### References

- [1] I.G. Brown - J. Vac. Sci. Technol, **A 11**, 1480 (1993)
- [2] D.E. Cusack, W.M. Glashen, H.R. Steglich - Trans. of 2nd Int. High Temperature Electronics Conf. (HiTEC), Session III, 17 (1994)
- [3] R.J. Trew, J.B. Yan, P.M. Mock: Proc. IEEE **79**, 598 (1991)
- [4] Advanced Technology Materials, Inc., 7 Commerce Drive, Danbury, CT 06810-4169
- [5] E.G. Wang - Physica **B185**, 85 (1993)
- [6] W. Wesch - Nucl. Instr. Meth., **B 116**, 305 (1996)
- [7] R.F. Davies, G. Kelner, M. Shur, J.W. Palmour, J.A. Edmond - Proc. IEEE, **79**, 677 (1991)

# A NEW DIRECT METHOD FOR CALCULATING INTENSITIES OF ELECTRIC AND MAGNETIC FIELDS AT RF PLASMAS

I.Abdoullin<sup>1</sup>, L.Aboutalipova<sup>1</sup> and V.Jeltoukhine<sup>2</sup>

<sup>1</sup>*Light Industries Department of Kazan State Technological University, Kazan, Russia*

<sup>2</sup>*Computing Mathematics Department of Kazan State University, Kazan, Russia*

Inductive, capacitive, or hybrid (both inductive and capacitive) coupled RF plasmas in cylindrical discharge tube is considered. It is assumed that vectors of electric and magnetic intensities  $\mathbf{E}, \mathbf{H} = \exp(i\omega t)$ ,  $\mathbf{E} = (E_r, E_\varphi, E_z)$ ,  $\mathbf{H} = (H_r, H_\varphi, H_z)$ , and all the plasma features, such as conduction  $\sigma$ , relative permittivity  $\varepsilon$ ,  $\mathbf{E}, \mathbf{H}$  components, are symmetrical about the discharge tube axis. This means that  $\sigma = \sigma(r, z)$ ,  $\varepsilon = \varepsilon(r, z)$ ,  $H_r = H_r(r, z)$ , etc., where  $r, z$  are cylindrical co-ordinates. Using the electromagnetic field conservation law, the Maxwellian equations is transformed to the following equation system

$$\nabla \cdot \left( \frac{\sigma}{s^2} \nabla H_\beta^2 - 2\mathbf{w}(\mathbf{h}_\beta, \phi_{\mathbf{H}, \beta}, \sigma, \varepsilon, \omega) H_\beta^2 \right) = 2\sigma E_\beta^2 \quad (1)$$

$$\nabla \cdot (\nabla E_\beta^2 - 2\mathbf{q}(\mathbf{e}_\beta) E_\beta^2) + 2 \frac{\varepsilon \omega^2}{c} E_\beta^2 = 2(\mu_0 \omega)^2 H_\beta^2, \quad (2)$$

$$\Delta \gamma_{\mathbf{k}(\beta)} = G_{\mathbf{k}(\beta)}(E_\beta, H_\beta, \sigma, \varepsilon, \omega, \delta \phi_{\mathbf{K}, \beta}, \gamma_{\mathbf{k}(\beta)}), \quad (3)$$

$$\Delta \phi_{\mathbf{K}, \beta} = F_{\mathbf{K}, \beta}(E_\beta, H_\beta, \sigma, \varepsilon, \omega, \delta \phi_{\mathbf{K}, \beta}, \gamma_{\mathbf{k}(\beta)}) \quad (4)$$

Here  $s^2 = \sigma^2 + (\varepsilon_0 \varepsilon \omega)^2$ ,  $E_\beta = |\mathbf{E}_\beta|$ ,  $H_\beta = |\mathbf{H}_\beta|$ , index  $\beta = \{L | C\}$  mean «capacitive» (C) or «inductive» (L) component of  $\mathbf{E}, \mathbf{H}$  so that  $\mathbf{H} = \mathbf{H}_L + \mathbf{H}_C$ ,  $\mathbf{E} = \mathbf{E}_L + \mathbf{E}_C$ :  $\mathbf{H}_L = (H_r, 0, H_z)$ ,  $\mathbf{H}_C = (0, H_\varphi, 0)$ ,  $\mathbf{E}_L = (0, E_\varphi, 0)$ ,  $\mathbf{E}_C = (E_r, 0, E_z)$ . Besides,  $\mathbf{h}_\beta = \mathbf{H}_\beta / H_\beta$ ,  $\mathbf{e}_\beta = \mathbf{E}_\beta / E_\beta$ ,  $c$  is the light speed;  $\gamma_{\mathbf{k}(\beta)}$  is the angle of  $\mathbf{k}(\beta)$  with  $Oz$  axis,  $\mathbf{k}(L) = \mathbf{h}_L$ ,  $\mathbf{k}(C) = \mathbf{e}_C$ ,  $\phi_{\mathbf{K}, \beta}$  is the phase of  $\mathbf{K}$  vectors, where  $\mathbf{K} = \{\mathbf{E} | \mathbf{H}\}$ ; vectors  $\mathbf{w}(\mathbf{a}, \phi, \sigma, \varepsilon, \omega) = \{\sigma \mathbf{q}(\mathbf{a}) - \varepsilon_0 \varepsilon \omega [(\mathbf{a} \cdot \nabla \phi) \mathbf{a} - \nabla \phi]\} / s^2$ ,  $\mathbf{q}(\mathbf{a}) = (\mathbf{a} \cdot \nabla) \mathbf{a} - \mathbf{a}(\nabla \cdot \mathbf{a})$  for any  $\mathbf{a}, \phi$ ;  $\delta \phi_{\mathbf{K}, \beta} = \phi_{\mathbf{K}, \beta} - \phi_{\mathbf{K}, \beta}$ ;  $F_{\mathbf{K}, \beta}$ ,  $G_{\mathbf{K}, \beta}$  are non-linear functions. Mixed type physical correct boundary conditions are formulated to these equations.

At first sight the new system of boundary-value problem are very difficult. Yet, every equation and boundary condition has clear physical meaning. Modern computational methods are solved similar problems very efficiently. Thus, in this way we'll find  $\mathbf{E}, \mathbf{H}$  magnitudes and directions at RF plasmas without any added transform.

# Construction of three-phase single-chamber plasma torch with tubular copper electrodes for work on air and oxidizing media

Ph.G. Rutberg, A.A.Safronov, V.N.Shiryaev, V.E. Kuznetsov

*Institute of Problems of Electrophysics RAS, Saint-Petersburg, Russia*

## Abstract

All industrially developed countries, first of all the USA, Germany, Canada, France, Japan has become interested in application of plasma chemical technology for destruction of various type of toxic wastes.

The similar systems are developed and produced in the Institute of Problems of Electrophysics of RAS and plasma torches of PT series are characteristic example of such devices [1].

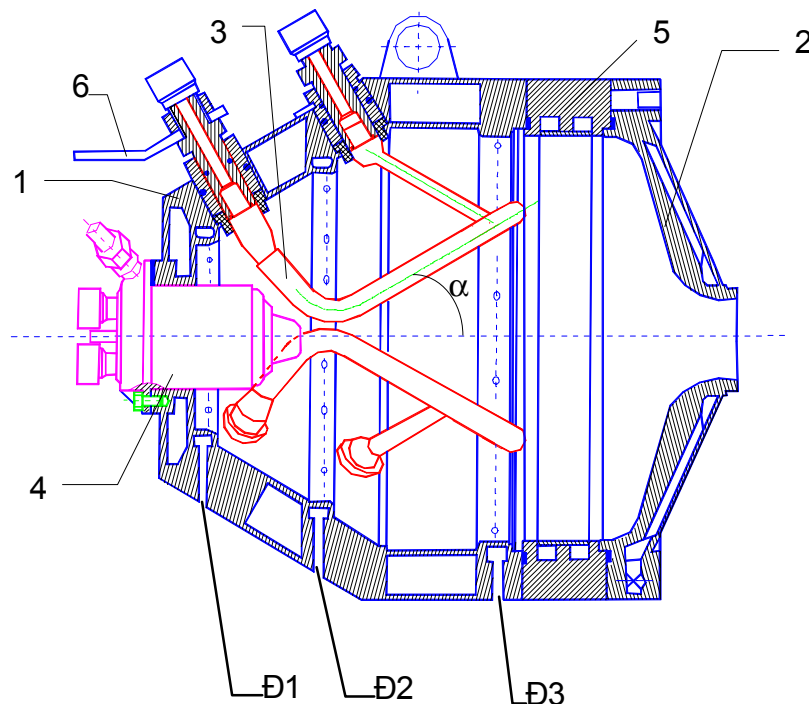
## Introduction

The basic advantage of AC plasma torches is simplicity of the power supply system, its low cost, possibility of automation of control procedures and high reliability of the system as a whole. Due to these peculiarities the use of AC plasma torches for solution of ecological tasks is not only perspective, but also an economically sound step.

The principle of plasma torch work is based on use of electrodynamic movement of the electrical arc in the electromagnetic field created by own arc current (rail gun effect). The arc after interelectrode breakdown moves along tubular electrodes up to their end and extinguishes at the place, where the interelectrode distance becomes more than working one. Three-phase system of electrodes and their configuration allows avoiding arc breakaway and current break. Thus the rail gun effect ensures distribution of thermal load along the electrode length. Intensive water cooling of tubular copper electrodes allows passing large currents with essential increase of lifetime of electrode operation and minimization of gas medium contamination.

## 1. Description

Three-phase AC plasma torch, fig.1, consists of



**Fig.A. Three-phase plasma torch PT-4.**

1 – electric discharge chamber case, 2 – outlet flange with a nozzle 3 – electrode unit, 4 - injector, 5 - intermediate ring, 6 - terminal of power supply voltage, P1-P3 - outlines of working gas input, P1 - injector inlet, P2 - basic inlet, P3 – nozzle inlet,  $\alpha$  - angle of electrode opening.

- water cooling electric discharge chamber 1 with a system of tangential gas feeding 5,
  - water cooling outlet flange with the nozzle 2
  - electrode unit 3,
  - plasma injector 4,
  - Intermediate ring 6.
1. The electric discharge chamber is intended for forming of interior gas current ensuring effective heat exchange between the electric arc and working gas and protection of near wall from arc attachment. Due to three independent outlines of working gas inlet and possibility of chamber geometry variation (with the help of special intermediate rings), this construction can work in a broad range of power and working gas flowrate.
  2. Water cooling outlet flange with the nozzle serves for forming of a plasma jet with defined physical parameters depending on the technological requirements.
  3. Electrode unit is intended for electric arc creation. The magnitude of angle opening and construction of electrodes is determined in dependence on electric power of the plasma torch.
  4. The plasma injector is necessary to ensure steady ignition of arcs in interelectrode gap.
  5. The intermediate ring ensures reaching of optimum gasdynamic conditions for flow in the electric discharge chamber at plasma torch power more than 150 kW or use of a series of electrode constructions designed on increased lifetime, prevents attachment and electrical arc shorting on the outlet flange of the plasma torch.

The case of the plasma torch is made of stainless steel and it geometrically represents unclosed volume formed by junction of the cylinder and two truncated cones in the walls of which there are cavities for cooling fluid.

## 2. Principle of operation

The rail gun effect is put in a basis of plasma torch work i.e. principal of electrical arc moving in a field of its own current.

Due to one-sided power supply through the terminal 7 fig.1 the arcs, appearing in the electric discharge chambers of the plasma torch, move along the electrodes under the action of electrodynamic forces, appearing as a result of interactions of arc current with its own magnetic field. Besides, due to three-phase feeding voltage, the arc transfers from electrode to electrode with change of anode and cathode phases with frequency 300 Hz.

The injector creates a stream of plasma ensuring concentration of electrons  $n_e \sim 10^{14} \div 10^{16} \text{ cm}^{-3}$  in a zone of minimum distance between basic electrodes  $\sim 0.5 \text{ cm}$ , that is sufficient for ignition of basic arcs at comparatively low voltage of power supply  $\sim 300\text{-}500 \text{ V}$ . Appearing arcs move along divergent electrodes with velocity 10-30 m/s depending on current magnitude and angle of electrode declination. In the near wall area the concentration of charged particles sharply drops and, thus, the insulating area is created at reaching of which the arc extinguishes and the process is repeated. With arc movement along the electrodes their velocity noticeably drops. It is explained by quadratic decrease of current magnetic field with a distance from the electrode that is not compensated by linear growth of arc length. Thus the working zone of electrode at a current, for example,  $\sim 850$  makes a few centimeters.

Arcs, the combustion regime of which has a diffuse character fig. 2, fill in the majority of the discharge chamber moving in longitudinal and transversal directions. That is why it is possible to obtain a comparatively large thermal efficiency of the plasma torch (up to 85 % depending on operating conditions).

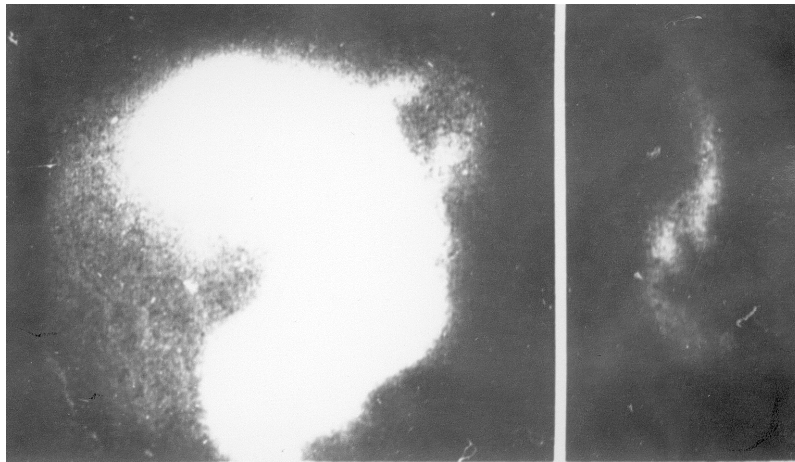


Fig.2. Contracted and diffuse combustion regime of an electrical arc of the AC plasma torch

The injector and use of rail gun effect allow to have low voltage of the power supply and comparatively high voltage on arcs, i.e.  $\cos \varphi$  of the unit is 0.6-0.7, thus there are no peaks of ignition and the form of voltage on the arcs is close to sinusoidal.

### 3. Some characteristics of the plasma torch

Volt-ampere characteristics of the arc discharge, defining dependence of voltage drop from current at various flowrates of air are represented in fig. 3.

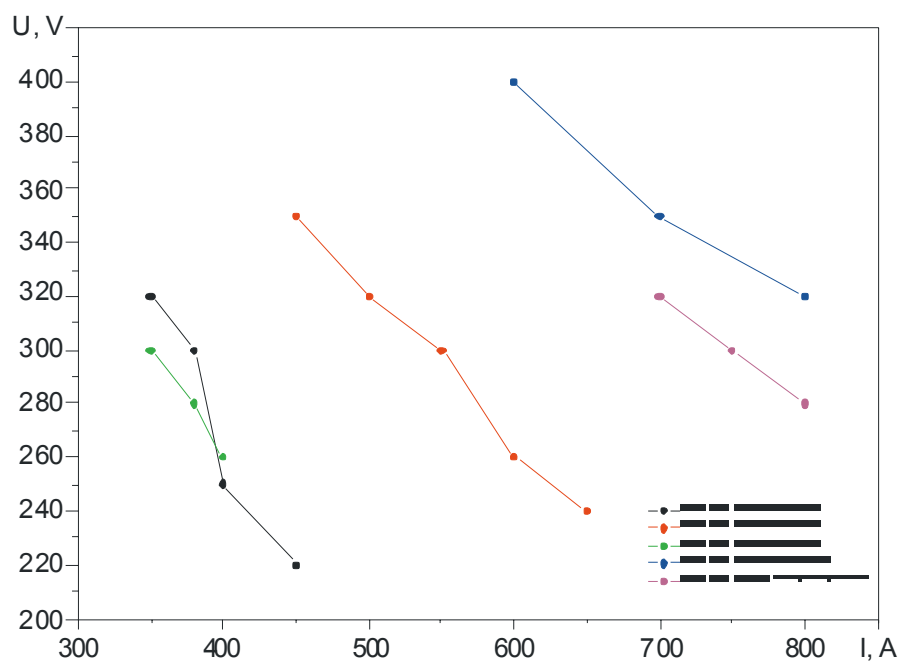


Fig3. Static volt-ampere characteristics of the plasma torch

Such form of the curve can be explained by combustion regime of arcs in the electric discharge chamber of the plasma torch. It has a diffuse-turbulent character. The dependence of the plasma torch efficiency of the electric power is represented in fig. 4.



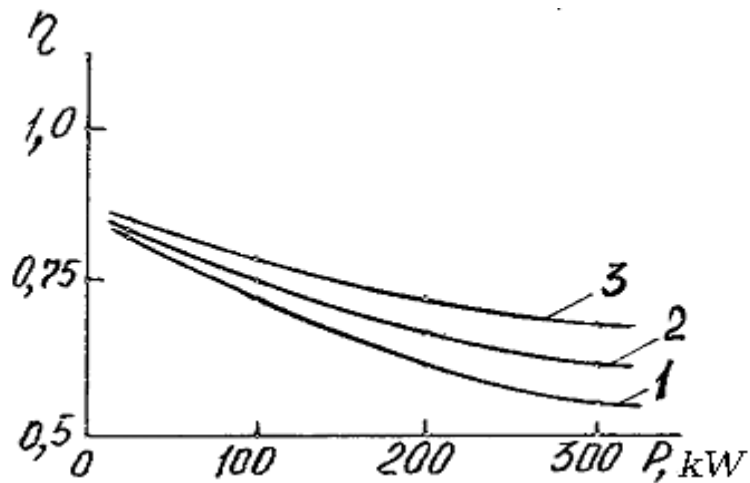


Fig4. The relationship of the plasma torch efficiency and the electric power  
1-flowrate 20 g/s, 2- flowrate 40 g/s, 3- flowrate 60 g/s

As may be seen from the figure the efficiency a little bit drops with increase of efficiency. It is natural, since average mass temperature and temperature in arcs grows, that results in increase of losses, first of all at the expense of losses on radiation. It is obvious that a reverse phenomenon is observed at growth of gas flow rate (of course these results concern the concrete cooling system). The estimations of dependence of the average mass temperature of gas in the discharge chamber from power are represented in fig.5. The obtained results satisfactory coincide with the experimental data.

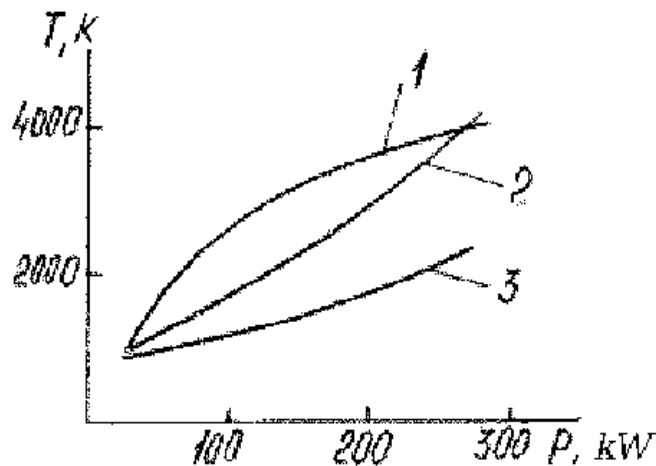


Fig 5. Calculated dependencies of average mass temperature  
1-flowrate 20 g/s, 2- flowrate 40 g/s, 3- flowrate 60 g/s

## References

1. I.A.Glebov, Ph.G.Rutberg. Power plasma generators., M.: Energoatomizdat, 1985 (in Russian)
2. Ph.G.Rutberg, A.A.Safronov, V.L.Goryachev. Strong-Current Arc Discharge of Alternating Current. IEEE Transactions on Plasma Science, August 1998, v.26, #4, ITPSBD, ISSN 0093-3813, p.1297-1306.
3. Ph.G.Rutberg A.A.Safronov, V.N.Shiryaev, V.E.Kuznetsov, Power AC plasma generator, Transactions of Conference on Physics of Low Temperature Plasma, 20-26 June,1995, Petrozavodsk. (in Russian)

# **Plasma Treatment of Different Type Waste in the Interests of Enviroment Protection**

Ph.G. Rutberg, A. N. Bratsev, I. I. Kumkova, A.A. Safronov

*Institute of Problems of Electrophysics RAS, Saint-Petersburg, Russia*

A treatment of municipal, medical and industrial waste by use of methods of high temperature chemical oxidizing or plasma pyrolysis and gasification with temperatures of 1200-1600deg C are considered. Different types of plasma reactors with productivity of 0.1-5 t/hr are discussed.

Estimations of parameters of reactors, of parts of the systems and plasma generators and produced syngas. are presented. Preliminary results of the experiments with test units are described.

Examples of IPE RAS installations for treatment of medical waste and destruction of high toxic waste are considered in detail.

The installation for treatment (high temperature oxidizing) of medical waste is constructed for 150-200kg/hr productivity. The principles of technically perfect organization of the thermal destruction of waste are proposed as follows: two stage thermal destruction with dwell time of flue gases in the reactor no less than 2 s; obligatory quenching (fast cooling) of flue gases; multistage cleaning of flue gases of flue ash, vapors of heavy metals, acid gases, and dioxins and furans; absence of waste waters; automatic control of mode parameters, emissions into the atmosphere and control of the whole technological process; low consumption coefficients on power engineering and using reagents.

A rotating furnace with direct motion of waste and gases is proposed as an aggregate for plasma destruction. As a gas cleaning method and in view of small productivity of the installation, a wet method of cleaning from flue ash, compounds of heavy metals and acid gases is applied and also adsorption method for absorption of residual vapors of heavy metals compounds and dioxins are used. The organization of reduction zones in the rotating furnace and in the dry scrubber for suppression of emission of nitrogen oxides is considered. The following waste are formed as a result of operation of the plant: cleaned flue gases — 846 kg/hr — are removed into the atmosphere; slag — 6.2 kg/hr;

Moreover there is presented a description of the unit and results of investigation of destruction and neutralization of complex, liquid, Cl-, F-, C-containing waste.

All units described are used multi-phase AC plasma torch as a plasma generator, what results to reduction of cost of the system.

# Biological activity of water created by pulse electrical discharge

Ph.Rutberg, A.N.Bratsev, V.E. Popov, S.V. Shtengel, V.A.Kolikov

*Institute of Problems of Electrophysics Russian Academy of Science, Saint-Petersburg, Russia*

A new unique method of producing biologically active water has been detected in IPE RAS. The essence of the invention is to apply a pulse high-voltage discharge to the water resulting in a new quality of it. The discharge is characterized by low energy in pulse. The average specific density of energy is  $1 - 5 \text{ J/cm}^3$ .

Generally all detected features of water treated by pulse electrical discharge with low energy in pulse have been defined the biological activity of water and the water itself can be called biologically active water (BAW).

Results of a few experiments are described as examples of the manifestations of the biological activity of water. Distilled water was used in the experiments described.

The physiological solution has been made using the treated water (BAW). Equal quantities of bacteria E.Coli and S.aurens, in concentration of  $10^3 - 10^7 \text{ 1/ml}$  were introduced into two solutions: the physiological solution using BAW and a regular physiological solution using untreated water. Twenty-four hours later the quantity of bacteria consisted of 0-4 1/ml in the solution using BAW whereas the concentration did not change in the regular solution. A check one year later showed that bacteria were absent in the solution using BAW.

Another experiment was performed with syringes. Non-sterilized needles and syringes were put into BAW and into untreated water. Six days later an increased quantity of microbes was observed in the untreated water. Ten days later this water was infected completely. Over the same time BAW was absolutely pure.

At present IPE RAS carries out investigations of detected events. Experiments are performed with electrodes of different materials, with different constructions of discharge chambers and so on. In these experiments such parameters as the pH value after the discharge effect, the concentration of metal particles in the water, the structure and size of micro particles created in the water, are measured by methods of electron and tunnel microscopy.

Sterilizing features of BAW need technological tests before being used in the practice, for sterilization of medical equipment and instruments such as rubber and plastic articles that cannot be subjected to thermal treatment. Moreover articles of other types can be sterilized in BAW at the preliminary stage without the use of chemical agents.

Some preliminary research on the effects of BAW was carried out. Biological objects of different types were the subject of the research:

- \* cell level - bull spermatozoa, rat mast cells, cell culture of fibroblast L929, microorganisms E. Coli, S. aurens, K. penmonial, P. aeruginosa;
- \* protozoa - Daphnia magna;
- \* mammals - white rats, guinea-pigs, rabbits.

Methods used in the research correspond to safety requirements brought to medical articles.

The results of the biological and chemical research on BAW confirmed the following:

1. The water has powerful sterilizing features;
2. Toxical and mutational reactions were not present during use in food;
3. No allergic reactions have been detected when applied directly on the skin and mucous membrane;
4. Biological solutions using BAW have a very strong effect on the concentration of several ferments in blood when injected into experimental animal blood.
5. The water reveals a capacity to reduce the rate of increase of cancer cells when injected into the experimental animal blood.
6. Biological activity of BAW has been observed on human blood. Defined dosage of BAW decreases activity of lymphocytes and influences on thrombocytes aggregation function in complicate mode being liable to activate or slow down aggregation.

# Temperature Distribution Induced by Electron Beam in a Closed Cavity

A.G. Molhem and S. Sh. Soulayman

*Department of Applied Physics, Higher Institute for Applied sciences and Technology, Damascus, P.O.Box 31983,  
Syria*

*Email: [ssoulayman@netcourrier.com](mailto:ssoulayman@netcourrier.com)*

It is well known that, the collision of electron beam (EB) with gas's atoms and molecules is of fundamental interest in plasma physics, as it plays an important role in many applications. In order to investigate heat transfer phenomena induced by EB in a closed cavity an experimental arrangement is used for this purpose. This arrangement allows generating and focusing an electron beam in to closed cavity within 1 mm in diameter as well as to measure gas temperature all over any perpendicular section to the EB. The measurement is accomplished by locating a copper sphere of diameter smaller than 9 mm (here it should be mentioned that we used spheres of 4mm and 5 mm additionally). The temperature of the spheres were measured using a special thermocouple inserted in each of them. The analysis of the experimental data shows that there is tow distinguishable regions of heat transfer behavior around the EB. The first one appears just near the EB, where the ionizations and excitations take place, while the other region is located far from the axis of the EB by about of 10mm depending on the conditions of experiment. The difficulty of treating of these results by available theoretical models enforced us to do some suitable modifications which ameliorate the agreement between theoretical interpretation and experimental data.

# Barrier films on polymers from low-pressure microwave excited plasmas

M. Walker, J. Schneider, K. Bazzoun, J. Feichtinger, A. Schulz and U. Schumacher

*Institute of Plasma Research, University of Stuttgart, Pfaffenwaldring 31,  
D-70569 Stuttgart, Germany*

## Abstract

This paper mainly deals with the development and characterization of plasma polymerized barrier films on polymeric packaging materials and on Nafion membranes for direct methanol fuel cells (DMFC). Two examples of barrier coatings will be described in detail: A surface treatment to reduce the permeation of methanol through Nafion and a surface coating of polyethylene (PE) foils to improve the barrier properties to oxygen.

## 1. Introduction

In recent years, low-pressure and low-temperature plasmas have received increasing attention mainly in the different fields of plasma processing. Especially for polymeric materials, the plasma technique offers a broad spectrum of applications. The gas discharge treatments of polymer surfaces are used, for example, for the improvement of wettability, paintability and adhesion. An important application results from the barrier performance of polymers like polyethylene (PE), polypropylene (PP) and polyethyleneterephthalate (PET), which can be strongly improved by plasma polymerized thin films [1]. Commonly, organosilicon compounds, such as hexamethyldisiloxane (HMDSO), hexamethylsilane (HMDS), trimethylsilane (TMS) or tetraethoxysilane (TEOS) in mixtures with O<sub>2</sub> are used as deposition gases. These films produce excellent results in terms of transparency and of barrier properties [2]. An other interesting example is the surface modification of Nafion membranes for direct methanol fuel cells (DMFC). Nafion is an ionomer consisting of carbonfluorine chains with perfluoro side chains containing –SO<sub>3</sub>H groups, which support the proton transport. A critical point in the use of Nafion as membranes for DMFC's is the high methanol permeability, known as methanol crossover in the literature. This methanol crossover leads to multiple negative effects resulting in poorer cell performance and worse fuel cell efficiency [3]. This work shows, that a surface treatment in a H<sub>2</sub> plasma can improve the barrier properties of such Nafion membranes.

## 2. Diffusion processes through polymers

The theoretical description of the permeation behaviour of the polymers as well as of the barrier layers is given by the two Fick's laws [4]. Assuming a one-dimensional diffusion process, where x is perpendicular to the polymer film surface, the first Fick's law is given by

$$j_x = -D(c) \frac{dc}{dx} \quad (1)$$

Here c is the concentration of the permeant, D(c) is the diffusion coefficient, which generally depends on c, and j<sub>x</sub> is the flux of the permeating molecules through the polymer surface.

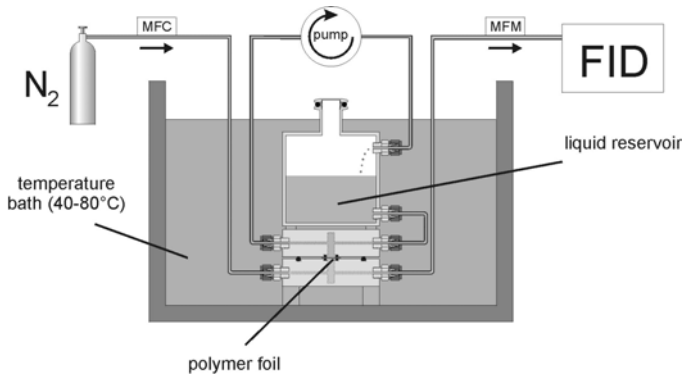
Fick's second law describes the non-steady state and can be written as

$$\frac{dc}{dt} = \frac{d}{dx} \left( D(c) \frac{dc}{dx} \right) \quad (2)$$

If the interactions between the permeating molecules and the polymer are small, then the diffusion coefficient D is independent of the concentration c. This holds for many permanent gases at room temperature and at moderate pressures and is a good approximation for the diffusion of O<sub>2</sub> through PE and PET. But, especially in the case of the diffusion of organic liquids and vapours in a series of polymers, the sorbed molecules swells the polymer, resulting in a strong increase of the diffusion coefficient. Then, the diffusion coefficient is a function of c and can often be written as [4]

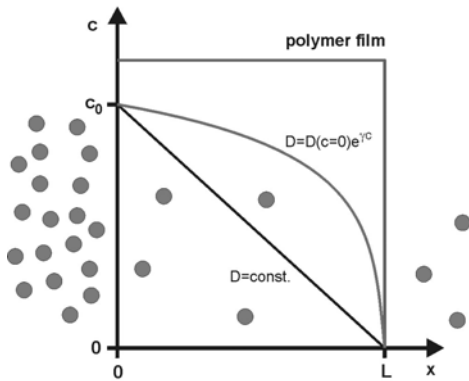
$$D(c) = D(c = 0) \exp(\gamma c), \quad (3)$$

where  $\gamma$  is a characteristic parameter of the specific polymer-permeant system and  $D(c=0)$  is the diffusion coefficient  $D$  in the limit of  $c=0$ .



**Fig. 1:** Schematic view of the permeation experiment.

In a typical and often used permeation experiment, the polymer film separates two chambers, which contain the gas, vapour or liquid at different concentrations. Then the molecules diffuse from the high concentration chamber with  $c_0$  to the low concentration chamber with  $c_1$ . In the so-called carrier gas method the experimental condition is:  $c_0 \gg c_1 \approx 0$ . The experimental set-up of such a permeation experiment is shown in Fig. 1. The permeant is introduced into the upper compartment. Through the lower compartment a carrier gas, e.g.  $N_2$ , flows with a constant rate. It sweeps the diffusing molecules to a detector. For the permeation experiments with the Nafion membranes, we use a flame ionisation detector (FID), which is highly sensitive to methanol. In the case of the measurements concerning the  $O_2$  barrier layers on PE foils a ceramic ( $ZrO_2$ ) detector instead of the FID was installed. Additionally, the liquid reservoir was replaced by an oxygen gas equipment.



**Fig. 2:** Boundary conditions in the permeation experiment of Fig. 1 and a steady state concentration profile for  $D=\text{const.}$  and  $D=D(c=0) \cdot \exp(\gamma c)$ .

According to Fig. 2, the boundary conditions can be written as  $c(x=0, t)=c_0$  and  $c(x=L, t)=0$ , where  $c_0$  is the concentration of the gas or liquid at the upper compartment, and  $L$  is the thickness of the PE foil or Nafion membrane, respectively. In the steady state and in the case of a constant  $D$ , the second Fick's law can be directly integrated, and the concentration distribution is given by

$$c_s(x) = c_0 \left( 1 - \frac{x}{L} \right) \quad (4)$$

This means, that the concentration decreases linearly within the polymer (see Fig. 2). A substitution into Fick's first law yields the stationary flux:

$$j_s(x=L) = D \frac{c_0}{L} \quad (5)$$

In the case of the concentration dependence of  $D$  according to eq. (3), the stationary concentration profile and the stationary permeation flux are given by

$$c_s(x) = \frac{1}{\gamma} \ln \left[ \left( 1 - \frac{x}{L} \right) e^{\gamma c_0} + \frac{x}{L} \right] \quad (6)$$

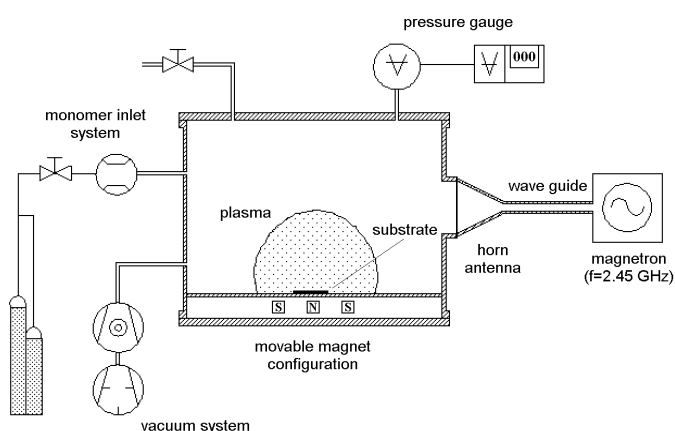
and

$$j_s(x=L) = \frac{D(c=o)}{L} (e^{\gamma c_0} - 1), \quad (7)$$

respectively. To obtain the time dependent flux  $j(x=L, t)$  of the permeating molecules through the polymers as well as through the barrier films at the position  $x=L$  and at any time  $t$  we solved the 1. and 2. Fick's law with a numerical method. Therefore, we used Mathlab<sup>®</sup> with the additional finite element program package Femlab<sup>®</sup>.

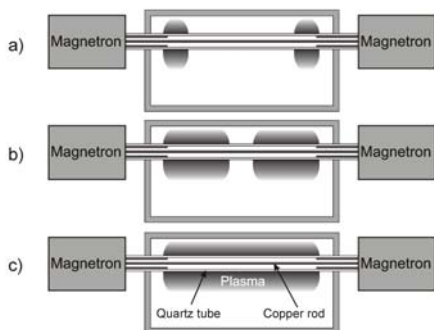
### 3. Plasma sources

For the deposition of the barrier layers two types of microwave sources, an electron cyclotron resonance heated (ECR) plasma and the Duo-Plasmaline are used. In the case of the ECR heated plasma, microwaves at a frequency of  $f=2.45$  GHz are radiated via a horn antenna into a vacuum chamber. The experimental set-up is shown in Fig. 3.

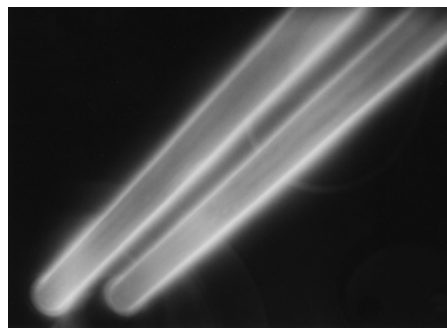


**Fig. 3:** Schematic view of an ECR heated plasma.

On the bottom of the recipient a magnet arrangement of cobalt-samarium permanent magnets is installed, which produces a magnetic field strength of 0.0875 T. In this region, the electron cyclotron frequency  $\omega_{c,e}=eB/m_e$  is equal to the applied microwave frequency  $\omega_{mw} = 2\pi/f=2.45$  GHz and the ECR condition  $\omega_{c,e}=\omega_{mw}$  is fulfilled. Here the plasma is preferentially produced and heated. The gases for the deposition process, i.e. HMDSO and  $O_2$ , are supplied to the recipient by means of mass flow controllers and mass flow meters. The typical pressure range for plasma operation is 1 to 20 Pa, and the microwave power is 3 kW. For our experiments we use a power modulated plasma with a typical on-off pulse cycle of 100  $\mu$ s to 900  $\mu$ s. The polymer foils are placed directly on the bottom of the recipient.



**Fig 4:** Side view of the Duo-Plasmaline for increasing microwave power (from top to bottom).



**Fig 5:** A photograph of an array of plasmalines.

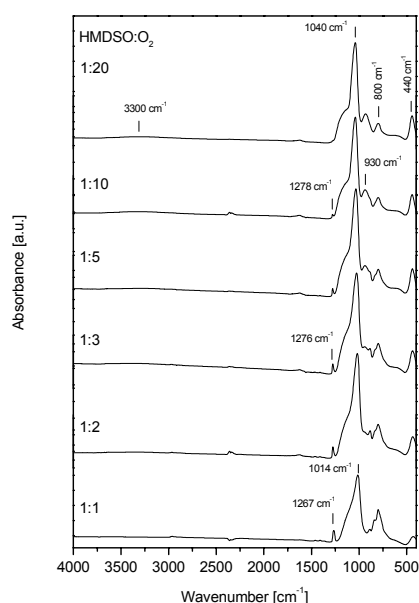
To improve the barrier properties of Nafion membranes we use another type of microwave plasma source, which is called Duo-Plasmaline and which is well described in the literature [5, 6]. The Duo-Plasmaline is a

„direct“ microwave discharge without using a magnetic field. In this concept, microwaves are fed into a copper rod, which is centered in a glass or quartz tube. The inside of the tube is at atmospheric pressure, whereas the outside is at low pressure. When the electric field strength exceeds the breakdown field strength, a discharge outside the glass tube is ignited. At low microwave power, the plasma is concentrated at the ends of the tubes only (see Fig. 4a). With increasing microwave power the plasma grows from both ends along the tubes (see Fig. 4b), and an axially homogeneous plasma is formed (see Fig. 4c). A combination of several of such plasmalines can be used to obtain a two-dimensional plasma array. Fig. 5 shows a photograph of an array consisting of two plasmalines with a length of 80 cm and a distance of 10 cm arranged in parallel. Both plasma sources allow a homogeneous deposition over large areas. Furthermore, they can be used to generate a plasma directly in the inside of a hollow body, for example in a container or in a bottle.

## 4. Results and Discussion

### 4.1 Gas barrier layers on PE foils

In the case of the O<sub>2</sub> gas barrier layers hexamethyldisiloxane (HMDSO) in mixtures with oxygen (O<sub>2</sub>) are used as deposition gases. Some typical infrared (ir) absorption spectra of SiO<sub>x</sub> films plasma polymerized



**Fig. 6:** IR spectra of SiO<sub>x</sub> films grown at different O<sub>2</sub> flow rates [6].

with different HMDSO:O<sub>2</sub> mixture ratios are displayed in Fig. 6 [6]. The films with a thickness of about 1 μm were deposited on aluminium foils. The ir spectra were recorded on a Vector 22 spectrometer from Bruker instruments using the ATR technique. Fig. 6 shows that the intensity of the symmetric –CH<sub>3</sub> deformation band at about 1270cm<sup>-1</sup> decreases with increasing O<sub>2</sub> concentration in the gas mixture. In the case of a HMDSO:O<sub>2</sub> mixture ratio of 1:20 the –CH<sub>3</sub> absorption band disappears. This film shows the three characteristic SiOSi bands at 440cm<sup>-1</sup>, 800cm<sup>-1</sup> and 1040cm<sup>-1</sup>, which correspond to rocking, bending and stretching vibrations, respectively. The addition of O<sub>2</sub> causes an oxidation of the CH-groups to, for example, CO, CO<sub>2</sub> and C-OH. The latter compound produces an absorption band at 930 cm<sup>-1</sup> and 3300 cm<sup>-1</sup> in the ir spectra. Thus, the balance of organic/inorganic content in such films can be adjusted by the HMDSO:O<sub>2</sub> mixture ratio.

The deposition of the O<sub>2</sub> barrier layers on the polymer foils was performed in the plasma equipment shown in Fig. 3. The thickness of the PE foil was 118 μm.

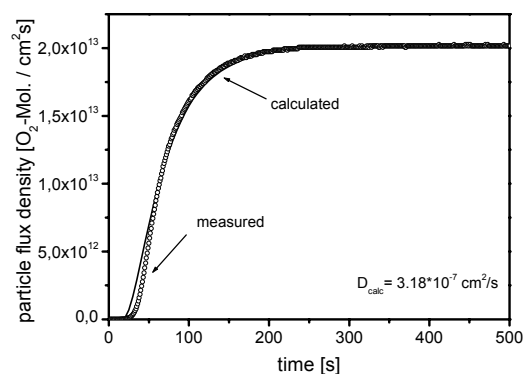
The O<sub>2</sub> permeability of the uncoated and coated foils was measured with the described permeation experiment using the ZrO<sub>2</sub> detector. The O<sub>2</sub> flux density through an uncoated PE foil versus the time is shown in Fig. 7. Additionally, the figure shows a comparison of the experimental data with the calculated results.

For the theoretical description of the measured permeation curve we use a constant D. Then, we solve Fick's second law numerically with the boundary conditions given in Fig. 2 and the initial condition  $c(x, t=0)=0$ . As a result we obtain the concentration profiles  $c(x, t)$ . Some typical concentration-distance profiles for different times are displayed in Fig. 8. A substitution of these concentration profiles into Fick's first law yields the time dependent O<sub>2</sub> flux at the position  $x=L$ . For the calculations we used the following values:  $D=3.18 \cdot 10^{-7}$  cm<sup>2</sup>/s and  $c_0=7.45 \cdot 10^{17}$  O<sub>2</sub>-Mol./cm<sup>3</sup>. The figure shows, that the theoretical results are able to describe the experimental values quite well.

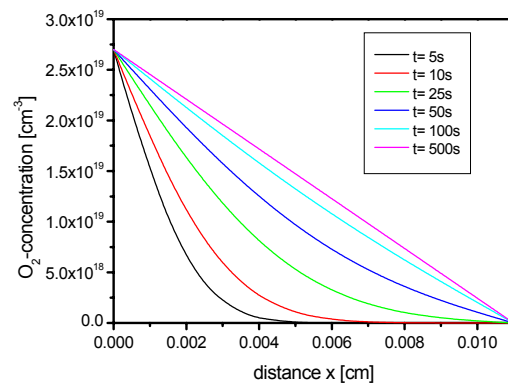
In order to improve the barrier properties of PE to O<sub>2</sub> we deposited thin films from different HMDSO:O<sub>2</sub> gas mixture ratios. All these films have a thickness of approximately 150 nm. Fig. 9 shows the steady state flux for an uncoated PE foil and for different plasma polymerized barrier films.

It can be seen, that the permeation flux first decreases with increasing O<sub>2</sub> concentration in the gas mixture. Then, at a HMDSO:O<sub>2</sub> mixture ratio of  $\approx 5:35$ ,  $j_s$  reaches a minimum value and with higher O<sub>2</sub> concentration the permeation flux increases again.



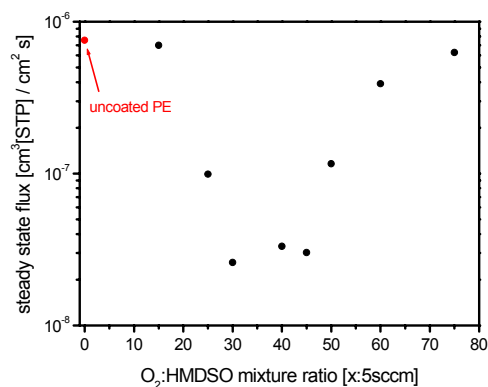


**Fig. 7:** A comparison of the experimental permeation flux of O<sub>2</sub> through PE with the calculated results.

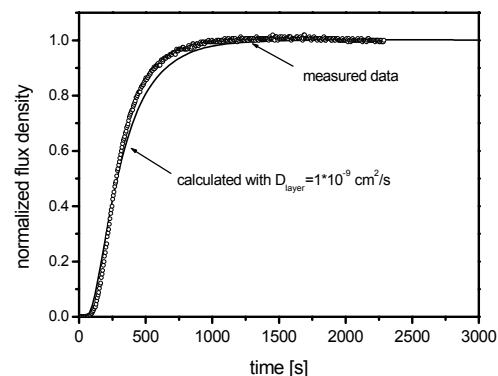


**Fig. 8:** Typical concentration-distance profiles for  $D= 3.0 \cdot 10^{-7} \text{ cm}^2/\text{s}$ ,  $c_0= 2.7 \cdot 10^{19} \text{ O}_2\text{-Mol./cm}^3$  and  $L=110 \text{ }\mu\text{m}$ .

A barrier layer of “pure” HMDSO leads to no significant reduction of the O<sub>2</sub> permeation. The ir spectrum in Fig. 6 shows, that such a film contains many CH groups. This film is polymer-like, so that no barrier effect can be measured. With increasing O<sub>2</sub> concentration the film properties change to a hard, inorganic film. The density of such films is higher and the structure is more crosslinked. Both properties affect the permeability of O<sub>2</sub>, resulting in a reduction of the steady state flux. But, if the organic/inorganic balance of the films is shifted more and more to the inorganic part, the deposited films show many cracks and pinholes. One reason for this is a thermal mismatch of the barrier film with the polymer foil. Thus, the permeation behaviour is mainly determined by the film defects [2].



**Fig. 9:** Steady state flux of different barrier films.



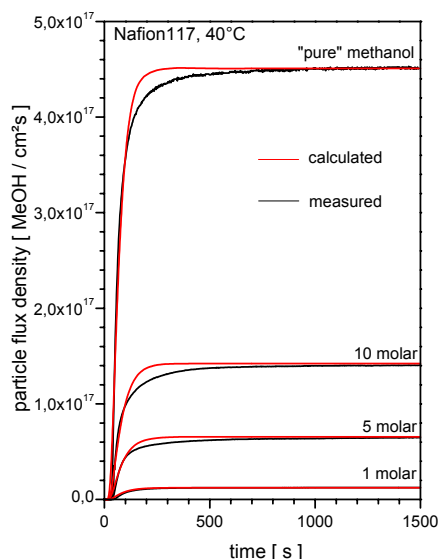
**Fig. 10:** Simulation of the permeation flux through a PE foil with a barrier layer.

For the theoretical description of the barrier layers we use the previous determined diffusion coefficient  $D$  of the PE foil. Then we optimized the diffusion coefficient  $D_{\text{layer}}$  of the barrier film. Fig. 10 shows an example of such a numerical calculation. It can be seen, that with a  $D_{\text{layer}}= 1 \cdot 10^{-9} \text{ cm}^2/\text{s}$  the agreement between the experimental data and the calculated results is quite well. But the value of  $D_{\text{layer}}$  is only an average value, because of the cracks and pinholes in the barrier film. That means, that the diffusion coefficient of a defect free layer is much higher.

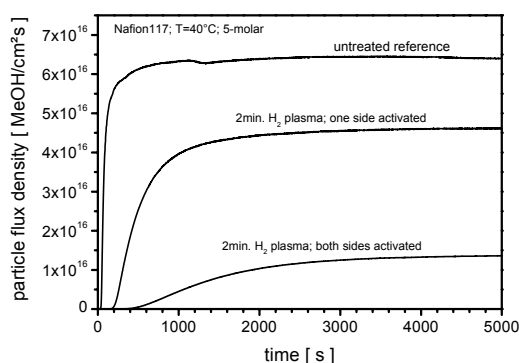
#### 4.2. Barrier layers on Nafion membranes

A 180 $\mu\text{m}$  thick Nafion membrane, supplied by Du Pont Chemicals, was used as substrate for the barrier layers. The methanol permeability was measured with the permeation device shown in Fig. 1. To measure at different methanol-water concentrations, the permeation experiment consists of a 200 ml reservoir and a circulating pump. This set-up was chosen to keep a constant concentration of the methanol-water mixture in the upper compartment of the permeation cell.

Fig. 11 shows the methanol flux density through the untreated Nafion membrane vs. time for different methanol solutions. Additionally, a comparison of the experimental data with the calculated results is given.



**Fig. 11:** A comparison of the experimental permeation flux of methanol through Nafion with the calculated results.



**Fig. 12:** Methanol particle flux density through Nafion for untreated and plasma treated membranes.

All permeation plots show a strong rise in the first 200 s. Then after 300 to 500 s they reach a stationary value between  $1.3 \cdot 10^{16}$  MeOH/cm<sup>2</sup> s for a 1-molar solution and  $4.5 \cdot 10^{17}$  MeOH/cm<sup>2</sup> s for pure methanol (MeOH means number of methanol molecules). The strong rise of the methanol flux is due to the swelling of the membrane, that leads to a strongly increasing of the diffusion coefficient of the material.

For the theoretical description of the measured permeation curves we use the diffusion function given in eq. (3) with  $D(c=0) = 6.1 \cdot 10^{-7}$  cm<sup>2</sup>/s and  $\gamma = 8.5 \cdot 10^{-23}$  cm<sup>3</sup>. The figure shows, that the theoretical results are able to describe the experimental values quite well. However, for the higher molar solutions a deviation can be observed in the transition of the unsteady state to the steady state part of the permeation curves. A reason for this deviation might be, that the diffusion function is not adequate to describe the whole concentration behaviour from small to high concentrations.

To improve the barrier properties of the Nafion membranes to methanol, we investigate a surface treatment in a H<sub>2</sub> plasma.

The treatment was performed in the Duo-Plasmaline equipment described in section 3. The commonly investigated fuel cells works with solutions of methanol in water, typically in the molar range. Therefore, we used a 5-molar solution as permeant. Referring to Fig. 12 it can be seen, that in the case of the surface treatments, the resulting steady state methanol flux is reduced from  $6.7 \cdot 10^{16}$  MeOH/cm<sup>2</sup> s for the untreated reference to  $4.6 \cdot 10^{16}$  MeOH/cm<sup>2</sup> s for a Nafion membrane treated on one side and to  $1.4 \cdot 10^{16}$  MeOH/cm<sup>2</sup> s for Nafion treated on both sides. This results show, that a plasma treatment in a H<sub>2</sub> plasma reduces the methanol permeation of Nafion by a factor of nearly 5.

## 5. Conclusions

The article contributes to the problem of diffusion through polymers and through plasma polymerized barrier films. It is shown, that the permeation behaviour can be described by the two Fick's laws. For the Nafion / methanol permeation system, the diffusion coefficient is a function of the sorbed methanol concentration. This is due to the swelling of the polymer and leads to high methanol permeabilities. In the case of the O<sub>2</sub> permeation through PE foils the diffusion coefficient is nearly constant.

## References

- [1] M. Walker, Recent Res. Devel. Appl. Pol. Sci., **1**, 281(2002).
- [2] G. Czeremuszkin, M. Latreche, M. R. Wertheimer, A.S. Sobrinho da Silva, Plasmas and Polymers, **6**, 107(2001).
- [3] X. Ren, T. E. Springer, T. A. Zawodzinski, S. Gottesfeld, J. Electrochem. Soc., **147**(2), 466(2000).
- [4] J. Comyn, Polymer Permeability, Elsevier Applied Science, Kidlington, UK, 1988.
- [5] E. R  uchle, J. Phys., **8**, 99(1998).
- [6] M. Walker, K. Baumg  rtner, J. Feichtinger, M. Kaiser, A. Schulz, E. R  uchle, Vacuum, **57**, 387(2000).

# Consequences of Long Term Transients in Large Area High Density Plasma Processing: A 3-dimensional Computational Investigation

Pramod Subramonium<sup>1</sup> and Mark J. Kushner<sup>2</sup>

<sup>1</sup>*Dept. of Chemical and Biomolecular Engr., University of Illinois, Urbana, IL 61801 USA, email: subramon@uiuc.edu*

<sup>2</sup>*Dept. of Electrical and Computer Engr., University of Illinois, Urbana, IL 61801 USA email: mjk@uiuc.edu*

**Abstract:** Continuous wave (CW) operation of inductively coupled plasma (ICP) reactors with geometrical asymmetries may result in asymmetric densities of radicals and fluxes to the substrate. In this paper, we discuss the effects of long-term transients during pulsed operation of ICPs on side-to-side asymmetries of radical and ion densities, and fluxes. We found that non-uniformities in species densities feed back through the plasma conductivity resulting in a non-uniform power deposition, which produces larger asymmetries. This positive feedback is reduced during the afterglow of pulsed plasmas making the densities more uniform.

## Introduction

Low temperature, high plasma density reactors are widely used for etching and deposition for microelectronics fabrication.[1] As the semiconductor industry transitions to larger wafers (300 mm), the requirement for highly symmetric and uniform reactant fluxes becomes more critical. The consequences of gas injection and pumping on reactant fluxes are well-characterized in high pressure ( $> 100$ s mTorr) systems. However the impacts of the symmetry of gas injection and pumping on the uniformity in low pressure ( $< 10$ s mTorr) systems are less well known. Many of the inductively coupled plasma (ICP) systems used for etching and deposition applications have discrete nozzles and single sided asymmetric pumping under the assumption that at low pressure, transport is diffusion dominated.[1-3] In this operating regime, the gas sources and sinks appear as volume averages, and so their asymmetries should not detrimentally affect the uniformity of reactants to the substrate. However, previous experimental [4] and computational investigations [5,6] of ICP reactors show that reactor asymmetries such as pumping can result in azimuthally asymmetric reactant densities. These asymmetric reactant densities translate to asymmetric ion fluxes to the substrate which results in non-uniform etch yields. The asymmetries introduced by gas inlets, pumping ports, and non-uniform power deposition become more important as wafer sizes increase.[6]

Kim et. al [4] measured the radial and azimuthal variation of the ion flux impinging on the wafer in Ar/SF<sub>6</sub> and Ar/Cl<sub>2</sub> ICP discharges using a 2-dimensional array of planar Langmuir probes on a 200 mm wafer. Typical conditions were 200 W, flow rate of 200 sccm and pressure of 10 mTorr. They observed that the ion flux had a local maximum near the pump port which they attributed to reduced ion losses by wall recombination. In Ar, they obtained a nearly azimuthally uniform ion flux distribution on the wafer while with the addition of electronegative gases ion fluxes increases near the pump port. Kushner investigated consequences of asymmetric pumping in Cl<sub>2</sub> ICPs employing 3-dimensional plasma equipment model.[5] The typical conditions were a pressure of 10 mTorr, 400 W and flow rate of 150 sccm. He concluded that ion densities and fluxes to the substrate are generally more uniform than their neutral counterparts due to the dominance of ambipolar forces.

In this paper, the consequences of long-term transients during pulsed operation of ICPs on side-to-side asymmetries of radical and ion densities, and fluxes will be discussed. These long-term phenomena are difficult to resolve in multi-dimensional plasma equipment models due to the large computational burden. In this regard, we have developed a 3-dimensional moderately parallel implementation of the Hybrid Plasma Equipment Model (HPEM3D) to investigate long-term transients in pulsed ICPs sustained in mixtures of CF<sub>4</sub>/C<sub>2</sub>F<sub>6</sub> and Ar/Cl<sub>2</sub>. We found that non-uniformities in species densities feed back through the plasma conductivity resulting in a non-uniform power deposition which leads to larger asymmetries. This positive feedback is reduced during the afterglow of pulsed plasmas making the densities more spatially uniform.

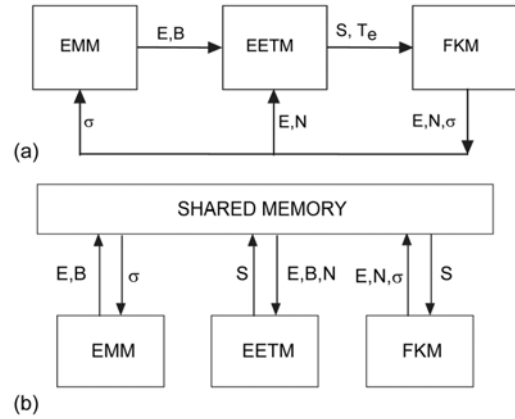
## Description of Model

The model developed for this investigation is a moderately parallel implementation of the 3-d Hybrid Plasma Equipment Model.[7] HPEM3D is a modular simulation which iteratively achieves a quasi-steady state solution. A flowchart of the HPEM3D is shown in Fig. 1a. The main body of HPEM3D consists of the Electromagnetics Module (EMM), the Electron Energy Transport Module (EETM) and the Fluid Kinetics Module (FKM). The EMM calculates inductively coupled electric and magnetic fields as well as static magnetic fields produced by the inductive coils and permanent magnets. The EETM uses these fields to spatially resolve electron energy transport by solving the electron energy conservation equation. Electron transport coefficients and rate coefficients for use in the electron energy equation are obtained by solving Boltzmann's equation using a two-term spherical harmonic expansion. The electron impact source functions produced by the EETM are used in the FKM during its next execution. The FKM solves continuity, momentum and energy equations coupled with Poisson's equation to determine the spatially dependent density of charged and neutral species, and electrostatic fields. The densities produced by the FKM are used to calculate the conductivity for the EMM and collision frequencies in the EETM. The modules are iterated to a quasi-steady state (average over an rf cycle).

In the computationally serial version of HPEM3D, each module receives updates from other modules at best once each iteration through the model. Although short term transients (e.g., during one rf cycle) are separately captured in each module since the integration time resolves the rf period, the exchange of parameters on longer scales is limited by the "looping time" between modules. To properly capture true transients, this looping time must be small compared to the time scale of the transients. In doing so, the expediency of the serial hybrid technique is defeated.

Since the time scales in plasma simulations are so disparate (e.g., rf dynamics vs gas residence time or plasma decay time), it is our working premise that some type of hybrid scheme is required to model long term transients. To achieve that goal in the parallel implementation of HPEM3D, each of the major modules (EMM, EETM, FKM) is executed simultaneously on different processors of a moderately parallel computer. (See Figure 1b.) This methodology is built upon task parallel algorithms developed for the 2-d HPEM.[8] In doing so, parameters from the different modules can be exchanged on a frequent basis without interrupting the time evolving calculation being performed in any given module. For example, the plasma conductivity and collision frequency are continuously updated during the execution of FKM. These updated parameters are made available in shared memory as they are computed so that they can be accessed by the EMM to produce nearly continuous updates of the electromagnetic fields. These more frequent updates of the electromagnetic fields are then made available to the EETM through shared memory, along with parameters from the FKM, updating electron impact source functions and transport coefficients. The electron impact source functions and transport coefficients computed in the EETM are then transferred to the FKM through shared memory as they are updated to compute densities, fluxes and electrostatic fields. Using this methodology, the parameters required by different modules are readily made available "on the fly" from other modules.

This method for addressing transients based on moderate parallelism directly interfaces the short plasma time scales with the long-term neutral time scales. Fluid properties (e.g., changes in pressure, mole fractions, and flow fields) which slowly evolve over time are made available to the simultaneous calculation of more rapidly changing plasma properties (e.g., electron and ion density, electrostatic fields) through shared memory. The plasma properties will therefore "track" (in an almost adiabatic sense) the more slowly varying fluid properties while continually updating electron impact sources.



**Figure 1** - (a) Schematic of the main body of the serial HPEM3D which sequentially exchanges plasma parameters. (b) Schematic of the parallel implementation of HPEM3D, which simultaneously exchanges plasma the parameters through shared memory.

## Consequences of Asymmetric Pumping During CW ICP Operation

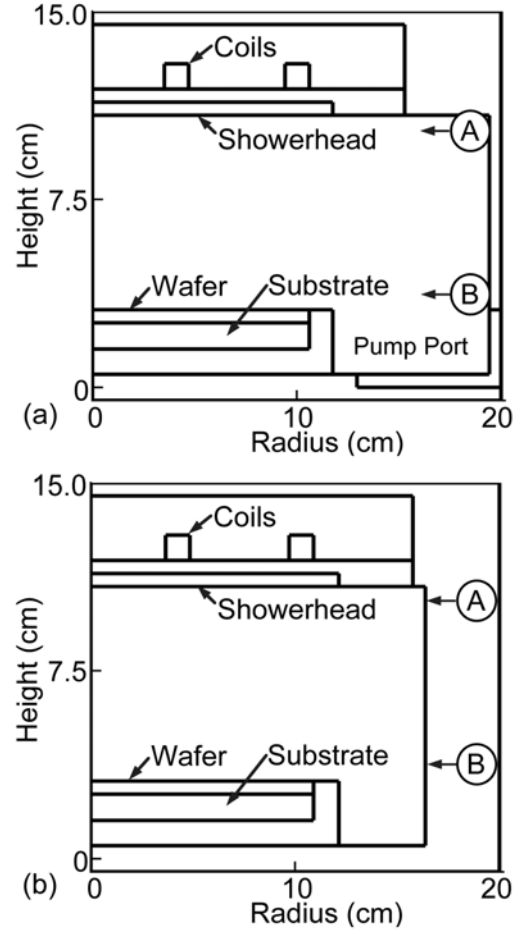
The system we investigated is an ICP etching reactor schematically shown in Fig. 2. The antenna is a two-turn coil set on top of a dielectric window. To eliminate asymmetries which may result from either transmission line effects in the antenna or the shape of the antenna, we specified that the coil conduction currents be uniform along the entire length of the coil and that the antenna is simply two nested annuli without azimuthal variation. To isolate the effects of gas flow the reactor is otherwise geometrically azimuthally symmetric with the exception of an asymmetric pump port. The gas injection is through a showerhead placed below the coils. The azimuthal asymmetries are quantified by an asymmetry factor at a given radius,[5]

$$\beta(r) = \max \frac{|\phi(\theta) - \bar{\phi}(r)|}{\bar{\phi}(r)},$$

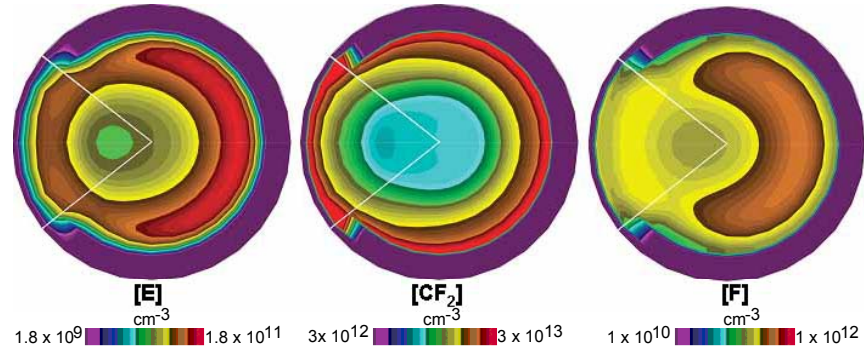
where  $\bar{\phi}$  is the average value of  $\phi$  as a function of azimuth at a given radius, and the max function denotes that we take the maximum value of  $\beta$  as a function of the azimuthal location. Smaller values of  $\beta$  are more uniform.

The feedstock gas injected through the nozzles is a mixture of  $C_2F_6$  and  $CF_4$  (40/60). The base case conditions are a CW ICP power of 600 W at 13.56 MHz, pressure of 5 mTorr and flow rate of 160 sccm. The gas phase reaction mechanism is similar to that reported by Abrams et. al [9] with additional reactions for  $CF$ ,  $CF_2^+$  and for dissociation (both neutral and dissociative attachment) of  $F_2$ . Species densities, temperatures and fluxes are inspected in the  $(r, \theta)$  plane at Height-B shown in Fig. 2, approximately 1 cm above the plane of the wafer. Electron impact sources, plasma conductivity and plasma power deposition are inspected at Height-A approximately 1 cm below the showerhead.

As expected, using the base case conditions in a symmetric reactor the plasma properties were azimuthally symmetric throughout the reactor. However, we observed significant azimuthal asymmetries in species densities at the plane of the wafer with the asymmetric pump port as shown in Fig. 3. The electron density is larger at locations further away from the pump port. This is due to the power deposition peaking further away from the pump port resulting in a larger source of electrons from electron



**Figure 2-** Schematics of the ICP reactor in the  $(r,z)$  plane. The section markers show the height at which densities in the  $(r, \theta)$  will be shown. The asymmetric reactor has the geometry shown in (a) for  $60^\circ$  azimuthally and the geometry shown in (b) for  $300^\circ$ .



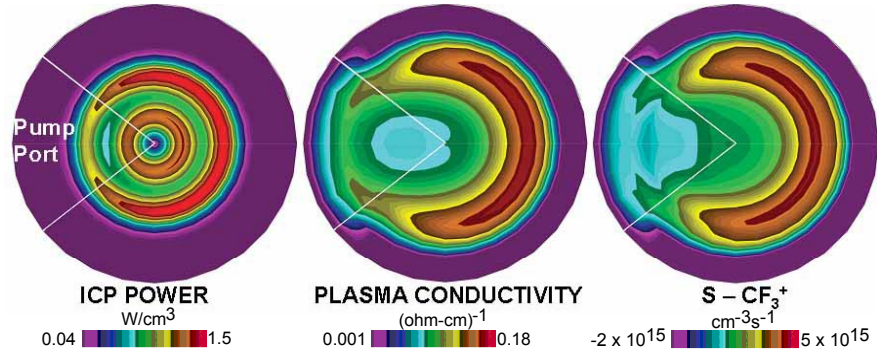
**Figure 3-** Densities of species at Height B for the base case conditions. (left) Electron density, (center)  $CF_2$  density and (right)  $F$  density. The electron density peaks further away from the pump port.



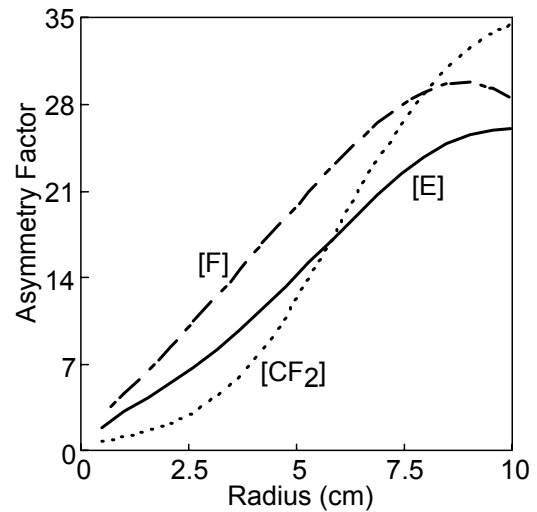
impact ionization as shown in Fig. 4. The residence time for the gas is larger further from the pump port due to dead zones in the reactor, resulting in a greater likelihood for electron impact ionization and dissociation. Wall recombination of  $\text{CF}_2^+$  results in a virtual source of  $\text{CF}_2$  at the walls as shown in Fig. 3. The returning  $\text{CF}_2$  radicals undergo further electron

impact dissociation forming CF radicals and F atoms. Due to these higher rates of dissociation, a peak in the F atom density occurs away from the pump port. The asymmetry factor for the species densities at Height-B is about 25% at a radius of 10 cm as shown in Fig. 5.

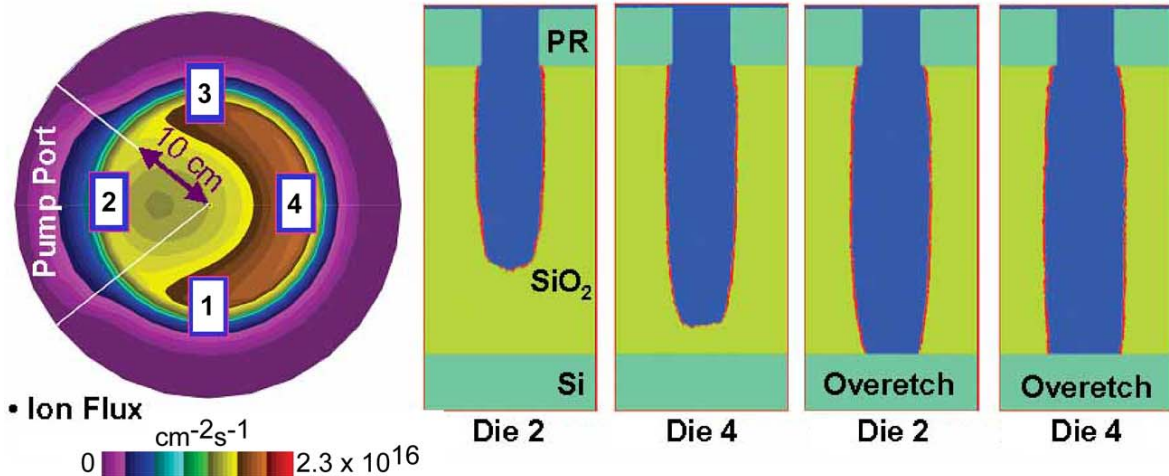
During CW ICP operation, the asymmetries are pronounced due to a positive feedback loop between the non-uniform electron density and plasma power deposition. Asymmetric pumping results in a non-uniform neutral density, which then provides a non-uniform source for ions, radicals and electrons. The non-uniform electron density results in an asymmetric plasma conductivity, which in-turn results in a non-uniform power deposition, as shown in Fig. 4. Owing to a non-uniform power deposition, the electron impact sources for ionization and dissociation reactions become azimuthally asymmetric, thus further reinforcing the asymmetries caused by pumping. The asymmetry factor is about 45% for plasma conductivity, 25% for power deposition and 45% for electron impact sources 1 cm below the showerhead



**Figure 4-** Plasma parameters at Height A just below the showerhead for the base case conditions. (left) Power deposition, (center) plasma conductivity, and (right) source of  $\text{CF}_3^+$ . Non-uniform power deposition results from a non-uniform plasma conductivity.



**Figure 5-** Asymmetry factor for F atoms, electrons and  $\text{CF}_2$  radicals as a function of radius at Height-B above the plane of the wafer. Asymmetries increases with radius.



**Figure 6-** (left) Ion flux to the substrate and the location of dies on the wafer. (right) Etch profiles in  $\text{SiO}_2$  over a Si substrate as defined by a hard photoresist (PR) mask for die locations 2 (near the pump port) and 4 (opposite the pump port). The left profiles show the disparity in etch rates, 20% slower for die location 2. The right profiles show the differences resulting from overetching to clear both features.

(Height-A). The asymmetry factor in species densities at Height-B, increases almost linearly as a function of radius as shown in Fig. 5. The ion densities and fluxes also show a similar trend.

These asymmetric densities which produce asymmetric reactant fluxes to the substrate can have significant effects on the resulting etch rates. In particular, azimuthal asymmetries can produce different etch yields at different azimuthal locations on the wafer. For example, the reactant fluxes at different locations on the wafer were used as input to the Monte Carlo Feature Profile Model to predict etch rates and feature shapes.[10] Etch profiles for SiO<sub>2</sub> are shown in Fig. 6 for die locations adjacent to and opposite to the pump port. There is a 20% reduction in etch rate near the pump port due to the reduced ion fluxes. The end result is that over-etching for some dies is required to complete etching locations on the wafer the ion flux is lower. This results in increased undercutting of the feature at locations having higher ion fluxes.

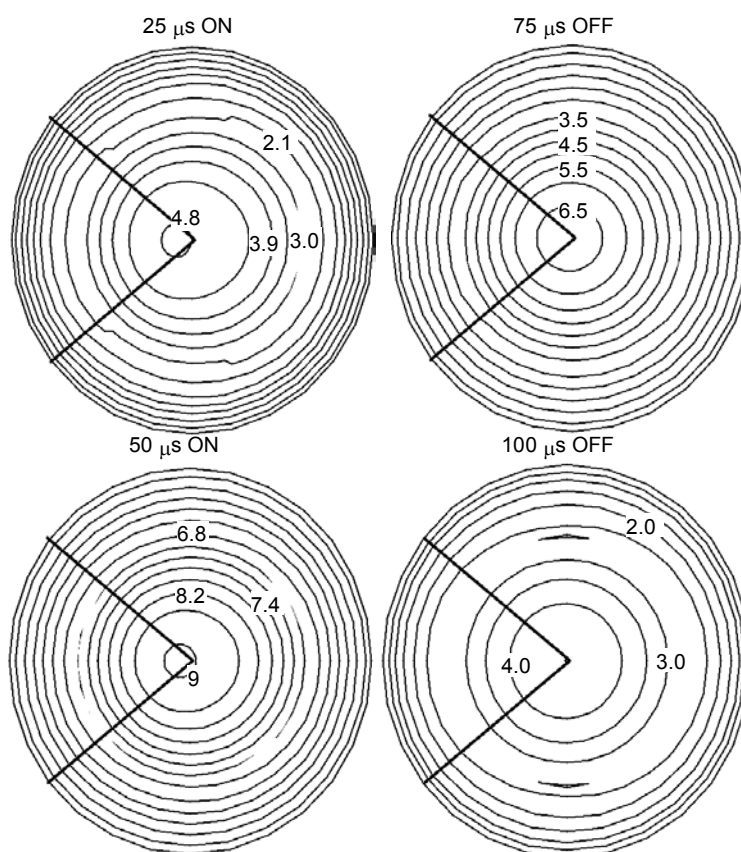
### Effect of Long Term Transients on Reactor Asymmetries for Ar/Cl<sub>2</sub> Plasmas

The asymmetries in reactant fluxes produced by gas injection and pumping may be addressed by pulsed plasma processing. The operating characteristics of ICP sources can be additionally tailored by modulating the radio frequency (rf) power. In this mode of operation, typically referred to as a “pulsed plasma,” the rf power to the coil is modulated on-off at pulse repetition frequencies (PRF) of 10s – 100s of kHz and duty cycles of 30 - 70%.

For the initial 3-d investigation of pulsed plasma operation, Ar/Cl<sub>2</sub> mixtures were used to leverage previous 2-d studies using this mixture.[8] The base case conditions are Ar/Cl<sub>2</sub> = 60/40, peak ICP power of 400 W at 13.56 MHz, pressure of 5 mTorr, flow rate of 160 sccm, PRF of 10 kHz and duty cycle of 50%. It is our premise that if we can reduce the positive feedback loop between non-uniform electron density and non-uniform power deposition, we can improve the azimuthal symmetry of plasma properties.

The electron density at different times during a pulse is shown in Fig. 7. As the ICP power is turned on the asymmetric neutral densities produce

asymmetric electron impact sources resulting in non-uniform electron densities and electron temperatures below the showerhead. Since the electron density is azimuthally asymmetric, further power deposition into the plasma becomes asymmetric making the densities more asymmetric. These asymmetries are shown at 25  $\mu$ s and 50  $\mu$ s during the activeglow or power on phase. After the power is turned off (the afterglow) electrons are lost by dissociative attachment and diffusion to the walls. As diffusion progresses, the electron density becomes azimuthally more uniform as shown at 75  $\mu$ s and 100  $\mu$ s during the afterglow. This more uniform initial plasma density for the next power on period produces more uniform power deposition compared to CW operation. All plasma properties are generally more uniform in the activeglow and afterglow of pulsed operation, compared to CW operation. For example, the Cl density also shows improved symmetry during pulsed operation as shown in Fig. 8. The more uniform initial conditions and reduced



**Figure 7-** Electron density ( $\times 10^{10} \text{ cm}^{-3}$ ) at different times during a pulse. The asymmetries present during the activeglow phase (25  $\mu$ s, 50  $\mu$ s) are dissipated during the afterglow (75  $\mu$ s, 100  $\mu$ s).

positive feedback between non-uniform conductivity and power deposition during pulsed operation of ICPs should enable a wider range of acceptable operating conditions compared to CW operation.

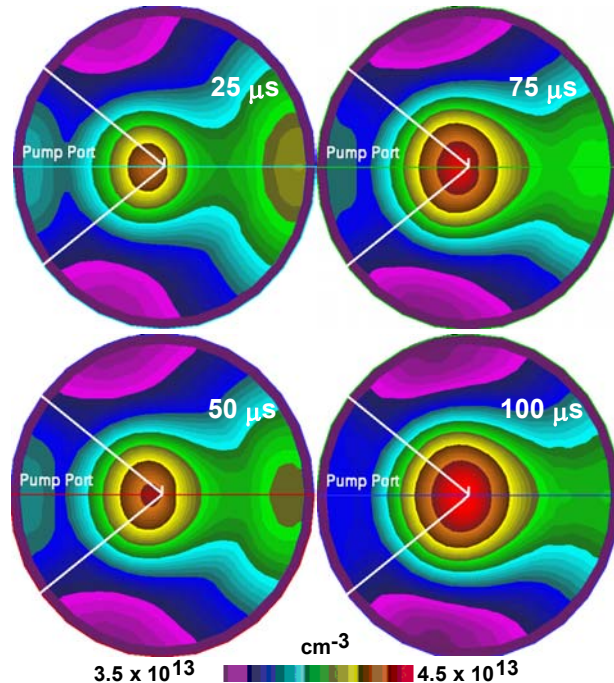
### Concluding Remarks

CW operation of ICP reactors with geometrical asymmetries such as pumping results in asymmetric densities of radicals and fluxes to the substrate. These asymmetric fluxes ultimately translate into asymmetric etch properties. For example, reductions in etch rates at one azimuth requires overetching at another azimuth to clear both features. The end result is loss of profile control. These azimuthal asymmetries in plasma properties are more pronounced during CW operation of ICPs due to a positive feedback loop between species densities and power deposition. Pulsed plasma operation of ICPs can be employed as a potential method for reducing these azimuthal asymmetries by reducing this feedback effect.

**Acknowledgements:** This work is supported by the National Science Foundation (CTS99-74962), the Semiconductor Research Corp, and Applied Materials.

### References

- [1] J. H. Keller, J. C. Forster, and M. S. Barnes, *J. Vac. Sci. Technol. A* **11**, 2487 (1993).
- [2] J. Hopwood, *Plasma Sources Science and Technology* **3**, 460 (1994).
- [3] T. H. Ahn, K. Nakamura, and H. Sugai, *Plasma Sources Science and Technology* **5**, 139 (1996).
- [4] T. A. Kim and E. S. Aydil, *J. Appl. Phys.* **92**, 6444 (2002).
- [5] M. J. Kushner, *J. Appl. Phys.* **82**, 5312 (1997).
- [6] D. J. Economou, T. L. Panagopoulos, and M. Meyyappan, *Micro* **16**, 108 (1998).
- [7] M. J. Kushner, W. Z. Collison, M. J. Grapperhaus, J. P. Holland, and M. S. Barnes, *J. Appl. Phys.* **80**, 1337 (1996).
- [8] P. Subramonium and M. J. Kushner, *J. Vac. Sci. Technol. A* **20**, 313 (2002).
- [9] C. F. Abrams and D. B. Graves, *J. Appl. Phys.* **86**, 5938-5948 (1999).
- [10] R. J. Hoekstra and M. J. Kushner, *J. Appl. Phys.* **79**, 2275-2286 (1996).



**Figure 8-** Cl density at different times during a pulse. The densities become more uniform during the afterglow. The Cl density increases in the afterglow due to increased rates of dissociative attachment.



# A New Concept of Plasma Furnace for Aluminum Recycling

V.F. Alves, E. Batista, O.W. Bender, A.C. Doring, N. Jansinski, H. Toku, and A.C. da Cruz

*Institute for Technological Research of the State of São Paulo - IPT  
São Paulo, SP, Brazil*

The traditional process for Al reclaiming from dross and scrap is based on salt rotary furnaces heated by combustion flames. To improve the efficiency of metal recovery, a salt mixture (typically 50%NaCl/50%KCl) is added to the furnace load at a ratio of 100 to 400 kg for each 1000 kg of raw material processed. Because the salt is easily leached, the solid residue of the process (black dross or salt cake) must be disposed into industrial land filling sites, wherever this practice is allowed.

The objectives of the present research are to study and develop a proprietary process (Fig. 1) for the salt free recovery of aluminum from a broad range of raw materials, including primary dross and several classes of scrap. A plasma heated fully tiltable rotary furnace of 300 kg nominal capacity was built and tested to process around 22 tons of different Al rich raw materials over the past year.



Fig. 1 – Overview of plasma heated Al recovery furnace, 300 kg capacity.

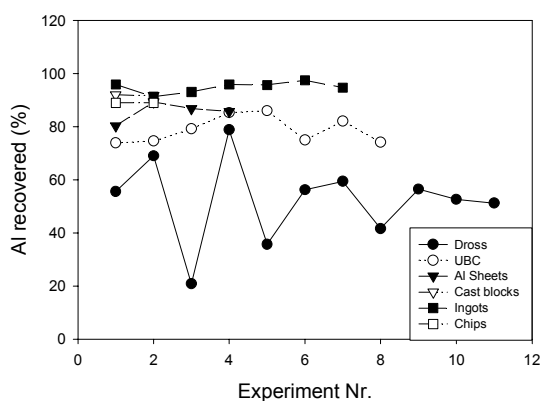


Fig. 2 – Percentage of Al recovered from several Al scrap classes.

A specific energy consumption in the range of 445 kWh to 550 kWh per ton of processed material has been consistently obtained, which is about 3% of the total energy consumption required for the electrolytic reduction of aluminum oxide to produce primary aluminum.

Concerning energy balance, a comparative evaluation was carried out which shows that the plasma process studied is far more efficient than other forms of heat sources. Experiment results of heavy scrap processing have consistently shown high Al recovery rates (Fig. 2). On the other hand, Al recovery rates from light scrap (UBC) were not as good, possibly because of higher contamination observed in this type of scrap and longer loading period of time required. An oxidation level (aluminum loss) smaller than 3% was determined based on the fusion of aluminum ingots.

# Low-pressure Generation of Microplasma by Harmonic ECR

Hiroshi Fujiyama, Masanori Matsushita and Yoshinobu Matsuda

Faculty of Engineering, Nagasaki University, 1-14 Bunkyo-machi, Nagasaki 852-8521

We will present that microplasma generation less than 1mm gap length is possible at the pressures less than 0.1Torr by using harmonic electron cyclotron resonance. In the present paper, we report both the numerical and experimental results of Harmonic ECR microplasma generation.

## Calculation Results

Figure 1 shows our calculation model. The electrodes are coaxial tube. We assumed that the part of dashed line is a parallel plate. To breakdown for microwave plasma generation, it is necessary to trap an initial electron in a short-gap length.

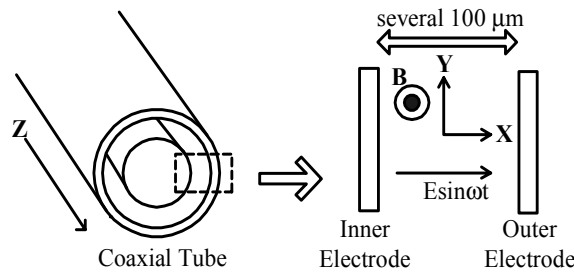


Fig.1 The calculation model of short gap length microwave discharge in a magnetic field

Figure 2 shows the typical calculation results for gap length dependence of breakdown, non-trapping and minimum ionization electric field. In this calculation, we used Ar gas at the pressure of 0.1Torr and the externally applied normalized magnetic field of  $\omega_{ce}/\omega=0.5$ . In the figure plasma generation is possible in the area where the electric field is larger than breakdown electric field and minimum ionization electric field and smaller than non-trapping electric field. Therefore, the minimum gap length for plasma generation is intersection point of minimum ionization electric field and non-trapping electric field. In this calculation result, plasma generation is possible for the minimum gap length of 486 $\mu\text{m}$ , and breakdown voltage of only 46V. These calculation results showed microplasma generation is possible for low-voltage conditions less than 50V.

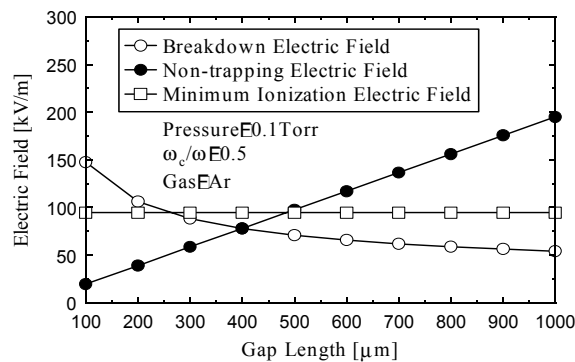


Fig.2 Gap Length dependence of the breakdown, non-trapping and minimum ionization electric fields at the pressure of 0.1Torr

## Experiment Results

Figure 3 shows the experimental results showing pressure dependence of breakdown magnetic fields. It

was confirmed the microplasma generation less than 1mm was possible at harmonic ECR conditions ( $\omega=2\omega_{ce}$ ).

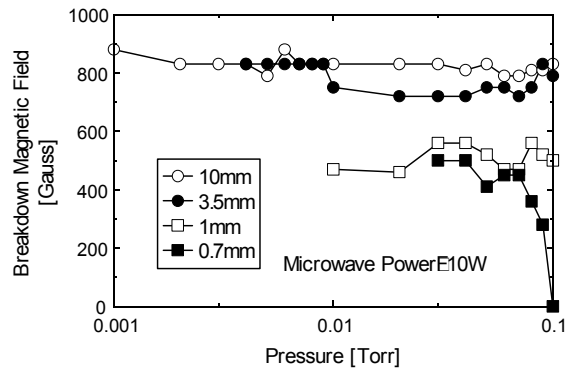


Fig.3 Experimental Results of the pressure dependence of breakdown magnetic field for gap length of 10mm, 3.5mm, 1mm, 0.7mm and microwave power of 10W

### Reference

- [1]H.Fujiyama, M.Miyazaki, M.Matsushita and Y.Matsuda, Proc. of the 25<sup>th</sup> Int. Conf. On Phenomena in Ionized Gases, Nagoya, Vol.1, p.271.(2001).
- [2]M.Matsusita, Y.Matsuda and H.Fujiyama, Thin Solid Films (2003) to be published

# Synthesis of Fulllurene-like Particles and Nanotubes by Arc Discharge in Cold Liquid

Noriaki Sano<sup>1+</sup>, Manish Chhowalla<sup>2</sup>, Haolan Wang<sup>3</sup>, Kenji Iimura<sup>1</sup>,  
Gehan.A.J.Amaratunga<sup>3</sup>, Tatsuo Kanki<sup>1</sup>

<sup>1</sup> Department of Chemical Engineering, Himeji Institute of Technology, 2167 Shosha, Himeji, Hyogo, 671-2201 Japan  
<sup>+</sup>sano@mech.eng.himeji-tech.ac.jp

<sup>2</sup> Rutgers University, Department of Ceramic and Materials Engineering, 607 Taylor Road, Piscataway, NJ 08854-8065 USA

<sup>3</sup> University of Cambridge, Engineering Department, Trumpington Street, Cambridge CB2 1PZ, UK.

## Abstract

Multi-walled fulllurene-like particles and nanotubes of carbon were synthesized using arc discharge in water or liquid nitrogen. Here the gas bubble formed from the hot arc plasma in the cold liquid successfully provides reaction field to rapidly quench the carbon vapor to produce carbon nano materials. Using the presented method, not only nano carbons but also we can produce fulllurene-like materials from other lamellar structural materials, such as MoS<sub>2</sub> and WS<sub>2</sub>.

## 1. Introduction

Fabrication and application of nano-tube related materials has been significantly developed since fullerenes and carbon nanotubes were discovered [1,2]. These nano materials are considered to have potential abilities to use for several industrial applications as (1) micro electronic circuits, (2) field emission devices, (3) reinforced composite materials, (4) adsorption media to store hydrogen, and (5) high quality lubricants. However, in spite of these interesting characteristics, industrial applications have been still difficult because of the high cost of the fabrication. Under this circumstance, it is demanded to develop cost-effective fabrication methods. In one of the common methods to produce such nanocarbons, graphite rods are used as electrodes and arc discharge is generated between these electrodes under controlled pressures in inert gas environment [3]. Carbon nanotubes are produced in a core of the deposits formed on the cathode tip. Though this method is easy to be performed, separation of nanotubes from the final products is a crucial problem. Also, vacuum systems are required to set up the reaction field, which is costly. Other well known methods to fabricate carbon nano materials, such as laser ablation method [4] and CVD [5], also require pressure controlling systems. Very recently, a new method using *arc discharge in water* was proposed [6, 7]. This method is outstanding in a point that it does not require inert gas and vacuum system so that the setting cost is extremely low.

## 2. Synthesis of nano materials by arc discharge in liquid

In our method, arc discharge is generated between graphite electrodes submerged in water. Figure 1 shows the schematic of the reactor system. In our method, a direct current (DC) arc discharge was generated in water between two carbon electrodes. Our apparatus consisted of two graphite electrodes submerged in water or liquid nitrogen. The arc discharge was initiated by contacting the grounded anode (typically 6 mm diameter) with the cathode (typically 12 mm diameter). The discharge voltage were around 25 V to generate 30-80 A. The cathode-anode gap of  $\approx 1$  mm must be kept to continue the arc discharge. The discharge in our case can be characterized as an anodic arc as only the anode electrode is consumed. The evaporated carbon from anode is quenched to form nano particles, and they are separated into floating fine powders and largely agglomerated deposits which sink to the reactor bottom.

It is shown in Fig. 1 that there is a plasma zone between electrodes surrounded by a gas bubble due to vaporization of the surrounding liquid as the arc temperature is estimated to be around 4000 K (sublimation temperature of carbon). In fact, this gas bubble can be regarded as a micro water-cooling reaction chamber that enables the rapid quenching of the arc discharge. When water is used as liquid, the main gas components CO and H<sub>2</sub> are produced by the reaction of C atomic vapor with H<sub>2</sub>O at the gas-liquid interface as [8]:



The extremely sharp temperature gradient in this gas bubble from the hot plasma region to the gas-water interface is essential to cause rapid solidification of the vaporized carbon.

At a experimental condition, the expansion rate of C vapor from hot plasma zone to cold region can be estimated by a simple approximation. If all the graphite consumed in the anode is assumed to be converted to C vapor, a volumetric C vapor expansion rate is calculated to be  $5.30 \times 10^{-5} \text{ m}^3/\text{s}$  at 4000K if ideal gas conditions with 1 atmospheric pressure are assumed. If the hot plasma zone between electrodes with 1mm gap is assumed as a cylindrical zone with 2mm diameter, the expansion velocity can be obtained by dividing this volumetric expansion rate by the surface area of this assumed hot plasma zone, resulting in a velocity of 4.2 m/s. This high expansion velocity enables C vapor to transfer into the cold zone of the bubble readily. The reaction zone can be categorized into two parts: (I) where ion current is significant in or adjacent to the plasma zone, and (II) without ion current outside the plasma zone in the gas bubble. In zone (I), elongated structures such as nanotubes are expected to be produced because of their epitaxial growth in the C ion current. On the other hand, in the zone (II), 3-dimensional isotropic growth of nano-particles is preferable because of the absence of an axis of symmetry. In this case, onion-like nano particles may be produced.

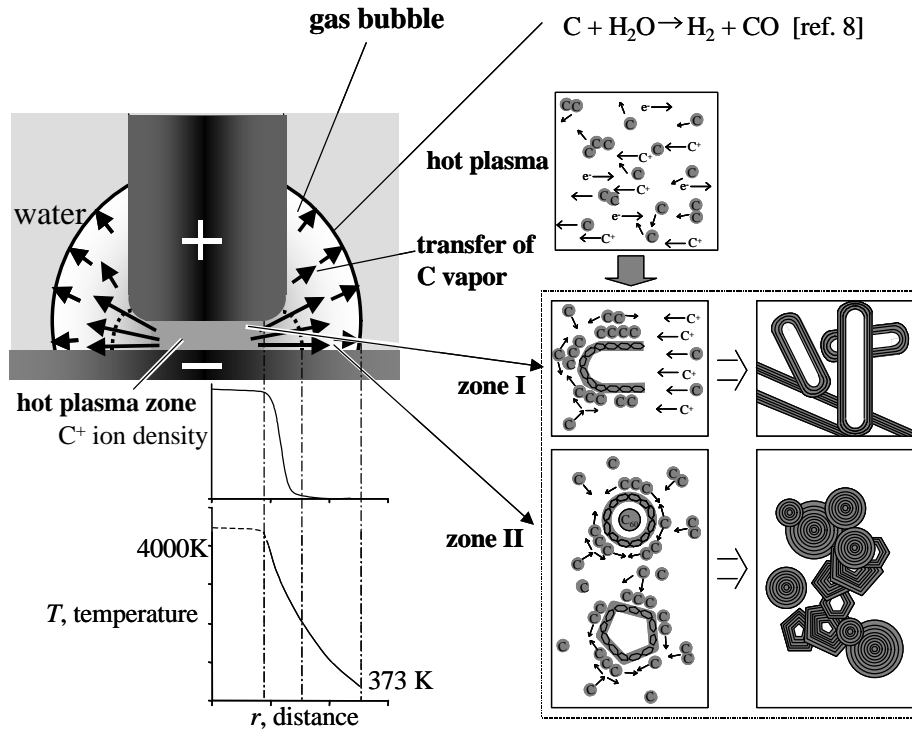


Fig. 1. Diagram of reaction system to produce nano materials by arc in cold liquid.

### 3. Results and discussion

#### 3.1. Nano carbons produced by arc discharge in water

##### 3.1.1 Carbon nano onions

Some typical views of carbon nano structural materials produced by arc discharge in water in transmission electron microscopy (TEM) are shown Figs. 2-5. Figures 2 and 3 respectively show low and high magnification images of spherical multi-shelled carbon particles (carbon 'nano onions') collected from the floating fine powder. A part of Fig. 2 marked by a square is shown in Fig. 3. The TEM specimen was prepared by sprinkling the powder dispersed in toluene with 1 minutes-ultrasound onto a carbon TEM grids. The particle diameter seems to ranging from 20 to 60 nm. It is shown that the spherical particle is a multi-

shelled particle in which distance between layers is approximately 0.34 nm. This interlayer distance corresponds to graphite structure.

### 3.2. Multi-walled carbon nanotubes

Figure 4 shows multi-walled carbon nanotubes collected from deposits which settled down to the reactor bottom. The deposit had a disk-like shape of approximately 1mm thickness and similar diameter to anode rod. It is considered that the deposit containing multi-walled carbon nanotubes are formed on the cathode tip, and the deposit is peeled away from there by pressure swing caused from bubble formation. In the TEM observation, the concentration of the multi-walled carbon nanotubes in the deposit seems to be very high.

### 3.3 Metal-including carbon nanocapsules

Figure 5 shows a carbon nanocapsule produced by arc discharge in water. The dark central core represent Fe included in a particle. It is also shown that this core is surrounded by graphitic layers. Such metal including nanocapsules can be produced by dissolving metallic ions in water or using composite carbon anode with metallic impurity.

### 3.4. Nano carbons produced by arc discharge in liquid nitrogen

Nano structural carbon materials can be produced also by arc discharge in liquid nitrogen. Multi-walled carbon nanotubes were produced by this method, and showed similar TEM images to Fig. 2. In addition, so far, high concentration carbon nanohorns have been successfully produced [14]. The arc discharge in liquid nitrogen is more stable than in water. The mechanism to form multi-walled carbon nanotubes in liquid nitrogen is considered to be the same as in water.

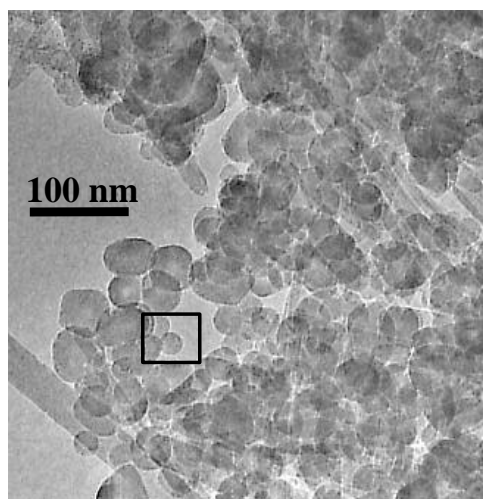


Fig. 2. Agglomerated carbon nano onions produced by arc in water.

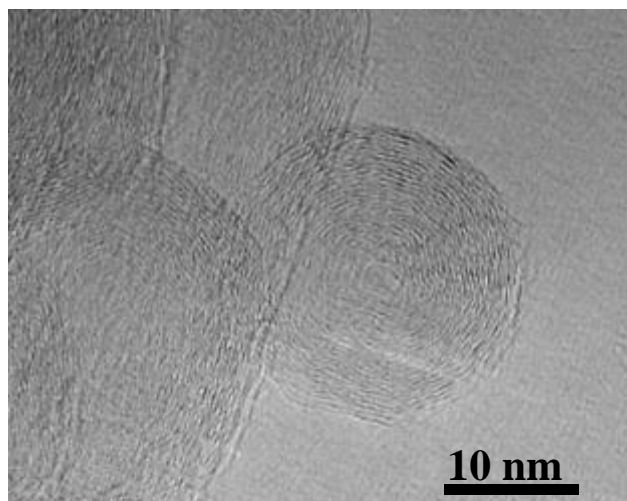


Fig. 3 High magnification image of the intersection of Fig. 2.

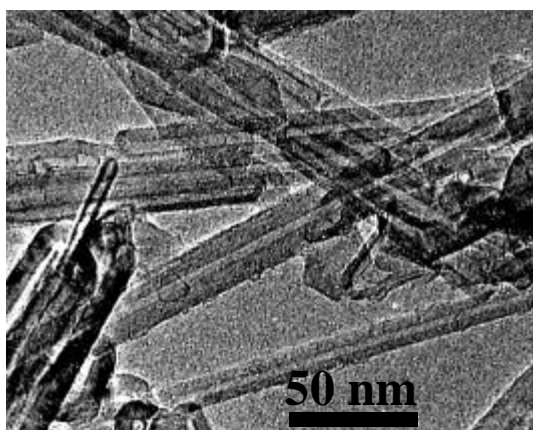


Fig. 4. Multi-walled carbon nanotubes produced by arc in water.

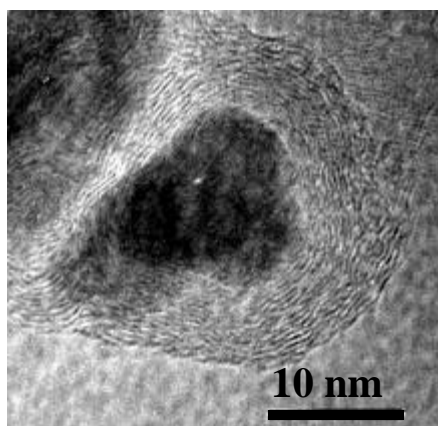


Fig. 5. Fe-including carbon nanocapsule produced by arc in water.

### 3.5. Specific surface area of onions powders produced by arc in water

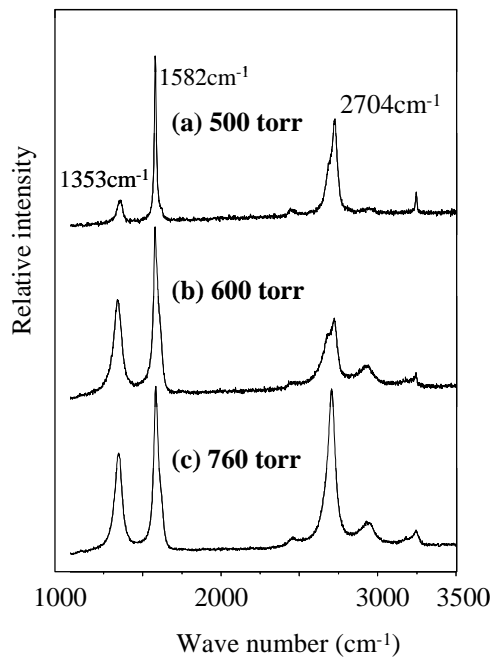
The specific surface area of the sample powder containing carbon nano onions produced with 30A and 18V (12mm diameter cathode and 6mm diameter anode) was measured by BET adsorption isotherm using nitrogen gas at 77K. The surface area result is shown in Table 1 together with multi-walled carbon nanotubes (MWCNT) and sinble-walled carbon nanotubes (SWCNT) produced by other methods. The surface area of the nano carbons produced by our method is extremely large as 934 m<sup>2</sup>/g, which is approximately 3-5 times as others. This result indicates that the particles produced by our method may be suitable for the application of hydrogen storage or other adsorption media.

### 3.6. Pressure effect on the structure of nanotubes formed by arc in water

It is interesting subject to examine whether the conditions of arc discharge in liquid may affect the structure of the nano structural products. One of the important parameter is pressure because the pressure may control the expansion rate of the gas bubbles formed from the arc zone. The quenching rate of the evaporated carbon should be retarded by reducing the pressure because the distance between hot arc spot and the gas-liquid interface should becomes longer with reducing pressure. Figure 6 shows one example of pressure effect on the physical properties of multi-walled carbon nanotubes produced by arc in water with varied pressures. It is shown that the peak at 1353 cm<sup>-1</sup> indicating disordered structure is significantly reduced when the pressure is lowered. The importance suggested by this result is that the physical properties of nano materials produced by arc in liquid can be tuned by varying some arc parameter, for example pressure.

**Table 1.** Specific surface areas of the particles obtained arc-in-water and other nanotubes

Reference:	This work	Hernadi et al. [13]	Inoue et al. [14]	Ye et al. [15]
sample	carbon onion & MWCNT	SWCNT & MWCNT	MWCNT	bundles of SWCNT
specific surface area	<b>984 m<sup>2</sup>/g</b>	312 m <sup>2</sup> /g	178 m <sup>2</sup> /g	285 m <sup>2</sup> /g



**Fig. 6.** Raman spectra of multi-walled carbon nanotubes produced by arc in water at 500, 600, 760 torr.

### 3.7. Inorganic multi-shelled fullerenes produced by arc discharge in water

Using the same method with different material electrodes, it is expected to produce onions or nanotube structures of non-carbon materials [9]. Figs. 7 and 8 show multi-shelled fullerene-like particles of  $\text{MoS}_2$  and  $\text{WS}_2$ , respectively, produced by our method using arc discharge in water. In these images, one can clearly see polyhedral multi-shelled particles together with lamellar fragments of  $\text{MoS}_2$  or  $\text{WS}_2$ . These structures can be consisted by closing the lamellar sheets of  $\text{MoS}_2$  or  $\text{WS}_2$ . Fig. 9 shows closed-cage  $\text{MoS}_2$  particle model matching with some TEM images. These results are significant because they promise the possibility that new fullerene-like nano particles can be produced using anodes of variety of materials.

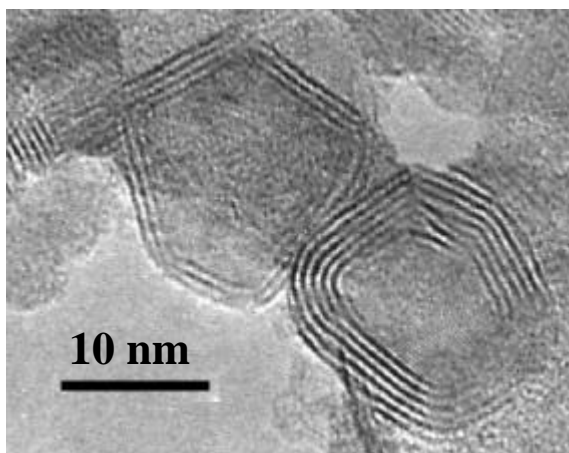


Fig. 7 Multi-shelled  $\text{MoS}_2$  fullerens produced by arc discharge in water.

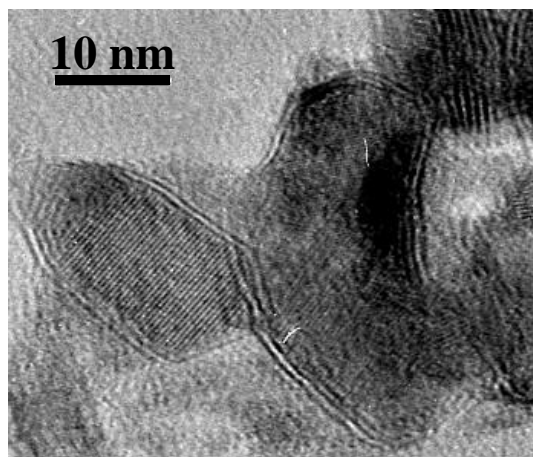


Fig. 8. Multi-shelled  $\text{WS}_2$  fullerens produced by arc discharge in water.

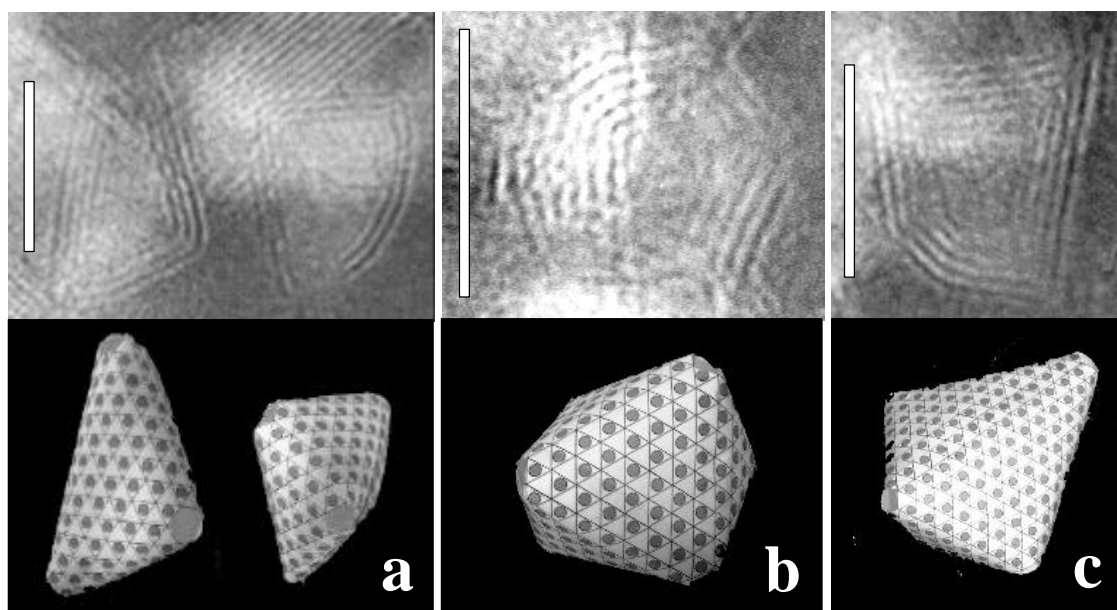


Fig. 9. Closed  $\text{MoS}_2$  sheet models, in which  $\text{MoS}_2$  surfaces are connected seamlessly with round edges. (a, right), (b), (c) are elongated octahedrons and (a, left) is elongated hexahedron. The scale bar in each figure corresponds to 10 nm.

## 5. Conclusions

A method to synthesize fullerene-like particles and nanotubes using arc discharge in liquid (water and liquid nitrogen) was demonstrated. Using this method, we successfully produced multi-walled fullerene-like



carbon particles (Nano Onions), metal including nanocapsules, and nanotubes. The specific surface area was measured on carbon onions sample, revealing that the carbon particles produced by our method has a large specific surface area, 984 m<sup>2</sup>/g, from which we expect our particles to be suitable for hydrogen storage application or some other application as adsorption media. It was shown that Raman spectra of multi-walled carbon nanotubes is changed by varying pressure of the arc in water, which suggests that the physical properties of nano structural products can be tuned by varying some arc parameters. Using the presented method, not only nano carbons but also we could successfully produced fullere-like materials from other lamellar structural materials, such as MoS<sub>2</sub> and WS<sub>2</sub>.

### Acknowledgement

Financial support by Grant-in-Aid for Young Scientists (B) of Japan Society for the Promotion of Science (JSPS) (No. 14750618), Kawanishi-Kinen-Shinmeiwa-Kyoiku Foundation (2002), and Kinki-Chiho-Hatsumei Center (2002) are acknowledged.

### References

- [1] H. W. Kroto, J. R. Heath, S. C. O'Brien, R. F. Curl, R. E. Smalley - *Nature*, **318**, 162 (1985).
- [2] S. Iijima - *Nature*, **354**, 56 (1991).
- [3] T. W. Ebbesen, P. M. Ajayan - *Nature*, **358**, 220 (1992).
- [4] A. Thess, R. Lee, P. Nikolaev, H. Dai, P. Petit, J. Robert, C. Xu, Y. H. Lee, S. G. Kim, A. G. Rinzler, D. T. Colbert, G. E. Scuseria, D. Tomanek, J. E. Fischer, R. E. Smalley, *Science*, **273**, 483 (1996).
- [5] M. Chhowalla, K. B. K. Teo, C. Ducati, N. L. Rupasinghe, G. A. J. Amaratunga, A. C. Ferrari, D. Roy, J. Robertson, W. I. Milne - *J. Appl. Phys.* **90**, 5308 (2001).
- [6] N. Sano, H. Wang, M. Chhowalla, I. Alexandrou, G. A. J. Amaratunga - *Nature* **414**, 506 (2001)
- [7] N. Sano, H. Wang, I. Alexandrou, M. Chhowalla, K. B. K. Teo, G. A. J. Amaratunga, K. Iimura - *J. Appl. Phys.*, **92**, 2783 (2002).
- [8] Y. L. Hsin, K. C. Hwang, Fu-Rong Chen, Ji-Jung Kai - *Advanced Materials*, **13**, 830 (2001)
- [9] N. Sano, H. Wang, M. Chhowalla, I. Alexandrou, G. A. J. Amaratunga, M. Naito, T. Kanki - *Chem. Phys. Lett.* **368**, 331 (2002).
- [10] K. Hernadi, A. Fonseca, J. B. Nagy, A. Fudala, D. Bernaerts, I. Kiricsi - *Appl. Catalysis A* **228**, 103 (2002).
- [11] S. Inoue, N. Ichikuni, T. Suzuki, T. Uematsu, K. Kaneko - *J. Phys. Chem. B.* **102**, 4689 (1998).
- [12] Y. Ye, C. C. Ahn, C. Witham, B. Fultz, J. Liu, A. G. Rinzler, D. Colbert, K. A. Smith, R. E. Smalley - *Appl. Phys. Lett.* **74**, 2307 (1999).
- [13] K. Hernadi, et al. *Zeolites*. **17**, 416 (1996).
- [14] H. Wang, N. Sano, S. Jia, M. Chhowalla, G. A. J. Amaratunga - *Chem. Phys. Lett.* Submitted.

# Simulation of hydrogen-rich gas production by plasma reforming of hydrocarbon fuels

M. S. Benilov<sup>1</sup>, G. V. Naidis<sup>1,2</sup>

<sup>1</sup> Departamento de Física, Universidade da Madeira, Largo do Municipio, 9000 Funchal, Portugal

<sup>2</sup> Institute for High Temperatures, Russian Academy of Sciences, Moscow 127412, Russia

## Abstract

The work is concerned with the simulation of plasma reforming of methane and octane. Results of simulation are compared with available experimental data. An amount of produced hydrogen is calculated for a wide range of control parameters: mixture composition and temperature at the reactor entrance, and the discharge power.

## 1. Introduction

Plasma-chemical methods of hydrogen production from natural gas and liquid hydrocarbon fuels through partial oxidation and steam reforming processes are considered among the most promising [1]. Recently a number of works have appeared on the experimental study of plasma reforming of mixtures of hydrocarbons with air and water vapour by means of gas discharges of various types. The highest efficiency of hydrogen production has been obtained using gliding arc discharges [2,3], operating at gas pressures of about 1 bar or higher, in the power range lower than 1 kW. In this work, results of simulation of plasma reforming of methane and octane under these conditions are presented.

## 2. The model

To simulate the plasma reforming process, a simple approach is used in which the discharge is accounted for as an additional, with respect to chemical processes, energy source inside the reactor. Calculation of chemical transformations is based on assumption of a perfect mixing of species inside the reactor chamber. The processes in the reactor are simulated using the code PSR from CHEMKIN-II package [4]. Input parameters for the code are the gas composition and temperature  $T_{\text{ent}}$  at the reactor entrance, pressure  $p$ , the reactor volume  $V$ , the total mass flow rate  $G$  and the power loss from the reactor  $W_{\text{loss}}$ . To account for the energy input from the discharge, in our calculations the value of  $W_{\text{loss}}$  is taken negative,  $W_{\text{loss}} = -W$ , where  $W$  is the discharge power. Output parameters are the gas composition at the reactor exit and the temperature  $T_{\text{react}}$  inside the reactor.

Partial oxidation of two hydrocarbon fuels has been simulated, methane and octane (the latter is commonly considered as a substitute of gasoline, e.g., [5]), in empty reactors, in the absence of catalysts inside the reactor chamber. Kinetic schemes of reforming are based on available in the literature mechanisms on fuel combustion. No discharge-related non-equilibrium reactions are taken into account.

For simulation of methane reforming, three various kinetic schemes of methane combustion have been used: GRI-Mech 3.0 [6], Leeds mechanism [7], and Warnatz mechanism [8]. Simulation of octane reforming has been performed using the kinetic scheme [9].

Composition of the mixture of hydrocarbon  $C_nH_m$  with air and water vapour at the reactor entrance is characterized by two parameters, O/C ratio, defined as  $2[O_2]/n[C_nH_m]$ , and  $H_2O/C$  ratio, defined as  $[H_2O]/n[C_nH_m]$ , where  $[O_2]$ ,  $[H_2O]$  and  $[C_nH_m]$  are volume flow rates of oxygen, water and hydrocarbon.

## 3. Results of simulation

Reforming of mixtures of methane with air has been simulated for conditions close to those of experiment [2]: at pressure  $p = 1$  bar, reactor volume  $V = 1$  l, discharge power  $W = 1$  kW, entrance temperature  $T_{\text{ent}} = 300$  K, total volume flow rate  $1.7 \text{ m}^3(\text{n})/\text{h}$ . The parameter SEI, defined in [2] as the ratio of the discharge power to the total volume flow rate, in these conditions is equal to  $0.59 \text{ kWh}/\text{m}^3(\text{n})$ . The O/C ratio was varied from 0.4 to 0.8, corresponding to the change of the total mass flow rate  $G$  from 0.47 to 0.53 g/s. In figure 1 the ratio is given of the molar fractions of  $H_2$  and CO in the reforming products versus the O/C ratio, calculated using three mentioned mechanisms of methane combustion. In the same figure experimental data are shown ([2], table 10, variants 3 and 4). It is seen that all the kinetic schemes give the values of  $H_2/CO$  ratio rather

close to those measured. However, the decrease of  $H_2/CO$  ratio with increase of  $O/C$  ratio, observed in [2], is predicted only by Leeds scheme [7].

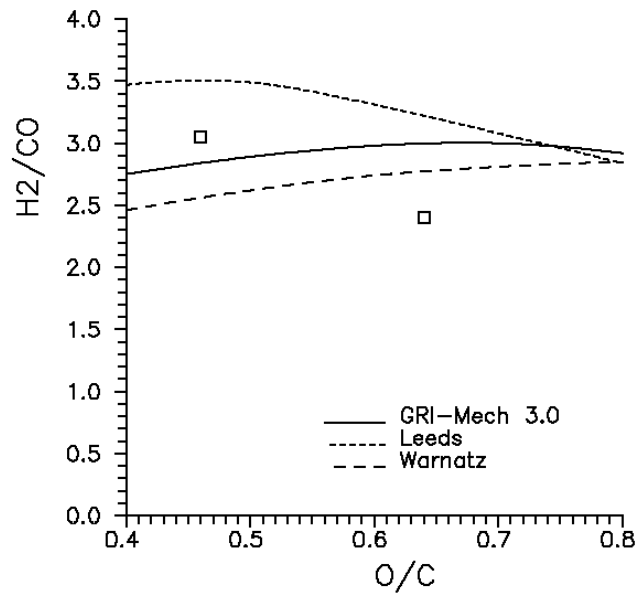


Figure 1. The  $H_2/CO$  ratio at methane reforming versus  $O/C$  ratio. Lines – simulation, points – experiment [2].

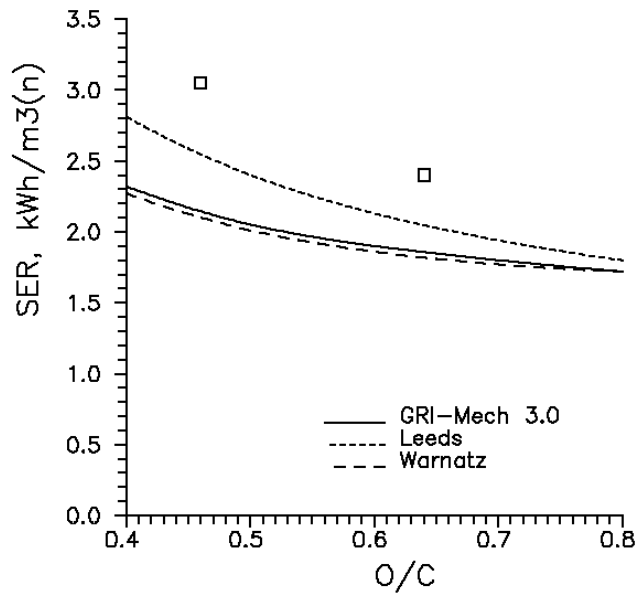


Figure 2. The ratio of the discharge power to the sum of volume flow rates of produced  $H_2$  and  $CO$  at methane reforming versus  $O/C$  ratio. Lines – simulation, points – experiment [2].

In figure 2 the parameter SER, defined in [2] as the ratio of the discharge power to the sum of volume flow rates of produced  $H_2$  and  $CO$ , is shown versus  $O/C$  ratio. Again, the Leeds scheme [7] gives the results closest to those measured in [2].

In figure 3 the composition of products of octane reforming is given versus O/C ratio, simulated for conditions of experiment [3]: pressure 1 bar, reactor volume 2 l, discharge power 0.27 kW, entrance temperature 300 K, fuel mass flow rate 0.26 g/s, at  $H_2O/C$  ratio equal to zero. In the same figure the molar fractions are presented, measured in [3] at O/C ratio equal to 1.32. It is seen that calculated molar fractions of products are consistent with those obtained in experiment.

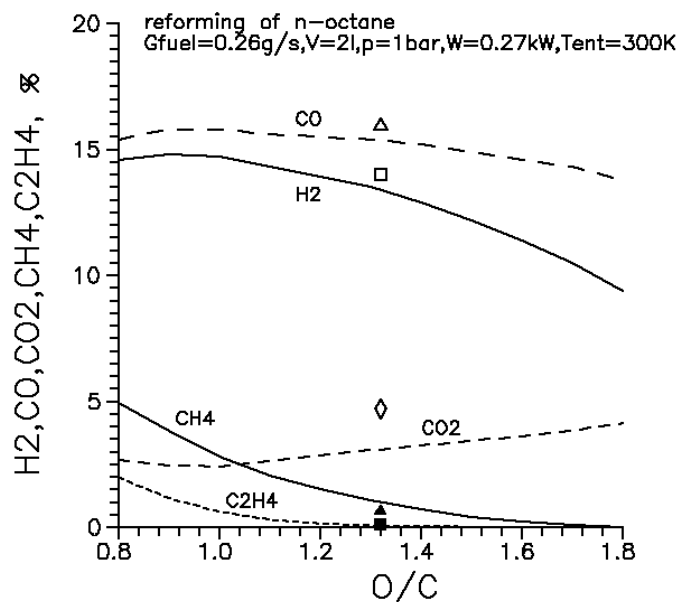


Figure 3. The molar fractions of products (in %) versus O/C ratio.  
Lines – simulation; points – experiment [3]: □ -  $H_2$ , Δ - CO, ◇ -  $CO_2$ , ▲ -  $CH_4$ , ■ -  $C_2H_4$

Carbon monoxide obtained at partial oxidation of a hydrocarbon fuel may produce hydrogen in water shift reaction  $CO + H_2O \rightarrow CO_2 + H_2$ . (Note that the equilibrium in water shift process is shifted to the right-hand side only at rather low temperatures,  $T < 800$  K. As, in the absence of catalysts, partial oxidation proceeds effectively at much higher temperatures inside the reactor chamber, the stage of water shift can proceed only after cooling of partial oxidation products. At the stage of water shift the use of a catalyst is required.) One of the parameters characterising the efficiency of reforming process is the ratio  $G_{H_2}/G_{fuel}$  of the mass flow rate of produced hydrogen, potentially accessible after water shift, to the mass flow rate of fuel. In figure 4 the ratio  $G_{H_2}/G_{fuel}$  is given versus O/C ratio, calculated for octane-air mixture (without water) at  $p = 2$  bar,  $V = 3$  l,  $G_{fuel} = 1$  g/s, and various values of  $T_{ent}$  and  $W$ . It is seen that optimal values of O/C ratio, resulting in the highest hydrogen yield, are in the range 1.3-1.5, corresponding to the ratio of air and fuel mass flow rates at the reactor entrance  $G_{air}/G_{fuel} = 6-7$ .

It is seen that preheating of air-fuel mixture results in noticeable increase of hydrogen yield. The effect of the discharge power is relatively weak, due to smallness of the energy input provided by the discharge in comparison with the chemical energy released in partial oxidation process. The role of the discharge in these conditions is, evidently, mainly in formation of high-temperature regions where an ignition of the reacting mixture occurs.

The effect of addition of water to fuel-air mixture at the reactor entrance is illustrated by figure 5, where the composition of products is given versus  $H_2O/C$  ratio, calculated for O/C ratio equal to 1.4, reactor volume 3 l, pressure 2 bar, entrance temperature 800 K, discharge power 0.3 kW, fuel mass flow rate 1 g/s. Increase of  $H_2O/C$  ratio results in decrease of the molar fraction of CO and increase of that of  $H_2O$ .

At small values of  $H_2O/C$  ratio the molar fraction of  $H_2O$  in the products of partial oxidation is smaller than that of CO. In this case an additional amount of water should be injected before the water shift stage. Figure 5 shows that using mixtures with  $H_2O/C$  ratio about 0.5 (corresponding to the ratio of water and fuel mass flow rates at the reactor entrance  $G_{H_2O}/G_{fuel}$  about 0.6) allows one to get, after partial oxidation, the mixture with nearly equal molar fractions of  $H_2O$  and CO. Note that the effect of  $H_2O/C$  ratio on hydrogen yield is

not substantial. It follows that the amount of water required for water shift process may be added to the fuel-air mixture not necessarily after fuel reforming in partial oxidation process, but already at the first stage, before reforming.

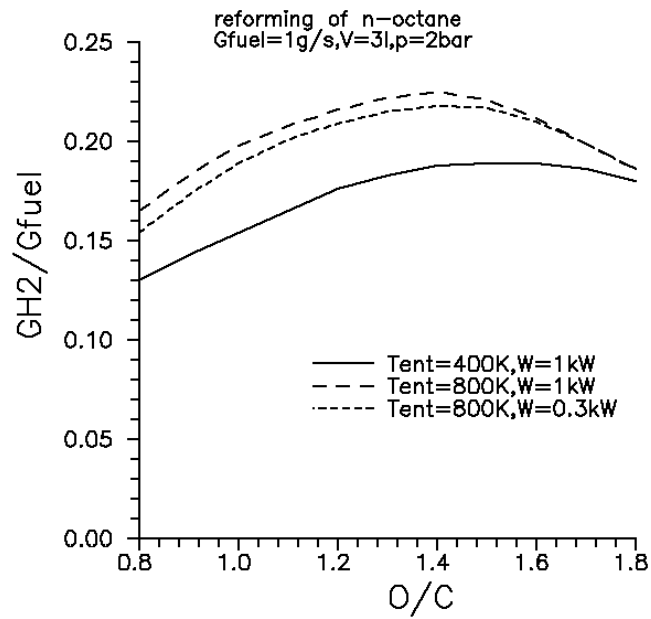


Figure 4. The ratio  $G_{\text{H}_2}/G_{\text{fuel}}$  versus  $\text{O}/\text{C}$  ratio.

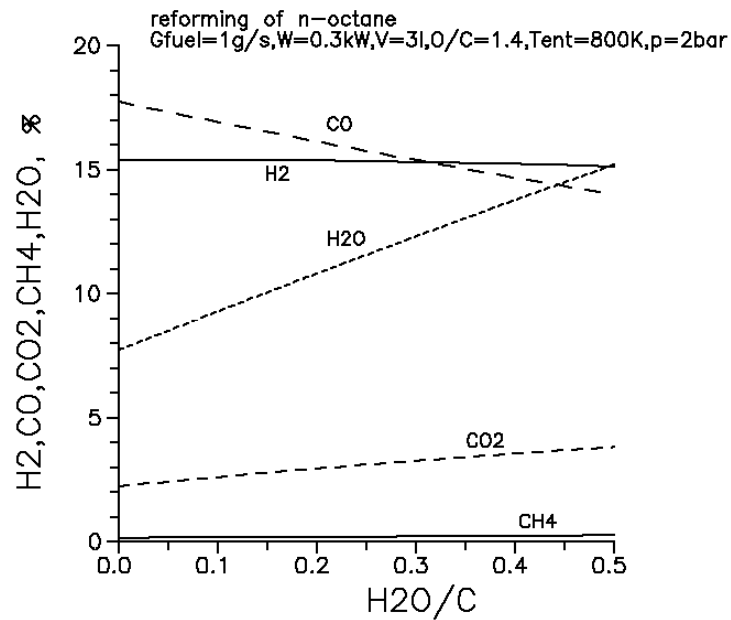


Figure 5. The molar fractions of products (in %) versus  $\text{H}_2\text{O}/\text{C}$  ratio.

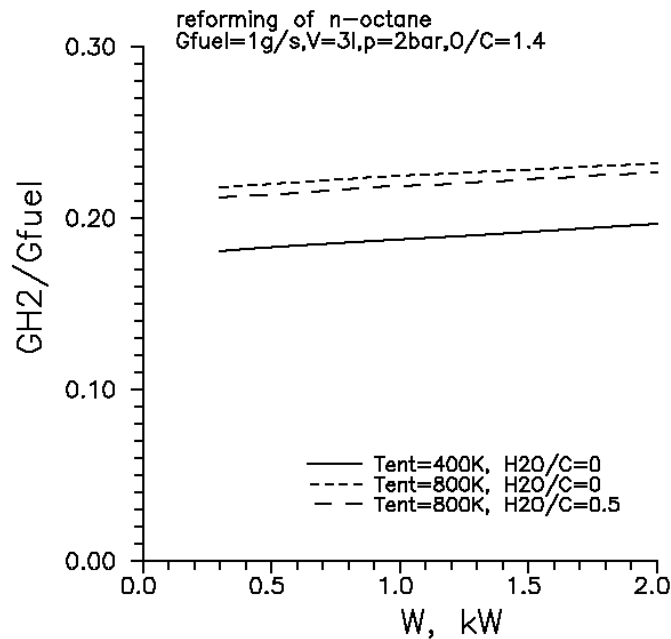


Figure 6. The ratio  $G_{H2}/G_{fuel}$  versus the discharge power.

The effect of discharge power on hydrogen yield is shown in figure 6 where the ratio  $G_{H2}/G_{fuel}$ , potentially accessible after water shift, is given versus  $W$ , for  $O/C$  ratio equal to 1.4,  $p = 2$  bar,  $V = 3$  l, and various values of  $T_{ent}$  and  $H_2O/C$  ratio. It is seen that increase of  $W$  by about an order of magnitude results in increase of  $G_{H2}$  not exceeding 10%. Such weak effect of  $W$  is due to smallness of the energy input provided by the discharge in comparison with the chemical energy released in partial oxidation process.

A use of regimes with high  $O/C$  ratios, where the required energy is provided by exothermic chemical reactions of oxidation of fuel, allows one to work at relatively low discharge powers. In these regimes the role of discharge is mainly in mixture ignition, like in spark-ignited gasoline engines. Some threshold value of the discharge power must exist, required to provide ignition. Extrapolation of experimental data [3] gives, for the fuel mass flow rate 1 g/s, the discharge power, sufficient for ignition, about 1 kW. Corresponding value of the energy consumption for hydrogen production is about 5 kJ/g.

### Acknowledgment

The work was supported by the EC through the project N° ENK5-CT-2000-00346.

### References

- [1] J.M. Cormier, I. Rusu - J. Phys. D: Appl. Phys. **34**, 2798 (2001).
- [2] A. Czernichowski - Oil and Gas Sci. Technol. **56**, 181 (2001).
- [3] L. Bromberg, D.R. Cohn, A. Rabinovich, J. Heywood - Int. J. Hydrogen Energy **26**, 1115 (2001).
- [4] R.J. Kee, F.M. Rupley, J.A. Miller - Sandia Report SAND89-8009 (1989).
- [5] L. Bromberg, D.R. Cohn, A. Rabinovich, J.E. Surma, J. Virden - Int. J. Hydrogen Energy **24**, 341 (1999).
- [6] G.P. Smith, D.M. Golden, M. Frenklach, N.W. Moriarty, B. Eiteneer, M. Goldenberg, C.T. Bowman, R.K. Hanson, S. Song, W.C. Gardiner, V.V. Lissianski, Z. Qin - [http://www.me.berkeley.edu/gri\\_mech/](http://www.me.berkeley.edu/gri_mech/)
- [7] M.J. Pilling, T. Turanyi, K.J. Hughes, A.R. Clague - <http://chem.leeds.ac.uk/Combustion/metan14.dat>
- [8] J. Warnatz, V. Karbach - <http://www.ca.sandia.gov/tdf/3rdWorkshop/ChemMech/JW-C297.mec.html>
- [9] P.A. Glaude, V. Warth, R. Fournet, F. Battin-Leclerc, G. Scacchi, G.M. Côme - Int. J. Chem. Kinetics **30**, 949 (1998); <http://www.ensic.u-nancy.fr/ENSIC/DCPR/cinetique/Chimieinfo/TEXTES/mecanooctane.htm>

# Modeling of a capacitive coupled RF O<sub>2</sub> plasma for SiO<sub>2</sub> deposition

M.Goujon<sup>1,2</sup>, R.Hugon<sup>2</sup>, T.Belmonte<sup>1</sup>, G.Henrion<sup>2</sup>

<sup>1</sup> LSGS (UMR 7570)- INPL-Ecole des Mines-Parc de Saurupt-54042 Nancy Cedex - France

<sup>2</sup> LPMIA (UMR 7040) Univ. H. Poincaré -BP239-54506 Vandoeuvre les Nancy - France

## Abstract

A transient fluid model in one dimension describing a RadioFrequency O<sub>2</sub> plasma between two metallic electrodes is presented. The adopted kinetic description of the electrons is done by considering separately two groups of electrons. The first one consists of the bulk electrons at moderate energy while the second one corresponds to the fast electrons that are described as a monoenergetic electron beam, mainly issued from the metallic electrodes.

## 1. Introduction

Capacitive coupled RF glow discharges are widely used for plasma assisted surface processing. In particular, electronegative oxygen plasmas are used in surface treatments for the deposition of thin oxide films on various materials.

In many processes, TEOS/O<sub>2</sub> or HMDSO/O<sub>2</sub> [1-5] plasmas are used in which the organometallic precursors are highly diluted to ensure a good quality of the deposited SiO<sub>x</sub> layer. Though these processes have been studied for many years, they are not completely understood and it is not yet possible to scale up the reactors. To achieve this purpose, one way consists in modeling the plasma reactor to get a good knowledge of the discharge and the behavior of the species.

We are mainly interested in the modeling of a RF HMDSO/O<sub>2</sub> plasma used for the deposition of SiO<sub>x</sub> thin films onto moving metallic surfaces. Owing to the complexity of the HMDSO molecule, and consequently of the HMDSO/O<sub>2</sub> plasmas, this first approach is devoted to the modeling of a pure O<sub>2</sub> plasma. Indeed, the dilution rate of HMDSO in O<sub>2</sub> is less or equal to 10% and it is reasonable to assume that the main part of the plasma kinetics is governed by O<sub>2</sub>, especially for charged particle kinetics.

The model developed herein is based on the solution of the first three moments of the Boltzmann's equation describing the transport of the charged particles. These equations are coupled with the Poisson's equation, for the electric field.

In this fluid approach, some assumptions have to be made in order to close the set of moment equations. Efforts have been made to describe the ionization mechanisms and attachment processes as accurately as possible. As a consequence, it is of major importance to choose the corresponding rates very carefully.

This model provides the evolution of parameters like the charged particle density, the electric field, and help us to point out the dominant regime of the discharge.

The first part of this paper presents the two electron group model, and the set of equations that are solved for the charged particles as well as the boundary conditions and the numerical method.

The second part discusses the results. Attention is paid to the variations of the dominant parameters of the discharge such as the electric field, the electron and ion number density, the RF voltage and current and the ionization rates as well.

## 2. Two electron group model

### 2.1 Basic equations

The equations describing the transport of the charged particles are coupled to the Poisson's equation for the electric field. In order to describe the transport of the electrons and the ions, a fluid model is used. This model is based on the three moments of the Boltzmann's equation written under the following assumptions:

- we consider that the heat flux is negligible, and we assume that the local field approximation applies,
- in order to account for two possible ionization mechanisms, the model considers two groups of electrons [6-9]. One group is composed by the fast electrons, emitted by each electrode under ion bombardment ; this group forms a monoenergetic beam. There is one beam for each electrode, hereafter referred to by subscript  $f_1$  and  $f_2$ . The second one is made by the "bulk" electrons, created in the negative glow (NG) from ionization by the fast electrons.

- We consider that the electrons created by ionization in the cathode-fall (CF) region belong to the fast electron group, whereas the electrons created by ionization in the NG belong to the bulk electron group.
- if the beam energy in the NG is lower than the ionization threshold, the electrons join the bulk electron group.
- Finally, the electron distribution function is assumed to be Maxwellian.

The transport of the fast electrons is described by a continuity equation and an energy equation:

$$\begin{cases} \frac{\partial n_f}{\partial t} + \frac{\partial(n_f u_f)}{\partial x} = S_f - P_f \\ \frac{\partial(n_f m \varepsilon_f)}{\partial t} + \frac{\partial(n_f m u_f \varepsilon_f)}{\partial x} - n_f q u_f E = S_f - P_f \end{cases} \quad (1)$$

The transport of the bulk electrons is described by a continuity equation, a momentum-transfer equation and an energy equation:

$$\begin{cases} \frac{\partial n_e}{\partial t} + \frac{\partial(n_e u_e)}{\partial x} = S_e + P_f + SDI - P_e + C_e \\ \frac{\partial(n_e m u_e)}{\partial t} + \frac{\partial(n_e m u_e u_e)}{\partial x} + \frac{\partial(P)}{\partial x} - n_e q E = S_e - P_e \\ \frac{\partial(n_e m \varepsilon)}{\partial t} + \frac{\partial(n_e m u_e \varepsilon)}{\partial x} + \frac{\partial(P u_e)}{\partial x} - n_e q u_e E = S_e - P_e \end{cases} \quad (2)$$

The transport equations for the positive ions ( $O_2^+$  and  $O^+$ ) consist of a continuity equation and a mobility equation:

$$\begin{cases} \frac{\partial n_p}{\partial t} + \frac{\partial(n_p u_p)}{\partial x} = SDI - P_p \\ n_p u_p = n_p w_p - \frac{\partial(n_p D_p)}{\partial x} \end{cases} \quad (3)$$

As oxygen is an electronegative gas, the negative ions  $O_2^-$  and  $O^-$  must be considered and their transport equations are:

$$\begin{cases} \frac{\partial n_n}{\partial t} + \frac{\partial(n_n u_n)}{\partial x} = SDI + S_n - P_n \\ n_n u_n = n_n w_n - \frac{\partial(n_n D_n)}{\partial x} \end{cases} \quad (4)$$

All these equations are coupled with the Poisson's equation for the electric field:

$$\frac{\partial E}{\partial x} = \frac{|e|}{\varepsilon_0} (n_p - n_e - n_f - n_n) \quad (5)$$

The subscript "f" designates the beams, "e" the bulk electrons, "p" the positive ions, "n" the negative ions.

- S and P are the source and loss terms,
- C is the balance term for the reactions of  $O_2$ , as presented below.
- n, u,  $\varepsilon$ , w, D are respectively the density, the average velocity, the energy, the drift velocity and the diffusion rate

The ionization source term is  $SDI = N \times n_e \times \frac{\int v f(v) \sigma(v) dv}{\int f(v) dv}$ ,  $\sigma(v)$  is the ionization cross section, for  $O_2$  and O



The oxygen plasma chemistry is described in table 1 [11].

Table 1 : Set of the reactions used in the model.

Reaction	rate
$O_2 + e^- \rightarrow O + O^-$	$K_1 = 7.74 \cdot 10^{-12} \text{ cm}^3 \cdot \text{s}^{-1}$
$O^- + O_2 \rightarrow O_2^- + O$	$K_2 = 1.00 \cdot 10^{-30} \text{ cm}^3 \cdot \text{s}^{-1}$
$O^- + O \rightarrow e^- + O_2$	$K_3 = 1.40 \cdot 10^{-10} \text{ cm}^3 \cdot \text{s}^{-1}$
$O_2^- + O \rightarrow O^- + O_2$	$K_4 = 3.30 \cdot 10^{-10} \text{ cm}^3 \cdot \text{s}^{-1}$
$e^- + O_2^+ \rightarrow 2O$	$K_5 = 2.10 \cdot 10^{-7} \text{ cm}^3 \cdot \text{s}^{-1}$
$O^- + O_2^+ \rightarrow O + O_2$	$K_6 = 9.60 \cdot 10^{-8} \text{ cm}^3 \cdot \text{s}^{-1}$
$O_2^- + O_2^+ \rightarrow 2O_2$	$K_7 = 4.20 \cdot 10^{-7} \text{ cm}^3 \cdot \text{s}^{-1}$
$e^- + O_2 \rightarrow e^- + O + O$	$K_8 = 3.91 \cdot 10^{-11} \text{ cm}^3 \cdot \text{s}^{-1}$
$e^- + O_2 + O_2 \rightarrow O_2 + O_2^-$	$K_9 = 1.82 \cdot 10^{-31} \text{ cm}^3 \cdot \text{s}^{-1}$

## 2.2 Boundary conditions

The following boundary conditions are used:

- The flux of electrons emitted by each electrode is:

$$n_{f1} v_{f1} = -\gamma n_p(x=0) \langle v_p(x=0) \rangle$$

$$n_{f2} v_{f2} = -\gamma n_p(x=d) \langle v_p(x=d) \rangle$$

where  $\langle v_p \rangle$  is the average velocity for the positive ions and  $\gamma$  the secondary emission coefficient.

- The sheath-glow boundary is supposed to be situated at the point where the electric field is less than 10V/cm (arbitrary value).
- The mean energy of electron emitted by the electrodes is:

$$\varepsilon_{f1}(x=0) = \varepsilon_{f2}(x=d) = 1 \text{ eV}$$

- The potential drop between the electrodes :  $V(x=d) = V_{RF} \cos(\omega t)$

## 2.3 Numerical method

The method adopted to solve numerically the transport equations is based on a finite-difference algorithm, with a centered scheme corrected by the FCT method (Flux corrected Transport) [12]. The space mesh is described by N cells (N=160 in our case). The time step must be small enough to satisfy the condition

$$u \frac{\Delta t}{\Delta x} \leq \frac{1}{2}. \text{ In our case, } \Delta t = 5 \cdot 10^{-11} \text{ s.}$$

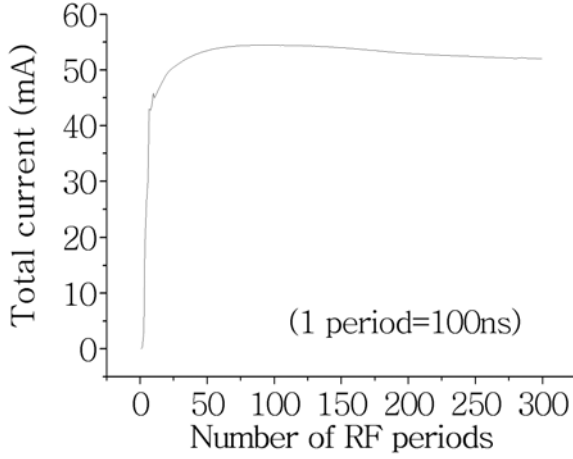
## 3. Results

The presented results have been obtained under the following conditions. The electrodes are metallic parallel plates. The pressure is 0.6 Torr (80 Pa). The gap length is  $d=4 \text{ cm}$  and the frequency is 10 MHz. The amplitude  $V_{RF}$  of the applied voltage is 1000 V.

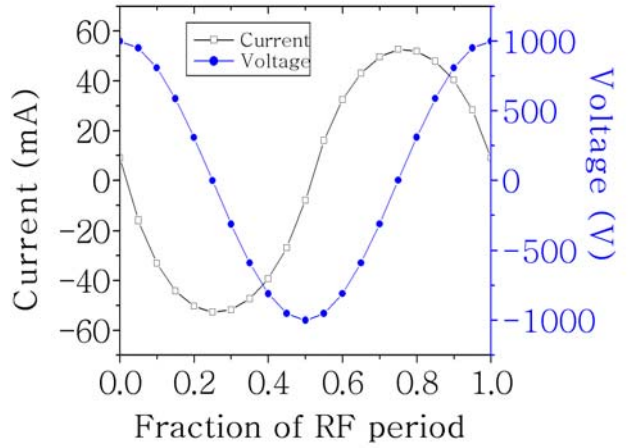
The secondary emission coefficient was taken equal to  $\gamma=5 \cdot 10^{-2}$ . It corresponds to the value used in [13] on iron electrodes for a  $N_2$ - $CO_2$  discharge.

Fig. 1 shows the variation of the current as a function of the number of RF cycles. It appears that a quasi-stationary state is reached after about 5  $\mu\text{s}$ . All the following results have been obtained after 300 RF cycles to ensure the stationary state is achieved.

The variations of the total RF current and voltage as a function of the interelectrode position are plotted in Fig. 2. The figure shows the dephasing between the two parameters. Indeed, the discharge is capacitive and the phase shift between the current and the applied voltage is close to  $\pi/2$ .

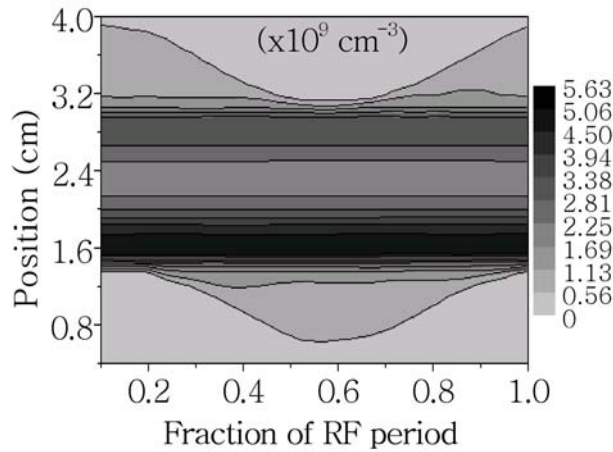


**Fig. 1 :** Variation of the RF current as a function of the number of RF cycles.

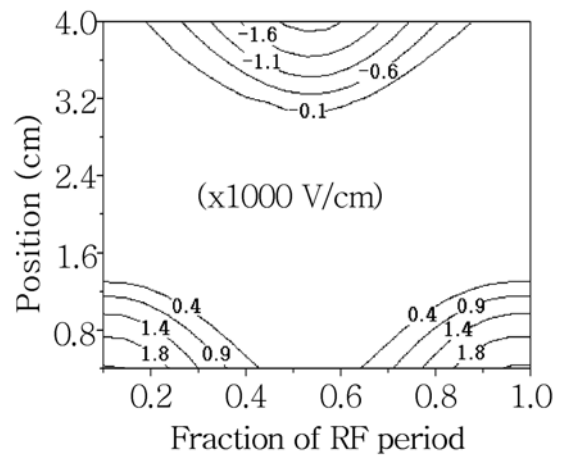


**Fig. 2 :** Variation of the RF current and voltage over one RF period.

The bulk electrons tend to be confined in the central part of the reactor rather than at the electrodes (Fig. 3). The bulk electron density is modulated in the sheaths. This oscillation is related to the successive contraction and expansion of the sheath on each electrode (Fig. 4).



**Fig. 3 :** Variation of the bulk electron number density as a function of the time fraction during one RF period and the position in the interelectrode space



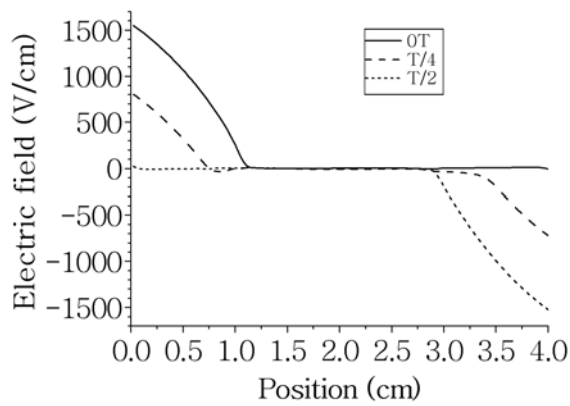
**Fig. 4 :** Contour plot of the electric field as a function of the time fraction during one RF period and the position in the interelectrode space

As deduced from the depicted variation of the electric field in Fig. 5, the sheath is on the electrode which behaves as an anode ( $z=0$ ) at the beginning of the RF period ( $T$ ). Then, at  $T/4$ , two sheaths simultaneously exist on each electrode. One of them contracts on one electrode while the other one expands on the other electrode. At  $T/2$ , the anodic sheath has disappeared and the cathodic sheath reaches its maximum.

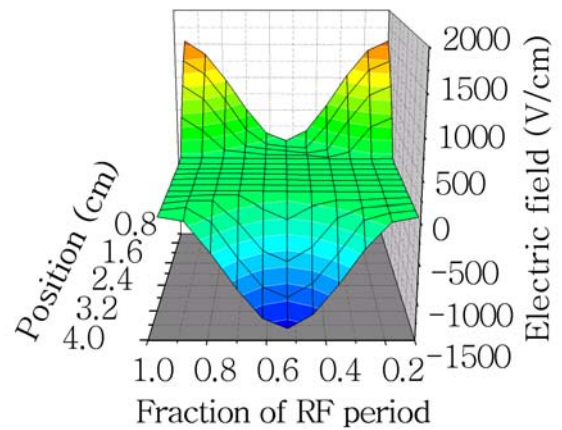
During a RF cycle, the electrodes alternatively play the role of the cathode. Fig. 6 shows the motion of the sheath during a RF cycle as a function of the interelectrode position.

The movement of the ions is almost frozen. Indeed, the ions cannot respond to the instantaneous variations of the electric field and their modulation is negligible. Figs. 7 and 8 show the evolution of the number densities of the positive ions  $O_2^+$  and  $O^+$  as a function of the RF cycle and the interelectrode position.

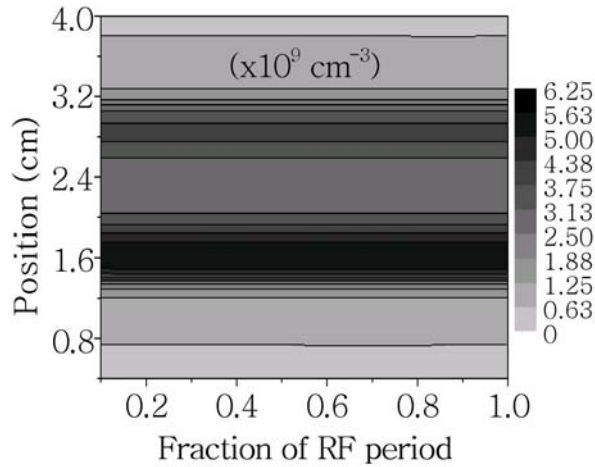
The evolution of the negative ions  $O_2^-$  and  $O^-$  density is similar to that of the positive ions (Figs. 9 and 10). They move much more slowly than the electrons.



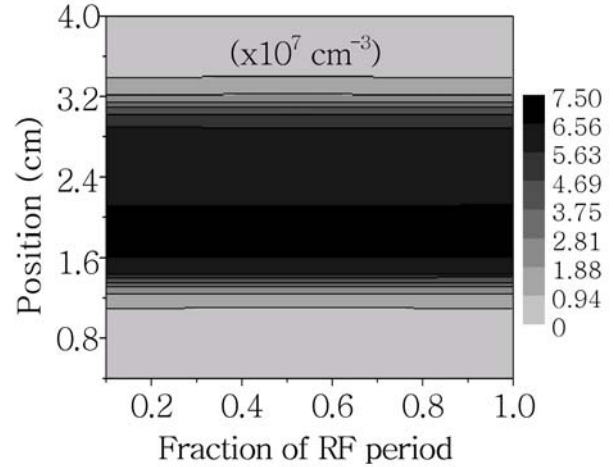
**Fig. 5 :** Variation of the electric field as a function of the interelectrode distance at different fractions of time during one RF period.



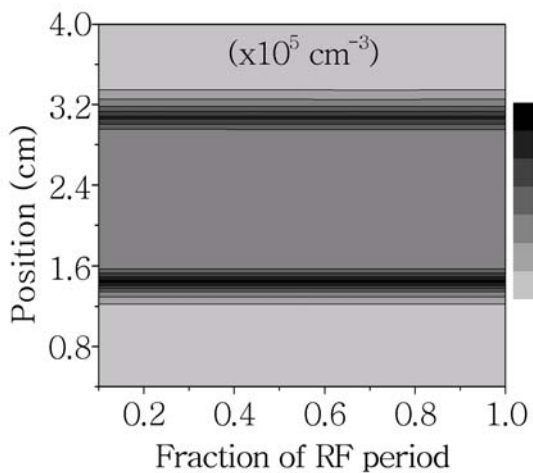
**Fig. 6 :** Variation of the electric field as a function of the interelectrode distance and the fraction of time during one RF period.



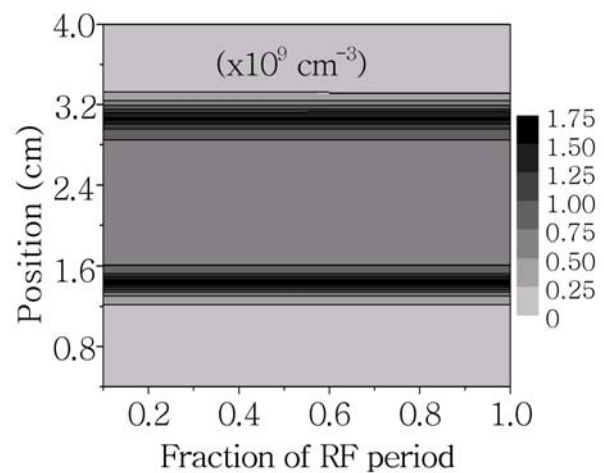
**Fig. 7 :** Variation of  $O_2^+$  number density as a function of the interelectrode distance and the fraction of time during one RF period.



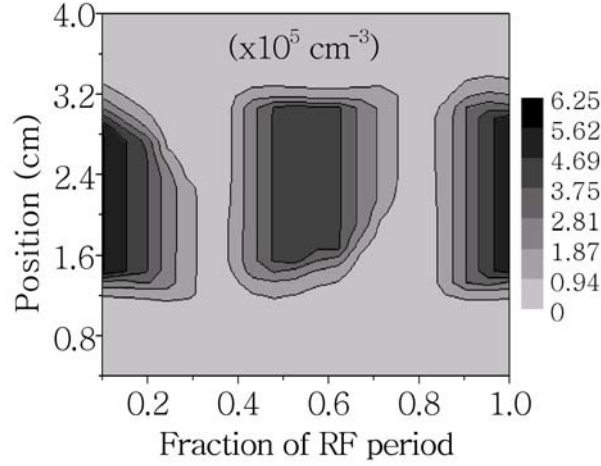
**Fig. 8 :** Variation of  $O^+$  number density as a function of the interelectrode distance and the fraction of time during one RF period.



**Fig. 9 :** Variation of  $O_2^-$  number density as a function of the interelectrode distance and the fraction of time during one RF period.



**Fig. 10 :** Variation of  $O^-$  number density as a function of the interelectrode distance and the fraction of time during one RF period.

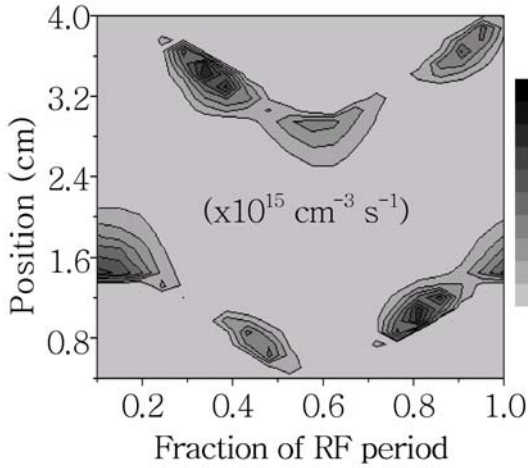


**Fig. 11 :** Variation of the fast electron number density as a function of the interelectrode distance and the fraction of time during one RF period.

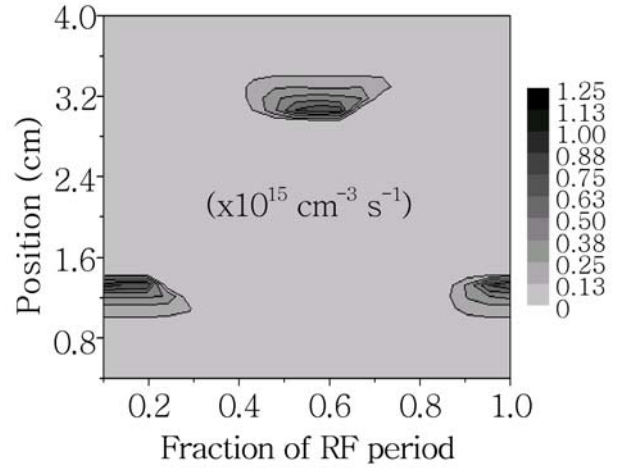
The fast electrons issued from each electrode are accelerated by an intense electric field in the sheath and release their energy by collision with the heavy particles in the discharge. The evolution of the density of the beams is shown in Fig. 11.

There are two different operating regimes of the discharge. The first one is the "wave-riding" regime, in which the sheath can be considered as a potential wall on which the electrons are reflected. In our case, it is the dominant regime. Fig. 12 represents the contour plot of the ionization rate for the "wave-riding" regime. The maximum ionization rate occurs in the sheath boundary during the sheath expansion.

The second regime is the "secondary electron" regime. In this regime, the maximum ionization rate is reached when the sheath length and the sheath potential are maximum (Fig. 13).



**Fig. 12 :** Wave riding ionization rate as a function of the interelectrode distance and the fraction of time during one RF period.



**Fig. 13 :** Secondary electron ionization rate as a function of the interelectrode distance and the fraction of time during one RF period.

The principal way the electrons gain energy is related to the sheath expansion, in the case of the "wave-riding" regime, while for the "secondary electron" regime, the electrons created by ion bombardment on one electrode are responsible for the discharge sustaining.

#### 4. Conclusion

This fluid model consists of equations describing the transport of charged particles coupled with the Poisson's equation for the electric field. The electron kinetics is described by considering two electron groups. It allows us to obtain the dominant parameters of the RF discharge, as the charged particles densities, the variations of the electric field, the ionization rates. The experimental validations of this model are in progress.

#### References

- [1] N. Benissad, C. Boisse-Laporte, C. Vallée, A. Granier, A. Goullet, Surf. Coat. Technol., **116-119**, 868 (1999)
- [2] K. Aumaille, C. Vallée, A. Granier, A. Goullet, F. Gaboriau, G. Turban, Thin Solid Films, **359**, 188 (2000)
- [3] R. Lamendola, R. D'Agostino, F. Fracassi, Plasmas Polym., **2**, 147 (1997)
- [4] M. Creatore, F. Palumbo, R. D'Agostino, Plasmas Polym., **7**, 291 (2002)
- [5] A. Granier, M. Vervloet, K. Aumaille, C. Vallée, Plasmas Sources Sci. Technol., **12**, 89 (2002)
- [6] P. Belenguer, thesis Univ. H. Poincaré, Nancy I, France (1990)
- [7] J.H. Ingold, "In gaseous electronics", M.N. Hirsh and H.J. Orskam (Ed), Academic Press, New York (1978)
- [8] A.V. Phelps, B.M. Jelenkovic, L.C. Pitchford, Phys. Rev. A, **36**, 5327 (1987)
- [9] E. Guiberteau, G. Bonhomme, R. Hugon, G. Henrion, Surf. Coat. Technol. **97**, 552, (1997)
- [10] W. Hwang, Y.K. Kim and M.E. Rudd, J. Chem. Phys., **104**, 2956 (1996)
- [11] G. Fournier, in "Réactivité dans les plasmas", Les Editions de Physique, Paris (1984), p. 297
- [12] J.P. Boris, D.L. Book, J. Comput. Phys., **11**, 38 (1973)
- [13] P. Bayle, J. Vacquie, M. Bayle, Phys. Rev. A, **34**, 360 (1986)

# Homogeneous and Micro-patterned plasma-deposited PEO-like coatings for biomedical surfaces

E.Sardella<sup>1</sup>, R. Gristina, G.S. Senesi, A. Delvecchio, R. d'Agostino, P. Favia

<sup>1</sup>*Department of Chemistry, University of Bari  
Istituto di Metodologie Inorganiche e dei Plasmi- Bari, CNR  
Via Orabona 4, 70126, Bari, Italy*

## Abstract

Polyethylene oxide (PEO)-like coatings were deposited on polystyrene (PS) by RF (13.56 MHz) glow discharges, increasing the input power in the range from 5W to 15W. Cell adhesion and morphology of keratinocytes and fibroblasts cell lines were observed and related to the chemical characteristics of the coatings. Further, micro-arrangement of cells was observed on micro-patterned substrates containing cell-adhesive zones alternated to totally cell repulsive ones, obtained with a sequence of PEO-like deposition processes.

## 1. Introduction

Biological responses induced by a material immersed in a physiological liquid are localised at molecular level in a narrow interface (<1nm depth) where the adsorption of a protein layer precedes any further biological event. Chemical [1] and topographical [2] properties of the material as well as the specific properties of individual proteins dramatically impact the organisation of the adsorbed protein layer, whose nature drives the cellular responses to the surfaces. One of the purposes of biomaterial science is to control the interactions of proteins with the material interface, for modulating morphology and physiology of adhered cells in biomedical applications. Polystyrene (PS), for example, a material non suitable for cell adhesion, is functionalised with oxygen and nitrogen containing groups [3,4] to improve its protein- and cell-adhesive property in manufacturing cell culture Petri dishes. On the other hand, highly or totally protein- and cell-repulsive substrates are demanded in a wide range of applications in water media ranging from extra corporal therapy [5] to solid phase diagnostics [6] and drug delivery [7]. Chemically non-adhesive surfaces for cells are generally represented by carbohydrates (i.e. agarose [9], mannitol [10]), proteins (i.e. albumin [11]) and synthetic polymers (i.e. polyacrylamide [12], pluronics [13] and poly (ethylene oxide) [14]) as shown by Nelson et al. [8]. Polymer surfaces incorporating PEO or PEG chains appear to be effective in resisting protein-adsorption and cell-attachment in water media [15]. The passive (unfouling) nature of these surfaces in water has led to increased interest in fouling resistant interfaces for biomedical/biotechnological devices, and, as a result, a number of methods were developed to immobilize PEO moieties on biomaterials [16]. Conventional methods for producing PEO surfaces may be limited by complex synthesis protocols and/or by the mismatch of the properties (i.e. mechanical) of the PEO-containing materials with certain substrates. The direct deposition of an over layer of fouling resistant films by RF-glow discharges may overcome this disadvantages, since this produces thin layers covalently bond to the substrate with peculiar chemical-physical characteristics. Volatile corona ethers [20], and glycols [21] are generally used as gas feed in RF-glow discharges aimed to deposit "PEO-like" coatings, i.e. thin film not only composed by EO units, like in conventional PEO polymers, but also by other moieties, including a certain cross-linking degree. The percentage of EO units in the film network usually indicates quantitatively how much the structure of the coating is close to a conventional PEO. This PEO character can be measured by means of X-ray Photoelectron Spectroscopy (XPS) from the contribution of ether carbons (C1 component) to the C1s signal. The higher the content of EO units in the coating, the higher its PEO-character, the better its non-fouling properties [14]. Only a PEO-character higher than 75-80% results in non-fouling properties, and this can be obtained in discharges run at low monomer fragmentation conditions [17-19]. Our present results show the possibility to drastically change the attitude of PEO-like coated PS to discourage cell attachment by tuning the fragmentation conditions in the discharge with the RF power input. An evident correlation between the chemical composition of plasma deposited PEO-like coatings and their biological responses were observed. Differently cell-adhesive domains can be spatially micro-arranged on polymer biomedical materials to address cell spreading along predefined directions. Cell cultures spatially arranged on substrates can be designed for a wide range of commercial applications, including biosensors and diagnostics. In the literature,

chemical patterns in which hydrophilic zones are alternated with hydrophobic ones is proposed as a possible method for patterning surfaces [22]. In our procedure, two different PEO-like coatings both hydrophilic and with drastically different bio-adhesive properties were used for micro-structuring PS samples. A very simple procedure of patterning has been applied by means of plasma processes. It consists of exposing only few zones of the substrate to a plasma process through a laser-cut micro-structured physical mask (e.g. metal grids for TEM analysis). PEO-like coatings with different composition and cell-adhesive properties were deposited in a micro-arranged configuration and the resulting morphology of cells on micro-patterns has been observed.

## 2. Materials and Methods

### 2.1 Surface modifications

Cristalline PS discs (diameter 12mm, thickness 1.2mm; Goodfellow) were used as substrates. PEO-like coatings were deposited from a gas feed mixture of di-ethylene glycole dimethyl ether (DEGDME, Sigma Aldrich) vapors and Argon (0.40 sccm DEGDME, 5 sccm Ar) at 400 mTorr. DEGDME was utilised after several freeze-thaw cycles to get rid of air dissolved. RF glow discharges were run for 1h, at different (5W; 10W; 15W) power input values. The name of the PEO-like coatings indicates the power of deposition, for example PEO-like coatings deposited at 5W as input power were named PEO5W. Micro-structuring procedures were performed by depositing the PEO-like coating with the best non fouling properties (PEO5W) onto native PS or plasma-deposited cell-adhesive surfaces (*i.e.* PEO10W, PEO15W coatings) through TEM round copper grids (3mm Ø; <10µm thick) with thin bars separated by large holes and positioned in close contact with the substrate. The grids for micro patterning were G50p (80µm bars; 400µm holes).

### 2.2 Surface diagnostic

XPS analyses were performed within the first hour after each plasma process, by a PHI 5300 ESCA instrument equipped with non-monochromatized MgK $\alpha$  and AlK $\alpha$  radiation sources. The take-off angle was 45°, resulting in a sampling depth analysis of about 7 nm. XPS wide-scan (B.E.=0-1000eV) and high resolution C1s and O1s spectra were registered for each sample using a pass energy of 89.45 eV and 34.75 eV, respectively. C1s signals were best-fitted into four peak. Before charging correction, the positions of the peaks were fixed at +1.6eV (C1; C-OH(C)), +3.6 eV (C2; (C=O, O-C-O) and +4.2 eV (C3; COOH(C)) respectively to the hydrocarbon C0 (C-H(C)) peak component. This peak was set at 285.0 eV for charging correction. A Gaussian percent of 85-100% and FWHM values in the range 1.5-2.1 eV were used in the fitting. An AXIS Ultra (Kratos instrument) instrument has been used to obtain spectroscopic information at high space resolution from selected areas of plasma microstructured PS. The image detection (chemical map) of the patterned area has been realised on the whole investigated field setting the detector of the instrument on the C0 contribute or on the C1 contribute of the C1s signals. The detector coordinates were set, by software, to collect an image of the tracks in the patterns. The minimum electron spot diameter (Ø 27µm) allowed a high spatial resolution to investigate chemical composition within the different domains realised. WCA measurements were realised in our lab with a Ramé-Hart 100-00 goniometer. Advancing WCA ( $\theta_a$ ) were measured by increasing the volume of the water drop, 2µl steps, until WCA remained constant. Receding WCA ( $\theta_r$ ) were measured by decreasing the volume of the drop until WCA value remained constant and the solid/liquid interface starts to decrease. WCA values reported are the mean value of at least 5 individual measurements on each sample performed within 10 min after the processes. FT-IR spectra of coatings deposited onto polished silicon substrate, were acquired in the transmission mode with Bruker Equinox 55 spectrometer. The C-O (1000-1300cm<sup>-1</sup> wave number) and C-H (2800-3000cm<sup>-1</sup>) characteristic stretching bands of conventional PEO polymers were investigated. Atomic Force Microscopy (Autoprobe CP, firma Park Scientific) measurements were performed in non-contact mode, at a very tip load (~10-12 N), as needed for “soft” materials, to investigate the topography of the surfaces at nanometer scale resolution.

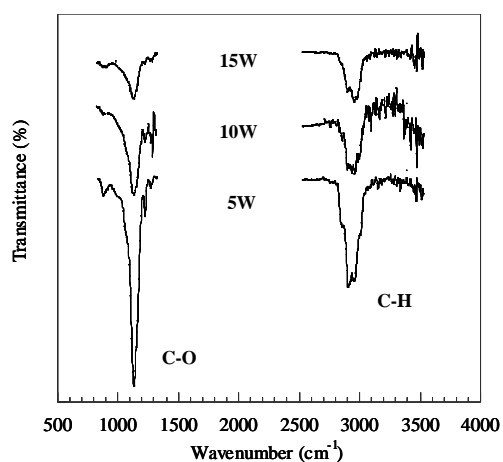
### 2.3 Cell Culture.

Throughout the experiments three cell lines were used: the NCTC 2544 human keratinocyte, the hTERT and 3T3 fibroblast cell lines. Each experiment was performed on at least four samples of each structured or non-structured modified sample, and also included control samples of plain cell culture treated polystyrene and

12 mm diameter native polystyrene cover slip. Cells were obtained after trypsinization of confluent or near-confluent culture and seeded at  $2 \times 10^4$  cells/well in suspension on all test material and incubated at 37°C and 5% CO<sub>2</sub>/95% air atmosphere in Dulbecco's modified Eagle's medium (DMEM) supplemented with 10% fetal bovine. Number and morphology of attached cells was determined at various time intervals using digital images acquired from a phase contrast light microscope (Leica DM IL). The number of adherent cells was manually determined in at least 10 areas of 0.8 mm<sup>2</sup>/sample. For morphological studies cells were divided with respect of their shapes in round and spread cells. Unpaired Student's t-test was used to evaluate statistical significative differences between test samples. Data were taken to be significant when a  $p < 0,05$  was obtained. For scanning electron microscopy cells fixed with 1% glutaraldehyde /0.1M sodium cacodylate and dehydrated through a series of alcohol solutions, were sputter coated with gold before examination with Hitachi S800 field emission SEM at an accelerating voltage of 10keV.

### 3. Results and discussion

#### 3.1 PE-CVD of PEO-like coatings



**Figure 1:** FT-IR transmittance spectra of PEO-like films obtained from DEGDME. The power ranges from 5W to 15W, maintaining the other plasma parameters constant (5sccm Ar, 0,4sccm DEGDME, 400mTorr, 1h). In the figure two characteristics zones have been shown: C-O stretching vibration at 1100cm<sup>-1</sup>; C-H stretching vibration at 2800- 3000cm<sup>-1</sup>.

Sample	C/O	PEO-character	$\theta_{adv}$	$\theta_{rec}$
PEO5W	2.4	80.7±0.8	56±5	37±5
PEO10W	2.7	67.8±1.7	67±5	46±5
PEO15W	4	41±2	71±5	50±5

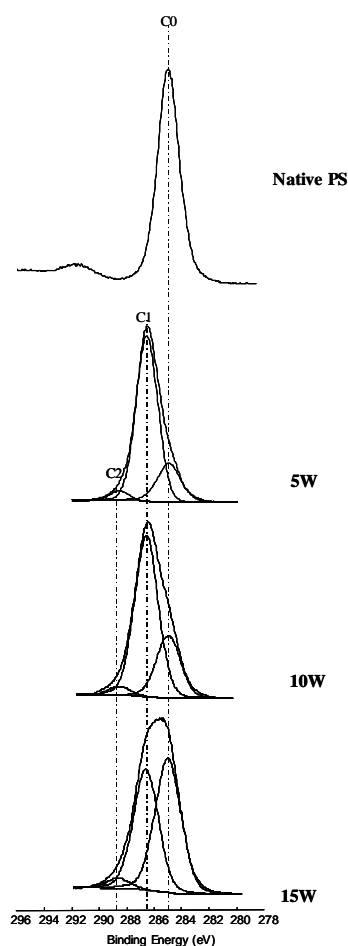
**Table 1:** XPS and WCA results of deposited PEO-like coatings deposited at 5W (PEO5W) 10W (PEO10W) and 15W (PEO15W) of power input.

*et al.* [19] shown that almost 80% PEO character was achieved using TEGDME monomer at low input power values. Since XPS and FT-IR data are in good agreement, it is possible to state that the observed effect is homogeneous through the entire thickness of our coatings.

PEO and PEO-like coatings generally exhibit hydrophilic properties due to the interactions of EO units, and other polar groups eventually present in the coating, with water molecules. We investigated the hydrophilic character of our plasma deposited PEO-like coatings with WCA measurements. As shown in Table 1,  $\theta_{adv}$  decreases from 71°±5 for PEO15W to 56°±5 for PEO5W. A decrease for  $\theta_{rec}$  values was observed as the power input decreases. The higher wettability of coatings deposited at lower power respect to coatings

The effect of the power on the chemical composition of the coatings through their entire thickness was analysed by FT-IR spectroscopy. Interesting variations in the relative intensity of the C-O and C-H characteristic stretching bands were observed for PEO5W, PEO10W and PEO15W films, has shown in Figure 1. A decrease of the C-O band is revealed as the input power increases, while the C-H band increases. This finding evidences the enhanced fragmentation of the monomer in the plasma when the power is increased, thus resulting in coatings with reduced PEO-character. It is worth to mention that the fragmentation of the monomer is labelled by the emission of CO and CH excited species in the plasma, that the fragmentation of the monomer can be easily monitored *in situ* by means of Optical Emission Spectroscopy of CO and CH excited species produced in the plasma from the fragmentation of the monomer. Previous experiments [22] realised in our laboratory shown that the higher the relative density of such species in the plasma (high EO monomer fragmentation), the lower is the resulting PEO character of the coating. XPS data for PEO5W coatings show a C/O ratio very close to 2, which is the stoichiometric C/O ratio of the DEGDME monomer (table 1). The C/O increases with the power, up to the value of about 4 (PEO15W; see table1), loss of oxygen moieties and increased cross-linking, due to the high DEGDME fragmentation in the plasma. As for FT-IR data, XPS results suggest that many intact EO units are present in the PEO5W coating, due to the low monomer fragmentation conditions utilized. Figure 2 shows the C1s spectra of PEO-like coatings soon after the deposition process. The relative importance of the C1 peak (PEO-character) is increased with the power, while the C0 peak increases. Analogous results were shown in the literature, using various ethers as the gas feed. Johnston



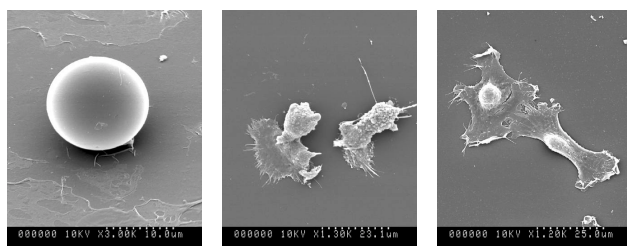


**Figure 2** C1s XPS spectra of PEO-like films obtained from discharges characterised by different power input (5W,10W and 15W). The other experimental parameters (5sccmAr, 0.4sccmDEGDME, 5W, 400mTorr,1h) have been kept constant.

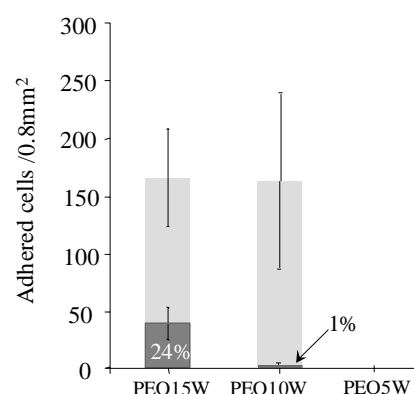
deposited at high power, is likely due to their higher content of EO units and oxygen-containing groups. PEO5W, PEO10W and PEO15W samples were scanned by means of non-contact mode AFM, and  $R_{RMS}$  values were calculated.  $R_{RMS}$  values compatible with roughness at molecular level were measured, ranging from 1.70 nm for PEO5W to 0.55 nm for PEO15W films. Due to the low and similar  $R_{RMS}$  values for all samples tested, roughness was considered not important, respect to features like PEO- and hydrophilic character, in driving the behaviour of cells at the surface of PEO-like coatings.

The results of cell culture experiments were resumed in the histogram of figure 3. After 24 hours of cell culture (light grey), no significant difference in the number of adhered cells was found on PEO10W and PEO15W surfaces, while no cells were found on PEO5W coatings. Nevertheless, a considerable difference in the number of spread cells was observed (dark grey). Considering that spreading of cells generally indicates a certain degree of affinity with the substrate, we can conclude that PEO15W provides the most suitable coating for cell adhesion among our PEO-like coatings, with almost 24% of the adhered cells spread on the surface, while PEO5W can be considered cell-repulsive. SEM investigations of hTERT human fibroblasts grown on different PEO-like coatings show relevant differences in cell morphology, depending on the surface (fig. 4). When the substrate is more suitable for keratinocytes (fibroblasts) adhesion, they exhibit a more spread morphology, and some fillopodia extending across the substrate as shown for fibroblasts seeded on PEO15W. Cells adhering on PEO10W show a lower cell /material interfacing area, and do not appear well spread. Occasionally, very few “adhered” cells (*e.g.* a single cell on the entire area monitored) were observed on cell-repulsive PEO5W samples. In these cases cells show, a perfect globular morphology, that minimizes the membrane/material, thus all possible cell/substrate interactions. The perfectly smooth cellular membrane, differently from cells on PEO10W

samples, witness for the absence of cellular motility, in fact no fillopodia were produced to search a better spot to adhere, probably because only “negative signals” to cell adhesion derive from the surrounding material.



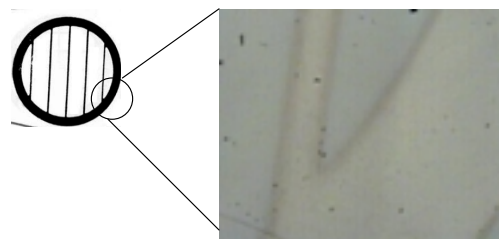
**Figure 4:** SEM images of hTERT fibroblasts cells on PEO5W (left), PEO10W (middle) and PEO15W(right) coatings after 24hrs of incubation. On PEO15W coatings cells are spreader than the ones adhered on PEO10W coatings. When a cell adhere on a PEO5W it appears to minimise cell/material contact.



**Figure 3:** The histograms show the number of adhered cells/area (light grey) and the percentage of spread cells (dark grey) on PEO-like coatings deposited on PS. A significative difference in the number of spread adhered cells is present between PEO15W and PEO10W samples. No cells adhered on PEO5W coatings (Student’s T-test,  $p < 0.05$ ).

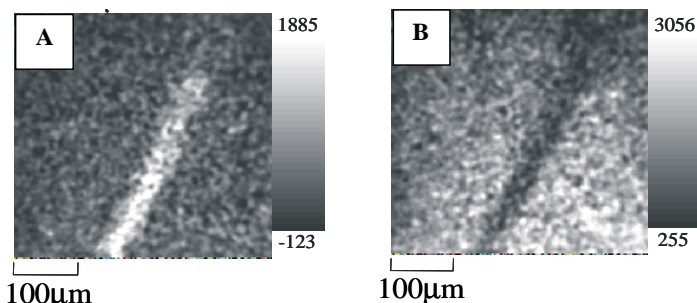
### 3.2 Micro-patterning of PEO-like coatings

Micro-structured samples consisted of a micro-arrangement of zones of native PS or containing PEO-like coatings deposited at higher input power (PEO10W, PEO15W), alternated to the ones deposited at the lowest supplied power (PEO5W) corresponding to the uncovered zones of the substrate by the physical mask, during the patterning procedure. The first step of the chemical-physical characterisation of the patterned substrates consisted in checking the transfer of the pattern on polystyrene by optical microscopy. As shown in figure 5 the pattern transferred on polystyrene is denoted by a slight colour difference between the lines and the large zones of the pattern. On the contrary it was not possible to distinguish the resulting two domains on



**Figure 5:** Optical micro-photo of patterned PEO-like coating on native PS (Goodfellow, UK), by means of G50p physical mask.

the pattern consisted of two different PEO-like zones probably due to the similar refractive indices of the two PEO-like coatings. Chemical characterisation of patterned substrates was realised by means of ESCA analysis. When a large X-ray spot ( $800\mu\text{m} \times 800\mu\text{m}$ ) was utilised, no elements other than carbon and oxygen were detected on the whole patterned zone of the substrate. Chemical differences in the investigated zone of the pattern were highlighted by graded contrast in a chemical map depending on the C1s peak chosen for



**Figure 6** Detecting image of patterned PEO5W on native PS obtained by set the B.E. of the detector at the values corresponding to the C0 (A) and C1 (B) components of C1s signal.

detecting the image (fig.6). When the image was acquired setting on the detector the B.E. of the C0-contribute (fig.6a), a light stripe corresponding to a zone with an higher content of hydroxyl carbon (high C0 percentage) respect to the surrounding zones was highlighted.

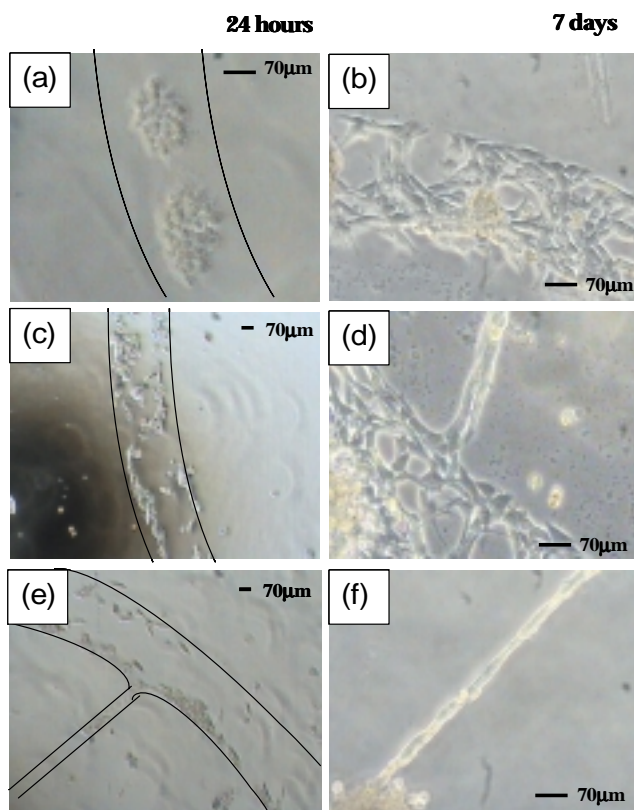
A complementary image was detected when the B.E. set on the detector was corresponding to the C1 component of C1s signal (fig.6b). In the latter case an higher content of hydrocarburic carbon was highlighted with respect to the surrounding zones of the track. These results confirm the transferring of the pattern on PS because the tracks that correspond to the uncovered PS zones of the pattern contain a greater C0 contribution to the C1s signal than the other PEO-like coated surrounding zones.

Micro-probing of different domains by means of  $\mu$ -spot ( $\varnothing 25 \mu\text{m}$ ) X-ray, was employed to collect chemical composition data from very small areas. By appropriately setting the coordinates of the detector, it was possible to investigate within and outside the track shown in Figure 6. The results of the chemical analysis

Position of the spot	C/O	C0	C1	C2
Inside of the stripe	2.7	45.8	50.3	3.9
Outside of the stripe	2.0	15.1	80.4	4.5

**Figure7:** Carbon to Oxygen ratio and percentage of the C1s components acquired by XPS analysis.

attest that a chemical difference characterises the two investigated zones (Fig.7). In fact the percentage of the C1 component is higher outside than inside the track, confirming the results of the image detection experiments. Nevertheless chemical composition inside the stripe results different from the one observed on the native PS in which the contribute of C1 component is negligible ( $\sim 3\%$ ) due to the presence of a certain oxygen impurity. This result makes evidence of a presence of a PEO-like coating also in some points within the stripe. An evidence of the pattern transferring was shown by cell culture tests. 3T3 murine fibroblasts adhere to the “adhesive” tracks (native PS, PEO 10W and PEO 15W ones) respect to PEO5W coated PS (fig. 7). Time lapse optical microscopy observations from 24hrs to 7 days shown that, after 24hrs of incubation, in the uncoated PS zones of the mask only round shaped adhered cells were present, since native PS represents a “bad” substrate for cell adhesion. After about 50hrs of culture was possible to observe spindle shaped cells



**Figure 8:** 3T3 Murine fibroblasts after 24h (left) and 7days (right) on patterned substrates realised by plasma processes. PEO5W coatings were deposited through a G50P mask on native PS (a-b) and PEO10W (c-d), PEO15W (e-f) coatings. As shown, different chemical composition of the cell-adhesive tracks of the pattern appear to induce different cell-morphology on seeded cells after 24hs of cell culture. After 7days arrangement of cells in confluent layer is observed on the adhesive tracks.

especially on the edge of the large boarder and on the tracks of the pattern. On other patterned substrates it was shown that in the first 24hrs most of the adhered cells exhibit a round shape, especially on PS zones. Only cells on the edge of the board, and on the thin lines of the structure, shown a spindle-aligned shape. There was a greater number of spindle shaped and spread cells on PEO15W zones. During the first hours of culture the chemical composition of the adhesive tracks appear to be affective in cell morphology. After 60 hrs of cell culture, the adhered cells were characterised by the same morphology whatever the “adhesive” substrate. The presence of cells inside the “adhesive” tracks of the patterns near the non-fouling PEO-like zones attests for the non-toxicity of this coating.

#### 4. Conclusions

Drastically different chemical characteristics results on PEO-like coatings that were plasma-deposited at different RF power input. A very high PEO-character can be obtained at very low power, which results in good cell repulsive PEO-like coatings. The chemical composition of PEO-like coatings appears much more important than roughness in controlling cell adhesion. Micro-domains of PEO-like coatings of different composition can be assembled at the surface of PS and other materials

by means of plasma deposition processes run through physical masks. Cells seeded on such patterned substrates adhere only on PEO-like coatings deposited in high-fragmentation conditions, while do not on coatings characterized by an high PEO character. This micro-patterning technique is quite simple, and could be utilized, in principle, for different biomedical applications such as bio-MEMS, tissue engineering and biosensors. Large areas could be patterned with this technique, in a cost effective way.

#### Acknowledgments

Dr. Christian Oehr and Dr. Michael Müller of the Fraunhofer Institute for Interfacial Engineering and Biotechnology, Stuttgart, Germany, are gratefully acknowledged for their assistance in  $\mu$ -spot XPS facilities. The COST 527 Action “Plasma polymers and related materials” is acknowledged for funding some analytical characterisation of the surface at the Fraunhofer Institute. Prof. A. Curtis and the University of Glasgow are gratefully acknowledged for SEM analysis. The 5th FP project “Nanobiotechnology and medicine” (NANOMED) is finally acknowledged for its financial support.

#### References

- [1] J. H. Griesser, C. R. Chatelier, T. R. Gengebach, G. Johnson, J. G. Steele; *J. Biomater. Sci. Polymer Edn.* 5-6 (1994) 531-554 [2] A. Curtis, M. Riehle; *Phys. Med. Biol.* 46 (2001) R47-R65 [3] B. W. Callen, R. N. S. Sodhi, R. M. Shelton and J. E. Davies, *J. Biomed. Mater. Res.*, 27 (1993) 851. [4] A. S. G. Curtis, J. V. Forrester and P. Clark, *J. Cell. Sci.*, 86 (1986) 9. [5] M. Malmsten (Ed.), *Biopolymers at Interfaces*, Surfactant Science Series, New York (1998) [6] M. Malmsten, B. Lassen, K. Holmberg, V. Thomas, G. Quash, *J. Colloidal Interface Sci.* 177 (1996) 70 [7] H. M. Patel, *Crit. Rev. Ther. Drug. Carrier Syst.*, 9 (1992) 39 [8] C. M. Nelson, S. Raghavan, J. L. Tan, C. S. Chen; *Langmuir*, 19 (2003) 1493 and ref. therein [9] C. Nelson, C. S. Chen, *FEBS Lett.* 514 (2002) 238 [10] Y. Luk, M. Kato, M. Mrksich, *Langmuir*; 16 (2000) 9604 [11] E. Ostuni, R. Kane, C. S. Chen, D. E. Ingber, G. M. Whitesides; *Langmuir*, 16 (2000) 7811 [12] C. H. Thomas, J.-B. Lhoest, D. G. Castner, C. D. McFarland, K. E. Healy; *J. Biomech. Eng.* 121 (1999) 40 [13] V. A. Liu, W. E. Jastromb, S. N. Bhatia, *J. Biomed. Mater. Res.* 60 (2002) 126 [14] M. Morra in: *Water in Biomaterials Surface Science*, M. Morra (Ed.); John Wiley and Sons, LTD, 12 (2001) 307 [15] P. Kingshott, H. J. Griesser; *Current Opinion in Solid State and Mater. Sci.* 4 (1999) 403 [16] J. H. Lee, J. Kopecek, J. Andrade; *ACS Polym. Mater. Sci. Eng.*, 57 (1987) [17] G. P. Lopez, B. D. Ratner, C. D. Tidwell, C. L. Haycox, R. J. Rapoza, T. A. Horbett; *J. Biomed. Mat. Res.* 26 (1992) 415 [18] R. d'Agostino, L. Martinu, V. Pische; *Plasma Chem. Plasma Proc.*, 11 (1991) 1 [19] E. E. Johnston, B. D. Ratner, J. D. Bryers in: *Plasma Processing of Polymers*; R. d'Agostino P. Favia, F. Fracassi eds., NATO ASI Series E: Applied Sciences, 346, Kluwer Acad. Publ. (1997) [20] Y. J. Wu, A. J. Griggs, J. S. Jen, S. Monolache, F. S. Denes, R. B. Timmons; *Plasmas and Polymers*, 6-3 (2001) 123-191 [21] F. Palumbo, P. Favia, M. Vulpio, R. d'Agostino; *Plasmas and Polymers*, 6-3 (2001) 163 [22] T. Matsuda, K. Inoue, T. Sugawara; *Trans. Am. Soc. Artif. Inter. Organs* 36 (1990) M559

# PLASMA CHARACTERIZATION IN CONNECTION WITH THE CHARACTERISTICS OF PULSED MPACVD DEPOSITED DIAMOND FILMS.

T. Lamara, M. Belmahi, G. Henrion, J. Bougdira, L. Depouques, M. Remy

*Lab. Physique des Milieux Ionisés et Applications – CNRS UMR 7040  
Université Henri Poincaré – BP 239 – 54506 VANDOEUVRE les NANCY cedex (France)*

Previous works [1, 2] showed that using a pulsed plasma greatly modifies the quality and the growth rate of diamond films synthesized by means of a microwave plasma assisted chemical vapour deposition (MPACVD) process. In particular, the importance of the right choice of the plasma pulse and afterglow duration was pointed out. Nevertheless, the optimum value of the on- and off-time is strongly depends on the plasma reactor configuration and the working conditions as well. It is thus necessary to know the influence of the power pulse duration and repetition rate on the plasma behaviour. To achieve this, the time- and space-resolved plasma characterization can give valuable insights into the variation of the reactive species concentration which may be related to the evolution observed on the diamond layer properties.

The presented results deal with the study of a high power (up to 6 kW)  $H_2/CH_4$  pulsed MPACVD reactor in order to improve the knowledge of the fundamental processes occurring in such a discharge which govern the kinetics of reactive species during both the discharge phase and the afterglow.

The radiative states are probed by means of emission spectroscopy, while laser induced fluorescence and the double pulse technique [3, 4] are used to determine and to study the behaviour of the ground states of the reactive species. We pay a particular attention to H atom,  $CH_x$ - and  $C_2H_y$  radicals which are well known to be responsible of the etching of graphite, the deposition of diamond and of graphite respectively. As the addition of a small amount of nitrogen in the gas mixture showed an improvement of the deposited layer quality [5], particular studies of N atom and CN- radical are performed for a better understanding of the role of nitrogen on the diamond deposition process.

The results of plasma characterization are explained in terms of the kinetic processes occurring in the plasma bulk and in the close vicinity of the substrate surface, and are correlated with the analyses of the synthesized diamond layers. A comparison of similar studies performed with two different reactor geometries and different working conditions points out the necessity of having a good knowledge of the species density and behaviour in order to optimise and better control the process.

## References.

- [1] L. de Pouques, PhD thesis, Université Henri Poincaré, Nancy 1, (2000)
- [2] T. Lamara, M. Belmahi, J. Bougdira, F. Bénédic, G. Henrion, M. Rémy  
8th Int. Conf. Plasma Surface Engineering (PSE'2002), Garmisch-Partenkirchen, (2002)
- [3] A. Bouchoule and P. Ranson, J. Vac. Sci. Technol. **A9** (1991) 317
- [4] P. Veis and G. Cernogora, Czech. J. Phys. **48** (1998) 75
- [5] F. Bénédic, PhD thesis, Université Henri Poincaré, Nancy 1, (2000)

# PLASMA STERILIZATION: FEASIBILITY AND MECHANISMS

J. Feichtinger<sup>1\*</sup>, H. Hägele<sup>1</sup>, J. Rauschnabel<sup>1</sup>, J. Schneider<sup>2</sup>, A. Schulz<sup>2</sup>,  
K.M. Baumgärtner<sup>3</sup>, H. Muegge<sup>3</sup>, P. Awakowicz<sup>4</sup>, P. Messerer<sup>4</sup>, O. Franken<sup>5</sup>,  
M. Heise<sup>6</sup>, W. Neff<sup>6</sup>, P. Muranyi<sup>7</sup>, J. Wunderlich<sup>7</sup>

<sup>1</sup> Robert Bosch GmbH, Stuttgart, Germany

<sup>2</sup> Institute of Plasma Research, University of Stuttgart, Stuttgart, Germany

<sup>3</sup> Muegge Electronic GmbH, Reichelsheim, Germany

<sup>4</sup> Plasma Group at the Chair of Physics for Electrotechnology,  
University of Technology, Munich, Germany

<sup>5</sup> Lehrstuhl für Lasertechnik, RWTH Aachen, Aachen, Germany

<sup>6</sup> Fraunhofer Institut Lasertechnik, Aachen, Germany

<sup>7</sup> Fraunhofer Institut Verfahrenstechnik und Verpackung, Freising, Germany

\* corresponding author, e-mail: jochen.feichtinger@de.bosch.com

State of the art sterilization applications use dry heat, hot steam, chemicals or UV light as sterilization agents. The article shows, that the sterilization with plasma processes is an alternative sterilization method with several advantages.

Several types of plasma sources were used for the sterilization process. The effect of low-pressure plasmas using microwaves or rf-power for excitation as well as atmospheric pressure plasmas based on a dielectric barrier discharge were investigated. Compared to the state of the art sterilization methods the plasma processes lead to low thermal loads of the sterilized materials and no dangerous or toxic chemicals have to be used. A further advantage are the fast treatment times of only a few seconds to reach six orders of spore reduction.

All plasma sources were used to treat test substrates with a defined initial contamination of approximately  $10^6$  spores. Therefore, the four test spores *Bacillus subtilis*, *Aspergillus niger*, *Bacillus stearothermophilus* and *Saccharomyces cerevisiae* were sprayed homogeneously on the test samples. As relevant substrates for food packaging applications PET foils and bottles were used. After the sterilization treatment in the different plasma sources the surviving colony forming units were counted.

Presented are spore reduction kinetics for all test spores obtained with the different plasma sources. After proving the feasibility of plasma sterilization the consortium focused on the study of the main spore reduction mechanisms and the effects of the plasma treatment on the properties of the packaging materials.

The presentation summarizes the results of the project “Fundamental study of plasma processes for the sterilization of food packaging materials” founded by the German Ministry of Education and Research.



# Structure and Mechanical Properties of VPS Ti-6Al-4V

H.R. Salimijazi<sup>1</sup>, T.W. Coyle<sup>1</sup>, J. Mostaghimi<sup>1</sup>, and L. Leblanc<sup>2</sup>

<sup>1</sup> Centre for Advanced Coating Technologies, University of Toronto, Toronto, Canada

<sup>2</sup> PyroGenesis Inc., Montreal, Canada

## Abstract

The vacuum plasma spray (VPS) process is capable of depositing even reactive metals and alloys such as titanium alloys with little oxidation. The extension of this process to form near net shape structural components requires improvements in the structure and mechanical properties of the deposited material. In this study the internal microstructure of individual splats, the chemical and phase composition, and the mechanical properties of Ti-6Al-4V deposited by VPS were studied. Both as-deposited material and material subjected to several post-deposition heat treatment schedules were examined.

## 1. Introduction

The vacuum plasma spray (VPS) process has been used for over 20 years to deposit coatings on a variety of substrates in order to improve their surface properties. Recently, vacuum plasma spray forming (VPSF) has emerged as one of the leading technologies for manufacturing near-net shape components, capable of forming complicated shapes with multi-layered and composite structures.

Ti-6Al-4V alloys are widely used in the aerospace, chemical, biomedical, and automotive industries because of good stability at high temperature, high specific strength, especially for high temperature operation, and high corrosion resistance in many corrosive media [1-4]. In this study VPSF is used to manufacture near-net shape structures of Ti-6Al-4V alloy.

Since the quality requirements for sprayed structural components are different than for coatings, the standard characterization tests used for coating structures do not fully address the microstructure requirements which must be met to assure acceptable properties. As with any structural material, metallurgical considerations such as grain size, phase composition, phase distribution, etc. must be considered for the VPSF structures. Because of the absence of convective heat transfer from the substrate or prior deposition and more interaction between the plasma jet and substrate, the VPSF deposit is maintained at a high temperature (up to 1000 °C) during the process. This results in self annealing, recrystallization, polygonization, and stress relief of within the structure and therefore enhances intersplat bonding relative to air plasma sprayed materials [5]. In order to study solidification during VPS, researchers have examined a number of nickel-base alloys [1-5]. Their results show that a rapid solidification of the molten droplets occurs during deposition in a low-pressure environment, with the deposits achieving nearly theoretical density. They reported that even in the case of heating the substrate up to 900 °C during the deposition, the cooling rates were likely equivalent to that of rapid solidification processes ( $10^6$ - $10^7$  K/s). Several studies have reported particle temperature, velocity and solidification during VPS. P.S. Grant et al. [1,2] have developed a numerical model to calculate the distribution of plasma gas temperature, enthalpy, and velocity under a range of plasma current, gas flow rate, and chamber pressure for Ti particles in VPS. S. Sampath and H. Herman [5] have reviewed solidification parameters, morphological stabilities, and cooling rates for Ni, Al, and Mo using various techniques such as dendrite arm spacing and splat thickness correlation. They reported cooling rate on the order of  $10^7$  to  $10^8$  K/s for splat solidification during VPS. Literature show that the splat cooling rates are depend upon not only substrate or prior deposit temperature but also substrate thermal conductivity. The deposition on the low thermal conductivity substrate or prior coating as well as high temperature of substrate show an order of magnitude lower cooling rates as compare to the lower substrate temperature and higher thermal conductivity as well [5].

## 2. Experimental procedure

Various powder sizes of standard feedstock Ti-6Al-4V powders (Table 1) produced by PyroGenesis Inc. [13] were used for vacuum plasma spraying. An F4VB gun from Plasma-Technik, Switzerland, was used in a low pressure controlled atmosphere chamber to deposit the material. The temperature of the mandrel as well as prior deposits was kept at approximately 750°C during the spraying. Spray conditions and deposition procedure were described elsewhere [12, 13].

The oxygen content of the powders was determined by carrier hot gas extraction (LECO). Chemical compositions of the alloy elements in the powders and as-sprayed structures were obtained by atomic absorption spectroscopy. Two techniques of porosity measurement were used, mercury intrusion porosimetry

(MIP) and image analysis (IA) on cross sections by optical and scanning electron microscopy. A Nikon Measurescope-11 was used for optical microscopy and scanning electron microscopy (SEM) was conducted on a Hitachi S-4500 to observe the structures. Two types of specimens were prepared from the deposit for transmission electron microscopy (TEM); cross sections and lateral sections (parallel to surface). X-ray diffractometry was performed by a Siemens D5000 Diffractometer System, using a high power Cu-K $\alpha$  source operating at 50kV/35mA over an angular range of 30°<2 $\theta$ <90°. Surface hardness measurements were conducted using a Vickers indenter in a Zwick hardness tester under a load of 2000 gf.

Table 1. Chemical composition of Ti-6Al-4V powders

Element	Composition, wt%			Element	Composition, PPM		
	25-45 $\mu\text{m}$	45-63 $\mu\text{m}$	63-75 $\mu\text{m}$		25-45 $\mu\text{m}$	45-63 $\mu\text{m}$	63-75 $\mu\text{m}$
Al	5.94	6.02	5.87	C	240	<100	210
V	3.95	3.98	3.99	O <sub>2</sub>	980	820	750
Fe	0.084	0.086	0.082	H <sub>2</sub>	27	10	15
Ni	0.016	0.017	0.017	N <sub>2</sub>	80	70	80
Cr	0.019	0.019	0.018				
Ti	Bal.	Bal.	Bal.				

### 3. Results and Discussion

#### *Physical and Mechanical Properties*

The plasma sprayed deposits consist of billions of individual splats which are connected together by mechanical and chemical bonding. The inter-lamellae boundaries are also associated with significant porosity which depends on the thermal spray process parameters. Therefore, the physical and mechanical properties of such deposits are mainly dependent on the cohesive strength between the splats, the size and morphology of the porosity, the cracks and defects, and less on the microstructure within the splats themselves. The cooling and solidification rates for a plasma sprayed structure depend on the solidification condition of individual splats as well as substrate conditions. Chemical compositions of the as-spray structures using various sizes of initial powders are shown in Table 2.

Table 2. Chemical composition of as-sprayed Ti-6Al-4V alloy.

Element	Composition, wt%			Element	Composition, PPM		
	25-45 $\mu\text{m}$	45-63 $\mu\text{m}$	63-75 $\mu\text{m}$		25-45 $\mu\text{m}$	45-63 $\mu\text{m}$	63-75 $\mu\text{m}$
Al	4.6	5.28	5.7	C	160	<100	170
V	4.25	4.02	4.16	O <sub>2</sub>	1380	1110	1260
Fe	0.092	0.082	0.07	H <sub>2</sub>	1030	840	670
Ni	0.02	0.017	0.011	N <sub>2</sub>	1290	750	850
Cr	0.014	0.016	0.015				
Ti	Bal.	Bal.	Bal.				

Decomposition of the initial powders during the plasma process causes a decrease in the aluminum content in the as-sprayed samples. Because hydrogen is used as a part of the plasma gas and leakage of oxygen into the system, a pick up of hydrogen and oxygen can be observed. As Fig. 1 illustrates, a line scan through about 70  $\mu\text{m}$  of the cross section of the VPSF structure, which consists of about 8 individual splats, verifies the very uniform distribution of alloy elements even in the lamellae boundaries. There are some variations of the alloy elements such as Al in the pores which are located across the lamellae boundaries as well as within the splats.

The measurement of porosity level by IA shows that the as-sprayed structures have an average porosity of 3%. Moreover, IA shows that the porosity slightly increases with increasing the initial powder size. However, the MIP results show that the amount of open porosity is varies slightly with the different powder sizes: 0.7%, 1.8%, and 0.08% for fine, medium and coarse powder size respectively.

Hardness measurements on cross sections indicate the inter-splat strength within the structure and are reflective of the intersplat boundary strength, phases present, and porosity distribution and content. The hardness data are 271 HV, 285 HV, and 301 HV for fine, medium and coarse powder size respectively.

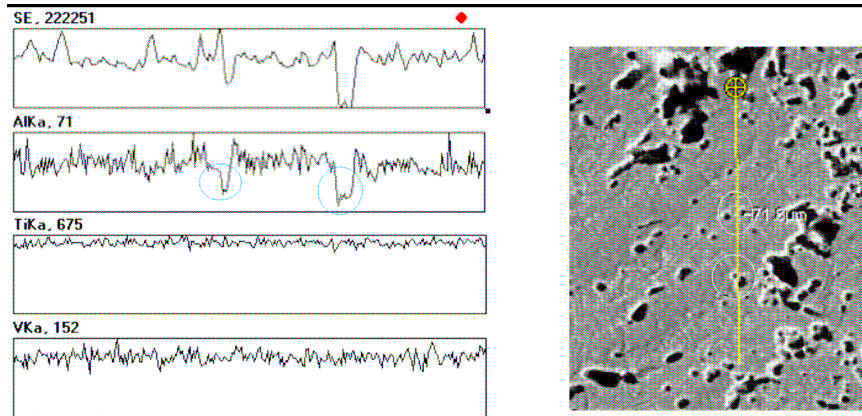


Fig. 1: Line scan from cross section of as-sprayed Ti-6Al-4V alloy.

Tensile strength tests confirm that the tensile strength and yield strength of materials deposited using the two larger particle size distributions were significantly higher than the material deposited using the smallest particle size powder (880-900 MPa). Results show that although the value of the tensile strength for the samples deposited using the two largest particle size were close to the conventional Ti-6Al-4V specimens but the ductility was as low as 1%, compare to 10-15% in the conventional materials [13].

### **Microstructure Formation**

Microstructural formation during VPSF depends primarily on the solidification history of the individual splats as well as their position in the deposit. Recent models confirm that columnar grain structures are expected in the central region of the splat [5]. Figure 2 shows typical scanning electron microscope (SEM) micrographs of etched, as-deposited VPSF Ti-6Al-4V alloy. The micrographs show clearly the columnar grain structures within the centre core of the splat oriented in the direction of heat transfer into the prior splats. The higher magnification image shows the presence of two phases. The gray regions are the  $\alpha'$  lathes, separated by small white regions of remnant  $\beta$  phase. The scale of the structure is quite fine, with the width of the  $\alpha'$  lathes on the order of 0.5  $\mu\text{m}$ . The micrographs also indicate fusion or microwelding areas across three individual splats which improve the cohesive strength of the structure, necessary in order to form a sufficient thickness of free standing components. Moreover, some internal porosity within and between splats can be observed. In the lower magnification image shown in Fig. 3b, a few isolated larger pores, 10-15  $\mu\text{m}$  in diameter, can be seen. The lamellae boundaries are not as distinct as in APS coatings. The high temperature of particles during the deposition due to the high temperature of the flame as well as greater interaction between the powders and the flame leads to some interdiffusion and recrystallization during the deposition. On the other hand, there are some unmelted and partially melted particles in the as-sprayed structure, especially using the course powder size (Fig. 3a).

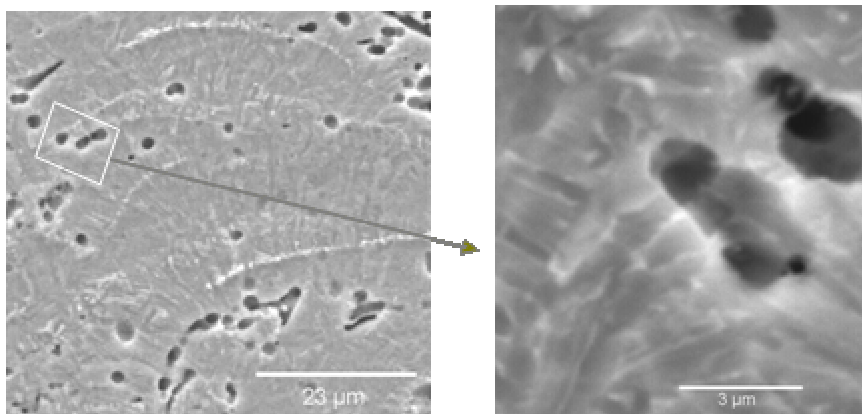


Fig. 2: SEM micrographs from cross section of the VPSF Ti-6Al-4V alloy.



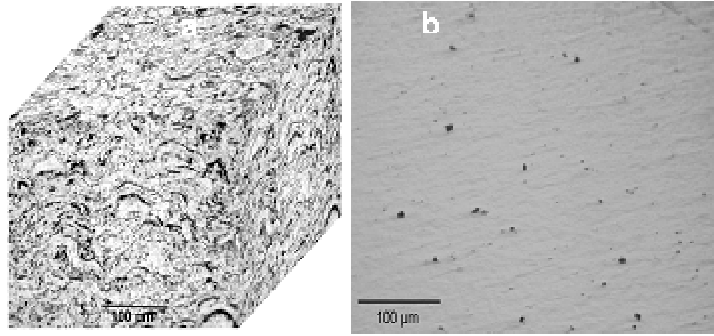


Fig. 3: Optical micrographs from cross section of the VPSF Ti-6Al-4V alloy.  
a) Etched, b) Unetched

The most frequently observed structures in the TEM examinations of the lateral and cross sections of the as-sprayed samples were irregularly shaped fine equiaxed grains and platelet structures (Fig. 4). The width of the platelets is between 200 and 800nm. The grain size is in the range of 100 nm to 1 µm. Polyganized cells are also observed within the equiaxed grains, indicating recrystallization during the deposition. It is generally accepted that the fine equiaxed grains were found as a result of self annealing and recrystallization of the deposit during the spraying.

The X-ray diffraction pattern of the as-sprayed sample is plotted in Fig. 5 compared with the calculated reference patterns of both  $\alpha$ -hexagonal and  $\beta$ -bcc Ti. A closer examination of the {002} reflection of the main phase reveals a shoulder due to some overlapping. Its position, marked with an arrow, matches well with the strongest reflection {110} of  $\beta$ -Ti. A detailed profile fitting analysis of this region of the pattern confirms the presence of  $\beta$ -Ti as a minor phase in the sample.

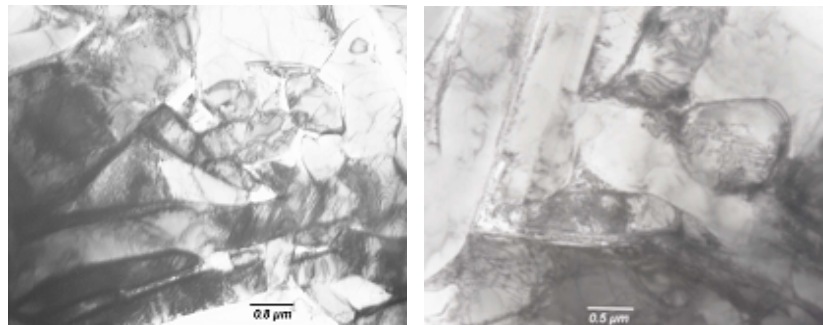


Fig. 4: TEM micrograph from lamellae and equiaxed grains in the VPSF Ti-6Al-4V alloy

A quantitative analysis reveals approximately 90 % wt of  $\alpha'$ -Ti against less than 10 % wt. of  $\beta$ -Ti. The main phase,  $\alpha'$ -Ti, has lattice parameters smaller than that of the  $\alpha$ -Ti reference. The unit cell least square refinement yields the lattice parameters as the following:  $a = 2.932(5) \text{ \AA}$ ,  $c = 4.675(9) \text{ \AA}$ ,  $V = 34.8(9) \text{ \AA}^3$ . All reflections are quite broadened. This is consistent with the interpretation that in the as-sprayed structure the major phase is a meta-stable  $\alpha'$ -Ti, which forms due to a martensitic transformation during cooling.

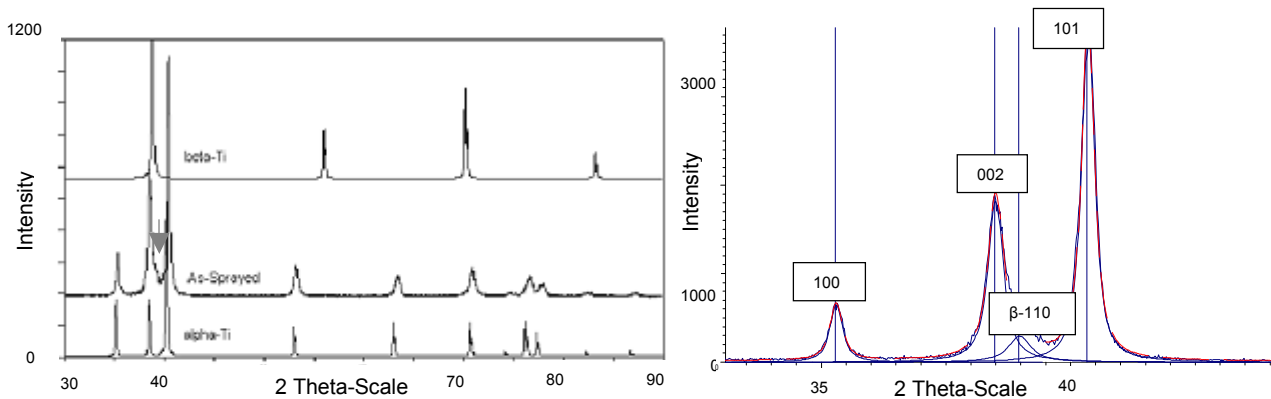


Fig. 5: XRD pattern of as-sprayed Ti-6Al-4V alloy. The position of an overlapped peak that could belong to the main 110 reflection of bcc  $\beta$ -Ti is marked with an arrow.

### Post-Deposition Heat Treatments

Given the as-sprayed microstructure and low elongation of the materials fabricated by VPSF, post deposition heat treatments should increase the cohesion across the splat boundaries and decrease the level of porosity between the splats. Simultaneously, the decomposition of the metastable  $\alpha'$  must be controlled to yield a desirable stable phase assemblage. The microstructure of the as-sprayed deposit is different than conventionally processed materials; therefore the response of the material to heat treatments is different than for conventionally processed Ti-6Al-4V alloy. The first aim in heat treatment is to enhance the cohesion between the splats boundaries as well to reduce the level of porosity in the as-sprayed structure. Based on the typical heat treatments used for conventional Ti-6Al-4V alloys, two modified heat treatment cycles were applied to the as-sprayed structure. Details of the heat treatment schedules are given in Fig. 6.

The first heat treatment was similar to mill annealing; cyclic heating in the  $\alpha$  plus  $\beta$  region, water quenching followed by tempering at 520 °C. No evidence of the splat structure could be seen after the heat treatment. The microstructure formed (Fig. 7) consists of recrystallized fine equiaxed  $\alpha$ -grains (light) with decomposed martensite regions (dark) between the  $\alpha$ -grains containing a vanadium enriched  $\beta$  phase due to the high cooling rate and aging. Subsequent tempering causes some platelet formation from the martensite structures. The average  $\alpha$ -grain size is about 4-5  $\mu\text{m}$  and porosity remains as low as 0.3-0.5%. The measured hardness of the structure before and after tempering was 266 HV and 320 HV respectively which is close to that reported for completely acicular microstructure in cast parts [9].

The second heat treatment cycle (duplex) was carried out in order to obtain uniform acicular  $\alpha$  grain structure. Again, after the heat treatment, due to diffusion of the alloy elements at high temperature, the original splat structure could not be seen. A uniform cross-hatched acicular  $\alpha$  structure was obtained as shown in figure 8. A short hold slightly below the  $\beta$ -transus temperature ( $\sim 980$  °C) causes nucleation of  $\alpha$  grains on the  $\beta$  grain boundaries while avoiding formation of a continuous  $\alpha_{\text{GB}}$  phase. On quenching from 700°C, the vanadium enriched inter-lamellae  $\beta$  phase regions transformed to the  $\alpha'$  or soft  $\alpha''$  martensite phases [8]. After the tempering, the martensite changes to a very fine  $\alpha$  plus  $\beta$  structure.

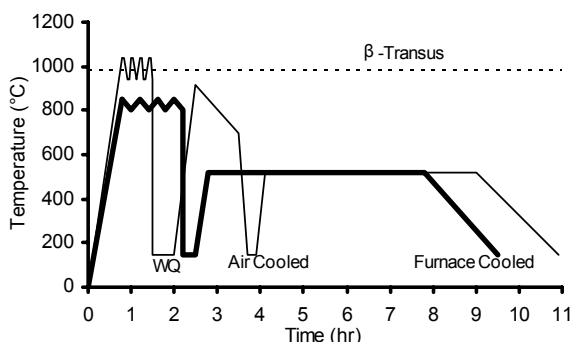


Fig. 6: Heat treatment cycles for VPSF Ti-6Al-4V alloy.

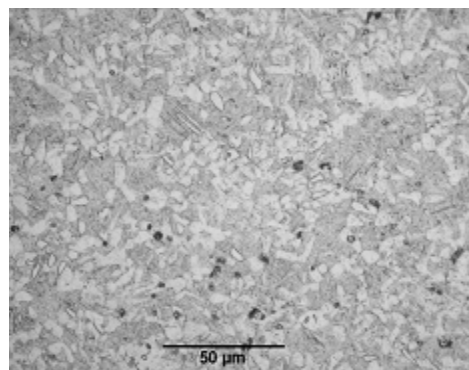


Fig. 7: Optical micrographs from cross section of mill annealed VPSF Ti-6Al-4V alloy (bi-modal).

Therefore the final microstructure consists of a fine platelet  $\alpha$  structure with an average prior  $\beta$  grain size about 20  $\mu\text{m}$ . The measured hardness of the structure before and after tempering was 270 HV and 300 HV respectively which is close to that reported for completely acicular microstructure in cast parts [9].

X-ray diffraction patterns of the heat treated structures show only hexagonal  $\alpha$ -Ti phase. The unit cell least square refinement yields the lattice parameters as the following:  $a = 2.912(2)$  Å,  $c = 4.664(4)$  Å, and  $V = 34.4(4)$  Å<sup>3</sup>. Regarding the crystallographic characterization of the sample, it appears that the unit cell shrank about 2.8 vol. % due to solid solution effects. Energy dispersive spectroscopy (EDS) reveals an increase in vanadium content in the regions between the  $\alpha$  platelets compared with the grain: 6.4% and 2.7% respectively. As V is a strong  $\beta$  stabilizer, this correlates with the presence of decomposed martensite in these regions.

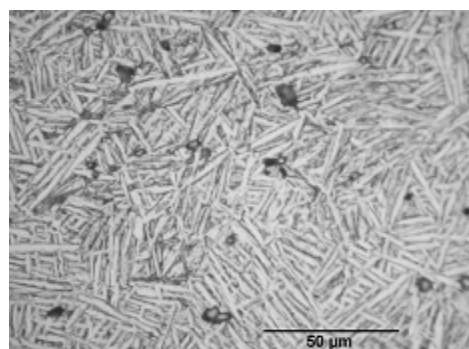


Fig. 8: Optical micrographs from cross section of duplex treatment of VPSF Ti-6Al-4V alloy.

Energy dispersive spectroscopy (EDS) reveals an increase in vanadium content in the regions between the  $\alpha$  platelets compared with the grain: 6.4% and 2.7% respectively. As V is a strong  $\beta$  stabilizer, this correlates with the presence of decomposed martensite in these regions.

The results of tensile testing indicated that the ductility of the materials were significantly improved (up to 5.8%) by both heat treatments. Duplex heat treated samples have higher ductility than that of bi-modal structures. The ultimate tensile strength of materials deposited with the smallest particle size distribution were increased from 690 MPa to approximately 880 MPa by the heat treatments while the tensile strength of materials deposited using the two larger particle sizes increased slightly from 860 MPa to approximately 900 MPa. Other heat treatment cycles have been described elsewhere [12, 13], the most successful of which yielded similar tensile strengths with elongation approaching 10%.

#### 4. Conclusion

As-sprayed microstructure and the response of the sprayed structure to the heat treatment cycles were discussed. The as-sprayed structure of material deposited by VPSF consists of approximately 90%  $\alpha'$  plus residual  $\beta$  with a porosity level of 3-5%, located primarily at splat boundaries and adjacent to unmelted particles. The splat structure of the deposits was eliminated by heat treatments, and the porosity was reduced to below 1%. Eliminating the splat structure characteristic of plasma sprayed deposits and thereby removing the relatively weak splat boundary regions and reducing the porosity located at the boundaries is the most important consideration in improving the ductility of these materials. Two heat treated structures were developed: (1) fine equiaxed  $\alpha$ -grains (light) with decomposed martensite regions (dark) between the  $\alpha$ -grains, and (2) a fine  $\alpha$  platelet structure. The tensile strength and ductility of the materials was significantly improved over the as-deposited case. The tensile strength of the two types of structures were similar, while the platelet structure exhibited slightly higher elongation of nearly 5%.

#### References

- [1] P. S. Grant et al., "Modeling and experimental analysis of vacuum plasma spraying part I: Prediction of initial plasma properties at plasma gun exit", *Modeling Simul. Mater. Sci. Eng.* 8 (2000).
- [2] P. S. Grant et al., "Modeling and experimental analysis of vacuum plasma spraying part II: prediction of temperatures and velocities of plasma gases and Ti particles in a plasma jet", *Modeling Simul. Mater. Sci. Eng.* 8 (2000).
- [3] T. McKechnie, "Near-net shape spray forming-metals", *Thermal spray proceeding 2000*, Alabama, USA (2000).
- [4] R. P. Krepski, "Thermal spray coating applications in the chemical process industries", MTI publication No. 42, Georgetown, PA, USA (1993).
- [5] S. Sampath and H. Herman, "Rapid solidification and microstructure development during plasma spray deposition", *Journal of Thermal Spray Technology*, Vol. 5(4) (1996).
- [6] Cullity, B.D., 1978, *Elements of X-ray Diffraction*, Addison-Wesley Publ. Inc
- [7] H.D. Steffens, M. Dvork, "Structure and electrochemical behavior of vacuum plasma sprayed titanium and plasma beam alloyed titanium coatings", ITSC (1990).
- [8] *Materials Properties Handbook: Titanium Alloys*, S. Lampman, ASM International, Metals Park, Ohio, USA (1998).
- [9] K. OI, H. Terashima, and K. Suzuki, "Control of Microstructure in Ti-6Al-4V Castparts", *Metallurgy and Technology of Practical Titanium Alloys*, S. Fujishiro, D. Eylon, and T. Kishi, TMS (1994).
- [10] *Metals Handbook Ninth Edition, Fractography*, K. Mills, ASM International, Metals Park, Ohio, USA, 12 (1987).
- [11] J.A. Hines, J.O. Peters, and G. Lutjering, "Microcrack propagation in Ti-6Al-4V alloys", *Fatigue behavior of titanium alloys*, *Proceeding of an international symposium*, TMS, Warrendale, Pennsylvania, USA (1999).
- [12] Hamid R. Salimijai, T.W. Coyle, J. Mostaghimi, and L. Leblanc, "Microstructural formation of VPSF Ti-6Al-4V alloys", ITSC, Florida, USA (2003).
- [13] L. Leblanc, Hamid R. Salimijazi, J. Mostaghimi, and T.W. Coyle, "On vacuum plasma spray forming of Ti-6Al-4V", ITSC, Florida, USA (2003).
- [14] R. Wood and P. A. Russo, "Heat treatment of titanium alloys", *Advanced in the science and technology of titanium alloy processing* (1997).
- [15] R.R. Boyer et al., "Heat treatment of titanium alloys: overview", *Advanced in the science and technology of titanium alloy processing* (1997).

# Pulsed positive corona discharge in point-to-plate configuration for VOC's decomposition

M. Magureanu, N. B. Mandache, C. Ruset

*National Institute for Lasers, Plasma and Radiation Physics,  
Str. Atomistilor, 111, 76900, Bucharest, Romania*

## Abstract

Experimental investigations of a pulsed corona discharge with positive polarity, in multipoint-to-plate configuration are reported. The aim of this experiment is to remove small amounts of volatile organic compounds, in particular toluene, from contaminated air streams. When the discharge was operated at voltages up to 28 kV, the discharge current was up to 0.5 A, the pulse frequency was approximately 450 Hz and the energy per pulse was 1.2 mJ. Under these conditions, a conversion rate of toluene up to 43% was obtained.

## 1. Introduction

Air pollution by volatile organic compounds (VOC's) enhances the greenhouse effect and contributes to the destruction of the ozone layer. Moreover, some of the VOC's are toxic and are responsible for the formation of photochemical smog.

Conventional VOC's removal techniques are thermal and catalytic oxidation and carbon adsorption. Thermal oxidation destroys the organic compounds in contaminated air streams at high operating temperatures (700-900 °C). The addition of a catalyst (noble metals: Pt, Pd, or metal oxides of Ni, Cu, Mg) accelerates the rate of oxidation on the catalyst surface and enables the reaction to occur at a much lower temperatures (300-600 °C). This technique was reported to effectively destroy both non-halogenated and several halogenated VOC's. However, catalyst poisoning by sulfur, chlorinated compounds or heavy particulate loadings present in the gas stream limit the performances due to catalyst deactivation.

In the carbon adsorption technique the pollutants are removed from the air stream by physical adsorption onto activated carbon grains. However, this method is not recommendable to remove high contaminant concentrations and there are several factors that affect the adsorption, including temperature, type of carbon and of contaminant, and residence time. In addition, the spent carbon must be disposed of and the adsorbed contaminants must be destroyed. This often involves thermal treatment, which increase the cost of the air cleaning process.

Non-thermal, atmospheric pressure plasmas have been subject to extensive investigation, both from a theoretical point of view [1-3] and in connection to their numerous applications [4]. With regard to pollution control and gas cleaning, the interest in corona discharges increased considerably in the past two decades. Most of the studies were focused on removal of nitrogen oxides and sulfur dioxide from mobile gas exhaust and other combustion sources [5,6]. More recently, low concentration volatile organic compounds emission control receives also considerable interest [7,8]. Despite these investigations, the corona discharges, as well as the chemical processes occurring in the plasma, are not completely understood, therefore being still studied both experimentally and theoretically.

The treatment of VOC's emissions by using a non-thermal plasma represents an attractive alternative to conventional removal techniques, since it can be used at high flow rates for various organic compounds, including chlorinated hydrocarbons, and it has little operation problems when SO<sub>2</sub> and/or particulate material are also present in the gas stream. Non-equilibrium discharges have the essential advantage of using the available energy selectively for generating high energy electrons, while the gas remains cold, close to room temperature. The energetic electrons excite and dissociate the background gas molecules, creating chemically active species (radicals, ions), that in turn lead to the decomposition of pollutant compounds.

The present paper reports investigations of a pulsed corona discharge with positive polarity in multipoint-to-plate geometry, with the aim of obtaining an efficient decomposition of VOC's, in particular toluene. The current-voltage characteristics were studied and the input energy per pulse was determined. Preliminary experiments were performed for a mixture of air and toluene and the toluene removal in the presence of the corona discharge was monitored by mass spectrometry.

## 2. Experimental set-up

The electrical circuit and the electrode configuration are shown in Figure 1.

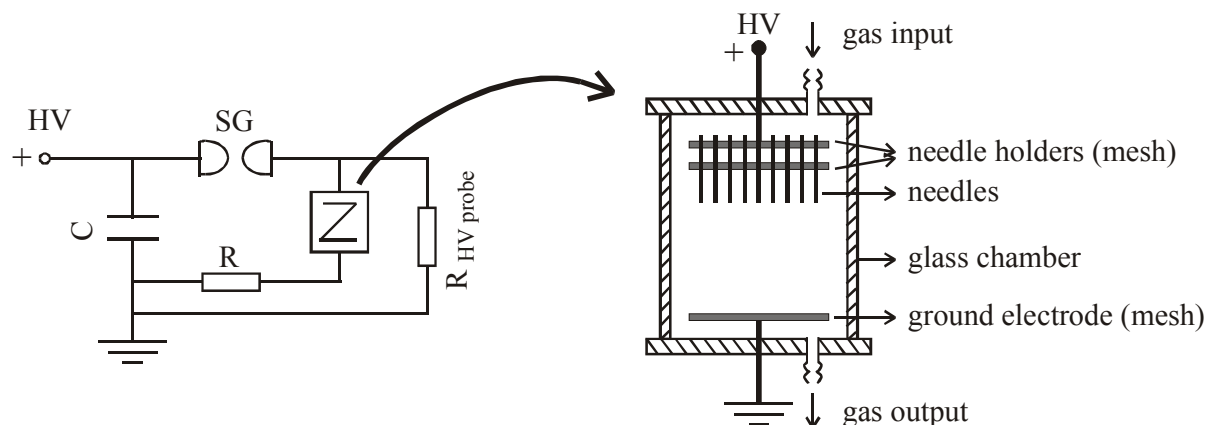


Figure 1. Electrical circuit and electrode configuration used for the corona discharge

The experiments were carried out in a cylindrical discharge chamber made of glass, of 6.5 cm inner diameter and 8 cm height. The high voltage electrode consists in an array of 33 tungsten needles, of 50  $\mu\text{m}$  tip diameter and 15 mm length, with the distance between neighboring needles of approximately 10 mm. The distance between the needles and the other electrode, a grounded circular grid, can be varied, and in the present experiments was 3-4 cm.

The voltage generator supplies up to 30 kV, charging the capacitor  $C = 1 \text{ nF}$ , which is discharged by means of a self-triggered spark-gap switch (SG). The discharge voltage was measured by a high voltage probe (Tektronix P6015,  $R_p = 100 \text{ M}\Omega$ ) and the discharge current was determined from the voltage fall on a  $50 \text{ }\Omega$  resistor in series with the grid electrode. The voltage and current waveforms are monitored by an oscilloscope (Tektronix TDS 320). The radiation emitted by the plasma is collected by an optical fiber and monitored with a photomultiplier (RCA7265).

The experiments were performed at atmospheric pressure, either in air, or in a mixture of air and toluene (toluene concentration in air 1%), flowing continuously through the discharge reactor with a rate of 100 sccm.

A HAL200 gas analyzer equipped with a quadrupole mass spectrometer, supplied by Hiden Analytical Ltd., was used to monitor the gas composition at the output of the reactor. The gas sample was transported to the spectrometer ionization chamber through a capillary of 2 m length. This allows the original gas composition to be preserved during transportation. A molecular leak, mounted at the entrance of the spectrometer chamber reduces the flow rate of the entering gas mixture without affecting its composition. Typical sample consumption rate in this regime is  $0.25 \text{ mbar}\cdot\text{l}\cdot\text{s}^{-1}$ . A bypass rotary pump is used for high flow rates or to reduce the pumping time when different gas mixtures have to be analyzed in succession. Typical mass resolution is 1 amu and the minimum detectable partial pressure is  $10^{-11} \text{ mbar}$ . The detector is a Faraday cup. The following gases were monitored: toluene ( $m/z$  91), nitrogen ( $m/z$  28), oxygen ( $m/z$  32), carbon dioxide ( $m/z$  44), hydrogen ( $m/z$  2), benzene ( $m/z$  78) and methane ( $m/z$  15 was used in order to avoid interference from water that can contribute to the signal at  $m/z$  16). The toluene concentration was calibrated by passing the carrier gas (air) through a temperature controlled vessel containing toluene. The air was saturated with toluene to a partial pressure determined by the temperature and the concentration was determined from the saturated vapours partial pressure diagram.

## 3. Results and discussion

Experiments carried out at constant applied voltage by varying the number of needles of the high voltage electrode have shown that the discharge current increases when more needles are used [9]. In addition, when more needles are used, the active volume occupied by the discharge is higher, therefore a higher efficiency of the chemical reactions could be expected. The maximum current at constant number of needles is obtained for a distance of approximately 10 mm between adjacent needles [9]. Lower values of this distance lead to interference effects on the electric field distributions near neighboring needles, consisting in the reduction of the electron density and electric field in the streamer head [10,11]. In the present experimental configuration,

a maximum of 33 needles can be placed in the discharge reactor, maintaining the distance between adjacent needles at the optimum value.

Typical voltage and current waveforms are shown in Figure 2a and 2b, respectively, for discharge voltages of 24 and 28 kV. The photomultiplier signal for 28 kV is shown in Figure 2c.

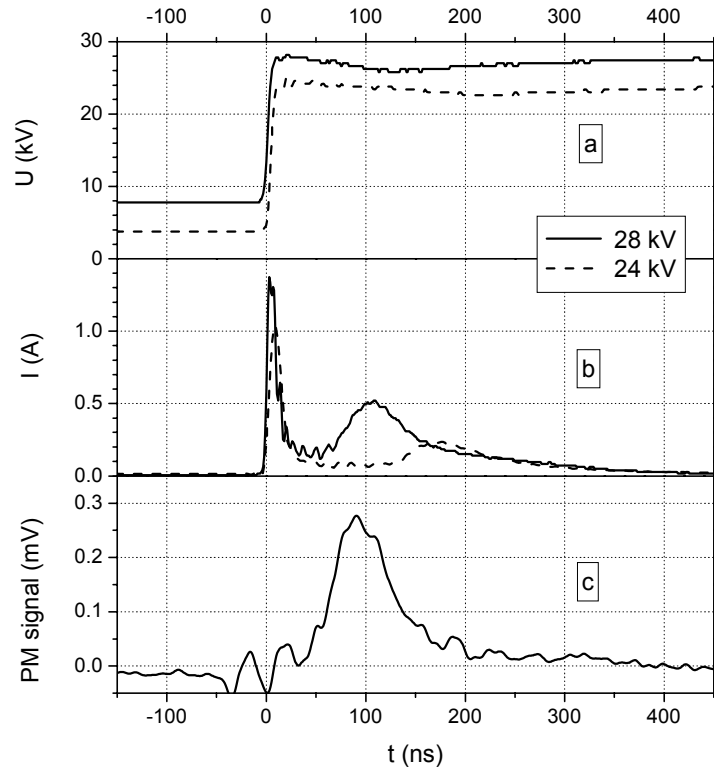


Figure 2. a – voltage waveform; b – current waveform for discharge voltages of 24 and 28 kV; c – photomultiplier signal for 28 kV discharge voltage

The rise time of the voltage (from 10 to 90%) is approximately 8 ns, corresponding to a voltage rise rate of 2 kV/ns. Due to the characteristics of the electric circuit and to the operation regime of the spark-gap switch, the voltage does not usually decrease to zero between consecutive pulses. The voltage decrease is slow, being determined by the time needed to discharge the capacitance of the electrode system through the resistance of the high voltage probe. The distance between the electrodes of the spark-gap switch used in most experiments was 7 mm, therefore a potential difference of approximately 20 kV between them is sufficient for the spark-gap breakdown. This operation regime leads to a shape of the discharge voltage as shown in Figure 2a: pulses of 20 kV height are superimposed on a “continuous” voltage of several kV. With increasing the applied voltage the amplitude of the voltage pulses remains the same, only the level of the continuous voltage changes, so the pulses are shifted at higher voltages.

The current consists of two parts. The first narrow peak, is a displacement (or capacitive) current, and represents the current charging the capacitance of the electrode arrangement [12]. The geometrical capacitance can be determined from the equation:

$$C \frac{dV}{dt} = I \quad (1)$$

by fitting the calculated  $dV/dt$  to the first current peak. For the present discharge configuration  $C \approx 1$  pF has been found.

The second part of the current is the real discharge current, which is confirmed also by the temporal correspondence with the radiation emitted from the plasma (see Figure 2b and 2c). In Figure 2c, the photomultiplier signal was corrected by the delay produced by its response time (50 ns). The current increases from 230 mA to 520 mA with increasing the discharge voltage from 24 to 28 kV.

The current duration is determined by the time needed for the streamers to cross the gap between the needles and the plate electrodes. The streamer velocity can be estimated at  $2 \times 10^5$  m/s for a gap length of 3.5 cm at 28 kV discharge voltage.

The energy in the second current pulse (the real discharge current) was calculated from:

$$E = \int I(t)U(t)dt \quad (2)$$

For 28 kV discharge voltage the energy per pulse was 1.2 mJ.

The frequency of the pulses is determined by the resistor connecting the spark-gap to ground and by the gap length (the distance between the electrodes) of the spark-gap switch. In most experiments the spark-gap is grounded through the resistance of the high voltage probe (100 M $\Omega$ ) and the gap length was 7 mm. Under these conditions, a pulse repetition rate of 450 Hz was obtained. When the gap length was reduced to 3 mm, keeping all the other parameters constant, the pulse frequency increases to 1400 Hz. In Figure 3 the voltage and current waveforms for the two gap lengths, for a discharge voltage of 28 kV are shown.

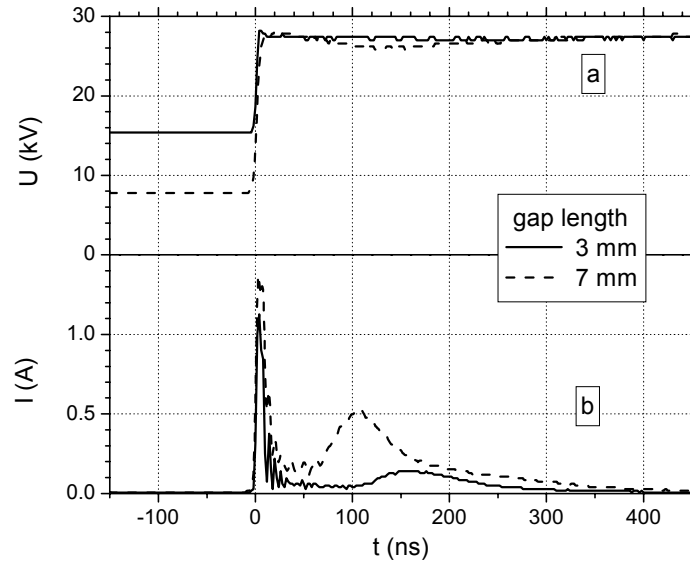


Figure 3. a – voltage waveforms; b – current waveforms, for 3 mm and 7 mm gap length of the switch

For the small gap length, a relatively low potential difference between the electrodes of the switch ( $\sim 12$  kV) is sufficient for breakdown, resulting in a smaller height of the voltage pulses and a higher continuous voltage, as compared to the longer gap length. In this case the discharge current is lower (140 mA) than the current obtained for the 7 mm gap length (520 mA), reflecting that the height of the voltage pulses has a more important influence on the current value than the continuous voltage.

For the 3 mm gap length the energy per pulse is only 0.4 mJ, three times lower than that obtained for the longer gap length. Since the energy is an important parameter for the chemical reactions in the plasma, in the following experiments only the gap length of 7 mm was used. The time interval between consecutive corona pulses is in this case much smaller than the residence time of the gas in the discharge region, as will be shown below. Even for a much higher flow rate of the gas than the one used in these experiments, the pulse repetition frequency would be sufficient so that the gas is subject to a large number of discharge pulses while crossing the gap between the electrodes.

The reactive species produced in the plasma by electron collisions with the gas molecules and subsequent reactions: oxygen and nitrogen atoms (O, N), ozone ( $O_3$ ), hydroxyl radicals (OH), ions ( $O^+$ ,  $O_3^+$ , etc.) and UV photons, react with the toluene molecules and are responsible for their decomposition.

Atomic oxygen is generated by dissociation of molecular oxygen according to the reaction:



The required energy for this reaction is 5.2 eV. Although atomic oxygen is a strong oxidizer, its stability is very limited. Due to fast re-association processes the lifetime of oxygen atoms is only a few microseconds at atmospheric pressure.

Atomic oxygen reacts also with molecular oxygen in three-body collisions, forming ozone by the following reaction:



The activation energy for this reaction is only 16.7 kJ/mol.

Ozone is a more stable molecule; its lifetime at room temperature is several days. It reacts directly with aromatic compounds by electrophilic addition to unsaturated bonds. The products are carboxylic acids, aldehydes or ketones [13]. Ozone is destroyed by OH radicals, that can be present in the discharge at high air humidity:



The net reaction is the conversion of ozone back to molecular oxygen.

The OH radicals, produced by water dissociation according to the reaction:



are also powerful oxidizers, which attack regions of high electron density of the organic molecules. Therefore, in the case of aromatic compounds, they add to unsaturated bonds of the rings. The final products are unsaturated aliphatic hydrocarbons with polyfunctional groups (carboxyl, aldehyde, carbonyl or alkanol groups) [13].

Preliminary experiments were carried out in a mixture of air and toluene (1% toluene) flowing with a rate of 100 sccm through the discharge reactor. The residence time of the gas in the active volume of the discharge is around 1 min. The discharge voltage was 25 kV in these experiments and the current was 240 mA. For a repetition rate of the pulses of approximately 450 Hz obtained in these experimental conditions, a gas molecule experiences about 27000 pulses while passing through the discharge zone.

The influence of the corona discharge on the gas composition at the output of the reactor is shown in Figure 4. The partial pressures have been measured in the spectrometer chamber, but they are proportional to the real ones existing in the gas stream, due to the gas sampling method. The MS signals for  $\text{N}_2$ ,  $\text{O}_2$ ,  $\text{C}_7\text{H}_8$ ,  $\text{H}_2$  and  $\text{CO}_2$  with and without the discharge were monitored.

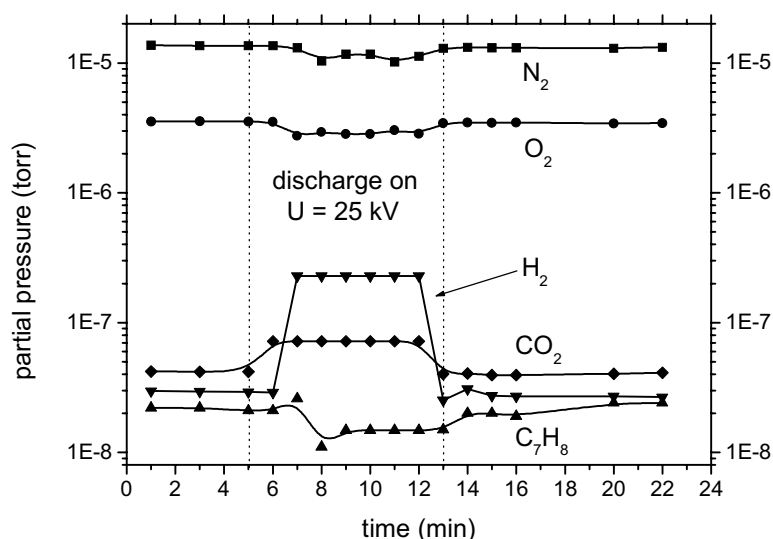


Figure 4. Temporal evolution of the  $\text{N}_2$ ,  $\text{O}_2$ ,  $\text{C}_7\text{H}_8$ ,  $\text{H}_2$  and  $\text{CO}_2$  concentrations in the presence of the corona discharge

In the presence of the discharge (the interval from 5 to 13 min) the toluene partial pressure decreases with 36% as compared to its value without discharge. A decrease was also observed in the oxygen and nitrogen concentrations, of 19% and 25% respectively. By increasing the discharge voltage to 28 kV the toluene conversion rate increases to 43%.

From the reaction products, only carbon dioxide and hydrogen were monitored in this stage of experiments. Although their concentration was not quantified, under the present experimental conditions complete oxidation of toluene to  $\text{CO}_2$  is unlikely. Benzene and methane were also observed, but with much lower partial pressures, therefore they were not included in the figure for clarity reasons.



In order to establish the reaction mechanism responsible for toluene decomposition in the plasma, the identification and quantification of all the reaction products is required. However, interferences of the mass spectra for complex compounds, due to fragmentation of the molecules in the spectrometer, would make this operation difficult. Therefore, the combination of mass spectrometry with a second detection method, like gas chromatography, would provide more accurate information about the chemical processes occurring in the plasma.

## Conclusions

A pulsed positive corona discharge was investigated with the aim of decomposing volatile organic compounds, especially toluene. The discharge voltage, up to 28 kV, with a rise rate of 2 kV/ns, consist of pulses of maximum 20 kV height superimposed on a continuous voltage of several kV. Current pulses up to 520 mA were obtained, with durations of 100-150 ns. Under these conditions, the energy per pulse was up to 1.2 mJ and the pulse repetition rate was 450 Hz. The operation of the spark-gap switch determines the pulse frequency. An increase up to 1400 Hz can be obtained by decreasing the gap length of the switch. However, this results in a decreased amplitude of the voltage pulses for constant discharge voltage, and consequently, lower discharge currents and energy per pulse are obtained.

Preliminary experiments performed in a mixture of toluene and air show the potential capability of the corona discharge to decompose toluene. A toluene conversion up to 43% was obtained. An increased toluene conversion is expected either by using higher discharge voltages or by increasing the amplitude of the voltage pulses. An optimization of the discharge configuration in order to maximize the discharge current is likely to improve the results.

## References

- [1] A. A. Kulikovsky, IEEE Trans. Plasma Sci. **25** (1997) 439
- [2] J. Chen and J. H. Davidson, Plasma Chem. Plasma Process. **22** (2002) 1
- [3] R. Morrow and T. R. Blackburn, J. Phys. D: Appl. Phys **35** (2002) 3199
- [4] J.-S. Chang, P. A. Lawless and T. Yamamoto, IEEE Trans. Plasma Sci. **19** (1991) 1152
- [5] Y. L. M. Creyghton, Pulsed positive corona discharges: fundamental study and application to flue gas cleaning, PhD Thesis, Technical University Eindhoven, 1994, ISBN 90-9007232-3
- [6] B. Penetrante et al, Pure Appl. Chem. **71** (1999) 1829
- [7] N. Hayashi et al, Jpn. J. Appl. Phys. **40** (2001) 6104
- [8] R. Vertriest et al, Proc. HAKONE 8, 21-25.07.2002, p. 342
- [9] M. Magureanu and N. B. Mandache, submitted to XXVI International Conference on Phenomena in Ionized Gases (ICPIG 2003), July 15-20, 2003, Greifswald, Germany
- [10] Y.-H. Kim and S. H. Hong, IEEE Trans. Plasma Sci. **30** (2002) 168.
- [11] G. V. Naidis, J. Phys. D: Appl. Phys **29** (1996) 779
- [12] E. M. van Veldhuizen and W. R. Rutgers, J.Phys. D: Appl. Phys. **35** (2002) 2169
- [13] W. F. L. M. Hoeben, Pulsed corona-induced degradation of organic materials in water, PhD Thesis, Technical University Eindhoven, 2000, ISBN 90-386-1549-3

# Double chamber radiofrequency discharge in nitrogen operating as a high pressure plasma jet

D. Crintea, M.C. Petcu, S.I. Vizireanu., B.M. Mitu, G. Dinescu

*National Institute for Laser, Plasma and Radiation Physics, Magurele MG-36, 76900, Bucharest, Romania;  
e-mail: dinescug@alpha1.infim.ro*

## Abstract

The operation of a RF (13.56 MHz) nitrogen plasma beam generated in a double chamber configuration in the high pressure region (1 - 760 mbar) is reported. The discharge is sustained mainly in a small space created between a cylindrical electrode and a planar nozzle and it expands outside the discharge chamber as a plasma beam. The occurrence of plasma expansion as function of electrode geometry, pressure, RF power was studied. The spectra modification as a result of the passage from the low pressure to the high pressure regime is discussed.

## 1. Introduction

The perspective of low cost plasma equipments which do not include vacuum systems is of large practical importance. Various types of atmospheric-pressure plasmas are known for a long time, as example high gas temperature sources like thermal torches and plasma arcs or low gas temperature sources like corona discharges and silent discharges. Nevertheless, their use in applications is limited due to the high temperature or the micro-filamentary aspect of these discharges. Low temperature discharges at high pressure is of large interest and strongly encourages the research devoted to the extension of the operation range of glow discharges at high pressure. This is a challenging task as many difficulties are related to the operation of glow discharge plasma sources at high pressure. The high voltage needed for breakdown and the prevention of instabilities leading to arc transition ask for the use of small interelectrode spaces, placement of dielectric barriers between electrodes and the flowing of special gases. In addition, the use of low or high frequency voltage is necessary.

Low pressure RF plasma jets generated in various configurations have been reported and used by many authors [1-5]. Also, the operation of the double chamber RF plasma source in nitrogen flow at low pressure was described previously [6] and extensively used in material processing [7,8]. Several groups reported on the operation of non equilibrium radiofrequency (RF) plasma sources at high pressure, as example based on planar discharges, discharges without dielectric barrier in parallel plate [9], or in capillary [10] configurations. An atmospheric plasma jet, in cylindrical geometry, tested for etching of materials was also previously reported [11].

In this work we report on the operation of a RF (13.56 MHz) nitrogen plasma jet generated in a double chamber configuration in the high pressure region (1 - 760 torr). The emission characteristics in nitrogen are also studied in relation with the working conditions.

## 2. Experimental

The schematic view of the source is shown in Figure 1. The source operation is based on system with two chamber; an active chamber and an expansion chamber. The geometry of the electrodes is shown to the right part of figure. The powered electrode is shaped as a cylinder (12 mm diameter, 12-16 mm length) hold in a quartz tube (16 mm inner diameter) which defines the active chamber wall. A grounded planar nozzle with a cylindrical aperture separates the two chambers. The discharge is mainly sustained in the narrow gap delimited by the powered RF electrode and the planar nozzle, but can extend through the nozzle in the grounded stainless steel expansion chamber (0.2 m diameter, 1.2 m length).

The gas is admitted in the active chamber via a mass flow controller. The system is pumped by a rotary pump and a Roots pump. Gas flows in the range 50- 2000 sccm can be used, with the expansion allowed in

closed space or under continuous pumping regime. Stationary pressure values in the range of  $10^{-3}$  torr - 760 torr can be established in the active chamber and/or expansion chamber.

The stability of the expanded discharge as a plasma jet was investigated for a nozzle aperture of 1.5 mm diameter and several gap values (2 - 10 mm) in order to find the optimal geometric parameters leading to operation in the high pressure regime. The active chamber was water cooled and power values up to 500 W were safely applied.

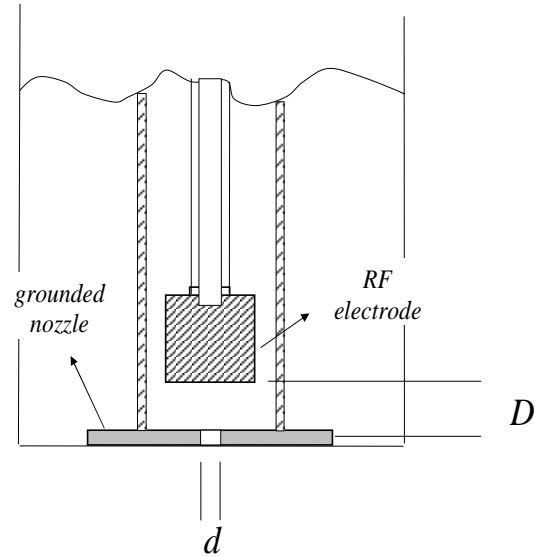
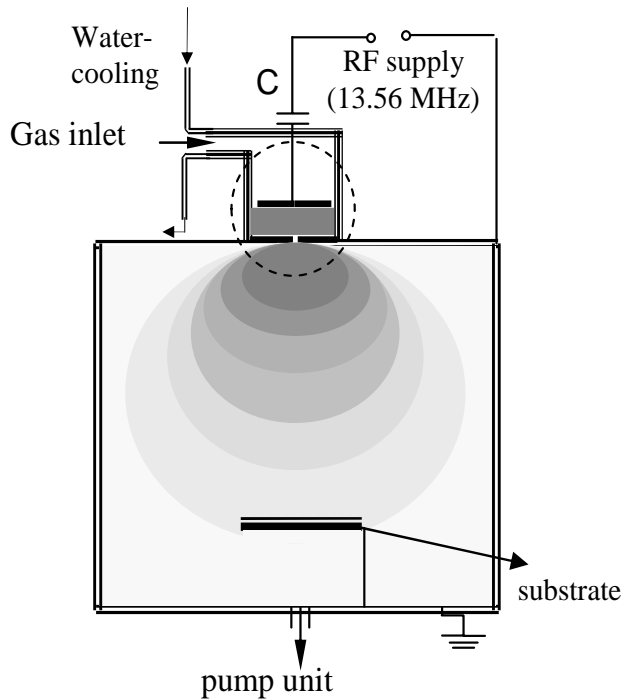


Fig. 1 The schematic view of the experimental set-up. Right: the view of the active chamber

The wall of the expansion chamber is provided with quartz windows that allow optical investigation along the plasma beam. The emission of plasma expansion was studied with a set-up consisting of quartz optics, monochromator (SPM-2, Carl Zeiss, grating  $1200 \text{ mm}^{-1}$ ) photomultiplier (QB 9958) and data acquisition system (acquisition card Advantech 818HG).

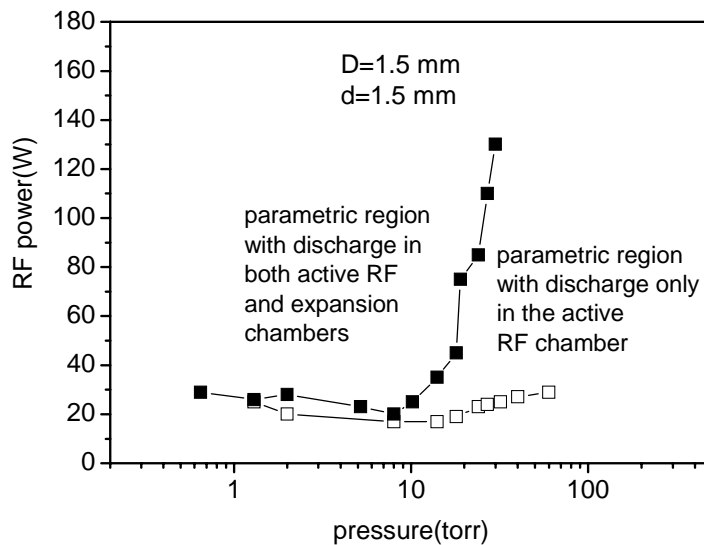


Figure 2. Example of breakdown and transfer curves

### 3. Operation in static conditions

In static conditions the pressure is the same in both active and expanding chambers. In a previous work with a similar discharge configuration [6], we have shown that the operation of the RF discharge in the double chamber system can be described in the power versus pressure axes. Two types of curves, corresponding to breakdown in the interelectrode space (curves of breakdown) and to the transfer of discharge in the expansion chamber (curves of transfer) is defined. Such curves are shown in Figure 2. The transfer of discharge in expansion is related to

the condition of sheath formation inside the nozzle aperture, meaning that the transfer occurs for plasma parameters leading to a sheath thickness smaller than the aperture radius. Parametric regions corresponding to the presence of discharge only in the active electrode chamber or in both chambers are then established. The discharge is present in the expansion chamber, only for pressure and power values corresponding to points situated above the transfer curves. The curves in Figure 3 have been obtained by increasing gradually the power, and the hysteresis behavior of the discharge after transfer, when the power is gradually decreased, was not studied.

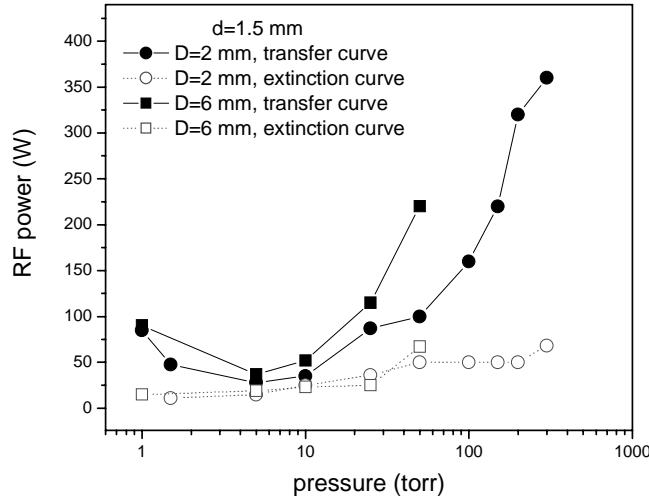


Figure 3. Examples of expansion and extinction curves

distances the hysteresis effect which characterizes the expanded discharge: after the transfer threshold was reached the plasma remains transferred for much lower power values.

The above mentioned hysteresis effect suggests that an way to extend the plasma operation to high pressure is to switch it first at low pressure, followed by gradually increase of the pressure. The gradual increase of the pressure was done by flowing a gas through the plasma source, so operating it in dynamic conditions, leading to an RF plasma jet.

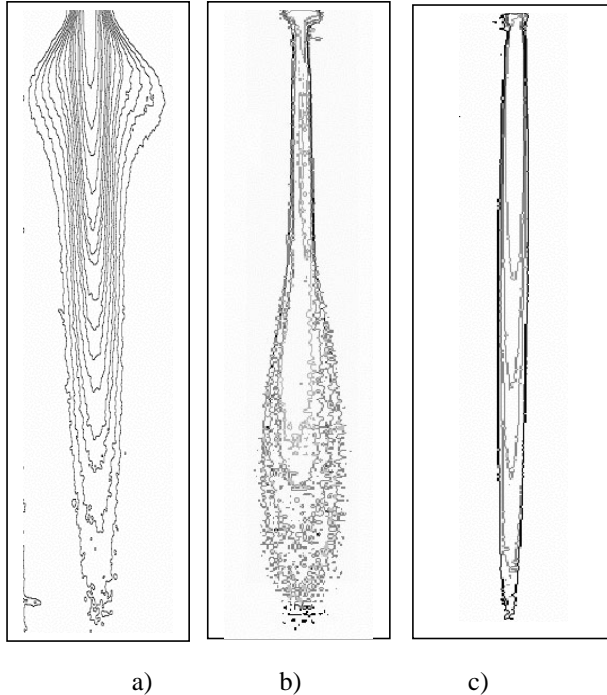


Figure 4. Processed images of the plasma jet: a)  $p=5$  torr, b)  $p=350$  torr, c) atmospheric pressure

Presently, the occurrence of the discharge in the expansion chamber was observed by the side quartz window. By gradually increasing the RF power, at given pressure, we recorded the power values corresponding to plasma transfer in expansion. After transfer, by gradually decreasing the RF power the values for which the extinction occurs were established. The obtained results, for electrode-nozzle distances ( $D$ ) of 2 mm and 6 mm and a nozzle diameter ( $d$ ) of 1.5 mm are shown in Figure 3. From the curves it is seen that higher pressures and larger distances ask for higher power values for transfer. As example, by using maximum 400 watts (value limited by the source heating) the transfer at  $D=2$  mm was possible up to 300 torr, and only up to 50 torr in the case of  $D=6$  mm. Besides, the curves show for the two

#### 4. Operation in dynamic conditions

By gradually increasing of pressure, stable operation of the source in the expansion regime was obtained up to atmospheric pressure. The experiments were performed at constant mass flow by controlling the pumping speed. Spectra have been recorded at the nozzle exit and in various positions along the plasma beam. As reference, the pressure in the expansion chamber was considered.

Processed images of the plasma expansion, at various pressure values are presented in Figure 4. The plasma luminosity is described by lines of equal intensity. Images are from the low pressure (5 torr), intermediate pressure (350 torr) and atmospheric pressure, respectively. At low pressure the contribution of the expansion chamber walls to the discharge is important. The wall behaves like a grounded electrode, connected to the active electrode through the nozzle aperture. In

Figure 4 this is seen as an enlargement of the plasma zone in the vicinity of the top of the metallic expansion chamber. That corresponds to an asymmetric discharge and the expected negative selfbias of the active RF electrode was indeed noticed. By increasing the pressure the discharge detaches from the walls and the formed plasma jet shows an enlargement at the end which is associated to collision with the stagnant atmosphere existing in the expansion chamber (Figure 4b). The enlargement at the end is a frozen image of turbulent flow. Finally, in the case of open atmospheric pressure (Figure 4c), the air mixing in the expansion produces a partial extinction of the intensity and the recorded image shows plasma jet with a conical end shape.

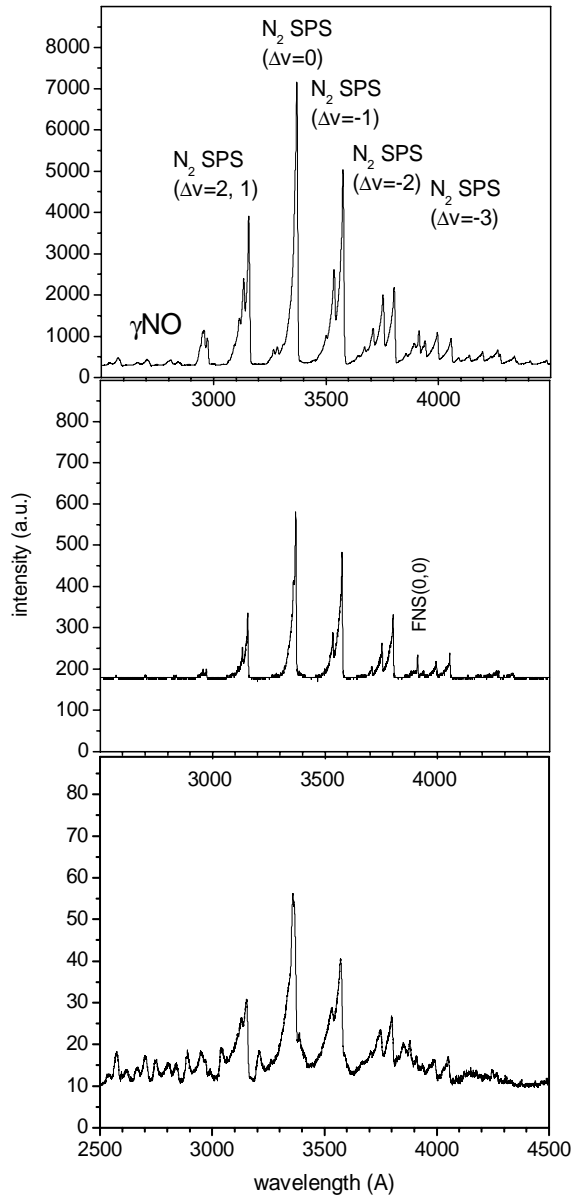


Figure 5. Aspect of spectra at: a) 10 torr, b) 300 torr and c) 760 torr ;300watts, D=10mm..

nitrogen excitation (excitation energy of the SPS system is  $\sim 11$  eV).

Various interelectrode distances, in the range 2 - 10 mm have been used for plasma generation up to atmospheric pressure. The spectra in Figures 5, 6 corresponded to an interelectrode distance of 10 mm. By comparison, a spectrum at atmospheric pressure recorded at the nozzle level for a interelectrode distance of 2 mm is presented in Figure 7. In the spectrum very strong atomic lines, assigned to iron (Fe I, Fe II) are

## 5. Plasma species identification

The plasma emission characteristics depend strongly on pressure. In the low pressure region ( $10^{-2}$  - 50 torr) the emission is dominated by the 2-nd positive system (SPS) of the molecular nitrogen in the violet part of the spectrum and the 1-st positive system (FPS) in the red part. The presence of  $N_2^+$  ions is revealed by the emission of FNS system. Impurities emission (from NO, NH, OH, CN) is observed as well.

A typical spectrum, recorded for the 2500 Å - 4500 Å is shown in Figure 5a. The pressure increasing produces an intensity decrease, but the general aspect of spectra do not change, as can be observed in Figure 5b, recorded for a pressure of 300 torr. In the atmospheric pressure case (Figure 5c) the overall emission is also much lower than at low pressure and a stronger fingerprint of emission of NO impurity relative to the nitrogen emission is observed. This change in the spectrum appearance is assigned to air mixing in the nitrogen jet and to NO radical creation and excitation.

The spectra also depend on the sampling position along the flow axis. In Figure 6 spectra recorded at various distances from nozzle are shown. In those spectra the relative increase of the impurities emission against of nitrogen emission is noticeable. This behavior indicates a mixing of air. In addition, it may be assigned to a decrease of the electronic temperature along the flow axis. That will favor the excitation of species with low excitation energies ( $\gamma$ NO, CN, OH have excitation energies of 2 - 4 eV), against

present, indicating local heating and evaporation of the stainless steel electrodes. These results suggest that an arc discharge is probably established in the active RF chamber in this case.

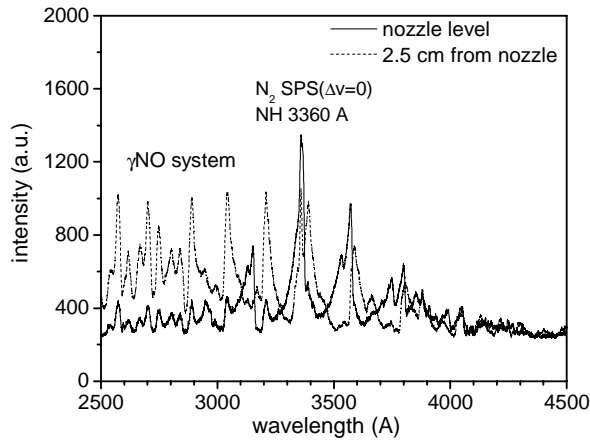


Figure 6. The spectra behavior along the flow axis (atmospheric pressure,  $D=10$  mm, 300 W)

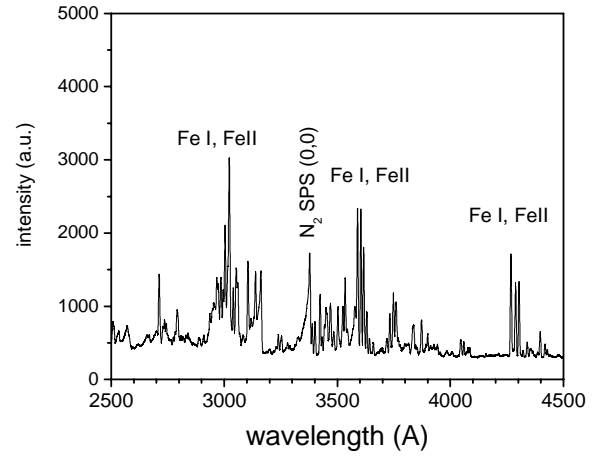


Figure 7. Atomic line presence observed at low interelectrode distance ( $D=2$  mm, 300 W)

## 6. Rotational and vibrational temperatures

For rotational and vibrational temperature measurements the method of spectra fitting was used. To this aim the nitrogen SPS spectra were computed for the spectral range 4200-4800 Å, and compared to the experimental ones. The method, which calculates the rotational and vibrational temperatures, implies the assumption of equilibrium distributions of the vibrational and rotational populations.

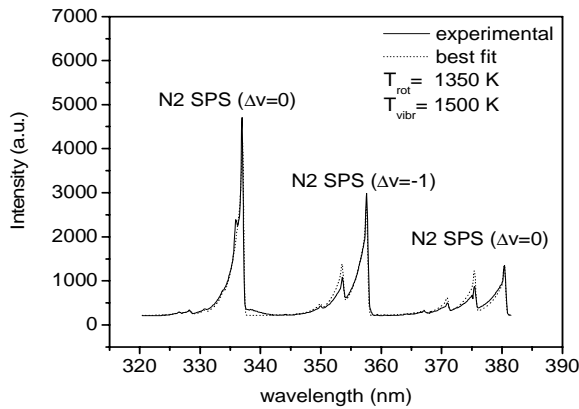


Figure 8. An experimental spectrum (pressure 300 torr, RF power 400 W, recorded at nozzle exit) and its best fit

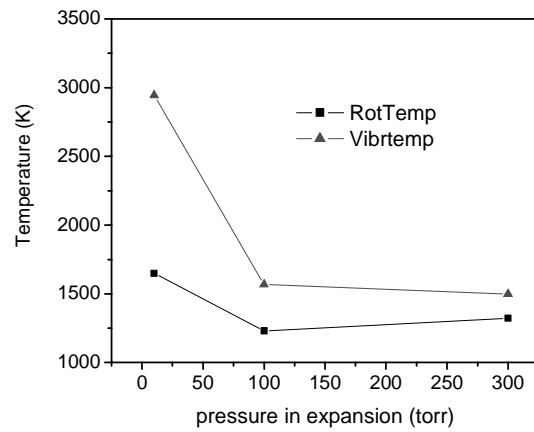


Figure 9. The behavior of rotational and vibrational temperatures with pressure increase (RF power 300 W, mass flow 1000 sccm,  $D=6$  mm, nozzle exit)

An example of fitted and experimental spectra is shown in Figure 8. The applicability of the method is limited when strong emission of impurities is present, as is the case of spectra recorded at atmospheric pressure and along the plasma flow axis. Consequently, spectra recorded at the nozzle level and at low and intermediate pressures were processed. The results are shown in Figure 9. Both the rotational and vibrational

temperatures decrease by increasing the pressure, and a tendency to converge to a common value is observed. Generally, the rotational temperature is associated to the gas temperature and the vibrational temperature to electrons temperature. Accordingly, the tendency to convergence is a good indication that a trend to equilibrium of electrons and heavy particles temperatures, which is expected for plasmas at high pressure, indeed occurs.

## 7. Conclusions

Stable operation of a double chamber radiofrequency plasma source from low pressure ( $10^{-2}$  torr) up to atmospheric pressure was obtained in nitrogen by gradually increase of pressure at constant gas flow (range of 500-1500 sccm) and constant power (range of 250-400 watts). In static regime (no gas flow) the operation at high pressure is limited by the source heating. By flowing a gas across the source the plasma expands as a beam. At low pressure the discharge uses the inner walls of the expansion chamber as grounded electrode. At high pressure values plasma detaches from the inner walls of the expansion chamber and the main discharge is constricted to the active chamber.

The plasma emission shows the usual nitrogen spectral systems, accompanied by impurities emission, the strongest coming from the NO radical. From the present measurements it results that for all used interelectrode distances, in the pressure range 1-350 torr, the discharge is a non-equilibrium one. As concerning the high pressure region the results suggest that the discharge type (cold or thermal) may depend on the interelectrode distance. The spectra obtained at low interelectrode distance (2 mm) exhibit atomic lines of electrodes material and suggests that a radiofrequency arc discharge was established in this case. In case of large interelectrode distance (10 mm) the atomic lines are hardly seen and the discharge character (glow or arc) has to be established by further measurements.

## Acknowledgments

The authors are grateful to Dr. E. Aldea for the spectra fitting procedure. Gabriel Stefan Vlad is highly appreciated for his skilful technical assistance.

## References (Times 11, bold)

- [1] S.J. Sibener, R. J. Buss, C.Y. Ng, Y.T. Lee, Rev. Sci. Instrum, 51 (2) (1980) 167-182
- [2] J.E. Pollard, Rev. Sci. Instrumen. 63 (2) (1992) 1771-1779
- [3] M. Tichy, M. Sicha, L. Bardos, L. Soukup, L. Jastrabik, K. Kapoun, J. Tous, Z. Mazanek, R. J. Soukup, Contrib. Plasma Phys. 34 (96) (1994) 765-772
- [4] H. Barankova, L. Bardos, S. Berg, J. Vac. Sci. Technol A (14) (6) (1996) 3033-3038
- [5] G. Dinescu, O. Maris, G. Musa, Contrib. Plasma Phys. 31 (1) (1991) 49-61
- [6] G. Dinescu, B. Mitu, E. Aldea, M. Dinescu, Vacuum 56 (2000) 83-86
- [7] G. Dinescu, E. Aldea, P. Boieriu, G. Musa, A. Aurel, M. Dinescu, G. J. H. Brussard, R. J. Severens, M. C. M. van de Sanden, D. C. Schram, Nuclear Instruments and Methods in Physics Research B 120 (1996) 298-302
- [8] G. Dinescu, E. Aldea, G. Musa, M.C.M. van de Sanden, A. de Graaf, C. Ghica, M. Gartner, A. Andrei, Thin Solid Films 325 (1-2) 123-129 (1998)
- [9] J. Park, I. Henins, H.W. Herrman, G.S. Selwyn, J. Appl. Phys, Vol. 89, 1 (2001) 15-19
- [10] H. Baránková and L. Bárdoš, Appl. Phys. Lett, 76, 3 (2000) 285-287
- [11] J.Y. Jeong, S.E. Babayan, V. J. Tu, J. Park, I. Henins, R. F. Hicks, G. S. Selwyn, Plasma Sources Sci. Technol. 7 (1998) 282-285

# CHARACTERIZATION OF A PULSED ELECTRON BEAM SOURCE USED FOR MATERIALS ABLATION

M.Nistor, M.Magureanu, F.Gherendi, N.B.Mandache

*National Institute for Lasers, Plasma and Radiation Physics, L 22, P.O.Box MG-36, 76900 Bucharest, Romania*

*E-mail: mnistor@alpha2.infim.ro*

## Abstract

In this work, a compact pulsed electron beam source based on a channel-spark discharge was studied in order to find optimum operating conditions for an efficient ablation of hydroxyapatite and thin-film deposition. Electron beam ablation of the hydroxyapatite target was investigated by time-resolved spectroscopic measurements of the optical emission of the plume plasma.

## 1. Introduction

A compact, pulsed electron beam source based on a channel-spark discharge was studied in order to find the optimum operating conditions for an efficient ablation of hydroxyapatite (HA). Due to its excellent biocompatibility and chemical reactivity to a variety of biomaterials, this ceramic is highly recommendable for coatings of orthopaedic implants, and in the last years it became subject of extensive research in the field of material science. Several methods for HA thin films deposition are known, most often sputtering and pulsed laser ablation being mentioned [1].

A channel-spark discharge is a transient hollow cathode discharge working at low-pressure and high-voltages characterized by the generation during the breakdown phase of the discharge of a pulsed intense electron beam, which propagates in a self-focused way due to the space-charge neutralisation [2]. It was already proved that these electron beams could be used for ablation of materials at higher fluences (up to few J/cm<sup>2</sup>) as compared to preionized controlled open-ended hollow cathode discharges previously studied by the authors [3,4]. A comparative study on intense electron beams generated in different transient hollow cathode discharges is presented in [5].

Electron beam parameters, such as current intensity, pulse length, beam diameter and radial profile of the current density were measured.

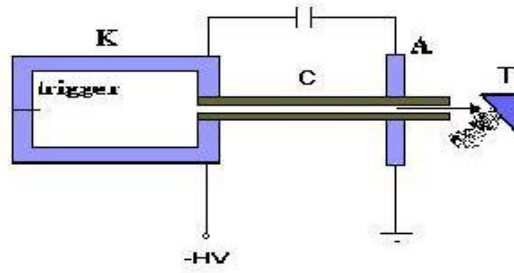
The pulsed electron beam interaction with the HA target leads to a plasma plume due to ablation, which was studied by time-resolved optical emission spectroscopy.

## 2. Experimental setup

The pulsed electron beam source based on a channel-spark discharge consists of a hollow cathode, a quartz tube and a grounded anode (figure 1). A 16 nF capacitance is discharged between the cathode and the anode, with a frequency of 1-2 Hz. A capillary tube of 6 mm diameter was used. The applied voltage, in the range 12-18 kV, was measured with a Tektronix P6015A probe. The working gas was argon at a pressure of 10<sup>-3</sup>-10<sup>-2</sup> mbar.

The electron beam current collected by a Faraday cup was measured on a 0.3  $\Omega$  shunt resistor. The Faraday cup was positioned axially at 10 mm from the anodic end of the capillary tube. In order to determine the radial profile of the electron beam, measurements were made with several apertures (2 - 6 mm diameter) placed in front of the Faraday cup.





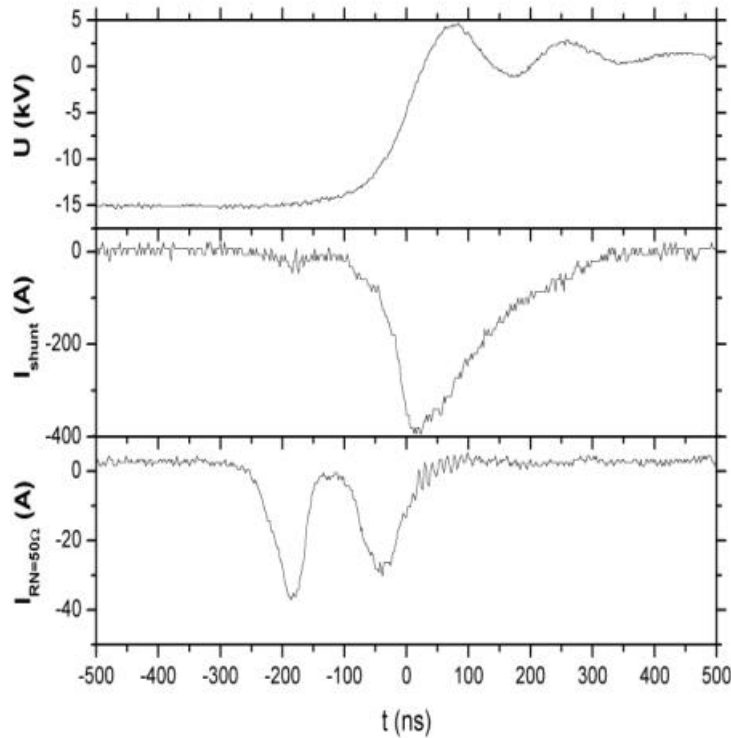
**Figure 1** Experimental set-up: K – hollow cathode, C –capillary tube, A – anode, T – target

In order to study the ablation the Faraday cup was replaced with a HA target, positioned at  $45^\circ$  with respect to the beam axis (figure 1). The plasma emission spectrum was analysed with a Czerny-Turner spectrograph (Acton SpectraPro-750I – 750 mm focal length), coupled with an intensified charge-coupled device (ICCD) detector (512x512 pixels). Two gratings were used: 300 lines/mm and 1200 lines/mm, with a blaze wavelength of 500 nm, and 350 nm, respectively. The investigated spectral range was between 350 nm and 750 nm. The plasma was observed perpendicularly to the direction of the electron beam and imaged on the entrance slit of the spectrograph by using an optical fiber. The ICCD detector was operated in an externally gated mode, synchronized with the HV signal. The measurements were performed with 100 ns exposure time, with trigger delays varying in steps of 100 ns. All spectra were averaged over 100 discharges.

### 3. Experimental results and discussions

#### 3.1 Electron beam parameters

The electron beam parameters were studied in two distinct discharge regimes: a low pressure and a high pressure regime, respectively. An aperture of 6 mm diameter was placed in front of the Faraday cup.



**Figure 2** Temporal evolution of discharge voltage (top) and beam currents for shunt and for  $R_N=50\Omega$

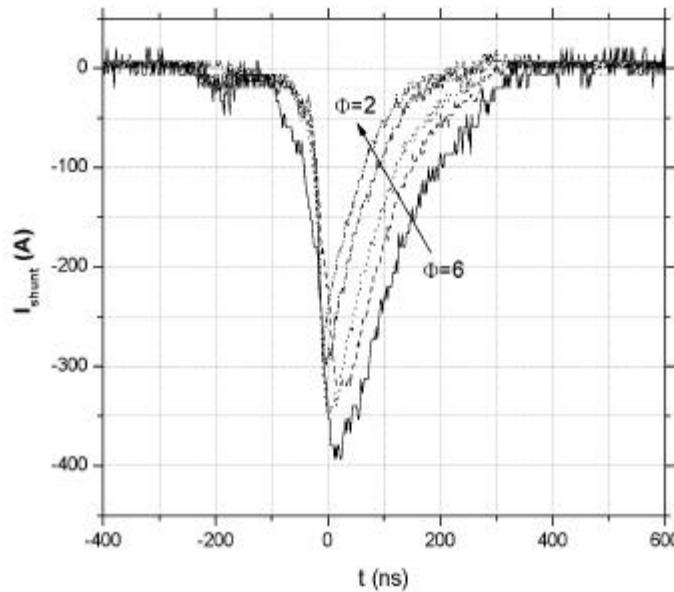
In the low pressure regime ( $6 \times 10^{-3}$  mbar) the electron beam current has a double-peaked structure (figure 2). The first current peak ( $\sim 40$  A) appears early on the voltage fall and represents the contribution of high-energy electrons, with energies comparable to the maximum discharge voltage (15 kV). The second current peak ( $\sim 400$  A) corresponds to lower voltages, and is due to lower energy electrons, with energies between zero and the maximum discharge voltage.

The energy characterization of the electron beam was made using the method described in [6]. A Faraday cup connected to ground through a resistor ( $R_N$ ), in series with the shunt, is self-biased with respect to ground to a negative potential  $V_N = R_N \times I(t)$ , where  $I(t)$  is the electron beam current. Hence, the slow electrons are repelled and only the electrons with energies higher than  $eV_N$  are collected by the Faraday cup.

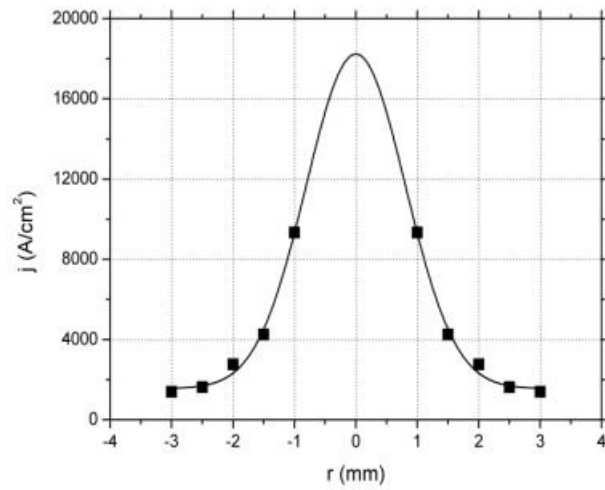
The electron beam current measured for  $R_N = 50 \Omega$  is shown in figure 2c. Both the maximum value and duration of the second current pulse decrease, suggesting that most of the electrons responsible for this pulse have relatively low energies. The current of the first pulse remains practically the same, suggesting that the pulse corresponds to electrons having higher energies.

With increasing pressure, the temporal separation between the two current peaks decreases until they superpose at a pressure of  $10^{-2}$  mbar. This high pressure regime is characterized by only one current pulse having a shorter duration ( $\sim 70$  ns).

Measurements of the electron beam current for several apertures (2-6 mm diameter), placed in front of the Faraday cup, are presented in figure 3. The radial profile of the electron beam current density (second peak) determined from these measurements is presented in figure 4.



**Figure 3.** Electron beam current for several apertures ,  $\Phi_A = 2 - 6$  mm



**Figure 4** The radial profile of the electron beam current density

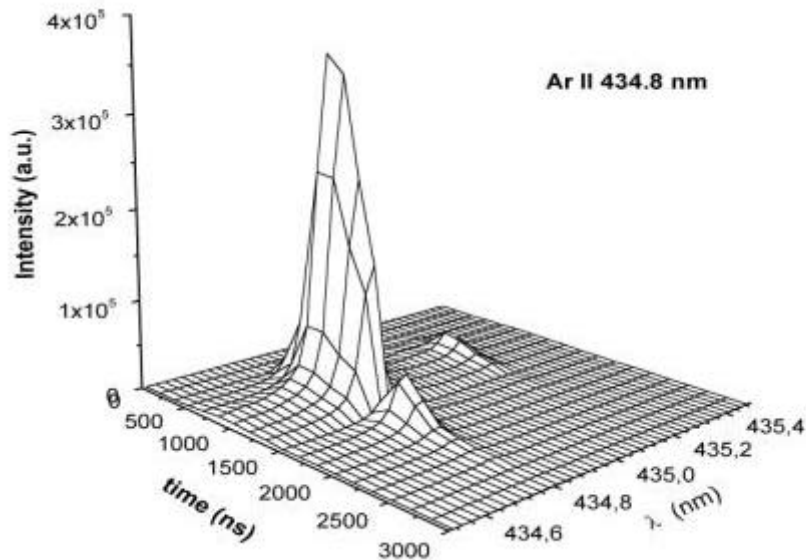
The radial profile is well approximated by a gaussian function having the full width at half maximum of 2 mm. Most of the higher energy electrons in the beam are concentrated in a diameter smaller than 2 mm, in accordance with the trace observed on the target after the beam interaction.

### 3.2 Spectroscopic measurements

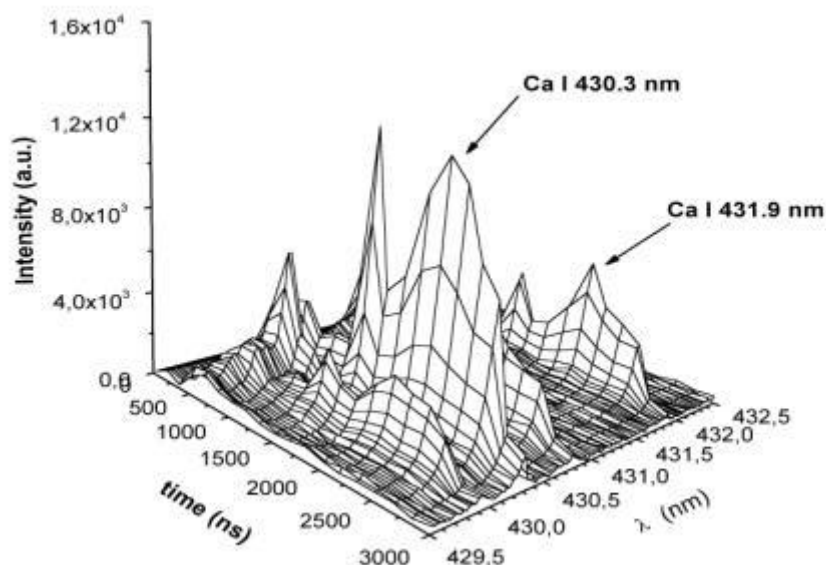
The plasma plume which appears at the interaction of the electron beam with the HA target was studied by time-resolved optical emission spectroscopy. Spectral lines of working gas and target species were identified and their temporal evolution was monitored.

The delay time “zero” correspond to the first current peak (figure 2). An important luminous emission is correlated with the increase of the second current peak.

Figure 5 shows the temporal evolution of the emission spectrum of the plasma in front of the HA target. One can notice the different temporal behaviour of singly ionized argon line (figure 5 a) in comparison with calcium atomic lines (figure 5 b).



**Figure 5a** Temporal evolution of Ar II 434.8 nm line



**Figure 5b** Temporal evolution of Ca I 430.3 nm and 431.9 nm lines

Atomic calcium lines (430.25 nm, 431.86 nm) appear simultaneously with the emission of singly ionized argon lines, but their intensity is relatively weak during the first 600 ns and increases significantly in the following hundreds of ns. The Ca I lines last about 3000 ns, much after the argon lines extinction. Thus the thin-film deposition takes place in the presence of excited calcium atoms.

#### 4. Conclusions

Electron beam parameters characterization and time-resolved optical spectroscopy were performed in a channel-spark discharge configuration to find the optimum operating conditions for hydroxyapatite ablation and thin-film deposition. The electron beam fluence is high enough for an efficient ablation. The discharge configuration determines a long lasting plasma, as proved by temporal evolution of excited calcium atoms.

#### Acknowledgements

The authors greatly acknowledge Dr. Gabriela Pavelescu for providing the Acton SpectraPro-750I spectrograph.

#### References:

- [1] R.Gilgenbach, S.D.Kovaleski, J.S.Lash, L.K.Ang, and Y.T.Lau, IEEE Trans.Pl.Sci. **27** 150 (1999)
- [2] F. Hoffmann, M. Konijberg, C. Schultheiß, M. Schwall, K. Mittag, G. Müller, KfK. Nachr. Jahrg. **24** 254 (1992)
- [3] M.Nistor, A.M.Pointu, Y.Vitel, Proceedings of the 15th International Symposium on Plasma Chemistry, Orleans, France, vol. VI, 2167 (2001)
- [4] M.Nistor, P. Charles, M.Ganciu, M. Lamoureux, N.B. Mandache and A.M.Pointu, Plasma Sources Sci.Technol. **11** 183 (2002)
- [5] E.Dewald, K.Frank, D.H.H. Hoffmann and A. Tauschwitz, IEEE Trans. Pl.Sci. **30** 1820 (2002)
- [6] G.Modreanu, NB Mandache, AM Pointu, M.Ganciu and I.I.Popescu, J. Phys.D: Appl. Phys. **33** 819 (2000)

# Modeling Relaxation Oscillations in Microhollowcathode Microplasmas

David B. Graves<sup>1</sup>, Pascal Chabert<sup>2</sup>, and David Hsu<sup>1</sup>

<sup>1</sup> *Department of Chemical Engineering, University of California at Berkeley, Berkeley, CA USA 94720*

<sup>2</sup> *Laboratoire de Physique et Technologie des Plasmas, Ecole Polytechnique, Palaiseau, France*

Microplasmas are of increasing interest due in part to the possibility of operating a glow discharge at atmospheric pressure. We have studied microhollowcathode (MHC) plasmas that employ metallic thin films coating each side of a thin (~1 mm thick) dielectric material. A hole of typically several hundred micron diameter is drilled through the metal films and dielectric material. The MHC is connected in series with a ballast resistor and a commercial dc power supply. Applying a dc voltage across the metallic films results in a discharge at pressures as high as atmospheric pressure under the proper conditions. The cylindrical geometry approximates a hollow cathode configuration and explains in part the intense nature of the discharge.

Under some conditions, the discharge operates in pulsed mode, showing relaxation oscillation-type dynamics. Evidently, this is the result of the voltage drop across the ballast resistor dropping the applied discharge voltage below the discharge sustaining voltage, resulting in the discharge extinguishing. The power supply then charges the cathode electrode until the breakdown voltage is reached, and the cycle repeats. Although this explains the phenomenology, it provides no predictive power in determining when relaxation oscillations will occur, or how they depend on discharge or external circuit characteristics.

We have developed an equivalent circuit model of the discharge as a non-linear resistor in series with an inductor, in which the resistance can be negative. Coupled with the other circuit elements, we show how this model predicts the onset and nature of the relaxation oscillations. Linear stability theory is used to predict the values of discharge and circuit characteristics that correspond to oscillatory or stable conditions. The crucial importance of the proper treatment of discharge negative differential resistance is emphasized in modeling the relaxation oscillations properly. Finally, the importance of manipulating discharge pulsing for various applications such as chemical processing and optical emission-based sensing is discussed.

# Broad band absorption diagnostics on a low-voltage circuit breaker

J.M. Bauchire<sup>1</sup>, D. Hong<sup>1</sup>, S. Guillot<sup>1</sup>, E. Le Menn<sup>1</sup>, G. Pavelescu<sup>2</sup>, F. Gentils<sup>3</sup>, C. Fiévet<sup>3</sup> and C. Fleurier<sup>1</sup>

<sup>1</sup> GREMI, Université d'Orléans, B.P. 6744, 45067 Orléans Cedex 2, France

<sup>2</sup> National Institute for Optoelectronics, 76900 Bucarest-Magurele, Romania

<sup>3</sup> Schneider Electric, Centre de Recherche, 38050 Grenoble Cedex 9, France

## Abstract

The electric arc created in a low voltage circuit breaker has been studied by means of broad band absorption spectroscopy. From absorption spectra in the 510-523 nm range, copper atom and silver atom concentrations have been determined as well as electron temperature using the LTE assumption. The iron atom density and the temperature have also been determined using iron spectrum in the 430 nm region.

## 1. Introduction

In a low voltage circuit breaker, the arc established at contacts opening is usually pisted, by self-generated force towards the quenching area. The development and the modelling of such devices require a detailed knowledge of the behaviour and of the properties of the moving arc. Because of the very complex processes involved, many experimental investigations and computer simulations of the arc in low voltage circuit breaker have been achieved by several teams (see [1] and its references). In a previous paper [2], it was shown with time resolved optical emission spectroscopy and imaging measurements in a low voltage circuit breaker filled with air that metallic atoms (Copper, Silver and Iron) were present in the electric arc. In order to determine the concentrations of these atoms, we have performed a diagnostic based on broad band absorption spectroscopy measurements using a bright radiation source specially developed for this purpose [3]. In this paper, we present the experimental set-up used for these measurements and the results obtained.

## 2. Experimental set-up

The low voltage circuit breaker studied here is shown in figure 1 and described in [2]. This device, symmetrical about the vertical median plane, is composed of two mobile contacts, two fixed contacts and two quenching chambers. Materials of the contacts on copper fixed and movable electrodes are respectively silver-carbon and silver-carbon-tungsten. The quenching chambers consist of parallel arc splitter plates of different lengths which are disposed on plastic holders. This kind of design leads to the simultaneous creation of two electric arcs at the moment of contacts separation. Then the two arcs expand and reach the respective quenching areas.

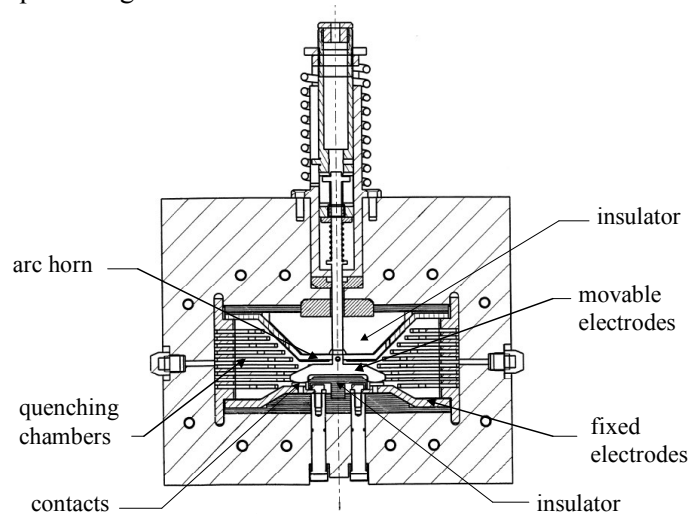


Fig. 1: Sketch of the nearly industrial low voltage circuit breaker.

Because the electric arcs in circuit breakers are rapidly transient and also because circuit breakers are single shot devices, the absorption spectroscopy technique requires an intense and broad band radiation source. Such a source was developed in our laboratory. It consists in a fast electrical discharge called Z-pinch as described by Hong *et al* [3]. Under specific conditions and at the moment of the maximal self-compression of the plasma, called pinch time, the radiation is extremely intense while the spectral lines are totally smeared out in the continuum. The whole spectrum of this source, in the spectral range 350-750 nm, acquired at pinch time, is shown in figure 2.

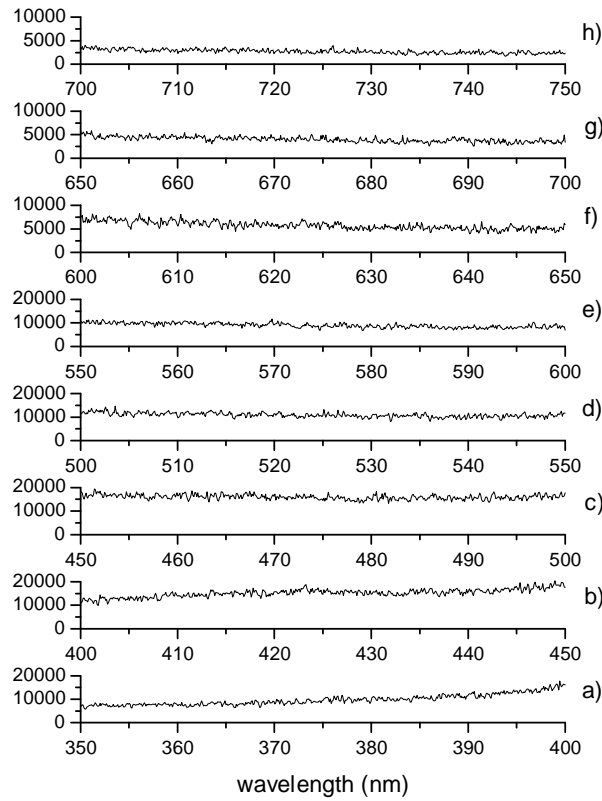


Fig. 2: Spectrum of the light source at pinch time

The absorption measurements are performed by means of the optical set-up illustrated in figure 3. The light coming from the Z-pinch source is driven by an optical fibre called  $OF_z$  and forms a parallel beam with a lens. This beam becomes polarized thanks to the polarizer P1 before going through the absorption medium, i.e. the electric arc. On the opposite side of the absorption medium, the light collection system using a second polarizer and two optical fibres allows to separate the transmitted light from the Z-pinch and the light emitted by the arc of the circuit breaker. The optical fibre  $OF_{trans}$  collects the transmitted light from the Z-pinch and one half of light (polarisation p) emitted by the arc, while the fibre  $OF_{emi}$  collects the other half of light (polarisation s) emitted by the arc. A spectrometer coupled to an intensified 2D CCD camera is used to record simultaneously the two spectra of these two fibres. Subsequently, the subtraction of the two spectra yields the transmission spectrum. More details concerning this acquisition system are given in references [2,3]. In cases where the radiation of the absorbing medium can be neglected, a more simpler optical set-up can be used [3]. The results presented below are obtained for an optical opening time of 1  $\mu s$  of the ICCD camera.

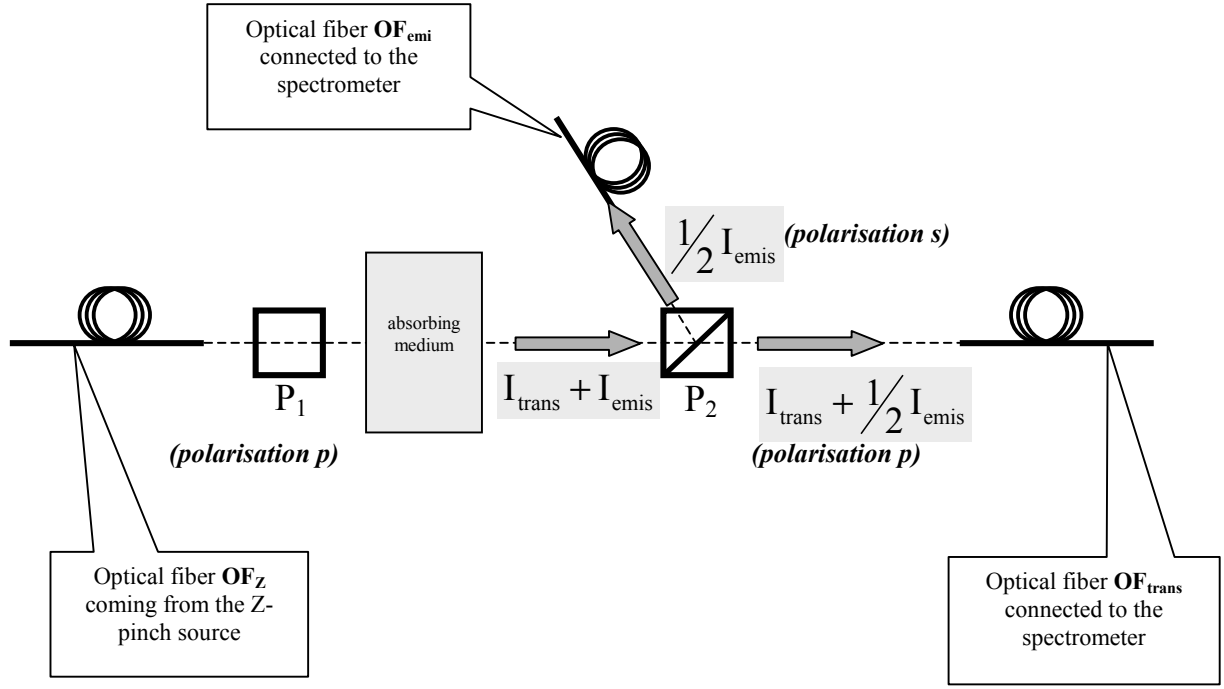


Fig. 3: Optical absorption measurement set-up.

### 3. Results and discussions

Figure 4a) represents the spectrum acquired in the spectral range 510-523 nm from the Z-pinch light source alone. Figure 4b) shown the spectra collected by the fibres  $OF_{trans}$  and  $OF_{emi}$  respectively, simultaneously acquired when an arc is present in the circuit breaker. Measurement was performed 3 ms after the current start (i.e. 2 ms after the opening of the contacts). The current peak value was about 5 kA.

The spectral transmission coefficient shown in figure 5 is derived from these spectra. The five absorption lines shown in figure 4b) are respectively CuI 510.55, 515.32, 521.82, 522.01 nm and AgI 520.91 nm.

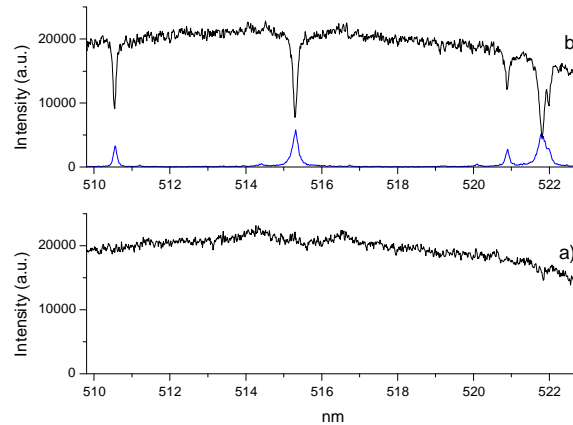


Fig. 4: a) spectrum acquired without arc, b) spectra from  $OF_{trans}$  and  $OF_{emi}$  respectively.



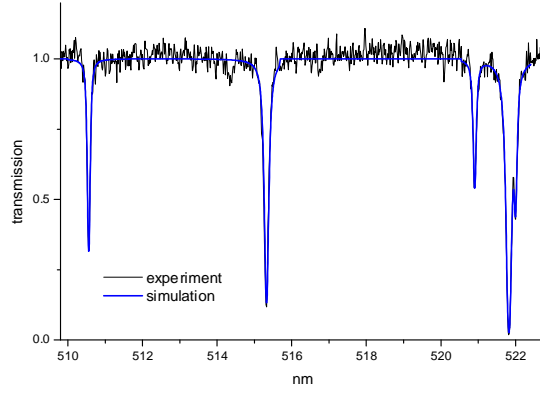


Fig. 5. Spectral transmission coefficient and its best fit.

This spectral transmission coefficient is then fitted by a synthesised spectrum given by the convolution operation :

$$t = e^{-\alpha_T(\lambda) L} * F_a$$

where  $L$  is the length of the absorbing medium,  $F_a$  is the apparatus function of detection system. Here an important approximation must be made concerning the homogeneity of the absorbing medium. The theoretical value of the absorption coefficient  $\alpha_T$  is given by the following relation :

$$\alpha_T(\lambda) = \frac{\lambda^4 A_{ul}}{8\pi c} \frac{g_u}{g_l} N_l S(\lambda)$$

here  $\lambda$  is the wavelength,  $A_{ul}$  is the transition probability between the upper level  $u$  and the lower level  $l$ ,  $g_l$  and  $g_u$  are respectively the statistical weights of these two levels,  $c$  is the speed of light in vacuum and finally,  $N_l$  is the population of the atom in lower level. For this calculation the stimulated emission term is neglected.  $S(\lambda)$  represents the normalised true line profile which has a nearly Lorentzian shape in our case.

$$S(\lambda) = \frac{1}{\pi} \frac{w}{(\lambda - \lambda_0)^2 + w^2}$$

where  $\lambda_0$  is the wavelength at line centre and  $w$  is the HWHM of the true line profile. So, the best fit of line transmission spectrum enables us to determine the population of atoms in the lower energy level of the corresponding transition.

The best fit shown in figure 5 yields copper atom density in the excited states listed below in the table I with an uncertainty estimated at 20% for a given value of the absorbing medium length  $L$ .

Table I: Spectroscopy data and population in lower level of CuI lines

CuI line (nm)	Config.	Desig.	$E_l$ (eV)	$g_l$	$A_{ul} (s^{-1})$	$N_l (m^{-3})$
510.55	$3d^9 4s^2$	$4s^2 {}^2D$	1.39	6	$1.949 \times 10^6$	$3.9 \times 10^{20}$
515.32	$3d^{10} ({}^1S) 4p$	$4p {}^2P^\circ$	3.79	2	$1.034 \times 10^8$	$5.4 \times 10^{18}$
521.82	$3d^{10} ({}^1S) 4p$	$4p {}^2P^\circ$	3.82	4	$1.221 \times 10^8$	$1.1 \times 10^{19}$
522.01	$3d^{10} ({}^1S) 4p$	$4p {}^2P^\circ$	3.82	4	$2.180 \times 10^7$	$1.2 \times 10^{19}$

Considering local thermodynamic equilibrium assumption, the population of excited and fundamental levels are linked by the Boltzmann's law. In this case, the plot of the quantity  $\ln(N_l/g_l)$  as a function of  $E_l$ ,

yields the electron temperature  $T_e$ . In the case of copper lines, the Boltzmann's plot shown in figure 6, yields an electron temperature of 0.77 eV. Since the energy gap between the two lower levels of the two CuI lines (510.55 and 515.32 nm) is as large as 2.4 eV, the uncertainty is quite good, and is estimated to be 15%. The uncertainty comes mainly from the fact that only two groups of levels are used here. In these conditions, the total population of copper atom is estimated to be  $1.4 \times 10^{21} \text{ m}^{-3}$ .

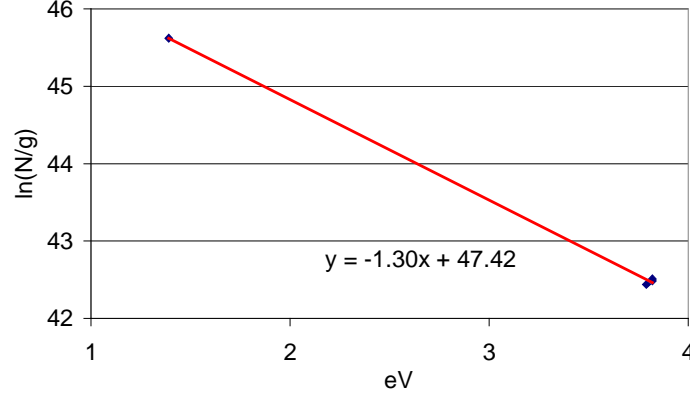


Fig.6: Boltzmann's plot from four CuI lines

From the best fit in figure 5, we can also estimate the lower level population of the line AgI 520.91 nm to be of about  $2.0 \times 10^{18} \text{ m}^{-3}$  which gives a total Ag atom population of  $2.5 \times 10^{20} \text{ m}^{-3}$ .

Measurements were also performed for iron lines lying in the spectral range around 430 nm. Four isolated FeI lines (426.05, 430.79, 432.58 et 438.35 nm) were chosen in figure 7. The measured populations are given in table II. The electron temperature is estimated to be about 0.72 eV from the Boltzmann's plot shown in figure 8. This temperature is in good agreement with the one deduced from the copper lines absorption.

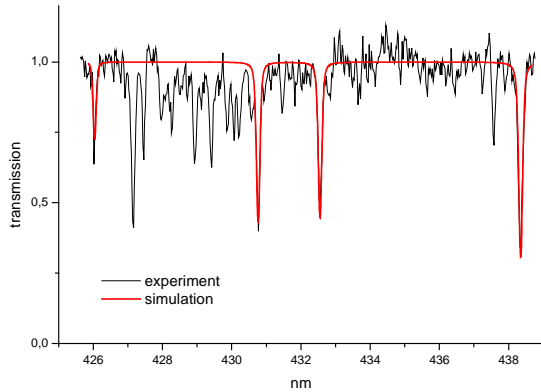


Fig. 7: Transmission spectrum in 425-439 nm range lines and the best fit for four chosen FeI lines.

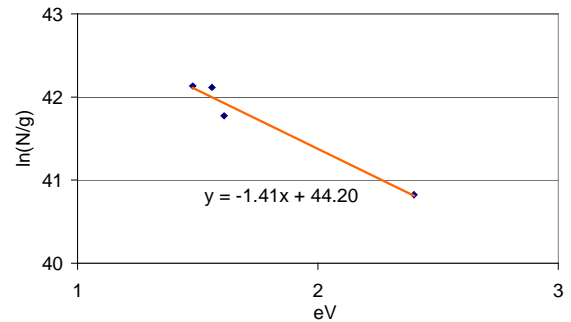


Fig.8: Boltzmann's plot from four FeI

Table II: Spectroscopy data and population in lower level of FeI lines

FeI line (nm)	Config.	Desig.	$E_l$ (eV)	$g_l$	$A_{ul} (\text{s}^{-1})$	$N_l (\text{m}^{-3})$
426.05	$3d^6 4s(a^6D)4p$	$z^7D^o$	2.4	11	$3.2 \times 10^7$	$5.8 \times 10^{18}$
430.80	$3d^7 (a^4F)4s$	$a^3F$	1.56	7	$3.4 \times 10^7$	$1.4 \times 10^{19}$
432.58	$3d^7 (a^4F)4s$	$a^3F$	1.61	5	$5.0 \times 10^7$	$7.0 \times 10^{18}$
438.35	$3d^7 (a^4F)4s$	$a^3F$	1.48	9	$5.0 \times 10^7$	$1.8 \times 10^{19}$

#### **4. Conclusion**

Optical absorption spectroscopy measurements were performed on a low voltage circuit breaker using a Z-pinch discharge as broad band light source. Copper, Silver and Iron spectrum were used to estimate atom densities and temperature of the electric arc of about 0.75 eV for this particular instant of the arc. It has been demonstrated that optical absorption spectroscopy could be a useful tool not only for the diagnostic of hot gases with low level of radiation but also for very bright medium like electric arcs.

#### **5. Acknowledgements**

This work has been partially supported by the NATO Science For Peace LOVARC project and by Electricité de France (EDF)

#### **6. References**

- [1] M. Lindmayer, Complete Simulation of Moving Arcs in Low-Voltage Switchgear, proceedings of the XIV Int. Conf. on Gas Discharges and their Applications, **2** (2002) 318-324.
- [2] S. Guillot, J. M. Bauchire, E. Le Menn, C. Fleurier, C. Fiévet and F. Gentils, Experimental Diagnostic of A Low-Voltage Circuit Breaker, proceedings of 15<sup>th</sup> ISPC, **III** (2001) 1097-1100.
- [3] D. Hong, G. Sandolache, K. Lan, J. M. Bauchire, E. Le Menn and C. Fleurier, A Radiation Source Developed for Broad Band Optical Absorption Spectroscopy Measurements, Plasma Sources Science and Technology, **12** (2003) 1-7.

# Isotropic Plasma Etch of Silicon for Bubble-Trench Formation

L. Rubino<sup>1</sup>, G. Arena<sup>1</sup>, G. Fallica<sup>1</sup> and P. Vasquez<sup>1</sup>

<sup>1</sup>*STMicroelectronics – Stradale Primosole 50, 95100 Catania, Italy*

During the last twenty years, SOI technology has made impressive progress from the first laser recrystallization experiments to CMOS circuits operating at multigigahertz frequencies, withstanding high temperatures or surviving several megarads of radiation.

This technology has some limitation due to high substrates costs.

In this work a new approach for *low-cost* SOI formation is showed. It consists in large cavities (Bubble-Trench) formation into silicon single crystal by means of an isotropic plasma process. The sidewall thermal oxidation of the buried cavities and the subsequent filling with a dielectric material leads to a dielectrically isolated region in the silicon substrate.

Moreover, this solution allows to integrate in the same device about all the elementary components without any interaction or parasitic effects: mos transistors, bjt, power transistor, etc. In particular it is possible to integrate a power transistor with vertical current flow and a bicmos control circuit.

# A Novel Plasma Process for Cobalt Silicide /Polysilicon Stack Etch

G.Arena<sup>1</sup>, A.Scandurra<sup>2</sup>, C.Tringali<sup>1</sup>, G.Beique<sup>3</sup>, S.Ravesi<sup>1</sup> and P.Vasquez<sup>1</sup>

<sup>1</sup>STMicroelectronics – Stradale Primosole 50, 95100 Catania, Italy

<sup>2</sup>Laboratorio Superfici ed Interfasi - Consorzio Catania Ricerche c/o STMicroelectronics, Stradale Primosole 50, 95100 Catania, Italy

<sup>3</sup>Tegal Corporation, Petaluma, California, USA

## Abstract

The resistivity of a polycide gate structure (i.e. silicide on polysilicon) is controlled by the silicide layer. The self-aligned silicide (SALICIDE) process is widely used in the ULSI technology for many applications. Among leading silicides, cobalt disilicide ( $\text{CoSi}_2$ ) is most attractive due to its low resistivity ( $15\text{--}20\ \mu\Omega\ \text{X cm}$ ), linewidth-independence sheet resistance and easy formation by thermal sinterization of metal sputtered on polysilicon layer.

Since in many application the cobalt silicide / polysilicon gate stack patterning is required, the dry etching characteristics of this silicide layer have to be evaluated. However, while for other silicide ( $\text{WSi}$ ,  $\text{TiSi}_2$ ) fluorine and/or chlorine based etching chemistry are able to dry etch these materials,  $\text{CoSi}_2$  is an hard-to-etch materials, due to the inherent low volatility of cobalt by-products (i.e.  $\text{CoCl}_x$ ).

In this work the ability to etch  $\text{CoSi}_2$  /polysilicon stack with good etching characteristics using a low-pressure, high density plasma etcher was achieved and the role of both plasma chemistry, DC bias voltage, process pressure, and wafer temperature control in  $\text{CoSi}_2$  etch performances is also showed. Finally, both X-ray Photoelectron Spectroscopy (XPS) and morphological characterization have been used in order to point out a possible reaction mechanism.

## Introduction

The resistivity of a polycide gate structure (i.e. silicide on polysilicon) is controlled by the silicide layer. The self-aligned silicide (SALICIDE) process is widely used in the ULSI technology for many applications<sup>1</sup>. Among leading silicides, cobalt disilicide ( $\text{CoSi}_2$ ) is most attractive due to its low resistivity ( $15\text{--}20\ \mu\Omega\ \text{X cm}$ )<sup>2,3</sup>, linewidth-independence sheet resistance and easy formation by thermal sinterization of metal sputtered on polysilicon layer. All these characteristics lead to a promising candidate for gate electrode formation in electronic devices<sup>4</sup>.

Since in many application the cobalt silicide / polysilicon gate stack patterning is required, the dry etching characteristics of this silicide layer have to be evaluated.

While for other silicide ( $\text{WSi}$ ,  $\text{TiSi}_2$ ) fluorine and/or chlorine based etching chemistry are able to dry etch these materials,  $\text{CoSi}_2$  is an hard-to-etch materials, due to the inherent low volatility of cobalt by-products (i.e.  $\text{CoCl}_x$ ) that causes increasing of cobalt concentration in the silicide layer during the etch and leads to metal residuals on the wafer surface<sup>5</sup>.

Even if the cobalt silicide etch with chlorine based chemistry is reported, poor etching rate values were observed and other chemistries show a behaviour similar to the argon plasma (pure physical sputtering)<sup>5</sup>.

In this work the ability to etch  $\text{CoSi}_2$  layer with good etching characteristics using a low-pressure, high density plasma etcher is achieved. The role of both DC bias voltage, process pressure, chemistries and wafer temperature control in  $\text{CoSi}_2$  etch performances is also shown.

## Experimental

Cobalt silicide samples were prepared by cobalt sputtering (250Å) on polysilicon layers (3kÅ). Samples were annealed at 540°C, etched in a HCl/H<sub>2</sub>O<sub>2</sub>/H<sub>2</sub>O solution in order to remove the unreacted Co, and finally annealed at 800°C. This procedure resulted in the formation of 1500Å of CoSi<sub>2</sub> layer. Experiments have been performed using both patterned and blanket cobalt silicide wafer. Patterned wafers preparation has been performed by 5kÅ of APCVD silicon oxide and windows of 0.6µm width were opened by a photolithography process. APCVD oxide has been etched in CF<sub>4</sub>/CHF<sub>3</sub>/Ar plasma and resist removal has been performed by O<sub>2</sub> plasma. CoSi<sub>2</sub>/Poly stack etch has been performed through the APCVD oxide hard mask and patterned wafers were used for process characterization.

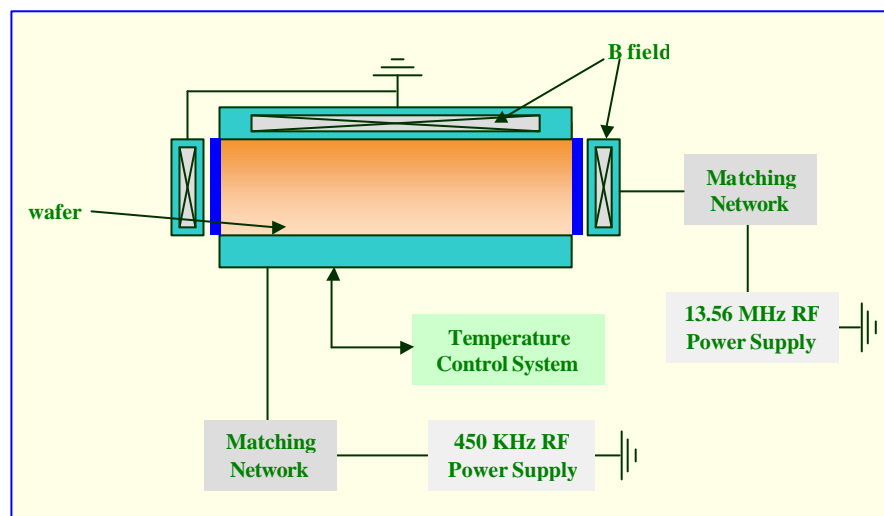
CoSi<sub>2</sub> blanket wafers were used for XPS analysis and this set of samples was prepared performing the cobalt silicide partial etch at different etching temperature as reported in table 1:

Sample	Etching Temperature [°C]
#1	Not etched (reference)
#2	150
#3	190
#4	240

**Table 1:** Cobalt silicide blanket wafers preparation for XPS analysis

## The Reactor

CoSi<sub>2</sub>/poly stack etching process has been performed with a TEGAL 65xx HRe<sup>+</sup> (High Reflected electrons) low-pressure process module with a tri-electrode configuration (figure.1)



**Figure 1** TEGAL 6540 HRe- Reactor Chamber configuration

The etch process module has a symmetric multipolar magnetic confinement, to minimize electrons losses to chamber walls. It also has a symmetric high-conductance pumping system capable of greater than 500 litres/sec at the wafer plane. The system uses high frequency (13.56MHz) for ion generation and low frequency (450KHz) to control ion energy. The etcher operates at low pressure of ion mill systems in order to balance the amount of physical and chemical etch. Finally, the wafer temperature can be increased up to 400 °C, in order to increase the cobalt by-product volatility. Wafer temperature control is performed by an optical pyrometer.

XPS analysis of several partially etched samples (see table 1) has been performed using an AXIS-HS Kratos Spectrometer equipped with Mg and Al dual anode x ray source. The instruments

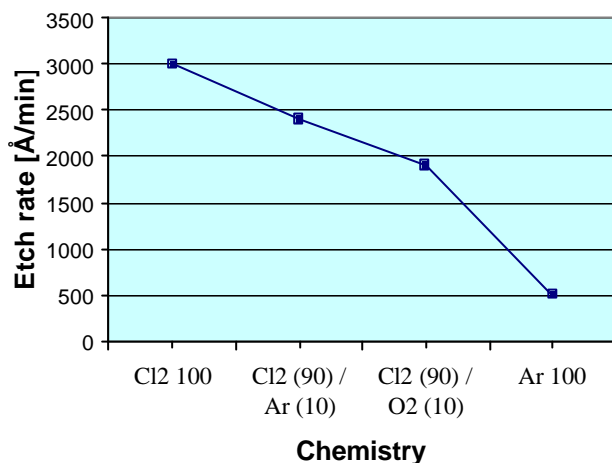
operates in Fixed Analyser Transmission (FAT) mode; the pass energy of 40 eV was used. The spectra were acquired using  $Mg_{K\alpha}$  radiation of 1253.6 eV.

## Results and Discussion

### Etching Chemistry

Cobalt silicide etching rate variation with the used etching chemistry has been evaluated. The experiments were performed keeping constant the process pressure (2 mTorr), the total gases flow (25sccm) and both the high- frequency (1100 Watts), the low-frequency (200Watts) powers and etching temperature (240°C).

$CoSi_2$  etching rate variation versus plasma composition is reported in figure 2.

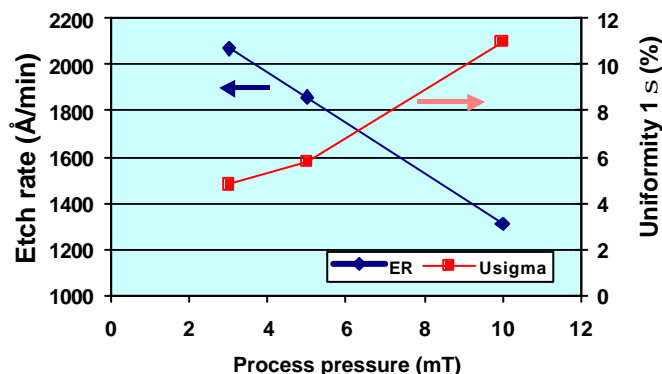


**Figure 2**  $CoSi_2$  etch rate variation vs. etching chemistries- DC Bias values was 890V per each process

Higher etch rate is observed for 100%  $Cl_2$  plasma (3000Å/min). Using a 90%  $Cl_2$  / 10% Ar plasma chemistry etch rate decreasing has been observed (from 3000Å/min to 2400Å/min). This could be due to the less chlorine radicals concentration in the plasma phase. Using  $Cl_2/O_2$ , instead of  $Cl_2/Ar$ , etch rate is decreased to 1900Å/min. This effect could be explained considering the reaction between chlorine and oxygen in the plasma environment and with the surface oxidation due to the oxygen presence.

### Process Pressure

Process pressure variation on etching performances is shown by the next graph.



**Figure 3**  $CoSi_2$  etch rate and etch non-uniformity variation vs. process pressure

Experiments were performed using  $\text{Cl}_2$  chemistry, a source power of 530W, a bottom power of 200W and an etching temperature of 190°C.

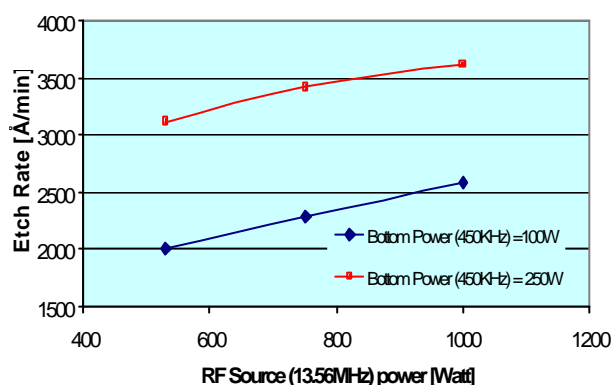
From previous graph, an etch rate enhancement has been observed with the process pressure increasing. At the same time etch non-uniformity also increases.

These effects are related to the greater ion bombardment energy achieved operating at lower pressure.

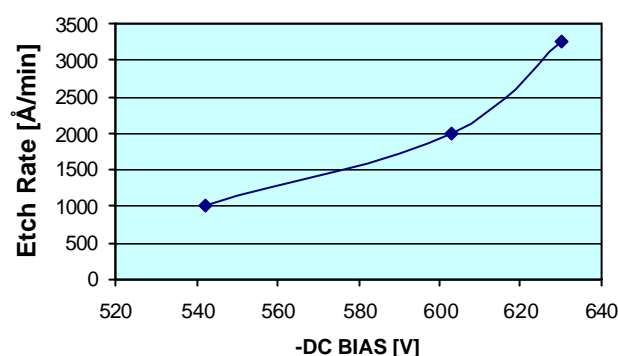
### RF Power

In the graph of figure 4 ER variation versus the source power (13.56MHz) is reported. This evaluation has been performed at two different bottom powers (450 KHz).

Increasing the MHz power the ion density is also increased and this cause a linear etch rate enhancement.



**Figure 4** CoSi<sub>2</sub> etch rate variation vs. MHz Power at two different Bottom power values



**Figure 5** CoSi<sub>2</sub> etch rate variation vs. DC Bias Voltage

Moreover, increasing the DC bias voltage, the etch rate value is also increased. The effect is clear from previous figure 5.

### Process Temperature

In order to investigate about the role of the wafer heating on the reaction mechanism, XPS analyses of different plasma treated samples have been performed.

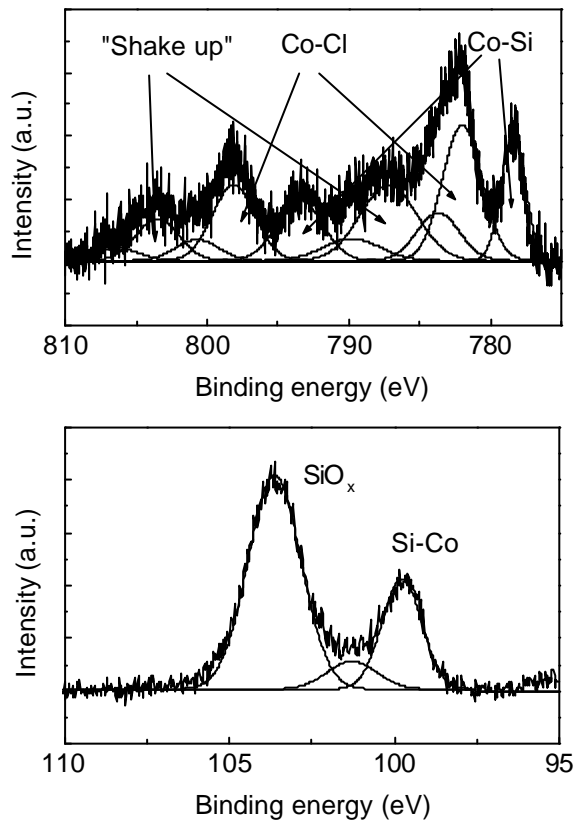
In particular, the following samples were analyzed:

- 1) not etched sample;
- 2) sample etched at 150 °C
- 3) sample etched at 190 °C
- 4) sample etched at 240 °C for 10 and 20 sec respectively.

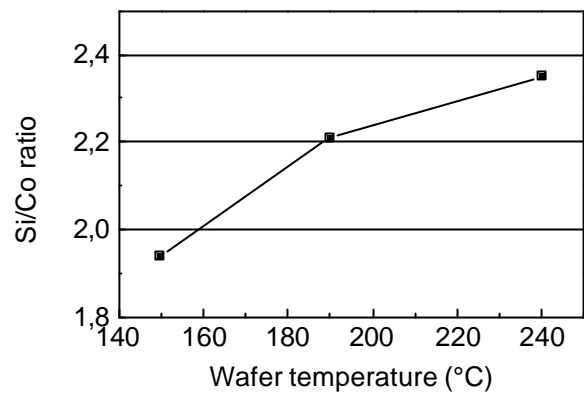
The survey spectra of surfaces show the Co, Si, O and Cl signals (this absent in the case of not etched sample). Fig. 6 reports the Co2p and Si2p signals obtained for the sample etched at 240 °C for 20 sec. The spectrum of Co2p is formed by the components assigned to Co-Si and to Co-Cl chemical bonds. Moreover, associated to the main components, in the spectrum are present the “shake up” satellites. The spectrum of Si2p shows the signals due to SiO<sub>2</sub> and CoSi<sub>2</sub>.



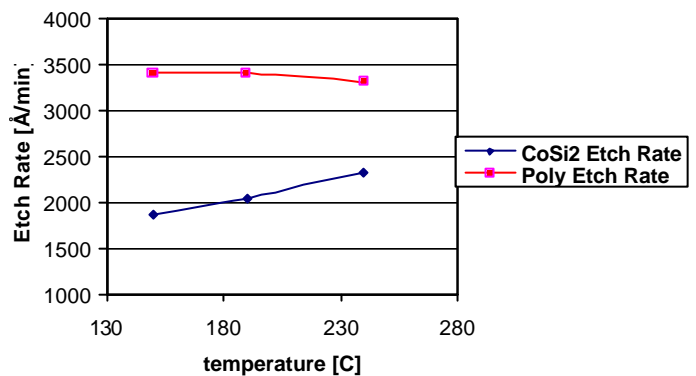
Fig. 7 reports the Si/Co atomic ratio (normalized after  $\text{SiO}_2$  and  $\text{CoCl}_x$  contributions subtraction), as a function of wafer temperature. It shows that the increase of the wafer temperature small variation of Si/Co ratio in the range of 1.9-2.35.



**Fig. 6.** Co2p and Si2p XPS spectra of CoSi<sub>2</sub> surface after etching at 240 °C for 20 sec.



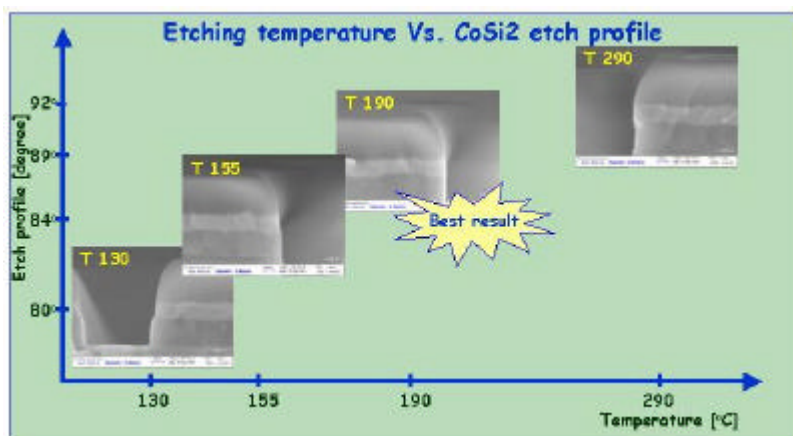
**Fig.7.** Si/Co atomic ratio measured by XPS as function of wafer temperature.



**Figure 8** CoSi<sub>2</sub> and Polysilicon etch rate values versus etching temperature

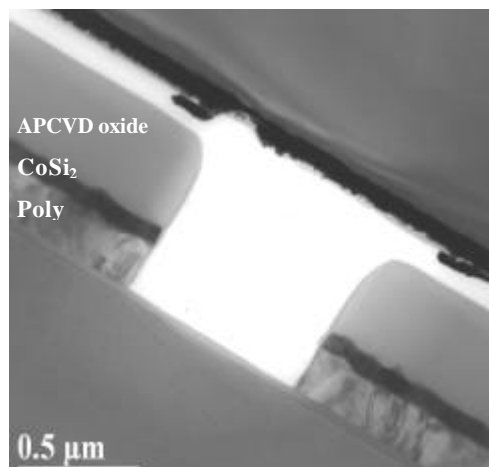
Figure 8 reports the cobalt silicide and polysilicon etch rates variation versus the etching temperature. This picture shows that increasing the temperature CoSi<sub>2</sub> etch rate is also increased, while polysilicon etch rate remains almost constant at about 3400 Å/min.

Figure 9 shows the CoSi<sub>2</sub>/polysilicon stack profile etch variation at different etchin temperature.



**Figure 9:** X-SEMs of CoSi<sub>2</sub>/Polysilicon stack vs. etching temperature

The best etch performances were obtained at 190°C etching temperature, as it is clear from next TEM cross-section of Fig. 10.



**Figure 10:** X-TEM of CoSi<sub>2</sub>/ poly stack. The result has been achieved operating at 190°C etching temperature

## Conclusions

Cobalt di-silicide is a very promising candidate for gate electrode formation in electronic devices. However, while for other silicide (WSi, TiSi<sub>2</sub>) fluorine and/or chlorine based etching chemistry are able to dry etch these materials, CoSi<sub>2</sub> is a hard-to-etch material, due to the inherent low volatility of cobalt by-products (i.e. CoCl<sub>x</sub>) that causes increasing of cobalt concentration in the silicide layer during the etch and leads to metal residuals on the wafer surface.

In this work the ability to etch CoSi<sub>2</sub> /polysilicon stack with good etching characteristics using a low-pressure, high density plasma etcher was achieved and the role of both plasma chemistry, DC bias voltage, process pressure, and wafer temperature control in CoSi<sub>2</sub> etch performances is also shown.

The combination of the 100% chlorine etching chemistry with the low pressure, high density conditions and the wafer temperature control allowed to avoid the cobalt concentration increasing in the silicide layer during the etching, leading to a reliable dry etch process.

## References

- 1) H. Sung Rhee, B.Tae Ahn and D.K. Sohn – J. of Appl. Phys Vol. 86 n.6 15 Sept 1999 pp3452 - 3459
- 2) A.Alberti, F.LaVia and S.Ravesi J.Vac. Sci. Technol. May/Jun 2002 pp 880-884
- 3) W.Town Sun, M. Chi Liaw, K.Chieng Hsieh and C. Ching-Hsiang Hsu, IEEE Transaction on Electronics Devices Vol. 45 NO9 Sept 1998 pp.1912-1919
- 4) H.S.P. Wong IBM J.Res. & Dev. Vol 46 NO2/3 March/May 2002 pp133-153
- 5) F.Fracassi, R.D'Agostino, R. Lamendola, A.Filippo, C.Rapisarda and P.Vasquez, J. Electrochem. Soc. Vol.143 No.2 (1996).
- 6) C.Tringali, ST Microelectronics Internal Report - 5 Mar 2002.
- 7) G.Arena, ST Microelectronics Internal Report – 1 Sept 2000.

# Experimental program for pulsed corona processing of biomass derived fuel gases at 850 degr.C

A.J.M. Pemen<sup>1</sup>, S.A. Nair<sup>1</sup>, F.M. van Gompel<sup>1</sup>, H.E.M. van Leuken<sup>1</sup>, F.A.J. Mertens<sup>1</sup>,  
V. Lekx<sup>1</sup>, K. Yan<sup>1</sup>, E.J.M. van Heesch<sup>1</sup>, K.J. Ptasinski<sup>2</sup>,  
H.P.E. Thieman<sup>3</sup>, T.C.J. Geutjes<sup>3</sup>, P. Leijendeckers<sup>4</sup>

<sup>1</sup>*Eindhoven University of Technology, Faculty of Electrical Engineering,  
P.O.Box 513, 5600 MB Eindhoven, The Netherlands*

*Phone: +31(0)40 2474492, Fax: +31(0)40 2450735, E-mail: a.j.m.pemen@tue.nl*

<sup>2</sup>*Eindhoven University of Technology, Faculty of Chemical Engineering, The Netherlands*

<sup>3</sup>*Vicoma, Roermond, The Netherlands, <sup>4</sup>Montair Andersen, Sevenum, The Netherlands*

**Abstract** - To supply combustion engines, gasturbines or fuel cells with fuel gas obtained from biomass gasification, it is necessary to clean the biogas. Also the production of chemicals requires a high gas quality. Especially heavy aromatic hydrocarbons ("tars") must be removed. In this work we present investigations on tar removal by pulsed corona discharges. A new pulsed corona tar removal system will be described, which can operate at gas temperatures up to 850 degr.C.

## 1. Introduction

To supply combustion engines, gasturbines or fuel cells with fuel gas obtained from biomass gasification, it is necessary to clean the biogas. Also the production of chemicals by processes such as Fisher-Tropsch requires a high gas quality. Especially heavy aromatic hydrocarbons ("tars") must be removed. Biomass gasification has a significant higher biomass to power efficiency than biomass combustion. The produced fuel gas has a low heating value of typically 4-6 MJ/Nm<sup>3</sup> and mainly consists of H<sub>2</sub>, CO, CH<sub>4</sub>, CO<sub>2</sub> and N<sub>2</sub>. Tars are formed during thermal conversion of biomass. Condensation of tar can block filters and can seriously decrease the lifetime of the engine. As a consequence, tars in the biogas must be removed until the dew point temperature is lower than the lowest temperature in the process. Hence it is necessary to reduce the aromatic content of the gasses. Reviews of tar removal methods can be found in [1,2].

In this work, we present investigations on tar removal by pulsed corona discharges as an alternative approach to catalytic or thermal tar cracking. Experiments (at a gas temperature of 200 degr.C) show that tar removal by pulsed corona processing is possible. Energy requirements vary from 400-500 J/L for naphthalene removal, while phenol removal requires 900-1000 J/L. In this paper we discuss the main reactions paths for tar removal. A reaction scheme will be outlined, showing that tar removal mainly occurs via dissociation of CO<sub>2</sub>. The energy density requirement is influenced by termination of O radicals by background CO.

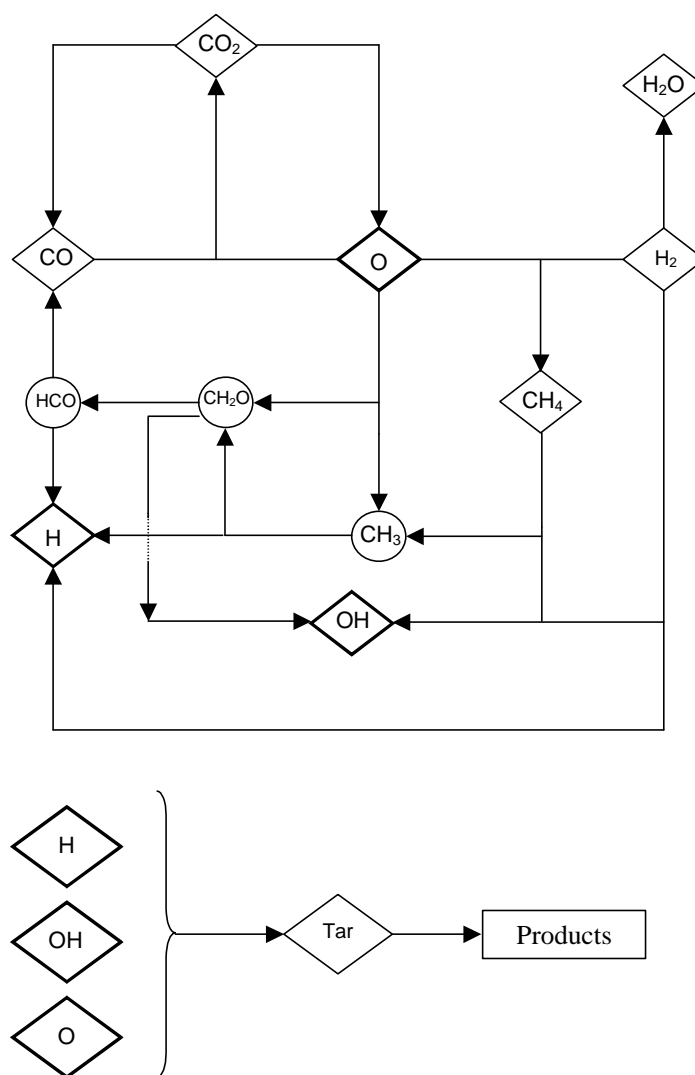
More efficient tar removal is expected at higher temperatures (>400 degr.C). This paper describes a pulsed corona system that can operate at temperatures up to 850 degr.C. Interesting engineering problems will be highlighted, for instance the high-temperature high-voltage feedthrough of the reactor. We will show that pulsed corona runs excellently at temperatures of 850 degr.C. For high-temperature corona operation, pulsed power is the only method for avoiding spark breakdown. The experimental program will focus on: (i) the effects of temperature, tar concentration and tar composition, (ii) the effect of additives, (iii) properties of the pulse-source and corona reactor geometry on streamer properties and tar removal efficiency.

## 2. Tar removal by pulsed corona discharges

We showed the feasibility of pulsed corona tar removal during field tests, where a pulsed corona reactor was coupled to a wood gasifier [3,4]. At an energy density of 160 J/L about 70 % of the heavy tars was converted into lighter ones. In addition, laboratory studies in fuel gas at 200 degr.C show a >90 % removal of tar

components as naphthalene, toluene, phenanthrene and phenol [5,6], at corona energy densities varying from 400-1000 J/L. A global kinetic model for tar removal is given in [6]. Insight into the chemical processes involved has been obtained by determining the energy needed for tar removal in various gas mixtures [5,6].

Based on the above mentioned results, 106 chemical reactions involved in tar removal from fuel gas have been identified [7]. By means of kinetic modeling and sensitivity analysis, reference [7] indicates that 10 reactions dominate the process and are more important than the others. Figure 1 shows these important reaction pathways. Of course, these reactions are not sufficient to describe the complete process, but these are the ones, that represent the important pathways encountered by the radicals formed.



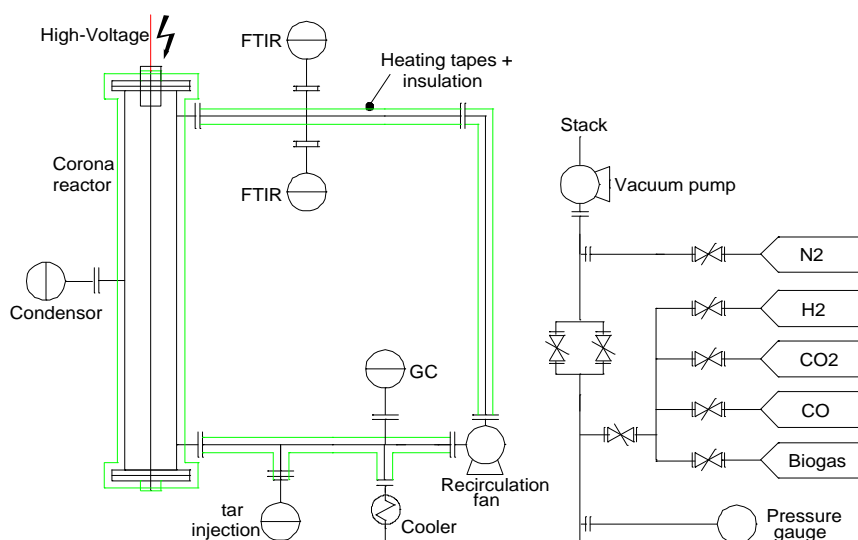
**Figure 1** Reaction scheme for tar (heavy hydrocarbon of PAH) removal from fuel gas obtained from biomass gasification.

The primary process starts with the formation of oxidizing species, viz, O via dissociation of CO<sub>2</sub> with the main competing step being its termination by CO. In addition, favorable production of secondary radicals occurs via its reaction with H<sub>2</sub> to form reactive species such as OH and H. This step in fact performs a balancing act for the consumption of O by H<sub>2</sub>. Since both those species perform the same role in case of naphthalene removal as done by O. On the other hand, the calculations indicated sensitivity to the dissociation step of HCO as well as its reaction with CH<sub>4</sub>, which were not seen so explicitly by experimentation. Perhaps, higher concentrations of CH<sub>4</sub> can therefore have an impact on the process, but not verified experimentally. Like wise, HCO decomposition has also been indicated to be a significant producer of CO, in combustion studies as well [8]. Hence, all paths leading to production of HCO therefore assumes

importance. Indirectly, this also has a negative influence, since it involves trapping of the more reactive O atom in CO. The path depicted thus outlines the flow of energy in the system, since every radical produced involves consumption of energy and therefore every radical terminated results in loss of energy. The scheme thus shows a more or less complete picture of radical behavior at 200 degr.C, supported by experimental results as well. Product distribution in case of naphthalene removal indicates ring opening via an oxidation mechanism as well. For coupling to an actual working gasifier, an ideal gas cleaning (tar removal system) should operate at higher temperatures (>400 degr.C). At these conditions, the radical pathway would definitely depend on its kinetics, but more on the radical concentrations, which are difficult to predict. In addition, a technical challenge is also to create a non-thermal plasma at such severe conditions.

### 3. A high temperature pulsed corona set up

The experimental set-up (Fig. 2) consists of a pulsed power supply and a wire-cylinder type corona reactor. The reactor has a diameter of 160 mm and is 1 m in length. The reactor is part of a closed loop circulation system, driven by a fan with variable speed adjustment. This fan, manufactured by Piller-Germany, can operate up to 850 degr.C and at a pressure range from 1-1000 mbar. The internal gas flow rates can be adjusted between 6-12 m/s or 400-900 Nm<sup>3</sup>/hr and the volume of the system is 100 liters. The entire set-up is heated by means of heating lines, along with adequate thermal insulation and temperature control. The maximum operating gas temperature is 850 degr.C. The heating rate is determined by the capacity of the heating and insulation system, reactor materials, flanges, feedthrough e.d. The system can be heated up from 20 degr.C to 850 degr.C in about 4 hours. In order to prevent any condensation of tars, cold-spots (e.g. at flanges or the fan-axis) have a temperature of at least 220 degr.C. Flanges allow flexible connection of e.g. diagnostics, tar injector, gas supply, vacuum pump, and their temperatures are adjusted to 220 degr.C.



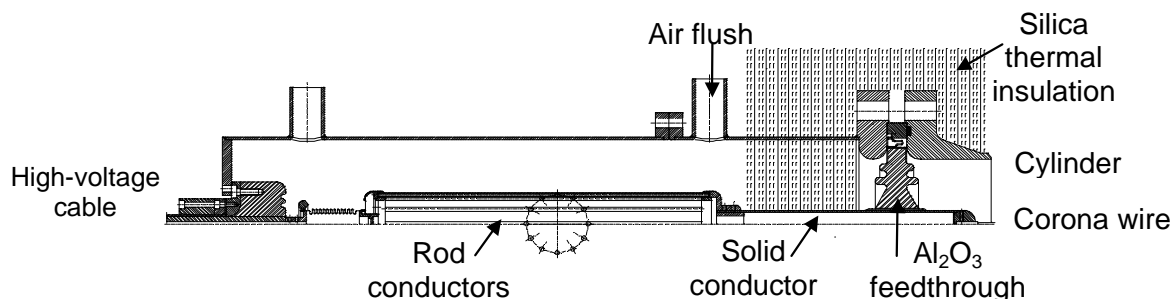
**Figure 2** *Experimental setup. The corona reactor has a diameter of 160 mm and a length of 1 m. The reactor is part of a closed loop circulation system, and can operate at gas temperatures up to 850 degr.C and a pressure range from 1-1000 mbar.*

Prior to filling the system with fuel gas, all air will be evacuated by means of a vacuum pump (1 mbar). Evacuation can also be done when the system is already heated up. This saves a lot of time, since various experiments can now be done without first cooling down the system and heating it up again. However, stainless steel loses mechanical strength at higher temperatures. Finite element analysis was used to evaluate the mechanical strength of the system under operating and fault conditions, as complete combustion of the fuel gas. Based on these results, stainless steel ASTM A-312 was selected for the reactor and the flow system (wall thickness 12 resp. 8 mm). For safety reasons, a brake plate is used in the flow system.

The system can be filled with a synthetic fuel gas of composition 20 % CO, 12 % CO<sub>2</sub>, 17 % H<sub>2</sub>, 1 % CH<sub>4</sub>, rest N<sub>2</sub> and heated up to about 850 degr.C, at a pressure of 1 bar. Apart from this, individual gases can be added via separate gas injection ports. Filling the system with each individual gas and monitoring its partial pressure can make the required gas composition. All gas-cylinders are stored in safety cabins, equipped with safety valves, fire protection and appropriate gas sensors. Tar injection is done by means of a boiler. A weighed amount of the component can be added and vaporized into the flowing gas stream.

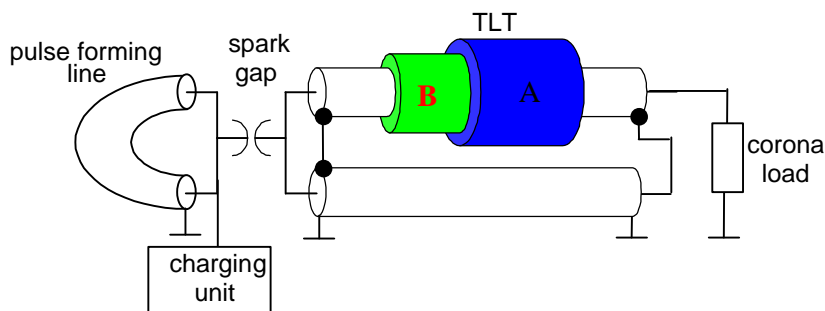
Tar measurements can be done by both FTIR (Bruker Vector22) and a GC (HP5890). The GC is equipped with a FID and a Chrompack CP-Sil 5 CB fused silica WCOT (Wall Coated Open Tubular) column for measurement of heavy hydrocarbons. Additionally a condenser is connected to the corona reactor, via a temperature controlled sample line. The condensate can be analyzed by means of GC-MS for hydrocarbons, that can be intermediates formed during the corona processing. In the near future, optical access to the corona reactor will be possible, e.g. for optical measurements on streamer properties.

A very complicated component is the high-voltage feedthrough of the corona reactor. The feedthrough must have the following requirements: (i) withstand an electrical stress of up to 30 kV/cm, (ii) high temperature of 850 degr.C, (iii) pressure range from 1-1000 mbar, (iv) the thermal expansion must be well controlled, and (v) acts as a thermal barrier between the high temperatures inside the reactor whereas the connection to the pulsed power supply can only withstand room temperature. A detailed drawing of the feedthrough is given in Fig. 3. The main feedthrough is an alumina part, hold between two metal flanges (with bolts having the same thermal expansion coefficient as the alumina). This whole part is embedded in silica thermal insulation. A coaxial high-voltage cable (on left side) is connected via a number of parallel rods, in order to reduce the temperature. The rods are flushed with ambient air. The characteristic impedance of the whole structure equals the impedance of the cable.



**Figure 3** *High-temperature high voltage feedthrough*

An experiment starts with switching on the heating and filling the system with the desired gas composition. After allowing sufficient time to ensure uniform gas composition and temperature distribution, tar is vaporized into the gas stream and again the system is allowed to attain uniform tar concentration. This can be monitored from the FTIR spectrum. This spectrum is taken as the background for further analysis. Pulsed corona discharges are then run for a particular time interval. After every run, both GC and FTIR analysis are done for the tar component removed.

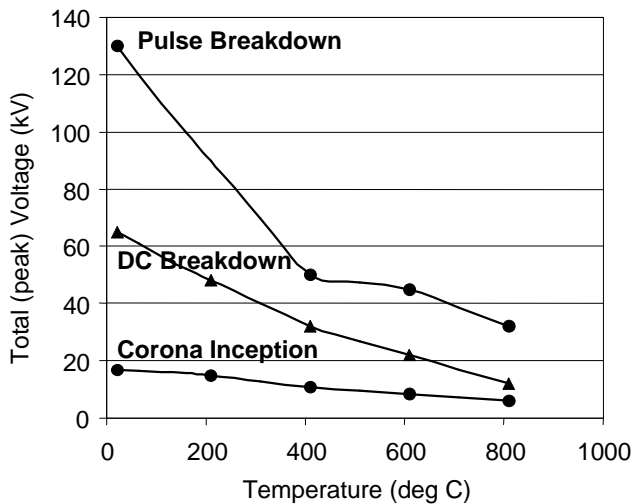


**Figure 4** *Pulsed power generator*

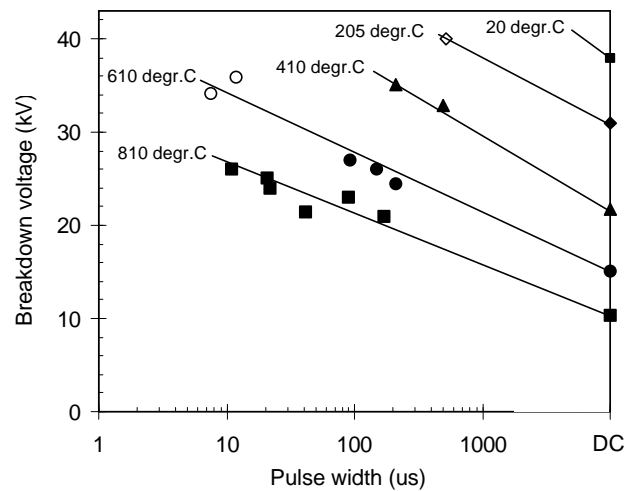
The pulsed power supply is shown in Fig. 4. A 10 m long pulse forming line (RG218 coaxial cable) is charged via a resonant charging unit. The charging voltage  $V$  can be varied between 20-40 kV. After charging, the spark gap is automatically triggered, using the RLC trigger method (see [9]). Now the pulse forming line is discharged, forming a pulse with an amplitude of  $\frac{1}{2}V$  and a width of  $2\tau$  (where  $\tau$  is the transit time of the pulse forming line:  $2 \times 5 \text{ ns/m} \times 10 \text{ m} = 100 \text{ ns}$  width). The rise time is about 5 ns. The energy-per-pulse is  $\frac{1}{2}CV^2$  (where  $C$  is the capacitance of the pulse forming line ( $100 \text{ pF/m} \times 10 \text{ m} = 1 \text{ nF}$ ) and varies between 0.2-0.8 J/pulse, depending on the charging voltage. Proper impedance matching between the generator and the corona reactor is necessary for good energy transfer efficiency. A good matching (energy transfer  $>90\%$ ) can be obtained by a proper choice of the peak-voltage [9]. The pulse repetition rate can be adjusted up to 1000 pps. The length of the pulse forming line can easily be varied, thus varying the pulse width (in practice about one order, between 20 and 200 ns).

Since the output voltage is only half the charging voltage, a transmission-line-transformer (TLT) is used. Detailed descriptions of a TLT are given in [9]. The TLT used here consists of two coaxial transmission lines (RG218), with a length of 2.5 m. At the sparkgap-side, both lines are connected in parallel, thus providing a matched impedance for the charged line (25 ohm). At the reactor-side, the lines are connected in series. This output impedance of 100 ohm provides a better matching with a corona reactor. In addition, the output voltage will be doubled, thus the pulse voltage will now be equal to the charging voltage  $V$ . The performance of a TLT depends on the choice of magnetic cores. An energy efficiency of about 97 % has been obtained using Metglas cores with a microgap. High resistivity ferrite cores are used to absorb remaining energy in the circuit after plasma quenching, and to limit the switching currents during short-circuits or breakdowns in the reactor. The main functions of the TLT used in this work can be summarized as: (i) achieve a higher output impedance for better matching with a corona reactor, (ii) double the output voltage, and (iii) protection of the switch against short-circuits and breakdowns.

Pulsed corona runs excellently at temperatures of 800 deg.C and higher, even under polluted conditions, see Fig. 5 [10]. This figure shows the applied peak corona voltage as a function of temperature for three cases: (i) corona inception, (ii) DC breakdown and (iii) breakdown with microsecond pulses (1-5  $\mu\text{s}$  pulses in a 30 cm diameter 1 m long reactor). Figure 6 shows that, also at higher temperatures, the breakdown voltage increases significantly with decreasing pulse width. For nano-second pulses the breakdown voltage is expected to be even higher. For high-temperature corona operation pulsed power is the only method for avoiding spark breakdown.



**Figure 5** Pulsed corona existence at higher temperatures for a wire-cylinder reactor of 30 cm diameter and 1 m length. Pulse-width for pulse breakdown is 1-5  $\mu\text{s}$ .



**Figure 6** Breakdown voltage versus pulse width for a 30 cm wire-cylinder reactor at various temperatures. At open markers, no breakdown yet.

#### 4. Conclusions

Tars can be removed from biogas by means of pulsed corona processing. The important reaction pathways involved have been identified for a gas temperature of 200 degr.C. A chemical reaction scheme has been set up. The tar removal process mainly occurs via O radicals, obtained from dissociation of CO<sub>2</sub>. The main competing reaction is termination of the O radical by background CO.

Further research will focus on further reducing the energy consumption for tar removal. More efficient tar removal is expected at higher temperatures. An experimental setup has been build, which can operate at temperatures up to 850 degr.C. Pulsed corona runs excellent at these high gas temperatures. The setup allows great flexibility in gas compositions, tar compositions and concentrations and pulsed power parameters.

**Acknowledgements** - The authors acknowledge the support of SDE (Dutch foundation for sustainable energy) and the Dutch Energy Research Center ECN.

#### References

- [1] J.P.A. Neeft, H.A.M. Knoef, P. Onaji: "Behavior of Tar in biomass gasification systems. Tar related problems and their solutions", Novem report No. 9919. Energy from Waste and Biomass (EWAB), The Netherlands. 1999.
- [2] T.A. Milne, R.J. Evans: "Biomass Gasification tars: their nature, formation and conversion", NREL, Golden, Colorado, USA. Report No. NREL/TP-570-25357, 1998.
- [3] E.J.M. van Heesch, A.J.M. Pemen, K. Yan, S.V.B. van Paasen, K.J. Ptasinski, P.A.H.J. Huijbrechts: "Pulsed corona tar cracker", IEEE Transactions on Plasma Science, 28 (2000), 1571-1575.
- [4] S.A. Nair, A.J.M. Pemen, K. Yan, F.M. van Gompel, H.E.M. van Leuken, E.J.M. van Heesch, K.J. Ptasinski, A.A.H. Drinkenburg: "Tar removal from biomass derived fuel gas by pulsed corona discharges", accepted for Fuel Processing Technology, January 2003.
- [5] S.A. Nair, A.J.M. Pemen, K. Yan, E.J.M. van Heesch, K.J. Ptasinski, A.A.H. Drinkenburg: "Chemical processes in tar removal from biomass derived fuel gas by pulsed corona discharges", accepted for Plasma Chemistry and Plasma Processing, December 2002.
- [6] A.J.M. Pemen, S.A. Nair, K. Yan, E.J.M. van Heesch, K.J. Ptasinski, A.A.H. Drinkenburg: "Pulsed corona discharges for tar removal from biogas derived fuel gas", submitted to Plasmas and Polymers, February 2003.
- [7] S.A. Nair, K. Yan, A.J.M. Pemen, E.J.M. van Heesch, K.J. Ptasinski, A.A.H. Drinkenburg: "Chemical Kinetic Modeling of Tar Removal from Biomass Derived Fuel gas by Pulsed Corona Discharges", to be presented at this conference ISPC16.
- [8] N.M. Marinov, W.J. Pitz, C.K. Westbrook, A.M. Vincitore, M.J. Castaldi, S.M. Senkan, C.F. Melius: "Aromatic and polyaromatic hydrocarbon formation in a laminar premixed n-butane flame, Combust. Flame 1998, 114, 192-213.
- [9] K. Yan, "Corona Plasma Generation", Ph.D.-Thesis, Eindhoven University of Technology, 2001, ISBN 90-386-1870-0.
- [10] E.J.M. van Heesch, A.J.M. Pemen, P.C.T. van der Laan: "Pulsed Corona Existence up to 850°C ", Proceedings of 6th Int. Symp. On High-Voltage Eng., New Orleans, paper 42.23, 4p, 1989.



**Plasma Etch Process for Ferroelectric Capacitor formation**  
G. Béique<sup>1</sup>, G. Arena<sup>2</sup>, S Ross<sup>1</sup>, S Ravesi<sup>2</sup>, C Tringali<sup>2</sup>, P Vasquez<sup>2</sup>  
1-Tegal Corporation, Petaluma, California, USA  
2-STMicroelectronics, Catania, Sicily, Italy

**Abstract**

The patterning of FeRAM capacitor stacks has proven challenging for both the electrode and ferroelectric layers typically used in these device structures. Noble metals, including platinum and iridium, are used as electrodes in the capacitor structure, while high-dielectric constant materials, such as lead zirconium titanate (PZT) and strontium bismuth tantalate (SBT) are used for their ferroelectric properties. Because of the chemical behavior of all these materials the etch processes require entirely new technologies and approaches. This is due to the inherent low volatility of the etch by-products. Strong ion bombardment energies and high temperatures are required for the etching of these materials.

One of the main issues in ferroelectric materials is related to the control of the critical dimension (CD) and the veil deposition on the sidewall. In order to achieve steep profiles with a veil-free process two approaches are reported in this work.

**Introduction**

First and second generation FeRAM devices have been successfully produced using photoresist masks for cell features as small as 0.5 microns. In order to preserve the mask, moderate wafer temperatures must be used (<200C). This results in an etch regime dominated by physical etching and the tendency to re-deposition on the mask sidewall. Most approaches in this category employ two or three masks.

As the device size decreases looking to third generation FeRAM, the pattern transfer becomes increasingly difficult. For smaller geometries, the focus of the stack etching has shifted to the use of a single mask process.

This study reports process performance for individual layers and full stack etching.

**Experimental Procedure**

**A. Sample preparation**

The present study is based on 3 sets of samples, described below:

A ferroelectric material strontium bismuth tantalate (SBT) was spun coated onto BPSG/Si substrates by a sol-gel method to a thickness of 1200Å.

A top electrode Pt was sputtered to a thickness of 1000Å onto TiN/BPSG/Si substrate.

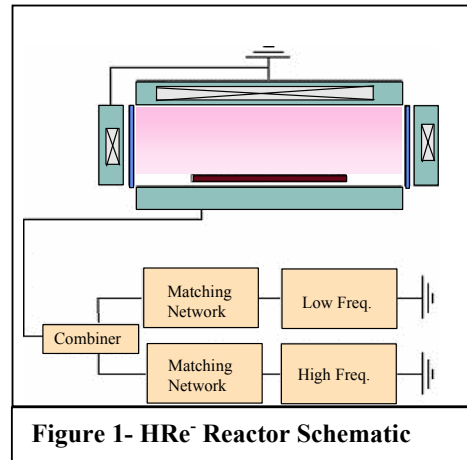
A full stack of Pt/SBT/Pt was processed onto TiO<sub>2</sub>/oxide/si substrate, where each layer measured approximately 2000Å.

All stacks were dry etched by means of a Tegal 6540 HRe-™ cluster tool. Etch rates for different conditions were measured with Tencor™ profilometer. Process performances were characterized using scanning electron microscopy (SEM) techniques.

## B. FeRAM Etch Reactor Development

The initial phases of the development program that produced this etch technology focused on selecting among the known reactor types (i.e., ICP, ECR, capacitively-coupled, etc.) and reactor configurations the one best suited for etching FeRAM materials. The result of this development work is the HRe<sup>-</sup> (Figure 1), a magnetically confined, dual frequency (Tegal patented), capacitively-coupled reactor. This reactor produces uniform, high density, low pressure plasmas and supports high gas flow rates.

The reactor design of the HRe<sup>-</sup> makes it uniquely well suited for etching FeRAM materials. The reactor is capacitively-coupled, which is to say that the RF excitation that sustains the discharge is applied directly to an electrode that is interior to the reactor's vacuum vessel. Further, the feature that makes the reactor uniquely well suited for etching FeRAM material is Tegal's patented use of dual frequency. As shown in Figure 1, both of the RF frequencies are applied to the wafer platen. Our experiments have shown that the fundamental trade-off of profile vs. re-deposited etch product side wall is much easier to manage with this RF configuration than any configuration in which the dual frequencies are applied to different electrodes.<sup>1,2</sup>



**Figure 1- HRe<sup>-</sup> Reactor Schematic**

## Results

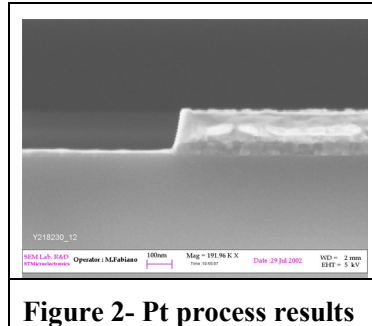
### A. Platinum Etch

Platinum has been typically used for the electrode in ferroelectric capacitor structures for thermal stability and resistivity considerations. Independent of the type of reactor used for dry etching the platinum, most common approaches to etch platinum utilizes halogen-containing gas mixtures such as CF<sub>4</sub>/Ar, Cl<sub>2</sub>/O<sub>2</sub>, Cl<sub>2</sub>/Ar, and Cl<sub>2</sub>/CF<sub>4</sub>. These gas mixtures form a variety of halogen compounds with platinum, though they are typically non-volatile.<sup>3</sup> Here lies the major difficulty associated with the low temperature process necessary for photoresist etch mask application. The choice of mask limits the increase of wafer temperature to increase the volatility of FeRAM materials.

In the present study, we point out, among others, a few process parameters that allow the etching of Pt to yield a profile angle of 84° without fences using photoresist masks.

To obtain a veil-free process, it is essential to control the resist erosion, where too much erosion will yield in shallow profile angle, and too little in Pt re-deposition on the resist sidewall. As previously shown,<sup>4</sup> the size of the veils can be controlled to some extent by chlorine flow and resist thickness. Increasing the flow results in higher erosion of the photoresist. This will result in more sloped profile angle of Pt, which in turns decreases the veils that build up on the sidewalls.

Figure 2, shows a result that was achieved after optimizing the resist thickness, the chlorine flow and other parameters. The SEM shows the post etch (with resist mask removed) profile that was achieved on a Pt/TiO<sub>2</sub> layer stopping on BPSG. The Pt etch rate was above 2000Å/minute, the profile angle measures 84°. The process has been demonstrated on a 1.0µm structure line width.



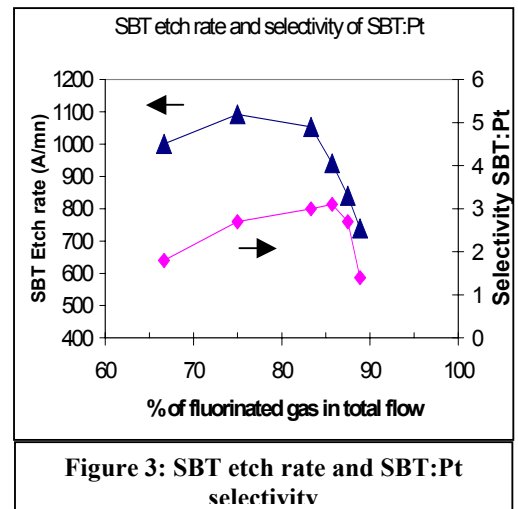
**Figure 2- Pt process results**

## B. SBT Etch

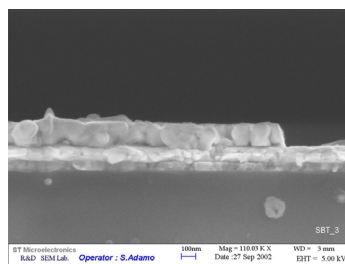
Like platinum, the by-products of SBT etching in a chlorine and in a fluorine chemistry have melting points well above the temperature range allowed by the use of photoresist masks. Again, the process performance will depend on balancing the chemical and physical component of the etch, and may require a compromise to profile angle for a veil-free process. The SBT etch process must fulfill a number of requirements: sufficient etch profile control, selectivity to the underlying layers; adequate high etch rates for acceptable productivity, and no post-etch veils.

Chlorinated and fluorinated chemistries together with several additives were investigated for SBT etching in terms of etch rate, profile angle and selectivity to Pt.

Dry etching of SBT has been performed in a variety of gases, e.g.  $\text{NF}_3/\text{Cl}_2/\text{Ar}/\text{O}_2$  and  $\text{Cl}_2/\text{CF}_4/\text{Ar}$ .<sup>5,6</sup> It was found that a fluorine-based chemistry yields better results in the HRe-™ reactor. Using a fluorinated chemistry, the dry etching of SBT thin films was studied by varying the gas ratio of fluorinated gas in the total gas flow. It was found that the addition of the fluorinated gas increased the selectivity of the dielectric to Pt and the SBT etch rate up to a maximum value; as shown in Figure 3 as the concentration of the fluorinated gas increase further, both parameters (etch rate and selectivity) decrease. The decrease in etch rate could be indicating that an excess of etching gas inhibits sputtering of ions to the film surfaces.



The etching process developed for the SBT thin film yields reasonable etch rate ( $> 800\text{\AA}/\text{minute}$ ), and a selectivity of SBT to Pt higher than 2.5:1. The profile angle was on the order of  $70^\circ$  without redeposit or residues. The results are shown in Figure 4.

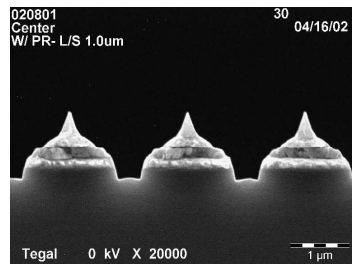


**Figure 4- SBT process results**

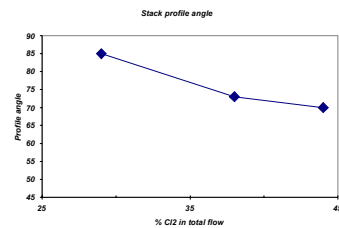
### C. Pt/STB/Pt Stack Etch

An alternative approach to individually etching each component of the FeRAM capacitor is to etch the entire MFM capacitor with one mask.

As per etching the individual layers, it is important to balance out the resist thickness and the thickness of the materials to be etched. If the resist erosion is too severe during etch, the full stack profile angle will be sloped and in an extreme case, this will result in excessive corner rounding of the platinum top electrode material. The following graph shows the relation between profile angle and chlorine concentration; while the following SEM shows an extreme case of resist erosion and consequently of the top electrode.

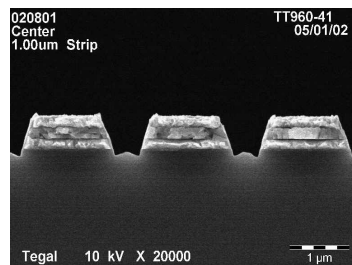


**Figure 5: Full stack etching with too much resist erosion**

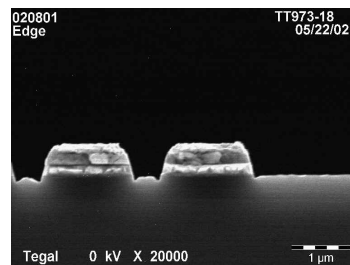


**Figure 6. Stack profile angle vs chlorine flow**

After optimizing the chlorine ratio in the total gas flow, among other process parameters, the full stack was etched with a two step process. The first step allowed controlling the resist thickness and slope while the second step was engineered to remove any sidewall re-deposition. The best results were presented in figures 7 and 8.



**Figure 7. Full stack best results**



**Figure 8. End of array for full stack etching**

The SEM shows the post etch (with resist mask removed) profile that was achieved on a Pt/STB/Pt/TiO<sub>2</sub> layer stopping on oxide. The Pt and STB etch rate are above 2000Å/minute and 500Å/mn respectively, the profile angle measures 76°. The process has been demonstrated on a 0.5µm structure line width.

## CONCLUSION

Veil-free processes for Pt and SBT etch using photoresist masks, either as an individual layer or part of a stack, are the results of the right balance between resist thickness and the thickness of the materials to be etched. For a thick resist, the platinum chloride by-product will redeposit on the resist sidewall, causing veils or horns. The resist thickness needs to be engineered for the stack to be etched, and the dry etch process needs careful control of resist erosion to balance out the integrity of the Pt corner in a veil free process.

Veil free processes were demonstrated for individual layers etch of Pt and SBT and for a Pt/SBT/Pt stack. For Pt and SBT individual layer etching a profile angle of 84deg and 70deg, respectively, was obtained, while for a full stack of Pt/SBT/Pt, a profile of 76deg was obtained, without any sign of sidewall redeposition. The process performances were proven down to 0.5um line and space geometries, improving further the process performances of FeRAM structures with photoresist masks.

---

<sup>1</sup> C. E. Farrell, et. al., *Integr. Ferroelectr.*, **16**, 109 (1997)

<sup>2</sup> Y. C. Jeon, et. al., *Integr. Ferroelectr.*, **17**, 489 (1997)

<sup>3</sup> Jin Hong Kim et al., *IEEE TRANSACTIONS ON ELECTRON DEVICES*, VOL. 46, NO. 5, MAY 1999, p 984,

<sup>4</sup> G. Beique et al. *XVI congresso nazionale sulla scienza e tecnologia del vuoto*, Oct. 2002. Proceedings to be published

<sup>5</sup> Y. H. Im, et al. *J. Vac. Sci. Technol. A* 19 (4 ), Jul Aug 2001 -1315

<sup>6</sup> DP Kim et al, paper presented *at AVS 48<sup>th</sup> International Symposium* in Nov 2001

# EVALUATE ON MECHANICAL, OPTICAL PROPERTIES AND CHEMISTRY PROPERTIES OF THE ULTRA WATER-REPELLENT THIN FILMS PREPARED BY METHOD OF TMMOS + CO<sub>2</sub> PLASMA

Yunying Wu<sup>1,2</sup>, Makoto Bekke<sup>4</sup>Yasushi Inoue<sup>3</sup>, Hiroyuki Sugimur<sup>4</sup> and Osamu Takai<sup>1</sup>

<sup>1</sup> Center for Integrated Research in Science and Engineering, Nagoya University, Nagoya 464-8603, Japan

<sup>2</sup> Aichi Science & Technology Foundation, Nagoya 460-0002, Japan

<sup>3</sup> Department of Materials Processing Engineering, Nagoya University,  
Nagoya 464-8603, Japan

<sup>4</sup> Research Center for Nuclear Materials Recycle, Nagoya University,  
Nagoya 464-8603, Japan

E-mail: [wu@plasma.numse.nagoya-u.ac.jp](mailto:wu@plasma.numse.nagoya-u.ac.jp)

## Abstract

In this work we present the results on the evaluation about the mechanical property, optical property and chemical composition of hard ultra water repellent film by means of microwave plasma-enhanced CVD (MPECVD). The results demonstrate the feasibility of obtaining the ultra water repellent film of the transparent and better mechanical properties. In particular we show that control of total deposition pressure is as effective as the techniques.

*Key words:* microwave plasma-enhanced CVD, silicon dioxide, hard thin film, ultra water-repellency, mechanical properties.

## 1. Introduction

Recently, various coatings on glasses have been frequently conducted in order to provide some new functions. Water repellent glasses fabricated by coating a water repellent film maintaining the original optical property of the glass have a wide variety of applications, for example, eyeglasses, lenses, windows of automobiles, etc. Optical transparency and the durability, such as wear resistance, of the films are of particular importance. Furthermore, it is favorable that such films are prepared at a low temperature below 373K in order to provide ultra water-repellency to optical parts made of polymeric materials. Plasma-enhanced CVD (PECVD) using organosilicon compounds as raw materials is a useful deposition method of producing water-repellant silicon oxide ones at low substrate temperature less than 373K [1]. But the thin film produced by this method is very soft. The ultra water repellent film with both mechanical durability and the good optical property was still unrealizable.

By introducing oxygen into the films, the films were effectively hardened. However, the hard films become hydrophilic (water contact angle below 10 degrees) because of hydroxyl groups existed at the surface. Moreover, surface roughness decreased due to dense formation of the films. The control of surface nanotextures of the deposited films to obtain ultra water-repellency is difficult therefore we cannot use oxygen to increase hardness [2]. In this research we have used CO<sub>2</sub> to harden silicon oxide films instead of O<sub>2</sub>. We first prepared a hard thin film by using CO<sub>2</sub> as an additive gas by means of MPECVD. Second, the film was treated by a chemical method, preparation of self-assembled monolayers of fluoroalkylsilane on the film. By this treatment, the water contact angle of the film increased up to 150 degrees. This paper reports the results of the evaluation about the mechanical property, optical property and chemical composition of ultra water repellent film by using CO<sub>2</sub> as an additive gas by means of MPECVD.

## 2. Experimental

### 2.1. Films Preparation

The film was prepared by the MPECVD system [2]. We used a gas mixture of trimethylmethoxysilane (TMMOS; (CH<sub>3</sub>)<sub>3</sub>SiOCH<sub>3</sub>) and CO<sub>2</sub>. Substrates were glass and Si wafers. During deposition for 15 min, the substrate temperature remained below 373 K. The films prepared with various deposition condition such as  $P_{\text{total}} = 80 \sim 188$  Pa with constant partial pressure ratio  $P_{\text{TMMOS}} / P_{\text{CO}_2} = 0.37$ , and  $P_{\text{TMMOS}} / P_{\text{CO}_2} = 0.21 \sim 1.56$  with

constant total pressure  $P_{\text{total}} = 160$  Pa. Self-assembled monolayers of fluoroalkylsilane were prepared by CVD using heptadecafluoro-1,1,2,2-tetrahydro-decyl-1-trimethoxysilane [FAS17;  $\text{CF}_3(\text{CF}_2)_7(\text{CH}_2)_2\text{Si}(\text{OCH}_3)_3$ ] as a precursor. The CVD vessel was sealed with a cap and then heated for 5 hours in an oven maintained at 373K. Details of this chemical method have been described elsewhere [3].

## 2.2. Properties evaluation

Water contact angles of deposited film surfaces were measured with a contact angle meter (Kyowa Interface Science, CA-D) based on the sessile water drop measuring method with a water drop of 2 mm in diameter. The measurements were conducted at 298 K in air.

Mechanical properties, hardness, Young's modulus ( $E_r$ ) and wear resistance, of the films were measured with a nanoindenter (Hysitron, TriboScope) interfaced with an atomic force microscope (AFM; Park Scientific Instruments, Autoprobe-LS). We used a Berkovich-type diamond tip. A force-displacement curve of each sample was measured at a maximum load of 200  $\mu\text{N}$ . The wear resistance of the films was measured as follows. First, each film surface was scanned with the same diamond tip at a constant load of 20  $\mu\text{N}$ . The tip scanning was repeated 10 times in a 1  $\mu\text{m}$ -square region with 512 lines at a scanning rate of 2  $\mu\text{m/s}$ . After this tip scanning, the film surface was observed in AFM mode at a contact load of 3  $\mu\text{N}$  using the same Berkovich tip. The mechanical durability test was conducted by rubbing the coated surface with flannel cloth under load of 200 g. the durability was evaluated by measuring the change in contact angle.

Optical transmittance and reflectance of the films were evaluated with spectrophotometers (Hitachi, U-4000 and Olympus, UMPS).

Chemical compositions and structures of the films were analyzed by Fourier transform infrared spectroscopy (FTIR; Biorad, FTS-175C) and X-ray photoelectron spectroscopy (XPS; Shimadzu-Kratos, AXIS). Depth profiles of the films were measured by XPS with Ar ion etching.

Surface morphologies of the films were observed with a field emission scanning electron microscope (FESEM; JOEL, JSM-6330F).

## 3. Results and Discussion

**3.1. Water repellency** Water repellency of films depend on the deposited conditions (pressure ratio ( $P_{\text{TMMOS}} / P_{\text{total}}$ ) and total pressure) as shown in Fig.1. The water contact angle increased with increased pressure ratio ( $P_{\text{TMMOS}} / P_{\text{total}}$ ) and total pressure  $P_{\text{total}}$ . This is showed that deposited pressure influences film structure. Different surface structure made with different pressure are shown in Fig.2 and 3.

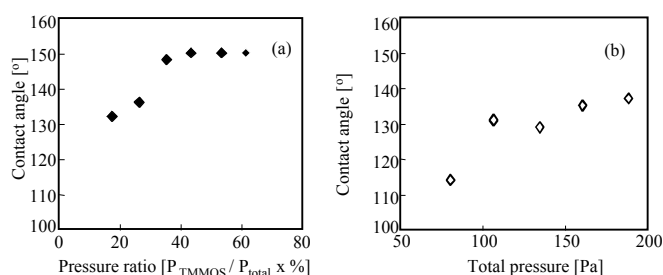


Fig. 1. Water repellency of films depend on the deposited conditions.  
(a) total pressure was 160 Pa, pressure ratio ( $P_{\text{TMMOS}} / P_{\text{total}}$ ) was changed.  
(b) pressure ratio ( $P_{\text{TMMOS}} / P_{\text{total}}$ ) was 26%, total pressure was changed.

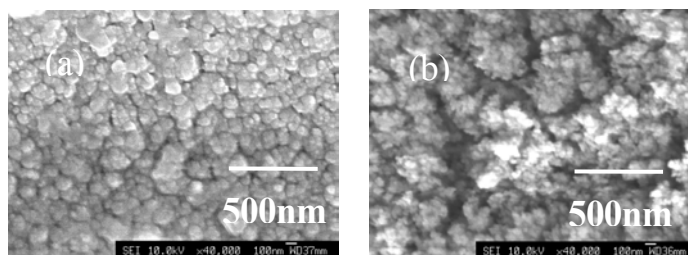


Fig. 2. FESEM images of the films surface.

- (a) pressure ratio ( $P_{\text{TMMOS}} / P_{\text{total}}$ ) was 17%, total pressure was 160 Pa.  
(b) pressure ratio ( $P_{\text{TMMOS}} / P_{\text{total}}$ ) was 61%, total pressure was 160 Pa

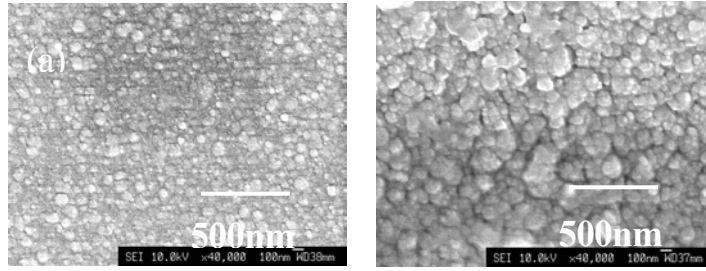


Fig. 3. FESEM images of the films surface.  
(a) total pressure was 80 Pa, pressure ratio ( $P_{\text{TMMOS}} / P_{\text{total}}$ ) was 26%.  
(b) total pressure was 188 Pa, pressure ratio ( $P_{\text{TMMOS}} / P_{\text{total}}$ ) was 26%

**3.2. Hardness and wear resistance** Figures 4 and 5 shows the mechanical properties of the deposited films. Hardness and wear resistance increased with decreasing total pressure  $P_{\text{total}}$ . On the other hand, roughness of

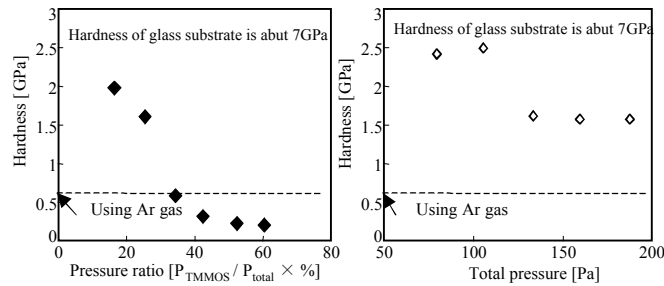


Fig. 4 Hardness of the deposited films

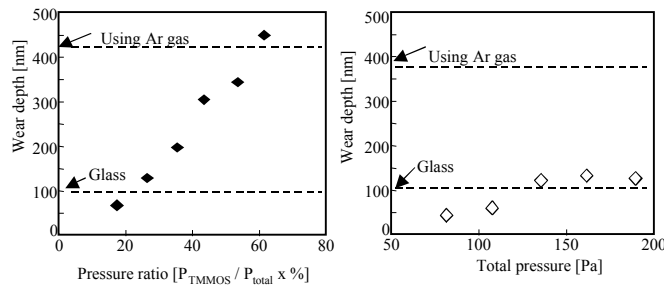


Fig. 5 Wear resistance of the deposited films

the film surface fell down (seen in Fig.3), that is water contact angle decreases. Hardness and wear resistance also increase in with decreasing of pressure ratio ( $P_{\text{TMMOS}} / P_{\text{total}}$ ). But the cluster size which dominate surface roughness decreased with partial pressure of TMMOS ( $P_{\text{TMMOS}}$ ). As a result, roughness of the film surface fell down and water contact angle decreased with increasing of  $P_{\text{TMMOS}}$ . The water contact angle prepared at the optimal condition ( $P_{\text{Total}} = 107 \text{ Pa}$ ,  $P_{\text{TMMOS}} / P_{\text{CO}_2} = 0.37$ ) was 150-135 degrees (after the hydrophobic treatment to form the self assembled monolayer of fluoroalkylsilane(FAS17) which give low surface energy). The hardness here was 2.48 GPa. Although it was quite low compared with the hardness of substrate glass (7GPa), it is improved about 8 times than that of the films prepared by Ar as a mixing gas [2]. The wear depth was about 58 nm, and lower compared with the wear depth of substrate glass (80-110 nm). Wear resistance is better than that of the glass substrate.

**3.3. Mechanical durability** Figure. 6 shows the dependence of water repellency of ultra water repellent film deposited on the three types of glass substrates upon repeating the rubbing with flannel cloth. The water repellency on all the substrates has a critical rubbing cycle at which the contact angle begin to decrease remarkably. This critical rubbing cycle was different for each samples. Among the substrates having almost the same surface roughness, the ultra water repellent film deposited using  $\text{CO}_2$  as an additive gas showed the best durability against rubbing. After 3000 times cycle, the contact angle of the ultra water repellent film deposited using  $\text{CO}_2$  as an



additive gas is maintained to 132 °. The decrease in water repellency after mechanical durability tests can be ascribed to breakdown of the tip part of film structure and to the decrease in fluorine surface density due to the gradual peeling of water repellent molecules (seen in Fig. 7).

3.4. *Optical transmittance* The photograph of a water drop on the chemically-treated film prepared with CO<sub>2</sub>

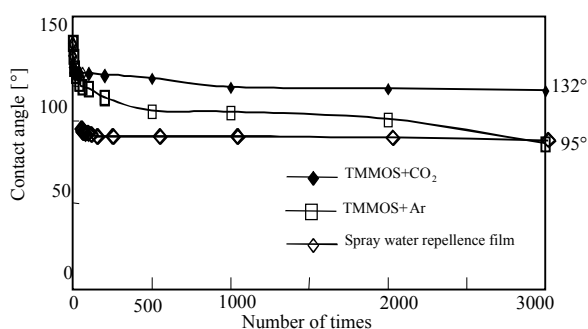


Fig. 6 Results of mechanical durability test

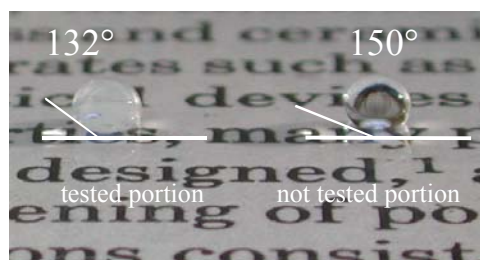


Fig. 7 Images of samples after test.

on glass is shown in Fig. 5. The printed characters can be read clearly through the film. The optical transmittance of the film was more than 90% in the visible range of 300 nm ~ 800 nm. The reflectance of the film was 0.3% and lower than that of the glass substrate (3~5%). However the trace worn out by the eye is not seen after a 3000 times wear test..

3.5. *Chemical compositions* Concentration of an element by XPS spectrum of these films was shown in Fig. 8. FTIR spectra of the films prepared with CO<sub>2</sub> and O<sub>2</sub> are shown in Fig. 9. From the XPS analysis the O/Si ratio

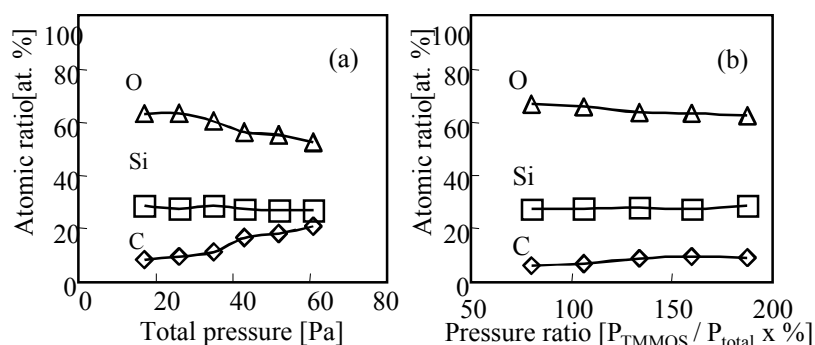


Fig. 8 Atomic ratio of the films by XPS analysis

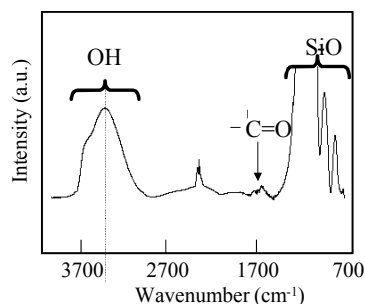


Fig. 9 FT-IR spectra of the films

of the film prepared with CO<sub>2</sub> is ca. 2.2 and higher than those of the films prepared with Ar and O<sub>2</sub>. Moreover, the results of XPS and FTIR analyses also showed the existence of a small amount of -COOH group in the film prepared with CO<sub>2</sub>. The peaks due to -COOH groups (288.5eV) were observed in the C1s spectrum [4]. In the FTIR spectrum of the film, small but distinct peaks due to C=O were found at 1640 cm<sup>-1</sup> ~ 1900 cm<sup>-1</sup> and the broad peak due to OH was appeared at ca. 3450 ~ 3700 cm<sup>-1</sup> [5, 6]. Because of the inclusion of a small amount of -COOH groups into the film prepared with CO<sub>2</sub>, the O/ Si ratio of the film exceeded a little the stoichiometric value of SiO<sub>2</sub>.

#### 4. Conclusions

Hard thin films with ultra water-repellency and optical transparency were prepared by the method of MPECVD using TMMOS and CO<sub>2</sub> as source gases and then the hydrophobidizing treatment using fluoroalkylsilane. Mechanical properties, hardness and wear resistance were improved largely compared with the films prepared with TMMOS and Ar. The addition of CO<sub>2</sub> is remarkable to improve the mechanical properties of the ultra water-repellent films. The film of wear resistance is better than that of the glass substrate and the permeability of visible light is high.

#### Acknowledgements

This work is supported in part by “Advanced Cooperative Research Project” of Aichi Science & Technology Foundation and Research Project "Biomimetic Materials Processing" (No. JSPS-RFTF 99R13101), Research for the Future (RFTF) Program, Japan Society for the Promotion of Science.

We also thank to the TOKAI RIKA CO.,LTD., who conducted the wear experiment in this research.

#### References

- [1] A. Hozumi, H. Sekoguchi, N. Kakinoki, O. Takai -J. Mater. Sci. **32**, 4253 (1997).
- [2] Yuning Wu, Yasushi Inoue, Hiroyuki Sugimura, Osamu Takai - Proc. Materials Research Society 2001, (U.S.A.) **711**, 283 (2001).
- [3] H. Sugimura, N. Nakagiri, J. Photopolym -Sci. Technol., **661**, 10(1997).
- [4] G.Beamson, D.Briggs - “High Resolution XPS of Organic Polymers The Scienta ESCA300 Database”, John Wiley & Sons, (1992).
- [5] C. Rau -Thin Solid Films **249**, 28 (1994).
- [6] R. M. Silverstein, G. Clayton Bassler, Terence C. Morrill -“Spectrometric Identification of Organic Compounds”, John Wiley & Sons, (1992).

# Pulsed RF Excited Argon-Oxygen Discharges and the Influence of Metastable Oxygen Molecules

H.M. Katsch, C. Manthey, and H.F. Döbele

*Institut für Experimentelle Physik, Universität Essen, D-45117 Essen, Germany  
e-mail: katsch@uni-essen.de*

## Abstract

The temporal behavior of negative oxygen ions was investigated in the afterglow of a pulsed inductively excited rf discharge in oxygen-argon mixtures. Collisions of O-minus ions with O atoms and metastable oxygen molecules lead to considerable electron production in the afterglow. An increase of the absolute O-minus density is observed with increasing argon fraction. It is likely that additional negative ions are generated by dissociative attachment of metastable oxygen molecules.

## 1. Introduction

Oxygen radio frequency discharges with capacitive and inductive coupling are of considerable technological relevance. This is reflected by an impressive number of publications on the basic properties and phenomena both from the experimental and the theoretical point of view. These publications consider, however, in the majority of cases rf discharges with capacitive coupling. Nevertheless rf discharges in oxygen with inductive coupling are clearly finding increasing interest. Measurements and theoretical predictions of oxygen rf discharge properties with capacitive coupling show that the density of atomic oxygen and metastable oxygen molecules can have a strong influence on the density of negative ions and vice versa. It is an open question in how far experience gained with capacitive discharges can be applied to inductive discharges, since the plasma densities are higher by one or two orders of magnitude. Additional loss processes of negative ions such as electron detachment and ion-ion neutralization of negative ions with positive ions have to be considered at higher plasma densities. The resulting negative ion density and the spatial structure are therefore dependent on a number of parameters. The validation of existing models requires reliable experimental information on negative oxygen ions. Pulsing the rf discharge provides a means to gain insight into basic phenomena of inductive oxygen discharge.

## 2. Experimental set-up

The measurements were performed at a GEC reference cell which is well documented in the literature [1]. The plasma is generated by inductive excitation at an rf frequency of 13.56 MHz. The standard pressure at which the majority of the measurements was performed was 10 Pa at a standard power of 250 W. All power data refer to the “on” phase. The fraction of the power that is coupled to the plasma as compared to the fraction dissipated in the coil and the surrounding metal mantling has not been determined. Some of the shown measurements were performed in a modified reference cell. In this configuration the inductive excitation coil is enclosed in a quartz vessel. The measurements have been performed in most cases with a pulse duration of 1 ms and an interpulse pause of 1 ms.

A plasma monitor (Hiden EQP) was installed at one of the side walls of the reactor chamber. The plasma monitor allows us to determine both the masses and the energies of particles and metastable oxygen molecules by appearance potential mass spectrometry.

Negative ions are detected by photo-detachment whereby the generated electrons are collected by a Langmuir probe. The frequency doubled output of an Nd:YAG laser ( $\tau \sim 15$  ns;  $E \sim 360$  mJ), shaped by a mask of suitable diameter (between 0.2 – 1.2 mm), enters the discharge chamber. The Langmuir probe is irradiated coaxially. The temporal distribution of atomic oxygen was achieved with two photon absorbed laser induced fluorescence spectroscopy (TALIF) (226 nm) using a Nd:YAG pumped dye-laser [2].

The density of positive ions, electrons were measured with a second Langmuir probe system (Scientific Systems Smart Probe). The Boxcar option of this system allows us to perform time resolved determinations of these quantities.

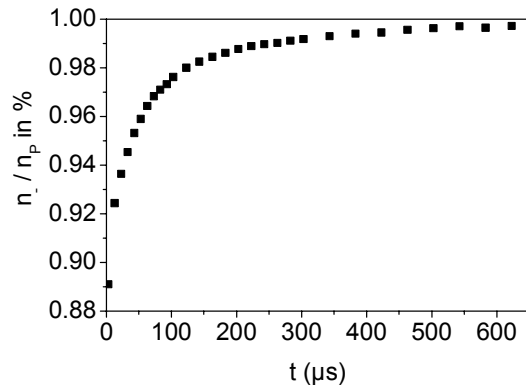
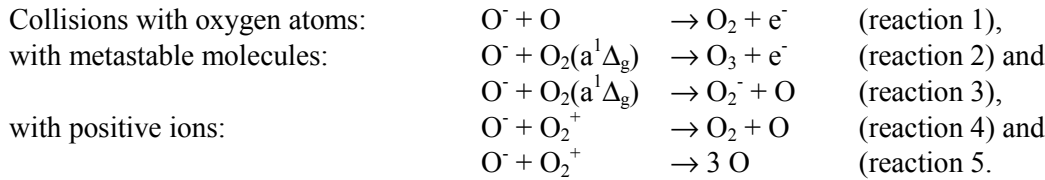
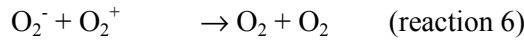


Fig. 1. relative density of negative oxygen ions ( $O^-$  and  $O_2^-$ ) in the afterglow

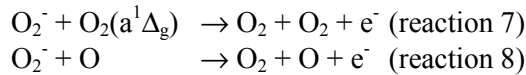
negative ions in the afterglow could be observed. The following reactions are candidates for losses of negative ions:



The  $O_2^-$  ions generated during the discharge and during the early afterglow are annihilated at high plasma densities predominantly by reactions with positive ions



and in the later afterglow by the reactions



The rate constants are taken from Lieberman and Lichtenberg [4] and the references there in.

Note: with photo-detachment we have measured as well the atomic negative ions as molecular negative ions.

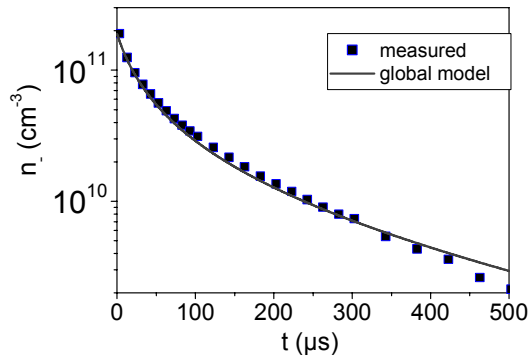
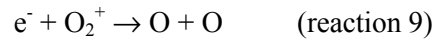


Fig. 2. density of negative oxygen ions ( $O^-$  and  $O_2^-$ ) in the afterglow

### 3. Charge carrier distribution in the decay phase of the discharge

Figure 1 shows the ratio of negative ions to plasma density measured with the uncompensated probe by photo-detachment. This measurement indicates the formation of an ion-ion plasma (electron free plasma) after approximately 500  $\mu s$  within the frame of the measurement error. The density distribution of negative ions is shown in figure 2 in comparison with a global model, see below. We assume that the negative ions are trapped in the positive plasma potential (not shown: measurements have been made with the smart probe system) up to 500  $\mu s$  (see [3] for the self-confinement of negative ions). Thus the density decay of negative ions must be explained by volume loss reactions alone. No formation of

The decay of the positive ions is determined by ion-ion neutralization according to reaction 4 and recombination with electrons, see fig. 3,



and diffusion. The first fast density decay is dominated by ion-ion neutralization at plasma densities range of  $10^{11} \text{ cm}^{-3}$ , the ambipolar diffusion dominates at later times.

The decay of the electrons (fig. 4) is given by recombination with  $O_2^+$  ions and by diffusion while the negative ions are trapped in the afterglow [3].

The measurements shown in fig. 2, 3 and 4, are compared with a global model basing on the reactions given above, and the measured initial conditions at

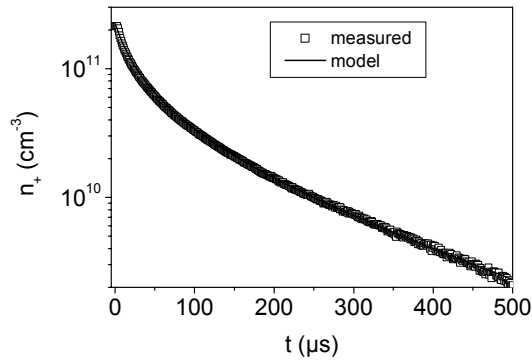


Fig. 3. density of positive oxygen ions in the afterglow

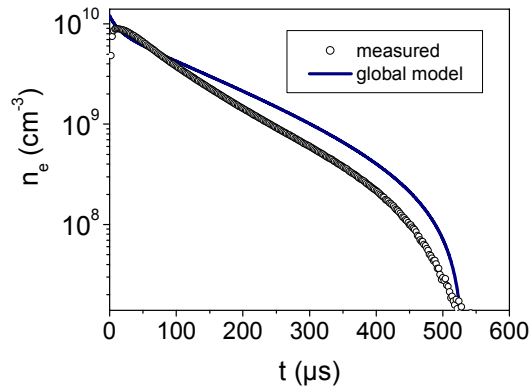


Fig. 4. density of electrons in the afterglow

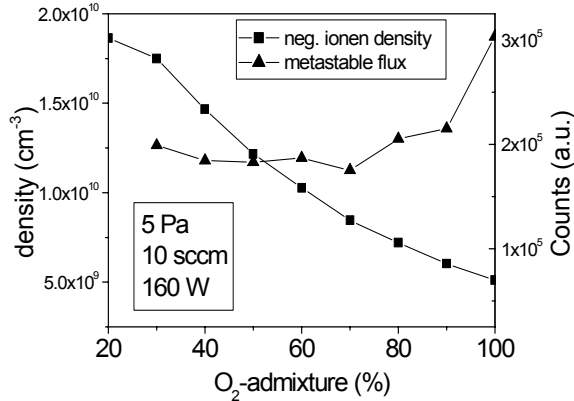


Fig. 5. density of negative oxygen ions 50  $\mu$ s after switch off and flux of metastable oxygen molecules

both cases we obtained an increasing density of the negative ions with decreasing partial pressure of oxygen, see fig 5. This findings are in contrast to the predictions of a global model of C. Lee and M. A. Lieberman [7]. The relative density of the negative ions (negative ion density to plasma density) increases as well, see fig. 6.

The main loss mechanism for negative oxygen ions during the discharge and in the early afterglow is given by ion-ion neutralization with positive ions. According to the predictions of the model [7] it is therefore unlikely that the density of the negative ions should increase with decreasing oxygen fraction. It is, therefore, necessary to consider an additional production reaction channel for the negative ions in order to explain the

$t = 0$ , plasma density, negative ion density and electron density in the afterglow.

The temporal distribution of the atomic density in the afterglow is given from TALIF-measurements. The decay of the positive ions by ambipolar diffusion is taken from the decay of the positive ions in the late afterglow. The unknown density of the metastables is used as a fit parameter assuming that the lifetime of the  $O_2(a^1\Delta_g)$  molecules is much longer than 1 ms [5].

The model yields fairly good agreement with the experimentally determined decays. Model calculations indicate that the early pronounced density decay of the negative ions is caused predominantly by the ion-ion neutralization with positive  $O_2^+$  ions.

In the late afterglow ( $t > 150 \mu s$ ) the density of the atomic oxygen is still sufficiently high so that the further decay of negative ions is dominated by collisions with oxygen atoms and metastables. Note that these reactions can represent a considerable source of electron production in the shut-off phase of the discharge.

In an electropositive plasma the temporal change of the electron density is equal to the decay of the positive ions due to quasineutrality. For the present case of the plasma potential being also positive during the afterglow, the negative ions with low temperature can not leave the plasma. This allows the electrons to escape quickly, since the negative ions are still left to provide quasineutrality [6]. Although the approach to describe the temporal behaviour of the electrons adopted here shows clearly the significance of the electron producing channel in the afterglow (see reactions, 1, 2, 7, and 8) leading to the formation of an ion-ion plasma later than expected. Note this transition is strongly affected by the metastable density and the decay of the atomic density.

#### 4. Density of negative oxygen ions in argon-oxygen mixtures

According to the above shown measurements the density of negative oxygen ions was determined in different argon-oxygen mixtures. The measurement has been carried out as well as for fixed input power as for controlled constant plasma density. In

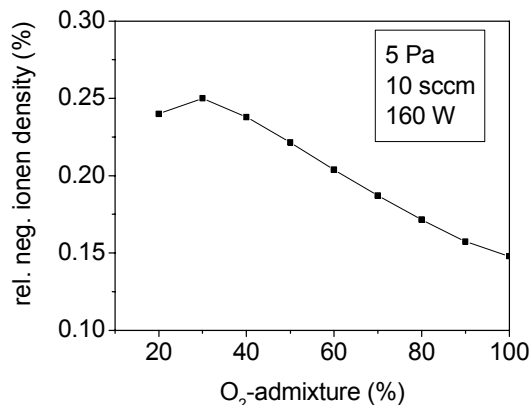


Fig. 6. relative density negative oxygen ions in the afterglow 50  $\mu$ s after switch off

important generation mechanism of electrons – have also been found to be important. The production of electrons in the afterglow inhibits the early establishment of the ion-ion plasma state. This transition to an ion-ion-plasma occurs, however, very fast and is an immediate manifestation for the diffusion behavior of electrons in electronegative gases. The metastable  $O_2(a^1\Delta_g)$  molecules can have a strong influence on the spatio-temporal diffusion of the primarily formed  $O^-$  ions to the walls and can lead to the formation of  $O_2^-$  ions.

In argon-oxygen mixtures we found an increasing negative ion density with decreasing oxygen fraction. We suppose that this behavior is caused by an additional production reaction due to dissociative attachment of metastable oxygen molecules.

### Acknowledgments

This work was supported by the “Bundesminister für Bildung und Forschung“ in the frame the “Verbundprojekt: Analyse und Modellierung der Einwirkung gepulster Plasmen auf Oberflächen, Teilvorhaben: Analyse der Wechselwirkung gepulster elektronegativer Plasmen mit Oberflächen”.

### References

- [1] P. J. Hargis, et al., Rev. Sci. Instrum., **65** (1994) 140
- [2] A. Goehlich, T. Kawetzki, and H.F. Döbele, Journal of Chemical Physics, **108** (1998) 9362
- [3] E. A. Bogdanov, A.A. Kudryavtsev and L.D. Tsendin, Tech. Phys. Lett., **27** (2001) 652
- [4] M. A. Liebermann and A. J. Lichtenberg, Principles of plasma discharges and materials processing, John Wiley & Sons, New York (1996)
- [5] H.-M. Katsch, et al., Plasma Sources Sci. Technology, **9** (2000) 323
- [6] A.A. Kudryavtsev, Tech. Phys. Lett., **22** (1996) 693
- [7] C. Lee and M. A. Lieberman, J. Vac. Sci. Technol., **A 13** (1995) 368
- [8] D. Hayashi and K. Kadota, J. Appl. Phys., **83** (1998) 697

measured increase of the negative ion density. Appearance potential mass spectroscopy measurements show a nearly constant flux of metastable oxygen molecules with increasing argon fraction (note: with this method different metastable states of the oxygen molecules could not clearly distinguished). It is, therefore, likely that additional negative ions are generated by dissociative attachment of metastable oxygen molecules [8].

### 5. Conclusions

We could identify the ion-ion neutralization of positive oxygen ions with negative oxygen ions as the main loss mechanism for the latter during the discharge and in the early afterglow. Losses of negative ions in collisions with oxygen atoms and metastable oxygen molecules – representing

# An Industrial 10-30 kW Corona Plasma System

G.J.J. Winands, R.C.J. Smetsers, A.J.M. Pemen, K. Yan, S.A. Nair and E.J.M. van Heesch.

*EPS Group, Department of Electrical Engineering, Eindhoven University of Technology,  
Eindhoven, 5600 MB, The Netherlands  
[g.j.j.winands@tue.nl](mailto:g.j.j.winands@tue.nl)*

## Abstract

This paper discusses an industrial corona-induced plasma system for gas cleaning (odor control, VOCs removal). A hybrid (= pulses superimposed on DC voltage) high-voltage pulsed power source for up to 30 kW output is being developed. Sixteen wire-cylinder reactors (1000 x 160 mm each) in parallel are used to match the source. We have seen that the energy per pulse increases as a function of the DC voltage level. No increase in matching was found, since the system was already well matched, even without DC bias superposition.

## 1. Introduction

The work of many authors has already shown the beneficial use of corona discharges for several pollutant removal processes (like tars, VOCs, bacteria's and odor specimens) [1-5]. The radicals produced by the corona discharge enhance several chemical reactions leading to a decrease in the pollutant concentration. Due to the chemical reactions, the species are transformed into other molecules, which are more easy to remove or less harmful.

To make corona plasma systems an industrial application which is compatible or even better than other contaminant removal processes (like ozone treatment, acid washing, etc.) a lot of research has still to be performed.

Since most industrial applications will be on large scale we considered it useful to investigate the possibilities to enlarge the present systems. Several possibilities to handle larger quantities of contaminants come to hand:

- Use many small pulsed power sources in parallel or in series. Of course this will not be a feasible, industrial, option since the installation costs will be extremely large.
- Increase the corona power. In doing so, it should be possible to increase the number of produced radicals and thereby the flow through the system (since more gas-flow can be treated at the same time). Of course the corona energy density cannot be increased infinitely due to physical limitations.
- Increase the corona power and the volume (so the flow can be enlarged) of the reactor, thereby keeping the average energy density constant. Although this seems a fairly logic possibility, some care has to be taken. Many of the theoretical calculations in the past are based on the assumption of uniformity (in both axial and radial direction) of the energy density. For larger reactor volumes this assumption will not necessarily be correct. In the future, experiments will be performed on the energy distribution of the plasma inside a wire cylinder reactor as function of the spatial position.
- Increase the corona power and use several reactors in series or in parallel. In this way the uniformity of the energy density is assured and only one power source is needed (thereby reducing the installation costs).

This paper discusses the developed 10-30 kW set-up and the first measurements performed to validate the feasibility of the last option. The set-up does have an increased average power and 16 reactors in parallel are used to match the pulse source. Initial measurements of the recently finished set-up are analyzed and presented.

Our first interest was in determining whether or not the superposition of a DC bias voltage on the energy pulses leads to an improved matching [6] between the power source and the reactor, and an increase in the energy density per pulse. The results of these measurements will be described below (in section 3) as well as the details of the set-up (section 2).

## 2. Experimental set-up: The 10-30kW hybrid set-up.

The concept of the experimental set-up was described in [6]. A schematic overview can be seen in figure 1. The set-up consists of the following parts:

- 1) *Low voltage part.* This part converts the 3 phase 380 VAC voltage into approximately 25  $\mu$ s wide voltage pulses of about 1 kV and 1 kA (peak).
- 2) *Pulse transformer.* The transformer has a winding ratio of 36. It converts the pulses from the low voltage part into high voltage pulses. These pulses are stored in the high voltage capacitor  $C_H$ . As can be seen in figure 1, the high voltage capacitor  $C_H$  is resonantly charged through the inductor  $L_2$  and the pulse transformer. The used pulse transformer was fabricated by the North Star Research Company.

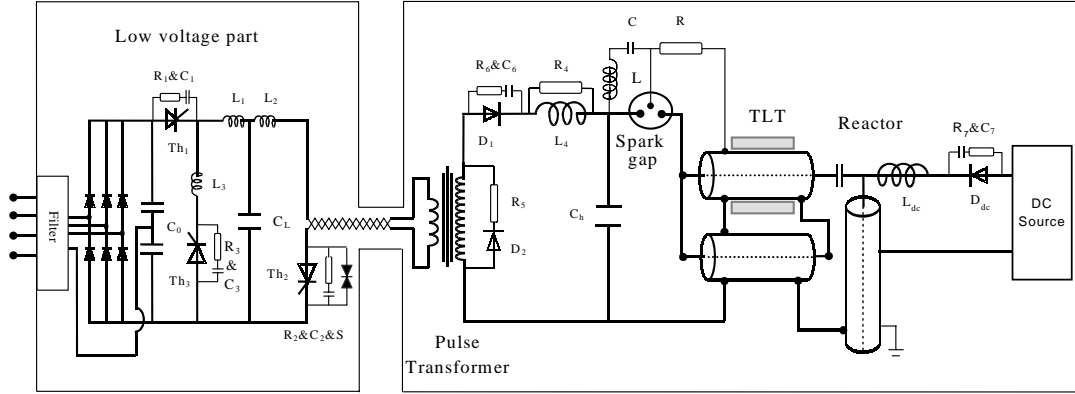


Figure 1: Schematic representation of the developed 10-30 kW hybrid pulsed power set-up.

- 3) *Spark gap.* This air flushed (4 bars, 0-100 m<sup>3</sup>/h), heavy duty (30 kV, 8 kA), high repetition rate (<1000 pps) switch is used to discharge the high voltage capacitor  $C_H$  into the TLT. The switch is triggered by means of the RLC circuit (see below). Since the transferred power in the gap is large, the electrode material will erode. As a result, the distance between the electrodes will increase, eventually leading to misfiring of the gap. Of course this should be avoided. Thus when constructing a spark gap, attention should be paid to the used electrode material and to the electrode geometry (to optimize the uniformity of the erosion). The present spark gap has an estimated lifetime of 1-year (continuous operation, 1000 pps) [6]. A concept for an improved spark gap has also been made. This new spark gap has an estimated lifetime of more than 5 years.
- 4) *RLC trigger circuit.* For continuous and stable performance of the spark gap it is important that the spark gap fires just after the high voltage capacitor has been completely charged. Pre-firing and mis-firing leads to several unwanted effects and should be avoided. The developed fail-safe RLC trigger method is described in [6].
- 5) *Transmission Line Transformer (TLT).* The TLT is used for several reasons: Firstly to match the power source with the reactor, secondly to multiply the output voltage or current, thirdly to easily super-impose a DC bias voltage onto the high voltage pulses. A schematic overview of the TLT can be seen in figure 2.

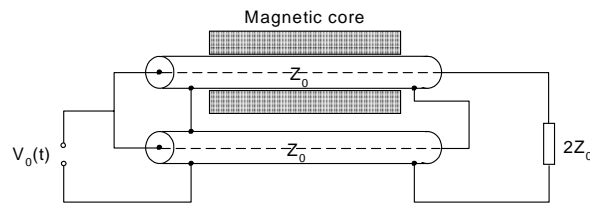


Figure 2: Schematic representation of the transmission line transformer.

As can easily be seen in figure 2, the output voltage of this two stage TLT is twice the input voltage. By changing the connection configuration it is also possible to multiply the output current by a factor 2 (i.e. by connecting the input side in series and connecting the output side in parallel).

The magnetic cores around the upper cable are added to significantly reduce the secondary mode current and thus reducing the energy losses. For our set-up, Ferrite CMD 5005 Toroid magnetic cores were used. It was also chosen to not use cables (RG218) for the TLT, but to use a concentric cylindrical



construction to fabricate the TLT. Detailed calculations for this TLT are given in [6]. The output impedance of our system is around 20 Ohms.

- 6) *Reactor*. Our reactor consists of 16 wire-cylinder reactors in parallel. The dimensions (length and diameter) of each cylinder are: 1000 x 160 mm. The reactor is constructed from stainless steel and has its axis in vertical direction.
- 7) *DC-power source*. For our experiments we used a water cooled Lambda EMI LC1202 High Voltage power source for supplying DC voltages up to 30 kV.

The complete set-up was made EMC proof by following the concept of an EMC wall and well-separated differential and common mode current paths.

The experimental set-up is equipped with several D/I measuring units, to be able to measure the voltage and the current on the input of the reactor. By means of an Agilent Infinium oscilloscope, the measured signals were recorded.

### 3. Measurements and results

In first instance we only used 1/4th ( $=12.6$  nF) of the available high voltage capacitors ( $C_H$ , see figure 1) to perform the measurements. This implies that the maximum average output power of 30kW has not yet been obtained. The reason we used only 1/4th of the capacitors was that we first needed to calibrate the complete system and to check if there weren't any constructional problems.

As a first measurement we determined the voltage over the spark gap. The result can be seen in figure 3. The voltage first rises continuously to a value of approximately 35kV. If the spark gap is triggered correctly than it will only fire once the voltage reaches the maximum value. The moment of triggering can be adjusted by varying the pressure and flow rate in the spark gap [6], or by changing the parameters of the RLC trigger circuit. The pulse repetition rate was kept as low as 50Hz during this measurement. It can be seen in figure 3 that the spark gap triggers at the right moment.

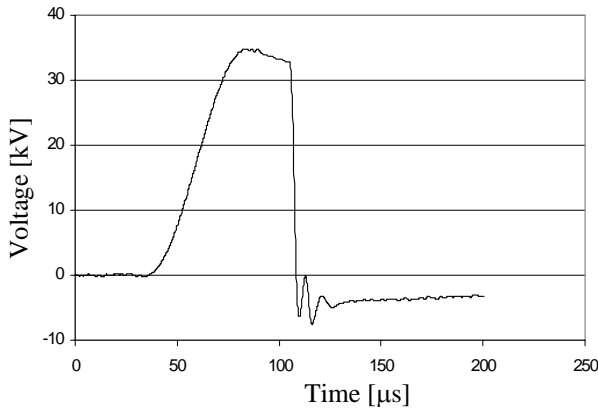


Figure 3: Voltage on the spark gap. Pulse repetition rate is 50 Hz.  $C_H$  is 12.6 nF.

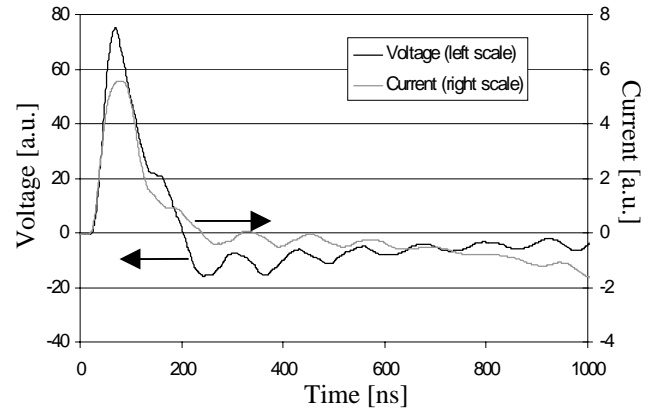


Figure 4: Typical voltage and current waveform. DC bias voltage is zero. Pulse repetition rate is 30 Hz  $C_H$  is 12.6 nF.

The energy stored in the high voltage capacitor  $C_H$  ( $=\frac{1}{2}C_H V^2 = 7.7$  J) is delivered to the reactor by means of the TLT system. This TLT will double the voltage (if designed and connected correctly). A typical result of a voltage pulse and a current pulse is shown in figure 4. The pulse repetition rate is 30 Hz and there is no DC bias superimposed. Unfortunately the calibration of the D-I measuring system turned out to be incorrect. Because we noticed this problem only shortly before the submission date of this paper we were not able to correct all the measurements. As a result the vertical axes of all the plots in the remainder of this paper will be given in arbitrary units.

The pulse duration would be around 65 ns based on the RC-time of the high voltage capacitors (12.6 nF) and the input impedance of the TLT ( $=5$  Ohm). Looking at the FWHM value of the curves in figure 4 it can be seen that the pulse duration is equal to approximately 60-70 ns.

When calculating the product of the voltage and the current the power will result. For the same pulse as shown in figure 4 the power is calculated in figure 5. In figure 6 the energy for this pulse is calculated by integrating the power waveform.

In figure 5 it can be seen that even without a DC bias voltage, there is no reflected (negative) power. This means that the power source and the reactor are already well matched. After the pulse, no energy will flow back into the TLT and the spark gap. The superposition of a DC bias voltage onto the pulses will therefore have no influence on the matching.

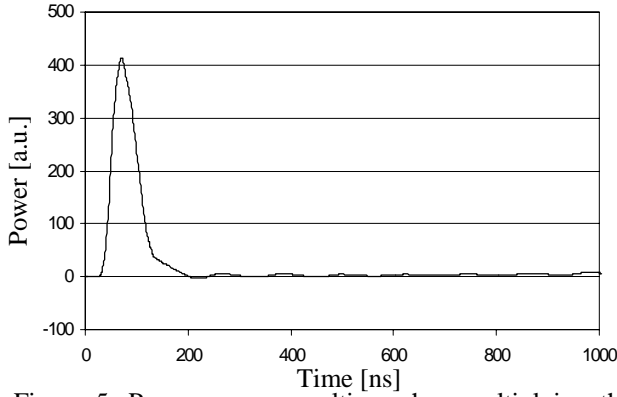


Figure 5: Power curve, resulting when multiplying the voltage and the current waveforms from figure 4.

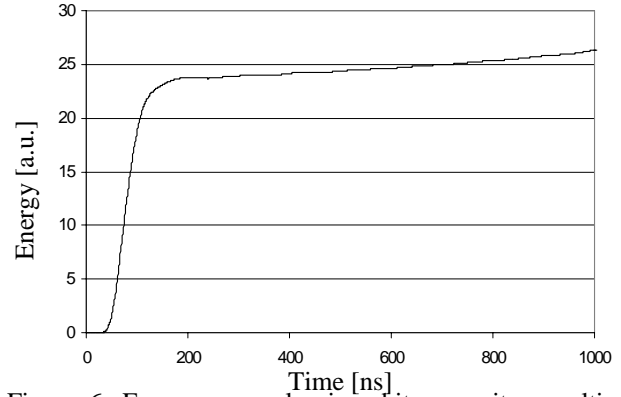


Figure 6: Energy per pulse in arbitrary units, resulting when integrating the power waveform from figure 5.

Looking at the energy per pulse (figure 6) we can see that the energy keeps increasing slightly after the voltage pulse has been applied. This is not a real physical result, but it is due to a numerical adjustment for the low frequency part of the signals that still has to be made, resulting in a more accurate representation of the actual properties of the reactor. This will most probably lead to a constant amount of energy per pulse after a pulse.

The second set of measurements concerns the influence of the superposition of a DC bias on the matching and the energy per pulse.

To perform the measurements, again only 1/4th of the available capacitors was used. The pulse repetition rate was 30 Hz and the DC voltage was varied between 0 kV and 15 kV.

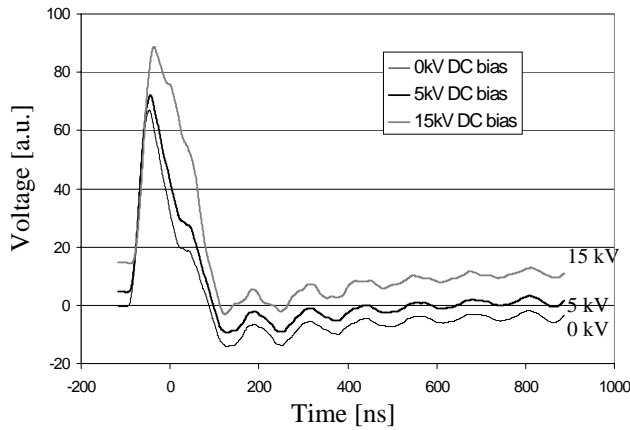


Figure 7: The influence of a DC bias voltage on the voltage waveforms. The pulse repetition rate was 30 Hz. The DC voltage was varied in the range of 0-15 kV.

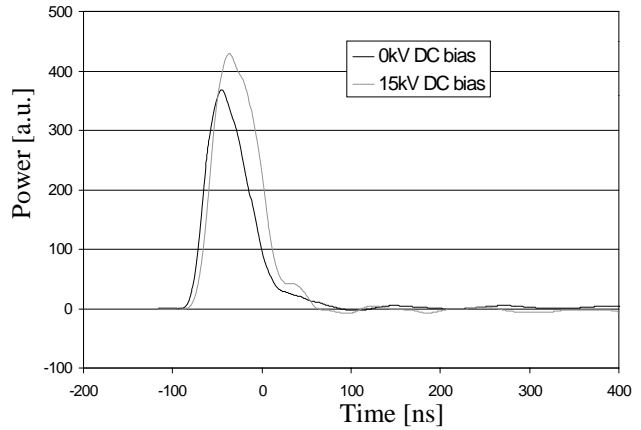


Figure 8: Influence of a DC bias voltage on the power waveforms. These waveforms are obtained by multiplying the voltage waveforms from figure 7 with the corresponding current waveforms (not shown in this paper).

Looking at figure 8 it can be seen that the power increases with increasing DC bias voltage. This is also apparent in figures 9-10. Thus by superimposing a DC bias the energy density inside the reactor can be increased. The matching between the reactor and the power source is not increased, since the matching is already good for no DC bias voltage (see figure 5).

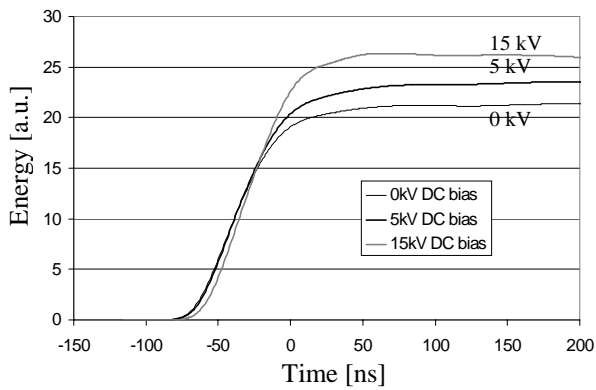


Figure 9: Influence of a DC bias voltage on the energy per pulse. The energy is determined by integrating the power waveforms from figure 8.

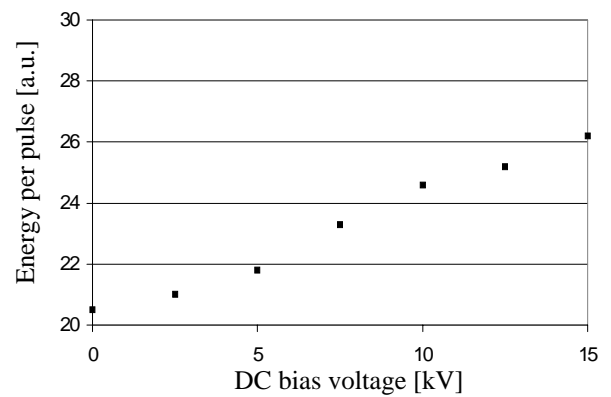


Figure 10: Influence of DC bias voltage on the energy per pulse.

#### 4. Conclusions

The most important conclusion so far (besides that the developed set-up is working) concerns the effects of the superimposed DC bias voltage. As could readily be seen in figures 9 and 10, the energy per pulse increases with increasing DC bias voltage. Since the matching between the power source and the reactor is already good without DC bias voltage (no reflected energy can be seen), the influence of the DC bias voltage on the matching could not be determined.

The problems we encountered with the calibration of the electrical measurement system will be solved in near future. At that moment we will be able to make more quantitative statements concerning our experiments.

#### 5. Future developments and goals:

For the near future we have set the following goals:

- Increasing the average output power of the set-up to 30 kW
- Optimizing the system in terms of its components and settings
- Optimizing the matching between reactor and power source (both experimentally and theoretically)
- Performing field measurements at a compost manufacturer in the Netherlands, to investigate the opportunities to treat 250.000 m<sup>3</sup>/hour of odor contaminated air (investigating the industrial possibilities of this corona unit)
- Looking at the energy/corona distribution inside the reactor (in both radial and axial direction)
- Developing a system that can deliver even more power (100kW average power).

#### References

- [1] A. J. M. Pemen, I. V. Grekhov, E. J. M. van Heesch, K. Yan and S. A. Nair, "Repetitive high-voltage pulse generation using a solid-state opening switch". 13th international symposium on High-Voltage Engineering (ISH), Delft, The Netherlands (2003).
- [2] B. E. J. M. Van Heesch, G. A. J. M. Pemen, K. Yan, S. V. B. van Paasen, K. J. Ptasiński and P. A. H. J. Huijbrechts, "Pulsed corona tar cracker". IEEE Transactions on Plasma Science, vol. 28, no. 0093-3813, pp. 1571-1575, (2000).
- [3] E. J. M. van Heesch, A. J. M. Pemen, K. Yan, P. P. M. Blom, P. A. H. J. Huijbrechts and P. C. T. van der Laan, "Pulsed corona for sustainable technology". Journal of Technical Physics, vol. 41, no. 1 (special issue), pp. 273-292, (2000).
- [4] K. Yan, E. J. M. van Heesch and A. J. M. Pemen, "Corona induced Non-thermal plasma for Pollution Control and Sustainable Technology". ISESP 2. Proceedings of the 8th international conference on Electrostatic Precipitation, (2001).
- [5] K. Yan, T. Yamamoto, S. Kanazawa, T. Ohkubo, Y. Nomoto, and J. S. Chang, "Control of Flow Stabilized Positive Corona Discharge Modes and NO Removal Characteristics in Dry Air by CO<sub>2</sub> Injections". Journal of Electrostatics, vol. 46, no. 2-3, pp. 207-219, (1999).
- [6] K. Yan, "Corona Plasma generation". Ph.D. thesis, Eindhoven University of Technology, The Netherlands (2001).

# Deposition of polymer films in the diffuse coplanar surface discharge

M. Šimor<sup>2</sup>, P. Stáhel<sup>1</sup>, A. Brablec<sup>1</sup>, Z. Navrátil<sup>1</sup>, D. Kováčik<sup>2</sup>, A. Zahoranová<sup>2</sup>  
V. Buršíková<sup>1</sup> and M. Černák<sup>2</sup>

<sup>1</sup> Department of Physical Electronics, Masaryk University, Brno, Czech Republic

<sup>2</sup> Faculty of Mathematics, Physics and Informatics, Comenius University, Bratislava, Slovakia

## Abstract

The coplanar diffuse surface discharge is used for deposition of thin hydrophobic films. The films were deposited on a filter paper substrate from mixture of nitrogen and HMDSZ. The discharge was investigated by emission spectroscopy while the composition of deposited films was studied by IR spectrometry and mechanical properties were studied by depth sensing indentation technique. Surface energy and wettability of thin polymer - like layers were also estimated. Then, a significant decrease of free surface energy was achieved (from 53 mJ/m<sup>2</sup> for the uncoated paper to about 11 - 23 mJ/m<sup>2</sup>).

## 1. Introduction

Over the past two decades the plasma technique for surface activation of polymeric materials has been extensively reported, including the surface treatment of paper [1 - 3]. The majority of applications were made at reduced pressures (see, for example [1, 2]), where the spatially homogeneous low-temperature plasma can easily be generated and brought into direct contact with the treated surfaces. However, the use of expensive vacuum systems that force batch processing has discouraged this application of low-pressure plasmas in larger industrial scale for treatment of low-cost materials. Additional disadvantages of the low-pressure plasma technique are high power consumption, long processing times, and difficulty to scale-up of an experimental set-up to a large production reactor. Thus it is apparent that such low-pressure plasma treaters cannot be used in line with standard paper production lines. In a contrast, atmospheric-pressure plasma processes offer different advantages for the finishing of low-cost materials: costly vacuum equipment is unnecessary, processing times are reduced, and the plasma finishing is simpler in an in-line process.

The most common systems tested are modifications of barrier ("silent" or "industrial-corona") discharge treaters widely used for the treatment of polymeric film [3]. In these cases the discharge is generated by applying a high frequency, high voltage signal to an electrode separated from a grounded plane by a discharge gap and a dielectric barrier. The treated material as, for example paper, is localised on the dielectric barrier surface. The main drawback of the barrier discharge devices is that the useful plasma conditions are achieved only in small volume plasma channels termed "streamers" developing perpendicularly to the paper surface. As a consequence, the plasma is in a very limited contact with the surface, which results in low processing speeds, typically in the order of 1 m/min. Moreover, because the plasma channels and arcing is an intrinsic phenomenon associated with this discharge type, localised arcing results in the formation of pinholes in the material being treated.

To remedy the mentioned shortcomings of the standard barrier discharge treaters, a novel surface discharge type (the coplanar diffuse surface discharge – CDSD) has been developed, whose major advantage is the generation of a thin layer of uniform atmospheric-pressure plasma with the power density as high as 100 W/cm<sup>3</sup> [4]. This system is protected by patent pending, and the laboratory tests have demonstrated the feasibility of the CDSD technique for surface activation of polypropylene and polyester nonwoven fabrics. In this paper preliminary results on surface using this novel discharge type are presented.

## 2. Experimental

The experimental arrangement including the discharge electrode system is illustrated by Figure 1. The electrode system consisted of two systems of parallel striplike electrodes (1- mm wide, 50 µm thick, 150 mm long, 0.5 mm strip-to-strip; molybdenum) were embedded in 96 % alumina using a green tape technique. The thickness of the ceramic layer between the plasma and electrodes was 0.4 mm. A sinusoidal high- frequency high voltage (6 kHz, up to 10 kV peak) was applied between both electrode systems. Such a discharge electrode arrangement and energisation were found to generate visually almost uniform plasmas of some

0.3 mm thickness in nitrogen and ambient air at atmospheric pressure. The power density of 50 W/cm<sup>3</sup> was kept in all experiments of this study.

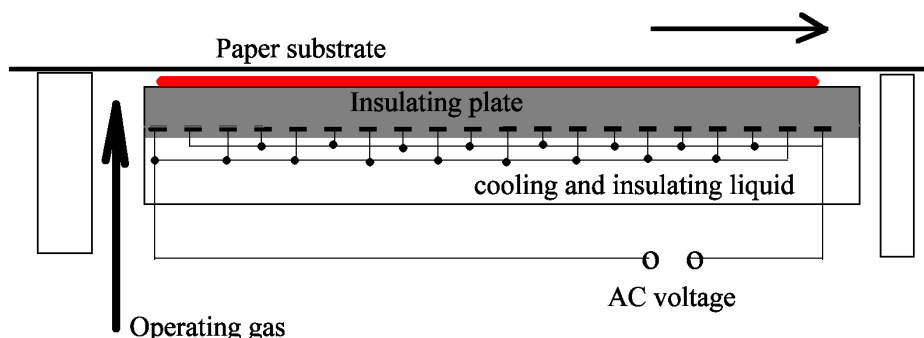


Fig.1 Arrangement of coplanar barrier discharge reactor.

The films were deposited on a filter paper substrate from the mixtures of hexamethyldisilazane - C<sub>6</sub>H<sub>19</sub>Si<sub>2</sub>N (HMDSZ) with nitrogen. Pure nitrogen was added to the mixture of HMDSZ and nitrogen. The HMDSZ vapours were obtained bubbling of the nitrogen through glass bottle containing the monomer. Filter paper strips were used as the substrates. The paper was pulled 0.4 mm above the insulating plate and 0.1 mm above the discharge with constant rate in the zone of after-glow. For characterisation of the mechanical properties polycarbonate and glass substrates were used.

The total surface energy of the deposited film was investigated by means of the sessile drop technique using the Surface Energy Evaluation System (SEE System) [5, 6]. The contact angles were measured directly from the image of the solid-liquid meniscus of a liquid drop set taken with CCD camera. For the determination of total free surface energy from the contact angle measurement the so-called “acid-base” theory we used. This theory [7, 8] enables to determine polar and apolar part of free surface energy and the electron-acceptor and electron-donor parameters of the surface tension. Wetting properties were studied by means of industrial permeability tests. The permeability was measured as a time necessary for penetration of 5 ml of testing liquid through the sample to special wettable paper ERT FF3. This test is consistent with tests ISO 9073-8-1995

The composition of the film was studied by means of Infrared Spectroscopy (IR). The spectra were taken from the filter papers samples by a Bruker Spectra 22 Spectrometer, using a ZnSe crystal, with a 45° incidence angle. 20 scans were co-added for all samples to reduce noise-to-signal ratio. The resolution was 2 cm<sup>-1</sup>. From each sample were taken 3 spectra, which were furthermore manipulated by means of spectrometer software: spectra were averaged, normalised and after then were devise differential spectra with standard sample.

The mechanical properties were studied by means of the depth sensing indentation technique using a Fischerscope H100 tester. The Jobin – YVON TRIAX 550 monochromator equipped with the CCD detector, recorded the spectra emitted by the discharge.

### 3. Results and discussion

In the first part of the presented study, the discharge properties are investigated by optical emission spectroscopy. The free surface energy and wettability of the coated papers are studied in second part. Chemical composition of deposited films is investigated in the next subsection while mechanical properties of the systems are presented in last part.

#### 3.1 Optical emission spectroscopy

Emission spectra of the discharge in nitrogen were recorded in the range 300 – 800 nm. Typical spectra of the discharge created in the mixture of nitrogen and HMDSZ vapours are shown in the Fig.2. The spectrum is plotted in the range 300 - 500 nm, because above 500 nm only the second spectral order was registered.

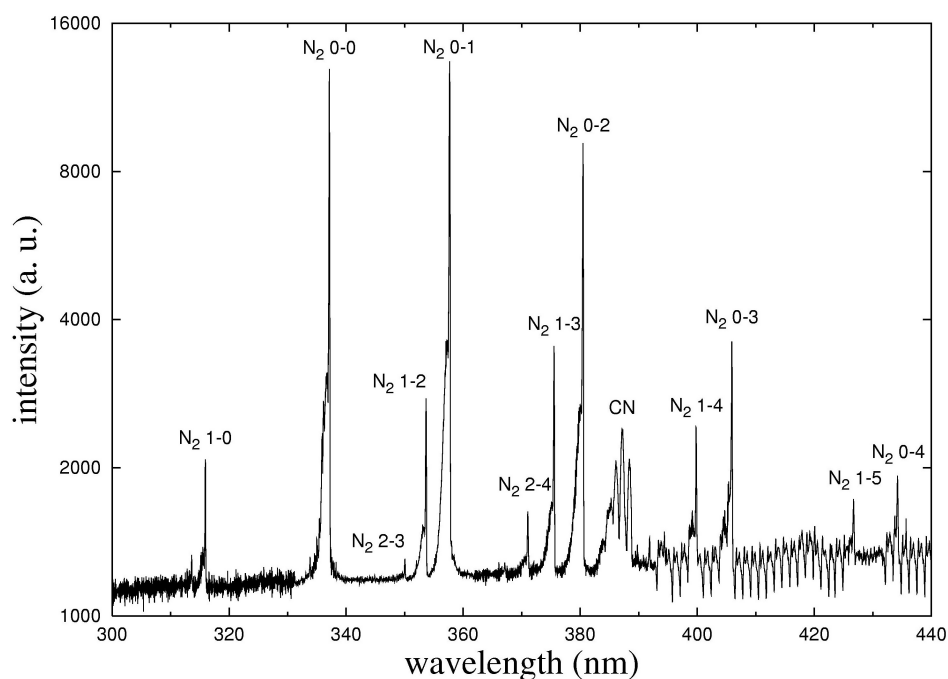


Fig.2: The emission spectrum of the surface discharge burning in nitrogen with admixture of HMDSZ.

The spectra consist of the molecular bands of second positive system of nitrogen ( $C^3\Pi_u \rightarrow B^3\Pi_g$ ). When the monomer was added into the nitrogen, intensive bands of CN violet system ( $^2\Pi \rightarrow ^2\Sigma$ ) at 388 nm and 422 nm were observed.

Intensity of  $N_2$  and CN system depended on the flow rate of organosilicon. Therefore integrated intensity of the CN band at 388 nm and integrated intensity of  $N_2$  system was calculated. The integrated intensity CN/ $N_2$  ratio as a function of the flow rate of HMDSZ admixed to the 6 l/min of pure nitrogen is shown in the Fig. 3.

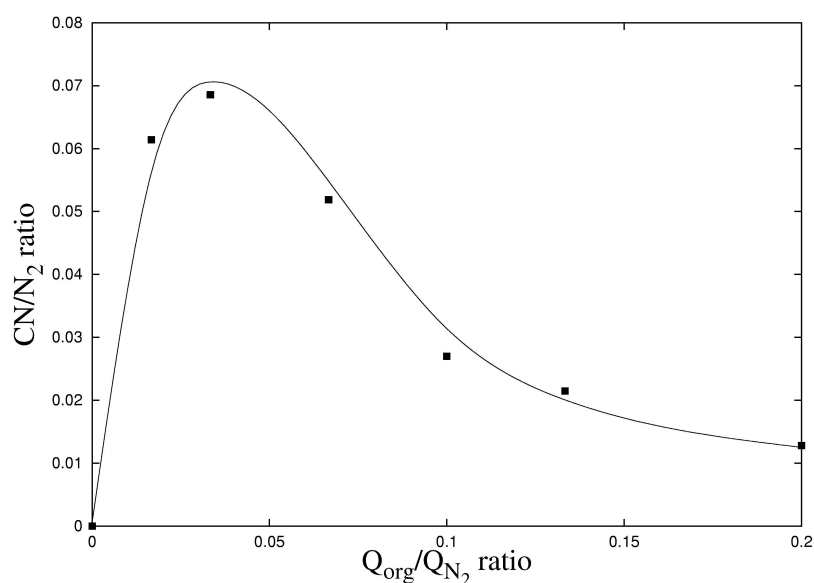


Fig.3: Ratio of integrated intensities of CN and  $N_2$  bands for different flow rates HMDSZ. The full line serves as a guide of eyes

The CN/N<sub>2</sub> ratio in the beginning increases with increasing flow rate of organosilicon, than it decreases. The maximal decomposition of monomer is at 0.03 flow rate ratio. The vibrational temperature was calculated from the bands of second positive system of nitrogen N<sub>2</sub> 0-2, N<sub>2</sub> 1-3 and N<sub>2</sub> 2-4. The value of the vibrational temperature varied only slightly with flow rate of organosilicon admixed to pure nitrogen, and its value was at about 1800 K in all cases.

### 3.2 Surface energy and wettability

Thin polymer-like layers were deposited on the filter paper substrate in order to reduce the water penetration and decrease the free surface energy. In Fig. 4 the total surface free energy and its polar and apolar parts are shown as a function of flow rate ratio HMDSZ/N<sub>2</sub>.

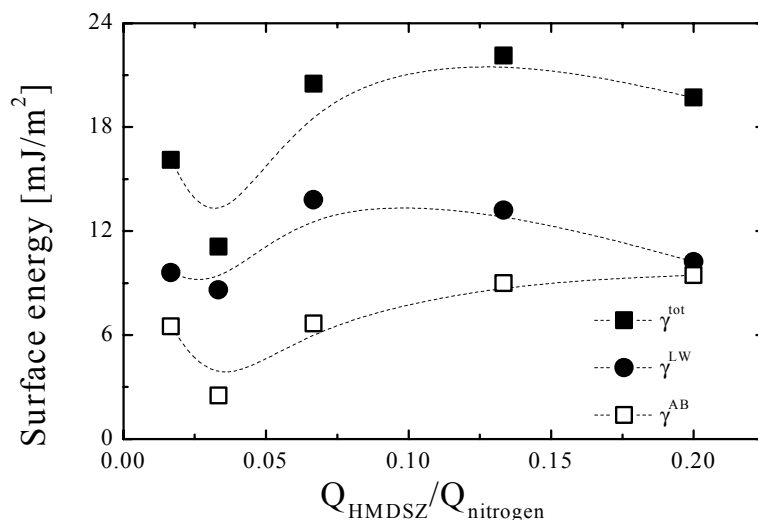


Fig.4 Total surface energy  $\gamma^{\text{tot}}$  and its polar  $\gamma^{\text{AB}}$  and a polar  $\gamma^{\text{LW}}$  part of samples deposited from different gas mixtures. The dash lines serve as a guide of eyes.

There was observed a significant decrease in surface free energy for the whole range HMDSZ to nitrogen flow rate ratio ( $0.017 < Q_{\text{HMDSZ}}/Q_{\text{O}_2} < 0.20$ ) comparing to the paper surface energy (53 mJ/m<sup>2</sup>). At first, the surface energy decreases (in the range from  $Q_{\text{HMDSZ}}/Q_{\text{O}_2} = 0.017$  up to 0.034) but then the increase is observed for higher concentration of HMDSZ in nitrogen. Similar dependencies were observed for the polar and the apolar part of the surface energy. The total surface free energy and its components increased when CN/N<sub>2</sub> ratio (see Fig. 3) decreased and the dependencies show the similar evolution. The acid and basic component of the polar part of free surface energy is not plotted.

The Fig. 5 shows the images of the water drop set on the coated and uncoated substrate. In case of uncoated paper the contact angle is at about 60°, however after the deposition the water contact angle increased to 120°.

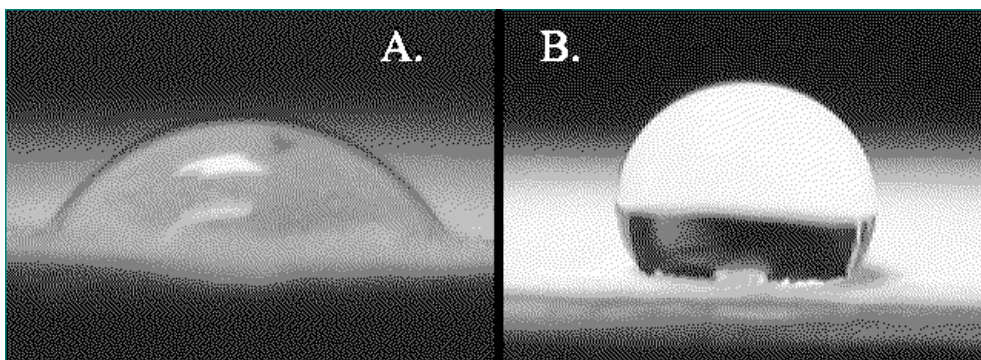


Fig.5: Image of the uncoated paper substrate (A.) and coated filter paper (B.)

The water penetration time for deposited film is given in Table 1. It is necessary to say that the water permeability depends not only on the surface properties but also on the thickness of the deposited film and roughness of the substrate. In case of big substrate roughness the thickness of the film plays crucial role. The Table shows that water penetration time increases with increasing flow rate ratio. The film deposited from higher concentration of HMDSZ vapours is characterised by small water permeability. This effect can be explained with different structure and higher thickness of the deposited film compare to films deposited from the lower concentration of HMDSZ and N<sub>2</sub>.

	$Q_{\text{HMDSZ}}/Q_{\text{N}_2}$	Penetration time [s]
0	Filter paper	3
1	0.0017	111
2	0.033	432
3	0.067	159
4	0.13	2002

Table 1. Penetration times corresponding to films deposited from different gas mixtures

### 3.3. Chemical composition

The attenuated total reflectance Fourier transform infrared spectroscopy (ATR - FTIR) was used in order to monitor and to specify the functional groups on the surface after the plasma treatment. The characteristic spectra of the film deposited from HMDSZ are shown on the figure 6. Most dominant are absorption peaks at 760 - 860 cm<sup>-1</sup> corresponding to Si-C stretching bonds. The increase at 1000-1130 cm<sup>-1</sup> can be correlated with Si-O-Si or Si-O-C stretching bonds. The CH<sub>3</sub> bonds represent the absorption peak at 1255 - 1280 cm<sup>-1</sup>.

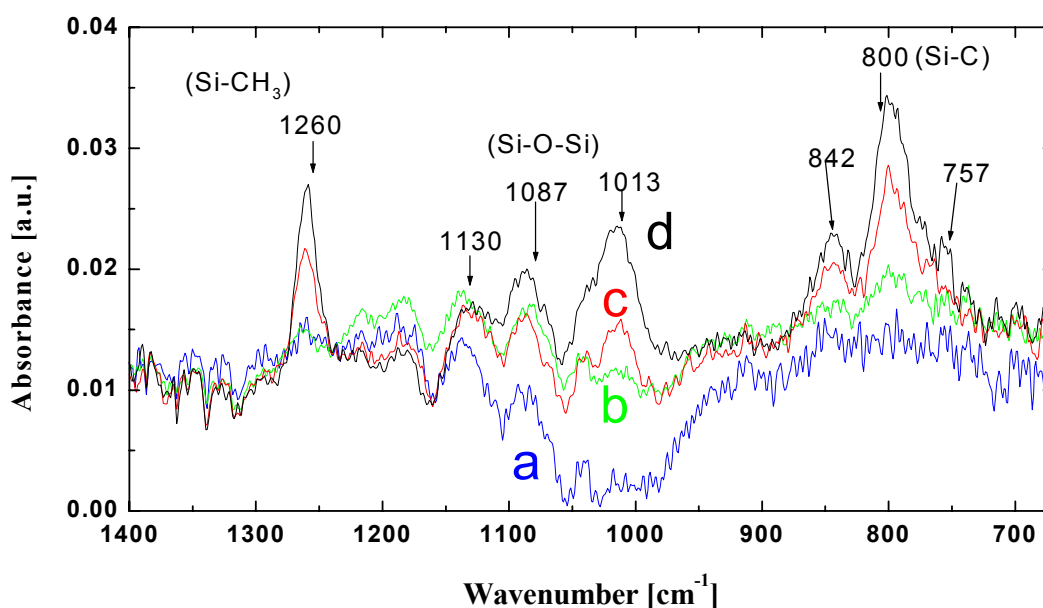


Fig.6: FTIR spectra of the coated films deposited on the paper substrate for different flow rate ratio monomer/nitrogen: 1 – 0.016, 2 – 0.032, 3 – 0.128, 4 – 0.2.

### 3.4 Structure, morphology and mechanical properties

As in the case of films deposited in surface discharge [6], the plasma deposition of that hydrophobic films did not affect the appearance of the paper surface, i.e. we did not observe any yellowing of the substrate material as it was referred in [9]. The coatings exhibited good abrasion resistance and the microhardness of the films. The mechanical properties of films were measured on films deposited on polycarbonate plate, and



microhardness was determined to about 0.1-0.2 GPa. This value is comparable with the microhardness of plastics.

#### 4. Conclusion

A new deposition technique based on atmospheric pressure coplanar barrier discharge was developed in order to protect the paper surface against air pollutant, humidity and UV radiation. Highly hydrophobic plasma polymer coatings were deposited on the filter paper substrate from mixtures of HMDSZ with nitrogen. The free surface energy decreased from 53 mJ/m<sup>2</sup> for the uncoated paper to about 11 - 23 mJ/m<sup>2</sup>. A substantial decrease of the water permeability was achieved in all cases. After the optimisation of deposition conditions this deposition technique may be used for example for the protection of the surfaces of wood, paper or other nature wettable materials.

#### Acknowledgement

This work has been supported by Grant Agency of Czech Republic under the contract numbers. 202/03/0708 and 202/02/D097.

#### References

- [1] Z. Q. Hua, R. Sitaru, F. Denes, and R. A. Young: *Plasmas and Polymers* **2(3)**, 196-220 (1998).
- [2] F. Denes and R. A. Young, Surface Modification of Polysaccharides under Cold Plasma Conditions, in *Structural Diversity and Functional Versatility of Polysaccharides*, Ed. Severian Dumitriu, Marcel Dekker Inc., New York, Basel, Hong Kong (1998).
- [3] S. D. Lee, S. Manolache, M. Sarmadi and F. Denes, Deposition of High Fluorine Content Macromolecular Thin Layers under Continuous-Flow-System Corona Discharge Conditions, *Polymer Bulletin* **43**, 409-416 (1999).
- [4] M Šimor, J. Ráhel J., P. Vojtek, M. Černák, A. Brablec, *Appl. Physics Letters* **81** (2002) 2716.
- [5] <http://www.seesystems.wz.cz>
- [6] P. St'ahel, V. Buršíková, Z. Navrátil, A. Záhoranová, J. Janča, this conference
- [7] R. J. Good: *Contact Angle, Wettability and Adhesion* ed. K. L. Mittal **3** (1993).
- [8] N. Inagaki, *Plasma Surface Modification and Plasma Polymerisation*, Technomic Publication Company, Lancaster (1996).
- [9] L. Ruys, A. Saey, M. Van Lancker, Y. Rogister, J. Knott, 3. Internationale Fachtagung N-D-Plasma-Technologie, Wuppertal (1995).

# Processing of hazardous organic materials in RF thermal plasmas

J. Szépvölgyi

*Research Laboratory of Materials and Environmental Chemistry, Chemical Research Centre  
Hungarian Academy of Sciences, Budapest, Hungary*

## Abstract

Decomposition of hazardous organic materials such as hexane, toluene,  $\text{CCl}_4$ ,  $\text{CHCl}_3$  and  $\text{CFCl}_3$  was investigated in an RF thermal plasma reactor. Studies performed in argon atmosphere were aiming at having deeper insight into the decomposition of given compounds at high temperatures. Rather complicated decomposition and recombination mechanisms were identified in all cases. Plasma conditions and chemical nature of the models proved to be important factors both in terms of thermal decomposition and product formation.

## 1. Introduction

Modern economies are „producing” various organic wastes including chemical by-products, pesticides, herbicides, waste solvents, waste oils, hospital wastes, military wastes etc. in large quantities. In chemical terms these wastes consist of hydrocarbons, aromatic compounds, miscellaneous oxygen-containing compounds, and organohalide, organosulfur or organonitrogen compounds [1]. Due to their chemical and biological effects particular wastes may have serious environmental impacts to the atmosphere, the hydrosphere or the geosphere. In order to minimize danger of pollution, they should be handled and processed with special care. Processing implies transformation of organic wastes into less hazardous and less voluminous materials on the one hand, and utilisation of their valuable constituents on the other. In the latter case wastes can be regarded as secondary raw materials, and waste destruction is combined with generation of valuable products. Thermal methods, namely incineration and pyrolysis belong to the most wide-spread processing ways of organic wastes. High temperature thermal plasmas seem to be especially suitable tools for the thermal treatment of hazardous organic wastes. As compared to competing technologies, thermal plasma processing offers a number of advantages [2]:

- Very high heating rates and high temperatures that can be achieved in thermal plasmas make possible fast and actually complete decomposition of organic materials.
- Fragments formed on thermal decomposition are cooling very rapidly downwards the plasma flame region; products of special chemical and morphological properties are produced in these conditions.
- The high energy densities in plasma reactors allow small installations for comparable waste throughputs, thus reducing capital costs and favouring construction of small mobile units.
- The total gas throughput of thermal plasma reactors is relatively low with a consequence of reduced capacity for off-gas treatment.
- RF thermal plasmas offer wide choice of process gases, independently of plasma temperature; it improves the control over the process chemistry.
- Ultraviolet radiation emitted by thermal plasmas enhances destruction of organohalide compounds.

Different methods have been developed for plasma processing of various volatile organic compounds more recently [3, 4]. Hexane and toluene studied in this work can be regarded as models of VOC's. Chlorinated hydrocarbons and chlorofluorocarbons were broadly used as solvents and refrigeration fluids, respectively in the last decades. These compounds when emitted into the atmosphere reacted with the stratospheric ozone layer. It resulted in the leakage of ozone layer and thus, increased UV radiation on the surface of earth. In order to eliminate CFC emission, broad research was initiated on the decomposition of chlorinated and fluorinated hydrocarbons. One of the most promising ways is plasma-assisted decomposition [5-7].

## 2. Experimental

The experiments were performed in an RF induction plasma torch of standard design with a quartz glass plasma confinement tube of 27 mm I.D. The torch was connected to an air-cooled quenching chamber and a dust separator unit. The plasma power was provided by a 3-turn induction coil from an RF generator operating at oscillator frequency of 27.17 MHz. High-purity argon was used as plasma gas ( $8 \text{ l}\cdot\text{min}^{-1}$  (STP)) and sheath gas ( $21 \text{ l}\cdot\text{min}^{-1}$  (STP)), respectively. Argon was applied as carrier gas of model compounds, as well.

Starting materials of analytical grade were injected in a swirl direction through a transverse slot into the plasma tail flame region. After having reached the steady-state operation samples were taken from the off-gas, and they were immediately analyzed by GC-MS. Solid soot was also formed on cooling of the gas-vapour stream. It mainly condensed on the reactor wall. Morphology of the soot was characterized by SEM micrographs. The soot might contain adsorbed organic compounds, as well. For their separation the soot was extracted by toluene using the Soxhlet method. Extracts were also subjected to GC-MS analysis.

The off-gases and the extracts were analysed by HP5890 gas chromatograph connected to VG-ZAB2-SEQ mass spectrometer. A 50m long HP-5MS fused silica capillary column was used for GC separation. Helium was applied as carrier gas with a flow rate of 2 ml·min<sup>-1</sup>. Temperature program of the column was set as follows: 80°C for 4 min then increased by 5°C·min<sup>-1</sup> up to 250°C and kept there for 10 min. The mass range of mass spectrometer was 30-800 m/z.

In addition to analysis and characterisation of products, experiments were evaluated by calculating the specific energy of processing ( $E_{sp}$ ) defined as plasma plate power related to feed rate of model compounds. The soot yield ( $Y_s$ ) was calculated as the ratio of the rate of soot formation against feed rate of starting materials. The extract yield (E/S) was characterised by the mass of extract related to the mass of soot.

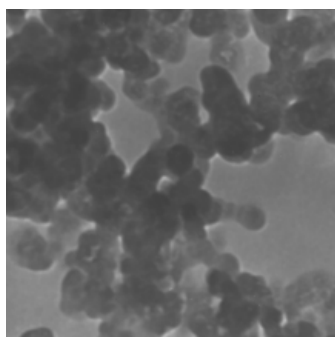
### 3. Results and discussion

The experimental conditions and the soot and extract yields, respectively are summarized in Table 1.

**Table 1.** Conditions and results of experiments

Model compound	Initial comp. (m/m %)		$E_{sp}$ (kWh·g <sup>-1</sup> )	$Y_s$ (%)	E/S (%)
	Model	Argon			
C <sub>6</sub> H <sub>14</sub>	1.4	98.6	0.085	0.4	56.8
			0.096	1.4	55.1
			0.119	5.9	54.3
C <sub>7</sub> H <sub>8</sub>	1.4	98.6	0.142	7.1	58.5
			0.187	18.7	40.2
			0.206	13.3	41.4
CHCl <sub>3</sub>	1.15	98.85	0.045	4.7	23.3
			0.057	4.3	15.2
			0.074	5.5	35.5
CFCl <sub>3</sub>	1.15	98.85	0.016	2.7	50.8
			0.022	3.4	40.2
			0.134	7.8	50.0
CCl <sub>4</sub>	0.93	99.07	0.061	1.7	51.0
			0.072	1.7	26.3
			0.089	3.0	21.6

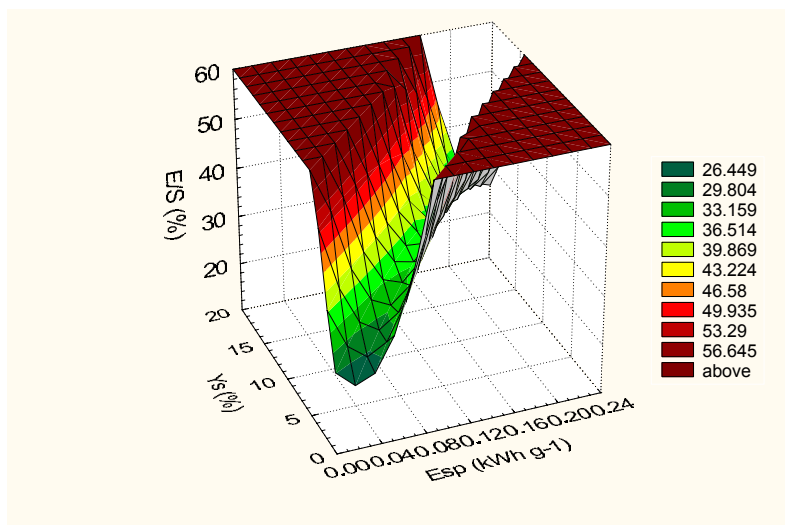
As it can be seen from Table 1, more or less soot has been formed from all model compounds on thermal plasma treatment, in conditions as above. The soot always contained extractable fraction in reasonable amounts. SEM studies revealed that the soot mostly consisted of spherical grains having mean particle size of 20-40 nm and specific surface area of 150-170 m<sup>2</sup>·g<sup>-1</sup> (Fig. 1). The soot particles loosely agglomerated due to surface forces.



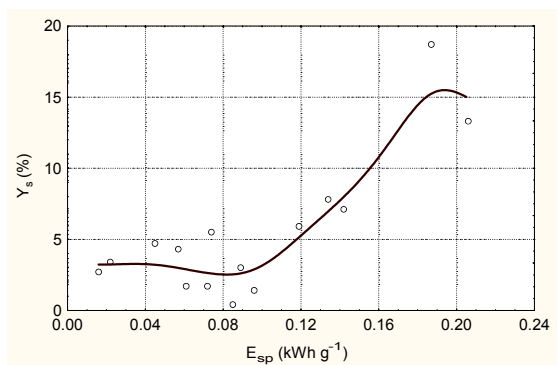
**Fig. 1** SEM micrograph of soot from n-hexane. Magnification: 50,000 x

Plotting of  $Y_s$  and E/S values against  $E_{sp}$  in 3D (Fig. 2) gives a general picture on correlations among process parameters and soot and extract yields, respectively. Fig. 2 refers to rather complicated relationships among variables. Soot yield is increasing with  $E_{sp}$  i.e. the greater is plate power the more complete is decomposition, and hence, more soot is formed (Fig. 3). However, the extract yield has a minimum against  $E_{sp}$  (Fig. 4). Most probably, it is due to the complexity of decomposition and recombination processes.

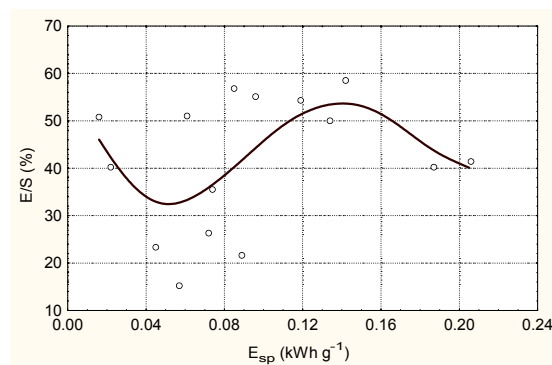
At lower  $E_{sp}$  values (i.e. at lower plate power related to unit feed) decomposition of starting materials, while at higher  $E_{sp}$  values recombination of fragments determine the amount of extractable products.



**Fig. 2**  $Y_s$  and  $E/S$  as plotted against  $E_{sp}$



**Fig. 3** Soot yield plotted against specific energy



**Fig. 4** Extract yield plotted against specific energy

The specific energy ( $E_{sp}$ ) can be regarded as a measure of the energy content of plasma flame and thus, in some extent, it characterizes the temperature and flow patterns in the reactor. Based on this consideration, we can conclude that operating parameters of the plasma torch determine both decomposition and recombination phenomena in a great extent.

However, this general picture is modulated by the chemical nature of models, as it can be seen from the scattering of data in Figs. 3 and 4. Results of off-gas analysis (Table 2) support this finding. The off-gas compositions from various runs with different models significantly differ from each other. In the toluene case some toluene, as well as benzene and naphthalene derivatives were detected in the off-gas.

During decomposition of chloroform off-gases of much simpler composition were formed. However, very hazardous compounds such as hexachloro-butadiene and hexachloro-benzene were detected in the off-gas.

Thermal plasma destruction of carbon-tetrachloride seems to be an efficient process: only  $CCl_4$ ,  $C_2Cl_4$  and  $C_4Cl_6$  were identified as gaseous products.

Off-gas of very complex composition was formed on destructing  $CHCl_3$ . Products included poly-chlorinated and poly-fluorinated hydrocarbons and aromatic compounds, as well. If we compare the off-gas compositions for the  $CHCl_3$  and  $CFCl_3$  cases, the role of hydrogen and fluorine in decomposition and recombination, respectively can be distinguished. Fluorine atoms and radicals facilitate formation of more complex compounds such as poly-halogenated aromatics.

Results of extracts analysis (Table 3) are actually in agreement with the above findings. Extracts of most complicated composition were obtained in  $C_7H_8$  and  $CFCl_3$  cases. Presence of hydrogen in chlorinated hydrocarbons, as it was discussed previously, improves product distribution due to extraction of chlorine from the reaction system as  $HCl$ .

Formation of poly-aromatics and poly-halogenated aromatics of high molecular mass was observed during destruction of  $CFCl_3$ . Further investigations are required to elucidate the mechanism and kinetics of  $CFCl_3$  destruction in thermal plasma conditions.

**Table 2** Summary of the results of off-gas analysis

Products detected in the off-gas	m/z	Models			
		$C_7H_8$	$CHCl_3$	$CFCl_3$	$CCl_4$
HCl	35		+		
$Cl_2$	70			+	
Toluene	92	+			
$CF_3Cl$	104			+	
Benzene, ethyl	106	+			
1H-Indene	116	+			
$CF_2Cl_2$	120			+	
Naphthalene	128	+			
Benzene, 1-methyl-4(1-propyl)	130	+			
$CFCl_3$	136			+	
4H-Indene, 1-methyl	140	+			
Naphthalene, $\alpha$ -methyl	142	+			
Naphthalene, $\beta$ -methyl	142	+			
$C_2Cl_3F$	148			+	
$CCl_4$	152			+	+
Acenaphthylene	152	+			
Benzene, 1,3 dichloro-2-fluoro	164			+	
$C_2Cl_4$	166			+	
Fluorine	166	+			
Ethene, tetrachloro	166		+		+
$C_2Cl_4F_2$	167			+	
Ethane, hexachloro	201			+	
Benzene, chloro-pentafluoro	202			+	
Benzene, dichloro, tetrafluoro	218			+	
Butadiene, pentachloro	224			+	
Benzene, trichloro, trifluoro	234			+	
Benzene, 1-chloro-4-(pentachloroethyl)	240			+	
Xilene, tetrachloro	244			+	
Benzene, tetrachloro, difluoro	252			+	
1,3-Butadiene, 1,1,2,3,4,4-hexachloro	260		+	+	+
Benzene, pentachloro, fluoro	268			+	
Xilene, 1,2,3,5 tetrachloro-4,6 dimethyl	272			+	
1,3-Cyclopentadiene, 1,2,3,4,5,5-hexachloro	272		+	+	
Benzene, 1,4-bis(trichloromethyl)	277			+	
Benzene, hexachloro	284		+	+	
Toluene, 3-dichlorofluormethyl-heptafluoro	285			+	

**Table 3** Summary of the results of extracts analysis

Products detected in the extract of the soot	m/z	Models			
		C <sub>7</sub> H <sub>8</sub>	CHCl <sub>3</sub>	CFCl <sub>3</sub>	CCl <sub>4</sub>
Benzene, ethyl	106	+			
Benzene, o-dimethyl	106		+		+
Benzene, m-dimethyl	106				+
Benzene, p-dimethyl	106			+	+
Cyclohexane, dimethyl	112			+	
Benzene, ethyl, methyl	120			+	
Benzene, 1,4-bis (ethynyl)	126	+			
Naphthalene	128	+			
Biphenyl	154	+			
C <sub>2</sub> Cl <sub>4</sub>	166			+	
Fluorine	166	+			
Ethane, tetrachloro	166		+		
Anthracene	178	+			
Phenantrene	178	+			
Dibenzyl	182	+			
Benzene, 1-methyl, 4-methylphenyl	182				+
Phenantrene, cyclopenta	190	+			
Ethane, hexachloro	201				+
Pyrene	202	+			
Fluoranthene	202	+			
Benzene, tris-izopropyl	204	+			
Indeno-2,1,6-indole	206	+			
o-Terphenyl	230	+			
Benzene, trichloro, trifluoro	234			+	
Benzene, dichloro, tetrafluoro	252			+	
1,3-Butadiene, 1,1,2,3,4,4-hexachloro	260		+	+	
Benzene, chloro-pentafluoro	268			+	
Cyclopentadiene, perchloro	270		+		
Benzene, hexachloro	284		+	+	
Cyclobutane, 1,2-dichloro 3,4-bis (dichloro-methylene)	284				+
Biphenyl, hexachloro	362				
Styrene, perchloro	378			+	
Benzene, pentachloro (trichloroethenyl)-perchloro-styrene	380				+
Fluoranthene	385			+	
Biphenyl, heptachloro	394			+	
Naphthalene, octachloro	404			+	+
Benzene, tris-trichloromethyl	427			+	

## Conclusions

Our comparative studies on decomposition of methyl-benzene, trichloro-methane, trichlorofluoro-methane and tetrachloro-methane in RF thermal plasma reactor revealed that

- Particular compounds were mostly decomposed even at low plate power i.e. at low specific energies related to unit feed.
- Amount and composition of condensed products and composition of gaseous ones greatly depended on the operating parameters of the plasma reactor.
- Decomposition mechanism and product distribution were affected by the chemical nature of models, as well.
- In the presence of fluorine a more complex product distribution was obtained as compared to its absence.

- There is a chance of the formation of poly-halogenated aromatic and poly-aromatic compounds in plasma pyrolysis performed in argon atmosphere.

### **Acknowledgment**

This work has been supported by Hungarian Scientific Research Fund (Project No. T29734)

### **References**

- [1] S. E. Manahan – Environmental Chemistry (7<sup>th</sup> edition). Lewis. Boca Raton. 2000.
- [2] E. Pfender – Plasma Chem. Plasma Process. **19**, 1 (1999)
- [3] Y. Wen, X. Jiang – Plasma Chem. Plasma Process. **20**, 343 (2000)
- [4] L. W. Sieck, T. J. Buckley, J. T. Herron, D. S. Green – Plasma Chem. Plasma Process. **21**, 441 (2001)
- [5] H. Sekiguchi, T. Honda, A. Kanzawa – Plasma Chem. Plasma Process. **13**, 463 (1993)
- [6] L. S. Hsieh, W. J. Lee, C. Y. Chen, M. B. Chang – Plasma Chem. Plasma Process. **18**, 215 (1998)
- [7] E. Bergeron, G. Soucy, M. Boulos – Proc. ISPC 12. University of Minnesota. Vol. II. 1033 (1995)

# Plasma Induced Functional Properties of Thin Layer PE films

S. Bronco<sup>1,2</sup>, M. Bertoldo<sup>1,2</sup>, Ciardelli<sup>2</sup>, C. Cepek<sup>3</sup>

<sup>1</sup> INFN, UdR Pisa, [simona@dccl.unipi.it](mailto:simona@dccl.unipi.it)

<sup>2</sup> Department of Chemistry and Industrial Chemistry, University of Pisa, via Risorgimento 35, 56126 Pisa, Italy

<sup>3</sup> National Laboratory TASC-INFN, Area Science Park - Basovizza, Edificio MM, Strada Statale 14, Km.163.5 I-34012 Trieste, Italy

In the last years, the packaging sector showed a growing interest for easy processable polymers that are able to substitute traditional materials such as paper, glass and metals. These materials have good bulk properties and are available at low cost but require selective modifications of their surface properties (inertness and hydrophobicity). Surface treatment (chemical functionalization, cleaning, etching) can lead to an increase in the reactivity of the surface, improving wettability, dyeing properties, adhesion to other polymers or metals, barrier properties, while bulk properties are usually not affected. The most attractive techniques to carry out these tasks are hot and cold plasmas, corona or glow discharge, irradiation with X-ray, electron or ionic beams because of their low environmental impact and limited degradation.

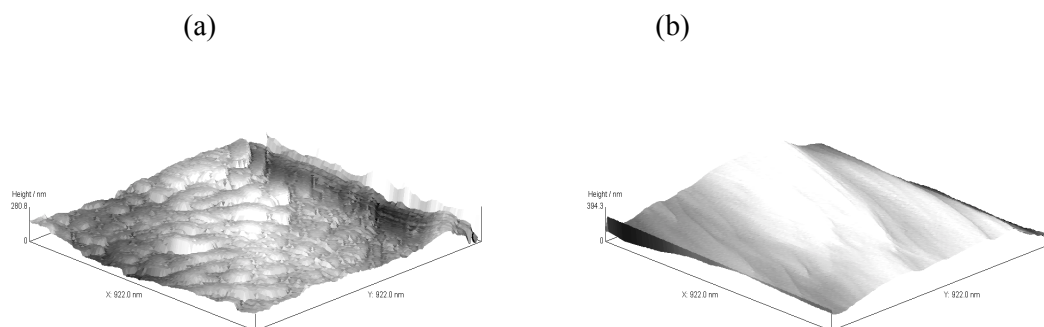
In this work, O<sub>2</sub> and N<sub>2</sub> cold plasma treatment was applied to LDPE films in order to improve, by inducing a higher surface polarity to the thin layer, the deposition of a catalyst for a polyurethane adhesive water formulation.

The effect of the O<sub>2</sub> treatment during different exposition time (60 sec., 120 sec., 180 sec. e 375 sec.) at different temperature (room temperature and 70 °C), at 2.0x10<sup>-2</sup> torr was investigated. Before and after each treatment the surface composition of the film via XPS measurements was evaluated. The photoemission spectra were collected up to 1100 eV of bounding energy and for the C 1s and O 1s levels. The homogeneity and the aging of the films was also monitored. The results showed that: **1-** for exposition time longer than 60sec, the presence of ester, carboxylic and anhydride groups appear, **2-** The effects of the treatment decrease after 375sec; **3-** the dishomogeneity produced on the film are lower than 2-3%, **4-** the aging of the film did not affected the homogeneity.

Similarly, the effect of N<sub>2</sub> treatment was studied during different exposition time (15, 60, 120, 240, 300, 360 and 420 sec.). The presence of polar groups such as C-N, C=N e C≡N was observed. In this case the C 1s, O 1s, and N 1s spectra were analyzed.

The effect produced by the application of different gases was monitored by AFM analysis as shown in Figure 1. The different morphology did not affect the wettability of the film according to the ASTM D882-91.

Figure.1 AFM imagines of LDPE films treated with plasma of O<sub>2</sub> (a) and N<sub>2</sub> (b).



The polymerization of a polyurethane adhesive on the film surface after deposition of a suitable catalyst was monitored by following the decrease in the isocyanate peak through FT-IR spectroscopy with time. The value of  $t_{1/2}$  for a reaction with a first order decay has been considered indicative of the polymerization rate. On the treated film the  $t_{1/2}$  values decreases of about 60% giving indication of a more efficient blocking of the catalyst on the LDPE surface treated with the O<sub>2</sub> plasma.



# **Investigating in blood compatibility of DLC films on cylindrical inner wall, fabricated by (r.f.) plasma CVD processing**

Y. Ohgoe, S. Takada, T. Saito and K. K. Hirakuri

*Department of Electronic & Computer Engineering, Tokyo Denki University,  
Ishizaka, Hatoyama, Saitama, 350-0394, Japan*

Radio frequency (r.f.) glow discharges have been widely used in plasma processing for plasma chemical vapor deposition (CVD), sputtering by plasma, plasma etching and ion plating. r.f. plasma conditions are routinely controlled by plasma excitation parameters (input of power, gas pressure and gas flow rate) and these generation conditions have been progressively optimized from studies of plasma processing. In r.f. plasma processing the most common system consists of two capacitively coupled planar reactor for wide area deposition and etching. Moreover, deposition of a functional thin film, surface modification, and fine pattern etching are available by the r.f. plasma CVD processing at low temperature. Specifically, diamond-like carbon (DLC) films can be easily fabricated by CVD techniques. Above all, the r.f. plasma CVD processing is very useful for the deposition and etching processes because it is able to be fabricated on most substrates that are conductor and/or insulator substrates at room temperatures. DLC films have attractive characteristics, such as high resistance, extreme hardness, low friction, high thermal conductivity and prevention of corrosion against acids and alkaline solutions. Furthermore, DLC films can be deposited on polymeric materials as biomedical applications. However, there are big problems of the application of this process because it is difficult to generate the uniform plasma on the insulator material surface with complicated (3-dimensional) structure.

Uniform fabricating process of DLC films should be realized to 3-dimensional object. The properties are predominately dependent on the ion kinetic energy of ion flux in the plasma that reached to the substrate surface. Special substrate holder is proposed to keep the thickness of the ion sheath. This support is referred to as "improved electrode". In order to apply the DLC films to new biomaterials, 3-dimensional coating technique will be establish during CVD process. It is most important to estimate the biomaterial applications. Therefore, we have developed improved electrode that can fix all of the cylindrical substrates. This improved electrode is electrically conducted to the cathode.

The DLC films were fabricated by the r.f. plasma CVD processing with the improved electrode process. In estimation of uniformity of DLC films, thickness was measured by the cross section of scanning electron microscope (SEM) images. The DLC films were fabricated by cylindrical electrode. In this, the DLC films were deposited at 10 Pa ( $\text{CH}_4$  gas pressure), and deposition time was 10 min. Using the improved electrode process, the thickness of DLC films was kept uniform at approximately 300 nm. As an application of the deposited the DLC films on cylindrical inner wall, it evaluated about the blood conformity. The cylindrical substrate was made of polycarbonate. The thrombosis was measured the platelet adhesion on the sample surfaces by SEM images. This estimation used whole human blood. As the result, the DLC films coating on substrates reduced the volume of the platelet adhesion. It could be seen that DLC films would improve the blood compatibility of cylindrical polymeric materials.

It could be seen that DLC films would improve the blood compatibility of cylindrical polymeric materials. The creation of a DLC film to a 3-dimensional structure was attained. The application nature as a biomechanical material of a DLC film is expected very much.

# Evaluation of HDPCVD and SACVD oxide deposition for Shallow Trench Isolation application in ULSI CMOS

S.Cascio<sup>1</sup>, C.Demuro<sup>1</sup>, C.D'Acerno<sup>1</sup>, M.Vulpio<sup>1</sup>

<sup>1</sup> CR&D Catania, STMicroelectronics Srl, Catania, Italy

## Abstract

With the shrinking of the microelectronic devices, trench filling process represents an important aspect of isolation scheme: in fact, deposition oxide with good fill property is necessary to ensure a good isolation. In this paper USG by HDPCVD and SACVD process has been morphologically evaluated for STI applications in ULSI CMOS; it has been demonstrated that SACVD process represents a promising method for STI applications.

## 1. Introduction

With the shrinking of technologies, STI (Shallow Trench Isolation) module has replaced the traditional LOCOS (Local Oxidation of Silicon) to isolate contiguous active areas. Trench filling process represents an important aspect of this isolation scheme: in fact, deposition oxide with good gap fill and planarization property is necessary to ensure a good isolation and integration of module in the process flow.

HDPCVD (High Density Plasma Chemical Vapor Deposition) process allows the oxide deposition with good quality and gap fill capability such as it can be used to perform trench filling isolation, especially on devices with a higher aspect ratio: in fact, in function of device dimensions, HDPCVD deposition technique gives the possibility to fill aggressive structures, tuning D/S (deposition to sputter) value. HDPCVD is a plasma chemistry technique due to a reaction between  $\text{SiH}_4$  and  $\text{O}_2$  together with Argon gas that sputters the oxide during its deposition. The value of D/S must be always  $> 1$  to have oxide deposition. The main drawback of this technique is that, decreasing D/S ratio, plasma damage and dislocation defectivity on silicon increase.

For critical device dimensions in terms of trench (width and depth), STI filling process by HDPCVD has been considered, using a recipe with two deposition steps at different deposition/sputter ratio (the second D/S ratio more aggressive than the first one) to improve film gap fill efficiency and better planarization.

In alternative SACVD (Sub Atmospheric Chemical Vapor Deposition) oxide, usually used in a PMD (Pre Metal Dielectric) level for his excellent morphological properties, has also been considered instead of HDPCVD film, using  $\text{O}_2$  flow and a low TEOS (Tetra Ethyl Ortho Silicate) flow during deposition step to improve filling performances and obtain a better step coverage and film conformity; SACVD is a typical deposition technique by reaction of vapour source (TEOS) with  $\text{O}_3$  gas.

In this paper, HDPCVD and SACVD oxide have been morphological evaluated for STI process, and in particular, it has been demonstrated that SACVD process represents a promising method for STI applications. The test vehicle, chosen to study gap fill properties of different dielectric films deposited by HDPCVD and SACVD, is a device with critical dimensions (Tab.1).

Tab.1: critical dimensions of considered structures (STI level)

Critical Dimensions	
Active Area	180 nm
Active Area Pitch	350 nm
Nitride top	190 nm
Nitride bottom	200 nm
Depth Trench	360 nm
Width Trench	170 nm

## 2. Process A: USG STI filling by HDPCVD

USG (Undoped Silicate Glass) by HDPCVD can be used for STI applications for its good quality, gap fill capability and planarization properties. This last aspect of deposition technique is really important in direct STI approach [1, 2].

Deposition of USG in STI process was performed on HDPCVD Centura chambers (Applied Materials) with 24 gas nozzles injectors (to obtain a better film uniformity respect to 18 gas nozzles chambers), using a no Helium cooling of wafers to improve oxide quality; the deposition process temperature was about 750°C.

The gap fill capability for a given aspect ratio depends on D/S, which is the ratio between silicon oxide deposition and Argon sputtering processes, that are performed simultaneously; in general, the use of a lower D/S ratio enhances the filling of a structure with a higher aspect ratio [3].

So we investigated STI filling process using a deposition recipe by HDPCVD which consisted of two steps by different deposition/sputter ratio:

- I step deposited USG layer (4000 Å) using a D/S = 5.0, to cover completely active areas and prevent risks of the nitride sputtering with the second step;
- II step deposited USG layer (2000 Å) with a D/S = 2.5, more aggressive than the first one, necessary for a better planarization and to improve the film gap fill efficiency so in order to prevent voids formations.

Experimental conditions of HDPCVD steps deposition process was reported (Tab. 2).

Tab.2: experimental conditions of HDPCVD process

Experimental Conditions	I step (D/S 5.0)	II step (D/S 2.5)
Pressure (mTorr)	~12	~7
RF top (Watt)	1300	1300
RF side (Watt)	3100	3100
RF bias (Watt)	3500	3500
O <sub>2</sub> (sccm)	302	132
SiH <sub>4</sub> top (sccm)	18	9
SiH <sub>4</sub> side (sccm)	132	62

Morphological analysis on STI filling process by HDPCVD showed that these experimental conditions were not able to fill efficiently structures with pitch 0.35µm, giving voids formation. (Fig. 1).

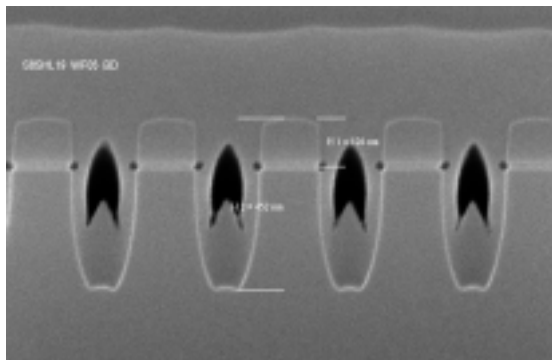


Fig. 1: morphological analysis on STI filling process by HDPCVD (I step D/S = 5.0; II step D/S = 2.5)

So we tested a recipe using the first step with a  $D/S = 4.0$ , more aggressive than the previous one and leaving the second step unchanged: in this case, morphological analysis showed not only the presence of voids in field oxide but even sputtered nitride on active areas, probably because of a very aggressive  $D/S$  on the first step (Fig. 2)

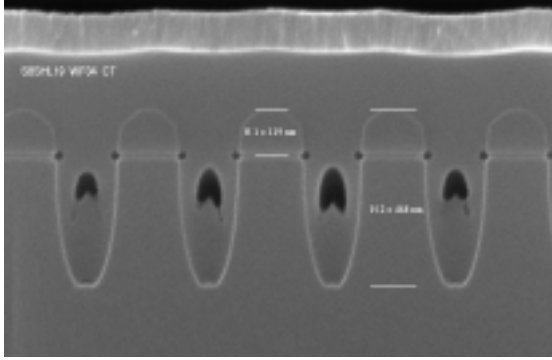


Fig. 2: morphological analysis on STI filling process by HDPCVD (I step  $D/S = 4.0$ ; II step  $D/S = 2.5$ )

In order to set up a good trench filling by HDPCVD process, step by step study has been performed to determinate:

- the correct thickness in the first step, for a sufficiently covering of active areas to avoid nitride sputtering during the second deposition step;
- the correct  $D/S$  ratio of the second step, for a good planarization and film gap fill efficiency.

This study allowed the set up of a correct process using a recipe with two deposition steps:

- I step, USG layer ( $2500\text{\AA}$ ) deposited with a  $D/S = 5.0$
- II step, USG layer ( $3500\text{\AA}$ ) deposited with a  $D/S = 3.4$

Experimental conditions of HDPCVD deposition steps and morphological analysis were reported (Tab. 3 and Fig.3, respectively).

Tab. 3: experimental conditions of HDPCVD process

Experimental Conditions	I step ( $D/S = 5.0$ )	II step ( $D/S = 3.4$ )
Pressure (mTorr)	~12	~7
RF top (Watt)	1300	1300
RF side (Watt)	3100	3100
RF bias (Watt)	3500	3500
$O_2$ (sccm)	302	132
$SiH_4$ top (sccm)	18	11
$SiH_4$ side (sccm)	132	86

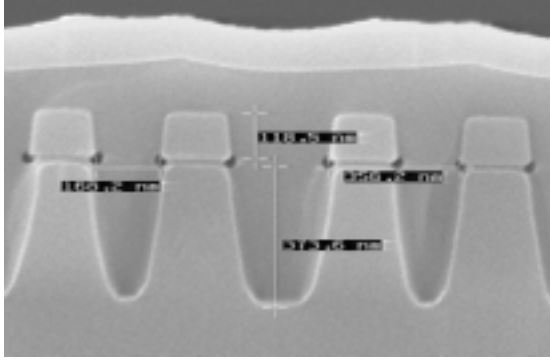


Fig. 3: morphological analysis on STI filling process by HDPCVD (I step D/S = 5.0; II step D/S = 3.4)

In order to obtain a stable and reproducible deposition process, we are evaluating the process window of integrated HDPCVD deposition, varying thickness of the first step ( $2500\text{\AA} \pm 200\text{\AA}$ ) and D/S of the second step ( $3.4 \pm 0.2$ ). Preliminary results were not encouraging because the process latitude found was not large enough to avoid risk of the nitride sputtering and to ensure the film gap fill efficiency. However, we have started to test a new alternative film to fill the trench with silicon oxide by SACVD deposited.

### 3. Process B: USG STI filling by SACVD

In alternative of HDPCVD film, we evaluated SACVD one, generally used at PMD level for its excellent morphological properties: in fact, in SACVD process, ozone induces a higher surface mobility of the TEOS molecules and this gives an excellent conformality and gapfill capability to the SACVD oxide film.

USG deposition in STI process was performed on SACVD DXZ chambers (Giga Fill Applied Materials) at  $550^\circ\text{C}$ , using a different process recipe respect to the standard process used for PMD applications:

- $\text{O}_2$  flow (4000sccm), to improve oxide quality and gap filling performances [4];
- lower TEOS flow (700 mgm), to decrease deposition rate and to obtain a better conformality and step coverage.

Morphological analysis on STI filling process by SACVD showed as the use of SACVD oxide efficiently allowed the trench filling without the voids formation during deposition process (Fig. 4).

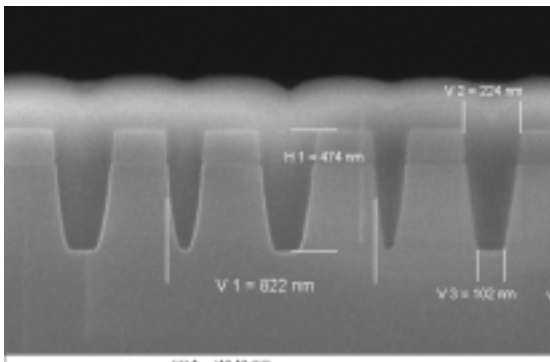


Fig. 4: morphological analysis on STI filling process by SACVD

### 4. Process results

The oxide films characterization by HDPCVD and SACVD process, used for STI applications, was reported (Tab. 4).

Tab. 4: process parameters comparison between different process recipes

Parameters	USG by HDPCVD	USG by SACVD
Deposition Rate (Å/min)	~ 6100	~ 370
Uniformity	< 1.7%	< 1.7%
Refractive Index	1.46±0.01	1.45±0.01
Stress (Dyne/cm <sup>2</sup> )		
Without ann. treatment	-1.38E09	1.59E09
With ann. treatment (1160°C)	-2.83E09	-2.60E09
WERR (BOE)		
Without ann. treatment	1.6	6.3
With ann. treatment (1160°C)	1.0	1.0

Higher WERR (Wet Etch Rate Ratio) value and tensile stress of USG by SACVD confirmed the low film quality (porous, absorbs moisture), compared with HDPCVD film; moreover, low deposition rate decreased process throughput, but a thermal treatment on USG SACVD film deposited (annealing process at 1160 °C, in N<sub>2</sub> ambient for 30 min), made the same dense and removed moisture, ensuring a better quality of oxide deposited, comparable with HDPCVD film.

## 5. Conclusions

USG by HDPCVD and SACVD process have been morphologically evaluated for STI applications.

A step by step study performed on structures with critical dimensions, using USG gap fill property by HDPCVD, allowed to set up a correct process for the trench filling without voids formation, and also to ensure a good planarization performance. However the process latitude we found was not large enough.

On the contrary the study performed on STI filling process by SACVD showed that USG by SACVD can be considered an important alternative for STI applications, showing good oxide properties in terms of gap fill and planarization performance, and good compatibility with nitride without adhesion problems between the two films. As far as the density of the film is concerned, by a proper thermal treatment we could ensure a suitable quality of the deposited oxide, comparable with the HDPCVD film.

Although the integration of SACVD deposition process with the CMP module and the electrical device characterization have still to be evaluated, at least at morphological level we can conclude that USG by SACVD process represents a promising alternative for STI applications.

## 6. Acknowledgements

We are grateful to the litho, process integration and etching teams of Catania CR&D (Central Research and Development) for their support in realizing this work. Moreover, thanks to M5 SEM (Scanning Electron Microscopy) Group for its participation to cross section embody in the report.

## References

- [1] B.Fazio, G.Curro', N.Nastasi – Patent Nr 00122102.7-2203 (2000).
- [2] P.Colpani, S.Ratti, D.Berselli – Counter Mask and CMP Optimization for CMOST8STI – CR&D Agrate-Technology Development, T.R. 130.1034 (2000).
- [3] S.V.Nguyen – Plasma Processing , 0018-8646 IBM, **43**, 1-2 (1999).
- [4] J.Franck – CTLib ID:13873 (2001).

# Ti<sub>x</sub>TiN film used as cap layer in the CoSi<sub>2</sub> growth to improve silicide properties

D. Fazio<sup>1</sup>, M. Bileci<sup>1</sup>, D. Mello<sup>2</sup>, R. Ricciari<sup>2</sup>, C. Gerardi<sup>1</sup>, M. Vulpio<sup>1</sup>

<sup>1</sup> Catania Central R&D, STMicroelectronics, Catania, Italy

<sup>2</sup> Q.A. & Physics Lab., STMicroelectronics, Catania, Italy

## Abstract

The use of cobalt, to form CoSi<sub>2</sub>, allows the formation of good quality silicide layers in ultra-scaled CMOS technologies. Due to the difficulty of cleaning the silicide surface and to the non-reproducibility of the process itself, a capping layer on cobalt is always used. Ti and TiN layers, separately, are widely used for different reasons. In the present work, we investigate the use of a mixed cap layer, Ti<sub>x</sub>TiN, which has features in between Ti and TiN and therefore matches the advantages of both cap layers.

## 1. Introduction

The formation of CoSi<sub>2</sub> obtained starting from cobalt layer deposition on silicon, has revealed unsuitable for manufacturing processes because of the hard difficulties to clean the silicide surface and the non-reproducibility of the process itself [1]. The use of a cap layer on cobalt avoids these problems. Titanium has been widely used both as a cap layer and as an interlayer, enhancing the epitaxial growth of CoSi<sub>2</sub> [2] and exhibiting a large process window [3], [4], [5].

During cobalt silicide formation one serious issue is the growth of native oxide on the Si surface. The use of Titanium strongly reduces the possibility of native oxide growth, therefore facilitating the diffusion of cobalt into silicon. At the same time it captures H<sub>2</sub>O or other gases from the silicon surface during the deposition of a cobalt layer [6]. Unfortunately Ti strongly competes with Co in the formation of the silicide.

On the other hand, the use of TiN cap layer, presents some advantages as well. First of all it allows a large process window for what concerns the lateral growth of the silicide, thus preventing problems of wordline-substrate leakage [7]. Even though it appears that its use gives line width dependence [6], and that it is not able to reduce the native silicon oxide [8], TiN is a good diffusion barrier and reduces the roughness of the CoSi film [9]. In addition, titanium nitride introduces nitrogen in the cobalt silicide, preventing the film from surface diffusion [10]. Finally, TiN does not participate to the self-aligned silicidation.

Some authors have recently reported studies on the simultaneous use of both Ti and TiN materials, on the top of the cobalt layer [11] with the purpose of combining the advantages from both the materials.

In this work we propose the use of a mixed layer (Ti<sub>x</sub>TiN) having features in between Ti and the TiN films. The stoichiometry of such a film is not well defined. The layer is obtained, in fact, depositing a first layer (Tix) in the same chamber in which TiN is deposited, but using only argon as gas inside the chamber. The target is nitrided, so part of the film contains TiN, but since N<sub>2</sub> is not present in this first step, the deposited film is titanium rich. In a second step, N<sub>2</sub> is flowed into the chamber and TiN is sputter-deposited.

## 2. Experimental

Co was sputter deposited on p-type (100) Si 8 inches wafers in an AMAT Endura HP 5500. *In situ*, Ti (std PVD), Ti<sub>x</sub>TiN or TiN (std PVD) have been deposited in a Ti or TiN chamber of the same tool. For the Ti<sub>x</sub>TiN film, the Tix layer was deposited by sputtering the TiN target only with Ar. For Ti and TiN films, a standard procedure was used. Subsequent, the *ex situ* annealing was carried out in an AMAT Centura in N<sub>2</sub> for 30 sec. at 450-700°C, to obtain the sensitivity curves, and at 550°C for the wafers used for the films analysis. The four wafers used for the CoSi film analysis have been treated with a SC1/SC2/SC1 scheme in a FSI Mercury MP, for the stripping process. The depth profiles of the elements were obtained by Auger analysis electron microscopy (AES) in a Physical Electronics SMART200. The energies of the electron and ion beams used are respectively 20kV and 2kV. SIMS profiles were obtained in a CAMECA WF-SC Ultra, using Cs<sup>+</sup> as primary beam, with impact energy of 1keV. The structures were characterized using Transmission Electron Microscopy (TEM) in a Tecnai F 20 equipped with a Field Emission Gun (FEG) and Gatan energy filter (GIF). TXRF analyses were performed on Rigaku TXRF300 equipment.

### 3. Results

In order to investigate the mixed  $\text{Ti}_x\text{TiN}$  cap layers, four wafers have been prepared depositing on pure silicon  $150\text{\AA}$  of cobalt and  $\text{Ti}_x\text{TiN}$  with different ratios (reported in table I). The cobalt layer does not react with silicon, since no thermal annealing is performed on the samples.

Table I: Scheme of deposition for samples **I-IV**.

Sample	Stacks
<b>I</b>	Co $150\text{\AA}$ $\text{Ti}_x$ $50\text{\AA}$ TiN $100\text{\AA}$
<b>II</b>	Co $150\text{\AA}$ $\text{Ti}_x$ $100\text{\AA}$ TiN $50\text{\AA}$
<b>III</b>	Co $150\text{\AA}$ $\text{Ti}_x$ $80\text{\AA}$ TiN $70\text{\AA}$
<b>IV</b>	Co $150\text{\AA}$ Ti $50\text{\AA}$ TiN $100\text{\AA}$

On these samples TEM, SIMS and Auger analysis have been performed. The thickness of the films **I-IV** has been measured by TEM and it is reported in table II. As observed, the values found are slightly different from the real thickness deposited.

Table II: Thickness of the samples I-IV measured by TEM.

Sample	Thickness ( $\text{\AA}$ )		
	Co	$\text{Ti}_x$	TiN
<b>I</b>	150	-	<b>150</b>
<b>II</b>	150	<b>60</b>	<b>70</b>
<b>III</b>	150	<b>60</b>	<b>70</b>
<b>IV</b>	150	50	100

Figure 1 shows a TEM cross section of sample IV, in this sample the interface between the two capping layers is clearly visible.

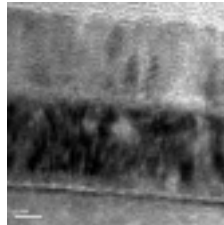


Figure 1: TEM section of sample **IV**

In order to distinguish the interface between the  $\text{Ti}_x$  and the TiN layers an energy filter was used (GIF). In this way elemental maps of samples **I-IV** were obtained, determining the presence of nitrogen in the  $\text{Ti}_x$  film (Fig. 2).

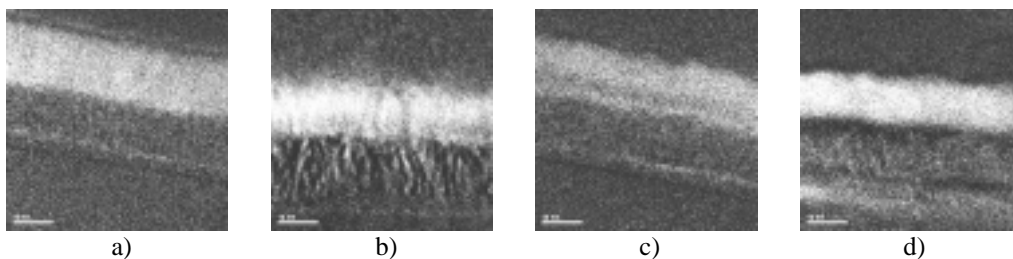


Figure 2: TEM elemental maps of samples **I** (a), **II** (b), **III** (c) and **IV** (d)

In particular, in sample **I** (Fig. 2a), the distribution of nitrogen is clearly detected. It is interesting to notice a decrease of nitrogen concentration within the TiN film for samples **II** and **III** (darker liner within the lighter part of fig. 2b and 2c). This darker liner represents the  $\text{Ti}_x$  film and actually it has been observed even by the AES and SIMS analysis, discussed later. In particular SIMS analysis reveals the  $\text{Ti}_x$  sheet even in sample **I**.



This phenomenon is related to the method of deposition of the  $\text{Ti}_x\text{TiN}$  film and it is clearer in samples **II** and **III** rather than in sample **I**. Only for sample **II** the phenomenon falls within the sensibility range of TEM and it can be clearly observed. Auger depth profiles have been obtained on the four samples and they are shown in figure 3.

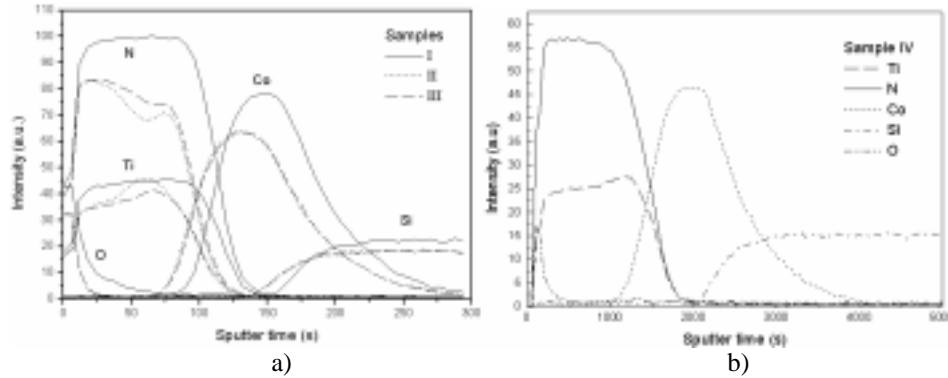


Figure 3: Ti/TiN depth profiles for a): Co/Ti<sub>50</sub>/TiN100 (**I**), Co/Ti<sub>100</sub>/TiN 50 (**II**), Co/Ti<sub>80</sub>/TiN 70 (**III**), and b): Co/Ti 50/TiN100 (**IV**)

No difference between the  $\text{Ti}_x$  and TiN layers can be observed in sample **I**, and only the TiN film can be revealed on cobalt. In samples **II** and **III** nitrogen is detected between Co layer and  $\text{Ti}_x$  layer and it is easy to distinguish the two films ( $\text{Ti}_x$  and TiN), with thickness values similar to the nominal ones.

The only thing that can be surely stated for sample **IV** is that a Ti film below the TiN film is clearly observed experimentally.

SIMS depth profiles for the samples **I-III** are shown in figure 4.

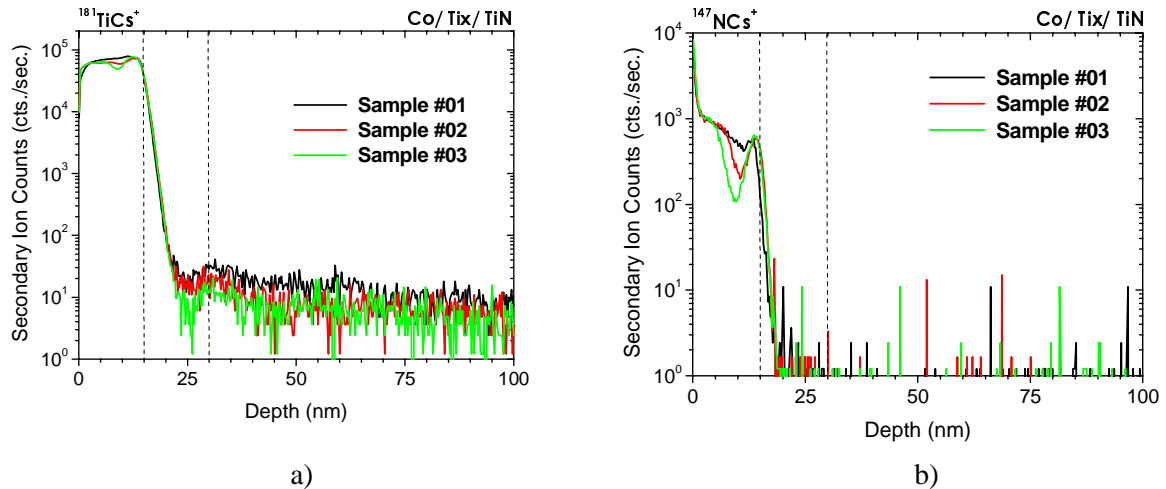


Figure 4: SIMS spectra for the capping samples **I-III**. a) Ti depth profile; b) N depth profile

Comparing the titanium depth profiles for the 3 samples (figure 4a) we can just observe that only for sample **III** there is a clear interface between the TiN and the  $\text{Ti}_x$  layers. In general the intensity of the titanium signal grows from the surface to the interface with cobalt indicating that the  $\text{Ti}_x$  layer (the one closer to cobalt) is richer in titanium compared to the TiN film.

From the nitrogen depth profiles is instead easier to distinguish the interface between  $\text{Ti}_x$  and TiN. It appears, in fact, that the intensity of the nitrogen signal decreases to a minimum value at the interface between TiN and  $\text{Ti}_x$  and it increases again at the interface between  $\text{Ti}_x$  and cobalt. This is mainly due to the deposition recipe for the  $\text{Ti}_x\text{TiN}$  film.

In order to evaluate the influence of these capping layers on the formation of cobalt silicide, other four samples have been prepared by sputter-deposition of  $150\text{\AA}$  of cobalt on pure silicon. Different cap-layers have been used on cobalt and they are described in table III. The wafers have been then annealed to favor the formation of  $\text{CoSi}$ . With a subsequent stripping process the unreacted cobalt and the cap layers have been removed.

Table III: Scheme of deposition for samples 1-4.

Sample	Stacks	T <sub>Annealing</sub>
1	Co 150Å_TiN100Å	550°C
2	Co 150Å_Tix 50Å_TiN 100Å	550°C
3	Co 150Å_Tix 100Å_TiN 50Å	550°C
4	Co 150Å_Ti 50Å_TiN 100Å	550°C

Rs measurements of the four wafers at three different steps (as-deposited, after the rapid thermal processing and after stripping) show the influence on the formation of CoSi of the different cap layers (Fig. 5).

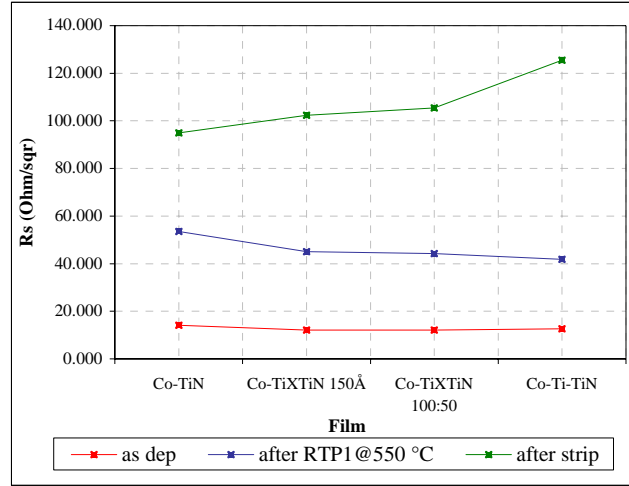


Figure 5: Rs values for samples 1, 2, 3, 4 after deposition, RTP1 and stripping.

In general, we observe that the Rs values are comparable for all the deposited capping layers. When CoSi is formed, the CoSi/TiN film gives a higher Rs value compared to the other films. This is probably due to the higher Rs value of the TiN cap layer with respect to the other three capping layers.

The last curve in figure 5 shows Rs values for the same four films after stripping. In this case only CoSi is present on all the wafers and therefore the differences can be directly attributed to the thickness of the formed CoSi. The film formed from the Co/TiN stack shows the lowest Rs, indicating that the grown CoSi film is thicker. Higher values are found for the other three films and the maximum Rs is found for the sample with the Co/Ti/TiN stack, indicating that this sample has a thinner formed CoSi layer.

The influence of the cap layers on the formation of the cobalt silicide has been also investigated by plotting the sensitivity curves for the four films over a wide range of temperature (400-700°C).

Figure 6 shows the sensitivity curves for the rapid thermal process for all the four stacks.

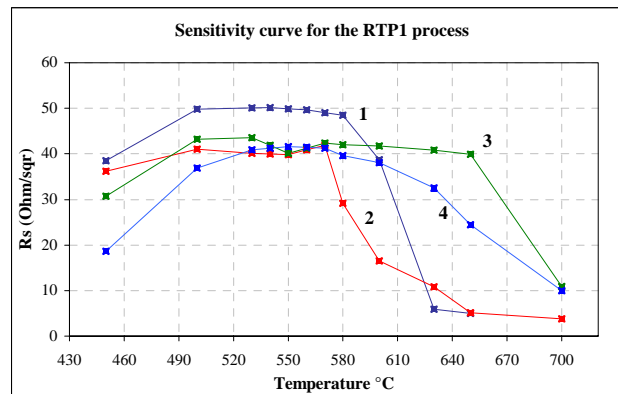


Figure 6: Sensitivity curves for the RTP1 process of Co/150Å/cappings wafers. 1) Co/TiN100Å, 2) Co/Tix50Å/TiN100Å, 3) Co/Tix100Å/TiN50Å, 4) Co/ Ti50Å/TiN100Å

Curve **1**, represents the Co/TiN wafers and the values are in good agreement with those found in literature [12]. At 450°C the formation of CoSi starts and remains more or less stable over a range of about 130°C (450°C-580°C). At 600°C the transformation into CoSi<sub>2</sub> starts, revealed from the sudden increase of the standard deviation. Curve **2** shows the same type of graphic for the Co/Ti<sub>x</sub> 50Å/TiN 100Å stack. In this case the process window is comparable to the one for the Co/TiN stack, even though the Rs values are generally lower, as already observed. The decrease of Rs values of about 10 Ohm/[ ] between the first curve (Co TiN stack) and the other three curves is probably imputable to the difference in the total thickness of the deposited capping layers. In the case the sensitivity curve for the Co/Ti<sub>x</sub> 100Å/TiN 50Å stack (curve **3**) CoSi species can be formed over a wider range of temperature. No change can be detected all over the range, since the standard deviation and the Rs values are more or less constant for all the range. These values are comparable with those found in literature for a Co/Ti stack. In fact the presence of Ti, enlarges the process window. A similar effect is, in fact, observed for the sensitivity curve of the last film, Co/Ti/TiN (plot **4**).

#### 4. Discussions

As a first result from all the spectroscopic analysis carried out on the samples **I-IV**, for the characterization of the cappings, it appears that the nominal thickness values for Ti<sub>x</sub>TiN do not correspond to the real deposited thickness. In particular, sample **I** is thicker than **II** and **III**, and the presence of Ti<sub>x</sub> is detected only by the high sensitivity SIMS analysis.

In samples **II**, **III** and **IV** the interface between Ti and TiN is quite well defined, even if the values of the thickness of Ti<sub>x</sub> are smaller than the expected ones. The smaller thickness of the cappings for sample **II** and **III** compared to sample **I** can be attributed to the deposition process and to the relative packing of the crystals at the Ti/TiN interface. This phenomenon, in fact, is not observed for sample **IV** since Ti and TiN are deposited separately. A more accurate SIMS analysis and a TEM analysis of the elemental maps reveal the presence of a TiN underlayer between Ti<sub>x</sub> and Co in samples **I**, **II** and **III**. This can be explained with the characteristics of the Ti<sub>x</sub>TiN deposition recipe, since in the first few seconds of Ti<sub>x</sub> sputtering, the target of the deposition chamber is anyway nitrated.

Concerning the results of the analysis carried out on the 4 samples with CoSi (**1-4**), we can say that the different cap layers influence the formation of CoSi depending on the concentration of titanium present in the capping film. In the case of the first sample, TiN does not participate to the CoSi formation. The sheet resistance of the film formed measured after stripping is the lowest found among the 4 samples, probably due to the formation of a thicker CoSi film. Regarding samples **2** and **3** (Co/Ti<sub>x</sub>TiN), the presence of a percentage of titanium influence the CoSi formation and the Rs measured after stripping is higher. As a result the process window gradually becomes bigger (resembling the one found in literature for the CoSi formed from a Co/Ti stack), titanium is probably present within the silicide film, and even if in small quantity, the Ti<sub>x</sub> present in the cap layer can compete with cobalt in the formation of CoSi. In sample **4**, for which a cap layer of standard Ti and standard TiN has been used, the influence of titanium in the formation of CoSi is much stronger. The Rs value after stripping is the highest found. Actually, from the studies carried out on the cappings we can argue that, if the thickness of Ti in the capping was the only factor influencing the formation of CoSi, then sample **3** and **4** should be the same (or even more, sample **3** should be more resistive than **4**). The apparent discrepancy of the results can be explained thanks to the observation of the TiN as underlayer noticed in the SIMS and Auger analysis of the capping samples in which Ti<sub>x</sub> is deposited. This explains even why samples **1** and **2** are similar concerning Rs values of CoSi. Considering the deposition recipe for the Ti<sub>x</sub>TiN cappings, we can argue that the concentration of Ti in samples **2** and **3** within the CoSi film must be quite low, but still enough to influence the silicide formation and its electrical properties (*i.e.* Rs values). At the same time it is responsible for the widening of the process window. The process window for the Ti<sub>x</sub>TiN cap layers (especially the Ti<sub>x</sub> 100Å/TiN 50Å) is as large as the one reported in literature for samples using Ti 80Å as cap layer [13], but with the advantage that the use of a Ti<sub>x</sub>TiN film can exploit the good qualities of both the Ti and the TiN cappings mentioned in the introduction to this work.

#### 5. Conclusions

In this paper we have proposed and characterized a new process that uses a cap layer of Ti<sub>x</sub>TiN deposited on a Co layer to promote the formation of cobalt silicide. The proposed process has been compared with conventional processes, which employ Ti and TiN as capping layer.

In particular, the Ti<sub>x</sub>TiN (100:50) film shows intermediate features between standard Ti and standard TiN, concerning Rs values of CoSi formed and process window for the silicide formation. The process window is wide and there is a well-defined transition to CoSi<sub>2</sub>.

The process proposed here combines the advantages of using Ti cap layer- which implies good junction leakage control, better process window- with the ones given by the employ of TiN –which has a negligible dependence on morphology and a very low resistivity.

## 6. Acknowledgements

We acknowledge M.Bersani and L.Vanzetti from IRST for SIMS and XPS analysis. F.Cordiano from STMicroelectronics for TXRF analysis, M.Sacchi from STMicroelectronics and M.Fragala' from Applied Materials for their support on thermal processes.

## References

- [1] Q.F. Wang, A. Lauwers, B. Deweerdt, R. Verbeeck, F. Loosen, K. Maex – IEEE Trans., Semiconductor Manufact., **8**, 449 (1995).
- [2] M.L.A. Dass, D.F. Fraser, C.S. Wei - Appl. Phys. Lett., **58**, 1308 (1991).
- [3] Q.F. Wang, K. Maex, S. Kubicek, R. Jonckheere, B. Kerkwijk, R. Verbeeck, S. Biesemans, K. De Meyer - Proc. Symp. VLSI Technology, Kyoto, Japan, 17 (1995).
- [4] Q.F. Wang, K. Maex - US Patent 5780362, pending.
- [5] A. Lauwers, P. Besser, M. de Potter, E. Kondoh, N. Roelandts, A. Steegen, M. Stucchi, K. Maex - Proc. IEEE Int. Interconnect Technology Conf. (IITC), San Francisco, Ca, 99 (1998).
- [6] K. Maex, A. Lauwers, P. Besser, E. Kondoh, M. de Potter, A. Steegen - IEEE Trans. Electron Devices, **46**, 1545 (1999).
- [7] a) A.C. Berti, V. Bolkhovsky - Proc. VLSI Multi Level Metal Integration Conf. (VMIC), 267 (1992);  
b) P. Apte, A. Paranjpe, G. Pollack - IEEE Electron Device Lett., **17**, 506 (1996).
- [8] M. Yoshimaru, T. Yoshie, M. Kageyama, K. Shimokawa, Y. Fukuda, H. Onoda, M. Ino - IEEE (1995).
- [9] G.P. Ru, J. Liu, X.P. Qu, B.Z. Li, C. Detavernier, R.L. Van Meirhaeghe, F. Cardon - An atomic force microscopy study of thin CoSi<sub>2</sub> films formed by solid state reaction - IEEE, 328 (1998).
- [10] S. Ogawa, T. Yoshida, T. Kouzaki - Appl. Phys. Lett., **56**, 725 (1990).
- [11] S.A Yoshikawa, Z. Wang, W.G. Catabay - US Patent 5902129, (1999).
- [12] G. Pares, unpublished work.
- [13] D. Saigal, G. Lai, L.Yang, J. Su, K. Ngan, M. Narashiman, F. Chen, A. Singhal, D. Lopes, S. Lian, W. Cao, K. Tsai, P. Lo, S.K. Lee, J. Shih - Study of capping layers, cleaning method and rapid thermal processing temperature on cobalt silicide formation.

# Role of polymerization on etch profile evolution: comparison between $C_4F_6$ and $C_4F_8$ chemistry

G. Garozzo<sup>1</sup>, A. La Magna<sup>2</sup>, C. Bellecci<sup>1</sup>, S. Cavaleri<sup>1</sup>, F. Beffumo<sup>1</sup>

<sup>1</sup> Central R&D, St-Microelectronics, Stradale Primosole 50, 95121 Catania, Italy. Phone +39 095 7405915 Fax +39 095 7405740

<sup>2</sup> CNR-IMM Sez. Catania, Stradale Primosole 50, 95121 Catania, Italy. Phone +39 095 591212 Fax +39 095 7139154

## Abstract

In this work we show the results obtained by a set of experiments, performed in order to study the ARDE (Aspect Ratio Dependence Etch) effects in dry-etching processes of silicon dioxide substrates [1]. In particular, we investigated the effect of the reagent and polymer flux modifications in different geometric conditions using two different gases:  $C_4F_8$  and  $C_4F_6$ . Finally, using a dry etch simulator [2,3] we are able to evaluate the different polymerizing conditions and to predict the overall profile evolution.

## 1. Introduction

The dry-etch is a critical process step for the microelectronic devices manufacturing. In particular, in the back-end on line technology (BEOL) we have to define the interconnections through inter-layer dielectric (ILD) between multilevel metallizations. The evolution of integrated circuits and the scaling down of the device feature-size has resulted in ever increasing demand of the etching processes because of the complexity of pattern to be defined. We usually have to etch patterns with different geometry, that is large in an one-dimensional or two-dimensional (trench and “infinite zone”) and small contact-hole features on the same substrate.

The pattern dependence on etch rate uniformities, in particular the ARDE effects (RIE-Lag, [4]) is a relevant aspect on our processes. This effect can result in a higher etch rate in the hole compare to large zone (Inverse RIE-Lag).

The etch rate in medium-high density fluorocarbon plasmas is believed to be the result of a concurrent etching (of the  $SiO_2$  substrate) and deposition (of a fluorocarbon film) phenomena [1,2]. Our efforts were focus on emphasizing the dependence of the etchant /polymer flux ratio on fluorocarbon gas. For this reason we have analyzed the different etch profiles obtained using  $C_4F_8$  and  $C_4F_6$  mixture gas. Finally in this work comparing experimental and theoretical profiles obtained by a dry etch simulator, we can compute the reagent/polymer flux ratio for both chemistry and study its correlation with RIE lag performance.

## 2. Experiments

In order to investigate the RIE-Lag phenomenon we etched oxide substrates and we studied the variations in the etch rate on the different feature-sizes.

For this purpose we used PECVD oxide film (deposited by plasma enhanced chemical vapor deposition); the wafers were patterned with a DUV photoresist to transfer on the substrate holes (0.16  $\mu m$  diameter), narrow lines (0.30  $\mu m \times 18 \mu m$  trench) and “infinite zones” (18  $\mu m \times 18 \mu m$ , large exposed area). These wafers were etched in a dual frequency diode reactor for 60 seconds, having a gap spacing of 1.6 cm, 27MHz top electrode RF frequency and 2 MHz bottom electrode RF frequency.

The etching gases were  $C_4F_6/O_2/Ar$  and  $C_4F_8/O_2/Ar$  gas mixtures. The wafer area pressure was 55mT and the total flux was 325 sccm (standard centimeter cubic minute) for both gas compositions to guarantee the same plasma density and resident time. The etch depth and profile of each features defined were evaluated by scanning electron microscopy (SEM).

First of all we studied the  $C_4F_6/O_2$  mix behavior. Tuning this ratio we were able to find the critical point in which the polymer deposition rate favors the inverse RIE-Lag.

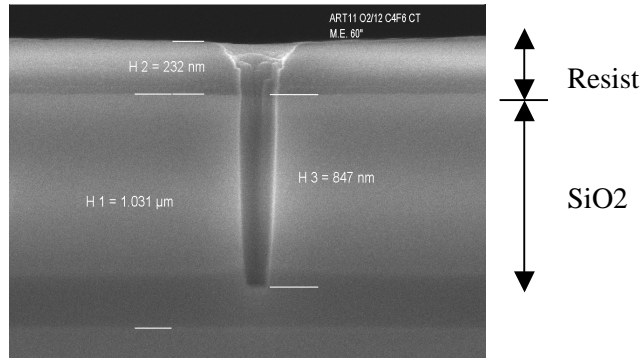


Fig.1 Etched contact profile at hole-size of 190 nm AD<sup>1</sup> with C<sub>4</sub>F<sub>6</sub>/O<sub>2</sub> mixture. Etch depth: 847 nm

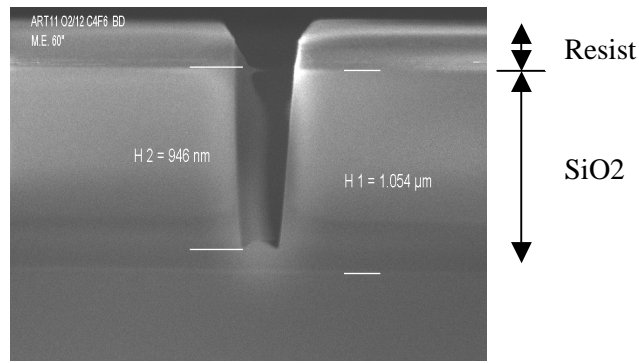


Fig.2 Etched trench profile, at feature-size of 300 nm AD in one direction and “infinite” in the other, with C<sub>4</sub>F<sub>6</sub>/O<sub>2</sub> mixture. Etch depth: 946 nm

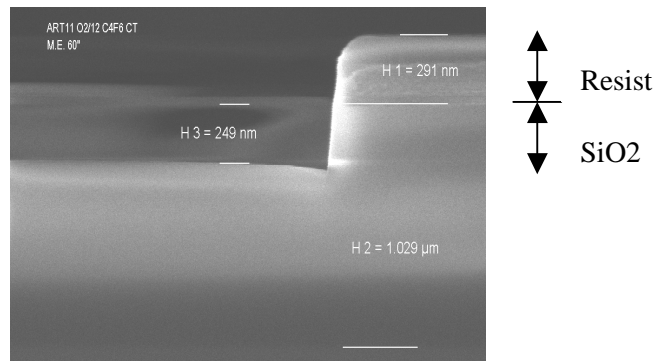


Fig.3 Etched scribe profile, at infinite feature-size in all directions, with C<sub>4</sub>F<sub>6</sub>/O<sub>2</sub> mixture. Etch depth: 249 nm

Studying the equivalent processes with  $C_4F_8$  (i.e. performed at the same ratio  $C_4F_8/O_2$ , and at the same flux of  $O_2$  and  $Ar$ ) we observed different effects on the geometry etched profile. These differences should be due to the different ratio between reagent and polymer flux in the  $C_4F_6$  chemistry case with respect to the  $C_4F_8$  chemistry case.

<sup>1</sup> After development mask

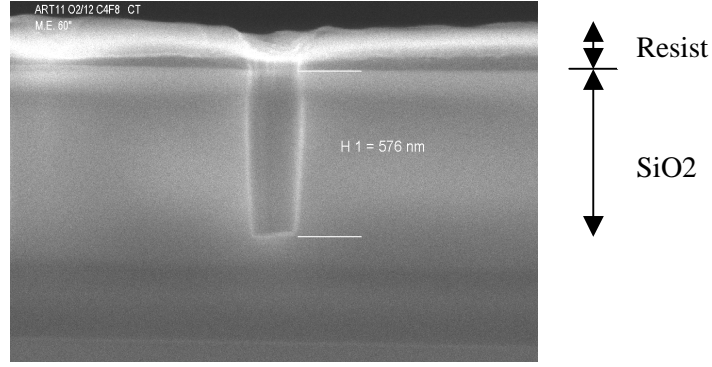


Fig.4 Etched contact profile at hole-size of 190 nm AD with C4F8/O2 mixture. Etch depth: 576nm

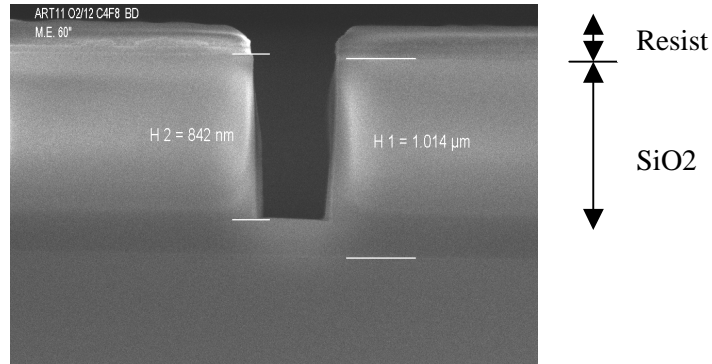


Fig.5 Etched trench profile, at feature-size of 300 nm AD in one direction and “infinite” in the other, with C4F8/O2 mixture. Etch depth: 842nm

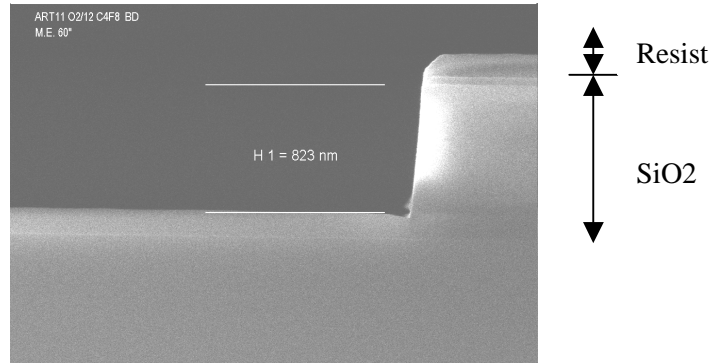


Fig.3 Etched scribe profile, at infinite feature-size in all directions, with C4F8/O2 mixture. Etch depth: 823nm

### 3. Etch model

In our model we consider a single active specie (namely the etchant), a single inhibitor specie (namely the polymer) and a single ion specie. More exactly, we assume that only chemical sputtering causes polymer etching, then the polymer film etch rate is

$$ER_p = AJ_i \Theta_{e/p}$$

where  $J_i$  is the ion flux,  $A$  a parameter depending on polymer density and yield, and  $\Theta_{e/p}$  is the polymer coverage.

The polymer deposition rate is

$$DR_p = BJ_p$$

where  $J_p$  is the polymer flux, and  $B$  a parameter depending on polymer density and yield.

If  $DR_p > ER_p$  the inhibitor polymer film will soon cover the whole surface elements and the oxide etch is stopped.

The etch rate on oxide depend on ion flux and dielectric coverage then in generally we can write:

$$ER_{ox} = ER_{ox}(J_i, J_n, \Theta_e)$$

where  $J_n$  is the reagent flux and  $\Theta_e$  is the coverage reagent on dielectric.

An balance equation link  $\Theta_e$  by  $\Theta_{e/p}$  [1,2]. So, taking into account the polymer deposition the final etch can be write in this way:

$$ER = ER_{ox} \left( 1 - \frac{ER_p}{DR_p} \right)$$

Of course the ion, neutral and polymer flux depend on visibility angle. This is very low in the hole, about  $\pi$  in one direction of the trench and about  $4\pi$  in the “infinite zone”.

#### 4. Results and Discussion

In order to understand the experimental features previously presented we have simulated our plasma-etching process using our simulator NOSTRADAMUS described in detail in the Refs. [2,3,5]. The phenomenon of the inverse RIE-lag has been explain using the model implemented in the our simulation code which considers the concurrent ion enhanced chemical etching of the reagent adsorbed film and the deposition of an inhibitor compound (polymer) film. Indeed in particular etching conditions the geometric constrain which, usually cause a decrease of the overall etching yield, can favor the plasma enhanced erosion since a lower local deposition of the inhibitor film is expected in this case. The balance between ion, reagent and polymer components impinging locally in the profile point given the profile geometry cannot be described qualitatively and must be evaluated by means the computational tool. In our experimental condition machine parameter does not vary, indeed only the gas moistures distinguish the two cases. In these conditions only reagent and the polymer fluxes can vary being the other parameter fixed (see again ref [2] for the derivation of model parameter from the machine parameter). In Fig.7 we show and compare with the relative SEM analysis, the profile evolution during the plasma etching in the case of  $C_4F_8/O_2$  moisture for the hole case. The model predict in this case  $\sim 850$  nm total erosion depth for the scribe (infinite) zone in good agreement with the measured one. In this case the balance between the reagent and polymer fluxes leads to a RIE-lag effect with the visibility is reduced from the scribe to the hole geometry. Moreover a good agreement between SEM and simulated etched profile can be observed.

In the  $C_4F_8/O_2$  case the fragmentation process in the plasma should be more efficient in the production of both reagent and polymer component, which derive from two different fragmentation path of the same ( $C_4F_6$  specie). However experiments show that using the  $C_4F_8/O_2$  we are near a stop etch condition while erosion occurs in hole geometry. In order to considered the moisture change we have simulated the profile evolution considering a reagent flux  $\sim 2$  times the and a polymer flux  $\sim 8$  times the  $C_4F_8/O_2$  case. In this condition our model foresees a stop-etch for the scribe case. The simulation for the hole geometry is shown in Fig. 8. Note the etch occurs in this condition, revealing that the balance between the reagent and polymer fluxes leads to a *inverse* RIE-lag phenomenon.



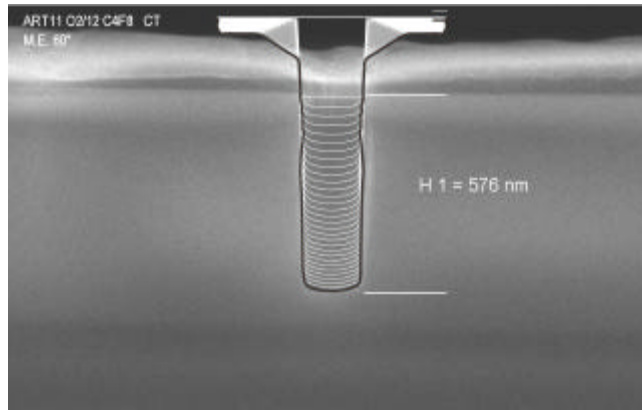


Fig.7 Comparison between numerical and experimental profile for hole etched with C4F8/O2 mixture.

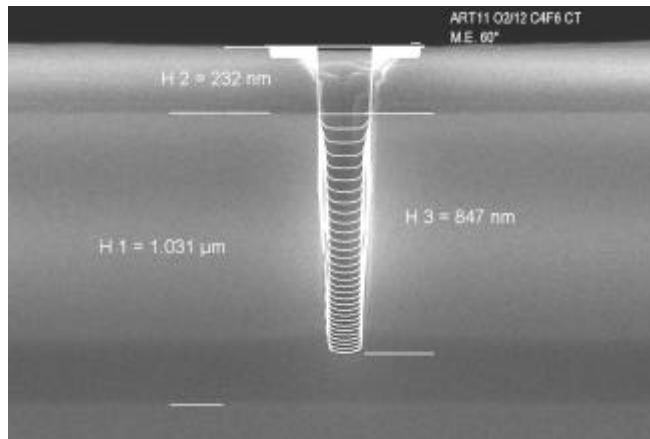


Fig.8 Comparison between numerical and experimental profile for hole etched with C4F6/O2 mixture.

## References

- [1] E. Gogolides, P. Vauvert, G. Kokkoris, G. Turban, A. Boudouvis - J. Appl. Phys. **88**, 5570 (2000).
- [2] G. Garozzo, A. La Magna - Proceeding SCI\_2002. **6**, 40 (2002).
- [3] G. Garozzo, A. La Magna, S. Coffa, G. D'Arrigo, N. Parasole, M. Renna and C. Spinella, Comp. Mat. Sci. **24**, 246 (2002).
- [4] R.A. Gottscho, C.W. Jurgensen, D.J. Vitkavage – J. Vac. Sci. Technol.B. **10**, (1992).
- [5] A. La Magna, G. Garozzo - Proceeding ISPC\_2003. **n° 183** (2003).

# PE-CVD Modification of PVC Intubation Tubes to Control Bacterial Adhesion: Ag/PEO-like Coatings

D.J. Balazs<sup>1</sup>, K. Triandafillu<sup>2</sup>, E. Sardella<sup>3</sup>, G. Iacoviello<sup>3</sup>, P. Favia<sup>3</sup>,  
R. d'Agostino<sup>3</sup>, and H.J. Mathieu<sup>1</sup>

<sup>1</sup> Materials Science Department, Swiss Federal Institute of Technology, Lausanne, Switzerland

<sup>2</sup> Department of Environmental Science and Technology, Swiss Federal Institute of Technology, Lausanne, Switzerland

<sup>3</sup> Department of Chemistry, University of Bari, Bari, Italy

*Pseudomonas aeruginosa* (*P. aeruginosa*) is one of the most prevalent bacterial strains in a clinical environment, responsible for 30% of pneumonia cases occurring in intubated and mechanically ventilated patients [1]. Colonization of the intubation tube often leads to mortality, despite aggressive antibiotic therapy. Therefore, a strategy to reduce bacterial adhesion to intubation tubes is desirable. We are developing an approach based on the surface modification of the polymer used for this application, medical grade poly(vinyl chloride) (PVC). This paper investigates a method to prevent protein adsorption and bacterial adhesion, as protein adhesion is believed to be a key event responsible for the specific adhesion of bacteria.

The strategy is to mask the PVC substrate with a plasma-deposited Ag/PEO-like coating, which combines the non-fouling properties of conventional poly(ethylene-oxide) materials [2] and the well-known bacterial toxic effects of silver [3]. Nanocomposite Ag/PEO-like coatings are plasma deposited in a mixed RF PE-CVD/sputtering process [4], and consist of Ag clusters of nanometric dimensions embedded in a hydrophilic PEO-like matrix. Thin Ag/PEO-like coatings were deposited on PVC substrates through RF PE-CVD methods, employing a silver cathode in an asymmetric RF PE-CVD reactor, DiEthylGlycol-DiMethyl-Ether (DEGDME) vapors as a monomer, and Ar as a buffer gas [4]. PEO-like films without Ag clusters were also produced using a stainless steel cathode and proper experimental conditions that prevent sputtering from the cathode; these samples served as controls to identify the origin of the anti-bacterial effects of the films. The PVC substrates were 1cm<sup>2</sup> sections cut from Mallinckrodt Hi-Lo<sup>TM</sup> endotracheal tubes, which were flattened to allow the eventual microscopic counting of bacteria. X-ray photoelectron spectroscopy (XPS) analysis was used to investigate the chemical nature of the films. Surface wettability was determined by contact angle measurements of deionized water sessile drops. Protein adhesion to the various surfaces was studied by incubating the samples in bovine serum albumin and fibrinogen. Bacterial adhesion studies were completed using four different strains of *P. aeruginosa*.

A systematic study of the deposition parameters, which are known to be important in determining the PEO-like character (C\*-O-C/total C1s) and Ag-content of the coatings, was completed using XPS analysis. The Ar flow rate (10–30 sccm) and RF input power (15–25 W) were varied, until a coating that yielded the highest Ag-content, while maintaining a certain PEO-like character was obtained. It was determined that glow discharges operating at high power result in a high Ag-content, but a decreased PEO-like character due to the increased dissociation of the DEGDME monomer. A similar phenomenon was observed for films deposited with high Ar flow rates, where higher flow rates yielded films with a very low PEO character, but a high silver content. Films with the highest Ag-content, while maintaining a certain PEO-like character, were obtained at a moderate flow rate and power, 20 sccm and 20 W respectively; samples were mass-produced for bacterial adhesion studies using these conditions.

The Ag-free films with the highest possible PEO character produced at 5W were completely non-fouling and prevented adsorption of both albumin and fibrinogen. It was determined that Ag/PEO-like films had similar protein adsorption properties to those of Ag-free films PEO-like produced at 15W and demonstrated minimal adsorption of albumin and fibrinogen. The Ag/PEO-like films completely prevented the adhesion of the four *P. aeruginosa* strains tested, whereas the Ag-free PEO-like films were not nearly as effective in preventing bacterial adhesion. This indicates that it is the silver content of the Ag/PEO-like films that is essential to the anti-bacterial properties of these coatings.

[1] J.L. Vincent, D.J. Bihari, P.M. Suter, *et al.* – *JAMA.* **274**, 639 (1995).

[2] S.I. Jeon, J.H. Lee, J.D. Andrade, *et al.* – *J. Colloid. Interf. Sci.* **142**, 149 (1991).

[3] R.L. Davies, S.F. Etris – *Catalysis Today*, **3**, 107 (1997).

[4] P. Favia, M. Vulpio, R. Marino, R. d'Agostino, *et al.* – *Plasmas and Polym.* **5**, 1 (2000).

# **NO<sub>x</sub> decomposition and re-synthesis in nitrogen-oxygen mixtures containing vapor in barrier discharge**

M. Wronski, I. Pollo

*Dept. of Chemical Technology, Lublin Technical University,  
ul.Nadbystrzycka 40; 20-618 Lublin, Poland*

Rapidly developing methods for NO<sub>x</sub> removal from flue gases and prospects of an application of processes using non-equilibrium plasma for this purpose induce a necessity of gaining a thorough knowledge about the mechanism of the processes. When discharges occur under the influence of high voltage in the discharge volume simultaneously with the processes of nitrogen decomposition processes of nitrogen oxides re-synthesis occur. A recognition of the effect of electrical parameters of a HV feeder and of a gas composition on the synthesis can help to obtain a higher degree of NO decomposition and more efficient utilization of electrical energy that feeds a reactor. Tests have been performed on a flat reactor with a quartz dielectric (discharge gap of 1mm) fed with alternate voltage of 50-4500Hz up to the value of 8.0kV. Feeding gas has contained from 9 to 95% of O<sub>2</sub>, 0- 8,000ppm of H<sub>2</sub>O with the remaining part being nitrogen.

An analysis of a gas composition at the reactor outlet has been performed with a mass spectrometer and it has shown that among the synthesis products aside with ozone there also are N<sub>2</sub>O, NO, NO<sub>2</sub> and N<sub>2</sub>O<sub>5</sub>. The highest total NO<sub>x</sub> concentration values have been obtained at the ca 50% oxygen content in the mixture. Further increase of the oxygen content in the mixture causes a decrease of the N<sub>2</sub>O and N<sub>2</sub>O<sub>5</sub> content. The highest NO<sub>2</sub> concentration values have been obtained for a mixture of 55% of O<sub>2</sub> and 45% of N<sub>2</sub>. For testing the effect of vapor content a mixture of 21% of O<sub>2</sub>, 0- 8,000ppm of H<sub>2</sub>O, and nitrogen being the remaining part has been applied. An increase of the vapor content has caused a decrease of the N<sub>2</sub>O concentration and a an increase of the N<sub>2</sub>O<sub>5</sub> concentration. For the H<sub>2</sub>O concentration of 3,500ppm the highest values of the NO concentration and the lowest values of the NO<sub>2</sub> concentration occur. Along with the growing feeding voltage value the total NO<sub>x</sub> concentration increases but for higher frequency values (4,500Hz) the increase gets smaller. The obtained results indicate that in the process of a NO<sub>x</sub> removal from flue gases it is possible to limit a re-synthesis of NO<sub>x</sub> by an adequate selection of the HV feeder parameters and of the composition of gas that is subdued to the discharge action.

## Reactions of S<sub>2</sub>F<sub>10</sub> and benzenes in a low temperature plasma

A. Jesih, M. Remškar, T. Skapin, D. Žigon and B. Kralj

*Jožef Stefan Institute, Jamova 39, 1111 Ljubljana, Slovenia*

Pentafluorosulfanyl, SF<sub>5</sub>, group containing organic compounds are potentially useful in a number of applications, which includes high temperature polymers and energetic materials. Pentafluorosulfanyl group containing polymers show lower dielectric constant, greater solubility, increased hydrophobicity, less colour and improved tensile properties in comparison to trifluoromethyl group containing polymers [1], while replacement of nitro group with pentafluorosulfanyl group in energetic materials reduces the shock sensitivity of energetic materials [2]. The low yields of production of pentafluorosulfanylbenzenes inhibit the use of these compounds. Recently the formation of pentafluorosulfanylbenzenes in a low temperature plasma of sulfur fluorides SF<sub>6</sub>, SF<sub>5</sub>Cl, SF<sub>5</sub>CF<sub>3</sub> and benzenes has been reported. Products consisted mainly of halogenated benzenes, but C<sub>6</sub>H<sub>5</sub>SF<sub>5</sub> was found in all cases in minor quantities [3].

In a low temperature plasma sulfur fluoride S<sub>2</sub>F<sub>10</sub> was allowed to react with benzenes C<sub>6</sub>H<sub>6</sub>, C<sub>6</sub>H<sub>5</sub>Br and C<sub>6</sub>H<sub>5</sub>Cl. The reaction products were trapped at 77 K and subsequently analysed by GC-MS and GC-FTIR spectroscopy. In reaction products pentafluorosulfanybenzenes appeared in minor quantities besides fluorinated benzenes, biphenyl and sulfides.

[1] A. Jesih, A. M. Sipyagin, L. F. Chen, W. D. Hong, J. S. Thrasher, Polymer Prepr. (Am. Chem. Soc., Rev. Polym. Chem.) **34**, 383 (1993).

[2] H. Sitzmann, W. H. Gilligan, D. L. Ornellas, J. S. Thrasher, J. Energ. Mat. **8**, 352 (1990).

[3] P. Klampfer, T. Skapin, B. Kralj, D. Žigon, A. Jesih, Acta Chim. Slov. In Press.

# Chlorinated hydrocarbons destruction by plasma chemical reactor with double transferred arc torch (DTAT)

O. Tukhto<sup>1</sup>, I. Kuropyatnik<sup>2</sup>, Ye. Chasovskikh<sup>2</sup>, M. Predtechensky<sup>2</sup>

<sup>1</sup> *Institute of Thermophysics SB RAS, Novosibirsk, Russia*

<sup>2</sup> *International Scientific Center on Thermophysics and Engineering, Novosibirsk, Russia*

## Abstract

This work concerns the chlorinated hydrocarbons destruction in plasma chemical reactor with a plasma double transfer arc torch (DTAT). The experimental destruction of PCB (trichlorobiphenyl) transformer oil showed that the concentration of dioxins in the synthesis gas does not exceed 0.05 ng/m<sup>3</sup> (EPA standard is 0.1 ng/m<sup>3</sup>), which implies that the plasmochemical reactor is fully applicable to the destruction of organochlorine wastes. Gas exhaust complies with the ecological requirements.

## 1. Introduction

The most promising technologies for the treatment of toxic waste is plasma chemical technology based on high-temperature plasmochemical treatment and complete decomposition of the treated wastes by means of arc plasma yielding a valuable energy resource, i.e., synthesis gas, which is a mixture of CO and H<sub>2</sub>. The main advantage of plasmochemical technology is that it can universally be applied to various kinds of waste and can be implemented in relatively small-sized mobile technological modules.

At the same time, wide practical application of plasma technologies is hindered by the absence of powerful and reliable arc plasma torches with a sufficiently long service life. The existing torches require costly inert gases as plasma-forming agent, whereas, from the viewpoint of plasmochemical reactions, the optimum plasma-forming gas is actually steam. An electric arc in powerful plasma torches results in the erosion of electrodes, which are to be replaced periodically thus necessitating stoppages of the plant. The solution of these problems, in particular, provision of new plasma sources, could secure a new higher level of plasma technologies. Our work presents a plasmochemical reactor with a novel source of arc plasma free from the above-mentioned drawbacks. Treatment of polychlorinated biphenyls is demonstrated with the dioxin content synthesis gas produced in the reactor being in compliance with ecological standards.

## 2. Plasma reactor with liquid-metal electrodes: schematic representation

Figure 1 shows schematic representation of the plasmochemical reactor. Inside a steel airtight case lined with refractory bricks there are two reaction chambers with special baths [1]. Prior to starting the operation of the plasmochemical reactor, metal scrap is fed to the baths. An electric arc is generated between these bath and as it is burning. The metal melts. A special unit stabilizes the arc. The waste is fed to the melt surface. Plasmochemical reaction of gasification proceeds in the reactor chambers at the temperature of 1300-1500°C. Gasification products are removed from the chambers of the plasmochemical reactor and fed to the system of gas purification.

During the operation, a layer of molten slag is formed on the metal surface. The slag is removed as it is accumulated or continuously for high-capacity plants by means of a special slag-removing device.

The new reactor has some strategic advantages over plasmochemical reactors based on the traditional plasma torches:

- 1) There is no erosion of electrodes.

The surface of molten metal serving as electrodes is not subject to erosion; therefore the service life of the new plasmochemical reactor is characterized by practically unrestricted service life of the electrodes.

- 2) Steam can be used as a plasma-forming gas.

In known analogues argon, nitrogen or air are usually used as a plasma-forming gas. Then the corresponding air or nitrogen plasma is mixed with reactants, i.e., steam, and waste. In order to improve the efficiency of the reactor operation, steam is to be used as a plasma-forming gas. However, when steam is used it intensifies the erosion of the electrodes. In our case, liquid metal employed as electrodes makes it possible using steam as a plasma-forming gas.

- 3) The reactor capacity can be increased practically without restriction.

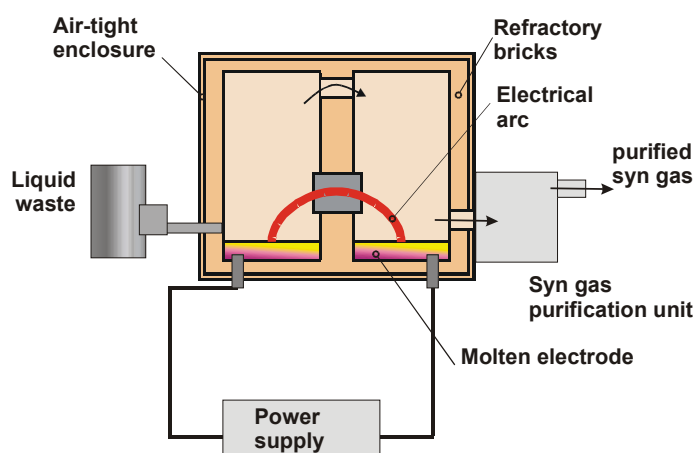


Fig. 1. Plasma chemical reactor for toxic waste destruction: flow chart.

As is known, the plasma torch capacity can be enhanced by increasing the discharge current. The discharge current increase also intensifies the erosion of electrodes. Making use of liquid electrodes, which are not subject to erosion, gives new potential of increasing capacity.

### 3. Plasma reactor with liquid-metal electrodes: pilot plant

A pilot plant for waste destruction based on the new plasma chemical reactor has been produced and installed. Its photograph is shown in Figure 3. The plant includes the following components:

- Plasma chemical reactor;
- Power supply;
- Steam generating unit;
- Waste feed system;
- Cooling system;
- System of synthesis gas quenching and purification;
- Gas control desk;
- Control board.

Main parameters of the plant are presented in Table 1.

Table 1. Main parameters of the plant for toxic waste treatment.

Capacity	up to 40 kg/h
Electric arc power	up to 150 kW (limited by the available power supply)
Plasma-forming gas	nitrogen, air, CO <sub>2</sub> , steam
Plasma-forming gas rate	3-5 g/s.
Operating temperature in reaction chambers	1300°C

The procedure of the reactor tests was in two variant.

Fist variant. Mixture simulating chlorine-containing waste (iso-propil alcohol – 60%, benzine – 25%, chlormethane – 15%) was fed to the reaction chamber to the melt surface. Gasification reaction between the waste and the steam yields synthesis gas (a mixture of hydrogen, CO and HCl). The produced synthesis gas is promptly cooled and quenched simultaneously being purified from HCl in centrifugal bubbling scrubber. The analysis the synthesis gas has shown that the dioxin/furan concentration does not exceed TEQ=0.02 ng/m<sup>3</sup>.



Fig. 2. Pilot plant for waste destruction based on the new plasma chemical reactor.

In second variant the PCB containing transformer oil (90% trichlorobiphenil) was used for test. The experimental destruction of PCB (trichlorobiphenyl) transformer oil showed that the dioxin/furan concentration in the synthesis gas does not exceed  $0.05 \text{ ng/m}^3$  (EPA standard is  $0.1 \text{ ng/m}^3$ ), which implies that the plasmochemical reactor is fully applicable to the destruction of organochlorine wastes.

#### 4. Conclusion

The developed plasmochemical reactor has important strategic advantages providing its higher viability in comparison with the traditional technologies of toxic waste destruction. The tests on the destruction of hazardous highly toxic wastes, polychlorinated biphenyl, proved very successful. The gas exhaust complies with international standards of environmental protection.

#### References

- [1] M. Predtechensky, O. Tukhto, I. Kuropyatnik, Ye. Chasovskikh. Plasma double transfer arc torch (DTAT). ISPC-16.

# Plasma double transferred arc torch (DTAT)

M. Predtechensky<sup>1</sup>, O. Tukhto<sup>2</sup>, I. Kuropyatnik<sup>1</sup>, E. Chasovskikh<sup>1</sup>

<sup>1</sup> *International Scientific Center on Thermophysics and Energetics, Novosibirsk, Russia*

<sup>2</sup> *Institute of Thermophysics SB RAS, Novosibirsk, Russia*

## Abstract

The plasma chemical reactor is presented based on a new type of DC arc plasma source, i.e., plasma double transferred arc torch (DTAT). The influence of the feed rate of plasma forming gas on the arc characteristics is investigated. The range of parameters (arc current, feed rate of plasma forming gas) is determined providing steady arc burning.

## 1. Introduction

The development of plasma technologies is hindered by the absence of powerful and reliable arc torches with a sufficiently long service life of electrodes. An electric powerful arc results in the erosion of electrodes and plasma torches are to be stopped periodically to replace them. The development of plasma technologies are directly connected with the provision of new low-temperature plasma sources with long service life of electrodes. The electrode service life of high power plasma torch usually does not exceed 100-300 hours. Various methods are proposed to decrease the erosion of electrodes. In our work novel arc plasma source where electrodes are not subject to erosion is described. Unlike traditional transferred arc which is used in a number of plasmochemical reactors and plasma furnaces, both ends of an arc in our torch rest on a melt (plasma double transferred arc torch, DTAT). Molten surface is not subject to erosion and so novel plasma source has unlimited service life of electrodes which provides its broad applications. The present work presents the research data of electrophysical properties of DTAT and the analysis of intended industrial applications.

## 2. DTAT

DTAT is realized in the plasmochemical reactor (Fig.1). Inside a steel airtight case lined with refractory bricks there are two chambers with special baths with metal serving as electrodes (anode and cathode). An electric arc is burning between the electrodes and melting them. The central part of an arc is placed in a water-cooling channel in the partition which divides two chambers, near electrodes in an open space. This new electric arc is a new object for investigation. Using liquid metal electrodes determines specific properties of this arc.

Electrical characteristics of DTAT were tested on a pilot plant of plasmochemical reactor with capacity up to 200 kWt. At start-up of DTAT the air was used as plasma-forming gas. When steam is introduced, the air is cancelled. During the operation of DTAT the electrodes are melted and the arc tension decreases.

Figure 2 shows volt-ampere (V-A) characteristics of DTAT while the electrodes are melting and when they have been melted. Steam is used as plasma forming gas. Steam rate - 2 g/sec. The total length of the arc - 40 cm. The length of open parts of the arc - 6 cm. The open part of the arc is transformed in a luminous cord. It is seen that while the electrodes are melting VA characteristics are changing, arc voltage decreases at the same current values.

Figure 3 shows V-A characteristics of DTAT under various air flow rate. It is seen that electrical strength of arc is growing with the increasing of plasma-forming gas rate. Voltage fluctuations are within the limits of 2%. Arc voltage is more growing when current is decreasing at high gas rate. The curves are converging at high values of current discharge. Large diameter of the channel (5,4 cm) provides the decrease of arc voltage.

Long-term test of DTAT prove its high reliability. It has been operating more than 1500 hours. Complete lack of electrode erosion opens wide possibilities for the industrial applications of a novel DTAT.



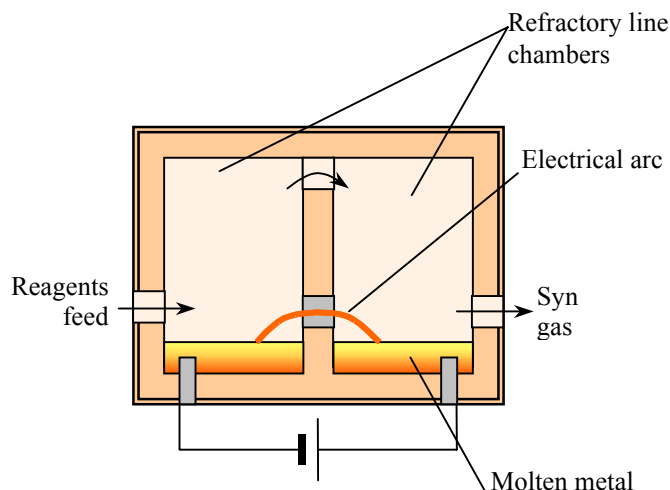


Fig. 1. Scheme of plasma chemical reactor with double transfer arc torch DTAT.

### 3. Business prospects of the suggested development and its commercial use

The major application of novel plasmachemical reactor is **the destruction of hazardous and toxic waste**, which are difficult or impossible to destroy using traditional technologies or because of environmental damage. It makes it possible to destroy chlorinated and fluorinated carbohydrates, pesticides, chemical weapon, medical waste, food contaminants, plastic packages, chemical production waste, disposed chemical reactants, confiscated drugs, etc.

There exist other areas where our plasmachemical reactor can be applied:

#### 1) Processing of solid domestic waste using coal gasification.

Large plant produced on the basis of plasmachemical reactor with the capacity over 100,000 tons per a

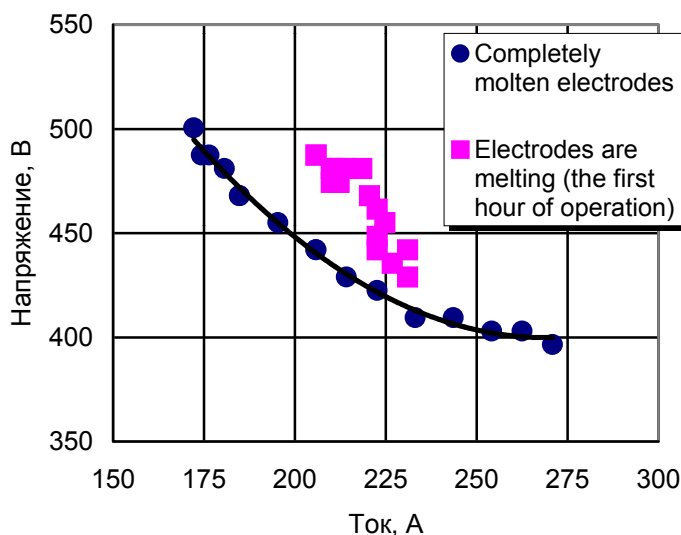


Fig 2. Variation of V-A characteristics at electrode melting. The flow rate of plasma-forming gas (steam) – 1,8 g/sec.

year will yield great profit producing energy obtained by synthesis-gas burning. The problem of open dump pollution is becoming more and more urgent with every year, and such plant will make it possible to get rid of waste, but also to produce heat and electric energy and building materials made of chemically inert gas.

## **2) Ash vitrification.**

Long-term traditional waste incineration results in the accumulation of huge amount of ash. At present the plants for plasma ash melting are being constructed in Europe, USA and Japan. Our plasma reactor can be effectively applied in this technology.

## **3) Coal gasification.**

Ecologically safe power engineering with coal gasification combined cycle using modern steam and gas turbines is of fundamental importance now because the quality of coal is being steadily worsening and the demand for coal in power engineering steadily increases. However, the development of large-tonnage plasma gasifiers is hindered by the absence of powerful plasmotrones with long service life. The application of our plasmochemical reactor with long service life and unlimited power augmentation makes it possible to solve a problem of the development of powerful and reliable plasma gasifiers.

## **4) Plasma metallurgy.**

The development of the furnaces for melting stainless and high-alloy steel

## **References (Times 11, bold)**

[1] M.R. Predtechensky, I.N. Kuropyatnik, O.M. Tukhto. ISPC-15, 1187-1190, (2001).

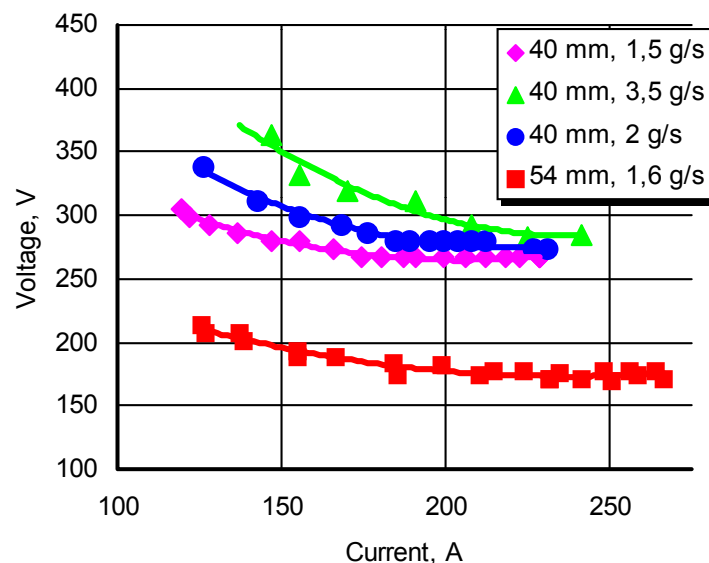


Fig. 3. V-A characteristics of DTAT at various flow rates of plasma-forming gas (channel diameter – 40 and 54 mm).

# Plasma Etching of FeRAM Materials: New Developments in High Temperature

S. Marks<sup>1</sup>, G. Beique<sup>1</sup>, J. P. Almerico<sup>1</sup>

<sup>1</sup> Tegal Corporation, Petaluma, California, U.S.A.

## Abstract

We discuss our motivations for pursuing the high temperature plasma etching of Ferroelectrics films. We show results of our work at high wafer temperature. We present details showing an effective combination of the capabilities of dual frequency plasma etching with high wafer temperature etching in a capacitively coupled plasma reactor. These capabilities allow fine-line geometries to be etched for advanced FeRAM structures. Key Words: FeRAM, Ferroelectric, Ir, IrO<sub>2</sub>, PZT, BST.

## 1. Introduction

The plasma etching of Ferroelectric Electrodes (Pt, Ir, IrO<sub>x</sub>, Ru,...) and Dielectrics (PZT, Y1,...) presents some challenges not encountered in the etching of the familiar materials in a standard CMOS process. First, the volatility of the etch products is very low compared to the etch products of etching silicon or aluminum in halogen chemistries, making it difficult to achieve high etch rates or vertical etch profiles. Secondly, the sputtering yields of the Ferroelectric materials are significantly below that of the standard CMOS materials, so even a reactive etch with a strong physical component may not work so readily as it does with the more familiar films.

In this study, we achieved steep profiles and high etch rates of Ir and PZT films using a capacitively coupled plasma reactor at elevated wafer temperatures. We measured profiles and angles as a function of wafer temperature, and optimized our etch process for 0.13μm features. We also present our observations on temperature dependent etch-rates on BST (a High k dielectric) films.

## 2. Equipment – Electrostatic Chuck

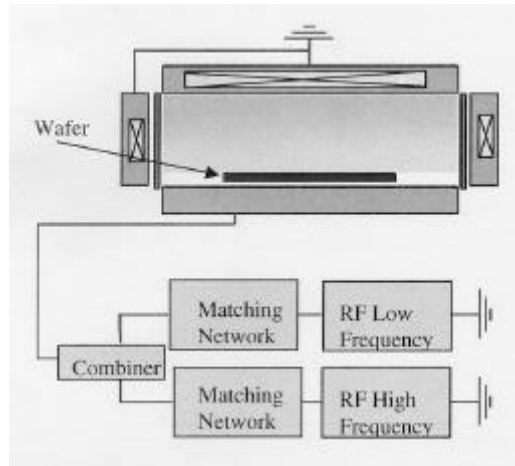
This work was done on a magnetically confined capacitively-coupled reactor, the Tegal 6540 HRe<sup>TM</sup> (a High density Reflected Electron plasma etch reactor). This reactor produces a dense and uniform plasma and is optimized for low-pressure operation. The main feature of the reactor explored in the current study was the ability to achieve and control elevated wafer temperatures (350 – 400°C) during plasma etch. The etch reactor is configured with an electrically heated electrode capable of operation to greater than 450°C. In addition, the ESC module has the ability to control the wafer temperature using sensors that directly monitor the wafer temperature to supply information to a wafer temperature control feedback loop.

The salient features of the present ElectroStatic Chuck (ESC) design are as follows:

- 1) Jonsen-Rahbek Ceramic design (monopolar) which accommodates any material or wafer backside.
- 2) A patented Auto-Clamp feature that assures that each wafer is optimally clamped.
- 3) Wide operating temperature range (200 to 500°C) capability.
- 4) Direct sensing of wafer temperature in addition to direct sensing of electrode temperature.

## 3. Equipment – RF Delivery

A diagram of the RF power delivery used in our work is shown in Figure 1 below:



**Figure 1. RF Delivery Schematic of the Tegal 6540 HRe™.**

A key item of note for the RF transmission in this capacitively coupled reactor design is that RF power is *not* delivered through a dielectric window. This important feature of capacitively coupled reactors has particular bearing on the plasma etch of nonvolatile metals, as the following table indicates.

**Table 1. Comparison of Capacitively Coupled and Inductively Coupled (ICP) methods of RF delivery.**

Parameter	Capacitively Coupled 6540 HRe™ RF System	Inductively Coupled (ICP) RF system with dielectric window
Is RF power transfer affected by electrically non-conducting film that deposits as a result of etching by-products?	No	No
Is RF power transfer affected by electrically <i>conducting</i> film that deposits as a result of etching by-products?	No	Yes – RF power transfer is attenuated by the conducting film, resulting in decreasing etch rates. Etch uniformity is also affected, due to non-uniform buildup of this deposited film.

Since most FeRAM structures contain materials like Ir, Pt, Ru, and PZT, the etch by-products usually deposited on the interior surface of the plasma reactor are electrically conducting layers. This deposition will attenuate the effective transmitted RF power in systems where the RF power driving the plasma couples through a dielectric window. As a result, wafer-to-wafer etch reproducibility is adversely affected by this conducting layer. Furthermore, since depositions tend to build up faster in the center of the window, the uniformity is also adversely affected. The capacitively coupled approach to plasma reactor design and RF power transmission avoids this effect and delivers a reproducible process over large numbers of etched wafers.

### 3. Motivation for High Temperature Etching

For standard CMOS films such as silicon, polysilicon and aluminum alloys, the wafer temperatures needed to volatilize the etch products created in halogenated etch chemistries are modest. However, to volatilize the etch products of FeRAM materials a much higher temperature is required. Table 2 below contrasts the etch product properties of some well-established CMOS films to the etch products expected from the components of the ferroelectric material Lead Zirconate Titanate (PZT).

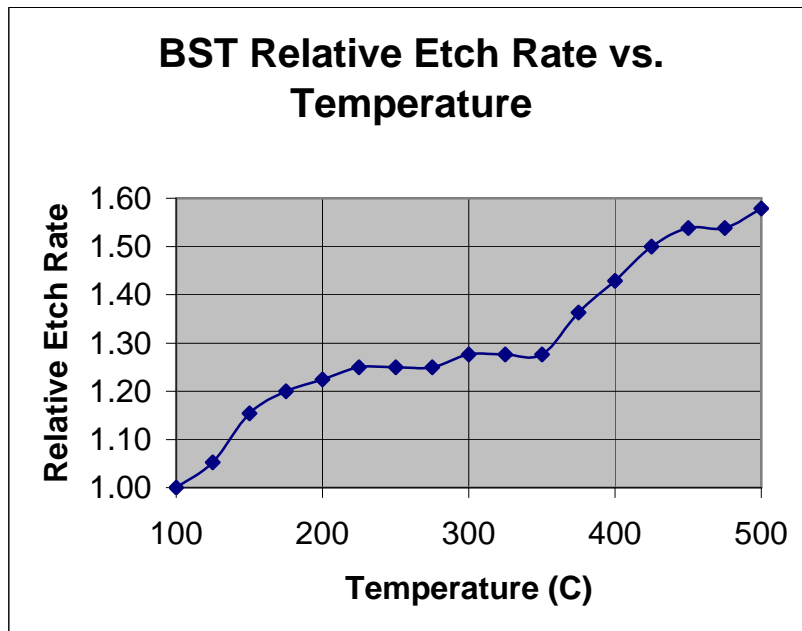
**Table 2. Etch product volatilities**

Element	Chloride Boiling Point (°C)	Fluoride Boiling Point (°C)
Si	58	-86
Al	70	
Pb	360	1290
Zr	331	58
Ti	136	284

As Table 2 shows, there is a significantly higher temperature range needed to volatilize PZT etch products than compared to silicon or aluminum.

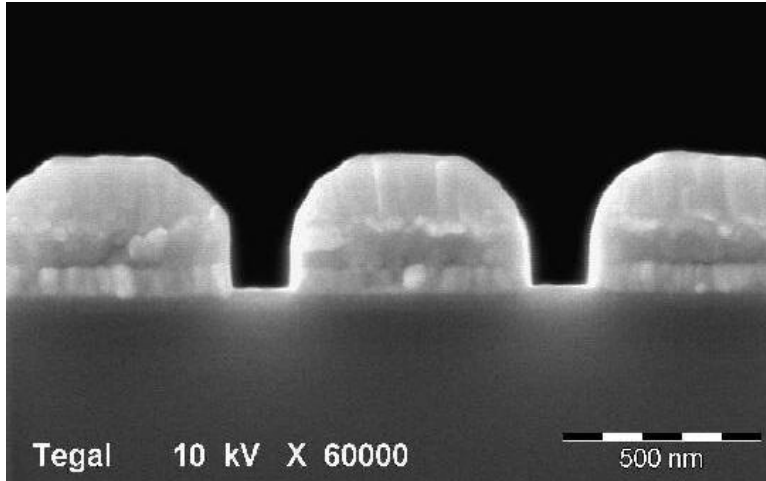
#### 4. High Temperature Results

The High k material BST or (Ba,Sr)TiO<sub>3</sub> is a technologically important film for microwave and RF tuner applications, along with advanced DRAM structures. In prior work we have observed the etch rate of BST to increase significantly with wafer temperature as plotted in Figure 2.



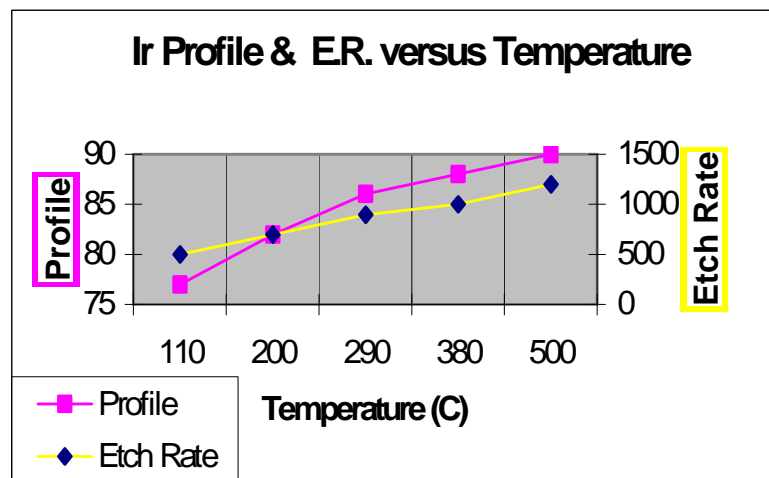
**Figure 2. BST Etch-Rate versus Temperature.** It appears as though the Titanate part of BST experiences an enhanced etch-rate to 200°C.

The main thrust of this paper is to report on results obtained on 200-mm wafers for the FeRAM stack Ir/IrO<sub>2</sub>/PZT/Ir at 0.13-micron geometries. These wafers were provided to us by Texas Instruments and represent the most technologically demanding FeRAM structure currently being produced [1]. We were able to realize the full capabilities of our etch system by utilizing the heated electrode at 500°C, where we can produce vertical (90-degree) profiles in an FeRAM stack using a single mask etch. This result is illustrated in Figure 3:



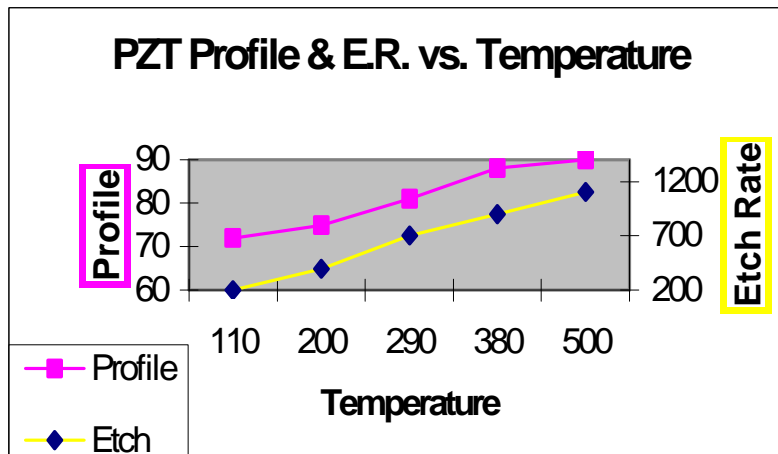
**Figure 3. 90-Degree Profiles on the Ir/IrO<sub>2</sub>/PZT/Ir stack at 130-nm spacing.** The hard mask is rounded but the ferroelectric stack itself is at 90 degree after etch.

To show the enhanced reactive effect of etch chemistry as a function of wafer temperature an etch-rate and profile study was conducted at various temperatures. Results of etching just the upper electrode from the above stack (Ir/IrO<sub>2</sub>) are shown in Figure 4:



**Figure 4. Enhancement of both the Etch-Rate and Profile of the Ir/IrO<sub>2</sub> Stack.** The profile improves from 77 degrees to 90 degrees across the temperature range studied. The etch rate increased from 500 to 1200 Angstroms/Min. over the same temperature range.

In a similar manner, the temperature of the PZT etch was varied to produce the results illustrated in Figure 5:



**Figure 5. Enhancement of both the Profile and Etch Rate of PZT with increasing temperature.** PZT results are even more dramatic than Iridium. The profile increased 72 degrees to 90 degrees and the Etch Rate improved from 200 to 1000 Angstroms/Minute.

It is beyond the scope of this paper to present the details on electrical device testing; please refer to the paper cited in [2]. Suffice to say that a process was identified with steep profile, good switched charge and low leakage.

## 5. Summary

A key event in plasma etching is the desorption and volatilization of the etch products. For emerging materials such as ferroelectrics the temperatures needed to markedly affect that desorption and volatilization are significantly higher than the wafer temperatures encountered in plasma etching of most familiar CMOS materials. We have demonstrated that at elevated wafer temperatures (up to 500°C) the etch product desorption for FeRAM stack etching can be enhanced with significant resulting improvements in etch profile and etch-rate.

## References

- [1] Embedded Ferroelectric Memory With 0.58  $\mu\text{m}^2$  Cell Size Using 130nm, 5LM Cu/FSG Logic Process, S. Summerfelt *et al.*, paper 1.1.5-I of the 15<sup>th</sup> International Symposium on Integrated Ferroelectrics (2003) – to be published in Conference Proceedings.
- [2] Profile and Device Characterization of Ir/PZT/Ir Stacks Etched at High Wafer Temperature, S. Marks, J. P. Almerico, F. Celli, paper 1.2.7-C of the 15<sup>th</sup> International Symposium on Integrated Ferroelectrics (2003) – to be published in Conference Proceedings.

# Protection of silver-based alloys from tarnishing by means of PECVD coatings

S. Grassini<sup>1</sup>, R.d'Agostino<sup>2</sup>, E. Angelini<sup>1</sup>, F. Fracassi<sup>2</sup>, G.M. Ingo<sup>3</sup>, N. Lionetti<sup>2</sup>, F. Palumbo<sup>4</sup>,  
F. Rosalbino<sup>1</sup>

<sup>1</sup>*Department of Materials Science and Chemical Engineering, Polytechnic of Turin, Turin, Italy*

<sup>2</sup>*Department of Chemistry, University of Bari, Bari, Italy*

<sup>3</sup>*CNR-ISMN, Monterotondo, Roma, Italy*

<sup>4</sup>*Institute for Inorganic Methodologies and Plasmas, CNR, Bari, Italy*

## Abstract

This paper describes the preliminary results on the utilisation of SiO<sub>x</sub>-like thin films in the field of protection of silver artefacts against tarnishing. The coatings deposition has been carried out on silver-based alloys in a home-made reactor with tetraethoxysilane-oxygen-argon mixture. Tarnishing tests have been performed in 0.1 M Na<sub>2</sub>S solution at room temperature. Coating tarnishing protection increases with increasing the O<sub>2</sub> flux of the feeding gas and the discharge power density and by performing surface H<sub>2</sub>-plasma pre-treatment.

## 1. Introduction

Silver has been used since ancient times in the fabrication of decorative and functional objects because of its working properties and pleasant colour and shine.

Silver may be shaped by hammering, embellished by engraving, or insert with gems or plated with gold. Many artefacts are not constituted by pure silver but by an alloy with other metals, as copper. As a decorative item silver often appears in association with polished hardwoods, ivory or other metals of contrasting colour. Gold may discolour but usually because of changes in alloying metals; other metals, as bronzes, may assume various coatings and colour changes with time: unless these represent active corrosion that alters the character and properties of alloys, some coatings contribute to highly valued patinas that must not be cleaned off.

Although highly lustrous when first polished, silver and silver-based alloys gradually darken and become less shiny during air exposures. This happens because silver undergoes chemical reactions with sulphur-containing compounds present in the environment. For this reason historic-artistic artefacts are subjected to a gradual discolouration and loss of polished finish; the metal surface turning first to pink, then darkening to brown before ending up as a very dark grey or black with a slight sheen. Silver's tarnish is rarely regarded as a valuable patina and generally detracts from its qualities, for this reason tarnish film has to be removed or its formation hindered.

The removal of the tarnished layer may be carried out by means of commercial liquid cleaners if the surface is decorated or intricately shaped, or by means of creams, that are not however the first choice for conservators because they contain abrasive compounds that remove a very thin layer of silver along with the tarnish; moreover repeated cleaning may increase the damage.

Methods involving dissolving away the silver sulphide, such as the use of potassium cyanide solution, have been abandoned because the chemicals are highly toxic.

Other methods using "silver dip" type solutions containing an inorganic acid plus thiourea allow to obtain good results, but usually are not used because of the possibility of damaging the image. One damage is that traces of thiourea may cause a rapid local retarnishing [1].

Moreover, a freshly cleaned silver surface is very reactive and will quickly tarnish again, so the artefact has to be periodically cleaned and protected or maintained in controlled environment.

At present there is not any ideal methodology for the elimination of the never-ending problem of cleaning and protecting silver artefacts. In this contest the high chemical stability, the low permeability and the optical transparency of PECVD organosilicon thin films render them particularly promising for a possible employ in the field of protection of silver artefacts from tarnishing [2].



Figure 1 - Shell-shape box for cosmetic powders. Hellenistic period - IV century b.c.



## 2. Experiment

The experimental apparatus employed in this study is a home-made parallel-plate-reactor with an asymmetric electrode configuration. It consists of a vacuum chamber made of stainless steel, a powered electrode connected to a RF power supply through an impedance matching unit and a grounded electrode. Gas and organosilicon vapour flow rates are controlled by mass-flow and vapour source controllers, respectively, while a turbomolecular pump backed by a rotary pump, a throttle valve, and a pressure gauge allow to keep the pressure fixed at the selected value.

SiO<sub>x</sub>-like thin films have been deposited by PECVD on silver-copper alloys which composition is reported in Table 1. The Ag-based alloys have been melted in a graphite crucible under a reducing atmosphere in order to avoid oxidising atmosphere and in particular, the presence of oxygen. Indeed, we have to take into account that during the melting or the casting of the gold or silver alloys, a slight oxidising environment could be present, and therefore, a considerable amount of oxygen can be dissolved in the minor elements of the alloy, i.e. copper.

This oxygen could form Cu<sub>2</sub>O and likely also Ag<sub>2</sub>O. Indeed, as copper is more reactive than silver, they tend to act as deoxidant and in particular, copper and oxygen form a copper-cuprous oxide eutectic with 3.5 % Cu<sub>2</sub>O (melting point 1066°C) at the grain boundaries of the solidifying metal.

Furthermore, it is worth noting that molten silver at the melting point absorbs about 20 times its own volume of oxygen that is released during metal solidification. This information must be considered in processing silver and its alloys in order to avoid a defective structure characterised by oxides of alloying elements oxides as well by porosity [3].

Silver-based specimens (20 mm dia. x 2 mm disks), mirror finishing, were positioned on the ground electrode at the floating temperature reached by the plasma (T<50°C), by applying the electromagnetic radiation to a gas mixture containing tetraethoxysilane (TEOS) oxygen and argon. SiO<sub>x</sub>-like films have been deposited in different experimental conditions, summarized in Table 2, in order to find out the best protective performances. The depositions have been performed on as received samples and on samples subjected to a surface treatment carried out in hydrogen-containing plasma.

Table 1 – Chemical composition of the silver-copper alloys (wt%)

	Ag	Cu
Alloy A	90	10
Alloy B	50	50
Alloy C	10	90

Table 2 - Experimental conditions for PECVD on silver-based alloys

Parameters	Pre-treatment	SiO <sub>x</sub> deposition
Pressure (mTorr)	1000	100
Input Power (W)	50	50 - 200
TEOS flux (sccm)	-	3
O <sub>2</sub> flux (sccm)	-	10 - 50
H <sub>2</sub> flux (sccm)	15	-
Ar flux (sccm)	-	36
Treatment Time (min)	30	30 - 60
Coating thickness (nm)	-	600 - 1200

Surface chemical and morphological characterisation of coatings has been carried out by means of X-Ray Photoelectron Spectroscopy (XPS), Fourier Transformed Infrared Spectroscopy (FT-IR) and Scanning Electron Microscopy equipped with an X-ray spectrometer (SEM-EDS).

XPS analyses have been performed with a non monochromatized PHI 5300 spectrometer. In order to gather information on the effect of hydrogen plasma treatment some samples were coated with a very thin SiO<sub>x</sub>-like film after the pre-treatment step, to protect the surface against the detrimental effect of air exposure. The film was easily removed in the XPS chamber by means of 3 keV Ar-ion sputtering.

The film thickness has been evaluated by means of a  $\alpha$ -step Tencor Profilometer.

Tarnishing tests have been carried out in 0.1 M Na<sub>2</sub>S aerated solution at room temperature. Intermittent exposures to air and sulfide solution immersions for 24, 48 and 72 hours have been carried out. Tarnishing is evaluated by visually comparing coated and uncoated samples. Using this test, the tarnishing susceptibility of coated samples is directly related to the extent of the surface area interested by the corrosion process.

### 3. Results

Silver-base alloys are characterised by high tarnishing susceptibility. As a matter of facts, the three uncoated alloys under study blacken very rapidly during the exposure to the  $\text{Na}_2\text{S}$  solution, as it is possible to observe in Figure 2a. The silver tarnishing begins immediately after the immersion of the specimens in the aggressive solution.

If the exposure time is extended, also alloys sample coated with  $\text{SiO}_x$  thin film begin to blacken. This is visible in Figure 2b showing a silver-base alloy (Ag10Cu90) coated with  $\text{SiO}_x$ -like film deposited at 200W of input power in oxygen rich plasma, after 24h immersion in the sulfide containing solution. Film thickness is about 900 nm.



Figure 2 - Silver-base alloy samples (Ag90Cu10) after 24h of immersion in 0.1M  $\text{Na}_2\text{S}$ : (a) uncoated; (b) coated with 900 nm PECVD  $\text{SiO}_x$ -like film (TEOS 3 sccm,  $\text{O}_2$  50 sccm, Ar 36 sccm, at 200W); (c) coated after  $\text{H}_2$ -plasma treatment

This poor protective effectiveness can be correlated to the high defectivity degree of the coating and to its poor adhesion to the metal surface as confirmed by the SEM micrograph reported in Figure 3. Defects allow the penetration of the electrolyte and consequently the beginning of the corrosion process at the metal/coating interface. The formation of sulfide corrosion products causes the delamination of the film and its detaching from the metal substrate.

On the contrary, a very negligible tarnishing is observed, in the first 24h of immersion, for silver alloy samples coated with  $\text{SiO}_x$ -like thin film deposited in the same conditions after hydrogen plasma treatment (Figure 2c). SEM observation shows that the  $\text{SiO}_x$ -like films cover uniformly the surface. The film is a pinhole free layer with a high degree of adaptability to the underlying substrate (Figure 4a).

The hydrogen plasma pre-treatment allow increasing the adhesion of the film on the metal surface and consequently increasing its protective properties. As a matter of facts, only a very limited portion of the sample surface is blackened. The tarnishing process starts at few defects point and no evidences of coating delamination can be observed (Figure 4b).

The same behaviour has been observed for the two silver alloys characterised by a less Ag content.

The infrared spectroscopy characterisation of  $\text{SiO}_x$ -like thin film evidences that good barrier effects against tarnishing can be correlated to the inorganic nature of deposited coating.

Infrared spectra have been recorded on coatings deposited by increasing the oxygen flux of the feeding gas mixture and the input power density. Increasing the oxygen/monomer flow ratio only the absorption bands of Si-O group (stretching at  $1070\text{ cm}^{-1}$ , bending at  $820\text{ cm}^{-1}$ ) are detected, while peaks due to organic groups disappear (e.g. C-H stretching at  $2950\text{ cm}^{-1}$ , Si- $\text{CH}_3$  wagging at  $1250\text{ cm}^{-1}$ , Si-( $\text{CH}_3$ ) $_x$  stretching at  $840$  and  $885\text{ cm}^{-1}$ ). The input power too affects the chemical structure of deposited coating. Increasing the input power not only the above-mentioned C-H and Si- $\text{CH}_3$  peaks disappear, but also the absorption bands of silanols (single SiO-H stretching at  $3650\text{ cm}^{-1}$  and Si-OH stretching at  $900$ - $920\text{ cm}^{-1}$ ) reduce their intensity.

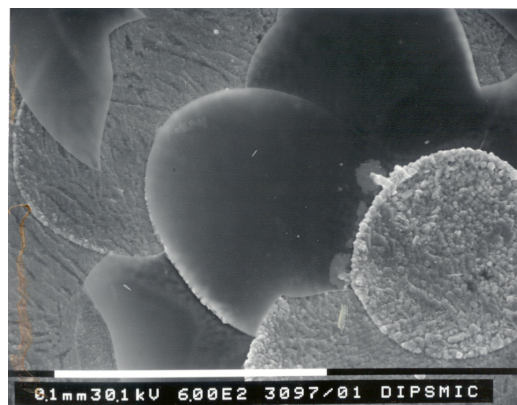


Figure 3 - SEM micrograph of silver-based alloy samples (Ag90Cu10) coated with 900 nm thick  $\text{SiO}_x$  film (TEOS 3 sccm,  $\text{O}_2$  50 sccm, Ar 36 sccm, at 200W) after 24h of immersion in 0.1M  $\text{Na}_2\text{S}$  solution.

The increase in the protective effectiveness can be also correlated to a decrease of silanols groups content which probably renders the coating more idrophobic [4].

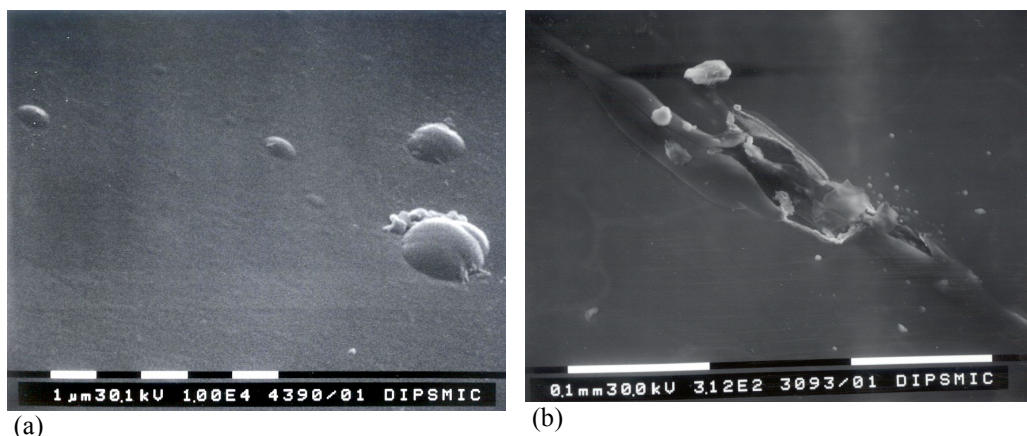


Figure 4 - SEM micrographs of silver-based alloy samples (Ag90Cu10) coated with 900 nm thick SiO<sub>x</sub> film (TEOS 3 sccm, O<sub>2</sub> 50 sccm, Ar 36 sccm, at 200W) after H<sub>2</sub>-plasma treatment: (a) as deposited; (b) after 24h immersion in 0.1M Na<sub>2</sub>S solution

The resistance against tarnishing strongly depends on the coating thickness. As a matter of facts, increasing the film thickness, a slight tarnishing is observed after 48h of immersion in the 0.1M Na<sub>2</sub>S solution (Figure 5a). The silver tarnishing becomes noticeable after 72h of immersion in the aggressive environment (Figure 5b).

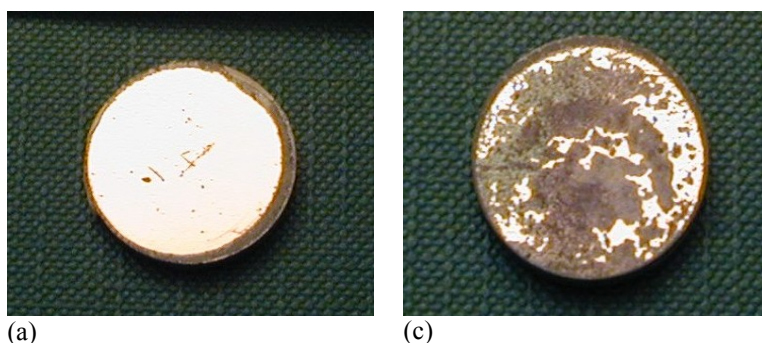


Figure 5 - Silver-base alloy samples (Ag90Cu10) coated with 1200 nm PECVD SiO<sub>x</sub>-like film (TEOS 3 sccm, O<sub>2</sub> 50 sccm, Ar 36 sccm, at 200W) after H<sub>2</sub>-plasma pre-treatment: (a) after 48h and (b) after 72h of immersion in 0.1M Na<sub>2</sub>S solution

In order to evaluate the effects of substrate pre-treatment in hydrogen plasma, thin SiO<sub>x</sub> layers have been deposited with and without hydrogen plasma treatment. After PECVD process the samples have been immediately transferred in the analysis chamber of the XPS spectrometer. The thin SiO<sub>x</sub> layers were progressively removed with ion sputtering (Ar<sup>+</sup> 3 Kev) and surface analyses were performed every 5 min of sputtering. In all cases the silver-based alloy surface is highly oxidized.

In the case of copper-richer alloys (Ag10Cu90 and Ag50Cu50), the evolution of Cu2p region as a function of the sputtering time show, at the metal/coating interface, the presence of CuO ( 933.4 eV), of Cu(OH)<sub>2</sub> (934.8 eV) and of Cu (932.8 eV). Instead, the Ag3d<sub>5/2</sub> peak and the Auger transition signal, Ag<sub>M4VV</sub>, confirm the presence of Ag<sub>2</sub>O layer on the surface of the silver-rich alloy (Ag90Cu10).

As expected the extent of the oxidation is reduced during the hydrogen plasma discharge as confirmed by the disappearance of the Cu<sup>++</sup> peaks and by the position of the Ag3d<sub>5/2</sub> and Ag<sub>M4VV</sub> signals that indicate the presence of Ag in the lower oxidation state.

Moreover, the H<sub>2</sub>-plasma pre-treatment remove the surface contamination and consequently enhances the adhesion of the film to the metal surface.

#### 4. Conclusions

The preliminary results reported in this paper show the good barrier effects that render PECVD coatings particularly promising for a possible employ in the field of protection of silver artefacts against tarnishing. As a matter of facts, serious tarnishing has been observed only after 72 h of immersion in the Na<sub>2</sub>S solution. The protective effectiveness increases with increasing the oxygen to monomer ratio in the feeding gas mixture and with increasing the input power density. The coating adhesion increases if the deposition process is performed after a hydrogen plasma treatment.

Further experimental work is in progress in order to test the coatings resistance in accelerated ageing conditions in H<sub>2</sub>S containing climatic chamber, which allow the variation of the temperature and relative humidity. CIE L\*a\*b\* colorimetry measurements for a quantitative evaluation of tarnishing susceptibility are also in progress.

Finally, the efficiency of coating could also be regarded as a function of the sample surface roughness. This kind of coating could also be deposited on the lacquers or varnishes already used in conservation to further improve their impermeability to tarnishing agents.

#### 5. References

- [1] A. Lins, N. McMahon – Current Problem in the Conservation of Metal Antiquities (1993).
- [2] L. Favre-Quattropani, P. Groening, D. Ramseyer, L. Schlapbach – Surf. Coat. Tech. **125**, 377 (2003)
- [3] A.J. Dornblatt - Silver in Industry (1940)
- [4] E. Angelini, S. Grassini, F. Rosalbino, F. Fracassi, R. d'Agostino – Surface and Interface Analysis **34**, 155 (2002)

# Plasma deposited acrylic acid coatings for biomedical devices: adapting the interface with flat and nano-structured substrates for improved water resistance and cell culture

L. Detomaso<sup>1</sup>, R. Gristina<sup>2</sup>, G.S. Senesi<sup>2</sup>, D. Sutherland<sup>3</sup>, H. Agheli<sup>3</sup>, R. d'Agostino<sup>2</sup>, P. Favia<sup>2</sup>

<sup>1</sup>*Department of Chemistry, University of Bari, Bari, Italy*

<sup>2</sup>*Institute of Inorganic Methodologies and Plasmas (IMIP), CNR Bari, Italy*

<sup>3</sup>*Department of Applied Physics, Chalmers University of Technology, Gothenburg, Sweden*

## Abstract

Thin coatings with different chemical properties were plasma-deposited from Acrylic Acid (pdAA) vapours on flat and nano-structured surfaces. Highly hydrophilic films were inhomogeneous and non conformal due to poor adhesion to substrates. Plasma-pretreatments of substrates, however, resulted in improved surface/coatings interfaces and in homogeneous, conformal pdAA films. It was also shown that only pdAA coating with low COOH content and high cross-linking degree were stable after soaking in water.

## 1. Introduction

Many plasma deposited organic coatings have been proposed to modify the surface of biomedical polymers in order to drive the adhesion, spreading and proliferation of cells. Hydrophilic, functional coatings with tuneable surface density of –COOH groups, such as pdAA coatings, have been investigated as cell-adhesive layers [1] and primer functional layers for biomolecule immobilization [2]. To control the surface density of carboxylic groups and their related surface properties, AA coatings can be deposited from glow discharges in different fragmentation regimes. Low monomer fragmentation conditions generally result in highly hydrophilic, highly –COOH surface dense but poorly homogeneous layers; pre-treatments of polymers in NH<sub>3</sub> RF (13.56 MHz) Glow Discharges were successfully utilized to improve compatibility and adhesion with the thin pdAA coatings to be deposited later. High fragmentation regime leads, on the contrary, to coatings with lower hydrophilicity, better substrate adhesion and water stability [3].

Micro- and nano-patterning techniques produce surfaces with pre-determined morphology able, in principle, to drive and control adhesion-spreading and growth of cells in tissue engineering [4]. This approach has determined, in the last ten years, an escalation in the biomedical research aimed to deliver affordable fabrication techniques for producing large areas of “smart” micro- and nano-patterned biomedical surfaces with controlled morphology and chemistry. In this contest, the present research is aimed to provide conformal and stable cell-adhesive layers of controlled chemical composition (i.e., COOH surface density) on polymers nano-patterned by means of polymer de-mixing [5,6] or colloidal lithography [7] techniques.

## 2. Experimental

Silicon, glass, and polystyrene (PS) flat substrates were coated with pdAA, as well as polyethyleneterephthalate (PET) and PS/Polybromostyrene (PS/PBrS) samples structured with features of nanometric sizes by means of colloidal lithography (cones) and polymer de-mixing (bumps), respectively. Nano-structured samples were utilized to assess the conformity of pdAA coatings with and without NH<sub>3</sub> plasma pre-treatments, also after prolonged soaking in bidistilled water.

A stainless steel parallel-plate plasma reactor was utilized for pdAA deposition from an AA (3 sccm) / Ar (20 sccm) mixture feed at a pressure of 200 mTorr. AA was degassed with freeze-thaw cycles. Substrates were cleaned in ethyl alcohol and dried at room temperature. RF discharges were ignited between the upper (stainless steel, shielded, RF connected) and the lower (grounded, sample holder) electrode. A RF (13.56 MHz) generator was utilized at 20 or 100 W of RF power in continuous (CW) or modulated mode. A pulse generator was utilized to modulate on/off (time on =  $t_{on}$ ; time off =  $t_{off}$ ) AA/Ar discharges, with variable duty cycle (D.C. % =  $100 t_{on} / (t_{on} + t_{off})$ ). Results shown for modulated pdAA deposition were obtained with a period,  $t_{on} + t_{off}$ , of 100 ms [8]. PdAA coatings in lower monomer fragmentation regime were obtained at 20 W of power and 3% D.C. for 1 minute; 100 W CW mode discharges performed for 5 minutes were utilized to deposit pdAA coatings in a higher fragmentation regime. The discharge duration was always kept low enough to obtain very thin pdAA coatings that do not alter the morphology of the underneath substrate. NH<sub>3</sub>



plasma pre-treatments of flat and nano-structured polymer substrates were performed in a tubular Pyrex parallel plate RF reactor (CW mode, 20 W, 10 sccm  $\text{NH}_3$ , 200 mTorr, 1 min) with the substrates positioned on the ground lower electrode.

X-ray Photoelectron Spectroscopy (XPS), water contact angle (WCA), profilometry and Atomic Force Microscopy (AFM) were utilized to characterize plasma-processed surfaces. Wide scan and high-resolution (C1s, O1s and N1s) unmonochromatized  $\text{AlK}\alpha$  XPS spectra were acquired with a PHI 5300 spectrometer at an electron take-off angle of  $45^\circ$ , within one hour after each process. Sample charging was corrected by setting the hydrocarbon component of the C1s signal at 285.0 eV. C1s spectra of pdAA coatings were best-fitted with four peak-components (FWHM = 2.00 eV), corresponding to C-atoms with zero, one, two and three carbon-oxygen bonds: C0 (C-H(C); BE = 285.0 eV, reference), C1 (C-OH (OC); BE =  $286.6 \pm 0.2$  eV), C2 (O-C-O, C=O; BE =  $288.2 \pm 0.2$  eV) and C3 (COOH, COOR; BE =  $289.1 \pm 0.2$  eV). Static WCA measurements were carried out just after each processes with a Ramé-Hart NRL 100 goniometer by using bidistilled water. Thickness and deposition rate of pdAA were measured with an Alpha-Step® 500 Surface Profiler on silicon samples pdAA-coated through a physical mask. AFM (Autoprobe CP-Research) and profilometry were utilized to control the conformity of pdAA thin films deposited on nano-structured samples. Images were acquired in non-contact mode AFM using commercial, unmodified silicon nitride tips. To evaluate the effect of water on pdAA films in terms of leaching of soluble components and/or surface restructuring, duplicate samples were XPS, WCA and AFM analysed before and after soaking in 7 ml of bidistilled water, followed by overnight drying at room temperature.

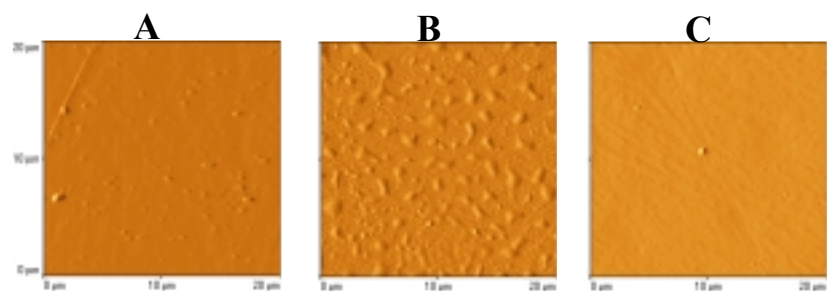
Cell culture experiments were performed on pdAA coatings deposited on flat, 12 mm diameter, crystalline PS cover-slips and on 12 mm diameter flat and nano-patterned PET samples. NCTC 2544 human keratinocytes and hTERT BJ1 fibroblasts cell lines were utilized. All cells were obtained from stocks routinely grown in DMEM medium supplemented with 10% fetal bovine serum, 50 IU/ml penicillin, 50 IU/ml streptomycin and 200 mM glutamine, under 5%  $\text{CO}_2$ /95% air atmosphere at  $37^\circ\text{C}$ .

All plasma-processed and control samples were placed, modified side up, in 24 wells culture plates (Iwaki 24 wells). Cells were obtained after trypsinization of confluent or near-confluent culture and seeded at  $2 \times 10^4$  cells/well in suspension on all test material and incubated at  $37^\circ\text{C}$  under 5%  $\text{CO}_2$ /95% air atmosphere. After 24 hours of incubation, fixed and dehydrated samples were sputter coated with gold before examination with a Hitachi S800 field emission SEM at an accelerating voltage of 10 keV. Cell attachment, distribution and morphology were determined at various time intervals using digital images acquired from a phase contrast light microscope (Leica DM IL). The number of adherent cells was determined in at least 10 areas of  $0.8 \text{ mm}^2$ /sample. For morphological studies cells were divided in cells with and without laminae. Unpaired Student's t-test was used to evaluate statistical significant differences among tests performed on at least four repeated samples for each experiment. Data were taken to be significant when a  $p < 0.05$  was obtained.

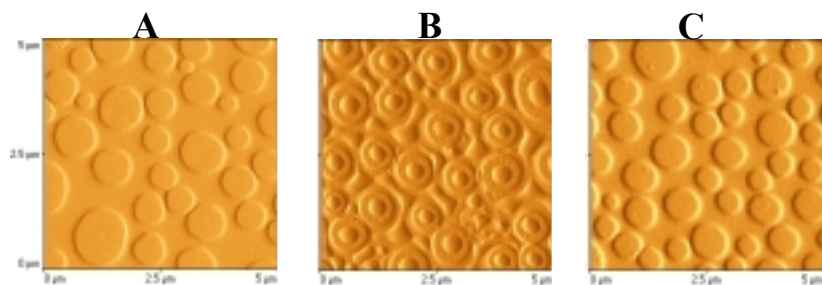
### 3. Results and discussion

Two fragmentation regimes were investigated to obtain homogeneous, conformal, water stable and cell adhesive pdAA coatings: 20 W, 3% D.C. and 100 W CW.

Very thin ( $< 5 \text{ nm}$ ) pdAA layers, deposited onto different surfaces in lower fragmentation conditions (20 W 3% D.C.), resulted in a partial coverage of flat substrates and in a non conformal coatings on nano-structured substrates, as shown by AFM (Figures 1 and 2, case B). The non-homogeneity of the coating was also attested from the fact that the underneath substrates chemistry affected both WCA values and chemical composition of pdAA layers, as revealed by XPS analysis (data not shown). This phenomenon was recorded for pdAA films deposited either on hydrophilic or on hydrophobic materials. Pre-treatments of substrates in  $\text{NH}_3$  glow discharges were found extremely beneficial in solving this problem. Figures 1 and 2 display two cases of substrates plasma-coated with pdAA films, where it is evident that  $\text{NH}_3$ -plasma pre-treatments offered a much better pdAA/substrate interface and lead to complete coverage and conformity of the deposited layer. On  $\text{NH}_3$  pre-treated pdAA coatings, WCA value was close to  $10^\circ$  with the C3 component close to 18% whatever the substrate. Besides, an O/C ratio very close to characteristic value of conventional polyacrylic acid was recorded, thus highlighting considerable monomer structure retention. The N1s XPS signal was drastically reduced after pdAA deposition, thus emphasising a homogeneous and complete coverage of underneath substrate.

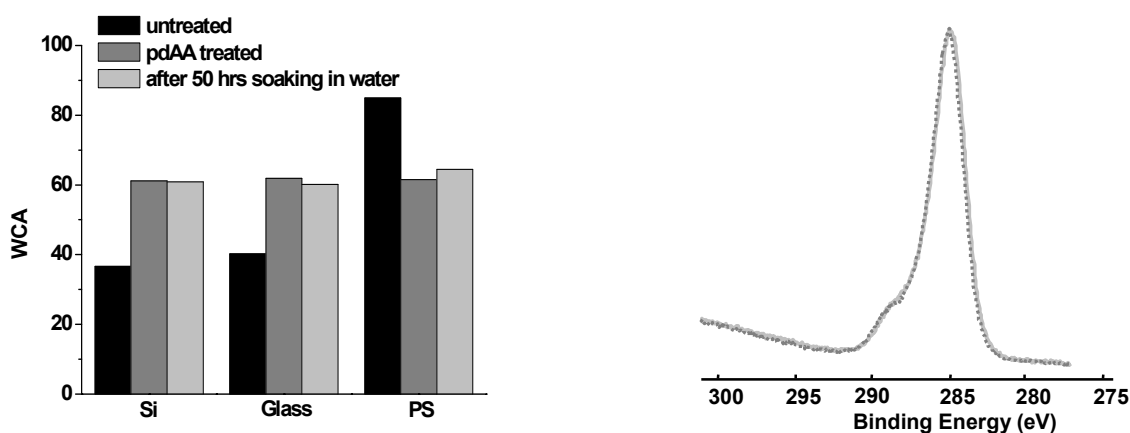


**Figure 1:** Nc-AFM error signal of very thin pdAA coatings deposited on untreated and  $\text{NH}_3$ -plasma pre-treated flat PS: untreated **a**); pdAA coated (3% D.C. 20 W) without **b**) and with **c**)  $\text{NH}_3$ -plasma pre-treatment.



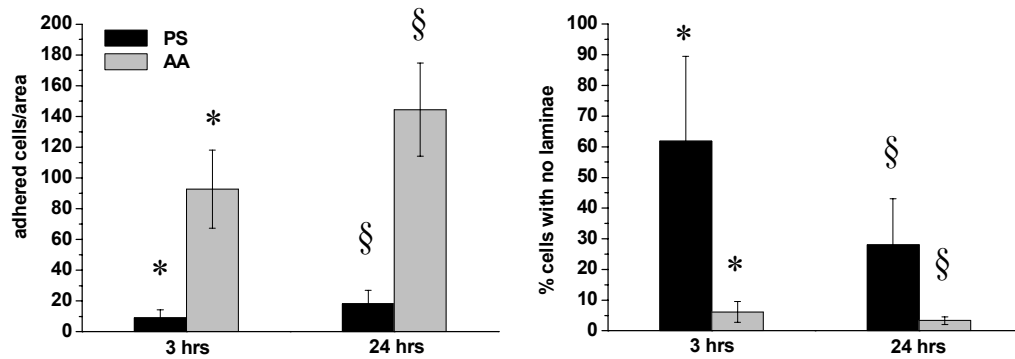
**Figure 2:** Nc-AFM error signal of very thin pdAA coatings deposited on untreated and  $\text{NH}_3$ -plasma pre-treated 35 nm bumps PS/PBrS nano-structured substrates: untreated **a**); pdAA coated (3% D.C. 20 W) without **b**) and with **c**)  $\text{NH}_3$ -plasma pre-treatment.

To verify the resistance of the  $\text{NH}_3$ /pdAA coatings to water, samples were soaked in bidistilled water for different periods of time. It was observed that less than 50 hours were necessary for pdAA delamination and/or for changes of the surface composition to occur. This was attested by the increase of WCA values close to the value of untreated substrates, by a relevant decrease of the C3 component (from 18% to 4%) in the C1s signal, by a drastic change of the O/C XPS ratio and by the appearance, in the wide scan XPS spectra, of the native substrates signal. The high surface density of COOH groups, characteristic of pdAA coatings deposited in very low fragmentation conditions, might lead to a strong water/pdAA interactions (e.g., hydrogen bonds, swelling) that combined with the low cross-linking degree of the coatings may causes delamination and/or leach of hydrophilic moieties. To reduce carboxylic surface percentage and to obtain more cross-linked pdAA coatings, discharges with increased fragmentation regime (100 W, CW) were performed. In this condition a 3 % of C3 component and WCA values close to  $63^\circ$  were recorded whatever the substrate. Figure 3 shows WCA measurements and XPS analysis performed on 100 W pdAA films before and after soaking in water. Differently from coatings synthesised in low fragmentation conditions, the effect of substrate was negligible and the films resulted more homogeneous also after water soaking.



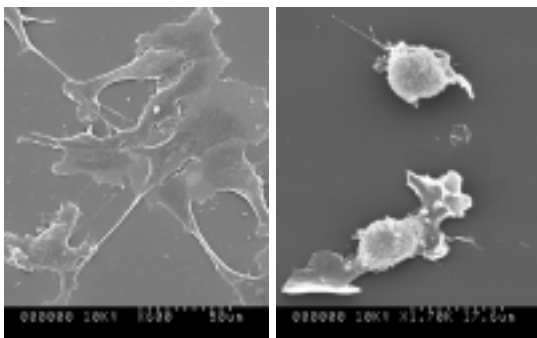
**Figure 3:** On the left: WCA values on 100 W pdAA before and after 50 hrs in  $\text{H}_2\text{O}$ ; on the right: C1s XPS signal of 100 W pdAA before..... and after — 50 hrs in  $\text{H}_2\text{O}$ .

HTERT BJ1 fibroblasts were cultured on 100 W pdAA coated flat PS, using native PS as control substrate. As shown in Figure 4 (left), few cells adhered onto uncoated PS, while much more cells were observed on 100 W pdAA after 3 and 24 hours of culture. Figure 4 (right) shows that the number of unspread cells (i.e., without laminae) on pdAA was much lower than that on uncoated PS.



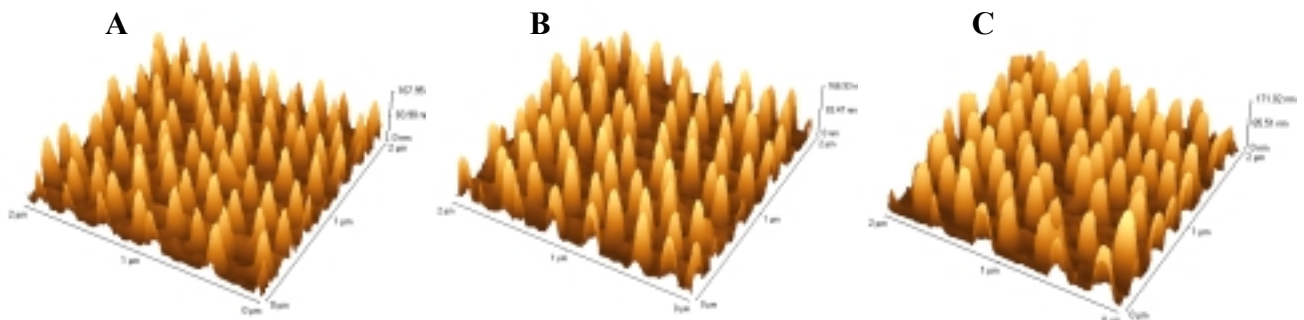
**Figure 4:** hTERT BJ1 fibroblasts on native and on 100 W pdAA coated PS. Adhered cells/area (left) and % of cells without laminae (right); \*, §=p < 0.05.

In Figure 5 are displayed SEM images of cells after 24 hours of incubation on 100 W pdAA and on uncoated PS. The much more flat appearance of cells on pdAA attests that pdAA coatings are very suitable to improve cells attachment and proliferation.



**Figure 5:** SEM images of hTERT BJ1 fibroblasts on 100 W pdAA coated PS (left) and on uncoated PS (right).

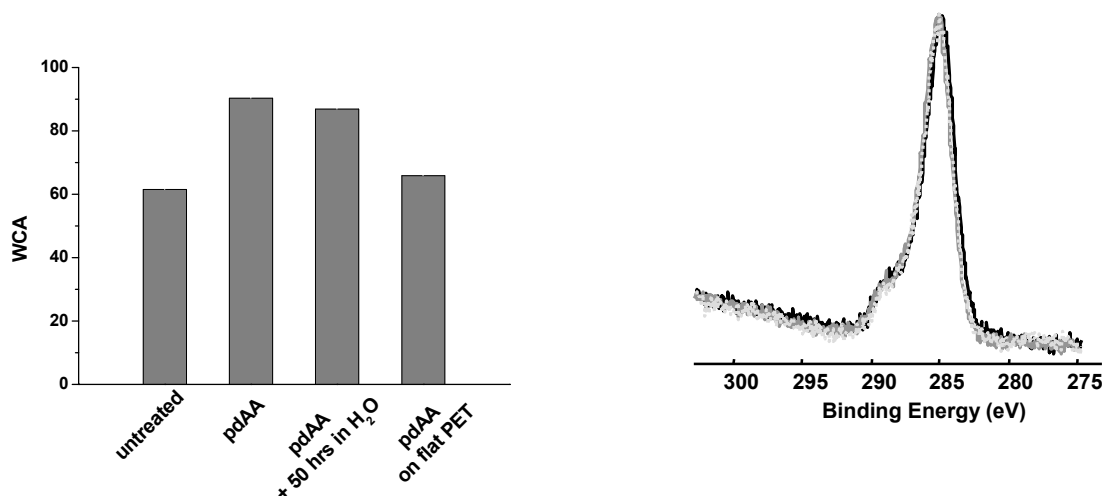
To assess the conformity of 100 W pdAA films, the deposition processes were performed on nano-structured materials (PET samples nano-patterned by colloidal lithography). AFM 3D representations (Figure 6) show that pdAA coatings did not affect significantly the morphology of the nano-features. Soaking in bidistilled water slightly changed the shape of the nano-domains, probably due to the swelling of the pdAA layer and/or to the leach of acrylic acid oligomers or similar fragments not covalently bonded.



**Figure 6:** 3D nc-AFM images of conical nano-features on PET: untreated (A); 100 W pdAA coated (B); 100 W pdAA coated after 50 hrs soaking in water (C).

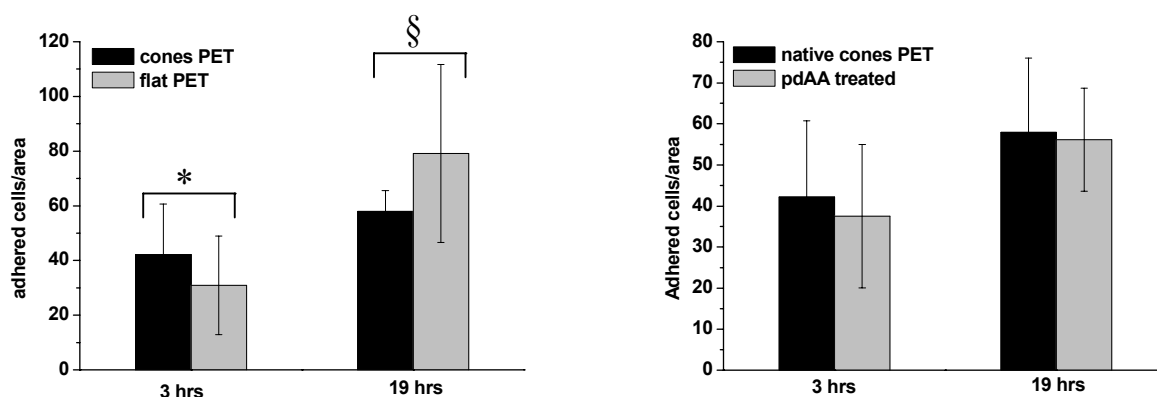


WCA data of Figure 7 (left) show that the wettability of pdAA deposited on flat PET substrates was different from that achieved on patterned ones while the chemical composition (Figure 7, right) was retained. After 50 hours soaking in water, the WCA of nano-structured samples did not change significantly.



**Figure 7:** On the left: WCA values on 100 W pdAA coated cones and flat PET samples; on the right: C1s XPS signal of 100 W pdAA on cones PET before — and after ..... 50 hrs in H<sub>2</sub>O, of 100 W pdAA on flat PET — .

Cell culture experiments performed with NCTC 2544 keratynocytes on flat and nano-structured PET samples showed that after 3 hours of incubation more cells adhered on nano-patterned surfaces respect to flat ones as shown in Figure 8 (left). After 19 hours of incubation time on the contrary, cell proliferation was more enhanced on flat PET than on nano-structured one. This phenomenon may be due to a larger surface area of nano-features respect to flat surfaces which probably improves cell attachment to the substrate. Subsequently, during cell growth the nano-domains seem to obstruct the spreading and proliferation of cells. As shown in Figure 8 (right), pdAA coatings affected cell adhesion on nano-structured PET as well as uncoated samples. This may be due to the similar chemical composition between PET and pdAA films.



**Figure 8:** NCTC 2544 keratynocytes on cones and flat native PET (left) and on native and pdAA coated cones PET (right) samples. \*, §=p < 0.05.

## Conclusions

PdAA deposition is a very suitable method to enhance cells attachment and proliferation onto a variety of materials not suitable to promote cell adhesion on their surface. Interface optimisation may be needed, in certain cases, and has been found beneficial for flat and nano-structured surfaces coated with highly hydrophilic films. When the fragmentations conditions (i.e., power input and/or D.C. of modulated discharges) are increased, the COOH surface density decreases and the adhesion to the surface and water stability of pdAA coatings improve.

## Acknowledgements

Prof. S. Affrossman (University of Strathclyde, UK) is acknowledged for having provided polymer de-mixed samples.

Laboratory of Prof. Curtis (University of Glasgow, UK) is acknowledged for experiments with hTERT BJ1 fibroblasts.

The EC project Nanobiotechnology and Medicine "NANOMED" (QLK3-CT-2000-01500, EC 5thFP Quality of Life) is acknowledged for funding this research.

## References

- [1] R. Daw, S. Condon, A.J. Beck, A.J. Devlin, I.M. Brook, S. MacNeil, R.A. Dawson, R.D. Short; *Biomaterials*, 19 (1998) 1717-1725.
- [2] P. Favia, F. Palumbo, R. d'Agostino, S. Lamponi, A. Magnani, R. Barbucci; *Plasmas and Polymers*, 3 (1998) 77-95.
- [3] M.R. Alexander, T.M. Duc; *Polymer*, 40 (1999) 5479-5488.
- [4] M.J. Dalby, S.J. Yarwood, M.O. Riehle, H.J.H. Johnstone, S. Affrossman, A.S.G. Curtis; *Experimental cell Research*, 276 (2002) 1-9.
- [5] M.J. Dalby, M.O. Riehle, H.J.H. Johnstone, S. Affrossman, A.S.G. Curtis; *Biomaterials*, 23 (2002) 2945-2954.
- [6] M.J. Dalby, M. Riehle, H.J.H. Johnstone, J. Gallagher, M.A. Wood, B. Casey, K. McGhee, S. Affrossman, C.D.W. Wilkinson, A.S.G. Curtis; *Materials Research Society Proceedings*, 705 (2002) Y5.1.1-Y5.1.11.
- [7] M. Riehle, M.J. Dalby, H. Agheli, D. Sutherland, A.S.G. Curtis; Joint Open Nanomed/Magnanomed Meeting on 21 September 2002, Glasgow.
- [8] P. Favia, E. Sardella, R. Gristina, A. Milella, R. d'Agostino; *Journal of photopolymer Science and Technology*, 15 (2002) 341-350.

# **Modelling of Fracture in Coating Systems Subjected to Thermal Loading: Use of Finite Element Technique**

**\*A Mimaroglu, , I Taymaz, S. Ercan and A Ozel**

*\*University of Sakarya, Faculty of Engineering, Esentepe Kampusu, Adapazari, Turkey  
Tel: (90) 264-3460354, Fax: (90) 264- 3460351, e-mail: mimarog@sakarya.edu.tr*

In engineering, severe operating conditions such as thermal loading tends to result to fracture problems due to heat transfer conditions. Plasma coating system is one of the engineering systems, which face this problem. Plasma coating systems are used for many severe engineering applications. Most of these applications are in the form of thermal barrier coatings, which allow higher engine temperatures and better efficiency. Coating materials, which are used as a thermal barrier, has two failure mechanisms, namely, interfacial oxidation and fracture under thermal stress. In case of large thickness coatings, failure is mainly due to fracture rather than interfacial oxidation. In this study the general purpose finite element code ANSYS has been employed to analysis fracture in ceramic coating subjected to thermal loadings. Coupled (thermal and structural) finite element solution was used. In this study substrate material Tungsten and coating materials Diamond,  $\text{Si}_3\text{N}_4$  coating systems were modelled. Coatings with interlayer materials NiAl were also modelled. The aim was to evaluate the stress intensity factors in different coating systems. The normalized stress intensity factors were obtained and compared. The result showed that the shorter the crack length and the thinner the coating, the sounder is the coatings. It is also concluded that the finite element technique can be used to optimise the design and the processing of ceramic coatings.

# Comparison of Two-Color and Three-Color Pyrometry for Measuring Velocity, Surface Temperature and Size of Single Particle in Plasma Flow

O. Solonenko, A. Mikhachenko, and E. Kartaev,

*Institute of Theoretical and Applied Mechanics, SB RAS, 4/1 Institutskaya str., Novosibirsk, 630090, Russia*

## Abstract

The comparative analysis of two-color and three-color pyrometry for determining the temperature of single alumina particles in high-temperature dust-laden flows has been carried out. It is shown that satisfactory restoring of temperature based on known radiation characteristics enables one to determine average size of particle ensemble. The estimates of temperature and size by means of modeling of measurement of particle thermal radiation have been obtained.

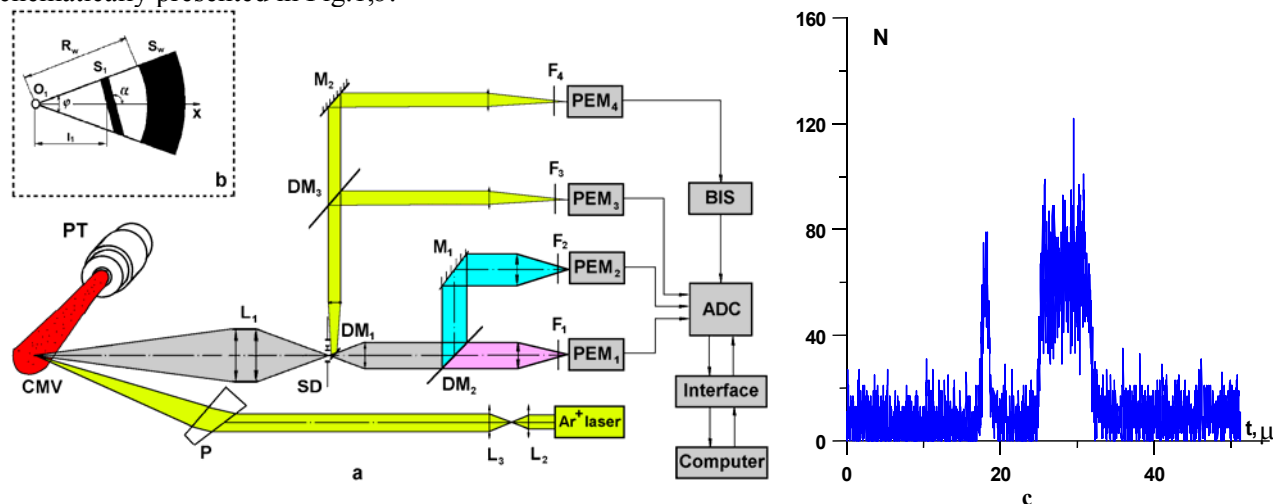
## 1. Introduction

In high-temperature dust-laden flow particle temperature can be determined by measuring its thermal radiation. As a rule, the procedure includes an in-situ measurement of radiation intensities at two close wavelengths; the ratio between these intensities gives the so-called color temperature of the particle. The main advantage of that method of two-color pyrometry is considered the relativity of measurement. Nevertheless, the inaccuracy in determination of the two-color temperature substantially depends on the spectral region chosen to perform the measurements, as well as on the emissivity spectrum of the particle, which normally is not known beforehand. In order to reduce both procedural error and that of the method, it is generally recommended to use more operating wavelengths.

The goal of the present study was to test the method of polychromatic pyrometry by means of registering thermal radiation at three spectral regions and to perform a comparative analysis of gained data on temperatures and sizes of alumina particles in low-temperature plasma flow.

## 2. Diagnostic complex and data acquisition

The principal diagram of the setup is shown in Fig.1,a. The image of luminous particle with the help of an intake lens  $L_1$  is projected on two-slit diaphragm SD (henceforth – control measuring volume (CMV)) schematically presented in Fig.1,b.



**Fig. 1.** Schematic of the setup: *a* – diagnostic complex; *b* – multi-slit diaphragm. PT – plasma torch;  $L_1$ ,  $L_2$ ,  $L_3$  – lenses; P – deflecting prism; SD – diaphragm;  $DM_1$ ,  $DM_2$ ,  $DM_3$  – dichroic mirrors,  $M_1$ ,  $M_2$  – mirrors;  $F_1$ ,  $F_2$ ,  $F_3$ ,  $F_4$  – light filters;  $PEM_1$ ,  $PEM_2$ ,  $PEM_3$ ,  $PEM_4$  – photo-electronic multipliers; BIS – discriminator; ADC – analog-to-digital converter; *c* – typical oscillogram of pyrometric signal detected for selected spectral region.

While crossing CMV particle radiation via dichroic mirrors  $DM_1$ ,  $DM_2$ ,  $DM_3$  and transmitting optics is projected onto photocathode of  $PEM_1$ ,  $PEM_2$ ,  $PEM_3$  in front of which light filters  $F_1$ ,  $F_2$ ,  $F_3$  transmitting light in narrow spectral regions are set. To start up the diagnostic equipment the highlighting of plasma jet is applied

using single laser beam. Circular orifice  $O_1$  with diameter of  $\cong 160 \mu\text{m}$  of sector diaphragm is intended to receive the laser radiation scattered by particle. With the help of dichroic mirrors  $DM_1$ ,  $DM_3$ ,  $M_2$  and transmitting optics the scattered laser radiation is subsequently transmitted onto photocathode  $PEM_4$  in front of which interference filter  $F_4$  transmitting light at laser wavelength is set.

Using sector diaphragm  $SD$  (Fig.1,b) in the image plane of traveling particle enables simultaneous determination of temperature, size, and velocity vector of single particle [1]. Amplified signals from photo detectors  $PEM_1$ ,  $PEM_2$ ,  $PEM_3$  are entered two synchronized 2-channel analog-to-digital converters (ADC). Amplified signal generated by  $PEM_4$  (detecting scattered laser radiation) is entered the discriminator (BIS) generating standard start-up signal for ADC if the level of scattered light signal exceeds some programmable threshold.

### 3. Methods of measuring the particle characteristics

In order to measure above-mentioned parameters the thermal radiation of particle has been analyzed in three spectral regions:  $\lambda_1=0.6328 \mu\text{m}$ ,  $\lambda_2= 0.721 \mu\text{m}$ ,  $\lambda_3 = 0.8906 \mu\text{m}$ .

Typical oscillogram of pyrometric signal is drawn in Fig.1,c (the amplitude  $N$  of the signals is expressed in counts, scale of time on axis of abscissa – in microseconds).

Parameters of single particle are determined by means of correlation analysis of real and model pyrometric signals in combination with estimating the characteristics by the least-squares method [1].

For each operating spectral region, the model pyrometric signals are computed according to the formula

$$U_i = \xi(\lambda_i) f(D_p, u_p, t) \varepsilon(\lambda_i, T) \int_{\lambda_i - \Delta\lambda_i}^{\lambda_i + \Delta\lambda_i} \Phi_i(\lambda) \frac{C_1 d\lambda}{\lambda^5 [\exp(C_2 / \lambda T) - 1]}, i=1,2,3 \quad (1)$$

where  $f(D_p, u_p, t)$  is the function that describes passage of the image of a spherical particle of diameter  $D_p$  in the plane of the intake diaphragm  $SD$  in time as a function of its velocity  $u_p$  (this function is proportional to the area of the particle image sequentially truncated by slits  $S_1$  and  $S_w$  of the intake diaphragm (see Fig.1, b));  $\varepsilon(\lambda_i, T_p)$ , ( $i=1,2,3$ ) is emissivity of particle substance at the center of the spectral region of the  $i$ -th interference filter with measured transmission factor  $\Phi_i(\lambda)$ ,  $\lambda \in [\lambda_i - \Delta\lambda_i/2; \lambda_i + \Delta\lambda_i/2]$  (if the emission power is unknown, the black body approximation is used);  $\xi(\lambda_i)$  is the transmission factor of the  $i$ -th optico-electronic channel determined beforehand, this factor relates radiation fluxes emitting by the particle with registered values of the analog signals.

The algorithm of processing the experimental information (realization) obtained for the selected particle is the following. First, the axial velocity  $u_p$  is to be estimated by maximization of the cross-correlation function between the given physical realization and the family of model (test) realizations of test particles with velocities to be varied, with the averages of size  $\bar{D}_p = (D_{p,min} + D_{p,max})/2$  and temperature  $\bar{T}_p = (T_{p,min} + T_{p,max})/2$  being calculated in compliance with the ranges of these parameters.

With the particle velocity found one can reveal the position of the constant component (under actual conditions of a noised “plateau”) of trapezoidal pulses and determine the color temperature of the particle  $T_c$  in two couples of operating spectral regions from the relation (“gray” body approximation):

$$\bar{U}_j \xi(\lambda_i) \int_{\lambda_i - \Delta\lambda_i/2}^{\lambda_i + \Delta\lambda_i/2} \Phi_i(\lambda) \frac{C_1 d\lambda}{\lambda^5 [\exp(C_2 / \lambda T_{cij}) - 1]} = \bar{U}_i \xi(\lambda_j) \int_{\lambda_j - \Delta\lambda_j/2}^{\lambda_j + \Delta\lambda_j/2} \Phi_j(\lambda) \frac{C_1 d\lambda}{\lambda^5 [\exp(C_2 / \lambda T_{cij}) - 1]}, \quad (2)$$

where  $\bar{U}_i$  and  $\bar{U}_j$  are average amplitudes corresponding to the plateaus in the spectral regions of interest,  $i < j$ .

In addition, the algorithm proposed in [2,3] based on analysis of deviation of experimentally measured thermal radiation from model one in 3 operating spectral regions:  $\lambda_1=0.6328 \mu\text{m}$ ,  $\lambda_2= 0.721 \mu\text{m}$ ,  $\lambda_3 = 0.8906 \mu\text{m}$  by least square method is implemented, namely the minimum of following function is to be found

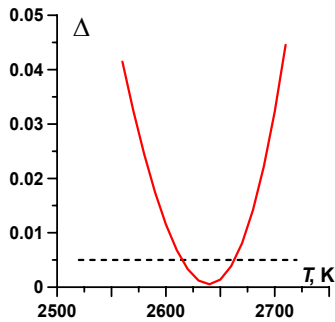
$$\Delta(r_p, \varepsilon, T) = \sum_{i=1}^3 \left\{ \pi r_p^2 \varepsilon(\lambda_i, T) \xi(\lambda_i) \int_{\lambda_i - \Delta\lambda_i/2}^{\lambda_i + \Delta\lambda_i/2} \Phi_i(\lambda) \frac{C_1 d\lambda}{\lambda^5 [\exp(C_2 / \lambda T) - 1]} - U_i \right\}^2 / \sum_{i=1}^3 U_i^2 \quad (3)$$

It is of common knowledge [2, 3] that minimal value  $\Delta(r_p, \varepsilon, T)$  is specified in the best way if linear approximation  $\varepsilon(\lambda) = a_0 + a_1 \lambda$  is fitted. Since, in the case of consideration, effective particle radius  $r_p$  is not known *a priori* (only the typical range of variation of size is preliminarily set), then, as previously, the “gray” body approximation  $\varepsilon(\lambda) = a_0 = \text{const}$  has been stated in the framework of three-color pyrometry method.

The temperature  $T$  can be determined by finding the minimum of the function (3). To this end, the domain of the parameters  $q = \varepsilon(\lambda, T) \pi r_p^2$  and  $T$  was covered with a 2D grid with nodes  $(q_i, T_j)$ ,  $i=1, \dots, N_1$ ,  $j=1, \dots, N_2$ , each of

the nodes corresponding to a certain value of  $\Delta_{ij}$ . The sought values  $q^*, T^*$  are desired for  $\Delta^* = \min \Delta_{ij}$ , i.e. at  $T_{c3} = T^*$ , whereas  $\delta_{appr}$  to be estimated from  $\Delta^* = \delta_{appr}^2 / \sum_{i=1}^3 U_i^2$  evaluates the absolute error in fitting the experimental data with the adopted theoretical dependence.

As is well known the error of estimate of average amplitude of trapezoidal signal within “plateau” depends on noise variance  $\sigma_{ni}^2$  (in our case PEM shot noise variance and plasma background noise) and also total number of sampled counts in amplitude averaging [4]. In view of this, one can estimate root-mean-square error  $\delta$  of amplitudes of pyrometric signals  $\delta^2 = \sum_{i=1}^3 \frac{\sigma_{ni}^2}{N} = \frac{1}{(N-1)N} \sum_{i=1}^3 \sum_{k=1}^N \left\{ U_k(\lambda_i) - \frac{1}{N} \sum_{k=1}^N U_k(\lambda_i) \right\}^2$ , where  $N$  – number of indications of sampled signals to be averaged. Being the result of minimization of  $\Delta(q^*, T^*)$  the values  $q^*, T^*$  are assumed to be adequate to registered amplitudes of signals  $\{U_i\}$ ,  $i=1,2,3$  if  $\delta_{appr} \leq \delta$  (Fig.2).



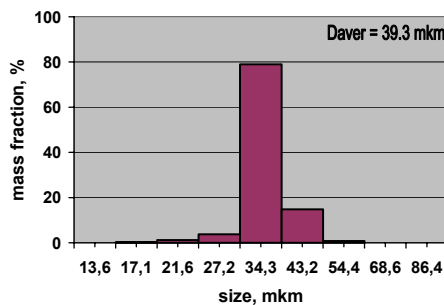
**Fig.2.** Functional relationship  $\Delta(q^*, T)$  for desired  $q^*$ , dotted line denotes values of noise variance.

Determination of particle size  $D_p$  is fulfilled with the help of least squares procedure for experimental and model signals. Taking into consideration the particle emissivity at  $\lambda_2=0.721 \mu\text{m}$ , the model realization is computed for estimated  $u_p$  and  $T$  ( $T_{c13}$ ,  $T_{c23}$ ,  $T_{c3}$ ) within the plateau area of trapezoidal pyrometric signal.

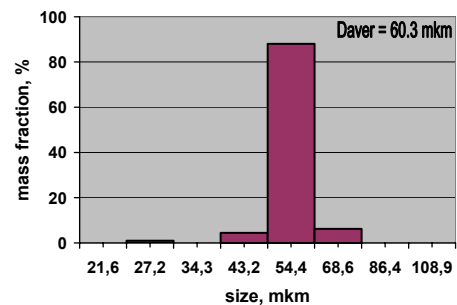
The estimate of emissivity has been yielded providing validity of assumption of thermodynamic equilibrium of spherical particle given by the Kirchhof law [5]:  $\varepsilon(\lambda, T) = Q_{\text{abs}}(\lambda)$ , where the absorption efficiency factor  $Q_{\text{abs}}(\lambda)$  varies depending on complex refractive index of particle substance  $m=n-i\eta$  and scattering parameter  $\rho=2\pi r_p/\lambda$ .

#### 4. Comparative analysis of measurement methods of particle parameters

The analysis of the above methods has been carried out for  $\text{Al}_2\text{O}_3$  particles since its optical properties in broad spectral region for variety of temperatures are well known. The emissivity was estimated from the approximation formula valid for  $\eta < 0.1$  and  $n \leq 1.7$  and derived in geometrical optics approximation [6, 7] using referred values of optical parameters [8]. Alumina powder has been beforehand spheroidized and dispersed with the help of set of mesh sieves. As result two powder fractions have been obtained - 45-50  $\mu\text{m}$  (fraction #1) and 63-71  $\mu\text{m}$  (fraction #2). Complementary research of particle size distributions of the two fractions has been carried out using COULTER COUNTER TA-II apparatus. The data gained of the research are indicated in Figs. 3 and 4 ( $D_{\text{aver}}$  is average diameter).

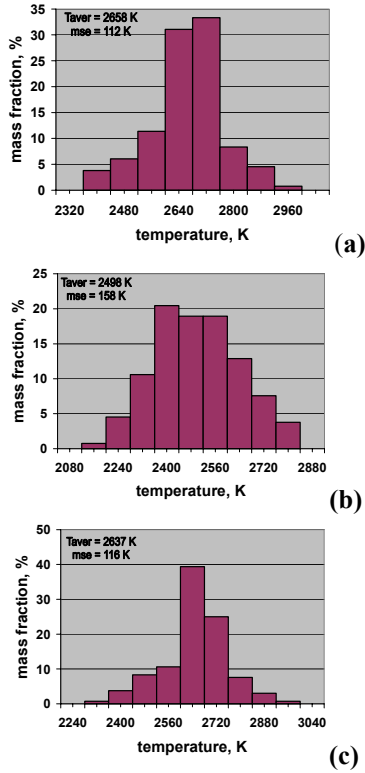


**Fig. 3.** Particle size bar chart of  $\text{Al}_2\text{O}_3$  powder of fraction 1.

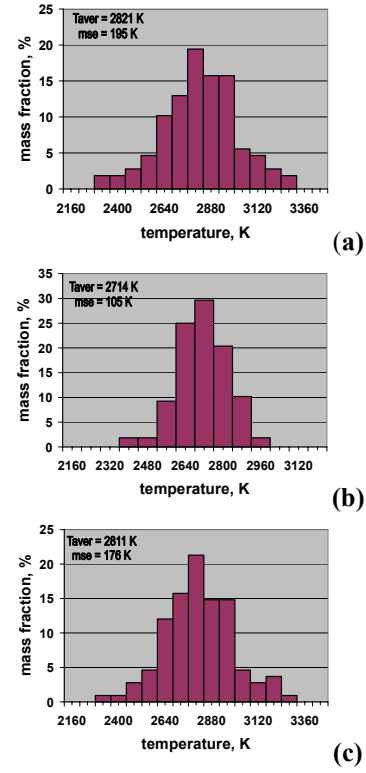


**Fig. 4.** Particle size bar chart of  $\text{Al}_2\text{O}_3$  powder of fraction 2.

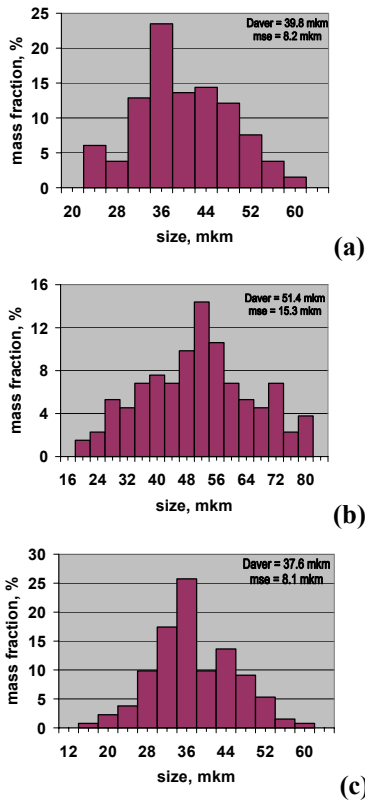
The model test using the plasma gun of 50 kW nominal power with inter-electrode insert [9] was performed. Powder was fed at nozzle exit section being 180 mm away from the measuring volume on the jet axis. Fraction #1 was treated in plasma torch under following operating parameters: current  $I=250 \text{ A}$ , arc voltage  $U=197 \text{ V}$ , plasma-forming gas flow rate (air)  $G=0.8 \text{ g/sec}$ , carrier gas flow rate (air)  $G_{tr}=0.05 \text{ g/sec}$ , powder feed rate  $G_p=0.15 \text{ g/sec}$ . Operating parameters for fraction #2 were as follows:  $I=250 \text{ A}$ ,  $U=260 \text{ V}$ ,  $G=1.7 \text{ g/sec}$ ,  $G_{tr}=0.05 \text{ g/sec}$ ,  $G_p=0.2 \text{ g/sec}$ .



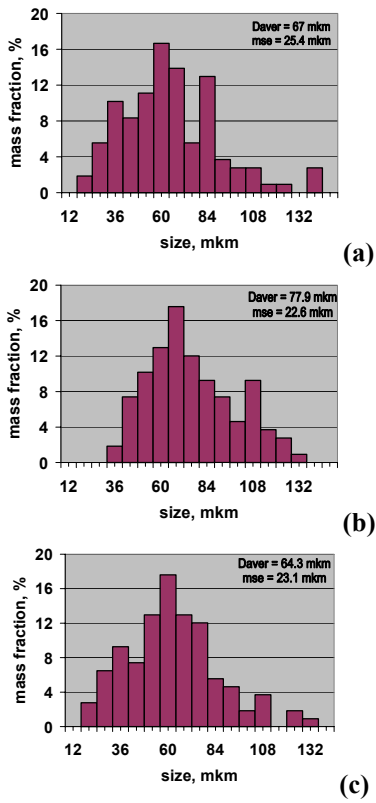
**Fig. 5.** Bar charts of particle temperature distributions of 1<sup>st</sup> fraction powder: *a*, *b* – color temperatures  $T_{c13}$  and  $T_{c23}$ ; *c* –  $T_{c3}$  calculated from the data taken from three spectral regions.



**Fig. 6.** Bar charts of particle temperature distributions of 2<sup>nd</sup> fraction powder: *a*, *b* – color temperatures  $T_{c13}$  and  $T_{c23}$ ; *c* –  $T_{c3}$  calculated from the data taken from three spectral regions.



**Fig. 7.** Particle size bar charts for the Al<sub>2</sub>O<sub>3</sub> powder of fraction 1 corresponding to the color temperatures  $T_{c13}$  (a),  $T_{c23}$  (b), and  $T_{c3}$  (c).



**Fig. 8.** Particle size bar charts of the Al<sub>2</sub>O<sub>3</sub> powder of fraction 2 corresponding to the color temperatures  $T_{c13}$  (a),  $T_{c23}$  (b), and  $T_{c3}$  (c).

The statistical distributions of particle temperatures  $T_{c13}$ ,  $T_{c23}$  and  $T_{c3}$  acquired for fractions #1 and #2 are demonstrated in Figs.5 and 6, respectively ( $T_{aver}$  is average temperature,  $mse$  is root-mean-square error). It is seen that the distributions of color temperatures  $T_{c13}$  and  $T_{c23}$  differ in both absolute value and width of the sample bars. This discrepancy can be interpreted by differing quantities of error of method and instrumental error, while the distributions  $T_{c13}$  and  $T_{c3}$  are close (Fig.5,a,c and 6,a,c).

In Figs. 7 and 8 the size distributions obtained from both pyrometric signals' amplitudes are demonstrated taking into account found temperatures:  $a,b$  – color temperatures  $T_{c13}$  and  $T_{c23}$ ;  $c$  – particle temperature  $T_{c3}$ . These distributions indirectly allow one to make up a conclusion about accuracy in estimating the temperatures. In particular, one can notify that color temperature  $T_{c23}$  is systematically underestimated compared with  $T_{c13}$  and  $T_{c3}$  as well as perhaps compared with actual temperatures of particles. This is the case both for the mean particle sizes of both fractions and for their size limits, although within these limits stated distributions are different. Widening of acquired distributions is caused by instrumental error of temperature measurement.

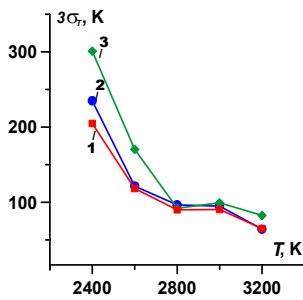
## 5. Modeling of measuring the particle parameters

Registering the particle thermal radiation at 3 spectral regions allows one to improve capability of temperature measurement due to spreading of spectral regions of interest and implementing two independent techniques of signal processing as well. The basic sources of temperature inaccuracies are the following: PEM shot noise and ground plasma noise bars, inconsistency of assumption of the actual emissivity spectrum of the particle to the “gray”-body approximation.

To clarify the influence of noise factor of registering pyrometric signals on accuracy of temperature estimates the computer simulation of the procedure of measuring this parameter for various levels of noise has been conducted. Initial parameters were particle size, temperature and velocity, plasma temperature. Particle diameter, its velocity as well as plasma temperature were fixed ones:  $D_p = 50 \mu\text{m}$ ,  $u_p = 200 \text{ m/sec}$ ,  $T_g = 2000 \text{ K}$ ; with particle temperature being varied within  $T_p = 2400 \div 3200 \text{ K}$ . The calculation of model signal for each operating bandwidth was executed according to (1). Afterwards, an additive noise was superimposed onto the calculated signal; the noise was assumed distributed according to the normal distribution law with the relative root-mean-square deviation given by the formula

$$\sigma_{ni} / \bar{U}_i = P_0^{-1} \sqrt{PkT_g \Delta f + 2e(P_0 + P)(1+B)\Delta f / S_{\lambda i}}, \quad (4)$$

where  $P_0$  and  $P$  are the mean thermal radiation powers of particle and plasma, respectively, of  $i$ -th spectral region;  $k=1.38 \cdot 10^{-23} \text{ [J/K]}$  is the Boltzmann constant,  $e=1.6 \cdot 10^{-19} \text{ [A} \cdot \text{sec]}$  is the electron charge;  $(1+B)=2.5$  is the coefficient of this sort of PEM dynode shot noise;  $S_{\lambda i} \text{ [A/W]}$  is a photocathode spectral sensitivity;  $\Delta f=20 \text{ MHz}$  is an electronic channel bandwidth. For particle temperature  $T_p=2400 \text{ K}$  the signals were noised maximally ( $\sigma_{n1} / \bar{U}_1 = 0.35$ ,  $\sigma_{n2} / \bar{U}_2 = 0.23$ ,  $\sigma_{n3} / \bar{U}_3 = 0.17$ ): the relative noise intensity decreases with increasing temperature.

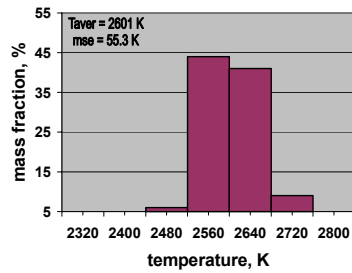


**Fig. 9.** Instrumental error in estimating the particle temperatures versus temperature: 1,2 – color temperatures color temperature  $T_{c13}$  and  $T_{c3}$ ; 3 – color temperature  $T_{c23}$ .

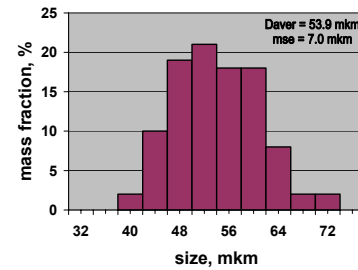
With fixed particle temperatures  $T_p = 2400, 2600, 2800, 3000, 3200 \text{ K}$ , 100 in-flight particles with independent noise bars have been simulated to subsequently reconstruct the color particle temperatures  $T_{c13}$ ,  $T_{c23}$ , and  $T_{3c}$ . Here, test particle emissivity is supposed to be “grey” radiator ( $\epsilon_\lambda = \text{const}$ ) with absolute value being close to  $\text{Al}_2\text{O}_3$  particle thermal radiation  $D_p = 50 \text{ MKM}$  at given temperature. The temperatures  $T_{aver}$  averaged over the particle ensemble and their mean-square deviations  $\sigma_T$  were calculated. The calculated mean temperatures are close comparatively to initial “true” temperatures within 10 K. The curve of maximum error  $\Delta T = 3 \cdot \sigma_T$ , K of temperature estimates  $T_{c13}$ ,  $T_{c23}$  and  $T_{c3}$  for single realization as function of true particle temperature is depicted in Fig.9.

Distribution of temperature  $T_{c3}$  after restoring the particle initial parameters at  $T_p=2600 \text{ K}$  is illustrated in Fig.10. The error of temperature restoration from single noised realization lies within the range  $2600 \pm 160 \text{ K}$ , resulting in an inaccuracy in reconstructing the particle size of  $50 \pm 21 \mu\text{m}$  (see Fig. 11). Hence, particle size measurements provide acceptable estimates of ensemble-averaged sizes of particles (within 10%), although being up to 50 % for a single realization.





**Fig. 10.** Bar chart showing the distribution of particles over the temperature  $T_{c3}$ ; the bar chart was obtained through reconstruction of initial particle parameters for  $T_p=2600$  K.



**Fig. 11.** Bar chart showing the particle-size distribution reconstructed for the mean temperature  $T_p=2600$  K and for the likely error of  $\pm 160$  K.

## 6. Summary

The conducted analysis of polychromatic pyrometry method and the comparison between the “measured” and “true” sizes and temperatures of alumina particles with well-known optical properties in broad spectral region for vast variety of temperatures show that this method is efficient (sharp minimum of root-mean-square deviation of model and experimental spectra of thermal radiation) assuming “gray” body nature of radiation. Using linear approximation of emissivity  $\varepsilon(\lambda, T) = a_0 + a_1\lambda$  results in occurrence of several minima within the “grass” of experimental spectrum. This can be dealt with the fact that number of unknown parameters (temperature, size, coefficients of polynomial of emissivity approximation) is greater than number of available measurement data acquired from three operating spectral regions. measure the particle temperature by two independent methods and perform a comparison between three color temperatures gained with different instrumental and methodical errors. The results of the comparison make it possible to draw conclusions about the nature of the emission.

## Acknowledgement

This work was supported by Siberian Branch of the Russian Academy of Sciences (Interdisciplinary Program on 2000-2002, Project No.45).

## References

- [1] O.P. Solonenko, A.A. Mikhilchenko, V.A. Gavrilov, E.V. Kartaeu – Proc. of 14th Intern. Symposium on Plasma Chemistry, Aug. 2-6, 1999, Praha, Czech Republic. **2** (1999).
- [2] D.Ya. Svet, Yu.N. Pyrkov, V.G. Plotnichenko – Reports of Russian Academy of Sciences. **361**, 5 (1998) (in Russian).
- [3] A.S. Leonov, S.P. Rusin – J. of Thermophysics and Aeromechanics. **8**, 3 (2001) (in Russian).
- [4] J. Max. Methods and techniques of processing of signals for physical measuring applications, Moscow, Mir Publishing House. **1** (1983).
- [5] C. Bohren, D. Huffman. Absorption and Scattering of Light by Small Particles, Moscow, Mir Publishing House (1986).
- [6] V.P. Pinchuk, N.P. Romanov – J. of Appl. Spectroscopy. **27**, 1 (1977) (in Russian).
- [7] L.A. Dombrovsky – J. of Thermophysics of High Temperature. **28**, 6 (1990) (in Russian).
- [8] A.B. Shigapov – J. of Thermophysics of High Temperature. **36**, 1 (1998) (in Russian).
- [9] O.P. Solonenko, A.P. Alkhimov, V.V. Marusin et al. High-energy processes of treatment of materials. Low-temperature plasma, **18**, Novosibirsk, Nauka, Siberian publishing house (2000) (in Russian).

# Some peculiarities of YSZ splats formation under plasma spraying of thermal barrier

O. Solonenko<sup>1</sup>, A. Mikhachenko<sup>1</sup>, E. Kartaev<sup>1</sup>,  
K. Ogawa<sup>2</sup>, T. Shoji<sup>2</sup>, and M. Tanno<sup>2</sup>

<sup>1</sup> *Institute of Theoretical and Applied Mechanics, Siberian Branch, Russian Academy of Sciences,  
4/1 Institutskaya str., Novosibirsk, 630090, Russia*

<sup>2</sup> *Fracture Research Institute, School of Engineering, Tohoku University,  
Aoba-yama 01, Sendai, 980-8579, Japan*

## Abstract

A new theoretical solution for prediction the thickness and diameter of the metal oxide splats under plasma spraying has been experimentally tested. Towards this end the collection of model experimental splats of yttria stabilized zirconia (YSZ) deposited on the polished metallic substrates at fully controlled key physical parameters (KPPs) was obtained. The results of comparison show a wholly satisfactory agreement between predicted and measured thickness and diameter of splats without introducing any empirical constant.

## 1. Introduction

During the last decade, there has been a considerable interest in the metal oxide coatings ( $\text{Al}_2\text{O}_3$ ,  $\text{ZrO}_2$ ,  $\text{TiO}_2$ ,  $\text{Cr}_2\text{O}_3$  and others) thermally sprayed onto solid surfaces [1-6]. It was recognized that further progress in improving the quality and structure of sprayed materials largely depends on the understanding of processes that occur during the interaction of molten particles, carried by a high-temperature jet, with substrates. Therefore, it is necessary to derive a set of analytical solutions for splat characteristics that can be obtained under these or those particular conditions characterized by KPPs of the process (velocity  $u_{po}$ , diameter  $D_p$ , surface temperature  $T_{po}$  and phase state of particle, and temperature  $T_{bo}$  and surface state of the substrate). For metal splats deposited onto polished substrates ( $\text{Pr} = \nu_{pm}^{(l)} / a_{pm}^{(l)} \ll 1$ ,  $\nu_{pm}^{(l)}$  and  $a_{pm}^{(l)} = \lambda_{pm}^{(l)} / \rho_{pm}^{(l)} c_{pm}^{(l)}$  are the kinematic viscosity and the thermal diffusivity of the melt at melting point,  $\rho_{pm}^{(l)}$  and  $c_{pm}^{(l)}$  are its density and heat capacity), this problem was recently solved in a first approximation in [7, 8].

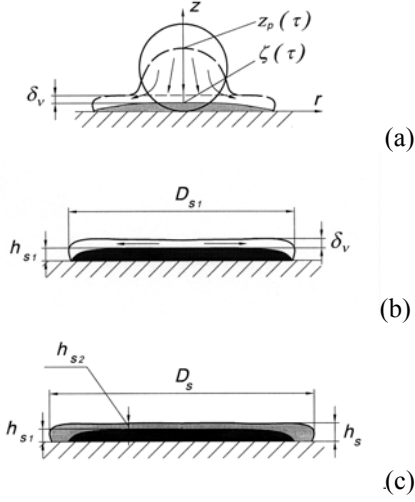
A new theoretical solution for the thickness and diameter of plasma-sprayed alumina splats ( $\text{Pr} > 1$ ) was obtained and experimentally tested in [9, 10]. It was shown that the solution allows one to predict the splat characteristics without introducing any empirical constant. The theoretical approach developed is based on a two-stage description of the splat formation process (initially ideal and consequently viscous spreading of the melt over the previously solidified layer of the material). In the present work, we have continued the experimental testing of theoretical solution and have obtained a set of model experimental YSZ splats deposited onto substrates under fully controlled KPPs. Scanning electron microscopy and profilometry were used to reveal the morphology of the model splats. As before, a comparison shows a satisfactory agreement between the predicted and measured splat thickness and diameter.

## 2. Theoretical background

Apparently, any description of the conductive-convective heat transfer between a metal or metal-oxide melt and a solid substrate should be based on two different model approaches. To devise such a description, it is required to consider axisymmetric and non-isothermal spreading of a melted droplet over a substrate in a vicinity of the stagnation point. Here, only the transitional period should be considered during which the melt flattens to reach its final thickness. If the viscosity of the melt is high and its thermal conductivity is low ( $\text{Pr} > 1$ ), the thermal boundary layer, in which the temperature varies along the direction normal to the wall (solidification front) from  $T_{pm}$  to  $T_{po}$ , turns out to be submerged into a viscous near-wall flow. Over the viscous near-wall flow, at sufficiently high Reynolds and Weber numbers ( $\text{Re} = D_p u_{po} / \nu_{pm}^{(l)} > 100$ ,

$\text{We} = \rho_{pm}^{(l)} D_p u_{po}^2 / \sigma_{pm}^{(l)} > 100$ , where  $\sigma_{pm}^{(l)}$  is the surface tension of the melt) we have a flow much the same as ideal spreading of a liquid having an initial temperature equal to  $T_{po}$  (here, the emission from the free surface is ignored). Hence, in this case the heat-transfer regularities are fully determined by the hydrodynamic features of the flow in the viscous sub-layer, and we have to consider a model heat-transfer problem about a viscous liquid normally impinging on a non-isothermal wall. The physical model for the process of interest

developed rests on the assumptions formulated in [9]. To obtain an approximate solution that characterizes deformation and solidification of a metal oxide droplet on a solid substrate we consider, in succession, the following two stages:



**Fig.1.** Successive splat formation stages during impact interaction of a metal – oxide droplet with a substrate.

- the stage of ideal impact spreading of the melt over the quasi-stationary viscous layer; this layer being simultaneously displaced by the solidification front that propagates from the substrate (Fig.1,a); this stage comes to an end when the top  $z_p$  of the liquid droplet reaches the external boundary of the viscous layer (Fig.1,b);
- the stage of subsequent inertial spreading of the already formed thin viscous layer of a melt; this stage turns out to be completed when the solidification front meets the free surface (Fig.1,c).

**Potential spreading stage.** This stage is restricted to the droplet potential spreading period that starts at the moment  $t=0$  (Fig.1,a) and finishes at the moment  $t_1^*$ , at which time the top  $z_p$  of the spreading droplet reaches the external boundary of the viscous layer (Fig.1,b). As a first approximation, we may adopt an assumption that during this stage the droplet top moves with a constant velocity  $u_{po}$ , and its current coordinate may be represented as  $z_p(t) = D_p - u_{po}t$ .

Introducing the non-dimensional time and space variables  $\tau = \sqrt[3]{a_{pm}^{(l)}\beta^2}t$ ,  $\eta = \sqrt[3]{\beta/a_{pm}^{(l)}}z$ , we obtain a bi-quadratic equation for the duration of the first stage. This equation, with due regard for [9], may be written as

$$\tau + \frac{c_\zeta}{\kappa}\sqrt{\tau} - \frac{(1-\eta_v)\bar{D}_p}{\kappa} = 0, \quad \kappa = u_{po} / \sqrt[3]{\beta(a_{pm}^{(l)})^2}, \quad (1)$$

where  $\beta = (2/\chi)\alpha\sqrt{\alpha/\nu_{pm}^{(l)}}$ ,  $\alpha$  is a parameter that characterizes the ideal flow of the melt in the vicinity of the stagnation point. The solidification rate  $c_\zeta$  will be defined below. Solving the equation (1), we have

$$t_1^*/t_d = (c_\zeta^2/4Pe)[\sqrt{1+4Pe(1-\eta_v)/c_\zeta^2} - 1]^2, \quad h_{s1}/D_p = (c_\zeta^2/2Pe)[\sqrt{1+4Pe(1-\eta_v)/c_\zeta^2} - 1], \quad (2)$$

$\eta_v = \delta_{v,eff}/D_p$ ,  $t_d = D_p/u_{po}$ ,  $Pe = D_p u_{po} / a_{pm}^{(l)}$  is the Peclet number.

**Viscous spreading stage.** This stage begins at the moment  $t = t_1^*$  (Fig.1,b) and finishes at the moment  $t = t_1^* + t_2^*$ , when the upper boundary of the viscous layer meets the solidification front, i.e.  $z_p(t_1^* + t_2^*) = h_{s1} + h_{s2}$  (Fig.1,c). The current coordinate of this boundary, on the assumption that it continues the motion in the velocity field of the initial viscous flow, may be determined as  $z_p(t') = \delta_{v,eff}/(1 + \beta\delta_{v,eff}t')$ ,  $t' = t - t_1^*$ ,  $t \geq t_1^*$ , and the thickness of the layer solidified at this stage may be found as  $h_{s2} = \zeta(t_1^* + t_2^*) - \zeta(t_1^*)$ . Hence, the duration of the second stage may be found from the equation

$$\bar{\delta}_{v,eff}/(1 + \bar{\delta}_{v,eff}\tau) + \bar{h}_{s1} = c_\zeta\sqrt{\tau_1^* + \tau}, \quad (3)$$

The dash over the quantities indicates non-dimensional space variables. Re-arranging this equation in order to get an equation for the variable  $y = \tau_1^* + \tau$ , we obtain a full cubic equation

$$ay^{3/2} + by + cy^{1/2} + d = 0, \quad a = c_\zeta\bar{\delta}_{v,eff}, \quad b = -\bar{\delta}_{v,eff}\bar{h}_{s1}, \quad c = c_\zeta(1 - \bar{\delta}_{v,eff}\tau_1^*), \quad d = -[\bar{\delta}_{v,eff} + (1 - \bar{\delta}_{v,eff}\tau_1^*)\bar{h}_{s1}]. \quad (4)$$

Introducing the variable  $\sqrt{y} = w - b/3a$ , we bring the equation (4) to the canonical form

$$w^3 + pw + q = 0, \quad w = \sqrt{\tau_1^* + \tau} - \bar{h}_{s1}/3c_\zeta, \quad p = -b^2/3a^2 + c/a, \quad q = 2b^3/27a^3 - bc/3a^2 + d/a. \quad (5)$$

To find the roots of this equation, we may use the Cardano formula [11]. Equation (5) has only one real root, whereas two other roots are complex conjugated, provided that  $D = -27q^2(1 + 4p^3/27q^2) < 0$ . In this case, the real root of interest is

$$w^* = \sqrt[3]{|q|/2} \cdot \left( \sqrt[3]{\sqrt{1+\kappa_2} + 1} - \sqrt[3]{\sqrt{1+\kappa_2} - 1} \right), 1+\kappa_2 \geq 1; \quad w^* = \sqrt[3]{|q|/2} \cdot \left( \sqrt[3]{\sqrt{1+\kappa_2} + 1} + \sqrt[3]{1 - \sqrt{1+\kappa_2}} \right), 1+\kappa_2 < 1, \quad (6)$$

where  $\kappa_2 = 4p^3/27q^2$ . As a result, for the total duration of the splat formation process and for the final splat thickness we have the formulas

$$t_s^*/t_d = \sqrt[3]{2\chi^2 \text{Pr}} (y_* + \bar{h}_{s1}/3c_\zeta)^2, \quad h_s/D_p = \sqrt[3]{\chi\sqrt{2}c_\zeta} (y_* + \bar{h}_{s1}/3c_\zeta) / \sqrt[3]{\text{Pe}\sqrt{\text{Re}}}. \quad (7)$$

According to [9], the resultant solution for the parameter  $c_\zeta$ , characterizing the melt solidification rate, is

$$\bar{\zeta}(\tau) = c_\zeta \sqrt{\tau}, \quad c_\zeta = P[\sqrt{1+4Q/P^2} - 1]/2, \quad (8)$$

$$P = \frac{\pi\lambda_{p,p}^{(s,l)} \text{Ku}_p^{(l)} + 2(1+\alpha_c) \text{K}_\varepsilon^{(b,p)} (\mathcal{G}_{po} - 1)}{\sqrt{\pi} \text{K}_\varepsilon^{(b,p)} \text{Ku}_p^{(l)}}, \quad Q = \frac{2\lambda_{p,p}^{(s,l)} (1 - \mathcal{G}_{bo})}{\text{Ku}_p^{(l)}} \cdot \left[ 1 - \frac{(1+\alpha_c)(\mathcal{G}_{po} - 1)}{(1 - \mathcal{G}_{bo}) \text{K}_\varepsilon^{(b,p)}} \right], \quad (9)$$

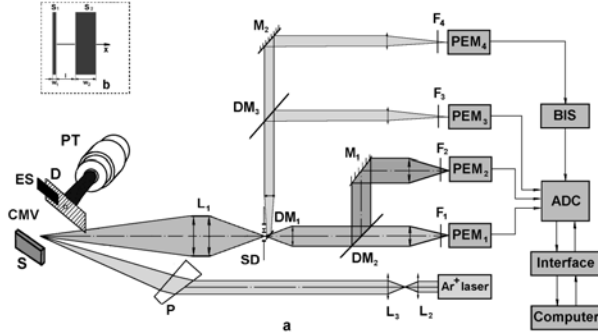
$$\mathcal{G}_c = (\sqrt{\pi} \lambda_{p,p}^{(s,l)} + c_\zeta \text{K}_\varepsilon^{(b,p)} \mathcal{G}_{bo}) / (\sqrt{\pi} \lambda_{p,p}^{(s,l)} + c_\zeta \text{K}_\varepsilon^{(b,p)}), \quad (10)$$

where  $\text{Ku}_p^{(l)} = L_{pm}/c_{pm}^{(l)} T_{pm}$  is the Stefan – Kutateladze criterion for the phase transition,  $\text{K}_\varepsilon^{(b,p)} = \lambda_{b,p}^{(s,l)} \sqrt{a_{p,b}^{(l,s)}}$  is the thermal activity criterion for particle and substrate materials,  $\lambda_{p,p}^{(s,l)} = \lambda_{pm}^{(s)}/\lambda_{pm}^{(l)}$ ,  $\alpha_c \cong \tau_d(1 + \tau_d/18)/4$ ,  $\tau_d = t_d/t_o$ ,  $t_d = D_p/u_{po}$ ,  $t_o = 1/\sqrt[3]{a_{pm}^{(l)} \beta^2}$ . The effective thickness  $\delta_{v,eff}$  of the viscous boundary layer is given by the following expression [9]:

$$\delta_{v,eff} = 2(2 - c_{\zeta 0}/\sqrt{\text{Pr}}) D_p / 3\sqrt{\text{Re}}, \quad (11)$$

where the parameter  $c_{\zeta 0}$  is determined using dependencies (8) and (9) with due regard for the additional condition  $\alpha_c = 0$ . The final splat diameter  $D_s$  (Fig.1,c) may be found, under an assumption that the droplet solidifies as a cylinder, from the full balance condition for the particle mass prior to and after the particle interaction with the substrate.

### 3. Experimental procedures



**Fig. 2.** Schematic diagram of the model setup. (a) – diagnostic apparatus; (b) – two-slit diaphragm; PT – plasma torch; D – diaphragm; ES – solenoid-driven shutter; S – substrate;  $L_1, L_2, L_3$  – lenses; P – deflecting prism; SD – diaphragm; DM<sub>1</sub>, DM<sub>2</sub>, DM<sub>3</sub> – dichroic mirrors; SD – light splitter; M<sub>1</sub>, M<sub>2</sub> – mirrors; F<sub>1</sub>, F<sub>2</sub>, F<sub>3</sub>, F<sub>4</sub> – light filters; PEM<sub>1</sub>, PEM<sub>2</sub>, PEM<sub>3</sub>, PEM<sub>4</sub> – photo-electronic multipliers; BIS – discriminator; ADC – analog-to-digital converter.

To simultaneous measuring the particle velocity, temperature and size we employed a technique based on time-of-flight method and three-color pyrometer [13] realized in one and the same CMV. The CMV was located 5 mm away from the water-cooled diaphragm D. The detailed description of the particle-in-flight diagnostic apparatus is given in the paper [13].

A powder of spherical yttria-stabilized zirconia particles (Zulzer Metco NS 204, particle sizes 20-120  $\mu\text{m}$ ) was used as the initial powder for splats deposition. Prior to using it in the experiments, powder was sieved to obtain narrow cuts with particle diameters 45-50, 50-56, 56-63, 63-71, 71-80, 80-90, and 90-100  $\mu\text{m}$ .

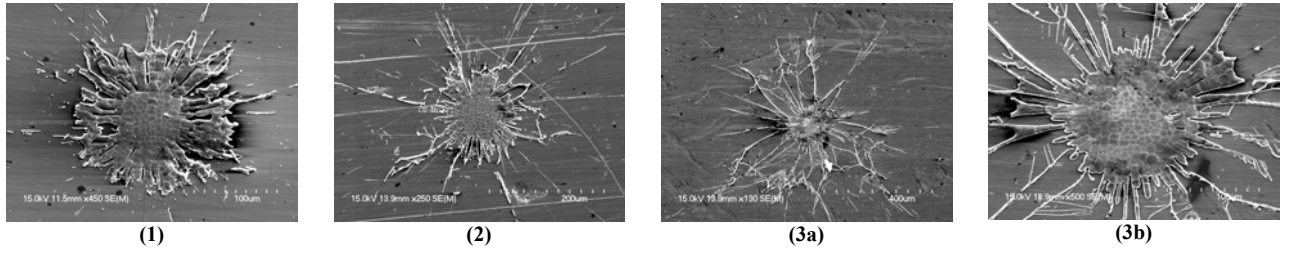
Nowadays, the experimental studying the melted particle–substrate interaction under fully controlled KPPs of the process attracts a considerable interest. To heat the particles of YSZ powder, we used a plasma torch operating in turbulent, transient and quasi-laminar jet outflow regimes [12].

To study the interaction of melted particles with the substrate, individual heated particles were isolated from the dusted plasma jet with the help of a water-cooled diaphragm. Afterwards, the velocity, temperature, and size of the isolated particle were measured prior to its impingement onto the substrate whose temperature was also controlled with good accuracy. The diagram of the setup used is shown in Fig.2. As a molten particle passes the 1-mm-diameter opening in the diaphragm D and subsequently traverses the control measurement volume (CMV), the solenoid-driven shutter ES blocks the opening thus isolating this particle.

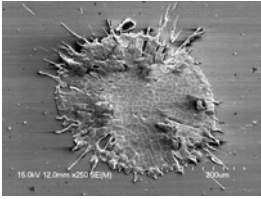
The isolated melted particles were deposited onto both the stainless-steel substrates and Ni-super-alloy substrates coated by CoNiCrAlY sub-layer using LPPS. Finally, these substrates were polished to a mirror state. The splats' morphology was studied using the HITACHI S-4700 scanning electron microscope (Capture resolution 1280x960) and the Surfcoorder SE-2300 profilograph, Kosaka Laboratory Ltd., Japan.

#### 4. Discussion

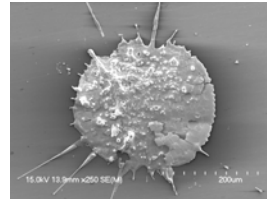
The purpose of the present study was to tackle the following scope of problems: (1) to obtain a set of experimental YSZ splats deposited onto above-mentioned substrates under fully controlled KPPs; 2) to study the morphology of the splats thus obtained by means of scanning electron microscopy and profilometry; 3) to compare the theoretically predicted and experimentally measured splats' thickness and diameter in order to verify the developed theoretical foundations. In the set of splats obtained, two types of splats could be distinguished, splats with a regular and with an irregular morphology. Typical irregular splats deposited onto relatively cold stainless-steel substrates ( $T_{bo} \leq 475$  K) are shown in Fig.3.



**Fig. 3.** Typical splats deposited on relatively cold stainless-steel substrates. 1 –  $u_{po}=146$  m/s,  $T_{po}=3610$  K,  $T_{bo}=478$  K (45-50  $\mu\text{m}$  fraction); 2 –  $u_{po}=138$  m/s,  $T_{po}=3240$  K,  $T_{bo}=475$  K (63-71  $\mu\text{m}$  fraction); 3 –  $u_{po}=146$  m/s,  $T_{po}=3480$  K,  $T_{bo}=473$  K (63-71  $\mu\text{m}$  fraction); 3,a – general view; 3,b – central part of splat.



**Fig. 4.** The splashing with fingering that gives rise to splats formed on the verge of stable and unstable splat formation regions with  $u_{po}=130$  m/s,  $T_{po}=3510$  K,  $T_{bo}=584$  K, (80-90  $\mu\text{m}$  fraction).



**Fig. 5.** The splat formed from a partially melted particle (with a quasi-solid internal core) that demonstrates peripheral fingers ( $u_{po}=98$  m/s,  $T_{po}=3030$  K,  $T_{bo}=574$  K, (63-71  $\mu\text{m}$  fraction).

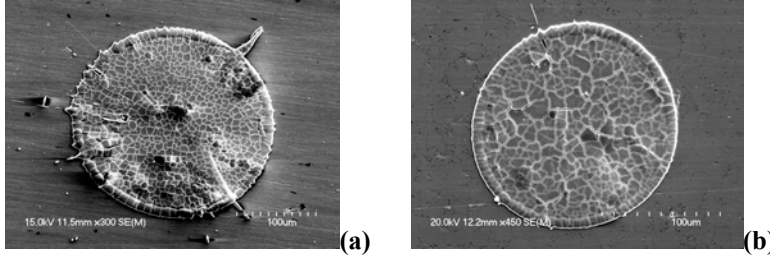
**Table 1.** The experimentally determined values of the KPPs for YSZ splats deposited on polished stainless-steel substrates (#1-5) and polished CoNiCrAlY sub-layer sprayed on Ni-super-alloy substrates (#6-15).

No.	$T_{bo}$ , K	$u_{po}$ , m/s	$T_{po}$ , K	$D_p$ , $\mu\text{m}$	$D_{s,exp}$ , $\mu\text{m}$	$D_{s,calc}$ , $\mu\text{m}$	$h_{s,exp}$ , $\mu\text{m}$	$h_{s,calc}$ , $\mu\text{m}$
1	581	130	2980	45.6	180	190	1.96	1.75
2	586	114	3120	37.9	253	247	1.45	1.48
3	475	138	3210	56.9	158	156	1.91	2.01
4	584	122	3390	52.8	223	238	1.97	1.74
5	591	130	3400	57.0	251	266	1.96	1.74
6	620	122	2980	39.4	152	155	1.68	1.71
7	598	162	3330	42.9	199	195	1.33	1.43
8	522	138	3540	39.9	174	176	1.40	1.44
9	630	146	3300	42.7	191	190	1.42	1.51
10	612	130	3540	36.0	150	154	1.38	1.38
11	592	154	3310	52.4	250	242	1.55	1.63
12	624	146	3380	54.3	253	261	1.66	1.68
13	624	138	2950	57.1	256	257	1.89	1.97
14	617	178	3170	42.2	197	189	1.29	1.40
15	682	146	3610	63.2	314	317	1.71	1.67

As is seen from the photographs shown in Fig.3, even well heated droplets, when being deposited onto insufficiently heated substrates, form the splats with corrupted internal material continuity and a finger-like peripheral structure. For splats obtained from droplets with almost identical impingement velocities and temperatures, the instability in their formation process is manifested most distinctly with increasing droplet

diameter. However, in all cases the splats display a continuous structure in a vicinity of the stagnation point ( $2r \leq D_p$ ). Another unstable splat formation mechanism arises in the case of large particles with liquid and overheated shell and only partially melted core that consists of individual solid fragments. When such particles impinge onto the substrate, the melt spreads over the substrate whereas the quasi-solid core disintegrates into fragments that block the normal melt spreading and give rise to peripheral splashes of the particle material (Figs. 4 and 5). Of course, the above-described unstable splat formation mechanisms do not exhaust the whole variety of reasons leading to the formation of irregular zirconia splats. This point has always been the object of much concentrated attention and it still invites further investigation.

Figure 6 illustrates the typical view of YSZ splats having a regular morphology flattened and solidified on the polished metallic substrates. The splats are seen to have a cracked cellular structure caused by fluid contraction. The cells represent irregular polygons. The orientation of the cell boundaries along the substrate polishing direction is seen to inherit the surface texture (Fig.6, a). The characteristic transverse size of the cells seems to be determined by the melt cooling rate and by the solidification-front velocity. Generally, the cellular splat structure is rather uniform over the splat surface. Only in the peripheral regions the cells are elongated along the melt-flow direction, this difference however being rather small. In our opinion, the latter observation supports the point of view that, under the adopted spray conditions, the droplets spread over the substrate and solidify almost simultaneously.



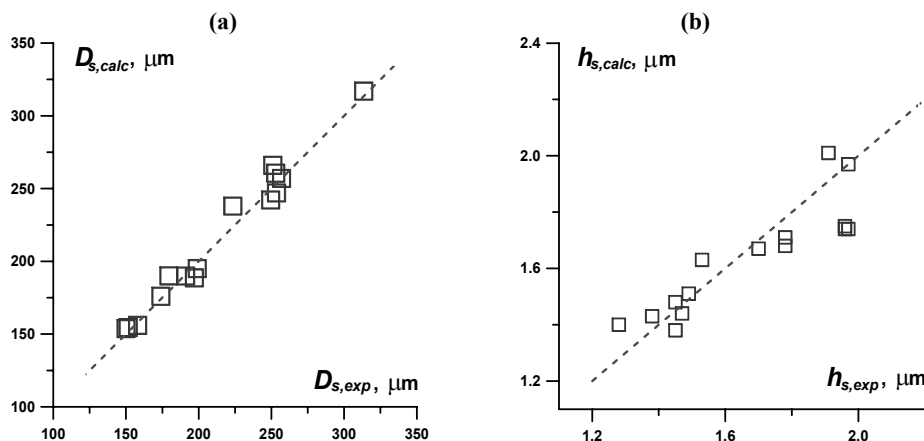
**Fig. 6.** Typical view of YSZ splats with regular morphology deposited on polished metallic substrate. (a) – stainless-steel substrate:  $u_{po}=130$  m/s,  $T_{po}=3400$  K,  $T_{bo}=591$  K, (71-80  $\mu$ m fraction); (b) – Ni-super-alloy substrate coated by layer of CoNiCrAlY using LPPS:  $u_{po}=138$  m/s,  $T_{po}=3540$  K,  $T_{bo}=522$  K, (50-56  $\mu$ m fraction).

To determine the temperature of YSZ particles prior to their impingement onto substrates, we independently measured the color temperatures for two wavelength pairs:  $\lambda_1=0.6328$   $\mu$ m,  $\lambda_3 = 0.8906$   $\mu$ m, and  $\lambda_2= 0.721$   $\mu$ m,  $\lambda_3 = 0.8906$   $\mu$ m. In addition, to determine the temperature of the particles, we used the algorithm described in [13]. It is based on the minimization of the sum of squared deviations of experimentally measured emission intensities at the above-indicated wavelengths from their theoretical values.

The data thus obtained showed the extracted three-color temperature to be always in excess of the ordinary color temperature by approximately 300 K. Since at high temperatures the optical characteristics of zirconia (refractive index and absorption coefficient) are unknown, the particle size could not be reliably deduced from the pyrometric data using the temperature obtained. This conclusion is supported by the fact that estimates of particle sizes even in the blackbody approximation ( $\epsilon(\lambda, T)=1$ ) always yielded a particle size in excess of the grain size of the powder fraction used. The latter shows that the surface temperature of the particles extracted from the pyrometric data, including the found three-color temperature, is lower than the actual volume-averaged temperature. This deduction may be indicative of a considerable temperature gradient present inside the zirconia particles.

In this connection, to verify the developed theoretical foundations for metal oxide splats, we performed the following additional tests. From the obtained set of splats, fifteen splats were selected (see Table 1) for which their surface profilograms in two mutually perpendicular directions were recorded on the Surfcomer SE-2300 profilograph (Kosaka Laboratory Ltd., Japan). Properly treating the data obtained, we determined the mean splat thickness, which, together with the diameters measured with the help of the HITACHI S-4700B scanning electron microscope, were used to subsequently access the splat volume under the assumption that the splats solidify as cylinders. Using the balance relation for the mass of a spherical droplet prior and after its impingement onto the surface  $\pi D_p^3 / 6 = \pi D_s^2 h_s / 4$ , we estimated the diameter of liquid droplets which were subsequently used to theoretically estimate the splats' diameter. In Table 1 there are represented the experimentally determined values of the KPPs of the interaction between melted YSZ particles and two kinds of substrates. The theoretically predicted and experimentally measured diameter and thickness of splats selected are also listed in Table 1.

As is seen from Fig.7, the theoretically predicted splat diameters and thickness compare well with the values estimated from the experimental data. The finding that measured in-flight diameter of zirconia particle always exceeds a particle diameter reconstructed from the measured profilograms also deserves mention.



**Fig. 7.** Comparison between the experimentally measured and theoretically predicted splats' diameter (a) and thickness (b).

## 5. Conclusions

We have continued the testing of new theoretical fundamentals in order to predict splats' thickness and diameter in thermal spray processes (including plasma spraying) as applied to YSZ powder. To verify the analytical solution derived, experimental data obtained under fully controlled KPPs of the plasma spray process were invoked. Scanning electron microscopy and profilometry were used to study the morphology of obtained model splats. A fairly good agreement between the predicted and measured splats' thickness and diameter was obtained without introducing any empirical parameter.

## Acknowledgements

This work was supported by the Grant-in-Aid for Scientific Research (B) (No. 13450041) and COE (Center of excellence) Research (No. 11CE2003) of the Ministry of Education, Culture, Sports, Science and Technology, Japan and by Siberian Branch of the Russian Academy of Sciences (Interdisciplinary Program on 2000-2002, Project No.45).

## References

- [1] M. Vardelle, A. Vardelle, K.-I. Li, P. Fauchais, and N.J. Themelis – Pure and Applied Chemistry. **68**, 5 (1996).
- [2] P. Fauchais, M. Vardelle, A. Vardelle, L. Bianchi, and A.C. Leger – Plasma Chemistry and Plasma Processing. **16**, 1 (Supplement) (1996).
- [3] J. Matejcek, S. Sampath, and H. Herman – Thermal Spray. Meeting the Challenges of the 21th Century, ASM International, USA (1998).
- [4] X. Fan, F. Gitzhofer, and M. Boulos – J. of Thermal Spray Technology. **7**, 2 (1998).
- [5] K. Shinoda, P. Han, and T. Yoshida – Proc. of ISPC-15, 9-13 July 2001, Orleans, France. **6** (2001).
- [6] O.P. Solonenko, V.A. Neronov, A.V. Smirnov, and V.I. Kuz'min – Proc. of ISPC-14, 2-6 August 1999, Prague, Czech Republic. **4** (1999).
- [7] O.P. Solonenko – In coll. Thermal Plasma Torches and Technologies, Vol.2. Thermal Plasma and Allied Technologies: Research and Development, Ed. by O.P. Solonenko, Cambridge International Science Publishing, Cambridge, England (2001).
- [8] O.P. Solonenko, and A.V. Smirnov – Ibid.
- [9] O.P. Solonenko – J. of Physical Mesomechanics. **4**, 6 (2001).
- [10] O.P. Solonenko, A.A. Golovin, E.P. Shurina, A.A. Mikhachenko, A.V. Smirnov, and E.V. Kartaev – Proc. of the 1<sup>st</sup> Intern. Symp. on Advanced Fluid Information, 4-5 October 2001, Sendai, Japan (2001).
- [11] Mathematical encyclopedia, Ed. by I.M. Vinogradov, Moscow, Soviet Encyclopedia (1979).
- [12] O.P. Solonenko, A.P. Alkhimov, V.V. Marusin et al – High-Energy Processes of Materials Treatment, Novosibirsk, Science, Sib. Publishing House of RAS (in Russian) (2000).
- [13] O.P. Solonenko, A.A. Mikhachenko, and E.V. Kartaev – Comparison of Two-Color and Three-Color Pyrometry for Measuring Velocity, Surface Temperature and Size of Single Particle in Plasma Flow (see this Proceedings).

# Theoretical analysis and computer simulation of thermophysical processes under removal of oxide layer on metal surface by a vacuum arc

K. Takeda<sup>1</sup>, O.P. Solonenko<sup>2</sup>, and A.A. Golovin<sup>2</sup>

<sup>1</sup> - Akita Prefecture University, Honjyo, Akita, 015-0055, Japan

<sup>2</sup> - Institute of Theoretical and Applied Mechanics SB RAS, 4/1 Institutskaya str., Novosibirsk, 630090, Russia,

## Abstract

A calculation procedure and software tools for modeling processes of non-stationary conjugated conductive heat transfer, oxide-layer evaporation, and simultaneous metal-substrate melting under impact a vacuum-arc spot, and also subsequent cooling and solidification of the melted metal-substrate layer, are developed. The computation algorithm is based on the finite-element method. Numerical results, which are of interest for cleaning substrates from oxide layers, are reported.

## 1. Introduction

Interesting properties of cathode spot regarding the removal of oxide layer from metal surface by vacuum arc were investigated in [1]. The cathode spots attack the oxides selectively and remove them by evaporation. The observed removal rate of the oxide layer increases in proportion to the arc current and in inverse proportion to the thickness of the oxide layer. In order to gain a better insight into the parameters governing the descaling action of the arc, the authors of [1, 2] developed simplified models using a relation for the energy balance at a cathode spot.

For more precise control of the process, often used for surface cleaning and purposeful decreasing residual roughness of base-metal surfaces, it is necessary to develop a more adequate theoretical approach taking into account non-stationary conjugate heat transfer into the oxide layer and into the basic metal, and phase transitions that occur in the system, at a power density of the heat flux ranging in the interval  $10^{10}$ - $10^{14}$  W/m<sup>2</sup> typical for vacuum arc removal of oxide layers.

The numerical study was performed with the use of the finite-element method developed in [3]. Different scenarios of evolved processes that include heating, evaporation of the oxide layer and simultaneous melting of the base, cooling and solidification of the melted layer are studied. In the numerical algorithm, constructed for possibly more accurate computation of the solidification phenomenon, a proper consideration was given to the melting interface and to the dynamics of the free surface of the oxide layer. In this connection, a novel procedure for dynamic adaptive triangulation of domains involved in the numerical solution by the given moment of time and characterizing different phase states (liquid or solid) of the materials was developed.

## 2. One-dimensional analysis of thermophysical processes

We assume that, at the time  $t=0$ , a constant heat flux of a power density  $q$  is fed to the surface of an infinite metal plate having a temperature  $T_{b0}$  and thickness  $H$  and covered by a very thin base-metal oxide layer of thickness  $\Delta_f \ll H$  (see Fig.1). The plate is assumed to be sufficiently thick, i.e.  $H \gg L = \lambda_{f0} T_{fe} / q$ , where  $\lambda_{f0}$  is the oxide thermal conductivity at the initial temperature,  $T_{fe}$  is the oxide evaporation point, and  $L$  is the characteristic internal linear scale of the problem. In what follows, to denote parameters, we use the following subscripts: the subscripts “ $f$ ” and “ $b$ ” refer respectively to layer and base parameters, and the subscripts “ $m$ ” and “ $e$ ” are additional superscripts that refer to problem parameters under melting and evaporation points. We are going to gain approximate solutions and estimates for heating and phase-transition processes for a model problem of vacuum arc cleaning of the surface of a base prepared from SUS 430 stainless steel covered by a 5  $\mu$ m thick Cr<sub>2</sub>O<sub>3</sub> oxide layer. The properties of involved materials are given below in Table 1.

It is known [1] that, at a pressure of  $10^5$  Pa, solid chromium oxide undergoes melting at a temperature of 2700 K and evaporation at a temperature of 3300 K. However, under a pressure of  $10^2$  Pa, typical for vacuum arc-assisted surface cleaning, solid chromium oxide evaporates bypassing melting right into the gas phase already at the temperature  $T_{fe}=2400$  K. According to reference data, the energy required for heating and evaporation of Cr<sub>2</sub>O<sub>3</sub> is  $L_{fe}=1.92 \cdot 10^7$  J/kg.



**Table 1.** Thermophysical properties of SUS 430 stainless steel and chromium oxide.

Material	$\rho$ kg/m <sup>3</sup>	$C$ J/kg·K	$\lambda$ W/m·K	$a=\lambda/\rho c$ m <sup>2</sup> /s	$T_m$ K	$T_e$ K	$L_m$ J/kg	$L_e$ J/kg
Stainless steel SUS 430	7700	585	26	$5.77 \cdot 10^{-6}$	1767	-	250000 <sup>(1)</sup>	-
Cr <sub>2</sub> O <sub>3</sub>	5210	795	13.2	$3.19 \cdot 10^{-6}$	2705	3280	$6.9 \cdot 10^5$	$3.86 \cdot 10^6$

<sup>(1)</sup> – As the latent heat for melting the SUS 430 stainless steel, the latent melting heat of pure iron is adopted.

In view of the afore-said, to perform a qualitative analysis of thermophysical processes in an oxide layer of thickness  $\Delta \sim 5 \mu\text{m}$  and in the metal substrate under various heat-flux power densities in the interval  $q=10^{10} \div 10^{14} \text{ W/m}^2$ , we may restrict the present consideration to the following sequence of time stages:

- 1) heating of the oxide-layer surface from initial temperature  $T_{f0}$  to the boiling point 2400 K during a time  $t_1$ ;
- 2) complete evaporation of the oxide layer during a time  $t_2$  with possible sub-melting of the metal base;
- 3) solidification of the melt formed on the base surface during the time  $t_3$ .

There were obtained the limiting estimates for the above stages, which are of interest for constructing an optimum computation algorithm by the finite-element method. In particular, these estimates include:

(i) the time  $t_1$  required for heating the oxide-surface layer to the evaporation point  $T_{fe}$ :

$$t_1 = 3[\lambda_{f0} \cdot (T_{fe} - T_{f0}) / q]^2 / 4a_{f0}, \quad (1)$$

(ii) lower estimate for the time  $t_2$  of complete evaporation of the oxide layer under an assumption that all the input heat goes into evaporation of this layer:

$$t_2 \cong \rho_{f0} L_{fe} \Delta_f / q, \quad (2)$$

(iii) lower estimate for the time  $t_3$  of solidification of the molten layer formed on the surface of the metal base under an assumption that this layer, of thickness  $\Delta_b$ , is heated uniformly and has a melting point  $T_{bm}$ :

$$t_3 = \left( 2\sqrt{2} \Delta_b L_{bm} / 3c_{b0} \sqrt{a_{b0}} (T_{bm} - T_{b0}) + \sqrt{t_1 + t_2} \right)^2 - (t_1 + t_2). \quad (3)$$

### 3. Computer two-dimensional simulation of the thermophysical processes

#### 3.1. Formulating the boundary-value problem

Let us formulate an axisymmetric boundary-value problem for the heating and phase transition processes that occur during the interaction of a vacuum arc spot with the surface of an oxide layer placed onto the surface of a semi-infinite metal base. Figure 1 shows a sketch of the calculation domain (here, the  $r$ -axis coincides with the interface between the layers, and the origin lies under the centre of the arc spot).

The boundary-value problem includes the following equations and boundary and initial conditions:

– heat conduction equation for the oxide layer and the substrate:

$$\rho_i c_i \partial T_i / \partial t = \text{div}(\lambda_i \text{grad } T_i), \quad i = f, b, \quad (4)$$

where  $\rho_i$ ,  $c_i$ , and  $\lambda_i$  are the density, heat capacity, and thermal conductivity of the  $i$ -th material;

– conjugating conditions for the temperature fields at the interface between the layers:

$$(\lambda_b \partial T_b / \partial n)_{-0} + (\lambda_f \partial T_f / \partial n)_{+0} = 0, \quad (T_b)_{n=0} = (T_f)_{n=0}; \quad (5)$$

– equation of steady evaporation for the oxide layer, included into the boundary-value problem from the moment at which the surface of the layer reaches the temperature  $T_{fe}$ :

$$\rho_{fe} L_{fe} d\zeta_f / dt = (\lambda_f \partial T_f / \partial n)_{-0} - q(t, r, \zeta_f), \quad T_f(t, r, \zeta_f) = T_{fe}, \quad (6)$$

where  $\mathbf{n}$  is the external normal to the evaporation-front surface;

– equation of steady melting of the metal layer, included into the boundary-value problem from the moment at which the layer-base interface reaches the melting point  $T_{bm}$  of the base material:

$$L_{bm} \rho_{bm} d\zeta_b / dt = (\lambda_b \partial T_b / \partial n)_{-0} + (\lambda_b \partial T_b / \partial n)_{+0}, \quad T_b = T_{bm}, \quad (7)$$

– initial conditions ( $t=0$ ):

$$\begin{aligned} T_f(r, z) &= T_{f0}, \quad (r, z) \in \{(r, z) / 0 \leq r \leq \infty; 0 \leq z \leq \Delta_f\}, \\ T_b(r, z) &= T_{b0}, \quad (r, z) \in \{(r, z) / 0 \leq r \leq \infty; -\infty \leq z \leq 0\}, \quad T_{f0} = T_{b0}; \end{aligned} \quad (8)$$

– boundary conditions, which specify:

a) heat flux at the arc-oxide layer contact spot:

$$(\lambda_f \partial T_f / \partial n)_{\Delta_f+0} = q(r), \quad (9)$$

b) uniform second-kind condition, set at all other boundaries:

$$\partial T / \partial n = 0. \quad (10)$$

From the arc-oxide layer contact spot, an axisymmetric heat flux with a known radial distribution of  $q=q(r)$  enters the calculation domain. In a simplest case,  $q(r)$  is set in the form of a step function  $q(r)=q_0\chi(r_0-r)$ , where  $\chi(r_0-r)$  is the Heaviside function defined as  $\chi(r)=1, r\geq 0, \chi(r)=0, r<0$ , and  $r_0$  is the radius of the arc spot.

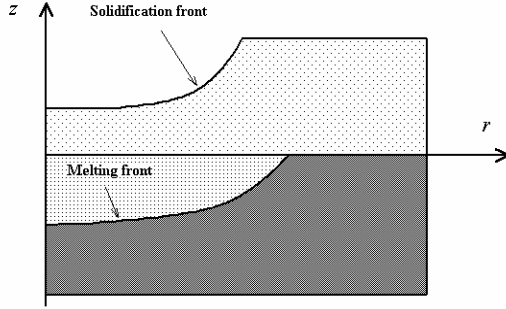


Fig. 1. Schematic of the calculation domain.

### 3.2. Determination of position of the phase-transition boundaries

The accuracy in solving the boundary-value problem (4)-(10) is largely determined by the accuracy in determining the position of the oxide-layer evaporation surface, for any point of which conditions (6) should be fulfilled. To construct the computation algorithm, we rewrite these conditions as

$$\begin{aligned} 1) & (\lambda_f \partial T_f / \partial n)_{\zeta_f+0} = q(t, r, \zeta_f), \\ 2) & (\lambda_f \partial T_f / \partial n)_{\zeta_f-0} = \rho_{fe} L_{fe} \cdot d\zeta_f / dt + (\lambda_f \partial T_f / \partial n)_{\zeta_f+0}, \\ 3) & T_f(t, r, \zeta_f) = T_{fe}. \end{aligned}$$

The first and second conditions are used as boundary conditions for Eq. (4). Hence, the calculated temperature fields will satisfy these conditions automatically. As for the third condition, it will be satisfied only if the position of the evaporation surface will be found with a sufficient accuracy. Since the computation-domain boundaries are approximated in the finite-element method as polygons, the evaporation surface will be represented by a broken line (see Fig. 2). Thus, we assume that the third condition is satisfied if this condition holds with a prescribed accuracy at all nodal points of the broken line.

To ensure the required accuracy in calculating the  $j$ -th time layer ( $j \geq 1$ ), we use the following iteration procedure for determining the evaporation-front position:

$$z_{j,n}^{(i+1)} = z_{j,n}^{(i)} - f_{j,n}^{(i)} \cdot (z_{j,n}^{(i)} - z_{j,n}^{(i-1)}) / (f_{j,n}^{(i)} - f_{j,n}^{(i-1)}), \quad r_{j,n}^{(i+1)} = r_{j,n}^{(i)} - f_{j,n}^{(i)} \cdot (r_{j,n}^{(i)} - r_{j,n}^{(i-1)}) / (f_{j,n}^{(i)} - f_{j,n}^{(i-1)}), \quad n = \overline{1, N}. \quad (11)$$

Here  $f_{j,n}^{(i)} = T_f(r_{j,n}^{(i)}, z_{j,n}^{(i)}) - T_{fe}$  is the residual function for the front temperature in the course of the iterations.

As a zero-order approximation ( $i=0$ ) for the coordinates of the front at the  $j$ -th time layer, we use the data gained at the previous,  $(j-1)$ -th layer, i.e.,  $z_{j,n}^{(0)} = \zeta_{j-1,n}$ . As a first-order approximation ( $i=1$ ), we use the estimate obtained by solving problem (9), i.e.

$$z_{j,n}^{(1)} = z_{j,n}^{(0)} - q_n \Delta t_j \cos \varphi_{z,j-1,n} / \rho_{f0} L_{fe}, \quad r_{j,n}^{(1)} = r_{j,n}^{(0)} - q_n \Delta t_j \cos \varphi_{r,j-1,n} / \rho_{f0} L_{fe},$$

where  $\varphi_{z,j-1,n}$  and  $\varphi_{r,j-1,n}$  are the local nodes formed by the normal to the evaporation-front surface and by the coordinate axes at the time  $t_{j-1}$ , and  $\Delta t_j$  is the step in time.

Since for  $i=0$  the heat conduction equations are modeled for the computation-domain geometry obtained at the previous time layer, then, apparently, in the near-surface region of the oxide layer there will appear a zone overheated above the boiling point  $T_{fe}$ .

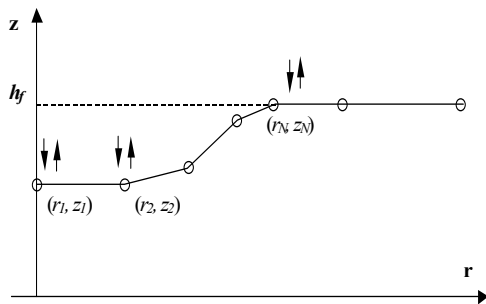


Fig. 2. Representation of the evaporation-front surface.

This zone will certainly be wider than the actual evaporation surface, since, as the oxide-layer evaporation surface moves down, there occurs heat absorption. It is also probable that part of grid points initially having fallen into the overheated zone subsequently will not be lying on the evaporation front, since, with the evaporation process taken into account, the temperature at these point may become lower than the temperature  $T_{fe}$ . Nevertheless, these points are not excluded from the iteration process because after minimization of the function  $f_{j,n}^{(i)} = T_f(r_{j,n}^{(i)}, z_{j,n}^{(i)}) - T_{fe}$  these points may happen to return to their initial position.

The iteration procedure for determining the coordinates of the melting/solidification front in the substrate is analogous to the above-described procedure, except for the fact that, unlike the evaporation surface, which gives off mass into environment, the melting/solidification front can move in the course of the iterations in an arbitrary direction.

### 3.3. General computation scheme

The modeling procedure for the physical processes in the system “stationary vacuum-arc spot – oxide layer – metal substrate” is based on the finite-element method and includes the following main stages: setting of initial conditions and thermophysical properties of materials, estimation of characteristic times of processes, construction of non-structured grids in sub-domains, organization of the computing process in time, and performing iterations for determining the temperature fields and position of phase-transition times (evaporation, melting/solidification) at a current time layer.

As it follows from the analysis performed, the processes proceeding as an arc spot interacts with a solid-body surface may have different time and spatial scales, and these scales may suffer drastic changes. The latter imposes substantial restrictions on time and spatial steps that can be used to solve the problem. In addition, the solution domain of the problem posed contains moving boundaries whose position and shape are the function of the solution. In view of this, we have developed a triangulation algorithm for arbitrarily shaped composite domains that belongs to the class of frontal algorithms and allows one to break a solution domain into triangles based only on its boundaries. This procedure makes it possible to use arbitrary grid steps in different materials, and also set local densening regions, which can be necessary, for instance, for ensuring a required accuracy in calculating temperature fields with high temperature gradients and at the moments at which evaporation, melting, or solidification fronts appear or disappear in the system. In performing solution-region triangulation, the requirement is also to be taken into account that deformation of different sub-regions of the solution domain for one step in time both in the horizontal and vertical direction must not exceed the grid step. The developed triangulation procedure previously was approbated by the present authors in modeling the dynamics and phase transitions during impingement of a melt drop onto a solid surface [3, 4].

To describe the general numerical algorithm for solving the boundary-value problem (4)-(10), we use induction with respect to  $j$ , where  $j$  is the subscript denoting the current time layer. Suppose that we have already obtained the numerical solution of the boundary-value problem at the moment  $t_{j-1}$ ,  $j \geq 1$ . If  $j=1$ , then, as the solution at the previous layer, we use the initial conditions (8). Under the solution, we mean the geometry of the region defined by the position of the phase-transition fronts and the temperature field. To gain the solution at the moment  $t_j = t_{j-1} + \Delta t_j$  ( $j \geq 1$ ,  $t_0 = 0$ ), we use the following algorithm:

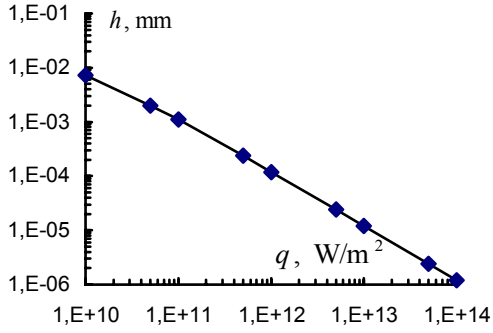
1. If the iteration number is  $i=0$ , then, as the computation-domain geometry, we use the geometry obtained at the  $(j-1)$ -th time step.
2. Then, we solve the heat conduction problem at the time step  $t_j$ .
3. We calculate the function  $f_{j,n}^{(i)} = T(r_{j,n}^{(i)}, z_{j,n}^{(i)}) - T_{fe}$  for all nodes that lie at the free surface of the oxide layer.
4. We check if the condition for convergence of the iteration process at the current time layer is satisfied. If the relative inaccuracies in determining the temperature field and the position of phase-transition fronts are smaller than a preliminarily set value, then we pass to calculation of the next time layer and then to Step 1; otherwise, we pass to Step 5.
5. If the iteration number is  $i=0$ , we determine all the nodes on the free surface of the oxide layer for which the inequality  $f_{j,n}^{(i)} = T(r_{j,n}^{(i)}, z_{j,n}^{(i)}) - T_{fe} > 0$  holds.
6. For all newly found nodes, we calculate their new coordinates; for  $i=1$ , we put  $z_{j,n}^{(1)} = z_{j,n}^{(0)} - q_n \Delta t_j \cos \varphi_{z,j-1,n} / \rho_{f0} L_{fe}$ ,  $r_{j,n}^{(1)} = r_{j,n}^{(0)} - q_n \Delta t_j \cos \varphi_{r,j-1,n} / \rho_{f0} L_{fe}$ ; for  $i \geq 1$ , to calculate the coordinates, we use formulas (11).
7. We pass to Step 2.

### 4. Some numerical results

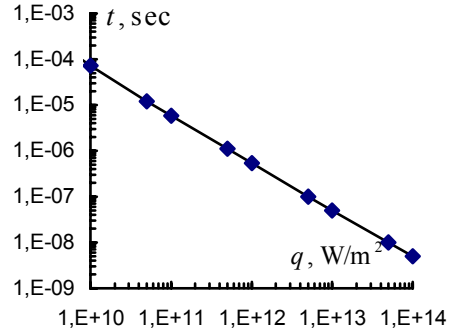
The authors of [2], using a simplified one-dimensional model disregarding the conjugate heat transfer between the oxide layer and the substrate and phase transitions in the substrate, attempted an estimate of the depth of substrate melting achieved by the moment of complete evaporation of the oxide layer in a wide range of heat-flux power densities in the arc spot.

Figure 3 shows results of the present similar study, performed using the above-formulated model and the proposed method for its numerical examination. As in [2], the oxide-layer thickness is taken to be  $\Delta_j = 5$  mkm. The adopted thermophysical properties are listed in Table 1, and the heat for chromium-oxide evaporation was taken to equal that previously used in [2],  $L_{fe} = 1.92 \cdot 10^7$  J/kg. The arc-spot radius is taken to equal the

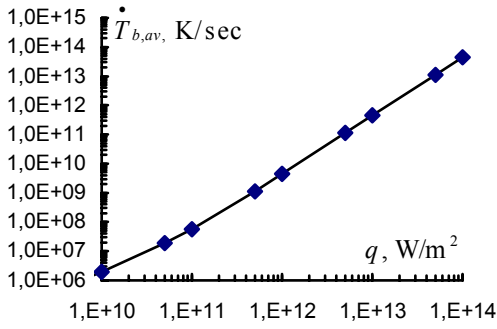
oxide-layer thickness,  $r_0=\Delta_f$ , and the heat flux is assumed to be uniform over the arc-spot area. For the chosen conditions, the computations were terminated when a complete evaporation of the oxide layer at  $r=0$  was achieved.



**Fig. 3.** Depth of the molten layer on the metal substrate as a function of the heat-flux power density.



**Fig. 4.** Time required for complete removal of the oxide layer at the center of the art spot as a function of the heat-flux power density.



**Fig. 5.** Mean cooling rate of the melt versus the heat-flux power density.

A substantial, both qualitative and quantitative, discrepancy between our results and the results previously obtained in [2] is worth noting. First, we found that, at the minimum heat-flux power density of  $q=10^8$  W/m<sup>2</sup>, substrate melting does take place but no oxide-layer evaporation occurs at all, whereas in [2] such evaporation was found to occur. Second, the thickness of the molten layer on the metal substrate at a fixed heat-flux density in the present study was found to be smaller than in [2], which difference can be explained by more adequate description of the simultaneously occurring physical processes in the present model. Figure 4 shows the predicted time for complete removal of the oxide layer at the symmetry axis of the arc spot as a function of the heat-flux density.

These data refine the data previously obtained in [1]. It is known that [1] after complete evaporation of a thin oxide layer by an arc spot; this spot changes its position on the substrate surface. Hence, just after the removal of the thermal flux, cooling and solidification of the melt previously formed at the surface of the metal substrate take place. It is of interest to estimate the local cooling rate of the melted layer due to heat removal into the substrate (auto quenching regime), since it is this parameter that governs the final microstructure of the molten layer.

According to [5], the current cooling rate during melt solidification can be represented as  $\dot{T}_b(t) = (\partial T_b / \partial z)_{z=\xi_b+0} \cdot (d\xi_b / dt)$ , where  $(\partial T_b / \partial z)_{z=\xi_b+0}$  is the temperature gradient in the melt at the solidification front at the time  $t$  and  $d\xi_b / dt$  is the solidification-front propagation velocity.

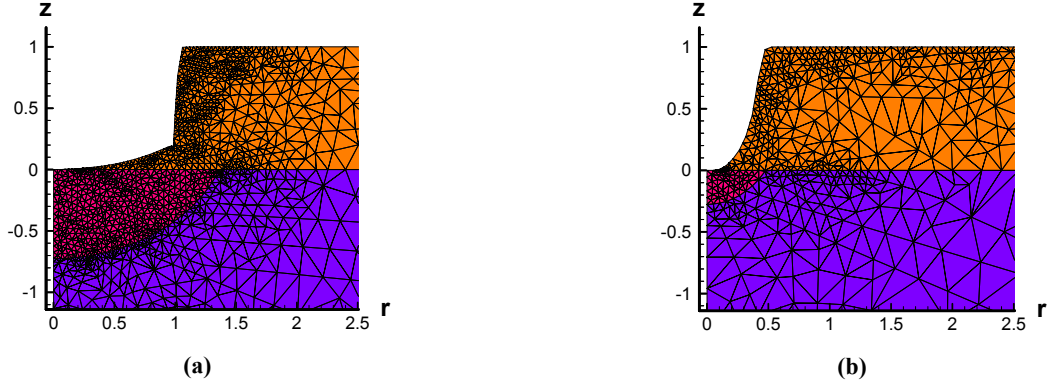
Let us perform the estimate for the symmetry axis, where the melt thickness is maximal. If  $t_3$  is the total time required for the melt to solidify, then the local mean cooling rate can be evaluated as

$$\dot{T}_{b,av} = (1/t_3) \int_0^{t_3} \dot{T}_b(t) dt = (1/t_3) \int_0^{t_3} (\partial T_b / \partial z)_{z=\xi_b+0} \cdot (d\xi_b / dt) \cdot dt.$$

Figure 5 shows the mean rate of melt cooling during solidification of the melt formed during the evaporation period of the oxide layer as a function of the heat-flux density. As is seen from Fig. 5, the cooling rate varies in rather a broad range of values (approximately from  $10^6$  to  $10^{13}$  K/sec). Hence, after the cleaning procedure the quenched near-surface layer of the substrate may display a structure ranging from microcrystalline to amorphous one.

All other things being equal, it is also of interest to examine the shape of the crater formed after the local oxide-layer evaporation and also the characteristics of the molten layer on the surface of the metal substrate for different distributions of the heat-flux intensity over the area of the vacuum-arc spot. To this end, along

with the case of a uniform areal distribution of the heat-flux density  $q_{eff}=10^{10}$  W/m<sup>2</sup> for  $r \leq r_0$ , we consider a normally distributed specific flux of the form  $q(r) = q_m \cdot \exp(-kr^2)$ , where  $q_m$  is the maximum local heat-flux density at the center of the arc spot,  $k$  is the heat-flux distribution parameter that defines the shape of the normal distribution, and  $r$  is the radial coordinate reckoned from the center of the arc spot. The results of computations performed for the above-indicated initial data and  $q_{eff}=10^{10}$  W/m<sup>2</sup>,  $k=9$ ,  $q_m \approx 2.89 \cdot 10^{10}$  W/m<sup>2</sup>, and  $r_s=1.535$   $\mu$ m are shown in Fig. 6.



**Fig. 6.** Effect of shape of the areal distribution of the heat-flux power density on the shape of the evaporation surface in the oxide layer and of the melting surface in the metal substrate. (a) – uniform heat flux, (b) – normally distributed heat flux.

As a criterion for terminating the computations, we used the condition of complete evaporation of the oxide layer at the axis of the arc spot. It is seen that, all other conditions being identical, the shape of the craters formed after the oxide-layer evaporation largely inherits the shape of the heat-flux distribution. The more concentrated heat flux with the chosen parameter  $k$  results in melting of a smaller microvolume of the metal substrate, which feature can be explained by the fact that the time necessary for complete evaporation of the oxide layer at the center of the arc spot in this case is substantially shorter than in the case with the uniform heat flux.

## 5. Conclusions

The results obtained in the present study can be summarized as follows:

- (1) A two-dimensional axisymmetric physico-mathematical model is developed, and a numerical method is proposed for studying the processes that take place during surface cleaning of metal substrates from oxide layers. The model makes it possible, in terms of non-stationary conjugate conductive heat transfer, to study oxide-layer evaporation with simultaneous melting, and subsequent cooling and solidification of the substrate microvolume under the arc spot, which seems to be essential for furnishing an adequate description for the thermophysical processes and for reliable prognostication of the state of the surface after the cleaning procedure.
- (2) Model computing experiments are performed; these experiments allowed us: (a) to find the melting depth of a stainless-steel substrate, initially covered by a 5- $\mu$ m thick chromium oxide layer as a function of the power density of the heat flux given to the substrate, for a fixed radius of the arc spot; (b) to compare the times required for complete evaporation of the oxide layer under various power densities of the heat flux in the arc spot as calculated by the proposed model with the analogous times predicted by the simplified one-dimensional model of [2]; (c) to estimate, for the first time, the cooling rate of the melted metal-substrate layer for various heat-flux densities; (d) to illustrate the influence of heat-flux non-uniformity on the shape of the evaporation surface in the oxide layer and characteristics of the metal-substrate microvolume melted by the moment of complete evaporation of the oxide layer.

## References

- [1] K.Takeda and S.Takeuchi – Materials Transactions, JIM. **38**, 7 ( 1997).
- [2] K.Takeda and S.Takeuchi – Thin Solid Films. **407** (2002).
- [3] O.P. Solonenko, E.P. Shurina and A.A. Golovin – Preprint 5-2000, ITAM SB RAS (2000).
- [4] O.P. Solonenko, E.P. Shurina and A.A. Golovin – Physical Mesomechanics. **4**, 1 (2001).
- [5] B. Chalmers. – Solidification, ASM, Metals Park, OH (1971).

# On electric physical measurements in electron beam air plasmas at moderate pressure

A. Ardelyan<sup>1</sup>, V. Bychkov<sup>1</sup>, O. Gordeev<sup>2</sup>

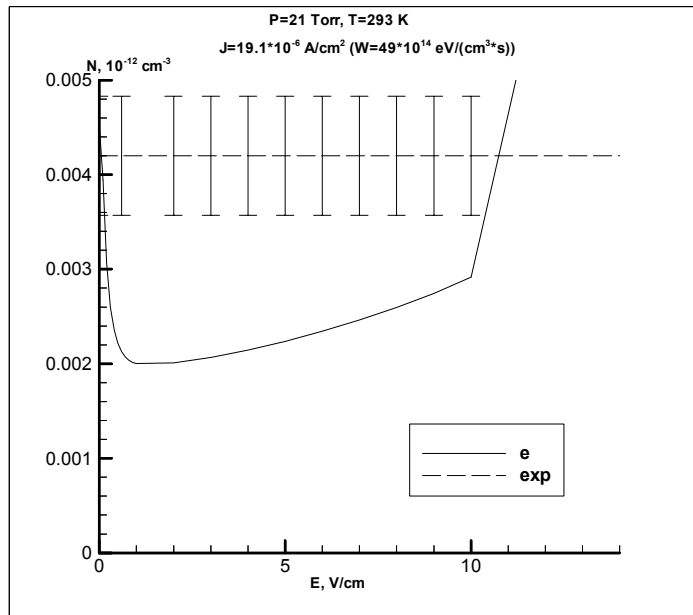
<sup>1</sup>Department of Physics, Moscow State University, Moscow, Russia

<sup>2</sup>Department of Physics, Moscow Aviation University, Moscow, Russia

Electron beam air plasmas is applied for creation of new materials, sterilization, treatment of waste gases etc. So it is necessary to have reliable data on electron concentrations or conductivity which are obtained with a help of antennas, resonator and other methods with applied external electric field [1,2]. In order to eliminate the influence of electric field the external power is usually chosen to be about of tens mW, this power is considered to weakly effect on increasing of electron temperature and is usually is not considered. However, in air plasmas at electron ionization level  $N_e/N < 10^{-6}$  the disregarding of external electric fields can lead to considerable mistakes due to electron energy dependence of the three-body electron attachment process with the participation of oxygen molecules [3]  $e + O_2 + O_2 \rightarrow O_2^- + O_2$  with the rate constant:

$$K_{att} = 1.7 \cdot 10^{-31} \cdot \sum_{j=1}^8 \frac{\alpha_j \cdot f(\varepsilon_j)}{1 + b_j \cdot (N_{O_2}, \text{cm}^{-3})}, \text{cm}^6 / \text{s}, \quad (1)$$

where  $f(\varepsilon_j) = \frac{2 \cdot e^{-\frac{\varepsilon_j}{T_e}}}{\sqrt{\pi} \cdot T_e^{3/2}}$ ,  $\varepsilon_j, \alpha_j, b_j$  are some coefficients, accounting creation of the ion in  $j$ - auto-ionizing state,  $T_e$  is electron temperature. This formula satisfies experiments, it shows the sharp increase at  $T_e \sim 0.09$  eV, and the rate constant decreasing with pressure. It is different from usually used formulae from [4]. Electron temperature in the range 0.06-1.3 eV corresponds to  $E/N$  parameter range 0.3-0.8 Td. So it is necessary to consider even low electric fields at analysis of electron beam plasmas.



In Fig.1 we represent our calculation results for electron-beam air plasmas including the components  $e_b, e, O_2^+, NO^+, O^+, O^-, O_2^-, O_3^-$ ,  $O, N, O_2(\Delta), O_2(v), N_2(v), N_2(A^3\Sigma_u^+), NO, O_3$ , equations for electron and gas temperatures were also applied for conditions of experiments [1] under the influence of external electric field at the electron beam excitation level  $W = 49 \cdot 10^{14} \text{ eV}/(\text{cm}^2 \text{ s})$ .

One can see that the external electric field can lead both to decrease and to increase of electron concentration. Difference between results at absence of low external electric field and with it can reach the factor of 2 and more. This proves necessity of accounting of electric fields at electric physical measurements of electron concentrations or conductivity in electron beam air plasmas.

Fig.1 Comparison of our calculations of electron air plasma concentrations with experiment [1] at  $P=21$  torr,  $T=293$  K,  $E_b=100$  keV for electron beam current density  $J_b=19.1 \cdot 10^{-6} \text{ A}/\text{cm}^2$ . Vertical lines with caps show the dispersion of experimental data.

[1] S.M. Antipov, V.N. Kononov, A.S. Koroteev - *Teplofizika Vysokikh Temperatur*. **23**, 170 (1985).

[2] R.R. Kikvidze, I.M. Minaev, A.A. Rukhadze, A.G. Shvarkunets- *Fizika Plazmy*. **10**, 976 (1984).

[3] N.L. Alexandrov-*Uspekhi Fizicheskikh Nauk*. **154**, 177, (1988).

[4] H. Matzing *Chemical kinetics of flue gas cleaning by electron beam*. Karlsruhe, 1989.

# Fabrication of Diamond-Like Carbon Films on Microextrusion Dies by Pulse Plasma Enhanced CVD

X.D. Yang<sup>1</sup>, Y. Inami<sup>1</sup>, N. Ohtake<sup>1</sup>, T. Saito<sup>2</sup>, Y. Nakamura<sup>2</sup> and Y. Kondo<sup>2</sup>

<sup>1</sup>*Department of Mechanical Sciences and Engineering, Tokyo Institute of Technology, Tokyo, Japan*

<sup>2</sup>*NGK INSULATORS, LTD., Nagoya, Japan.*

## Abstract

In order to improve wear resistance of microextrusion dies with numerous imperceptible holes, DLC film was deposited on the inner wall surface of model dies with holes of 2 mm, 0.9 mm in diameter and 20 mm in depth by using pulse plasma-enhanced CVD method. Wear resistance was evaluated by extrusion experiments using clay materials of cordierite composition ( $2\text{MgO}\cdot 2\text{Al}_2\text{O}_3\cdot 5\text{SiO}_2$ ). It was clearly shown that wear resistance of the inner wall surface against cordierite clay was significantly improved.

**Key words:** DLC, Pulse plasma, CVD, Inner wall surface, Microextrusion dies, Wear resistant

## 1. Introduction

Diamond-like carbon (DLC) films consist of amorphous carbon mixture with  $\text{sp}^3$  and  $\text{sp}^2$  bonding structures. As all of surface treatment materials, much attention has been paid to DLC film for its superior tribological characteristics decided by the  $\text{sp}^3$  bonding ingredient, such as its low coefficient of friction and high wear resistance [1-3]. Now, DLC film is significantly increasingly applied as a protective coating on the surface of devices such as hard disks and dies [4-5].

On the other hand, as represented by the dies employed in making the honeycomb ceramics used to treat exhaust gas generated in vehicles, it is very important to reduce the wear of microextrusion dies with numerous holes of about 1 mm diameter and 10 mm depth. Although a coating method has been desired to improve the wear resistance of the die, there still exists the problem that it is very difficult to coat DLC inside the inner wall surface because of the presence of numerous imperceptible holes. Therefore, as a kind of industrial application, it is very important to investigate the friction and wear action of inner wall surface of the holes.

In this paper, in order to improve the lifetime of stainless steel SUS630 (17-4PH) microextrusion dies which is used to extrude clay materials, DLC film was deposited on the inner wall surface of model dies with five holes of about 2 mm diameter and 20 mm depth by using pulse plasma-enhanced CVD method, then DLC film was estimated by Raman spectroscopy. Furthermore, in order to study friction and wear characteristic of DLC film, the ball-on-disk experiment was conducted after DLC film was deposited on Si wafer by using acetylene and methane. And then, the wear resistant performance of the die which was coated by DLC film was investigated through extrusion experiments of the clay materials.

## 2. Experimental

Fig.1 shows a schematic illustration of deposition apparatus. The apparatus consists of a pair of cathode and anode, a substrate holder and a vacuum chamber. By applying a negative pulse power with pulse repetition rates of 5 kHz and pulse duration of 20  $\mu\text{s}$ , the substrate holder is negatively charged to generate plasma. Acetylene was first used as the source gas and the pressure was controlled at a constant level during the deposition. In the actual die, although coating to a thin hole is the first subject of this research, the optimal deposition condition was not established yet. First of all, we experimented using a

model die since it is easy to evaluate various physical-properties values. The die has five holes of 2 mm in diameter and 20 mm in depth, and can be split into two parts through the central lines of holes. As shown in Fig.2, a Si wafer was inserted between the divided dies as a monitor substrate in order to characterize the properties in depth direction of DLC film which was deposited on the inner wall surface of die. And another Si wafer which attached to bottom surface of the dies was prepared as back cover of the holes to evaluate thickness distribution of DLC film. Before the deposition, stainless steel die with the inner wall surface roughness of  $R_z=400$  nm, which was cleaned ultrasonically in acetone for 10 minutes after fine grinding, was used it as the substrate.

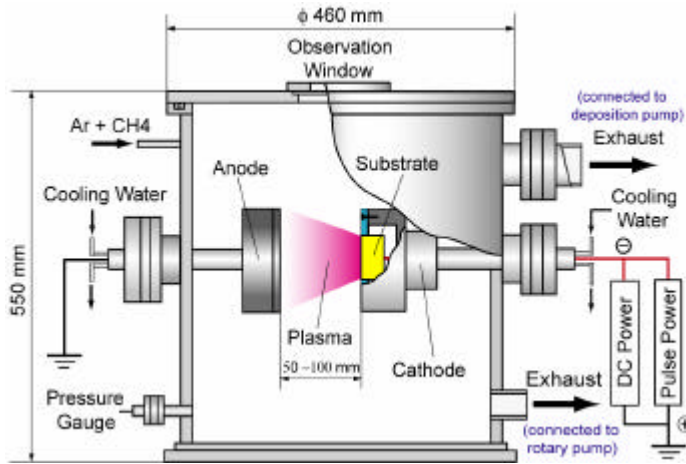


Fig. 1 Schematic illustration of deposition apparatus.

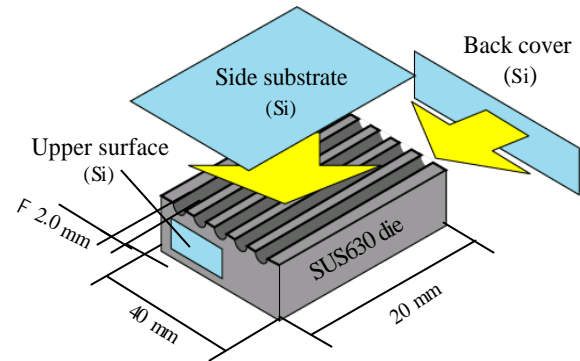


Fig. 2 Schematic illustration of the die and Si wafers.

Table 1 Deposition conditions

Pulse voltage (kV)	-4	-6	-8
Pressure (Pa)	3		
C <sub>2</sub> H <sub>2</sub> flow rate (cm <sup>3</sup> /min)	25		
Deposition time (min)	60		

First, the DLC film was deposited under deposition conditions of Table 1. In order to investigate the influence of pulse voltage to DLC film deposition, only the voltage was changed and pressure, gas kind, gas flux and deposition time were held to constant values. The chemical structure information of the deposited films was studied by Raman spectroscopy (JASCO, NRS-1000). The hardness of the DLC film was measured by using a nanoindenter (SHIMADZU, DUH-50) under the load of 14.7 mN (1.5 gf).

Then, thickness distribution of the DLC film deposited on Si back cover was measured. Two dies with holes diameters of 2 mm and 0.9 mm were used.

The friction and wear resistance characteristics are very important parameters for the microextrusion die. Before conducting an actual extrusion experiment using clay material to the die, a ball-on-disc experiment was conducted to investigating friction coefficient and ratio of wear volume of the DLC film deposited on Si wafer. The Si substrate with area about 30 mm × 30mm were stuck on the surface of cathode which applied with negative voltage of -8 kV, and DLC films were deposited on the Si substrates with acetylene and methane under the deposition conditions as shown in Table 2. Here, we have two reasons for using methane as one of source gas. One was to check whether there is any bombard effect to the Si substrates by using methane during the DLC film deposition. And other one was to distinguish the effect of methane and acetylene from viewpoint of wear resistant. Coefficient of friction and wear resistance were measured by the ball-on-disc method in our laboratory. All of the experiments were performed under un-lubricated conditions at the speed of 100 mm/s for a sliding distance of 500 m and the



normal load of 1.5 N. Stainless steel ball (SUS630, 5 mm diameter) slid against the film surface in the dry air condition. After the experiments, the coefficient of friction was defined as the ratio of measured tangential force with load cell divided by the normal force and wear tracks were observed and analyzed by atomic force microscope (AFM: SII, SPA300).

### 3. Results and discussion

Fig.3 shows the photographs of Si wafer which was inserted between the divided dies after the deposition under the conditions as shown in Table1. Length of the DLC film deposited on the surface of Si wafer was increased with the increasing of negative pulse bias voltages from -4 kV to -8kV. The Raman spectroscopic analysis and hardness measurement were performed every 2 mm along depth direction of the films from upper surface of the dies to Si back cover which was coated under the voltage of -8 kV.

Fig.4 shows the Raman spectra corresponding to the points in the depth direction of the films shown in Fig.3(c). Almost all spectrums which were observed along the depth direction are consisting of the G peak and D peak, which indicates that the films are confirmed to be the typical DLC film.

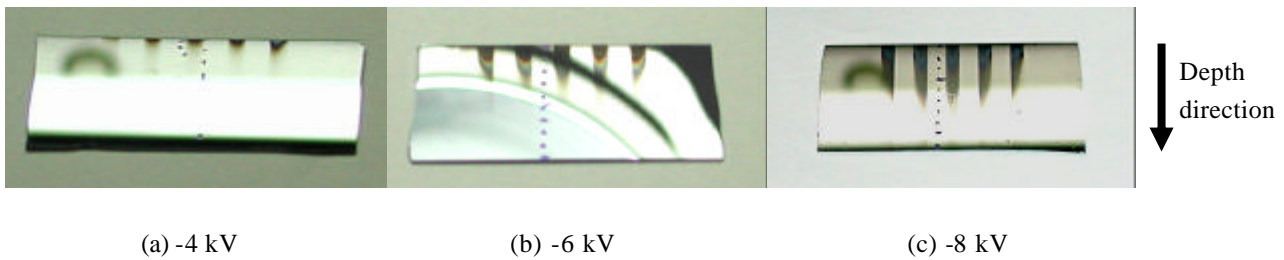


Fig.3 Photographs of side Si monitor substrate inserted between the divided dies after the DLC coating.

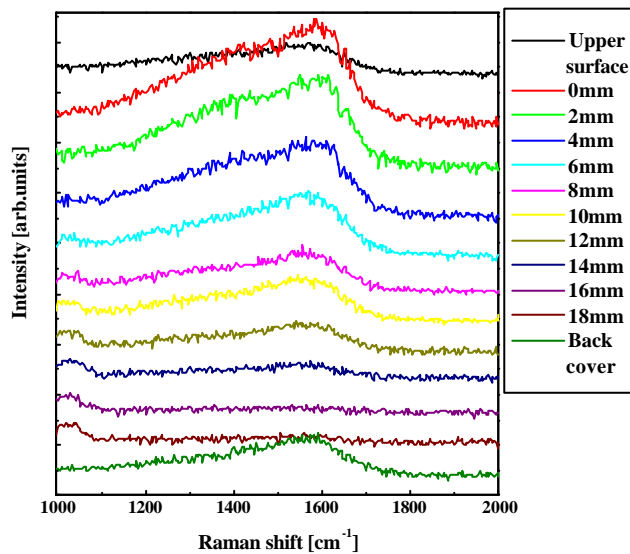


Fig.4 Raman spectra of DLC films deposited on side Si monitor substrate under the voltage of -8 kV.

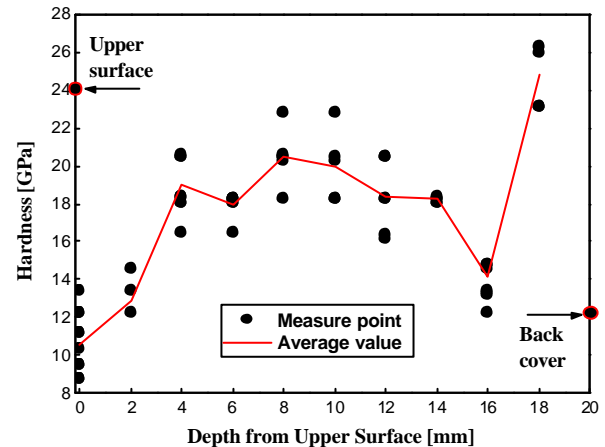


Fig.5 Hardness distribution of DLC films deposited on side Si monitor substrate along depth direction from under the voltage of -8 kV.

Moreover, hardness evaluation of the films was performed by using Si monitor substrate. In each position along the length direction of the films, the hardness was measured 20 times. Among these data, five maximum and five minimum values were omitted. At last, the hardness of the films which were deposited on the Si monitor substrate was calculated as average value from the ten remaining data. The result was showed in Fig.5. It was clearly that hardness increased sharply in the place near the Si back cover. It was thought that Electric field here tends to be concentrate when the Si back cover.

The hole with a diameter of 2 mm was studied above, but for the actually used die, there are many

kind of holes with different diameter, it is also very important to deposit DLC film on the bottom of different kind of hole. Here, we used two dies which have five holes with diameter of 0.9mm and 2mm respectively to investigate thickness distribution of the films which were deposited on the Si back cover. The films were deposited under the same conditions of the voltage of -8kv which was shown in Table 1. The photographs of the films deposited on the Si back cover were shown in Fig. 6. It is clarified that the film deposited clearly on the Si back cover which attached to the bottom surface of the dies. Through the Raman spectroscopic analysis, the deposited films are confirmed to be DLC film. The thickness distribution of the films was also measured. As shown in Fig. 6, we can see that the thickness of DLC film which was deposited in bottom of center hole corresponding to each die is the thickest with about  $0.7\ \mu\text{m}$ . Since the size of the cathode and the dies are almost the same, the intensity of plasma was most strong in the center of cathode, and then became weak gradually from the center to edge of the dies. In order to obtain a uniform thickness distribution of the films on the bottom of the dies which has many holes, it is necessary to consider size relation of cathode and die in future research.

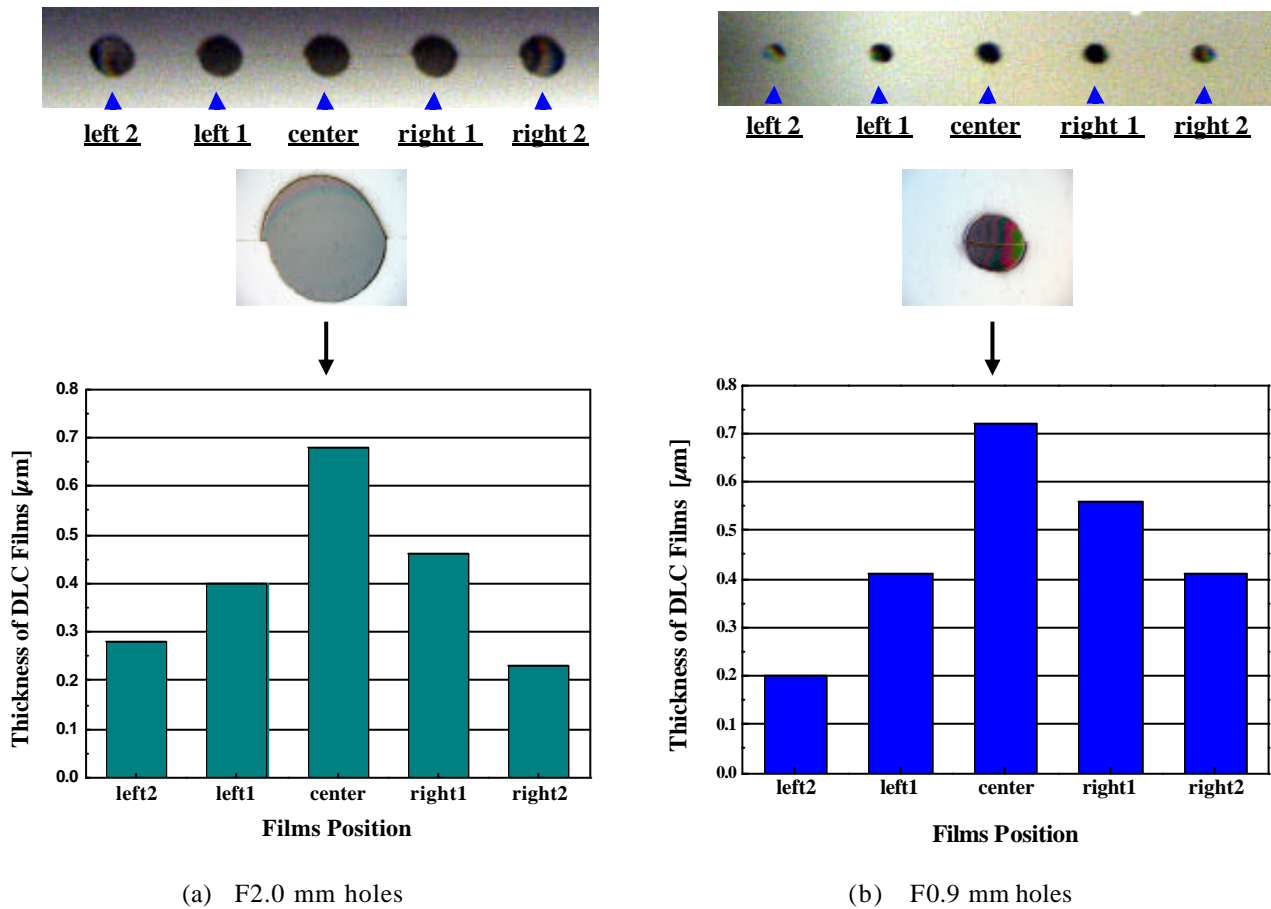
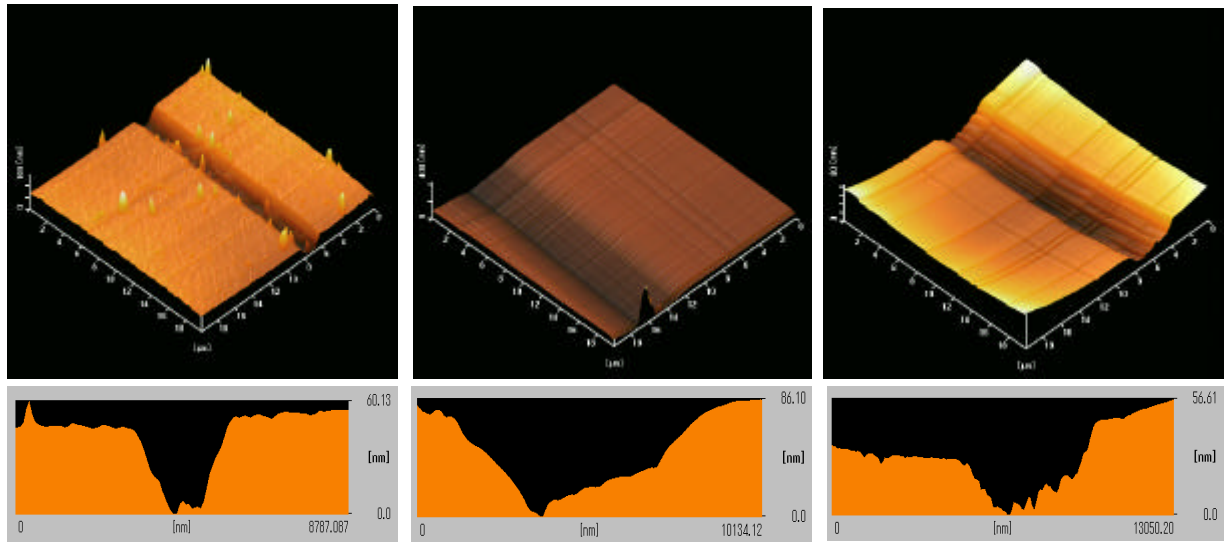


Fig. 6 Photographs and thickness distribution of DLC films deposited on Si back cover

The results of ball-on-disc experiment were shown in Fig. 8. Since the experiment was performed under dry air conditions, so the results showed high and unstable. The average coefficient of friction was about 0.28. Although the effect of using methane and acetylene was not clear enough, we can see the friction coefficient of DLC film which was deposited by using acetylene become the smallest after sliding distance exceed 150m. Wear tracks were analyzed by AFM, and the result was shown in Fig. 7. The surface of DLC film deposited by using acetylene and methane seems to be smooth. From the AFM result about the cross-section of wear tracks, we deduced the ratio of wear volume corresponding to the film before and after the ball-on-disc experiment. Compared with the other film deposited by using methane, the ratio of wear volume of the film deposited only using acetylene is the smallest. This result was clarified in Fig. 9.

Table 2 Deposition conditions

	Sample name	1	2	3
	Pressure (Pa)	3		
	Pulse voltage (kV)		-8	
	CH <sub>4</sub> flow rate (cm <sup>3</sup> /min)		28	
	Deposition time (min)		60	
	Pulse voltage (kV)	-8		
	C <sub>2</sub> H <sub>2</sub> flow rate (cm <sup>3</sup> /min)	25		
	Deposition time (min)	60		120



(a) C<sub>2</sub>H<sub>2</sub>, 60 minutes

(b) CH<sub>4</sub>, 60 minutes,  
C<sub>2</sub>H<sub>2</sub>, 60 minutes

(c) CH<sub>4</sub>, 60 minutes,  
C<sub>2</sub>H<sub>2</sub>, 120 minutes

Fig. 7 AFM images of wear tracks of DLC films after ball-on-disc experimental.

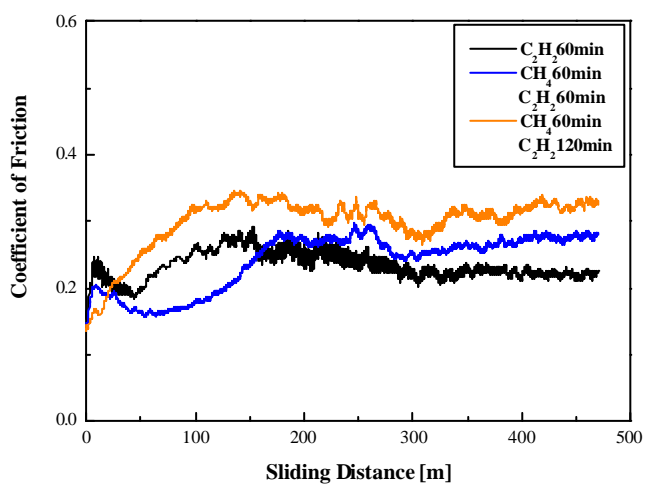


Fig.8 Frictional behavior of DLC films in dry air.

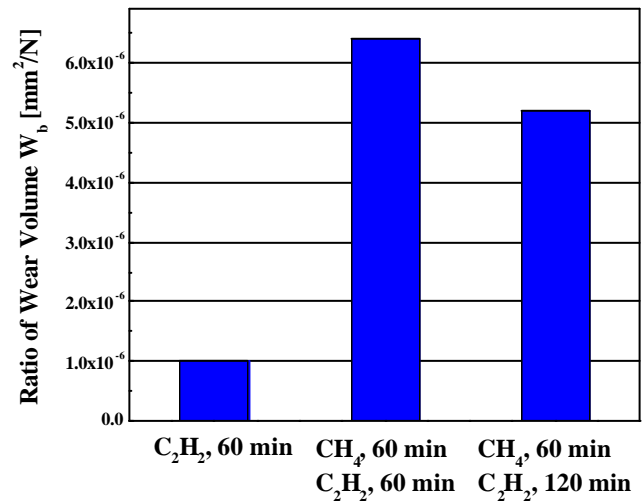


Fig.9 Ratio of wear volume of DLC films after ball-on-disc experimental.

Based on the above results, we decided to coat DLC films on an actual model microextrusion die, the optimal conditions is depositing 60 minutes under -8 kV by using only acetylene. The schematic illustration of one side of the microextrusion die was shown in Fig. 10(c). The die has only one hole of 2 mm in diameter and 20 mm in depth. It has the same composition as SUS630. In the die, flow is reduced through a 50  $\mu\text{m}$  slit near the bottom of hole. The die can be split into two parts through the central line of hole. In order to improve the adhesion between DLC film and inner wall surface of the die for extrusion examination, NiP buffer layer was employed between the DLC film and considered surface of the die. DLC film was deposited directly on the inner wall surface of the hole under the optimal conditions. After the deposition, the divided dies were jointed to evaluate wear resistance of DLC film by observing the optical micrographs of the position of reduced flow at the bottom of the hole. The extrusion experiments were conducted using clay materials with cordierite composition ( $2\text{MgO}\cdot 2\text{Al}_2\text{O}_3\cdot 5\text{SiO}_2$ ). Wear resistance was evaluated by observing the wear of DLC films at the position of reduced flow by optical microscope. The extrusion conditions were  $3\times 10^{-2}$  m/s extrusion speed and 5 ton extrusion force. Fig. 10 (a) shows photographs of one side of the dies after DLC coating. Furthermore, Enlargement photographs of the reduction flow position after DLC coating was shown in Fig. 10(b). No wear of the DLC film is observed after 1000 m extrusion experimental. It clearly shows not only the wear resistance of DLC film but also the adhesion strength between the DLC film and the microextrusion die can be improved greatly by using NiP buffer layer.

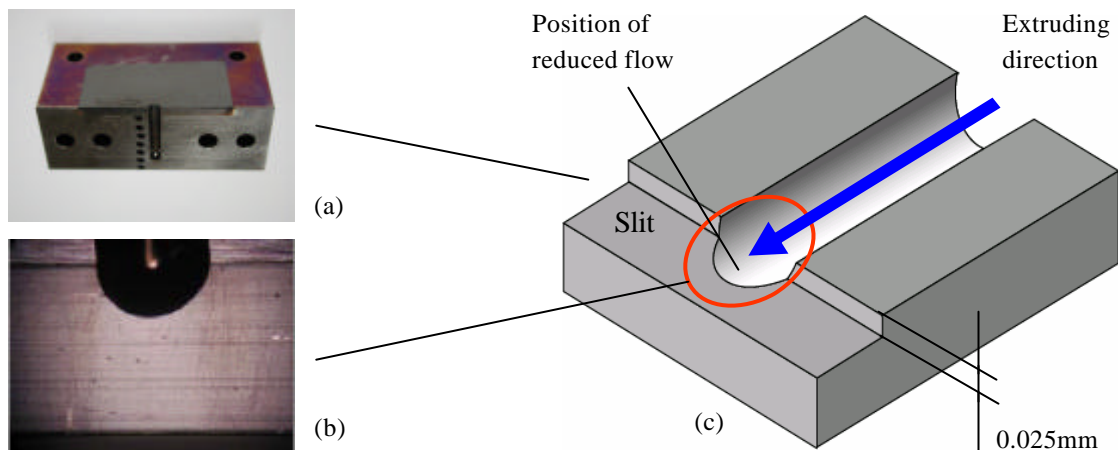


Fig.10 Photographs of position of reduced flow of the actual model microextrusion die after extrusion.

(a) Photographs of dies after DLC coating (b) DLC coated (c) Schematic illustration of the die

#### 4. Conclusions

DLC film was deposited successfully not only on the inner wall surface but also the bottom of the closed holes of 2 mm, 0.9 mm in diameter and 20 mm in depth by pulse plasma CVD. Furthermore, DLC was coated on the inner wall surface and reduction flow position of the model microextrusion dies with holes of 2 mm in diameter and 20 mm in depth. Wear resistance of the dies during extrusion was found to be significantly improved. The adhesion strength between the DLC film and the stainless microextrusion dies was improved notably applying NiP buffer layer. It was confirmed that the DLC film has excellent wear resistance against cordierite clay in the microextrusion process.

#### References

- [1] K. Miyoshi: Surf. Coat. Technol. 44 (1990) 799.
- [2] J. Robertson: Phys. Rev. Lett. 68 (1992) 220.
- [3] Al. H. Lettington: Carbon 36, No. 5-6, (1998) 555.
- [4] H. C. Tsai and D. B. Bogy: J. Vac. Sci. Technol. A 5(1987)3287.
- [5] A. Matthews and S. S. Eskildsen: Diamond Relat. Mater. 3(1994)902.

# 2D model of an rf hydrogen plasma and comparison with ion energy distribution measurements

R. Zorat, D. O'Connell, D. Vender, M.M. Turner and A.R. Ellingboe

*Plasma Research Laboratory,  
School of Physical Sciences and National Centre for Plasma Science and Technology,  
Dublin City University, Glasnevin, Dublin 9, Ireland*

## Abstract

An explanation of a numerical scheme coupling PIC simulation and a suitable global model of the simulated plasma is given. This scheme is used to model a capacitively coupled rf  $H_2$  discharge. IEDs for  $H_3^+$ ,  $H_2^+$  and  $H^+$  are presented, discussed, and compared with IEDs measured experimentally. The ion flux is mainly composed of  $H_3^+$ .  $H_2^+$  distributions are strongly affected by charge-exchange collisions in the rf sheath.

## 1. Introduction

Radio-frequency (rf) hydrogen plasma discharges are of interest for high performance injectors on next-generation hadron accelerators and in the research on negative ion sources to be used in neutral beam injection systems for heating and current drive in magnetically confined fusion plasma reactors. An important negative ion production mechanism in  $H_2$  plasmas is electron dissociative attachment (DA) of  $H_2(v)$ , with  $v$  being the vibrational excitation level of the hydrogen molecule. By increasing the value of  $v$  the cross section of this process increases dramatically [1,2], moreover the threshold energy decreases. Both effects increase the rate constant of the collision process. Usually, in Particle-In-Cell Monte Carlo Collisions (PIC-MCC) simulations of rf plasmas [3,4] only charged species are simulated, while neutral species are assumed to have a constant and uniform density, to be set arbitrarily. In PIC codes neutral densities are only used to calculate the collision probability of the computational plasma particles with these neutral species. The neutral densities are not calculated in the simulation, but to calculate the  $H^-$  production rate by DA, for a certain value of  $v$ , in  $H_2$  plasma discharges, it is necessary to also know the  $H_2(v)$  density, therefore modelling self-consistently the negative ion production by DA in a standard PIC simulation is not possible. In order to solve this problem a numerical scheme able to handle the chemistry of a plasma discharge has been developed [5]. In this scheme PIC simulation and a suitable global model of the simulated plasma interact iteratively by exchanging information. Some of the data exchanged are the neutral densities calculated by the global model and then delivered to the PIC. A further advantage of this scheme is that significantly less computational time is needed for the convergence of the simulated plasma towards its steady state than in a standard PIC simulation. This may be important for 2D simulations like the ones performed for this work.

Rf hydrogen plasma discharges are also of interest for their industrial applications. In processing plasmas the energy distribution of the positive ions arriving at the wall of the discharge chamber is an important factor in the effectiveness of processes such as plasma enhanced deposition and etching. Before hitting the surface of the chamber, positive ions are accelerated in the sheath, the positively charged region that forms between the plasma and the chamber wall. In rf plasmas the rf sheath dynamics, the rf modulation of the sheath potential and collisions in the sheath can have an important influence on the ion energy distribution (IED) of particles hitting the surface of the chamber wall. To study these effects, approximate analytical models, Monte Carlo and PIC simulations were developed, for a review see [6].

In this work first an explanation of the coupling scheme between PIC simulation and the suitable global model of the simulated plasma is given. Second, the experimental system is described and some specific information about the numerical method used is given. Third, species density profiles, IED and flux of the positive ion species simulated are presented and discussed. Finally, experimental IED measurements are compared with some of the IEDs obtained numerically.

## 2. The coupling scheme between PIC simulation and global model

Coupling a global model with a PIC simulation allows modelling of RF capacitively coupled plasma discharges with complex chemistry. As previously explained, the handling of the chemistry will be necessary if negative ions are to be included in the simulated hydrogen plasma. But the scheme also reduces significantly the computational time needed by the simulated plasma to converge towards its steady state.

Global models [7-9] have been used to study the gas-phase kinetics and the plasma chemistry in rf plasma discharges. By solving a set of non-linear equations composed of the species particle balance equations, the power balance equation and the quasi-neutrality condition, the averaged densities of the various species and the averaged electron temperature in the steady state can be calculated. The idea of this numerical scheme is to use the results of a global model of the PIC simulated plasma, which has some significant differences from a standard global model, to obtain an estimation of the densities of both charged and neutral species at the steady state. The effects of all volume collision processes included in the PIC have also to be included in the global model. Moreover, the effects of the collision processes needed to model the kinetics of the neutrals have to be included in the global model but not in the PIC. Since the global model can use the electron energy probability function (EEPF) obtained from the simulation, it makes sense to eliminate the electron temperature as an unknown in the set of equations of the global model. Consequently, the particle balance equation of one of the positive ion species has to be excluded as well from the set of equations. Another significant change to be made in the global model to make it interact with the PIC is the inclusion of an equation setting the ratio between positive and negative charge present in the system equal to the value of this quantity obtained from the PIC. The quasi-neutrality condition must be replaced by this new equation, because the former is satisfied only in the plasma bulk, not in the whole system simulated.

In the scheme, the PIC and the global model interact cyclically as follows: the PIC simulated plasma evolves for a time interval sufficiently long and a number of physical quantities are calculated in the simulation. Some of them are the EEPF, the rates of the collision processes, the averaged densities of the simulated species and the rates of their surface losses. The calculated quantities are used as input data for the global model of the same simulated rf plasma discharge. Then the global model calculates the densities of charged and neutral species to be used as input data for the PIC simulation. That information is used for both setting the neutral densities to be used in the PIC and eventually modifying the densities of the charged species before the PIC simulated plasma is made to evolve again.

### 3. Experimental and simulated system

The system modelled in this work is a capacitively coupled rf hydrogen plasma discharge created between two parallel-plate electrodes of equal area of diameter 140 mm and separated by a 50 mm gap. The discharge is radially confined between the electrodes by a cylindrical quartz tube, that both shields the discharge from the chamber walls and creates a pressure differential between the inside and the outside of the tube. Gas is introduced into the chamber through a shower-head arrangement in the grounded electrode. A 10  $\mu\text{m}$  orifice at the centre of the grounded electrode allows for the sampling of particles impinging on its surface by diagnostic systems. To measure the energy distribution of the particles arriving at the electrode for the different ion species present in the discharge, a two stage differentially pumped Hiden EQP is installed. This system is composed of an electrostatic ion energy analyser and a quadrupole mass spectrometer.

To model this system a 2D bounded electrostatic PIC simulation in cylindrical geometry ( $r, z$ ), coupled with a global model as previously described, was used. One of the electrodes is driven by an external voltage source while the other one is grounded. The simulated species are electrons and the three positive ions  $\text{H}^+$ ,  $\text{H}_2^+$  and  $\text{H}_3^+$ . The background neutral species included are  $\text{H}_2$ ,  $\text{H}_2(v=1)$ ,  $\text{H}_2(v=2)$ ,  $\text{H}$  and  $\text{H}^*(2s)$ . The collision process kinds included in the PIC simulation are ionization, electronic and vibrational excitation, dissociation, elastic scattering, charge exchange, collision induced dissociative (CID) reaction and the interchange reaction  $\text{H}_2^+ + \text{H}_2 \longrightarrow \text{H}_3^+ + \text{H}$ .

### 4. Results and discussion

All numerical results presented in this paper are obtained by setting a peak voltage of 200 Volt for the external rf power source in both the experiment and the simulation. Figure 1 shows the density profiles of the electron species and of the 3 positive ions included in the model at a pressure of 49 mTorr. In those graphs the x-axis is associated to  $r$ , the radial coordinate, while the y-axis is associated to  $z$ , the axial coordinate. The latter axis is actually the symmetry axis of the cylindrical chamber.  $\text{H}_3^+$  is the dominant positive ion species. In the plasma bulk  $\text{H}_2^+$  particles produced by electron ionization of  $\text{H}_2$  are efficiently converted into  $\text{H}_3^+$  particles through the interchange reaction previously mentioned. On the symmetry axis of the chamber ( $r = 0$ )  $\text{H}_3^+$  and electron density behave as expected; moving from the centre of the chamber to either of the electrodes ( $z = 0$  or  $z = 0.05$ ) those densities drop monotonically. In contrast, the  $\text{H}_2^+$  density is flattened in the plasma bulk, because the interchange reaction cross section is very high at energies less than 1 eV, but monotonically decreases very strongly if the energy increases. Therefore, slow  $\text{H}_2^+$  particles in the plasma

bulk are lost more efficiently through this reaction than fast  $H_2^+$  particles already accelerated in the sheath.  $H^+$  density even increases by moving from the plasma bulk to the electrodes. This happens because  $H^+$  particles are mainly produced through the CID reaction  $H_3^+ + H_2 \longrightarrow H^+ + H_2 + H_2$ . This process has higher cross section values at the energies positive ions typically have in the sheath than in the bulk, therefore a fraction of the  $H_3^+$  particles is converted to  $H^+$  particles and this happens more often in the sheath than in the bulk.

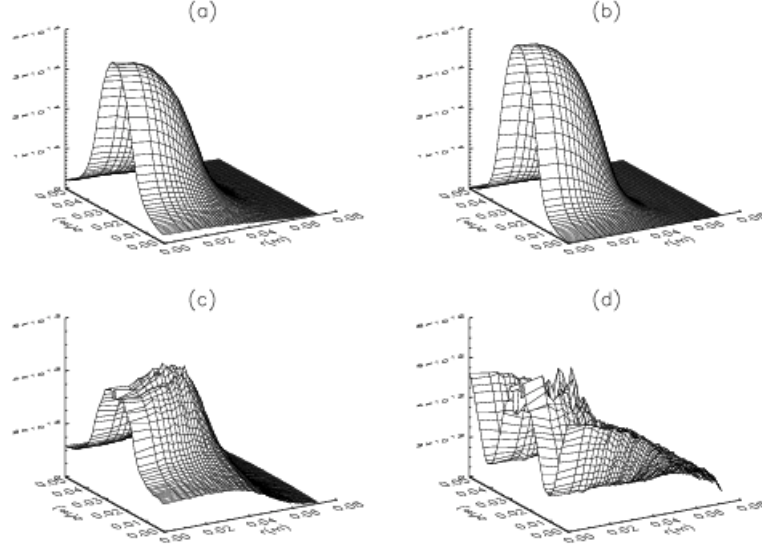


Figure 1: Time-averaged density vs. position ( $r,z$ ) of (a)  $H_3^+$ , (b)  $e$ , (c)  $H_2^+$  and (d)  $H^+$ ;  $p = 49$  mTorr,  $f = 13.56$  MHz

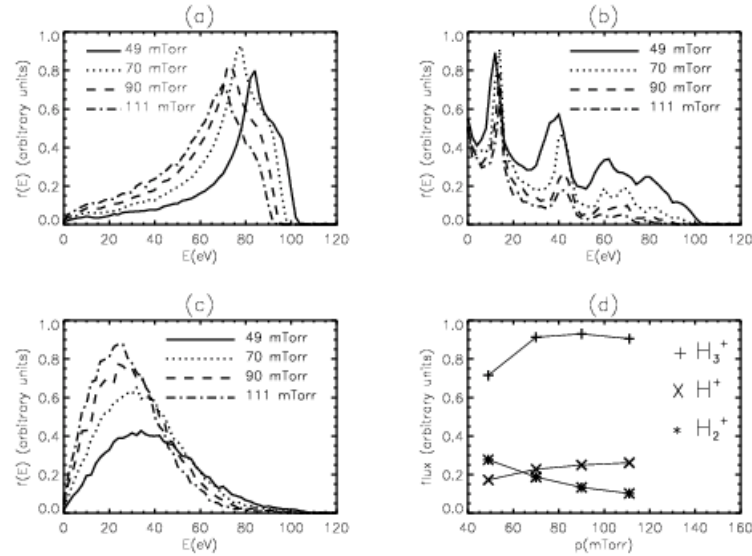


Figure 2: Energy distribution function of particles arriving at the central region of the grounded electrode at different pressures for (a)  $H_3^+$ , (b)  $H_2^+$ , (c)  $H^+$  species and (d) flux vs. pressure for the same species;  $f = 13.56$  MHz

In rf collisionless sheaths the ratio  $\beta = \tau_{ion}/\tau_{rf}$  between the ion transit time in the rf sheath,  $\tau_{ion}$ , and the rf period,  $\tau_{rf}$ , is a crucial parameter in determining the shape of the IED. If the ion transit time is a small fraction of the rf period ( $\beta \ll 1$ ), the sheath ion dynamics is in a low-frequency regime and the ions respond to the instantaneous sheath voltage. The resultant IEDF has a double peak structure, with the energy halfway between the two peaks being the time-averaged sheath voltage. The higher energy peak is produced by ions entering the sheath when the sheath voltage is near its maximum value during the rf cycle, while the lower



energy peak is produced by ions entering the sheath when the sheath voltage is near its minimum value in the cycle. In the high frequency regime ( $\beta \gg 1$ ) the ions respond only to the time-averaged sheath voltage, because they need many rf periods to cross the sheath. This makes the two peaks approach each other and if the value of  $\beta$  is high enough they will merge to form a single peak at the time-averaged sheath potential.

The flux of particles arriving at the grounded electrode and their IED were obtained for each positive ion species simulated. These IEDs were obtained for several values of pressure at the rf voltage source frequency  $f = 13.56$  MHz and are plotted in figure 2(a)-(d). All IEDs obtained from the PIC simulation shown in this paper are calculated by using the energies of positive ions hitting the electrode in its central region ( $0 < r < 0.035$ ). In the experiment the collection area in the centre of the grounded electrode is much smaller. But if the same region had been chosen in the simulation it would have taken a much longer computational time to obtain an acceptable sampling of the distributions, especially for the minority species  $H^+$  and  $H_2^+$ . The  $H_3^+$  distributions in figure 2a have a shape similar to the saddle-shaped expected for the low-frequency regime, although the second peak is missing. The remaining low-energy peak is placed at a value of the energy distinctly less than the average sheath potential, as expected. By increasing the pressure the average energy of the particles decreases, due to the decreasing average sheath potential. Moreover, the low energy tail becomes more pronounced because of the increased probability of producing less energetic  $H_3^+$  than their  $H_2^+$  parents in the sheath through the interchange reaction.  $H_2^+$  distributions in figure 2b have very pronounced peaks at energies much lower than the time-averaged sheath potential. These are produced by  $H_2^+$  charge exchange reaction in the sheath, efficiently converting fast  $H_2^+$  into slow  $H_2^+$ . By increasing the pressure the peaks become more pronounced. The dependence of the energy, of positive ions hitting the electrode, on the position where it enters the oscillating rf sheath and on the sheath oscillation phase when this happens determines the position of the peaks [10].  $H^+$  distributions shown in figure 2c have a single maximum at energies below 40 eV, indicating that  $H^+$  particles are efficiently created in the sheath. Figure 2d shows the ion fluxes at different pressures at the central region of the grounded electrode. The total flux in this region, being the sum of the 3 fluxes plotted, does not vary very much with increasing pressure.  $H_3^+$  is the main component of the flux.  $H_2^+$  flux significantly decreases with increasing pressure and the  $H^+$  flux increases. This is due to the bigger efficiency of the interchange reaction and of the CID process, converting  $H_2^+$  into  $H_3^+$  and  $H_3^+$  into  $H^+$ .

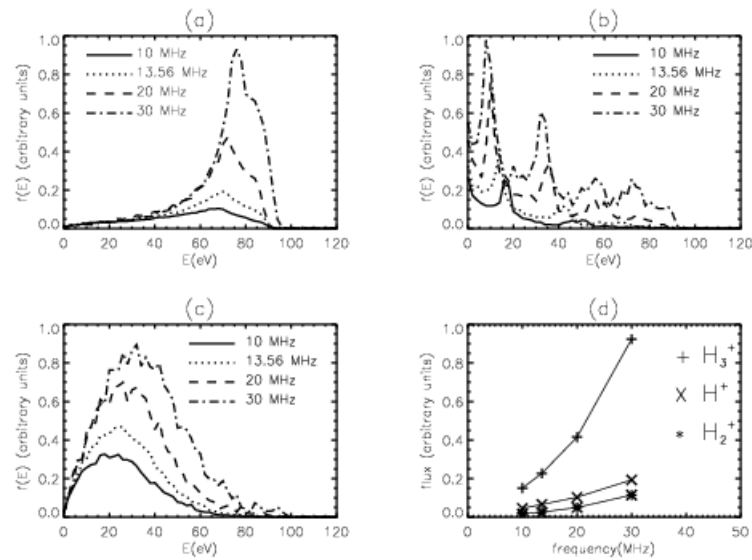


Figure 3: Energy distributions of particles arriving at the central region of the grounded electrode at different driving frequencies at  $p = 111$  mTorr for (a)  $H_3^+$ , (b)  $H_2^+$ , (c)  $H^+$  species and (d) flux vs. frequency for the same species.

The flux of particles arriving at the grounded electrode and their IED were obtained for each positive ion species simulated. These IEDs were obtained for several values of rf frequency at the pressure  $p = 111$  mTorr and are plotted in figure 3(a)-(d). By increasing the rf frequency the time-averaged sheath potential remains around 80 eV. The  $H_3^+$  distributions shown in figure 3a have a low energy peak. This peak is distinctly



below 80 eV.

The distributions become narrower by increasing the frequency and consequently increasing  $\tau_{rf} = 1/f$ , due to an increase in the value of  $\beta$ . The distributions of  $H_2^+$  are plotted in figure 3b. The peaks become more pronounced by increasing the frequency and at 30 MHz there is also a significant contribution to the IED at energies around the average sheath potential.  $H^+$  distributions in figure 3c have a single maximum at energies below 40 eV, once again it indicates that  $H^+$  particles are efficiently produced in the sheath. The fluxes plotted in figure 3d show that for all positive ion species the flux increases with increasing frequency, due to the increasing plasma density, and the  $H_3^+$  component of the total flux is the most important at all frequencies.

## 5. Comparison with ion energy distribution experimental measurements

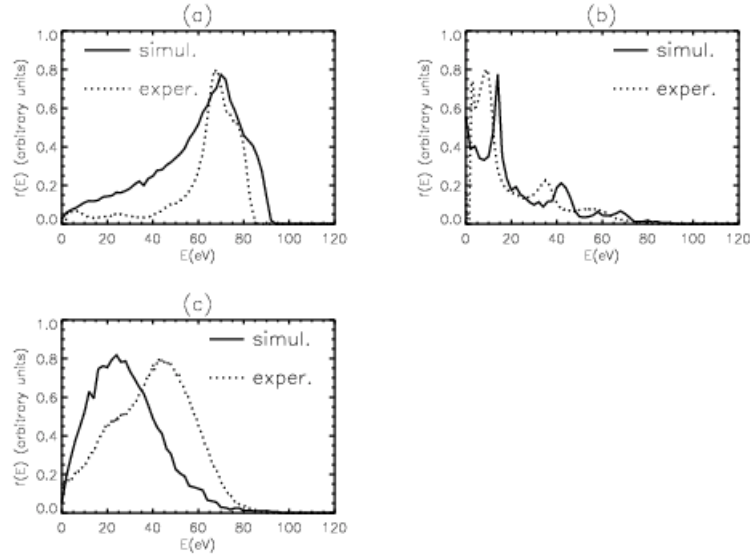


Figure 4: Energy distributions for particles of the species (a)  $H_3^+$ , (b)  $H_2^+$  and (c)  $H^+$  arriving at the central region of the grounded electrode compared with experimental measurements at  $p = 111$  mTorr,  $V = 200$  Volt and  $f = 13.56$  MHz

In figure 4(a)-(c) IEDs measured experimentally in an rf capacitively coupled  $H_2$  discharge at  $V = 200$  Volt,  $p = 111$  mTorr and  $f = 13.56$  MHz are compared with the IEDs obtained from the numerical model at the same operating conditions. The shapes of the two  $H_3^+$  distributions shown in figure 4 have many similarities. The low energy peak is placed nearly at the same energy and at higher energies the trend of the distribution is the same. The difference at lower energies may be explained by the different particle sampling in the simulation and in the experiment.  $H_3^+$  particles deflected by collisions in the sheath may arrive at the electrode with a velocity component parallel to the electrode too big with respect to the perpendicular component to allow sampling in the experiment. But in the simulation the particles are sampled regardless of their colliding angle. In figure 4b both  $H_2^+$  distributions have the same structure in the whole energy range, except for energies less than 10 eV. In the experiment the peaks are positioned at lower energies than in the simulation, possibly due to power losses, resulting in a lower effective peak voltage in the experiment. This would also explain the difference in the peak position in the  $H_3^+$  distribution. In figure 4c the two  $H^+$  distributions do not look as similar as the  $H_3^+$  and the  $H_2^+$  ones where the distance between the corresponding peaks is just a few eV. In fact, in this case the peak distance is nearly 20 eV.

## 6. Conclusions

In this work an explanation of the coupling scheme between a PIC simulation and a suitable global model of the simulated plasma was given. Species density profiles, IEDs and fluxes of the positive ion species arriving at the central region of the grounded electrode in a capacitively coupled rf hydrogen discharge, modelled using this numerical model were presented. The averaged density profiles of the positive ion species simulated exhibit significant differences, due to the different mechanisms for their production and loss and to

their different efficiency in the different regions of the discharge.  $H_3^+$  is the main component of the ion flux in the central region of the grounded electrode. In the  $H_3^+$  energy distributions presented the distribution monotonically decreases from the low energy peak to lower energies in the pressure and frequency regimes considered. Therefore, collisions in the sheath just create a higher tail at low energies, but do not distort the shape of the distribution. In contrast,  $H_2^+$  distributions are strongly affected by charge-exchange collisions in the sheath, presenting pronounced secondary peaks at energies significantly less than the time-averaged sheath voltage.  $H^+$  are mainly produced in the sheath and their IED peaks at energies always less than half the time-averaged sheath voltage. Comparison of experimental IED measurements with some of the IEDs obtained numerically give reasonably good agreement, particularly for  $H_3^+$  and  $H_2^+$ .

### Acknowledgment

This work is supported by Association EURATOM DCU Contract ERB 5004 CT960011

### References

- [1] M. Allan, S.F.Wong, Phys. Rev. Lett. **41**, 1791 (1979).
- [2] J.M. Wadhera, J.N. Bardsley, Phys. Rev. Lett. **41**, 1795 (1979).
- [3] C.K. Birdsall, IEEE Trans. Plasma Sci. **19**, 65 (1991).
- [4] M. Surendra, D.B. Graves, IEEE Trans. Plasma Sci. **19**, 144 (1991)
- [5] R. Zorat, D. Vender, M.M. Turner, 16<sup>th</sup> ESCAMPIG and 5<sup>th</sup> ICRP proceedings **2**, 255 (2002).
- [6] E. Kawamura, V. Vahedi, M.A. Lieberman, C.K. Birdsall, Plasma Sources Sci. Technol. **8**, R45, (1999)
- [7] C. Lee, D.B. Graves, M.A. Lieberman, D.W. Hess, J. Electrochem.Soc. **141**, 1547, (1994)
- [8] C. Lee, M.A. Lieberman, J. Vac. Sci. Technol. A **13**, 368, (1995)
- [9] R. Zorat, D. Vender, J. Phys. D: Appl. Phys. **33**, 1728, (2000)
- [10] C. Wild, P. Koidl, J. Appl. Phys. **69**, 2909 (1991)

# Numerical characterization of converging jet in a triple torch plasma system

K. Ramachandran, H. Nishiyama

*Institute of Fluid Science, Tohoku University, Sendai, Japan*

## Abstract

Triple torch plasma system is used for material processes to increase the process efficiency. A numerical model is developed to characterize the structure of the thermo-fluid fields of the converging plasma jet in a triple torch plasma system. The thermo-fluid fields of the converging plasma jet are symmetric with three symmetric sections at an interval 120°. Symmetry and uniformity of thermo-fluid fields are improved in the downstream. Central gas injection decreases the temperature of the converging jet at the geometric center.

## 1. Introduction

Thermal plasma torches are being used in wide range of industrial applications [1], such as plasma spraying, waste treatment, chemical vapor deposition and production of ultra-fine particles. The steep temperature and velocity gradients in the plasma jet and small plasma volume are disadvantages for the material processing. To overcome these disadvantages, a triple torch plasma system is used for spraying [2] and new material synthesis [3] etc. Three individual plasma jets are coalesced and form a converged jet in a triple torch plasma system. Asmann *et al* [4] have carried out enthalpy probe measurements on converging plasma jet in a triple torch plasma reactor. Another experimental study using spectroscopic technique on this topic is found in the literature [5]. However, these experimental studies could not provide the complete structure of the converging plasma jet. The numerical modeling is being used to clarify the complex flow structures. However, there is no modeling work on converging plasma jet at present. The objective of the present work is to investigate the converging plasma jet structure in the triple torch plasma system numerically. The complete geometry and experimental parameters of the triple torch plasma system, used for the measurements [4, 5], are not available in the literature. Hence, as a first step, we clarify the converging plasma jet complex structure for given geometry and process parameters in the present study.

## 2. Description of the model

The following assumptions are included in the converging plasma jet model:

1. The plasma is in local thermodynamic equilibrium (LTE) and optically thin.
2. Turbulent argon plasma jets discharge into argon at atmospheric pressure.
3. Unsteadiness due to the interaction of plasma jets is negligible.

The general form of governing equations used to simulate the converging plasma jet is given in equation (1).

$$\text{div}(\rho \mathbf{V} \phi) = \text{div}(\Gamma_{\phi} \text{grad} \phi) + S_{\phi} \quad (1)$$

where  $\rho$  and  $\mathbf{V}$  are density and velocity vector respectively. The exchange coefficients ( $\Gamma_{\phi}$ ) for the solved variables ( $\phi$ ) are

$$\Gamma_{\mathbf{V}} = \mu_l + \mu_t ; \Gamma_h = \mu_l / \text{Pr}_l + \mu_t / \text{Pr}_t \quad (2)$$

The subscripts l and t denote laminar and turbulent.  $\text{Pr}$ ,  $\mu$  and  $h$  are Prandtl number, viscosity and enthalpy respectively. The turbulent Prandtl number ( $\text{Pr}_t$ ) is fixed to 0.70. The pressure gradient in the momentum equations and radiation of heat in energy equation are source terms ( $S_{\phi}$ ). The standard k- $\epsilon$  model is used to take into account the turbulent characteristics of the plasma jets. The exchange coefficients and source terms for turbulent kinetic energy ( $k$ ) and dissipation rate ( $\epsilon$ ) used here are same as used by Eichert *et al* [6]. The size of the computational domain in the present model is 15 cm in the axial (Z), 4.5 cm in the radial (Y) and  $2\pi$  rad in the azimuthal (X) directions. In this preliminary study, we employed 160,000 elliptic-staggered grid points in the computational domain (50 in Z, 40 in Y and 80 in X directions).

In the present model, inlets (nozzle exits) having a diameter of 6.35 mm are set at the top boundary with an interval of  $120^\circ$  in X direction. The remaining top boundary is open. The distance between the geometric center and axis of the each torch is 1.27 cm. The angle of convergence ( $\alpha$ ) of the each plasma jet is set to be  $45^\circ$ ,  $30^\circ$  or  $15^\circ$ . At bottom and side boundaries, pressure is fixed at atmospheric pressure and flow can move to either direction. The effective power and mass flow rate of argon for each plasma torch are 3.64 kW and  $7.02 \times 10^{-4}$  kg/s respectively. A flat temperature and velocity profiles are given at an inlets for simplicity. Radial ( $v$ ) and axial ( $w$ ) velocities are derived from resultant velocity, calculated from mass flow rate of the plasma gas.

$$v = R \sin \alpha \text{ and } w = R \cos \alpha \quad (3)$$

The turbulent kinetic energy and dissipation rate at the inlets are assumed to be  $0.005R^2$  and  $0.1k^2$  respectively. To investigate the effect of central gas injection, cold argon is injected as a central gas at the geometric center. Radius of the central gas inlet is 0.733 mm. Mass flow rate of the central gas is 14.25 % of total mass flow rate of the plasma gas. Phoenix CFD code [7] is used to solve continuity, momentum, energy, turbulent kinetic energy, and dissipation rate equations.

### 3. Results and discussion

Figures 1(a) and 1(b) show the simulated converging plasma jet temperature and axial velocity fields respectively. In this case, three individual plasma jets are converged with an angle of convergence of  $30^\circ$ . Outline of the jet represents the temperature of 1000 K and velocity of 50 m/s.

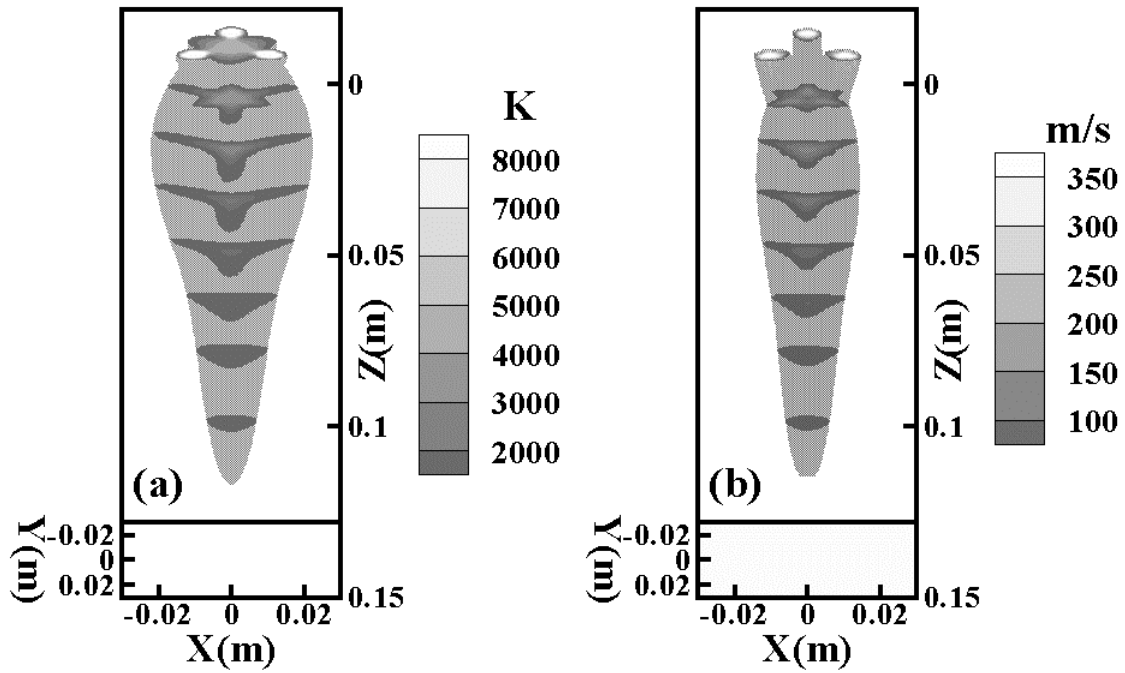


Figure 1. Converging jet (a) temperature and (b) axial velocity fields ( $\alpha = 30^\circ$ )

The temperature and axial velocity fields appear to be axially symmetric. But the radial cross sections of these fields show the three symmetric sections at an interval of  $120^\circ$  in an X direction that reflect the input boundary conditions. The interaction among plasma jets increases with increasing axial distance from the nozzle exit. The maximum strength of interaction appears around the converging point (the point at which all torch axes crossing in an axial direction). Here, radial flow of heat and radial transfer of momentum are higher than that in other places. Beyond this distance, the strength of interaction decreases with increasing axial distance. The symmetry and uniformity of the converging plasma jets temperature and axial velocity fields are improved in the downstream.

Figures 2(a) and 2(b) show the radial distribution of temperature of the converging plasma jet for an angle of convergence of  $45^\circ$  and  $15^\circ$  respectively. Results are shown along the line defined by the projection of the axis of one of the torches onto the horizontal plane. The converging point of three jets in an axial direction is  $Z = 1.27$  cm for  $\alpha = 45^\circ$  and is  $Z = 4.74$  cm for  $\alpha = 15^\circ$ . The interaction between the plasma jets is higher at larger  $\alpha$  than at smaller  $\alpha$ . Also the plasma jets are mixed more rapidly at larger  $\alpha$  than at lower  $\alpha$ . The flow of heat in the radial direction is higher at larger  $\alpha$  whereas the flow of heat is higher in axial direction at lower  $\alpha$ . The symmetry and uniformity of the converging jet temperature are improved at the converging point or in the downstream for lower  $\alpha$  (figure 2(b)). Also the length and volume of converging plasma jet is increased at lower  $\alpha$ . The strength of interaction, which determines structure of the converging jet, between the plasma jets depends on  $\alpha$ .

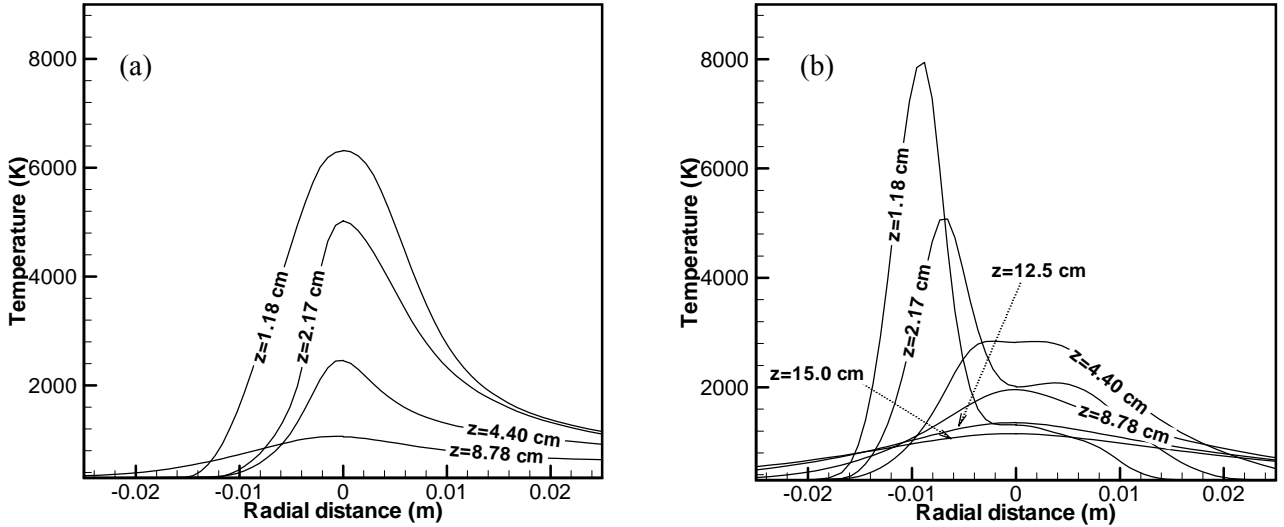


Figure 2. Radial distribution of the converging plasma jet temperature at an angle of convergence (a)  $45^\circ$  and (b)  $15^\circ$

Figures 3(a) and 3(b) show the radial distribution of the converging jet axial velocity for an angle of convergence of  $45^\circ$  and  $15^\circ$  respectively along the line defined by the projection of the axis of one of the torches onto the horizontal plane. The radial distribution of axial velocity shows a small dip at the geometric center at  $Z=1.18$  cm in the case of  $\alpha = 45^\circ$ . The dip does not appear beyond this distance or in the temperature distribution (figure 2(a)). The dip in the velocity corresponds to slower mixing of velocity fields than temperature fields. Since mixing is improved in the downstream, the dip is disappeared.

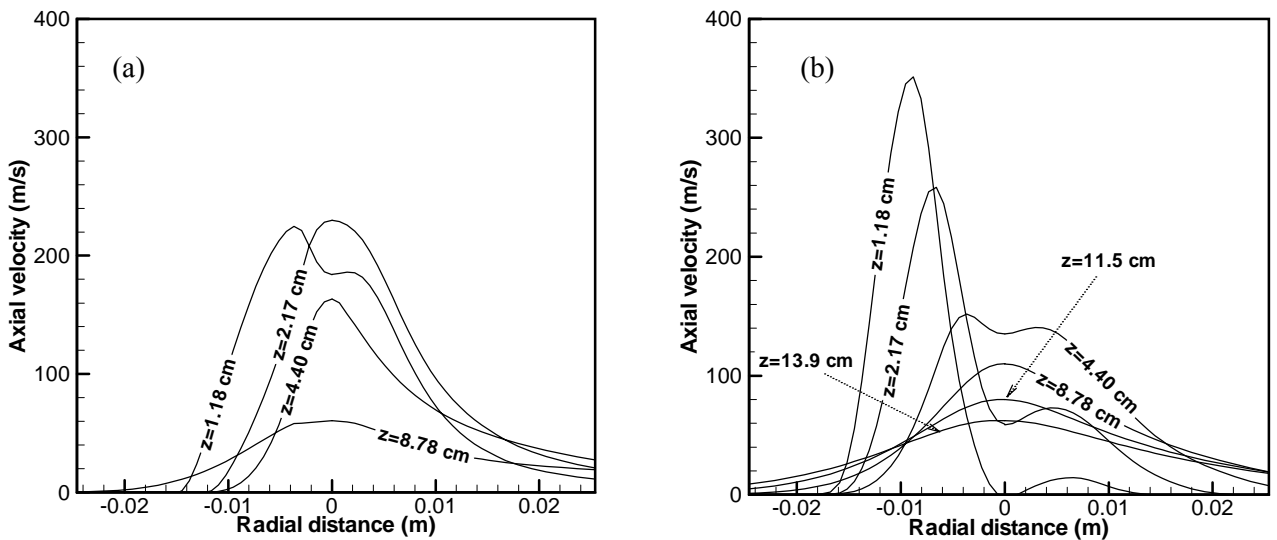


Figure 3. Radial distribution of the converging jet axial velocity at an angle of convergence (a)  $45^\circ$  and (b)  $15^\circ$

The dip decreases with increasing axial distance (figure 3(b)). The dip does not appear beyond the converging point. The axial velocity also shows improved symmetry and uniformity in the downstream. Figures 4(a) and 4(b) show the radial cross-section of converging jet temperature with velocity vectors at  $Z=2.17$  cm for  $\alpha = 45^\circ$  and  $\alpha = 15^\circ$  respectively. It is noticed that the angle of convergence plays important role to determine the form of the converging jet temperature fields. Three plasma jets are mixed at larger  $\alpha$  whereas the mixing is on half way at smaller  $\alpha$ . The complete mixing of temperature takes long axial distance at smaller  $\alpha$ . Figures 5(a) and 5(b) show the radial cross-section of converging jet axial velocity with velocity vectors at  $Z=2.17$  cm for  $\alpha = 45^\circ$  and  $\alpha = 15^\circ$  respectively. The results of axial velocity are similar to that of temperature. At a given angle of convergence, slower mixing of axial velocity than temperature is noticed by comparing the figures 4 and 5. No entrainment of cold gas from surroundings to the geometric center is evident from velocity vectors. Hence the presence of dip in the axial velocity is due to poor mixing of three individual plasma jets velocity fields. The poor mixing may be due to lower velocity gradients and lower turbulent and laminar exchange coefficients.

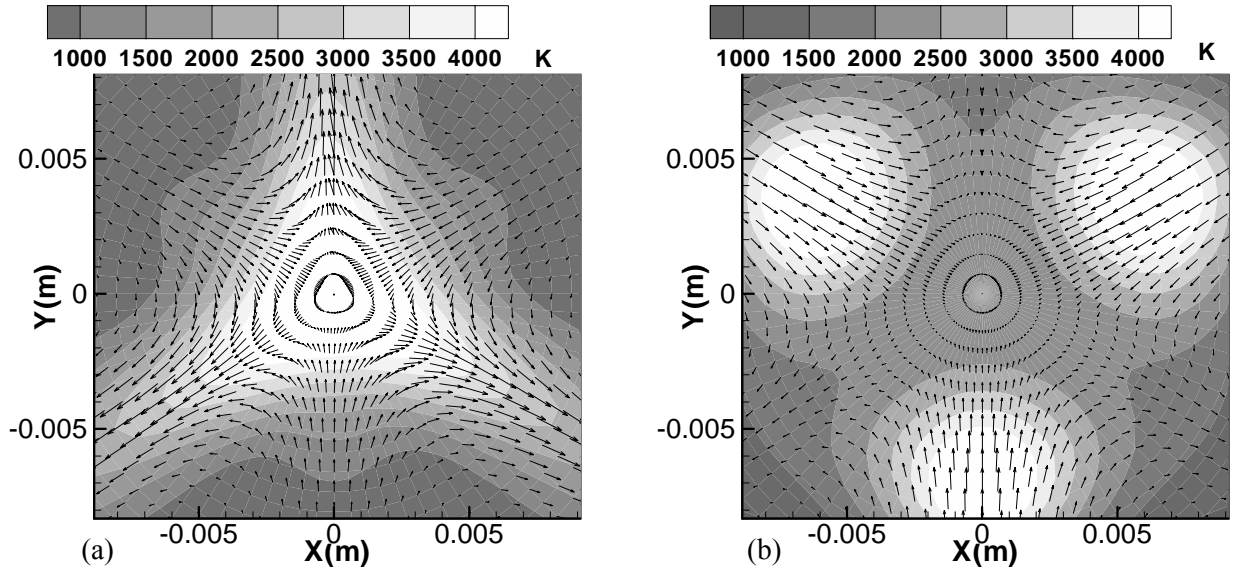


Figure 4. Radial cross-section of temperature with velocity vectors (at  $Z=2.17$  cm) at (a)  $\alpha = 45^\circ$  and (b)  $\alpha = 15^\circ$

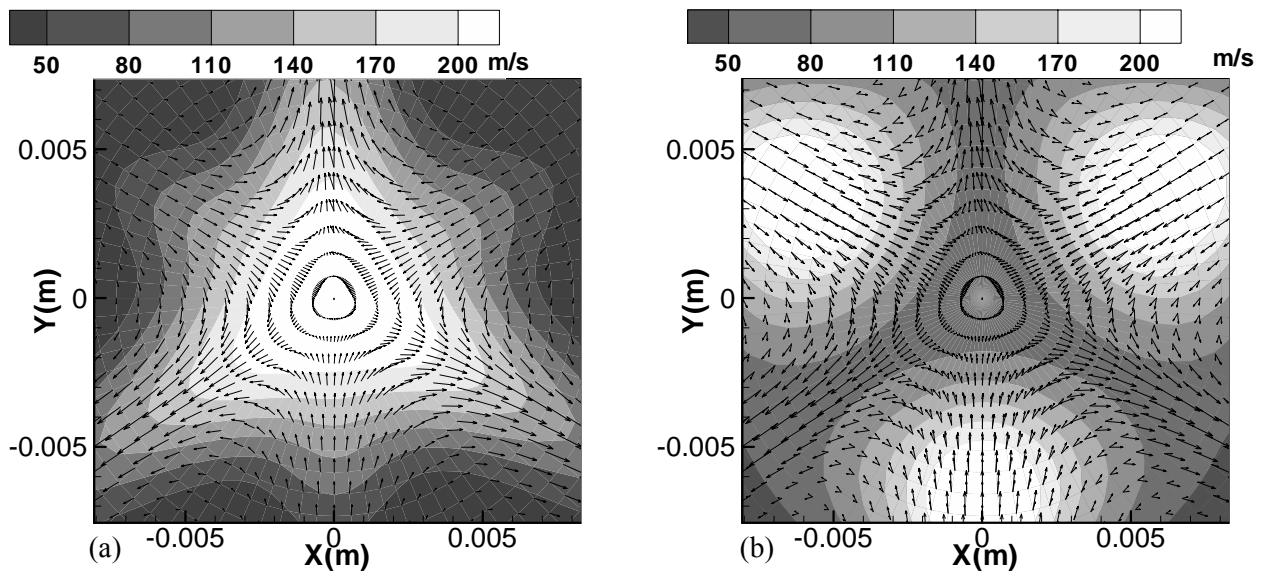


Figure 5. Radial cross-section of axial velocity with velocity vectors (at  $Z=2.17$  cm) at (a)  $\alpha = 45^\circ$  and (b)  $\alpha = 15^\circ$

Figures 6(a) and 6(b) show the radial distribution of the converging jet temperature and axial velocity at  $\alpha = 30^\circ$  for with and without central gas injection respectively. Results are shown along the line defined by the projection of the axis of one of the torches onto the horizontal plane. A dip in the axial velocity is disappeared whereas a dip in the temperature is appeared at the geometric center by the central injection of cold argon into the converging jet. Results show that the effect of central gas injection on the converging jet temperature is more significant than that of axial velocity. While mixing of cold gas with high temperature gas, the variation of thermal conductivity is larger than that of viscosity with temperature.

The boundary conditions used in this model are different from operating conditions and configuration of the triple torch plasma system used for the measurements [4]. This is a reason for the differences between predictions of the model and measurements. Also present model predicts the results for an ideal case. But the results of measurements show that experiment is not an ideal case. Hence the differences between the predictions of the model and measurements are reasonable.

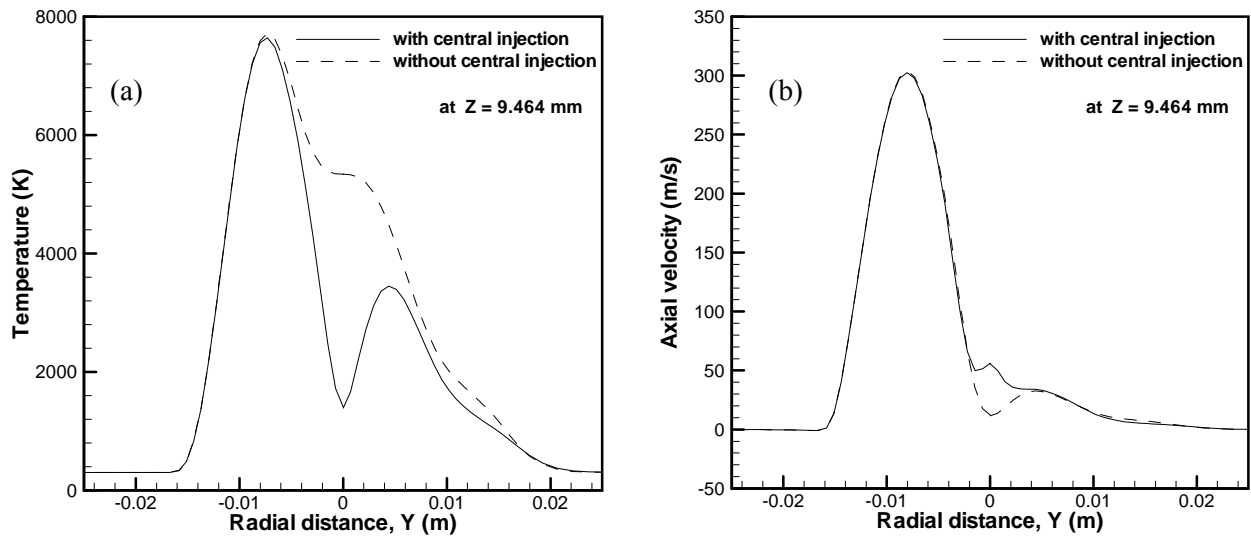


Figure 6. Radial distribution of converging jet (a) temperature and (b) axial velocity for with and without central gas injection ( $\alpha = 30^\circ$ )

#### 4. Conclusion

We simulate the converging plasma jet in a triple torch plasma system and characterize the structure of the thermo-fluid fields of the converging plasma jet for given geometry and process parameters. The following are conclusions in the present study.

1. The thermo-fluid fields of converging plasma jet are symmetric with three symmetric sections at an interval  $120^\circ$ . The symmetry and uniformity of the thermo-fluid fields are improved well at  $\alpha = 15^\circ$  in the downstream.
2. Velocity fields of three individual plasma jets are mixed slower than temperature fields of the same. The angle of convergence determines the structure of the temperature and velocity fields of converging plasma jet.
3. The effect of central cold gas injection on the converging plasma jet temperature is more significant than axial velocity.

#### References

- [1] E. Pfender - Plasma Chem. Plasma Process. **19**, 1 (1999).
- [2] H.C. Chen, E. Pfender, J. Heberlein - Thin Solid Films **315**,159 (1998).

- [3] P. Lu, J. Heberlein, E. Pfender - Plasma Chem. Plasma Process. **12**, 35 (1992).
- [4] M. Asmann, A. Wank, H. Kim, J. Heberlein, E. Pfender - Plasma Chem. Plasma Process. **21**, 37 (2001).
- [5] D. Bendix, D. Hebecker - Proc.14th Int. Symp. on Plasma Chemistry (Prague, Czech) ed M Hrabovsky, M Konrad and V Kopecky (Institute of Plasma Physics AS CR) pp. 2809 (1999).
- [6] P. Eichert, M. Imbert, C. Coddet - J. Thermal Spray Technol. **7**, 505 (2000).
- [7] The Phoenix Reference Manual, CHAM/TR200, CHAM, London, UK
- [8] R. Bolot, C. Coddet, M. Imbert - Phoenix J. Comp. Fluid Dyn. Appl. **10**, 335 (1997).



# THE SIMULATION OF ATMOSPHERIC PRESSURE PLASMA JET BY LATTICE BOLTZMANN METHOD

ZHANG Hai-Ou   ZHU Jie-Ying   WANG Gui-Lan

*State Key Lab of Plastic Forming Simulation and Die. & Mold Tech. , Huazhong Univ. of Sci. & Tech.,  
Huazhong Univ. of Sci. & Tech., Wuhan 430074, China.*

## Abstracts

A new model is proposed to calculate velocity and temperature field of plasma jet by hexagonal 7-bit Lattice Boltzmann method (LBM) in this paper. The macro equations have been derived by selecting two opportune equilibrium distribution functions and with Chapman-Enskog expansion and multi scale expansion. The LBM is found effective and simpler than FDM. It can be concluded that reducing flow turbulent viscosity and increasing Re number at exit can increase energy density and plasma jet length.

**Key words:** Lattice Boltzmann method, simulation, plasma jet, temperature, velocity

## 1 Introduction

Plasma spraying has already been widely used to corrosion-, heat-, and abrasion-resistant coatings to the production of monolithic and near-net shapes of metallic and ceramic parts [2]. And Direct Rapid Metal Tooling by plasma spraying is a new oriental method of RP (Rapid Prototyping). The two main effects that plasma does on particle are sufficient heating and enough momentum to spread and binding force at the substrate. So temperature and velocity field of plasma jet effects loading particle, thus affects the sprayed-coating. Because high temperature (up to 104K) and flow velocity (up to 103m/s) are too difficult to diagnose, many researchers have carried out the modeling and simulation of plasma jet by SIMPLE algorithm, or CFD software such as LAVA, FLUENT, PHOENICS [3-6]. But these models are on finite difference method and their unsuitable pressure must be eliminated, still the program is complex. So by the new developed LBM, an effective and simple model to calculate the field of plasma jet is given in this paper.

Lattice Boltzmann was put forward with real variables in 1988[7], which is developed from Boolean Lattice Gas Automata. Latter the single relaxed Lattice BGK [8] simplifies LB equation and has more flexibility and efficiency. Since then the LB Method has been widely used for modeling physical systems [9] and solving partial differential equations especially in compute fluid dynamics [10]. Unlike conventional numerical schemes based on discretization of macroscopic continuum equations, LBM is to construct simplified kinetic models that incorporated the essential physics of microscopic or mesoscopic processes so that the averaged properties obey the desired macroscopic partial differential equation. The special character of Lattice Boltzmann method is its simple idea and instinctive physical picture. It also provides easily implemented fully parallel algorithms and the capability of handling complicated boundaries.

## 2 Numerical Model

### 2.1 LB model of plasma jet

The atmospheric plasma jet is laminar in the center and turbulent in the boundary. There are two-fluid model [11] and  $k-\epsilon$  model to simulate the plasma turbulence. In fact the turbulence degree of plasma jet has connection with structure of the gun, the ratio of work gas supply and the mode of supplying gas et al [6].

The  $k-\mathbf{e}$  functions aren't calculated in this paper, but the contribution of turbulence is included by turbulent diffusion coefficient.

The basic assumption: the jet is in a local thermodynamic equilibrium state and optical thin.

The calculation domain is the section parallel to axis shown in Fig.1. It shows the calculating model of grid division. It's a hexagonal and the vectors are expressed as:

$$\bar{c}_i = \begin{cases} C(\cos a_i, \sin a_i); & i = 1, \dots, 6 \\ 0; & i = 0 \end{cases} \quad \text{where} \quad a_i = \mathbf{p}(2i-1)/6;$$

and  $C$  is unit velocity of grid.

Because the fluid field of plasma jet includes both velocity and temperature, in tradition a multi-speed thermal lattice Boltzmann method [9] is used to model temperature change. In this paper two sets of Lattice Boltzmann equation with BGK collision operator are given as:

$$f_i(\bar{x} + \bar{c}_i \mathbf{e}, t + \mathbf{e}) - f_i(\bar{x}, t) = -\frac{1}{t_r} [f_i(\bar{x}, t) - f_i^{(0)}(\bar{x}, t)], \quad T_i(\bar{x} + \bar{c}_i \mathbf{e}, t + \mathbf{e}) - T_i(\bar{x}, t) = -\frac{1}{t_r} [T_i(\bar{x}, t) - T_i^{(0)}(\bar{x}, t)] - \frac{\dot{q} \mathbf{a}_i}{r c_p} \quad (1)$$

Where  $i$  and  $\mathbf{a}_i$  are the direction number particles moving and percent of the  $i$  direction particles;  $f_i$  and  $T_i$  are distribution of density and temperature respectively,  $f_i^{(0)}$  and  $T_i^{(0)}$  are the local equilibrium distribution of  $f_i$  and  $T_i$ ,  $t$  and  $t_r$  are relaxation factors;  $\bar{x}$ ,  $\bar{c}_i$  and  $\mathbf{e}$  are position vector, velocity vector and time step which has a minimal value; and  $\dot{q}$  is the radiance per unit volume of plasma jet. Then  $f_i^{(0)}$  and  $T_i^{(0)}$  are chosen as following:

$$f_i^{(0)} = A_0 - A_1 v^2 + A_2 (\bar{c}_i \bullet \bar{v}) + A_3 (\bar{c}_i \bullet \bar{v})^2, \quad f_0^{(0)} = D_0 - D_1 v^2, \quad T_i^{(0)} = B_0 + B_1 (\bar{c}_i \bullet \bar{v}), \quad T_0^{(0)} = E_0, \quad (i=1,2,3,4,5,6); \quad (2)$$

To derive the macro equation of plasma jet, coefficient of Eqs. (2) must satisfy Eqs. (3)

$$\left. \begin{aligned} \sum_i f_i &= \mathbf{r}, \quad \sum_i f_i c_{ik} = \mathbf{r} v_{ik}, \quad \sum_i T_i = T, \quad \sum_i T_i c_{ia} = T v_a, \\ \sum_i f_i c_{im} c_{in} &= \mathbf{r} v_m v_n + p \mathbf{d}_{mn}, \quad \sum_i f_i c_{il} c_{im} c_{in} = (\mathbf{r} u_l u_m u_n) + \mathbf{r} c_s^2 (u_l \mathbf{d}_{nm} + u_m \mathbf{d}_{ln} + u_n \mathbf{d}_{ml}) \end{aligned} \right\} \quad (3)$$

where  $\mathbf{d}_{ij}$  is Kronecker delta, pressure  $p = \mathbf{r} c_s^2$  and  $c_s$  is the local sound speed.

To give the macro function, the left items of Eqs. (1) are expanded by Taylor series and multi-scale method (Eq.(5)) while the right items are expanded by Chapman-Enskog method (Eqs.(4)). Summations of all direction particles are gave on every grid by reference to Eqs. (3). The expansion is truncated to  $\mathbf{e}^2$  (about  $10^{-12}$  magnitude). When the simulation field evolve to steady state, the macro quantities of the same position don't vary with time and their differential coefficient with time is zero. Still, density gradient in energy conservation equation is neglected because it's too small when comparing to velocity gradient and temperature gradient. Finally the macro continuity equation, momentum conservation and energy conservation equation is obtained as following Eqs. (6).

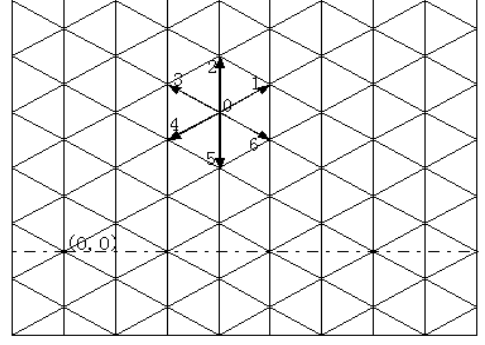


Fig.1 Lattice grid model of fluid field

$$f_i = f_i^{(0)} + \mathbf{e} f_i^{(1)} + \mathbf{e}^2 f_i^{(2)} + \mathbf{e}^3 f_i^{(3)} + \dots, \quad T_i = T_i^{(0)} + \mathbf{e} T_i^{(1)} + \mathbf{e}^2 T_i^{(2)} + \mathbf{e}^3 T_i^{(3)} + \dots \quad (4)$$

$$\frac{\partial}{\partial t} = \frac{\partial}{\partial t_0} + \mathbf{e} \frac{\partial}{\partial t_1} \quad (5)$$

$$\nabla \cdot (\mathbf{r} \bar{\mathbf{v}}) = 0, \quad \nabla \cdot (\mathbf{r} \bar{\mathbf{v}} \bar{\mathbf{v}} + p \mathbf{d}_{ij}) = \frac{\partial}{\partial x_j} \left[ \mathbf{m} \left[ \frac{\partial v_i}{\partial x_j} + \frac{\partial v_j}{\partial x_i} \right] \right], \quad \nabla \cdot [\bar{\mathbf{v}} (\mathbf{r} T)] = \nabla \cdot [\Gamma_e \nabla T] - \dot{q} / C_p \quad (6)$$

Where  $\mathbf{m}_e = \mathbf{m} + \mathbf{m}_t$ ,  $\Gamma_e = \Gamma + \Gamma_t = \mathbf{l} / C_p + \mathbf{m}_t / \text{Pr}_t$ , and  $\mathbf{m}$  is laminar viscosity decided by working gas property  $\mathbf{m}_t$  is effective turbulent viscosity decided by gun structure and around environment,  $\mathbf{l}$  is thermal conductivity,  $C_p$  is specific heat and  $\text{Pr}_t$  equals 0.9.

At the same time, coefficient of Eqs.(2) is obtained as:

$$A_0 = \mathbf{r} / 12, \quad A_1 = \mathbf{r} / 6, \quad A_2 = \mathbf{r} / 3, \quad A_3 = 2\mathbf{r} / 3, \quad D_0 = 0.5\mathbf{r}, \quad D_1 = \mathbf{r}, \quad B_0 = 0.15T, \quad B_1 = T / 3, \quad E_0 = 0.1T;$$

In the deducing process, relaxation factors are obtained as:

$$t_T = 0.5 + 2\Gamma_e / (\mathbf{a} C^2 \mathbf{e}), \quad t = 0.5 + \mathbf{m}_t / (\mathbf{r} C_s^2 \mathbf{e}), \quad \mathbf{a} \text{ is the portion of non-static particles.}$$

For conventional Lattice Boltzmann, the diffusion coefficient is constant in evolution. But for the full length of plasma jet, the temperature varies to ten thousands degree and physical parameters such as  $\mathbf{m}, \mathbf{l}, C_p$  and  $\dot{q}$  are temperature-dependent. To satisfy this condition, the following steps are done. First the discrete data in literature [4] is fitted to curves by malab. Then a proper grid length is chosen to make the diffusion coefficient of LB to the real coefficient magnitude. Last, regulating the relaxation to the true coefficient at each grid. To insure the computing is valid, the fluid must be subsonic for LB.

The atmospheric pressure plasma jet satisfies this because the temperature of Ar plasma jet is up to  $10^4 \text{K}$  and its max velocity is under  $1000 \text{m/s}$

## 2.2 Boundary conditions

For the symmetry of plasma jet, half calculating region is plotted in fig.2. The left side OB is fixed bound expressed in Eqs.(7). Left-up side BC adopts non-slip rebound side. The central line OA is employed to symmetry side, the right AD and the upper side CD are regarded as free bound.

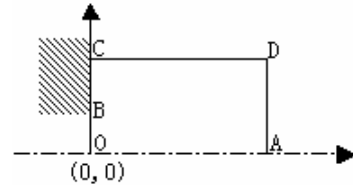


Fig 2. The Bound Condition side

$$v = v_0 \left[ 1 - (r/R)^2 \right], \quad T = (T_0 - T_w) \left[ 1 - (r/R)^4 \right] + T_w \quad (7)$$

Where  $v_0$  and  $T_0$  are maximum values of plasma axial velocity and temperature at exit respectively.  $T_w$  is the wall temperature of the gun.

## 2.3 Calculating process

1. Give the initial value of densities, temperatures and velocities on the whole field
2. Calculate the values of left bound according to Eqs. (7), the inner equilibrium distributions of density and temperature according Eqs. (2), inner distributions for fly according to Eqs.(1), then the distributions of bound.
3. The particles move a step, and record the fly-in distributions of density and temperature.
4. Calculate macro qualities such as mass, momentum, temperature according to Eqs.(3), if the absolute difference of values between this and last is higher than the given small value, go to 2.

5. Save and output the values of temperature and velocity of the whole field.

Because the whole calculating process includes the collision and the fly of particles, it has direct physical background.

### 3 Results and Discussions

The compute region is  $8\text{mm} \times (130 \sim 216.5\text{mm})$ ; The grid division is  $(16 \times 150 \sim 250) \times n$ , where  $n$  is decided by diffusion coefficient magnitude. The Beginning values are given as:  $\bar{v} = 0$ ,  $r = 0.02\text{kg}/\text{m}^3$ ,  $T = 300\text{K}$ . For convenience, dimensionless parameters are used.

#### 3.1 Validation of this model

The computing conditions are: the plasma is spraying in the air, the working gas is Ar, exit diameter of the gun is 8mm, and the turbulent viscosity is assumed as:  $\bar{m} = (0.1 - b \times 10^{-6} T) r$

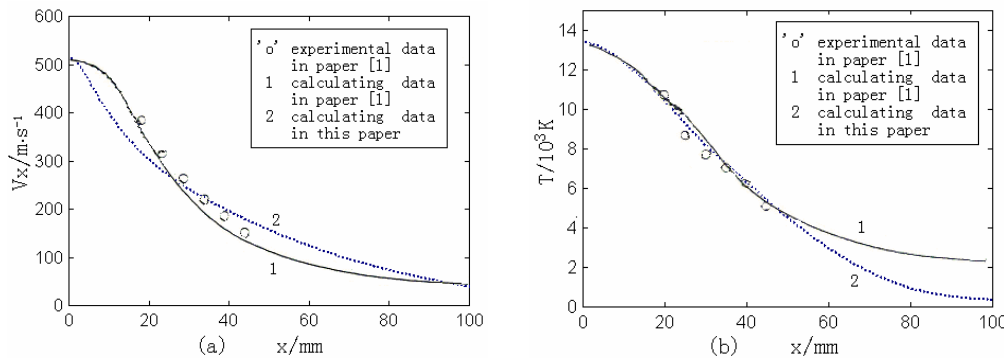


Fig.4 Velocity and temperature distribution along the jet centerline

When  $b$  equals 4, our result is compared with paper [1] in Fig. 4. The distribution trend of this paper is almost the same to that of paper [1]. The temperature of the down jet in our calculating is smaller than that of paper [1] because when the mean velocity is small, the real turbulent coefficient is smaller than the computing value. The difference in the velocity field is because a simple expression of  $\bar{m}$  can't be quite fit with the model used in paper [1]. Still, the turbulence varies with outer condition frequently.

#### 3.2 Turbulence on jet

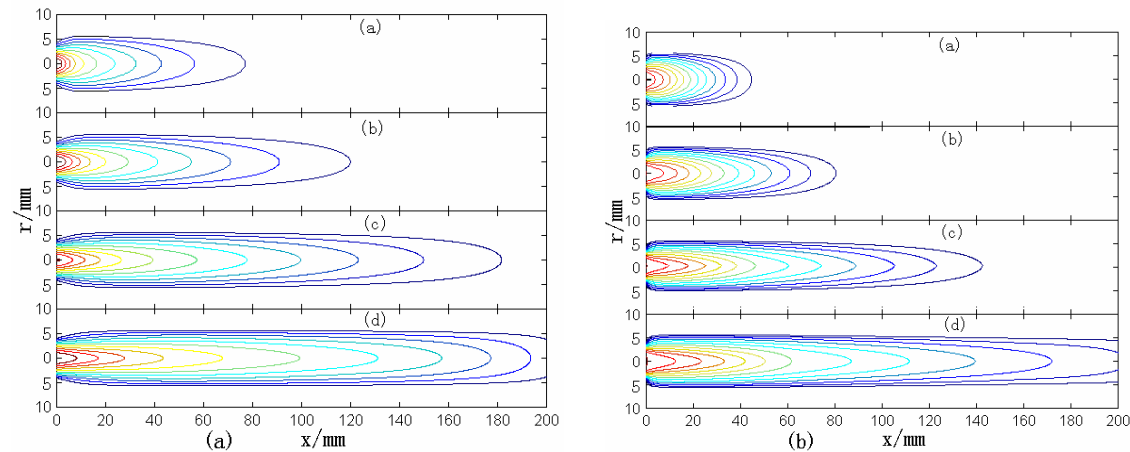


Fig.5 (a) Velocity distribution with different turbulent viscosity, 50m/s for both the outer line and interval

(b) Temperature distribution with different turbulent viscosity, 1000K for both the outer line and interval

In Fig. (5),  $v_0 = 600\text{m/s}$ ,  $T_0 = 14000\text{K}$ ,  $\bar{m} = 0.02 r$   $\bar{m}^t = 8\bar{m}$ ,  $\bar{m}^b = 4\bar{m}$ ,  $\bar{m}^c = 2\bar{m}$ ,  $\bar{m}^d = \bar{m}$

Fig. (5) shows that when other conditions are the same, the less the turbulent viscosity, the longer the fields

of high temperature and high velocity. Torch structure, gas feeding, and power supply are all important factors affecting the length and the stability of an atmospheric plasma jet. To reduce the turbulence and entrainment of surrounding air, the torch structure of the gun should be improved [6], and protecting gas or shrouding wall can be used around the jet. With the decrease of turbulence by plasma jet, the consumption of jet heat and kinetic energy is reduced, thus heating and accelerating of loaded powder is strengthened.

### 3.3 Re number on jet

The Re number is given as:  $Re = r v_0 d / m_e$ , where  $d$  is diameter of the nozzle.

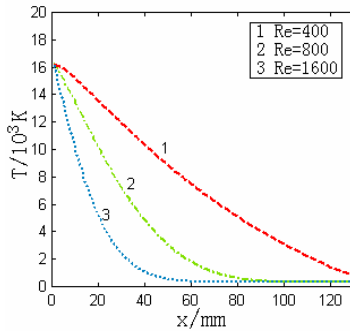


Fig.6 Temperature distribution along the center line

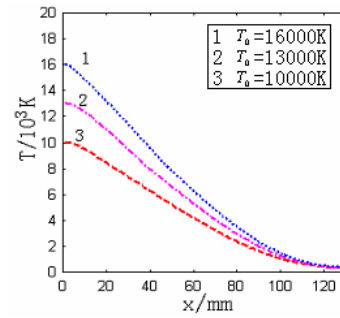


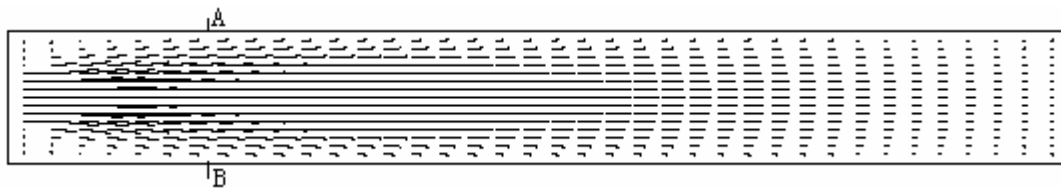
Fig.7 Temperature distribution along centerline

Fig.6 shows the larger Re number is, the slower temperature decline, and the longer the high temperature region is. Reducing the viscosity is helpful to increase the jet length. For common gases such as Ar, H<sub>2</sub>, and N<sub>2</sub>, the viscosity of Hydrogen is smallest, so its portion can be properly raised. Using the convergent-divergent nozzle can also increase the velocity of exit.

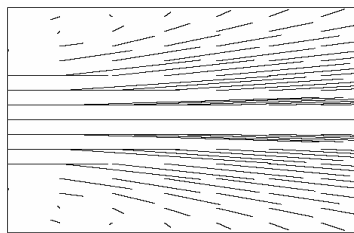
### 3.4 Exit temperature on jet

Fig.7 shows that with the same exit velocity, those with higher temperature declined faster, but temperature of the same position with higher exit temperature is still higher along the centerline. So properly enhancing electric current can increase the temperature of the jet.

### 3.5 Flow field of velocity



(a) Jet flow field



(b) local enlarged flow field at exit

Fig.8 Flow field

Fig.8(a) shows that from upper part of the jet to down part, it changed from normal distribution to parabolic distribution. The entrainment of air at the outside of exit can also be seen from Fig.8 (b)

#### 4. Conclusion

- (1) The LB method is simpler than the traditional SIMPLE (or SIMPLEC) method. There is no need to solve the large equations set and to use stagger grids, still the bound by LB is easy to determined. The method is feasible when  $v_0$  is less than the local sound, for which the atmospheric pressure plasma jet meets.
- (2) The statistic of LB equation depends on the time, so it's convenient for computing non-steady fluid and also feasible for steady fluid. In this paper, the fluid field can reach steady state after twenty times of axial grid number step.
- (3) For atmospheric plasma spray, reducing turbulent viscosity and properly increasing the velocity and temperature at exit can increase energy density and plasma jet length.

#### Acknowledgements

This research was funded by the Ministry of Science and Technology of the Chinese government and the National Natural Science Foundation of China through research grants 2001AA421150 and 50075032, respectively.

#### Reference

- [1] Pfender E., Chang C.H., Plasma Spray jet and plasma-particulate interaction: modeling and experiments, Thermal spray: meeting the challenges of the 21st century, ed. by Christian Coddet. ASM International, USA, 1:315-226 (1998).
- [2] Zhang Haiou, Wang Guilan, Y. Luo , Takeo Nakga . Rapid Hard Tooling by Plasma Spraying for Injection Molding and Sheet Metal Forming . Thin Solid Films **390**(2001) 7-12
- [3] He-Ping Li, Xi Chen, Three-dimentional simulation of a plasma jet with transverse particle and carrier gas injection, Thin Solid Films. **390**:175-180( 2001)
- [4] Boulos M, Fauchais P, Pfender E. Thermal Plasmas. New York: Plenum, **1**: 388-392(1995).
- [5] Bertrand Jodoin, Pierre Proulx., Yves Mercadier, Numerical study of supersonic direct current plasma nozzle flow, AIAA Journal, **36**(4): 578-584(1998).
- [6] Wenxia Pan, Wenhua Zhang, Wenhong Zhang, and Chengkang Wu, Generation of Long, Laminar Plasma Jets at Atmospheric Pressure and Effects of Flow Turbulence, Plasma Chemistry and Plasma Processing, **21**(1):23-35 (2001).
- [7] G McNamara, G Zanetti, Use of the Boltzmann Equation to Simulate Lattice-gas Automata. Phys. Rev. Lett. **61**: 2332 - 2337(1988).
- [8] Y H Qian et al. Lattice BGK Models for Navier-Stokes Equation. Europhys. Lett. **17**:479 - 484(1992).
- [9] Chris Teixeira, Hudong Chen, David M. Freed, Multi-speed thermal lattice Boltzmann method stabilization via equilibrium under-relaxation, Computer Physics Communications, **129**: 207-226(2000).
- [10] Shiyi Chen and Gary D. Doolen, Lattice Boltzmann method for fluid flows, Annu. Rev. Fluid Mech., **30**:329-364 (1998).
- [11] P.C. Huang, J. Heberlein, E. Pfender, Particle behavior in a two-fluid turbulent plasma jet, Surface and Coatings Technology **73**:143-151(1995).

# EFFECT OF ROBOTIC PATH PLANNING ON PLASMA SPRAY COATING

Haiou Zhang, Guangchao Han, Guilan Wang

*State Key Lab. of Plastic Forming Simulation and Die & Mould Tech*

*Huazhong University of Science & Technology, Wuhan 430074, P.R.China*

*Tel: +86-27-87543493, Fax: +86-27-87554405,*

*E-mail: hangc@21cn.com, zholab@mail.hust.edu.cn*

**Abstract:** Plasma spray tooling has received more attention because it is not limited by pattern's size or material<sup>[1]</sup>. One of the key of the method is to make the temperature and the stress fields of the metal coating as possible as uniform during the spraying process besides the thickness of the film, which is affected greatly by the path planning. In this paper, a robotic path planning method is developed to confirm the optimal trajectory by comparing the four types of robotic plasma spraying paths.

**Key words:** Robot, Path planning, Plasma spray coating

## 1. Introduction

Robot used for rapid plasma spray tooling is effective to improve the automation and the coating's quality, which is greatly effected by the robotic path planning. The study of robotic path plan on the spray paint has been widely carried, such as Automatic Trajectory Planning System (ATPS) by Suk et al.<sup>[2]</sup>; a frame work for optimal trajectory planning to deal with the optimal paint thickness problem by Antonio et al.<sup>[3]</sup>; a surface forming algorithm to cover free-form surface and achieve satisfactory thickness by Heping Chen et al.<sup>[4,5]</sup>. Compared with the path planning of the spray painting, whose main goal is to get the possible uniform thickness, the plasma spray coating process is more complex (such as high temperature, high residual stress etc.), so the robotic path plan must be fit for its special characters and requirement.

## 2. Automatic path planning

The robotic path planning is important for robotic plasma spray process. It has two main methods: teaching and off-line program. With the development of the industrial automation and the requirement of the fabrication of complex parts, the off-line path planning has become more and more popular. The main content of the plasma spray path planning including spray deposition model, path interval and path type etc.

Three dimensional geometry model of the pattern can be described by many 3D-CAD program systems, such as UG, Pro/Engineer and Solidworks etc. So the STL files of the 3D-CAD model can be getting. A program to convert the STL files to the dispersed coordinate values and the normal vectors of the target points on the pattern's surface has been developed. After the path planning, the robotic spray trajectory according the target point's value can be generated. Finally the path files are transferred to the robotic controller to realize the plasma spraying coating.

## 3. Experiment and discussion

### 3.1 Experimental condition

In this study, a 6DOF industrial robot of SG-MOTOMAN (UP20, shown in fig 1) is used, whose payload is 20kg. The experiment parameters are shown in table .

Table : The parameters of the plasma spray path

Power(kw)	Powder	Substrate	Diameter(eye)
20	Ni matrix alloy	90 × 90 × 3mm	180-220

The material of the substrate is steel. The powder deposition efficiency from the gun to the substrate is 0.753. The spraying speed is 1200mm/min.



Fig 1 : View of the 6-DOF robot

### 3.2 Spray deposition model

The trajectory of a 6-DOF robot can be defined by a six-dimension vector  $p \in R^6$ ,  $p = [p_x, p_y, p_z, p_f, p_y, p_q]^T$ , which specifies the position and orientation of the gun at each instant time, where  $p_x, p_y, p_z$  represent the position of the gun, others represent the gesture on the position. The gun is often attached to the end-effector of the robot, whose spraying model is often assumed as a spraying cone shown in Figure 2. During the spraying, the gun should be kept normal to the substrate's surface to get ideal property of the film. On the other hand, it is important to keep the gun's muzzle normal to the substrate at a fix distance. In this study, the fix distance is kept as 120mm.

The profile of the deposition thickness can be approximated by Gaussian function. A single line-spraying path of the robot has been tested and the surface curve is measured by the REPLICA 1000-laser scanner. The experiment datum line and the function's fitting curve are shown in Figure 3, which fit each other very well. The bell type normal (Gaussian) probability distribution function is :

$$y = y_0 + \frac{A}{w \cdot \sqrt{\pi/2}} e^{-\frac{2(x-x_0)^2}{w^2}} \quad (1).$$

Where A is the total area under the curve from the baseline, w is 2 "sigma", approximately 0.849 the width of the peak at half height.



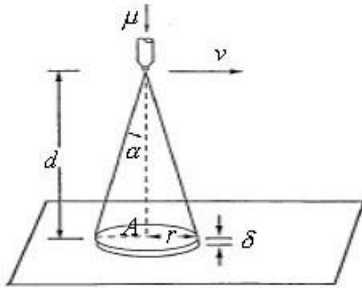


Figure 2 : The gun model

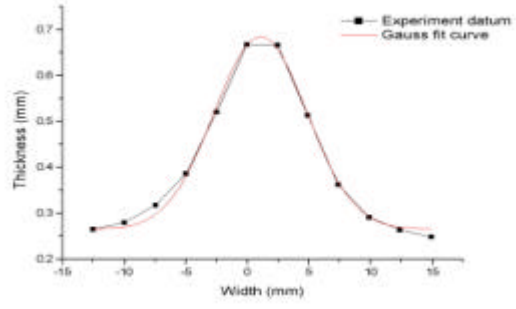


Figure 3 : The Gaussian fit of the profile

### 3.3 Path interval

During the plasma spray process, the thickness of a point is mainly affected by two neighbor paths (shown in Figure 4). Where  $r$  is the radius of the spray cone and  $d$  is the overlap distance between two neighbors. The function of the thickness distribution is:

$$q(x) = \begin{cases} q_1(x) & 0 \leq x \leq r-d \\ q_1(x) + q_2(x) & r-d < x \leq r \\ q_2(x) & r < x \leq 2r-d \end{cases} \quad (2)$$

Where  $q_1(x)$  and  $q_2(x)$  represents the spray thickness of two paths separately.

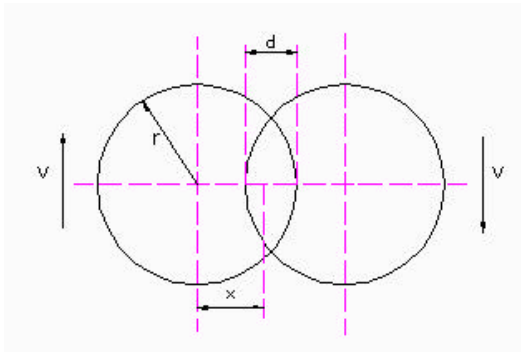


Figure 4: The scheme of neighbor path overlap

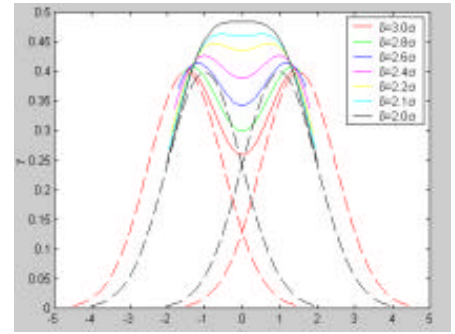


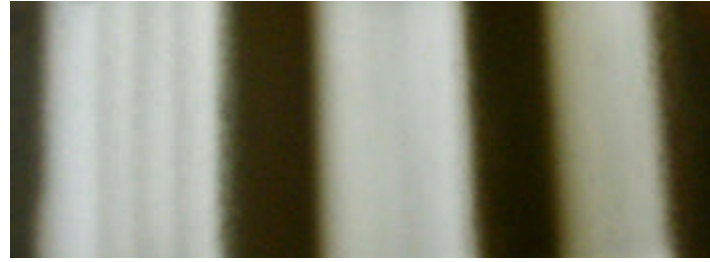
Figure 5 :The scheme of across section thickness overlap

As the final thickness of the coating is accumulated layer by layer, the thickness of a single layer should be made as uniform as possible and the thickness wave should be permitted in an allowable scope for getting the optimal path interval for uniform coating. When the path interval  $d$  equal to  $2s_0$ , the single layer has the most uniform thickness between the two neighbors shown in Figure 5, which is the optimum path interval. According to the equation (1),

$$w = 2s_0 = d \quad (3)$$

Where  $s_0$  is a parameter of the normal (Gaussian) probability distribution function.

The optimum path interval is  $d = w = 8$  mm in this study. Experiments of different path interval (8, 11, 14mm) were performed to be verified. In the figure 6, the path interval increases from right to left and the surface of the interval 8 mm is the most uniform path obviously.



interval=14mm                      11mm                      8mm

Figure 6 : The scheme of different path intervals

### 3.4 Path type

After confirming the spray parameters, the plasma spray trajectory type will be decided. In the spray paint, the path of raster type is used mostly <sup>[2-6]</sup>. Teng Gong-yong adopt a subarea changing-direction scanning method to enhance the scan forming efficiency of the rapid prototyping method SLS<sup>[7]</sup>. Stephen Duncan used a mirror spray path to depress the asymmetry temperature distribution<sup>[8]</sup>. In order to get uniform distribution of the stress field of the plasma spray metal coating, a new rotating raster path was developed. In each layer, the spray path type is still raster type. The angle of the raster increases by degree  $q$  with the accumulating of the spray layers. Figure 7 shows the rotating angle gradually changing with the  $q$ . The base angle  $q$  is designed as  $0^\circ$ 、 $45^\circ$ 、 $60^\circ$ 、 $90^\circ$  respectively. When  $q=0^\circ$ , the path is raster type.

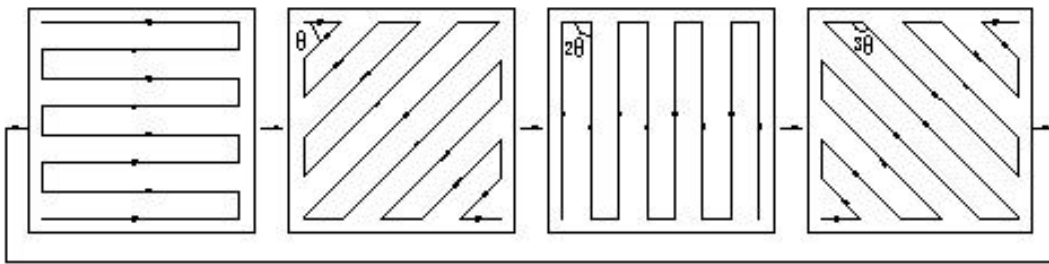


Figure 7 : The path changes with the rotating  $q$

### 3.5 Residual stress

The D/max - C x ray diffraction gauge is used to examine the distribution of the residual stress on the film by  $(2q - \sin^2 j)$  method. With the increasing of the base angle, the residual stress of the film reduces distinctly shown in Figure 8, and the coating has the lowest residual stress when  $q = 90^\circ$ . It is considered that the anisotropy with the increasing of the base angle makes the coating's stress distribution more uniform. The lower residual stress can decrease the distortion of the metal coating during the spraying process and enhance spray formability of the coating.

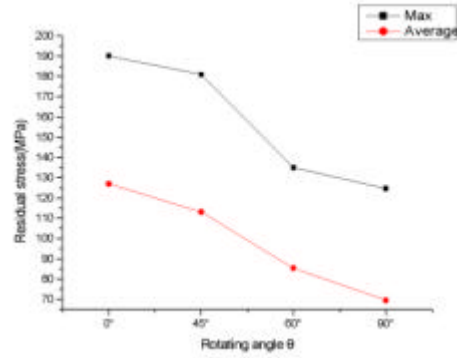


Figure 8: Relationship between residual stress with rotating angle

### 3.6 Surface roughness

The REPLICA 1000-laser scanner which has 0.05mm resolution ratio is used to measure the coating surface roughness for four types of base angles. Figure 9 and Figure 10 show the surface roughness of rotating angles 0 ° and 90 ° respectively. It is clear that the coating surface roughness was hardly affected by the changing of the base rotating angles.

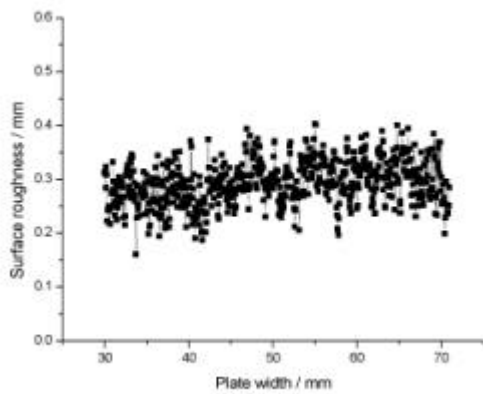


Figure 9: Coating surface roughness of 0 °

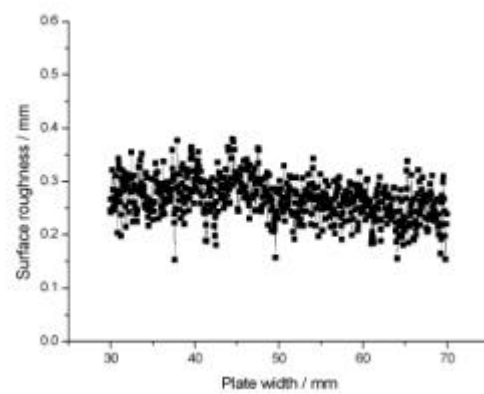


Figure 10: Coating surface roughness of 90 °

## 4. Conclusion

In this paper, a robotic path planning method is developed. The results are as follows:

- (1) It is confirmed experimentally that the normal (Gaussian) probability distribution is reasonable as spray deposition model and the optimum path interval is about 8 mm;
- (2) The effect of path type on the residual stress in the spray coating is investigated. The results show that the residual stress is affected greatly by the rotating base angle and the 90 ° angle is the best;
- (3) The coating surface roughness appears similar character with the increasing of the base angle.

## Acknowledgements

This research was funded by the Ministry of Science and Technology of the Chinese government and the National Natural Science Foundation of China through research grants 2001AA421150 and 50075032, respectively.

**Reference :**

- [1] Zhang Haiou, Wang Guilan, Y. Luo , Takeo Nakga . Rapid Hard Tooling by Plasma Spraying for Injection Molding and Sheet Metal Forming . *Thin Solid Films* **390**(2001) 7-12
- [2] Suk-Hwan Suh, In-Kee Woo, and Sung-Kee Noh Development of An Automatic Trajectory Planning System (ATPS) for Spray Painting Robots *Proc. of the 1991 IEEE Int. Conf on Robotics and Automation* pp : 1948-1954
- [3] John K. Antonio Optimal Trajectory Planning for Spray Coating *Proc. of the 1994 IEEE Int. Conf on Robotics and Automation* pp : 2570-2577
- [4] Heping Chen, Weihua Sheng, Ning Xi Automated Robot Trajectory Planning for Spray Painting of Free-From Surface in Automotive Manufacturing *Proc. Of the 2002 IEEE Int. Conf on Robotics and Automation* pp : 450-455
- [5] Weihua Sheng, Ning Xi Automated CAD-Guided Robot Path Planning for Spray Painting of Compound Surfaces *Proc. Of the 2000 IEEE Int. Conf on Robotics and Automation* pp : 1918-1923
- [6] Naoki Asakawa, Yoshimi Takeuchi Teachingless Spray-Painting of Sculptured Surface by an Industrial Robot *Proc. of the 1997 IEEE Int. Conf on Robotics and Automation* pp : 1875-1879
- [7] Teng Gong-yong, Wang cong-jun etc. Factors Effect the Development of SLS and Measures to Improve it. *Journal of Hubei Automotive Industries Institute*. Vol 15 No 2 June 2001 pp : 12-15
- [8] Stephen Duncan, Paul Jones etc. The Sprayform Tooling Process The 6th International Tooling Conference, 2002.9

# Measurement of negative oxygen radicals in pulsed corona plasma near the atmospheric pressure

Masateru Nishioka, Takamasa Seta, Yukimasa Baba, Masayoshi Sadakata

*Department of Chemical System Engineering,  
The University of Tokyo*

Non-thermal plasma such as pulsed corona discharge are used as an advanced oxidation process, and applied for industry, air cleaning (deNO<sub>x</sub>, Soot oxidation etc.) and sterilization. It was considered that the most effective oxidation species is hydroxyl radical (OH). However, most of negative oxygen radicals and these clusters have very powerful oxidation ability (ex. for SO<sub>2</sub> oxidation, O<sup>-</sup> negative anion is 10<sup>3</sup> times faster than the OH radical)

The O<sup>-</sup> negative anion is one of the most active, and therefore, useful radicals for potential applications such as oxidation of thin film and chemical syntheses. The method conventionally used to generate an O<sup>-</sup> is the attachment of a free low-energy electron to a molecule or negative ion/molecule reactions, which can occur in a plasma process, electron impact or laser irradiation on molecules in gas phase.

However, there are no good tools to measure the negative ions under the atmospheric pressure. An electrometer has been used to measure the polarity and amount of ion concentration, but could not distinguish the chemical species. The mass-spectrometer with differential vacuum system has been applied to investigate the ion species under the atmospheric pressure. However, the signals from mass-spectrometer are not corresponded to the atmospheric ion distribution because the ions are lost and/or generated while the differential vacuum zone.

We have proposed a simple technique by using an opt-galvanic (OG) method to measure the oxygen anion radicals (O<sup>-</sup> and O<sub>2</sub><sup>-</sup>). The OG method was widely used at low-pressure plasma diagnosis (less than 1 Torr, typically 10 mTorr). When the negative anions are absorbed the energy more than electron affinity energy, the electron is detached from anions. The detached electron can be measured by a suitable electrode. We modified the Langmuir probe to detect the detached electron and applied the energy by Nd-YAG pumped dye laser (wavelength: 848nm).

As the result the O<sup>-</sup> and O<sub>2</sub><sup>-</sup> signals were detected near the atmospheric pressure (100 Torr). We applied this analysis technique to diagnosis pulsed corona discharge plasma. The O<sup>-</sup> anion density was measured as 2×10<sup>5</sup>/cm<sup>3</sup> after 500μsec delay from turn off the plasma (plasma condition: 100% oxygen, applied field: 3kV/cm, 10μsec pulse, pressure: 100 Torr). The negative anion density was also investigated as the function of the pressure. The pressure dependence was compared with Monte-Carlo Simulation (13 molecules and 140 elemental reactions) and it had good relation between experimental result and calculation.

# Hydrophilization of PTFE by treatment with a dielectric discharge

Z. Andronache, C.Mihesan, N. Dumitrascu, G. Popa

*Faculty of Physics, "Al. I. Cuza" University  
Bd. Carol I, no. 11, Iasi, Romania*

The PTFE film were treated by a dielectric barrier discharge (DBD), frequently used to the wettability of the polymer surfaces and to hydrophilize or to optimize basic physical and chemical processes.

Experimental set-up consists of 2 electrodes (point-plane geometry) separated by a dielectric barrier of air and the polymer film. The thickness of dielectric barrier was of 1cm and a sinusoidal high voltage with peak-to peak voltage of 28KV, at the frequency of 13.5KHz was used. The power dissipated in the discharge was computed from the typical voltage and current waveforms. The PTFE samples (Goodfellow Co., thickness 0.05mm) were washed with ethanol and dried in a vacuum oven to eliminate surface contamination. The contact angles were measured before and after the treatments. Treatments were performed in helium, with spectral purity, at atmospheric pressure with a flow rate of 30cm<sup>3</sup>/min. The energetic surface characteristics (adhesion work, components of surface energy, surface polarity) were considered at the room temperature and evaluated by using the sessile drop technique. These evaluations proved that after the DBD treatments for 20sec, the hydrophilization of the PTFE surface is increased with 70%. A study of the aging effect upon the exposure at DBD permits to conclude that after 3days this hydrophilization is stabilized. To complete this study we followed the surface morphology (by AFM), dependent on the time of treatment and it has been found (by ATR-FTIR) the polar groups responsible for the hydrophilization.

Dielectric barrier discharge in helium can be a very attractive technique applicable for PTFE hydrophilization by a very short time of the treatment. The main advantage is that the treatments are effective at atmospheric pressure but the area of the treated surface is aprox. of 2mm<sup>2</sup>.

# Thermal Plasma of Free Burning Electric Arc between Composition Electrodes in Air

A.N.Veklich<sup>1</sup>, I.L.Babich<sup>1</sup>, V.Ye.Osidach<sup>1</sup>, L.A.Kryachko<sup>2</sup>, R.V.Minakova<sup>2</sup>

<sup>1</sup>*Taras Shevchenko Kyiv National University, Kyiv, Ukraine*

<sup>2</sup>*Institute of Materials Technology Problems NAS of Ukraine, Kyiv, Ukraine*

A problem of developing of reliable interrupting devices, where ignition of electric arc often is realised, can not be resolved without careful analysis of processes which take place in the arc and its electrodes. Furthermore, an electric arc, being generated at contact disconnection, results in considerable material erosion of contacts. This causes the decrease of device efficiency and limits reliability of its activity.

In this paper the processes occurred in a free burning electric arc in air between electrodes from composite materials on the base of cooper (*Cu*, *Cu-W*, *Cu-Mo*, *Cu-Mo-LaB<sub>6</sub>*) and silver (*Ag*, *Ag - CdO*, *Ag - Ni*) were studied. Such arc is model of arcs arising between contacts of current disconnectors of electric circuits.

Techniques of plasma diagnostics of electric arcs between copper electrodes with usage of copper spectral lines were developed earlier [1,2]. Therefore at the first stage the applicability of these methods for plasma diagnostics of an electric arc between composite electrodes was studied.

It was found, that the diagnostics copper lines in radiation spectrums of investigated plasma are not overlapped with lines of other elements. Therefore, the developed spectroscopic techniques can be applicable for diagnostics in our case.

Because of the discharge spatial and temporal instability the method of the single tomographic recording of the spectral line emission was used. A 3000-pixel CCD linear image sensor (B/W) Sony ILX526A accomplished fast scanning of spatial distributions of radiation intensity. It allows recording the radial distributions of nonstationary arc radiation intensity in arbitrary spatial sections simultaneously. In a combination with a Fabry-Perot interferometer (FPI) the spectrometer provides simultaneous registration of spatial and spectral distribution of radiation intensities. Thus, the spectrometer allows measuring contours of spectral lines in different spatial points of plasma volume.

The ISA interface slot of IBM PC in a control and data exchange is used. The hardware and software was especially designed for laboratory and industry plasma investigations.

The radial profiles of temperature and electron density were determined in the average cross section of the discharge gap  $l_{ak} = 2, 4, 6$  and  $8$  mm in air at arc currents  $3.5$  and  $30$  A. The temperature profiles are obtained from relative intensities of spectral lines CuI  $510.5$  and  $521.8$  nm or CdI  $479.9$ ,  $508.5$  and  $643.8$  nm. The electron density profiles are obtained from the width of the spectral line CuI  $465.1$  nm or AgI  $466.8$  nm.

Based of spatial profiles of the temperature and electron density the model of the investigated plasma can be developed. It is visible from the analysis of the obtained results that the processes occurred in the discharge gap are determined by erosion of the electrode material and condition of its surface.

[1] A.N.Veklich, V.A.Zhovtyansky – J. Appl. Spectroscopy (translated from Russian), **50**, 359 (1989).

[2] I.L.Babich, A.N.Veklich, V.A.Zhovtyansky – J. Appl. Spectroscopy (translated from Russian), **51**, 10281 (1990).

[3] I.L. Babich, V.Ye. Osidach, V.I.Sobovoy, A.N.Veklich – Proceedings of the 20th Symposium on Plasma Physics and Technology. June, 10-13, 2002, Prague, Czech Republic: in Czechoslovak Journal of Physics, **52**, Supplement D, D731 (2002).

# Enhancement of excited-atom flux in downstream portion of pulse-modulated induction thermal plasma

Tadahiro Sakuta and Yasunori Tanaka

*Department of Electrical and Electronic Engineering, Kanazawa University,  
2-40-20, Kodatsuno, Kanazawa 920-8667, JAPAN*

## Abstract

Time variation in the number of excited Ar atom was studied especially at downstream portion in the reaction chamber as well as the main thermal plasma region of the pulse-modulated induction thermal plasma (PMITP) system by spectroscopic observation. From this observation, influence of ‘shimmer current level (SCL)’, which is a ratio of lower to higher level of the coil-current in the modulated operation, on excited atom flux into the chamber was investigated. The experimental results indicated that the current-modulation could enhance the excited particle flux into the reaction chamber in Ar or Ar-H<sub>2</sub> PMITP.

## 1. Introduction

An inductively coupled thermal plasma (thermal ICP or ICTP) around atmospheric pressure is used to various plasma processing fields such as analytical chemistry, thermal spray coating of metals and ceramics, chemical vapor deposition of diamond films, fullerene synthesis, etc [1]-[6]. This is because an ICTP has some advantages of high enthalpy, high chemical activity with high reaction rates and cleanliness. For the purpose of applying the ICTP to material processing fields, much effort has been made so far to sustain the ICTP statically under steady condition. However, a steady ICTP has some disadvantages of uncontrollable and remarkably high enthalpy which can cause damages on substrates and/or production materials. To encounter this high thermal flux problems and also to introduce a new function to an ICTP, we have developed a new operation to the ICTP system [7]-[16]. This new system is called ‘pulse-modulated induction thermal plasma (PMITP)’ system [13, 15]. This system can modulate the amplitude of the 450 kHz coil-current sustaining an ICTP, periodically by switching a MOSFET inverter power supply. This pulse-modulation of the coil-current can control average input power to the thermal plasma, and can decay the average plasma-temperature in time domain, with keeping high reaction activity of the thermal plasma [13, 15]. Furthermore, the coil-current modulation may induce chemically non-equilibrium effects in the thermal plasma [16], and also thermal non-equilibrium effects [12]. Up to now, our group has diagnosed transient aspect of the PMITP with various additional gases both experimentally and theoretically [7]-[16]. In these works, attention was paid to the main thermal plasma region of PMITP, i.e. high-temperature region. The reason is that one of our research purposes is to achieve stable operation of the PMITP, and to control the high-temperature of the thermal plasma by pulse-modulated operation. The stable operation of the PMITP with a MOSFET inverter power supply has been confirmed for various additional gases [13]. And also, the control of plasma-temperature can be achieved by setting, for example, SCL [13, 15].

On the other hand, for plasma material processings, the number density of radicals and excited particles related with some reactions is quite important factor in the reaction chamber installed at downstream portion of the torch. Then in the present work, special attention is paid to the downstream portion in the reaction chamber rather than the main thermal plasma region of the Ar PMITP system, and a time-dependent radiation intensity from excited Ar atom was measured there. Influence of the pulse-modulation in the coil-current on the excited particle flux into the reaction chamber was investigated by changing SCL. Four kind of gases H<sub>2</sub>, O<sub>2</sub>, N<sub>2</sub> and CO<sub>2</sub> was selected as an additional gas. As a result, it was found that decreasing SCL up to around 80% enhanced excited particle flux into the reaction chamber in Ar or Ar-H<sub>2</sub> PMITP. This enhancement originates from the pulse-modulation, and that has been not obtained in the conventional continuous operation mode.

## 2. Experimental setup

### 2.1. Pulse-modulated induction thermal plasma torch, reaction chamber and power supply

Figure 1 illustrates a schematic diagram of the plasma torch and the reaction chamber used in the experiment. Note that the left of this schematic diagram in Fig.1 corresponds to the actual top side. The torch is composed of two coaxial quartz tubes with a 330 mm length. The inner tube has a inside diameter of 70 mm. Between the inner and outer tubes, cooling water flows from bottom to top side with a swirl to keep wall-temperature around 300 K. The reaction chamber made of SUS304 is installed at downstream of the plasma torch. The wall of the chamber is water-cooled and tapered as seen in Fig.1. Argon-additional gas mixture is supplied as a sheath gas



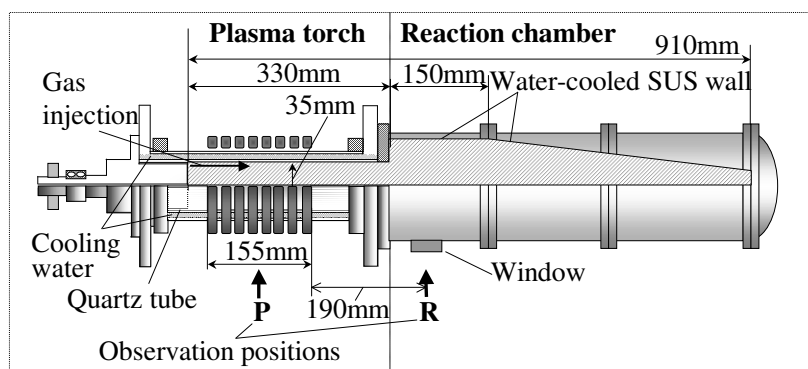


Fig. 1. Plasma torch and reaction chamber.

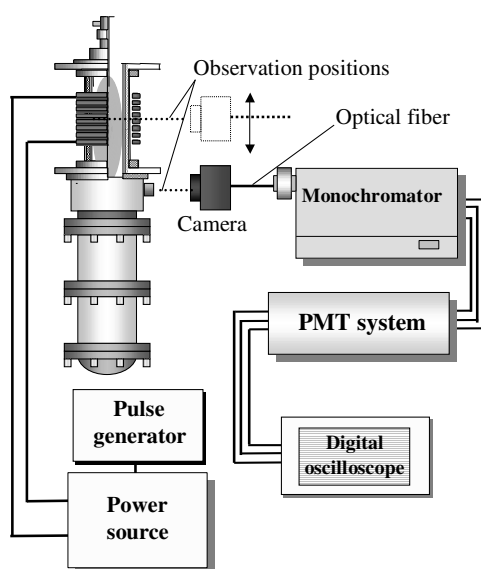


Fig. 2. Spectroscopic observation system.

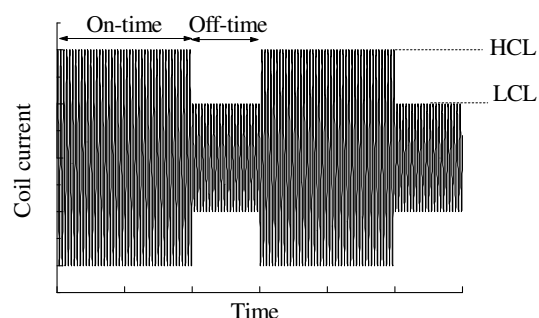


Fig. 3. Pulse-modulated coil-current waveform.

along the inner tube wall of the torch with a swirl to prevent the plasma from contacting the inner tube. This torch has an eight-turns induction coil. With this coil, a high frequency power supply with a MOSFET inverter unit is connected through a matching circuit. The matching circuit is comprised of a matching transformer and series capacitor [15]. The electric current flowing in the coil has a frequency of 450 kHz. This inverter power supply has a rated power of 50 kW and a rated current of 460A. The plasma in the tube is sustained by receiving an rf-power from the induction-coil by electromagnetic coupling. This power supply has an ability of coil-current amplitude modulation.

## 2.2. Spectroscopic observation system

The spectroscopic observation was carried out at two positions in the present work. One of the positions is at the middle of the plasma torch as denoted by P in Fig.1. The other is at 190 mm below the coil-end in the reaction chamber as designated by R in Fig.1. Figure 2 shows the optical measurement system. The light radiated from one of the observation positions is transmitted through a camera lens and an optical fiber to the slit of a monochromator. The light into a monochromator is splitted in terms of wavelength. At a focal plane of the monochromator, three optical fiber bundles are installed to capture lights at three different wavelengths, simultaneously. At each of another ends of the fiber bundles, photomultipliers are set to convert radiation intensity of the captured lights into electrical signals. This signals are memorized with a digital oscilloscope with a sampling time of  $0.5 \mu\text{s}$ . The wavelength width observed by this system is 1.0 nm for each of detecting channels. The whole optical system was calibrated using tungsten-halide lamp. In this experiment,

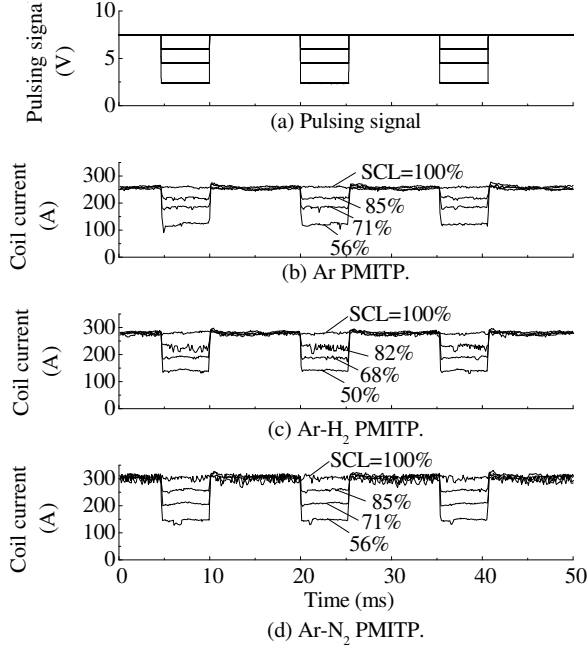


Fig. 4. Coil-current waveform.

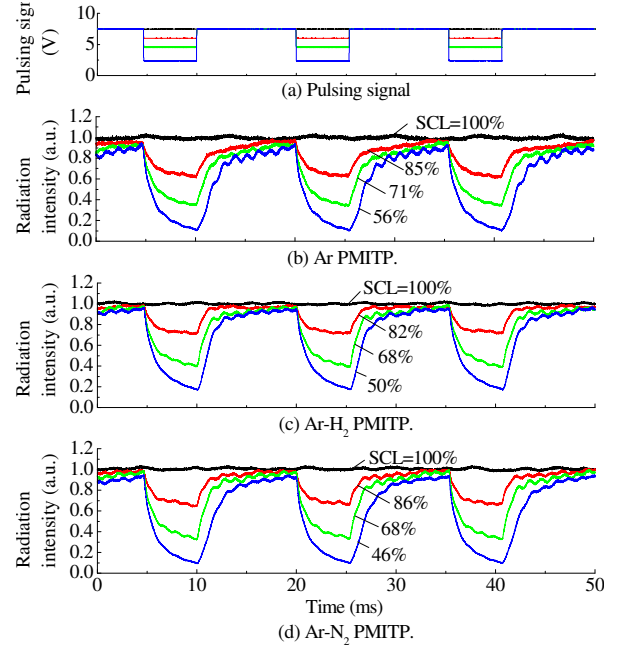


Fig. 5. Time evolution in radiation intensity of Ar spectral line at a wavelength of 751.465 nm measured at the middle of the coil.

we measured an Ar atomic spectral line at 751.465 nm and a neighbor wavelength for continuum at 755.0 nm.

### 2.3. Parameter definition and experimental condition

Figure 3 depicts a diagram of pulse-modulated coil-current. The pulse-modulation of the coil-current induces four parameters. They are ‘HCL’ which is the higher current level, ‘LCL’ the lower current level, ‘on-time’ the time period with the higher current level and ‘off-time’ the time period with the lower current level. We also define ‘SCL; shimmer current level’ as a ratio LCL/HCL. These parameters have a relationship for stable operation of the PMITP [13]. With control of these parameters, the following feasibilities and effects are expected: (i) control of average power and temperature/enthalpy of the thermal plasma in time domain, (ii) extremely high or low electromagnetic field operation can be made, (iii) thermally and/or chemically non-equilibrium effects in thermal plasma could be introduced.

In this paper, the ‘on-time’ was fixed at 10 ms, and the HCL was set to a value corresponding to an input power 30 kW for each of gas ICTP in steady state. Pressure inside the torch was fixed to 0.1 MPa by an automatic feed-back pressure control unit. Gas flow rate is set to 100/2.5 liters/min for Ar/additional gases.

## 3. Results and discussions

### 3.1. Coil current

Figure 4 indicates measured waveforms of the modulated coil-current peaks in Ar, Ar-H<sub>2</sub>, Ar-N<sub>2</sub> PMITPs as examples. The LCL or SCL is taken as a parameter with a fixed HCL. The amplitude of the coil-current for these three kinds of gas inclusions can be modulated into an almost square-waveform corresponding directly to the pulsing control signal. This tendency was also found for Ar-O<sub>2</sub> and Ar-CO<sub>2</sub> PMITPs. The stepped change in the coil-current requires around 80  $\mu$ s for any gas plasmas. This time order of the stepped change is much shorter than thermal plasma inertia treated here, then we can study an inherent dynamic behavior of the thermal plasma.

### 3.2. Main thermal plasma region

#### 3.2.1. Relationship between radiation intensity and number of excited atom

Let us remind that the radiation intensity  $I$  of Ar atomic spectral line is in proportion to the number of Ar atom excited to an upper level in observation region  $\Omega$ . This relation is expressed by

$$I = \int_{\Omega} N_m A_{mn} h \nu_{mn} dV = A_{mn} h \nu_{mn} \int_{\Omega} N_m dV = A_{mn} h \nu_{mn} \bar{N}_m \quad (1)$$

where subscripts  $m, n$  are the indices of the upper and lower levels,  $N_m$  is the number of excited Ar atom of an upper level,  $A_{mn}$  is the transition probability from  $m$  to  $n$ ,  $h$  is the Planck constant and  $\nu_{mn}$  is the frequency of emitted light,  $dV$  is the differential volume,  $\bar{N}_m$  is the whole number of excited Ar atom in the observation region  $\Omega$ . In the present work, we measured the radiation intensity of an Ar line at 751.465 nm whose upper level is  $107054 \text{ cm}^{-1}$ , the configuration is  $3p^5(2P_{1/2}^0)4p$ . This level is not metastable, and thus the time variation in the radiation intensity can be considered due to transient behavior of the bulk thermal plasma.

#### 3.2.2. Modulation of number of excited atom

Figures 5(a),(b) and (c) indicate time evolutions in the radiation intensity of the Ar spectral line at a wavelength of 751.465 nm at the main thermal plasma portion P, i.e. at the middle of the coil region in Ar, Ar-H<sub>2</sub> and Ar-N<sub>2</sub> PMITPs, respectively. The radiation intensities are normalized by those of SCL=100%, the steady state condition values. In this figure, the radiation intensities can be found to change periodically with a modulation of the coil-current. This means that the number of excited Ar atom  $\bar{N}_m$  can be modulated in the observation region by pulse-modulation of the coil-current. However, the waveform is not a square form. This is attributed to the thermal inertia of the thermal plasma itself. On the other hand, the additional gas kind hardly affects the radiation intensity waveform at this main plasma region. This is because the additional molecules are almost completely dissociated into atoms, which have similar thermal properties, in this high-temperature region.

As seen in Fig.5, decreasing SCL decays the minimum radiation intensity in a modulation cycle, for example, around at 10, 25, 40 ms, although the maximum is recovered in on-operation. Figure 6 shows the maximum and minimum radiation intensity of the Ar line in a modulation cycle as a function of SCL. From this figure, we can find that the maximum of the radiation intensity scarcely changes with SCL. This means that a high-temperature plasma can be re-established by on-operation periodically. On the other hand, the minimum of the radiation intensity decreases with a reduction of SCL. This indicates that we can control minimum value of the number of excited particle by setting SCL with keeping its maximum value constant.

### 3.3. Reaction chamber region

#### 3.3.1. Enhancement of excited atom flux by pulse-modulation

Radicals and excited particles into the reaction chamber is of great importance for various processing of materials. Figure 7 indicates time evolution in the radiation intensity of the Ar line measured at the reaction chamber R in cases of Ar, Ar-H<sub>2</sub> and Ar-N<sub>2</sub> PMITPs. It should be noticed that the waveform of the radiation intensity measured in Ar or Ar-H<sub>2</sub> PMITP at SCL<100% seems a triangular form. This form is quite different from those measured in the plasma torch. In particular, we emphasize that the peak value of the radiation intensity at SCL<100% is much higher than that at SCL=100%, i.e. continuous mode in Ar and Ar-H<sub>2</sub> PMITP. In other words, the instantaneous peak magnitude of the number of the excited Ar atom is enhanced by pulse-modulation of the coil-current. However in an Ar-N<sub>2</sub> PMITP case, such an enhancement cannot be seen in Fig.7 (d).

#### 3.3.2. Effects of shimmer current level and additional gas kind

Effect of the shimmer current level SCL on the enhancement was investigated here. Figure 8(a) shows the radiation intensity peak value as a function of SCL for different gas PMITPs at off-time of 5 ms. Each of the radiation intensity is normalized by that at SCL=100%. In this figure, decreasing SCL from 100% enhances the radiation intensity peak value for Ar PMITP. Such an enhancement in the radiation intensity peak value cannot be obtained in those measured at the main thermal plasma region as indicated in Figs.5 and 6. This may be caused by a puffer advection of high-temperature gas from the torch into the reaction chamber by rapid pulse-on operation. On the other hand, for Ar-H<sub>2</sub> PMITP, decreasing SCL up to 70% also enhances the radiation intensity, and however a further decrease in SCL decays the radiation intensity peak value as represented in Fig.8(a). This means that there is an adequate SCL for enhancing the radiation intensity peak value into the

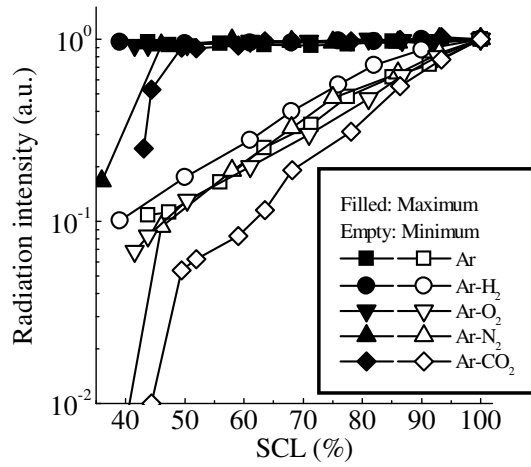


Fig. 6. Dependence of maximum and minimum value of radiation intensity at 751 nm on shimmer current level.

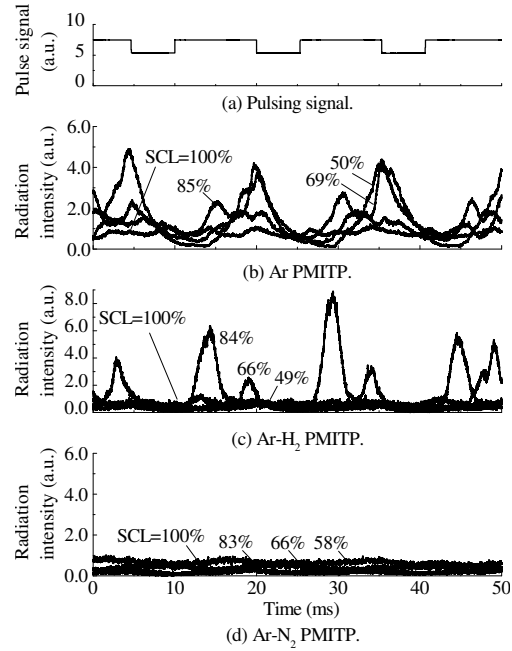


Fig. 7. Time evolution in radiation intensity of Ar line at 751 nm measured at 190 mm below the coil end in the reaction chamber. Off-time is 5 ms.

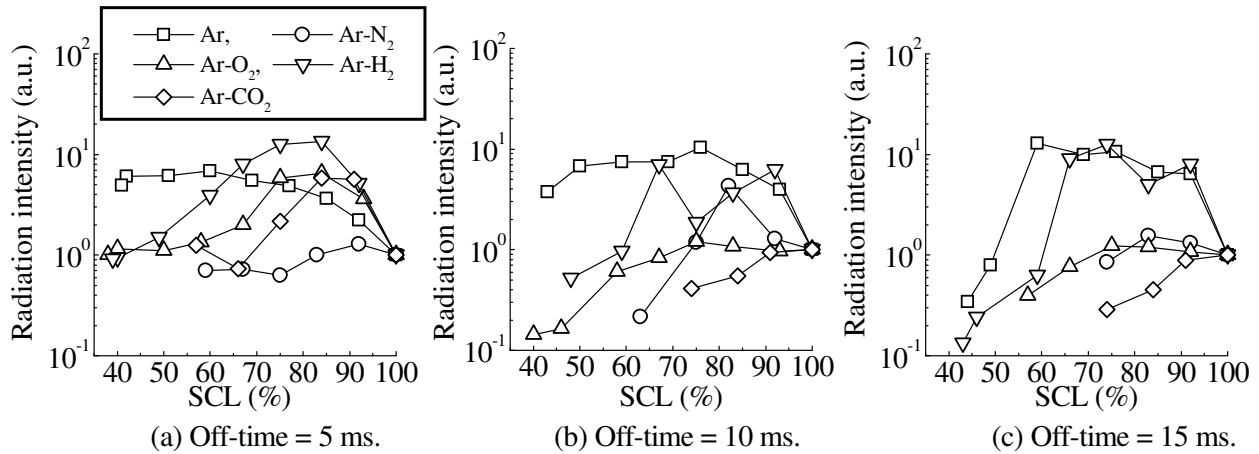


Fig. 8. Peak of relative number of excited Ar atom versus shimmer current level.

reaction chamber. For Ar-O<sub>2</sub> and Ar-CO<sub>2</sub> PMITPs, similar tendency to Ar-H<sub>2</sub> one can be found. Whereas in N<sub>2</sub> inclusion case, decreasing SCL does not enhance the radiation intensity.

It should be again noted that such an enhancement in the radiation intensity corresponds to the enhancement of excited atom flux. Therefore, the above results indicates that pulse-modulation of the coil-current can enhance the instantaneous number of the excited Ar atom into the reaction chamber.

### 3.3.3. Off-time effect

The PMITP has a parameter of ‘off-time’ as well as SCL. In order to study ‘off-time’ effect on the above enhancement of radiation intensity, off-time is increased from 5 to 15 ms with on-time=10 ms fixed. Figures 8(b) and (c) show the radiation intensity peaks at off-times of 10 and 15 ms, respectively. In case of Ar PMITP at off-time of 10 and 15 ms, the radiation peak is increased by reducing SCL to around 70 %, and then that is decreased by a reduction of SCL from about 70 %. Such an enhancement in the radiation intensity peak can be found for off-times of 5–15 ms in Ar and Ar-H<sub>2</sub> PMITP. However, in additional gas such as O<sub>2</sub>, N<sub>2</sub> and CO<sub>2</sub> inclusion cases, the radiation intensity is not always enhanced especially at long off-time.

#### 4. Conclusions

Spectroscopic observation was carried at the downstream in the reaction chamber of the pulse-modulated induction thermal plasma (PMITP) system to investigate effect of pulse-modulation of coil-current upon excited particle flux into the reaction chamber. Time variation in the radiation intensity of Ar line at 751.465 nm was measured for this purpose. Four testing gas such as H<sub>2</sub>, O<sub>2</sub>, N<sub>2</sub> and CO<sub>2</sub> were selected as an additional gas. Off-time is set to three value of 5, 10 and 15 ms. From the results, we found that the radiation intensity peak value was enhanced by the pulse-modulation of coil-current in cases of Ar and Ar-H<sub>2</sub> PMITP. This means that the excited Ar atom flux was enhanced by the pulse-modulation. This enhancement might also enhance the possibility of application of the PMITP.

#### References

- [1] I.Carzard-Juvernât, D.Morvan, J.Amouroux - Proc. 13th European Photovoltaic Solar Energy Conf., 2451 (1995).
- [2] H.Hamatani, H.Kumaoka, T.Yahata, T.Yoshida - J.Japan Inst. Metals, **55**, 1240 (1991).
- [3] S.Takeuchi, K.Takeda, N.Uematsu, H.Komaki, K.Mizuno, T.Yoshida - Proc. 12th Int. Symp. on Plasma Chem., 1021 (1995).
- [4] J.W.McKelliget, N.El-Kaddah - J.Appl.Phys., **64**, 2948 (1988).
- [5] C.Wang,A.Inazaki, T.Shirai, Y.Tanaka, T.Sakuta, H.Takikawa, H.Matsuo - Thin Solid Film, **425**, 42 (2003).
- [6] C.Wang, T.Imahori, Y.Tanaka, T.Sakuta, H.Takikawa, H.Matsuo - Thin Solid Film, **407**, 72 (2002)
- [7] T.Ishigaki, F.Xiaobao, T.Sakuta, T.Banjo, Y.Shibuya - Appl. Phys. Lett., **71**, 3787 (1997).
- [8] T.Sakuta, K.C.Paul, K.Katsuki, T.Ishigaki - J. Appl. Phys., **85**, 1372 (1999).
- [9] T.Ishigaki, T.Sakuta - J. Intelligent Mater. Syst. & Struct., **10**, 565 (1999).
- [10] M.M.Hossain, K.C.Paul, Y.Tanaka, T.Sakuta, T.Ishigaki - J. Phys. D: Appl. Phys., **33**, 1843 (2000).
- [11] K.C.Paul, J.Mostaghimi, T.Ishigaki, T.Sakuta - Plasma Chem. Plasma Process., **21**, 371(2001).
- [12] M.M.Hossain, Y.Tanaka, Y.Hashimoto, K.C.Paul, T.Sakuta - IEEE Trans. Plasma Sci., **3**, 327 (2002)
- [13] Y.Tanaka, T.Sakuta - Trans. IEE of Japan, **123-A**,469 (2002)
- [14] M.M.Hossain, Y.Tanaka, T.Sakuta - Plasma Sources Sci & Tech., **12**, 22 (2003)
- [15] Y.Tanaka, T.Sakuta - Plasma Sources Sci. & Tech., **12**, 69 (2003)
- [16] Y.Tanaka, T.Sakuta - Proc. 14th Int. Conf. on Plasma Chem., **I**, 245 (1999)

# Novel Chromate-Replacement Paint Pigments based on Water-Soluble Inhibitors Coated with a Plasma-Polymerized Membrane Film

W.J. van Ooij, Hai Yang, Haichuan Mu and Rick Manian

*Department of Chemical and Materials Engineering, University of Cincinnati, Cincinnati, OH 45221-0012, USA*

## Abstract

In this paper, we present a unique method for developing pigments that can be tailored to the substrate metal by modifying selected water-soluble corrosion inhibitor particles using a plasma polymerization technique. TOF-SIMS, SEM, TEM and contact angle data confirmed the successful deposition of the plasma-polymerized membrane film. Using immersion tests, we have demonstrated that the encapsulated water-soluble inhibitor can slowly release into the environment to protect a metal as needed.

## Introduction

Paint pigments based on chromates are very effective in protecting substrate metals from corrosion but they will be phased out in the near future because of their toxic and carcinogenic nature. Due to the urgent need to eliminate chromate pigment mandated by Environmental Protection Agency (EPA) [1], the pigment industry is seeking an equally effective while environmentally benign inhibitor. Different triazole derivative inhibitors including tolyltriazole (TTA), benzotriazole (BTA) and 1,2,4-triazole (TA) itself, are effective organic inhibitors for preventing corrosion of commonly used aerospace Al alloys. These inhibitors are known to adsorb onto copper-rich phases [2,3,4,5,6] and work by inhibiting the cathodic reaction of the corrosion process [7]. Cerium acetate is also an effective inorganic corrosion inhibitor. These inhibitors are soluble in water, thus they cannot be used in paints, as they would cause blistering of organic coatings when in contact with moisture. Therefore, they cannot be used directly as pigments in organic coatings. The individual inhibitor particles have to be surface-treated, modified or encapsulated to serve as slow-release pigment similar to chromate pigments. A possible way of attaining this purpose is to use a plasma polymerization technique to encapsulate the pigments. Recently, a plasma technique has been used to modify inorganic or organic nanoparticles to achieve unique mechanical, physical, biochemical and chemical properties etc [8,9,10]. It is a commonly used technique for surface modification for substrates such as metals, ceramics, paper and even powdered materials for the purpose of changing the hydrophilicity, hydrophobicity, adhesion and also anti-corrosion property of these materials. It is also used for reinforcement of automobile tires by modifying polyester fabrics [11]. Plasma polymerization is a relatively simple process to generate a thin polymer film on almost all types of substrates.

In this study, three potential inhibitors were used as pigments and three monomers, pyrrole, perfluorohexane and acetylene, were used as precursor. The plasma-treated pigments were dispersed into a water-based epoxy coating and applied onto AA2024-T3 panels. The plasma treatment process, the polymer thin film surface characterization, and the corrosion behavior of AA2024-T3 with pigmented epoxy coating are discussed.

## Experimental

**Materials** AA2024-T3 metals were obtained from ACT Laboratories, Inc.. Chemicals BTA, TA, pyrrole, perfluorohexane, cerium acetate, barium chromate and potassium dichromate were obtained from Aldrich Chemical Company, Inc.. TTA was obtained from PMC Specialties Group, Inc. and acetylene from Aga Gas Inc.. The epoxy resin used in this study was Shell EPON Resin 828, from Miller-Stephenson Chemical CO., Inc., and the curing agent was EPI-Cure 8290-Y-60 Curing Agent from Resolution Performance Products.

**Plasma Polymerization** The plasma reactor is schematically shown in Figure 1. The vacuum chamber consisted of a Pyrex glass column 55 cm in height and 6 cm in internal diameter. The organic corrosion inhibitor powder was put on the bottom of the glass flask and stirred by a magnetic stirrer bar to expose the particles uniformly to the plasma. The flask was connected to a vacuum pump (Welch Vacuum, Thomas Industries Inc., model 1402B-01) and the system pressure was measured by a Denton Vacuum Gauge (model: DV-515). The monomers were introduced from the monomer inlet during plasma treatment. The power system consisted of an RF generator

(model: LTA-302). Once ionized, excited gas species react with the surface of the powders placed in the reaction chamber and the powders were vigorously stirred.

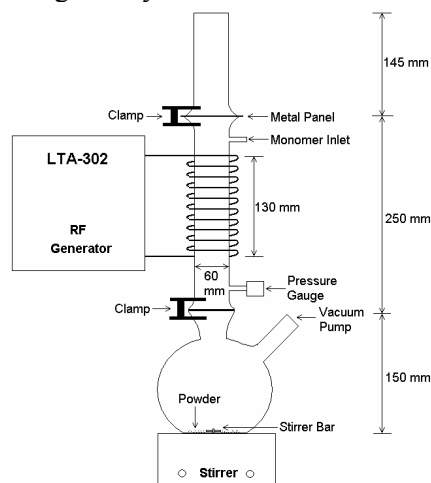


Figure 1: Schematic view of the vertical plasma reactor.

Before the plasma treatment the base pressure was pumped down to around 5 Pa. The desired monomer was then introduced into the reactor chamber and the power was applied. The detailed plasma treatment conditions are shown in Table 1.

Table 1: Conditions of plasma polymerization

Sample #		1	2	3	4	5	6		
Inhibitor	cerium acetate	TTA	TTA	TTA	TTA		BTAA	Inner layer	Outer layer
Monomer	C <sub>6</sub> F <sub>14</sub>	C <sub>2</sub> H <sub>2</sub>	C <sub>6</sub> F <sub>14</sub>	C <sub>6</sub> F <sub>14</sub>	C <sub>6</sub> F <sub>14</sub>	C <sub>4</sub> H <sub>5</sub> N	C <sub>6</sub> F <sub>14</sub>	C <sub>6</sub> F <sub>14</sub>	C <sub>4</sub> H <sub>5</sub> N
Initial Weight (g)	10	10	10	10	10	10	5	5	5
Base Pressure (Pa)	5	5	5	5	5	5	5	5	5
Monomer Pressure (Pa)	50	50	50	50	50	40	50	50	40
Input Power (w)	80	30	80	80	80	40	80	80	40
Treatment Time (minutes)	120	60	60	15	60	60	30	15	15

**Time-of-flight secondary ion mass spectroscopy (TOFSIMS).** After the plasma treatment, the polymeric film was examined by TOFSIMS using a CAMECA ION-TOF spectrometer. This instrument is equipped with a reflection-type time-of-flight mass analyzer and a pulsed 25 kV primary source of monoisotopic <sup>69</sup>Ga<sup>+</sup> ions, with a minimum beam size of 50 nm.

**Scanning electron microscopy (SEM).** SEM was performed on a Hitachi S-900 scanning electron microscope using 3 kV acceleration voltage.

**Transmission electron microscopy (TEM).** TEM was performed on a JEOL JEM-2000FX Electron Microscope equipped with a LaB<sub>6</sub> gun. The polymeric films could be observed clearly and the thickness was measured.

**Contact Angle.** The dynamic wicking properties of untreated and plasma treated powder were determined by a Lesca dynamic wicking meter. Contact angle between powder and water can be calculated by measuring the penetration rate of water into a tapped column of particles. The principle of dynamic wicking meter as well as the specific experimental procedures has been described in detail by Inagaki [12].

**Immersion Test.** Untreated and plasma-treated organic corrosion inhibitors and barium chromate were added to the water-based epoxy paint as pigments by stirring for 10 minutes at the level of 1 wt.%. BaCrO<sub>4</sub> and K<sub>2</sub>CrO<sub>7</sub> powders served as control and an epoxy coating without pigments was also tested. The epoxy resins without and with pigments were applied on cleaned AA2024-T3 panels and dried at 60°C for 2 hours. After curing, the coated side of panels was then scribed by a carbide tip. The edges and the uncoated side of the panels were sealed by wax. The panels were then immersed in DI water or 3.5 wt.% NaCl solution.

**Release Rate Test.** The plasma-treated cerium acetate was added to the 3.5 wt.% NaCl solution and stirred by a magnetic stirrer continuously. Every 24 hours, fresh AA2024-T3 panels were immersed into the solution for 1 hour and then tested by DC polarization.

## Results

TOFSIMS spectra were recorded of untreated and plasma-treated triazole (sample 6) and are shown in Figure 2. The peak assignments for all the significant peaks are marked in the figures. Figure 2-a and 2-b are the negative SIMS spectra of untreated and plasma-treated triazole, respectively. In Figure 2-b, peaks F<sup>-</sup>, F<sub>2</sub><sup>-</sup>, CF<sub>2</sub><sup>-</sup> and CF<sub>3</sub><sup>-</sup> are seen which confirms the formation of PFH (plasma-polymerized perfluorohexane) on the surface. The peaks CN<sup>-</sup>, CNO<sup>-</sup> and CHNO<sup>-</sup> indicate the formation of PPy (plasma-polymerized pyrrole) at the surface. Therefore, the double-layered polymeric films had been formed using plasma polymerization technique and the surface of the triazole had been modified successfully.

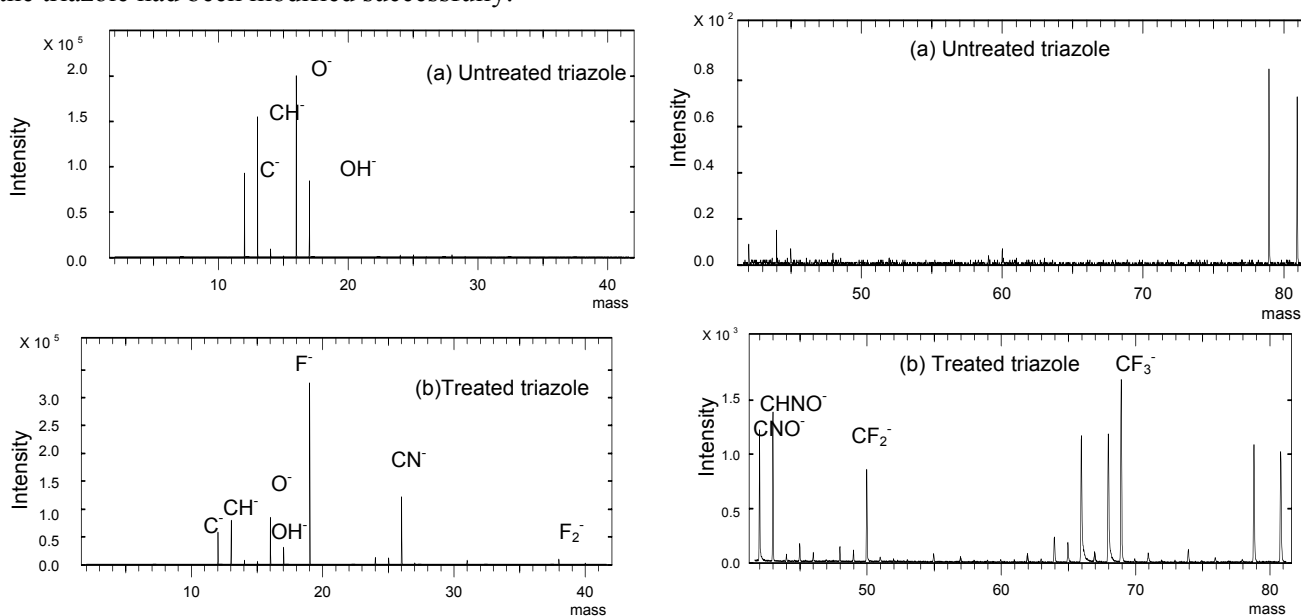


Figure 2: Negative SIMS spectrum of (a) untreated triazole, (b) plasma-treated triazole

SEM images of untreated and plasma-treated BTA (sample 5) are shown in Figure 3, where (a) and (b) are at lower magnification and (c) and (d) are at higher magnification. The difference between untreated and treated powder is obvious. As shown in (a) and (b), the untreated BTA powder has a smooth surface, while the treated



powder shows plasma-roughening. As shown in more detail in (d), the PP-PFH-coated powder has a rough and cauliflower-like surface.

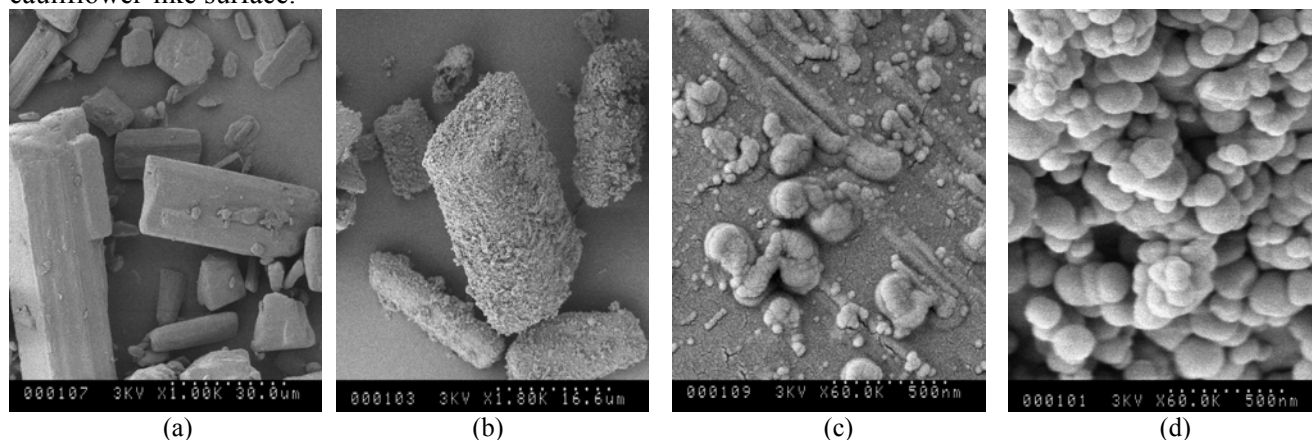


Figure 3: SEM images of untreated (a and c) and plasma-treated (b and d) benzotriazole (sample 5)

Figure 4 shows the TEM images of plasma-treated TTA by perfluorohexane for 1 hour. It can be concluded that the surfaces of treated TTA powders are completely and uniformly covered with PP-PFH films. The thickness of the PP-PFH film is measured to be 4 nm after 1 hour of plasma polymerization duration. The average deposition rate of PP-PFH film on TTA powders is therefore approximately 0.07 nm/min.

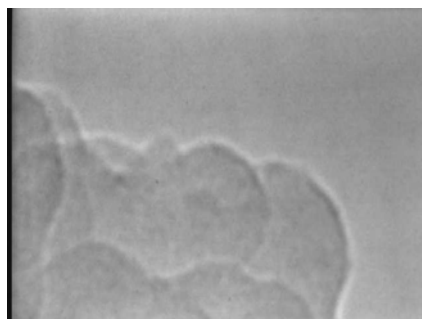


Figure 4: TEM images of plasma-treated tolyltriazole by perfluorohexane for 1 hour (sample 2) (X600K)

Table 2: Wicking properties of untreated and plasma-treated corrosion inhibitors

Powder	Porosity of powder column	Total weight of penetrating water (g)	Contact angle of water (degree)
Untreated tolyltriazole	0.413	0.95	13
Sample 1	0.337	0.17	54
Sample 2	0.377	0	> 90
Sample 3	0.377	0.05	90
Sample 4	0.315	0.17	52
Untreated benzotriazole	0.532	0.57	70
Sample 5	0.377	0	> 90
Untreated triazole	0.278	0.22	0
Sample 6	0.440	0.20	87
Barium chromate	0.717	0.19	90

Table 2 shows the results of wicking properties of untreated and plasma-treated corrosion inhibitors. From the contact angles obtained, the hydrophobicity of each corrosion inhibitor was increased after plasma treatment.

Figure 5 shows the scanned images of epoxy-coated AA2024-T3 panels after 30 days of immersion in DI-water and 3.5 wt.% NaCl solution. As shown in DI-water immersion test, the panels of (b), (d), (f) and (g) showed blisters phenomena, especially panel g, which is pigmented by potassium dichromate. The coating in (a) and (i) was peeled off from the metal, especially for the epoxy control. Photograph (c), (e) and (h), which are epoxy pigmented with treated TTA, BTA and TA, respectively, showed no blister or delamination. As shown in the salt immersion test, after 30 days immersion, the epoxy without pigment panel (a) as well as epoxy pigmented with untreated TA (i) had corroded heavily and peeled off from the substrate. The panels pigmented with  $\text{BaCrO}_4$ ,  $\text{K}_2\text{CrO}_7$  and treated corrosion inhibitors showed almost the same anti-corrosion behavior. When we compare (c) and (d) or (e) and (f) or (h) and (i), it is seen that the paints with plasma-treated pigments showed less corrosion than those with untreated pigments

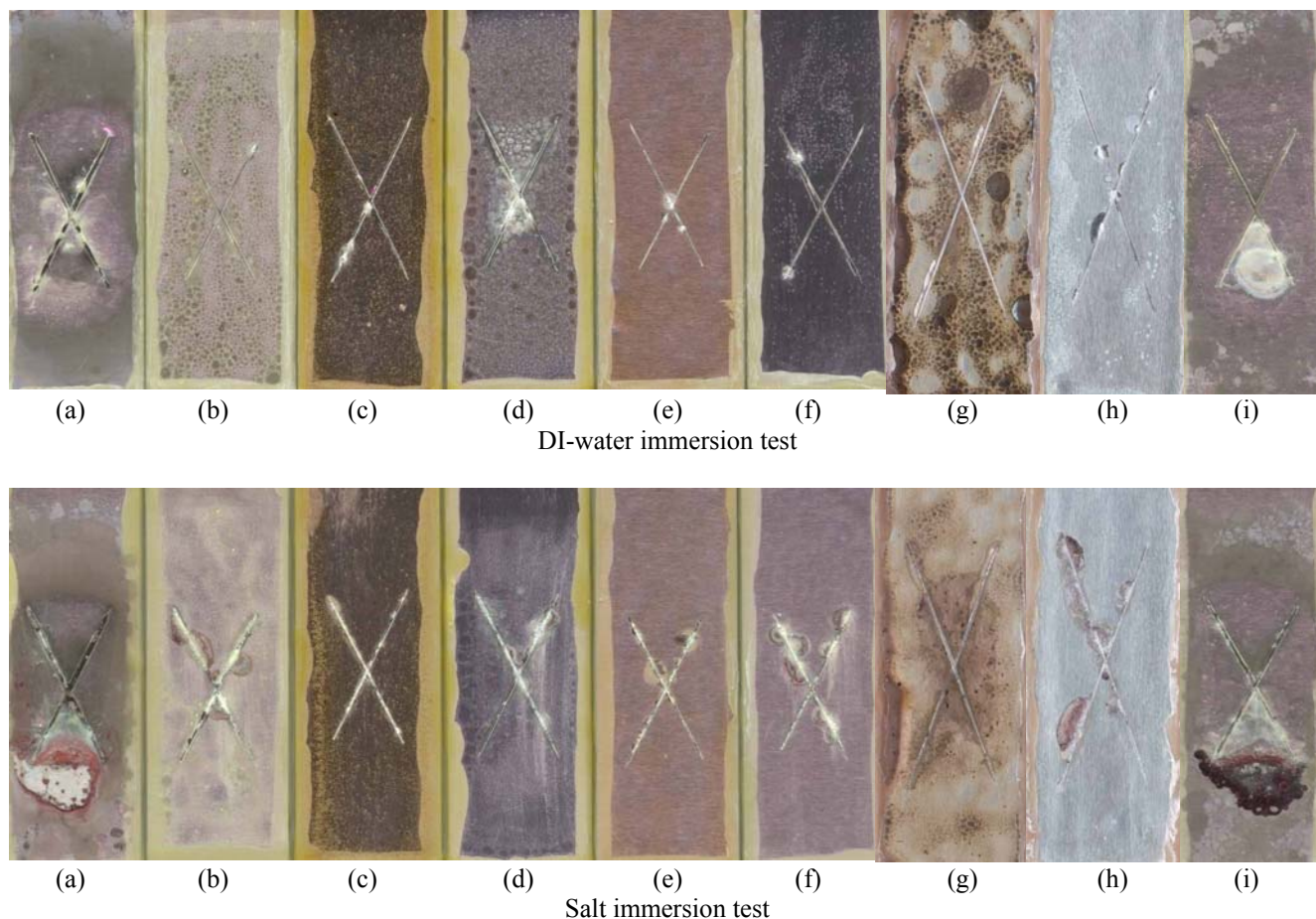


Figure 5: DI-water and salt immersion test (3.5 wt.% NaCl Solution) for AA2024-T3 with coatings: (a) epoxy control, (b) epoxy +  $\text{BaCrO}_4$ , (c) epoxy + treated TTA, (d) epoxy + untreated TTA, (e) epoxy + treated BTA, (f) epoxy + untreated BTA, (g) epoxy +  $\text{K}_2\text{CrO}_7$ , (h) epoxy + treated TA, (i) epoxy + untreated TA (immersion time: 30 days)

**DC Polarization.** In Figure 6, we can observe a gradual shift of the DC curve with the increase of the dissolution time of the  $\text{C}_6\text{F}_{14}$  treated cerium acetate, which indicated the gradual improvement of the anti-corrosion performance. Such improvement can be attributed to the slow release of the cerium acetate in the solution with time. The effect influence of the outerlayer  $\text{C}_6\text{F}_{14}$  coatings on the corrosion behavior was demonstrated.

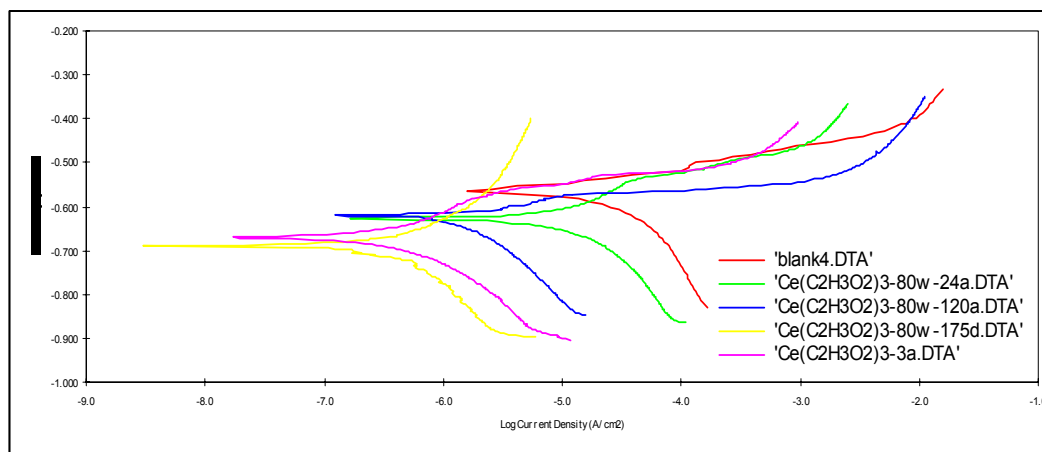


Figure 6: DC polarization curve of plasma treated  $\text{Ce}(\text{C}_2\text{H}_3\text{O}_2)_3$  powder (400mTorr, 80w, 2 hours)

## Conclusions

Using plasma polymerization, polymeric thin films were successfully obtained on the surface of TTA, BTA, TA and cerium acetate powdered organic corrosion inhibitors. TOFSIMS, SEM and TEM confirmed the presence of the polymeric films. By measuring the contact angle with water, the surfaces of these particles were confirmed to be modified from hydrophilic to hydrophobic. Using immersion tests, we have demonstrated that the encapsulated water-soluble inhibitors can slowly release into the environment and protect AA2024-T3 panels. They are as effective as chromate pigments. Thus this technology offers promise to replace chromates in various applications.

1. EPA Federal Register, *National Emission Standards for Hazardous Air Pollutants for Source Categories: Aerospace Manufacturing and Rework Facilities*, **60**, 45947 (1995)
2. W. Qafaoui, Ch. Blanc, N. Pebere, A. Srhiri and G. Mankowski, *J. App. Electrochem.*, **30**, 959 (2000)
3. W. Qafaoui, Ch. Blanc, N. Pebere, H. Takenouti, A. Srhiri and G. Mankowski, *Electrochimica Acta*, **47**, 4339 (2002)
4. C. Chen and C. Lin, *Analytica Chimica Acta*, **321**, 215 (1996)
5. A.M.S. Abdennabi, A.I. Abdulhadi and S. Abu-Orabi, *Anti-Corros. Meth. Mat.*, **45**, 102 (1998)
6. S.L. Cohen, V.A. Brusic, F.B. Kaufman, G.S. Frankel, S. Motakef and B. Rush, *J.Vac. Sci. Technol.* **A8(3)**, 2417 (1990)
7. A.N. Önal and A.A. Aksüt, *Anti-corros. Meth. Mat.*, **47**, 339 (2000)
8. D. Shi, S. Wang, W.J. van Ooij, L.M. Wang, J. Zhao and Z. Yu, *Appl. Phys. Lett.*, **78**, 1243 (2001)
9. F. Homilius, A. Heilmann and C. von Borczyskowski, *Surf. Coat. Tech.* **74**, 594 (1995)
10. D. Vollath and D.V. Szobó, *J. Nanoparticle Research*, **1**, 235 (1999)
11. J. Janca, P. Stahel, J. Buchta, D. Subedi, F. Krcma and J. Pryckova, *Plasmas and Polymers*, **6**, 15 (2001)
12. N. Inagaki, S. Tasaka, and H. Abe, *J. Appl. Pol. Sci.*, **46**, 595 (1992)

# Comparison of Remote and Direct Plasma Techniques to Remove NO from High Temperature Diesel Exhaust Gases

Y.Yoshioka<sup>1</sup>, R.Takenaka, J.Shimasaki<sup>2</sup>

<sup>1</sup> Kanazawa Institute of Technology, Ishikawa, Japan  
<sup>2</sup> Hokuriku Electric Power C., Toyama, Japan

## Abstract

Direct and remote plasma techniques were applied to remove NO from high temperature diesel exhaust gases. The tests were carried out at the temperature up to 220°C. It was found that NO removal efficiency by direct plasma method is higher in the temperature range between 90 to 130°C and gradually decreases with temperature above 130°C. There is a small temperature effect of the efficiency improvement by HC addition to exhaust gases. It was also found that we could remove NO by ozone injection method up to at least 220°C.

## 1. Introduction

Diesel exhaust gases are one of the causes of severe atmospheric pollutions. Selective catalytic reduction of NO<sub>x</sub>, which is widely adopted for gasoline engines, is very difficult to apply to diesel exhaust gases, because the gases contain considerable amount of oxygen and suspended particulate matters. Alternatively, non-thermal plasma techniques have been investigated in various institutes or universities [1]~[5]. The authors group has been investigating this method from various directions [6]~[9]. The principal issues are that as direct plasma techniques, barrier discharge reactor can remove NO with efficiency of 20 to 25 g/kWh and as remote plasma techniques, ozone injection method also can remove NO with efficiency of 25 to 30 g/kWh. In order to increase the efficiency, hydrocarbon addition to exhaust gases is effective and in this case the efficiency is almost 2 times higher than that of without HC addition. Hydrocarbon addition to ozone injection method has no effect or an opposite effect [10]. The effective way to improve efficiency in ozone injection method is to use pure oxygen or oxygen enhanced air as an ozonizer source gas [11]. The efficiency in the case of pure oxygen becomes almost 60 to 70 g/kWh, which is very close to a research target of 80 g/kWh [12]. However, all these experiments were carried out at the temperature range of 30 to 60 °C. Usually, chemical reactions are temperature sensitive and so if high temperature gases are treated by plasma, the efficiency may change hopefully to higher values. There is almost no literature, which described the temperature effect of NO removal efficiency.

In this paper, we are going to investigate the temperature effect of NO removal efficiency for both remote plasma (ozone injection) and direct plasma method.

## 2. Experimental apparatus

### 2.1 Experimental apparatus of direct plasma method

Exhaust gases from a 2.4kVA diesel engine generator were used as the target of plasma treatments. This engine exhausts 20Nm<sup>3</sup>/h gases and gas components change with electric load as shown in Fig.1. Highest NO concentration appears at the maximum electric power output and the concentration is around 310ppm. Oxygen at this power remains about 14%. The amount of suspended particulate matters is about 3.3 g/h. The NO removal system by direct plasma techniques is shown in Fig.2. Exhaust gases from engine flow through a gas cooler to control gas temperature and come into plasma reactor based on barrier discharge. Fig.3 shows the system for higher gas temperature, where the gas cooler is omitted. Fig.4 shows a barrier discharge device. It consists of a stack of six pilex-glass plates of 3mm thickness pasted aluminum foil electrode on them and with 3mm thick spacer. The stack is set inside of the stainless steel vessel. High voltage transformer (max 30kVrms) driven by a variable voltage and frequency power source was used to apply high

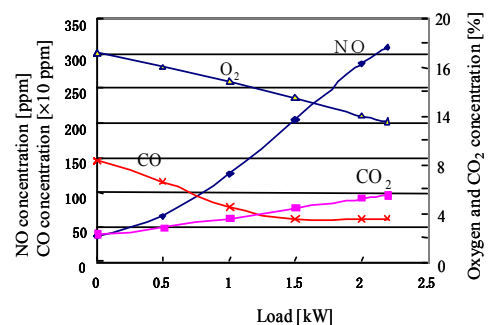


Fig.1 Gas components and their variation with engine load



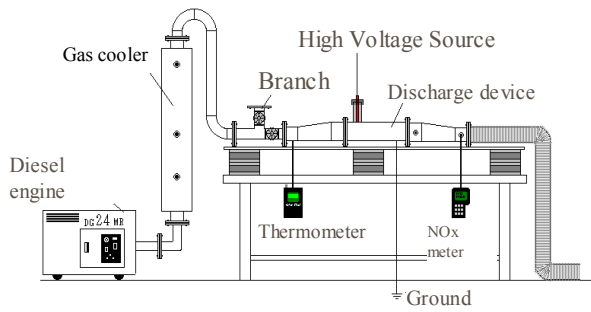


Fig.2 Experimental setup-1 for medium temperature exhaust gas treatment

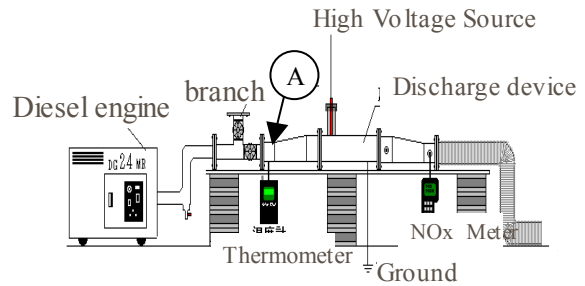


Fig.3 Experimental setup-2 for high temperature exhaust gas treatment

voltage to the discharge device through a small bushing.

Discharge power was calculated from voltage-charge lissajous figure. Gas flow rate was measured by the pressure difference at an orifice located in the gas flow line. NO, NO<sub>2</sub>, NO<sub>x</sub>, CO, CO<sub>2</sub> were measured by NO<sub>x</sub> meter (Testo. Co). Hydrocarbon (HC) addition port is located at the upstream portion (see mark A) and HC concentration was measured by HC meter ( Horiba Co.) at rear portion of the plasma reactor. Behind the system we used scrubber to absorb NO<sub>2</sub> converted from NO.

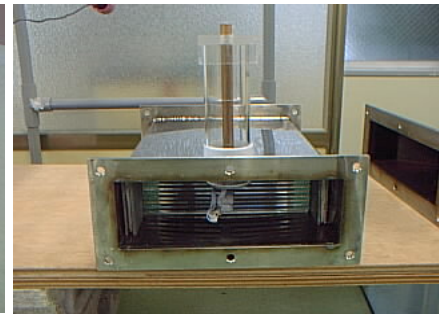
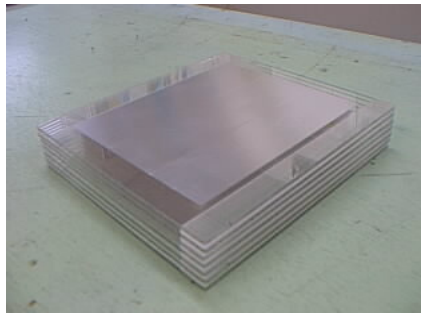


Fig.4 Barrier discharge device consists of a stack of electrode and barrier (left) and barrier discharge device set in a vessel (right)

## 2.2 Experimental apparatus of remote plasma method

We used an ozone injection method as remote plasma technique. The reason why this belongs to remote plasma method is that plasma is not used directly in the exhaust gases. Fig. 5 shows the experimental setup. An ozonizer (a barrier discharge device) consists of 10 soda-glass plates pasted aluminum foil electrode on them and stacked with 3mm gap. A blower feeds air to the ozonizer. Ozonized air is injected into high temperature exhaust gases. Airflow rate to the ozonizer was changed as a parameter. Total gas flow rate after injecting ozonized gas increases up to the sum of exhaust gases and ozonized gas. Ozone concentration was measured by ozone monitor ( Ebara Jitugyo Co.). All other things are same as in direct plasma method.

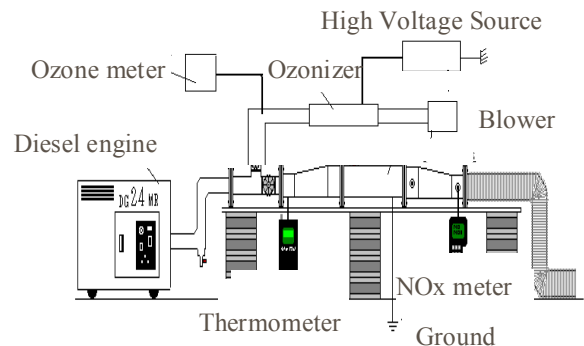


Fig.5 Experimental setup of remote plasma method (ozone injection method)

## 3. Experimental result

### 3.1 Direct plasma method

A series of experiments was carried out at the following conditions; namely engine load of 1kW (half

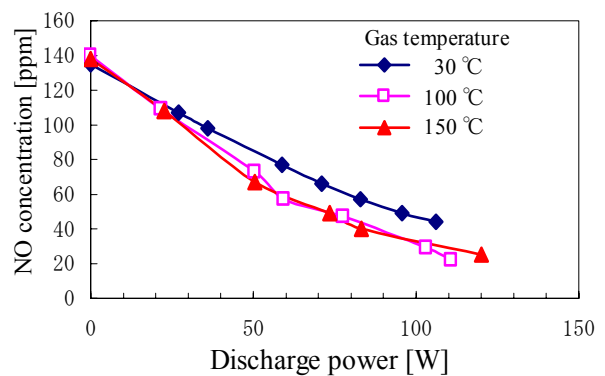


Fig.6 NO removal characteristics at different gas temperature

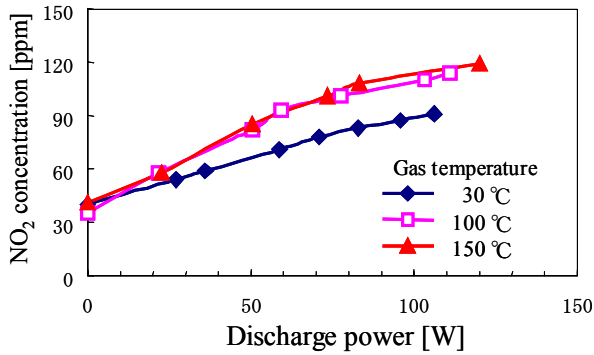


Fig.7 NO<sub>2</sub> formation at different gas temperature

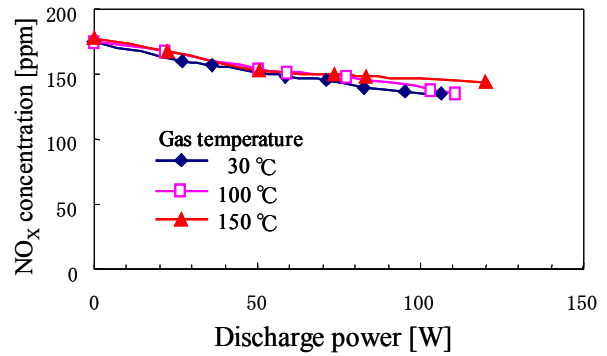


Fig.8 NO<sub>x</sub> removal at different gas temperature

load), applied voltage of 10 to 14kV and frequency of 50 to 250Hz depending on the discharge power, gas temperature range between 30 and 155 °C, and gas flow rate of 20m<sup>3</sup>/h.

Fig.6 shows NO removal characteristics at 3 different gas temperatures of 30, 100 and 150 °C. It is clearly seen that at higher temperature, NO decrease faster with the increase of discharge power. Fig.7 shows formation of NO<sub>2</sub> in the same experiment. NO<sub>2</sub> is formed by an oxidation of NO and the NO<sub>2</sub> formation is more active at higher temperature. Fig. 8 shows NO<sub>x</sub> concentration as a function of discharge power. It is seen that decrease of NO<sub>x</sub> is smaller than NO, because most part of NO<sub>2</sub> is formed from NO and NO<sub>x</sub> is a sum of NO and NO<sub>2</sub>. Fig.9 shows relation between NO removal efficiency and NO removal rate. The efficiency at high temperature as 100 and 150 °C is about 35% higher than that at low temperature. In order to know the temperature dependency of NO removal efficiency more clearly, we carried out another experiment. This experiment was carried out at fixed discharge power of 60W and by changing gas temperature by adjusting gas cooler. Fig.10 shows the result. It is seen that in the temperature range between 80 and 120 °C, the efficiency becomes high as around 40g/kWh.

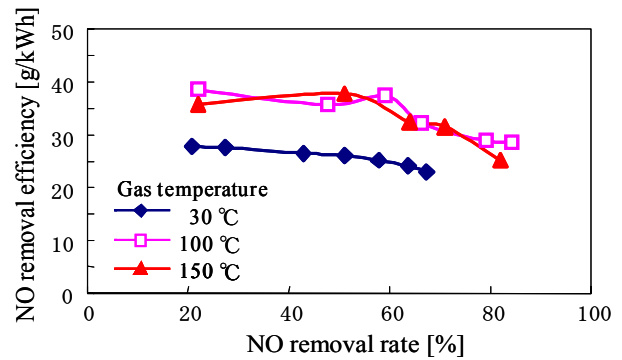


Fig.9 NO removal efficiency at different gas temperature

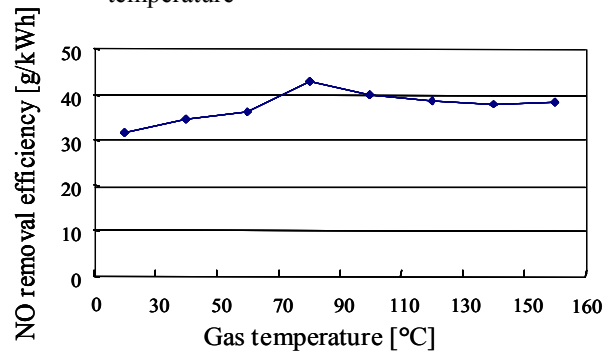


Fig.10 NO removal efficiency as a function of gas temperature (discharge power was fixed on 60W)

### 3.2 Direct plasma method with HC addition

It is well known that HC addition improves the efficiency considerably. Here we investigated the effect of HC addition at high temperature. Fig.11 shows NO removal characteristics when HC of 300 and 500ppm were added into exhaust gases at gas temperature of 150 °C. It shows clearly that by HC addition of 300 and 500ppm, NO decreases quickly with the increase of discharge power. Fig.12 shows the NO removal efficiency of this experiment. The efficiency is improved about 52% to 62% by HC addition. The HC addition experiment was carried out

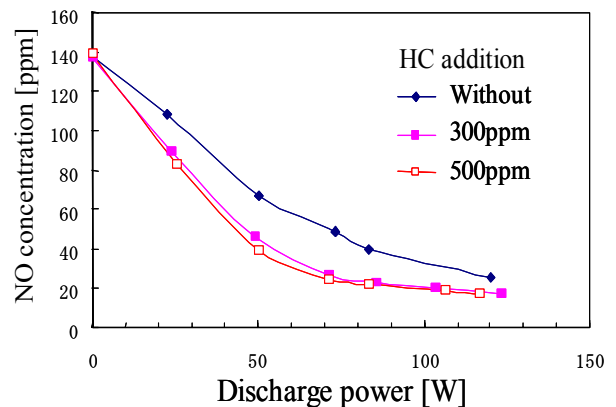


Fig.11 NO removal characteristics with HC addition

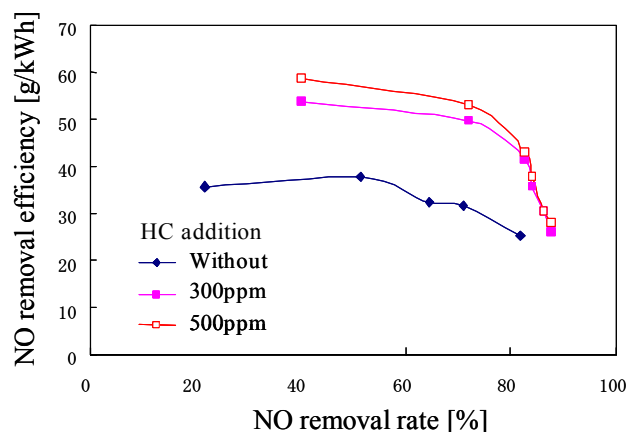


Fig.12 NO removal efficiency as a function of NO removal rate

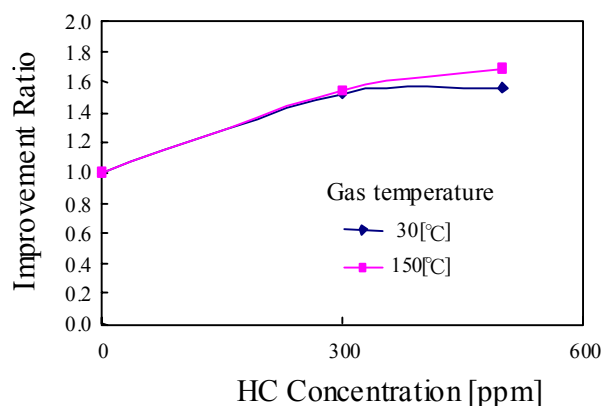


Fig.13 Improvement of NO removal efficiency by HC addition

at 30 °C also, and Fig.13 shows a comparison of the effect of HC addition at 30 and 150°C. It is seen that there is almost no temperature effect of HC addition on the NO removal efficiency at 300ppm but the effect increases a bit at 500ppm.

### 3.3 Remote plasma method (ozone injection)

In the remote plasma method, discharge device is set apart from exhaust gases. This is a big advantage; because the discharge device is not contaminated by suspended particulate matters contained in exhaust gases. The principle to remove NO is an oxidation of NO by ozone. Our previous investigation showed that the NO removal efficiency is a bit higher than the direct plasma method [6]. However, whether this ozone injection method is applicable to exhaust gas treatment of high temperature or not is very interesting, because ozone is said to be thermally dissociated above around 200 °C.

Experiments were carried out using the experimental setup shown in Fig.5. The experimental conditions were as follows. Exhaust gas flow rate was 20m<sup>3</sup>/h, engine load was 2kW, air flow rate to ozonizer was 8 to 20m<sup>3</sup>/h, applied voltage was 10 to 14kV and the frequency was 50 to 300Hz. Table 1 shows ozone formation characteristics taken at the discharge power of 150W. Air flow rate was changed from 8 m<sup>3</sup>/h to 20m<sup>3</sup>/h, and ozone yield was maximum at the air flow rate of 16m<sup>3</sup>/h. Efficiency of ozone yield is around 60g/kWh and this value is usual as a conventional ozonizer, while modern ozonizers have much higher efficiency. Fig.14 shows the experimental result carried out at gas temperature of 150°C. Here gas temperature is not the exhaust

Table 1 Ozone yield and its efficiency (discharge power 150W)

Flow rate [m <sup>3</sup> /h]	8	10	13	16	20
Ozone concentration [ppm]	510	410	322	275	180
Ozone yield [g/h]	8.74	8.78	8.97	9.42	7.71
Efficiency of Ozone yield [g/kWh]	58.3	58.6	59.8	62.9	51.4

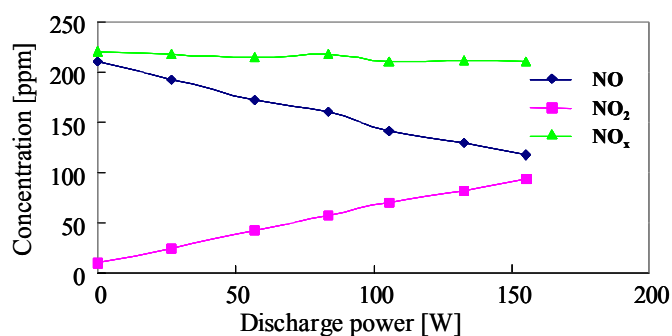


Fig.14 NO removal and NO<sub>2</sub> formation characteristics by ozone injection method

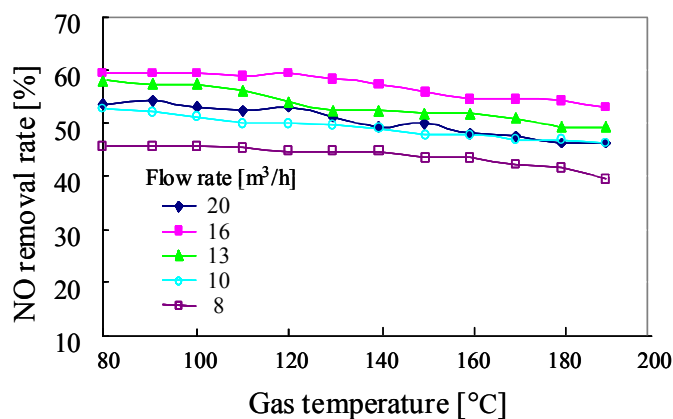


Fig.15 NO removal rate as a function of gas temperature

gas temperature but gas temperature after mixing with ozonized air. It was a little surprise that even at 150°C, NO decreases and NO<sub>2</sub> increases linearly with discharge power, because exhaust gas temperature seems to be around 250°C. Next, Fig.15 shows the NO removal rate at various gas temperatures. In this experiment, we fixed the discharge power at 150W, and changed gas temperature by adjusting gas-cooler. From this figure, we see that NO removal rate is highest at airflow rate of 16m<sup>3</sup>/h, and it decreases at lower airflow rates. It is also seen that NO removal rate gradually decreases at the temperature above around 130 °C. Difference of NO removal rate by airflow rate is explained partly by the difference of ozone yield shown in Table 1. The decrease of NO removal rate at the temperature above 130°C may be ozone dissociation at high temperature. Fig.16 shows NO removal efficiency of this experiment. As it is expected from figure 15, NO removal efficiency gradually decreases above 130°C, but the efficiency is about 33g/kWh at 190°C and at 60% NO removal rate. It is a bit low in comparison with the efficiency of 38g/kWh obtained by direct plasma method (see figure 9). The reason of the degradation of efficiency at high temperature is analyzed from ozone reaction rate with NO shown in Fig.16. In this figure, the ozone reaction rate decreases gradually at the temperature of above 130°C, which means perhaps that some of ozone injected into high temperature exhaust gases dissociate before oxidize NO. However, ozone reaction rate is more than 80% except at air flow rate of 8m<sup>3</sup>/h. An additional experiment was carried out up to 220°C; the decrease of NO removal efficiency was within 9% compared with that at 180°C.

#### 4. Discussion

##### 4.1 Comparison of remote and direct plasma method

Ozone injection method is classified as a typical remote plasma method and in case of lower gas temperature like below 60°C, it was very attractive from both high NO removal efficiency and contamination free from suspended particulate matter in exhaust gases. Present experiments were carried out at higher gas temperature from 80 to 220°C. We started the experiment with a suspicion that ozone injection does not work at such a high temperature. However we could confirm this method can be applied at least up to 220°C and the NO removal efficiency of around 33g/kWh was obtained although the value is a bit lower than at low temperature. On the other hand, direct plasma method using barrier discharge showed high efficiency of 40g/kWh at around 90 to 130°C and if HC was added, the efficiency increased up to 58g/kWh. From these data, we will soon think that direct plasma method is better than remote plasma method. However, in the course of experiments, we have experienced much trouble in direct plasma method. Principal trouble was a contamination of discharge device by suspended particulate matter in exhaust gases. High voltage connection to the discharge device and high temperature operation were also sources of trouble. So as for practical application, remote plasma method would be better than direct plasma method even applied to high temperature exhaust gases.

##### 4.2 Ozone dissociation at high temperature

It is said that ozone dissociates thermally at high temperature. From the reference, we see that ozone dissociation is a secondary reaction shown in the following equations

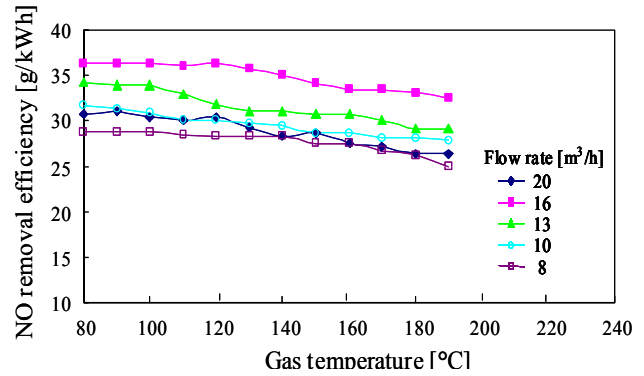


Fig.16 NO removal efficiency by ozone injection method

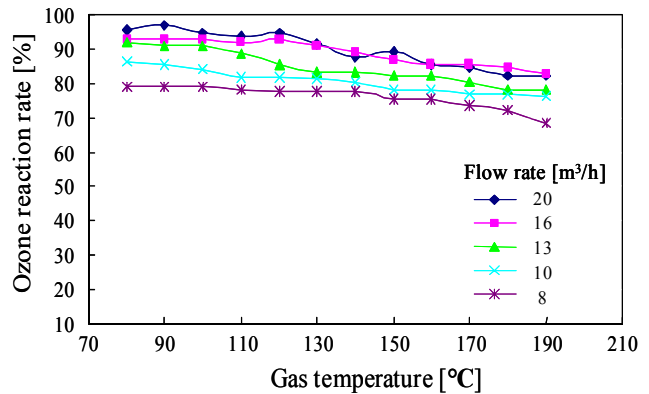
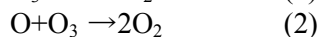
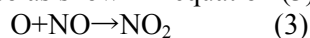


Fig.17 Ozone reaction rate as a function of gas temperature





The reaction speed increases one order higher level by every 25°C increase, which means the reaction speed increases 6th order high from 50°C to 200°C [13]. However, O radical formed in equation (1) can react with NO also as shown in equation (3).



So dissociation of O<sub>3</sub> contributes to remove NO also. So in spite of our suspicion, ozone injection method can be applied to high temperature exhaust gases.

## 5. Conclusion

In order to remove NO from high temperature diesel exhaust gases, Ozone injection method and direct discharge method were investigated, and NO removal efficiency of two methods was compared each other. The conclusions that we obtained are as follows.

- (1) NO removal efficiency by direct discharge method increases at a temperature range of 90 to 130°C and reaches to 42g/kWh, and above this temperature the efficiency gradually decreases but keeps about 38 to 40g/kWh at 180°C.
- (2) Addition of HC of 300ppm to 500ppm into high temperature exhaust gases increases the NO removal efficiency up to 52 to 55g/kWh, but the increase of efficiency is not so different from the one at low temperature.
- (3) Ozone injection method is applicable to high temperature exhaust gases of at least 220°C in spite of the suspicion that ozone dissociates and does not work at high temperature. This method has big advantages that the discharge device is free from the contamination of suspended particulate matters and needs not to be operated at high temperature. The NO removal efficiency of 33g/kWh is a bit smaller than the direct method, however the value is fairly good in comparison with that of direct discharge method at lower temperature.

## Acknowledgement

The author's express sincere thanks to students, Mr. K.Tokunaga, O.Miwa, K.Takanami, K.Takahasi and S.Saeki for their contribution to experiments. This work was supported by a Grand-in Aid for Scientific research (c) of JSPS.

## References

- [1] J.W.Rogers, A.J.Nezezchelh, G.E.Rolader, S.P.Federle, D.M.Littrell, W.C.Neely and E.I.Newhouse, J. Adv. Oxid. Technol. Vol.2, pp353-363, (1997)
- [2] J.Ryu, B.Chum, H.Lee, K.Chum and K.Lee, Proceeding, ISNPT-3, pp114-118, (2001)
- [3] B.M.Penetrante, B.M.Brusasco, B.T.Merritt, W.J.Pitz and G.E.Vogtlin, SAE, SP-1483, pp45-50, (1999)
- [4] R.Wegst, M.Neiger, H.Russ and S.Liu, SAE, SP-1483, pp103-110, (1999)
- [5] R.Dorai and M.J.Kushner, SAE, SP-1483, pp81-87, (1999)
- [6] Y.Yoshioka, K.Sano and K.Teshima, Proceeding, ISNPT-3, pp119-124, (2001)
- [7] Y.Yoshioka and T.Shinkawa, T.IEE Japan, Vol.120-A, pp250-255, (2000)
- [8] Y.Yoshioka, T.Yukitake, M.Nakai, K.Souma, K.Tuchya, K.Annou and Y.Hor, Comb. Sci. and Tech, Vol.133, pp13-29, (1998)
- [9] T.Shinkawa, J.Shimasaki, K.Sano and Y.Yoshioka, T.IEE Japan, Vol.122-A, NO.9, pp832-839, (2002)
- [10] Y.Yoshioka, K.Sano and T.Shinkawa, ISPC-15, VII-pp3149-3154, (2001)
- [11] K.Sano and Y.Yoshioka, Meeting of Discharge Research, JIEE, ED-01-143, pp59-64, (2001)
- [12] Y.Yoshioka, T.IEE Japan, Vol.122-A, No.7, pp676-682, (2002)
- [13] E.Warburg, Ann.Phys (4), 9, 1286, (1902)

# Modelling of processes accompanying a treatment of surfaces in gas discharge: influence of sputtering and implantation on working gas composition

A. I. Lyapin

Mogilev State Technical University, Mogilev, Belarus, [lyapin@mgtu.mogilev.unibel.by](mailto:lyapin@mgtu.mogilev.unibel.by)

Composition of working gas plays an important role in surface processing in gas discharge. The ratio of gas components determines the direction and the rate of reactions in gas [1]. Sputtering and implantation are the dominant processes during the surface treatment of materials in the presence of accelerating potential on the pattern being processed [2, 3]. Sputtering results in acceleration of various phase reorganizations in the implanted layer [4-6]. Besides sputtering may influence the composition of gas and the parameters of the discharge as it provides the inflowing of a new (additional) portion of gas into the discharge. In this paper we try to establish the correlation between the working gas composition and distribution of the implanted atoms, which are subjected to the subsequent sputtering.

The following preconditions lie in the basis of the model: (i) sputtering and implantation take place together with the processes necessary for maintenance of the discharge; (ii) ionization degree of gas is high enough [2]; (iii) the pumping rate of the working chamber is constant and the pressure in the chamber is determined only by sputtering and implantation; (iiii) sputtering and implantation do not influence the "independence" of the discharge. Sputtering provides inflow of particles into the discharge. Whereas implantation provides outflow of particles from the discharge. The sputtered atoms leave a surface being neutral. Both atoms of the pattern being processed and implanted atoms of an impurity are exposed to sputtering. Part of the sputtered atoms are ionized and come back to the "cathode".

The equations for the partial pressures and the current densities are obtained on the basis of the assumptions given above. The parameters included in the equations are connected with the discharge parameters and the characteristics of the treated material. In this paper only some calculation results are given. The change of the partial pressures caused by implantation and sputtering is given in Figure 1.

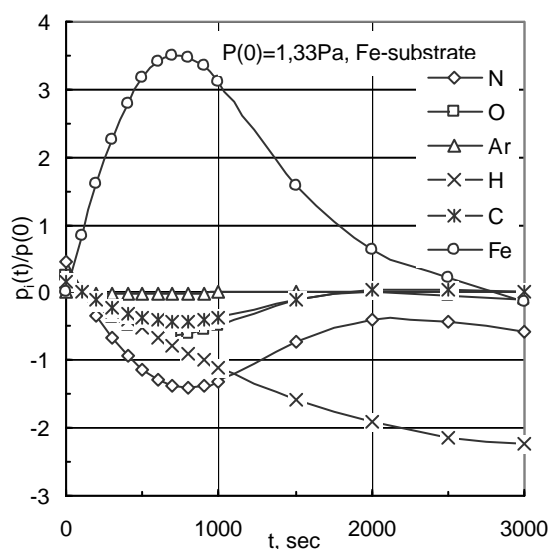


Figure 1. The change of the partial pressures as a function of the treatment time

The received results show, that the ratio of working gas components essentially changes as a result of implantation and sputtering. There is an initial transitive stage of the process after which a certain ratio of the gas components is established. Obviously, the duration of the specified stage is determined both by the parameters of the discharge (accelerating potential, current density) and the parameters of distribution of atoms implanted into the matrix (by the gas - substrate combination).

Model calculations lead to physically motivated results. The characteristic parameters of the ion-target combination and the irradiation conditions are taken into account in the model in question. This means that the model can be used for other combinations. Certainly, the numerical significance should be precise experimentally.

## References

- [1] M. Capitelly, R. Celiberto, F. Esposito et al Plasma Sources Sci. Technol. **11** 3A (2002)
- [2] L.I. Kiselevskii, A.I. Lyapin - ICPIG-XIX, **1** (1989)
- [3] A.I. Lyapin- ICPIG-XXV, **1** (2001)
- [4] A.A. Katkalo, A.I. Lyapin- ICPIG-XXIII, **2**, (1997)
- [5] A.I. Lyapin- IRS-99, Proc. Third Intern. Conference. **2**, (1999) Minsk, Belarus.
- [6] A.I. Lyapin- Modelling Simul. Mater. Sci. Eng. **8**, (2000). Printed in the UK

# Phenomena on Electrodes of Compact Fluorescent Lamps at End-of-Life

Yoshio Watanabe, Yo Ooishi and Yoshiki Kurokawa

*Department of Electrical, Electronics and Information Engineering, Kanagawa University, Yokohama, Japan*

## 1. Introduction

For various reasons, compact fluorescent lamps are mainly operated on the high-frequency electronic ballast called “Half-bridge Inverter”. It is reported that the electrodes driven by an electronic ballast will be exposed to serious ion bombardments during ignition process and the electrode may be broken even if emitter still remains [1]. It is also reported that the glass envelop of the lamp accidentally melts down at the end-of-life due to the discharge formed at the broken electrode [2]. In this study, erosion phenomena of the tungsten-coil electrode during ignition phase are investigated.

## 2. Experiment

A fluorescent lamp will reach to end-of-life when the emitter coated on the coil-electrode is exhausted. In this study, the lamp of which one of the electrodes is without emitter is employed instead of the lamp at end-of-life. The view of the test lamp is shown in Fig.1. The specification of the test lamp is also shown in Table 1.

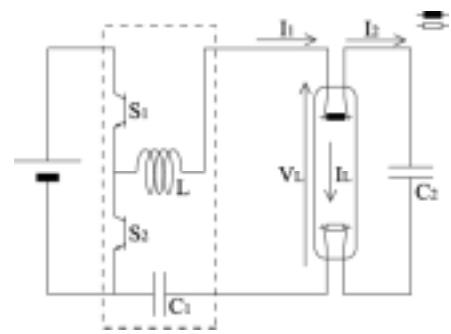


**Fig.1 View of the test lamp**

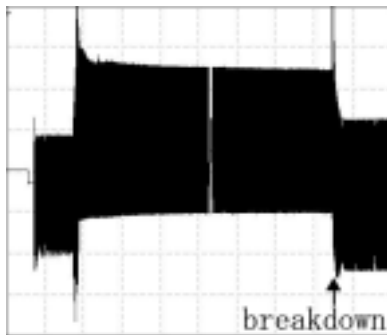
**Table 1 Specification of the test lamp**

Type	FPL36EX-N
Rated wattage	36 W
Rated discharge current	0.435 A
Tube diameter	20 mm
Discharge length	740 mm

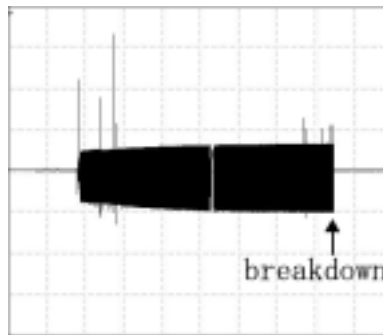
The employed operating circuit is shown in Fig.2. The circuit operation is as follows. When the switch  $S_1$  is closed and  $S_2$  is open, the current  $I_1$  flows from the power source to the capacitors  $C_2$  and  $C_1$  (where  $C_1 \gg C_2$ ) through the inductor  $L$  and the electrodes. Then  $C_2$  and  $C_1$  are charged up. In turn,  $S_1$  is open and  $S_2$  is closed, the charges stored in  $C_2$  and  $C_1$  begin to discharge through  $L$  and  $S_2$ . If the switching frequency of  $S_1$  and  $S_2$  are chosen to the resonance frequency determined by  $C_2$ ,  $C_1$  and  $L$ , the voltage appeared across  $C_2$  increases enough to ignite the lamp while the current  $I_2$  flowing through  $C_2$  serves for heating the electrodes. After ignition, the operating frequency will shift to the resonance frequency determined by  $L$  and  $C_1$ . As the half-bridge inverter employs the resonance circuit construction, the output current shows almost constant-current characteristics.



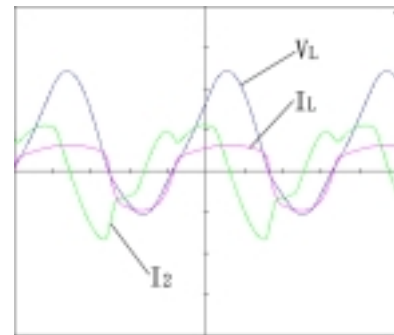
**Fig.2 Half-bridge inverter circuit**



(a) discharge voltage  $V_L$   
(150V/div., 1sec./div.)



(b) discharge current  $I_L$   
(0.5A/div., 1sec./div.)



(c)  $V_L$ ,  $I_L$ ,  $I_2$ ,  
(0.5A/div., 150V/div., 4μs/div.)

**Fig.3 Discharge voltage and current waveforms of the test lamp**

The discharge voltage  $V_L$  and current  $I_L$  waveforms of the test lamp during lamp operation are shown in Fig.3(a) and (b). At first, the pre-heating mode starts about one second. After the pre-heating mode, high voltage is applied across the lamp so that the lamp ignites immediately. Fig.3(c) shows the voltage  $V_L$  and current  $I_L$  and  $I_2$  waveforms after ignition. The amplitude of the discharge voltage is asymmetry since one electrode is with emitter and the other is without emitter, while DC component of the discharge current is zero since  $C_2$  and  $C_1$  are inserted in series in the circuit. The electrode breakdown occurs at the emitter-less electrode at about 8 seconds. Then discharge ceases.

The view of the electrode at which breakdown is taken place is shown in Fig.4. The breakdown place is always at the connecting point of the tungsten coil and a thick Ni-Fe pole, which supports the coil electrode. The enlarge view of the breakdown point is shown in Fig.5 which is taken just before breakdown occurs. At the connecting point with the supporting pole, the basket wire was lost and the center wire of the coil was eroded.

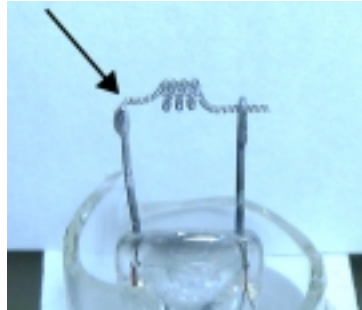


Fig.4 View of breakdown electrode

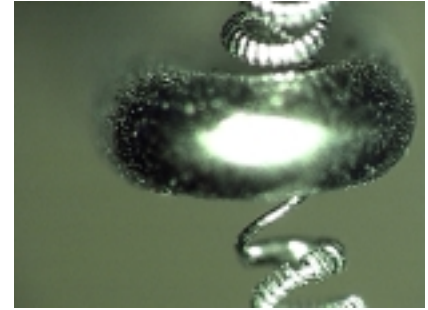


Fig.5 View of breakdown point

The top surface of the supporting pole looks like being polished and shows lustrous surface.

Next, the test circuit II shown in Fig.6 is employed to investigate the influence of the current  $I_2$  on the electrode erosion, since  $I_2$  should increase at end-of-life since discharge voltage that is equal to the voltage across  $C_2$  will increase. In the test circuit II,  $I_2$  does not flow through the emitter-less electrode. The discharge voltage  $V_L$  and current  $I_L$  waveforms during lamp operation are shown in Fig.7(a) and (b). The observed phenomena are fundamentally the same with those obtained by the circuit in Fig.2. The electrode breakdown occurs at the connecting point of the

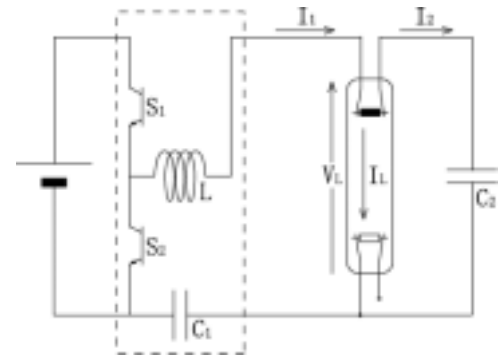
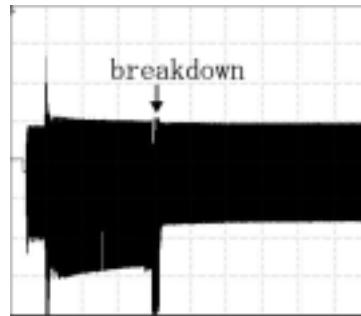
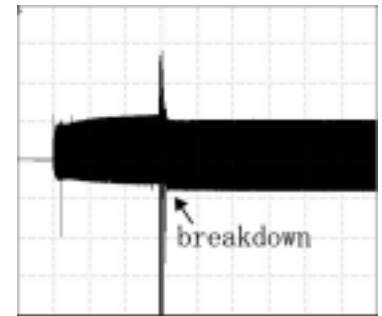


Fig.6 Test circuit II

emitter-less electrode with the supporting pole within 8 seconds. This result indicates that  $I_2$  does not affect the electrode breakdown mechanism. When the electrode breakdown takes place at the right side of the filament coil (open terminal) in Fig.6, the free end of the tungsten coil wire acts as a thermal electrode. Then discharge voltage drops to almost normal voltage as shown in Fig.7. This case was found to be majority (6/8 lamps). On the other hand, when electrode breakdown takes place at the left side of the filament coil (connecting terminal to the circuit), the supporting pole acts as an electrode and melts down abruptly. Discharge ceases when the pole melts down completely. This case was found to be minority (2/8 lamps).



(a) discharge voltage  $V_L$   
(150V/div., 2sec./div.)



(b) discharge current  $I_L$   
(0.5A/div., 2sec./div.)

Fig.7 Voltage and current waveforms at the test circuit II

Next, which cycle the electrode breakdown will take place in cathode- or anode-cycle is investigated. The test circuit III shown in Fig.8 is employed. The test lamp has two emitter-less electrodes in one end of the lamp. Each emitter-less electrode is connected to the operating circuit through a diode respectively in order to operate as a cathode or an anode independently. The discharge voltage waveform during lamp operation is shown in Fig.9(a), and  $I_L$  and  $V_L$  waveforms are also shown in Fig.9(b). The electrode breakdown occurs within

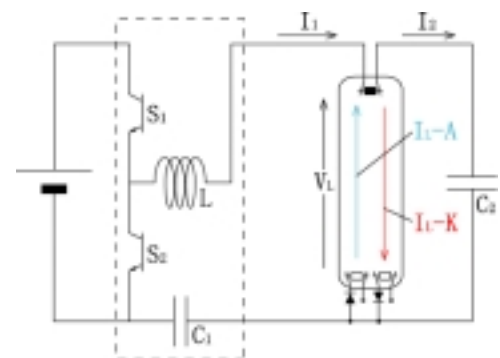


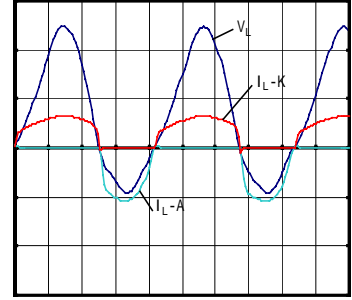
Fig.8 Test circuit III

8 seconds always at the cathode-cycle electrode. The observed phenomena are fundamentally the same with those obtained by the circuit in Fig.2 and the test circuit II in Fig.6.

The obtained data by the three experiments are summarized in Table 2. There is no significant difference in the discharge voltage and current characteristics between the three experiments. For the breakdown time, the time obtained by the circuit shown in Figs.6 and 8 are rather short compared with the one by the circuit shown in Fig.2. The coil breakdown always occurs at the connecting point with the thick pole supporting the coil electrode.



(a) discharge voltage  
(150V/div., 1sec./div.)



(b)  $I_L$ ,  $I_{L-K}$ ,  $I_{L-A}$  and  $V_L$   
(0.5A/div., 150V/div., 4μs/div.)

**Fig.9 Voltage and current waveforms at the test circuit III**

**Table 2** Discharge voltage, current and breaking time by three experiments

Test circuit	Number of test lamps	Discharge voltage (Vp-p)	Discharge current (Ap-p)	Breakdown time (sec.)
Fig.2	23	537	0.80	8.31
Fig.6	8	588	0.86	7.70
Fig.8	7	545	0.90	7.60

### 3. Cathode fall characteristics

Cathode-fall voltage  $V_K$  and the power  $P(T_K)$  which flows into the emitter-less electrode during cathode-cycle are estimated using a simulation model. The energy balance in cathode cycle is given as follows.

$$P(T_K) = I_p(V_K + V_i - \phi) - I_e\phi = \alpha(T_K - T_0) + \beta(T_K^4 - T_0^4) \quad (1)$$

where  $I_p$ : ion current,  $I_e$ : electron current,  $V_i$ : ionization potential,  $\phi$ : work function of the electrode material,  $T_K$ : cathode temperature,  $T_0$ : ambient temperature,  $\alpha$ : convection coefficient and  $\beta$ : radiation coefficient for the electrode.

To calculate  $T_K$  by Eq.(1), the values  $V_K$  and the electron current ratio  $\eta = I_e/(I_e + I_p)$  is needed to know.  $V_K$  is estimated by two methods. The first method is as follows. Discharge voltage consists of anode-fall voltage, positive column voltage  $V_c$  and cathode-fall voltage. When the lamp is operated at high frequency, anode-fall voltage could be neglected. The cathode-fall voltage for the electrode with emitter is also neglected since it is much smaller than the cathode-fall voltage  $V_K$  for the emitter-less electrode and positive column voltage. Thus following approximation is obtained for anode- and cathode-cycle respectively.

$$\text{For the cycle when the emitter-less electrode acts as an anode: } V_{L-A} \approx V_c' \quad (2)$$

$$\text{For the cycle when the emitter-less electrode acts as a cathode: } V_{L-K} = V_K + V_c \quad (3)$$

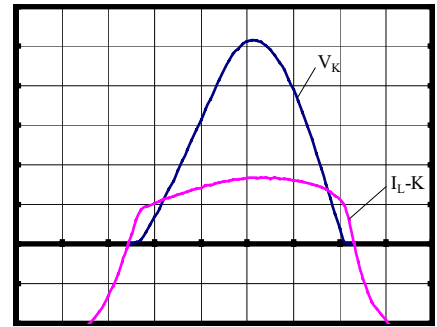
where  $V_{L-K}$  and  $V_{L-A}$  are discharge voltages in cathode- and anode-cycle respectively. The positive column (plasma) resistance can be regarded as constant during anode- and cathode-cycle in the case of high frequency operation. Thus  $V_c/V_c' = I_{L-K}/I_{L-A}$  is established, where  $I_{L-K}$  and  $I_{L-A}$  are discharge currents in cathode- and anode-cycle respectively. Then  $V_K$  is given by the following equation.

$$V_K = V_{L-K} - \frac{I_{L-K}}{I_{L-A}} V_{L-A} \quad (4)$$

Using the measured discharge voltage ( $V_{L-A}$ ,  $V_{L-K}$ ) and current ( $I_{L-K}$ ,  $I_{L-A}$ ) waveforms,  $V_K$  is calculated to be 269V<sub>0-p</sub> in average for 5 lamps.

The second method is a direct measurement using a probe. The probe (0.5mm in diameter and 2mm length) is inserted in front of the emitter-less electrode. The cathode voltage  $V_K$  estimated by the probe voltage and discharge current  $I_{L-K}$  waveforms during cathode cycle of the emitter-less electrode are shown in Fig.10. The obtained cathode voltage is also 269V<sub>0-p</sub> in average for 5 lamps.

Next, the electron current ratio is estimated using the simulation model. The simulation model consists of “ion-sheath model” and “negative-glow model”. The model is applied for a direct current.

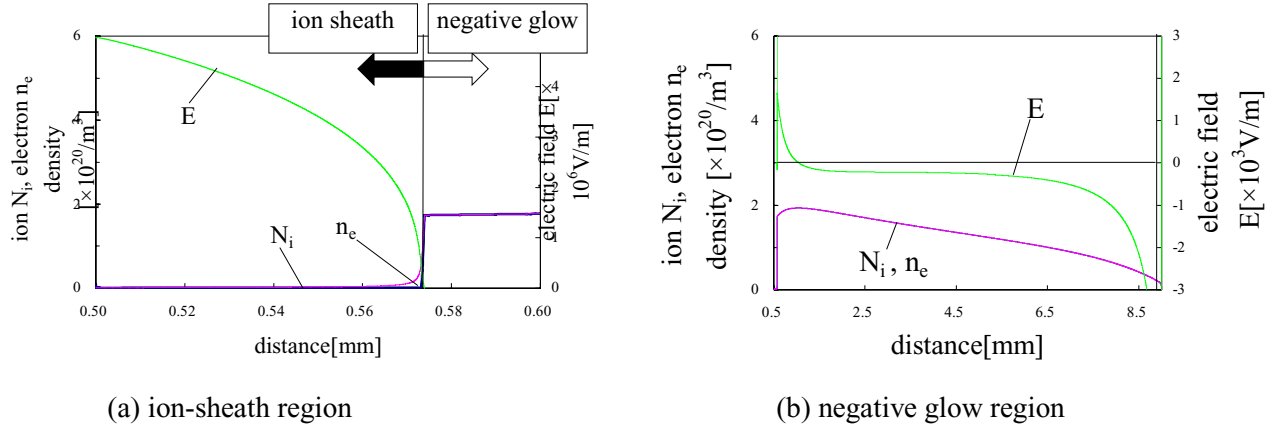


(50V/div., 0.2A/div., 2μs/div.)

**Fig.10 Cathode voltage  $V_K$  and discharge current  $I_{L-K}$**



Calculation condition is as follows. The tube inner diameter is 18mm. The cathode is assumed to be the ball shape of which diameter is 1mm and work function  $\phi$  is 4.7eV for tungsten. Ionization atoms are mercury ( $V_i=10.4\text{eV}$ ). Penning effect between argon and mercury atoms is taken into account in this model. The calculated results for the distribution of electron density  $n_e$ , ion density  $N_i$ , and electric field  $E$  at  $I_L=0.32\text{A}$



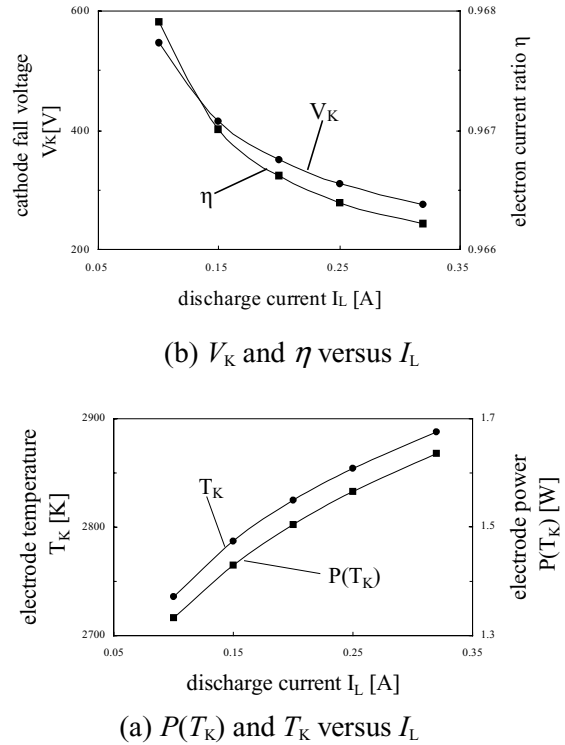
**Fig.11 Distribution of electron density  $n_e$ , ion density  $N_i$ , and electric field  $E$  in the cathode fall**

and  $V_K=269\text{V}$  are shown in Fig.11. Fig.11(a) is in the ion-sheath region and Fig.11(b) is in the negative glow region. The calculated results for cathode-fall voltage  $V_K$ , the power  $P(T_K)$  flowing into the cathode and cathode temperature  $T_K$  as a function of discharge current  $I_L$  are shown in Fig.12.  $V_K=269\text{V}$ ,  $\eta=0.966$ ,  $P(T_K)=1.64\text{W}$  and  $T_K=2888\text{K}$  at  $I_L=0.32\text{A}$ . Since the peak value of the discharge current was  $0.32\text{A}$  as shown in Fig.10, the average cathode temperature must be lower than  $2800\text{K}$ . This value would be not enough for rapid meltdown for the tungsten coil. The cathode temperature for the electrode with emitter is also calculated using the same model. The result is as follows:  $V_K=16\text{V}$ ,  $P(T_K)=0.082\text{W}$  and  $T_K=1202\text{K}$  at  $I_L=0.46\text{A}$ .

#### 4. Discussion

Two mechanisms could be possible for the breakdown mechanisms of the filament-coil electrode. One is “meltdown” due to high temperature. The other is “spattering” by high-energy ion bombardment. Following estimation can be derived from the data shown in Table 2. The discharge voltage-current characteristics, the breakdown time and its position are fundamentally the same between the three experiments. These facts suggest that the mechanism of the electrode breakdown in the three experiments is essentially the same. Namely the electrode breakdown is governed by the discharge current in cathode-cycle, while the current  $I_2$  flowing through the electrode and the discharge current in anode-cycle do not contribute for electrode breakdown. This result indicates that the breakdown mechanism is not meltdown due to high temperature, since less current flowing through the electrode is enough for meltdown. The coil breakdown always occurs at the connecting point with a thick pole supporting the coil electrode. The temperature at this portion hardly increases since the thick pole acts as a radiator. This fact also supports that the meltdown due to high temperature will hardly occur. Thus the electrode erosion must be caused by ion bombardments. The photograph shown in Fig.5 also supports this conclusion.

Next, cathode fall characteristics are discussed. The thermo-electronic emission current from the cathode surface,  $i_{e0}$  including Schottky effect is given by Eq.(5)



**Fig.12 Calculated cathode fall characteristics**

$$i_{\text{co}} = AT_K^2 \exp \left[ -\frac{q\phi - q\sqrt{qE_0 / 4\pi\epsilon_0}}{kT_K} \right] \quad (5)$$

where:  $q$ : elementary charge,  $E_0$ : electric field at cathode surface,  $\epsilon_0$ : dielectric constant,  $k$ : Boltzmann constant. At end-of-life, work function  $\phi$  of the electrode will increase from 1.7eV (for barium) to 4.7eV (for tungsten) due to barium emitter exhaustion. Since the half-bridge inverter circuit has constant output current characteristics, discharge current would not decrease so much even if discharge voltage increases. Thus the increment of  $\phi$  causes the increment of  $E_0$ , hence  $V_K$ . In turn,  $T_K$  increases since the power related  $V_K$  is increased. Overall the increment in  $\phi$  should be compensated by increasing  $E_0$  from Eq.(5). Thus the cathode spot should be formed at the place where high electric field can be produced. The reasons why cathode spot is formed at the connecting point of tungsten coil and the supporting pole in the case of emitter-less electrode are not clear up to now: One might be due to the geometry effect, and the other might be due to the work function of Fe-Ni (about 4.0eV) which is lower than that of tungsten.

## 5. Conclusion

When ignition voltage is applied across the emitter-less electrode, discharge current tends to concentrate at the connecting point of tungsten coil and the supporting pole. Then, the electrode erosion by ion bombardments will occur at this point due to the high accelerating voltage and current concentration. The meltdown due to high temperature would not take place as breakdown mechanism. The reason why discharge current concentrates such portion might be due to the formation of high electric field produced by geometry effect.

## 6. References

- [1] M. Haverlag, et al., Proc. of 9<sup>th</sup> Int. Symp. Sci. & Tech. of Light Sources, 144:P, p.441, NY, USA (2001)
- [2] M. Myojo, et al., Proc. of 2002 Conf. Illum. Engng. of Jpn., No.5, p.55, Nagoya, Japan (2002).

# SiO<sub>x</sub>-like thin films deposited by PECVD for improving the corrosion behaviour of Mg alloys

E. Angelini<sup>1</sup>, F. Fracassi, S. Grassini<sup>1</sup>, F. Palumbo<sup>2</sup>, F. Rosalbino<sup>1</sup>, F. Spada<sup>2</sup>

<sup>1</sup> Department of Materials Science and Chemical Engineering, Polytechnic of Turin, Turin, Italy

<sup>2</sup> Department of Chemistry, University of Bari, Bari, Italy

## Abstract

In this work the corrosion behaviour of a magnesium alloy, WE43, coated with SiO<sub>x</sub>-like films was investigated. The coatings were prepared by Plasma Enhanced Chemical Vapour Deposition (PECVD), using Tetraethoxysilane (TEOS)-O<sub>2</sub>-Ar mixtures. The deposition process was performed at 200 W input power after a hydrogen plasma treatment. Electrochemical impedance spectroscopy was used to predict corrosion protective properties of deposited films. Different TEOS/O<sub>2</sub> ratios in the mixture provide varying degree of corrosion protection, however an increase in the film thickness gives the better protective properties.

## 1. Introduction

Magnesium alloys have some advantageous properties that make them an excellent choice for a number of applications: high strength/weight ratio, high thermal conductivity, good electromagnetic shielding characteristics, high damping characteristics, high dimensional stability and good machinability [1]. These properties make magnesium alloys valuable in a number of applications including automobile and computer parts, aerospace components, mobile phones, sporting goods, handheld tools and household equipment. Due to environmental problems associated with fuel emission products, there is a push in the automotive industry to make cars lighter in order to decrease fuel consumption. The use of magnesium alloys can significantly decrease the weight of automobiles without sacrificing structural strength. Unfortunately, magnesium alloys have a number of undesirable properties including poor corrosion and wear resistance, poor creep resistance and high chemical reactivity that have hindered their widespread use in many applications. One of the main challenges in the use of magnesium alloys, particularly for outdoor applications, is their poor corrosion resistance. Magnesium alloys are extremely susceptible to galvanic corrosion, which can cause severe pitting in the metal resulting in decrease of mechanical stability and an unattractive appearance [2]. One of the most effective ways to prevent corrosion is to coat the base material. Coatings can protect a substrate by providing a barrier between the metal and its environment and/or through the presence of corrosion inhibiting chemicals in them. In order for a coating to provide adequate corrosion protection, the coating must be uniform, well adhered, pore free and self-healing for applications where physical damage to the coating may occur. One of the problems with magnesium alloys is their chemical reactivity. As soon as they come in contact with air or water an oxide/hydroxide layer forms on the surface which can have a detrimental effect on coating adhesion and uniformity [3]. Thus, the pre-cleaning process plays a critical role in the development of a good protecting coating on magnesium alloys. The use of pre-treatments prior to painting or adhesive bonding is an essential technology in many industrial sectors (e.g. automotive and aerospace industries). However, the pre-treatments used on magnesium alloys which are vital to ensure reliable long-term performance, often comprise a range of environmentally objectionable chemicals, such as solvents and chromates, some of which are carcinogenic. The plasma deposition of thin coatings on magnesium alloys could be an alternative to the traditional chromate-based treatments. It is envisaged that plasma cleaning, etching and deposition could be carried out in a single plasma reactor, providing a complete preparation cycle before painting and avoiding the use, handling and disposal of hazardous materials [4, 5]. Plasma coatings from hexamethyldisiloxane (HMDSO) and add-gases such as O<sub>2</sub> have proven to be an attractive treatment technique for the surface modification of magnesium alloys in order to increase their corrosion resistance [6, 7].

In the present work, Electrochemical Impedance Spectroscopy (EIS) was used to evaluate the corrosion behaviour of WE43 alloy coated with SiO<sub>x</sub>-like thin films prepared by Plasma Enhanced Chemical Vapour Deposition (PECVD), using Tetraethoxysilane (TEOS) as monomer. This work is included in wider project,



whose main objective is the evaluation of the corrosion and adhesion properties of plasma-polymerised coatings prepared under different experimental conditions [6 - 10].

## 2. Experimental

SiO<sub>x</sub>-like films were deposited using the PECVD technique in a home-made parallel-plate-reactor described elsewhere [6, 10]. The precursor gases for the deposition were O<sub>2</sub> and TEOS, and Ar was used as a diluent gas. The deposition substrate was a Mg alloy, WE43, employed in the automotive industry, whose chemical composition in wt % is: 94.16 Mg, 3.42 Y, 2.41 Nd. The plasma processing consisted of two stages: pre-treatment and deposition. In the first stage, the Mg alloy samples were cleaned in H<sub>2</sub> plasma for 30 min at 1000 mTorr pressure. The deposition process was performed at 25°C by varying the TEOS : O<sub>2</sub> flow rate ratio at 200 W input power and 100 mTorr pressure. The experimental conditions employed during the experiments are summarised in Table 1. The film thickness was evaluated by means of a Tencor Profilometer .

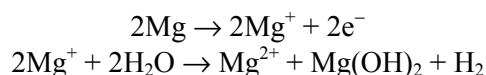
Parameters	Pre-treatment	SiO <sub>x</sub> -like deposition
Pressure (mTorr)	1000	100
Input Power (W)	15	200
TEOS flux (sccm)	-	3
O <sub>2</sub> flux (sccm)	-	30 - 50
H <sub>2</sub> flux (sccm)	15	
Ar flux (sccm)	-	36
Treatment Time (min)	30	48 - 96
Coating thickness (nm)	-	960 - 1920

Table 1- Experimental conditions for PECVD on WE43 substrates

The corrosion behaviour of WE43 coated samples was assessed by means of electrochemical impedance measurements performed in aerated 0.1 M NaCl solution at 25°C. Untreated WE43 alloy was also tested. The experimental set-up for these tests comprised a Gamry EIS300 Frequency Response Analyser controlled by a PC-compatible computer that also performed the data acquisition and processing. The measurements were carried out at the open circuit potential by applying a 10 mV (RMS) sine wave with frequencies in the range 100 kHz -10 mHz (5 points per decade). A silver-silver chloride (Ag-AgCl) electrode as reference and a titanium counter electrode were employed. The exposed samples area 12.6 cm<sup>2</sup>. Impedance spectra were analysed using a suitable fitting procedure in order to obtain the values of the charge transfer resistance (R<sub>ct</sub>) and of the double layer capacitance (C<sub>dl</sub>) which may be directly related to the protective properties of the coating.

## 3. Results and discussion

Figure 1 shows the Nyquist plot of the uncoated WE43 alloy after 24 h exposure to 0.1 M NaCl solution. The shape of the diagram is similar to that obtained on pure magnesium in the same solution [11]: the high frequencies part is related to charge transfer, while the low frequencies one is attributed to the presence of corrosion products. Fitting of the experimental data allows to determine an equivalent electrical circuit which is representative of the physical processes taking place in the system under investigation. An accurate analysis of the impedance spectrum was achieved using the equivalent circuit model reported in Figure 2; R<sub>e</sub> is the solution resistance, R<sub>ct</sub> the charge transfer resistance of the corrosion process [12]:



occurring at the metal surface, in parallel with the double layer capacitance C<sub>dl</sub>; R<sub>diff</sub> is the diffusion resistance related to relaxation of mass transport in the solid phase due to the growth of the corrosion product layer, in parallel with a constant-phase element (CPE) [13]. The impedance of a CPE is represented by the equation :

$$Z = C \cdot 1 / (i \omega)^\alpha$$

where  $C$  is a constant depending on the specific analyzed system,  $i = \sqrt{-1}$ ,  $\alpha$  is a coefficient ranging between 0 and 1, and  $\omega$  is the angular frequency. CPE is usually interpreted as a general diffusion-related element to depict the geometric fractal nature of an electrochemical interface [14]. The values of  $C_{dl}$  and  $R_{ct}$  determined by fitting the experimental data are respectively  $5.3 \cdot 10^{-4} \text{ F} \cdot \text{cm}^{-2}$  and  $85 \Omega \cdot \text{cm}^2$ , thus indicating a poor corrosion resistance of WE43 alloy in the aggressive environment considered.

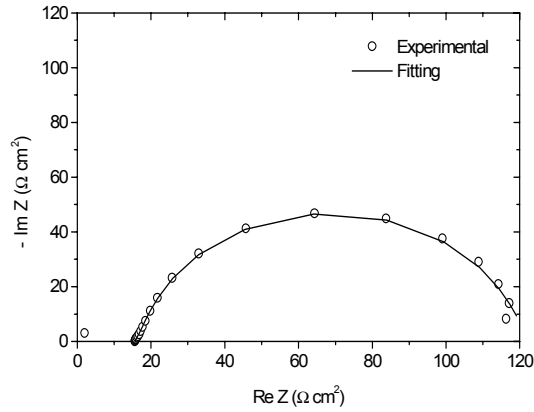


Figure 1 - Nyquist plot of the uncoated WE43 alloy after 24 h exposure to 0.1 M NaCl solution

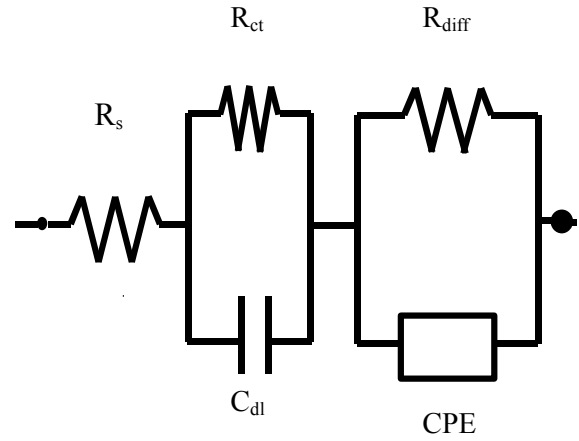
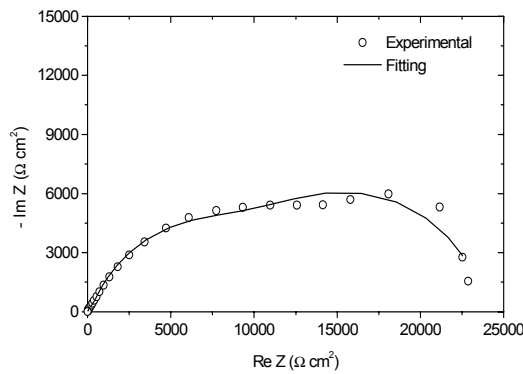
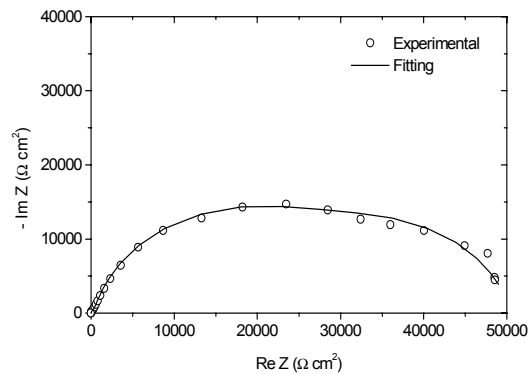


Figure 2 - Equivalent circuit model used for fitting the impedance spectrum of the uncoated WE43 alloy

Figure 3a,b shows the Nyquist plots of WE43 alloy coated with a 960 nm thick  $\text{SiO}_x$ -like film deposited in plasma fed with different TEOS :  $\text{O}_2$  flow rate ratio, after 24 h exposure to 0.1 M NaCl solution. The deposition process was performed at 200 W input power after a hydrogen plasma treatment that enhances the adhesion of film to magnesium substrate as a consequence of simultaneous cleaning and native oxide reduction [6].



(a)

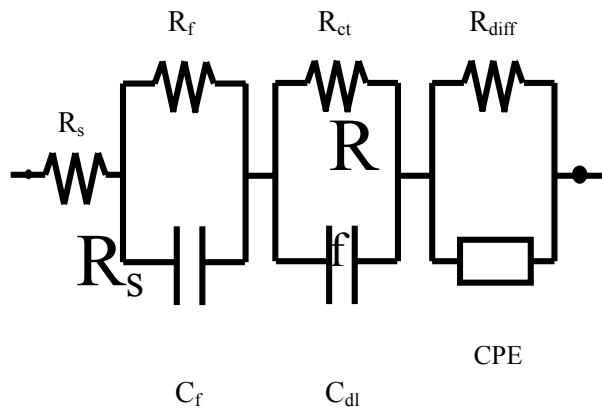


(b)

Figure 3 - Nyquist plots of WE43 alloy coated with a 600 nm thick  $\text{SiO}_x$ -like film deposited in plasma fed with: (a) 3 sccm TEOS and 50 sccm  $\text{O}_2$ ; (b) 3 sccm TEOS and 30 sccm  $\text{O}_2$ , after 24 h exposure to 0.1 M NaCl solution

The shape of the impedance diagrams is similar to that obtained for the uncoated alloy, however fitting of experimental data gives good results when the electrical equivalent circuit shown in Figure 4 is used, where  $R_c$  is the coating resistance resulting from the penetration of the electrolyte solution and  $C_c$  is the corresponding capacitance [15]. Calculated values of the charge transfer resistance,  $R_{ct}$ , and the double layer capacitance,  $C_{dl}$ , are reported in Table 2. In comparison with the uncoated alloy, the increase of  $R_{ct}$  and

decrease of  $C_{dl}$  are indicative of a significant slowing down of the corrosion process occurring at the coating/metal interface. As evidenced in Table 2, plasmas fed with lower oxygen content give rise to films with improved protective properties, while an opposite trend is observed in the case of HMDSO [6, 10].



	50 sccm O <sub>2</sub>	30 sccm O <sub>2</sub>
$R_{ct}$ (k $\Omega$ cm <sup>2</sup> )	13.5	28.7
$C_{dl}$ (F cm <sup>-2</sup> )	$1.2 \cdot 10^{-5}$	$7.8 \cdot 10^{-6}$

Figure 4 - Equivalent circuit model used for fitting the impedance spectra of coated WE43 alloy samples

Table 2 -  $R_{ct}$  and  $C_{dl}$  values for coated WE43 alloy samples after 24 h exposure to 0.1 M NaCl solution

The better barrier efficiency of SiO<sub>x</sub>-like films deposited in plasmas fed with reduced oxygen content may be ascribed to the presence of a reduced defects number: pores, pinholes or other defects generated by microcracks due to unreleased compressive stresses [16], which allow contact between the aggressive environment and the bare metal, thus involving localised corrosion phenomena at the coating/metal interface. A noticeable enhancement of the corrosion behaviour of WE43 alloy can be achieved by increasing the film thickness. Figure 5 reports the Nyquist plot of WE43 alloy coated with a 1960 nm thick SiO<sub>x</sub>-like film deposited in plasma fed with 3 sccm TEOS and 50 sccm O<sub>2</sub>, after 24 h exposure to 0.1 M NaCl solution. The shape of the impedance spectrum consists of two or three interacting capacitive loops. In this case, fitting of experimental data with the equivalent circuit model reported in Fig. 4 yields the following values:  $R_{ct} = 119.6$  k $\Omega \cdot \text{cm}^2$  and  $C_{dl} = 2.8 \cdot 10^{-7}$  F $\cdot \text{cm}^{-2}$ , which are indicative of a marked inhibiting action toward the kinetic of the electrochemical reactions occurring at the metal substrate, as a consequence of the reduced penetration rate of charged (ions) and uncharged (water molecules, oxygen) species through local defects within the coating.

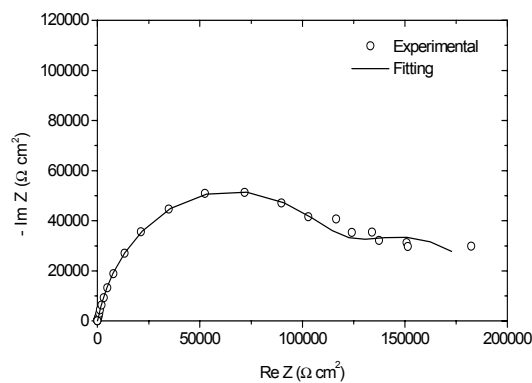


Figure 5 - Nyquist plots of WE43 alloy coated with a 1200 nm thick SiO<sub>x</sub>-like film deposited in plasma fed with 3 sccm TEOS and 50 sccm O<sub>2</sub>, after 24 h exposure to 0.1 M NaCl solution

The influence of film thickness on the corrosion behaviour of WE43 alloy is also evidenced in Table 3 which reports the calculated values of disbonded area,  $A_d$ , of the coating/metal interface where the corrosion takes place [17]:

$$A_d = C_{dl} / C_{dl}^0$$

where  $C_{dl}^0$  is the double layer capacitance of the uncoated metal.

TEOS / O <sub>2</sub> ratio	Thickness (nm)	Disbonded Area (%)
3 / 50	600	2.3
3 / 30	600	1.5
3 / 50	1200	0.05

Table 3 – Percentage of disbonded area

As can be seen, the better corrosion protective properties of thicker films are testified by a drastic decrease of the disbonded area.

#### 4. Conclusions

In this work, EIS investigations were carried out to assess the corrosion behaviour of a Mg alloy, WE43, coated with SiO<sub>x</sub>-like films obtained by the plasma deposition of TEOS. The obtained results show that PECVD coatings improve the corrosion resistance of WE43.

The barrier performance of SiO<sub>x</sub>-like films is affected by the TEOS/O<sub>2</sub> ratio, and to a larger extent by the film thickness. As a matter of fact, thicker films exhibit better barrier properties giving rise to improved corrosion protection. This may be ascribed to the lower permeation rate of H<sub>2</sub>O, O<sub>2</sub>, Na<sup>+</sup> and Cl<sup>-</sup> through local defects within the coating, as a consequence of its higher homogeneity degree.

#### 5. References

- [1] Y. Kojima, *Mater. Sci. Forum*, **350-351** (2000), 3
- [2] G.L. Song, A. Atrens, *Advanced Engineering Materials*, 1999
- [3] W.J. Van Ooij, K.D. Connors, P.J. Barto, *Mittal Festschrift*, 1998, 355
- [4] J. Schwarz, M. Schmidt, A. Ohl, *Surf. Coat. Tech.*, **98** (1998), 859
- [5] Y. Iriyama, T. Ihara, M. Kiboku, *Thin Solid Films*, **287** (1996), 169
- [6] E. Angelini, S. Grassini, F. Rosalbino, F. Fracassi, R. d'Agostino, *Progr. Org. Coat.*, **1-5** (2003), 1260
- [7] E. Angelini, S. Grassini, F. Rosalbino, F. Fracassi, R. D'Agostino, in *Proc. 15<sup>th</sup> ICC, International Corrosion Congress, Frontiers in Corrosion Science and Technology*, Granada (Spain) 22-27 september 2002, paper 362, pp. 1-10
- [8] F. Fracassi, R. d'Agostino, A. Buccolieri, V. Colaprico, E. Angelini, S. Grassini, F. Rosalbino, in *Proc. ISPC15*, Orleans, 9-13 July 2001, pp. 27-32
- [9] E. Angelini, S. Grassini, F. Rosalbino, F. Fracassi, R. d'Agostino, in *Proc. EUROCORR 2001*, Riva del Garda, 30 September – 4 October 2001, pp.130-139
- [10] E. Angelini, R. d'Agostino, F. Fracassi, S. Grassini, F. Rosalbino, *Surf. Interface Anal.*, **34** (2002), 155
- [11] A. Yu Simaranov, I. Sokolova, A.I. Marshakov, N. Mikhailovskii, *Protection of Metals*, **27** (1992), 329
- [12] M.R. Bothwell, *The Corrosion of Light Metals*, John Wiley and Sons, New York (1967), 257
- [13] G. Baril, C. Deslouis, N. Pébère, in *7th Symposium of Electrochemical Methods in Corrosion Research*, CD-Rom Paper N° 007 (2000)
- [14] B.A. Boukamp, A.C.-impittance Analysis Sysyem, Version 3.97, Copyright B.A. Boukamp/UT'85-89, Faculty of Chemical Technology, University of Twente, The Netherlands, 1989
- [15] G.W. Walter, *Corros. Sci.* **26** (1986), 681
- [16] W. Kern, G.L. Svchnable, A.W. Taylor, *RCA Rev.*, **37** (1976), 3
- [17] S. Haruyama, M. Asari, T. Tsuru, in *Proc. Symp. Corrosion Protection by Organic Coatings*, The Electrochemical Society, USA (1987), 197

# Numerical Analysis of Carbon Isotope Separation By Plasma Chemical Reactions in CO Glow Discharge

S. Mori and M. Suzuki

*Department of Chemical Engineering, Tokyo Institute of Technology, Tokyo, Japan*

## Abstract

The separation of carbon isotopes in CO glow discharge has been studied, in which the formation of stable products enriched in heavier carbon isotopes is analyzed by the numerical simulation of kinetic model. Vibrational kinetic rate equation for CO molecules, rate equations for chemical species, and the spatially homogeneous Boltzmann equation for the velocity distribution of electrons are solved numerically. The influence of electron energy distribution function on isotope enrichment is also evaluated.

## 1. Introduction

In the previous study, we reported experimental results of carbon isotope separation by plasma chemical reactions in CO glow discharge [1]. This isotope separation method is due to vibration-to-vibration (V-V) energy exchange among the vibrational states of molecular gases. The detailed explanation for the principle of this isotope separation method is presented by Ploenjes *et al.* in Ref. [2]. Since this isotope separation method was first suggested by Belenov *et al.* in 1971, there have been a large number of papers on this isotope separation phenomena [3]. Theoretical analyses have shown its attractive potential as practical isotope separation method in which the reaction yields and separation factors are relatively high and the energy expenditure per separated atom is quite low. And a few experimental studies have shown the evidence of this isotope separation phenomena [3]. However, there is a large difference between experimental separation factors and those of theoretical predictions. The main reason for this discrepancy would be that the stable products are diluted by the unenriched products yielded by the isotopically nonselective reactions and isotope scrambling reactions [4]. In our previous studies, the maximum separation factor for  $^{13}\text{C}$  in  $\text{C}_3\text{O}_2$  polymers of 2.31 has been obtained by using CO/Ar glow discharge plasma and the kinetic model in which the electron energy distribution function (EEDF) is assumed to be Maxwellian distribution can reproduce experimental isotope enrichment qualitatively [1,4,5].

In this study, we developed a much detailed kinetic model for  $^{12}\text{C}^{16}\text{O}$ ,  $^{13}\text{C}^{16}\text{O}$ , and  $^{14}\text{C}^{16}\text{O}$  in which the rate equations for the density of vibrational quantum levels of CO molecules, rate equations for reaction products, and Boltzmann equation for the electron velocity distribution are solved numerically as a function of discharge parameters such as reduced electric field, current density and gas compositions. In the rate equations for the density of vibrational quantum levels of CO molecules used in the present study, the vibrational kinetics of CO molecules, vibrationally induced chemical reactions of CO molecules, and electron impact reactions are considered. In the rate equations for the reaction products, vibrationally induced chemical reactions, electron impact reactions, surface reactions on the discharge wall, and isotope scrambling reactions are included. The rate constants of some elementary processes are unknown with sufficient accuracy and those values are estimated by requiring best agreement between calculated and experimental results. The final isotope enrichment and reaction yield of the stable products are derived as a function of discharge parameters. By using this calculation model, the carbon-14 separation factor is estimated. The influence of electron energy distribution function on isotope enrichment is also evaluated.

## 2. Kinetic Modeling

The kinetic model in the present study is based on previous publications [3,6-12] and developed to describe isotope enrichment in stable products by including much detailed atomic and molecular processes. The master vibrational rate equations for the density of the vibrational levels of the isotopic molecules can be written in the following form:

$$\frac{dN_i^v}{dt} = (e - V)_i^v + (V - V')_i^v + (V - V'')_i^v + (V - T)_i^v + (SRD)_i^v + (V - E)_i^v + (Chem.)_i^v, \\ i = 1, 2, 3, v = 0, 1, \dots, v_{\max}, \quad (1)$$

where  $N_i^v$  is the number density of molecules of species  $i$  in vibrational quantum level  $v$  ( $v_{\max} = 50$  in our calculation) in  $\text{cm}^{-3}$ ,  $i = 1, 2, 3$  represents respectively the isotopic species  $^{12}\text{C}^{16}\text{O}$ ,  $^{13}\text{C}^{16}\text{O}$ ,  $^{14}\text{C}^{16}\text{O}$ . The term  $(e-V)_i^v$  represents the net rate of change in  $N_i^v$  due to electron impact. The term  $(V-V)_i^v$  and  $(V-V')_i^v$  represent the net rate of change in  $N_i^v$  due to V-V exchange process between the single isotopic species and two isotopic species, respectively. And the term  $(V-T)_i^v$ ,  $(\text{SRD})_i^v$ ,  $(V-E)_i^v$ , and  $(\text{Chem.})_i^v$  represent the rate of change in  $N_i^v$  caused by V-T processes in collisions with other species, spontaneous radiative decay, vibration-electronic transfer process, and chemical reactions, respectively. The detailed rate form for those reactions are presented in Ref. [5]. The kinetic processes and chemical reactions considered in this model are listed in tables 1 and 2. Reaction R6 produces the isotopically enriched products,  $\text{CO}_2$  and  $\text{C}$ , because heavier  $\text{CO}$  molecules are excited preferentially. On the other hand, products formed by reactions R8, R9, R11 and R12 are not isotopically enriched and moreover these reactions initiate the successive de-enriching processes by forming atomic oxygen. The rate constants of heterogeneous reactions R15, R18, and R19 can be expressed by using reaction probabilities [5]. In this study, reaction probabilities for R18 and R19 are determined by the diffusion characteristic time of  $\text{C}$  and  $\text{CO}_2$  as  $1 \times 10^{-2}$  and  $1 \times 10^{-3}$ , respectively. Reaction probability for reaction R15 was left as an adjustable parameter and determined to be  $1 \times 10^{-3}$  by requiring the best agreement between experimental and calculated values of both separation factors and reaction yields. The importance of vibration-electronic transfer in kinetic modeling has attracted a growing interest during last two decades. A V-E transfer to the electronic  $a^3\Pi$ -state has been examined by Farrenq *et al.* [16] and to the electronic  $A^1\Pi$ -state has been applied to the numerical simulation model by Deleon *et al.* [11]. Recently, from the comparison of calculated vibrational distribution functions (VDFs) with experimental one, Porshnev *et al.* concluded that the V-E transfer to the  $a^3\Pi$ -state is much probable process to depopulate the vibrational states of ground electric state  $\text{CO}$  at  $v > 25$  [8]. Therefore, V-E transfer to the  $a^3\Pi$ -state is included in our kinetic model. The term  $(V-E)_i^v$  represents the rate of change in  $N_i^v$  caused by collision-induced V-E transfer of  $\text{CO}$  molecules of ground electronic state  $X^1\Sigma^+$  to the electronic state  $a^3\Pi$ . The  $a^3\Pi$ -state is a metastable one with a radiative time about 10 ms [8]. The system of equation (1) has been solved numerically using the Runge-Kutta method starting from the Boltzmann population distribution at the gas temperature,  $T_g$ .

Table 1 Vibrational kinetic processes

Reactions	Rate constant
R1. $\text{CO}(v) + e \rightarrow \text{CO}(w) + e$	[5]
R2. $\text{CO}(v) + \text{CO}(w) \rightarrow \text{CO}(v') + \text{CO}(w')$	[11,12]
R3. $\text{CO}(v) + \text{CO}(w) \rightarrow \text{CO}(v') + \text{CO}(w')$	[5]
R4. $\text{CO}(v) + \text{M} \rightarrow \text{CO}(v-1) + \text{M}$	[11-14]
R5. $\text{CO}(v) \rightarrow \text{CO}(v-1) + h\nu$	[12,15]
R6. $\text{CO}(v) + \text{CO}(w) \rightarrow \text{C} + \text{CO}_2 (E_v < E_w)$	[5]
R7. $\text{CO}(v) + \text{CO}(w) \rightarrow \text{CO}(a^3\Pi) + \text{CO}$	[5]

Table 2 Chemical reactions

Reactions	Rate constant
R8. $\text{CO} + e \rightarrow \text{C} + \text{O} + e$	$f(E/N)$
R9. $\text{CO} + e \rightarrow \text{C} + \text{O}^\cdot$	$f(E/N)$
R10. $\text{CO} + e \rightarrow \text{CO}(a^3\Pi) + e$	$f(E/N)$
R11. $\text{CO}_2 + e \rightarrow \text{CO} + \text{O} + e$	$f(E/N)$
R12. $\text{O}_2 + e \rightarrow \text{O} + \text{O} + e$	$f(E/N)$
R13. $\text{CO}(a^3\Pi) + \text{CO} \rightarrow 2\text{CO}$	[5]
R14. $\text{CO} + \text{O}^\cdot \rightarrow \text{CO}_2 + e$	[17]
R15. $\text{C} + \text{O} + \text{Wall} \rightarrow \text{CO} + \text{Wall}$	text
R16. $\text{CO} + \text{O} + \text{Wall} \rightarrow \text{CO}_2(\text{s}) + \text{Wall}$	[18]
R17. $\text{O} + \text{O} + \text{Wall} \rightarrow \text{O}_2(\text{s}) + \text{Wall}$	[19]
R18. $\text{C} + \text{Wall} \rightarrow \text{C}(\text{s}) + \text{Wall}$	text
R19. $\text{CO}_2 + \text{Wall} \rightarrow \text{CO}_2(\text{s}) + \text{Wall}$	text

Electron energy distribution and electron density used in the calculation have been obtained by solving the spatially homogeneous Boltzmann equation for the velocity distribution of the electrons.

$$\frac{\partial F}{\partial t} = (e_0/m)\mathbf{E} \frac{\partial}{\partial \mathbf{v}} F + C^{el} + \sum_k C_k^{in}, \quad d n_e(t) = F(\mathbf{v}, t) d\mathbf{v}, \quad (2)$$

where  $F$  is the velocity distribution,  $\mathbf{E}$  is the applied electric field,  $e_0$  is the modulus of the electron charge,  $m$  is the mass of electrons,  $\mathbf{v}$  is the velocity of electrons,  $n_e$  is the electron density, and  $C^{el}$  and  $C^{in}$  represent the elastic and inelastic binary electron-neutral particle collision processes, respectively. To derive simply the

isotropic and anisotropic velocity distribution of electrons, the two-term approximation is used in this study [20-22].

The number density of the system is determined by the typical value of total discharge pressure,  $N_0=5.8 \times 10^{17} \text{ cm}^{-3}$  (0.80 kPa, 100 K), of our experiment. The translational temperature of the system,  $T_g$ , is estimated as 100 K from the temperature of the reactant gas and reactor wall which are assumed to be identical with liquid nitrogen coolant one.

### 3. Results and Discussion

Figure 1 shows the calculated results of vibrational distribution functions of CO molecules. The preferential excitation of heavier isotopic specie  $^{13}\text{C}^{16}\text{O}$  is produced by our kinetic model. Calculated VDFs by using different EEDFs are compared in the Fig. 1 and it is found that the difference among those results is not significant. As a consequence, the inference of difference in EEDFs on the isotope selectivity for the vibrational excitation is not significant.

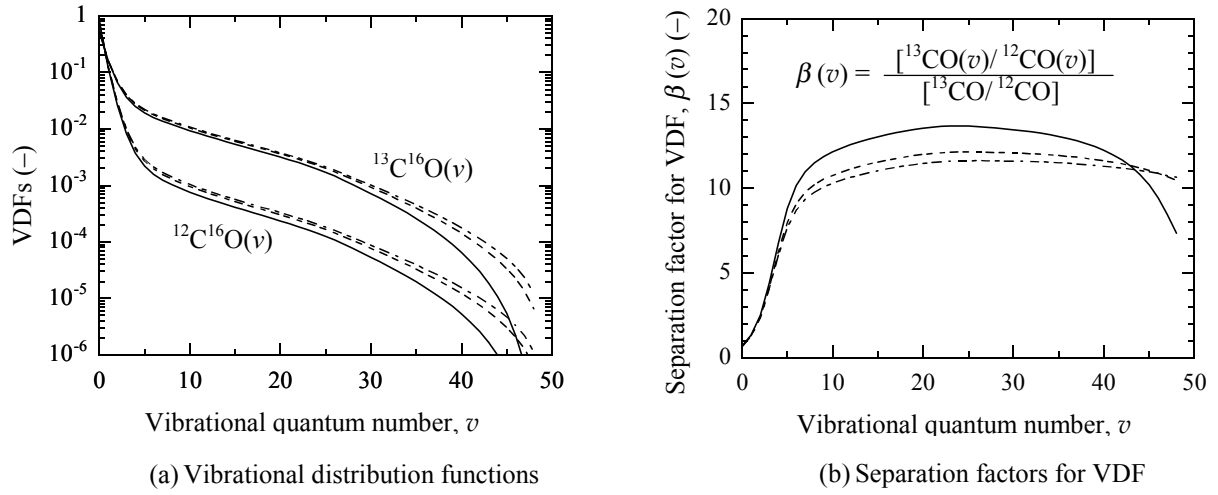


Fig. 1 Calculated results of VDFs by using different EEDF: Maxwellian distribution (-----), Druyvesteyn distribution (— · —), and EEDF obtained by solving Boltzmann equation (—). (CO/Ar=50/50,  $E/N=6 \times 10^{-16} \text{ Vcm}^2$ ,  $j=5.2 \text{ mA/cm}^2$ ,  $N_0=5.8 \times 10^{17} \text{ cm}^{-3}$ , Mean electron energy: 1.0 eV).

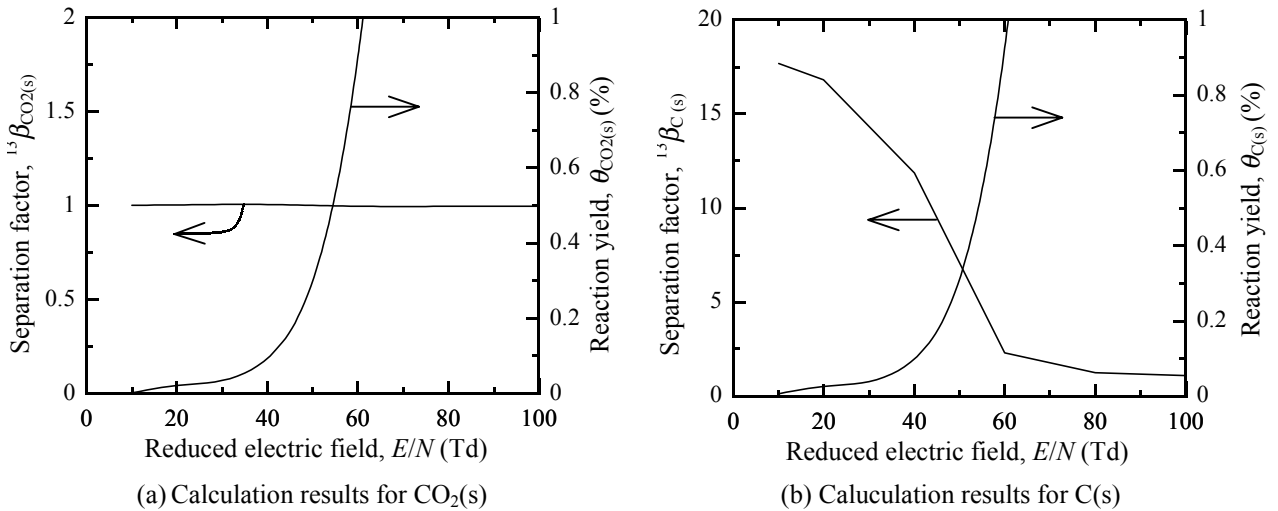


Fig. 2 Calculated results of isotope enrichment and reaction yields of stable products  $\text{CO}_2(\text{s})$  and  $\text{C}(\text{s})$  as a function of reduced electric field with (CO/Ar=50/50,  $j=5.2 \text{ mA/cm}^2$ ,  $N_0=5.8 \times 10^{17} \text{ cm}^{-3}$ ,  $T_g=100 \text{ K}$  residence time: 1 s).

Figure 2 shows final isotope enrichment and reaction yield of stable products. Here, reaction yields of stable products are defined as follows:

$$\theta_{C(s)} = n_{C(s)}/n_{CO}, \quad (3)$$

$$\theta_{CO_2(s)} = n_{CO_2(s)}/n_{CO}, \quad (4)$$

where  $\theta_{C(s)}$  and  $\theta_{CO_2(s)}$  are the C(s) and CO<sub>2</sub>(s) yields,  $n_{C(s)}$  and  $n_{CO_2(s)}$  are the amount of C(s) and CO<sub>2</sub>(s), respectively. Isotope separation factors of stable products are defined as follows:

$$\beta_{C(s)} = [n_{^{13}C(s)}/n_{^{12}C(s)}]/[n_{^{13}CO}/n_{^{12}CO}], \quad (5)$$

$$\beta_{CO_2(s)} = [n_{^{13}CO_2(s)}/n_{^{12}CO_2(s)}]/[n_{^{13}CO}/n_{^{12}CO}], \quad (6)$$

where  $\beta_{C(stable)}$  and  $\beta_{CO_2(stable)}$  are <sup>13</sup>C separation factors for the C(s) and CO<sub>2</sub>(s),  $n_{^{12}C(s)}$ ,  $n_{^{13}C(s)}$ ,  $n_{^{12}CO_2(s)}$ , and  $n_{^{13}CO_2(s)}$  are the amount of <sup>12</sup>C(s), <sup>13</sup>C(s), <sup>12</sup>CO<sub>2</sub>(s), and <sup>13</sup>CO<sub>2</sub>(s), respectively.

Separation factor for CO<sub>2</sub> is about 1 for the calculated range tested, which corresponds to our experimental results. On the other hand,  $\beta_{C(stable)}$  decreases with increasing reduced electric field. This reduction of separation factor is explained by the dilution mechanism in which isotope scrambling reactions and reaction products formed through reaction path other than isotope selective reaction R6 dilute the isotope enrichment in the stable products. Reaction yields for CO<sub>2</sub> and C atom reasonably increase with increasing reduced electric fields, which is explained by the increase of direct electron impact dissociation of CO.

Figure 3 shows the comparison between our experimental results for atomic carbon and calculated ones. Experimental data for atomic carbon shown in Figs. 3 are derived from our experimental data for deposited polymer on the discharge wall in the 50 Hz CO glow discharge, by subtracting the contribution from the end carbons of C<sub>3</sub>O<sub>2</sub> (OCCCCO) in the polymer [4,23]. As can be seen in Fig. 3, if we performed the calculation with  $E/N = 60$  Td ( $1 \text{ Td} = 1 \times 10^{-17} \text{ V cm}^2$ ), calculation model can reproduce the experimental results. However, the reduced electric fields of the experiments calculated by using averaged discharge voltage measured by the digital multimeter are about 20 Td. It is difficult to determine whether this discrepancy is due to limited accuracy of rate constants we used, to the presence of other elementary processes which are not taken into account, or the inaccuracy of the measurements of the discharge voltage. For example, the agreement between experimental results and calculations could be improved by introducing other atomic carbon formation path such as:

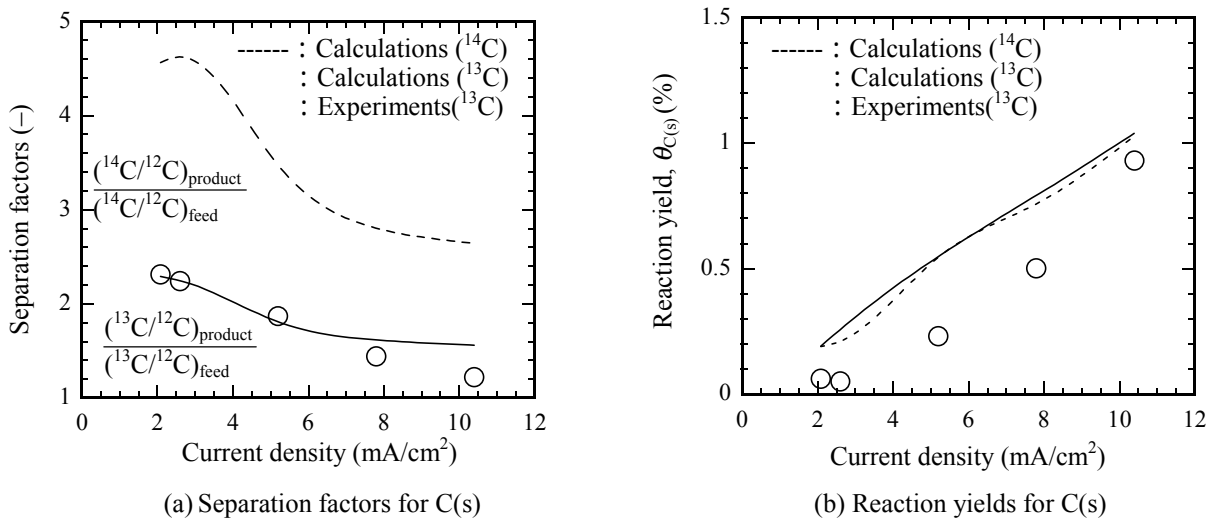
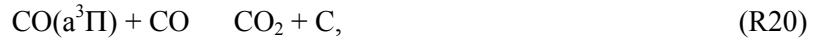


Fig. 3 Comparison between our experimental results for atomic carbon and calculated ones.  
(CO/Ar=50/50,  $E/N=2 \times 10^{-16} \text{ V cm}^2$ ,  $N_0=5.8 \times 10^{17} \text{ cm}^{-3}$ )





However, the lack of information on rate constants for those reactions makes further development difficult. By using this developed kinetic model, calculations of  $^{14}\text{C}$  separation factors of this isotope separation method have also been performed and it is estimated that the  $^{14}\text{C}$  separation factor of 4.6 is obtained in the case of same discharge conditions as those of maximum  $^{13}\text{C}$  separation factor, 2.31, we obtained.

The influence of difference in EEDFs on isotope enrichment of stable products is also evaluated as shown in Figure 4. It is found that the difference among those results is significant for stable products. This is explained by the EEDF around its tail area. Figure 5 shows the calculated results of EEDF in the CO/Ar gas mixture. The difference of EEDF around the tail is significant and the direct electron impact dissociation which causes isotope scrambling reactions depends on the EEDF tail.

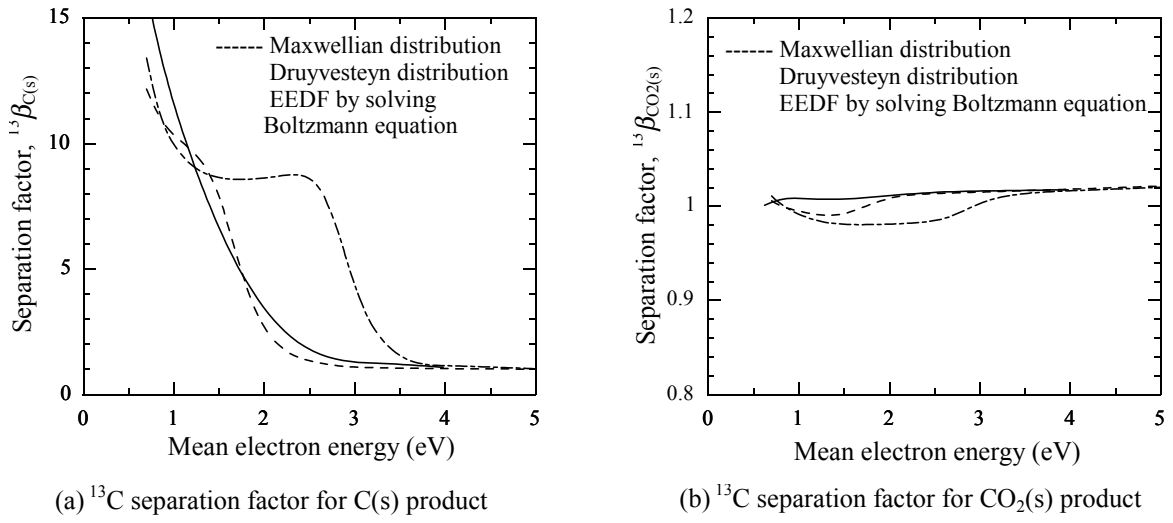


Fig. 4 Influence of EEDF on separation factor.  
( $N_e=10^{10} \text{ cm}^{-3}$ , residence time: 1.0 s CO/Ar=50/50,  $N_0=5.8 \times 10^{17} \text{ cm}^{-3}$ ,  $T_g=100 \text{ K}$ ).

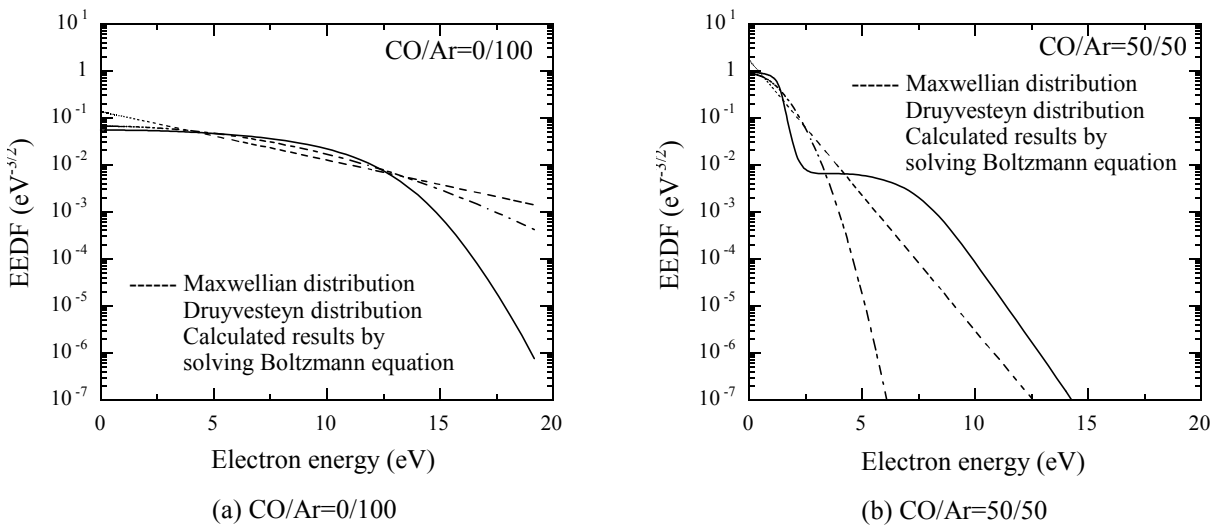


Fig. 5 Calculated results of EEDF as a function of electron energy for different Ar mole fraction ( $E/N=40 \text{ Td}$ ,  $j=5.2 \text{ mA/cm}^2$ ,  $N_0=5.8 \times 10^{17} \text{ cm}^{-3}$ )

#### 4. Conclusions

The separation of carbon isotopes in CO glow discharge has been studied, in which the formation of stable products enriched in heavier carbon isotopes is analyzed by the numerical simulation of kinetic model. The calculation model can reproduce our experimental results and, by using this calculation model, the calculation of  $^{14}\text{C}$  separation factor is also performed. It is estimated that the  $^{14}\text{C}$  separation factor of 4.6 is obtained in the case of same discharge conditions as those of maximum  $^{13}\text{C}$  separation factor 2.31 we obtained. The influence of electron energy distribution function on isotope enrichment is negligible for VDF but significant for the stable products because the difference of EEDF around the EEDF tail is significant and the direct electron impact dissociation which causes isotope scrambling reactions depends on the EEDF tail.

#### References

- [1] S. Mori, H. Akatsuka, M. Suzuki, *Proc. 15th Int. Symp. on Plasma Chemistry (ISPC15)*, 647 (2001).
- [2] E. Ploenjes, I. Adamovich, V.V. Subramaniam, J.W. Rich, *AIAA Paper* 98-0993, Jan. (1998).
- [3] M. Capitelli, *Nonequilibrium Vibrational Kinetics*, Springer, Berlin, 271 (1986).
- [4] S. Mori, H. Akatsuka, M. Suzuki, *J. Nucl. Sci. Technol.*, **38**[10], 850 (2001).
- [5] S. Mori, H. Akatsuka, M. Suzuki, *J. Nucl. Sci. Technol.*, **39**[6], 637 (2002).
- [6] V.I. Dolinina, A.N. Oraevskii, F.F. Suckhov, *et al.*, *Sov. Phys.-Tech. Phys.*, **23**[5], 574(1978).
- [7] V.M. Akulintsev, N.M. Gorshunov, Yu.P. Neshchimenko, *High Energy Chem.*, **16**, 67 (1982).
- [8] P.I. Porshnev, H. Wallaart, M.Y. Perrin, J.P. Martin, *Chem. Phys.*, **222**, 289 (1997).
- [9] C. Gorse, M. Cacciatore, M. Capitelli, *Chem. Phys.*, **85**, 165 (1984).
- [10] C. Gorse, S.de Benedictis, M.Cacciatore, *et al.*, *Gazz. Chim. Ital.*, **113**, 615 (1983).
- [11] R.L. Deleon, J.W. Rich, *Chem. Phys.*, **107**, 283 (1986).
- [12] C. Flament, T. George, K.A. Meister, *et al.*, *Chem. Phys.*, **163**, 241 (1992).
- [13] M. Cacciatore, G.D. Billing, *Chem. Phys.*, **58**, 395 (1981).
- [14] M. Capitelli, *Nonequilibrium Vibrational Kinetics*, Springer, Berlin, 85 (1986).
- [15] H. Dunnwald, E. Siegel, W. Urban, *et al.*, *Chem. Phys.*, **94**, 195 (1985).
- [16] R. Farrenq, C. Rossetti, G.Guelachvili, W. Urban, *Chem. Phys.*, **92**, 401 (1985).
- [17] L.S. Polak, Yu A Lebedev, *Plasma Chemistry*, Cambridge International Science, Cambridge (1998).
- [18] W. Choi, M.T. Leu, *Geophys. Res. Lett.*, **24**[23], 2957 (1997).
- [19] L. Magne, H. Coitout, G. Cernogora, G. Gousset, *J. Phys. III France*, **3**, 1871 (1993).
- [20] V.E. Golant, A.P. Zhilinsky and I.E. Sakharov, *Fundamentals of plasma physics*, John Wiley and Sons, New York (1980).
- [21] R. Winkler, H. Deutsch, J. Wilhelm, C. Wilke, *Beitr. Plasmaphys.*, **24**, 285 (1984).
- [22] R. Winkler, J. Wilhelm, A. Hess, *Ann. Phys.*, **42**, 537 (1985).
- [23] O. Dunn, P. Harteck, S. Dondes, *J. Phys. Chem.*, **77**[7], 878 (1973).

# Nitrogen Atom Recombination on Silica Surface: Recombination Probability and Energy Flows

M. Cacciatore and M. Rutigliano

*CNR-IMIP(Istituto di Metodologie Inorganiche e dei Plasmi) di Bari  
c/o Chemistry Department of University of Bari, Via Orabona,4 70126 Bari –Italy*

N. Pieretti and N. Sanna

*CASPUR – Consorzio interuniversitario per le Applicazioni di Supercalcolo per Università e Ricerca  
Via dei Tizii, 6b, 00185 Roma – Italy*

## Abstract

Molecular dynamics simulation, in connection with electronic structure calculations for N, N<sub>2</sub> interacting with a silica cluster, has been performed to study the most basic dynamical behaviour of N<sub>2</sub> formation after atom recombination on  $\beta$ -cristobalite *via* Eley-Rideal mechanism.

## 1. Introduction

This contribution concerns the investigation of recombination probability and energy flows in the Eley-Rideal ( E-R ) recombination reaction of nitrogen atom on silica surface.



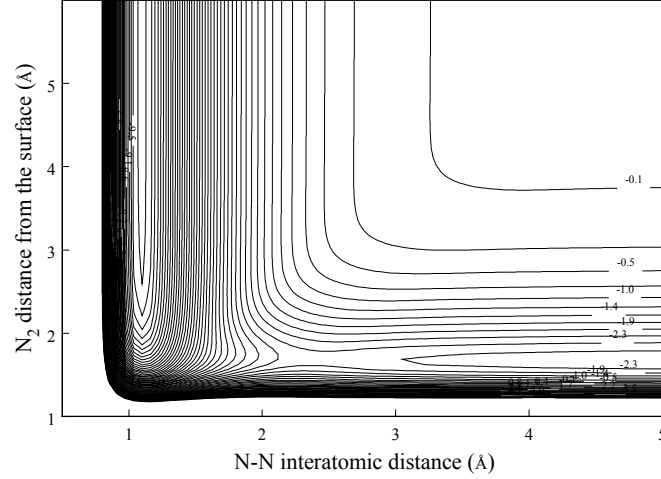
According to this mechanism the recombination occurs between a nitrogen atom impinging the silica substrate from the gas-phase, propagating on the surface and then eventually recombining with an adsorbed nitrogen atom to form N<sub>2</sub> in a specific vibro-rotational state (v,j). The reaction is strongly exothermic, so that a fraction of the exothermic recombination energy,  $\Delta E_{\text{exo}}$ , can be shared among the translational and internal states of the formed nitrogen molecules while the remaining part can be transferred to the silica surface as heat flux.

The need to calculate the recombination probability and the reaction energy partitioning is very important with regard to many laboratory plasma processes and in aero-thermodynamics for the thermal protection system of space-shuttles under re-entry conditions.

## 2. Molecular Dynamics Simulation

We have made a theoretical study of the reaction (1) in the framework of Molecular Dynamics calculation by using a complex semiclassical collisional method [1]. To determine the forces exerted between the interacting chemical species, that is between the two N atoms and the atoms of the solid substrate, we have followed a fully ab initio DFT electronic structure calculations [2] using different Si<sub>x</sub>O<sub>y</sub> cluster. The results obtained for N and N<sub>2</sub> interacting with a silicon atom of the Si<sub>3</sub>O<sub>4</sub> cluster show that N<sub>2</sub> is slightly or not physisorbed while atomic nitrogen is strongly chemisorbed. In the equilibrium geometry the N-Si distance is 1.65 Å with a binding energy of 2.75 eV.

From the calculated adsorption energies the interaction potential for N, N<sub>2</sub>/silica is obtained as a LEPS potential surface. In Figure 1 is shown a contour plot of the potential energy surface for N<sub>2</sub> interacting perpendicularly on a Si atom. The potential energy surface exhibits an energetic barrier of 0.3eV for the recombination reaction.



**Figure 2:** Potential contour map for N<sub>2</sub> interacting with the active Si surface atom in the perpendicular geometry. The interaction potential is plotted as a function of the distance from the N atom closest to the surface and the N-N bond distance. The contours energies are in eV

The molecular dynamics simulation is carried out using the semiclassical collisional method according to which the dynamics of the chemical particles, N and N<sub>2</sub>, interacting with the silica surface is described by solving self-consistently the classical Hamilton's equations of motion of the two nitrogen atoms and the quantum dynamics of the vibrational motions of the silica surface atoms. Thus the 'effective' classical Hamiltonian is given by:

$$H_{\text{eff}} = \frac{1}{2} \sum_{i,\gamma} \frac{1}{m_i} P_{i,\gamma}^2 + V_{N_2}(r_{N-N}) + V_0 + \sum_k V_k^{(1)} \eta_k(t) \quad (2)$$

where  $P_{i,\gamma}$  is the  $\gamma$ -th cartesian component of the momentum of atom  $i$  having mass  $m_i$ ,  $V_{N_2}$  is the interaction potential for the free N<sub>2</sub> molecule and  $V_0$  is the static interaction potential. The last term of the right-hand side is the additional term to the classical Hamiltonian and it is given in terms of the Fourier transform,  $I_{c,k}(t)$ , of the interacting forces[1]:

$$\eta_k(t) = - \int dt' (\hbar \omega_k)^{-1} \frac{d}{d\rho_k} (\Delta E_k^+ + \Delta E_k^-) \times [I_{c,k}(t') \cos(\Theta_k(t', \omega_k)) + I_{s,k}(t') \sin(\Theta_k(t', \omega_k))] \quad (3)$$

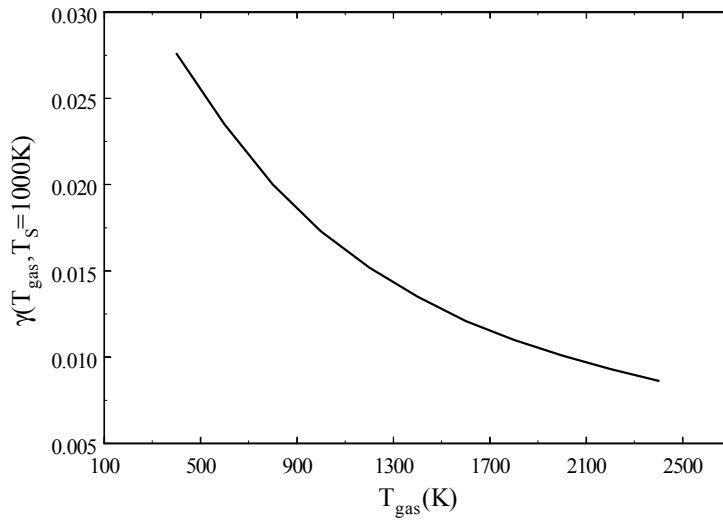
$V_k^{(1)}$  is the first derivative of the interaction potential with respect to the phonon normal mode coordinates.

$\Delta E_k^{+/-}$  is the energy loss (-) or gained (+) from the surface phonons.  $\omega_k$  is the frequency of the k-th phonon normal mode,  $\Theta_k \sim \omega_k t$ .

In the simulation the silica surface consists of 149 arranged according to the  $\beta$ -cristobalite unitary cell. The adsorbed nitrogen atom is placed at a distance of 1.65Å from an active Si atom, in thermal equilibrium with the surface whose temperature is fixed at  $T_S=1000K$ . The kinetic energy of  $N_{gas}$  is varied between 0.01eV and 2.5 eV

### 3. Results

Some important collisional coefficients relevant to the recombination reaction are calculated, such as the recombination probability as a function of the impact energy, the state-selected recombination coefficient  $\gamma(v, T_S)$  relevant to the  $N_2$  formation in a specific vibrational state, the global coefficient  $\gamma(T_{gas}, T_S=1000K)$ .

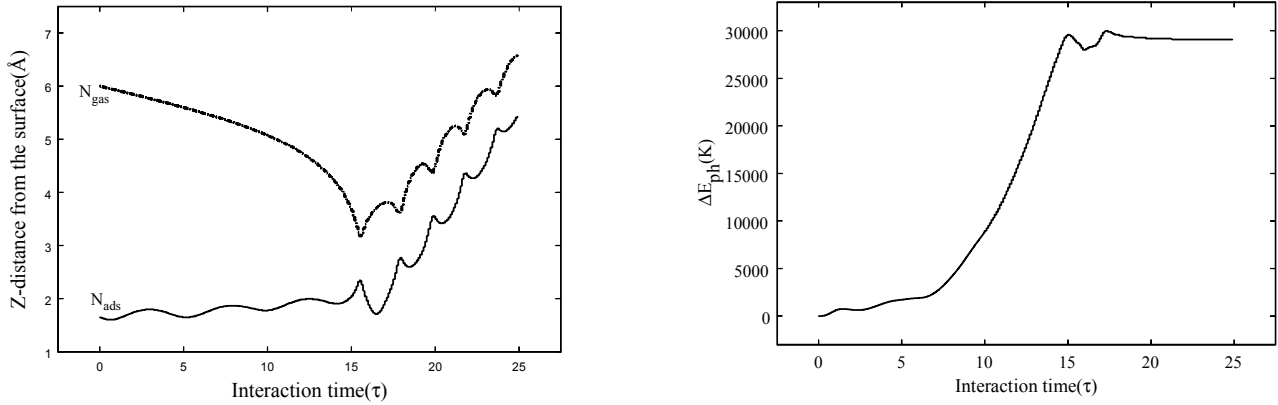


**Figure 2:** Recombination coefficient as a function of gas temperature

Figure 2 shows the recombination coefficient  $\gamma$  as a function of the gas temperature at  $T_S=1000K$ . At  $T_{gas}=T_S$  we get  $\gamma=1.73 \times 10^{-2}$ , which is comparable with the experimental values,  $\gamma=9.0 \times 10^{-3}$  and  $\gamma=4.0 \times 10^{-4}$ , obtained in Ref.[3] and Ref.[4] but for  $N_2$  formation on RGD and pure silica respectively.

In Figure 3 a typical trajectory is shown for a collisional event:  $N_{ad} * silica + N_{gas} \rightarrow N_2(v=36, j=23) + silica$ , where  $N_2$  is formed in the roto-vibrationally excited state ( $v=36, j=23$ ).

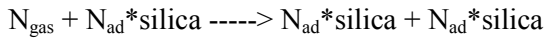
From Figure 3 it is evident that the adsorbed nitrogen atom is temporary trapped at the silica surface and that the recombination occurs close to the solid substrate: as a consequence a large fraction of the exothermic energy released in the recombination reaction is transferred to the surface as phonon excitation. The energy flux to the surface for this specific reactive collision is shown in the right-hand side Figure 3.



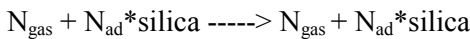
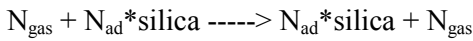
**Figure 3:** Figure on the left shows a typical trajectory for the reaction:  $N_{ad} \cdot \text{silica} + N_{gas} \rightarrow N_2(v=36, j=23) + \text{silica}$ . The  $Z(t)$  coordinate of the two N atoms is reported as a function of the collision interaction time ( in units of  $\tau=10^{-14}$  s ). The nitrogen gas atom hits the surface with an impact energy  $E_{kin}=0.04\text{eV}$ . The energy transferred to the silica surface in the recombination reaction is shown in the right-hand side figure.

In addition to the  $N_2$  formation at surface, a great variety of surface process can occur that are in competition with each other:

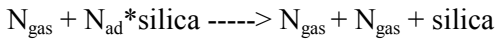
-- adsorption processes, that is processes where both N atoms are finally adsorbed at the surface



-- adsorption/desorption processes with one atom adsorbed and the other reflected into the gas-phase



-- direct inelastic surface processes with both atoms scattered in the gas-phase



In Table 1 we have reported the probability for these processes calculated as a function of the impact energy of the gas-phase nitrogen atom.

From the given results one can see that at high collisional energies the adsorption/desorption processes are the only active ones, while the recombination process is very effective in a rather narrow range of impact energies, between 0.02 and 0.04 eV. This is due to the changing of the energy exchange mechanism between the silica substrate and the nitrogen atoms. In fact, at the higher collisional energies the energy loss of the

two nitrogen atoms to the surface is stronger such that the probability for  $N_{\text{gas}}$  to be finally adsorbed increases considerably.

**Table 1:** Probability for the different processes at the surface.

$E_{\text{kin}}$	E-R recombination	Adsorption	Ads/Des	Inelastic
0.01	0.0	0.0	1.0	0.0
0.02	1.75(-2)	5.71(-1)	4.08(-1)	5.00(-3)
0.03	4.25(-2)	7.62(-1)	1.85(-1)	1.08(-2)
0.04	1.16(-1)	6.5(-1)	2.25(-1)	9.17(-3)
0.055	0.0	0.0	1.0	0.0
0.07	0.0	0.0	1.0	0.0
0.1	0.0	0.0	1.0	0.0
0.2	0.0	0.0	1.0	0.0
0.5	0.0	0.0	1.0	0.0
1.0	0.0	0.0	1.0	0.0

### Acknowledgements

Part of this work was supported by the Italian Space Agency (ASI) in the framework of the project: “Dynamics and Kinetics of Elementary Processes in Hypersonic Flows”.

### References

- [1] E. g. see: G. D. Billing, "Dynamics of Molecule Surface Interactions", Wiley, 2000;  
M. Cacciatore and G.D.Billing, Surf.Sci.**232**,35(1990); M. Rutigliano, M. Cacciatore, G.D. Billing, Chem. Phys. Lett., **340**, 13 (2001).
- [2] H. J. Ae. Jensen, P. Jorgensen and T. U. Helgaker, J. Chem. Phys., **85**, 3917 (1986).
- [3] C. D. Scott, “*Catalytic Recombination of Nitrogen and Oxygen on High Temperature Reusable Surface Insulation*”, in Aero and Planetary Entry, ed. A. L. Crosbie, Vol. 77 Progress in Astronautics and Aeronautics, AIAA , p.192, **1981**.
- [4] Y.C. Kim and M.Boudart, Langmuir **1991**,7,2999

# Numerical Modeling of the Performances of an Arc With Multiple Anode Contraction

V.M. Lelevkin, V.F. Semenov

Kyrgyz-Russian Slavic University, Bishkek, Kyrgyz Republic

## Abstract

On the basis of the equations of magnetic gas dynamics the calculation of the performances of an unclosed high-current arc, burning from the conical cathode up to the flat anode in an argon of atmospheric pressure depending on a current strength, anode sizes and interelectrode distance, is carried out. A possibility of a split of arc near the anode to current conducting channels with contraction by time references to electrode surface is defined. The results of calculation are qualitatively agreed with experimental data.

## 1. Introduction

Electric arcs, burning between rod electrode and item, executing a role of a second electrode, have received a wide circulation. The arc generates streams of plasma [1], in forming of which ones a noticeable role play a current intensity and geometry of welding rods [2]. The equations of magnetic gas dynamics (MGD) are applied for theoretical exposition of performances of a high-current arc [2]. Interaction of arc plasma with a surface of a welding rod can result in development of instabilities

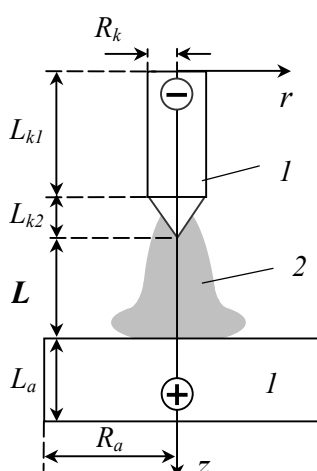


Fig. 1. The settlement plan of an arc,  
1 - welding rods, 2 - pole of an arc.

(phenomenon of a multiple contraction). Experimental researches of an arc [3-4] show, that the formation of multiple contraction on the anode is connected with gas-dynamic interaction of a stream of plasma and a welding rod surface as well as with development of instability of an overheating type. The similar phenomenon is implemented in a cavity of a cylindrical cathode [6], where the gas-dynamics of fluxion of gas promotes division of an arc near a welding rod.

Registration of near-electrode processes together with the phenomena of split of arc makes a problem of calculation of its performances extremely difficult. At model operation of an arc on the basis MGD of the equations the near-electrode processes are partially taken into account by engaging experimental data (radius of binding of an arc to welding rods, distribution of temperature etc.), or by requirements on the basis of the solution of model tasks [7]. From comparison of account results with the experiment [8-10] it is visible, that influence of near-electrode processes to performances of extended arcs of atmospheric pressure is localized in narrow locations and

quickly moves from electrodes surface.

The purpose of the work is to make on the basis of MGD equations a calculation of arc performances "from cathode to anode" and establish the conditions of realization of definite arc burning regimens in near-anode area (split, diffuse, contraction).

## 2. Model

The unclosed electric arc, burning between a conic tungsten cathode and flat surface of the copper anode (fig. 1) is considered. It is supposed: the flowing processes are stationary, the flow rotationally symmetric, laminar, the plasma is in a state of a local thermodynamic equilibrium, the radiation is volumetric. System MGD of the equations [2] in a cylindrical frame looks like:

$$\frac{\partial}{\partial r}(F_r h) + \frac{\partial}{\partial z}(F_z h) = \frac{1}{\sigma r} \left[ \left( \frac{\partial \chi}{\partial r} \right)^2 + \left( \frac{\partial \chi}{\partial z} \right)^2 \right] - r \psi + \frac{\partial}{\partial r} \left( r \frac{\lambda}{C_p} \frac{\partial h}{\partial r} \right) + \frac{\partial}{\partial z} \left( r \frac{\lambda}{C_p} \frac{\partial h}{\partial z} \right);$$



$$\begin{aligned}
\frac{\partial}{\partial r}(F_r v) + \frac{\partial}{\partial z}(F_z v) &= -r \frac{\partial P}{\partial r} - r j_z \mu H_\varphi + 2 \frac{\partial}{\partial r} \left( r \eta \frac{\partial v}{\partial r} \right) - \frac{2 \eta v}{r} + \\
&\quad \frac{\partial}{\partial z} \left[ r \eta \left( \frac{\partial u}{\partial r} + \frac{\partial v}{\partial z} \right) \right] - r \frac{\partial}{\partial r} \left[ \frac{2}{3} \eta \left( \frac{1}{r} \frac{\partial r v}{\partial r} + \frac{\partial u}{\partial z} \right) \right], \\
\frac{\partial}{\partial r}(F_r u) + \frac{\partial}{\partial z}(F_z u) &= -r \frac{\partial P}{\partial z} + r j_r \mu H_\varphi + 2 \frac{\partial}{\partial z} \left( r \eta \frac{\partial u}{\partial z} \right) + r(\rho - \rho_\infty)g + \\
&\quad \frac{\partial}{\partial r} \left[ r \eta \left( \frac{\partial u}{\partial r} + \frac{\partial v}{\partial z} \right) \right] - \frac{\partial}{\partial z} \left[ \frac{2}{3} \eta r \left( \frac{1}{r} \frac{\partial r v}{\partial r} + \frac{\partial u}{\partial z} \right) \right]; \\
\frac{\partial F_r}{\partial r} + \frac{\partial F_z}{\partial z} &= 0; \quad \frac{\partial}{\partial z} \left( \frac{1}{\sigma r} \frac{\partial \chi}{\partial z} \right) + \frac{\partial}{\partial r} \left( \frac{1}{\sigma r} \frac{\partial \chi}{\partial r} \right) = 0,
\end{aligned}$$

Here Ohm's law and the Maxwell equations are reduced to the equation for function  $\chi = r H_\varphi$ . The system is supplemented by expression for a current of arc  $I = 2\pi \int_0^R j_z r dr$ , dependencies of transport coefficients and thermal properties of plasma from temperature at atmospheric pressure taken from the same sources, as [2].

The boundary conditions are set on all contour of accounting calculated area (fig. 1):

$$\begin{aligned}
z = 0, \quad 0 < r < R_k: \quad v = u = 0, \quad h = h_R, \quad \chi = Ir^2 / (2\pi R_k^2); \\
R_k < r < R: \quad P = P_0, \quad v = 0, \quad h = h_R, \quad \chi = I / 2\pi; \\
0 < z < L_z, \quad r = 0: \quad v = 0, \quad \partial u / \partial r = 0, \quad \partial P / \partial r = 0, \quad \partial h / \partial r = 0, \quad \chi = 0; \\
r = R: \quad u = 0, \quad P = P_0, \quad \partial h / \partial r = 0, \quad \chi = I / 2\pi; \\
z = L_z, \quad 0 < r < R: \quad v = u = 0, \quad h = h_R, \quad \partial \chi / \partial z = 0.
\end{aligned}$$

Labels:  $F_r = r v r$ ,  $F_z = r u r$ ,  $V(v, u, 0)$  - velocity,  $h$  - enthalpy,  $P$  - pressure,  $E(E_r, E_z, 0)$ ,  $H(0, 0, H_\varphi)$  - intensity of electrical and magnetic fields,  $j(j_r, j_z, 0)$  - density of electric current,  $\mu$  - magnetic constant,  $\rho$ ,  $\sigma$ ,  $\lambda$ ,  $\psi$ ,  $\eta$ ,  $C_p$  - density, electrical conductivity, thermal conductivity, emissive power, viscosity and specific thermal capacity at constant pressure. The coefficients  $r$ ,  $z$ ,  $\varphi$  - correspond to axes of coordinates;  $k$ ,  $a$  - values on the cathode and anode,  $R$  - on exterior boundary.

### 3. Method of the solution

The solution of system of the differential equations is carried out by a method of finite differences in physical variables. The digitization of the equations is carried out on a nonuniform grid by a method of control volume. The boundaries of welding rods coincide with sides of control volumes. In all calculated settlement area including welding rods, the cold gas, plasma, procedure of calculation is applied a uniform (method of the open score), grounded on an account of change of medium properties on a demarcation welding rod - plasma (gas) by usage of medial harmonic coefficient [11]. In the field of welding rods the thermal properties of a material with a rather "large" viscosity is used, and on a contact surface the plasma - welding rod a limiting condition for a design temperature not exceeding melting point of a welding rod is put. The solution of difference equations is carried on iteratively using the methods of a under-relaxation and running in a radial direction. The field of fluxion is calculated with the help of a routine SIMPLE [11]. The sizes and arrangement of cathode and anode time references of arc, distribution allocation of a current density and temperature in near-electrode areas are the calculated parameters of a problem, which one are established during a numerical solution depending on a given current intensity, geometry of welding rods and interelectrode distance.

### 4. Results of calculation

The calculation of the performances of an arc in an argon of atmospheric pressure is carried out at following data (fig. 1):  $L_{k1} = 8$  mm,  $L_{k2} = 2$  mm,  $L = 10$  and  $20$  mm,  $L_a = 10$  mm,  $R_a = 2-20$  mm,  $R_k = 2$  mm,  $r_a = 1-10$  mm,  $T_R = 300$  kK,  $I = 50-400$  A.

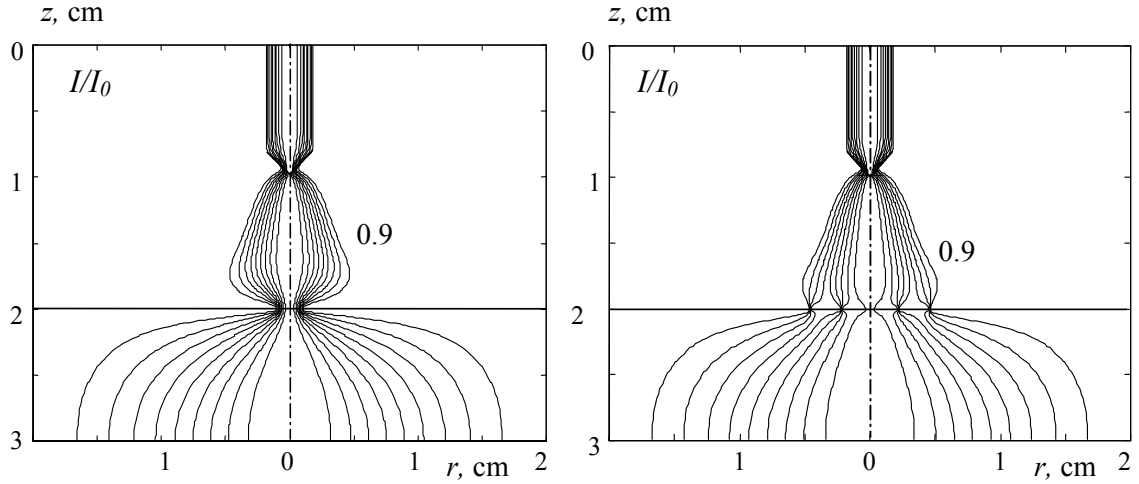


Fig. 2. Lines of an electric current  $I/I_0$  (step 0.1) for contraction (a) and split (b) arc in near-anode area,  $I=100$  A,  $L=10$  mm.

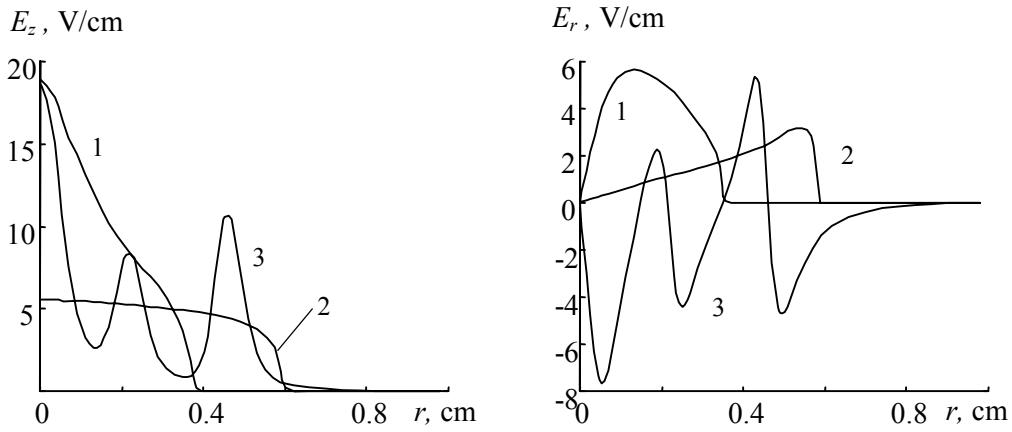


Fig. 3. Radial allocation of electric intensity in sections  $z=1$  (1),  $5$  (2),  $9.5$  (3) mm from an cathode cut,  $I=100$  A,  $L=10$  mm.

As it follows from the outcomes (fig. 2), the behaviour of the performances of arc for the anode depend on a current intensity, radius of binding of an arc to a welding rod  $r_a$  and interelectrode distance. Depending on change of  $r_a$  at  $I < 100$  A two steady solutions (fig. 2) are formed: with contraction ( $r_a < 4$  mm) trunk of an arc for the anode and its split ( $r_a > 4$  mm) it to a surface of the anode. The latter is implemented at setting the initial diffuse binding of an arc to the anode by the way of homogeneous current-conducting stratum ( $T = 6-10$  kK) for a flat surface of a welding rod. During solution of equations near the anode area formed of accumulation of electric current lines, which are joined in narrow ring locations with a practically rectangular distribution of a current and a surface electrode allocation (analog of anode spots, fig. 2 b). Herewith blanket current channel with minimum medial value  $E_z$  in near-anode area is realized. The split, apparently, is connected with hydromagnetic instability of diffuse binding of an arc to the anode and electromagnetic interaction of contraction current-conducting jets between them as well as with a surface of a welding rod. The extent of area of split of an arc does not exceed  $0.5$  mm from the anode surface. The radial distribution of an electric intensity in the section has a complex nature (fig. 3). It is less expressed is exhibited in temperature, pressure variations and axial velocity. The similar results of a mode of multiple contractions at burning arc in a xenon are obtained as a result of experiments [4].

With increase of a current intensity ( $I > 200$  A,  $r_a = \text{const}$ ), due to an operation of own electromagnetic forces [2] the intensity of plasma stream from the cathode, flowing to a flat anodes increases, killing "anode spots", reducing anode falling intensity and ensuring a steady diffuse binding of an arc to a welding rod. With  $r_a$  increase the diffuse binding of an arc to the anode exists together with

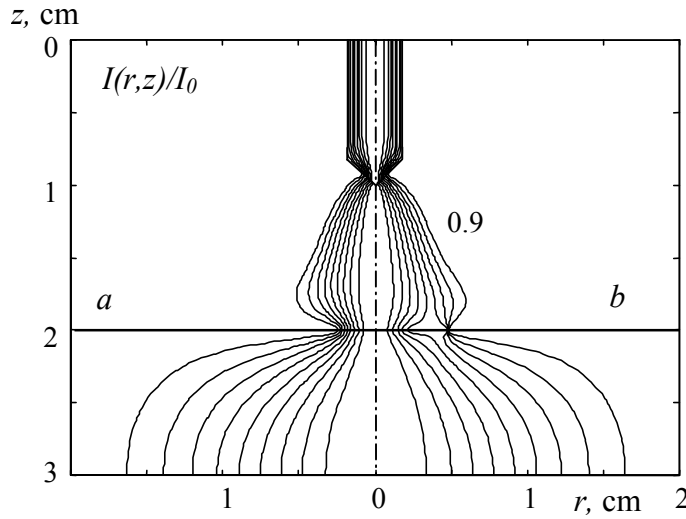


Fig. 4. Allocation  $I(r, z)/I_0$  (step 0.1) depending on initial binding of an arc to the anode:  $r_a < 5$  mm (a),  $r_a = 6$  mm (b),  $I = 200$  A.

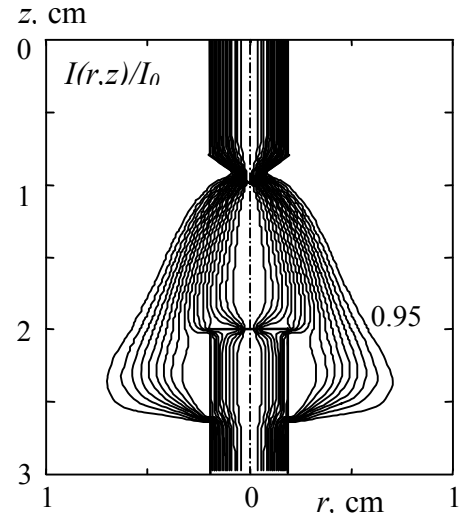


Fig. 5. Allocation  $I(r, z)/I_0$  (step 0.05) at,  $I = 100$  A,  $R_a = 2$  mm

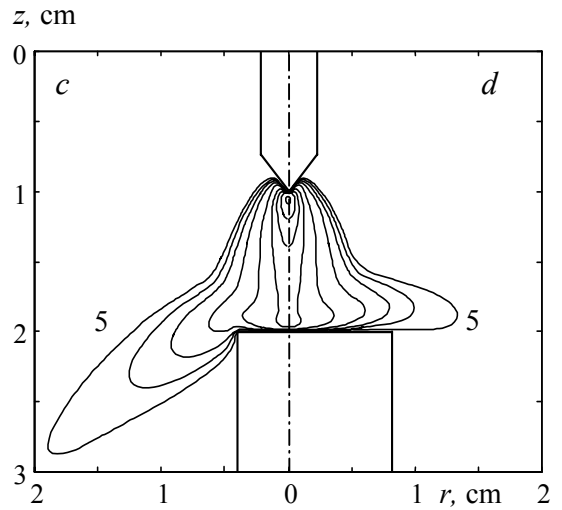
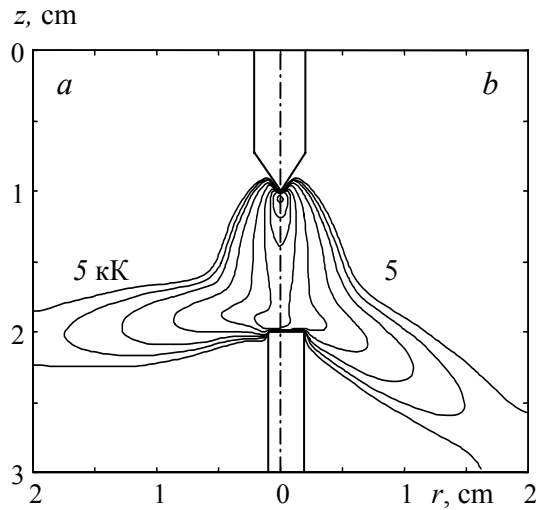


Fig. 6. Allocations of isotherms (step 2 kK) depending on radius of the cylindrical anode  $R_a$  = 1 (a), 2 (b), 4 (c), 8 (d) mm;  $I = 200$  A.

"anode spots" generated on a rim of a discharge (a fig. 4). At magnification of interelectrode distance the intensity MGD of a jet from the cathode decreases and the formation of "anode spots" in near-axial area is supervised at higher currents.

The diminution of the initial sizes  $r_a$  leads to forming contraction ( $I < 100$  A), or diffuse ( $I > 200$  A) time references of an arc to a welding rod. For interelectrode distance  $L = 10$  mm the maximum values  $r_a$ , at which an arc does not split in near-anode area, are restricted by the following conditions:  $r_a < 2$  mm at  $I = 50$  A,  $r_a < 4$  mm at  $I = 100$  A,  $r_a < 6$  mm at  $I = 200$  A,  $r_a < 10$  mm at  $I = 400$  A. So, a modification of interval  $r_a$  increases with a magnification of current intensity and anode arc does not split. For example, at  $I = 400$  A,  $r_a = 1-10$  mm the numerical solution converges to the same values with  $r_a \sim 5$  mm. With diminution of a current intensity the probability of split of an arc increases, which one is realized at minor resizing of current-conducting area near the anode ( $\Delta r_a \sim 1$  mm). At currents values  $I < 100$  A,  $r_a < 4$  mm one consider a growth of electric field strength near the anode and a contraction arc binding to a welding rod with the brightly expressed anode spot (fig. 2 a). Narrowing of an arc gives to a welding rod surface leads to a magnification of temperature of plasma near the anode and forming of near-axis toroidal vortex.

With magnification of interelectrode distance the intensity of a stream of plasma from the cathode decreases and the intensity of a vortex motion near the anode increases. The consent of results of calculation for different requirements of binding of an arc to the anode (split, diffuse or contraction) at a given current intensity takes place on distances of 1-2 mm from a surface of the anode. Unlike the anode area, the performances of an arc near the cathode practically do not depend on sizes of interelectrode distance and dynamics of development of an arc in near-anode area. It is explained by influencing of a gasdynamics of fluxion of plasma, as because of geometry and material of welding rods the forming of a stream of plasma by electromagnetic forces goes from the cathode to the anode.

With diminution of a current intensity the intensity of a cathode jet and its influencing on near-anode area decreases. At  $I < 100$  A "the arc anode binding" becomes a contraction one, a current density, temperature of plasma, electric intensity and impulse of an anode jet increase near a welding rod. This reduces in a displacement of area of interaction of "electrode jets" towards a cathode, increase of vortex gas circulation in toroidal vortex, which promotes arc contraction to anode and its expansion in an interaction section of cathode and anode plasma jets.

The intensity of a vortex motion of gas near to the anode increases at magnification of interelectrode distance, whereas temperature of plasma for the cathode is inflected insignificantly. It points to a noticeable role of a cathode jet on the performances of an arc of this area, that is in agreement with deductions of operation [11] and experiments [3]. With magnification of a current the intensity of a cathode jet increases, which one at  $I > 200$  A kills the anode one, flows on a surface of the anode and takes out a heat from the arc in a radial direction. Under the cathode jet the band of a recycling of gas fades, the anode drop of potential is moderated and the diffuse binding of an arc to the anode takes place. The influencing of the anode to performances of an arc is localized in immediate proximity from a surface, and a discharge itself practically is completely shaped by a cathode jet (see experiments [3]).

The geometry of welding rods essentially influences the performances of a stream of plasma. At a flat face of the cathode the sizes of an arc for a welding rod increase and consequently, axial velocity of a cathode jet (with 300 up to 30 m/s,  $I=200$  A), temperature (with 21 up to 15 kK) and pressure of plasma (with 1,5 up to 0,4 kPa) decrease. At usage of welding rods of identical radius ( $R_k=R_a$ , fig. 6) the arc is stronger contracted for a copper anode, as temperature of its surface is less, than for a tungsten cathode and the electromagnetic forces construct more intensive anode jet, which displaces an interaction range of streams of plasma closer to the cathode. With magnification  $R_a$  the intensity of an anode jet decreases, and a cathode jet flow around the anode (fig. 6). At  $R_a > 8$  mm a field of isotherms becomes like that one, which is realized at burning an arc on a flat plate. At fast submersion of a cylindrical anode in plasma a split of an arc on a series of current channels, convergented to the anode, with a formation of local areas of increased temperature of plasma near a welding rod surface also takes place (fig. 5).

## 5. Conclusion

At solution of MGD equations a method "of an open score" allows to determine the performances of a high-current arc, burning between welding rods with arbitrary geometry and material of welding rods without engaging near-electrode of processes, model problems building or other experimental information. At certain conditions near a surface of a welding rod a split of an arc in near-anode area is supervised, or a diffuse or contraction bindings of an arc to a welding rod are realized, that is agreed with the experiment.

## References

- [1] O.B. Bron and L.K. Sushkov - Plasma Flows in Electric Arc of Switch-off Devices, Energiya, Leningrad, (1975).
- [2] V.S. Engelscht, V.Ts. Gurovich, G.A. Desyatkov et al. - The Theory of Electric Arc Column, Nauka, Novosibirsk, (1990).
- [3] G.A. Dyuzhev, N.K. Mitrofanov, and S.M. Shkolnik - Zhurn. Tekhn. Fiz., **67**, 35 (1997).
- [4] F.G. Baksht, G.A. Dyuzhev, N.K. Mitrofanov et al. - Zhurn. Tekhn. Fiz., **67**, 41 (1997).
- [5] J.M. Sobrino, J.F. Coudert, P. Fauchais - ISPC-12, Minneapolis, Minnesota, **3**, 1455 (1995).
- [6] M.F., Zhukov, I.M. Zasyplin, et al. - Electric Arc Generators of Thermal Plasma, Nauka, Novosibirsk, (1999).
- [7] I.G. Panevin, V.I. Khvesyuk, I.P. Nazarenko et al. - Ttheory and Calculation of Near-Electrode Processes, Nauka, Novosibirsk (1992).

- [8] K.C. Hsu, K. Etemadi, E. Pfender J. Appl. Phys. **54** 1293 (1983).
- [9] V.M. Lelevkin, V.F. Semenov - Thermophysics and Aeromechanics, **9**, 2 (2002).
- [10] V.M. Lelevkin, V.F. Semenov – Phys. High Temp. **40**, 698 (2002).
- [11] S. Patankar, Numerical Heat Transfer and Fluid Flow, Hemisphere Publ. Corp., N. Y. (1980).
- [12] V. Neyman - in Experimental Studies of Plasmatorches, Nauka, Novosibirsk, 253 (1977).

# Surface modification of polymer powders in a fluidized bed plasma reactor

F. Brétagne<sup>1</sup>, M. Tatoulian<sup>1</sup>, F. Arefi-Khonsari<sup>1</sup>, G. Lorang<sup>2</sup> and J. Amouroux<sup>1</sup>

<sup>1</sup> LGPPTS, Université Pierre et Marie Curie, ENSCP, 11 rue Pierre et Marie Curie, 75005 Paris, France

<sup>2</sup> Centre d'Etude de Chimie et de Métallurgie, C.N.R.S, 15, rue Georges Urbain, 94407 Vitry Seine, France

## Abstract

A combination of a fluidized bed and a low pressure plasma has been used for the surface modification of polyethylene (PE) powders. XPS and contact angle measurements were used to reveal surface modification of nitrogen and ammonia plasma treatment of PE powders. Both nitrogen and ammonia plasma treatment show an increase of the hydrophilic character of the surface treated powders. XPS analysis show the incorporation of new functional moieties including C-N, C=O and C=N groups on the surface of treated powders. Nitrogen plasma treatment as compared as to ammonia plasma leads to a better incorporation of nitrogenated containing functional groups.

## 1. Introduction

Cold plasma processing of polymeric materials is a very efficient and practical method to modify the topmost layer without altering their bulk properties. Powders are useful as raw materials in many fields such as in electronic and paint industries, but also in biotechnology (enzymes, antibodies or DNA immobilization...). However, the control of the surface functionality of the powders is an important step for the success of these applications. The desired functionality can be obtained either by grafting of new chemical moieties [1-4] or by plasma polymerization of a polymeric film [5-10]. Many groups have studied surface treatment of powders in rotary drum with low-energy plasmas [4, 11-13]: significant disadvantages appear with regard to treatment homogeneity, because the residence time distribution is similar to a stirred reactor and, in the case of fine powders (below 100  $\mu\text{m}$ ) agglomeration can occur [14]. Fluidization is known as one of the most effective techniques available for treatment of particles. Fluidized bed reactors offer the possibility to minimize all aggregation phenomenon and give rise to an excellent mass and heat transfer rate between the gas and the particles.

In this paper, we report the effect of nitrogen and ammonia plasma treatment in the surface modifications of Low Density Polyethylene (LDPE) powders. Optical emission Spectroscopy was used to determine the nature of the excited chemical species as well as the energetic character of the discharge: the role of the introduction of the powders in the reactor has been thus discussed. Moreover, XPS and contact angle measurements were used to reveal the surface modifications of powder particles.

## 2. Experimental

### 2.1 Fluidized bed reactor

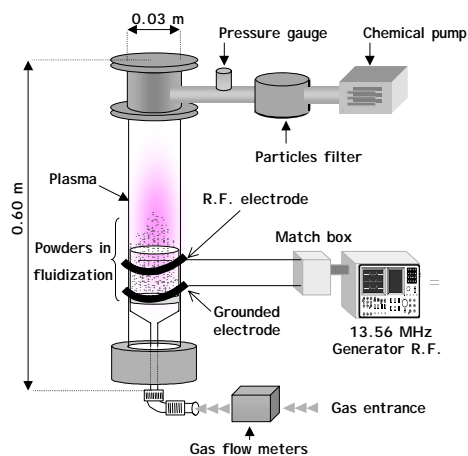
The fluidized bed reactor (FBR) consists of a cylindrical Pyrex glass tube of 30 mm internal diameter and 600 mm high as shown in figure 1. Low Density Polyethylene (LDPE) powders (density : 920  $\text{kg.m}^{-3}$ ; diameter : 350  $\mu\text{m}$ ) were fluidized by  $\text{N}_2$  or  $\text{NH}_3$  gases that passed through a porous glass plate. Gas flow rates were regulated by MKS mass flow controllers and the pressure was controlled by an EDWARDS Pirani type vacuum gauge. The low pressure in the reactor was maintained by a 18 two stages EDWARDS chemical pump. A capacitive coupled system composed of two external electrodes (distance between the two electrodes : 6 cm) was placed at the same level as the fluidized bed. The plasma is maintained by radio frequency energy generated by a SAIREM generator (power range from 0-300 W) with a matching box Incident and reflected powers were controlled by a wattmeter (impedance : 50 Ohms) and reflected power was adjusted at its minimum value (~1% of incident power). To prevent the powders from damaging the pump, a dust trap has been installed.

The flow rate of fluidization has been chosen carefully. When the gas flow rate is under a specific value corresponding to the minimum fluidization state, there is some dead zone in the bed where powders do not move. When the flow rate is higher than the minimum fluidization, new states

of fluidization can be observed (aggregative, bubbling fluidization or pneumatic transport) which could disturb the homogeneity of the plasma discharge [15]. The flow rate, corresponding to the minimum of fluidization state has been thus determined by measuring the pressure drop versus the gas flow rate. The minimum fluidization flow rate corresponding to the maximum of the pressure drop was found around 30 sccm at a working pressure of 50 Pa with both  $N_2$  and  $NH_3$  gases.

Moreover, in order to have a better understanding of the behavior of particles involved in the fluidized bed, we have used *L.D.A* (Laser Doppler Anemometry), which is a non intrusive method. This technique allows to determine the concentration of particles as well as their velocity. The principle of the technique and the system have been described in a previous work [16]. The determination of the residence time of LDPE powders in the fluidized bed has shown that in our experimental conditions, LDPE powder were treated only 35 % of the total treatment time.

Finally, plasma emission was controlled by an optical fiber (diameter : 200  $\mu m$ , Incident angle =  $47^\circ$ ). The radiations transmitted were analyzed by a spectrophotometer SpectraPro-500i (Acton Research Corporation) equipped with a 3600 and 1200 grooves/mm holographic grating for the analysis of the 300-450 nm spectral domain.



**Figure 1:** Experimental set-up of the FBR used for the surface treatment of LDPE powders

## 2.2 Surface analysis of powders

X-ray photoelectron spectroscopy investigations were performed at the CECM laboratory of Vitry (CNRS) with a Cameca MAC II analyser operating in the constant analyser energy mode (156 eV pass energy, 1.0 energy resolution). The  $Al-K\alpha$  anode (1486.6 eV) of the X-ray source ( $57^\circ$  mean incidence angle) working at a power of 325 W was presently employed. The spectrometer energy scale was calibrated with respect to the C-1s (C-C, C-H) component set at 285.0 eV.

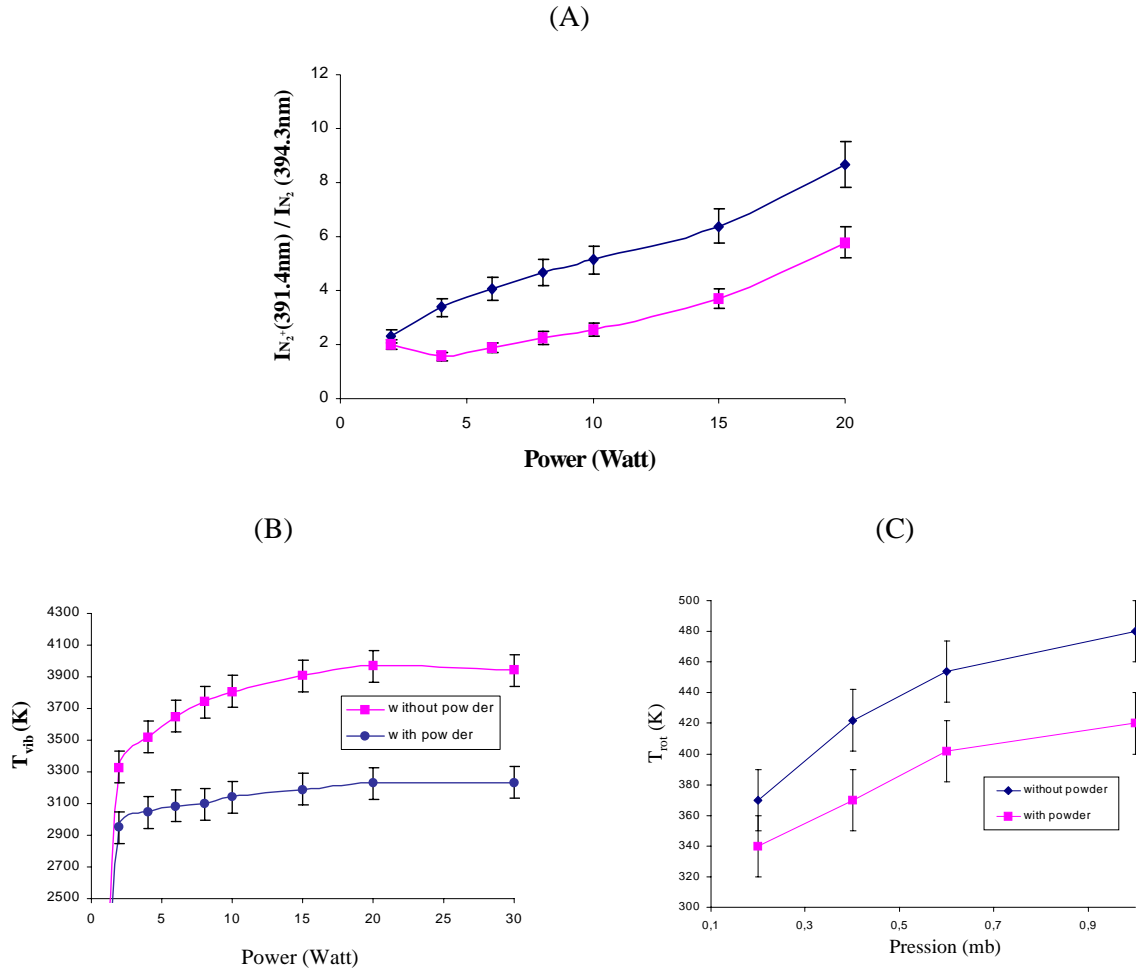
Contact angle measurements were performed on compacted plates and on uncompacted powder stucked on fixed glass support. The uncompacted powder scotched on the glass plate gave more realistic values for the surface energy of the powders than the compacted plate approach. According to these results, the hydrophilicity of the treated LDPE powders was investigated by contact angle measurements (sessile drop method). The samples holder was covered with a double face adhesive tape. Powders were brushed onto the adhesive and the excess of powders was blown off using compressed air. Contact angle measurements were performed with an image processing system using bi-distilled water liquid (liquid droplet : 2  $\mu L$ ). The reported values correspond to the average of six measurements of the advancing contact angle, on different parts of the sample.

## 3. Results and discussion

### 3.1 Plasma phase characterization by Optical Emission Spectroscopy

The radiation from the discharge was recorded by an optical fiber placed in the inter-electrode gap. For both  $NH_3$  and  $N_2$  discharges, the spectra showed the characteristic lines of the second positive system of  $N_2$  ( $C^3\Pi_u \rightarrow B^3\Pi_g$ ) as well as the first negative system of  $N_2^+$  (B) [17]. When LDPE powders were introduced into the plasma discharge, no new peak corresponding to new volatile products (such as hydrogen or carbon dioxide) were detected. However, we can note that the intensity of all peaks

decreased with the introduction of LDPE powders. Fig.3 shows that the presence of powders leads to an important modification of the energetic characteristic of the discharge. The ratio of the first negative system of  $N_2^+$  (B) line at 391.4 nm and that of the second positive system of  $N_2$ (C) at 394.3 nm have been used to estimate the energetic aspect (electronic temperature) of our discharge [18, 19]. First of all, one can note that by increasing the power, both the electron temperature and electron density increase. On the other hand, the presence of the powders leads to a decrease of the intensity of all of the emission peaks, since the powders pump the electron energy. However, a closer look at the two different temperatures measured, shows that the vibrational and the rotational temperature decreased whereas the electronic temperature increased when powders are introducing. This phenomenon could be explained by the fact since the powders absorbed electron, present in the plasma discharge, this will give rise to a decrease of electron density. Therefore, for the same power input the mean electronic temperature increases. On the contrary, vibrational and rotational temperature decreased (for a same power input).



**Figure 2 :** Influence of the presence of the LDPE powder in the nitrogen plasma discharge in the FBR on the energetic characteristics [(A)  $T_e$  ; (B)  $T_{vib}$  and (C)  $T_{rot}$ ].

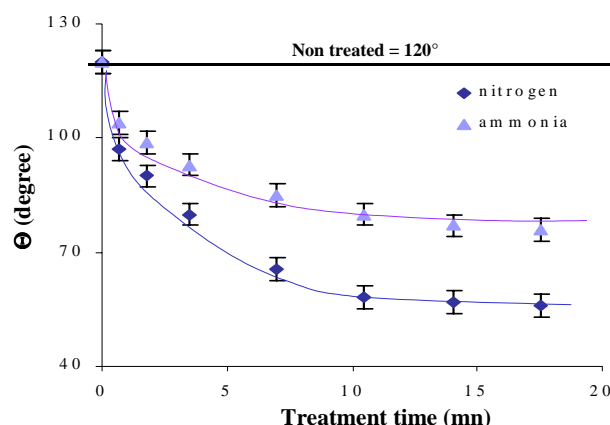
( $N_2$  flow rate = 30 sccm, Pressure = 50 Pa, 3 grams of LDPE powders,  $f = 13.56$  MHz)

### 3.2 Surface properties of plasma treated LDPE powders

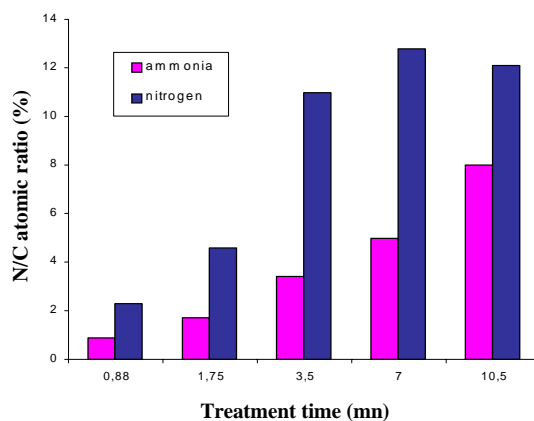
In agreement with literature [25], the wettability of plasma treated powders have been determine by the sessile drop method. Comparison of contact angle measurements of  $N_2$  and  $NH_3$  plasma treated LDPE powders is shown in figure 3. The contact angle determined by the sessile drop method is around  $120^\circ \pm 3^\circ$  for untreated LDPE powders which reveals the high hydrophobic character of the powders. The contact angle of plasma treated LDPE powders with water decreases with the increase of treatment time for both gases. This indicates that the surface becomes more hydrophilic. However, the



contact angle remained constant after a treatment time of around 10 minutes for both gases. This leveling corresponds to the competition between the functionalization and degradation phenomena which is a well known process in the plasma processing of polymers. The results confirm also that  $\text{NH}_3$  plasma treatment of powders is less effective in terms of hydrophilicity since contact angles of  $\text{N}_2$  plasma treated powders were smaller than those obtained with ammonia (respectively  $76^\circ$  compared to  $57^\circ$ ). XPS analyses show that this difference could be explained by a higher nitrogen uptake on the surface with nitrogen plasma treatment (Fig.4). However, the efficiency of nitriding of PP films in a low frequency discharge (70 kHz) and non symmetrical configuration of electrodes showed an opposite effect i.e. better results for  $\text{NH}_3$  compared to  $\text{N}_2$  plasma, revealing the important role of the excitation frequency on the kinetics of nitrogen incorporation [17, 20].

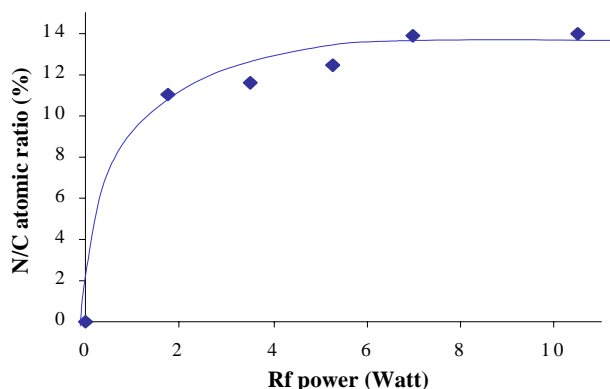


**Figure 3 :** Variation of contact angle measurements on LDPE powders after  $\text{N}_2$  and  $\text{NH}_3$  plasma treatments in the low pressure FBR  
( $\text{N}_2$  and  $\text{NH}_3$  flow rate = 30 sccm, Pressure = 50 Pa, Power = 5 W, 3 grams of LDPE,  $f = 13.56$  MHz)



**Figure 4 :** Comparison of N/C atomic ratio measured by XPS on LDPE powders after  $\text{N}_2$  and  $\text{NH}_3$  plasma treatment in a low pressure FBR  
( $\text{N}_2$  and  $\text{NH}_3$  flow rate = 30 sccm, Pressure = 50 Pa, Power = 5 W, 3 grams of LDPE,  $f = 13.56$  MHz)

The RF power plays also an important role in the incorporation of nitrogen moieties. As shown before, when the plasma power is increased, both electron energy and density are increased, and particles became more energetic. S. H Park and co-workers have shown that the increase of RF power in an O<sub>2</sub> discharge leads to a higher uptake of oxygen groups on the surface of HDPE powders [21]. The effect of RF power on the nitrogen incorporation for plasma treated LDPE powders in the fluidized bed reactor is shown in figure 5. The N/C atomic ratio increases with RF power until a value of 13.9 % for 20 W, and then the ratio remains constant. These results are in good agreement with those reported by Jama and co-workers who demonstrated that contact angle on polyethylene powders after a cold remote nitrogen plasma treatment increased until a given power value beyond which the contact angle remained constant [1].



**Figure 5 :** Variation of the nitrogen incorporation versus RF power on surface of LDPE powders after a nitrogen plasma treatment in the low pressure FBR  
(t = 3.5 minutes, N<sub>2</sub> flow rate = 30 sccm, Pressure = 50 Pa, 3 grams of LDPE, f = 13.56 MHz)

We can observe clearly by comparing plasma treated and non treated samples the presence of new nitrogen and oxygen moieties detected on the surface of LDPE powders after only one minute of N<sub>2</sub> plasma treatment. The evolution of the oxygen and nitrogen uptake on the surface after N<sub>2</sub> plasma treatment is summarized in Table 1. The O/C atomic ratio increases with the treatment time and reached a plateau at 14 % after a treatment time of ten minutes. A non negligible amount of oxygen atoms was incorporated on the surface of the plasma treated LDPE powders. Some studies made with an oxygen plasma <sup>18</sup>O<sub>2</sub> have shown that the incorporation of oxygen on the surface of polymer may have come either from the residual <sup>16</sup>O<sub>2</sub> present in the reactor during the plasma treatment or from the post oxidation reaction between the free radicals created by the plasma treatment on the surface and atmospheric oxygen <sup>16</sup>O<sub>2</sub> [22, 23]. Concerning the nitrogen incorporation, N/C atomic ratio increases from 0 to 12.8 % by increasing the treatment duration and a plateau is obtained for treatment times above 5 minutes.

treatment time (minute)	Atomic ratios		C <sub>1s</sub> component (Peak position and peak area)		
	O/C (%)	N/C (%)	Peak 1 (285 eV)	Peak 2 (285.8 eV)	Peak 3 (287.8 eV)
0	1.4	0	90	10	0
0.35	3.2	1.4	75.8	23.8	0.4
0.88	5.2	2.3	75.4	22.8	1.8
1.75	8.8	4.6	65.5	28.2	6.3
3.5	14	11	60.3	30.2	9.5
5.25	12.4	9.6	53.5	36.7	9.8
7	13.6	12.8	51.8	38.2	10
10.5	14.1	12.1	50	39.6	10.3

**Table 1 :** XPS results of plasma treated LDPE powders in the low pressure fluidized bed

(Nitrogen flow rate = 30 sccm, Pressure = 50 Pa, Power = 5 W, 3 grams of LDPE, f = 13.56 MHz)

High resolution spectra analyses of untreated LDPE powders, shows that the C<sub>1s</sub> peak is relatively sharp and symmetrical. It can be deconvoluted into a main component at 285.0 eV due to C-C groups and a very small component at 285.8 eV assigned to C-O groups. The latter represents 1.4 % of the total C<sub>1s</sub> peak, probably due to polymer additives. After a N<sub>2</sub> plasma treatment, two new components appear corresponding to alcohol or amine groups (285.8 eV) and to carbonyl or imine groups (287.8) eV. In order to have a better understanding in the discrimination between amine and other grafted functional groups, we are developing a derivatization method using different specific coupling agents. The quantification is based on UV-visible absorption measurement in solution [24].

## Conclusion

Both XPS analysis and contact angle measurements have confirmed that treatment of LDPE powders by N<sub>2</sub> or NH<sub>3</sub> plasma in a fluidized bed was an efficient method to incorporate nitrogen functional groups at the outmost layer of the surface of powders. Comparison between nitrogen and ammonia plasmas shows that in our plasma reactor configuration, the nitrogen plasma is more efficient than the ammonia plasma in order to incorporate new nitrogen moieties. After plasma treatment in the low pressure fluidized bed reactor, LDPE powders show a considerable increase in terms of hydrophilic character due to the incorporation of new functional groups. It has been shown that the hydrophilicity and the nitrogen incorporation on the surface of LDPE powders increase both with treatment time and RF power. Optical Emission Spectroscopy has shown that the powders absorb a large part of the electron present in the plasma discharge, revealing the necessity of using high RF power to maintain a high level of electron density.

## References

- [1] C. Jama, G. Breton, B. Mutuel, O. Dessaux and P. Goudmand, ISPC-14, vol 3 , 1287-1292, (1999)
- [2] S. H. Park and S. D. Kim, Colloids and Surfaces, A: Physicochemical and Engineering Aspects **133**, 33-39 (1998)
- [3] S. P. Godfrey, E. Kinmond and J. P. S. Badyal, Chem. Mater., **13**, 513-518, (2001)
- [4] S. P. Godfrey, E. J. Kinmond, J. P. S Badyal, I. R. Little, Chem. Mater, **13**, 513-518, (2001)
- [5] F. Denes, Trends Polym. Sci., **5**, 23, (1997)
- [6] G. Fye, V. Roucoules, A. M. Cameron, L. J. Oates, N. R. Cameron, P. G. Steel and J. P. S. Badyal, B. G. Davis, D. Coe, and R. Cox, Langmuir, **18**, 8996-8999, (2002)
- [7] W.J. Van Ooij and A.Chityala, Polymer Surface Modification : Relevance to Adhesion, **2**, 243-253, (2000)
- [8] M. Karches, Ch. Bayer, Ph. Rudolf von Rohr, Surface and coatings Technology **116-119**, 879-885 (1999)
- [9] N.Inagaki, S. Tasaka, K. Ishii, Journal of Applied Polymer Science, **48**, 1433-1440, (1993)
- [10] C. Bayer, M. Karches, A. Matthews and P. von Rohr, Chem. Eng. Technol., **21**, 427 (1998)
- [11] T. Tsugeki, S. Yan, H Maeda, K. Kusakabe, S. Morooka, Journal of Materials Science letters, **13**, 43-45, (1994)
- [12] T. Ihara, S. Ito, M. Kiboku, Chemistry letters, 675-678, (1986)
- [13] K. Tsutsui, K. Nishizwa, S. Ikeda, Journal of Coatings Technology, **60**, 765, oct (1998)
- [14] C. Bayer, M. Karches, A. Matthews, P.R. von Rohr, Chem.Eng. Technol, **21**, 427-430, (1998)
- [15] Kunii & Levenspiel, "fluidisation engineering", kriegel, (1977)
- [16] E. Francke, F. Bourg, M. Benmansour, D. Morvan, J. Amouroux, D. Ballutaud 15<sup>th</sup> International Symposium on Plasma Chemistry, Vol VI, P2521-2526, (2001)
- [17] F. Arefi, M. Tatoulian, V. Andre, J. Amouroux, G. Lorang ; Metallized Plastics 3: Fundamental and Applied Aspects, 243-256 -Edited by K.L Mittal - Plenum Press, New York (1992)
- [18] A Ricard, Ann. Chem. Fr. **8**, 303-318, (1983)
- [19] A. Ricard, "réactivité dans les plasmas" Ed, Phys, **56**, (1983)
- [20] F. Arefi-Khonsari, M. Tatoulian, N. Shahidzadeh, J. Amouroux, Plasma Processing of Polymers, 165-207, (1997)
- [21] S.H. Park and S.D. Kim, polymer bulletin, **33**, 249-256, (1994)
- [22] E. Occhielle, M. Morra, G. Morini, F. Garbassi, P. Humphrey, J. of Appl. Polym. Sci, **42**, 551, (1991)

- [23] F. Clouet, M. K Shi, R. Prat, Y. Holl, P. Marie, D. Leonard, Y. De Puydt, P. Bertrand, J. L. Dewez, A. Doren, J. Adhesion Sci. Technol. **8**, n°4, 329-361, (1994)
- [24] O. Bouloussa, F. Brétagne, M. Tatoulian, F. Arefi-Khonsari, J. Amouroux, F. Rondelez  
Submitted to langmuir (2003)
- [25] N. Marilyn Ahfat, G. Buckton, R. Burrows, M. D. Ticehurst, European Journal of pharmaceutical Science, **9**, 271-276, 2000

# DIAGNOSTICS OF ELECTRON BEAM EXCITED $\text{CF}_4/\text{Ar}$ PLASMAS FOR SILICON OXIDE ETCHING

Masafumi Ito<sup>1</sup>, Takayuki Kawanabe<sup>1</sup>, Tatsuo Shiina<sup>1</sup>, Yasuyuki Okamura<sup>1</sup>,  
Hisao Nagai<sup>2</sup>, Masaru Hori<sup>2</sup> and Toshio Goto<sup>2</sup>

<sup>1</sup>Faculty of systems Eng., Wakayama University, 930 Sakaedani, Wakayama 640-8510, Japan

<sup>2</sup>Dept. of Quantum Eng., Nagoya University, Furo-cho, Chikusa-ku, Nagoya 464-8603, Japan

## Abstract

We have evaluated silicon oxide ( $\text{SiO}_2$ ) etching using an electron beam excited plasmas (EBEP) for a micromachining process and have achieved the  $\text{SiO}_2$  etch rate of 117 nm/min without any additional bias power supply. From  $\text{CF}_4/\text{Ar}$  plasma diagnostics using a Langmuir probe and an optical emission spectroscopy, it was found that the electron beam current for generating plasmas limits the plasma density and self-bias voltage, resulting in the saturation of etch rate.

## 1. Introduction

Recently, new micro optical mechanical devices or micro total analysis system devices attract much attention [1],[2]. Micromachinings of optical fiber or non-planer thick dielectric materials are necessary to fabricate such devices. In such micromachinings, fast atomic beam etching and ion beam etching are employed because the RF self-biasing in the conventional reactive ion etching (RIE) is not applicable to non-planer dielectric materials. However, the etch rates of these processes are very low compared with the RIE and higher etch rate is required to improve processing time. On the other hand, an electron beam excited plasma (EBEP) has an excellent potential for applying self-bias to the non-planer dielectrics by using the electron beam. As an etching process using the electron beam of the EBEP, T. Hara et al. and M. Roji et al. reported poly-Si and GaAs etching processes [3], [4]. However,  $\text{SiO}_2$  etching characteristics were never reported. Therefore, we have examined the  $\text{SiO}_2$  etching characteristics using self-biasing assisted by an electron beam of the EBEP. Moreover, we have carried out the plasma diagnostics using a Langmuir probe and an optical emission spectroscopy. From these results, the etching mechanism in the EBEP is discussed to improve the etch rate.

## 2. Experimental setup

Figure 1 shows the experimental setup using the EBEP. Ar gas is fed to the plasma cathode region, where the electrons emitted from  $\text{LaB}_6$  produce the DC Ar plasma. The discharge current of the DC plasma is controlled by the electron current  $I_d$ . The electrons are extracted from the plasma cathode region and are accelerated in the electron acceleration region. The electron acceleration energy is controlled by the DC voltage  $V_A$ .

Electromagnet A and B produce mirror magnetic field, which guide the electrons into the aperture of the final electrode. The accelerated electrons are injected into the EBEP region.  $\text{CF}_4$  gas diluted by Ar gas was fed to the EBEP region. The accelerated electrons irradiate a thermally oxidized silicon ( $\text{SiO}_2$ ) substrate, which is located at 210mm from the final electrode and is mounted on the water-cooled substrate

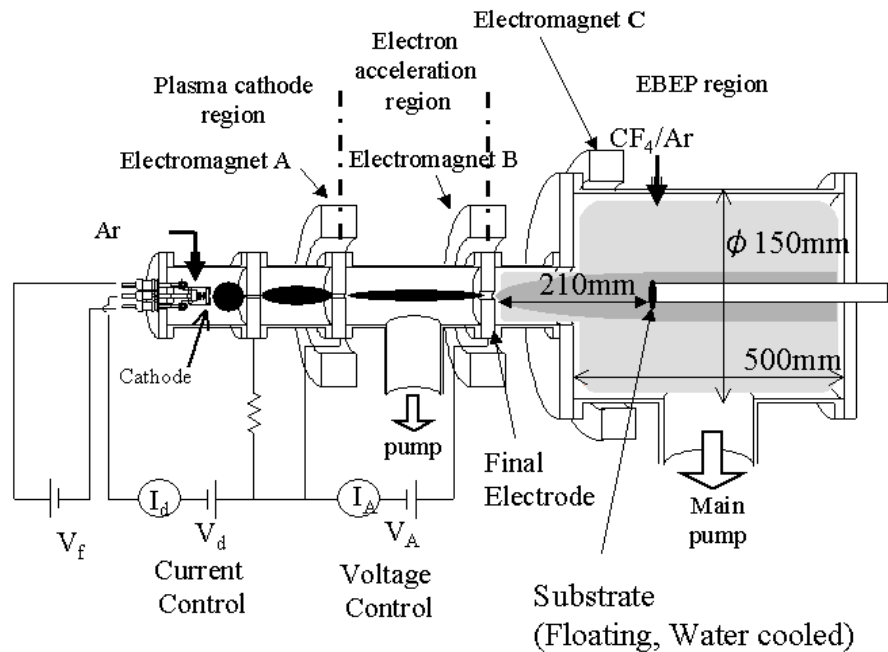


Fig.1 Experimental setup

holder. The holder is made of a cylindrical stainless tube with a diameter of 20mm and its sidewall is covered by the quartz tube to prevent the holder from being electrically connected to the plasma. The potentials of the substrate and the holder are electrically floating. The electromagnet C is employed to produce uniform ion current density and electron density on the substrate. The solenoid coil in the magnet C is bound up to the EBEP chamber with a diameter of 150 mm. The electron density, the ion current density and the space potential were evaluated by Langmuir single probe. In this work, the electron density was calculated from the electron saturation current of the probe. Since the beam current which flows directly into the probe was substantially smaller than the electron saturation current under the conditions in this study, the measured electron density was not largely affected by the beam current.<sup>4)</sup> The probe was set 1 cm above the substrate. Optical actinometry for the F density and optical emission spectroscopy of CF<sub>2</sub> were carried out above the substrate.

### 3. Results and Discussion

To improve the etch uniformity, the magnetic field was modified by using the electromagnet C. The distributions of the ion current density and the electron density on the substrate were evaluated by using the Langmuir probe. Figures 2(a)-(c) show the distributions of ion current density and electron density on the substrate. The currents of electromagnet C in Figs 2(a), (b) and (c) were 0A, 2A, -2A, respectively. The center of the substrate with a diameter of 20mm corresponds to the probe position of 0 mm. The cusp type magnetic field and the mirror type magnetic field are produced at the substrate by setting the current of magnet C to be 2A in Fig. 2(b) and -2A in Fig. 2(c), respectively. From these results, the ion current density and electron density exhibit uniform distributions at the cusp type magnetic field as shown in Fig. 2(b) while they decreased compared with those at no additional magnetic field and mirror type magnetic field (Fig. 2(a) and (c)). The etch characteristics were investigated in the condition of the cusp type magnetic field.

The SiO<sub>2</sub> etch rate and self-bias voltage (Vdc) were evaluated as a function of total pressure. Figure 3 shows the etch rate and the Vdc of the SiO<sub>2</sub> substrate as a function of total pressure. The total pressure was controlled by

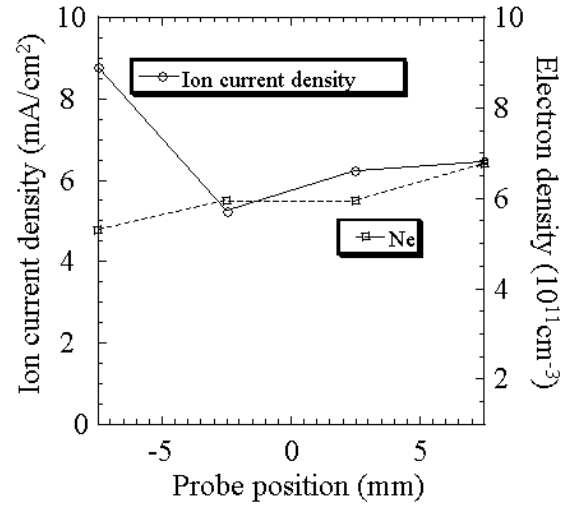


Fig.2 (a) Distributions of ion current density and electron density on a substrate (No additional magnetic field)

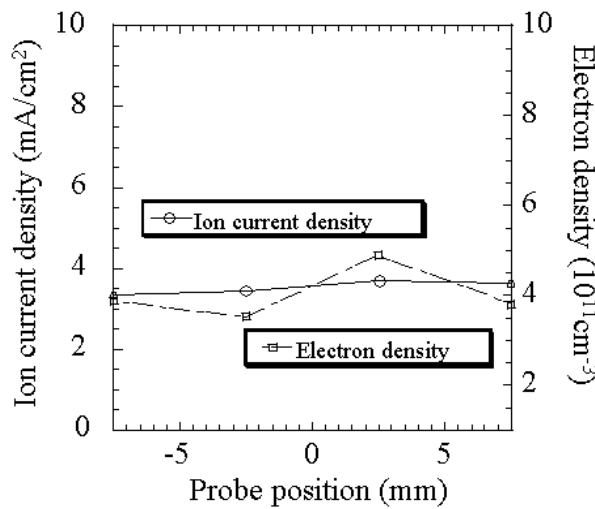


Fig.2 (b) Distributions of ion current density and electron density on a substrate (Cusp type magnetic field)

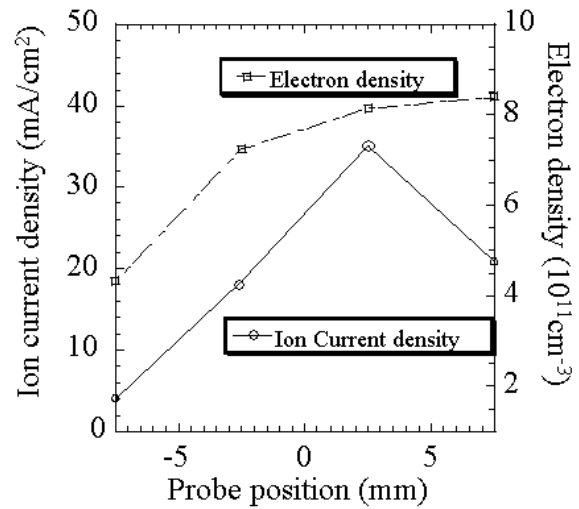


Fig.2 (c) Distributions of ion current density and electron density on a substrate (Mirror type magnetic field)

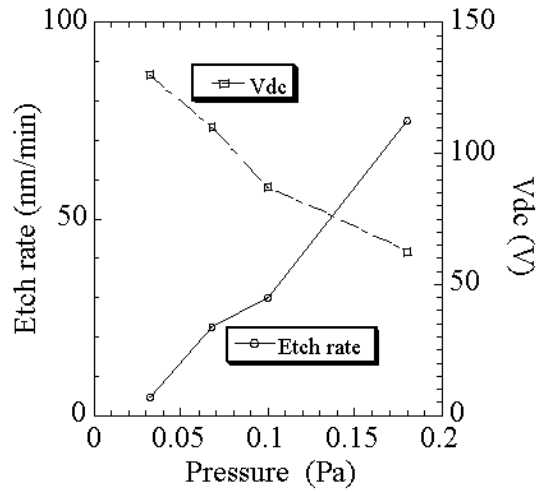


Fig.3 Etch rate and self-bias voltage (Vdc) as a function of total pressure

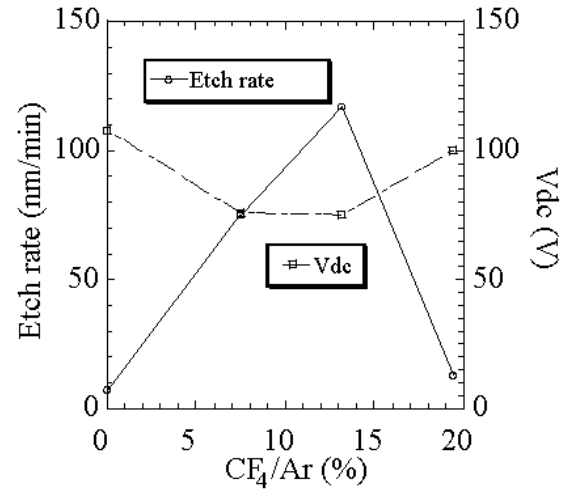


Fig.4 Etch rate and self-bias voltage (Vdc) as a function of CF<sub>4</sub>/Ar

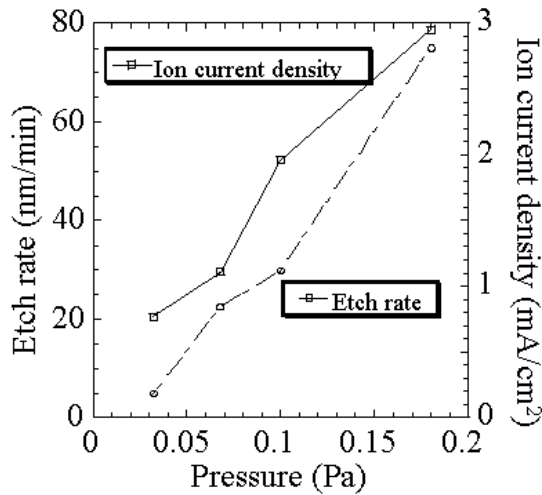


Fig.5 Etch rate and ion current density as a function of pressure

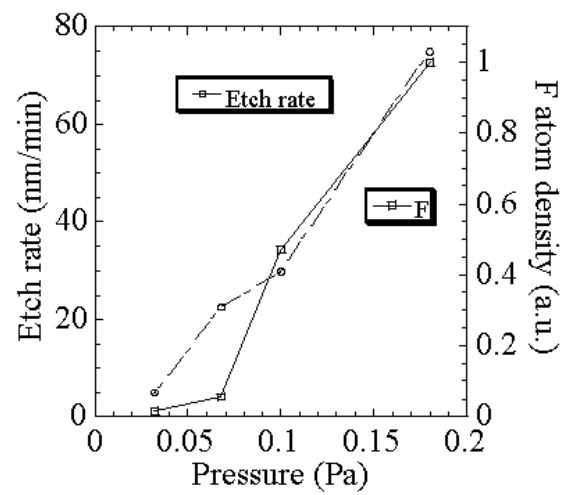


Fig.6 Etch rate, atom density and CF<sub>2</sub> emission intensity as a function of pressure

changing the total flow rate. The flow rate ratio of CF<sub>4</sub>/Ar was maintained to be 3/40. The etch rate increases while the Vdc decreases as the total pressure increases. The electron beam current  $I_A$  and the electron acceleration current were fixed to be 9.5 A and 100 V because of the upper limit of power supply.

Figure 4 shows the etch rate and Vdc as a function of the flow rate ratio of CF<sub>4</sub> to Ar (CF<sub>4</sub>/Ar) with the total flow rate of 43 standard cubic centimeter per minute (sccm). The operating pressure was maintained to be 0.18 Pa. The etch rate has a maximum point at about 13% of CF<sub>4</sub>/Ar while the Vdc decreases from ~100 to 75 V in the high etch rate region.

From these results, the highest etch rate of 117nm/min was obtained, which was about 10 times higher than that in the conventional fast atom beam or ion beam etching process.

The behaviors of ion current density and F atom density were compared with that of the etch rate as a function of the pressure as shown in Figs. 5 and 6. The behavior of the etch rate is similar to those of the ion current density and F atom density.

Figures 7 and 8 show the behaviors of ion current density, F atom density and CF<sub>2</sub> emission intensity compared with that of the etch rate as a function of CF<sub>4</sub>/Ar. The ion current density decreases and is saturated as the CF<sub>4</sub>/Ar increases while the etch rate has a maximum. F atom density and CF<sub>2</sub> emission intensity increase as the CF<sub>4</sub>/Ar

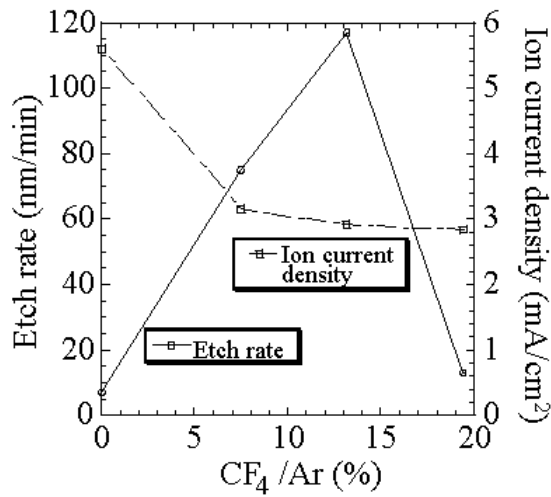


Fig.7 Etch rate and ion current density as a function of CF<sub>4</sub>/Ar

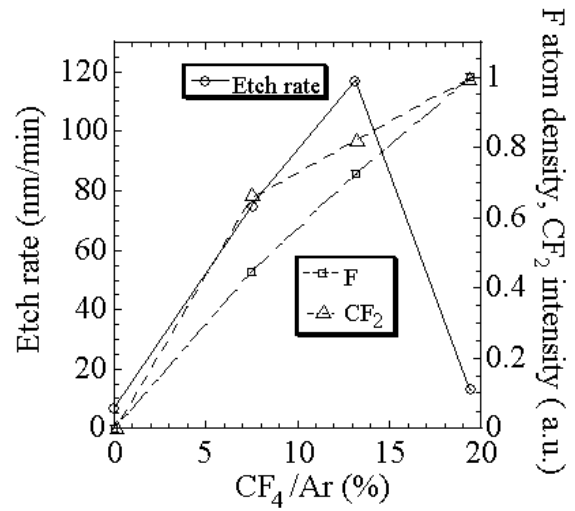


Fig.8 Etch rate and ion current density as a function of CF<sub>4</sub>/Ar

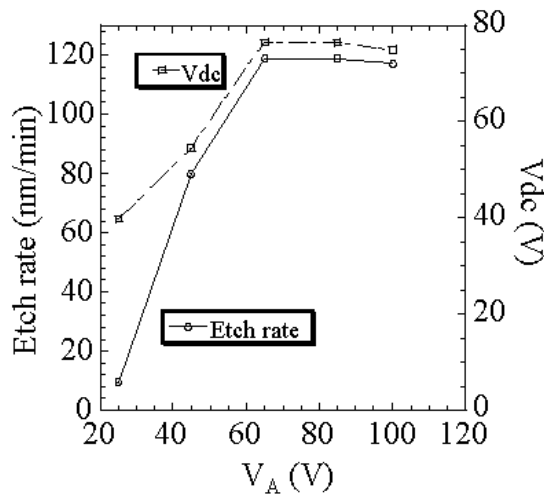


Fig.9 Etch rate and V<sub>dc</sub> as a function of V<sub>A</sub>

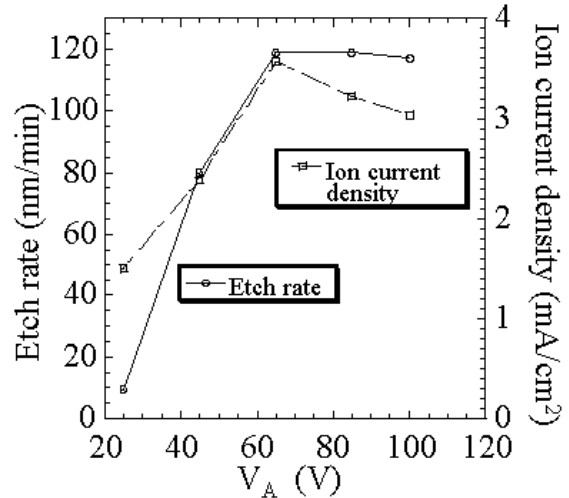


Fig.10 Etch rate and ion current density as a function of V<sub>A</sub>

Ar increases.

From the results as shown in Figs. 5 and 6, the etch mechanism seems to be due to the ion assisted etching and the chemical etching by F atoms. However, the behavior of ion current density in Fig. 7 has no relationship with that of the etch rate. On the other hand, the behavior of F atom density has a correlation with that of the etch rate up to 13% in CF<sub>4</sub>/Ar as shown in Fig. 8. However, the etch rate decreases while the F atom density increases as the CF<sub>4</sub>/Ar increases. The CF<sub>2</sub> emission intensity roughly corresponds to the production rate of the CF<sub>x</sub> radicals. This means that not only CF<sub>x</sub> radicals but also F atoms increase with the increase of CF<sub>4</sub>/Ar. The CF<sub>x</sub> radicals are well known as a precursor of CF<sub>x</sub> film as an etch protection layer. The deposition of the CF<sub>x</sub> film seems to be due to the decrease of the etch rate. Therefore, the chemical etching by F atoms seems to be dominant under the condition of the highest etch rate. The effect of ion-assisted etching as well as the chemical etching is necessary for obtaining higher etch rate. Therefore, the higher ion current density and higher V<sub>dc</sub> are considered to be important to improve the etch rate.

The V<sub>dc</sub> can be usually controlled by the electron acceleration voltage (V<sub>A</sub>) of the electron beam in the EBEP [5]. Figure 9 shows the V<sub>dc</sub> as a function of the V<sub>A</sub> in the condition obtained the highest etch rate. The flow rates of CF<sub>4</sub> and Ar were 5 and 38 sccm, respectively. The total pressure was 0.18 Pa. The V<sub>dc</sub> is saturated at the V<sub>A</sub> of 65 V. The behavior of V<sub>dc</sub> is similar to that of etch rate. The ion current density, F atom density and CF<sub>2</sub>



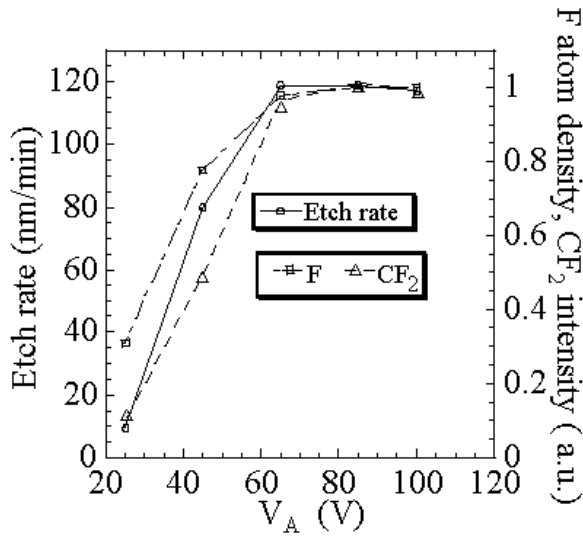


Fig.11 Etch rate, F atom density and  $\text{CF}_2$  emission intensity as a function of  $V_A$

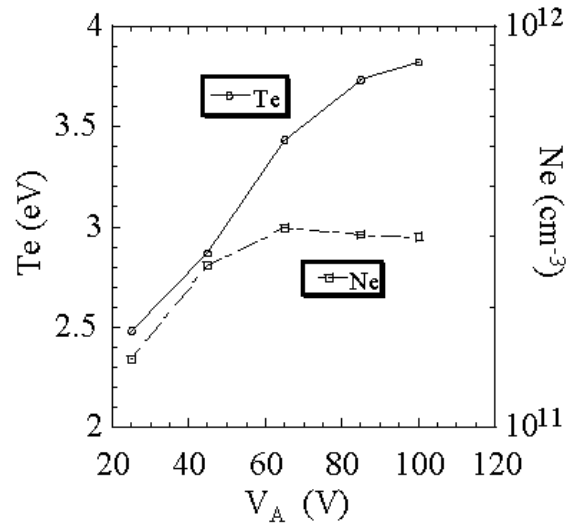


Fig.12 Electron temperature  $T_e$  and electron density  $N_e$  as a function of  $V_A$

emission intensity as a function of the  $V_A$  are shown in Figs.10 and 11. The ion current density increases up to the  $V_A$  of 65 V and is saturated as the  $V_A$  increases. F atom density and  $\text{CF}_2$  emission intensity increase with the increase of  $V_A$  and are saturated at the  $V_A$  of 65 V.

Figure 12 shows the electron temperature ( $T_e$ ) and electron density ( $N_e$ ) as a function of  $V_A$ . The  $T_e$  increases linearly up to the  $V_A$  of 65 V and the gradient of  $T_e$  gradually decreases. The  $N_e$  increases up to the  $V_A$  of 65 V and is saturated. Figure 13 shows the Vdc and the electron beam current  $I_A$  as a function of the  $V_A$ . The  $I_A$  is saturated at the  $V_A$  of 45V and is restricted by the upper limit of the power supply while the Vdc is saturated at the  $V_A$  of 65 V, which indicates that the  $N_e$ , the ion current density, the F atom density and the  $\text{CF}_2$  emission intensity are not determined by the only  $I_A$ .

As shown in Fig.12, the  $T_e$  increases slightly over the  $V_A$  of 65 V but the  $\text{CF}_4$  and Ar are dissociated or ionized by the electron beam in the EBEP unlike the conventional plasmas. The dissociation and ionization are almost constant above 60 eV [6], [7]. Therefore, the plasma densities such as the  $N_e$  and so on are saturated at the  $V_A$  of 65 V as shown in Figs. 10 and 11 and seem to be restricted by the  $I_A$  above the  $V_A$  of 65 V.

On the other hand, the Vdc should increase with the increase of the  $V_A$ . However, the Vdc is saturated as the etch rate is as shown in Fig. 9. Even in Fig. 4, the Vdc has a tendency of the decrease at higher etch rates. From these results, the electron beam might discharge the etch by-products into ions in the ion sheath region under the condition of high etch rate, resulting in the saturation of the Vdc because of constant electron beam current. In a deposition process using EBEP employed  $\text{C}_7\text{H}_8$  as a source gas, the disappear of ion sheath was reported and was speculated to be due to the discharge of the CH molecules [8]. The sufficient supply of the beam electron will exceed the generation of ions in the ion sheath, resulting in higher Vdc even under the condition of higher etch rate.

To achieve higher etch rate of  $\text{SiO}_2$ , higher plasma density and higher Vdc are necessary. The plasma density and the Vdc are restricted by the upper limit of  $I_A$  in this study. Therefore, the higher electron beam current without heating damage will be necessary in  $\text{SiO}_2$  etching process assisted by the electron beam of the EBEP.

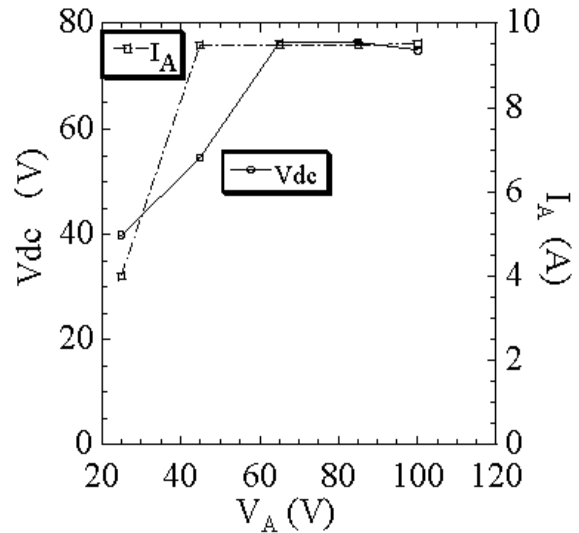


Fig.13 The Vdc and the electron beam current  $I_A$  as a function of  $V_A$

## Acknowledgments

This work was partly supported by the Grant-in-Aid for Scientific Research from Ministry of Education, Scientific, Sports, and Culture of Japan.(12131209)

## References

- [1]K. Hane et al., Si micromechanical fiber-optic switch with shape memory alloy microactuator, Transducers'99, 790793(1999).
- [2] T. Ujiie, T. Kikuchi, T. Ichiki and Y. Horiike, Fabrication of Quartz microcapillary electrophoresis chips using plasma etching, Jpn. J Appl. Phys., **39**, 3677(2000).
- [3] T. Hara, M. Hamagaki, A. Sanda, Y. Aoyagi, and S. Namba, J. Vac. Sci. & Technol. **B5**, 366 (1987).
- [4] M. Ryoji, T. Hara, K. Ohnishi, M. Hamagaki, Y. Dake, M. Tohkai, and Y. Aoyagi, New etching system with a large diameter using electron beam excited plasma, Jpn. J. Appl. Phys. **31**, 4257 (1992).
- [5] M. Hamagaki and T. Hara, Potential profiles in an Electron –beam-excited plasma, Jpn. J. Appl. Phys. **33**, 4369(1994).
- [6]H. F. Winters and M. Inokuti, Phys. Rev. A, Total dissociation cross section of CF<sub>3</sub> and other fluorocarbons for electron impact, **25**,1420(1982).
- [7]M. Kurachi and H. Nakamura, Proc. 13<sup>th</sup> Symp. Ion-Sources and Ion-assisted Technology, Kyoto, ed T. Takagi, 205 (1990).
- [8]S. Tada, M. Ito, M. Hamagaki, M. Hori, T. Goto, Deposition of Diamond-Like Carbon Using Compact Electron-Beam-Excited Plasma Source, Jpn. J. Appl. Phys., **41**, 5408(2002).

# Thermodynamic state and fluctuations of a nitrogen arc plasma

L. Delair, B. G. Chéron

UMR 6614 – CORIA - UFR des Sciences et Techniques de Rouen  
76801 Saint Etienne du Rouvray Cedex (France)

## Abstract

An original DC double arc nitrogen plasma source is analyzed from its optical and electrical signals. Plasma temperature and composition are determined inside the first and second arc chambers. In spite of the steep axial pressure gradient the plasma characteristics remain close to those of a LTE state. Besides electrical supply LF fluctuations the temporal series exhibit a 6.7 kHz peak which is attributed to the generation of acoustic waves by the arc column movements.

## Introduction

Previous studies in our laboratory have been focused on the characterization of a supersonic low pressure nitrogen plasma jet. These experimental works were intended to validate free jet and boundary layer kinetic schemes involved in the numerical simulation of space shuttle re-entries<sup>[1]</sup>. To that end an original stable and long lifetime plasma source has been devised. The plasma is created by following a two step procedure : at first, a primary arc is ignited between the tip of a cone shaped tungsten cathode and the throat of a nozzle shaped copper anode. Then the plasma is reheated by another arc ignited between the cathode tip and an annular copper anode set in the extension of the primary anode divergence. The aerodynamic stability and spectral intensity of the plasma jet are greatly enhanced by the latter ignition. The electrical operating conditions are typically 35V / 200 to 400 A for the primary arc, and 40V / 50 to 200 A for the secondary arc. The flow rate varies between 5 to 30 slm. The static pressure successively falls from 27 kPa to 3 kPa when passing from the first to the second arc chamber, then to 100 Pa in the test chamber.

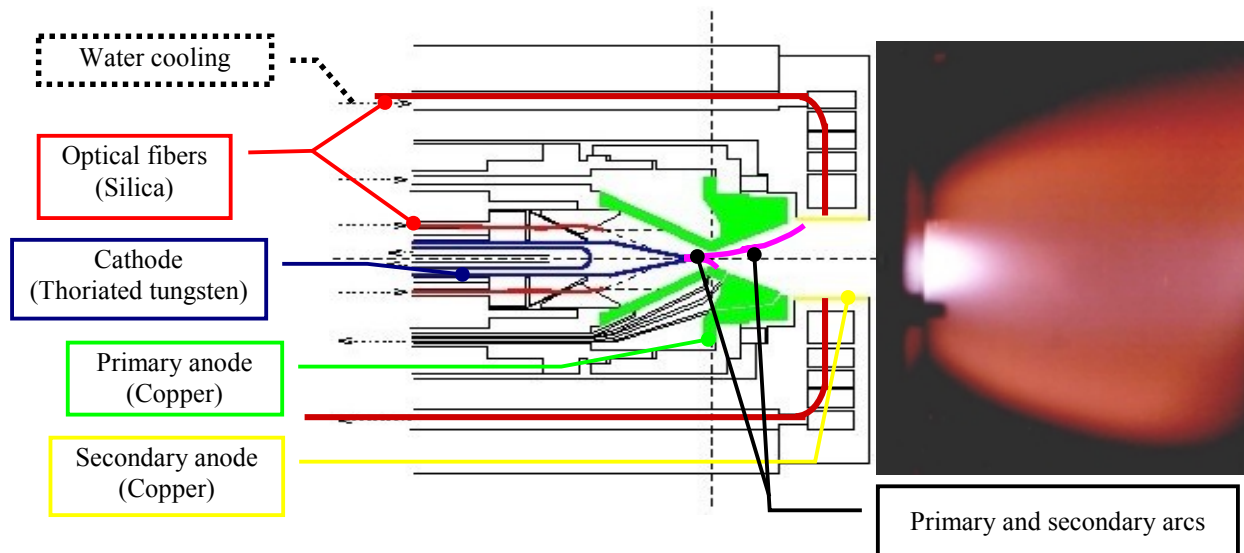


Figure 1 : Plasma torch

The arc chamber has been equipped with six 600  $\mu\text{m}$  in diameter VUV silica optical fibers : four are inserted above the primary anode throat and two are set at the secondary anode level. They are connected to an imaging spectrograph (Acton SP758i) set for a 0,03 nm resolution within the 200 nm - 900 nm range (Figure 1). By this way it is possible to watch the plasma and to detect the eventual movements of its anodic roots.

The dynamical behavior of the plasma is analyzed by means of classical tools (FFT, correlation functions and PDF) applied to the following temporal series : primary and secondary arc current intensity and voltage, plasma jet floating potential, and spectral intensity collected by the optical fibers. Conversely the electrical HF fluctuations of the plasma are used to measure the flow velocity at the outlet of the plasma source by using electrostatic probes.

## Thermodynamic state : results and comments

### 1. Specific enthalpy and energetic efficiency

The plasma source is water-cooled. From the measurement of the temperature difference  $\Delta T_{wj}$  between the inlet and the outlet of the cooling circuits, we deduce the specific enthalpy of the plasma flow. In our standard operating conditions ( $q_{N_2} = 0,22 \text{ g.s}^{-1}$ ,  $I_1 = 250\text{A}$ ,  $I_2 = 100 \text{ A}$ ), this enthalpy is about  $32 \text{ MJ.kg}^{-1}$ . Another important parameter of the plasma source is its energetic efficiency expressed as (1) :

$$h_p = \frac{\sum_{i=1}^2 U_i I_i - \sum_{j=1}^4 q_{wj} C_w \Delta T_{wj}}{q_{N_2}} \quad \text{and} \quad \eta = \frac{h_p q_{N_2}}{\sum_{i=1}^2 U_i I_i} \quad (1)$$

where  $U_i$  and  $I_i$  are the electrical potential and intensity (first and second stage of the plasma source),  $q_{wj}$  and  $C_w$  are respectively the cooling water mass flows (cathode, first and second anode, body) and specific heat. For a constant nitrogen flow rate this efficiency is almost constant ( $\eta = 0.5 \pm 0.05$ ) when the injected electrical power ranges from 10 to 24 kW. It can be increased up to 0.7 when increasing the mass flow rate up to  $0,45 \text{ g.s}^{-1}$ , but this gain is paid in return by a severe reduction of the electrode lifetime.

### 2. Excitation temperatures

The spectral scans at the first and second stage of the plasma source are very much alike. Both are dominated by the numerous  $N^+$  lines emitted in the near UV and visible range. Some  $N^{++}$  lines are also detected, which indicates a strong excitation level. In our optical conditions, a measurement of the absolute intensity of these lines is not possible. Nevertheless Boltzmann diagrams may be drawn from their relative values. The energetic range of the emitting levels spreads over a large range (20 to 32 eV) which allows to verify with a good accuracy the electron excitation equilibrium hypothesis.

The results are presented in the Table 1 : when only the first arc is ignited, the electron temperature  $T_e$  slightly decreases from 26 to 25000 K between the first and the second anode. As expected, this tendency is inversed (28 to 29000 K) when the plasma is reheated by the secondary arc.

The observed molecular spectra belong to the  $N_2^+$  first negative system and  $N_2$  second positive system. Their experimental shape and intensity have been compared to theoretical spectral simulations. The best fit reveals rather low internal excitation temperatures :  $5000 \pm 1500 \text{ K}$  for the vibration and  $2500 \pm 1000 \text{ K}$  for the rotation. The relevant inaccuracy may be ascribed either to the rotational excitation mode (particularly for  $N_2^+$ ) or to the strong molecular density gradients along the line of sight. Actually, as it will be shown further,  $N_2^+$  and  $N_2$  number densities are very weak in the plasma core.

### 3. Electron and ion densities

In the first arc chamber the electron density is derived from the lorentzian broadenings<sup>[2] [3] [4]</sup> of some  $N^+$  lines (404.13 nm, 444.20 nm, 453.04 nm, ...) which are clearly larger than the apparatus function of the spectrometer. At the second stage of the plasma source this procedure cannot be used because these line broadenings have become too weak. By adding few percent of hydrogen in the nitrogen flow we have derived the electron density in this region from the  $H_\alpha$  Stark broadening. Results are presented in Table 1. When the pressure falls from 27 kPa to about 3 kPa between the first and the second stage, the decrease of the electron density is only 40%. The lighting of the second arc enhanced the electron density by about 20%

in both chambers. At the entrance in the test chamber ( $P = 100$  Pa) previous works<sup>[5]</sup> based on electrostatic probe technique have shown that the electron density strongly falls down to  $5 \cdot 10^{20} \text{ m}^{-3}$ .

		first arc only	first and second arcs
Te	First chamber	26000 K	28000 K
	Second chamber	25000 K	29000 K
Ne	First chamber	$1,3 \cdot 10^{22} \text{ m}^{-3}$	$1,6 \cdot 10^{22} \text{ m}^{-3}$
	Second chamber	$0,8 \cdot 10^{22} \text{ m}^{-3}$	$0,9 \cdot 10^{22} \text{ m}^{-3}$

Table 1

Our spectroscopic measurements have been compared to the results of a simple equilibrium kinetic model involving six species ( $\text{N}$ ,  $\text{N}^+$ ,  $\text{N}^{++}$ ,  $\text{N}_2$ ,  $\text{N}_2^+$ , and  $\text{e}^-$ ) bound by the classical Dalton, electroneutrality and mass action laws. The composition of a nitrogen plasma in a complete equilibrium state is displayed in Figure 2. In our operating conditions ( $I_1 = 250$  A and  $I_2 = 100$  A) the major species in both chambers are  $\text{N}^+$ ,  $\text{N}^{++}$  and free electrons. The calculated values are comparable with the electron density deduced from spectroscopic measurement. The main chemical reactions are almost frozen between the two chambers and the evolution of the densities may be imputed to the only pressure gradient.

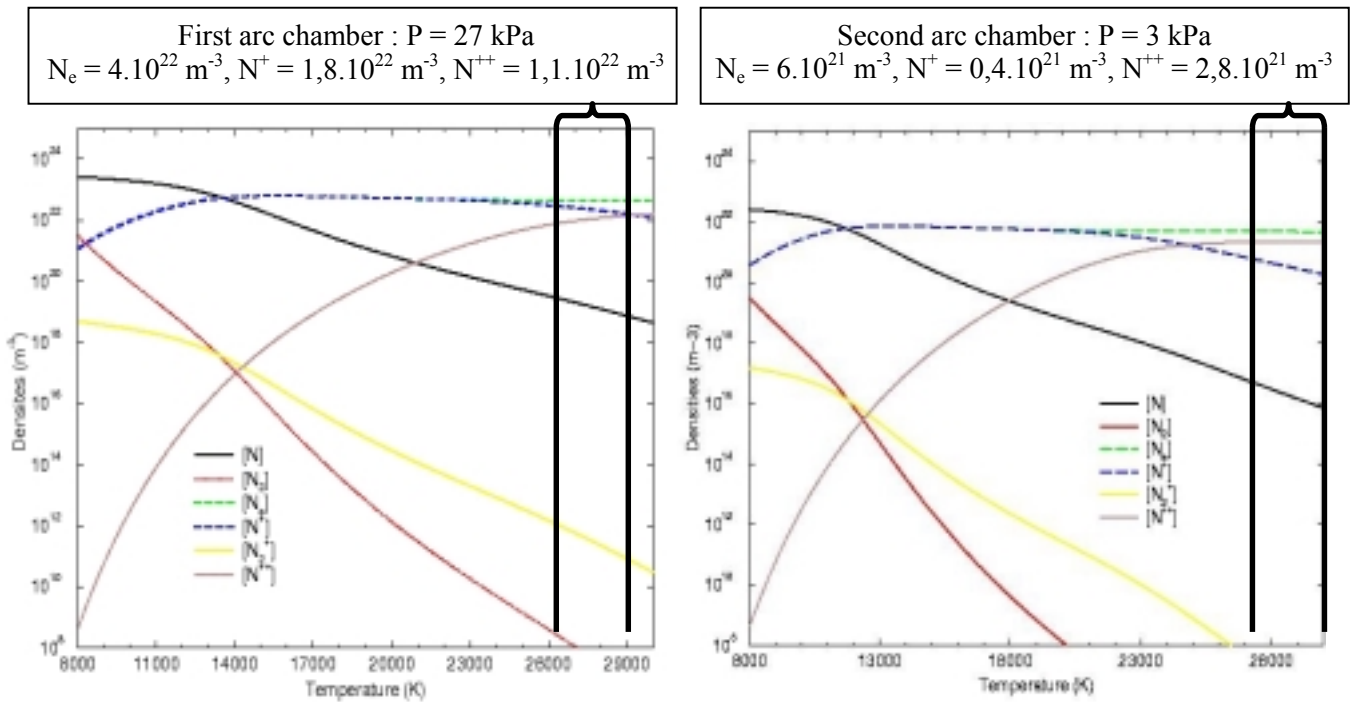


Fig. 2 : LTE Nitrogen plasma composition

## Fluctuations : results and comments

### 1- Harmonic analysis

The temporal fluctuations of the voltages ( $U_1$  and  $U_2$ ), current intensities ( $I_1$  and  $I_2$ ), radiation collected by the optical fibers ( $L_1$  and  $L_2$ ) and floating potential ( $V_F$ ) inside the plasma jet are analyzed by using classical tools. They have pointed out a large redundancy between all these parameters. The Fast Fourier Transformation (FFT) exhibits the characteristic frequencies of the undulation of the torch power supply

(150 Hz and its harmonics) and these are independent of any change of the working conditions. From any temporal series except the current intensity ones, another peak emerges in the HF range at about 6.7 kHz.

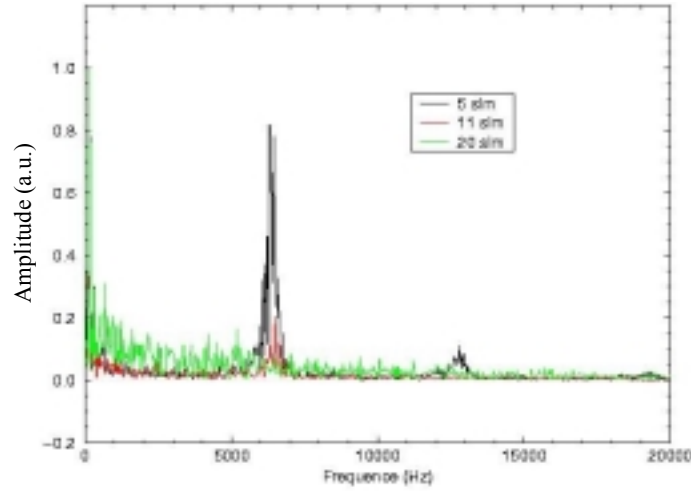


Fig. 3 : Fast Fourier Transforms of  $U_2$

The voltage signals do not exhibit the same sawtooth shape as observed in atmospheric plasma sources<sup>[6]</sup>. Such a behavior is characteristic of the arcing between the arc column and the anode wall. In fact, under the actions of the drag and electromagnetic forces acting on it, the arc attachment at the plasma column is pushed downstream as long as arcing does not occur at a shorter distance. The arc root moves only when arcing occurs between the plasma column and the anode wall. Such breakdowns result in HF peaks generally located in the 1-10 kHz range, the frequency of which increases with a rise of the current intensity.

So, the origin of the 6.7 kHz oscillations that we observe must be found by another way. When switching off the second arc this peak disappears from the FFT spectra. Its intensity is particularly sensitive to flow rate variations and its second harmonic appears around 13 kHz when the flow rate is lowered down to 5 slm.

## 2- Time correlations

Time correlation calculations have been achieved in the purpose to characterize the resemblance between different signals and between any signal with itself through time shift. Obviously, the BF (150 Hz) oscillations are quite reproducible. After subtraction of this carrier wave, the correlation functions are calculated and the influence of the flow rate is studied. As seen within the first millisecond shift (Fig 4) all the recorded signals become more and more stochastic as the flow rate increases.

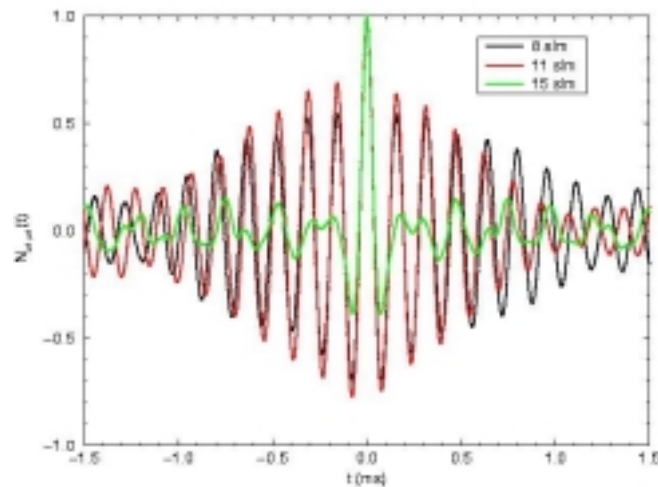


Fig. 4 : Autocorrelation of  $U_2$

These FFT and correlation analyses lead to ascribe the HF fluctuations to aerodynamic effects. In the arc chamber where steep pressure gradients are involved, their origin may be found either in acoustic waves or in turbulence induced in the vicinity of the electrodes. As exhibited by the  $V_F$  floating potential signals, these fluctuations are carried outside the arc chamber over the first centimeters of the supersonic plasma jet expansion. Moreover, in this region, camera pictures have revealed that the spatial variations of the  $V_F$  FFT peak amplitude are similar to the number density ones.

As previously mentioned, the first arc radiation is observed by using four optical fibers symmetrically displayed above the anode nozzle throat. The time correlation of the relevant temporal series do not exhibit any difference in phase. Consequently the primary arc root can be considered as quite stable and diffusely attached along the anode throat perimeter.

The  $U_1$  and  $U_2$  voltage density probability functions (PDF) have also been calculated. Typical shapes are presented on Fig.5. Assuming that the electrical strength is constant along the arc, this work gives access to the arc column length variations. One remarks the rise of modal shapes over 15 slm.

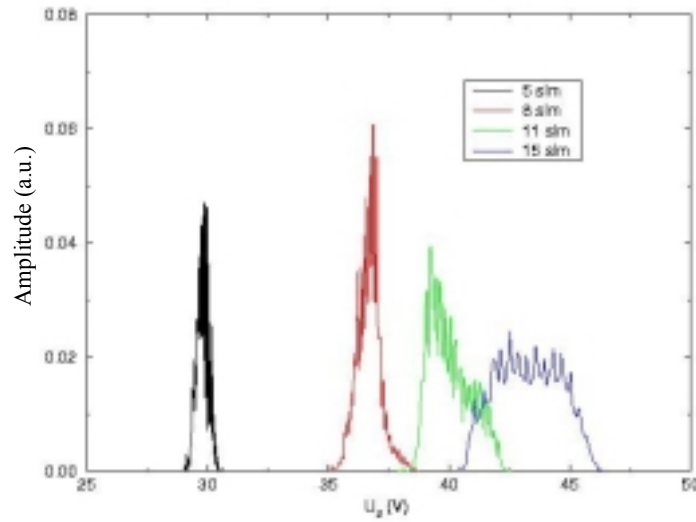


Fig. 5 : Self-correlation of  $U_2$

These distributions can be quantified by a “fluctuation intensity”  $Q(U)$ , defined as the ratio of the voltage RMS to its mean value. In our case,  $Q(U_2)$  and  $Q(U_1)$  are roughly insensitive to the variations of the electric power ( $Q(U_2) \approx 0,05$  and  $Q(U_1) \approx 0,03$ ), but strongly increase with a rise of the flow rate.

So, the aerodynamic origin of the HF is now well established. Considering all these results and the fact that the erosion of the second anode is hardly perceptible after tens working hours, the existence of a single local arc root on it must be discarded. The arc attachment can be regarded as diffuse and stable. Consequently the FFT 6.7 kHz peaks, which disappear when the second arc is switched off, show up the plasma column movements between the nozzle throat and the annular second anode.

In the plasma jet, the electron number density fluctuations can be used to measure the flow velocity. By raising to the local plasma potential two close and parallel Langmuir probes, we have derived the axial velocity from the temporal shift of their current signals. In the supersonic expansion zone, at 60 millimeters downstream the torch outlet, the so obtained velocity ( $2,5 \text{ km.s}^{-1}$ ) confirms the results published by H. Tahara<sup>[7]</sup> in closely aerodynamic conditions.

## Conclusion

An original double arc chamber have been devised which creates a very stable and energetic nitrogen low pressure plasma jet. Spectroscopic and signal treatment techniques have clearly shown that in our configuration the arc roots are diffusely attached to anode walls. The HF Fourier analysis have exhibited a single peak located around 6.7 kHz the source of which is imputed to aerodynamic effects. When the second arc is lighted the related increase of the electron number density and temperature (11000 K) at the exit of the torch raises the viscosity of the plasma up to its maximum value. Consequently the velocity field and shock structures are modified and the surrounding cold gas engulfment is clearly reduced which leads to a better stability of the free plasma jet.

The extension of this low pressure plasma torch to the atmospheric pressure is currently undertaken with the aim of achieving solid particle treatment. By another hand a physical model capable to describe and explain the aerodynamic behavior of this double arc plasma source has to be done.

## References

- [1] A. Bultel, B. G. Chéron - Measurement of the ground state and metastable atomic nitrogen number density in a low-pressure plasma jet. *Plasma Sources Sci. Technol.* **4** (1995) 597-605.
- [2] : Dimitrijevic M.S., and Konjevic N., 1980, *J. Quant. Spectrosc. Radiat. Transfer*, **24**, 451
- [3] Mar S., Aparicio J. A., de la Rosa M.I., and al – Measurement of Stark broadening and shift of visible NII lines. *J. Phys. B : At. Mol. Opt. Phys.* **33**, 1169-1184, (2000).
- [4] Griem H. R. – *Spectral line broadening by plasmas*. Academic press New York (1974).
- [5] L. Robin, P. Vervisch and B. G. Chéron – Experimental study of a supersonic low pressure nitrogen plasma jet. *Phys. Plasmas*. **1** (2), 444-458, 1994.
- [6] J. F. Coudert, M. P. Planche, P. Fauchais : Anode-arc attachment instabilities in a spray plasma torch, *J. of High temperature Chemical processes* **3** (1994) 639.
- [7] H. Tahara, K. Komiko, T. Yonezawa, Y. Andoh, T. Yoshikawa : Thermodynamical nonequilibrium nitrogen plasmas in a direct-current arcjet engine nozzle, *IEEE Transactions on plasma science*, **24** (1), 1996.



# **Surface modification with dielectric barrier discharge (DBD) running at atmospheric pressure**

I.P. Vinogradov, and A. Lunk

*Institut für Plasmaforschung, Universität Stuttgart, Germany*

In this paper investigations of surface modifications with intermittent dielectric barrier discharges running at atmospheric pressure in fluorocarbon mixtures are presented.

Results of the following discharge diagnostics will be discussed: FTIR absorption spectroscopy in Ar/fluorocarbon gas mixtures, diagnostics of the UV- and VIS- radiation and UV- absorption of DBD.

Diagnostics were performed in DBD containing Ar with admixtures of fluorocarbons. The following fluorocarbon molecules have been studied:  $\text{CF}_4$ ,  $\text{C}_2\text{H}_2\text{F}_4$ ,  $\text{C}_3\text{F}_8$ ,  $\text{C}_3\text{HF}_7$ , and  $\text{c-C}_4\text{F}_8$ . Emission and absorption spectroscopy performed simultaneously in combination with electrical measurements of the discharge characteristics is a suitable diagnostic tool for evaluating relevant process parameters. In the case of DBD in Ar/ $\text{CF}_4$ , or Ar/ $\text{c-C}_4\text{F}_8$  mixtures  $\text{CF}_3$  radicals or  $\text{CF}_2$  (carben), respectively, were detected as main products.

*Ex situ* fluorocarbon film diagnostics were performed using:

XPS,

FTIR absorption spectroscopy,

SEM,

Surface tension measurements.

Fluorocarbon films were deposited on Si plates, polymer foils, and textile. A small amount of admixture gases as hydrogen and oxygen molecules shows considerable effects on polymer film production and will be discussed in detail.

# Erosion Behavior of W-Pd Bimetallic System under Nitrogen Plasma Impact

G.P. Glazunov<sup>1</sup>, A.A. Andreev<sup>1</sup>, D.I. Baron<sup>1</sup>, E.D. Volkov<sup>1</sup>,  
K.M. Kitaevskiy<sup>1</sup>, A.L. Konotopskiy<sup>1</sup>, A.Hassanein<sup>2</sup>

<sup>1</sup> *Institute of Plasma Physics of National Science Center  
"Kharkov Institute of Physics and Technology", 61108 Kharkov, Ukraine*

<sup>2</sup> *Argonne National Laboratory, 60439 Argonne, IL, USA*

It was suggested earlier [1] to use two-layer (bimetallic) diffusion systems, which comprise of rather thick palladium substrate and erosion resistant coating, e.g., tungsten on the plasma facing surface, for active control of hydrogen recycling process in thermonuclear fusion devices. In order to choose the optimal performances of tungsten-palladium bimetallic system, it is needed to carry out thorough investigations of its properties under plasma impact, in particular, its erosion behavior in hydrogen saturated or non-saturated states. Such researches could be useful not only for fusion problem, but for numerous plasma applications (hydrogen power engineering, plasma chemistry, biomedical applications, etc.), when above mentioned diffusion system could be used for hydrogen isotopes puffing through cathodes directly in reaction zone.

Tungsten protective coatings on palladium substrate were produced by vacuum-arc method and by sputtering in coaxial Penning discharge in argon atmosphere (so-called "rodtron" configuration). So the different W-film structures and morphologies were realized. For a comparison also investigated were virgin samples made of pure Pd. The experimental setup for plasma impact studies was device with mirror Penning discharge, which was ignited at magnetic field 0.05T in nitrogen at pressure  $2 \cdot 10^{-3}$  Torr. The ion energy values were 0.8 keV – 1.6 keV, irradiation doses were  $10^{18}$ - $10^{20}$  ions/cm<sup>2</sup>. Erosion coefficient values were measured by weight loss method. Before sputtering experiments under nitrogen plasma impact, the current-voltage characteristics were measured with and without small hydrogen admixture. It was shown that there is no significant influence of hydrogen admixture in the working gas on plasma performances. Such behavior is explained by the fact that plasma column in mirror Penning discharge has no contact with the wall surface, so surface reactions, influencing recombination rate, do not play an essential role. It was shown that erosion coefficient weakly depends on ion energy for both Pd and W-Pd system and its value (1.3 at./ion for Pd and 0.2 at./ion for W) is in a good agreement with literature data on sputtering by monoenergetic N<sup>+</sup> ions. But practical independence of sputtering rate on hydrogen saturation up to concentration about H/Pd = 0.65 was unexpected result. The point is that in some recent works, e.g., [2] it was shown the possibility to decrease material erosion by hydrogen/deuterium saturation to high concentration. Possible mechanism is discussed to understand the reason of such differences in an erosion behavior. For hydrogen saturated W-Pd system the new kind of radiation damages were observed caused by not homogeneous adhesion of relatively thick ( $\approx 10\mu$ ) W-films. The measured dose dependencies are different for coatings made by different methods. For W-films made by vacuum-arc sputtering, the erosion coefficient value is near to that for bulk tungsten, and it does not change to dose about  $4 \cdot 10^{19}$  ion/cm<sup>2</sup>. At the further dose increase, sputtering rate increases extremely up to typical values for bare palladium due to full film disruption. In the case of W-coatings made in Penning discharge, erosion coefficient monotone increases on exposure time. Mechanisms are suggested and discussed to explain such erosion behavior.

[1] G.P.Glazunov, E.D.Volkov, A.Hassanein. In: Hydrogen and Helium Recycling at Plasma Facing Materials. NATO Science Series II: Mathematics, Physics and Chemistry, **54**, 163 (2002).

[2] J.P. Alain, D.N. Ruzic. Nucl. Fusion, **42**, 202 (2002).

# Initiation of plasma chemistry reaction with electron beam, produced by plasma electron gun.

V. Burdovitsin, Yu. Burachevsky, E. Oks, S. Rabotkin, M. Fedorov

*Tomsk State University of Control Systems and Radio-Electronics, Tomsk, Russia*

## Abstract

The experimental results of plasma generation by electron beam and plasma-chemistry decomposition of methane in beam-plasma discharge are presented. Electron beam was produced by electron gun on the basis of hollow cathode discharge. This gun can operate at pressures favorable for beam-plasma discharge initiation. C-H films were deposited at substrates, disposed in discharge plasma. Films growth rate and properties strongly depend on distances between plasma axis and substrate.

## 1. Introduction

Beam-plasma discharge may be successfully used for plasma-chemical application [1]. Usual methods of plasma chemical reactions initiation in gas phase such as glow and RF discharges have some disadvantages. Main of them are: existence of electrodes in reaction chamber in DC glow discharge and absence of abrupt plasma boundary in both types of discharges. This has result in uncontrolled plasma influence at substrate surface, if using for film deposition. Besides it is difficult to maintain large area uniform plasma. At the same time discharge, initiated by electron beam may produce plasma which form is defined only by electron beam configuration. This allows to maintain abrupt plasma boundary and to remove electrodes from reaction chamber. It is possible also to produce large area plasma in case of using ribbon like electron beam. However electron gun, used in this method, must be able to operate in “bad” vacuum and in presence of reaction gas. At this reason it is not possible to use thermo-cathode gun, and only plasma cathode gun may be used. In our laboratory plasma electron gun on the basis of hollow cathode discharge was designed which can operate at pressure range from 5 to 13 Pa [2]. Two modifications of guns were made. One of them produces cylindrical electron beam and other – ribbon one. In this paper we report some details about plasma producing and its parameters. Examples of this plasma application for C-H films deposition are also presented.

## 2. Experimental set-up

Details of cylindrical beam gun construction were reported earlier [3]. Main elements of ribbon like beam gun are the same. It consists of rectangular hollow cathode 1 with dimensions 4 x 8 x 30 cm (Fig. 1), flat anode 2 with 1 x 25 cm window crossed by metal mesh 3 and extractor 4. Electrodes were electrically separated one from another by organic insulators 5, 6 which were screened from discharge plasma influence. For plasma distribution investigation 30 probes 7 were inserted in near anode area through insulator 5 between hollow cathode and anode. Beam current density distribution along beam width was measured by movable collector 8 disposed in electron beam. Collector had 1 mm collimating split

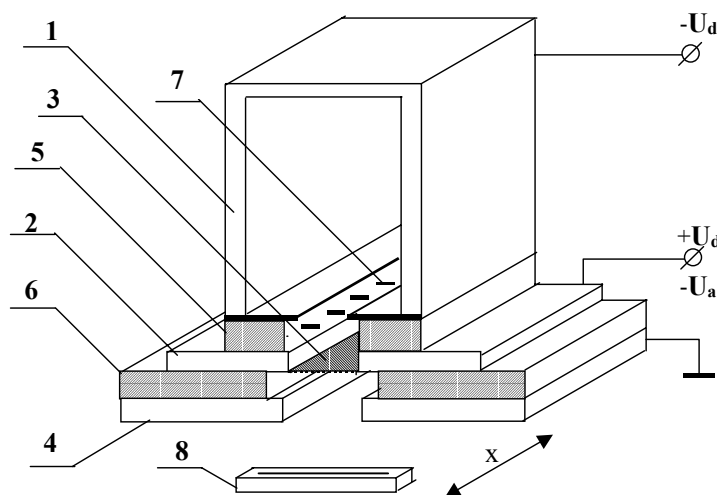


Fig.1. Scheme of ribbon beam electron gun

which were oriented perpendicular to beam flatness. Collector current was registered by recorder. Plasma

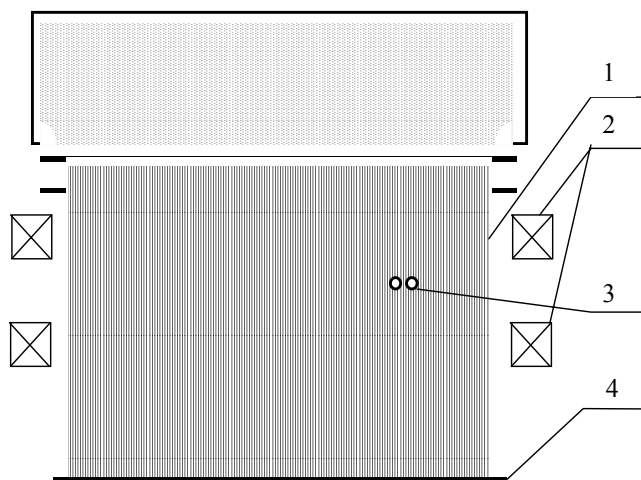


Figure 2. Scheme of beam plasma parameters measurements.

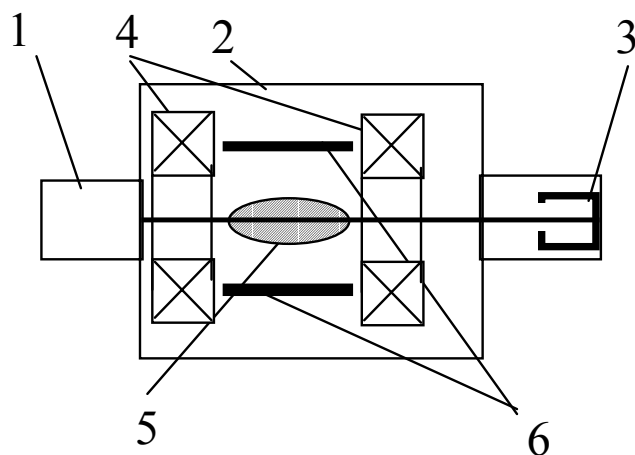


Figure 3. Scheme of film deposition.

producing was realized in scheme, shown in Fig. 2. Electron beam 1 was propagated in magnetic field about 10 mT, created by two coils 2. This field served as for beam focusing so for plasma confining. Plasma, produced by electron beam was sheet like form which was looked about uniform luminescence. Plasma properties investigations were provided by double probe 3 inserted in plasma so that beam electrons could not get probe. This probe was able to move in two directions: along beam width X and across beam plane Y. Beam was directed to collector 4 which was cooled by running water. At last, plasma maintained by cylindrical beam in methane gas was used for carbon films deposition. This scheme is shown at Fig. 3. Electron gun 1 was mounted at the wall of vacuum chamber 2. Faraday cup collected beam. Magnetic field, produced by coils 4, compressed beam and promoted plasma 5 generation and its confining. Glass substrates 6 were disposed around beam at different distances from beam axis.

### 3. Results and discussion

An important feature of the ribbon beam is its uniformity along the width. To obtain this characteristic, measurement of the current directed to collector 8 (Fig. 1) was carried out. Characteristic curves of linear current density distribution to the collector are presented in Fig. 4. Coordinate X was measured from the edge of hollow. First experiments show beam non-uniformity rises with the pressure increase and at pressures 4 Pa or more beam consisted of several beams – streams. Plasma density distribution in hollow, measured by probes 7 (Fig. 1),

also has maximums, however their relative heights are much less than maximums of beam current. More of that, in absence of emission, i.e. at zero accelerating voltage plasma density non-uniformity is not more than 10 percents at any pressures. The rise of plasma non-uniformity takes place at presence of emission mostly at high pressures. It allows us to propose the following explanation of “amplifying” plasma and beam non-uniformity. As it was shown earlier [4], especially for fore-pump pressure range gas ionization in accelerating gap provides intense back-stream ion flow. Penetrated to the plasma these ions provide increase of the plasma density, recharging at gas molecules. Because of positive feed back a small initial plasma non-uniformity converts to more stronger one. This results in electron beam non-uniformity. At any case beam non-uniformity is more than plasma one. The reason of local beam density maximums is not only because of plasma density distribution, but also due to different thickness of space charge sheath between plasma and mesh. This thickness determines open plasma surface in every mesh sell. So better beam uniformity can be reached by better stabilization of plasma emission surface. Another way is defocusing of back ion streams. It

weakens positive feed back due to absence of coincidence between plasma maximums sites and sites of back ion streams maximums. This defocusing may be ensured by anode mesh configuration. It allows to reduce

beam non-uniformity to admissible values 10 – 15 %.

Propagating beam produces gas ionization and forms plasma. Visual observation of luminescence allow to judge qualitatively about plasma density distribution and plasma is seemed to be uniform enough. As it was reported earlier, beam plasma parameters were measured by double probe (Fig. 2). Plasma density distribution and electron temperatures profiles are presented at Fig. 5 and 6, if working gas was argon. As it may be seen, electron temperatures are in interval 2 – 3

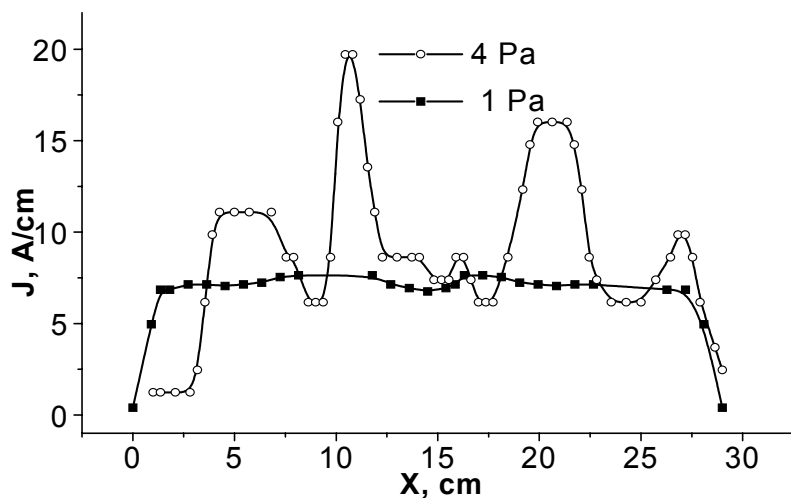


Figure 4. Beam linear density distribution along beam width for different pressures.

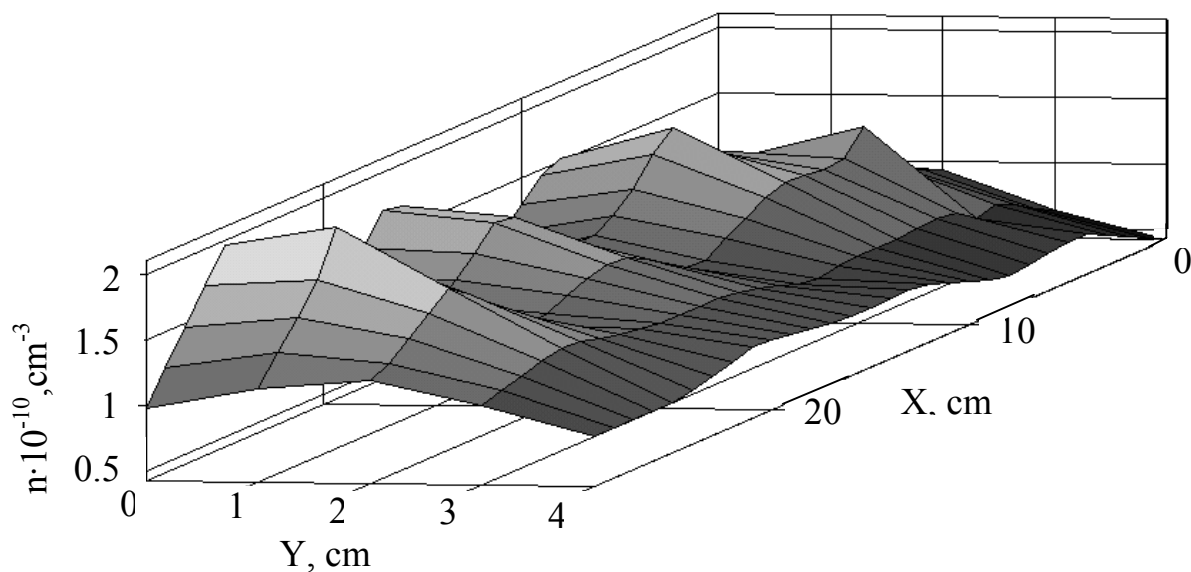


Figure 5. Plasma density distribution at beam cross-section

eV. It differs from values, presented in [5], where about 1 eV temperatures are reported. Fig. 5 shows remarkable non-uniformity of plasma density distribution. Its value is in interval  $(1 - 2) \times 10^{10} \text{ cm}^{-3}$ , i. e. changes two times in different sites of plasma cross section. These differences are much more than beam non-uniformity. Possible reason of it is in our opinion influence of magnetic field, which obstacles plasma electrons motion and therefore prevent from profile smoothing. May be also magnetic field, created by short coils, is not uniform enough, and it leads to different electron beam focusing at different sites of beam cross section.

As it was reported in sec. 2, cylindrical electron beam was used for film deposition by methane decomposition in beam discharge. Films were transparent light brown. Their deposition rates are strongly depends on distance between substrate and plasma axis (Fig. 7) and is as lower as distance is more. But deposition rate was falling also at small distances. First explanation of it was substrate heating, which really takes place. However film deposition at hot substrate, heated specially had no result in rate falling. The most probable

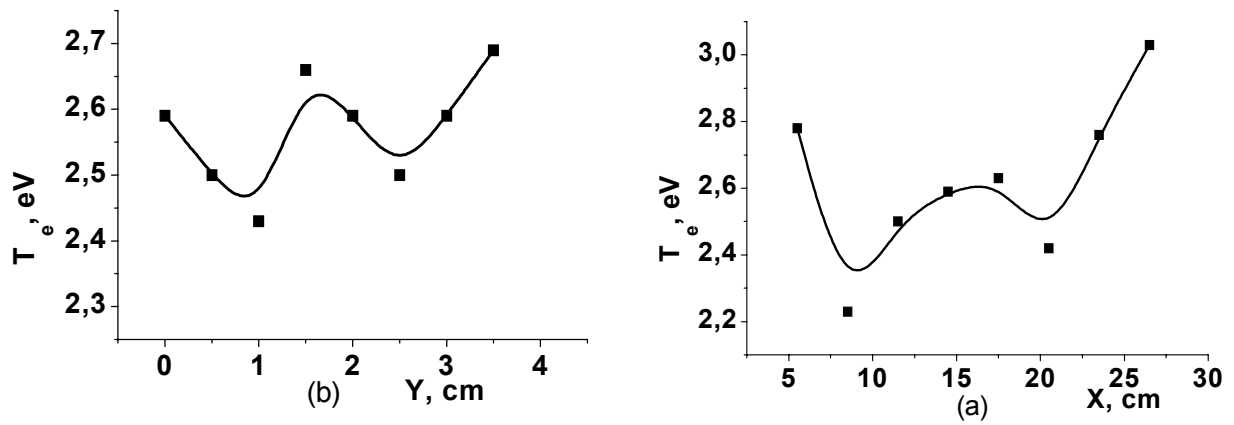


Figure 6. Electron temperature profile along beam width (a) and across the beam (b). Gas (Ar) pressure  $p = 8$  Pa, total beam current  $I_b = 300$  mA.

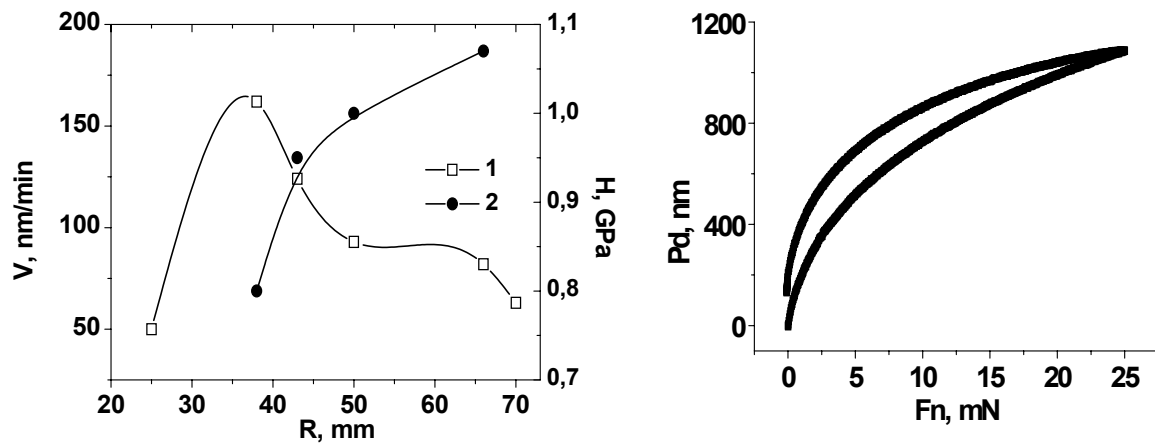


Figure 7. Film deposition rate  $V$  (1) and hardness  $H$  (2) as function of radial coordinate.

Figure 8. Penetration depth  $Pd$  as function of normal force  $F_n$ .

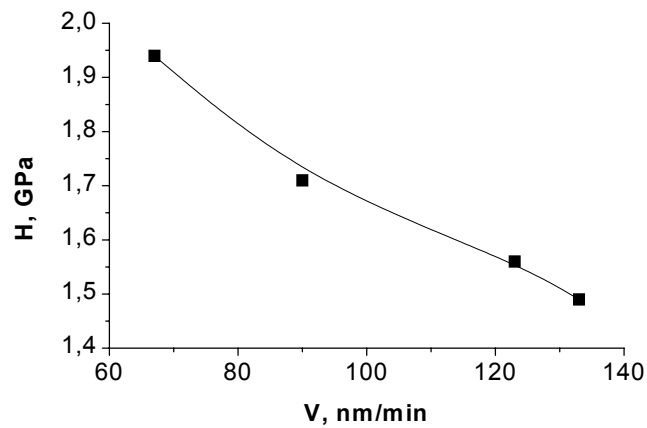


Figure 9. Film hardness as function of deposition rate at negative pulse potential, applied to substrate holder.

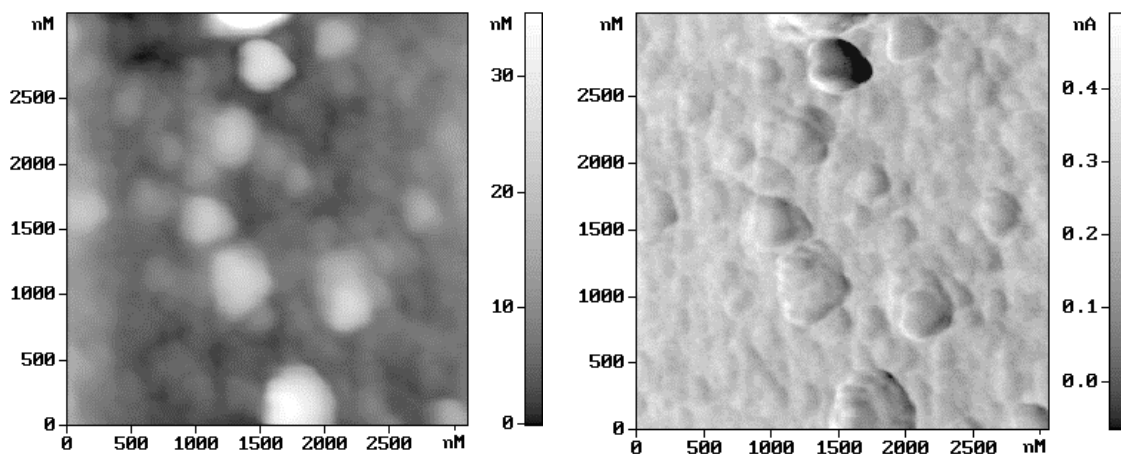


Figure 10. AFM pictures of prepared films

explaining of it is, in our mind, ion sputtering of growing (or existing) film. Ions acquire their energy due to potential difference between plasma and substrate. Value of substrate floating potential is in interval 5 – 15 volts negative to grounded walls of vacuum chamber. Plasma potential is as usual near zero or several volts positive. These values are enough for ion acceleration to energies, sufficient for film sputtering.

Ion bombardment, being the reason of film destroying, is at the same time the instrument of film properties controlling. This can be realized by pulse negative potential applying to substrate holder. Some properties such as Hardness and Yung Module were measured in prepared films. Both these characteristics were measured by instrument NHT-S-AX-000X. All of prepared films were elastic as illustrated by Fig. 8, in which typical loading - unloading curves are presented. Films were not hard. Their hardness were about 1 - 2 GPa. Yung modules were 15 - 25 Gpa (Fig. 7, 9). It allows concluding that films are polymers with great hydrogen contents. Applying of negative pulses about 100 V amplitude in time of deposition resulted in films growth rate falling and simultaneously in increasing of their hardness (Fig.9). It may be explained by more dense film structure formation during ion bombardment. Films morphology was investigated by AFM methods. According to these measurements, films consist of 400 - 500 nm grains (Fig. 10). It allows assuming film deposition mechanism based on macromolecular species forming in gaseous phase.

## References

- [1] A.A.Ivanov, A.A. Serov, et al, Plasma Physics Reports, **25**, 1, 46-52, (1999).
- [2] V.A. Burdovitsin and E.M. Oks // Rev.Sci.Instrum.. 70, 2975-2778, (1999).
- [3] Y.A. Burachevsky, V.A. Burdovitsin, E.O. Oks et al, Proc. of 15<sup>th</sup> Int. Symp. on Plasma Chemistry, Orleans, France, p.1301-1304, (2001).
- [4] V.A. Burdovitsin, M.N. Kuzemchenko and E.M. Oks, Technical Physics, 47, 926-928, (2002).
- [5] D.D. Blackwell, S.G. Walton, D. Leonhardt et al, J. Vac. Sci. Technol. A, **Vol. 19**, No. 4, Jul/Aug (2001).

# Metallic contamination in dry-etch system

M.Cavallaro<sup>(1)</sup>, D.Pirnaci<sup>(1)</sup>

STMicroelectronics, Catania, Italy

## Abstract

This paper deals with the results of metallic contamination measurements in dry-etch equipments performed with surface photo voltage technique. Measurements were made in different downstream equipments, used for photo resist removal, and in reactive ion etching. This kind of measurements is affected by problems due to possible damage of superficial layer. It will be shown that it is possible to measure metallic contamination even in process condition, that means with plasma on.

## Introduction

The metallic impurities are highly mobile and diffuse long distance in the crystal even at moderate process temperatures (for example, copper can diffuse 600  $\mu\text{m}$  in 1 minute at 900  $^{\circ}\text{C}$ , and iron 3000  $\mu\text{m}$  in 30 min at 1000  $^{\circ}\text{C}$ ) and have a high probability of encountering defects sites and being captured by them. Moreover these impurities, located in the interstices of the lattice, introduce energy states in the forbidden gap reducing the diffusion length of carriers.

It's obvious, from these considerations, that metallic contamination can degrade devices properties reducing the yield of them. Thus it has become more important to reduce and control the metallic impurities that can be introduced during the various wafer fabrication process. In this paper will be exposed the results of metallic contamination measurements in dry-etch equipments performed with SPV (surface photo voltage) technique. In this kind of equipments metallic contamination is generally monitored with plasma off during process (leaving only process gas).

This choice is realized to avoid the possible damage of superficial layer that can alters the SPV signal. In this report, two different techniques have been found and described to valuate the contribution of plasma damage to iron measurements, showing that it is possible to measure metallic contamination even in process condition, that means with plasma on.

## Measurement technique and equipment

In this section, the technique used to measure metallic contamination is briefly described. For the monitoring of iron content we used a surface photovoltage (SPV) method by FAaST 230 SDI system. With the SPV method we measure the diffusion length ( $L_D$ ) of minority carrier. In this technique, the variation of surface potential upon illumination is measured for various light wavelengths, hence for various light penetration depths. Diffusion length is obtained from the dependence of the SPV signal ( $\Delta V$ ) on light penetration depths ( $z$ ) according the equation:

$$\frac{1}{\Delta V} \propto \left( v + S_F \right) \left( 1 + \frac{z}{L_D} \right) \quad (1)$$

with  $v$  and  $S_F$  are respectively diffusion velocity and front surface recombination

Moreover FAaST 230 tools includes the optical *Fe activation* step which decreases the diffusion length value due to enhancement of Fe's contribution to the recombination process. Activation proceeds by liberating Fe from Fe-B pairs (therefore Fe measurements must be done on p-type, B-doped silicon). The iron concentration is calculated from the expression:

$$N_{Fe} = C \left[ \left( 1 / L_D^{Aft} \right)^2 - \left( 1 / L_D^{Bef} \right)^2 \right] \quad (2)$$

Where  $C (=1.1\text{E}16)$  is the calibration constant, which is dependent on the type of activation, while  $L_D^{Aft}$  and  $L_D^{Bef}$  are respectively diffusion length after and before iron activation.



## Results

All experiments were carried out using wafers p-type (B doped) 6 inch, with resistivity  $1.5 \div 4 \Omega \cdot \text{cm}$  and oxygen content  $9 \div 20 \text{ ppm}$

Wafers were processed either in equipments downstream (FUSION, IPC GASONICS), used for photo resist removal, or in reactive ion etching R.I.E. (LAM 490, LAM 590) used to etch poly, oxide and nitride. After this chemical process, all samples were diffused in R.T.P (rapid thermal process) furnace to realize a drive-in process (180 seconds at  $1100^\circ\text{C}$  in  $\text{O}_2$ ) and then measured in FAaST 230 equipment.

In some of them was grown a sacrificial oxide ( $620 \text{ \AA}$ ), and again measured.

Results are showed distinguishing the data from wafers processed in plasma downstream entities and from the RIE ones.

### - Downstream Plasma

Table 1 reports the measurements relative to the wafers processed in FUSION GEMINI ES

Table1

Equipment	Plasma	Iron average concentration (E10 cm-3)	Iron max concentration (E10 cm-3)	Notes
FUSIONR304	Off	12.3	122.2	
FUSIONR304	On	15.54	164	
FUSIONR304	On	15.67	267	wafer processed upside-down

As showed in table, in Fusion the iron distribution on wafers test is below  $1\text{E}12 \text{ atoms/cm}^3$ . It's important to notice, that the damage is negligible (there isn't different between iron measured on wafer processed with plasma off from one with plasma on), and so it is possible to check iron also in process conditions (with plasma turned on).

This result is enhanced from the value of iron concentration of wafer processed upside-down (last row in table1).

In table 2 are reported the measurements relative to GASONICS IPC; some maps relative to the measurements are shown in figure 1 and 2.

Table 2

Equipment	Plasma	Average iron concentration (E10 cm-3)	Max iron concentration (E10 cm-3)
IPC112	On	65.32	350.2
IPC112	Off	79.54	373.5
IPC403	On	44.34	410.3
IPC403	Off	79,62	509.88

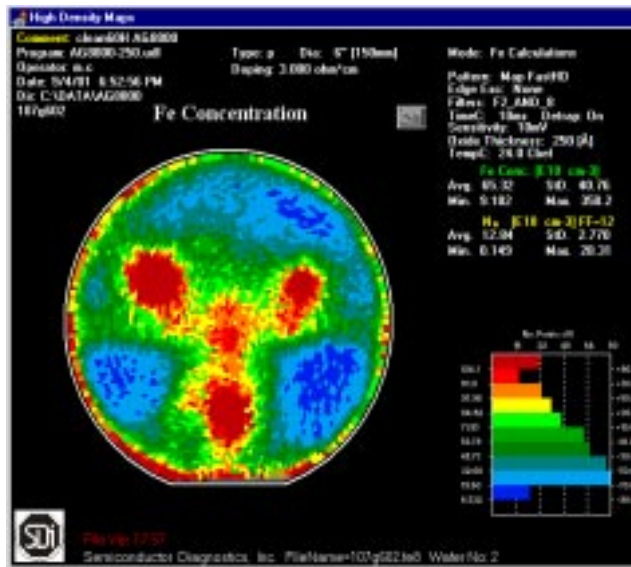


Figure1: Iron map realized with plasma on

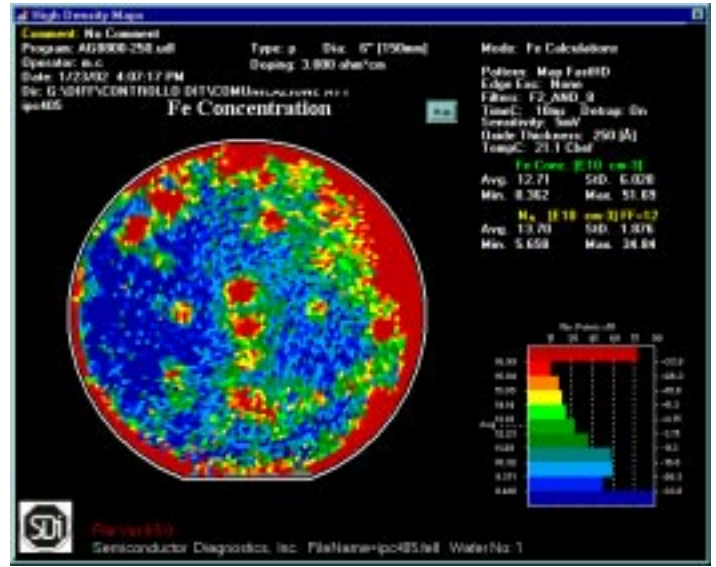


Figure2: Iron map realized in same condition of fig1 after cleaning pin

Data reported in table 2 show again that there isn't difference in the measurements if we use plasma on or off. This indicates there isn't plasma damage.

Moreover, as illustrated in figure 1, in all measurements realized on IPC was found an iron concentration ( $\approx 4 \text{ E}12$ ) located preferentially in particular zones of the wafers. Source of this contamination was found due to the pins on which is placed the wafer during the process. In figure 2 is reported the measure realized in the same condition of map in figure1 after cleaning of the pin: there isn't evidence of the pin contamination and Fe concentration is below  $1 \text{ E}12$  on all wafers. This important result has led us to be more careful in cleaning of hardware components of chamber process.

### - Plasma RIE

For this type of dry etch entities, in which plasma damage is bigger (in fact plasma is generated in process chamber), tests have been articulated considering different etching chemistry: polysilicon and oxide etch chemistry. In table 3 are shown the measurements obtained processing wafers test on LAM590 AUTOETCH (oxide chemistry). To remove the surficial layer, eventually damaged, to the wafers was performed an oxidation and then measured again.

Table3

Equipment	Plasma	Iron average concentration (E10 cm-3)	Iron max concentration (E10 cm-3)	Process Notes
LAM590	ON	468.3	1680	Only etch
LAM590	ON	578.7	2707	Etch + 620 A oxide
LAM590O102	Off	28.3	201.6	Only etch
LAM590O102	Off	99.3	8655	Etch + 620 A oxide
LAM590O212	ON	425.6	2821	Only etch
LAM590O212	ON	457.2	1738	etch + 620 A oxide

From table it's evident that iron concentration before and after the growing of the oxide is the same. These results show how plasma damage is limited. To have an exhaustive evaluation of damage it has been also analysed the behaviour of the signal  $\Delta V$  varying the different light penetration  $Z$ . How we have seen  $\Delta V - Z$  are related by equation 1 thus, measurements of  $L_d$  are reliable if  $\Delta V$  and  $Z$  satisfy to a linear equation. In figure 3 and 4 are shown SPV plots relative to a wafer processed on LAM590 AUTOETCH with oxide etch chemistry before and after the growth of a 620 A oxide.

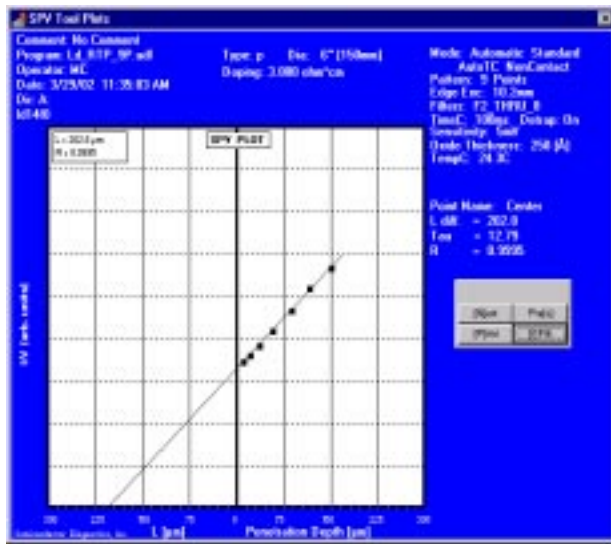


Figure3: SPV PLOT of measure realized before oxide grown

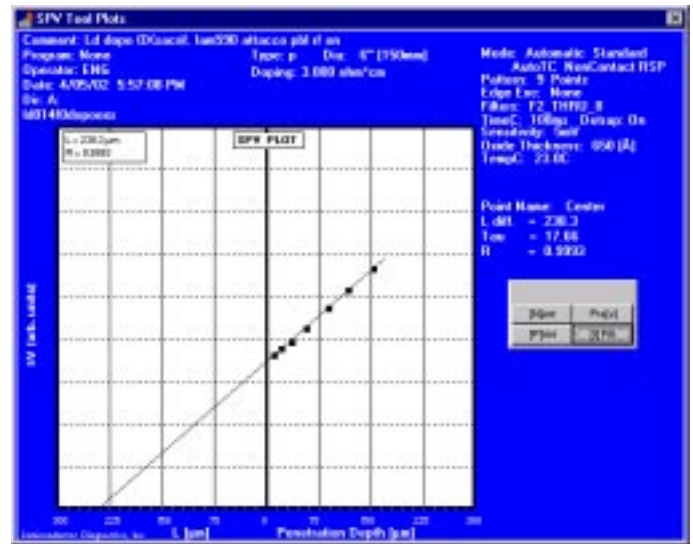


Figure 4: SPV PLOT of measure realized after oxide grown

Comparing figure 3 and 4, the relation between  $\Delta V$  and  $Z$  is nearly linear either before or after the removal of the damaged layer. This is also confirmed by the coefficients of linear (relation) ( $R$ ), near 1, reported in every plot.

By the data obtained, we have come to the conclusion that, in this case, is possible realize a Fe measurements also in process condition (plasma on). With an oxide etch chemistry the plasma damage of superficial layer is negligible, this show the possibility to use processes with plasma turned on in entities that use  $CF_4/CHF_3$  chemistry to measure Fe concentration.

The results of the measurements using LAM490, which uses a polysilicon and nitride etch chemistry, are shown in table 4

Table4

Equipment	Plasma	Iron average concentration (E10 cm-3)	Iron max concentration (E10 cm-3)	Notes
LAM490P106	ON	Undefined	Undefined	Only etch
LAM490P106	ON	112.6	762.7	Etch + Oxide 620 A
LAM490P106	Off	21.25	101.8	
LAM490P106	ON	1041	5378	Plasma with inert gas
LAM490P106	ON	112.6	762.7	Etch + Oxide 620 A

For this kind of dry etch equipments the tests realized turning on plasma and using a SF6 chemistry (nitride etch chemistry), show values of Fe concentration absolutely not reliable (see table 4). Also in this case it was decided to realize the growth of an oxide with the aim to eliminate the superficial damaged layer. The value of Fe concentration is now measurable (second row) and this confirm how SF6 chemistry damages wafer surface. In fact measures one processing with plasma turned off and the other with plasma on and with inert gas we have obtained reliable measurements of Fe concentration (see row 3 and 4 table 4) As in the precedent case, SPV plot has been analysed (figure 5 and 6 ).

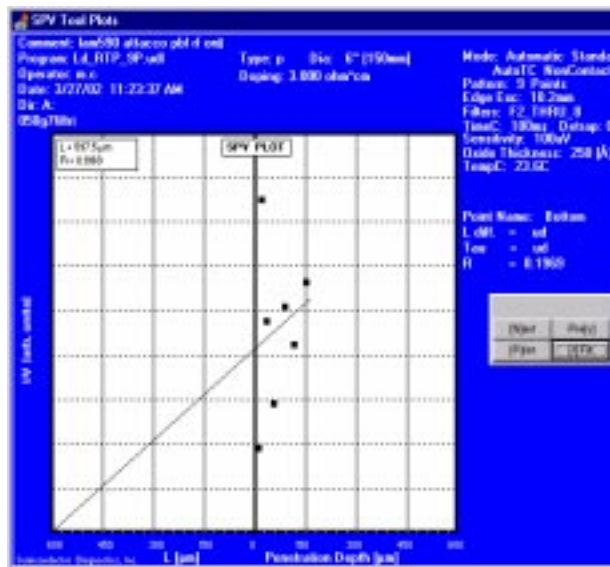


Figure5: SPV plot for a wafer processed with SF6 chemistry

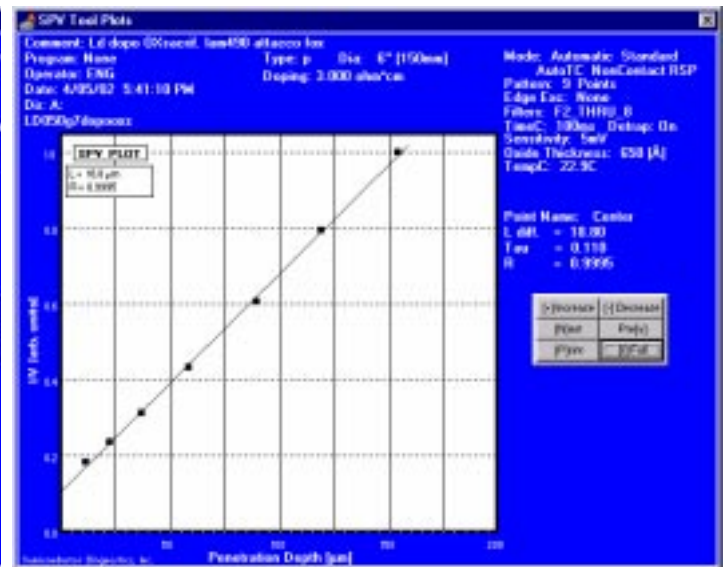


Figure 6: Same SPV-plot obtained after the growth of a 620 A oxide

In the figure 5 is reported SPV plot for a wafer processed with SF<sub>6</sub> chemistry. As you can see, between  $\Delta V$  and Z there isn't, in this measurements, a linear relation .

This is confirmed by R factor (0.19) far from the unity. This shows that, in this case, metallic contamination measurement isn't reliable due to an high plasma damage.

In figure 6 is shown the same plot obtained after the growth of a 620 Å oxide on wafer, and thus the removal of damaged layer.

There is, in this case, a linearity between  $\Delta V$  and Z (R=0.99) to demonstrate that the 620 Å oxide has been enough to remove part of the damaged layer. This fact confirms the previous conclusion.

In this way the analysis of SPV plot, introduced in this work, seems a good mean to evaluate the damage of superficial layer and can be extended to other uses.

Resuming we can conclude that, in standard condition, it isn't possible to realize Fe measurements: only after the growth of an oxide that removes the damaged layer is possible to measure Fe concentration.

## Conclusion

In this paper have been exposed results of metallic contamination in dry-etch equipments. Two different techniques have been found to valuate the contribution of plasma damage of superficial layer.

The results have shown that for the equipments that use plasma downstream there is no problems with plasma damage. Thence is possible to realize measure of metallic contamination in process condition (that means with plasma on.). Even for the RIE equipments that perform oxide etch ( use CF<sub>4</sub>/CHF<sub>3</sub>) there is not evidence of silicon damage and, moreover, the iron content is lower than downstream tools.

Instead, in the RIE equipments that use poly etch chemical (SF<sub>6</sub>), it is evident a strong damage of superficial layer that can't permit to get reliable iron measurements.

However it's been shown in this paper , with SPV plot, that it's sufficient to grow an oxide to remove the layer plasma damaged . In this way it's possible to measure the iron concentration in etch equipments, even with plasma off, that use SF<sub>6</sub> during the process.

# Calculation of silicon particles dynamics, heat and mass transfers in thermal plasmas. Effect of particles vaporization

J. Amouroux<sup>1</sup>, S. Dresvin<sup>2</sup>, D. Morvan<sup>1</sup>, L. Ouvrelle<sup>1</sup>, D. Ivanov<sup>2</sup>

<sup>1</sup> LGPPTS, ENSCP, 11 rue P. & M. Curie, 75005 Paris, France

<sup>2</sup> SPb State Polytechnic University, Polytechnic Str 29, 195251 Saint Petersburg, Russia

Plasma is used to heat small particles or droplets in a number of technologies such as the spraying of refractory coating, powder spheroidization, spectrochemical analysis. In this paper there were calculated the motion and the heating of a silicon particle in the RF ICP torch which is used in the Laboratoire de Génie des Procédés Plasmas et Traitement de Surfaces (Université P. et M. Curie, France) for powder treatment.

The investigation of the behavior of the small particle in plasma can be divided into two problems.

The first problem is the investigation of the particle dynamics which include the calculation of the trajectory and velocity of the particle. The model takes into account the following forces acting on the particle in plasma: the drag force and the gravity force.

The second problem is the investigation of the particle heat and mass transfer which include the calculation of changes in temperature and diameter of the particle. The model for the particle heating takes into account the following processes: the particle heating, its melting, vaporization (including losses of energy by vaporization and heating of the vapor cloud) and evaporation (boiling). The temperature inside the particle is supposed uniform. The model also takes into account the mass losses by vaporization and by boiling.

The boiling and vaporization rates are described by the following formulas:

$$\dot{m}_{\text{boil}} = \frac{P_p - P_{\text{rad}}}{\Delta H_{\text{boil}} + \bar{c}_{p_{\text{vapor}}} (T_p) \cdot (T_p - T_{\text{boil}})} \quad (1)$$

$$\dot{m}_{\text{vap}} = h_m \cdot S_{\text{surface}} \cdot p \cdot \ln \left( \frac{p}{p - p_v(T_s)} \right) \quad (2)$$

If the particle temperature is close to the boiling temperature then the calculation using formula (2) will give a mistake. Therefore we propose to calculate the mass losses by vaporization by the following formula:

$$\dot{m} = \frac{\dot{m}_{\text{vap}} \cdot \dot{m}_{\text{boil}}}{\dot{m}_{\text{vap}} + \dot{m}_{\text{boil}}} \quad (3)$$

where  $\dot{m}_{\text{vap}}$  is the vaporization rate given by the formula (2),  $\dot{m}_{\text{boil}}$  is the boiling rate given by the formula (1).

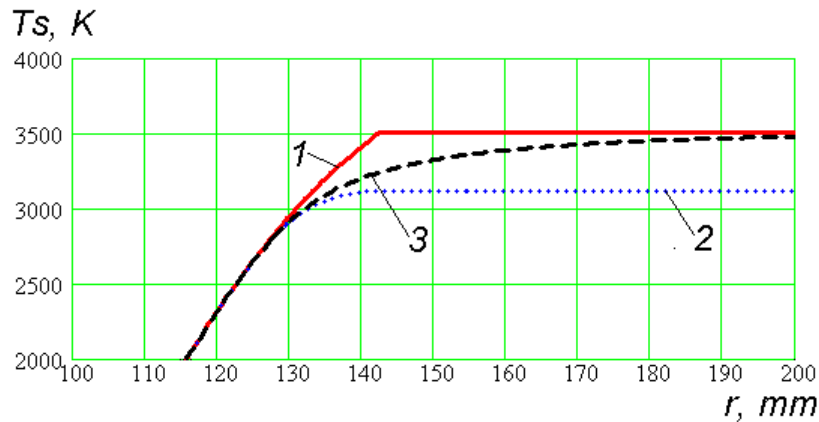


Figure. The particle temperature near the boiling temperature for three variants of calculation: 1 – without taking into account vaporization, 2 - calculation using formula (2), 3 – calculation using formula (3).

The results of the calculations are compared with experimental data.

# Thermal modelling of multilayer sprayed particles under plasma conditions

M. El Ganaoui<sup>1</sup>, M. Bouneder<sup>2</sup>, B. Pateyron<sup>1</sup>, P. Fauchais<sup>1</sup>

<sup>1</sup> SPCTS UMR 6638 CNRS, Faculté des Sciences et Techniques. 123 Albert Thomas, 87060 Limoges Cedex.

<sup>2</sup> Institut d'Aéronautique, Université Saad Dahleb. Route de Soumaa B.P 270, Blida, Algérie.

**Abstract:** A model predicting the temperature profiles of the sprayed particles during their flight in the plasma jet is developed. Lumped thermal capacitance method is compared to full simulation taking into account the dependency of physical parameters on temperature. Coated particles composed of two materials are considered for spray applications showing the influence of the possible thermal contact resistance between both materials.

## 1. Introduction

Thermal spray processes involve many physical phenomena strongly conditioning the quality of industrial applications. The powder morphologies and their injection within the hot jet as well as their reactions with the environment have an important influence on the particles flattening, splats layering, residual stresses, coating microstructure and properties. Such processes admits several control variables [1] (arc current, plasma forming gases, flow rates and composition, stand-off distance, powder feed rate, etc.) and quantitative knowledge of the thermal behaviour of a particle in a plasma jet is fundamental to optimise the operating parameters.

The coating technology concerns a large scale of commercial products. It is proven industrially that when spraying two-layer particles made of a metal coated by a ceramic, the uniform distribution of ceramic splats within coating improve the wear resistance under high temperature working conditions [2]. An alumina coating on stainless-steel particles shows experimentally the improvement of the hardness and cohesion of the final coating [3].

Various studies have previously modelled the thermal behaviour of a single homogeneous particle in thermal plasmas with different properties and temperature jumps [4, 5, 7, 8]. Coated particles recently became considered in many modelling works. In [6] a global system investigation exhibits the behaviour of metal and ceramic particles co-sprayed through a plasma jet by using a fluid dynamics model in which the particles are considered as discrete Lagrangian entities. The specific knowledge of the heat transfer in coated particles is required to improve the physical accuracy of the global modelling from plasma torch to deposited layers [6, 9-11].

This work focus on the particles heated under plasma conditions. A comparison between lumped capacitance methods and full numerical simulation is achieved for the thermal conductivity and the heat transfer coefficient depending on the temperature.

## 2. Modeling

### 2.1 Lumped capacitance method

The lumped capacitance model gives a quick estimate of the temperature evolution. The essence of this method is the assumption that the temperature of the solid is spatially uniform at any instant during the transient process [14]. This assumption permits to neglect the temperature gradient within the solid. Defining the Biot number  $Bi = k_{\infty}/k$ , where  $k_{\infty}$  is the averaged thermal conductivity of the plasma outside the boundary layer and  $k$  that of the particle. Classical references deals with a Biot value of 0.01 as a limit of this assumption [13]. An experimental estimate of the limit of this assumption is given for  $Bi \leq 0.03$  for solid particles quenched suddenly in a plasma environment [9].

For a spherical particle of radius  $R$  in an infinite medium of temperature  $T_e$ , the energy balance allow to write:

$$\rho.V.c_p \frac{dT}{dt} = [h(T_{\infty} - T) - \varepsilon\sigma(T^4 - T_e^4)]A \quad (1)$$

where  $T(0) = T_{ini}$ , is an initial condition,  $\rho$  is the density,  $V$  the volume,  $c_p$  the heat capacity,  $A$  the cross section,  $\sigma$ 's the Stefan constant and  $\varepsilon$  the emissivity.

In Stokes regime the heat is transferred in a conductive mode, the Nusselt number is then constant  $Nu = 2$ . The convective heat exchange coefficient  $h$  is estimated by a method commonly used for thermal spray applications [9].

$$h = \frac{1}{R(T_\infty - T)} \int_T^{T_\infty} k_\infty(T) dT \quad (2)$$

where  $k_\infty(T)$  is the thermal conductivity of the plasma gas at the temperature  $T$ . For plasma composed of 15% hydrogen and 45% argon ( $Ar-H_2/45-15$  slm) the thermal conductivity is evaluated by using a fourth order Runge Kutta integration formula giving the non linear profile represented on figure 1.

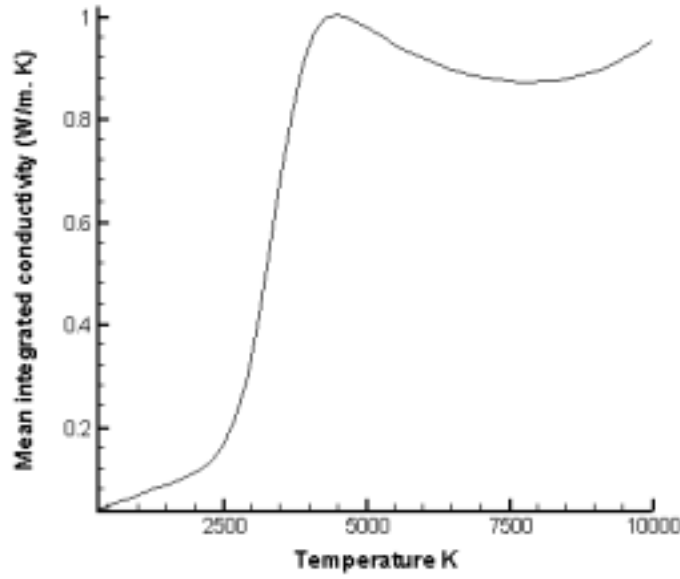


Figure 1: Averaged thermal conductivity for  $Ar-H_2/45-15$  slm plasma

## 2.1 Full model

For the full model, the particle is supposed to occupy spherical domain where heat transfer equation is solved. The physical domain is assumed homogeneous and isotropic. The energy equation is written as:

$$\rho.C_p \cdot \frac{\partial T}{\partial \tau} = \frac{1}{r^2} \cdot \frac{\partial}{\partial r} (r^2 k_p \cdot \frac{\partial T}{\partial r}) \quad (3)$$

with the initial conditions:

$$T(r,0) = f(r) \quad (4)$$

and the radiative and convective boundary conditions:

$$k \frac{\partial T}{\partial r}(R,t) = h(T(R,t) - T_\infty) - \epsilon \sigma (T(R,t)^4 - T_e^4) \quad (5)$$

A symmetrical geometry is assumed:

$$\frac{\partial T}{\partial r}(0,t) = 0 \quad (6)$$

The numerical solution is obtained by using the classical finite differences approximation with a linearization of the dependency of the heat transfer coefficient on the temperature.



When considering more than one layer, the transmission conditions must be written at the interface between the layers  $\Sigma$ , namely, if the symbol  $[ ]$  define the jump of any quantity at the interface, the perfect contact will be represented by the continuity of the temperature field and the heat flux

$$\left[ k \frac{\partial T}{\partial r} \right]_{\Sigma} = 0 \text{ and } [T]_{\Sigma} = 0 \quad (7)$$

The imperfect contact will be taken into account by using a thermal contact resistance  $R_{th}$  coupling the temperature jump and the heat flux as:

$$k \frac{\partial T}{\partial r} \Big|_{\Sigma} = -\frac{1}{R_{th}} [T] \quad (8)$$

### 3 Results

#### 3.1 Comparisons between lumped capacitance model and full model

Comparison between the two models is achieved for particles typically used during experiments (spherical steel and alumina particles  $30 \mu m$  to  $90 \mu m$  in diameter initially at  $300 K$ ) immersed in an infinite  $Ar-H_2/45-15 slm$  plasma at the temperature of  $5000 K$ .

Figure 2 corresponds to an averaged Biot number of  $0.001$  corresponding to a spherical steel particle of  $30$  micrometer diameter. It shows that very close profiles are obtained by using the lumped capacitance model and the full simulation model. Figure 3 corresponds to an averaged Biot number of  $0.268$  corresponding to an alumina particle of  $90 \mu m$  in diameter, the lumped capacitance model shows an important difference and appears to give a middle temperature between that of the centre and the surface of the particle.

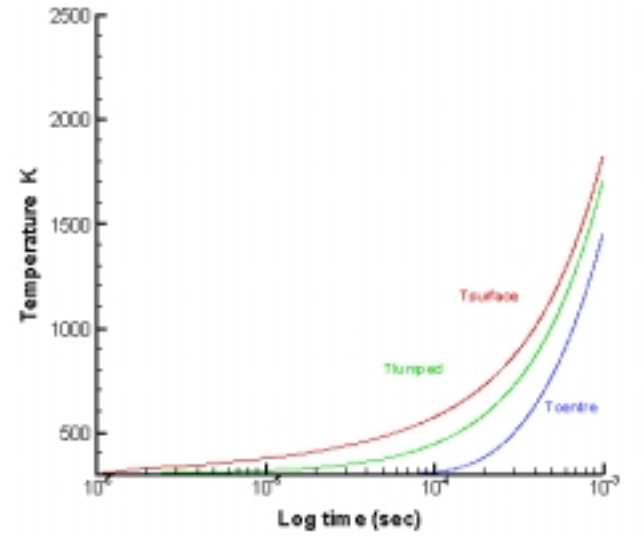
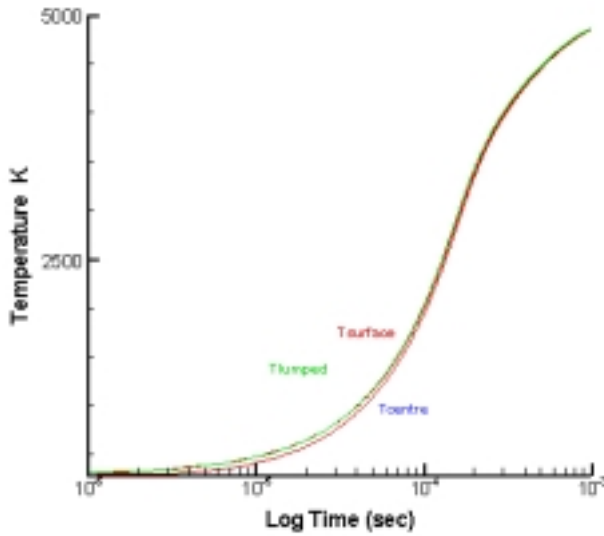


Fig. 2: Temperature time evolution of a spherical Fe particle  $30 \mu m$  in diameter at an initial temperature of  $300 K$  ( $Bi=0.001$ ).

Fig. 3: Temperature time evolution of a spherical  $Al_2O_3$  particles of  $90 \mu m$  in diameter at initial temperature of  $300 K$  ( $Bi=0.268$ ).

### 3.2 Two-layers and thermal contact resistance effect

Figure 4 shows the radial distribution of temperature for particles of  $60\ \mu\text{m}$  in diameter, the comparison concerns monolayer steel, monolayer alumina and two-layers steel-alumina (for an aspect ratio  $E/R=0.6$  and  $0.2$  where  $E$  is the steel thickness). It is to be noted that the heat transfer intensify in presence of alumina. This remark is confirmed in the figure 5 for the two layers  $\text{Fe-Al}_2\text{O}_3$  ( $6\ \mu\text{m}$  of  $\text{Al}_2\text{O}_3$ ) after  $1\ \text{ms}$  of transfer.

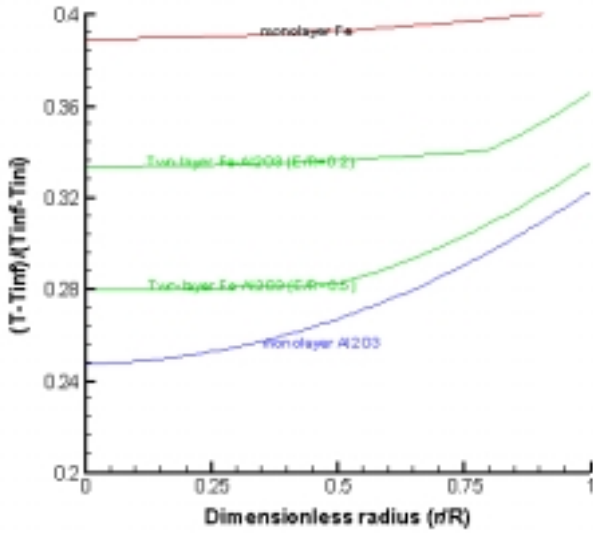


Fig. 4: Heat transfer in mono and two-layers medias.

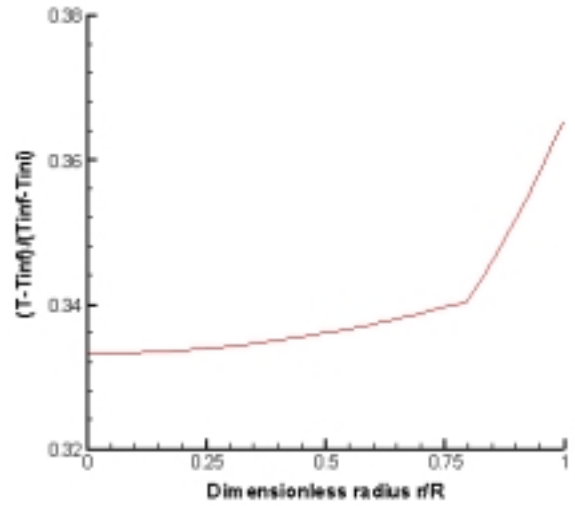


Fig. 5: Radial distribution of temperature in a two-layers  $\text{Fe-Al}_2\text{O}_3$ .

Figures 6 and 7 present the evolution of the surface, the interface and the centre temperature respectively for two aspect ratio  $E/R=0.5$  and  $0.2$ . It is shown that the centre and the contact line temperature are very close. The alumina layer plays an insulating role on reducing the heat transfer to the centre of the particle. Figures 8 presents results when contact resistance between steel and alumina is taken into account. The temperature jump and the heat transfer are noticeably modified at the interface. In the case of a thermal resistance  $R_{th}=1.e^{-6}\ \text{m}^2\ \text{K/W}$  a temperature jump of  $160\ \text{K}$  is observed; however for a  $R_{th}=1.e^{-8}\ \text{m}^2\ \text{K/W}$  the contact is close to the perfect case one.

### 3. Conclusions

A computational model has been developed to simulate the temperature profiles of particles used in plasma spray experiments. The model takes into account mono-layer and two-layer materials. Applications are considered for steel-alumina particles immersed in an infinite  $\text{Ar-H}_2/45-15\ \text{slm}$  plasma at  $5000\ \text{K}$ . The need of full particles simulation is underlined to characterize global heat transfer of the composite system.

The consideration of the thermal contact resistance shows an important jump of the temperature field for  $R_{th}=1.e^{-6}\ \text{m}^2\ \text{K/W}$ ; however for  $R_{th}=1.e^{-8}\ \text{m}^2\ \text{K/W}$  the system is close to a perfect thermal contact. This work follows in providing general comparison between the full model and homogenized lumped capacitance model for heat transfer estimate under plasma spray conditions.

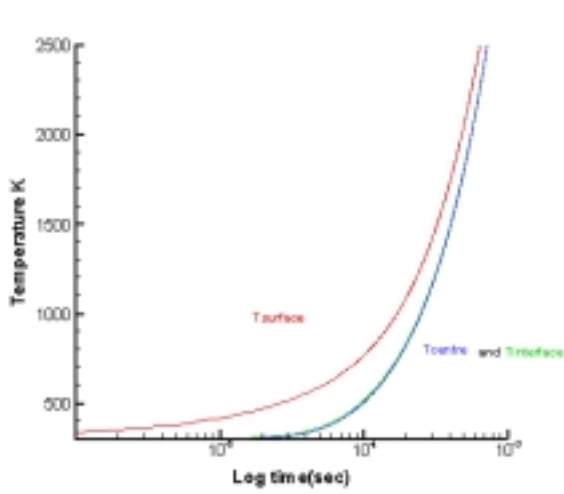


Figure 6: Two-layer Fe-Al<sub>2</sub>O<sub>3</sub>  $E/R=0.5$

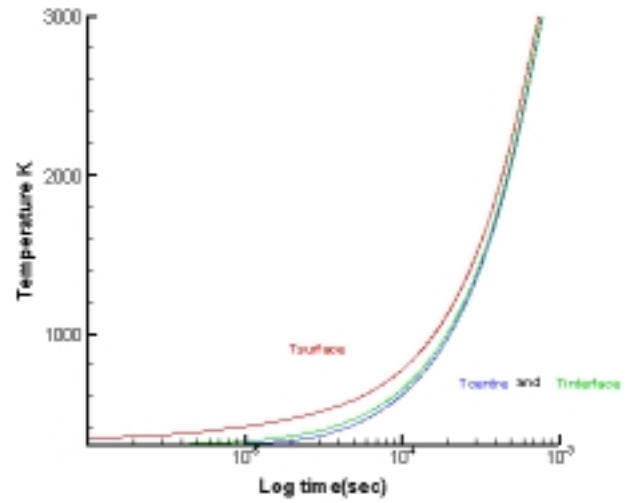


Figure 7: Two-layer Fe-Al<sub>2</sub>O<sub>3</sub>,  $E/R=0.2$

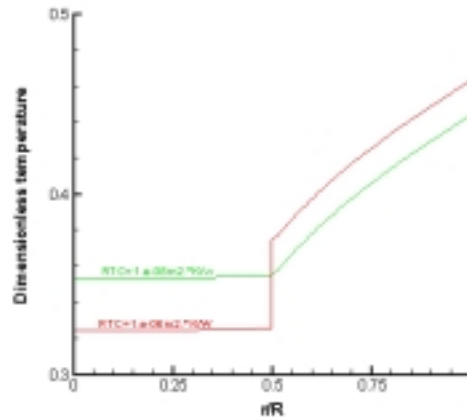


Figure 8: Contact effect for two-layer particle.  $R_{th} = 1.e^{-6} m^2 K/W$ ,  $E/R=0.5$ .

#### 4. References

- [1] P. Fauchais, A. Vardelle and B. Dussoubs Quo Vadis Thermal Spraying?, Journal of Thermal Spray Technology, Volume 10, Issue 1, March 2001, Pages 44-66.
- [2] S. P. Yan, F. A. Mohamed, E. J. Lavernia and T. S. Srivatsan, Influence of spray atomisation and deposition processing on microstructure and mechanical behaviour of an aluminium alloy matrix composite. J. Mater. Sci., 30, pp. 4726-4736, 1995.

- [3] H. Ageorges and P. Fauchais, Plasma spraying of stainless-steel particles coated with an alumina shell, *Thin Solid Films*, Volume 370, Issues 1-2, 17 July 2000, Pages 213-222.
- [4] Fiszdon J. K. Melting of powder grains in a plasma flame, *International Journal of Heat and Mass Transfer*, Volume 22, Issue 5, May 1979, Pages 749-761.
- [5] Lee Y. C. Chyou Y. P. And Pfender E. Particles dynamics and particle heat and mass transfer in thermal plasmas, *Plasma Chem. Plasma process.* 5, pp. 391-415.
- [6] B. Dussoubs, A. Vardelle, G. Mariaux, P. Fauchais and N. J. Themelis, Modelling of Plasma Spraying of Two Powders, *Journal of Thermal Spray Technology*, Volume 10, Issue 1, March 2001, Pages 105-110.
- [7] Pfender E., Particle behavior in thermal plasmas, *Plasma Chemistry and Plasma Processing*, Vol 9. N 1, 167-195, 1989.
- [8] Chen X.I, Pfender E., *J. Plasma Chem. and Plasma Processing*, Vol.2, N° 293, 1982.
- [9] Bourdin E., Fauchais P, Boulos M.I, Transient heat conduction under plasma conditions, *International Journal of Heat and Mass Transfer*, Volume 26, Issue 4, April 1983, pages 567-582.
- [10] Vardelle M., Vardelle A., Fauchais P. and Boulos M., Plasma particle momentum and heat transfer: Modelling and measurement, *AIChE Journal*, 1983, 29 N. 2, 236-243.
- [11] Demetriou M. D., Lavine A. S., and Ghoniem N. M. Feasibility of plasma spraying in developing MMC coating: modelling the heating of coated powder particle. *J. of Manufac. Sci. and Eng., Trans. ASME*, Feb.2002, Vol. 124, pp 58-64.
- [12] Holman J.P. *Heat Transfer*, Fifth edition, Mac-Graw Hill N. Y., 1979.
- [13] Carslaw H.S, Jaeger J.C., *Conduction of Heat in solids*, Oxford University Press, 1959.
- [14] F. P. Incropera, D. P. DeWitt, *Fundamentals of Heat Transfer*, Fifth edition, J. Wiley and sons N. Y., 2002.

# **Deposition of Diamond Films on Mirror-smooth Glass Substrates**

Wang Jianhua, Ma Zhibin, Wang Chuanxin, Man Weidong

*Department of Materials Science & Technology, Wuhan Institute of Chemical Technology, Wuhan, 430073, China*

Diamond films have been deposition on mirror-smooth glass substrates at low substrate temperature. For improving the nucleation density, interlayer such as  $\text{TiO}_2$  has been used. The reductive pretreatment using hydrogen plasma on the  $\text{TiO}_2$  intermediate layer may significantly increase the nucleation density and the adhesion of the diamond films. The enhancement of the nucleation is postulated to be a result of appearance of low valence Ti even metal Ti on the growth surface after the hydrogen plasma treatment. The film adhesion improvement may be due to the formation of Ti-C chemical bonding between the  $\text{TiO}_2$  intermediate layer and the deposited diamond film.

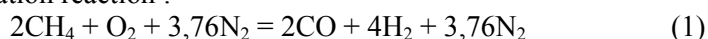
# Plasma assisted partial oxidation of methane in microwave discharge

B.V. Potapkin, M.A. Deminsky, V.K. Zhivotov, A.S. Moskovsky,  
E.N.Gerasimov, O.V. Sytnov, R.V. Smirnov and V.D.Rusanov

*RRC "Kurchatov Institute", Kurchatov Sq. 1, 123182, Moscow, Russia*

The partial oxidation of methane in the air is perspective method of syn-gas production for the needs of transport, chemical manufacturing and energetic. This process is interesting also from fundamental point of view where effect of the plasma can essentially accelerate process of hydrocarbons conversion [1]. In this paper the effect of stimulation of methane partial oxidation in the air by plasma of microwave discharge is under consideration.

The process of partial oxidation proceeds via preliminary oxidation and decomposition of methane in the flame front and further slow transformation of products in the syn-gas. The influence of plasma on acceleration of transformation processes behind flame front were investigated elsewhere [1]. There we investigated the influence of plasma effect on the first stage of conversion process: stabilization of flame front. The ignition limits of the methane-air mixture at the normal conditions are 5% and 15%. However the stoichiometry of partial oxidation reaction :



corresponds to 30% content of methane. Thus the realization of reaction (1) demands additional stimulation which can be carried out by plasma action. The experiments of methane partial oxidation were performed in two type of microwave discharges: pulse-periodic (wave length is 3 cm, pulse duration is 1 $\mu$ s, frequency of pulse repletion is 1kHz, pulse power is 300 KW) and continuous (frequency 2.5 GHz, power 1-5 KW). Reagents (mixture of methane and air) were preheated up to 800 C in the pulse periodic and up to 600 C in the continuous cases and inputted in the reaction chamber where zones of plasma and combustion front were overlapped.

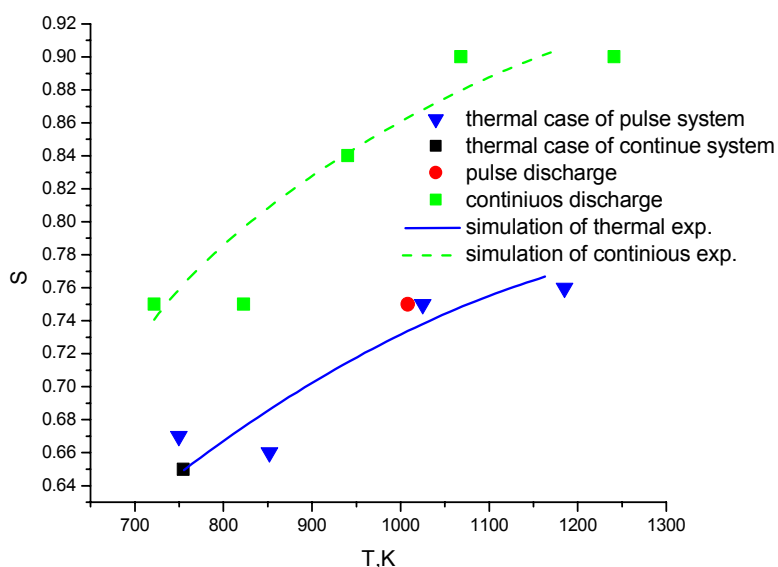


Fig.1 Change of combustion limits for the methane-air mixture.

It was shown that effect of continuous discharge essentially shifts the ignition limits in the direction methane rich mixture whereas effect of pulse-periodic discharge is comparable with thermal case. The simulation of mixture ignition and flame stabilization in frame of elementary theory of Semenov was carried out. The simulation results for thermal and plasma cases are performed on the Fig.1. It was shown that plasma effect leads to decreasing of effective activation energy of overall process ( $\Delta E=1300$  K) and accelerates endo-thermic processes of methane decomposition and acetylene formation in the flame front.

References:

1. M.Deminsky, V.Jivotov, B. Potapkin and V.Rusanov, Pure Appl. Chem., 74 (2002) 413

The criteria of ignition of mixture was absent of oxygen in the products. The experimental results like dependence of limits of ignition ( $S=[\text{CH}_4]/[2\text{O}_2]$  –describes stoichiometry deviation vs partial oxidation) on initial temperature for the thermal case are shown on the Fig.1. The two other experiments with pulse-periodic and continuous discharges also indicated. To provide correct comparison between different experimental conditions the plasma energy input of these experiments was recalculated in to the temperature based on initial chemical composition of mixture.

# **Synthesis of aligned carbon nanotubes by microwave plasma chemical vapor deposition**

Jianhua Wang, Shenggao Wang

*Province key laboratory of plasma chemistry & advanced materials, Wuhan institute of chemical technology, Wuhan,  
People's Republic of China*

In this paper, aligned carbon nanotubes were synthesized on different substrate through microwave plasma chemical vapor deposition at the low temperature of 550°C. It is shown that carbon nanotubes can be grown in a direction always perpendicular to the surface under the effect of plasma. It was found that randomly oriented carbon nanotubes grown when the substrate was not in contact with plasma. Our results indicate that the self-bias imposed on the surface of substrate plays a very important role in the alignment of carbon nanotubes.

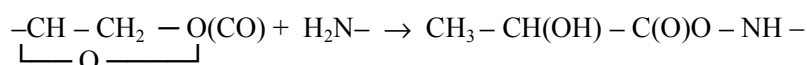
## The Intensification of the process of organic tannage by low temperature HFE-plasma of reduced pressure

Sysoev V.A., Abdullin I.S., Abutalipova L.N., Salimova A.I., Pankova E.A.

*The Kazan State Technological University*

The obtaining of available, non-toxic tanning compounds providing the required properties of skin and fur semifinished item represents scientific and practical interest. As an alternative to chromium tannage we offer to use multifunctional alkylencarbonates - laprolates, having the average functionality equal to 2,5. The indicated compounds are capable to interact with collagen aminogroups under moderate temperatures according to the reaction of uretanoformation.

Aminolysis alkylencarbonates appertains to reactions of nucleophilic joining and takes place under rather mild conditions according to the following:



In the process of tannage the temperature should not exceed 40C<sup>0</sup>, and practically all aminogroups are in toned state when the process takes place. These circumstances considerably reduce the velocity of interaction of laprolate with protein aminogroups.

As it is known, the process of treating fibre-porous materials, skin tissues of hide considered to be included into them, by low-temperature gas-discharged plasma, results in their structural modifications promoting the intensification of liquid processes, mainly due to the acceleration of the diffusion of solution components into internal stratum of treated material. Besides, in our case, the electrons of HFE-PLASMA should neutralize the positive charge at protein aminogroups considerably having increased the nucleophilic of nitrogen of these groups. On the whole both these factors are aimed to increase the degree of collagen filaments of skin tissue.

The in-data of the unit used by us, were changing in the following ranges: the expenditure of plasmofforming gas (argon) G = 0,1-0,6 gramm/sec.; the capacity of the discharge Wp = 0,2 - 2,0 kw; frequency of the generator f = of 13,56 MHz; pressure P = 13,3 - 133 Pascal.

The conducted tests have allowed to determine the optimum modes of plasma influence on thermostability of skin tissue characterized by the temperature of welding. In particular, for budge samples, treated by HFE-PLASMA with the parameters: G = 0,04; Wp = 1,22 kw; f = 13,56 MHz and pressure 19,95 Pascal, the increase of welding temperature was 19C<sup>0</sup>. This parameter reached 82C<sup>0</sup> and is sufficient to perform safely the consequent operations.



# **The Treatment of the Porous – Fibrous materials with the radio-frequency charge in Reduced pressures**

I. Sh. Abdullin<sup>1</sup>, L.N. Abutalipova<sup>1</sup>, F.A. Gizatullina<sup>2</sup>, M.F. Shaekhov<sup>1</sup>

<sup>1</sup> *Kazan, The Kazan State Technological University*

<sup>2</sup> *Kazan, The Kazan State Technical University named after A.N. Tupolev*

Natural fibrous-porous materials leather end fur are used in everyday life. Among one can name a considerable low grade raw material output, a rather lengthy production cycle and a use of the ecologically harmful substances.

Research on the changes of the properties of natural fibrous - porous material in radio-frequency charge of the reduced pressure has been carried out. The furs of shipskin, ondatra, horseskin, cattle skin, pigskin have been treated.

The research was carried out on the radio-frequency plasma installation with the generations frequency of 13,56 MHz, the charge strength 1,5 - 3,2 kW, with the dynamic vacuum from 13 to 26 Pa, the plasmaproducing gas consumption from 0 to 0,08 g/s. Argon, oxygen, and nitrogen were used as a plasmaproducing gas. The rate of the vacuum pumping 5-50 dm<sup>3</sup>/s.

The Modified material added to the strength. A change in the chemical properties of the reaction of the hair and leather tissue with the dye and the tanning substances has been observed. However there has been no chemical changes in the porous – fibrous materials.

The absorption of the liquid in the samples increased twice. The adhesion of the hair to the leather tissue increased by 20%. The tensile strength of the leather increased by 15%.

The tanning time of the leather material decrease twice.

The colour of the dyed hair and the leather material has become more homogenous, the dyeing rate increased by 1,2 times. The Consumption of the dyes decreased by 1,5 times.

From the comparative analysis of the elementary processes of the interaction the layer of the positive charge of the radio-frequency charge in the reduced pressure one can name a number of processes affecting the treatment namely: ion bombarding, the surfaces ion recombination, the thermal current.

# **Transport of macroparticles in weakly ionized dusty plasma of gas discharges**

Olga S. Vaulina, Oleg F. Petrov, Andrey V. Gavrikov, Iya A. Shakhova and Vladimir E. Fortov

*Institute for High Energy Densities, Russian Academy of Sciences, Moscow, Russia*

Dusty plasma consists of neutral gas, ions, electrons, and micron-size particles that have a negative charge, when emission processes are negligible. The combined effect of interactions of the grains between themselves as well as with the ambient plasma can lead to the formation of both stationary structures (similar to liquid or crystal) and composite oscillatory, or chaotic regimes. Dissipation plays a basic role for the particle dynamics, and self-organizing of dust in bulk of plasma. The basic reasons of dissipation in low-ionized dusty plasma are the impacts of dust with the neutrals of surrounding gas. Diffusion is the basic transport process, which determines the energy losses, the phase state, the wave propagation and the formation of different instabilities in dusty plasma systems.

The dynamics of charged macro-particles in complex “dusty” plasma is numerically investigated for the conditions of laboratory experiments on weakly ionized gas discharges. The expression for the dust diffusion coefficient in strongly correlated liquid-type Yukawa system has been obtained from analysis of our numerical data on base of “jump theory” for molecular fluids. This result has been used for non-perturbative diagnostics of the non-ideality parameter, macroparticle charges and plasma screening lengths in laboratory dusty plasma. The experiments have been performed for macroparticles in rf- and dc-glow discharges (including the space experiments) over a wide range of plasma parameters (dust temperatures and sizes, gas pressure etc.). The dust concentration, the pair correlation function, the dust temperatures and diffusion coefficients have been measured. The coupling parameter, characteristic dust frequency and particle charges have been obtained.

This work was supported by the Russian Foundation for Basic Research, Grant No. 01-02-16658, and by INTAS, Grant No. 2001-0391.

# Numerical simulation of Si/C/N Nano-powder synthesis

M. Amara, D. Hourlier, M. El Ganaoui

*SPCTS, UMR 6638. Faculté des Sciences et Techniques, 123 Albert Thomas  
87 060 Limoges*

**Abstract:** A numerical model was developed for the ceramic powder synthesis by the laser pyrolysis, in order to study the experiment feasibility and to optimise the process. This model takes into account heat and mass transfers during the experiment.

## 1. Introduction

For manufacturing nanocomposite ceramics, the synthesis of powders with a nanometric scale, is a promising candidate for structural applications allowing higher temperature values than those allowed by metallic super-alloys.

This synthesis was developed by CVD, arc-plasma-heated or laser pyrolysis processes [1, 2]. The last approach is a consequence of the interaction between an infrared laser beam and a gas precursor or a liquid in aerosol form. The principle is based on the resonance phenomena between the emitted laser frequency (continuous  $CO_2$ ,  $\lambda=10.59 \mu m$ ) with at least one of the reactant band absorption. The powder obtained by this method shows very interesting characteristics, the small reaction volume and the ability to maintain steep temperature gradients allow the accurate control of the nucleation rate, permitting the formation of fine particles.

The control of these powders during their synthesis requires the understanding of coupled physical and chemical phenomena. Indeed, the nucleation and the growth of the particles depend directly on the resulting temperature field, dynamic field and particles concentration. These parameters are related to the operating conditions including conductive, convective and radiative heat transfers. The goal of the present work is to develop a three dimensional model of the reactor and to characterize the influence of the various thermal parameters involved during the process. The validation and the qualification at this stage are essential for any extension including the chemical processes and particles growth.

## 2. The problem

Except Akmandor work at the beginning of the eighties [3], the majority of the published researches focused on the development of the experimental part of the process. The author built a simplified model, incorporating the gas dynamics and the chemical reactions. The simulations were limited in the fact that, the thermal heat transfer did not take into account the mixture between the carrying and the reactive gas. The later is very important in the cooling processes of the reactive gas. The simulations were limited to a 2D-axisymmetrical geometry on a domain around the jet, whereas the real experiment is three-dimensional and the powder synthesis may be influenced by supposed minor phenomena taking place in the full reactor in the Akmandor calculations [4].

In order to understand the solid particles formation mechanism and the relationship which exist between experimental parameters (laser power, pressure, etc) and resulting powders characteristics, three-dimensional simulations is achieved.

Nowadays, powerful calculation means are developed in such a way that complex geometries are taken into account, incorporating the deep analysis of the physical phenomena. An industrial Computational Fluid Dynamic (CFD) package is used [5]; this software is based on finite volume element approximation, allowing the modelling of various fluid flows in more or less complex geometries, and particularly including reactive flow.

### 3. Modelling

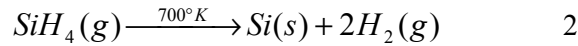
This work deals with the laser radiation and the reactive gases interaction. The majority of the sources yield their energy without any discrimination concerning vibration states. For the laser pyrolysis synthesis of silane, the system uses a well defined quantity of energy, the brought energy is not sufficient on the one hand to break down the molecular bonds via the electronic states excitation. On the other hand, all states are very largely excited.

Hence a condition is necessary so that, the reaction rate is significant, in which the excitation energy is in the same order magnitude of the activation energy, relative to the silane decomposition, which lies between  $E_a = 100\text{--}380 \text{ kJ/mol}$  ( $1\text{--}4 \text{ eV/molecule}$ ). The used photons ( $\lambda = 10.6 \text{ mm}$ ), transport an energy of  $1.90 \cdot 10^{-20} \text{ J}$  ( $0.12 \text{ eV}$ ). 30 photons are roughly needed for the silane decomposition in the case of producing  $\text{SiH}_3$  and  $\text{H}$  ( $E_a \approx 318 \text{ kJ/mol}$ ,  $3.3 \text{ eV/molecule}$ ). This means that several mechanisms (collisions, radiations) must be involved to reach this dissociation. From the macroscopic point of view, absorption of laser radiation occurs according to Beer-Lambert law [6, 7]:

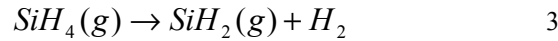
$$q = q_0 [1 - \exp(-\alpha_{abs} P \Delta L)] \quad 1$$

$q_0$  being the energy density brought by the laser,  $\alpha_{abs}$  the absorption coefficient,  $P$  the total pressure and  $\Delta L$  the absorption length. The absorption coefficient depends on the temperature by broadening effect, but its value is not tabulated; however an average value of  $0.005 \text{ N/m}$  will be taken in this study [3].

The thermal decomposition reaction at  $700 \text{ K}$  can be schemed as:



It was shown that this decomposition is a result of 120 intermediate steps [7], which gives rise to many radicals such as  $\text{SiH}_2$  or  $\text{C}_2\text{H}_6$ , but the global decomposition is limited by the reaction producing the silylene:



The rate of reaction 3 is given by [6]:

$$\frac{d[\text{SiH}_4]}{dt} = [\text{SiH}_4] 5 \times 10^{12} e^{\frac{-52.2 \text{ Kcal/mol}}{RT}} \quad 4$$

Where  $[x]$  is the concentration ( $\text{kg/m}^3$ ) of the species  $x$ .

In the developed numerical model, only the initial reaction leading to the dominant component formation of (silylene) will be taken into account. This assumption is justified by comparing characteristic time scales of the various involved phenomena: convective time scale based on a fluid characteristic distance (in our case the diameter of the laser beam) to the flow characteristic speed (inlet speed) giving  $t_{\text{convection}} \approx 1 \text{ s}$ . The reaction time scale is based on the rate of the reaction. In the case of silylene decomposition,  $t_{\text{reaction}} \approx 10^{-6} \text{ s}$ . It is noted that the reactive transfers are infinitely faster than the convective transfers.

### 4. Numerical approach

A model was developed to represent the laser pyrolysis synthesis. Steady state solution of fluid flow is a required condition to have a good reproducibility of the synthesis process and especially for the powder characteristics.

As a first step, the energy loss of the system by the particles thermal radiation is not taken into account. The system incorporating the chemical species and the solid particles is under development.

The model consists on coupled conservation laws involving Navier-Stokes, energy and species equations. The systems of Partial Differential Equations (PDE) formulated on primitive variables and approximated using finite elements approximation on unstructured grid. The simulations use CFX<sup>R</sup> industrial software [5].

The investigated configuration concerns a cylindrical geometry (figure 1. a), with a silane jet surrounded by an annular argon flow (carrier gas). The laser has a fixed diameter permitting the use of focused or unfocused ray. These dimensions correspond to those of Flint experimental model [5]. Two experimental values of power density corresponding to  $180\text{ W}$  and  $510\text{ W}$  are used. The flow rates of gases and the cell pressure are maintained constant (table 1).

CFX-5 automatically performs the volume meshing. Delaunay algorithm for specified geometry. This speeds up preprocessing enormously and products high quality meshes ensuring faster convergence [5]. A grid dependency study is performed and a cell meshing of 36635 nodes is carried out with refinement in the vicinity of the strong gradients areas as the laser source and the laser/gas interaction (figures 1-b).

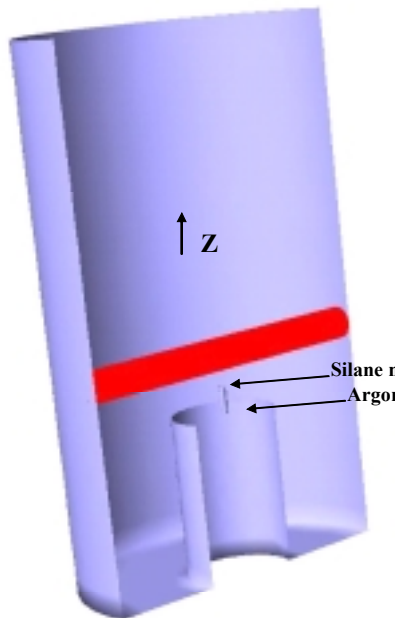


Figure 1a: Geometry of the reactor.

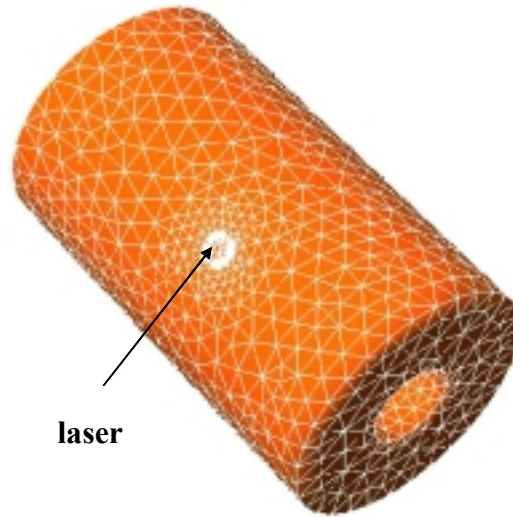


Figure 1b : Meshing of the domain.

Table 1 : Physical parameters

Silane (cc/min)	38
Argon (cc/min)	$10^3$
Pressure (Pa)	$2 \cdot 10^4$
Silane nozzle diameter (mm)	1.2
Argon nozzle diameter (mm)	19.7

## 5. Results and discussion

Figure 2, shows the axial speed variation of the fluid, according to the distance relatively to the silane nozzle. The velocity of the jet is equal to  $3\text{ m/s}$ , this result is agreement within the same order of magnitude with Akmandor calculations [3]. It has to be noted that at about the beginning of the reaction region, the speed increases with the power; this increase is due to the heating of the gas.

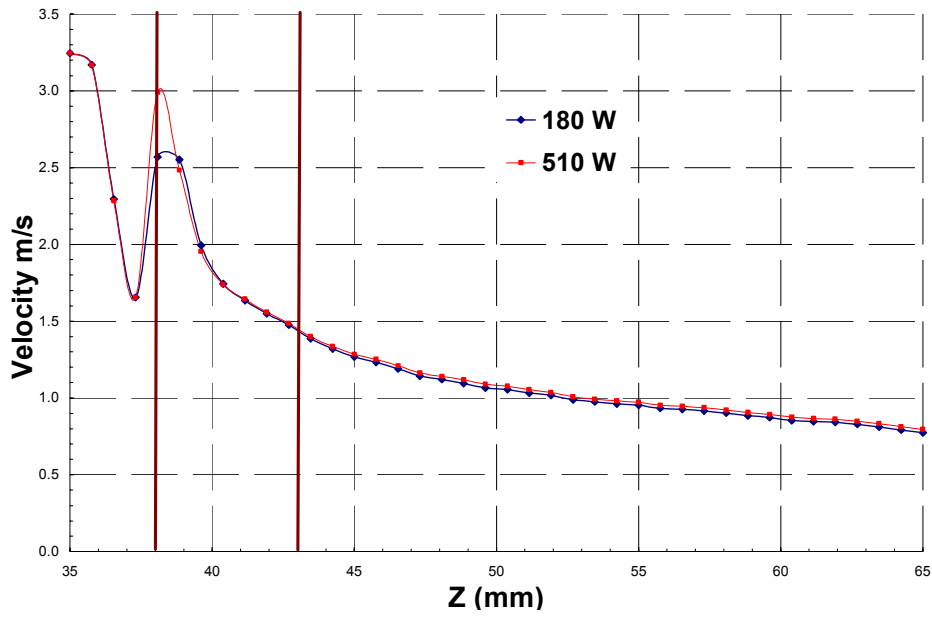


Figure 2: Gas speed versus silane nozzle distance.

The developed calculations show a small recirculation cell of the gases (figure 3). It is important to outline that the existence of a recirculation zone may induce a poor characteristic for particles growth and powder collections.

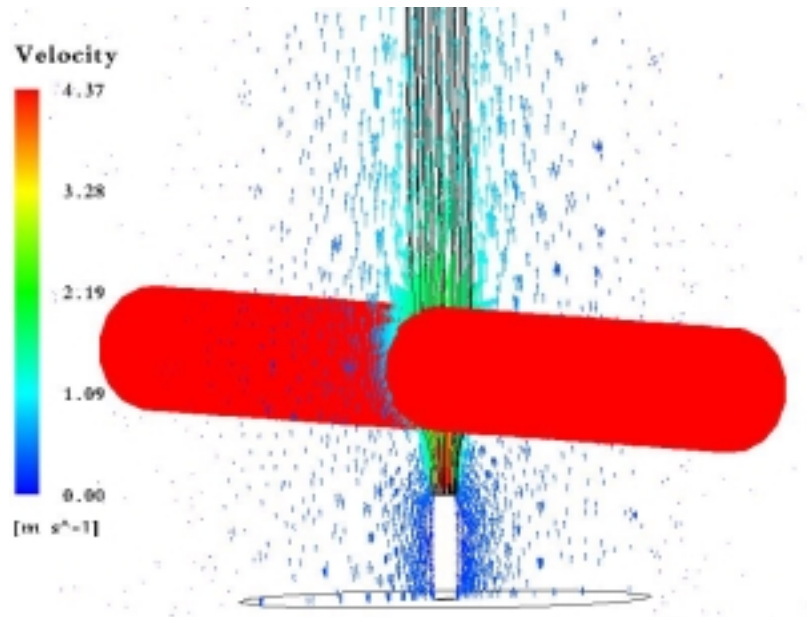


Figure 3: Gas speed Field inside the reactor versus silane nozzle distance.

Figure 4 gives the temperature field, in  $XY$  plane. It is remarked the small reaction region size (a few centimetres order). The flame is limited by the isotherm line at 800 K.

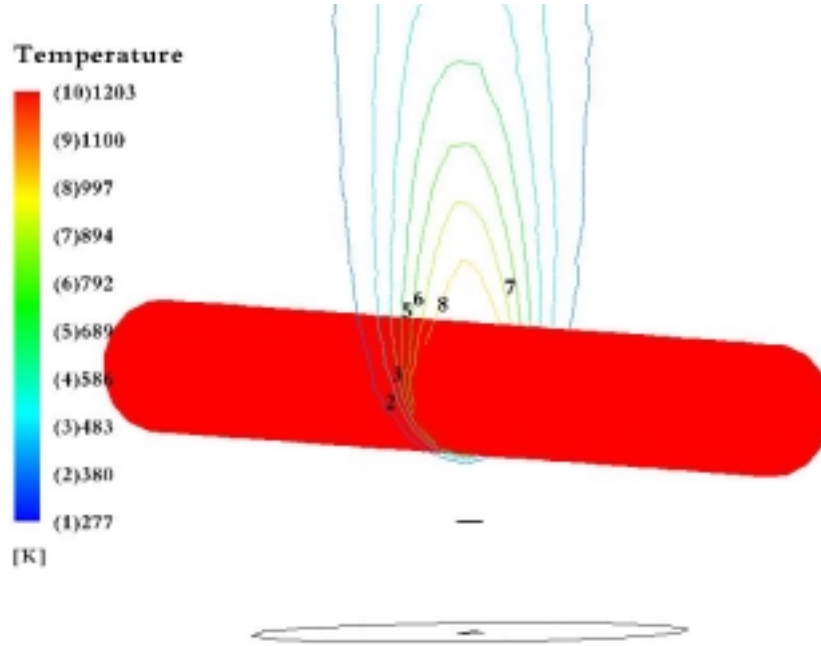


Figure 4: Isotherms ( $P = 510 \text{ W}$ ).

Moreover the reaction region is confined by the carrier gas, as shown in figure 4. This implies the importance of the carrier gas to prevent the powders contamination, and especially their cooling effect. Indeed, they stop the growth of the grains, and lead to nanometre size of particles [8].

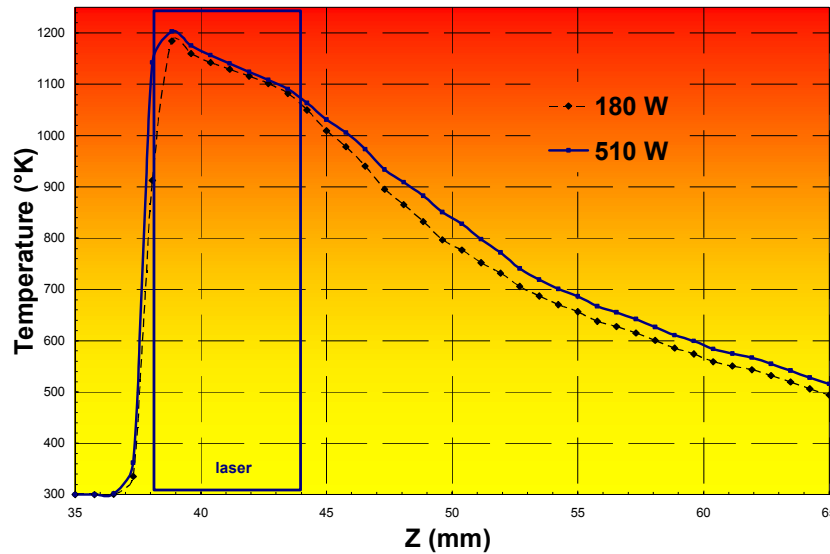


Figure 5: Axial temperature evolution with the distance from the silane nozzle exit.

Figure 5, shows that the temperature presents a maximum value. Its value increases with the laser power and the position of maximum moves towards the nozzle. This phenomenon induces a variation on the particles residence time inside the reaction zone [8]. Moreover the temperature increases with the power dissipated and the maximum approaches the nozzle. Indeed, the gas is heated in the zone of pre-reaction (1/3 of the preheated region); this is explained by the heat transfer by conduction, which grows with laser intensity. These results are confirmed by the silane decomposition study along the jet axis and it is noticed, that silane breaks up completely (figure-6).

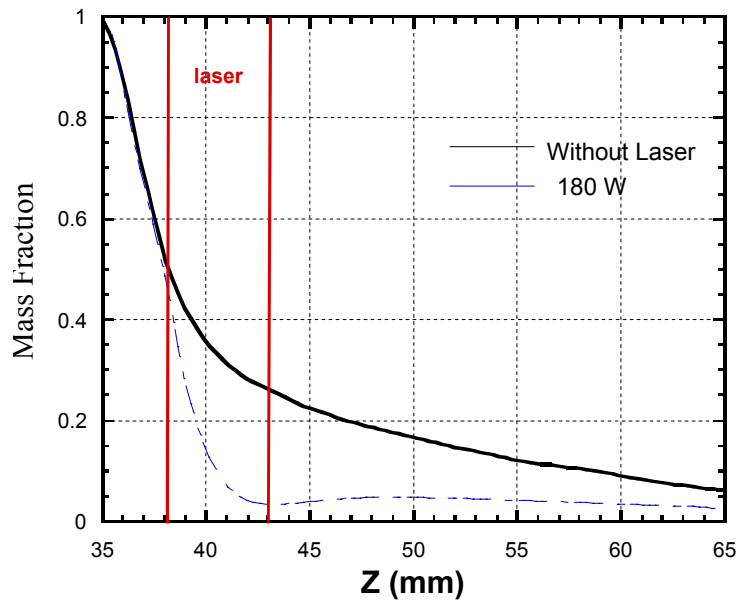


Figure 6: Axial mass fraction of silane.

## 6. Conclusion

A three-dimensional model which take into account both, thermal transfers and silane chemical reactions decomposition gas has been developed. The temperature fields, dynamic field, and decomposition of the chemical species are calculated. The goal of this work resides in the fact that these calculations are carried out in three dimensions, and takes into account the thermal transfers by convection and conduction and the gravity influence. These results correspond to an extension of those of Akmandor's limited to a two-dimensional axisymmetric geometry, and are in agreement with experiments. This work follows on clarifying the behaviour of the several reagents gas mixture ( $SiH_4$ ,  $CH_4$ ,  $NH_3$ , ...) in the laser beam, in order to approach as well as possible the synthesis conditions of  $SiCN$  powders.

**Acknowledgements :** Authors thank Denis Lécuyer (AEA Technology/CFX-France) for invaluable help concerning CFX software and Professor P. Fauchais (University of Limoges) for comments and discussions.

## References

- [1] Suhas V. Patankar, and Spalding, D. B., 1970, Heat and Mass Transfer in Boundary Layers, 2<sup>nd</sup> Edition, Intertext Books, London.
- [2] W. R. Cannon SCD, J. S. Haggerty, R. A. Marra. Sinterible Ceramic Powders from Laser-Driven Reactions: II, Powder Characteristics and Process Variables. Journal of the American Ceramics Society. 65 (7):330 (1982).
- [3] Akmandor I. S. Theoretical and Computational Models of Reacting Silane Gas Flows: laser Driven Pyrolysis of Subsonic and Supersonic Jets [PhD]. Cambridge, MIT (1985).
- [4] Amara M., Hourlier D., El Ganaoui M., Laser driven synthesis of Si/C/N nanopowder. In proceedings of 2<sup>nd</sup> Int. Conf. Physique des Interactions Rayonnement Matière PIRMII. 19-21 Février 2003. Settat/Marrakech, Maroc, p. 46-47.
- [5] CFX5, developed by AEA technology. <http://www.software.aeat.com/>
- [6] Flint JH. Powder Temperature in Laser Driven Reactions, M.S. Thesis, MIT (1982)
- [7] Michel E. Coltrin RJM, James A. Millerr. A Mathematical Model of the Coupled Fluid Mechanics and Chemical Kinetics in a Chemical Vapor Deposition Reactor. J. Electrochem Soc. 131:425-434 (1984).
- [8] Marra RA. Homogenous nucleation and growth of silicon powder from laser heated gaz phase reaction [PhD], MIT; 1983.



# Surface Modification of Polymer Substrates Using Vacuum Ultraviolet Light Generated by Dielectric Barrier Discharge

A. Hozumi, Y. Yokogawa and T. Kameyama

*National Institute of Advanced Industrial Science and Technology (AIST), Nagoya, Japan*

The surface modification of polymeric materials through photochemical processes has attracted much attention due to its wide variety of applications, such as microstructure fabrication, photochemical etching, and improvement of the wettability and biocompatibility. Among the various light sources available, vacuum ultraviolet (VUV) light, whose wavelength is much shorter than 200 nm, is of particular interest for polymer surface processing. Although extensive research has been reported on polymer surface modification with VUV light using plasma, or synchrotron radiation, as well as on modification using UV or VUV excimer lasers, studies on surface processing employing a dielectric barrier discharge VUV excimer lamp have been few [1-3].

In this study, we report on the surface modification of poly (methyl methacrylate) (PMMA) using two types of dielectric barrier discharge excimer lamps filled with Ar<sub>2</sub> and Xe<sub>2</sub> gasses. These lamps radiate VUV light of 126 and 172 nm in wavelength, respectively. In this study, we have particularly focused on the effects of wavelength and atmospheric pressure during VUV irradiation on the surface wettability, chemical structure, morphology and photoetching rate of the PMMA surfaces.

Each of sample substrates cut from a commercial PMMA sheet was placed in a vacuum chamber evacuated by a rotary pump. The pressure in the chamber was controlled at 10, 10<sup>3</sup> or 10<sup>5</sup> Pa. The PMMA substrate was then irradiated for 5~50 min with one of two types of VUV light at distance of about 20 mm from the lamp window to the sample surface. Substrate temperature was measured by a thermocouple and remained at less than 40 °C, even when irradiation was prolonged up to 50 min. Furthermore, in order to fabricate microstructures on the PMMA substrates, some of the samples were irradiated with either 126 or 172 nm VUV light through a mesh-mask contacting the substrate surface. This VUV-irradiation was conducted for 30 min at 10, 10<sup>3</sup> or 10<sup>5</sup> Pa. Moreover, such microstructured samples were applied to the arrangement of antibodies labeled with fluorescent on the PMMA surfaces.

VUV irradiation of the PMMA substrates resulted in the sample surfaces becoming hydrophilic. However, photooxidation rate and degree of hydrophilicity of the treated sample surface markedly depended on VUV light wavelength and atmospheric pressure. The minimum water-contact angle of the samples was about 25° when 172 nm VUV light was irradiated to the sample under the reduced pressure of 10<sup>3</sup> Pa. Based on this result, microfabrication of PMMA substrate was demonstrated using simple mask-contacting method. As confirmed by atomic force microscope, microwells of about 2 μm in diameter and 350 nm in depth were successfully formed on the samples. Finally, this sample was immersed in a solution containing antibodies for 30 min. After this, it was rinsed with MilliQ water and then blown dry with a N<sub>2</sub> gas stream. Fluorescence optical micrograph clearly indicates that antibodies were selectively deposited on the microwells, while the surrounding regions remained free of deposits. This area-selectivity was probably due to the difference in chemical reactivity, e.g., hydrophobic/hydrophilic property, between the microwells and the surrounding regions [4]. This microstructured PMMA sample is expected to be applicable for a low-cost polymeric biochip.

## References

- [1] H. Esrom, U. Kogelschatz, *Thin Solid Films*, **218**, 231 (1992).
- [2] J.-Y. Zhang, H. Esrom, U. Kogelschatz, G. Emig, *J. Adhes. Sci. Technol.*, **8**, 1179 (1994).
- [3] C. Fuchs, O. Goetzberger, R. Henck, E. Fogarassy, *Appl. Phys. A*, **60**, 505 (1995).
- [4] A. Hozumi, T. Masuda, K. Hayashi, H. Sugimura, O. Takai, T. Kameyama, *Langmuir*, **18**, 9022 (2002).

# Research on Chemical Reaction of Long-range Plasma

Chen Jierong<sup>1</sup> Yan Jinglian<sup>1</sup> Zhang Yunze<sup>1</sup>

<sup>1</sup>Environmental & Chemical Engineering Institute, Xi'an Jiaotong University, China

**Abstract:** Based on the theory of “Long-range Plasma”; a kinetic model of long-range oxygen plasma with low pressure, low flux and high-concentration radicals is constructed according to one-dimensional mass continuity equation. The distribution and transportation of electrons, ions and radicals in long-range plasma field are analyzed. And the model was tested by the plasma treatment on medical PVC.

**Keywords:** Long-range plasma      Kinetic model      PVC

## 1. Introduction

As it contains many highly activated species, plasma reaction is relatively complex, repeatable and unstable. So far, a general convincing mechanical model<sup>[1-5]</sup> has not yet been set up. Accordingly, it is the key step of promoting its application in many areas to control and strengthen the objective reaction, to set up an applied model of plasma reaction theory, to forecast the diffusion and distribution of different species in plasma, to provide theoretical support for plasma reaction design and control.

## 2. Modeling

### 2.1 The Basic Theory of Modeling

Complex and various plasma reactions can be divided into three groups: (1) Collision between electron and material; (2) Recombination between ion and electron; (3) Recombination between two radicals. The rate constants of the latter two reactions are  $10^{-7}\text{cm}^3/\text{s}$  and  $10^{-33}\text{cm}^6/\text{s}$ <sup>[6]</sup> respectively, which means that ions and electrons disappear immediately while radicals have long life. Therefore, high-concentration radicals can be obtained at certain positions away from the plasma source, which make the surface modification (radical reactions) dominant, electron and ionic etching reactions inhibited and more desirable surface modification effect can be acquired than conventional plasma treatment. The above is the long-range plasma theory<sup>[7]</sup>.

### 2.2 Model Development

A cylindrical glass tube with a diameter of  $R$  and a length of  $L$  ( $L \gg R$ ) is set up. The tube is a stable flow field without returning and mixing; the concentration of species is diverse along with the length of the tube, independent of time. As shown in Figure1, the model simulates the different behavior of species.

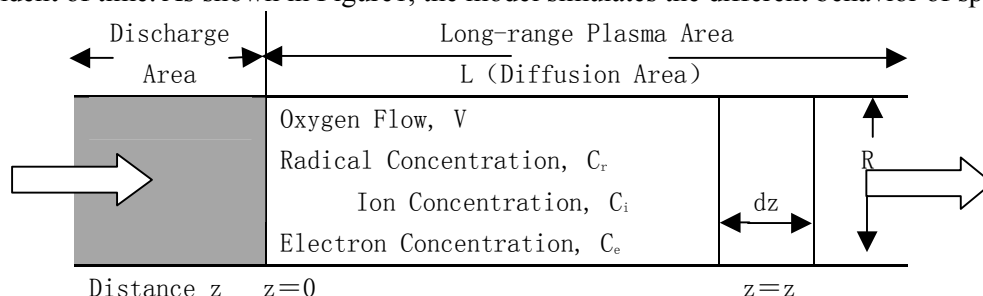


Figure 1. Long-range Plasma Model

Project 20174030 supported by National Natural Science Foundation of China

Doctor Foundation from Ministry of Education (20010698007)

Returned Personnel Foundation from Ministry of Education (2001[345])

Oxygen gas is flowed at a constant velocity of  $V$  from the discharge area to the end of the tube. And the position of  $z$  is defined as the distance away from the end of the discharge area along with the tube.

In developing the model, we have the following assumptions:

1. Activated species are generated only in the discharge area, and never generated at  $z > 0$ , the concentration of activated species is a function of  $Z$ .

2. At  $z > 0$ , radicals are drifted by the oxygen flux and diffusion. Ions and electrons are drifted by oxygen flux, diffusion and electric field.

### 2.2.1 Concentration Distribution of Oxygen Radicals

As shown in Figure 1, a tiny unit with thickness of  $dz$  and area of  $\pi r^2$  was selected, the differential coefficient ( $dJ_r/dz$ ) of oxygen radical flux at the distance of  $z$  is equal to the generation rate ( $R_g$ ) minus the combination rate ( $R_r$ ) of oxygen radicals

$$\frac{dJ_r}{dz} = R_g - R_r \quad (1)$$

The oxygen radical flux at  $z$  is given by the two modes, oxygen flux and diffusion:

$$J_r = C_r V - D_r dc / dz \quad (2)$$

Where  $C_r$ ,  $V$  and  $D_r$  are the oxygen radical concentration, the velocity of oxygen flux and the diffusion coefficient of oxygen radicals, respectively. The flowing result can be deduced (more detail can be got from reference [8]):

$$C_r = C_r^0 \exp(-0.27 \times 10^{-4} z) \quad (3)$$

Where  $C_r^0$  is the concentration of oxygen radicals at  $z$ .

### 2.2.2 Concentration Distribution of Electrons and Ions

A similar one-dimensional mass balance can be considered with regard to the electron flux ( $J_e$ ) and ion flux ( $J_i$ ).

$$dJ_e / dz = R_g - R_e \quad (4)$$

$$dJ_i / dz = R_g - R_i \quad (5)$$

The electron flux ( $J_e$ ) and oxygen ion flux ( $J_i$ ) are given by the three modes, oxygen flux, diffusion and electric field:

$$J_e = C_e V - D_e dC_e / dz - C_e \mu_e E \quad (6)$$

$$J_i = C_i V - D_i dC_i / dz + C_i \mu_i E \quad (7)$$

Where  $C_e$  and  $C_i$  are the electron and oxygen ion concentration;  $D_e$  and  $D_i$  are the diffusion coefficients of electrons and ions;  $\mu_e$  and  $\mu_i$  are the velocity of electrons and ions driven by electric field, respectively. The concentration of electrons and ions can be concluded as follows (more detail can be got from reference [8]):

$$\frac{C_e}{C_e^0} = \frac{1}{[1 + 3.62 \times 10^{-2} z]^2} \quad (8)$$

## 2.3 Theoretical Concentration Distributions of Activated Species

According to equation (3) and equation (8), we can select some points to calculate. The calculation result is shown in Figure 2, which shows the theoretical concentration distribution of radicals, ions and electrons in plasma field.

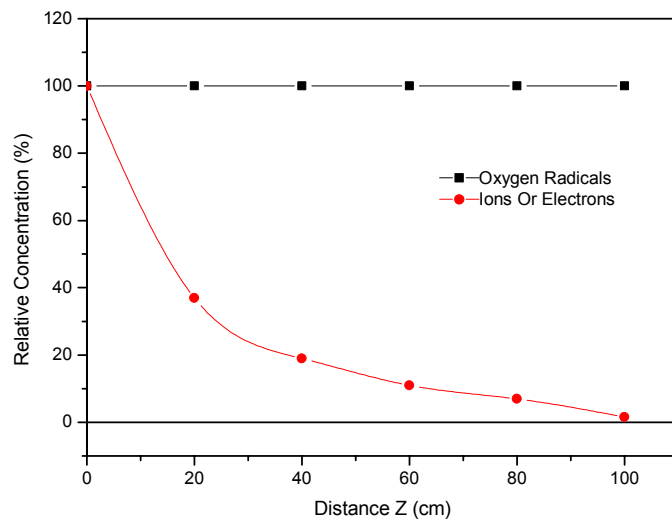


Figure 2 shows that the relative concentration of oxygen radical ( $C_r/C_r^0$ ) almost remain unchanged with the increase of distance. At  $z=60, 80$  and  $100\text{cm}$ , the relative concentration is still above 99%. While the relative concentration of ions and electrons decreases rapidly with the distance, at  $z=80$  and  $100\text{ cm}$ , the relative concentration is about 6.6% and 1.4% respectively in which the combination disappear is above 95%. This comparison shows that we can get relatively high concentration of radicals and strengthen radical reactions at

Figure 2. Relative Concentration Distribution

long distance while inhibit ion and electrons reactions. As follows, the reliability of the model is tested by experiment of PVC surface modification by oxygen plasma.

### 3. Experimental Section

#### 3.1 Long-range Plasma Treatment

The medical PVC film (made by Blood Center of Shanghai City), which is cut into pieces with dimension of  $40\text{mm} \times 35\text{mm}$  each. The PVC sheets were positioned on a glass plate at a constant distance of 0, 200, 400, 600 and 800mm from the center of the inductance coil to distinguish long-range plasma treatment from conventional plasma treatment (discharge zone).

#### 3.2 Weight Loss Rate

Sample weights before and after treatment are obtained by electron analytical balance (Mettler AE240). Weight loss rate can be calculated by the following equation:

$$W = (m_1 - m_2) / S \quad (9)$$

Where  $W$ ,  $m_1$ ,  $m_2$ , and  $S$  are the weight loss rate ( $\mu\text{g}/\text{cm}^2$ ), sample mass of before treatment and after treatment ( $\mu\text{g}$ ), the areas of sample ( $\text{cm}^2$ ).

#### 3.3 Contact Angle Measurement

The contact angle was measured by a contact angle meter JY-82 (made in Chengde, China). To lessen the effect of gravity, the volume of each drop was regulated to about 0.2cc by a microsyringe. The measurement was carried out at a temperature of  $20^\circ\text{C}$  and at a humidity of 45%RH. Each sample was measured at different points 20 times, and the contact angle was determined by their average values.

The liquids used in measuring the contact angle of the film are shown in Table1. According to Yamaish<sup>[7]</sup>, the surface tension  $\gamma_L$  of the liquid can be divided into three components: dispersion force  $\gamma_L^a$ , polar force  $\gamma_L^b$ , and hydrogen bonding force  $\gamma_L^c$ . The surface tension of PVC can be evaluated by the extended Fowkes equation as follows:

$$\gamma_L(1 + \cos\theta) = 2\sqrt{\gamma_s^a \gamma_L^a} + 2\sqrt{\gamma_s^b \gamma_L^b} + 2\sqrt{\gamma_s^c \gamma_L^c} \quad (10)$$

where subscript S represent solid to be measured, superscript a、b、c represents dispersion, polar and hydrogen bond components of surface tension respectively. Above equation can be solved by using three-dimensional determinant<sup>[9]</sup>.

Table1. Dispersion, polar and hydrogen bond components of surface tension of reference liquids at 20°C

		Surface tension ( $\times 10^{-5} \text{N} \cdot \text{cm}^{-1}$ )				
No.	Liquids	$\gamma_L^a$	$\gamma_L^b$	$\gamma_L^c$	$\gamma_L^n$	$\gamma_L$
1	Water	29.1	1.3	42.4	43.7	72.8
2	Glycerin	37.4	0.2	25.8	26.0	63.4
3	Formamide	35.1	1.6	21.5	23.1	58.2
4	Methyleneiodide	46.8	4.0	0.0	4.0	50.8
5	Ethyleneglycol	30.1	0.0	17.6	17.6	47.7

$$\gamma_L^n = \gamma_L^b + \gamma_L^c \text{ (nondispersion, polar)} \quad \gamma_L = \gamma_L^a + \gamma_L^b + \gamma_L^c$$

### 3.4 XPS

The XPS (PHI5400ESCA, Perkin-Elmer Co.) was conducted to analyze chemical compositions of surface layers of the PVC film at a pressure lower than  $5 \times 10^{-8} \text{Pa}$ .  $\text{MgK}_{\alpha}$  X-ray was used as the source.

## 4. Results and Discussion

### 4.1 Effect of plasma treatment condition on weight loss rate of PVC

Figure3~5 show effects of treatment power, exposure time and oxygen flux on weight loss rate of PVC respectively. With the increase of power and time, PVC weight loss rate enhances from Figure3 and 4. The reason is that when activated species of oxygen plasma attack PVC surface, etching action occurs, which makes large molecule chain rupture and remove, and lead to PVC weight loss. With power increase, the energy of particles increase, etching action strengthens. While with the residue time increase, weight loss rate also increase for etching action accumulates. Figure 5 is effect of  $\text{O}_2$  flux on weight loss rate of PVC film.

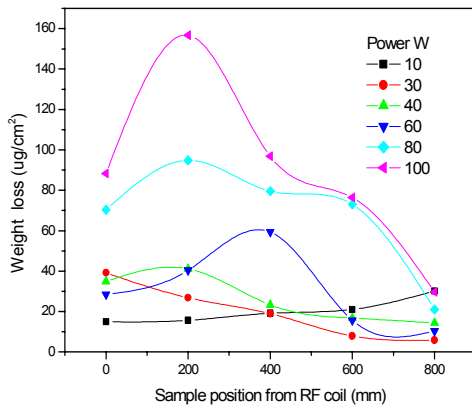


Figure 3. Effect of RF power on weight loss rate (treatment time 60s;  $\text{O}_2$  flux 30sccm)

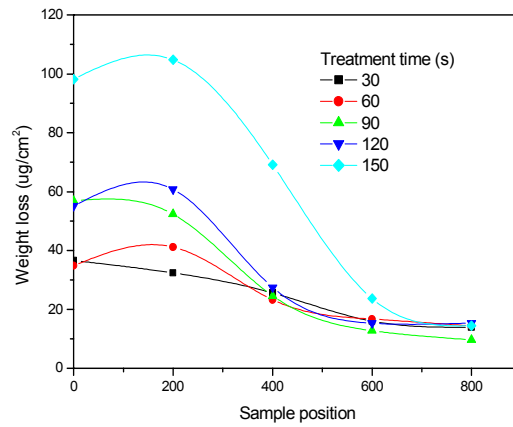


Figure 4. Effect of treatment time on weight loss rate (Power 40w;  $\text{O}_2$  flux 30sccm )

When treatment power and time are fixed, the energy of system received is a constant. At low flux, though the number of particles, which collide with the surface, is less than that of high flux. However, the average energy of particles is higher than that of high flux. At low O<sub>2</sub> flux, the probability to collide with the surface of each particle increases, so etching actions strengths, weight loss rate also increases. While at high O<sub>2</sub> flux, the number of particles is large but the average energy and residue time is low, the etching action is comparatively small. Thus, when oxygen fluxes changes, while other conditions fixed, etching action is interaction effect of the energy and the amount of activated species and residue time. It shows that weight loss rate of sample in long-range zone is much lower than that of conventional plasma zone, namely etching action of electrons and ions in long-range zone are inhibited to a certain extent.

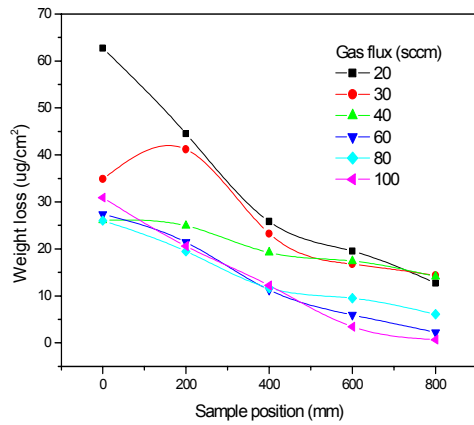


Figure 5 Effect of O<sub>2</sub> flux on weight loss rate  
(power: 40W; treatment time: 60 s)

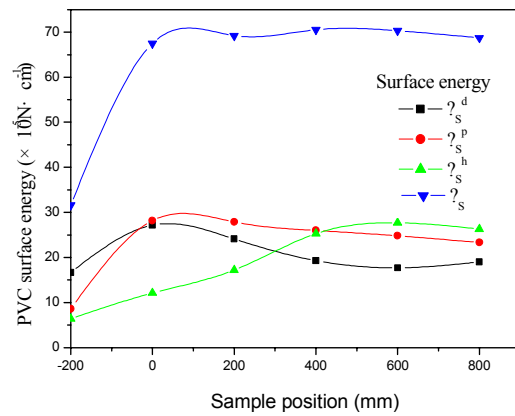


Figure 6. Effect of plasma treatment on surface energy  
(power 40W, time 60s, O<sub>2</sub> flux 30 sccm, sample position of -200 represent untreated sample)

#### 4.2 Effect of plasma surface modification on surface energy of PVC

Figure 6 shows the surface free energy and its components of the PVC. It shows that the medical PVC's surface energy is increased after modification by long-range plasma. Compared with untreated sample, its surface energy increased more than two times. The surface energy's polar and hydrogen components increase from 27.2%, 20.3% to about 36.2%, 29% respectively, and the degree of increase has relation with the sample's position. Dispersion is almost unchanged. From which, it can be concluded that, the improved wettability of surface largely lies in the increase of the surface polarity ingredient. From this figure, we can also find that the 0mm position is very different from other positions: dispersion suddenly increased to the maximum, however other positions are almost unchanged; the surface free energy of that point is lower than other points. This is because the sample at 0mm is located in the discharge area, free radical density is relatively low; electrons, ions have a strong etching effect, but other points lie in the long-range area where the effect of the etching is restrained, and free radical reaction intensified which introduce many polar groups to the surface, enhancing material's polarity. According to Andrade et al<sup>[10-11]</sup>, the biocompatibility with blood of material can be improved obviously by reducing the surface free energy, forming the hydrophilic surface and micro-phase separate structure and so on. Therefore, the biocompatibility with blood of PVC can be improved by long-range plasma treatment, as the treatment can improve the hydrophilicity of the surface.

#### 4.3 Chemical composition of the surface of PVC

Surface chemical composition of PVC treated with long-range plasma is analyzed by XPS. The content of groups and O/C are given in Table 2. That oxygen content increases shows that C=O etc oxygen-contained groups are introduced into material surface, especially in long-range position 40cm and 60cm. So, in long-range area polarity and hydrophilicity of the surface increase more. This can be explained that radical

reactions are intensified in long-range area. From above, it can be seen that to enhance surface hydrophilicity of PVC, long-range plasma treatment is more desirable than conventional plasma treatment. It is consistent with above surface free energy analysis.

Table2 C<sub>1s</sub> of XPS for plasma modified PVC film

Sample position	—CH <sub>n</sub>	—C—Cl —C—O	C=O	O—C=O	O <sub>1s</sub> /C <sub>1s</sub>	Cl <sub>2p</sub> /C <sub>1s</sub>
Untreated	27.4	59.1	8.0	5.5	0.508	0.081
0 cm	31.2	54.7	10.7	3.4	0.577	0.048
20cm	47.1	40.0	10.4	2.5	0.562	0.066
40cm	23.9	54.8	17.1	4.2	0.659	0.054
60cm	33.6	46.1	17.7	2.7	0.603	0.055
80cm	61.3	27.5	11.2	0	0.545	0.040

Power: 40W; treatment time: 60s; gas flux: 30 sccm..

## 5. Conclusion

Experimental results are summarized as follows:

- (1) A kinetic model of long-range oxygen plasma is developed according to one-dimensional mass continuity equation. The concentration distribution and transportation of electrons, ions and radicals in long-range plasma field can be got form the model.
- (2) Long-range plasma treatment can enhance radical reactions and inhibit electron and ion etching reactions.
- (3) Both long-range and conventional plasma can improve the hydrophilicity of PVC surface, however, the increase of oxygen-contained groups of the surface treated by long-range plasma is much higher than treated by conventional plasma. It shows that long-range plasma treatment is more effective in surface modification. Surface modification effects depend on long-range distance, discharge power, and exposure time and oxygen flux.

## 6.Reference

- [1] Kushner, M.J. J.Appl. Phys.1988, 63, 2532.
- [2] B Eliasson, M Hirth and U Kogelschatz. Ozone Synthesis from Oxygen in Dislectric Barrier Discharges. J. Appl. Phys. (20) 1987,1421.
- [3] Fongray Frank Young and Chwan-Hwa Wu. Comparisons of One- and Two-dimensional Three-moment Fluid Models for RF Glow Discharges. J.Appl.Phys. Vol74.2 (1993), 839.
- [4] Rau.H, Picht.F. Description of Microwave Discharges in Hydrogen. J. Appl. Phys. (26) 1993,1260.
- [5] Deson,J,Halous,F,Lalo,C,Rousseau.A,Veniard V. Detection of H Atoms in the Flowing Afterglow of a H<sub>2</sub> Microwave Plasma by Multiphoton Laser- induced Fluoresence: Atom-removal Kinetics. J.Appl.Phys. (27) 1994, 2320.
- [6] Goldman A, Amouroux J., Electrical Breakdown and Discharge in Gases, Macroscopic Processess and Discharge; Kunhardt, E. E., Luessen, L. H., Eds.; Plenum: New York, 1983, 293.
- [7] 陈杰榕, 低温等离子体化学及应用, 北京: 科学出版社, 2001
- [8] 张云泽, 远程等离子体及其对医用 PVC 的表面改性研究, 硕士论文, 2002, 24
- [9] Chen Jie-rong. Chem. J. Chinese of University, 1997, 18(3):466-471
- [10] Andrade J.D et al. Trans Amer Soc Artif InterOrgans, 1973, 19:1
- [11] Okano T et al. J Biomed Mater Res, 1981, 15:393

# Preparation of composites of plasma-synthesized fine ferrite particles dispersed in porous silica and its application to a new VOC treatment technique

N. Kikukawa, S. Kobayashi, M. Sugasawa, K. Kosuge, M. Takemori, and Y. Nagano

*National Institute of Advanced Industrial Science and Technology (AIST), Tsukuba 305-8569, Japan*

## Abstract

In order to develop a new VOC treatment technique suitable for small factories, we have proposed a new adsorption-desorption technique utilizing the heating effects of magnetic porous materials. Firstly, we synthesized zinc-substituted spinel-type ferrite fine particles by RF thermal plasma, secondly, we synthesized silica porous materials incorporating ferrite fine particles. The properties of magnetic fine particles and porous materials were characterized and were compared with those made by wet method.

## 1. Introduction

Control technology to prevent emission of volatile organic compounds (VOCs) is very important for environmental improvement, since VOCs such as benzene, trichloroethylene are known as hazardous air pollutants. Although there are several conventional technologies, none of them are available to small factories, because the facilities required for these technologies are too expensive and too large in scale. For example, the adsorption technique is widely used because of its relative inexpensiveness. However, since steam is usually used for recovering the adsorbate, the facility must become big and auxiliary facilities treating waste water must be necessary. Therefore, it is necessary to develop a new treatment technique suitable for small factories.

The purpose of this study is to develop a novel technique utilizing the heating effects of magnetic porous materials (that is, magnetic hysteresis energy losses) for recovering the VOCs in the exhaust gas economically.

For this end, we have been conducting following researches: (1) to develop magnetic porous materials, (2) to develop an adsorption-desorption technique for VOCs using the magnetic heating effects.

In order to prepare silica porous materials containing magnetic fine particles, we have investigated two-step synthesis, in which first we prepare zinc-substituted spinel-type ferrite fine particles by RF thermal plasma method, then we synthesize silica porous materials incorporating the magnetic fine particles. In order to investigate the feasibility of the new adsorption-desorption technique, we constructed a lab-scale high-frequency (HF, 56 kHz) magnetic field generator.

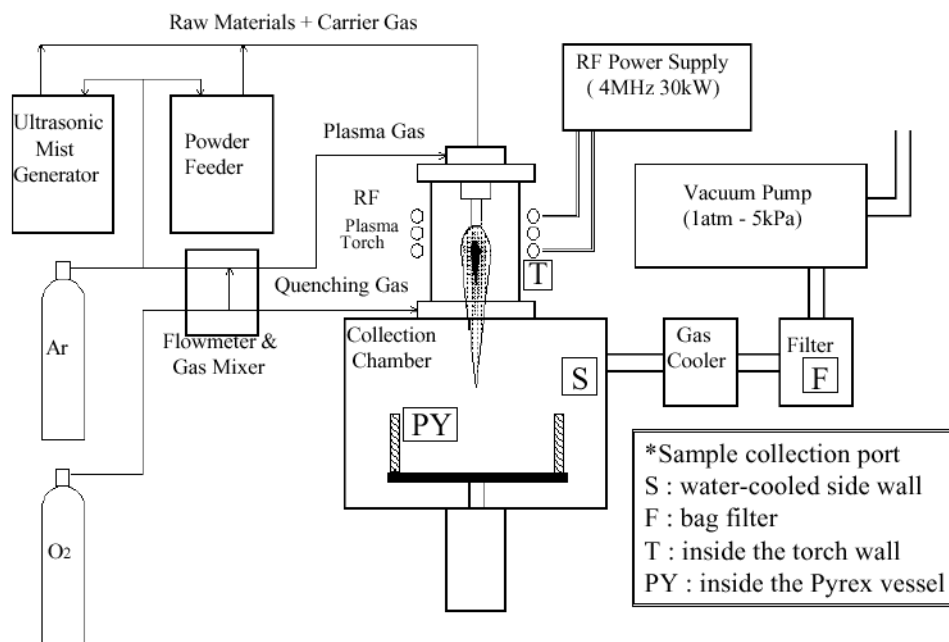


Fig.1 Schematic of the RF plasma reactor



In this paper, the properties of the synthesized magnetic porous materials are mainly described and the preliminary results about the adsorption-desorption characteristics are also presented.

## 2. Experimental

### 2.1 Magnetic Fine Particles Preparation

The magnetic fine particles must have following properties. First, they must be well crystallized, second the stoichiometry of them is important because the Curie points of spinel-type ferrites are strongly affected by the zinc contents. Moreover, the size of ferrite particles should be in the range of 10 – 100 nm through the consideration of coercive force.

We prepared well-crystallized ferrite fine particles by RF thermal plasma method using amorphous citrate gel as precursor[1]. The Citrate gel precursor was prepared as follows. Nitrates of each metal element were dissolved in an aqueous solution of citric acid containing ethylene glycol. The solution was kept at 80 °C in a rotary evaporator until the gel reaction was completed. The gel was successively heated at 110 °C for 36 h in a vacuum oven, then was pulverized to powder less than 40 µm and kept in dry until being fed to RF plasma. The RF plasma reactor (4MHz-60kW) is schematically drawn in Fig.1. The citrate gel powder was fed into Ar-O<sub>2</sub> plasma with feeding rate of 0.3-0.7 g/min. The collected powder products were characterized with XRD, TEM/EDX, VSM, etc. In addition to plasma powder, magnetite (Fe<sub>3</sub>O<sub>4</sub>) fine particles were prepared by coprecipitation method[2] for comparison.

### 2.2 Magnetic Porous Materials Preparation

Secondly, we synthesized spherical silica porous materials using a sol-gel method[3] incorporating magnetic fine particles. The silica source was tetrabutoxysilane (TBOS) and cetyltrimethylammonium bromide (CTAB) was used as structure-directed reagent. The magnetic particles, plasma-synthesized particles and wet-method magnetite particles, were suspended in an aqueous solution of CTAB and sodium hydroxide with continuous stirring. After adding TBOS, the solution was stirred at room temperature for about 16 h. Finally, thus obtained spherical precursor was calcined at 500°C in air for 12h. The produced magnetic porous materials were characterized by XRD, VSM, and BET specific surface area measurement.

### 2.3 Heating Characterization by High-Frequency Magnetic Field

The magnetic heating effects of the magnetic fine particles and the magnetic porous materials were characterized using HF generator (Daiichi Koshuha, HighHeater 4005, 56 kHz) and a magnetic coil, as shown in Fig. 2. Up to 500 Oe of alternating magnetic field was generated. The temperature of magnetic materials was measured by fluorescent-type optical fiber thermometer (Anritsu Meter, FL2000).

For the experiments of VOC adsorption-desorption, a mixed gas of benzene (100 ppm) and nitrogen was flown through the magnetic porous material with the flow rate of 1 ml/s. The concentration of benzene in the effluent gas was monitored by quadrupole mass spectrometer (MKS Instruments, Microvision Plus)

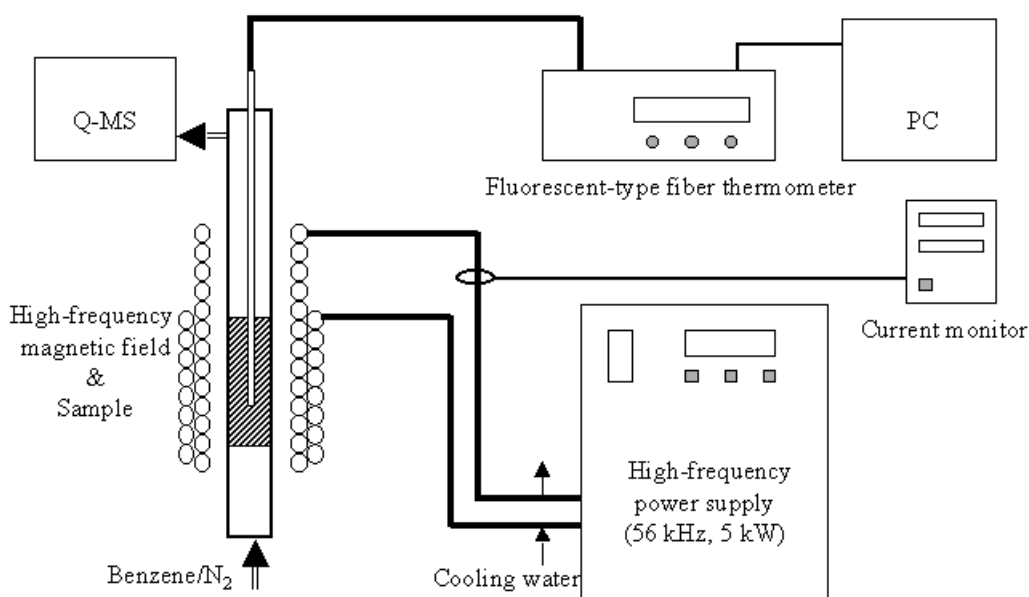


Fig.2 High-frequency magnetic field experimental apparatus.

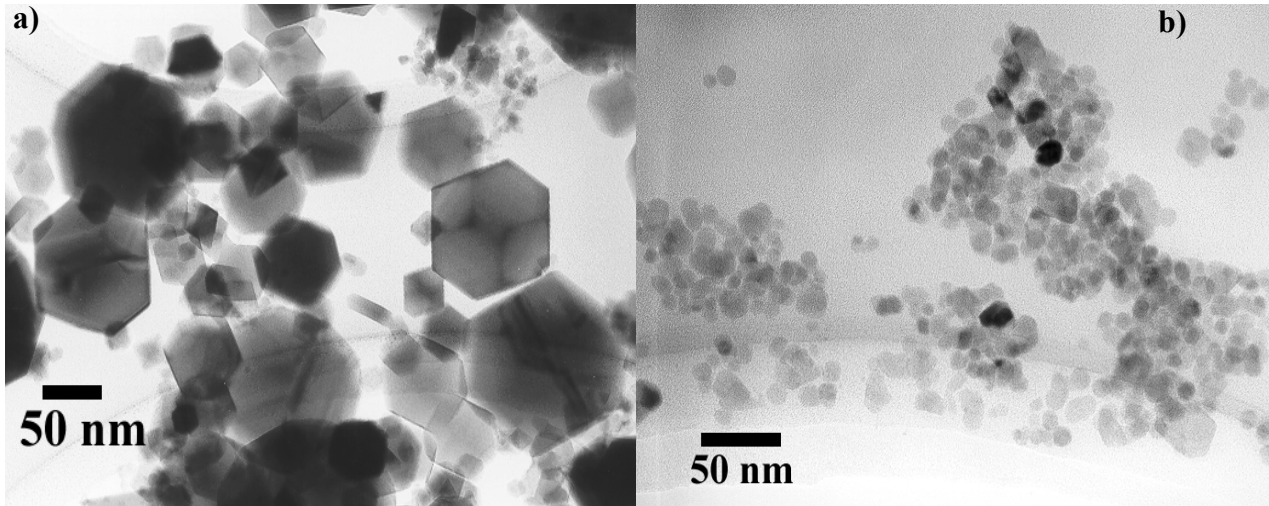


Fig. 3 TEM images of a) plasma-synthesized  $\text{Ni}_{0.5}\text{Zn}_{0.5}\text{Fe}_2\text{O}_4$ , and b)  $\text{Fe}_3\text{O}_4$  synthesized by coprecipitation method.

### 3. Results and Discussions

#### 3.1 Properties of Magnetic Fine Particles and Magnetic Porous Materials

The product powder was mono phase spinel-type ferrite. TEM image shown in Fig. 3a) indicates clear crystal habit. The average diameter was 50 nm from TEM images, while that of wet-method magnetite was about 15 nm shown in Fig. 3b). Table 1 shows some magnetic properties of plasma-synthesized ferrite particles.

The resulting porous materials containing plasma particles had following properties; BET specific surface areas ( $S_{\text{BET}}$ ) were 370 - 1300  $\text{m}^2/\text{g}$ , saturation magnetization ( $M_s$ ) ranged 5.2 - 13  $\text{emu/g}$ , and ferrite concentrations were 12 - 21  $\text{wt}\%$ . The shape of the magnetic porous materials were 0.5 - 2 mm spheres.

Figure 4 shows the  $M-H$  curve of the magnetic porous material containing plasma-synthesized  $\text{Ni}_{0.5}\text{Zn}_{0.5}\text{Fe}_2\text{O}_4$  and magnetic fluid (wet method magnetite dispersed in water). Since magnetic hysteresis heating strongly depends on the loop area of  $M-H$  curve, the value of the coercive force is important. So the produced magnetic porous materials seems to be more suitable.

The SEM image of the cross section of magnetic porous material, shown in Fig. 5a), indicates the finely distributed composite aspect of bright ferrite particles, aggregated less than  $1\mu\text{m}$ , dispersed in dark porous silica matrix. On the contrary, when incorporating coprecipitated magnetite particles for comparison, large agglomerates of magnetite were observed (Fig. 5b)). The reason is not yet clear and the factors affecting the magnetic particle dispersion are still being examined.

Table 1 Properties of plasma-synthesized ferrite fine particles.

Properties	$\text{Mn}_{0.5}\text{Zn}_{0.5}\text{Fe}_2\text{O}_4$	$\text{Cu}_{0.7}\text{Zn}_{0.3}\text{Fe}_2\text{O}_4$	$\text{Ni}_{0.5}\text{Zn}_{0.5}\text{Fe}_2\text{O}_4$
Lattice constant ( $\text{\AA}$ )	8.454	8.403	8.389
Saturation magnetization ( $\text{emu/g}$ )	40	52	62
Coercive force (Oe)	45	69	71
Residual magnetization ( $\text{emu/g}$ )	4.1	6.6	6.2
Curie point (K)	527	648	651

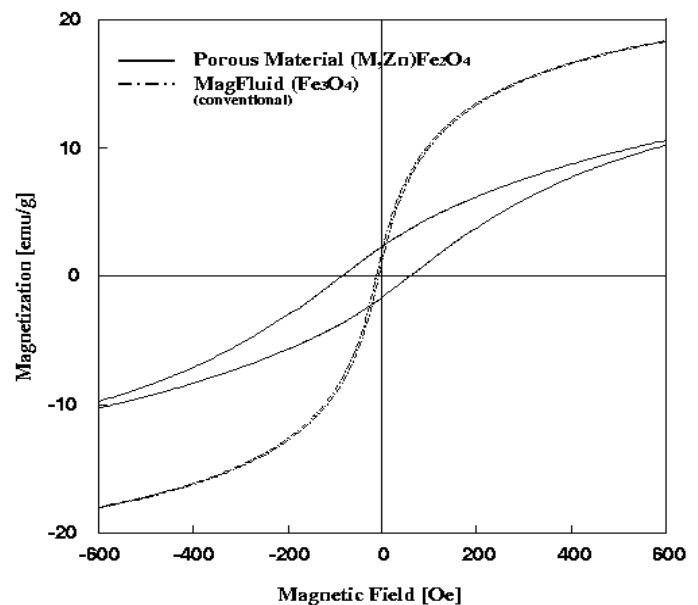


Fig. 4  $M-H$  curves of magnetic porous material and magnetic fluid by wet-method.

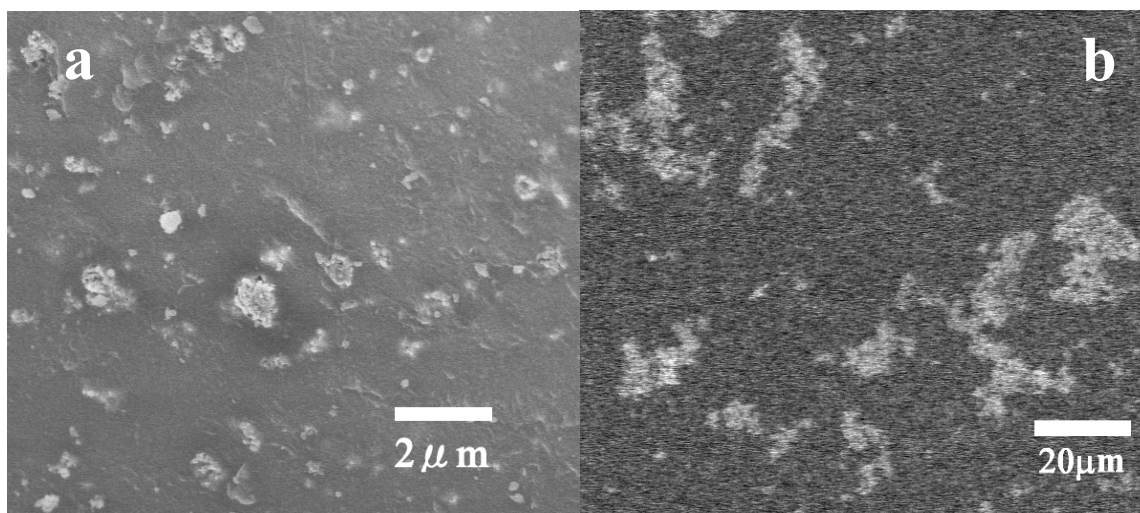


Fig. 5 SEM images of the cross section of magnetic porous material, containing a) plasma-synthesized ferrite particles ( $S_{\text{BET}}$ : 1300 m<sup>2</sup>/g,  $M_s$ : 5.2 emu/g, Coercive force( $H_c$ ): 62 Oe) and b) coprecipitated magnetite particles ( $S_{\text{BET}}$ : 550 m<sup>2</sup>/g,  $M_s$ : 14 emu/g,  $H_c$ : 11 Oe).

### 3.2 Heating Characteristics of Magnetic Fine Particles and Magnetic Porous Materials

Figure 6 shows the examples of the heating characteristics of the magnetic porous material under 56 kHz alternating magnetic fields. The magnetic porous materials rapidly reached a constant temperature below their Curie temperature. That means that the adsorbent itself has auto-regulation function and that the Curie point plays a role of "safety valve". These results strongly suggest the proposed heating method using magnetic heating effects is an excellent way of heating suitable for recovering VOCs from adsorbed porous materials.

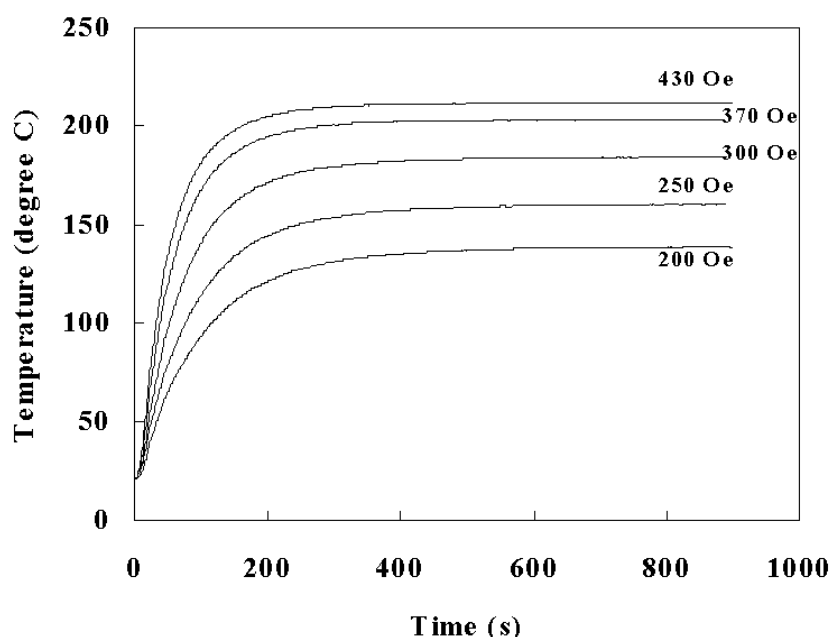


Fig. 6 Heating characteristic of magnetic porous material under 56 kHz magnetic field. ( $S_{\text{BET}}$ : 570 m<sup>2</sup>/g,  $M_s$ : 13 emu/g,  $H_c$ : 64 Oe, Curie point( $T_c$ ): 378 °C, no carrier gas)

To demonstrate the adsorption-desorption properties of proposed VOC treatment technique, we made an experiment of adsorption of diluted benzene at room temperature and desorption of adsorbed benzene. Figure 7 shows the desorption characteristics of magnetic porous materials by HF magnetic heating (solid line) and electric-furnace heating (broken line). From this figure, the adsorbate was desorbed in a shorter time and at higher concentration in the case of HF magnetic heating. Higher concentration is crucially important for VOC recovery procedure. From these results, though this work is still in its preliminary stage, we believe this technique is suitable for VOC treatment at small factories.

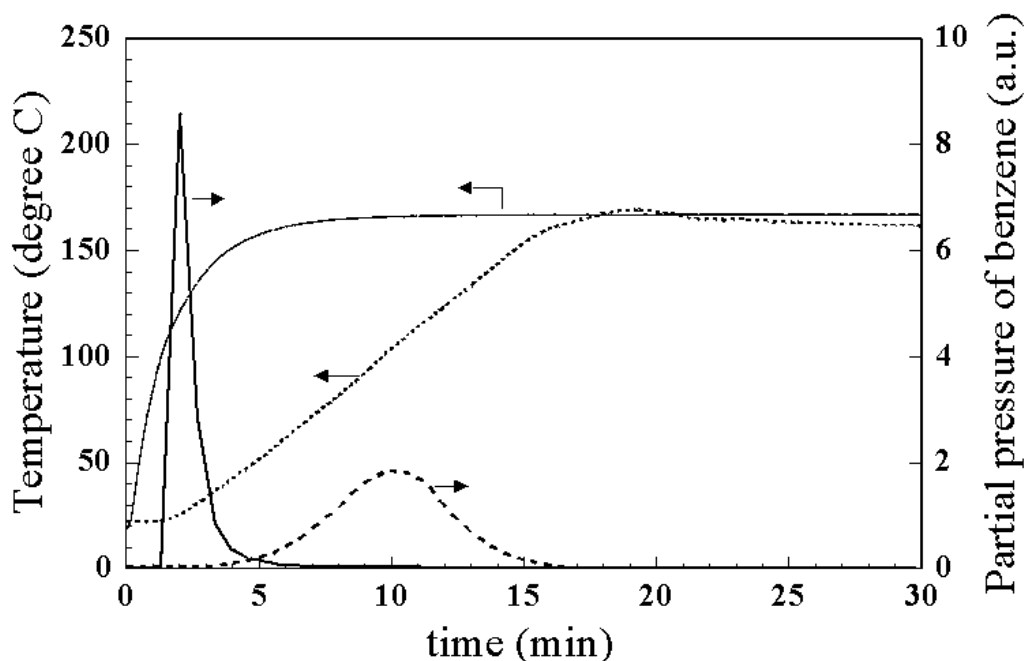


Fig. 7 Desorption characteristic of magnetic porous material heated by HF magnetic field (solid line) compared with electric-furnace heating (broken line). Same porous material as Fig.6 was used. (carrier N<sub>2</sub> flow rate: 1 ml/s, magnetic field: 470 Oe)

#### 4. Conclusion

In order to develop a new VOC treatment technique suitable for small factories, we have proposed a new adsorption-desorption technique utilizing the heating effects of magnetic porous materials. For this purpose, we conducted the experiments on magnetic fine particles and magnetic porous materials preparations and obtained following results.

Plasma powder synthesis with citrate gel precursors was found to yield well-crystallized, mono-phase zinc-substituted spinel-type ferrite particles with the average diameter of 50 nm.

The magnetic particles was found to be successfully incorporated into silica porous materials by a modified sol-gel method.

The efficient desorption characteristic through magnetic hysteresis heating was demonstrated by applying 56 kHz alternating magnetic field.

#### References

- [1] N. Kikukawa et al., *Proc ISPC-15*, 2787-2791(Orléans, 2001); *Jpn J. Appl. Phys.*, **41**, 5991(2002).
- [2] J. Shimoizaka et al., *J. Chem. Soc. Jpn.*, 1976, 1.
- [3] Q.S. Huo et al., *Chem. Mater.*, **9**, 14 (1997).

# **Carbon Nanotube Growth by Plasma Enhanced CVD**

M. Meyyappan

*NASA Ames Research Center, MS 229-3, Moffett Field, CA 94035  
Ph: 650 604 2616 Fax: 650 604 5244 email: [meyya@orbit.arc.nasa.gov](mailto:meyya@orbit.arc.nasa.gov)*

Carbon nanotubes (CNTs) exhibit extraordinary mechanical and unique electronic properties and hence have been receiving much attention in recent years for their potential in nanoelectronics, field emission devices, scanning probes, high strength composites and many more applications.

In the early years of CNT research, the primary approaches to produce nanotubes consisted of laser vaporization and arc-evaporation of graphite electrodes. More recently, catalytic decomposition of hydrocarbon or CO feedstock with the aid of supported transition metal catalysts - also known as chemical vapor deposition (CVD) – has become popular. CVD provides a simple approach to growing CNTs on patterned substrates and proceeds at temperatures below 1000° C, substantially lower than in laser ablation and carbon arc processes. More recently, low temperature plasmas have been used in growing CNTs. The conventional wisdom for plasma processing in microelectronics is that it allows preparation of thin films at substrate temperatures significantly lower than that possible with thermal CVD. Such an advantage is highly desirable in many applications that stand to lose certain characteristics of the processed substrate at elevated temperatures (for example, charring of the photoresist). This advantage of the plasma may not be realizable in CNT growth since the catalyst activity is significant only above a temperature of 550°C. Nevertheless, a plasma process is useful as it grows more vertically aligned nanotubes than thermal CVD.

We have used ion beam sputtering (IBS) for the deposition of the metal catalyst for the growth of single walled carbon nanotubes (SWNTs), multi-walled carbon nanotubes (MWNTs), and multi-walled carbon nanofibers (MWNFs). IBS allows for the deposition of the catalyst over a large area with uniform deposition and for the shadow masking or lithographic patterning of the catalyst. By controlling the catalyst formulation and the growth conditions, the type and density of the CNTs grown can be controlled. This flexibility of growth allows for the construction of a variety of different structures and applications based upon CNTs.

In this presentation, we will present our results on SWNT, MWNT, and MWNF growth using PECVD. Characterization of these structures has been performed using SEM, TEM, Raman spectroscopy, and EDX. The catalyst surface has been characterized using AFM and STM to determine the particle size. We have been able to develop an understanding of the effects of catalyst composition as well as layer thickness on the resulting structure of the CNTs. In addition, we have also conducted parametric studies varying pressure, feedstock composition, growth temperature, and applied power (in PECVD) to determine their influence on the growth characteristics.

The aim of this invited talk is to present important results on PECVD of nanotubes along with the application potential, while emphasizing the need for diagnostics and modeling.

# Treatment of fly ash model by PTA : experimental results modeling of pollutants evaporation

S. Bernard<sup>1</sup>, P. Fauchais<sup>2</sup>, J. Jarrige<sup>2</sup>, J. P. Lecompte<sup>2</sup>

<sup>1</sup> *Laboratoire d'Energétique Explosion et Structures (LEES), UPRES EA CNRS 1205,  
IUT GMP, 63, avenue de Lattre de Tassigny - 18000 Bourges - France*

<sup>2</sup> *Sciences des Procédés Céramiques et des Traitements de Surface (SPCTS), CNRS UMR 6638,  
Faculté des Sciences et Techniques de Limoges, 123, av. Albert Thomas - 87060 Limoges Cedex - France*

**Abstract :** A plasma transferred arc reactor was designed to follow on-line by ICP the evaporation of zinc chlorides and sulfates impregnated in a zeolite matrix (fly ash model). The zeolite granules were injected in a graphite crucible on which the arc, in argon atmosphere, was transferred. The modeling of the zinc evaporation by using a first order law, allowed to determine the corresponding evaporation constant  $k$  and provided a good agreement with experimental results.

## 1.Introduction

The incineration of the household refuse generates residual materials named fly ashes. After burning, the produced fumes are cleaned and specific filters relieve fly ashes. These particles are composed of a porous matrix of alumina, silica, calcia... and contain pollutants trapped in them such as heavy and volatile metals (Pb, Zn, Cd, Hg...) associated to different anions : chlorides, sulfates, and nitrates but also toxic organic molecules such as dioxin, phosgen, HAP [1]... Even if the 2002 dead line for the storage in landfills is exceeded, no other treatments are developing. However, one solution to this problem is to convert fly ashes in an inert material trapping residual pollutants in a glassy matrix while the more volatile metals are evaporated and collected by condensers, to be recycled, and the toxic organic molecules destroyed [2].

The developed process uses a transferred arc working in an atmospheric pressure plasma reactor under an argon atmosphere. The fly ashes are injected and treated in batch in a graphite crucible. During the treatment, the reactor atmosphere is analyzed, on-line, by an ICP system, which allows characterizing the different elements evaporation.

This study presents a model of kinetic evaporation phenomenon of the pollutant species (Pb, Zn, Cl, S, ...). By considering the melting bath at thermal equilibrium and the evaporation laws (experimentally determined), the time evolution of the pollutant concentration in the gaseous phase resulting from the reaction is calculated and compared to the ICP measurements.

## 2.Experimental device

The plasma reactor (Figure 1) is described in details in [3][4][5][6]. It is composed of a water-cooled controlled atmosphere chamber where a transferred arc, stabilized by an argon flow rate of 20 slm, works in an argon atmosphere slightly above room pressure. In the fly ash model no dioxin and phosgenic species have been introduced for safety reasons and assuming that such molecules are completely destroyed at  $T > 2000$  K [8][9] which is the case in plasma furnaces.

Fly ashes are introduced into the crucible during the treatment with the help of a powder feeder and driven by an alumina tube to the bath surface to be treated there. As shown in [3][4], the bath temperature is the key parameter which governs all the reaction process. This parameter is directly controlled by the arc current intensity [4].

During the sample treatment, the reactor atmosphere is analyzed on-line by an ICP system coupled to emission spectroscopy [10]. The gas sample is picked up near the plasma and driven to the RF torch ( $P=3.5$  kW and  $f=63$  MHz) by a peristaltic pump to be analyzed [5]. The calibration of the system is achieved with standard solutions of zinc and chlorine, which are nebulized by an ultrasonic set-up coupled to a desolvator and a condenser.



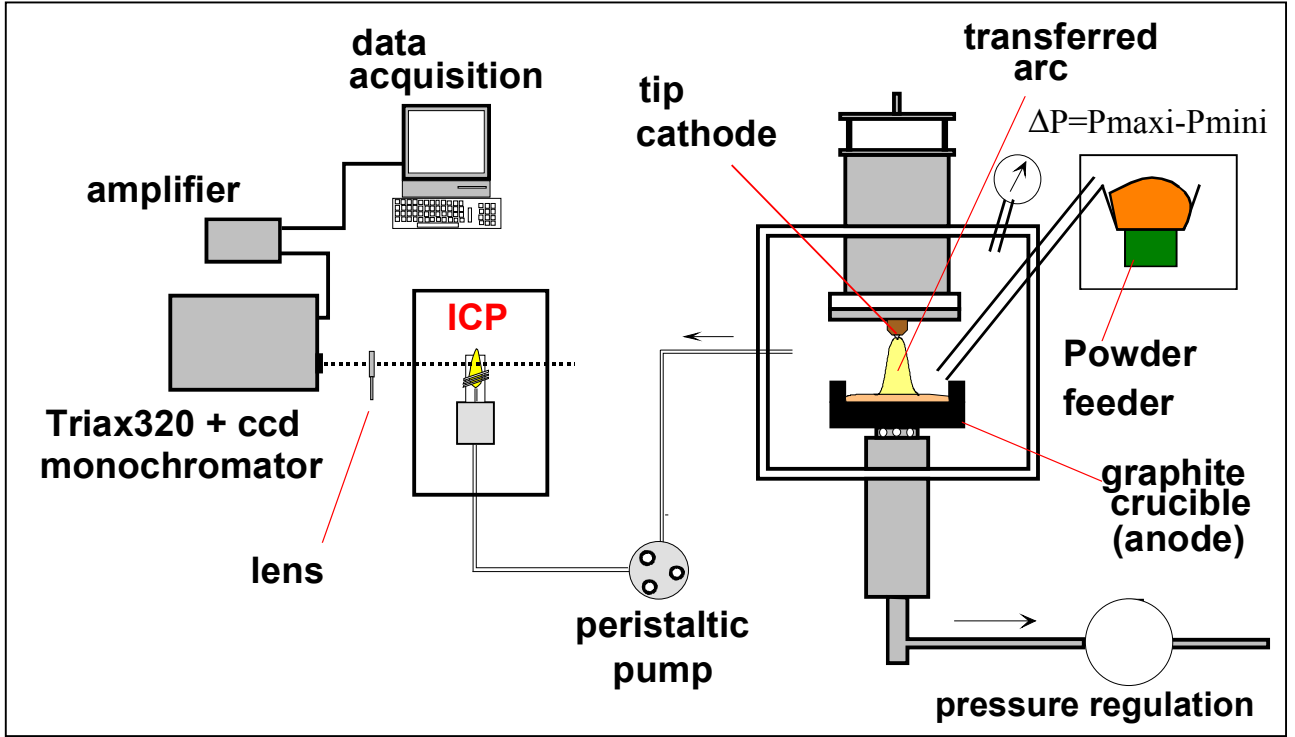


Figure 1 : Experimental device

This experimental device analysis system (ICP) allows us to follow on-line evaporation phenomena and possible synergies, but it does not allow yet the determination of the constant  $k$  (in  $s^{-1}$ ) of the evaporation law (Eqn.1) for each elements as shown in [3].

$$\ln \frac{M(t)}{m_0} = -kt \quad \text{Eqn. 1}$$

Where  $m_0$  (in kg) represent the initial mass of the element in the crucible and  $M(t)$  (in kg) describe the time evolution of the element mass present in the crucible.

The ICP signal results of the competition between two terms. The first one is a term due to the evaporation of elements coming from the molten bath and the second represents the renewing of the reactor atmosphere (due to the plasma gas flow and the vacuum pump group). One sample of the time evolution of the ICP signal is given in 2.

### 3. Modeling

By considering the dimensionsof the reaction volume of the chamber and the evaporation law determined previously, this part aims in determining a simple law to calculate the  $k$  constant by using the ICP signal.

In this first approach, the reactor is represented as a closed volume  $V_0$  ( $m^3$ ), where a flow rate  $D_0$  ( $m^3.s^{-1}$ ) of argon is injected continuously. The pressure is maintained constant slightly ( $\sim 10kPa$ ) over the room pressure by evacuating gases with a flow rate of  $D_0$ . This flow rate results from the argon plasma forming gas flow rate and the element evaporation. The atmosphere of the reactor is not instantaneously replaced and materials previously evaporated are still present in the gaseous phase few moments later.

The purpose of this section is to calculate the mass variation ( $dm$ ) of a given element in the gaseous phase. At  $t$ , the mass variation is the difference between these both sources.

$$dm = -dm_1 + dm_2 \quad \text{Eqn. 2}$$

Where  $dm_1$  is the mass pumped by vacuum group, and  $dm_2$  the mass due to the evaporation in the crucible and obtained with the evaporation law given in Eqn.1.

By assuming that  $m_1$ , the concentration at time  $t$  of the considered element, is nearly the same everywhere in the reactor, it can be defined as :

$$dm_1 = \frac{m(t)}{V_0} \cdot D_0 \cdot dt \quad \text{Eqn. 3}$$

where  $D_0$  represents the gas plasma flow rate,  $m(t)$  represent the mass of the evaporated element at  $t$  in the gaseous phase.

Thus Eqn.2 can be written as a first order differential equation where the second member is not constant and is a function of time :

$$\frac{dm}{dt} + \frac{m(t)}{V_0} D_0 = m_0 \cdot k \cdot e^{-kt} \quad \text{Eqn. 4}$$

The solution of Eqn.4 is given by Eqn.5 :

$$m(t) = m_0 \frac{V_0 \cdot k}{D_0 - k \cdot V_0} (e^{-kt} - e^{-\frac{D_0}{V_0}t}) \quad \text{Eqn. 5}$$

The determination of  $k$  is possible by calculating the tangent at the time  $t = 0$  of the ICP signal curve. This tangent  $p$  is equal to the derivative of the Eqn.5 expression for  $t = 0$ , its expression is given by Eqn.6.

$$k = \frac{V_0 \cdot p}{m_0} \quad \text{Eqn. 6}$$

This model was compared to the ICP signal obtained during the treatment of zeolites impregnated [7] with a mixture of zinc chloride and zinc sulfate.

The ICP signal represented in Figure 2 is obtained during the treatment of the zeolite matrix impregnated with a mixture of zinc sulfate and zinc chloride (5 w% Zn).

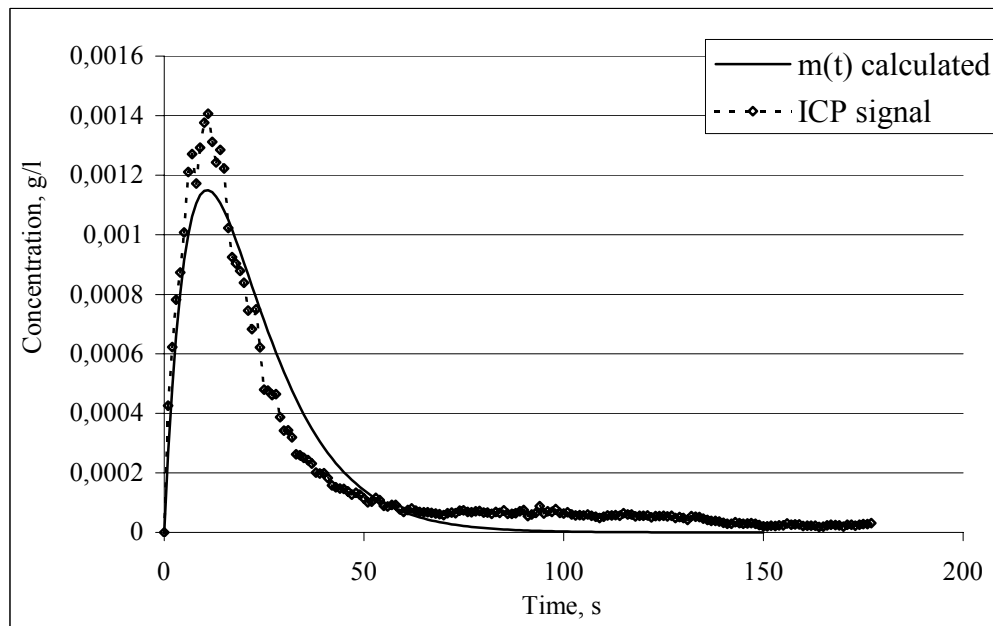


Figure 2 : Calculated and measured ICP signal in the case of impregnated zeolites with a mixture of zinc sulfate and zinc chloride,  $D_0$  is constant with time.



The contribution of the sulfate to the total mass of zinc is the same than that of the chlorine one. The treatment was realized with an arc current of 400 A. The calculation by using Eqn.6 gives :  $k = 0,0807 \text{ s}^{-1}$ . This value was used to calculate the time evolution of the zinc concentration in the gaseous phase of the reactor and compared to its measurement by ICP. These results are presented in Figure .

The determination of the constant  $k$  value by using the tangent of the ICP signal provides a good agreement between measurement at the beginning of the treatment but at the end, the model tends towards zero before the experimental curve.

This phenomenon is probably due to the assumption on the vacuum group flow rate ( $D_0$ ) which is considered as constant during the experiment. In fact  $D_0$  is composed of two parts : the first one  $D_1$  is the plasma gas flow rate and the second one  $D_2$  is due to the evaporated materials. By considering that  $D_0$  is constant the second part is neglected compared to the plasma gas flow rate which is not the case as shown in Figure .

The evolution of the vacuum group flow rate is obtained by solving the expression where  $D_0$  is solution at each time of the Eqn.6.

$$m_{ICP}(t) = m_0 \frac{V_0 \cdot k}{D_0 - k \cdot V_0} (e^{-kt} - e^{-\frac{D_0}{V_0}t}) \quad \text{Eqn. 7}$$

and  $m_{ICP}(t)$  the mass measured with the ICP.

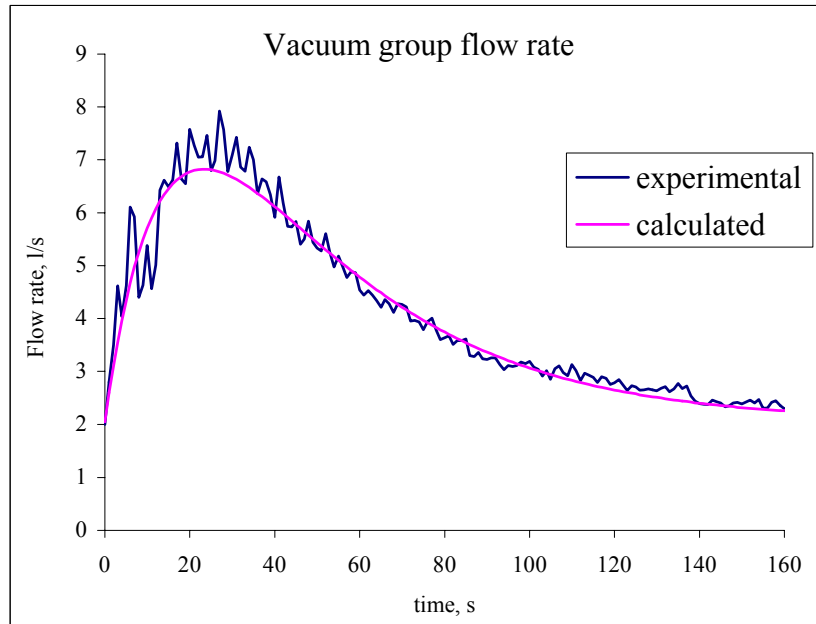


Figure 3 : Calculated and experimental vacuum group flow rate in the case of impregnated zeolites with a mixture of zinc sulfate and zinc chloride

During the experiment  $D_1$  is constant and it is  $D_2$  which varies and corresponds to the evaporation of all the elements. To represent this phenomenon it is necessary to use the same function as that used for the evaporation. This expression is given by

$$D_0(t) = A(e^{-k_1 t} - e^{-k_2 t}) + D_1 \quad \text{Eqn. 8}$$

where  $A$ ,  $k_1$  and  $k_2$  are calculated constants.

The function (Eqn.8) is represented in 3 and provide a good agreement with the vacuum group flow rate time evolution.

Thus  $D_0$  is replaced in the Eqn.5 by the expression of Eqn.8 with  $A=15.5 \text{ l.s}^{-1}$ ,  $k_1=0.027 \text{ s}^{-1}$ ,  $k_2=0.064 \text{ s}^{-1}$  and  $D_1=2.05 \text{ l.s}^{-1}$ .

The result of the calculated  $m(t)$  is given in 4 which shows that the model is in good agreement with the experimental results obtained with the ICP.

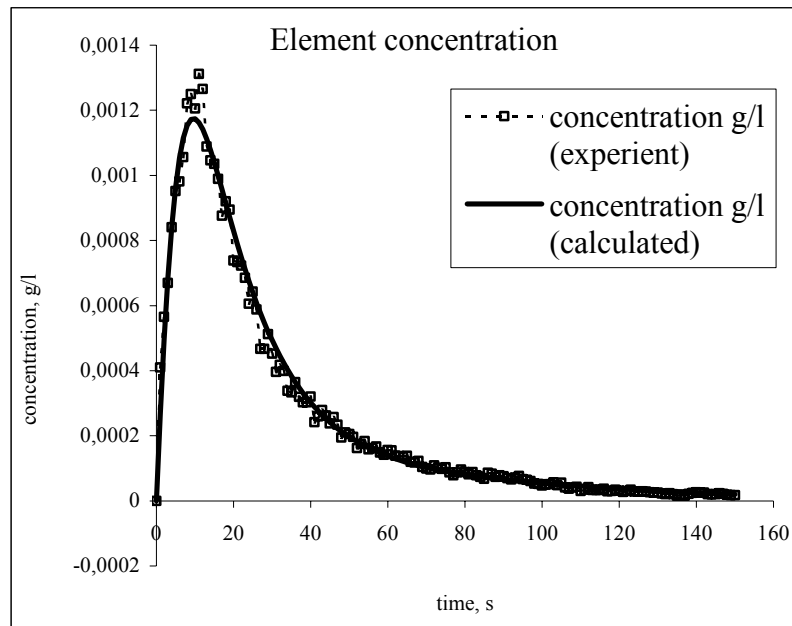


Figure 4 : Calculated and measured ICP signals in the case of impregnated zeolites with a mixture of zinc sulfate and zinc chloride,  $D_0$  is a function of time defined by Eqn.8.

#### 4. Discussion and Summary

The proposed model allows to represent the evaporation of an element in the studied plasma reactor. It allows to determine very easily the evaporation constant  $k$  and gives a realistic time evolution of the evaporation. These first calculation have to be extended to other experimental results collected with the ICP. Moreover, in our model the flow rate  $D_0$  of the vacuum group is considered to be nearly equal to the plasma gas, this assumption relying on the assumption that the volume evaporated element is negligible compared to  $D_0$ . But, due to the evaporation of chloride and sulfate, the flow rate of the vacuum group is greater than the plasma flow rate in the first steps of the treatment.

A second step would be to take into account the injection of the treated material during few minutes and not few seconds (less than 10 second) such as in this study.

The final step would be to link the applied power to the  $k$  constant, so in these conditions the process would be completely described and it would become possible to determine on-line the time treatment when the injection phase is achieved.

#### 5. References

- [1] Moo-been Chang, Yun-Tai Chang, Chemosphere, Vol 36, (9), (1998), 1959-1968.
- [2] E. Pfender, Plasma Chemistry and Plasma Processing, Vol 19, (1999), 1-31.
- [3] S. Bernard, P. Fauchais, J. Jarrige, J. P. Lecompte, Journal of High Temperature and Material Processes, vol 5, n°2, (2001), p 183-197.
- [4] S. Bernard, P. Fauchais, J. Jarrige, J. P. Lecompte, Journal of High Temperature and Material Processes, vol 5, n°2, (2001), p 199-217.
- [5] S. Bernard, M. EL Ganaoui, P. Fauchais, J. Jarrige, J. P. Lecompte, Progress in Plasma Processing of Materials 2001, (ed.) P. Fauchais, J. Amouroux, M.F. Elchinger (Pub.) Begell House NY, (2001), 662-672.
- [6] S. Bernard, P. Fauchais, J. Jarrige, J.P. Lecompte, P. Denoirjean, In the Proceedings of Heat and Mass Transfert under Plasma Conditions, (Ed.) P. Fauchais, (Pub.) Begell House NY, (2000), 164-173.
- [7] S. Bernard., F. Petit, P. Fauchais, J. Jarrige, J.P. Lecompte, Progress in Plasma Processing of Materials 1999, (ed.) P. Fauchais, (Pub.) Begell House NY, (1999), 709-718.

- [8] A. B. Murphy, Plasma destruction of gaseous and liquids wastes, In Heat and Mass Transfert under Plasma Condition (Ed.) P. Fauchais, (Pub.) Annals of the New York Academy of Science, (2000), 106-123.
- [9] S. BERNARD, Contribution to the study of the treatment by a transferred arc plasma reactor of fly ashes (REFIOM), Study of the evaporation synergies, (in French), Ph. D. thesis of the Univ. of Limoges, France, (2000).
- [10] Trassy C. R. and Diemiaszonek, Journal of Analytical Atomic Spectrometry, Vol 10, (1995), 661-669.

### 3-Dimensional Transition Map of Flattening Behavior in Thermal Spray Process

M. Fukumoto, M. Shiiba, H. Kaji and T. Yasui

*Department of Production Systems Engineering, Toyohashi University of Technology, Toyohashi, Japan*

As a flattening behavior of thermal sprayed particle impinged onto the flat substrate surface can be recognized as a fundamental phenomenon of the coating formation of the thermal spray process, a clarification of the flattening behavior of an individual particle is essential. Theoretical models, such as Madjeski's equation [1], indicate that both in-flight temperature and velocity of the particle are the dominating factors in the flattening of the sprayed particles, and thus for controlling the thermal spray process. However, we have pointed out in our previous reports that the particle/substrate interface related factors, such as the substrate temperature, affect more significantly the flattening behavior of the sprayed particles. Especially, our experimental results has revealed that a splat shape of most metallic and ceramic material onto a flat substrate surface has a transitional changing tendency from a distorted with splash to a lenticular without splash at a narrow temperature range with an increase of the substrate temperature [2-3]. The transition temperature,  $T_t$ , at which the particle's splat pattern change to the form without splashing from the one with splashing was defined and introduced by the authors [4]. The drastic change in the splat pattern nearby the transition temperature has become of the great concern in recent years. Moreover, we have pointed out that the changing tendency in the splat morphology with substrate temperature increasing corresponds quite well to that in the adhesion strength of the coating [5].

On the other hand, our experiments have also revealed that the transition behaviour from the splash splat to the disk one can be recognized in the low pressure plasma spraying by reducing the chamber pressure [6]. The transition pressure,  $P_t$ , at which the particle's splat pattern change to the disk type from the splash type was also defined and introduced by the authors. From the fact that the dependence of  $T_t$  and  $P_t$  on the particle material has a similar tendency, it is indicated that both substrate temperature and chamber pressure have an equivalent effect on the transition. The dependence of fraction of disk splat both on the substrate temperature and chamber pressure may be summarized schematically as **Fig. 1**. By selecting the moderate operating conditions in both factors in the thermal spraying, we can controll the coating structure and some other properties. Based on the experimental, analytical or numerical data, unified explanation has been tried to be made on the transition behavior. As the most possible domination, the role of solidification [7], wetting [2-3], and desorption of the adsorbates [8] on the flattening has been mainly investigated. The feasibility of each domination for the transition behavior in the flattening will be discussed.

[1] J.Madejski, Int. J. Heat and Mass Transfer, **19**, 1009(1976)

[2] Y. Tanaka and M. Fukumoto, Surface and Coatings Technology, **120-121**, 124 (1999)

[3] M. Fukumoto, Y. Huang, M. Ohwatari, Thermal Spray, Meeting the Challenges of the 21<sup>st</sup> Century, edited by C. Coddet, ASM International, **1**, 401 (1998)

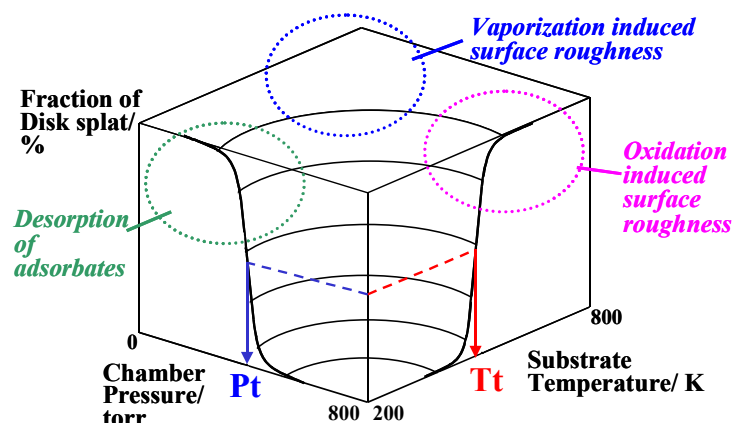
[4] M. Fukumoto, S. Katoh, I. Okane, Proc. of 14<sup>th</sup> ITSC, **1**, 353(1995)

[5] M. Fukumoto, H. Hayashi, T. Yokoyama, J. Japan Thermal Spray Society, **32-3**, 149 (1995)

[6] M. Fukumoto, H. Kaji, M. Shiiba, T. Yasui, Proc. Annl. Meeting of JTSS, **1**, 49(2002)

[7] M. P-Fard, V. Pershin, S. Chandra, J. Mostaghimi, JTST, **11(2)**, 206(2002)

[8] X. Jiang, Y. Wang, H. Herman, S. Sampath, Thin Solid Films, **385-1**, 132(2001)



**Fig. 1** 3-D Transition Map in

# Ozone generation in negative corona discharge fed by mixtures of nitrous oxide with oxygen and air

J. D. Skalný<sup>1</sup>, S. Matejčík<sup>1</sup>, B. Gulejová<sup>1</sup>, N. J. Mason<sup>2</sup> and S. Eden<sup>2</sup>

<sup>1</sup>*Department of Plasma Physics, Comenius University Bratislava, Bratislava, Slovakia*

<sup>2</sup>*Department of Physics and Astronomy, University College London, London, United Kingdom*

## Abstract

The ozone generation in the negative corona discharge between coaxial cylindrical electrodes has been experimentally investigated in flowing mixtures of N<sub>2</sub>O + O<sub>2</sub> and N<sub>2</sub>O + air at a constant flow velocity of 1 cm.s<sup>-1</sup> and an ambient temperature. The rate of the ozone generation and the saturated ozone concentration were considerably reduced with an increasing content of nitrous oxide both in oxygen and air. Such changes were accompanied with a considerable decrease in a mean discharge current at a constant voltage applied on electrodes.

## 1. Introduction

The effect of chemical compounds on ozone formation has been investigated recently in a negative corona discharge fed by mixtures of oxygen with several chemicals [1, 2]. In CO<sub>2</sub> + O<sub>2</sub> mixtures the higher experimentally measured values of ozone concentration at a constant input power density were detected than those predicted by Vasiljev-Eremin formula [1]. Even in pure CO<sub>2</sub> gas the saturated ozone concentration was hundreds of ppm. Ozone was produced due to the electron impact dissociation of carbon dioxide molecules followed by associative process forming molecular oxygen. The analogous effects can be expected when a tree-atomic N<sub>2</sub>O gas containing oxygen in molecule is mixed with oxygen and treated in the negative corona discharge. A linear structure and a biogenic character are typical for both of molecules, which influence the infrared absorption in the Earth atmosphere. It must be noted however that there are remarkable differences between CO<sub>2</sub> and N<sub>2</sub>O molecules as regards of interactions with low energy electrons typical for the drift region of negative corona discharge. The dissociative electron attachment to carbon dioxide exhibits its maximum at relatively high electron energies (around 4 eV) [3]. Hence the process is confined only to glow region. In contrast to this two clearly resolved features were observed in the O<sup>-</sup> yield in N<sub>2</sub>O with peak energies 0.55 and 2.4 eV [4]. Therefore one could expect a remarkable differences in electrical parameters of the negative corona discharge in these two gases.

In the present study an effect of N<sub>2</sub>O admixture in oxygen and dry air on the process of ozone formation by negative corona discharge has been investigated experimentally. Moreover the electrical parameters of the negative corona discharge in pure N<sub>2</sub>O and its mixtures with oxygen and air were measured.

## 2. Experimental apparatus and diagnostics

The experiments have been carried out at atmospheric pressure and ambient temperature by using experimental apparatus schematically shown in Fig. 1. The system of stainless steel coaxial electrodes, an inner wire electrode of 125 µm and an outer cylindrical electrode of 15-mm diameter, was used in experiments. The active length of electrodes was of 100 mm. The experiments were performed at a constant flow rate of the gaseous mixture (100 cm<sup>3</sup> per minute), which corresponds to the transport velocity of approx. 1 cm.s<sup>-1</sup>. Hence the retention time of gas in the active zone of the discharge reactor was of 10 seconds. The ozone concentration in gas mixture was measured at the outlet of the reactor by FTIR spectrometer Vector Brucker. The spectrometer was also used for a detection of eventual other expected chemical product, especially nitrogen oxides in higher oxidation steps. In the case of pure N<sub>2</sub>O the gas after treatment was also analysed by UV spectrometer SPECORD. The dependence of ozone concentration on input energy density, so called Becker parameter  $\eta$ , was measured for each gas mixture. The Becker parameter was calculated by the formula

$$\eta = \frac{U \cdot I}{Q} \quad (1)$$

where U is the voltage on the electrodes, I is the total mean discharge current and Q is the flow rate.

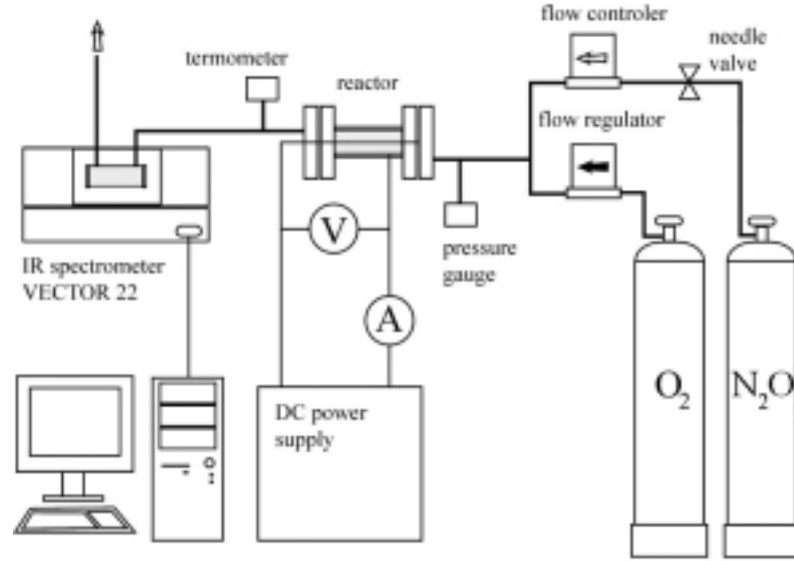


Fig. 1 Schema of experimental apparatus

### 3. Experimental results and discussion.

#### 3.1. Discharge parameters

The onset voltage of corona discharge was found to be at  $4.2 \pm 0.05$  kV in air and  $4.35 \pm 0.05$  kV in pure oxygen respectively. With increasing content of  $N_2O$  the onset voltage was slightly increased in both mixtures. The value  $4.85 \pm 0.05$  kV was detected in pure nitrous oxide. The flow speed of the mixture did not shown any remarkable effect on the onset voltage.

The dependence of mean discharge current per one cm length of the outer electrode  $I_a$  on voltage  $U$  (current voltage characteristics) shown in Fig. 2 and 3 followed the well-known quadratic dependence of the current on the voltage applied on electrodes.

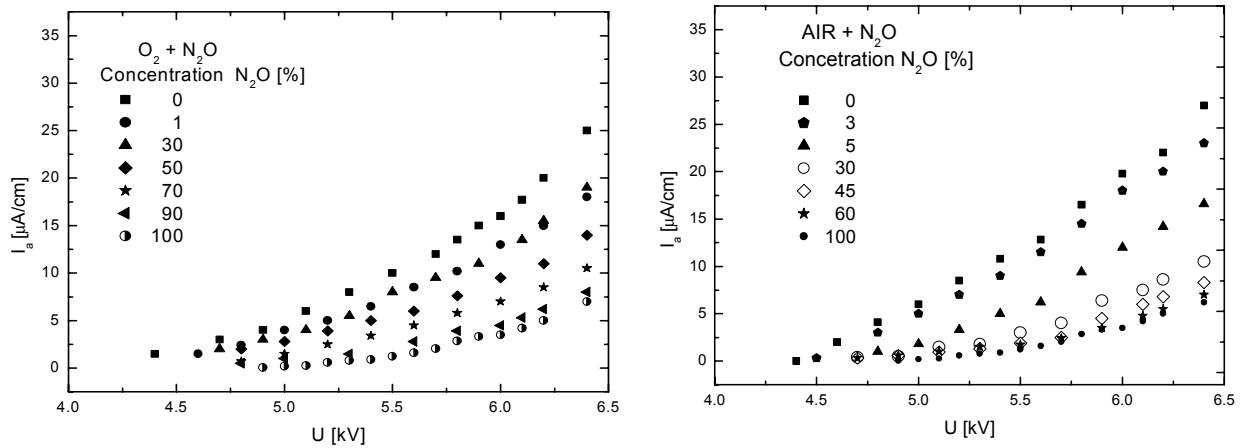


Fig. 3 Current-voltage characteristics in mixtures of air with nitrous oxide

The Townsend formula for the CV characteristic was used to calculate the average mobility of negatively charged particles in the drift region of the negative corona discharge in pure nitrous oxide and its mixtures with oxygen and/or air [5]. The results are shown in Fig. 4.

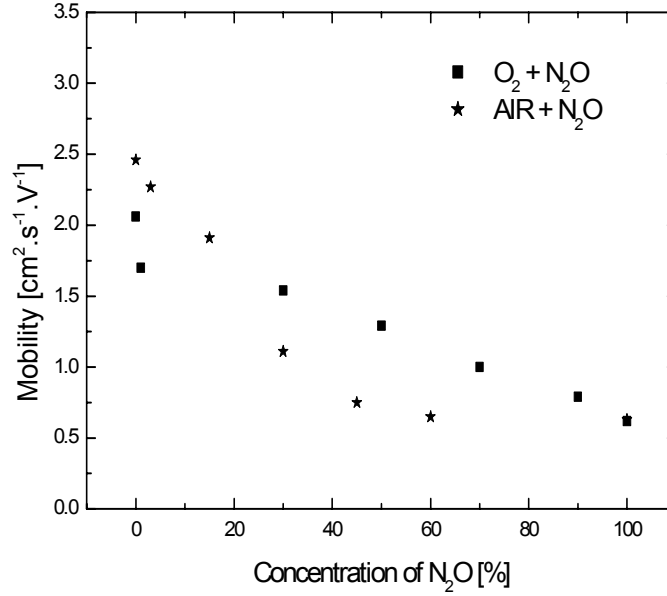
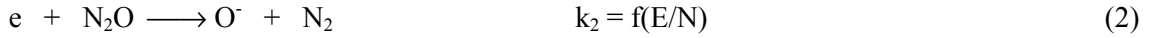
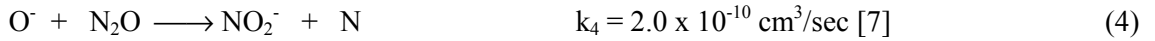
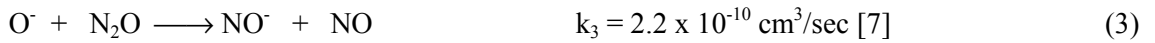


Fig. 4 Calculated average mobility of charge carriers in mixtures of oxygen and air with nitrous oxide

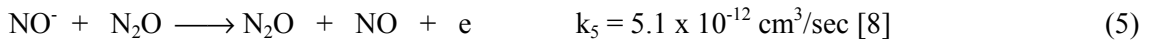
The value of the average mobility calculated from the CV characteristics of negative corona discharge in pure nitrous oxide ( $0.62 \text{ cm}^2 \cdot \text{V}^{-1} \cdot \text{s}^{-1}$ ) is remarkably below the value corresponding to the ion  $\text{O}^-$  generated in the discharge gap. The ions  $\text{O}^-$  are formed via dissociative electron attachment [4]



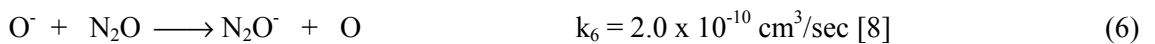
The mobility of  $\text{O}^-$  ions should be  $4.7 \text{ cm}^2 \cdot \text{V}^{-1} \cdot \text{s}^{-1}$  at the boundary between glow and drift region and  $3.2 \text{ cm}^2 \cdot \text{V}^{-1} \cdot \text{s}^{-1}$  at a surface of the outer cylindrical electrode [6]. The process (2) is effective practically in the whole discharge gap because the maximum in the electron attachment cross section is reached at energies 0.55 and 2.4 eV [4]. In pure nitrous oxide the ions  $\text{O}^-$  can undergo fast ion-molecule reactions producing either  $\text{NO}^-$  or  $\text{NO}_2^-$  ions



The ions  $\text{NO}^-$  are not stable because undergo fairly fast detachment process

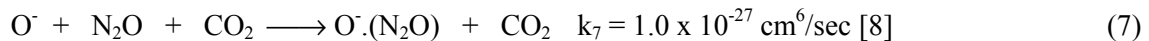


Thus the lifetime of  $\text{NO}^-$  ions at atmospherical pressure in  $\text{N}_2\text{O}$  is of order of 10 nsec. Hence the ions  $\text{NO}_2^-$  should be the dominant ions in the drift region of the discharge. If the energy of  $\text{O}^-$  ions is above of 1 eV the formation of  $\text{N}_2\text{O}^-$  ions is possible via charge transfer process



but this is not the case of corona discharge. The mobility of  $\text{NO}_2^-$  ions at nearly zero electric field and ambient temperature 300 K is  $2.55 \text{ cm}^2 \cdot \text{V}^{-1} \cdot \text{s}^{-1}$  [9]. The low values of experimentally found mobility of charge carriers in the drift region of negative corona discharge fed by nitrous oxide are remarkably below this value. The lower values of mobility can be explained by a formation of clusters  $\text{O}^-(\text{N}_2\text{O})_n$  [10]. The statement is based on an existence of the permanent dipole moment of  $\text{N}_2\text{O}$  molecule to be equal to 0.167 D.

Therefore relatively stable clusters can be most likely formed not only in the drift region of the discharge but also in the glow region. There is a lack of data on the production of such clusters. Only the three body generation process of the first of them  $O^-(N_2O)$  is referred in the book of data for ion-molecule reactions [8]



The rate of the process (7) is larger by two orders of magnitude than the process (3) and (4). It must be noted that the process (7) is even more effective than the generation of  $CO_3^-$  ions via

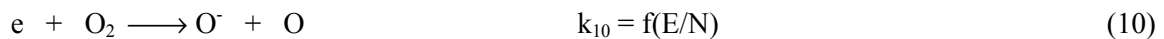


what is probably due to absence of permanent dipole moment in the case of  $CO_2$ . It can be easily presumed that the formation of clusters  $O^-(N_2O)_n$  with  $n > 1$  is most likely active too. There are no data on a mobility of  $O^-(N_2O)_n$  clusters but one can easily surmise that this must be smaller than the mobility of parent  $O^-$  ions.

The addition of nitrous oxide into the pure oxygen and air leads to decrease in the discharge current at the constant voltage on electrodes. Hence the average mobility of charge carriers is decreasing. The discharge in oxygen is more sensitive to the presence of nitrous oxide than in air (Fig. 2 and 3). The drop in current caused by addition of only one percent of nitrous oxide is dramatic. The further increase in  $N_2O$  content in the mixture up to 30% does not considerably effect the current. For higher concentrations the current decreases continuously. The extremely high rate constant of process (7) can explain observed phenomena. In pure oxygen ions  $O^-$  are predominately converted to  $O_3^-$  ions [6] by associative process



If the concentration of nitrous oxide in the mixture with oxygen is approaching  $\approx 1\%$  the rate of processes (7) and (9) is comparable and the formation of  $O^-(N_2O)_n$  clusters prevails. The reactions of minor ions  $O_2^-$  and  $O_4^-$  do not play an important role. The ion-molecule reactions of those ions lead to the formation of stable  $NO_3^-$  ion, which however can easily form clusters with  $N_2O$  molecules. At low concentration of nitrous oxide in oxygen the primary source of  $O^-$  is the dissociative electron attachment to oxygen molecules

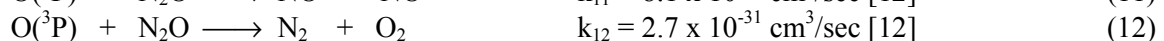
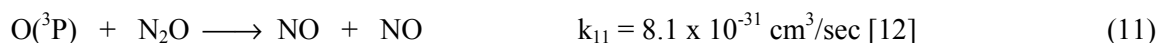


but with increasing content of nitrous oxide in the mixture the process (2) starts to be dominant. Because the rate constant of (2) is higher than that of process (10), especially at low electron energy of [11], the number of free electrons in the discharge gap is reduced effectively with increasing concentration of nitrous oxide. That is why the values of calculated mobility are decreasing with increasing content of  $N_2O$  in mixture.

The situation in air is rather different because of high efficiency of process (8). This is most likely the reason why the current of negative corona in air was not so sensitive to the addition of the nitrous oxide.

### 3.2. Ozone production

The results are summarised in Fig.5 a, b and 6. It must be noted however that contrary to pure carbon dioxide the formation of ozone in pure nitrous oxide was not observed. Both in air and oxygen mixtures with  $N_2O$  the rate of ozone concentration and the value of ozone concentration were affected by concentration of nitrous oxide. The increase in  $N_2O$  concentration caused the considerable reduction in ozone concentration. When the  $N_2O$  concentration reached a critical value (70 % in oxygen and 40% in air), the ozone concentration was found being below the threshold sensitivity of diagnostic used for determination of the ozone concentration (2 ppm). The obtained dependencies, in air +  $N_2O$  within whole range of used concentration and  $O_2 + N_2O$  up to 45 %, can be fairly well fitted by Vasiljev-Eremin formula [1] It is evident that processes





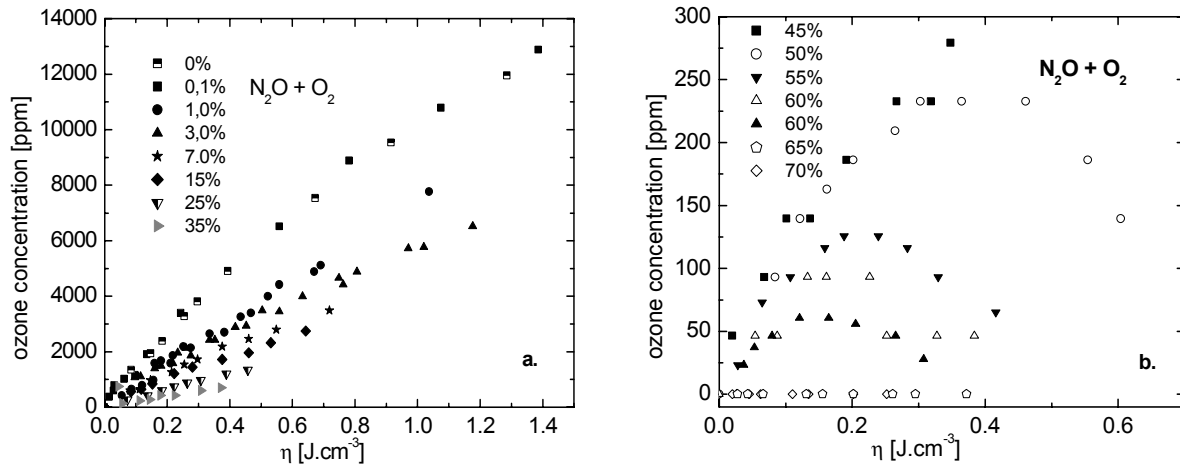


Fig. 5a. and 5b. Dependence of ozone concentration on mean input energy density in mixtures  $O_2 + N_2O$

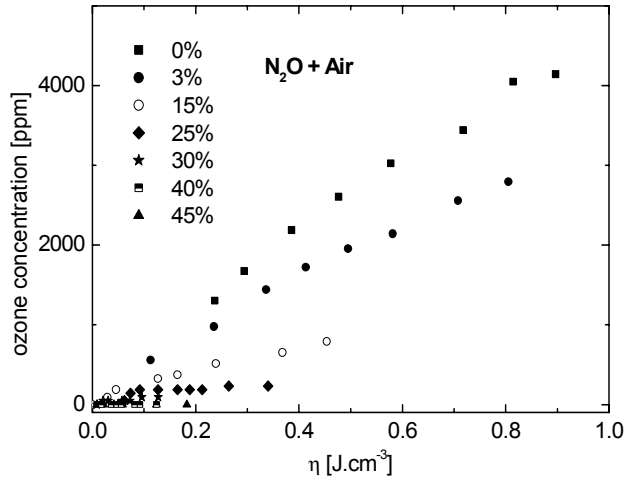
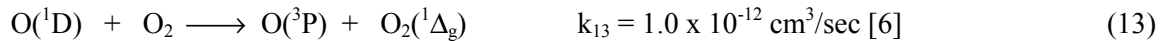


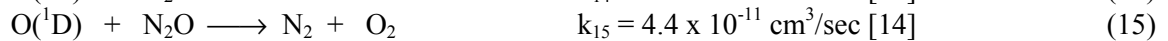
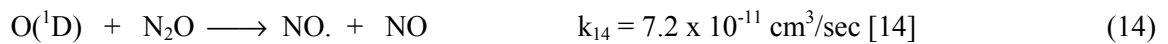
Fig. 6 Dependence of ozone concentration on mean input energy density in mixtures air +  $N_2O$

can hardly explain observed effect because the rate constants for mentioned processes are extremely low. Therefore the oxygen atoms produced by a direct dissociation of molecular oxygen in ground stage  $O(^3P)$  predominately form ozone molecules. Contrary to the low reaction activity of atomic oxygen in the ground stage the atoms  $O(^1D)$  can react with nitrous oxide very effectively. It must be noted that at conditions typical for the glow region of negative corona discharge in oxygen ( $E/N > 100$  Td) the process of electron impact dissociation of oxygen generating excited atoms of oxygen is faster than process leading to  $O(^3P)$  production. The rate constant corresponding to this is twice of that producing oxygen atom in ground stage [6].

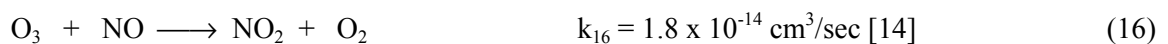
Therefore practically 90% of oxygen atoms is generated in  $O(^1D)$  stage [13]. In pure oxygen they are quenched in collisions with oxygen molecules



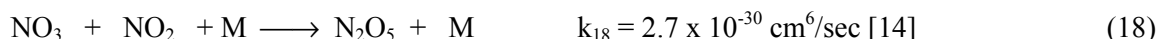
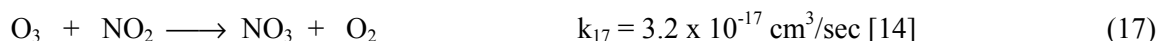
The rate constants for processes (14) and (15) are fairly high



Therefore at concentrations of  $N_2O$  higher than one percent a considerable part of oxygen atoms is consumed in processes (14) and (15) what is most likely the primary reason for the experimentally observed decrease in the ozone concentration. The secondary effects can be contributed to reaction of NO oxide with ozone. It is well known that NO oxide is effective scavenger of ozone molecules via process

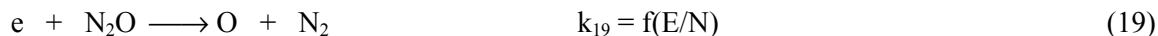


This is followed by a step reaction schema



$\text{N}_2\text{O}_5$  is a typical gaseous product observed at generation of ozone by ozonizers fed by air.

Moreover the excited nitrogen molecules, which are generated by direct electron impact dissociation of nitrous oxide



can be active in decomposition of ozone. The most probable is the process leading to formation of  $\text{N}_2(\text{A}^3\Sigma_u^+)$  [15]. Unfortunately there is a lack of data both for the cross section data for the process (19) [16] and the reactions of excited nitrogen molecules with ozone required for a quantitative analysis. The idea about the active role of excited molecules of nitrogen in destroying of ozone molecules is supported by the fact that the inhibition effect of  $\text{N}_2\text{O}$  admixture was more pronounced in mixtures with air.

#### 4. Conclusions

The admixture of nitrous oxide significantly inhibits the production of ozone if this is added into oxygen or air although there is not known any direct chemical reaction of  $\text{N}_2\text{O}$  with ozone. The concentration of produced ozone was below its detectable limit when 40 % or 70 % of  $\text{N}_2\text{O}$  was added into air or oxygen respectively. The reactions of excited  $\text{O}(^1\text{D})$  atoms with nitrous oxide is most likely are responsible for reduction in ozone production. The decrease in discharge current caused by  $\text{N}_2\text{O}$  admixture is explained by formation of  $\text{O}^-(\text{N}_2\text{O})_n$  clusters.

#### 5. Acknowledgements

The authors are pleased to acknowledge the financial assistance of Slovak Grant Agency under the project 1/765920, the UK EPSRC (Grant GM/98944) and European Commission Brussels.

#### 5. References

- [1] J.S. Skalny, T. Mikoviny, N.J. Mason, V. Sobek, *Ozone Sci. & Engineering* **23** 29 (2002).
- [2] J.D. Skalny, N.J. Mason, *Ozone Sci. & Engineering* **23** 329 (2002).
- [3] P. Cicman, G. Senn, G. Denifl, D. Muigg, J.D. Skalny, P. Lukac, A. Stamatovic, T.D. Märk, *Czech. J. Phys.* **48** 1135 (1998).
- [4] F. Brüning, S. Matejcik, E. Illenberger, Y. Chu, G. Senn, D. Muigg, G. Denifl, T.D. Märk, *Chem. Phys. Lett.* **292** 177 (1998).
- [5] L.B. Loeb, *Electrical Coronas* (Berkeley, CA: University of California Press) (1965).
- [6] B. Eliasson, *Electrical discharge in oxygen, Part 1: Basic data, rate coefficients and cross sections*, Forschungsbericht KLR 83-40 C, (Brown Boveri, Baden, Switzerland) (1985).
- [7] D.L. Albritton, *Atom. Data and Nuclear Data Tab.* **22** 1 (1978).
- [8] L.I. Virin, R.V. Dyagaspanyan, G.V. Karatchevsev, V.K. Potapov, V.L. Talrose, *Ion-molekularnyie reakcii v gazach*, (Isdatelstvo NAUKA, Moscow ) (1978).
- [9] M.D. Perkins, F.L. Eisele, E.W. McDaniel, *74* 4206 (1981).
- [10] G. Hanel, T. Fiegele, A. Stamatovic, T.D. Märk, *Int. J. Mass Spectrom.* **205** 65 (2001).
- [11] L.G. Lee, F. Li, *J. Appl. Phys.* **56** 3169 (1984).
- [12] F.E. Niles, *J. Chem. Phys.* **52** 408 (1970).
- [13] B.M. Penetrante, H.C. Hsiao, J.N. Bardsley, B.T. Meritt, G.E. Vogtlin, A. Kuthi, C.P. Burkhardt, J.R. Bayless, *Plasma Source Sci. and Technol.* **6** 251 (1997).
- [14] R. Atkinson, D.L. Baulch, R.F. Hampson, J.A. Kerr, M. J. Rossi, T. Troe, *J. Phys. Chem. Ref. Data* **26** 521 (1997).
- [15] S.M. Barnett, N.J. Mason, W.R. Newell, *Chem. Phys.* **153** 283 (1991).
- [16] A. Zecca, G.P. Karwasz, R.S. Brusa, T. Wroblewski, *Int. J. Mass Spectrom.* **223-224** 205 (2003).

# **Plasma methods for technology of pesticide treatment in a triple torchs electric-arc reactor**

A. L.Mosse, A.V. Gorbunov, E. M. Ermolaeva.

*Institute of Heat and Mass Transfer, National Academy of Sciences of Belarus,  
P.Brovka str. 15, 220072 Minsk, Belarus, Fax: +375-172-322513  
E-mail: [mosse@itmo.by](mailto:mosse@itmo.by)*

Alternative to conventional low-temperature methods of toxic wastes incineration is their destruction in thermal plasma, which takes place at high temperatures. Using electric arc and other plasma methods of delivering temperature of the order of 5000 K, makes possible to destruct organic and unorganic compounds with high efficiency even without oxygen. The other merit is possibility of good mixing in plasmochemical reactor, this is the important factor of wastes thermal processing. This process can be realized in the multi-jet plasma reactor which provides good mixing of plasma with treated waste particles.

Continue experimental study of thermal plasma neutralization of some of pesticides with a expired term of validity was carried out in the triple torchs plasma reactor . Except pesticides – isophene and concentrate of butyl ether of 2,4 – dichlorphenoacetic acid investigations are also metaldehyde and pentatiuram.

Different physical-chemical methods were used for analysis of products of waste processing products. The detailed analysis of gases at the outlet of plasma reactor was carried. The automatical spectral complex and the methods of chromato- mass-spectrometry and absorption spectroscopy in ultraviolet (UVR), visible and infrared (IR) wavelength range are used. The detailed analysis of condensed phase at the outlet of plasma reactor included of element chemical analysis and micro X-ray spectral analysis.

It was shown that plasma process provides effective destruction of toxic wastes and is an environmental pure technology.

# SYNTHESIS OF NANO-DISPERSED POWDERS OF ALUMINUM OXIDE FROM SOLUTIONS IN PLASMA REACTOR

A.L.Mosse, A.V. Gorbunov, E M. Ermolaeva

*Institute of Heat and Mass Transfer, National Academy of Sciences of Belarus,  
P.Brovka str. 15, 220072 Minsk, Belarus, Fax: +375-172-322513  
E-mail: [mosse@itmo.by](mailto:mosse@itmo.by)*

Thermal dissociation of salts is one of the most common methods of obtaining dispersed oxides of metals. Traditional industrial technology usually includes the stages of settling salt from solution, its filtration, washing, drying, calcination, i.e the technology is multistage and demands bulky equipment. Intensification of processes is possible by heating dispersed solutions with streams of hot burning gases or by heating in furnaces. However, utilization of low-temperature (thermal) plasma for obtaining oxides of metals from salts, solutions or suspensions is most promising technology. Utilization of plasma heat carriers with initial averaged-mass temperature 4000-6000K, permits implementation of processes with the deeper degree of physical and chemistry transformations of basic raw material, up to vaporization and sublimation of resultant oxides of metals. Furthermore, obtaining of nano-dimensional powders of oxides of metals is possible if particle size is regulated. This technology makes it possible to use equipment of smaller size and weight; economic indices are also acceptable.

During the experimental investigation of plasma-chemical synthesis of oxide powders  $\text{Al}_2\text{O}_3$  from sulfate solutions in the flow of air plasma, the primary attention was directed toward formation of the end products of condensation processes for the purpose of obtaining nano-dimensional powders. Therefore the content of salts in the stock solutions was assigned not high: 10 - 40 %, and aqueous solution of aluminum sulfate was used as the basic raw material. Investigations were executed in the plasma reactor with triple-jet mixing chamber, for which three electric arc plasmatrons of direct current worked. The supplied electric power was 180 kW, the total flow of plasma-forming gas (air) was 10 g/s, the calculated averaged-mass temperature of plasma flow - 5800 K, the consumption of the basic raw material - 2,0 g/s (7,2 kg/h). The injector for dispersion and charge of aluminum sulfate into the reactor was established at the upper point of the mixing chamber along the axis of the reactor. The raw material in the form of small drops was transported by air into the reactor, where it was mixed with the plasma flow, formed in the triple-jet mixing chamber.

The obtained powders of aluminum oxide were analyzed by BET method (by low-temperature adsorption of nitrogen vapors) on the tool "Acusorb -2100" (firm Micromeritics, USA). The powder of aluminum oxide, assembled in the intermediate bin, has specific surface area  $S_w = 12,91 \text{ m}^2/\text{g}$ . The powder of aluminum oxide, assembled on the filter, has specific surface area  $S_w = 59,37 \text{ m}^2/\text{g}$ . The obtained results are analyzed.

# PLASMACHEMICAL PROCESS FOR THE FABRICATION OF SOFC AND HEATING DEVICES COMPONENTS BASED ON NEW DOPED ABO<sub>3</sub>-MATERIALS

A.V. Gorbunov\*, V.A. Gorbunova\*\*, A.L. Mosse<sup>\*</sup>, A. Marotta<sup>†</sup>, G.I. Novikov\*\*

\* - Heat & Mass Transfer Institute (HMTI) - Academy of Sciences - 220072 Minsk - Belarus

Tel.: 375 017 2841223, Fax: 375 017 2322513, e-mail: mosse@itmo.by

\*\* - Belarussian State University of Technology, 220630 Minsk, Belarus

<sup>†</sup> - Institute of Physics, University of Campinas - UNICAMP, SP, Brazil

Semiconducting ceramic materials based on oxides with perovskite ABO<sub>3</sub>-structure (e.g. doped chromites, manganites, cobaltites of lanthanum or other lanthanides) are widely investigated as materials for various energy conversion technologies. It is expected that the technologies based on electrochemical fuel cells and particularly on solid oxide fuel cells (SOFC) will gain an important position in future stationary electric power generation.

Besides conventional techniques based on thermal synthesis of ceramic ABO<sub>3</sub>-materials the advanced plasma (DC- and RF-type) processes are developed for preparation of these materials as components of SOFC and heating semiconducting devices [1]. The new spray process for the preparation of powders of La-Ca-Al-Cr-O-system (which is one of the most suitable for SOFC' interconnections as well as high-temperature air heaters) using 200 kW triple torch electric arc plasma reactor (TTPR) [2] was developed in HMTI. The process was also modified for the fabrication of new type of air electrode of high temperature SOFCs, which cost is strong lower in comparison with conventional LSM-cathodes (e.g. porous La<sub>0.7</sub>Sr<sub>0.3</sub>MnO<sub>3</sub>), based on mixed lanthanide manganites (simultaneously doped in A- and B-sites) of La<sub>0.8-x</sub>Ln<sub>x</sub>Ca<sub>0.2</sub>Mn<sub>0.94</sub>Cr<sub>0.04</sub>Ni<sub>0.02</sub>O<sub>3</sub>-system [3]. In this paper the TTPR operating regimes and heat transfer parameters under the preparation of powders and thick films of this system as well as the data on charge transport and microstructure of these advanced oxide materials are presented. The plasmachemical process using the TTPR was tested in our laboratory for the fabrication of cathodes for tube-type SOFC (with 0.9ZrO<sub>2</sub>+0.1Y<sub>2</sub>O<sub>3</sub>-electrolyte) operated with alcohol-ammonia and coal combustion gas fuels at 1070-1270 K. It can be also used for the fabrication of manganite- and chromite-based heating elements on metal and others substrates which are operated in air. The heating film thickness varied as 20-50 μm for the plasma processing variant with nitrate solution spraying.

*This work was partially supported by Foundation of basic researches of Belarus (grant X01-188).*

[1] Henne R.H., Lang M., Muller M. et al. // Heat and mass transfer under plasma conditions. - Ed. P.Fauchais et al. (Annals of the New York Acad. Sci. - V.891). 1999, pp.124-136.

[2]. A.L. Mosse, A.V. Gorbunov, A. Marotta et al. // Proceedings of the "14<sup>th</sup> International Symposium on Plasma Chemistry", Czech Republic, Prague, 1999, Vol.4, pp.2253-2258.

[3] N.M. Gamanovitch, V.A. Gorbunova, G.I. Novikov // Russian J.Appl.Chem. 2001, V.74, pp.870-873

# Development of Superhard Nanocomposite Coatings for Dry, Hard Machining and of the Coating Technology for Industrial Production

M. Jilek<sup>1</sup>, T. Cselle<sup>2</sup>, P. Holubar<sup>1</sup>, M. Morstein<sup>2</sup>, M. G. J. Veprek-Heijman<sup>3</sup> and Stan Veprek<sup>3</sup>

<sup>1</sup> SHM Ltd., CZ-78803 Nový Malín 266, Czech Republic

<sup>2</sup> PLATIT AG, Moosstr. 68, CH-2540 Grenchen, Switzerland

<sup>3</sup> Institute for Chemistry of Inorganic Materials, Technical University Munich, Lichtenbergstr. 4, D-85747 Garching/Munich, Germany

## Abstract

The development of novel superhard nanocomposite – nanolayer coatings and of the coating technology based on vacuum arc evaporation is briefly summarized. The nc-(Al<sub>1-x</sub>Ti<sub>x</sub>)N/a-Si<sub>3</sub>N<sub>4</sub> coatings in which the nanocrystals of the Al-rich solid solution with the fcc crystal structure of TiN are imbedded into a thin matrix of amorphous silicon nitride show an excellent performance in dry, fast machining that is superior to the state-of-the-art (Ti<sub>1-x</sub>Al<sub>x</sub>)N coatings.

## 1. Introduction

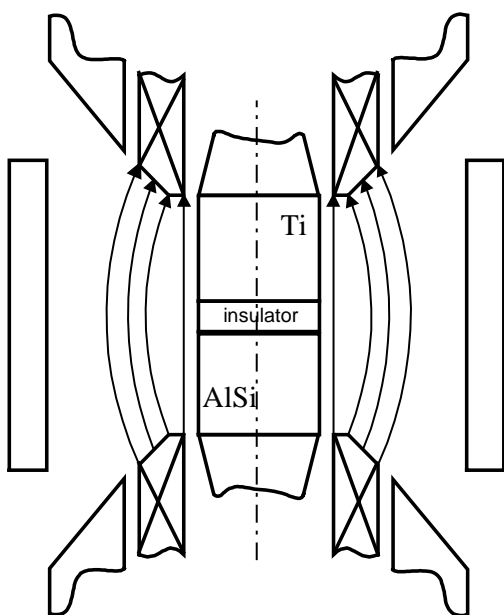
The demand on the improvement of machining technology in terms of higher cutting speed, better quality of the machined surface, lower consumption of lubricants and coolants calls for the development of new wear resistant coatings for machining tools. Because the costs of environmentally friendly recycling and disposal of the coolants represents a significant part of the total machining costs, the ultimate goal is dry, high speed machining. Under such conditions, the temperature of the cutting tool and of the coatings can reach 800°C or more. This poses strong requirements on the quality of the coatings, such as a high hardness combined with a high resistance against crack formation and adherence to the substrate, high temperature stability and oxidation resistance, low coefficient of friction, absence of reaction with the material being machined and others. For these reasons, the earlier developed (Ti<sub>1-x</sub>Al<sub>x</sub>)N coatings [1, 2] and more recent (Ti<sub>x</sub>Al<sub>1-y</sub>Y<sub>z</sub>)N, (Ti<sub>x</sub>Al<sub>y</sub>Y<sub>z</sub>Cr<sub>c</sub>)N coatings with a high oxidation resistance [3, 4] and similar coatings alloyed with Hf, Zr, V and other elements in order to improve the cutting performance are progressively replacing TiN (for lack of available space we don't discuss here other dedicated coatings, such as heterostructures, self-lubricant hard coatings, low friction coatings for bearings and others). In the present paper we shall show that the recently developed superhard nanocomposites, which are formed according to the generic design principle [5, 6] by self-organisation due to thermodynamically driven spinodal phase segregation, meet the requirements for a new generation of advanced wear resistant and tribological coatings.

SHM Ltd. was established in 1993 as a small company producing a variety of specialised products, such as a special coating for spark plugs that enables a more uniform ignition of the gasoline-air mixture in the engine, diamond dressers and others. In 1994 the development of the nc-(Ti<sub>1-x</sub>Al<sub>x</sub>)N/a-Si<sub>3</sub>N<sub>4</sub> begun motivated by the work of Li Shizhi et al. [7]. Later on, when the generic principle for the design of the nanocomposites was published by Veprek et al. [5], a collaboration between SHM and the Technical University of Munich begun. In 1996 the first coatings on indexable inserts made of cemented carbide were introduced on the market. In 1999 the further developed coating “MARWIN<sup>®</sup>” were commercialised in collaboration with the company PRAMET, a Czech manufacturer of machining tools made of cemented carbide. In parallel to the development of the materials also the new coating technology based on rotating arc cathodes was developed because of the requirement for an uniform erosion of that cathode and a high density plasma. According to the generic design principle [5, 6] these conditions are needed for the formation of the nanocomposites with a high thermal stability and also to evaporate pure aluminium which is not possible with conventional cathodes. This technology was recently included into a new advanced coating system  $\pi^{80}$  that utilizes a new **L**ateral **R**otating **A**RC Cathodes **LARC**<sup>®</sup> technology developed together with the company PLATIT (Switzerland), a well established manufacturer of coating units. The asymmetric arrangement of the cathodes with respect to the coated tools provides automatically a nano-layered structure of the coatings and enables a pre-cleaning of the cathodes by means of **Virtual Shutter**<sup>®</sup> that significantly improves the performance of the coatings. This enabled us to significantly improve the cutting performance. Examples will be presented in order to demonstrate that the nanolayered-nanocomposite nc-(Al<sub>1-x</sub>Ti<sub>x</sub>)N/a-Si<sub>3</sub>N<sub>4</sub> coatings display excellent cutting performance that is superior to the state-of-the-art (Ti<sub>1-x</sub>Al<sub>x</sub>)N coatings.

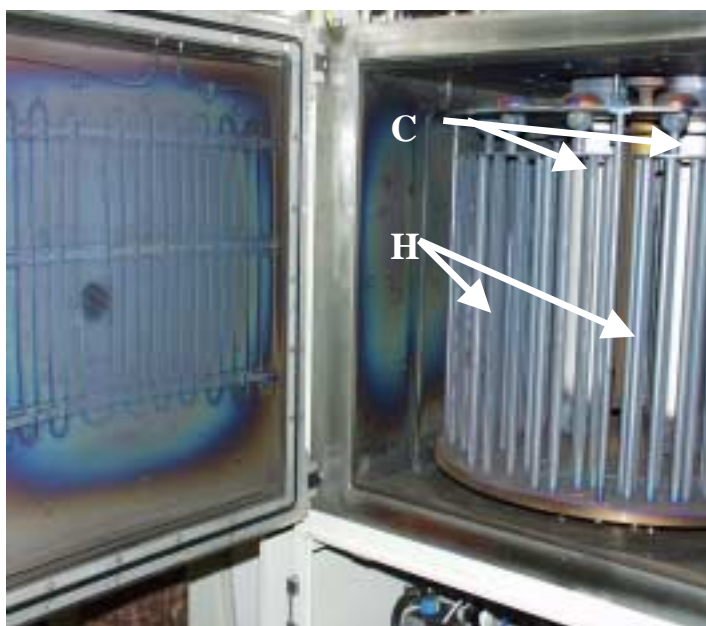
## 2. The Development of the Coating Technology

According to the generic principle for their design [5, 6], the formation of the nanocomposites with a high thermal stability requires a sufficiently high chemical activity of nitrogen in order to assure the segregation of stoichiometric phases, such as nc-(Ti<sub>1-x</sub>Al<sub>x</sub>)N and a-Si<sub>3</sub>N<sub>4</sub>. This is achieved in an intense plasma at a sufficiently high nitrogen pressure [5, 6]. A deposition temperature of  $\geq 500$  °C is required in order to make the thermodynamically driven segregation to proceed fast. Because such conditions are rather difficult to achieve in conventional PVD coating systems with planar electrodes, SHM developed a new vacuum arc technology based on a central cathode.

Figure 1 shows a schematics of the axially symmetric central cathode consisting of two independent segments, one made of pure titanium and the other one of AlSi alloy of the eutectic composition of 11,8 wt (11,3 at) % of Si. The axially symmetric magnetic field together with the perpendicular electric field at the cathode provide the Lorenzian force which results in a fast rotational movement of the cathodic spot on the surface around that axis. By an appropriate change of the axially symmetric magnetic field in the axial direction, the arc can be moved from one segment to the other one with a frequency of the order of kHz. In such a way, atomically mixed (Ti<sub>1-x</sub>Al<sub>x</sub>)N/a-Si<sub>3</sub>N<sub>4</sub> coatings of a chosen stoichiometry are deposited on substrates that are fixed on holders undergoing a planetary motion. The arrangement also allows us a simple deposition of multilayers with sharp interfaces. It was successfully operating in the production with a relatively low emission of droplets<sup>1</sup>. The recently developed more advanced system [8] is shown in Fig. 2. It consists of two (or more) independent cylindrical, rotating cathodes with a very strong magnetic field. This enables us to achieve very high plasma density at the substrates (coated tools) and also a very uniform erosion of the cathodes. Because of the uniformity of the erosion the cylindrical cathodes reach 5 to 7 times longer life time than the planar ones of a similar total area.



**Fig. 1:** Schematics of the central cathode with two separate and independently operated vacuum arcs

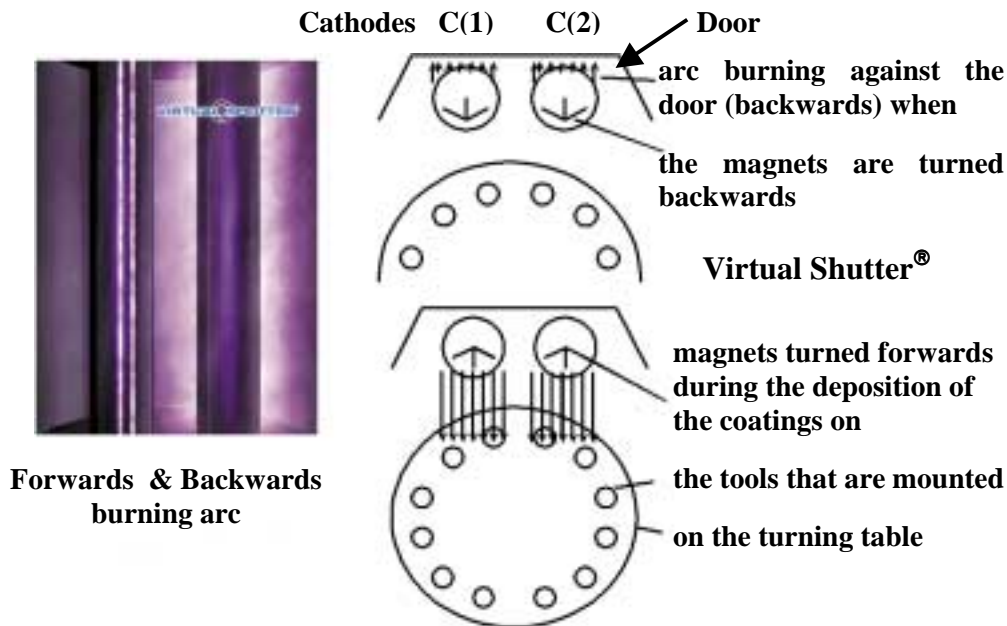


**Fig. 2:** Coating unit "MARWIN" with two rotating central cathodes C and the tool holders H.

In autumn 2002 the Swiss company PLATIT introduced the new coating unit " $\pi^{80}$ " on the market. The new **LARC**<sup>®</sup> technology (**L**ateral **R**otating **A**RC **C**athodes) was developed by the partners SHM and PLATIT especially for this unit. This technology combines the advantages of the rotating cathodes and their positioning on the side of the chamber (Fig. 3) [9]. The asymmetric position of the cathodes in the door for loading and unloading of the tools results automatically in a deposition of nanolayered nanocomposite coatings. Another advantage is the possibility of the pre-cleaning of the cathodes by means of a **Virtual Shut-**

<sup>1</sup> Droplets are liquid particles emitted from the hot cathodic spot due to the large magnetohydrodynamic forces. In the case of vacuum arc they cannot be fully eliminated but only reduced. The advantage of vacuum arc evaporation are the high deposition rates which can be achieved.

ter<sup>®</sup> [8] when the evaporated material is directed away from the substrates prior to the deposition of the coatings. The advanced design and high magnetic field enables one to reliably operate and evaporate even a pure aluminium cathode.

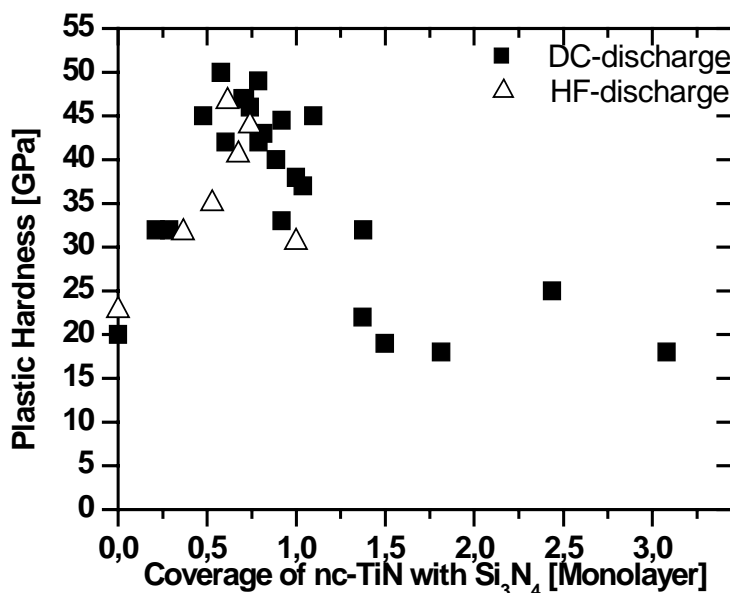


**Fig. 3:** The new coating unit  $\pi^{80}$  that was developed jointly by PLATIT AG and SHM Ltd. [9].

### 3. Properties of the Coatings

#### The Binding State of Silicon

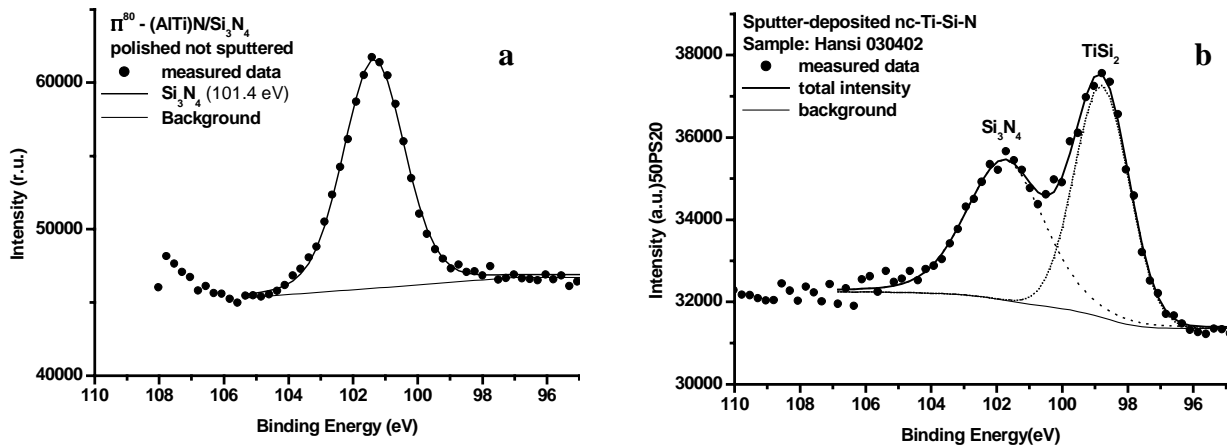
Figure 4 shows the dependence of the hardness of nc-TiN/a-Si<sub>3</sub>N<sub>4</sub> nanocomposite coatings on the coverage of the TiN nanocrystals with Si<sub>3</sub>N<sub>4</sub>. In order to estimate the coverage, the specific interface area was determined from the crystallite size assuming – in agreement with studies by means of high resolution transmission electron microscopy – a regular shape of the nanocrystals and the volume fraction of Si<sub>3</sub>N<sub>4</sub> that was measured by a combination of elastic recoil detection spectroscopy and X-ray photoelectron spectroscopy. The maximum hardness is achieved at about one monolayer coverage. The Si<sub>3</sub>N<sub>4</sub> acts as a “glue” between the TiN nanocrystals decreasing the interface grain boundary energy and thus stabilising it against the grain boundary sliding. Without this stabilisation, softening is observed at a crystallite size decreasing below 10-20 nm (“reverse Hall-Petch”) [10, 11]. At a larger coverage, when the interfacial Si<sub>3</sub>N<sub>4</sub> matrix becomes thicker, the incoherency strain destabilises the nanostructure and the hardness decreases again.



**Fig. 4:** Dependence of the hardness of the nc-TiN/a-Si<sub>3</sub>N<sub>4</sub> coatings on the coverage of the surface of the TiN nanocrystals with Si<sub>3</sub>N<sub>4</sub>.



Similar results were found in all other nanocomposites, such as nc-W<sub>2</sub>N/a-Si<sub>3</sub>N<sub>4</sub>, nc-VN/a-Si<sub>3</sub>N<sub>4</sub>, nc-TiN/a-Si<sub>3</sub>N<sub>4</sub>/a- and nc-TiSi<sub>2</sub>, nc-TiN/a-BN and nc-TiN/a-BN/a-TiB<sub>2</sub>, which were investigated in detail so far [12, 13]. In the present study, it was therefore important to verify if the silicon in the coatings is incorporated as Si<sub>3</sub>N<sub>4</sub> or in a “metallic” form, such as Si dissolved in (TiAl)N, free silicon precipitates or as TiSi<sub>x</sub>. This was done by means of X-ray photoelectron spectroscopy, XPS. Although the Al K<sub>α</sub> radiation provides a good signal-to-noise ratio, the Si 2p region, which is of the fundamental interest here, is interfered by the K<sub>α3,4</sub> satellite of the Al 2s line and by the Al KLL Auger signal, which position overlaps with the Si 2p signal from TiSi<sub>2</sub> and elemental Si. When using the Mg K<sub>α</sub> radiation, the Al KLL Auger signal is shifted away of the Si 2p region but new problems arise: Firstly, because the Mg anode has to be operated at a much smaller power a significantly longer time for the measurement is necessary in order to obtain a sufficient signal-to-noise ratio. Secondly, the weak second satellite Mg K<sub>α5,6</sub> of the Al 2s XPS signal overlaps with the Si 2p signal from TiSi<sub>2</sub> and elemental silicon. Therefore we have investigated if the signal with binding energy of about 98.8 eV (which was attributed to TiSi<sub>2</sub> by several researcher including our studies) is due to TiSi<sub>2</sub> phase or to the Al 2s Mg K<sub>α5,6</sub> satellite. For nc-(Ti<sub>1-x</sub>Al<sub>x</sub>)N/a-Si<sub>3</sub>N<sub>4</sub> coatings deposited in the unit “MAR-WIN” (Fig. 2) we have shown that there is no noticeable amount of such “metallic Si” phase [14]. Figure 5a shows a typical example of XPS spectra of the Si 2p region for coatings deposited in the new  $\pi^{80}$  unit. One can see that the only peak is due to “non-metallic Si” bonded as in Si<sub>3</sub>N<sub>4</sub> and there is no any noticeable contribution of the “metallic Si” phase. For comparison, Fig. 5b shows a nc-Ti-Si-N coating deposited by magnetron sputtering at a low pressure of nitrogen that contains as a dominant Si - phase the “metallic” TiSi<sub>2</sub>.

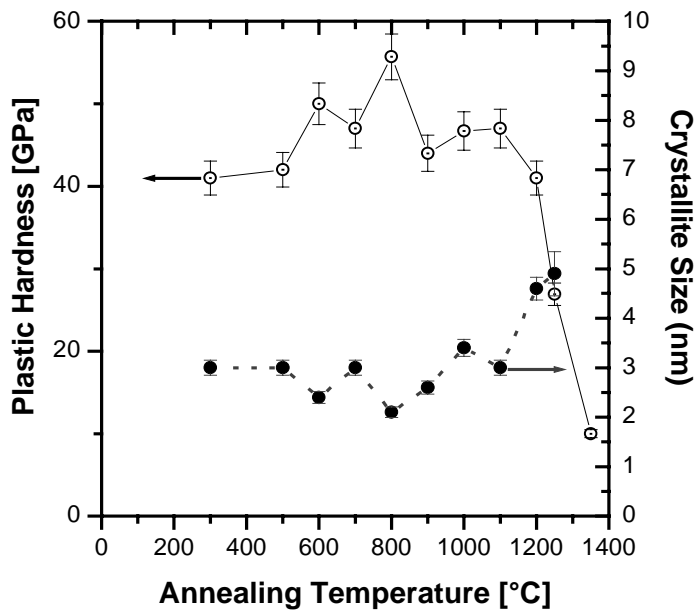


**Fig. 5:** XPS spectra from the Si2p region showing the non-metallic Si<sub>3</sub>N<sub>4</sub> phase in the nc-(Al<sub>1-x</sub>Ti<sub>x</sub>)N/a-Si<sub>3</sub>N<sub>4</sub> coatings from the  $\pi^{80}$  unit (Fig. a) and the dominant “metallic Si” phase TiSi<sub>2</sub> in coatings deposited by magnetron sputtering at a low pressure of nitrogen (Fig. b).

### Thermal Stability

It is well known that solid solution (Ti<sub>1-x</sub>Al<sub>x</sub>)N with the fcc structure of TiN decomposes into (TiAl)N and h-AlN when the Al content is too high, typically for  $x \geq 0.7$ . The presence of the a-Si<sub>3</sub>N<sub>4</sub> tissue reduces this decomposition and allows us to prepare coatings with a higher Al content and therefore with a higher oxidation resistance. Of particular interest is the high thermal stability of the nanostructure and concomitant stability of the hardness because one would generally expect a recrystallisation and coarsening (Ostwald ripening) to occur at a much lower temperature. Figure 6 shows one of many examples of the high stability of the nc-(Al<sub>1-x</sub>Ti<sub>x</sub>)N/a-Si<sub>3</sub>N<sub>4</sub> coatings up to a temperature of  $\geq 1100$  °C. The spinodal nature of the decomposition stabilizes the nanostructure against coarsening (for details see [6, 11-14]). It is interesting to note the **self-hardening upon annealing** that was already reported earlier by us for these coatings [15, 16] and by other researcher for mixed nitrides that undergo spinodal decomposition [17, 18]. The relatively complex behavior of the crystallite size and hardness upon isochronal annealing as seen in Fig. 6 indicates a complex, multi-step structural relaxation to occur in our coatings. This may be due to a combination of annealing of defects induced by energetic ion bombardment during the deposition [19], spinodal decomposition

of the (TiAl)N nanocrystals [20, 21] and completion of the formation of the nc-(Al<sub>1-x</sub>Ti<sub>x</sub>)N/a-Si<sub>3</sub>N<sub>4</sub> nanos-structure [12, 16].

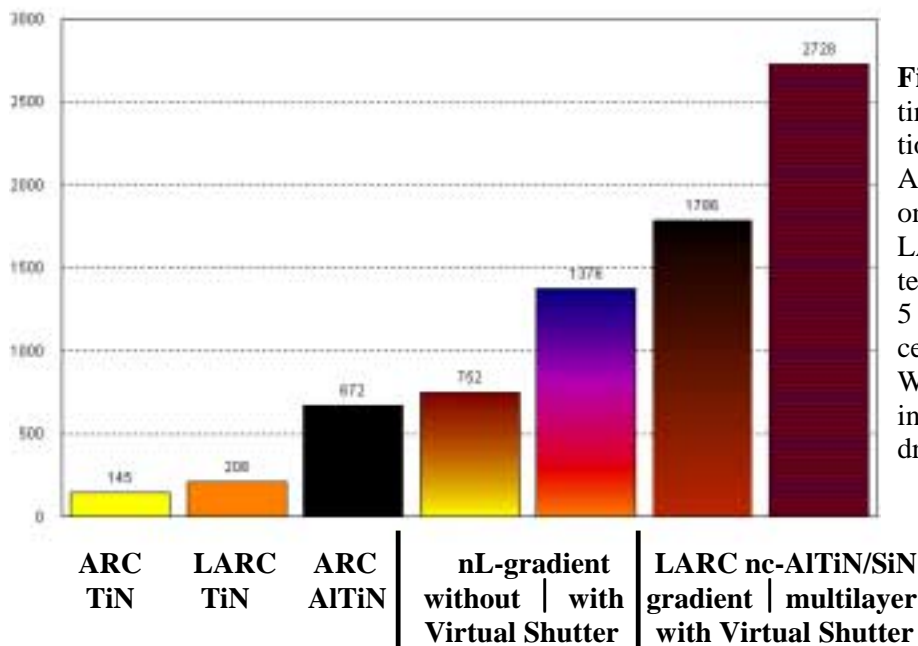


**Fig. 6:** Example of a high thermal stability of superhard nc-(Ti<sub>1-x</sub>Al<sub>x</sub>)N/a-Si<sub>3</sub>N<sub>4</sub> coatings deposited on cemented carbide. The onset of the coarsening and of the decrease of the hardness coincide with the onset of the diffusion of cobalt from the substrate into the coatings.

### Single- and Multilayers and Improvement of the Cutting Performance

The composition and properties of wear resistant coatings have to be adapted to a given machining operation. For interrupted machining, such as milling, high impact hardness is more important than the static indentation one. This is achieved by multilayers MARWIN MT<sup>®</sup> which consist of nc-(Ti<sub>1-x</sub>Al<sub>x</sub>)N/a-Si<sub>3</sub>N<sub>4</sub> with varying x and TiN interlayers inbetween (for details see [14]). The somewhat softer but more elastic TiN layers improve the resistance of the coatings against the impact in the interrupted milling and the hard nc-(Ti<sub>1-x</sub>Al<sub>x</sub>)N/a-Si<sub>3</sub>N<sub>4</sub> layers improve the abrasive wear resistance. The multilayered structure of coatings improves also their resistance against failure due to cracks propagation because the cracks are deflected at the interfaces between the individual layers.

The successful development of the new  $\pi^{80}$  LARC<sup>®</sup> coating technology with the **Virtual Shutter**<sup>®</sup> and asymmetric arrangement of the cathodes provides structurally modulated nc-(Al<sub>1-x</sub>Ti<sub>x</sub>)N/a-Si<sub>3</sub>N<sub>4</sub> nanocomposites-nanolayers that show a superior cutting performance as illustrated in Fig. 7.



**Fig. 7:** Comparison of the cutting performance of conventional, state-of-the-art TiN and AlTiN coatings with the new ones prepared by means of the LARC coating technology (see text). Dry drilling of steel with 5 mm diameter drill made of cemented carbide with Corner Wear = 200  $\mu$ m. The numbers indicate the total number of drilled holes.

One can see that already the TiN coatings deposited by the LARC<sup>®</sup> technology show a better performance

than the conventional arc (see ARC). The importance of the **Virtual Shutter**<sup>®</sup> is illustrated by comparison of the state-of-the-art AlTiN deposited with arc, those with nc-gradient without and with the **Virtual Shutter**<sup>®</sup>; in the latter case, the life time of the tool is more than factor of 2 longer as compared with the standard AlTiN. Here, "nL" and "nc" stands for the nanolayers and nanolayered-nanocomposites, respectively. The significant improvement the cutting performance of the nc-(Al<sub>1-x</sub>Ti<sub>x</sub>)N/a-Si<sub>3</sub>N<sub>4</sub> nanocomposites is illustrated by the last two columns: The **LARC**<sup>®</sup> technology results in an improvement of the gradient layer by a factor of 2.7 and in the case of the multilayers more than 4. Significant improvement of the life time of the tools was also documented for dry milling and turning (not shown here for lack of space).

#### 4. Conclusions

The superhard nanocomposites prepared according to the generic design principle due to a **self-organization of the nanostructure** that occurs during the strong spinodal phase segregation show a high hardness, thermal and oxidation (not shown here for lack of space, see [5]) stability. The extraordinary mechanical properties of these nanocomposites whose tensile strength approaches the ideal one of 10 to 40 GPa [22] was recently explained in terms of conventional fracture physics scaled to the dimensions of few nm [23]. Because of the generic nature of that design concept, they can be prepared in a variety of chemical composition. The recently developed **LARC**<sup>®</sup> coating technology that utilizes the **Virtual Shutter**<sup>®</sup> for the pre-cleaning of the cathodes enables one to coat a variety of tools at a price comparable with the state-of-the-art (Ti<sub>1-x</sub>Al<sub>x</sub>)N coatings but with a significantly improved life time by a factor of 2 to 4.

#### 5. Acknowledgment

This work has been supported in part by the European Commission under Growth Programme in the frame of the 5<sup>th</sup> RTD Framework Programme under the contract number G5RD-CT-2000-0222 Project "NACODRY", by the NATO SfP Project No. 972379 "Protection Coatings" and by the Swiss National Research Project TOPNANO.

#### References

- [1] W.-D. Münz, J. Vac. Sci. Technol. **A 4**, 2717 (1986).
- [2] O. Knotek, M. Böhmer and T. Leyendecker, J. Vac. Sci. Technol. **A 4**, 2695 (1986).
- [3] W.-D. Münz, Werkstoffe und Korrosion **41**, 753 (1990).
- [4] L. A. Donohue, I.J. Smith, W.-D. Münz, I. Petrov and J. Green, Surf. Coat. Technol. **94-95**, 226 (1997).
- [5] S. Veprek and S. Reiprich, Thin Solid Films **268**, 64 (1995).
- [6] S. Veprek, J. Vac. Sci. Technol. **A 17**, 2401 (1999).
- [7] Li Shizhi, Shi Yulong and Peng Hongrui Plasma Chem. Plasma Process. **12**, 287 (1992).
- [8] Patent pending
- [9] <http://www.platit.ch>.
- [10] R.W. Siegel and G.E. Fougere, Mater. Res. Soc. Symp. Proc. **362**, 219 (1995).
- [11] J.Schiotz, F.D.Di Tolla & K.W. Jacobsen, Nature **391**, 561 (1998).
- [12] A. Niederhofer, T. Bolom, P. Nesladek, K.Moto, C. Eggs, D. S. Patil and S. Veprek, Surf. Coat. Technol. **146-147**, 183 (2001).
- [13] P. Karvankova, M. G. J. Veprek-Heijman, O. Zindulka, A. Bergmaier and S. Veprek, Surf. Coat. Technol. **163-164**, 149 (2003).
- [14] M. Jilek, P. Holubar, M. G. J. Veprek-Heijman and S. Veprek, MRS Symp. Proc. **697**, (2003) in press.
- [15] P. Holubar, M. Jilek and M. Sima, Surf. Coat. Technol. **133-134**, 145 (2000).
- [16] H.-D. Männling, D. Patil, K. Moto, M. Jilek and S. Veprek, Surf. Coat. Technol. **146-147**, 263 (2001).
- [17] O. Knotek and A. Barimani, Thin Solid Films **174**, 51 (1989).
- [18] R. A. Andrievski, I. A. Anisimova and V. P. Anisimov, Thin Solid Films **205**, 171 (1991).
- [19] L. Hultman, Vacuum **57**, 1 (2000).
- [20] F. Adibi, I. Petrov, L. Hultman, U. Wahlström, T. Shimizu, D. McIntyre, J. E. Greene and J.-E. Sundgren, J. Appl. Phys. **69**, 6437 (1991).
- [21] A. Hörling, L. Hultman, M. Odén, J. Sjöln and L. Karlsson, J. Vac. Sci. Technol. **A 20**, 1815 (2002).
- [22] S. Veprek, S. Mukherjee, P. Karvankova, H.-D. Männling, J. L. He, K. Moto, J. Prochazka and A. S. Argon, J. Vac. Sci. Technol. **A 21**, May/June (2003), in press.
- [23] S. Veprek and A. S. Argon, J. Vac. Sci. Technol. **B 20**, 650 (2002).

# Electrical polarization of the PMMA films treated by a DBD in helium

N. Dumitraşcu, P. Tuluc, I. Topală, N. Apetroaei, G. Popa

*Plasma Physics Department, "A. I. Cuza" University, Iasi – 6600, Romania*

## Abstract

Interactions between the biomaterials and biological environments (living tissues, blood, sinovial liquid, plasma proteins, aminoacids etc.) are complex and include various physico-chemical processes at the interface such as physical adsorption, scission bonds, chemical reactions, enzymatic processes etc. These processes depend on the mechanical, physical, chemical and energetic properties of the surface and in particular on the distribution of electrical charges on the surface. We used a dielectric barrier discharge in helium at atmospheric to add polar groups on the polymeric surfaces of poly(methyl methacrylate) films and important surface modifications have been observed. After the treatments the surface energy and its polarity are increased, morphology is modified with a new distribution and density of grains. The electrical charge density is increased on the surface and changes in the refraction index and absorption coefficient are also observed.

## 1. Introduction

Living tissues and biological fluids are usually in contact with the biomaterials and might generate physico chemical processes at the interface including physical adsorption, van der Waals and electrostatic forces which are in general different to that of the bulk of material. In the system-human environment these interfaces generate significant problems which are often critical for good results in the medical act [1, 2]. These processes depend on the mechanical, physical, energetic and chemical properties of the surface and, in particular, on the surface charge distribution. All of these characteristics govern the stability of the biomaterial-tissue interface and could predict the biocompatibility of an implant. For the biomaterials, the electrostatic interactions between the polar sites presented on the surface and the components of blood (a strong electrolyte) could be dangerous, because they can induce thromboembolic processes. On the other hand, creation of anionic and cationic sites is a necessary condition for biological species (drugs, antibodies, enzymes etc.) immobilization on these surfaces. Presence of functional electrical groups can improve the efficiency and selectivity of the filtration membrane that may select and control the salt and water fluxes by the interface [3]. Cell adhesion and its proliferation, plasma proteins adsorption etc. imply also the surface charge distribution and the electrostatic interactions at interface [4, 5], this depending also on water content in polymer structure [6].

The electrical characterization of biomaterials and the electrokinetic parameters such as surface charge density, salt and ionic permeability, zeta potential etc. are usually obtained by measurements of the sedimentation potential, streaming potential etc. For ex., the electrical potential at the plane of shear in the liquid, named zeta potential, is only detectable in a dynamic system because the liquid is moving in relation to the surface. A new non-destructive technique for characterizing materials and interfaces, in particular for analysis of layers with different electrical properties, is an electrochemical impedance spectroscopy that permit to evaluate ceratin electrokinetic parameters at interface [7].

One of the solutions to increase the polarity is the plasma treatment that produces not only a perturbation of the surface charges distribution but also new positive and negative functional groups on the surface [8]. This charge accumulation on the surface and injection into the dielectric during formation of a discharge could also be very important on the subsequent development of the discharge [9].

To conclude, the plasma treatments are capable to increase the electrical polarization by creating of new polar sites on the surface that subsequently may produce favorable changes at the interface between the biological environment and the implant. Finally, biocompatibility characteristics of the materials are strongly dependent on the processes at biomaterial-tissue interface and its time evolution.

We used a dielectric barrier discharge (DBD) in helium at atmospheric pressure with the aim to increase the surface polarity and to provoke a controlled electrical polarization of the polymer surface, as a first step to a subsequent immobilization of active species (drugs and enzymes) implied in the medical act. Dielectric barrier discharge (DBD) is known as one of the technique suitable for modifying polymer surfaces and

improving their surface property [10]. Usually, DBD improves the adhesion properties, functionalization and crosslinking of polymer surfaces in the depth to several 100Å, without affecting the bulk properties.

The material used for experiments was PMMA, characterized by a very good light transmittance, toughness and stability, qualities which makes it a preferred material for medical applications in ophthalmology, respectively for intraocular and contact lens [11, 12].

The characterization of the surface is made before and after the DBD treatments by AFM, contact angle measurements correlated with certain electrokinetic and ellipsometric measurements.

## 2. Experimental

The experimental arrangement for the DBD treatments has been presented elsewhere [10].

The PMMA films (Goodfellow Co., 0.250mm thickness) were cleaned with alcohol to remove organic material whereupon rinsed with deionized water and dried in the oven at 50°C for 1h.

We consider flat and smooth polymer surface, with less roughness or chemical heterogeneity. The surfaces of PMMA were treated 10sec by a DBD in helium at atmospheric pressure and stored in air under room conditions.

The experimental set up used to measure capacitive currents through the PMMA is presented in Fig. 1 [13]. The film of PMMA was placed in a cell test, over an aperture (4 mm in diameter) between aqueous phases contained in two Teflon chambers (100x150x100 mm<sup>3</sup>) filled with 10 mM KCl solution. An Axopatch 200B (Axon Instruments) amplifier was used to apply rectangular pulses of potential difference (50mV) across the polymer sheet. In order to measure capacitive currents elicited through polymer we used two reversible Ag/AgCl electrodes. Due to the fact that very low currents had to be measured across the polymer, it was necessary to confine the entire set-up in a Faraday cage. The capacitive current signal was amplified and sent to an A/D converter; the resulting digitized data was further stored on a PC computer. The equivalent circuit consists of a parallel association of a resistance and a non ideal capacitor (PMMA film) in the total circuit PMMA film and electrolyte solution.

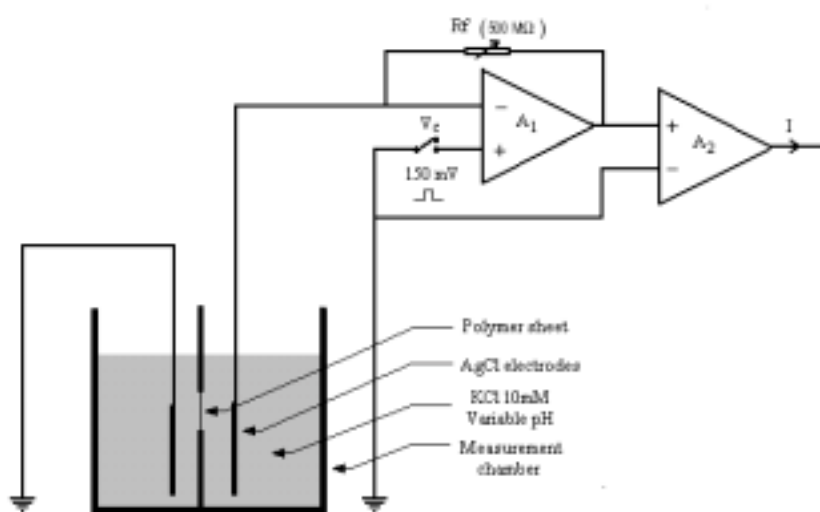


Fig. 1. Experimental set-up for electrical measurements on PMMA films in electrolyte solutions.

Measurements of contact angle were made by the sessile drop method with a 1μl volume of liquid.

Contact angle titration measurements were made using solutions of 10mM KCl and pH was adjusted by small additions either HCl or KOH solutions. Experiments was conducted at different pH values above and below the pI (isoelectric point), i. e., at 2, 4, 6, 8 10 and 12 and contact angle was determined as function of pH. The measurements were made at room temperature (22-25°C) and all the solutions were in thermal equilibrium with environment. The response of the material to the various pH of the solutions has been found immediately after the DBD treatment.

The surface morphology was observed by means of AFM working in the tapping mode. We used a standard silicon nitride cantilever (NSC21) and tip radius less than 7nm. In our experiments the roughness of samples is verified by statistic AFM estimations and the images covers various area, from 70μm x 70μm to 3μm x

3 $\mu$ m. AFM measurements are extended to different sites of the sample and are repeated in same conditions at room temperature and ambient atmosphere.

Energetic characteristics of the surface have been evaluated by Owens methods and additional analysis by ellipsometry was made using an EL X-01R ellipsometer, which permit to evaluate the refraction index and absorption coefficient of the films. We analyzed the ellipsometric response in two perpendicular directions taking into account the possible optical anisotropy of PMMA films. Slides of SiO<sub>2</sub> are used as substrates, each substrate having 1cm wide and 1cm long.

### 3. Results and discussion

It is known that surfaces may be charged for various reasons, for ex., during processing or by adsorbing of charged molecules onto the surface [1]. In particular the most polymer surfaces are polar surfaces due to the both acidic and basic sites distributed free and bonded on the surface giving its acidic or basic character. Due to the ester groups, our surface of PMMA film has a slow basic character. When this material with a charge distributed on the surface is placed into a solution with positive and negative ions an electrical double layer is established and electrokinetic phenomena appear at the interface. In this respect, in a biological environment the surface of an implant will be electrical polarized and this new interface is very important generating various consequences benefic or not for the medical act. For this reason the surface of the implant is usually covered with biological active species to assure the biocompatibility with the human.

The AFM images have shown morphological changes of the PMMA surfaces after the treatments (Figs. 2.a. and 2.b.). The root mean square roughness of the treated surfaces are not essentially modified, the grains are relatively uniform distributed on the surface, density of grains is the same, but their dimensions are increased after the treatment (Table 1).

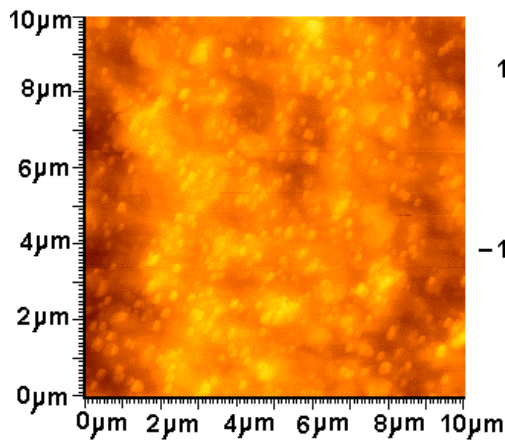


Fig.2.a. AFM image of untreated PMMA films; 10x10 $\mu$ m<sup>2</sup>.

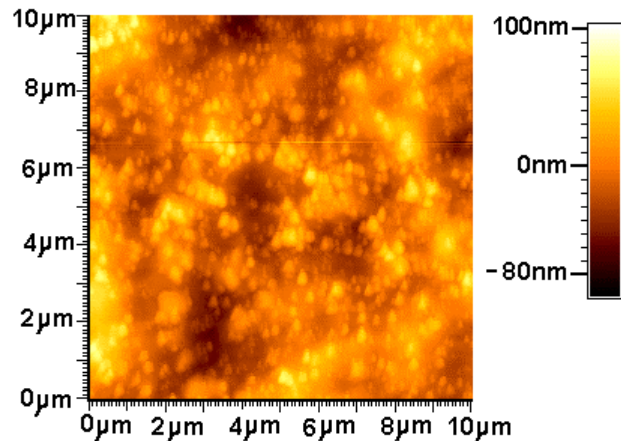


Fig.2.b. AFM image of treated PMMA films; 10s duration of DBD treatment; 10x10 $\mu$ m<sup>2</sup>.

The increasing of polar groups at the polymer surface after the DBD treatments is proved by evaluation of surface polarity and the polar and dispersive components (Table 2). Surface polarity and the polar components of surface energy are increased after the treatment due to various interactions at the polymer surface interaction with the plasma particles.

Table 1. Surface morphology modifications of PMMA films after DBD treatments.

Sample	Density of grains (grains/cm <sup>2</sup> )	Diameter of grains (nm)
Untreated PMMA	4x10 <sup>8</sup>	184
Treated PMMA ( 10s )	4.2x10 <sup>8</sup>	230

Table 2. Surface energetic properties of PMMA films before and after DBD treatments (measured after 1h).

Sample	$\gamma_{SV}^p$ (mN/m)	$\gamma_{SV}^d$ (mN/m)	$P = \frac{\gamma_{SV}^p}{\gamma_{SV}^p + \gamma_{SV}^d}$
Untreated PMMA	3.12	27.33	0.099
Treated PMMA (10s)	16.15	25.66	0.38

Introduction of new polar groups and functionalities were observed also by contact angle titration measurements (Fig. 3 and Fig. 4). We observe a variation of the contact angles in the presence of different concentrations of positive and negative ions, expected taking into account that polymer chains have a greater mobility at the surface allowing the dipoles to reorient in response to different pH environments. It is clear that the electrostatic forces between the surface and the liquid induce instability at the interface. After the DBD treatment the contact angles decrease because other polar groups are added at the surface and this new charge density distribution appear to be more stable in the presence of various pH solutions (Fig. 3). Similar results are obtained by surface charge measurements (Fig. 4). So, after the treatment the charge density accumulated on the surface is increased and a new acid-base equilibrium is established. The change in the pH of the solution induces changes in the acid-base equilibrium at interface but the electrical charge on the surface theoretically remains increased but uniformly distributed. Variations/fluctuations of the charge density at different pH can be attributed to the reorientation of dipoles at the boundary surface-electrolyte and charge migration and diffusion of them from the surface into the electrolyte solutions.

We assume/suppose that the acid and basic ions are not attack the surface by chemically bounds.

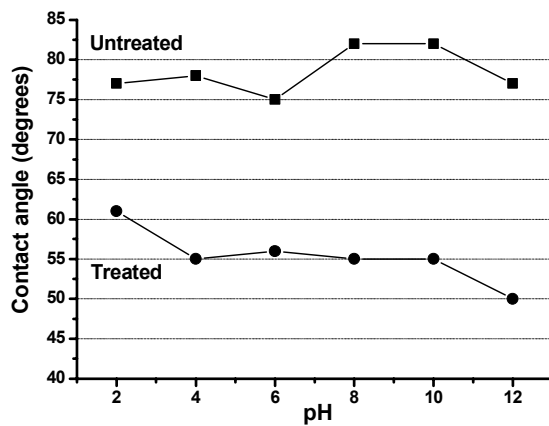


Fig. 3. Contact angle before and after DBD treatment as function of solution pH (10mM KCl).

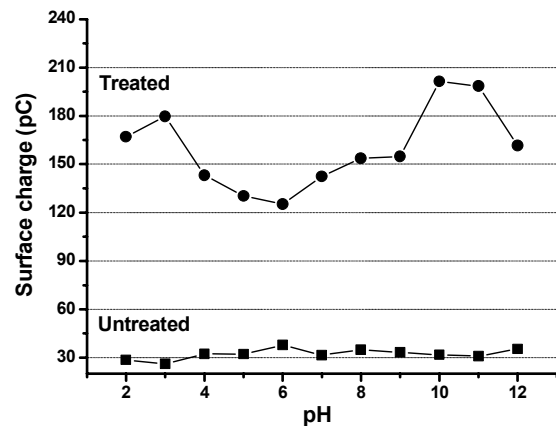


Fig. 4. Surface charge of PMMA films before and after DBD treatment as function of solution pH (10mM KCl).

From the ellipsometric measurements we can emphasize that refractive index and absorption coefficient are modified after the DBD treatments providing that we could use this method in the improving and controlling of certain optical properties of the polymer surfaces. After the treatments the ellipsometric response of PMMA films appear to be more stable in time (Table 3).

Measurements by AFM show a strong anisotropy at the surface before the treatments but after 7 days the surface appears to be more uniform, in good agreement with ellipsometric measurements. A more uniform distribution of grains due to a reorganization of processes in the atmospheric environment is observed after the treatments (Figs. 5.a. and 5.b.).



Table 3. Optical properties of PMMA films before and after DBD treatments.

PMMA	Refractive index (n)		Absorption coefficient (k)	
	<i>parallel</i>	<i>normal</i>	<i>parallel</i>	<i>normal</i>
Untreated	1.7274	1.7161	0.8920	0.9735
Treated (measured after 1 hour)	1.4550	1.4293	0.3294	1.9783
Treated (measured after 1 day)	1.4139	1.4019	0.5120	0.6826
Treated (measured after 7 days)	1.3552	1.3581	0.5751	0.5981

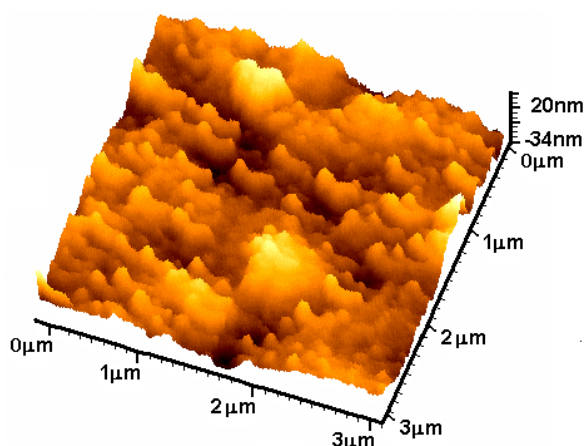


Fig.5.a. AFM image of untreated PMMA film, 3x3μm<sup>2</sup>.

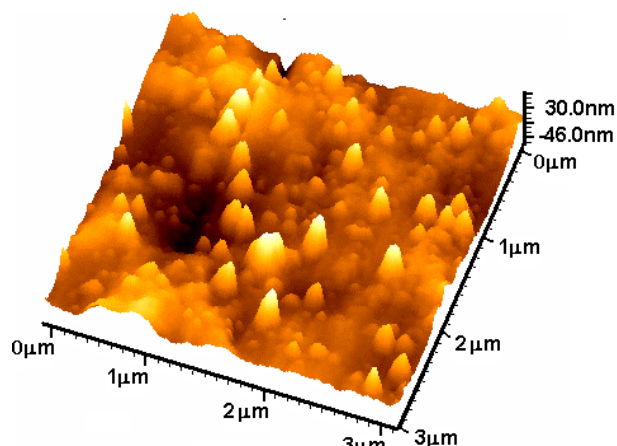


Fig.5.b. AFM image of treated PMMA film, 3x3μm<sup>2</sup>.

#### 4. Conclusions

We summarize the following results:

- morphology, the dimensions and density of grains after the DBD treatments are modified;
- surface polarity (defined by polar component/energy surface) is increased after the DBD treatments;
- more polar groups are introduced and the surface charge density is increased after the DBD treatments;
- pH of the biological liquids induces changes in the electrical layer at the surface;
- refraction index and adsorption coefficient are modified after the treatments and their stabilization is assured after 7 days.

#### References

- [1] F. Garbassi, M. Morra, E. Occhiello, Polymer surfaces, From Physics to Technology, John Wiley&Sons, New York, 1998.
- [2] P. Favia, R. d'Agostino, Proc. of ISPC 14, Praha, August 2-6, 2761 (1999).
- [3] F. Pincet, E. Perez, G. Belfort, Langmuir **11**, 1229 (1995).
- [4] *Biomaterials Science, An introduction to Materials in Medicine*, Eds B. D. Ratner et al., Academic Press, San Diego, 1996.
- [5] H. Shirahama, T. Suzawa, J. Coll. and Interface Sci. **104**, 416 (1985).
- [6] S. Hatorri, J. D. Andrade, J. B. Hibbs, Jr., D. E. Gregonis, R.N. King, J. Coll. Inter. Sci. **104**, 72 (1985).
- [7] A. Canas, M. J. Ariza, J. Benavente, J. of Membrane Science **183**, 135 (2001)
- [8] L. Tusek, M. Nitschke, C. Werner, K. S. Kleinschek V. Ribitsch, Colloids and SurfacesA **195**, 81 (2001).
- [9] V. Nikonov, R. Bartnikas, M. R. Wertheimer, IEEE Trans. on Plasma Science, **29**, 866 (2001).
- [10] N. Dumitrascu, G. Borcia, N. Apetroaei, G. Popa, Plasma Sci. Technol. **11**, 1 (2002).
- [11] M. T. Cuberes, H. E. Assender, G. A. D. Briggs, O. V. Kolosov, J. Phys. D: Appl. Phys **33**, 2347 (2000).
- [12] J.S.Cho, Y.W. Beag, S. Han, K.H.Kim, J. Cho, S.K.Koh, Surf. and Coat. Technol. **128/129**, 66 (2000).
- [13] N. Dumitrascu, T. Luchian, N. Apetroaei, V. Bancia, C. Pavel, G. Popa, Entropy **239/240**, 168 (2002).



# Treatment of flexible polyethylene with low pressure plasma to improve its painting

A. Martínez-García, A. Segura-Domingo and A. Sánchez-Reche

*AIJU, Product and Test Engineering Department, Ibi (Alicante), Spain*

## Abstract

In this study, low pressure plasma was selected as a surface treatment to improve the painting properties of a elastomeric polyethylene (PE). Several experimental variables in the low pressure synthetic air plasma treatment of elastomeric PE were considered: treatment time, plasma power and the duration of the treatment effects. After plasma treatment, the paint was adhered to the material, and the surface modifications were maintained during four hours after the treatment.

## 1. Introduction

Elastomeric polyolefinic materials, as elastomeric polyethylene, are very flexible materials with low hardness. Due to these good mechanical properties they can be successfully used in the manufacturing of toys and child care articles. Because of the low surface energy of polyethylene, adhesion and painting problems are commonly encountered [1]. And this decoration (painting) problem limits the use of these new thermoplastics in some industrial sectors. Surface modifications should be an adequate method to improve the wettability and painting properties of polyolefins, and the low pressure plasma treatment is one of the most commonly used treatments for low surface energy polymers [2]. This treatment is fast, can be easily adapted to industrial production, and produces an increase in adhesion properties [3-6].

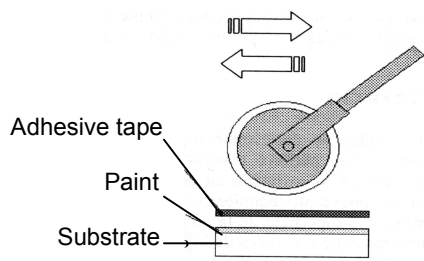
Thus, one of the objectives of this study was the improvement in the painting properties of a 4 mm thick elastomeric polyethylene using low pressure plasma as surface treatment. The efficiency of the treatment is a consequence of different experimental parameters [7-9], so in this study, the treatment time and the plasma power on the elastomeric polyethylene treatment were considered. Also, the time for which the effect of the treatment remains on the polyethylene surface is other important parameter to be considered. The present paper includes the results of one of these variables, the treatment time.

## 2. Experimental

### 2.1. Materials

An elastomeric polyethylene (PE) supplied by DOW PLASTICS was used in this study. Their melt flow index is 5 g/10 min and its Shore A hardness is 75 (data supplied by DOW PLASTICS). The PE polymer was received as pellets and moulded using a DEMAG Ergotech 110-430h/310V injection machine to obtain test samples of 150 mm length, 60 mm width and 4 mm thickness. The following injection conditions were used: temperature = 170-185 °C; injection time = 12 s; injection pressure = 48 bar (1 bar=10<sup>5</sup> Pa); mould temperature = 15 °C. The injection moulded pieces were cut into test samples of sizes 20×30×4 mm for characterisation and 150×30×4 mm for painting tests.

An acrylic and flexible paint supplied by PINTURAS BLATEM (Torrent, Valencia) was used to perform the T-peel test. The paint was applied on the treated samples with a brush and dried for three hours in open air to facilitate the evaporation of the solvent. Then a polyisoprene-styrene adhesive tape of 30 mm width was applied on the painted samples to evaluate the paint-substrate adhesion. The adhesive tape was applied by pressing it on the substrate using a roller as shown in Figure 1.



**Figure 1.** Application of the adhesive tape to the painted substrate [10].

## 2.2. Experimental techniques

**Low pressure plasma equipment** A Tantec Vacuted Plasma System model HV 2000 generator was used to modify the PE. The radiofrequency unit was set at 13 kHz. The samples were placed on an aluminium plate inside the chamber. During the experiments the pressure inside the chamber was 10 mbar and all the treatments were performed in synthetic air supplied by Abelló Linde, S.A. (Barcelona). The treatment time was varied from 1 second to 120 seconds, and the plasma power was varied between 100 and 700 W. The duration of the effects produced by the treatment on the PE samples was studied by applying the adhesive tape from 30 minutes to 10 weeks after the treatment.

**Contact angle measurements.** Advancing contact angles on the treated PE were measured at 25 °C using a Ramé-Hart 100-0 equipment by placing 4 µl drops of deionized and doubly distilled water on the surface. The contact angle values were measured immediately after the low pressure plasma treatment. The experimental error was  $\pm 2$  degrees.

**Infrared spectroscopy using ATR.** ATR-IR spectra of low pressure plasma-treated PE, before and after T-peel tests, were obtained using a Nicolet FTIR 550 spectrometer. To avoid deep penetration of the IR radiation into the sample, the attenuated total multiple reflection method was employed using a KRS-5 (thallium bromide) crystal. The incident angle of the IR radiation was 45°. The resolution was 4 cm<sup>-1</sup> and 100 scans were averaged.

**X-ray photoelectron spectroscopy (XPS).** XPS spectra of low pressure plasma-treated PE were obtained with a Vacuum Generator (VG) Scientific Microtech Multilab spectrometer, using Mg K<sub>α</sub> X-ray source (hν=1253.6 eV) operating at 15 keV and 300 W. The analyser was operated in the constant transmission mode. The pressure inside the analysis chamber was held below 5x10<sup>-7</sup> torr (6.6 x 10<sup>-5</sup> Pa) during the course of the analysis. Rectangular sample pieces (10 mm x 20 mm) were used. The measurements were carried out at a take-off angle of 45°. Survey scans were taken in the range of 0-1100 eV and high-resolution scans were obtained on all significant peaks in the survey spectra. Binding energies of all photopeaks were referenced to C1s at 285.0 eV. Multi-component C1s photopeaks were curve fitted by using a Gaussian function with a full-width-at-half maximum (FWHM) of 1.6±0.1 eV.

**Scanning electron microscopy (SEM).** SEM micrographs of the as-received and low pressure plasma-treated PE were obtained in a JEOL SEM J840 instrument using an electron beam energy of 20 kV. The samples were coated with gold.

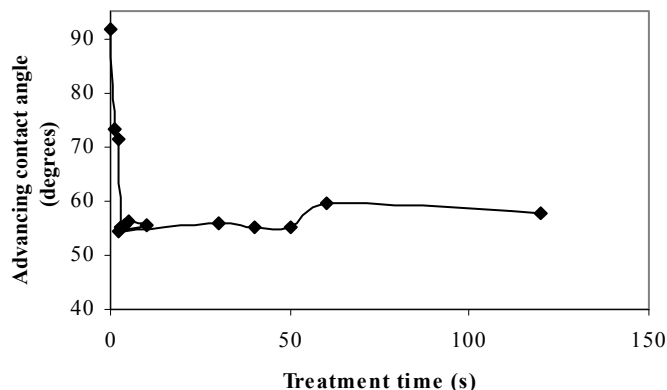
**T-peel strength measurements.** The pint-substrate adhesion was evaluated from T-peel tests (72 hours after bond formation) using an Instron 6025 instrument; a crosshead speed of 0.1 m/min was used. Five replicates for each experimental variable were obtained and data were averaged with an error less than  $\pm 0.5$  kN/m. In order to more precisely assess the loci of failure of the joints, the failed surfaces obtained after peel tests were analyzed using ATR-IR spectroscopy and SEM.

## 3. Results

### 3.1. Effect of treatment time

Different treatment time (from 1 to 120 seconds) were used in this study for treatment of elastomeric PE, at a plasma power of 500 W and a partial pressure of the gas of 10 mbar. Figure 2 shows the variation of the contact angle values on the low pressure plasma treated PE as a function of the treatment time using water as test liquid. The contact angle value on as-received PE is high (92°) and decreases considerably (to 55°) after 3 seconds of treatment due to the introduction of polar groups on the PE surface after the treatment [11,12]. From 3 to 50 seconds of treatment the contact angles remain similar and slightly increase to 60°, from 60 seconds of treatment, due probably to an excessive treatment. Therefore, the treatment with low pressure plasma increases the wettability of elastomeric PE.

XPS, a sensitive surface analysis technique [7,13,14] was used to assess the chemical modifications produced by the treatment. Table 1 shows the elemental composition of the as-received and some low pressure plasma-treated PE obtained using XPS. The elemental composition of the as-received PE surface mainly corresponds to carbon and oxygen. Small amount of silicon are also obtained which are most likely due to surface contamination. The plasma treatment produces a decrease in carbon and an increase in oxygen and in the O/C ratio due to the introduction of oxygenated moieties on the PE surface [15] (Table 1) during the first 3 seconds of treatment. The increase in the treatment time (50 s) slightly decreases both the amount of oxygen-containing moieties on the PE surface and the O/C ratio. In previous studies [16,17] the plasma treatment using air produces an increase in the nitrogen content; as shown in Table 1, this content is higher with long treatment times.



**Figure 2.** Advancing contact angles (water, 25° C) on low pressure plasma-treated elastomeric PE treated as a function of the treatment time (500 W, 10 mbar).

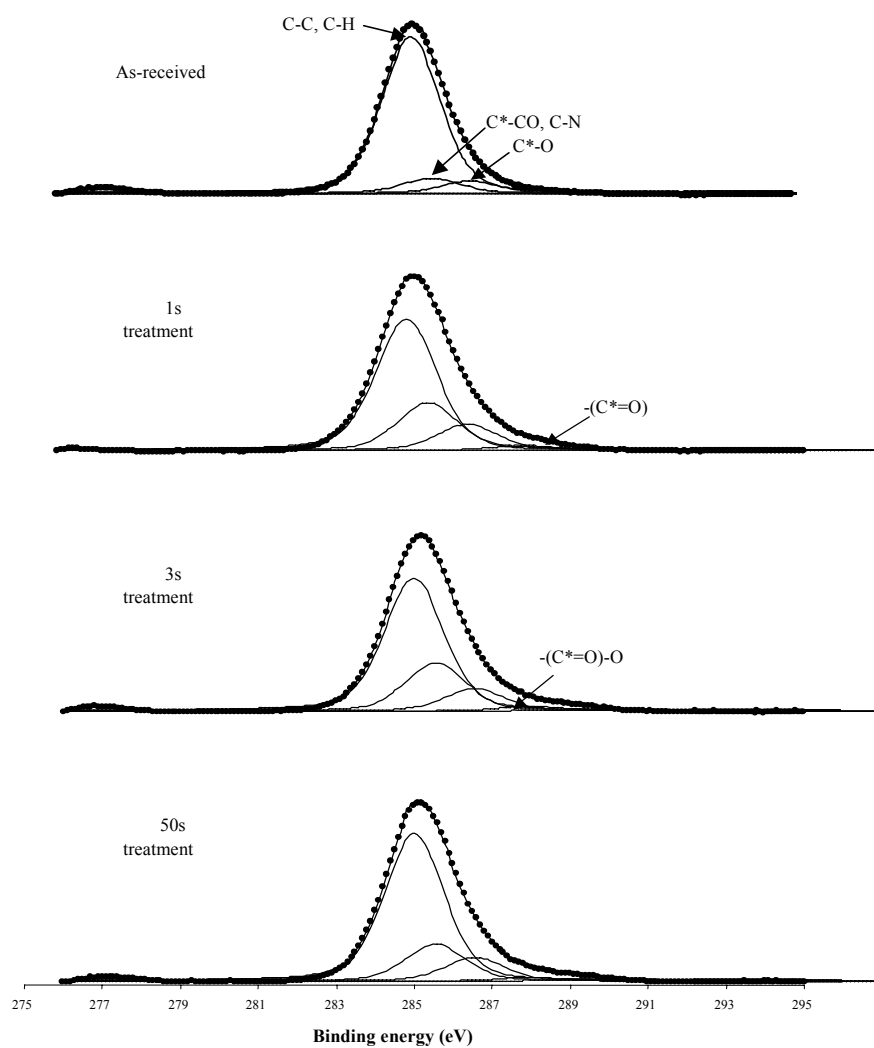
**Table 1.** Elemental composition (atomic %) of as-received and some low pressure plasma treated elastomeric PE. (500 W, 10 mbar).

Element	As-received (at %)	1s (at %)	3s (at %)	50s (at %)
C	92,22	86,70	85,95	86,16
O	5,73	11,92	12,67	12,29
N	0,14	0,37	0,34	0,81
Si	1,73	1,02	1,04	0,73
O/C	<b>0,062</b>	<b>0,137</b>	<b>0,147</b>	<b>0,143</b>

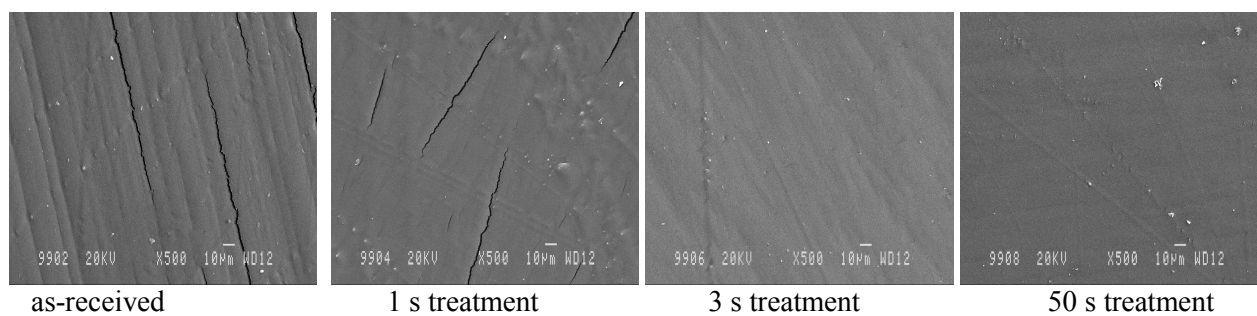
According to Figure 3, the plasma treatment creates new  $\text{C=O}$  and  $\text{COO}$  moieties [16,18] (bands at 288.0 eV and 289.3 eV, respectively) and the bands of polyethylene are also modified: a decrease in the band at 285 eV is observed due probably to the cracking of C-C, C-H bonds, and tends to increase with longer treatment times. Bands associated to C-O and C-N groups (285,7 and 286,9 eV) are markedly increased.

The surface topography of elastomeric PE was modified by low pressure plasma treatment. SEM micrographs (Figure 4) show some cracks on the surface of the as-received PE surface; the low pressure plasma treatment produces surface degradation and the modifications are more marked as the treatment time increases, indicating that surface ablation [18, 19] is favoured by increasing the length of the treatment, which leads to the removal of the outermost polymer surface, and obtaining a rather smooth surface.

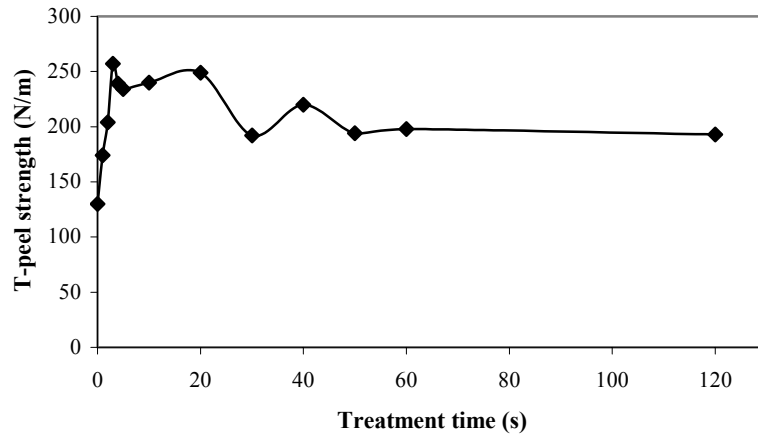
T-peel strength values of paint-substrate joints (Figure 5) indicate that the as-received elastomeric PE has a low adhesion capacity, according to their low surface energy. Treatment with low pressure plasma increases the peel strength values from 130 N/m, the as-received material, to 260 N/m, 3 s treated PE; this value decrease until 30 s treatment and remains similar (about 200 N/m) for longer treatment times. This decrease could be produced by a surface cross-linking, which can act as a weak boundary layer that difficult the adhesion of the paint. The ultraviolet radiation generated in the plasma treatment could produce a crosslinked surface layer [20, 21]. However, in all cases the T-peel values are higher that in the as-received material.



**Figure 3.** Carbon 1s XPS spectra of as-received and low pressure plasma-treated elastomeric PE at different treatment time. (500 W, 10 mbar).



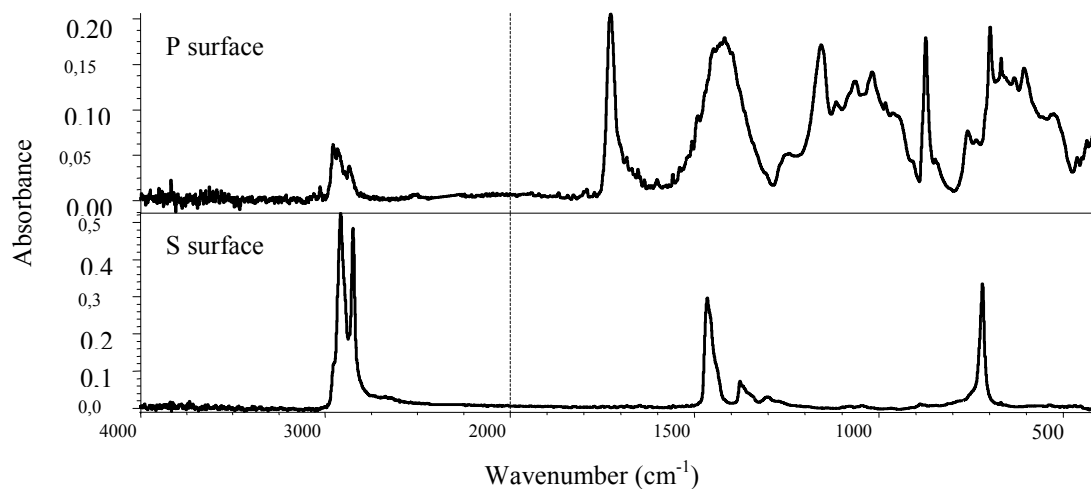
**Figure 4.** SEM micrographs of as-received and low pressure plasma-treated elastomeric PE as a function of the treatment time. (500 W, 10 mbar).



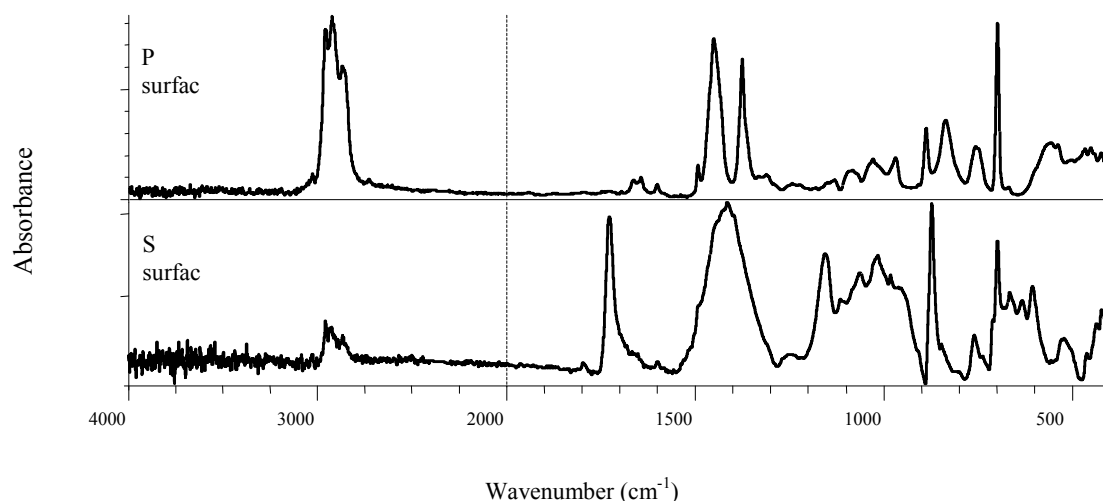
**Figure 5.** T-peel strength of as-received and low pressure plasma-treated PE/paint joints as a function of treatment time. (500 W, 10 mbar).

The loci of failure of the paint joints were assessed by characterization of the failed surfaces obtained after peel tests using ATR-IR spectroscopy. In this study, S surface corresponds to the failed surface that visually corresponds to the PE substrate and P surface to that visually corresponding to the paint-adhesive tape part. For the paint joint produced with the as-received PE (Figure 6), an adhesional paint-substrate failure was obtained, because the ATR-IR spectrum of the P surface is the same as that of the paint, and the ATR-IR spectrum of the S surface corresponds to the ATR-IR spectrum of PE. This indicates that the paint is not adhered to the elastomeric PE.

The loci of failure of the low pressure plasma treated PE/paint joints are different. The ATR-IR spectra of the failed surfaces for the joint produced with PE treated 3 s are shown in Figure 7 as an example. Whereas the ATR-IR spectrum of S surface mainly corresponds to that of paint, the ATR-IR spectrum of the P surface corresponds to the adhesive tape, indicating that an adhesional failure between the paint and the adhesive tape was obtained. Therefore, during peel test the paint remained on the elastomeric PE, achieving the objective of the present work. This failure is the same as the treatment time increases. Consequently, from the obtained results, we can conclude that 3 s of low pressure plasma treatment are enough to modify the surface of the elastomeric PE and improve their painting properties.



**Figure 6.** ATR-IR spectra of failed surfaces after peel tests on as-received elastomeric PE/paint joint.



**Figure 7.** ATR-IR spectra of failed surfaces after peel tests on low pressure plasma-treated elastomeric PE/paint joint.

### Acknowledgements

We would like to thank J.M. Martín Martínez from the Adhesion and Adhesives Laboratory for his help in XPS analysis.

### References

- [1] A. Zisman, *Ing. Eng Chem*, **50**(10), 19 (1963).
- [2] M.J. Owen, P.J. Smith, *Polymer surface modification: Relevance to adhesion*. Ed. K.L. Mittal, pp.3-15, Utrecht, The Netherlands (1996).
- [3] M.D. Landete, J.A. Martínez, M.A. Rodríguez, J.A. de Saja, J.M. Martín Martínez, *J.Adhesion Sci. Technol.*, **16**, 1073-1101 (2002).
- [4] S. Sapieha, J. Cerny, J.E. Klemberg-Sapieha, L. Martinu, *J. Adhesion*, **42**, 91-102 (1993).
- [5] O.D. Greenwood, R.D. Boyd, J.Hopkins, J.P.S. Badyal, *Polymer Surface Modification: Relevance to adhesion*, 17-32 K.L. Mittal Ed. (1995).
- [6] H.F. Webster, J.P. Wightman, *J.Adhesion Sci. Technol.*, **5**, no1, 93-106 (1991).
- [7] T M. Charbonnier, M. Romand, M. Alami, Tran minh Duc, *Polymer surface modification: Relevance to adhesión*, Ed. K.L. Mittal, Vol.2 pp.3-27, Utrecht, The Netherlands (2000).
- [8] Q. Quoc Toan Le, J.J. Pireaux, R. Caudano, *J. Adhesión Sci. Technol.*, **11**, 735, (1997).
- [9] A. Nihlstrand, T. Hjertberg, H.P. Schreiber, J.E. Klemberg-Sapieha, *J. Adhesión Sci. Technol.*, **10**, 651, (1996).
- [10] M.D. Landete, J.M. Martín-Martínez, A. Martínez-García, II Jornadas sobre adhesivos. Alicante University, (2001).
- [11] A. Martínez-García, *Estudio preliminar del tratamiento de copolímeros EVA mediante descarga corona*. Tesis licenciatura, Alicante (1998).
- [12] J.W. Chin, J.P. Wightman, *Surface characterization of plasma-modified*. H.M. Clearfield Editor, Blacksburg, Virginia, (1991).
- [13] H.F. Webster and J.P. Wightman, *J. Adhesion Sci. Technol.* **5**, 93 (1993).
- [14] T. Hjertberg, B.A. Sultan and E.M. Sorvik, *J. Appl. Polym. Sci.* **37**, 1183 (1989).
- [15] F. Arranz, *Revista de plásticos modernos*, **410**, 221 (1990).
- [16] E.M. Liston, L. Martinu, M.R. Wertheimer, *J. Adhesión Sci. Technol.*, **7**, No.10, 1091-1127, (1993).
- [17] R. Foerch, G. Kill, M.J.Walzak, *J. Adhesión Sci. Technol.*, **7**, No.10, 1077-1089, (1993).
- [18] C.M. Cepeda-Jiménez,, PhD, Alicante (2001).
- [19] M. Morra, E. Ochiello, F. Garbassi, *J. Adhesion Sci. Technol.*, **7**, 1051 (1993).
- [20] A.K. Taraija, G.A. Orchard, I.M. Ward, *Plastics, rubber composites processing applications*, **19**, 273, (1993).
- [21] A.V. Popoola, *J. Appl. Polym. Sci.*, **49**, 2115, (1993).

# A PARAMETRIC STUDY OF A ARGON/OXYGEN RF DISCHARGES USING ONE-DIMENSIONAL COUPLED MODELS OF DISCHARGE DYNAMICS AND SPECIES TRANSPORT

W. Morscheidt<sup>1,2</sup>, K. Hassouni<sup>1</sup>, F. Aréfi-Khonsari<sup>2</sup>, J. Amouroux<sup>2</sup>

<sup>1</sup> *Laboratoire d'Ingénierie des Matériaux et des Hautes Pressions, CNRS-UPR1311, Université Paris Nord, 99 Avenue J. B. Clément, 93430 Villetaneuse, France*

<sup>2</sup> *Laboratoire de Génie des Procédés Plasmas et Traitements de Surfaces, ENSCP, 11 Rue P. et M. Curie, 75231 Paris Cedex 05, France*

## Abstract

A 1D self consistent numerical model of glow discharges obtained in parallel plate capacitively coupled device is used to investigate an argon-oxygen plasma obtained in the conditions relevant to SnO<sub>2</sub> deposition by PECVD. In this paper, we discuss the effect of RF voltage, DC bias voltage and flow velocity on the species densities, electron average energy and discharge dynamics. For this purpose, several simulations were performed for a 66% Oxygen - 34% Argon feed gas at a pressure of 15 Pa.

## 1. Introduction

Applications for thin SnO<sub>2</sub> films cover several fields such as the fabrication of solar cells, transparent heating elements and, more recently, toxic gas sensors or anti-fouling coatings [1]. PACVD technique have been successfully employed for the deposition of SnO<sub>2</sub> thin films (300nm) using parallel plate radio-frequency discharges in a Ar/O<sub>2</sub>/Sn(CH<sub>3</sub>)<sub>4</sub> mixture containing a very low percentage of Sn(CH<sub>3</sub>)<sub>4</sub> (< 2%) [2,3]. The SnO<sub>2</sub> films obtained present a wide range of conductivities obtained in a one step process, which presents an important advantage when compared to other existing processes. The use of the plasma technique to obtain thin films with controllable properties requires in deep understanding of the mechanisms involved in the process. For this purpose it is necessary to carry out modelling of the discharge dealing with the investigation of the coupled phenomena namely the power deposition, species and energy transport, electron and heavy species kinetics in the plasma reactor. A step by step approach has been chosen. Some authors [4] have reported the importance of the role of electrons, O-atom and metastable states in similar deposition processes. As the precursor represents less than 2% of the gas flow, this model deals with, as a first step, Ar-O<sub>2</sub> mixture.

The modelling of the electron kinetics, chemistry and energy transfer for argon-oxygen plasmas was carried out under discharge conditions corresponding to SnO<sub>2</sub> deposition experiments in previous studies [3,5-6]. The present work represents the continuation of the latter and deals with the self consistent one-dimensional modelling of electric field, transport phenomena, electron kinetics and chemistry in argon/oxygen discharges obtained in the same conditions. In the present paper we will mainly focus on the investigation of the RF voltage, the self-bias voltage and gas flow velocity effects on the molar fraction of the major species.

## 2. Model Overview

The discharge considered in this work is obtained using a parallel plate capacitively coupled reactor sustained by a 13.56 MHz radio-frequency electric field. The discharge is processed for a pressure of 15 Pa (100 mTorr). The chemistry in the investigated discharge may be well described using the following 15 species O<sub>2</sub>(X<sup>3</sup>Σ), O<sub>2</sub>(<sup>1</sup>Δ<sub>g</sub>), O<sub>2</sub>(<sup>1</sup>Σ<sub>g</sub>), O<sub>3</sub>, O(<sup>3</sup>P), O(<sup>1</sup>D), O(<sup>1</sup>S), Ar\*, Ar, O<sub>2</sub><sup>+</sup>, O<sub>2</sub><sup>-</sup>, O<sup>-</sup>, O<sup>+</sup>, Ar<sup>+</sup> and e<sup>-</sup>. These species are linked by a set of 68 reactions that consists of excitation-de-excitation reactions for O<sub>2</sub> and Ar metastables, electron impact dissociation and ionization reactions, electron impact dissociative attachment for O<sub>2</sub>, ion conversion, mutual neutralization and recombination processes. The reaction rate constant and electron transport coefficients are calculated as a function of the electron mean energy, from the EEDF solution of the two term expansion of the Boltzmann equation. These values are calculated off-line for several feed gas compositions. Ions transport coefficient are estimated as a function of the reduced electric field (E/n) from published data [7, 8].

The discharge conditions considered in this work are such that the mean free paths of the different plasma species are much smaller than the characteristic discharge dimensions. Therefore, the fluid approximation may be used to describe the discharge dynamics and composition. The fluid model developed in the frame of

this work distinguishes two main modules: a discharge module that describes the RF field and charged species dynamics and a transport-chemistry module that describes the coupled chemistry and transport phenomena for neutral species.

### 2.1. Discharge module

The discharge module is used to solve the coupled set of Poisson's equation, electron energy equation and charged species continuity equations. The Poisson's equation links the electrical potential to the density of charged species as follows :

$$\left( \frac{\epsilon_0}{e} \right) \Delta V = n_e - \sum_{\text{ions}} z_i n_i \quad (1)$$

Where  $n_e$  is the electron density,  $z_i$  and  $n_i$  are the number of charges and the densities of ions. The boundary condition for the Poisson's equation at the electrodes are:

$$V_{\text{RF}} = V_0 \sin(\omega t) + V_{\text{bias}} \quad \text{and} \quad V_{\text{ground}} = 0 \quad (2)$$

Due to the relatively high frequency, only electrons can follow the RF electric field  $\vec{E} = -\vec{\text{grad}}(V)$ . The heavy ions shows an important inertia and doesn't instantaneously respond to the RF electric field. The drift of these species takes place in a damped effective electric field  $E_{\text{eff}}$  given by :

$$\frac{\partial \vec{E}_{\text{eff}}}{\partial t} = -v_i (\vec{E}_{\text{eff}} - \vec{E}) \quad (3)$$

Where  $v_i$  is the collision frequency between ions and neutrals.

The charged species densities required for solving the Poisson's equation are estimated from the continuity equations that may be written :

$$\frac{\partial n_s}{\partial t} = -\nabla \cdot (-D_s \nabla n_s + z_s \mu_s E_s n_s) + S_s \quad (4)$$

where 's' is a species that may be either an electron or an ion.  $D_s$ ,  $\mu_s$  and  $S_s$  represent the diffusion coefficient, the mobility and the collisional production rate of the considered charged species respectively. The source terms  $S_s$  are estimated using the rate constants determined on the basis of the solution of the two-term expansion of Boltzman equation.  $\vec{E}_s$  is the electric field experienced by the considered species, i. e.  $\vec{E}_s = \vec{E}$  for electron and for each ion  $\vec{E}_s$  is the effective electric field obtained from equation (3). The transport coefficients are assumed to be a function of the reduced electric field using the transport data from references [7] and [8]. For the electrons, we used the transport coefficients estimated from an off-line Boltzmann solver. The discharge module also solves the electron energy conservation equations assuming a Maxwellian EEDF with a mean electron temperature  $T_e$ . This equation may be written as the following:

$$\frac{\partial n_e \epsilon_e}{\partial t} = -\nabla \cdot \left( -\frac{2}{3} \kappa_e \nabla \epsilon_e + \frac{5}{3} J_e \epsilon_e \right) - e J_e \cdot \vec{E} - \sum_{\text{coll}} k_{\text{coll}} n_e n < E_{\text{th-coll}} > \quad (5)$$

$\epsilon_e$ ,  $\kappa_e$  and  $J_e$  are the average energy, the thermal conductivity and the flux of electrons respectively.  $k_{\text{coll}}$  and  $<E_{\text{th-coll}}>$  represents the reaction rate constant and the energy threshold for the collision 'coll'.

The right hand side (RHS) of equation (5) involves a flux divergence term that takes into account the energy transport through energy conduction and electron diffusion. It also contains a source term that involves the rate of energy gain from the high frequency electric field and the rate of energy loss through collisions.

### 2.2. Neutral species transport-chemistry module

The transport chemistry module solves the stationary continuity equation of neutral species that may be formulated as follows :

$$-\nabla \cdot (-D_s \nabla n_s + u n_s) + <S_s> = 0 \quad (6)$$

$u$  is the gas flow velocity and  $<S_s>$  is the time averaged source terms for species s.  $u$  has been determine from off-line calculation using Fluent© CFD software. The value of  $u$  will be precised in the third section of this paper. The diffusion coefficient for neutrals is estimated using a Lennard-Jones interaction potential [9]. The solution of the stationary transport equation for neutral species was motivated by the resulting strong reduction of the computation time without alteration of the physics of the considered discharge. As a matter of fact, the dynamics of neutral species (chemistry and transport) is much longer than that of the RF field or the charged species. The spatial distribution of these species may be therefore deduced from time-averaged electron density and electron-impact rate constants.



The boundary conditions for the different conservation equations are similar to those reported in [10]. They basically express the balance between the rate of transport flux at the electrode surface and the rate of surface processes.

The system of equations was solved by time-advancing a finite difference form of the charged species transport equation, Poisson's equation being solved at each time step. At the end of each period the steady state axial profiles of the neutral species corresponding to the time averaged electron density and electron-impact rate constants are determined from the solution of the stationary continuity equation (6). The procedure is then iterated for another RF cycle. Typically, 3000 RF cycles, sometimes less, are needed to obtain the convergence of the whole system of equations.

### 3. Results and discussion

#### 3.1. RF voltage

The effects of the RF voltage in the range of 200 V to 500 V on the electron average energy, the electron, O and O-atom densities have been investigated. Figure 1 shows the time averaged profiles for electrons molar fraction estimated for four values of the RF voltage amplitude ( $V_0$ ). The ionisation rate in the center of the discharge changes from  $2 \times 10^{-7}$  to  $6 \times 10^{-7}$  for  $V_0$  in the range of 200 to 500 V. Greater variations are observed in the central part of the discharge for higher voltages. These smoother profiles are attributed to a more efficient diffusion of electrons, in the case of lower voltage, due to the higher reduced electric field obtained in the center of the discharge for  $V_0 = 200$  V. The evolution of the time-averaged electron energy profiles are given for  $V_0$  in the range of 200 V to 500 V in figure 2. In the center of the discharge, the time-averaged electron energy is independent of the  $V_0$  applied. The estimated value is about 2.16 eV. In the lateral part of the discharge we observe two maxima that increase from 10 to 30 eV for  $V_0$  in the range of 200 V to 500 V. This increase leads to a global enhancement of the ionisation rate in the discharge. We observed that the mean electron energy is well correlated to the increase of the reduced electric field in the sheath.

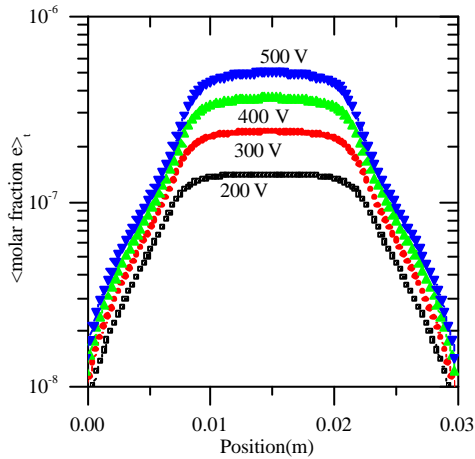


Figure 1 : Evolution of the time averaged electron molar fraction profile for different value of  $V_0$

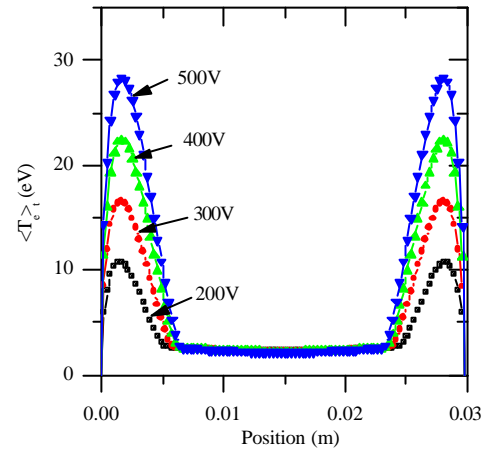


Figure 2 : Evolution of the time averaged electron energy profile for different value of  $V_0$

The distribution of the neutral species in the inter-electrode gap are almost constant. The variation of the time and space averaged molar fraction for O-atom and  $O_2(^1\Delta_g)$  are given in figure 3 as a function of  $V_0$ . The O-atom molar fractions increases by a factor of four between  $2 \times 10^{-2}$  to  $8 \times 10^{-2}$  for  $V_0$  in the range of 200 V to 500 V. It has been found that this increase is well correlated to the increase of the dissipated power. These results can be explained considering the former results [6] which showed that dissociative collisions represent 80 % of electrons energy loss. The increase of O-atom density and dissipated power are due to the increase of electron density and mean energy, when the  $V_0$  is changed from 200 V to 500 V. The change of  $O_2(^1\Delta_g)$  is less significant than electrons and change by only a factor two. This result is explained by the increase of the electron mean energy in the sheath. The  $O_2(^1\Delta_g)$  kinetics is governed by electron excitation of the fundamental state and by dissociation of the metastable state,  $O_2(^1\Delta_g)$ . The mass balance then showed that the  $O_2(^1\Delta_g)$  density is directly related to the electron energy through the ratio of rate constants of the above cited reactions.

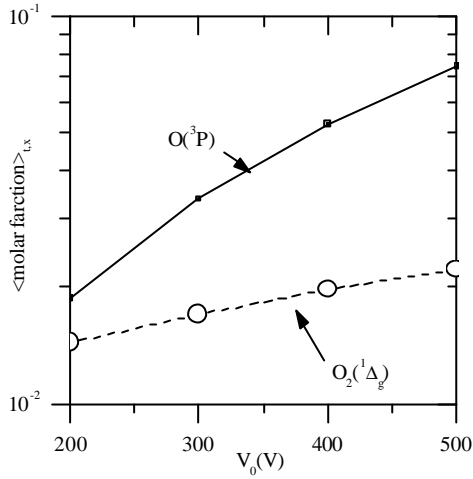


Figure 3 : Variation of the time and space averaged O-atom and  $\text{O}_2(^1\Delta_g)$  molar fraction profiles versus RF voltage.

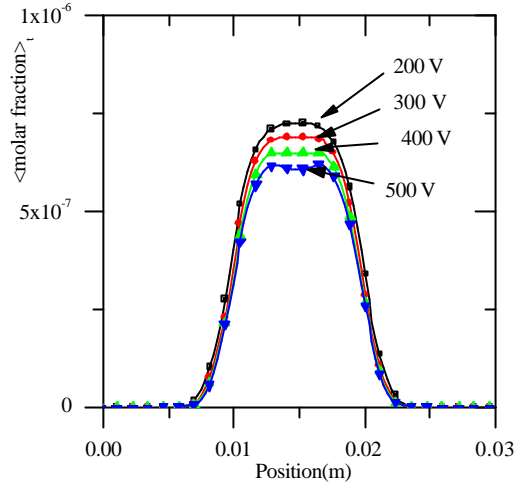


Fig. 4 : Evolution of the time averaged O molar fraction profile for different values of  $V_0$

Molar fractions of ions are also affected by RF voltage. The  $\text{O}^+$  molar fraction decreased from  $7.3 \times 10^{-7}$  to  $6.1 \times 10^{-7}$  for  $V_0$  in the range of 200 V and 500 V. The  $\text{O}^+$  ions are produced through dissociative attachment reactions in the center of the discharge and are consumed by detachment reaction with O-atom. The observed decrease can then be justified by the increase of O-atom with RF voltage. The decrease of the  $\text{O}^+$  densities associated with the increase of ionisation rate leads to a shift from a high electronegative discharge at low RF voltage to a low electronegative one for high voltages.

### 3.2. DC bias voltage

The variation of the reduced electric field induced by the self bias voltage leads to a considerable variation of the average electron energy profile. On the grounded electrode side, the electron energy maximum decreases from 15 to 7 eV when  $|V_{DC}|$  increase from 0 to 300 V. On the RF electrode side, where the self-bias voltage is apply, the average electron energy increases from 15 eV to 47 eV (figure 5). We can note also that the electron energy in the core of the plasma remains unchanged. The electric field profile leads to important changes in the electron molar fraction profile, shown in figure 6. The value of electron molar fraction in the center of the discharge decreases around 40 % for the same increase of the  $V_{DC}$ .

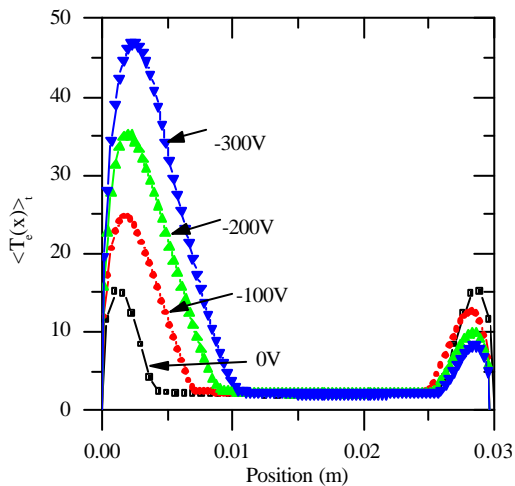


Figure 5 : Evolution of the time averaged electron mean energy profile for different value of  $V_{DC}$ .

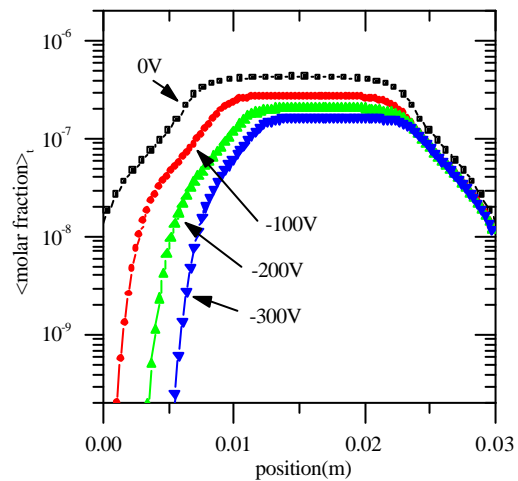


Figure 6 : Evolution of the time averaged electron molar fraction profile for different value of  $V_{DC}$ .

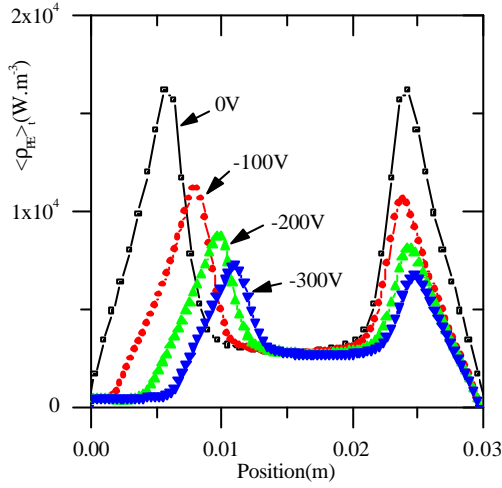


Figure 7 : Evolution of the time averaged power deposition profile for different  $V_{\text{DC}}$  value.

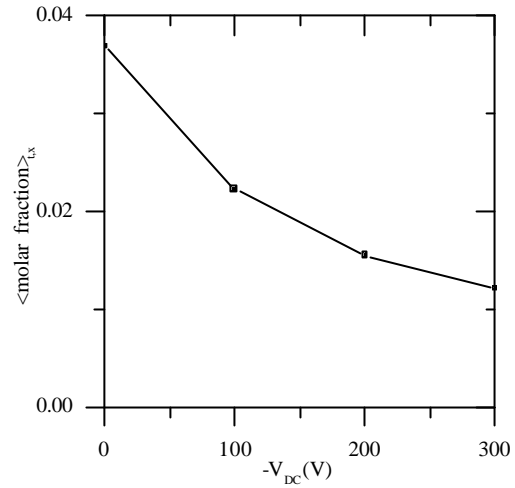


Figure 8 : Variation of the time and space averaged O-atom molar fraction profiles versus  $V_{\text{DC}}$ .

The coupling of electron density and electric field variations results in a strong decrease of electron heating (figure 7) from  $6 \times 10^{-3}$  to  $3 \times 10^{-3} \text{ W.m}^{-3}$ . As the O-atom and the dissipated energies are closely linked, the decrease of the absorbed power results in a decrease of O-atom molar fraction. For  $V_{\text{DC}}$  in the range of 0 to  $-300 \text{ V}$ , the time and space molar fraction averages of O-atom changes from  $3.7 \times 10^{-2}$  to  $1.2 \times 10^{-2}$ .

### 3.3. flow velocity effects

Usually the models presented in the literature assume that the neutral transport is diffusive and neglect the gas flow hydrodynamics. This approximation is valid if the value of peclet number calculated from the gas flow velocity is less than 2. The diffusion coefficient for O-atom is in the range of  $0.12 \text{ m}^2.\text{s}^{-1}$  at 15 Pa which point out that for a 3 cm inter-electrode gap that the diffusion is dominant if the gas flow velocity is less than  $10 \text{ m.s}^{-1}$ . In the experimental setup, the gas is introduced at the RF electrode either by a simple hole (3 mm), or by a shower-head type electrode with 80 holes (0.5 mm each). The typical flow rate is in the range of 10 sccm. This leads to a gas flow velocity at the inlet as high as  $250 \text{ m.s}^{-1}$ . The followings results shows the comparison between results obtained with and without neglecting the gas flow velocity.

The gas flow velocity has been estimated from calculations performed with the Fluent® 5.4 CFD software. The axial gas flow velocity profile between the two electrodes, on the symmetry axis, is given in figure 9. The velocity when entering the reactor is about  $250 \text{ m.s}^{-1}$ . At  $x=3 \text{ cm}$  the velocity is zero, due to the stagnation point formed by the grounded electrode. Between the two electrodes, the gas velocity decreases exponentially down to  $10 \text{ m.s}^{-1}$  for  $x$  in the range  $x=0$  to  $x=8 \text{ mm}$ .

The estimation of the  $\text{e}^-$  molar fraction when the flow velocity is considered is 50% lower than the one in a purely diffusive regime. Similar effects have been observed for ions. Despite the high velocity of charged species, their densities are sensitive to the gas flow velocity. This effect is attributed to the important coupling between the chemistry and discharge dynamics. The neutral species molar fractions are also modified when taking into account the gas flow velocity. Figure 10 shows the comparison of molar fraction estimation of O-atom and  $\text{O}_2(^1\Delta_g)$  species for the two cases studied namely  $u=0$  and  $u=f(x)$ . In the first case, the profile obtained is almost flat and presents some symmetry according to the center. For  $u=f(x)$ , the molar fractions of O-atom and  $\text{O}_2(^1\Delta_g)$  are severely affected by the gas flow velocity which induces some asymmetric profiles. The molar fraction increase from the injection zone at the RF electrode to the grounded electrode. The increase is in particularly high in the first third of the discharge while the molar fraction are almost flat in rest of the discharge. These profiles lead to an increase of the O-atom molar fraction.

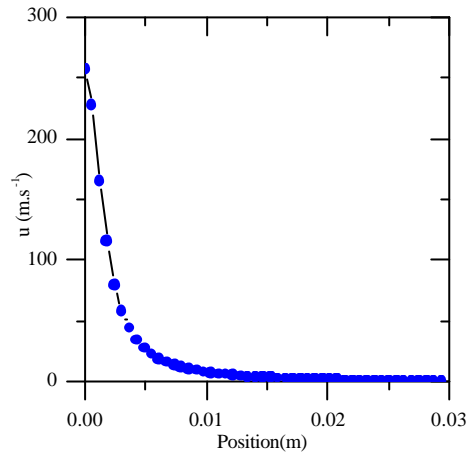


Figure 9 : Axial velocity.

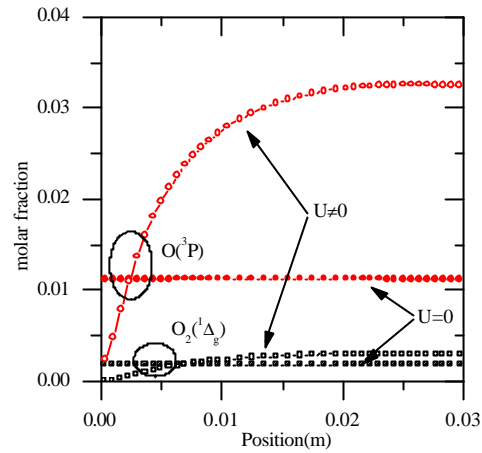


Figure 10 : Comparison between time averaged profile for O-atom and  $O_2(^1\Delta_g)$  molar fractions obtained with and without taking into account the flow velocity.

#### 4. Conclusion

A one-dimensional self consistent numerical model of glow discharges obtained in parallel plate capacitively coupled devices have been used to investigate the composition of argon-oxygen plasmas obtained under pressure and input power conditions relevant to  $SnO_2$  deposition by PECVD.

In this paper, we discussed the effect of RF voltage, DC bias voltage and flow velocity on the species densities, electron average energy and discharge dynamics. Results showed that the increase of the RF voltage leads to an increase of the electron density in the bulk of the discharge, while the density of the negative  $O^-$  ion remains almost constant. The electron average energy in the sheaths strongly increases from 10 to 30 eV for the same RF voltage variation. Its value in the bulk of the discharge remains however constant. This behavior leads to a significant increase of the O-atom density. The magnitude of the DC bias voltage mainly affect the spatial profiles of electron temperature and density that are quite sensitive to the potential distribution in the discharge. Higher values of the DC bias voltage leads to smaller RF power dissipation on electrons. A large DC bias yields smaller dissociation degrees. The flow rate in the discharge has also a significant effect on the discharge composition. The O-atom and metastable densities are particularly sensitive to the gas velocity at the gap inlet.

#### References :

- [1]. J.Pulpytel, M.Ghassami, H.Cachet, D.Festy, F.Arefi-Khonsari, *to be published in Proc of ISPC 16*, Taormina, June 22-27,(2003).
- [2]. F. Arefi-Khonsari, F. Hellegouarc'h and J. Amouroux, *J. Vac. Sci. Technol. A*, **16**(4), (1998), 2240-2244.
- [3]. W.Morscheidt, K.Hassouni, N.Bauduin, F.Arefi-Khonsari, J.Amouroux, *Plasma Chemistry and Plasma Processing*, **23** (1), ( 2003),117-140
- [4]. A. Granier, F. Nicolazo, C. Vallée, A. Goullet, G. Turban, B. Grolleau, *Plasma Sources Sci. Technol.***6**, (1997),pp 147-156
- [5]. W.Morscheidt, K.Hassouni, J.Amouroux, F.Arefi-Konsari, *Proc of ISPC 15*, Orleans, July 12-16, (2001), 2161-2166
- [6]. W.Morscheidt, K.Hassouni, N.Bauduin, J.Amouroux, F.Arefi-Konsari, *Proc of ISPC 14*, Prague, August 2-6, (1999), 771-776
- [7]. M. Yousfi, A.Hennad, O.Eichwald, *J. Appl. Phys.*, **84**(1) (1998), 107-114
- [8]. B. Eliasson and U. Kogelschatz, 'Basic Data for Modelling Electrical Discharges in Gases : Oxygen', KLR 86-11 C Report of Brown Boveri Forschungszentrum, Baden, Switzerland, (1986).
- [9]. R.B. Bird, W.E.Stewart, E.N.Lightfoot, 'Transport phenomena', John Wiley & Sons, 1960
- [10]. E. Gogolides, H. H. Sawin, *J. Appl. Phys.***72**(9) (1992), 3971-3986.

# Hydrogen production from hydrocarbon using atmospheric pure steam plasma generated by microwave discharge

H.Sekiguchi<sup>1</sup>, S.Nakanishi<sup>1</sup>, K.Fukuda<sup>2</sup> and H.Inagaki<sup>2</sup>

<sup>1</sup> *Department of Chemical Engineering, Tokyo Institute of Technology, Tokyo, Japan*

<sup>2</sup> *WE-NET Center, The Institute of Applied Energy, Tokyo, Japan*

## Abstract

Steam plasma reforming of hexane under atmospheric pressure was investigated to generate hydrogen using microwave discharge. Experiments were carried out with 2.0kW microwave power followed by the process simulation considering equilibrium condition. The results showed that rapid reforming of hexane and production of hydrogen were achieved without catalyst. Energy conversion efficiency evaluated with the experimental data was not sufficient compared with conventional reforming methods.

## 1. Introduction

Fuel cell system is being significantly developed for high efficient and decentralized electric power source. The power system can be applied widely in commercial uses, especially for automobiles. A major concern in developing fuel cell system is how to get hydrogen as fuel and many systems have been proposed for hydrogen generation. The reformation of hydrocarbons is conventional method, however this should be done because present situation on hydrogen supply and demand is well balanced. Usual reforming of hydrocarbon is carried out thermally with steam and oxygen where partial oxidation of hydrocarbon takes place to provide reaction heat because the reforming reaction with steam is endothermic. Noble metal catalysts are usually required to enhance the reaction rate. Hence the reforming system is sensible to impurities in the source which deactivates catalysts.

One of attracting methods for reforming hydrocarbon is to use plasma [1,2]. Plasma contains reactive radicals, ions and electrons. High reactivity caused by these species enhances the reaction rate and eliminates catalysts. These advantages as well as its high energy density ensure the compactness of the plasma reformer. Moreover the plasma system is adapted for various hydrocarbons including natural gas, gasoline, heavy oils and biofuels. Fast response time can be also achieved because the plasma is operated by electricity. However the utilization of electricity seems a disadvantage from the viewpoint of energy efficiency. When steam is used for plasma supporting gas, radicals such as H, OH, and O give both reductive and oxidative circumstances, and the plasma is effective for various treatments of materials. The authors have already studied on the reforming of hydrocarbon using atmospheric pure steam plasma using microwave discharge [3]. Microwave discharge is one of the techniques to get non-equilibrium plasma even under atmospheric pressure where the electron temperature has around 4000 - 6000 K, while the heavy particle temperature around 2000K [4]. This non-equilibrium may cause the efficient reformation comparing equilibrium plasma system. The continuing study on steam plasma reforming has been carried out here with various experimental conditions. Hexane was used here as a model of hydrocarbon.

## 2. Process Evaluation

To determine suitable conditions on the reforming of hexane, process calculation was carried out using chemical process simulator (Aspen Tech., Hysys Plant) assuming the reactions took place in equilibrium. Figure 1 shows the system diagram for the simulation. The plasma reformer was connected to the sift reactor which could convert CO into CO<sub>2</sub> and H<sub>2</sub> with additional H<sub>2</sub>O. Three heat exchangers were equipped to recover heat. The simulation results are shown in Figs.2-5 where the flow rates of hexane and steam are respectively 1.5 and 9 mmol/s. Figure 2 shows the composition at the exit of the plasma reformer. Hydrogen and CO are dominantly produced and increase with microwave power. However these amounts become

constant above about 2000W because supplied energy is enough to reach complete reforming. This result can be confirmed in Fig.3 where the temperature of the plasma reformer increases steeply from 2000W. Figure 4 shows the composition after the shift reactor where CO is completely converted into CO<sub>2</sub>.

Energy conversion efficiencies based on higher and lower heating values (HHV, LHV) are defined by the following equations:

$$h_{HHV} = \frac{F_{H2}H_{H2}}{W_i + F_{C6}H_{C6}} \quad (1)$$

$$h_{LHV} = \frac{F_{H2}L_{H2}}{W_i + F_{C6}L_{C6}} \quad (2)$$

where  $F$  denotes flow rate,  $H$  and  $L$  respectively mean higher heating value (HHV) and lower heating value (LHV), and  $W_i$  is input power for microwave discharge. The subscripts C6 and H2 mean hexane and hydrogen. As shown in Fig.5, maximum efficiency is obtained at about 2000W. Maximum efficiency could not attain to unity because CH<sub>4</sub> is a little formed in the product gas. Therefore, 2000W is ideal input power for the reforming at the present calculation condition (hexane: 1.5mmol/s, steam: 9.0mmol/s).

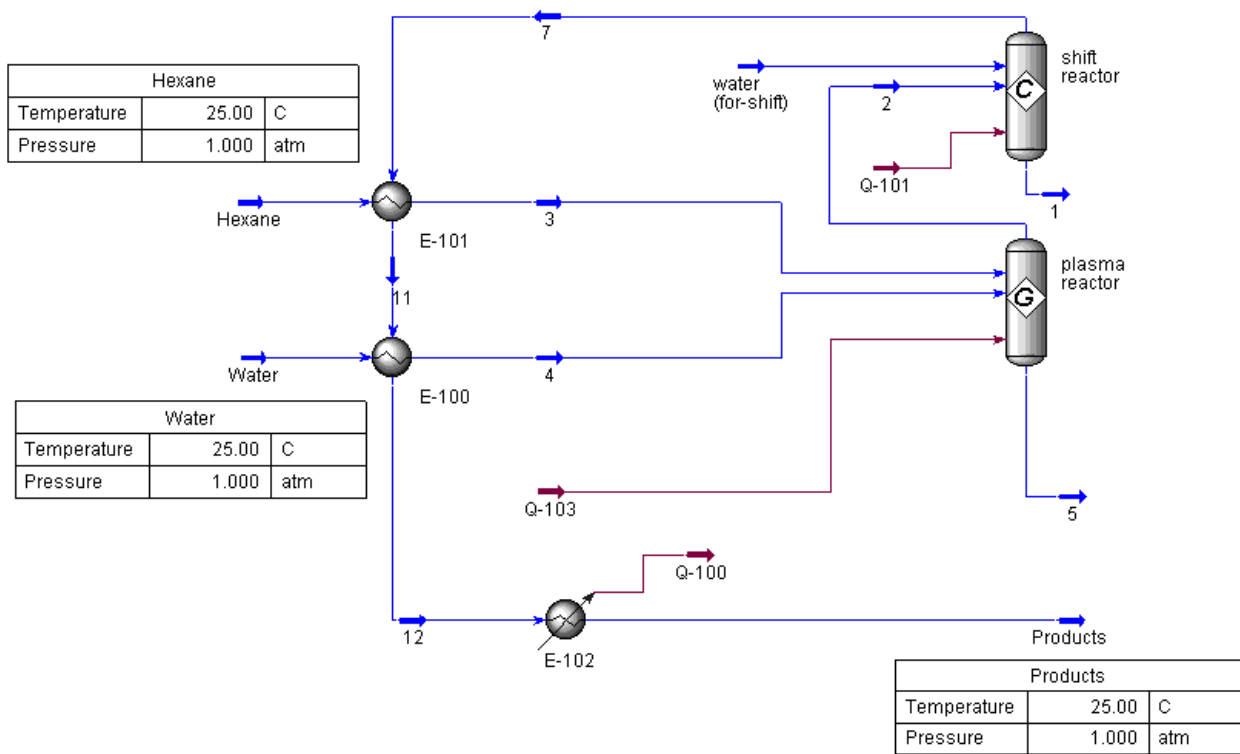


Fig.1 Process simulation diagram for plasma reforming

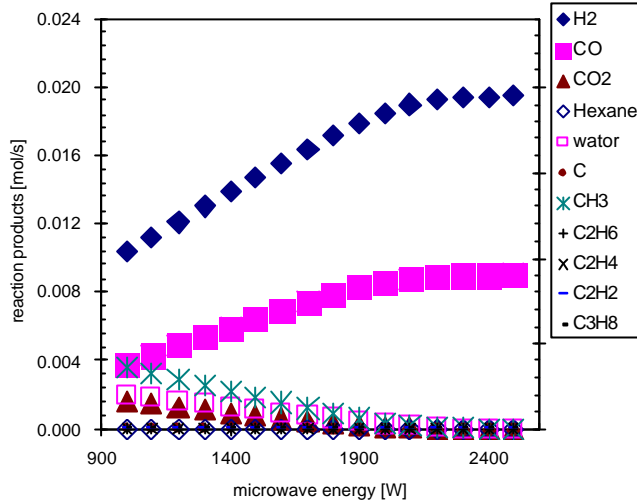


Fig.2 Effects of input power on product gas composition

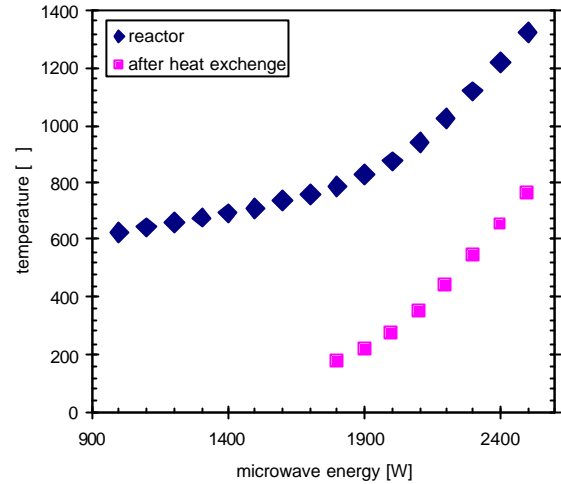


Fig.3 Effects of input power on plasma reformer temperature

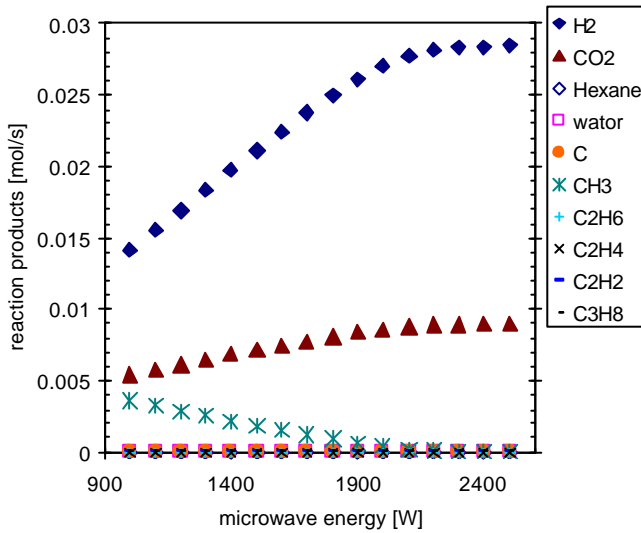


Fig.4 Effects of input power on product gas composition after sift reactor

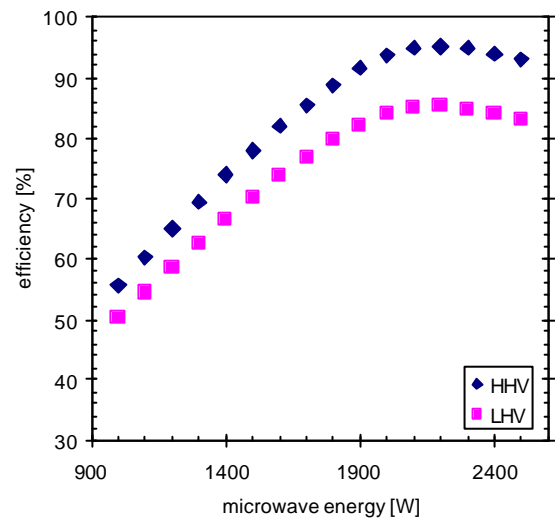


Fig.5 Effects of input power on energy conversion efficiency

### 3. Experimental

The experimental apparatus shown in Fig.6 was almost the same as that in our previous work [3]. The experiment was conducted with 2.45GHz microwave power supply and the power was set 2.0kW in all the experiment. A quartz tube reactor having a inner diameter of 10 mm was used. Hexane, used as a model of hydrocarbon, was preheated and mixed with steam before the injection into the reactor. The composition of the product was analyzed by gas chromatography and continuous gas analyzer. The experimental conditions are summarized in Table 1. The flow rates of hexane and steam were increased as compared with those in the previous work because the process simulation suggested the suitable conditions mentioned above. The sift reactor was not equipped in the experiment.



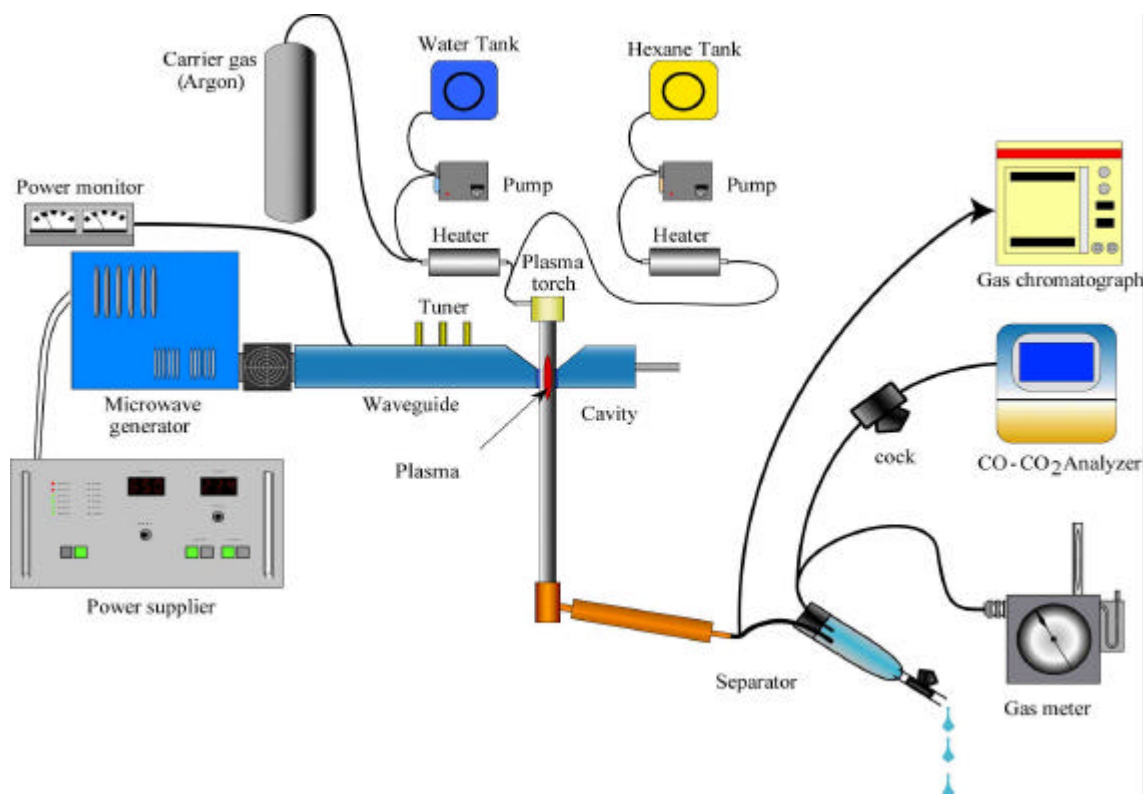


Fig.6 Schematic of experimental apparatus

Table 1 Experimental conditions

Reaction Tube (quartz)	O.D. 12mm, I.D. 10mm, Length 500mm
C <sub>6</sub> H <sub>14</sub> flow rate	1 – 1.4 mmol/s
H <sub>2</sub> O flow rate	4.8-8.4 mmol/s
O/C ratio	0.8 – 1.4
Input power	2 kW

#### 4. Results and Discussion

The results showed that H<sub>2</sub> and CO were dominantly produced and was similar to those in the previous work [3]. Figure 7 shows the product gas composition with varying hexane flow rate where the ratio of oxygen to carbon (O/C) in the feed gas is unity. The figure also indicates the estimation by the process simulation described above. The production rate was almost independent of the flow rate nevertheless the increases in H<sub>2</sub> and CO were estimated in the ideal condition. The conversions of hexane and steam were decreased with increasing flow rate as shown in Fig.8. An agreement in both the conversions is observed, suggesting that the following reaction takes place in the plasma reactor:



Energy conversion efficiency based on HHV and estimated from the experimental results is shown in Fig.9 assuming that the existing CO in the product is equivalent to H<sub>2</sub> because the shift reactor can convert CO into H<sub>2</sub> with additional steam under the reaction;  $\text{CO} + \text{H}_2\text{O} \rightarrow \text{CO}_2 + \text{H}_2$ . The efficiency is decreased with increasing flow rate. Figure 10 shows modified energy conversion efficiency with the consideration of power supply efficiency. This is more realistic than the previous one because an energy loss is caused at microwave



generation. The power supply efficiency is assumed 0.5 here, hence we substitute 4000W for  $W_i$  in Eq.1 to estimate efficiency at a microwave power of 2000W. The modified efficiency is slightly decreases with increasing flow rate.

Figure 11 shows the effect of O/C on conversions of hexane and steam where hexane flow rate is 1.0 mmol/s. The conversion of steam is decreased with increasing O/C because excess steam is supplied in regard to the stoichiometry indicated in R1. However the conversion of hexane is not significantly affected by O/C. This may be ascribed to the change in flow condition in the reaction tube. The increase in O/C corresponding to much increase in steam flow rate uniformizes temperature field, resulting in the improvement of hexane conversion. Figure 12 shows the modified energy conversion efficiency corresponding to the condition of Fig.11. The efficiency also indicates almost constant about 0.4.

As indicated in Figs.10 and 12, the performance based on the experimental data is too low to supply enough hydrogen for fuel cell system compared with the conventional reforming methods. However rapid reforming of hexane can be achieved without catalyst in compact power supply system. Improvement on flow condition may enhance the efficiency.

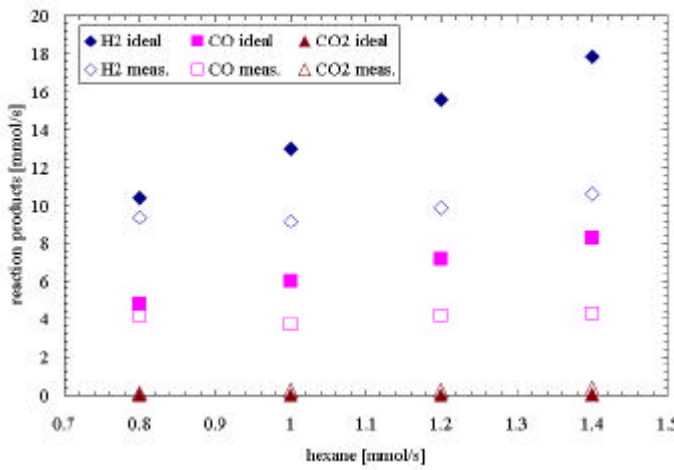


Fig.7 Effects of hexane flow rate on product composition where O/C=1, ideal: simulation, meas: experiment

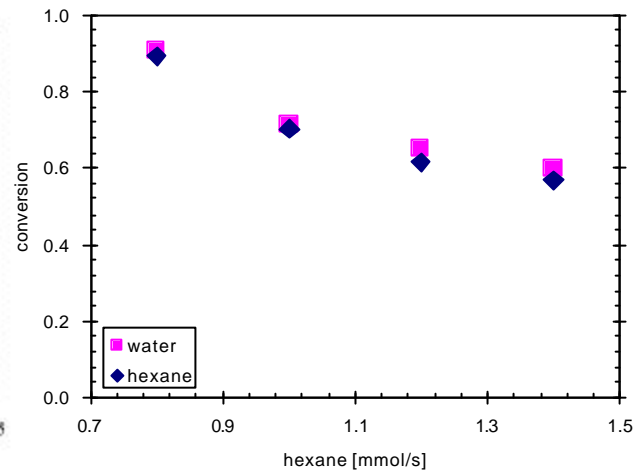


Fig.8 Effects of hexane flow rate on conversion where O/C=1

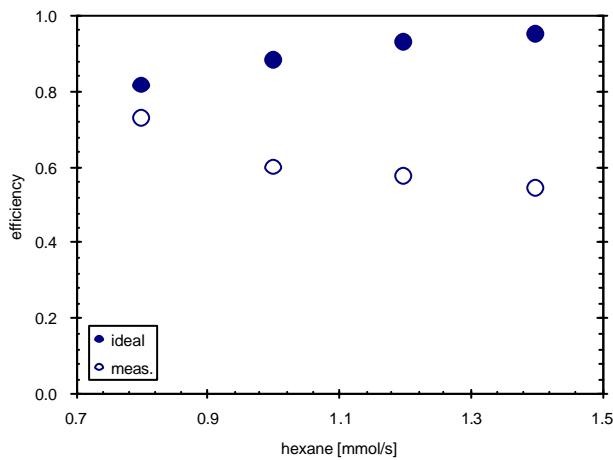


Fig.9 Effects of hexane flow rate on energy conversion efficiency (HHV) where O/C=1, ideal: simulation, meas: experiment

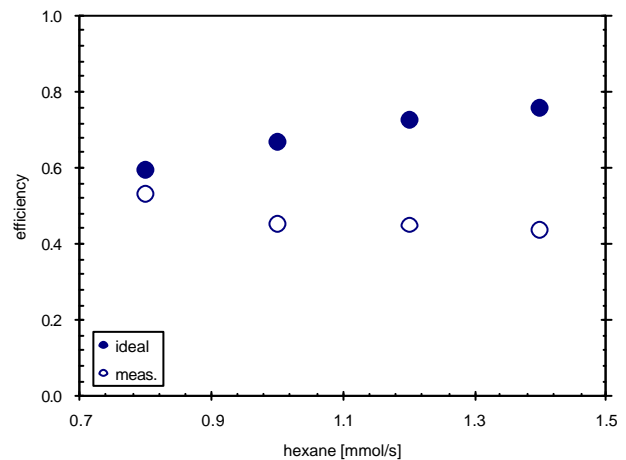


Fig.10 Effects of hexane flow rate on modified energy conversion efficiency (HHV) where O/C=1 assuming power supply efficiency is 0.5

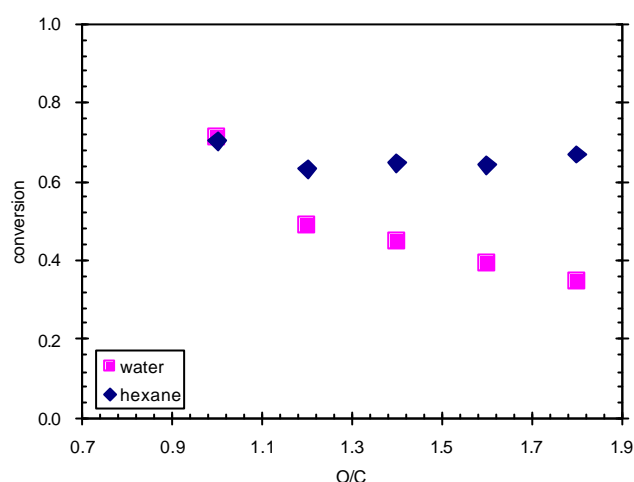


Fig.11 Effects of O/C on conversion where hexane flow rate is 1.0mmol/s

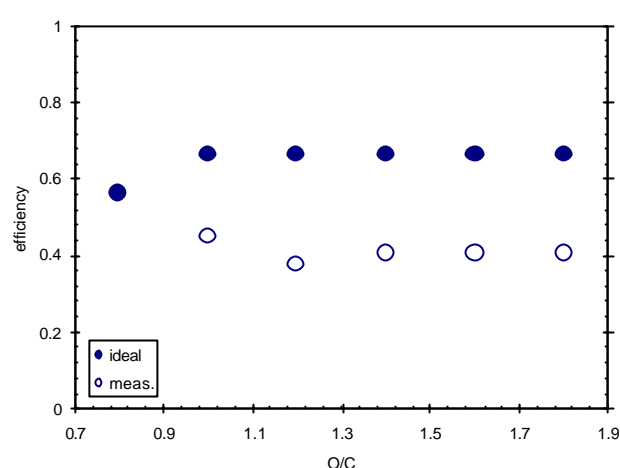


Fig.12 Effects of O/C on modified energy Conversion efficiency (HHV) where Hexane flow rate is 1.0mmol/s assuming power supply efficiency is 0.5

## 5. Conclusion

The atmospheric pure steam plasma generated by microwave discharge was applied to the reforming of hexane. The results indicated the reforming was achieved and confirmed the advantages of the proposed method. However insufficient efficiency was concluded from the experimental data and improvement should be required for the development of the plasma reforming method.

## Acknowledgments

This research was partially supported by New Energy and Industrial Technology Development Organization (NEDO) under WE-NET project and the Ministry of Education Science, Sport and Culture under Grant-in-Aid for Scientific Research (b)No.13558054.

## References

- [1] L.Bromberg, D.R.Cohn and A.Rabinovich, *Int.J.Hydrogen Energy*, **22**, 83(1997).
- [2] L.Bromberg, D.R.Cohn, A.Rabinovich, N.Alexeev, A.Samokhin, R.Ramprasad, and S. Tamhankar, *Int.J.Hydrogen Energy*, **25**, 1157 (2000).
- [3] H.Sekiguchi and Y.Mori, *Thin Solid Films*, in press, (2003).
- [4] M.D.Calzada, M.Moisan A.Gamero, and A.Sola, *J.Appl.Phys.*, **80**, 1(1996).

# ABOUT MODELLING PLASMA PHENOMENA DUE TO SWITCHING OF CAPACITOR BANKS

P. Tusaliu<sup>1</sup>, I. Carstea<sup>1</sup>, V. Tusaliu<sup>2</sup>, D.Carstea<sup>3</sup>,  
M. Tusaliu<sup>1</sup>, D. Tusaliu<sup>1</sup>

<sup>1</sup>*University of Craiova, Lapus Street No.5, Craiova, 1100, Romania*

<sup>2</sup>*National College of Craiova, I.Maiorescu, Craiova*

<sup>3</sup>*Energetical School, Amaradia Street No.93-95, Craiova*

E-mail: [ptusaliu@yahoo.com](mailto:ptusaliu@yahoo.com)

The breakers are used both in the normal and damage regimes in the Electrical Power Systems. In both regimes of commutations, the electrical arc appears between the breakers contacts in the extinction chamber. This is not a desired phenomenon because it produces heating, melting and a fat damage of the commutation contacts, supplementary to the thermal and electromagnetic solicitations of the damage current. The electrical arc is characterized by the reduced cathode potential drops and high current densities ( $10^2$ - $10^7$  A/cm<sup>2</sup>). The arc legs are supported o reduces surfaces of the electrode, generating so- called cathode spots. The temperature of the arc column can reach values of the order 5-10.000 K and in some cases can reach values until 50.000 K. The state of the gas in the arc column, essentially an ionized gas, is called plasma (the 4 states of the matter). In the electrical arc column high temperature drops appear. For the thermal field there are same characteristic ranges of the electrical arc :(1) the central zone is characterized by a high thermal ionization, so that a strong dissociation of the atom in positive ions and electrons appears; (2) the second range around the central region is characterized by the molecules brakes in atoms; (3) in the third region (towards the periphery of the electrical arc) the medium of the development of the arc is decomposed in molecules.

In commutation apparatus in the extinction of the electrical arc it is of the great importance both the extinction medium (oil, compressed air, SF<sub>6</sub>) and the thermal conductivity of the deferent regions in which the electrical arc burns and the voltage drop of the electrical arc column [6]. In this sense, the ionization strength of plasma with respect to the temperature represents one of the fundamental aspects of the electrical arc extinction.

The study presents the modelling of plasma phenomena and the main disturbances, generated by the transient phenomena at the switching of capacitor banks in Power Systems with circuit breakers. This stress evaluation and modelling are based on adequate numerical programs concerning certain equipment and capacitor banks. There are presented the mathematical model for plasma, an algorithm for solving of equation and the diagram of thermal conductivity for Nitrogen and for SF<sub>6</sub> , that principal medium for extinction of electrical arc. The final part of this study contains proposals and recommendations for construction, function, and operation of the assembly capacitor banks-circuit breaker-network, to limit the level of stress and to raise the security in function.

# Investigation of a pulsed corona discharge initiated with a nanosecond voltage pulse

N. Aggadi, X. Duten, , K. Hassouni, M. Beauverger

*LIMHP, CNRS-UPRI311, Université Paris 13, 99 Avenue J. B. Clément 93430 Villetaneuse, France.*

## Abstract

We present an investigation of a pulsed corona discharge processed in the nanosecond regime. The experimental device used to generate the nanosecond voltage pulse is presented and the resulting pulsed discharge are analyzed in term of their voltage-current characteristics. Analysis of the major energy dissipation channels under the measured electric fields is then carried out by solving the electron Boltzmann equation for the investigated conditions.

## 1. Introduction

Pulsed corona discharge are now widely used and investigated for applications that requires the transient generation of chemically active species to enhance or alter the reactivity of the investigated system. Such applications include assisted combustion, pollutant removal and surface treatment [1-3].

The production of active species in corona discharges is mainly based on electron impact processes that enables the dissociation and ionization of the feed gas, the kinetic of which is particularly enhanced when the reduced electric field,  $E/N$ , is very high and leads to high values of the electron impact rate constants. Several, investigations were therefore carried out to develop systems that insure very high reduced field even for low duration. Among this system pulsed corona discharges with very short voltage rise time were especially investigated. The idea was to insure fast enough voltage rise to achieve very high electric field value before the ignition of the discharge. In this way the first electron of the discharge can experience very high electric field, undergo strong heating and achieve an average energy that enable a strong excitation, dissociation and ionization kinetics.

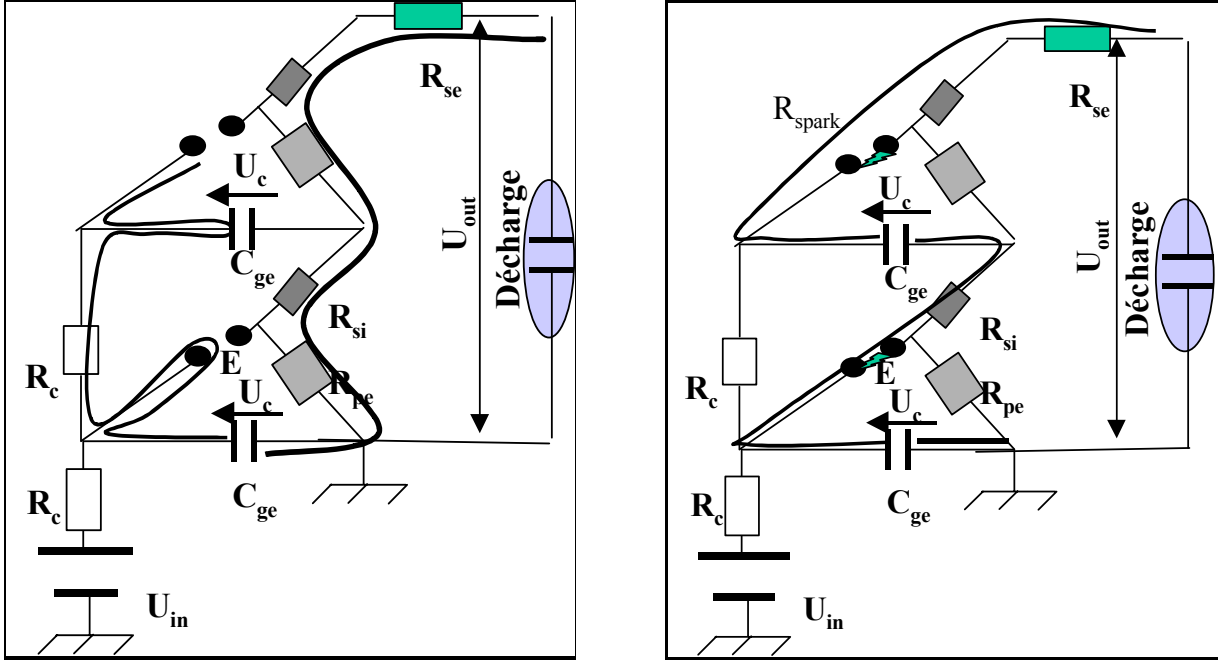
In this paper we discuss the main features of a system that provides very steep voltage pulse and we analyse its properties in term of voltage-current characteristics.

## 2. Discharge generation.

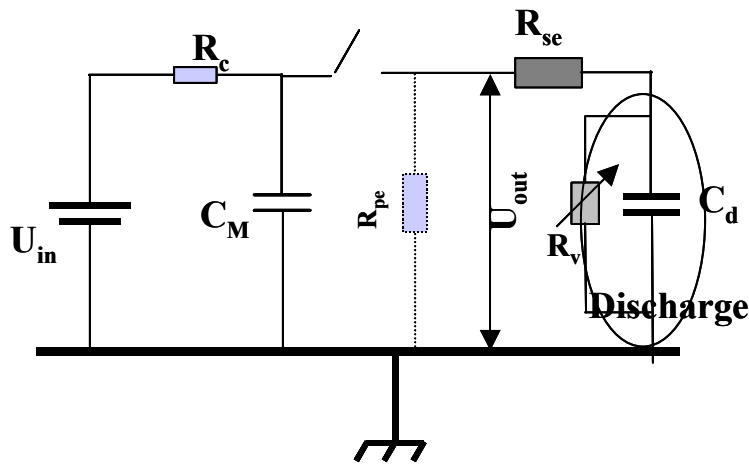
One of the methods that are widely used to generate very high voltage chocs with very short rise time is based on the use of Marx generator. In this system, the voltage pulse is obtained by charging a stack of capacitances in parallel and discharging them in series. Usually, the capacitance circuit is switched from parallel to a series configuration thanks to spark gap that enable a switching time as short as 1 ns [4]. The gap is disposed between two capacitors and the gap distance is set in such a way to initiate a spark at the desired voltage level. Therefore a charge/discharge cycle for the two stage Marx generator sketched in figure 1 consists of charging the capacitors  $C_M$  up to the desired voltage which coincides with the sparking voltage of the first gap. A spark is therefore initiated in the gap which becomes conducting and switch the capacitors circuit from parallel to series configuration. The voltage at the spark gap of the second stage suddenly transitions from  $U_{in}$  to  $2xU_{in}$ . A second spark can be initiated in this gap that becomes also conducting. As a result, the voltage at the investigated electrode system would jump from 0 to almost 2  $U_{in}$  in few nanoseconds (see figure 1). Of course the scenario reported here is quite ideal and the voltage pulse delivered by the Marx generator is less than  $2xU_{in}$ . Marx generators is characterized by the number of capacitors placed in parallel, which is usually called the number of stages, and the charging voltage which defines the amplitude level of the voltage pulse.

The equivalent circuit of a Marx generator connected to a point-to-plane electrode system is shown in figure 2. During the charging phase the rise time of the voltage output is given by the product of the tail resistance  $R_{se}$  and the electrode system capacitance. Assuming a value of 10 pF for the electrode system capacitance a rise time of 10 ns would require a tail resistance below 1 k $\Omega$ . The energy output per cycle is another controlling parameter for Marx generators. It depends on the charging capacitance value and the voltage delivered by the primary source ( $W=n_{stage}C_MV^2/2$ ). The primary source used in this work may deliver up to 30 kV with a charging current of 30 mA. For 50% duty, the maximum power input is therefore 450 W and for a repetition rate of 100 Hz, the two-stage Marx generator of figure 1 would deliver 4.5 J per cycle. This yield a maximum capacitance value of 5 nF. In the experiments discussed in this paper, the charging capacitors were varied between 50 pF and 1 nF. The charging resistor  $R_c$  is chosen so as the energy

dissipated through ohmic heating remains negligible with respect the total energy delivered by the generator (less than 10%). The resistance should however be high enough to avoid any reverse flow of the current to the power source. The optimum value found for our device is 100 k $\Omega$ . A parallel resistance has to be used for evacuating the residual charges at the end of each charge/discharge cycle. This parallel resistance has to be high enough to force the current flow in the discharge and avoid too much charge loss to the earth during the discharge phase. A value of 30 k $\Omega$  was chosen for these resistors.



**Figure 1** : schematic of a two-stage Marx generator indicating the charge flow during the charge (left) and discharge (right) phases.  $U_{in}$  is the primary DC voltage,  $R_c$  are the charging resistors,  $E$  are the two spark gaps,  $C_{ge}$  are the charging capacitance.  $R_{si}$  and  $R_{pe}$  are the series and parallel resistance of the Marx circuit, respectively.  $R_{se}$  is the tail resistance.  $U_{out}$  is the output voltage the amplitude of which is ideally  $2xU_{in}$  for a two-stage generator.



**Figure 2** : equivalent circuit for the Marx generator.  $C_M$ ,  $R_c$ ,  $R_{pe}$  and  $R_{se}$  are the equivalent charge capacitance, charging resistance, parallel resistance and series resistance of the whole Marx generator. The electrode gap / discharge system is modelled by a parallel capacitor/variable resistor circuit. The system is purely capacitive (gap resistance is infinite) during the charging phase and becomes almost purely conductive during the discharge phase (gap resistance is given by the discharge resistance)

### 3. Discharge investigation

#### 3. 1. Discharge circuit characterisation

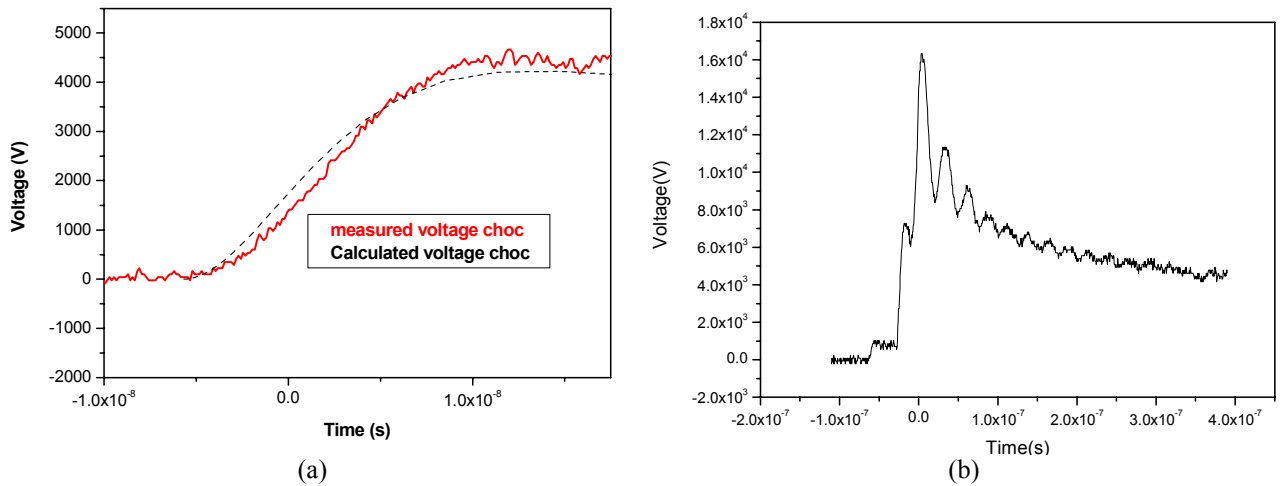
The circuit design discussed in the last paragraph assumed a values of 10 pF for the electrode system capacitance and zero inductance circuit. The value of the tail resistance that would lead to a 10 ns voltage choc determined using this assumption is certainly much more an upper limit than a suitable value to achieve

the desired rise-time. Indeed the total discharge capacitance includes an additional stray capacitance that may be much greater than the electrode capacitance and the circuit is probably inductive in nature. To determine the total capacitance of the circuits an inductive coil of 1 mH, a value that is likely to exceed the whole device inductance, was introduced in the circuit and the resonance frequency of the obtained device was measured. The total circuit capacitance, including the stray capacitance, determined from the measured frequency is 5.5 pF. Knowing the actual capacitance, the circuit inductance could be determined by measuring the resonance frequency, i. e. 202 MHz. A value of 4.5  $\mu$ H was found. The circuit equations was then solved again to determine the tail resistance value that would insure a 10 ns rise time. An upper limit of 500  $\Omega$  was found and we actually used 200  $\Omega$  tail resistance in the Marx generator investigated here.

### 3. 2 Voltage rise-time

Figure 3.a shows a typical voltage pulse obtained with a 1 stage Marx generator with the parameters described in the last section. This voltage was measured using a LeCroy LC584AM 1GHz/ 8 GS/s oscilloscope along with Lecroy P6015 voltage probe. The calculated voltage pulse for the same electrical parameters is also shown. The measured pulse is in good agreement with that predicted by solving the circuit equation and the rise time is indeed below 10 ns as expected from the calculation.

Figure 3b shows a similar voltage pulse obtained from a three-stage generator with the same characteristics as the previous one except that the charging voltage is 6 kV. The voltage rise time is again less than 10 ns and the voltage amplitude is around 17 kV, which shows that the losses in the circuit remain quite limited and that the rise time does almost not depend on the number of stage and the voltage amplitude.

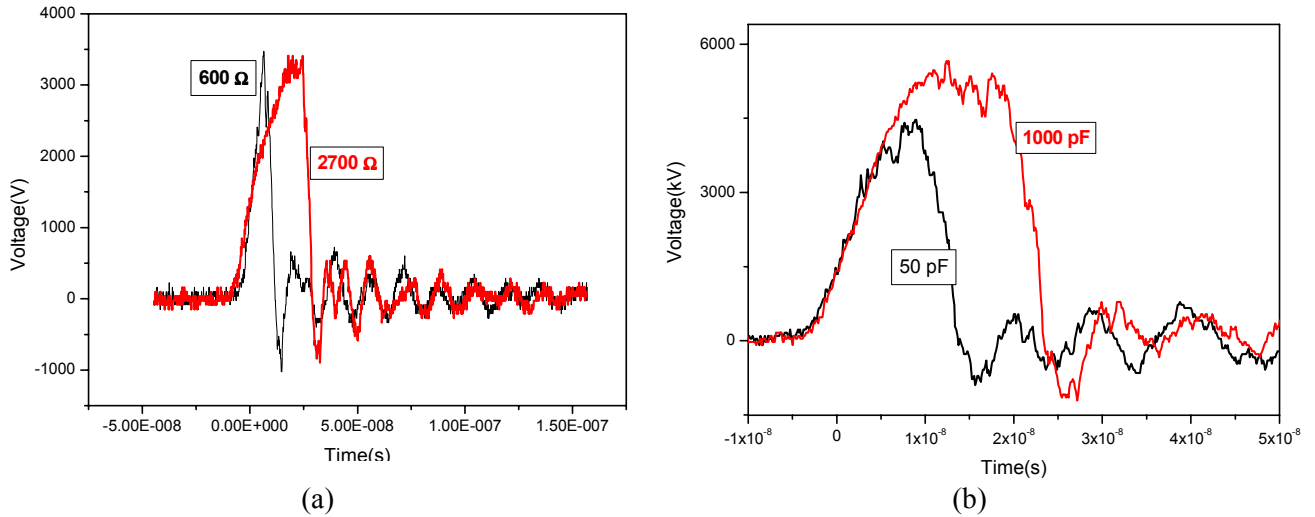


**Figure 3 :** (a) Calculated and measured voltage pulses for one-stage generator. (b) Measured voltage pulse for three-stage generator with 6 kV primary voltage. The kink observed on the beginning of the pulse (around 6 kV) corresponds to the switching from parallel to series configuration of the first two stages.

The effect of the tail resistance on the voltage rise-time may be seen in figure 4 where we have presented the measured voltage pulse for tail resistance values of 600 and 2700  $\Omega$ . The rise-times for these two values are respectively 12 ns and 30 ns, respectively. The pulse duration is almost not affected by this parameter. The charging capacitance values also affect the shape of the voltage pulse. The pulse amplitude and duration for higher charging capacitance are always greater. Note that the rise time is not affected by this parameter.

### 3. 3. Current behaviour

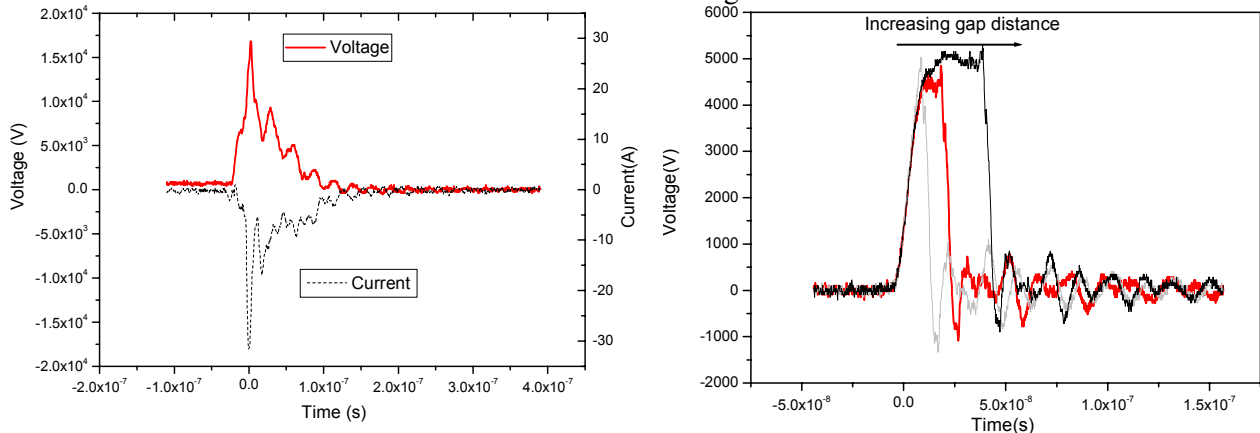
The current collected by the plane cathode is measured with a 2 ns rise-time Pearson current probe (Model 2877) that converts the transient current pulse to a voltage pulse with a sensitivity of 1V/A. The maximum current value that may be determined with this probe is 100 A. Figure 5 shows the current evolution resulting from a 17 kV voltage pulse for a point-to-plane system. The current exhibits two major components, the first one corresponds to the displacement current and results from the steep variation of the voltage. The second current pulse and the exponentially decreasing part that follows this first peak are due to streamer conduction current. At this voltage level the current reaches a value of 20 A, which indicates the existence of branching phenomena that lead to the formation of several streamers [5]. Note that for a voltage value of the order of 5-10 kV the current collected at the anode is much smaller than this value and remains below 1 A.



**Figure 4 :** Measured voltage pulses for one-stage generator and two values of the tail resistance (a) and charging capacitances (b).

### 3. 4. Effect of the gap distance

Figure 6 shows the voltage pulse evolution for different gap distance values. The voltage rise-time is not affected by the gap distance, while the pulse duration significantly decreases when this parameter is reduced. The gap-distance values investigated in this paper are rather small and range between 300  $\mu\text{m}$  and 1 mm. They lead to a voltage pulse duration that vary between 20 and 50 ns. These durations are rather low and may be increased by inserting a resistor between the cathode and the earth in such a way to limit the current and increase the time needed for the evacuation of all the charges from the circuit.



**Figure 5 :** Voltage/Current waveform generated by a three-stage generator with a primary voltage of 6 kV

**Figure 6 :** Effect of the gap distance on the voltage waveform.

### 3. 5. Effect of current limitation on voltage and current waveforms

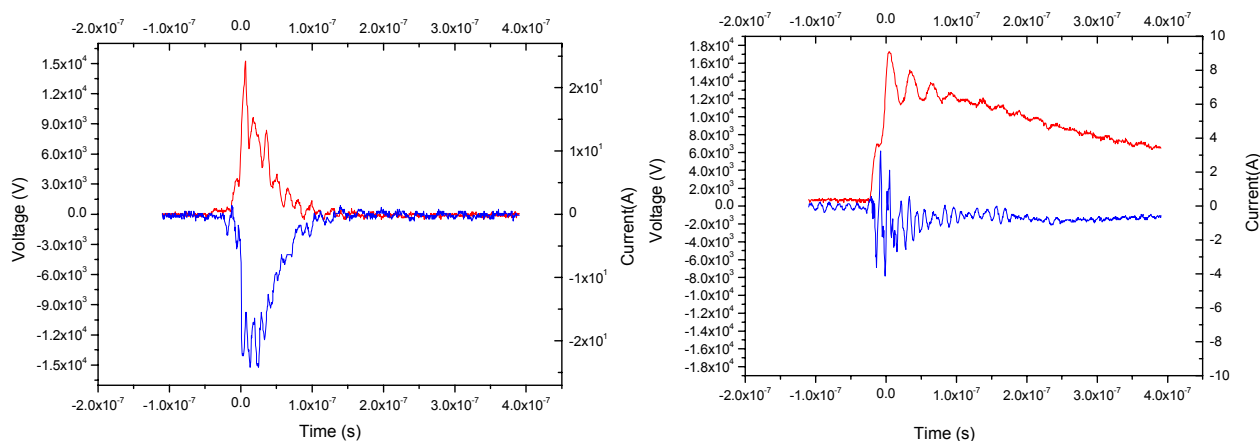
Figure 7 shows the pulse waveform when 200  $\Omega$  and 10 k $\Omega$  resistors are inserted behind the cathode plane. The pulse duration increases with the resistance value and the current tends to decrease. The voltage/current waveforms exhibit several narrow oscillations which would correspond to several streamer developments. A large fraction of the observed total current is however due to the displacement current and not to the streamer discharges in the point-to-plane gap.

### 3.6 Comparison between point-to-plane and multipoint-to-plane electrode systems.

The relatively high current density obtained in point-to-plane system often results in a transition from a cold streamer regime to a spark regime. In this regime, a substantial part of the energy is lost in heating the background gas and chemical activation of the gas is much less efficient than in the case of the intermittent streamer regime that may be obtained using a pulsed mode [1]. As discussed above, the current density may be decreased through the limitation of the total current by the use of a current limiting resistor between the cathode and the earth. This solution presents a drawback since the total energy input in the system may become limited. The local current density may be also decreased by increasing the surface over which the



discharge can take place. This may be achieved by using a wire-to-cylinder, wire-to-plane or multipoint-to-plane systems. This last system was chosen to investigate the effect of electrode geometry.



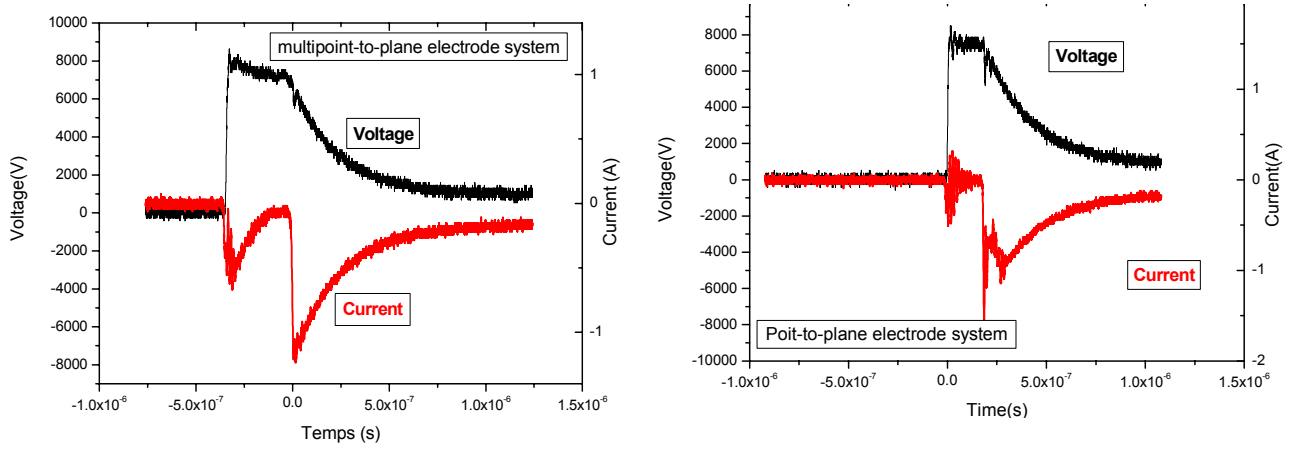
**Figure 7 :** Voltage/current waveforms for 200  $\Omega$  (left) and 10 k $\Omega$  (right) current limiting resistors

Figure 8 shows the current-voltage waveforms for point-to-plane and multipoint-to-plane electrode systems. The two systems present similar behaviours from the qualitative point of view. The voltage pulses are characterized by a fast increase, less than 10 ns, a plateau, and then a relatively long decrease that lasts for 500 ns. The only difference between the two system is related to the duration of the plateau which is longer for the multipoint-to-plane configuration. The current waveforms also show similar trends with a first current peak at the early stage of the voltage pulse and a second more significant pulse at the end of the voltage plateau. The current values show similar amplitudes and remain below 2 A for the two systems. since the multipoint-to-plane system is made of few tens of points, the corresponding local current density should be much lower and the transition to spark less probable than in the case of point-to-plane configuration. Note also that the second current peak is smoother for multi-point-to-plane configuration, which indicates that the streamer discharges are well distributed over the anodic points. The very narrow oscillations observed on the second peak in the case of the point-to-plane configuration would indicate the initiation and development of several streamer and the existence of branching phenomena.

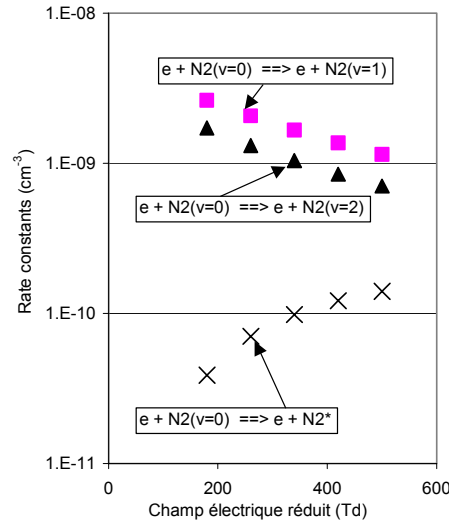
#### 4. Consequences on the chemical kinetics in the discharge.

The implication of the electric field value achieved in the investigated discharge on the chemical kinetics that may occur in the discharge can be analysed in term of the rate constant of the chemical processes that presents a practical interest. Usually pulsed corona are used to generate active species such as oxygen and nitrogen atoms and OH radicals. These processes have an intermediate energy threshold, i. e. 5-10 eV, that are significantly above the energy threshold of inelastic vibrational excitation process (0.1-1 eV) and remain below the energy threshold of the ionization (>12 eV). Low electric field value will yield small electron average energy and favours an energy dissipation through vibrational excitation of nitrogen. The rate constants of vibrational excitation processes show indeed pronounced maxima for electron average energy in the range 1-2 eV. If the electric field is high enough, the participation of intermediate energy threshold process to the energy dissipation becomes more significant. To determine the fraction of energy dissipated in the interesting dissociation processes, we solved the electron Boltzmann equation under its two-term expansion form for a nitrogen/oxygen mixture and for electric field values corresponding to those obtained in the pulsed discharge investigated in this work (up to 900 Td). The rate constants for the excitation of the first two vibrational levels and dissociation of nitrogen are presented in figure 9. this shows that at 200 Td more than 99 % of the energy is dissipated in the vibrational excitation of  $N_2$  which mainly lead through non resonant v-v relaxation and v-t transfer to the gas heating. The situation is somewhat different at 600 Td, since almost 15-20 % of the energy is dissipated in the dissociation of  $N_2$  which can therefore take benefit from significant fraction of the energy deposited in the discharge.





**Figure 8 :** comparison between current and voltage waveforms obtained for point-to-plane and multipoint-to-plane electrode systems



**Figure 9 :** Nitrogen vibrational excitation and dissociation constants as function of the reduced electric field

## 5. Conclusion

The pulse generator discussed in this paper enabled to obtain voltage choc with less than 10 ns rise-time. The effect of the generator characteristics on the corona discharges current-voltage waveform was also investigated. It was shown that for a given primary dc voltage tail resistance significantly affects the voltage rise-time, while the charging capacitance may influence the voltage amplitude and the plateau duration. The current waveform exhibits two major components corresponding to the displacement and streamer conduction currents. Finally two solutions were investigated to minimize the local current density and to avoid the transition from low current streamer regime to high current spark regime. These consisted either in limiting the total current by the use of resistors between the collecting cathode and the earth or the use of a multipoint-to-plane configuration that provide larger discharge area. Finally, estimation of the rate constants for the main energy dissipation processes showed that the energy dissipated in dissociating nitrogen becomes significant only for electric field values as high as 600 Td

## References

- [1] 'Non thermal plasma techniques for pollution control', Part A & B, NATO ASI series, Eds. B. M. Penetrante et S. E. Shultheis, Springer, Berlin, 1993
- [2] H. Conrads et M. shmidt, Plasma sources science and technology, **9**, pp. 441-454 (2000).
- [3] N Foulon-Belkacemi and R Coelho J. Phys. D: Appl. Phys. **28** (5), pp 1001-1008 (1995).
- [4] J. Craggs and R. Meek, High Voltage Laboratory Technique, Butterworth Scientific Publishers, London, 1954
- [5] E M van Veldhuizen and W R Rutgers J. Phys. D: Appl. Phys. **35** (17), 2169-2179 (2002).

# Investigation of PAHs and soot formation in moderate pressure Ar/H<sub>2</sub>/CH<sub>4</sub> microwave plasmas

F. Mohasseb, K. Hassouni, G. Lombardi, F. Bénédic, A. Gicquel

LIMHP, CNRS UPR 1311, Université Paris 13, 99 Avenue J. B. Clément 93430 Villetaneuse, France

## Abstract

In this paper we report the modeling results of Poly-Aromatic Hydrocarbons (PAH) and soot formation through homogeneous chemistry in moderate pressure Ar/H<sub>2</sub>/CH<sub>4</sub> microwave discharges used for the deposition of nanocrystalline diamond films. A parametric study was carried out to investigate the effect of gas temperature ( $T_g$ ) and composition on the rate of soot production in the discharge.

## 1. Introduction

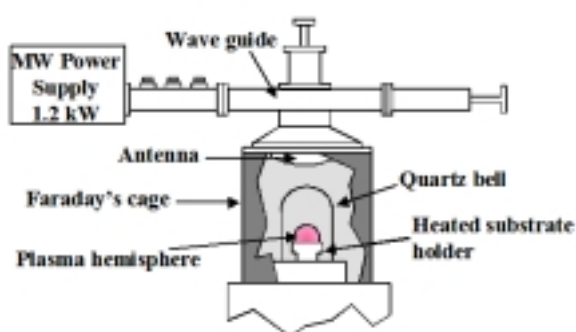
A significant amount of soot particles may appear in moderate pressure Ar/H<sub>2</sub>/CH<sub>4</sub> microwave discharges used for the deposition of nanocrystalline diamond (NCD). The soot formation often results in the appearance of some instabilities in the deposition plasma, which make process control and film properties optimization quite difficult. The achievement of a stable, reproducible and optimal deposition process for nanocrystalline diamond growth synthesis would therefore require to avoid soot formation during the deposition experiment.

Soot particles formation in Ar/H<sub>2</sub>/CH<sub>4</sub> discharge may result from either heterogeneous process involving the carbonaceous deposits on the substrate and the reactor wall, or homogeneous gas phase chemistry similar to the one characterizing hydrocarbon pyrolysis. The objective of the present study was to investigate through numerical modeling if the homogeneous gas phase chemistry channel may explain the soot formation observed under nanocrystalline diamond deposition discharge conditions.

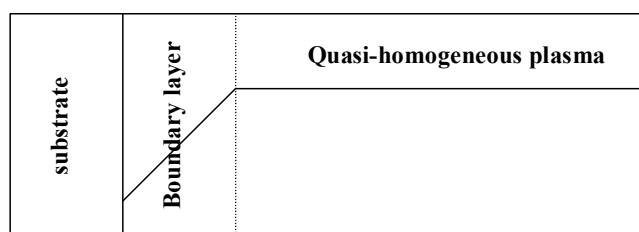
## 2. Investigated plasma device

The experimental set-up mainly consists of a quartz bell jar low pressure chamber surrounded by a Faraday cage (figure.1). The gas is activated by a 1200 W, 2.45 GHz microwave power supply. Substrates are heated by the plasma and by an additional heating source that enables to control the substrate temperature. The input power was varied in the ranges 100-800 W for a pressure of 20000 Pa. Since we are interested in depositing nanocrystalline diamond by Microwave Plasma Assisted Chemical Vapour Deposition (MPACVD) process, we used an Ar/H<sub>2</sub>/CH<sub>4</sub> feed gas mixture with a large amount of Argon <sup>[1]</sup>.

The substrates used in the present experiments are (100) silicon wafers. In order to generate high nucleation density, the substrates were pre-treated in an ultrasonic bath of ethanol with a suspension of diamond powder of approximately 45  $\mu\text{m}$  in size.



**Figure.1:** Schematic of the MPACVD apparatus used for NCD growth.



**Figure.3 :** Schematic principle of a quasi-homogeneous plasma model

## 3. Moderate pressure Ar/H<sub>2</sub>/CH<sub>4</sub> plasma model

### 3.1 Thermochemical model

The studied plasmas are characterized by a strong thermal and chemical non-equilibrium. We distinguish two different energy modes : the heavy species translation-rotation mode (t-r) characterized by the gas temperature ( $T_g$ ) and the electron translation mode (e). Due to the relatively high pressure, a thermal equilibrium was assumed between the vibrational modes of molecular species and the 't-r' mode.

In principle, the electron energy distribution function (eedf) deviates from a Maxwellian distribution for the considered discharges. Previous studies have however shown that, for moderate pressure discharges, the electron-heavy species reaction rate constants only depend on the electron average energy and that the knowledge of the whole electron energy distribution function is not necessary to estimate the rate constants and the energy dissipation frequency. This brings an important simplification to our model, since instead of considering an electron Boltzmann equation to estimate the rate constants, we just need to deal with an electron average energy equation. The dependence between the rate constant and the electron average energy can be determined independently by using an offline Boltzmann solver.

### 3.2 Chemical model

One of the main objective behind the chemical kinetics investigation of the discharge presented in this paper is to analyze the formation of heavy hydrocarbons and soot particles under various discharge conditions (pressure and input power). For this purpose, we developed a thermochemical model that distinguishes four subgroups of model.

#### 3.2.1 $H_2/CH_4$ sub-model

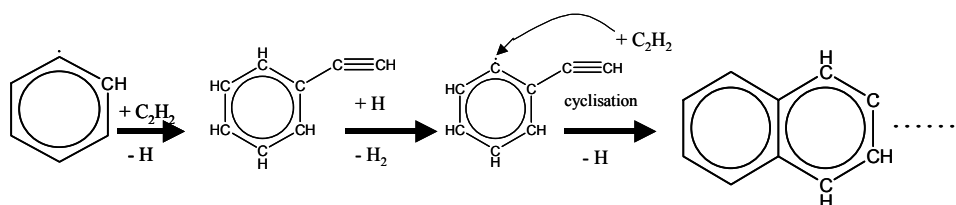
The first sub-model which was the starting point of the work described here is a kinetic model that was previously developed to describe the chemical kinetics of moderate pressure  $H_2/CH_4$  microwave discharges used for the deposition of polycrystalline diamond films <sup>[2]</sup>. This model takes into account molecular and atomic hydrogen and their ions, the first two excited states of H-atom, neutral hydrocarbon species with up to two carbon atoms ( $C_{1-2}H_{0-6}$ ), the most significant hydrocarbon ions ( $CH_3^+$ ,  $CH_4^+$ ,  $CH_5^+$ ,  $C_2H^+$ ,  $C_2H_2^+$ ,  $C_2H_3^+$ ,  $C_2H_4^+$ ,  $C_2H_5^+$ ,  $C_2H_6^+$ ) and the electrons. These species are linked by chemical reactions that include electron-impact dissociation and ionization of hydrogen and hydrocarbon species, thermal chemistry that only involves heavy species and leads to  $H_2$  dissociation and hydrocarbons conversion, a large number of ion conversion processes that favor the formation of some hydrocarbon ions even for low methane concentration in the feed gas and dissociative recombination processes for  $H_3^+$  and hydrocarbon ions.

#### 3.2.2 Ar/ $H_2/CH_4$ sub-model

Beside the species of the first sub-model, the second group of reactions includes all argon based compounds. These are Ar,  $Ar^*$ ,  $Ar^+$ ,  $ArH^+$  and  $ArH^{+*}$ . The production of  $Ar^+$  and  $Ar^*$  species is due to the electron impact ionization and excitation of argon.  $ArH^+$  is obtained through ion conversion process that involve  $Ar^+$  and  $H_2$ . Note also that in the presence of hydrocarbon,  $Ar^+$ -ion will tend to undergo charge transfer reaction with hydrocarbon molecules that leads to a significant amount of hydrocarbon ions even at the low methane percentage that characterizes the investigated discharges.

#### 3.2.3 PAHs sub-model

The third group of reactions describes the formation of large aliphatic and aromatic neutral hydrocarbons. This group of reactions is essentially thermal in nature and do not include electron impact process. It is derived from the work of Wang and Frenklach <sup>[3]</sup>. Up to 6 carbon aliphatic species and four-rings aromatic species are taken into account in this sub-model. The first aromatic ring is produced through the  $C_4H_3$  (1-buten-3-yne-1-yl radical) and acetylene mechanism, then production of larger aromatic compounds proceeds through the Hydrogen Abstraction Carbon Addition (HACA) mechanism described in figure 2. In principle this mechanism would lead to very large PAHs and kinetic models taking into account the formation of PAH with up to 9 aromatic rings have been already developed. We will however restrict ourselves to 4 ring aromatic compounds in this work.



**Figure. 2** : HACA mechanism

### 3.2.4. Soot nucleation sub-model

Following the approach of Revzan and Frenklach<sup>[4]</sup>, soot nucleation is assumed to result from the condensation of two large PAH molecules. This nucleation mechanism is still subject to a large controversy<sup>[5]</sup> since the formation of two-PAH complex is insured by Van der Waals type bonds which requires very large PAH (i.e. to insure a large surface attraction and therefore strong enough Van der Waals bonds) to be stable at temperatures as high as those encountered in our discharge. Nevertheless, taking into account nucleation mechanism from the condensation of two pyrene molecules would give the main qualitative features of the soot nucleation mechanism.

Finally we should mention that the aerosol dynamics and soot growth, coagulation and aggregation are not considered in the present model which only yield information on the rate of nucleation of soot particles.

The nucleation constant rate was determined using the method given by Revzan and Frenklach<sup>[4]</sup>.

The four sub-models described above leads to the description of argon-methane-hydrogen discharges in term of 101 species-352 chemical reaction mechanisms.

### 3.3 Quasi-homogeneous plasma model

The thermochemical model described in the last sections was used to investigate argon/hydrogen/methane microwave plasma used for NCD deposition under quasi-homogenous plasma assumption. The principle of the numerical model resulting for the use of this assumption was largely discussed by Hassouni et al.<sup>[2]</sup>. To summarize, the model assumes that the plasma is made of two regions : a homogenous plasma bulk where all the plasma characteristics are constant, and a boundary layer where the species density and plasma temperature vary linearly (figure.3). For a given discharge conditions, i.e. microwave power density, pressure and feed gas composition, the steady state plasma composition is calculated by time-integrating the coupled set of species and energy balance equations. The integration is stopped once the species densities and the electron and gas temperature reach the steady state.

## 4. Results and discussion

Simulations were performed for a feed gas composition of 1% CH<sub>4</sub>, 2% H<sub>2</sub> and 97% argon at a pressure of 20000 Pa and input power values of 10, 25, 50, 75, 100, 350 and 500 W. The investigation of several power values enables us to analyze the effect of gas temperature (T<sub>g</sub>) on the PAHs formation and soot nucleation. Indeed, each value of the input power corresponds to steady state gas temperature in the plasma bulk. The dependence between input power and T<sub>g</sub> is shown in figure.4 that shows that the gas temperature may vary between 1200 K and 4200 K in the investigated power domain.

The evolution of H<sub>2</sub> and H-atom densities as a function of the gas temperature are shown in figure.5. At low power density the molecular hydrogen is almost not dissociated and H-atom mole fraction is below 10<sup>-3</sup>. When the power increases, H<sub>2</sub> dissociation is enhanced and almost all the hydrogen is in the atomic form. In fact H-atom density even exceeds two time the H<sub>2</sub> mole fraction in the feed gas. This is due to the fact that a fraction of H-atom present in the discharge comes from the conversion of CH<sub>4</sub>. Figure.6 presents the major hydrocarbon species with one and two carbon atoms. These are CH<sub>4</sub>, C, C<sub>2</sub>H<sub>4</sub>, C<sub>2</sub>H<sub>2</sub> and C<sub>2</sub>. The relative predominance of these species depends on the power density. CH<sub>4</sub> remains the major hydrocarbon species up to a temperature of 1460 K, which corresponds to an input power of 25W. Then, methane is converted to ethylene, then acetylene that becomes the major species above a temperature of 1500 K. When the power is further increased C<sub>2</sub>H<sub>2</sub> is converted to C<sub>2</sub> and C. This later is the only significant carbon species at high power and above 3500 K.

As far as aromatic species are concerned, their density are significant only for temperature below 1500 K, i.e. power density of 25 W. For this conditions, benzene (A1) is always by far the major aromatic species with a mole fraction that reaches 10<sup>-4</sup>. The other significant hydrocarbon species are naphthalene (A2) and

phenanthrene (A3) that shows mole fraction values two orders of magnitude less than that of benzene (see figure 7).

The mole fraction of A4 species shown in figure.7 permits to estimate the rate of soot formation through the condensation of 2 pyrene molecules. The time-evolution of the nucleation rate is given in figure.8. This shows that the time-scale for soot formation is around hundred seconds. This is much greater than the time necessary for the lighter hydrocarbon species and the gas temperature to achieve the steady state (of the order of 1s, see Figure.8 for  $T_g$ ). The variation of the average mass production rate as a function of the gas temperature is given in figure.9 that shows that the soot production rate is quite high and almost constant for temperature between 1200 K and 1500 K and strongly decreases for higher temperature.

The results presented in figure 9 are in term of mass production rate, which is different from the usually adopted representation in term of particle density. To have an estimate of the particle density that would result from such mass production rate, we assumed that the soot is made of 100 nm spherical particles and that the soot material density is  $2000 \text{ kg.m}^{-3}$ . With such assumption the soot mass production rate at 1500 K corresponds to a particle production rate of  $9.5 \times 10^7 \text{ particle/cm}^3/\text{h}$ . If these particles remain in the plasma bulk the particle density obtained if the discharge is processed during 4 hours would be around  $3.8 \times 10^8 \text{ particle/cm}^3$ . This particle density is quite significant and we can therefore conclude that the homogenous nucleation mechanism that involves only neutral chemistry and more specifically the HACA mechanism of Wang and Frenklach, may explain formation of soot particles in discharges with gas temperature less than 1500 K.

Actually, this mechanism may also take place in the cold region of discharges obtained at higher power density, and can as well explain the soot formation in these conditions as well.

Of course other nucleation sources such as heterogeneous soot formation on the substrate surface and the reactor wall, or homogenous nucleation through condensation of charged species may also be significant. These mechanism and especially the homogeneous ionic nucleation will be the scope of a future investigation.

## 5. Conclusion

The modeling study presented in this paper allowed to analyze the main features of moderate pressure microwave Ar/H<sub>2</sub>/CH<sub>4</sub> used for nanocrystalline diamond film deposition.

We tried in particular to account for the formation of PAH and soot nucleation phenomena. The results of the model showed that significant production of PAH and soot can take place when the gas temperature is lower than 1500 K. Under such conditions, the molecular hydrogen is almost not dissociated and acetylene and methane are the major hydrocarbon species in the discharge. Although the present model makes use of a quasi-homogenous plasma assumption and give information only on the bulk of the discharge, it may give some additional qualitative information with respect to soot formation under NCD deposition discharge conditions. The model particularly shows that for high power density discharges actually used for NCD deposition, the soot cannot be formed in the bulk of the discharge. The only reactor regions where homogeneous nucleation, based on the HACA mechanism, may take place are the cold region situated just above the substrate surface and at the edge of the discharge zone. The fact that nuclei may form just near the growing film may have a significant effect on the deposition process and should be considered more thoroughly in the frame of process optimization.

Of course the conclusion drawn in this study should be considered only from a qualitative point of view. A more quantitative conclusion requires an improvement of the present model by coupling the aerosol dynamics, including growth, aggregation and transport of particles, by taking into account the soot formation through an ionic mechanism and by using at least a one dimensional model. The latter point is crucial in order to describe species and energy transport and to take into account the plasma non-uniformity.

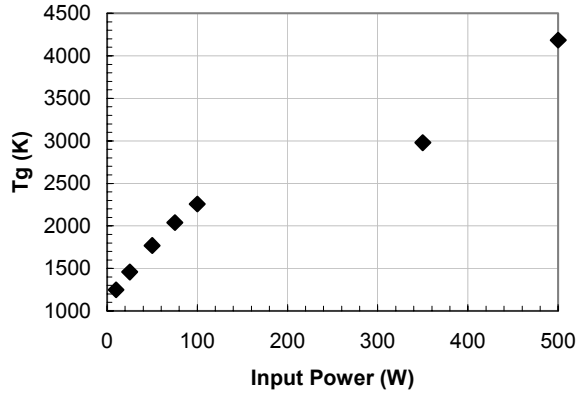


Figure 4: Evolution of the gas temperature as a function of the input power

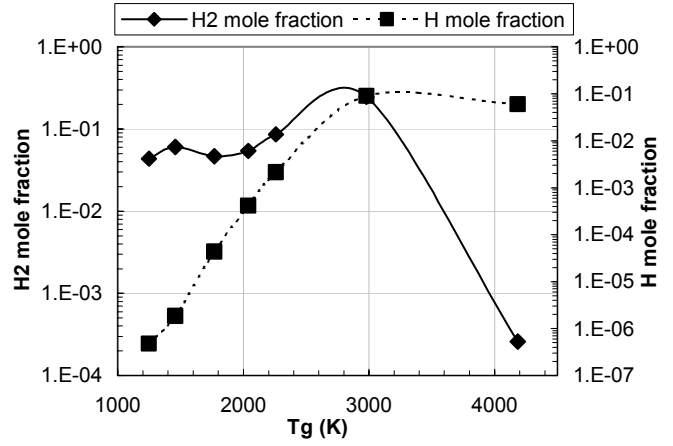


Figure 5: Evolution of  $H_2$  and H mole fractions as a function of the gas temperature

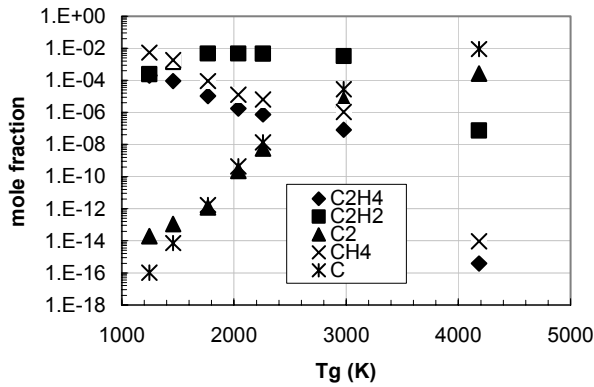


Figure 6: Evolution of the  $C_2H_4$ ,  $C_2H_2$ ,  $C_2$ ,  $CH_4$  and C mole fractions as a function of  $T_g$  at Ar/ $H_2$ / $CH_4$  (97/2/1%)

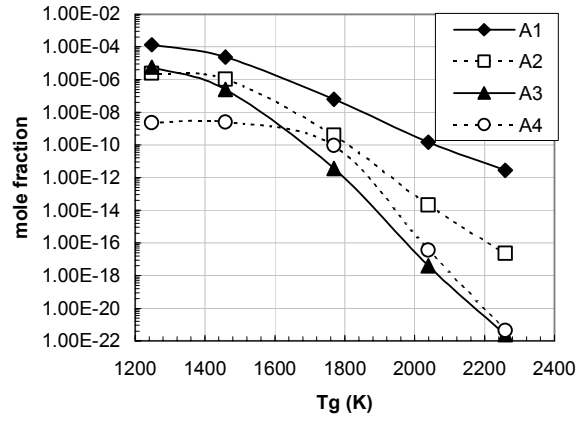


Figure 7: Evolution of the aromatic rings mole fraction as a function of  $T_g$  at Ar/ $H_2$ / $CH_4$  (97/2/1%)

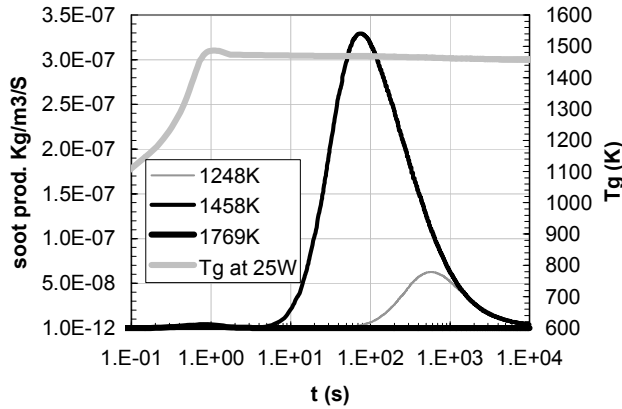


Figure 8: Evolution of the soot production rate as a function of  $T_g$  and time, and the evolution of  $T_g$  at 25W as a function of time

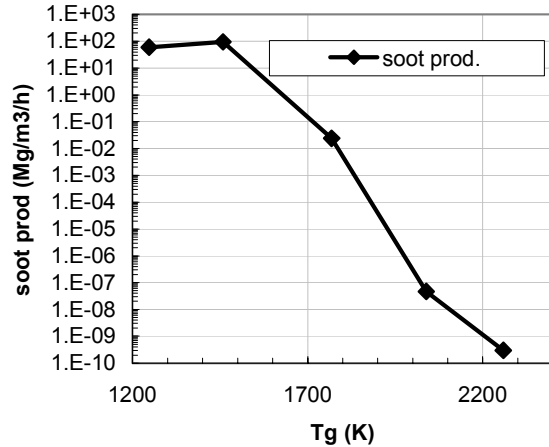


Figure 9: Evolution of the soot production rate as a function of  $T_g$  at Ar/ $H_2$ / $CH_4$  (97/2/1%)

## References

- <sup>1</sup> D. Zhou, D. M. Gruen, L. C. Qin, T. G. McCauley, and A. R. Krauss, J. Appl. Phys. **84**, 1981-89 (1998).
- <sup>2</sup> K. Hassouni, O. Leroy, S. Farhat, and A. Gicquel, Plasma Chem. and Plasma Process. **18**, 325-362 (1998).
- <sup>3</sup> H. Wang and M. Frenklach, Comb. and Flame **110**, 173-221 (1997).
- <sup>4</sup> K. L. Revzan and M. Frenklach, <http://www.me.berkeley.edu/soot/codes/soot.f> (2002).
- <sup>5</sup> H. F. Calcote, Comb. and Flame **42**, 215-242 (1981).

# Plasma treatment of dental caries

E. Stoffels, R.E.J. Sladek, R. Walraven, P.J.A. Tielbeek

*Department of Biomedical Engineering, Eindhoven University of Technology, Eindhoven, The Netherlands*

## Abstract

Non-thermal plasmas generated under atmospheric pressures can efficiently sterilize heat-sensitive surfaces. We consider a new application of plasma-aided bacterial decontamination: *in vivo* treatment of dental caries. Plasma sterilization of infected dental cavities may provide a novel tissue-saving method in dentistry. In this work we investigate some important side effects of such treatment, e.g. thermal effects (heating of the pulp leading to irritation of the nerve), and pain perception in case of sensitive teeth.

## 1. Introduction

In traditional treatment of dental caries, the infected tissue is mechanically removed by drilling. The resulting cavity is chemically treated prior to restoration. During mechanical drilling the dental pulp and the nerve are significantly heated, and consequently the patient experiences intense pain. Even though the pain may be reduced by local anesthesia, the noise and vibration of the drilling tool cause much discomfort. Moreover, in this procedure excessive tissue removal takes place to ensure that no bacteria are left over in the (porous) dental tissue; the prepared cavity is much larger than the original one. Considering all these disadvantages of traditional caries treatment, there is vital interest in development of less destructive therapeutic methods. Successful attempts of cavity preparation have been made by means of laser ablation of infected tissue [1]. In laser treatment of caries, high-power pulsed lasers like Nd:YAG or Er:YAG are used with typical pulse energies in the order of 0.1 – 0.4 J. In more than the half of studied cases, the patient does not experience excessive pain, but only minor discomfort. However, in order to prevent pulp heating, the repetition rate of the laser must be kept low, which considerably prolongs the treatment (up to several minutes are needed for the preparation of a cavity). Moreover, ablation event is followed by a shock wave, which can inflict mechanical damage to the tooth (cracks). Finally, the major drawback of laser techniques is the high cost of lasers.

Laser ablation is in fact an alternative technique of material removal. However, the infected tissue need not always be removed. Once the cavity interior is sterilized, the opening (being often a narrow fissure) must be sealed to prevent further bacterial attack, and the natural healing and remineralization can commence. Thus, the problem of healing caries should be posed in another way: is there a method to sterilize an irregular surface inside the cavity, without involving hazardous chemicals and without irritating the nerve? Plasma sterilization may be the right answer to the needs of dentistry. Non-thermal plasma is the only medium that combines exceptional chemical activity with mild, non-destructive character. Plasma chemistry can be well controlled by introducing a desired amount of an active gas; in this way unique (often short-living) radical species can be obtained. These radicals can spread over an irregular surface, penetrate narrow channels and to some extent also propagate in the liquid phase. Bacterial decontamination by means of treatment with non-thermal plasmas is well-documented in the literature [2,3]. The mechanism of deactivation is explained as a joint action of active radicals and plasma-produced UV radiation, but in principle the radicals alone are also capable of killing microorganisms. Various tests on heat-sensitive materials have been performed using large-area electric discharges, but so far plasmas have not been applied to sterilize living tissues. In this work we present a novel plasma source (plasma needle [4]) which is much more flexible than the hitherto developed large-area reactors for bacterial decontamination. This source is truly non-thermal (operating at room temperature), and it poses no hazard of an electric shock. Thanks to its compactness it can operate with high precision in difficult to reach places, like the oral cavity. It can be safely applied to human skin and teeth.

## 2. Plasma setup

In this section the novel small-size plasma source for fine biomedical treatment will be briefly introduced. A detailed description is given elsewhere [4]. The discharge type is an atmospheric radio-frequency (RF) glow.

In case of RF excitation, the active plasma zone is created only at the powered electrode (see Figure 1); a bipolar configuration is not necessary. In our arrangement the powered electrode is a thin (0.3 mm diameter) tungsten wire; the remote surrounding acts as the counter-electrode (ground). When the plasma is brought in the vicinity of a grounded object, it evolves into a bipolar mode, where the glow spreads over the object's surface. In this type of discharges, voltage fall occurs in the closest vicinity of the powered electrode. In the outer plasma zones, which make contact with biological samples, only small rest electric fields are present. This guarantees no electric hazard during treatment. Dependent on the desired chemical effect, various gases can be used: air, nitrogen, hydrogen and many others. However, it is recommended that the buffer gas be helium. There are many advantages of using helium: the operating voltages are lower than in other gases and the gas temperature is low due to high thermal conductivity of helium. Moreover, helium is inert and non-toxic. The last feature allows to keep a good control of plasma chemistry, because active gases can be carefully dosed into the buffer gas.

Treatment of tissues, including samples of human teeth, is performed with a flexible plasma needle configuration shown in Figure 2. Basically, the setup consists of a tungsten wire inserted coaxially into a plastic tube. Helium throughput and rf connection are visible at the right hand side of the picture. Helium flow through the tube is 2 l/min. The tube can be moved along the axis, so that the tip of the needle can be exposed or pushed back inside the tube. This allows to determine the distance from the tip to the treated object, and to regulate the air content in the plasma (e.g. to enhance or suppress radical generation).

The new plasma source has been characterized in terms of basic physical properties. Operating voltages and powers have been determined and temperature in the plasma as well as at the exposed surface has been measured. The minimum voltage to operate this plasma is 200 V peak-to peak; typical power consumption is about 100 mW.

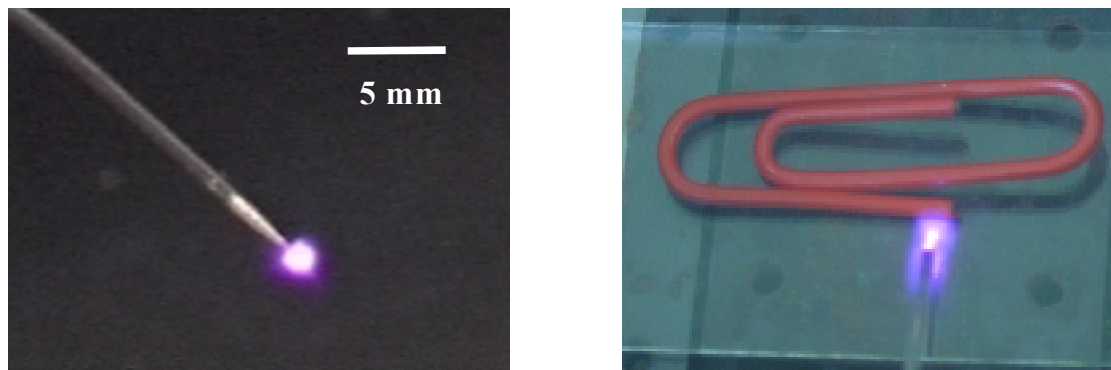


Figure 1: left – plasma needle in the unipolar mode, right – plasma glow in contact with a surface.



Figure 2: The plasma needle used for tissue treatment: left – helium-filled moveable plastic tube surrounding the needle, down – helium inlet, right – rf connection.



### 3. Thermal properties of the plasma

Thermal load is an essential property of a plasma, and our intended application of plasma needle in dentistry makes a thorough study of thermal effects even more urgent than in other plasma sources. In the past we performed spectroscopic temperature measurements by analyzing emission bands of nitrogen [4]. From these measurements it follows that the gas temperature in the plasma can be kept low, even as low as room temperature, provided the power dissipation does not exceed 1-2 W. However, optical emission spectroscopy, being essentially a plasma physical technique, does not provide the accuracy which is needed for the characterization of a biomedical plasma source. In treatment of heat sensitive objects it is important to record even smallest temperature effects, in the order of a fraction of degree. Besides, the actual temperature increase in the tissue is more relevant than the temperature in the gas phase. Therefore we have performed thorough measurements of surface temperature using thermocouples. The data shown in Figure 3

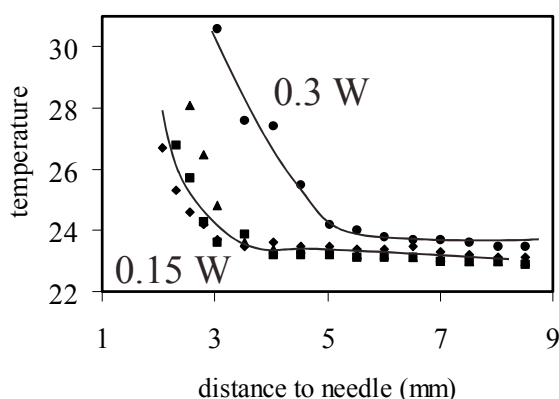


Figure 3: The temperature determined by a thermocouple placed at various distances from the needle tip.

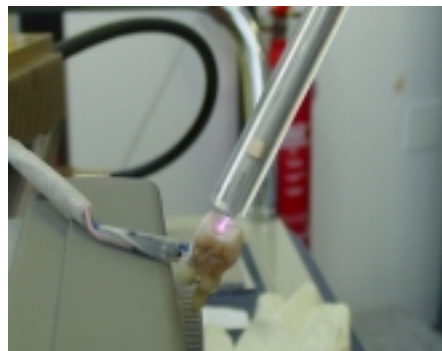


Figure 4: Temperature measurements inside the tooth (central). Above – plasma glow, right – electrical connection of the thermocouple.

result from steady state temperature recording for several distances between the needle and the thermocouple head. It is clear that thermal effects are directly related to the power input. At the applied power levels the temperature increase is tolerable, but preferably the power should not exceed 0.2 W.

Stabilization of the temperature is reached after a considerably long time of treatment (100 – 200 s). In practice, treatment times will lie in the range of seconds rather than minutes, so that heating suffered by the tissue will be much less than one could deduce from Fig. 3. Therefore we have performed a dynamic measurement of temperature inside the tissue. In order to make this more realistic, we have used a real tooth (see Figure 4) with a drilled out root channel, and inserted a thermocouple into the channel. The head of the thermocouple is positioned in the middle of the tooth, about 3 mm under the upper (chewing) surface. The needle is brought as close as possible to the surface. Temperature as a function of time is shown in Figure 5 for various plasma parameters (rf voltages). Again, it can be seen that the temperature increase is moderate, and at low voltages even negligible. Since deactivation of microorganisms using atmospheric pressure plasma takes typically several seconds [3], we can conclude that within reasonable treatment times the dental nerve will not be significantly irritated by the plasma heat. Last but not least, one of the authors has *in vivo* verified that the exposure of teeth to the plasma (including sensitive teeth and gingiva) is entirely painless, even for prolonged exposure times (see Figure 6).

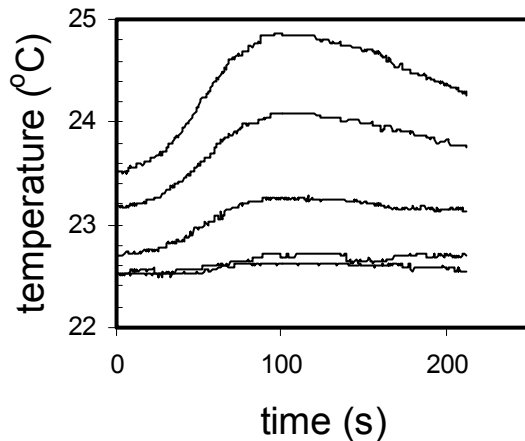


Figure 5: The temperature recorded by a thermocouple inserted in the root channel of a tooth as a function of time. The curves correspond to different peak-to-peak rf voltages (from bottom to top curve): 200, 230, 270, 300 and 340 V. Plasma is switched off at  $t=100$  s, afterwards the tissue cools down.

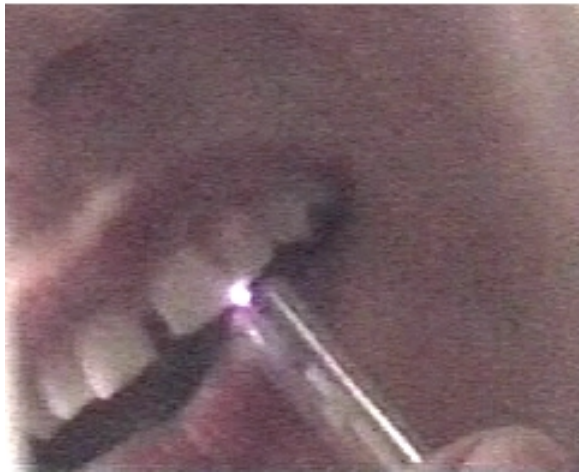


Figure 6: First *in vivo* plasma treatment: the plasma is brought in very close vicinity of a tooth. Here the glow actually penetrates the space between two teeth. However, the person involved in the experiment did not experience any pain whatsoever.

#### 4. Conclusion

Plasma needle is a non-thermal source, operating under ambient pressure and at room temperature. By means of thermocouples we have performed thorough measurements of plasma-induced heating of various surfaces, both in the steady state and as a function of treatment time. Thermal effects during treatment of surfaces appear to be negligible. This remains true even for biological objects, which are otherwise extremely heat-sensitive. We intend to introduce plasma treatment as a novel technique in dentistry, for the preparation of cavities in treatment of dental caries. *In vivo* sterilization of infected cavities may become a genuine tissue-saving technique that could replace painful and destructive mechanical drilling. Plasma interactions with dental tissue are entirely painless.

#### References

- [1] U. Keller, R. Hibst, *Lasers in Surgery and Medicine* **20**, 32 (1997).
- [2] M. Moisan, J. Barbeau, S. Moreau, J. Pelletier, M. Tabrizian, L'H. Yahia, *Int. Journal of Pharmaceutics* **226**, 1 (2001).
- [3] J. Reece Roth, D.M. Sherman, R. Ben Gadri, F. Karakaya, Z. Chen, T.C. Montie, K. Kelly-Winterberg, *IEEE Trans. Plasma Sci.* **28**, 56 (2001).
- [4] E. Stoffels, A.J. Flikweert, W.W. Stoffels, G.M.W. Kroesen, *Plasma Sources Sci. Technol.* **11**, 383 (2002).

# On the improvement of ozone efficiency for NO to NO<sub>2</sub> conversion in polluted air

S. Dupré, A. Goldman\*, M. Goldman

*Laboratoire de Physique des Gaz et des Plasmas (Université Paris-Sud / CNRS)*

*Equipe Décharges Electriques et Environnement*

*SUPELEC, 3 rue Joliot-Curie, 91192 Gif-sur-Yvette Cedex, France*

*\*Electronic address: [alice.goldman@lpgp.u-psud.fr](mailto:alice.goldman@lpgp.u-psud.fr)*

## Abstract

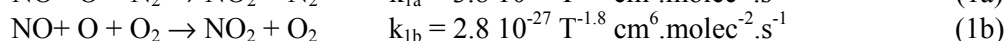
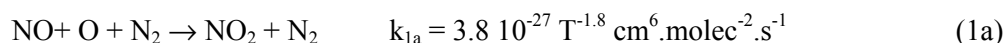
The paper shows the limits in efficiency for NO to NO<sub>2</sub> conversion when a same chamber is used, as usually, for both the production of the oxidizing species and for the NO oxidation by them. On the other hand, it also shows, with some quantitative data as examples, the gain of efficiency that can be obtained by using separate chambers for the two purposes.

## References

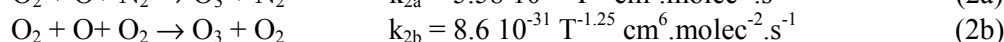
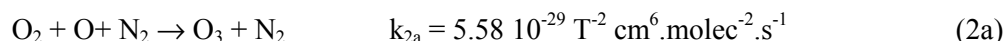
- [1] B.M. Penetrante, J.N. Bardsley, M.C. Hsiao - Japanese Journal of Applied Physics **36**, 5007-5017 (1997).
- [2] L.G. Krishtopa, L.N. Krasnoperov – Proc. SAE Fuel & Labs 98 (1998).
- [3] Y.S. Mok, S.W. Ham - Journal of Chemical Engineering Science **53**, 1667-1678 (1998).
- [4] K. Takaki, M.A. Jani, T. Fujiwara - IEEE Trans. on Plasma Science **27**, 1137-1145 (1999).
- [5] K. Yan, T. Kanazawa, T. Ohkubo, Y. Nomoto - Plasma Chemistry and Plasma Processing **19**, 421-443 (1999).
- [6] S. Dupré, C. Deniset, A. Goldman, M. Goldman, E. Marode – Proc. 8<sup>th</sup> Intern. Symp. on High Pressure, Low Temperature Plasma Chemistry (Hakone VIII), Estonia, 355-359 (2002).
- [7] K. Toda, K. Takaki, T. Fujiwara, S. Kato, Y. Akama, A. Sasaki – Proc. 3<sup>rd</sup> Intern. Symp. on Non-Thermal Plasma Technology for Pollution Control, Korea, 111-1118 (2001).
- [8] Y. Yoshioka, K. Sano, K. Teshima – same Proc., 119-124 (2001).

## 1. Introduction

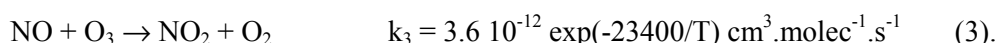
It is now well known [1-5] that NO remediation from polluted atmospheres primarily proceeds by conversion of NO to NO<sub>2</sub> according to a reaction scheme of the production of O atoms by the discharge and then of their consumption by the gas to be cleaned. The oxidation of NO can proceed directly via the reactions:



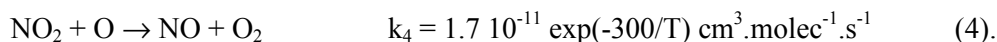
or indirectly, and it was proved with more efficiency [6], via in a first step the production of O<sub>3</sub> according to the reactions:



and then in a second step its consumption by NO via the reaction:



This led us and other researchers [6-8] to proceed with separate chambers, one for the production of O<sub>3</sub> and another for its use for the NO removal in order to optimize O<sub>3</sub> production and to avoid reverse reactions such as:



Our aim in this paper will be to compare the two modes of gas treatment, the standard one, using a unique chamber for the reactants production and for the NO treatment, which will be referred to as “*the standard process*” and the other one with two separate chambers, referred to as “*the indirect process*”. The comparison will be made through considerations on the efficiency of the discharge characterized by two factors: (i) the number  $[\text{O}^*]_{\text{needed}} / [\text{NO}]_{\text{conv.}}$  of O atoms needed to convert 1 NO molecule to 1 NO<sub>2</sub> molecule according to the definition that will be given later on for an evaluation of the O atoms production and (ii) the number  $[\text{NO}_2]_{\text{formed}} / [\text{NO}]_{\text{conv.}}$  of NO<sub>2</sub> molecules formed per molecule of NO converted.

## 2. Experimental

Simple synoptic diagrams are provided in Figure 1 for the arrangements corresponding to both systems of treatment. The same discharge reactor was used for both of them. It consisted of a point-to-plane electrode system. The point electrode, made of stainless steel, was connected to a 64 kHz ac high voltage supply and the plane electrode, covered with a 4 mm thick alumina-silicate ceramics, was connected to ground. The gap length between the active electrode and the ceramics was set to 1 mm for all experiments concerned with the paper. Most experiments were carried out in dry air, containing or not NO, with a total flow rate fixed to 0.3 l/min. A high voltage probe (1:1000) was used for the voltage measurements V(t), and the discharge current I(t) was determined from the voltage drop through a 50 Ω resistance placed between the plane electrode and the earth. Signals were stored on a 500 MHz numerical oscilloscope. The power injected in the discharge was calculated by the product of the instantaneous values of the discharge current and of the applied voltage. The resulting signal was integrated over 10 periods and the power values were obtained by multiplying this result by the generator frequency. The different chemical species were identified and their evolution studied by using a FTIR absorption spectrometer (Vector 22 from Brüker Instruments) which permits, with a resolution of 0.5 cm<sup>-1</sup>, to quantify the nitrogen oxides (NO, NO<sub>2</sub>, N<sub>2</sub>O<sub>5</sub>, N<sub>2</sub>O), the acids (HNO<sub>3</sub>, HNO<sub>2</sub>) and ozone (O<sub>3</sub>). The cell we used has an optical path length of 10 cm and CAF<sub>2</sub> windows (4000-1000 cm<sup>-1</sup> spectral bandwidth).

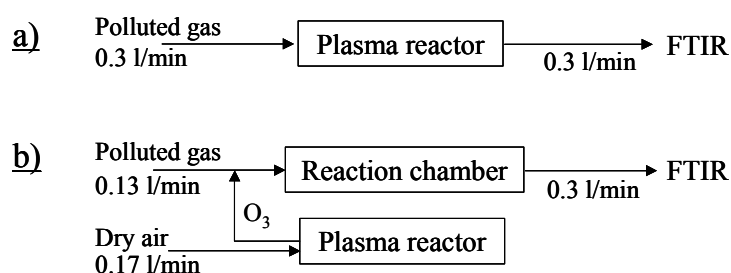


Figure 1: Schematic arrangements for the two types of treatment: a) the standard process with the same chamber for the production of the reactive species and for the NO treatment; b) the indirect process with one chamber for ozone production and another one for the NO treatment

## 3. Experimental results

### 3.1. Results in the standard process

Figure 2 shows, as a function of the power consumption, the influence of  $[\text{NO}]_i$  (NO initial content) on the efficiency of the NO removal.

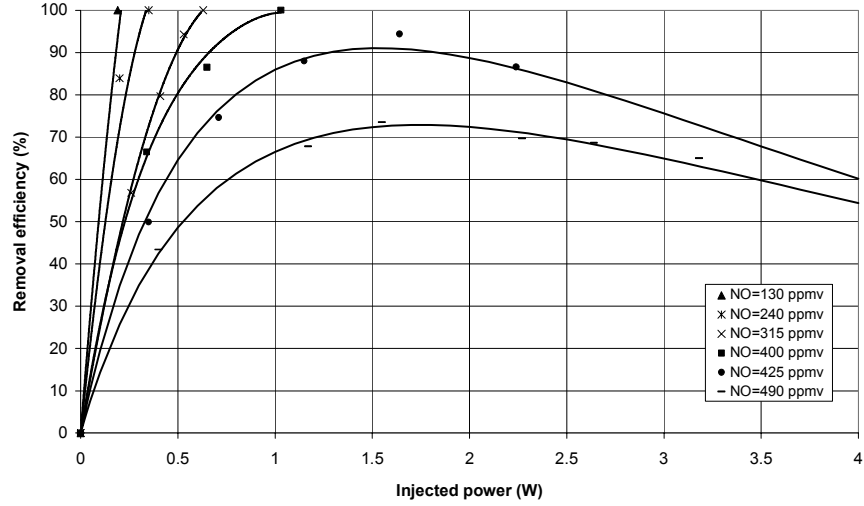


Figure 2: Evolution, as a function of the injected power and of the initial NO concentration, of its removal efficiency in the standard process

- (i) For initial NO concentrations at maximum equal to 400 ppmv, the production of O atoms is sufficient to convert the totality of NO to NO<sub>2</sub>, the power  $P_{100\%}$  needed for a total consumption of NO increasing with the initial NO concentration. As long as  $P < P_{100\%}$ , O<sub>3</sub> is not observed since consumed as soon as produced, but as soon as P exceeds  $P_{100\%}$ , O<sub>3</sub> is observed.
- (ii) For initial NO concentrations larger than 400 ppmv, the discharge is no more able to provide enough oxygen atoms to oxidize the totality of NO and, in this case, ozone is never detected downstream.

Let us now more thoroughly consider the  $[O_3] = f(P)$  curves of Figure 3 which shows O<sub>3</sub> concentrations measured (i) for dry air without NO (upper curve), (ii) for dry air enriched with NO in different concentrations (all other curves).

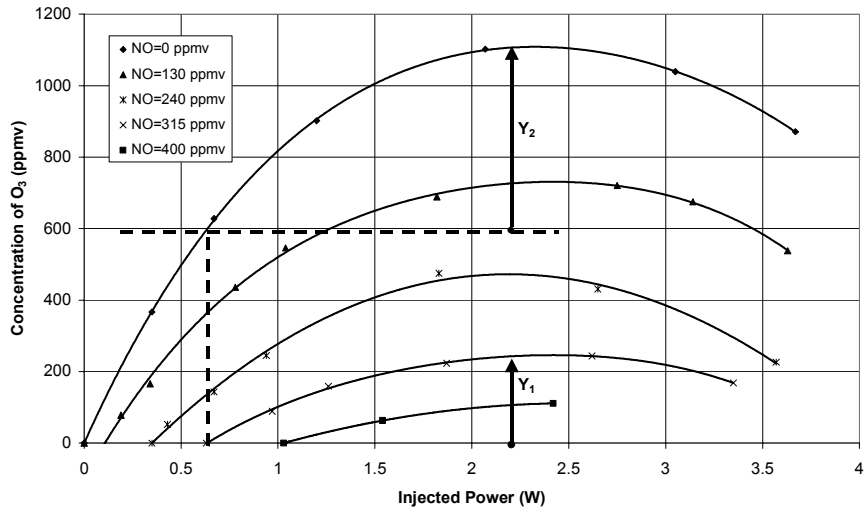


Figure 3 : Evolution, as a function of the injected power and of the NO initial concentration, of the ozone concentration measured in the standard process

If O<sub>3</sub> production was not dependent on the presence of NO, the last curves for dry air with NO should coincide with the curve  $[O_3]_{[NO]_i=0}$  corresponding to  $[NO]_i = 0$  after subtraction from it of the O<sub>3</sub> concentration just needed for a complete conversion, for instance  $[O_3]_{100\%} = 590$  ppmv for  $[NO]_i = 315$  ppmv. But in fact the  $[O_3]$  curves for  $[NO]_i \neq 0$  give lower values, that shows that a part of the reactions (2a) and (2b) of O<sub>3</sub> formation are replaced by other reactions consuming O atoms. To characterize this effect, we can introduce a factor  $R = y_1 / y_2$  defined, as shown in Fig. 3, by the ratio between the  $[O_3]$  curves effectively obtained for  $[NO]_i \neq 0$  and that ones which should be obtained without this effect. Doing so gives R values diminishing

linearly with the increase of  $[\text{NO}]_i$ , independently of the injected power, approximately from the value  $R = 1$  for  $[\text{NO}]_i = 0$  to the value  $R = 0$  for the maximum of  $[\text{NO}]_i$  for which a complete conversion can be obtained (Figure 4). In agreement with our modelling results presented in [6], this  $R$  value shows the efficiency losses, with the increase of  $[\text{NO}]_i$ , for the oxidation of NO by  $\text{O}_3$  according to the reaction (5), to the benefit of its oxidation directly through O atoms (reactions (1) and (2) less efficient). Finally, this leads us to consider the values of  $[\text{O}_3]_{R=1}$ , i.e. the values of  $[\text{O}_3]$  produced in air without NO, as representative, to some extent, of the production of O atoms by the discharge.

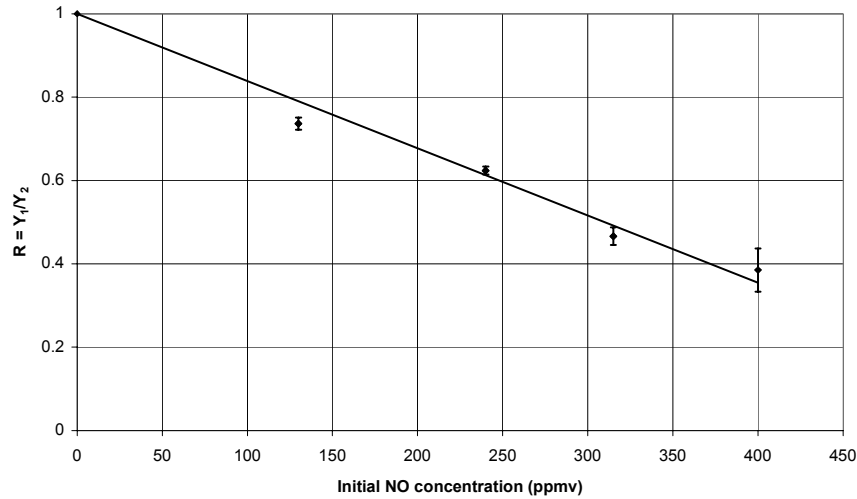


Figure 4: Evolution of the parameter  $R = y_1 / y_2$  as a function of the initial NO concentration in the standard process

### 3.2. Results in the indirect process

Using the same reactor and the same operating conditions as before in the standard process, but now only for the production of ozone in dry air without NO and then injecting it in the reaction chamber (Figure 1b) leads, in terms of NO removal efficiency, to curves presenting the same shapes as in the previous process (Figure 2), but with better results for same values of the injected power. Typically, for instance :

- (i) a complete conversion of NO to  $\text{NO}_2$  is now obtained with  $P = 1.1$  W for  $[\text{NO}]_i = 660$  ppmv and with  $P = 1.2$  W for  $[\text{NO}]_i = 730$  ppmv.
- (ii) a 80 % maximum conversion of  $[\text{NO}]_i = 960$  ppmv is obtained with  $P = 1.8$  W.

If  $\text{O}_3$  production efficiency is increased, obviously the NO removal efficiency increases. So, if the ozone is produced in a 80 %  $\text{O}_2$  - 20 % Ar mixture instead of air, a complete conversion of  $[\text{NO}]_i = 930$  ppmv is now obtained with only 0.4 W then producing 1500 ppmv  $\text{O}_3$  instead of 700 ppmv in air with the same gas flow (here 0.17 l/min).

### 3.3. Results comparison between the two processes

Figures 5 and 6 give a general view on the variations of  $[\text{NO}]_{\text{conv.}}$  and  $[\text{NO}_2]_{\text{formed}}$  as functions of the parameter  $[\text{O}_3]_{R=1}$  as defined in Section 3.1. For the curves illustrating the standard process,  $\text{O}_3$  values correspond to  $[\text{O}_3]_{R=1}$  measurements, i.e. to concentrations of O atoms primarily into play. For those illustrating the indirect process, they correspond to  $\text{O}_3$  concentrations in the reaction chamber without NO put inside, i.e. to the  $\text{O}_3$  concentration effectively in action.

First of all, the similarity exhibited by the curves of Figs 5 and 6 shows that the efficiency yield is doubled with the indirect process compared to the standard one, while the number of  $\text{NO}_2$  molecules formed per NO molecule converted remains close to 1 in all cases, with only small differences between the two processes, as we will now see in more details.

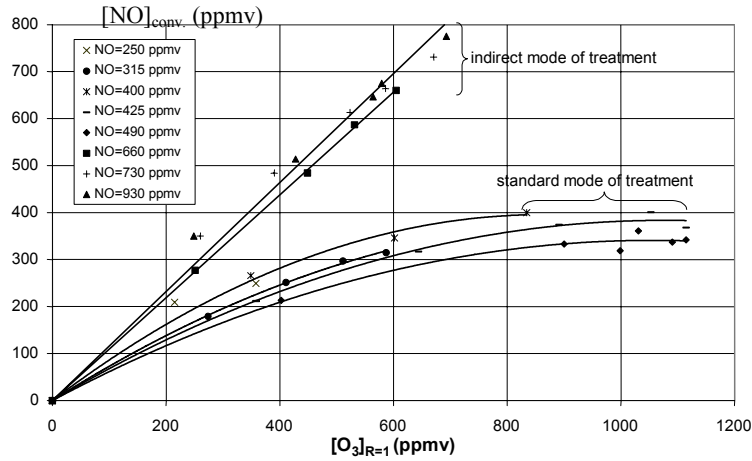


Figure 5 : Evolution of the quantity of NO converted for various initial NO concentrations.

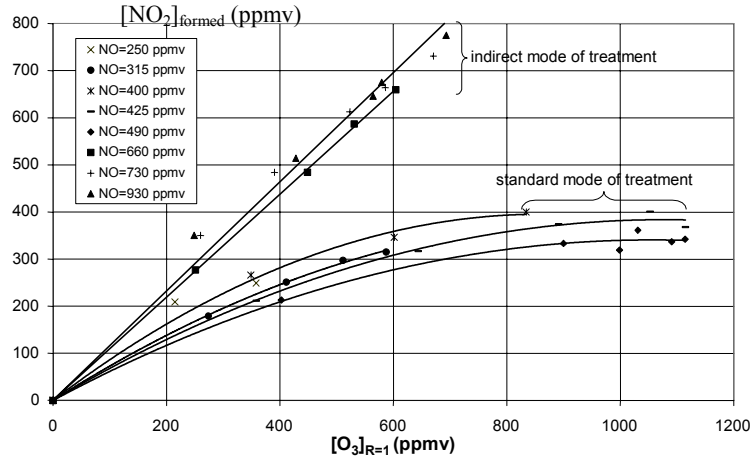
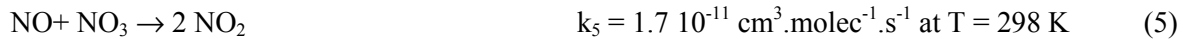


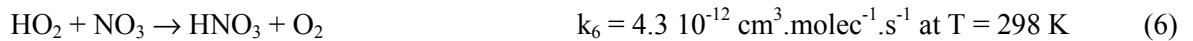
Figure 6 : Evolution of the quantity of NO<sub>2</sub> formed for various initial NO concentrations.

In the standard process, the quantity of O atoms needed for the oxidation of 1 NO molecule increases from 1 to more than 2 with the increase of the injected power, i.e. with the increase of the NO removal, but does not show very significant variations with  $[\text{NO}]_i$  for values allowing a total conversion ( $[\text{NO}]_i < 425$  ppmv) or not. As for the number of NO<sub>2</sub> molecules formed for 1 NO molecule converted, it always exceeds 1, but not by much.

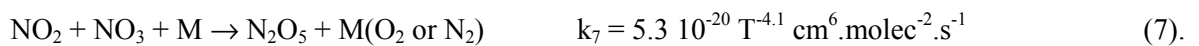
In practice, the excess of NO<sub>2</sub> molecules production with regard to NO molecules consumption shows that in the standard process, other reactions than (1a), (1b) and (3) enter into play. Another possible way for the oxidation of NO to NO<sub>2</sub> is via the reaction:



which produces two times more NO<sub>2</sub> than NO is consumed. In fact, NO<sub>3</sub> is never observed, neither with nor without NO introduced in the vessel. But without NO, one observes HNO<sub>3</sub> and N<sub>2</sub>O<sub>5</sub> that implies NO<sub>3</sub> as an intermediate species for their production according to the following reactions:



and



With the introduction of NO, HNO<sub>3</sub> and N<sub>2</sub>O<sub>5</sub> also appear, but only when NO is almost completely removed. This suggests that reaction (5), that implies NO<sub>3</sub> as the only corona product and that presents a relatively high reaction speed, could rather occur in this case.

*In the indirect process*, whatever [NO]<sub>i</sub> allowing a total conversion ([NO]<sub>i</sub> < 960 ppmv) or not and whatever the quantity of ozone available, i.e. the power put in use, the oxidation of 1 NO molecule always gives exactly 1 NO<sub>2</sub> molecule, needing a little less than 1 molecule ozone (about 10 % to 15 % less in our experiments) for this conversion. This was verified to remain valid even in the case of polluted gaseous mixtures closer to practical situations; this was for instance the case when treating 305 ppmv NO in a 70 % N<sub>2</sub> + 12 % O<sub>2</sub> + 10 % CO<sub>2</sub> + 8 % H<sub>2</sub>O + 310 ppmv CO + 220 ppmv C<sub>3</sub>H<sub>6</sub> gaseous mixture at 80 °C with a gas flow of 3 l/min, a 60 % maximum conversion rate being obtained in this case with 0.9 W injected power.

To explain the overstepping of the number of NO molecules converted with regard to the number of O<sub>3</sub> molecules consumed, we should have to take other oxidants into account, typically for instance HO• radicals.

#### **4. Conclusion**

We have shown that mixing the polluted gas with pre-formed O<sub>3</sub> gives much better results for the conversion of NO in NO<sub>2</sub> than introducing the polluted gas in the reactor designed for the production of oxidizing species, as it is usually done. The reason is that in the last case if a first part of the O atoms produced by the discharge are consumed by NO to form NO<sub>2</sub> by direct oxidation and a second part by O<sub>2</sub> to produce O<sub>3</sub> which in turn react with NO to form also NO<sub>2</sub>, a third part is engaged in inverse reactions which bring back NO<sub>2</sub> to NO, and this all the more as the NO initial concentration in the polluted gas is high and as a higher conversion rate is looked for.

Next step for further improvements will lie in the gain that can be obtained in the ozone production, especially via the reactor geometry.

At last, our study has been carried out with O<sub>3</sub> produced in dry conditions. For some applications, it should be interesting to optimise its production in ambient air, always charged with water vapour.

#### **Acknowledgments**

The authors want to acknowledge Peugeot and Renault Companies and the CNRS for financial support.



# Transient plasma parameters of pulsed inductively coupled planar rf plasmas at 27 MHz

R. Schwefel, P. Awakowicz

*Technical University Munich, Physics of Elektrotechnology, Germany*

## Abstract

The transient behaviour of an inductively coupled plasma source (ICP) at 27 MHz was investigated. Plasma on and off phases at 1 kHz repetition rate and 50% duty cycle were analysed by two synchronised diagnostic systems: An APS 3 Langmuir probe system and a Hiden EQP 300 energy mass spectrometer. The temporal behaviour of the electron density, mean electron energy, plasma- and floating potentials, ion energies and ion currents of Ar, Kr, H<sub>2</sub>, and Ar/H<sub>2</sub> plasmas are shown.

## Introduction

Inductively coupled plasmas operated at low pressures have been intensely investigated in recent years [1, 2, 3]. In the majority, publications deal with permanently driven plasmas neglecting the transient behavior of charged particles transport and chemical reactions. A first publication dealing with modelling a GEC-ICP filled with argon has been found [4].

As different ingredients of plasmas combined with different processes are liable to strongly different time constants, these fact may be used for many technological applications. Pulsed magnetron sputtering technique for instance is used to deposit thin films or pulsed high power ICP for the production of negative ions in fusion research.

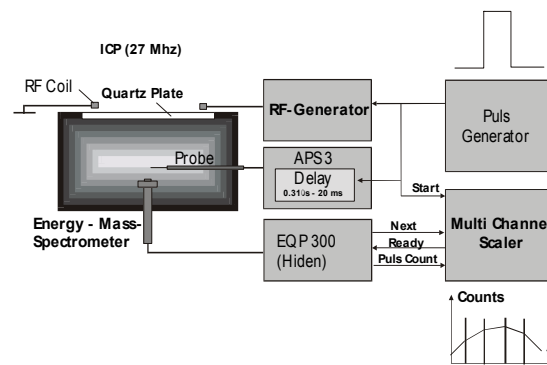
## Experimental Setup

All experiments were performed using an inductively coupled plasma chamber (200 mm diameter, 38 mm height). RF power was coupled into the plasma by an planar coil above a quartz window. Additionally, a Faraday shield (not shown in fig. 1) was used to ensure mainly inductive coupling. The system was powered by an Dressler Caesar 2720 RF Generator. An external pulse generator was used to generate the RF pulses and synchronize the diagnostics. The timing was deduced from a 10 MHz base clock. All experiments were done by using 1 kHz pulses and 50 % duty cycle.

To enable time resolved plasma diagnostics, the reactor is equipped with two diagnostics systems.

The APS3 automatic Langmuir probe system [5] is directly prepared for time resolved measurements. It already includes a programmable delay unit to acquire automatically trigger delay series of the plasma parameters (plasma potential, floating potential, electron density and energy). Time resolution of the system was adjusted to be better than 5  $\mu$ s. The delay quantisation is 310 ns. In order to obtain time resolved energy distribution functions of positive and negative ions coming out of the plasma, a Hiden EQP 300 plasma monitor was used in combination with a Fast Comtech MCD-2 multichannel scaler with a time resolution of 125 ns.

Scripting language programs running in the mass spectrometer and the multichannel scaler were used to automatically acquire the whole ion energy distribution function in one experiment by using the handshake signals “ready” and “next” (see fig. 1).



**Figure 1:** ICP reactor equipped with time resolved plasma diagnostics.

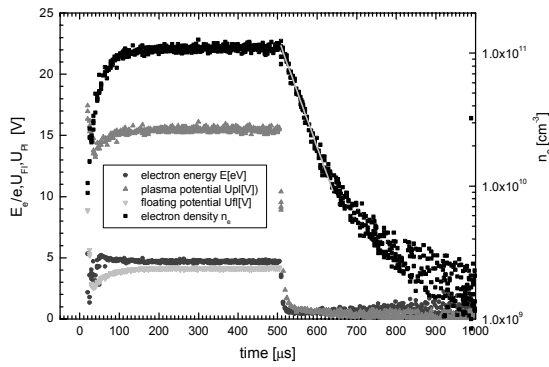
The time resolution of the acquired data is limited by the travel time spread in the EQP 300. By using improved operating parameters it was possible to reduce this time spread from about 25  $\mu\text{s}$  to 2.7  $\mu\text{s}$  for argon ions. Ion travel times have been eliminated by calculation.

## Results

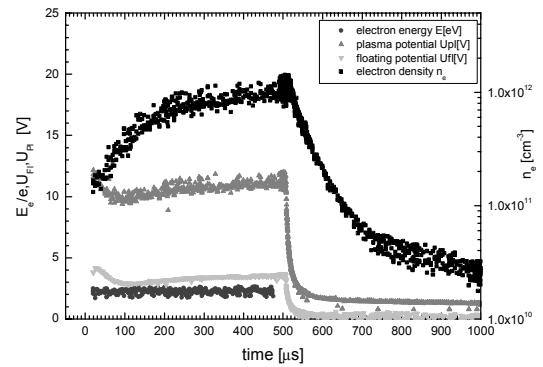
Fig. 2 and fig. 3 show the transient behaviour of electron density and energy of a pulsed argon plasma at 1 Pa and a pulsed krypton plasma at 3 Pa measured by the APS3 Langmuir probe. In addition, the temporal change of plasma and floating potential is displayed.

After ignition there is a very fast rise of both potentials and the mean electron energy caused by the fact that due to the low electron density in the beginning the skin effect is negligible. Therefore a strong heating of the (few) electrons takes place leading to an overshoot in plasma potential at very early times ( $\approx 1\mu\text{s}$ ) after switch on. The steady state in mean electron energy is reached after around 20  $\mu\text{s}$ , only to drop steeply after switch off with time constants from 2 to 20  $\mu\text{s}$  depending on the filling gas or gas mixture (see tab. 1).

In contrast, the increase of electron density is much slower. At switch-off time (at 500  $\mu\text{s}$ ) there is a (in log-scale nearly invisible) density peak, caused by switch-off currents in the coils of the rf-generator. After switch-off potentials and electron energy are decaying quickly. Mean electron energy is dropping down to a value little below 1 eV. The time constants are evaluated by fitting lines in log-scale.



**Figure 2:** Pulsed argon plasma 1 Pa 100 W 1 kHz 50 % duty cycle. Time resolved Langmuir probe measurement.



**Figure 3:** Pulsed krypton plasma 3 Pa 100 W 1 kHz 50 % duty cycle. Time resolved Langmuir probe measurement.

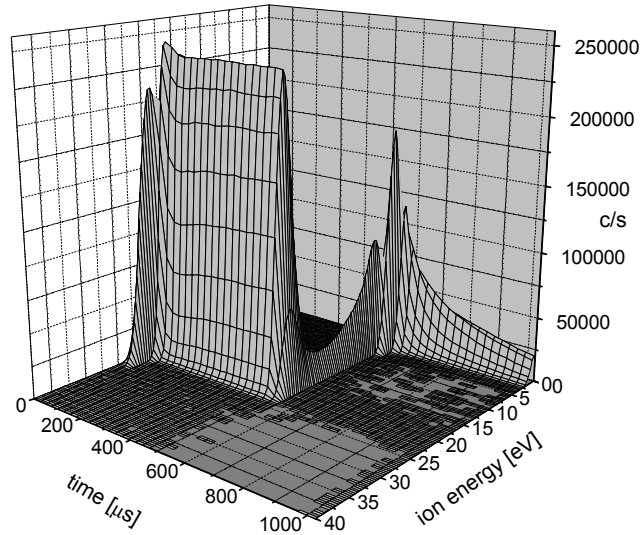
The time constants in the afterglow for different atomic and molecular gases at various plasma conditions are shown in tab. 1. As a result, an increase in pressure leads to longer decay time constants for the charged particles densities, caused by an increase in collisions with neutrals. Since the decay rate of the electrons (ions) is governed by ambipolar diffusion, helium and hydrogen densities decay faster because of their low masses leading to higher ion mobility and therefore to a more effective transport to the walls. Admixture of molecular gases like nitrogen and hydrogen, having a lot of vibrational and rotational molecular energy levels, speeds up decay of electron energy.

In all experiments, two different time constants of density decay are visible where the first (and fast) one for the different gases and mixtures are in the range from 10 to 200  $\mu\text{s}$ . These results partly agree with the estimated time constant for ambipolar diffusion [6]. The second (and slow) time constants are in the range from 280 up to more than 800  $\mu\text{s}$ . These time constants are equal and longer than those for binary diffusion, i.e. diffusion without an ambipolar electric field. This behavior might be due to the fact that the ambipolar transport decreases since electron temperature rapidly decreases. The mean electron energy (fig. 2, 3) does not decrease much below 1 eV in the afterglow since the large energy sink of inelastic collisions is not longer effective. Additionally, superelastic collisions, where the excitation energy of a metastable atom heats the colliding electron, take place and deliver energy back to the electrons.

**Tab. 1:** Afterglow time constants for potentials, electron energies and densities obtained from time resolved Langmuir probe measurements.

Gas	Mass [amu]	Pressure [Pa]	Power [W]	$\tau_{\text{Ee}}$ [ $\mu\text{s}$ ]	$\tau_{\text{Upl}}$ [ $\mu\text{s}$ ]	$\tau_{\text{Un}}$ [ $\mu\text{s}$ ]	$\tau_{\text{ne1}}$ [ $\mu\text{s}$ ]	$\tau_{\text{ne2}}$ [ $\mu\text{s}$ ]
Ar	40	1	100	14.7	18.4	16.2	122	555.6
Ar	40	3	100	15.4	22.43	11.99	143	769
Ar	40	10	100	22.75	33	25.25	336	961
He	4	10	500	5.26	6.67	8.33	<5	308.6
Kr	84	3	100	33.6	34.6	26.1	126.1	830
H <sub>2</sub>	1,2,3	10	1000	2.47	3.83	3.8	58.5	290
Ar/N <sub>2</sub> (2%)	14,28,40,54	3	100	10.76	11.4	6.37	171.8	-
Ar/H <sub>2</sub> (2%)	1-3,40,41	3	100	19	18.3	18	165	285
Ar/H <sub>2</sub> (10%)	1-3,40,41	3	100	7.57	12.1	-	180	280

The time resolved ion energy distribution function in a pulsed argon plasma at 1 Pa and 100 W obtained from energy and mass spectrometry is shown in fig. 4. At any time, a narrow energy distribution with a single maximum around 15 eV can be observed as it is typical for inductively coupled plasmas. Shortly after rf is switched on ( $t = 0 \mu\text{s}$ ) an energy overshoot at around 20 eV is visible. After approx. 70  $\mu\text{s}$  steady state is reached. At 500  $\mu\text{s}$  rf is switched off and the energy peak is shifted within 20  $\mu\text{s}$  to very low energies below 2 eV. The ion current decay is much slower.



**Figure 4:** Temporal development of the ion energy distribution function in a pulsed Ar plasma at 1 Pa 100 W

As the ion energy distribution function contains very detailed information, the temporal behavior of the ion current and the mean ion energy as more technological relevant parameters are evaluated.

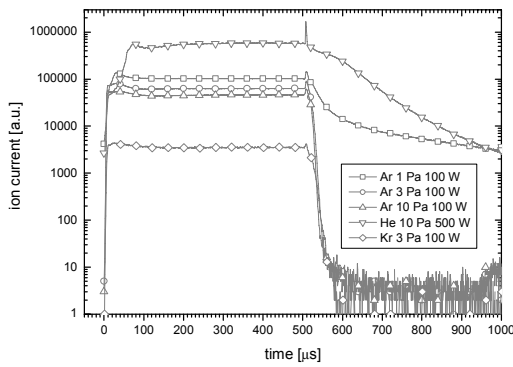
Fig. 5 shows the time resolved results from energy and mass spectrometry of different noble gas plasmas. The time development of the ion current (5a) has a narrow peak at switch-off time which is already discussed above. Clearly visible is the much longer decay time in dependence of pressure since elastic collisions with neutrals decelerate the transport of the ions.

The ion energy (5b) has the expected overshoot shortly after plasma ignition, and shortly after the peak in plasma potential. The higher mobility of the light weight electrons leads to a temporal peak of the ambipolar electric field. This peak is compensated later by the positive ions travelling to the wall. After around 200  $\mu\text{s}$  steady state is reached for all pressures and gases used here.

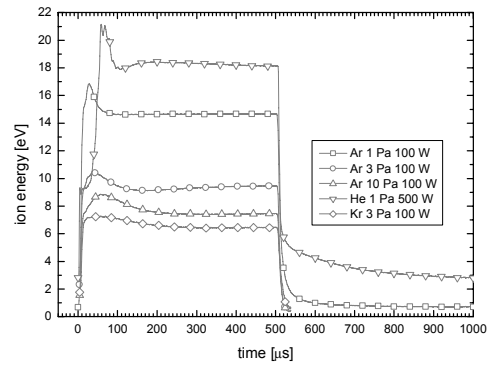
As aforementioned, in the afterglow different time constants for ion energy and current can be observed depending on the plasma conditions.

The results for a mixed argon hydrogen plasma are presented in fig 6. The ion currents (6a) are plotted versus time for six different ion species, including negative  $H^-$  ions. Clearly visible is the fast decrease of the heavy ion currents ( $Ar^+$  and  $ArH^+$ ) with a fast time constant around  $5\ \mu s$  and a slow one around  $50$  ( $ArH^+$ ) up to  $140\ \mu s$  ( $Ar^+$ ) (see tab. 2). The first time constant is equal or shorter than the ambipolar time constant, the second one is in the order of the binary diffusion time constant.

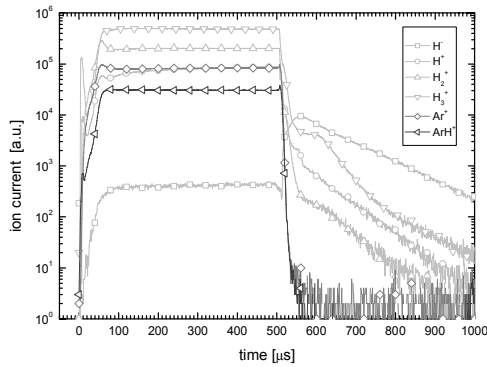
Remarkable in fig. 6a is the increase of  $H^-$  ions in the afterglow: during plasma-on time the negative  $H^-$  ions are trapped by the ambipolar electric field. Only minorities, generated in the vicinity of the walls escape and can be detected. A bulk of negative  $H^-$  ions escapes after rf is switched off and the ambipolar electric field is collapsed.



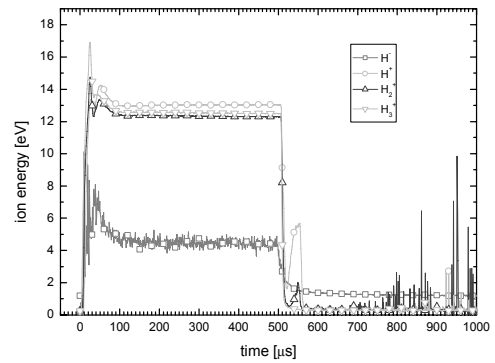
**Figure 5a:** Time resolved ion currents from various pulsed noble gas plasmas.



**Figure 5b:** Time resolved ion energies in various noble gas plasmas.



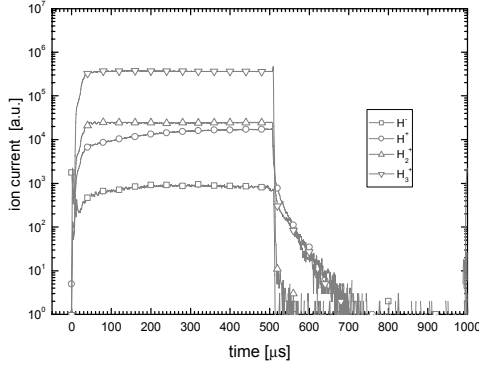
**Figure 6a:** Pulsed  $Ar/H_2$  plasma. Time resolved ion currents of positive species and  $H^-$ .



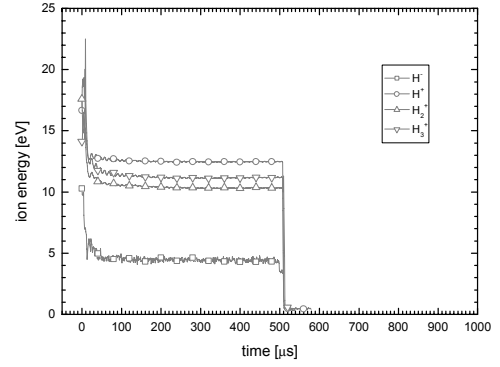
**Figure 6b:** Pulsed  $Ar/H_2$  plasma. Time resolved ion energies of hydrogen species.

The ion energies of the hydrogen species in an  $Ar/H_2$  plasma are shown in fig. 6b. All energies have the above discussed ignition peak. In the afterglow the species  $H_2^+$  and  $H^+$  show a peak in energy after the main energy drops. This peak occurs at exactly the same time as the  $H^-$  ion current has a maximum. High rate reactions like  $H+H_3^+\rightarrow 2H+H_2$  and the charge exchange  $Ar^++H_2\rightarrow Ar+H^+, H_2^+$  could be responsible for generating the observed energetic particles. The second reaction could also be responsible for the fast decrease of argon ions given in fig. 6a.

In pure  $H_2$  plasmas (fig. 7a, b) without Ar admixture, no significant amount of  $H^-$  ions could be observed in the afterglow. Only a small  $H^-$  ion current is observable during plasma-on phase. The rise times for  $H^-$ ,  $H_2^+$  and  $H_3^+$  are in the region of 20  $\mu s$ ,  $H^+$  needs more than 300  $\mu s$  to reach a steady state in the on phase. In the afterglow, all hydrogen ion currents show two time constants (see tab. 2), the first around 5 to 20  $\mu s$  and the second from 50 up to 250  $\mu s$ . In the moment, this temporal behavior remains unclear and may not be described only by regarding the transport times of the different species. In this respect it necessary to implement the complex reaction mechanism in order to simulate the time dependencies.

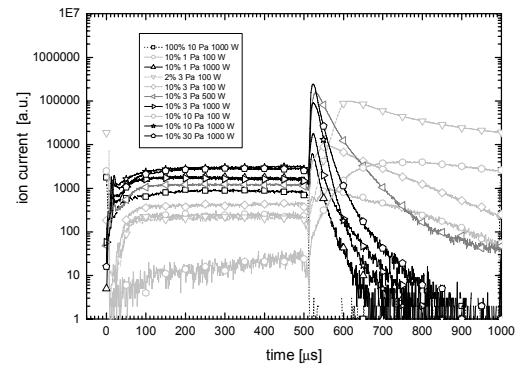


**Figure 7a:** Time resolved ion currents of different species in a pulsed pure hydrogen plasma.



**Figure 7b:** Time resolved ion energies of different species in a pulsed pure hydrogen plasma.

The influence of various plasma conditions on the yield of  $H^-$  ion production in the afterglow is shown in fig. 8. The time development of the corresponding energy is not evaluated (tab. 2). The time constants of the ion current decay are mainly influenced by the rf power in the pulse. A lower rf power leads to slower decay which might be due to the initially lower electron density at switch off time. By increasing the total pressure and power the peak in ion current shortly after switch off is increased. Additionally, regarding the time constants of the high power decays in the afterglow, time constants are reduced with decreasing pressure. Reducing the hydrogen content from 10% to 2% an increase in  $H^-$  peak current in the afterglow is observed without leading to faster decay. Without Ar admixture there is no  $H^-$  current observable in the afterglow.



**Figure 8:** Influence of external parameters on  $H^-$  ion currents.

All afterglow time constants obtained by energy mass spectrometry are summarized in tab. 2.

In general, a zero dimensional approximation in [6] in conjunction with cross sections from [7] and [8] leads to the following diffusion times: Ambipolar diffusion ranges from 3 to 20  $\mu s$ , binary diffusion from 30 to 150  $\mu s$ , reactor residence time from 5 to 200 ms and time constants caused by electron ion recombination from 80 to 5000 ms.

## Conclusion

Different time constants for the electron densities, mean electron energies, ion currents and ion energies in pulsed ICP plasmas with argon, hydrogen and mixtures have been investigated. The switch on time constant for the mean electron energy is in the order of 1  $\mu s$  and below, the switch off or afterglow time constant lies in between 10 and 50  $\mu s$  depending on plasma conditions. After 500  $\mu s$  the electron energy remains at around 1 eV since the excitation sink is nearly not available and superelastic collisions prevent the electrons from cooling.

The electron density shows two afterglow time constants, a fast one which is due to ambipolar diffusion and a slow one which is longer than typical binary diffusion time constants. Ion current studies reveal that decay time constants depend strongly on the puls parameters like puls power and pressure. Negative hydrogen ions in the afterglow will only be observed with argon admixtures. In this respect, there exists an optimum parameter range for  $H^-$  production.

**Tab. 2:** Afterglow ion time constants obtained from energy resolved mass spectroscopy.

Gas	Mass [amu]	Pressure [Pa]	Power [W]	$\tau_{i1}$ [ $\mu$ s]	$\tau_{i2}$ [ $\mu$ s]	$\tau_E$ [ $\mu$ s]
Ar	40+	1	100	68.9	743	18.48
Ar	40+	3	100	7.68	163.2	13.4
Ar	40+	10	100	7.4	191.7	14.65
He	4+	10	500	228	182	11.66
Kr	84+	3	100	15.8	29.1	23.9
H <sub>2</sub>	1-	10	1000	1.2	-	<2
	1+	10	1000	5.6	72.25	<2
	2+	10	1000	3.3	69.5	<2
	3+	10	1000	17.12	67.65	<2
Ar/H2(2%)	1-	3	100	349.7	793.7	-
Ar/H2(10%)	1-	1	100	415	274	-
Ar/H2(10%)	1-	3	100	273.8	-	-
	1+	3	100	17.43	176.6	-
	2+	3	100	18.01	153.37	-
	3+	3	100	20.3	251.8	-
	40+	3	100	4.76	143.8	-
	41+	3	100	4.9	53.8	-
Ar/H2(10%)	1-	10	100	1002	-	-
Ar/H2(10%)	1-	3	500	60.5	297.6	-
Ar/H2(10%)	1-	1	1000	30.2	62.5	-
Ar/H2(10%)	1-	3	1000	25.7	89.6	-
Ar/H2(10%)	1-	10	1000	22.6	78	-
Ar/H2(10%)	1-	30	1000	27.3	117.2	-

### Acknowledgement

The Authors want to acknowledge the financial funding of this work by the Dr. Johannes Heidenhain Stiftung.

### References

- [1] R. Stewart, P. Vitello, and D.Graves, J. Vac. Sci. Technol. B **12**, 478 (1994)
- [2] U. Kortshagen, I. Pukrowski, and M. Zethoff, J. Appl. Phys. **76**, 2048 (1994)
- [3] P. Ventzek, R. Hoekstra, and M. Kushner, J. Vac. Sci. Technol. B **12**, 461 (1994)
- [4] B. Ramamurthi, D. J. Economou, Plasma Sources Sci. Technol. (2002) 324-332
- [5] P. Scheubert, U. Fantz, P. Awakowicz, and H. Paulin, J. Appl. Phys.**90**, 587-598 (2001)
- [6] P. Awakowicz, Habilitationsschrift, Technische Universitaet Muenchen (1998)
- [7] NIFS database AMDIS, <http://dpc.nifs.ac.jp/>, National Institute for Fusion Science, Japan (2002)
- [8] NIFS database CHART, <http://dpc.nifs.ac.jp/>, National Institute for Fusion Science, Japan (2002)

# Plasma Sources for Electrochemical Reactors

Eugen Hnatiuc<sup>1,2</sup>, Jean-Louis Brisset<sup>1</sup>, Bogdan Hnatiuc<sup>2</sup>, Radu Burlica<sup>2</sup>

*1 Laboratoire d'Electrochimie (L.E.I.C.A.) UFR Sciences, University of Rouen  
76821 Mont-Saint-Aignan (France)*

*2 Faculty of Electrical Engineering, Technical University "Gh. Asachi" of Iasi  
51-53 Blvd. D. Mangeron, 6600 Iasi (Romania)*

## Abstract

Electric non-thermal plasma are more and more extensively used for a variety of interesting applications for pollutant abatement. A different type of the discharges needs HV sources ranging from 1 kV to 100 kV. But for HV plasma sources the isolation costs are expensive and can reach 35% of the total costs of the devices. A new view concerning the HV plasma sources and the criteria of the best choose is now really necessary.

## 1. Introduction

There are many electrical discharges that generate cold plasma, which proved their feasibility for application concerning the pollutants removal from environment.

- Corona discharge
- Lighting discharge
- Gliding arc discharge (Glidarc)

In the last time the dielectric, pulse corona and Glow discharges tried to find their place in the pollutants removal technologies. Every type of these discharges needs a power supply (rectified or pulsed high voltage, alternative current, single-phase or tri-phase or high frequency), well adapted for the cold plasma electrochemical reactors.

The cold plasma can be obtained from an electrical discharge between two electrodes supplied by a HV power supply and placed into a close insulated tube with gas at a pressure  $p$ , like is shown in Fig.1.

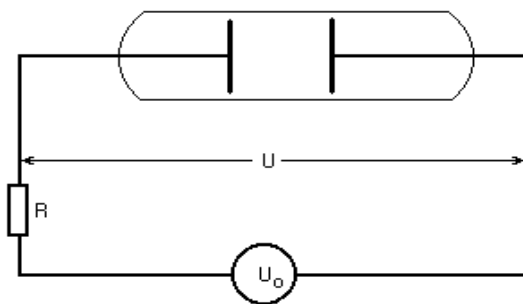


Fig. 1

The characteristic of an electrical discharge depends on: the gas used as support for electrical discharge, its pressure  $p$  and temperature  $T$ , the distance between electrodes,  $d$ , the resistance  $R$  of the electrical circuit, etc. Also, we must take into account the voltage of the power supply  $U_0$ , and the voltage of the electrical discharge,  $U$ .

If we look to the characteristics of the electrical discharge in the gas phase and the dynamic characteristic of the electrical circuit, Fig.2, it is obvious that the choosing of certain plasma generator parameters can aloud us to obtain one or another type of electrical discharge (and even the same discharge for

different parameters). So, it is necessary to choose the appropriate electrical discharge type for a specific treatment of the pollutant, despite the large utilization domain for each type of discharge, announced some time as an advantage, but not a guarantee for an optimal utilization of the reactor.

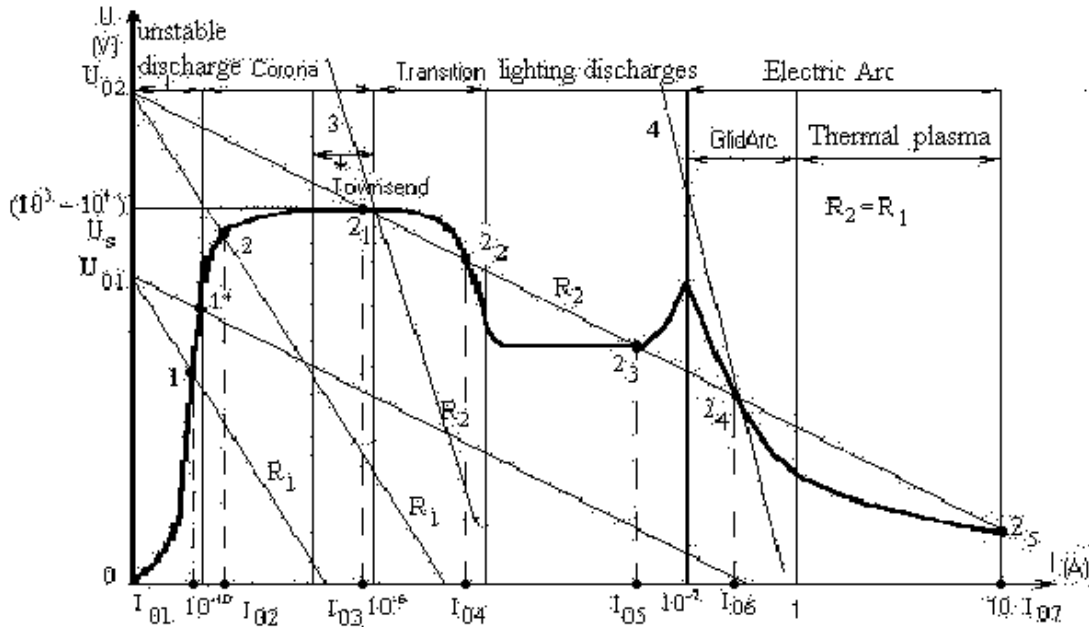


Fig. 2.

The voltage break down for each electrical discharge respects the Paschen curves and for few usual gases the influence of the factor (pd) is emphasized in Fig.3.

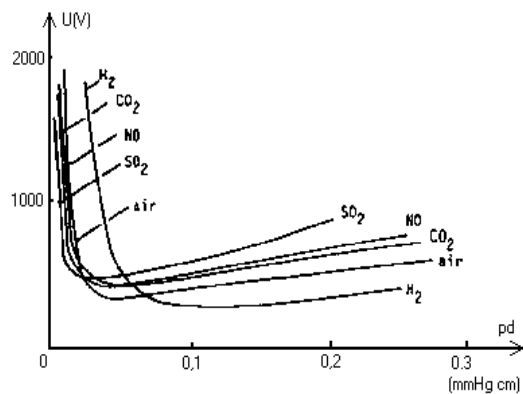


Fig. 3

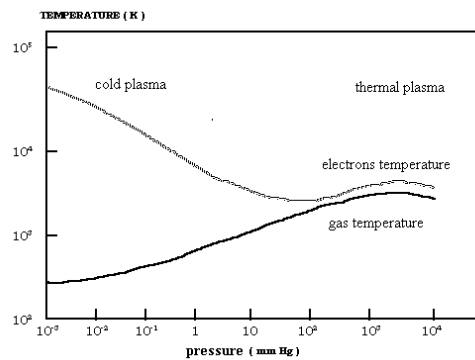


Fig. 4.

The pollutant removal in a cold plasma electrochemical reactor, Fig.4 takes place in the presence of different electrochemical active species generated by an electrical discharge between two electrodes, in a gas flow. There are a lot of cold plasma electrochemical reactor types and finding some criteria to choose the appropriate type of the reactor for a certain application demands a laborious research.



## 2. Power supplies for electrochemical reactors.

A power supply for electrochemical reactor consists in a HV electrical transformer, characterized by its electrical power and also in this case by its voltage, in the absence of the load,  $U_0$ . At the beginning, there are the corona electrical discharges that have proved their feasibility for the pollutant treatment. We have to mention that this type of electrical discharge demands very high voltage, between 10 KV and 100 KV, and low values for the continuous current (1  $\mu$ A to 10 mA). Therefore, one obtains low values for the electrical discharge power, but the work in rectified current and the high value of the voltage determine the high price of these installations.

An important step in the pollutants removal by electrical discharges at industrial scale is the utilization of the Glidarc, [1]. At the beginning, the power supplies were electrical transformers with magnetic shunt which have the outlet volt-ampere characteristic well adapted to the electrical discharges due to the fact that their voltage is about 10 KV without load and became about 1 KV after the electrical discharge is settled between the electrodes, for 100 mA alternative current. That leads to an over-dimensioning of the insulation with respect to the electrical power used by the electrical discharge (about 100W) and in consequence the electrical efficiency is very low (10%). Though there are promising results at the laboratory scale these are far from the industrial requirements.

In order to fulfill these requirements the efficiency of the electrochemical reactors must be increased.

The electrical discharge voltage,  $U$ , is described by the Ayrton relation:

$$(1) \quad U = a + c \cdot l + \frac{b + d \cdot l}{i},$$

The parameters of equation 1 are:  $a$ ,  $b$ ,  $c$  are constants related to the electrodes material,  $l$  is the electrical discharge length,  $i$  is the electrical current.

The electrical power of the discharge has the expression:

$$(2) \quad P_d = (a + c \cdot l) \cdot i + b + d \cdot l.$$

Obviously, in order to increase the electrical power of the discharge we must increase or the current value, which can lead to a thermal status of the plasma or the length of the electrical discharge  $l$ , but that could request a higher voltage of the power supply and a better electrical insulation, therefore a higher cost of the installation.

A first solution was proposed by Harry, [3]. He used an auxiliary electrodes, A, connected to one of the two main electrodes, E1 for example, in order to reduce the initial break down distance of the discharge,  $d_0$ , Fig.5.

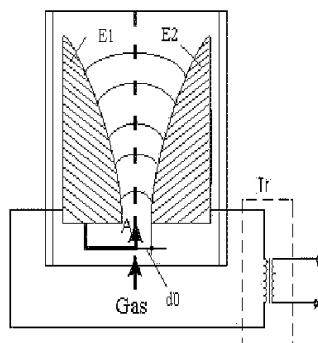


Fig. 5

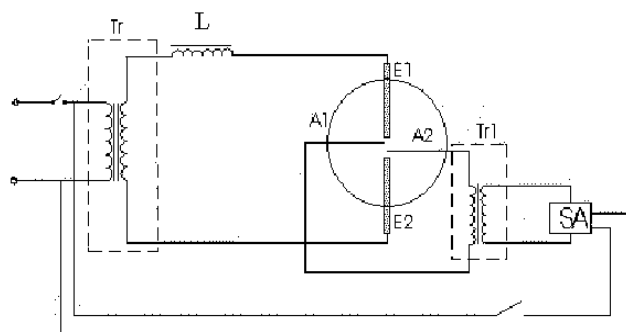


Fig. 6.

A better solution was proposed by the romanian research team of Technical University “Gh. Asachi” Iasi, [2], which used an auxiliary electrical discharge, of very low power, between two electrodes A1, A2, connected to a special power supply, SA, Fig.6.

This solution permits to obtain a higher power of the electrical discharge (2.5KW-5KW) for currents between 1A and 2A, even for a lower voltage of the main power supply.

Other solutions proposed to increase the energy in the electrical discharge area due to the radioactive particles, the gas pre-heating or electromagnetic waves. These solutions are more difficult to set-up and the cost is too high.

The main advantage of the solution proposed by the roumanian team is that, for special design of the auxiliary source, it is possible to control the power of the discharge not only its starting time, like the solution proposed by Janovski, [4]. More, the efficiency considered being the rapport between the power of the electrical discharge and the power of the main source can reach values between 65% and 75%, which becomes interesting for industrial scale application. In the same time is possible to use standard transformers, with a rigid characteristic volt-ampere. In this case it must be used auxiliary circuits L-R in order to limit the electrical discharge current.

In the last time the effect of the pulse discharges on the pollutants removal have been studied. The power supply provides the short HV pulses that require an enhancement of the electrical insulation and very complex electrical equipment. There are many promising results but it must take into account, also, the rapport efficiency/costs and the treatment time of the pollutant.

### 3.Non-thermal plasma reactors

The cold plasma electrochemical reactors were used from the beginning for the treatment of the pollutants from air and aqueous solution. The reactors geometry evolutes and lead to the new solutions to increase the interface between the active species from the plasma and the fluid being treated. To build efficient equipment it must be considered the assembly power supply-electrochemical reactor.

For example we will present only the electrochemical reactors Glidarc type because they provide the highest specific energy injected by the non-thermal plasma, Table 1.

Table 1

Electrical discharge	corona	Pulse discharge	Glidarc
Specific energy[J/L]	10	10-30	500-700

The first non-thermal electrochemical reactors were used for the air depollution. They had a plane geometry, with two divergent metallic electrodes connected to a HV power supply. The electrical discharge took place between these two electrodes in a gas flux, Fig. 7.

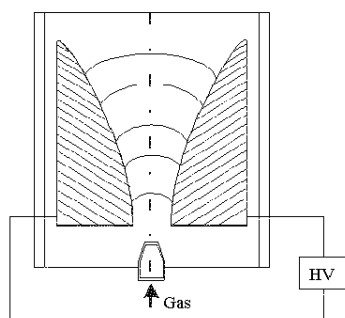


Fig.7

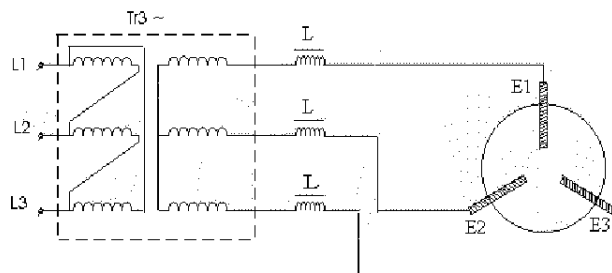


Fig.8

The first step to improve this type of reactors was the utilization of the tri-phase power supply, Fig. 8, which provide an larger interface between the plasma and the gas being treated, a great power of the electrical discharge and less harmonic perturbation in the power network due the connection star-triangle of the transformer. Also in this case is possible to use auxiliary electrodes in order to control the discharge and to increase the power of the reactor.

In the last time the cylindrical geometry of the reactor become the most appropriate for the air treatment due to the rotary electrical discharge imposed by the tangential injection of the gas being treated or to the presence of the magnetic field. The interface between the gas and the plasma is even bigger and is related to the gas aerodynamic behavior.

The main problems linked to the non-thermal electrochemical reactors industrial utilization is:

- The shape and the material of the electrodes
- Improvement of the gas aerodynamics
- Finding the factors responsible for one or another active species in the plasma

This approach requires the parameters optimization of the power supply and the reactor in the same time, in order to have choosing criteria for different applications, for air and as well for solution. We must say that for now the power supply and some time the reactor are the same for very different application.

### 3. Conclusions

1. To obtain a non-thermal discharge is necessary to use HV power supply and if the voltage is lower also the costs of the insulation are lower.
2. Instead to increase the voltage and the power of the discharge is preferable to increase its length by using an auxiliary discharge.
3. The cylindrical shape of the reactor with the rotary discharge increases the interface between the fluid being treated and the active species from the plasma.
4. The power supplies for the electrochemical reactors are in general the same for air treatment or aqueous solution but there are some specific particularities for each case.
5. The power supplies for the Glidarc electrochemical reactors are usually standard transformers and the reactors work at atmospheric pressure. It is necessary to pass now to tri-phase transformers and also to a modular technology for the reactors.
6. The research concerning the factors that determine the presence of certain active species in the plasma is very important.
7. A performing reactor requires the optimization of the assembly power supply-electrochemical reactor (the influence of the shape and material of the electrodes, gas aerodynamics, etc.).
8. The confirmation of the electrochemical reactors performances is done by the pollutant removal efficiency and it to find the appropriate indicators.
9. A fundamental research is necessary to optimize the set-up of the assembly power supply-electrochemical reactor for a certain application.

### References

- [1]. A. Czernichowski, Gliding Arc Applications to Engineering and Environment Control, Pure & Appl. Chem., **66**, 6, (1994)
- [2]. E. Hnatiuc *et al.*, Procédés électriques de mesure et de traitement des polluants, Edition Lavoisier Tec&Doc, Paris, (2002)
- [3]. J.E. Harry, Knight R., Investigation of the Intensity Distribution of Large Volume Multiple Arc Discharges, J. Phys.D., Appl. Phys., **17**, (1984)
- [4]. Strycwska H.D., Janowski T., Integrated Supplying System of Non-Thermal Plasma Generator, Proceedings of International Conference OPTIM '96, Brasov, Romania, (1996)

# Spent extraction solvents removing by a gliding arc plasma

D. Moussa and J.L. Brisset

*Laboratoire d'Electrochimie (LEICA), University of Rouen, 76821 Mont Saint-Aignan, France*

## Abstract

Trilaurylamine (TLA) and dodecane used as an extraction solvent in Pu analysis. Nowadays no defined outlet to treat the contaminated organic part of the aqueous mixture is available. A new technique to degrade TLA and dodecane using a wet air gliding discharge at atmospheric pressure and low temperature is tested in a batch reactor. A plasma treated mixture of  $C_{12}H_{26} + H_2O$  gives carbon oxides (CO,  $CO_2$ ). TLA is by far more difficult to degrade compared with TPH (hydrogenated tetrapropylene) and TBP (tributylphosphate). Reaction mechanisms are proposed.

## 1.Introduction

Mixtures of trilaurylamine (i.e. TLA) and N.dodecane  $C_{12}H_{26}$  are used as plutonium extractant to achieve plutonium analysis in nuclear fuel reprocessing field <sup>[1,2]</sup>. Thus these mixtures constitute a contaminated organic solution without any well defined outlet that must be degraded before waste conditioning. TLA is very difficult to degrade due to its structure, so that the disposal of this solvent is an actual problem in radioactive liquid waste management. We focused on the gliding arc discharge (i.e. glidarc) in wet air since it is a cheap source of  $HO^\bullet$ ,  $HO_2^\bullet$  and NO species <sup>[3-5]</sup> which are able to degrade organic compounds <sup>[6,7]</sup>. Another advantage of the glidarc technique lies in the required working conditions (i.e., atmospheric pressure and near room temperature). It is described elsewhere and was successfully applied to the treatment of gases <sup>[8]</sup>, aqueous solutes <sup>[9]</sup> and even tributylphosphate (TBP) <sup>[10-12]</sup>, additionally to solids. TBP is another complexing solvent used in uranium and plutonium recovery from spent nuclear fuel: it was converted mainly into phosphoric acid,  $CO_2$  and phosphorus oxide <sup>[10-12]</sup>. This communication is devoted to adapting the glidarc technique to the treatment of TLA and dodecane.

## 2.Experimental section

### 2.1. Dodecane

The experimental device used is the same as for TBP treatment <sup>[10-12]</sup> and consists in a one-liter glass reactor with water cooling jacket (Fig.1). The reactor includes two metal diverging electrodes disposed symmetrically around a blowing nozzle. This nozzle is fed by wet air obtained by bubbling the gas through a water filled Durand flask. When the electrodes are raised to a convenient voltage, an electric discharge forms at the electrode gap and the arc moves along the conductors owing to the air flow. It breaks when short-circuited by a new arc and gives a quenched plasma trail which licks an upper layer of solvent (25 mL) disposed on water (560 mL). The distance between electrodes and target must be long enough to prevent dodecane from catching fire.

The outlet gases are washed with potassium hydroxide solution (350 mL) disposed in a trap. CO and  $CO_2$  are monitored by a COSMA analytical infrared station protected by a Peletier dryer. After the treatment both the reactor and washing trap contents are cooled, acidified with (2M) sulphuric acid and treated with sulfamic acid to eliminate the nitrous acid formed. Remaining dodecane is thus extracted by ether, and analysed by capillary column gas chromatography (GPC). Acidic organic fraction is extracted from the bulk ether phase by stirring with NaOH (1M) solution. The resulting aqueous phase, which contains the sodium salts of the acids, is acidified with (2M) sulphuric acid and saturated with NaCl. Acids are thus extracted by

ether, the solvent is removed in vacuum. The residue is treated with a solution of boron trifluoride in methanol to make the methyl ester derivatives <sup>[13]</sup> and therefore identified by GPC, by comparing the obtained retention times with those of carboxylic acid standards samples prepared with the same method.

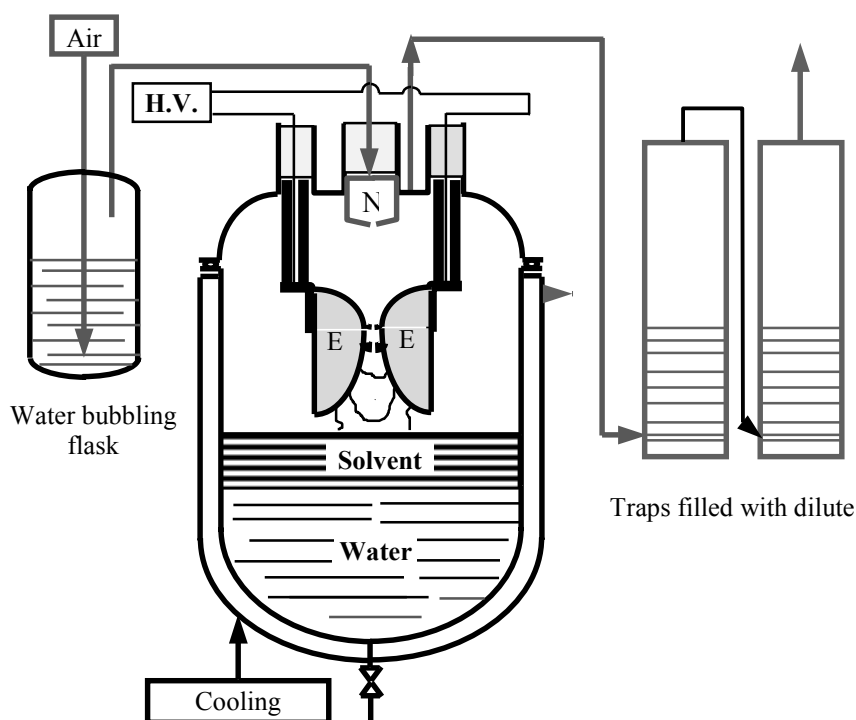


Fig.1: Batch glidarc reactor used for the treatment of dodecane

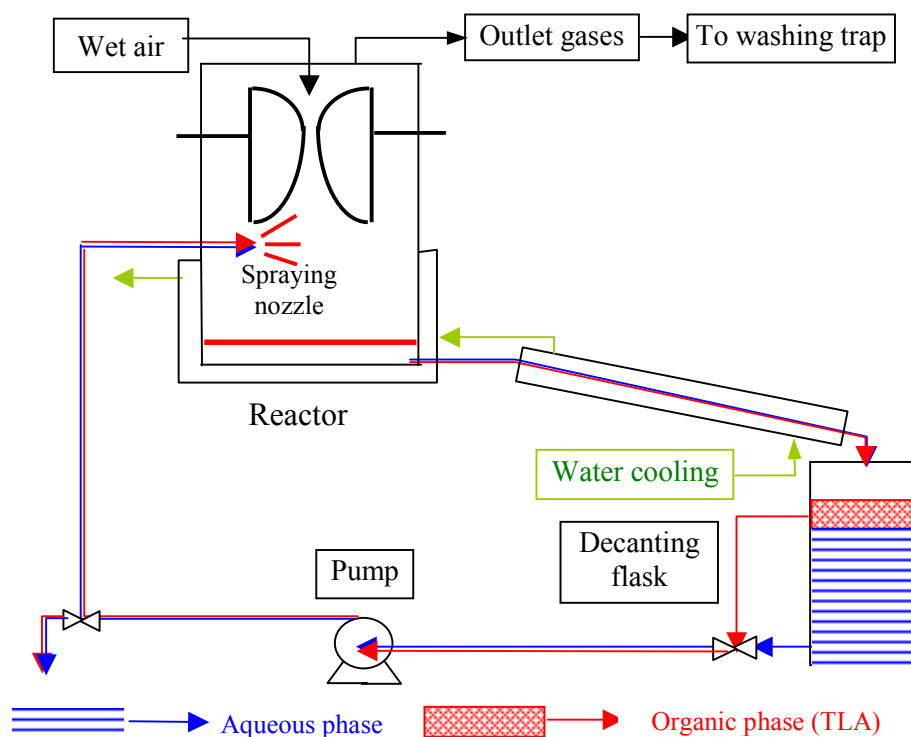


Fig.2: Pump recycled target reactor for the TLA treatment

## 2.2. Trilaurylamine (TLA) treatment

TLA is initially an oily liquid. In a batch glidarc treatment, it gets waxy due to trilaurylammonium salts formation caused by the plasmachemical acidification. We have thus experimented a circulation reactor (Fig.2) which allows recycling of the liquid target.

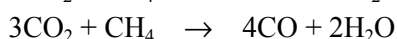
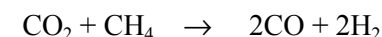
The TLA (60mL, non-miscible with water and less dense) is treated with (1M) sodium hydroxide solution (590mL). The mixture is cooled by a heat exchange tube, and poured into a decanting flask from where the liquid is pumped near the liquid surface of the plasma reactor. Therefore only TLA-rich fraction is recycled and re-injected in the reactor, between the electrodes, through a spraying nozzle. Sodium hydroxide prevents trilaurylammonium salts formation, so the target remains fluid. After the treatment, the remaining TLA is extracted with chloroform and titrated by spectrophotometry, by means of forming a blue complex with cobalt (II) nitrate and potassium thiocyanate. The carboxylic acids produced in the treatment are separated and identified by GPC, as for the dodecane treatment.

## 3.Results and discussion

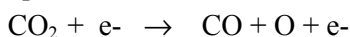
### 3.1.Dodecane treatment

The dodecane present in the reactor disappears within only 20 minutes. The CO<sub>2</sub> emission exhibits two strong peaks respectively at the beginning (2.3 min) and the end (11.8 min) of the treatment (Fig.3), while CO flow seems to have only one maximum and to be an important product around the middle time. The CO flow curve is truncated since the range of the used sensor was too narrow.

Complete oxidation of the hydrocarbon to CO<sub>2</sub> occurs when the vapour concentration in organic compound over the liquid is low enough. For high vapour pressures in organics, the oxidation of hydrocarbon is limited to CO, due to the reducing power of hydrocarbons (or hydrogen). Such a plasmachemical process was already described for methane [8]:



CO<sub>2</sub> may also undergo dissociation in the plasma [14, 15]:



which participates to the general degradation scheme.

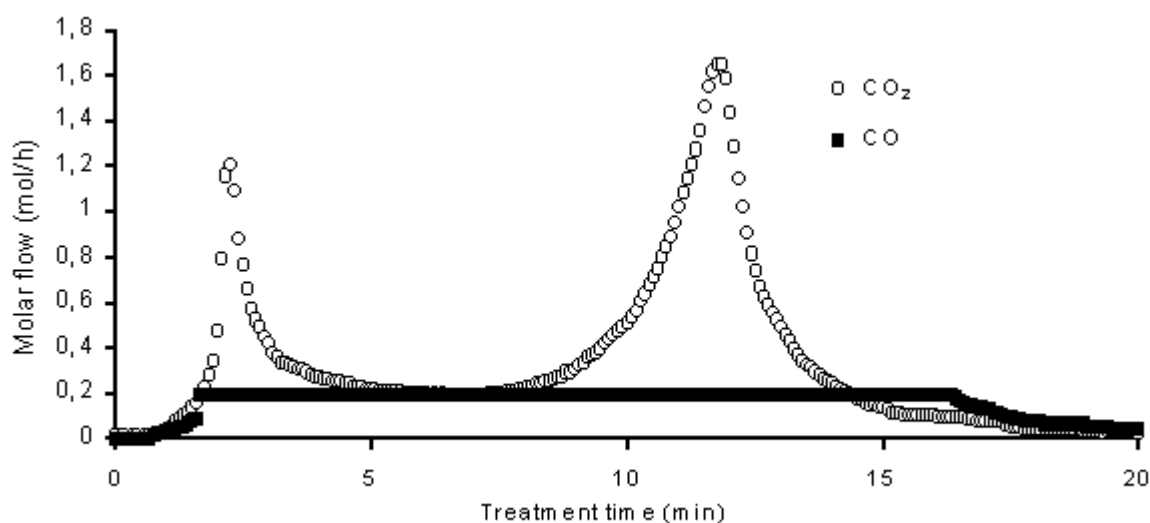


Fig.3: CO and CO<sub>2</sub> release in dodecane treatment

During the plasma treatment, dodecane strongly evaporates, so that about 25% of non-degraded dodecane was found in the trap. This is caused by the heat produced by the discharge combined with the air flow. An improved treatment was undertaken with stirring the mixture to distribute heat in the entire medium and thus prevent surface heating and dodecane evaporation. Much more CO<sub>2</sub> is produced and less than 2% of the initial dodecane is found in the outlet trap.

Carboxylic acids ranging from acetic to dodecanoic are found both in the reactor and in the outlet trap after the treatment. A mechanism (Fig.4) based on the literature data relevant to the HO• and NO properties toward aliphatic chains<sup>[6,7]</sup> is suitable to explain their formation.

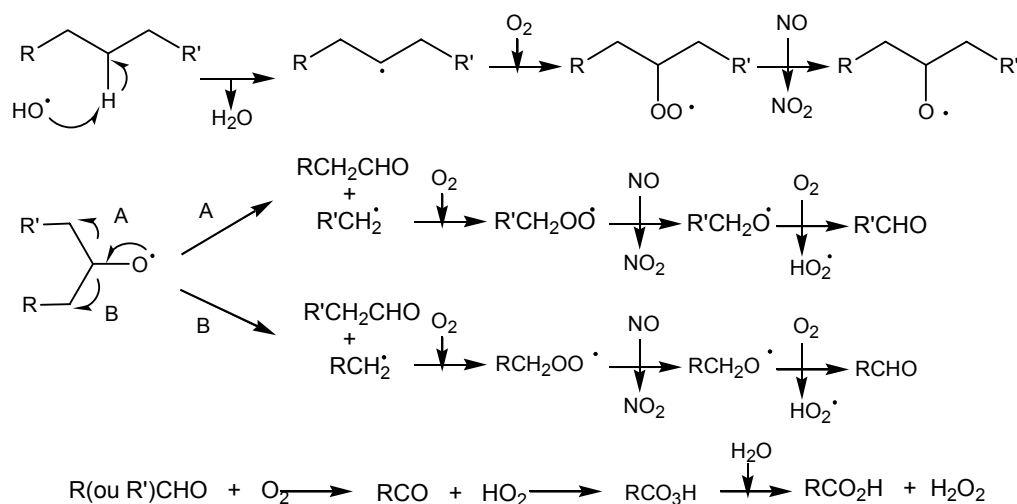


Fig.4: Suggested mechanism for an alkane (e.g., dodecane treatment)

### 3.1.TLA treatment

TLA is much less volatile than dodecane and its three hydrocarbon chains hinder the nitrogen atom. The degradation rate of the compound is therefore much slower (Fig.5) than that of dodecane.

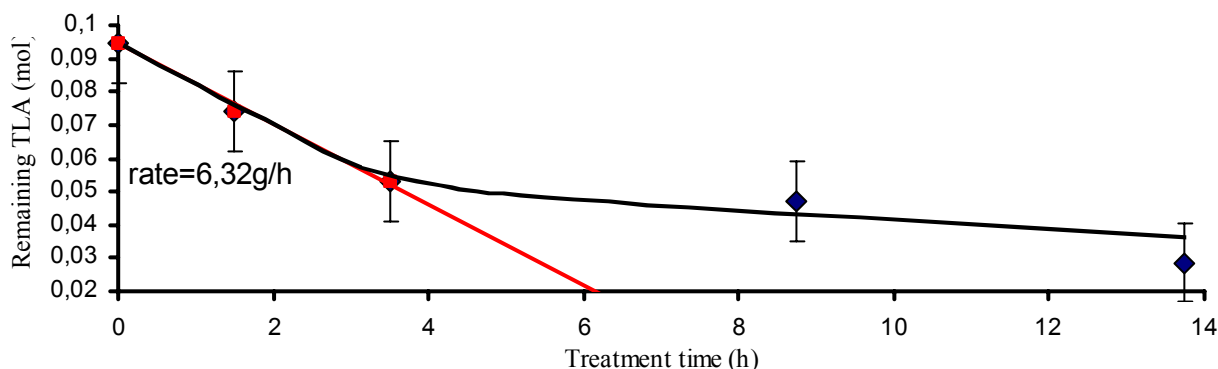


Fig.5: Kinetics of TLA degradation

It needs about 14 hours and first involves a zero-order step within zero and 3.5 h. This step is followed by a rate decrease which takes place when not any enough TLA remains to ensure a good and constant contact with the plasma. In the acidic fraction we identified several carboxylic acids ranging from C<sub>8</sub>H<sub>17</sub>COOH to C<sub>11</sub>H<sub>23</sub>COOH, which is the major compound. The following mechanism (Fig.6) aims to ex-

plain their formation. The hydrogen removal by the  $\text{HO}^\bullet$  radical is favoured on the carbon in  $\alpha$  position from the nitrogen atom <sup>[6,7]</sup>. The alkoxy radical formed leads either to a cleavage giving undecanal, which is oxidised to yield undecanoic acid (path A), or to the amide, which is hydrolysed to give dodecanoic acid (path B).

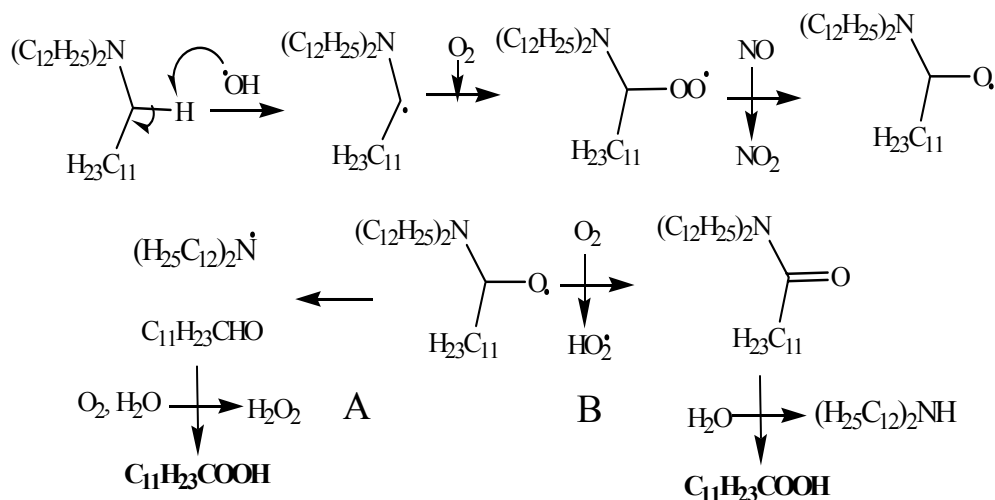


Fig.6: Suggested mechanism for TLA treatment

Lighter acids (i.e.,  $\text{C}_8\text{H}_{17}\text{COOH}$  and  $\text{C}_9\text{H}_{19}\text{COOH}$ ) result from hydrogen removal respectively at the carbon atoms in  $\beta$  and  $\gamma$  position, followed by a mechanism similar to path A.

#### 4. Conclusion

We designed new wet air gliding arc devices to degrade spent organic solvents. They were successfully tested the technique with particular organic solvents which are widely used in nuclear industry, and compared with a range of other possible techniques (incineration, destruction by a powerful oxidiser such as silver (II), supercritical process, ...), the main advantages of the gliding arc process are the operational parameters which are atmospheric pressure and room temperature. The degradation products confirm the properties of  $\text{HO}^\bullet$  and  $\text{NO}$  species toward hydrocarbon chains. Work is in progress to improve the degradation rates and the  $\text{CO}_2$  yields.

#### Literature cited

- [1] K. Bunzl, W. Kracke, *J. Radioanal. Nucl. Chem., Letters*, **186**, (1994), 401-413.
- [2] W. Schimmack, K. Auerswald, K. Bunzl, *Environ. Radioactivity*, **53**(1), (2001), 41-57.
- [3] R. Peyrous, *Ozone Sci. Eng.* **12**(1), (1990), 19-40.
- [4] M. Garcia, B. Chang, *Proc. 12th Int. Symp. Plasma Chem.*, (Minneapolis, USA, 1995) **2**, 813-818.
- [5] B. Benstaali, P. Boubert, B.G. Chéron, A. Addou, J.L. Brisset, *Plasma Chem. Plasma Proc.*, **22**(4), (2002), 553-571.
- [6] R. Atkinson, *Chem. Rev.*, **85** (1985) 69-201.



- [7] M. Veillerot, P. Foster, R. Guillermo, J.C. Galloo, *Int. J. Chem. Kinet.*, 28, (1996), 235-243.
- [8] A. Czernichowski, *Pure Appl. Chem.*, 66(6), (1994), 1301-1310.
- [9] B. Beenstaali, D. Moussa, A. Addou, J.L. Brisset, *Eur. Phys. J. AP*, 4, (1998), 171-179.
- [10] D. Moussa, J.L. Brisset, *J. Hazard. Mat.* (in press)
- [11] D. Moussa, J.L. Brisset, *Proc. 14th Int. Symp. Plasma Chem.*(Praga, Czech Rep., 1999) Ed. M. Hrabovsky, M. Konrad, V. Kopecky, 5, 2539-2544.
- [12] D. Moussa, J.L. Brisset, S. Barges, «*Destruction d'un solvant organique par plasma froid*», French Pat. N° 98.13439.
- [13] L.D. Metcalfe, A.A. Schmitz, *Anal. Chem.*, 33 (1951), 363.
- [14] S.Y. Savinov, H. Lee, H.K. Song, B.K. Na, *Ind. Eng. Chem. Res.* 38(7), (1999), 2540-2547.
- [15] C.J. Liu, G.H. Xu, T. Wang, *Fuel Process. Technol.*, 58, (1999), 119-134.

# Temporal post-discharge reactions in the gliding arc treatment of aqueous solutions

A. Doubla<sup>1</sup>, F. Abdelmalek<sup>2</sup>, A. Addou<sup>2</sup>, E. Hnatiuc<sup>3,4</sup>, J.L. Brisset<sup>4</sup>

1- *Inorganic Chemistry Laboratory; University of Yaounde-I; Cameroon*

2- *STEVA Laboratory; University of Mostaganem; Algeria*

3- *Technical University G. Asashi; 6600-Iasi; Romania*

4- *Electrochemistry Laboratory (LEICA) University of Rouen; 76821 Mont St. Aignan; France*

## Summary

The reaction between  $\text{Fe}^{2+}$  and  $\text{SCN}^-$  aquoions in a humid air gliding arc discharge is checked as a new suitable test for evaluating the efficiency of the reactor for oxidising treatment of solutes.  $\text{Fe}^{2+}$  is oxidised to  $\text{Fe}^{3+}$  which forms the coloured complex  $\text{FeSCN}^{2+}$ . The relevant kinetics was studied, additionally to the evolution of the solution after switching off the discharge and removing the liquid from the reactor. The temporal post-discharge (TPD) phenomena are described and arguments for a possible mechanism are given.

## 1- Introduction

Due to their particular working conditions (i.e, quasi-ambient temperature and atmospheric pressure) two non-thermal plasma techniques (i.e., the corona and the gliding arc discharges) are strongly attractive both for scientists and for industrials, since they accept gaseous, liquid and solid targets. They are now more and more often involved in pollution abatement processes, so that they now take place aside the emerging advanced oxidation processes (AOPs). Their use in the field is related to the chemical properties of the main gaseous species formed in the discharge, which were identified as  $\cdot\text{OH}$  and  $\text{NO}$  radicals for humid air plasmas [1] and found responsible for oxidising or acid properties.

The increasing use of these plasma devices led us to look for chemical tests that could account for the efficiency of the plasmachemical reactors operated in humid air. One of them is based on the acid properties [2]. The present paper deals with a matching easy to make test based on the oxidising properties of the plasma species. The reaction involves i) the oxidation of  $\text{Fe(II)}$  to  $\text{Fe(III)}$  and ii) the complex formation between  $\text{Fe(III)}$  and  $\text{SCN}^-$  in a plasma treated solution. These reactions are based on the following assumptions, which are widely accepted in solution chemistry: i) the oxidation reaction is rapid and governed by the discharge (or by the active species formed in the discharge), ii) the complex formation reaction occurs rapidly and may be easily examined by the stopped flow technique, iii) the complex formation reaction is very sensitive since the complex is detected for trace concentrations ( $10^{-6}$  M).

We focus here on the gliding arc device as the plasma device, because this plasma source appears to more efficient than the corona discharge. The gliding arc discharge ("glidarc") belongs to the restricted family of the non-thermal plasmas, and is actually a quenched plasma with practically no thermal matching effect at the macroscopic scale.

## 2- Experimental section

The glidarc system is described elsewhere [3]. It involves a couple of diverging electrodes raised to a suitable potential fall (by a few kV), so that an arc forms at the minimum gap (Fig. 1). This arc is gently pushed along the electrodes by a gas flow directed along the axis of the reactor. The arc length increases until it is short-circuited by a new arc and breaks into a plume. The feeding gas is water saturated air.

The plasma plume licks the magnetically stirred liquid target which is disposed in front of the gas input.

The liquid target is a mixture of  $\text{Fe(II)}$  (e.g., the Mohr salt) and potassium thiocyanate aqueous solutions at the same concentration (2.5 mM) and is placed in a thermostatted cell to prevent from any temperature effects.

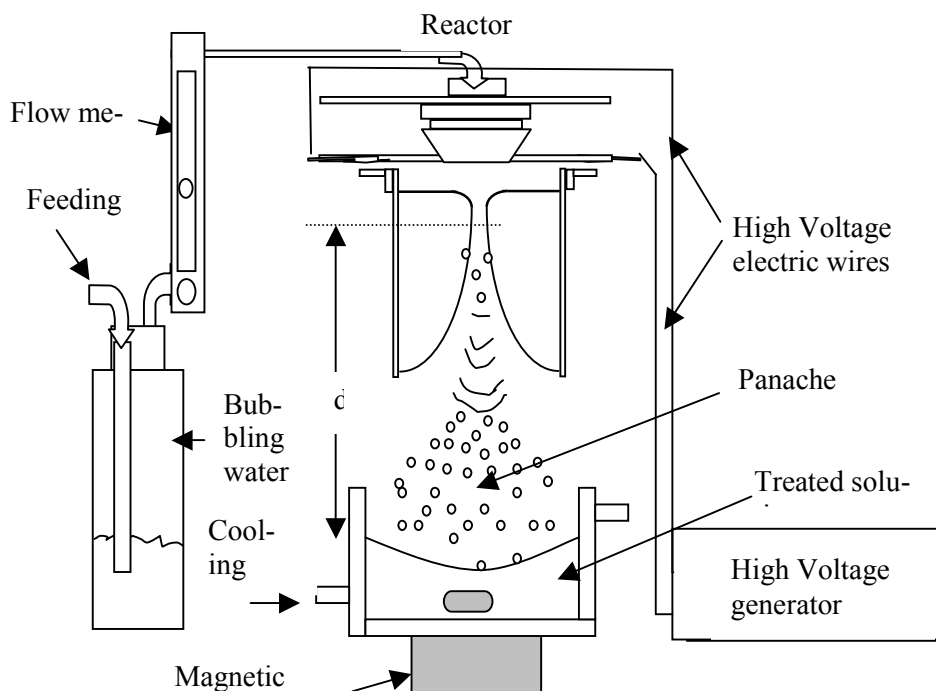


Fig. 1. General scheme of the gliding arc reactor.

Analysis of the plasma-treated solution is performed by sampling known aliquots of liquid for absorbance measurements at the absorption peak of the coloured complex ( $\lambda = 450$  nm) for various exposure times to the plasma, and by standard electrochemical methods.

### 3- Results and Discussion

#### 3.1- Preliminary and instant reaction

An aqueous solution of ( $1\text{g.L}^{-1}$ ) Fe(II) is exposed to the discharge for various given treatment times  $t$  (min). When the discharge is switched off, the potential of the treated solution is measured at a platinum electrode and increases with  $t$ . (Fig. 2). This evidences that the ratio  $C_{\text{Fe(III)}}/C_{\text{Fe(II)}}$  increases with  $t$  and confirms the oxidising power of the plasma species. For about 10 min-treatment, the solution potential stabilises, which accounts for the occurrence of a buffered system (i.e.,  $\text{Fe}^{2+}/\text{Fe}^{3+}$ ). For  $t \approx 30$  min, a steep increase in the potential shows that the concentration in the matching reducing species  $\text{Fe}^{2+}$  is close to zero. For long exposure times ( $t > 40$  min) a new oxidation-reduction buffer occurs and stabilises the potential. Relevant candidates might be the systems  $\text{HNO}_2/\text{NO}_3^-$  ( $E^\circ = 0.94$  V) or  $\text{NO}/\text{NO}_3^-$  ( $E^\circ = 0.96$  V).

Additionally, the target liquid readily turns to reddish on adding an excess of  $\text{SCN}^-$  solution to aliquots of the plasma treated solution. This shows that Fe (II) is oxidised to Fe(III) and that the coloured complex  $\text{FeSCN}^{2+}$  forms. The absorbance  $A_{450}$  of the solution measured at 450 nm indicates that the concentration in oxidised iron increases with  $t$ , and tends to a limit, so that the log plot associated to  $C_{\text{FeSCN}^{2+}}$  vs.  $t$  reflects a 1<sup>st</sup> order kinetic, with the rate  $k = 8.8 \cdot 10^{-4} \text{ s}^{-1}$  (Fig. 3).

Similarly, the colour of an aqueous mixture of Fe(II) and  $\text{SCN}^-$  exposed to the gliding arc discharge for  $t$  (min), readily becomes reddish, which confirms the formation of the Fe(III)-SCN complex  $\text{FeSCN}^{2+}$  and again accounts for the oxidation of the  $\text{Fe}^{2+}$  aquoions by the plasma species.

The absorbance of the solution was measured at 450 nm after switching off the discharge and sampling, after various plasma treatment times  $t$  (min). The relevant values provide the concentration  $C_{\text{FeSCN}^{2+}}$  in the complex as an increasing function of  $t$ . The log plots associated to  $C_{\text{FeSCN}^{2+}}$  vs  $t$  reflect a 1<sup>st</sup> order kinetic with a rate very close to that reported above for single Fe(II) solutions, and may be related to a slight difference in the temperature.

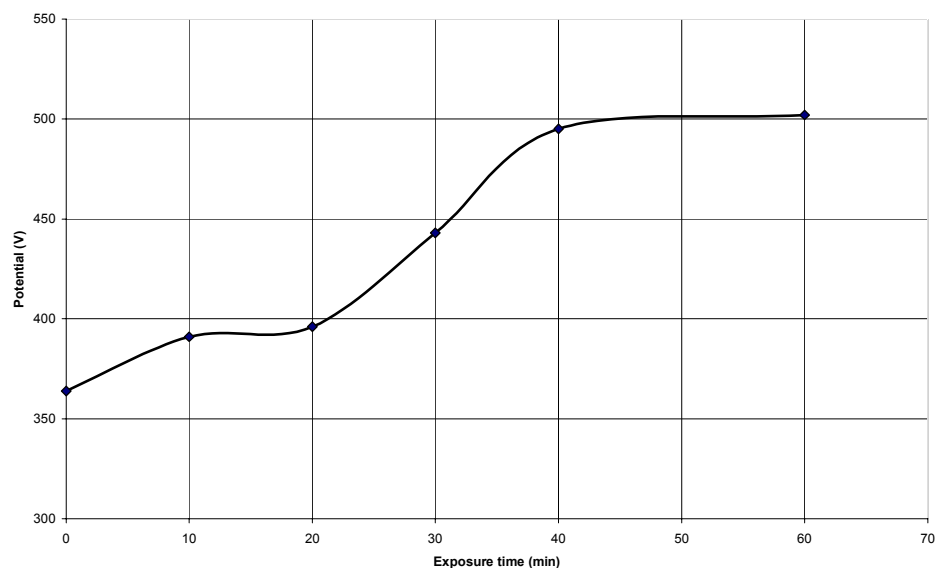


Fig.2- Evolution with time of the solution potential

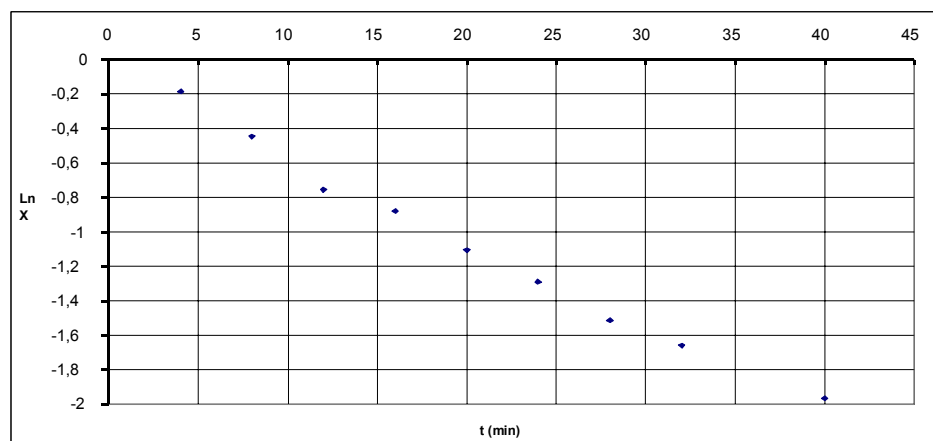
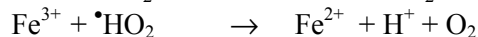
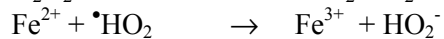
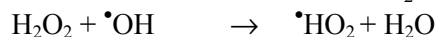
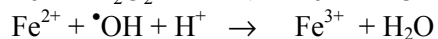
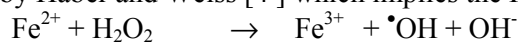
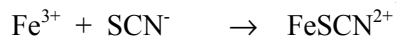
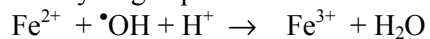


Fig. 3- Kinetic plot  $\text{Ln } X = f(t)$ , with  $X = 1 - C_{\text{FeSCN}^{2+}} / C^0$

Oxidation of Fe(II) solutions exposed to an electric discharge was already recognised [3] on exposing the solution to the neutral species of a corona discharge. This is directly related with the mechanism suggested by Haber and Weiss [4] which implies the Fenton's reaction as the first step:



The oxidation reaction of Fe(II) by  $\text{H}_2\text{O}_2$  and  $\cdot\text{OH}$  allows the subsequent formation of the complex  $\text{FeSCN}^{2+}$ . The main oxidising species is  $\cdot\text{OH}$  ( $E^\circ(\cdot\text{OH}/\text{H}_2\text{O}) = 2.85 \text{ V/NHE}$ ) which also results from the dissociation of hydrogen peroxide. Hence the overall reaction should be:



The rate determining step is probably the production in hydroxy radicals which directly depends on the plasma treatment time and on the electric power dispensed in the discharge.

### 3.2 - Temporal Post-Discharge Reactions

As mentioned, the complex  $\text{FeSCN}^{2+}$  results from exposing the tested solution  $\text{Fe}^{2+} + \text{SCN}^-$  to the discharge, and this is considered as an instant reaction. A more careful examination of the absorbance of the solution immediately after switching off the discharge confirms that  $A_{450}$  is an increasing function of the exposure time  $t$ . However the instant absorbance value is linearly related to  $t$ , with the slope  $3.4 \cdot 10^{-4} \text{ s}^{-1}$ . The main difference with the previously reported results lies in the reaction overall mechanism which is now zero-order.

A matching and subsequent evolution may be then observed out of the discharge and is referred to as Temporal Post Discharge (TPD) phenomena.

Aliquots of the solution were sampled and disposed outside the reactor, and in the absence of any source of energy (thermal or light) after the discharge was switched off. The absorbance of the solutions changes with the post discharge time  $t^*$  (min), which shows that the concentration in the complex is modified.

For moderate exposure times  $t$  to the discharge (i.e.,  $t < 30 \text{ min}$ ), the absorbance of the solution goes on increasing with the post discharge time  $t^*$  (Fig. 4), and so does the concentration in the complex. The relevant kinetic plots are linear functions of  $t^*$  at the beginning of the evolution, which indicates an initial zero-order process. For longer  $t^*$  values, the kinetic process gently gets slower, tends to a limit value and the zero-order process is no more observed.

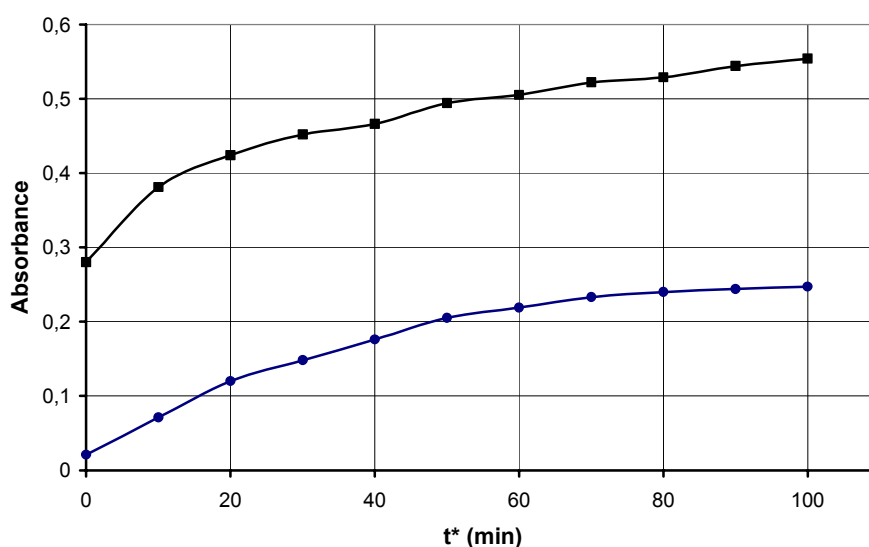


Fig.4 – Post discharge evolution of the absorbance with time for moderately treated solutions ( $t = 3 \text{ min}$ : diamonds;  $t = 10 \text{ min}$ : filled squares)

Thus,  $d C_{\text{FeSCN}^{2+}} / dt^* = k$

and the associated slope  $k$  is a linear function of the instant absorbance of the complex  $A_{450}$ .

$$k = 4 \cdot 10^{-4} A_{450} + 7 \cdot 10^{-5} \quad (r^2 = 0.92)$$

which means that  $k$  is directly related to the instant concentration in complex:

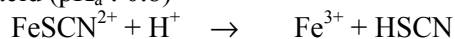
$$k = \alpha C_{\text{FeSCN}^{2+}} + \beta$$

Therefore, the post discharge kinetics of complex formation reasonably obeys a 1<sup>st</sup> order mechanism at the very beginning of the TPD.

This feature may be related to a more general kinetic model involving diffusion phenomena in the liquid phase. On impinging the liquid surface at  $\text{Fe}^{2+}$  ions, the OH radicals directly oxidise the metal species to  $\text{Fe}^{3+}$  ions which are now able to drift in the solution, react with the available ligands and yield the coloured complex. Additionally, the OH radicals form hydrogen peroxide molecules which drift in the liquid phase and slowly react then as oxidising species (in acidic medium).

For long exposure times  $t$  to the discharge (i.e., for  $t > 30$  min), the absorbance of the solution changes again when the sample is removed from the reactor, decreases with  $t^*$  and tends to a steady value  $A^*_{450}$  which depends on the exposure time to the plasma (Fig 5), according to a process close to a 1<sup>st</sup> order kinetic mechanism. Since the  $A^*_{450}$  values are proportional to the instant concentrations in complex when the TPD starts, this means that the complex disappears. Such a feature may result from two matching mechanisms which must be considered:

i) the increase in the acidity of the solution destroys the complex and yields thiocyanic acid which behaves as a quasi strong acid ( $pK_a : 0.8$ )



ii) the ligand  $\text{SCN}^-$  is oxidised to sulphate and cyanate. No evidence of such a degradation is confirmed by the plasma treatment of synthetic complex solutions, since no trace of sulphate is detected. Therefore the relevant assumption must be discarded.

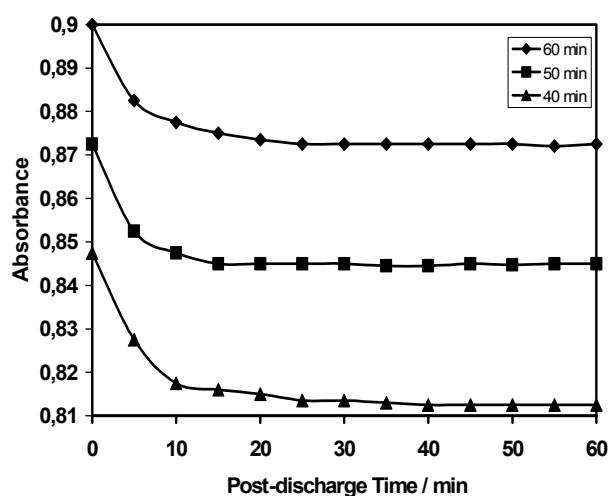


Fig 5. Evolution with the post discharge time of the absorbance of the plasma treated solution (Exposures: 40; 50 and 60 min)

For very long post discharge times  $t^*$ , the absorbance values stabilise and tend to steady values corresponding to the end of the post-discharge evolution, that is the  $A^*_{450, \infty}$  relevant to  $t_{\infty}^*$ . One can then plot the evolution of  $A^*_{450, t_{\infty}}$  with the exposure time to the plasma (Fig. 6). The matching log transform is linear, which indicates a 1<sup>st</sup>-order mechanism, with the rate constant  $k$  :

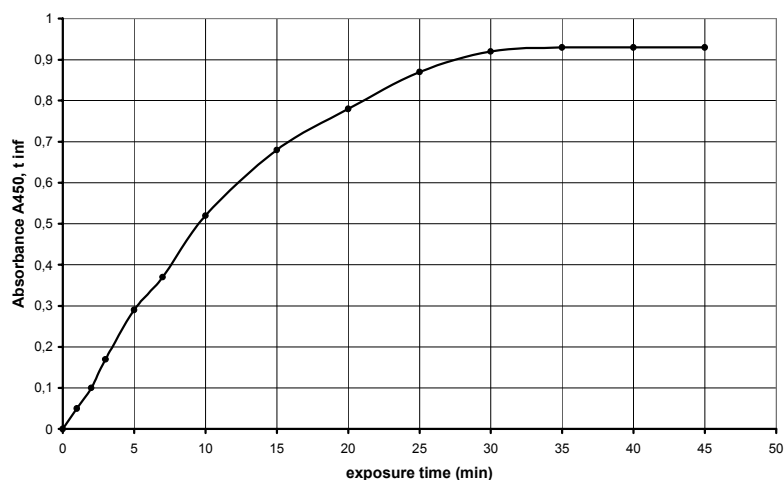


Fig 6. Evolution of the absorbance of the treated solution 3 days after the discharge was switched off. The reported values are considered as stabilised and account for an overall 1<sup>st</sup> order reaction ( $k \approx 10^{-3} \text{ s}^{-1}$ ).

### 3.3- Discussion

The plasmachemical oxidation of solutes is attributed to the occurrence of the OH radicals formed in the discharge, since  $\bullet\text{OH}/\text{H}_2\text{O}$  is the most oxidising system after  $\text{F}_2/\text{F}^-$ :  $E^\circ(\bullet\text{OH}/\text{H}_2\text{O}) = 2.85 \text{ V/NHE}$ . The reactivity of the OH radicals may account for the very first evolution of the solute after a limited exposure to the plasma. Then, any impinging  $\bullet\text{OH}$  reacts with a target  $\text{Fe}^{2+}$  ion the concentration of which is then in large excess. For long exposure times, the  $\text{Fe}^{2+}$  are not so concentrated at the liquid surface and the oxidation kinetics is governed by the diffusion of the target ions.

A matching feature is the formation of hydrogen peroxide which acts as a strong oxidising agent in acidic medium, but the relevant kinetics are usually slow, so that they can be associated with 1<sup>st</sup> order reactions.

Two reaction paths are thus concerned and result from the plasma treatment: the immediate oxidation reaction by  $\bullet\text{OH}$  and the delayed reaction by  $\text{H}_2\text{O}_2$  may be interpreted as zero and 1<sup>st</sup> order reaction steps respectively, that the overall reaction is 1<sup>st</sup> order, and involves diffusion phenomena.

Such a feature seems however to present a more general character, since multi-steps kinetics were observed and reported for the plasma degradation of organic dyes [5] or waste waters. In these cases, the Fenton's reaction has not to be considered since no metal ion is present in solution. However it can be guessed that the first kinetic step is connected with the occurrence of  $\bullet\text{OH}$  and the second one with that of hydrogen peroxide which usually reacts with organic compounds more slowly than  $\bullet\text{OH}$ .

### 4- Conclusions

One of our starting aims was to find an easy to use chemical test for plasma reactors devoted to pollution abatement of liquid effluents. The expected test could match and confirm the "acid test" for evaluating the efficiency of some plasmachemical reactors, and the gliding arc device in particular. We choose a very simple, sensitive and well known reaction based on the oxidation of  $\text{Fe}^{2+}$  ions in solution and the subsequent formation of a coloured complex with  $\text{SCN}^-$  ligands.

We actually failed because of unexpected results, although the oxidising properties of the humid air gliding arc discharge are confirmed. Post-discharge oxidation of the solute is observed long after the target solution is removed from the reactor and the first kinetic information are given and prevents using the reaction as a handy test.

This feature is assigned to the occurrence of  $\bullet\text{OH}$  and other oxidising species (such as  $\text{H}_2\text{O}_2$  or  $\text{NO}_3^-$ ) generated by the discharge. Temporal post discharge phenomena seem to present a more general character, because several reaction steps also observed for the pollution abatement of liquid wastes may be also related to the same reason. In any case, a more acute reflection must start on the residence time of plasma-treated targets which could be drastically reduced and thus substantially lower the treatment costs.

### 4- Literature cited

- 1- B. Benstaali, P. Boubert, B.G. Chéron, A. Addou and J.L. Brisset; *Plasma Chem Plasma Process.* **22** (2002) 553-571.
- 2- D. Moussa, H. Vitrac, F. Abdelmalek, B. Benstaali, A. Addou, E. Hnatiuc J.L. Brisset; *Plasma & Polym.* (submitted)
- 3- J.L. Brisset, N. Dubreuil, J. Lelièvre; *Proc. 3<sup>rd</sup> Int. Symp. High Pressure Low Temp. Plasma Chem.* (Strasbourg, France, 1991) 91-96
- 4- F. Haber, J. Weiss; *Proc. Royal Soc.* (1934) **A147**, 332
- 5- F. Abdelmalek, S. Gharbi, B. Benstaali, A. Addou, J.L. Brisset, *Water Res.* (submitted)

# **RF- plasma co- polymerization of the ferrocene with silanes/xylene monomers**

**I. Stamatiu, Anca Dumitru, C. Panaiotu, Claudiu Serban**

*University of Bucharest, Faculty of Physics, Diamond Films, Plasma Polymerization & Novel carbon lab, Bucharest-Magurele, MG-11, Romania*

In recent years, the development of metal-containing polymers has been a topic of interest because of the wide range of magnetic, electrical, optical, and catalytic properties that are associated with metal centers. The recent developed co-polymers, poly(ferrocenylsilanes) with backbone of ferrocene and organo-silane units are currently being investigated as charge- transport - dissipation materials and as precursors to magnetic nanostructured ceramics. Poly (ferrocenylsilane) are representatives to investigate the molecular motions in different synthesis schemes or transition-metal-catalyzed ring-opening polymerization of strained metallocenophane monomers. Well established, polycarbosilanes produced of hexamethyldisilanes (HMDS) are usual applied as precursors for SiC ceramics. Also poly(ferrocene) are currently chemical synthesized and, recently, few reports have produced with plasma polymerization. The needs to develop co-polymers to be applied as precursors, catalysts for the precision control of polymerisation in building of supramolecular architectures, fuel cells elements, impose an enlarged search to combination of the pi-conjugated polymers and d- organo metallic compound. We present a new poly(ferrocene) class based on the insertion of carbosilane (from HMDS), silazane (from HMDSz) and spiroconjugated blocks using p-xylene monomers.

These kind of co- polymers are synthesized by plasma etching of ferrocene pellets using monomer carriers HMDS, HMDSz and p-xylene. The RF reactor, 2.5Mhz, inductive coupled has at one of head an external heater up to 800<sup>0</sup>C, the polymerization reaction being controlled in many ways. The deposition conditions are moderates, p=1-5 torr with a monomer flux of 1-5 ml/h at 50-100 W power discharge. The results, in powder form, have been investigated by xrd, raman, FT- IR and XPS. Beside the insertion of Si-C and Si-N groups into ferrocene – backbone, has been observed, in case of p-xylene, an effect of spiroconjugation from aromatics groups.



# Characterization of carbon nitrides by UV Raman spectroscopy

R. Ohta<sup>1</sup>, S. Okazaki<sup>1</sup>, N. Saito<sup>1</sup>, Y. Inoue<sup>2</sup>, H. Sugimura<sup>1</sup> and O. Takai<sup>3</sup>

<sup>1</sup> Department of Materials Processing Engineering, Graduate School of Engineering, Nagoya University, Nagoya, Japan

<sup>2</sup> Research Center for Nuclear Materials Recycle, Nagoya University, Nagoya, Japan

<sup>3</sup> Center for Integrated Research in Science and Engineering, Nagoya University, Japan

## Abstract

Hydrogenated amorphous carbon nitride films were mainly characterized by UV-Raman spectroscopy. UV-Raman spectroscopy is a powerful tool to obtain the chemical bonding states of the films, which are partly undetected by visible-Raman spectroscopy. The chemical bonding states obtained by UV- and visible-Raman spectroscopy and infrared spectroscopy were correlated with the nanohardness of hydrogenated amorphous carbon nitride obtained by nanoindentation test.

## 1. Introduction

Amorphous carbon nitrides (a-CN<sub>x</sub>) [1] are attracting attentions of many researchers for their favorable mechanical properties of hardness and wear resistance. These properties are due to the chemical bonding states. The chemical bonding states of a-CN<sub>x</sub> are frequently analyzed by visible Raman spectroscopy (visible-RS) [2,3,4], Infrared spectroscopy (IR) [3-8], X-ray photoelectron spectroscopy (XPS) [9-12], electron energy loss spectroscopy (EELS) [7,8], etc. However, an accurate structure model of CN<sub>x</sub> has not been proposed yet, since a-CN<sub>x</sub> have complex amorphous structures. Although the determination of the structures is difficult with those analysis methods, some other analysis methods can provide more detail knowledge of the chemical bonding states in a-CN<sub>x</sub>.

Recently, UV Raman spectroscopy (UV-RS) has been frequently used in the characterization of carbon related materials as amorphous carbon [13-15] and carbon nanotubes [16]. UV-RS provides some important information of chemical bonding states in carbon related materials undetected by visible-RS, since the resonance Raman effect depends on the wavelength of the excitation laser. In visible-RS, *sp*<sup>3</sup> orbital hybridization is underestimated compared to *sp*<sup>2</sup> orbital hybridization, since energy of the visible light is not enough to excite *sp*<sup>3</sup> orbital hybridization [17,18]. Therefore, two bands, G band around 1550 cm<sup>-1</sup> and D band around 1350 cm<sup>-1</sup>, assigned to the chemical bonding states including *sp*<sup>2</sup> orbital hybridization have been mainly discussed in visible-RS spectra [3,19]. On the other hand, T peak assigned to stretching vibration mode in *sp*<sup>3</sup>C-*sp*<sup>3</sup>C bonds can be observed at around 1000 cm<sup>-1</sup> in UV-RS spectra, since UV can excite *sp*<sup>2</sup> and *sp*<sup>3</sup> orbital hybridizations equivalently [13-15]. Therefore, using UV-RS, we can simultaneously obtain information of chemical bonding states of both *sp*<sup>2</sup> and *sp*<sup>3</sup> orbital hybridization in carbon related materials. However, there are only a few reports using UV-RS for the characterization of a-CN<sub>x</sub> [7,20,21].

In this research, we aimed to characterize the chemical bonding states of hydrogenated amorphous carbon nitride (a-CN<sub>x</sub>:H) by visible- and UV-RS and IR. IR and Raman vibrational modes in a-CN<sub>x</sub>:H are observed in the following three regions; 900-2000 cm<sup>-1</sup> (region I) which is assigned to stretching vibration modes of C=C, C=N, C-C, C-N, etc., and bending vibration modes of C-H, N-H, etc., 2000-2300 cm<sup>-1</sup> (region II) which is assigned to stretching vibration modes of C≡C, C≡N, C=C=N, etc., and 2800-3800 cm<sup>-1</sup> (region III) which is assigned to stretching vibration modes of C-H, N-H, etc. In the analyses of vibration spectra in a-CN<sub>x</sub>:H, we focus on the region I, in which G and D bands and T peak in RS spectra appear. We discussed in detail the assignments of the bands observed in the region I. Finally, we correlated the chemical bonding states with the nanohardness of the films obtained by nanoindentation test.

## 2. Experiment

a-CN<sub>x</sub>:H films were prepared by inductively coupled plasma chemical vapor deposition (ICP-CVD) under the following conditions. The feed gas was nitrogen and benzene. Cleaned n-type Si (100) wafers were used as substrates. The chamber was filled with nitrogen and benzene to the pressure 1 Pa after evacuating to 4.0x10<sup>-3</sup> Pa. The pressure ratio of nitrogen to benzene was kept at 1 during the film deposition. The radio frequency power was 1 kHz and substrate bias voltage was varied between 0 and -1000 V.

In RS measurements (Tokyo Instruments, Nanofinder®), second harmonic light of Ar<sup>+</sup> laser (λ=244 nm) and Nd:YAG laser (λ=532 nm) were used as excited sources of UV- and visible-RS. The laser power

irradiated on the film surface was 100  $\mu\text{W}$  in both RS measurements. The RS spectra were collected from the backscattering light of the laser irradiated on the surface of  $\text{a-CN}_x\text{:H}$  films. IR spectra were measured using Fourier-transform infrared (FT-IR) spectrometer (BIO-RAD, 175C). IR spectra were obtained as transmittance spectra of the film by subtracting the spectra of Si (100) substrate before film deposition as a background. XPS measurements (AXIS, Shimazu-Kratos) were performed under the following conditions. The  $\text{MgK}\alpha$  X-ray source was operated at 10 mA and 12 kV. The pass energy was 10 eV and the electron take-off angle was  $90^\circ$ . N/C ratios of the films were estimated from each component's peak area after normalizing with the respective relative sensitivity factor [22].

Nanohardness of the films were measured by a nanoindenter (Hysitron, TriboScope) interfaced with an atomic force microscope (AFM, Park Scientific Instruments, Autoprobe-LS) using a trigonal diamond tip (Berkovich type:  $65.3^\circ$  of half angle). A force-displacement curve was measured with a peak load force of 500  $\mu\text{N}$ . Nanohardness was defined as the indentation load divided by the projected contact area of the indentation. Five nanoindentation tests were conducted to each film in determining the nanohardness [23].

### 3. Results and Discussion

#### 3.1 Assignments of bands in visible- and UV-RS and IR spectra

Figures 1, 2 and 3 show visible- and UV-RS and IR spectra of  $\text{a-CN}_x\text{:H}$  films at given substrate bias voltages during film depositions, respectively. In comparing the visible- and UV-RS spectra, we focused on two typical bands. One is G1 band located at around  $1550\text{ cm}^{-1}$ , and the other is G2 band located at around  $1620\text{ cm}^{-1}$ . G1 band was assigned to  $sp^2$  orbital hybridization in  $\pi$ -conjugated ring structures, and G2 band was assigned to  $sp^2$  orbital hybridization in olefinic structures [15]. In the visible-RS spectra, G2 band as well as T peak is underestimated. On the other hand, in the UV-RS spectra, G1 and G2 are detected equivalently for the resonant Raman effects of  $sp^2$  orbital hybridization in both olefinic structures and  $\pi$ -conjugated ring structures.

In the IR spectra, we focused on band (i) located at around  $1000\text{ cm}^{-1}$ , band (ii) located at around  $1300\text{ cm}^{-1}$ , band (iii) located at around  $1600\text{ cm}^{-1}$  and band (iv) located at around  $1700\text{ cm}^{-1}$ . In this research, we did not take into account of the following peaks:  $\text{SiO}_2$  str. ( $1100\text{ cm}^{-1}$ ) and C-H bend. ( $1400\text{--}1500\text{ cm}^{-1}$ ). We assigned band (i) to a stretching vibration mode of  $sp^3\text{C}\text{--}sp^3\text{N}$  bonds, since hexamethylenetetramine (HMTA) have the same mode at the same position [24]. Kaufmann et al. reported that band (ii) at around  $1300\text{ cm}^{-1}$  and band (iii) at around  $1600\text{ cm}^{-1}$  appeared by the IR activation of D and G bands in the RS spectra as a consequence of symmetry break induced by the substitution of heteroatom in the graphite structure [3]. Band (iii) appeared at the wavenumber close to G2 band, so we followed their assignments for this band. However, band (ii) appeared at the wavenumber about  $50\text{ cm}^{-1}$  lower than D band. Moreover, intensity of band (ii) increased greater than that of D band. Therefore, band (ii) is not only assigned to the IR activated chemical bonding states of  $\pi$ -conjugated ring structures.  $sp^2\text{C}\text{--}sp^3\text{N}$  or  $sp^2\text{C}\text{--}sp^2\text{N}$  ( $sp^2\text{C}$  in aromatic ring) bonds can also be assigned to band (ii), since the IR spectra of polyaniline include peak at around  $1270\text{--}1300\text{ cm}^{-1}$  which is assigned to stretching vibration mode of these bonds [25,26,27]. Therefore, we assigned band (ii) to the following two chemical bonding states;  $\pi$ -conjugated ring structures and  $sp^2\text{C}\text{--}sp^3\text{N}$  or  $sp^2\text{C}\text{--}sp^2\text{N}$  ( $sp^2\text{C}$  in aromatic ring) bonds. In the IR spectra of  $\text{a-CN}_x\text{:H}$  prepared with the bias voltages

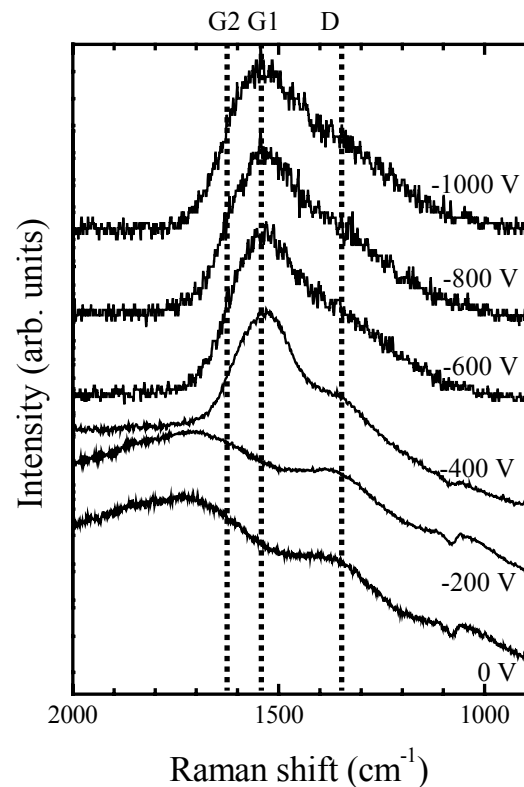


Figure 1. Visible-RS spectra of  $\text{a-CN}_x\text{:H}$  films prepared at given substrate bias voltages during film deposition.

of 0 and -200 V, band (iv) is observed at around 1700  $\text{cm}^{-1}$ . This band was not observed in the visible- and UV-RS spectra. Moreover, the intensity of this band decreased, while the intensities of bands (i) and (ii), which are assigned to C-N bonds, increased. Therefore, band (iv) is mainly assigned to  $sp^2\text{C}=sp^2\text{N}$  bonds in olefinic structures. Moreover, band (iii) and G2 band are mainly assigned to  $sp^2\text{C}=sp^2\text{C}$  bonds in olefinic structures. The intensities of bands (i), (ii) and (iv) are relatively strong for the films of small N/C ratios (N/C ratios of a- $\text{CN}_x\text{:H}$  films prepared at the bias voltages of 0, -200, -400, -800 and -1000 V corresponded to 0.085, 0.074, 0.054, 0.059, 0.060 and 0.043, respectively). These strong intensities are due to the larger polarization of bonds between carbon and nitrogen than ones between carbon and carbon.

3.2 Structural change of a- $\text{CN}_x\text{:H}$  films by increasing the bias voltage during film deposition

In the visible-RS spectra of a- $\text{CN}_x\text{:H}$  films prepared at the bias voltages of 0 and -200 V, only D band was slightly observed due to a large interference of luminescence, which indicates that these a- $\text{CN}_x\text{:H}$  films possess few  $\pi$ -conjugated ring structures. By applying higher substrate bias voltages, G1 band appeared and intensity of D band increased. This spectral change suggests that the  $\pi$ -conjugated ring structures appeared by applying higher bias voltages.

In the UV-RS spectra, the intensities of G1 and D bands also increased. G2 bands were seen in the spectra of a- $\text{CN}_x\text{:H}$  films prepared at all bias voltages. Even in the spectra of a- $\text{CN}_x\text{:H}$  films prepared at the bias voltages of 0 and -200 V, G2 band had strong intensities. This indicates that all the samples contain  $sp^2\text{C}=sp^2\text{C}$  bonds in olefinic structures.  $sp^3\text{C}-sp^3\text{C}$  bonds were not confirmed, since T peak at around 1000  $\text{cm}^{-1}$  was not observed in the UV-RS spectra.

In the IR spectra, band (i) appeared by increasing the bias voltage, and intensity of this band was maximized at the bias voltage of -800 V. The decrease of band (iv) and the increase of band (ii) were also observed. These changes in the intensities of the bands indicate that  $sp^2\text{C}=sp^2\text{N}$  bonds in olefinic structure decreased, and  $\pi$ -conjugated ring structures,  $sp^3\text{C}-sp^3\text{N}$  bonds and  $sp^2\text{C}-sp^3\text{N}$  or  $sp^2\text{C}-sp^2\text{N}$  ( $sp^2\text{C}$  in aromatic rings) bonds increased. The fraction of  $sp^3\text{C}-sp^3\text{N}$  bonds was maximized at the bias voltage of -800 V.

From the visible- and UV-RS and IR spectra, the effects of the different bias voltages during film preparation on the chemical bonding states in a- $\text{CN}_x\text{:H}$  are concluded as follows.

- (1) a- $\text{CN}_x\text{:H}$  films prepared at the bias voltages of 0 and -200 V, in particular, showed that there were few  $\pi$ -conjugated  $sp^2\text{C}=sp^2\text{C}$  bonds in ring structures and many olefinic  $sp^2\text{C}=sp^2\text{C}$  bonds.

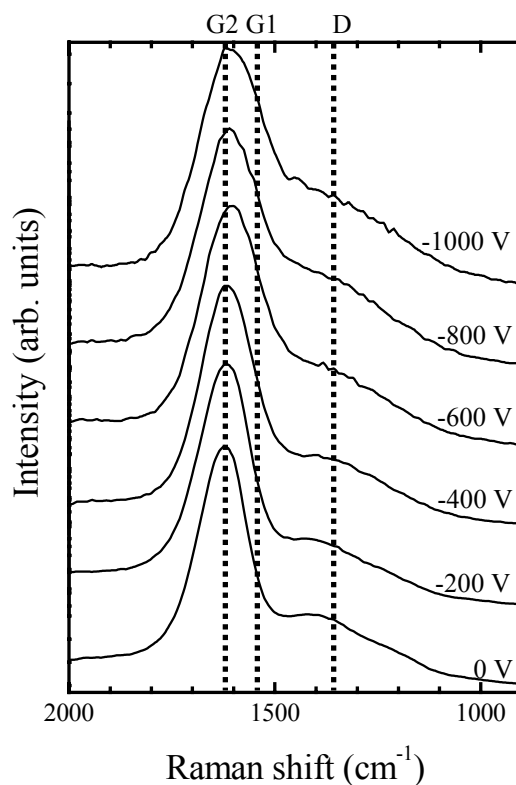


Figure 2. UV-RS spectra of a- $\text{CN}_x\text{:H}$  films prepared at given substrate bias voltages during film deposition.

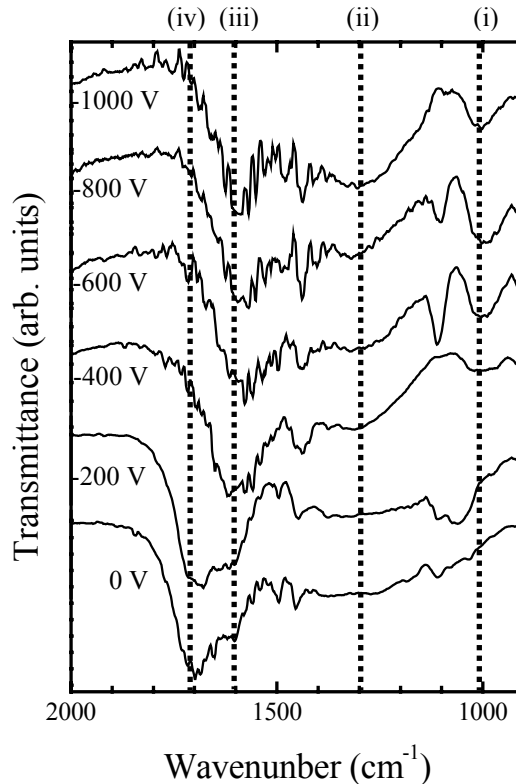


Figure 3. IR spectra of a- $\text{CN}_x\text{:H}$  films prepared at given substrate bias voltages during film deposition.

- (2)  $sp^2C=sp^2N$  bonds in olefinic structures decreased by applying higher bias voltages.
- (3)  $\pi$  conjugated ring structures,  $sp^3C-sp^3N$  bonds and  $sp^2C-sp^3N$  or  $sp^2C-sp^2N$  ( $sp^2C$  in aromatic rings) bonds increased by applying higher bias voltages.
- (4) The most  $sp^3C-sp^3N$  bonds rich a- $CN_x:H$  film was the one prepared at the bias voltage of -800 V.

### 3.3 Correlation between chemical bonding states of a- $CN_x:H$ films and nanohardness

The nanohardness of each a- $CN_x:H$  films at given bias voltages obtained by nanoindentation test is shown in Fig. 4. The hardness of TiN, Si (100) and Quartz are also shown in the figure for the comparison. The hardness of a- $CN_x:H$  films increased by applying higher bias voltage. The sample prepared at bias voltage of -800 V showed the largest hardness (17.2 GPa). From the analysis results of IR and visible- and UV-RS, the small hardness is due to the large amount of  $sp^2$  orbital hybridization in olefinic structures and small amount of  $\pi$ -conjugated ring structures. The hardness of a- $CN_x:H$  films become larger with the decrease of  $sp^2$  orbital hybridization in olefinic structures, and increase of  $\pi$ -conjugated ring structures,  $sp^3C-sp^3N$  bonds and  $sp^2C-sp^3N$  or  $sp^2C-sp^2N$  ( $sp^2C$  in aromatic rings) bonds. The hardest film was most  $sp^3C-sp^3N$  bonds rich one. We proposed that the nanohardness of a- $CN_x:H$  films strongly depends on the presence of the  $\pi$ -conjugated ring structures and the crosslinkings of these structures by  $sp^3C-sp^3N$  bonds and  $sp^2C-sp^3N$  or  $sp^2C-sp^2N$  ( $sp^2C$  in aromatic rings) bonds.

## 4. Conclusion

In interpreting the spectral changes in the visible- and UV-RS spectra, we referred to the assignments of G1, G2 and D bands proposed by Ferrari et al. The assignments of four bands in the IR spectra were determined as follows. Band (i) located at around  $1000\text{ cm}^{-1}$ , band (ii) located at around  $1300\text{ cm}^{-1}$ , band (iii) located at around  $1600\text{ cm}^{-1}$  and band (iv) located at around  $1700\text{ cm}^{-1}$ , are assigned to (i)  $sp^3C-sp^3N$  bonds, (ii)  $\pi$ -conjugated ring structures (IR activated G1 band) and  $sp^2C-sp^3N$  or  $sp^2C-sp^2N$  ( $sp^2C$  in aromatic rings), (iii)  $sp^2C=sp^2C$  bonds in olefinic structures (IR activated G2 band) and (iv)  $sp^2C=sp^2N$  bonds in olefinic structures, respectively. From the visible- and UV-RS spectra, a- $CN_x:H$  films prepared at the bias voltages of 0 and -200 V particularly had few  $\pi$ -conjugated  $sp^2C=sp^2C$  bonds in ring structures and many  $sp^2C=sp^2C$  bonds in olefinic structures.  $\pi$ -conjugated ring structures increased by applying higher bias voltages.  $sp^3C-sp^3C$  bonds were not confirmed in all a- $CN_x:H$  films, since T peak at around  $1000\text{ cm}^{-1}$  was not observed in the UV-RS spectra. From the IR spectra,  $sp^2C=sp^2N$  in olefinic structures decreased and  $\pi$ -conjugated ring structures,  $sp^3C-sp^3N$  bonds and  $sp^2C-sp^3N$  or  $sp^2C-sp^2N$  ( $sp^2C$  in aromatic rings) bonds increased. The most  $sp^3C-sp^3N$  bonds rich a- $CN_x:H$  film was the one prepared at the bias voltage of -800 V. The nanohardness of a- $CN_x:H$  films obtained by nanoindentation test increased by applying higher bias voltage and was maximized with the a- $CN_x:H$  films prepared at the bias voltage of -800 V. The nanohardness of a- $CN_x:H$  films strongly depended on the presence of the  $\pi$ -conjugated ring structures and the crosslinkings of these structures by  $sp^3C-sp^3N$  bonds and  $sp^2C-sp^3N$  or  $sp^2C-sp^2N$  ( $sp^2C$  in aromatic rings) bonds.

## References

- [1] E.G. Wang - Prog. Mater. Sci. 41, 241 (1997).
- [2] P.N. Wang, Z.Guo, X.T. Ying, J.H. Chen, X.M. Xu, F.M. Li - Phys. Rev. B 59, 13347 (1999)
- [3] J.H. Kaufman, S. Metin, D.D. Saperstein - Phys. Rev. B 39, 13053 (1989)
- [4] S.E. Rodil, A.C. Ferrari, J. Robertson, W.I. Milne - J. Appl. Phys. 89, 5425 (2001)

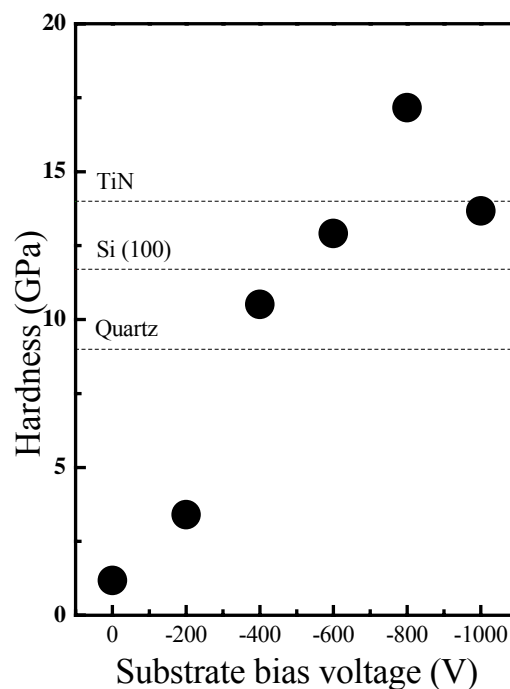


Figure 4. Hardness of a- $CN_x:H$  films prepared at given substrate bias voltages during film deposition.

- [5] S. Liu, S. Gangopadhyay, G. Sreenivas, S.S. Ang, H.A. Naseem - Phys. Rev. B 55, 13020 (1997)
- [6] T. Szorenyi, C. Fuchs, E. Fogarassy, J. Hommet, F. Le. Normand - Surf. Coat. Tech. 125, 308 (2000)
- [7] S.E. Rodil, A.C. Ferrari, J. Robertson, S. Muhl - Thin Solid Films 420-421, 122 (2002)
- [8] A. Fernandez, P. Prieto, C. Quiros, J.M. Sanz, J.M. Martin, B. Vacher - Appl. Phys. Lett. 69, 764 (1996)
- [9] D. Marton, K.J. Boyd, A.H. Al-Bayati, S.S. Todorov, J.W. Rabalais - Phys. Rev. Lett. 73, 118 (1994)
- [10] S. Souto, M. Pickholz, M.C. dos Santos, F. Alvarez - Phys. Rev. B 57, 2536 (1998)
- [11] J.M. Ripalda, E. Roman, N. Diaz, L. Galan, I. Montero, G. Comelli, A. Baraldi, S. Lizzit, A. Goldoni, G. Paolucci - Phys. Rev. B 60, R3705 (1999)
- [12] F. Le Normand, J. Hommet, T. Szorenyi, C. Fuchs, E. Fogarassy - Phys. Rev. B 64, 235416 (2001)
- [13] V.I. Merkulov, J.S. Lannin, C.H. Munro, S.A. Asher, V.S. Veerasamy, W.I. Milne - Phys. Rev. Lett. 78, 4869 (1997)
- [14] K.W.R. Gilkes, H.S. Sands, D.N. Batchelder, J. Robertson, W.I. Milne - Appl. Phys. Lett. 70, 1980 (1997)
- [15] A.C. Ferrari, J. Robertson - Phys. Rev. B 64, 075414 (2001)
- [16] T.R. Ravindran, B.R. Jackson, J.V. Badding - Chem. Mater. 13, 4187 (2001)
- [17] N. Wada, P.J. Gaczi, A. Solin - J. Non-Cryst. Solids 35&36, 543 (1980)
- [18] S.R. Sails, D.J. Gardiner, M. Bowden, J. Savage, D. Rodway - Diamond Relat. Mater 5, 589 (1996)
- [19] A.C. Ferrari, J. Robertson - Phys. Rev. B 61, 14095 (2000)
- [20] J.R. Shi, X. Shi, Z. Sun, E. Liu, B.K. Tay, S.P. Lau - Thin Solid Films 366, 169 (2000)
- [21] Y.H. Cheng, B.K. Tay, S.P. Lau, X. Shi, X.L. Qiao, J.G. Chen, Y.P. Wu, C.S. Wie - Appl. Phys. A – Mater. 73, 341 (2001)
- [22] D. Briggs, M.P. Seah - Practical Surface Analysis by Auger and X-ray Photoelectron Spectroscopy, Wiley (1983)
- [23] W.C. Oliver, G.M. Pharr - J. Mater. Res. 7, 1564 (1992)
- [24] J.O. Jensen - Spectrochim. Acta A 58, 1347 (2002)
- [25] M. Ilic, E. Koglin, A. Pohlmeier, H.D. Narres, M.J. Schwuger - Langmuir 16, 8946 (2000)
- [26] M. Kertesz, C.H. Choi, S.Y. Hong - Synthetic Met. 85, 1073 (1997)
- [27] R. Mathew, B.R. Mattes, M.P. Espe - Synthetic Met. 131, 141 (2002)

# CHEMICAL BONDING STATES OF CARBON NITRIDES: SPECTROSCOPIC STUDIES USING NUCLEAR MAGNETIC RESONANCE

O. Takai<sup>3</sup>, R. Ohta<sup>1</sup>, N. Saito<sup>1</sup>, Y. Inoue<sup>2</sup> and H. Sugimura<sup>1</sup>

<sup>1</sup>*Department of Materials Processing Engineering, Nagoya University, Nagoya, Japan*

<sup>2</sup>*Research Center for Nuclear materials Recycle, Nagoya University, Nagoya, Japan*

<sup>3</sup>*Center for Integrated Research in Science and Engineering, Nagoya University, Nagoya, Japan*

## Abstract

The hardness of amorphous carbon nitride (CN) was investigated by solid-state nuclear magnetic resonance (NMR) spectroscopy and Fourier transform infrared spectroscopy (FT-IR). The results of NMR measurements showed that  $sp^2$  and/or  $sp$  hybrid orbitals controlled the hardness of amorphous-CN films, which we had determined by nanoindentation tests. The intensity of the C-H and CN stretching modes observed in the FT-IR spectra was the weakest in the hardest sample. The decreases of  $-CH_3$  and  $-CH_2$  groups indicated that the amorphous network had increased. The  $sp^2$  hybrid orbital forms a “cross-linker” which plays an important role in improving of the hardness of the film.

## 1. Introduction

Amorphous carbon nitride (CN) is well known as a hard coating material and is applied, for example, to coat the heads of hard disk drives.<sup>1</sup> As the capacity of hard disk drives increases and data is stored at higher and higher densities, amorphous-CN films become both thinner and harder. The hardness of such extremely thin film can not be examined by current techniques such as nanoindentation since the measured property is greatly influenced by the substrate. For this reason, the amorphous-CN film must also be evaluated by other means. The chemical bonding states of amorphous-CN have frequently been examined using X-ray photoelectron spectroscopy (XPS)<sup>2-4</sup>, Raman spectroscopy<sup>5-7</sup> and electron energy loss spectroscopy (EELS)<sup>8-10</sup> in order to correlate with the hardness. In particular, the  $sp^2$  and  $sp^3$  orbital hybridization ratio is considered to correlate with the hardness of the film. However, since the above-mentioned analyses do not provide us with sufficient information regarding orbital hybridization, it remains controversial as to whether the  $sp^2$  or the  $sp^3$  orbital component contributes most to hardness. In order to control the hardness and other properties of extremely thin films, it is vital that accurate information be obtained concerning chemical bonding states. In the present study, we have aimed to investigate hardness through detailed analyses of the chemical bonding states of amorphous-CN films using solid-state nuclear magnetic resonance (NMR) and Fourier transform infrared spectroscopy (FT-IR). In particular, NMR provides us with information on orbital hybridization since the peaks originating from  $sp^2$  and/or  $sp$  orbitals are independent of that from  $sp^3$  orbitals.<sup>11-13</sup>

## 2. Experimental procedures

Amorphous-CN films were prepared with an inductively coupled plasma chemical vapor deposition apparatus. Benzene ( $C_6H_6$ , 99.5%, Kishida Chemical Co. Ltd.) and nitrogen ( $N_2$ , 99.9999%, Nippon Sanso Co.) were used as source material. Silicon wafers (n-type (100) [Shinestu Chemical Co.]) were used as substrates. The partial pressures of benzene and nitrogen were 0.5 and 0.5 Pa, respectively. The distance between the substrate and plasma center was about 310 mm. High frequency output power was 1.0 kW.

The atomic ratio of the amorphous-CN was determined by XPS (AXIS, Shimadzu-Kartos). The MgK $\alpha$  X-ray source was operated at 10 mA at 12 kV. The pass energy was 10 eV and the electron take-off angle was 90°. Hardness was evaluated by nanoindentation with a scanning probe microscopy (Triboscope, Hysitron Co. + JEOL Co.). A Berkovich-type diamond tip with a radius of less than 100 nm, was used for the nanoindentation measurements. A load-displacement curve was obtained for each sample with a maximum load of 250  $\mu$ N. The loading, holding and unloading times for each nanoindentation were 2.5, 0 and 2.5 s, respectively. The hardness was determined from five measurements.  $^{13}\text{C}$ -NMR spectra based on the cross polarization magic angle spinning (CPMAS) method were obtained by solid-state NMR (Chemagnetics, CMX-300). FT-IR spectroscopy (Biorad Co., FTS-175C) was also employed to reveal the chemical bonds in the amorphous-CN films.

### 3. Results and discussion

Figure 1 shows the hardness of amorphous-CN films prepared at bias voltages from 0 to -1000 V. The hardness increased as the bias voltage became reduced to less than the value obtained at -800 V. The hardness at -800 V was 16 GPa. At -1000 V, the hardness became lower than the value in -800 V. Figure 2 shows the atomic fraction of nitrogen determined by XPS in the amorphous-CN films prepared at bias voltages of 0, -800 and -1000 V. The amount of nitrogen in the films decreased as the bias voltage became more negative. This phenomenon originated from sputtering on the sample surface.

In order to understand the origin of the amorphous-CN films' hardness, we examined the  $^{13}\text{C}$ -NMR and FT-IR spectra of films prepared at the bias voltages of 0, -800 and -1000 V. Figure 3 shows the  $^{13}\text{C}$ -NMR spectra in the CPMAS mode and the chemical bonding states assigned to the chemical shifts. Chemical shifts less than 70 ppm corresponds to the chemical bonding state of  $\text{sp}^3$  hybrid orbitals. On the other hand, chemical shifts above 70 ppm correspond to the bonding states of  $\text{sp}^2$  and  $\text{sp}$  hybrid orbitals. The ratios of chemical shifts indicating  $\text{sp}^2$  and/or  $\text{sp}$  to those indicating  $\text{sp}^3$  at the bias voltages of 0, -800, -1000 V were 0.71, 0.81 and 0.76, respectively.  $\text{sp}^2$  and/or  $\text{sp}$  orbital hybridization predominated in the chemical bonding states of the amorphous-CN film prepared at the bias voltages of 0 V. Moreover, some sharp peaks can be seen in this spectrum, which probably indicate that the structure of the film succeeded to that of the precursor. In comparison with the film obtained at 0 V, the relative amount of  $\text{sp}^3$  hybrid orbitals decreased in the film prepared at -800 V. Moreover, the spectrum of this amorphous-CN film was broader. These results show that the film's structure had become complex, not taking over the structure of the precursor since the increase in bias voltage increases the ion bombardment of the sample. Unsaturated bonds and a form of random structure resulted in the film prepared at this voltage. In particular, the  $\text{sp}^2$  bonds may work as a bond "cross-linker" to promote hardness. On the other hand,  $\text{sp}^2$  and/or  $\text{sp}$  orbital hybridization decreased in the film prepared at -1000 V.  $\text{sp}^2$  bonds were broken due to excessive ion bombardment. Thus, the decrease of hardness at -1000 V originated from the reduction of cross-linking  $\text{sp}^2$  bonds.

Figure 4 shows FT-IR spectra for films prepared at the bias voltages of 0, -800 and -1000 V. The intensity of the N-H stretching mode became weaker at the increase of negative bias voltage. This decrease in intensity can be understood considering the change in the atomic fraction of N obtained by XPS analysis (Fig.2). The intensity of the C-H and CN stretching mode was weakest at -800 V, since unsaturated bonds, such as  $\text{sp}^2$  and/or  $\text{sp}$  bonds, increased at the more negative bias voltage. This change in chemical bonding states agrees with our NMR measurement results.

In summary, the hardness of amorphous-CN films was found to increase due to an increase in  $\text{sp}^2$  orbital hybridization. Cross-linkers composed of  $\text{sp}^2$  hybrid orbitals play an important role in improving the film's hardness. We have demonstrated here that NMR is a promising technique to elucidate the relationship between hardness and chemical bonding states.

## Acknowledgements

This work has been supported by the "Biomimetic Materials Processing" (No. JSPS-RFTF 99R13101), Research for the Future (RFTF) Program, Japan Society for the Promotion of Science.

## References

- [1] E. G. Wang, *Progress in Material Science* 41, 241-298 (1997).
- [2] K. Ogata, J. F. D. Chubaci, and F. Fujimoto, *J. Appl. Phys.* 76, 3791-3796 (1994).
- [3] B. C. Holloway, O. Kraft, D. K. Shuh, M. A. Kelly, W. D. Nix, P. Pianetta, and S. Hagström, *Appl. Phys. Lett.* 74, 3290-3292 (1999).
- [4] H. Ohta, A. Matsumuro, and Y. Takahashi, *Jpn. J. Appl. Phys., Part 1* 41, 7455-7461 (2002).
- [5] N. Hellgren, M. P. Johansson, E. Broitman, L. Hultman, and J.-E. Sundgren, *Phys. Rev. B* 59, 5162-5169 (1999).
- [6] Y. Ohkawara, S. Ohshio, T. Suzuki, H. Ito, K. Yatsui, and H. Saitoh, *Jpn. J. Appl. Phys., Part 1* 40, 7007-7012 (2001).
- [7] Y. Ohkawara, H. Akasaka, K.-i. C. Namiki, S. Ohshio, H. Ito, and H. Saitoh, *Jpn. J. Appl. Phys., Part 1* 42, 254-258 (2003).
- [8] S. Csillag, R. Rätty, W. Y. Zou, H. Sjöström, J.-E. Sundgren, and C. Colliex, *J. Appl. Phys.* 82, 666-669 (1997).
- [9] M. Mattesini and S. F. Matar, *Phys. Rev. B* 65, 075110-07524 (2002).
- [10] S. E. Rodil, W. I. Milne, J. Robertson, and L. M. Brown, *Appl. Phys. Lett.* 77, 1458-1460 (2000).
- [11] Y.-G. Yoon, B. G. Pfrommer, F. Mauri, and S. G. Louie, *Phys. Rev. Lett.* 80, 3388-3391 (1998).
- [12] J. C. Sánchez-López, C. Donnet, F. Lefèbvre, C. Fernández-Ramos, and A. Fernández, *Journal of Applied Physics* 90, 675-681 (2001).
- [13] W. J. Gammon, D. I. Malyarenko, O. Kraft, G. L. Hoatson, A. C. Reilly, and B. C. Holloway, *Phys. Rev. B* 66, 153402-153406 (2002).



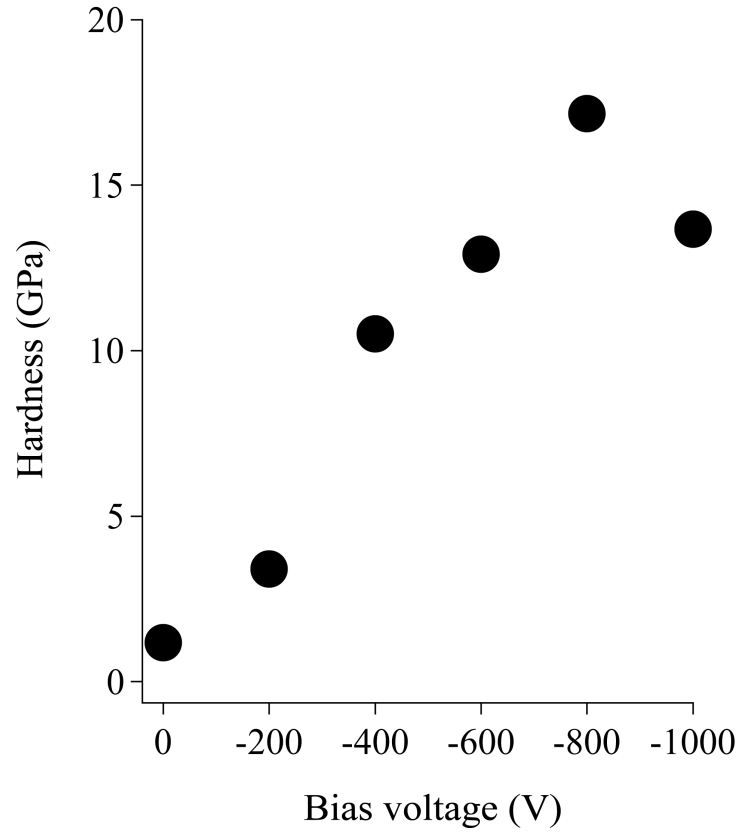


FIG. 1 Relationship between the hardness of amorphous-CN film and the bias voltage applied during the preparation.

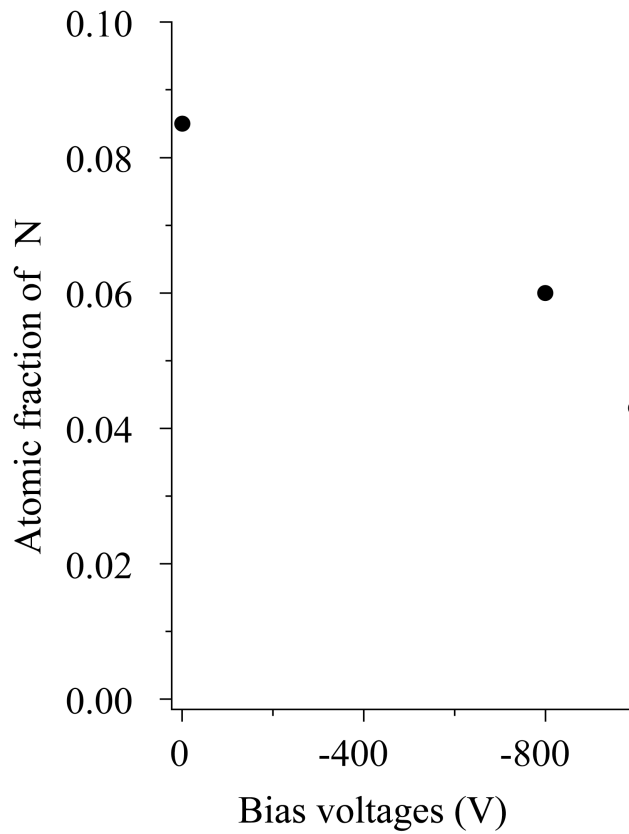


FIG. 2 Atomic fraction of nitrogen in amorphous-CN film prepared at bias voltages of 0, -800 and -1000 V.

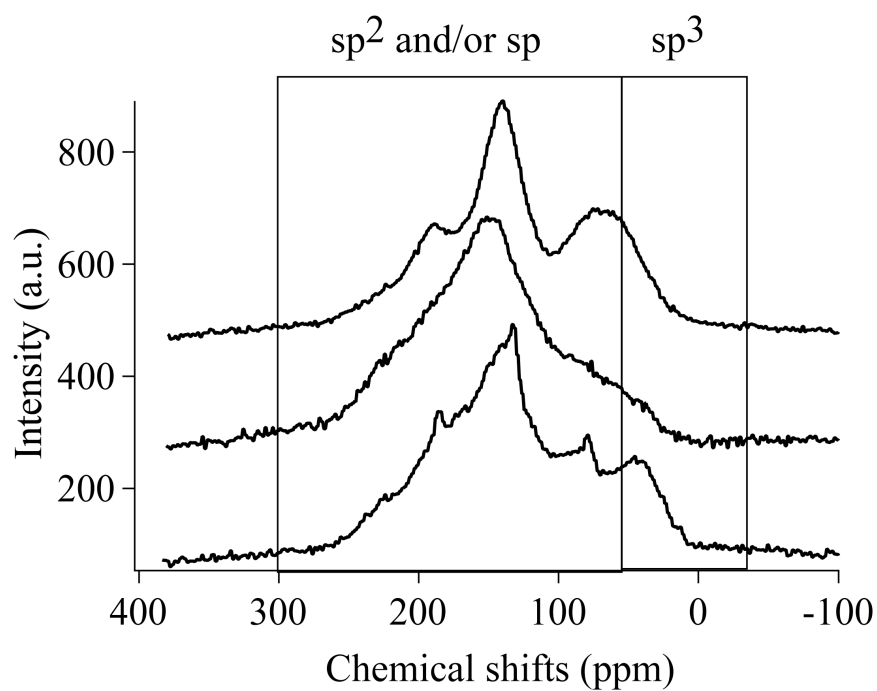


FIG. 3 NMR spectra of amorphous-CN films prepared at bias voltages of 0, -800 and -1000 V.

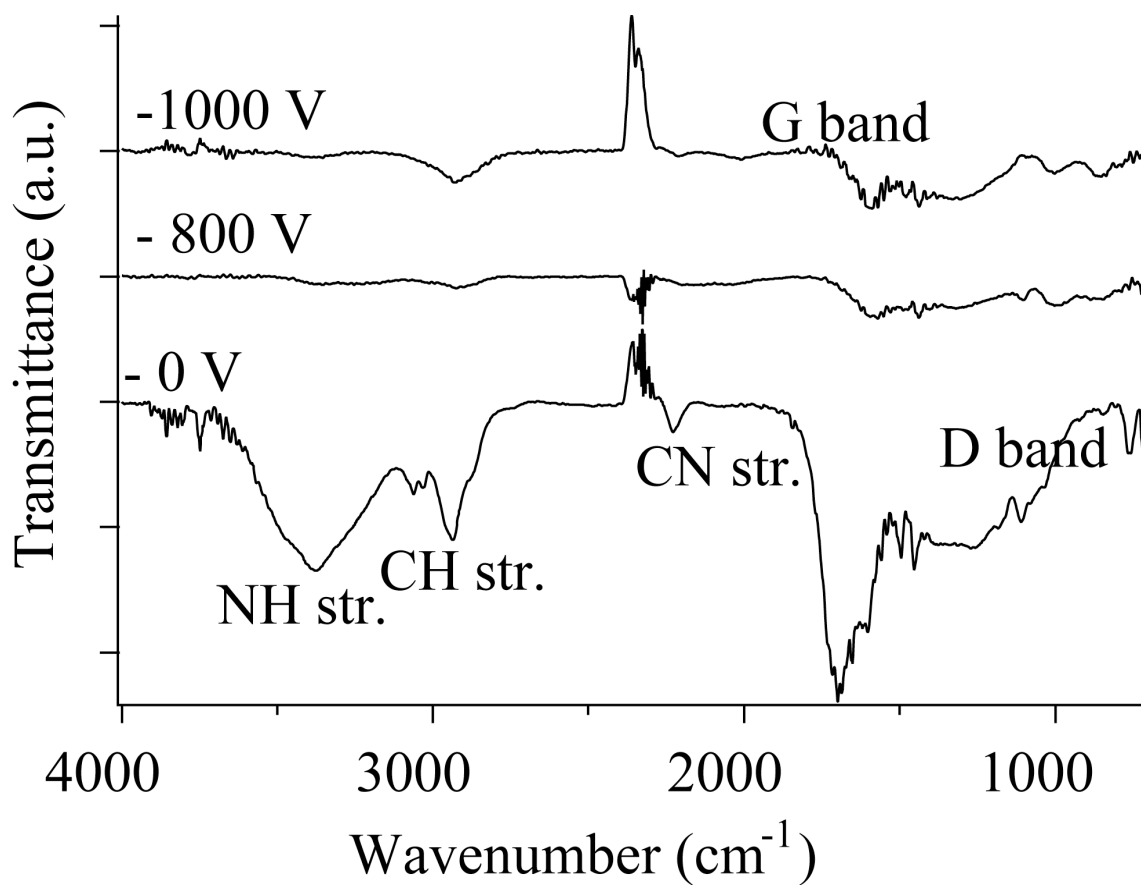


FIG. 4 FT-IR spectra of amorphous-CN films prepared at bias voltages of 0, -800 and -1000 V.

# Photochemical Vapor Deposition of Carbon Nitrides Using 172 nm Xe<sub>2</sub>\* Excimer lamp Radiation

N. Saito<sup>1</sup>, T. Kamikawa<sup>1</sup>, Y. Inoue<sup>2</sup>, H. Sugimura<sup>1</sup>, O. Takai<sup>3</sup>

<sup>1</sup>Department of Materials Processing Engineering, Nagoya University, Nagoya, Japan

<sup>2</sup>Research Center for Nuclear materials Recycle, Nagoya University, Nagoya, Japan

<sup>3</sup>Center for Integrated Research in Science and Engineering, Nagoya University, Nagoya, Japan

## Abstract

Amorphous carbon nitrides (CN) films were prepared from pyrazine through photochemical vapor deposition (photo-CVD) with a 172 nm Xe<sub>2</sub>\* excimer lamp. The photo-CVD process was examined by in-situ quadruple mass spectroscopy (Q-MASS) and in-situ FT-IR spectroscopy. Furthermore, amorphous-CN films were analyzed by x-ray photoelectron spectroscopy (XPS). This photo-CVD process allows us to prepare the amorphous-CN films at the room temperature.

## 1. Introduction

Amorphous carbon nitride (CN) film [1] is an attractive material in the field of hard and wear-resistance coating for head parts in hard disk drives. Moreover, the amorphous-CN films can be applied in the coating of medical appliances and artificial bones within the living body. The amorphous-CN has been prepared by many methods, for examples, arc ion plating, plasma chemical vapor deposition and sputter deposition. These methods frequently require the conditions of bias voltage, substrate heating and reaction system with excess energy. Under these conditions, they are difficult to prepare amorphous-CN films on the insulative substrate and polymer material. In particular, it is a serious problem that the excess energy of the synthesis process cause the heavy damages to samples in the case of polymer material. The coating techniques of amorphous-CN on polymer materials would be necessary since polymer materials are expected to be applied in the medical appliances and the artificial bones.

Photo chemical vapor deposition (photo-CVD) have a potential for the synthesis of amorphous-CN film at low energy and temperature since photochemical reaction proceeds based on the absorbance of characteristic photon energy. Thus, photo-CVD is a promising process for the coating on the polymer substrate. We tried to prepare the amorphous-CN films though photo-CVD, and reveal the reaction mechanism of deposition.

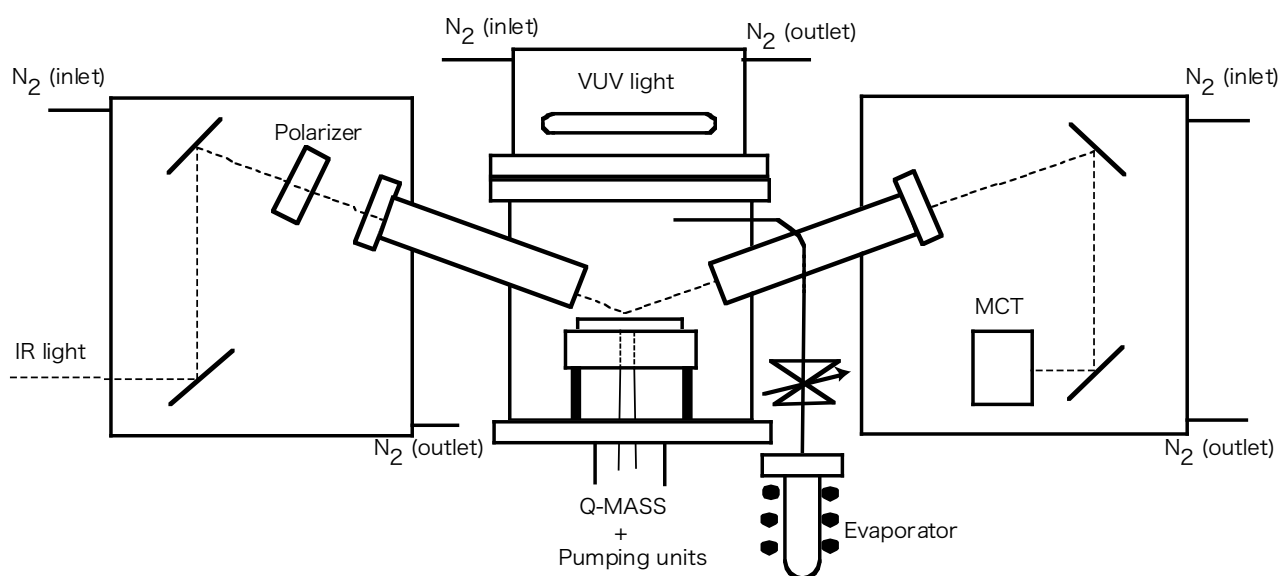


Figure 1. Schematic diagram of photo-CVD system with in-situ FT-IR spectroscopy.

## 2. Experimental procedures

Amorphous-CN films were prepared by photo-CVD under the following conditions. Figure 1 shows a schematic diagram of photo-CVD system with in-situ FT-IR spectroscopy (Bio-Rad Co., FTS-170C) and in-situ Q-mass spectroscopy (Extrel Co., MEXM-100-60H). Light source was an excimer lamp of  $\lambda = 172$  nm at  $10 \text{ mW/cm}^2$  (Ushio Electric, UER20-172V). This wavelength is categorized by vacuum ultra violet (VUV) light. Pyrazine ( $\text{C}_4\text{H}_4\text{N}_2$ , Tokyo Kasei Co. Ltd.) was used as a raw material. Cleaned Au coated n-type Si (100) wafers were used as substrates. The chamber was evacuated until  $1 \times 10^{-4}$  Pa and filled with pyrazine to reaction pressures. The source gas and the substrate in the reactor were simultaneously irradiated by VUV light. The reaction pressures were 10 and 20 Pa. In the IR measurements, a p-polarized IR beam was used.

Figure 2 shows the molecular structure and property of pyrazine. The excited energy and molecular orbital of pyrazine were obtained by ab-initio molecular orbital (MO) calculations. The calculation level was CIS/6-31(g). From these results, pyrazine have a light absorbance at 217 nm based on  $\pi \rightarrow \pi^*$ . The  $\text{Xe}_2^*$  excimer lamp can excite pyrazine molecules although the absorption coefficient is small. The excited state

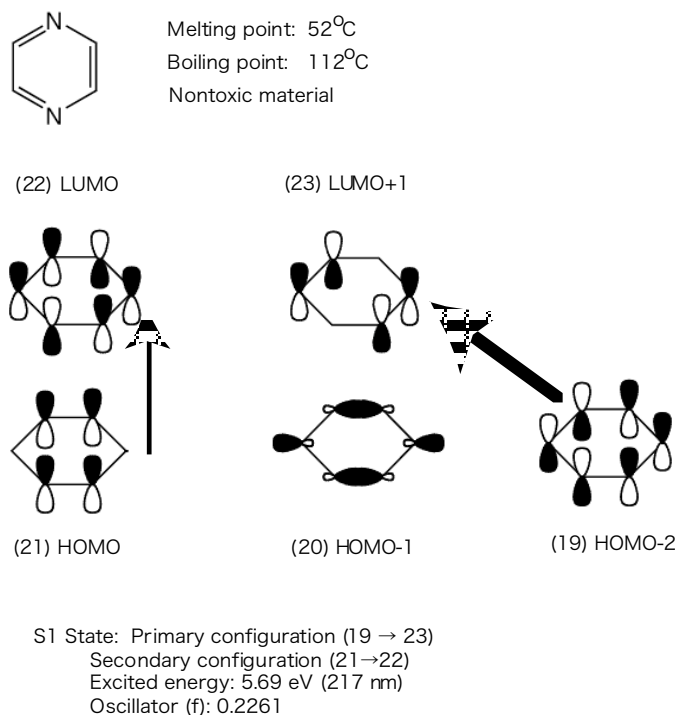


Figure 2. the molecular structure and property of pyrazine obtained by ab-initio MO calculations.

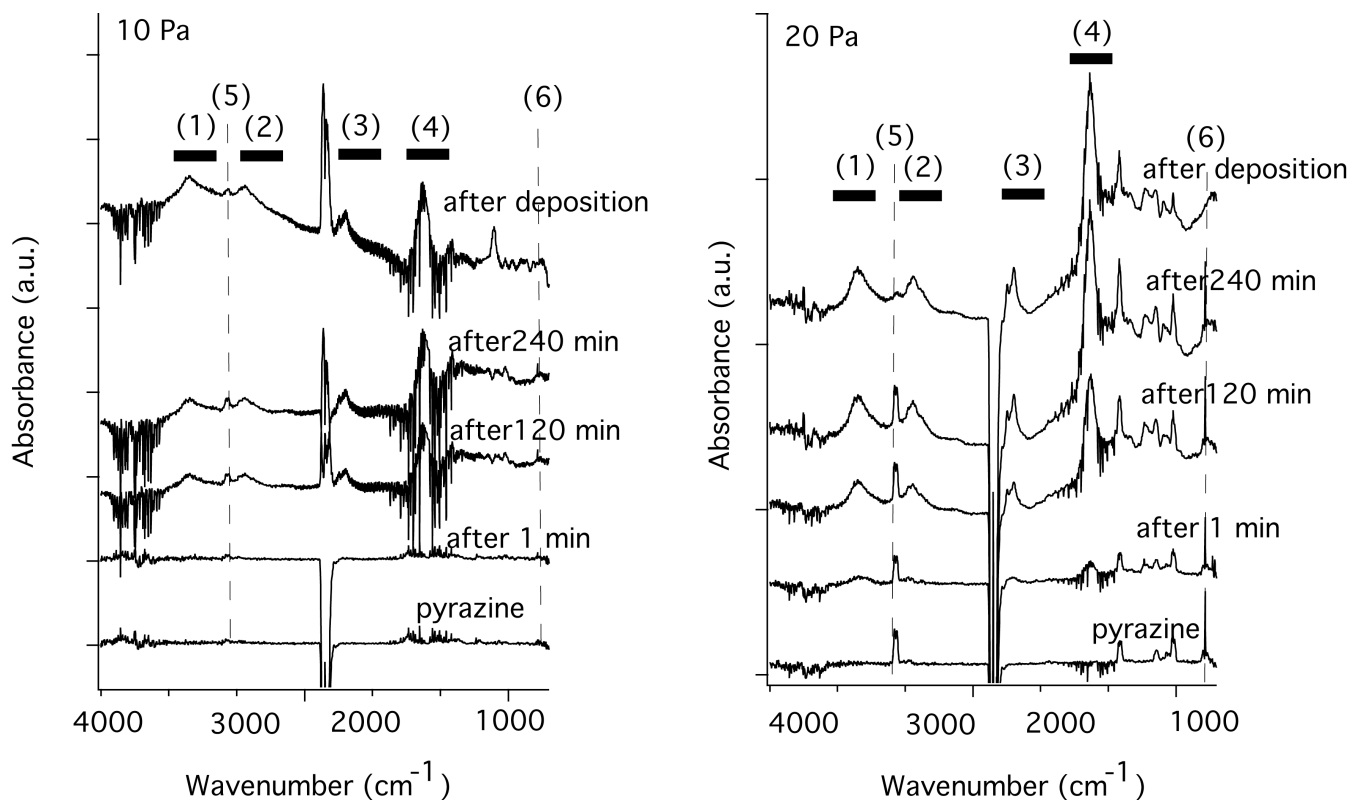


Figure 3. In-situ IR spectra of amorphous-CN films prepared at 10 and 20 Pa

consists of two electron configurations (the transition from a highest occupied molecular orbital (HOMO) and a lowest occupied molecular orbital (LUMO), and the transition from HOMO-2 to LUMO+1). This electron configuration indicates the photodecomposition reaction of pyrazine starts as follows.



XPS (AXIS, Shimadzu-Kartos) measurements were performed under the following conditions. The MgK $\alpha$  X-ray source was operated at 10 mA and 12 kV. The pass energy was 10 eV and the electron take-off angle was 90°. All binding energies were referenced to Au (4f7/2) at 83.98 eV.

### 3. Results and discussion

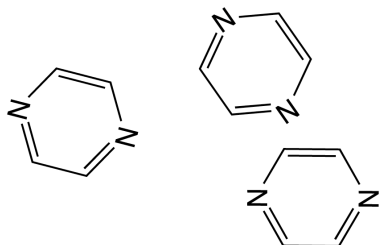
Figure 1 (a) to (c) show in-situ IR spectra in preparations at the total pressure of 10 and 20 Pa. The common peaks were observed in all the spectra. From this, the total pressure has no influence on the vibration aspects of the films. The peaks of 1 to 6 are assigned to the vibrational mode listed in Table 1. The peaks of 1 to 4 were observed during the preparation and after the preparation. Thus, these peaks mainly originated from the chemical bonding of the deposited films. On the other hand, the peaks of 5 and 6 were measured during only the VUV irradiation. This shows that these peaks originated from the chemical bonding of the gas species.

Table 1. Peak assignment of amorphous-CN films

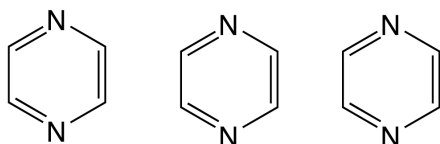
1. NH str., NH<sub>2</sub> sym. (asym.) str.
2. CH str., CH<sub>2</sub> sym. (asym.) str., CH<sub>3</sub> sym. (asym.) str.
3. CN str, NH def., C=C str.
4. CH aromatic str.
5. C-H out of plane def.

In particular, we found the strong intensity of peak 5 (C-H out of plane def.). Generally, the

Gas phase



Surface



intensity is not so strong. Generally, p-polarized beam enhance an intensity of vibrational mode in a perpendicular motion with the beam on the substrate. Thus, the pyrazine might adsorb on the surface of film as shown in Fig. 4. From this, probably, the deposition process is governed by surface reaction, as follows.



[\* = Active site on the surface]

Figure 4. Estimated adsorption geometry of pyrazine molecules onto the sample surface.

measured. The significant change of intensity was seen only in the m/e corresponding to HCN and

In order to confirm the reaction mechanism, in-situ Q-MAS spectra were

CN\*. Figure 5 shows the Q-MAS spectra at the total pressure of 10 and 20 Pa. The signal intensities saturated at 1 min, that is, the deposition reaction became a steady state. These results bear out the above-mentioned reaction mechanism. Furthermore, the atomic ratio of N to C is expected to be 1 to 3 when the reaction mechanism is reasonable.

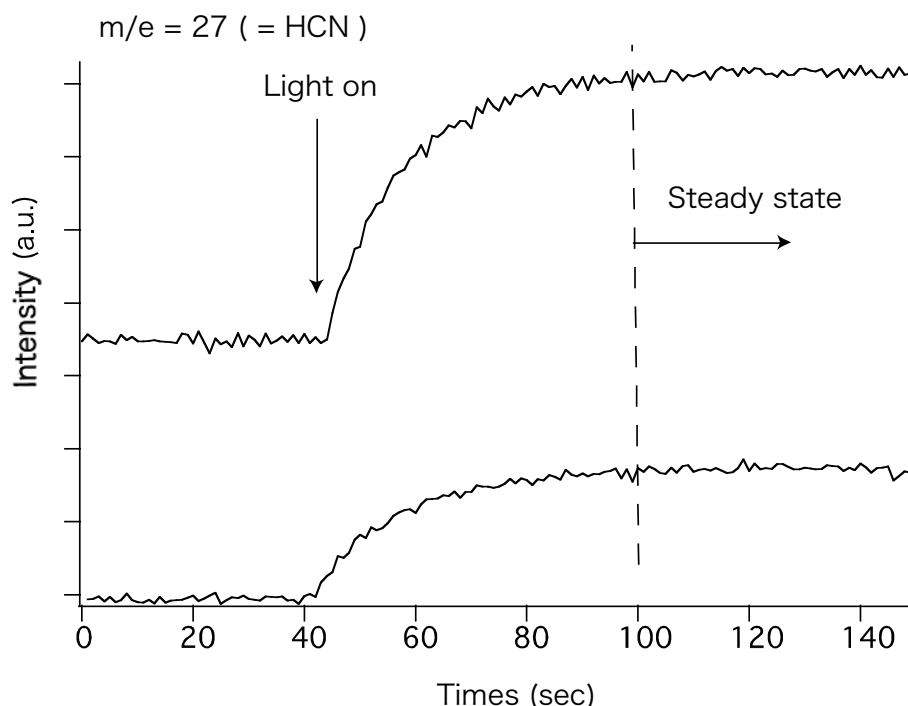


Figure 5. Q-MAS spectra at the total pressure of 10 and 20 Pa.

The atomic ratios obtained by XPS measurements were approximately 1 to 4. This ratio indicates that the reactions 3 and 5 partially proceed. Furthermore, the XPS measurements also show that the amorphous-CN films are deposited from the viewpoint of chemical bonding states. However, the amorphous-CN films must be characterized by mechanical property and electronic property in the future.

#### 4. Summary

We are successful to prepare amorphous-CN films through a VUV-CVD process, and propose a reasonable reaction mechanism. This process can be applied in the coat of amorphous-CN to polymer substrate.

#### Acknowledgements

This work has been supported by the "Biomimetic Materials Processing" (No. JSPS-RFTF 99R13101), Research for the Future (RFTF) Program, Japan Society for the Promotion of Science.

#### References

- [1] E. G. Wang, Progress in Material Science 41, 241-298 (1997).

# Removal of Fluorocarbons by Surface Discharge Plasma Reactor with Catalysts and Various Additives

A. OGATA<sup>1</sup>, H.-H. KIM<sup>1</sup>, S. FUTAMURA<sup>1</sup>, S. KUSHIYAMA<sup>1</sup>, and K. MIZUNO<sup>2</sup>

<sup>1</sup> *Research Institute for Environmental Management Technology, National Institute of Advanced Industrial Science and Technology, Tsukuba, Japan*

<sup>2</sup> *Industrial Technology Center of Nagasaki, Nagasaki, Japan*

## Abstract

The decomposition of  $\text{CClF}_3$  in Ar at atmospheric pressure was investigated using a surface discharge type plasma reactor. In particular, in order to enhance the effectiveness of plasma chemical processing, we investigated the effects of catalysts packed in the reactor and additives in the reactant. The removal rate increased in the plasma reactor packed with  $\text{TiO}_2$  pellets. Furthermore, the removal rate was also enhanced when the water vapor, oxygen, or hydrogen was added in the reactant.

## 1. Introduction

There are many methods for the decomposition of chlorofluorocarbons (CFCs), such as liquid injection incineration, reactor cracking process, gaseous/fume oxidation, rotary kiln incineration, municipal solid waste incinerator, cement kilns, catalytic destruction, thermal plasma destruction, chemical destruction, etc. [1]. On the other hand, the advanced technologies, such as nonthermal plasma, photochemical destruction, supercritical water oxidation, bio-catalytic system, ultrasonic irradiation, etc., have been developed due to their advantages such as low cost, high decomposition efficiency, small space volume requirement, application for other halocarbons, etc. [1].

Among them, the decomposition of fluorocarbons (FCs) using nonthermal plasma techniques was investigated by many researchers and was found to be excellent in the performance [2-16]. However, the researches done at atmospheric pressure were not so much [2-10]. Oda and co-workers studied the decomposition of CFCs, such as trichlorotrifluoroethane ( $\text{C}_2\text{Cl}_3\text{F}_3$ ) and dichlorodifluoromethane ( $\text{CCl}_2\text{F}_2$ ), using a surface discharge [2-4]. Chang also studied the decomposition of hexafluoroethane ( $\text{C}_2\text{F}_6$ ) using dielectric barrier discharge (DBD) and combined plasma catalysis (CPC) [5]. We also carried out the decomposition of diluted various FCs such as CFCs, hydrochlorofluorocarbons (HCFCs), hydrofluorocarbons (HFCs) and perfluorocarbons (PFCs) and obtained the similar performance [8]. Most of them were investigated under the low FCs concentration conditions, such as several tens ppm to several thousands ppm. On the other hand, Kang has reported recently the excellent removal rate in the decomposition of  $\text{CCl}_2\text{F}_2$  (100 ppm to 1.0 %), whereas the analysis of byproducts was not enough to evaluate as the true environmental technique [6].

In this study, we attempted to decompose the highly concentrated FCs (percent order) with surface discharge at atmospheric pressure and evaluated the significance of a nonthermal plasma technique through the byproduct analysis. Also, the effects of combined catalysts and additives were investigated in order to accelerate the decomposition of FCs with nonthermal plasma.

## 2. Experimental

### 2.1 Plasma system

The configuration of the surface discharge reactor is illustrated in Fig. 1(a). Pyrex, quartz, and alumina tubes were used as the dielectric barrier. Spiral stainless steel wire coil (70 turns in 150 mm) of 0.4 mm diameter was set in contact with the inner wall of the barrier tube. Copper sheet was wrapped on the outside of the dielectric tube as the ground electrode.

Two types of  $\text{Al}_2\text{O}_3$  (corundum) and  $\text{TiO}_2$  (rutile) pellets were used as catalysts. These pellets were not porous, i.e., lower specific surface area, which enable us to invest the net contribution by the plasma alone because of their low adsorption capacity. The catalyst was housed in the reactor as shown in Fig. 1(b).

The reactant gas [1.0%  $\text{CClF}_3$ , 0.0-0.5%  $\text{H}_2\text{O}$ , 0.0-1.0%  $\text{O}_2$  and 0.0-2.0%  $\text{H}_2$  + Ar] was fed into the reactor at a flow rate of 100  $\text{cm}^3/\text{min}$ , and a high-voltage ac was applied across the electrodes using a 24kHz neon transformer (S-light Co., Ltd.: model alpha-NEON M-5). The input power (plug-in power) was measured

with a digital power meter (Yokogawa Analytical Systems: model WT110). Specific energy density (SED: J/L) was derived from the input power (plug-in power) and flow rate.

Emission spectrum during plasma discharge was measured in the range of 250-850 nm with a multi-spectrophotometer (Bunkoukeiki Co. Ltd.: ATRAS-25GT).

## 2.2 Product analysis

Gas samples ( $0.5 \text{ cm}^3$ ) were obtained from the effluent by a micro syringe and were analyzed. Normally, the sampling for GC was carried out at the downstream during plasma discharge for 5 min. Unreacted FCs and their reaction products were analyzed by two gas chromatographs (Shimadzu, GC14A and GC14B) equipped with a hydrogen flame ionization detector and a thermal conductivity detector. Methane and  $\text{CF}_4$  were separated with a 2 m Porapak Q column and Porapak N column at 40 to 150 °C. Chlorotrifluoromethane ( $\text{CClF}_3$ ),  $\text{CHClF}_2$ ,  $\text{CHF}_3$ ,  $\text{CCl}_2\text{F}_2$ , and  $\text{CF}_4$  were separated with a 2 m Gaskuropack 54 column at 40 to 150 °C. Minor products were measured with a GC-MS (HP5971A) equipped with a 24 m Poraplot Q capillary column at 40 to 150 °C.

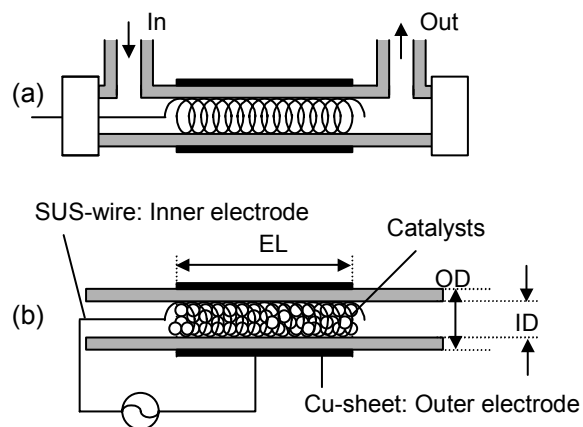
In this work, we could not obtain the information of  $\text{CO}_2$  formation (the total amount of  $\text{CO}_x$  formed), since an alkaline-scrubber ( $\text{Ca}(\text{OH})_2$  soln.) was installed between the plasma reactor and sampling port to remove harmful products such as  $\text{HCl}$ ,  $\text{HF}$ ,  $\text{COF}_2$ , and  $\text{SiF}_4$ . Therefore, the removal rates (conversion) of FCs were shown as an index of their reactivities.

## 3. Results and discussion

### 3.1 Basic properties of a surface discharge-type plasma reactor on the removal of $\text{CClF}_3$

We investigated the basic properties of our plasma reactor without any catalyst or additives. Three kinds of the reactors having different dielectric tubes such as Pyrex, quartz, and alumina were tested for the decomposition of  $\text{CClF}_3$ . Fig. 2 shows the removal rate of  $\text{CClF}_3$  as a function of the input energy (SED). All the reactors showed the same performances, although the removal rate for the reactor made of Pyrex was slightly lower than the other ones. Furthermore, it was found that the removal rate saturated with increasing the input energy.

It was reported that stable plasma discharge was not maintained after long time operation of toluene decomposition due to the carbon deposition of inside wall of the reactor [9]. However, the removal rate did not change at all even after 5 hrs, when we investigated the performance of the plasma reactor for a prolonged plasma discharge at 3.0 kJ/L of SED. Therefore, the saturation behavior was not ascribed to the contamination of inside wall of the reactor.



Barrier	Pyrex	Quartz	Alumina
OD(cm)	1.27	1.26	1.34
ID(cm)	0.97	0.96	0.90
EL(cm)	15	5-15	15
Coil(turn)	70	12-70	70

Fig.1 The configurations of surface discharge plasma reactors: (a) normal type and (b) catalyst-packing type.

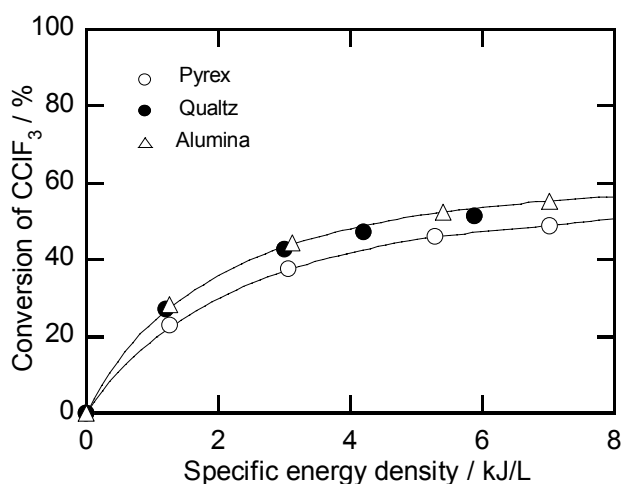


Fig.2 Conversion of  $\text{CClF}_3$  using the surface discharge plasma reactor with (a) Pyrex, (b) quartz, and (c) alumina as dielectric tubes.



On the other hand, it was considered that the plasma did not work effectively for the reaction at the internal position far from reactor wall, because the gases flow at the laminar flow (Reynolds' number < 2,000) normally under these conditions. In order to confirm them, a Pyrex rod in outer diameter of 7.0 mm was inserted in the central position of the reactor tube (alumina) in inner diameter of 9.0 mm. However, the  $\text{CClF}_3$  reactivity did not change regardless of the presence of the inner rod. Furthermore, the effect of residence time was investigated by changing the outer electrode length (5, 10, and 15cm) at a constant flow rate. Removal rate of  $\text{CClF}_3$  was almost the same in all of the reactors at the constant input energy. That is, the removal rate in the decomposition of  $\text{CClF}_3$  depended only on SED. The laminar flow in the reactor is also not responsible for the saturation of removal rate at high input energy. The agitation of the gas seems to occur by plasma discharge (applied high voltage).

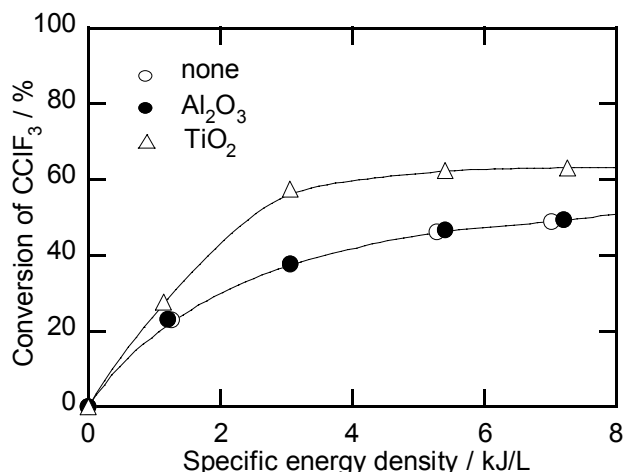


Fig.3 Conversion of  $\text{CClF}_3$  in the plasma reactor packed with (a) none (b)  $\text{Al}_2\text{O}_3$ , and (c)  $\text{TiO}_2$  pellets.

### 3.2 Combination effect of catalysts on the decomposition of $\text{CClF}_3$

The effect of catalysts under plasma discharge was investigated using the plasma reactor packed with  $\text{Al}_2\text{O}_3$  and  $\text{TiO}_2$  pellets (Fig.1(b)), because these oxides were one of the effective catalysts for the decomposition of CFCs and HCFCs at 400-500 °C [17-19]. Fig.3 shows that  $\text{TiO}_2$  pellets enhanced the removal rate. In contrast,  $\text{Al}_2\text{O}_3$  did not affect the removal rate of  $\text{CClF}_3$ . Several researchers reported the enhancing effect of  $\text{TiO}_2$  on the plasma decomposition of various VOCs [20-22]. The reason of its effect under plasma discharge has not been yet fully understood. The emission spectrum was measured during plasma discharge, since  $\text{TiO}_2$  is a well-known photocatalyst. However, significant emissions in the region of lower wavelength were not observed in this plasma reactor. In addition,  $\text{TiO}_2$  used have the rutile structure, whose photocatalytic activity was lower than that of  $\text{TiO}_2$  with the anatase structure. Furthermore, the temperature in the reactor was about 65 °C, while thermal activation of  $\text{TiO}_2$  catalysts requires normally temperature higher than 400 °C. On the basis of these findings, promoting effect by  $\text{TiO}_2$  was not ascribed to either photocatalysis or to thermal catalysis. The catalytic effect seems to be derived from the direct activation of  $\text{TiO}_2$  surface by plasma discharge.

To obtain the evidence for the direct activation by plasma discharge, chemical species released in gas phase during plasma discharge were measured by a mass-spectrometer (MS) under an Ar flow without FCs, since activated species on the catalysts could not be measured directly in situ. A small amount of  $\text{O}_2$  molecule alone was consequently observed during plasma discharge. Fig. 4 shows the intensity change of  $m/e=32$  peak in the reactors packed with  $\text{Al}_2\text{O}_3$  and  $\text{TiO}_2$  pellets. The peak intensity with  $\text{TiO}_2$  was larger than that with  $\text{Al}_2\text{O}_3$ . This  $\text{O}_2$  molecule seems to be derived from the activated atomic oxygen species, such as  $\text{O}$ ,  $\text{O}^+$ , and  $\text{O}^{2+}$  ( $2\text{O} \rightarrow \text{O}_2$ ). These species were released from a lattice oxygen in the oxide surface, because oxygen sources did not exist originally under an Ar flow except for a trace amount of  $\text{H}_2\text{O}$  adsorbed on the

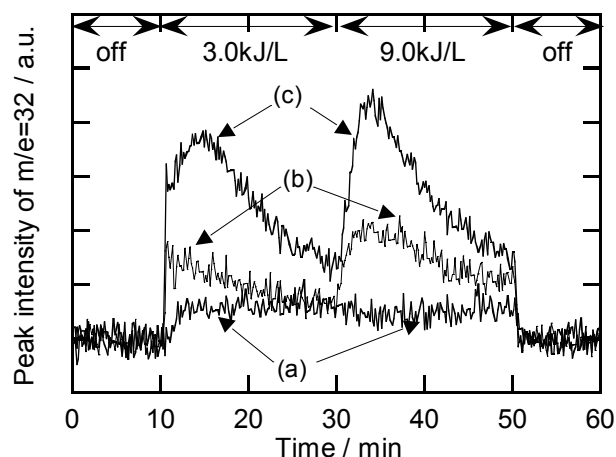


Fig.4 Intensity change of  $m/e=32$  peak on the plasma reactors packed with (a) none, (b)  $\text{Al}_2\text{O}_3$ , and (c)  $\text{TiO}_2$  pellets under an Ar flow.

reactor wall and pellets. As shown in the figure, the amount of released  $O_2$  decrease with discharge time. Moreover, the removal rate of  $CClF_3$  decreased similarly with discharge time. On the basis of these observations, we concluded that lattice oxygen atoms of  $TiO_2$  pellet surface were activated by plasma discharge more easily than those of  $Al_2O_3$  pellet surface. The different of reactivities of  $CClF_3$  with  $Al_2O_3$  and  $TiO_2$  in plasma reflect the difference degrees of the activation ease of a lattice oxygen on the solid surface. Titanium dioxides could be activated not only by UV-irradiation and thermal heating but also by plasma discharge.

### 3.3 The effect of co-existing substances (additives) on the decomposition of $CClF_3$

In order to completely decompose  $CClF_3$  into the stable products such as  $CO_2$ ,  $HCl$ , and  $HF$ , the hydrogen and oxygen sources are needed for this reaction system. Then, it was found that the decomposition rate was enhanced, when  $H_2O$ ,  $O_2$ , and  $H_2$  as the reaction accelerator were added in the reactant (Fig.5). Furthermore, product analysis was carried out under various conditions. Table 1 summarizes the byproducts in the decomposition of  $CClF_3$ , which were identified qualitatively by GC-MS analysis. The major byproducts were  $CF_4$  and  $CCl_2F_2$  as shown in Figs. 6 and 7, which were analyzed quantitatively by GC. From these formation profiles, it was suggested that the byproducts in the reaction without the additives were higher than those with the additives, resulting in the saturation of removal rate at high input energy in the decomposition of  $CClF_3$  without the additives. Also, various FCs including H-atom were produced, although removal rate became extremely high by adding  $H_2$  in the reactant.

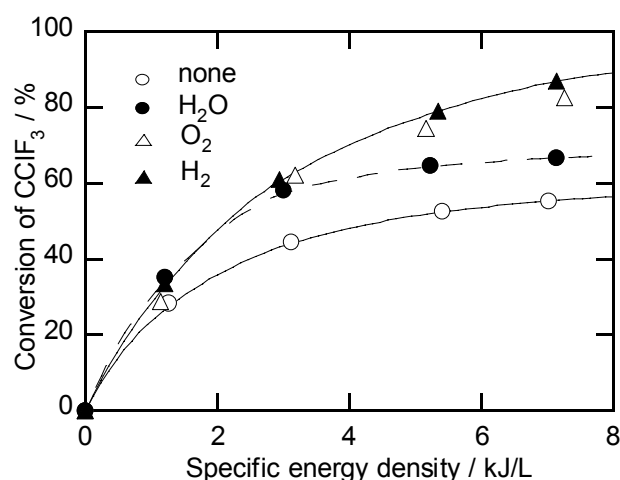


Fig.5 Removal rate of  $CClF_3$  with additives: (a) none, (b)  $H_2O$ , (c)  $O_2$ , and (c)  $H_2$ .

Table 1 Relative intensity of byproducts observed by GC - MS analysis on the decomposition of  $CClF_3$ : 6.0kJ/L

Byproducts	none	$H_2O$	$O_2$	$H_2$
$CF_4$	Medium	Medium	Medium	Small
$CHF_3$	Small	Small	n.d. (no detection)	Very small
$CCl_2F_2$	Large	Large	Very small	Very small
$CHClF_2$	n.d.	n.d.	n.d.	Very small
$CH_2ClF$	n.d.	n.d.	n.d.	Small
$CHCl_2F$	n.d.	n.d.	n.d.	Very small
$CH_2Cl_2$	n.d.	n.d.	n.d.	Very small
$CClF_2-CHF_2$	n.d.	n.d.	n.d.	Very small
$CHF_2-CHF_2$	n.d.	n.d.	n.d.	Very small
$CClF_2-CH_2F$	n.d.	n.d.	n.d.	Very small
$CClF_2-CHClF$	n.d.	n.d.	n.d.	Very small
$CClF_2-CHCl_2$	n.d.	n.d.	n.d.	Very small

It is already known that the introduction of additives suppresses the removal rate of  $CClF_3$  in lower concentrations [8]. In contrast, in higher concentrations, suitable amounts of additives are very effective in removing  $CClF_3$  and suppressing the formation of byproducts. Therefore, in the case of lower FCs concentrations, i.e., the quantity of the additives is excess for the target molecules (FCs), loss of effective fast electrons for the reaction seems to increase due to quenching by additives.

#### 4. Conclusion

Additives such as  $\text{H}_2\text{O}$ ,  $\text{O}_2$ , and  $\text{H}_2$  increased FCs conversions in their decomposition due to scavenging of FCs fragments by these additives before those fragments reproduces stable FCs such as  $\text{CF}_4$ . Furthermore, it was suggested that the lattice oxygen of  $\text{TiO}_2$  activated by plasma scavenged the decomposition fragments of FCs as well as the additives, and enhanced the removal rate. Titanium dioxides can be activated as a catalyst not only by UV-irradiation and thermal heating but also by plasma discharge at room temperature.

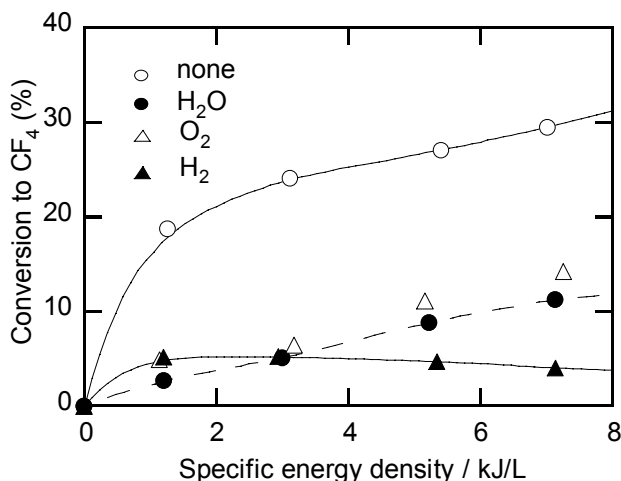


Fig.6 Conversion of  $\text{CClF}_3$  to  $\text{CF}_4$  with additives:  
(a) none (b)  $\text{H}_2\text{O}$ , (c)  $\text{O}_2$ , and (d)  $\text{H}_2$ .

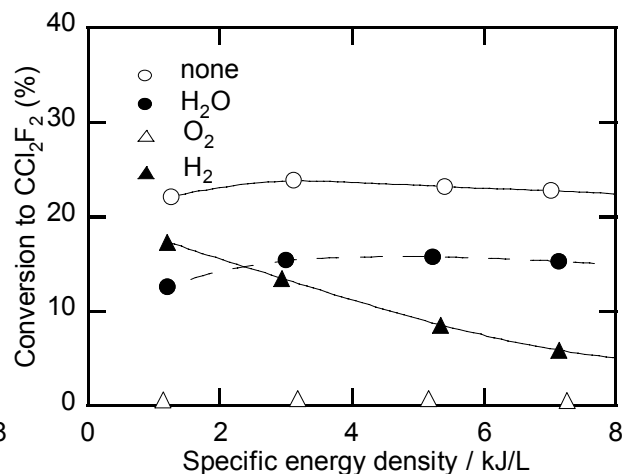


Fig.7 Conversion of  $\text{CClF}_3$  to  $\text{CCl}_2\text{F}_2$  with additives:  
(a) none (b)  $\text{H}_2\text{O}$ , (c)  $\text{O}_2$ , and (d)  $\text{H}_2$ .

#### References

- [1] UNEP April 2002 report on the technology and economic assessment panel, vol.3B.
- [2] T. Oda, T. Takahashi, H. Nakao, S. Masuda, IEEE Trans. Ind. Applicat., **29**, 787 (1993).
- [3] T. Oda, R. Yamashita, K. Tanaka, T. Takahashi, S. Masuda, IEEE Trans. Ind. Applicat., **32**, 1044 (1996).
- [4] T. Oda, R. Yamashita, T. Takahashi, S. Masuda, IEEE Trans. Ind. Applicat., **32**, 227 (1996).
- [5] M. B. Chang and S. J. Yu, Environ. Sci. Technol., **35**, 1587 (2001).
- [6] H.-C Kang, J. Ind. Eng. Chem., **8**, 488 (2002).
- [7] S. Futamura, H. Einaga, A. Zhang, IEEE Trans. Ind. Applicat., **37**, 978 (2001).
- [8] A. Ogata, T. Tanaka, K. Mizuno, S. Kushiya, A. Obuchi, M. Tezuka, Proceedings of 2000 Annual Meeting of the Institute of Electrostatics Japan, pp.191-183, 2000
- [9] S. Masuda, S. Hosokawa, X. Tu, Z. Wang, J. Electrostat., **34**, 415 (1995).
- [10] S. J. Yen, M. B. Chang, Plasma Chem. Plasma Process., **21**, 469 (2001).
- [11] Y.-F. Fen, W. J. Lee, C.-Y. Chen, L.-T. Hsieh, Environ. Sci. Technol., **33**, 2234 (1999).
- [12] Y.-F. Fen, W. J. Lee, C.-Y. Chen, L.-T. Hsieh, Ind. Eng. Chem. Res., **38**, 3199 (1999).
- [13] B. A. Wofford, M. W. Jackson, C. Hartz, J. W. Bevan, Env. Sci. Technol., **33**, 1892 (1999).
- [14] C. Hartz, J.W. Bevan, M. W. Jackson, B. A. Wofford, Env. Sci. Technol., **32**, 682 (1998).
- [15] F. W. Breitbarth, D. Berg, K. Dumke, H.-J. Tiller, Plasma Chem. Plasma Process., **17**, 39 (1997).
- [16] Y.-F. Wang, W.-J. Lee, C.-Y. Chen, Y.-P. G. Wu, G.-P. Chang-Chien, Plasma Chem. Plasma Process., **20**, 469 (2000).
- [17] M. Tajima, M. Niwa, Y. Fujii, Y. Koinuma, R. Aizawa, S. Kushiya, S. Kobayashi, K. Mizuno, H. Ohuchi, Appl. Catal. B: Environ., **9**, 167 (1996).
- [18] S. Imamura, T. Shiomi, S. Ishida, K. Utani, Ind. Eng. Chem. Res., **29**, 1758 (1990).
- [19] G.-L. Li, T. Ishihara, Y. Moro-oka, Y. Takita, Appl. Catal. B:Environ., **9**, 239 (1996).
- [20] D.-W. Park, S.-H. Yoon, G.-J. Kim, H. Sekiguchi, J. Ind. Eng. Chem., **18**, 393 (2002).
- [21] M. Kang, B.-J. Kim, S. M. Cho, C.-H. Chung, B.-W. Kim, G.Y. Han, K. J. Yoon, J. Molec. Catal. A: Chemical, **180**, 125 (2002).
- [22] D. Li, D. Yakushiji, S. Kanazawa, T. Ohkubo, Y. Nomoto, J. Electrostat., **55**, 311 (2002).

# **A Novel Cross-Field Plasma Switch**

Deng Xinlu<sup>\*</sup>, Xu Jun, Wang Younian, Xia Yuanliang,  
Wang Jingang, Liu Chengsen, Zhang Jialiang, Zhong Fu

*State Key Lab for Materials Modification, Dept. of Physics  
Dalian University of Technology  
Dalian 116024, P. R. China  
<sup>\*</sup>e-mail: [xldeng@dlut.edu.cn](mailto:xldeng@dlut.edu.cn)*

This paper introduces a novel planar cross-field plasma switch. Besides anode, cathode, source grid and control grid, it contains a corrugated chrome plate attached to the cathode for creating more second electrons and an additional magnetic ring placed near the source grid. This magnetic ring combined with the two magnetic rings beneath the cathode forms an unbalanced magnetic bottle for confining the plasma in the switch. By this way the plasma density in the switch increased greatly. This is beneficial to reduction of the volume of the switch and increase of switching speed.

A modulator based on this planar cross-field plasma switch was built and tested. Trigger circuit used for control grid was described. The strategy for resolving the problem of “shoot throu” of the plasma switches (i.e. switching failure caused by arc running through from plasma load to the switch interior) was offered.

# Preparation of DLC films on the inner wall of the long stainless steel tubes by using PIII

Deng Xinlu<sup>a\*</sup>, Wang Jingang<sup>a</sup>, Ma Guojia<sup>a</sup>, Chen Xi<sup>b</sup>, Li Xin<sup>a</sup>, Dong Chuang<sup>a</sup>, Li Changsheng<sup>b</sup>

<sup>a</sup>*State Key Lab for Materials Modification, Plasma Lab of Dept of Physics  
Dalian University of Technology Dalian 116024, P. R. China*

<sup>b</sup>*Center of micro/nano science and technology Jiangsu University  
212013 Dantu Road 301 Zhenjiang city Jiangsu province China*

\*e-mail: [xldeng@dlut.edu.cn](mailto:xldeng@dlut.edu.cn)

We prepared Diamond like carbon films(DLC) on the inner wall of the long stainless steel tubes by using plasma immersion ion implantation (PIII). In order for uniform implantation on the inner wall, a ground-connected metal wire was installed at central line of the tube. Methane(CH<sub>4</sub>) was used as working gases for micro-wave ECR plasma. High negative voltage pulses of -20kv~-30kv was applied to the substrate. Chemical composition and chemical structure of the DLC films was measured by Raman spectroscopy and FT-IR spectroscopy. Meanwhile corrosion-resistant peroperties, mechanical properties and the surface morphology information of DLC were obtained. The results showed that the corrosion-resistant peroperties, hardness and the friction of the inner wall of the stainless steel tube were modified.

# Surface modification of polyethylene (PE) powders using a remote nitrogen plasma and a fluidized bed reactor

Brigitte Mutel<sup>1</sup>, Nouria Fatah<sup>2</sup>, Hervé Vezin<sup>3</sup> and J. Grimblot<sup>2</sup>

<sup>1</sup>Laboratoire de Génie des Procédés d'Interactions Fluides réactifs-Matériaux (UPRES-EA 2698)

<sup>2</sup>Laboratoire de catalyse de Lille (UMR CNRS 8010)

<sup>3</sup>Laboratoire de Chimie Organique et Macromoléculaire (UMR 8009)

Université des Sciences et Technologies de Lille, 59655 Villeneuve d'Ascq cedex, France

## Abstract

The coupling between fluidized bed and far cold remote nitrogen plasma processes is efficient to modify surface properties of a PE powder which wettability increases, and the increase is as better as 0.75 % of O<sub>2</sub> is added to the nitrogen flow. XPS studies give evidence for the incorporation of oxygenated and nitrogenated functions, while ESR analyses reveal the presence of a mixture of alkyl and allyl radicals.

## 1. Introduction

Taking into account their low surface energy, polymers often require a modification of their surface properties before any use. Cold plasma treatments are a convenient way to obtain these modifications by introducing new surface chemical groups without affecting the bulk properties. For last fifteen years, the efficiency of the far cold remote nitrogen plasma technology to modify polymers surfaces was clearly evidenced in our group [1-4]. This medium, located far from the excitation zone and exempt of ions, electrons and charged particules is characterized by a gas temperature about the ambient [5]. Its main reactive species are atomic nitrogen in the ground state N(<sup>4</sup>S) and vibrationally and/or electronically excited nitrogen molecules. The long lifetime of N(<sup>4</sup>S), due to a redissociation of nitrogen molecules [6], allows a large volume expansion of this remote plasma. The addition of O<sub>2</sub> to the N<sub>2</sub> plasma gas allows the introduction of oxygen atoms without destroying the large volume expansion providing that the O<sub>2</sub> rate remains lower than 2%. The efficiency of the process rely on a good contact between the polymer surface and the plasma; so, classical plasma reactor cannot be used to modify polymers powders. Aggregation of the grains has to be eliminated and to reach this aim, a coupling between fluidized bed and plasma processes was successfully carried on in a previous work [7] to treat a polyethylene (PE) powder (GURX 132 from Hostalen). Because of the small size of the reactor used during this study, it was not possible to operate with more than 5 g of sample by treatment. So, it was difficult to study the homogeneity of the treatment as well as flowing properties of treated powders. In this paper, a larger reactor, allowing the treatment of mass reaching 100 g was used. The evolutions of wettability, flowability and physical properties of the powder versus various conditions of plasma treatment are reported. Modifications induced in the best conditions (leading to the best wettability) are investigated by X-ray photoelectron Spectroscopy (XPS) and by Electron Spin Resonance (ESR).

## 2. Experimental details

**2.1. The reactor.** The experimental set-up was previously described [8]. The gaseous flow (N<sub>2</sub> or N<sub>2</sub> + O<sub>2</sub>), created by a continuous pumping (33 m<sup>3</sup>/h), was excited by an electrodeless discharge by means of a microwave generator (2450 MHz) which could deliver an incident power (P) up to 1.5 kW. The discharge was produced in a quartz tube (32 mm diameter) connected to the fluidized bed reactor through a 90° elbow. This reactor was constituted of a vertical cylindrical Pyrex glass tube (height: h = 1 m; inner diameter: D = 0.15 m) with a porous plate at the bottom to support the powder bed. This porous plate has to be made with a material which does not destroy the reactive species of the plasma. In this work, it was made of PE and its pore diameter was equal to 17 μm. Nitrogen and oxygen (Industrial quality, U grade, Air Liquide) flow rates (Q<sub>N2</sub> and Q<sub>O2</sub> respectively) were adjusted by mass flow regulators. In this work, the addition of oxygen to nitrogen was always lower or equal to 1 %. To simplify the text, the far cold remote nitrogen and the far cold nitrogen + oxygen plasma will be denoted by FCRN and FCRNO plasma respectively. The pressure was measured at the top of the

column thanks to a Pirani type vacuum gauge. The distance ( $d$ ) between the discharge and the porous plate was 0.65 m, so that the PE powder was fluidized by the FCRN (or FCRNO) plasma.

**2.2. Contact angle measurements.** The wettability of the plasma-treated PE powder was determined from dynamic contact angle measurements according to the Washburn method [9] with a Krüss K12 tensiometer. A 5 mm inside diameter glass tube, bottom closed with a porous glass plate, was filled with 1 g of powder. The bottom of the tube was then put in close contact with a chosen liquid which penetrates up into the PE powder column by capillarity rising. The weight  $W$  of the penetrating liquid was measured as a function of time  $T$  after contact of the porous glass plate with the liquid. The contact angle  $\theta$  at the powder surface was determined according to the Washburn equation:

$$W^2 / T = (K \rho^2 \gamma_L \cos \theta) / 2\eta \quad (1)$$

$\rho$ ,  $\eta$  and  $\gamma_L$  are the density, the viscosity and the surface tension of the liquid respectively. The empirical constant  $K$ , which depends on the particles size and on their degree of packing, was experimentally determined using a liquid that perfectly wets the powder. In that case, the contact angle against the powder is assumed to be  $0^\circ$  and  $\cos \theta = 1$ . In this work, the  $K$  value was determined with heptane.

**2.3. Flow properties.** The powder flowability can be described as the collective movement of particles. It is the more easy as the particles can move freely one with respect to another and it can be altered or complicated by interparticle forces as Van der Waals (only for cohesive powders), electrostatic or capillary forces. The powders flowability was studied using an empirical test: the Hausner index (HR), defined as the ratio of bulk density of particles after prolonged tapping ( $\rho_t$ ) over aerated density ( $\rho_a$ ), and governed by the friction and the interparticle forces.

$$HR = \rho_t / \rho_a = V_a / V_t \quad (2)$$

The experiment was performed in a graduated glass cylinder with a 100 ml capacity. The volume of powder before tapping was  $V_a = 40$  ml for all the experiments, then it was submitted to vertical tapping until no change in the volume ( $V_t$ ) was observed.

HR allows to distinguish the powders as follows:

- for  $HR > 1.4$ , the powder can be classified in group C of Geldart [10] (cohesive powder and non free flowing)
- for  $HR < 1.2$ , the powder can be classified in group A, B or D of Geldart (non cohesive powder and free flowing)
- for  $1.2 < HR < 1.4$ , the powder exhibits the behaviour of both groups.

The test was repeated six times. The given values correspond to the average of six measurements. The experiences were carried out at room temperature ( $\approx 20^\circ \text{C}$ ) and with a relative humidity ranging from 60 % to 65 %.

**2.4. Textural properties.** The density or specific gravity ( $\rho_p$ ) of powders were measured with a helium gas pycnometer (Micrometrics, Accupyc 1330). The average diameter (Sauter diameter,  $d_p$ ) was measured by a light-scattering laser instrument (Beckman-Coulter LS230).

**2.5. XPS study.** Analyses were performed in a Leybold LHS 10 spectrometer. The unmonochromated Al  $K\alpha$  (1486.6 eV) X-ray source was operated at 13 kV and 20 mA current emission. The binding energies were calculated by reference to aliphatic carbon of the untreated polymer, located at 285.0 eV. For two components A and B, the atomic ratio were calculated from the corresponding peak area, assuming a homogeneous distribution within the analysed depth.

**2.6. ESR study.** ESR measurements were made at 100 K in a Bruker ELEXYS 580<sup>E</sup> spectrometer operating at 9 GHz microwave frequency. Spectra were recorded at non-saturating microwave power (3.1 mW) and with a frequency and a modulation of the magnetic field respectively equal to 100 KHz and 10 G. Each ESR spectrum consists in three accumulations and corresponds to the derivative of the absorption spectrum. The absolute magnitude of the free radicals population of the treated powder was determined by comparison of the area under the ESR absorption curve with the one of a reference material, a pitch in KCl standard. The ESR spectra were simulated using Winsim 2000<sup>®</sup>, the hyperfine

splitting constants and the calculation of the radicals ratio were performed using automatic simplex algorithm implemented in the software.

After the plasma treatment, the PE powder was removed from the reactor, exposed to the ambient air for a duration denoted by  $\delta$  (aging time), then, dipped in liquid nitrogen to stop the aging.

### 3. Results.

**3.1. Determination of fluidization conditions.** At first, experimental conditions were chosen in order to obtain a good compromise between the plasma intensity and the apparent fluidization. It leads to a nitrogen flow rate equal to 0.35 NL/min and a pressure equal to 1.9 mbar for treating 45 g of PE (with a microwave power of 600 W).

The good quality of a fluidized bed is the result of a good gas-solid mixing. It leads to the optimum contact between the solid particles and the flowing gas. The fluidization has to be performed with a gas fluidization velocity ( $U$ ) higher than the minimum fluidization velocity ( $U_{mf}$ ) and lower than the particles terminal velocity ( $U_t$ ):  $U_{mf} < U < U_t$ . In these conditions, dead zones and elutriation phenomenon (powder entrainment) are avoided. So, it was necessary to check the respect of these conditions in our experiment. So,  $U$ , calculated from the flow rate in working conditions and the cross section area of the column is equal to 0.186 m/s.

$U_{mf}$  was estimated from one of the correlations given in the literature. In our conditions, the Reynolds number ( $Re$ ), (calculated from  $d_p = 283 \mu\text{m}$ , see §3.3) and  $U = 0.186 \text{ m/s}$ , was equal to  $6.5 \cdot 10^{-3}$ . This low value indicates a laminar regime for both fluidization state and minimum fluidization velocity. So  $U_{mf}$  could be estimated using the Wen *et al.* [11] correlation obtained at ambient pressure:

$$U_{mf} = \frac{d_p^2 g (\rho_p - \rho_g)}{1650 \mu_g} \quad (3)$$

where  $\mu_g$  is the gas viscosity,  $\rho_g$  the gas density and  $g$  the acceleration of gravity.

In the Stocke's law region, the terminal velocity [12] ( $U_t$ ) is given by:

$$U_t = \frac{(\rho_p - \rho_g) g d_p^2}{18 \mu_g} \quad (4)$$

Within our experimental conditions,  $U_{mf} = 0.0256 \text{ m/s}$  and  $U_t = 2.35 \text{ m/s}$ . Therefore, the relationship  $U_{mf} < U < U_t$  is verified.

**3.2 Study of PE wettability.** The PE wettability was followed from contact angle measurements performed with ethylene glycol ( $\theta_{eg}$ ) whose surface tension ( $\gamma_L$ ) is equal to 47.3 mN/m. For the untreated powder,  $\theta_{eg}$  could not be determined as the liquid did not penetrate through the powder column, but it was expected to be equal to  $90^\circ$ . The aim of the study was to obtain a  $\theta_{eg}$  value at least as good as the one obtained for the PE powder chemically treated by the Hostalen Compagny ( $\theta_{eg} = 0^\circ$ ). Each  $\theta$  value corresponds to the average of 4 measurements. The accuracy of the results is  $\pm 2^\circ$ . The evolution of  $\theta_{eg}$  values was studied versus  $t$ , and the percentage of oxygen added to nitrogen (denoted by  $\chi$ ) for  $Q_{(N_2+O_2)} = 0.35 \text{ NL/min}$ . Results are shown in Table 1. For  $\chi = 0$ ,  $\theta_{eg}$  decreases when  $t$  increases from 0 to 25 min, then  $\theta_{eg}$  reaches a limit value equal to  $67^\circ \pm 2^\circ$ . For  $t = 25 \text{ min}$ , the wettability is strongly improved by addition of oxygen to nitrogen. The best wettability, ( $\theta_{eg} = 0^\circ$ ), is reached for  $\chi = 0.75 \%$ . This wettability remains stable within an ageing at least equal to 3 days. Contact angles measurement performed with water ( $\gamma_L = 72.8 \text{ mN/m}$ ) allowed to give evidence for the efficiency of the plasma treatment in comparison with the chemical one: for  $t$  and  $\chi$  values respectively equal to 25 min and 0.75 %, , the  $\theta_{water}$  value reaches  $50^\circ$ ; it is equal to  $70^\circ$  for the chemically treated PE.

t (min)	0	5	10	15	20	25	30
$\theta_{eg} (^\circ)$	> 90	> 90	> 90	> 90	86	67	68

Table 1: Evolution of  $\theta_{eg}$  vs treatment time ( $t$ ) for  $\chi = 0 \%$

$\chi (\%)$	0	0.5	0.75	1.0
$\theta_{eg} (^\circ)$	67	59	0	30

Table 2: Evolution of  $\theta_{eg}$  vs  $\chi$ ;  $t = 25 \text{ min}$ .



In the following study, modifications of the PE powder induced by the plasma treatment were studied by comparing three sets of powders: the untreated PE (denoted by PE), the powder treated by a FCRN plasma (denoted by PE-N) and the powder treated by a FCRNO plasma with a  $\chi$  value equal to 0.75 % (denoted by PE-NO).

**3.3. Study of textural properties.** For PE, PE-N and PE-NO, neither the BET surface area, equal to  $0.5 \text{ m}^2/\text{g}$ , nor the powder density, equal to  $\rho_p = 960 \text{ kg/m}^3$ , was affected by the plasma treatment. On the other hand, a small variation of the average diameter of the powder (Sauter diameter  $d_p$ ) could be noticed [8]. It varies from  $283 \text{ }\mu\text{m}$  for PE to  $312 \text{ }\mu\text{m}$  for PE-N and PE-NO. This increase could be explained [8] by the elutriation of the finest particles during the plasma treatment. Taking into account  $\rho_p$ ,  $\rho_g$  and  $d_p$  values, the three sets of powders can be included in the B group of Geldard exhibiting homogeneous fluidizing bed.

**3.4. Powder flowability.** A free flow was observed with PE (HR = 1.15), whereas the flowability seems to be altered for PE-N (HR = 1.2) and PE-NO (HR = 1.24). These results are in good agreement with the wettability increase obtained for PE-N and PE-NO. Indeed, the hydrophilic powder can lead to the formation of agglomerates due to capillary forces, thus affecting the results of HR test performed at 62 % relative humidity. According to HR, PE-N and PE-NO powders acquired a behavior more close to the C-A group of Geldart than of the B one.

**3.5. XPS study.** A single C 1s photopeak was detected on PE, while the presence of N 1s and O 1s photopeaks were evidenced both on PE-N and PE-NO. Atomic ratio, calculated for the three sets of powder are shown in Table 3. These, ratio remain stable within an ageing at least equal to 3 days.

	PE	PE-N	PE-NO
nO/ nC	0	0.02	0.28
nN/ nC	0	0.04	0.09

Table 3: Atomic ratio for the three sets of powder

**3.6. ESR Study.** ESR studies were performed on PE-N and PE-NO. In both conditions, ESR spectra, characterized by a six lines pattern, are similar and have the same intensity for  $\delta = 0$ . The influence of  $\delta$  on the ESR integrated signal was performed on PE-NO.

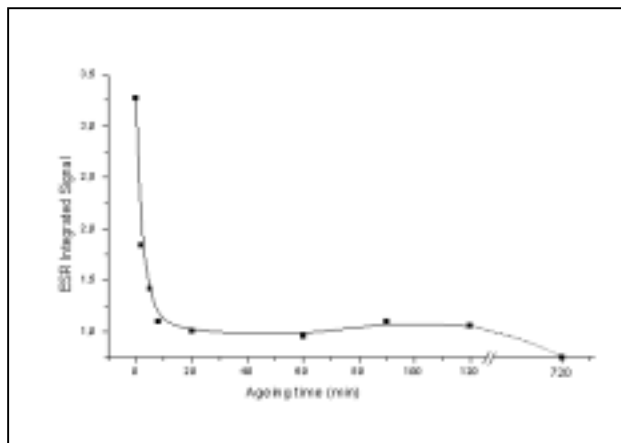


Figure 1 shows that the radical concentration decreases very quickly and reaches 50 % as soon as 2 minutes. For  $\delta$  values higher than 2 hours, the integrated ESR signal was very weak. It was no more detected after an aging time equal to 12 hours. However, the spectra are not modified during the aging in open air and the sextet pattern remained. The peroxy radical, described by Hori *et al.* [13] as typically a broad asymmetric single line (10 G) was not detected in our conditions.

Figure 1 : Evolution of the ESR integrated signal (a.u.) versus ageing

The ESR spectrum, characterized by a sextet is similar to the one already obtained by O'Neill *et al.* [14] by  $\gamma$  irradiation (11.25 Mrad) of PE surfaces. According to these authors, the spectrum obtained is presumed to be the result of either the alkyl free radical  $-\text{CH}_2-\text{CH}^\bullet-\text{CH}_2-$ , the allyl radical  $-\text{CH}_2-\text{C}_{(1)}\text{H}=\text{C}_{(2)}\text{H}-\text{C}_{(1)}\text{H}^\bullet-\text{CH}_2- \leftrightarrow -\text{CH}_2-\text{C}_{(1)}\text{H}^\bullet-\text{C}_{(2)}\text{H}=\text{C}_{(1)}\text{H}-\text{CH}_2-$  or the polyenyl radical  $-\text{CH}_2-(\text{CH}=\text{CH})_n-\text{CH}^\bullet-\text{CH}_2-$ , or a combination of two or more of these. In the case of allyl radical, the unpaired electron spin density on the  $\text{C}_{(1)}$  and  $\text{C}_{(2)}$  atoms are respectively equal to 0.622 and  $-0.231$  [15,16].

In our study, several hypotheses were taken into account. The comparison between the simulated spectrum of the alkyl radical and the experimental one is shown Figure 2.

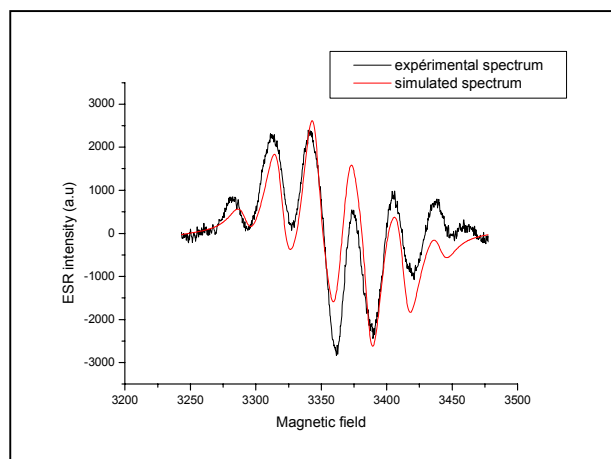


Figure 2: Comparison between simulated spectrum of the alkyl radical and the experimental one

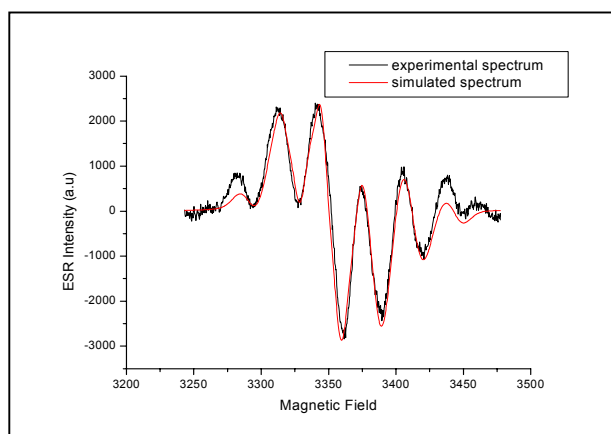


Figure 3: Comparison between the experimental spectrum and the simulated one based on a combinaison of alkyl (65 %) and allyl (35 %) radicals.

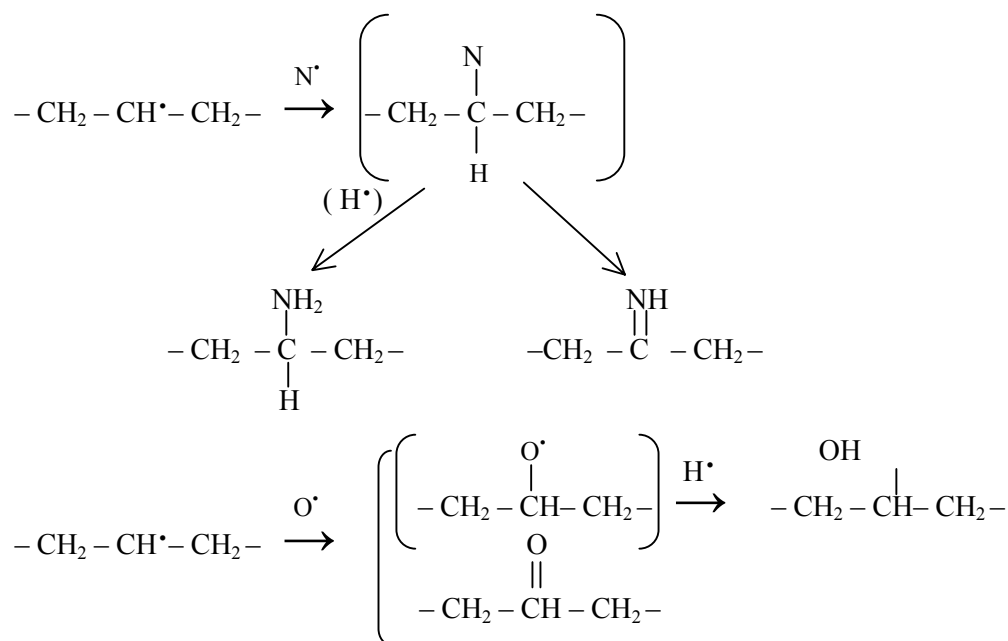
#### 4. Discussion and conclusion

From the results presented in this work, it is confirmed that the coupling between fluidized bed and far cold remote nitrogen plasma processes is efficient to modify surface properties of a PE powder. Its wettability increases, and the increase is better when 0.75 % of  $O_2$  is added to the nitrogen flow. BET surface area and powder density are not modified by the treatment; the average diameter of the particles increases from 283  $\mu m$  (before the treatment) to 312  $\mu m$  (after the treatment) due to the elutriation of the finest particles. The flowability of the powder is slightly altered by the treatment, due to the wettability increase which can lead to the formation of agglomerates due to capillary forces. XPS studies give evidence for the surface incorporation of oxygenated and nitrogenated functions, while ESR analyses reveal the presence of a mixture of alkyl and allyl radicals. An ageing in open air during 12 hours does not affect neither contact angle values nor grafted nitrogen and oxygen rates, while radicals are completely disappeared. So, the wettability seems mainly to be due to the fixation of new chemicals functions rather than the presence of radicals. On the other hand, these radicals can initiate the fixation of the new functions. In a previous work, performed in a smaller reactor [7], we gave evidence that new nitrogen and oxygen incorporated functions were amine, imine, amide and alcohol and carbonyl respectively. For instance, alkyl radicals can react with nitrogen atoms to produce the imine or amine function, with some hydrogen transfer and/or oxygen to produce alcohol and carbonyl groups according to the sequences:

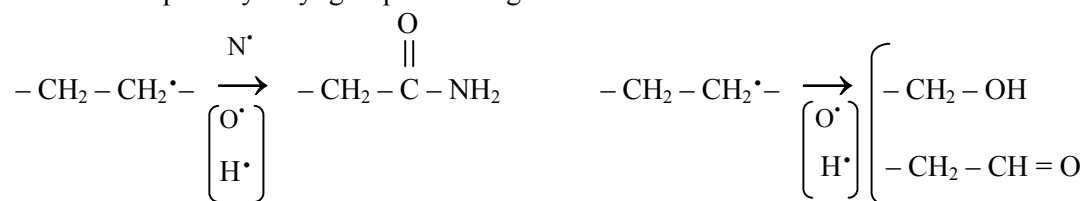
This fit is not as good as the one based on a combination of alkyl and allyl radicals. The best results were obtained (Fig.3) for a combination based on 65 % of alkyl radicals and 35 % of allyl radicals. For the alkyl radicals, the splitting can occur with the four equivalent  $H_\beta$  proton and the  $H_\alpha$  proton (the  $\alpha$  carbon is the atom on which the unpaired electron is primary located). The splitting constants, respectively equal to  $a_{H_\alpha} = 25.80$  G and  $a_{H_\beta} = 33.05$  G agree with literature data [14] which quote the  $a_{H_\alpha}$  value in the range 12-22 Gauss and the  $a_{H_\beta}$  value in the range 28-33 Gauss. For the allyl radical, the splitting constants, respectively equal to  $a_{H_\alpha} = 20.1$  G and  $a_{H_{\alpha'}} = 9.8$  G for  $H_\alpha$  and  $H_{\alpha'}$  protons agree also with data given by O'Neill *et al.*[14] (to  $a_{H_\alpha} = 20.2$  G and  $a_{H_{\alpha'}} = 7.5$  G).

As the XPS results give evidence for a nitrogen fixation on the treated PE (see Table 3), the hypothesis taking into account a splitting with a nitrogen atom was also considered, but had to be given up.

For  $\delta = 0$ , the treated PE-NO contains  $5.7 \cdot 10^{15}$  radicals per gram; as the polymer weight is  $4 \cdot 10^6$  gram / mol, it is equivalent to about 0.04 radicals per chain.



The imine function, exposed to wet air after the plasma treatment and before XPS analysis, may also be partly hydrolysed to form amide group. The amide, alcohol and carbonyl functions can also be created from a primary alkyl group according to:



These reactions, occurring in the plasma, can explain the weak level of radicals detected on the PE after the treatment, which only originate from the bulk. Disappearance of the ESR signal during the ageing after the plasma treatment is probably due to electron migration along the polymer chain and then paired.

## References

- [1] B. Mutel, O. Dessaux, P. Goudmand, F. Luchier Rev. Phys. Appl. **25**, 1019 (1990)
- [2] B. Mutel, C. Hoyez, P. Goudmand, O. Dessaux, L. Gengembre, J. Grimblot ISPC-12, Minneapolis, 167 (1995)
- [3] B. Mutel, J. Grimblot, P. Goudmand, O. Dessaux Surf. Interf. Anal. **30**, 401 (2000)
- [4] B. Mutel, J. Grimblot, V. Moineau, T. Colson, P. Goudmand, O. Dessaux Surf. Interf. Anal. **30**, 415 (2000)
- [5] P. Supiot, O. Dessaux, P. Goudmand, J. Phys. D: Appl. Phys. **28**, 1826 (1995)
- [6] O. Dessaux, P. Goudmand, B. Mutel, J. Quant. Spectrosc. Radiat. Transfer **29**, 49 (1983)
- [7] C. Vivien, C. Wartelle, B. Mutel, J. Grimblot, Surf. Interf. Anal. **34**, 575 (2002)
- [8] J. B. Leroy, N. Fatah, B. Mutel, J. Grimblot, Plasma and polym. In press
- [9] E. W. Washburn, Phys. Rev. Ser. 2, **17**, 273 (1921)
- [10] D. Geldart, Powder Technol. **7**, 285 (1973)
- [11] C. Y. Wen, Y. H. Yu, Aich E symposium. Ser. **62**, 100 (1966)
- [12] D. Geldart, Gas Fluidization Technology, J. Wiley, Chichester, England, p. 130 (1986)
- [13] Y. Hori, S. Shimada, H. Kashiwabara, Polymer **20**, 181 (1979)
- [14] P. O'Neill, C. Birkinshaw, J. J. Leahy, R. Barklie, Polym. Degrad. and Stab. **63**, 31 (1999)
- [15] H. C. Lefkowitz, J. Fain, F. A. Matsen, J. Chem. Phys. **23**, 1690 (1955)
- [16] C. Heller, H. K. McConnell, J. Chem. Phys., **32**, 1535 (1960)

# Nitriding of aluminum alloyed with magnesium by a DECR nitrogen plasma

Y. Bouvier<sup>1,2</sup>, D. Balloy<sup>3</sup>, B. Mutel<sup>1</sup>, J. Grimblot<sup>2</sup>

<sup>1</sup>Laboratoire de Génie des Procédés d'Interactions Fluides réactifs-Matériaux (UPRES-EA 2698)

<sup>2</sup>Laboratoire de catalyse de Lille (UMR CNRS 8010)

Université des Sciences et Technologies de Lille, 59655 Villeneuve d'Ascq cedex, France

<sup>3</sup>Laboratoire de Sciences des Matériaux

Ecole Centrale de Lille, BP 48, 59651 Villeneuve d'Ascq cedex, France

## Abstract

Aluminum alloyed with magnesium was nitrided using a Distributed Electron Cyclotron Resonance (DECR) nitrogen plasma. During the process, which included a pre-treatment by an Ar-H<sub>2</sub> plasma and a nitridation step, a negative bias voltage was applied to the substrate. The influence of the bias voltage value was investigated by Scanning Electron Microscopy and Electron Dispersion Spectroscopy. A nitrided layer 3  $\mu\text{m}$  thick has been obtained at the surface of the alloy and was analyzed by X-ray Photoelectron Spectroscopy.

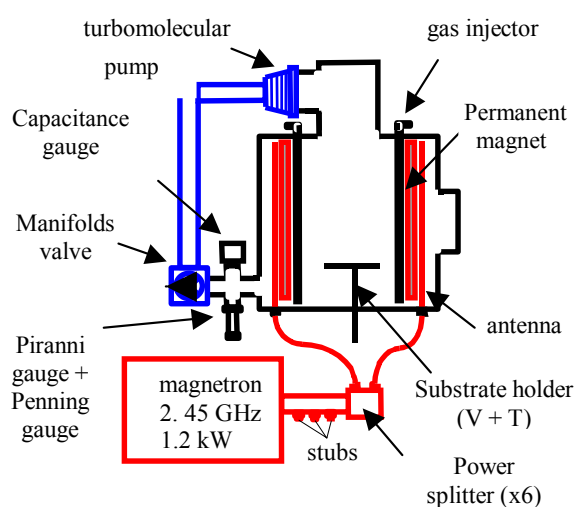
## 1. Introduction

At the present time, aluminum and its alloys, which have attractive properties such as low specific weight, corrosion resistance and good machinability, are considered as one of the most important materials in various fields. However, owing to their low surface hardness and wear resistance, modifications of their surface are necessary to develop future applications. So, recently, the aim of many studies was to improve the surface properties of Al and its alloys by the formation of an AlN layer which is known to have very interesting mechanical and physical properties. To reach this aim, ion beam implantation at low [1,2] and high energy [3-6] and plasma technologies [7-16] are largely involved.

In a previous work [14-16], we have shown that it was possible to obtain a dense AlN layer (6 nm thick) followed by a diffusion layer (0.3  $\mu\text{m}$  thick) when aluminum samples were treated by a Distributed Electron Cyclotron Resonance (DECR) nitrogen plasma. The substrate was biased with a D.C. negative voltage equal to -120 V and was always pre-treated for 1 hour by a Ar-H<sub>2</sub> plasma. The nitridation was performed at 500 °C.

In the present work, such a plasma is used to nitride aluminum alloyed with magnesium (4.5 % at.). Indeed, it seems that the presence of elements such as Mg, Si or Zn makes the aluminum nitridation easier [17], acting as catalysts or as oxygen traps. Treated samples are studied by X-ray Photoelectron Spectroscopy (XPS), Scanning Electron Microscopy (SEM) and Energy Dispersion Spectroscopy (EDS).

## 2. Experimental details



**The reactor:** the DECR plasma reactor is shown Fig.1. The vacuum system included a turbomolecular pump (500 NL/s) allowing a base pressure ( $p$ ) around  $10^{-5}$  Pa and an operating pressure around 0.1 Pa. The pressure was measured by a Pirani-Penning gauge and by a capacitance manometer. The microwave power ( $P$ ) was fed through six antenna rods located inside the periphery of the cylindrical stainless steel reactor (280 mm high, 400 mm diameter) and close to its wall. Six pairs of permanent magnets with alternated polarities were settled in front of the antenna and provided the magnetic field (875 Gauss) required to obtain the ECR coupling. Six injectors allowed to introduce the gases (which flow,  $Q$ , are regulated by mass flow controller) on the whole height of the reactor.

Figure 1: The DECR plasma reactor

**The sample treatment procedure:** substrates were commercial Al-5083 alloy (from Hoogovens Aluminium France), which atomic composition is shown Table 1.

Elements	Mg	Si	Fe	Mn	Cr	Zn	Cu	Ti	Al
at. %	4.94	0.38	0.19	0.34	0.08	0.10	0.04	0.08	94.00

Table 1: average atomic composition of Al-5083 alloy

At first, samples (19x7 mm<sup>2</sup>, 1 mm thick) were mechanically cleaned (using 28  $\mu$ m, 7  $\mu$ m and 3  $\mu$ m grit silicon carbide paper), polished to mirror finish using 3  $\mu$ m diamond past, ultrasonically cleaned in methanol (10 min at 25°C) and dried for 2 min at 60°C. Then, they were introduced in the DECR plasma reactor, and the process was conducted as follow:

1. Evacuation of the chamber to  $p \approx 10^{-4}$  Pa
2. Pre-treatment of the substrate with an Ar-H<sub>2</sub> plasma (Ar purity > 99.999 % , H<sub>2</sub> purity > 99.9999 % , Q<sub>Ar</sub> = 5 sccm and Q<sub>H2</sub> = 10 sccm, p<sub>Total</sub> = 1 Pa, P<sub>transmitted</sub> = 800W). During this step, which duration was 1 hour, the substrate was biased with a negative D.C. voltage (denoted by V<sub>p</sub>) and heated from 20°C to 475°C with a rate equal to 7.6°C/min.
3. Nitriding of the substrate with a nitrogen plasma for arbitrarily 1 hour (N<sub>2</sub> purity > 99.999 % , Q<sub>N2</sub> = 16 sccm, p<sub>Total</sub> = 0.2 Pa, P<sub>transmitted</sub> = 800 W). The substrate temperature remained equal to 475°C and was biased with a negative D.C. voltage denoted by V<sub>n</sub>.
4. Cooling of the substrate to 20°C for 12 hours under a pressure around 10<sup>-4</sup> Pa.
5. Removing of the substrate out of the reactor. In case of XPS analysis, the exposure to ambient air never exceeded 10 minutes.

**Surface characterization:** XPS analyses were performed using a Leybold LHS 10 system ( Al K $\alpha$  X- ray source: 1486.6 eV, anode voltage 13 kV, current emission: 20 mA). In order to obtain a depth profile of the samples, Ar<sup>+</sup> etching sequences were performed in the spectrometer (7 mA, 600 V, 2 kV). The angle between the Ar<sup>+</sup> beam and the sample was 90°. The spectra were curve fitted using the peak fit<sup>®</sup> software. Shirley background and Gaussian-Lorentzian curve type were used for data fitting.

Samples were examined using a Scanning Electron Microscope Hitachi 2500 with an attached energy dispersive X-ray micro-analysis system Kevex to provide local atomic composition. The accelerated voltage was 15 keV.

### 3. Results and discussion

**Samples after mechanical polishing:** XPS analysis of the mechanically polished Al-5083 substrate reveals

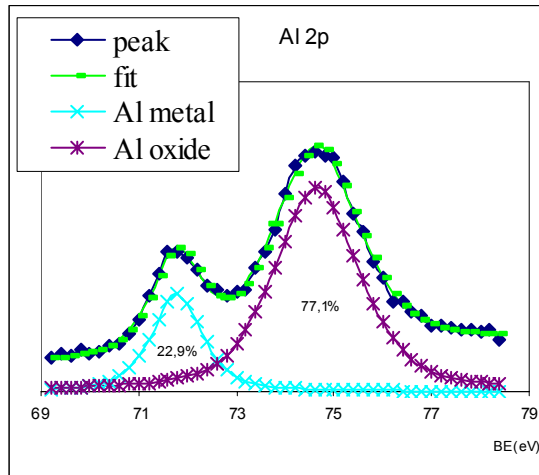


Figure 2: Decomposition of the Al 2p peak after the mechanical polishing step

an important oxygen rate (57%) at the surface samples. The decomposition of the Al 2p peak (Fig.2) reveals that 77 % of Al is in an oxide environment (Binding Energy (BE) = 74.6 eV ) and 23 % is in a metallic state (BE = 71.8 eV). These results confirms that a pre-treatment of the substrate with an Ar-H<sub>2</sub> plasma is required after polishing and before the nitridation step in order to reduce the native oxide layer. Streaks due to the polishing step can be seen by SEM (Fig.3a). EDS analysis confirms manufacturer composition data.

**Pre-treated samples:** During the pre-treatment step by the Ar-N<sub>2</sub> plasma, two V<sub>p</sub> values were used (-120 V and - 450 V) and at first, their influences were studied by XPS. The surface of the sample pre-treated at V<sub>p</sub> = - 120 V is constituted by magnesium oxide (60 %), aluminum oxide (25 %) and metallic aluminum (15%). These calculations agree with the decomposition of the Al 2p peak shown in Fig.4. The migration of Mg towards the surface is due both to the high temperature effect and to the radiation induced segregation effect [18]. Then the

Mg present at the surface of the alloy can react with the Al<sub>2</sub>O<sub>3</sub> layer to form MgO according to the reaction:  $3 \text{ Mg} + \text{Al}_2\text{O}_3 \rightarrow 3 \text{ MgO} + 2 \text{ Al}$  for which the Gibbs energy formation is equal to - 45 kcal [19]



For the sample pre-treated with  $V_p = -450$  V, metallic Al amount is approximately equal to 40 %, while the percentage of Mg and aluminum oxides are equivalent and equal to 30 %. The strong decrease of magnesium oxide percentage can be explained by the high sputtering yield of MgO in comparison with the  $Al_2O_3$  one [19]. The destruction of MgO could lead to the one of  $Al_2O_3$  and explain the increase of the metallic aluminum rate. However, it is to note that the samples being exposed to ambient air before the analysis, the true composition of the sample surface before the nitriding step may be slightly different (less oxidized). SEM micrographs of the surface samples shows that streaks due to the polishing step are no more visible. Hollows containing Mn (3 %), Fe (1 %) and a high level of Si (ranging from 33 to 40 %) can be seen (Fig.3b) whatever the  $V_p$  value, but they are more numerous for samples treated at  $V_p = -450$  V.

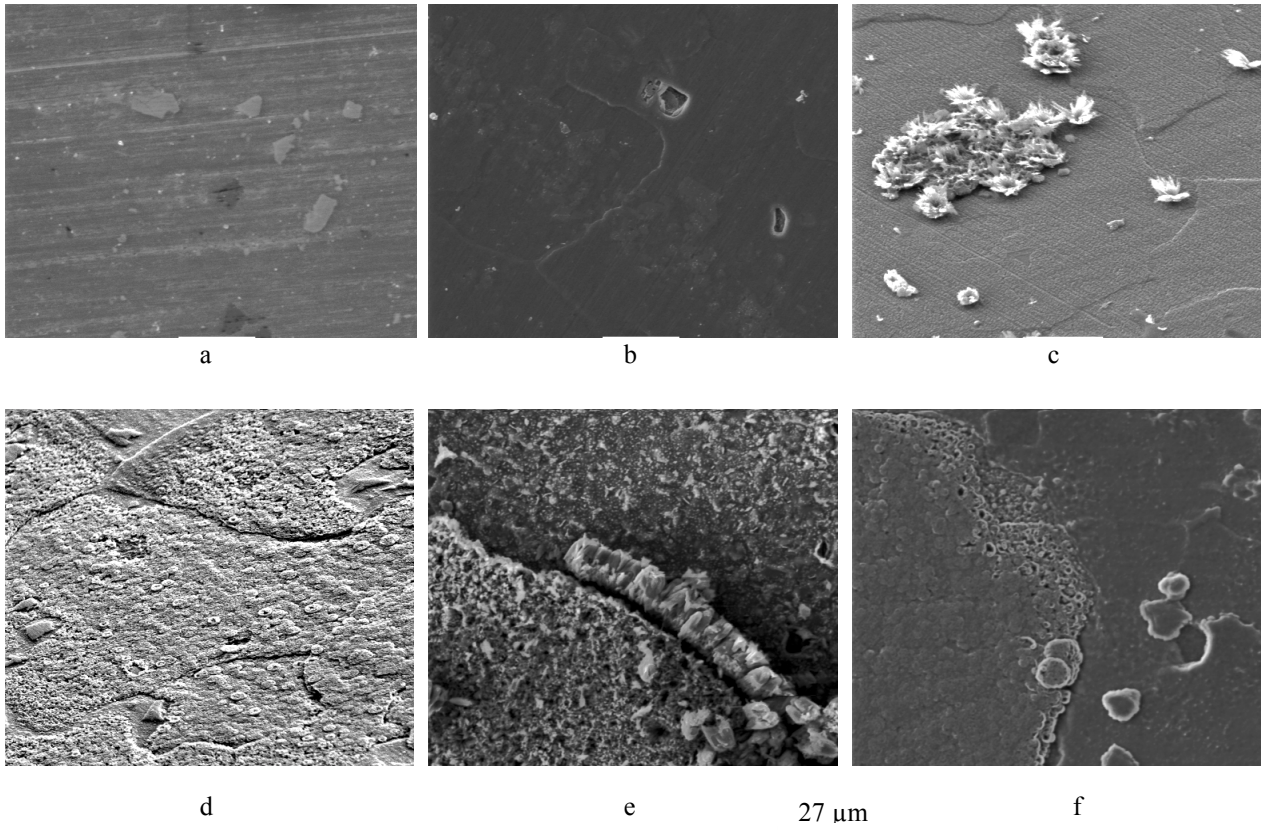


Figure 3: SEM micrographs of the Al - 5083 surface (x 1010); a: after the mechanical polishing; b: pre-treated at  $V_p = -120$  V; c: treated with  $V_p = -120$  V,  $V_n = -120$  V (C1); d: treated with  $V_p = -120$  V,  $V_n = -450$  V (C2); e: treated with  $V_p = -450$  V,  $V_n = -120$  V (C3); f: treated with  $V_p = -450$  V,  $V_n = -450$  V (C4).

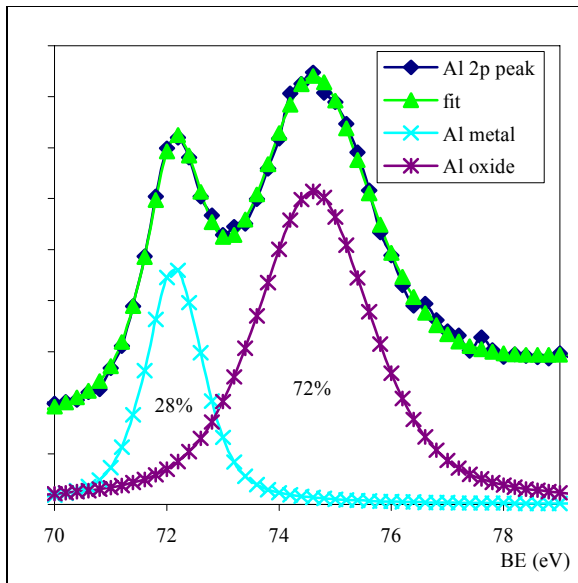


Figure 4: Decomposition of the Al 2p peak of the sample pre-treated at  $V_p = -120$  V

**Nitrided samples:** Four nitriding conditions (denoted by C1, C2, C3, C4) were used in this study (C1:  $V_p = -120$  V,  $V_n = -120$  V; C2:  $V_p = -120$  V,  $V_n = -450$  V; C3:  $V_p = -450$  V,  $V_n = -120$  V; C4:  $V_p = -450$  V,  $V_n = -450$  V). The nitrided samples were firstly studied by SEM and EDS.

A lot of protuberances containing about 14 % of N and 12 % of Mg can be seen at the surface of the C1 nitrided sample (Fig.3c). The cross-sectional EDS analysis, not shown in this paper, gives evidence for a segregation of Mg at the uppermost surface, but no layer or diffusion zone containing nitrogen is observed.

The surface of the C2 nitrided sample (Fig.3d) is mainly constitute of grains which diameter is  $\leq 3\mu\text{m}$ .

The distribution of these grains is not uniform and the presence of terraces and hollows (containing Si, Mn and Fe) can be noticed.

The cross-section analysis (Fig.5 ) reveals the formation of a layer, about 3 $\mu$ m thick and mainly constituted of Al (55 %) and N (39 %).

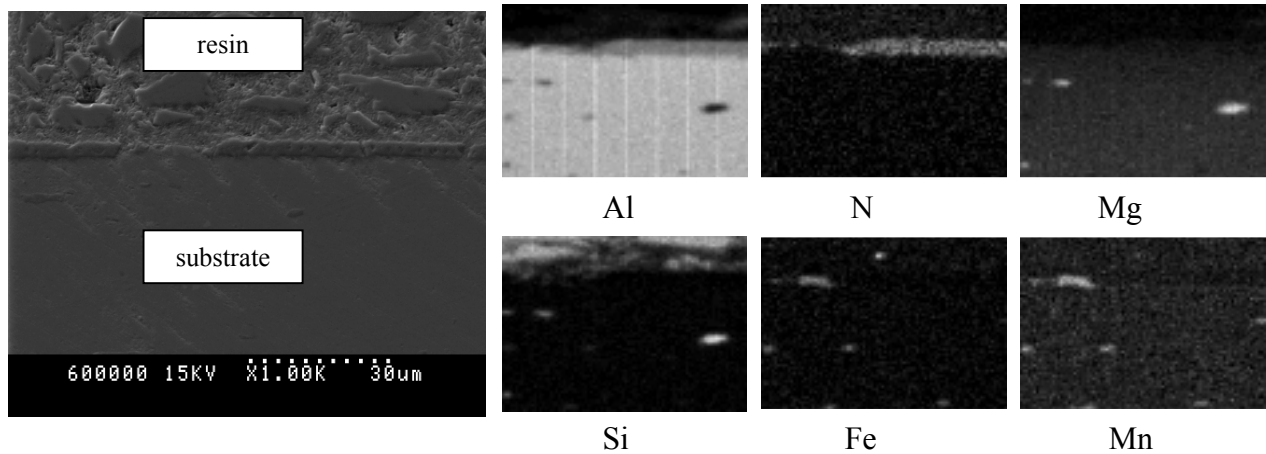


Figure 5: Cross-section analysis of the C2 nitrided sample.

The surface of the C3 nitrided sample (Fig.3e) looks very porous and a lot of cracks can be seen. The cross section analysis (Fig.6) reveals a layer which contains about 25 % of N and 75 % of Al.

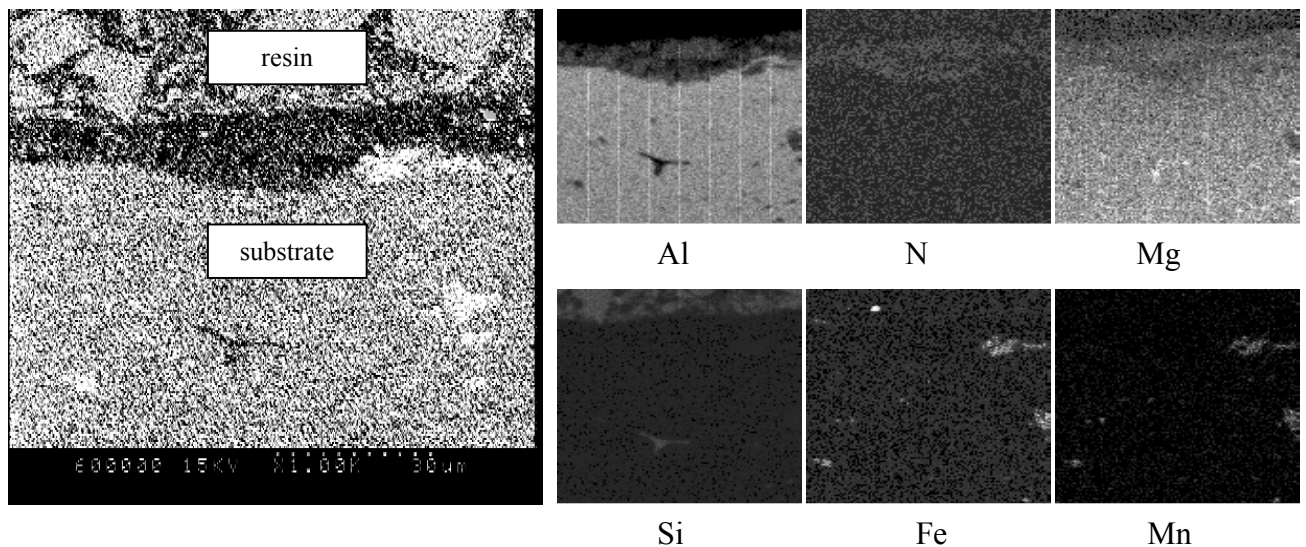


Figure 6: Cross-section analysis of the C3 nitrided sample

Its thickness is ranging from 10 to 20  $\mu$ m, but its adhesion to the substrate is rather poor. The numerous Mn and Fe inclusions which were observed at the surface of the sample pre-treated at  $V_p = -450$  V may be potential nuclei where the aluminum nitride begins to grow.

Some hollows can be seen on the surface of the C4 nitrided sample (Fig.3f), but the adhesion is rather good. A layer which thickness is ranging from 3 to 7  $\mu$ m is formed. This layer is mainly constituted by 66 % of Al and 33 % of N.

From these studies, it seems that the best nitridation was obtained with condition C2. Sample nitrided in these conditions were studied by XPS. N 1s, Al 2p, O 1s, Mg 1s and Mg 2p peaks were detected.

The BE(N 1s) – BE(Al 2p) difference equal to 323.0 eV, gives evidence for the presence of aluminum nitride [20]. The full width at half maximum (FWHM) of N 1s and Al 2p peak are respectively equal to 2.1 and 2.2 eV and remain stable whatever the duration ( $\delta$ ) of the  $Ar^+$  etching sequence in the spectrometer.

As it can be seen in Fig.7, the atomic percentages (x) of Al, O, N and Mg are quite stable whatever  $\delta$  ( $x_{Al} \approx 50\%$ ,  $x_N \approx 36\%$ ,  $x_{Mg} \approx 1\%$ ,  $x_O \approx 19\%$ ) and are in good agreement with the EDS analysis.

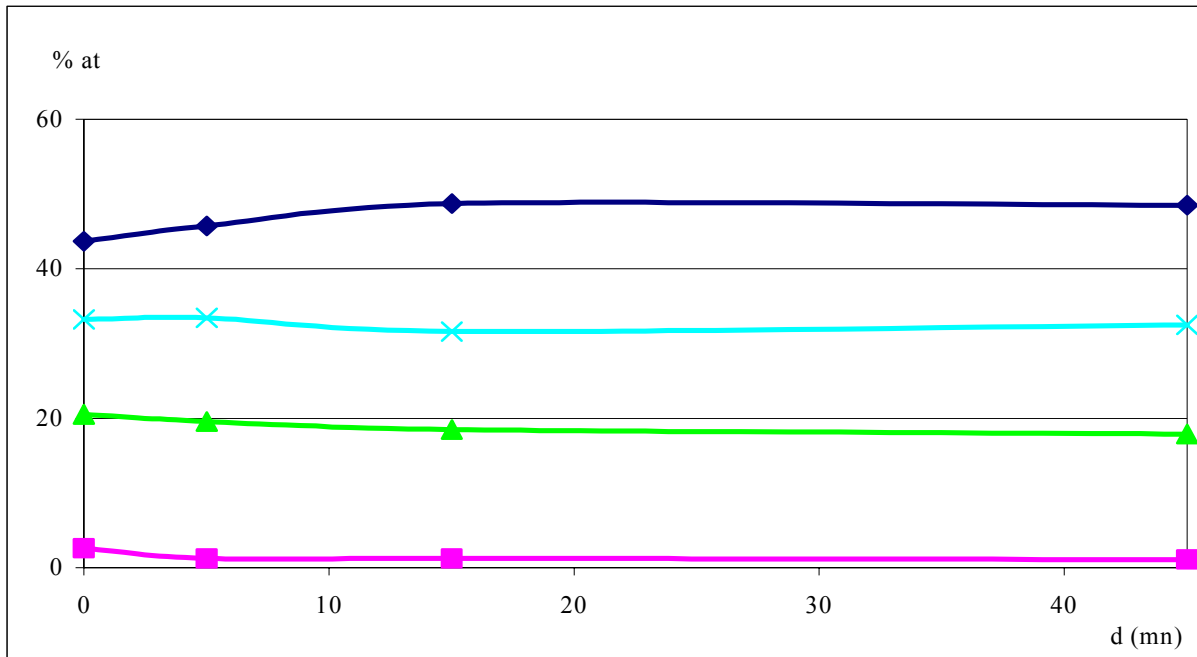
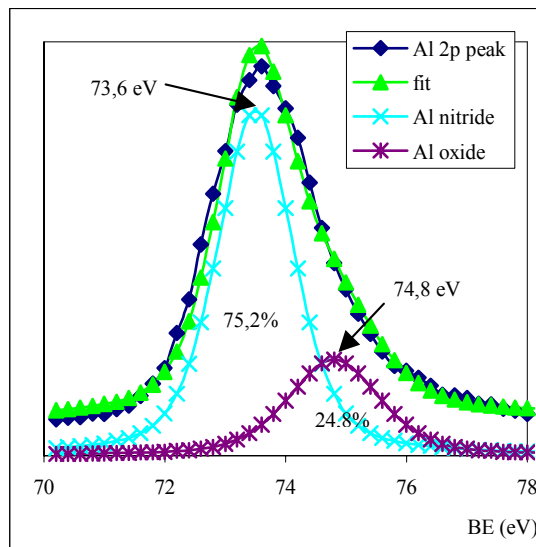


Figure 7: Profile of the C2 nitrided sample, legende:  $\blacklozenge$  Al;  $\times$  N;  $\blacktriangle$  O;  $\blacksquare$  Mg



The decomposition of the Al 2p peak (Fig.8) shows that about 75 % of the aluminum is in a nitride environment and 25 % is in an oxide one. From that decomposition and atomic percentages, it appears that the surface of the C2 nitrided sample is constituted by AlN ( 78 % ),  $Al_2O_3$  ( 14.6 % ), MgO ( 4.9 % ) and  $Mg_3N_2$  ( 2.4 % ). The nitridation of magnesium was evidenced from its Auger parameter [21]. The strong decrease of MgO and  $Al_2O_3$  percentage in comparison with these observed after the pre-treatment step can be due to a sputtering effect during the nitridation which occurs at  $-450$  V. As no diffusion layer was observed, it seems that the nitride layer grows due to the Al diffusion from the underlying bulk toward the surface. Such a mechanism was evidenced by T.Telbizowa *et al.* thanks to the implantation of  $N^{14}$  and  $N^{15}$  [22].

Figure 8: Decomposition of the Al 2p peak of the C2 nitrided sample

## Conclusion

A nitrided layer  $3\mu m$  thick can be obtained at the surface of an Al-5083 substrate treated by a DECR plasma including a pre-treatment by a Ar- $H_2$  plasma and the nitridation by a  $N_2$  plasma. The process performed at  $475^\circ C$  required a negative dc bias voltage polarization. Taking into account our experimental results, it seems that the different steps occuring during the process involved in this paper can be summarized as follows:



- during the pre-treatment :
  - i, magnesium segregation towards the surface under thermal and radiation effect,
  - ii, reaction between Mg and  $\text{Al}_2\text{O}_3$  to form  $\text{MgO}$ ,
  - iii, an increase of bias voltage favours  $\text{MgO}$  sputtering as well as the appearance of Fe, Mn and Si inclusions at the surface.
- during the nitridation:
  - i, adsorption and/or implantation of nitrogen ions or molecules at the surface,
  - ii, diffusion of Al towards the surface under the temperature effect,
  - iii, formation of  $\text{AlN}$  nuclei,
  - iv, growth of the  $\text{AlN}$  layer either by an increase of the  $\text{AlN}$  nuclei (low  $V_n$  value), or by implantation (high  $V_n$  voltage),
  - v, the nitrided layer constituted a barrier to the diffusion of Al.

## References

- [1] T. Reier, J.W. Schultze, W. österle, Chr. Buchal, Surf. Coat. Technol. **103-104**, 415 (1998).
- [2] S. Simson, T. Reier, J.W. Schultze, Chr. Buchal, Surf. Coat. Technol. **83**,49 (1996)
- [3] V.V. Uglov, N.N. Cherenda, A.L. Danilyuk, V.V. Khodasevich, A. Wenzel, J. Gerlach, B. Raushenbach, Surf. Coat. Technol. **103-104**, 312 (1998)
- [4] A.P. Matthews, M. Iwaki, Y. Horino, M. Satou, K. Yabe, Nucl. Instr. Meth. **B59/60**, 671 (1991)
- [5] S. Lucas, J. Chevalier, Surf. Coat. Technol. **51**,441 (1992)
- [6] H.L. Lu, W.F. Sommer, M.J. Borden, J.R. Tesmer, X.D. Wu, Thin Solid Films, **289**,17 (1996)
- [7] M. Quast, P. Mayr, H.R. Stock, H. Podlesak, B. Wielage, , Surf. Coat. Technol., **135**, 238 (2001)
- [8] N. Renevier, T. Czerwec, A. Billard, J. Von Stebut, H. Michel, Surf. Coat. Technol. **116-119**, 380 (1999)
- [9] T Arai, H. Fujita, H. Tachikawa, 1<sup>st</sup> Intern.Conf. Ion Nitriding, T. Spalvins (Ed).Cleveland, USA, 37 (1986)
- [10] H.R. Stock, C. Jarns, F. Seidel, J.E. Döring, Surf. Coat. Technol. **94-95**, 247 (1997)
- [11] T Ebisawa, R. Saikudo, Surf. Coat. Technol. **86-87**, 622 (1996)
- [12] S. Greedelj, A.R. Gerson, S. Kumar, G. P. Cavallaro, Appl. Surf. Sci. **174**, 240 (2001)
- [13] P. W. Wang, S. Sui, W. Wang,, W. Durrer, Thin Solid Films, **295**, 142 (1997)
- [14] N. Duez, B. Mutel, J. Grimblot, O. Dessaux, P. Goudmand, C. R. Acad. Sci. Paris, **t. 327, serie II b**:1191 (1999).
- [15] N. Duez, B. Mutel, O. Dessaux, P. Goudmand, J. Grimblot, Surf. Coat. Technol. **125**,79 (2000).
- [16] N. Duez, B. Mutel, C. Vivien, L. Gengembre, P. Goudmand, O. Dessaux, J. Grimblot, Surf. Sci. **482-485**,220 (2001).
- [17] H. Scholz, P. Greil, J. Mat. Science, **26**, 669 (1991)
- [18] S. Schoser, G. Brauchle, J. Forget, T. Weber, J. Voigt, Surf. Coat. Technol., **103-104**, 222 (1998).
- [19] R. A. Swalin, Thermodynamics of solids, John Wiley and Sons, New York, London, Toronto (1972)
- [20] G. Betz, G.K. Wehner, Sputtering by Particle Bombardement, R. Behrisch (Ed.), 2, Berlin (1983)
- [21] H.K. Sanghera, J.L. Sullivan, Surf; Interf. Anal; **27**, 678 (1999)
- [22] B. Mutel, Y. Bouvier, J. Grimblot, E-MRS, Strasbourg (2003)
- [23] T. Telbizova, S. Parascandola,U. Kreissig, G. Günzel, W; Möller, Appl. Phys. Lett. **76**, 1404 (2000)

# **$\text{N}_2(\text{C}^3\Pi, v''=0,1,2,3,4)$ emissions in the Short Lived Afterglow of a pulsed microwave nitrogen discharge**

M. Grushin, C. Foissac, C. Dupret, and P. Supiot

*Laboratoire de Génie des Procédés Fluides Réactifs-Matériaux UPRES EA 2698  
Université des Sciences et Technologies de Lille, 59 655 Villeneuve d'Ascq Cedex, France.*

## **Abstract**

This paper presents the study of the so-called Short-Lived Afterglow induced under long duration pulsed conditions downstream from a nitrogen microwave discharge (pressure of 2-3 Torr) mainly through  $\text{N}_2(\text{C}^3\Pi, v'=0-4)$  emissions. The kinetics of the excitation processes of this specie in the SLA is discussed.

## **1. Introduction**

Fundamental aspects of nitrogen discharge kinetics are now quite well understood concerning the controlling parameters and electron energy delivery. The so-called Short-Lived Afterglow (SLA) taking place downstream from the discharge is a very exciting medium for new data determination as model inputs. Previous special investigations [1,2,3] were carried out concerning the relaxation of the Electron Energy Distribution Function (EEDF) and of the electron density and neutral species excitation in the SLA. The probe measurements compared with the results of a detailed kinetic model for the post-discharge showed the presence in the SLA of the electrons with energy less than 6 eV. Indeed, progress in model accuracy could arise by taking account of secondary processes among which energy exchanges between low-energy electrons and neutral species and between neutrals.

The scope of the present work is to analyse the SLA induced under pulsed conditions. The present study is focused on  $\text{N}_2(\text{C}^3\Pi_u)$  emissions observed also in the SLA region. These emissions are characteristic of the second positive emission system of  $\text{N}_2(2^+)$ . The high energy level of this specie ( $E > 11$  eV) allows us to discuss the kinetics of the excitation processes in the SLA.

## **2. Experimental section**

Spectroscopic experiments on dynamics of different transitions of the second positive system of nitrogen were carried out during discharge pulse and post-discharge periods from the discharge zone to the bulk of the SLA.

A sketch of experimental set up is shown in Fig. 1. The discharge is generated by a 433 MHz or 2450 MHz coaxial resonant cavities (Fig. 1) in flowing nitrogen in a Pyrex tube (38 mm inner diameter). Experiments were performed at gas pressures ranging from 2 - 3 Torr and flow-rate 0.72, 1.45 and 2.0 slpm. A rectangular signal triggering generator allows to deliver modulated microwave pulses from the power supply (microwave generator: 433 MHz (2450 MHz), max  $P_{\text{out}}$  400 W). The discharge pulse duration ( $T$ ) and frequency ( $\nu$ ) were varied from 160 to 400 ms and 5 - 1 Hz in order to reach steady state regime. The microwave power transmitted to the discharge pulses was 300 W. Rise time of the peak power from 0 to 300 W is 1 ms, down time - 5  $\mu\text{s}$ . Thus, pulse duration (160 - 400 ms) was long enough to reach a steady state of emissions.

The emissions from the discharge to the bulk of the SLA are collected by a lens and an optical fibre situated on the lens focal distance (Fig. 1). Each position of this optical system is described by the distance  $L$  from the gap centre ( $L=0$ ) to that of the studied volume. The collected signal is recorded with a long-focal-length monochromator THR-1000 ( $f=1$  m, 1200 grooves per mm grating) equipped with R446 photomultiplier (PMT). Minimal temporal resolution of 2  $\mu\text{s}$  was obtained. Signal from PMT was recorded with digital oscilloscope triggered from down front of the pulse by the rectangular pulses generator. Resulting spatial resolution of the optical system is about 0.5 cm.

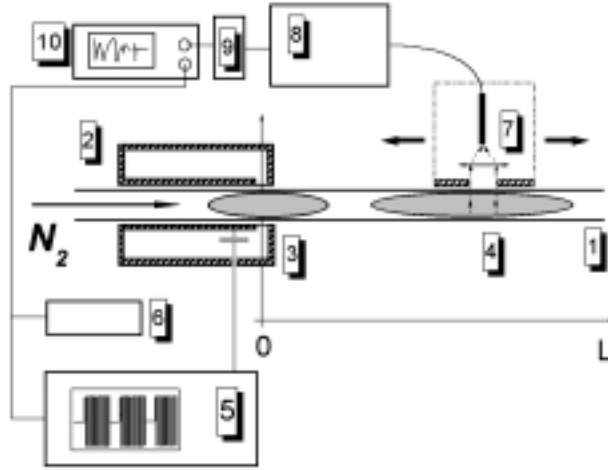


Fig. 1: experimental set-up :1) Pyrex tube; 2) microwave cavity; 3) discharge; 4) SLA; 5) microwave generator;6) triggering generator of rectangular pulses; 7) optical fibres and lens; 8) monochromator; 9) PMT; 10) oscilloscope.

### 3. Experimental results:

The relative intensity axial profiles of the emission of the second positive system during the discharge pulse obtained by moving the optical system at 1.44 slpm are shown on Fig. 2. The resulting profiles typically reproduce the shape previously obtained with the complete steady system [4]. These normalised curves show slight differences essentially due to microwave coupling device properties.

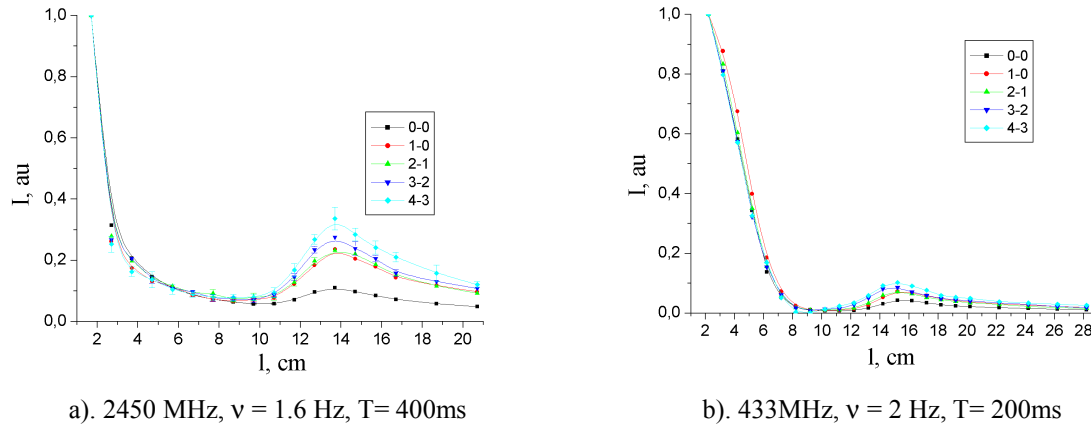
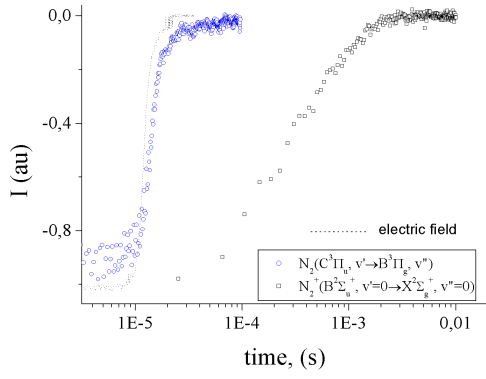


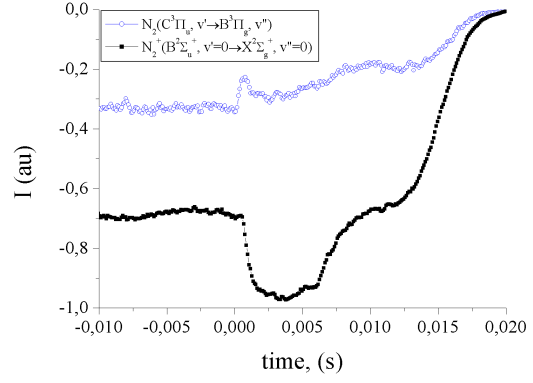
Fig. 2:  $N_2(C^3\Pi_u, v'' \rightarrow B^3\Pi_g, v')$  transition emission intensity along the tube during the discharge pulse ( $P = 3$  Torr, 1.44 slpm)

We can observe on Fig. 3 different temporal behaviours of the second positive and first negative ( $1^-$ ) emission systems for two distances along the gas flow (a)  $L=2$ cm, (b)  $L= 13.2$  cm: a fast drop of the  $2^+$  emission intensity correlatively with the electric field amplitude is seen for both positions ; and a long lived afterglow (about 2 ms) in discharge zone for  $1^-$  system and a much longer duration for both emissions (about 20 ms) due to both kinetics and gas carrying.

Dynamics of different transitions of the second positive system for different distances  $L$  (cm) after switching-off discharge pulse are shown on Fig. 4 – 7 (2450MHz, 1.44 slpm, 3 Torr,  $\nu = 1.6$  Hz,  $T = 400$ ms). Time  $t = 0$  s corresponds to down front of the rectangular pulse.

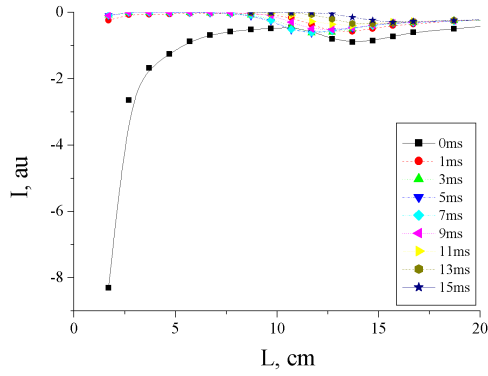


(a) discharge region

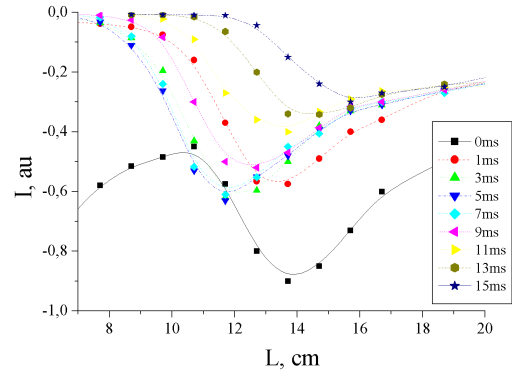


(b)  $L = 13.2$  cm

Fig. 3: temporal evolution of the emission intensity of  $N_2^+(B^2\Sigma_u^+, v'=0 \rightarrow X^2\Sigma_g^+, v''=0)$ ,  $N_2(C^3\Pi_u, v' \rightarrow B^3\Pi_g, v'')$  transitions ( $P = 3$  Torr,  $1.44$  slpm,  $v = 2$  Hz,  $T=400$ ms).

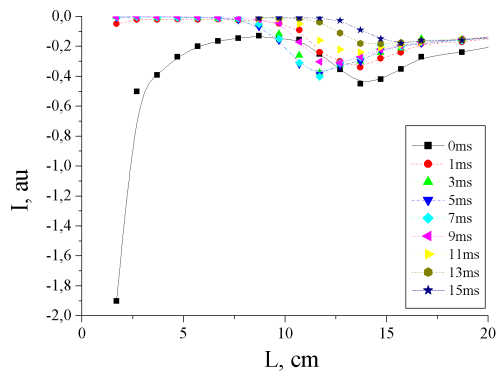


(a) Full scale picture

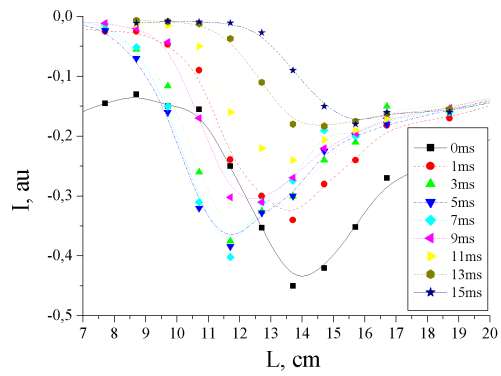


(b) Zoomed picture

Fig. 4. Spatial-temporal behaviour of  $N_2(C)$  emissions ( $\lambda = 3371\text{\AA}$ , 0-0)

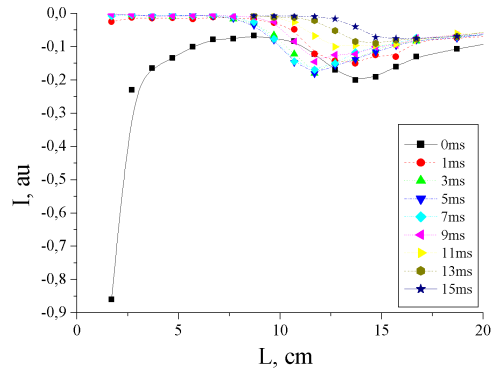


(a) Full scale picture

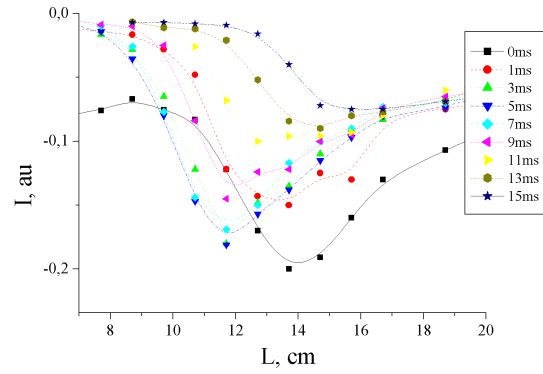


(b) Zoomed picture

Fig. 5. Spatial-temporal behaviour of  $N_2(C)$  emissions ( $\lambda = 3159\text{\AA}$ , 1-0)

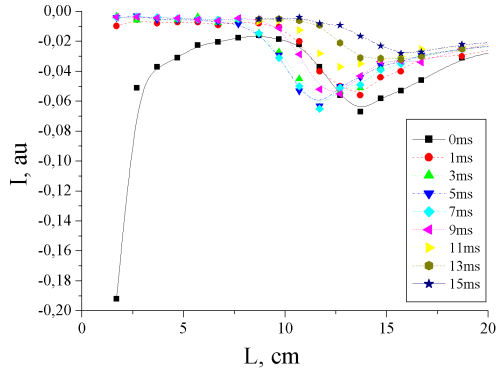


(a) Full scale picture

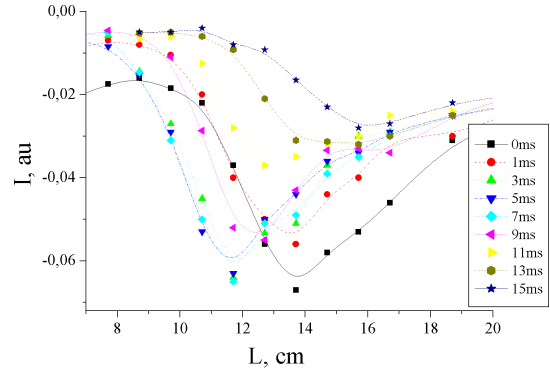


(b) Zoomed picture

Fig. 6. Spatial-temporal behaviour of  $N_2(C)$  emissions ( $\lambda = 3136\text{\AA}$ , 2-1)



(a) Full scale picture



(b) Zoomed picture

Fig. 7. Spatial-temporal behaviour of  $N_2(C)$  emissions ( $\lambda = 3104\text{\AA}$ , 4-3)

Experiments were made for different flow rates, repetition frequencies and pulse duration. One should notice that these shapes and emission dynamics of the second positive system after discharge pulse do not depend on the pulse duration.

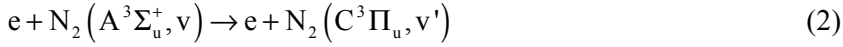
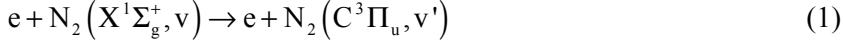
One can emphasise two common characteristic features of measured dynamics of  $N_2(C^3\Pi_u, v'=0,1,2,3,4)$  populations for all conditions. The first one is a rapid emission fall after the discharge switching-off in the discharge zone and in the dark region (Fig. 3) ; the second one is a small emission decrease and movement to positions closer to cavity in SLA region during first 5ms after discharge pulse switching-off. This shift is about 2 cm. Besides there are some differences in dynamics of different vibrational levels of the  $N_2(C^3\Pi_u)$  state in SLA region. Firstly, one could see on Fig. 2. that during discharge pulse the high levels are more intensively populated than the lower ones. Secondly, after switching off the discharge pulse the population of the  $v'=0$  level decreases more strongly than that of the levels  $v'=1-4$ , the latest one being much less affected.

Fig. 4 –7 also show that after 5 ms the position of maximum emission intensity for each emitter is stabilised during approximately 3 – 4ms. Within this period the signal relative to  $v'=0$  is roughly a third less than during the discharge pulse ( $t=0\text{ms}$ ). On the contrary, for level  $v'=4$ , the intensity level is unchanged.

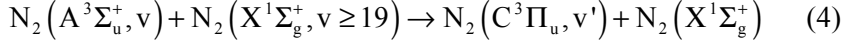
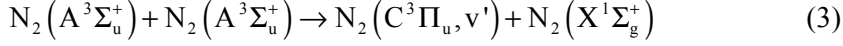
#### 4. Discussion:

The  $N_2(C^3\Pi_u, v')$  excitation occurs through two different mechanisms:

- direct electron impact excitation:



- pumping by metastable molecule interaction.



From profiles of the fast drop of the  $2^+$  emission signal with decreasing the electric field (Fig.3.a) one can conclude that processes (1) and (2) play a main role in  $N_2(C^3\Pi_u, v')$  states excitation during discharge pulse in discharge region.

On the contrary, the remaining of a high intensity of  $N_2(C^3\Pi_u, v')$  emission in the SLA after the discharge pulse switching-off (Fig.3.b and Fig.4-7) shows the predomination of metastable molecules in the  $N_2(C^3\Pi_u, v')$  pumping process (channels (3) and (4)). As shown by the long-life dynamics of the first negative system (Fig. 3 a, b), large amount of metastable molecules like  $N_2(X^1\Sigma_g^+, v \geq 12)$  and  $N_2(A^3\Sigma_u^+)$  [5] are leaving the discharge region. In previous investigations [6], the axial profile of the absolute density of  $N_2(A^3\Sigma_u^+)$  was determined under steady state conditions and showed the presence this molecule at equivalent time as large as 1 ms.

One should notice the small but quick decrease of  $N_2(C^3\Pi_u, v')$  emission intensity after switching-off the discharge pulse simultaneously with the electric field (Fig. 3b – 7). This suggests that electrons could be responsible of this contribution to the  $N_2(C^3\Pi_u, v')$  excitation. Previous work through electrostatic probes measurements [1,2,3] showed the presence of low energy electrons was shown (less than 6 eV) in the SLA. Obviously, this behaviour of  $N_2(C^3\Pi_u, v')$  arises from the influence of the interaction of the low energy electrons and  $N_2(A^3\Sigma_u^+, v)$  molecules (process (2)) in SLA during discharge pulse. As a consequence this demonstrates that there is a small heating of the electrons also within the SLA. This region is then not completely field free. This fact also makes proof of the contribution of processes involving neutral species to excitation of  $N_2(C^3\Pi_u, v')$ . From Fig. 4-7 which shows the trend of these emissions, we can conclude that roughly a third of  $N_2(C^3\Pi_u, v'=0,1)$  species is produced by process (2) and two thirds by processes (3) and (4) during the discharge pulse. This interpretation is qualitatively consistent with the decrease of the population field-sensitivity when increasing  $v'$  as undoubtedly shown by Fig. 7. Indeed according to Franck-Condon principle, the  $v'=0, 1$  levels significantly production by electron impact on the contrary of level  $v'=4$  which is mainly produced by pooling reactions (3) and (4). It is not presently possible to identify the dominant process among the previously mentioned (3) and (4) ones, despite the fact that reaction (3) is much more considered in the literature for pumping by metastable interaction.

Modelling investigations [5,7] have shown that the vibrationally excited molecules  $N_2(X^1\Sigma_g^+)$ , at high levels, play a major role in the appearance of SLA due to an efficient near resonant Vibration-Vibration energy-exchange collisions (V-V). V-V and Vibration-Translation (V-T) rates are strongly dependent on the gas temperature. Translation relaxation favours the V-V pumping within the  $N_2(X^1\Sigma_g^+)$  manifold. We suppose that in conditions of the pulse discharge the gas temperature decreases more faster than in steady-state regime. It can explain SLA spatial moving to positions closer to cavity after switching of the discharge pulse (Fig. 4 – 7). This result shows good quality agreement with theoretical calculations [7].

#### 5. Conclusions:

Experimental studies on population dynamics for numerous levels of  $N_2(C^3\Pi_u)$  ( $v' \leq 4$ ) were performed by optical emission spectroscopic measurements on long pulse microwave discharges in pure nitrogen and in afterglow at pressure 2-3 Torr. Specific features in time behaviour of levels populations  $N_2(C^3\Pi_u)$  was revealed, a main one being a unambiguous evidence of excitation by electron impact from the  $N_2(A^3\Sigma_u^+, v)$ . Results of comparison between the obtained experimental data and theory show a good qualitative agreement, while further detailed studies are necessary to achieve a numerical coincidence of predicted and measured quantities.

## References:

- [1] F.M. Dias, P. Supiot, V. Guerra, C. Dupret, T. Popov, P.A. Sá and J. Loureiro, Proceedings of 15<sup>th</sup> International Symposium on Plasma Chemistry, (2001) Orléans – France p.545-550
- [2] E. Eslami, A. Campargue, C. Foissac, P. Supiot, and N. Sadeghi, 15<sup>th</sup> International Symposium on Plasma Chemistry, Taormina – Italy (2003)
- [3] V. Guerra, F.M. Dias, C. Dupret, P. Supiot, T. Popov, P.A. Sá and J. Loureiro, IEEE Plasma Transaction (2003) (to be published)
- [4] P Supiot, D Blois, S De Benedictis *et al*, J. Phys.D:Appl.Phys., **31** (1998) 2521.
- [5] J. Loureiro, P. Sá, and V. Guerra, J. Phys. D: Appl. Phys., **34** (2001) 1769.
- [6] N. Sadeghi, C. Foissac, and P.Supiot, J.Phys.D:Appl.Phys. **34** (2001)1779–178
- [7] P. Sá, V. Guerra, P. Supiot and J. Loureiro, Proceedings of 15th Int. Symp. Plasma Chem., ISPC 15, Orléans, France, July 9-13, (2001) 985-990

# Plasma polymer coatings deposited from hexamethyldisilazane downstream a microwave nitrogen plasma jet.

C. Vivien<sup>1</sup>, R. Mascart<sup>1</sup>, C. Dupret<sup>1</sup>, P. Dhamelincourt<sup>2</sup>, L. Gengembre<sup>3</sup>, and P. Supiot<sup>1</sup>

<sup>1</sup> Laboratoire de Génie des Procédés Fluides Réactifs-Matériaux UPRES EA 2698

<sup>2</sup> Laboratoire de Spectrochimie Infrarouge et Raman UMR-CNRS 8516

<sup>3</sup> Laboratoire de Catalyse de Lille UPRESA-CNRS 8010

Université des Sciences et Technologies de Lille, 59 655 Villeneuve d'Ascq Cedex, France.

## Abstract

Plasma polymerized hexamethyldisilazane deposits have been obtained downstream a microwave nitrogen plasma jet. In dependence on the growth conditions, types of chemical bonds of the polymer coatings are studied by IRTF. IR spectra revealed the formation of SiH, NH, OH, Si-O-Si, Si-NH-Si and Si(CH<sub>3</sub>)<sub>n</sub> groups but the most interesting feature is the emergence of large amounts of C≡N bonds. However, their structures change dramatically on ageing. Then, XPS and Raman analyses show a three dimensional silicon oxide SiO<sub>x</sub> like structure.

## 1. Introduction

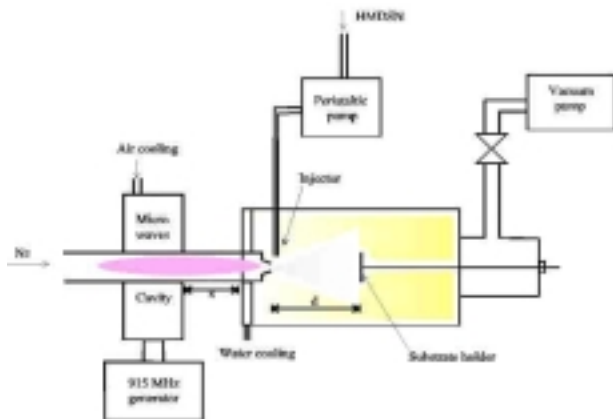
RPECVD assisted polymerisation of organosilicon precursors is well known as a suitable technique for polymer deposits. Previous studies showed that Cold Remote Nitrogen Plasma (CRNP) obtained by a microwave discharge with a pressure range of 100 – 5000 Pa gives exciting results according to polymer structure [1]. Excited nitrogen molecules and nitrogen atoms in ground state N(<sup>4</sup>S) mainly compose the CRNP and make this medium very reactive. This reactivity was used to induce plasma polymerisation from organosilicon monomers which leads to silicon oxide films.

In this work, we tried to turn to account and to optimise the reactivity of the nitrogen species by the use of a nozzle just at the exit of the discharge. The originality of the present approach is to utilise the increase of energy and density of the active species of nitrogen created by the plasma jet for a better incorporation of nitrogen in the deposits and why not for ceramics deposition.

The influences of different parameters as the distance  $d$  between the nozzle and the substrate, the precursor flow  $\phi$ , the time of deposition  $t$  and the effect of a pre- or post-treatment of the substrate are studied by IRTF, XPS, and Raman analyses.

## 2. Experimental set-up

Figure 1 shows the experimental set-up of a microwave plasma jet assisted deposition reactor.



**Table 1 : Process parameters**

Parameter	Values
Power [kW]	2.5
Nitrogen [slpm]	1.5
Chamber pressure [Pa]	350
Precursor flow rate ( $\phi$ ) [sccm]	0.16 – 4
Deposition time ( $t$ ) [min]	10 – 30
Distance nozzle-substrate ( $d$ ) [cm]	4 – 22
Distance cavity-nozzle ( $x$ ) [cm]	0
Substrates	Glossy aluminium disks

**Figure 1 : Scheme of the experimental set-up**

The microwave discharge is sustained by a 915 MHz cavity in a constant nitrogen flow in a quartz tube (28 mm inner diameter). The quartz nozzle (3 mm inner diameter at the exit) allowing creation of the jet is



placed at the end of the tube of discharge just at the entrance of the Pyrex deposition chamber (108 mm inner diameter, 250 mm of length). The nozzle is cooled by water circulation in the flask. The liquid precursor is injected in the plasma jet just at the exit of the nozzle through an aluminium tube. The substrate holder is placed in the axis of the jet with the possibility for the distance ( $d$ ) between the nozzle and the substrate to be varied in the range of 4 – 22 cm.

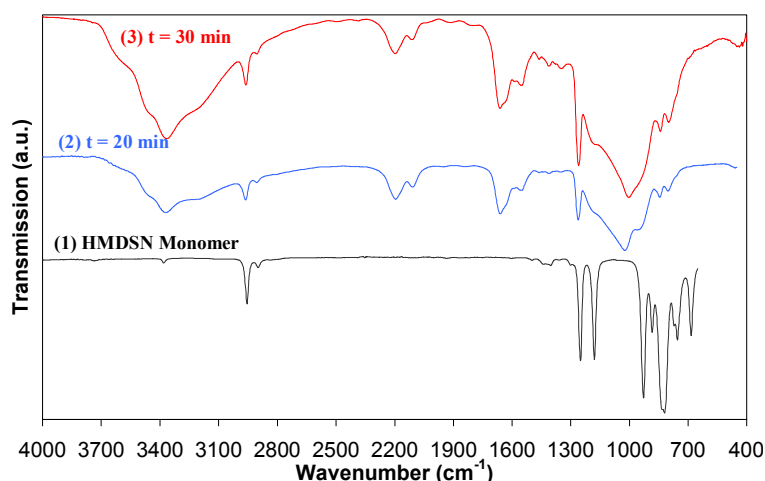
Nitrogen (industrial quality, U grade, Air Liquide) flow rate is regulated by a Alphagaz RDM 280 mass flow regulator. The pressure upstream the discharge is controlled by a HPS Pirani type vacuum gauge (MKS). The substrates for plasma deposition are glossy aluminium disks (2.54 cm diameter, 1 mm thick). Plasma polymer films are deposited using Hexamethyldisilazane  $(\text{CH}_3)_3\text{Si-NH-Si}(\text{CH}_3)_3$  (HMDSN, 99% electronic grade, Lancaster). HMDSN flow rate ( $\phi$ ) is regulated by a user-definable peristaltic pump (Ismatec). The process parameters used are listed in Table1.

Deposits were analyzed by a Perkin-Elmer FT-IR Spectrum One spectrometer with a variable angle specular reflection device. The angle for analyses was fixed to  $45^\circ$ . Spectra were performed in the  $4000\text{--}400\text{ cm}^{-1}$  wavenumber range with a resolution of  $4\text{ cm}^{-1}$ . Raman spectra were recorded with a LABRAM microspectrometer (Jobin Yvon) equipped with an internal He-Ne laser (632.8 nm) and a liquid nitrogen cooled CCD detector. XPS analyses were performed in a Leybold LHS10 spectrometer equipped with Al X-ray source (1486.6 eV). The binding energies (BEs) were calibrated by reference to the aliphatic carbon located at 285.0 eV (C1s photopeak).

### 3. Results and discussion

#### Influence of deposition time $t$ :

The FTIR spectra of HMDSN monomer and of the plasma polymerized coatings (ppHMDSN) obtained for two different times  $t$  are shown in Figure 2. On this picture, one can see the spectra only for  $t = 20$  min and 30 min because for  $t$  lower than 20 min no significant deposit is observed. By increasing deposition time  $t$ , absorption bands increased as shown in Figure 2. As it can be noted, IR spectra of ppHMDSN have common absorption peaks with those of the HMDSN monomer : The N-H stretching at  $3380\text{ cm}^{-1}$ , the asymmetric and symmetric C-H stretch of methyl groups at  $2955\text{ cm}^{-1}$  and  $2896\text{ cm}^{-1}$  respectively, the  $-\text{CH}_3$  asymmetric and symmetric bending of the methyl groups in  $\text{Si-CH}_3$  at  $1400\text{ cm}^{-1}$  and  $1250\text{ cm}^{-1}$ , the N-H bending and the asymmetric stretching mode of Si-N-Si in Si-NH-Si at  $1177\text{ cm}^{-1}$  and  $930\text{ cm}^{-1}$  respectively, and a group of absorption bands between  $900\text{ cm}^{-1}$  and  $800\text{ cm}^{-1}$  assigned to the methyl rocking mode in  $\text{Si}(\text{CH}_3)_3$  and a second one between  $770\text{ cm}^{-1}$  and  $650\text{ cm}^{-1}$  assigned to the Si-C stretching modes.



**Figure 2 :** IR absorption spectra of (1) HMDSN monomer (HATR), (2) ppHMDSN for  $t = 20$  min, and (3) ppHMDSN for  $t = 30$  min ( $\phi = 2\text{ sccm}$ ,  $d = 10\text{ cm}$ ).

In addition, the ppHMDSN spectra show bands that are absent from the monomer spectrum. This can be summarized as follows : (a) New  $\text{CH}_2$  absorption bands in  $\text{Si}-(\text{CH}_2)_n\text{-Si}$  ( $n = 1, 2$ ) groups appear at  $1457\text{ cm}^{-1}$  and  $1345\text{ cm}^{-1}$  attributed to the asymmetric bending modes and near  $1030\text{ cm}^{-1}$  corresponding to the wagging mode; (b) The absorption bands assigned to the  $\text{CH}_3$  rocking modes in  $\text{Si}(\text{CH}_3)_n$  ( $n = 1, 2$ ) newly appear while the intensity of the bands corresponding to the rocking mode of the  $\text{CH}_3$  in  $\text{Si}(\text{CH}_3)_3$  and the bands attributed to the Si-C stretching mode seem to decrease; (c) The band intensity assigned to the N-H group at  $3366\text{ cm}^{-1}$  and  $1177$

$\text{cm}^{-1}$  increases and the band is broadened as well as for the  $942 \text{ cm}^{-1}$  absorption band corresponding to Si-N-Si; (d) New absorption bands due to the oxidized structure appear which correspond to the O-H stretching modes at  $3613 \text{ cm}^{-1}$  and  $3460 \text{ cm}^{-1}$ , to the Si-O-Si asymmetric stretching mode between  $1100\text{-}1000 \text{ cm}^{-1}$ , overlapped with the asymmetric stretching mode of Si-O-C, and to the rocking mode of Si-O-Si at  $440 \text{ cm}^{-1}$ ; (e) An interesting spectral range is situated between  $1660 \text{ cm}^{-1}$  and  $1550 \text{ cm}^{-1}$ . The absorption bands are always present in any IR spectra and are located around  $1660 \text{ cm}^{-1}$ ,  $1630\text{-}1620 \text{ cm}^{-1}$  and  $1550 \text{ cm}^{-1}$ . They can be assigned to C=C and C=N stretching modes for the  $1600 \text{ cm}^{-1}$  region and to  $\text{NH}_2$  bending modes in Si- $\text{NH}_2$  for the band observed at  $1550 \text{ cm}^{-1}$ . But as it will be seen later, these bands in this particular spectral region increase and become asymmetric with a maximum located at  $1660 \text{ cm}^{-1}$ . As this increase follows the increase in the  $3360 \text{ cm}^{-1}$  region, S. Rodil *et al.* [2] attributed this band observed between  $1660\text{-}1550 \text{ cm}^{-1}$  to olefinic bonds ( $=\text{N-C}$ ;  $=\text{N-H}$  and  $\text{RNH}_2$ ) rather than only due to the C=C and C=N bonds. And then, the most interesting band appears at  $2190 \text{ cm}^{-1}$  which can be assigned to  $\text{C}\equiv\text{N}$  (sp hybridization) in Si- $\text{C}\equiv\text{N}$  with a shoulder around  $2150\text{-}2080 \text{ cm}^{-1}$  which can be assigned to the Si-H stretching mode. The band corresponding to the single C-N bonds might be overlapped with that observed at  $1360 \text{ cm}^{-1}$  corresponding to the Si $\text{CH}_3$  bending modes.

**Table 2 :** Band assignement of FTIR spectra [3, 4, 5, 6, 7]

Material	Peak position (cm <sup>-1</sup> )	Assignments	Material	Peak position (cm <sup>-1</sup> )	Assignments
HMDSN monomer	3380	v(N-H)	ppHMDSN deposit	3613	v(O-H), free Si-OH
	2955	v <sub>a</sub> (C-H), Si-CH <sub>3</sub>		3460	v(O-H), H- bonded OH
	2896	v <sub>s</sub> (C-H), CH <sub>3</sub>		3366	v(N-H)
	1400	δ <sub>a</sub> (CH <sub>3</sub> ), Si-CH <sub>3</sub>		2957	v <sub>a</sub> (C-H), Si-CH <sub>3</sub>
	1250	δ <sub>s</sub> (CH <sub>3</sub> ), Si-CH <sub>3</sub>		2900	v <sub>s</sub> (C-H), CH <sub>3</sub>
	1177	δ(N-H), Si-NH-Si		2190	C≡N
	930	v <sub>a</sub> (Si-N-Si), Si-NH-Si		2150 – 2080	v(Si-H)
	880, 830	ρ(CH <sub>3</sub> ), Si-(CH <sub>3</sub> ) <sub>3</sub>		1658	C=C
	770 – 650	v(Si-C)		1627	C=N
(v) stretching, (δ) bending, (ρ) rocking, (ω) wagging, (a) asymmetric, (s) symmetric mode.				1547	NH <sub>2</sub> , Si-NH <sub>2</sub>
		1457		δ <sub>a</sub> (CH <sub>2</sub> ), Si-CH <sub>2</sub> -CH <sub>2</sub> -Si	
		1410		δ <sub>a</sub> (CH <sub>3</sub> ), Si-CH <sub>3</sub>	
		1345		δ <sub>a</sub> (CH <sub>2</sub> ), Si-CH <sub>2</sub> -Si	
		1258		δ <sub>s</sub> (CH <sub>3</sub> ), Si-CH <sub>3</sub> , C-N	
		1177		δ(N-H), Si-NH-Si	
		1100 – 1000		v <sub>a</sub> (Si-O-Si), v <sub>a</sub> (Si-O-C)	
		1030		ω(CH <sub>2</sub> ), Si-(CH <sub>2</sub> ) <sub>n</sub> -Si, n=1, 2	
		942		v <sub>a</sub> (Si-N-Si), Si-NH-Si	
		840		ρ(CH <sub>3</sub> ), Si-(CH <sub>3</sub> ) <sub>n</sub> , n = 2, 3	
		794		ρ(CH <sub>3</sub> ), Si-(CH <sub>3</sub> ) <sub>n</sub> , n = 1, 2	
		440		ρ(Si-O-Si)	

All these bands exhibit a monomer fragmentation via abstraction of methyl from silicon and hydrogen from methyl groups into the plasma jet. The observation of CN bands underscores the fact that the monomer molecules introduced into the plasma jet are activated into reactive fragments which recombine to form new chemical bonds. Hydrogen atoms are certainly abstracted by active nitrogen atoms  $\text{N}^4\text{S}$  in the plasma jet to form ammonia and also NH bonds on the substrate. Then the extract carbon is captured to form the CN bonds.

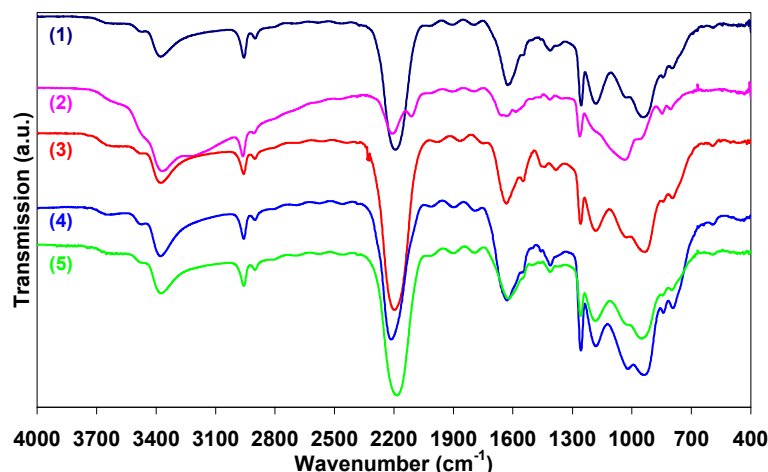
As the time of deposition makes no significant change in the structural observations of ppHMDSN,  $t$  is kept equal to 20 min in all the other experiments presented here.

#### Influence of plasma treatment :

In order to see the influence of plasma pre- or post-treatment and of the monomer injection alternately with plasma treatment, some ppHMDSN have been made for different combinations between the injection of the monomer for the deposit and the plasma treatment. All the different sequences have been made in order to keep the total time of monomer injection equals to 20 min.

Figure 3 presents the IR spectra of ppHMDSN coatings obtained for different sequences, which are summarized in the table. Firstly, we can observe that the IR spectra are marked by the intensity increase of the band assigned to the CN stretching mode. Spectra (1) and (2) (fig3) show that plasma post-treatment is good to reduce the intensity of the SiOSi/SiOC and then the NH and OH bands only for few minutes of plasma treatment. Long plasma post-treatment increases the oxygen incorporation in the deposit and tends to reduce the intensity of the bands assigned to the CN bond in the side of which the SiH band reappears. Spectra (3), (4) and

(5) (fig.3) present different sequences for deposit and plasma treatment. The same conclusion is made : the longer is the plasma treatment, the more oxide is the deposit with the increase of SiOSi/SiOC absorption and also the absorption bands of SiNH<sub>2</sub>Si. The deposit which presents a better ratio between containing more CN bonds and less oxide and/or SiNH<sub>2</sub>Si is the deposit represented by (3) : A deposit of 20 minutes with a pre- and a post-treatment of 5 minutes.



**Figure 3** : Effects of plasma treatment on the IR absorption spectra of ppHMDSN deposits ( $\phi = 2$  sccm,  $d = 10$  cm).

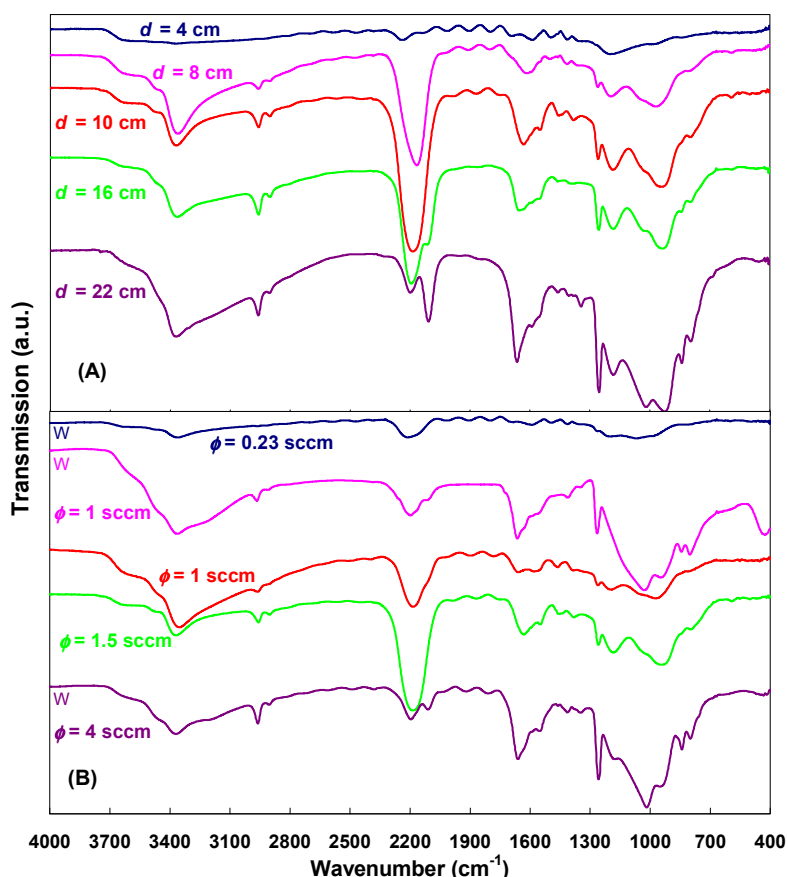
IR spectra	Plasma pre-treatment	Deposition	Plasma post-treatment
(1)	—	20 min	5 min
(2)	—	20 min	20 min
(3)	5 min	20 min	5 min
(4)	—	10 min	10 min (2 times, alternate)
(5)	—	5 min	5 min (4 times, alternate)

To diminish the incorporation of oxygen and also the presence of SiNH<sub>2</sub>Si bonds in the ppHMDSN, the addition of 0.1 % or 0.2 % of hydrogen in the discharge before, during or after the deposition of ppHMDSN coatings has been tried without success. The hydrogen added during or after deposition leads to increasing the intensity of the bands assigned to the SiOSi/SiOC, OH, and then SiH bonds while the intensity of the band corresponding to the CN bonds decreases. A plasma pre-treatment with hydrogen addition shows no change compared with ppHMDSN deposit realized with pre- and post-treatment of nitrogen plasma of 5 minutes. These last experiments with hydrogen demonstrate that the incorporation of nitrogen in the ppHMDSN deposits is due mainly by the activity of nitrogen species in the remote plasma but also to a thermal effect on the surface.

#### Influence of $d$ and $\phi$ :

The influence of the distance  $d$  between the nozzle and the substrate and also the flow rate  $\phi$  of HMDSN monomer injected in the plasma has been studied.

Figure 4A shows the effect of  $d$  at a fixed  $\phi$  (1.5 sccm) and Figure 4B, the effect of  $\phi$  at a fixed  $d$  (10 cm). It can be seen that the structural changes by increasing  $d$  or  $\phi$  seem to be similar. When the distance  $d$  increases at fixed  $\phi$  (fig 4A), three different zones can be defined as follow : The first one for  $d$  lower than 8 cm where deposits are not significant with the presence of the bands corresponding to the OH and SiNH<sub>2</sub>Si bonds. May be this absence of deposit is due to a bombardment of the substrate by the nitrogen species of the plasma jet and/or to the fact that the HMDSN monomer molecule is not broken in the plasma for this short distance. The second zone is located between 8 and 16 cm with a progressive intensification of the bands appearing in the 1660-800 cm<sup>-1</sup> spectral range with  $d$  but with a marked distance at 10 cm for which the band intensity corresponding to the C≡N vibrations is higher and the intensity of the band assigned to the OH bonds seem to decrease. The last zone, for  $d$  greater than 16 cm, all the band intensities are increased except for the band assigned to the C≡N stretching mode which is reduced drastically.



**Figure 4 :** Effects of (A)  $d$  ( $\phi = 1.5$  sccm) and (B)  $\phi$  ( $d = 10$  cm, w signifieate without plasma treatment) on the IR absorption spectra of ppHMDSN deposits.

The same feature is observed when the HMDSN monomer flow rate  $\phi$  is increased at fixed  $d$  (fig 4B). For  $\phi$  lower than 0.5 sccm, no significant deposit is observed certainly because of the lack of reactant. In the range of 0.5-1 sccm and for  $\phi$  greater than 2 sccm, the absorption intensities increase with  $\phi$  but there is always more intensity of NH, OH, SiH, SiOSi/SiOC and SiNHSi bands compared with those attributed to CN stretching vibrations, even if a plasma treatment is done. ppHMDSN deposits realized for  $\phi$  between 1.5 and 2 sccm are similar with superimposable spectra. In this case, CN vibrations absorption peaks show good intensity compared with those of SiOSi/ SiOC and SiNHSi vibration bands.

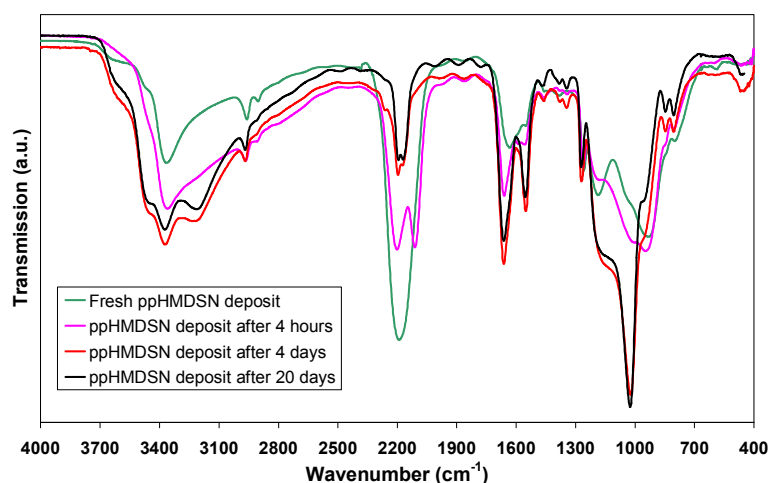
In the same optic, as for the influence of  $d$ , the distance  $x$  between the cavity and the nozzle has been changed from 0 to 8 cm. FTIR spectra of ppHMDSN coatings show a decrease of deposit with increasing  $x$  what which can be explain by the removal of the discharge from the nozzle and then of the kinetic energy of the nitrogen species.

#### Structural changes during ageing :

Whatever the experimental conditions, as reported before by Gengenbach *et al.* [6] for glow discharge polymerisation experiments with HMDSN monomer, the structure of the coatings changes dramatically on ageing.

Figure 5 presents the changes of the IR spectra recorded at different time after deposition of the ppHMDSN coatings. The most pronounced change is the important increase of the intensity of the bands corresponding to the SiOSi, OH, NH and NH<sub>2</sub> groups with the simultaneous reduction of the intensity of band assigned to the C≡N mode. As polymer coatings realized by Gengenbach *et al.* [6] appear to age by loss of silazane groups and their replacement with siloxane cross-links over time, our ppHMDSN coatings can see the evolution in time of their composition vary with different delays depending on the moisture in air. Then their structure stop changing and all the ppHMDSN have near the same final IR spectrum as represented in Figure 5. The conclusion which can be made is that those ppHMDSN deposits are very sensitive to water because of the

presence of the Si-N- bond which can react with H-O-H molecule to form Si-NH, Si-NH<sub>2</sub>, Si-OH and Si-O-bonds, what is shown with the IR spectra recorded.



**Figure 5 :** Evolution of IR absorption spectra over time of ppHMDSN deposit.

To confirm this structural change, XPS and Raman analyses have been performed. The Si KLL Auger spectra recorded for BEs between 1600 and 1620 eV show a peak generally centred around 1608.5 and 1609 eV which is characteristic of SiO<sub>x</sub> and SiO<sub>2</sub> structure. Then Raman spectra show the presence of bands which are assigned to the CH<sub>3</sub>, NH or NH<sub>2</sub>, SiH, C≡N and (SiOSi)<sub>n</sub> stretching and bending modes. The intensity of the band corresponding to the (SiOSi)<sub>n</sub> mode is significant of a three-dimensional SiO<sub>x</sub> film.

In comparison of all these analyses, the final structure of ppHMDSN deposits leads to a polysiloxane which can be compared with coatings made with other monomer precursors as Tetraethoxysilane, Tetramethyldisiloxane or Hexamethyldisiloxane.

#### 4. Conclusion

Plasma polymerization of Hexamethyldisilazane (HMDSN) monomer has been performed downstream a microwave plasma jet. The effects of the deposition conditions on the composition of ppHMDSN coatings have been investigated. Depending on the parameters, the IR spectra of the different substrates revealed the formation of SiH, NH, NH<sub>2</sub>, OH, Si-O-Si, Si-NH-Si, Si(CH<sub>3</sub>)<sub>n</sub> and Si(CH<sub>2</sub>)<sub>n</sub> groups with variable quantity but the most interesting feature is the emergence of large amounts of C≡N bonds. When the bands corresponding to inorganic bonds as Si-O, Si-N and Si-C become more intense and broader, this is indicative of a more inorganic film with cross-linking structure. All the bands assigned to the NH, NH<sub>2</sub>, Si-O-Si, Si(CH<sub>3</sub>)<sub>n</sub> and Si(CH<sub>2</sub>)<sub>n</sub> groups and then to the CN are significant of the reactivity of the remote nitrogen plasma jet for abstraction of hydrogen, methyl or other groups to form new bonds among which the most interesting is C≡N. However, even if conditions which are giving a ppHMDSN deposit with a large amount of C≡N have been determined, the structure of ppHMDSN coating is extremely unstable over time : A rapid increase in the concentration of hydrogen and oxygen depending on the moisture in air exhibit a highly hydrolytic recomposition of the deposit which leads to a polysiloxane structure.

#### References

- [1] F. Callebort, B. Revel, O. Dessaux and P. Goudmand – High Temp. Chem. Processes **4**, 59 (1995).
- [2] S. Rodil, N.A. Morrison, W.I. Milne, J. Robertson, V. Stolojan, and D.N. Jayawardane – Diam. Rel. Mat. **9**, 524 (2000).
- [3] D.R. Anderson, in Infrared, Raman and Ultraviolet Spectroscopy, Analysis of silicones – Wiley-interscience, A. Lee Smith, Ed., New York, (1974).
- [4] A.M. Wrobel, M.R. Wertheimer, J. Dib and H.P. Schreiber – J. Macromol. Sci. Chem. **A14(3)**, 321, (1980).
- [5] S.Y. Park, N. Kim, U.Y. Kim, S.I. Hong and H. Sasabe – Polymer Journal **22 (3)**, 242, (1990).
- [6] T.R. Gengenbach and H.J. Griesser – Polymer **40**, 5079 (1999).
- [7] F. Benitez, E. Martinez and J. Esteve – Thin Solid Films **377-378**, 109, (2000).

# Surface Modification of Activated Carbons by Atmospheric-Pressure Glow Discharge

Satoshi Kodama and Hidetoshi Sekiguchi

*Department of Chemical Engineering, Tokyo Institute of Technology, Japan*

## Abstract

Granular activated carbon was treated by oxygen non-thermal plasma. The activated carbon was fluidized in the tubular reactor, and it was treated with oxygen plasma induced by atmospheric pressure glow discharge or dielectric barrier discharge. After the treatment, the samples were characterized by selective neutralization and the concentration of acidic functional groups was determined. Effects of the discharge on the change of the activated carbon were discussed.

## 1. Introduction

Activated carbon is widely used as adsorbents because of their well-developed porous structure. Activated carbon is essentially nonpolar material, therefore, it is used as adsorbent for organics in water. On the other hand, there are many reports about treating the activated carbon in various ways to modify the surface chemistry [1, 2]. In our previous study, granular activated carbon was treated by oxygen non-thermal plasma induced by dielectric barrier discharge (DBD) [3]. Plasma was generated by loading high voltage alternating current to the parallel-plate electrodes. The sample was treated by oxygen plasma varying the treatment time. The changes of the samples in adsorbability for the copper ion in aqueous solutions were measured. The results showed that the saturated adsorption amount of copper ion was increased by the treatment. This was caused by the introduction of functional groups on the activated carbon. It was concluded that the DBD treatment with the equipment was effective to introduce acidic functional groups on activated carbon. The method used in the study had advantages that the treatment was easy to operate and small power consumption. However, it also had the disadvantages of small capacity of the sample and long treatment time.

Recently, atmospheric pressure glow (APG) discharge has been applied for the surface treatment of materials [4]. The discharge generates plasma by applying high frequency alternative current to electrodes; one of which is at least covered with dielectric materials. In this study, the APG discharge plasma was applied for the surface modification of activated carbon. The activated carbon was treated with two types of the reactor, and the samples were compared with the activated carbon modified by the DBD treatment.

## 2. Experimental

### 2.1 Materials

Commercial granular activated carbon (20-48 mesh, Takeda chemical industries) was used in this study that contains fewer impurities and less acidic functional groups compared with that used in our previous work. The activated carbon was befit to emphasize the effect of the plasma treatment. Though this activated carbon contains fewer impurities, the suspension of the as-received activated carbon showed alkalescency because of the ash exists in raw material. Therefore, the activated carbon was rinsed with distilled water until the pH of it was near neutral and then dried at 40 °C in an oven for 5 days.

### 2.2 Plasma treatment of the samples

#### (a) plasma jet reactor

Figure 1(a) shows the coaxial type plasma jet reactor. The reactor consisted of plasma generation section and fluidized bed section. The plasma generation section was made of quartz glass tube (6 mm outer diameter, 4 mm outer diameter and 40 mm length), inner electrode (3 mm diameter and 80 mm length) and outer electrode (20 mm in length). Inner electrode, which was made of tungsten, was located coaxially at the center of the quartz glass tube. Outer electrode, which was made of stainless sheet, was wrapped around the

tube. The experimental conditions are shown in table 1(a). Helium (6 L/min) and oxygen (1 L/min) gases were mixed and introduced into the section. The plasma jet was generated by loading high-frequency alternating current (500kHz, 3kV) to the electrodes using the high-frequency power supply (ASTECH, LG-10S) was used in the experiment. The washed activated carbon sample weighed 1g was fluidized in the tubular reactor (quartz glass tube, 21mm outer diameter, 18mm of inner diameter, and 300 mm length). The plasma generation section was connected at the bottom of the fluidized bed section. The sample was treated by the plasma for 60 min. A cyclone was connected at the top of the fluidized bed reactor to recover the sample. There was some loss of the sample during the treatment and the yield of this experiment was approximately 75 %. Figure 2 (a) shows the waveform of the voltage and the current loaded to the reactor. There exists some current pulse after the large pulses. This discharge would be the mixture of the APG and DBD [5, 6], however, the discharge seemed to be uniform, therefore it was called as APG in this study. The voltage loaded to the reactor and the current were measured with digital oscilloscope (Tektronix, TD-3012)

#### *(b) Coaxial discharge reactor*

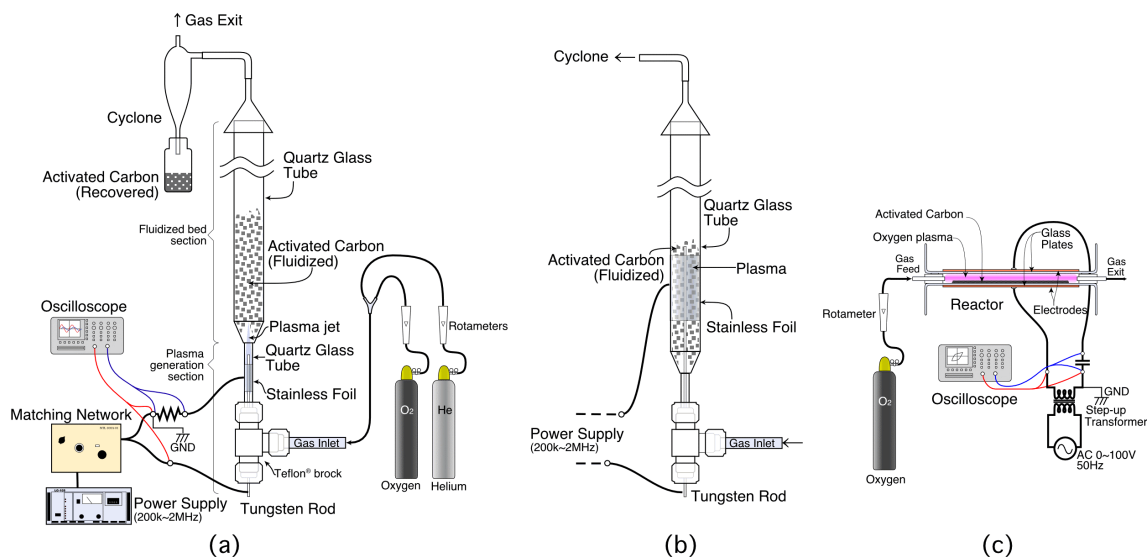
Figure 1(b) shows the coaxial discharge reactor. The equipment was essentially the same as (a), except for the length of the inner electrode and the position of the outer electrode. The length of the inner electrode was 160 mm, and the outer electrode was wrapped around the fluidized section. Thus, discharge area was at the fluidized section. The experimental conditions were shown in table 1(b). The washed activated carbon weighed 1g was fluidized in it. The sample was burnt by the treatment time of 1 hour, therefore, the treatment time was set to 30 min. The yield was 40% approximately. Figure 2(b) shows the waveform of the voltage and the current loaded to the reactor. This is alike to the waveform of DBD [5], however, the waveform of APG discharge was observed after the treatment time of 20 min. Then, the amount of activated carbon fluidized in the reactor was smaller because of the burned-out.

#### *(c) DBD parallel-plate reactor.*

The schematic of the experimental apparatus for the DBD parallel-plate reactor is shown in fig. 1(c), and the experimental conditions are shown in table 1(c). The reactor (c) was similar to that used in our previous work [3]. The gap between the electrodes was 8.5 mm and the thickness of the dielectrics was 1.5 mm. The washed activated carbon weighed 0.4g was put on the lower dielectric. Oxygen gas flow rate was set as 12 mL/min and the pressure in the reactor was 1 atm. The dielectrics were made of glass and the electrodes were made of copper. The plasma was generated at a discharge voltage of 21 kV and a frequency of 50 Hz. Figure 2(c) shows the waveform of the voltage and the current loaded to the reactor. The power consumption in the reactor was 2.5 W measured with a digital oscilloscope from the Lissajous figure. The yield was approximately 100 %.

### *2.3 Characterization*

Acid functional groups on the activated carbon surface were determined by the method proposed elsewhere [2, 7]. The solutions of NaOEt, NaOH, Na<sub>2</sub>CO<sub>3</sub>, and NaHCO<sub>3</sub> were prepared using decarboxylized water. Concentration of the each samples were 0.02N. The activated carbon samples weighed 0.1g were mixed with the solutions in Erlenmeyer flasks. The flasks were shaken at the temperature of 20 °C for 3 days enough to reach equilibrium. The solutions were filtered with membrane filters (ADVANTEC, 0.5 um pore size) to separate the activated carbon from the solution. The concentrations of base in the filtrates were determined by back-titration with titrator (Metrohm, 798 MPT Titrino) using 0.1N of HCl solution. The concentration of the acidic functional groups on the activated carbon was determined from the amount of consumption of the bases.

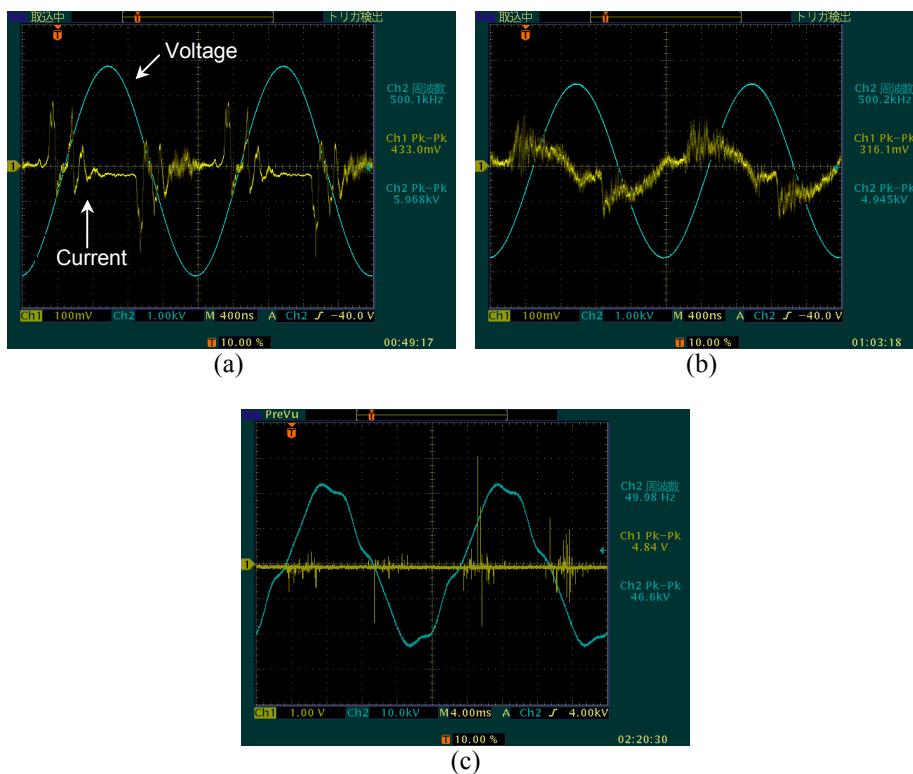


Figs. 1. Experimental apparatus.

(a) Coaxial plasma jet reactor, (b) Coaxial discharge reactor,  
(c) DBD parallel-plate electrodes reactor.

Table 1. Experimental Conditions

Experimental equipment	(a)	(b)	(c)
Used sample	20-48 mesh granular activated carbon		
Treatment time	60min	30min	60min
Power consumption	60 W	120 W	2.5 W
Power supply	500kHz, 3kV	500kHz, 2.5kV	50Hz, 23kV
Distance between the electrodes	1.5mm	7.5mm	8.5mm
Amount of the sample/batch	1g		
Gas flow rate	He:6 L/min, O <sub>2</sub> : 1L/min		O <sub>2</sub> 12mL/min



Figs. 2. Waveforms of the voltages and currents loaded to the reactor.

(a):Coaxial plasma jet, 3kV, (b): Coaxial discharge, 2.5kV, treatment time of 5 min  
(c): DBD parallel-plate type, 23kV



### 3. Results and Discussion

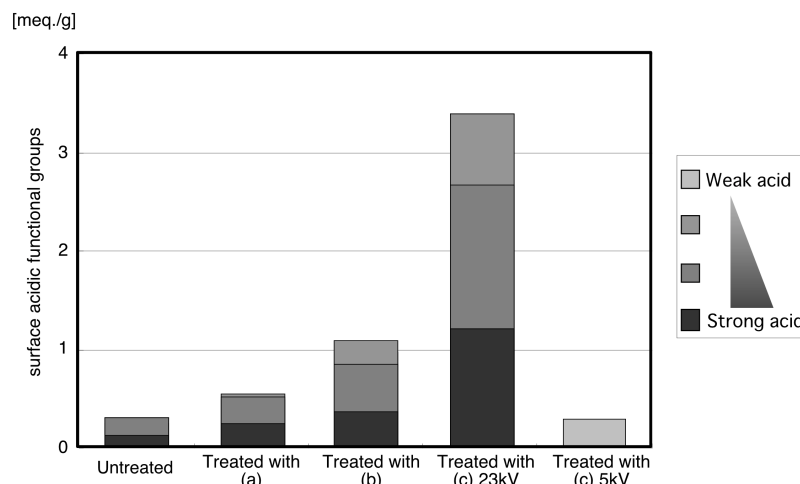


Fig. 3. Variation in the content of surface functional groups of the activated carbons.

\* The bar of 'DBD-5kV' is total amount of acidic functional groups.

Figure 3 shows the variation in the content of surface functional groups of the activated carbons. The results show that the samples treated by the equipment (a) and (b) were introduced acidic functional groups on its surface. The concentration of functional groups is higher in the sample treated with (b). In our previous work, it was suggested that ions, radicals, and electrons existing in the oxygen plasma modified the activated carbon. Oxygen should be excited in the plasma jet of (a) according to the results of spectroscopic analysis. Therefore, we suppose that the discharge onto the surface of the activated carbon corresponding to the condition of (b) helped the generation of acidic functional groups. On the other hand, the treatment by the equipment (c) was introduced much amount of acidic functional groups on activated carbon compared with the sample treated by the equipment (a) and (b) though they consumed much power than with (c). The equipment (c) was smaller power consumption, however, it was loaded higher voltage. Electron temperature of the plasmas was not measured in this study, however, it should be higher in the reactor of the equipment (c). The results should be compared with the treatment with equipment (c) in 5kV. The result is shown in fig. 3, whose value is total amount of acidic functional groups and the treatment introduced less functional group on the surface of the sample. The results mentioned above indicated that the introduction of the acidic functional groups requires the plasma with high electron temperature and discharge onto the surface.

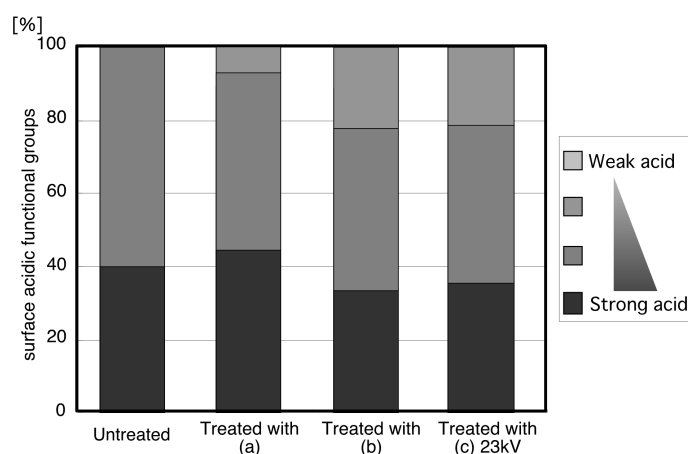


Fig. 4. Ratios in the content of the surface functional groups of the activated carbon

Figure 4 shows the ratios in the content of the acidic functional groups of the activated carbon. It is found that the ratio of sample treated with (b) is similar to the rate of treated with (c) though the frequency of their power supply and power consumption during the treatment were different. These samples were treated in discharging zone. This also suggests that the introduction mechanisms of acidic functional groups onto the

surface of the activated carbon are differing from with and without the discharge onto the surface of activated carbon.

#### **4. Conclusion**

Oxygen plasma jet induced by APG discharge was applied to treat granular activated carbon in fluidized bed reactor. The acidic functional groups were introduced on the sample, however, the amount of the functional groups was smaller than the sample treated by DBD parallel-plates electrodes reactor. In addition, coaxial type direct discharge reactor improved the treatment. The experiment using DBD-parallel electrode reactor with low voltage was also carried out. The sample treated by the experiment has the little amount of acidic functional groups. These results indicate that the direct discharge with high voltage onto the activated carbon plays an important role in the introduction of acidic functional groups on the activated carbon.

#### **Acknowledgement**

Financial supports by 'National Institute of Advanced Industrial Science and Technology' and 'The 21st Century COE Program (Chemistry Field), Tokyo Institute of Technology' are gratefully acknowledged.

#### **References**

- [1] J.L. Figueiredo, M.F.R. Pereira, M.M.A. Freitas, J.J.M. Órfão, Carbon, **32**, 1379, (1999)
- [2] H. Valdés, M. Sánchez-Polo, J. Rivera-Utrilla, C.A. Zaror, Langmuir, **18**, 2111, (2002)
- [3] S. Kodama, J. Kawasaki, H. Sekiguchi, H. Habaki - Thin Solid Films, **407**, 151, (2002)
- [4] K. Tanaka, T. Inomata, M. Kogoma - Plasmas and Polymers **4**, 269, (1999)
- [5] T. Nozaki, Y. Miyazaki, Y. Unno, K. Okazaki, J. Phys. D: Appl. Phys., **34**, 3383, (2001)
- [6] F Massines, G. Gouda, J. Phys. D: Appl. Phys., **31**, 3411, (1998)
- [7] H. P. Boehm, Carbon, **32**, 759, (1994)

# Influence of plasma chemistry in high-pressure ceramic envelope metal halide lamps on the mass transport coefficients

J.B. Rouffet, G. Zissis, M. Aubes, J.J. Damelincourt

*Centre de physique des plasmas et de leurs applications de Toulouse, Université Paul Sabatier, Toulouse 3, France*

## Abstract

In high-pressure lamps, discharge is maintained in an enclosure in which the wall temperature can change. This temperature determines some parameters of the discharge. Its influence on transport coefficients and thermodynamics properties of the gases discharge is examined in this paper.

## 1. Introduction

To study the influence of plasmas chemistry on gas discharge properties in high-pressure lamps, we decided to change the wall temperature  $T_w$ . Indeed, if this temperature is rather low, condensed phases can exist. This involves a modification of the amount of atoms number of each element in the gas phase. In the case of the high-pressure lamps, we consider that the pressure is constant in each point of the system. The wall temperature, fixes the system pressure. We study, in this paper, the influence of this temperature in the case of a mixture made up of mercury, thallium and iodine. We make this study for a lamp of volume  $V_{\text{lamp}}=1.57.10^{-6}\text{m}^3$ , containing 10 mg of mercury and 5 mg of thallium iodide. We consider, moreover, the assumption of local thermodynamic equilibrium (LTE). The goal of this paper is to show the importance of the wall temperature on the discharge gas properties in the high-pressure lamps.

## 2. Influence of wall temperature on system pressure and on the amount of mercury, iodine and thallium.

Plasma existing in high pressure (atmospheric or more) lamps, is often described within the framework of local thermodynamic equilibrium (LTE). This assumption allows us to simplify calculations and to determine rapidly the macroscopic variables: densities of particles, transport coefficient. Moreover, it enables to know the thermodynamic variables versus only two parameters, which are temperature and pressure. Using LTE assumption, the equation set describing the plasma is:

- Saha law for ionic equilibrium
- Guldberg and Waage law for dissociation equilibrium
- Boltzmann law for populations of excited level
- Dalton law for the relations between densities, pressure and temperature.

In a ceramic metal halide lamp (C-MHL), several hundreds chemical reactions take place simultaneously. To calculate chemical composition of the mixture, we use the free enthalpy  $G$  minimization method [1,2,3]. For a fixed temperature  $T$  and pressure  $P$ , thermodynamic balance is found when  $G$  is minimum. For a system made up of  $N$  elements, whose chemical potential with the reference pressure  $P_0$  is  $\bar{G}_i^0$ ,  $G$  is given by the relation [4]:

$$G = \sum_{i=1}^N n_i \bar{G}_i^0 + RT \ln \left( \frac{n_i}{\sum_{i=1}^N n_i} \right) + RT \ln \left( \frac{P}{P_0} \right) + \sum_{i=1}^N \bar{G}_i^{\text{Debye-Hückel}} = \sum_{i=1}^N \bar{G}_i^0 + G^{\text{Debye-Hückel}} \quad (1)$$

$R$  is here the constant of perfect gases ( $R=8,315 \text{ J.K}^{-1}.\text{mol}^{-1}$ ),  $n_i$  is the molar density of species  $i$ , and  $\bar{G}_i^{\text{Debye-Hückel}}$  accounts for the effects due to the charged particles interactions. In the approximation of Debye-Hückel [5], this correction is written:

$$\bar{G}_i^{\text{Debye-Hückel}} = \frac{V k_B T}{8 \epsilon_0 \epsilon_d} \quad \text{with} \quad \epsilon_d^2 = \frac{e^2}{\epsilon_0 k_B T} \sum_{i=1}^N z_i^2 n_i \quad (2)$$

$V$  is the volume,  $\epsilon_d$  represents the Debye length,  $z_i$  is the number of elementary charge of the species  $i$ ,  $\epsilon_d$  is the dielectric permittivity of the vacuum,  $k_B$  is the Boltzmann constant, and  $e$  is the electron charge [5]. Densities  $n_i$  have to minimize free enthalpy functions, but also satisfy the Dalton and electrical neutrality laws:

$$P = \sum_{i=1}^N n_i k_B T \quad \text{with} \quad P = \frac{k_B T}{24 \epsilon_d^2} \quad \text{and} \quad \sum_i n_i Z_i = 0 \quad (3)$$

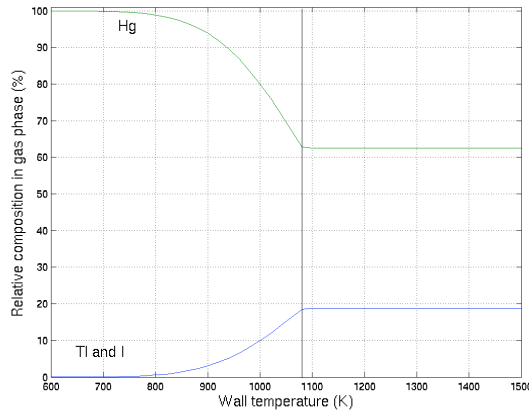
where  $\bar{G}_i^{\text{Debye-Hückel}}$  is the Debye-Hückel correction of pressure [5]. An other way to write  $G$  is:

$$G = RT \sum_{j=1}^N n_j \left[ C_j + \ln \frac{n_j}{n} \right] \text{ where } C_j = \frac{G_j}{RT} + \ln P \quad (4)$$

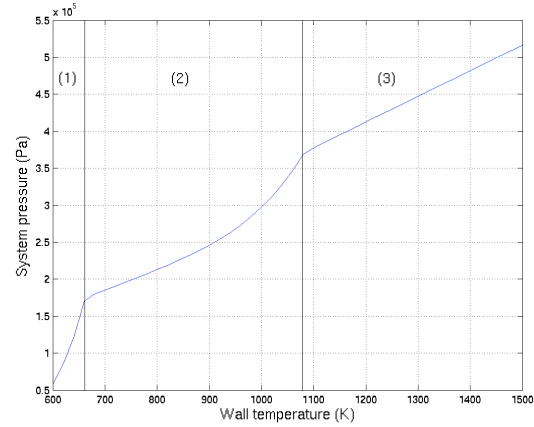
$$\bar{n} = \sum_{j=1}^N n_j$$

$G_j$  is the free enthalpy of formation of each component. The research of the equilibrium chemical composition of the system at the temperature  $T$  and the pressure  $P$ , consists in minimizing the system (4) under constraints (3), by using for example the Lagrange multipliers method [2].

Let us study the evolution of the discharge gas composition and pressure versus wall temperature  $T_w$ . By supposing that  $T_w$  is the cold point temperature in the lamps, condensed phases will be formed on the wall. To know proportions of elements in gas phase, we study the system with constant volume  $V_{\text{lamp}}$ , at the uniform temperature  $T_w$ , containing 10 mg of mercury and 5 mg of thallium iodide.



**figure 1.** Evolution of the relative proportion of elements in gas phase versus wall temperature.



**figure 2.** Evolution of system pressure versus wall temperature.

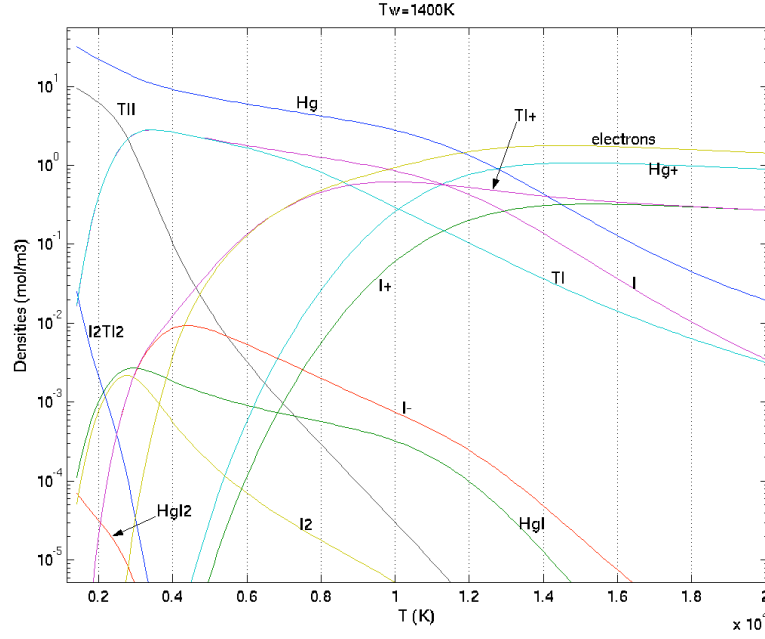
Figure 1 shows the evolution of the proportion of elements in gas phase versus wall temperature. We see that for temperatures lower than 1090K the existence of thallium iodide in condensed phase modifies proportions of iodine and thallium in gas phase. This proportion increases with the temperature, under the effect of thallium iodide vaporization, until the complete vaporization, which takes place at 1090K. At the top of this temperature, proportions in gas phase remain constant.

Figure 2 presents the evolution of the system pressure versus wall temperature. When temperature is lower than 680K (area 1), the vaporization of mercury occurs. The increase in the pressure is thus more significant than in the case of a perfect gas only. At the top of this temperature, all the mercury is in the gas phase. For  $T_w < 1090K$  (areas 1 and 2) the vaporization of thallium iodide creates this high variation of pressure. At the top of 1090K (area 3), we find a linear variation corresponding to a perfect gas in which the number of mole and the volume are constant.

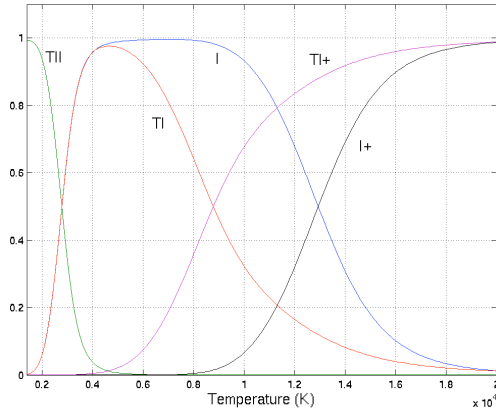
### 3. Calculation of chemical composition in gas phase

In the case of gas discharge in high-pressure lamps, we consider the pressure equal in any points of the system. We assume that the proportion of each element is constant too. Thus, the wall temperature fixes proportion of each element in gas phase and the system pressure. To calculate the evolution of the densities of the elements taken into accounts, we use, the free enthalpy minimization method. We choose to study more accurately what occurs when the wall temperature is 1400K. This enables us to highlight the mechanisms influencing transport coefficients and thermodynamic properties.

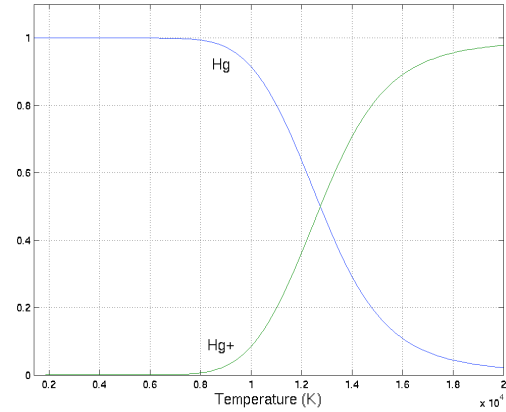
On figure 3 we present the evolution of densities of the various species taken into account versus temperature for a wall temperature of 1400K. Figures 4 and 5 enable us to understand what occurs in the gas for the majority species when the temperature increases. First of all we have the thallium iodide dissociation, which increases the number of thallium and iodine atoms. Then comes the thallium ionization and then the iodine and mercury ionization at the same time.



**figure 3.** Densities evolution versus temperature, for a wall temperature of 1400K.



**figure 4.** Evolution of the number of moles of the prevalent species containing thallium and iodine normalized in volume versus temperature, for a wall temperature of wall of 1400K.



**figure 5.** Evolution of the number of moles of mercury and its ion normalized in volume versus temperature, for a wall temperature of 1400K.

#### 4. Calculation and evolution of transport coefficients versus wall temperature.

Transport coefficients are calculated using Chapman-Enskog method [6,7,8], which is based on an approximation solution of the Boltzmann equation. Expressions for the transport coefficients are derived as function of the collision integrals, which are averages over Maxwellian distribution of the binary cross sections. Collisions integrals are required for each pair of species (i,j) present in the plasma. They are defined as follows:

$$\bar{\Omega}_{ij}^{(s)} = \frac{4(\bar{\Omega} + 1)}{(s+1)!(2\bar{\Omega} + 1 - \bar{\Omega})} \int_0^{\bar{\Omega}} e^{-\bar{\Omega}^2} \bar{\Omega}^{2s+3} Q_{ij}^{(\bar{\Omega})} d\bar{\Omega} \quad (5)$$

Transport cross-sections are given by:

$$Q_{ij}^{(\bar{\Omega})} = 2\bar{\Omega} \int_0^{\bar{\Omega}} (1 - \cos \bar{\Omega}) b db \quad (6)$$

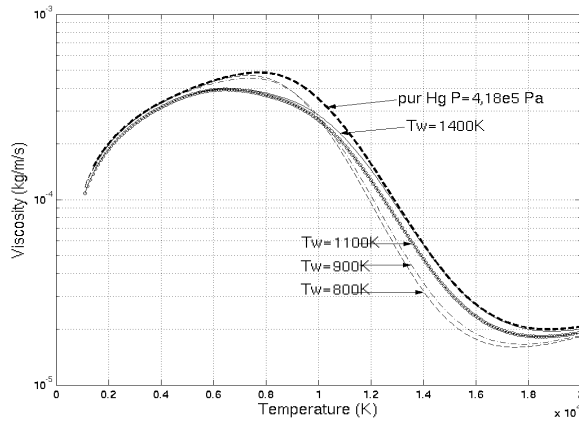
where  $b$  and  $\bar{\Omega}$  are, respectively, the impact parameter and the angle of deflection. For neutral-neutral collisions, we use a Lennard-Jones interaction potential, that collision integrals are tabulated [6,8]. The collision integrals for charged-charged interaction were calculated using the screened Coulomb

potential [9]. For neutral-ion interaction we use polarizability potential [10,11]. For electron-neutral collisions we integrate directly the formula (5), starting from cross sections found in literature. For an  $M-M^+$  interaction, the resonant charge exchange occurs when  $\ell$  is odd in collision integrals. The charge exchange cross section can be written [12] as:

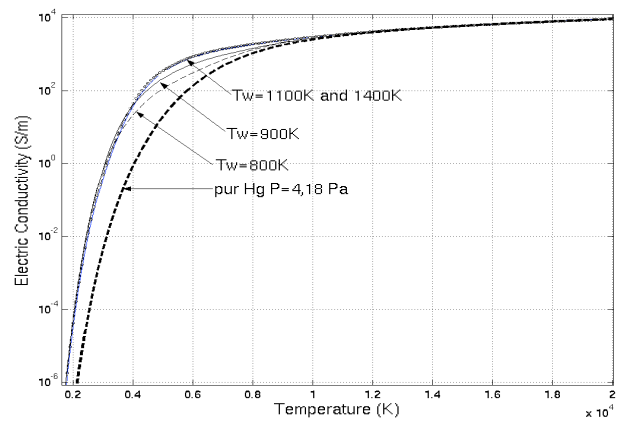
$$Q_{ex} = \frac{1}{2} (A \ell B \ln g)^2 \quad (7)$$

where  $g$  is the relative velocity. The constants  $A$  and  $B$  are adjusted following a calculation of the difference between potentials of the "gerade" and "ungerade" states [13]. The expression of Devoto [12] then allows us to calculate the collisions integrals as function of  $A$  and  $B$ .

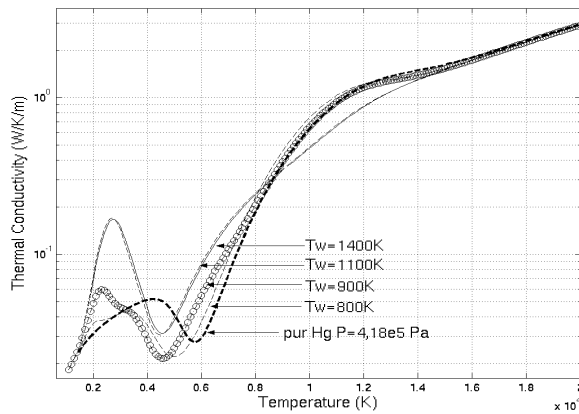
On the figure 7 we can observe that at low temperatures (less than 10kK), the electrical conductivity of the mixture is higher for the same wall temperature than for a pure gas of mercury



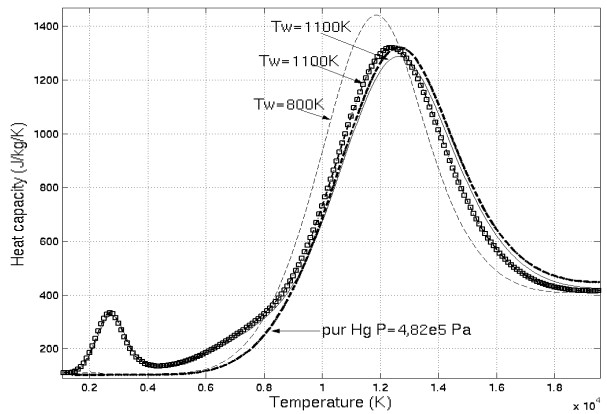
**figure 6.** Viscosity evolution versus temperature for various wall temperatures.



**figure 7.** Electrical conductivity evolution versus temperature for various wall temperatures.



**figure 8.** Thermal conductivity evolution versus temperature for various wall temperatures.



**figure 9.** Heat capacity at constant pressure evolution versus temperature for various wall temperatures.

Electrical conductivity also increases with the wall temperature. On figures 4 and 5, we can notice that thallium ionization takes place at temperatures lower than for mercury. Thus, the more the wall temperature is high, the more the number of electrons is significant at low temperatures. We thus explain the increase in electrical conductivity at low temperatures (which are those where we place ourselves in the case of the high pressure lamps).

On figure 8 we can note that, the more the wall temperature is weak the more we approach the case pure mercury. When we look at figure 4, we realize that for temperatures lower than 5000K, there is the thallium iodide dissociation. This reaction is responsible for the peak observed on the figure-9 at low temperatures of the heat capacity with constant pressure.

Thermal conductivity is the sum of three terms: thermal conductivity of translation, of reaction and internal thermal conductivity. At low temperatures, the peak of heat capacity involves an increase in the thermal conductivity of reaction, other terms remaining practically unchanged. Moreover, the more quantity of one compound is significant in a mixture, the more its properties will influence those of the system. Thus when Tl and I are in very small quantity in the system, we approach the pure mercury case. The largest peak of the figure-9 is with ionizations of the atoms especially for the mercury. The shift of these peaks towards the high temperatures when  $T_w$  increases is an effect of the pressure.

## 5. Conclusion.

This study enabled us to highlight the importance of the wall temperature and of the various phases existing in the high-pressure lamps. The higher the temperature of wall is, the more the electrical conductivity increases. We understand the interest of the use of ceramics to manufacture the enclosures of the lamps. In fact it allows to reach temperatures about 1400K on the walls. We can notice that the metal iodide addition changes the properties of high-pressure plasmas.

## Acknowledgments

This work is supported by the project EU-FP5-"NumeLiTe" and the European COST-529 network. Authors are indebted to Dr Stuart Mucklejohn (GE Lighting UK) for all useful discussions and advices.

## References

- [1] P. Sutre, J.P. Malenge - J. Chem. Phys. **5**, 285 (1968)
- [2] A. Sanon - thesis, "Contribution au calcul des propriétés thermodynamiques et des coefficients de transport de plasmas thermiques de mélange Ar/H<sub>2</sub>/CH<sub>4</sub>", UPS France (1988)
- [3] J.J. Lowke, A.B. Murphy - "The Handbook of Fluid Dynamics" R.W. Johnson (1998)
- [4] P. André - J Phys D: Appl. Phys. **30** 475-493 (1997)
- [5] M.I. Boulos P. Fauchais E. Pfender - "Thermal plasmas", Press New York (1994)
- [6] J.O. Hirschfelder, C.F. Curtis, R.B. Bird - "Molecular theory of gases and liquids", Wiley, New York (1964)
- [7] A.B. Murphy - J. Phys. D: Appl. Phys. **34**, R151-R173 (2001)
- [8] Y. Cressault - thesis "Propriétés des plasmas thermiques dans des mélanges argon-Hydrogène-cuivre", UPS France (2001)
- [9] R.I. Liboff - Phys. Fluids **2**, 40 (1959)
- [10] J. Aubreton, C. Bonefoi, J. Mexmain - Rev. Phys. App. **21** (1986)
- [11] C.W. Tan - thesis, 64, 6163, Illinois (1963)
- [12] R.S. Devoto - phys. Fluid. **10**, 354-64 (1967)
- [13] E.A. Mason, J.T. Vanderslice - Phys. of fluids **2**, 698 (1959)

# Absolute measurements of metastable Ar atom density using diode laser atomic absorption spectroscopy

D.Alexandroaie<sup>1</sup>, A.C.Ciocan<sup>2</sup>, I.Motrescu<sup>1</sup>, L.Musteata<sup>2</sup> and G.Popa<sup>1</sup>

<sup>1</sup>Department of Plasma Physics, "A.I.Cuza" University, Iasi, Romania

<sup>2</sup>Department of Optics and Spectroscopy, "A.I.Cuza" University, Iasi, Romania

## Abstract

Absolute measurements of metastable Ar atom density using diode laser atomic absorption spectroscopy have been done using a DL 100 Toptica system. A Littrow grating stabilized external resonator is used for tuning the wavelength of laser emission. This configuration allows a 1MHz spectral profile of the diode laser, which makes the system suitable and performant spectroscopic tool for plasma diagnostics.

## Introduction

Besides production of charge particles (electrons and both positive and negative ions) plasma is largely used for producing of other active species as radicals, metastables, molecular fragments and so on. [1]. One of the major problem of such applications is to measure the concentration of different species of the neutral particles and their density in different energetic states. Laser absorption techniques as ring down spectroscopy (RDS) [2] and laser induced fluorescence (LIF) [3] offer good solutions for finding concentration of some excited species.

Much of the current absorption atomic physics spectroscopy involves diode lasers, which can be tuned to a certain wavelength very precisely. While a typical diode laser has a spectral line width of 100MHz an External Cavity Diode Laser (ECDL) system using a diffraction grating can reach 1MHz. Toptica has recently developed an ECDL system, which allows many applications in atomic physics. In our laboratory we used such a system to measure absolute Ar metastable density in a DC discharge by absorption spectroscopy. Such kind of experiments have been done also before using different types of discharges taking the advantage that diode lasers are well-established tools for absorption spectroscopy particularly in plasma diagnostics [4]. The DC discharge of our system is a common geometry for application in plasma chemistry and plasma processing.

## Experimental

In this paper plasma parameters of a DC glow discharge were measured using Langmuir probe and absorption of a laser radiation using a DL 100 system.

The DC discharge was produced between two hollow electrodes made from copper, connected at  $U=800-1000V$ , with the current intensity in the range of 10-20mA and the argon pressure variable from 0.2Torr to 0.6Torr. The distance between electrodes was of 50cm. The electrodes were placed at the ends of a cylindrical glass tube (diameter of 3cm and 60 cm length). The discharge tube was terminated at both sides by optical glass windows, set at Brewster angle. The experimental set-up used in our work can be seen in Fig.1.

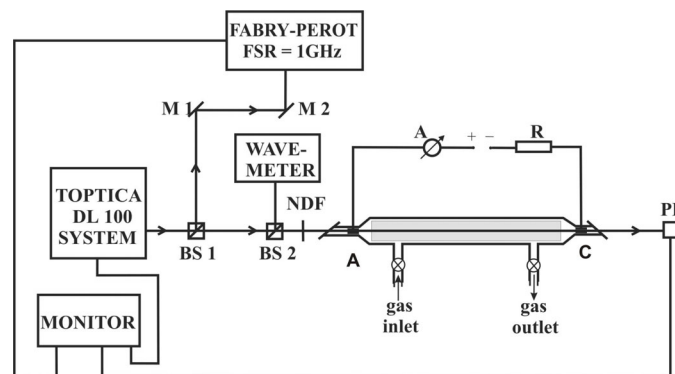
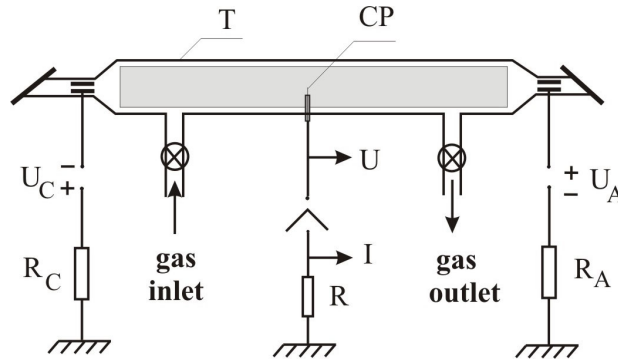


Fig.1 Experimental set-up



A wavemeter from Coherent allows a precision of 0.005 nm for the wavelength measurements but it was enough to assure the position of absorption resonance line. A Fabry-Perot interferometer with a Free Spectral Range (FSR) of 1GHz has been used in order to find the mode hope free of the system by using a Feed Forward operation [5]. This application consists of using the Scan Control unit and varying very carefully the diode laser current, so the ratio between the current applied on the piezo (which changes the angle of the grating) and the current applied on the diode itself, leads to a single mode operation of the system. This element has a typical maximum linear extension of more then 5  $\mu\text{m}$ , i.e. 33 nm/V. A photodiode and an amplifier measure the signal from the diode laser after passing along the plasma positive column. The laser head has incorporated a photodiode in order to monitors the radiation coming from the diode laser. This signal coming from the photodiode together with the signal from the Fabry-Perot and the signal amplified from the photodiode, which measures the absorption signal, were visualized on Le Croy Oscilloscope simultaneously. When the fringes from the interferometer are equidistant and equally in amplitude, the system is working in the single mode

Diagnosis of the positive column plasma was performed by Langmuir probe. The experimental set-up used in this measurement can be seen in Fig.2 where  $R_C=20\text{K}\Omega$ ,  $R=1.5\text{K}\Omega$  and  $R_A=20\text{K}\Omega$ ,  $U_C=800\text{V}$ ,  $U_A=200\text{V}$ . Mean free path of the electrons is in the order of 1.1mm so that collisionless model was used for probe processing[6].



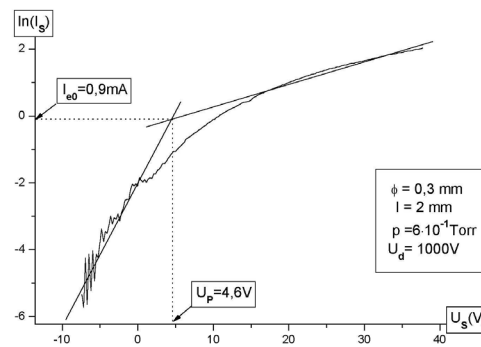
**Fig.2** Experimental set-up with electrical probe

## Results and discussions

### a) Plasma parameters by electrical probe measurements

In Fig.3 a typical semilogarithmic characteristic of a Langmuir probe is represented. The electron number density and electron temperature can be measured. By standard procedure [7] it has been obtained an electron temperature of  $T_e=2.35\text{eV}$  and  $n_e=1.25 \cdot 10^{10}\text{cm}^{-3}$ . Consequently plasma of the positive column has a

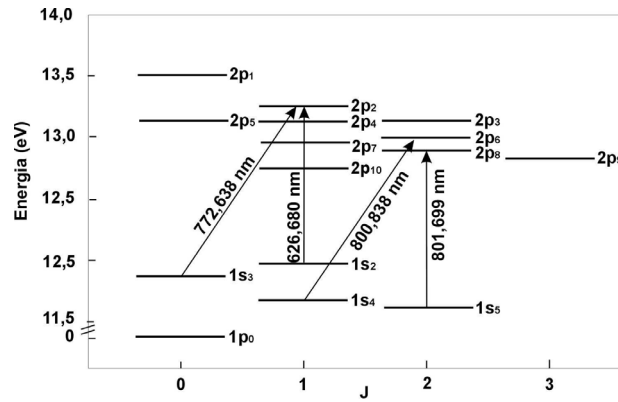
degree of ionization of  $\frac{n_i}{n_i + n_n} = 6.5 \cdot 10^{-5}\%$ .



**Fig.3** Semilogarithmic characteristic of I-U for a Langmuir probe

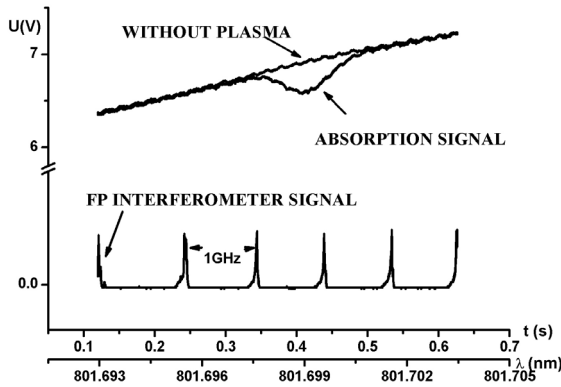
## b) Spectral measurements

The spectral measurements allow the calculation of the absolute density of metastable argon atoms in the energetic state  $(3p^5 4s)^3P_2(1s_5)$ . The lifetime of this argon metastable state is 55.9s [8]. In Fig.4 it is shown the partial diagram of energy levels of Ar including that which is of interest for our measurements.

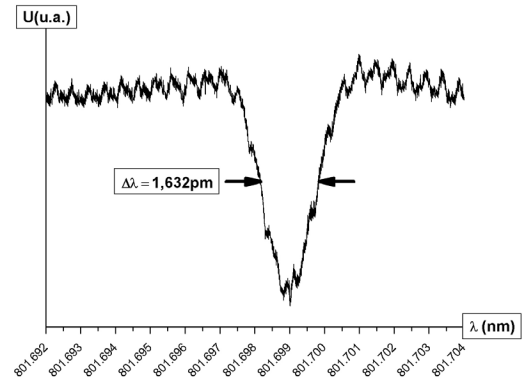


**Fig.4** Partial energy level diagram of Ar and the transitions for interest

Scanning the wavelength of the laser radiation emitted in a range of 10-12pm around 801,699nm gives the profile of the absorption line of the transition from metastable level  $(3p^5 4s)^3P_2(1s_5)$  to  $2p_8$  level. The absorption signal was obtained in typical conditions of diode temperature 24.6°C and diode laser current 69mA. A typical absorption profile with and without plasma can be observed in Fig.5.a and 5b.



**Fig.5a** Typical experimental signals



**Fig.5b** Typical absorption line profile

The absolute concentration of the argon metastable was calculated (using formula (1)) [9]. Using the profile obtained under the conditions mentioned above, the density of the argon atom in metastable state is  $2 \times 10^8 \text{ cm}^{-3}$ .

$$N_i = \frac{\int k_v dv}{\lambda_{0i}^2 (g_j / g_i) (A_{ji} / 8\pi)} \quad (1)$$

where for the i-j transition  $\lambda_{0i} = 801.699 \text{ nm}$  is the central wavelength,  $g_i$  and  $g_j$  are the statistical weights of the lower and upper level,  $A_{ji}$  the spontaneous emission probability and  $k_v$  is the absorption coefficient. The constant value in the equation (1) is:  $\lambda_{0i}^2 (g_j / g_i) \times (A_{ji} / 8\pi) = 2.4 \times 10^{-7} (\text{m}^2 \text{ s}^{-1})$  [9].

As a result the percentage of metastable with respect to gas density is  $\frac{n_m}{n} = 10^{-6}\%$  and with respect to plasma density is  $\frac{n_m}{n_i} = 1.6\%$

Assuming that the line width from Fig.5b is given mainly by Doppler profile, we may calculate the gas temperature. Standard formula for Doppler line is given by equation (2) [10].

$$\Delta\lambda_D = \frac{\lambda_0}{c} \sqrt{\frac{2RT \ln 2}{M}} = 7.16 \cdot 10^{-7} \lambda_0 \sqrt{\frac{T}{M}} \quad (2)$$

where  $\lambda_0$  is 801.699nm,  $\Delta\lambda_D=1.6$ pm,  $M=40$  for argon and  $T$  is the gas temperature. Using the equation (2) we obtained  $T=323$ K. It means that metastable atoms are in equilibrium with neutral gas within the discharge tube so their temperature is close to room temperature.

The results express the simplicity of the experimental set-up for plasma diagnosis, the stability of the system and the possibility to work for different types of discharges and different gases. The method has also analytical capabilities allowing detection of trace elements. The potential of the Toptica DL 100 has still to be used at its full capacity in a various types of experiments in atomic physics and plasma physics.

### Acknowledgements

This research was supported by the grant 39699 of CNCSIS-MEC.

We would like to thank Dr. M.Miclea from ISAS-Germany for very fruitful discussions and also to Toptica for professional support during installing the system.

### References

- [1].S.M.Rossnagel, J.J. Cuomo, W.D. Westwood, *Handbook of Plasma Processing Technology*, Noyes Publications, N.J., (1990)
- [2].T.Motylewski, M.Linnartz, Rev. Sci. Instrum., **70**, 1305 (1999)
- [3].A.Kono, N.Koike, K.Okuda, T.Goto, Jpn. J. Appl. Phys., **32**, L543 (1993)
- [4].H. Scheibner, St. Franke, Samir Solyman, J.F. Behnke and C. Wilke, Rev. Sci. Instrum., **73**, 378 (2001)
- [5].\*\*\*\**Diode Laser System DL 100 Manual* – TOPTICA Photonics AG, Germany
- [6].G.Popa, K.Ohe and N.Dumitrascu, J.Phys.D:Appl.Phys.**22**, 1327 (1989)
- [7].R.H.Huddleston, S.C.Leonard, *Plasma diagnostics techniques*, Acad. Press., NY (1965).
- [8]. Norma E. Small-Warren and Lue-Yung Chow Chiu – Phys. Rev. A **11**, 1777 (1975)
- [9]. C. Penache, M. Miclea, A. Brauening-Demian, O. Hohn, S. Schosler, T. Janke, K. Niemax and H. Schmidt-Boecking – Plasma Sources Sci. Technol. **11**, 476-483 (2002)
- [10]. M.Miclea, PhD Thesis:”*Study of the dielectric barrier discharge using diode laser spectroscopy*”, Bucharest, Romania (2001).

# COMPARATIVE SURFACE STUDIES OF PLASMA TREATED FLUORINATED ETHYLENE PROPYLENE (FEP) AND POLYPROPYLENE (PP)

R.K. Pitrus, A. Soliman, N. Brack, P.J. Pigram and J. Liesegang

*Department of Physics and Centre for Materials and Surface Science La Trobe University VIC 3086, AUSTRALIA.*

## Abstract:

The effects of air plasma treatment on FEP and PP are explored. Variation in surface electrical conductivity with plasma treatment and ageing time is measured and related to results from XPS and contact-angle measurements. Despite chemical and structural differences, FEP and PP show remarkably, broadly similar resistivity and wettability behaviour.

## 1. Introduction

FEP and PP play an important role in many technological applications such as substrates for printed circuit boards, non-stick coatings for kitchen utensils and adhesive tapes [1-4]. Improvement in the characteristics of FEP and PP will lead to an expanded range of applications; for example in biomedical encapsulation technology (such as protein-phobic surfaces).

Specific techniques are required for understanding the plasma surface modification of polymers aimed at improving wettability and adhesion. These include X-ray Photoelectron Spectroscopy (XPS), resistivity and contact angle (CA) measurement [5-10].

The interaction of air and oxygen plasma with PP films creates C-O, C=O and COOH groups [8,11,12], while with FEP co-polymer films it forms C-C, C-O and C=O. Ageing of plasma-treated polymers has been investigated by several workers and the chemical changes induced by the plasma treatment are often found to be only partially reversible with time [13-17]. This work investigates the effects of air plasma treatment (APT) of FEP and PP surfaces and subsequent ageing effects; in particular, surface resistivity is monitored.

## 2. Experimental

FEP and PP films (GoodFellow, UK) were used. PP samples were ultrasonicated in ethanol for 30 minutes, rinsed with ethanol and air dried. FEP samples were ultrasonicated in toluene for 10 minutes and rinsed with toluene and then ultrasonicated with acetone for 10 minutes and rinsed with acetone again and finally rinsed with ethanol twice and air dried.

Films (sample size 50 x 30 x 0.04 mm) received APT as follows:  $10^{-1}$  torr FEP; 1 torr PP; with RF power 30 W for various treatment times (0-180s) (Harrick model PDC-3XG). Dielectric constant was measured by a capacitive method; the values are necessary for resistivity determinations as described in reference [18] which provides a method of measurement of the volume resistivity of the sample in its surface region.

XPS analyses were performed using a Kratos AXIS Ultra imaging XPS instrument using a monochromated Al K $\alpha$  X-ray source (1486.6 eV) operated at 150W. The sample analysis area was approximately 700  $\mu\text{m}$   $\times$  300  $\mu\text{m}$ ; pass energies of 160 and 20 eV were used for acquiring survey and region spectra, respectively.

Air/water contact angles (sample size 20 x 15 x 0.04 mm) were measured using de-ionised Milli-Q water (10  $\mu\text{L}$  drops at 20°C) with a Data physics OCA20 instrument incorporating a reversible drive to allow determination of advancing (ACA), sessile (SCA) and receding (RCA) contact angles.

## 3. Results and discussion

### 3.1 Wettability Measurements

The ACA, SCA and RCA on the untreated, cleaned FEP were 117, 108 and 100 ( $\pm 2$ ) degrees, respectively and were compared with literature values [17, 19, 20]. The same angles for untreated cleaned PP films were 106, 95 and 78 degrees, respectively.

Sessile and dynamic contact angle measurements were performed on cleaned, APT-FEP co-polymer. Figure 1 shows average of left and right angles for SCA as a function of APT time for FEP and PP samples. From this figure it may be seen that the SCA decreases sharply for less than 10 seconds APT for FEP and then approximately stabilizes, but shows slower decreasing tendency for PP. In both cases, wettability is significantly enhanced. Similar behaviour has been reported for water plasma treatment of FEP [17], and air plasma treatment of PP [11, 20].

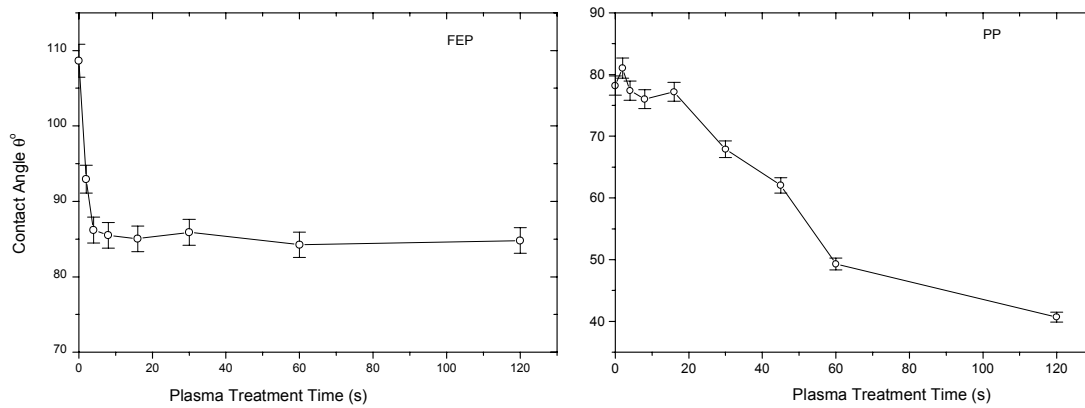


Figure 1. SCA of de-ionized water drops on FEP and PP as a function of APT time.

Figure 2 represents the average of left and right SCA as a function of ageing time after APT. The results show that there are no significant ageing variations within the experimental error, but it may be noted that the ageing trend lines cluster differently for the two samples. For FEP, the clustering is due to the rapid initial fall in CA seen in Figure 1 (FEP) while the slower decrease of CA in Figure 1 (PP) also accounts for less clustering in Figure 2 (PP).

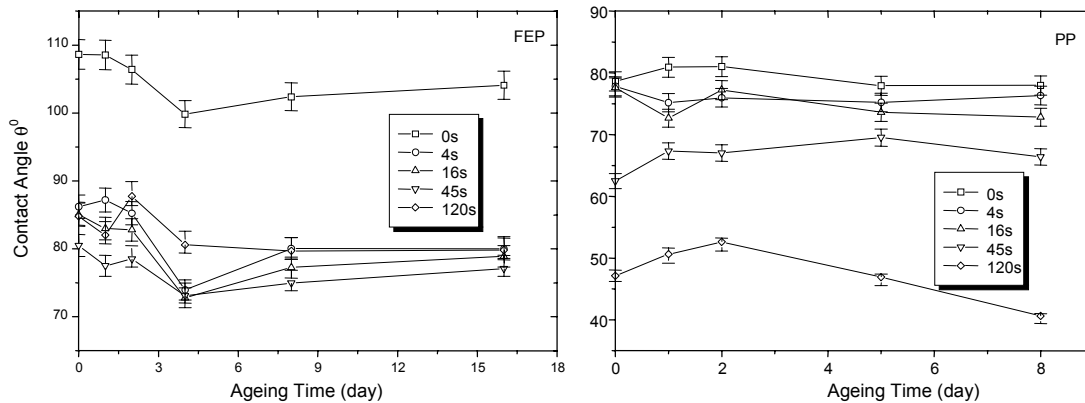


Figure 2. Average of left and right SCA as a function of ageing time for different APT times shown.

### 3.2 Resistivity Measurements

Resistivity in the surface region of the samples was determined using the method of Liesegang *et al.* [18]. The results are shown in Figure 3 for different APT times. Both samples show that the resistivity is reduced by approximate factors of 1.3 (FEP) and 1.5 (PP). Resistivity variation with APT time for FEP levels out, but for PP it appears to decrease.

Resistivity measurements were carried out for cleaned, APT and aged, APT films. The results obtained are shown in Figure 4. Plasma treatment times of 0, 4, 16, 45 and 120 s were used. From Figure 4 it may be seen that there is slight decrease in resistivity with ageing, and this is discussed later in the section on XPS measurements.

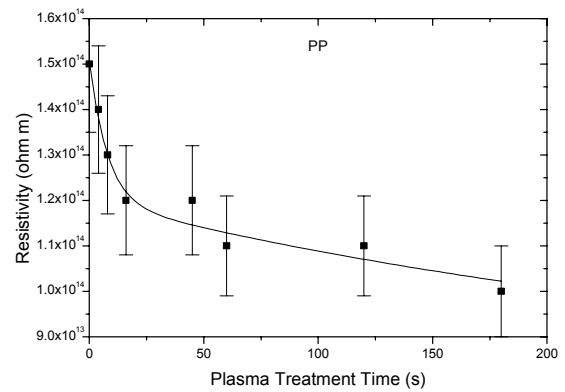
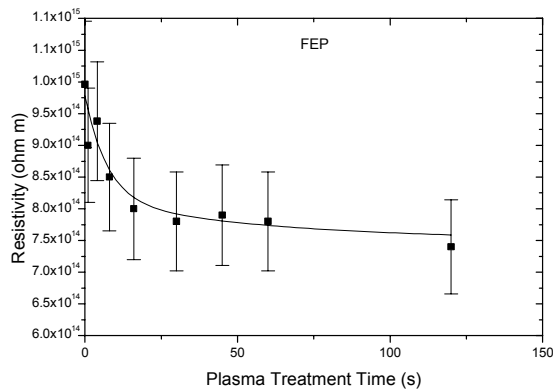


Figure 3. Resistivity versus plasma treatment time of cleaned FEP and PP.

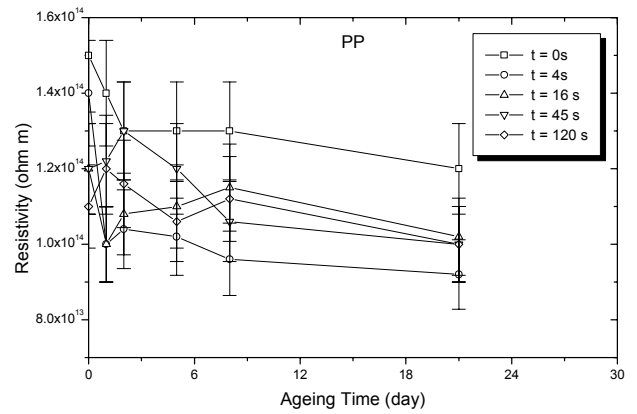
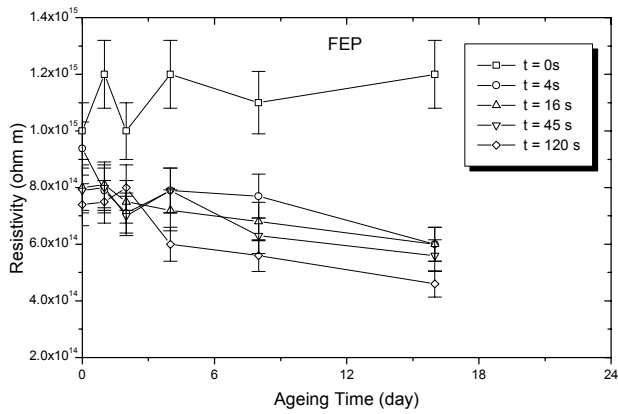


Figure 4. Resistivity versus ageing time for FEP and PP samples for different plasma treatment times as indicated.

### 3.3 XPS Measurements

A survey scan (not shown) and region scans (Figure 5) for the FEP film as-received were acquired using XPS. (The survey scan showed two major peaks: C 1s and F 1s; and some adventitious carbon contamination, while quite small, was detectable as a hydrocarbon signal at 285.0 eV.

From Figure 5, it may also be seen that the spectrum for the treated sample has been divided into 6 component peaks with binding energies at: 292.0, 293.9, 290.2, 285.0, 287.0 and 288.6 eV representing  $\text{CF}_2$ ,  $\text{CF}_3$ , CF, C-C, C-O and C=O respectively. The changes in the atomic ratios (F/C and O/C) of FEP and PP films with increasing plasma treatment time, ranging from 1 to 180 seconds, are plotted in Figure 6. It may be noted that the decrease in F/C ratio coincides with increase in O/C ratio for FEP. In terms of actual O/C values, PP oxidized more easily under APT.

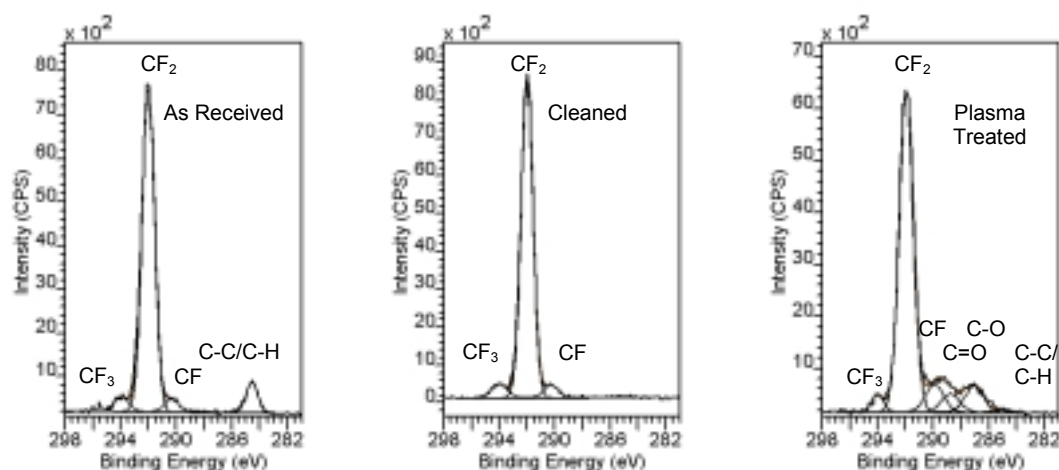


Figure 5: High resolution C 1s spectra for as received, solvent cleaned and 120 s air plasma treated FEP samples.

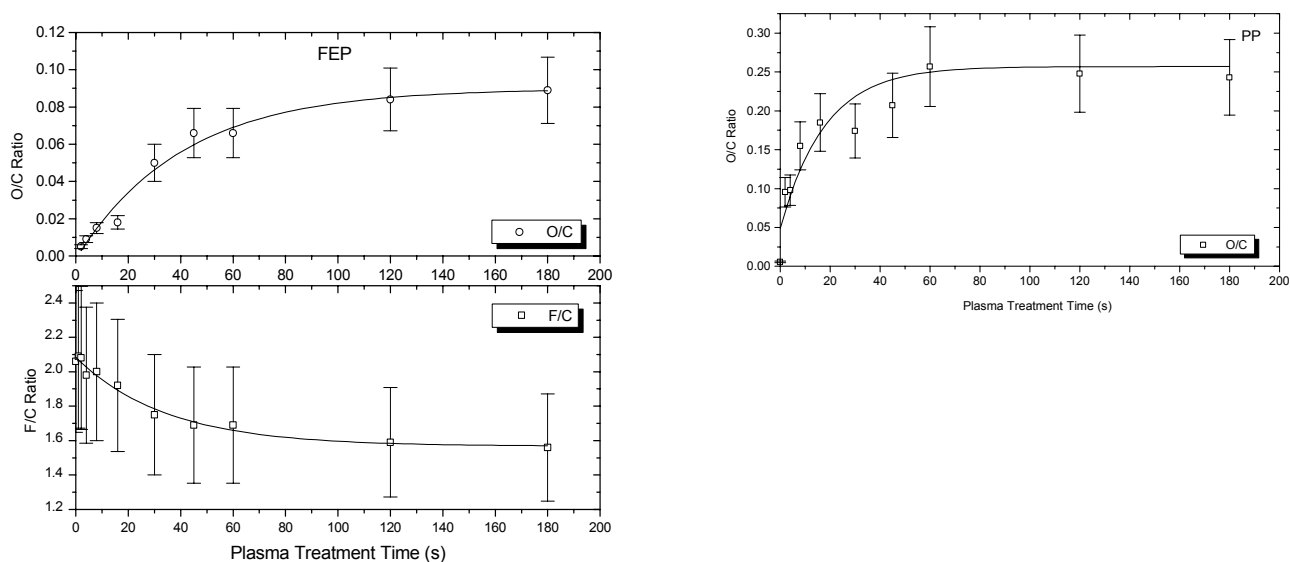


Figure 6. Atomic surface composition ratios for FEP and PP samples.

Cleaned PP was also examined by XPS and found to be free from contaminating N and O. The spectrum of cleaned samples may be well fitted with three significant peaks (Figure 7). The hydrocarbon signal shows a two peak structure at binding energies 285.0 and 285.3 eV. This is attributed to vibrational broadening resulting from the removal of the core level C 1s electrons from the orbital during photoelectron excitation [20].

It may be seen from C1s region scans for PP film at different APT times (4s shown only in Figure 7), that higher binding energy carbon species and other additional oxidized species start to appear and extend to 290.0 eV. Oxygen-containing polar functional groups incorporated into the surface have been identified as hydroxyl (C-OH) (286.5 eV), peroxy (C-O-O) (287.1 eV), carbonyl (C=O) (287.9 eV), ester (C-O-C=O) (288.6 eV) and carboxylic acid (HOC=O) (289.5 eV), as described previously, for example [8]. These peaks vary in intensity depending on treatment time.

During APT the surface becomes significantly rougher [11] and more oxidized, consistent with the initial changes in contact angle and resistivity results. In addition, the F/C and O/C ratios for FEP and the O/C ratio for PP show little variation with ageing (not shown), consistent with approximate levelling out of the resistivity (Fig. 4) and SCA (Fig. 2).

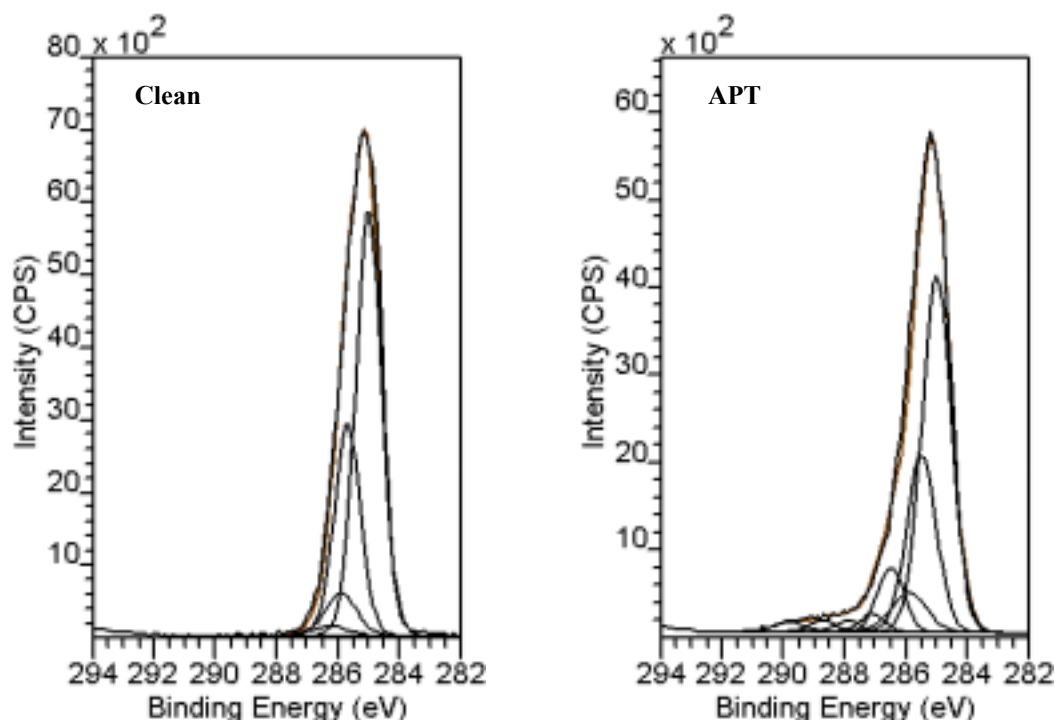


Figure 7: High resolution C 1s spectra of clean PP (left) and 4s APT-PP (right).

Surface roughening and the production of polar functional groups as a result of APT will account for the initial fall in SCA for both FEP and PP as shown in Figure 1. It is also known (from water plasma treatment) [17] that the modification layer is deep for FEP, which hinders polymer chain re-orientation and is unfavourable for mobility of the functional groups towards the bulk. We similarly assert that such a process will account for the leveling out of the SCA data for APT-FEP with ageing (Fig. 2).

In PP, however, the polar groups produced by APT are more labile. Hydroperoxide groups, for example, can more easily reorientate and are more easily pushed below as non-polar chains move to the surface to lower the surface energy during the ageing process [17, 21]. It seems that this process of partial surface recovery or return to hydrophobic nature is more applicable to corona discharge treatment [11] than to the APT used in this work. It may be noted that the SCA data reported here appear not to exhibit such recovery.

The resistivity trends for both FEP and PP at low APT times would also appear to be in accord with polar functional group production. But for FEP, the O/C ratio reaches 8% while for PP it reaches 25% under APT. That both materials exhibit approximately similar reduction factors in resistivity is therefore surprising. The surface electrical transport mechanism would seem to be independent of O/C ratio. The slight decrease in resistivity with ageing in air of both APT-FEP and APT-PP could be accounted for by adventitious water adsorption.

#### 4. References

- [1] I. Mathieson, D.M. Brewis and I. Suther, *J. Adhesion*, **46**, 49 (1994).
- [2] C.A. Chang, J.E.E. Baglin, A.G. Schrott and K.C. Lin, *Appl. Phys. Lett.*, **51**, 103 (1987).
- [3] C.A. Chang, C.J. Chan and F. J. Jones, *Appl. Phys. Lett.*, **59**, 1069 (1991).
- [4] R.K. Sung, *J. Appl. Polym. Sci.*, **77**, 1913 (2000).
- [5] D. Briggs, D.M. Brewis, R.H. Dahm and I.W. Fletcher, *Surface and Interface Analysis*, **35**, 156 (2003).
- [6] F.A. Rasoul, D.S. Hill, G.A. George and O. Donnell, *Polymers for Advanced Technologies*, **9**, 24 (1998).
- [7] N. Medard, M. Aouinti, E. Pocin and P. Bertrand, *Surface and Interface Analysis*, **31**, 1042 (2001).



- [8] A. Lesley, L. Stuart and P. Bhakan, *Surface and Interface Analysis*, **33**, 335 (2002).
- [9] D. Simon, J. Liesegang, P.J. Pigram, N. Brack and J.L. Pura, *Surface and Interface Analysis*, **32**, 148 (2001)
- [10] J. Liesegang, B.C. Senn, P.J. Pigram, E.T. Kang, K.L. Tan and K.G. Neoh, *Surface and Interface Analysis*, **28**, 20 (1999).
- [11] S. Süzer, A. Argun, O. Vatnarsever and O. Aral, *J. Appl. Polym. Sci.*, **74**, 1846 (1999).
- [12] F. Garbassi, M. Morra, E. Occhiello, L. Barino and R. Scordamaglia, *Surface and Interface Analysis*, **14**, 585 (1989).
- [13] G. Suhanes, A. Terlingen, F. Hermina, G. Gerristan, A.S. Hoffman and J. Feijen, *J. Appl. Polym. Sci.*, **57**, 969 (1995).
- [14] P. Wittenbeck and A. Wokanov, *J. Appl. Polym. Sci.*, **50**, 187 (1993).
- [15] H. Yasuda, *J. Polymer Sci.*, **19**, 1255 (1981).
- [16] R.C. Chatelier, X. Xie, T.R. Gengenbach and H.J. Griesser, *Langmuir*, **11**, 2576 (1995).
- [17] X. Xie, T.R. Gengenbach and H.J. Griesser, *J. Adhesion Sci. Technol.*, **6**, 1411 (1992).
- [18] J. Liesegang, B.C. Senn and E.R. Smith, *J. Appl. Phys.*, **77**, 11 (1995).
- [19] A.W. Adamson and A.P. Gast, *Physical Chemistry of Surfaces*, 6<sup>th</sup> ed., John Wiley and Sons Inc. 365 (1997).
- [20] N.Y. Cui and N.M.D. Brown, *Applied Surface Science*, **189**, 31 (2002).
- [21] P. Wittenbeck and A. Wokaun, *J. Appl. Polym. Sci.*, **50**, 187 (1993).

# Molecular Dynamic Simulation of Polymer Etching by H<sub>2</sub> and N<sub>2</sub> plasmas

Hideaki Yamada<sup>†</sup> and Satoshi Hamaguchi

*Department of Fundamental Energy Science, Graduate School of Energy Science, Kyoto University, Uji, Kyoto, Japan*

<sup>†</sup>h-yama@center.iae.kyoto-u.ac.jp

## Abstract

We have constructed an interatomic potential model for classical molecular dynamics (MD) simulation to study interaction of H<sub>2</sub>/N<sub>2</sub> plasmas with organic polymer surfaces. The obtained potential functions for (H,C,N) systems are of generalized Stillinger-Weber type. The structure of the potential functions and a sample calculation of atom-molecule interaction are presented.

## 1. Introduction

Reducing the dielectric constants of insulating materials for interconnect circuits is of significant importance for the manufacturing of fast computer chips based on copper wiring. For this purpose, organic polymers with low dielectric constants have been studied recently as an alternative to SiO<sub>2</sub>. Polymers are also used for other applications, such as substrates for healthcare chips and optical waveguides for optical wiring. Hydrogen and nitrogen based plasmas such as N<sub>2</sub>+H<sub>2</sub> or NH<sub>3</sub> plasmas are often used to etch such polymer surfaces with micron and submicron structures [1,2].

The goal of this work is to study plasma-surface interactions of polymer etching process, especially to evaluate etching rates, etching products, and the degree of surface modification, using classical molecular dynamics (MD) simulations[3,4]. To represent surface reactions correctly, it is critical to employ realistic interatomic potential functions for MD simulations. Many classical interatomic potential functions have been proposed for MD simulations for various materials. Among them, we find that the Stillinger-Weber (SW) potential [5] and Abel–Tersoff–Brenner potential [6] are particularly useful for MD simulations of plasma-surface interactions. For polymer etching simulations mentioned above, however, there had not been good interatomic potential models readily available to the authors. In this work, therefore, we present interatomic potential functions for (H,C,N) systems that we have recently developed. The newly developed potential functions are seemingly of Stillinger-Weber type, but the atomic interactions are limited to those of covalent bonds. In the aspect of the latter, our potential is also similar to the Abel-Tersoff-Brenner potential. Similar potential functions for (Si, O, C, F) systems are given in Ref. [7].

## 2. Classical interatomic potential

To perform the MD simulations, we have constructed a classical interatomic potential model of the (H,C,N) system. In general, potential functions can be expanded into many body interactions using the cluster expansion technique, such as  $U(\mathbf{r}_1, \mathbf{r}_2, \mathbf{r}_3, \mathbf{r}_4, \dots) = \sum V_{ij}(\mathbf{r}_i, \mathbf{r}_j) + \sum V_{ijk}(\mathbf{r}_i, \mathbf{r}_j, \mathbf{r}_k) + \dots + \sum V_{ijkl}(\mathbf{r}_i, \mathbf{r}_j, \mathbf{r}_k, \mathbf{r}_l) + \dots$ , where summations are taken over  $i, j, k, \ell, \dots$ . Neglecting higher order interactions, the Stillinger-Weber (SW) potential consists of the 2- and 3-body interatomic potential functions [4] as

$$U = \sum_i \sum_{j(<i)} V_{ij}(r_{ij}) + \sum_i \sum_{j(<i)} \sum_{k(<j)} W_{ijk}(\mathbf{r}_i, \mathbf{r}_j, \mathbf{r}_k), \quad (1)$$

where  $V_{ij}$  and  $W_{ijk}$  are

$$V_{ij}(r_{ij}) = \frac{a_{ij}}{r_{ij}^{p_{ij}}} \exp[c_{ij}/(r_{ij} - r_{cij})] - \frac{b_{ij}}{r_{ij}^{q_{ij}}} \exp[d_{ij}/(r_{ij} - r_{cij})] \quad (2)$$

and

$$W_{ijk}(\mathbf{r}_i, \mathbf{r}_j, \mathbf{r}_k) = h_{kij} + h_{ijk} + h_{jki} \quad (3)$$

with

$$h_{kij} = \left[ \lambda_{kij} |\cos \theta_{kij} - \cos \theta_{0kij}|^{2\sigma_{kij}} \right] \exp \left[ \frac{\sigma_{kij}^{(k)}}{(r_{ki} - a_{kij}^{(k)})} + \frac{\sigma_{kij}^{(j)}}{(r_{ij} - a_{kij}^{(j)})} \right]. \quad (4)$$

Here  $r_{ij}$  represents the distance between the  $i$ -th and  $j$ -th atoms and  $\theta_{kij}$  represents the bond angle spanned by vectors  $\mathbf{r}_k - \mathbf{r}_i$  and  $\mathbf{r}_j - \mathbf{r}_i$ . An example of the 2-body potential between C and N atoms in  $\text{CH}_3\text{NH}_2$  molecule is shown in Fig.1, where the horizontal axis represents the distance between the C and N atoms as shown in the inset and the vertical axis represents the 2-body potential function, i.e.,  $V_{\text{NC}}$ . The filled circles represent the data from the quantum mechanical (*ab initio*) calculations [9]. The parameters  $a_{ij}, b_{ij}, \dots$  of  $V_{ij}$  of Eq. (3) are determined from the fit to *ab initio* data and the solid curve of Fig.1 is the fitting curve. The cut-off length of this function is taken to be somewhat shorter than the *ab initio* data in order to form realistic covalent bonds when many atoms are present to form molecules. The angular dependence of 3-body potential for H, C and N atoms in  $\text{CH}_3\text{NH}_2$  molecule is shown in Fig.2, where the horizontal axis represents the angle between C-H and C-N bonds as shown in the inset. The vertical axis represents the sum of the 2- and 3-body potentials, i.e.  $U = V_{\text{CH}} + V_{\text{CN}} + W_{\text{HCN}}$ . Here squares represent *ab initio* data obtained with the most stable H-N and N-C lengths while circles and triangles represent *ab initio* data obtained with 20% shorter and longer bond lengths, respectively.

It is not easy to fit the standard SW-type functional form to interatomic potential data of (H,C,N) systems in order to obtain a classical potential model. First, in the standard SW-type potential, all pairs and triplets of atoms are assumed to interact as long as their relative distances are within the cut-off lengths, even if no covalent bonds are considered to be formed among some of these atoms. Under this approximation, together with the approximation of eliminating the higher order terms in the cluster expansion, the standard SW-type potential function sometimes fails to represent the absence of covalent bonds correctly, e.g., the case where the coordination number of an atom is larger than the number of its valence electrons. Second, the functions  $V_{ij}$  and  $W_{ijk}$  of Eqs. (2) and (3) do not depend on the bond kinds while C and N can form double and triple bonds. Thus the standard SW-type potential can not be applied directly to systems with multiple bonds.

To solve such problems, we generalize SW-type potential functions as

$$U = \sum_m \sum_i \sum_{j(<i)} A_{ij}^m(N_{bij}) V_{ij}^m(r_{ij}) + \sum_i \sum_{j(<i)} \sum_{k(<j<i)} \sum_{m,n} \left[ \begin{aligned} &B_{ijk}^{m,n}(N_{bij}, N_{bjk}) h_{ijk}^{m,n}(r_{ij}, r_{jk}, \theta_{ijk}) \\ &+ B_{kij}^{\ell,m}(N_{bki}, N_{bij}) h_{kij}^{\ell,m}(r_{ki}, r_{ij}, \theta_{kij}) \\ &+ B_{jki}^{n,\ell}(N_{bjk}, N_{bki}) h_{jki}^{n,\ell}(r_{jk}, r_{ki}, \theta_{jki}) \end{aligned} \right], \quad (5)$$

where  $N_{bij}$  represents the multiplicity of bond between the  $i$ -th and  $j$ -th atoms; for example,  $N_{bij}=0$  for no covalent bond and  $N_{bij}=2$  for a double bond. The parameter  $N_{bij}$  is chosen to be a smooth function of the atomic configuration. The weight functions  $A_{ij}^m$  and  $B_{ijk}^{m,n}$  are smooth functions of their arguments that satisfy  $A_{ij}^m(N_{bij} = m) = 1$ ,  $A_{ij}^m(N_{bij} \neq m) = 0$ ,  $B_{ijk}^{m,n}(N_{bij} = m, N_{bjk} = n) = 1$  and  $B_{ijk}^{m,n}(m', n') = 0$  if  $m' \neq m$  or  $n' \neq n$  with  $m, n, m'$ , and  $n'$  being integers. Clearly if  $ij = \text{CC}$  or  $\text{NN}$ , then  $1 \leq m, n \leq 3$ . If  $i$  or  $j$  is H, then we set  $A_{ij}^m(N) = 0$  for  $m=2,3$ . The formation of a covalent bond (which is represented by nonzero  $N_{bij}$ ) is determined based on the following two conditions: 1) each atom preferentially form bonds with closer atoms and 2) the number of bonds at each atom does not exceed the number of its valence electrons. Details of the potential functions we have constructed will be published elsewhere. Sample calculations based on our potential functions are shown in Fig.3, where three H atoms are arranged in line. For  $Y=5.0$  [Å], the center H forms a bond with the left H if bond length  $X$  is shorter than the H-H cut-off length (Fig.3a). For the other two cases with  $Y < 0.74$ , the center H forms a bond with the right H and the left H is repulsed (Figs.3b and 3c). It is seen that our potential function (solid line) reproduces the *ab initio* data (cross symbols) well despite the fact that data points shown here were not used when the values of fitting parameters were determined.

### 3. MD simulation

Many of commercial low dielectric organic polymers contain benzene rings [1,2]. In order to study polymer etching by MD simulations, therefore, we have selected poly (1,4-phenylene)  $[C_6H_4]_n$  as our model substrate since it is one of the simplest polymers with benzene rings. Figure 4 shows the geometry of the our simulation cell. Here the side lengths of the simulation box in x and y directions are 17.3 and 25.1  $\text{\AA}$ . White and black spheres represent hydrogen and carbon atoms respectively. In the horizontal direction, the periodic boundary conditions are imposed. Incident atoms and molecules are directed toward the substrate surface from the upper side of the box .

### 4. Summary

We have constructed classical interatomic potential functions for (H,C,N) systems, using interatomic data obtained from quantum mechanical calculations. The potential functions are made to satisfy that (1) each atom preferentially forms bonds with closer atoms and (2) the number of bonds of each atom does not exceed the number of its valence electrons. Further the new model functions can also represent multiple bonds. MD simulations results based on these potential functions for poly (1,4-phenylene) substrates will be presented elsewhere. This work was supported by the Semiconductor Technology Academic Research Center (STARC).

### References

- [1] H. Nagai, et.al., J.App.Phys.**91**, 2615(2002);
- [2] M. Hukasawa, et.al., Proceedings of Symposium on Dry Process (Waseda Univ., Japan, Nov.11-13, 1998), pp.175.
- [3] S. Hamaguchi and H. Ohta, Vacuum **66**, 189 (2002).
- [4] H. Ohta and S. Hamaguchi, J. Vac. Sci. Technol. A**19**, 2373 (2001); J. Chem. Phys.**115**, 6679 (2001).
- [5] F. H. Stillinger and T. A. Weber, Phys. Rev. B**31**, 5262 (1985).
- [6] D. W. Brenner, Phys. Rev. B **15**, 9458 (1990).
- [7] H. Ohta, S. Hamaguchi, M. Wakatani, and H. Yamada, proceedings of 26th international conference on phenomena in ionized gases (Greifwald, Germany, July 15-20, 2003).
- [8] H. Yamada and S. Hamaguchi, Proceedings of international symposium on dry process (Univ. of Tokyo, Japan, Oct.10-11, 2002), pp.189; Proceedings of the 20th symposium on plasma processing (Nagaoka, Japan, Jan.29-31, 2003), pp.191.
- [9] M. J. Frisch, et.al., "Gaussian 98, Revision A.11.1," Gaussian, Inc., Pittsburgh PA, (2001).

### Figures

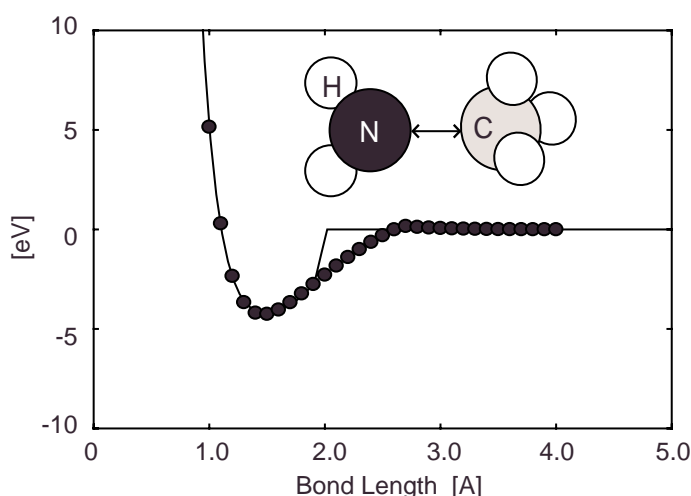


Fig.1 The 2-body potential function  $V_{NC}$  (solid line) as a function of the interatomic distance. Filled circles represent *ab initio* data.

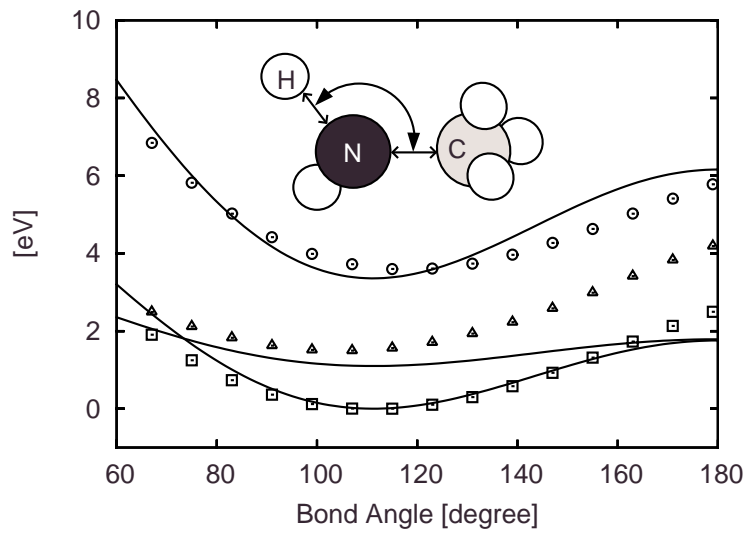


Fig.2 The potential function,  $V_{CH}+V_{CN}+W_{HCN}$  (solid line) as functions of the bond angle shown in the inset. Open circles, triangles, squares represent *ab initio* data.

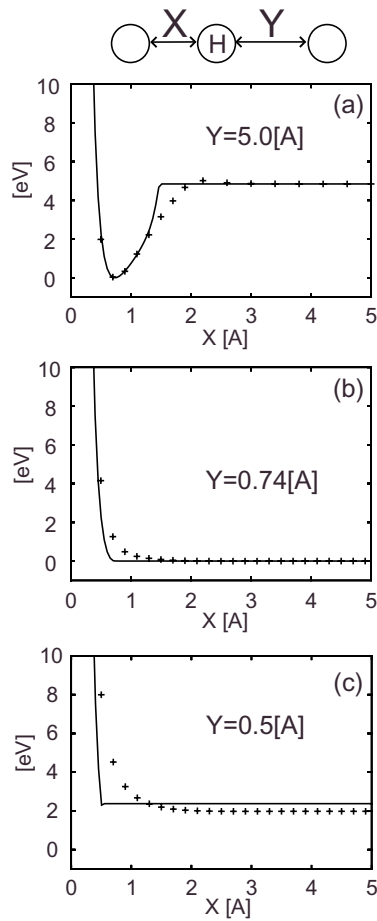


Fig.3 The potential  $U$  for  $H_3$  cluster as functions of the interatomic distances. The cross symbols represent *ab initio* data. The parameters of the potential function were determined by fitting  $V_{HH}$  of Eq. (2) to the *ab initio* data given in (a). The obtained function (solid curves) is shown to be in reasonable agreement of the *ab initio* data given in (b) and (c).

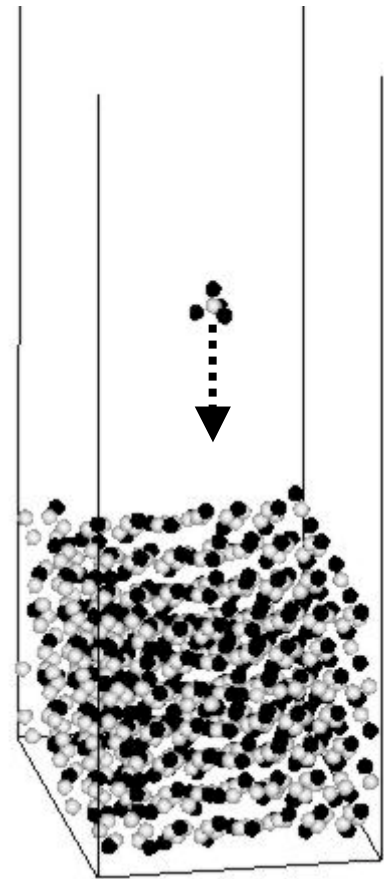


Fig.4 The geometry of the initial data of our MD simulations for poly (1,4-phenylene),  $[C_6H_4]_n$ . etching. White and black spheres represent carbon and hydrogen atoms. In horizontal direction, the periodic boundary conditions are imposed. Incident particles come from the upper side of the simulation box. The incident molecule shown here is  $CH_4$ .

# Amorphous fluorocarbon polymer films prepared in perfluorooctane (C<sub>8</sub>F<sub>18</sub>) vapor plasma CVD for an application of electrical insulation

C. Biloiu<sup>1,2</sup>, I. A. Biloiu<sup>1,2</sup>, Y. Sakai<sup>1</sup>, Y. Suda<sup>1</sup> and A. Ohta<sup>1</sup>

<sup>1</sup> Division of Electronics and Information Engineering, Hokkaido University, Sapporo 060-8628, Japan

<sup>2</sup> On leave from Faculty of Physics, Bucharest University, Bucharest-Magurele, P.O.Box MG-11, 76900, Romania  
(sakaiy@eng.hokudai.ac.jp)

## ABSTRACT

Amorphous fluorocarbon polymer films (a-C:F) were prepared in perfluorooctane (C<sub>8</sub>F<sub>18</sub>) vapor plasma enhanced chemical vapor deposition. The deposition rate in the C<sub>8</sub>F<sub>18</sub> vapor and the vapor diluted by 10% Ar gas reached 200-300 nm/min for the thickness  $h$  from 1  $\mu$ m to 12  $\mu$ m. The dielectric constant and dielectric loss in a frequency range between 120 Hz and 1 MHz were  $\sim 2.5$  and  $\leq 3 \times 10^{-2}$  respectively. The dielectric strength  $E_B$  against  $h$  was  $E_B \sim h^{-0.53}$  ( $E_B = 2.7$  MV/cm at  $h = 1$   $\mu$ m and  $E_B = 0.9$  MV/cm at 12  $\mu$ m). The chemical properties of the film were also analyzed.

## 1. INTRODUCTION

Amorphous fluorocarbon polymer films (a-C:F) have attracted great interest as a promising material for interlayer dielectrics in ultra-large scale integrated circuits[1,2], biocompatible materials production[3,4], and recently, electrical insulation in electric apparatus[5,6], because of their unique properties, such as low dielectric constant, high dielectric strength, high protein binding capability, low surface energy, high hydrophobicity, and chemical inertness. Usually, these films are prepared using plasma enhanced chemical vapor deposition (PECVD) methods. In the obtained film, a C–C cross-linked structure brings high thermal stability and fluorination makes dielectric constant lower.

Stoffels et al [7] indicated that the densities of large C<sub>x</sub>F<sub>y</sub> polymers in the film increased with increasing the size of feedstock molecule and that the saturation level of polymerization decreased with decreasing the amount of fluorine in the molecule, namely, a feedstock monomer with higher molecular weight makes possible to achieve polymerization with a large amount of CF<sub>2</sub> bonds. Consequently, the electrical properties of the film are expected to be close to those of polytetrafluoroethylene (PTFE). However, only a few attempts to obtain a-C:F films using high molecular weight monomers such as: C<sub>7</sub>F<sub>14</sub>, C<sub>7</sub>F<sub>16</sub>, [(C<sub>6</sub>F<sub>5</sub>)CF<sub>2</sub>CF=CF<sub>2</sub>], and (C<sub>3</sub>F<sub>7</sub>)<sub>3</sub>N/(C<sub>4</sub>F<sub>9</sub>)<sub>3</sub>N have been reported [8-10], since these fluorocarbon monomers are liquid at room temperature. But actually, their saturation vapor pressures are relatively high, i.e. a few tens of Torr. The fluorocarbon vapor PECVD brought high deposition rate of 200-300 nm/min, which were one order of magnitude higher than those obtained in conventional CF<sub>4</sub> and C<sub>2</sub>F<sub>6</sub> gases. Furthermore, the dielectric strength was larger and dielectric constant was smaller than the films obtained in CF<sub>4</sub> and C<sub>2</sub>F<sub>6</sub> gases [9].

In the present work we study the electrical and chemical properties of a-C:F films prepared in perfluorooctane (C<sub>8</sub>F<sub>18</sub>) vapor PECVD, and examine a possibility of application of the film to electrical insulator for electrical apparatus.

## 2. EXPERIMENTAL

Fig.1 shows the present experimental set-up. a-C:F films were prepared in a parallel-plate, capacitively coupled, 13.56 MHz PECVD reactor (base pressure 10<sup>-6</sup> Torr) with a size of 400 mm in diameter and 560 mm in height. The electrodes are made of stainless steel discs of 15 cm diameter, and their distance is 2 cm. The input power into the plasma is between 50 and 300 W. C<sub>8</sub>F<sub>18</sub> is used as a feedstock monomer, which is introduced into the reactor through a Koffloc-type mass flow controller (Fuji Electric Co.) at a flow rate of 15 sccm under the pressure between 0.2 and 1 Torr. Then, the residence time of C<sub>8</sub>F<sub>18</sub> monomer in the reactor is estimated between 1 and 10 minutes. The substrates used are Si n-type (111) wafer, glass, copper foil and stainless steel disc mounted on the grounded electrode. They are cleaned using an ultrasonic bath in acetone and ethanol, and then

in deionized water. Before deposition starts, the substrate is exposed to a 0.2-Torr Ar dc discharge for 15 minutes.

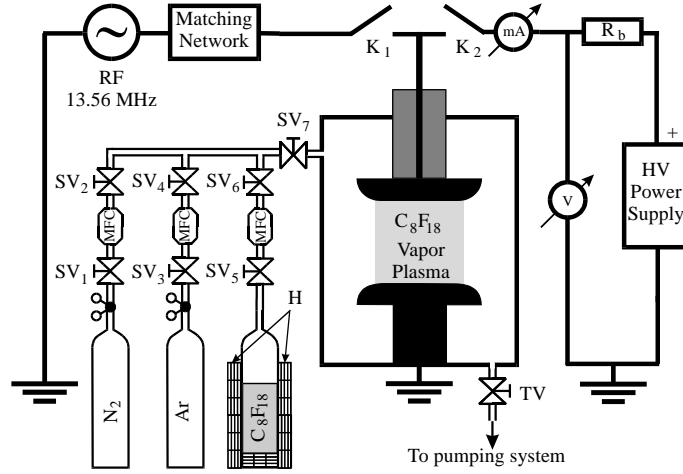


Fig.1 Experimental set-up for a-C:F film deposition and dielectric strength measurement

For the film analysis, we use a scanning electron microscope (SEM) to obtain the surface morphology and thickness of the film, X-ray photoelectron microscope (XPS) to obtain the relative elemental composition and chemical bonding structure of the film, and Fourier Transform Infrared Spectroscopy (FTIR) to gain insights about different vibration modes of chemical species contained in the film, and ellipsometry to measure the refractive index of the film.

For capacitance-voltage (*C-V*) measurements, small Cu/a-C:F film/Au (MIM) sandwich structures were prepared by masking the film surface, which was previously deposited on copper foils (2×2 cm area, 0.1 mm thick), and then coating with gold by evaporation under ultrahigh vacuum condition. MIM capacitors were employed in the dielectric constant and dielectric loss measurements using a 2340 LCZ meter (NF Electronic Instruments).

The MIM structures were also used for *I-V* measurements using an ultra high resistance meter (model R8430, Advantest Co.). From these measurements the dependence of leakage current *J* against electric field strength *E*, and the breakdown voltage *V<sub>B</sub>* of the film were obtained.

Complementary characterization of the film dielectric strength has been accomplished by measuring *V<sub>B</sub>* through a test electrode placed on the film surface. For this measurement, a high voltage dc supply was connected to the test electrode, and the applied voltage was increased at a constant rate of 10 volts per second till the film breakdown occurred. The breakdown moment was noticed by the sudden jump of the current with the drop of the voltage.

### 3. RESULTS AND DISCUSSION

#### 3.1 Dielectric constant

Fig.2 shows the capacity of the MIM element as a function of  $d^2$ , where *d* is the diameter of the Au electrode. The dielectric constant  $\epsilon_r$  of the a-C:F film is calculated using the following equation:

$$\epsilon_r = \frac{4h \tan \alpha}{\pi \epsilon_0} \quad (1)$$

where *h* is the film thickness,  $\epsilon_0$  is the permittivity in vacuum ( $=8.85410 \text{ F/m}$ ), and  $\tan \alpha$  is the slope of linear dependency in Fig.2. The dielectric constant of the a-C:F film as a function of frequency *f*, along with Tefzel® and Teflon®FEP(PTFE) films [11] for comparison, are shown in Fig.3. As it is well known, overall dielectric constant  $\epsilon$  is given by a sum of the following three components:

$$\epsilon = \epsilon_{\text{electronic}} + \epsilon_{\text{ionic}} + \epsilon_{\text{oriental}} \quad (2)$$

The first term is due to electronic polarization, and is defined as  $\epsilon_{\text{electronic}} = n^{1/2}$  ( $n$  : the optical refractive index). Endo et al [12] showed that, in the case of fluorocarbon polymer films, the dielectric constant is determined mainly by electronic polarization. In the present case, the ellipsometric measurement gave that  $n=1.38$ . With this value, electronic polarization accounts for about 80% of the dielectric constant. Since oriental polarization comes from the presence of C-O bonds or O-H bonds [13] and the XPS analysis reveals a small amount of oxygen contained in our films, we could say that the ionic polarization accounts for 20% of overall dielectric constant. A tendency of the slight decrease in  $\epsilon$  with  $f$  is regarded as incomplete dielectric relaxation occurring at  $f$  higher than 10 kHz [2]. The present results are consistent with previous observation that an increase in the fluorine to carbon ratio in the film leads to a lower dielectric constant [12]. In the case of Teflon<sup>®</sup>FEP film with a dielectric constant of about 2, the F/C ratio is 2 because these films consist in  $(-\text{CF}_2-)_n$  linear chains. The present films show a dielectric constant of about 2.48, but the F/C ratio revealed by XPS analysis is 1.75.

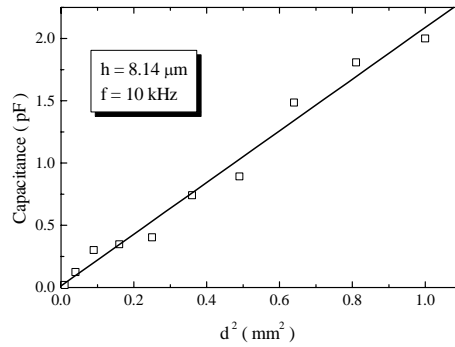


Fig. 2. Linear dependency of MIM element capacitance vs the square of the MIM electrode diameter

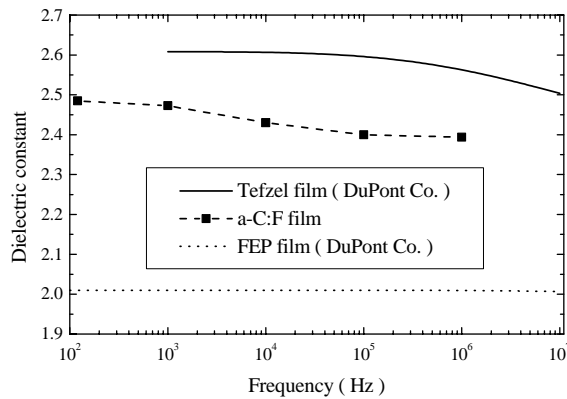


Fig. 3. Dielectric constant against frequency for a-C:F film and Teflon<sup>®</sup>FEP and Tefzel<sup>®</sup> films for comparison

### 3.2 Dielectric loss

Fig. 4 shows the dielectric loss factor,  $\tan \delta$ , as a function of  $f$  for the a-C:F films, together with Teflon<sup>®</sup>FEP and Tefzel<sup>®</sup> film cases [11]. The increasing trend in the low  $f$  may come from the fact that dielectric losses dominated the resistive loss. In other words, the dielectric loss increases slowly with increasing  $f$ , since mobile charges contained in the film cannot follow the high frequency field. The present  $\tan \delta$  of about  $3 \times 10^{-3}$  is from two to six times lower than those of plasma polymerized films using  $\text{CF}_4$  and  $\text{C}_2\text{F}_6$  [14] or  $\text{C}_2\text{H}_2\text{F}_4$ ,  $\text{CH}_2\text{F}_4$  and  $\text{CHClF}_4$  [15] as feedstock monomers, but about one order of magnitude higher than those reported for Teflon<sup>®</sup>FEP [11].



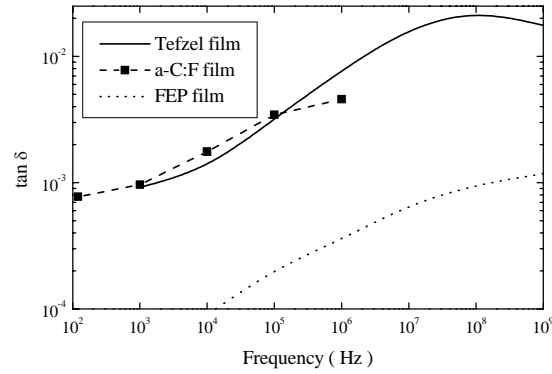


Fig. 4. Dielectric loss against frequency for a-C:F films and Teflon<sup>®</sup>FEP and Tefzel<sup>®</sup> films for comparison

### 3.3 Leakage current

$J$ - $E$  curves of the MIM (Cu/a-C:F/Au) element are shown in Fig. 5. The present  $J$  is appreciably lower than that of Ding *et al.* [16] and the  $E_B$  becomes also higher than that of Ding *et al.* The  $J$ - $E$  characteristics may be expressed, in general, as  $[\ln(J) \text{ vs } E^{1/2}]$  (Schottky type) or  $[\ln(J/E) \text{ vs } E^{1/2}]$  (Poole-Frenkel type) in high  $E$  region. However, though in the case of Poole Frenkel model, the estimated dielectric constant becomes far away from measured value, in the case of the Schottky model, the inferred dielectric constant becomes 2.6 which is close to the value 2.5 obtained in Fig.2) for  $E$  from 0.4 MV/cm to 0.9 MV/cm and 3.7 for  $E$  from 0.9 MV/cm to 1.4 MV/cm. But, in this case the Schottky barrier height is only 0.94 eV, which is too low compared with typical metal-insulator barrier heights. So, we may conclude that neither Poole-Frenkel nor Schottky conduction mechanisms are valid. A remaining model could be a space charge limited conduction (SCLC) mechanism, as is shown by Suh *et al.* [17], when  $J$  is proportional with  $E^m$ . If  $m=2$  the current density is given by [18]

$$J = (9/8)\epsilon_0\epsilon_r\mu V^2 / h^3 \quad (3)$$

where  $\mu$  is the effective charge mobility.

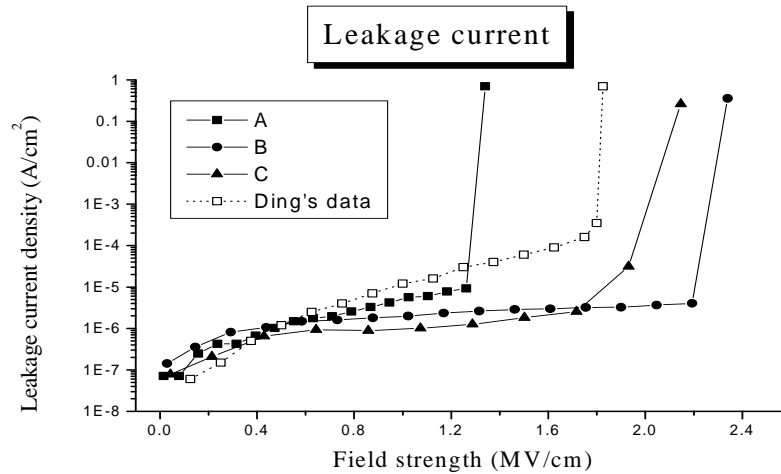


Fig.5 Leakage current vs field strength of the a:C-F films

For the present a-C:F films we found, from the slope of linear representation  $[\ln(J) \text{ vs } \ln(E)]$ , the  $m$  value to be 3.5 for the low electric field region and 2.7 for the high electric field region. It suggests that electrical conduction is governed by a trap modulated space charge limited conduction mechanism [19]. This result is

consistent with the observation that plasma polymerized films contain many dangling bonds [14,20] and, in the view of electrical conduction mechanism, these dangling bonds act as traps of carriers hopping from one dangling bond to a nearby bond.

### 3.4 Dielectric strength

The directly measured breakdown strength  $E_B$  of a-C:F film against  $h$  is shown in Fig.6. The tendency of  $E_B$  against  $h$  of the a-C:F film exhibits a similar trend of other insulating fluorocarbon films as

$$E_B \propto h^{-k} \quad (4)$$

where  $k$  is the fitting parameter. For the present film thickness of 1-12  $\mu\text{m}$ ,  $k$  becomes 0.53. This is about half of the value reported for PTFE sample of 1  $\mu\text{m}$  thickness [21]. The  $E_B$  measured by this method is about 10-20% higher than those obtained from the leakage current measurement.

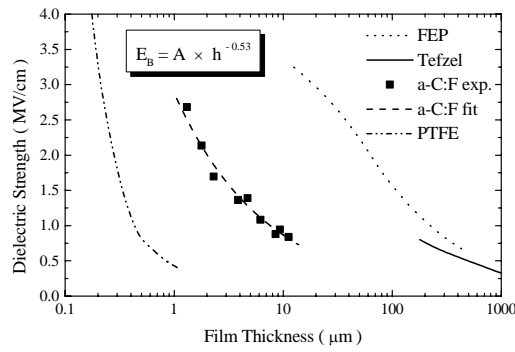


Fig.6 Dielectric strength  $E_B$  vs film thickness  $h$  for a-C:F film obtained from direct breakdown voltage measurement, and Teflon®FEP and Tefzel® and PTFE for comparison.

### 3.5 Chemical properties

Table 1 shows the elemental composition of the film prepared from  $\text{C}_8\text{F}_{18}$  monomer and  $\text{C}_8\text{F}_{18}/10\% \text{ Ar}$ , and PTFE for comparison. In the a-C:F films three bonding states for fluorine, as  $-\text{CF}_3$ ,  $-\text{CF}_2$  and  $-\text{CF}$  exist. The  $\text{CF}_2$  state, which shows PTFE-like bonding, is about 29 % in both  $\text{C}_8\text{F}_{18}$  and  $\text{C}_8\text{F}_{18}/10\% \text{ Ar}$ . While the  $\text{CF}_3$  state, which indicates endings of the polymer chains, is 16 % for  $\text{C}_8\text{F}_{18}$  monomer and 11% for  $\text{C}_8\text{F}_{18}/10\% \text{ Ar}$ . The present results are consistent with previously reported works for feed monomers, such as  $\text{C}_4\text{F}_8$ ,  $\text{C}_3\text{F}_8$ ,  $\text{C}_2\text{F}_6$  and  $\text{CF}_4$  [22,23], where it is shown that Ar dilution extends the high-energy tail in the electron energy distribution function toward higher energies and enhances the electron impact ionization. A similar tendency is expected for the present  $\text{C}_8\text{F}_{18}/10\% \text{ Ar}$  plasma. Thus, a large number of F and CF radicals could be produced in the plasma. On the other hand in the case of  $\text{C}_8\text{F}_{18}$  plasma, a larger amount of  $\text{CF}_2$  and  $\text{CF}_3$  radicals may be generated and the amount of F atoms would be small.

Table I: Compositions of elements and C (1s) bonding states obtained by XPS analysis

Material	Source gas	Elemental composition (%)			F/C <sup>a)</sup>	C <sub>1s</sub> bonding environment (%)					F/C <sup>b)</sup>	Degree of cross-linking <sup>c)</sup>
		F	C	O		C-C-	C-CF <sub>n</sub>	CF	CF <sub>2</sub>	CF <sub>3</sub>		
a-C:F	$\text{C}_8\text{F}_{18}$	62.9	35.9	2.2	1.75	2.7	31.3	21.1	28.6	16.3	1.27	34
a-C:F	$\text{C}_8\text{F}_{18}/\text{Ar}$	59.7	37.9	2.4	1.57	14.3	24.8	18.5	31.3	11.1	1.07	39.1
PTFE	-	66.3	32.6	1.1	2	-	-	-	100	-	2	-

<sup>a)</sup> F/C ratios calculated from total integrated intensities using:  $(F/C) = (A_F / S_F) / (A_C / S_C)$

<sup>b)</sup> F/C ratios calculated from the C (1s) spectra using:  $(F/C) = (3 \times A_{\text{CF}_3} + 2 \times A_{\text{CF}_2} + A_{\text{CF}}) / A_{\text{C}(1s)}$

<sup>c)</sup> Calculated values from C (1s) spectra by : % crosslink degree= [%(-C-C) + % (-C-CF<sub>n</sub>)] [24]

#### 4. CONCLUSIONS

Electrical properties of a-C:F films prepared in C<sub>8</sub>F<sub>18</sub> vapor PECVD were investigated by means of *C-V*, *J-E* and *V<sub>B</sub>* measurements, and an ellipsometric method. Chemical properties were also measured by SEM, XPS and FTIR. It was shown that the film has a low dielectric constant ( $\sim 2.5$ ) and a low dielectric loss (below  $3 \times 10^{-2}$ ) in the frequency range of 120 Hz-1 MHz. These values are comparable with those for Teflon<sup>®</sup>FEP and Tefzel<sup>®</sup> films. The leakage current was below  $10^{-7}$  A/cm<sup>2</sup> at 1 MV/cm. The film resistivity was two orders of magnitude lower than the Teflon<sup>™</sup> film. The dielectric strength of the film was as  $E_B \sim h^n$  ( $n = -0.53$ ) for *h* ranging from 1-12  $\mu$ m. Overall, the a-C:F film showed good electrical proprieties as an insulating material.

#### ACKNOWLEDGEMENT

The authors thank Professor H. Sugawara and Dr. M. A. Bratescu for helpful discussion. Dr. C. Biloiu has carried out of this work under the auspices of a postdoctoral fellowship from Japan Society for Promotion of Science, No. P00712. This work was supported in part by a Grant-in Aid for Scientific Research (B) of JSPS.

#### REFERENCES

- [1] K.Endo and T.Tatsumi, Appl. Phys. Lett. **68**, 3656 (1996)
- [2] L.M.Han, R.B.Timmons, and W.W.Lee, J. Vac. Sci. & Technol. B **18**, 799 (2000)
- [3] S.Limb, K.Gleason, D.J.Edell, and E.F.Gleason, J. Vac. Sci. & Technol. A **15**, 1814 (1997)
- [4] M.D.Garrison, R.Luginbuhl, R.M.Overney, and B.D.Ratner, Thin Solid Films **352**, 13 (1999)
- [5] Y.Sakai, *Gaseous Dielectrics IX*, edited by L. G. Christophorou, (Kluwer Academic, 2001) p.285
- [6] C.Biloiu, I.A.Biloiu, Y.Sakai, Y.Suda, and M.Nakajima, Jap. J. Appl. Phys. **42** (Part 2, No. 2B), L 201 (2003)
- [7] W.W. Stoffels, E. Stoffels, and K. Tachibana, J. Vac. Sci. Technol. A **16**, 87 (1998)
- [8] T.W.Mountsier and J.A.Samuels, Thin Solid Films 332, 362 (1998)
- [9] C.P.Lungu, A.M.Lungu, M.Akazawa, Y.Sakai, H.Sugawara, and M.Tabata, Jpn. J. Appl. Phys. **38**, L1544 (1999)
- [10] C.P.Lungu, A.M.Lungu, Y.Sakai, H.Sugawara, M.Tabata, M.Akazawa, and M.Miyamoto, Vacuum **59**, 210 (2000)
- [11] Du Pont Nemour Co., *Product Catalog*, <http://www.dupont.com/teflon/chemical>
- [12] K.Endo, K. Shinoda, and T.Tatsumi, J. Appl. Phys. **86**, 2739 (1999)
- [13] T. Fukuda, N. Aoi, and H. Matsunaga, Jpn. J. Appl. Phys. **41**, (Part 2, No. 3B) L307 (2002)
- [14] K.Endo and T.Tatsumi, Appl. Phys. Lett. **68**, 2864 (1996)
- [15] C.B.Labelle and K.Gleason, J. Vac. Sci. & Technol. A **17**, 445 (1999)
- [16] S.J.Ding, P.F.Wang, X.G.Wang, D.W.Zhang, J.T.Wang, and W.W.Lee, Material Sciences & Engineering B **83**, 130 (2001)
- [17] K.S.Suh, J.E.Kim, W.J.Oh, and H.G. Yoon, J. Appl. Phys. **87**, 7333 (2000)
- [18] K.C.Kao and W.Hwang, *Electrical Transport in Solids*, (Pergamon, Oxford, 1981), p. 151
- [19] A. J. Campbell, D. D. C. Bradley, and D. G. Lidzey, J. Appl. Phys. **82**, 6326 (1997)
- [20] C.B.Labelle, S.J.Limb and K. Gleason, J. Appl. Phys. **82**, 1784 (1997)
- [21] H.K.Kim and F.G.Shi, IEEE Trans. on Dielectrics and Electrical Insulation **8**, 248 (2001)
- [22] S.Samukawa and T.Nakano, J. Vac. Sci. & Technol. A **17**, 500 (1999)
- [23] S.J.Ding, P.F.Wang, D.W.Zhang, J.T.Wang, and W.W.Lee, J. Phys. D: Appl. Phys. **34**, 155 (2001)
- [24] J.P.Chang, H.W.Krauter, W.Zhu, R.L.Opila, and C.S.Pai, J. Vac. Sci. & Technol. A **17**, 2969 (1999)

# STRUCTURE AND PROPERTIES OF MULTI-FUNCTIONAL COATINGS $\text{Al}_2\text{O}_3$ WHICH HAD BEEN DEPOSITED ON ALUMINUM ALLOY

A.D.Pogrebnjak<sup>1</sup>, V.S.Kshnyakin<sup>1</sup>, S.V.Sokolov<sup>2</sup>, A.G.Boyko<sup>1</sup>, A.P.Kobzev<sup>3</sup>, Yu.N.Tyurin<sup>4</sup>

<sup>1</sup>*Sumy Institute for Surface Modification, St.Romenskaya 87, Bld. "M", 40030 Sumy, Ukraine*

<sup>2</sup>*Sumy State University, St.Rimskogo-Korsakova 2, Bld. "AET", 40007 Sumy, Ukraine*

<sup>3</sup>*Joint Institute for Nuclear Researches, Dubna, Moscow Region, Russia*

<sup>4</sup>*Institute for Electric Welding NAN of Ukraine, Ukraine*

## Abstract

Using nuclear-physics and physical methods of analysis: XRD, SEM, SIMS, RBS, ERDA and measurements of micro-hardness, we had investigated the structure and properties of  $\text{Al}_2\text{O}_3$  coating, which was deposited to the aluminum alloy substrate Al-Mg-Mn using the micro-arc oxidation. It has been shown that together with aluminum oxide, which existed in the  $\alpha$ -phase, a small amount of chromium oxide  $\text{CrO}_3$  also appeared.

## 1.Introduction

Aluminum alloys combine many positive properties: a low density, a high strength, a high electrical- and thermal conductivity and viscosity, a high corrosion resistance of many organic acids, seawater, good adaptability to manufacturing [1,2]. This makes them indispensable for many industries. For example, one can hardly imagine the aviation industry, food industry, power industry, building, etc. without application of aluminum alloys. At the same time there is a number of disadvantages as their low hardness, low module of elasticity, high chemical activity with many non-organic acids, low wear resistance. To avoid these disadvantages, one can produce aluminum oxide ( $\text{Al}_2\text{O}_3$ ) on tool surfaces, since this coating is very hard and has high corrosion resistance. One of the known methods, which allow one to do this, is a micro-arc oxidation of the aluminum alloy by an electric arc in a special electrolyte [3].

The micro-arc oxidation (MAO) is one of the most promising types of surface treatment, which recently has been widely applied for production of multi-functional coatings, which found their application in many different industries. The micro-arc oxidation relates to electro-chemical processes, but its feature is application of energy of electrical micro-discharges in an electrolyte in the surface of treated tools, which allows one to produce coatings of special properties. This allows one to improve the ceramics-like coatings with a composition, structure and properties which can be regulated in a wide range, as well as to apply these coatings as wear and corrosion resistant, electric-insulating, heat-resistant as well as decorating coatings [4,5]. In such a way, the goal of this work was to investigate the structure and properties of  $\text{Al}_2\text{O}_3$  coatings, which had been deposited to the Al-Mg-Mn alloy substrate using the micro-arc oxidation.

## Methods of Deposition and Investigation

An alloy Al-Mg-Mn, which can hardly be treated using the thermal type of treatment [1], has been chosen as the substrate (base) for micro-oxidation. Samples of this alloy of 14 x 20 mm<sup>2</sup> dimensions have been subjected to the micro-arc oxidation in  $\text{KOH} + \text{Na}_2\text{SiO}_3 + \text{SiO}_2 \cdot n\text{H}_2\text{O} + \text{Cr}(\text{OH})_3$  solution. The current density of oxidation was .....A/cm<sup>2</sup>, its time was .....min.

To investigate the element composition, we applied methods of secondary ion mass-spectrometry (MC-7201, Selmi, Sumy, Ukraine), Rutherford back-scattering (RBS), the elastic recoil detection analysis (ERDA). To investigate the phase composition we applied the diffraction of X-rays (DRON-2.0, S-Peterbourg, Russia), to investigate the surface morphology, we applied the scanning electron microscope (REM-102Э, Selmi, Sumy, Ukraine) and the metallography optic microscope (MIM-7, S-Peterbourg, Russia). To study mechanical properties, we measured micro-hardness (PTM-3, S-Peterbourg, Russia).

## 2.Results and Discussion

### 1. Analysis of the Sample Element Composition

We applied the method of secondary ion mass-spectrometry (SIMS) to analyze the element composition of aluminum alloys in the initial state and after treatment using the method of micro-arc oxidation.

In the initial state the mass spectrum (SIMS) of sample has shown peaks of such metals as  $\text{Al}^+$ ,  $\text{Mg}^+$ ,  $\text{Mn}^+$ ,  $\text{V}^+$  and  $\text{Fe}^+$ . Manganese, magnesium and vanadium are doping elements of the alloy, but iron is an inevitable contaminant of the system Al-Mg-Mn [1].

Also we found small peaks of contaminants  $\text{Na}^+$ ,  $\text{Ca}^+$ ,  $\text{K}^+$ ,  $\text{H}_2\text{O}^+$  and  $\text{C}^+$  in the surface of the investigated alloy. These elements appeared in the surface as the result of sample treatment during its preparation to investigations.

The presence of peak  $\text{Ar}^+$  in the mass-spectrum is related to the application of Ar beam for ion etching applied in SIMS method.

In addition to it, we observed small peaks of  $\text{Al}^+$  and  $\text{AlO}^+$  clusters, which confirmed the presence of an oxide  $\text{Al}_2\text{O}_3$  film in the surface of the investigated alloy [3].

The mass-spectrum of the aluminum alloy after micro-arc oxidation in the  $\text{KOH} + \text{Na}_2\text{SiO}_3 + \text{SiO}_2 \cdot n\text{H}_2\text{O} + \text{Cr}(\text{OH})_3$  solution is presented in Fig.1.

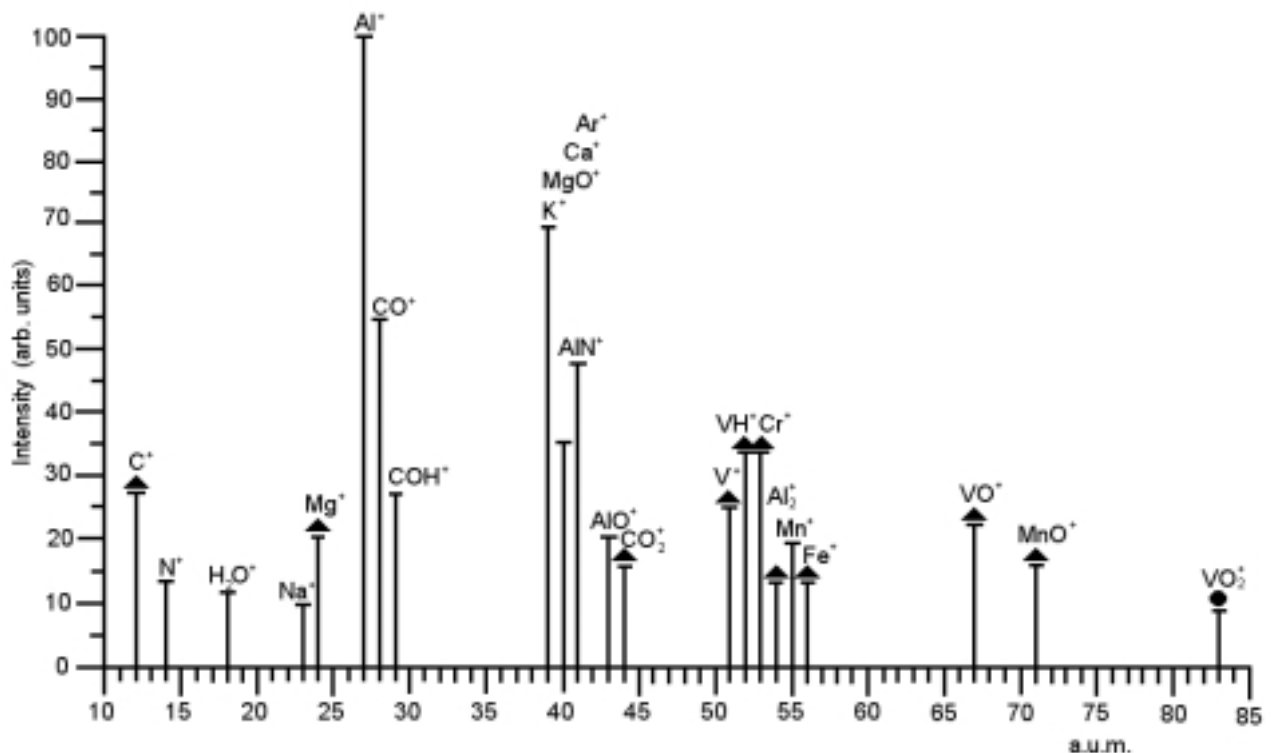


Figure 1. Mass-spectrum of secondary ion clusters obtained for aluminum alloy using argon beam bombardment after micro-arc oxidation. Line intensity marked as ▲ was magnified by a factor of 5; those marked as ● was magnified by a factor of 20.

In contrast to the mass-spectrum of the initial aluminum alloy, here we observed new peaks of  $\text{Cr}^+$ ,  $\text{VO}^+$ ,  $\text{MnO}^+$ ,  $\text{MgO}^+$  and the intensity of  $\text{AlO}^+$  peak increased essentially.

These oxide peaks evidence about surface oxidation of the investigated alloy, and the increase in  $\text{AlO}^+$  peak intensity evidences about an increase in aluminum oxide concentration in the surface.

Clusters of higher molar mass in the mass spectrum were not found due to a low sensitivity of SIMS in the range exceeding 90 atomic units of mass and lower amount of two- and three-atomic clusters [6].

These results are confirmed and added by methods of elastic recoil detection analysis (ERDA) and Rutherford back-scattering (RBS).

As it is seen in the spectra of (ERDA) (Figure 2a) and Rutherford back-scattering (Figure 2b), together with aluminum oxide, which stoichiometry is close to  $\text{Al}_2\text{O}_3$  (which is evidenced by formation of the step in Al and O peaks) one can observe a significant concentration of Mg and  $\text{MgO}$  and a small amount of Cl, Fe, and V in the oxide layer.

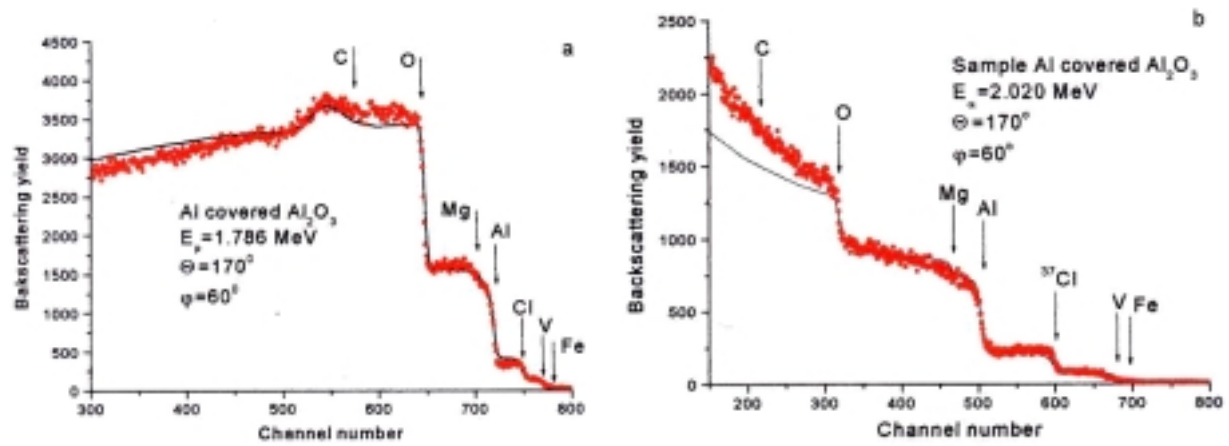


Figure 2. Spectra: (a) from elastic resonance on protons measured for Al<sub>2</sub>O<sub>3</sub> coating; (b) from Rutherford back scattering.

The Table 1 presents results of analysis obtained from RBS and ERDA spectra scanned over the coating depth. As one can see from the Table, the element composition does not change till almost 26.6μm depth, which speaks about stability in the coating composition obtained as a result of micro-arc oxidation.

**Element Concentrations (at%)**

Depth, nm	Fe	V	Cl	Al	Mg	O	C
205.3	.39	.92	5.88	30.54	9.33	52.02	.92
615.8	.39	.92	5.88	30.54	9.33	52.02	.92
1026.3	.39	.92	5.88	30.54	9.33	52.02	.92
2052.3	.39	.92	5.88	30.54	9.33	52.02	.92
4105.0	.39	.92	5.88	30.54	9.33	52.02	.92
14367.6	.39	.92	5.88	30.54	9.33	52.02	.92
24630.1	.39	.92	5.88	30.54	9.33	52.02	.92
26682.6	.39	.92	5.88	30.54	9.33	52.02	.92

## 2. Investigation of Phase Composition

Investigation of the phase composition of Al-Mn-Mg-V-Fe alloy in the initial state and after micro-arc oxidation has been performed using the X-ray analysis.

In spite of Mg and Mn intensity in SIMS mass-spectrum, the diffraction pattern corresponding to these metals did not show peaks corresponding to these metals, because they had been dissolved in the aluminum matrix [1]. In the initial state we observed only aluminum peaks.

After micro-arc oxidation of the aluminum alloy the picture in the diffraction patterns had changed (Figure 3). We found sharply expressed peaks of α-Al<sub>2</sub>O<sub>3</sub> (202), α-Al<sub>2</sub>O<sub>3</sub> (234) and α-Al<sub>2</sub>O<sub>3</sub> (204) with a rhombohedron lattice of  $a = 0.3253 \pm 0.0022$  nm parameter and  $\alpha = 56.65 \pm 0.80$  angle [7-9]. And the peak intensities of Al(200), Al(311) and Al(400) of a cubic fcc-lattice with  $a = 0.4032 \pm 0.0303$  nm lattice parameter [7-9] decreased essentially. This evidences about formation of a thick film Al<sub>2</sub>O<sub>3</sub> in the alloy surface.

In addition, we found small CrO<sub>3</sub> peaks. They are the result of chromium electrolysis from the electrolyte solution into the surface layers of the treated alloy.

Results obtained by XRD, RBS, ERDA correlate with SIMS results (showing those peaks of ions, which are present in RBS and ERDA data). At the same time one should pay attention that almost all the elements in this coating are in their oxide form, starting from MgO and finishing with MnO, Table 1, however, their concentration is not high in comparison with the aluminum oxide.

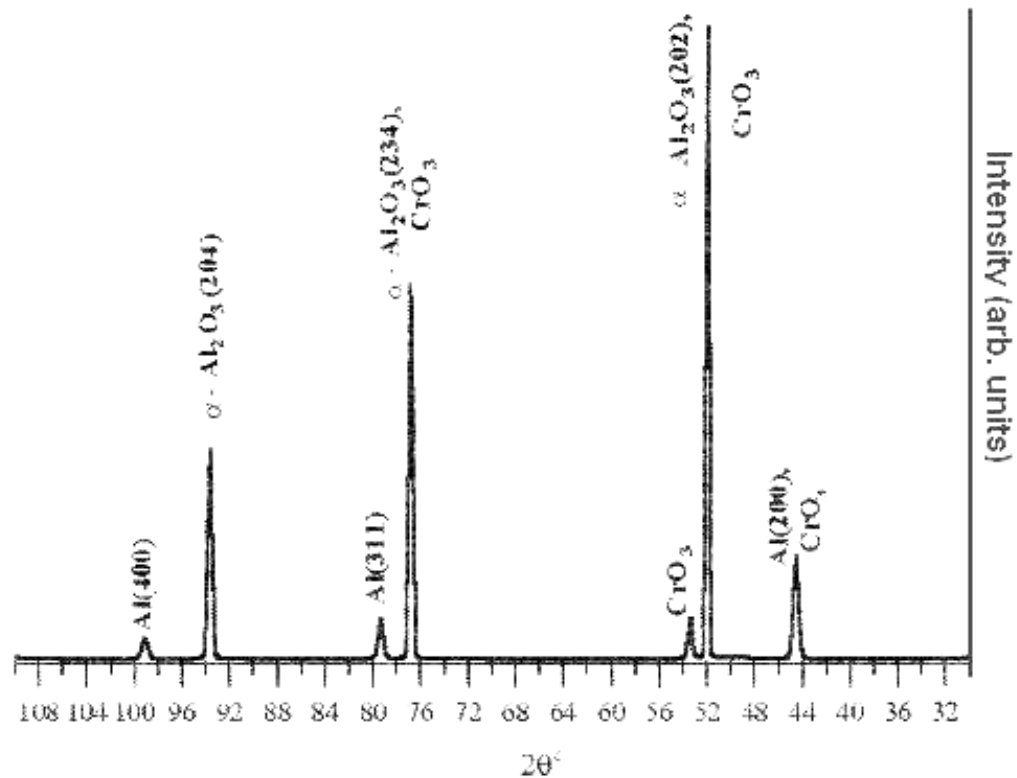


Figure 3. The diffraction pattern for aluminum alloy after micro-arc oxidation (from the coating side).

### 3. Analysis of Investigation of Sample Surface Morphology

Investigations of the surface morphology and the angular cross-section of the treated aluminum alloy were performed using the scanning electron microscope REM-102Э and metallography microscope MIM-7. Significant difference in investigations obtained using these REM-102Э and MIM-7 microscopes were not found. The quality of MIM photos is essentially worse than those of REM, therefore in this work we do not present MIM photos.

Investigating the surface morphology of the aluminum alloy using the scanning microscopy, we found foreign regions. One can see them in REM photos made for the treated sample surface (Fig.4a) and in the angular cross-section (Fig.4b). Investigations of the structure and morphology of the oxide layer (coating) performed over the transversal cross-section demonstrated dark and light regions in the coating, the coating itself being of fairly high porosity. These photos show that the oxide film is not uniform in thickness, which can be explained as non-uniform oxidation of different regions of the alloy surface.

Taking into account results of SIMS and XRD, one can assume that drops seen in the grey background (i.e. in  $\text{Al}_2\text{O}_3$ ) (Fig.4a) are inclusions of  $\text{CrO}_3$  phase.

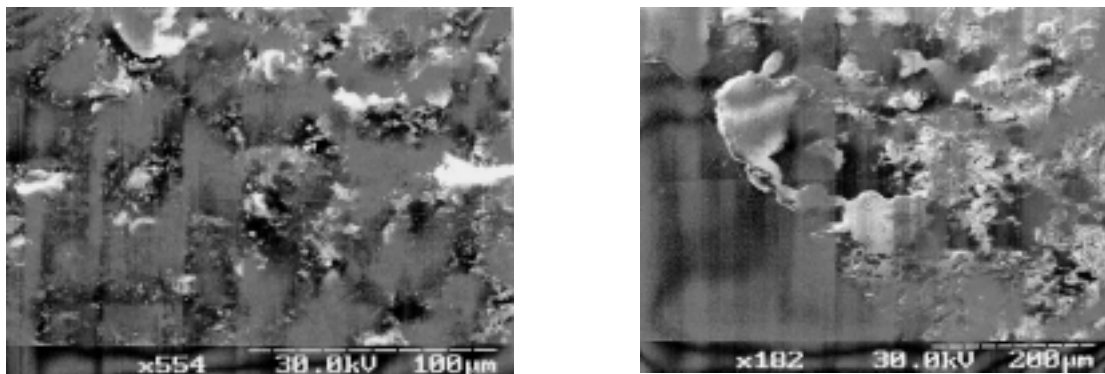


Figure 4. Scanning electron microscopy image for the aluminum alloy surface after micro-arc oxidation: (a) 554 time magnification; (b) cross-section of aluminum alloy after micro-arc oxidation. 182 time magnification

#### *4. Analysis of Micro-hardness Investigations*

To investigate the influence of micro-arc oxidation on properties of the aluminum alloy, we had measured the micro-hardness using the apparatus PMT-3 with 10g load.

The micro-hardness of initial non-treated region was about 12.6kPa. We failed to measure the micro-hardness of treated regions, because solid regions of  $\alpha$ - $\text{Al}_2\text{O}_3$  phase were brittle and flaked.

Taking the above mentioned, we could make a conclusion that the micro-arc oxidation of aluminum alloy resulted in the formation of a very solid phase  $\text{Al}_2\text{O}_3$  in the surface of investigated sample.

The disadvantage of this type of treatment (we mean the concrete regimes of oxidation) is high brittleness of this very hard coating and its bad adhesion (relating to the presence of the inter-phase boundary between the obtained phase and the basic material matrix).

#### **Conclusions**

1. Using the method of micro-arc oxidation for treatment of the aluminum alloy in  $\text{KOH} + \text{Na}_2\text{SiO}_3 + \text{SiO}_2 \cdot n\text{H}_2\text{O} + \text{Cr}(\text{OH})_3$  solution, we produced  $\text{Al}_2\text{O}_3$  coating with uniform element concentration over the whole depth. Phases  $\text{CrO}_3$  were present in the sample surface.

2. Disadvantages of this type of treatment for selected regimes are high brittleness of this coating and bad adhesion.

#### **Acknowledgements**

Authors are pleased to acknowledge Dr. V.I. Perekriostov, Dr. V.A. Pchelintseva, Dr. A.I. Saltykova for their help in experiments.

This work was partly funded by the Project 1472 STCU and 2M/0145-2001 of the Ministry of Science and Education of Ukraine.

#### **References**

1. Guliaev A.P. *Metallovedeniye* (rus). Moscow: Metallurgy. 1977. 645P.
2. Lakhtin Yu.M., Leontieva V.P. *Materialovedeniye* (rus). Moscow: Mashinostrojenije. 1990. 528P.
3. Vernik S.A., Pinner R. *Chemical and Electrolyte Treatment of Aluminum and its Alloys* (rus). Leningrad: Sudpromgiz. 1960. 388P.
4. Rozen A.E., Artemiev A.Yu. *Hardening of Tool Surfaces Made of Aluminum, Titanium and Zirconium Alloys Using Micro-Arc Oxidation* (rus). Moscow: Nauka. 1998. 145P.
5. Fiodorov V.A., Beloziorov V.V. *Composition and Structure of Hardened Surface Layer of Aluminum Alloys Produced Using Micro-Arc Oxidation* (rus). *Physika i Khimiya Obrabotki Materialov*. 1988. N4. P.92-98.
6. *Methods of Surface Analysis* (rus). Ed. By Zandera. Moscow: MIR. 1979. 582P.
7. Mirkin L.I. *X-Ray Analysis. Production and Measurements of X-Ray Patterns. Reference Book* (rus). Moscow: MIR. 1976. 326P.
8. Smittles K.J. *Metals. Reference Book. Russian Translation*. Moscow: Metallurgy. 1980. 447P.
9. Gorelik S.S., Rastorgujev L.L., et al. *Roentgenographic and Electron-Optical Analysis. Appendix* (rus). Moscow: Metallurgy. 1970. 170P.





# STRUCTURE AND PROPERTIES OF $\text{Cr}_3\text{C}_2$ + Ni COATINGS DEPOSITED ON METALLIC WORKPIECES USING HIGH-VELOCITY PLASMA JET

A.D.Pogrebnjak<sup>1</sup>, M.V.Ilyashenko<sup>1</sup>, V.S.Kshnyakin<sup>1</sup>

<sup>1</sup>Sumy Institute for Surface Modification, 40030 Sumy, Ukraine

## Abstract

Using the high-velocity plasma jet and specially calculated plasmatron regimes, coatings of chromium dioxide with nickel had been deposited on the substrate of a technical copper. The performed analysis of the obtained coating had demonstrated the formation of a solid solution on Ni base, formation of a complex chromium carbide ( $\text{Cr}_7\text{C}_3$ ) and the fcc-phase with the lattice parameter 3.614 Å. A characteristic relief relating to the dynamical interaction of melted and fused powder particles had been found. The coating surface hardness and its depth one reached  $66 \pm 2.5$  HRC. The adhesion power reached 25 to 300MPa.

## 1.Introduction

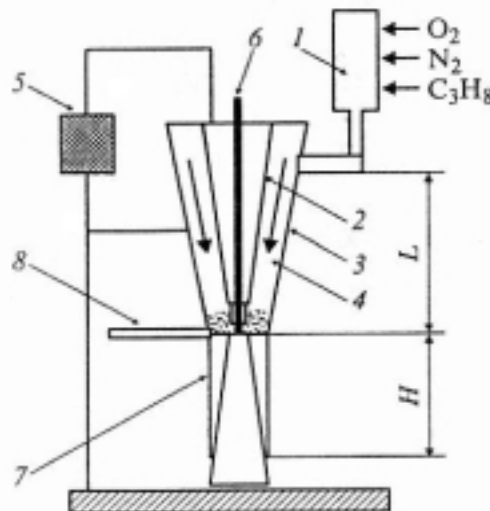
Recently, the methods of surface treatment using particle beams, plasma and light are considered as the efficient means to improve the reliability of tools and to increase their life. The most popular type of such kind of hardening is the deposition of different films and coatings. One of new technologies providing the possibility of surface modification of construction materials, deposition of coatings with protective and other functions on them is the pulsed plasma-detonation deposition [1-4].

The plasma-detonation technology is based on application of pulsed plasma jets, which are transported by a detonation wave as a plasma pulse.

## 2. Results and Discussion

As it is known from [2,3], to form a dense coating, fairly adhering to the tool surface (even without heating), one needs 100 to 1000m/s velocity of particles for alloy on metal base. Recently the devices applied for coating deposition with powder feeding from their side and gas-dynamical control systems had been developed [1,4]. Gases and powders are fed periodically after ejection of the high-velocity jet when the pressure in the combustion chamber becomes low. Mixing of the components and detonation of the combustion gas mixture are offered to be realized in a special combustion chamber (1), Fig.1, which is separated from the plasmatron itself. The plasmatron comprises the inside conical electrode (2) and the outside electrode-cathode (3). Between two coaxial electrodes in the inter-electrode gap [5,6] of L length, we applied the electric field E using the source of high voltage (5). A melted metallic rod (6) is positioned in the central electrode. This rod, as a rule, is manufactured of a refractory material (W, Mo, Ta, Hf, etc.). The pulsed plasmatron comprises the pipe for acceleration and heating of the powder. Its length H depends on the element composition and powder dispersion. For example, we calculated that for deposition of oxides its length should be  $H \approx 380\text{mm}$ . The powder is fed to this pipe through the pipe-line [7].

Fig.1. Scheme of the device operation designed for pulsed plasma-detonation treatment and coating deposition on



metallic substrates.

The frequency of pulse repetition was 4Hz. The capacity was  $C = 600\mu\text{F}$ , the distance between the samples and the plasmatron nozzle was  $H = 380\text{mm}$ , the velocity  $V$  was  $0.6\text{cm/s}$ , the number of passes was 1 to 4. The powder particle dimensions were 25 to  $56\mu\text{m}$  (the composition was  $\text{Cr}_3\text{C}_2 + 30\text{wt.}\%\text{Ni}$ ).

To investigate the coating phase composition we applied the apparatus DRON-2 (St.Peterburg, Russia) in cobalt emission. The surface morphology was studied and the micro-analysis (SEM with EDS) was performed using the scanning electron microscope REMMA-2M (Selmi, Sumy, Ukraine) and CXA-733 JEOL. The element analysis was performed using the secondary ion mass-spectrometry (SIMS) by the apparatus MC-7201M (Selmi, Sumy, Ukraine) with Ar ion beam of to 20keV energy. The coating Rockwell hardness was measured in HRC units, the adhesion power was determined by diamond pyramid scrubbing over the transversal and angular cross-sections.

Analysis of the coating diffraction patterns measured using the DRON-2 apparatus in cobalt emission had demonstrated that only one phase – a solid solution on Ni base with the lattice period  $a = 3.525\text{\AA}$ , was present in the coating (table value for Ni is  $a = 3.524\text{\AA}$ ). Also we found the compound  $\text{Cr}_7\text{C}_3$ , however, the peak intensity of this phase was weaker. There was one more phase, the data for which were absent: the fcc-phase with the lattice parameter  $3.614\text{\AA}$ .

Fig.2a,b presents images of the coating surface (a) and that of the coating fracture (b). The structure and morphology of the coating significantly differ in the depth: there are light regions (which are characteristic for chromium carbide) and glittering dark regions (which are characteristic for the metallic nickel phase). Microanalysis of these regions (Fig.2c) had demonstrated the presence of Cr, Ni, O, Cu, and Fe in the coating. There were also glittering regions, in which only Ni was present with a small amount of Cr and Cu. In those regions, where we found glittering, there were about 96% of Ni and about 4% of Cr. In these regions we found the powder grains or nickel powder particles with a small amount of Cr, which seemed to appear as a result of melting of Ni powder particles and mixing of Cr and Ni, i.e. there was the diffusion in the liquid phase at the moment of plasma jet fly or during the gas-plasma state. In the regions with a grey background the atomic concentration of Cr was about 61%, that of Ni – about 8.5%, oxygen – about 5.6%, copper – about 13.3%, iron – about 2.6% and aluminum exceeded 5%, sulphur, calcium and silicon amounted less than 1%. We assumed that Cu penetrated from the substrate as a result of dynamical and temperature action of the plasma jet, therefore the fcc-phase with the lattice parameter  $3.614\text{\AA}$  related to Cu.

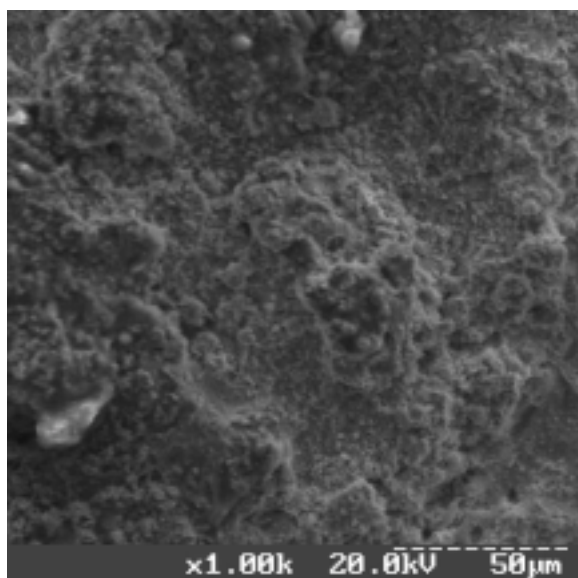


Fig.2a. The morphology of the coating  $\text{Cr}_3\text{C}_2 + 30\text{wt.}\%\text{Ni}$  surface obtained using the scanning electron microscope.

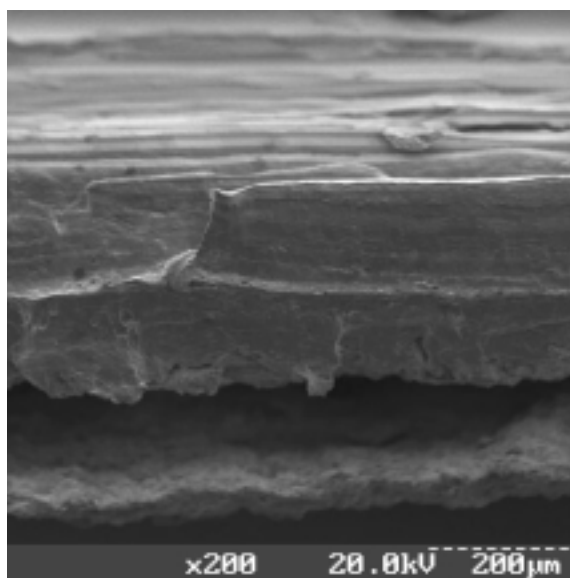


Fig.2b. The structure of  $\text{Cr}_3\text{C}_2 + 30\text{wt.}\%\text{Ni}$  coating in the fracture.

Measurements of the coating hardness over the coating transversal cross-section had demonstrated that the maximum hardness value in the light regions ( $\text{Cr}_7\text{C}_3$  was the basic phase) was  $66 \pm 2.5\text{HRC}$ , that in the dark regions with prevailing Ni solid solution was  $45 \pm 1.5\text{HRC}$ . Measurements of the coating-substrate

adhesion power, which were performed using the diamond pyramid scrubbing over the transversal and angular cross-sections, demonstrated that these values strongly differed and reached 25 to 300MPa.

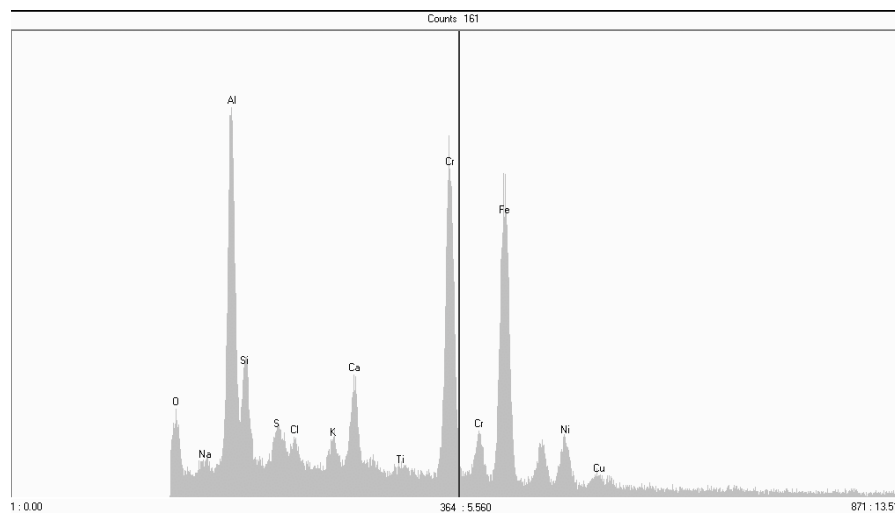


Fig.2c. The X-ray spectra obtained for the coating and measured using the apparatus REMMA-2M with dispersion Over the energy (at the point of mixed composition – the grey color).

Table 1 presents surface hardness values for various pyramid loads. Analysis of the measured results for hardness allows one to conclude that the indentation depth of the pyramid is several tens of micro-meter, and dimensions of the powder particles are of the same order.

Table 1. Results of Rockwell hardness measurements in the coating surface under various loads on pyramid.

N of Testing Series	Load in gram	Hardness in HRC	Notes
1 – 4	50	$58 \pm 1$	Grey field
	100	$51 \pm 3$	
	200	$48 \pm 5$	
6, 8, 9, 12	50	$62 \pm 4$	A uniform grey field
	100	$56 \pm 1$	
	200	$50 \pm 1$	
10, 11, 13	50	$27 \pm 7$	A light field
	100	$35 \pm 3$	
	200	$50 \pm 12$	

Figure 2d presents the dependence of the coating hardness on the depth (the angular cross-section) for the same pyramid load. Measurements were performed only in the grey coating regions, in order that to have true information about the hardness over the depth of deposited coating.

In such a way, in this report we demonstrated that under optimum calculated deposition regimes, from chromium carbide with 30wt.%Ni one could produce coatings of essentially good quality, with high hardness reaching 66HRC and good adhesion reaching 300MPa. In this case the coating may comprise a solid solution on Ni base, complex carbides of Cr ( $\text{Cr}_7\text{C}_3$ ) and the fcc-phase on Cu basis ( $3.614\text{\AA}$ ).

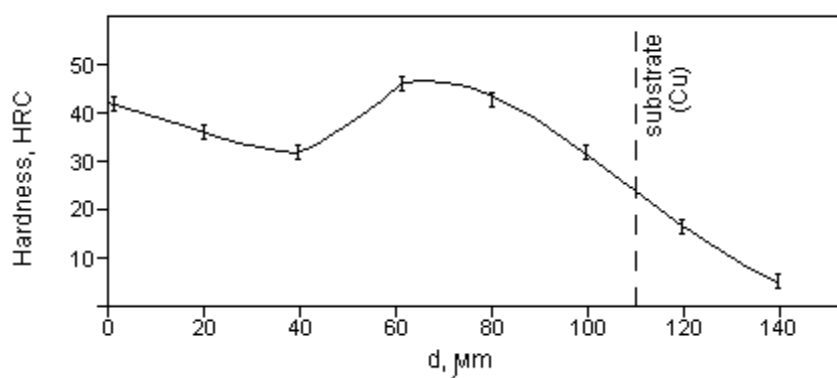


Fig.2d. Dependence of hardness on the coating depth (the transversal cross-section) under 50g load.

Testing of units of thermal power stations such as impeller blades pipe surfaces in boilers working in an oxidizing atmosphere (in air), in a slag medium (slag particles) under high temperatures of 300 to 800°C, which had been covered by  $\text{Cr}_3\text{C}_2 + \text{Ni}$  coating deposited using the pulsed plasma jet, demonstrated good resistance and work-ability.

### Acknowledges

The authors are pleased to acknowledge O.V.Kolisnichenko for the help in experimental work. The work was partly funded by the Project 2M/0145-2001 and 2M/076-2000 of the Ministry of Education and Science of Ukraine.

### REFERENCES

1. A.D.Pogrebnyak, M.V.Ilyashenko, O.P.Kul'ment'eva, etc. Journal Tech.Phys. (rus). Vol. **21**. Vyp.8. P.111 (2001).
2. S.Kuroda. Proc. of the 10<sup>th</sup> Inter.Thermal Spray Conf., May 25-29 France. P.539 (1999).
3. A.I.Zverev, S.Yu.Sharivker, E.A.Astakhov. Detonation Deposition of Coatings. Leningrad: Sudostrojenije. P. 178 (1979).
4. Yu.N.Tyurin, A.D.Pogrebnyak. Surf.Coat.Tech.. V.**111**. P.269 (1999).
5. A.D.Pogrebnyak, M.V.Ilyashenko, V.S.Kshnyakin, etc. Pisma v Journal Tech.Phys. (rus) Vol. **27**. Vyp.17. P.82. (2001).
6. A.D.Pogrebnyak, Yu.N.Tyurin, Yu.F.Ivanov, etc. Pisma v Journal Tech. Phys.. Vol. **26**. Vyp. 21. P.58 (2000).
7. A.D.Pogrebnyak, M.V.Ilyashenko, O.P.Kul'ment'eva, et al. Vacuum.. Vol.**62**. P.21 (2001).

# Effect of bias voltage on the growth and properties of PECVD hydrogenated amorphous carbon films

G. Cicala<sup>1</sup>, P. Bruno<sup>2</sup>, A. M. Losacco<sup>3</sup> and G.S. Senesi<sup>1</sup>

<sup>1</sup>*IMIP-CNR Sezione di Bari w/o Department of Chemistry, University of Bari, Italy*

<sup>2</sup>*Department of Chemistry, University of Bari, Italy*

<sup>3</sup>*Centro Laser, S.P. Casamassima km3 70010 Valenzano Bari) Italy*

## Abstract

Hydrogenated amorphous carbon films are produced via radiofrequency plasma enhanced chemical vapour deposition technique under the effect of bias voltage. The deposition rate, the hydrogen incorporation, the surface roughness and morphology of the film are analyzed. The sessile drop method is used to investigate the changes on the surface free energy of carbon film induced by the effect of bias voltage. The resultant wetting properties are found to be affected both by the density of C-H bonds and the surface roughness of the hydrogenated amorphous carbon films.

## 1. Introduction

Thin hydrogenated amorphous carbon (a-C:H) films, produced using the plasma enhanced chemical vapour deposition (PECVD) technique, are highly functional materials with chemical and physical properties ranging from graphite-like and diamond-like to polymer-like character. For this reason, the growth of a-C:H films can be tailored for definite applications. Specifically, a-C:H films are used as scratch resistant, wear protective and biocompatible coatings, permeation barriers, functionalized surfaces for packaging applications and low-k dielectrics for microelectronics [1,2]. The main aim of this work was to investigate the effect of bias voltage on the growth and properties of a-C:H films obtained starting from CH<sub>4</sub>-Ar plasmas. The correlation between the deposition parameters (deposition rate, pressure, r.f.power) and the film properties (composition, structure, surface roughness, morphology and wettability) is discussed.

## 2. Experimental

Plasma deposition of a-C:H films was performed in a typical capacitive ion etching reactor (RIE Plasma Tech DP800) with a parallel plate configuration of the two aluminium electrodes (15 cm in diameter and 6 cm far away). The negative d.c. self-bias voltage ( $V_b$ ) developed on the powered electrode has been tuned through the pressure (P) and rf power (W) variation according to the following relationship [3]:

$$V_b \propto \left( \frac{W}{P} \right)^{1/2} \quad (1)$$

which allows to change substantially the ion bombardment of the growing film surface. The pressure, the flow rate and the r.f. power (supplied by ENI-ModelACG-5 generator) were continuously monitored during the process. The growth of a-C:H films was performed on silicon substrates placed on the bottom powered electrode, which was water-cooled in order to avoid the self-heating of its surface exposed to plasma and to maintain constant the electrode temperature during the deposition process. Two runs of a-C:H coatings were obtained by varying the working pressure and the radiofrequency (r.f. = 13.56 MHz) power as listed in Table I, and keeping constant the following experimental parameters: CH<sub>4</sub> flow rate, 15 sccm; Ar flow rate, 55 sccm; deposition temperature, 25°C; and time deposition, 30 minutes.

Table I. Experimental conditions for the growth of a-C:H films deposited on double polished crystalline silicon at fixed total flow rate of 70 sccm and variable r.f. power and pressure.

Run	Sample No.	d.c. self-bias voltage (Volt)	Pressure (mTorr)	r.f. power (Watt)	Hydrogen content (%)	Thickness (Å)
<b>1</b>	40	-60	300	<b>50</b>	29.8	3200
	47	-120	300	<b>100</b>	23	4300
	27	-220	300	<b>250</b>	25.7	3100
	37	-250	300	<b>300</b>	13.7	2500
	36	-270	300	<b>350</b>	13	500
<b>2</b>	33	-400	<b>50</b>	250	11.8	2100
	30	-280	<b>200</b>	250	28.1	3300
	27	-220	<b>300</b>	250	25.7	3100
	41	-200	<b>400</b>	250	34.1	3700
	29	-170	<b>500</b>	250	---	4200

A Fourier Transform Infrared (FTIR) spectrophotometer (NICOLET IMPACT 400 D) was utilized for the structural and compositional characterization. FTIR spectra covering the range 400 - 4000 cm<sup>-1</sup> were collected with a resolution of 4 cm<sup>-1</sup>. The hydrogen content was estimated from the integrated area of the C-H stretching band at about 2900 cm<sup>-1</sup>.

Atomic force microscopy (AFM, Thermomicroscopes Autoprobe CP) was performed in air and the images were obtained in contact mode using commercial and unmodified silicon nitride tips. Each sample was analysed on two different regions using three spatial resolutions: 2x2, 10x10 and 20x20µm<sup>2</sup>. The rms (root mean square) surface roughness (σ<sub>s</sub>) was evaluated on a squared 20x20µm<sup>2</sup> area of the sample surface.

Water contact angles (WCA) were measured by a Rame'Hart contact-angle goniometer (mod.A-100) at 25 °C in static and dynamic modes using the sessile drop technique (a double distilled water

droplet of 2 $\mu$ l). The dynamic advancing and receding angles ( $\theta_A$ ,  $\theta_R$ ) were recorded as the probe water was added to and withdrawn from the drop, respectively. The average values of WCA angles were evaluated by performing three independent measurements on the coating surface.

A surface profiler (KLA-TENCOR® P-10) was used to measure the thickness and the surface roughness of the films.

### 3. Results and discussion

The d.c. self-bias voltage ( $V_b$ ) is directly related to r.f. power (Fig.1 left) and inversely related to

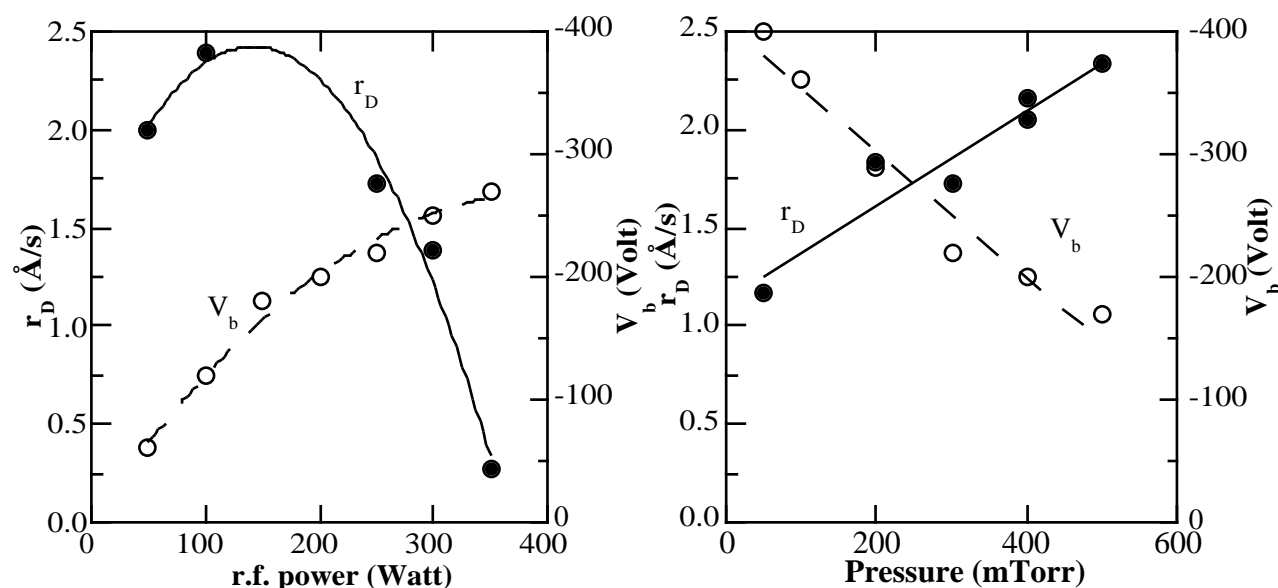


Figure 1 Deposition rate  $r_D$  and negative d.c. self-bias voltage ( $V_b$ ) as a function of r.f. power (left) and pressure (right).

pressure (Fig.1 right), as expected from eq. (1) quoted in the experimental section. The deposition rate ( $r_D$ ) increases slightly with increasing r.f. power up to about 150 Watt, and then decreases abruptly (Fig.1 left); whereas it increases linearly as the pressure increases (Fig.1 right).

The surfaces of a-C:H films were studied by measuring their wetting properties. Figure 2 shows advancing and receding water contact angles for coatings deposited at various rf power and pressure values. The films exhibit  $\theta_A$  and  $\theta_R$  that vary in the range from 60 to 80° and from 40 to 55°, respectively. The water contact angle hysteresis ( $\theta_A - \theta_R$ ) is about 20, and remains almost constant by changing either r.f. power or pressure. Thus, the WCA hysteresis appears to be not significantly affected by the negative d.c. self-bias voltage.

The AFM images and topographies obtained on the two sets of samples studied are qualitatively similar. The AFM images of two representative a-C:H films obtained at low (-100 Volt) and high (-250 Volt) negative d.c. self-bias voltage are shown in Figs. 3a and 3b, respectively. The rms surface roughness, obtained on a squared 2x2 $\mu\text{m}^2$  area under these experimental conditions are equal to



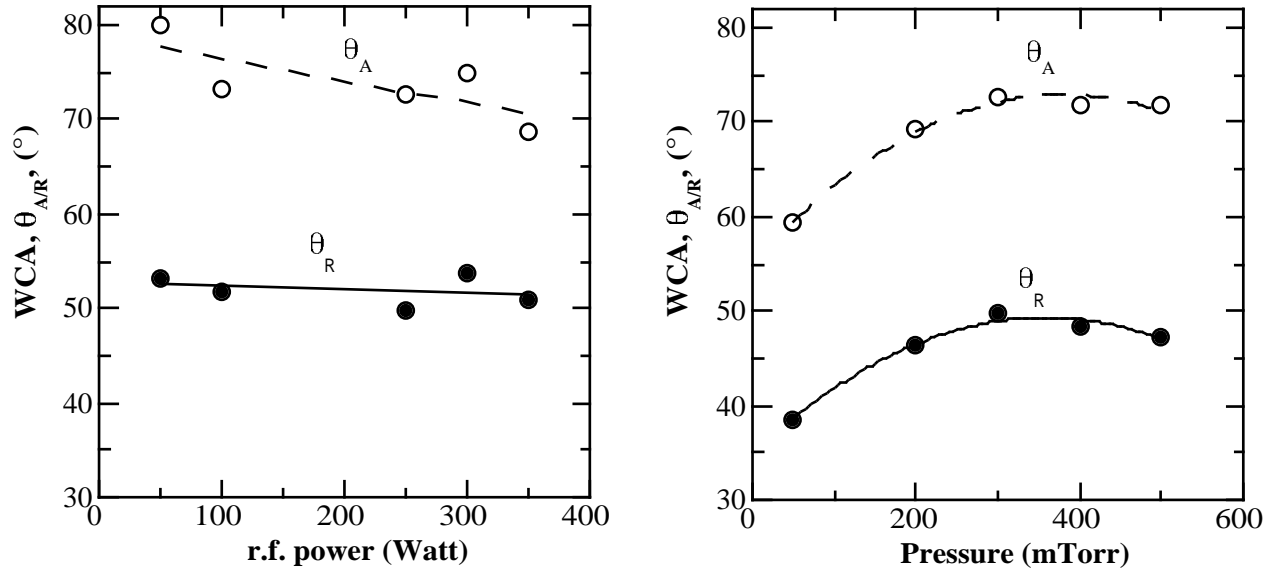


Figure 2 Advancing ( $\theta_A$ ) and receding ( $\theta_R$ ) water contact angle (WCA) as a function of r.f. power (left) and pressure (right).

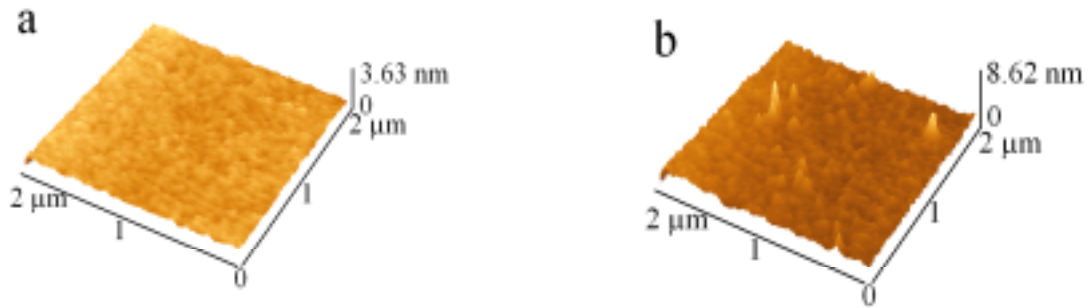


Figure 3 The 2x2 $\mu\text{m}^2$  AFM topography images of a-C:H films obtained by varying the r.f. power at negative d.c. self-bias voltage (a) low (-100 Volt) and (b) high (-250 Volt).

0.2987 nm (a) and 0.64596 nm (b). The surface roughness modifications measured as a function of r.f. power and pressure are reported in Fig. 4, in which the  $\sigma_s$  values are quantified on a larger squared area of 20x20 $\mu\text{m}^2$ .

Results obtained by measuring the effects of r.f. power and pressure on the deposition rate and properties of a-C:H films indicate that the negative d.c. self-bias voltage controls and determines univocally the trends of  $r_D$ , WCA,  $\sigma_s$  and hydrogen content as reported in Figs. 1, 2, 4 and Table I.

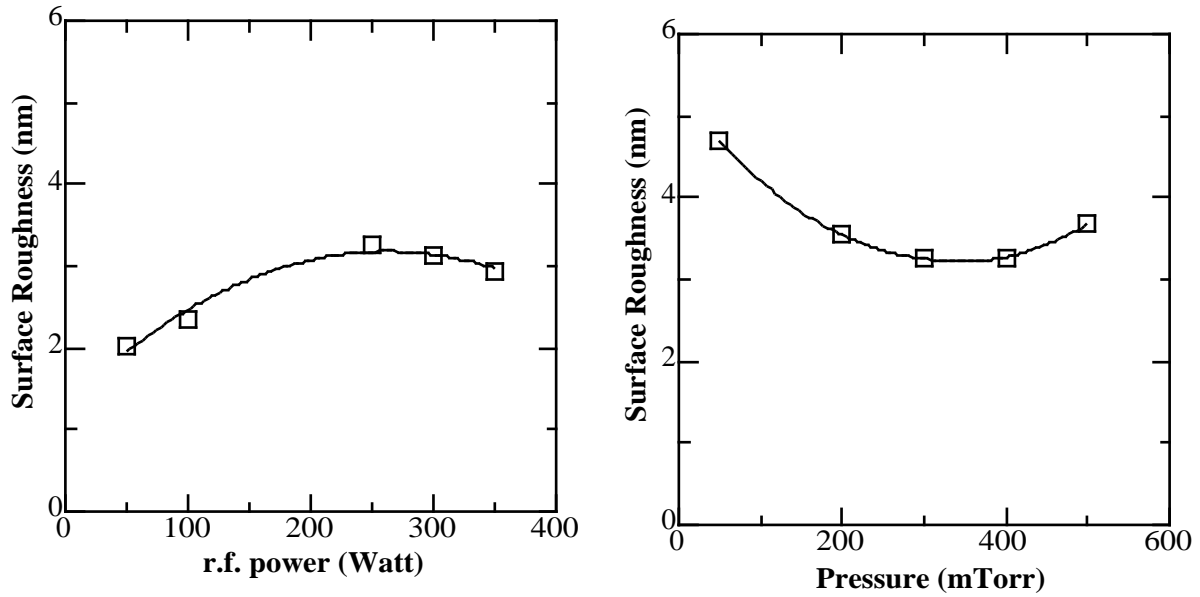


Figure 4 Root mean square (rms) surface roughness ( $\sigma_z$ ) determined by AFM measurements (scale  $20 \times 20 \mu\text{m}^2$ ) of a-C:H films obtained by varying r.f. power (left) and pressure (right).

The decrease of deposition rate is always observed when the negative d.c. self-bias voltage increases (Fig. 1). In particular, at low values of  $V_b$  (from -60 to -120 Volt) (Fig.1 left), the deposition rate increases with  $V_b$  and reaches a maximum value at about -180 Volt that corresponds to 150 Watt. At higher  $V_b$  values the  $r_D$  decreases abruptly down to  $0.28 \text{ \AA/s}$ . This trend can be explained by considering that the degree of dissociation/ionization of  $\text{CH}_4$  and Ar gases and the energy of the impinging ions increase by increasing  $V_b$ . The first process leads to the production of  $\text{CH}_x$  (with  $x=0-3$ ) radicals and H atoms responsible for a-C:H growth, whereas the second one favors the sputtering [4] and/or etching [5] of growing films. The film formation from  $\text{CH}_x$  and H species can be explained by a growth mechanism, which was previously proposed in a-Si:X ( $X=\text{Cl}, \text{F}, \text{H}$ ; see ref.[6] and references therein) and a-C:H deposition [5, 7-10]), and which is based on the chemisorption of  $\text{CH}_x$  active species and subsequent surface free bond creation via abstraction reaction by incoming H atoms. Furthermore, a change of relative amounts of  $\text{CH}_x$  radicals and H atoms can cause the decrease of the deposition rate as a function of r.f. power and pressure (Fig. 1). Thus, the net deposition rate, which is given by the difference between the growth rate and the etching rate, is indicative of a growth/etching competition. Further, as the a-C:H coatings are grown on the cathode, ions arriving at the surface of the growing film can play a key role in modifying the deposition rate, the structure and the properties of the material by sputtering loosely bonded species and in promoting the physical subplantation process of the ions as claimed by J. Robertson [2]. The modifications of the film composition, surface free energy, roughness and morphology are found to depend principally on the energy of ion bombardment, too. An attempt to quantify the

changes in wetting properties of the a-C:H coatings has been done. In this respect, the assessment of surface energy based on the film wettability is important to characterize the coating stability and, therefore, the processes taking place at the water-film interface. The wetting properties show a correlation with the surface roughness and the hydrogen incorporated in the films which vary as a function of pressure and rf power (Fig. 4 and Table I). In particular, at high pressure and low r.f. power the WCA angles increase by indicating that the reduced ion bombardment increases the hydrogen in the bulk sample as well as at its surface and decreases the surface roughness. The roughness decrease induces an increase of WCA, according to the Wenzel equation [11] because the measured contact angle is less than 90°:

$$\cos \theta_r = r \cdot \cos \theta_s \quad (2)$$

where  $r$  is the roughness factor (defined as the ratio between the increased area of the rough surface and the geometrical surface area) and  $\theta_r$  and  $\theta_s$  are the contact angles for a rough and smooth surface, respectively. In conclusion, higher values of WCA, i.e., lower values of surface free energy, are indicative of a weak interaction between the water and the coating and of good protective properties.

#### 4. Conclusions

The deposition rate, the composition, the surface wetting properties and the surface roughness of a-C:H films on silicon substrates produced from CH<sub>4</sub>-Ar plasmas are studied as a function of r.f. power and pressure. Similar trends of deposition rate and properties of a-C:H films are obtained under the effect of negative d.c. self-bias voltage.

The wettability variations appear to be related to the different degree of surface passivation with hydrogen and to surface roughness. In addition, the wetting properties of a-C:H, influenced by the outermost surface layers, are evaluated to monitor the surface reactivity of the film and the quality of their protective action.

#### References

- [1] A. Grill – Diam. Rel. Mater. **8**, 428 (1999).
- [2] J. Robertson – Mater. Sci. & Engineering R **37**, 129 (2002).
- [3] Y. Catherine, P. Couderc - Thin Solid Films **144**, 265 (1986).
- [4] K. Kobayashi, K. Yamamoto, N. Mutsukura, Y. Machi, Thin Solid Films **185**, 71 (1990).
- [5] J. Koppers – Surf. Sci. Rep. **22**, 249 (1995).
- [6] G. Bruno, P. Capezzuto, G. Cicala in Plasma Deposition of Amorphous silicon-based materials ed. G. Bruno, P. Capezzuto and A. Madan, Chapter I pp. 1-62 (1995) Academic Press .
- [7] N. V. Mautzaris, E. Goloides, A. G. Bardouvis, G. Turban – J. Appl. Phys. **79**, 3718 (1996).
- [8] J. Perrin, M. Shiratani, P. Mae-Nune, H. Videllot, J. Jolly, J. Guillon J. Vac. Sci. Technol. **A16**, 278 (1998).
- [9] W. Jacob - Thin Solid Films **326**, 1 (1998).
- [10] A. von Keudell, T. Schwarz-Selinger, M. Meier, J. Jacob - Appl. Phys. Lett. **76**, 676 (2000).
- [11] R. N. Wenzel - J. Phys. Colloid Chem. **53**, 1466 (1949).

# THEORETICAL STUDY OF THE NON – STEADY DISCHARGE AT ATMOSPHERIC PRESSURE IN PIN-PLATE SYSTEM AND ITS APPLICATION FOR OZONE PRODUCTION

V.I. Karas<sup>1</sup>, V.I. Golota<sup>1</sup>, V.P. Mal'khanov<sup>2</sup>, I.F. Potapenko<sup>3</sup>, O.N. Shulika<sup>1</sup>

<sup>1</sup>National Science Center "Kharkov Institute of Physics & Technology", Kharkov, Ukraine,

<sup>2</sup>TurboDEn, Moscow, Russia

<sup>3</sup>Keldysh Institute of Applied Mathematics of the RAS, Moscow, Russia

## Abstract

As a result of the numerical simulation we established following main conclusions: (i) for humid air at increasing pressure of  $1.0133 \cdot 10^5$  Pa until  $5.0665 \cdot 10^5$  Pa ozone concentrations during  $2 \cdot 10^{-3}$ s become higher in 22 times. In this case the harmful  $NO_x$  concentrations are 2-3 order lower than ozone one; (ii) it is shown that nitrogen is useful to ozone production in the discharge; (iii) based on ion collection we cleared increasing ignition discharge voltage at growing ozone concentrations even with low ozone concentrations.

## 1. Introduction

Electrodynamic and plasma-chemical processes at high-pressure glow discharge conditions have a very complicated, many-factor character, because in the discharge gap there occur nearly simultaneously a great many separate streamer discharges, which cross the discharge space parallel to each other. Generally, one can expect that the discharge characteristics are determined by the energy put into the gas flow. However, it is evident that the resulting gradients of the discharge parameters along the gas flow are not too great, because the specific power density is not high. Therefore the variations in the gas discharge parameters from one local streamer discharge to another can be neglected. By contrast, the nonuniformity in the discharge parameters in the direction from one electrode to the other should be expected to be very strong. Really, the radius of current channel near the needle is several orders of magnitude smaller than the period of needle separation along the gas flow. This means that the gradients of both the electric field strength and the charged particle density are great, particularly in the vicinity of the needle electrode. So, the two-dimensional model for the glow discharge can be constructed by taking one PCR structure element and formulating the equations, which describe the propagation of the discharge from the needle electrode to the plane electrode.

In atmospheric-pressure air, the nonlocality effects of electron/ion distributions, and also, of diffusion, can play a certain role only at a very small distance from the electrode (cathode dark space). Bearing in mind the insensibility of the parameter of the cathode layer to the choice of the kinetic model, we have chosen the simplest model [1-5 and references therein], where all the transport coefficients and the kinetic coefficients are the local-importance functions of the reduced electric field  $E/N$  ( $E$  is the electric field strength,  $N$  is the gas particle density).

## 2. Mathematical model and main equations

The basic parameters of any electrical discharge in gas are mainly determined by the energy distribution of electrons. The knowledge of electron kinetics of the low-temperature plasma is of great importance for simulation of plasma-chemical processes in the glow discharge in air. For example, the average energy or the temperature of electrons governs the rate of plasma-chemical processes and the discharge power distribution between different channels. A more exact analysis can be performed with the use of the electron energy distribution function (EEDF). A typical theoretical approach to determination of the EEDF in a gas plasma is the solution of the Boltzmann equation in the two-body approximation. This approach appears rather simple and reliable; it is confirmed by comparison with more substantiated methods of simulation, e.g., the Monte-Carlo method. The electron motion in gas under the action of the external electric field  $E$  is determined by the frequency of collision with molecules and other charged particles. The electron-electron collisions become to play a certain role at a relatively high degree of gas ionization, generally, starting from  $10^{-4}$  -  $10^{-3}$ . Typical electron densities in the discharge are substantially less than  $10^{15} \text{ cm}^{-3}$ , therefore the electron-electron interaction can be neglected to a high accuracy. . In consequence of a rather small energy contribution to the gas, the variations in the gas composition and temperatures can be neglected. The electron-electron, electron-ion collisions and any other collisions can also be neglected. In this case, all kinetic coefficients for the pro

cesses involving electrons are the functions of the reduced electric field  $E/N$  and the gas composition. The mathematical model of discharge, developed here, makes it possible to calculate the evolution of many important plasma components: ions ( $N_2^+$ ,  $O_2^+$ ,  $O_4^+$ ,  $O^-$ ,  $O_2^-$ ,  $O_3^-$ ), electron-excited particles ( $N_2(A^3\Sigma_u^+)$ ,  $N_2^*$ ,  $O_2(a^1\Delta)$ ,  $O_2(b^1\Sigma)$ ,  $O(^1D)$ ), atoms ( $N$ ,  $O$ ), ozone ( $O_3$ ), nitrogen oxides ( $NO$ ,  $N_2O$ ,  $NO_2$ ,  $NO_3$ ,  $N_2O_5$ ) and electrons. Here  $N_2^*$  denotes the electron-excited molecule of nitrogen at any level, except for  $A^3\Sigma_u^+$ . In humid air, electrons attach to molecules to form negative ions. The negative ions of most importance are  $O^-$ ,  $O_2^-$ ,  $O_3^-$ ,  $O_4^-$ ,  $H^-$ ,  $OH^-$ ,  $NO_2^-$ ,  $NO_3^-$ ,  $O_2^-(H_2O)$ ,  $O_2^-(H_2O)_2$ ,  $OH^-(H_2O)$  and  $OH^-(H_2O)_2$ . The electron detachment from negative ions is of great importance, because it influences the plasma conductivity. At a measured average electric field strength of  $\sim 10^4$  V/cm in the discharge gap, the attachment rate is appreciably higher than the electron-impact ionization rate. The other process that leads to electron losses is the electron-ion recombination. The only process that can, in principle, compensate the electron losses is the electron detachment from negative ions. The processes of electron detachment include a simple electron detachment, the associated detachment and photodetachment. For the atmospheric plasma, the last process can be neglected. It is well known that the addition of water vapor to any weakly ionized gas or plasma exerts a considerable effect on the content of positive and negative ions, and the cluster water ions become the predominant ions. This changes the properties of a weakly ionized environment, because (i) the process of electron detachment from negative cluster ions proceeds very slowly, (ii) the process of dissociative recombination of electrons with positive cluster ions of water goes much quicker than with simple positive ions. The both effects lead to a decrease in the electron density, and hence, in the degree of ionization. Therefore, it is of importance to know the rate constants for cluster water ion formation and breakdown. In simulation, the processes of  $H_2O$  molecule ionization and dissociative attachment, being of greatest importance for the plasma balance, were characterized by the rate constants in the form of functions of the reduced electric field, which were calculated through the solution of the Boltzmann equation for electrons. At a critical reduced electric field value  $(E/N)_c = 12.4 \cdot 10^{-16} \text{ Vxcm}^2$ , the processes of ionization and attachment equalize each other. This value is often called the equilibrium point. In the absence of detachment processes in the collisions, the equilibrium value of the reduced electric field must be no less than  $(E/N)_c$ . The detachment processes provide an additional amount of electrons as if from an external ionization source, that gives the possibility to maintain the discharge burning at an electric field lower than the equilibrium value. The continuity equations for electrons and basic positive and negative ions are solved with the 1D - model, that can be briefly described as follows. The geometry of discharge is symmetrical with respect to the discharge axis. This means that the continuity equation can be solved in terms of the variables  $(x, r)$ , where  $x$  is the distance from the cathode along the discharge axis,  $r$  is the radius. However, the solution of the two-dimensional nonstationary problem in the physics of discharge is still a serious challenge to computer potentialities. On the other hand, the presentation and treatment of calculations also presents difficulties. The present report deals with a quasi-one-dimensional numerical model. To derive the equations of this model, we make an assumption that all physical parameters ( $E$ ,  $n_e$ ,  $n_p$ ,  $n_n$ ) are constants in each cross section for the discharge current. This approximation was used, for example, by R. Morrow [1], who assumed the discharge channel to have the cylindrical shape. However, from a great many experiments it is well known that the discharge current is concentrated as a small spot on the needle and occupies a comparatively large area on a flat cathode. If the radius of the current channel is introduced, then it strongly increases from the rod to the plane. The ratio of current channel radii on the negative and positive electrodes makes about  $10^3$ . We consider the radius of the current channel to be the function of the axial coordinate  $x$ . The problem of choosing the channel shape will be discussed separately. Then, integrating the equation with respect to the cylinder of radius  $r$  and height  $dx$  and taking into account the mentioned constancy of the physical parameters, one can obtain the following equations [2,3]:

$$\frac{\partial n_e}{\partial t} + \frac{1}{S} \frac{\partial}{\partial x} (S n_e w_e) = (v_i - v_a) n_e + v_d n_n, \quad (1)$$

$$\frac{\partial n_p}{\partial t} - \frac{1}{S} \frac{\partial}{\partial x} (S n_p w_p) = v_i n_e, \quad (1)$$

$$\frac{\partial n_n}{\partial t} + \frac{1}{S} \frac{\partial}{\partial x} (S n_n w_n) = v_a n_e - v_d n_n, \quad (2)$$

$$\frac{1}{S} \frac{\partial}{\partial x} (SE) = - (n_p - n_e - n_n) \frac{e}{\epsilon_0}, \quad (4)$$

where  $S(x)$  is the cross-sectional area of the current channel, which is considered to be the known function of the coordinate  $x$ . The introduction of this function is the key point of our model. Equations (1) - (4) should be supplemented by boundary conditions. The boundary conditions for positive and negative ions are obvious: their concentrations equal zero at the anode and at the cathode, respectively. For electrons, in contrast to R. Morrow [1], we [2-5] consider only the secondary electron emission caused by the ions. Really, some particular processes in air that would yield an essential amount of secondary photoelectrons are unknown. Therefore, it appears reasonable to neglect them at all. Then the boundary condition for electrons is formulated through the introduction of the secondary ion emission coefficient  $\gamma$ :

$$j_e(0, t) = \gamma j_p(0, t), \quad (3)$$

where  $j_e = n_e w_e$ ,  $j_p = n_p w_p$ . The boundary conditions for the electric field strength were determined directly from eqs. (1) - (4) at each time step. The procedure and a detailed description of the numerical algorithm for the solution of the set of eqs. (1)-(4) can be found in ref. [2]. The solution of the above-described set of equations is a complicated task because of a great difference between the characteristic times of the physical processes, and because of the fact that the parameters to be calculated (electric field, charged particle density) strongly vary in the space between the electrodes. For the numerical solution we use the implicit numerical scheme. The space grid is nonuniform, having a smaller step in the vicinity of the electrodes (in particular, close to the needle tip). The integration step in time  $\tau$  is limited by three conditions:

$$\tau < \min(\Delta/(\mu_e E)), \quad \tau < \min(1/v_i, 1/v_a), \quad \tau < \tau_M, \quad (6)$$

where  $\Delta$  is the local grid size in space,  $\tau_M = 1/(4\pi\sigma)$  is the Maxwellian time,  $\sigma$  is the plasma conductivity. To avoid the numerical instability, we put the time dependence of the supply voltage in the following form:

$$U_{suppl} = U_0 \left( 1 - 0.9 \exp(-t/\tau_{suppl}) \right), \quad (7)$$

where  $\tau_{suppl} = 20\mu s$  can be considered as a characteristic time of the establishment of steady-state conditions. If it is compared with the time intervals, for which the calculations are made, it can be seen that except for the very beginning, the calculations are performed with a practically stable supply voltage, as is also the case in experiment. Typically, the total number of numerical grid nodes was 160. The real time integration step ranged between  $10^{-12}$  -  $10^{-11}$  s.

The calculations of concentrations of basic charged components are performed by the above-described one-dimensional model, where the equations were averaged in the approximation of the given discharge shape, i.e., relying on some experimental data or some other physical concepts we assign the shape of the current channel, over which the continuity equations are averaged. In this case, it is also assumed that all the parameters do not vary in the discharge cross section, but are dependent only on the longitudinal coordinate. The Poisson equation, as opposed to other approaches, is solved in the two-dimensional space (in parabolic coordinates) with the help of integration of the algebraic sum of charged component concentrations using the known Green function [6].

$$G = \frac{1}{R} = 2 \sum_{m=0}^{\infty} \chi_m \cos[m(\phi - \phi_0)] \int_0^{\infty} J_m(k\lambda) J_m(k\lambda_0) I_m(k\mu) K_m(k\mu_0) k dk, \quad \mu_0 > \mu, \quad (8)$$

where  $\lambda$ ,  $\mu$  are the paraboloid characteristics,  $J_m$  is the first-order Bessel function,  $I_m$ ,  $K_m$  are the modified Bessel functions of the imaginary argument.

The resulting from this integration spatial distribution of the potential determines the distribution of the reduced electric field  $E/N$ . The knowledge of this distribution permits the use of a locally zero-dimensional model of chemical kinetics, which takes into account about 100 chemical reactions, owing to the local dependence of the rate constants of the main processes (ionization, attachment, detachment, associative recombination, dissociative recombination, etc.), this being due to the presence of the small parameter  $b = l/\lambda_e$  (where  $l$  is the characteristic electrode size and separation,  $\lambda_e$  is the free path length of the electron between the successive collisions) on account of a high pressure of the gas mixture. The quantitative and qualitative compositions of plasma components, between which collisions occur, are substantially dependent on the degree of nonequilibrium of the system, i.e., on the appreciable excess of the average electron energy over the energies of ions, neutral molecules and atoms. Not to overload the problem, we do not take into account the nonequilibrium in the vibrational level distribution. This can be done at a not too high specific power of the discharge, i.e., for the ozonizers with a high gas flow rate as in our case.

### 3. Results and discussion

The distribution of gas-mixture chemical components, found at the previous stage, makes it possible to find the space distribution of the electron distribution function and, in accordance with the above-described procedure, to find the space distribution of the ionization, detachment, attachment, etc. coefficients which enter into the set of continuity equations for the main charged components. At our experimental conditions, we can restrict ourselves to the equations for electrons, negative ozone ions ( $O_3^-$ ) and positive oxygen ions ( $O_2^+$ ), the concentrations of which considerably exceed the concentrations of other ions. In our case of rather low concentrations of water vapor (no more than 1%), the  $OH^-$  concentration, as indicated by the calculations of the local chemical kinetics, does not approach  $O_3^-$ , and therefore, we calculate only three mentioned kinds of charged particles. Note that the electron concentration is often several orders of magnitude lower than the ion concentrations, yet, owing to a high mobility of electrons and large cross sections for the processes involving electrons, the equation for electrons is major in the set. Among reactive particles, of most interest for our consideration is ozone which is produced in the discharge as a result of oxygen molecule dissociation. It is well known that for the destruction of ozone produced in the discharge two catalytic cycles are of importance: one is associated with nitrogen oxides, and the other - with hydrogen radicals. The first cycle can play a significant role only at a great energy contribution, that was not attained in the calculations. The other can be the cause of the ozone destruction also at a rather great energy contribution and a high content of water vapor. The introduction of a small quantity of water vapor may cause the ozone concentration to increase, because, first of all, the discharge voltage increases at the same current value. At a higher voltage, the rate of oxygen molecule dissociation is higher, and this fact plays a positive role for the efficiency of ozone generation.

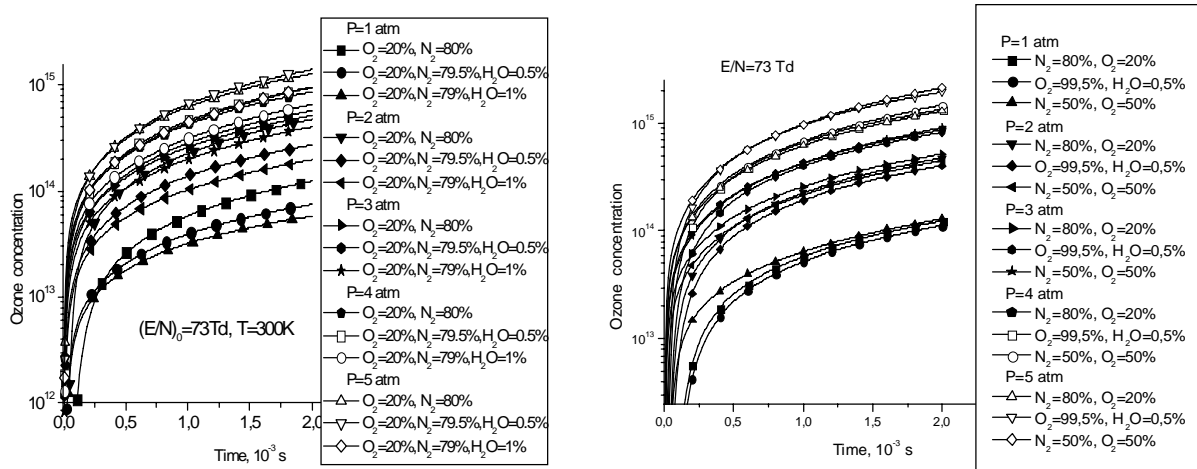


Fig. 1. Ozone concentrations for gas mixtures of various compositions at different pressures

The real ozone yield is the result of competition between two effects: (i) voltage increase and (ii) the ozone breakdown in the corresponding catalytic cycle. As it is obvious, for our conditions the other aspect of the water vapor effect (that leads to a decreased ozone concentration) becomes of greater importance at  $H_2O$  concentration higher than 1%. Higher (see Fig. 1) we give the time evolution of the ozone concentration for various gas mixtures (dry and humid air, combined mixtures) at different parameters (pressure, initial reduced electric field values). The temperature was chosen to be 300 K. For air with a 1% water content, as the pressure rises from 1 atm. to 5 atm., the ozone concentration increases 22 times (see Fig. 1) at a reduced electric field strength  $E/N \approx 73$  Td ( $1 \text{ Td} = 10^{-17} \text{ V/cm}^2$ ), i.e., an approximately square pressure dependence of ozone concentration takes place, that can be explained on the basis of the structure of basic reactions, where ozone is synthesized. In this case, the concentration of harmful  $NO_x$  compounds is 2-3 orders of magnitude lower than the ozone concentration.

Therefore, no excess of boundary-admissible concentrations of  $NO_x$  can be provided at rather high ozone concentrations. For the gas mixture  $O_2 : H_2O = 99,5 : 0,5$  at a 5-fold rise in pressure, the ozone concentration increases by a factor of 15 at a voltage even slightly higher than the reduced electric field. The temperature dependence of the ozone concentration obviously shows that this concentration increases with temperature lowering (corresponding increase of neutral particle density in the gas mixture). However, it should be noted that in this case the specific efficiency remains nearly constant, i.e., the use of cooling may appear expedient to create ozonizers with a higher ozone concentration. We note that here we did not take into account the consumption of energy for cooling, that might be a significant part of the total power expended. For dry air, with a five-fold rise in pressure the electron concentration increases 35 times (from  $2 \cdot 10^6$  to  $7 \cdot 10^7 \text{ cm}^{-3}$ ). And for the mixture  $O_2 : H_2O = 99,5 : 0,5$  at the same rise in pressure the increase in the electron concentration does not exceed a factor of 6. As to the gas mixture  $N_2 : O_2 = 50 : 50$ , here the increase in the electron concentration does not exceed a factor of 3 at a five-fold rise in pressure. The comparison of the obtained numerical results shows the following trends: (i) the higher is the humidity, the lower is the discharge current at the same voltage, or a higher voltage is required to maintain the same current value; (ii) the total quantity of nitrogen oxides decreases with a successive replacement of the basic sort of oxide, i.e.,  $N_2O$  by  $NO$ ; (iii) the variations in the concentrations and composition of hydrogen-containing particles are comparatively small. At a higher humidity, the discharge in air approaches the thermodynamically equilibrium discharge. At 2% of  $H_2O$  and higher, it is  $OH$  that becomes the main negative ion. It is of interest to note that for 1% and 2% of  $H_2O$ , the evolution of electron concentrations is not monotone. Among the particles produced in the discharge, the  $OH$  radicals are the most reactive. It can be seen that their concentration first increases, then reaches maximum and decreases. However, the duration of the increase strongly depends on the water vapor content. This behavior results in a complicated dependence of the maximum  $OH^-$  radical concentrations on time and the water vapor content. The electron energy dependence of the electron distribution function is a very illustrative characteristic of the discharge (see Fig. 6). Thus, it can be seen that the distribution function reaches the energy up to 5 - 6 eV with an increase in the reduced electric field from  $E/N \approx 62$  Td up to 350 Td. However, in this case, the behavior of the distribution function very strongly depends on the gas mixture composition. In particular, for the mixture  $O_2 : H_2O = 99,5 : 0,5$  the distribution function is nearly constant in a wide energy range (up to 10 eV). This indicates that there is no effective channel of energy loss by electrons almost up to 10 eV. The phenomenon known but not explained in the literature, namely, the rise in the discharge ignition voltage with an increasing ozone concentration, can be rather well accounted for relying on two facts: (i) the ion current is 20 to 40 times higher than the electron current, and (ii) as a result of a great cross section for attachment, the  $O_3^-$  ions are the basic ions, their concentration is more than 3 orders of magnitude higher than the concentration of electrons. Therefore, despite the fact that the ozone concentration makes about a few tenths of percent of the oxygen molecule concentration, the both gases are electronegative; a high concentration of  $O_3^-$  ions (they are just responsible for the basic current transfer in the discharge) exerts a cardinal effect on the current-voltage characteristic of the discharge, specifically, on the ignition voltage. The role of negative  $OH^-$  ions is very



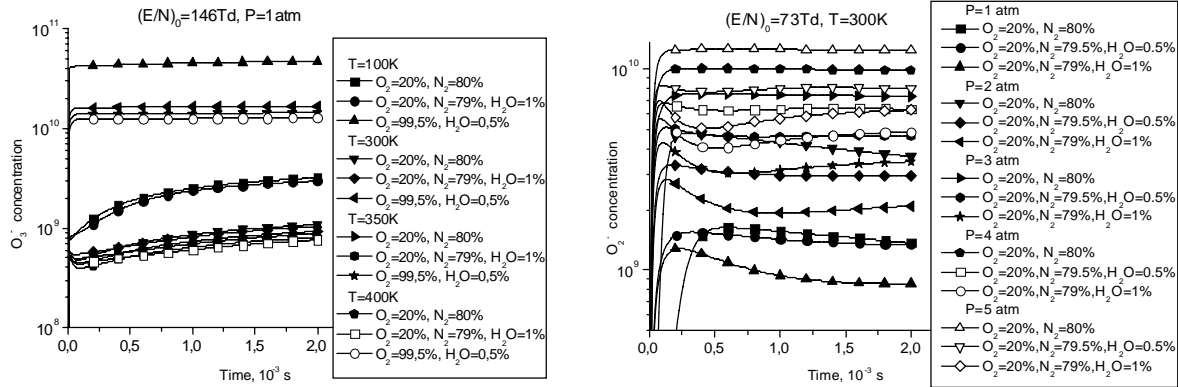


Fig.2. Concentration of negative ions  $O_3^-$  for various gas mixtures at different temperatures and pressures.

significant even at a low water content in the gas mixture. These ions assist the decrease of electrons in the discharge, take up a substantial portion of ion current and lead to the formation of complex cluster ions.

#### 4. Conclusion

Relying on the undertaken numerical simulation we have established that for humid air (with 1% water vapor content) with pressure rising from 1 atm. to 5 atm., the ozone concentration increases by a factor of 22 for a time of  $2 \times 10^{-3}$  s at a reduced electric field strength  $E/N \approx 73$  Td. The known fact of the rise in the discharge ignition voltage with an increasing ozone concentration was proposed to be treated relying on two facts: (i) the ion current is 20 to 40 times higher than the electron current, and (ii) as a result of a great cross section for attachment, the  $O_3^-$  ions are the basic ions, their concentration is more than 3 orders of magnitude higher than the concentration of electrons. Therefore, despite the fact that the ozone concentration makes about a few tenths of percent of the oxygen molecule concentration, and the both gases are electronegative, a high concentration of  $O_3^-$  ions (they are just responsible for the basic current transfer in the discharge) exerts a cardinal effect on the current-voltage characteristic of the discharge, specifically, on the ignition voltage. It has been shown that the initial reduced electric field value does not remain constant, but within a very short time ( $10^{-8}$  s) almost reaches its steady-state value that depends on the external electric circuit and the discharge gap resistance. So, it has been demonstrated that the transition to elevated pressures appears very expedient, because this transition provides considerably higher ozone concentrations even with lower expenditures of energy. The investigation of the ion composition has allowed us for the first time to explain the dependence of the discharge gap voltage on the ozone concentration. It has been shown that the presence of nitrogen in the mixture is favorable for ozone generation in the discharge. In this case, the concentration of harmful  $NO_x$  compounds can be substantially reduced by an appropriate choice of the optimum conditions of discharge burning.

This work was supported by Science and Technology Center in Ukraine (grant # 1069).

#### References

1. R. Morrow. Phys. Rev. A. **32**, 1799 (1985).
2. Yu.S. Akishev, N.N. Elkin, A.P. Napartovich. Plasma Physics Reports **12**, 1225 (1986).
3. Yu.S. Akishev, I.V. Kochetov, A.I. Loboyko, A.P. Napartovich. Plasma Phys. Reports **28**, 1136 (2002).
4. V.I. Golota, V.I. Karas', V.P. Mal'khanov, I.F. Potapenko, O.N. Shulika Proc. XXVIII Zvenigorod Conf. on Plasma Physics and CTF. Moscow, abstracts, 161 (2001).
5. V.I. Golota, V.I. Karas', V.P. Mal'khanov, I.F. Potapenko, O.N. Shulika Proc. XXIX Zvenigorod Conf. on Plasma Physics and CTF. Moscow, abstracts, 164 (2002).
6. P.M. Morse, H. Feshbach. Methods of Theoretical Physics. New York, Toronto, London. McGraw-Hill Book Company, Inc., 1953.

# **Operate on the Kinetics of a Diamond Films Plasma Chemical Synthesis by Means of Reversible Metal Hydrides**

Klochko Ye.V.<sup>1</sup>, Pashnev V.V.<sup>2</sup>, Shmal'ko Yu.F.<sup>1</sup>, Strel'nitsky V.Ye.<sup>2</sup>

<sup>1</sup>*A.N.Podgorny Institute for Mechanical Engineering Problems of National Academy of Sciences of the Ukraine, Kharkov, Ukraine*

<sup>2</sup>*National Sciences Center "Kharkov Institute for Physics and Technology", Kharkov, Ukraine*

Author's results of experimental researches of influence of the metal hydride activations effect of hydrogen on the kinetics of a diamond films plasma chemical synthesis from a gas phase are submitted. Was prescribed, that use of metal hydride hydrogen activators as additional to the gas discharge of means of an intensification of process, considerably allows to increase quality of a synthesized film at moderate expenses of energy. Use multifunctional metal hydride elements which are entered in a plasma chemical reactors structure is shown, that, allows, besides improvement of quality of a synthesized diamond films, effectively to solve auxiliary tasks of compact and safe storage of necessary quantity of hydrogen, its clearing of gas impurity and programming letting-to-hydrogen in a working zone of reactor.

# Film Deposition in Parallel Plate RF Discharges Containing Hydrocarbons

N. Bibinov<sup>1</sup>, V. Kudrle<sup>1,2</sup>, L. Zajicková<sup>2</sup>, Z. Donkó<sup>3</sup> and K. Wiese<sup>1</sup>

<sup>1</sup>*Ruhr-Universität Bochum, Experimentalphysik insbes. Reaktive Plasmen, 44780 Bochum, Germany*

<sup>2</sup>*Masaryk University, Department of Physical Electronics, Kotlářská 2, 611 37 Brno, Czech Republic*

<sup>3</sup>*Research Institute for Solid State Physics and Optics, Hungarian Academy of Sciences, H-1525 Budapest, Hungary*

## Abstract

The processes accompanying hydrocarbon film deposition are studied in a capacitively coupled RF discharge in He,Ar/C<sub>2</sub>H<sub>2</sub> and He,Ar/CH<sub>4</sub> mixtures. About 200 ms after discharge ignition acetylene disappears completely from the plasma, while the electron temperature increases because of negative ion production. The hydrophilic/ hydrophobic character of the films can be influenced by the discharge parameters. It depends on the surface roughness and on the polarizability of the molecules and radicals at the surface.

## 1. Introduction

RF discharges containing hydrocarbons are often used for tailoring surface coatings with respect to physical and chemical properties. Recently this method is used for coatings of tools and materials for biomedical applications because plasma polymer coating is a dry process and the process temperature is low. It is important to understand and control the interactions at the interface between synthetic components and biological materials because - depending on its function - the surface must meet various demands. An important quantity in this respect constitutes the surface wettability. It can be modified as a result of electron and ion bombardment. The wettability also depends on the surface roughness, which in turn can be modified by properly choosing the plasma parameters. In the present work we study the plasma processes in RF discharges in rare gas / hydrocarbon mixtures with respect to their influence on desired and non-desired properties of hydrocarbon films.

## 2. Experiment

We deposited hydrocarbon films in pulsed and continuous 13.56 MHz parallel plate RF discharges in Ar, He/C<sub>2</sub>H<sub>2</sub> and Ar, He/CH<sub>4</sub> mixtures. The pulse lengths were of the order of 50 to 1000 ms. The frequency we choose close to 0.5 Hz for ascertaining the discharge gas to be completely exchanged between two successive discharge pulses. The processes occurring in the plasma we investigated spectroscopically using a SpectraPro-500i<sup>®</sup> spectrometer with 500 mm focal length - see fig. 1. Using at the entrance of our spectrometer a moveable optical fibre with a collimator head we measured space ( $\Delta x \approx 0.5$  cm) and time resolved ( $\Delta t = 1-10$  ms) emission spectra with a spectral resolution of  $\Delta \lambda \approx 0.1$  nm. The wettability of the created hydrocarbon films we characterized by measuring the contact angle of special test fluid drops, using a DSA 10 Mk2<sup>®</sup> drop shape analysis system (Kruess).

The temporal behaviour of the acetylene concentration in a pulsed discharge we obtained by means of absorption measurements in the VUV. For this purpose we used a Xe resonance lamp and a photomultiplier of the Russian type PhMT-154 and measured the absorption of acetylene along a radial line-of-sight at different positions along the axis of the gas chamber - see fig. 1. With the PhMT-154 we measured also the VUV emission. It consists mainly of the H<sub>2</sub> emission bands.

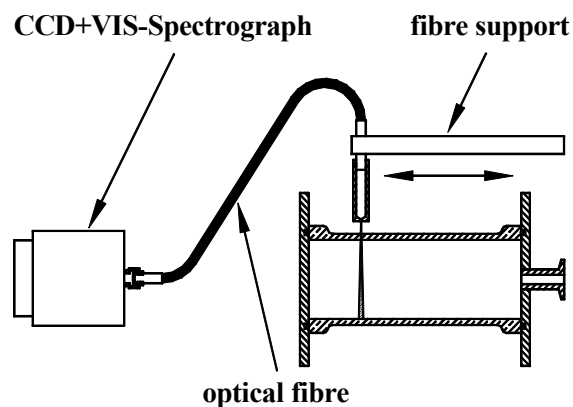


Fig. 1 Optical set-up for plasma spectroscopy. The plasma of a parallel plate RF discharge is viewed through the glass wall of the discharge vessel. The end flanges constitute the electrodes.

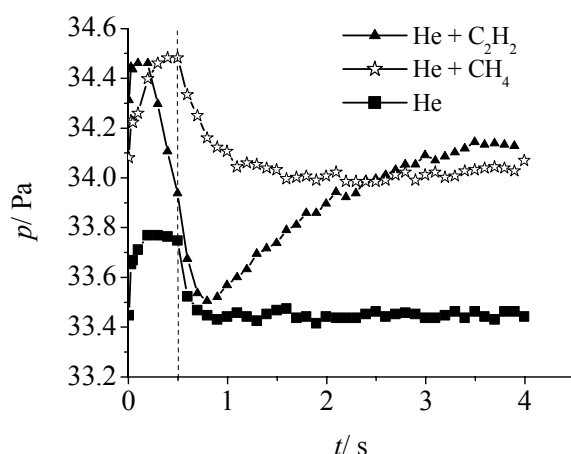


Fig.2 Gas pressure in pulsed discharges in He/C<sub>2</sub>H<sub>2</sub> and He/CH<sub>4</sub> mixtures (He flow 17 sccm, C<sub>2</sub>H<sub>2</sub> and CH<sub>4</sub> flows 0.6 sccm, RF power 20 W, discharge pulse duration 500 ms)

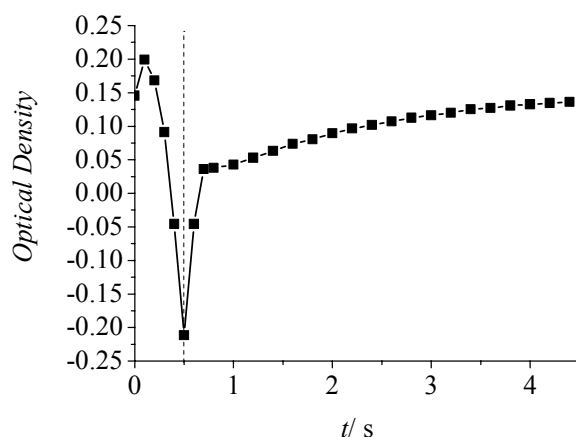


Fig.3 VUV-optical density in a pulsed discharge in a He/C<sub>2</sub>H<sub>2</sub> mixture (He flow 17 sccm, C<sub>2</sub>H<sub>2</sub> flow 0.6 sccm, RF power 20 W, discharge pulse duration 500 ms) the dotted line indicates the end of the pulse.

### 3. Results

When igniting a discharge, usually the gas pressure rises due to gas heating and/or dissociation. After some time the pressure reaches a constant value and starts to decrease immediately after switching off the discharge power. Such behaviour we observed in discharges in pure rare gases or in rare gas/ methane mixtures – see the respective curves in fig. 2. In mixtures of He or Ar with acetylene, however, the

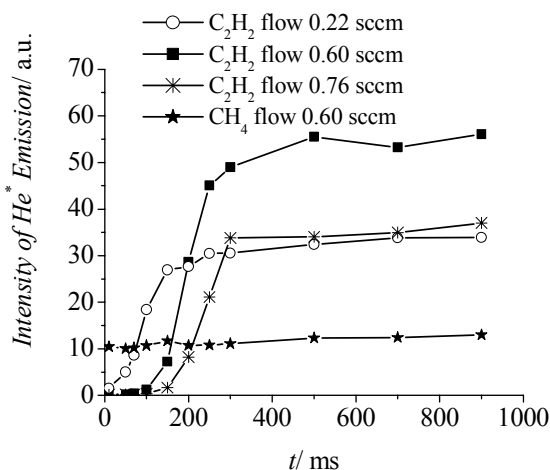


Fig.4 Time dependences of He atom emission intensities in pulsed He/hydrocarbon discharges (He flow 17 sccm, RF power 20 W, gas pressure 34 Pa)

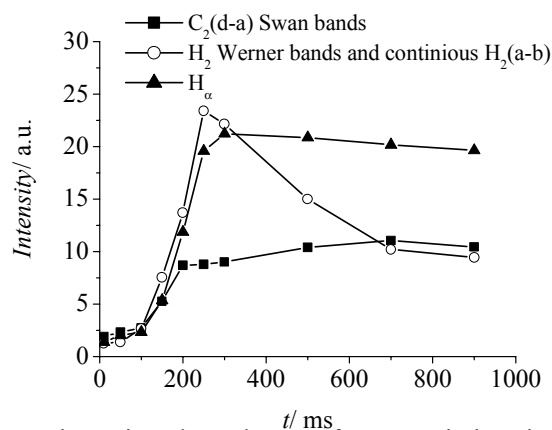


Fig.5 Time dependences of some emissions intensities in pulsed He/C<sub>2</sub>H<sub>2</sub> discharges (He flow 17 sccm, C<sub>2</sub>H<sub>2</sub> flow 0.6 sccm, RF power 20 W, gas pressure 34 Pa)

behaviour of the pressure was quite different. In the first 200 ms we observed also a pressure rise to a constant value. Then the pressure started to decrease with running discharge and continued to decrease for some time even after switching off the discharge. After exhibiting a minimum after some seconds the pressure rose again to reach finally the value characteristic for the system before starting a discharge – see fig. 2. During the decrease of the pressure also the VUV optical density exhibits a minimum as shown in fig. 3 (the apparent negative values of the optical density are due to the influence of plasma emission). This minimum indicates a strong reduction of the acetylene concentration. This anomalous behaviour of pressure and optical density is accompanied by a slow increasing of the intensities of rare

gas atomic lines in the visible, the intensities of the  $C_2$ -Swan bands, of the H atomic lines in the visible and of the VUV and UV emission of  $H_2$  (Werner bands and  $H_2(a-b)$  continuum). All these emission intensities rise with characteristic times of tens of milliseconds and then saturate. Only the intensity of the  $H_2$  emission exhibits a maximum and then decreases again – see figs. 4 and 5.

After switching off the acetylene supply while the discharge kept running it takes minutes before the increased emission of the rare gas lines levels off. However the emission drops within less than a second to its value of a pure rare gas discharge, if the discharge is switched off shortly and then immediately re-ignited – see figs. 6 and 7.

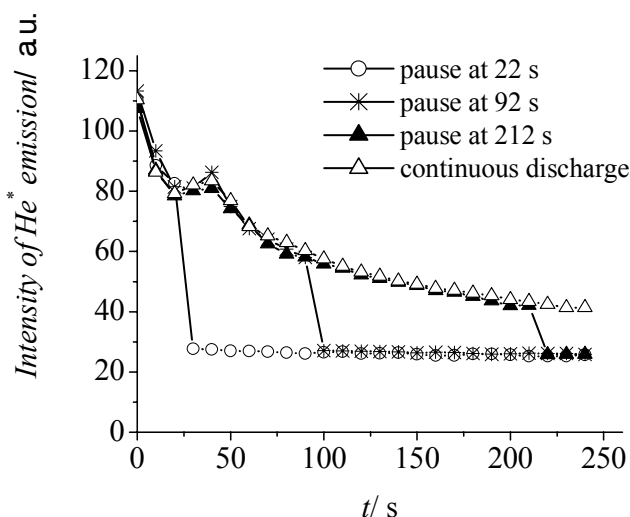


Fig. 6. Time dependence of the He atom emission intensity in He discharges after stopping the acetylene flow (He flow 17 sccm, RF power 20 W, pause duration 1 s)

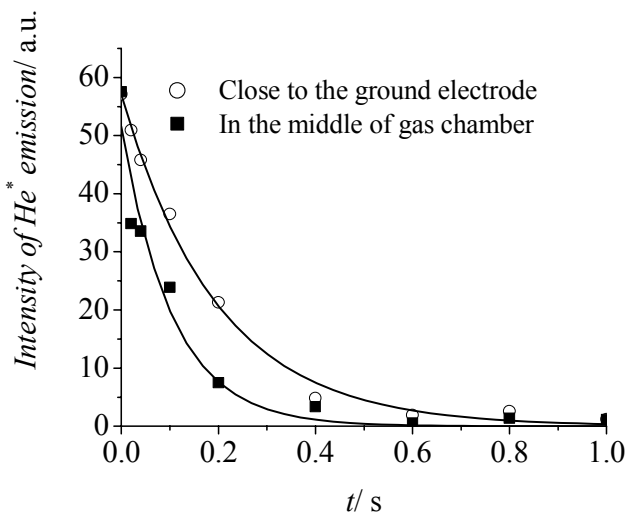


Fig. 7. Dependence of the He atom emission intensity on the pause duration. Discharge conditions were the same as in fig. 5. The time after stopping of the acetylene flow was 10 s.

The decay of the intensity during the discharge pause we measured by first switching off the acetylene supply and then interrupting the discharge for a short time of less than a second and measuring the intensity immediately after re-ignition as a function of the duration of the pause – see fig. 7.

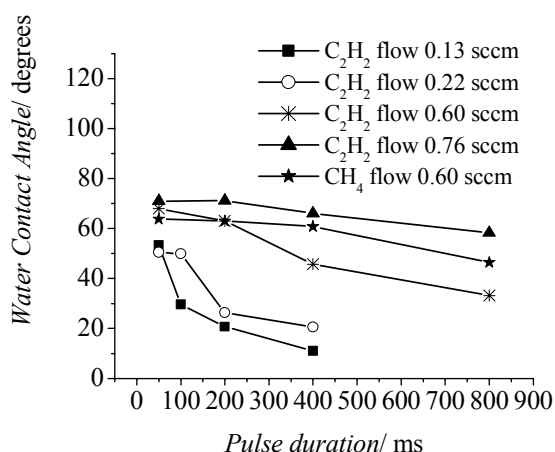


Fig. 8. Water contact angle measured on hydrocarbon films created in pulsed He/hydrocarbon discharges (He flow 17 sccm, gas pressure 34 Pa, RF power 20 W).

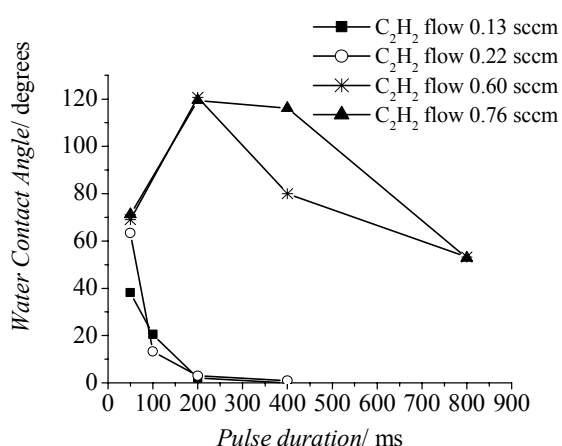


Fig. 9. Water contact angle measured on hydrocarbon films created in pulsed Ar/ $C_2H_2$  discharges (Ar flow 10 sccm, gas pressure 35 Pa, RF power 20 W).

The wettability of the created hydrocarbon films we characterized by measuring the water contact angle. By properly choosing the gas mixture and the duration of the discharge pulses we could produce either hydrophilic or highly hydrophobic films in acetylene containing discharges - see figs. 8 and 9. The wid-

est range of water contact angles that is from 0 to 120 degrees we measured on films deposited in Ar/C<sub>2</sub>H<sub>2</sub> mixtures. In the case of He/C<sub>2</sub>H<sub>2</sub> mixture the range of contact angle variation ranges from 10 to 70 degrees, that means it is narrower than in the case of argon - acetylene mixtures. A much weaker variation of the water contact angle with the pulse duration we observed also on films deposited in methane containing discharges - see fig.8.

#### 4. Discussion

Our observations reveal a fundamental difference between discharges containing methane and those containing acetylene. The anomalies in acetylene containing discharges come to pass on time scales characteristic for heavy particle reactions (tens of milliseconds). They must be due to a characteristic feature of acetylene. Such a characteristic feature is the triply bond C<sub>2</sub> group, which is known to be very stable. Further C<sub>2</sub> forms one of the most stable negative ions having even electronically excited states and thus a characteristic emission spectrum. Mass spectrometric studies of acetylene containing plasmas reveal the formation of long hydrocarbon chains probably with alternating triple and single bonds [1]. Such molecules have delocalised electronic wave functions. As a consequence the attachment cross sections should be high and also the polarizability of these chains. Besides film deposition the formation of these molecules may be the reason for the disappearance of acetylene and the pressure decrease. The increase of the optical density at the beginning of the discharge pulse is also due to a creation of hydrocarbon chains (for example C<sub>4</sub>H<sub>2</sub> molecules) absorbing the emission of the Xe resonance lamp as effectively as C<sub>2</sub>H<sub>2</sub> molecules [2]. Immediately after switching off the discharge the acetylene concentration (and thus the optical density measured in the VUV) begins to increase again. That is due

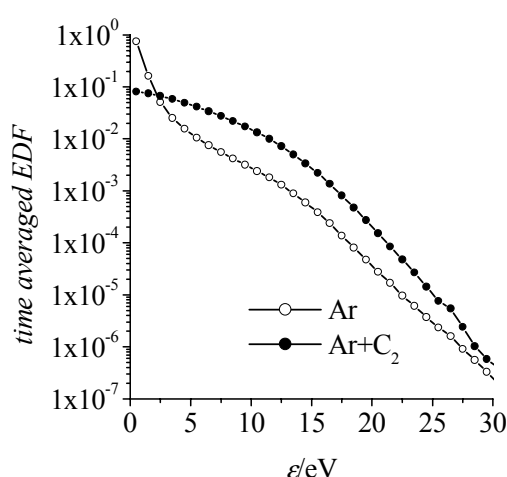


Fig.10 Electron distribution function in an Ar RF discharge with (full circles) and without (open circles) C<sub>2</sub><sup>-</sup> ions ( gas pressure 13 Pa, electrode separation 2 cm, stationary C<sub>2</sub> -concentration 10<sup>11</sup> cm<sup>-3</sup>).

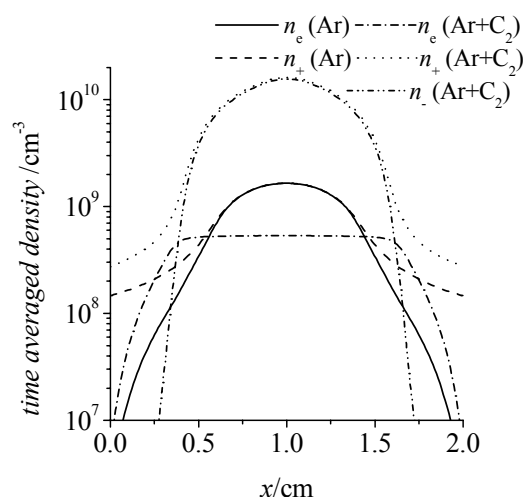


Fig.11 Time averaged density of charged particles calculated for Ar RF discharges: conditions as in fig. 10.

to the gas flow.

The reduction of the acetylene concentration is accompanied by an increase of the density of high-energy plasma electrons (active electrons), as can be seen by the increase of the intensities of the optical emission of the discharge. We think that attachment processes acting as a sink for low energy electrons are the reason of this effect. As mentioned above the large hydrocarbon molecules have very large attachment cross-sections for low energy electrons [3]. Thus a deficit of low energy electrons will be established if large numbers of these molecules are present in the plasma. This makes the heating of high-energy electrons more efficient and their number increases in spite of the decrease of the total electron density. This involves an increase of the intensity of the optical emission.

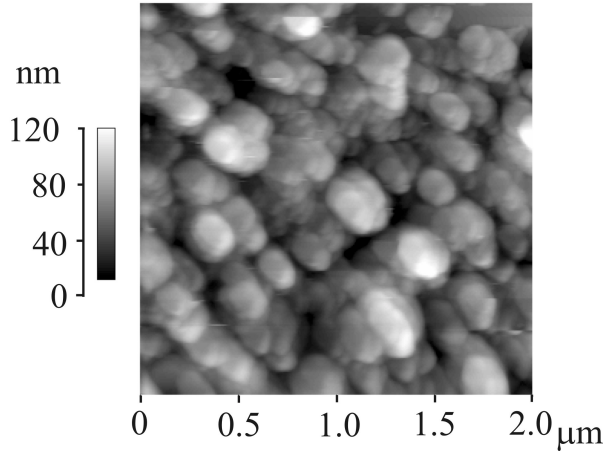
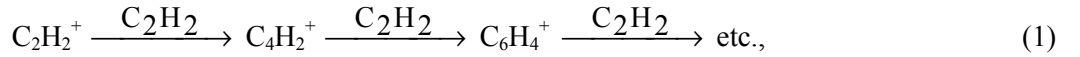


Fig.12 SEM micrograph of the surface of a film on a silicon substrate deposited in a pulsed Ar/C<sub>2</sub>H<sub>2</sub> RF discharge (pulse duration 125 ms, Ar flow 10 sccm, C<sub>2</sub>H<sub>2</sub> flow 0.60 sccm, gas pressure 34 Pa, RF power 20 W)

In order to investigate through simulations this effect of C<sub>2</sub>H<sub>2</sub> on the Ar discharge we have developed a 1-dimensional particle-in-cell computer simulation code. We simulate a number of superparticles in the order of 10<sup>4</sup>: electrons and Ar<sup>+</sup> ions, as well as C<sub>2</sub><sup>-</sup> molecules in the presence of the acetylene admixture. The model incorporates several simplifying assumptions due to the lack of information about cross sections of elementary processes and about details of the chemistry taking place in the Ar+C<sub>2</sub>H<sub>2</sub> discharge. The effect of acetylene is modelled by assuming a constant spatial concentration (10<sup>11</sup> cm<sup>-3</sup>) of C<sub>2</sub> molecules. Electrons with low energy attach to these molecules this way depleting the electron density in the bulk plasma. The resulting C<sub>2</sub><sup>-</sup> molecules are assumed to have a lifetime of 5 ms, which accounts for their losses by detachment and chemical reactions. The results of the simulations are presented in figs. 10 and 11 for a

constant RF voltage at the powered electrode of  $V_{RF} = 80$  V, a pressure  $p = 100$  mTorr and an electrode separation  $L = 2$  cm. An unexpected result is the increase of the total ion density by a factor of 10, see fig. 11.

It follows from these considerations that the negative ions in rare gas/acetylene discharges have severe consequences for the gas phase chemistry, namely (i) a decrease of the total electron density, (ii) an increase of the concentration of high-energy electrons (active electrons), (iii) a decrease of the loss rates of positive ions on the chamber walls and thus an increase of the ion densities. A consequence may be an increase of the probability of participation of positive and negative ions in polymerisation processes: polymerisation by acetylene attachment to positive ions:



and polymerisation by mutual neutralisation:



When switching off the acetylene supply the optical emission intensity decreases very slowly. As shown in fig. 6 the characteristic time of decay amounts to several minutes. However, when switching off the discharge the phenomenon disappears in one second. This is a further hint to the important role of negative ions, which are almost perfectly contained in the potential of a discharge. However, also the decay time in the discharge pause is relatively long and can be taken as an indication of the high mass of the responsible particles.

The saturation of the optical emission intensity indicates that a constant density of the electrons and radiating species is reached. However, the anomaly of the H<sub>2</sub> emission indicates two counteracting effects: It is formed in reactions of the type



When the acetylene concentration decreases the rate of H<sub>2</sub> formation decreases too, while the loss processes (transport by the gas stream out of the discharge vessel) have constant efficiency.

We observe no anomalous behaviour of the optical emission in methane containing discharges. When switching on the methane supply in a running noble gas discharge the emission intensities immediately decrease and remain constant as long as methane is admitted. This indicates very low concentrations of negative ions in these discharges.

The wettability of the hydrocarbon films depends on the surface polarizability and on the surface structure. Hydrophobia is dominated by the strong self-association of water molecules excluding the association with non-polar surfaces. Surfaces created from fluorocarbon and saturated hydrocarbon molecules are mostly hydrophobic. The molecules or groups on these surfaces cannot form hydrogen bonds and do not interact with water drops. Otherwise the surface has a hydrophilic character. The limit between hydrophobia and a hydrophilic character is usually taken at a water contact angle of 65° [4].

A further important surface characteristic with respect to wettability is roughness. The combination of polar or non-polar films and surface roughness can lead to changes of the water contact angle between 0 to 160-175 degrees [5].

AFM and SEM micrographs showed that the surface roughness of films, created in pulsed Ar/acetylene discharges, changed dramatically with the pulse duration [6] - see fig. 12. Films deposited with 50 ms pulses had very smooth surfaces. The roughness was comparable to the roughness of the quartz and silicon substrates. But with increasing pulse duration the roughness rapidly increased. We observed an increased deposition rate at any electric field inhomogeneity and at edges. Further we observed that the surface roughness grows self-organized [7]. This can be explained by a high polarizability of the molecules and radicals building up the film. Due to their induced dipole momentum such molecules are attracted by inhomogeneities of the electric field. This same property of the surface may also explain that it

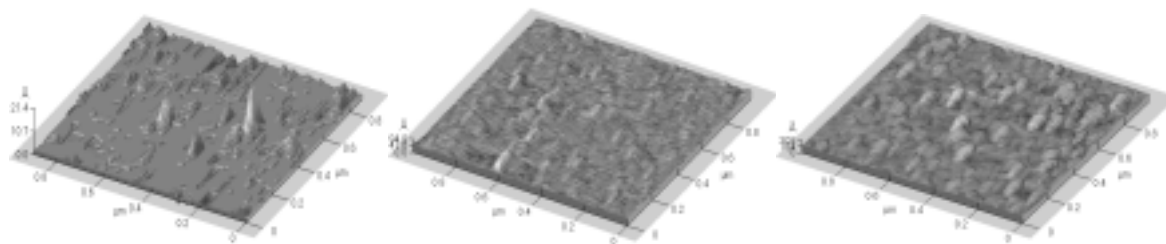


Fig. 13 Self-organized growth of surface roughness of a plasma deposited polymer film [7]. From left to right: surface after 10 plasma pulses, after 100 pulses and after 500 pulses. Pulse duration 100 ms, 10 sccm Ar, 2 sccm  $C_2H_2$ ,  $p_{tot}$  34 Pa, RF power 20 Watt. Please, notice the change of scale in the direction vertical to the surface.

is possible to obtain totally hydrophilic films. However, the latter explanation must be further checked. Before measuring contact angles we must expose our films to air. We cannot exclude that the surface changes during that exposure. A hydrophobic surface will be created when saturated hydrocarbon molecules adsorb at the surface. For saturation one needs hydrogen, which is created by reaction (3) at high acetylene concentrations. This may explain the influence of the acetylene flow on the water contact angle. These problems will be the subject of our further investigations.

## 5. Conclusion

In pulsed He,Ar/ $CH_4$ , $C_2H_2$  RF-discharges we have studied the processes in relation to the wettability of plasma deposited hydrocarbon films. The acetylene concentration decreases dramatically during the discharge pulse. In discharges containing acetylene negative ions determine the temporal behaviour of discharge parameters and the efficacy of excitation and ionisation processes. The polar character of the deposited hydrocarbon films depends on the acetylene flow and the duration of the discharge pulses. One reason for this dependence is the strong influence of the pulse length on the surface roughness.

This work was supported by Ministerium für Schule, Weiterbildung und Forschung, Nordrhein-Westfalen under grant 315-108 004 02, by OTKA, Hungary under grant OTKA-T-34156 and by the Ministry of Education of the Czech Republic under contracts MSM143100003 and COST 527.20.

## References

- [1] Ch. Deschenaux, A. Affolter, D. Magni, Ch. Hollenstein and P. Fayet, J. Phys. D: Appl. Phys. **32**, 1876 (1999)
- [2] H. Okabe, J. Chem. Phys. **75**, 2772 (1981)
- [3] I. I. Fabrikant and H. Hotop, Phys. Rev A **63** (2001) 022706 and private communication
- [4] E. A. Volger, Adv. Coll. Int. Sci **74**, 69 (1998)
- [5] R. d'Agostino, P. Favia, R. Gristina, E. Sargella, Proc. APP Spring Meeting "Biomedical Aspects of Plasma Physics", APP Spring meeting 2003, Bad Honnef, Germany, 1 (2003).
- [6] L. Zajicková, S. Rudakowski, H.-W. Becker, D. Meyer, M. Valtr and K. Wiesemann, Study of plasma polymerisation from acetylene in pulsed RF discharges, thin solid films 2003, in print.
- [7] S. Rudakowski, Diagnostik an einer gepulsten RF-Entladung zur Erzeugung dünner a:C-H Schichten, Dissertation Ruhr-Universität Bochum 2002 (in German)



# STUDY OF THE PLASMA ARC TORCH WITH ANTIVORTEX GENERATOR FOR CUTTING METALS

T. Stanciu, V. Pogora and I. Protuc

*Technical University of Moldova, 168, bd. Stefan cel Mare,  
Chisinau, MD-2004, Republic of Moldova*

## Abstract

An experimental study of the influence of the antivortex generator on the gas dynamic characteristics of plasma arc torch for cutting metals is presented. On the base of this study an adequate mathematical model was elaborated. The utilization of the antivortex generator ensures the increase of the deep and the velocity of cutting by 20 – 40 % in comparison with the ordinary plasma arc torch.

## 1. Introduction

In the plasma arc torch for cutting metals with the vortex stabilization of the electric arc [1,4] the integral pressure of the plasma jet, in which the tangential component of the velocity predominates over the axial one, quickly decreases from the exit of the nozzle. At the same time the diameter of this jet significantly increases. Consequently the velocity and the deep of cutting diminish but the width of the cut increases.

For the elimination of these disadvantages a new plasma arc torch with the antivortex generator was elaborated, the principle of the work and its application for cutting metals is given below.

## 2. Experimental set-up and diagnostics

The principal scheme of the plasma arc torch is shown in figure 1. The main particularity of this torch in comparison with the other torch [1] is the utilization of a metallic antivortex generator 4 installed between the vortex generator 3 and the nozzle 2. On the both sides of this antivortex generator the chambers 5 and 6 are created in which the gas arrives by means of the tangential channels 7. The channels on the both sides are in opposite directions necessary for creating two opposite vortices.

The vortex created in the chamber 6, which has the opposite direction will compensate partially or totally the gas vortex issues from the chamber 5 to the nozzle. Consequently the tangential component of the velocity of the plasma jet decreases but the axial component increases on the issue of the nozzle. The vortex generator 3 ensures the insulation between the copper electrode with the cavity 1 and the nozzle 2.

The diagnostics includes the capacitive pickup 8 with a Pitot tube for measurement of the integral pressure, the camera with the filters 9 to take pictures and the microphotometer 10 to study the distribution of the radiation intensity and the radial distribution of the temperature of the outgoing plasma arc jet 11. The radial distribution of the radiation intensity was calculated by means of the Abel inversion

$$I(x) = 2 \int_{r=x}^R \frac{I(r)r dr}{\sqrt{r^2 - x^2}}, \quad (1)$$

where  $I(r)$ ,  $I(x)$  are respectively the radial and “transversal” radiation intensity distribution;  $R$  is the radius of plasma arc jet.

The radial distribution of the temperature of plasma arc jet was obtained using the radial distribution of the radiation intensity and the pyrometric curves for air [2].

The velocity of plasma arc jet was calculated using the results of measurement of the integral pressure and the temperature by the following expression

$$V = \sqrt{\frac{2(P_i - P_s)}{\rho}}, \quad (2)$$

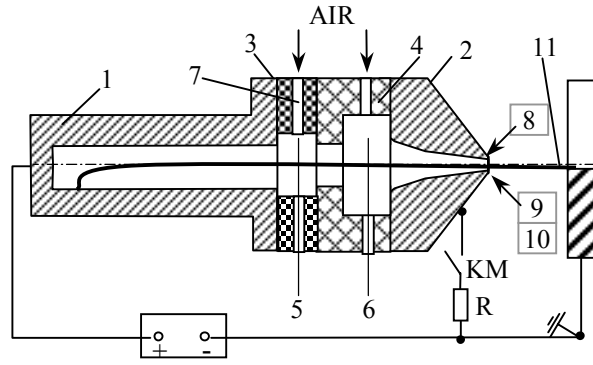


Figure 1. Experimental set-up

where  $P_i$  and  $P_s$  are respectively the integral and static pressures;  $\rho$  is the density of plasma arc jet. The density was obtained using the dependences  $\rho = f(T)$  given in [3]. The static pressure of the plasma arc jet was calculated using the relation [2]

$$P_s = \frac{I_a^2}{\pi R^4} (R^2 - r^2), \quad (3)$$

where  $I_a$  is the arcing current.

### 3. Experimental results

The experiments were made for three values of the arcing current 200, 250 and 300 A, three values of the flow rate 1.0, 1.35 and 1.7 g·s<sup>-1</sup>. The diameter of the nozzle channel was respectively 4.0, 4.5 and 5.0 mm. Each point is the result of the middle value of three experiments.

The dependencies between the maximum value of the integral pressure of the outgoing plasma arc jet and the distance from the nozzle to the Pitot tube for different values of the arcing current are presented in figure 2. When increasing the value of the arcing current the integral pressure increases. While increasing the arcing current from 200 to 300 A (curves 1 and 3) the integral pressure, for the distance from the exit of the nozzle 3 mm, increases from  $3 \cdot 10^4$  to  $6 \cdot 10^4$  N·m<sup>-2</sup>.

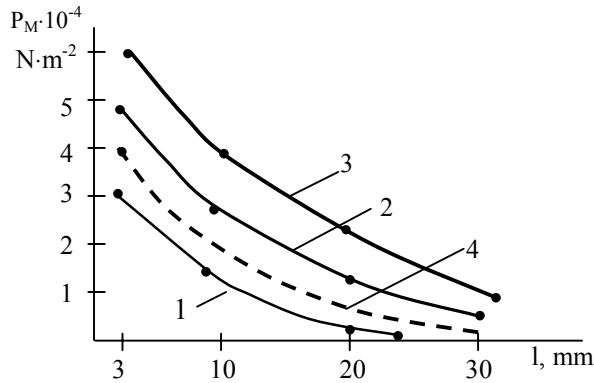


Fig.2. Distribution of the integral pressure of the plasma arc torch with antivortex generator of the arcing current, A: 1 -200; 2 -250; 3 -300; 4 -250 (without antivortex generator [4])

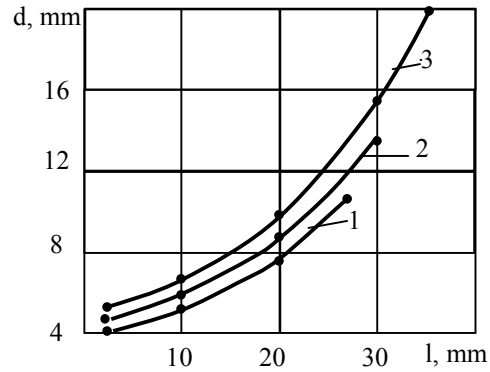


Fig.3. Dependence of the diameter of the plasma arc jet on the distance from the exit of the nozzle for arcing current, A: 1 – 200; 2-250; 3-300.

The diameter of the outgoing plasma arc jet increases more quickly for the great value of the arcing current (fig.3).

While increasing the flow rate of the air the maximum value of the integral pressure of the plasma arc jet increases (fig.4, curves 1,2 and 3,4). For the same values of the arcing current and the flow rate the integral pressure, in the presence of the antivortex generator, is from 1,2 to 1,45 greater (curves 1 and 3) then in the absence of this one (curves 2 and 4).

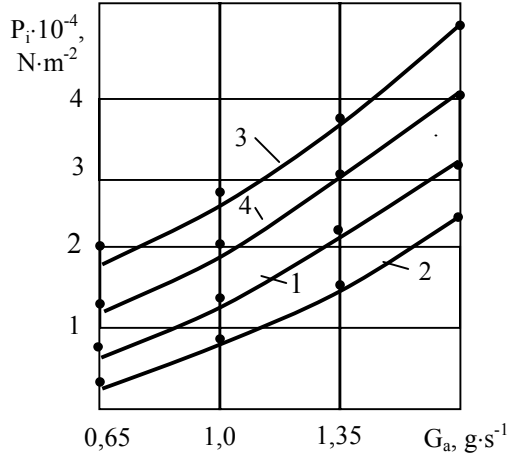


Fig.4. The influence of the flow rate upon the integral pressure of the plasma arc jet for the nozzle channel 4 mm and the distance 5 mm for the arcing current, A: 1, 2 – 200; 3, 4 – 300A; 1, 3– in the presence of the antivortex generator; 2, 4 –in the absence of this one.

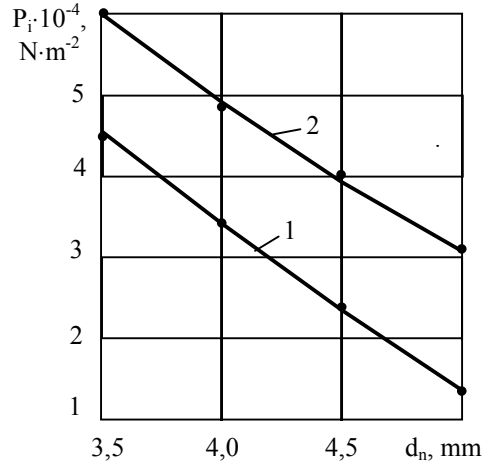


Fig.5. The influence of the diameter of nozzle channel upon the integral pressure of the plasma jet for the flow rate 1,5 g·s⁻¹, the distance 5 mm, for arcing current, A: 1-200; 2-300

The influence of the diameter of the nozzle channel on the maximum value of the integral pressure of the plasma arc jet for the flow rate 1,35 g·s⁻¹ and the distance from the exit of the nozzle to the Pitot tube 5 mm is presented in figure 5. When decreasing the diameter of the channel from 5 to 3,5 mm the integral pressure of the outgoing plasma arc jet increases from  $3.1 \cdot 10^4$  N/m² to  $6.4 \cdot 10^4$  N/m² for the arcing current 300 A (curve 1). But it is necessary to mention that the decreasing of the diameter of the nozzle channel is limited by the conditions of the appearance of the double arc that is very dangerous for the nozzle.

The radial distribution of the velocity and the temperature of the outgoing plasma arc jet for the arcing current 200 and 300 A respectively, the flow rate 1.35 g·s⁻¹ and the diameter of the nozzle channel 4.0 mm is given in figure 6. While increasing the intensity of the arcing current from 200 to 300 A the velocity of the outgoing plasma arc jet in the axial zone increases from  $1.8 \cdot 10^3$  to  $4.0 \cdot 10^3$  m·s⁻¹. The value of the temperature in the axial zone of the plasma jet is approximately the same but the radial distribution of the temperature significantly changes. A zone with a high temperature dilates while increasing the temperature.

A study of the influence of the geometry of the antivortex generator upon the maximum value of the integral pressure and the diameter of the outgoing plasma arc jet was made using the method of the mathematical planned experiment.

The regression equations was obtained respectively for the integral pressure and the diameter of the plasma arc jet for the distance 3 mm of the exit of the nozzle:

a) the integral pressure of the plasma arc jet

$$P_i^{(3)} = (2,29 + 0,52 I_a + 0,34 G_a - 0,41 d_n - 0,24 d_{ca} + 0,25 \cdot d_v + 0,32 \cdot S_a + 0,41 I \cdot d_v - 0,52 G_a \cdot S_a + 0,41 \cdot d_{ca} \cdot S_a) \cdot 10^4, N \cdot m^{-2} \quad (4)$$

b) the diameter of the plasma arc jet

$$d^{(3)} = (4,3 + 0,5 d_n + 0,28 d_{ca} + 0,24 S_a - 0,14 I_a \cdot G_a - 0,5 I \cdot d_v - 0,19 G_a \cdot d_v - 0,14 d_n \cdot d_{ca} - 0,19 d_n \cdot S_a - 0,5 d_{ca} \cdot S_a), mm \quad (5)$$

where  $G_a$  is a flow rate of the air,  $\text{g}\cdot\text{s}^{-1}$ ;  $d_n$  is the diameter of the nozzle channel, mm;  $d_{ca}$  is the diameter of the channels of the antivortex generator, mm;  $d_v$  is the diameter of the vortex chamber, mm;  $S_a$  is the total cross-section of the antivortex generator's channels,  $\text{mm}^2$ .

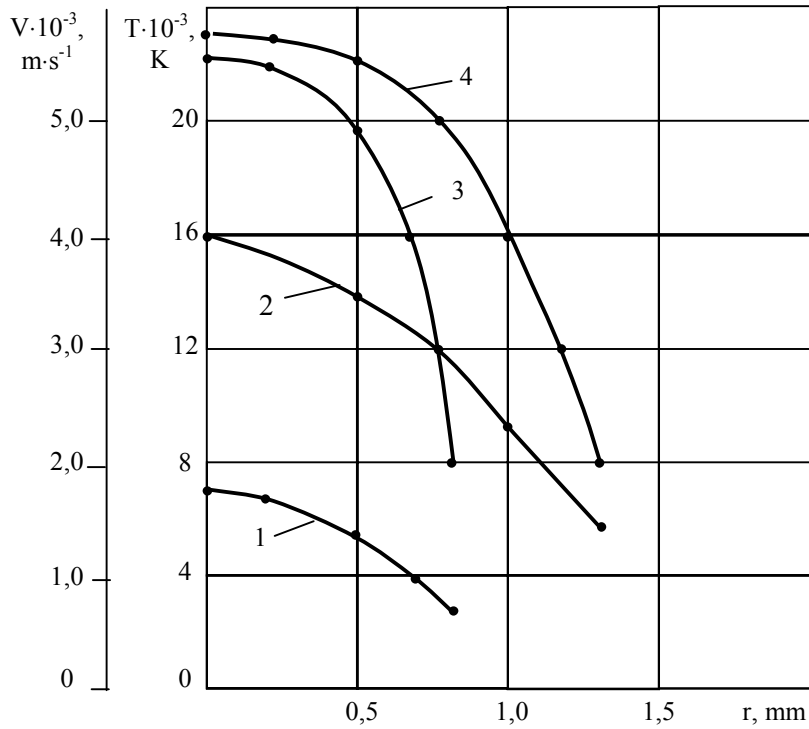


Fig.6. The radial distribution of the velocity (1,2) and the temperature (3,4) for the flow rate of the air  $1\text{g}\cdot\text{s}^{-1}$ , the diameter of the nozzle channel 4 mm and the arcing current, A: 200 (1,3) and 300 (2,4)

The analysis of the equations (4) and (5) shows the important influence of the intensity of the arcing current, the flow rate of the air and the diameter of the nozzle channel upon the integral pressure and the diameter of the plasma arc jet. A significant influence over the integral pressure has the diameter of the channels, the diameter of the vortex chamber and the total cross-section of the channels of the antivortex generator.

For increasing the integral pressure of the plasma arc jet it is necessary to diminish the diameter of the channel, to increase the diameter of the vortex chamber and the total cross-section of the channels of the antivortex generator. While decreasing the diameter of the channel of the antivortex generator the degree of compression of the column arc increases and, hence the velocity, the dynamic and the integral pressures increase too. The rise of the integral pressure of the plasma arc jet when the increasing of the diameter of the vortex chamber of the antivortex generator is due to the amelioration of gas dynamic characteristics of the axial component of the plasma arc jet.

While increasing the cross-section of the antivortex generator the integral pressure increases that is due to the supplementary compression ensured by this generator. As a result of the supplementary compression the velocity and the integral pressure of the plasma arc jet rise.

Comparing the regression equations of the integral pressure and the diameter of the plasma arc jet without antivortex generator and the equations (4) and (5) we can underline that in the presence of the antivortex generator the free coefficient of the integral pressure is greater with 39%. The diameter of the plasma jet in the presence of the antivortex generator is with 12 – 16% less then in the absence of this one.

The experimental study of the deep of cutting and the width of cut was made for the same parameters: the arcing current, the flow rate of the air, the diameter of the nozzle channels and the parameters of the antivortex generator. The adequate mathematical model was elaborated which gives a relation between the deep of cutting and the width of cut and the parameters mentioned above while cutting stainless steel:

a) for the deep of cutting

$$\delta = (65,3 + 9,8 I_a + 2,3 G_a - 4,1 d_n - 1,3 d_{ca} + 1,1 d_v - 1,6 S_a), mm \quad (6)$$

b) for the width of cut

$$b = (7,5 - 0,1 I_a + 0,2 G_a + 0,7 d_n - 0,2 d_{ca} + 0,3 d_v + 0,4 S_a), mm \quad (7)$$

The analyses of this equations show that the great influence on the deep of cutting have the arcing current, the flow rate, the diameter of the nozzle channel and the total cross-section of channels of the antivortex generator.

#### 4. Conclusions

The utilization of the antivortex generator in the plasma arc torch, having a cooper electrode with the cavity, ensures the increasing of the integral pressure with 39% and the decreasing of the diameter of the outgoing plasma arc jet with 12-14%. As the result in comparison with the ordinary plasma arc torch the deep of cutting rises with 20 – 40% and the width of the cut decreases with 12-16 %.

#### 5. References

- [1] V. Pogora, I. Protsouc, T. Stanchou. Etude et optimisation de l'Installation de coupage des Metaux par la Torche à plasma d'air. UIE Congress on Electricity Applications, 1 Birmingham, UK (1996).
- [2] S.V. Dresvin, A.V. Donskoi, V.M. Golidfarb, V.S. Klubnikin. Physics and technics of the low temperature plasma (in Russian). M., Atomizdat, 1972.
- [3] N.B. Vargaftic. Spravochnik po teplofizicheskim svoistvam gazov i jidkosti, Moskva, Fizmatgiz, 1972.
- [4] Iu.I. Kisseliov, I.A. Protuc, T.P. Stanciu, I.Z. Terzi. Study and optimization of the process of the plasma cutting metals (in Russian), Chisinau, Stiinta, 1986.

# Investigations of Kr-I<sub>2</sub>, Xe-I<sub>2</sub> barrier discharges plasma processes

G.Zvereva

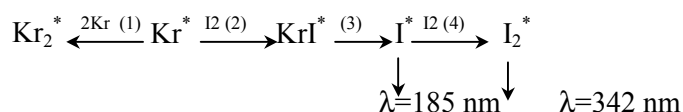
*S.I.Vavilov State Optical Institute, St-Petersburg, Russia*

Investigations of Kr-I<sub>2</sub>, Xe-I<sub>2</sub> dielectric barrier discharges (DBD) are important for the development of a new mercury-free UV DBD light sources [1]. These mixtures can produce radiation with the same wavelengths as mercury: Xe-I<sub>2</sub> DBD lamp is a promising source at the wavelength  $\lambda=253$  nm (XeI\* B(1/2)-X(1/2)) excimer band) and Kr-I<sub>2</sub> DBD lamp – at the region  $\lambda=185$  nm (I\* p<sup>4</sup>s-p<sup>5</sup> atomic transitions). These types of mixtures aren't good investigated, among works, devoted to them it is possible to point out [2-4].

Optimization of the lamps parameters demands plasma chemical characteristics knowledge. In this work calculations of plasma components concentrations, analysis of radiating species (XeI\*, I\*) formation and destruction channels were carried out. For these purposes plasma was represented consisting of 14 (Kr-I<sub>2</sub> mixture) and 15 (Xe-I<sub>2</sub> mixture) different components: I (5p<sup>5</sup> <sup>2</sup>P<sub>3/2</sub>), I\* (6s<sup>4</sup>P, <sup>2</sup>P), I<sup>+</sup>, I<sup>-</sup>, I<sub>2</sub><sup>+</sup>, I<sub>2</sub><sup>\*</sup> (D' <sup>3</sup>Π<sub>2g</sub>), Kr\*(Xe\*) (<sup>3</sup>P low excited levels), Kr(Xe), Kr\*\* (Xe\*\*) – higher excited levels, Kr<sup>+</sup> (Xe<sup>+</sup>), Kr<sub>2m</sub><sup>\*</sup> and Kr<sub>2r</sub><sup>\*</sup> (Xe<sub>2m</sub><sup>\*</sup> and Xe<sub>2r</sub><sup>\*</sup>) – low excited <sup>3</sup>Σ<sub>u</sub><sup>+</sup> и <sup>1</sup>Σ<sub>u</sub><sup>+</sup> states, Kr<sub>2</sub><sup>\*\*</sup> (Xe<sub>2</sub><sup>\*\*</sup>) – higher excited states, Kr<sub>2</sub><sup>+</sup> (Xe<sub>2</sub><sup>+</sup>), KrI\* (XeI\*)- low excited excimer state, Xe<sub>2</sub>I\*. During calculations uniform model of gas discharge was used: electric field was represented as a step function with 20 ns duration, about 100 reactions taking place in gas volume were considered, mixtures with 200-600 torr of rare gas and 0.1-10 torr of I<sub>2</sub> were taking in to account, initial conditions were chosen in accordance with experimental electric current values.

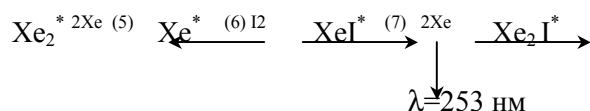
Calculations show, that iodine atomic concentration dominates above others ones reaching value  $1 \cdot 10^{15}$  cm<sup>-3</sup>, XeI\* excimer concentration and I\* excited atom one reach values about  $1 \cdot 10^{13}$  cm<sup>-3</sup>, components: I (5p<sup>5</sup> <sup>2</sup>P<sub>3/2</sub>), I<sup>-</sup>, I<sub>2</sub><sup>+</sup> and I\* have long decay times in the volume, this tells about important role of diffusion processes and reactions on the walls in the chemical plasma balance.

Analysis shows that I\* formation takes place in accordance with following kinetic scheme:



with reactions :  $\text{Kr}^* + 2\text{Kr} = \text{Kr}_2^* + \text{Kr}$  ( $k=2.3 \cdot 10^{-32} (300/T_g)^{1/2}$ ) (1),  $\text{Kr}^* + \text{I}_2 = \text{KrI}^* + \text{I}$  ( $k=5 \cdot 10^{-10} \text{ cm}^3 \text{ c}$ ) (2),  $\text{KrI}^* = \text{Kr} + \text{I}^*$  (3),  $\text{I}^* + \text{I}_2 = \text{I}_2^* + \text{I}$  ( $k=10^{-9} \text{ cm}^3 \text{ c}$ ) (4). Optimum Kr and I<sub>2</sub> pressures values restricted by reaction (1) and (4) was found to be equal to 300 torr and 0.1 torr correspondingly.

Excimer XeI\* formation will take place in accordance with kinetic scheme:



with reactions :  $\text{Xe}^* + 2\text{Xe} = \text{Xe}_2^* + \text{Xe}$  ( $k=2 \cdot 10^{-32} \text{ cm}^6 \text{ c}$ ) (5),  $\text{Xe}^* + \text{I}_2 = \text{XeI}^* + \text{I}$  ( $k=5 \cdot 10^{-10} \text{ cm}^3 \text{ c}$ ) (6),  $\text{XeI}^* + 2\text{Xe} = \text{Xe}_2\text{I}^* + \text{Xe}$  ( $k=10^{-9} \text{ cm}^3 \text{ c}$ ) (7). Optimum Xe pressure restricted by reaction (7) was found to be about 600 torr. I<sub>2</sub> pressure isn't restricted by reactions in the volume. Calculated UV radiation efficiency  $\lambda=253$  nm at the optimum conditions was determined to be equal to 20%.

Xe-I<sub>2</sub> DBD calculations results are in good agreement with experimental ones of the work [3].

As an application water disinfection experiments by means of these light sources and mercury ones were carried out. These experiments have shown comparable germicidal efficiency of Kr-I<sub>2</sub>, Xe-I<sub>2</sub> lamps with mercury ones.

[1] U. Kogelschatz, Proceeding of XXIII ICPIG, 1997, Toulouse, France.

[2] B.Gellert, U. Kogelschatz, Appl. Phys. B, v.52, p.14-21, 1991

[3] J.-Y.Zhang, I.W.Boyd, J. Appl. Phys., v.84,N3,p.1174, 1998.

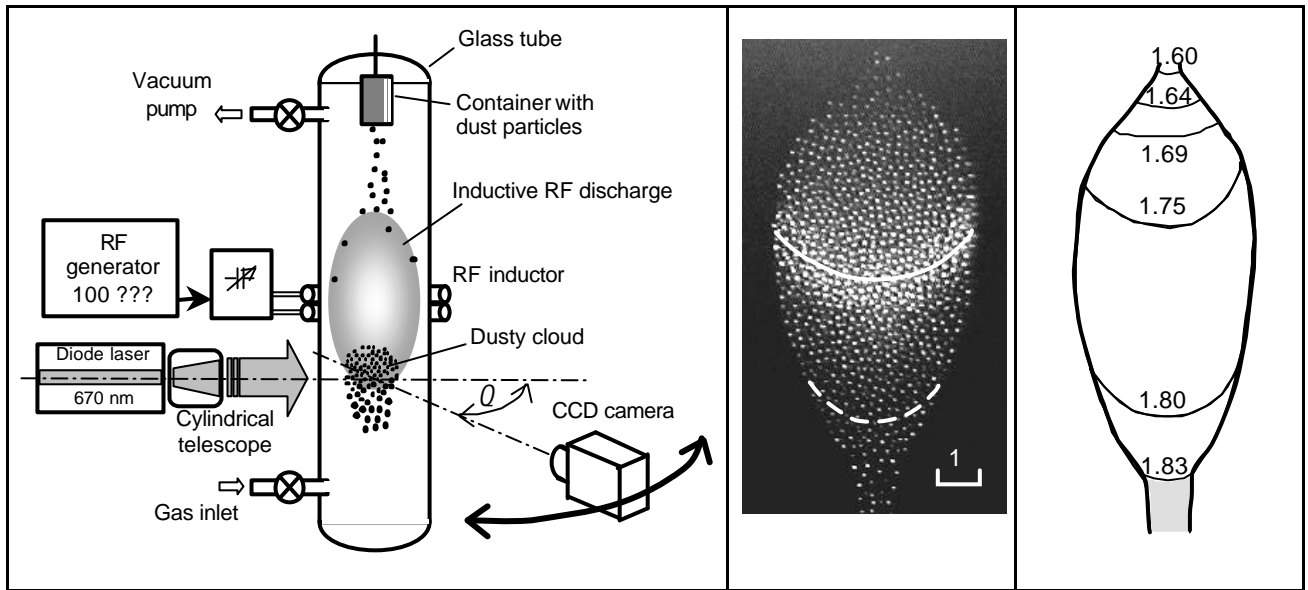
[4] U W. Frame, P.C. John and oth. , Appl. Phys. Lett., v.72, N21, p.2634, 1998.

# Particle sizing and time evolution of dust grain size distribution in a diffuse edge of an rf inductive low-pressure discharge plasma.

V. Fortov, A. Zobnin, A. Usachev, and O. Petrov.

*Institute for High Energy Densities Russian Academy of Sciences  
Izhorskaya 13/19, 127412, Moscow, Russia*

In present study a technique for measuring *in situ* 2D-spatial distribution of the polymeric (melamine formaldehyde) spherical particles by their size in complex plasma is presented. For this purpose monodisperse particles of the two original diameters ( $0.99 \pm 0.04$  and  $1.87 \pm 0.04$   $\mu\text{m}$ ,  $n = 1.68$ ,  $r = 1.51$   $\text{g}/\text{cm}^3$ ) were used. These particles were inserted into an rf inductively coupled gas discharge in neon (Fig.1)



**FIGURE 1.** The scheme of dusty cloud formation at the diffuse edge of rf inductive discharge and 2D diagnostics of particle size distribution in dusty cloud.

**FIGURE 2.** The view of MF-1.87 dusty cloud at  $\theta = 74^\circ$  with respect to the detecting laser beam. Solid (dashed) white line shows the area with maximum (minimum) intensity of scattered laser light.

**FIGURE 3.** The measured spatial distribution of particles on their sizes in case of using MF-1.87: Hatched areas mean the cloud region with coupled particles.

and suspended there [1]. The determination of particle sizes was based on measurements of the angular distribution of scattered light intensity and further interpretation of the measured data within a framework of Mie theory. For simultaneous measurements of scattered light intensity from different parts of all powder cloud it was illuminated by a diode laser sheet ( $\lambda = 670$  nm) with the cross-section size  $15 \times 0.4$   $\text{mm}^2$ , and the intensity of scattered light was measured by means of CCD video camera from each particle separately.

It was found that the particles are decreased in size during an exposition in rf discharge plasma. The rate of particle size etching was found to depend on particle position along the vertical axis  $H$  of dusty cloud. The comparison of the rate dependence  $R(H)$  with the electron density dependence  $n_e(H)$  have shown that the ratio  $R(H)/n_e(H)$  is constant for all possible  $H$  and  $R/n_e = 3 \times 10^{-9}$   $\text{\AA} \times \text{s}^{-1} \times \text{cm}^{-3}$ . That means the sublimation of dust material occurs due to bombardment of the MF particles by charged atomic plasma species – ions and electrons.

[1] V.E. Fortov, A.P. Nefedov, V.A. Sinel'shchikov, A.D. Usachev, A.V. Zobnin. Physics Letters, **A267**, 179 (2000).

# Continuous and modulated deposition of fluorocarbon films by means of c-C<sub>4</sub>F<sub>8</sub> plasmas

A. Milella<sup>1</sup>, F. Palumbo<sup>2</sup>, P. Favia<sup>1</sup>, G. Cicala<sup>2</sup>, R. d'Agostino<sup>1</sup>

<sup>1</sup> Dipartimento di Chimica, Università di Bari, via Orabona4, 70126 Bari, Italia

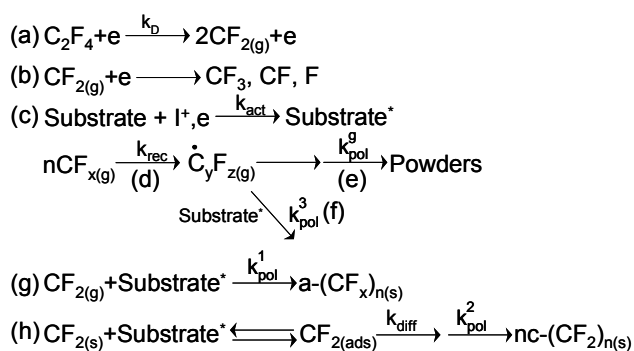
<sup>2</sup> Istituto di Metodologie Inorganiche e dei Plasmi, CNR-IMIP, via Orabona4, 70126 Bari, Italia

## Abstract

Continuous and modulated c-C<sub>4</sub>F<sub>8</sub> plasmas were used to deposit thin PTFE-like films. Gas phase and film composition and structure were investigated and the results were rationalized using the deposition mechanism developed, in a previous work, for the C<sub>2</sub>F<sub>4</sub> plasmas. The morphology and the chemistry of the surface change continuously when the modulation parameters are varied.

## 1. Introduction

Modulated Discharges (MD) fed with fluorocarbons allow to deposit, under particular discharge regime, films with superior characteristics and with remarkable monomer structure retention degree. Properties such as low dielectric constant, low friction coefficient, high flexibility, high hydrophobic/oleophobic character can be granted by such coatings, as well as applications in textiles, packaging, biomaterials, microelectronics and other fields [1-4]. Albeit surface chemistry of MD fluorinated films have been extensively analysed, few works deal with the investigation of the plasma phase and of the material morphology. In a companion work dealing with the deposition of fluorocarbon films from continuous and modulated tetrafluoroethylene (C<sub>2</sub>F<sub>4</sub>) plasmas, the plasma phase and film chemical composition and structure were deeply investigated as a function of various discharge parameters and finally we developed the deposition mechanism reported in figure 1 [5]. Briefly describing, the depletion of the monomer by electron impact (reaction a), produces CF<sub>2</sub> radicals which then undergo recombination or electron impact reactions leading to the formation of small



**Figure 1:** Scheme of the deposition mechanism developed for C<sub>2</sub>F<sub>4</sub> plasmas.

radicals as CF, CF<sub>3</sub> and F. When the gas phase CF<sub>x</sub> radicals concentration is high, recombination reactions proceed at a very high rate and heavier fragments are formed according to route d. This reaction can also keep on, mainly at high pressure, resulting in powders formation. Depending on the discharge regime, film growth can take place according to the two paths (g) and (h). In particular (g) refers to the high rate formation of amorphous and crosslinked film (a-(CF<sub>x</sub>)<sub>n</sub>), according to the Activated Growth Model (AGM) [6] occurring in continuous discharge and, in modulated ones, at high duty cycle. In low CF<sub>2</sub>-radicals concentration regime (route h), that is

very low value of duty cycle, the deposition rate and positive ion bombardment are drastically reduced and the few adsorbed CF<sub>2</sub> radicals have enough time to diffuse on the surface and to reach the activated sites before the arrival of other radicals (beginning of the on time), thus forming nucleation centers which become a preferential attachment site for the other incoming CF<sub>2</sub> radicals. In this regimes an anisotropic growth process takes place which finally leads to a film characterized by the presence of Teflon-like nano-/micro-crystalline ribbon-like structures. At higher duty cycle, instead, the morphology is characterized by spherical nanosized aggregates, while in continuous mode smooth coatings can be deposited.

This paper reports on the deposition of fluorocarbon films from continuous and modulated discharges fed with perfluorocyclobutane (c-C<sub>4</sub>F<sub>8</sub>). The results obtained are analysed in comparison with those obtained by C<sub>2</sub>F<sub>4</sub> plasmas and interpreted with the above reported deposition mechanism.



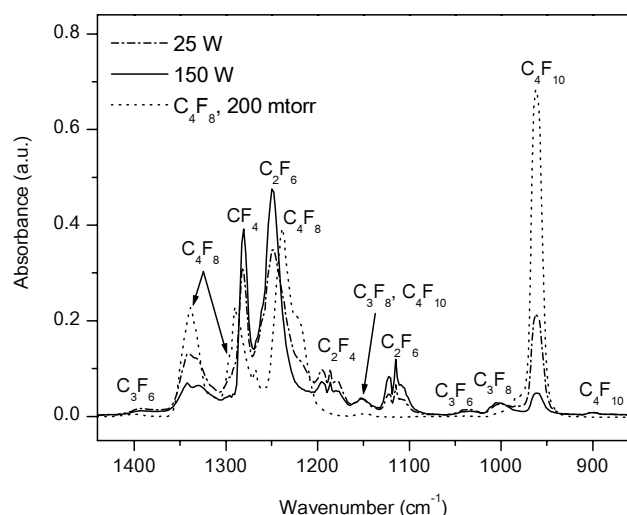
## 2. Experimental

Plasma deposition experiments were carried out in a cylindrical parallel plate stainless steel reactor (20 cm diameter, 27 cm high). The upper powered electrode (12 cm in diameter) and the lower grounded one (diameter of 19 cm) are spaced 5 cm apart with samples placed on the grounded electrode. The plasma is ignited with a 13.56 MHz power supply (RF POWER PRODUCTS, model RF5). Impedance matching is accomplished with a LC network (ULVAC, model 002A). For working in MD mode, the RF power input is modulated using a pulse generator implemented into the RF generator which allows to change both the on time and the duty cycle. An oscilloscope (TEKTRONIX, model TDS 200) is used to monitor the pulse duration and amplitude and a second channel allows also to monitor the RF wave. The gas flow rate is metered by means of electronic mass flow controllers (MKS), and the pressure in the system is monitored by mean of a (MKS Baratron. The system is continuously pumped down by a rotary pump which allows a base pressure of  $10^{-3}$  Torr. The gas phase diagnostics is carried out through ZnSe and sapphire windows for Fourier Transform Infrared Absorption Spectroscopy (FT-IRAS) and Optical Emission Spectroscopy (OES). In order to avoid contaminations due to film deposition, the windows were mounted onto 20 cm long side tubes and heated up to 60°C, by means of heating tapes. Experiments were carried out changing the input power, pressure and deposition time in continuous plasmas while duty cycle, period and deposition time were the process parameters changed in modulated ones.

Infrared spectra of the gas phase were recorded from 500 to 7500  $\text{cm}^{-1}$  with a spectral resolution of 4  $\text{cm}^{-1}$  over 1000 scans. Semi-quantitative density trends of light emitting species as a function of the experimental parameters were obtained by means of Actinometric Optical Emission Spectroscopy (AOES, actinometry), using an Ar/He mixture (1:1) as actinometers at a total flow rate of 0.6 sccm. Film chemical composition was investigated by FT-IR and X-ray Photoelectron Spectroscopy (XPS). The latter were performed using a PHI ESCA 5300 with a non-monochromatic Mg  $K_{\alpha}$  radiation (1253.6 eV). High resolution spectra of the regions C 1s, O 1s, F 1s were acquired at a pass energy of 35.75 eV and the C1s XPS spectra were fitted using five components corresponding to:  $\text{CF}_3$  ( $294.5 \pm 0.2$  eV),  $\text{CF}_2$  ( $292.5 \pm 0.2$  eV),  $\text{CF}$  ( $290.0 \pm 0.2$  eV), C-CF ( $288.0 \pm 0.2$  eV) and C-C ( $285.0 \pm 0.2$  eV). Changes in surface morphology with process parameters were assessed by atomic force microscopy (AFM). The AFM images were acquired with a microscope (Thermomicroscopes Autoprobe CP) in non contact mode using a gold-coated silicon conical high resonance frequency (280 kHz) probe tip.

## 3. Results and discussion

Figure 2 shows the FT-IRAS spectra of c- $\text{C}_4\text{F}_8$  continuous plasmas sustained at two different power values of 25 W and 150 W and at fixed pressure (200 mtorr). By comparing plasma spectra with those of the



**Figure 2:** FT-IRAS spectra of c- $\text{C}_4\text{F}_8$  gas and of continuous plasmas at 25 W and 150 W at a pressure of 200 mtorr and flow rate of 6 sccm.

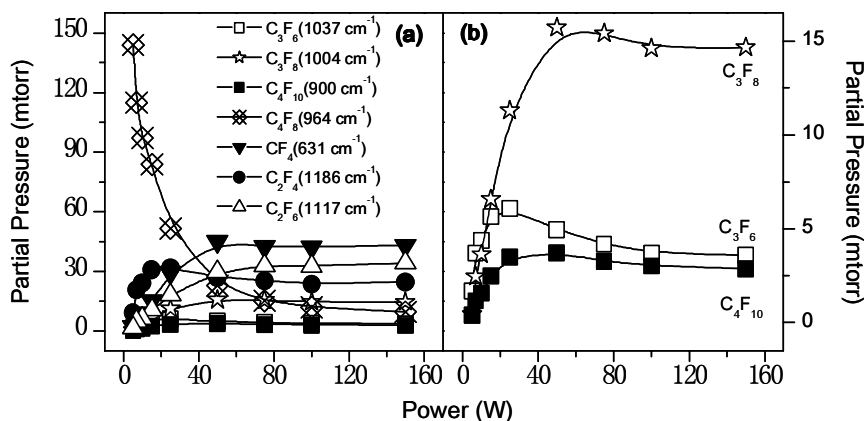
fluorocarbon gases, it is possible to recognize the species formed within the plasmas. At 1281  $\text{cm}^{-1}$  the main signal of  $\text{CF}_4$  and at 1250  $\text{cm}^{-1}$  that of  $\text{C}_2\text{F}_6$ , which partially overlap, can be found. The presence of undissociated monomer can be observed from the signal at 964  $\text{cm}^{-1}$ , while the bands between 1200 and 1350  $\text{cm}^{-1}$  are almost completely overlapped to those of  $\text{CF}_4$  and  $\text{C}_2\text{F}_6$ . The band at 1117  $\text{cm}^{-1}$  is also due to  $\text{C}_2\text{F}_6$  absorption, while the ones at 1337  $\text{cm}^{-1}$  and 1186  $\text{cm}^{-1}$  are due to  $\text{C}_2\text{F}_4$ . A certain amount of  $\text{C}_3\text{F}_8$  in the plasma is also produced as evident from the low absorption at 1004  $\text{cm}^{-1}$ . The main  $\text{C}_3\text{F}_8$  band gas at 1261  $\text{cm}^{-1}$  is which is hidden by  $\text{CF}_4$  and  $\text{C}_2\text{F}_6$  absorptions. The small absorption band at 900  $\text{cm}^{-1}$  is due to  $\text{C}_4\text{F}_{10}$ , while those at 1396  $\text{cm}^{-1}$  and 1037  $\text{cm}^{-1}$  can be assigned to  $\text{C}_3\text{F}_6$ . Between 800 and 600  $\text{cm}^{-1}$  (not shown) it can

be found features assigned to  $\text{C}_2\text{F}_6$ ,  $\text{C}_4\text{F}_{10}$  and  $\text{C}_3\text{F}_8$ . In order to develop a semi-quantitative analysis of the

recombination species in the plasma, the spectrum of the monomer was subtracted from that of the plasma according to the equation (1):

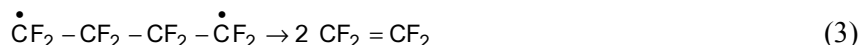
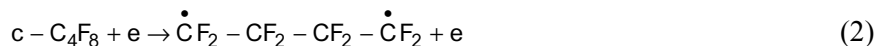
$$A_{\text{sub}} = A_{\text{plasma}} - k \cdot A_{\text{gas}} \quad (1)$$

where  $A_{\text{sub}}$ ,  $A_{\text{plasma}}$  and  $A_{\text{gas}}$  are, for a certain wavenumber, the absorbance in the calculated spectrum, that in the plasma and the one in the monomer gas at the working pressure, respectively. The factor  $k$ , instead, is obtained empirically, in a way that the integral of the band at  $964 \text{ cm}^{-1}$  is zeroed. Once the absorption integrals were evaluated, the partial pressure for each species was calculated by means of calibration curves. Figure 3 shows the effect of input power on the partial pressures of all the species detected by the FT-IRAS.

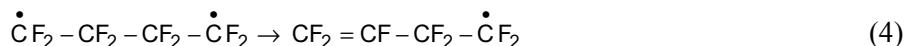


**Figure 3:** Effect of input power, at a pressure of 200 mtorr, on the partial pressures of all the species detected by FT-IRAS (a) and of the minority species (b).

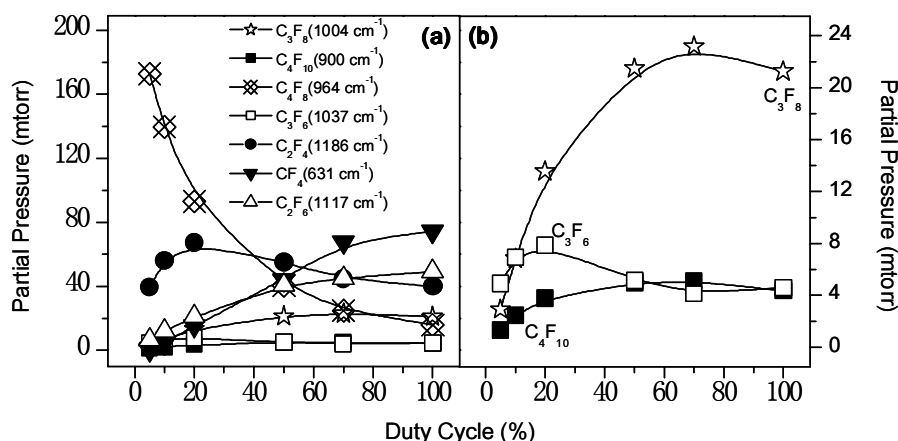
It is worth to note that the monomer steeply decreases up to 50 W while it is almost constant for higher values of power. Moreover all the saturated products increases and then reach a plateau at 50 W, the unsaturated ones ( $\text{C}_2\text{F}_4$  and  $\text{C}_3\text{F}_6$ ), instead, show a maximum and this is consistent with the reactivity of the double bonds. Up to 25 W the main product in the plasma phase is  $\text{C}_2\text{F}_4$ . Its production likely follows  $\text{C}_4\text{F}_8$  ring opening by electron impact, according to the following reaction path:



As an alternative reaction path, the bi-radical formed from reaction (2) could rearrange resulting into a more stable mono-radical and this is believed to be more likely to occur at very low values of RF power:



Another proposed electron impact dissociation reaction for  $\text{c} - \text{C}_4\text{F}_8$  leads to the formation of  $\text{C}_3\text{F}_6$  and  $\text{CF}_2$ :

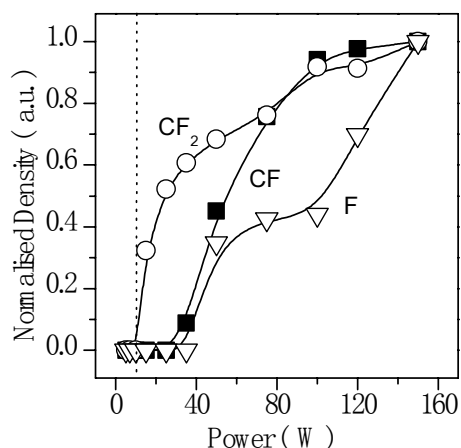


**Figure 4:** Effect of duty cycle (at 320 ms of period, 100 W and 300 mtorr) on the partial pressures of the species detected by FT-IRAS.

However the latter reaction path can be considered negligible, as the  $\text{C}_3\text{F}_6$  concentration is low. For power values higher than 50 W,  $\text{CF}_4$  and  $\text{C}_2\text{F}_6$  become the main recombination products. FT-IRAS was also utilized to check the production of powders inside the plasma but their presence was excluded since no baseline deviation in the spectra, at high wavenumbers, was observed [7-9].

Switching to modulated plasmas leads to the result

that the same recombination products were detected and, as shown in figure 4, the partial pressure trends as a function of duty cycle are close to those observed in continuous plasmas. This result can be explained



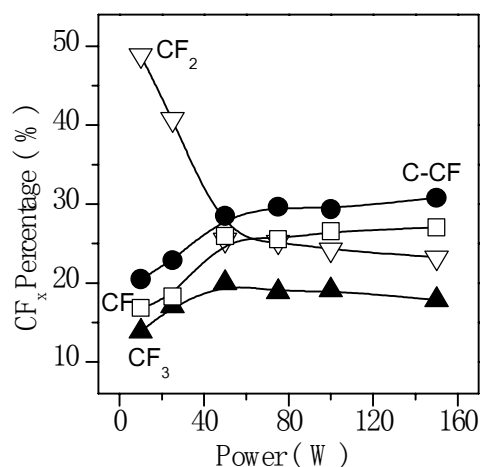
**Figure 5:** CF<sub>2</sub>, CF and F actinometric density trends as a function of input power. Actinometry can be safely used for all species only above 10 W (dotted line). The discharge was sustained at 200 mtorr and 6 sccm.

considering that FT-IRAS is a non time resolved technique and thus allows to obtain only time-averaged species absorbance.

Figure 5 shows the density trends of the main emitting radicals in the continuous plasma, i.e. CF<sub>2</sub>, CF and F atoms obtained by means of AOES, as a function of input power. Since the actinometers emission ratio (not shown) is independent from the input power only for input power values higher than 10 W, the actinometric correction can be safely utilized for all emitting species in the plasma, only above this threshold. The relative density of all species increase with the input power but in the case of CF<sub>2</sub> is quite evident that from about 40 W this increase proceeds at lower rate.

Studying the effect of input power on film chemical composition it was observed by FT-IR analyses (not shown) that massive composition is almost the same while differences in surface composition may be deduced by XPS analyses. CF<sub>x</sub> area percentages determined by the curve fitting of the XPS C1s spectra are reported in figure 6. The F/C ratio calculated by the curve fitting changes from 1.6 to 1.3 in the range 10-150 W. The CF<sub>2</sub> content in the film decreases progressively while the trends of CF<sub>3</sub>, CF and C-CF are approximately the opposite. These

results point out to a more crosslinked surface at higher powers mainly ascribed to a higher ion bombardment of the growing film. Film chemical composition can be tuned in a larger range using modulated plasmas. Figure 7 shows the normalized FTIR spectra of films deposited for 90 minutes at different duty cycles, with period sets at 320 ms. The input power and the gas feed pressure were fixed at 100 W and 300 mtorr, respectively. The absorption band between 1400 and 1000 cm<sup>-1</sup>, due to CF<sub>x</sub> absorptions, becomes progressively sharper and at a duty cycle value of 5% a clear doublet structure can be evidenced. Then the

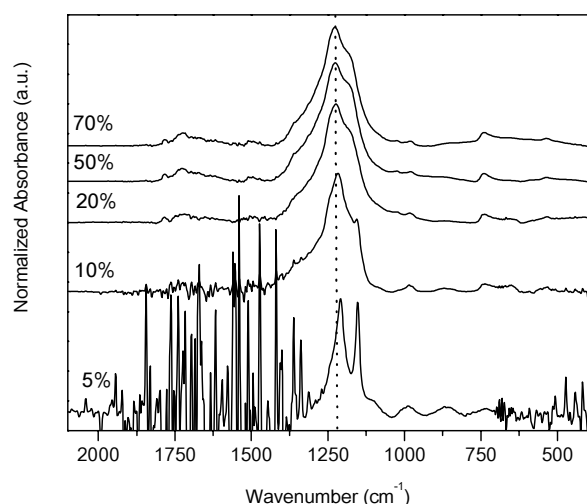


**Figure 6:** CF<sub>x</sub> percentages as a function of input power for films deposited by continuous discharges sustained at 200 mtorr, 6 sccm and 15 min duration time.

changed band profile is coupled to a shift of the maximum wavelength position from 1230 to 1215 cm<sup>-1</sup>. For a better evaluation of this effect the original positions of the maximum and of the shoulder are indicated in the figure by the dashed lines. The peaks at 1215 and 1152 cm<sup>-1</sup> are assigned to CF<sub>2</sub> asymmetric and symmetric stretching vibrations, respectively. Another significant feature characterizing film deposited at lower duty cycle, is the reduction of the broad absorptions between 1500 and 1800 cm<sup>-1</sup> due to double bonds along with the more resolved but less pronounced shoulder at about 1340 cm<sup>-1</sup>, assigned to CF stretch. The decrease in CF content is also evident in the less pronounced tail at 1070 cm<sup>-1</sup> and from the small peak at 1030 cm<sup>-1</sup> which progressively extinguishes. It should also be noticed that lowering the duty cycle results in films with less CF<sub>3</sub> groups and this feature is highlighted by the slight broadening of the peak at 980 cm<sup>-1</sup>. Finally, the bands at 640 and 530 cm<sup>-1</sup>, indicated in figure 7 by the dotted line, are due to CF<sub>2</sub> wagging mode and becomes stronger and sharper at lower duty cycle. It is important to remember that

wagging and rocking vibrations are generally ascribed to the crystalline phase of PTFE. Thus, summarizing the information depicted by FTIR analysis, it can be affirmed that coatings deposited at lower duty cycle, are characterized by a sharper distribution of the chemical groups, higher content of CF<sub>2</sub> with respect to CF or CF<sub>3</sub> moieties, and a less disordered structure. These data are confirmed by XPS ones. It is worth to highlight the very high Teflon-like character in the film deposited at 5% as witnessed by the F/C ratio of 1.9. The increased Teflon-like character with the decreasing of the duty cycle can be ascribed to the reduced ion bombardment of the film.

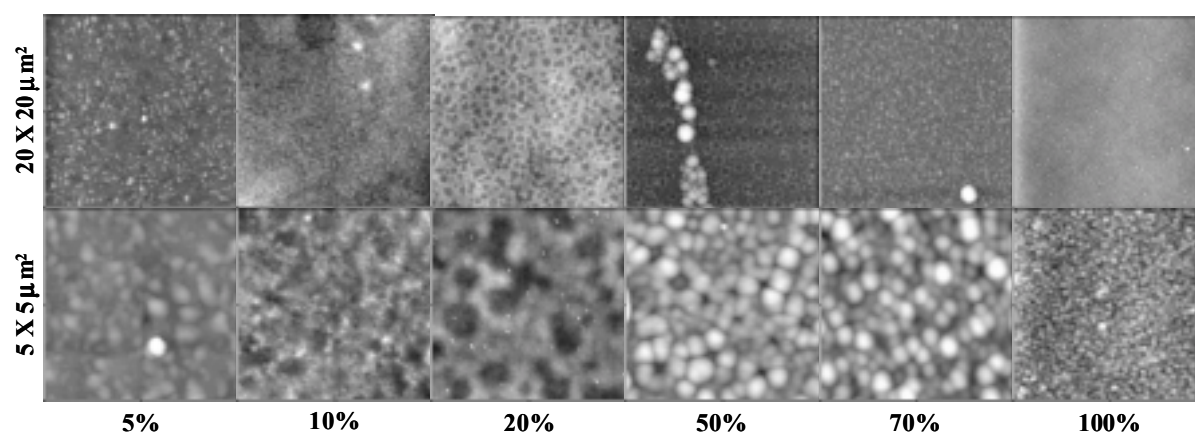
The 2-D and 3-D non contact AFM images of film deposited at different duty cycles are shown in figure 8. Images at different magnification are reported in order to understand both the overall appearance of the film surface and the structure of the morphological features. At 5% of duty cycle the film surface is covered by



**Figure 7:** FT-IR spectra of film deposited for 90 min at different duty cycles and at 320 ms of period. Input power and pressure are 100 W and 300 mtorr, respectively.

quasi spherical nuclei almost uniformly distributed and the RMS roughness, estimated from the  $20 \times 20 \mu\text{m}^2$  image, is 9.4 nm. When the DC is increased up to 10%, the roughness decreases to 2.0 nm and the surface appears populated by islands with irregular shape. At 20% of duty cycle the morphology is mainly characterized by small cavities conferring a sponge-like appearance and the roughness further decreases to 1.5 nm. At 50% and 70% the spherical nuclei appear again and, in the case of 50%, they give rise to sporadic organized linear aggregates, no further visible at 70%. Finally, the RMS roughness values for these two samples are 18.4 nm and 10.2 nm, respectively. The film deposited in continuous mode shows a surface rich in small, uniform in size islands, and the roughness was found to be 3.4 nm. A rationale of the coating morphology, obtained by means of  $\text{C}_4\text{F}_8$  modulated plasmas, can be achieved using

the deposition mechanism proposed for the  $\text{C}_2\text{F}_4$ .



**Figure 8:** Non contact AFM images of film deposited from modulated discharges at different duty cycle (100 W input power, 300 mtorr pressure).

Varying the DC in the range 100-50%, the transition from a surface rich in small nuclei homogeneous in size to the formation of larger nuclei and clusters with a broad range of sizes, can be explained with a progressively reduced number of both  $\text{CF}_2$  radicals impinging on the surface and of activated sites produced by the ion bombardment. Thus, the adsorbed radicals have more time to diffuse, during the off time, and to arrange on the activated nuclei which can grow bigger and bigger and give origin also to aligned cluster (50% of DC). The sponge-like morphology observed at 20%, instead, is at the moment not completely clear, even if it is believed to be the result of a competition between radicals impinging rate and their diffusion across the surface: it is possible that a key role is played by the heavier precursors with 3 or 4 carbon atoms (resulting from reaction 2 and 4). The latter should diffuse across the surface at much lower rate than  $\text{CF}_2$  radicals, thus resulting into the sponge-like architecture.

Analyzing the images at 5% of duty cycle in comparison with those obtained using  $\text{C}_2\text{F}_4$  plasmas, where the ribbon-like structures appeared, the question to be answered is: why does not any ribbon-like structure appear? Is it only a matter of deposition time or is there another key point to be taken into account? In order to find out a possible explanation, longer deposition times were investigated, in the range 5400-15300 s.

However at 15300 s simply a rougher surface where no clear regular structure growth was observed, though at 5400 and 10800 s small islands structures can be identified. On the basis of these latter results and of those relative to film and plasma composition, it has been thought to explain the morphology at duty cycle of 5%, as due to a different film precursors. In fact, it is likely that, at such low values of duty cycle, the  $\text{CF}_2$  radical is not the main film precursor, as the monomer dissociation is lower than that at higher DC. Since only light absorbing radicals can guarantee a certain species diffusion on the surface, regular structures or clusters cannot be obtained. Conversely heavier precursors formed directly by the  $\text{c-C}_4\text{F}_8$  ring opening, can play a key role in the deposition of the film. The relevance of this kind of precursor in the film formation is demonstrated by the high Teflon-like character of the coating shown by XPS and FTIR analyses. Once again, as this radical is heavier than  $\text{CF}_2$ , it has a limited surface mobility necessary for ribbon-like structures growth. Increasing the duty cycle, the monomer depletion increases as well, until the partial pressures of  $\text{C}_2\text{F}_4$ , which is the main source of  $\text{CF}_2$ , becomes greater than the one of  $\text{C}_4\text{F}_8$ . Thus the light  $\text{CF}_2$  likely becomes the main film precursor, and regular cluster can be deposited as observed from 50% of duty cycle on.

#### 4. Conclusions

PTFE-like films were deposited both by continuous and modulated discharges fed with  $\text{c-C}_4\text{F}_8$ . Plasma phase composition was studied by FT-IRAS and OES. As input power increases, the monomer depletion increases too and many recombination reactions take place at progressively higher rates, leading to the formation of  $\text{CF}_4$ ,  $\text{C}_2\text{F}_4$ ,  $\text{C}_2\text{F}_6$ ,  $\text{C}_3\text{F}_6$ ,  $\text{C}_3\text{F}_8$ ,  $\text{C}_4\text{F}_{10}$ . Accordingly the  $\text{CF}_2$ , CF and F density increase. Concerning the film composition, it was found that lowering the RF power results in less crosslinked and  $\text{CF}_2$  richer films. Modulating the discharge introduces two further parameters, duty cycle and period, which allow to tune film chemical composition and structure in a way that is otherwise impossible to achieve. In particular, at low duty cycle (5%) and high period (320 ms), films more similar to Teflon were obtained with F/C ratio as high as 1.9. The film formation mechanism proposed to explain the different morphological evolutions in  $\text{C}_2\text{F}_4$  discharges, was used also to explain the growth of coatings deposited by means of  $\text{c-C}_4\text{F}_8$ . The lack of ribbons at low duty cycle and high period was explained considering a film precursor different from  $\text{CF}_2$  which can be the heavier bi-radical or similar mono-radical resulting from the rearrangement of the opened  $\text{c-C}_4\text{F}_8$  cycle.

#### References

- [1] V. Panchalingam, B. Poon, H.H. Huo, C.R. Savage, R.C. Eberart; *J. Biomat. Sci. Polym. Ed.*, **5**, 131 (1993).
- [2] S.J. Limb, K.K. Gleason, D.J. Edell, E.F. Gleason; *J. Vac. Sci. Tech. A*, **15** 1814 (1997).
- [3] S.R. Coulson, I. S. Woodward, S.A. Brewer, C. Willis, J.P.B. Badyal; *Chem. Mater.*, **12**, 2031 (2000).
- [4] S.J. Limb, K.K.S. Lau, D.J. Edell, E.F. Gleason, K.K. Gleason; *Plasmas and Polymers*, **4**, 21 (1999).
- [5] G. Cicala, A. Milella, F. Palumbo, P. Rossini, P. Favia, R. d'Agostino; *Macromolecules*, **35**, 8920 (2002).
- [6] R. d'Agostino, F. Cramarossa, F. Fracassi, F. Illuzzi, in *Plasma Deposition, Treatment and Etching of Polymers*, d'Agostino R. ed., Acad. Press (1990).
- [7] W. Stoffels, E. Stoffels, G. Kroesen, M. Haverlag, J. den Boer, F. Hoog, *Plasma Sources Sci. Technol.*; **3**, 320 (1994).
- [8] M. Haverlag, E. Stoffels, W. Stoffels, H. den Boer, G. Kroesen, F. de Hoog; *Jpn. J. Appl. Phys.*, **33**, 4202 (1994).
- [9] P.R. i Cabarrocas, A. F. i Morral, S. Lebib, Y. Poissant, *Pure Appl. Chem.*, **74**, 359 (2002).

# The Potential of Surface Radicals for Polymer Functionalization

A. Meyer-Plath, R. Mix, G. Kühn, J. Friedrich

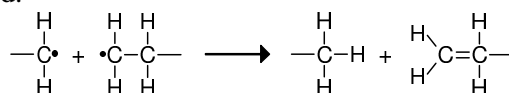
Bundesanstalt für Materialforschung und –prüfung, Berlin, Germany

## Abstract

A new approach to radical-rich polymer surfaces was evaluated for radical-initiated surface functionalization. Radical-containing polymer films have been deposited by plasma polymerization from five different unsaturated monomers: ethylene, acetylene, dicyclopentadiene (DCP), styrene, and toluene. Surface densities of radicals up to 4.5 % were quantified by XPS after exposition of the surface to nitric oxide (NO). In parallel, the post plasma oxidation behaviour of the films was monitored. A fast and a slow oxidation component were identified and could be attributed to primary and secondary, and tertiary radicals, respectively. One surface radical gave rise to an average incorporation of about 5 oxygen atoms.

## 1. Introduction

Radicals in polymers are created by mechanical stress or bombardment with energetic particles and photons. Processes like scission of polymer backbones, side group or hydrogen abstraction, and opening of multiple bonds create two radical-terminated fragments. The term radical denotes an atom with an unpaired electron. The two radicals may recombine with their former partner or another radical species, or abstract an atom or group in bimolecular reactions. An important termination process is disproportionation, depicted in Scheme 1, where a double bond is formed.



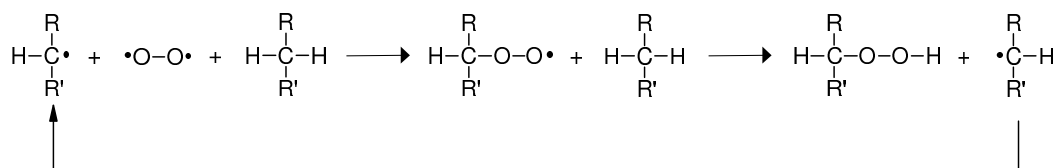
Scheme 1: Disproportionation of two radicals.

During and after radical formation, a generally unwanted change of polymer structure results due to lowering of molecular weight by chain scission and group abstraction [1], crosslinking of polymer chains, double bond formation, and oxidation phenomena on air. These processes are traditionally denoted as “ageing” since they affect the mechanical, optical, and chemical properties of the material.

From an alternative point of view, the creation of radicals offers a way to overcome the high chemical inertness of many polymers which is a consequence of the unpolar character of C–C and C–H covalent bonds. Radicals enhance the reactivity of a polymer surface to liquid or gaseous monomers. For the functionalization of polymer surfaces the following three approaches have been developed in the literature:

- (1) Molecules with *permanent* radical character like NO, the biradical oxygen molecule ( $\bullet\text{O}-\text{O}\bullet$ ), or 2,2-diphenyl-1-picrylhydrazyl (DPPH) can be incorporated by radical recombination reactions.
- (2) Similarly, *transient* radicals like  $\bullet\text{OH}$  or  $\bullet\text{NH}_2$ , supplied by thermal dissociation, photolysis, or plasmas, can be recombined with surface radicals [2].
- (3) Last, not least, under appropriate conditions, monomers with easily-activatable multiple bonds that carry functional groups can be graft polymerized to surface radicals.

The oxidation of surface radicals by reaction with  $\text{O}_2$ , a process of type (1), will be called post oxidation in the following. It occurs spontaneously at contact to air via peroxy radical formation and enhances the surface energy and the reactivity of the polymer. Abstraction of a hydrogen radical by the peroxy radical from the molecule itself or a neighbouring chain creates a hydroperoxy group and may transfer the radical for several subsequent reaction cycles, see Scheme 2.



Scheme 2: Peroxy radical induced post oxidation.

Nowadays, an improved control of the type of generated surface functionality is becoming increasingly important, for instance in biomaterial applications where unspecific adherence has to be minimized. This motivated the intensive research on surface radical induced graft polymerization. i.e. method (3), during the last years. At present, it is the most versatile approach of the three. The performance of numerous vinyl, allyl, acryl, and methacryl compounds of different chemical functionality has been studied on various polymer substrates. The spectrum of successfully grafted chemical functionalities includes: carboxy (from acrylic acid) [3][4][5][6], ester (from methyl acrylate) [3], epoxy (from glycidyl methacrylate) [7][8], alcohol (from allyl alcohol) [9], aldehyde (from acrolein), amide (from acryl amide) [10][11]. The grafting efficiency critically depends on the reactivity of the precursor. For some monomers, peroxy radicals or thermally instable hydroperoxy groups can initiate graft polymerization. For others, contact to oxygen must be avoided since carbon-centered radicals are required as starters of grafting. In order to enhance the grafting efficiency, some authors added initiators like benzoyl peroxide [12] or photoactivators like benzophenone [4][13] to the monomer, worked at elevated reaction temperatures, or under UV irradiation. Another approach towards higher grafting efficiency is to increase the density of reactive sites. Various mechanisms for the generation of surface radicals are being studied in the literature. They include mechanical stress [14], irradiation with energetic particles from ion [11] or electron beams [6], UV/VUV irradiation [1][7][15] (often in presence of the precursor), ozone exposition [16], and plasma activation<sup>1</sup> [3][9][12][17][18]. A review is given in ref. [19]. However, little data can be found on the density of surface radicals resulting from the different approaches: Maximum surface densities of polymer radicals determined by the NO method are about 1.5 at.% after VUV irradiation of polypropylene (PP) [20], and about 2 at.% after Ar plasma activation of polystyrene (PS) [21].

**New approach** In the following paper, a new approach to radical-containing polymer surfaces will be investigated. It is based on the plasma polymerization of unsaturated monomers under high power input. A low degree of structure retention is intended in order to deposit a polymer with a high density of radical sites resulting from (partly) scissioned multiple bonds. This strategy was motivated by findings of Kuzuya et al. [22][23] that the nature of radical formation by plasma activation is affected by the polymer structure in a very sensitive way: Branched LDPE yielded considerably higher densities of primary radicals than HDPE.

**Polymer radicals** Polymer radicals can be classified as given in Table 1. Their reactivity depends on many factors: Type and density, structural parameters of the polymer, temperature, and reaction environment. Mid-chain alkyl radicals are, for instance, under vacuum thermally less stable than primary radicals and survive mainly in crystalline regions of the polymer [22]. However, primary radicals, also known as dangling bonds, are very susceptible to oxygen and instantly react at ambient pressure [23]. Tertiary carbon-centered radicals are generally less reactive than secondary and primary ones. The motility of allyl radicals along the polymer is enhanced by the double bonds. This is believed to enhance their reaction probability in bimolecular reactions of polymers, e.g. leading to crosslinking [24]. Effective crosslinking may reduce post process oxidation.

primary	secondary	tertiary	alkyl	allyl	oxy	peroxy
$\begin{array}{c} \text{H} \\   \\ \text{R}-\text{C}\cdot \\   \\ \text{H} \end{array}$	$\begin{array}{c} \text{R} \\   \\ \text{H}-\text{C}\cdot \\   \\ \text{R}' \end{array}$	$\begin{array}{c} \text{R}' \\   \\ \text{R}-\text{C}\cdot \\   \\ \text{R}'' \end{array}$	$\begin{array}{c} \text{H} \quad \quad \text{H} \\   \quad \quad   \\ \text{R}-\text{C}-\text{C}\cdot-\text{C}-\text{R}' \\   \quad   \quad   \\ \text{H} \quad \text{H} \quad \text{H} \end{array}$	$\begin{array}{c} \text{H} \quad \quad \text{H} \\   \quad \quad   \\ \text{R}-\text{C}=\text{C}-\text{C}\cdot-\text{C}-\text{R}' \\   \quad   \quad   \\ \text{H} \quad \text{H} \quad \text{H} \end{array}$	$\begin{array}{c} \text{R}' \\   \\ \text{R}-\text{C}-\text{O}\cdot \\   \\ \text{R}'' \end{array}$	$\begin{array}{c} \text{R}' \\   \\ \text{R}-\text{C}-\text{O}-\text{O}\cdot \\   \\ \text{R}'' \end{array}$

**Table 1:** Classification of carbon- and oxygen-centered radicals.

Other important polymer radicals are the oxy radical and the peroxy radical, mentioned before. Polymer oxy radicals are products of decomposed hydroperoxy groups, or the recombination of two tertiary peroxy radicals. Hydrogen abstraction by oxy or peroxy groups predominantly occurs from tertiary carbon atoms. Important stable products of reactions of oxy radicals, peroxy radicals, and polymers are epoxy, aldehyde, ketone, and hydroxy groups. Also crosslinking of polymers via  $-\text{C}-\text{O}-\text{O}-\text{C}-$  peroxy bonds may result.

**Radical identification and quantification** Radicals can be analysed by means of electron spin resonance (ESR) spectroscopy [22]. The detection threshold of ESR lies in the order of  $10^{12}$  spins/cm<sup>3</sup> and is generally not sufficient for surface radical quantification on films. The standard method for carbon-centered surface radicals therefore is labelling with nitric oxide (NO). Primary and secondary radicals react with NO to

<sup>1</sup>During the plasma activation step, impurities desorbing from the plasma chamber walls may be plasma grafted efficiently, thus faking successful radical-initiated grafting.

oximes, whereas tertiary radicals react to nitro, nitroso, or nitrate groups [24]. Their surface density can be quantified by means of X-ray photoelectron spectroscopy (XPS), see below, or infrared absorption (FTIR) spectroscopy [25][26]. Alternatively, bromine may be reacted with carbon radicals, however, it also adds to double bonds and phenyl rings [24] to form dibromides. Other methods use DPPH or iodine consumption from a solution to quantify surface radicals and/or peroxy radicals, respectively [17][18]. However, results from DPPH consumption are difficult to compare to results from the NO method since the DPPH method is sensitive to radicals in greater depth than XPS.

## 2. Experimental

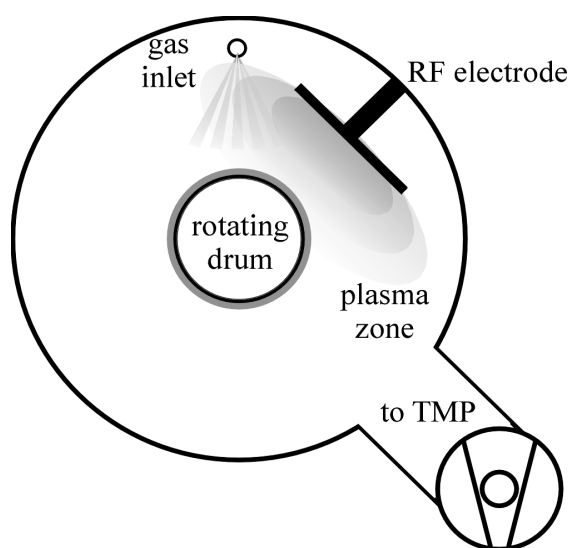
**Plasma reactor** The reactor used for this study is depicted in Figure 1. Briefly, it is a viton-sealed high vacuum reactor of 50 l volume equipped with a turbo molecular and a backing pump. Radio frequency (RF) excitation at 13.56 MHz sustains a plasma between a grounded rotating steel drum of about A4 surface area and a home-built electrode. Liquid monomers are introduced via liquid flow controllers (Bronkhorst, Ruurlo, The Netherlands) and are evaporated at the entry to the gas distribution system of the reactor. For gaseous monomers mass flow controllers (MKS Instruments, Andover, U.S.A.) are used.

**Surface analysis** X-ray photoelectron spectroscopy (XPS) was performed using a Sage 100 spectrometer (Specs GmbH, Berlin, Germany) at 300 W Mg  $k_{\alpha}$  x-ray radiation and 0° electron take-off angle with respect to the surface normal. Exposure durations were below 15 min. During the transport to the XPS, the plasma-treated samples were exposed to air for at least 10 min.

**Radical analysis** Within 1 min of the end of the plasma process, the polymer film was exposed for 15 min to 25 hPa nitric oxide (NO) that was introduced to the evacuated reactor (pressure below 0.1 Pa). Primary and secondary radicals were distinguished from tertiary radicals via their N 1s XPS-subpeaks according to the method of ref. [15]. Nitrates (C–O–NO<sub>2</sub> at 408 eV), nitro (C–NO<sub>2</sub> at 406 eV), and nitroso groups (C–N=O at 404 eV) are products of reactions of NO and tertiary radicals, whereas primary and secondary radicals react to oxime groups (C=N–OH at 400.3 eV). However, the separation of N 1s XPS peaks of oximes and nitriles or amines (both at 399 eV), just 1.3 eV apart, could not be reliably achieved with our XPS device of about 2.2 eV energy resolution. Therefore, quantification of surface radicals could not be performed on samples that contained nitrogen groups originating from plasma activation.

**Thin film deposition** All plasma polymers were deposited on polypropylene (PP) film of 100 µm thickness supplied by Goodfellow GmbH, Bad Nauheim, Germany. Manufacturing additives inside the film were extracted in freshly-distilled diethyl ether prior to usage. Plasma polymerization was performed at a continuous wave RF power of 30 W and a process pressure of 25 Pa. The deposited films had a thickness of 50 nm. Gases (H<sub>2</sub>, C<sub>2</sub>H<sub>2</sub>, C<sub>2</sub>H<sub>4</sub>) were supplied by Messer GmbH, Berlin, Germany, and liquid monomers (DCP, styrene, toluene) by Sigma-Aldrich GmbH, Munich, Germany. All chemicals were of the highest commercially available purity grade. Each experiment was performed twice. The first sample was used for the post oxidation study, being cut down to many small pieces for time delayed XPS analysis, the second sample was derivatized in situ with NO for radical quantification. After each cycle the reactor was cleaned thoroughly. For all plasma polymer films, the level of nitrogen background caused by the plasma process was well below 0.3 nitrogen atoms per 100 carbon.

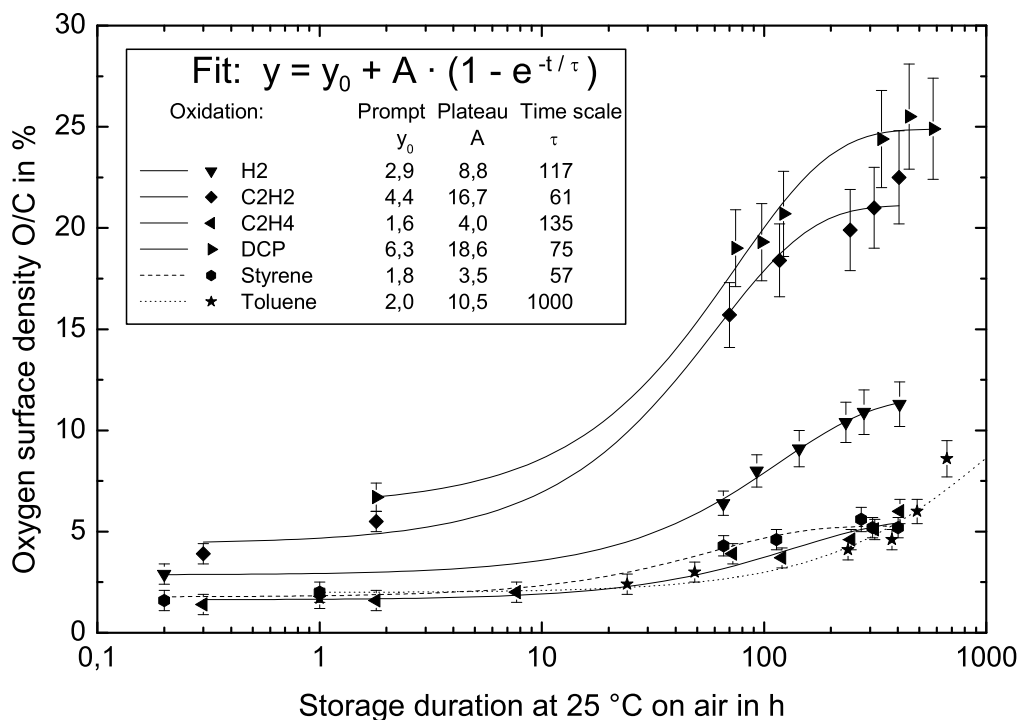
**Surface activation** For performance comparison to the plasma polymerization approach, hydrogen and noble gas plasma activation of PP was performed. However, pure noble gas plasma activation of polymers performed in the reactor gave rise to a significant nitrogen surface density of 3–6 nitrogen atoms per 100 carbon: Smallest nitrogen impurities from the reaction environment are efficiently activated and incorporated to the polymer. For the reasons given above, radical analysis was only possible after hydrogen plasma activation.



**Figure 1:** Schematic drawing of the reactor used.



### 3. Results and Discussion



**Figure 2:** Post oxidation behaviour of plasma polymerized films and a hydrogen plasma activated polypropylene film during storage on air. The data is fitted with  $y = y_0 + A (1 - \exp(-t / \tau))$  to find the levels of prompt ( $y_0$ ) and long-term oxidation ( $A$ ) as well as the time scale  $\tau$  of oxidation. The error on  $y$  is  $\Delta y = \max(0.1 \cdot y, 0.5 \%)$ , and  $\Delta t = 5$  min on  $t$ . For the fit to oxidation data of the film from toluene a time scale of  $\tau = 1000$  h was assumed.

The post oxidation of the plasma polymers deposited in this work and of the H<sub>2</sub> plasma activated PP film during storage at 25 °C on air is shown in Figure 2. The oxidation behaviour of the surface can be parametrized by the following function

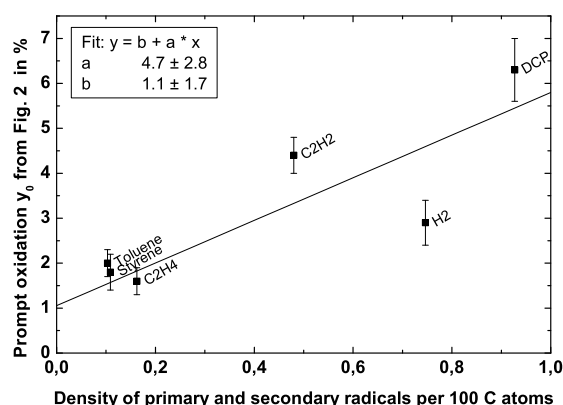
$$y = y_0 + A \cdot (1 - \exp(-t / \tau)) \quad (1)$$

The offset  $y_0$  can be interpreted to be due to a fast oxidation process, called prompt oxidation in the following. It was finished faster than the samples could be transferred (in air) to the XPS, so its time scale could not be determined. The second term describes a slower, saturating oxidation process approaching the plateau value  $A$ . It proceeds on a time scale  $\tau$  and consumes radicals, denoted by  $R$ , in a first order process, i.e.  $d[R]/dt \propto [R]$ .

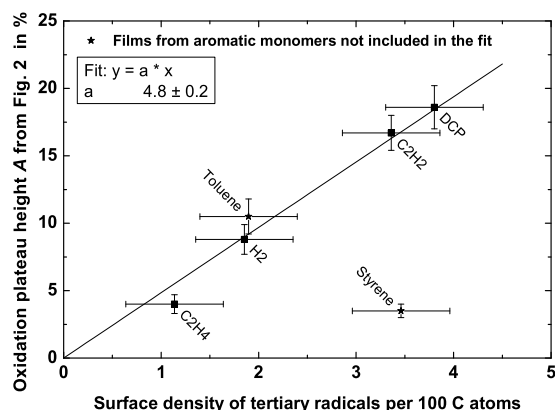
Figure 3 suggests the hypothesis that the amount of prompt oxidation  $y_0$  determined in Figure 2 can be attributed to oxidation induced by primary and/or secondary surface radicals. Likewise, tertiary radicals can be made responsible for the slower oxidation that occurs on time scales of days, as Figure 4 shows.

However, the plasma polymer made from the aromatic precursor toluene forms an exception: Its post oxidation appears to be extremely slow. It did not approach the plateau within more than 500 h. If the time constant of post oxidation due to tertiary radicals of  $\tau = 1000$  h is assumed, the fit *predicts* a post oxidation plateau  $A$  for toluene that is in accord to the other data in Figure 4. Such a slow oxidation behaviour may result from tertiary radicals that are of reduced reactivity due to resonance-stabilization by a neighbouring phenyl ring. Also for the plasma polymer deposited from the other aromatic monomer styrene, an anomaly is found: Here, the post oxidation appears to saturate faster but the oxidation plateau  $A$  value is far lower than expected from the density of tertiary radicals in the film, see Figure 4. A possible explanation may be that plasma polymers made from styrene exhibit a strong propensity for crosslinking, similar to chemically polymerized PS, so that crosslinking becomes more probable than oxidation. In order to test this hypothesis, longer storage on air will be needed.

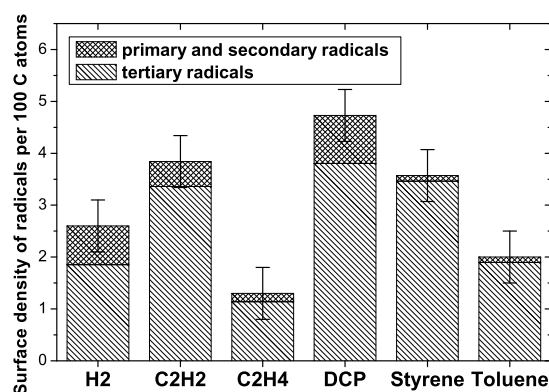
The density of radicals determined by NO labeling is summarized in Figure 5. From Figure 3 and Figure 4 follows that one primary or secondary, or tertiary radical gives rise to a prompt incorporation of about 5 oxygen atoms to the polymer. Only tertiary radicals in styrene plasma polymer films from an exception. The time scale  $\tau$  of the slow post oxidation, given in Figure 6, should be characteristic for the polymer structure resulting from the plasma treatment. However, no dramatic deviations were found with respect to the experimental error of the time scale determined by the fit.



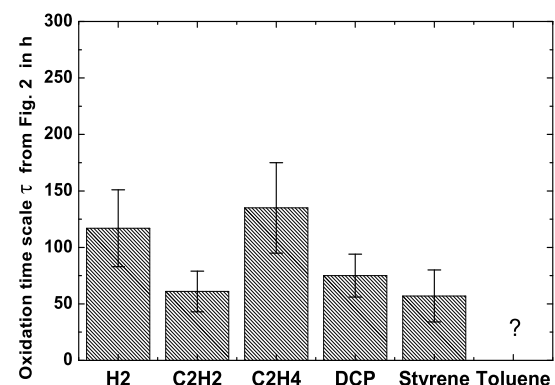
**Figure 3:** In Figure 2 a fast oxidation component  $y_0$  was determined. It correlates to the surface density of primary radicals. A finite oxygen level, not caused by radicals, is admitted. It is determined by the fit to  $b = 1.1$  %.



**Figure 4:** In Figure 2 a slow oxidation component to a plateau level A was determined. For films from non-aromatic precursors, it correlates to the surface density of tertiary radicals. The data of was predicted from the fit in Figure 2 by assuming a time scale of  $\tau = 1000$  h.



**Figure 5:** Surface density of the two classes of radicals that can be distinguished by NO labeling determined by XPS. An experimental error of 0.5 % was assumed.



**Figure 6:** The post oxidation proceeds on a time scale  $\tau$  that was determined in Figure 2. No time scale could be determined from the oxidation data of films from toluene.

**Functionalization-related remarks** Radicals of low reactivity are likely *not* to react during a subsequent surface functionalization step, e.g. a graft polymerization. However, they will induce post oxidation during storage of the functionalized surface. This will in general deteriorate the selectivity of the surface functionalization. The ratio of primary (and secondary) to tertiary radicals should therefore be further optimized.

**Reliability of radical quantification** The reliability of radical quantification requires additional discussion. NO does not react with polyolefins or polystyrene [15][26]. However, in presence of oxygen groups on the surface, NO can react with hydroxy, hydroperoxy, and peroxy groups to give nitrite (C-ONO), peroxy, and nitrates groups, respectively [25][26]. Residual oxygen in the reaction environment therefore deserves our special attention: First, it can produce hydroxy groups directly from the plasma and thus fake carbon-centered surface radicals via a nitrite signature, which is indistinguishable from nitro groups by XPS. Second, oxygen quickly reacts with primary radicals to peroxy groups, which were then be

taken for tertiary radicals via the nitrates forming with NO. Third, NO reacts with O<sub>2</sub> to NO<sub>2</sub>, NO<sub>2</sub> would react with primary radicals to nitro groups, being interpreted as the signature for tertiary radicals. In other words, oxygen impurities imply an underestimation of primary and secondary radicals whereas tertiary tend to become overestimated. In situ XPS measurements may be of help to quantify the level of oxygen incorporation before NO labeling. For future research, it is desirable to develop a radical labeling XPS-based technique capable of reliably distinguishing primary from secondary radicals.

#### 4. Conclusions

Deposition of unsaturated monomers by high power plasma polymerization is a promising new approach to radical-containing surfaces. Compared to radical densities obtained by VUV or Ar plasma activation, as cited in the introduction, plasma polymerized films from C<sub>2</sub>H<sub>2</sub> and DCP exhibit a significantly higher radical density of 4–5 %.

The post oxidation behaviour of the studied surfaces can be interpreted to result from the different reaction rates of primary and secondary radicals, as well as tertiary ones. One surface radical gives rise to the incorporation of about 5 oxygen atoms to the polymer. The hypothesis that primary radicals are responsible for prompt surface oxidation at ambient air is in accord to findings of Kuzuya et al. [23]. The rather slow post oxidation is attributed to reactions of tertiary radicals. A possible oxidation of double bonds had not to be considered on the storage time scale investigated for the present work.

The higher reactivity of primary (and secondary) radicals makes them attractive for radical-initiated surface functionalization purposes. The ratio of primary and secondary to tertiary radicals should therefore be further enhanced.

#### Acknowledgements

Financial support by Bundesministerium für Wirtschaft und Technologie (FKZ VI A 2-22) is gratefully acknowledged.

#### References

- [1] A.C. Fozza, J. Roch, J.E. Klember-Sapieha, A. Kruse, A. Holländer, M.R. Wertheimer, *Nucl. Instr. Meth. B* **131**, 205-210 (1997).
- [2] W.M. Lau, *Nucl. Instr. Meth. B* **131**, 341-349 (1997).
- [3] K. Johnsen, S. Kirkhorn, K. Olafsen, K. Redford, A. Stori, *J. Appl. Polym. Sci.* **59**, 1651-1657 (1996).
- [4] B. Rånby, *Int. J. Adhes. Adhesives* **19**, 337-343 (1999).
- [5] B. Gupta, C. Plummer, I. Bisson, P. Frey, J. Hilborn, *Biomaterials* **23**, 863-871 (2002).
- [6] F. Poncin-Epaillard, B. Chevet, J.C. Brosse, *J. Appl. Polym. Sci.* **53** (10), 1291-1306 (1994).
- [7] K. Allmér, A. Hult, B. Rånby, *J. Polym. Sci. A: Polym. Chem.* **27**, 3405-3417 (1989).
- [8] G.H. Yang, E.T. Kang, K.G. Neoh, *J. Adhes. Sci. Technol.* **15** (6), 727-746 (2001).
- [9] C. Oehr, M. Müller, B. Elkin, D. Hegemann, U. Vohrer, *Surf. Coat. Tech.* **116-119**, 25-35 (1999).
- [10] P.Y. Zhang, B. Rånby, *J. Appl. Polym. Sci.* **40**, 1647-61 (1990).
- [11] Y. Zhang, A.C.H. Huan, K.L. Tan, E.T. Kang, *Nucl. Instrum. Meth. B* **168** (1), 29-39 (2000).
- [12] C.Y. Huang, W.L. Lu, Y.C. Feng, *Surf. Coat. Tech.* **167**, 1-10 (2003).
- [13] H. Ma, R.H. Davis, C.N. Bowman, *Macromolecules* **33** (2), 331-335 (2000).
- [14] G. Scott, *Polym. Degrad. Stabil.* **48** (3), 315-324 (1995).
- [15] R. Wilken, A. Holländer, J. Behnisch, *Macromolecules* **31** (22), 7613-7617 (1998).
- [16] R. Foerch, N.S. McIntyre, D.H. Hunter, *J. Polym. Sci. A: Polym. Chem.* **28**, 803-809 (1990).
- [17] I.L.J. Dogué, N. Mermilliod, R. Foerch, *Nucl. Instr. Meth. B* **105**, 164-167 (1995).
- [18] R. Teng, H.K. Yasuda, *Plasmas Polym.* **7** (1), 57-69 (2002).
- [19] K. Kato, E. Uchida, E.T. Kang, Y. Uyama, Y. Ikada, *Prog. Polym. Sci.* **28**, 209-259 (2003).
- [20] A. Holländer, R. Wilken, J. Behnisch, *Surf. Coat. Tech.* **116-119**, 788-791 (1999).
- [21] B. Finke, A. Meyer-Plath, K. Schröder, A. Ohl, *Proceedings of the ISPC-16*, Filecode 285 (2003).
- [22] M. Kuzuya, S. Kondo, M. Sugito, T. Yamashiro, M. Mouri, *Macromolecules* **31** (10), 3235-3239 (1998).
- [23] M. Kuzuya, S. Kondo, M. Sugito, T. Yamashiro, *Macromolecules* **31** (10), 3230-3234 (1998).
- [24] R. Wilken, A. Holländer, J. Behnisch, *Plasmas Polym.* **7** (1), 19-39 (2002).
- [25] Y.J. Yu, F.W. Shen, H.A. McKellop, R. Salovey, *J. Polym. Sci. A: Polym. Chem.* **37**, 3009-3316 (1999).
- [26] J.F. Rabek, *Polymer Photodegradation*, Chapman & Hall (1995).

# Pulsed plasma initiated homo and copolymerisation – characterization of thin plasma polymer layers by dielectric relaxation spectroscopy

A. Schönhals<sup>1</sup>, A. Fritz<sup>2</sup>, R. Mix<sup>1</sup>, G. Kühn<sup>1</sup>, J. Friedrich<sup>1</sup>

<sup>1</sup>Federal Institute for Materials Research and Testing, Unter den Eichen 87, D-12205 Berlin, Germany

<sup>2</sup>Technical University Wildau, Friedrich Engels Straße 63, D-15745 Wildau, Germany

## Abstract

The aim of our work to pulsed plasma-initiated radical homo and copolymerisation was the composition and the structural design of such macromolecules to converge to those of classic polymers as much as possible. However, pulsed plasma polymerisation is a compromise between hard polymerisation conditions of the continuous wave plasma, characterized by total monomer fragmentation and random recombination of these fragments to irregularly structured polymers, and the plasma-less chemical gasphase polymerisation, leading to defined but amorphous products. Using allyl and diene comonomers for pulsed plasma copolymerisation the chemical contribution to the resulting copolymers should be not very high. Additionally, the short plasma pulses disturb also the regularity of the structure. Thus, the polymer bulk should be investigated for the characterization of regular and irregular structures using the method of dielectric relaxation spectroscopy. Moreover, all plasma polymers contain trapped radicals, which can react with oxygen from air, and other unstable defect centres. Therefore, the dielectric relaxation spectroscopy should identify such defects in the polymer layers and characterize their stability.

## 1. Introduction

Functionalized polymer surfaces are applied in biochemistry, in chromatography or in metal-polymer composites. The most important recent advantage was the highly dense functionalisation with exclusively one type of functional groups (specific functionalization). For many applications a low defect concentration or regular structures at these functionalised surface is a prerequisite. The new method consists of the deposition of thin plasma polymer layers (20 to 200 nm) of functional group carrying monomers in a pulsed plasma. Thus, using allyl alcohol in maximum 31 OH groups per 100 C atoms were measured with a selectivity (retention of functional groups introduced with the monomer) of about 95% and a significant stability at long-time exposure to air. Allyl amine was used to produce primary amino groups in concentrations of at least 18 NH<sub>2</sub> per 100 C atoms in maximum. Side reactions were observed during the storage in air such as the formation of secondary amines and oxidations at the  $\alpha$ -C atom of the amino groups. Carboxylic groups could be synthesised using acrylic acid with a maximum concentration of 24 COOH per 100 C atoms. The most prominent side reaction was the decarbonylation/decarboxylation of the acid group during the plasma deposition.

The variation of the density of functional groups is possible applying a pulsed plasma and initiating a radical copolymerization with monomers extending the length of the chain as ethylene or acting as crosslinker like butadiene. The density of functional groups could be continuously adjusted (0 to 31 OH, 0 to 18 NH<sub>2</sub> and 0 to 24 COOH groups per 100 C atoms). The ethylene homopolymer was free of oxidations by exposure to air but shows a significant high degree of branched and crosslinked structures which is also found for butadiene. Generally, plasma polymer layers can be prepared either by using the continuous wave plasma or the pulsed plasma technique introduced by Tiller [1]. Applying the first method, plasma polymers are often irregular both in structure and in chemical composition, because of the high energy input and fragmentation of the monomers during plasma-on time. In addition, most of these polymer layers are extremely cross-linked and nearly insoluble in all organic solvents. For further processing, polymer layers with defined chemical structure and low degree of cross-linking are desired. These properties can be obtained by controlling the processing parameters as pressure, gas flow or energy input. The pulsed plasma polymerisation has the benefit that significantly smaller amounts of power are introduced into the system. During the plasma-on time, radical polymerisation should ideally start without fragmentation of the monomer. The chain propagation takes place throughout the plasma-off period. Thereby, fragmentation and cross-linking are (slightly) depressed. Polymers produced by this method should be more comparable in composition and structure to conventional polymerized polymers than those made by continuous plasma technique (see Fig. 1). This was approved for different monomers with XPS, NEXAFS, IR, FFF etc. [2,3].

It was proven by many works that dielectric spectroscopy is a very powerful tool to investigate the molecular mobility and the structure of polymers [4]. This is especially true for the investigation of thin and ultra thin polymeric films or layers because the sensitivity of dielectric spectroscopy increases with decreasing thickness of the capacitor [5]. In this work dielectric spectroscopy is applied to study thin plasma polymerised copolymer layers synthesised from butadiene and allyl alcohol. It was known for plasma polymerised homopolymers of ethylene, butadiene and styrene that the structure of pulsed plasma prepared polymers differs from that of the conventional synthesised ones [6]. This is further investigated by dielectric spectroscopy for the selected system including the thermal stability of the layers. Moreover the composition dependence of dielectric properties is studied in detail which leads to new information concerning the structure of the synthesised products.

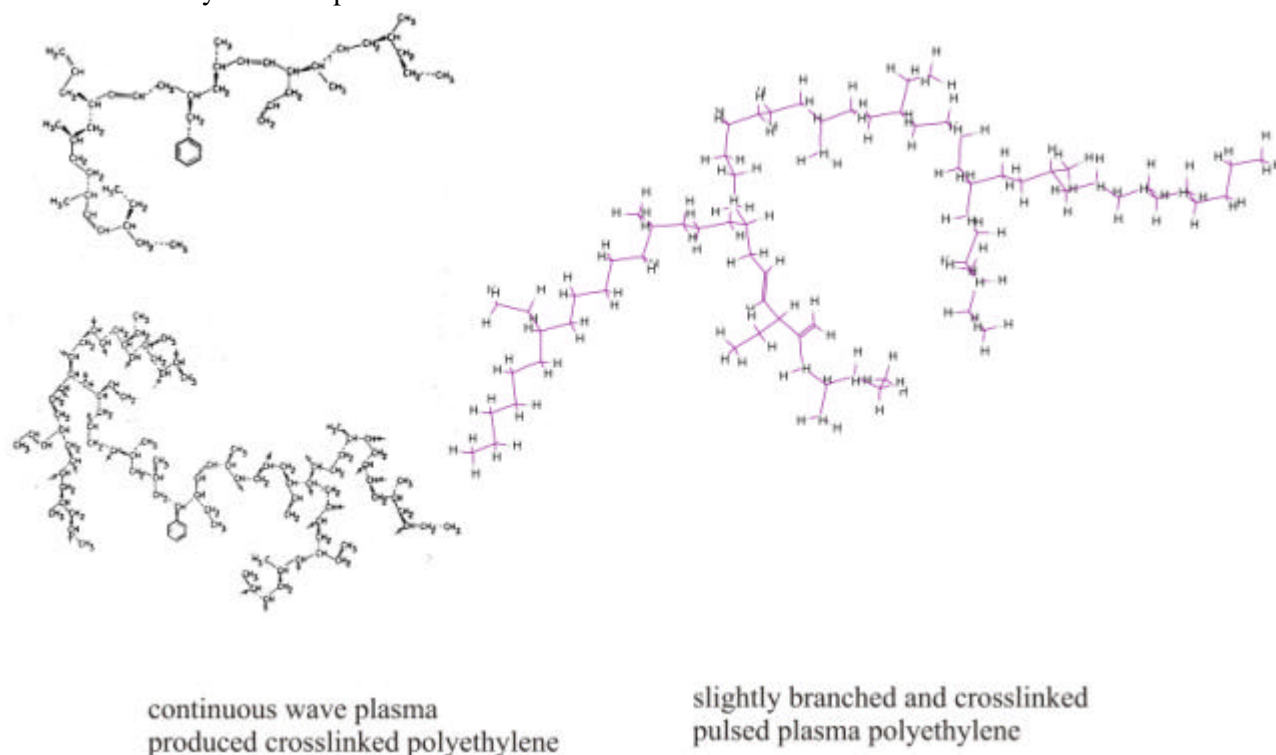


Fig. 1: Proposed models of plasma polyethylene produced by continuous wave plasma [1] according to [7] and pulsed plasma polyethylene as modelled by us using data presented in [6].

## 2. Experimental

### 2.1 Materials

1,3-butadiene and allyl alcohol (Merck, Germany) were freshly distilled before use. Tetrahydrofuran (THF, p.a., Merck, Germany) was filtered and degassed before application. In addition to the plasma polymers an anionic synthesized poly(1,2-butadiene) ( $M_n=11000$  g/mol) purchased from Polymer Standard Service Mainz was investigated by dielectric spectroscopy for comparison.

### 2.2 Plasma polymerisation

Polymerisation and copolymerisation of 1,3-butadiene and allyl alcohol were performed using a plasma reactor Labovac Implasma 1200 (Saskia, Ilmenau, Germany). The set-up of the reactor was described in detail in [8]. Low pressure conditions were achieved with an oil-pump connected to a turbo molecular pump. The plasma was generated with a high frequency electrode implemented in the reactor vessel. In order to establish a pulsed plasma mode a generator (CESAR 136 RF Power Generator, Dressler, Germany) was used. The duty cycles (plasma-on time to plasma-on plus plasma-off time) were 0.1 with a frequency of 1000 Hz. Styrene was polymerised with a continuous plasma (3 W) and a pulsed plasma with an energy input of 30 W (3 W effective using a duty cycle of 0.1). For allyl alcohol only a pulsed plasma was applied (300 W, 30 W effective). The copolymers were prepared by pulsed plasma technique with 100 W and 300 W (10 W and 30 W effective).

### 2.3. Dielectric relaxation spectroscopy

To form a condenser in parallel plate geometry a strip-like electrode of aluminium (bottom electrode, width 2 mm) was evaporated onto a glass substrate. After that a thin polymer layer with a thickness of several 100 nm was deposited by plasma polymerisation directly onto that substrate. In the last step a second aluminium strip-like electrode (top electrode) was evaporated perpendicular to the first one. The crossover area of the both electrodes defines the capacitor for the dielectric measurement.

The complex dielectric function

$$\epsilon(f) = \epsilon'(f) - i\epsilon''(f) \quad (1)$$

( $f$ -frequency,  $\epsilon'$ -real part,  $\epsilon''$ -imaginary or loss part,  $i = \sqrt{-1}$ ) was measured in the frequency range from  $10^{-1}$  Hz to  $10^5$  Hz by a lock-in amplifier (Stanford Research 810) interfaced to the sample by a broadband dielectric interface (BDC, Novocontrol). The temperature of the sample was varied from 173 K to 380 K by a custom-made liquid nitrogen cooled cryostat. The accuracy was  $\Delta T = 0.02$  K. A detailed description of the dielectric equipment to measure the dielectric function can be found elsewhere [9]. The data have been analysed by the fitting of the Havriliak / Negami (HN-) function [10] to the data. From this fit the position of the maximum of dielectric loss (relaxation rate  $f_p$ ) and the dielectric strength  $\Delta\epsilon$  have been extracted for each process. The HN-function reads

$$\epsilon_{HN}^*(f) = \epsilon_{\infty} + \frac{\Delta\epsilon}{(1 + (if/f_{HN})^{\beta})^{\gamma}} \quad (2)$$

where  $f_{HN}$  is a characteristic frequency related to  $f_p$ . For the fractional shape-parameters  $\beta$  and  $\gamma$ , which describe the symmetric and asymmetric broadening of the complex dielectric function,  $0 < \beta, \beta\gamma \leq 1$  holds.

### 3. Results and Discussion

The dielectric spectra versus temperature at a fixed frequency of a pulsed plasma homo polymerised polybutadiene displays several peaks indicating different relaxation processes taking place in the sample (cf. Fig. 2). The increase of  $\epsilon''$  at high temperatures is related to conductivity due to the migration of charge carriers. Moreover, Fig. 2 compares the dielectric loss for an anionic polymerised poly(1,2-butadiene) with a product obtained by plasma polymerisation. The spectra reveal strong differences between the both polymers. It is known that also the properties of polybutadiene depend strongly on the microstructure of the chain. For instance a strong dependence of the glass transition temperature and the dielectric strength on the vinyl content of statistical poly(1,2-butadiene-stat-1,4 butadiene) copolymers was observed [11].

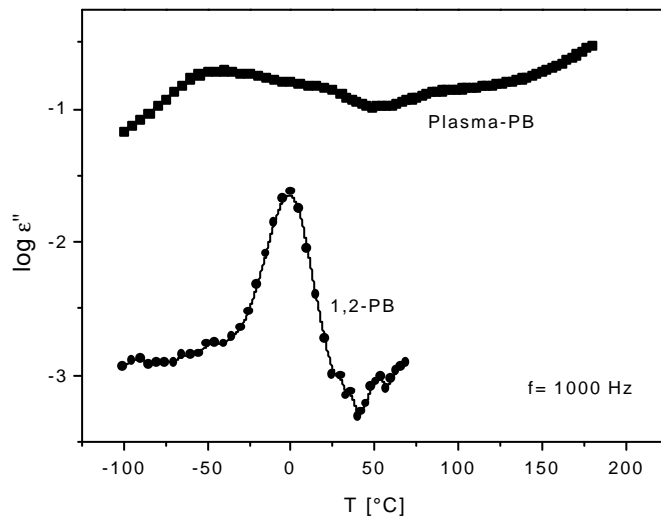


Fig. 2: Dielectric loss  $\epsilon''$  versus temperature at a frequency of 1000 Hz for a pulsed plasma homo polymerised polybutadiene (■) and an anionic polymerised pol(1,2-butadiene) (●). Lines are guides for the eyes.

So Fig. 2 indicates firstly that the microstructure of the product obtained by the pulsed plasma polymerisation of butadiene is quite different from that obtained by conventional polymerisation techniques. Probably, a highly cross-linked structure is obtained because the plasma process can activate both double

bonds present in butadiene. Additionally, 1,2- or 1,4- trans/cis-sequences can be present. Secondly, the dielectric loss of the pulsed plasma polymer is at least one order of magnitude higher than that of poly(1,2-butadiene). So it has to be concluded that the plasma process creates a number of unsaturated radicals, which can react with oxygen at exposure to air. The consequence is the formation of various oxygen containing polar groups, which are not present in a conventional synthesised polybutadiene.

This line of argumentation leads to the hypothesis that the synthesised products are not thermally stable because the unsaturated radicals can be converted at higher temperatures. This is demonstrated by Fig. 3, where the first heating run is compared with a second one for plasma polymerised copolymer with 20 / 80 (1,3-butadiene / allyl alcohol) in the formulation. In the second run the dielectric loss is dramatically reduced because the polar radicals are converted into less polar groups. Moreover the relaxation process around 75°C seems to disappear in the second run indicating also a change in structure. Therefore, only the low temperature process is further analysed and its peculiarities are discussed in dependence of the formulation.

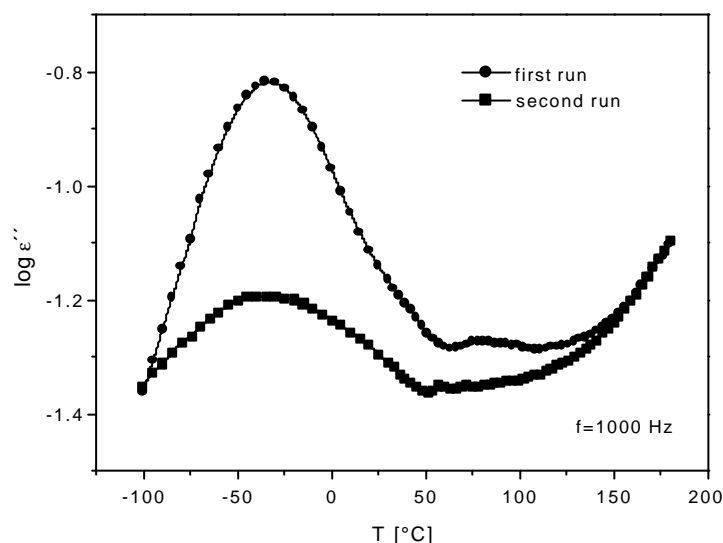
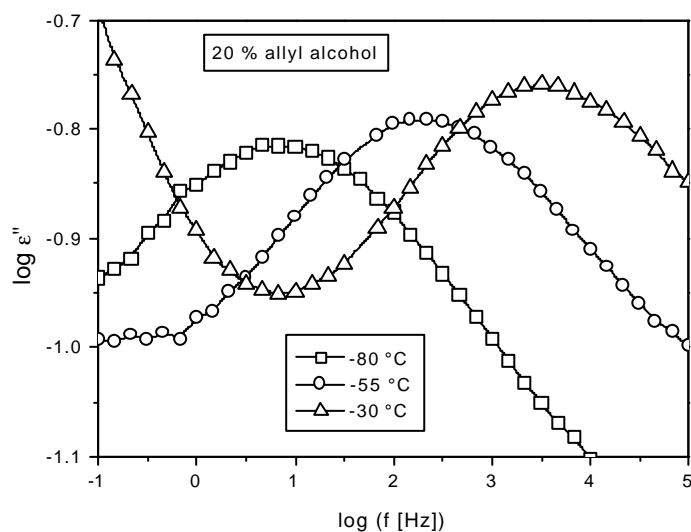


Fig. 3: Dielectric loss  $\epsilon''$  versus temperature at a frequency of 1000 Hz for a pulsed plasma copolymer with 20 / 80 (1,3-butadiene / allyl alcohol) in the formulation: ● - first run; ■ - second run.



With increasing temperature the position of this low temperature peak shifts to higher frequencies and increases in intensity (see Fig. 4).

Fig. 4: Dielectric loss  $\epsilon''$  versus frequency at the indicated temperatures for a pulsed plasma copolymer with 80 / 20 (1,3-butadiene / allyl alcohol) in the formulation. Lines are fits of the HN-function to the data including a low frequency tail.

The temperature dependence of the relaxation rate can be described by an Arrhenius law (Fig. 5). For the plasma synthesized polybutadiene a value 40 kJ mol<sup>-1</sup> is obtained which compares well with that for the  $\beta$ -relaxation of conventional polymerised 1,2- and 1,4-polybutadiene (41 and 37 kJ mol<sup>-1</sup> [11]). This indicates a

localised motional process like the  $\beta$ -relaxation in conventional synthesised polymers [12]. This is also consistent with the increase of  $\Delta\epsilon$  with temperature (see inset Fig. 5).

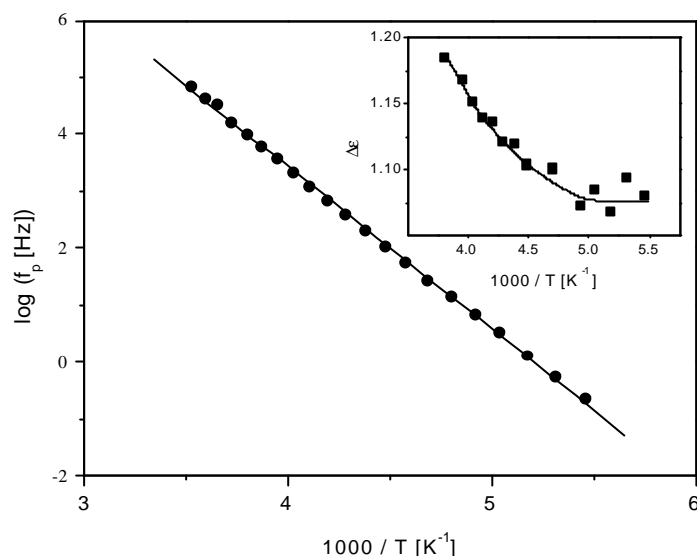


Fig. 5: Relaxation rates  $f_p$  versus inverse temperatures for a pulsed plasma copolymer with 10 / 90 (1,3-butadien / allyl alcohol) in the formulation. The line is a fit of the Arrhenius equation to the data. The inset gives the temperature dependence of the dielectric strength for the same polymer. The line is a guide to the eyes.

$E_A$  increases systematically with the content of allyl alcohol (see Fig. 6). This points to additional interaction cause by the allyl alcohol groups which hinders the molecular fluctuations. Moreover this systematic variation indicates also that the both monomers are incorporated according to its concentration in the formulation.

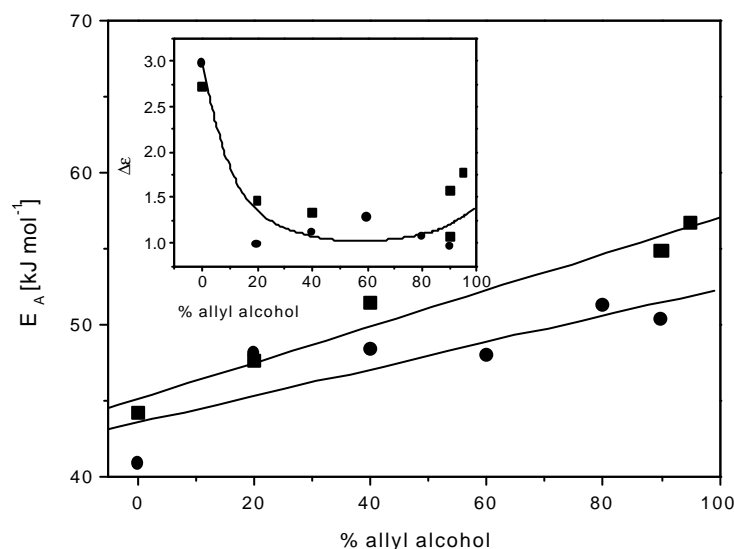


Fig. 6: Dependence of the activation energy  $E_A$  on the composition of the formulation.: ■-first run, ●-run. The line is a linear regression to the data. The inset gives the composition dependence of the dielectric strength at  $T = -55^\circ\text{C}$ : ■-first run, ●-run. The line is a guide to the eyes.

The dependence of the dielectric strength  $\Delta\epsilon$  on the concentration of allyl alcohol in the mixture is plotted in the inset of Fig. 6.  $\Delta\epsilon$  is proportional to the mean squared dipole moment  $\mu^2$  and to the mobility of dipoles. Pure plasma polymerised polybutadiene shows a high value of  $\Delta\epsilon$ . A minimum of  $\Delta\epsilon$  was found around the equimolar composition of the mixture of the both monomers. At the first glance this is unexpected because the dipole moment of allyl alcohol should be higher than that of butadiene. Therefore it is concluded that the increasing interactions of hydroxyl groups restricts the molecular mobility. To higher percentages of allyl alcohol an increase of  $\Delta\epsilon$  was measured, which is interpreted as an increase of the dipole moment  $\mu$  at high concentrations of OH groups. This interpretation is in agreement with the dependence of the activation energy on the concentration of allyl alcohol. At the end it should be stressed again that both dielectric



quantities vary systematically with the composition. Because dielectric spectroscopy is a “bulk method” this result points to a homogenous composition of the layers.

#### Acknowledgements

The financial support by VDI-TZ Düsseldorf (grant 13N7776) is highly acknowledged.

---

#### 4. References

- [1] J. Meisel, H.-J. Tiller - Z. Chem. **7**, 275 (1972).
- [2] J. Friedrich, I. Retzko, G. Kühn, W. Unger, A. Lippitz - Metallized Plastics 7: Fundamental and Applied Aspects, K. L. Mittal (Editor), VSP, Utrecht, 2001, 117-142.
- [3] G. Kühn, I. Retzko, A. Lippitz, W. Unger, J. Friedrich - Surf. Coat. Technol. **142-144**, 494 (2001).
- [4] Dielectric Spectroscopy of Polymeric Materials, J.P. Runt, J.J. Fitzgerald (Editors) ACS books Washington DC (1997).
- [5] L. Hartmann, K. Fukao, F. Kremer “Molecular Dynamics in Thin Polymer Films” in Broadband Dielectric Spectroscopy, F. Kremer, A. Schönhals (Editors) Springer Verlag Berlin (2002) p 433.
- [6] J. Friedrich, G. Kühn, R. Mix, I. Retzko, V. Gerstung, St. Weidner, R.-D. Schulze, W. Unger “Plasma Polymer Adhesion Promoters to be used for Metal-Polymer Composites” in: Polyimides and Other High Temperature Polymers: Synthesis, Characterization and Application, Vol. 2, K. L. Mittal (Editor.), VSP, Utrecht, in press.
- [7] J. M. Tibbitt, M. Shen and A. T. Bell - J. Macromol. Sci., Chem. **A10**, 1623 (1976).
- [8] St. Weidner, G. Kühn, R. Decker, D. Roessner, J. Friedrich - J. Polym. Sci.: Part A: Polym. Chem. **36**, 1639 (1998).
- [9] F. Kremer, A. Schönhals „Broadband Dielectric Measurement Techniques“ in Broadband Dielectric Spectroscopy, F. Kremer, A. Schönhals (Editors) Springer Verlag Berlin (2002) p 35.
- [10] S. Havriliak, S. Negami J. Polym. Sci. Part C **14**, 99 (1966).
- [11] A. Hofmann, A. Alegria, J. Colmenero, L. Willner, E. Buscaglia, N. Hadjichristidis - Macromolecules **29**, 129 (1996).
- [12] A. Schönhals “Molecular Dynamics in Polymeric Model Systems” in Broadband Dielectric Spectroscopy, F. Kremer, A. Schönhals (Editors) Springer Verlag Berlin (2002) p 225.

# Detonation and Combustion Waves in Heterogeneous Medium with Charged Dusts and Drops

Oleg Sinkevich, Emin Isakaev

*Associated Institute for High Temperatures, Russian Academy of Sciences*

## **Abstract**

The processes of charged dust crystal formation are discussed. Such processes take very often place in low - temperature plasmas and lead to formation of fractal structures that are consisted of sub- micron charged solid aerosol particles and charged hydrated clusters. It is shown that in such charged fractal structures detonation-like and combustion-like waves may propagate. Expressions for velocities of combustion and detonation waves propagating in charged fractal structure of quasi-crystal filaments are obtained.

## **1. Introduction**

The heterogeneous medium containing positive and negative hydrated ion clusters is often formed during a linear lightning discharge in the plasma channel of lightning. Hydrated ion clusters are created when ions and electrons are diffusing from the lightning channel and actively hydrated due to the humidity of the surrounding air. The dust from hydrated-ion clusters can store sufficiently high energy and the observed existence time of the hydrated ions substantially exceeds the recombination time of free ions and electrons [1]. Another type of charged dust could be assembled from polymer particles containing electrons and ions. The remaining positive and negative hydrated ion clusters may condense to liquid drops or solid dust. In the next stage liquid drops and solid dust may built up the fractal charged structure. Charged fractal objects may be synthesized as a result of evolution of a weakly ionized plasma in an external A or D electric field. The radius of independent charged and uncharged particles is small compared with the free path length of gaseous molecules. So, the moving gas could to penetrate inside fractal objects. In Earth atmosphere fractal charged heterogeneous structures often consist of metallic particles aggregated in filaments, polymer films, liquid droplets, quasi-crystal filaments of hydrated ions, excited atoms, and dusty plasmas [2, 3]. Such situation could arise in turbulent, non-equilibrium plasma during very fast non-adiabatic expansion processes. The non- equilibrium mechanism of recombination of free electrons and ions in such expansion may differ appreciably from equilibrium one.

Fractal structures of independent charged particles are formed in laboratory experiments as a result of MW or laser evaporation of metallic surface, in erosion discharges and in the Earth atmosphere during of solid cluster coagulation [2]. The charged fractal structures, that lifetime are exceeding the time of free electron - ion recombination, are similar to aerogels, but have a much lower density. The lifetime of negative and positive charged fractal structures consists of the diffusion time of free charges from the region of their initial formation, the time of charged clusters formation, the time of formation of the liquid or solid phase from clusters, the time of evaporation of droplets or disintegration of crystal, and, finally, the short time of recombination negative and positive charges of different sign. This long existed formation could to storage big energy. It is possible to give classification of mechanisms of formation long-lived negative and positive charged structures and to describe main characteristics of such structures: dimension, stored energy, and characteristic lifetime.

## **2. Formation of ordered structures**

### ***a. Analytical results***

Here we consider only one mechanism of charged fractal structures formation. This mechanism of spatial ordered quasi - crystal structure formation might be taken place in low - temperature plasmas that are containing heavy dust particles [4]. Often in plasma physics and physics of solids, the set of Vlasov - Poisson equations is used for numerical simulation of dust charging and mechanisms of dust interaction. But the most important part of the considered problem is connected with finding the condition of quasi - crystal structure formation. Vlasov himself have derived from the kinetic equation the condition of the steady- state, a space-periodic structure formation [5]. The Vlasov criterion of crystallization differs from the well known Lindemann formula. But for using Vlasov's criterion of a space-periodic structure formation for dust

particles in plasmas, we should know the electrostatic energy of two charged dust particle surrounded by electrons and ions.

Further, for finding the electrostatic energy of two charged dust particle surrounded by electrons and ions we'll follow our work [6]. Very often in electrical discharges in the Earth atmosphere all components of plasmas: charged dust particles, negative and positive ions and atoms have the same temperature [4]. Ions and electrons are surrounding any dust particle and shielding the particle charge. The formation of a dust crystal occurs as a result of the Coulomb interaction of electrons and ions with dust. A dust crystal is the non-equilibrium, open system that is taking place in external electrical and gravitational fields. Long-time exiting of such crystal is possible only in that case if the weight force is counterbalanced by force forming by an external electrical field or by gas motion through the dust structures. In plasmas two charged dust particles repel each other and at the same time attract charges from the clouds of the neighboring particle. Such interaction may results either in the repulsion of the particles if they are inside of the region of plasma charges that shields them or in their attraction if the particles are sufficiently removed from each other. If the foregoing picture is correct, then both lower and upper limitations on the mean distance between the particles for the formation of a stable plasma crystal exist. The shielding occurs at a distance of the order of Debye's shielding distance  $r_D$ , so the minimum distance between the particles must be  $\sim 2r_D$ . The electrostatic energy of two dust particles in plasmas may be found, using the obtained from the Poisson equation distribution of an electrical potential of each dust particle.

For deriving of the energy of dust particles interaction, one could use Poisson's equation for an isolated dust particle. The charge of a particle or the potential of its surface that could be used as boundary conditions for the Poisson equation is the self-consistent parameter of problem. In order to determine this parameter, one has to know the particle properties and, first of all, the emission properties which are usually unknown. Here we consider the particle charge as an external quantity for this problem. The potential distribution in the vicinity of a single charged dusty particle is represented in the form

$$\varphi(r) = \varphi_s(r_s^*) \exp(r_s^* - r^*). \quad (1)$$

where  $\varphi = e\Phi/k_B T$  is the dimensionless electrical potential,  $\varphi_s$  is the dimensionless electrical potential of the dust particle surface,  $e$  is an electron charge,  $T$  is temperature,  $r^* = r/r_D$  is the dimensionless distances from the dust particle center,  $r_D = (\epsilon_0 k_B T / 2n_0 e^2)^{1/2}$  is Debye's radius,  $n_0$  is the ions density.

Foregoing restrictions on the particle charge and size are valid for distribution (1). This foregoing assumption about the interaction of charged dust particles enables one to treat the interaction of two particles and clouds of electrons and ions that shield those particles and present the interaction energy as

$$U(r) = \Phi(r)eZ + \int \Phi(r; x, y, z) \rho_e(x, y, z) dx dy dz, \quad (2)$$

where  $\rho_e = -2en_0\Delta\Phi$  is density of electrical charges.

In (2) the first term describes the repulsion of the particles, and the second term describes their attraction owing to the interaction of one particle with the ions cloud of the other particle. A similar expression was used in [7], where the criterion of crystallization was estimated from the Lindemann formula. In fact, the use of the left-hand side of Poisson's equation  $-2en_0\Delta\Phi$  instead of the real distribution of electrical charge density  $\rho_e$ , with due regard for the approximate character of the solution for  $\Phi$ , introduces an additional error into the solution. However, for the above-identified values of potential  $\Phi_s \sim 3$  and radius  $r_s^* \sim 0.05$ , this error does not exceed 10%, which is approximately twice less than the regular error of experimental data.

Substituting the potential (1) and the space charge distribution  $\rho_e$  into (2) we obtain the interaction energy of two dust particles. The interaction energy of two dust particles may be represented in the next form

$$U(r^*)/U_0 = 2(1 + r_s^* + r_s^{*2} \exp r_s^*) r^{*-1} \exp(-r^*) - \exp(r_s^* - r^*), \quad (3)$$

where  $U_0 = 4\pi k_B T n_0 r_D^3 \Phi_s^2 r_s^2 \exp r_s^*$ . Spatial distribution of the interaction energy of two dust particle is represented in the Fig. 1. The interaction energy of two dust particles (3) contains a potential well whose depth, for  $r_s^* \ll 1$ , is

$$U_m = -U_0(1 - 2/r_m^*) \exp(-r_m^*).$$

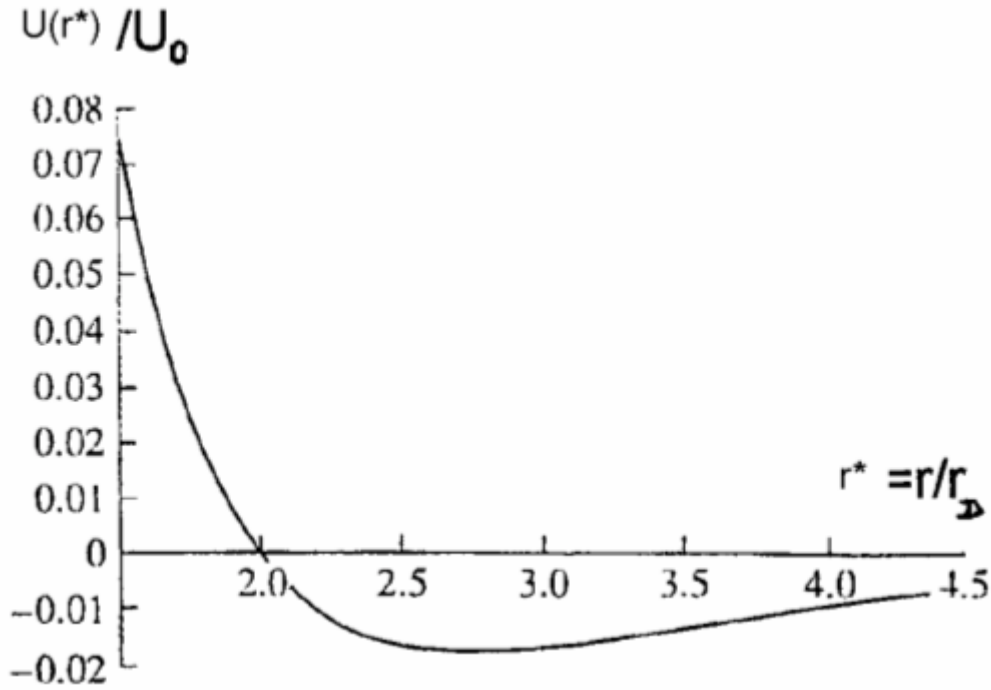


Fig. 1 Spatial distribution of the interaction energy of two dust particle.

As it is clear from Fig. 1 the electrostatic energy as a function of distance is non-monotonic one: the repulsion for the small radii and attraction for the big one. The position of the minimum of potential energy  $r_m^* = 1 + 3^{1/3}$  defines the characteristic scale of the mean distance between particles in a dust crystal and corresponds to the reasoning given at the beginning of this section. Therefore, it is possible to identify the unified mechanism of interaction of charged dust particles in air with negative and positive ions, which includes both the repulsion and the attraction of the particles, and derive the expression of the energy of such interaction. Given the latter, one can describe the effect of ordered structure formation in an atmosphere.

Now we may use the Vlasov criterion [5] for finding the dust crystal formation condition. This Vlasov condition for finding criterion of dust crystal formation may be represented in the next from

$$-(4\pi n_d r_D^3 / k_B T) \int_{r_s}^{\infty} U(s) \frac{\sin Ks}{Ks} s^2 ds = 1. \quad (4)$$

Here  $K^{-1}$  is the dimensionless period of emerging stricture.

Solution (4) was derived by Vlasov as a result of linearization of the input nonlinear equation for the particle interaction energy, which places a certain restriction on the parameter  $U_m$ , i.e.,  $U_m / kT \ll 1$ . Note Vlasov obtained condition (4), under assumption that the bifurcation of the solution of the problem on the space structure of a system of interacting particles corresponds to the formation of a crystal. The bifurcation parameter (dimensionless complex) is the eigenvalue of the linear problem. Apparently, Vlasov was the first who use the physical treatment of eigenvalue of the nonlinear problem for finding the condition of crystal formation. Criterion (4) corresponds to the formation of a crystal with central symmetry.

Using expression (4) one could obtain criterion of dust crystal formation. So, for a crystal with an infinite period ( $K \Rightarrow 0$ ), the expression (4) transforms to

$$-(4\pi n_d r_D^3 / k_B T) \int_{r_s}^{\infty} U(s) s^2 ds = 1. \quad (5)$$

In (4) and (5),  $U(s)$  is the energy of pair interaction of particles, which is found in the previous section, and  $n_d$  is the dust particle concentration. When integrating to infinity, it is assumed that the effect of the boundaries is ignored. Estimation shows [6] that the thermolization time of the dust component occurs very rapidly compared with the characteristic times of experiments.

As follows from (4) and (5), the necessary requirement for the existence of a crystal with an arbitrary dimensionless period  $K$  may be found from next relation

$$n_d/n_0 = 4/F(r_s, K), \quad (6)$$

where  $n_d$  is the dust particles concentration, and

$$F(r_s, K) = \frac{\{ \cos(2r_s^* K) K^{-1} [(2 + r_s^*) r_s^* K - 2K^3] + \sin(2r_s^* K) K^{-1} (r_s^* (1 - K^2) - 1 - 3K^3) \}}{(1 + K^2)^2}. \quad (7)$$

The solutions of a physical meaning are restricted by the inequality  $F(r_s, K) > 0$ , which is valid only for small values of  $K$ . When  $K \rightarrow 0$ , the formula (6) defines the minimum concentration of dust particles at which crystallization of the dust component may occur in a plasma with considered parameters. If  $F(r_s, K) \rightarrow 3 r_s^*$ , criterion (6) may be rewritten in a more customary form, namely, in terms of the parameter characterizing the ratio between the electrostatic and thermal energy

$$\Gamma_s \equiv (eZ)^2 n_d r_s^2 / 4\pi\epsilon_0 k_B T = 1/6\pi. \quad (8)$$

The dust particle radius  $r_s$ , which the characteristic length scale is provided by the quantity  $(n_d r_s^2)^{-1}$  instead of the mean distance between particles  $\langle r \rangle$ . The equation (8) yields the expression for the "regular" critical interaction parameter or the parameter of non-ideality of plasmas

$$\Gamma = \Gamma_s \langle r \rangle^2 / r_s^2 = \langle r \rangle^2 / 6\pi r_s^2, \quad (9)$$

where  $\langle r \rangle = n_d^{-1/3}$ .

As it follows from (9) for "crystallization" of dust the critical interaction parameter have always be greater than unity. This restriction is not always mentioned in the case when the method of kinetic equation is applied to the dust component. Generally speaking [6], it is correct to use the kinetic equation for one-particle distribution function only in the case of weak correlation between particles, which places a restriction on the particle interaction energy. In our case, this criterion is provided by the quantity  $U_m/k_B T$  rather than by the interaction parameter. Such a restriction was already mentioned above in connection with the linearity of the problem whose solution is provided by (5). That enables one to perform analyses of the dust component within the framework of either the kinetic equation or Vlasov's collisionless approximation. Otherwise, the results of calculations by the foregoing- formulas may only be regarded as estimates. Using the correlation between the crystal period and the plasma parameters, one can treat the stability of the new formation and the effect of external stimulation (such as a radio frequency and electric fields) on the dust crystal structure.

### b. Numerical simulation

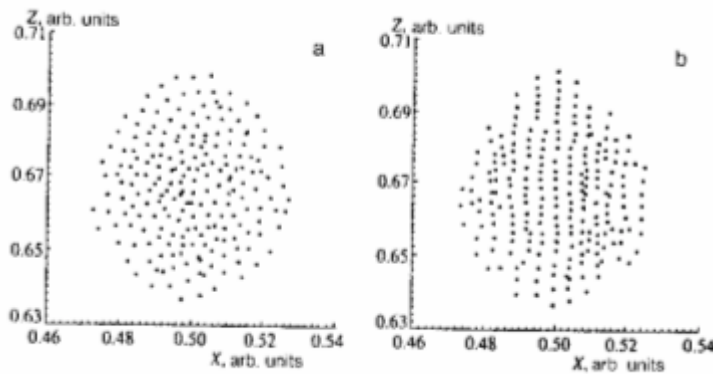


Fig. 2 Picture of vertical structures of the dust cloud: a)  $\chi = 22$ ; b)  $\chi = 7$

Here following our work [7] we give short presentation of numerical simulation of ordered structures formation in dust plasmas. In this calculation numerical modeling of low - temperature plasma with dust particles was performed by the standard Monte Carlo method. It was considered a finite number of particles (3000 particles) distributed over a cell of extent  $L = 700 r_D$ . The parameters of the external electric fields and its spatial distribution were chosen to be close to the real situation. Some of these numerical calculations are presented in Fig. 2,3. Fig. 2 shows a

properly scaled picture of vertical structures of the dust cloud: a)  $\chi = 22$ ; b)  $\chi = 7$ . Fig. 3 gives an axial cross section of the dust cloud: a)  $\chi = 22$ , b)  $\chi = 7$ . Here,  $\chi$  is the mean ratio of charges in the pair. Distance along the z-axis is plotted along the vertical external electric field. Axes x and y are plotted along the horizontal cross section.

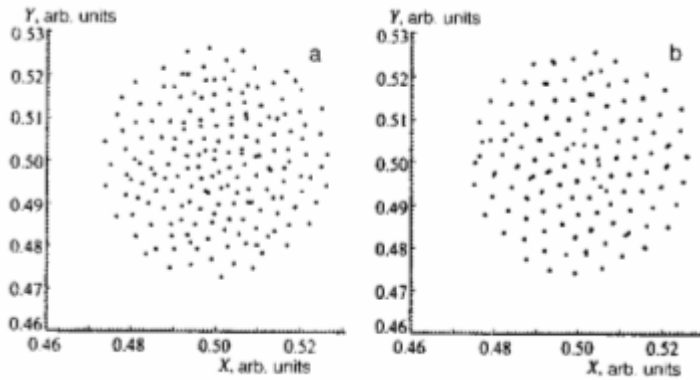


Fig. 3 Axial cross section of the dust cloud: a)  $\chi = 22$ , b)  $\chi = 7$

Monte Carlo simulations could explain the experimentally observed formation of threadlike structures in low - temperature plasmas with dusts, liquid drops, clusters and “crystallization” of these “treads” under real atmospheric conditions.

### 3. Destruction of fractal charged structures by detonation and combustion waves

The process of destruction of fractal negative and positive charged structures may be accompanied by detonation and combustion and may vary

at different stages in time because of predominance of those or either recombination mechanisms. Destruction of the charged fractal structures with quasi-crystal filaments may have a slow decay that is connected with the combustion- like wave propagation or the explosion one that is connected with the detonation-like wave -explosion of the fractal charged structure [8]. The velocity of the combustion wave propagating through a domain of a size  $l$  may be estimated from the next expression

$$V_c \geq 2 \sqrt{\frac{\chi_g \mathcal{E}_r}{k_B n} \frac{d(n_c^{+,-} / \tau_c)}{dT}}.$$

Here  $n_c^{+,-}$  is the density of charged clusters,  $n$  is the number density of gaseous molecules,  $k_B$  is the Boltzmann constant,  $\mathcal{E}_r$  is recombination energy of charged clusters,  $\tau_c$  is time of cluster destruction,  $\chi_g$  is temperature conductivity of gas.

There exist several mechanisms of initiation of detonation in the charged fractal structures some of them are connected with the electric fields but not only. The velocity of the detonation wave propagating through a domain of a size  $l$  may be estimated from the next expression

$$V_D \cong \sqrt{\frac{\mathcal{E}_r n_c^{+,-}}{k_B n m_e}}.$$

Here  $m_e = (m_g + m_f)/m_g$ ,  $m_g$  is the mass of the gaseous molecule,  $m_f$  is the mass of the particle forming the charged cluster. Both the velocity of the combustion wave and the velocity of the detonation wave are

proportional to  $\approx \sqrt{\frac{n_c^{+,-}}{n}} \approx \sqrt{(l/r_f)^d}$ , where  $r_f$  is the radius of the particle forming the charged cluster,

and  $d$  is the fractal dimension. The methods of experimental generation of fractal negative and positive charged structures under laboratory and full-scale experimental conditions and its destruction by combustion or detonation may be investigated in laboratory.

### 4. Conclusion

The processes of dust crystal formation are discussed. Such processes may be taken place in low - temperature plasmas when fractal structures (fractal aggregates, fractal tangles, aerogels) are forming from sub- micron charged solid aerosol particles and charged hydrated clusters. It is shown that the disintegration

of the charged fractal structures may be connected with propagation of the “combustion” or the “detonation” wave. Expressions for velocities of such combustion and detonation waves propagating in charged fractal structures of quasi-crystal filaments are obtained.

### References

- [1] S.A. Mayorov, A. N. Tkachev, S.I. Yakovlenko. *Physica Scripta*. **51**, P. 498 (1995).
- [2] M. DePaz, A.G. Giardini, L. Friedman. *J. Chem. Phys.* **52**,7, (1970).
- [3] J.D. Sartor. *Journal-of-Geophysical-Research*. **75**, 36, (1970).
- [4] V.N. Tsytovich. *Usp. Fiz. Nauk*. **167**, 1, (1997).
- [5] A.A. Vlasov. *Non - local Statistical Mechanic* (in Russian). Moscow, Nauka (1978).
- [6] D.N. Gerasimov, O.A. Sinkevich. *High Temperature*. **37**, 6 (1999).
- [7] E.A. Allahvarov, L.I. Podloubny, P.P.J.M. Schram, S.A. Triger. *Phvsica A*. **220**, P. 349 (1995).
- [8] O.M. Belotserkovskii, I.E. Zakharov, A.P. Nefedov, V.S. Filinov, V.E. Fortov, O.A. Sinkevich. *J.Experimantal and Theoretical Phys. (ZETF)* **88**, 3 (1999).
- [9] O.A. Sinkevich. *Detonation and Combustion Waves in Charged Fractal Structures. Control of Detonation Processes*. Eds. G. Roy, S. Frolov, D. Netzer, A. Borisov. Moscow, Elex-KM Publisher, (2000).

# Pulsed plasma initiated homo and copolymerisation – deposition rates and plasma diagnostics in dependence on the pulse length and frequency

R.-D. Schulze, R. Mix, G. Kühn, J. Friedrich

*Bundesanstalt für Materialforschung und –prüfung (BAM) / Federal Institute for Materials Research and Testing, Unter den Eichen 87, D-12205 Berlin, Germany*

## Abstract

Pulsed low-pressure r.f. plasmas were used to deposit homo and copolymer films. Investigations on the deposition rate of monomer gases, mixtures of comonomers as functional groups carrying monomers and chain extending comonomers were performed in dependence on the plasma-on time using a given plasma-on time. Moreover, some parameters of the ignited plasma pulses were measured by means of SEERS (Self-Excited Electron Resonance Spectroscopy) in the equivalent time sampling mode.

## 1. Introduction

Several applications require polymer surfaces with functional groups of defined type and concentration. The plasma polymer deposition, using the pulsed low-pressure r.f. plasma, is a suitable tool to deposit such tailor-made coatings [1]. This pulsed plasma technique was introduced by Tiller et al. in 1972 [2] and enhanced by Yasuda in 1977 [3] and Shen and Bell [4].

The inelastic collisions in the plasma and the particle bombardment of the substrate generate reactive radicals by activation of double bonds, hydrogen abstraction or C-C bond dissociation. These radicals are the preponderance for starting the radical polymerisation to produce stoichiometric composed polymers. However, UV irradiation from the plasma and the plasma particle bombardment destroy the molecular structure of polymeric substrates. Extended plasma-off time ( $T_{\text{off}}$ , also denoted as delay time) between the periodic plasma pulses (plasma-on time  $T_{\text{on}}$  within the period  $T$ , equivalent to the pulse frequency  $f_p$ ) allows to start the chemical chain propagation using chemically polymerizable monomers, for example acryloyl chloride in [5] or styrene. The thus deposited plasma polymer layers show a chemical composition and structure, which is near to those of classic polymers, i.e. the structure and the functional group of the monomer is retained in the polymer. The pulse regime and the input power have the most important influence on the resulting structure and stoichiometry of deposited polymer layers as was observed in preliminary tests. Therefore, these parameters have to be optimised for every system.

The concentration of functional groups in polymers can be adjusted applying the plasma initiated radical copolymerisation in the pulsed plasma mode. This process is not a simple mixing of two organic monomers and their polymerisation in the continuous wave plasma as performed by Yasuda [6]. Hereby, the reactivities of the two comonomers must be considered. This is known from polymer chemistry where the copolymerisation parameters describe the qualification of comonomers for copolymerisation. The principal procedure for designing the functional group carrying copolymers is to link a functional group containing comonomer with a chain extending comonomers of similar copolymerisation tendency preferentially by the radical copolymerisation initiated by the pulsed plasma and propagated during the plasma-off time. In such a plasma copolymerisation mixtures of two (or more) comonomer gases or vapours are used, which react at the substrate surface. The different reactivities of such a pair of comonomers affect the composition of resulting plasma copolymers additionally [7,8]. The influence of the different comonomer ratios on the deposition rate was also investigated.

Varying the external process parameters it is very useful to get concrete information on the real time behaviour of plasma species during the short pulses and the following reactions in the delay time. A plasma diagnostic method, which can be applied in this field, has to measure plasma parameters with a time-resolution of a few microseconds and has to be resistant to all problems of wall and sensor contamination by deposited plasma polymer layers.

The Self-Excited Electron Resonance Spectroscopy (SEERS) meets these requirements. Here, a capacitively coupled sensor as part of the chamber wall is used to measure the damped high frequency vibrations of the plasma bulk, generated in every peak period of the powered r.f. sinusoidal wave. This sensor signal and the measured peak voltage at the power electrode, taking in account the chamber geometry the electron density ( $n_e$ ) and electron collision rate ( $\nu_e$ ) can be modelled. These parameters are calculated by



special software based on the theory of the resulting plasma potential of r.f. discharges sustained in diode type reactors [9]. The results are volume-averaged values. They are very sensitive to changes in the plasma. Such commercially available systems [10] work with a data acquisition time of only 1  $\mu$ s and are widely used in continuous plasma applications in semiconductor industry [11].

## 2. Experimental setup

In this investigations a plasma chamber with a volume  $V=50$  l and equipped with an r.f. electrode of 300 cm<sup>2</sup> was used. A fomblin oil filled rotary pump and a turbomolecular pump were used to evacuate the chamber to a base pressure of about  $10^{-3}$  Pa. Working with permanent gases, for example nitrogen or oxygen, a second reactor was used with a volume of 1.5 l and an r.f. electrode with an area of 15 cm<sup>2</sup>. This recipient was equipped with a turbo molecular pump, which allows to reach a base pressure of  $10^{-7}$  Pa. The r.f. power was produced by a 13.56 MHz/600W generator Cesar 136, which was connected with a matchbox from Dressler (Stolberg, Germany). The r.f. supply works in the mode of constant power supply to the electrode and in the auto bias mode. To manage the gas injection mass flow controllers were used from MKS (Munich, Germany) and for adjusting the vapour flow of liquid monomers the DLI injection system (MKS, Munich, Germany) or Liquid-Flows (Bronkhorst, Ruurlo, The Netherlands) were used. The pressure was measured by full range gauges (Pirani and cold cathode) or by a capacitance gauge (Balzers, Liechtenstein).

SEERS diagnostic was performed using a modified Hercules system from ASI (Berlin, Germany). It is equipped with a trigger module. In the equivalent time sampling mode it was possible to evaluate the plasma data in short pulses with a time-resolution of 1  $\mu$ s. Using the implemented 500 MHz digital storage oscilloscope the characteristics of the anode voltage during the r.f. pulse could be measured.

## 3. Results

### 3.1. Influence of delay time on deposition rate

To study the fraction of chemical polymer deposition in the plasma-less dark time (plasma-off) a short plasma pulse of 30  $\mu$ s was given and then the plasma-off time was varied. Corresponding to the lower effective energy input with prolonged plasma-off times, referenced to the total cycle duration, the deposition rate  $r$  decreased for a few monomers as allyl alcohol, shown in Fig. 1.

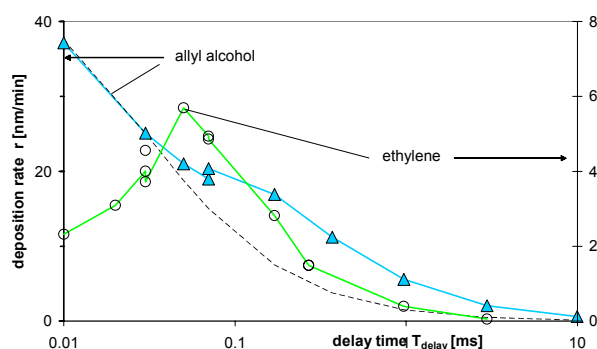


Fig. 1 Deposition rates for allyl alcohol and ethylene using 30  $\mu$ s r.f. pulse duration and 100 W varied with delay time, pressure of 27 Pa

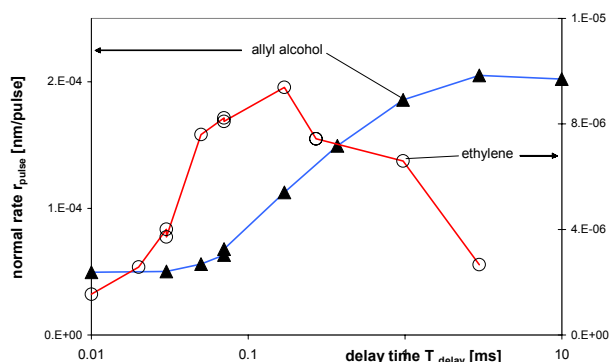


Fig. 2 Normalized deposition rates per r.f. pulse  $r_p$  of allyl alcohol and ethylene as derived from Fig. 1

Ethylene shows a significant increase of  $r$  near 70  $\mu$ s clearly evidencing the chemical contribution to the polymerisation reaction. However, a more detailed view shows for all monomers a decline from the pure plasma time reduction (proportional to  $T_{on}/(T_{on}+T_{off})$  dashed line, also known as duty cycle). This can be better expressed by normalisation of the rate per pulse  $r_p$  in Fig. 2. The increase of the deposition rate with the delay time reflects the capability to undergo a pure chemical chain propagation in the plasma-less period ( $T_{off}$ ). It has to be concluded that the time to reach the maximal deposition rate differs for each monomer.

The increase of deposition rate with prolonged pulse time for ethylene (Fig. 3) or higher input power for  $T_{on}/T_{off}$  times of 100/900  $\mu$ s (Fig. 4) confirms the suggestion of producing a higher concentration of starting radicals during the plasma pulses. For different monomers the influence of the power varies. Increasing the power input from 100 to 300 W, ethylene and 1,3-butadiene show a deposition rate, which is much more

increased (superproportional) than the power input (dashed line). In contrast to those monomers, acetylene and allyl alcohol did not reach a proportional increase of their deposition rates compared with the increase of power (saturation behaviour).

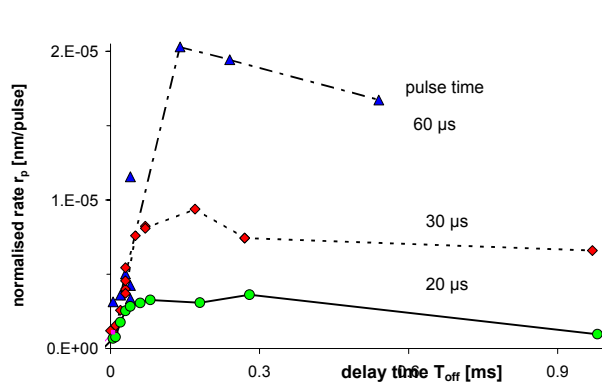


Fig. 3 Normalized deposition rate for ethylene as in Fig. 1 for a different pulse length

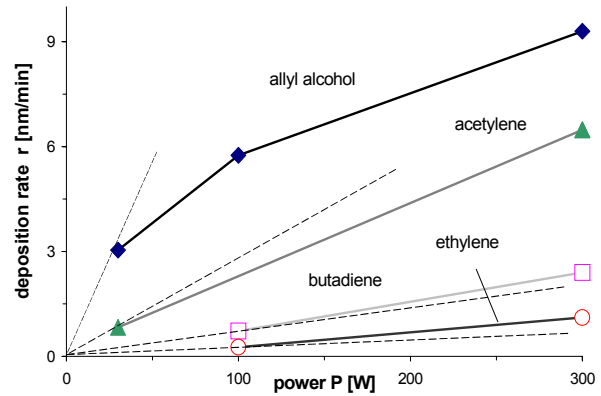


Fig. 4 Deposition rates of pure monomers as function power at  $p=26$  Pa,  $T_{\text{total}} = 1000$   $\mu\text{s}$ ,  $T_{\text{on}}=100$   $\mu\text{s}$

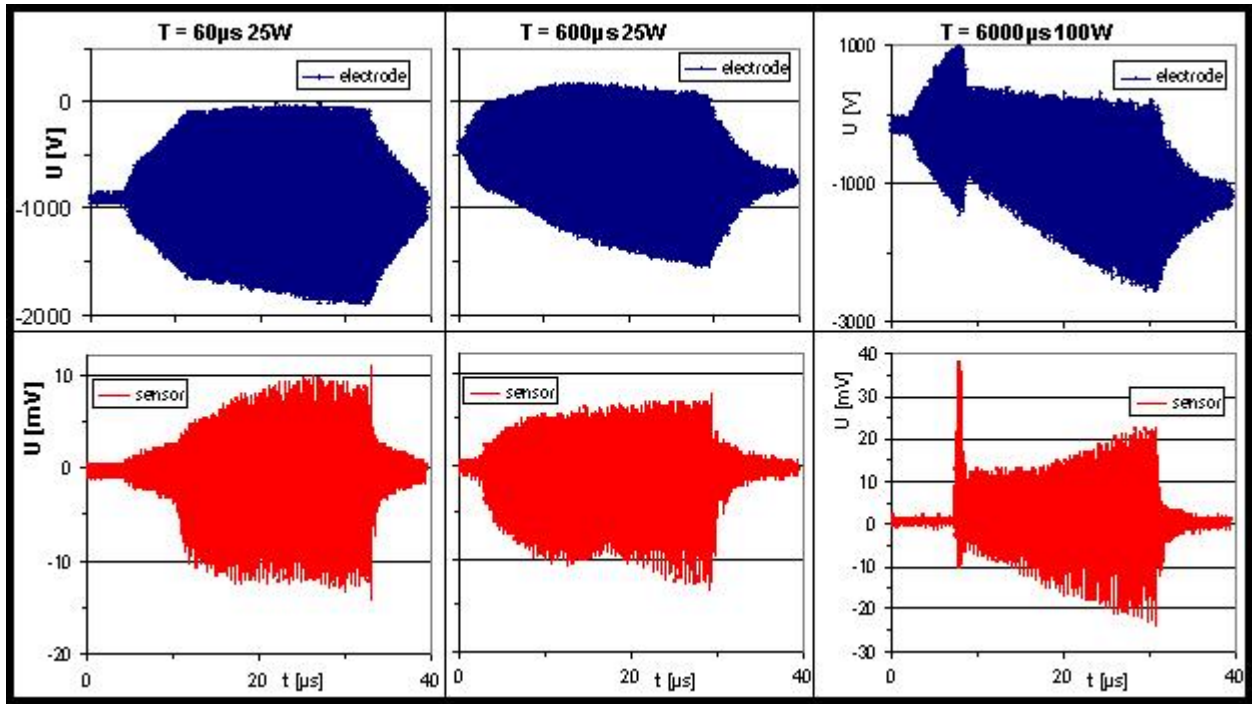


Fig. 5 Anode voltage and plasma signal for 30  $\mu\text{s}$  plasma pulses for delay times of 60, 600  $\mu\text{s}$  (25 W) and 6000  $\mu\text{s}$  (100 W) (nitrogen, 5 Pa)

Surprisingly, for prolonged delay time the normalized deposition rates does not converge to a constant value, as assumed for the termination of the polymerisation reaction. After reaching the maximum they fall exponentially with increasing plasma-off time (Fig. 2). It can be assumed that this effect is caused by a plasma effect or by desorption of low-molecular weight substances and monomers during prolonged  $T_{\text{off}}$ . Referring to this mentioned plasma effect it can be suggested that adverse conditions for plasma ignition at every pulse are the reason why. These improper plasma conditions are due to the recombination/relaxation of all excited molecules at surfaces and also in gas. Therefore, this is the idea, the isolating surface hinders the new ignition of the following pulse. Additionally, as result of the self-bias voltage discharge in the plasma-less period, a higher a.c. voltage has to be necessary to ignite the plasma again (resulting peak voltage = bias voltage + a.c. amplitude).

In Fig. 5  $U/t$  measurements in nitrogen pulsed plasma are shown. Applying pulses of  $T_{\text{on}}=30$   $\mu\text{s}$  within a full time ( $T_{\text{total}}$ ) of 600  $\mu\text{s}$  the bias at ignition of the pulse amounts less than half of its saturation

(normal) value, at 6000  $\mu\text{s}$  the bias is nearly completely discharged. It takes 30  $\mu\text{s}$  of plasma time to reload the bias to normal plasma (continuous wave) conditions. Under consideration of the above discussed pulse plasma effects and post-plasma reactions/relaxations following conditions for copolymerisation and using monomer mixtures following are preferred: pulses of 100  $\mu\text{s}$  duration and a delay time of 900  $\mu\text{s}$  ( $T_{\text{total}} = 1000 \mu\text{s}$ ).

### 3.2. Influence of monomer composition on deposition rate

The deposition rates during the pulse plasma-initiated copolymerisation of a functional group carrying comonomer and a chain-extending or (chemically) bifunctional crosslinking comonomer were determined controlling the pressure by a Pirani gauge (uncorrected). The pressure was adjusted to 26 Pa, the pulse duration to 100  $\mu\text{s}$  and the repetition rate to 1000 Hz. The nominal input power was 300 W or 100 W (30 W for acetylene). The deposition rates show characteristic deviations from the linearity in dependence with the molar ratio of the comonomer mixtures. This is known from copolymerisation chemistry, which is characteristic for the excess or deficiency of one of the comonomers due to differences in the copolymerisation coefficients of the comonomers.

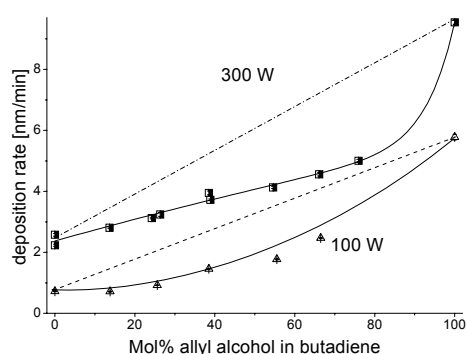


Fig. 6 Deposition rates for monomer mixtures from butadiene/allyl alcohol at  $p = 26 \text{ Pa}$ ,  $f = 1000 \text{ Hz}$ , pulse duration = 100  $\mu\text{s}$

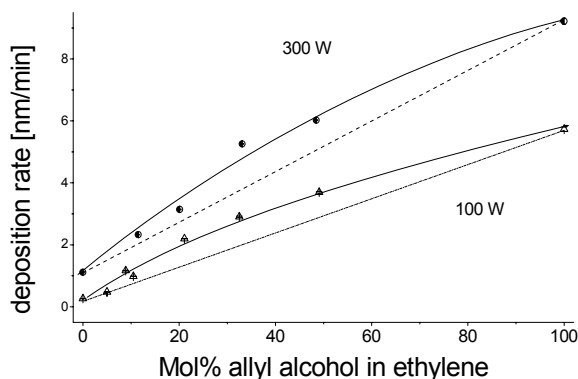


Fig. 7 Deposition rate for ethylene/allyl alcohol as in Fig. 6

Summarizing these results, slope and shape of rates as a function input power change generally. This behaviour is also known from chemical copolymerisation. Variations of pressure, gas flow and chamber geometry induce additional effects on deposition conditions.

### 3.3. Plasma diagnostic by SEERS

SEERS (Self-Excited Electron Resonance Spectroscopy) is a convenient method to measure a few of plasma characteristic parameters, is insensitive towards the deposition of plasma polymers and does not disturb the

The butadiene-allyl alcohol comonomer plasma exhibits a lower deposition rate than given by the linear interpolation of the rates for the pure monomers. Fig 6 shows the result for a nominal power  $P=300 \text{ W}$  and 100 W.

The ethylene-allyl alcohol comonomer plasma generates a higher deposition rate than given by the interpolation (Fig. 7).

For acetylene-allyl alcohol comonomer mixtures, as shown in Fig. 8, the measured rates are higher than the rates of the pure monomers.

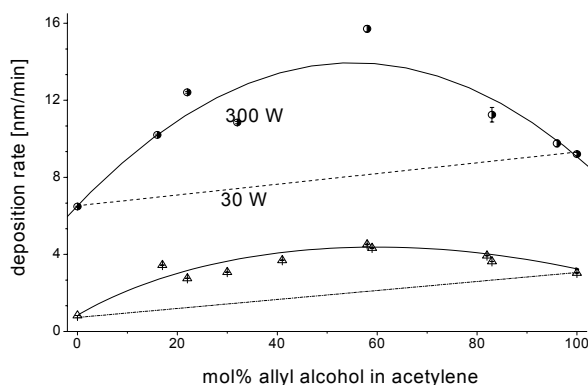


Fig. 8 Deposition rate for acetylene/allyl alcohol as shown in Fig. 6

plasma. This diagnostic allows it to measure the electron density ( $n_e$ ), collision rate ( $\mu_e$ ) and the bias in a time-resolved mode for characterizing pulsed plasmas. SEERS measurements are completed by a few ion energy measurements using a plasma mass spectrometric monitor (EQP, Hidden Analytical, Warrington, United Kingdom). For non-depositing gas plasmas as nitrogen or oxygen the plasma density grows after ignition within short period of 30  $\mu$ s (Fig. 9). A nearly constant electron collision rate produces a continuous increase of the electron density until a limit.

For the nitrogen plasma the values at the end of the pulse  $T_{on}/T_{off} = 30 \mu s/70 \mu s$  pulses are presented in Fig. 10 as function of gas pressure ( $P = 20$  W, gas flow 45 sccm) and as function of power ( $p=5$  Pa, gas flow 30sccm).  $n_e$  increases strongly with both the pressure and the wattage as expected.  $n_e$  increases proportionally to the pressure and therefore to the number of atoms/molecules in the plasma.  $v_e$  undergoes less changes.

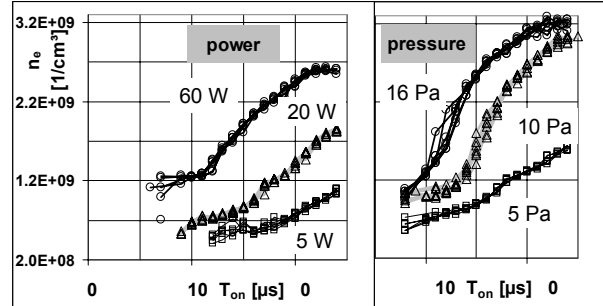


Fig. 9 electron density of pulses/period nitrogen plasma with  $T_{on}/T_{off}=30 \mu s/70 \mu s$  at power ( $p=5$  Pa) and pressure variation ( $P=20$  W)

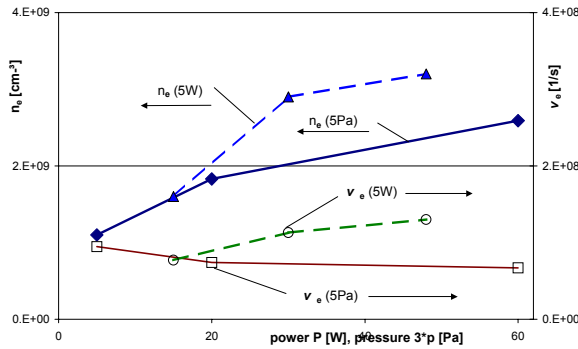


Fig. 10 Values at the end of 30  $\mu$ s ( $T_{off}=70 \mu$ s) pulses/period nitrogen plasma: electron density and electron collision rate as function of power ( $p=5$  Pa) and of pressure ( $P=5$  W)

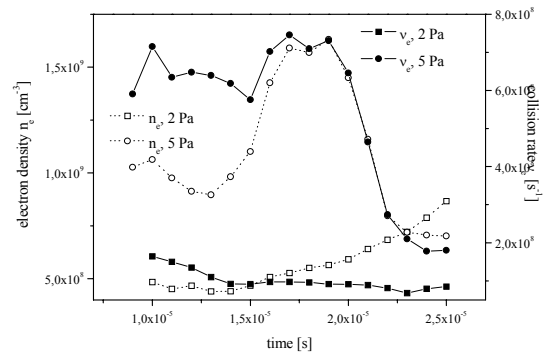


Fig. 11  $n_e$  and  $v_e$  in dependence on time within a 25  $\mu$ s plasma pulse of styrene

Different polymer-depositing plasmas were investigated as such with the improper monomer acetylene, the moderately qualified ethylene, and the best-qualified styrene, deduced from their qualification in chemical radical polymerisation. Pulse lengths longer than the above mentioned time of adjusting the steady-state after ignition of the plasma have an insignificant influence on the electron density for both the ethylene and the styrene plasma. Looking to one single pulse of 25  $\mu$ s in the styrene plasma in more detail (Fig. 11), differences in the time-dependence of  $n_e$  and  $v_e$  during the plasma pulse for the pulse polymerisation at 2 or 5 Pa are obvious. Thus, the process can be easily controlled and reproduced.

### 3.4. Control of plasma characteristics using SEERS

SEERS was applied in our work as convenient diagnostic for polymer depositing pulsed plasmas. One important mechanism, which should be controlled, is the ignition and the adjustment of steady-plasma in the beginning of each pulse. This mechanism depends on the electrode geometry as well as on the wall/electrode isolation by the deposited plasma polymer. For styrene pulse plasma with  $T_{on}/T_{off} = 100 \mu s/900 \mu s$ , 20 W and 5 Pa the well-reproduced variation of plasma parameters in the first 40  $\mu$ s are shown in Fig. 11. Afterwards the electron density is nearly constant and the collision rate slightly increases. Changing the process gas and using oxygen as shown in Fig. 12, a successive transition in parameter curves was observed within the first

40  $\mu\text{s}$  of the pulse time. After 5 min electron density and collision rate reach the characteristic behaviour of the clean (or oxygen cleaned) chamber walls.

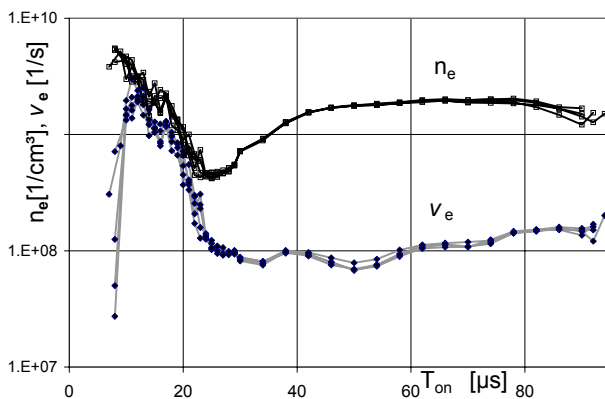


Fig. 11  $n_e$  and  $v_e$  in dependence on time within a 25  $\mu\text{s}$  plasma pulse  $T_{\text{on}}/T_{\text{off}} = 100 \mu\text{s}/900 \mu\text{s}$  5 Pa, 20W of styrene

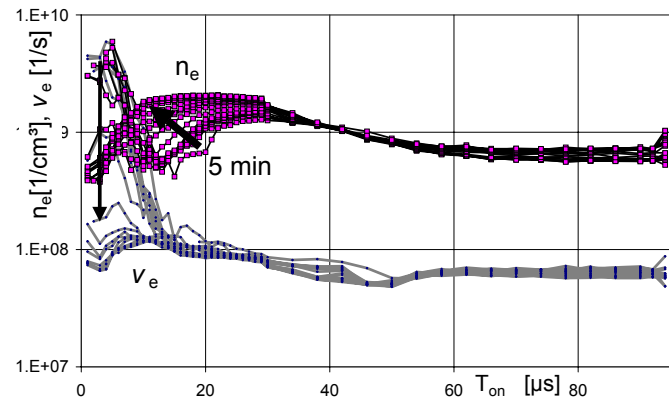


Fig. 12 as in Fig. 11 pulsed oxygen plasma, followed after styrene deposition of fig.11 - changes during 5 min

The second parameter, which can be controlled, is the measurement of the established steady-state plasma conditions in the second region of the pulse. This parameter represents the actual content of particles in the plasma. Every increase of impurities in the plasma gas can be detected in the such a way.

### Acknowledgements

This work was financed by VDI-TZ Düsseldorf under grant 13N7776

### References

- [1] C. R. Savage and R. B. Timmons, Polym. Mater. Sci. Eng., **64**, 95 (1991)
- [2] J. Meisel and H.-J. Tiller, Z. Chem., **7**, 275 (1972)
- [3] H. Yasuda and T. Hsu, J. Polym. Sci., Polym. Chem. Ed., **15**, 81 (1977)
- [4] J. W. Vinzant, M. Shen and A. T. Bell, ACS Polymer Preprints, **19**, 453 (1978)
- [5] J. G. Calderon and R. B. Timmons, Macromolecules, **31**, 10, 3216, (1998)
- [6] H. Yasuda, H. C. Marsh, M. O. Bumgarner and N. Morosoff, J. Appl. Polym. Sci., **19**, 2845 (1975)
- [7] A. Fritz, A. Schönhals, R. Mix, G. Kühn, J. F. Friedrich, Dielectric spectroscopy of plasma copolymers or the system allyl alcohol/alkene, Eighth International Conference on Plasma Surface Engineering PSE 2002, Garmisch-Partenkirchen 9-13.09.2002 Abstracts VDI-Technologiezentrum, 112 (2002)
- [8] J. F. Friedrich, R. Mix, G. Kühn, D. Schulze, R.-D. Schulze, I. Retzko, W. Unger:: Functional groups bearing plasma homo and copolymer layers as adhesion promoters in metal-polymer composites, Eighth International Conference on Plasma Surface Engineering PSE 2002, Garmisch-Partenkirchen 9-13.09.2002 Abstracts, VDI-Technologiezentrum, (2002)
- [9] M. Klick et al., Jpn.J.Appl.Phys., Part I, **36**, 7B, 4625 (1997)
- [10] [www://ASInst.com](http://www://ASInst.com)
- [11] Second Workshop on Self Excited Electron Plasma Resonance Spectroscopy, Dresden 1999, CD published by the AEC/APC Workshop Europe Organisation Committee Dresden, Germany, 5(2002)

# Development of new vascular prostheses : PVDF multifilament yarns grafted with polystyrene induced by plasma

P. Marmey<sup>1</sup>, F. Rossi<sup>2</sup>, M. C. Porté-Durrieu<sup>1</sup>, H. Blanchard<sup>3</sup>, Ch. Baquey<sup>1</sup>

<sup>1</sup> INSERM U. 443, Université Victor Segalen Bordeaux 2, 146, rue Léo-Saignat, 33076 Bordeaux cedex, France

<sup>2</sup> European Commission Joint Research Center, IHCP, 21020 Ispra (VA), Italy

<sup>3</sup> SNPE Propulsion, Av. Gay Lussac, 33167 Saint-Médard-en-Jalles cedex, France

There is great interest in developing an alternative prosthesis material because the successful substitution of small diameter arteries ( $\varnothing < 5$  mm) by Polyester (PET) and Expanded Teflon (PTFEe) vascular grafts has not been achieved in humans. In order to reach this objective, we have chosen to work with new biomaterial, multifilament yarns, from polyvinylidene fluoride (PVDF) which present suitable mechanical properties, *i. e.*, lower tensile modulus than PET and PTFEe. The need for more h mocompatible materials leads to modify its surface with so-called “heparin-like” treatment and then modify its level of thrombogenicity [1]. A four steps method is necessary to implement this “heparin-like” surface transformation [2]. The first step, consisting in grafting polystyrene (PS) on the PVDF surface, is currently achieved using radiochemical grafting techniques. But  $\gamma$ -rays impairs the mechanical properties especially the toughness of the final “heparin-like” materials for high doses (upper than 25 kGy).

The relevance of plasma treatment as an alternative to a  $\gamma$  irradiation was evaluated in this work.

Different MW (post-discharge) and RF atmospheric plasma treatments were tried, with several Ar/O<sub>2</sub> or Ar/H<sub>2</sub> gas mixtures. This work has been carried out on commercial PVDF multifilament yarns. Evolution of the mechanical properties was investigated with tensile tests. The Young modulus and the fracture toughness variations were studied in order to compare the influence of each treatment. Surface modification in each case was investigated by XPS, as well.

As expected, plasma treatment has weaker influence on the Young modulus and fracture toughness than  $\gamma$ -irradiation.

But up to now, plasma treatments did not allow to obtain grafting yield as important as  $\gamma$ -rays treatment. This is confirmed by XPS results, which shows a partial covering of the surface since fluorine is still detectable after treatment.

These results encourage us to investigate new grafting plasma parameters (power, time, gas mixtures) in order to get higher grafting yields and biomaterials with preserved mechanical properties as well.

Future prospects are (i) preparation of knitted yarns based tubular constructs, (ii) mechanical behaviour under dynamic stress and (iii) *in vivo* biomechanical investigations.

## References :

- [1] C. Fougnot, J. Jozefonvicz, M. Samama, L. Bara, - Ann. Biomed. Eng. **7**, 429-439 (1979).
- [2] M. C. Port -Durrieu, C. Aymes-Chodur, N. Betz, C. Baquey, - J Biomed Mater Res. **52**, 119-127 (2000).

# Comparison of different plasmachemical processes for the formation of monotype functionalized polymer surfaces

J. Friedrich, A. Meyer-Plath, I. Retzko, G. Kühn, R. Mix

*Bundesanstalt für Materialforschung und –prüfung (BAM), 12200 Berlin, Germany*

## Abstract

Several approaches were investigated to produce monotype functionalized polymer surfaces with a high density and homogeneity of functional groups: (1) Plasma oxidation followed by wet-chemical reduction, (2) the attachment of molecules with permanent radical character onto plasma-produced radical sites, (3) the plasma bromination followed by (4) Williamson, Gabriel-like or other synthesis of spacer and biomolecules, (5) the pulsed plasma polymerization of functional groups bearing monomers and, moreover, (6) the plasma-initiated copolymerization of functional group carrying monomers with chain extenders or crosslinkers. The abundance of hydroxyl (OH), primary amino (NH<sub>2</sub>), and carboxyl (COOH) groups at surfaces was studied in detail.

The oxygen plasma treatment in a low-pressure non-isothermal glow discharge results in the formation of a wide variety of O functional groups, polymer degradation and crosslinking. Low power densities and short exposure times (0.1 to 2 s) are required to functionalize a polymer surface while preserving the original polymer structure. Carbonate, ester, and aromatic groups of the polymer are rapidly degraded by an extensive oxygen plasma treatment. Furthermore, scissions of polymer backbones and losses in molecular weight are also of importance. Moreover, the formation of 8 to 16 monomer units membered macrocycles was observed. Isolated as well as conjugated C=C bonds were also observed in a region of around 4 nm in depth (NEXAFS spectroscopy). The investigated polymers could be classified by their degradation behaviour during exposure to the oxygen plasma.

In order to maximize the process selectivity for OH groups, the variety of oxygen functionalities formed by the oxygen plasma was wet-chemically reduced by diborane, vitride™ (Na complex), and LiAlH<sub>4</sub>. Typical yields were 7 to 14 OH groups per 100 carbon atoms at surfaces of polyethylene and polypropylene.

Typical yields of quenching the plasma-produced radical sites with NO were 4 to 8 NO reaction products per 100 C atoms. Using organic molecules with functional groups and a permanent radical site the yield of grafting reached 2 to 3 grafted functionalities per 100 C atoms. Furthermore, this reaction with NO was successfully applied to plasma polymers to suppress their ageing during exposure to air by quenching the trapped radicals.

Plasma bromination (40 Br per 100 C atoms) of polymer surfaces, followed by grafting of spacer molecules, has been proved to be a direct and very efficient way of polymer surface functionalization with high selectivity.

Another way to produce high densities of monotype functionalities was the pulsed plasma polymerization of functional group bearing monomers such as allyl amine, allyl alcohol or acrylic acid. The retention of chemical structure and functional groups during plasma polymerization was achieved by using low power densities and a pulsing technique. The maximum yields were 31 OH, 18 NH<sub>2</sub>, or 24 COOH groups per 100 C atoms. To vary the density of functional groups a chemical copolymerization with “chain-extending” comonomers such as butadiene and ethylene was initiated in the pulsed plasma.

## 1. Introduction

The intention of this paper is to compare the efficiency of investigated plasma processes for producing monotype functional groups of different type and density at the surface of polymers. Polymers offer a number of advantageous properties and, therefore, they are widely used in many products such as applied in medicine or in the automotive industry. However, polymer surfaces are often chemically inert and don't undergo interactions with other materials. This behaviour is due to the absence of reactive groups at the surface. The simplest way to enhance the interactivity of a polymer surface is the introduction of polar groups by chemical oxidation, flame or plasma treatment. Two disadvantages are immanent using such pretreatments, the great variety of different functional groups and the degradation of the macromolecules near the surface resulting in a mechanically unstable surface layer (weak boundary layer). Such an introduction of different types of functional groups is designated as *unspecific functionalization*. Therefore, we look for a soft treatment that can produce a high-density monotype functionalization of polymer surfaces, which is consequently called *specific functionalization* (cf. Fig. 1). To overcome this disadvantage mild plasma conditions or

remote plasma are applied. An alternative way is the application of pulsed plasma. Such plasma can be characterized as non-destructive regarding the polymer substrate and regarding the selectivity of monotype functionalization.

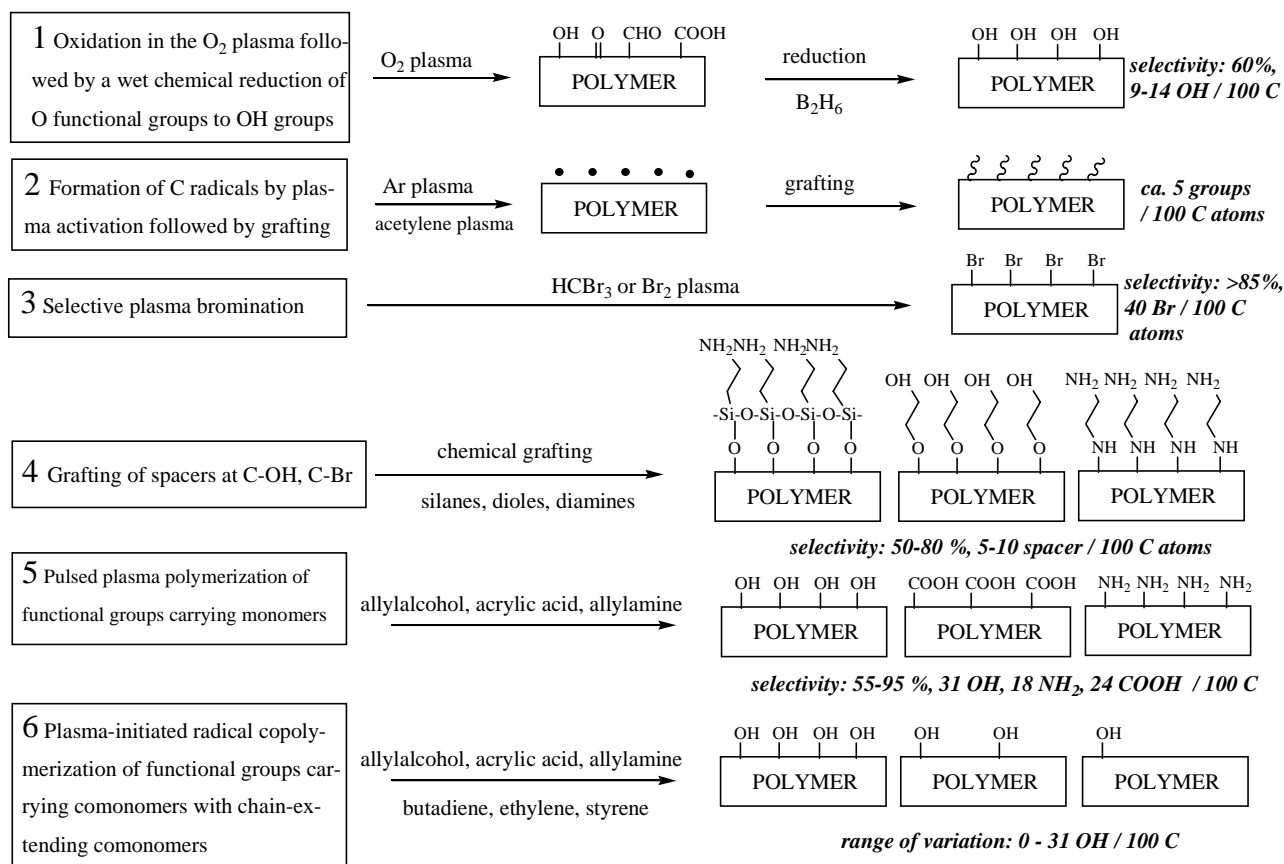
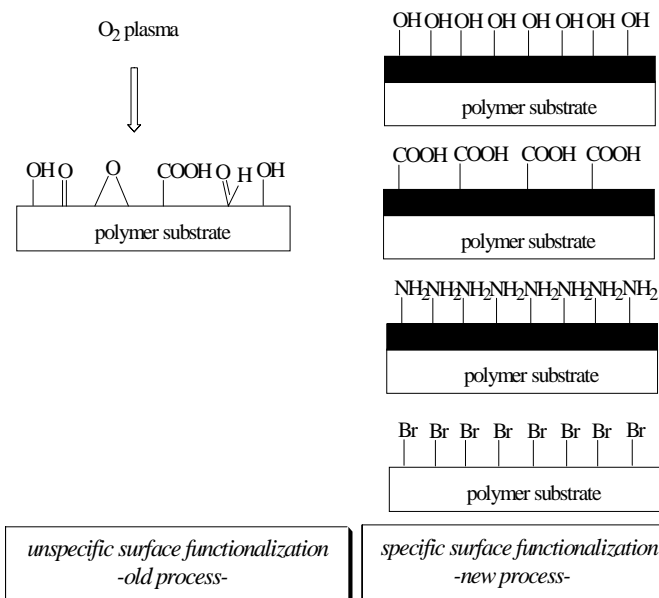


Fig. 1 Schematic comparison of different plasmachemical processes for the formation of monotype functionalized polymer surfaces



A number of different ways for functionalization of polymer surfaces with exclusively one sort of functional groups such as OH, COOH,  $NH_2$  or Br were investigated (Fig. 1, processes 1-3, 5,6). The first way (1) is to create a *plasma gas specific surface functionalization*.

Fig. 2 Specific and unspecific functionalization

This variety of functional groups of one basic element is obviously an *unspecific functionalization* (cf. Fig. 2). It can be transferred into a *specific functionalization* (of exclusively one type of functional group) by (immediately) following by

a subsequence of a chemical conversion of the different coexisting functional groups to preferably one type of functional groups. This approach was introduced by Nuzzo and Smolinsky in 1984 [1]. Plasma bromination (40 Br per 100 C atoms) of polymer surfaces, followed by grafting of spacer molecules, has been proved to be a direct and very efficient way of polymer surface functionalization with high selectivity.

A further way to produce high densities of monotype functionalities was the pulsed plasma polymerization of functional group bearing monomers such as allyl amine, allyl alcohol or acrylic acid [2-4] based



on works of Tiller and Yasuda [5,6]. The retention of chemical structure and functional groups during plasma polymerization was achieved by using low power densities and a pulsing technique. The maximum yields were 31 OH, 18 NH<sub>2</sub>, or 24 COOH groups per 100 C atoms. To vary the density of functional groups a genuine chemical copolymerization of functional group carrying comonomers with “chain-extending” comonomers such as ethylene or “crosslinking” comonomers such as butadiene was initiated in the pulsed plasma.

## 2. Experimental

Plasma functionalizations of polymer surfaces were carried out in a plasma reactor described earlier [7]. The pumping system comprised an oil-free membrane pump connected to a turbomolecular pump. Polymer samples were treated in an r.f. (13.56 MHz, also in the pulsed mode) oxygen low-pressure plasma. The samples were fixed to a rotating sample holder [8] in order to achieve a more uniform treatment. To avoid polymer degradation, the discharge power used was below 50 W in the continuous wave mode and 0.3 to 10 W in the pulsed r.f. mode. The base pressure was about 10<sup>-4</sup> Pa. Most experiments were performed at a pressure of 6 Pa. The gas flux was 7 dm<sup>3</sup>/h. Plasma brominations were performed using bromoform or bromine vapour as plasma gas.

Plasma polymerizations were carried out in the same plasma reactor as described before. A pulsable r.f. generator with an automatic matching unit was used to ignite the plasma. The duty cycles (plasma-on [ms] / plasma-off [ms] + plasma-on [ms]) were varied from 0.01 to 1 with frequencies from 10 to 10<sup>5</sup> Hz. The power input was varied from a few Watts to 300 W. The effective power ( $W_{\text{eff}}$ ) applied was calculated by taking into account the plasma-on time. Copolymerizations were performed in the same manner injecting two gases or vapours simultaneously.

The derivatization of OH groups was performed using trifluoroacetic anhydride (TFAA) or m-trifluoromethylphenylisocyanate (TMPI), that of NH<sub>2</sub> by applying pentafluorobenzaldehyde (PFBA) or 4-trifluoromethylbenzaldehyde (TFMBA) and that of COOH by exposure to trifluoroethanol (TFE). The number of functional groups was calculated by considering the percentage of the introduced fluorine (F1s peak) and the theoretical stoichiometry of the derivatized polymer. It was supposed that the XPS analyzed outermost layer ( $\approx 3$  nm) was homogeneously derivatized. The completeness of the derivatization and the absence of non-consumed functional groups in the deposited polymer layer were checked using the ATR-FTIR spectroscopy. Further methods were the C1s peak fitting (CF<sub>3</sub>, COOR) or the measuring of the concentrations of introduced oxygen (OH, COOH – O1s peak) or introduced nitrogen (NH<sub>2</sub> - N1s peak).

## 3. Results

### 3.1. O<sub>2</sub> plasma and chemical reduction

Using the oxygen r.f. pulsed-plasma modification the oxygen incorporation onto the surface of PP can be shown by a series of ATR-FTIR spectra. A strong carbonyl band ( $\approx 1700$  cm<sup>-1</sup>), alcoholic structures ( $\approx 1100$ -1200 cm<sup>-1</sup>), a broad OH peak and adsorbed water related features ( $\approx 3100$ -3500 cm<sup>-1</sup>) appear within an exposure to the O<sub>2</sub> plasma of shorter than 2 s. Surfaces with a O/C ratio of about 0.2 were used for further chemical processing. In Fig. 3 the XP spectra of PP are shown for as received, after low-pressure oxygen plasma pretreatment, diborane reduction and derivatization with TFAA. After plasma treatment the appearance of a strong O1s peak can be seen. After TFAA derivatization of plasma generated OH groups a small F1s peak at a binding energy of 689 eV is detected at the PP surface. The origin of this limited OH group formation in oxygen plasma can be attributed only to the existence of additional hydrogen sources such as abstracted hydrogen from polymer backbone and hydrogen from dissociation of desorbed water. It is clearly identifiable by comparing the F1s peaks in the survey scans with and without diborane reduction (cf. Fig. 3) that the diborane reduction strongly increases the yield of OH groups. Quantification of this optimized process shows an improvement in OH yield of nearly 4% without further chemical post-plasma treatment to 13-14 % maximum after chemical reduction with diborane under the best conditions (Fig. 3). These conditions were the diborane reduction followed by hydrolysis with H<sub>2</sub>O<sub>2</sub> in the presence of NaOH for the hydroxylation of C=C. LiAlH<sub>4</sub> (or vitride<sup>TM</sup> = sodium bis (2-methoxyethoxy)aluminium hydride) additionally reduces the C-O-C bonds as evidenced by the model reaction of polyethylene oxide degradation. Nevertheless, the yield in OH groups was not increased because of the partial reduction of O functional groups to CH<sub>2</sub> groups.

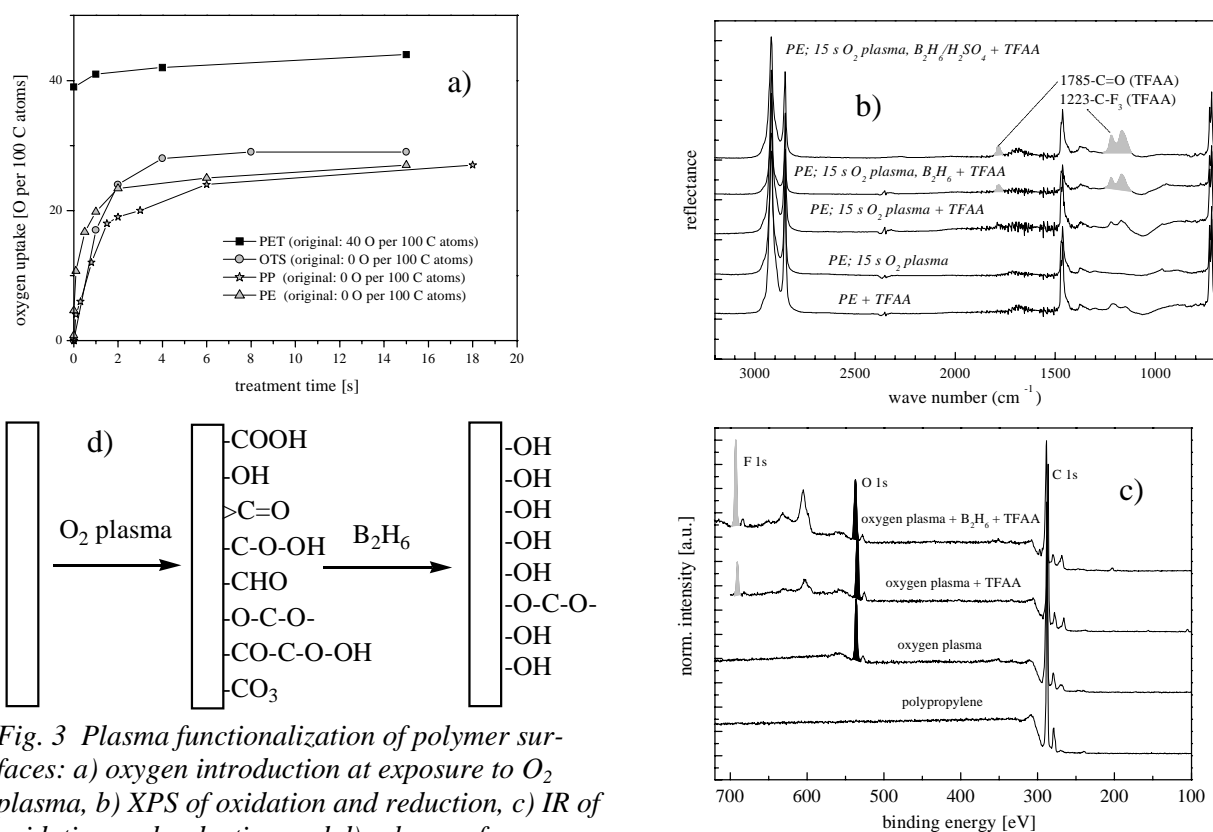


Fig. 3 Plasma functionalization of polymer surfaces: a) oxygen introduction at exposure to O<sub>2</sub> plasma, b) XPS of oxidation and reduction, c) IR of oxidation and reduction and d) scheme of processes

### 3.2. Bromination

The plasma surface bromination and chlorination with HCBBr<sub>3</sub> or CCl<sub>4</sub> are much more selective than the oxidation in the O<sub>2</sub> plasma. Modifying polymer surfaces in the plasma it is very seldom or nearly impossible to find a process with such a high selectivity of more than 85 %. In this work, up to 40 Br per 100 C atoms have been introduced (Fig. 4).

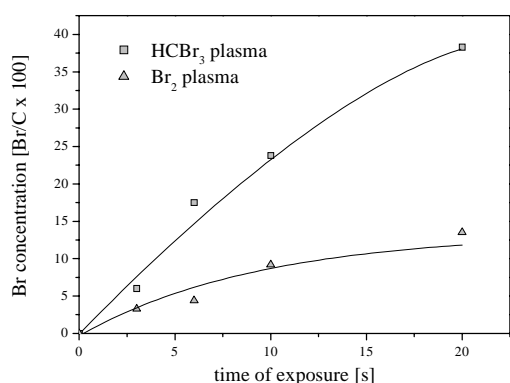


Fig. 4 Plasma bromination with HCBBr<sub>3</sub> and Br<sub>2</sub>

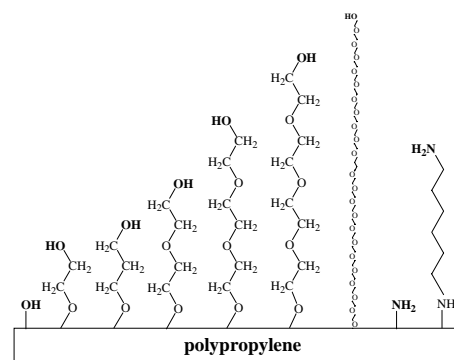
### 3.3. Spacer introduction

Subsequent wet-chemical synthesis after Williamson or Gabriel-like open a way to exploit the high selectivity of the initial bromination step to achieve a highly selective OH or NH<sub>2</sub> functionalization bonded to a spacer molecule with a chain length of free choice (Fig. 5). The yield was 6 NH<sub>2</sub> or 6 OH terminated spacers (cf. Fig. 5). Using undecenylsilane as spacer, linked to OH groups, in maximum 9 spacer molecules could be grafted.

Fig. 5 Schematics of grafted spacers onto C-Br groups

### 3.4. Radical quenching

Vinyl monomers were grafted after precedent Ar plasma treatment. The degree of grafting was measured by XPS. However, homopolymerization influences the results. 2 to 5 monomer molecules could be grafted after finishing the Ar plasma and introducing the monomer vinylsilane. Using NO as small permanent radical the same number of C radical sites at the polymer surface were derivatized. The concentration of introduced NO onto acetylene plasma polymer layers was in the range of 5 to 8 sites per 100 C



atoms.

### 3.5. Plasma polymerization of functional group carrying monomers

The new functionalization method consists of the deposition of very thin plasma polymer layers (20 to 100 nm) of functional group carrying monomers in pulsed plasma. Thus, with allyl alcohol in maximum 31 OH groups per 100 C atoms were measured with a selectivity of about 95% and a significant stability at long-time exposure to the air. Allyl amine was used to produce primary amino groups in concentrations of at least 18 NH<sub>2</sub> per 100 C atoms in maximum. Side reactions were observed during the storage in air such as oxidation of the amino groups. Carboxylic groups could be produced using acrylic acid with a maximum concentration of 24 COOH per 100 C atoms. The most prominent side reaction was the decarbonyla-

tion/decarboxylation of the acid group during the plasma deposition. Fig. 6 shows the C1s signals of homopolymers before and after derivatization.

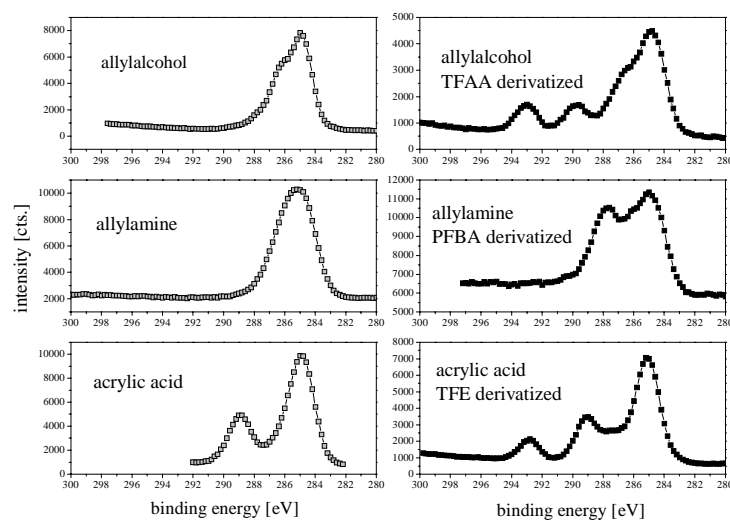


Fig. 6  
C1s signals of functional groups carrying polymers before and after derivatization

### 3.6. Copolymerization for adjusting the exact concentration of functional groups

The variation of the density of functional groups using the pulsed plasma polymerization of functional group bearing monomers was possible by the plasma chemically initi-

ated radical copolymerization with a chain-extending monomer such as ethylene or a crosslinker such as butadiene. The density of functional groups could be continuously adjusted (0 to 30 OH, 0 to 18 NH<sub>2</sub> and 0 to 24 COOH groups per 100 C atoms). However, the re-

activity of both comonomers must be similar, which can be expressed in terms of copolymerisation parameters as known from classic polymer chemistry. In Fig. 7 the copolymerisation of allyl alcohol and styrene is presented showing from 0 to 60 % allyl alcohol in the precursor mixture homopolymerization and from 60 to 100% copolymerization.

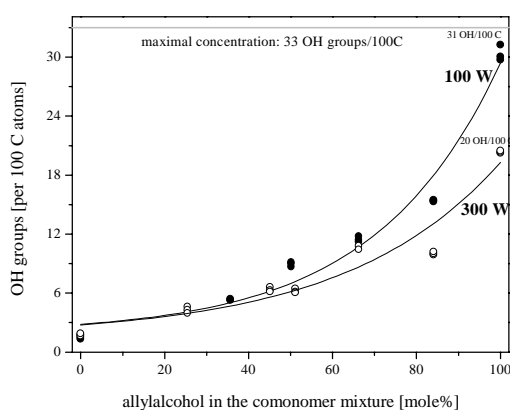


Fig. 7  
Example for the copolymerization of allyl alcohol and styrene as comonomers

## Conclusions

Aim of this work was to compare the efficiency of different routes of plasmachemical formation of functional groups at polymer surfaces. Thereby, the maximal obtainable concentration of functional groups (yield), the percentage of the wished functional group among all formed functional groups (selectivity) and the simplicity of the used plasmachemical process were taken into consideration.

The plasma modification of polymers is able to break covalent bonds at surface (and also in the surface-near layers). This is a prerequisite for the covalent bonding of plasma gas-specific functional groups onto carbon atoms at the surface. However, the unavoidable scission of covalent bonds of the polymer backbone results in polymer degradation and crosslinking simultaneously as

well as formation of (trapped) radical sites followed by formation of peroxy groups and auto-oxidation of the polymer. The consequence is a loss in mechanical strength (formation of a weak boundary layer) and, on the other hand, the formation of a broad variety of functional groups. It could be shown that only a compromise leads to an acceptable functionalizing of polymer surfaces without a significant loss in mechanical strength. This could be realized by low power-input and maximum exposure times to the plasmas of about 2 s [2]. To qualify the broad variety of functional groups could be limited using post-plasma chemical reduction as a second process. In addition, the bromination of polymer surfaces proved to be a very selective single-step plasma process. C-Br groups are well suited for further chemical processing.

The general concept for the plasma polymerization was to lower the power-input as much as possible and, therefore, the average energy input per monomer molecule to  $<0.1$  eV. Using chemically reactive monomers, which are qualified to undergo a classic radical chain propagation only one activation incident with  $\approx 1.5$  eV is required to start a chain polymerization with a resulting molar mass of 100.000 and the respective polymerization degree of  $X \approx 1000$ . Therefore, 0.0015 eV per monomer are needed to initiate a chemical polymerization. The advantage of a chemically produced polymer compared to a plasmachemically synthesized material is the defined structure, the exact stoichiometry, the presence of a supermolecular structure (crystallinity), the defined properties and the significantly better ageing stability. Thus, we intend to exclusively initiate such a chemical polymerization through the plasma. The chain propagation should be performed on such a pure chemical way. In practice, the low pressure and the low collision rate of monomers with a radical site of a growing macromolecular chain limit the propagation. Terminations as radical recombination, chain transfer and disproportionation limit the chain length. Therefore, the use of pulsed plasma is necessary. Precondition of such a chemical chain reaction are monomers with active double bonds as vinyl or acrylic groups or moderately suited allyl groups and dienes.

All results are summarized in Table 1.

	<b>Process</b>	<b>Yield [%]</b>	<b>Selectivity [%]</b>
1	O <sub>2</sub> plasma and B <sub>2</sub> H <sub>6</sub> reduction	10...14	55
2	Grafting to radicals	2...7	$\approx 35$
3	Bromination	20...40	85
4	Grafting of spacers	4...9	80
5	Homopolymerization-OH	28...31	85-95
5	Homopolymerization-NH <sub>2</sub>	12...18	40-55
5	Homopolymerization-COOH	18...24	55-75
6	Copolymerization	0-31	55-95

Tab. 1 Comparison of yield and selectivity of different plasma methods for introducing functional groups

## References

- [1] R. G. Nuzzo and G. Smolinsky, *Macromolecules*, **17**, 1013 (1984)
- [2] J. Friedrich, I. Retzko, G. Kühn, W. Unger and A. Lippitz, in: *Metallized Plastics 7: Fundamentals and Applied Aspects*, K. L. Mittal (Ed.), pp. 117-142, VSP, Utrecht (2001)
- [3] I. Retzko, J. F. Friedrich, A. Lippitz and W. E. S. Unger, *J. Electr. Spectr. Rel. Phenom.* **121**, 111 (2001)
- [4] G. Kühn, I. Retzko, A. Lippitz, W. Unger and J. Friedrich, *Surface Coatings Technol.* **142-144**, 494 (2001) J. Friedrich, I. Retzko, G. Kühn, W. Unger and A. Lippitz, in: *Metallized Plastics 7: Fundamentals and Applied Aspects*, K. L. Mittal (Ed.), pp. 117-142, VSP, Utrecht (2001)
- [5] J. Meisel and H.-J. Tiller, *Z. Chem.*, **7**, 275 (1972)
- [6] H. Yasuda and T. Hsu, *J. Appl. Polym. Sci.*, **20**, 1769 (1976)
- [7] J. Friedrich, G. Kühn, R. Mix, I. Retzko, V. Gerstung, St. Weidner, R.-D. Schulze and W. Unger, in: *Polyimides and Other High Temperature Polymers: Synthesis, Characterization and Application*, Vol. 2, K. L. Mittal (Ed.), VSP, Utrecht, in press.
- [8] J. F. Friedrich, W. E. S. Unger, A. Lippitz, Th. Gross, P. Rohrer, W. Saur, J. Erdmann and H.-V. Gorsler, *J. Adhesion Sci. Technol.*, **9**, 575 (1995).

## Acknowledgment

This work was financed by VDI-TZ Düsseldorf under grant 13N7779.

# Pulsed plasma initiated homo- and copolymerisation - molar masses

J. Friedrich, V. Gerstung, R. Mix, G. Kühn, St. Weidner

*Bundesanstalt für Materialforschung und -prüfung (BAM) / Federal Institute for Materials Research and Testing, Unter den Eichen 87, D-12205 Berlin, Germany*

## Abstract

Molar masses (MM) and molar mass distributions (MMD) of plasma polymerised styrene, allyl alcohol, and their copolymers were investigated by means of thermal field-flow fractionation (ThFFF). The influence of various plasma parameters (continuous or pulsed plasma and various wattage) on molar mass and molar mass distribution was analysed in terms of changes of the relative amount of polymeric and highly cross-linked compounds. Molar masses were estimated by comparison with polystyrene standards.

## 1. Introduction

Plasma polymer layers can be prepared either by the usage of continuous wave plasma or using the pulsed plasma technique introduced by Tiller [1]. Synthesized by the first method, plasma polymers are often irregular in structure and chemical composition, because of relative high energy input and fragmentation of monomers during plasma-on time. In addition, most of these polymer layers are highly cross-linked and insoluble in nearly all organic solvents. But for further processing, polymer layers with defined chemical structure and degree of cross-linking are desired. These properties can be obtained by controlling of processing parameters, like pressure, gas flow or energy input. Especially the energy input is quite different for both methods. The pulsed plasma polymerisation has the benefit that smaller amounts of power are inserted in the system. During the plasma-on time, radical polymerisation should only be started without fragmentation of the monomer. The chain propagation takes place throughout the plasma-off period. Thereby, fragmentation and cross-linking are repressed. Polymers produced by this method are more comparable in composition and structure to commercial polymers than those made by continuous plasma technique. This was approved for different monomers with XPS, NEXAFS, IR, etc. [2, 3].

The pulsed plasma was produced by using a radio-frequency discharge, which was pulsed with duty cycles in the range of 0.1 to 1 and frequencies of  $10^1$  to  $10^5$  Hz. The power input was 3 to 300 W and the pressure amount 25 Pa. The substrate has floating potential and was placed within the plasma glow. Details of the experimental design are summarized in [1-3].

Besides branched or cross-linked structures, plasma polymer products also contain oligomers, polymers, high molar mass compounds, and gel particles. Molar mass and chemical heterogeneity of the polymer system complicates the characterisation. Analysis with chromatographic standard methods like size exclusion chromatography (SEC) or high performance liquid chromatography (HPLC) can only be accomplished for soluble products. However, soluble polymers with very high molar masses can not be analysed with these two methods due to the necessity of stationary phases and the problems which arise therewith, for example blocking of columns, exclusion limits, adsorption, and shear degradation.

Field-flow fractionation (FFF) provides one approach to solve these problems, because FFF is not subjected to restrictions of the column material. This method represents an "expansion" of SEC into the range of ultrahigh molar masses [4]. Due to the fact that this method is still not popular, it shall be briefly reported here.

The field-flow fractionation is a chromatography-like method described by J. C. Giddings in 1966 [5]. Separation is carried out in a small channel, which is formed by a spacer between two parallel plates. The driving force for fractionation is caused by an external field applied perpendicular to the channel and therefore, stationary phases are not essential. As a result of this special build-up, field-flow fractionation can be used for separation and characterisation of polymers with very high molar masses, up to  $10^{18}$  Da. Suspended or colloidal particles, supramolecular structures, aggregates, polymer networks, latices, and micro or macro gels in organic or aqueous solvents can be analysed without filtering and loss of information.

In this investigation a thermal field was applied and the method is called thermal field-flow fractionation (ThFFF). A temperature gradient is applied across the channel by electrical heating of the upper plate and cooling the bottom plate (accumulation wall) with running tap water. This temperature difference causes a migration of particles towards the accumulation wall due to thermal diffusion. As a result, a concentration gradient is formed at this wall. The normal diffusion counteracts this formation and in the

stationary state an equilibration between these two forces is reached. Depending on the quotient of both forces, particles were arranged at different distances to the cold wall. Because of the parabolic flow profile in the channel, they elute at different retention times.

The thermal diffusion coefficient is nearly independent of the molar mass, but it depends on the chemical composition of polymer and solvent [6, 7]. In contrast to that, ordinary diffusion depends on molar mass. Thus, polymers in ThFFF are fractionated according to chemical composition and molar mass. If polymers with similar chemical composition are analysed, separation only takes place according to molar mass. In that case large particles will be longer retained because of the smaller ordinary diffusion coefficient.

In this work molar masses respectively molar mass distributions of plasma polymerised styrene, allyl alcohol, and their copolymers were determined. For polystyrene the influence of different plasma parameters (continuous or pulsed plasma) on MM and MMD was analysed. The effect of different wattage and percentages of reactant monomers for pulsed plasma copolymerisation of styrene and allyl alcohol was investigated. The amount of ultrahigh molar mass polymers and polymers, which are comparable in molar mass and distribution to polymers synthesized by standard polymerisation methods, should be proved. A multiangle laser light scattering (MALLS) detector was used for detection.

## **2. Experimental**

### **2.1 Materials**

Styrene and allyl alcohol (Merck, Germany) were freshly distilled before use. Tetrahydrofuran (THF, p.a., Merck, Germany) was filtered and degassed before application. Polystyrene standards Easical (Polymer Labs, U. K.) were used as purchased.

### **2.2 Plasma polymerisation**

Polymerisation and copolymerisation of styrene and allyl alcohol were realised with a plasma reactor Labovac Ilm plasma 1200 (Saskia, Ilmenau, Germany). The construction of the reactor was described in detail in [8]. Low pressure conditions were achieved with an oil-pump connected to a turbo molecular pump. The plasma was generated with a high frequency electrode implemented in the reactor vessel. In order to establish a pulsed plasma mode a generator (CESAR 136 RF Power Generator, Dressler, Germany) was used. The duty cycles (plasma-on time to plasma-on plus plasma-off time) were 0.1 with a frequency of 1000 Hz. Styrene was polymerised with a continuous plasma (3 W) and a pulsed plasma with an energy input of 30 W (3 W effective using a duty cycle of 0.1). For allyl alcohol only pulsed plasma was applied (300 W, 30 W effective). The copolymers were prepared by pulsed plasma technique with 100 W and 300 W (10 W and 30 W effective). All plasma polymers were deposited on glass targets. For analysis, the thin polymer films were removed by scratching.

### **2.3 Thermal Field-Flow Fractionation/Multiangle Laser Light Scattering (ThFFF/MALLS) Analysis**

The investigation of the MM and MMD of cross-linked products has been carried out with thermal field-flow fractionation (Polymer Fractionator Model T-100, FFFractionation, LLC, Salt Lake City, Utah, USA). The amount of low and ultrahigh molecular weight polymers was measured with a MALLS detector (DAWN DSP, Wyatt Technology Corp., Santa Barbara, California, USA).

Polymer solutions were prepared by dissolving or suspending of 2 mg (homopolymers) or 5 mg (copolymers) of the raw product in 1 ml THF. Solutions were shaken for 12 to 18 hours and analysed without filtering. The injected sample volume was 20 µl (homopolymers) or 100 µl (copolymers) and the flow rate was 0.2 ml/min. The start temperature difference of the temperature program was 70° C. The investigation of polyallyl alcohol could only be accomplished for the soluble fraction, because these polymers are highly cross-linked and were inadequately dissolved. The concentration of polystyrene standard solutions was 1 mg/ml in THF.

## **3. Results and discussion**

### **3.1 Homopolymerisation**

The insets in Fig. 1 show two fractograms of the plasma polymerised styrenes (PS). Analysis by ThFFF results in two peaks and very high molar masses for both plasma processes. Molar masses and distributions were comparable for either method. The main difference could be observed in the intensity of peaks (MALLS detector, 90° signal), i. e. for the concentration of the produced plasma polystyrenes. The first peak, linear and weakly branched polymers with a molar mass of about 20 kDa, has a higher intensity for the

pulsed plasma polystyrenes than for those synthesized with the continuous plasma method (inset 1). The molar mass and molar mass distribution are comparable to polymers made by standard polymerisation techniques.

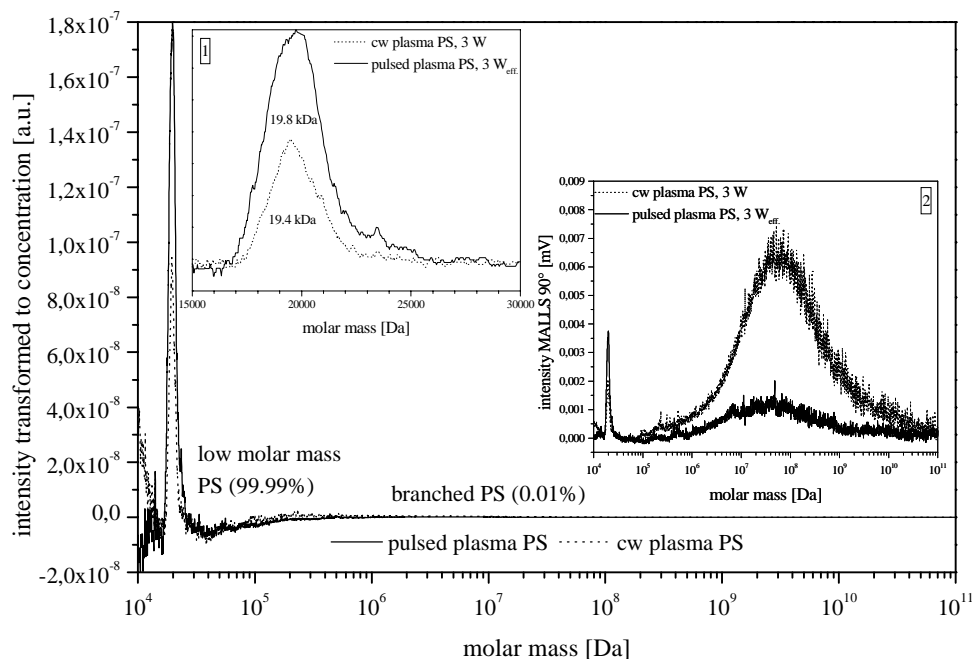


Fig. 1. Fractograms of plasma polymerised styrene (continuous wave and pulsed plasma technique), MALLS 90° signal transformed to concentration. (Insets show original MALLS 90° signal intensity.)

The lower intensity of the second peak, which can be attributed to branched and cross-linked polymers with a molar mass about 44 MDa, clarifies that using the pulsed plasma polymerisation the rate of ultra-high molar masses and cross-linked structures can be diminished.

To verify these results, a transformation of the MALLS 90° signal to concentration was accomplished with polystyrene standards (Easical®). The light scattering intensity is the product of molar mass and concentration. Therefore, very high molar masses are overemphasised. With this approach, it becomes clear that more than 99% of the plasma polymerised styrene has a molar mass about 20 kDa (Fig.1). Beside this low molar mass fraction, only very small quantities of ultra high molar mass polystyrene exist.

The homopolymerisation of allyl alcohol was exclusively realised with the pulsed plasma method, because the products emerging by the continuous wave method are highly cross-linked and can not even be suspended. Even using the pulsed plasma technique, cross-linked and indissoluble polymers were generated. Thus, only the soluble fraction was analysed by ThFFF. However, as well for this solution very high molar masses were found (Fig. 2). The first peak in the fractogram, with a molar mass about 80 kDa, can be interpreted as linear, weakly branched homopolymer. The second peak with broad distribution represents high molar mass polymers. This peak and the shoulder on the right hand side can be accounted for branched and weakly cross-linked polymers. A comparison with polystyrene standards Easical® gives a molar mass about 2 MDa.

Due to the fact that polyallyl alcohol standards are not available, polystyrene standards were used for this estimation. It must be considered that this procedure can only be a relative comparison, because polymers with different chemical composition were compared with each other. Mainly for ThFFF, which separates compounds subjected to molar mass and chemical composition, this fact must be taken into account. Furthermore it can not be neglected that polystyrene standards consist of linear macromolecules, whereas plasma polymers contain a high ratio of branched and cross-linked structures. Hence, different conformations and hydrodynamic volumes result. So, for all molar mass estimations of plasma polymers only limited statements about molar masses are possible.

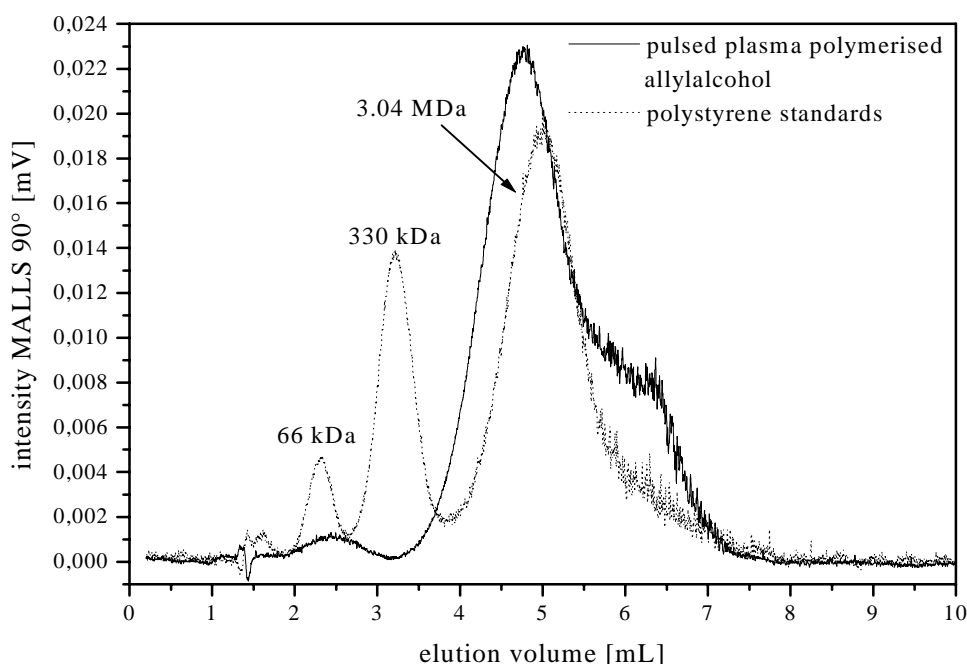


Fig. 2. Fractograms of pulsed plasma polymerised allyl alcohol and polystyrene standards Easical<sup>®</sup>. (Comparison was done for the estimation of molar masses of polyallyl alcohol.)

### 3.2 Copolymerisation

Styrene and allyl alcohol were copolymerised in a pulsed plasma with different percentages of monomers and wattage. With the pulsed plasma technique, functional groups can be inserted into the plasma polymer layers under structural retention. The density of functional groups on the surface is important for further processing and for surface characteristics. It can be controlled by the content of chain extending monomer (styrene) in the reaction system and consequently in the polymer layer. So the various percentages of monomers were used to synthesise copolymers with a graded amount of functional groups. With ThFFF the influence of different wattage should be studied regarding to MM and MMD for the different compositions.

In Fig. 3 the fractograms of pulsed plasma polystyrene, two allyl alcohol/styrene pulsed plasma copolymers (66.2 and 84.1 mol-% allyl alcohol,  $300\text{ W} \triangleq 30\text{ W}_{\text{eff}}$ ), and polystyrene standards Easical<sup>®</sup> are shown. For all plasma polymerised polymers two peaks were detected. The first peak in each fractogram can be attributed to a molar mass about 20 kDa. This was estimated using polystyrene standards. Their molar mass distributions are comparable to commercial polymers. However, the signal intensity, i. e. the concentration, is different for all three samples. The highest intensity showed the peak representing the copolymer with 66.2 mol-% allyl alcohol. The intensity of the other copolymer (84.1 mol-% allyl alcohol) is nearly three times smaller. In addition to the low molar mass polymers, very high molar mass compounds with broad distributions were detected. The highest intensity was found for plasma polymerised polystyrene. Its molar mass range is about 1 to 10 MDa compared with the polystyrene standards. For the copolymer with 66.2 mol-% allyl alcohol a very broad molar mass distribution was measured, too. The peak maximum is approximately 1 MDa. The peak corresponding to the second copolymer shows a narrow distribution with a peak maximum of about 4 MDa. In this place, it should be pointed out, that the same restrictions for estimation of molar masses of chemically and structurally different (polystyrene) standards have to be considered as described for the polymerisation of allyl alcohol.

Beside the different molar masses and distributions for the plasma polymerised high molecular weight polymers the ratio of the signal intensities of low and very high molar mass compounds varies for different percentages of reactant monomers. The intensities of the high molar mass peaks of the copolymers are nearly the same and both smaller than the intensities of the low molar mass peaks. But the latter



intensities are quite different for the two copolymers. The amount of polymers structurally comparable to conventional polymers is much higher for the copolymer with the lower mol-% content of allyl alcohol in the starting mixture. In combination with the high molar mass fraction it can be stated that the ratio of low to high molar mass polymers is much higher for the reactant mixture with the lower mol-% of allyl alcohol. The signal intensities for the two polystyrene peaks show a different situation. The signal of the high molar mass polymer is very intensive and nearly two times higher than that for the low molar mass polymer. It can be concluded that the amount of branching and cross-linking is much higher for the plasma homopolymerisation of styrene.

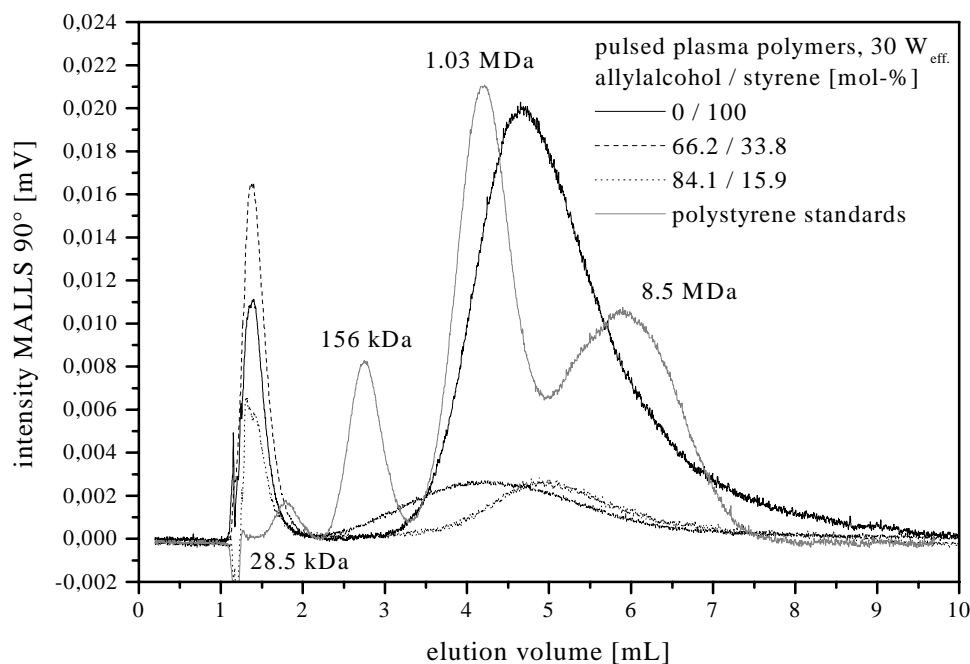


Fig. 3 Fractograms of pulsed plasma polymerised styrene and pulsed plasma copolymerised allyl alcohol/styrene with different percentages of reactant monomers (30  $W_{\text{eff.}}$ ). Comparison with polystyrene standards Easical®.

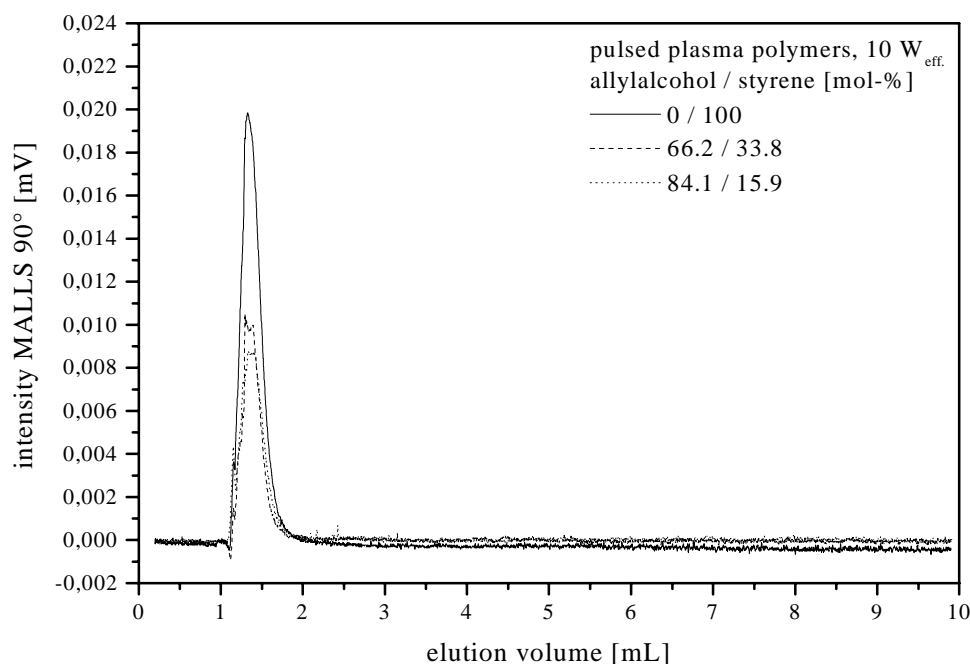


Fig. 4 Fractograms of pulsed plasma polymerised styrene and pulsed plasma copolymerised allyl alcohol/styrene with different percentages of reactant monomers (10  $W_{\text{eff.}}$ ).

Interestingly, the pulsed plasma polymerisation at 10  $W_{\text{eff}}$  of the same monomers and mol-% led to different results (Fig. 4). High molar mass polymers were not detectable. The reduction of the effective input power from 30  $W_{\text{eff}}$  to 10  $W_{\text{eff}}$  totally changes the composition of the obtained polymer products. Compared to the polymers synthesized at 30  $W_{\text{eff}}$ , the low molar mass polymers elute at the same retention volume and show similar MMD. The highest signal intensity was obtained for polystyrene. This signal was almost twice as intense as for the 30  $W_{\text{eff}}$  product. The amounts of pulsed plasma copolymerised products are comparable for both monomer percentages. In contrast to the polymerisation at 30 W, the amount of copolymers formed at lower allyl alcohol concentrations decreases. For the higher allyl alcohol concentration their amount increases slightly.

#### 4. Conclusion

Compared to the continuous wave plasma polymerisation mode the principle of pulsed plasma polymerisation can be used to diminish the amount of highly cross-linked products and to enhance the low or moderate molar mass fraction. This was demonstrated for the homopolymerisation of styrene.

Using this method, polymers with MM and MMD comparable to commercial polymers can be obtained. Different plasma parameters were applied in order to control the characteristics of the products, such as the amount of high molar mass polymers and branched or cross-linked compounds. This was shown for the copolymerisation of allyl alcohol and styrene.

The characterisation of formed high molar mass and structurally heterogeneous polymers was performed with ThFFF. Only field-flow fractionation is capable to separate these ultra high molar mass polymers without loss of information. Low molar mass polymers could be detected along with branched and cross-linked products. For the latter the comparison with polystyrene standards results in molar masses above 40 MDa. With the same approach molar masses about 20 kDa were detected for polymers with moderate molar masses. Their MM and MMD are close to conventionally synthesized polymers.

A separation of this fraction can be carried out by ThFFF, which enables their characterisation by SEC or matrix-assisted laser desorption/ionisation time of flight mass spectrometry (MALDI-TOF MS). First attempts were carried out, though further investigations are necessary.

#### Acknowledgements

This work was financed by VDI-TZ Düsseldorf under grant 13N7776.

#### References

- [1] J. Meisel and H.-J. Tiller - Z. Chem., **7**, 275 (1972).
- [2] J. Friedrich, I. Retzko, G. Kühn, W. Unger and A. Lippitz - Metallized Plastics 7: Fundamental and Applied Aspects, K. L. Mittal (ed.), VSP, Utrecht, 2001, 117-142.
- [3] G. Kühn, I. Retzko, A. Lippitz, W. Unger and J. Friedrich - Surf. Coat. Technol., **142-144** (2001) 494-500.
- [4] J. C. Giddings - J. Chrom., **125** (1976) 3-16.
- [5] J. C. Giddings - Sep. Sci., **1**, 123 (1966).
- [6] M. E. Schimpf and J. C. Giddings - Macromolecules, **1987**, 20, 1561.
- [7] M. E. Schimpf and J. C. Giddings - J. Polym. Sci.: Part B: Polym. Phys., **27**, 1317 (1989).
- [8] St. Weidner, G. Kühn, R. Decker, D. Roessner and J. Friedrich - J. Polym. Sci.: Part A: Polym. Chem., **36**, 1639 (1998).

# **Pulsed corona discharges: Fundamentals and environmental applications**

E. M. van Veldhuizen

*Department of Physics, Technische Universiteit Eindhoven, The Netherlands*

## **Abstract**

This paper describes the state-of-the-art of the knowledge on pulsed positive coronas as used nowadays in environmental applications. The demands on the pulsed power source are a rise time of tens of nanoseconds and a duration of far less than one microsecond. This leads to efficient radical production and negligible gas heating. It is shown that the modeling of this type of discharge is still only in an initial phase. Applications are emerging at industrial scale in areas such as removal of  $\text{NO}_x$ , bad smell and tar, also due to the appearance of pulsed power supplies with sufficient power (up to 100 kW), good efficiency ( $\sim 90\%$ ) and long life time.

## **1. Introduction**

Corona discharges appear in a large variety, their main common features are an asymmetric electrode pair and atmospheric working pressure. Differences are found in electrode shape, gap distance, pulse shape and level of the applied voltage and gas composition. Even pulsed corona discharges are distinguished according to their rise time. In precipitators pulsed or “intermittent” discharges are used with millisecond rise time, microsecond rise times are used in “square wave” excited barrier discharges. The fastest rise times used are in the range of tens of nanoseconds. This last case is of particular use in environmental applications [1]; therefore it is the specific topic of this contribution.

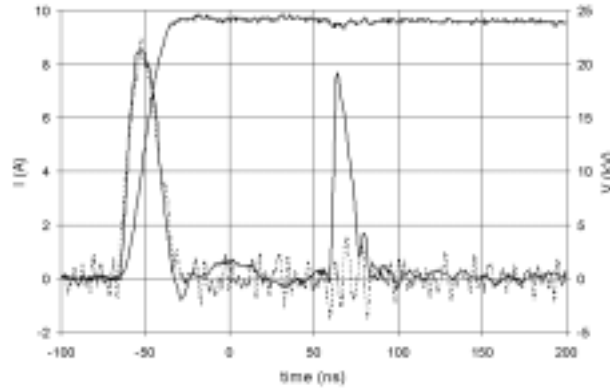
This paper gives an overview of fundamental studies on pulsed positive corona made in the past [1-2]. It is striking that up to now still a lot of new information can be obtained by just taking photos [3-5]. The required resolution in space and time, i.e. micrometers and nanoseconds resp., is still not easily obtained and detailed measurements of plasma parameters have been performed only sporadically under limited conditions. The theoretical description encounters the same difficulties: steep gradients in time and space in combination with complicated and unknown boundary conditions. The state-of-the-art is 2D simulation using a drift-diffusion fluid model [1, 6]. These models of positive streamers are still quite limited, i.e. they use very small gaps, too high fields and they do not show branching of streamers. A recently developed model of the negative streamer does show instability in a deterministic 2D model [7] that looks to be the onset of branching. Again, the model requires unrealistically high electric field strength.

The particular feature of the pulsed corona discharge with the fast rise time is its high efficiency for radical production. This makes it suitable for chemical applications where ozone generation is one of the best-known examples. Other possibilities are treatment of waste gases for the removal of  $\text{SO}_2$ ,  $\text{NO}_x$ , VOCs, etc. [1, 8]. In all these cases the corona oxidizes the undesired species, not only by the ozone that it creates but also by O and OH radicals and UV photons. Recent improvements in the pulsed power supplied bring medium scale applications within range [8]. Removals of bad smell, solvents and  $\text{NO}_x$  in small industries are the most promising opportunities at present. A second, less developed subject is water cleaning. Removal of phenol from water is demonstrated with a good efficiency [9]. Up scaling of this process is under investigation [10].

## **2. Fundamental measurements**

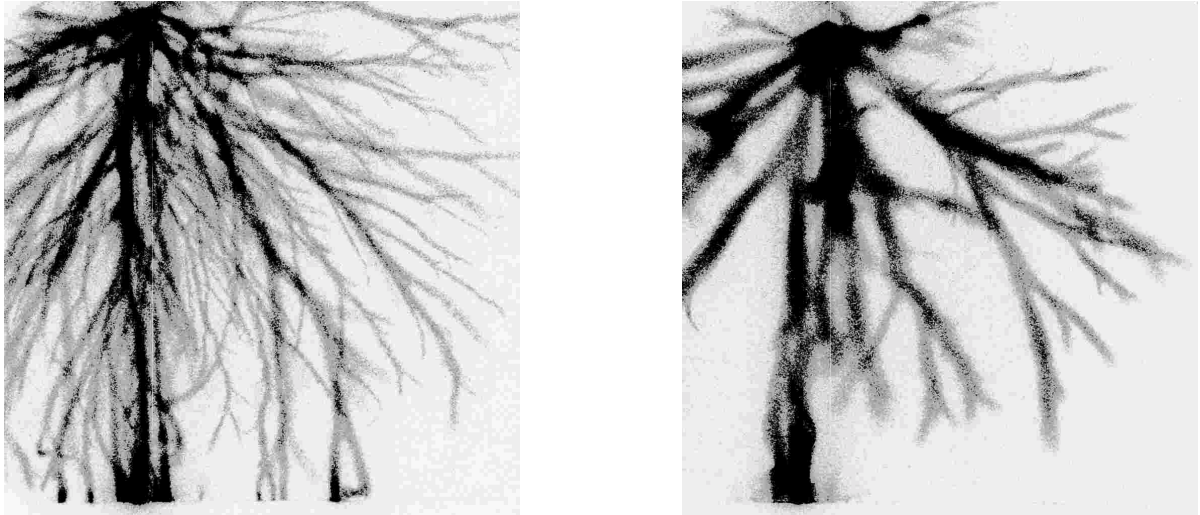
The pulsed corona discharge requires a specific power supply. The main parameters are the rise time and the maximum level. The voltage level at which corona occurs depends evidently on the electrode geometry and the discharge medium but further it depends on the rise time and there is an influence of the impedance of the pulsed power source. This leads to a great emphasis on what the requirements are for the pulse rise time. Since the corona discharge develops in the form of streamers, one requirement results from the fact that the streamer propagation velocity is in the range of 0.1-1 mm/ns. This gives a transition time across the gap in the range of 50-200 ns for most practical situations, so a rise time shorter than 50 ns seems appropriate. Values of 20-30 ns are readily achieved by spark gap fired pulsed power sources [1, 2]. An upper limit seems to appear when the

voltage rate of rise becomes greater than 10 kV/ns. The diameter of the streamer then becomes much larger, i.e.  $\sim 10$  mm; this phenomenon is called ionization wave [3]. This type of discharge is up to now only very rarely applied on gas cleaning. It is expected that the electron energy will be higher but the overall efficiency is not yet determined. To stay in the usual streamer region a lower limit of the rise time is roughly 10 ns. An example of the electrical characteristics of a positive corona pulse is given in fig. 1. It shows the voltage and current of a 25 mm point-plane gap in air. The first current peak is purely capacitive charging of the electrodes; the second peak is the corona discharge. The time delay for corona initiation is stochastic; this case is for clarity an example of an extremely long delay, usually both current pulses overlap.



*Fig. 1: Voltage (upper line) and current of a typical pulsed corona discharge (straight line total current, dotted line calculated capacitive current)*

The appearance of corona discharge also shows a large variety, as is known for a long time [11]. Recent improvements of CCD cameras with gated image intensifiers have greatly increased the investigation possibilities [3]. Fig. 2 gives two examples of photos taken from the same gap as in fig. 1, both at 25 kV pulse maximum. The only difference in making these photos is that for fig. 2a the power supply was fitted with a semiconductor switch and for fig. 2b a spark gap. In [3] it is argued that the most probable cause is that the semiconductor switch is resistive and the spark gap is inductive.



*Fig. 2: Examples of branching of pulsed corona streamers*

Point-plane corona is often thought of as one thin channel between anode and cathode. This situation can be obtained, e.g. with a self-repetitive DC corona. It is also always encountered in numerical simulations where it is due to the rotational symmetry of the 2-D model. The branching is, however, well known since the first

investigations of these discharges [11]. The extreme amount of branching as seen in fig. 2a is obtained at a voltage that is just below breakdown voltage. Such a voltage level is required in cleaning applications to obtain the shortest possible residence time in the reactor thereby limiting the investment cost of the equipment. Breakdown on the other hand must be avoided because the high current of the spark may damage the electrodes and the power supply and the energy that goes into it is wasted. At present pulsed power supplies up to 100 kW with high efficiency and long life time are being developed [8], [12].

Detailed information of processes inside the corona is very limited [1], [11]. Emission spectroscopy has been applied and from its spectrum one can derive some information on plasma parameters [2]. Fig. 3 and 4 show two examples of spectra from corona in air in the near UV range. The spectrum is dominated by nitrogen. In fig. 3 several peaks are seen of the nitrogen Second Positive System that originates from the  $C \rightarrow B$  transition of neutral nitrogen. Each line has an asymmetric rotational fine structure. At 391.4 nm one line is observed of the nitrogen ion  $A \rightarrow X$  transition (First Negative System). The ratio of the intensities of ion and neutral lines is a measure of the average electron energy of the electrons that cause the optical emission. From fig. 3 a value of 10 eV is estimated [2]. This value must be assigned to the streamer head, which is by far the strongest emitting part. By specifically looking at later time stages the electron energy of the streamer channel can also be obtained, this is found to be  $\sim 1$  eV [2]. Similar results are obtained recently in barrier discharges using cross correlation spectroscopy [13].

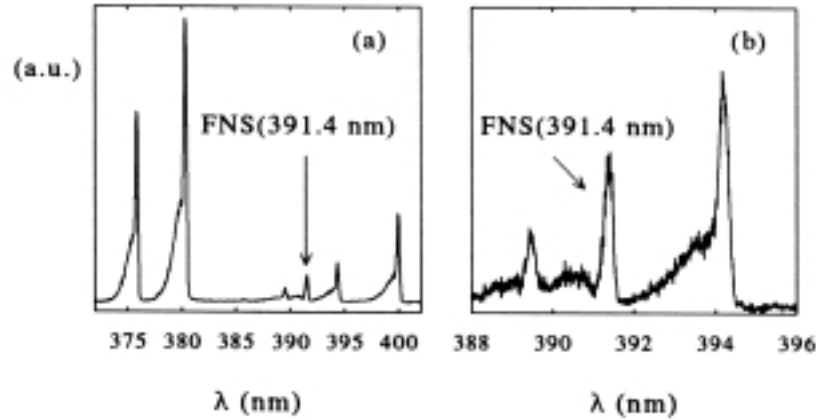


Fig. 3: Spectrally resolved optical emission of pulsed corona discharges in a wire-plane gap [2].

In fig. 4 the rotational fine structure of the strongest nitrogen neutral line is shown in more detail (upper curve). The upper curve is measured; the lower is simulated using a gas temperature of 300 K. This spectrum is recorded in a time interval of 50-200 ns after corona initiation. It shows that here the gas is still at room temperature so the corona current does not heat it.

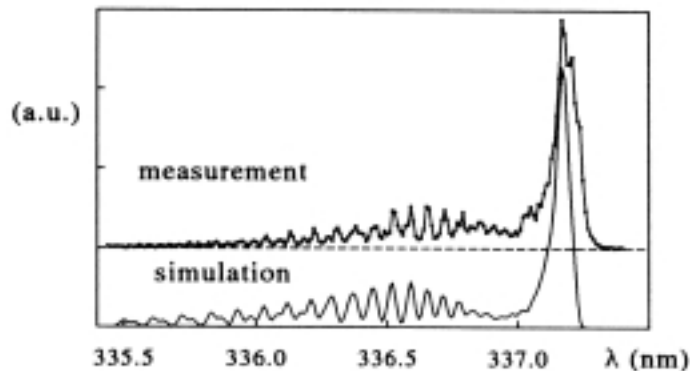


Fig. 4 Rotational structure of the (0,0)-transition of  $N_2$  in a wire-plane corona discharge [2].

It was also observed by Schlieren photography that after  $\sim 1 \mu s$  no discharge paths were visible. At later times heated channels are seen and they are most pronounced during  $\sim 50-100 \mu s$  after the discharge start. This heating

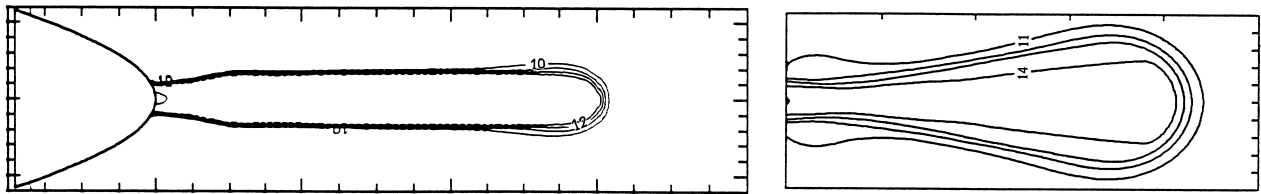
is probably due to deexcitation of vibrationally excited molecules that have a decay time in this range. The highest temperature observed inside the channels due to this effect is  $\sim 350$  K, so still a modest increase. Higher temperatures are sometimes recorded in different situations. For the self-repetitive DC-corona 600 K is reported, in this case the discharge takes the same path for each pulse, which gradually increases the temperature. In barrier discharge it is possible to use the discharge current to control the temperature rise. In this way temperatures up to 2000 K have been obtained [1, ch. 11].

Another parameter that is occasionally determined from experiments is the electron density. Up to now this is only done from Stark broadening of hydrogen line. The results are in the range of  $1\text{--}3 \cdot 10^{15} \text{ cm}^{-3}$  [14, 15], these values are more than an order of magnitude higher than those obtained in numerical simulations as can be seen in the next section. Besides these basic plasma parameters many measurements have been performed on products that evolve. Radicals are of course a main issue but they are not easily measured. Advanced methods such as LIF are required [1, ch. 7].

### 3. Simulations

Corona discharges are also studied theoretically but, due to their complex structure with large gradients in space and time, the possibilities for analytical treatment are limited [1, ch. 3]. Numerical models have been created already in the 1960's, but also these must be strongly restricted to stay within the limits of the memory and the calculation speed of contemporary computers. Practically all simulations use the approximation of the fluid model. These are based on conservation equations for the concentrations of charged particles, which includes at least electrons and positive ions and sometimes also negative ions. The transport parameters in these equations are given as a function of the local reduced electric field. The underlying assumption is that all these processes are in equilibrium with the local condition, or in other words the particles under consideration have a distribution function corresponding to the local conditions. This assumption has been validated by comparison with Monte Carlo simulations and it turned out that even with streamer propagation on nanosecond time scale it is not really violated.

Also the geometry of the calculation must be limited. 2-D simulations of a single streamer having rotational symmetry are still state-of-the-art. For gaps larger than 10 cm still only 1.5-D calculations have been reported, i.e. the streamer has a fixed diameter as input variable [16, 17]. A very small amount of 3-D simulations have appeared but only with very limited results [18, 19]. A typical result of a 2-D simulation is given in fig. 5. It shows a streamer on the left in a point-plane gap and on the right in a plane-plane gap. The first case shows a constant streamer diameter and the second an increasing one. These effects are seen also in simulations by other authors. They are, however, not observed in experiments.



*Fig. 5: Simulations of positive corona streamers in a point-plane gap (left) and a plane-plane gap.*

A typical value found for the streamer diameter is  $200 \mu\text{m}$ ; this is similar to experimental values. Occasionally a much larger value of  $\sim 1$  cm is found [6] which is also observed in experiments but under very different conditions.

Very interesting results have recently been obtained using a very basic model for propagation of negative streamer in a non-attaching gas [7]. Under these conditions both negative ions and photo ionization can be left out from the equations. A uniform electrical field strength of  $50 \text{ kV/cm}$  is applied. This leads to instability in the streamer front as shown in fig. 6. In this figure all parameters are indicated in normalized, dimensionless units. The model uses a 2-D approach with cylinder symmetry. The instability develops from a completely deterministic set of equations. It is argued that in a complete 3-D calculation instabilities will develop easier than in this case so probably also at lower field strength.

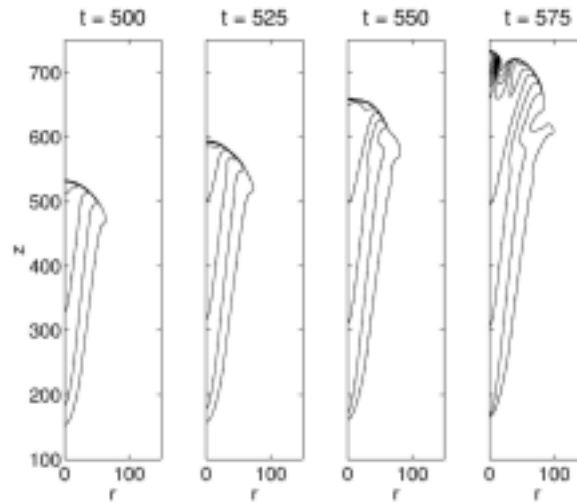
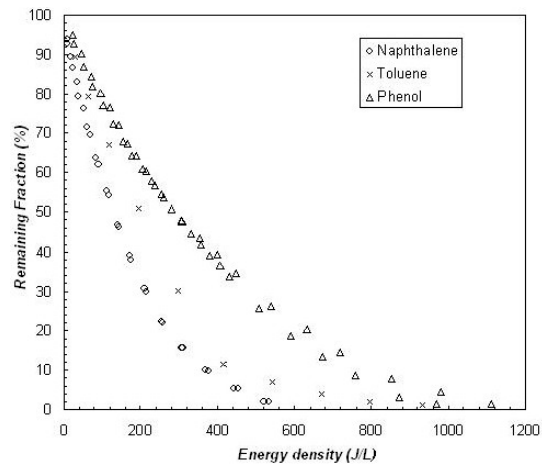
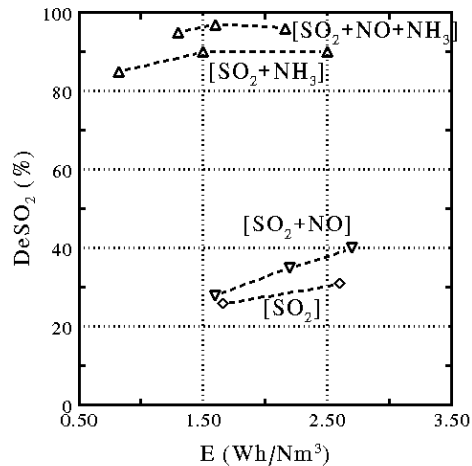


Fig. 6: Simulation of negative streamers in a plane-plane gap at 50 kV/cm.

At present there are still large discrepancies between simulations and experiments and they cover different parts of the parameter space. This is more clearly the case with the applied field strength, which is up to 50 kV/cm in simulations, whereas in experiments 10 kV/cm is an upper limit [3].

#### 4. Applications

Corona discharges are in use in two categories of purposes. One is the production and transfer of electric charge. This process is used worldwide in copiers, laser printers and dust precipitators [1]. The second is the initiation of chemical reactions. The oldest example here is ozone generation [1]. About 15 years ago other applications will be given here. The major topics on gas 1 of VOCs [1, 8, 20], see fig. 7.



$\gamma_2$  removal from simulated flue gas (left [1]) biogas (right)[20].

Recently NO removal from diesel engines has gained a lot of interest, the main line of the investigations is the plasma-enhanced selective catalytic reduction [21]. Water cleaning is reported much less frequent, two methods are distinguished: the discharge can be made in the water [22] or above it [9]. Fig. 8 gives an example of phenol degradation as determined with LIF.

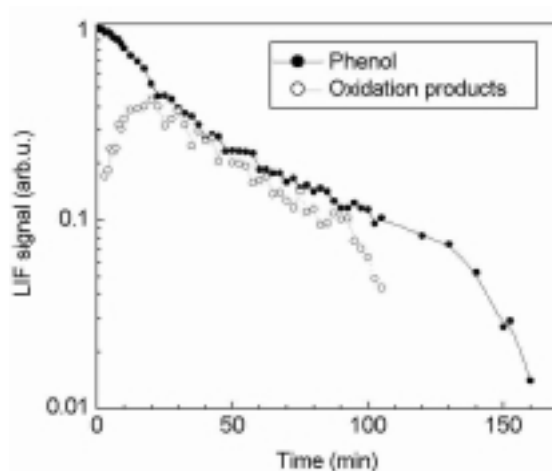


Fig. 8: Breakdown of phenol by corona discharges above water [9]

## Conclusion

The knowledge on pulsed coronas is limited. Up to now optimization of applications is performed empirically. New measurement methods are required to determine in-situ plasma parameters. More detailed simulations can probably help to understand and maybe control processes such as branching. The chemistry that follows after the nanosecond discharge is not discussed in this short paper but it also requires a major effort [1]. Considering the fact that pulsed power supplies of 100 kW with good efficiency and life time are becoming available [8], the time is ripe for pilot studies that will bring the knowledge for well designed large scale applications.

## References

- [1] E.M. van Veldhuizen (editor), *"Electrical Discharges for Environmental Purposes: Fundamentals and Applications"*, Nova Science Publ., New York, 1999, ISBN 1-56072-743-8.
- [2] Y.L.M. Creyghton, PhD thesis, Eindhoven : Technische Universiteit Eindhoven, 1994.
- [3] E.M. van Veldhuizen, W.R. Rutgers, J. Phys. D: Appl. Phys. **35**(2002)2169.
- [4] W.J. Yi, P.F. Williams, J. Phys. D: Appl. Phys. **35**(2002)205.
- [5] P. Tardiveau, E. Marode, A. Agneray, J. Phys. D: Appl. Phys. **35**(2002)2823.
- [6] A.A. Kulikovskii, Phys. Rev. E **57**, 7066 (1998).
- [7] A. Rocco, U. Ebert, W. Hundsdorfer, Phys. Rev. E **66**, 035102(2002).
- [8] K. Yan, PhD thesis, Eindhoven : Technische Universiteit Eindhoven, 2001.
- [9] W.F.L.M. Hoebe, E.M. van Veldhuizen, W.R. Rutgers, C.A.M.G. Cramers, G.M.W. Kroesen, Plasma Sources Sci. Technol. **9**(2000)361-369.
- [10] [www.phys.tue.nl/EPG/YTRID](http://www.phys.tue.nl/EPG/YTRID)
- [11] J.M. Meek, J.D. Craggs, "Electrical breakdown of gases", Chichester : Wiley-Interscience, 1978.
- [12] A.J.M. Pemen, this conference proceedings.
- [13] K.V. Kozlov, H.-E. Wagner, R. Brandenburg, P. Michel, J. Phys. D: Appl. Phys. **34**(2001)3164.
- [14] F. Bastien, E. Marode, J. Phys. D: Appl. Phys. **12**(1979)249.
- [15] E. Gerova, S. Muller, in: Proc. XXIII ICPIG (ed. J. Berger), Toulouse, France, 1979, p. IV-120.
- [16] N.L. Alexandrov, E.M. Bazelyan, R.B. Carpenter Jr., M.M. Drabkin and Yu. P. Raizer, J. Phys. D: Appl. Phys. **34**(2001)3256.
- [17] R. Morrow, T.R. Blackburn, J. Phys. D: Appl. Phys. **35**(2002)3199.
- [18] A.A. Kulikovskii, Physics Letters **A245**(1998)445.
- [19] J.M. Park, Y.-H. Kim, S.H. Hong, Proc. Hakone VIII (ed. A. Haljaste), Pühajärve, Estonia, 2002, p. 104.
- [20] S.A. Nair, K. Yan, A.J.M. Pemen, E.J.M. v. Heesch, K.J. Ptasinski, A.A.H. Drinkenburg, this proceedings.
- [21] T. Hammer, Plasma Sources Sci. Technol. **11**(2002)A196.
- [22] P. Lukes, A.T. Appleton, B.R. Locke, IEEE Ind. Appl. Conf. **37**(2002)1816.



# Bistable State of Filamentary pattern in Dielectric Barrier Discharge in Atmosphere

Zengqian Yin<sup>1</sup>, Lifang Dong<sup>1</sup>, Xuechen Li<sup>2</sup>, Yafeng He<sup>1</sup>, Zhifang Chai<sup>1</sup>, Long Wang<sup>2</sup>

<sup>1</sup>College of Physics Science & Technology, Hebei University, Baoding 071002, China

<sup>2</sup>Institute of Physics, Chinese Academy of Sciences, Beijing 100080, China

Bistable character refers that the pattern can remain stable as the applied condition varying within certain range, it is the essential character of pattern. Although the bistable state in PDP (plasma display panels) has been investigated for decades[1], there is no report on the bistable state of pattern formation in DBD (dielectric barrier discharges). In this paper, the dynamics of bistable state of pattern formation is investigated in detail by using a novel DBD setup with water electrodes, which is favorable to optical measurement. The experimental results have been explained by the proposed breakdown and quench model theoretically.

In experiment, cleaning discharge technology is used to obtain a stable pattern. A pattern can still remain stable when the applied voltage is decreased or the gas gap is increased very slowly, the waveforms of applied voltage and the light emission from one individual filament are measured. On the one hand, the experimental results show that the intervals of adjacent breakdown moments vary between long one and short one alternatively. On the other hand the net field at breakdown moments of the same filament under different condition (applied voltage or width of gas gap) is maintained to the same almost, although the breakdown moments vary with the condition, which results in the bistable behavior. In addition, when the applied voltage is decreased to so small (or the width of gas gap is increased so large) that the filament will expires. All experimental results can be interpreted by the breakdown-and-quench model, which is indicated as the following equations:

$$E_0 \sin \omega t_1 - E_c = E_m \quad (1)$$

$$E_0 \sin \omega t_2 + E_c = E_b \quad (2)$$

where  $E_0$  and  $\omega$  are the peak value and the circular frequency of the applied field respectively,  $E_c$  is the electric field of the surface charges which quenches the discharge of this half cycle and will help the next breakdown.  $E_m$  is the critical quench field and  $E_b$  is the critical breakdown field, under most circumstances  $E_m$  and  $E_b$  remain constant,  $t_1$  and  $t_2$  are the moments of quench and breakdown of the discharges respectively. According to equation (1) and (2), it is obvious that  $t_2$  increases as  $t_1$  decreasing when  $E_0$  (so as applied voltage and gas gap width) is constant, which results in the short and long intervals. While if  $E_0$  is decreased (the applied voltage is decreased or the width of gas gap is increased) after the first breakdown (the approximate breakdown moment is  $t_1$ ), the second breakdown moment ( $t_2$ ) will be increased in order to meet equation (2). So the discharge moment will lag behind when the gap width is increased and the applied voltage is decreased very slowly. Of course, if  $E_0$  is decreased to so small that the equation (2) can't be met any more, that is, the breakdown condition can't be satisfied and the filament will expire.

In conclusion, the bistable behavior of pattern in DBDs is investigated experimentally and theoretically. The theoretical analyze is in agreement with the experimental results.

# Hybrid type dielectric barrier discharge for VOC decomposition and defect detection of Teflon coated metal

Kenji Ebihara, Yukari Shibuya, Takahiro Tanaka, Ryutaro Maki and Tomoaki Ikegami

*Department of Electrical and Computer Engineering and Graduate School of Science and Technology,  
Kumamoto University, Kurokami 2-39-1, Kumamoto 860-8555, Japan*

## Abstract

The hybrid type high frequency power source was developed to generate the dielectric barrier discharge for environmental purification processes such as VOC reduction and NO removal. The pulse width and position of HF 10kHz power supply superimposed on the commercial 60 Hz controlled to increase the energy efficiency due to the decreased dielectric energy loss.

## 1.Introduction

A dielectric barrier discharge(DBD) has been widely used for the effective generation process of radical ozone and the decomposition of NO<sub>x</sub> and volatile organic compounds(VOCs)[1]. Environmental pollutant VOCs have been decomposed by various methods including DBD process generating non-thermal plasma state. However, the decomposition of VOC and NO<sub>x</sub> using the non-equilibrium thermal plasma has the problems of the energy efficiency and by-products. In this paper, we developed a hybrid type power supply in which high frequency power of 10kHz was superimposed on the commercial frequency of 60Hz. Controlling the pulse width and the time sequence contributed to the increase of the energy efficiency for decomposition of the environmental treatment. Alternative application of the DBD to evaluation of the surface quality of the Teflon coated stainless tube was also proposed.

## 2. Characteristics of hybrid type high frequency power source

A hybrid high frequency power source used here consists of 10kHz high frequency generator and a commercial power. Fig.1 shows the voltage wave diagram of superimposed high-frequency voltage( $V_p$ ) and commercial voltage( $V_{60}$ )[2].  $T$  shows the pulse duration of the high frequency voltage, and  $\Delta\Phi$  is phase difference between high frequency power and 60 Hz power. The typical applied voltage and current waveforms of the hybrid type high-frequency power source are shown in Fig.2 (a) and (b), respectively. Here, the hybrid type power source

supplied the voltage to the coaxial screw type electrode. High frequency voltage (10 kHz) with the pulse width of 1.0 ms is 4.4 kV, and commercial voltage (60 Hz) is 3.0 kV. NO/N<sub>2</sub> (485 ppm) gas flow rate was 1.0 *lit./min*. The phase difference  $\Delta\Phi$  is 90°. The resultant voltage waveform consists of high frequency voltage  $V_f$  and commercial voltage  $V_{60}$ .

The current waveform shows the generation of a large number of microdischarge at the time duration (4.2 ms) when high frequency voltage was superimposed on the commercial voltage. Also, a few current pulses were detected during 9-12 ms. When only commercial voltage of 3.0 kV was applied, the discharge did not appear in 9-12 ms. Referring this discharge characteristic using the hybrid type high frequency power source, it is shown that it is possible to generate simultaneously microdischarges by high frequency voltage as well as commercial voltage in one cycle of commercial voltage.

Fig. 3 shows the NOx concentration as a function of phase difference. It is found that much amount of NO decomposition occurs at the large ratio of high frequency voltage ( $\Delta\Phi=0$ ). Here, high frequency of 10 kHz (the pulse width 1.0 ms), commercial voltage ( $V_{60}$ ) of 2.0 kV and NO/N<sub>2</sub> gas flow rate of 1.0 *lit./min* were used. Total applied voltage ( $V_f+V_{60}$ ) was kept at 8.0 kV by changing the voltage ratio of  $V_f/V_{60}$ . The high decomposition of NO at  $\Delta\Phi=0$  ( $V_f=8\text{kV}$ ) is attributed to the increase of number of microdischarges at large voltage ratio of  $V_f/V_{60}$ .

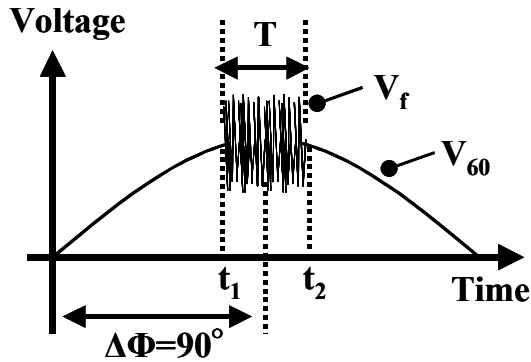


Fig.1 Diagram of the superimposed high-frequency voltage

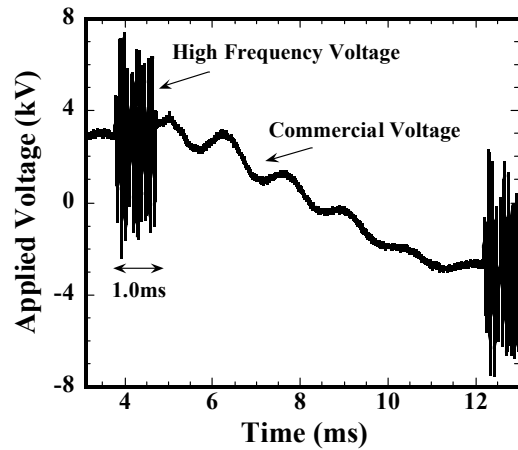


Fig.2 (a) Voltage waveform generated by the hybrid type high-frequency power

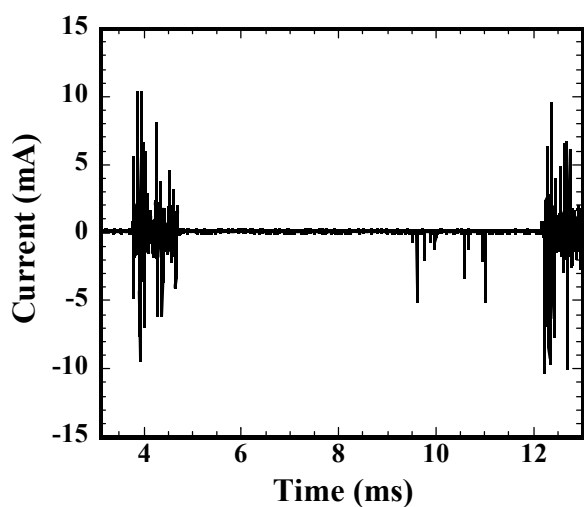


Fig.2(b) Current waveform generated by the hybrid type high-frequency power source

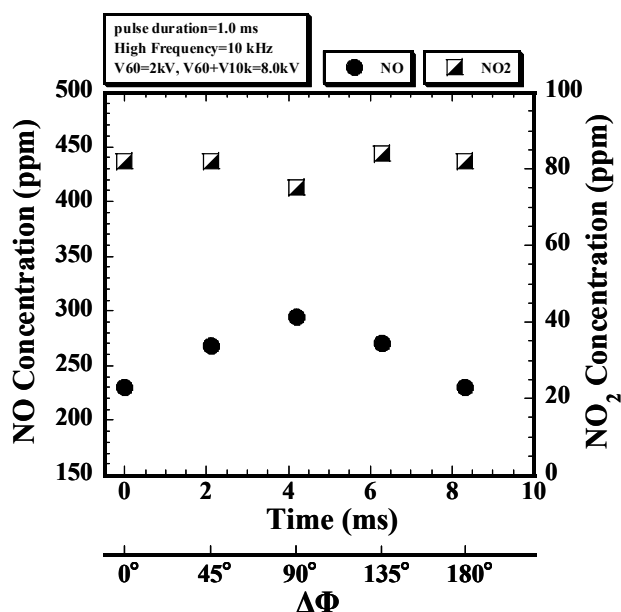


Fig.3 NOx concentration as a function of phase difference

### 3 .VOC decomposition by the high frequency DBD

A schematic diagram of the experimental equipment for VOC decomposition is shown in Fig.4[3].  $N_2$  diluted toluene ( $C_6H_5CH_3/N_2$ , 100ppm) as a typical VOC was fed into the discharge reactor through a gas flow meter. Additive oxygen gas controlled flow rate was mixed with toluene gas by mass flow controller. The structures of a screw type electrode and a pyramid type electrode(Fig.5) were used for the decomposition of VOC. The inner electrode is a pyramid or a screw structure of stainless steel rod ( $\Phi$  6mm). The ground electrode is aluminum foil wrapped around the dielectric quartz glass tube ( $\Phi$  8mm). The gap separation between the inner electrode and the insulator tube was kept at 1mm. Outside diameter of a pyramid type electrode is also same as the screw type electrode. High frequency power sources (Denki Kogyo CX-O3CP-Z 10kHz;Denki Kogyo MH-O3Y 20kV 50mA 50kHz) were used to generate the DBD.

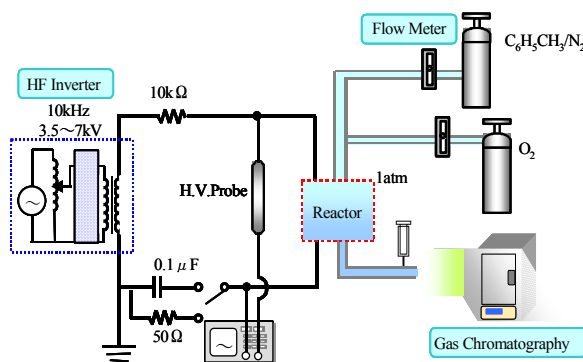
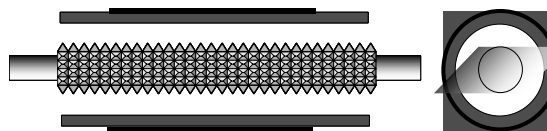


Fig. 4 A schematic diagram of experimental equipment

Time-resolved waveforms of discharge current and voltage were measured through a high voltage probe and a resistor of  $50\Omega$ , respectively and recorded on a digitizing oscilloscope (Tektronix TDS-3034). Discharge power was estimated from the Q-V Lissajous figure obtained by measuring the capacitor voltage of  $1\mu\text{F}$ . The concentration of toluene before and after discharge decomposition was analyzed by the gas chromatography (Shimazu FID GC-14B).



pyramid-electrode type reactor

**Fig. 5 Structure of discharge electrodes**

Fig.6 shows voltage-current waveform of dielectric barrier discharge by the pyramid type electrode. The applied voltage of 10kHz power source is 5kV and the electrode axial length is 100mm. This is typical waveform of dielectric barrier discharge that current waveform advances by about  $90^\circ$  from voltage waveform. The initial breakdown voltages for a screw type electrode and a pyramid type electrode were about 4 - 4.5kV and 3 - 3.5kV, respectively. It was noticed that a pyramid type electrode could initiate the discharge at lower voltage than at that for a screw type electrode.

Fig.7 shows the decomposition rate as a function of discharge power when toluene was decomposed using screw type electrode and pyramid type electrode. The decomposition rate when using the pyramid type electrode was higher than at a screw type electrode. Therefore, the effective decomposition of toluene was obtained by the pyramid type electrode. It is noticed that the number of microdischarges of a pyramid type electrode is more than that in the screw type electrode.

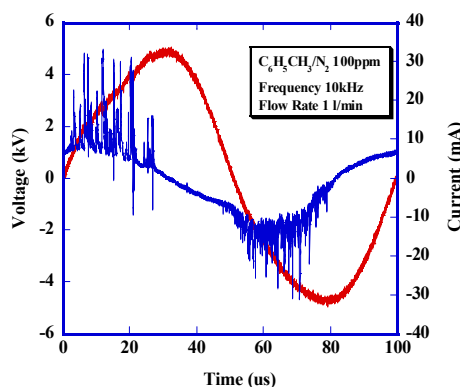


Fig.6 Current wave form at Pyramid type inner electrode.

Fig.8 shows the FT-IR spectra measured at the inlet and the outlet of the reactor. After the VOC treatment the absorption corresponding to the toluene mostly disappears and the strong absorption of  $\text{CO}_2$  and CO appears. Small absorption signals are considered to be due to existence of Azides and Amine.

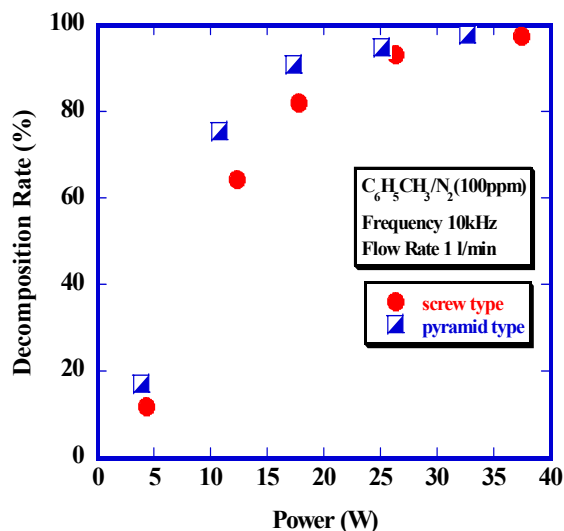


Fig. 7 Toluene decomposition rate

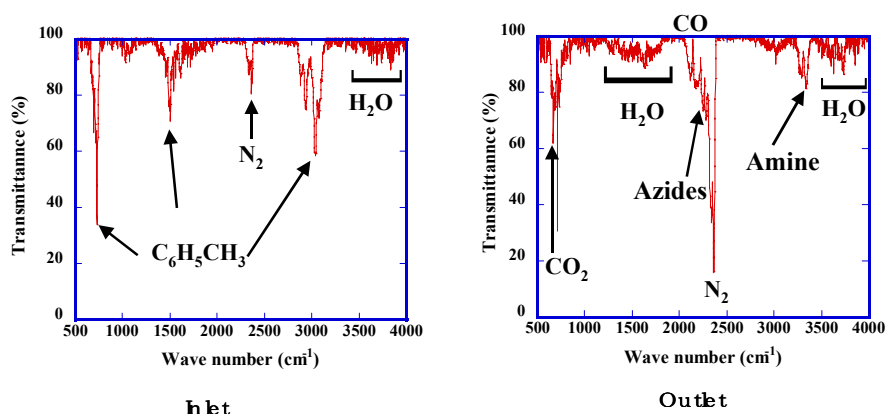


Fig.8 FT-IR spectra at the inlet and the outlet of the reactor.

#### 4. The defect detection of Teflon coated stainless steel

Fig. 9 shows the schematic diagram of the defect detection system[4]. The conducting liquid electrode as a ground electrode is grounded through the stainless steel flange. Stainless point electrodes (diameter : 2.5 mm, point angle : 45 angles and diameter : 0.84 mm), and stainless point electrode (diameter : 0.84 mm) coated by Pyrex glass were used as a powered electrode. The 10 kHz oscillator was used to generate the dielectric barrier discharge. The water level in Pyrex glass tube (external diameter : 25 mm, inside diameter : 21 mm) is controlled by adjusting a valve of the water container. Two point electrodes were placed with a vertical separation of 60mm and the distance from the glass tube was 1mm. Fig.10 is the current signals when the water level approached the lower point electrode at 8kV. When the water level was elevated to reach the upper electrode, the pulse current increases in amplitude and most of microdischarges appears within 18μs.

This result suggests that the current amplitude and occurrence of the microdischarges provides the information of the defective parts of the Teflon coated steel.

Fig.9. Defect detection system

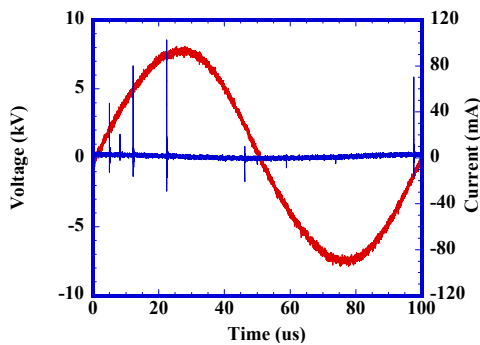
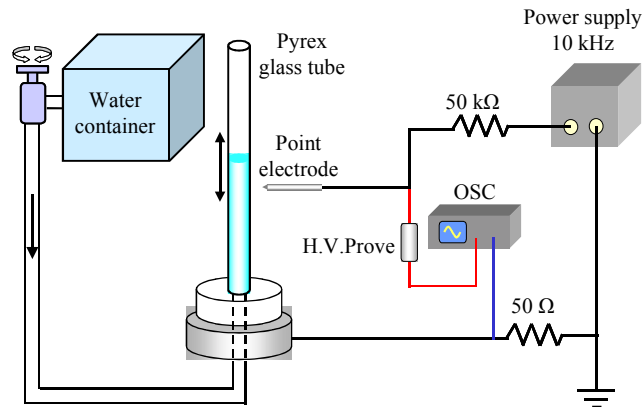


Fig.10 Current pulse at lower point electrode.

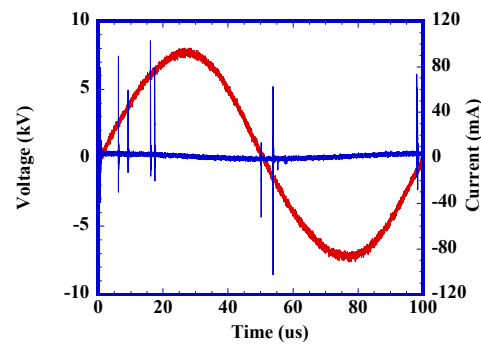


Fig.11 Current pulse at upper electrode.

## 5. Conclusion

We report here the development of hybrid power source to decrease dielectric loss. NO decomposition was performed at high efficiency when the ratio of 10kHz voltage was increases. With respect to the VOC treatment, the most part of toluene was decomposed using a pyramid type electrode in the cylindrical dielectric barrier discharge.

The proposed detection technique using the conducting liquid electrode is useful to inspect the surface state of insulator coated metal.

## Reference

- [1]Yukihiko Yamagata, Ken-ichi Murayma, Tomoaki Ikegami, and Kenji Ebihara,,Journal of Advanced oxidation Technology,61(2003)
- [2]Ryutaro Maki, Yukari Shibuya,Kenji Ebihara, Yukihiko Yamagata, Proceedings of 2002 Joint Conference of Asian Conference on Electric Discharge & Korean-Japan Symposium on Electrical Discharge and High Voltage Engineering(November 17-20,2002,Seoul, Korea),262(2002).
- [3]Yukari Shibuya, Ryutaro Maki, Takahiro Tanaka, Tomoaki Ikegami, Kenji Ebihara, Proceedings of 2002 Joint Conference of Asian Conference on Electric Discharge & Korean-Japan Symposium on Electrical Discharge and High Voltage Engineering(November 17-20,2002,Seoul, Korea),270(2002).
- [4]Takahiro Tanaka, Kenji Ebihara, Yukihiko Yamagata, Makoto Mizukami, Kazutaka Yamashita, Yoshifumi Oyama,Proceedings of 2002 Joint Conference of Asian Conference on Electric Discharge & Korean-Japan Symposium on Electrical Discharge and High Voltage Engineering(November 17-20,2002,Seoul, Korea),279(2002).

# Organic and inorganic light emitting thin films using pulsed laser ablation in nitrogen and oxygen radical atmosphere

Kenji Ebihara<sup>1</sup>, Paik-Kyun Shin<sup>2</sup>, Tamiko Ohshima<sup>1</sup>, and Tomoaki Ikegami<sup>1</sup>

<sup>1</sup> Department of Electrical and Computer Engineering and Graduate School of Science and Technology,  
Kumamoto University, Kumamoto, Japan

<sup>2</sup> Acrosens Co.Ltd, Seoul, Korea

## Abstract

Organic thin films of Alq<sub>3</sub> and TPD were fabricated by laser ablation technique using Nd:YAG ( $\lambda=532$  nm) laser and KrF excimer ( $\lambda=248$  nm) laser without substrate heating. The optical absorption spectra of organic films deposited at lower laser fluence were similar to those of films deposited by the vacuum evaporation method. The preparation of inorganic p-type ZnO thin films has been attempted by N-doping using NO gas. The deposited ZnO films showed p-type conduction having high resistivity and low carrier density.

## 1. Introduction

Organic electroluminescence (EL) is promising for large area displays capable of low voltage operation [1]. Alq<sub>3</sub> (aluminum tris-8-hydroxyquinoline) has attracted a great deal of attention as a material for an organic EL material. This compound is one of the most reliable electron conducting and light emitting organic material. Alq<sub>3</sub> has been widely used as a light emitting layer in organic EL. Another EL material TPD (N, N'-diphenyl-N, N'-bis(3methylphenyl) -(1,1'-biphenyle) -4, 4'-diamine), which has high hole mobility, is usually used in the hole transportation layer of EL devices. The formation of organic films is generally carried out by the vacuum evaporation technique. Because TPD is easily decomposed at low temperature due to a low glass transition temperature of 60 °C, the structure of the films prepared by vacuum evaporation may be changed at high processing temperature. Therefore a low process temperature is required for growth of organic films.

Laser ablation has several advantages of low process temperature, good reproducibility and highly purified deposition with low impurity level. By understanding the reaction of the plasma plume emitted from the target and ambient gas, it becomes possible to control the plasma plume and to prepare high quality films. Recently there are some papers about preparation of organic films by laser ablation, but the effect of the deposition conditions on film properties has not been examined in detail [2-4].

In this paper, we have prepared organic films of Alq<sub>3</sub> and TPD by laser ablation technique using Nd:YAG laser and KrF excimer laser on the quartz glass substrate at room temperature (RT) and vacuum of  $4 \times 10^{-5}$  Torr. We have investigated the effect of the difference of laser wavelength on the structure of the deposited films. In order to obtain high quality organic films, we have investigated the optimum in deposition conditions.

As for inorganic devices of the blue luminescent materials, ZnO (Zinc Oxide) has the unique properties of direct band gap (3.3 eV) at RT and a large excitation binding energy (60 meV). Therefore ZnO seems a promising candidate for short-wavelength optoelectronic applications such as light emitting diodes (LED's) and laser diodes (LD's). Generally ZnO indicates n-type conduction due to the oxygen deficiency resulting from vapor pressure difference between Zn and O atoms. To realize optical devices based on ZnO, it is necessary to grow p-type ZnO. In this paper, we have attempted to fabricate p-type ZnO films by N-doping under NO gas ambience.

## 2. Experiment

Figure 1 shows the experimental setup used in this study. Second harmonic light of a Nd:YAG laser ( $\lambda=532$  nm,  $\tau=7$  ns) and a KrF excimer laser ( $\lambda=248$  nm,  $\tau=25$  ns) were used as the ablation light source. A stainless steel vacuum chamber was evacuated to a base pressure ( $4 \times 10^{-5}$  Torr) by a turbo molecular pump. Powdered Alq<sub>3</sub> and TPD (Dojindo Laboratories) were pressed to form a disk target (dia.12 mm $\times$ 0.8 mm thick). The densities of the Alq<sub>3</sub> and TPD targets were 1.08 g/cm<sup>3</sup> and 1.20 g/cm<sup>3</sup>, respectively. Films were deposited on quartz glass substrates placed at a distance of 25 mm from the target in vacuum of  $4 \times 10^{-5}$  Torr. For film deposition, the targets were ablated at the different laser fluences. Table 1 shows the depositions condition of the Alq<sub>3</sub> and TPD films. X-ray diffraction (XRD; RIGAKU, RINT2100/PC), atomic force microscopy



(AFM; Seiko Instruments, SPI3800N) were used to measure the structure of the deposited films. Optical absorption spectrum of the films was measured by UV/visible photometry (Shimazu, UV-160). Photoluminescence (PL) measurement was carried out using a 3rd harmonic light of Nd:YAG laser ( $\lambda=355$  nm,  $\tau=3$  ns). The luminescence from the films is collected on the optical fiber by the lens ( $f=80$  mm), and it is analyzed by the monochromator (Acton Research, SpectraPro-308i) equipped with an ICCD (Princeton Inc., ICCD-576G) camera.

For the attempt to fabricate p-ZnO, we have used NO gas (purity 99 %) to dope acceptors. NO is easily dissociated into N and O atoms at lower energy (6.5 eV) than  $N_2$  (9.1 eV). Therefore it is expected that single N atoms are doped into the film. ZnO films were deposited on quartz glass substrates by ablating a metallic Zn target at the substrate temperature of 400 °C and various NO gas pressure of 50-200 mTorr. For N-doped ZnO deposition, the laser fluence and the number of laser shots of KrF excimer laser were fixed at 2 J/cm<sup>2</sup> and 9000 shots (thickness~ 200 nm), respectively. The structural properties of films were studied using XRD and AFM. Electrical property was investigated by Hall measurement using van der Pauw method at RT and the magnetic field of 3 kG. To confirm the carrier type of the film, Seebeck coefficient measurement was also carried out at RT and  $\Delta T=15$  K. The emission spectra of the plasma plumes produced during film deposition were recorded using the monochromator.

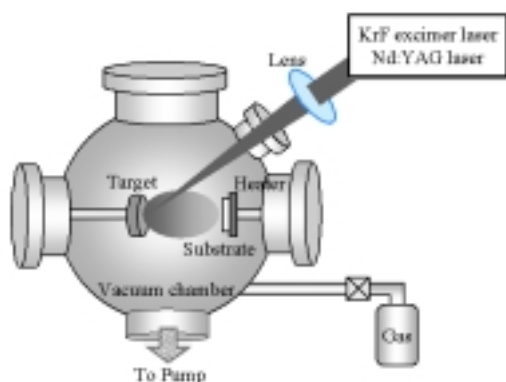


Fig. 1. Laser ablation apparatus.

Table 1. Deposition conditions of Alq<sub>3</sub> and TPD films.

Laser wavelength (nm)	Organic material	Laser fluence (mJ/cm <sup>2</sup> )	Ambient gas	Substrate temperature	Laser pulses (shots)	Deposition rate (pm/shot)
532	Alq <sub>3</sub>	201	Vacuum	Room temperature	6000	
		403				2.5
		497				8.6
		604				
		104				
248	Alq <sub>3</sub>	195				
		324				
		25				3.9
		36				8.3
		67				9.6
		91				11.5
	TPD	23				
		37				
		68				
		80				

### 3. Results and discussion

#### 3.1 Preparation of organic Alq<sub>3</sub> and TPD films

Most of the deposited films showed amorphous structure by XRD measurement while the target had polycrystalline structures. In Alq<sub>3</sub> preparation using Nd:YAG laser, the films were hardly deposited below the laser fluence of 201 mJ/cm<sup>2</sup>. The films were gradually deposited above the laser fluence of 403 mJ/cm<sup>2</sup> as shown in Table 1. Light yellowish films were deposited at low laser fluence. With increasing the laser fluence, the films became dark yellow. At using KrF excimer, the films began to grow at lower laser fluence than by Nd:YAG laser. However, the film color prepared by KrF excimer laser became brownish. Because the photon energy (5.0 eV) of KrF excimer laser is much larger than that (2.3 eV) of Nd:YAG laser, a combination of organic elements might be broken by the KrF excimer laser. According to the AFM measurement, the films deposited by Nd:YAG laser were very rough and the particles like a powder were found in the films. The surface of the films deposited by KrF excimer laser was smooth and similar to that of the film by vacuum evaporation. Figures 2 (a) - (c) show UV/visible light transmission spectra of Alq<sub>3</sub> films deposited using different laser wavelength ablations and vacuum evaporation. The film prepared by vacuum evaporation shows large absorption at about  $\lambda=400$  nm. The films deposited using Nd:YAG laser also show the faint absorption at the same wavelength as Fig. 2 (a). This absorption wavelength agrees with the previous report by C. Hong et al [1]. However the intensity is very weak, and films deposited using the 248 nm KrF excimer laser do not show any absorption at  $\lambda=400$  nm. Figure 3 shows PL spectra of Alq<sub>3</sub> films by vacuum evaporation and KrF excimer laser ablation. The film by vacuum evaporation shows the PL spectrum around  $\lambda=520$  nm. This wavelength shows the 10 nm red-shift comparing with the PL spectrum ( $\lambda=510$  nm) for the Alq<sub>3</sub> target. **This red-shift is due to the high pressure for the effect during the Alq<sub>3</sub> disk target fabrication [1].** In case of film deposited by KrF laser, any PL peaks cannot be seen because the molecular structure is decomposed due to high photon energy.

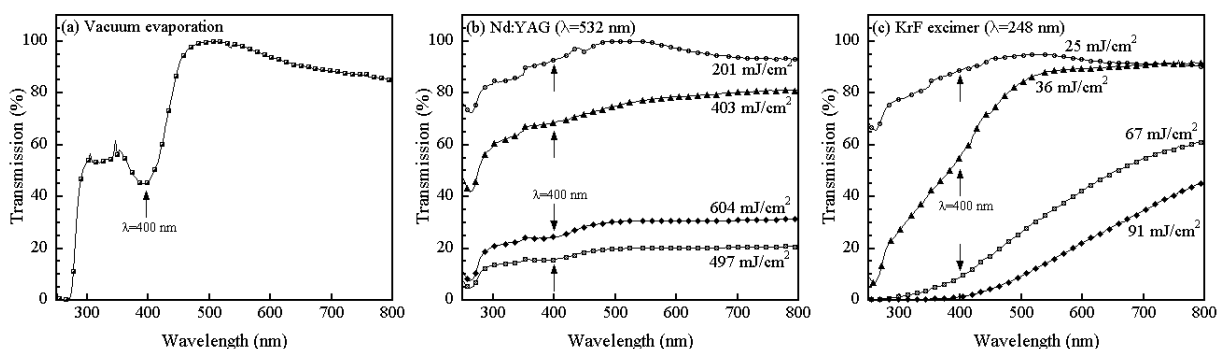


Fig. 2. Optical transmission spectra of Alq<sub>3</sub> films deposited by (a) vacuum evaporation, (b) 532 nm Nd:YAG laser ablation, and (c) 248 nm KrF excimer laser ablation.

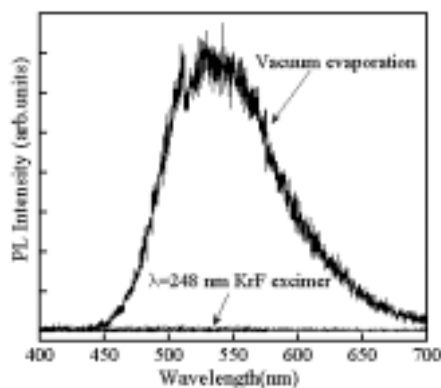


Fig. 3. PL spectra of Alq<sub>3</sub> films deposited by vacuum evaporation and 248 nm KrF excimer laser ablation.

Figures 4 (a) – (c) show UV/visible light transmission spectra of the TPD films. The film by vacuum evaporation shows large absorption spectrum containing two peaks at  $\lambda=320$  nm and  $\lambda=360$  nm. The films prepared using the Nd:YAG laser and KrF excimer laser also show the similar absorption spectra. In the Nd:YAG laser ablation, all deposited films are transparent, and the weak absorption of the film deposited at low laser fluence of  $104 \text{ mJ/cm}^2$  results from its thin film thickness. By increasing the laser fluence, the absorption becomes large. In the case of KrF excimer laser ablation, the film deposited at  $25 \text{ mJ/cm}^2$  shows the large absorption, and the peak of absorption becomes unclear with increase of the laser fluence. Moreover, the film changed from transparent to dark with increasing the laser fluence. For AFM images measured in the region of  $5 \times 5 \text{ mm}^2$ , the surface roughness increased with the laser fluence. RMS (root mean square) roughness of the films deposited at the laser fluence of 23, 37, 68 and  $80 \text{ mJ/cm}^2$  are 1.1, 1.1, 3.1 and  $6.2 \text{ nm}$ , respectively.

Figures 5 (a) and (b) show PL spectra of the TPD films deposited by vacuum evaporation and KrF excimer laser ablation. As seen in Fig. 5 (a), two PL peaks centered around  $\lambda=400$  and  $420$  nm are observed, and the PL peak at  $\lambda=420$  nm is sharper and stronger than the PL peak at  $\lambda=400$  nm. Since the PL spectrum at  $\lambda=420$  nm is seen in the TPD target, the film structure by vacuum evaporation is similar to the target. At the PL spectra of the film by KrF excimer laser, the PL peak around  $\lambda=415$  nm is blue-shifted compared with the PL spectra of Fig. 5 (a). Similar blue-shift behavior was reported in the TPD films deposited by ArF excimer laser ( $\lambda=193 \text{ nm}$ ) ablation [5].

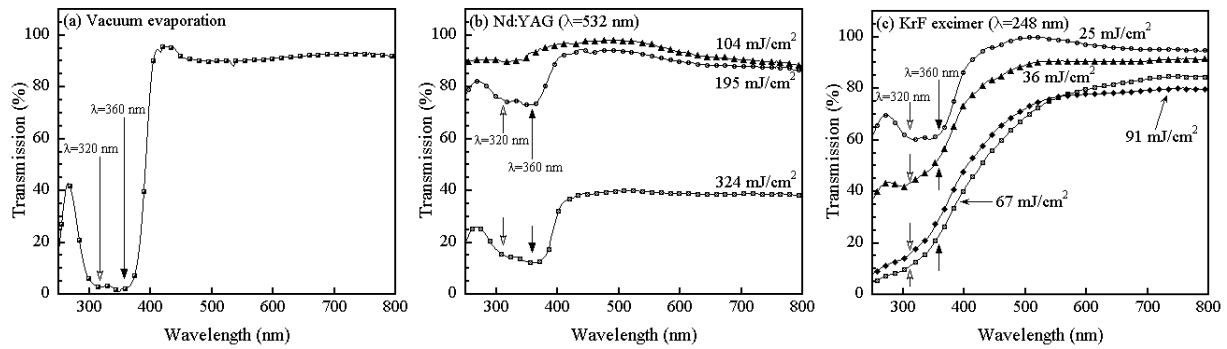


Fig. 4. Optical transmission spectra of TPD films deposited by (a) vacuum evaporation, (b) 532 nm Nd:YAG laser ablation, and (c) 248 nm KrF excimer laser ablation.

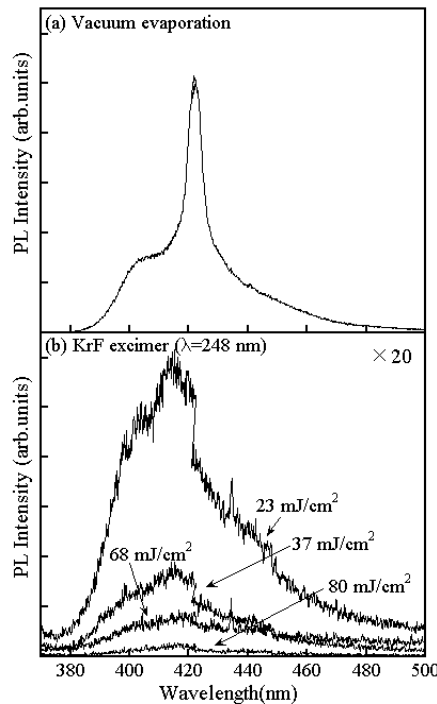


Fig. 5. PL spectra of TPD films deposited by (a) vacuum evaporation and (b) 248 nm KrF excimer laser ablation.

### 3.2 Attempt to fabricate N-doped ZnO film

In order to investigate the behavior of a plasma plume produced by laser ablation, optical emission spectra of the plasma plume were monitored at various delay times ( $\tau_d$ ) after laser irradiation and at several distances ( $d$ ) away from the target. Fig. 6 shows optical emission spectra of the plume acquired at  $\tau_d=100$  ns, NO gas pressure of 100 mTorr and  $d=5$  mm. Emission lines corresponding to N or O radicals are seen. For the ablation of the metallic Zn target at vacuum, strong Zn I and Zn II emission lines were observed[6]. Therefore, it is thought that the emission lines in Fig. 6 result from the dissociation and ionization of NO by the energetic species ablated from the target. However, because the intensity of these emission lines decreases rapidly with increase of  $\tau_d$  and  $d$ , reactions between ablated species and NO gas seem to occur at early time after ablation.

Electrical property of ZnO films prepared in ambient of NO gas was investigated by Hall effect measurement using van der Pauw method. The ZnO film deposited at NO gas pressure of 200 mTorr was indicated p-type conduction having high resistivity of 16  $\Omega\text{cm}$  and low carrier concentration of  $6 \times 10^{14} \text{ cm}^{-3}$ . We also confirmed the conduction type of the film by Seebeck coefficient ( $S$ ) measurement for  $\Delta T=15$  K at around RT. Figure 7 shows the potential difference ( $\Delta V$ ) due to the temperature difference ( $\Delta T$ ), and then  $S$  is calculated using  $S=-(\Delta V/\Delta T)$ . The Seebeck coefficient of the ZnO film was  $S=+32 \mu\text{V/K}$  and it was similar to those of other II-VI wide band gap semiconductors as p-type (LaO)CuS [7]. However, the electrical properties of the ZnO films prepared at NO gas pressure excepting 200 mTorr could not be obtained due to their high surface resistivity.

Structural property and surface morphology of the ZnO films deposited in NO gas ambience did not show remarkable difference compared with undoped ZnO films reported at the previous work [8]. The XRD for all ZnO films prepared in this study showed (002) and (004) c-axis orientations.

Optical transmission spectra of the ZnO films showed large transparency above 80 % in visible region. The optical band gap of 3.15-3.22 eV were obtained, and these values were similar to those of the undoped ZnO film of 3.25 eV.

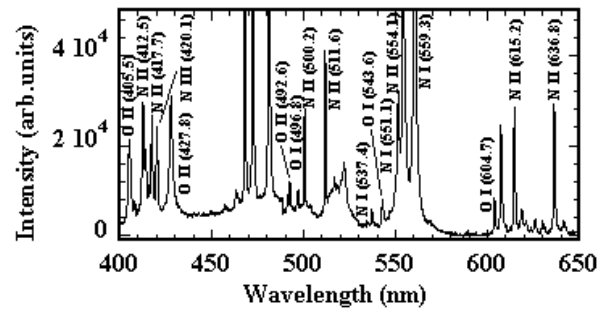


Fig. 6. Optical emission spectra measured at NO gas pressure of 100 mTorr,  $d=5$  mm and the delay time of  $\tau_d=100$  ns.

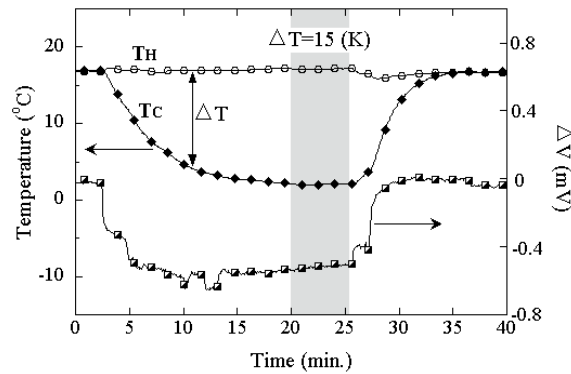


Fig. 7 Seebeck coefficient measurement.

#### 4. Conclusion

We have prepared organic Alq<sub>3</sub> and TPD films by Nd:YAG (532 nm) and KrF excimer (248 nm) laser ablation techniques. At low laser fluence, organic films were successfully deposited. The Alq<sub>3</sub> films by Nd:YAG laser showed weak absorption at  $\lambda=400$  nm. While the Alq<sub>3</sub> film by vacuum evaporation showed the PL spectrum centered at  $\lambda=520$  nm, films prepared by KrF laser did not show any PL spectra. It is thought that molecular structure of the films is broken by KrF excimer laser due to its high photon energy. TPD films prepared by Nd:YAG laser and KrF excimer laser showed two absorption peaks at  $\lambda=320$  nm and  $\lambda=360$  nm as well as the film by vacuum evaporation. The TPD film by KrF excimer laser showed the PL spectrum around  $\lambda=415$  nm.

We have also tried to prepare inorganic p-type ZnO films in NO ambient gas for N-doping into the films. The ZnO film deposited at NO gas pressure of 200 mTorr displayed p-type conduction by Hall effect and Seebeck coefficient measurements. Laser ablation in NO gas, which was used as a dopant owing to its low dissociation energy, realized the N-doping into the ZnO films.

#### 5. References

- [1] C. Hong, H.B. Chae, K.H. Lee, S.K. Ahn, C.K. Kim, T.W. Kim, N.I. Cho, S.O. Kim, *Thin Solid Films* **409**, 37 (2002)
- [2] X. Yang, Y. Tang, M. Yu, Q. Qin, *Thin Solid Films* **358**, 187 (2000)
- [3] H. Kim, C.M. Gilmore, J.S. Horwitz, A. Piqu , H. Murata, G.P. Kushto, R. Schlaf, Z.H. Kafafi, D.B. Chrisey, *Appl. Phys. Lett.* **76**, 259 (2000)
- [4] X. Yang, X. Xu, *Appl. Phys. Lett.*, **77**, 797 (2000)
- [5] L.D. Wang, H.S. Kwok, *Thin Solid Films* **363**, 58 (2000)
- [6] T. Ohshima, P.K. Shin, K. Ebihara, T. Ikegami, R.K. Thareja, *J. Phys. D* (submitted)
- [7] K. Takase, M. Koyano, T. Shimizu, K. Makihara, Y. Takahashi, Y. Takano, K. Sekizawa, *Solid State Communications* **123**, 531 (2002)
- [8] T. Ohshima, R. K. Thareja, Y. Yamagata, T. Ikegami, K. Ebihara, *Mat. Res. Soc. Symp. Proc.* **666**, F3.20.1-6 (2001)

# Plasma Polymerization Technique to Overcome Cerebrospinal Fluid Shunt Infections

M. Mutlu<sup>1</sup> and H. Caner<sup>2</sup>

<sup>1</sup>Hacettepe University, Institute for Pure and Applied Sciences, Bioengineering Division  
Beytepe Campus, 06532, Ankara, Turkey

<sup>2</sup>Baskent University, School of Medicine, Department of Neurosurgery, Bahçelievler, 06490, Ankara, Turkey

The incidence of cerebrospinal fluid shunt infections remains high. The majority of these infections are caused by *Staphylococcus epidermidis*. In recent years the effect of surface chemistry on bacterial adhesion has been studied intensively and hydrophilic uncharged surfaces and electrostatic charges showed the resistance to protein and microorganism adsorption.

The present investigation focus on the effect of cold plasma modification of polymers and deposition of thin polymer films on catheter surface in order to prevent *Staphylococcus epidermidis* adherence to the shunt catheter. Cold-plasma modification is a branch of science characterized by an increasing popularity. The unique advantage is that the product feature "surfaces" with tailored and unusual properties, which enable their use where otherwise would be impossible to conventional materials. Plasma modified-polymers are considered an entirely novel class of materials showing chemical inertness or enhanced reactivity, hydrophobicity and -philicity, adhesivity, bacterial infection resistance, etc. Shunt catheters were placed on to the ground electrode in the reactor. A 13.6 MHz RF generator was used to sustain the plasma. The reactor was evacuated to  $10^{-3}$ - $10^{-4}$  mbar, and hydroxyethylmetacrylate (HEMA) vapors allowed to feed the reactor at a constant flow rate of 60 ml/min. for 15 minutes at a discharge power of 15 W. This polymerized with HEMA (n:10) and normal (Control group n:10) catheters are re-sterilized and incubated in triptych soy broth medium suspension of  $5 \times 10^7$  colony forming unit/ml of slime producing strain of *Staphylococcus epidermidis* for two hours at 37 °C. After incubation the catheters were rinsed and settled in saline vortex for 2 minutes and 0.3 ml of the suspension was inoculated to blood agar and incubated at 37 °C for 18 hours.

- The surfaces were characterised by Contact angle measurements and AFM images before and after modification with plasma polymerisation and interaction with microorganism.
- Plates were contained PlzP-HEMA modified catheter suspension yielded bacterial colony counts averaging 2.00 log scales per catheter lower than control samples.

# Underwater oxidation of organic compounds using thermal plasma

M. Violier, N. Cerqueira, C. Vandensteendam and J.M. Baronnet

*Laboratory of Plasma Chemistry, University of Limoges,  
123 avenue Albert Thomas, 87060 Limoges, France*

## Abstract

This work is concerned with decontamination of wastewater spoiled by organic, such as phenols, cyanides, organophosphorus compounds, chlorinated aliphatic and aromatic chemicals, oil products and others. The process is based on an arc plasma jet immersed in the waste aqueous solution; the oxidation results of interaction of organic with active oxidants, atoms and radicals, present in the plasma in large concentration.

The experimental set-up consists of a cylindrical vertical reactor filled with a few liters of water in which a few grams of organic compounds such as phenols, dyes and so...are added. At the bottom of the reactor, a high velocity oxygen/argon plasma jet is provided by a plasmatron: the gas-liquid system shows an intense turbulence resulting in a fast fragmentation of the jet into small-sized bubbles.

The electrical power of the plasma torch is about 10 kW with current intensity between 200 and 400 A. The argon flow-rate is 30 NL/min, the oxygen one is in the range of 0 to 50 NL/min.. The concentrations versus time of phenol or methylene-blue and of hydrogen peroxide are measured and the results discussed.

## Introduction

Preserving and restoring water purity is a major step of sustainable development: elimination from industrial waste water of dangerous organic impurities such as organophosphorus compounds, aromatic and aliphatic chlorinated compounds, cyanides or phenols is a major task to ensure the quality of our environment. Various fields of industrial activities are concerned such as surface treatment, tanneries, pharmaceutical, paper industry and so...

In the more recent processes, the organic compounds are destroyed or mineralized using oxidizing attack of free radicals, specially hydroxyl radicals which are an oxidizing agent much more efficient than usual ones: reaction rates of HO radicals with organic compounds in aqueous solution are from  $10^6$  to  $10^9$  mol.L<sup>-1</sup>.s<sup>-1</sup> [1].

In addition to chlorination, physicochemical processes allowing oxidation of these organic compounds appeared during the last ten years:

- ozonization including two possible ways of oxidation, either direct oxidation by ozone O<sub>3</sub> or an oxidation by HO radicals resulting from ozone decomposition into water,
- photo-catalytic oxidation [2] finding niches for example for the water treatment of the tertiary circuit of nuclear thermal power stations. Only UV destroy molecular bounds: thus, coupling of UV with hydrogen peroxide or with ozone, allows molecules breaking and hydroxyl radicals formation,
- more recently, HO radicals have also been obtained by ultrasonic treatment [3] inducing in an aqueous solution, local variations of pressure leading to the phenomenon of cavitations and thus to small steam bubbles formation. During the implosion of these steam bubbles, the rise in temperature and pressure (5000 K, 1000 bar) induces the water molecules to dissociate and consequently to form hydroxyl radicals,
- another physicochemical method of oxidation has been proposed and tested: high-tension pulsed electric discharges [4] [5]: in such discharges, a large part of the energy is consumed on formation of a thermal plasma channel; this channel emits UV radiation and its expansion against the surrounding water generates an intense shock wave producing reactive species ; so the oxidative degradation of organic molecules is attributed to three physical processes: UV photolysis, electrohydraulic cavitation and supercritical water oxidation.

However these different techniques offer restricted efficiency due to the limited capacities of the used sources to produce reactive species.

Recently, new processes based on plasma technologies appeared: not only on non-thermal plasmas [6] but also on thermal plasmas. In their pioneering works G. Soucy [7] [8] [9] and N.V. Alekseev [10] have shown the feasibility to decontaminate aqueous effluents polluted by particularly refractory organic compounds such as phenols or cyanides.

The aim of this work is to test the feasibility of the oxidation of soluble organic compounds - phenol and dyes such as methylene blue -, contained in water, using an underwater thermal plasma jet. Major advantages of the process concept are :

- the direct contact between the active species in the plasma jet and the aqueous phase,
- the high thermal gradients between the two phases increasing mass and energy transfer into the aqueous phase and also,
- the photo-catalytic action of the intense plasma UV radiation.

### The experimental set up

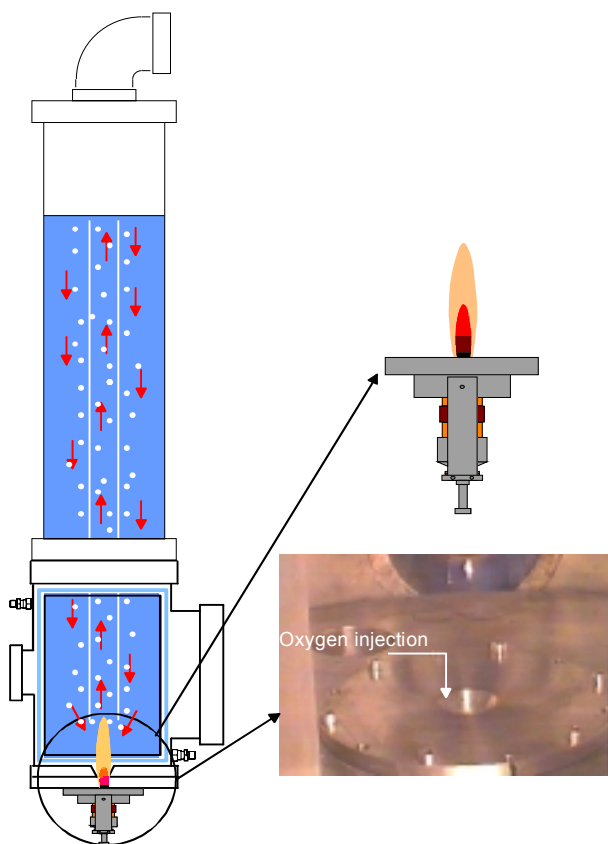


Figure 1: Experimental set up

The experimental set up is presented on figure 1; it consists in a vertical cylindrical reactor of about 20 liters, made of Plexiglas in its upper part; its diameter is  $\sim 14$  cm. It is equipped at its base with a plasma torch using argon as plasma gas. Oxygen can be injected at the periphery of the jet. The current intensity of the arc lies between 200 A and 400 A, the tension is  $\sim 25$  V; the flow of argon is 30 NL/min and oxygen one from 0 to 50 NL/min; the thermal efficiency of the torch is about 50 %. So the effective power – electrical power minus losses in electrodes cooling system – is in the range 2.5 to 5 kW. The reactor works in batch. Once the arc is established, the reactor is filled with the test solution –  $\sim 3$  or 18 liters of water added with a few tens milligrams of the tested compound: phenol or methylene blue-; an inner vertical tube accelerates the re-circulation of the solution in the closed vicinity of the plasma jet where it is aspirated and partially vaporized. The plasma jet, due to its high velocity -  $\sim 400$  m/s in the nozzle exit cross section – is disintegrated into a multitude of bubbles. Their number and their size ( $< 1$  mm) vary with the test parameters and time. These bubbles cause a major increase of the gas-liquid interface and of the rate of transport of the reactive species produced in the plasma jet towards the liquid phase.

At the end of the test, (duration  $\sim 1$  hour), the reactor is emptied before the arc is switched off. The increase of the solution temperature observed during the test does not exceed  $20^{\circ}\text{C}$ .

Solution samples are periodically collected for titration.

The methylene blue concentration is measured by molecular absorption spectrometry at the wavelength of 665 nm ; for phenol, the standard NF T 90.109 was used: phenol concentration is determined by molecular absorption spectrometry with 4-aminoantipyrine as complexing agent

### *Thermodynamics and kinetics approaches*

In order to determine the species generated by the plasma and their life time, the thermal dissociation of water has been modeled. To approach the operating conditions, i.e. argon plasma jet immersed in water, we supposed that water is aspirated in the jet in such a way that the mixture is immediately homogeneous and composed of 80 % of argon and 20 % of water. A quenching rate of  $10^8$  K/s has been used.



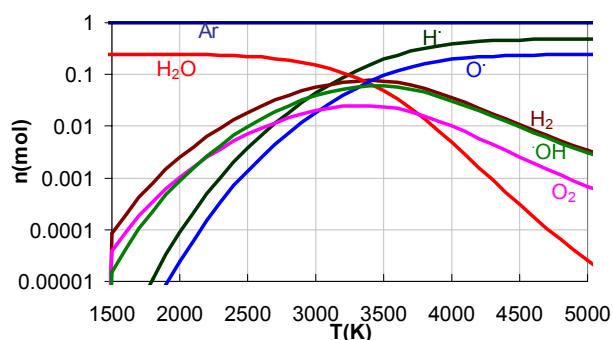


Figure 2: Composition Ar/H<sub>2</sub>O, 80/20 % mole

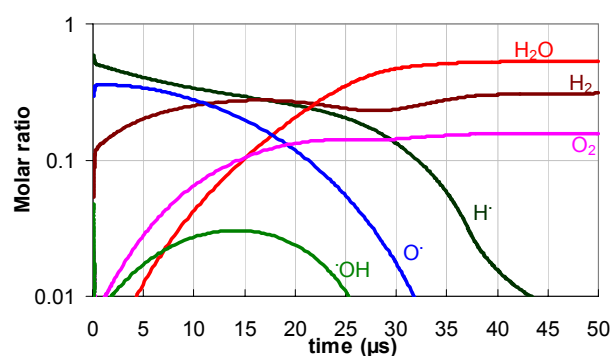


Figure 3: Evolution of the composition of the system Ar/H<sub>2</sub>O during the quench

that the system is quenched: more than 30 % of H<sub>2</sub>O are dissociated in H<sub>2</sub> and O<sub>2</sub>. So, even without injection of oxygen into the system, there are oxygen atoms are formed in the plasma jet.

## Results

In order to determine the parameters influencing the treatment rate of the organic compounds by the immersed plasma jet, preliminary experiments have been carried out on a test molecule. Methylene blue (cf figure 4) has been chosen for several reasons: because of its structure (benzene cycles) and its atomic composition (nitrogen, sulphur, chlorine), this molecule is similar to an organic waste. This colored compound is easily titrated by molecular absorption spectrometry.

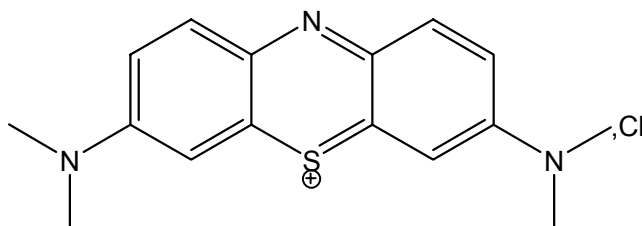


Figure 4: Methylene blue molecule

### Degradation of the methylene blue

Figure 5 presents, for an effective power about 3.75 kW, the destruction of methylene blue in 3 L of solution with an initial concentration of 27 mg/L. The methylene blue concentration seems to decrease exponentially and the solution appears colorless in less than 15 min. The final corresponding concentration is lower than 0.3 mg/L, a value corresponding to the limit authorized concentrations for a majority of organic compounds.

Assuming the system in thermodynamic equilibrium, by minimization of Gibbs energy, the system chemical composition is computed versus temperature (cf. Figure 2). It can be noticed that the dissociation of the molecules begins above 2000 K leading to the formation of H<sub>2</sub>, HO<sup>•</sup> and O<sub>2</sub>. Above approximately 4500 K, hydrogen and oxygen atomic are the major species; the content of HO radicals is of a few percents. 4500 K corresponds to the "mean enthalpy temperature" of the plasma jet, deduced from the calorimetric balance in the torch cooling system.

In order to coarsely simulate the quench of the plasma jet impacting the liquid phase, the evolution versus time of the composition of the gaseous phase has been calculated. The species H<sub>2</sub>O, H<sub>2</sub>, O<sub>2</sub>, H, O, HO... and a set of 18 reactions with their reaction rate [11] [12] have been taken into account. The initial composition at the quench beginning is supposed to be the equilibrium composition at 4500 K. The used computer code allows to vary the quenching rate. The results for a quenching rate of 10<sup>8</sup> K/s are presented on Figure 3. This rate is evaluated by considering a flow velocity of 400 m/s at the nozzle exit and a jet cooling rate of 10 000 K along 4 cm [13]. It can be observed that the life time of H and O atoms and of HO radicals is about a few tens of microseconds and

The rate of reaction of methylene blue has been calculated using a first order kinetics:

$$\ln\left(\frac{C_0}{C}\right) = k \cdot t \quad (1)$$

On Figure 6 two successive steps are observed in the process, each characterized by a particular rate: during the first one, the kinetics of disappearance of the methylene blue is the same with or without injection of oxygen; during the second step, when the concentration becomes lower than  $\sim 1$  mg/L, the rate decreases and is dependent on the introduction of oxygen into the system.

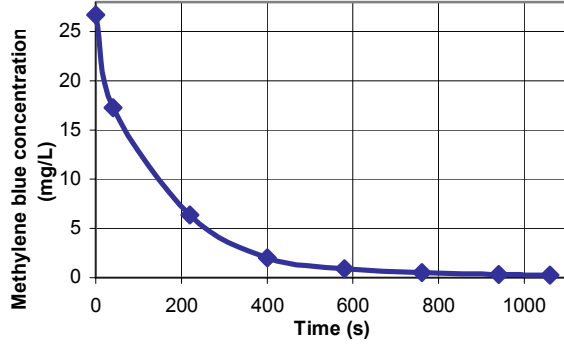


Figure 5: Degradation of methylene blue versus time

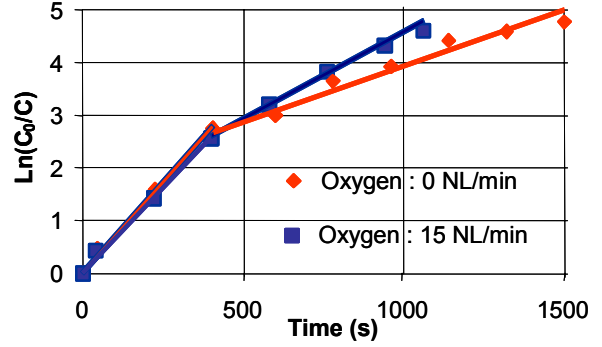


Figure 6: Kinetic of reaction of methylene blue

### *Influence of the batch volume*

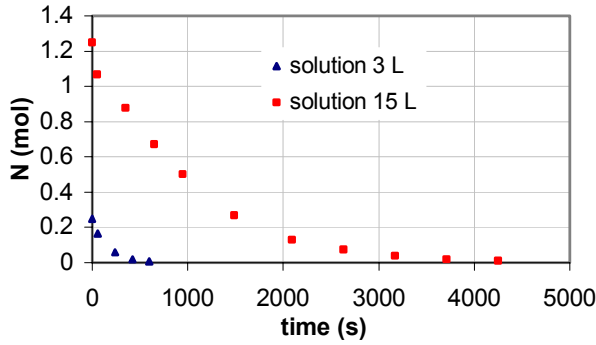


Figure 7: Methylene blue mole number versus time

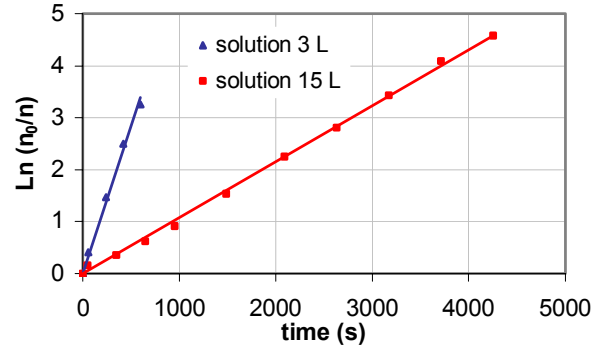


Figure 8: Comparison between the kinetics with 3 L solution and with 15 L solution

In order to compare the efficiency of treatment with different batch volumes, we proceeded with two tests without the inner tube: the one with a 3 L of methylene blue solution and the other with 15 L. The operating parameters for these two experiments were: an effective power about 3.25 kW, flow rates of argon and oxygen fixed to 30 NL/min, and the same concentration in methylene blue, i.e. 27 mg/L for the two solutions. The degradation of the methylene blue versus time and the associated kinetics (first order) are represented in figures 7 and 8. The comparison of the results obtained with 3 L and with 15 L of solution (with the same initial concentration) indicates that the processing time necessary for degradation of methylene blue is directly proportional to the volume treated. More over we may notice that during the first ten minutes, 0.6 moles are destroyed with a 15 L batch against 0.25 moles with a 3 L batch.

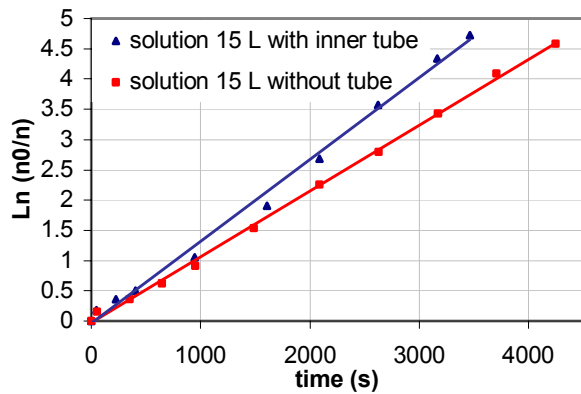


Figure 9: Comparison of the degradation kinetics with and without the inner tube

Figure 9 shows the influence of the inner tube : the degradation rate is higher with the inner

tube and it is all the higher that the methylene blue concentration is lower. So, due to the inner tube, organic compounds recirculation near the plasma jet is increased and an homogeneous repartition of the reactive species is obtained in the whole volume.

### Decomposition of phenol

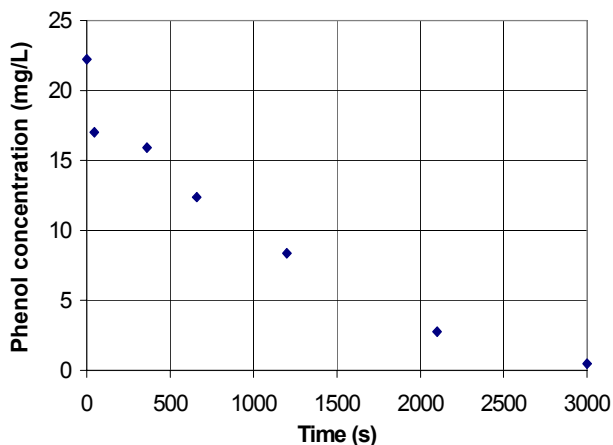


Figure 10: Phenol degradation versus time

### Formation of $H_2O_2$

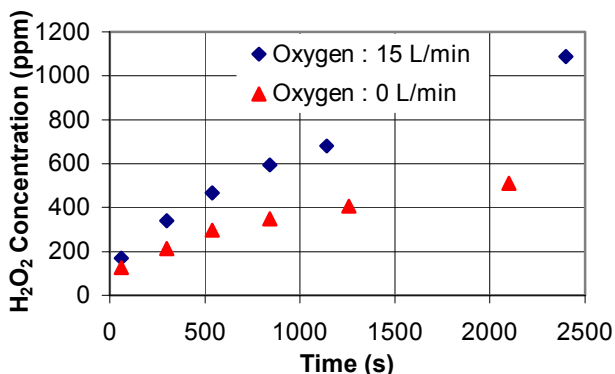


Figure 12: Formation of  $H_2O_2$  versus time

Figure 10 characterizes the degradation rate of 15 L of phenol solution with a 22 mg/L initial concentration. 30 NL/min of oxygen are injected around the argon plasma jet; the effective torch power is around 3.25 kW. The structure of phenol molecule is presented on figure 11. Now identification of the oxidation products is in progress. We have just noticed during experiment, the appearance, and then the disappearance, of a pink color.

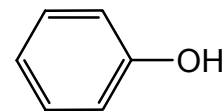


Figure 11: Phenol molecule

In order to point out the oxidant effect of the process, with or without introduction of oxygen, and also to study the influence of oxygen injection on the reactive species generated by the plasma,  $H_2O_2$  concentration in water has been measured as a function of time by titration with  $KMnO_4$  (cf. Figure 12). It can be first seen that without oxygen injection, i.e. with only Ar as plasma gas, 500 ppm of hydrogen peroxide are obtained in 30 minutes. Nevertheless with a gaseous flow rate of oxygen of 15 NL/min injected around the plasma jet, 900 ppm are obtained in the same time.

## Discussion

With this underwater plasma, HO radicals are supposed formed by water dissociation:



$O_2$  injected around the plasma is also dissociated and O atoms produced are as reactive as the hydroxyl radicals [14] for organic compounds such as aromatic ones:



More over, atomic oxygen reacts with water, increasing so HO active radicals concentration, while their recombination leads to formation of hydrogen peroxide, an oxidizing and stable molecule:



The introduction of oxygen at the periphery of the jet leads to higher concentrations of reactive species, due to reactions (3), (4) and (5).

The oxidation of organic compounds by reactive species, previously formed, takes place at the liquid-gas interface; it is then necessary that the transfer time of reactive species to this interface should be as short as possible compared to the recombination time. The immersed thermal plasma concept involves high gas flow rates (about 400 m/s) within the liquid, ensuring the formation of gas bubbles of small size, leading to unexpected mass transfer kinetics. The transferred dissociated species can thus take part in the reactions of oxidation with the liquid phase compounds.

About the pink color transitory appearance during phenol oxidation, we may suppose as in [15] that quinones are intermediate products towards acids, such as maleic acid and so., and to CO<sub>2</sub> and H<sub>2</sub>O.

From the results with different batch volumes, we may think that the reactive species generated by the plasma are present in the solution whole volume.

The inner tube is supposed to intensify the recirculation of the solution near the plasma jet where the concentration in reactive species is presumed to be the more important and consequently to increase the degradation kinetic.

## Conclusion

These first results have shown the potentiality of the process: the reactive species, atoms and molecular radicals, generated by the plasma jet, more particularly with oxygen injection, allow to obtain important kinetics of degradation: phenol concentration may be reduced to 0.2 mg/L from 25 mg/L in less than one hour in 15 L solution. The next experiments will take into account the identification of the intermediate products of degradation. The improvement of the hydro-dynamic geometry of the reactor will be a major point in our next studies too.

## Références

- [1] R. Farhataziz et al. Natl. Standard Ref. Data Ser. **59** (1977).
- [2] Y. Wang, Water Research. **34**, 3, 990-994 (2000).
- [3] N.H. Ince, G. Tezcanli et al., Applied Catalysis B : Environmental **29**, 167-176 (2001).
- [4] B. Sun, M. Sato et al., J. Phys. D : Appl. Phys. **32**, 1908-1915 (1999).
- [5] M. A. Malik, A. Ghaffar et al., Plasma Sources Sci. Technol. **10**, 82-91 (2001).
- [6] D. Moussa, J.L. Brisset, 14<sup>th</sup> ISPC, 2-6 august (1999) 2539-2543.
- [7] V. Yargeau, G. Soucy and M. Boulos, 14<sup>th</sup> ISPC, 2-6 august (1999) 2519-2524.
- [8] L. Fortin, G. Soucy et al., 14<sup>th</sup> ISPC, 2-6 august (1999) 2387.
- [9] J.L. Bernier, L. Fortin et al., Patent WO 97/22556.
- [10] N.V. Alekseev, A.V. Samokhin et al., High Energy Chemistry. **34**, 6, 389-393 (2000).
- [11] E. Meillot., "Contribution à l'étude d'un plasma d'arc de vapeur d'eau. Application à la gazéification de charbon pulvérisé" (1988), Ph.D. thesis, University Paul Sabatier, Toulouse, France
- [12] D.L. Baulch et al., Evaluated kinetic data for high temperature reactions (1976), 3, London.
- [13] M. Vardelle., "Etude de la structure des dépôts d'alumine obtenus par projection plasma en fonction des températures et des vitesses des particules au moment de leur impact sur la cible" (1980), Ph.D. thesis, University of Limoges, France.
- [14] J. Phys. Chem. Ref. Data. **21**, No. 3, (1992).
- [15] A.A. Joshi et al., Journal of Hazardous Materials. **41**, 3-30 (1995).

# DETERMINATION OF ROTATIONAL TEMPERATURES IN HIGH ENTHALPY ATMOSPHERIC PRESSURE NITROGEN PLASMA FLOWS USING $N_2^+$ ROVIBRONIC SPECTRA

A.A. Belevtsev, V.F. Chinnov, A.V. Fyodorov, E.Kh. Isakaev, A.M. Kukushkin

*Associated Institute for High Temperatures, Russian Academy of Sciences  
Izhorskaya 13/19, Moscow, 125412 RUSSIA Fax: (095) 4859777, E-mail: [v\\_chinnov@oivtran.iitp.ru](mailto:v_chinnov@oivtran.iitp.ru)*

## Abstract

The line-by-line numerical simulation of the (0-0) and (0-1) bands of the  $N_2^+$  First Negative System are applied to derive the rotational temperatures at different sections of an atmospheric pressure nitrogen plasma jet. Correlation to the electron temperatures at the respective sections and to the vibrational temperature at the lowest electronically excited state of CN molecules in the far relaxation zone of the jet is given.

## 1. Introduction

In the last few years there has been keen interest in energetic nitrogen plasma flows. First, they offer strong possibilities for a variety of studies on the atomic and molecular spectroscopy of nitrogen and on the nitrogen plasma kinetics at elevated temperatures. The latter is difficult if impossible under most other experimental conditions. Secondly, these plasmas are very promising for some novel technologies, such as plasma processing of materials, formation of nanostructures in the near-surface layers, etc. Of great importance are therefore measuring the nitrogen plasma parameters at extremely high temperatures. Applied to the electron component, this problem was solved in [1,2]. The present paper focuses on determining rotational temperatures in high enthalpy nitrogen plasma flows at atmospheric pressure.

In this paper, the rotational temperatures  $T_r$  are derived from the (0-0) and (0-1) vibronic bands of the First Negative System ( $B^2\Sigma_u^+ - X^2\Sigma_g^+$ ) of  $N_2^+$  molecular ion. Two different procedures are applied, each starting from the line-by-line numerical simulation of the rotational structure of the electronic transition. The first procedure consists in performing a global fit of the spectral regions of the bands (0-0) and (0-1), while the second one is in comparing the intensities of single lines to those of the band heads. Because of fairly high temperatures being typical of the flows being studied, the band segments comprising rotational lines with large rotational quantum numbers  $N' \sim 80-100$  should ordinarily be involved. This primary requirement imposes tight constraints on the measuring technique and equipment used. Specifically, a high-resolution spectral equipment has to be arranged for correctly resolving the partly overlapped vibronic bands.

The obtained values of  $T_r$  allow reasonable estimates of the translation temperatures  $T_m$  of heavy particles at different sections of the flow. Besides, several CN Violet System bands of the principal sequence ( $\Delta v=0$ ) are involved to assess the temperatures  $T_v$  of vibrational population of CN ( $B^2\Sigma_u^+$ ) molecules in the far relaxation zone. These three temperatures,  $T_m$ ,  $T_r$ , and  $T_v$ , are finally compared with the electron temperatures  $T_e$  derived at the respective sections of the plasma jet.

## 2. Experimental arrangement and measuring technique

High enthalpy atmospheric plasma flows are produced by an electric arc plasmatron ( $I=150\div 500A$ ) with a divergent channel-anode and vortex stabilization by a plasma-forming gas. The gas flow rates  $G$  range from 1 to 6g/s and the arc length is 20÷30mm. The densities of the deposited electric power are as great as 50kW/cm<sup>3</sup>.

For spectral measurements high-class spectral devices and optical detectors with a wide spectral sensitivity region are employed that allows the emission spectra in the 200-1000nm region with a spectral resolution of 0.01-0.02nm to be taken. The measuring complex is composed of two independent recording systems.

The first system consists of a small-sized monochromator MDR-41 with a high light-gathering power; a control unit that provides scanning with a given speed and control over the current wavelength; a photomultiplier tube FEU-100 and its supply unit; an electronic circuit converting the RS-232 protocol to RPS; an L-1250 computer ADC card; and the software. The operating wavelength range, limited by the FEU-100 photocathode, is 200-830nm.

The second system consists of a diffraction spectrograph DFS-452 and a multichannel optical spectrum analyzer MOAC-2. The analyzer incorporates two photometer heads with photodiode CCD arrays (TDS1250A by Toshiba), each photodiode array (PDA) containing about 3700 photosensitive elements 8μm in length and 200μm in height. One of the PDAs is used to record a spectrum, while the other PDA allows measuring the intensity distribution across the plasma jet at a given wavelength.

A great body of spectrometric information is processed with an automated SPEC\_MCD. 100 system developed on the basis of the Mathcad 7.03 Professional mathematical package. It permits resolution of overlapped spectral lines, determining basic spectral characteristics (transition probabilities, line widths, etc.), and deriving electron, rotational, and vibrational temperatures and electron number densities. Structurally, the system is a set of procedures, which are common all processed spectra, and calling modules, which are individual for each spectrum. Some further details can be found in papers [1,3].

### 3. Results and discussion

The rotational structures of the (0-0) and (0-1) bands of the  $N_2^+ B^2\Sigma_u^+ - X^2\Sigma_g^+$  transition most clearly manifest themselves at large distances  $Z$  from the plasmatron cathode and allow them to be modeled in detail. They are not masked by NI and/or NII lines in the associated spectral regions and narrow CuI lines (copper arises from evaporation of the channel wall) may easily be identified and offer no difficulties in comparing the measured and simulated spectra.

On modeling the rovibronic  $N_2^+$  spectrum, the fine structure of the bands due to the spin doubling was taken into account, so that the branches  $P_1$ ,  $P_2$ , and  $R_1$ ,  $R_2$  were distinguished. The line positions are taken in accord with data [4], which seem to be most reliable ones at present. The Honl-London factors  $S_{J,J'}$  are taken from [5]. All necessary spectroscopic constants are chosen accordingly to [6, 7]. The lines are shaped to Gauss with the apparatus function half-width of 0.025 nm. No account was taken of the rotation perturbation, so that the associated spectral regions were outside the comparison.

In Fig.1, the (0-0) band taken at  $Z=55$  mm is compared with the simulated spectra calculated at three different values of  $T_r$ . The same for two rotational temperatures is given in Fig.2 for the (0-1) band. It is seen that the global fit procedure does not allow one to decide between the rotational temperatures indicated in Fig.1 and Fig.2. The reason is that the spectral regions chosen contain the lines with the rotational numbers  $N' < 50$  for which the Boltzmann factor  $\exp \{-F(N')/kT_r\}$  ( $F(N')$  is the rotational energy), determining the relative line intensity distribution, is insensitive to varying  $T_r$  from 6000K to 8000K.

For larger values of  $N'$  the (0-0) and (0-1) bands are appreciably overlapped by other bands, which, therefore, should also be numerically simulated to permit the calculated and measured spectra to be compared. However there can be used a simpler procedure allowing more precise assessment of the rotational temperatures through comparing the intensities of single and not overlapped lines to that of the band head. As for the (0-0) band, it is, for instance, the complex  $P_{1,2}(97)+R_{1,2}(70)$  line [8]. This complex line both measured and simulated is shown at the upper left of Fig.3. Its intensity relative to that of the band head as a function of  $T_r$  is given at the upper right of Fig.3.

Of fundamental importance is the fact that the procedure being discusses is applicable even in the cases when the total spectrum within the spectral region of the (0-0) band cannot be fully resolved into its constituents. This is typical of the lower and moderate distances  $Z$  from the plasmatron cathode in the zone of energy deposition. As an example Fig.3 shows such a spectrum taken at  $Z=28$ mm and displaying the double-“relief” structure. It should be noted that the nature of these “reliefs” overlapping the (0-0) band has to be yet understood. This in particular was discussed in [9]. Nevertheless the method of the line to the band head intensity ratio allows one to get around the associated difficulties.

The obtained values of  $T_r$  allow estimates for the translation temperatures  $T_m$  of heavy particles, which are of primary importance for the understanding of the nitrogen plasma kinetics in high enthalpy flows. Because of effective rotation-translation (R-T) and translation-translation energy exchange processes, one can assume that  $T_m=T_r$ .

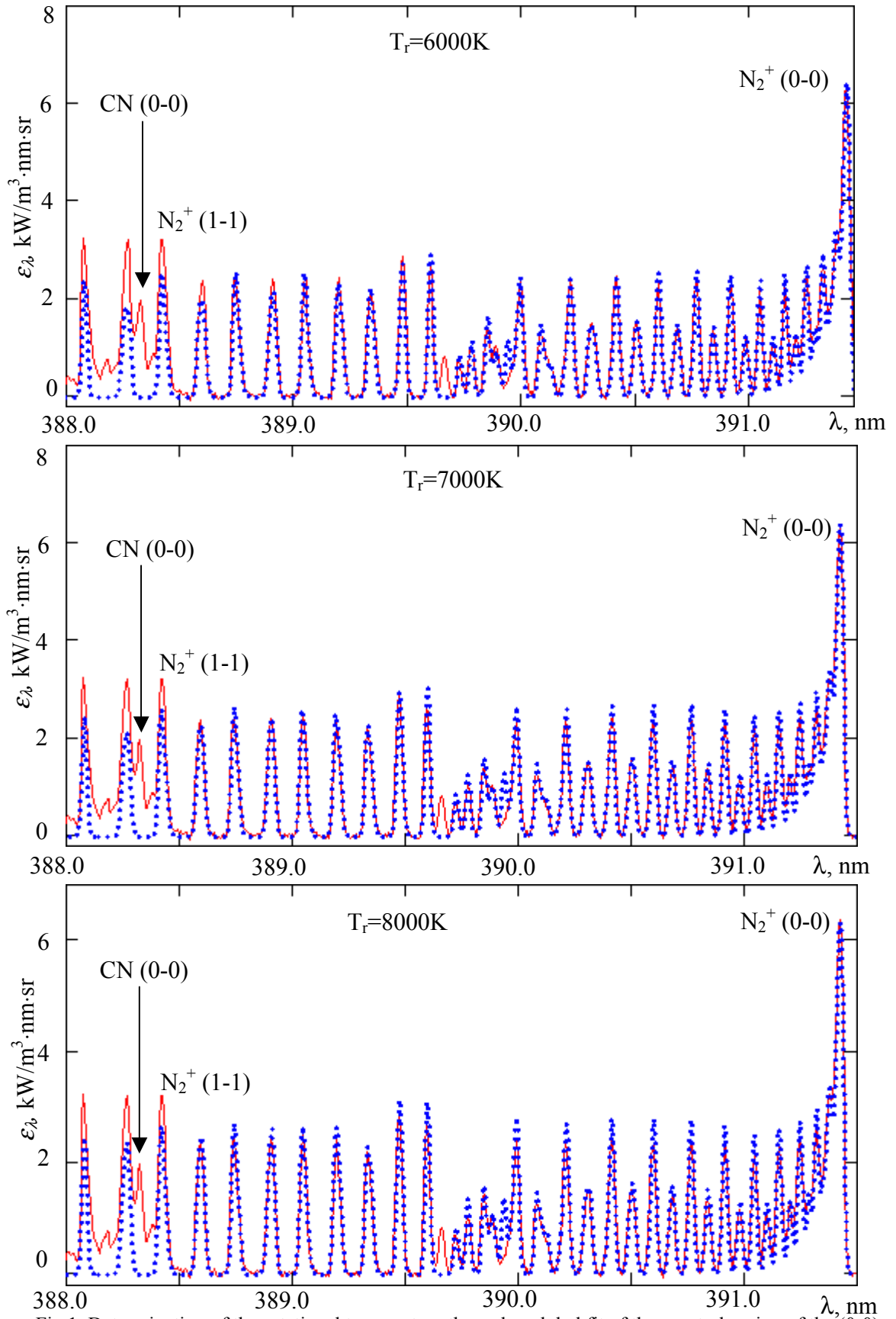


Fig.1. Determination of the rotational temperature through a global fit of the spectral region of the (0-0) band of the  $N_2^+ 1^-$  system.  $Z=55\text{mm}$ ,  $I=400\text{A}$ ,  $G=1\text{g/s}$ . Solid lines-measured spectra, broken lines-simulated spectra.

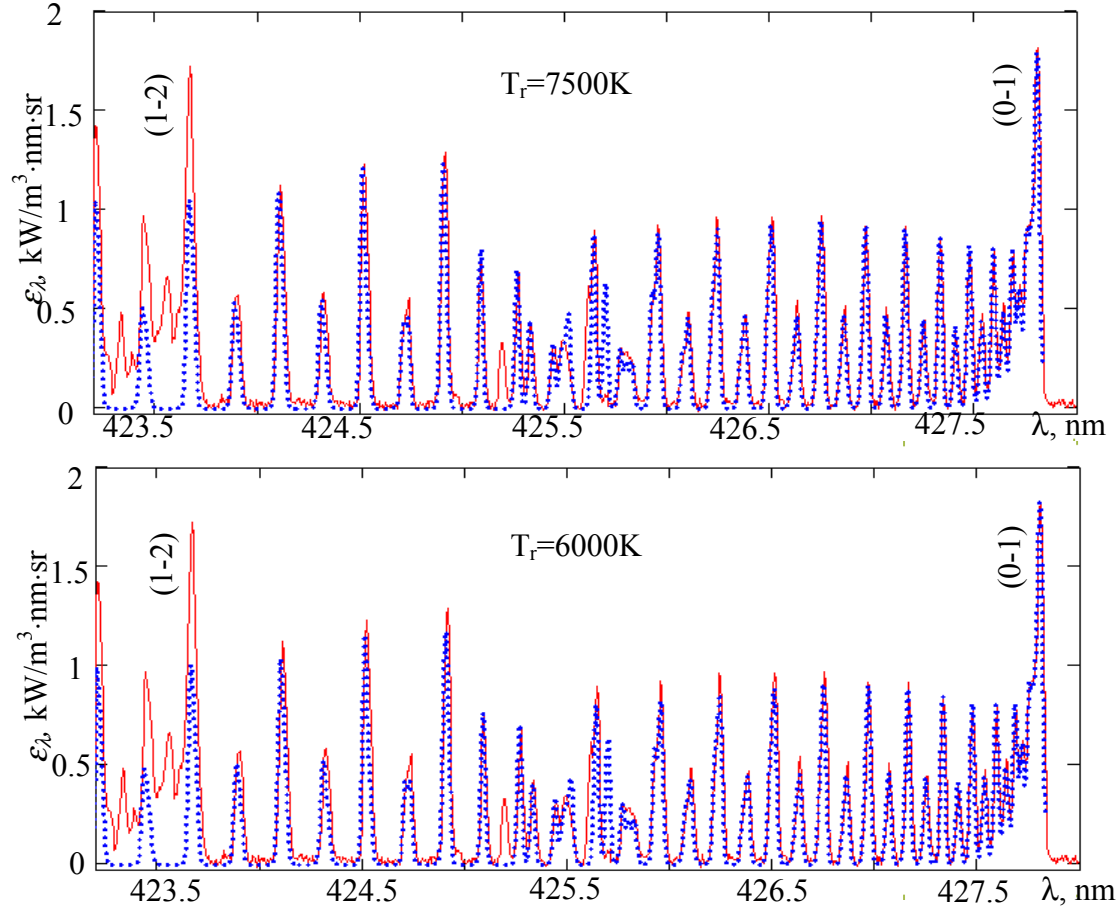


Fig.2. As in Fig.1 for the (0-1) band of the N<sub>2</sub><sup>+</sup> 1-system.

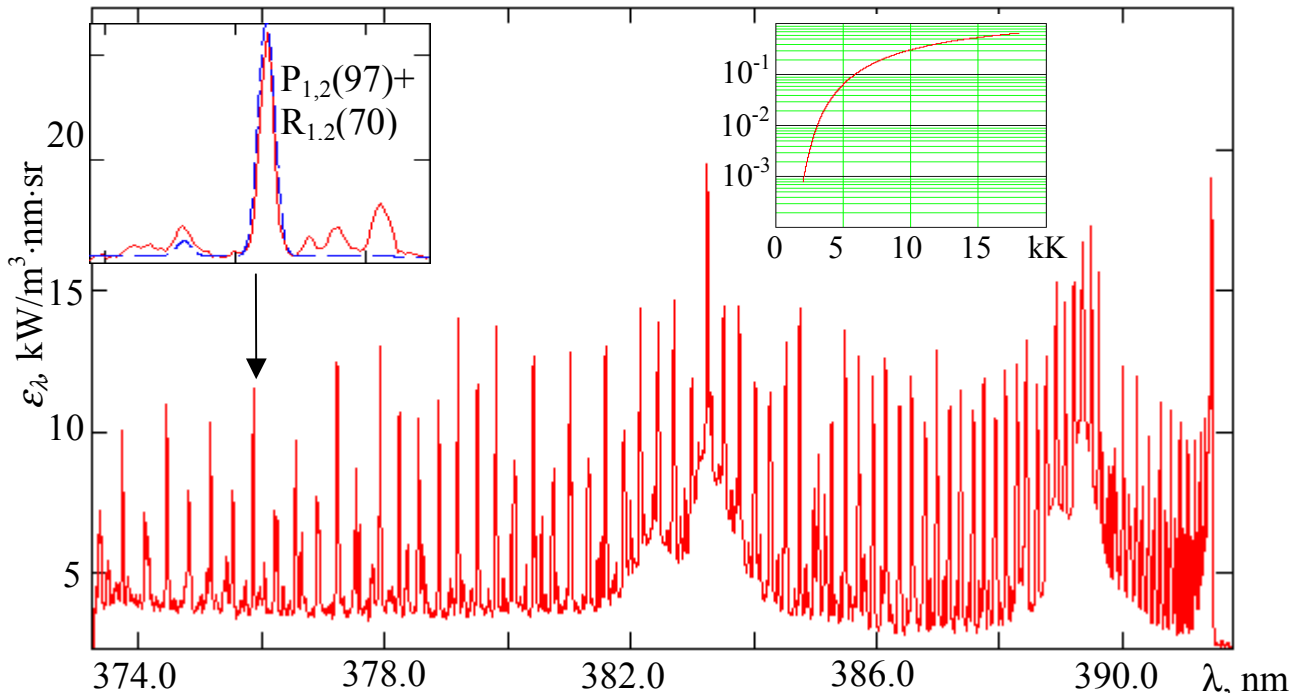


Fig.3. Determination of the rotational temperature using not fully identified spectrum in the spectral region of the (0-0) band of the N<sub>2</sub><sup>+</sup> 1-system.  $Z=28\text{mm}$ ,  $I=400\text{A}$ ,  $G=1\text{g/s}$ . The intensity of the complex line P<sub>1,2</sub>(97)+R<sub>1,2</sub>(70) (the upper left of the figure) is compared to that of the band head. At the upper right of the figure is shown the line to band head intensity ratio as a function of  $T_r$ . Solid line-measured spectrum, broken line-simulated spectrum.



Also important is the information about the vibrational temperatures  $T_v$ . It is clear that  $T_v$ -values are generally distinct not only for different kinds of molecules, but also for different electronic states of the same molecule. Nevertheless some reasonable conclusions about possible vibrational temperatures can be drawn if the spectrum shows the developed band sequences ( $\Delta v = \text{const}$ ) or  $v'$ -progressions whatever the molecule they belong to. Fig.4 illustrates determination of  $T_v(\text{CN } B^2\Sigma_u^+)$  through the use of the principal ( $\Delta v = 0$ ) sequence of CN molecules in the far relaxation zone at  $Z = 85\text{mm}$ . The line-by-line simulation of the  $\text{N}_2^+$  and CN

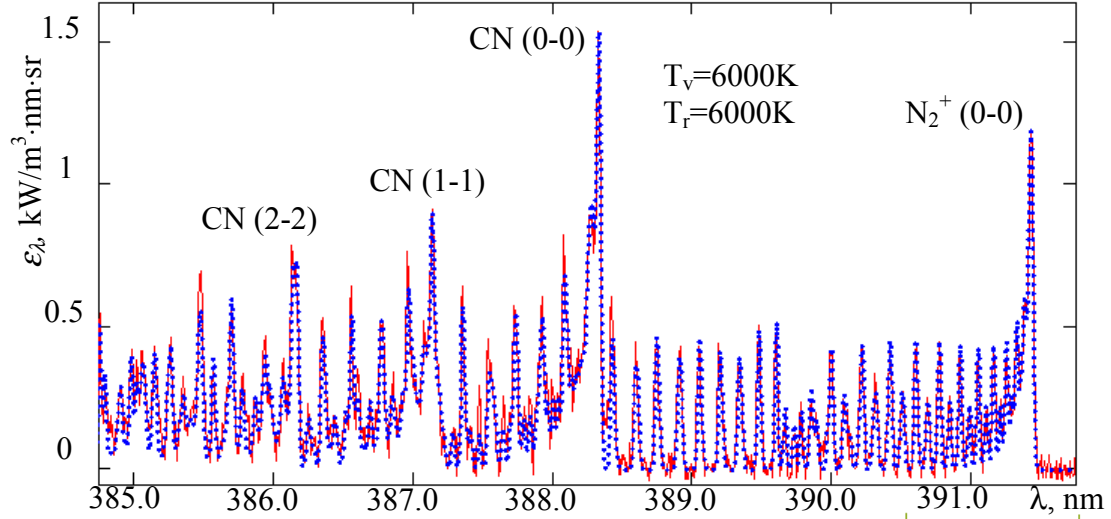


Fig.4. Determination of the rotational temperature using the principal ( $\Delta v = 0$ ) sequence of the CN Violet System.  $Z = 85\text{mm}$ ,  $I = 400\text{A}$ ,  $G = 1\text{g/s}$ . Solid lines-measured spectrum, broken lines-simulated spectrum.

spectra was applied to perform a global fit of the 385-391nm region. Choosing values of  $T_r$  and  $T_v$  being equal provides the best fit. Of interest is also to correlate the obtained  $T_r$ -values to the axial magnitudes of the electron temperature  $T_e(0)$  at several sections of the plasma jet. The latter are derived from relative intensities of NII and CuI lines [10]. Some results are presented in Table1.

Table1. Rotational and electron temperatures in high enthalpy nitrogen jet at different distances from the cathode.

Z, mm	Band (0-0)		Band (0-1)	Electron temperatures at the axis $T_e(0)$ , kK
	Global fit of spectral regions $T_r$ , kK	Line to bandhead relative intensity $T_r$ , kK	Global fit of spectral regions $T_r$ , kK	
28		13.5		$12.5 \pm 1$
55	6-8	7.3	7-8	$7.8 \pm 0.7$
70	6-8	7.4	6-7.5	$6.8 \pm 0.7$

#### 4. Conclusion

The experimental arrangement and measuring technique used in this paper allow reasonable assessment of the rotational temperatures at different sections of high enthalpy nitrogen flows at atmospheric pressure. These radius-averaged rotational temperatures do not appreciably deviate from the axial values of the electron temperatures at the respective sections. To compare these quantities in greater detail, the radial distributions of  $T_r$  have to be obtained. The approach applied offers no difficulties in this regard. In the far relaxation zone, the obtained rotational temperatures are in good agreement with the vibrational temperatures determined through the use of the CN Violet System.

## 5. References

- [1] A.A. Belevtsev, E.Kh. Isakaev, A.V. Markin, V.A. Khaimin, V.F. Chinnov - High Temp. **38**, 667 (2000).
- [2] V.M. Batenin, A.A. Belevtsev, V.F. Chinnov, E.Kh. Isakaev, A.V. Markin - Progress in Plasma Processing of Materials (Ed. P.Fauchais), Begell House, inc., New York, 199 (2001).
- [3] E.Kh. Isakaev, A.V. Markin, V.A. Khaimin, V.F. Chinnov - Instr.Exper.Techn. **44**, 32 (2002).
- [4] F. Michaud, F. Roux, S.P., Davis, A-D. Nguyen, C.O. Laux - J.Mol.Spectrosc. **203**, 1 (2000).
- [5] G. Herzberg - Molecular Spectra and Molecular Structure. Vol.1, Spectra of Diatomic Molecules/Van Nostrand, Princeton, NY, 1950.
- [6] A. Lofthus, P.H. Krupenie - J.Chem.Phys.Data. **6**, 113 (1977).
- [7] F. Michaud, F. Roux, S.P., Davis, A-D. Nguyen - Appl.Optics. **35**, 2867 (1996).
- [8] C.O. Laux, R.J. Gessman, C.H. Kruger, F. Roux, F. Michaud, S.P. Davis – JQSRT. **68**, 473 (2001).
- [9] V.F. Chinnov – High Temp. **40**, 489 (2002).
- [10] A.A. Belevtsev, V.F. Chinnov, E.Kh. Isakaev, A.V. Markin - Progress in Plasma Processing of Materials (Ed. P.Fauchais), Begell House, inc., New York, 393 (1999).

# ANALYSIS OF THE EFFECTIVENESS OF PLASMA GENERATORS WITH DIVERGENT CHANNELS

V.F. Chinnov, E.Kh. Isakaev

*Associated Institute for High Temperatures, Russian Academy of Sciences  
Izhorskaya 13/19, Moscow, 125412 RUSSIA Fax: (095) 4859777, E-mail: [v\\_chinnov@oivtran.iitp.ru](mailto:v_chinnov@oivtran.iitp.ru)*

## Abstract

For high arc currents and moderate plasma-forming gas flow rates, a stable laminar mode of arc burning with characteristic arc lengths of 20÷30mm is realized in argon and nitrogen. The arc current completes through a cold near-wall layer ionized by resonance VUV photons generated in a highly ionized ( $T_e(0) \sim 2\div 3\text{eV}$ ) arc core. In the near relaxation zone the processes of recombination of charged and atomic particles are insignificant because of high plasma flow velocities ( $\sim 100\div 200\text{m/s}$ ) and high electron temperatures. The plasma is overcooled and, in case of nitrogen, it is predominantly atomic ( $n_a > n_m$ ).

## 1. Introduction

Thermal high enthalpy atmospheric pressure plasma is one of the most technologically used media. Suffice it to mention about the large-ton plasma chemistry, plasma metallurgy, plasma processing of metals, and plasma pyrolysis. The chief advantages of plasma technology lying in high temperatures and high velocities of the working medium need the development of high-efficiency, high-power, and long-lived plasmatrons for being realized. One of promising technological plasmatrons is the d.c. plasma generator with a divergent channel-anode, vortex gas feed, and a self-setting length of the arc developed in Associated Institute for High Temperatures of the Russian Academy of Sciences [1]. Successfully employed in some technological processes, this plasmatron is very difficult to be modeled in view of some its peculiarities such as a short length of the jet segment with the unsteady-state plasma flow in a divergent channel, a variable current channel length and a complex pattern of completing the current through the anode under transverse (and vortex) gas flow over the arc. This plasmatron is capable of providing extremely high energy depositions in the arc plasma and heating atmospheric pressure plasma up to temperatures of 25-35kK. Double ionization is characteristic of these plasma temperatures.

## 2. Plasmatron description and the measuring system

The quest for creation of high efficiency technological plasmatrons has led the authors of [1] to designing a plasma generator with vortex stabilization and a divergent channel being the arc anode. The most important features of this geometry are ensuring great gas flow rates, effective heating of the working medium and low heat fluxes onto the water-cooled anode surface [1].

The plasmatron this kind of is distinguished by the ability for generating high enthalpy plasma flows with great gas flow rates and negligible arc lengths (20-40mm) at a high efficiency. Because maximum plasma temperatures in such generators with the 3-7 mm inlet anode opening diameters exceed 2eV and the mass-averaged temperatures at the outlet are 5000-10000K at gas flow rates of 1-5g/s, these plasmatrons are widely technologically used [4,5]. Their practical importance has impelled us to carry out comprehensive plasma investigations at different sections of the jet beginning with the near-anode region of the electric discharge with specific power depositions of  $\sim 50\text{-}100\text{kW/cm}^3$  and ending with the plasma relaxation zone at the distances of above 50 mm downstream from the anode. The effectiveness of converting the electric field energy of the arc into the heat energy of the plasma flow is promoted by jet vortex stabilization performed in these plasmatrons through a tangential feed of plasma-forming gas. In such discharges, the convective and conductive fluxes to the water-cooled wall of a divergent channel-anode decrease whilst the radiant losses whose role increases with increasing temperature come first.

The measuring complex comprises the system for spectral measurements, the system for high-speed visualization of the plasma filament, the system for calorimetrically measuring the heat fluxes removed from

the plasma through all water-cooled plasmatron elements, and also the system for measuring currents through each segment of the segmented anode.

The system for spectral measurements, represented schematically in Fig. 1, includes two subsystems. The first subsystem consists of a small-sized monochromator MDR-41 with a high light-gathering power; a control unit that provides scanning with a given speed and control over the current wavelength; a photomultiplier tube FEU-100 and its supply unit; an electronic circuit converting the RS-232 protocol to RPS; an L-1250 computer ADC card; and the software. The operating wavelength range is limited by the sensitivity of the FEU-100 photocathode and spans the 200-830 nm region. The second subsystem consists of a DFS-452 diffraction spectrograph and an MOAC-2 multichannel optical spectrum analyzer. The MOAC-2 analyzer incorporates two photometer heads with photodiode CCD arrays (TDS1250A by Toshiba) and an interface card inserted in a serial computer port. Each photodiode array (PDA) contains about 3700 photosensitive elements 8  $\mu\text{m}$  in length and 200  $\mu\text{m}$  in height. The spectral region of sensitivity is 190-1000 nm. The DFS-452 spectrograph permits operation throughout the sensitivity region of the PDAs. With gratings of 600 and 1200 grooves/mm, the reciprocal linear dispersion is 1.6 and 0.8 nm/mm, i.e., 0.013 and 0.0065 nm per PDA element. One of the PDAs is aligned with the direction of the spectrograph dispersion and is used to record a spectrum; the other PDA is perpendicular to this direction and is intended for measuring the intensity distribution over the slit height (and, accordingly, across the plasma jet) at a given wavelength.

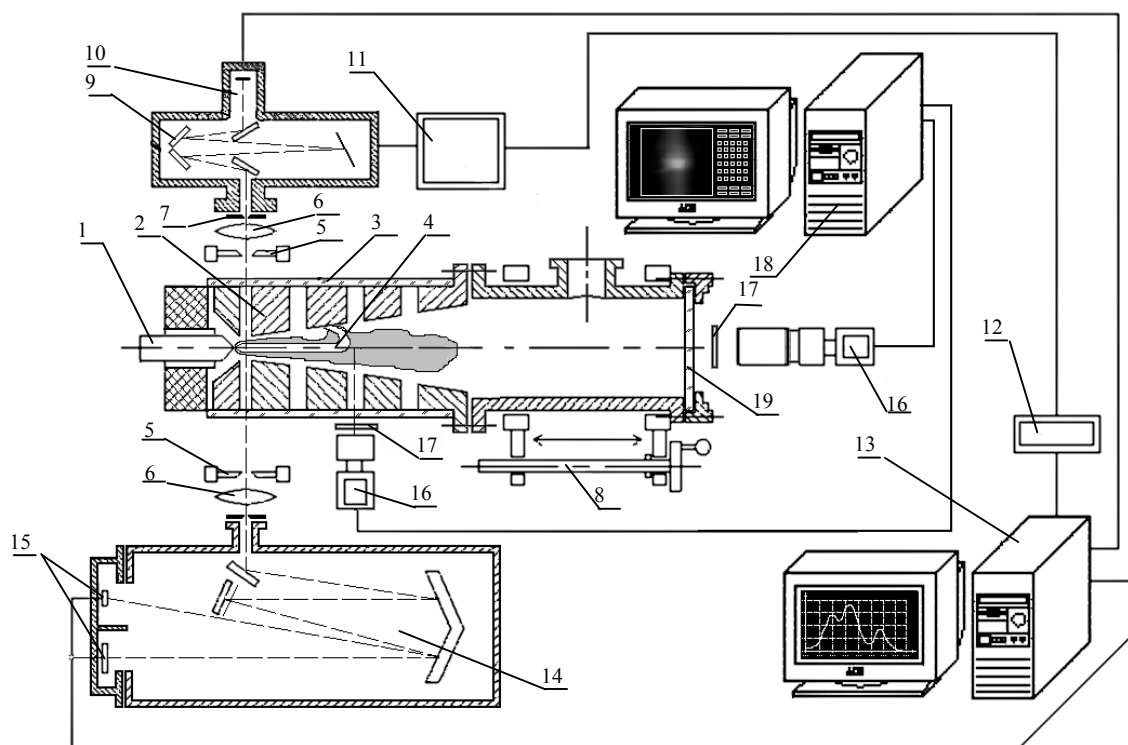


Fig. 1. Layout of optical measurements. 1-plasmatron cathode; 2-plasmatron anodes; 3-optical windows; 4-arc plasma; 5-diaphragm; 6-condenser; 7-Hartman screen; 8-mechanism for moving plasmatron; 9-MDR-41 monochromator; 10-FEU-100 photomultiplier tube; 11-monochromator controller; 12-interface card (for converting the RS-232 standard into RPS); 13-PC-AT computer with the interface and ADC cards; 14- DFS-452 spectrograph; 15-photometric heads with CCD arrays; 16-CCD-cameras; 17-light filter; 18-IBM PC-AT computer with CCD-camera interface; 19-end windows.

The applied spectral systems permit reliable processing of the lines whose half-widths are commensurable with or greater than  $\delta_{APP} \cong 0.025$  nm. The spectral resolution of these systems should be stressed to be better than 0.01 nm.

For investigating both longitudinal and transverse structures of the plasma filament during the exposure times comparable with the characteristic time of changing the filament configuration, the “VS-tandem/s54” system is employed. It consists of controller VS54 and CCD camera VsatTV on the basis of the SONY matrix. It is designed for high quality input of black-and-white images into IBM PC computers.

### 3. The results of measurements

The SPEC\_MCD.100 system for an automated processing of spectroscopic information allowing solution of the main issues of quantitative spectroscopy is developed and practically employed [6].

Most reliable methods are developed and substantiated for determining basic parameters of highly ionized argon and nitrogen plasmas including mathematical modeling of  $N_2^+$  rovibronic spectra to determine the vibrational and rotational temperatures of nitrogen plasma [2, 3, 7].

The absolute power flows irradiated by highly ionized Ar and  $N_2$  plasmas are measured and their role in the energy balance and the passage of current through a plasma with vortex stabilization by gas flow is revealed.

An experimental base is laid for creating unique database on the radiative properties of highly ionized Ar and  $N_2$  plasmas and on basic spectral characteristics like the optical transition probabilities and Stark constants of neutral and singly and doubly ionized argon and nitrogen. As an example, Fig.2 gives the distributions over the excited states in highly ionized argon and nitrogen plasmas.

Experimentally investigated is the character of the departure from the equilibrium state in the relaxation zone of plasma, which gives rise to its high chemical reactivity.

Along with the comprehensive spectral analysis, calorimetric measurements of the heat fluxes removed through the basic cooled elements of the plasmatron are performed. This permitted the enthalpy measurements at different sections of the plasma jet and assessments of the mass-averaged temperatures and velocities of Ar and  $N_2$  plasmas at the plasmatron outlet in the plasma relaxation zone.

### 4. Analysis of the results

The most important feature of the investigated high current arcs ( $I > 250$  A) in a divergent channel-anode are their low lengths of only 2-3 diameters of the inlet opening of the divergent channel. Accordingly to the estimates, the mode of a stabilized hydrodynamic flow is not realized in the plasmatron being investigated. However it is in this mode that high specific energy depositions ( $W_V > 60$  kW/cm<sup>3</sup>,  $W_L = 15-25$  kW/cm) and high heat efficiency  $\eta_T = hG/IU$  ( $h$  is the mass-averaged plasma enthalpy at the plasmatron outlet,  $G$  is the gas flow rate) are attained.

As shown in experiments with a segmented anode channel of 5-6 mm inlet anode opening (minimum diameter) and gas flow rates of 1-5 g/s, about 95% of the total arc current (250-500 A) in argon and nitrogen plasmas is removed through the first anode segment of 1 cm in length and the rest of 5% is withdrawn through the three subsequent segments. This character of the current removal is apparently caused by that there is a transverse (with respect to the vortex arc-stabilizing flow) electric field  $E_r \approx 30-50$  V/cm in the transition layer of  $\Delta$  depth between the current-bearing plasma filament of 5-5.5 mm optical diameter and the water-cooled anode wall of 6-7 mm diameter.

The pattern of the spatial distributions of the electric current and plasma parameters in the region of the current removal is given in Fig.3. The heat fluxes onto the water-cooled anode surface measured calorimetrically in nitrogen arc show that 2 kW of 6 kW heat power removed by cooling water from the first segment arrives at the anode with the current. A uniform, with no discontinuities and filaments, current extraction through the first anode segment is observed on visualization of the near-wall arc plasma at the medium section of this segment [8].

We now assess the number densities of electrons produced in the transition layer by the VUV-radiation generated in the high-temperature arc core and transferred to the discharge periphery in the wings of NII and NIII resonance lines [9]. For this purpose the results are involved of the experimental and calculated-theoretical analysis of changing the radiant flow divergence along the radius in a cylindrical

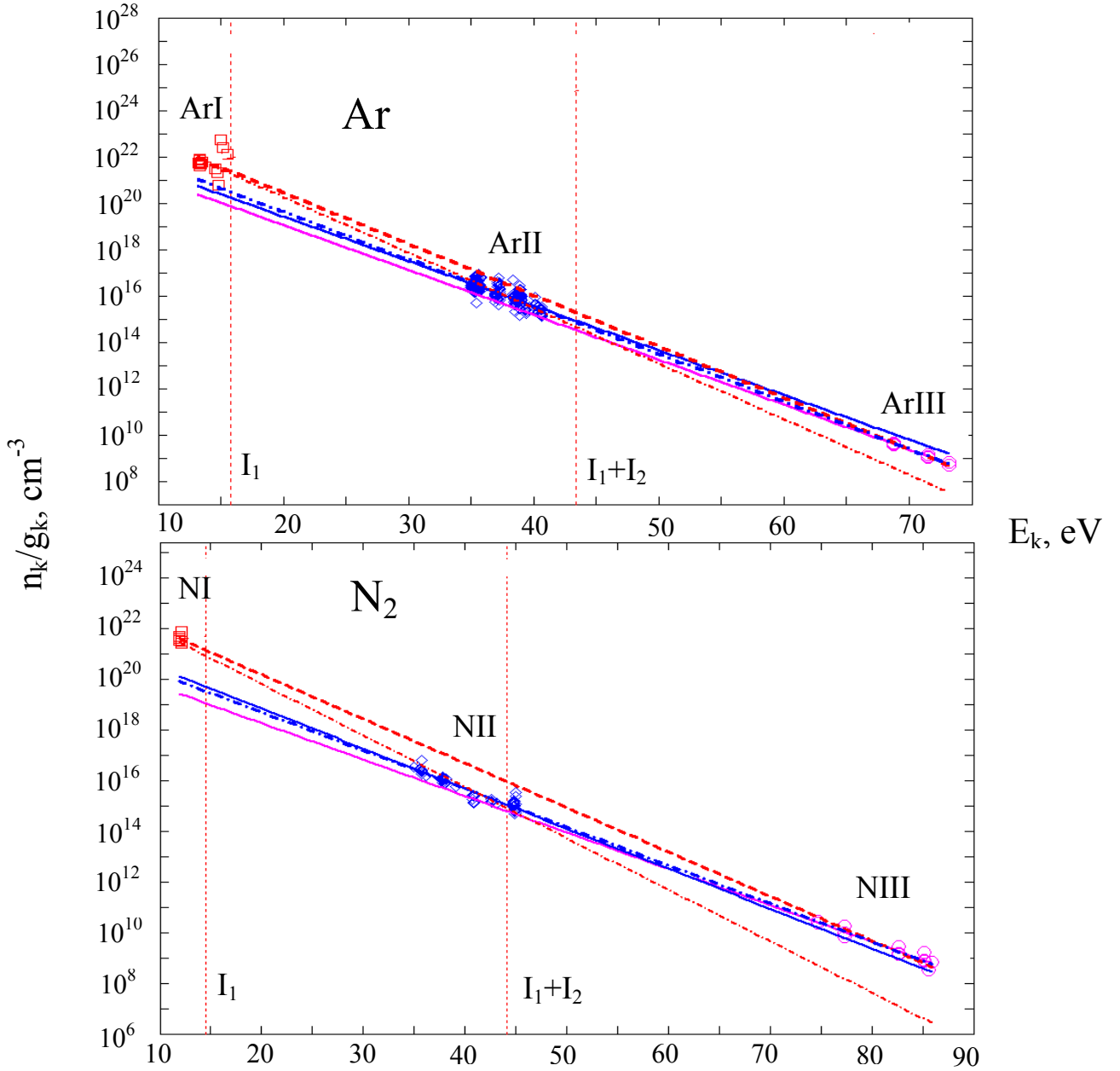


Fig.2. The reduced populations of atomic and ion excited states in argon and nitrogen plasmas near the arc axis. The excitation energies are reckoned from the ground states of atoms. Overpopulation of atoms is caused by the Larens effect. Arc current is 400A, the distance from the cathode is 4 mm.

nitrogen plasma arc column at a current of 350-400A, the channel diameter of 5 mm, and the axial temperature of 26000K [9, 10]. Ar and N<sub>2</sub> possess extremely high photoionization cross sections near their ionization thresholds  $I_i$  (i.e., at photon energies  $h\nu \geq I_i$ )

$$\sigma_{ph}(N_2) = 2.6 \cdot 10^{-17} \text{ cm}^2, \lambda_i \leq 79.8 \text{ nm}; \quad \sigma_{ph}(\text{Ar}) = 3.5 \cdot 10^{-17} \text{ cm}^2, \lambda_i \leq 78.7 \text{ nm}$$

VUV-radiation of argon and nitrogen plasmas contains great many spectral lines with the photon energies exceeding Ar and N<sub>2</sub> ionization potentials. The radiation flux arrives at the transition layer with high number densities of molecules  $[N_2] \geq 10^{18} \text{ cm}^{-3}$ , so that it is effectively absorbed in this layer

$$k_0 = \sigma_{ph} \cdot [N_2] \sim 30 \text{ cm}^{-1}$$

The electron balance in the transition layer allowing for the photoionization process may be written as

$$\frac{dn_e}{dt} = J^{ph} \frac{\sigma_{ph}[N_2]}{h\nu} - n_e \cdot n_i \alpha_{dr} = 0. \quad (1)$$

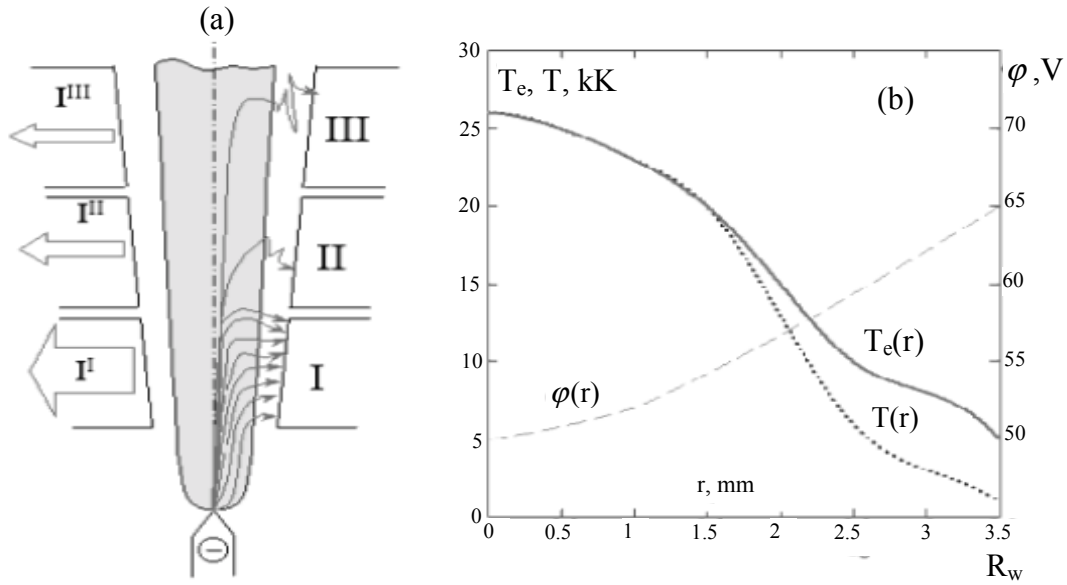


Fig.3. A qualitative pattern of the current lines (a) and of the spatial distribution of basic plasma parameters at the medium section of segment I (b).  $R_w$  is the associated channel radius. The arc current predominantly completes through the segment I of the anode as seen from Fig.3a..

Using the estimate for the total radiation flux density and the data [9, 10] about the fraction of the radiation with photon energies  $h\nu \geq I_i$  in this flux, one arrives at a magnitude of  $J^{ph} \cong 500 \text{ W/cm}^2$  for the density of the VUV-radiation flux providing photoionization. On the assumption that the charge losses in the absorbing layer are due to only dissociative recombination, the expression for the number density of electrons produced by photoionization reads

$$n_e \cong \sqrt{\frac{J^{ph} \sigma_{ph} [N_2]}{h\nu \alpha_{dr}(T)}}. \quad (2)$$

Substituting numerical values into Eq.(20) gives  $n_e \sim 10^{14} \text{ cm}^{-3}$ . This number density is sufficient for ensuring the required conductivity  $\sigma \cong 5 \text{ Ohm}^{-1} \cdot \text{cm}^{-1}$  in the layer. It means that the current in a high-current electric arc plasmatron with a divergent channel-anode completes through the anode due to photoionization of the transition “plasma-wall” layer by VUV-radiation generating in a highly ionized arc core. An uniform and diffuse character of the current removal arises from the combined effect of the radial electric field in the transition layer  $E_r \sim 40\text{-}50 \text{ V/cm}$ , ensuring the electron drift velocity  $w_d \sim 10^6 \text{ cm/s} \gg u$  greatly exceeding the mass-averaged gas flow velocity transverse to the current, and of the volume VUV-photoionization ( $1/k_0 \sim \Delta$ ) sustaining the required level of conductivity of the transition layer.

## 5. Conclusion

Conversion of the electric power into the enthalpy of working gas in a high-current electric arc plasmatron is performed in the following way. Hot highly ionized ( $T \cong 25 \text{ kK}$ ,  $n_e \sim 1.5 \cdot 10^{17} \text{ cm}^{-3}$ ) arc core transforms a considerable fraction of the specific electric power  $jE = 50\text{-}100 \text{ kW/cm}^3$  into the radiation of primarily VUV-range. The “transparent” component of this radiation reaches the anode channel walls and is the chief fraction of the energy losses. Optically dense VUV-radiation is transferred to the arc periphery in the wings of spectral lines and ionizes the near-wall layer of relatively cold gas, which is not transparent for this radiation. The plasma chemical reactor thus can be considered to operate at the initial segment of the anode channel, which convert electric energy to the gas enthalpy with the efficiency of no less than 70%. At a current of 400A the plasmatron provides the mass-averaged temperatures of 5-6 kK for nitrogen and of 9-10 kK for argon plasmas at the outlet.

In the near relaxation zone being of prime interest for technological applications, the processes of recombination of charged and atomic particles are insignificant because of high plasma flow velocities

(~100-200 m/s) and high electron temperatures. The plasma is overcooled, i.e.  $n_e \gg n^+ \gg n_e^{eq}(T_e)$ , and, in case of nitrogen,  $n_a > n_m > n_m^{eq}(T_e)$  [7]. This ensures high chemical reactivity of the investigated nitrogen plasmas, which is successfully used, for example, in hardening and nitriding of steels [5].

### References

- [1] E.Kh. Isakaev, R.R. Grigor'yants, N.O. Spector, A.S. Tyuftyaev – High Temp. **32**, 588 (1994).
- [2] A.A. Belevtsev, E.Kh. Isakaev, A.V. Markin, V.A. Khaimin, V.F. Chinnov - High Temp. **38**, 667 (2000).
- [3] A.A. Belevtsev, E.Kh. Isakaev, A.V. Markin, V.F. Chinnov - High Temp. **40**, 26 (2002).
- [4] A.A. Belevtsev, V.F. Chinnov, E.Kh. Isakaev, P.P. Ivanov - Proc. of the XIII Int. Conf. on Gas Discharges and their Applications, Glasgow, UK, Sept.3-8, 609 (2000).
- [5] Ivanov P.P., Isakaev E.Kh., Tyuftyaev A.S., Zhelobtsova G.A., Filippov G.A. - Progress in Plasma Processing of materials. 5<sup>th</sup> European Conference on Thermal Plasma Processes, St.Petersburg, 12-17 july 1998, Ed. P.Faushais and J. Amouroux, 393 (1999).
- [6] E.Kh. Isakaev, A.V. Markin, V.A. Khaimin, V.F. Chinnov - Instruments and Experimental Techniques. **44**, 1 (2001).
- [7]: A.A. Belevtsev, V.F. Chinnov, E.Kh. Isakaev, A.V. Markin, N.O. Spector - Proc.15<sup>th</sup> Symp. on Plasma Chemistry, Orleans, France, .765 (2001).
- [8] Chinnov –High Temp. **40**, 489 (2002).
- [9] Hermann W., Schade E. - JQSRT. **12**, 1257 (1972).
- [10]. Hermann W., Schade E. Zeitschrift fur Physik. - **B.233**, 333 (1970).



# A Theoretical Investigation of Underlying Dynamics in Arc Plasma Devices and Comparison with Experiment

S. Ghorui and A.K. Das

*Laser & Plasma Technology Division, Bhabha Atomic Research Center, Trombay, Mumbai, India*

Dynamic and static behaviors of arc plasma devices are subject of experimental study for a long time. Although the nature of behavior is investigated in depth, the origins of inherent fluctuations observed in such devices have not been explored. In this paper we present a general theory of such fluctuations using basic equations of dynamics and show that the theory is able to predict the fluctuations observed experimentally. A gradual transition of the dynamics from non-oscillatory to regular oscillatory to chaotic regime is predicted by the theory under current variation as a controlling parameter, which is in agreement with the experimentally observed transition. The formulation in terms of nondimensional parameters ensures the general applicability of the theory to other experimental systems also.

Non-dimensional set of governing equations in terms varying components of temperature, material concentration, magnetic field and velocity for an assumed cylindrical near arc root region of radial dimension  $R$  and height  $d$ , is as follows.

$$\frac{\partial \eta}{\partial t} = \Gamma(\psi, \eta) + \sigma \nabla^2 \eta - R_l \sigma \partial_r T + R_s \sigma \tau \partial_r S - \frac{2}{R} \sigma \xi Q \partial_z B$$

$$\frac{\partial T}{\partial t} = \Gamma(\psi, T) - \partial_r \psi + \nabla^2 T$$

$$\frac{\partial S}{\partial t} = \Gamma(\psi, S) - \partial_r \psi + \tau \nabla^2 S$$

$$\frac{\partial B}{\partial t} = \phi(v, B) - 2dR^{-1} \partial_z \psi + \xi \nabla^2 B$$

Where, all the parameters are dimensionless and  $R_l$ ,  $R_s$ ,  $\sigma$ ,  $\xi$ ,  $\tau$  and  $Q$  are Rayleigh number, solute Rayleigh number, Prandtl number, Magnetic Prandtl number, ratio of solute to thermal diffusivities and Chandrasekhar number respectively defined as:

$$R_l = \frac{g \alpha \Delta T d^3}{\kappa \nu}, \quad R_s = \frac{g \alpha \Delta S d^3}{\kappa \nu}, \quad \sigma = \frac{\nu}{k}, \quad \xi = \frac{\eta_B}{k},$$

$$\tau = \kappa_s / \kappa, \quad \eta_B = 1 / \mu_0 \sigma_C, \quad Q = \frac{B_0^2 d^2}{\mu \rho_0 \eta_B \nu}, \quad B_0 = \frac{\mu_0 J_0 R}{2}, \quad \kappa = k / \rho s.$$

$k$ ,  $\rho$ ,  $s$ ,  $S$ ,  $\kappa_s$ ,  $\nu$ ,  $J$  and  $\psi$  are thermal conductivity, density, specific heat, metal concentration, diffusivity of evaporated metal, viscosity, current density and stream function respectively. ACS (Arneodo, Coulet and Spiegel) technique for the derivation of amplitude equation gives rise to amplitude equation for the system:  $\ddot{F} + \Omega_2 \dot{F} + \Omega_1 F + \Omega_0 F = \pm F^3$ .

Coefficients of this equation are directly related to the experimental conditions via arc current and solution of the equation gives underlying nature of the instability existing in the system. The associated instability will be reflected in all measurable signals emitted from the plasma subject to other conditions. The electronic component of the plasma will instantaneously respond to the generated fluctuation in electric field and transfer a part of their energy to the neutrals through elastic collisions. The energy transfer, modulated according to fluctuation, induces pressure perturbation and generates an acoustic wave in the plasma which has been experimentally observed. Depending on dimension ( $\ell$ ) of the plasma, this acoustic signal can be detected mostly undistorted but enveloped by a response function  $f(\omega) = \omega^{-1} \sin(\omega \ell / 2c)$ . Accounting for all these, in our experiment (comprised of more than 250 runs under various conditions) it has been found that generated acoustic signal is directly proportional to  $F(t)$ . Once unenveloped acoustic signal  $[F(t)]$  is obtained, the fluctuating behavior of power inside the plasma is obtained just by integrating  $F(t)$ . Other associated signals are derived in similar fashion. Acoustic, voltage and optical signals generated from the theory are characterized in terms of invariants of dynamics like power spectra, phase portrait, fractal dimension and Lyapunov exponent. Remarkable similarity has been observed in these invariants when theoretical and corresponding experimental results are compared. The paper presents details of such comparisons.

# **Application of DC arc plasma torch as a tailored heat source for thermal-hydraulic simulation of proton beam-target interaction in accelerator driven sub critical systems (ADS)**

A. K. Das , P. S. S. Murty, S. N. Sahasrabudhe, N. S. Dixit, Srikumar Ghorui  
and P Satyamurthy

*Laser & Plasma Technology Division  
Bhabha Atomic Research Centre,  
Bombay, 400 085, India*

Plasma beams emanating from DC arc plasma torches are ideal concentrated energy flux (CEF) sources for a large number of industrial applications like cutting, melting, welding, spheroidization, materials synthesis, simulation of reentry conditions, treatment of radioactive wastes etc. Recently, transferred arc plasma beams have been proposed as one of the attractive CEF sources for thermal and hydraulic simulation of the proton beam – target (liquid metal) interaction in accelerator driven sub critical systems (ADS). Currently, research on accelerator driven sub critical (ADS) nuclear reactors have assumed extreme significance due to their high safety level and incredible potential in terms of both thorium utilization as well as nuclear waste transmutation. While the high energy - high current proton beams are being built; intensive efforts are being undertaken towards the development of complex lead bismuth eutectic (LBE) target systems in terms of thermal-hydraulic simulation facilities using equivalent easily controllable heat sources. The basic objective of the thermo hydraulic simulator is to simulate the effects of 1 GeV, 10 mA proton beam depositing 66% of its power in form of thermal energy in to the liquid metal control volume. The detailed computations show the power density to be  $2.5 \text{ kW/cm}^3$ . On the other hand, a plasma jet that impinges on a metal substrate (window), say for example copper-stainless steel window, creates a surface heat source and most of the thermal energy transmitted through this window is confined in the thermal boundary layer formed adjacent to the window on the liquid metal side. The surface heat fluxes necessary for simulation are of the order of  $1 \text{ kW/cm}^2$  to be spread uniformly on the ADS target. The paper describes the development of a transferred arc plasma source that is capable of delivering the requisite heat flux on to the target window. The plasma torch powered by a current regulated DC power source consists of a thoriated tungsten cathode located coaxially inside a copper anode in the form of a nozzle. Argon and mixtures of argon with either nitrogen or hydrogen are used as plasma gas. The 100 kW torch is encased in a 250 mm diameter SS pipe with a heat guard against the hot gases reflected from the target window. All the elements are intensively water-cooled. The target window, in keeping with the requirements of ADS system, is made up of a  $50 \text{ cm}^2$  water cooled copper block surrounded by a co-axial stainless steel disc-end of specified curvature. The plasma torch and the window assembly is qualified by using water as the heat transfer agent (target) in stead of the liquid metal. The uniformity in heat flux delivered to the target is achieved through use of magnetic field configurations to sweep/ rotate the plasma beam over the entire window surface. The paper presents the design and operational data of the plasma source including V-I characteristics, electro thermal efficiency and the heat source spatial distribution on the window during the qualification runs.. The experimental data is supported by computations using a 2D finite volume plasma column code. A plasma run at 60 kW with rotating magnetic field delivered a peak power of  $1.6 \text{ kW/cm}^2$  with a half width of 80mm at a standoff of 150 mm.

# **On synergetic effects at destroying of toluene and TCE by non-thermal plasma of DC glow discharge and streamer corona at atmospheric pressure.**

Yuri S. Akishev, Vladimir B. Karal'nik, Igor V. Kochetov, Anton E. Monich,  
Anatoly P. Napartovich, and Nikolay I. Trushkin

*State Research Center of RF Troitsk Institute for Innovation and Fusion Research,  
Troitsk, Moscow region, 142190, Russian Federation*

## **Abstract**

Results on toluene decomposition obtained from both experiments with DC glow discharge in gas flow and numerical calculations are compared in this report. In the case of a binary mixture of toluene and TCE (trichloroethylene), experiment shows synergetic effect, i.e. an addition of TCE in mixture increases the decomposition of toluene. The comparison of decomposition efficiencies between DC glow discharge and DC positive streamer corona is presented as well. In last case, the tested admixtures were toluene and TCE.

## **1. Introduction**

Atmospheric pressure non-thermal plasmas induced by DC glow discharge in diffusive mode and DC positive corona in streamer mode can be used for decomposition of different VOCs compounds in off-gases [1, 2]. Type of discharge producing the non-thermal plasma determines the efficiency of generation of chemically active species and therefore the energy cost of clean up process. The latter value can be found from experiment or estimated by numerical calculations. The completed model describing numerous reactions in waste gas under non-thermal plasma processing is absent yet. The main reason is scant information about paths and rate coefficients for many possible chemical reactions. Another reason is poor knowledge about influence of contaminants on charged particle kinetics in discharge plasma. We present both the experimental data proving strong impact of contaminants like toluene and TCE on the reduced electric field in glow discharge, and appropriate numerical model describing the decomposition of toluene by glow discharge in humid airflow.

## **2. Experiment**

Non-thermal plasma in humid airflow with dosed pollutants was created in a rectangular channel of 15 cm in width and 30 cm in length. The height of channel was 1.35 and 3.5 cm in the case of glow discharge and positive corona respectively. Gas flow velocity was 15-20 and 2.5 m/s in glow discharge and positive corona respectively. Humidity of airflow was varied up to 18% (volume concentration of water vapor). The electrode system consisted of 28 the paired elements (pin-to-crater) [2, 3] disposed evenly from each other. The pins served either as cathodes in the case of DC glow discharge or as anodes in the case of DC positive corona. Each pin had several emitting points. High-voltage power supply up to 30 kV was used to sustain both of the discharges mentioned above. Concentrations of toluene and TCE were varied from 15 to 500 ppm and measured with a gas chromatograph.

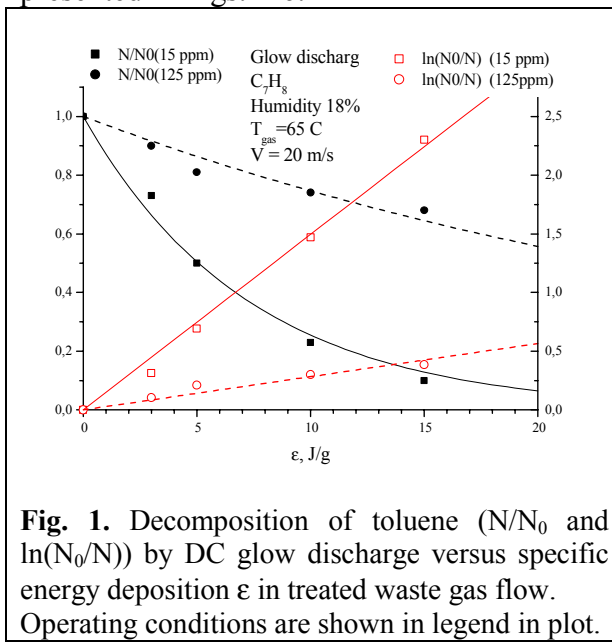
### ***Experimental results on non-thermal plasma destruction***

Additional increase  $\Delta E$  of the reduced electric field  $E/N$  in DC glow discharge due to admixtures of water vapor, toluene and TCE in airflow can be written by this empirical expression found from the processing experimental data:

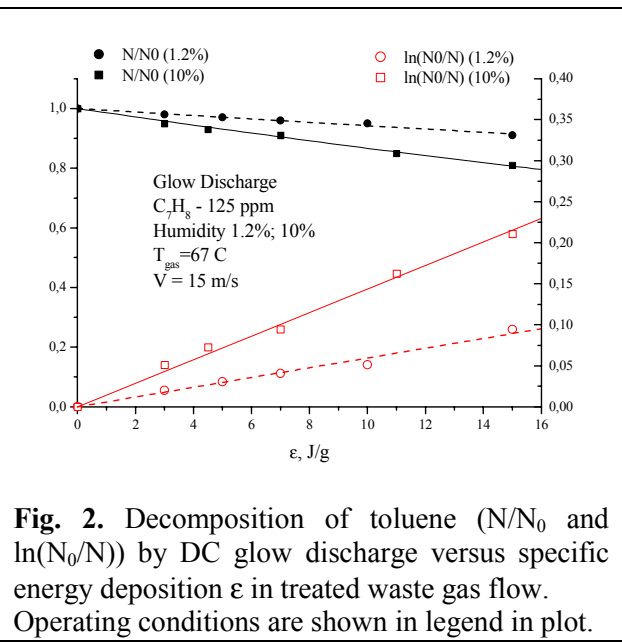
$$\Delta_{\Sigma} \cong \left( \frac{\theta_{H_2O}^{3/2}}{33} + \frac{\sqrt{(C_7H_8)_0}}{25} + \frac{\sqrt{(TCE)_0}}{11} \right) \cdot 10^{-16} \text{ V cm}^2$$

where  $(C_7H_8)_0$  and  $(TCE)_0$  are initial concentrations (in ppm) of toluene and TCE,  $\theta_{H_2O}$  is volume concentration (in %) of water vapor. One can see the TCE has strong impact on the E/N. In the case of positive corona, admixtures don't influence strongly average reduced field.

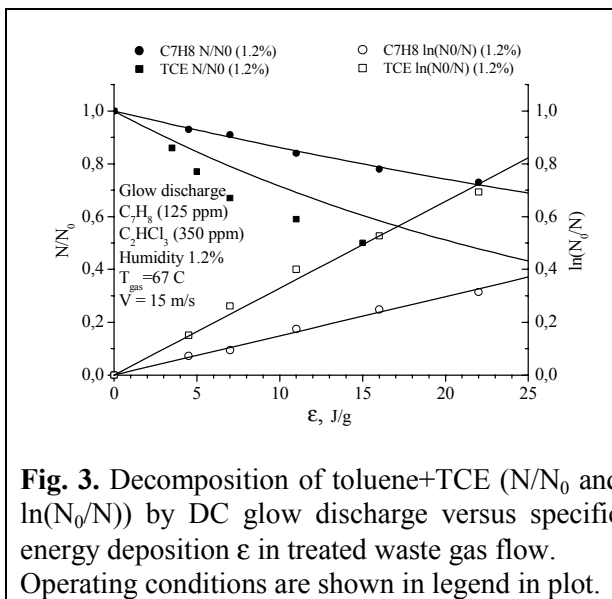
In many cases the pollutant decomposition in non-thermal plasma reactor can be expressed as exponential function [1]:  $N \cong N_0 \exp(-\varepsilon/\varepsilon_n)$ , where  $N_0$  and  $N$  are inlet and outlet volume concentrations of a pollutant numbered as  $n$ ,  $\varepsilon$  is a specific energy deposited into treated gas (in J/g),  $\varepsilon_n$  is an effective energy characterizing the decomposition of pollutant of the  $n$ -sort. We also treated our experimental data with use of exponential function. Some results on destruction of toluene and TCE by DC glow discharge and DC positive corona are presented in Figs. 1-6.



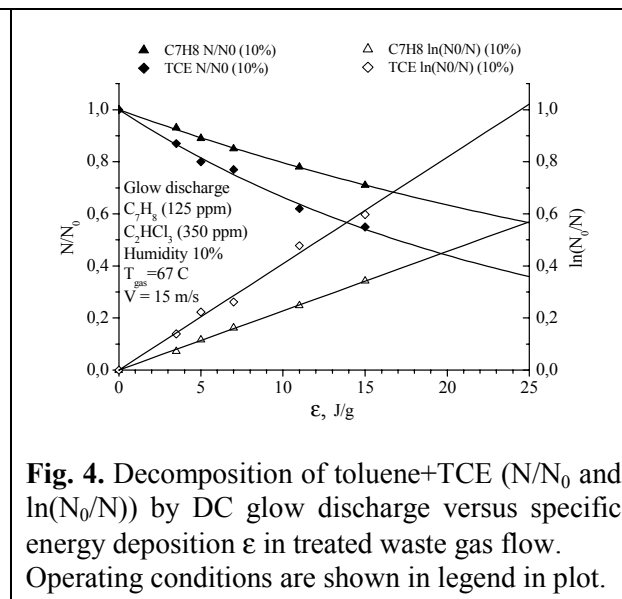
**Fig. 1.** Decomposition of toluene ( $N/N_0$  and  $\ln(N_0/N)$ ) by DC glow discharge versus specific energy deposition  $\varepsilon$  in treated waste gas flow. Operating conditions are shown in legend in plot.



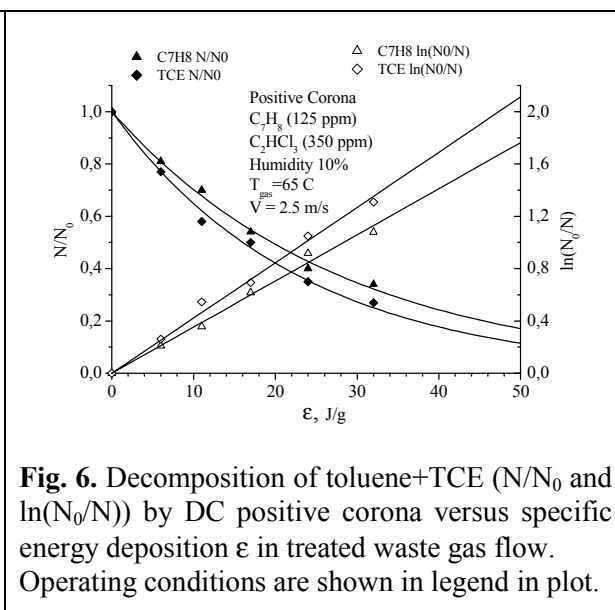
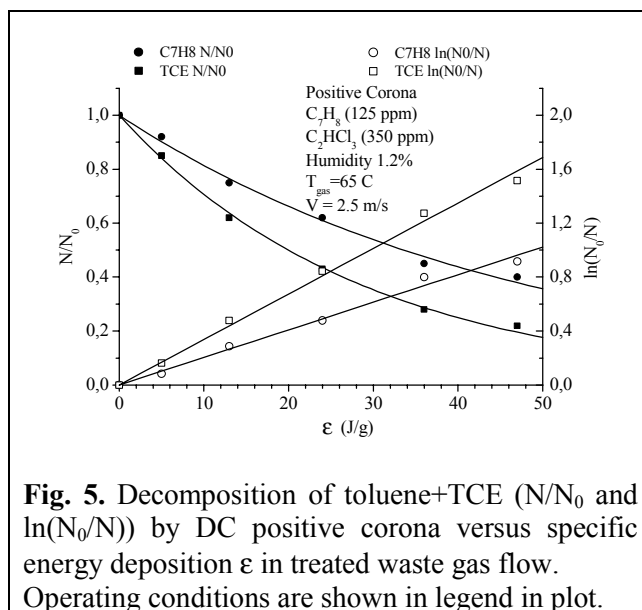
**Fig. 2.** Decomposition of toluene ( $N/N_0$  and  $\ln(N_0/N)$ ) by DC glow discharge versus specific energy deposition  $\varepsilon$  in treated waste gas flow. Operating conditions are shown in legend in plot.



**Fig. 3.** Decomposition of toluene+TCE ( $N/N_0$  and  $\ln(N_0/N)$ ) by DC glow discharge versus specific energy deposition  $\varepsilon$  in treated waste gas flow. Operating conditions are shown in legend in plot.



**Fig. 4.** Decomposition of toluene+TCE ( $N/N_0$  and  $\ln(N_0/N)$ ) by DC glow discharge versus specific energy deposition  $\varepsilon$  in treated waste gas flow. Operating conditions are shown in legend in plot.



### 3. Theory

DC glow discharge experimental system is hard for theoretical analysis. Also quite a little information is available about chemical and plasma-chemical reactions with participation of toluene molecules. Therefore, the theory can be developed by making reasonable assumptions verified by comparison of calculation results with experimental data. We use combination of two approaches: a rather complete zero-dimensional description of processes in discharge plasma, and 1.5-dimensional modeling of discharge spatial structure. Generally, the electrode system allows operating of discharge in different modes: at lower currents the discharge has a form of an array of separate coronas, at higher currents it transforms to more uniform glow discharge [2]. In conditions of present experiments on toluene destruction, the discharge regime is near the transition point, and inhomogeneity of current distribution may play a significant role in toluene removal efficiency.

#### *Spatial structure of DC glow discharge*

It was demonstrated earlier [2] that the transition from corona to glow regime for an array of negative pins with a common flat electrode can be described satisfactorily by 1.5-D model, where electric current cross section area was specified as a function of discharge axial distance from the pins, and continuity equations were solved for charged particle fluxes. The electric field was calculated from Poisson equation. The shape of the current channel was chosen according to visual observations. Possible variations in the shape of the current channel due to variations in the current value were neglected in calculations. In calculations, all of the parameters were reduced to the conditions referred to one pin. In total, the discharge was composed of 28 individual columns. The primary goal of modeling spatial structure of the discharge was to evaluate spatially averaged production rate of chemical radicals known to destruct toluene molecules. It was assumed that the each radical yield in the whole discharge is a sum of yields for individual sub-discharges. As a result of calculations, spatial distributions of electric field strength, electron, positive and negative ion number densities were found. Accuracy of modeling was controlled by comparison of calculated reduced electric field strength averaged over space,  $E/N$ , and the Reduced Voltage Current Characteristic (RVCC) with experimental measurements (see Fig. 7 and Fig. 8, respectively).

As mentioned above, an addition of toluene in amount of more than 10 ppm resulted in an increase of the discharge voltage at the same current. This effect can be attributed to influence of ion-molecule reactions involving toluene molecules, which result in formation of heavy ions with better stability and lower mobility. Because of lack of any data about such processes, we changed in the model ion mobility and negative ion destruction rate within a reasonable range to achieve the best agreement with experimental measurements of  $E/N$  and RVCC. Figs. 9-12 demonstrate calculated axial distributions for charged particle number densities, electric field strength, electron and ion currents as fractions of the total current and  $OH$  radicals production, respectively. All results are presented for the total discharge current of 7 mA (267  $\mu$ A per a single pin) and toluene concentration of 125 ppm. It is seen that the electron number density is about  $10^{-3}$  from the ion number density resulting in electron current fraction about 0.1 of the total current. The electric field strength is rather high what explains a good chemical efficiency of the discharge.

Plasmachemical model described below indicates that the most effective agent in destruction of toluene in experimental conditions is  $OH$  radical. To evaluate  $OH$  yield in the discharge, the electron impact dissociation of water molecules and production of two  $OH$  radicals in the reaction of  $O(^1D)$  metastables with water molecules were taken into account. Besides, dissociation of water molecules in collisions with electronically excited nitrogen molecules was included. Summing all these sources of  $OH$  radicals, the axial distribution of  $OH$  yield (in an assumption of 100% efficiency for each the reaction channel) in a single discharge is shown in Fig. 12. A very sharp peak of  $OH$  yield near to the cathode is explained by growth of electric field strength. The total yield of  $OH$  calculated with 1.5D discharge model is 28.5 and 26.6 ppm for  $C_7H_8$  concentration 15 and 125 ppm, respectively.

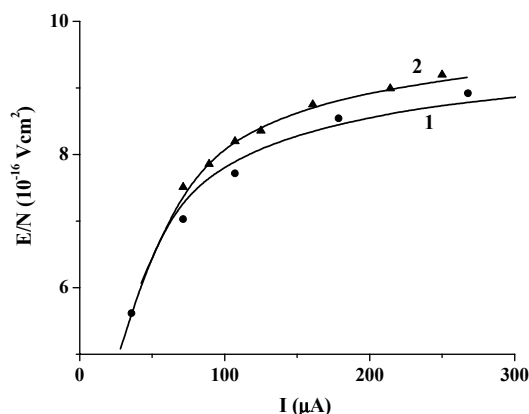
To evaluate finally the toluene destruction by the active particles produced in the discharge a much more detailed kinetic model is necessary. In particular, the real yield of  $OH$  radicals in the discharge should be evaluated accounting properly different channels in metastables energy conversion. Evidently, radicals produced in the discharge may react with other species diminishing efficiency of the toluene removal. It is the primary purpose of the full kinetic model described shortly below to find out the  $OH$  yield available in the discharge and what percentage of chemical radicals reacts with toluene. By that, an assumption is made that the result of the reaction is destruction of the toluene molecule.

### ***Modeling plasmachemical processes***

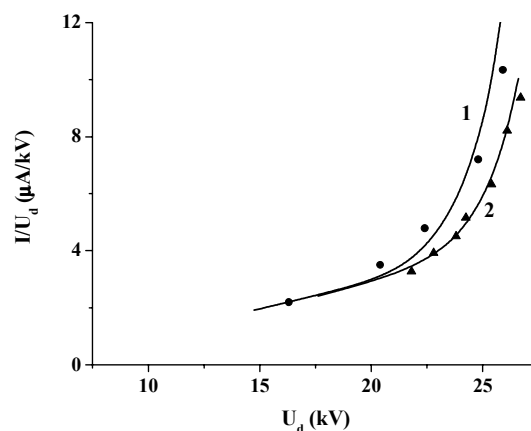
The full kinetic model of plasma in humid air is essentially the same as described in [3]. This model includes 227 reactions for components of humid air, molecular and atomic metastables, radicals and ions produced in plasma. Up to now, there is no reliable information about plasma ion composition at atmospheric pressure. The situation with air polluted by a Volatile Organic Compound (VOC), such as  $C_7H_8$ , is still more complicated due to low ionization potential and high electron affinity of these species and their fragments produced in the discharge. One may expect that fast ion-molecular reactions completely change ion composition even at a very low pollutant content. Actually, ion-molecular reactions cannot influence strongly on composition of chemical products in the discharge because of low ionization degree of plasma. Therefore, ignoring of unknown ion-molecular reactions in our model is expected to give a small error in the neutral species composition.

Efficiency of toluene removal is controlled by two factors: discharge production efficiency of chemical species involved in destruction of toluene and a number of removed toluene molecules per one molecule of active species,  $\eta_{chem}$ . Electric discharge is producing

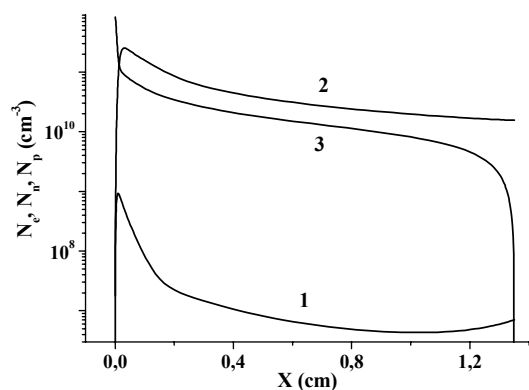
electronically excited molecules and radicals, which, in turn, react with stable molecules and with products of chemical reactions.



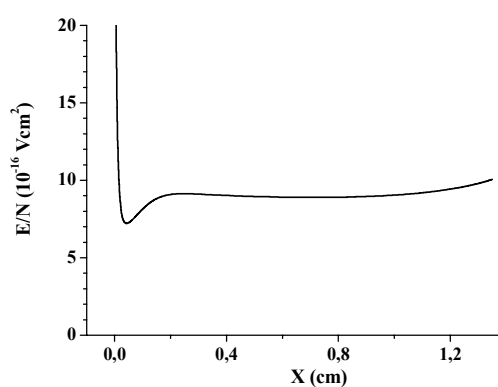
**Fig. 7.** The reduced electric field strength for gas mixture 18%  $H_2O$  - air.  $T = 338$  K,  $P = 753$  Torr,  $d = 1.35$  cm. Markers are experimental results, lines are results of 1.5D simulations (● and 1– 15 ppm  $C_7H_8$ , ▲ and 2– 125 ppm).



**Fig. 8.** RVCC per one pin for gas mixture 18%  $H_2O$  - air.  $T = 338$  K,  $P = 753$  Torr,  $d = 1.35$  cm. Markers are experimental results, lines are results of 1.5D simulations (● and 1– 15 ppm  $C_7H_8$ , ▲ and 2– 125 ppm).

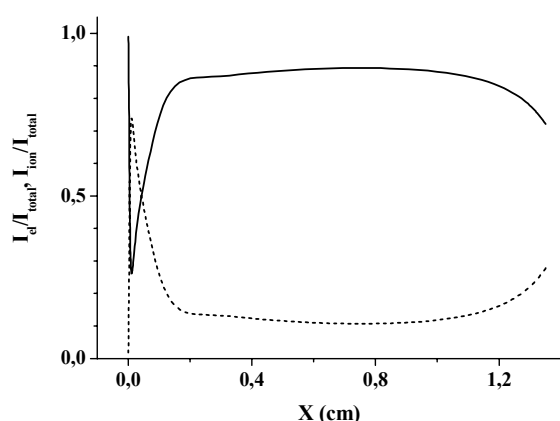


**Fig. 9.** Calculated axial distributions of a number density of charge particles: 1 – electrons, 2 – negative ions, 3 – positive ions.  $I = 267$   $\mu A$ , 125 ppm  $C_7H_8$ .

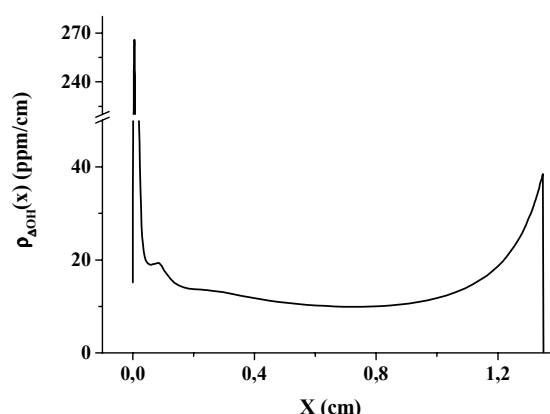


**Fig. 10.** Calculated axial distribution of the reduced electric field averaged over current area. Conditions are the same as in Fig. 3.

Simple estimations showed that the most effective agent in toluene removal is  $OH$  radical. There are known [4] rate coefficients for reactions of toluene with  $OH$ ,  $O$ , and  $O_3$ , which are equal to  $6.2 \cdot 10^{-12}$ ,  $7.6 \cdot 10^{-14}$  and  $4 \cdot 10^{-22}$   $cm^3/s$ , respectively. In our conditions, only  $OH$  is effective in destruction of toluene. Numerical simulations of evolution of gas portion coming through the discharge and receiving the reduced energy-loading equal to experimentally realized 10 J/g showed that formation of  $OH$  radicals in processes of nitrogen and atomic oxygen metastables quenching is rather effective. In particular, an efficiency of  $OH$  production with respect to ideal conversion of excited particles to  $OH$  is equal to 80% at toluene concentration 15 ppm and 86% at 125 ppm.



**Fig. 11.** Calculated axial distributions of electron (dashed line) and ion (solid line) current reduced to total current. Conditions are the same as in Fig. 9.



**Fig. 12.** Calculated axial distribution of the *OH* yield averaged over current area. Conditions are the same as in Fig. 9.

The next step is the evaluation of the  $\eta_{\text{chem}}$ . The full kinetic model predicted that 0.28 of a total *OH* yield is spent in reactions with toluene at its concentration 15 ppm, and 0.645 at the concentration 125 ppm. Multiplying the *OH* yield calculated with 1.5D model by the factor accounting losses in *OH* formation channels and by the  $\eta_{\text{chem}}$ , the total toluene removal by the discharge predicted by the theory is 6.4 and 14.8 ppm at toluene concentration 15 and 125 ppm, respectively.

#### 4. Discussion

Comparing theoretically predicted toluene removal with experimentally measured figures 11.7 and 31 ppm at toluene concentration 15 and 125 ppm, respectively, one may conclude that theoretical model underestimate the discharge efficiency. Bearing in mind an enormous complexity of the experimental situation (combination of spatial non-uniformities with complicated poor understood chemistry), this is not too surprising. Variation of rate coefficients of reactions for electronically excited molecules within limits of their uncertainty may result in some increase of predicted values, but it's hard to expect two-times enlargement of toluene removal efficiency without introduction of new channels. Our model indicates that the most effective mechanism of *OH* production is associated with  $N_2^*$  quenching by water molecules. Here  $N_2^*$  denotes nitrogen molecules excited to states above  $A^3\Sigma_u^+$ . Products of quenching these states may be excited, too (for example,  $O(^1D)$  atom), and produce *OH* radicals additionally.

#### 5. Conclusions

Experimental and theoretical studies performed show strong influence of admixtures on charged particle kinetics in discharge plasma that can result in synergetic effects at decomposition of contaminants.

#### References

1. L. Rossocha, -Proc. 2<sup>nd</sup> Int. Symp. on NTP Technol. for Pollut. Control, Salvador, Brazil, (1997), 1
2. Yu. S. Akishev, M. E. Grushin, I. V. Kochetov, A. P. Napartovich, M. V. Pan'kin, and N. I. Trushkin, *Plasma Physics Reports*, **26**, No. 2, 2000, pp. 157–163.
3. Yu. S. Akishev, A. A. Deryugin, V. B. Karal'nik, I. V. Kochetov, A. P. Napartovich, and N. I. Trushkin, *Fiz. Plazmy* **20**, 571 (1994) [*Plasma Physics Reports*, **20**, 511 (1994)].
4. <http://webbook.nist.gov/chemistry>



# Ion impact on surface modification of polymers - Low pressure plasma treatment versus ion implantation

G. Suchanec<sup>1</sup>, M. Guenther<sup>1</sup>, J. Sorber<sup>1</sup>, G. Gerlach<sup>1</sup>, K.-F. Arndt<sup>2</sup>, A. Deyneka<sup>3</sup>, L. Jastrabik<sup>3</sup>

<sup>1</sup>Dresden University of Technology, Institute for Solid State Electronics, 01062 Dresden, Germany

<sup>2</sup>Dresden University of Technology, Institute of Physical Chemistry and Electrochemistry,  
Mommstr. 13, 01062 Dresden, Germany

<sup>3</sup>Institute of Physics, Academy of Sciences of the Czech Republic, Na Slovance 2, 182 21 Prague 8, Czech Republic

## Abstract

In this work, a complex investigation of the film surface composition, chemical bonding, and optical properties of plasma modified polyimide and poly(vinylalcohol)/poly(acrylic acid) (PVA/PAA) thin films as well as of ion implanted polyimide thin films was carried out. Boron ions were implanted at 50-500 keV with irradiation doses between  $10^{13}$  and  $10^{16}$  B<sup>+</sup>/cm<sup>2</sup>, whereas plasma surface modification was performed using SF<sub>6</sub>, CHF<sub>3</sub>, SiH<sub>4</sub>/N<sub>2</sub>, NH<sub>3</sub> and N<sub>2</sub>O low pressure gas discharges.

## 1. Introduction

Polymer thin films find extensive use in microelectromechanical systems (MEMS) and electronic applications. For instance, bimorphic gas sensors make use of gas absorption-induced swelling of polyimide and polyethersulfone thin films [1,2]. The polymer's sensitivity to gas uptake is significantly increased by surface ion-beam modification [3] and plasma surface treatment [4]. Infrared bolometers comprising surface ion implanted polymer thin films were described in [5]. Polymeric hydrogels such as poly(vinylalcohol)/poly(acrylic acid) (PVA/PAA) blends change their conformation in dependence on pH-value, polarity of the solvent, temperature etc. converting thus chemical energy reversibly into mechanical one [6]. They are promising materials for bio-actuators, e.g., artificial muscles and lenses, vitreous bodies in ophthalmology, and for swell gel bio-sensors. On the other hand, the numerous -COOH groups of PAA easily form covalent bonds and thus a good interfacial bonding with other functionalities of polymers which may be used for designing polymer MEMS devices.

Preparation of organic thin films by plasma polymerization was reported more than 30 years ago in [7]. However, vacuum deposition of polymeric films is much more expensive than a simple spin coating process followed by a short-time surface modification. The latter process step tailors the physical properties of the polymer thin films for applications by altering the nature of the surface without changing the properties in the bulk.

Various species such as excited particles, radicals, ions or photons are involved in the surface property modification leading to three major effects [8]: surface cleaning by ablation, crosslinking, and functionalization, i.e., formation of covalent bonding suitable for attachment of an adherent. If condensable species are available, film deposition occurs at the polymer surface.

The structural transformation induced by plasma surface treatment occurs only over the penetration depth of the modifying species. Excited species and radicals are absorbed within the first monolayer. The ion range of 100 eV ions into polymers amounts just to a few monolayers. The chemical modification of the polymer surface by these species is well determined by X-ray photoelectron spectroscopy (XPS). However, due to the complex plasma-surface interaction, a separate consideration of ion bombardment is not possible.

On the other hand, the penetration depth of low energy electrons ( $E < 1$  keV) exceeds that one of ions by more than one order of magnitude. Moreover, due to the presence of excited species, low pressure plasmas generate a wide spectrum of electromagnetic radiation from the FIR to the VUV region. For polymer surface modification UV and VUV photons are sufficient which cause bond breaking and initiate chemical reactions. UV radiation is absorbed due to forbidden  $\pi$ - $\pi^*$  transitions of  $\pi$  bonds. By VUV radiation  $\sigma$  bonds are excited by allowed transitions. The penetration depth of VUV photons into polymers is known to be about 50 nm [9].

Recently, we have determined the effective modification depths of boron ions implanted into polyimide as 250-300 nm at an ion energy of 50 keV and 400-450 nm at an ion energy of 180 keV. To investigate the chemical modification at these larger penetration depths, we obtained refractive index profiles by variable

angle spectroscopic ellipsometry (VASE) as well as, hardness and Young's modulus profiles by Hysitron depth-sensing nanoindentation technique with a Berkovich indenter [10].

The effectiveness of a plasma-assisted surface treatment depends on a number of process parameters such as process gas composition, total gas flow rate, operation pressure and frequency of the electrical excitation source. The energy flux to the polymer surface in standard low pressure planar reactors is usually determined by the ion flux. Therefore, a deeper understanding of the role of ions in polymer surface modification is a crucial point of plasma chemistry and plasma processing.

## 2. Experimental

The polymers used in this work are summarized in Table 1. Polyimide and polyethersulfone thin films were deposited by spin coating of polyimide PI2566 [6FDA-ODA; hexafluoroisopropylidene bis(phthalic anhydride-oxydianiline)] precursor solutions (polyamic acids / N-methyl-2-pyrrolidone) and polyethersulfone (PES UltrasonE2010) solution (20 wt.% PES / NMP) onto silicon substrates. After deposition of the polymer films the solvent was removed at 90 °C for 30 min, and then polymer films were cured in nitrogen at 400° C for 60 min to convert into polyimide structure. The completion of this chemical reaction was checked by FTIR spectroscopy. The final film thickness amounted to typically between 1.0 and 3.5 µm. Poly(vinylalcohol) and poly(acrylic acid) polymers were dissolved separately in distilled water under stirring at 80°C (PVA 15 wt% and PAA 7.5 wt%). For hydrogel formation, the aqueous solutions of 80 wt% PVA and 20 wt% PAA were stirred for 1 h at 60°C to obtain a homogeneous solution. The polymer thin films of PVA, PAA and the hydrogel were deposited by spin-coating onto 3 in. silicon wafers coated with a 550 nm thick PECVD silicon oxide film which served as convenient substrates. Prior to deposition, the silicon wafers were prebaked at 90°C for 10 min. After deposition of the polymers the solvent was removed at 45°C for 90 min. In dependence on solution concentration and wafer rotation speed films with a thickness of 0.3 to 3 µm remained on the substrates. The dried hydrogel films were isothermally annealed in an oven at 130°C for 20 min.

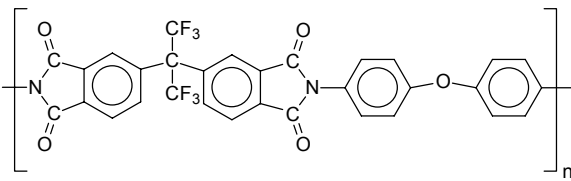
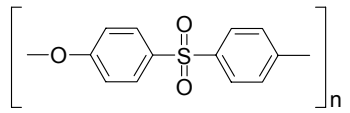
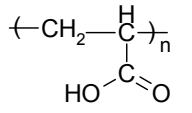
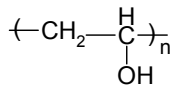
Abbreviated name	Structural formula	Polymer class	Manufacturer
PI2566		Polyimide	DuPont
PES UltrasonE2010		Polyethersulfone	BASF
PAA		Poly(acrylic acid)	Aldrich
PVA		Poly(vinylalcohol)	Aldrich

Table 1. Investigated polymers

Ion implantation was performed using a B<sup>+</sup> ion beam (energy: 50, 130, and 180 keV; dose: 10<sup>13</sup>...10<sup>16</sup> B<sup>+</sup>/cm<sup>2</sup>). Light elements like boron are good candidates for ion beam processing, if high-ionization linear energy transfer (LET), low displacement LET, and a long trajectory range are needed. The range of boron ions and the LET profiles were calculated using the public domain software SRIM-2000.39 [11].

Low-pressure SF<sub>6</sub> and CHF<sub>3</sub> plasma treatment of the deposited polymer films was performed using the RIE chamber of a Plasmalab 80<sup>+</sup> double chamber master/slave system (Oxford Plasma Technology) at a pressure of 13 Pa, a r.f. power (13.56 MHz) of 150 W and flow rates of 25 sccm. The SiH<sub>4</sub>/N<sub>2</sub> and NH<sub>3</sub> plasma

treatment was performed in the system's PECVD chamber at a pressure of 65 Pa, a r.f. power (13.56 MHz) of 20 W, and flow rates of 200, 40 and 100 sccm, respectively. The SiH<sub>4</sub> concentration in nitrogen was 2%. For dual-frequency treatment, two r.f. power supplies were used in a switched mode, a high-frequency unit (13.56 MHz) for a soft surface modification and a low-frequency unit (100 kHz) to enhance ion bombardment on the as-modified film surface. Thus, the influence of ion bombardment on surface modification was investigated. The low-frequency power was varied within 20 to 200 W, whereas the r.f. power was kept constant at 20 W. In the dual-frequency mode, high-frequency and low-frequency cycle times were chosen 10 s each. The typical plasma treatment was performed three minutes at a substrate temperature of 25°C. Beyond three minutes of treatment, the thickness of the modified layer further increases, but the results become more inconsistent.

Changes in chemical composition by surface modification were investigated by X-ray photoelectron spectroscopy (XPS) using the Mg K<sub>α</sub> (1253.6 eV) radiation of a Physical Electronics PHI 5702 electron spectrometer. The spectra were recorded at a take-off angle of 45° with respect to the sample surface. The sampling depth of this technique amounts to about 3 nm. The surface composition was determined by calculating peak areas of high resolution XP spectra. The atomic ratios of the elements were estimated using tabulated sensitivity factors. All XPS peaks were referenced to the C1s hydrocarbon signal at a binding energy of 285 eV. The core level peaks have been analyzed by means of a Gauss-Lorentz-fit algorithm with background subtraction. The curve-fitting quality was evaluated by chi-convergence. The position of the fitted peaks were determined with an accuracy of about 0.1 eV.

To investigate larger penetration depths, refractive and absorption index spectra and films anisotropy were calculated from main ellipsometric angles Δ and Ψ measured with J. A. Woollam spectroscopic ellipsometer. Measurements at ten different angles of incidence allowed us to perform the refractive index depth profile calculations. The experimental data were analyzed by means of the software package WVASE32, which is based on least-square regression analysis to minimize the differences between measured and calculated values.

### 3. Results and Discussion

Ion implantation and low pressure plasma surface treatment provide similar ion fluxes to the polymer surface. However, due to large differences in ion energy, the energy flux seen by the polymer surface is very different. The ion energy determines the penetration depth, while in the case of ion implantation, the energy flux may be changed by selecting the irradiation dose. Low pressure plasma treatment causes chemical attack on the polymer surface. The chemical modification of the plasma treated surface depends on the nature of the involved species. SF<sub>6</sub> was chosen to investigate the effect of fluorine attack on surface modification, while in a CHF<sub>3</sub> plasma an additional condensation of CF<sub>3</sub> radicals occurs. NH<sub>3</sub> low pressure plasmas emit UV radiation, N<sub>2</sub>O and atomic hydrogen emit VUV radiation.

Table 2 summarizes the changes of polymer surface composition caused by ion implantation [12,13] and low pressure plasma treatment [4,14].


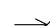
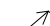
	PI2566[12]	PES[13]	PI2566 [4]	PAA [14]			
Surface treatment	Ion implantation		Low pressure plasma treatment				
	$10^{14} \dots 10^{16} \text{ B}^+/\text{cm}^2$		N <sub>2</sub> O	NH <sub>3</sub>	SF <sub>6</sub>	CHF <sub>3</sub>	NH <sub>3</sub>
C <sub>aromatic</sub>	↓↓	↓	↓	↓	-	-	-
C-C, C=C		↑	↓	→	↓↓	↓	↓
[O]		↓	↑	→	↑↑	↓↓	→
[N]	↓	-	↑	↑↑	-	-	↑↑
S=O	-	↓	-	-	-	-	-
C-O	↑	-	↑	↑↑	↓	↓↓	↓
C=O	↓	-	↓	↓↓	↑	↓↓	→
CF <sub>x</sub>	↓	-	↓	↓	↑	↑↑	-
O-H		n.A.	↓	↑↑	-	-	-
(O+N)/C	↓	-	↑↑	↑	↑↑	↓↓	↑

Table 2. Changes of polymer surface composition in dependence on surface treatment determined by XPS.

↑ - increase, ↑↑ - strong increase, ↗ increase followed by a decrease at higher doses, n.A. - not analyzed

The obtained surface restructuring by ion beam implantation is partly similar to that of surface modification by plasma exposure. By both ion bombardment and plasma treatment, carbonyl, sulphone, imide, and aromatic groups are partly destroyed and aromatic structures are degraded by hydrogen abstraction up to partial graphitization. The formation of graphite-like clusters enhances both surface conductivity and optical absorption at the surface [4,12]. A fingerprint of graphitization of PI2566 even by plasma surface treatment is the oscillator energy shift of the one-oscillator fit describing the spectral dependence of the refractive index from 7.3 eV, which corresponds to the  $^1A_{g1}$ - $^1E_{u1}$  transition of benzene, to 1.75 eV which is characteristic for  $\pi$  electrons bonded in more graphitic rings or delocalized over several rings [4]. A high ion energy flux destroys the anisotropic features of the refractive index of both polyimide [15] and polyethersulfone [13] films leading to its isotropization. At the same time, an absorbing visible and UV light surface layer forms characterized by extinction coefficients which are as high as 0.25 to 0.40 after receiving  $10^{16}$  B<sup>+</sup>/cm<sup>2</sup> [10]. Thus, the polymer bulk is screened from the electron flux and the UV-radiation and the chemical modification of the polymer bulk (crosslinking) are determined by the electronic process (ionization) related ion energy dissipation (linear energy transfer-LET) discussed below.

Contrary to ion beam modification, the (O+N)/C ratio at the surface increases after plasma treatment except the case of CHF<sub>3</sub> plasma treatment, where a CF<sub>x</sub> surface layer is formed [14]. Ellipsometry measurements give evidence that the increase of the (O+N)/C ratio is attributed to the formation of micro-voids and the pick-up of nitrogen, oxygen, and moisture from the ambient atmosphere. Using the effective medium approximation, the void fractions in the bulk were estimated as 2%, 0.68%, and 2.69% for CHF<sub>3</sub>-, NH<sub>3</sub>-, and dual-frequency NH<sub>3</sub>-treated PAA films. The hydrophobic nature of the CF<sub>x</sub> surface layer formed by CHF<sub>3</sub> plasma treatment obviously inhibits moisture absorption regardless of the large void fraction in the bulk of the PAA film. This argument is also based on the obtained rapid increase of the (O+N)/C ratio after SF<sub>6</sub> plasma treatment. On the other hand, the increase of both the void fraction in the bulk and the (O+N)/C ratio by dual frequency plasma treatment illustrates that enhanced ion bombardment increases also the chemical attack. This coincides with a significant increase of the fluorine reaction rate by plasma induced high energy VUV radiation [16]. Nonchemical ion attack can be excluded in this case due to a Ar<sup>+</sup> threshold energy of about 500 eV for chemical surface modification of polyimide [17].

Bombardment by energetic ions produces changes both of composition and bond structure since the linear transfer of energy is much larger than typical polymer bond energies. There are four possible mechanisms of energy transfer from an energetic incoming ion to the atoms of the polymer film [18]: (i) electronic excitation, (ii) nuclear displacement, (iii) phonon decay, and (iv) plasmon decay.

Electronic excitation includes the ejection of electrons and formation of excited states. This may cause a chemical bond to break, when the excited energy localizes in a particular chemical bond. Even this process is mainly responsible for the formation of unsaturated bonds and cross-linking and largely responsible for changes in optical density, electrical conductivity and hardness [3,10,12]. Nuclear displacement is the major cause for chain scissions. The interaction of light ions like boron with a polymer is distinguished by a high fraction of electronic excitation (ionization), a low fraction of nuclear displacement, and a long trajectory range. The energy deposition of one ion per unit path length is characterized by the linear energy transfer (LET) which in the case of boron ions in polyimide amounts to about 200 eV/nm [19]. This energy deposits in a very short time ( $10^{-14}$  to  $10^{-13}$  s) in a small volume surrounding the ion track. Figure 1 compares the ionization LET with the refractive index profile of PI2566 films ion implanted at  $10^{15}$  B<sup>+</sup>/cm<sup>2</sup>. At ion energies of 50 keV, the calculated ionization LET gives a correct estimation of the modification depth. However, at 180 keV the modification depth has about half the value as predicted. This is attributed to surface modification during ion bombardment changing the composition and density of the surface layer. On the other hand, the SRIM-calculation is based on the initial material properties, and it does not take the changes of material properties during ion bombardment into account. Consequently, the ions are expected to penetrate less deep, and the SRIM calculation should be performed in an iterative way where the increasing resistance to penetration is used as an input data after each increment of implantation dose. Otherwise, SRIM will only give reasonable results, if the material modification is small.

In the case of low pressure plasma treatment, the ion energies used for the calculations were selected as corresponding to the obtained self-bias of 103 V (545 V) of the SF<sub>6</sub> (CHF<sub>3</sub>) low pressure plasma. The calculated maximal ion penetration depths of 1.1 (3.0) nm are too small to be measured by variable angle spectroscopic ellipsometry. As a consequence, a film thickness independent refractive index was found which is smaller than the values of untreated films due to the formation of micro-voids discussed above.

Thus, the ion impact on surface modification of low pressure plasma treatment is limited just to a few monolayers.

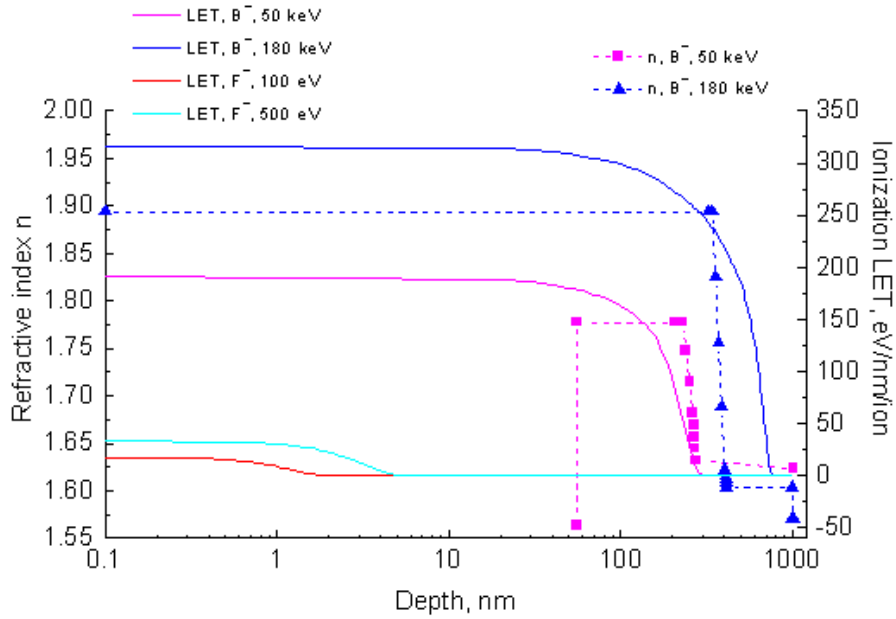


Figure 1: Refractive index and ionization LET profiles of ion implanted ( $10^{15}$  B<sup>+</sup>/cm<sup>2</sup>) and of SF<sub>6</sub> (100 eV) and CHF<sub>3</sub> (500 eV) low pressure plasma treatment PI2566 films

Plasma polymerization of acrylic acid in the high r.f. power monomer deficient regime was recently found to convert acid functionalities into ester ones [20]. We have investigated the ratio of carbonyl and ester oxygen after plasma treatment. Figure 2 illustrates the bond destruction at the surface of PAA films after NH<sub>3</sub> plasma treatment. The O1s peak of untreated PAA consists of a mixture of comparable amounts of carbonyl oxygen C=O (532.3 eV) and ester oxygen C-O (533.6 eV). After NH<sub>3</sub> plasma treatment the ester oxygen groups were partly destroyed while the peak area of carbonyl oxygen remains nearly constant. After SF<sub>6</sub> and CHF<sub>3</sub> plasma treatment only one O1s peak remains with was assigned to ester oxygen. Obviously, the impact of ion bombardment from NH<sub>3</sub> low pressure plasmas is smaller than that of fluorine containing ones. Indeed, ammonia discharges generate mainly neutral fragments of NH<sub>3</sub> molecules including NH, NH<sub>2</sub>, H, H<sub>2</sub> and N<sub>2</sub> [21].

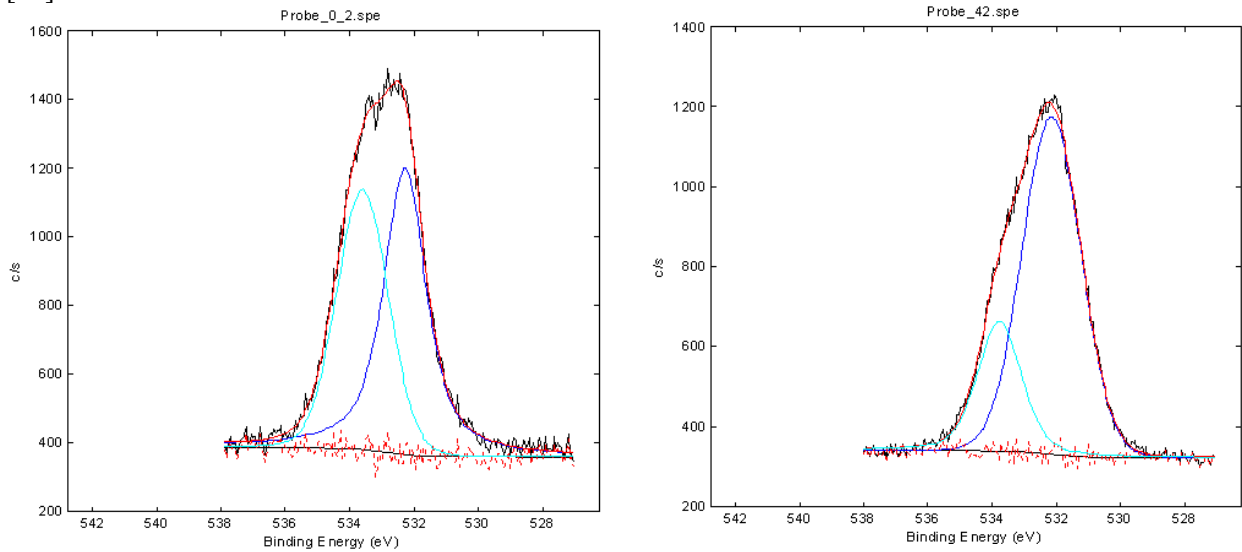


Fig. 4: XPS O1s spectra of (a) untreated PAA thin film, (b) PAA thin film after NH<sub>3</sub> low-pressure plasma treatment.

#### 4. Conclusions

The chemical modification of the plasma treated surface depends on the nature of the involved species. An enhanced ion bombardment increases also the chemical attack on the plasma treated surface. The obtained surface restructuring upon plasma exposure is similar to that of surface modification by ion beam implantation. By both plasma treatment and ion bombardment, imide, and aromatic groups are partly destroyed and aromatic structures are degraded by hydrogen abstraction up to partial graphitization. The formation of graphite-like clusters enhances both surface conductivity and optical absorption at the surface. The optical anisotropy of the surface layer is lost and a visible and UV light absorbing surface layer forms. Thus, the polymer bulk is screened from the electron flux and the UV-radiation. In this case, the chemical modification of the polymer bulk (crosslinking), which extends a few monolayer in the case of low pressure plasma treatment, is determined by the electronic process (ionization) related ion energy dissipation (linear energy transfer-LET). Contrary to ion beam modification, the O+N/C ratio at the surface increases after plasma treatment and exposure to air due to the absorption of nitrogen, oxygen, and moisture from the ambient atmosphere.

#### Acknowledgements

The authors gratefully acknowledge support of this work from the Deutsche Forschungsgemeinschaft (Grant Ge 779/6-2 and Collaborative Research Center (SFB) 287, Project C11), by Grants LN00A015 (Ministry of Education of the CR) and CZE00/002 (German Federal Ministry of Education and Research).

#### References

- [1] G. Gerlach, and K. Sager - Sensors and Actuators **A43**, 181 (1994).
- [2] R. Buchhold, A. Nakladal, G. Gerlach, M. Herold, G. Gauglitz, K. Sahre, K.-J. Eichhorn - Thin Solid Films **350**, 178 (1999).
- [3] M. Guenther, K. Sahre, G. Suchaneck, G. Gerlach, K.-J. Eichhorn - Surface and Coatings Technol. **142-144**, 482 (2001).
- [4] G. Suchaneck, M. Guenther, B. Adolphi, G. Gerlach, K. Sahre, K.-J. Eichhorn, A. Deineka, L. Jastrabik - ISPC-15, **VI**, 2485 (2001).
- [5] US Patents 5 629 665, 5 753 523.
- [6] K.-F. Arndt, A. Richter, S. Ludwig, J. Zimmermann, J. Kressler, D. Kuckling, H.-J. Adler - Acta Polym. **50**, 383 (1999).
- [7] A.P. Bradley - Ind. Chem. Prod. Res. Rev. **9**, 101 (1970).
- [8] F. Arefi-Khonsari, J. Kurdi, M. Tatoulian, J. Amouroux - Surface and Coatings Technol. **142-144**, 437 (2001).
- [9] G.A. Corbin, R.E. Cohen, R.F. Baddour - Macromolecules **18**, 98 (1985) 98.
- [10] M. Guenther, G. Gerlach, G. Suchaneck, K. Sahre, K.-J. Eichhorn, B. Wolf, A. Deineka, L. Jastrabik - Surface and Coatings Technol. **158-159**, 108 (2002).
- [11] J. F. Ziegler, J. P. Biersack, and U. Littmark, in J. F. Ziegler (ed) The Stopping and Range of Ions in Solids, Pergamon Press, New York, 1985, pp. 1-321.
- [12] M. Guether, G. Gerlach, G. Suchaneck, D. Schneider, B. Wolf, A. Deineka, L. Jastrabik - Macromolecular Symposia 2003 (in print).
- [13] K. Sahre, K.-J. Eichhorn, F. Simon, M. Guenther, G. Suchaneck, G. Gerlach - Mat. Res. Soc. Symp. Proc. 672, O1.18 (2001).
- [14] G. Suchaneck, M. Guenther, J. Sorber, G. Gerlach, K.-F. Arndt, A. Deineka, L. Jastrabik - Surface and Coating Technol. 2003 (in print).
- [15] K. Sahre, K.-J. Eichhorn, F. Simon, D. Pleul, A. Janke, G. Gerlach - Surface and Coatings Technol. **139**, 257 (2001).
- [16] W. Schwarzenbach, J. Derouard, N. Sadeghi - J. Appl. Phys. **90**, 5491 (2001).
- [17] G.A. Hishmesh, T.L. Barr, A. Sklyarov, S. Hardcastle - J. Vac. Sci. Technol. **A14**, 1330 (1996).
- [18] E.H. Lee - in: Polyimides/Eds. M. Ghosh, K. Mittal, Marcel Dekker, N.Y., 1996.
- [19] M.B. Lewis, E.H. Lee - Nucl. Instrum. Meth. Phys. Res. **B69**, 341 (1992).
- [20] M.R. Alexander, T.M. Duc - J. Mat. Chem. **8**, 937 (1998).
- [21] M. Creatore, P. Favia, G. Cicala, R. Lamendola, and R. d'Agostino - ISPC-14, **III**, 1203 (1999).

# Plasma Etching and Analysis of Inorganic SiO<sub>2</sub>-like Low Dielectric Constant Material

S. Marschmeyer, H.H. Richter, H. Silz, R. Barth, S. Günther, D. Krüger, D. Wolansky

IHP, Im Technologiepark 25, D-15236 Frankfurt (Oder), Germany

## Abstract

Dry etching results of carbon-doped low- $k$  layers in a CF<sub>4</sub>/CHF<sub>3</sub>/Ar plasma followed by an *in-situ* resist strip are presented. With these processes essential demands for low- $k$  integration into advanced back-end-of-line (BEOL) technologies are fulfilled. First, small tapered and bowing-free via profiles for optimum subsequent metalization step were realized. Second, low- $k$  dry etching is characterized by a sufficient selectivity to resist. Third, the  $k$  value variations caused by etching and subsequent strip process are negligible small.

## 1. Introduction

One of the most important challenges in semiconductor manufacturing is to develop integrated circuits with a higher performance. An important problem for current IC generation is that signals through metal interconnects are delayed by the resistance  $R$  in the metal lines and the capacitance  $C$  between vicinal lines. To optimize the IC performance at a higher packing density, low dielectric constant ( $k$ ) materials are being introduced to replace conventional dielectrics such as oxide or nitride [1]. An ideal low- $k$  material should have similar properties as SiO<sub>2</sub>, such as low thermal expansion coefficient, low leakage, high breakdown voltage and low film stress. Moreover, preferred materials must have the ability to simple integration into the manufacturing process and low cost of ownership. Unfortunately, low- $k$  materials have been difficult and expensive to integrate into production lines and are poor thermal conductors [2]. Table 1 is taken from the 2000 ITRS Roadmap for logic devices and shows how the effective dielectric constant is predicted to change with the technology node.

Table 1: Interconnect requirements for logic devices [3].

Interconnect requirements for logic devices					
Year of first product shipment	1997	1999	2002	2005	2008
Technology node (nm)	250	180	130	100	70
Number of metal levels	6	6-7	7-8	8-9	9
Effective dielectric constant	4.0	4.0 – 3.5	3.5 – 2.7	2.2 – 1.6	1.5

The situation is complicated by the variety of low- $k$  material types and deposition. Carbon-doped SiO<sub>2</sub> (also known as SiCOH film) is an important low- $k$  material which was used in our investigations. Here, the reduction in  $k$  is realized by simply doping silicon oxide with methyl (-CH<sub>3</sub>) groups. The originating Si-CH<sub>3</sub> bonds effectively terminate a portion of original Si-O chemical bonds resulting in an extensive “loosening” of the lattice. Finally, this leads to a reduction in isolator film density and a reduction in  $k$  value, respectively [4]. This paper discusses the development of low- $k$  material dry etch processes including a surface analysis directly after etching and after different ashing and cleaning procedures.

## 2. Experimental

Low- $k$  films for the following etch investigations were prepared by a conventional CVD process. The initial film thickness was always close to 1000 nm, deposited on a 50nm thick silicon riched oxide. For patterning, a VIA mask of a qualified quarter micron CMOS process with 800nm DUV resist thickness and a dielectric anti-reflective coating was used. The so prepared wafers were etched in a magnetically enhanced reactive ion

etch mode using a Centura MxP<sup>+</sup> chamber (Applied Materials). Surface information was obtained using x-ray photoelectron spectroscopy (XPS) on blanket low-*k* samples and on patterned wafers with different arrays of holes and trenches.

### 3. Dry Etch Requirements

In general, volatility and ion induced desorption of reaction products define the most important dry etching characteristics (anisotropy and selectivity). Plasma etching and the following resist ashing are the most critical steps for the successful integration of a low-*k* dielectric. Figure 1 illustrates a typical interlayer dielectric film stack.

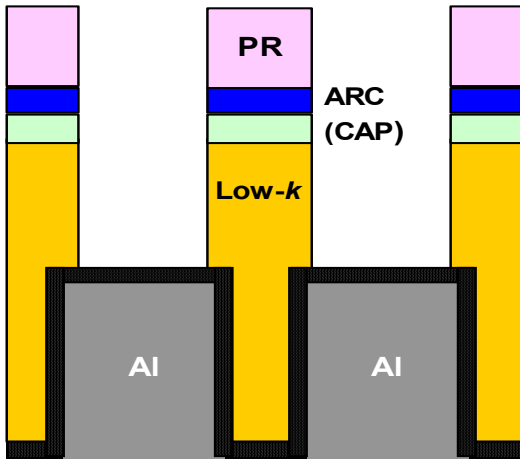


Fig. 1: Dielectric film stack [4] with low-*k* material which is to be patterned by a via etch process (PR: Photoresist; ARC: Antireflective Coating)

An acceptable etch process has to guarantee the following requirements [4]: (a) residue-free removal of dielectric film stack, (b) bowing-free profile for the subsequent metalization steps, (c) sufficient high selectivity to photoresist and underlayer, no *k* value variations in consequence of etching or stripping.

### 4. Results and Discussion

Etching of carbon-containing SiO<sub>2</sub>-like low-*k* material is compared to conventional SiO<sub>2</sub>. Only small modifications are necessary. Generally, due to the high Si:O ratio, discharges chosen are richer in F atoms than those for conventional oxides [4]. We have used a fluorocarbon plasma with the typical isolator etch gas combination CF<sub>4</sub>, CHF<sub>3</sub> and Ar. The etch process was controlled by monitoring a CO band using optical emission spectroscopy. Before patterning the low-*k* isolator film a short descum step in O<sub>2</sub>/Ar was introduced to remove “feet” caused by lithography, followed by etching the oxide cap layer. Here, there was a demand to preserve resist during these two steps so as to minimize the loss of critical dimension (CD) for the remaining low-*k* film. The result (Fig. 2) clearly shows that this multilayer stack can be etched by selection of classical isolator etch gases.

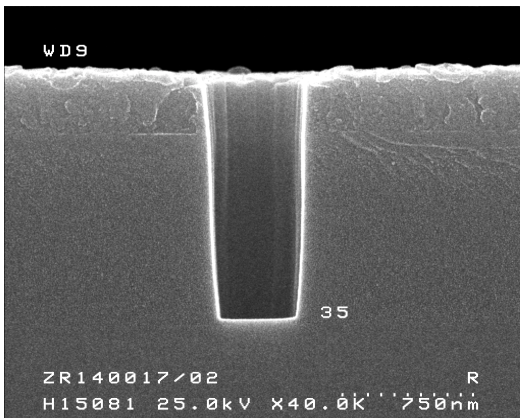


Fig. 2: SEM micrograph immediately after etching in CF<sub>4</sub>/CHF<sub>3</sub>/Ar plasma (without ash / clean steps).



The etch rate of the low- $k$  layer was  $\approx 300\text{nm/min}$ . The selectivity of low- $k$  material to the resist was 3-4:1. After etching a standard *ex-situ* ash for removing photoresist and cleaning the via holes was followed. This stripping procedure was realized in a oxygen/nitrogen plasma with a high  $\text{O}_2$  flow (2000sccm) at  $250^\circ\text{C}$  and 50mTorr.

Fig. 3 illustrates the structure after *ex-situ* ashing.

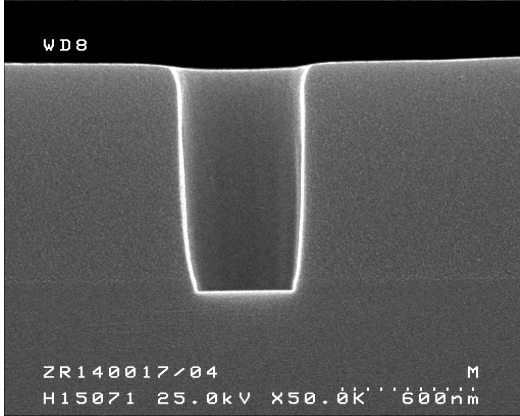


Fig. 3: SEM micrograph after etching and *ex-situ*  $\text{O}_2/\text{N}_2$  ashing.

In spite of a small bowing, for following technological steps purposes the etched hole profile is acceptable. A void free W plug deposition is realizable. But another problem has to be solved: The low- $k$  film must preserve its physical and chemical properties during all followed device fabrication steps. If this can not be achieved, then the perceived benefits of the low- $k$  film will never be realized [4]. Fig. 4 indicates an essential decrease in carbon concentration after *ex-situ* ash process.

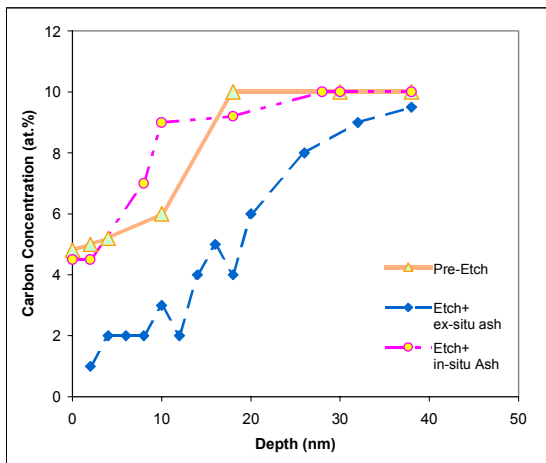


Fig. 4: Low- $k$  film carbon concentration before and after etching and *ex-situ* or *in-situ* ashing respectively.

During via hole etching, the sidewalls are passivated with a polymer layer. This fluorocarbon polymer protects the low- $k$  film from the plasma. But the following resist strip removes also the etch polymer as  $\text{CO}$ ,  $\text{CO}_2$ ,  $\text{COF}_x$  etc. During this step, there is a high risk that the carbon is striped out from the low- $k$  film.

Therefore, an ash process have to be find which maintains a constant carbon concentration. We have changed from an *ex-situ* oxygen dominating ashing to an *in-situ* plasma process at low chamber temperature and small oxygen portion in the ash step (Fig. 5). The XPS measurements, illustrated in Fig. 4, demonstrate the improvements.

Moreover, such profiles allow voidless via filling, which is conventionally realized by a combination of Ti/TiN and tungsten layers (Fig. 6).

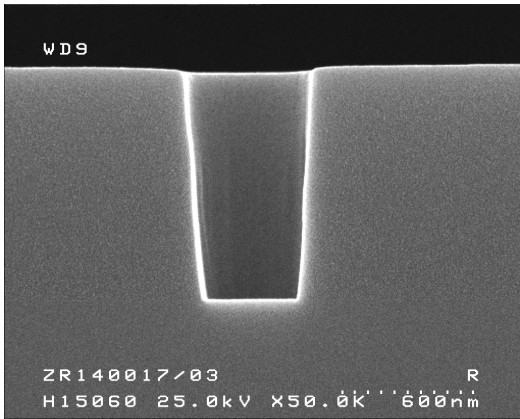


Fig. 5: SEM micrograph after etching and *in-situ* O<sub>2</sub>/Ar ashing.

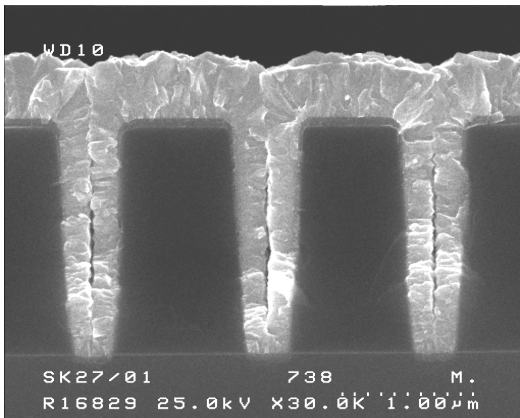


Fig. 6: SEM micrograph after via hole filling (Ti-IMP / TiN-PVD / W)

## 5. Conclusions

It has been demonstrated that carbon-containing SiO<sub>2</sub>-like low-*k* films can be successfully patterned in a magnetically enhanced plasma using conventional isolator etch gases. In contrast to *ex-situ* ashing an *in-situ* resist stripping does not effect the low-*k* film properties negatively.

## Acknowledgement

It is a great pleasure to acknowledge the excellent technical assistance of *C. Albrecht, D. Schinkel, G. Martins, D. Kehder and S. Orłowski*. The authors are also grateful to *A. Bauer and U. Haak* for stimulating discussions.

## References

- [1] T.E.F.M. Standaert, P.J. Matsuo, S.D. Allen, G.S. Oehrlein, T.J. Dalton - "Patterning of fluorine-, hydrogen-, and carbon-containing SiO<sub>2</sub>-like low dielectric constant materials in high-density fluorocarbon plasmas: Comparison with SiO<sub>2</sub>", J. Vac. Sci. Technol. A **17**(3), 741 (1999).
- [2] Status 2000 Integrated Circuit Industry Report, ICE-Integrated Circuit Engineering, 8 (2000).
- [3] 2000 ITRS Roadmap: Technology Needs.
- [4] D.J. Thomas, Y.P. Song, K. Powell - "Meeting ITRS Roadmap challenges with low-*k* dielectric etching", Solid State Technology, 107 (2001).

# Glow Discharge Stabilization of Material Surfaces for Bacteria Anti-fouling

K. Sarioglu, M. Mutlu

*Hacettepe University Engineering Faculty Food Engineering Department 06532 Beytepe Ankara Turkiye*

In recent years the effect of surface chemistry on bacterial adhesion has been studied intensively and hydrophilic uncharged surfaces and electrostatic charges showed the resistance to protein and microorganism adsorption [1], [2], [5].

In this study, we aimed to modify stainless steel and polyethylene model surfaces, which are widely used in food industry, by plasma polymerization technique [3]. To obtain Teflon like or hydrophilic surfaces, four different types of monomers; Hexafluoroisopropyl acrylate, (HFPA); Hydroxyethyl methacrylate (HEMA); Poly (ethyleneglycol) ethyl ether metacrylate (PEG-EEMA) Poly (ethyleneglycol) methacrylate (PEG-MA) [4]. In this group of monomers, the first one was used to create Teflon like and the rest were used for hydrophilic surfaces.

Glow discharge treatment parameters (exposure power and monomer flow rate) were varied to obtain different deposition rates of new coatings. All the experiments were proceed at 5,0 Pa base pressure. Maximum deposition rates were obtained at 20 W and 4,8 ccmSTP/min for HFPA; 20 W and 7,2 ccmSTP/min for HEMA; 20 W and 1,68 ccmSTP/min for PEG-EEMA and, 20 W and 1,68 ccmSTP/min for PEG-MA. After plasma polymerization, the surfaces were characterized with contact angel measurements and ATR-FTIR spectroscopy.

- [1] Jhon Tsibouklis at all, Biomaterials, **20** 1229-1236 (1999).
- [2] Christopher S.Andrews at all, Biomaterials, **22** 3225 –3233 (2001).
- [3] Susan A. Visser at all, Surface and Coatinns Technology **96** 210-222 (1997).
- [4] Seok Won Lee, Paul E. Laibinis, Biomaterials, **19** 1669-11675 (1998).
- [5] Mu Rong Yang at all, Material Chemistry and Physics, **48** 71-75 (1997).

# NON-THERMAL PLASMA TECHNIQUE APPLIED TO WASTE CARBONIZATION

Marcela Morvová<sup>1</sup>, Katarína Svetková<sup>1</sup>, Blanka Fógelová<sup>1</sup>, Mario Janda<sup>1</sup>,  
František Hanic<sup>3</sup>, Imrich Morva<sup>1</sup>, Peter Lukáč<sup>2</sup>

<sup>1</sup>*Institute of Physics, Faculty. of Mathematics, Physics and Informatics Comenius University  
Mlynská dolina F2, 84248 Bratislava, Slovakia*

<sup>2</sup>*Dept. of Plasma Physics, Faculty. of Mathematics, Physics and Informatics Comenius University  
Mlynská dolina F2, 84248 Bratislava, Slovakia*

<sup>3</sup>*Institute of Measurement Science, Slovak Academy of Sciences,  
Dúbravská cesta 9, 842 19 Bratislava, Slovakia*

## Abstract

Pyrolysis in an inert atmosphere with direct heating was applied for thermochemical waste degradation. The system enables poly-generation of energy and materials (heat, hydrogen, liquid hydrocarbons), the amorphous nano-sized carbon is formed from the carbonized material. The method for flue gas cleaning uses non-thermal plasma based pilot system for 50-250 m<sup>3</sup>/hour of gas flow. The applied method cleaned very efficiently the exhaust gas from variety of non-wanted compounds, CO<sub>2</sub> removal efficiency is as high as 40-99% and is connected with solidification of gas into proteinoid polymeric material.

## Introduction

Millions of tons of waste are produced worldwide every day. Waste has become a critical problem for industrial society, particularly in big cities and densely areas. However, still only about 10 % of waste are recycled, most of it goes to landfill (64 %) or is incinerated (18 %). The municipal waste carbonization inside high temperature combustion chamber using direct heating by exhaust gas flow in oxygen free atmosphere is an alternative to waste incineration [1]. Carbonization in comparison to incineration of waste creates only 2 molecules of CO<sub>2</sub> instead of 10 molecules from one average molecule of waste. During waste carbonization at lower temperatures (~350°C) the main process is cracking producing condensable liquid tar compounds, then at temperatures (~650°C) hydrogen is formed, at high temperatures (~950°C) the carbon char/active carbon is formed instead of ash. Formed active carbon, was tested by several authors [2]. We have tested carbon for wastewater treatment and as additive to soil. In spite of several advantages the carbonization of waste is rarely used because of environmentally hardly acceptable gas exhaust. This was the reason we focus our attention to complex treatment of carbonization exhaust. Non-thermal plasma based technique offers an innovative approach to this subject and was tested by several authors [3-9]. A multifunctional dry gas cleaning pilot system for 50-250 m<sup>3</sup>/hour of gas flow was applied; the system uses spontaneously pulsing transition type of discharge. The applied method cleaned very efficiently the exhaust from variety of non wanted compounds [15-19], utilizes CO<sub>2</sub>, [10-12] produces additional liquid hydrocarbons in process similar to hydro cracking method, produces solid proteinoid condensation product suitable for use as fertilizer and/or absorber material.

## Experimental

The carbonization chamber is heated directly using exhaust produced in natural gas oven with stoichiometric combustion and almost oxygen free flue gas. The carbonization zone (maximum temperature 950°C is placed 10cm above burners (temperature 975°C) A carbonization process of selected municipal waste arises in carbonization chamber in oxygen free atmosphere. When waste reach 350°C first volatile part is evaporated, then the thermal cracking starts producing hydrocarbons. At 500°C smaller hydrocarbons and its radicals and at 650°C hydrogen are produced. The waste contains large amounts of water and combustion exhaust additionally CO<sub>2</sub>. It together expands the formed carbon char to activated carbon.

Gas mixture exhausted from carbonization oven contains standard combustion exhaust, gas and liquid phase hydrocarbons and its radicals, oxidants and heterocyclic compounds, sulphur containing compounds, aerosol and

some other components. In the subsequent distillation unit the separation of hydrocarbons from gas into the liquid phase take place. The process is connected with the recuperation of heat. The non-condensable exhaust gases after distillation flow to the discharge equipment through cylindrical pipes with inner diameter of 15cm. The necessary gas flow is produced with 3 fans (flow 500 m<sup>3</sup>/h,  $\Delta p$  from 50 to 300 Pa) and measured using flow meters PREMA RPT3 with calibrated measuring range from 10 to 250 m<sup>3</sup>/h. On line diagnostic of air flow parameters is made using 2 pc of Testo 454 before and after discharge system. This make possible to measure gas flow velocity and its distribution, total gas flow evaluated from gas flow velocity distribution, static and dynamic pressure, temperature and humidity.

The multifunctional discharge system used for carbonization exhaust treatment operates on gas flow volume of 50-250 m<sup>3</sup>/hour and comprises in discharge system plurality of 24 discharge tubes connected parallel each other. The spontaneously regularly pulsing direct current electric discharge in streamer to spark transition regime was used. High voltage source with dc high voltage of both polarities up to 20 kV, maximum power 600 W and maximum current 30 mA was applied for discharge generation. The schema of pilot scale system is on Fig. 1

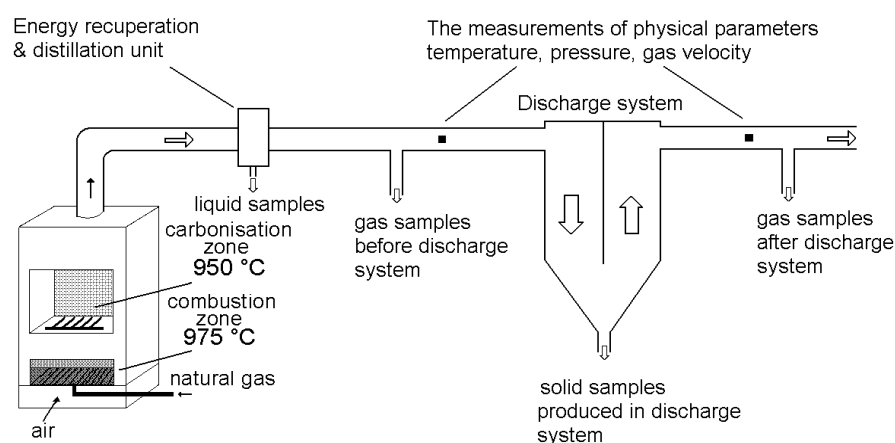


Fig. 1 The schema of oven used for carbonisation of selected municipal waste and pilot scale discharge system for flue gas cleaning built for gas flow volume of 50-250 Nm<sup>3</sup>/hour

Gas phase sampling was done using iso-kinetic method. The sample flow into IR gas cells was 30l/min both before and after discharge reactor. The gained samples were analysed by IR absorption spectrometry. We have used various IR techniques. The gases were analysed in 10 cm gas cell with KBr, CaF<sub>2</sub> or KRS5 windows. Liquids were analysed in liquid cell with variable path-length and KRS5 windows. For solid samples the KBr pellet technique was used. The sample is mixed with the KBr powder in the ratio approximately 0.2-1:100 and together pulverised in the vibration mill. The mixture is then pressed under pressure about 22 MPa to the metal ring and by this way the pellet is formed. From pellet the spectra are scanned. This method was used for analysis of solid product formed inside discharge system as well as for analysis of final carbon containing product from carbonization of waste inside oven.

## Results and its discussion

To study in details the carbonization processes in real conditions we have made a group of measurements of carbonization process applied to several types of waste. The produced carbonization gases undergo cleaning inside pilot scale non-thermal plasma based system. We have tested several typical types of waste, mostly rest of food as bones, bread and rolls, eggs shells, chicken rests, potato peels, leaves, rests of vegetables, nut shells, garlic rests, plastic (without chlorine) and a mixture of waste. The composition of carbonization exhaust differs with time, temperature i.e. with the stage of carbonization process. Additional changes occur due to type of processed waste, after distillation, after non-thermal plasma based processing.

At present stage it was possible to us to make only part of planed methods. It means that the gas phase analysis was made was not on-line, only isokinetic sampling followed by ex-post analysis of gas samples after oven,

before and after discharge system was made using IR absorption spectrometry as we see on Fig.2. From spectra before and after discharge system we can see the very high efficiency of CO<sub>2</sub>, CO, gas phase CH<sub>x</sub> and NO<sub>2</sub> removal (close to 99%). The carbon product from carbonization oven was analyzed permanently every day using KBr pellet technology for each type of waste separately.

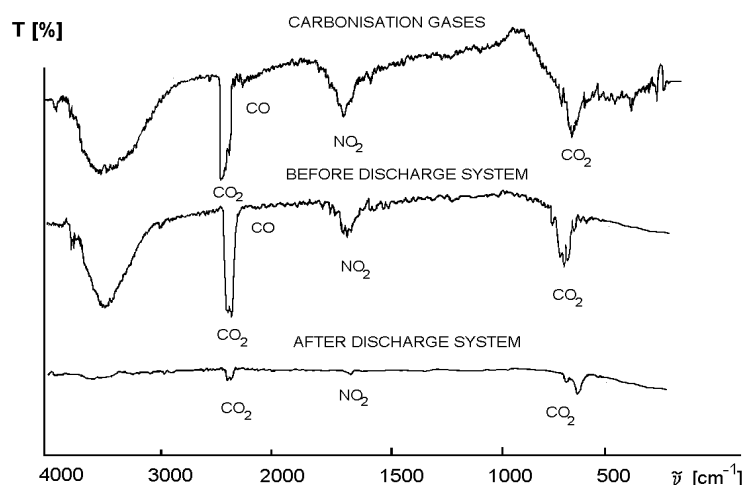


Fig. 2 IR absorption spectra of exhaust gases situated from top after carbonization oven, before and after discharge system made in gas cell with KBr windows

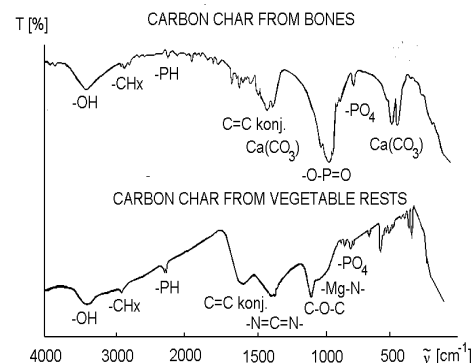


Fig. 3 IR absorption spectra of carbon char from carbonization oven produced from bones (top) and vegetable rest (bottom), the spectra are made using KBr pellet technique.

The produced carbon char in all cases has amorphous character, what was supported

also by scanned SEM photographs. From several magnification of SEM it was seen, that inside carbon are holes with radius changed in 3 order of magnitude. The walls of carbon cells were sub-nanometer sized. The active surface was 257m<sup>2</sup>/g measured by BET method using absorption of N<sub>2</sub>. The estimated density of amorphous carbon sample was approximately 0.3g/cm<sup>3</sup>.

In the case of each treated waste (bones, bread and rolls, eggs shells, chicken rests, potato peels, leafs, rests of vegetables, nut shells, garlic rests, plastics, mixture of waste without glass and metal) the char remains its texture from original material. The analysis made by IR absorption spectrometry using KBr pellet technique shows differences in the presence of mineral components and form how carbon intercalates with mineral components in produced carbon char. The biggest difference is seen between spectra of bones (top) & vegetable rests (bottom) as we see from Fig. 3. In the case of bones dominates calcium and phosphorus groups bonded to carbon as intercalates. In the case of vegetable rests the conjugated carbon chains, rests of sugar-like structures (C-O-C), rest of magnesium from chlorophyll bonded to carbon through nitrogen (Mg-N-, -N=C=N-) are most important features of spectrum. Structures with phosphoric acid are present only in small amounts, probable from DNA and RNA of plant cells.

The analysis made externally using AAS method shows following information about carbon char:

pH=8.7, P=7.1 g/kg, Na=13.4 g/kg, K=14.8 g/kg, Ca=29.0 g/kg, Mg=37.7 g/kg, Fe=25.3 g/kg, N=15.9 g/kg.

On the Fig.4 we see IR absorption spectra of solid product from discharge system after action electric discharge on carbonization gases. We can see small difference in composition of product on stressed and non-stressed electrode.

In the case of stressed electrode dominates proteinoid character of product. On non-stressed electrode product we see also a part of tar liquid products (levoglucosane, an condensable part of exhaust) separated from gas by electric wind and changed to solid due to polymerisation induced by the discharge action.

Comparison of solid samples with calibration IR absorption spectra of 27 pure amino acids help us to find amino acid components of solid product.

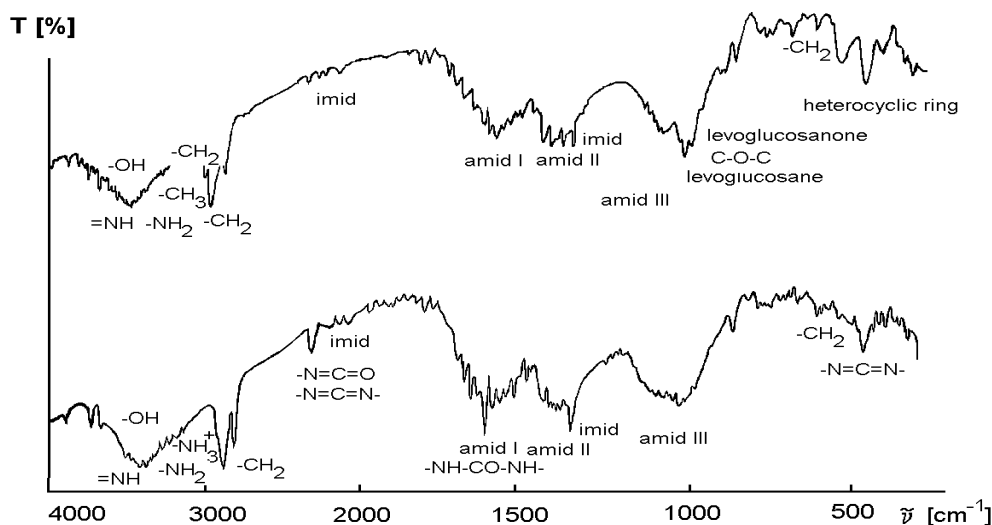


Fig. 4 IR absorption spectra of solid product collected from non stressed electrode (on the top) and stressed electrode (on the bottom) made using KBr pellet technique

## Conclusions

As we have used for carbonization the stoker fired type of oven, the waste treatment described in this contribution comprises several thermal decomposition forms of work (slow and fast pyrolysis, carbonisation) so produced exhaust comprises condensable as well as non-condensable portion of gas.

The release of energy from waste is postponed to the temperature when cracking begins ( $\sim 350^\circ\text{C}$ ). The chemical energy is separated in the form of liquid hydrocarbon in distillation unit (levoglucosane and other tar components). The cracking itself is exothermic process (breaking of chemical bonds), so the part of energy used earlier for heating of waste is possible to recuperate. The exhausts during this phase of process are similar to combustion exhaust enriched on large portion of rich variety of hydrocarbons. The treatment of such exhaust in non-thermal plasma systems is very effective.

By increasing the temperature up to  $\sim 550^\circ\text{C}$ , the release of hydrocarbons decreases and the composition of exhaust changes to typical combustion exhaust. The treatment of typical combustion exhaust in non-thermal plasma systems we have already described in earlier articles [10-12, 15 -19]. The important property of exhaust treatment is the formation of life important organic compounds in non-thermal plasma based systems.

Further heating of waste to temperature higher than  $\sim 650^\circ\text{C}$  causes formation of hydrogen. It is again conversion of energy from waste to chemical energy of hydrogen. It is necessary to find most suitable way how to store the released energy from hydrogen. We have prepared for tests the following possibility of hydrogen storage:

- absorption/desorption of hydrogen in carbon char with further use in PEM fuel cells,
- conversion of hydrogen in non thermal plasma based system to more suitable liquid compound as is hydrazine and/or hydrocarbons in system similar to hydrocrack (a part of hydrogen storage program was already realized).

The final active carbon char after release of all gas phase component is reached at temperature  $\sim 950^\circ\text{C}$ . The formed carbon was detailed analysed for several types of treated waste. The preliminary test of char use in future was tested for hydrogen storage, wastewater cleaning and as balancing additive to soil improving the vegetation growth.

The method of exhaust cleaning using non thermal based system was tested in regime when the released gases are rich on secondary tar components formed during cracking phase. The applied method cleaned very efficiently the exhaust gas from variety of non-wanted compounds and similar as in the case of only combustion

exhaust, the system utilises gases to solid product. The efficiency of treatment is very high. CO<sub>2</sub> and NO<sub>x</sub> removal efficiency vary in 40-99%. The process is connected as in the case of combustion exhaust with nitrogen fixation. The final solid amino acids condensation product (proteinoid) made in electric discharge was based on typical amid group as in the case of combustion exhaust only hydrocarbon part of product was enriched with radicals produced from tar components.

The knowledge of cracking process during waste carbonisation gives us the possibility to understand some processes taking later place in discharge system during solidification of carbonisation exhaust. The large part of municipal waste is composed of several poly saccharides. Thermal de-polymerisation and cracking leads to formation of  $\alpha$ -D-glucopyranose. In process of partial oxidation is  $\alpha$ -D-glucopyranose converted to levoglucosane or levoglucosanone that condense in distillation unit, only small portion is transported further into discharge system. The reactions taking place inside non-equilibrium plasma conditions in electric discharge are strongly influenced by the presence of electric field and heterogeneous catalysis on the electrode surface. The involved chemistry during final product formation can be divided into three important steps: • activation, • formation of energy rich intermediate species, • final product formation. The most important activation step is excitation of molecular nitrogen by repeated electron impact in electric discharge using in total energy close to 6.5eV. The described electronic state  $N_2^* A^3\Sigma_u^+$  has a lifetime between 1.3-1.9 sec [13] and that is why it can be involved with a great probability into chemical reaction. From IR spectra of product in Fig.4 and IR calibration spectra of arginine and lysine it comes out that the most probable amino acid in product is arginine. The formation of arginine from  $\alpha$ -D-glucopyranose in electric discharge under influence of metastable excited molecular nitrogen  $N_2^* A^3\Sigma_u^+$  is possible to see from following Fig 5. Similar process applied on cyclohexanone we have published in [15].

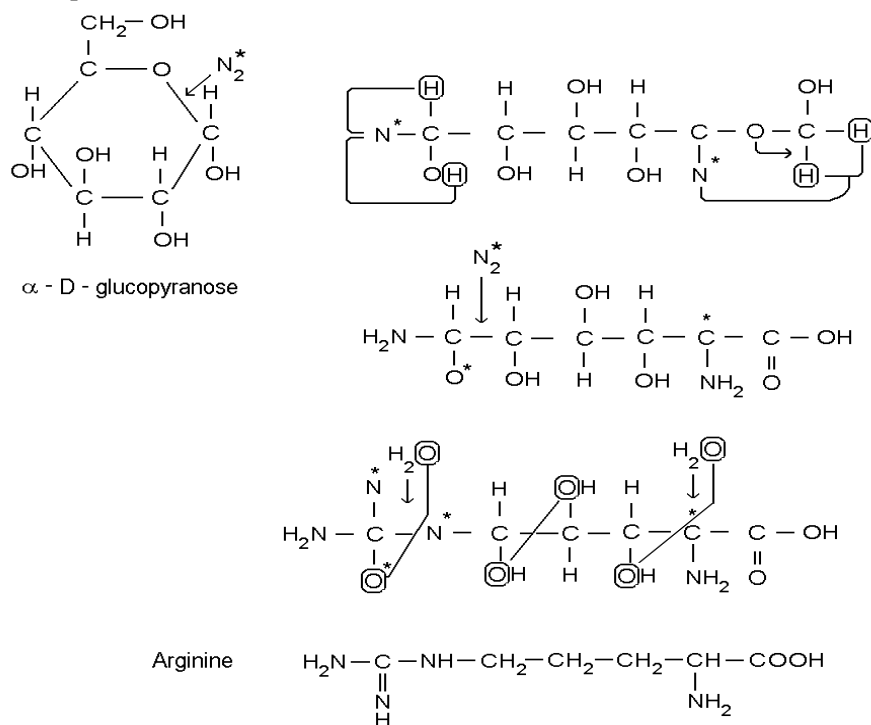


Fig 5 Formation of arginine from  $\alpha$ -D-glucopyranose in non-thermal plasma system

Similar processes responsible for formation of amino acids in strong and middle reducing primitive atmosphere during origin of life in Earth were described by S.L.Miller [14]. Combustion as well as carbonisation exhaust are from the point of view of composition relevant to neutral pre-biotic atmosphere.



## Acknowledgement

The authors wish to thank to the Slovak Scientific Grant Agency (VEGA) for the financial support given in projects 1/8312/01 and Agency for support of science and technology (AVPT) for financial support given to bilateral Slovak- US project No.027/2001.

## References

- [1]. A.V Bridgewater, G. V. C. Peacocke, Fast pyrolysis processes for biomass. *Renewable and Sustainable Reviews* 2000, 4, 1-73
- [2]. Valenzuela, C. C.; Gomez, S. V.; Hernandez, A. J.; Bernalte, G. A. Use of waste matter after olive grove pruning for the preparation of charcoal. The influence of the type of matter, particle size and pyrolysis temperature. *Bioresource Technol.* **1992**, 40, 17-22
- [3]. R McAdams: Prospects for non-thermal atmospheric plasmas for pollution abatement, *J. Phys. D: Appl. Phys.* **34** (2001) 2810–2821
- [4]. Civitano, L.: Industrial Application of Pulsed Corona Processing to Flue Gas 103-130, in *Non-Thermal Plasma Techniques for Pollution Control*, Edited by B.M.Penetrante and S.E.Schultheis, NATO ASI Series, Series G: Ecological Sciences, Vol.34, Part B, (Springer-Verlag, Heidelberg, 1993)
- [5]. Gallimberti I., *Pure Appl. Chem.* 60(1988), 663
- [6]. Mizuno A., Clements J.S., Davis R.H. *IEEE Trans.Ind.Appl.V.IA-22*(1986), 516-521
- [7]. Masuda S., *Pure Appl. Chem.* 60 (1988), 727
- [8]. Penetrante, B. M., Hsiao, M. C., Merritt, B. T., Vogtlin, G. E. and Wallman, P. H., *IEEE Trans. Plasma Sci.* **23**, 679 (1995).
- [9]. Higashi, M., Uchida, S., Suzuki and, N., Fujii, K., *IEEE. Trans. Plasma Sci.* **20**, 1 (1992)
- [10]. M. Morvová, I. Morva, F. Hanic: Single step removal of CO<sub>2</sub> incorporating CO<sub>2</sub> and nitrogen fixation from gas phase in electric discharge, *Greenhouse Gas Control Technologies, Proceedings of the 4<sup>th</sup> International Conference on Greenhouse Gas Control Technologies*, 30 August-2 September 1998, Interlaken, Switzerland, Ed. B.Elliasson, P. Riemer, A. Wokaun, Elsevier Science, Oxford, UK, 1999, ISBN: 008-043018-X, pp. 137-142
- [11]. M. Morvová, F. Hanic and I. Morva: Plasma Technologies for Reducing CO<sub>2</sub> Emissions from Combustion Exhaust with Toxic Admixtures to Utilisable Products, *Journal of Thermal Analysis and Calorimetry*, Vol.61 (2000), 273-287
- [12]. F. Hanic, M. Morvová and I. Morva: Thermochemical Aspects of the Conversion of Gaseous System CO<sub>2</sub>-N<sub>2</sub>-H<sub>2</sub>O into Solid Mixture of Amino Acids, *Journal of Thermal Analysis and Calorimetry*, Vol. 60 (2000), 1111-1121
- [13]. Lofthus, A., Krupenie, P.H., *J. Phys. Chem. Ref. Data* 6 (1977), 113-307
- [14]. Miller, S.L in "Major Events in the History of Life", Ed. By J.W.Schopf (Jones&Bartlett, Boston, Mass., 1992), Chap.1, pp. 1-28
- [15]. Z. Machala, M. Morvová, E. Marode, I. Morva: Removal of Cyclohexanone in Transition electric discharges at atmospheric pressure, *J.Phys.D: Appl.Phys.* Vol.33 No.24 (2000), pp. 3198–3213
- [16]. K.Hensel, M.Morvová: Removal of NO<sub>x</sub> in Corona Discharge at the Atmospheric Pressure with Inner Electrode Material Variation, *Contribution to Plasma Physics*, Vol. 36 (1996), No. 01, 51-61
- [17]. M. Kurdel, M. Morvová: DC corona discharge influence on chemical composition in mixtures of natural gas with air and its combustion exhaust with air, *Czechoslovak Journal of Physics*, Vol. 47 (1997), No. 2, pp. 205-215
- [18]. M. Morvová: DC corona discharge in CO<sub>2</sub> - air and CO - air mixtures for various electrode materials *J.Phys D: Appl.Phys* 31 (1998), pp. 1865-1874
- [19]. M. Morvová, The influence of water vapour and temperature on depletion of carbon monoxide in dc corona discharge, *Czech.J.Phys.* Vol.49, No.12 (1999), pp. 1703-1720

# THE MODEL FOR ORIGIN OF LIFE DUE TO EXHAUST UTILISATION IN ELECTRIC DISCHARGE.

Marcela Morvová, Imrich Morva, František Hanic\*

*Institute of Physics, Faculty of Mathematics, Physics and Informatics, Comenius University,  
Mlynská Dolina F2, 842 48 Bratislava, Slovakia*

*\* Institute of Measurement Science, Slovak Academy of Sciences, Dúbravská cesta 9, 842 19  
Bratislava, Slovakia*

## Abstract

The present paper describes process of CO<sub>2</sub> and combustion exhaust utilisation using transition electric discharge. The final solid product is proteinoid of various L-amino acids. The time and humidity causes reconfiguration of product producing microspheres. In polymerization process during quench the oxygen is released in measurable concentration. This process can be involved in ozonosphere formation on early Earth without need of photosynthesis. The technical application of exhaust utilization leads to CO<sub>2</sub> mitigation.

## Introduction

The early atmosphere consisted mainly of gases released by volcanic activity. The today composition of combustion exhaust is similar to the neutral primitive atmosphere i.e. CO<sub>2</sub>, CO, H<sub>2</sub>O, N<sub>2</sub>, traces NH<sub>3</sub>, H<sub>2</sub>, CH<sub>x</sub>. S. L. Miller performed the first successful synthesis of individual amino acids in strongly reducing atmosphere in apparatus with repeated spark discharges between two carbon electrodes (1952) [2]. Later (from 1972) in the same form of discharge was done an experimental work for middle reducing and (from 1987) for neutral primitive atmospheres [1]. As described in [1] it is hardly possible to form various biologically important macromolecules from monomers in polymerization processes without additional energy supply. From power sources present in Earth condition the most intensive is the terrestrial lightning with available energy (electrons up to ~20eV, UV radiation ~1-10eV, excited particles up to ~15eV). At present about 2x10<sup>6</sup> lightning is formed per a day. With rising concentration of CO<sub>2</sub> the number of lightning rise up, in prebiotic condition probably in 3-5 order of magnitude i.e. to about 10<sup>10</sup> lightning per day. The heterogeneous process leading to polymerization on charged rocks was proposed by L. E. Orgel in [4]. Also very probable form of energy source by submarine vents was proposed by J. P. Ferris [5]. A part of energy available in interstellar conditions (cosmic rays ~MeV, solar wind ~keV, UV radiation ~1-10eV) was described by M. P. Bernstein et al. [6]) can be used also on Earth in photochemical processes.

## Experimental

The small pilot equipment built for 50-250 Nm<sup>3</sup>/hour of exhaust gas flow operates with spontaneously pulsing electric discharge. The individual discharge channels quickly travel on the surface of stressed electrode. The discharge channels are connected with dielectric spots formed during discharge action and having enhanced dielectric constant and catalytic properties. The system was tested in gas flow regime using various exhaust types. The residence time in discharge zone was about ~2s.

The direct diagnostics of reacting gas before and after electric discharge reactor was done using IR absorption spectrometry. Final solid product was analyzed by IR absorption spectrometry, HPLC, X-ray diffraction and thermogravimetric analysis. The inside into conversion process, reaction kinetics, product development, amino acid formation and evolution of the catalytic surface spots on electrodes enabled in situ step by step time development measurements made inside small discharge reactor placed inside IR gas cell.

Activation of the gas system was performed by electric discharge; involved activating factors were electrons, excited heavy particles, photons and surface catalysis. The process starts in volume of the discharge zone by formation of electronically excited meta-stable molecular nitrogen  $A^3\Sigma_u^+$  with lifetime up to 2s. This excitation state could be achieved by repeated electron impact with total energy of ~6.8eV. Due to reaction of N<sub>2</sub>\* with CO<sub>2</sub> intermediate ON-NCO is formed. By reacting of ON-NCO with water amid radical is formed. Repeated radical polymerization then lead to the formation of final solid random polycondensate - proteinoid. As shows its analysis the solid product containing various amino acids (arginine, lysine, histidine, methionine, glycine alanine, serine and aspartic acid). From experiment came out the energetic pretension

necessary for conversion with value 2,3-4,7 Wh/m<sup>3</sup>, i.e. 8,3-16,9 kJ/m<sup>3</sup>. Due to disproportion in theoretical and experimental values of energy consumption we have tried to find out responsible catalytic effects.

Precise analysis of the non-stressed electrode by IR reflection spectrometry gave us more detailed information about catalyst. It seems that an important role might play oxamidato complexes (HNCO)<sub>4</sub> Cu. Also some other compounds on the electrode surface were found to have catalytic properties, namely heterocyclic structures containing pyrrole ring. The presence of metal complexes was supported by thermogravimetric analysis, showing 3-5% residue after heating in air up to 900°C. We have tried to analyse some details of these complicated structures. Comparing IR absorption spectrum of liquid pyrrole with single ring (down) and spectrum of electrode surface (up) on Fig.1 we could conclude that the surface products contain also oligo pyrrole compounds. The final product from pre-pilot equipment is a solid powder with fractal structure on microscopic level,

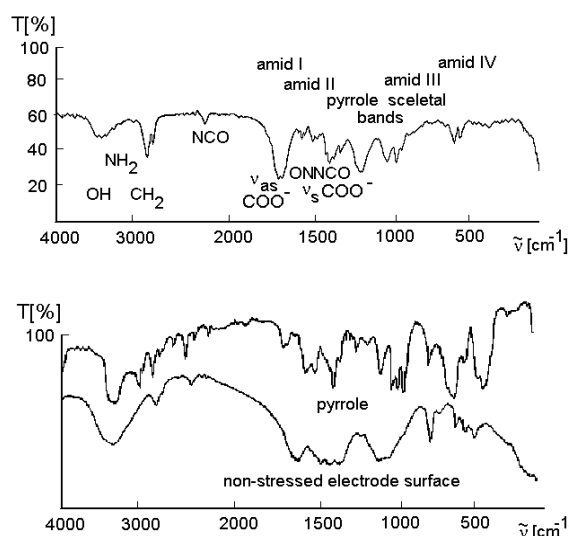


Fig.1 IR absorption spectra of solid condensation product, electrode surface and liquid pyrrole

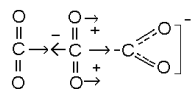
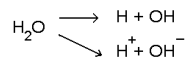
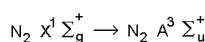
with low specific weight, consisting of chains of flakes as it is seen on optical microscopic photographs on left part of Fig.2. Reconfiguring of product under the influence of humidity and time lead to the formation of protocells as we see from SEM microscopic photographs on left part of Fig.2 in comparison to protocells on right part of Fig.2.



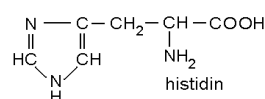
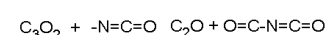
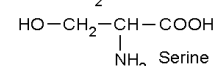
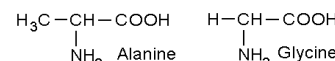
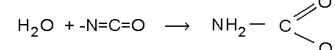
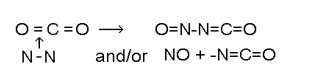
Fig.2 Left part of figure is microscopic photograph of solid product; magnification on left side 150 in middle 500 and on right side SEM photograph with magnification 8000; Right part of figure is SEM photograph of proteinoid protocells published by A.Pappelis & S.Fox [9]

#### Combustion exhaust reactions in electric discharge - formation of amino acids

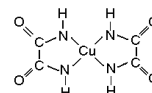
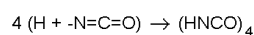
##### Activation processes



##### Volume reactions in discharge



##### Reactions on electrode surface



##### oxamidato complexes

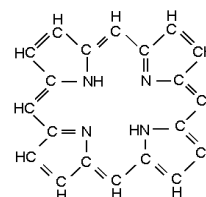


Fig.3 The processes involved in conversion of combustion exhaust in spontaneously pulsing electric discharge and formation of amino acid condensation product as well as catalytic active spots on the electrode surface

## The hypothesis

## 1. ACTIVATION BY TERRESTRIAL LIGHTNING

Here we want to show that the return stroke in the case when lightning beat into the water may have played the role of energy source necessary for the origin of life important compounds as well as polymers up to the proto-cell in pre-biotic Earth. Large amount of energy is transferred from spark channel into water and air surrounding. Due to adiabatic expansion of plasma channel the activated species (electrons, ions, meta-stable atoms, light, heat) are transported to zones, where the gas temperature is much lower. In dc electric field between cloud and see and additionally positive space charge of lightning streamer body in gas mixture of at least  $\text{N}_2\text{-CO}_2\text{-H}_2\text{O}$  and water droplets L amino acids may be formed from NCO radical. Additionally from ON-NCO in reaction with OC-CCO activated species pyrrole ring based compounds may be formed. These substances and various other fragments form polymeric fractal cluster by poly-condensation process in the colder part of discharge. The rest gas product is adsorbed. The free positive space charge expanded from lightning streamer body is attached inside formed fractal cluster. The stroke into the water is usually connected with huge water evaporation and sublimation of volatile aerosol impregnated by minerals from the see bottom. As the conductivity of Earth surface is relatively small a lot of negative charge is dissolved in water. From primary atmosphere only  $\text{CO}_2$  is highly soluble in water. This fact implicated the composition of gas slope inside stroke part of water to  $\text{CO}_2\text{-H}_2\text{O}$ -mineral part ( $\text{-PO}_4$ , K, Ca, Na)-negative space charge. As inside this slope the pressure is very high, the nitrogen from atmosphere cannot diffuse in. Due to composition and negative space charge the D form of sugars together with minerals may be formed. This can explain incorporation of  $\text{-PO}_4$  into further RNA, DNA, ADP and ATP. The high pressure in stroke slope transports the formed compound out in the trajectory crossing the trajectory of amino acid part of product formed in stroke outside water. In this way the fractal cluster containing L-amino acids, D-sugars, unsaturated organic acids, phosphate groups as well as various minerals attached free positive space charge and bonded positive and negative charge in common solid fractal product may be formed. Due to the electric wind from cloud to Earth in the zone with non disturbed electric field and no more high temperature, formed fractal clusters are transported to the water surface.

## 2. ORIGIN OF OZONOSPHERE

The formation of heterocyclic compounds from radicals and activated species generates several molecules of oxygen in each of the reaction step as we can see for adenine, cytosine and ribose formation in Fig.4.

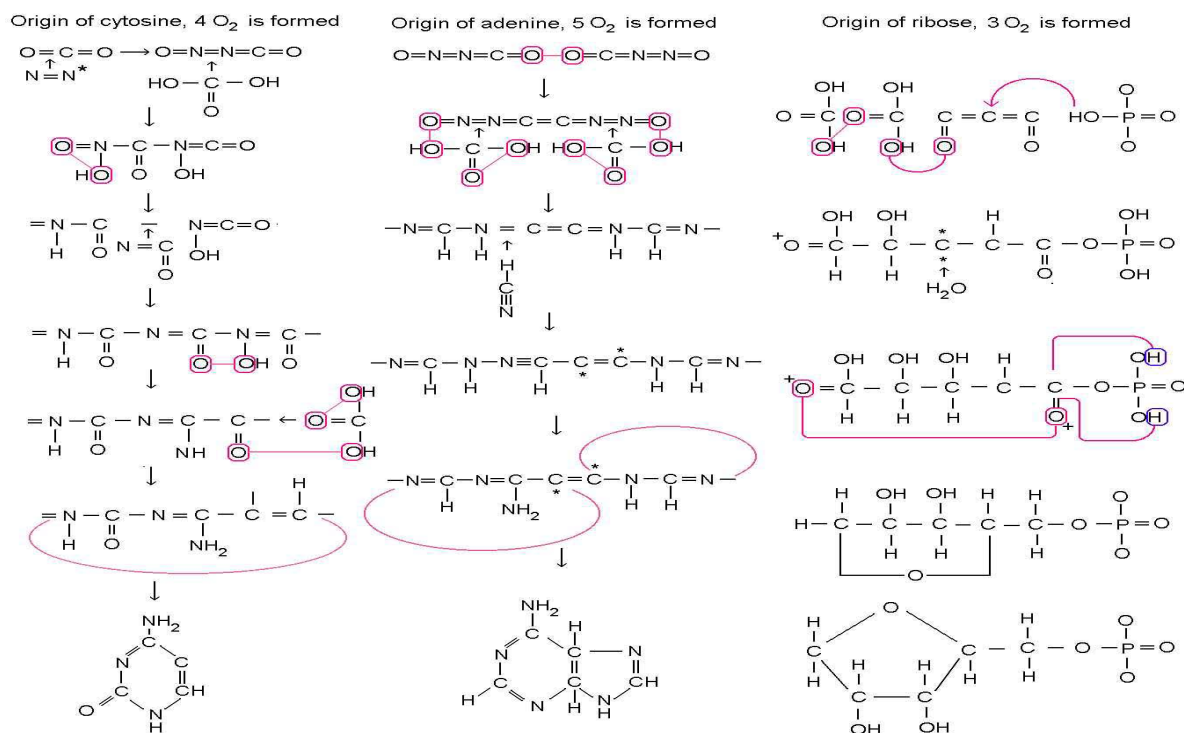


Fig.4 The formation of bases adenine, cytosine and sugar ribose from radicals and activated species leading to the formation of oxygen

We have generated in our experimental flowing system from oxygen free combustion exhaust oxygen after action of discharge (up to 5% by volume). Such oxygen can form ozonosphere even earlier than photosynthesis begin to work. In primary atmosphere the diffusion of formed oxygen to upper parts of atmosphere was much more probable due to high specific weight of rest atmospheric gases ( $\text{CO}_2$  molecular weight 44,  $\text{nH}_2\text{O}$  for  $n \geq 2$  molecular weight 36,  $\text{O}_2$  molecular weight 32). The solubility of oxygen in water is small and varies in between 4.9 and 1.7% (0-100°C). This implicates oxygen will diffuse up. To estimate the necessary time for ozonosphere origin we have evaluated the amount of ozone produced in one day from the number of lightning ( $\approx 10^{10}$  per day), the transported charge in one lightning ( $50\text{C} = 31.2 \times 10^{19}$  electrons), the probability of oxygen formation 0.1 to the value  $1.04 \times 10^{29}$  molecules. Then we have estimated the number of ozone molecules in today ozonosphere (in the case of 3mm thickness at atmospheric pressure, the high 25km, i.e. ozone volume  $4.637 \times 10^{12} \text{ m}^3$ ) to the value  $1.12 \times 10^{38}$  molecules. To generate such amount of ozone, when we additionally suppose that only 50% of oxygen will diffuse up and probability of ozone generation from oxygen due to UV radiation is 1%, we need  $2.154 \times 10^{11}$  days i.e. about  $6 \times 10^8$  years. The gained value 600 millions of years seems to be the realistic estimation for the time of ozone layer origin.

### 3. PROTOCELL ORIGIN (See Fig.5)

When fractal cluster with adsorbed gases and attached free positive space charge reach the water surface 1, water tries to introduce into cluster and gases try to go out. The attached positive space charge is set free and due to repulsive forces forms positive ball around fractal cluster. As the water is charged negative, due to electrostatic induction the electric bi-layer is formed. Inside this bi-layer the desorbed volatile compounds are oriented and create micelle like form. Inside this micelle rearrangement leads to the formation of plasma membrane, which covers fractal cluster in the form of microsphere 2. Splitting of proteinoid inside microsphere due to UV radiation leads to decrease of crosslinking degree and fragmentation of cluster structure 3. A part of fragments diffuse into plasma membrane bi-layer to create various membrane components. Smaller fragments solutes in water to produce cytoplasm. Middle size fragments can lead to the origin of enzymes. Large size fragments separate to produce histone type of compounds (RNA, DNA and pigments), protein types and various mixed types of compound. The conformation of fragment is still random 4. The individual polar parts of proteinoid fragment chain are surrounded by the charge of opposite polarity creating shielding layer in Debye length 5. Reconfiguration of random conformation to thermodynamically more stable (helical) structures 6 causes destruction of shielding layer around charged groups. The dipoles are formed due to hydrogen bonding between aminoacid zwitterions 7. Bonded positive as well as negative charge from shielding layer around charged groups is set free in reconfiguration process. Created free charge is redistributed and used to form intra-cellular membranes of organelles and create protocell 8. We have tried to evaluate the most important parts of charge redistribution inside cell. The charge of one sector of structures present in nucleus (histone components) is in total positive, so the nucleus is due to repulsive forces from cell plasma membrane in the centre of cell. The charge of tetrapyrrole structures present in thylacoids is in total negative, so thylacoids are due to attractive forces from cell plasma membrane situated close to inner part of membrane. The schema of protocell origin is on Fig.5.

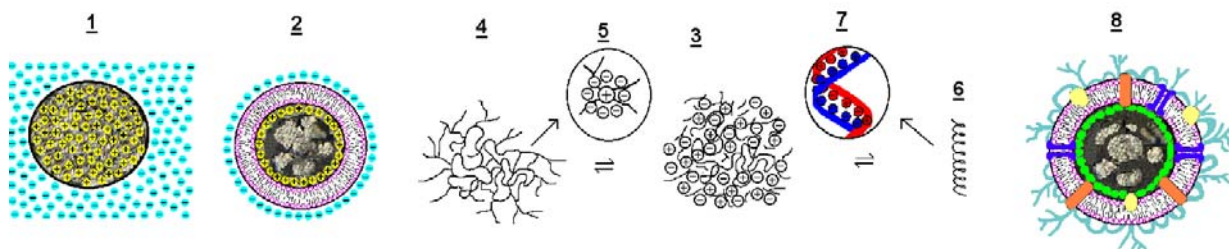


Fig.5 Development of plasma membrane around the fractal cluster after reaching water, formation of microsphere, redistribution of bonded charge and origin of protocell.

### Conclusions

The method reported here is interesting from the point of view of greenhouse effect limitation. The main advantage of described method is that in single system the full utilisation of combustion exhaust inclusive  $\text{CO}_2$  takes place. The observed utilisation efficiency is high (40-99% of  $\text{CO}_2$  is utilised) and the method works also on  $\text{NO}_x$  and  $\text{CH}_4$  with efficiency up to 95% [7]. The method is close connected with processes taking part in prebiotic chemistry as seen from [8].

We have collected in one model the most of points necessary for origin of life on Earth. Some valuable experimental results giving possible to create our hypothesis are:

1. We have shown how aminoacids and other life important substances and polymers can be formed.
2. We have produced proteinoid (~100 grams) in abiotic system i.e. by influencing the combustion exhaust (primary atmosphere) and charged water aerosol with spontaneously pulsing transient electric discharge.
3. We have produced oxygen from oxygen free combustion exhaust in electric discharge. We have shown the possibility of oxygen formation before onset of photosynthesis and estimated the probable time period necessary for the formation of ozonosphere to about 600 millions of years.
4. Due to charged water/water droplets the produced proteinoid can be converted into protocell, i.e. the plasma membrane can be formed.

### Acknowledgement

The authors wish to thank to the Slovak Scientific Grant Agency (VEGA) for the financial support given in projects 1/8312/01 and Agency for support of science and technology (AVPT) for financial support given to bilateral Slovak- US project No.027/2001.

### References

1. S.L.Miller in "Major Events in the History of Life", Ed. By J.W.Schopf (Jones&Bartlett, Boston, Mass., 1992), Chap.1, pp. 1-28
2. Miller, S.L, A Production of Amino Acids Under Possible Primitive Earth Conditions: *Science* 117 (1953), p. 528-529
3. Dolezalek, H., Discussion of the fundamental problem of atmospheric electricity, *Pure Appl.Geophys.*, 100, 8--43, 1972.
4. L.E.Orgel Orig. Life Evol. Biosphere 28 (1998), Polymerization on the Rocks: Theoretical Introduction, pp. 227-234
5. Ferris, J.P. 1992. Marine hydrothermal systems and the origin of life: Chemical markers of prebiotic chemistry in hydrothermal systems. *Origins Life Evol Biosphere* 22: 109-134
6. M.P.Bernstein, S.A.Sandford, L.J.Allamandola, S.Chang: *Astrophys.J.* Vol. 454 (1995), pp.327-344
7. M. Morvová, F. Hanic, I. Morva: Plasma Technologies for Reducing CO<sub>2</sub> Emissions from Combustion Exhaust with Toxic Admixtures to Utilisable Products, *Journal of Thermal Analysis and Calorimetry*, Vol.61(2000), 273-287
8. F. Hanic, M. Morvová and I. Morva: Thermochemical Aspects of the Conversion of Gaseous System CO<sub>2</sub>-N<sub>2</sub>-H<sub>2</sub>O into Solid Mixture of Amino Acids, *Journal of Thermal Analysis and Calorimetry*, Vol. 60 (2000), 1111-1121
9. A.Pappelis & S.Fox at <http://www.siu.edu/~protocell/photos.htm>

# Plasma-Fluorination Synthesis of High Surface Area Aluminum Trifluoride from Zeolite Precursors

J. L. Delattre, E. Hajime, A. M. Stacy

*Department of Chemistry, University of California – Berkeley, Berkeley CA, USA*

## Abstract

A method for the preparation of a high surface area aluminum trifluoride ( $\text{AlF}_3$ ) powder from aluminosilicates via a heterogeneous, perfluorocompound plasma fluorination/decomposition reaction has been developed. The flocculent product is nearly amorphous by powder x-ray diffraction and has an unusually high surface area ( $\sim 200 \text{ m}^2/\text{g}$ ). Based on  $^{27}\text{Al}$  and  $^{19}\text{F}$  NMR results, the local environment around aluminum appears to be more distorted in plasma-synthesized  $\text{AlF}_3$  than in traditionally prepared metastable phases. Structural changes associated with annealing were investigated using temperature programmed synchrotron radiation powder diffraction. The resulting material has an unusual nanostructure and Lewis acidity that is not found in aluminum fluoride prepared under more conventional conditions.

## 1. Introduction

Fluoride catalysts are often required in the manufacture of chlorofluorocarbons (CFCs), hydrochloro-fluorocarbons (HCFCs), hydrofluorocarbons (HFCs), and perfluorocarbons (PFCs) [1-4]. The first major development in this area occurred more than 100 years ago when Swarts discovered that  $\text{SbF}_5$  catalyzed the fluoro-dechlorination of chlorinated alkanes [5,6]. Subsequently, CFCs were identified as ‘ideal’ refrigerants and propellants because they are stable, nontoxic and nonflammable; mass production using Swarts catalysts soon followed [7]. In the early 1980s, the fluorinated oxides of trivalent metals such as  $\text{Cr}_2\text{O}_3$ ,  $\text{Fe}_2\text{O}_3$ , and  $\text{Al}_2\text{O}_3$  were adopted over  $\text{SbF}_5$ , as these materials also catalyze halogen exchange but are less toxic and more easily handled [8,9]. Interest in halogen exchange chemistry was renewed in the late 1980s when it was revealed that CFCs could deplete stratospheric ozone [10]. HFCs were identified as reasonable alternatives to CFCs for many applications because they do not generate ozone-depleting chlorine radicals. Because halogen exchange is the primary step for converting CFCs to ozone-safe HFCs, there has been an increase in the study of halogen exchange catalysts in the past ten years [11,12]. Most research efforts have focused on the preparation of new materials that are active catalysts, identification of the active species and the study the mechanism of halogen exchange.

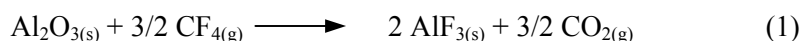
Of the industrial scale halogen exchange catalysts, fluorinated  $\gamma$ -alumina has been widely used for the manipulation of halocarbons because it is inexpensive and effectively catalyzes a variety of halogen exchange reactions, including isomerization and dismutation [9,13-16]. The structural and compositional changes associated with the fluorination pretreatment of  $\gamma$ -alumina have been studied extensively [17] in order to reveal the nature of the active surface species. XPS studies of  $\gamma$ -alumina pretreated with  $\text{CHF}_3$  at  $400^\circ\text{C}$  suggest that an amorphous form of  $\text{AlF}_3$  that is structurally similar to  $\beta$ - $\text{AlF}_3$ , a metastable phase of aluminum trifluoride, is the active catalyst. This result is in general agreement with a report on the pretreatment of  $\gamma$ -alumina with  $\text{CHClF}_2$  at  $500^\circ\text{C}$  that detected the formation of  $\beta$ - $\text{AlF}_3$  by XRD and determined this phase was the active catalyst [18].

The observation that  $\beta$ - $\text{AlF}_3$  is an active catalyst while the thermodynamically stable phase,  $\alpha$ - $\text{AlF}_3$ , is inactive fueled the search for additional metastable phases of  $\text{AlF}_3$ . Using wet chemistry techniques, a number of new metastable phases of  $\text{AlF}_3$  have been prepared [19,20]. Like  $\beta$ - $\text{AlF}_3$ , these new metastable phases are all derived from corner-sharing  $\text{AlF}_6$  octahedra, they are active halogen exchange catalysts and they irreversibly transform to  $\alpha$ - $\text{AlF}_3$  in the temperature range of  $450$  to  $700^\circ\text{C}$  [21]. Industrially, the use of pure  $\text{AlF}_3$  catalysts would mitigate the need for the use of corrosive fluorinating reagents and any induction period required for activation of the catalyst. Unfortunately, these new catalytically active phases of aluminum trifluoride are prepared using caustic reagents such as  $\text{HF}$ . Moreover, the surface areas of these fluoride materials are significantly lower than the corresponding oxides, reducing the efficiency of the catalyst in industrial application. Clearly, improved techniques for the preparation of high surface area, catalytically active phases of aluminum trifluoride are desirable.

Rather than approach this problem using traditional wet chemistry, we have developed a new synthetic method for the preparation of  $\text{AlF}_3$  based on the premise that heterogeneous reactions that use a perfluorocompound (PFC) plasma as a fluorinating agent could be used as a general route to solid fluorides



from oxides. For example, equation 1 shows an idealized reaction between CF<sub>4</sub> and Al<sub>2</sub>O<sub>3</sub> to yield solid AlF<sub>3</sub>.



Thermodynamic calculations for equation (1) yield  $\Delta G_f^\circ = -553$  kJ/mol and therefore the reaction should be spontaneous under standard conditions. However, not reflected in this calculation are the kinetic aspects of the reaction. An enormous activation barrier must be overcome in order to activate CF<sub>4</sub>, which will not react with  $\alpha$ -Al<sub>2</sub>O<sub>3</sub> below 800 °C. This activation barrier can be surmounted without high temperatures by ionizing the PFCs in a glow discharge. If relatively low substrate temperatures can be sustained during the fluorination process, metastable phases become accessible.

Before describing the results of our experiments, it is worthwhile to review other salient features of the plasma fluorination process and characteristics imparted on the catalytic materials so obtained. First, plasma fluorination is expected to be primarily a surface effect because the fluorinated surface, or passivation layer, may limit diffusion of the reactive components to the bulk of the material. Since catalytic reaction are surface mediated, this is satisfactory. Additionally, it is plausible that the instability of the molecular species within the plasma could be transferred to the catalyst surface in the form of surface-bound radicals or uncoordinated aluminum sites. These surface defects could lead to enhanced catalytic activity. Additionally, the rate of fluorination can be finely controlled by adjusting the rf power coupled to the plasma, which give access to a range of materials with varying fluoride content. Lastly, perfluorocompounds are quite inert and therefore much less toxic than conventional fluorinating agents such as HF and F<sub>2</sub>.

## 2. Experimental

Plasma reactions were carried out in an inductively coupled tubular reactor, consisting of a radio frequency power generator (ENI OEM-650A) operating at 13.56 MHz with variable power to ignite and sustain the plasma. The coil for inductively coupling power to the plasma was made of 1/4" o.d. copper tubing and was wrapped 3.5 times around a 1.5" o.d. alumina tube that acted as the reaction chamber. Cooling water was flowed through the copper tubing to prevent the reaction chamber from overheating. The temperature of the reactor exterior, measured using a thermocouple, did not exceed 180 °C. A mass flow controller was used to control the flow of PFCs into the reactor. The exit of the alumina reaction chamber was connected to a turbomolecular pump (Pfeiffer TPU 170, 170 l/s) and a backing pump. The pressure in the chamber was controlled by throttling the pumping speed with an automated butterfly valve (MKS 253A) in feedback with a capacitance manometer (MKS 222). The gaseous products were monitored continuously at the reactor exit by a Spectra Satellite quadrupole mass spectrometer. For each fluorination reaction, 200 mg of powdered precursor was weighed into an alumina boat, which was placed inside the reaction chamber prior to evacuation. The power was set at 150 W and the chamber pressure was maintained at 250 mTorr. The flow rate was 10 sccm for all reactions. The reactions ran until an endpoint was detected with the mass spectrometer – typically 10-20 minutes. Endpoints were marked by the disappearance of oxygen-containing and/or silicon-containing species in the effluent.

Halocarbon-14 (CF<sub>4</sub>), halocarbon-116 (C<sub>2</sub>F<sub>6</sub>) and nitrogen trifluoride (NF<sub>3</sub>) were used without further purification. Aluminum oxide precursors ( $\alpha$ -Al<sub>2</sub>O<sub>3</sub>,  $\gamma$ -Al<sub>2</sub>O<sub>3</sub>) and zeolite H-SSZ-32 (H<sub>1.3</sub>[Al<sub>1.3</sub>Si<sub>22.7</sub>O<sub>48</sub>], Chevron Central Research, zeolite type: MTT) were used without further purification. Surface areas of precursors and products were determined from nitrogen adsorption isotherms. Measurements were performed using a Quantachrome Autosorb-1 which gave specific surface areas (m<sup>2</sup>/g) based on multipoint BET theory. Low resolution images of a variety of precursors and fluorinated products were collected using a JEOL 6300 scanning electron microscope (SEM). Powder samples were attached to a brass sample stage using carbon tape. Simultaneous qualitative analysis of powder samples was performed using an energy-dispersive X-ray (EDX). High resolution images were collected using the Philips CM200 High Resolution Transmission Electron Microscope at the National Center for Electron Microscopy at Lawrence Berkeley National Laboratory. Amorphous plasma-AlF<sub>3</sub> was characterized by <sup>19</sup>F and <sup>27</sup>Al Magic Angle Spinning (MAS) Solid State NMR. Spectra were acquired using a double tuned Chemagnetics 3.2 mm probe with the assistance of Peter J. Chupas and Professor Clare P. Grey (SUNY – Stony Brook). Temperature programmed synchrotron X-ray powder diffraction data were collected at Beamline X7B of the National Synchrotron Light Source at Brookhaven National Laboratory with the assistance of Jonathon C. Hanson (NSLS staff) and Peter J. Chupas (SUNY – Stony Brook). Full circle powder diffraction profiles ( $\lambda = 0.9274$  Å) were collected on an image plate detector mounted perpendicular to the incident beam. Temperature programmed powder diffraction data collection was performed using a heated sapphire



capillary (0.8 mm o.d. / 0.6 mm i.d.) packed with the sample. The activity of plasma-AlF<sub>3</sub> toward halogen exchange was examined using a home-made gas flow reactor, with the CCl<sub>2</sub>F<sub>2</sub> reactant gas passing over a heated sample bed. Product gases were analyzed either by a gas chromatograph and or a mass spectrometer at the reactor exit. the temperature was ramped at 7.5 °C/min to 700 °C while the product gases were analyzed using mass spectrometry.

### 3. Results and Discussion

Preliminary attempts to prepare catalytically active, metastable phases of aluminum trifluoride via the fluorination of Al<sub>2</sub>O<sub>3</sub> were met with limited success. A wide range of reaction conditions were investigated but under all circumstances, only aluminum oxide starting materials and catalytically inactive α-AlF<sub>3</sub> were detected by X-ray diffraction. BET surface area measurements indicated that the fluorinated products had similar or lower specific surface areas than aluminum oxide starting materials [22].

Eventually, zeolites (aluminosilicates) were identified as more suitable starting materials for the synthesis of aluminum fluorides. The impetus for investigating the chemistry of aluminosilicate precursors came when we reasoned that the spatial density of aluminum cations in the solid precursors might influence the properties and phase of aluminum trifluoride products. We speculated that we could improve the likelihood of preparing open, metastable structures if the aluminum atoms were more sparingly distributed throughout the precursor solid. This would force the aluminum atoms to diffuse over larger distances as the oxygen atoms were volatilized and the aluminum-fluoride network condensed. It eventually became apparent that the desired type of spatial separation existed in aluminosilicates. Consider a plasma assisted reaction between NF<sub>3</sub> and a generic aluminosilicate, Al<sub>x</sub>Si<sub>y</sub>O<sub>z</sub>. We hypothesized that the aluminum oxide fraction would undergo a metathesis reaction,



forming a metastable phase of AlF<sub>3</sub> and NO<sub>x(g)</sub>, and the silicate fraction would be etched. Thus the silicate portion of the structure serves to dilute the concentration of aluminum atoms in the precursor. As an added advantage, aluminosilicates can be prepared with a wide range of Si:Al ratios, which gave us access to a range of aluminum densities. We also anticipated that under sufficiently mild reaction conditions high surface areas could be transferred from precursors to their aluminum fluoride products. Therefore a silicon-rich, high surface area aluminosilicate (H-SSZ-32, H<sub>1.3</sub>[Al<sub>1.3</sub>Si<sub>22.7</sub>O<sub>48</sub>], 100 m<sup>2</sup>/g) was studied as a precursor to high surface area AlF<sub>3</sub>.

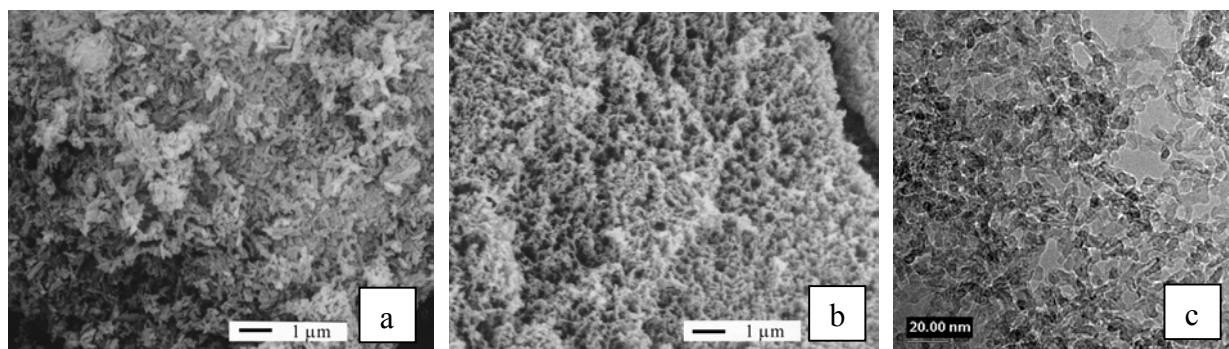
Fluorination of 200 mg of H-SSZ-32 with an NF<sub>3</sub> plasma at 250 mTorr and 250 W rf power for 45 min yielded a free-flowing, white to cream-colored powder. The BET surface area of 190 m<sup>2</sup>/g found for the fluorinated product was significantly greater than the surface area of the H-SSZ-32 starting material, which has a surface area of 100 m<sup>2</sup>/g. Table 1 shows the known phases of AlF<sub>3</sub> and the associated surface areas for each as reported in the literature. Only α-AlF<sub>3</sub> has been prepared with surface areas comparable to that of plasma-synthesized AlF<sub>3</sub>, however α-AlF<sub>3</sub> is known to be inactive for catalysis. Still, plasma-AlF<sub>3</sub> has an extraordinarily high surface area for an aluminum fluoride.

**Table 1.** Surface areas of the known phases of AlF<sub>3</sub> [21].

Phase	BET Surface Area (m <sup>2</sup> /g)
α-AlF <sub>3</sub>	120
β-AlF <sub>3</sub>	53
κ-AlF <sub>3</sub>	19
θ-AlF <sub>3</sub>	64
η-AlF <sub>3</sub>	58
‘plasma-AlF <sub>3</sub> ’	190

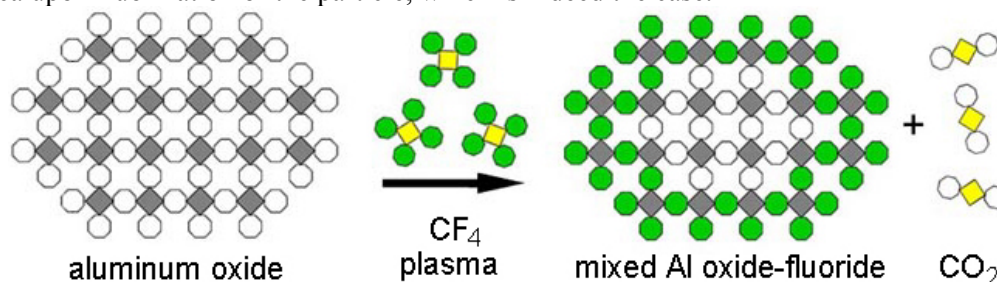
The H-SSZ-32 starting material and aluminum fluoride product were further examined using scanning electron microscopy (SEM) and energy dispersive X-ray spectroscopy (EDX) to assess the morphological and compositional changes associated with decomposition/fluorination. Figure 1a shows an SEM image of the H-SSZ-32 starting material. The zeolite is rather dense with well-defined crystallites, when compared to the aluminum fluoride product, shown in Figure 1b. The plasma-synthesized AlF<sub>3</sub> displays a significant void volume, undoubtedly a consequence of the selective removal of the silicate. High-resolution TEM imaging of plasma-AlF<sub>3</sub>, shown in Figure 1c, revealed a morphology of agglomerated particles of 3-5 nm, perhaps best described, in the spirit of this symposium, as ‘nanorisoitto’. EDX analysis showed that the material was composed of aluminum and fluorine; silicon and nitrogen were below detection limits. This suggests that fluorination of H-SSZ-32 is not merely a surface

effect, as was observed with other precursors, but a bulk fluorination. Mass balance calculations also indicated that conversion to  $\text{AlF}_3$  was quantitative.



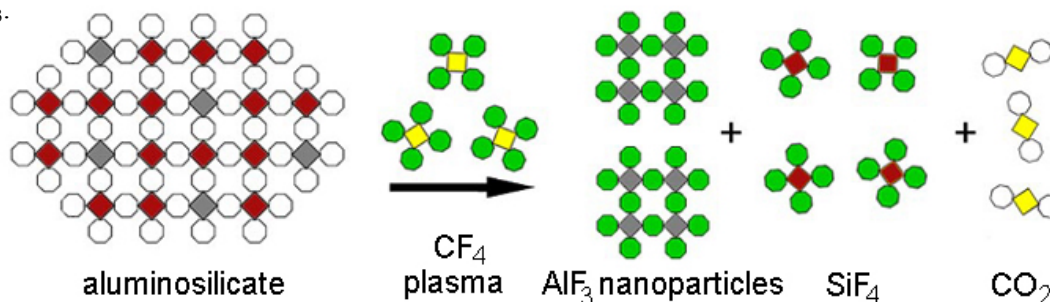
**Figure 1.** (a) SEM image of the H-SSZ-32 starting material and (b)  $\text{AlF}_3$  derived from H-SSZ-32. (c) HRTEM image of plasma- $\text{AlF}_3$  agglomerated nanoparticles.

The nanostructured, high surface area  $\text{AlF}_3$  obtained from zeolite precursors sharply contrasts with the low surface area oxide-fluoride mixtures obtained upon plasma fluorination of  $\text{Al}_2\text{O}_3$ . Figure 2 illustrates the plasma fluorination processes for (a) pure aluminum oxide and (b) aluminosilicate. This figure is idealized and not meant to indicate quantitative transformations; it does however present a simple model to explain the difference in the particle size and composition of the fluorinated products. Figure 2a shows the plasma-mediated reaction of  $\text{CF}_4$  with  $\text{Al}_2\text{O}_3$ . The surface of the  $\text{Al}_2\text{O}_3$  particle is fluorinated to yield a solid, mixed aluminium oxide-fluoride, while  $\text{CO}_2$  is formed as a gaseous byproduct. In such a case, one would expect a significant amount of aluminum oxide starting material to be retained and not expect an increase in the surface area upon fluorination of the particle, which is indeed the case.



**Figure 2a.** Schematic diagram of plasma fluorination of aluminum oxide. Incomplete fluorination is observed as a consequence of surface passivation.

In contrast, the plasma fluorination of aluminosilicate mimics in some ways the established soft chemistry (*chimie douce*) techniques that have been used successfully to prepare metastable materials. That is, more open, higher energy structures can be stabilized upon removal of a portion of the precursor at low temperature. The plasma fluorination of aluminosilicates, Figure 2b, loosely follows this design, in that the silicate portion of the structure is etched away, while the aluminate portion is fluorinated to give high surface area  $\text{AlF}_3$ .



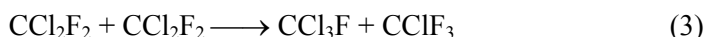
**Figure 2b.** Schematic diagram of plasma fluorination of aluminosilicate. The silicate fragment of the aluminosilicate is etched to yield pure, nanostructured  $\text{AlF}_3$ .

Thus, the divergent behavior observed upon fluorination of these two types of precursor materials can be attributed to the concurrent etching of the silica component of the zeolite.

After the successful preparation of metastable aluminum trifluoride, our focus shifted to the characterization of the structure and reactivity of  $\text{NF}_3$  plasma/zeolite-derived aluminum trifluoride, referred to as “plasma- $\text{AlF}_3$ ” throughout the remainder of this paper. Solid state NMR was used to probe the local environments of Al and F in the high surface area product of the plasma reaction with H-SSZ-32. The presence of a large sideband manifold in the  $^{27}\text{Al}$  MAS spectrum[22] spreading over more than 10,000 ppm, due to the satellite transitions, indicates a more distorted aluminum environment for plasma- $\text{AlF}_3$  compared with  $\alpha$ - or  $\beta$ - $\text{AlF}_3$ . With respect to catalysis, distorted aluminum environments are desirable as it suggests the possibility of open coordination sites with Lewis acid character.

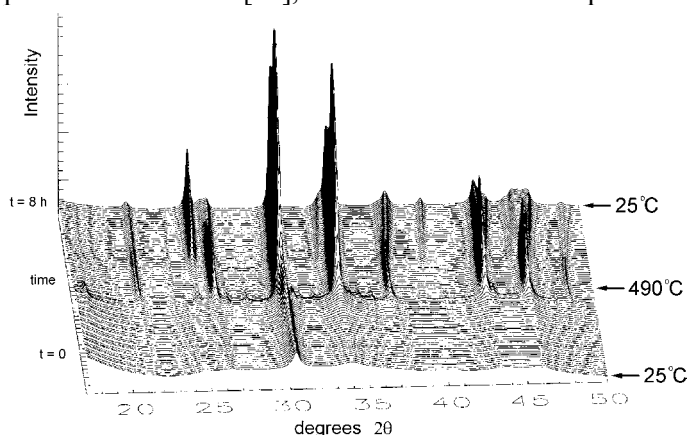
Halogen exchange reactions are carried out at elevated temperatures, so it is important to characterize the thermal stability of  $\text{AlF}_3$  catalysts. Structural changes associated with the annealing of plasma- $\text{AlF}_3$  were investigated using temperature programmed synchrotron radiation powder diffraction. Based on the diffraction data (Figure 3), plasma- $\text{AlF}_3$  is essentially amorphous as synthesized. The appearance of new reflections above 330 °C indicates crystallization of the amorphous phase. The formation of  $\beta$ - $\text{AlF}_3$  is evidenced by nine new reflections between 330 to 440 °C, with the broad 220 reflection at  $2\theta=17.8^\circ$  being the clearest example. At higher temperatures, the cubic phase of  $\alpha$ - $\text{AlF}_3$  dominates the diffraction pattern. The distorted aluminum environment detected by NMR, in addition to the presence of  $\beta$ - $\text{AlF}_3$  in the diffraction pattern provided strong evidence for catalytic activity in plasma- $\text{AlF}_3$ , so some simple halogen exchange test reactions were performed.

Temperature programmed reaction (TPR) studies of halogen exchange are a valuable way to determine the ‘thermal window’ for catalytic activity. Moreover, since halogen exchange is catalyzed by Lewis acid sites, TPR can be used to probe the relative strength of Lewis sites: reactivity that occurs at lower temperatures indicates strong Lewis sites while high temperature reactivity suggests weaker sites with greater thermal stability. The dismutation (or halogen scrambling) of  $\text{CCl}_2\text{F}_2$  was used as the model halogen exchange reaction to test the activity of plasma- $\text{AlF}_3$ .

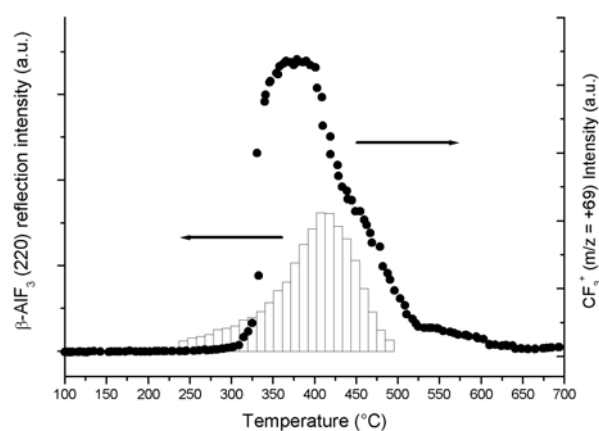


Dismutation was monitored by detection of the  $m/z = +69$  peak, which corresponds to the most intense mass spec fragment of  $\text{CClF}_3$ ,  $\text{CF}_3^+$ . This ion can only be attributed to the products of halogen exchange and thus is only detected when there is sufficient thermal energy to catalyze halogen exchange.

Figure 4 shows the TPR profile of  $\text{CCl}_2\text{F}_2$  overlaid with the intensity profile of the  $\beta$ - $\text{AlF}_3$  220 reflection observed during temperature programmed synchrotron powder diffraction of plasma- $\text{AlF}_3$ . It is useful to consider the TPR data in concert with thermally induced structural changes so structure-reactivity relationships can be established. The peak in the TPR profile is a clear indication that plasma- $\text{AlF}_3$  catalyzes halogen exchange. More interesting is that the peak maximum does not coincide with the maximum in  $\beta$ - $\text{AlF}_3$  content, but is observed at lower temperatures. We have performed more detailed catalytic studies, published elsewhere[23], and found that the TPR peak shown in Figure 4 is in fact two overlapping peaks;



**Figure 3.** Time-resolved synchrotron X-ray powder diffraction pattern for plasma- $\text{AlF}_3$ , ramped from 25 °C (foreground) to 490 °C over 4 h, then cooled back to 25 °C over a second 4 h interval.



**Figure 4.** Diffracted intensity of the  $\beta$ - $\text{AlF}_3$  220 reflections overlaid with the temperature programmed reaction profile of  $\text{CCl}_2\text{F}_2$  over plasma- $\text{AlF}_3$ .

an intense peak centered at  $\sim 350$  °C and a broader peak centered at  $\sim 420$  °C. Thus, two different active catalytic sites can be identified. The low temperature, and thus highly Lewis acidic, sites can be attributed to amorphous plasma-AlF<sub>3</sub>. The higher temperature reactivity coincides with the crystallization of  $\beta$ -AlF<sub>3</sub> and thus can be attributed to the well-documented Lewis acids sites found on the surface of  $\beta$ -AlF<sub>3</sub>. To summarize, plasma-AlF<sub>3</sub> displays two types of Lewis sites, highly active sites that are unique to the plasma-prepared catalyst, and a set of  $\beta$ -AlF<sub>3</sub> Lewis acid sites that form when plasma-AlF<sub>3</sub> is annealed.

#### 4. Conclusions

To conclude, we have developed a new method for the plasma synthesis aluminum trifluoride catalysts. The process involves the simultaneous fluorination/decomposition of zeolite starting material in a perfluorocompound plasma. The low temperature, non-equilibrium plasma environment makes accessible metastable, nanostructured material that can not be prepared using traditional synthetic techniques. Investigations of the structure-activity relationships revealed that plasma-AlF<sub>3</sub> displays two types of Lewis sites, highly active sites that are unique to the plasma-prepared catalyst, and a set of  $\beta$ -AlF<sub>3</sub> Lewis acid sites that form when plasma-AlF<sub>3</sub> is annealed.

#### References

- [1] F.J. Christoph, G. Teufer - *U. S. Pat.* **3,178,484** (1965).
- [2] F.J. Christoph, G. Teufer - *U. S. Pat.* **3,178,483** (1965).
- [3] J. Thomson, G. Webb, J. M. Winfield - *J. Chem. Soc.-Chem. Comm.* 323-324 (1991).
- [4] E. Kemnitz, D.H. Menz - *Prog. Solid State Chem.* **26**, 97-153 (1998).
- [5] F. Swartz - *Bull. Acad. R. Belg.* **24** (1892).
- [6] F. Swartz - *Mem. Cour. Acad. R. Belg.* **51** (1895).
- [7] T. Midgely, A.L. Henne - *Ind. Eng. Chem.* **22**, 542 (1930).
- [8] L. Kolditz, V. Nitzsche, G. Heller, R. Stosser - *Z. Anorg. Allg. Chem.* **476**, 23-32 (1981).
- [9] G.B. McVicker, C.J. Kim, J.J. Eggert - *J. Cat.* **80**, 315-327 (1983).
- [10] M.J. Molina, F.S. Rowland - *Nature* **249**, 810 (1974).
- [11] L.E. Manzer - *Science* **249**, 31-35 (1990).
- [12] L.E. Manzer, V.N.M. Rao - *Catalytic Synthesis of Chlorofluorocarbon Alternatives*; Academic Press Inc: San Diego, **39**, 329-350 (1993).
- [13] R.I. Hegde, M.A. Barteau - *J. Catal.* **120**, 387-400 (1989).
- [14] T. Skapin, E. Kemnitz - *Catal. Lett.* **40**, 241-247 (1996).
- [15] J.M. Saniger, N.A. Sanchez, J.O. Flores - *J. Fluorine Chem.* **88** 117-125 (1998).
- [16] E. Kemnitz, D.H. Menz - *Prog. Solid State Chem.* **26**, 97-153 (1998).
- [17] E. Kemnitz, J.M. Winfield - *Adv. Inorg. Fluorides*, 367-401 (2000).
- [18] A. Hess, E. Kemnitz, A. Lippitz, W.E.S. Unger, D.H. Menz - *J. Catal.* **148**, 270-280 (1994).
- [19] N. Herron, D.L. Thorn, R.L. Harlow, G.A. Jones, J.B. Parise, J.A. Fernandez-Baca, T. Vogt - *Chem. Mater.* **7**, 75-83 (1995).
- [20] A. Lebail, J.L. Fourquet, U. Bentrup - *J. Solid State Chem.* **100**, 151-159 (1992).
- [21] N. Herron, W.E. Farneth - *Adv. Mater.* **8**, 959-968 (1996).
- [22] J.L. Delattre, P.J. Chupas, C.P. Grey, A.M. Stacy - *J. Am. Chem. Soc.* **123**, 5364-5365 (2001).
- [23] E. Hajime, J.L. Delattre, A.M. Stacy - *submitted to J. Cat.* (2003).

# THE DISPERSION STUDY OF $\text{TiO}_2$ NANO-PARTICLES MODIFIED BY SURFACE TAILORING COATING OF PULSED RF PLASMA POLYMERIZATION

Feng Zhu, Qinyu Yang, Changnian Shi, Zhan Chen, Ying Guo, Hanqiu Ni,  
Rongming Zhou, Hankun Xie, Jing Zhang\*

*\*College of Sciences Donghua University  
1882 West Yan-Road - Shanghai 200051 P. R. China  
[jingzh@dhu.edu.cn](mailto:jingzh@dhu.edu.cn) Tel:0086-21-62373921*

Titania nanoparticle is one of the most studied transition metal oxide for various applications ranging from pigment, ultra violet light absorber, ultra violet light or even visible light photo-catalyst, gas sensors etc. Combined with other polymers such as polytetraphathethylene, polyethylene, polypropylene, functional composite with some special performance can be formed. Because of the very high surface energy of the nanoparticles, they agglomerate severely and cannot be well dispersed in the background polymers. Therefore most of these composite applications have the problems of agglomeration and dispersion. That is the “bottleneck” in the formation of nanoparticle-polymer composite.

Titania nanoparticle surface were modified by pulsed RF plasma polymerized coating. The ultra violet light absorbance of Titania-glycol solution were employed to express its dispersion behavior. It was found that the dispersion stability of coated Titania-glycol solution were improved. The particle size distribution was also observed to be narrowed towards the small particle size through the laser particle size analysis. The surface molecular structure was measured through some surface analysis tools such as XPS, FTIR and TOF-SIMS. The relationship of the dispersion with the surface structure and property were discussed. TG and DSC of the coated Titania nanoparticle were also used to measure their thermal stability.

# Comparison between different plasma processing for paper water repellency

S. Zanini<sup>1</sup>, C. Riccardi<sup>1</sup>, M. Orlandi<sup>1</sup>, C. Canevali<sup>1</sup>, L. Meda<sup>2</sup>

<sup>1</sup>*Universita' degli Studi di Milano-Bicocca*

*P.zza della Scienza 3, 20126 Milano-Italy*

<sup>2</sup>*Istituto Donegani, Polimerieuropa, Novara- Italy*

## Abstract

The water proof and grease proof properties and the gas barrier ability are the main interesting features required for every kind of packaging.

We applied the cold plasma technology for surface treatments of papers as an alternative technology to the standard chemical processes; more precisely we used plasmas in order to perform fluorine grafting and thin film deposition on the surface.

In this context we report some preliminary results concerning cold plasma treatments of paper surfaces to impart water proof properties: the grafting of fluorine through radical reactions and the deposition of teflon-like and silica-like polymeric films.

## 1 Introduction

Many surface properties of materials, such as wettability, adhesion or biocompatibility, can be tailored to specific applications by appropriate cold plasma treatments [1-3]. Such dry-processing methods have several advantages over more traditional treatments, since they are rapid, clean, and environmentally safe, depending on the chosen gas. Cold plasma treatments are known to induce physical and chemical surface changes in polymers through activation, etching, grafting, implantation, polymerisation and crosslinking processes [1-3], usually without interfering with their bulk properties.

In particular, in the present work we have investigated plasma processing in order to impart water repellence to paper.

The research has been performed at the Universita' degli Studi di Milano – Bicocca. In all cases, the plasma processing has been performed at low pressure. The reactor generates plasmas with a radio-frequency source [4] whose power is below 600 W; the gas pressure was ranging between 0.1 mbar and 1 mbar and three different gases were used. Typical time exposure was between 15'' and 2'.

Papers with different grains and hydrophilicity have been treated. After plasma treatment we analysed the compositions and the bonding characteristics of the films through XPS technique.

All samples showed an increasing of the water repellency after plasma treatments. In fact the water contact angle increases up to 120° and a water drop of 20 µl put on the treated surface is not absorbed but evaporates. However the properties strongly depend on the ageing of the paper and on the gas used.

Moreover, an optimisation study and a comparison between grafting and deposition have been carried out varying the relevant plasma source parameters.

SF<sub>6</sub> cold plasma treatments are known to impart water repellence to polymer surface by grafting of fluorine radicals; CF<sub>4</sub> cold plasma treatments impart water repellence both by grafting of fluorine radicals and by deposition of polymeric chains of CF<sub>x</sub> on the treated surface; HMDSO ( hexamethyldisiloxane) cold plasma treatments impart water repellence by deposition of C/Si polymers that can be modified in composition (to obtain silica-like deposit) by modulating the operating conditions.

The nature of the plasma-induced surface processes was investigated by correlating the properties of treated samples with the cold plasma parameters. The stability of the imparted surface properties obviously has great practical importance. Thus, surface modifications of differently plasma treated samples undergoing different ageing treatments were also systematically investigated in the present work. It turns out that the most promising plasma processing for paper water repellency is obtained by deposition.

## 2 Experimental

### 2.1 Materials

Two types of paper have been treated: an absorbent paper with water droplet absorption time instantaneous (paper A) and a paper with absorption time of 2 minutes (paper B).

### 2.2 Plasma reactor

The employed cold plasma reactor has been fully described and characterised in detail elsewhere. Briefly, it consists of three parts: *a)* a vacuum chamber connected to a pumping system; *b)* a plasma production system, composed of a radiofrequency (RF) power generator operating at 13.56 MHz, an RF matching network and a metallic antenna; *c)* plasma diagnostics (Langmuir probes) and sample holders. The system was especially devised to allow the evaluation of electron density both radially and longitudinally to the gas flow under different gas pressure and radiofrequency power conditions. For SF<sub>6</sub> plasma treatment of paper B, also a pulsed power supply was used.

## 3 Result and discussion

For all the plasma treatments, the effectiveness in imparting hydrorepellence to type A and B paper was verified by droplet absorption time. Water droplet absorption time was obtained as the average absorption time of four 20 µl water droplets deposited on different parts of each sample following a standard procedure. Samples were classified as totally hydrorepellent when, under the adopted standardised conditions, no water absorption occurred within the evaporation time of the droplets (*ca.* 120 min). The absorption time was also evaluated after different ageing treatment on each treated sample. For the ageing treatment, the samples were maintained for 2 hours at 40° C in a 100% humidity atmosphere. The ageing effect was evaluated for each sample by measuring the absorption time, at different time intervals from the plasma exposure: after a minimum of 5 days from the plasma exposure, to a maximum of 4 months. The absorption time was also evaluated after an ageing treatment of the sample.

The SF<sub>6</sub> plasma treatments were performed in the 0.2-0.4 mbar pressure range, and at distances from the antenna smaller than 10 cm, in full agreement with the result of SF<sub>6</sub> plasma diagnostics, which indicated a marked decrease in the fluorine radical concentration for  $d \geq 10$  cm.

For SF<sub>6</sub> plasma treated samples (both of paper A and B), the absorption time of a drop of 20 µl increased with respect to the untreated sample. The XPS analysis on paper A SF<sub>6</sub> plasma treated samples indicates grafting of fluorine radicals on the treated surface.

The best treatment for paper A was performed under these conditions: residual pressure =  $3.4 \times 10^{-7}$  mbar, operating pressure = 0.3 mbar, treatment time = 30 s, radiofrequency power = 50 W, distances from the antenna = 7.5 cm. After the treatment, the drops stayed on the surface of the paper sample for 105 min; after ageing of 5 days the absorption time fell to 5 s.

The same was shown for paper B, but in this case the best treatment conditions were: residual pressure =  $4 \times 10^{-6}$  mbar, operating pressure = 0.3 mbar, treatment time = 1 min, radiofrequency power = 50 W, distances from the antenna = 7.5 cm. After the treatment the drops stayed on the surface of the sample for 47 min; after ageing of 5 days the absorption time fell to 9 min.

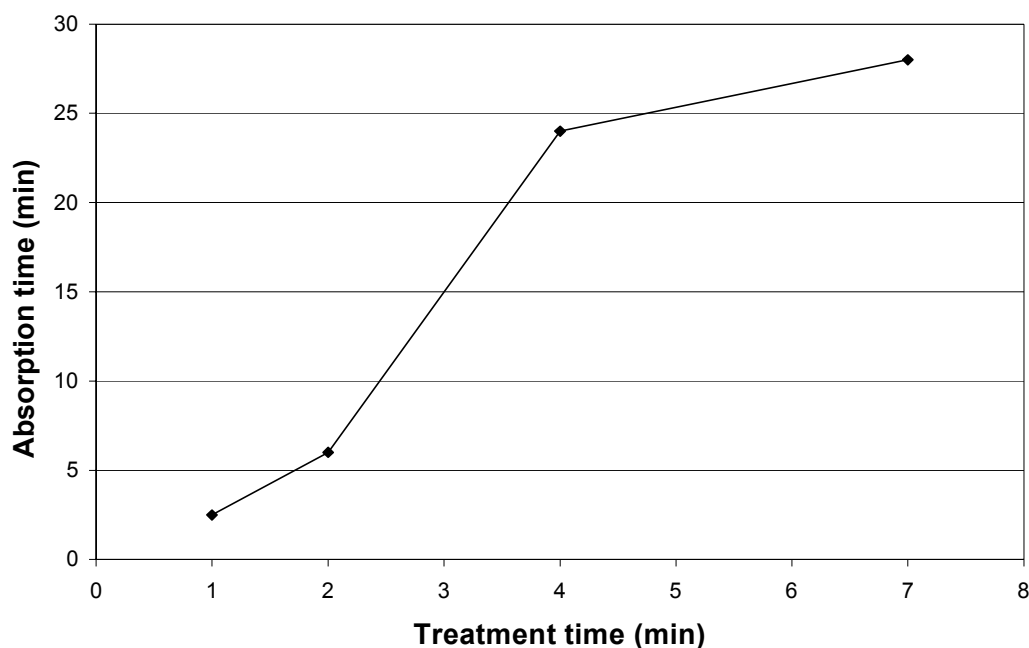
Table 1 shows the droplet absorption time for the best treated sample of paper B and for a sample treated with the same operating conditions but with the pulsed operating mode, measured immediately after the treatment and after 5 days. The pulse time was of 10 ms, while the pause time was of 100 µs.

**Table 1** Absorption time (min) of water droplets measured on paper B samples immediately after the SF<sub>6</sub> treatment ( $t_0$ ) and after having being stored in air for 5 days ( $t_5$ ).

	Untreated	SF <sub>6</sub> treated	
		<i>continuous</i>	<i>impulsed</i>
$t_0$ (min)	2	47	70
$t_5$ (min)	2	9	18

As you can see the pulsed operating mode increases the droplet absorption time measured immediately after the treatment and reduce the ageing effect on the SF<sub>6</sub> plasma treated samples. *The absorption time measured on sample 5 days after the treatment with the pulsed mode was the double (18 min) with respect to the absorption time measured on the sample treated with the continuous mode (9 min).*

By treating paper with CF<sub>4</sub> cold plasma, it is possible to obtain totally hydrorepellent sample by modulating the operating conditions. It was seen that the droplet absorption time increases with the pressure in the range 0.3-0.8 mbar and with the time in the range 30 s -120 s. Figure 1 shows the absorption time of the paper A CF<sub>4</sub> plasma treated samples versus the treatment time, measured immediately after the treatment. The operating conditions were: residual pressure =  $7 \times 10^{-6}$  mbar, operating pressure = 0.6 mbar, radiofrequency power = 50 W, distances from the antenna = 7.5 cm.



**Fig 1** Absorption time of water droplet measured immediately after the treatment on paper A CF<sub>4</sub> plasma treated samples versus the treatment time

As you can see and already written before, the absorption time measured immediately after the treatment increase with the treatment time. It is also possible to see that, with these operating conditions, the total hydrorepellence of the samples was not reached. With different operating conditions it is possible to reach the total hydrorepellence (fig.3, tab.2).

Figure 2 shows the droplet absorption time measured on HMDSO cold plasma treated samples versus the operating pressure. The four series refer to 2 radiofrequency powers (10 W and 25 W) and to the absorption time value measured immediately after the treatment and after ageing (2 hour 40° C / 100% humidity + 4 month in air at room temperature).

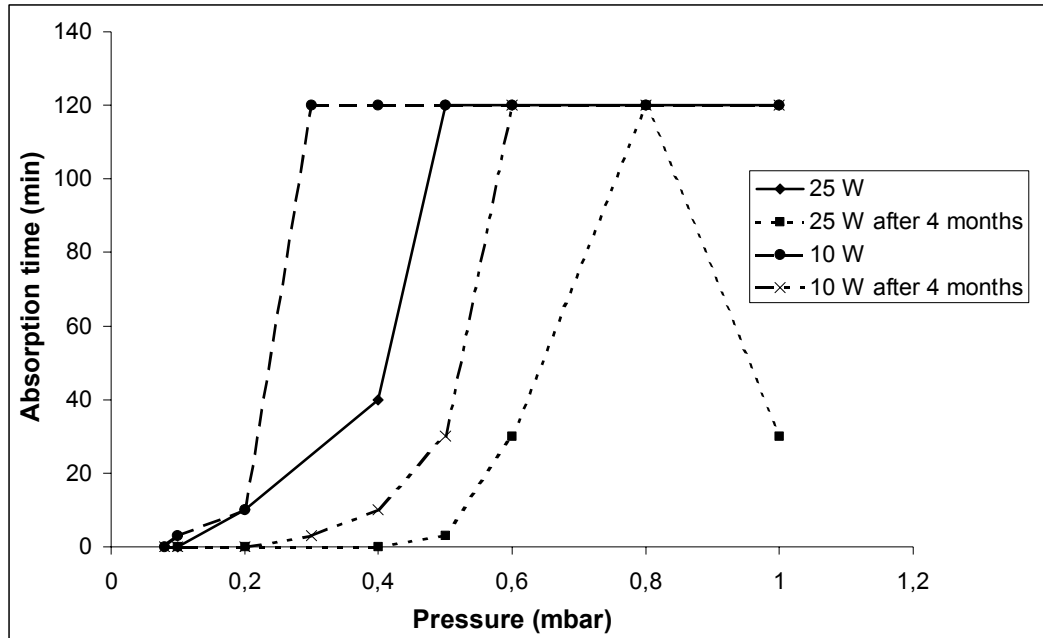
As you can see the absorption time increases with the pressure in the range 0.08-1 mbar.

The samples treated with a radiofrequency power of 25 W were totally hydrorepellent immediately after the treatment, when the operating pressure was greater than 0.5 mbar. After ageing, only the sample treated at operating pressure of 0.8 mbar remained totally hydrorepellent.

The samples treated with a radiofrequency power of 10 W were totally hydrorepellent immediately after the treatment, when the operating pressure was greater than 0.3 mbar. This indicates that the greater is the



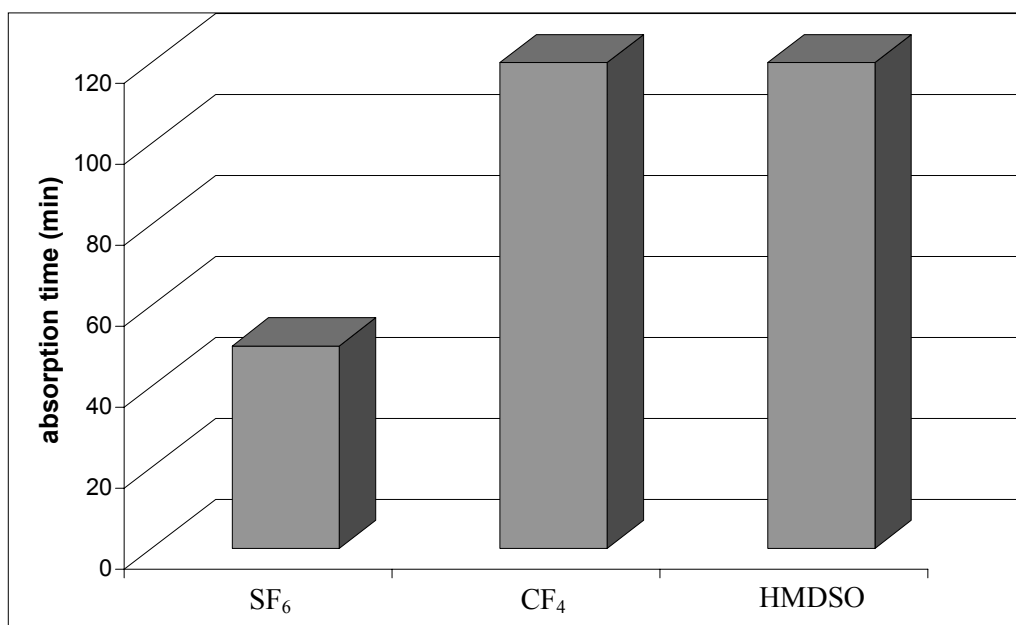
radiofrequency power, the greater is the pressure at which the treatment must be done in order to obtain totally hydrorepellent samples. After ageing, the samples treated at operating pressure greater than 0.6 mbar still showed a total hydrorepellence.



**Fig 2** Absorption time of water droplet measured on paper A HMDSO plasma treated samples versus the plasma operating pressure, immediately after the plasma treatment and after four months.

The same results were obtained for paper B: the operating pressure plays a key role for the effectiveness of the treatment. Another important parameter is the treatment time: as we have seen for the  $\text{CF}_4$  plasma treatment, the effectiveness of the HMDSO plasma treatment in imparting hydrorepellence increased when the treatment time increased in the range 30 s – 180 s. The best treatments have been obtained with treatment times above 120 s.

Figure 3 shows the droplet absorption time measured immediately after the treatment on the best paper B samples obtained after  $\text{SF}_6$ ,  $\text{CF}_4$  and HMDSO cold plasma treatment. The total hydrorepellence with  $\text{SF}_6$  plasma treatment hasn't been reached. Instead, samples treated with  $\text{CF}_4$  and HMDSO in the best conditions were totally hydrorepellent (absorption time of 120 min).



**Fig 3** Absorption time of water droplets measured immediately after the treatment on the best performing samples obtained by treating paper B with SF<sub>6</sub>, CF<sub>4</sub> and HMDSO plasma.

Table 2 shows that CF<sub>4</sub> and HMDSO plasma treatments were also more resistant against the ageing effect. This indicates that the most promising plasma processing for paper water repellency is obtained by deposition. The profilometer analysis suggests that the thickness of the deposited film is always lower than the typical roughness of the samples.

**Table 2** Absorption time (min) of water droplets measured immediately after the treatment and after 5 days on the best samples obtained by treating paper B with SF<sub>6</sub>, CF<sub>4</sub> and HMDSO plasma

Untreated	SF <sub>6</sub>		CF <sub>4</sub>		HMDSO	
	After treatment	After 5 days	After treatment	After 5 days	After treatment	After 5 days
2	47	9	120	120	120	120

#### 4 Conclusions

We have treated paper samples with different plasmas in order to impart hydrorepellence. The best treatments were obtained with CF<sub>4</sub> and HMDSO plasmas, which are known to impart hydrorepellence by deposition of thin polymeric films on the sample surface. With cold SF<sub>6</sub> the total hydrorepellence was not reached; moreover SF<sub>6</sub> plasma treated samples were more sensitive to the ageing effect.

#### References

- 1 U.Voher , M. Müller and C. Oehr, *Surf. Coat. Technol.*, 1998, **98**, 1128
- 2 J. Behnisch, *NATO ASI Ser., Ser. E*, 1997, 345
- 3 H. K. Yasuda, *Plasma polymerization and plasma treatment of polymers*, Wiley, New York, 1987
- 4 C.Riccardi et al. , *Modeling and diagnostic of SF<sub>6</sub> RF plasma at low pressure*, IEEE transaction on Plasma Science 28, 278-287 (2000).

# Interactions of Non-equilibrium Atmospheric Pressure Plasmas with Biological Media

M. Laroussi and F. Leipold

*Electrical & Computer Engineering Dept.  
Old Dominion University, Norfolk, VA 23529 USA*

## Abstract

Recently, non-equilibrium atmospheric pressure plasmas took center stage in several applications. Amongst the novel applications, the use of plasmas to decontaminate materials and media from biological contaminants generated heightened interest from both the plasma science research community and the biomedical research community. In this paper, the potential roles of the various plasma agents will be evaluated. In addition, an attempt to elucidate the physical and biochemical effects will be presented.

## 1. Introduction

Since the nineteen nineties, non-equilibrium atmospheric pressure plasmas took center stage in several applications such as UV sources [1], surface treatment [2], and the cleaning of flue gases [3]. Amongst the novel applications, the use of atmospheric pressure “cold” plasmas in the biomedical field is experiencing a heightened interest from both the plasma science research community and the biomedical research community. This is due to newly found applications of these plasmas in promising medical research such as wound healing [4], tissue engineering [5], surface modification of bio-compatible materials [6], and the sterilization of reusable heat sensitive medical instruments [7,8]. This paper focuses on the interaction of high-pressure, low temperature air plasmas with bacteria. The results of this line of research have direct implications in the areas of sterilization and decontamination of surfaces and media. Early research focused mainly on the quantification of the germicidal effects of plasmas. Little was known or understood regarding the role of each plasma agent in the inactivation process, and even less was known or understood regarding the cellular and sub-cellular effects that these agents may have. Today, our knowledge and understanding of the processes that enter into play during the interaction of plasmas with biological matter remains limited. However, in the last few years a great deal of information has been gained to allow scientists to begin to understand the physical and biochemical impacts that plasmas have on bacterial cells [8].

In this paper, first the germicidal effects of non-equilibrium atmospheric pressure plasmas will be briefly reviewed. Then, the role of each agent (i.e. UV radiation, free radicals, charged particles) will be assessed for the case of an air plasma. This will be followed by the determination of the physical effects resulting from the exposure of cells of representative gram-negative and gram-positive bacteria to the plasma. In this study, electron microscopy is used as a tool to inspect cells’ morphology. In the last part of this paper, the effects of plasma on the metabolism of bacteria will be investigated. It is believed that by understanding the plasma-induced alterations in the biochemical pathways of cells, new applications such as the controlled bio-manipulation of cells’ machinery can be possible [8,9].

## 2. Brief Review of the Germicidal Effects

Since it is generally impossible to provide the ideal conditions which inactivate all microorganisms, experimental investigation of the kinetics of cell inactivation is paramount in providing a reliable temporal measure of microbial destruction. One kinetics measurement parameter, which has been used extensively by researchers studying sterilization by plasma, is what is referred to as the “D” value (Decimal value). The D-value is the time required to reduce an original concentration of microorganisms by 90%. The D-value in this presentation is therefore expressed in the unit of time. Since survivor curves (Colony forming units versus treatment time) are plotted on semi-logarithmic scales, the D-value is determined as the time for a one  $\log_{10}$  reduction.

To date, the experimental work on the germicidal effects of cold, atmospheric pressure plasmas has shown that survivor curves take different shapes depending on the type of microorganism, the type of the medium supporting the microorganisms, and the method of exposure (*direct exposure*: samples are placed in direct contact with the plasma; *remote exposure*: samples are placed away from the discharge volume or in a second chamber. The reactive species from the plasma, but not the plasma itself, are allowed to diffuse and come in contact with the samples).

Single-slope survivor curves with D-values ranging from 4.5 seconds to 5 minutes were reported for both direct and remote exposure configurations [8]. Under direct exposure, two-slope survivor curves have been reported by various investigators [8], with the D-value of the second inactivation phase being consistently shorter than the D-value of the first phase. Finally, and similar to the results obtained by Moisan et al. [10] under low pressure conditions, three-slope survivors curves have also been reported [8] with each inactivation phase having a different D-value. Various researchers have attempted to explain each of the phases of the survivor curves but a clear consensus is yet to emerge. To learn more about this, the reader is referred to [8].

The questions that need to be answered in order to reach some level of understanding of what takes place during the inactivation of bacteria by plasma are basically the following: 1. What are the agents within the plasma that can potentially play a role in the inactivation process? This question can be answered by a plasma physicist after carrying out proper diagnostics; 2. What are the cellular and sub-cellular effects of each agent? This is a more difficult question than the first and a close collaboration between plasma physicists and microbiologists is required; 3. What are the synergistic effects of two or more inactivation agents? The following section is an attempt to answer the above questions, at least partially.

### 3. Plasma Inactivation Agents

Since the plasma generation method and the gas mixture used in the plasma play important roles, and since there are many different methods using various gas mixtures, we are restricting our presentation to the case of an air plasma generated by a dielectric barrier discharge (DBD).

#### UV radiation and its possible role

Amongst UV effects on cells of bacteria is the dimerisation of thymine bases in their DNA strands. This inhibits the bacteria's ability to replicate properly. Wavelengths in the 220 – 280 nm range and doses of several mW.s/cm<sup>2</sup> are known to have the optimum effect. Figure 1 shows the total UV output from an air plasma generated by a DBD.

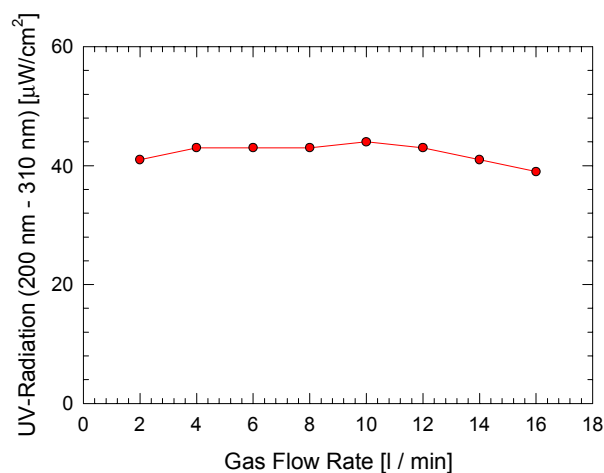


Fig.1 Total UV emission from a DBD in air

It is important to note that the UV emission resulting from the N<sub>2</sub> rotational bands (0-0) at 337 nm is about an order of magnitude higher than the UV level shown in Figure 1. However, based on the above measurements, the UV power density is below 1 mW/cm<sup>2</sup> (even if the N<sub>2</sub> emission at 337 nm is taken into account). At this low power density level, UV radiation by itself would not be expected to play a direct important role in the inactivation of bacteria.

#### Reactive species and their possible role

It has always been recognized that the reactive species, generated in a high-pressure non-equilibrium discharge through electron impact excitation and dissociation, play an important role in its germicidal characteristics. Amongst these are oxygen-based species such as atomic oxygen and ozone, NO<sub>x</sub>, and the hydroxyl radical (OH). Montie et al. [11] suggested three oxidation mechanisms caused by radicals which lead to cellular death: 1. Lipid peroxidation resulting from the susceptibility of unsaturated fatty acids to attacks by hydroxyl radicals; 2. Protein oxidation resulting from the susceptibility of amino acids to oxidation; 3. DNA oxidation resulting from the formation of base adducts which are generated through reactions with oxygen radicals. Ozone, O<sub>3</sub>, also plays an important role as an inactivation agent mainly because of its interference with cellular respiration. As illustration, Figure 2 and Figure 3 show the concentrations of two species, NO<sub>2</sub> and O<sub>3</sub>, in an air plasma generated by a DBD.

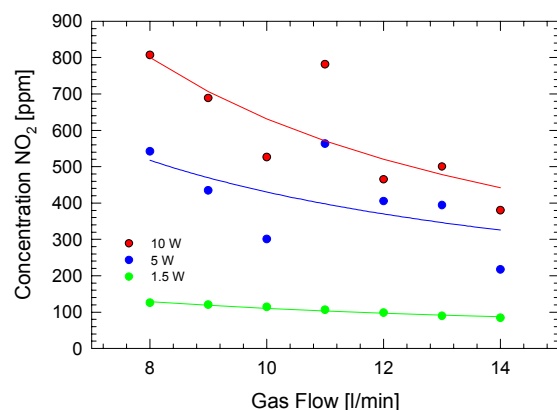


Fig.2 NO<sub>2</sub> concentration for various powers

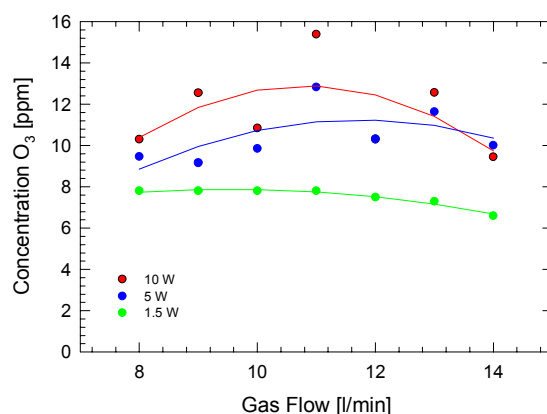


Fig.3 Ozone concentration for various powers

#### Charged species and their possible role

Mendis et al. [12] suggested that charged particles might play a very significant role in the rupture of the outer membrane of bacterial cells. By using a dusty plasma model, they showed that the electrostatic force caused by charge accumulation on the outer surface of the cell membrane could overcome the tensile strength of the membrane and cause its rupture. They claim that this scenario is more likely to occur for gram-negative bacteria, the membrane of which possesses an irregular surface.

#### Thermal effects

High temperatures can have deleterious effects on the cells of microorganisms. A substantial increase in the temperature of a biological sample can lead to the inactivation of bacterial cells in that sample. To monitor the temperature, a thermocouple probe can be used. In addition, in the case of an air plasma, the gas temperature in the discharge can be measured by evaluating the rotational band of the 0-0 transition of the second positive system of nitrogen. Figure 4 shows that the gas temperature in a DBD air plasma remains close to room temperature. Figure 5 shows the rise in sample temperature as a function of the power dissipated in the discharge. Based on these measurements no substantial thermal effects are expected.

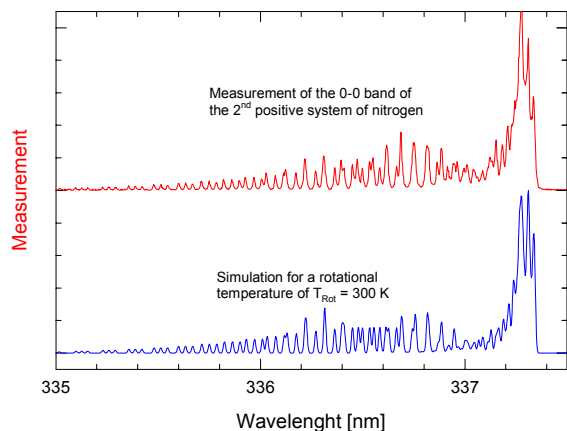


Fig.4 Evaluation of the gas temperature in a DBD air plasma by comparing the rotational band of nitrogen with a modeled spectrum.

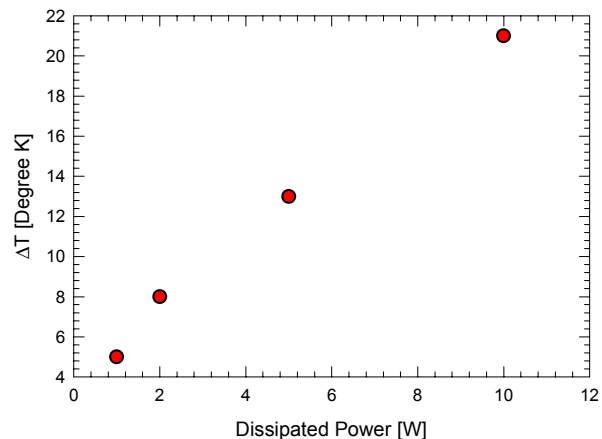


Fig.5 Change of the sample temperature versus the dissipated power. Air flow rate of 10 l/min.

#### 4. Morphological Studies

Laroussi et al. [13] and Montie et al. [11] reported that for *Escherichia.coli*, a gram negative bacterium, the outer membrane ruptures after short exposures (10-30 seconds) to plasma, followed by leakage of the cytoplasm. In addition, for longer exposure times, total cell fragmentation was observed. Gram positive bacteria such as *Bacillus subtilis* did not undergo any visible morphological changes [9]. However, reduction in cell viability was achieved on various such types of bacteria. This lead to the conclusion that cell lysis is not the only mechanism whereby bacterial cells are inactivated by plasma. As an illustration of these findings, Figures 6 & 7 show micrographs of *E. coli* and *B. subtilis* before and after plasma treatment.

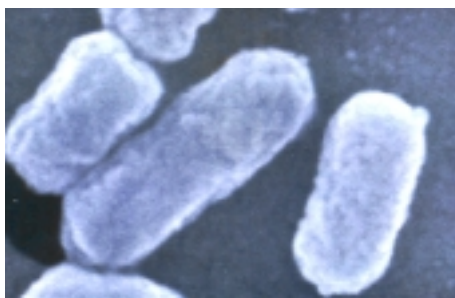


Fig.6a Micrograph of control *E. coli*.

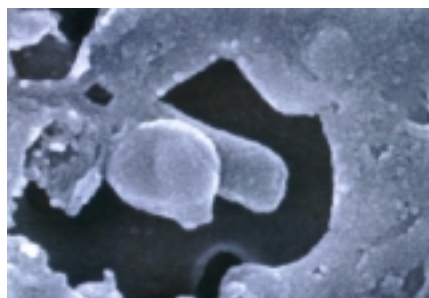


Fig.6b Micrograph of treated *E. coli*

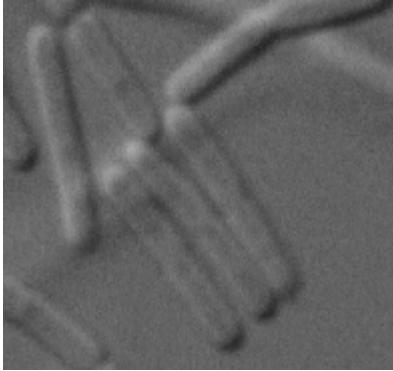


Fig.7a Micrograph of *B. subtilis*, control



Fig.7b Micrograph of treated *B. subtilis*

### 5. Effects of Plasma on Bacterial Cells Metabolism

Carrying out “sub-lethal” experiments, Laroussi et al. [9] reported that short exposures to plasma can affect the metabolic functions of cells without necessarily killing them. This was achieved by exposing *E. coli* cells to small doses of plasma and monitoring changes in their heterotrophic pathways, relative to those of unexposed cells (controls). A change in these pathways is indicative of changes in enzyme activities. Figure 8 shows cases of increased and decreased use of certain nutrients by exposed cells relative to control cells, respectively. These results indicate that plasma could be used just to alter the metabolic behavior of microorganisms, in applications where killing is not the desired result.

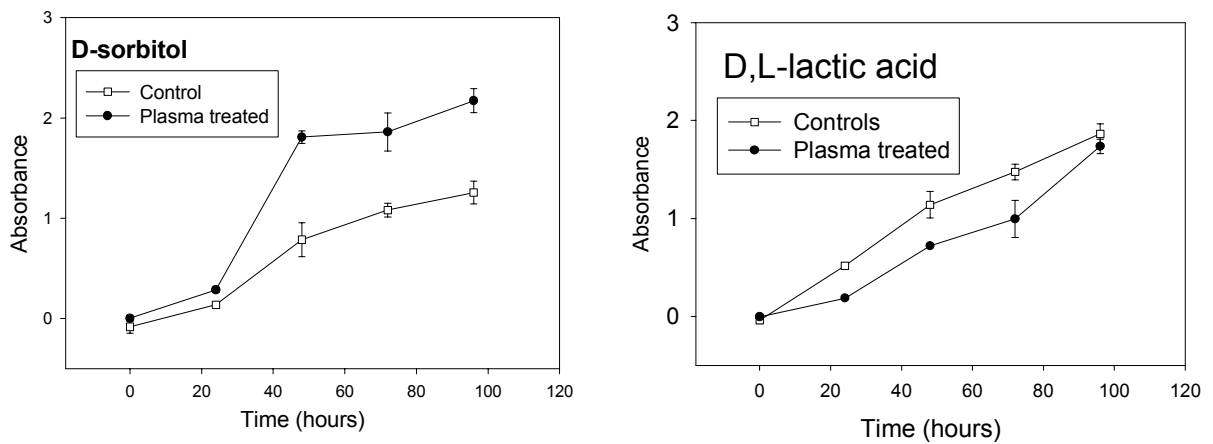


Fig.8 Increased (left) and decreased utilization of substrates by plasma-treated *E. coli* cells.

## 6. Conclusion

To understand the interaction of plasma with living cells in general, and with bacterial cells in the case of this particular study, requires a careful investigation which probes the effects on the cellular and sub-cellular levels. Since plasma is a source of charged particles, radicals, and radiation, it is expected that physical as well as biochemical effects enter into play. To a certain degree the role of various plasma agents can be separated and studied. However, when all of the agents are present simultaneously, as is in fact the case, one can expect that some level of synergy will exist. To date, no in-depth or systematic study of synergistic effects has emerged in the case of non-equilibrium, high-pressure, low temperature plasmas. Also, the specific effects of the plasma on sub-cellular components such as nucleoid, cytoplasm, ribosome, etc. have yet to be elucidated. Therefore, much remains to be done in this respect.

## References

- [1] B. Eliasson, and U. Kogelschatz, "Non-Equilibrium Volume Plasma Chemistry", *IEEE Trans. Plasma Sci.*, Vol. 19, No. 6, pp. 1063-1077, (1991).
- [2] F. Massines, C. Mayoux, R. Messaoudi, A. Rabehi, and P. Segur, "Experimental Study of an Atmospheric Pressure Glow Discharge: Application to Polymers Surface Treatment", *In Proc. Int. Conf. Gas Discharges & their Applications*, Swansee, U.K., (1992), pp.730-733.
- [3] E. Smulders, B. Van Heesch, and S. Van Paasen, "Pulsed Power Corona Discharges for Air Pollution Control", *IEEE Trans. Plasma Sci.*, Vol. 26, No. 5, pp. 1476-1484, (1998).
- [4] E. Stoffels "Biomedical Applications of Electric Gas Discharges", *High Temp. Material Proc.*, Vol. 6, No. 2, pp. 191-202, (2002).
- [5] E. A. Blakely, K. A. Bjornstad, J. E. Galvin, O. R. Monteiro, and I. G. Brown, "Selective Neuron Growth on Ion Implanted and Plasma Deposited Surfaces", *In Proc. IEEE Int. Conf. Plasma Sci.*, (2002), p. 253.
- [6] F. S. Sanchez-Estrada, H. Qiu, and R. B. Timmons, "Molecular Tailoring of Surfaces via RF Pulsed Plasma Polymerization: Biochemical and Other Applications", *In Proc. IEEE Int. Conf. Plasma Sci.*, (2002), p. 254.
- [7] M. Laroussi "Sterilization of Contaminated Matter with an Atmospheric Pressure Plasma", *IEEE Trans. Plasma Sci.*, Vol.24, No.3, pp. 1188-1191, (1996).
- [8] M. Laroussi, "Non-thermal Decontamination of Biological Media by Atmospheric Pressure Plasmas: Review, Analysis, and Prospects", *IEEE Trans. Plasma Sci.*, Vol. 30, No. 4, pp. 1409-1415, (2002).
- [9] M. Laroussi, J. P. Richardson, and F. C. Dobbs, "Effects of Non-Equilibrium Atmospheric Pressure Plasmas on the Heterotrophic Pathways of Bacteria and on their Cell Morphology", *Appl. Phys. Lett.* Vol. 81, No. 4, pp. 772-774, (2002).
- [10] M. Moisan, J. Barbeau, S. Moreau, J. Pelletier, M. Tabrizian, and L'H. Yahia, "Low Temperature Sterilization Using Gas Plasmas: A Review of the Experiments, and an Analysis of the Inactivation Mechanisms", *Int. J. Pharmaceutics*, Vol. 226, pp. 1-21, (2001).
- [11] T. C. Montie, K. Kelly-Wintenberg, and J. R. Roth, "An Overview of Research Using the One Atmosphere Uniform Glow Discharge Plasma (OAUGDP) for Sterilization of Surfaces and Materials", *IEEE Trans. Plasma Sci.*, Vol. 28, No. 1, pp. 41-50, (2000).
- [12] D. A. Mendis, M. Rosenberg, and F. Azam, "A Note on the Possible Electrostatic Disruption of Bacteria", *IEEE Trans. Plasma Sci.*, Vol. 28, No. 4, pp. 1304 – 1306, (2000).
- [13] M. Laroussi, G. Saylor, B. Galscock, B. McCurdy, M. Pearce, N. Bright, and C. Malott, "Images of Biological Samples Undergoing Sterilization by a Glow Discharge at Atmospheric Pressure", *IEEE Trans. Plasma Sci.*, Vol. 27, No. 1, pp. 34-35, (1999).





# HOMOGENEOUS MICROWAVE PLASMA FROM VACUUM TO ATMOSPHERIC PRESSURE – APPLICATIONS IN THE GASPHASE

Dr. Ralf Spitzl, Dr. Hildegard Sung-Spitzl

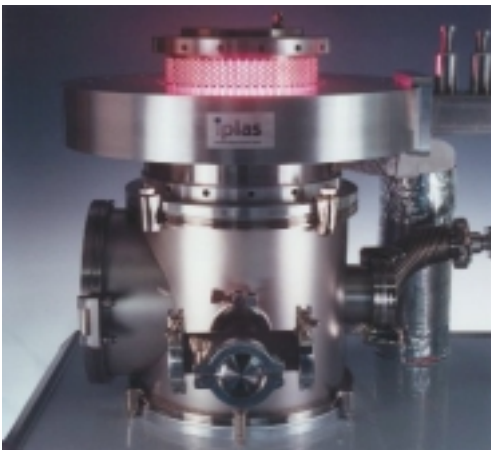
*Iplas innovative plasma systems gmbh, Troisdorf, Germany*

A Generation of microwave plasma with the *CYRANNUS*<sup>®</sup> (cylindrical resonator with annular slots) concept enables a bulk plasma with larger three dimensional extension at any pressure with arbitrary process gas. Various plasma processes have been investigated and compared to similar processes at low pressure. A remarkable increase of process speed has been found in the medium to atmospheric pressure range. At higher pressure such plasma is influenced by gas phase interactions. Plasma-wall interaction as a main effect in high vacuum becomes negligible.

Increase of pressure seems to be an over-proportional lever for efficiency of some processes. One explanation is the dramatic increase of neutral radicals in the medium or atmospheric pressure plasma. Due to high collision frequency the production of excited neutrals is enhanced and result in a highly reactive plasma gas. The share of neutral radicals can be 2 or three orders of magnitude higher compared to ionized radicals.

A transfer of high vacuum plasma processes to medium to atmospheric pressure processes frequently leads to an increase of process speed. Several new mechanisms in plasma gas dynamics are a threat for process development. This represents a great opportunity for optimized production but has to be controlled. Several plasma applications have been tested and optimized and compared with high vacuum plasma processes. As examples:

- cracking of molecules and chemical bonding / abatement
- synthesis of solid particles through condensation
- improvement of generation of new bonding as a preliminary step to enhance growth mechanisms
- use common gases to synthesize valuable gases
- chemical vapour deposition



The *CYRANNUS*<sup>®</sup> I plasma source

# MICROTRIBOLOGICAL INVESTIGATIONS ON FLUOROCARBON THIN FILMS DEPOSITED IN CONTINUOUS AND MODULATED C<sub>2</sub>F<sub>4</sub> RF GLOW DISCHARGES

Giuseppe Breglio<sup>zi</sup><sup>a)</sup>, Antonella Milella<sup>b)</sup>, Imad Ahmed<sup>a)</sup>, Fabio Palumbo<sup>b)</sup>,  
Pietro Favia<sup>b)</sup>, Riccardo d'Agostino<sup>b)</sup>, and Henry Haefke<sup>a)</sup>

*a) CSEM Swiss Center for Electronics and Microtechnology, Inc., Rue-Jaquet Droz 1, CH-2007 Neuchâtel, Switzerland*

*b) Department of Chemistry and IMIP-CNR., University of Bari, Bari, Italy Via Orabona 4, 70126, Bari, Italy*

## Abstract

The high adhesion (stiction), friction and wear occurring in silicon-based microsystems threaten to severely limit their technological potential. Consequently, there is a strong effort to reduce these detrimental effects. It has been observed that capillary forces are a major problem for microsystems. Thus, a main thrust in current research is to reduce capillarity by the application of various kinds of hydrophobic films. Among the various types of such films, fluorinated amorphous carbon films show promise as a stiction reducer. However, their frictional and wear properties need to be more thoroughly examined. This paper discusses the microtribological properties of such types of films. Here the hydrophobicity is controlled by also varying the microstructure of the film.

## 1. Introduction

Microtribological studies are needed to develop fundamental understanding of adhesion, friction and wear phenomena on a small scale for applications in fields such as magnetic storage and microelectromechanical systems (MEMS) [1]. Friction and wear of micro and nanocomponents are highly dependent on surface interactions. Due to the high adhesion and friction of silicon, with which most microsystems today are still fabricated, microtribological studies are needed to understand the influence of various characteristics such as surface forces, roughness etc. Such an understanding can lead to optimisation of the reliability and performance of microsystems. At present, the most common probe to evaluate the tribological properties of microsystems is contact mode AFM, where the lateral force signal is analysed to derive friction information and normal force detections used to measure pull-off forces, thereby measuring adhesion. While the AFM has provided and continues to provide new insights into the basic mechanisms of friction, in its ideal form it simulated a single asperity, which is quite different from most contact in MEMS [2]. Another feature unique to the AFM is that while the forces are very small (typically in the nN regime), contact pressure can easily approach gigaPascal (GPa), because of the sharp tip. Based on their size and geometry, many MEMS have contact pressures in the megaPascal (MPa) regime. Thus, a complete picture of MEMS tribological behaviour can only be obtained with complementary tribological information obtained using a microtribometer which is geared towards meeting the applied load and contact characteristic specific to MEMS. Microtribological studies are also valuable for providing micro-based understanding of macroscopic systems.

Due to the significant technological potential of MEMS, there have been many efforts to find viable solutions. The use of hydrophobic surface like, for example, H-terminated silicon surface [3-5], self assembled monolayers [6-7] and Langmuir-Blodgett [6] films have shown promising results. In microsystem applications, where low energy surfaces with favourable mechanical properties are required, fluorinated films may prove to be useful [8].

## 2 Experimental Details

### 2.1 Sample preparation and characterization

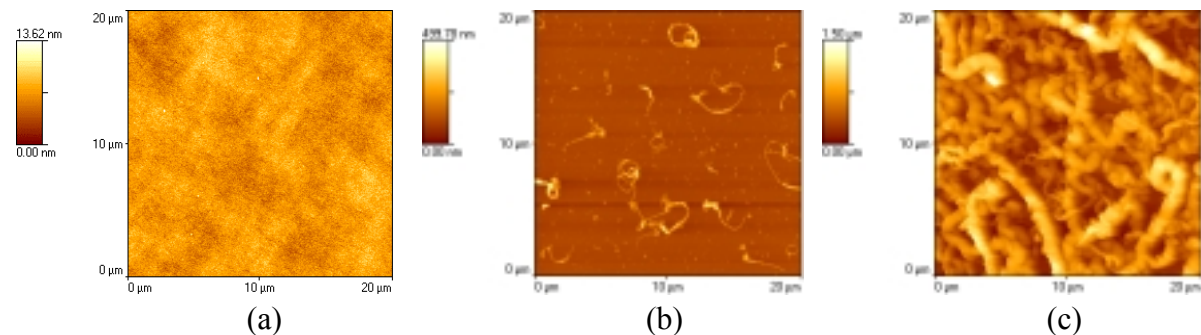
Thin fluorocarbon films were synthesized by C<sub>2</sub>F<sub>4</sub> plasma deposition both in continuous and modulated modes. The processes were carried out in a cylindrical parallel plate stainless steel reactor, with the upper

electrode powered and the lower one grounded. The plasma was ignited with a 13.56 MHz power supply (RF POWER PRODUCTS, model RF5) and an impedance matching LC network (ULVAC, model 002A). In the modulated mode, a pulse generator implemented into the RF generator was utilized, which allows to change both the on time and the duty cycle (ratio between on time and period) of the discharge. An oscilloscope (TEKTRONIX, model TDS 200) is used to monitor pulse duration and amplitude; a second channel allows also to monitor the RF wave. The gas flow rate is metered by electronic mass flow controllers (MKS), the pressure is monitored by a pressure transducer (MKS Baratron). The system is continuously pumped down by a rotary pump. Fluorocarbon films were obtained working in different regimes by changing the modulation period in the range 40-320 ms and the duty cycle from 5 to 100 %. Film chemical composition was characterized by FT-IR, XPS and ToF-SIMS analyses while film wettability was tested both by static and dynamic water contact angles measurements. Film morphology and structure were studied by AFM and XRD, respectively.

Working in continuous mode typically results in amorphous and highly cross-linked films characterized by a low fluorination degree (F/C ratio up to 1.4) and water contact angles of 110°. Switching to pulsed mode it becomes possible to deposit, within a certain range of experimental conditions, partially crystalline, highly fluorinated (F/C ratio up to 1.8) and nano-structured coatings, whose extremely high hydrophobic nature leads to water contact angle values of 160° and even higher.

From the morphological point of view, we report that films deposited in continuous mode are smooth, with no topographical features (surface roughness as low as 0.9 nm). On the contrary, those obtained in discharges modulated at duty cycle lower than 7% and period longer than 200 ms, exhibit ribbon-like micro-/nano-structures randomly distributed all over the surface. When the densities of such structures is high enough, above a certain threshold, the surface becomes extremely water repellent.

For the microtribological investigations a flat sample and two structured samples at different feature densities were examined. Figure 1 shows the AFM images of the three samples; in Table 1 the corresponding preparation method, characteristic and the advancing water contact angle are reported.



**Figure 1:** AFM images of the coatings investigated. **(a)** Film deposited for 15 min in continuous mode at 100 W, 200 mtorr, 6 sccm C<sub>2</sub>F<sub>4</sub>; **(b)** Film deposited in modulated discharge for 3000 s at 100 W, 200 mtorr, 6 sccm C<sub>2</sub>F<sub>4</sub>, 16 ms on time, 304 ms off time (DC=5%, Period=320 ms); **(c)** Film deposited in modulated discharge for 21600 s at 100 W, 200 mtorr, 6 sccm C<sub>2</sub>F<sub>4</sub>, 16 ms on time, 304 ms off time (DC=5%, Period=320 ms).

**Table 1:** Preparation method, characteristics and static water contact angles for the fluorocarbon films tested.

No.	Deposition Method	Characteristic	Water Contact Angle (°)
Sample A	Continuous Plasmas (CW)	Flat Amorphous	100°
Sample B	Modulated Plasmas (MD)	Scarcely dense of ribbon-like structures Partially crystalline	113°
Sample C	Modulated Plasmas (MD)	Highly dense of ribbon-like structures Partially crystalline	138°

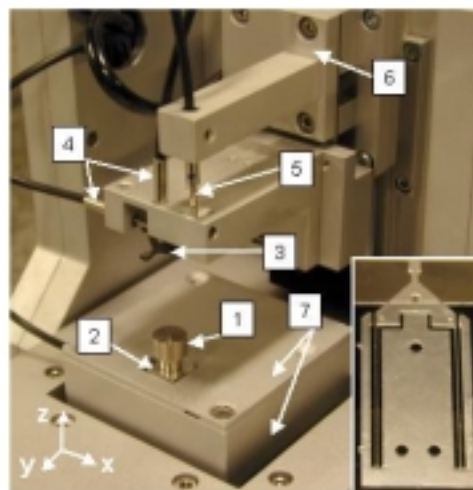
## 2.2 Microfriction tests

The precision microtribometer (Fig. 1a) used in this work consists of three basic units: 1) precision motion mechanisms 2) force transducer and 3) fiber-optic length detection system [9].

The precision motion mechanisms consist of various drives incorporated within the microtribometer for sample positioning, providing reciprocating motion and for normal force adjustment. The sample positioning drives are stepper motors, while the reciprocating unit consists of a piezobimorph element coupled to a linear guide providing a total stroke of around 1 mm. Coarse normal force adjustment is achieved manually by using a micrometer screw, while fine adjustment is performed using a piezo. A practical feature of the motion mechanisms is a built-in tilt adjustment system that allows samples to be aligned parallel to the reciprocating motion of the piezobimorph, thereby eliminating experimental artifacts introduced by measuring the friction between tilted samples.

A very important element of the system is the force transducer, which is made from photostructurable glass. The force transducer used in the microfriction tester is a double leaf spring, shown in the inset in figure 1. The length of the beam is about 1 cm, while the width of the beams can be varied during fabrication making the double leaf spring suited for measuring either small or medium friction forces. Typically, the width of the beam is set at 100  $\mu\text{m}$  for microtribological applications. With this width, the normal force constant is approximately 70-100 N/m and the lateral force constant 30 - 60 N/m. Note that the normal force constant is always higher than the lateral force. This feature makes the double leaf spring particularly suited for tribological experiments. With this design, coupling of normal and lateral forces, a problem in SFM cantilevers, is completely avoided or, at worse, considerably minimized.

Lateral and normal deflections of the photostructured glass bending element, the back and forth motion of the reciprocating unit as well as the vertical motion of the normal force adjustment drive are all measured using fiber-optic sensors based on the principle of reflection intensity variation.



**Fig. 2:** Image of the microfriction tester. The main components are marked: 1) Sample, 2) reciprocating unit, 3) force transducer, 4) fiber-optic sensors to detect normal and lateral deflections of the force transducer, 5) fiber-optic sensor for normal force adjustment detection, 6) precision drive to adjust normal force and 7) the yz micropositioning stages powered by stepper motors with an integrated sample tilt adjustment. The inset shows a photostructured glass spring.

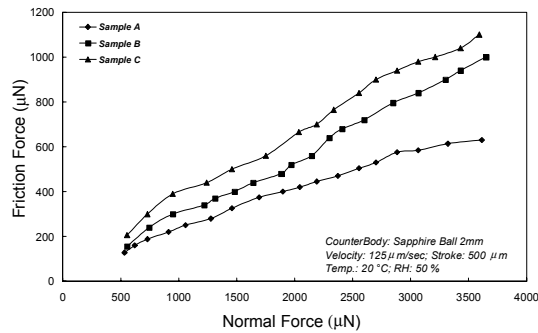
An important and distinctive feature of the double leaf spring is that it is easily calibrated. Both lateral as well as normal force constants need to be known to transform the length values read by the fiber-optic sensors to force values using  $F = kx$ , where  $k$  can be the lateral or normal force constant depending on whether the lateral ( $x_L$ ) or normal ( $x_N$ ) deflection is applied to the equation, respectively. The most simple calibration procedure is performed by placing known precision weights on the end of the double leaf spring and determining the deflection of the spring. The spring constant is obtained from the linear fit to the data. Also, since the assembly containing the bending element spring can be rotated by 90°, both normal as well as lateral force constants can be readily determined.

Three types of counterbodies were used for the tests, namely silicon (with a native oxide, which has been determined to be around 0.6 nm thick [10]), sapphire and steel balls, all with diameters of 2 mm. Prior to each experiment, the balls were sequentially cleaned with ultrasonic assistance first in acetone and then in isopropanol for 10 minutes each.

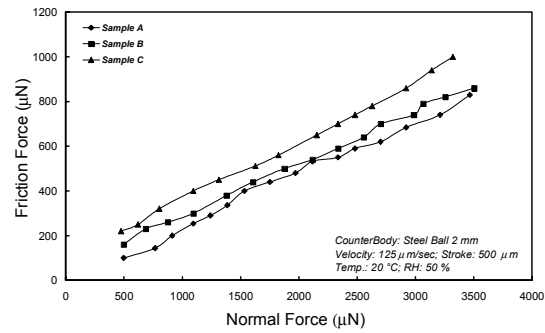
### 3 Results and discussion

Comparative microfriction studies were performed by measuring the friction force as a function of the applied normal force. All the measured values were then used to generate friction-load curves, as is typical in nanotribological studies [10-13], providing useful information about the microfrictional behavior of systems.

Figure 3(a) and 3(b) shows the friction-load curves obtained from the different fluorocarbon film using the 2 mm diameter sapphire ball and 2 mm diameter steel ball, respectively. As can be seen in the figure, the measured friction-load curve of the flat hydrophobic sample shows the lowest friction. Samples with the ribbon-like structures, although more hydrophobic, show a higher friction. This is attributed to the adhesion of the ribbons to the substrate due to which the ribbons are sheared away during the reciprocating motion.

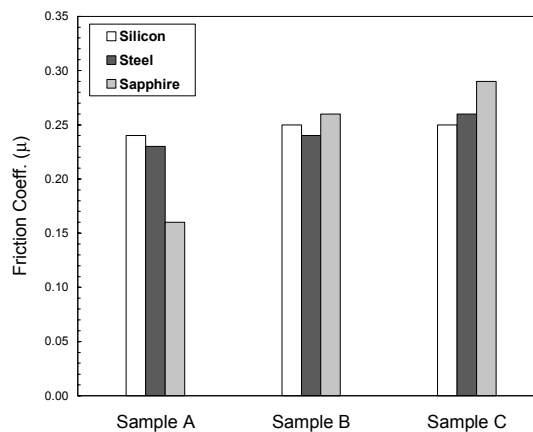


**Fig. 3(a):** Friction force versus the applied load for a 2 mm diameter sapphire ball sliding against various types of fluorocarbon films.



**Fig. 3(b):** Friction force versus the applied load for a 2 mm diameter steel ball sliding against various types of fluorocarbon films

The frictional behaviour of silicon against the various fluorocarbon films is qualitatively similar to the results obtained using the steel ball. However, the absolute friction force values at the corresponding loads are different. This can be observed in Figure 4, where the friction coefficient, determined by performing a linear fit to the friction-load curves, is plotted for the various tribosystems. It is also seen there that the friction of the fluorocarbon films is generally lower than that of native silicon oxide [5].

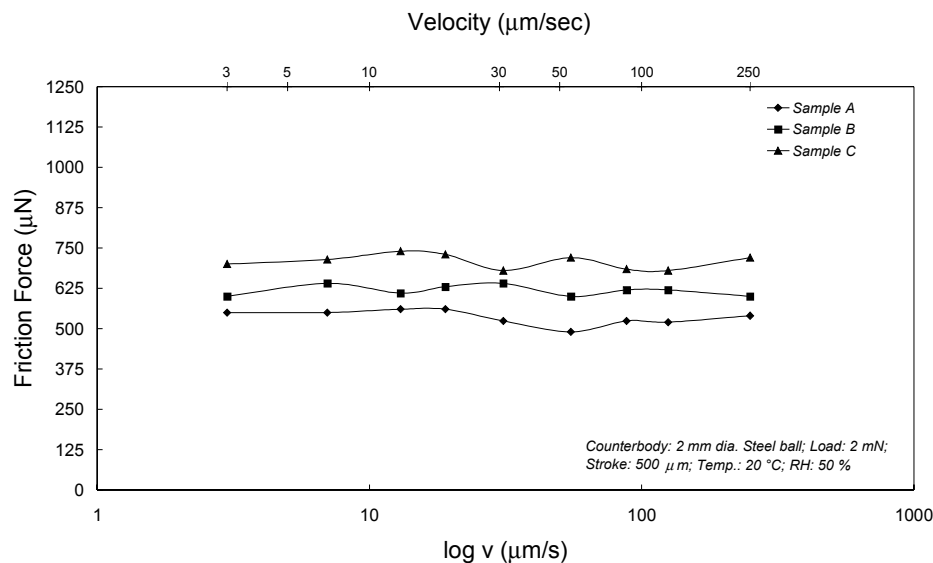


**Fig. 4:** Friction coefficient of 2 mm diameter sapphire, silicon and steel balls sliding against different samples. It illustrates differences in the friction behaviour for various tribosystems.

Wear on the samples as well as counterbodies was controlled using optical microscopy after all tests. A discoloration on the surface of sample B and C with accumulation of small debris particles on the counterbodies were detected at the end of each tests..

The dependence of the sliding velocity on the friction force was also examined. Figure 5 shows the friction force as a function of the sliding velocity at a normal load of 2000  $\mu\text{N}$  for the system steel against the various fluorocarbon films. No dependence on the sliding velocity on friction was determined also for the test with sapphire and silicon ball (not shown). Inspection of the curves reveals that the absolute values of the friction forces for a particular load are higher here than for the friction-load test. The reason is the time the samples are in contact prior to measurement. This time is longer than in the case of the friction-load curves. Due to this, the contact conditions are not the same and this results in some water condensation in the slit created when the sample and counterbody are in contact, leading to higher friction [14].

For flat samples, Scherge et al. [5] and Mate et al. [11] showed that there is a strong velocity dependence for hydrophilic samples (friction decreases with increasing sliding velocity) and negligible dependence for hydrophobic samples. However, this is true only when the samples are relatively flat. For rough hydrophilic samples no dependence of friction force on the sliding velocity was observed [5]. This observation holds true for these experiments as well, further indicating that the contact has a multi-asperity nature.



**Fig. 5:** Friction force plotted against different sliding velocities at a normal load of 2000 mN for the system steel against various types of fluorocarbon films. For the films tested, no dependence of sliding velocity on friction was determined.

## Conclusion

Different fluorocarbon films were characterized with respect to their microtribological properties. The results show that the friction of fluorocarbon films is generally less than that of native silicon oxide. The microfriction of the flat fluorocarbon films was the lowest. The ribbon-like fluorocarbon films with higher water contact angles indicative of better hydrophobicity showed higher friction. This is attributed to the adhesion of the ribbon-like structures to the substrate. Thus, further optimization of structured fluorocarbon films is needed to reap tribological benefits of their superior hydrophobic characteristics.

## References

- [1] B. Bhushan, *Tribology Issues and opportunities in MEMS*, ed. by B.Bhushan (Kluwer,Dordrecht,1998). 229-246.
- [2] M.N. Gardos, *Tribol .Issues and opportunities in MEMS*, ed. by B.Bushan (Kluwer,Dordrecht,1998). 341-365.
- [3] R. Maboudian, *Surface process in MEMS technology*, *Surf. Sci. Rep.* **30** (1998) 207.
- [4] C.H. Mastrangelo and C.H. Hsu, *J.Microelectromech. Syst.* **2**, 33 (1993)
- [5] M. Scherge, S.N. Gorb: *Biological Micro- and Nanotribology*, Springer-Verlag, Berlin 2001.
- [6] H. Liu, S.I.-U. Ahmed, M. Scherge, *Thin Solid Film*, **381**, (2001) 135.

- [7] S.I. Ahmed, M. Scherge, X. Li and J.A. Schaefer, Proc. Of GfT-Tribologie-Fachtagung "Reibung, Schmierung und Verschleiss" Göttingen, Deutschland, p.9, (1999).
- [8] R.S. Butter, D.R. Waterman, A.H. Lettington, R.T. Ramos, E.J. Fordham, *Thin Solid Film* **311** (1997).
- [9] M. Scherge, S.I. Ahmed, O. Mollenhauer, F. Spiller, *Technisches Messen*, **67** (2000) 324.
- [10] C.M. Mate, *Wear* **168** (1993) 17.
- [11] C.M. Mate, *Surf. Coat Technol.* **62** (1993) 373.
- [12] E. Riedo, J. Chevrier, F. Comin, H. Brune, *Surf. Sci.* **477** (2001) 25.
- [13] S.S. Pery, G.A. Somorjai, C.M. Mate and R.L. White, *Tribol. Lett.* **1** (1995) 135.
- [14] R.A. Nevshupa, M. Scherge, S.I.-U. Ahmed, *Surf Sci.* **517** (2002) 17.



# Mechanical Properties of Multilayer Coatings on Polycarbonates Prepared by PECVD

V. Buršíková<sup>1</sup>, L. Zajíčková<sup>1</sup>, J. Buršík<sup>2</sup> and J. Janča<sup>1</sup>

<sup>1</sup>Department of Physical Electronics, Faculty of Science, Masaryk University,  
Kotlářská 2, 611 37 Brno, Czech Republic, e-mail: [vilmab@physics.muni.cz](mailto:vilmab@physics.muni.cz)

<sup>2</sup>Institute of Physics of Materials, Academy of Sciences of the CR, Žitkova 22, 616 62 Brno, Czech Republic

## Abstract

In the present work, several different types of intermediate layers between the polycarbonate (PC) substrate and the plasma deposited hard SiO<sub>x</sub>-like protective coatings have been studied and their influence on the mechanical properties of the whole coating/substrate system has been compared. By the help of an optimized fracture resistant intermediate multilayer system and the hard SiO<sub>x</sub>-like protective coating the original PC surface hardness (~0.2 GPa) was increased by almost two orders of magnitude (5-9 GPa).

## 1. Introduction

There is a continuing interest in improving methods for deposition of hard coatings having still greater abrasion resistance while also exhibiting improvements in various other physical properties [1]. It is therefore an object of the present work to provide a method for forming protective coatings on the surfaces of plastics such as polycarbonates, having a high level of abrasion resistance, with improved resistance against cracking under exposure to thermal and mechanical stresses. It is another object of the present work to provide an improved method for applying smooth, hard, optically transparent layers with uniform thickness, high wear and ultraviolet yellowing resistance, without pinholes and microcracks over a surface of polycarbonate substrates. Plasma-chemical methods are generally using a mixture of hard-coating precursors (e.g. organosililicon or organosilazane mixtures with oxygen in the case of transparent coatings) in a high-frequency or corona discharges and depositing the product directly on a plastic substrate as a very thin film. However, inorganic hard-coatings such as silicon dioxide (SiO<sub>2</sub>) deposited directly onto plastics such as polycarbonate have performance problems when the system is subjected to stresses produced by mechanical or thermal effects. These problems are due to the difference in property characteristics of inorganic and plastic materials. Therefore, it is important to study the mechanical properties of *thin film – plastic substrate systems* in order to find their optimum composition.

There are several basic problems associated with the determination of the mechanical properties of systems consisting of hard inorganic coatings and viscoelastic-plastic substrates as are polycarbonates. The polymer-like films and the polycarbonate substrate exhibit significant creep (time dependent plastic) deformation at room temperatures. The determination of material parameters as elastic modulus and plastic hardness of both the protective film and the viscoelastic substrate is problematic in the case of thin film/substrate systems exhibiting, besides the elastic and plastic indentation response, also creep and anelastic (time dependent reversible) deformation. An elastic material on an easily deforming substrate exhibits so called “plate-bending” effect. If we load such system to a maximum load and keep a constant penetration depth, the load will relax under some plastic or viscoelastic response. Indentation prints obtained at low loads may recover and heal over with time. By measuring the relaxation-recovery process it is possible to obtain information about the internal stress. We attempted to take these effects into account.

## 2. Experimental

The SiO<sub>x</sub>C<sub>y</sub>H<sub>z</sub> films were prepared by plasma enhanced chemical vapour deposition (PECVD) from hexamethyldisiloxane (C<sub>6</sub>H<sub>18</sub>Si<sub>2</sub>O - HMDSO) and oxygen with oxygen-to-HMDSO flow rate ratio ( $q=Q_{O_2}/Q_{HMDSO}$ ) ranging from 0 to 20. The substrates were silicon wafers and polycarbonate (LEXAN-LS2) plates. Capacitive r.f. discharges (13.56 MHz) were generated in a parallel plate reactor. The HMDSO flow rate  $Q_{HMDSO}$  was 4 sccm, the oxygen flow rate was varied from 0 to 80 sccm. The working pressure was in the range from 1 to 40 Pa depending on  $q$ . The applied power  $P$  was varied from 50 to 450 W and the negative bias voltage was in the range from -25 to -400 V.

The optical parameters of the films were studied by means of UVISEL Jobin-Yvon phase modulated ellipsometer in spectral range from 240 to 830 nm with incidence angles from 55° to 75° by the step of 5°. A

Perkin Elmer spectrophotometer was used to measure the film reflectivity. The composition of the films was studied by FTIR, RBS and ERDA techniques.

The morphology of the film surface and the indentation prints was studied by means of Zeiss-Neophot optical microscope, a Nikon SMZ - 2T optical stereo-microscope, a Philips SEM 505 scanning electron microscope and by AFM. The surface energy of the deposited films was calculated from contact angle measurement.

The intermediate layers were deposited combining different discharge parameters in order to optimise the mechanical properties of the *hard protective SiO<sub>x</sub>-like film - intermediate layer (or system of layers) - PC substrate*. The first process was pretreatment of the PC surface in pure Ar or O<sub>2</sub> plasma. Thin layers using  $Q_{O_2}/Q_{HMDSO} < 5$  or systems of several thin layers with gradually changed  $Q_{O_2}/Q_{HMDSO}$  (constant HMDSO, increasing O<sub>2</sub> flow rate) were deposited onto PC surface with or without plasma pretreatment. The protective silicon oxide films were deposited after different sequences of the above-mentioned processes.

The Fischerscope H100 depth sensing indentation (DSI) tester equipped with Vickers indenter was used to study the mechanical properties of the coating-substrate systems. From the loading/unloading curves we obtained the universal hardness  $HU$  (measure of the resistance against elastic and plastic deformation), the elastic deformation work  $W_e$  and the irreversible dissipated indentation work  $W_{irr}$ :

$$HU = \frac{L}{26.43h^2}, \quad (1)$$

$$W_{total} = \int_{h=0}^{h_{max}} L_1(h)dh, \quad W_e = \int_{h_{min}}^{h_{max}} L_2(h)dh \quad \text{and} \quad W_{irr} = W_{total} - W_{el}, \quad (2)$$

where  $h$  is the penetration depth at applied load  $L$ ,  $L_1(h)$  is the loading curve and  $L_2(h)$  is the unloading curve. From the load-penetration curves it was possible to determine also the material resistance against plastic deformation  $H_{pl}$  (so called plastic hardness) and the elastic modulus  $Y$ .

$$H_{pl} = \frac{L_{max}}{26.43h_r^2}, \quad (3)$$

$h_r$  is the depth of the remained indentation print created by irreversible deformation under maximum load  $L_{max}$ . The indentation elastic modulus  $Y$  of the tested material can be calculated on the basis of the contact model in the following way:

$$\frac{1}{Y} = \frac{1}{E_r} - \frac{(1-\nu_i^2)}{E_i}, \quad E_r = \frac{\sqrt{\pi}}{2} \frac{dL(h_{max})/dh}{\sqrt{A}}, \quad A(h) = 26.43h^2. \quad (4)$$

Here  $E_r$  is the so called reduced elastic modulus,  $dL(h_{max})/dh$  is the slope of the unloading curve at maximum load (depth) and  $A(h)$  is the contact area of the indenter and the tested material. The contact model was derived on the basis of the homogeneous elastic half space assumption [2]. In the case of the relatively hard coating on the soft viscoelastic-plastic substrate this assumption is not fulfilled. Then the calculated value of the indentation elastic modulus  $Y$  represent an average of elastic constants of the coating and the substrate for the given indentation depth. This statement holds both for universal hardness and for plastic hardness.

The indentation creep and anelastic recovery values were calculated according to following formulae:

$$CR_1 = \frac{h_{max} - h_{CR1}}{h_{max}} 100\% \quad \text{and} \quad CR_2 = \frac{h_{min} - h_{CR2}}{h_{min}} 100\% \quad (5)$$

Here  $h_{CR1}$  or  $h_{CR2}$ , respectively, is the indentation depth after holding the maximum or minimum load, respectively, at constant value during a given time interval.

### 3. Results and discussion

The differences in structural and physical properties of coatings and the PC substrate result in tangential stresses at the coating-substrate interface. The internal stress may have compressive or tensile character. Due to high internal stress complete film delamination or spontaneous film cracking can occur. If the internal stress has rather compressive character, the films tend to delaminate, in the case of the tensile stress there is a tendency to initiation of film cracking. Our previous results carried out on a large number of different coatings showed, that the SiO<sub>x</sub>C<sub>y</sub>H<sub>z</sub> film prepared at higher HMDSO to O<sub>2</sub> flow rate ratio ( $q > 10$ ) exhibited

tensile stress. The tensile stress is increased with applied power  $P$  and negative self bias voltage  $U_b$ . For  $q > 16$  and  $P > 300$  W, the tensile stress is high enough to cause the spontaneous film cracking. When  $q$  approached 0, the intrinsic stress tended to compressive character. With increasing applied power this tendency was more and more evident. When the applied power exceeded 300 W, spontaneous delamination of films took place because of poor adhesion and high compressive stress. The compressive stress in films can be compensated by increased adhesion.

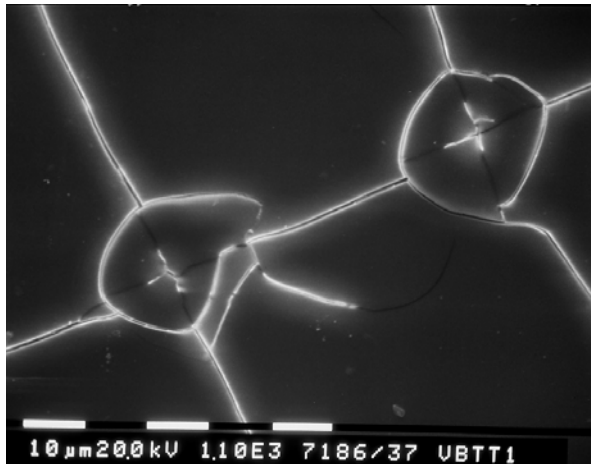


Fig. 1 SEM image of the indentation induced cracking of film with high tensile stress.



Fig. 2 SEM image of the crack network developed around the matrix of indentation prints.

The surface energy of the PC can be significantly increased by plasma treatment in Ar discharge as it was shown in [3]. The plasma treatment increased not only the surface energy but also the surface hardness and had stabilisation effect on the coating-substrate interface [4, 5]. The indentation tests performed on coating-substrate systems enable to study also the indentation induced film damage. In the case of high tensile stress creation of cracks at the corners of the indentation prints could be observed after the indentation test. In Fig. 1 the indentation induced film cracking is shown. Fig. 2 shows, that the cracks propagation and spreading into a large area around the indentation prints resulted in creation of crack network. The films were deposited at applied power  $P=400$  W, negative self bias of  $U_b = -300$  V. The flow rate ratio  $q$  was 14. The films were transparent, relatively hard with plastic hardness  $H_{pl}$  of about 7 GPa and had inorganic  $\text{SiO}_x$  character. Despite of these positive properties these types of coatings may not be deposited directly on the PC surface due to tensile cracking.

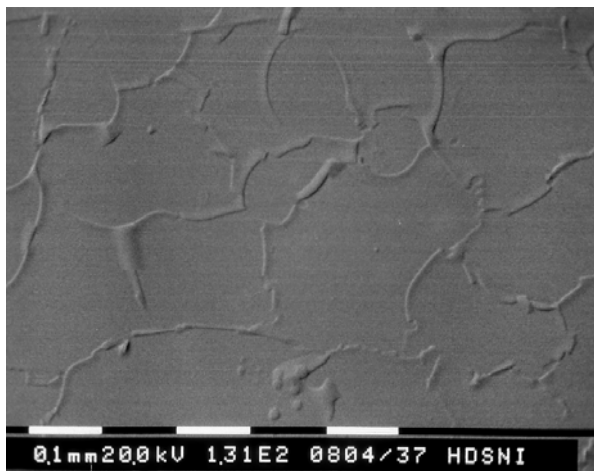


Fig. 3 SEM image of the wrinkling and buckling of PP-HMDSO film on PC substrate due to high compressive stress.

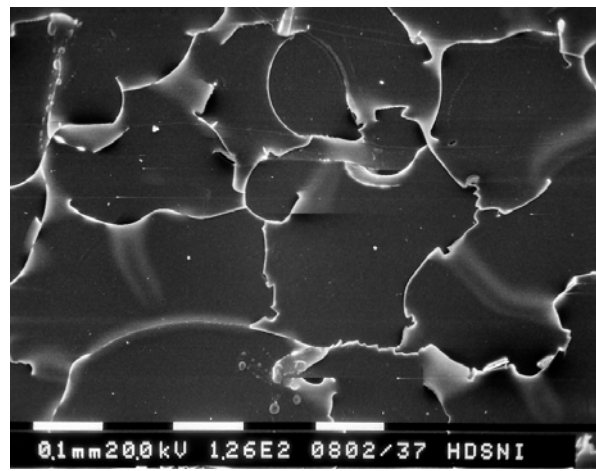


Fig. 4 SEM image of the cracking and delamination of the buckled parts of the PP-HMDSO coating initiated by local heating of the coating-substrate system.

The cracks propagated from the corner of the indentation prints without delamination indicated a rather strong adhesive strength between the coating and the substrate. The strong adhesive strength led to channeling of cracks in the coating rather than separation of the coating from the substrate. These kind of coatings can serve as protective when a system of intermediate layers providing gradual transition from polymer to inorganic properties is deposited on the PC surface before the  $\text{SiO}_x$ -like coating deposition.

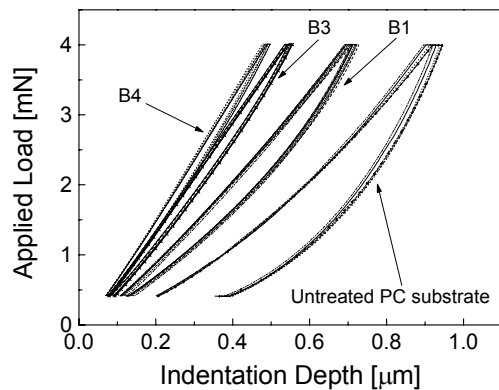


Fig. 5 Load-penetration curves carried out on three different systems of polymer-like coatings on PC substrate (for deposition conditions see Table 1) compared to load-penetration curve obtained for untreated PC sample.

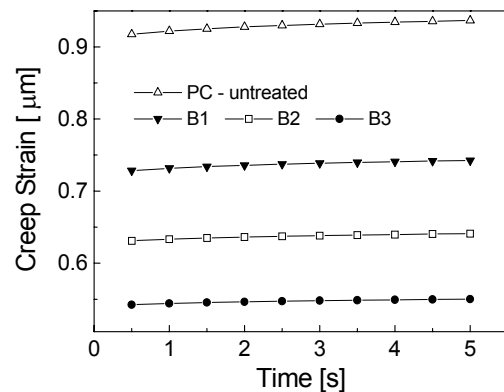


Fig. 6 Results of creep tests carried out on systems from Table 1, comparing to creep test obtained for untreated PC sample.

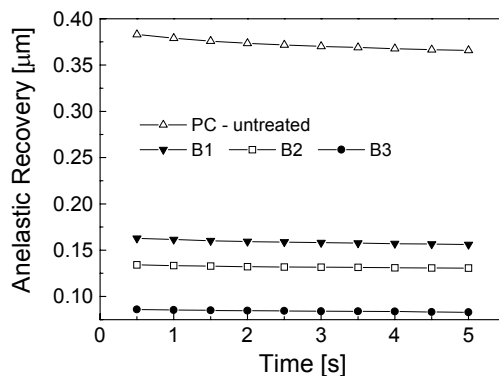


Fig. 7 Anelastic recovery at minimum load of 0.4 mN for coating-substrate systems from Table 1 compared to anelastic recovery of untreated PC sample.

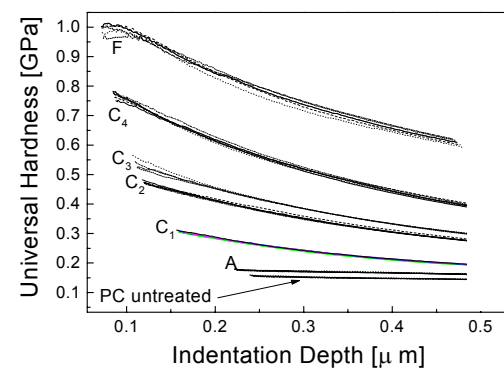


Fig. 8 Universal hardness versus indentation depth for several different coatings (A, C<sub>1</sub>-C<sub>4</sub>, see Table 2) on PC substrate and for their graded composition F.

In Fig. 3 and 4 the spontaneous delamination of PP-HMDSO film deposited from pure HMDSO without oxygen addition at applied power 400 W is illustrated. The initial wrinkling and buckling was followed by complete delamination, when the coating-substrate system was subjected to local heating due to electron beam in SEM.

The load-penetration curves in Fig. 5 show the results on depth sensing indentation tests performed on coated polycarbonate samples at maximum load of 4 mN. The polycarbonate substrate was treated in Ar plasma prior to deposition process. The argon flow rate was 5.7 sccm, the applied power was  $P=100$  W and the treatment time was 5 minutes. The deposition condition for illustrative series of coating-substrate systems are summarized in Table 1 together with the apparent material parameters as universal hardness  $H_U$ , plastic hardness  $H_{pl}$ , elastic modulus  $Y$ , creep strain  $CR_1$  and anelastic recovery  $CR_2$ .

	q	P[W]	U <sub>b</sub> [V]	t[μm]	HU[GPa]	H <sub>pl</sub> [GPa]	Y[GPa]	CR <sub>1</sub> [%]	CR <sub>2</sub> [%]
PC	-	-	-	-	0.15 ±0.01	0.24±0.01	3.0±0.1	2.1	-4.3
B <sub>1</sub>	2.5	100	-85	1.1	0.25±0.03	1.45±0.04	4.5±0.1	1.8	-3.6
B <sub>2</sub>	2.5	200	-135	1.2	0.30±0.03	2.23±0.06	5.8±0.1	1.5	-3.4
B <sub>3</sub>	2.5	300	-180	1.2	0.39±0.01	4.40±0.04	8.8±0.2	1.4	-2.7
B <sub>4</sub>	2.5	400	-230	1.2	0.41±0.01	5.40±0.20	10.5±0.3	1.1	-1.9

Table 1. Deposition conditions for polymer-like SiO<sub>x</sub>C<sub>y</sub>H<sub>z</sub> coatings B1–B4. *q* is the oxygen to HMDSO flow rate, *P* is the applied power, *U<sub>b</sub>* is the negative self bias voltage and *t* is the coating thickness. The apparent material parameters as universal hardness *HU*, plastic hardness *H<sub>pl</sub>*, elastic modulus *Y*, creep strain CR<sub>1</sub> and anelastic recovery CR<sub>2</sub> of the coating-substrate systems and the untreated PC substrate are also included.

For comparison, the material parameters of the uncoated PC substrate are included, too. As the maximum penetration depth in Fig. 5 was higher than one third of the film thickness, can be assumed, that the load-penetration curves obtained for the coated PC substrate were in each case influenced with the PC substrate. Even if there is still a substrate influence, the calculated plastic hardness is more than 20 times higher for systems B3 and B4 than the plastic hardness of the PC substrate.

Fig. 6 shows, that the maximum depth for the same maximum testing load of 4 mN was decreased from 0.92 μm to 0.5 μm. The creep deformation of the coating-PC substrate systems was caused mainly by the creep of the PC substrate (see also Table 1.). The creep deformation was significantly decreased using the coating B<sub>4</sub>. The remained plastic depth (depth of the remained plastic deformation) was decreased from 0.4 μm to 0.07 μm as it is shown in Fig. 7. The anelastic recovery was higher for uncoated PC substrate and decreased with increasing hardness and elastic modulus.

An example of indentation response of system (marked with F) consisting of intermediate layers and hard protective SiO<sub>x</sub>-like film deposited on PC substrate is shown in Fi. 8. The first process was pretreatment of the PC surface in pure Ar or O<sub>2</sub> plasma. The system of intermediate layers was deposited combining different discharge parameters. The deposition conditions together with the calculated material parameters are given in Table 2. Coatings A, C<sub>1</sub> – C<sub>4</sub> were used for preparation of the intermediate multilayered coating, which provided the transition between the polycarbonate substrate and the hard protective SiO<sub>x</sub>-like coating. The system showed high wear resistance, high fracture toughness and relatively high apparent plastic hardness. The measured material parameters are only averaged values of the material resistance of the particular coatings and the substrate.

	q	P[W]	U <sub>b</sub> [V]	t[μm]	Δt[nm]	H <sub>pl</sub> [GPa]	Y[GPa]	CR <sub>1</sub> [%]	CR <sub>2</sub> [%]
A	0	450	-130	0.6	50	0.30±0.01	3.3±0.1	2.0	-4.2
C <sub>1</sub>	5	100	-75	1.3	400	1.55±0.04	4.4±0.1	1.5	-3.8
C <sub>2</sub>	5	200	-105	1.0	300	4.25±0.03	4.9±0.1	1.4	-3.0
C <sub>3</sub>	5	300	-150	1.0	200	4.44±0.02	6.5±0.5	1.2	-2.7
C <sub>4</sub>	5	400	-195	0.9	100	6.50±0.05	7.5±0.3	1.2	-2.4
F	*	*	*	1.2	-	7.9±0.7	14.0±0.7	1.1	-1.9

Table 2 Deposition conditions for polymer-like SiO<sub>x</sub>C<sub>y</sub>H<sub>z</sub> coatings A and C<sub>1</sub>–C<sub>4</sub> and their apparent material parameters. \*F is a graded composition of coatings A, C<sub>1</sub>, C<sub>2</sub>, C<sub>3</sub>, C<sub>4</sub> and of a thin (150 nm) film deposited at applied power *P*=450 W, negative self bias of *U<sub>b</sub>* = -330 V and flow rate ratio 14. Δ*t* are the thicknesses of particular coatings in the graded composition F.

All deposited layers were transparent in the visible range. The refractive indices of films prepared with an addition of oxygen were slightly lower than the tabulated for SiO<sub>2</sub>. The refractive index of PP-HMDSO film A was higher, 1.5 at 600 nm. The absorption index of this film in UV region had non-zero values, it was 0.06, the film provided also protection against UV irradiation. FTIR spectra of the studied films showed [3] besides the characteristic silicon oxide absorption peaks (Si-O-Si stretching -1070 cm<sup>-1</sup>, Si-O-Si bending – 810 cm<sup>-1</sup> and Si-O-Si rocking – 450 cm<sup>-1</sup>) also peaks at 845 cm<sup>-1</sup> (Si-CH<sub>3</sub> symmetric rocking) and 2908 cm<sup>-1</sup> (CH<sub>2</sub> stretching). Moreover, the characteristic silicon-oxide peaks were overlapped probably by a Si-(CH<sub>3</sub>)<sub>3</sub> deformation from 760 to 860 cm<sup>-1</sup>. The film compositions was studied by RBS and ERDA methods [3]. The

polymer-like films are characterized by a relatively high content of hydrogen (from 66 to 20 %) and a carbon content below 20 %.

#### 4. Conclusion

Several different types of intermediate layers between the polycarbonate substrate and the plasma deposited hard SiO<sub>x</sub>-like protective coatings have been studied and their influence on the mechanical properties of the whole coating/substrate system has been compared. The best mechanical properties were obtained in the case of the following sequence of processes: *plasma pretreatment - deposition of intermediate multilayer system with graded increase of  $Q_{O_2}/Q_{HMDSO}$  in the range from 2 to 10 - deposition of the hard protective layer with  $Q_{O_2}/Q_{HMDSO} > 14$* . These types of systems increased the original PC surface hardness (~0.2 GPa) almost of two order of magnitude (5-9 GPa). The protective coatings prepared according to this procedure were well adherent and showed high resistance against indentation induced fracture and delamination.

#### Acknowledgement

This work has been supported with the Ministry of Education of the Czech Republic, contract J07/98:143100003, COST 527.20, ME489 and by the Grant Agency of Academy of Sciences of the Czech Republic under project S2041105.

#### References

- [1] T.O. See You, N. Ext June, I.N. Taormina - We. Hope. You. Enjoy. **22**, 6 (2003).
- [1] L. Martinu - Plasma Processing of Polymers, ed. by R.d'Agostino et.al. Kluwer Academic Publisher ) 247 (1997).
- [2] G.M.Pharr, W.C.Oliver, F.R. Brotzen - J. Mater. Res. 7, 613 (1992).
- [3] L. Zajíčková, V. Buršíková, V. Peřina, A. Macková, D.P.Subedi, J. Janča, S. Smirnov - Surface & coatings technology, **142-144**, 449 ( 2001).
- [4] A.S.S. Sobrinho, N. Schühler, J.E. Klemberg-Sapieha, M.R. Wertheimer, M. Andrews and S.C. Gujrathi – J. Vac. Sci. Technol. A. **16(4)**, (1998).
- [5] A. Bergeron, J.E. Klemberg-Sapieha, L. Martinu, J. Vac. Sci. Technol. A, **16(6)**, 3227 (1998).

# Production of WC and WTi in Inductively Coupled and Microwave plasma Reactor

J. Janča<sup>1</sup>, M. Eliáš<sup>1</sup>, Z. Frgala<sup>1</sup> and V. Brožek<sup>2</sup>

<sup>1</sup>Department of Physical Electronics, Masaryk University, Kotlářská 2, 611 37 Brno, Czech Republic

<sup>2</sup>Institute of Plasma Physics, Czech Academy of Sciences, Za Slovankou 3, CZ-18221 Praha, Czech Republic

## Abstract

The new plasma chemical reduction and carbidization techniques of tungsten precursors were investigated in order to produce tungsten carbide powder with high surface activity. The application of non-isothermal hydrogen/methane plasma allowed the initiation of reduction and carburization processes at relatively low temperature of neutral gas because the high electron temperature increased atomic hydrogen and carbon concentrations. The processes were monitored by optical emission spectroscopy to determine the end-point of the reduction.

## 1. Introduction

Tungsten and its alloys are important industrial materials. More than 40 % of tungsten is used for the production of tungstencarbide [1]. Tungsten carbide (WC) catalysts are prepared by direct synthesis of tungsten with gaseous hydrocarbons by pyrolysis of organometallic compounds. The use of hydrocarbons requires temperatures above 1000 °C [2]. Because of the known correlation between the reduction temperature and the value of specific surface or catalytic activity, there is an effort to carry out the WC synthesis at temperatures as low as possible. First experiments with the reduction of tungsten by plasma chemical methods showed a possibility to use the method for tungsten powder production. The application of non-isothermal plasma allows the initiation of reduction processes at a lower temperature of neutral gas and therefore lowers the temperature necessary for sintering. The main objective of the present work was to produce tungsten carbide using homogeneous and heterogeneous plasma chemical reactions.

## 2. Experimental

The powder of tungsten and/or tungsten carbide was prepared in inductively coupled r.f. (ICP) discharges (see Fig. 1) and microwave discharge (Fig. 2). Ammonium paratungstate powder  $(\text{NH}_4)_{10}[\text{H}_2\text{W}_{12}\text{O}_{42}] \cdot 4\text{H}_2\text{O}$  (APT) was inserted into the reactor as a source of tungsten.

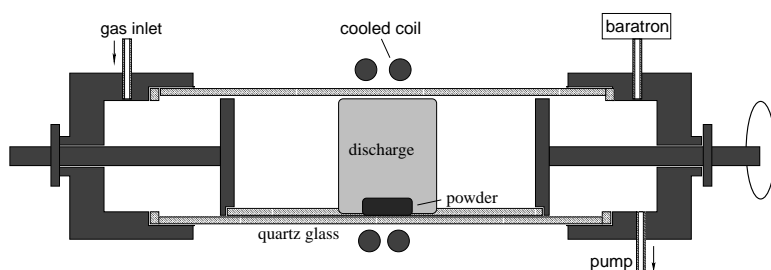


Figure 1: Schematic drawing of ICP reactor.

The ICP reactor was a quartz tube 500 mm long with the diameter of 80 mm. The frequency of the r.f. generator and applied power were 27.12 MHz and 1 kW, respectively. Hydrogen ( $\text{H}_2$ ), mixed with methane ( $\text{CH}_4$ ) in case of tungsten carbide preparation, flowed continuously through the reactor during the discharge. The  $\text{CH}_4$ -to- $\text{H}_2$  flow rate ratio varied from 0 to 0.25. The total flow rate of gases was kept at 90 sccm which corresponded to the pressure of 250 Pa. The powder was heated by the discharge itself to the temperature of 900 °C.

The preparation of tungsten powder doped with titanium was performed in a hydrogen plasma mixed with titanium tetrachloride in the ICP reactor. The flow rate of hydrogen was 90 sccm. The flow rate of titanium tetrachloride ( $\text{TiCl}_4$ ) vapour was varied by a needle valve in the range 0.5–2 sccm.

The microwave reactor was a conventional bell jar (ASTeX-type) reactor. The microwave generator operating at the frequency of 2.45 GHz with power of 1.3 kW. The total flow rate of gases was 300 sccm and total pressure 12 kPa. The  $\text{CH}_4$ -to- $\text{H}_2$  flow rate ratio was held at 0.06. The APT precursor was placed on the graphite holder in the middle of the microwave resonator and heated up to the temperature about 900 °C.

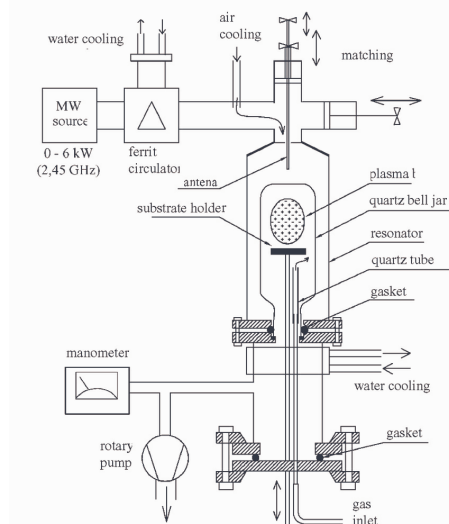


Figure 2: Schematic drawing of microwave reactor.

We recorded the emission spectra from the discharge during the reduction process by means of the monochromator TRIAX 320 equipped with a CCD detector. Solid powder products of the plasmachemical process were analysed by the X-ray diffraction (XRD) method.

### 3. Results and discussion

During the plasmachemical reduction of APT the emission spectra related to the reduction process such as  $\text{H}_\beta$  (486.13 nm) line,  $\text{NH}$  ( $A^3\Pi - X^3\Sigma^-$ , 336.01 nm),  $\text{OH}$  ( $A^2\Sigma^+ - X^2\Pi$ , 307.80 nm)  $\text{CN}$  (the violet system  $B^2\Sigma - X^2\Sigma$ , 388.34 nm) and  $\text{CH}$  ( $A^2\Delta - X^2\Pi$ , 431.42 nm) molecular bands were recorded.

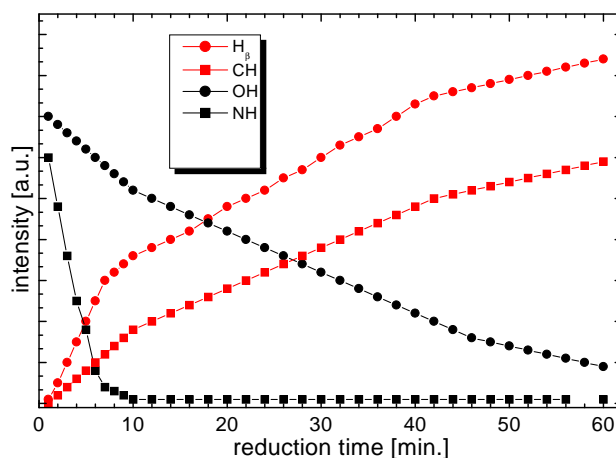


Figure 3: Intensities of chosen spectral features as function of reduction time in  $\text{CH}_4/\text{H}_2$  ICP discharge (rf input power was 1 kW and flow rate ratio  $Q_{\text{CH}_4}/Q_{\text{H}_2}$  was 0.1.)



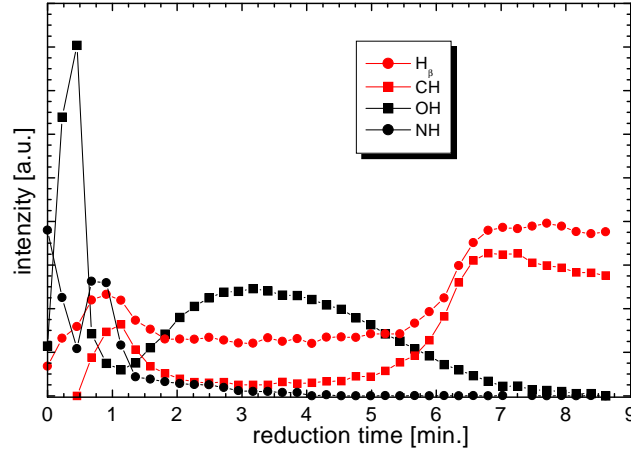


Figure 4: Intensities of selected spectral features as function of reduction time in  $\text{CH}_4/\text{H}_2$  microwave discharge

We observed that the intensities of OH and NH molecular bands generally decreased with increasing time of reduction. The intensities of  $\text{H}_\beta$  exhibited opposite behavior (see Fig. 3). The decrease of NH intensity can be explained by the removal of nitrogen from the APT precursor. Since this process takes place during the first minutes when the APT powder is heated to the final temperature of  $900^\circ\text{C}$  we suppose it is caused mainly by a thermal decomposition. From analogy with industrial processes we assume that the thermal decomposition is the main process of water removal too [2]. However, the OH emission decreases slowly because it is an indication of the water removal as well as the reduction of tungsten oxide. The latter is due to the reaction of hydrogen radicals produced in the discharge rather than the thermal processes. These two different mechanisms of reduction are clearly revealed in Fig. 4 from the time dependent intensity of OH radicals. We can see that the intensity of OH radicals exhibits two maxima. The first one occurs at the early beginning of the discharge due to the thermal decomposition of the powder. The second maximum appears after approx. 3 min of the discharge and is caused by plasma reduction processes. The increase in  $\text{H}_\beta$  emission intensity shows that less hydrogen is consumed as the oxide reduction proceeds with time. The intensity of CN and CH emission bands increased and decreased, respectively, with the reduction time. The CN intensity diminished similarly like NH but this is not shown in the figures in order to keep the lucidity of the graphs. However, we can see from the comparison of Figs. 3 and 4 that the process of oxide reduction is much faster in microwave discharge.

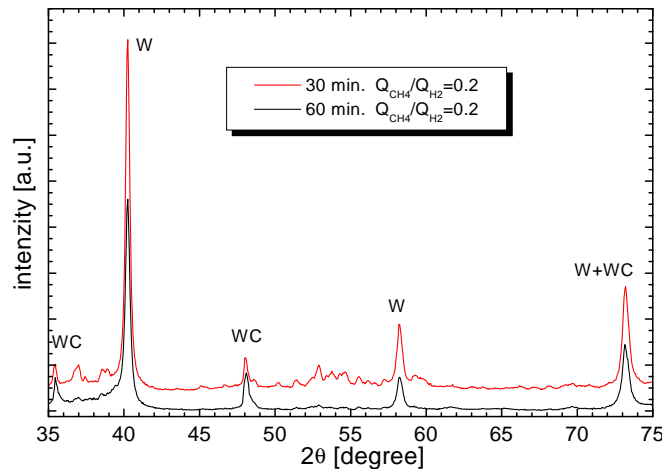


Figure 5: Comparison between XRD spectra of two powder materials produced by reduction in  $\text{CH}_4+\text{H}_2$  ICP discharge

In Fig. 5 there is a comparison between two XRD spectra of powder materials after reduction processes by ICP discharge. The diffraction patterns in the powder exposed to the pure hydrogen discharge shows the presence of tungsten and tungsten oxide. In particular, the peaks at  $2\Theta = 40.2^\circ$ ,  $58.3^\circ$ ,  $73.1^\circ$  correspond to (110), (200) and (211) orientations of tungsten and the broad peaks about  $37^\circ$ ,  $53^\circ$  and  $60^\circ$  were assigned to tungsten oxide [3]. Additional peaks in the XRD spectrum of powder exposed to  $H_2/CH_4$  discharge at  $2\Theta = 35.6^\circ$ ,  $48.3^\circ$ ,  $73.1^\circ$ ,  $75.4^\circ$  correspond to (100), (101), (111) and (200) orientations of tungsten carbide, respectively. This is a proof that WC materials can be produced by addition of hydrocarbon gas to hydrogen. Since in both spectra there is a signal from tungsten oxide we can see that after 30 min of reduction the original APT powder was not completely reduced.

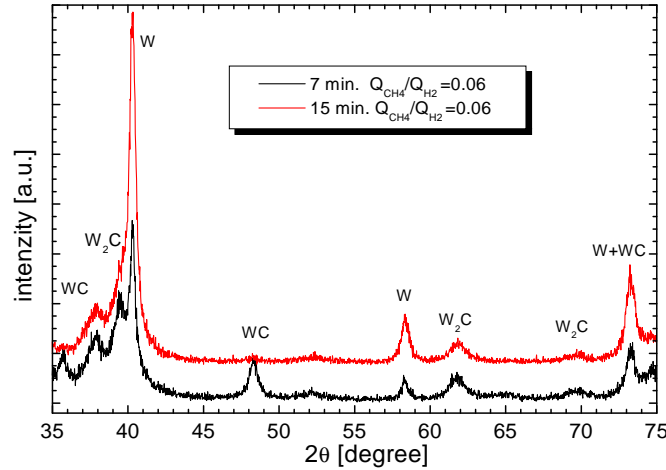


Figure 6: The XRD spectra of WC product from microwave discharge for different time.

Table 1: The percentage of tungsten carbide in the powder in dependence on carbidization conditions.

discharge	power	pressure	time of carbidization	CH <sub>4</sub> /H <sub>2</sub>	WC+W <sub>2</sub> C
	[kW]	[kPa]	[min.]		[%]
ICP	1.0	0.25	30	0.1	1.3
ICP	1.0	0.25	60	0.1	3.8
ICP	1.0	0.25	30	0.2	2.5
ICP	1.0	0.25	60	0.2	6.1
microwave	1.3	12.0	7	0.06	15.9
microwave	1.3	12.0	10	0.06	16.6
microwave	1.3	12.0	15	0.06	25.2

According to the above results we can describe the process of carbidization by two following consecutive steps: (i) the APT precursor is reduced to tungsten and its suboxides ( $WO_x$ ,  $x < 3$ ), (ii) tungsten and its suboxides are carbidized. As a result of the second step the percentage of tungsten and its suboxides percentage in the sample decrease [4]. In XRD (Fig. 6) spectra of the powder prepared by microwave discharge we can see patterns at  $2\Theta=39.6^\circ$ ,  $61.9^\circ$ ,  $69.7^\circ$  correspond to (102), (040) and (321) orientations of  $W_2C$ . Contrary to ICP discharge the powder treated in the microwave discharge is composed also of  $W_2C$  which is usually not a stable product. We believe that its presence is due to the rapid plasma carburization processes occurring in the microwave discharge as compared with ICP (Fig. 6). The maximum percentage of tungsten carbide in the powder was about 25 % (Tab. 1).

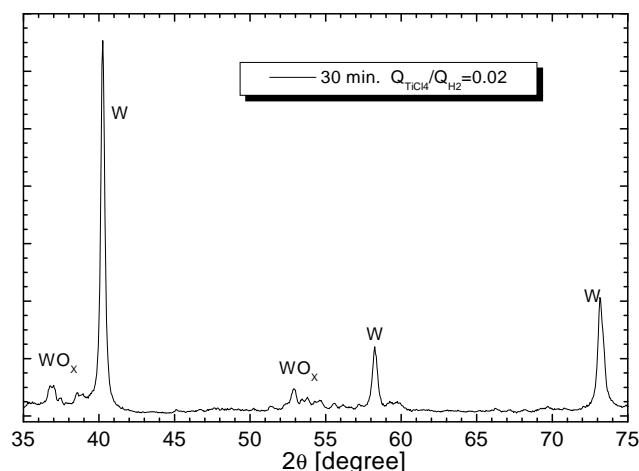


Figure 7: XRD spectra of titanium tungsten powder.

In Fig. 7 there is a typical XRD spectra of WTi. The detection of titanium in the sample using XRD is complicated because diffraction patterns of titanium are overlapped by the peaks of tungsten or tungsten oxide (e. g.  $38.4^\circ$  (002),  $40.2^\circ$  (101)). We did not observed any shift of the lattice constant of tungsten or titanium. Therefore we think that titanium does not create an alloy with tungsten and is a separated phase.

#### 4. Conclusion

Introductory experiment with applying the  $H_2 + CH_4$  plasmachemical activation for tungsten reduction and simultaneous carbidization indicated the possibility of further lowering the reduction and carbidization temperature in comparison with conventional technologies. The resulting powder consisted of a mixture of tungsten and tungsten carbide. The maximum percentage of  $WC + W_2C$  in the powder was about 25 %. The optical emission spectra of discharges were recorded during the reduction process in order to observe changes of the selected spectral line and band intensities. We determined the moment of the completed reduction from the intensity of OH band. This is an important result that can be applied for simple monitoring of the reduction process in the next similar experiments as well as in the industry.

#### Acknowledgment

This work was supported by the Grant Agency of the Czech Republic under contract 202/01/P106 and by the Czech Ministry of Education, contracts MSM 143100003 and OC 527.20.

#### References

- [1] S.W.H. Yin, Ch.T. Wang: Tungsten; Plenum Press, New York, 1979
- [2] E. Lassmer, W.D. Schubert: Tungsten; Kluwer Academic/Plenum Publishers New York, 1999
- [3] WinXPOW STOE & CIE GmbH 1998, Darmstadt
- [4] J.-M. Giraudon, P. Devassine, J.-F. Lamonier, L. Delannoy, L. Leclercq, G. Leclercq: Journal of Solid State Chemistry, 154 (2000), 412-426

# Non-Thermal Plasma BioPrinter with Nano-Scale Precision

Gregory Fridman, Gary Friedman, Alexander Gutsol, Alexander Fridman

*Drexel Plasma Institute, Drexel University, Philadelphia, USA*

## Abstract

We have developed a method of biochemical patterning which allows for micro and nano-scale resolution on non-planar substrates. In this method, bio molecules (including DNA) are delivered to charged locations on surfaces by charged water buffer droplets. Charging of water droplets is accomplished using Dielectric Barrier Discharge (DBD) plasma. DBD was effectively stabilized in the presence of high concentration of micron-size water droplets. Discussed in this paper are theoretical estimations as well as experimental data.

## 1. Introduction

Patterning of different biochemical molecules on surfaces has many applications ranging from biosensors, used in genetic discovery and monitoring of dangerous toxins, to tissue engineering constructs where surfaces control tissue assembly or adhesion of cells. Most existing methods of biochemical patterning are suitable only for planar surfaces. In addition, micro and nano-scale patterning often relies on complex sequences of lithography-based process steps.

Many methods are available for printing today. Two most common ones, that led us to our idea, are Inkjet and Laser printing technologies. Inkjet sprays ink droplets onto paper (Fig. 1) while in a Laser printer toner

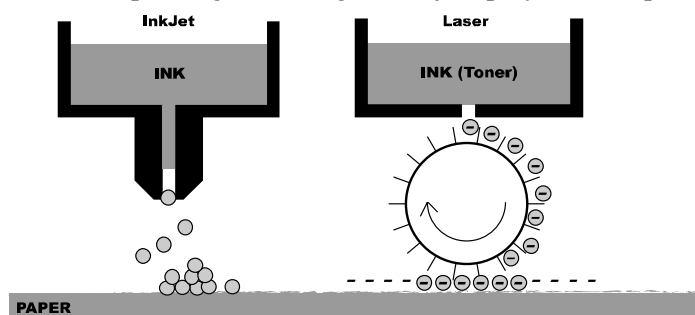


Fig. 1. Inkjet and Laser printing technologies as prototypes of the Plasma BioPrinter

particles are charged and then deposited onto paper in the pre-charged locations. Disadvantage of Inkjet printing technology is splashing caused by droplets accelerated to high speeds hitting target surface, low precision caused by diffusion, and, in many of the variations of the technology – like electrospraying – high dependence on chemical composition of the ink, i.e. printer having to be heavily modified to be able to print a slightly different substance. Laser printers address many of the issues brought up by Inkjets but raise many of their own. Toner particles

undergo high mechanical strains that biochemical molecules and DNA are likely to not survive. There also is a multitude of issues associated with heating.

After looking at the existing state-of-the-art technologies, we have developed a method of biochemical substance patterning, or printing, which allows for micro and nano-scale resolution on non-planar substrates. In this method we utilize ideas of both Inkjet and Laser printing technologies as well as a popular derivative of Inkjet printing – electrospraying technology. Our goal is to print biomolecules (including DNA), peptides, and cells. We accomplish this by creating droplets of the molecules or cells in their respective buffer solution, then charging the droplets in Dielectric Barrier Discharge (DBD) plasma, and finally delivering them onto substrate with pre-written charge (Fig. 2). DBD was selected as the plasma source because of its lower power – we are able to charge droplets in a more “gentle” way than competing technologies and more powerful plasma sources [1]. DBD is also a non-thermal discharge which is required for survival of most biochemicals. In addition, DBD design allows us to charge larger volumes and throughput more liquid than most available technologies resulting in faster printing. Finally, we have precise control of the droplet flow speed (carrier gas flow speed) and are able to virtually eliminate splashing problems that occur with other methods like electrospraying. Slower droplet speeds also allow for higher precision control in printing.

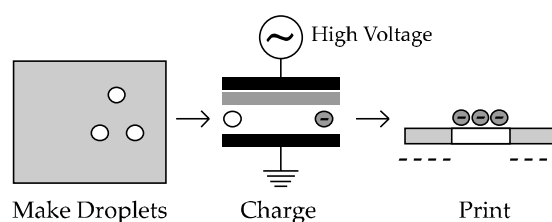


Fig. 2. Plasma “BioPrinter” prototype

## 2. Experimental setup

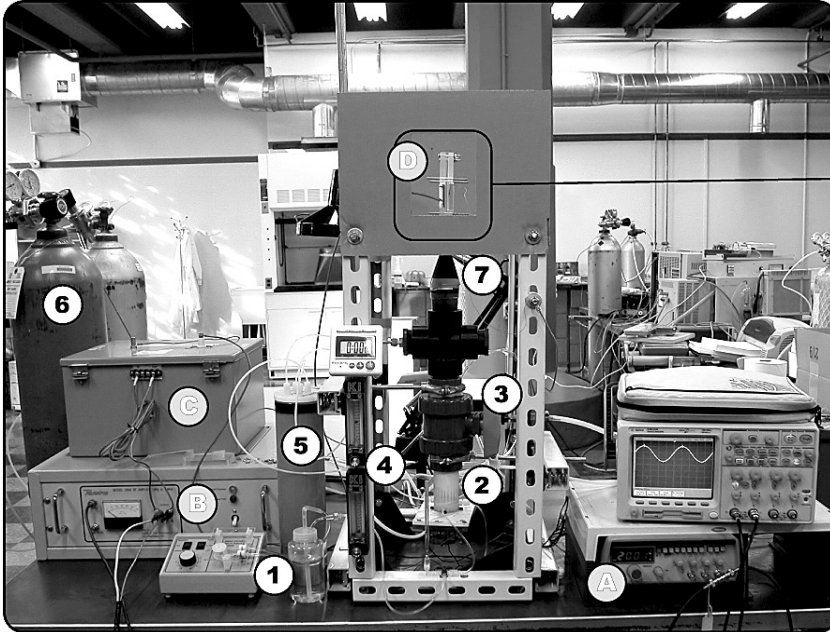


Fig. 3.1. Plasma BioPrinter Experimental Setup

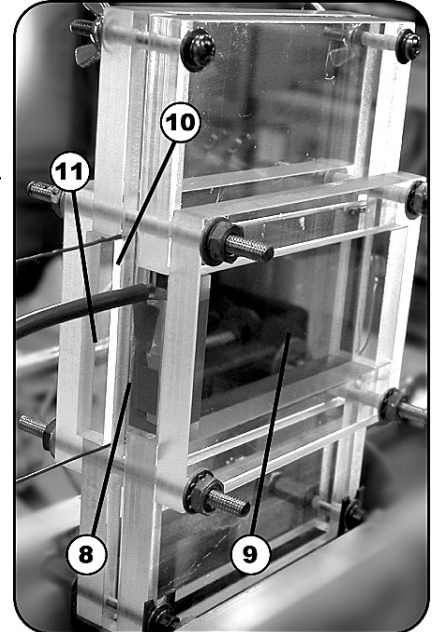


Fig. 3.2. Plasma Discharge & Printer Head

### Plasma Generation

10KV 20KHz AC is generated by:

- A. Signal generator (sine, triangle, square waveform)
- B. High frequency current amplifier
- C. Power transformer

Voltage is then applied to:

- D. Printer head

### Experimental Setup

- 1. Liquid supply (bottle and variable flow pump)
- 2. Piezoelectric “Ultrasonic Nebulizer”
- 3. Droplet flow control valve
- 4. Carrier gas flow control
- 5. Liquid Nitrogen cooler
- 6. Carrier gas supply
- 7. Flow conversion nozzle

### Printer Head

- 8. Quartz dielectric
- 9. High voltage electrode
- 10. Grounded mesh electrode
- 11. Target substrate

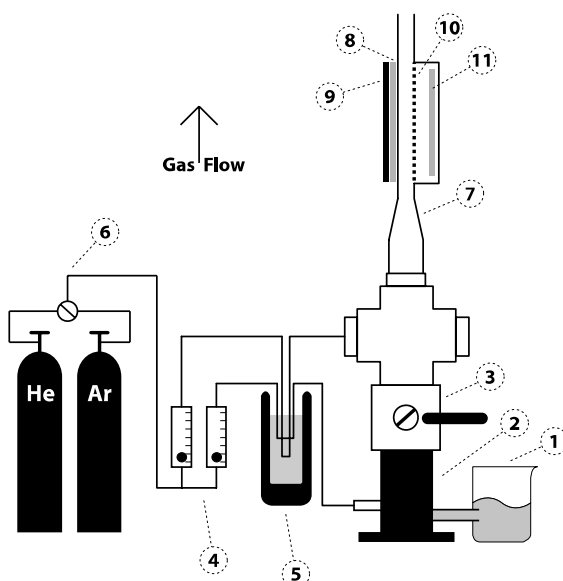


Fig. 3.3. Plasma BioPrinter Setup Schematic

Gold was thermally evaporated onto quartz to act as an electrode (#9). Second electrode in an

Schematic illustration of the Plasma BioPrinter is presented in Fig. 3.3 (all number are same on Fig. 3.1, 3.2, and 3.3). Experimental process is as follows. Liquid is supplied by a variable flow mini-pump at 130ml per hour (#1). Piezoelectric “Ultrasonic Nebulizer” (atomizer) then produces 1 up to 4 micrometer droplets (depending on the surface tension of the supplied liquid) (#2). Droplet flow into the system is controlled by the ball valve (#3) and by supplying carrier gas into the Nebulizer (#4). Carrier gas is supplied in two locations to allow for control of the flow speed as well as droplet concentration (#4). We have ability to test the system with air, Argon, or Helium as carrier gases (#6) which are cooled by liquid Nitrogen to ensure minimal water vaporization (#5). Our gas flow through plasma ranges from 1 up to 2 liters per minute (4 up to 8 cm per second in plasma), thus staying laminar with low Reynolds number; connection from Nebulizer to plasma is made in such a way as to ensure laminar flow (#7). Our plasma region consists of a 40x80x1 mm quartz dielectric barrier (#8). Gold was thermally evaporated onto quartz to act as an electrode (#9). Second electrode in an

open stainless steel mesh (#10) which provides us with the ability to extract charged droplets from plasma onto target substrate (#11) using an external electric field.

### 3. System parameters and estimations

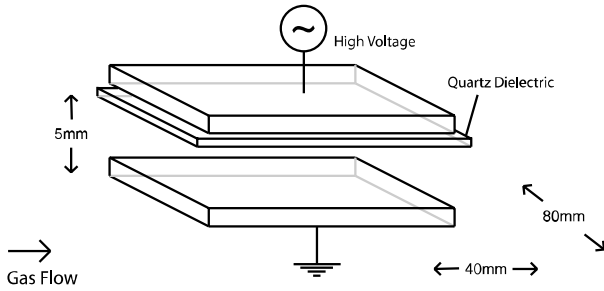


Fig. 4. Dielectric Barrier Discharge (DBD) plasma setup

Dielectric Barrier Discharge plasma is non-thermal, atmospheric pressure discharge. Water is an electro-negative liquid – water molecules arrange themselves in such a way that negative ends of the droplets are pointing outward and positive ends – inward, thus forming a charge layer close to surface, creating a potential drop between the layer itself and the outside [1]. DBD plasma is electron + positive ion gas so we have an abundance of charges to shield the potential drop thus charging the droplet negatively. Thus, water, in the ionized gas, will charge to its “chemical” potential that has been measured to be  $\Delta\phi = 0.26V$  [1]. In plasma, ion collisions are inelastic and ions easily transfer their kinetic energy to the surrounding gas. Electron collisions are very elastic due to electron’s small size, and thus electrons give up their energy slower. Ion temperatures are close to those of the surrounding gas while electrons are far more energetic. When droplet enters plasma region it gathers electrons for its potential is initially different from that of the plasma immediately surrounding it; thus the droplet attracts electrons, gaining negative charge. Positive ions start flowing to the negatively charged droplet, attracted by the newly created electric field, and balance the flow of energetic electrons, shielding the droplet from plasma. Some electrons, however, are energetic enough to overcome the barrier and stay on the droplet. As a result, droplet gets charged to a certain potential, referred to as “floating potential” – a potential at which flow of electrons is balanced out by the flow of positive ions. Bohm’s sheath model, describing behavior of a Langmuir probe, allows us to estimate the floating potential as  $\phi_{fl}$  (4.7 V at room temperature and pressure in electron + positive ion gas):

$$\phi_{fl} = -\frac{T_e}{2} \ln\left(\frac{M_i}{2\pi m_e}\right) = -4.7V \quad (1)$$

For a  $r=500nm$  droplet we can estimate its charge to be:

$$q_{drop} = \phi_{fl}C = \phi_{fl}4\pi\epsilon_0 r \approx 10^{-16}C \approx 1000electrons \quad (2)$$

In DBD discharge at room temperature and pressure in Argon number of electrons  $n_e \approx 10^{10}/cm^3$  and their speed  $v_e \approx 10^{10}cm/sec$  we can calculate electron flux [5]:

$$\Phi_e = 4\pi r^2 \frac{n_e v_e}{4} \approx 10^5 \text{ 1/sec} \quad (3)$$

Thus  $r=500nm$  droplet will gain 1000 electrons in approximately  $5 \cdot 10^{-3}$  seconds; and at our flow speed (4cm/sec through plasma) we can estimate that the droplet will charge after 0.02cm in plasma.

Some of the parameters specific to our plasma setup: plasma frequency:

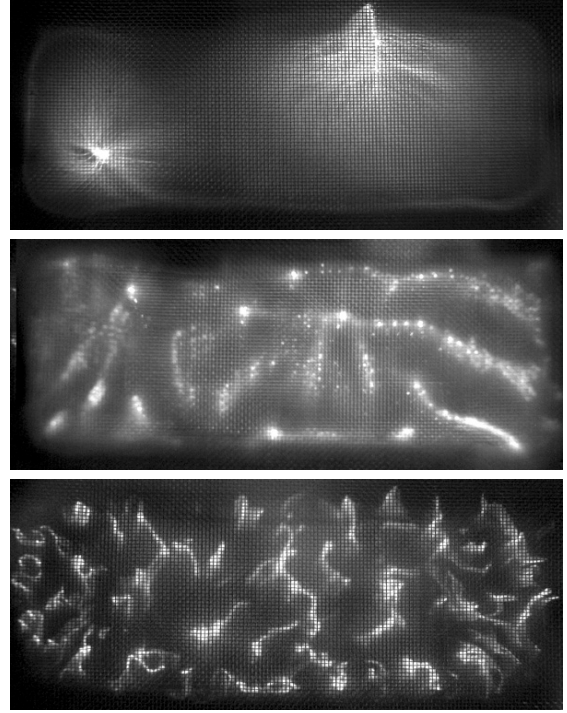


Fig. 5. DBD in (top to bottom) dry Argon, Helium with water aerosol and Argon with water aerosol



$$\omega_e = \frac{1}{2\pi} \sqrt{\frac{n_e e^2}{\epsilon_0 m_e}} \approx 10^9 \text{ Hz} \quad (4)$$

Debye radius:

$$\lambda_{de} = 7434 \sqrt{\frac{T_e}{n_e}} = 9.1 * 10^{-5} \text{ m} \quad (5)$$

With average droplet diameter of approximately  $d=1.7*10^{-6}\text{m}$  we can estimate distance between droplets  $D=9.2*10^{-6}\text{m}$ . Plasma non-ideality parameter  $\Gamma_d$ , designed to measure strength of interaction between dust particles in plasma (or droplets), shows us whether plasma will be closer to ideal state – complete chaos, or if droplets will “feel” each other forming structures. Estimating non-ideality parameter by a model with a shielded Debye potential, also known as Yukawa model, we obtain [1,4]:

$$\Gamma_d = \frac{Z_d^2 e^2 n_d^{1/3}}{4\pi\epsilon_0 T_d} e^{\left(-\frac{1}{n_d^{1/3} \lambda_{de}}\right)} = 3.63 * 10^4 \quad (6)$$

In our estimations we came over an interesting fact – many parameters signify to us that plasma will be in highly non-ideal state; i.e. Coulomb Crystals will form. Fig. 6 shows modelled droplet Coulomb Crystal formation. To verify this let us look at the Debye radius  $\lambda_{de}$  (5) and at the distance between droplets. Debye radius signifies distance at which droplets “feel” each other and we can see that it is an order of magnitude higher than our average distance between droplets. Plasma non-ideality parameter (6) also indicates a similar trend: when  $1 \leq \Gamma_d \ll 171$  plasma is considered to be in or close to ideal state but as  $\Gamma_d$  approaches 171 and higher plasma is said to be non-ideal and the order should be observed.  $\Gamma_d$  for our system is a few magnitudes higher than for ideal plasma [3]. Fig. 7 shows non-ideal behaviour of streamers in plasma: in both Argon and Helium with and without water and at varying power levels streamers “feel” each other especially in dry cold Argon where they are completely immobile and do not react to even significant changes in gas flow speed.

Let us get back to droplets. Piezoelectric crystal in Ultrasonic Nebulizer vibrates at 2.4MHz generating droplets of mostly 1.7 micrometer diameter [2]. Depending on the liquid surface tension average droplet diameter at room temperature and pressure is:

$$d = 0.73 \left( \frac{T_{liquid}}{rf^2} \right)^{1/3} \quad (7)$$

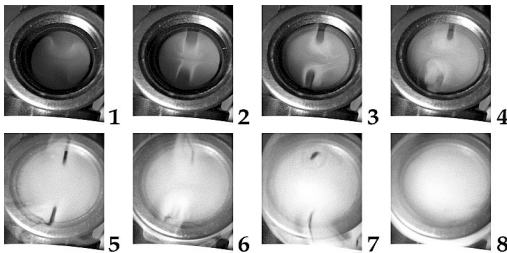


Fig. 8. Droplets exiting Nebulizer

slowly. Fig. 8 shows droplets exiting the Nebulizer at the flow rate of 1 liter of gas per minute (time interval between photos is 1/3 second).

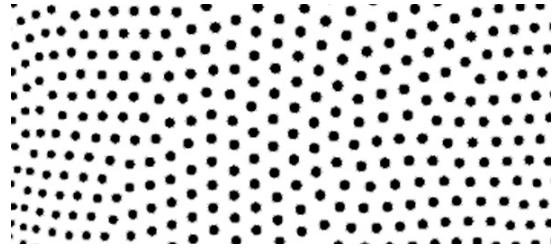


Fig. 6. Coulomb Crystals

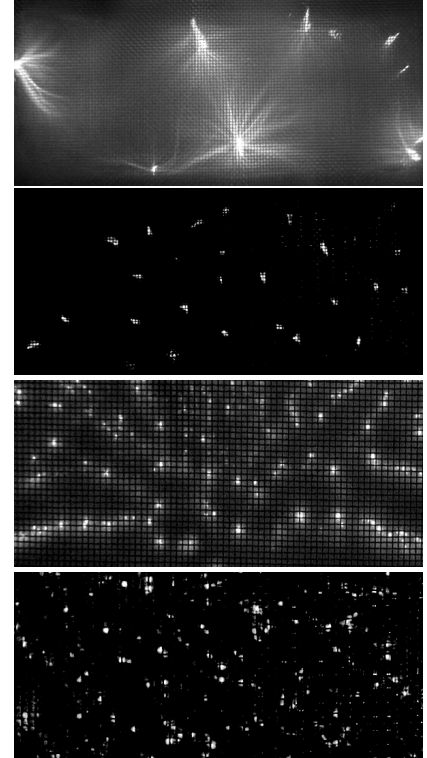


Fig. 7. Streamer patterns in (top to bottom) dry Argon, Argon in water aerosol, dry Helium, Helium in water aerosol.

Sonozap corp., makers of the crystal, measured droplet diameters to be in the 1 to 4 micrometer range (via light scattering). Assuming pure water we can estimate droplet concentration to  $7.8*10^8$  droplets per  $\text{cm}^3$ . Droplet plus carrier gas mixture is very dense and evaporates very

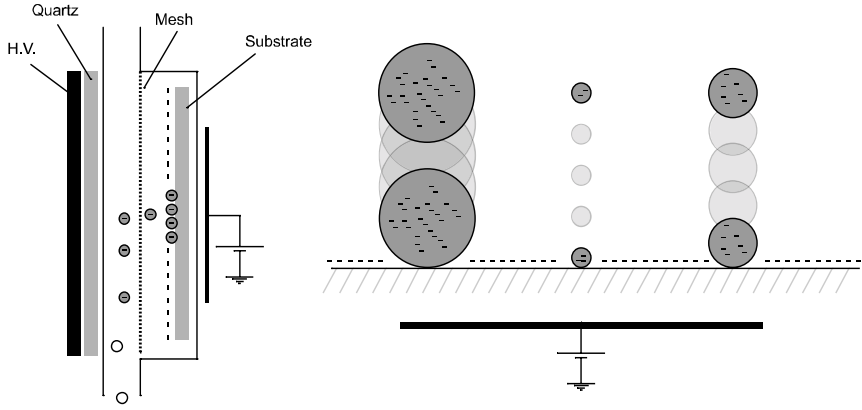


Fig. 9. Charged Droplet Deposition

Our droplets are too small to feel the effect of gravity in the time intervals that concern us [2,3]. Neglecting the effect of gravity we notice that the only two forces acting on the droplet are force exerted by the electric field pulling the droplet onto the substrate and drag force exerted by the gas on the droplet. To find droplet's terminal velocity let's equate  $Eq$  (force exerted by electric field  $E$  on charge  $q$ ) and

$$F_{drag} = 6\pi\eta r v \quad (\text{for low}$$

Reynolds number or Stoke's flow) [2]. Since we know that droplet charge  $q = \varphi c = \varphi 4\pi\epsilon_0 r$  we can solve for speed:

$$Eq = 6\pi\eta r v \Rightarrow E\varphi 4\pi\epsilon_0 r = 6\pi\eta r v \Rightarrow v = \frac{2}{3} \frac{\varphi\epsilon_0}{\eta} E \quad (8)$$

Thus we observe that charged droplet speed under the influence of electric field will not depend on the size of the droplet. This allows us to control droplets much more precisely as well as virtually eliminate splashing problems.

#### 4. Acknowledgements

We would like to thank the following for making this project possible: DARPA for supporting this work, and KODAK Corp. for supplying us with valuable experimental data.

1. A.Fridman, L.Kennedy, *Fundamentals of Plasma Physics and Plasma Chemistry*, Taylor & Francis, 2003.
2. W.A.Sirignano, *Fluid dynamics and transport of droplets and sprays*, Cambridge University Press, 1999.
3. A.V.Kozyrev, A.G.Sitnikov, *Evaporation of a spherical droplet in a moderate pressure gas*, Uspekhi Fizicheskikh Nauk, Russian Academy of Sciences, 2001.
4. V.E.Fortov, *Charge coupling and ordering in nonideal dusty plasmas*, Institute for High Energy Densities, Russian Academy of Sciences, 2000.
5. U.Kogelschatz, *Dielectric-barrier discharges: their history, discharge physics, and industrial applications*, Plasma Chemistry and Plasma Processing, Vol. 23, No. 1, Plenum Publishing, March 2003.



# Coupling of NMR and XPS analyses for the chemical characterization of plasma polysiloxane membranes

S. Roualdès<sup>1</sup>, R. Berjoan<sup>2</sup>, J. Durand<sup>1</sup>

<sup>1</sup> *Institut Européen des Membranes (UMR 5635), Université Montpellier II, CC047, Place Eugène Bataillon, 34095 Montpellier Cedex 5, France*

*Tél. : (33)4-67-14-91-81 - Fax : (33)4-67-14-91-19 - E-mail : Stephanie.Roualdes@iemm.univ-montp2.fr*

<sup>2</sup> *Institut de Science et de Génie des Matériaux et Procédés, CNRS, B.P 5 Odeillo, 66125 Font-Romeu, France*

Plasma polymerization has been recognized as a unique method for preparing thin, uniform, and pinhole-free polymeric films. This polymerization process is a powerful technique that allows to obtain highly cross-linked polymers from nonfunctional monomers that are not used in conventional polymer synthesis. Organosilicon compounds, especially alkylsiloxane ones, are widely used as monomers in low-pressure plasma deposition due to their availability, volatility at room temperature, safe handling and low cost.

In this study, thin polysiloxane films were deposited in a low-frequency plasma polymerization process using alkylsiloxane monomers with different sizes and geometries: linear monomers formed of two or three silicon atoms (hexamethyldisiloxane, octamethyltrisiloxane), and cyclic monomers with three or four silicon atoms (hexamethylcyclotrisiloxane, octamethylcyclotetrasiloxane). The nature and relative proportions of the different chemical environments in plasma polymers were characterized using two different spectroscopic analyses: the X-ray Photoelectron Spectroscopy (XPS) and the solid-state Nuclear Magnetic Resonance (NMR). The purpose of this work is to evidence the influence of the monomer molecular structure (siloxane chain geometry and length) and of plasma conditions on the chemical composition of deposited materials.

Both spectroscopic analyses show that it is possible to synthesize a wide range of materials depending on the more or less energetic character of the plasma and the precursor nature. Under soft plasma conditions (low input power and high monomer flux), the monomer structure is widely preserved; plasma films synthesized under such soft conditions are composed of a high proportion of  $[\text{Si}(\text{O})_2(\text{CH}_3)_2]$  environments characteristic of conventional polydimethylsiloxane polymers. This environment is all the more represented in polymers that the monomer siloxane chain is large; it is partly on the form of cyclic siloxane chains in materials deposited from cyclic precursors (whereas plasma films synthesized from linear monomers are exclusively composed of linear siloxane chains). At the opposite, plasma materials manufactured under drastic plasma conditions (high input power and low monomer flux) are very inorganic, mainly composed of  $[\text{Si}(\text{O})_4]$  environments; whatever the precursor nature may be, plasma films deposited under such drastic conditions are similar to amorph silica polluted by carbon.

Whatever plasma conditions may be, spectra obtained for the same material by both analysis methods are in agreement. The XPS analysis has the advantage of being perfectly adapted to the chemical characterization of thin films. Although the NMR analysis is difficult to perform on plasma materials, it allows to distinguish very closed environments and to display the possible presence of cyclic chains in polymers, more easily than the XPS analysis does. The coupling of both chemical analyses is actually a very powerful tool to precisely investigate the atomic arrangement of polysiloxane plasma materials.

# **Boltzmann solver for simulations of non-equilibrium effects in plasma chemistry**

Vladimir Kolobov and Robert Arslanbekov

*Computational Fluid Dynamics Research Corporation,  
Huntsville, AL 35805, USA*

The paper presents several examples of hybrid kinetic simulations of plasma systems ranging from low pressure inductively coupled and capacitively coupled plasma reactors to atmospheric pressure dielectric barrier discharges. The importance of non-equilibrium effects and consequences of non-Maxwellian electron distribution functions are discussed for different gases and different operating conditions.

## **Introduction**

Unique properties of cold plasmas are determined by its highly non-equilibrium state. The electron distribution function (EDF) substantially deviates from (equilibrium) Maxwellian distribution and the mean energy (temperature) of electrons usually exceeds the gas temperature by two orders of magnitude. This is true for both non-thermal atmospheric pressure discharges, and the low pressure plasma reactors widely used for semiconductor manufacturing applications. In the low pressure reactors, an additional factor further complicates the problem - the EDF becomes *non-local*, i.e. the EDF at a given spatial position is determined not only by the plasma characteristics at this point but also by the plasma properties in a certain vicinity of the point.

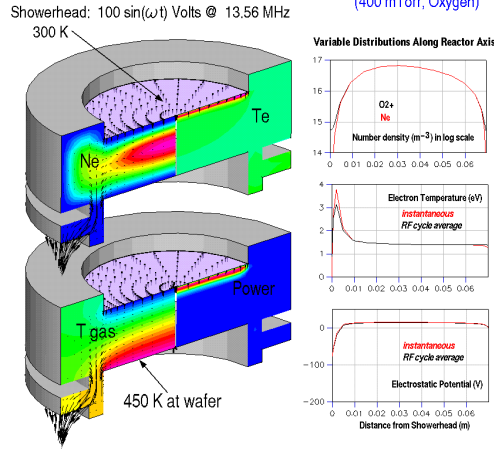
To account for *non-equilibrium* and *non-local* kinetic effects, we have developed a general purpose kinetic solver based on two-term Spherical Harmonics Expansion (SHE) of the Boltzmann Transport Equation (BTE). This approach reduces the 6D BTE to a four-dimensional (3 spatial coordinates + energy) Fokker Planck Equation (FPE) offering a very good compromise between physical accuracy and numerical efficiency. The kinetic module is coupled to electromagnetic, chemistry and other modules to enable self-consistent kinetic simulations of non-equilibrium plasmas. The FPE is solved for the Electron Energy Probability Function (EEPF) and provides macroscopic characteristics such as electron density, flux, and rates of electron induced chemical reactions. Using these quantities, the transport of ions and neutrals in multi-component plasmas is simulated using continuum model.

This paper presents several examples of hybrid kinetic simulations of plasma systems ranging from low pressure Inductively Coupled Plasma (ICP) and Capacitively Coupled Plasma (CCP) reactors used for microelectronics manufacturing, to atmospheric pressure dielectric barrier discharges (DBD) used for sterilization and decontamination. We discuss the importance of non-equilibrium effects and consequences of non-Maxwellian EEPF for different gases including oxygen, methane and nitrogen/oxygen mixtures. We also discuss specifics of electron kinetics and plasma chemistry at low and high pressures and peculiarities of plasma simulations under different conditions.

## **Plasma simulations with CFD-ACE**

CFD Research Corporation has developed commercial software CFD-ACE+Plasma for simulations of non-equilibrium plasmas for a variety of applications. Figure 1 shows examples of simulations low pressure CCP and ICP reactors used for semiconductor manufacturing.

### CFD-ACE+ 3D Simulation of Capacitively Coupled Plasma



### Inductively Coupled Plasma Reactor

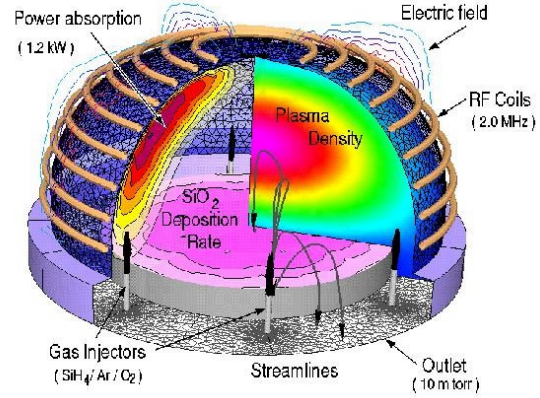


Figure 1. Examples of Plasma Reactor Simulations Using CFD-ACE

Simulations of low temperature, weakly-ionized plasmas are complicated due to strong interaction between gas flow, heat transfer, non-equilibrium gas phase/surface chemistry, and electromagnetic power coupling to charged particles. Moreover, under low pressure operating conditions, kinetic treatment of plasma species becomes important. The kinetic treatment is the most crucial for electrons because i) electron induced chemical reactions are very sensitive to the shape of the EEPF, ii) the EEPF is rather complex and almost always deviates from the Maxwellian EEPF typical to equilibrium systems, and iii) the electron energy relaxation length is much larger than the electron mean free path<sup>1</sup>. The non-local kinetic effects become important for electrons as soon as characteristic size of the system becomes smaller than the energy relaxation length<sup>2</sup>.

Recently, considerable attention has been devoted to the development of physical models for accurate description of kinetic effects at moderate numerical cost. The models based on two-term SHE of the BTE have emerged as a very good approximation valid as long as the dominant scattering process at the microscopic level is elastic or quasi elastic. Inelastic collision processes are easily incorporated in these models provided that they are weaker than the elastic ones, in other words, provided that the energy relaxation rate is much slower than the momentum relaxation rate. Even in situations where such a scaling is not obvious, the two-term SHE gives unexpectedly good results<sup>3</sup>. Kinetic treatment of electrons allows one to properly account for non-equilibrium and non-local effects and enhance the accuracy of plasma simulations.

### Kinetic Module

Kinetic module in CFD-ACE solves a generic Fokker Planck Equation in the form

$$\frac{\partial f}{\partial t} + \nabla \cdot [D_r \nabla f + \mathbf{V}_r f] + \frac{1}{\chi(u)} \frac{\partial}{\partial u} \left( \chi(u) \left[ D_u \frac{\partial f}{\partial u} + V_u f \right] \right) = S \quad (1)$$

Here  $\chi(u)$  denotes the density of states,  $D_r$  and  $\mathbf{V}_r$  are diffusion coefficient and drift velocity in physical space,  $D_u$  and  $V_u$  are diffusion coefficient and drift velocity along  $u$ -axis, and  $S$  is a source term. The variable  $u$  can have different meaning for different problems. For plasma

applications, function  $f$  in (1) denotes the EEPF,  $f_0$ ,  $u$  denotes energy, and  $\chi(u) = \sqrt{u}$ . Taking into account electrostatic field, the FPE for  $f_0$  can be written in the form:

$$\frac{\partial f_0}{\partial t} - \nabla \cdot \left[ D_r \left( \nabla f_0 + \nabla \phi \frac{\partial f_0}{\partial u} \right) \right] - \frac{1}{\chi} \frac{\partial}{\partial u} \left[ \chi D_r \nabla \phi \cdot \left( \nabla f_0 + \nabla \phi \frac{\partial f_0}{\partial u} \right) - \chi \left( V_u f_0 + D_u \frac{\partial f_0}{\partial u} \right) \right] = S \quad (2)$$

(a) (b) (c) (d)

Different terms in Eq. (2) describe: a) electron diffusion in configuration space with a diffusion coefficient  $D_r = v^2/3\nu$  and drift due to electrostatic field,  $\mathbf{E} = -\nabla \phi$ ; b) electron heating (cooling) due to the electrostatic field; c) quasi-elastic processes; d) inelastic collisions (excitation, ionization, attachment, etc.). The quasi-elastic processes including collisions with small energy change (elastic collisions of electrons with neutrals, excitation of molecular vibrations, Coulomb interactions among electrons and ions), and electron heating by electromagnetic fields are described in terms of diffusion and convection along the energy axis.

Using *total* energy  $\mathcal{E} = u - \phi$  as independent variable instead of *kinetic* energy  $u$ , the Fokker Planck equation (1) can be written in the following form<sup>4</sup>:

$$\frac{\partial f_0}{\partial t} - \frac{\partial \phi}{\partial t} \frac{\partial f_0}{\partial \mathcal{E}} - \nabla \cdot D_r \nabla f_0 + \frac{1}{\chi} \frac{\partial}{\partial \mathcal{E}} \left( \chi \left[ D_{\mathcal{E}}(\mathbf{r}, \mathcal{E}) \frac{\partial f_0}{\partial \mathcal{E}} + V_{\mathcal{E}}(\mathbf{r}, \mathcal{E}) f_0 \right] \right) = S \quad (3)$$

This method eliminates complicated cross-terms in Eq. (2) and in many cases simplifies the solution of the FPE. Having solved Eqs. (2) or (3) for  $f_0$ , one can calculate macroscopic properties of electrons (mobility and diffusion coefficients) and rates of electron induced chemical reactions. These quantities are communicated to other modules for self-consistent plasma simulations. For instance, electron density balance equation is usually solved together with the kinetic equation using the electron production rate and electron flux provided by the kinetic module. The electron number density calculated in such a way is used in Poisson and Maxwell equations for calculation of electrostatic and electromagnetic fields.

### Application of the FPE solver to plasma simulations

**Inductively coupled plasma** is maintained by electric fields induced by alternating current in the coil. We have simulated the Osram Sylvania ICP reactor driven by a planar coil. The experimental data for this reactor with argon gas are available for a wide range of discharge conditions (gas pressures  $p=10$ -100 mTorr, power absorbed in plasmas  $P=2$ -200W, and driving frequencies 6.8 and 13.56 MHz)<sup>5</sup>. Figure 2 shows an example of calculations for 13.56 MHz, 100 mTorr, and 100 W. The left part of the figure shows the EEPF at different axial positions at a radial position  $r=4$ cm (reactor radius  $R=10$  cm). It is seen that the "body" of the EEPF (up to energies 10 eV) depends only on total energy. The "tail" of the EEPF is enhanced by fast electrons in the skin layer (near the window, see the 1 cm curve), and is depleted near the plasma boundaries due to the escape of the fast electrons to the walls. The right part of the figure shows the spatial distributions of the electron density, electrostatic potential (upper part) and spatial distributions of electrons with different total energies 20.6 eV (left) and 5.6 eV (right). It is seen that the fast electrons with energies 20.6 eV are concentrated near the window where the RF heating takes place, whereas the electrons with *total* energy 5.6 eV are trapped inside the plasma.

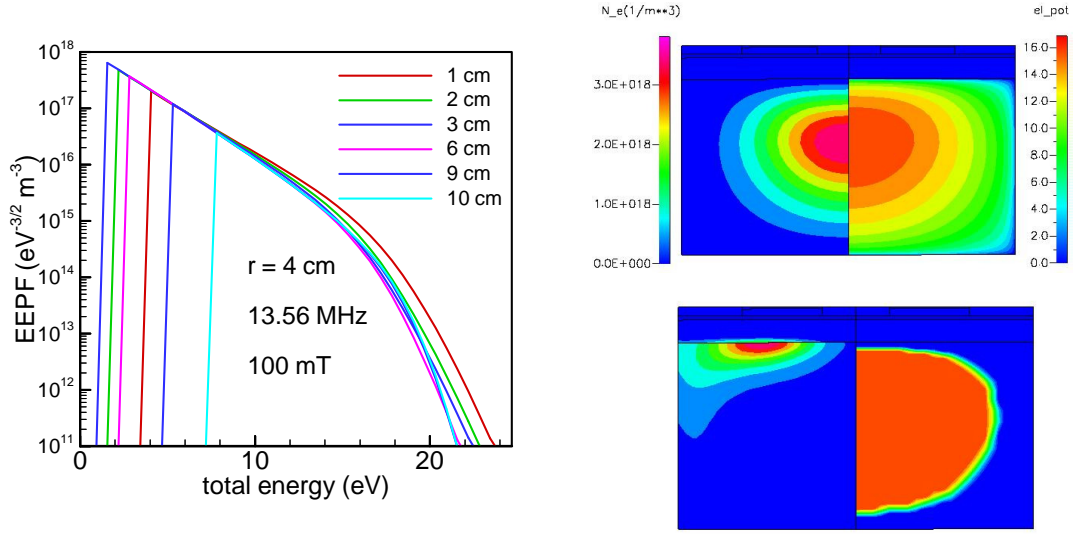


Figure 2. Kinetic ICP simulations. The left figure shows the EEPFs at different distances from the top reactor wall. The right figure shows 2D distributions of electron density and electrostatic potential (top figure), and the EDF with total energies 20.6 eV (left) and 5.6 eV (right) on bottom figure.

**Capacitively Coupled Plasma** is maintained by applying an alternating voltage between two electrodes. We have performed kinetic CCP simulations in  $\text{CH}_4$  gas for different operating conditions following Ivanov <sup>6</sup>. This type of plasmas is used, for instance, for deposition of diamond like carbon films. A 1D planar CCP reactor was considered with an inter-electrode distance of  $L = 3$  cm, the pressure of  $\text{CH}_4$  of 140 mTorr, and the RF voltage varied from 50 to 400 V. The 54-step gas phase reaction mechanism (with 23 species) was used as in [6]. The results of our simulations are presented in Figs. 3 and 4. For the 400V case, a large low-energy peak is formed on the EDF. This low-energy peak is more pronounced in [6] probably due to the absence of electron-electron collisions in [6].

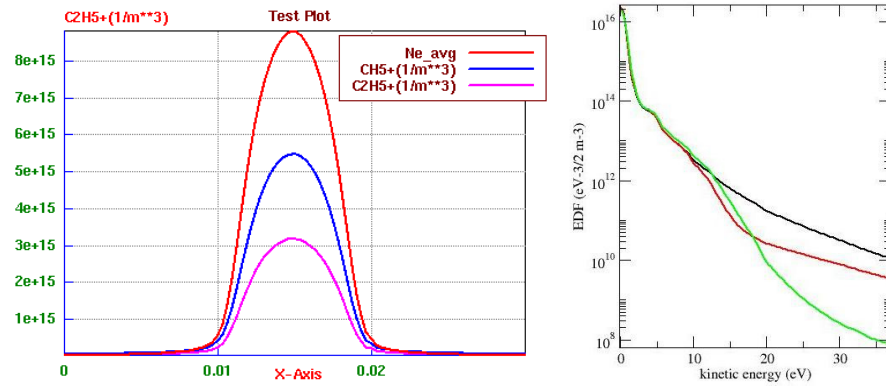


Figure 3.  $\text{CH}_4$  CCP discharge at 400 V. Spatial distributions of ion densities and cycle-averaged electron density (left) and the EDF  $f_0$  at the discharge center at 3 moments during RF cycle (right)

For the 50 V case, the electron temperature profile is drastically different from that obtained in the high current density case (with 400 V voltage): the electron temperature is maximum at the discharge center and the EDF does not exhibit any cold peak.

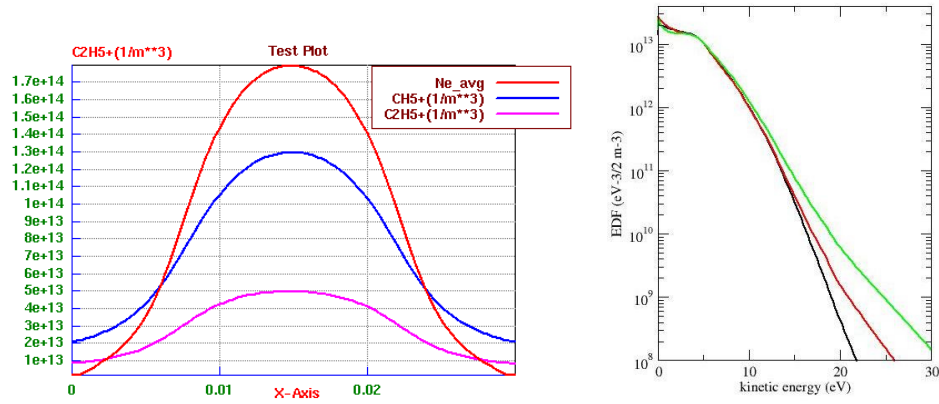


Figure 4. Same as in Fig 3 but for 50 V.

**Positive column** of a direct current (DC) glow discharge is a classical object of gas discharge physics. The PC plasma is maintained by an external electric field directed along the axis of the discharge tube. Such a plasma is widely used for fluorescent lamps. Electronegative gases such as oxygen, chlorine,  $C_xF_y$ ,  $SF_6$ , etc are commonly used in microelectronics manufacturing. The presence of negative ions profoundly affects the properties of plasmas: the plasmas are separated into regions of different compositions, an ion-ion core and an electron-ion shell. An example of kinetic simulations of an electronegative plasma is shown on Fig. 5 which displays the radial structure of positive column in Oxygen<sup>7</sup> for gas pressure of 0.15 Torr. In this low pressure case, the EDF depends solely on the total electron energy, so the EDFs at different radial positions coincide with each other when plotted versus the total energy (see the right part of Fig. 5). The plasma is strongly electronegative, the negative ions are trapped within the plasma, whereas the electron density is flat in the bulk of the plasma (see the left part of Fig. 5).

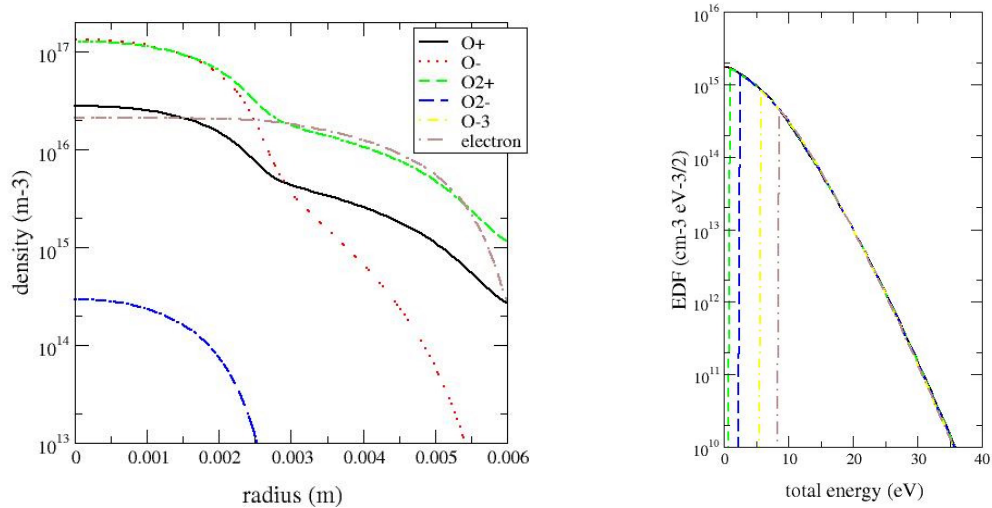
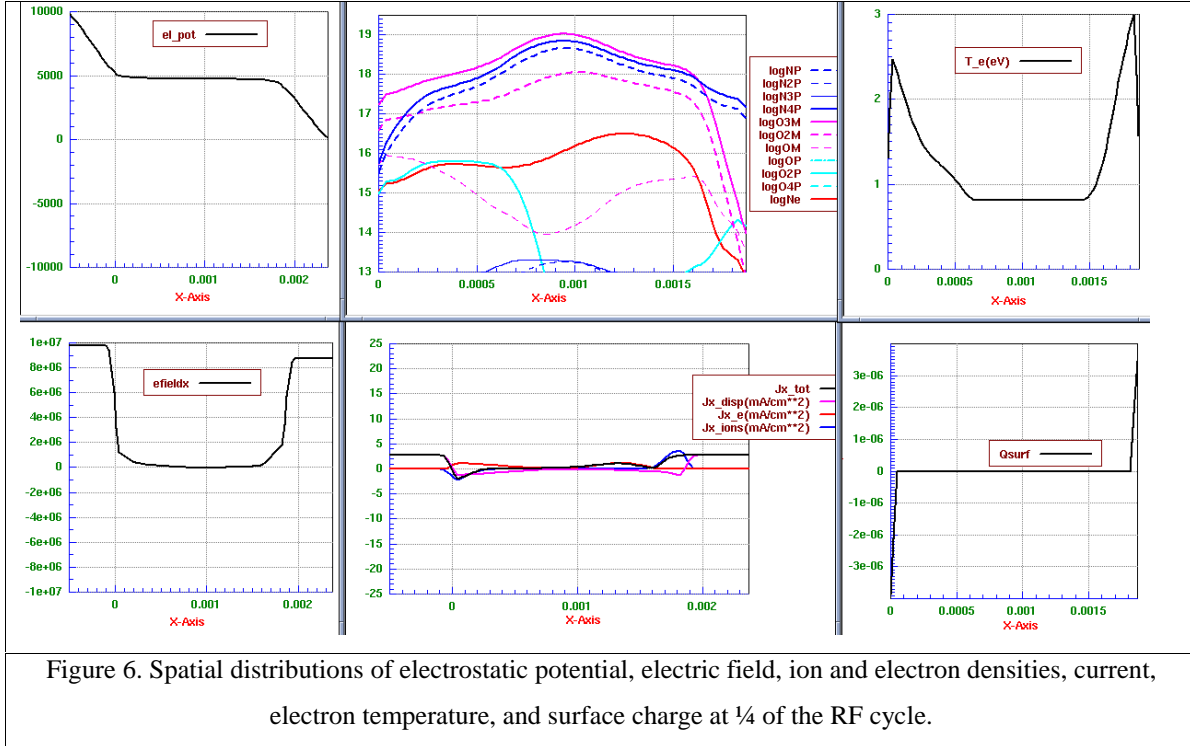


Figure 5. Oxygen,  $p = 0.15$  Torr,  $R = 0.6$  cm,  $E_z = 0.8$  kV/m

**Dielectric Barrier Discharges** For simulations of atmospheric pressure non-equilibrium plasmas we used so-called Lookup Tables (LUT). This feature is very useful when the EEPF is far from *equilibrium* (Maxwellian) but is close to *local*. The LUT technique consists in calculating tables of reaction rates vs average electron energy (or electron temperature) and electron density. The tables are calculated as a pre-processing step using Kinetic Module and are then used to find the reaction rates as functions of electron temperature and density during plasma simulations.

The DBD plasma composition and dynamics in air has been simulated using a mixture of Nitrogen and Oxygen. An example of simulations for RF power of 10kV, 100 kHz is shown in Figure 6. The major ion species are  $N_4^+$ ,  $N^+$ ,  $O_2^-$ ,  $O_3^-$ . The electron density is more than one-order of magnitude lower than the major negative ion species of oxygen. It is worth pointing out that at the RF frequency of 100 kHz, not only the electrons, but also much heavier ions oscillate following the instantaneous value of the electrostatic potential.



**Conclusion** We have presented several examples of hybrid kinetic simulations of plasmas using two-term spherical harmonics expansion of the Boltzmann transport equation for electrons. This approach offers a very good compromise between physical accuracy and numerical efficiency taking into account non-equilibrium and non-local effects and enhancing accuracy and fidelity of plasma simulations.

**Acknowledgements** Thanks are due to Drs H.Q.Yang and N.Zhou for their contributions to the development of the code. This work is funded by the NSF SBIR Project DMI-0091572.

## References

- <sup>1</sup> U.Kortshagen and L.D.Tsendin, Eds, *Electron Kinetics and Applications of Glow Discharges*, Plenum Press, Inc., New York, 1998.
- <sup>2</sup> V.I.Kolobov and V.A.Godyak. Nonlocal electron kinetics in collisional gas discharge plasmas (Review), IEEE Trans. Plasma Sci.23, 503 (1995).
- <sup>3</sup> P. Degond, Mathematical Models and Methods in Applied Science 11, 903 (2001)
- <sup>4</sup> J.R.Albritton, Phys.Rev.Lett 50, 2078 (1983)
- <sup>5</sup> V.A.Godyak, R.B.Piejak and B.M.Alexandrovich, Plasma Sources Science & Technology 11, 525 (2002)
- <sup>6</sup> V. Ivanov, O. Proshina, T. Rakhimova, A. Rakhimov, D. Herrebout and A. Bogaerts, J. Appl. Phys. **91**, 6296 (2002).
- <sup>7</sup> E.Bogdanov et al, submitted for publication in Tech Phys.



# Reactive Ion Etching of Diamond Films in a Narrow Gap Type

T. Misu, M.Goto and T. Arai

*Department of Electrical and Electronic Engineering,  
Kanagawa Institute of Technology, 1030 Shimo-ogino, Atsugi 243-0292, Japan*

Diamond films were etched using a reactive ion etching system in  $O_2/CF_4$  plasma with narrow electrode gap. The maximum etching rate was obtained with the addition of 20% $CF_4$  in  $O_2$  under conditions that the RF power was 100W, the gas pressure 20 Pa and the total flow rate 20sccm. Langmuir probe and actinometry technique were used to determine the plasma parameter. The electron temperature and O density had a peak around  $O_2/20\%CF_4$ .

## 1. Introduction

Diamond has excellent material properties for a variety of technological application including electronic devices, heat transport, and micromechanical devices. The reactive ion etching (RIE) in  $O_2$  plasma is suitable for patterning of diamond in a large area. Reactive ion etching of diamond films using  $O_2/CF_4$  plasma has yielded good etching rates [1], but the etching mechanism is not reported. Therefore, the plasma parameter is needed to clarify the etching mechanism in  $O_2/CF_4$  plasma.

In this study, using RIE of narrow electrode gap type, we investigated etching of polycrystalline diamond films in  $O_2/CF_4$  mixture plasma. Furthermore, the electron temperature and the relative O and F atom densities were measured in order to know the information of relationship between the etching rate of diamond and the plasma parameter.

## 2. Experimental

Figure 1 shows the schematic diagram of the radio frequency (RF) RIE plasma apparatus with

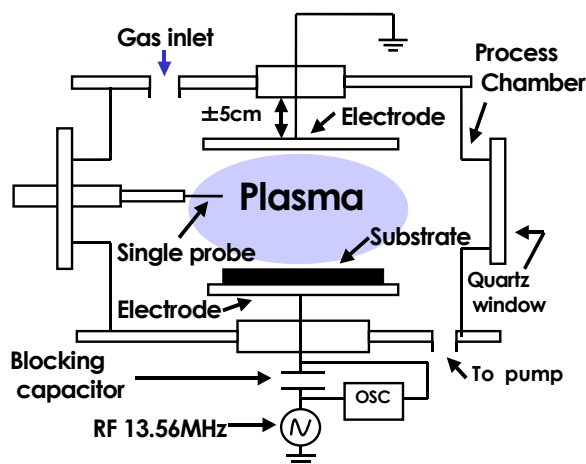


Fig.1 Schematic diagram of the plasma chamber.

single probe and optical access parts. The stainless steel chamber was 160mm in diameter and 250mm high. The stainless steel electrodes is 70mm in diameter, and their distance can be varied from 0.5 to 5.5cm. The background pressure in the process chamber was less than  $4 \times 10^{-4}$  Pa with a turbo molecular pump. The RF power (13.56MHz) is fixed at a constant 100W.  $O_2$  and  $CF_4$  were supplied by using two mass flow controllers. The polycrystalline diamond films of approximately 14 $\mu$ m thickness on silicon wafers (5x5mm) were used as samples. The samples to be etched are positioned on the power electrode. To determine the etching rate, the samples were coated with sputtered Al of 0.3 $\mu$ m thickness on one-half of the sample surfaces. The thickness of the etched films was determined with a stylus profilometer by measuring the step height. The etching rate was calculated from the etching time and etching thickness of the sample.

After etching, the samples were observed with scanning electron microscope (SEM). The electron temperature was measured by a Langmuir probe system (Hiden). The measurement probe was cylindrical tungsten rod and probe tip length 10mm and its diameter 0.15mm. The dc self-bias voltage of electrode was measured by oscilloscope using a voltage probe with 100x attenuation. Optical emission intensities of  $O^*$ ,  $F^*$  and  $Ar^*$  at 845, 703.7 and 750.4nm, respectively, were also measured as a function of  $CF_4$  concentration in order to detect relative O and F atom densities in the plasma by adding 3% Ar gas to the plasma using the actinometry technique[2].

## 3. Results and discussion

The etching rate of diamond and Al mask in  $O_2/CF_4$  plasma as a function of  $CF_4$  concentration is shown in Fig.2. The total flow rate, total pressure, and electrode distance were 20sccm, 20Pa, and 15mm. The etching rate of diamond increased from



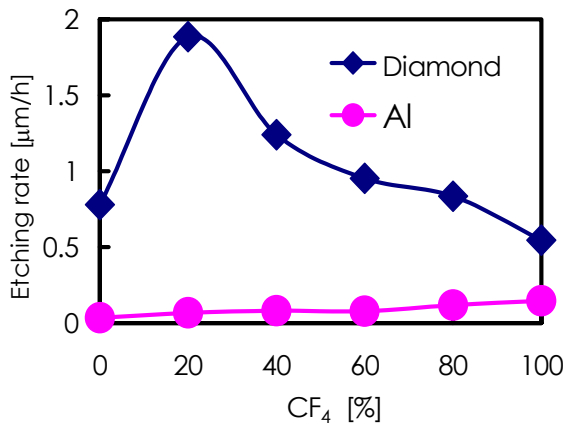


Fig.2. Etching rate as a function of the  $\text{CF}_4$  concentration in  $\text{O}_2/\text{CF}_4$  plasma. The total flow rate, total pressure and RF power are 20sccm, 20Pa and 100W, respectively.

0.5 to 1.9  $\mu\text{m}/\text{h}$  with decreases of the electrode gap from 55 to 15mm. The etching rate of diamond increases with  $\text{CF}_4$  concentration, has a peak around 20%  $\text{CF}_4$  concentrations and then slowly decreases. The etching rate of Al slightly increases with  $\text{CF}_4$  concentration.

Figure 3 shows the etching rate ratios of diamond/Al obtained under the same conditions as in Fig.2. The etching rate of up to 1.9  $\mu\text{m}/\text{h}$  for diamond was obtained at 20%  $\text{CF}_4$  concentration. The etching rate ratios of about 28 for diamond/Al were obtained at the optimal  $\text{CF}_4$  concentration.

Figure 4(a) and (b) are SEM micrographs of etched diamond surface for pure  $\text{O}_2$  and  $\text{O}_2/20\%\text{CF}_4$  plasma, respectively. The diamond surface and sidewall in an  $\text{O}_2/20\%\text{CF}_4$  plasma was smoother as compared with one in an  $\text{O}_2$  plasma. A further addition of  $\text{CF}_4$  led to a smooth etched surface, although the Al mask etched.

Figure 5 shows the dc self-bias voltage as a function of  $\text{CF}_4$  concentration under the same condition as in Fig.2. The dc self-bias voltage slightly decreases and then increased with an increase in the  $\text{CF}_4$  concentration. The dc self-bias voltages were -320V for pure  $\text{O}_2$  plasma, -220V for  $\text{O}_2/50\%\text{CF}_4$  plasma, and -280V for pure  $\text{CF}_4$  plasma.

Figure 6 shows the electron temperature as a function of  $\text{CF}_4$  concentration under the same condition as in Fig.2. In the  $\text{O}_2/\text{CF}_4$  plasma, the deposition of  $\text{CF}_x$  polymer occurs on the probe surface. This makes measurement by conventional probes difficult because the probe I-V characteristic is distorted by the deposited film. The electron

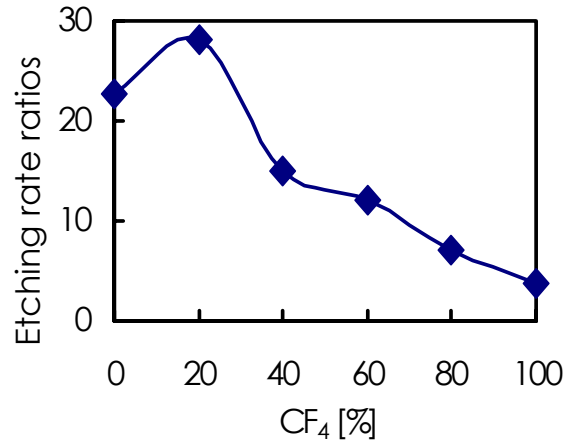


Fig.3. Etching rate ratios as a function of  $\text{CF}_4$  concentration under the same condition as in Fig.2.

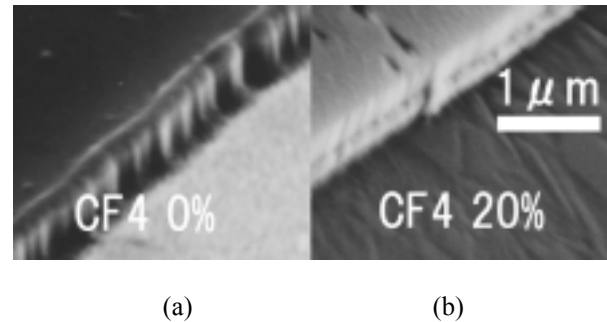


Fig.4. SEM micrographs of diamond etched in (a) pure  $\text{O}_2$  and (b)  $\text{O}_2/20\%\text{CF}_4$  plasma.

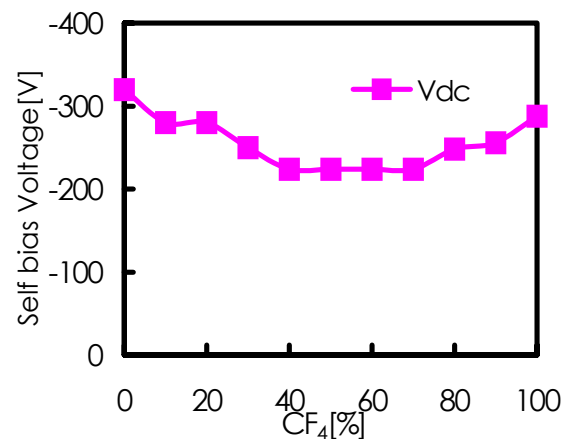


Fig.5. Self bias voltage as a function of  $\text{CF}_4$  concentration under the same condition as in Fig.2.

temperature was measured in the time of 5min, and the probe chip was exchanged to every measurement in order to prevent the film formation. The electron temperature has a maximum at 20%CF<sub>4</sub>, then decreases. The increase of the electron temperature is probably attributed to the increase in electron induced dissociation processes of O<sub>2</sub> and CF<sub>4</sub>.

Figure 7 shows O and F atom densities as a function of CF<sub>4</sub> concentration under the same condition as in Fig.2. The O atom density reaches a maximum at 20% CF<sub>4</sub>, then slowly decreases. The F atom density increases up to 80% CF<sub>4</sub>. Our observed density curve of O is similar to that obtained in the LIF [3]. The increase in O atom density occurs upon addition of 20%CF<sub>4</sub> to pure O<sub>2</sub> plasma. The change in O atom density is probably due to increase of the electron temperature. The addition of CF<sub>4</sub> into O<sub>2</sub> plasma greatly increases the etching rate of diamond. The dc self-bias voltage represents the ion bombardment energy. The measured dc self-bias voltage was not affected by the CF<sub>4</sub> concentration. The increase of the O atom density suggests that O atom plays a dominant role in the carbon removal process by forming CO or CO<sub>2</sub> via physical sputtering by ion bombardment.

The diamond etching rate appears to be controlled by a combination of physical (dc self-bias voltage) and chemical (O and F atom densities) mechanisms.

#### 4. Conclusions

Reactive ion etching of diamond films with O<sub>2</sub>/CF<sub>4</sub> plasma was studied using narrow gap. The maximum etching rate was obtained with O<sub>2</sub>/20%CF<sub>4</sub>. The diamond surface was very smooth by addition of 20%CF<sub>4</sub> in O<sub>2</sub>. The electron temperature and O atom density in O<sub>2</sub>/20%CF<sub>4</sub> plasma were about two times higher than that in pure O<sub>2</sub> plasma. The increase of the O atom density by addition of CF<sub>4</sub> can be one of the reasons for increasing the diamond etching rate.

#### 5. Reference

- [1] H. Shiomi : Jpn. J. Appl. Phys. **36** (1997) 7745.
- [2] J.W.Coburn and M.Chen: J. Appl. Phys. **51**(1980) 3134.
- [3] R. E. Walkup, K. L. Saenger and G. S. Selwyn: J. Chem. Phys. **84** (1986) 2668.

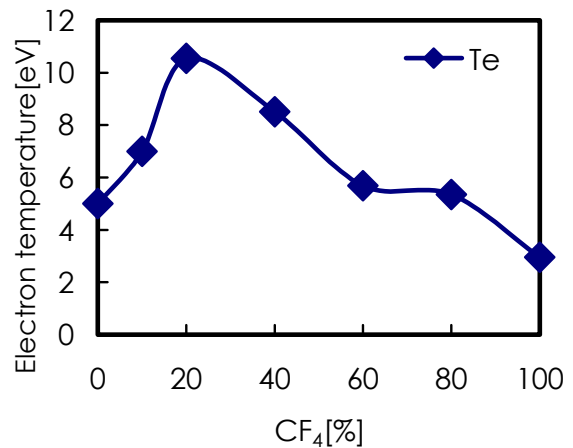


Fig.6. Electron temperature as a function of CF<sub>4</sub> concentration under the same condition as in Fig.2.

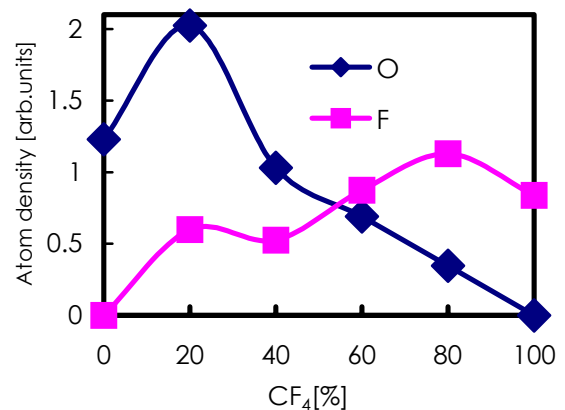


Fig.7. O and F atom densities as a function of CF<sub>4</sub> concentration under the same condition as in Fig.2.

# Polymer surface modification with monofunctional groups of different type and density

J. Friedrich, G. Kühn, R. Mix

Bundesanstalt für Materialforschung und –prüfung (BAM) / Federal Institute for Materials Research and Testing, Unter den Eichen 87, D-12205 Berlin, Germany

## Abstract

The retention of chemical structure and functional groups during the pulsed plasma polymerisation was used for producing adhesion-promoting plasma polymer layers with high concentrations of exclusively one sort of functional groups such as OH, NH<sub>2</sub>, or COOH. The maximum content of functional groups was 31 OH using allyl alcohol, 18 NH<sub>2</sub> using allyl amine, or 24 COOH groups per 100 C atoms using acrylic acid. To vary the density of functional groups a chemical copolymerisation with ethylene as “chain-extending” comonomer or butadiene as “chemical crosslinker” was initiated in the pulsed plasma.

The composition of these copolymers was investigated by XPS and IR spectroscopy. The concentrations of functionalities were measured by attaching fluorine-containing derivatizing reagents and use of XPS. These labelling reactions were audited with reference substances and different markers. A set of plasma parameters was found to be a compromise between a high number of functional groups and complete dissolubility in water, ethanol or THF as needed for further chemical processing. Here, these monotype functionalised surfaces are used in metal-polymer composites as adhesion-promoting interlayers to examine the influence of type and density of functional groups on the adhesion.

## 2. Introduction

The general concept for the plasma polymerization was to approximate the structure of plasma polymers to that of classic polymers as much as possible. Therefore, low power-input to the plasma, substrate and growing plasma polymer layer seem to be necessary because the average energy input per monomer molecule has to be <0.01 eV for a classic (pure chemical) radical polymerization. Thus, the constant energy flux in a continuous wave (cw) plasma is too high. Pulsed plasma with long off time offers an alternative.

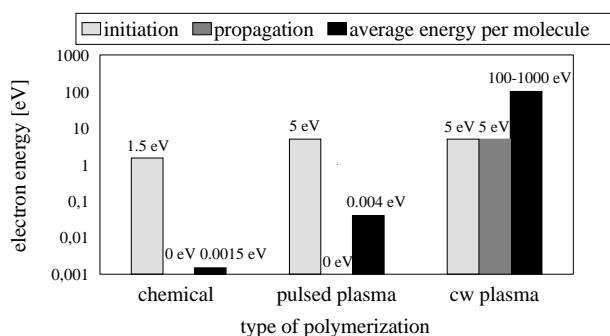


Fig. 1 Comparison of energies needed for the initiation of a radical polymerization and the average kinetic energies available in different modes of low-pressure glow discharge plasmas (pulsed plasma and cw=continuous wave plasma; without consideration of plasma UV, self-bias etc.)

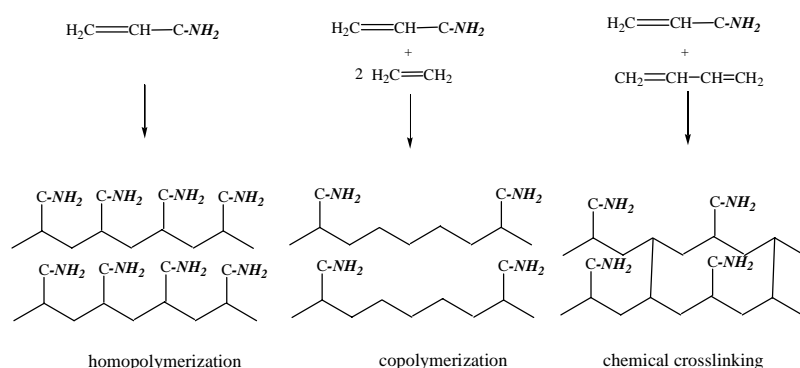
Using chemically reactive monomers, which are qualified to undergo a classic radical chain propagation only one activation incident with  $\approx 1.5$  eV is required to start a chain polymerization with a resulting molar mass of about 100.000 and the respective polymerization degree of  $X \approx 1000$ . Therefore, 0.0015 eV per monomer are needed to initiate and propagate a chemical polymerization. The advantage of a chemically produced polymer compared to a plasmachemically synthesized material is the defined structure, the exact stoichiometry, often the presence of a supermolecular structure (crystallinity), the defined properties and the significantly better ageing stability. Thus, we intend to exclusively initiate such a chemical polymerization through the plasma but the chain propagation should be performed on a pure chemical way. Monomers with active double bonds as vinyl or acrylic groups or moderately qualified allyl groups and dienes are precondition of such a chemical chain propagation. Using non-classic monomers and the cw mode only a non-chemical formation of low-quality polymer layers is possible. Examples for non-qualified monomers are alkanes (hexane), aromatic, cyclic etc. monomers.

In practice, the low pressure and, therefore, the low sticking rate of monomers with a radical site of a growing macromolecular chain limit the propagation. Terminations as radical recombination, chain transfer and disproportionation close the chain length. Therefore, the use of pulsed plasma is necessary to re-initiate the chain propagation. Short plasma pulses (0.01 to 1 ms) activate the monomer molecules and the surface of the growing polymer layer. During the plasma-off period reactive monomer molecules strike the radical sites at the polymer surface, graft and thus forming the growing macromolecular chain. The chain propagation is a pure chemical process. Using typical pulse conditions as 0.1 ms plasma-on and 1 ms plasma-off the very reactive monomer styrene forms polymer during every pulse of thinner than  $<0.1$ -monolayer styrene. Comparing the cw r.f. plasma and the pulsed plasma the yields of formed polymer differ in the ratio 1 : 2000 referenced to the same plasma-on durations. This difference in deposition rates demonstrates evidently the dominant role of the chemical chain propagation using the pulsed plasma. It is obviously that the plasma polymerization in the cw plasma mode can be characterized as a process of only slight preponderance of the deposition in comparison to the simultaneous plasma etching/sputtering of the growing polymer layer.

The structure of polymer sequences formed in the plasma-off period should be corresponding to those of classic polymers. However, the higher number of degrees of freedom for adsorbing molecules in the low-pressure gas phase compared to polymerizations in the liquid phase should hinder all types of supermolecular structure or tacticity. Only amorphous and atactic polymers are anticipated. Nevertheless, also such structures are chemically defined. However, these defined structures and compositions are strongly disturbed by every new plasma pulse due to the UV irradiation and particle bombardment. In addition, no hints for a significant contribution of ion-molecule reactions to the polymer formation were identified analyzing the polymer structure. The monomers used are all qualified for a radical and not for ionic polymerizations in the gas phase.

In 1971, A. R. Westwood found that the plasma polymers possess a chemically better defined structure and composition using low power-input, however, thus produced polymers are also characterized by inclusions of oligomers and monomers within the partially crosslinked polymer matrix [1]. Tibbitt et al. proposed a concrete model of such plasma polymer [2]. Pulsed low-power plasma helps to avoid the excessive monomer fragmentation in the plasma phase and reduces the number of plasma-induced damages in the polymers. This opens the way of enhancing the pure chemical radical polymerization in the gas phase or adsorption layer. Pulsed plasma polymerization was introduced first by Tiller in 1972 [3], later continued by Yasuda [4,5], Shen and Bell [6,7], and then further developed by Timmons [8,9] and our group [10-14].

The copolymerisation in pulsed plasmas was also designed as a plasma-initiated (chemical) radical chain propagation reaction preferentially in the plasma-off period [13,14]. This kind of copolymerisation is strictly different from those introduced by Schöler or Yasuda [15,16]. They simply mixed two gases or monomers without any consideration of their chemical reactivities. Using the cw plasma, which fragments all monomer molecules and allows their random recombination as non-defined plasma polymers, the reactivity of comonomers does not play any role. However, the more the chemical reactions dominate the more important becomes the chemical copolymerisation ability of comonomers. In polymer chemistry this behaviour is expressed in terms of copolymerisation parameters (coefficients)  $r_a$  and  $r_b$  for free radical copolymerizations to linear, branched or crosslinked copolymers [17]. For  $r_1=r_a$  and  $r_1=r_b$  two of five cases are important:  $r_1=1$  both comonomers add to any active centre with equal probability if  $[A]=[B]$  and  $r_1=\infty$  only homopolymerization occurs, no copolymerization. Hence, the pairs of comonomers must be accurately compiled to avoid homopolymerization. An example for a genuine classic copolymerisation is that of styrene and methylmethacrylate



with  $r_s=0.52$  and  $r_m=0.46$ . Vinyl, acrylic, allyl and diene comonomers are generally suited for plasma copolymerization. In Fig. 2 examples of co and homopolymerization as well as chemical crosslinking in the pulsed plasma are shown.

*Fig. 2 Schematics on the formation of functional group carrying homo and copolymers*

## 2. Experimental

Plasma polymerisations were carried out in a vacuum system with a base pressure of  $10^{-3}$  Pa or lower. The principal design of the plasma reactor was described earlier [12]. The r.f. power was varied from 50 to 300 W, the duty cycle from 0.1 to 1 and the pressure was 25 Pa. The samples are kept under floating potential. The XPS data acquisition was performed with a SAGE 150 Spectrometer (Specs, Berlin, Germany) using non-monochromatized  $MgK_{\alpha}$  or  $AlK_{\alpha}$  radiation with 12.5 kV and 250 W settings at a pressure  $\approx 10^{-7}$  Pa in the analysis chamber. This instrument is equipped with a plasma reactor separated by a gate valve from the UHV system, where surface treatments can be carried out at a pressure of  $10^1 - 10^{-7}$  Pa. XPS spectra were acquired in the constant analyser energy (CAE) mode at  $90^\circ$  take-off angle. Peak analysis was performed using the peak fit routine from Specs. The FTIR spectra were recorded with a NEXUS instrument (Nicolet, USA) using the ATR technique (Attenuated Total Reflectance) with a diamond cell ("Golden Gate", Specac, Kent, UK). Contact angle measurements were performed in the sessile drop mode using water, form amide, ethylene glycol, benzyl alcohol and diiodomethane as test liquids. The equipment consists of a G2 goniometer and the appropriate software (Krüss, Hamburg, Germany). The derivatization of OH groups was performed using trifluoroacetic anhydride (TFAA) or m-trifluoromethylphenylisocyanate (TMPI), that of  $NH_2$  by applying pentafluorobenzaldehyde (PFBA) or 4-trifluoromethylbenzaldehyde (TFMBA) and that of COOH by exposure to trifluoroethanol (TFE)[1]. The number of functional groups was calculated by considering the percentage of the introduced fluorine (F1s peak) and the theoretical stoichiometry of the derivatized polymer. It was supposed that the XPS analysed outermost layer ( $\approx 3$  nm) was homogeneously derivatized. The completeness of the derivatization and the absence of non-consumed functional groups in the deposited polymer layer were checked using the ATR-FTIR spectroscopy. Further methods were the C1s peak fitting ( $CF_3$ , COOR) or the measuring of the concentrations of introduced

oxygen (OH, COOH – O1s peak) or introduced nitrogen ( $NH_2$  – N1s peak). The metal evaporation onto plasma polymer modified PP foils was performed *in situ* by using a plasma reactor equipped with two sources for thermal evaporation (Ilm plasma 1200, Saskia, Ilmenau, Germany). This technique was applied for analytical purposes. For measuring the peel strength the samples are transferred to a metallizer equipped with the electron beam technique (Edwards, UK). The peeling technique of metal-PP composites follows DuPont's preparation and peeling procedure. It was described in detail elsewhere [18].

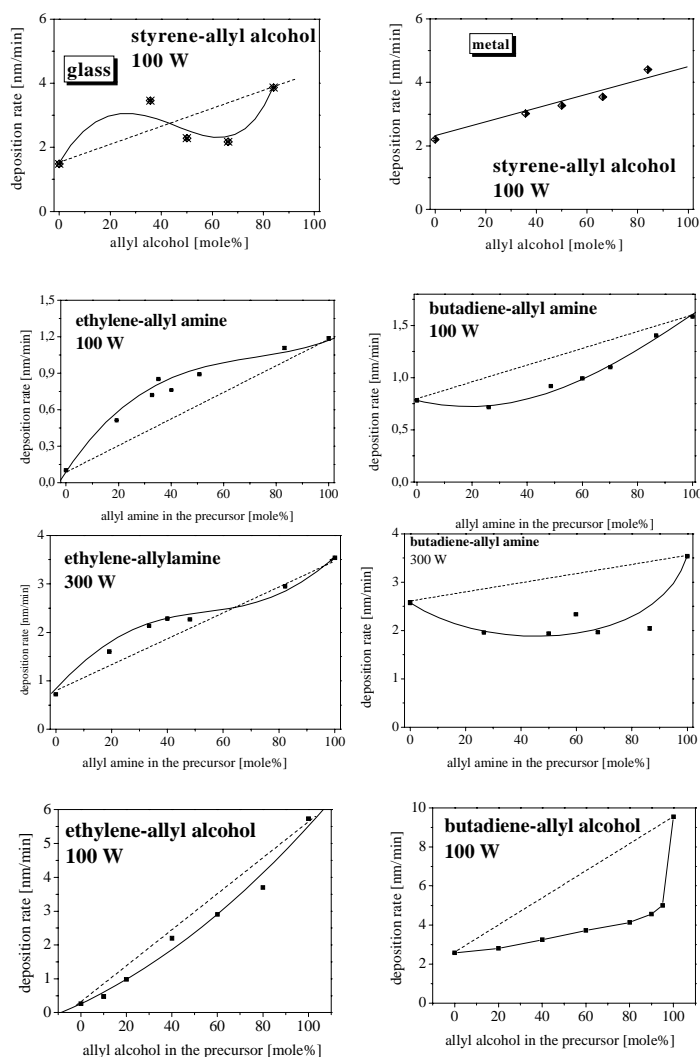


Fig. 3 Deposition rates vs. comonomer ratio on Si, glass or metal

## 3. Results

### 3.1. Kinetics of the deposition of copolymers

In Fig. 3 the deposition of different copolymerized mixtures of allyl alcohol and allyl amine with ethylene, styrene and butadiene are plotted as function of time. The deposition rates of these mixtures are shown to be almost not a linear combination of

those of the comonomers as expected for comonomers with different copolymerisation coefficients.

The curve regressions (non-linearity) are characteristic for chemical copolymerizations. However, they are not completely understood until now. Moreover, the type of substrate and therefore the possibility of dissipation of charges have influence on the deposition characteristics.

### 3.2. Kinetics of the copolymerisation

Ethylene and styrene as linear “chain extenders” and 1,3-butadiene as “chemical crosslinker” were copolymerized with allyl alcohol or allylamine. Thereby the composition of comonomer mixtures was systematically varied. Then the resulting number of OH or NH<sub>2</sub> groups in the copolymers were measured applying the derivatization methods in connection with the XPS and IR spectroscopy as described before. The structure of the copolymers is reflected in the respective C1s-XP spectra as shown for an ethylene-allyl alcohol copolymer (Fig. 4). The spectrum of the copolymer seems to be a linear superposition of the spectra of the homopolymers.

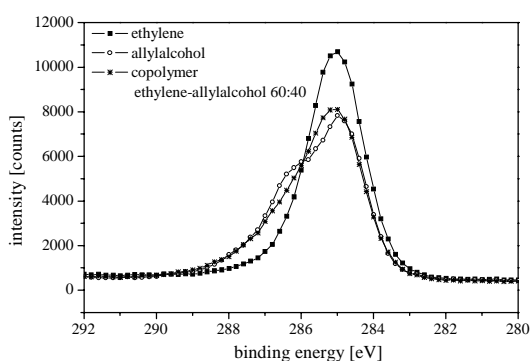


Fig. 4 XPS-C1s peaks of an allyl alcohol and ethylene homopolymer as well as of an allyl alcohol-ethylene copolymer

To determine the extent of retained functional groups the copolymers were derivatized in the same manner as the homopolymers. In Fig. 5 the number of OH groups of an ethylene-allyl alcohol copolymer after derivatization with TFAA is plotted. In the range of 60 to 100 % allyl alcohol in the gas-vapour mixture of ethylene only homopolymerization of allyl alcohol can be observed. From 0 to 60 % copolymerization occurs.

This behaviour can be observed for both the copolymerization at 100 W or 300 W. Using 300 W the maximum yield in OH groups is 23 per 100 C atoms whereas the maximum concentration is near 31 OH groups per 100 C atoms using 100 W. This can be interpreted as leaving the region of soft plasma power responsible for the preferred chemical chain propagation at polymer deposition and passing to the region of plasma parameters characteristic for the preferred fragmentation of monomers and the random recombination of fragments and atoms to irregular polymer structures. Therefore, the chemical structure of copolymers should change from a more chemically defined (100 W) to a more irregular (300 W).

In contrast to the ethylene-allyl alcohol system the copolymerization of butadiene-allyl alcohol is dominant in the full range of allyl alcohol in the gas/vapour comonomer mixture as shown by the (nearly) linear increase in the number of OH groups with growing percentage of allyl alcohol (Fig. 5).

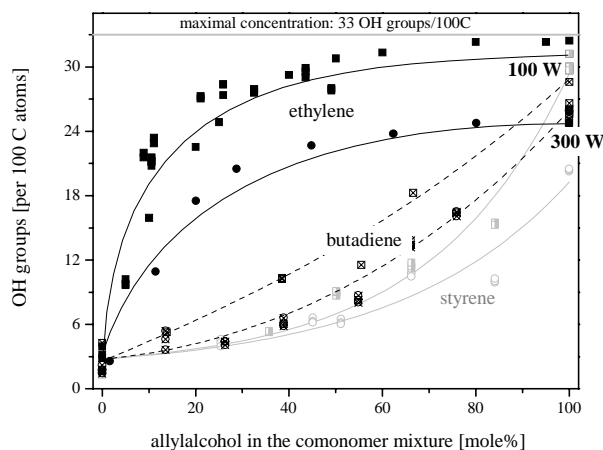


Fig. 5 Yield in OH groups at copolymerisation of allyl alcohol with different comonomers

Homopolymerization seems to be negligible. The difference in the maximum concentration of OH groups using 100 or 300 W is 29 to 23 OH per 100 C atoms. Copolymerization with styrene is dominated by its homopolymerization (0 to 50 mole% allyl alcohol).

The IR spectroscopy of the ethylene-allyl alcohol copolymer confirmed roughly the results of XPS measurements using 100 W power input. It should be mentioned that the recorded ATR signal collect the complete layer (200 nm). With increasing allyl alcohol percentage the  $\nu_{OH}$  intensity grows considerably in the range of 0 to 60 mole% allyl alcohol in the comonomer mixture. In the range of 60 to 100 mole% the absorbance of the  $\nu_{OH}$

signal remains constant. However, using 300 W power input, a linear dependence of the  $\nu_{OH}$  intensity on the chemical composition of the gas/vapour mixture is observed. The  $\nu_{OH}$  signal was referenced to the neighboured  $\nu_{as}CH_2$  vibrations at  $2925\text{ cm}^{-1}$ .

### 3.3. Structure and stability of copolymers

Studies on structure and stability of pulsed plasma polymers were performed using styrene as best qualified (vinyl) monomer. It could be shown using FFF (Field Flow Fractionation) that linear molecules with 20,000 Da molecular weight were synthesized. XPS and NEXAFS result corresponded completely to those of polystyrene standards [11-15]. However, deviations from classic composition and structure were found at the polymer backbone using FTIR spectroscopy. Here, branched structures were identified also using FFF ( $>10^8$  Da). Functional groups carrying homopolymers from allyl and acrylic monomers were completely soluble, thus showing the absence of crosslinked structures. Especially allyl alcohol was easily pulsed plasma polymerised under retention of 95% of all OH groups introduced with the monomer allyl alcohol, e.g. 31 OH groups per 100 C atoms were detected after derivatization with trifluoroacetic anhydride. The OH layers were stable during long-time exposure (1 year) to air. COOH groups introduced by acrylic acid decomposed partially in the pulsed plasma giving a selectivity of about 75%. The resulting layers were stable during storage. Primary amino groups were difficult to derivatize, react at the nitrogen by forming secondary amines and were oxidized at the  $\alpha$ -C atom in an auto-oxidation process resulting in an oxygen uptake up to 17 O per 100 C after 1 month exposure to air. The selectivity amounted 55%. Copolymers show similar properties, however, they were generally insoluble or fractionally soluble. The retention of functional groups was the same as with the homopolymerization. The number of functional groups could be continuously varied between 0 and the maximal number characteristic for the homopolymers.

### 3.4. Relation between functional groups of copolymers and surface energy

The surface energy increased with higher percentage of allyl alcohol in the mixtures with ethylene or butadiene as comonomers. The pure ethylene homopolymer shows a surface energy of  $36\text{ mJ/m}^2$ , which is slightly higher compared to that of conventional polyethylene ( $32\text{ mJ/m}^2$  [20]). However, the polar contribution is also near zero thus demonstrating the absence of polar groups (O functional

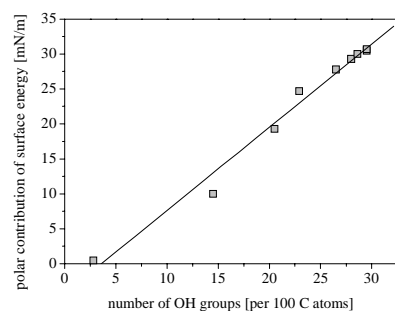


Fig. 6 Correlation of polar contribution vs. concentration of OH groups (allyl alcohol-ethylene copolymer)

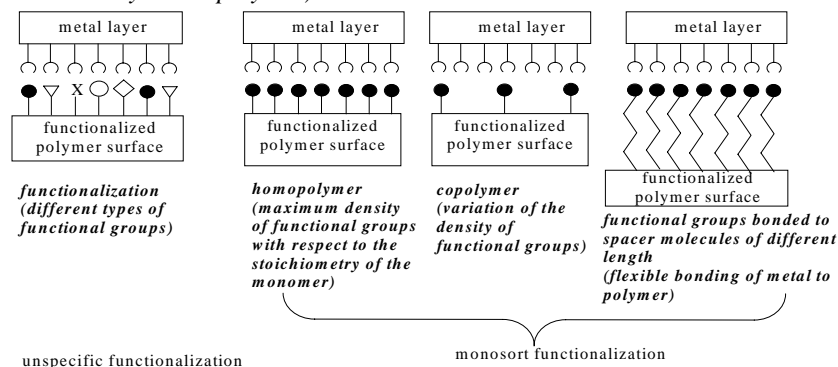


Fig. 7 Specific and unspecific functionalised polymer surface and the scheme of interactions to metal atoms

groups). This absence of the polar contribution in the pure ethylene homopolymer reflects its qualification as pure chain-extending component in the copolymer and the appropriateness of copolymers with ethylene sequences as model surfaces with variable concentrations of exclusively one type of functional group. The dispersive component is slightly increased ( $35\text{ mJ/m}^2$ ) compared to that of polyethylene ( $31\text{ mJ/m}^2$ ). It is argued that some imperfections in the structure of the ethylene homopolymer (C=C double bonds, branched structures and other inhomogeneities) increase the dispersive component. Pulsed plasma polymerized poly(allyl alcohol) homopolymer shows a surface energy of  $50\text{ mJ/m}^2$ . The characteristic shape of the polar component of surface energy

between 0 and 100 mole% allyl alcohol in the comonomer mixture with ethylene is completely coincident to the growing of the number of OH groups (cf. Fig. 6) and OH related IR features.

### 3.5. Relation between functional groups of copolymers and adhesion

Fig. 7 presents the differences between unspecific and specific functionalization

of polymer surfaces for evaluating the contribution of each functional group to the adhesion (interaction) between polymers and metals. Thus, homopolymers with OH, NH<sub>2</sub> and COOH groups are produced and the respective copolymers with ethylene or butadiene applied as adhesion-promoting interlayers in Al-PP composites. Such modified surfaces / interlayers are good models for studying the interaction between metal atoms and monotype functional groups in terms of metal-polymer peel strengths. Therefore, after evaporation of aluminium onto such model surfaces the peel strength of the Al-plasma polymer-PP composites were measured (Fig. 8) and the loci of failure were determined. The interactions between the monotype functional groups and aluminium depends strongly on the type of functional groups:

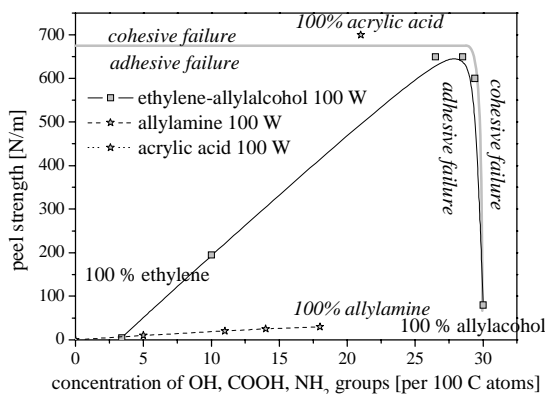


Fig. 8 Peel strength of Al-polymer composites with different types of adhesion-promoting interlayers

mers with increasing content of allyl alcohol (> 90 mole%). Pure allyl alcohol was tacky, completely soluble and shows a low coherent strength resulting in low peel strength and a cohesive failure within the allyl alcohol homopolymer layer. As expected from the chemical point of view, COOH groups showed the highest peel strengths to Al and NH<sub>2</sub> groups the lowest.

## References

- [1] J. Friedrich, W. Unger, G. Kühn, R. Mix, Extended Abstract of 11.NDVak Dresden, L. Blasek (ed.), Dresdner Transferstelle für Vakuumtechnik e.V., 2002, pp. 6-15
- [2] J. M. Tibbitt, M. Shen and A. T. Bell, J. Macromol. Sci., Chem. **A10**, 1623 (1976)
- [3] A. R. Westwood, Europ. Polym. J., **7**, 363 (1971)
- [4] J. Meisel and H.-J. Tiller, Z. Chem., **7**, 275 (1972)
- [5] H. Yasuda and T. Hsu, J. Appl. Polym. Sci., **20**, 1769 (1976)
- [6] H. Yasuda and T. Hsu, J. Polym. Sci., Polym. Chem. Ed., **15**, 81 (1977)
- [7] K. Nakajima, A. T. Bell, M. Shen and M. M. Millard, J. Appl. Polym. Sci., **23**, 2627 (1979).
- [8] J. W. Vinzant, M. Shen and A. T. Bell, ACS Polymer Preprints, **19**, 453 (1978)
- [9] C. R. Savage and R. B. Timmons, Polym. Mater. Sci. Eng., **64**, 95 (1991)
- [10] C. R. Savage, R. B. Timmons and J. W. Lin, Chem. Mater., **3**, 575 (1991)
- [11] G. Kühn, St. Weidner, R. Decker, A. Ghode and J. Friedrich, Surface Coatings Technol., **116-119**, 748 (1999)
- [12] J. Friedrich, I. Retzko, G. Kühn, W. Unger and A. Lippitz, in: *Metallized Plastics 7: Fundamentals and Applied Aspects*, K. L. Mittal (Ed.), pp. 117-142, VSP, Utrecht (2001)
- [13] I. Retzko, J. F. Friedrich, A. Lippitz and W. E. S. Unger, J. Electr. Spectr. Rel. Phenom. **121**, 111 (2001)
- [14] G. Kühn, I. Retzko, A. Lippitz, W. Unger and J. Friedrich, Surface Coatings Technol. **142-144**, 494 (2001)
- [15] H. Schüler and L. Reinebeck, Z. Naturforsch., **6a**, 271 (1951), **7a**, 285 (1952), **9a**, 350 (1954)
- [16] H. Schüler and L. Reinebeck, Z. Naturforsch., **6a**, 271 (1951), **7a**, 285 (1952), **9a**, 350 (1954)
- [17] H. G. Elias, An Introduction to Polymer Science, VCH, Weinheim, 1997
- [18] J. Friedrich, P. Rohrer, W. Saur, Th. Gross, A. Lippitz and W. Unger, Surf. Coatings Technol., **59**, 371 (1993)

## Acknowledgements

This work was financed by VDI-TZ Düsseldorf under grant 13N7776.



# High Velocity Thermal Spraying using 2.45GHz Microwave Plasma

P.Mavromatidis<sup>1</sup>, A. Al-Shamma'a<sup>1</sup>, J.Lucas<sup>1</sup>

<sup>1</sup>*Dept. of Electrical Engineering & Electronics, University of Liverpool, Liverpool*


## Abstract

This paper investigates the use of microwave plasma, at 2.45GHz frequency, to preheat nitrogen gas/coating powders when using a high velocity spray technique. In addition the design and construction of a unique system and its optimisation for automotive industry are presented. The heating process of this novel technique is obtained by the combination of dielectric and microwave plasma heating, as a result the thermal efficiency of the process will be as high as 50% compared with only 5% of the present commercial systems.

## 1. Introduction

The thermal spraying process made its first appearance in the early 20<sup>th</sup> century and for many years on, was used for heavy-duty components, bridges, tank cars and ships [1]. Today's spraying techniques, however, have been widely spread in a variety of industrial applications allowing many problems like corrosion, mechanical strength and durability to be resolved. These methods are mainly flame spraying, wire arc spraying, plasma spraying and HVOF spraying, with the two later dominating the world market. The evolution of emerging technologies has increased the demands of quality and reliable surface engineering creating a considerable academic interest in the research of improving current methods and applying new techniques. Current spraying methods are mainly based on the use of high kinetic energies to bring the particles at high velocities and project them onto the surface to create a bond with the surface, because of their small and fixed size of their heat zone [2,3]. As a result the coatings produced contain a small amount of non-molten particles that reduce the efficiency of the coating bond. Furthermore in order to reach these high velocities most spraying techniques resolve into the use of expensive gases like helium and hydrogen that significantly increase the cost of the spraying process and at the same time result in contamination of the coating by producing oxidised particles. The spraying technique introduced in this research program is a continuous melting spray technique using a different approach on performing the bond between the injected particle and the surface. It uses a long and high thermal interaction path to gradually and uniformly heat the particles above melting temperature and only then use the extra kinetic energy to project them onto the substrate surface creating a weld-bonded coat. This technique is based on the use of a low-pressure electrodeless gas discharge lamp operating at 2.45 GHz microwaves that will allow a controlled exploitation of the emitted temperature. Thus, allowing the use of nitrogen gas as the carrier gas of the powder particles delivering inexpensive and contamination free coatings. Table 1 gives a summary of currently used techniques.

Table 1 Thermal Spraying

Method	Heating Medium	Maximum Velocity (m/s)	Quality	Comment
Flame	Oxygen/Air and acetylene	50		Produces pollutants CO, NO <sub>x</sub> , HC, CO <sub>2</sub> substrate heated
Plasma	Electric Arc N <sub>2</sub> -He or Ar-H <sub>2</sub> gas	200		Low heating efficiency (~1%). Substrate not heated
HVOF	Oxygen with combinations of hydrogen, Propylene, Propane, Kerosene	800		Hydrogen preferred because pollutants CO, HC, CO <sub>2</sub> not produced with this gas. Substrate heated. High impact velocity.
Proposed Microwave Device	Nitrogen gas using microwave heating	1000		High heating efficiency (~50%) Substrate not heated High impact velocity.

## 2. Microwave thermal spraying system

The microwave system used in this project consists of the magnetron driven by a controller and a WG9A waveguide system, which in terms consists of the circulator, the matched load, the stub-tuner and the cavity (figure 1). The magnetron used, generates microwaves at 2.46 GHz and is driven by a high voltage power supply. The circulator is a specially formed waveguide configuration, which allows microwaves to leave through the waveguide towards the applicator, diverting any reflections to the matched load to protect the magnetron. The stub tuner is used to optimise the resonance at the cavity, where the heat source is housed, for maximum power absorption.

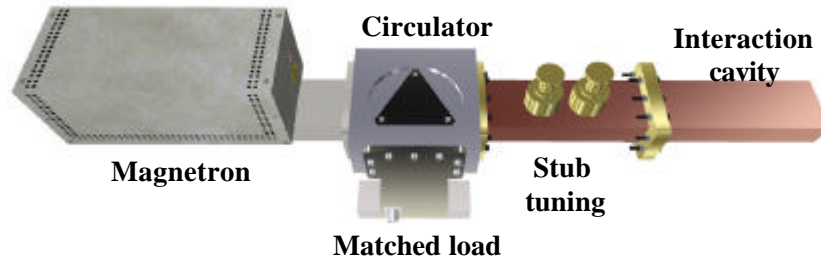


Figure 1: The microwave system

The heat source is that of an electrodeless, low-pressure gas discharge lamp also known as ultra violet (UV) lamp. When the low-pressure gas is disposed to microwaves its atoms are ionised creating a plasma discharge, which evolves heat and light [4]. Unlike commercial UV lamps that use electrodes to propagate power and produce plasma, this lamp is made of dielectric material allowing a dense discharge and exposure to larger powers. A spiral flow configuration surrounding the UV lamp will allow temperature transfer from heat source to the gas powder mixture flow. The advantage of this structure is not only to allow heat transfer but also to provide a long interaction path by keeping the mixture near the heat zone for a longer period of time and at the same time reduces heat losses that will cause the cavity to overheat and reach critical temperatures. Figure 2 depicts the experimental setup of the heat transfer system.

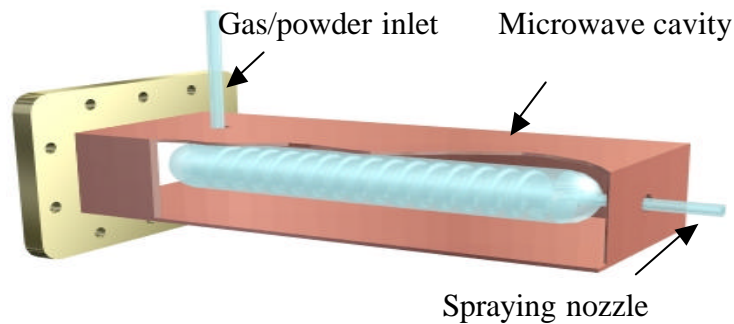


Figure 2: The heat source

## 3. System parameters

There are four parameters that affect the quality and efficiency of the coating during the process of the particles; system power and temperature, the gas flow, the amount of particles and the velocity of the spray. It is therefore necessary to perform a sequence of automated actions that will allow a controlled spraying path to be implemented. The emphasis of constructing a fully automated system, using a microcontroller, is on sensing the physical parameters, interacting all the feedback information, planning the task and programming to give perception of the overall process and to specify a sequence of actions.

In most spraying techniques, the spraying gun is a mobile part that controls the exposure of the surface to the coating process and allows flexibility for a precision coating. The movement of the surface is achieved by a combination of three joints, driven by two 4-phase step motors that form a Cartesian robot system with movement in the two dimensions (x, y axis). Their operation is set to full step drive mode to allow smooth movements and a build in dip-switch configuration determines the dissipating power of the motors

preventing friction and weight to stall the motors at high speeds. Direction and speed are controlled by a microcontroller allowing two modes of operation; off-line through a teach-pendant and on-line through a computer interface build in a Delphi programming environment. Two shaft encoders attached to each motor provide feedback information of speed and direction as well as error warnings on the operation of the motors. The movement of the surface with the amount of particles sprayed will determine the thickness of the coating and the spread of the molten particles on the surface. However, at the same time the movement of the surface in combination with the temperature and the gas flow of the carrier gas will determine the time duration of the actual bonding action between the powder particles and the surface, from the time of impact to the cooling instant. Consequently this will determine the physical structure of the adhesion. The gas flow control system consists of a gas flow controller whose outlet is connected in series with a digital flow meter. The data of the flow meter is fed to the microcontroller and a signal is sent to the flow controller to compensate for any instabilities of the main gas line or to adjust the flow according to the programming specifications of the coating process. The amount of powder sprayed onto the surface is controlled by the gas powder mixer. This consists of a grinded wheel driven by a servomotor. As the wheel rotates it picks up powder and drops it in the flow stream. Hence, by adjusting the speed of the motor, through a variable power supply, the amount of powder mixed with the carrier gas is controlled and therefore the thickness of the coating is determined.



Figure 3: Experimental setup for optical measurements

Finally, the temperature monitoring of the gas outlet is the most vital parameter of the whole process. It will determine whether the necessary condition for melting the powder is reached and will allow the initiation of the spraying process. The use of a thermocouple is impractical since it has to be manually removed before start spraying. However the temperature produced is directly proportional to the light emitted from the UV lamp as it indicates the strength of the plasma discharge and therefore the emitted energy [5]. Therefore, a photo sensor, using a simple photodiode, is used to measure the density of light from which the temperature is determined. It is placed at 30mm above a hole on the cavity, inside which the UV lamp system is placed at a distance, as shown in figure 3, which is calibrated so as to give a voltage corresponding to the actual temperature. Figure 4 shows the direct proportional relation of temperature and intensity versus incident power for both argon gas discharges. A tuning effect can be observed for argon discharge at 200 Watt to enhance the cavity Q factor. Similar observation can be seen for nitrogen discharge with a tuning effect at 220 Watt as shown in figure 5.

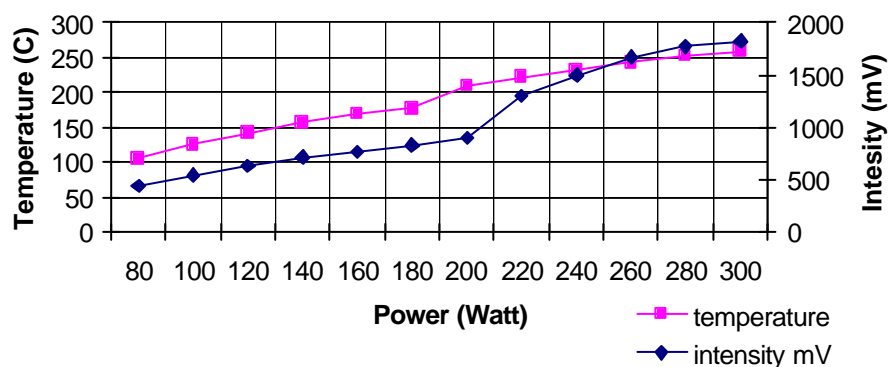


Figure 4: Temperature and intensity of argon discharge

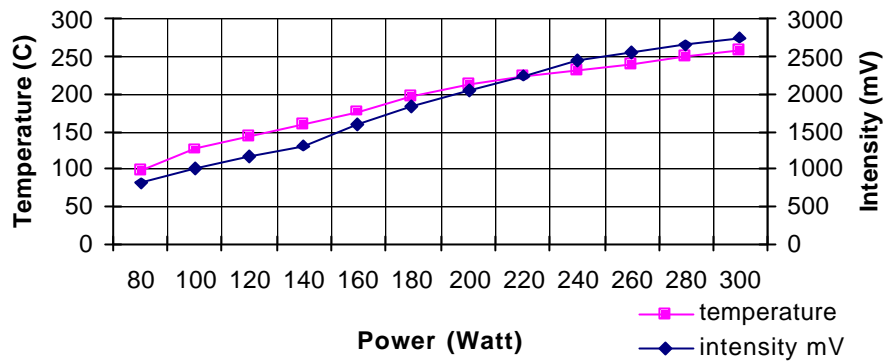


Figure 5: Temperature and intensity of nitrogen discharge

#### 4. Microcontroller Board

The power and the gas flow rate control voltages are each supplied by an 8-bit digital to analogue converter (DAC). In the case of the tuning stub, a digital switch is used to select the 12V, 0V or -12V signals that control the movement of the stub. In order to set the DACs voltage output and read the power feedback voltage via an analogue to digital converter (ADC), an 8-bit microcontroller board [6], shown in figure 6, is used. The board uses an Intel 80C32 CPU with a 12MHz clock that can access 32kB of RAM and 32kB of ROM (EPROM).

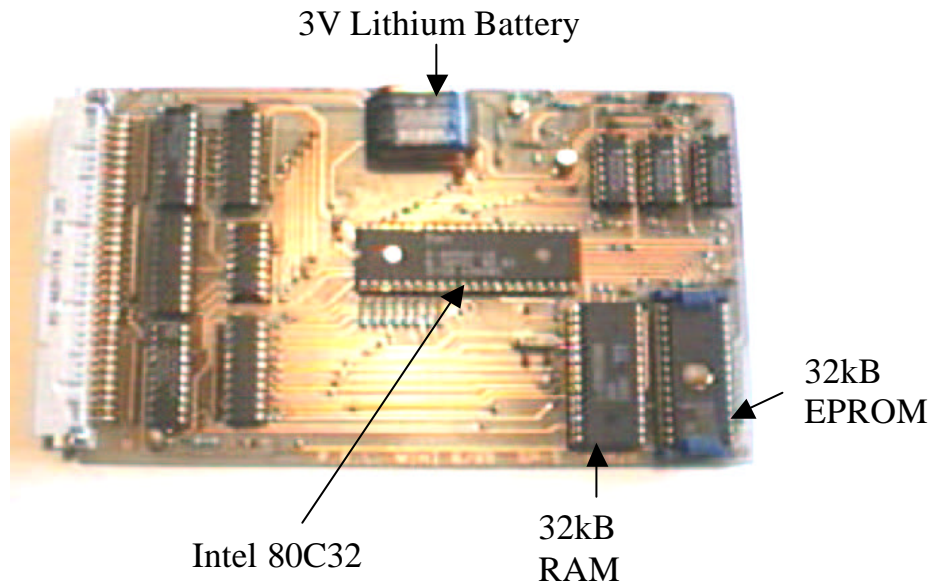


Figure 6: Microcontroller Board

The EPROM was programmed with a BASIC interpreter, downloaded from an Intel 8052. The RAM is battery-backed by a 3V lithium cell that will retain data in the event of a loss of mains derived power. The boards are designed for generic use, with additional circuit boards, connected through common 64-way a+c connectors, used for the DACs, ADC and the accompanying address decoding. The microcontroller board can address up to 256 input and output (I/O) devices (0C00H-0CFFH) and also provides an on-board TTL serial interface. The addition of a MAX 233 IC on one of the I/O boards enables RS-232 communication with a PC via the serial port at up to 19200 baud. This enables programs to be downloaded to the Microcontrollers RAM, and/or the PC to be used as a dumb terminal for setting variables, displaying output values, or for data logging. The complete control topology is shown schematically in figure 7.

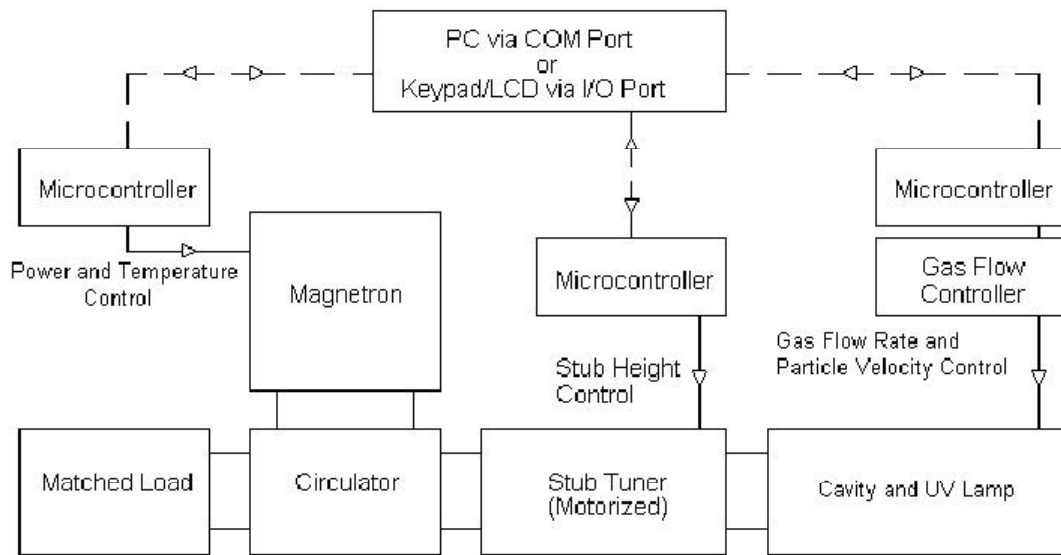


Figure 7: Control Schematic for Microwave Plasma

## 5. Experimental results

The experimental testing always starts with the gradual heating of Nitrogen gas measuring the actual temperature transferred at the gas rather than monitoring the temperature of the heat source like in most thermal spraying methods. A particular test is shown in figure 8 of a nitrogen discharge UV lamp at 0.11mbar pressure. At 20 litres/min the temperature output was monitored for a variation of microwave power.

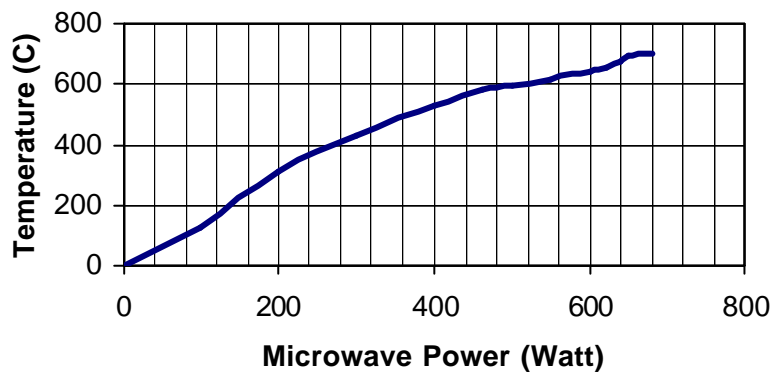


Figure 8: Power against carrier gas temperature

When the temperature of the carrier gas reached 420°C Tin powder was fed in the gas stream by diverting the flow through the gas powder mixer. The spraying nozzle was placed at a distance of 2 cm from a preheated surface. The forming coating is shown in figure 9, which provides an encouraging result and a step forward in the microwave plasma technology as a new source of thermal spraying.

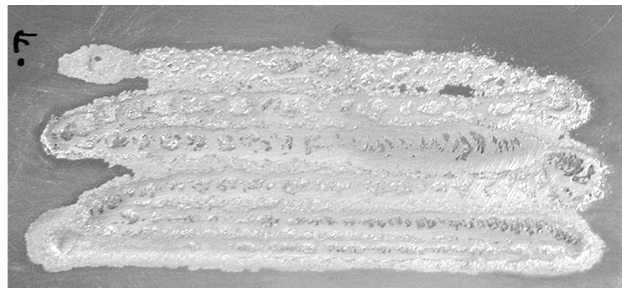


Figure 9: Tin coating on steel surface

## 6. Conclusions

The research so far has shown that the use of industrial microwaves in combination with the use of low-pressure plasma lamps provides the foundation of a new spraying method. This process has the further capability of being combined with high velocity oxygen free spraying technique providing the powder particles with a high kinetic and thermal energy at the same time. This is aimed to yield a highly strengthened bond between surface and projected particles minimizing the effects of oxidation and porosity.

## Acknowledgement

The authors would like to thank the Engineering and Physical Sciences Research Council (EPSRC) and the Department of Trade and Industry for their kind support.

## References

- [1] H. Herman, S. Sampath, and R. McCune, MRS Bulletin, 11, (2000).
- [2] B. Irving, Welding Journal, 42, (2000).
- [3] R. F. Smart and J. A. Catherall, "Plasma spraying", Mills & Boon Limited, (1972).
- [4] P. Mavromatidis, A.I. Al-Shamma'a, J. Lucas, R.A. Stuart, XIV Int. Conf. on Gas Discharges and their Applications, **2**, 28, (2002).
- [5] C. Fitzpatrick, P. Mavromatidis, E. Lewis, J. Lucas, A.I. Al-Shamma'a, J. Sensor Review ournal, **23**, 1, 44, (2003).



# Hybrid Microwave Plasma System for Material Processing

A.I. Al-Shamma'a<sup>1</sup>, S.R. Wylie<sup>1</sup>, J. Lucas<sup>1</sup>

<sup>1</sup>*Department of Electrical Engineering and Electronics, The University of Liverpool, Liverpool, UK*

## Abstract

The most common industrially used system for material processing is the high power lasers generated plasma. Their major disadvantages are the high capital cost and inefficient in terms of energy conversion. The microwave generated plasma torch, unlike the arc torch has no electrode but is based upon the use of a microwave resonance cavity. This paper presents the novel design and construction of a cost effective hybrid system combining the laser and microwave plasma torch systems.

## 1. Introduction

As the technology of material processing such as melting, cutting and welding develops in response to increasing commercial demands, the engineering margins are decreasing. There are several well-established ways of heating a gas to form plasma, including compression, magnetic field, shockwaves and direct heat exchange. Of the many types of discharges, the ones most used for material processing are the constricted arc, the open arc DC or AC and the radio frequency (rf) discharge [1-4]. Extensive research investigations were carried out on further plasma torches such as coaxial waveguide [5-7] and waveguide-based torches [8]. Most of the above torches suffer from a large amount of heat lost through out the waveguide walls, diffusion of plasma, restriction regarding the input energy and not fully automated and flexible for industrial applications. The inductively coupled plasma (ICP) torch is another popular plasma torch, which has been intensively investigated and applied [9,10]. The ICP system can only produce a large volume, low speed “plasma flame” which is not suitable for processes requiring high intensity heat energy, such as cutting and welding. Laser generated plasmas have good material processing characteristics for welding and cutting applications. Their major disadvantage is the high capital cost of the system. The rational behind this project was to research a more economical method of generating plasma for material processing applications.

## 2. Microwave Plasma System

The design of the system was based upon the use of a rectangular microwave waveguide to transport the microwaves and to develop the microwave resonance cavity [11]. The system is illustrated in figure 1.

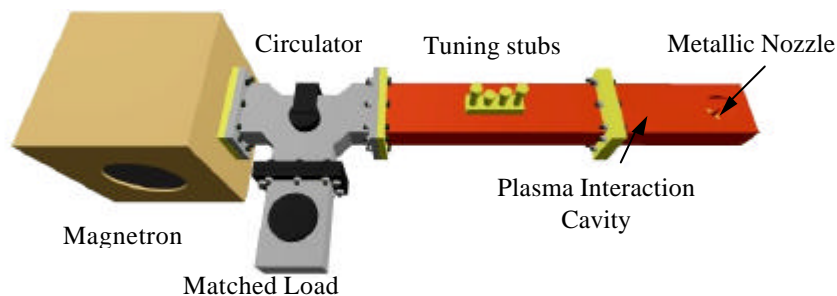


Figure 1: Microwave plasma system

The microwaves are transported by a waveguide from the microwave source via a circulator into a resonant section (cavity) of the waveguide. The cavity is tuned by using a motorised four-stub tuner and any reflected power from the cavity is passed, by the circulator, into the match load. This prevents





### 3. Microwave Plasma Cavity

Electromagnetic can propagate from one place to other through a medium. Changing the configuration and properties of the medium can alter power intensity distribution within the propagating medium. Consequently, it does not require the electrodes for the continuity of electrical current as are essential in DC plasma torches. Therefore, the plasma can be generated anywhere as long as the electromagnetic field intensity is sufficiently high to breakdown the gas and to maintain the discharge. In practice, microwave energy is launched into a resonant cavity and a quartz discharge vessel is placed within the cavity. In practice, it is preferred that the plasma torch is operated at atmospheric pressure with a substantial energy flux, producing a plasma temperature of around several thousands degrees Kelvin. Therefore, it is essential to use a metallic nozzle and a cooling system in order to handle the high temperature plasma. Although electromagnetic field cannot penetrate into the metal tube due to the skin effect, a dense electromagnetic field is induced at the end of cone shaped nozzle. The plasma is produced when a gas breakdown under a sufficiently high voltage. This is also true if the electric field has been produced by an electromagnetic wave. The breakdown of the working gas takes place at the end of nozzle rather than within the nozzle vessel [11,13]. The plasma interactive cavity of 2.45 GHz system consists of a section of waveguide that is terminated by a short circuit copper plate. The gas nozzle sits inside the cavity directly above an aperture in the waveguide, as shown in figure 1, one-quarter wavelength back from the short circuit, where the standing wave produces a maximum electric field. The gas supply could be any of these; compressed air, N<sub>2</sub>, argon, helium with various mixtures fed into the opposite end of the thinner nozzle section. The total length of the microwave plasma system, including the magnetron, is about 0.5m. The electric field distribution was modelled using the Vector Fields “Concerto” package [13-15]. While the plasma gas temperature was modelled using the Phoenix package [16]. Experimental results show that the electron number density in the bright region reaches the value as high as  $2 \times 10^{22} \text{m}^{-3}$  and the electron temperature is also higher than 11,000K.

### 4. Experimental Set-up

Figure 5 shows part of the 2.45GHz system set-up. As can be seen that the inert gas is inserted into the top section of the plasma nozzle and the work piece is moved relative to the plasma jet using the stepper motor driven linear traverse. Figure 6, shows an image of combined schematic diagram of the microwave plasma nozzle and a work piece with a plasma jet under cutting operation. One interesting characteristic of this systems is that the plasma jet appears to be concentric i.e. a focussed beam. However increasing the speed  $>2.5 \text{mm/s}$  lead to a smaller cut width  $<0.6 \text{mm}$  and cleaner top surface but there was still some dross formation on the back surface. For a 0.8mm mild steel sheet, similar quality cuts were achieved with 3 lpm of argon at 3kW and 3.75kW, with speeds of 3.5mm/s and 4.0mm/s respectively.

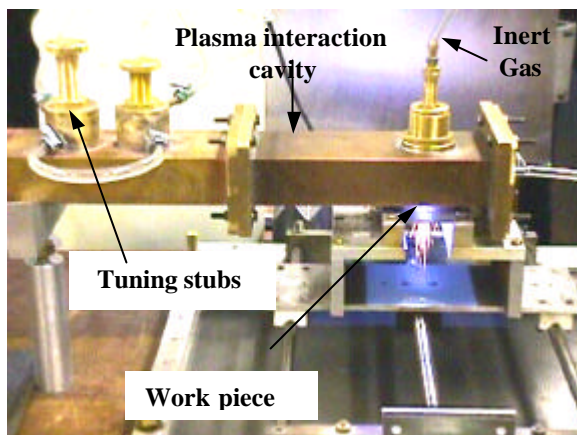


Figure 5: The microwave plasma under operation

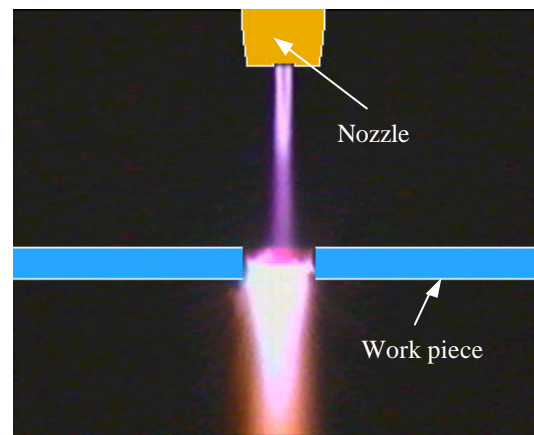


Figure 6: An image processing snap for the microwave plasma jet

## 5. Hybrid System

There is no doubt that lasers can produce a better quality cut due to their highly concentrated energy beams, but the efficiency could be low because of reflection of laser light by the work piece. Laser energy is still expensive at present and the price is approximately 50 to 100 times higher than that of a magnetron (microwave power source) at kW power level. Moreover, the price of lasers increases exponentially with output power. Nowadays, lasers are restricted to precision cutting. Since microwave energy is more affordable, a highly energy intensive plasma beam can be produced by a carefully designed nozzle and a matching microwave system. The cost saving means that the microwave plasma torch is a better choice for material cutting when precision is not critical. In order to maximise the qualities of both systems, a combination of microwave plasma and CO<sub>2</sub> laser systems has been investigated and shown in figures 7a and 7b. The use of the CO<sub>2</sub> laser is mainly due to the availability of the source and any other laser type should be applicable on the same principals. The MP system was easily adapted, due to the simplicity of the nozzle design, so that the focused laser beam could travel straight through the plasma nozzle and on to the work piece. The coupling arrangement of the hybrid system and in operation is shown in figure 8. The advantage of this approach was that the microwave system, which was used to provide the additional heat to the work piece, was always concentrated around the laser spot, regardless of the work piece height.

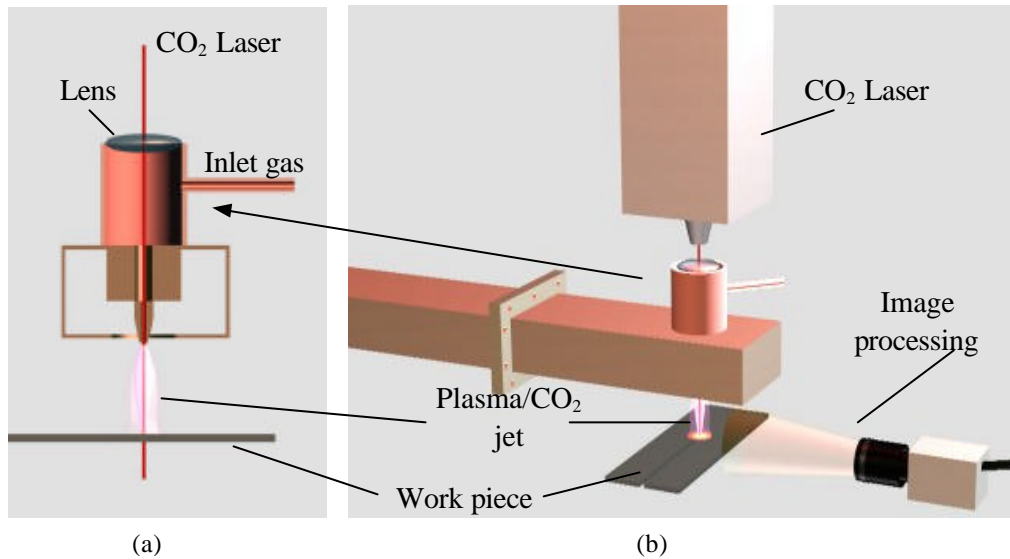


Figure 7: (a) Schematic diagram of the hybrid system (b) Laser beam and microwave plasma arrangement.

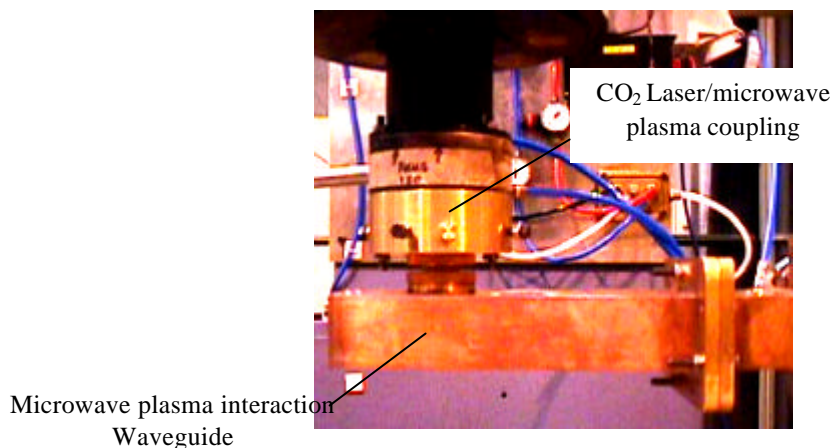


Figure 8: The hybrid CO<sub>2</sub>/MP systems set up

The laser was focused by a zinc selenide lens, which sat at the top of the nozzle section. The gas input was transferred to the side of the nozzle section, below the lens, which was fitted with an O-ring to

prevent gas leaks. Experiments were performed using laser powers ranging from 3kW to 5kW and microwave plasma of 1kW for both cutting and welding with speeds up to 100mm/sec. Figure 9a shows that when the microwave plasma jet of 1kW power is applied onto a 0.8mm mild steel sheet with a welding speed of 5mm/s, it gives a clean cut, which is 2mm wide. When using a 4kW laser and operated at 100m/s the much finer cut is obtained, as illustrated in Figure 9b. In order to obtain a relationship between microwave plasma power and CO<sub>2</sub> laser power a series of comparison experiments were undertaken by using almost penetrative welds. Figure 9c is shown that with 3kW of CO<sub>2</sub> laser power a cut/weld could not be achieved. However, combining the microwave plasma and the CO<sub>2</sub> systems appeared to be very effective where extra cut/weld penetration is achieved as shown in Figure 9d. This figure only shows the effect of combining microwave power and laser energy into a work piece. Various tests have been carried out with different combination of both systems resulting that a 1kW of microwave power could replace 800W of laser power in order to achieve the same laser cut quality in plates of both mild steel and aluminium for velocities up to 100mm/s.

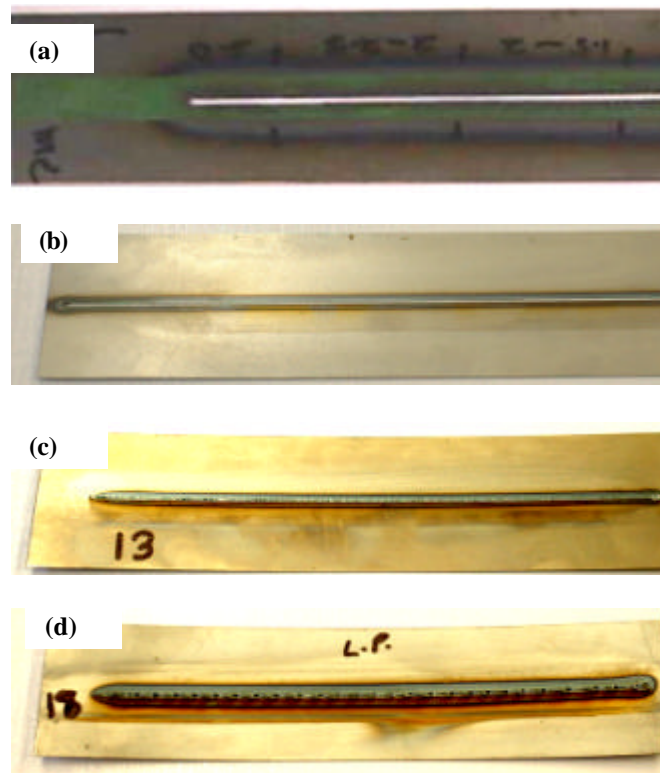


Figure 9: (a) Microwave plasma applied on 0.8mm mild steel at 8mm/sec (b) 4kW CO<sub>2</sub> laser applied on 0.8mm mild steel at 100mm/sec (c) A 3kW CO<sub>2</sub> laser applied on 0.8mm mild steel at 100mm/sec (with slight penetration) (d) 1kW microwave power and 3 kW CO<sub>2</sub> laser applied on 0.8mm mild steel at 100mm/sec (with penetration) but not a pure cut since 1kW plasma < 1kW laser.

## 5. Conclusion

The hybrid system has been successfully used to weld mild steel using various power ratings and up to 3kW for 3mm butt welds as illustrated in figure 10. When used with the activating flux it was found, that for the same microwave power, the welds were narrower but with deeper penetration. To conclude an overall hybrid system of microwave plasma torch and a central laser beam has produced a series of advantages over a conventional laser system for both welding and cutting of steels, see Table 1, as it was able to work with much lower laser powers hence very cost effective.

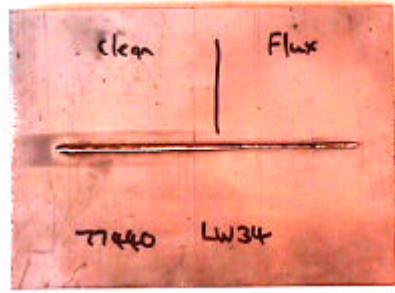


Figure 10: Laser and microwave plasma weld

Table 1: Comparison of Microwave and CO<sub>2</sub> plasmas

Item	Microwave Plasma	CO <sub>2</sub> laser
Cost for 8kW	£2,000 per kW	£30,000 per kW
Size	Compact and portable	Fixed structure
Welding	3mm steel plates	10mm steel plates
Cutting	2mm width in 3mm steel plate	0.25mm width in 3mm steel plate
Surface cleaning	Can be de-focussed to cover large area	Not suitable for large areas, it is too focused
Ceramic Fibre and Sphere Production	Ideal heat source	Too expensive and inefficient
Plasma/Laser Torch	This technique applies the best features of both sources to produce precision cutting and welding at much lower costs	

## Acknowledgement

The authors would like to thank the Engineering and Physical Sciences Research Council (EPSRC), The Welding Institute and Air Product Plc for their kind support.

## References

- [1] J.V.D. Mullen and J. Jonkers, Spectrochimica Acta, **54B**, 1017, (1999).
- [2] M. Huang, J. Microchemical, **53**, 79, (1996).
- [3] X. Chen, J. Phys. D: Appl. Phys., **22**, 361, (1989).
- [4] K. C. Hsu, J. Appl. Phys., **54**, 4359, (1983).
- [5] S. Murayama, J. of Appl. Physics, **39**, 5478, (1968).
- [6] L. Mollwo, Ann. Phys., **97**, (1958).
- [7] Y. Arata, S. Miyake, S. Takeuchi and A. Kobayashi, Transactions of JWRI, **4**, 31, (1975).
- [8] M. Moisan and J. Zakrzewski, J. Phys. D: Appl. Phys., **24**, 1025, (1991).
- [9] M.X. Ishii et al, Spectrochimica Acta, **49B**, 1111, (1994).
- [10] H.U. Eckert and D.C. Pridmore-Brown, J Appl. Phys., **42**, 5051, (1971).
- [11] A.I. Al-Shamma'a, S. Wylie and J. Lucas, J. Phys D: Appl. Phys. **34**, 2734, (2001).
- [12] S. Wylie, A.I. Al-Shamma'a, A. Shaw, J. Lucas, Proc., 8<sup>th</sup> International Conference on Computer Technology in Welding, Liverpool, UK, (1998).
- [13] C.F. Pau, J.D. Yan and S.R. Wylie, Int. Conf. on Phenomena in Ionised Gases (ICPG), Warsaw, (1999).
- [14] A.I. Al-Shamma'a, S.R. Wylie, J. Lucas, Proceedings of the XIV Int. Conf. on Gas Discharges and Their Applications, **2**, 24, (2002).
- [15] <http://www.vectorfield.co.uk>.
- [16] C.F. Pau, J.D. Yan, S. Wylie, OPTIM Conf., Romania, (2000).



# Theoretical Modeling and Experimental Results of 2.45 GHz Low Pressure Microwave UV Lamp

I. Pandithas<sup>1</sup>, J.J. Lowke<sup>2</sup>, M. Kong<sup>1</sup>, A.I. Al-Shamma'a<sup>1</sup>, J. Lucas<sup>1</sup>

<sup>1</sup>The University of Liverpool, Department of Electrical Engineering and Electronics, Liverpool, U.K.

<sup>2</sup>CSIRO, Division of Telecommunications and Industrial Physics, Sydney, Australia.

## Abstract

The microwave plasma ultraviolet (UV) lamp technology has no limitations in terms of power and shape of the lamp in contrast with the electrode configuration in which the power is constrained lengthwise. The microwave UV lamp is able to produce UV light at 254nm, the germicidal region, and 185nm, the Ozone forming region, simultaneously. This paper gives predictions that have been made of discharge properties; various aspects of the system apparatus and experimental results will be presented.

## 1. Introduction

The most common form of UV lamp technology is based upon an electrode discharge within a noble low-pressure gas. There is currently increasing interest in the development of new discharge lamps for the production of ultraviolet (UV)/Ozone radiation for sterilization purposes. It is desired to have improved sterilization methods for food, to obtain longer shelf life, and also for the removal of bacteria from water. UV radiation is a form of energy, which can be absorbed by and can bring about structural changes of systems [1]. The exposure of microbiological systems to UV radiation, within the wavelength range defined by figure 1, can dissociate the DNA, which are vital to metabolic and reproductive functions and thus inactivating the microorganisms. The very common fluorescent lamp tubes are basically an ultra violet light source producing a mercury line of 254 nm, which interacts with a phosphor coating the edge of the tubular fluorescent lamp to produce visible light. These discharge lamps without the fluorescent coating have been used for many years in the past as a source of ultra violet radiation for the sterilization of bacteria, for example in butcher shops. This common discharge lamp is basically a glow discharge in argon, with a small amount of mercury vapor. It is the mercury vapor, which produces the UV radiation. It is known that the common fluorescent lamp also produces strong radiation of 185 nm. Photons of this wavelength will be more energetic than those of 254 nm and may be more effective for sterilization. Furthermore the 185 nm photons have sufficient energy to dissociate oxygen molecules, which then react with normal oxygen to produce ozone.

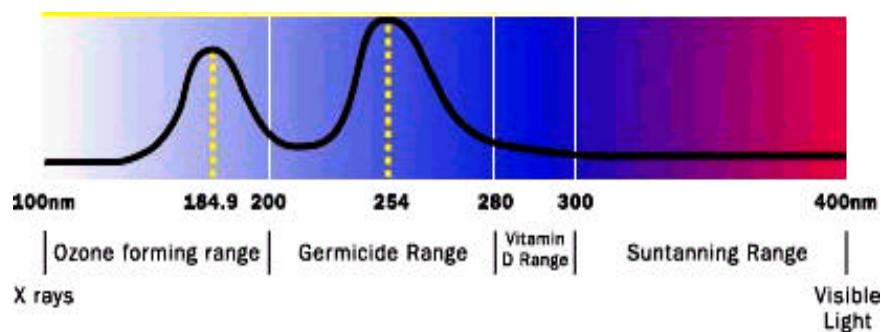


Figure 1: UV Radiation Spectrum

There are other exciting possibilities. The commercial popularity of microwave ovens has led to the development of inexpensive microwave power supplies. Experimental and theoretical investigations at the University of Liverpool [2-4] have been directed towards understanding gas discharges sustained by microwave excitation. The demand for microwave-generated plasma is increasing for many industrial applications as a high power source [5-8]. Microwave energy easily passes through the dielectric tube and so unlike the conventional lamps, they do not require electrodes which are not only a weakness for the longevity of conventional lamps but most importantly limit the amount of power per unit length that the lamp can produce which is in the order of 30W per unit meter. In a further development, recent

developments in gas lasers in inert gases have utilized radiation from excimer molecules. Excimer molecules are molecules in the discharge, which have an excited state but no stable ground state. Thus radiation from such excimers is not re-absorbed by the gas, as ground state molecules are not stable. It is such self-absorption that imposes the limitation of the total output power that is possible with a conventional mercury-argon discharge as occurs in a fluorescent lamp [9].

## 2. Germicidal Considerations of UV

### Germicidal Kinetics

The survival ( $S$ ) of microorganisms [1,10] when exposed to either UV or ozone is represented by two rates of decay [11] as shown in equations 1 and 2. This relationship is illustrated in figure 2.

$$S = C \exp^{(-KD)} \text{ for } D < D_o \quad (1)$$

$$S = C \exp^{(-mD)} \text{ for } D > D_o \quad (2)$$

The dosage  $D$  is the product of the UV or ozone intensity and duration ( $t$ ) of exposure. There is an initial rapid rate of kill ( $k$ ) to a level  $(1-C)$  and this is followed by a much slower kill rate ( $m$ ). The value of  $C$  is of the order of  $10^{-3}$ . Figure 3 shows a comparison of the dosages ( $D_o$ ) required for UV, ozone and chlorine required to achieve a 99.9% kill level when compared with the dosage for the Escherichia Coli (Ecoli) in water. They show comparative responses with a range of microorganisms. The most likely explanation for the tailing off of the survival curves is the clumping effect suggested by various investigators—the tendency of micron-sized particles to clump together naturally. The clumping of bacteria cells protect a small percentage of bacteria and causes them to behave as if they had much higher resistance to both UV and ozone.

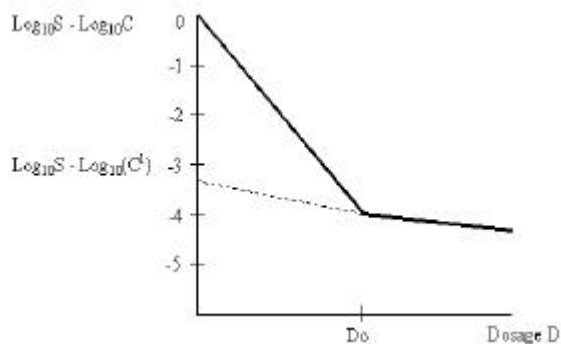


Figure 2: Fraction of Living Microorganisms ( $S$ )

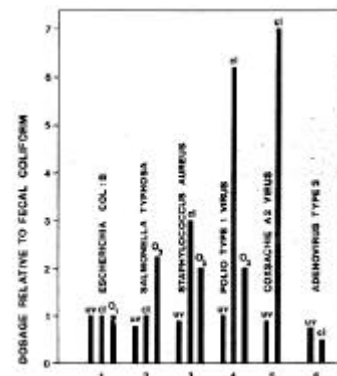


Figure 3: Mortalities of Bacteria and Pathogens in Serilisation of water

## 3. Microwave Lamp

Microwaves are high frequency electromagnetic waves, generated by magnetrons, which can be stored in a resonance cavity made of metal or dielectric material [12]. The principle is illustrated in figure 4 in which microwaves are launched into the lamp via a coupled metal cavity resonator [3,4]. The electric field ( $E$ ) ionizes the mercury vapour in the lamp to produce the UV emission. The microwave frequency is 2.45GHz and is the same as that used in a microwave oven. This allows low cost magnetrons to be used [8]. The lamps differ significantly from conventional UV lamps because they have no warm up time, do not deteriorate with age, have adaptable shapes and can be used in pulsed mode. There is also the ability of producing ozone and UV from the same lamp to produce a synergistic effect. Because the microwaves produce a transverse electric field compared with the longitudinal electric field of the conventional lamp, the microwave lamp is able to emit UV of an order of magnitude higher in intensity, e.g. at least 250W/m. Figure 5, shows the microwave UV lamp system set-up for bacteria killing experiments. The lamp has been positioned horizontally based up on the testing requirements. One end of the lamp is energised by the microwave power and the other end has a computer controlled stepping motor for lamp shutter in order to control the UV exposure time against various types of bacteria. The bacteria kill rate for the  $S$

aureus microorganism is given in figure 6 and shows the killing actions of ozone and UV/ozone jointly producing 4 log performance [Keith brown].

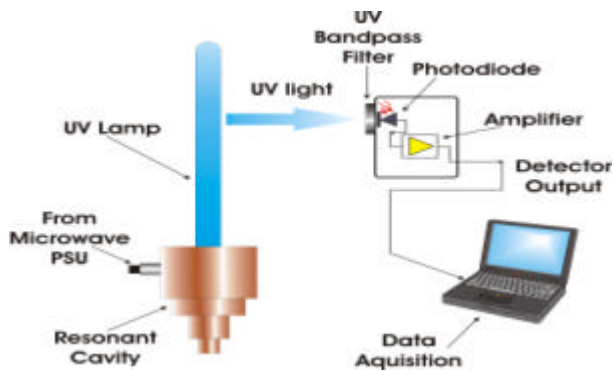


Figure 4: The Microwave UV Lamp

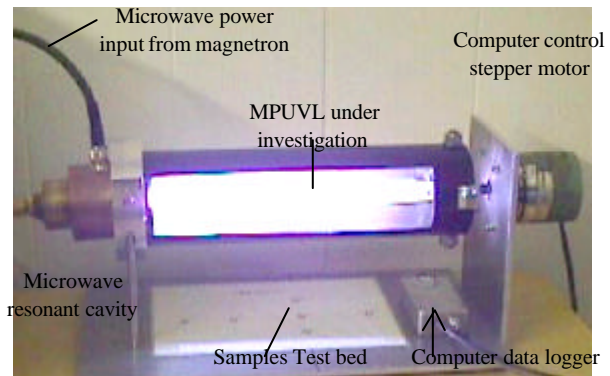


Figure 5: Microwave plasma UV lamp (MPUVL) under operation

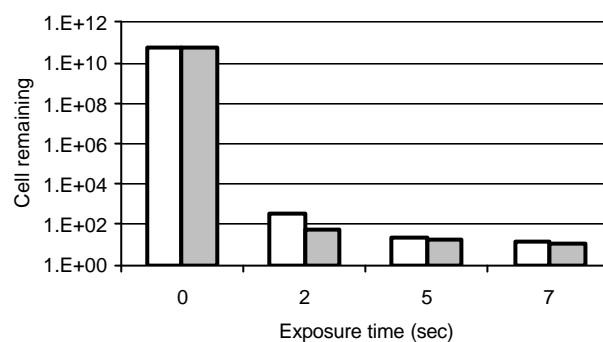


Figure 6: Repeated tests of Ecoil remaining cells under microwave UV lamp

#### 4. Prediction of Discharge Properties

Over the recent few decades, careful experiments of transport coefficients and also excitation cross sections at high energy using beam experiments, has made it possible to obtain complete sets of cross sections for the common gases. These cross sections range from very low energies of a few hundredths of a volt, appropriate to thermal energies at room temperature, to energies up to 100 V, which amply covers the range of laboratory plasma and discharge lamps. Of course there are dozens of different modes of excitation to the many high electronic states. In practice, only the first 5 or 6 levels are given explicitly. All remaining higher levels are lumped together to effectively represent their effect in a single cross section. We now have reasonably complete cross sections for gases such as argon, mercury, xenon, helium and neon, and also for molecular gases such as hydrogen, nitrogen, carbon dioxide and water vapor. Examples of such cross sections are given in figure 7 for argon and figure 8 for mercury.

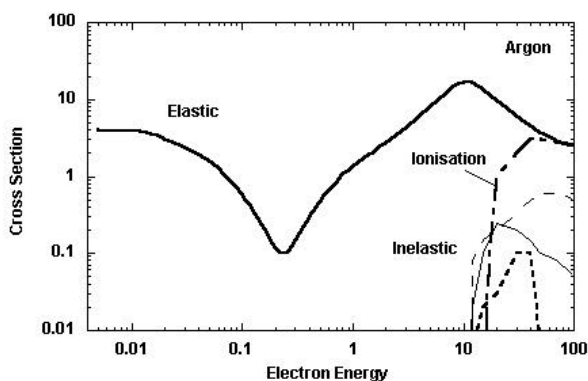


Figure 7: Argon elastic and inelastic cross sections

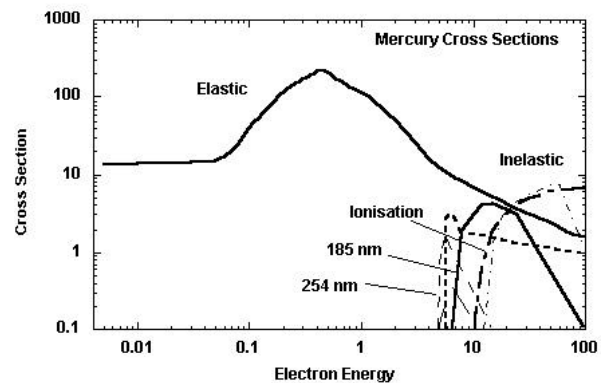


Figure 8: Elastic and Inelastic Cross Sections for Mercury

Each set of cross sections consists of the “momentum transfer” cross section, sometimes referred to as the “elastic” cross section, extending to zero energy. Above a threshold energy, which is of the order of 12 volts for argon and 5 volts for mercury, there are the various “inelastic” cross sections of each gas, corresponding to the various electronic excitation processes when electrons colliding with the atom, excite electrons from the outer orbits of these atoms to an excited state. The momentum transfer cross section is referred to as being “elastic”, because electrons lose only a fraction of about  $2m/M$  of their energy in collisions with the atom;  $m$  is the electron mass and  $M$  the heavy particle mass. The average electron energy in discharge lamps is a few electron volts. It is noticed from figure 7 and figure 8 that the momentum transfer cross-section for both argon and mercury varies by more than a factor of ten at low energies. In the “inelastic” collisions, however, they lose of the order of 12 or 5 volts or more, respectively for argon or mercury, because of the energy necessary to excite the electrons to an outer shell. A very important inelastic cross section is the cross section for ionisation, where the incident electron has sufficient energy to eject an electron from the atom with which it collides. The momentum transfer cross sections for argon at low energy were taken from the theoretical values of Petrovic et al [13] and the experimental values of Milloy et al [14], which are in agreement. The inelastic cross sections for argon are taken from Fiala et al [15]. A more complete listing of argon inelastic cross sections is given by Zecca [16]. The momentum transfers cross section for mercury was taken from England and Elford [17]. Inelastic cross sections of mercury were given by Boeuf and Sakai [18]. The cross sections of gases such as those shown in figure 7 and 8 were derived from properties of pure gases. It is now possible to use these cross-sections to derive properties of gas discharges for any value of  $E/N$ , including properties for any specified mixture of gases for which direct experiments have not been made;  $E$  is the electric field and  $N$  is the total gas number density. In particular it is possible to derive the proportion of electric power going into any particular excitation process to produce any particular wavelength of radiation. It is thus possible to derive the value of  $E/N$  for optimum efficiency of a given process.

## 5. The Boltzmann Transport Equation

The relative efficiency of the various excitation processes was obtained through a numerical solution of the Boltzmann transport equation to obtain the electron energy distribution function. The Boltzmann transport equation equates the gain in energy of electrons from the electric field with losses of energy of electrons through electron collisions with the gas molecules. Thus

$$\nabla_v \cdot (aF) = \text{Collision terms}; \quad (3)$$

the term  $\nabla_v = \mathbf{i}_x \partial/\partial v_x + \mathbf{i}_y \partial/\partial v_y + \mathbf{i}_z \partial/\partial v_z$  represents divergence with respect to velocity space with the terms  $\mathbf{i}_x$  being unit vectors;  $a$  is the acceleration of electrons due to the electric field  $E$ ,  $a = Ee/m$  where  $e$  is electronic charge and  $m$  is the mass of the electron;  $F = F(v_x, v_y, v_z)$  is the electron distribution function as a function of velocity versus equation (3) is analogous to the conventional continuity equation  $\nabla \cdot (vn) = \text{Source terms}$  in ordinary space where  $v$  is the velocity of flow,  $n$  is the particle density and  $\nabla$  is the divergence in space. The Boltzmann equation (3) has been the subject of much study [19]. Electrons in equilibrium with the electric field have an average drift velocity  $W$  in the direction of the electric field, but this velocity is only of the order of 1% of the average electron speed. A plot of contours of  $F$  for constant speed would give approximately spheres only slightly displaced from the origin in the direction of the field because, on average, there are almost as many electrons of a given speed traveling backwards, due to collisions, as there are traveling forwards. Equation (3), which is in 3 dimensions in velocity space, is simplified (a) by expressing it in terms of electron energy,  $\epsilon$ , rather than velocity  $v$ , (b) representing  $F(v) = f(\epsilon) + f_1(\epsilon)\cos\theta$ , where  $\theta$  is the angle of  $v$  with the electric field and (c) integrating the equation over all angles, thus eliminating  $\theta$ , and then obtaining a second equation by multiplying the equation by  $\cos\theta$  and again integrating all angles. Then  $f_1(\epsilon)$  is eliminated from these two equations to obtain a final equation just in  $f(\epsilon)$ , which is the following Boltzmann transport equation for electrons in gases [20].

$$\begin{aligned} & \frac{E^2}{3} \frac{d}{d\epsilon} \left( \frac{e}{NQ_m} \frac{df}{d\epsilon} \right) + \frac{2m}{M} \frac{d}{d\epsilon} (e^2 NQ_m) + \frac{2mkT}{Me} \frac{d}{d\epsilon} \left( e^2 NQ_m \frac{df}{d\epsilon} \right) \\ & + \sum_j (e + e_j) f(e + e_j) NQ_j(e + e_j) - e f(e) N \sum_j Q_j(e) = 0; \end{aligned} \quad (4)$$



$k$  is Boltzmann's constant and  $Q_m(\epsilon)$  the momentum transfer cross-section. The term in  $E^2$  in equation (4) accounts for the increase in the electron energy due to the electric field. The *Collision terms* of equation (3) are complex, there being different terms for the different collision processes. The second term of equation (4), with a factor  $2m/M$ , accounts for energy losses due to elastic collisions, as the fraction of energy loss of an electron of mass  $m$  with a heavy particle of mass  $M$  is, on average,  $2m/M$ . The third term, involving  $kT/e$ , accounts for the small gain in electron energy from collisions with the heavy particles due to the finite temperature  $T$ . This term ensures that for zero electric field, the solution of the Boltzmann equation gives a distribution function  $f$  having the classical Boltzmann distribution  $f \sim \exp(-\epsilon/kT)$ . The last terms involve a summation over each inelastic process, which will involve each inelastic collision cross section  $Q_i(\epsilon)$ . For an electronic excitation of energy  $\epsilon_j$ , the distribution function  $f$  for energy  $\epsilon$  is increased from electrons of energy  $\epsilon + \epsilon_j$  losing energy  $\epsilon_j$  in the inelastic collision. But, the distribution function  $f$  for energy  $\epsilon$  is reduced by other electrons losing energy  $\epsilon_j$  in the inelastic collision. Collisions involving gains of electron energy due to the de-excitation of atoms from the excitation processes  $Q_j$  have been omitted as they are negligible for the high excitation thresholds relative to thermal energies. The Boltzmann equation can be solved numerically to obtain the electron distribution function,  $f(\epsilon)$ , using the method and computer code developed by [20]. Once this distribution function is obtained, through the evaluation of various integrals involving the distribution function, the various transport coefficients can be obtained, and, in addition, the fractions of the electric power that are expended in the excitation of each electronic level. It is equation (4) that has been used by many previous workers to determine the cross sections at low energies from measurements of the drift velocity and diffusion coefficient for all common gases.

## 6. Results for mixtures of Mercury and Argon

The most common mercury-argon discharge is that of the ordinary fluorescent lamp. In this discharge a small amount of liquid mercury is added to a few Torr of argon. The percentage of mercury in argon then depends upon the temperature of the discharge tube, which determines the vapor pressure of the mercury in the gas mixture. At 20 °C, 40 °C and 60 °C the vapor pressures of mercury are respectively 0.0012, 0.006, 0.025 Torr. Calculations have been made as a function of  $E/N$  for

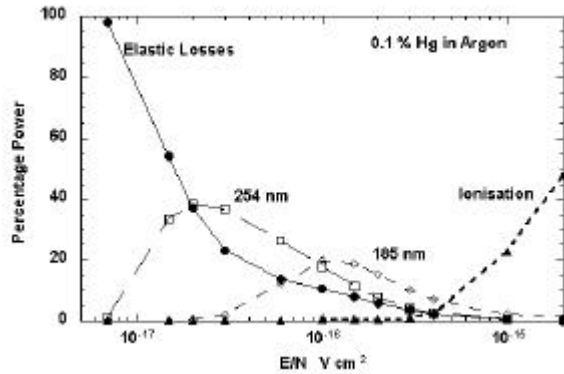


Figure 9: UV excitation of mercury lines of 254 nm and 185 nm as a function of  $E/N$  for 0.1% and 0.7 % of mercury vapor in argon.

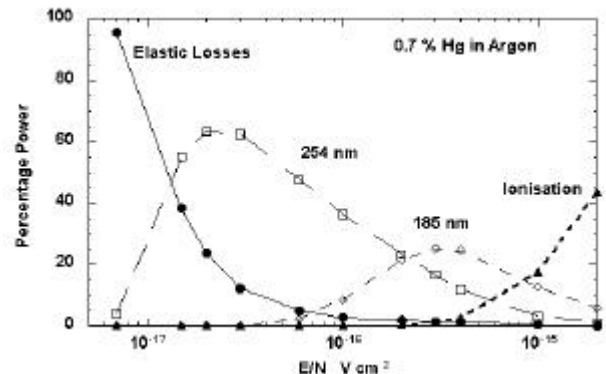


Figure 10: UV excitation of mercury lines of 254 nm and 185 nm as a function of  $E/N$  for 0.7 % of mercury vapor in argon.

Figures 9 and 10 show the calculated percentages of the input electric power expended in exciting the 254 nm radiations and 185 nm radiation, as a function of  $E/N$ . At 1 Torr and 20 C,  $N = 3.3 \times 10^{16}/\text{cc}$ . At values of  $E/N$  less than  $10^{-17} \text{ V cm}^2$ , electron energies are insufficient to excite the inelastic levels and almost all energy is lost in “elastic” collisions. At  $E/N$  values above  $10^{-15} \text{ V cm}^2$ , most energy is expended in the excitation of visible radiation and ionization. The excitation of 254 nm radiations takes place for lower  $E/N$  values than for 185 nm radiation, because of the lower threshold voltage required to excite the radiation for this radiation. The energy level diagrams for the transitions of the mercury atoms giving this radiation are given by [21]. As the percentage of mercury in the gas mixture is increased, the proportion of mercury radiation increases, because there are more mercury atoms radiating. However, as the percentage of mercury increases, there is an additional effect, not accounted for in the present

calculations, of absorption of emitted radiation from the center of the discharge by ground state mercury atoms in the outer region of the discharge. The calculated percentage efficiency for the generation of 254 nm radiations is up to 80%, but this figure will be reduced by the self-absorption effects.

## 7. Conclusion

There are several industrial applications for this type of plasma driven light source especially in the water, wastewater and food industry where it is necessary to kill life-threatening bacteria. In previous sections predictions have been made of the relative production of 254 and 185 nm radiations in mercury-argon discharges. But in evaluating the utility of this radiation, consideration must be given to the following loss processes: (a) Losses within the discharge due to the self-absorption of radiation. For the mercury-argon discharges producing 254 nm and 185 nm radiation, the absorption of these resonance lines by ground state mercury atoms is the limiting factor for the output of UV radiation from the lamp; Koedam et al [22]. (b) Losses within the confining quartz tube of the discharge. Conventional quartz tubing is reasonably transparent to 254 nm radiations. But for 185 nm radiation it is necessary to use special quartz, ultrasil or suprasil to avoid significant absorption of the radiation.

## Acknowledgement

The author would like to thank the Department for Environment, Food & Rural Affairs (DEFRA) with connections to the Engineering and Physical Sciences Research Council (EPSRC) for their support.

## References

- [1] L.R. Koller, Ultraviolet Radiation, 2<sup>nd</sup> Ed, John Wiley and Sons, (1965).
- [2] J. Lucas, Int. Patent W089/09068, (1996). J. Lucas, A.I. Al-Shamma'a, Patent P 407725GB, (2002).
- [3] A.I. Al-Shamma'a, I. Pandithas, J. Lucas, J. Phys D: Appl. Phys., 34, 14, 2775, (2001).
- [4] I. Pandithas, A.I. Al-Shamma'a, J.D. Cullen, J. Lucas, Proc. of the XIV Int. Conf. on Gas Discharges and Their Applications, 2, 124, (2002).
- [5] M Moisan and Z Zakrzewski, Plasma Sources Science & Technology, 4, 3, 379, (1995).
- [6] J.P.J. Van Dalen, P.A. De Lezenne Coulander, L. De Galan, Spect. Acta, 33a, 545, (1977).
- [7] V. Ibberson, New Scientist, 26, 103, (1984).
- [8] A. Kraszewski, Microwave gas discharge devices, Iliffe Books Ltd., second edition, (1967).
- [9] J.J Lowke and J.H. Parker, Phys Rev, 181, 302, (1969).
- [10] B.G. Oliver and J.H. Corey, J. Water Poll. Control Fed, 48, 11, 2618, (1976).
- [11] A. Wekhof, PDA J. of Pharmaceutical Science and Technology, 54, 3, 264, (2000).
- [12] F.A. Wilson, An Introduction to Microwaves, Bernard Babani (publishing) LTD, (1992).
- [13] Z.L. Petrovic, T.F. O'Malley, R.W. Crompton, J Phys B28, 3309, (1995).
- [14] H.B. Milloy, R.W. Crompton, J.A. Rees, A.G. Robertson, Aust J Phys., 30, 61, (1997).
- [15] A. Fiala, L.C. Pitchford, J.P. Boeuf, Phys Rev E, 49, 5607, (1994).
- [16] A. Zecca, G.P. Karwasz, R.S. Brusa, La Rivista del Nuovo Cimento, 19, 1, (1996).
- [17] J. England, M.T. Elford, Aust. J. Phys., 44, 647, (1991).
- [18] Y. Sakai, S. Sawada, H. Tagashira, J. Phys. D, 22, 276, (1989).
- [19] W.P. Allis, Handbuch der Physik, 21, 1956.
- [20] L.S. Frost, A.V. Phelps, Phys. Rev., 127, 1621, (1962).
- [21] J.F. Waymouth, Electric Discharge Lamps, MIT Press, (1971).
- [22] M. Koedam, A.A. Kruitthof, J. Riemens, Physica, 29, 565, (1963).

# **NANOMECHANICAL AND DECORATIVE PROPERTIES OF NANOCOMPOSITE SUPERHARD FILMS DEPOSITED BY PLASMA**

P. Jedrzejowski, L. Martinu , and J.E. Klemberg-Sapieha

*Engineering Physics Department, Ecole Polytechnique, Montreal, Canada*

There is a continuing need for new hard and superhard ( $H > 40$  GPa) materials for applications ranging from protective coatings in aerospace and automobile industries to MEMS.

Nanocomposite hard coatings fabricated by PECVD from  $\text{TiCl}_4/\text{SiH}_4/\text{N}_2/\text{H}_2/\text{Ar}$  gas mixtures offer unique properties such as superhardness, high toughness, and high thermal stability. The tribological and mechanical characteristics like wear resistance, hardness, Young's modulus, and adhesion were determined by a triboindenter and a nanoscratch tester. Film microstructure was studied by XRD, SEM, ERD-TOF, XPS, and AFM. Optical properties such as color, refractive index and extinction coefficient were evaluated using combined spectrophotometry and spectroscopic ellipsometry.

# **Quality of sputtered aluminum and plasmapolymerized corrosion resistant layers in an large scale coating machine for the production of car reflectors**

K.Nauenburg<sup>\*</sup>, G. Deppisch and W. Dicken

*<sup>\*</sup>Leybold Optics GmbH, Siemensstr.88, D-63755 Alzenau, Germany*

The Interpole-Target (IPT) sputter cathode is a powerful tool to metalize plastic parts in very short times with highly reflecting metal layers, mostly aluminum for head light reflectors. We intergated this tool into an one-chamber coater were up to five plasma processes – sputtering, mid-frequency plasma pretreatment and several steps of polymerization – are subsequently performed on a rotating vertical substrate holder to obtain full layer stacks for modern automotive reflectors within a few minutes.

Measurements and estimations of heat generation, done for the up-scaling of the IPT cathode are reported. Reflectivity, adhesion and humidity resistance of the layers are shown to be equal as obtained in short cycle coaters. Also ESCA-Analysis data, the distribution of layer thicknesses all over the reflectors and the pylon and the rates for aluminum and plasmapolymer deposition are reported.

# Plasma Treatments of Cellulose Fibers with Styrene for Composite Materials

J. Morales-Corona<sup>1</sup>, G. J. Cruz<sup>2</sup>, G. Olayo<sup>2</sup>, P. Herrera-Franco<sup>3</sup>, R. Olayo<sup>1</sup>

<sup>1</sup>*Departamento de Física, UAM, Apartado Postal 55-534, Iztapalapa, México, D.F.*

<sup>2</sup>*Departamento de Síntesis y Caracterización, ININ, Apdo. Postal 18-1027, Col. Escandón, México, D.F.*

<sup>3</sup>*Departamento de Polímeros, CICY, Apartado Postal 86; 97310, Cordemex, Yucatán, México.*

Mixtures of natural fibers and thermoplastics are studied with great interest because they offer the opportunity to enhance the properties of some natural fibers, and in this way, they can be useful in a wide number of applications. One of the problems involved in these composites is the chemical bonds between the fibers and the polymers at the interface. Superficial modification of fibers is used to improve the fiber-thermoplastic coupling interface to get stronger composites. Among other techniques, processing with glow discharges at low-pressure for superficial modification of different materials such as metals, natural fibers, ceramics and other materials is being studied to enhance the chemical bonds between those materials and polymers. The properties that can be modified by plasma are wettability, adhesion, superficial energy, etc.

In this work, cellulose henequen fibers were treated with styrene-plasma in order to increase the interfacial adhesion in polystyrene-fiber composites. The superficial treatment of the fibers was carried out in a tubular glass reactor with stainless steel electrodes. The cellulose fibers were located between the electrodes. The average temperature inside the reactor was around 90 °C. The electric discharges were applied with a capacitive coupling mechanism at 18 W, 13.56 MHz and  $5 \times 10^{-2}$  Torr. Two kinds of treatments were applied to the fibers, one with continuous and the other with pulsed glow discharges. The continuous treatment was applied with reaction times of 2, 4 and 6 min. For the pulsed treatment, the discharges were applied for 30 s and then the fibers were exposed 10 min with a styrene atmosphere without plasma. The cycles were repeated for 2, 4 and 6 min of discharges. Samples with 60 min of treatment were also done with this method. After the discharges ended, all the samples were kept in a styrene atmosphere for 2 hours to allow the reaction of the free radicals in the surface. Films of plasma polymerized styrene were obtained from the same reactions and analyzed by Fourier Transform Infrared spectroscopy (FTIR) and Thermo Gravimetric Analysis (TGA). Micro mechanical analysis was also done to the fibers to study the Young Modulus (YM), extension at rupture and peeling tension.

## **Plasma deposited graded index optical filters**

S. Larouche, R. Vernhes, A. Amassian, O. Zabeida, J.E. Klemberg-Sapieha, and L. Martinu

*Engineering Physics Department, Ecole Polytechnique, Montreal, Quebec, Canada*

Optical filters based on graded-index design possess unique characteristics which are impossible to obtain with traditional multilayer filters. This particularly includes the elimination of harmonics and sidelobes. They also offer better mechanical performance and wear resistance. Plasma-enhanced chemical vapor deposition (PECVD) is a very attractive technique to fabricate such graded-index filters since it allows one to control the refractive index,  $n$ , at every moment of the filter deposition by varying the concentration of precursors in the gas phase and the energy of bombarding ions.

In the present work, two PECVD approaches were applied to control the refractive index depth profile  $n(z)$  (@ 550 nm): a) continuous variation of the film composition in SiO<sub>2</sub>/TiO<sub>2</sub> mixtures with  $n$  ranging from 1.50 to 2.35, and b) continuous variation of film packing density (porosity) in a single material (SiN<sub>x</sub>) with  $n$  ranging from 1.60 to 2.00. We fabricated different graded index systems, including single- and multi-band rugate filters. Their performance and possible applications will be discussed. We also compare their characteristics with the properties of their multilayer counterparts. It will be shown that the graded-index filters possess additional advantages such as better tribological performance and lower light scattering. In addition, we demonstrate the use of in-situ spectroscopic ellipsometry as a very promising technique for real-time process control and monitoring.

# Sources of Non-equilibrium in Plasma Materials Processing

Mark J. Kushner

*University of Illinois, Dept. of Electrical and Computer Engineering, 1406 W. Green St., Urbana, IL 61801, USA*

Plasma materials processing occurs over a wide range of pressures and time scales, using a variety of geometry and plasma excitation mechanisms. In many cases, the fundamental plasma production mechanisms are inherently non-equilibrium, such as in low pressure inductively coupled plasmas (ICP) and high pressure dielectric barrier discharges (DBD). In other examples, chemical non-equilibrium may dominate, due to there being insufficient collisions or residence time for the system to come to equilibrium. The dynamics of these non-equilibrium processes are often necessary to obtain the final materials properties or have been empirically optimized through design-of-experiments to achieve a desired end product.

In this presentation, examples of non-equilibrium in plasma materials processing will be drawn from low pressure (e.g., ICP etching of dielectrics) and high pressure (e.g., DBD processing of polymers) systems. Results from multidimensional computer models of these systems will be used to illustrate how non-equilibrium dynamics have been leveraged, either deliberately or fortuitously, to optimize desired material processing characteristics. For example, in low pressure ICP systems, non-equilibrium in electron transport results primarily from the anomalous nature of the electromagnetic skin depth. The end result is the generation of spatial, time and angular harmonics in the electron energy distribution which, when optimized, dissociate feedstock gases through desirable channels. A source of chemical non-equilibrium is the evolving surface reactivity of walls whose sticking coefficients may change during a single etch process.

Non-equilibrium in high pressure DBDs largely results from the spatial dynamics of their propagating streamers and their non-uniform generation of radicals. More subtle sources of non-equilibrium occurs in the interaction of these streamers with surfaces. For example, in the corona or DBD processing of polymers, spatial inhomogeneity of functionalization of surface groups results from both the surface morphology and delivery of reactants to the surface.

This work was supported by the National Science Foundation, 3M Corporation and the Semiconductor Research Corporation. The author acknowledges contributions from. A. Sankaran, P. Subramonium, R. Dorai, A. Vasenkov, A. Bhoj and K. Rajaraman.

# Plasma Diagnostics by Electric Field Measurement

U. Czarnetzki

*Institute for Plasma and Atomic Physics, Ruhr-University Bochum, 44780 Bochum, Germany*

Electric fields play a vital role in gas discharges or plasmas in general. Electric power is coupled to the electrons and waves are driven via the field, the diffusion of electrons and ions is related to the ambipolar field, within the sheath in front of surfaces ions are accelerated to high energies and secondary electrons gain much higher energies than the majority of the bulk electrons, and last not least the random distribution of charges is the origin of stochastically distributed micro-fields. These fields are directed related to number of important parameters like e.g. voltages, currents, electron and ion densities and energy distributions.

Although it is obvious that measurement of these fields can provide a direct insight into the physics of discharges, it turns out to be experimentally a rather tricky business. Electrical diagnostic techniques are available for the induced electric field in inductively coupled plasmas by so-called B-dot-probes and the ambipolar field can be deduced from Langmuir probe measurements. In recent years a number of emission and laser spectroscopic techniques have been developed that allow the non-intrusive measurement of fields in plasmas [1-6].

Most laser spectroscopic techniques are based on the Stark effect on Rydberg states in atoms or molecules. Therefore, neutral particles in the plasma serve as probes that can be read out locally with high temporal resolution by the laser light. The mixing of states can lead to the appearance of 'forbidden' lines, especially in molecules, but in many cases the broadening and shift of lines is observed directly. Diatomic molecules, atomic hydrogen, and noble gases have been investigated as sensitive media for this kind of diagnostics so far. Nevertheless, there are number of over potential candidates like nitrogen, oxygen or chlorine. Present schemes allow a spatial resolution below 100  $\mu\text{m}$ , a temporal resolution of a few ns and a field sensitivity below 10 V/cm.

The concepts for analysing measured electric field distributions are essentially independent of the particular spectroscopic scheme but depend very much of the origin of the fields. Electric fields in low pressure discharges might be distinguished by six categories: 1) fields in the high voltage sheath free of electrons, 2) fields in the Debye sheath where the electron density is comparable but not identical to the ion density, 3) drift fields, 4) ambipolar fields, 5) microwave fields (or wave fields in general), 6) microfields in the quasi-neutral bulk of the plasma. Examples for the measurement and further analysis of these fields will be given with the exception of ambipolar fields that are beyond the sensitivity of present spectroscopic techniques.

It is the intention of this paper is to give an overview of the laser spectroscopic techniques available, the present range of applicability (gas, pressure, sensitivity, resolution), and, especially, to show the potential for plasma diagnostics. Particular emphasis will be on the further (scheme independent) analysis of the measured fields in order to infer plasma parameters and the combination with other diagnostics like ion energy analysers or Langmuir probes.

- [1] J.E. Lawler and D.A. Doughty, *Advances in Atomic, Molecular, and Optical Physics* 34, 171 (1994)
- [2] O.A. Evsin, E.B. Kupryanova, V.A. Ochkin, S.Yu. Savinov, and S.N. Tskhai, *Quant. Electr.* 25, 278 (1995)
- [3] Czarnetzki, D. Luggenhölscher, and H.F. Döbele, *Phys. Rev. Lett.* 81 (21). 4592 (1998)
- [4] V.P. Gavrilenko, H.J. Kim, T. Ikutake, et al., *Phys. Rev. E* 62, 7201 (2000)
- [5] K. Takizawa, K. Sasaki, and K. Kadota, *Jpn. J. Appl. Phys.* 41, L1285 (2002)
- [6] T.J. Jiang, M.D. Bowden, B. Visser, and G.M.W. Kroesen, *Proceedings Frontiers in Low Temperature Plasma Diagnostics V*, Villaggio Cardigliano, Italy (2003)



# **Diagnostics for advanced materials processing by plasma spraying**

C. Moreau, R. Lima And B. Marple

*National Research Council Canada, Boucherville (Quebec), Canada*

Advanced coatings deposited by plasma spraying are used in a large variety of industrial applications. The sprayed coatings are employed typically in the industry to protect parts from severe operating conditions or to produce surface with specific function. Efficient coatings are used typically to provide protection against degradation by high temperature, corrosion, abrasion and erosion. Applications are found in many industrial sectors such as aerospace, automobile, energy generation and biomedical implants.

Coatings are built by the successive deposition of molten or partially molten particles that flatten and solidify upon contact on the substrate forming lamellae. The coating properties are intimately linked to the properties of these lamellae, which in turn depend on in-flight particle properties before impact as well as the substrate temperature during spraying. Consequently, the development of diagnostic tools for monitoring and controlling these spray parameters provide the necessary information to study the coating formation process, optimize the coating properties and, eventually, control the spray process in production.

In this paper, a review of some recent developments of optical diagnostic techniques applied to measure in-flight particle temperature and velocity as well as monitor particle impact on a substrate are presented. First, time-resolved particle diagnostics is used to study the instabilities in particle parameters associated with plasma fluctuations due the cyclic movement of the arc root at the anode surface. It is shown that the particle instabilities affect the coating structure and deposition efficiency. Secondly, the influence of substrate temperature during spraying on the flattening and solidification of individual particles impacting on flat substrates is studied. It is found that the splat shape at impact depends strongly on the substrate temperature. Flattening ratio as high as 8 is observed on substrate at room temperature. In this case, the splat, after reaching its maximum extent, contracts rapidly due to the surface tension while it breaks into many secondary droplets or fingers. Finally, practical considerations related to the optimization and control of plasma spray process are discussed. To do so, examples of optimized properties of nanostructured coatings obtained under controlled in-flight particle conditions are given.

# Control of deposition profile of Cu for LSI interconnects by plasma chemical vapor deposition

Masaharu Shiratani, Kazunori Koga, and Yukio Watanabe

*Department of Electronics, Kyushu University, Japan*

Control of deposition profile in trenches and holes becomes important for fabrication of nanostructures such as ULSI interconnects, quantum dots and wires, and micro-electrochemical systems. Recently, using plasma chemical vapor deposition (CVD), we have realized not only subconformal and conformal deposition profiles but also anisotropic one, depositing material at the bottom of a trench while depositing nothing on the sidewalls as shown in Fig. 1. Subconformal deposition easily leads to a key hole in a narrow trench of a high aspect ratio. Conformal filling in such a trench results in a small crystal grain size below half of the trench width and in a seam where impurities of high concentration remain, although it is useful for formation of thin layer on all the surface of a trench. The anisotropic deposition profile has potentials to overcome the issues for the subconformal and conformal deposition profiles. Here, we focus on Cu deposition in trenches for ULSI interconnect application [1-4]. Our anisotropic deposition using plasma CVD has two additional attractive features. One is a self-limiting deposition by which deposition stops automatically just after filling completely a trench. The other is a fact that deposition rate increases with decreasing the width of a trench. We will also mention control of film properties such as purity, grain size, surface roughness, as well as adhesion strength using H atom irradiation during Cu film growth.

- [1] H. J. Jin, M. Shiratani, Y. Nakatake, T. Fukuzawa, T. Kinoshita, Y. Watanabe, and M. Toyofuku, Jpn. J. Appl. Phys. **38**, 4492 (1999).
- [2] H. J. Jin, M. Shiratani, T. Kawasaki, T. Fukuzawa, T. Kinoshita, Y. Watanabe, H. Kawasaki, and M. Toyofuku, J. Vac. Sci. Technol. **A 17**, 726 (1999).
- [3] M. Shiratani, H. J. Jin, K. Takenaka, K. Koga, T. Kinoshita, and Y. Watanabe, Sci. and Technol. of Adv. Mater. **2**, 505 (2002).
- [4] K. Takenaka, M. Shiratani, M. Onishi, M. Takeshita, T. Kinoshita, K. Koga, and Y. Watanabe, Matr. Sci. Semiconductor Processing **5**, 301 (2003) .

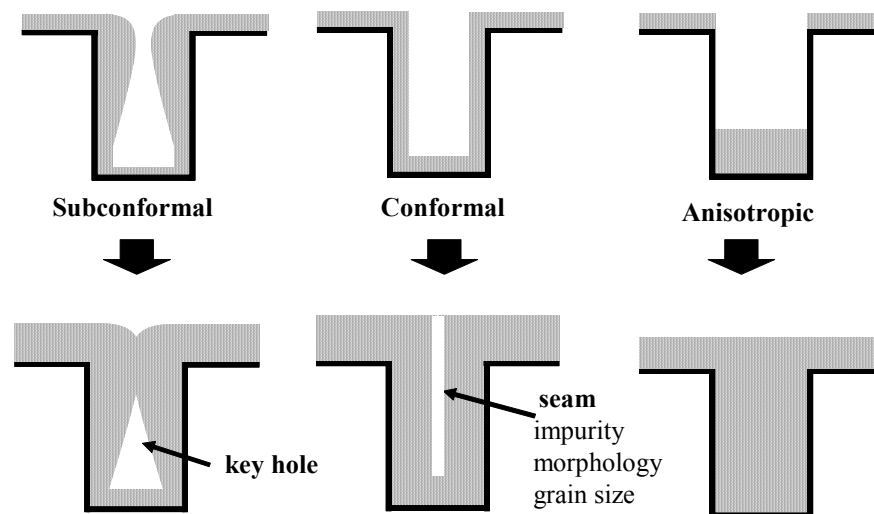


Fig. 1 Deposition profiles in a trench realized by plasma CVD.

## Plasmas and Polymers : from APGD to PECVD

M.R. Wertheimer, G. Dennler, and S. Guimond

*Groupe des Couches Minces and Department of Engineering Physics,  
Ecole Polytechnique, Montreal, Quebec H3C 3A7, Canada*

It is well known, even to non-specialists, that plasma has become an enabling technology in the production of advanced integrated circuits: it is now included in more than half of the processing steps. Over the past quarter century, plasma processing has also made remarkable, albeit less-known, inroads in polymer-based industries. Such processes include (i) surface modification for enhanced adhesion, (ii) etching, and (iii) plasma-assisted deposition of thin coatings on polymer webs or discrete parts. More recently, there has been a strong trend to develop such processes operating with “cold” plasmas at atmospheric pressure.

In this presentation we first discuss some of the particularities of plasma processing polymers, for example the effects of energetic UV photons and the generation of volatile species from the exposed polymer surfaces. Next, we review some ongoing research on plasmas and polymers in our laboratory at Ecole Polytechnique. A first example is surface nitriding of polyolefin films (polyethylene, polypropylene) by atmospheric pressure dielectric barrier discharges (BDB) in very pure nitrogen<sup>(1)</sup>. In this gas the atmospheric pressure glow discharge (APGD) is non-filamentary, contrary to conventional “corona” treatment in air. Unlike the latter, N<sub>2</sub> APGD can convey high surface energy values to the polymers, which remain stable over much longer periods of time in normal storage. An important second example is PECVD of silicon-compound coatings on polymer films, used for packaging, encapsulation of organic electronics, space technology, etc<sup>(2)</sup>. In this talk, we will focus on the very first instants of film growth on the polymer substrates, which we study by a combination of complementary surface – analytical techniques including RBS, ARXPS, and scanning electron microscopy combined with plasma-assisted etching<sup>(3)</sup>.

We close with some comments about the likely future of “plasmas and polymers”.

---

<sup>(1)</sup> S. Guimond et al, *Plasmas and Polymers* 7 (2002) 71.

<sup>(2)</sup> G. Czermuszkin et al, *Plasmas and Polymers* 6 (2001) 107.

<sup>(3)</sup> G. Dennler et al, *Plasmas and Polymers* 8 (2003) 41.

# **Recent Advances on Plasma Techniques for Bio-Medical and Drug-Engineering**

Masayuki Kuzuya

*Laboratory of Pharmaceutical Physical Chemistry, Gifu Pharmaceutical University,  
5-6-1, Mitahora-Higashi, Gifu 502-8585, Japan*

One of the advantages of plasma treatment is the fact that it is surface limited (500-1000 Å) so that only the surface properties can be changed without affecting the bulk properties. It is known that low temperature plasma of inert gas emits intense UV and/or VUV ray to cause an effective energy transfer to solid surface and gives rise to a large amount of stable free radicals on the polymer surface.

In view of the fact that surface reactions of plasma treatment are initiated by plasma-induced surface radicals, study of the resulting radicals is of utmost importance for understanding of the nature of plasma treatment. Thus, we have undertaken plasma-irradiation of a wide variety of polymers, synthetic and natural, and the surface radicals formed were studied in detail by electron spin resonance (ESR) coupled with the aid of systematic computer simulations. On the basis of the findings from a series of such studies, we were able to develop several novel biomedical and pharmaceutical application works.

For the most suitable therapy, development of sustained- and controlled-release systems for drug delivery is one of the most active areas today in the entire field of drug research. A wide variety of approaches of controlled-release drug delivery system (DDS) have been thus far investigated for oral application. Of these approaches, preparations of delayed-release systems have been also noted as orally applicable delivery systems that are useful for the time-controlled delivery of a drug in the gastrointestinal tract.

In this contribution, our novel application works in the field of drug engineering using plasma-irradiated organic polymers are presented, which include (1) preparation of multi-layered tablets applicable for reservoir-type DDS of sustained- and delayed- release, and (2) Development of Floating Drug Delivery System (FDDS) for oral controlled-release dosage forms possessing gastric retention capabilities. (3) Approach to Patient-Tailored DDS based on the combination of the above-mentioned devices, as well as brief overviews of ESR studies on plasma-induced surface radicals of several organic polymers relevant to the present study.

# Non-thermal Atmospheric Pressure Discharges: Physics and Applications

A.Fridman

*Drexel Plasma Institute, Department of Mechanical Engineering and Mechanics, Drexel University,  
Philadelphia, Pennsylvania, USA*

Non-thermal atmospheric pressure discharges attract last decade serious attention of fundamental scientists, engineers as well as very practically oriented people from industry. There are several reasons for that. First of all development of new diagnostic techniques and analytical approaches permit better understanding of very sophisticated physics of streamer-based corona and dielectric-barrier discharges. It helped in particular to make successful steps in understanding of micro-discharges, multi-streamer interaction in DBD, and development of atmospheric pressure glow discharges. Such progress stimulated even broader applications of the dielectric barrier discharges, probably - the most used today - non-thermal atmospheric pressure discharges. Traditional electron beam plasmas were also essentially developed in last decade. From the other hand, development of more effective, relatively cheap and powerful pulse power supplies opened good chances for large-scale industrial applications of pulse corona discharges in different configurations and modifications.

New achievements in physics of dielectric barrier and corona discharges are going to be discussed in the presentation. Especial attention will be paid to physics of multi-streamer interaction, patterning of streamers in DBD, and physical correlations between streamer and uniform configurations of the non-thermal atmospheric pressure discharges. In other words we are going to discuss transition between streamer discharges and atmospheric pressure glow discharges, which is probably one of the most challenging fundamental question of non-thermal atmospheric pressure plasma physics.

Especial attention will be obviously paid to new achievements in physics of the gliding arc discharges – the transitional thermal/non-thermal discharges, which are supposed to combine not disadvantages but advantages of thermal and non-thermal plasma systems. New experimental and computer modelling results regarding the gliding arc discharges trapped in the reverse vortex (tornado configuration) are to be presented and discussed.

Non-thermal atmospheric pressure plasmas have numerous successful industrial applications today. The most traditional between them are ozone production and surface modification. Mentioning some news regarding these traditional aspects of applied plasma chemistry, we are going to present also new application results related to use of the non-thermal plasma in environment control – in cleaning of gases and liquids from different pollutants. Especial attention is also going to be paid to biological applications of non-thermal atmospheric pressure plasmas, including in particular sterilization, bio-printing and bio-patterning for bio-sensors, drug delivery and tissue engineering.

# Exploration of the Deposition Limits of microcrystalline Silicon

D. Mataras

*Plasma Technology Laboratory, Dept. Chem. Engineering, University of Patras  
P.O.Box 1407, 26500 Patras, Greece, [dim@plasmatech.gr](mailto:dim@plasmatech.gr)*

Hydrogenated microcrystalline silicon ( $\mu\text{C-Si:H}$ ) has emerged in the last few years as an interesting addition in the amorphous silicon family of materials, used for the enhancement and the diversification of the range of thin-film devices that can be produced. The main advantage of  $\mu\text{C-Si:H}$  lies in the elimination or the minimization, depending on whether it is used without or with amorphous layers in the device, of stability issues that have been defaming amorphous silicon devices for many years [1].

Another advantage of  $\mu\text{C-Si:H}$  is that, in principle, it can be produced using the same equipment that is already used in the production of amorphous silicon with little modification. However, the process is only partially compatible with the amorphous silicon production process because it is based on the decomposition of highly diluted silane in hydrogen. Highly diluted silane discharges are completely different from pure silane discharges while they also differ in many ways from pure hydrogen discharges. Thus, although the existing production experience is useful, the extensive literature concerning the deposition of amorphous silicon is almost useless. Nevertheless, the need for studying these discharges does not rise from purely scientific interest only. There is one critical technical issue that needs to be solved rapidly, i.e. the deposition rate, together with a few, closely related, quality issues. Indeed, there is a need for at least a one order of magnitude increase of the deposition rate, while maintaining a high crystalline fraction, in order to be able to reach viable production conditions. This is due to the lower absorption of the material which imposes the need for thicker absorptive layers together with advanced light trapping techniques.

Many efforts were spent in this direction either by using conventional parametric optimization or other less production equipment compatible techniques [2-4]. In the paper we will review some of the continuing efforts done in the first direction. Namely, we will present the influence of parameters like the discharge power and frequency, the partial silane pressure and the total pressure, the discharge geometry and the addition of other silicon containing gases. The effect of each of these parameters will be isolated as much as possible from the other parameters, followed experimentally and analyzed using discharge diagnostics and finally correlated with the rest of the parameters through plasma modelling.

The ultimate goal is to bring to light the factors enhancing or limiting the deposition of  $\mu\text{C-Si:H}$ , especially in the amorphous/microcrystalline transition region, which seems to be of particular interest, through the understanding of the effect of the macroscopic parameters followed.

- [1] J. Meier, R. Fluckiger, H. Keppner, and A. Shah, Appl. Phys. Lett. 65, 860 (1994)
- [2] E. Amanatides, S. Stamou, D. Mataras, J. Appl. Phys. **90**, 5786 (2001)
- [3] E. Amanatides, D. Mataras, D. E. Rapakoulis, J. Appl. Phys. **90**, 5799 (2001)
- [4] E. Amanatides, D. Mataras, D. E. Rapakoulis, J. Vac. Sci. Technol. A **20**, 68 (2002)

# **Plasma spraying from thick to thin coatings and micro to nano structured coatings**

P. Fauchais<sup>1</sup>, J-F. Coudert<sup>1</sup>, J. Fazilleau<sup>1</sup>, C. Delbos<sup>1</sup>, L. Bianchi<sup>2</sup>, K. Wittmann-Ténèze<sup>2</sup>

<sup>1</sup>*Laboratoire Science des Procédés Céramiques et Traitements de Surface, Université de Limoges, Limoges, France*

<sup>2</sup>*Commissariat à l'Energie Atomique, Le Ripault, France*

Up to a recent period two types of coatings existed: thick coatings (from 100  $\mu\text{m}$  to a few mm) and thin coatings (up to a few  $\mu\text{m}$ ). The first ones are obtained by thermal spraying in general and plasma spraying in particular. They result from the flattening of molten particles (in the size range 10 to 100  $\mu\text{m}$ ) forming splats (a few  $\mu\text{m}$  in thickness) and their layering, a new particle impacting, the mostly, on an already solidified splat. Such coatings exhibit sub-micronic columnar structures in each splat, but the coating morphology is of micronic type. The second type of coatings is produced by plasma enhanced CVD, plasma vapor deposition, ion plating..., reactive species from gas phase being deposited as a solid coating. The deposition rate is of course a few orders of magnitude lower than in plasma spraying. However coatings are finely or even nano structured.

During the last decade great strides have been made in the spray process understanding both for particles in flight but also for their flattening and splat cooling. Simplified sensors, able to work in the harsh environment of spray booths, have been developed to monitor on-line the coating formation and improve its reliability and reproducibility. To achieve finely structured coatings, nanoparticles agglomerated to form particles in the tens of micrometers range are sprayed at velocities over 350 m/s, to have them impacting in a mushy state in order to keep the nanostructure. Concurrently, new spray techniques appeared with the injection in plasma jets either of liquid precursors (nitrates, isopropoxide, butoxide, acetate... dissolved in isopropanol, n-butanol...) or suspensions of nanoparticles. They result in coatings with a deposition rate close to that of plasma spraying with thicknesses in the range 3 to 100  $\mu\text{m}$  (bridging the gap between deposition from gas phase and liquid phase) and which are finely structured.

This paper presents what is the actual state of the art in these different fields, as well as the most recent developments in technology, measuring techniques and modeling.

# Study of fluorocarbon plasma etching and film deposition with mass separated $\text{CF}_x^+$ ion beam irradiation

M. Nakamura<sup>a)</sup>, K. Yanai, K. Kurihara, K. Karahashi\*, K. Ishikawa

*Environmentally benign Etching Technology laboratory (EEL), ASET, 3-1, Morinosato Wakamiya, Atsugi-shi, Kanagawa, 243-0198, Japan* <sup>a)</sup> e-mail: moritaka@eel-aset-unet.ocn.ne.jp

Fluorocarbon plasma has been widely used in dry etching for semiconductor devices fabrication. Its surface reaction mechanisms, however, have not yet been clarified well. Thus, we have developed a mass-analyzed ion beam apparatus. In this paper, we examined ion energy dependence of  $\text{SiO}_2$  etching yield by  $\text{F}^+$  or  $\text{CF}_x^+$  ion irradiation and the composition and energy distribution of desorbed products. Moreover, we studied the initial stage of a-C:F film deposition on  $\text{SiO}_2$  and  $\text{Si}_3\text{N}_4$  surfaces.

Mass analyzed pure ion beam of  $\text{F}^+$  or  $\text{CF}_x^+$  ( $x = 1\sim 3$ ) were irradiated on sample surface after precise control of ion energy. By using differential pumping, neutral radicals were effectively ejected. We estimated etching yield from the etch depth and ion dose measured by a movable Faraday cup set at the sample position. Ion irradiated sample surface was analyzed by XPS without air exposure.

Figure 1 shows the ion energy dependence of etching yield. It is clear that the ion energy and the presence of both carbon and fluorine in incident ion is significant for  $\text{SiO}_2$  etching. The saturation of etching yield at high energy is explainable by the shortage of chemical species from incident ion. We observed the desorbed species by mass spectrometer using  $^{13}\text{CF}_4$  gas.  $\text{SiF}_2$  was the major desorbed product by  $\text{CF}_x^+$  ion irradiation or by  $\text{CF}_4$  plasma beam irradiation to  $\text{SiO}_2$ . Composition of the desorbed products was almost independent on the ion energy or on the ratio of neutral flux to ion flux. Thus, the shortage of chemical species (F and C) from ion limited the chemical reaction.

With decreasing ion energy below 500 eV, etching yield abruptly dropped and fluorocarbon films grew on  $\text{SiO}_2$  surface. The film deposition takes place only by  $\text{CF}_x^+$  ion irradiation without neutral radicals. In these low energy conditions, we found that slight etching of  $\text{SiO}_2$  takes place first, and then the film growth started with increasing ion dose as shown in Fig. 2. Figure 3 shows the XPS spectra of C1s region. At low dosage of  $\text{CF}_1^+$  less than  $1\text{e}17$ , C-C bond (285 eV peak) was observed, and C-F<sub>x</sub> bond (288 and 291 eV peak) increased with the increase of ion dose. The same phenomenon of fluorocarbon film deposition after slight etching was also observed for  $\text{Si}_3\text{N}_4$  surfaces. From these results, we infer that the fluorocarbon film deposition takes place after carbon accumulation on the surface, which created by the reaction of fluorine and surface materials such as silicon in  $\text{SiO}_2$  or  $\text{Si}_3\text{N}_4$ . Finally, we would like to emphasize that “sticking coefficient” of incident species depends on the surface condition significantly and conventional deposition models

with unchanged sticking coefficient for each of incident species are apparently insufficient and misleading.

This work was supported by NEDO.

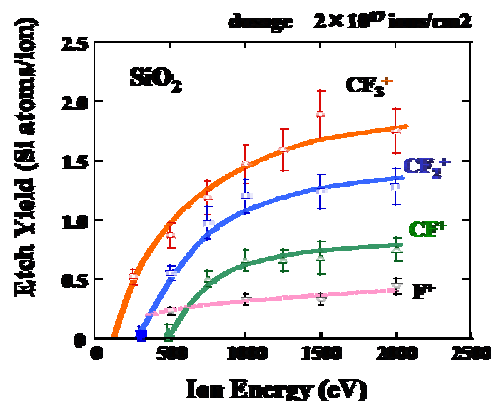


Fig. 1. Etching Yield vs. Ion energy.

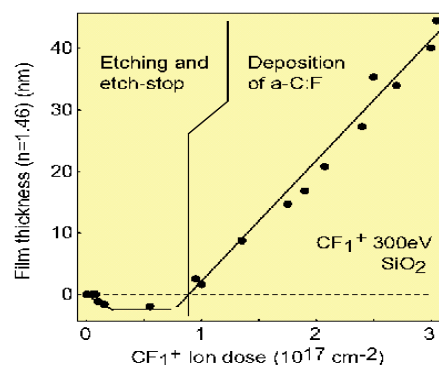


Fig. 2. a-C:F film deposition by 300 eV  $\text{CF}_1^+$  ion irradiation.

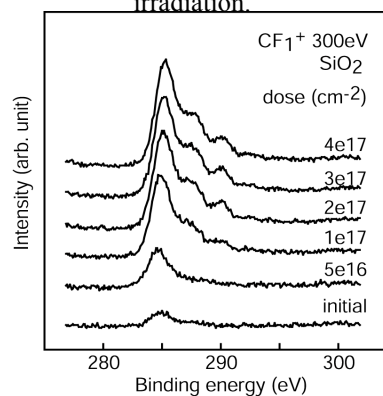


Fig. 3. XPS on  $\text{CF}_1^+$  ion irradiated  $\text{SiO}_2$  surface.

\* Present address: high-k, MIRAI, ASET, Tsukuba West7, Tsukuba, Ibaraki, 305-8569, Japan



# Dominant parameters in the physico-chemical modeling of filamentary high pressure discharge in air

C.Deniset, E.Marode

*LPG-, EDEE, Université Paris XI, Ecole Supelec Gif/Yvette*

## Abstract

A streamer induced filamentary discharge in air at atmospheric pressure is modeled. Diffusion, pressure expansion, and chemical reactions (41 species and 590 reactions) are treated. The treatment includes not only neutral species, but also excited species, ions, positive and negative. The model applies to the study of the processes occurring in the radial direction of the cylindrical plasma. The role of some relevant parameters will be stressed. Example of processes associated with excited species and ions will be given.

## 1. Introduction

At atmospheric pressure, it is known that tiny streamer ionizing waves, producing multiple filamentary streamer-induced plasma channels are the basis for producing non-thermal plasmas reactors. The length of the plasma channels ranges from millimeters up to centimeters while the filament cross-sections lie in the range of some tens of micrometers. In air, the streamer velocities are in the  $10^7$  cm/s range, so that they may cross discharge gaps from millimeters to centimeters within less than  $10^{-7}$ s. Streamer channels may thus operate in several type of discharge devices like DC initiated mesh to plane, dielectric discharge barrier (DBD) at some tens of kHz, pulse controlled axial wire to cylinder, brush of point electrodes against a plane electrode, etc.... Multiple targets guide the use of these plasmas reactors. Ozone production<sup>1</sup>, pollution control<sup>2</sup>, combustion triggering<sup>3</sup> are some examples. It is clear that all these applications use the fact that the electrical energy deposit within the gap trough the generated plasmas induces chemical conversion of species within a given gas flow. In each case the plasma device is aimed towards promoting a given set of chemical conversion for a specific result. This set is however mixed with a great number of chemical reactions, which interact on each other in an intricate time-dependant way. Moreover the interaction depends on the thermodynamic local parameters, such as temperature, densities, as well as their spatial gradients. While expert may help to optimize this situation, the complexity is such that modeling of the plasma-chemistry may help to derive the chemical tendencies in each cases.

In this presentation, the modeling is based on a filamentary discharge, following the axis of a centimeter positive point-to-plane gap in air at atmospheric pressure. It consists of computing the time resolved density distributions of all type of species, in the radial direction, perpendicularly to the discharge axis due to the physico-chemical processes. On the experimental side, it is known that single streamer-filaments are repeatedly generated, along the main central point-to-plane axis with a repetition rate of the order of hundred microseconds. Since single discharge duration is of the order of some hundred nanoseconds, it is assumed, for simplicity, that each discharge is generated in a virgin gas, not perturbed by a former one. First computations of such type of modeling has already been presented in conference form elsewhere<sup>4,5</sup>. A similar approach is developed in Toulouse, France<sup>6</sup>. However the obtained results depend drastically on the value taken for describing the initial conditions of the discharge. They are here different from those taken in Toulouse. More precisely, one of the difference consists in selectinf the radius of the discharge cross section. Actually, it define the energy density released by the discharge to the gas (here 20 micrometers against 200 in the Toulouse work). An example of results based on an approach including the ions species and neutral excited species will be presented here to illustrate some relevant parameter and problems associated with the modeling approach of filamentary discharges<sup>7</sup>.

## 2. The hydrodynamic physico-chemical model

Three groups of time resolved equations are applied along the radial coordinate  $r$  for each species: the groups of continuity equations, momentum transfer and energy transfer. They apply to electrons (e); Positive ions (+),

N<sup>+</sup>, N<sub>2</sub><sup>+</sup>, N<sub>3</sub><sup>+</sup>, N<sub>4</sub><sup>+</sup>, NO<sup>+</sup>, NO<sub>2</sub><sup>+</sup>, N<sub>2</sub>O<sup>+</sup>, N<sub>2</sub>O<sub>2</sub><sup>+</sup>, N<sub>3</sub>O<sup>+</sup>, NO<sub>3</sub><sup>+</sup>, O<sup>+</sup>, O<sub>2</sub><sup>+</sup>, O<sub>4</sub><sup>+</sup>, Negative ions (-): O<sup>-</sup>, O<sub>2</sub><sup>-</sup>, O<sub>3</sub><sup>-</sup>, O<sub>4</sub><sup>-</sup>, NO<sup>-</sup>, NO<sub>2</sub><sup>-</sup>, N<sub>2</sub>O<sup>-</sup>, NO<sub>3</sub><sup>-</sup> and neutral species (s): O, N, NO, NO<sub>2</sub>, NO<sub>3</sub>, N<sub>2</sub>, N<sub>2</sub>O, N<sub>2</sub>O<sub>5</sub>, O<sub>3</sub>, O<sub>2</sub>, which includes the excited species N(2D), N(2P), N<sub>2</sub>(A), N<sub>2</sub>(B), N<sub>2</sub>(C), N<sub>2</sub>(v), N<sub>2</sub>(a'), O(1D), O(1S), O<sub>2</sub>(A), O<sub>2</sub>(a), O<sub>2</sub>(b), O<sub>2</sub>(C), O<sub>2</sub>(c). The identification of the spectroscopic levels is simplified here in an obvious manner.

The continuity equations are:

$$\frac{\partial N_{e,+,-,s}}{\partial t} + \frac{1}{r} \frac{\partial}{\partial r} (r N_{e,+,-,s} V_{e,+,-,s}) = \sum_j \pm k_j(T) N_l N_m N_n + \sum_e \pm k_e(E_z / N_g) N_l N_e \quad (1)$$

where the subscript symbols correspond to the various species, and leads to 46 continuity equations.

The N's are the species densities, the V's are the species velocities, T is the heavy species temperature, E<sub>z</sub> is the axial field, and N<sub>g</sub> is the total density of the heavy species. The right hand sides are the source terms. They deal with 590 reactions. The k<sub>j</sub> are the various temperature dependent reaction rates between heavy species, while the k<sub>e</sub> corresponds to the electron collision rates which depends on the reduced field E<sub>z</sub>/N<sub>g</sub>.

The momentum equations for ions, positive and negative, are:

$$\frac{\partial}{\partial t} (N_{+,-} V_{+,-}) + \frac{1}{r} \frac{\partial}{\partial r} (r N_{+,-} V_{+,-}^2) + \frac{k}{m_{+,-}} \frac{\partial}{\partial r} (N_{+,-} T) - \frac{q E_r}{m_{+,-}} N_{+,-} = - \frac{1}{m_{+,-}} \sum_g \frac{kT}{D_{+,-}} N_{+,-} (V_{+,-} - V_g) \quad (2)$$

The m's are the masse of the ions, k is the Boltzman constant, the D's are the temperature dependent diffusion coefficients. The electron velocity sets very quickly to an equilibrium value defined by a balance between conduction and diffusion velocity. The following simplified equation has thus been adopted for them:

$$N_e V_e = q_e N_e \mu_e E_r - D_e \frac{\partial}{\partial r} (N_e) \quad (3)$$

The electron diffusion coefficient is a function of E<sub>z</sub>/N<sub>g</sub>.

For the neutral species, the field term (the forth term of the lhs of equation 2) drops so that, for them:

$$\frac{\partial (N_s V_s)}{\partial t} + \frac{1}{r} \frac{\partial}{\partial r} (r N_s V_s^2) + \frac{k}{m_s} \frac{\partial}{\partial r} (N_s T) = - \frac{1}{m_s} \sum_g \frac{kT}{D_s} N_s (V_s - V_g) \quad (4)$$

In all these equations, the temperature of the heavy species is supposed to be the same. It follows that only one equation is needed to determine the temperature T. It is the energy transfer equation:

$$\frac{5}{2} \frac{\partial}{\partial t} (NkT) + \frac{5}{2} \frac{1}{r} \frac{\partial}{\partial r} (r kT \sum_g N^g V^g) + \frac{kT}{r} \sum_g N^g \frac{\partial}{\partial r} (r V^g) - \frac{\lambda}{r} \frac{\partial}{\partial r} (r \frac{\partial T}{\partial r}) = S_2 \quad (5)$$

Where λ is the thermal conductivity. The rhs of equation 5 is:

$$S_2 = (f_e j_e + f_- j_- + f_+ j_+) E_z - \sum_g \frac{kT^s}{D^s} N^s (V^s - V^g) V^g \quad (6)$$

Where the f's are the fraction of the energy gained by the charged species and delivered to the heavy species as translational energy. Finally the radial field is derived from the poisson equation:

$$\frac{1}{r} \frac{\partial}{\partial r} (r E_r) = \frac{e(N_+ - N_e - N_-)}{\epsilon_0} \quad (7)$$

While the axial field E<sub>z</sub> is simply derived from the applied potential divided by the gap.

### 3. Initial conditions and computation process.

Figure 1 is a schematic sketch showing the elongation of the filamentary plasma at successive times. The streamer, at the plasma front, drives the filament extension towards the plane. The filamentary plasma is encapsulated within a positive space charge sheath, ensuring the plasma stability. The modeling aim is to compute the radial structure of the discharge around a given position z. Let us follow what happens around z.

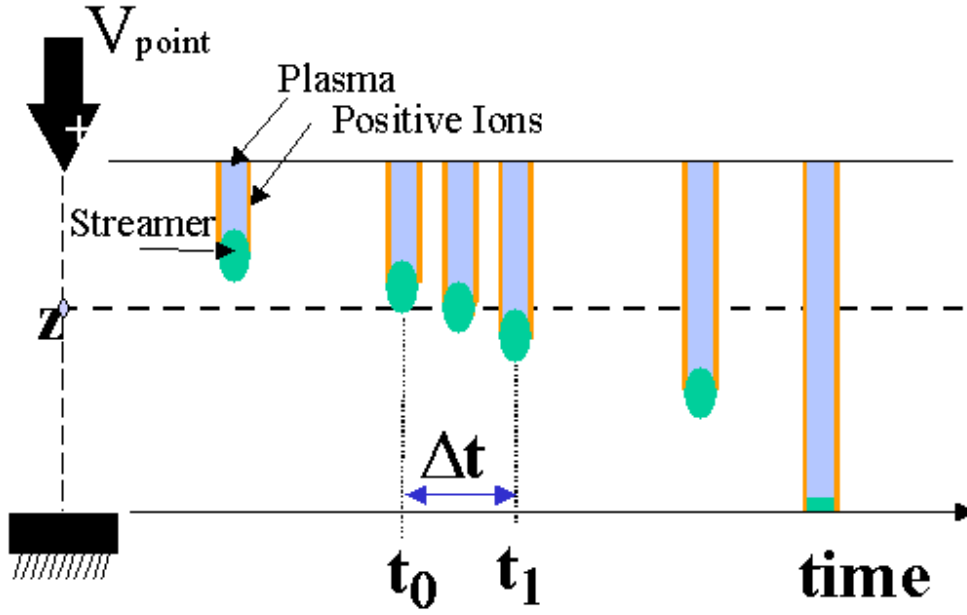


Figure 1: schematic sketch illustrating the computed sections

Obviously, as long as the streamer has not reached position  $z$ , nothing happens around  $z$ . At time  $t_0$  the streamer arrives at position  $z$ , and crosses this position from  $t_0$  to  $t_1$ . The time  $\Delta t = t_1 - t_0$  is very short,  $10^{-11}$ s. During that time a simplified computation of the streamer activity is made around  $z$ . This streamer computation gives the initials conditions allowing the full model to start at time  $t_1$ . An example of run is selected to discuss some of the relevant parameters of such approach. The results of this example will be used in all the following figures. The values used are the following for this run. The discharge radius is  $r_0 = 2 \cdot 10^{-5}$   $\mu\text{m}$  (see § 4). The discharge current  $I_d(t_1) = 2.4\text{mA}$ . The applied potential  $V_{\text{point}}(t_0) = 6.1\text{kV}$ . The gap is  $d = 3 \cdot 10^{-3}$  m.  $f_e = 5\%$  (thus  $E_z = 80\text{Td}$ ).  $\lambda = 2.7 \cdot 10^{-2}$   $\text{Jdeg}^{-1}\text{m}^{-1}\text{s}^{-1}$ . In addition, the potential evolution at the point is calculated using the value of the gap capacity  $C$ , equal to  $8\text{pF}$ , and the ballast resistor  $Z$  equal to  $10^6\Omega$ , set between the DC generator and the point. The rate constants for heavy species are mainly taken from the references <sup>8, 9, 10</sup>. The electron rate constants are obtained using a Boltzman solver provided by Segur<sup>11</sup>.  $f_e = 5\%$  (see § 5),  $f_i = f = 1$  since ions transfer into heat all their energy.

#### 4. Radius of the discharge cross-section and streamer treatment.

A still not solved problem is the value  $r_0$  of the radius of the filamentary discharge cross-section. It is not a second order question. Indeed for a given total discharge current, the energy density deposit along the filamentary plasma strongly depends on  $r_0$ . If  $r_0$  is small, the resulting rise of pressure and temperature inside the discharge will lead to a substantial pressure wave, a decrease of the species density  $N_g$ , and an increase of the reduced field  $E/N$ . All these processes have a first order influence on the gas chemistry. Let us discuss this question. Till recently, the 2D models of the filamentary induced streamer discharges lead to a value greater than  $100 \mu\text{m}$ <sup>12</sup>. These values contradict however former experimental results, based on spectroscopic measurements of  $H_\alpha$  broadening, which provided a value of  $20 \mu\text{m}$ <sup>13</sup>. Two subsequent results have been delivered which continue to feed the  $r_0$  story. Experimental result, based however on the total light emitted, gave this time rather  $100 \mu\text{m}$ <sup>14</sup>. In turn, recently, a 2D streamer-filament modeling using induced emission at the streamer front for gas photo-ionisation, gave a value of  $30 \mu\text{m}$  for  $r_0$ <sup>15</sup>. The option here is to take the experimental value  $r_0 = 20 \mu\text{m}$  as initial channel radius which is different from the 2D model (except the last one). From the 2D model however the mean value of the axial reduced field i.e.  $E_z/N_g$  of  $600 \text{Td}$  is adopted. The electron density is then deduced from the initial discharge current  $i_0 = 2.4 \text{mA}$ . The computed species evolution due to electron collision during the streamer passage at position  $z$  is then calculated assuming that a constant axial reduced field of  $600 \text{Td}$  is

applied during  $\Delta t = 10^{-11}$  (see figure 1). The resulting species distribution after the streamer passage is, in  $\text{m}^{-3}$  :  $N(\text{atomic nitrogen})/6.98 \cdot 10^{21}$ ,  $N(2D)/1.08 \cdot 10^{16}$ ,  $N(2P)/2.8 \cdot 10^{17}$ ,  $N_2(a'')/1.85 \cdot 10^{21}$ ,  $N_2(A)/1.28 \cdot 10^{21}$ ,  $N_2(B)/3.85 \cdot 10^{21}$ ,  $N_2(C)/1.58 \cdot 10^{21}$ ,  $N_2(v)/1.06 \cdot 10^{21}$ ,  $O(\text{atomic oxygen})/3.06 \cdot 10^{21}$ ,  $O(1D)/6.9 \cdot 10^{20}$ ,  $O(1S)/1.59 \cdot 10^{20}$ ,  $O_2(a)/9.81 \cdot 10^{16}$ ,  $O_2(b)/2.41 \cdot 10^{16}$ ,  $O_2(A)/4.37 \cdot 10^{14}$ ,  $O_2(C)/4.36 \cdot 10^{16}$ ,  $O_2(c)/4.36 \cdot 10^{16}$ . These values are injected as initial conditions for the main modeling of the radial filament description after the streamer passage.

## 5. Plasma potential

Along the plasma axis, the potential varies, from that at the point, +6100 V, to the negative plane (earthed).

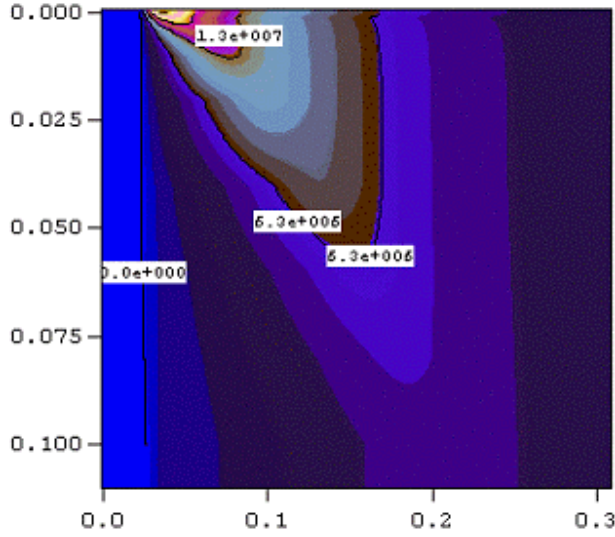


figure 2. Radial field distribution. Ordinate is time in  $\mu\text{s}$ , abscissa is position in mm.

Position  $z$  is selected to have an initial potential of 5000 V. Without any discharge the potential at  $z$  would be much lower, of the order of 1000V. The difference is due to positive ions around the discharge, which are keeping the electron inside the plasma. Figure 2 shows a clear limit at the edge of the discharge core, situated at 24  $\mu\text{m}$  from the axis. Inside, the value of the field (indicated in V/m) is zero, it is the plasma limit. Outside, for  $r > 24 \mu\text{m}$ , the radial field sets up, due to the positive unipolar space charge. The maximum field position, increases with time, due to the positive ion diffusion and repulsion. The direction of the radial field is such that the electrons cannot escape from the center where electron collisions are thus confined.

## 6. Hydrodynamics and fraction $f_e$ of electron heat release.

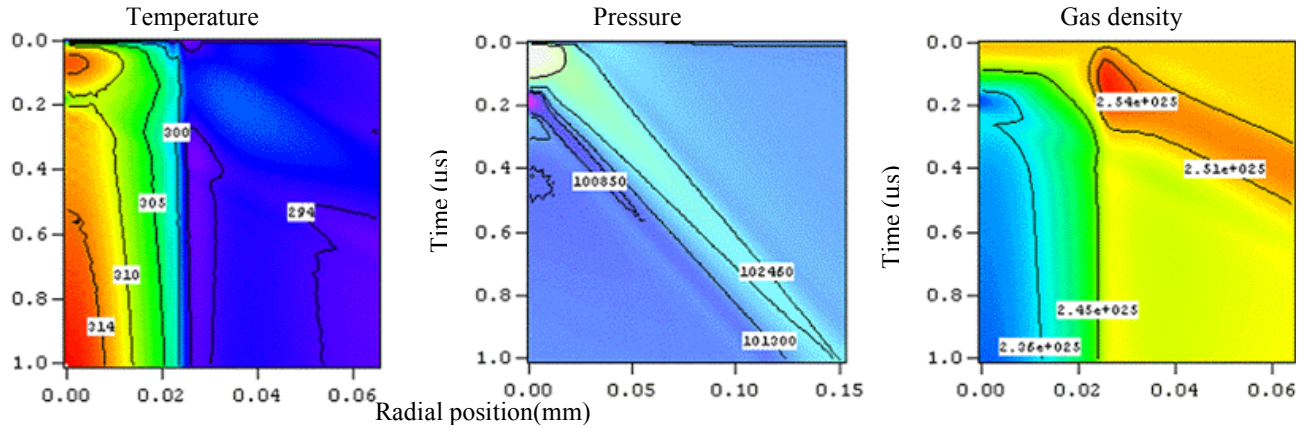


Figure 3. Temperature (in K), pressure (pascal), and density ( $\text{m}^{-3}$ ).

With an initial value of 2.4 mA, the discharge current decreases due to electron attachment. The current is practically negligible after  $50 \cdot 10^{-9}$  s. Thus, the electron existence time is confined within a thin range at the upper part of all figures in figure 3. This figures show thus the consequence of the perturbation introduced by the electron during a very small time compared to the 1  $\mu\text{s}$  of the time window presented. Following these radial distributions from left to right, we see that at first, the electrons rise the gas temperature within the discharge core. A simultaneous rise of pressure is induced which launch a pressure sound wave. An increase in density (red) goes with this pressure wave; but this, in turn, leads to a decrease of the density within the discharge

core (blue). Back to the temperature, we observe that the temperature passes through a minimum around 180 ns. This quick decrease in temperature cannot be due to thermal cooling, but to adiabatic expansion cooling. The subsequent rise of temperature is due to ion heating. The heating is associated with a decrease of gas density. Three parameters dominate all this behavior. The temperature gradient  $\nabla T$ , the value of  $r_0$ , and the value of  $f_e$ . Let us recall that a pressure gradient  $\nabla p \cong kT\nabla N + kN\nabla T$ , may correspond to a density gradient  $\nabla N$ , associated with diffusion and/or to a temperature gradient  $\nabla T$ . In this simulation, if the  $\nabla T$  term is dropped in the equation, no more pressure wave appears. This stresses the necessity to take into account, not only the diffusion, but also temperature gradient. The fact that a pressure wave is observed must be due to the large energy confinement in term of heat within the discharge core. But, a priori, the situation is not very good for such heat transfer. The electron loses their energy mainly in terms of inelastic collisions into exciting nitrogen vibrations. Into heat, is taken, elastic collisions (not heating very much, due to the mass difference between electrons and heavy species), rotational excitation (relaxing in the ns range), electron dissociation (inducing mutual repelling of the fragments). Not taken is the relaxation of vibration levels of nitrogen (occur in the 10  $\mu$ s range, not in the first 1  $\mu$ s expansion range). Finally, the fact that the pressure wave, and its associated density decrease, is obtained is due to the small value taken for  $r_0$ . It stresses one's more the necessity to carry on thinking about this parameter.

## 7. NO<sub>x</sub> formation

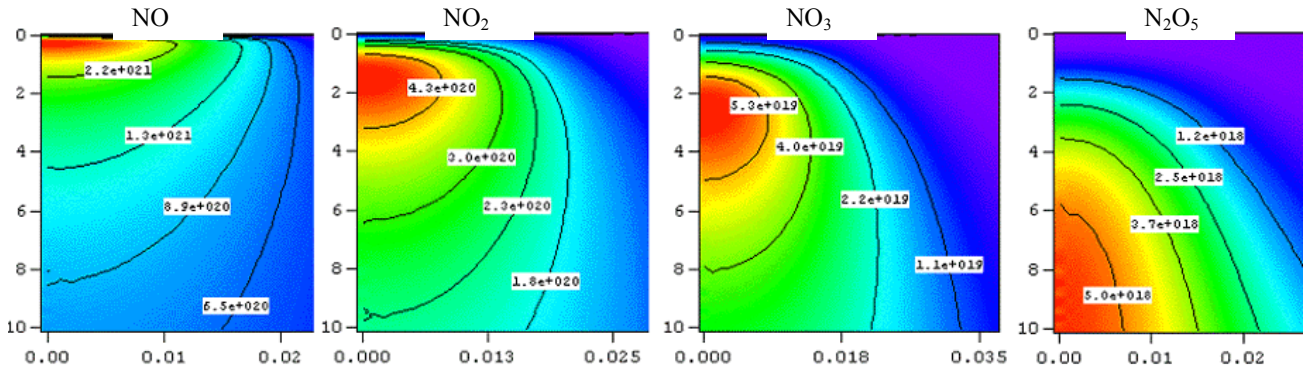
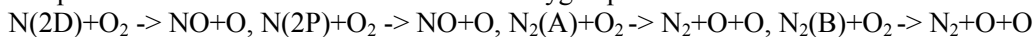


Figure 4: successive NO<sub>x</sub> formation

Atomic nitrogen and oxygen are the main radicals starting the whole chemical reactions story. They are initially produced by electron dissociation. After the initial atomic production by the streamer, the density of nitrogen at the axis increases from  $7.10^{21}$  to  $6.10^{22}$  at the axis, while the atomic oxygen from  $3.10^{21}$  to  $7.10^{22}$  in about 100 ns. The total number of atomic species, obtained by integrating the densities in the radial direction, increase up to 1  $\mu$ s. Nitride oxides appear successively, during the afterglow, in a more and more oxidation form (figure 4).

## 8. Some influence on the gas chemistry due to the excited states and the ions.

The time resolved radial density distribution of atomic oxygen, ozone, and temperature is shown in figure 5. There is a clear delay between oxygen formation and ozone formation. O<sub>3</sub> diffuse towards cooler region. The decrease in atomic oxygen with time could be due to diffusion without loss. But the integration of atomic oxygen density in the radial direction, i.e. the total amount of atomic oxygen per filament meter, shows losses. The left diagram shows that after 1  $\mu$ s, the total amount of oxygen decreases (plain blue curve), and is converted into ozone (plain red curve). If now, in the computation, all reactions involving excited states are removed, the dotted curve are obtained (labeled "sans"). Clearly the excited states play a role for ozone formation. Analyzing the computed data it is due to additional atomic oxygen production which come from the following processes:





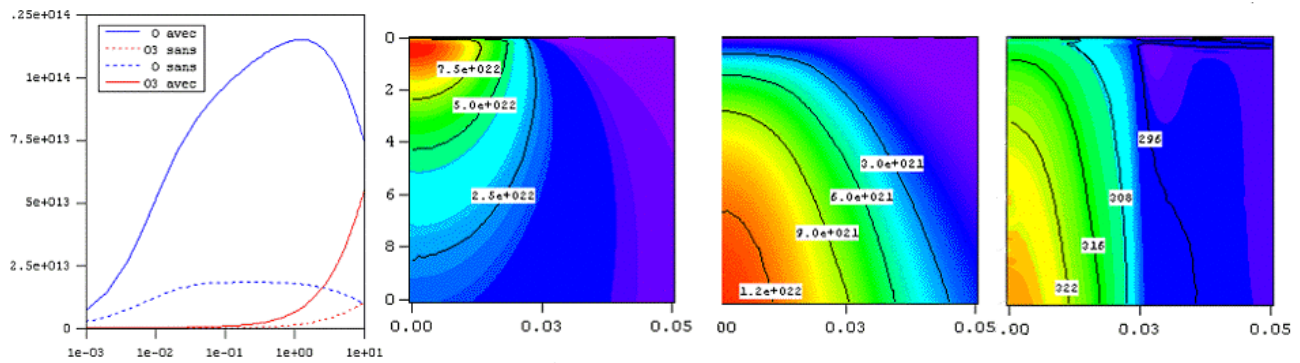


Figure 5: Left plot: Total amount of O and O<sub>3</sub> per filamentary plasma meters (abscissa time in μs). Distributions: from left to right, O, O<sub>3</sub> and T, ordinate time (μs), radial position (mm).

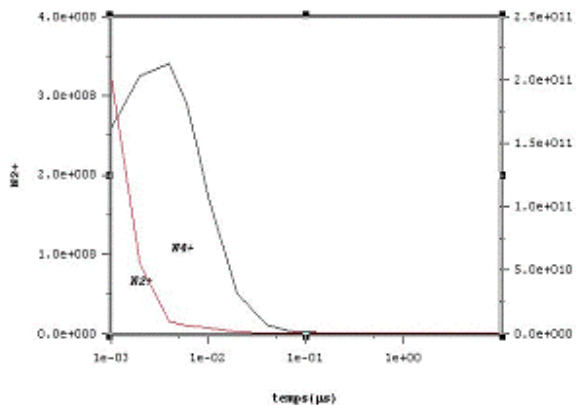


Figure 6 : Evolution of total number of N<sub>2</sub><sup>+</sup> and N<sub>4</sub><sup>+</sup> per meter.

As seen, N<sub>2</sub><sup>+</sup> is very quickly converted into N<sub>4</sub><sup>+</sup>. Since the electron recombination coefficient with N<sub>4</sub><sup>+</sup> is smaller than with N<sub>2</sub><sup>+</sup>, it follows that taking the nature of the ion into account leads to a larger duration of the discharge i.e. more electron activity.

## References

- [<sup>1</sup>] U. Kogelschatz, Process Technologies for water treatment, S. Stucki, Plenum, (1988)
- [<sup>2</sup>] S. Schultheis; Ed. B. Penetrante, Non-Thermal Plasma Techniques, NATO ASI Series, 34 G, Ecological Sciences, vol 1, 2, (1993)
- [<sup>3</sup>] P. Tardiveau, E. Marode, A. Agneray, M. Cheib, J. Phys. D: Appl. Phys. **35** No 21, 2823-2829 (nov 2002)
- [<sup>4</sup>] E. Marode, S. Samson, D. Djermoune, N. Deschamps, M. Touzeau, A. R. De Souza, J. AOT, vol. 4 No. 1, (1999).
- [<sup>5</sup>] E. Marode, D. Djermoune, S. Samson, C. Deniset. Modeling of the chemical dynamics in a streamer induced discharge, 11<sup>th</sup> symposium on elementary processes and chemical reactions in low temperature plasma, Low Tatras, Slovaquie, Invited paper book, p93, June, (1998)
- [<sup>6</sup>] O. Eichwald, N. A. Guntoro, M. Yousfi, M. Benhenni, J. Phys. D: Appl. Phys. **35** No 5 (7 March 2002) 439-450
- [<sup>7</sup>] C. Deniset, Activation physico-chimique par décharge couronne filamentaire, Thèse, Univ. Paris 11, déc (2003)
- [<sup>8</sup>] D. L. Baulch, et al J. Phys Chem. Ref Data, 11, 1259-1380, (1982)
- [<sup>9</sup>] Mätzing H., "Chemical kinetics of flue gas cleaning by irradiation with electrons.", Advances in Chemical Physics, vol LXXX, Edited by I. Prigogine and S. A. Rice, John Wiley & Sons, New York, 315-402, (1991)
- [<sup>10</sup>] I. A. Kossyi, A. Yu. Kostinsky, A. A. Matveyev, V. P. Silakov, Plasma Sources Sci. Technol., 1, p207-220, (1992)
- [<sup>11</sup>] P. Segur et al, J. Phys. D **17**, 2199, 1984
- [<sup>12</sup>] A. A. Kulikovskiy, J. Phys D: appl. Phys., **30**, 1515-1522, (1997), N. Yu. Babaeva, G. N. Naidis, J. Phys D: appl. Phys., 29, 2423-2431, (1996), D. Djermoune, E. Marode, P. Segur, Int. Conf. Phen. Ion. Gas, vol 1, 33-34 (1995)
- [<sup>13</sup>] F. Bastien, E. Marode, J. Phys. D: Appl. Phys. **12** p. 249-263 (1979)
- [<sup>14</sup>] A. Gibert, F. Bastien, J. Phys. D: Appl. Phys. **22** No 8 1078-1082 (1989)
- [<sup>15</sup>] P. Dessante, Modeling of streamer discharges, in air, at high pressure, Thesis, Versailles Univ. France (2000)

# High sensitivity laser-based techniques applied for plasma diagnostics

N. Sadeghi

*Laboratoire de Spectrométrie Physique (U.M.R. 5588), Université Joseph Fourier-Grenoble, France*

Since their introduction in 70<sup>th</sup>, tunable lasers became rapidly a very useful tool for atomic and molecular spectroscopy and for the species density determination in various gas phase media, including plasmas. Laser-based diagnostic techniques all rely on the absorption of laser radiation by a specific group of particles. Radiation from a pulsed dye laser, with a spectral bandwidth in the range of GHz ( $\sim$ pm), comparable to the Doppler width, interacts with all atoms or molecules of a single quantum state. For single-mode dye or diode lasers, which have a spectral bandwidth in the range of a few MHz ( $\sim 10^{-3}$  pm), much narrower than the Doppler width, only a group of particles of the quantum state, having the right velocity component along the laser propagation direction to fulfill the Doppler shift condition, can absorb laser photons. On the other side, when dealing with femtosecond lasers, whose fourier-transform bandwidth is in the range of a few nm, molecules in different vibrational and/or rotational levels of an electronic state are able to interact with the laser beam. Information about this laser-medium interaction can be deduced directly from the diminution of the transmitted intensity, absorption techniques, or by detecting radiation emitted from particles pumped to the upper electronic state, laser induced fluorescence (LIF) technique.

LIF could be a very sensitive technique, allowing to detect as low as 100 particles. But in the presence of strong plasma induced emissions, its sensitivity will be reduced by several orders of magnitude. Also, the determination of the absolute concentration of the absorbers requires very complicated calibration methods, often sullied by large experimental errors. In the opposite, absorption measurements can provide absolute concentrations of the species but suffer from a low sensitivity, particularly when dealing with low concentration of absorbers in excited states or when weak transitions are involved. The use of multipass cells was the first way to increase by almost two orders of magnitude the pathlength, thus the sensitivity of the measurements. But recently, new laser absorption techniques, that can artificially increase up to a few  $10^4$  times the number of passes through the absorbing medium, have been developed. Cavity RingDown (CRDS) [1] and Intracavity Laser Absorption (ICLAS) [2] are two of these powerful methods. Very recently, a new technique, which uses a mode-locked tunable femtosecond laser, has also been proposed [3]. It combines the broad spectral feature of the laser source with the multipass ability of the CRDS and can provide simultaneous measurement on several spectral lines with very high sensitivity.

To be non intrusive, a diagnostic technique shouldn't introduce any microscopic or macroscopic modification of the properties of the medium under study. But for laser-based diagnostics, this condition can never be fulfilled because particles absorbing the laser photons will be transferred from their initial state to the upper state of the transition. This process leads to both a reduced population in the lower state (depletion) and a lower absorption rate, related to the difference between populations of the lower and upper states of the transition (saturation).

In this lecture, different laser-based diagnostic techniques will be discussed and their main advantages and disadvantages will be compared. Supported by several examples, a special emphasis will be put on depletion and saturation phenomena and some other artifacts that can occur in laser-based experiments and lead to an erroneous interpretation of results.

[1] A. Campargue, D. Romanini and N. Sadeghi, *J. Phys. D : Appl. Phys.*, **31**, 1168 (1998).

[2] C. Foissac, P. Supiot, A. Campargue, A. Kachanov, G. Weirauch, and N. Sadeghi, *J. Phys D: Applied Phys.* **33**, 2434 (2000).

[3] T. Gherman, E. Eslami, D. Romanini, J.-C. Vial and N. Sadeghi, *To be published*

# Plasma pre-treatments and treatments for reducing the “hydrophobic recovery” and obtaining permanently wettable Polytetrafluoroethylene

A. Milella, A. Delvecchio, L. Iacobelli, E. Mesto, P. Favia, R. d’Agostino  
*Department of Chemistry, University of Bari, Via Orabona 4, 70126 Bari*

## Abstract

Different plasma treatments (NH<sub>3</sub>, O<sub>2</sub>) were carried out on polytetrafluoroethylene (PTFE) for grafting polar groups and obtaining a stable, permanent hydrophilic surface. Plasma pre-treatments (H<sub>2</sub> and Ar) were also utilized to limit the aging, including the hydrophobic recovery, of the treated surface with time. Dynamic Water Contact Angle (WCA) measurements and X-ray Photoelectron Spectroscopy (XPS) analyses were performed to study the in-depth chemical compositional changes as a function of ageing time. The results were expressed in terms of the fractions of mobile and immobile polar grafted groups.

## 1. Introduction

PTFE is widely nowadays used in many technological fields, including textiles and biomedical applications [1,2]. However, one disadvantage is its poor adhesion to other materials, molecules or biological systems, which could clearly extend its use. One possibility to overcome this drawback is to change the chemical composition of PTFE surface by grafting polar groups by means of a proper plasma process, a well known strategy for tuning surface properties of polymers. Grafting chemical groups and/or crosslinking by means of plasma treatments can deeply change the chemical characteristics and surface energy of polymers. Polar groups (*e.g.* -NH<sub>2</sub>, -OH, etc.) can be conveniently grafted, for example, to increase the wettability of biomedical polymers, or to improve the adhesion of evaporated/sputtered Al layers at the surface of polyester films, in packaging applications [3]. An important issue in this context, often crucial for industrial applications, is the *ageing* of plasma treated surfaces. In fact, when polar groups are covalently bound to the surface chains of a hydrophobic polymer (down to ~20 Å from the interface), a dynamic polymer/air interface is created which experiences, at different extent, the *hydrophobic recovery* of the original moieties of the polymer at its surface. In the case of treated polymers stored in air, in fact, rotational and translational motions, when permitted, allow the original hydrophobic moieties of the polymer to emerge at the interface thus minimizing the interfacial energy, while polar groups are moved immediately below. Due to this phenomenon, which is probably the most subtle among all processes (*i.e.*, oxidation, contamination, etc.) that lead usually to the ageing, treated polymer surfaces tend to loose, within days or hours, the properties conferred by the treatment.

In this paper we report results obtained by treating PTFE surfaces with NH<sub>3</sub> and O<sub>2</sub> RF (13.56 MHz) plasmas in several experimental conditions. Further, we have evaluated the capability of Ar and H<sub>2</sub> plasma pre-treatments of PTFE in reducing the hydrophobic recovery of the plasma-polymer PTFE surface. Contact angle measurement can provide a quantitative description of polymer surface dynamics since they probe the surface layers to a depth comparable with the range of the interfacial forces involved in surface restructuring processes. Moreover, such measurements can provide the fractions of non polar and polar structure elements stabilized at a polymer surface. Starting from the Cassie equation [4], Chatelier et al. [5-7], derived a time-dependent model to describe surface restructuring processes of polymer surfaces in terms of fraction of mobile (*i.e.*, able to rotate below the interface,  $f_{p,m}$ ) and immobile ( $f_{p,im}$ ) polar groups, and of apolar surface groups ( $f_{np}$ ); the method is based on dynamic WCA measurements as a function of the ageing time. Assuming an exponential decay for the fraction of mobile polar groups, the Cassie equation can be rewritten as in (1):

$$\theta_E(t) = \arccos[f_{p,im} + f_{p,m} e^{-t/\tau} + (1 - f_{p,im} - f_{p,m}) \cos \theta_E^{np}] \quad (1)$$

where  $\tau$  is the characteristic time constant for the aging process and  $\theta_E^{np}$  is the equilibrium WCA of the untreated polymer. Time dependent values of equilibrium contact angle,  $\theta_E(t)$ , can be calculated as the



average from the cosine values of the experimental advancing ( $\theta_A$ ) and receding ( $\theta_R$ ) WCA angles, according to equation (2). Since equation (1) contains three unknown restructuring parameters,  $f_{p, im}$ ,  $f_{p, m}$ , and  $\tau$ , no analytical solution is possible, only a numerical one based on the Marquardt-Levenberg algorithm.

$$\cos \theta_E(t) = \frac{\cos \theta_A(t) + \cos \theta_R(t)}{2} \quad (2)$$

## 2. Experimental

Plasma treatments were carried out in a parallel plate tubular pyrex reactor ( $\Phi=10$  cm,  $L=80$  cm). The upper electrode is connected to the RF generator (ENI ACG-10, 13.56 MHz) through a matching network; the lower one, 5 cm far apart, is grounded, and is used as sample holder. The reactor is continuously pumped by a rotative pump which allows a minimum pressure of  $10^{-3}$  Torr. Gas flow rates are controlled with mass flow meters (MKS); pressure is monitored with a baratron (MKS). All the discharges were sustained for 1 minute with a flow rate of 10 sccm and pressure of 200 mtorr. In the case of  $O_2$  and  $NH_3$  plasma treatments, an input RF power value of 100 W was used; 20 W  $NH_3$  treatments were also carried out. During Ar and  $H_2$  pre-treatments the input power was fixed at 40 W.

$5 \times 2$  cm<sup>2</sup> samples were cut from PTFE sheets; before plasma modification. Samples were cleaned in ethanol for 5 min. The disappearance of the hydrocarbon contaminants (C1s spectra, 285.0 eV peak) was checked by XPS analysis. After the treatments, samples were aged in lab air at room temperature, stored in tissue-culture polystyrene (TCP) boxes to reduce contaminations during the ageing. A fresh sample was used per each WCA measurement and each XPS analysis. Dynamic WCA measurements were carried out periodically at room temperature, according to the sessile drop method, using a Ramé-Hart A-100 manual goniometer. Contact angles were measured on both sides of five drops of double distilled water per each sample, the average value was calculated. For all WCA data an uncertainty of  $\pm 3^\circ$  was assumed. The changes of chemical composition during storage time were studied by XPS using a PHI ESCA 5300 spectrometer with a non-monochromatic Al  $K_\alpha$  radiation (1486.6 eV; 300 W). During polymer surface analysis the pressure in the analysis chamber typically was  $1 \times 10^{-8}$  torr. Atoms present were identified by survey (0 - 1000 eV) spectra run at a pass energy of 89.45 eV in the fixed analyser transmission mode. High resolution spectra of C1s, N1s, O1s, and F1s signals were recorded with a pass energy of 35.75 eV. The C1s peak component relative to  $CF_2$  groups (BE = 292.5 eV), was used as an internal standard for charging correction. XPS analyses were carried out at  $45^\circ$  and  $20^\circ$  take off angles (TOA) to reveal any in depth elemental distribution changes.

## 3. Results and discussion

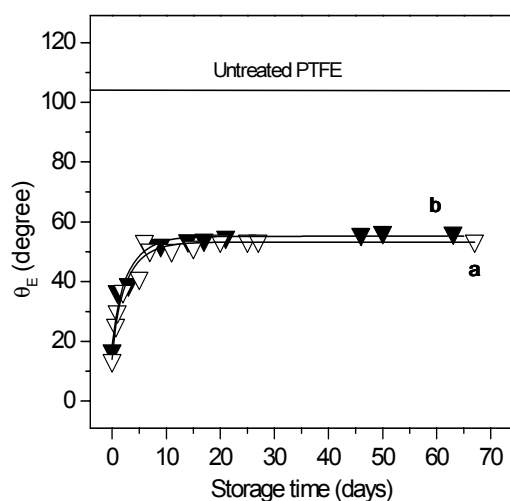
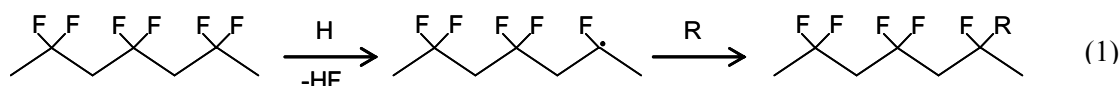
As a first step,  $NH_3$  plasma treatments, alone and coupled with  $H_2$  pre-treatments were investigated. The restructuring parameters are reported in Table 1, while WCA trends and curve fits are shown in Figure 1, where a case of negligible efficacy of the  $H_2$  plasma pre-treatment is shown.  $NH_3$  plasma treatment results in a hydrophilic PTFE surface. Equilibrium WCA, in fact, reach constant values of  $54^\circ$  within about ten days

**Table 1:** Process conditions and surface restructuring parameters for plasma modified PTFE.

Plasma treatment	$f_{p,m}$ (%)	$f_{p,im}$ (%)	$f_{np}$ (%)	$\tau$ (days)	$\theta_E(\infty)$ (degrees)
$NH_3$ (100 W)	$30 \pm 1$	$67 \pm 1$	$3 \pm 2$	$3.8 \pm 0.1$	$54 \pm 3$
1. $H_2$ (40 W) 2. $NH_3$ (100 W)	$30 \pm 1$	$64 \pm 1$	$6 \pm 2$	$3.6 \pm 0.5$	$56 \pm 3$

from the modification, thus lowering of more than 50% the original value for untreated PTFE. The fraction of immobile groups is 67% of the total fraction of polar grafted groups. It is also important to notice that immediately after the modification, PTFE is left very hydrophilic, as revealed by a WCA of  $14^\circ$ , and by a

non polar grafted groups fraction of only 3%. This is probably due to the presence of H atoms in  $NH_3$  plasma; they can, in fact, scavenge F atoms from PTFE, thus activating its surface toward the grafting of N-containing polar species, according to reaction 1. In this reaction, R represents a N-containing group, such as  $-NH_2$  or  $=NH$ , or a polymer chain radical; in this case it leads leading to cross-linking.



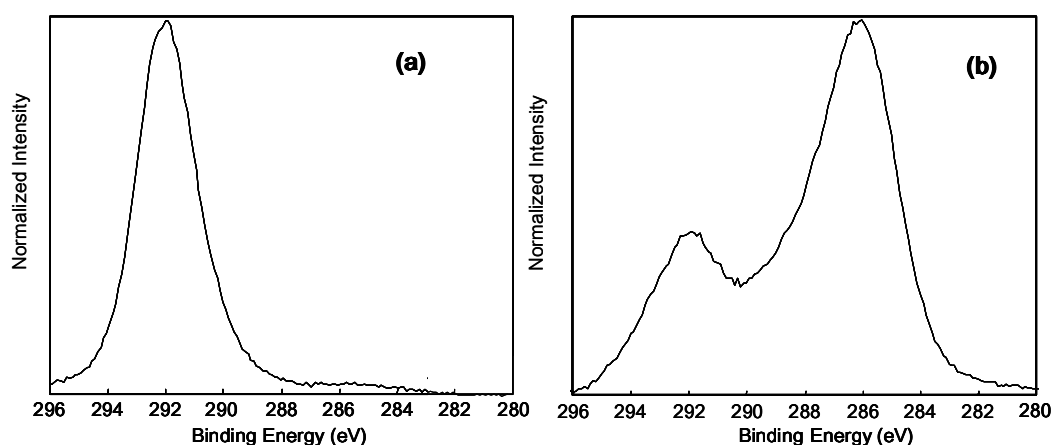
**Figure 1:** Equilibrium contact angles and best fitting curves as a function of storage time for (a) ammonia plasma (100 W) treated and (b) two step treated PTFE. Gas flow rate and pressure were fixed at 10 sccm and 200 mtorr, respectively.

Since WCA trends and restructuring parameters are almost the same for the two-steps process, it can be concluded that in the experimental conditions investigated  $\text{H}_2$  pre-treatment has no effect on limiting the hydrophobic recovery. In this case,  $\text{H}_2$  plasma pre-treated PTFE was tested with WCA and XPS measurements; advancing and receding WCA were found to be  $74^\circ$  and  $52^\circ$ , respectively. In any case these results show that a  $\text{NH}_3$  treatment is already somewhat successful in reducing the WCA value of PTFE. From XPS analysis it appears that  $\text{H}_2$  plasma pre-treatment drastically de-fluorinates the PTFE surface. The  $\text{C}1\text{s}$  peak (Figure 2) of  $\text{H}_2$  plasma pre-treated PTFE displays a strong decrease of the  $\text{CF}_2$  peak component at 292.5 eV, evidently due to a marked loss of fluorine abstracted from PTFE by H atoms formed in the plasma to form volatile HF. At the same time the  $\text{CF}$  and  $\text{C-CF}$  peak components increase their importance, and a contribution due

to  $\text{CF}_3$  groups appears at higher binding energy, as a result of chain rearrangement and reaction of F atoms.

Though  $\text{H}_2$  pre-treatment modifies PTFE extensively, and leads to a large extent of crosslinking, the trends shown in Figure 1 are very close thus reflecting, for this case, no benefits given by the  $\text{H}_2$  pre-treatments. Further experiments have shown that  $\text{NH}_3$  treatments at a low power performed on  $\text{H}_2$  pre-treated PTFE lead to much lower WCA stable values, as it will be shown. Very likely, drastic  $\text{NH}_3$  treatments (100 W, in our reactor) destroy the thin hydrogenated – cross-linked interface generated on PTFE by the  $\text{H}_2$  pre-treatment. The following two steps process has been investigated, then, with a low power (20 W)  $\text{NH}_3$  discharge:

- 1-  $\text{H}_2$  plasma pre-treatment at 40 W;
- 2-  $\text{NH}_3$  plasma treatment at 20 W.



**Figure 2:**  $\text{C}1\text{s}$  signal for (a) untreated PTFE and (b)  $\text{H}_2$  plasma (40 W, 200 mtorr, 10 sccm, 1 min) pre-treated PTFE, at  $45^\circ$  take off angle.

Restructuring parameters for this second treatment, listed in Table 2, have been obtained by fitting the WCA data. WCA trends are reported in Figure 3. These data show, with good evidence, how the  $\text{H}_2$  pre-treatment

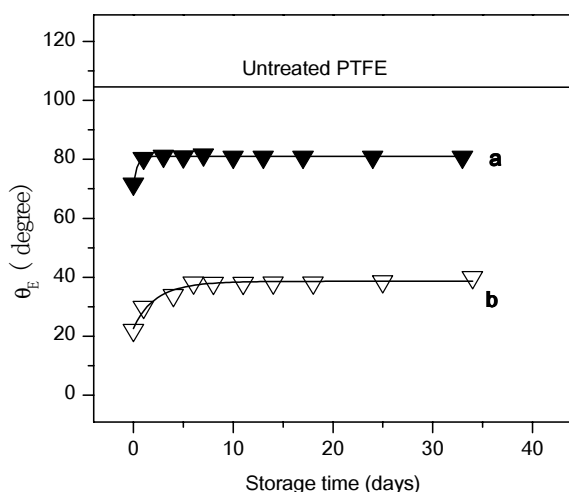
of PTFE is beneficial, in effect, but only when coupled to a low power  $\text{NH}_3$  treatment.

**Table 2:** Process conditions and surface restructuring parameters for plasma modified PTFE.

Plasma treatment	$f_{p,m}$ (%)	$f_{p,im}$ (%)	$f_{np}$ (%)	$\tau$ (days)	$\theta_E(\infty)$ (degrees)
$\text{NH}_3$ (20 W)	$13 \pm 1$	$31 \pm 1$	$56 \pm 2$	$0.37 \pm 0.06$	$81 \pm 3$
1. $\text{H}_2$ (40 W) 2. $\text{NH}_3$ (20 W)	$12 \pm 1$	$82 \pm 1$	$6 \pm 2$	$2.6 \pm 0.5$	$40 \pm 3$

The following comments can be expressed:

1.  $\text{H}_2$  pre-treatments are really effective (compare traces a and b in Figure 3) in preparing a surface more apt to retain  $\text{NH}_3$  plasma-grafted polar groups;
2. lower, stable WCA values are obtained (compare traces b in Figures 1 and 3) when low power  $\text{NH}_3$  treatments are performed
3. the fractions  $f_{np}$  and  $f_{p,m}$  are strongly reduced (compare Table 1 with Table 2);
4. the fraction of immobile polar groups,  $f_{p,im}$ , is strongly increased (compare Table 1 with Table 2);



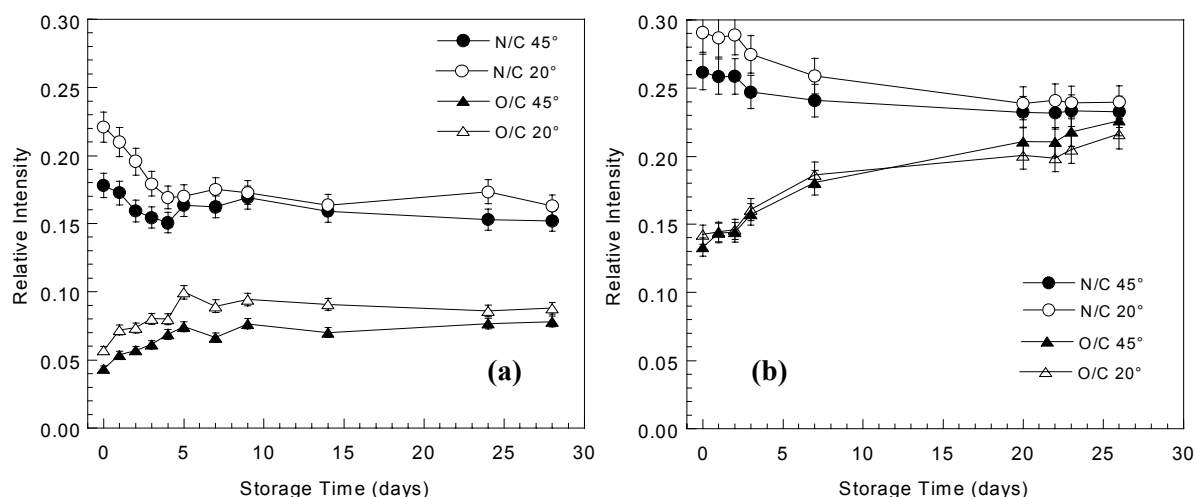
**Figure 3:** Equilibrium contact angles and best fitting curves as a function of storage time for (a)  $\text{NH}_3$  plasma treated PTFE (20 W) and (b) for the two step process. Gas flow rate and pressure were fixed to 10 sccm and 200 mtorr, respectively.

The inhibition of the surface restructuring process is evidenced also by the seven fold increase of  $\tau$  after the plasma  $\text{H}_2$  pre-treatment (see table 2). The pre-treatment is particularly successful probably due to the combined effect of H atoms (scavenging surface F atoms from PTFE) with UV radiation produced in  $\text{H}_2$  plasmas [8, 9]; both processes lead to a cross-linked PTFE surface, where the hydrophobic recovery of the untreated chains underneath is inhibited.

The evolution of O and N atom surface densities is reported for the two TOA, as a function of the ageing time, in Figure 4 (a), for  $\text{NH}_3$  (20 W) plasma treated PTFE. Both nitrogen and oxygen are present in the outer layer; the N density decreases with storage time due to chain/group restructuring motions at the polymer/air interface, and its density is higher in at the topmost layer of the surface, as attested by data at the lowest TOA. At the same time a continuous increase in oxygen concentration is observed as a function of the ageing, due to post-treatment oxidation of PTFE surface. This other process, part of the overall ageing,

can be ascribed both to reactions involving unsaturated radicals (dangling bonds) and to oxidation (oxygen insertion of some grafted groups (e.g., amines to amides). In particular, the oxygen incorporation is faster during the very first ageing days, as evident from the steep increase of the O/C ratio. Then a plateau is reached, as it happens also for WCA trends.

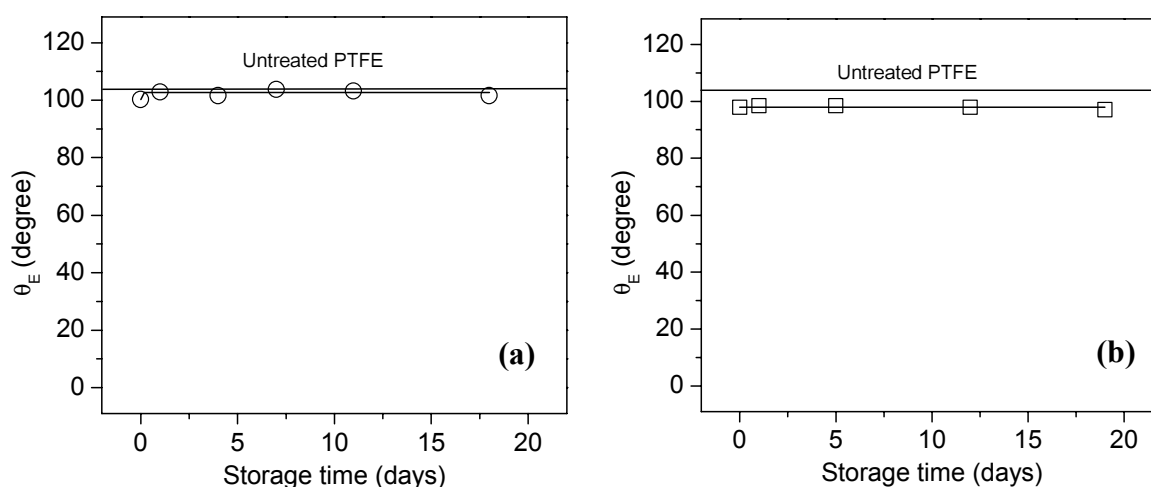
XPS density trends for  $\text{H}_2$  plasma pre-treated  $\text{NH}_3$  plasma (20 W) treated PTFE are shown in Figure 4 (b). By comparing these data with those in Figure 4 (a) one can clearly note how the hydrophobic recovery is now much slower. N/C trends, in fact, decrease less steeply in the pre-treated PTFE, attesting for a surface more polar and more rich in grafted N groups, very likely due to the more pronounced cross-linking of the PTFE surface, that reduces the hydrophobic recovery. The increase of the O/C ratio show that, also in this case, the oxidation of the surface is happening. XPS data are in good agreement with the restructuring data in Table 2. Pre-treatments have been performed also using argon as gas feed, in similar experimental conditions; in these cases WCA results obtained were found comparable, although slightly worse, to the case of  $\text{H}_2$ . XPS investigations, revealed a remarkable defluorination of PTFE soon after the Ar pre-treatment, most likely not for chemical abstraction, rather for the sputtering of the substrate. Ar pre-treatments result also in a cross-linked PTFE surface; the extent of de-fluorination, though, is lower respect to  $\text{H}_2$  pre-treatments.



**Figure 4:** XPS atomic ratios as a function of ageing time in air at take off angles of 20° and 45° for **(a)** NH<sub>3</sub> plasma treated (20 W) PTFE and **(b)** two step (NH<sub>3</sub>, 20W) treated PTFE.

Pre-treatments have been performed also using argon as gas feed, in similar experimental conditions; in these cases WCA results obtained were found comparable, although slightly worse, to the case of H<sub>2</sub>. XPS investigations, revealed a remarkable defluorination of PTFE soon after the Ar pre-treatment, most likely not for chemical abstraction, rather for the sputtering of the substrate. Ar pre-treatments result also in a cross-linked PTFE surface; the extent of de-fluorination, though, is lower respect to H<sub>2</sub> pre-treatments.

Figure 5 (a) shows equilibrium contact angle data as a function of storage time for oxygen plasma treated PTFE, using 100 W as input power.



**Figure 5:** Equilibrium contact angles and best fitting curves as a function of storage time for **(a)** O<sub>2</sub> plasma (100 W) treated PTFE and **(b)** two steps process (O<sub>2</sub>, 100 W) treated PTFE. Gas flow rate, pressure and treatment time were fixed at 10 sccm, 200 mtorr and 1 min, respectively.

It is well evident that the treatment was not effective at all in modifying the hydrophobic nature of PTFE, since WCA after the modification remained practically the same of the untreated polymer. This result could be expected, for the inertness of PTFE. As found by other authors [10, 11], in fact, the negligible degree of this modification probably reflects the preference of the radicals formed by the plasma on PTFE react with their neighbours rather than with oxygen containing species, in the plasma or in the atmosphere, after exposure to air. NH<sub>3</sub> treatments, instead, in the same discharge conditions, lead to a better hydrophilic surface character (see traces a in Figures 1 and 3) of PTFE surface. Very likely, this could be ascribed to the de-fluorination reaction of PTFE with H atoms generated by NH<sub>3</sub> molecules fragmented in the plasma, that activate the surface for the grafting of N groups. H<sub>2</sub> plasma pre-treatment (40 W) has been attempted, followed by O<sub>2</sub> plasma treatments (100 W). The resulting WCA ageing trends are reported in Figure 5 (b)

and show only a very little, negligible WCA decrease respect to PTFE untreated and O<sub>2</sub> plasma-treated in our conditions. Very likely, the de-fluorinated hydrogenated outmost PTFE layer produced with the H<sub>2</sub> pre-treatment has been etched away during the plasma-treatment in O<sub>2</sub>, thus revealing the untreated PTFE underneath with its wettability almost unchanged. Most likely, less drastic conditions of the O<sub>2</sub> Treatment (lower RF power input, lower discharge time, modulated plasma, etc.) may result in lower WCA values, provided the pre-treatment is performed before.

#### 4. Conclusions

A mathematical model describing the phenomenon of the hydrophobic recovery of PTFE chains after plasma treatments has been utilized for evaluating, quantitatively, the capability of O<sub>2</sub> and NH<sub>3</sub> plasma treatments, and of H<sub>2</sub> plasma pre-treatments, in obtaining stable wettable PTFE surfaces with limited ageing and long shelf life. Extremely promising results were obtaining by combining H<sub>2</sub> plasma pre-treatments with NH<sub>3</sub> plasma treatments at low RF power input. O<sub>2</sub> plasma treatments resulted, in the drastic experimental conditions tested, in no improvements of the PTFE wettability after H<sub>2</sub> pre-treatments; milder conditions may lead to lower WCA values.

#### References

- [1] E. M. Liston, L. Martinu, M.R. Wertheimer, in *Plasma Surface Modification of Polymers*, M. Strobel, C. Lyons, K. L. Mittal ed., VSP (1994).
- [2] F. Arefi-Khonsari, M. Tatoulian, J. Kurdi, J. Amouroux, *Vuoto*, **29**, 3-4 (2000).
- [3] M. Creatore, P. Favia, G. tenuto, A. Valentini, . d'Agostino, *Plasmas and Polymers*, **5**, 3/4 (2000).
- [4] A.B.D. Cassie, *Discuss. Faraday Soc.*, **3**, 11 (1948).
- [5] R.C. Chatelier, X. Xie, T.R. Gengenbach, H.J. Griesser, *Langmuir* **11**, 2576 (1995).
- [6] R.C. Chatelier, X. Xie, T.R. Gengenbach, H.J. Griesser, *Langmuir* **11**, 2585 (1995).
- [7] E.P. Everaert, R.C. Chatelier, H. C. Van der Mei, H.J. Bussecher, *Plasmas and Polym.* **2**, 41 (1997).
- [8] A. Hollander, R. Wilken, J. Behnisch, *Surface and Coatings Technology*, **116-119**, 788 (1999).
- [9] A. Hollander, J.E. Klemberg-Sapieha, M.R. Wertheimer, *J. Polymer Sci. A: Polymer Chem.*, **33**, 2013 (1995).
- [10] C. Baquey, F. Palumbo, M.C. Porte-Durrieu, G. Legeay, A. Tressaud, R. d'Agostino, *Nuclear Instruments and Methods in Physics Research B*, **151**, 255 (1999).
- [11] D. Youxian, H.J. Griesser, A.W.H Mau, R. Schmidt, J. Liesegang, *Polymer*, **32**, 1126 (1991).

# Smart BioSurfaces by Precision Chemical Control of Plasma Deposition

Buddy D. Ratner

*University of Washington Engineered Biomaterials (UWEB)  
Department of Bioengineering  
University of Washington  
Seattle, Washington 98195 USA*

In recent years, methods have evolved to deposit thin organic films from plasma environments that exhibit good control of chemistry along with the uniformity and substrate adhesion expected from plasma deposition. Three examples will be presented illustrating chemical control with special application to biomaterials.

Poly(*N*-isopropyl acrylamide) (pNIPAM) exhibits a solubility transition at 32 °C in an aqueous environment. When grafted onto a solid substrate, the pNIPAM phase transition produces a “smart” surface with strongly varying physical properties switchable with small temperature changes. Below the phase transition temperature, the surface is hydrophilic, swollen and nonfouling. As the temperature increases above the transition, the grafted polymer chains collapse and the surface becomes hydrophobic and protein-retentive. Vapor-phase deposition of plasma polymerized NIPAM (ppNIPAM) was used to produce conformal, sterile and pinhole-free pNIPAM coatings. The surface characteristics, protein adsorption properties and cell interactions of ppNIPAM were evaluated. The pNIPAM coating synthesized by plasma deposition is nonfouling at room temperature and highly protein-retentive at 37°C. The protein adsorption on ppNIPAM above its transition temperature is irreversible. Cells adhere and grow on ppNIPAM at 37°C and detach from the surface at room temperature. The ppNIPAM surfaces are non-toxic and excellent for cell growth. A microheater array can spatially control cell attachment to a ppNIPAM-treated chip. This suggests possibilities for cellomic and proteomic devices.

Since plasma environments destroy complex biomolecules, a new instrument has been constructed that combines electrospray ionization with plasma treatment of surfaces to produce a fast, efficient, flexible means to treat the surfaces of biomaterials with active biomolecules. The system has been successful in depositing intact, chemically bound hyaluronic acid (HA) onto plasma-activated stainless steel surfaces. HA is a naturally occurring polysaccharide that is found in the extracellular matrix, vitreous humor of the eye, synovial fluid, and has previously been shown to inhibit platelet activation and biological attachment to surfaces. These studies demonstrate that HA maintains these abilities after electrospray deposition onto plasma-activated surfaces.

Poly(L-lactic acid) (PLLA) has been widely applied in tissue engineering scaffolds or for delivery of bioactive molecules, as it breaks down in the body to lactic acid, a component of the normal metabolism. The pulsed plasma deposition technique has been used to form thin PLLA coatings using cyclic lactide monomer. Such films degrade in a phosphate buffer solution. These films and their degradation have been well characterized by XPS and TOF-SIMS.

# Atmospheric Pressure Plasma Technologies for Surface Modification of Polymers

Lesley-Ann O'Hare<sup>1</sup>, Stuart Leadley<sup>1</sup>, Bhukan Parbhoo<sup>2</sup>, Andy Goodwin<sup>1</sup>, Liam O'Neill

<sup>1</sup> *Dow Corning Plasma Solutions,*

*Dow Corning (Ireland) Ltd, Owenacurra Business Park, Midleton, Co. Cork, Republic of Ireland*

<sup>2</sup> *New Ventures Research and Development*

*Dow Corning (UK) Ltd, Cardiff Road, Barry, Vale of Glamorgan, CF63 2YL, UK*

## Abstract

The changes in the surface physico-chemistry of polypropylene and poly(ethylene terephthalate) films that are caused by corona discharge treatment have been described. A new approach of combining atmospheric pressure glow discharge (APGD) technology with a liquid delivery system to provide unique advantages over traditional plasma coating processes is also illustrated. True reel-to-reel processing of wide area flexible substrates with exciting possibilities in controlled chemistries is enabled.

## Introduction

Plasma enhanced coatings are a recognised route to well-adhered, high performance conformal coatings, but have been restricted to high value applications due to the need to carry out the process under vacuum. As a consequence, coating processes such as plasma enhanced chemical vapour deposition (PE-CVD) have found wide utility in the electronics industry but are not applied on a significant scale in industries which require high volume film, fibre or textile treatment.

Corona discharge treatment (CDT) is one form of atmospheric plasma, which has been widely used to modify polymer surfaces to obtain improved wettability and adhesion. The effects of corona discharge upon the surface physico-chemistry of polymer surfaces have been well characterised using a range of analytical techniques<sup>i</sup>. However, CDT does present some limitations, in that the modified surface can be heterogeneous, and can be damaged by this treatment. It also requires that activation and deposition be carried out in a multiple-stage process.

By combining atmospheric pressure glow discharge with a unique liquid precursor delivery system, Dow Corning Plasma Solutions are developing a new approach to coating technology- **atmospheric pressure plasma liquid deposition**. This process enables the treatment of wide area substrates in true reel-to-reel conditions. A summary of the apparatus and process will be presented, and the coating chemistry that is achieved will be summarised.

## Experimental

Corona Discharge Treatment was carried out on a GX10 corona treater manufactured by Sherman Treaters, Thame, Oxon. The treater is a bench-top dielectric barrier discharge instrument with a gap of 3mm between the electrode and the sample. Samples were treated at a constant speed of 10 mmmin<sup>-1</sup>, with varying powers to achieve treatment energy ranges from 0 – 15 kJm<sup>-2</sup>.

Plasma treatment was carried out using Dow Corning Plasma Solutions APGD equipment. This equipment is designed specifically for plasma processing of flexible substrates, operating in reel-to-reel conditions. The plasma source utilises parallel plate technology to generate a helium gas, glow discharge. Typical operating conditions are a voltage of 4-10 kV at a frequency of 10-50 kHz. The precursor is introduced as an atomised liquid directly into the glow discharge, enabling the use of a wide range of liquid precursors; not being restricted to gas or high volatility liquid precursors<sup>ii</sup>. The precursor may be chosen from a range of polymer precursors, unsaturated organic materials such as acrylates and alkenes are particularly favoured.

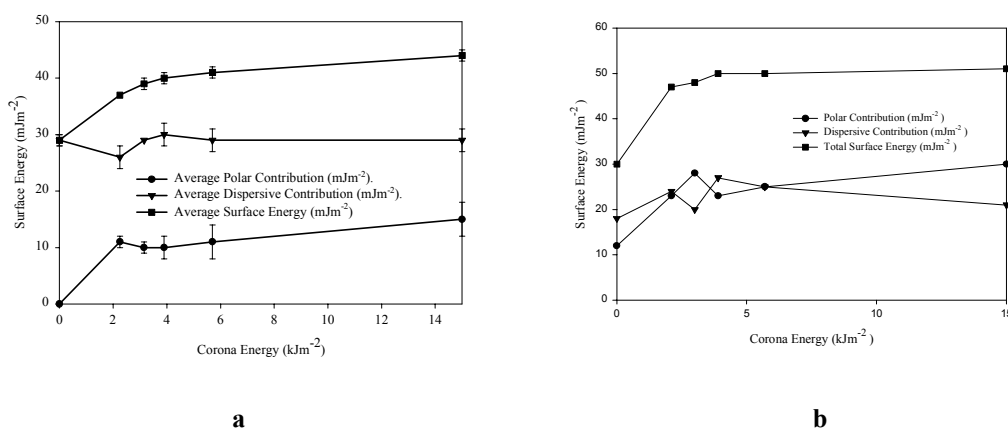
Video Contact Angle analysis was carried out on an Advanced Surface Technology VCA2500 system. 2μL drops of either Analar or HPLC grade probe liquids were used. Surface energies, when required, were then calculated using the geometric mean approach of Owens-Wendt and Kaelble.

X-ray photoelectron spectroscopy was performed on a Kratos Analytical Axis Ultra spectrometer. The spectrometer is equipped with a monochromated aluminium  $K\alpha$  K-ray source, and a magnesium/zirconium (Mg  $K\alpha$ /Zr  $L\alpha$ ) dual anode X-ray source. Samples were analysed at 300W, with a  $90^\circ$  take off angle, with respect to the sample surface.

Atomic force microscopy images were obtained using a Digital Instruments Dimension 3100 microscope in TappingMode® using a silicon tip.

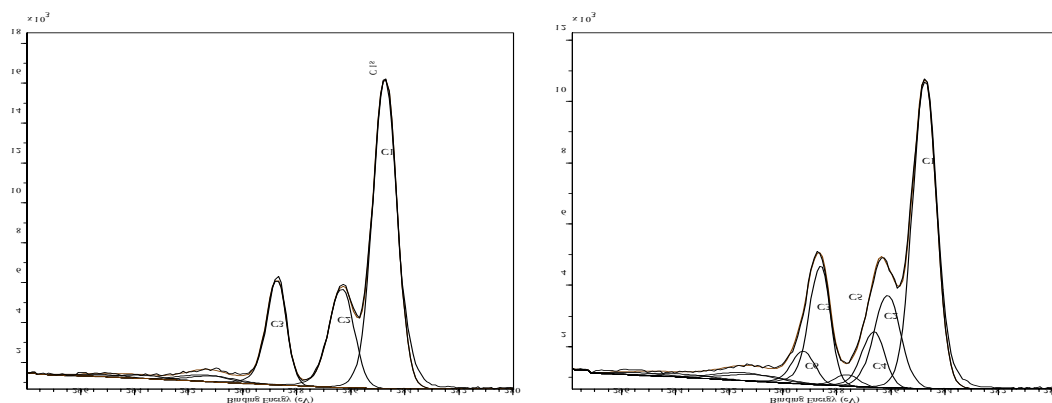
## Results and Discussion

Corona Discharge Treatment (CDT), when carried out in air brings about an increase in the surface energy of the treated polymeric substrate. This may be observed simply by noting a decrease in the contact angle that water makes with the surface. The use of additional probe liquids makes it possible to derive a specific value for the surface energy through the use of equations. Figure 1 presents the data for biaxially oriented polypropylene (BOPP) and poly(ethylene terephthalate) (PET) as a function of corona energy imparted to the surface of the film.



**Figure 1:** The surface energy ( $\gamma$ ), and its polar and dispersive components of corona discharge treated polymer films a) BOPP, b) PET

These surface energy changes may be further related to changes in the chemistry of the surface. These are investigated using X-ray Photoelectron Spectroscopy to determine, for example, the amount of a specific element incorporated into the surface. Using high resolution XPS, information about new functionalities introduced, or how existing functionalities are changed, may also be obtained. Figure 2 shows the carbon spectra for poly(ethylene terephthalate) **a)** as received, and **b)** after CDT at  $15 \text{ kJm}^{-2}$ .

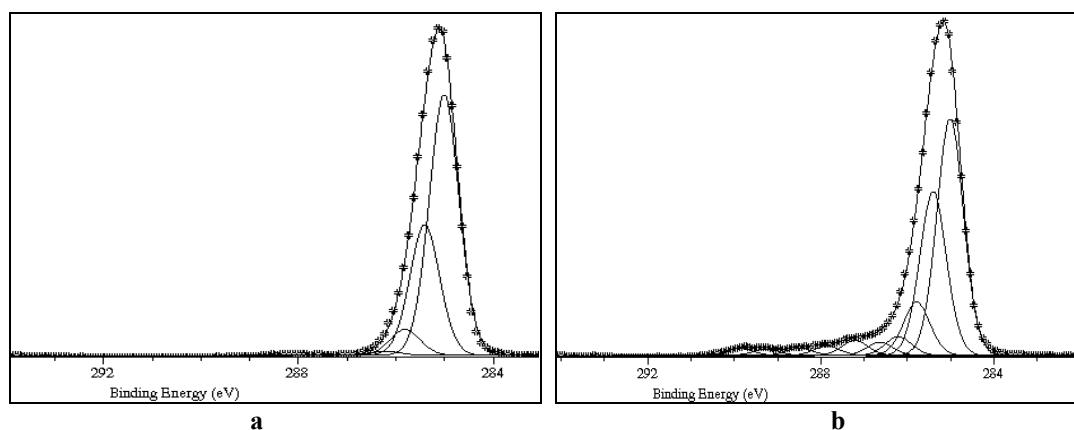


**Figure 2:** High-resolution carbon (C 1s) XPS spectra. a) 'As received' PET film, b) PET film corona discharge treated at an energy of  $15 \text{ kJm}^{-2}$



The assignment of three peaks in the original carbon spectrum (C1- aliphatic carbon, C2- aliphatic ester, C3- carboxyl) were as expected. Changes in the abundance of these three peaks were monitored as a function of CDT energy, and the addition of three components were required to provide a good fit of curves to the experimental envelope. The new functionalities were assigned as C4: phenolic-OH, C5: C=O, and C6: COOH.

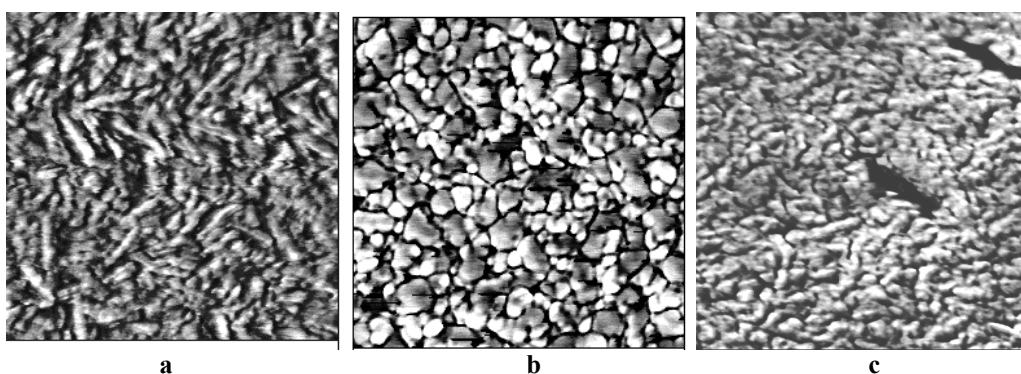
A similar procedure was used to identify the new functionalities on BOPP after CDT. The carbon spectrum for untreated BOPP has 4 peaks to represent the different vibrational states of carbon in the polymer backbone. After CDT, a shoulder on the high binding energy side of the spectrum is observed, indicating the incorporation of oxidised carbon species. The spectra for untreated BOPP, and BOPP exposed to a corona treatment at an energy of  $15 \text{ kJm}^{-2}$  are shown in Figure 3.



**Figure 3:** High-resolution carbon (C 1s) XPS spectra. a) Untreated BOPP film, b) BOPP film corona discharge treated at an energy of  $15 \text{ kJm}^{-2}$

The functionalities identified on the corona treated BOPP are C-OH, C-O-O, C=O, C-O-C\*=O, HOC=O and O-C(O)-O. These functionalities were present in varying concentrations dependent on the energy of the treatment.

Mechanisms were determined which accounted for incorporation of oxygen into the polymer backbone to generate some of these functionalities. Other functionalities were introduced through chain-scission of this oxidised polymer, leading to the creation of water-soluble, low molecular weight oxidised materials (LMWOM). The presence of such materials may be observed using AFM. Figure 4 shows images captured for a) untreated polypropylene b) BOPP after CDT, and c) BOPP after CDT and a 10s water wash.



**Figure 4:** Atomic force microscopy images of biaxially oriented polypropylene after various corona discharge treatment conditions. a) Untreated BOPP, b) BOPP after CDT at  $5.7 \text{ kJm}^{-2}$ , c) BOPP after CDT at  $5.7 \text{ kJm}^{-2}$ , followed by a 10 s water wash

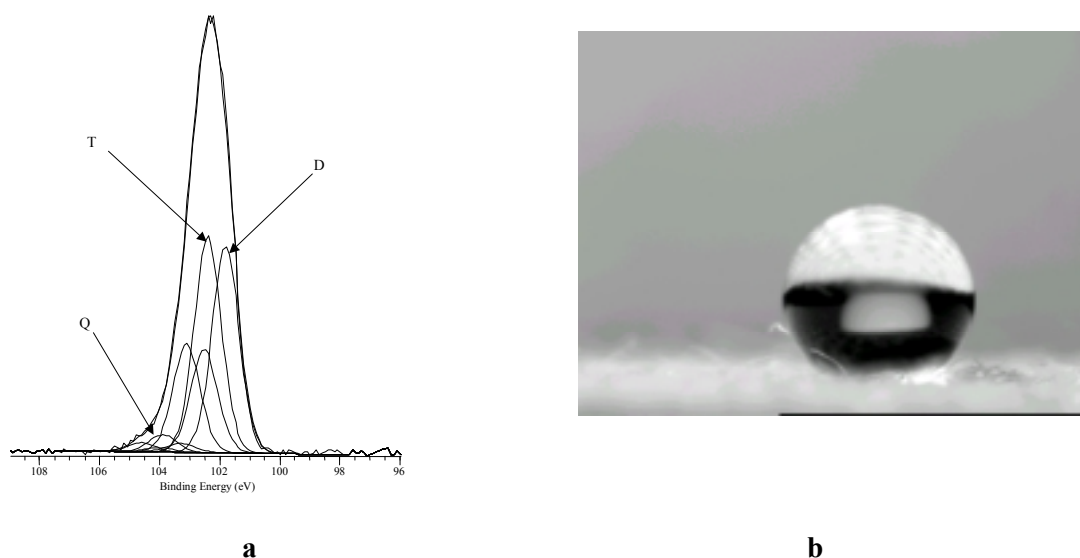
In Figure 4a, the biaxial orientation of the crystal structure of polypropylene is clearly visible. With corona treatment, this morphology is replaced with globular features, as can be observed in Figure 4b. The concentration and uniformity of these discrete globules increased with increasing energy of corona. That the LMWOM exist as globules is explained by differences in surface energy: the LMWOM will have a higher surface energy than the PP film, and as such would prefer to form a cohesive drop than to spread on the surface. Their water-soluble nature is also observed in Figure 4c. Here, although the structure of the film does not return to its untreated state, the globular features are removed. This is in agreement with work by Strobel *et al*, who observed similar effects with water washing experiments<sup>iii</sup>. The oxygen content also does not return to that of the untreated film- which suggests that oxidation is also occurring on a deeper and more permanent level than just in the outer, water-soluble layer. Also noted in Figure 4c is the appearance of two crevices, of ~200nm in length. It is surmised that these are areas of damage caused by localised arcs of high energy from the corona.

Atmospheric Pressure Glow Discharge offers a homogeneous surface treatment causing less surface damage to the substrate, when compared with traditional CDT. Working in collaboration with Professor Jas Pal Badyal at the University of Durham (UK), Dow Corning have developed a new coatings process which combines APGD with a liquid precursor delivery system<sup>ii</sup>. Operating at atmospheric pressure and ambient temperature, this process allows the use of a wide range of liquid precursors, delivering high coating rates onto flexible substrates. Patented APGD equipment enables the treatment of wide area substrates in true reel-to-reel conditions. Substrates can be either insulating (polymer films, non-wovens, fabrics and fibres) or conducting (metal foils, metallised films). Control of surface energy covers many applications, from water-wettable coatings on polyolefin films and non-wovens, to oleophobic treatments of films, fibres and fabrics. The possibility of introducing specific functionalities to polymeric substrates is also enabled, achieving such properties as barrier, adhesive, dielectric, conductivity and release.

#### Hydrophobic Coatings

Polydimethylsiloxane polymer coatings are widely used<sup>ii</sup> for their excellent hydrophobic properties, which increase water repellency, release and “hand”. Tetramethylcyclotetrasiloxane and octamethylcyclotetrasiloxane have been successfully used as precursors to produce polysiloxane coatings, which have excellent hydrophobicity.

Scrubbed cotton substrate was coated with polydimethylsiloxane, to give a hydrophobic, water repellent material. The octamethylcyclotetrasiloxane liquid precursor was introduced into the chamber at  $500 \mu\text{Lmin}^{-1}$  into a helium APGD with power  $1\text{Wcm}^{-2}$ . Figure 5a shows the silicon (Si 2p) XPS spectrum for the hydrophobic coating on scrubbed cotton, confirming the presence of D and T<sup>iv</sup> silicone polymer units, which indicates a cross-linked polymeric coating. This finding has also been reinforced by analysis by Fourier Transform Infra-Red Spectrometry and Nuclear Magnetic Resonance Spectroscopy (not presented here). Figure 5b presents an image of a water droplet on the surface of the cotton after the deposition of this polymeric coating. On an untreated cotton sample, water would wet out immediately.

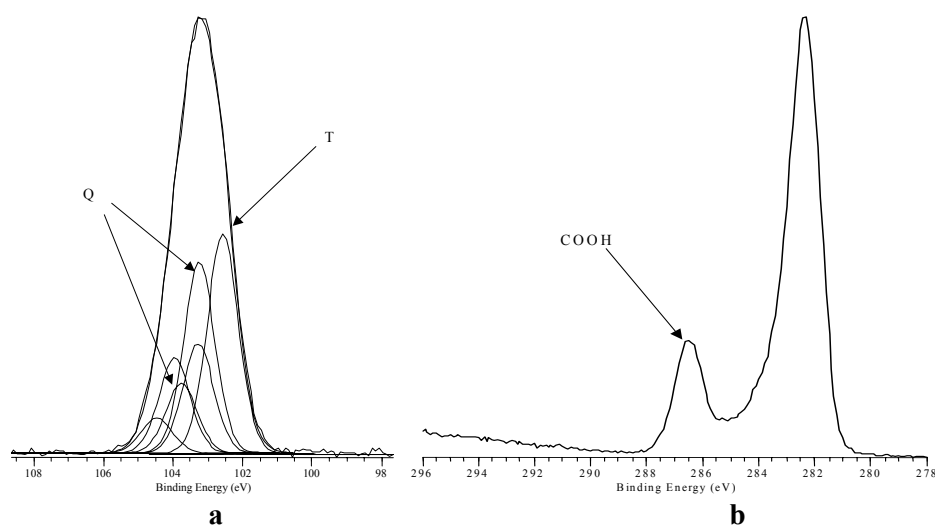


**Figure 5:** a) Silicon (Si 2p) XPS spectrum of a hydrophobic coating deposited from a siloxane precursor, b) Scrubbed cotton coated with polydimethylsiloxane. Water droplet on cotton substrate, with water contact angle 140 degrees, non-treated cotton wets immediately.

### Hydrophilic Coatings

The same siloxane precursors may also be used to prepare hydrophilic coatings. By changing to oxidising helium/oxygen APGD conditions, hydrophilic  $\text{SiO}_x$  coatings can be deposited in place of the hydrophobic coatings described previously. An example of the silicon (Si 2p) XPS spectrum for a hydrophilic coating deposited from a siloxane precursor is shown in Figure 6a. The chemical nature of the coating is  $\text{SiO}_{3/2}$  and  $\text{SiO}_{4/2}$ .

Polyacrylic acid (PAA) coatings are also widely regarded for their hydrophilicity, adhesion and biocompatibility. However, many challenges exist in the preparation of high quality PAA coatings, particularly in retention of  $-\text{COOH}$  functionality and coating durability. PAA coatings were prepared by Atmospheric Pressure Plasma Liquid Deposition to give highly hydrophilic coatings with high  $-\text{COOH}$  retention. For example, Figure 6b shows a carbon (C 1s) XPS spectrum for polypropylene film, coated by introduction of acrylic acid liquid precursor into the plasma at  $30 \mu\text{Lmin}^{-1}$ , substrate line speed of  $1 \text{ mmin}^{-1}$  in helium APGD with a power of  $0.4 \text{ Wcm}^{-2}$



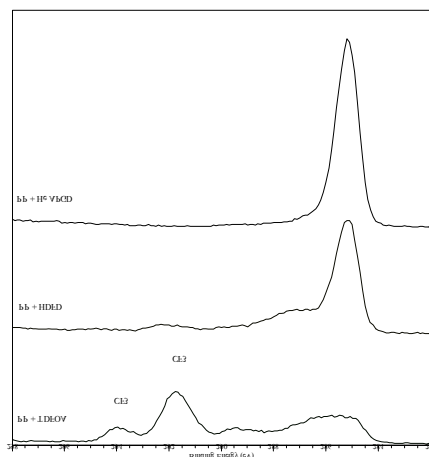
**Figure 6:** a) Silicon (Si 2p) spectrum of a hydrophilic coating deposited from a siloxane precursor, b) Carbon (C 1s) spectrum of a deposited Polyacrylic acid coating on polypropylene, with retention of  $-\text{COOH}$  functionality

### Oleophobic Coatings

Fluorocarbon coatings can be produced from perfluoroacrylate or perfluoroalkene precursors to provide highly oleophobic surfaces<sup>v,vi</sup>. Some simple examples of such coatings are presented here, where heptadecafluorodecene (HDFD) and tridecafluorooctylacrylate (TDFOA) precursors have been used to provide an oleophobic coating on polypropylene.

The high-resolution carbon (C 1s) spectra of atmospheric pressure plasma treated polypropylene and HDFD and TDFOA coatings on polypropylene are shown in Figure 7. Qualitatively, it is clear that with both precursors CF<sub>3</sub> and CF<sub>2</sub> functionality is retained. The hydrocarbon of the polypropylene substrate is clearly evident in the HDFD coated material but is absent from the TDFOA coatings.

Oil repellency was tested by the standard method, with an initial oil repellency of 6 being achieved, however this is degraded by washing in hot water.



**Figure 7:** High resolution carbon (C 1s) spectra of coated polypropylene films

### **Conclusions**

The changes in surface energy, chemistry and morphology of polypropylene and poly(ethylene terephthalate) films that are caused by corona discharge treatment have been described. It has been shown that damage to the substrate can be caused even under relatively mild conditions, due to localised arcing of discharge.

Combining atmospheric pressure glow discharge technology with a liquid delivery system provides unique advantages over traditional plasma coating processes. The Dow Corning APP liquid deposition equipment enables open perimeter, reel-to-reel processing of wide area flexible substrates. Liquid precursor introduction opens up exiting possibilities in controlled coating chemistries, with hydrophobic, hydrophilic and oleophobic coatings proven, and being continually developed.

### **References**

- <sup>i</sup> For detailed reference list see L.-A. O'Hare, S. Leadley, B. Parbhoo- Surf. Int. Anal. **33**, 335-342, (2002), and L.-A. O'Hare, J.A. Smith, S.R. Leadley, B.Parbhoo, A.J. Goodwin, J.F Watts- Surf. Int. Anal. **33**, 617-625, (2002)
- <sup>ii</sup> A.J. Goodwin, P.J. Merlin, J.P. Badyal, L. Ward, PCT Patent WO 02 28548, 11<sup>th</sup> April 2002
- <sup>iii</sup> M. Strobel, C. Dunatov, J.M. Strobel, C.S. Lyons, S.J. Perron, M.C. Morgan- J.Adhes. Sci. Technol. **6**, 423, (1989)
- <sup>iv</sup> Organosilicon notation, D= Si(Me)<sub>2</sub>O<sub>2/2</sub>, T = Si (Me)O<sub>3/2</sub>, Q = Si )<sub>4/2</sub>
- <sup>v</sup> S.R. Coulson, I.S. Woodward, J.P.S. Badyal, S.A. Brewis, C. Willis- Langmuir **16**, 6287-6293, (2000)
- <sup>vi</sup> S.R. Coulson, I.S. Woodward, J.P.S. Badyal, S.A. Brewis, C. Willis- Chem. Mater. **12**, 2031-2038, (2000)

# Dielectric barrier glow discharges: Science and applications

F. Massines<sup>1</sup>, P. Ségur<sup>2</sup>, N. Gherardi<sup>1</sup>, C. Kamphan<sup>2</sup>, C. Jimenez<sup>1</sup>, M. C. Bordage<sup>2</sup>,  
J.P. Cambronne<sup>1</sup>, N. Naudé<sup>1</sup>

<sup>1</sup> *Laboratoire de Génie Electrique de Toulouse, Université Paul Sabatier, Toulouse, France*

<sup>2</sup> *Centre de Physique des Plasmas et de leurs Applications de Toulouse, Université Paul Sabatier, Toulouse, France*

## Abstract

The development of a process based on Glow Dielectric Barrier Discharge (GDBD) requires a large understanding of the discharge physics and chemistry. After a rapid description of GDBD behaviour in He and N<sub>2</sub>, the mechanisms which enhance the cathode secondary emission to such a level that a Townsend breakdown occurs at atmospheric pressure will be discussed. Then, specific destabilisation of the nitrogen GDBD will be described. To finish, the specificities of dielectric barrier glow discharge will be analyzed in terms of advantages and drawback for surface treatment and gas chemistry.

## 1. Introduction

Cold plasma process appears as an answer to a lot of environmental problems like gas or surface decontamination and surface treatments. However, today, its application is partly limited by its condition of production. In several cases, low pressure plasmas lead to too much expensive solutions while atmospheric pressure plasmas lead to not enough controlled processes. Rather recently, a specific discharge working at atmospheric pressure and having most of the low pressure characteristics, the Atmospheric Pressure Glow Discharge (APGD) has been obtained and applied to different chemistry problems including thin film coatings [1-6]. This discharge is a dielectric barrier discharge (DBD): each electrode has to be covered by a solid dielectric. Its specificity is to be a glow like discharge having a section equal to that of the electrodes. Then, we call it Glow DBD (GDBD). The atmosphere, the excitation waveform and the shape of the electrodes and dielectrics have to be adapted to get it but GDBD is suitable with roll to roll surface treatment process working in controlled atmosphere. A better understanding of that discharge physics would help in the optimisation of new processes based on GDBD.

This presentation of GDBD will be limited to discharge obtained with plane electrodes. In such configuration, it is obtained in nitrogen and in noble gas if they contain at least some ppm of an other gas to realise a Penning mixture.

## 2. Experimental set-up and numerical model

The reactor used for this study is described in details elsewhere [7]. The discharge is obtained between two plane, flat, parallel electrodes coated on ceramic (Al<sub>2</sub>O<sub>3</sub>) plates which are or not covered by a silicon wafer or a polymer. The gas gap is 1 mm for the N<sub>2</sub> experiments and 5 mm for the He ones. The power supply is a low frequency sinusoidal voltage ranging from 200 Hz to 20 kHz and going up to 24 kV peak to peak. After outgassing the cell down to 10<sup>-1</sup> Pa the gas is introduced up to a pressure of 10<sup>5</sup> Pa. The maximum concentration of residual air is 1ppm. During the discharge, the gas flow can be vary from 0 to 10 l/min maintaining the pressure equal to 10<sup>5</sup> Pa.

The discharge current is measured through a 50 Ω resistor. From its value and that of the voltage applied to the electrode, the voltage applied to the gas is calculated assuming that the discharge uniformly covers the entire surface of the dielectric in front of the electrodes [8]. Time resolved pictures of the discharge gap are taken with a ultrahigh speed CCD camera.

The numerical model has been described in references [9,10]. It is a one-dimensional model based on the numerical solution of the electron and ion continuity and momentum transfer equations coupled to Poisson's equation. As usual in the case of high-pressure discharges, electrons and ions are assumed to be in equilibrium with the electric field. The model is self-consistent and gives the space and time variations of the electric field, the electron and ion densities. Time variations of gap voltage, memory voltage and current density are also obtained.

The charge accumulation on the dielectric as the discharge develops is carefully taken into account and the voltage boundary conditions for dielectrics are derived by considering the equivalent circuit of the gas gap in series with the equivalent capacitor of the dielectrics. The experimental electric circuit is also considered to

calculate the external voltage during the discharge pulse.

Data concerning the electron transport parameters and ionization and excitation coefficients were calculated from a numerical solution of the Boltzman equation. A detailed description of the data introduced in the GDBD model is given in [9] for He and in [10] for N<sub>2</sub>.

### 3. Similarity and difference between noble gases and nitrogen GDBD

Figure 1 presents the discharge current of a GDBD in He and in N<sub>2</sub>. In the two cases, the discharge is made of one pulse each half cycle. The specificity of GDBD is to have a duration of at least some microseconds and to be perfectly reproducible from one cycle to the following one. In nitrogen, the pulse duration is 5 time longer and its amplitude is 5 time lower. In argon and neon, the discharge is similar to that of helium.

Short exposure time pictures of the gas gap (Figure 2) confirms that the section of the discharge is equal to that of the electrodes and that there is no streamer. In He, the light distribution (Figure 2a) is that of a glow discharge with a cathode and a negative glows, a Faraday dark space and a positive column. Numerical model results (figure 3) confirm that interpretation and give the order of magnitude of the electrons and ions densities as well as the electrical field when the current is maximum. The cathode fall is about 400μm which is too large for an atmospheric pressure normal glow discharge. This discharge is a subnormal glow discharge. From the breakdown to the current maximum, the cathode fall becomes thinner and thinner i.e. the discharge turn Townsend into glow discharge but the discharge development is stopped before the normal glow discharge is reached. For a 5 mm gap, the positive column length is 3mm.

In N<sub>2</sub>, the light is maximum at the anode (figure 2b) which corresponds to the behavior of a Townsend discharge. Here again, numerical model results (figure 4) confirms this interpretation: even when the current is maximum, the ion density is too low to induce a significant space charge field. There is no positive column. The electrical field is quasi-homogeneous and the density of electrons increase exponentially in the gas gap.

The main difference between a noble gas and a nitrogen GDBD is the ionization level and consequently the formation of the positive column. In N<sub>2</sub>, the energy is mainly transferred near the anode while in noble gases the energy is mainly transferred near the cathode.

### 4. How a Townsend breakdown is obtained at atmospheric pressure ?

In the experimental conditions presented here, the product of the pressure and the gas gap is higher than 76 Torr.cm. The electron mean free path is about 1000 times shorter than the gas gap. So, the surface contribution to the ionization is so low compared to the gas bulk one that a large avalanche should be at the breakdown origin. The breakdown mechanism should be a streamer one. The production of a Townsend breakdown in these conditions supposes that the surface contribution, the  $\gamma$  secondary emission, is enhanced to be able to create the seed electrons and to induce the discharge development without a space charge localization in the gas bulk. The aim of this part is to discuss how this occurs i.e. which mechanism controls the breakdown. The case of noble gases and nitrogen will be successively considered.

In noble gases, the current density sufficiently increases to induce a positive column formation. It has been shown that the electrons and ions created during the discharge are trapped in this positive column from the end of the discharge to the electrode polarity reverse [10]. This reversal pushes the electrons and the ions to the electrodes which were respectively the cathode and the anode when they have been created and which are now respectively the anode and the cathode. If the breakdown occurs rather quickly after the gas voltage polarity inversion, the density of ions ( $n_i$ ) and electrons ( $n_e$ ), created during the previous discharge and still present in the gas gap when the next breakdown occurs, is rather high. As example, for a 10 kHz excitation,  $n_e$  is of some  $10^7/\text{cm}^3$  close to the anode while  $n_i$  is about  $10^9/\text{cm}^3$  in most of the gas gap. At contrario, at atmospheric pressure, the noble gas metastables have rather short life time (of the order of 10 μs) due to the formation of dimmers. Then, they can not contribute to the memory effect from one discharge to the following one.

This memory effect based on ions and electrons influences the breakdown through 3 mechanisms: (i) ion density is high enough to induce a significant gradient of the electrical field from the anode to the cathode (1.3 kV/cm to 2.6 kV/cm before the breakdown). (ii) ions will contribute through cathode secondary emission [11]. The ion flow at the cathode is around  $8.10^{13}/\text{cm}^2.\text{s}$ , if the secondary coefficient is 0.01 then the electron flow from the cathode will be of  $8.10^{11}/\text{cm}^2.\text{s}$ . These electrons increase the density of electrons in the gas gap before breakdown. (iii) The high concentration of trapped electrons will be at the origin of a high

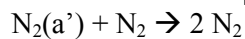
concentration of metastables before breakdown occurs because He metastables level is 5 eV lower than the ionization level. These metastables efficiently ionize the gas via Penning ionization ( $\text{He}(2^3\text{S}) + \text{A} \rightarrow \text{A}^+ + \text{e} + \text{He}$ ). The dimmers can also contribute. The ions created, will considerably increase the ion flow at the cathode before breakdown. In He, metastables are able to ionize all the other gases. Then the density of A is at least 1 ppm which corresponds to a density of  $2.10^{13}/\text{cm}^3$  and the contribution of Penning ionization is not negligible as shown in figure 5. Because of the space charge field, this ionization process occurs near the cathode and largely contribute to the cathode ion bombardment. These 3 steps mechanism: ions create electrons at the cathode, electrons create metastables in the gas, metastables create ions and electrons, as 2 consequences: (i) it allows a slow increase of the gas ionization before the voltage is high enough to induce the formation of a large avalanche. (ii) When the voltage is high enough to have a large contribution of direct ionization, seed electrons are mainly due to the cathode secondary emission.

In nitrogen, there is not a positive column. The electrons can not be trapped, but the life time of  $\text{N}_2(\text{A}^3\Sigma_u^+)$  metastables at atmospheric pressure is much longer than He metastable one. So the memory effect is based on that specie. During a discharge, the electric field is quasi-uniform and the electron density is maximum at the anode. Then the metastables are mainly created near the anode (Figure 4). Even if the order of magnitude of the mean free path is micron, part of them reach the dielectric surface as shown in figure 6 which represents the metastables flow on the surface of one dielectric during half a cycle. This flow is independent of the electrical field and only related to the concentration gradient of metastables. Then, after the end of the discharge, when the gas voltage polarity reverses which means that the dielectric which was on the anode is now on the cathode, the metastable flow on to the cathode is rather large. As metastables efficiently induces secondary emission, this mechanism will begin to produce electrons. Of course the electron emission depends on the cathode secondary emission coefficient of the dielectric surface. For kHz excitation the polarity of this surface changes at least every  $500\mu\text{s}$ . At this time scale, the dielectric surface can not reorganize: the electrons which have reached that surface when the dielectric was on the anode are trapped on shallow traps. The deepness of shallow traps is 1-2 eV from the void level while the valence band is at 6-8 eV. Then, these electrons are easily removed from the surface just after the polarity reverse. This is why, whatever the nature of the dielectric, the effective gamma coefficient does not significantly change. But it is necessary to have a dielectric on each electrode. An other point is that higher will be the field, higher will be the effective  $\gamma$  emission coefficient and then the contribution of that mechanism [12]. In  $\text{N}_2$  also, before breakdown voltage, the cathode largely contribute to the emission of electrons. Then, when the gas bulk ionization increases because of the increase of the  $\alpha$  ionization coefficient with the electrical field, these electrons are at the origin of the electronic avalanches. According to the numerical model, this mechanism allows to decrease the breakdown voltage of  $1/4$ . [10]

To summarize, in noble gases, because of excimer formation, the metastables life time is short compare to the time between two discharges then, a positive column is necessary to trap ions and electrons. Before breakdown, these ions and those created by Penning ionization due to the metastables created by the trapped electrons induce an ion bombardment of the cathode high enough to produce an amount of secondary electrons large enough to control the breakdown. In nitrogen, the  $\text{N}_2(\text{A}^3\Sigma_u^+)$  metastables life time is longer than the time between two discharges but these metastables can not make Penning ionization. However they are created so close to the dielectric surface which will be the cathode during the next breakdown that the cathode secondary emission due to the metastables bombardment control the breakdown.

In other words, if the discharge is a Townsend one, only metastables can be trapped in the gas gap as far as they have a long life time compared to the time between two discharges. If the discharge is a glow one electrons and ions trapped in the positive column will allow to ensure a large secondary emission through the creation of metastables and Penning ionization.

The formation of a positive column in a  $\text{N}_2$  GDBD is not so easy, probably because at atmospheric pressure, Penning ionization is low. The metastable state which is at the origin of Penning ionization in  $\text{N}_2$  is  $\text{N}_2(\text{a}')$ , and at atmospheric pressure this excited state is very efficiently quenched by  $\text{N}_2$  in the fundamental level. The quenching rate is 100 times higher than in helium. Moreover, in He, the dimmer ( $\text{He}_2$ ) can also contribute to the ionization [13]. Then the contribution of Penning ionization is really smaller in  $\text{N}_2$ .



$$k = 10^{-13} \text{ cm}^3/\text{s}$$

$$k = 3.10^{-15} \text{ cm}^3/\text{s at atmospheric pressure } ([\text{He}] = 2.3.10^{19} \text{ cm}^{-3})$$

## 5. Over GDBD destabilization mechanisms

In noble gases, if the breakdown is a Townsend breakdown, then the discharge is a glow one, probably because the gas voltage decreases too much to allow streamer development. In nitrogen, destabilization have been observed during the current increase when the current slope begin to decrease or around the current maximum. These destabilization have to be related to the discharge development.

At the beginning of the pulse, the current increase is due to the gas voltage increase (figure 7) i.e. to a higher value of  $\alpha$ , the ionization coefficient of the gas bulk. When the Townsend discharge is obtained the current can change a lot under a very small voltage variation [14]. From the point of view of the electrical circuit, during the current rise, the load connected to the power supply which are the solid dielectrics and the gas gap varies. If the voltage variation with time is too high, this variation is too quick, the electrical circuit oscillates and so the discharge [15].

The second destabilization which is a real transition to streamer occurs just after the current maximum when the power supply voltage ( $V_a$ ) is equal to that of the gas ( $V_g$ ) i.e. when the voltage applied to the solid dielectric ( $V_{sd}$ ) is equal to zero according to  $V_a = V_g + V_{sd}$ . This is explained by a decrease of the  $\gamma$  secondary emission coefficient. As explained previously, this coefficient depends on the density of electrons trapped in the dielectric shallow traps. During the current increase, these electrons are removed from the surface (cathode secondary emission) or neutralized by the ions. Then, that density decreases and so  $\gamma$  which decreases up to the point where all the shallow traps are free. This occurs when the charge of the dielectric surface is equal to zero i.e. when  $V_{sd}$  is equal to zero. A decrease of the  $\gamma$  coefficient can induce a decrease of the current or an increase of the  $\alpha$  ionization coefficient if the discharge is self sustained. A higher value of  $\alpha$  supposes a higher electrical field. This increase can be due to a gas voltage increase or to the formation of a thinner cathode fall which is a probable explanation of the light movement from the anode to the cathode which has been observed in certain conditions after the current maximum. However, if the  $\alpha$  has to increase too much, it seems that the only solution is a formation of large positive space charge and then a streamer development. When the gas gap is of 1mm this does not lead to a transition to a fully filamentary discharge but when the gas gap increases, the Townsend breakdown is no more obtained, probably because the electrical field distortion is too important and the metastables are created too far from the anode to efficiently reach the dielectric surface.

## 6. Characteristics of the GDBD

The understanding of GDBD principal allows to explain the limitation in that discharge conditions of production: the gas chemical composition as to be well controlled to ensure Penning ionization in noble gases and a metastables life time long enough in nitrogen. Dielectric layers on each electrode are necessary to have a high effective  $\gamma$  coefficient at the beginning of the discharge. The gas gap and the excitation frequency have to be high enough in noble gases to allow the positive column formation and the charge storage from one discharge to the following one. In  $N_2$ , the gas gap, the slope and the amplitude of the excitation are limited to avoid power supply oscillations and the formation of a positive space charge.

The first step of gas chemistry is the transformation of the electrical energy in energetic particles like electrons or metastables which will dissociate the reactive molecules. Then, it is interesting to compare these particles characteristics, in terms of creation kinetics, energy and space distribution.

The GDBD power is rather limited:  $0.01 \text{ W/cm}^2$  in He and  $3 \text{ W/cm}^2$  in  $N_2$ . These values have to be compared with the  $10 \text{ W/cm}^2$  typically used in a corona treater which is the more common roll to roll process. Remember that the discharge involved in a corona treater is a DBD made of a lot of filaments. The maximum of the electron density in the GDBD canal is very low compared to that of a filament:  $10^{11}/\text{cm}^3$  in He (fig. 3),  $10^9/\text{cm}^3$  in  $N_2$  (fig. 4), and about  $10^{14}/\text{cm}^3$  in a filament whatever the gas. These low values are balanced by the discharge duration: the order of magnitude are respectively  $5\mu\text{s}$ ,  $100 \mu\text{s}$ ,  $0.1\mu\text{s}$ , and the discharge radius is equal to that of the electrodes in GDBD while it is about  $200\mu\text{m}$  for a filament. Then, in a filament a lot of energy is injected during a very short time and in a small volume. Even if this energy is slowly dissipated in a channel which is typically 10 times larger than the initial one, a high density of primary radicals is created and these primary radicals largely recombine between them. In a GDBD, the energy is more slowly injected in all the volume at the same time. That means that the density of primary radicals is lower but the creation continues for a longer time. These differences affect radicals chemistry and the equilibrium between gas and surface chemistry.



An other important data is of course the energy of the particles which transport the energy. The N<sub>2</sub> GDBD being a Townsend discharge, it has a specific behavior. The electron energy is well define, E/N is constant on all the gap and during the most part of the discharge. Moreover, for a given gas gap, this field depends only on the temperature. Its typical value of 40kV/cm (fig. 4) corresponds to a mean electron energy of 4 eV. The other specificity of that discharge is that N<sub>2</sub>(A<sup>3</sup>Σ<sub>u</sub><sup>+</sup>) density is 5 orders of magnitude larger than the electron one. Then these metastables which have 6.2 eV highly participate to the chemistry. In He, He(2<sup>3</sup>S) and He<sub>2</sub> also play a dominant role. Their energy is 19.6 eV for He(2<sup>3</sup>S) and around 16 eV for He<sub>2</sub>. Due to the micrometric mean free paths, the over important point at atmospheric pressure is the position where the energy is dissipated. In the GDBD whatever the gas, most of the energy is dissipated close to one of the surface while in a filament a large part is dissipated in the gas gap. Then, GDBD appears as efficient discharge for surface treatment.

## 7. Conclusion

GDBD fundamentals are more and more understood. A GDBD is a discharge due to a Townsend breakdown. This atmospheric pressure discharge is very useful for surface treatment: it is very well controlled and uniform, the energy is mainly transferred near to the surface and the initial dissociation path way can be rather well controlled due to the large role of the main gas metastables. Moreover, production conditions compatible with roll to roll surface treatment have been found.

## References

- [1] S.F. Miralai, E. Monette, R. Bartnikas, G. Czeremuszkin, M. Latreche and M. R. Wertheimer, *Plasmas and Polymers* **5**(2), (2000)
- [2] C. P. Klages, R. Thyen and M. Vergohl, *Diamond-Materials. VI International Symposium Electrochemical Society* **99**, 64 (2000)
- [3] S. Okasaki, M. Kogoma, M. Uehara, and Y. Kimura, *J. Phys. D: Appl. Phys.* **26**, 889 (1993)
- [4] D. Trunec, A. Brablec, and F. Stastný, *Contrib. Plasma Phys.* **38**, 435 (1998)
- [5] F. Massines, G. Gouda, N. Gherardi, M. Duran and E. Croquesel, *Plasma and Polymers* **6** 35 (2001)
- [6] S. Martin, N. Gherardi, C. Jimenez et F. Massines, *Proc. 15<sup>th</sup> Int. Symp. Plasma Chemistry, ISPC 15*, Orléans (2001) p. 127
- [7] E. Croquesel, N. Gherardi, S. Martin, and F. Massines, *Proc. 7th Int. Symp. On High Pressure Low Temperature Plasma Chemistry, HAKONE VII*, Greifswald (2000) p. 88
- [8] F. Massines, Ph. Decomps, C. Mayoux, *Proc. 4th Int. Symp. On High Pressure Low Temperature Plasma Chemistry, HAKONE IV*, Bartislava (1993) p. 141
- [9] F. Massines, R. Ben Gadri, Ph. Decomps, A. Rabehi, P. Ségur, C. Mayoux, *J. Phys. D: Appl. Phys.* **38**, 2950 (1998)
- [10] C. Khamphan, P. Ségur, F. Massines, M.C. Bordage, N. Gherardi and Y.Cesses, *in this proceedings*
- [11] Y. Motoyama, H. Matsuzaki, H. Murakami, *IEEE Transactions on Electron Devices* **48**, 1568 (2001)
- [12] Y.Murakami,H.Matsuzaki,H.Murakami and N.Ikuta, *Jpn. J. Appl. Phys.* **40**, 3382 (2001)
- [13] Belikov A. E., *Chemical Physics* **215**, 97 (1997)
- [14] Y.P. Raizer, *in: Gas discharge physics*, Springer-Verlag, Berlin (1991)
- [15] N. Naudé, J.P. Cambronne, N. Gherardi, F. Massines, *in this proceedings*

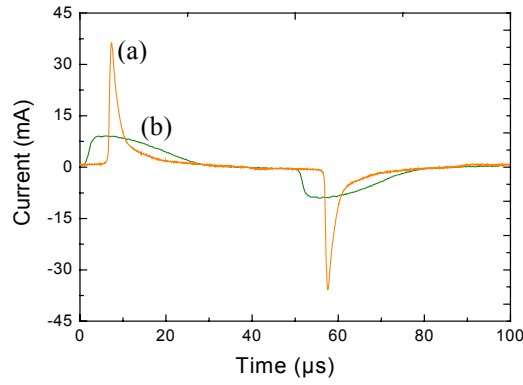


Figure 1: Measured current of GDBD  
a) helium, b) nitrogen

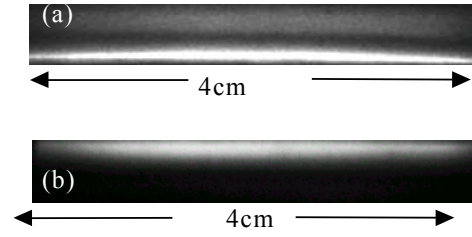


Figure 2: 10 ns exposure time photograph of a GDBD  
gas gap a) in helium, b) in nitrogen

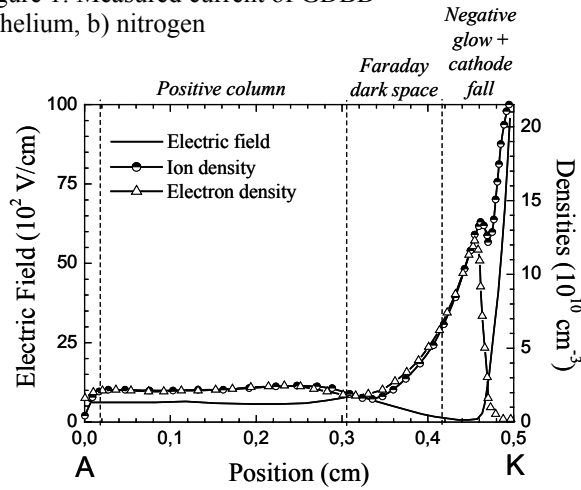


Figure 3: Density of electrons, ions and electrical field  
as function of the position from the anode to the  
cathode when the current of a He GDBD is maximum

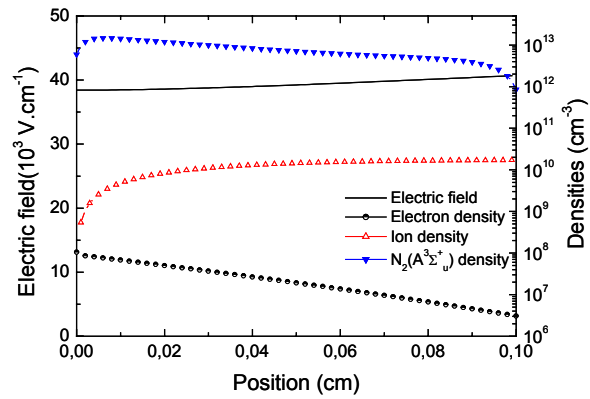


Figure 4: Density of electrons, ions and electrical field  
as function of the position from the anode to the  
cathode when the current of a N<sub>2</sub> GDBD is maximum

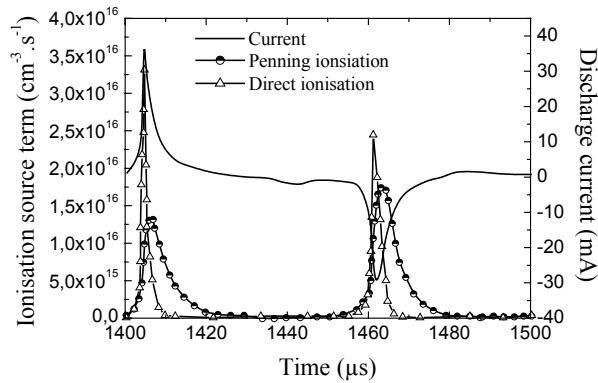


Figure 5: Source terms of the Penning ionization and  
the direct ionization during one cycle of a He GDBD

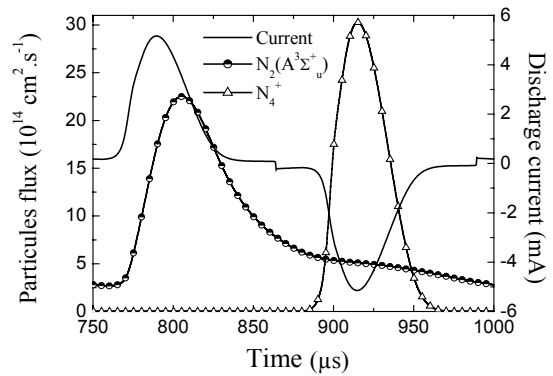
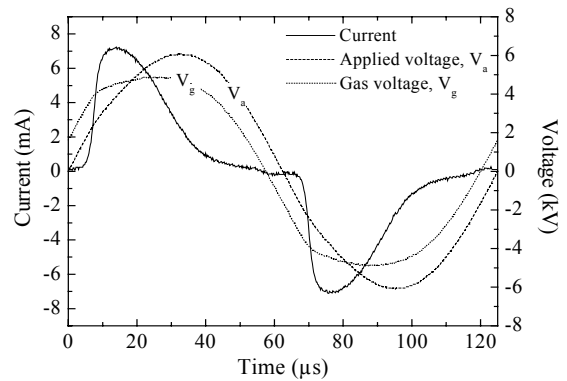


Figure 6: Metastable and ion fluxes on one of the  
dielectric surfaces during one cycle of a N<sub>2</sub> GDBD

Figure 7: N<sub>2</sub> GDBD oscillogram of the  
discharge current ant the voltages applied to the  
electrodes and to the gas



# Atmospheric pressure plasma deposition of thin films by dielectric barrier discharges

C.-P. Klages, M. Eichler, C. Geßner, C. Penache

*Fraunhofer Institute for Surface Engineering and Thin Films (IST), Braunschweig, Germany*

## Abstract

Dielectric barrier discharges can be used for the plasma-assisted deposition of thin films at atmospheric pressure. In contrast to low-pressure glow discharges, there is hardly any surface bombardment by energetic species in DBDs run at 1 bar. Therefore surface modifications and coatings requiring significant ion fluxes with energies in the order of 100 eV – hard diamond-like carbon deposition, for example – are generally not possible. On the other hand, thanks to the low mean free path of electrons at ambient pressure, DBDs can be sustained in very small volumes with linear dimensions down to of a few  $\mu\text{m}$ . This feature opens interesting new application opportunities, for example a conceptually very simple new direct-patterning surface modification process. Using pulsed excitation of the DBD, thin films with high retention of the monomer structure can be obtained from acrylic and methacrylic compounds.

## 1. Introduction

Dielectric barrier discharges (DBDs) are non-thermal transient gas discharges which can be maintained at atmospheric pressure between AC-powered electrodes separated by at least one dielectric barrier. Since decades DBDs are used industrially for ozone generation and the activation of polymer surfaces as a pretreatment before painting, printing or pasting. In these applications, DBDs usually appear a multitude of transient, localized microdischarges (filaments) of very short duration (several 10 ns), with filament diameters of about 0.1 mm and electron energies of typically 1-10 eV [1]. Within these microdischarges gases are electronically excited, ionized and dissociated and highly reactive species are formed without a significant increase of the average gas temperature, similar to low-pressure (typically 0.1 Pa to 1 kPa) glow discharges being in use, among other applications, for deposition of thin films by plasma-activated chemical vapor deposition (PACVD) processes. Due to the requirement of a vacuum system, low-pressure plasma processes of this kind are generally fairly cost-intensive. Run-through coating of large-sized products such as polymer foils, metal bands, textiles or papers requires either a large vacuum chamber accomodating take-off and take-up reels or a complicated cascade of pressure stages allowing an air-to-air process. For these reasons, the plasma-activated deposition of thin films at atmospheric pressure is a promising approach to a reduction of coating costs which is inevitable for finishing of low-cost products.

DBD-based PACVD at atmospheric pressure goes back to Donohoe and Wydeven which in 1979 reported about plasma polymerization from gas mixture of ethene and helium [2]. The present paper gives, from an application-oriented point of view, an overview of thin film deposition by DBD-based PACVD from hydrocarbon and Si-containing precursors, mainly based on IST work. In the 90s, the research in DBD applications was considerably intensified thanks to the results of Japanese (Okazaki, Kogoma et al.), French (Massines et al.) and American (Roth et al.) scientists proving that, aside from the filamented form, spatially uniform atmospheric pressure DBDs (“atmospheric pressure glow discharges”) can be generated under specific conditions. In the experiments reported here, no attempts have been made to generate uniform discharges. Film deposition results were usually uniform down to the  $\mu\text{m}$  scale, even though the discharge used was generally filamented.

## 2. Lack of ion bombardment in atmospheric pressure DBDs, consequences for thin film growth

In the literature on atmospheric pressure corona and dielectric barrier discharges, certain similarities between these discharges, closely related to each other, and low-pressure glow discharges have been pointed out, for example the formation of a transient cathode fall of several 100 V over a few  $\mu\text{m}$  thickness during the development of a microdischarge [3]-[5]. It has also been claimed, based on the detection of characteristic elemental lines in plasma emission spectra, that insulating [6] as well as metallic [7] surfaces are “sputtered” under the action of corona or barrier discharges.

For surface technological applications of DBDs it is an important question, if effects of ion bombardment can be utilized, e.g. for sputtering of materials or for the deposition of coatings requiring a certain amount of ion energy flux, like hard, “diamond-like” carbon-hydrogen coatings (“DLC”) [8].

A rough order-of-magnitude estimate of the average energies of ions hitting a surface during the transient cathode fall phase of the discharge (assuming a 1000 V cathode fall, 10  $\mu\text{m}$  cathode fall thickness, linear potential drop, 0.1  $\mu\text{m}$  mean free path and complete energy loss during collisions) yields a value of 10 eV. Figure 1 compares the corresponding ion flux energy distribution [9] to the sputter yield curves of Cu and SiO<sub>2</sub> [10]. Only a very small fraction of the ions have sufficient energy to sputter these materials with a yield of more than 1 %! In addition to the lack of sufficient ion energy flux, the small mean free path of sputtered particles at atmospheric pressure also is an obstacle to the utilization of atmospheric-pressure DBDs as sputter sources.

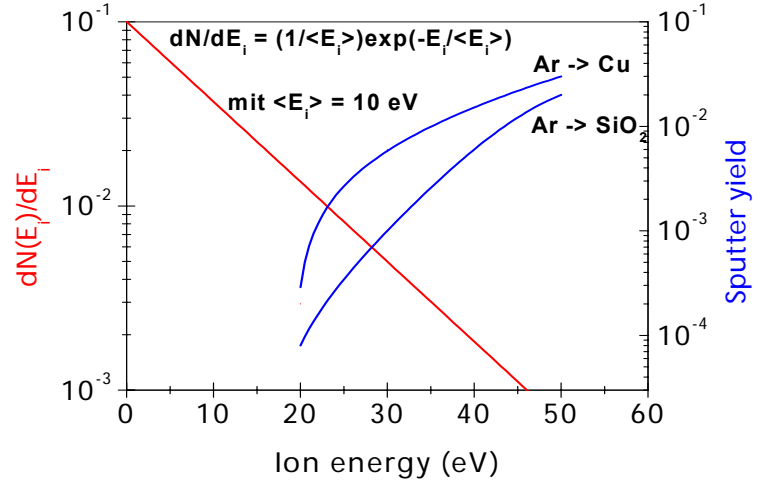


Fig. 1: Ion flux energy distribution with an average of 10 eV (red), sputter yield curves of Cu and SiO<sub>2</sub>, bombarded by Ar (blue; from [10]).

Figure 2 schematically shows a set-up as it is used for film deposition by DBD-based plasma-assisted chemical vapor deposition at ambient pressure at IST. In a series of experiments on amorphous hydrogenated carbon (a-C:H) coatings, deposited from methane and acetylene, respectively, diluted in Ar or N<sub>2</sub> as a carrier gas, the question of mechanical properties like hardness and elastic modulus of these coatings was addressed [11]. According to the present status of knowledge, a bombardment of the growing a-C:H film by energetic ions is inevitable if a hardness of at least 15-20 GPa is to be achieved. Using an indentation method with continuous registration of indentation depth and force on the indenter, maximum hardness and Youngs modulus values of 1.6 GPa and 9 GPa, respectively, were obtained in this study, which has to be compared to hardness values of roughly 20 GPa for DLC coatings deposited at low pressure by RF-plasma deposition. Infrared absorption spectra of the DBD-deposited films, taken in the region of C-H stretching vibrations around 3000 cm<sup>-1</sup>, indicate a hydrogen content of about 50 %, typically for a weakly crosslinked, “polymer-like” coating, as to be expected from the ion energy flux estimations made above.

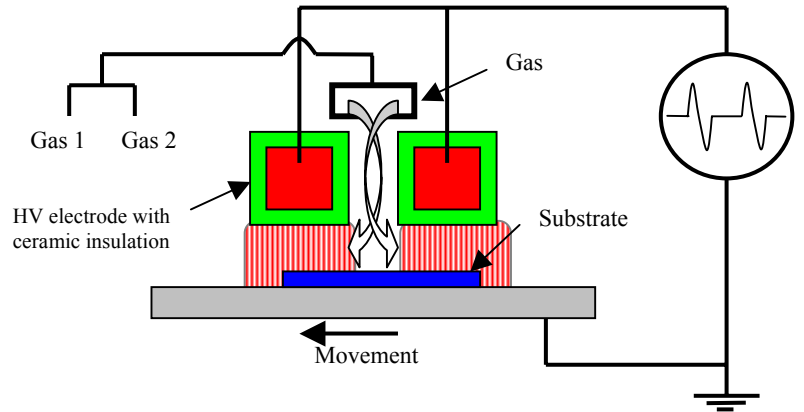


Fig. 2: Principal set-up used for film deposition by DBD-based plasma-assisted chemical vapor deposition at ambient pressure.

### 3. Pulse-plasma polymerization using DBDs

In recent years, the deposition of thin films by low-pressure pulse-plasma deposition from special, mostly unsaturated (allyl, vinyl, acryl, methacryl,...) monomeric precursors carrying functional groups like hydroxy, carboxy or epoxy has attracted increasing interest. A number of publications on this topic are referenced in a review article [12]. Using a pulsed excitation of the discharge, nearly monofunctional surfaces, i.e., surfaces carrying a high density of the functional groups contained in the precursor, have been obtained in many cases. The structural retention of the monomer usually increases with decreasing duty cycle ratio, because of decreasing damage to monomers and growing films by energetic plasma particles like electrons and ions.

Growth experiments with acrylic acid and methacrylic acid esters in Ar or N<sub>2</sub> carrier gases have shown, that similar mechanisms seem to be operative in DBD-based plasma deposition with pulsed excitation, too. Figure 3 shows the dependence of film growth rate as a function of the duty cycle for glycidyl methacrylate monomer, carrying epoxy groups, in nitrogen as a carrier gas. The deposition was performed using a sinusoidal mid-frequency (typically 30-50 kHz) excitation with a constant pulse length of 1 ms and varying pause durations. The maximum in the curve of Figure 3 shows that the growth rate is not simply proportional to the average power input to the discharge.

In Figure 4, infrared spectra are shown, taken from coatings on Si wafers, obtained in these experiments. The black curve is the spectrum of a thin film obtained from the commercial polymer poly(glycidyl methacrylate) ("Poly-GMA"). The series of spectra indicates, that an increasing retention of the monomeric structure is achieved upon increasing the pause duration.

A quantitative evaluation of the amount of epoxy groups in these coatings shows that up to 80 % of the functional groups originally contained in the monomer, are still present in the coating, if the pause duration is selected properly (see Figure 5). The plot of film thickness increment growing within one cycle (i.e. one pulse and one pause) versus the

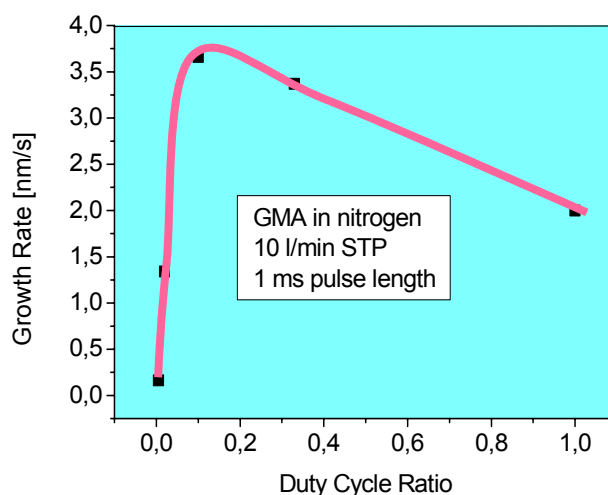


Fig. 3: Dependence of film growth rate on duty cycle for glycidyl methacrylate in nitrogen.

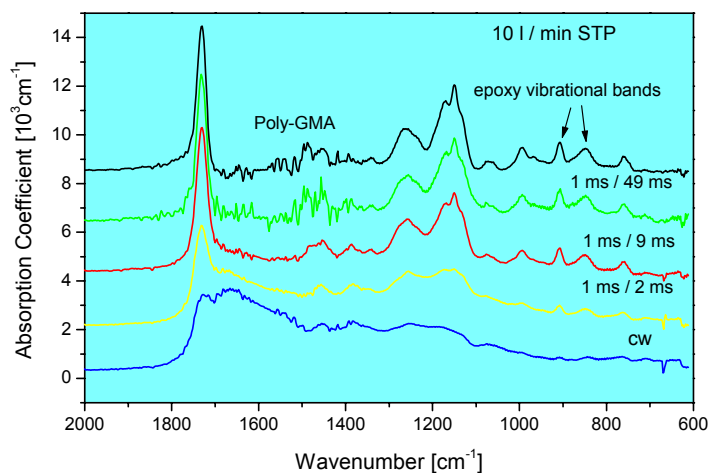


Fig. 4: IR spectra of poly-GMA and plasma deposited films for different pause lengths after 1 ms pulses at 10 l/min STP gas flow.

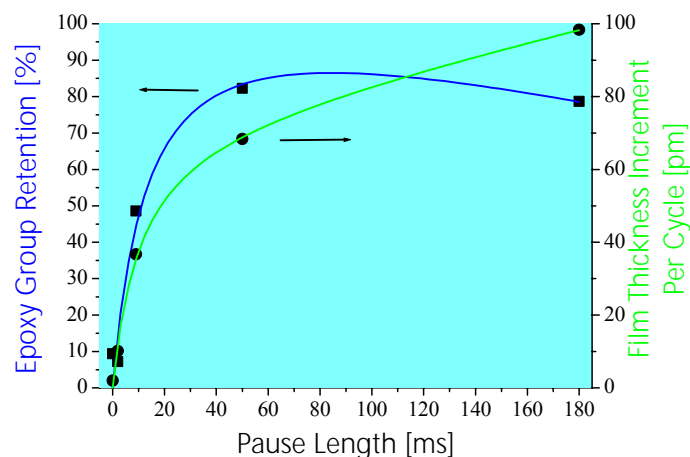


Fig. 5: Film thickness increment within one cycle and percentage of epoxy group retention as a function of pause lengths after 1 ms pulses, gas flow 10 l/min STP.

pause duration can be explained by long-lived radical species contributing to the film growth process during the plasma-off phase (Figure 5). From investigations of the influence of gas species residence times on the film growth rate further informations about the growth mechanism can be obtained: The increase of growth rate towards shorter residence times of the monomer species can be interpreted by a simple model in which active surface radicals, generated by the plasma pulse, react with intact monomer molecules during the pauses.

#### 4. Adhesion promotion and corrosion protection by ultrathin Si-based coatings

As an alternative to wet-chemical phosphating and chromating pretreatments prior to organic coating of metal surfaces, plasma polymerization at reduced pressure has frequently been investigated as a new method to improve the corrosion resistance of the painted metal by forming an adhesion-promoting interlayer [13],[14]. Although in some cases excellent corrosion resistance can be achieved after a replacement of chemical conversion of the metal surface by plasma polymerization, no process of this kind has so far been commercialized, probably due to the high costs involved in installing a vacuum section into a steel or aluminum sheet production line. Therefore it is of high interest to investigate if similarly good performance of a plasma polymer can be achieved by performing the film deposition process at atmospheric pressure using a dielectric barrier discharge.

The performance of ultra-thin silicon-based plasma polymers as adhesion-promoters for organic coatings on cold rolled steel (CRS), electrogalvanized steel (EG) and hot-dip galvanized steel (HDG) was investigated in a series of experiments. Superior results were obtained with powder-coated electrogalvanized steel: Using properly adjusted pretreatment and film deposition parameters, a very thin (10-30 nm) plasma polymer coating was sufficient to achieve salt spray test corrosion data which outperformed those of conventionally treated samples. In Figure 6, selected results of salt spray tests are shown which indicate the potential of ultra-thin plasma polymers. The EG coatings obtained with DBD-deposited plasma polymer interlayers are not only superior with respect to the corrosion resistances available; they also meet all other requirements (mechanical adhesion, bendability) of a state-of-the-art steel coating. On EG steel, silicon oxide coatings deposited from tetraethyl-orthosilicate (TEOS) were usually inferior to virtually oxygen-free silicon-based coatings grown from an inert or reducing gas ambient. In experiments with CRS, a different selection of monomer, carrier gas and deposition conditions was necessary to obtain reasonable corrosion results. This finding demonstrates the importance of a properly designed metal / polymer interface.

Silicon-based DBD plasma coatings do not only have considerable potential as adhesion-promoting coatings for subsequent organic coating; they can also be used as temporary corrosion protection under environmental conditions that are not too harsh. This is demonstrated by the two photographs in Figure 7, comparing two EG steel panels exposed for six weeks to the open air in the city of Braunschweig (October/November, 1997). After this

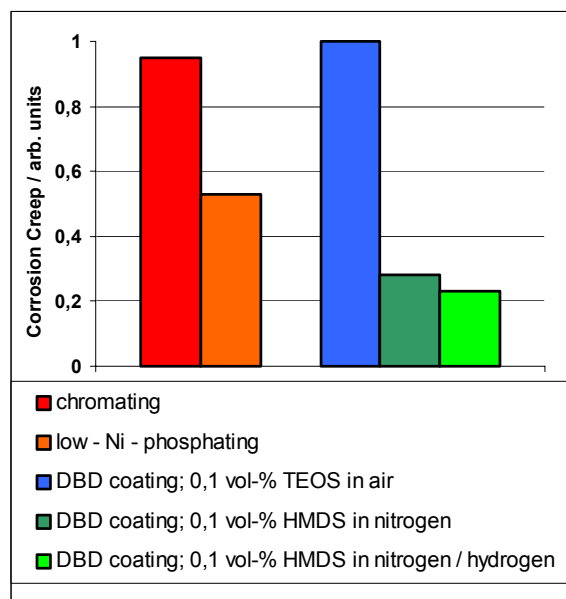


Fig. 6: Results of salt-spray corrosion tests on electrogalvanized steel sheets, powder-coated after different surface pretreatments. The bar height is a measure of the corrosive attack starting from a cut in the coating.

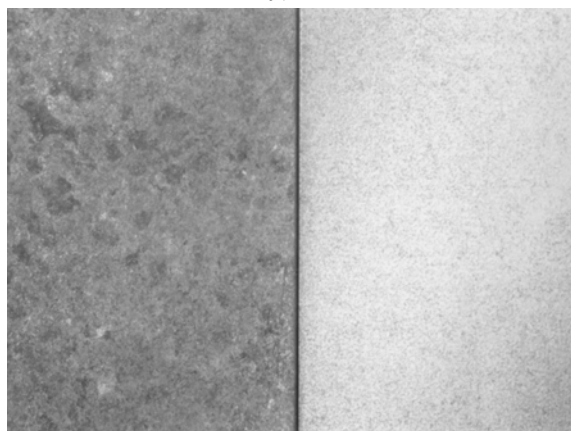


Fig. 7: Photographs of electrogalvanized steel sheets after 6 weeks storage at the open air (Braunschweig, october/november 1997). Left hand sheet uncoated, right hand sheet coated with 100 nm SiO<sub>x</sub> (DBD-PACVD from TEOS).



period the uncoated panel on the left had suffered strong corrosive attack, easily recognized by visual inspection, while the sample on the right, carrying a 100 nm  $\text{SiO}_x$  coating deposited by DBD plasma deposition, was virtually unchanged.

## 5. Utilization of micro-DBDs for plasma printing processes

Many technical applications require an area-selective film deposition or surface modification at predefined substrate positions. Presently this is normally achieved by photolithographical techniques requiring several process steps and costly chemicals and facilities. Atmospheric pressure DBD processes can not only decrease film deposition costs; compared to low-pressure processes they also have the advantage that DBDs can be generated in very tiny cavities with  $\mu\text{m}$ -dimensions, thanks to the small electron mean free path at ambient pressure of roughly 0,1  $\mu\text{m}$ . For example, DBDs can be implemented in a new surface modification process allowing very simple patterned treatment of, e.g., a polymer surface see Figure 8. This technique is similar to a printing process and involves a stamp, basically consisting of a suitably structured electrode / dielectric arrangement as shown schematically in Figure 9. Using a special design of the stamp, the cavities can be made accessible to a gas flow and coatings of several tens of nm thickness can be deposited locally.

Figure 10 is a photograph showing an array of ink drops, 500  $\mu\text{m}$  in diameter, wetting a polypropylene surface selectively at locations made hydrophilic by patterned deposition of  $\text{SiO}_2$ . Owing to their high chemical reactivity, freshly deposited  $\text{SiO}_2$  spots can be used to achieve a patterned functionalization by wet-chemical or vapor-phase silanization. An array of amino-functionalized circular dots was prepared and analyzed by the following sequence of steps:

- patterned deposition of an array of 400 m  $\text{SiO}_2$  dots on PP
- silanization with APTMS in ethanol
- reaction with fluoresceine-isothiocyanate in buffered aqueous solution
- detection of fluorescing spots in a biochip reader (Fraunhofer-IPM)

Although not all spots have an ideal circular shape and some residual fluorescence in the region between the spots is still to be seen, these results demonstrate the feasibility of a simple, cost effective new printing process which can be used to modify a polymer surface locally with respect to surface tension and surface chemical composition. Many other reactions schemes are possible to functionalize a surface locally using this process:

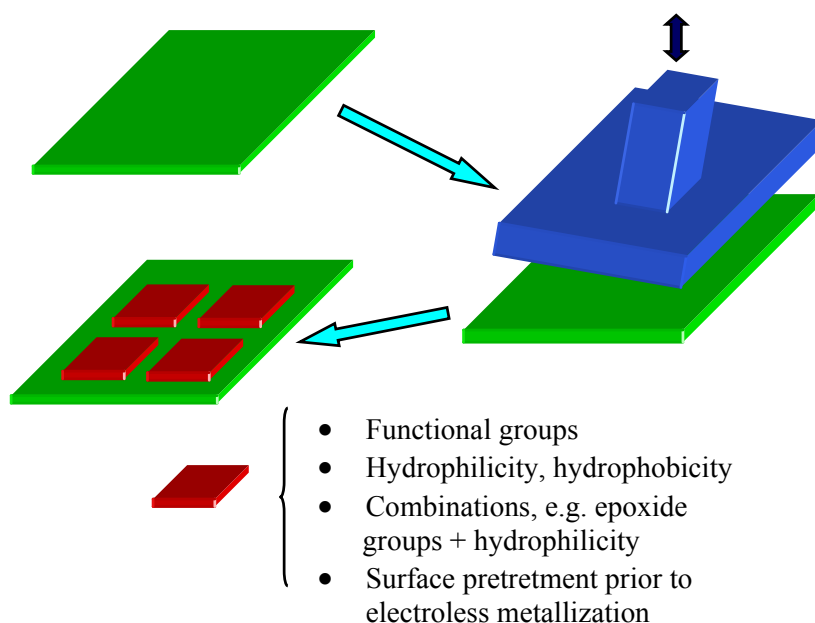


Fig. 8: Principle of "plasma printing" of physico-chemical surface functionalities

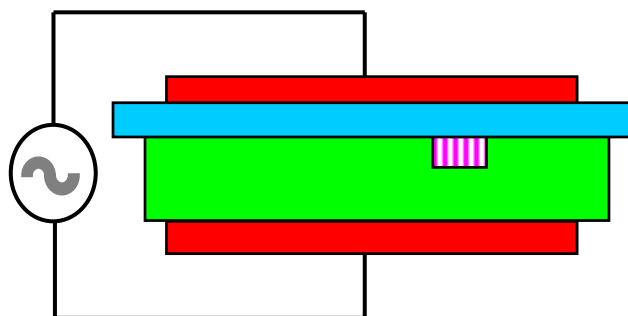


Fig. 9: Principle of plasma printing process for the patterned polymer surface modification: A small cavity is formed upon contact of the polymer (blue) with a patterned dielectric (green). A DBD within the cavity will modify the polymer surface locally.

For example, amino-functionalization is also possible

- by generation of epoxy groups (see above) and subsequent reaction with ammonia,
- by plasma polymerisation from a suitable precursor, carrying amino groups, like diamino-cyclohexane or allyl amine, and
- by a plasma modification of the polymer surface in nitrogen, ammonia, or hydrazine.

Fig. 10: Array of ink drops wetting a PP substrate locally at positions made hydrophilic by a plasma printing process with patterned dielectric. Spot diameter: 500  $\mu\text{m}$ .

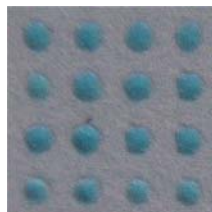
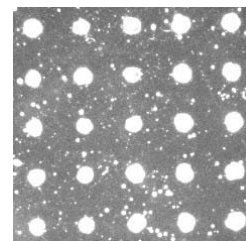


Fig. 11: Array of amino group containing dots (400  $\mu\text{m}$  diameter), prepared by  $\text{SiO}_2$  deposition and amino-silanization, made visible by fluorescence labeling.



## 6. Summary

Filamented dielectric barrier discharges run at atmospheric pressure have been used to deposit thin films from hydrocarbon and silicon-containing organic monomers. Because of the pronounced non-uniformity in space and time of the discharge formed by transient localized individual microdischarges and the small mean free path at atmospheric pressure, film deposition mechanisms are generally expected to differ from those prevalent in low-pressure plasmas: Without a sufficient flux of energetic ions, the deposition of DLC coatings with hardness values in the range of 20 GPa under typical conditions of DBDs at atmospheric pressure is not expected to be possible. On the other hand, the lack of energetic ion bombardment can be utilized to grow plasma polymers with high retention of specific functional groups from suitable unsaturated precursors, especially under pulsed plasma conditions. Silicon-based ultra-thin films obtained by DBD-assisted PA-CVD under suitably chosen conditions have been shown to have a high application potential as adhesion promoting interlayers between metal surfaces and organic coatings. A conceptually very simple new direct-patterning surface modification process can be realized using atmospheric pressure DBDs, thanks to the small dimensions sufficient for plasma generation.

## 7. Acknowledgements

The work reported here was partly funded by the Federal Ministry of Education, Research and Technology of Germany (BMBF) (FKZ: 13N7346/7) and by industrial sponsors.

## 8. References

- [1] B. Eliasson, U. Kogelschatz – IEEE Trans. Plasma Sci. **19**, 309 (1991).
- [2] K.G. Donohoe, T. Wydeven – J. Appl. Polym. Sci. **23**, 2591 (1979).
- [3] E. Marode - J. Appl. Phys. **46**, 2005 (1975).
- [4] M. Goldman, A. Goldman, J. Gallet - Proc. Int. Conf. Partial Discharge (Canterbury, UK, 1993) 11.
- [5] D. Braun, V. Gibalov, G. Pietsch - Plasma Sources Sci. Technol. **1**, 166 (1992).
- [6] J.J. Rodaro, C. Mayoux, A. Loubière - Rev. Gén. Electr. **85**, 697 (1976).
- [7] P.C. Johnson, G. Berger, M. Goldman - J. Phys. D: Appl. Phys. **10**, 2245 (1977).
- [8] J.C. Angus, P. Koidl, S. Domitz in: Plasma Deposited Thin Films, Ed. J. Mort and F. Jansen (CRC Press, Inc., Boca Raton, Florida, USA, 1986) 89.
- [9] G.J.M. Hagelaar, G.M.W. Kroesen, M.H. Klein – J. Appl. Phys. **88**, 2240 (2000).
- [10] B. Chapman, Glow Discharge Processes, Wiley & Sons, 1980.
- [11] C.-P. Klages, M. Eichler, R. Thyen - New Diamond and Frontier Carbon Technology, to be published
- [12] J. P. S. Badyal - IEE Seminar Plasma Polymerization - Processing for the Future (Ref. No.1999/026). - London, UK, UK: IEE, 1999, 56 p.2/1-4.
- [13] W.J. Van Ooij, K.D. Connors and P.J. Barto - Novel metal pretreatments for improved adhesion of paints using plasma methods in: Mittal Festschrift, Ed. W.J. Van Ooij and H.R. Anderson (VSP 1998) 355-371.
- [14] T.F. Wang, T.J. Lin, D.J. Yang, J.A. Antonelli and H.K. Yasuda - Prog. Org. Coat. **28**, 291 (1996).



# Atmospheric Pressure Non-Equilibrium Plasma Processes: History, Discharge Physics, Present Applications and Future Prospects

U. Kogelschatz

*Retired from ABB Corporate Research, Baden, Switzerland*

In 1857 Werner Siemens proposed a novel electric discharge configuration that has found a number of important industrial applications and has reached an annual market volume of several billion US\$. The original Siemens discharge apparatus consisted of two coaxial cylindrical glass tubes confining an annular discharge gap in between. An ac high voltage applied to external electrodes provided a radial electric field high enough to reach electrical breakdown in atmospheric-pressure gases. Air or oxygen passing through this annular discharge gap in the axial direction was partially converted to ozone in the discharge region.

The Siemens tube is still found in modern ozone generators and the discharge, now operated in many different gases, is referred to as the silent discharge, dielectric-barrier discharge, or simply barrier discharge. Its main advantage is the possibility to generate non-equilibrium plasmas at atmospheric pressure in a reliable and cost-effective way. In the majority of applications these conditions are reached only in tiny short-lived current filaments called microdischarges. More recently, also homogeneous and regularly patterned barrier discharges have been obtained [1]. The width of the discharge gap can range from  $\leq 0.1$  mm to several cm, the operating frequency from 50 Hz to several MHz. Glass, silica or ceramics are widely used materials for the dielectric barriers. As an alternative also enamel or polymer coatings can be used.

The generation of ozone, mainly used for water treatment, has for a long time been the major application of barrier discharges. Larger installations use thousands of discharge tubes and reach power levels of several MW. Similar installations can be used in pollution control applications for the treatment of gaseous pollutants and the elimination of odors. Smaller versions will soon be used in passenger cars for NO<sub>x</sub> and particle control of Diesel engine exhausts. Other industrial applications include corona treatment installations for conditioning and coating polymer surfaces, high-power CO<sub>2</sub> lasers for welding and cutting, and excimer lamps for the generation of narrow-band ultraviolet and vacuum ultraviolet (VUV) radiation. In mercury-free fluorescent lamps phosphor coatings on the inner surface of the lamp envelope are used to convert the UV radiation to visible light. Such excimer fluorescent lamps are used as image processing lamps in copiers and scanners and as flat planar panels in liquid crystal displays. The most recent, and as far as market volumes are concerned, the most important application of barrier discharges is in plasma displays panels (PDPs) which are used as large-area flat TV screens. Each pixel point of these displays is a miniature excimer lamp in which the VUV radiation from Xe<sub>2</sub><sup>\*</sup> excimers and from excited Xe<sup>\*</sup> atoms and is used to excite red, green or blue phosphors deposited on the internal walls of minute discharge cells of about 0.1 mm width and depth. The filling gas is Ne or He containing 5-10% Xe, the filling pressure is about 560 Torr. Typical operating voltages are about 100V, typical operating frequencies about 100 kHz (square wave). Although the first PDP factories started operation only in 1996, last year already 570'000 PDPs were sold worldwide. By the year 2005 the PDP market is expected to surpass US\$ 10 billion.

The recent progress in processes using barrier discharges has mainly two roots. A better understanding of the discharge physics allowed us to tailor the non-equilibrium plasma conditions for a given process. Advances in power semiconductors led to economic power supplies with integrated power conditioning process control. Current developments in high-voltage semiconductor modules will probably make the use of bulky high-voltage transformers obsolete for most barrier discharge applications. Recent investigations on mild cold plasmas, obtained in diffuse low-current-density barrier discharges, suggest novel applications for low-temperature sterilization, disinfection and decontamination of surfaces. Advanced manufacturing technologies for fine electrode and dielectric structures, developed originally for PDPs, will enable us to use much smaller configurations. Microstructured barrier discharges will find applications as large-area plasma electrodes, for diagnostic purposes and as a miniature laboratory on a chip. Further progress is expected from the use of ultra short pulses and a better understanding of the properties of surface discharges [2].

[1] U. Kogelschatz, IEEE Trans. Plasma Sci. **30**, 1400 (2002)

[2] U. Kogelschatz, Plasma Chem. Plasma Process. **23**, 1 (2003)

# Plasma sterilisation: Mechanisms overview and influence of discharge parameters

Francois Rossi<sup>1</sup>, Riccardo De Mitri<sup>1</sup>, Sophie Bobin<sup>2</sup> and Rosy Eloy<sup>2</sup>

<sup>1</sup>European Commission, Joint Research Centre, Institute for Health and Consumer Protection  
Via E. Fermi 1, 21020 Ispra (VA) Italy

<sup>2</sup>Biomatech, Zone Industrielle de L'Isloin, Rue Pasteur, 38670 Chasse sur Rhone  
France

**Abstract:** Mechanisms of plasma sterilisation are reviewed and analysed in terms of radiation induced desorption, UV radiation effects and etching. Different gas mixtures are analysed with Optical Emission Spectroscopy in order to find optimum conditions of UV emission and radicals production. The different gas mixtures are compared as a function of pressure, power and gas composition. Those effects are compared and related to effective sterilisation rates obtained from the literature and experimentally on *Bacillus subtilis*. It is shown that UV emission is the major contribution for sterilisation in Phase I, while the duration and kinetics of Phase II and III need further experiments to determine the influence of temperature and ion bombardment.

## 1. Introduction:

Manufacturers of medical devices can draw from a broad spectrum of techniques to sterilise medical components, but new physical and chemical processes are still needed and continue to be developed. A leading reason for this continued search for new methods is to meet the needs of an increasing number of cost-conscious hospital and clinical environments, which are forgoing the use of single-use, disposable devices in favour of devices that can be used more than once. The general trend is to suppress the wet sterilisation because of effluents and to substitute polymers to glass. In that case, a low temperature sterilisation method is required.

Traditional methods of sterilisation, like steam and ethylene oxide (EtO), successfully treat many devices but present the drawback of compatibility with materials (humidity, high temperature, corrosion, loss of polymer properties in the case of steam sterilisation) or problems linked to environment, safety of personnel and toxicity (in the case of EtO). The newer and most promising sterilisation techniques are based on the use of low temperature plasmas, such as the hydrogen peroxide gas plasma (Sterrad system, Johnson & Johnson). The advantage of plasma relies on the production of very active molecules in the discharge that permit, under specific conditions, a high efficiency sterilisation at low temperature using small concentrations of active product. However, the Sterrad system is more a conventional vapour sterilisation system since it was demonstrated that the use of plasma has *no effect* on the sterilisation kinetics, but was necessary to desorb and decompose the hydrogen peroxide adsorbed on the surfaces.

A large amount of work related to the use a plasma discharge, either in direct or post discharge has been made [1,2,3]. The mechanisms of plasma sterilisation were analysed in terms of action of UV emission and interaction with radicals produced in the plasma [4,5,6]. A very complete review of the mechanisms of plasma sterilisation can be found in [4], where it is proposed that the kinetics of sterilisation obeys 3 superimposed/successive mechanisms i) direct damage to the genetic material of micro-organisms by UV interaction, ii) erosion by intrinsic photo-desorption induced by UV and iii) etching of the micro-organism shell by radicals produced in the discharge. However, the model proposed is still qualitative in many aspects, and several experimental results are still difficult to explain, in particular the occurrence of phase 3 (direct etching of the spore material), which seems to occur with a latency period difficult to understand from the mechanisms proposed.

In an attempt to analyse and understand the different phenomena operating during plasma sterilisation, we try to correlate the UV emission flux and radicals of several gas mixtures used in a microwave plasma operating in the near post discharge, to the sterilisation rates obtained with *Bacillus subtilis*.

## 2. Experimental

The experimental plasma source used is represented in Fig.1 below. The Stainless steel chamber is a cylinder 200 mm in diameter and 380 mm in length with three 25 mm windows for *in situ* diagnostics, one window for

gas input ( $O_2$ ,  $CO_2$ ,  $H_2O$ , vapour pressures) and a 100 mm flange for pumping, on which is laid out a 25 mm window for optical spectroscopy. Different ports for diagnostic allow determining the species produced during the discharge and leading to sterilisation. The plasma is excited in the 0.1 to 1 Torr pressure range by microwave power supply working at 2.45 GHz introduced in the chamber through a silica window placed at the extremity of a circular 100 mm wave-guide. The microwave circuit includes the microwave supply (2 kW), a circulator, a three-stub impedance matching system, and a rectangular-circular wave-guide transition. The chamber is evacuated by a primary pump and a roots blower allowing a base vacuum of  $5 \cdot 10^{-2}$  Torr. The pressure is regulated by a throttle valve and measured by a baratron. The gas flows are controlled by Mass Flow controllers and the mixtures of Ar,  $O_2$ ,  $N_2$ ,  $H_2$  and  $H_2O$  have been studied.

Optical emission spectroscopy (OES) is performed with a Chromex 500is/sm spectrometer having a 50 cm focal length for a theoretical resolution of 0.08 nm. The associate detector is an air-cooled CCD camera (Dv401-uv ccd2477 Andor technology). A 600  $\mu$ m diameter fused silica optical fibre is used to transmit the signal to the spectrometer. The optical detection is made through a quartz window. A semi-quantitative evaluation of the species present in the different conditions is obtained by using the actinometric approach whenever applicable [7,8]. In that case, Argon was used as actinometer with a flux of 5 sccm.

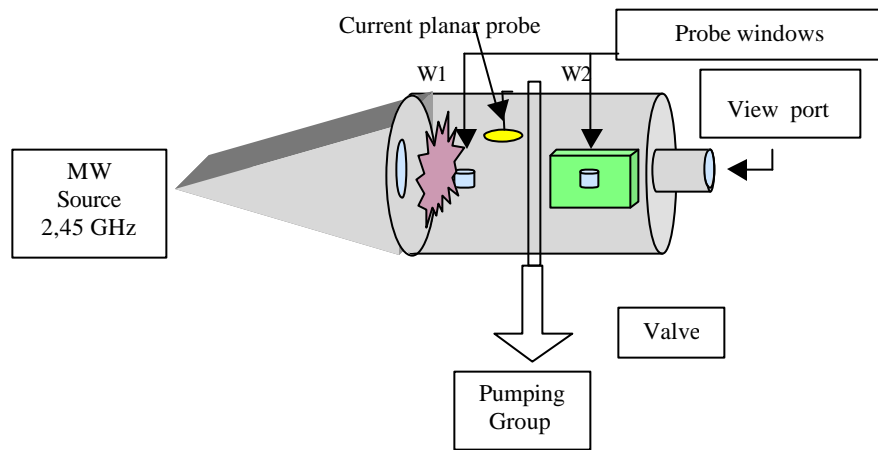


Figure 1: Experimental apparatus

The samples to be sterilized were glass bottles of 5cm height and 1 cm diameter. Validation of the bio burden estimation methodology was performed according to the ISO 11737-1 and NF/EN 1174 standards. After the selection of a technique for removal of micro organisms adapted to the devices, several factors were studied, for each assay on three samples:

- Evaluation of the efficiency of removal of microorganisms from samples. A correction factor for recovery efficiency was established. The inoculation method on the product was selected.
- Screening for the release of substances adversely affecting bio burden estimates.
- Validation of the culture conditions.

The following technique for removal of micro organisms has been chosen: the samples were filled up with 1 ml peptoned water with 0.05% polysorbate 80. They were then submitted to 1minute vortex agitation. 1 culture media have been validated (Tryptcase-soja agar plates under aerobic conditions). The absence of substance released from the device was demonstrated and due to the specificity of the product, a correction factor of 1.95 was determined.

In the experiments described below, the samples are placed at 10cm from the source and are thus treated in the plasma discharge.

In the first part of the experiments, the UV emission from different gas mixtures was evaluated. For this, OES spectra were acquired and the integral of the signal between 250 and 300nm was calculated. These values have been selected following the results of Munakata et al [9] who showed the efficiency of UV emission in this wavelength range. Fig. 2 indicates the value of the UV emission for the different gases used, at different

pressures. It can be seen that the highest UV emission is obtained for O<sub>2</sub>/N<sub>2</sub> mixtures between around 4 to 10% of oxygen. The lowest is obtained with Ar/O<sub>2</sub>. In all cases, the emission collected by the spectrometer is higher at lower pressures.

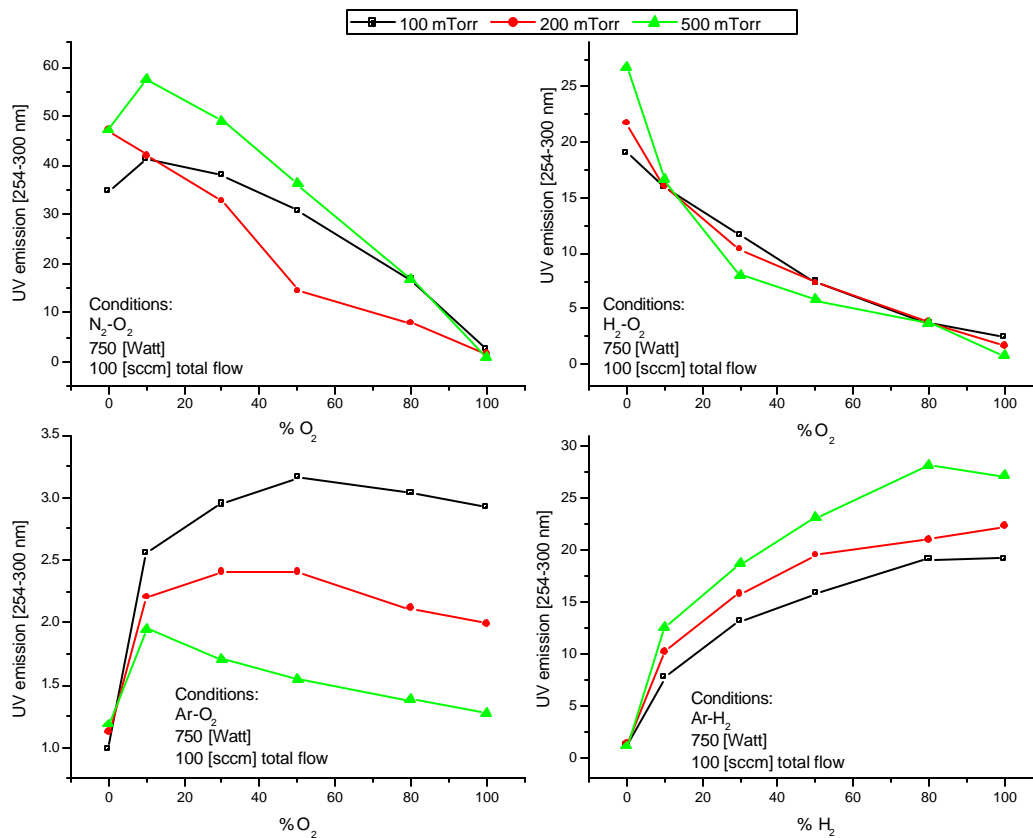


Figure 2: Integral of the UV spectra from 250 to 300nm for different gas mixtures at 100, 200 and 500mTorr.

The different gas mixtures have been used for sterilisation studies of *bacillus subtilis* for duration of 1, 2 and 5 min. at 500W and 500mTorr. Results of Log reduction vs time are presented in Figure 3a. It can be seen that the Log reduction of spores varies linearly with time. The slope of sterilisation rates have been reported vs UV emission (250-300nm) as presented in Fig. 2. It can be seen that the sterilisation rate is proportional to the UV emission, the largest effect being obtained with N<sub>2</sub>/O<sub>2</sub> mixtures.

The value of the O signal (777.19nm) as a function of power and pressure for N<sub>2</sub>/O<sub>2</sub> mixtures has also been measured. These values are proportional to the concentration of atomic oxygen in the discharge, for the conditions indicated. Fig. 4 shows the UV emission and O signal for the 3 gas mixtures tested, as a function of power. It can be seen that the UV emission is maximum around 8% while Po increases linearly with the discharge power.

Table 1 reports the results of sterilisation obtained for different conditions for 5min treatment time, i.e. corresponding to Phase I of Fig. 4. For the same conditions, the relative value of the O line intensity, at 777.1nm, normalized to the Ar 750.38nm line are reported, giving a relative value of the partial pressure of atomic oxygen in the discharge. The integral of the UV emission signal between 250-300nm is also reported. We find that sterilization efficiency is the highest for 4% O<sub>2</sub> in the gas mixture, similarly to what is reported above. The variation of sterilization efficiency vs O signal and UV emission are presented in Fig. 5.

Fig. 6 (a) shows the Log reduction in spore contamination as a function of time for different plasma treatments, at 4 and 8% of O<sub>2</sub> in a N<sub>2</sub>/O<sub>2</sub> mixture, at 350mTorr and different powers. It can also be seen that, like in the post discharge, 3 successive kinetics of spore destruction appear, more or less clearly depending on the power

applied. Comparison with the results of ref. [5] show that Phase I is faster in the discharge than in the post discharge, while the phase II kinetics are of similar magnitude, although the O concentrations are very different.

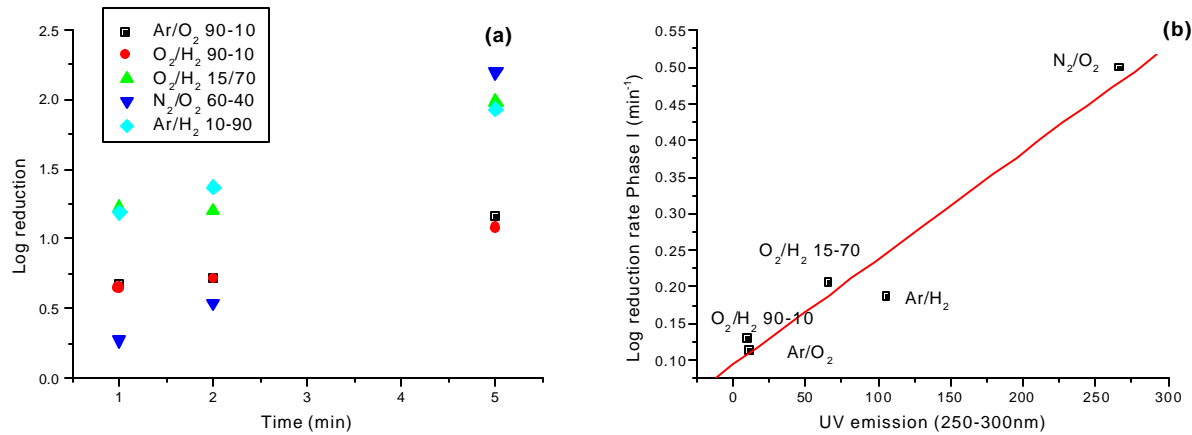


Figure 3: (a) Log reduction of *bac. subtilis* vs time for 5 different gas mixtures (500W, 500mTorr). (b) Log reduction rate as a function of UV emission (250-300nm)

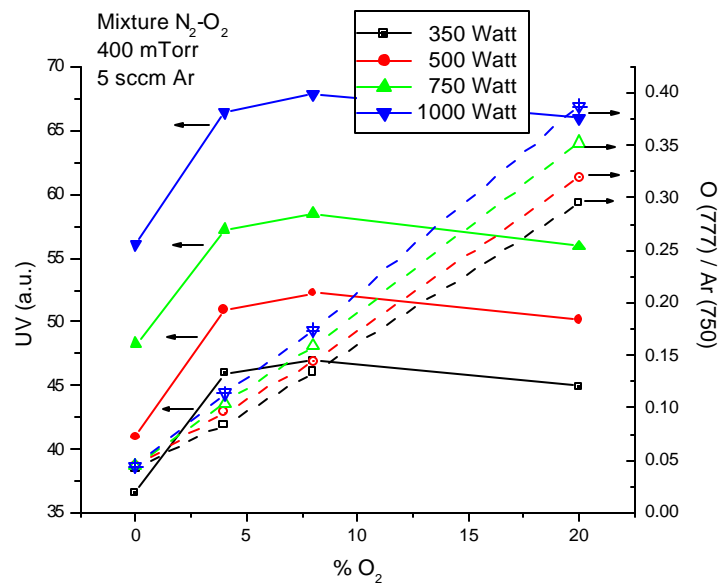


Figure 4: UV emission (250-300nm) and O(777)/Ar(750) signals as a function of gas composition for 4 different powers (N<sub>2</sub>/O<sub>2</sub> mixtures at 400 mTorr)

### 3. Discussion

The results above illustrate the influence of the O intensity line and UV emission on the sterilisation efficiency (Log reduction) for the different gas composition. Fig 5 confirms that there is a correlation between the UV emission and the sterilisation efficiency in Phase I, while no correlation exists with the O concentration. This confirms that Phase I is indeed related to UV destruction of genetic material of the spores. Fig. 6(a) gives more

contrasted results. It can be seen that for 4 and 8% concentration, the sterilisation kinetics increases strongly with the power applied. However, the fastest sterilisation is obtained for 4%O<sub>2</sub>, although Fig. 4 indicates that UV emission and P<sub>o</sub> are smaller for 4% than for 8%.

Gas mixture	Pressure (mTorr)	Total gas flow (sccm)	Power (W)	UV emission 250-300nm	O(777)/Ar(750)	Log reduction
N <sub>2</sub> -20% O <sub>2</sub>	920	1000	350	55.36	0.391	2.18
N <sub>2</sub> -20% O <sub>2</sub>	920	1000	500	56.11	0.438	2.36
N <sub>2</sub> -20% O <sub>2</sub>	920	1000	750	61.84	0.478	2.65
N <sub>2</sub> -4% O <sub>2</sub>	780	1000	350	51.04	0.124	2.15
N <sub>2</sub> -4% O <sub>2</sub>	780	1000	500	54.18	0.134	2.28
N <sub>2</sub> -4% O <sub>2</sub>	780	1000	750	60.56	0.150	3.38
N <sub>2</sub> -8% O <sub>2</sub>	790	1000	350	53.96	0.192	2.58
N <sub>2</sub> -8% O <sub>2</sub>	790	1000	500	56.11	0.210	2.69
N <sub>2</sub> -8% O <sub>2</sub>	790	1000	750	62.69	0.231	2.81

Table 1: Sterilisation results obtained for 5min. treatment with different gas mixtures and powers.

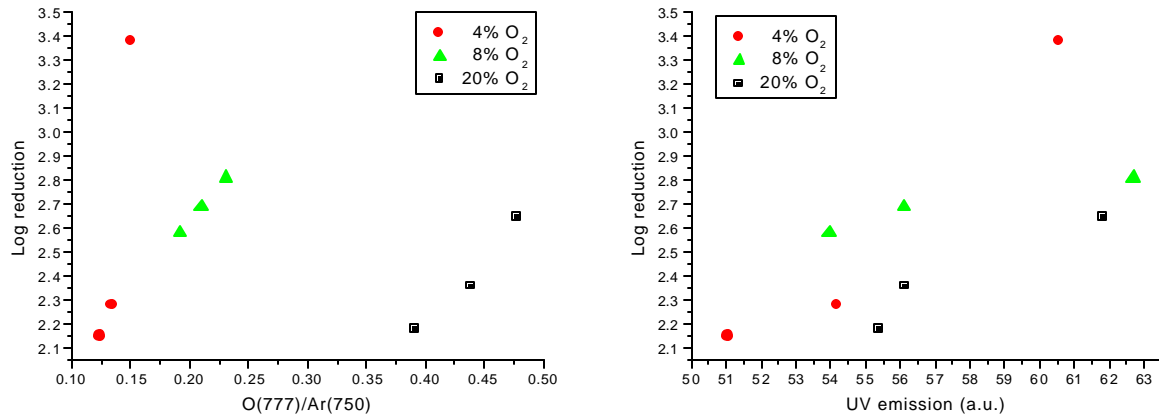


Figure 5: Sterilisation efficiency vs O signal and UV emission for 3 N<sub>2</sub>/O<sub>2</sub> compositions (values from Table I)

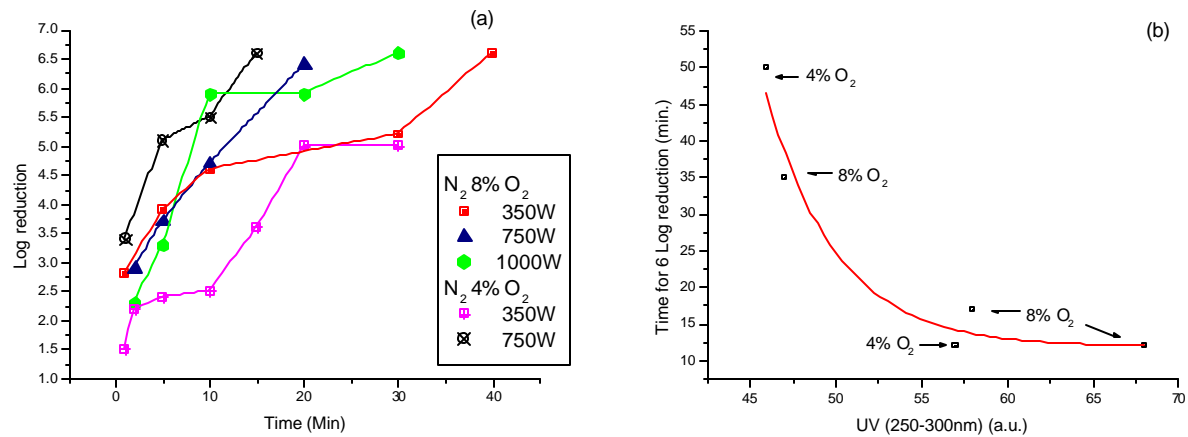


Figure 6: (a) Log reduction as a function of time for 4 and 8% of O<sub>2</sub> in N<sub>2</sub>/O<sub>2</sub> mixture. (b) Time needed for 6Log reduction as a function of UV emission.

This observation has to be taken with caution since the UV emission between 250 and 300nm increases of a few percents with O<sub>2</sub> concentration, while the Po increases by 50 to 60%. This illustrates that atomic oxygen plays a minor role in the overall sterilisation process. One possible explanation for the efficiency of the 4% mixture is related to the UV emission under 250nm, as suggested in other work and which we could not measure for experimental reasons. Fig. 6(b) shows the total time needed for a 6Log reduction from the data of Fig. 6a. A clear decrease of the overall sterilisation duration is observed with the UV emission as already mentioned. This figure seems also to indicate that the sterilisation time, based on the mixture N<sub>2</sub>/O<sub>2</sub> reaches a saturation level. The above observations can be used to optimise the sterilisation process by a microwave plasma discharge: In order to reduce the total sterilisation time, Phase I and II should lead to the maximum reduction of the spores' concentration. This can be achieved by maximizing UV emission, for instance with N<sub>2</sub>/O<sub>2</sub> mixtures at high power. Phase III requires atomic oxygen and also a maximum of UV, but our results do not explain the transition between Phase II and III, and above all, why should Phase III not start earlier. One of the factors that have been constantly overlooked is temperature, which might increase the surface etching kinetics while Phase I and II develop. Preliminary experiments using a fibre optics and a wave guide show that temperature of the samples varies strongly with the gas mixture and with time, giving a possible explanation for the increase of the sterilisation efficiency with Phase III. Further work is still needed to support this hypothesis.

#### 4. Conclusions

Sterilisation experiments have been performed with different gas mixtures. We have measured the UV emission between 250 and 300nm as well as the O (777nm) signal, representative of the O partial pressure in the discharge. Sterilisation experiments on *Bac. Subtilis* have been performed and compared to the literature. For low kinetics, we find a 3 stages sterilisation as reported elsewhere, while a linear sterilisation kinetics is observed at high powers. Our results suggest that UV emission is the major parameter for all stages of sterilisation, the oxygen partial pressure being necessary but playing a minor role. Future work will deal with sterilisation mechanism analysis under controlled temperature and with contrasting gas mixtures.

**Acknowledgements:** this work has been carried out within the EU Growth Project STERIPLAS (G1RD-CT-1999-00137). The authors would like to thank Roland Chery and Sophie Peyrouse from Biomatech, for technical support.

---

#### References

- [1] S. Moreau, M. Moisan, M. Tabrizian, J. Barbeau, J. Pelletier, A. Ricard and L'H. Yahia - J. Appl. Phys. Vol 88 No2 (2000) 1166-1174
- [2] S. Lerouge, M. Wertheimer, and L'H. Yahia - Plasma and Polymers Vol. 6 no3, (2001) 175-188
- [3] S. Hury, D.R. Vidal, F. Desor, J. Pelletier and T. Lagarde- Letters in Applied Microbiology (1998) **26** 417-421
- [4] S. Lerouge, A.C. Fozza, M.R. Wertheimer, R. Marchand and L'H. Yahia - Plasma and polymers Vol 5, No1 (2000) 31-46
- [5] M. Moisan, J. Barbeau, S. Moreau, J. Peletier, M. Tabrizian and L'H. Yahia, International Journal of Pharmaceutics, 226 (2001) 1-21
- [6] N. Philip, B. Saoudi, MA Crevier, M. Moisan, J. Barbeau and J. Pelletier, IEE transactions on Plasma Science Vol. 30, NO 4, (2002) 1429-1435
- [7] J. W. Coburn, M. J. Chen, *J. Appl. Phys.* **51**, 3134-3136, (1980).
- [8] R. d'Agostino, F. Cramarossa, S. De Benedictis, G. Ferraro, *J. Appl. Phys.* **52**, 1259-1265, (1981).
- [9] N. Munakata, M. Saito and K. Hieda, *Photochem. Photobiol.* **54** (5) 761 (1991)

# Plasma polymerised chemical patterns and gradients for biomedical applications

A. G. Shard<sup>1</sup>, S. A. Mitchell<sup>2</sup>, J. D. Whittle<sup>1</sup>, A. J. Beck<sup>1</sup>, S. MacNeil<sup>1</sup>, M. R. Alexander<sup>3</sup>, R. D. Short<sup>1</sup>

<sup>1</sup> *Department of Engineering Materials, Sir Robert Hadfield Building, University of Sheffield, Mappin Street, Sheffield S1 3JD, UK*

<sup>2</sup> *School of Life Sciences, Robert Gordon University, St Andrew Street, Aberdeen AB25 1HG, UK*

<sup>3</sup> *Corrosion and Protection Centre, UMIST, P.O.Box88, Manchester, M60 1QD, UK*

## Abstract

The production of chemical patterns and gradients by plasma polymerisation is described. Bifunctional patterns are generated by masking areas of the surface and depositing a plasma polymer onto the unmasked areas. We demonstrate that the resulting surfaces have a chemical heterogeneity and discuss some of the factors that limit the pattern resolution. Chemical gradients are produced using an aperture which is translated relative to the substrate whilst plasma parameters are simultaneously altered. These approaches are compared to alternative methods of pattern and gradient production.

It is well established that fibroblastic and epithelial cells adsorb preferentially to areas rich in oxygen or nitrogen derived functionalities, and poorly to hydrophobic surfaces. Areas of plasma polymers which have high heteroatom content within a matrix of hydrophobic plasma polymer are demonstrated to adsorb cells in a spatially selective manner. It is possible to produce these patterns with sufficient resolution to alter the shape of the cell, thus demonstrating that this approach may be used in studies of the relationship between cell shape and function. By altering the culture conditions it is possible to maintain fibroblasts within the patterns for up to a month, although the usual persistence of the pattern is a few days.

A useful extension to this approach is the independent and simultaneous spatial control of two phenotypes. This work is aimed at creating surfaces suitable for supporting the culture of keratinocytes and melanocytes on the same surface. Under normal co-culture conditions melanocyte function and number is down-regulated by keratinocytes. This impacts upon the normal appearance of autologous skin grafts, as pigmentation is different to the surrounding, healthy skin. In this ongoing work, suitable surface chemistries for patterning are selected followed by patterning of the two selected chemistries on a culture surface.

## 1. Introduction

Surface chemistry can be used to control the attachment and behaviour of mammalian cells in culture. It is generally thought that the chemistry of the surface influences the manner in which proteins in the culture media adsorb, which in turn influences cell behaviour. The fact that surface chemistry can influence both protein adsorption and activity has similarly been extensively reported. The preparation of surfaces with an heterogeneous chemistry is a topic of current interest. Such surfaces demonstrate a spatial variation in protein and cell interactions<sup>1</sup> which may be employed in advanced biomedical devices. Other approaches, such as the topology of a surface have also been employed,<sup>2</sup> although such methods do not so easily allow a specific control of cellular interactions, such as a different response from two cell types. For convenience, we divide heterogeneous chemistries into two classes, patterns and gradients. A pattern is a surface with two or more chemistries arranged in well defined areas, but within those areas is homogenous. A gradient is a continual variation in the surface concentration of a chemical group along the surface; this is distinct from a pattern in which concentration is ideally discontinuous at a boundary.

When chemical patterns and gradients are produced it is important to examine both the spatial and chemical control of the resulting surface. Many workers use self assembled monolayers (SAMs) for patterning because these offer excellent control over both parameters. SAMs have been patterned using both micro-contact printing<sup>3</sup> and photolithography<sup>4</sup> and sub micrometre features have been produced in this manner. The disadvantages of using SAMs are that they can be applied to a limited number of substrates and that they are laborious and time consuming to produce. Gradients of chemistry have been produced from SAMs using diffusive mixing,<sup>5</sup> although the spatial extent of the gradients in these cases is rather difficult to control with precision. There is also the potential problem of phase separation which, depending on domain size, may produce spurious results. The stability of SAMs, in particular alkanethiolate monolayers, is open to question.



Oxidation of the thiolate head<sup>6</sup> to produce weakly adsorbed species has been shown to occur and these observations indicate that shelf life may be an important issue for such systems.

The use of gas discharges to generate patterns and gradients has, until recently, been largely limited to non-polymerising gases.<sup>7,8</sup> By controlling the area of exposure it is possible to produce heterogeneous surface chemistry. In general, the substrates chosen for treatment have been polymers, the discharge serving to introduce polar and hydrogen bonding species into the surface with some attendant disruption of the original polymeric structure. In this manner it is possible to create variations in wettability and, to some extent charge on the polymer surface. Control of the surface chemistry produced by such treatments is limited. A number of functional groups are created, with little specificity, which largely depend upon the substrate polymer employed and the gas used. Treatment time and discharge power serve to control the concentration of such groups and these are the parameters used to create the chemical pattern or gradient. The major advantage of using gas discharges is the relative ease of manufacture this route offers.

Plasmas which deposit material have potential advantages over non-polymerising discharges. The film chemistry is largely independent of the substrate chemistry and there is usually a far greater control of the resulting chemistry. The techniques employed for non-polymerising gases can be directly transferred to polymerising plasmas with little or no modification. Topological micropatterns produced in this manner on the micrometre scale were reported several years ago,<sup>9</sup> yet only recently has there been evidence that patterns on such a scale display chemical heterogeneity at the surface.<sup>10,11</sup> One of the important technological questions to be addressed is the issue of pattern resolution, *i.e.* how well defined the boundary is between two chemical domains, currently there is little information available on this issue.

By exposing a limited area of the substrate to the plasma and translating the substrate relative to the masking aperture it is possible to create a continuous gradient. Non-polymerising discharges have been utilised in this manner to create gradients by changing the exposure time of the substrate to the plasma in a continual fashion.<sup>8</sup> The advantages of using polymerising plasmas in this manner are the greater control of film chemistry, as outlined above for patterns, the ease of mixing different chemical groups through copolymerisation and the ability to 'overwrite' previously deposited chemistries enabling complex heterochemical surfaces to be manufactured.

## 2. Plasma polymerised patterns

All patterns were produced in cylindrical glass reactors (typically 4 L volume) with inductive coupling, through a manual impedance matching network, to a 13.56 MHz radio frequency generator. The reactors were pumped with rotary vacuum pumps equipped with liquid nitrogen cold traps and the monomers were introduced to the chamber through a fine control leak valve. A range of volatile organic compounds were employed as monomers and typical operating conditions were 5-10 W power with a flow rate of 5-10 cm<sup>3</sup><sub>stp</sub>/min. In a typical patterning procedure, the substrate is coated with a plasma polymer of the first monomer, the chamber vented and a mask placed on the substrate, then a second monomer is plasma

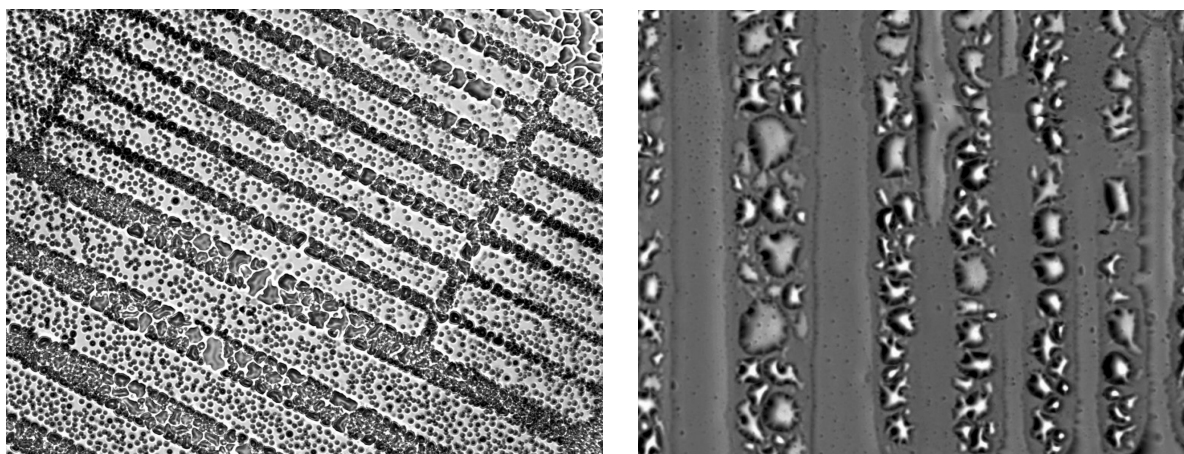


Figure 1: Water condensation on a plasma polymer patterns. Bar widths are approximately 50 and 100  $\mu\text{m}$ . Left; hydrophilic pp(allylamine) and hydrophobic pp(octadiene). Right; pp(acrylic acid) patterned with pp(octadiene) with the mask raised  $\sim 60 \mu\text{m}$  above the surface.

polymerised onto the unmasked areas of the substrate. At the end of the procedure the mask is removed to expose the chemistry deposited in the initial stage. Copper TEM grids were employed as masks with feature sizes ranging from 5 to 200  $\mu\text{m}$ .

If there is a significant difference in the hydrophobicity of the two surface chemistries it is possible to visualise the patterns by the simple expedient of breathing on them. Water condensed from the breath will form droplets of different size and shape on the two surfaces which are easily distinguishable in optical microscopy, as shown in figure 1. At the boundary between the two chemistries there is commonly a region devoid of water droplets and this may arise from movement of water droplets along the small scale chemical gradient formed at the edge of the mask. The movement of droplets along wettability gradients is due to the Marangoni effect and is particularly marked during condensation.<sup>12</sup> If this hypothesis is correct, the size of this depleted region can be used as an indication of the resolution of the chemical pattern and is typically found to be less than 15  $\mu\text{m}$ . This length scale is of the same order as found with AFM studies, which give topological information and indicate an edge resolution of better than 5  $\mu\text{m}$ , as indicated by the features shown in figure 2. One of the potentially important factors in pattern resolution is the distance between the mask and the substrate. We have found that for plasma polymerised (pp) octadiene features as small as 50  $\mu\text{m}$  are visible (following water condensation to visualise the patterns) even when the mask is raised more than 50  $\mu\text{m}$  above the substrate, as shown in figure 1. This has clear implications in terms of the mechanism of polymerisation. Positive ions are the only species in a plasma which can be collimated by the mask (since they are accelerated in the sheath and impact at close to normal incidence) and this observation

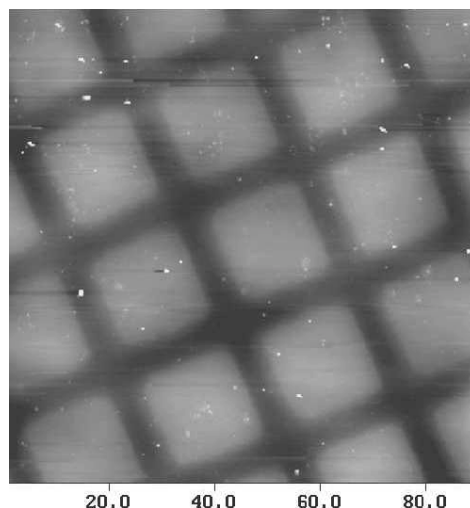


Figure 2: AFM image of a *pp*(*n*-hexane) pattern on silicon wafer. Depth of the deposited material is approximately 7 nm. Scale at bottom is in micrometres.

indicates that for this monomer at least, ions play an important role in the growth of the film. For other monomers, such as perfluorohexane, deposition under the mask (albeit at a much lower rate than on exposed areas) is found by imaging XPS which appear to be of a similar nature to the downstream deposits<sup>13</sup> from such plasmas.

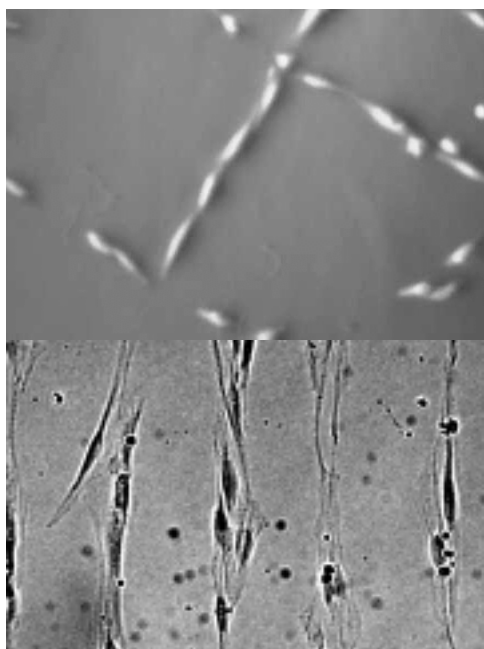


Figure 3: Cells grown on plasma polymer patterns. Top; chinese hamster ovarian cells on a tissue culture plastic surface with *pp*(*n*-hexane) squares. Bottom; human dermal fibroblasts after 20 days serum-free culture on *pp*(acrylic acid) stripes have not colonised *pp*(octadiene) areas.

The culture of cells on the plasma polymerised patterns followed standard protocols. In general, cells attach to hydrophilic and charged areas rather than hydrophobic areas. This effect can be used to control the spatial arrangement of cells on a surface by chemically patterning the substrate prior to culture. Figure 3 provides examples of the spatial control achieved. In the first image cells attach to a 5  $\mu\text{m}$  wide bar, which is smaller than the normal spreading dimensions of this type of cell. This leads to the cells being aligned and elongated in the direction of the bar. The second image shows cells after 20 days in culture still aligned in the bar direction. To achieve this the cells were cultured in serum-free conditions in which the cells were not highly proliferative and did not rapidly attach to the surface, presumably due to the lack of an adsorbed protein layer on the surface. In this case the fibroblasts appear able to attach to the acidic areas of the pattern, perhaps by secreting their own extra-cellular matrix proteins, but even after 30 days have not colonised the *pp*(octadiene) areas. Although these patterns can be successfully employed to create patterns in monoculture of a wide range of different cells, a more ambitious goal is to

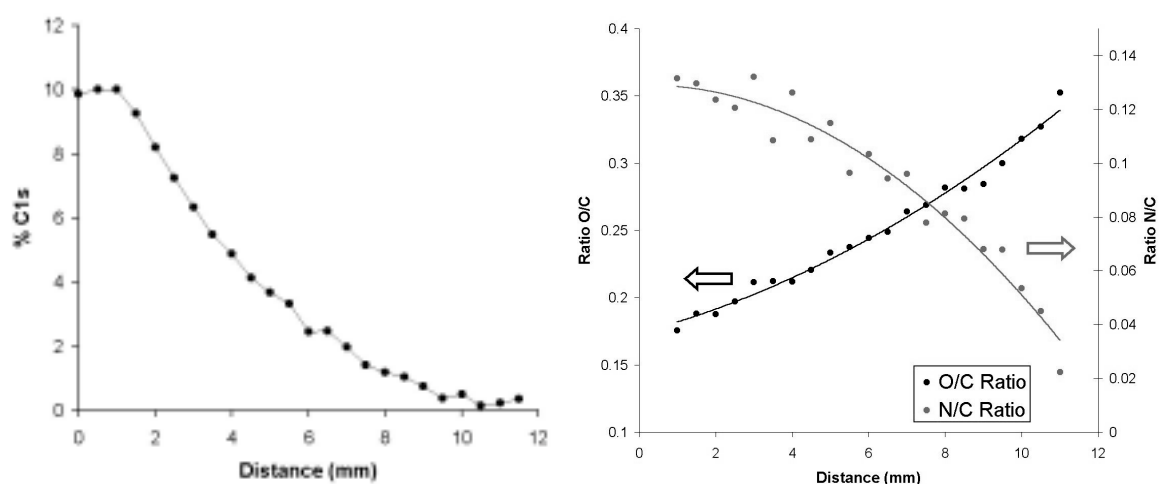


Figure 4: Elemental compositions obtained using small area ( $300\mu\text{m}$  in direction of variance) XPS along gradients. Left; pp(acrylic acid / octadiene) gradient showing decrease in Cls acid/ester environment from acid side (1mm) to octadiene side (11mm) of gradient. Right; pp(allylamine/acrylic acid) gradient showing changes in heteroatom composition from amine side (1mm) to acid side (11mm) of gradient.

spatially arrange and distinguish two different types of cells. This requires the identification of surfaces that are able to selectively attach one type of cell from a mixture. We are currently working to achieve this in co-cultures of melanocytes and keratinocytes, which meets a particular clinical requirement in the tissue engineering of skin. Most autologous skin grafts contain only keratinocytes, which when introduced to a wound bed provide the normal barrier properties of skin, however the grafted areas do not possess the functional aspects of skin, such as pigmentation. Attempts to co-culture melanocytes (pigment cells) with keratinocytes have met with limited success, as keratinocytes reduce both the number and function of melanocytes. By spatially isolating the melanocytes it is hypothesised that this regulation will be reduced. The plasma polymers to be used will be selected from our work on gradients (see below) and patterned using the methodologies outlined in this section.

Patterned plasma polymers offer a convenient route to the production of microengineered surfaces. Our group has demonstrated the spatially controlled adsorption of proteins and cells to such surfaces, the wide range of chemistries available from plasma polymerisation make this method an attractive option for device fabrication. Potential applications include protein-binding microarrays, surfaces to study cellular interactions and a generic method for functionalising microfluidic devices.

### 3. Plasma polymerised gradients

Gradients are produced by mounting the substrate on a movable drawer which is gradually closed as the plasma conditions are changed. Such devices have been employed previously with non-polymerising plasmas to produce gradients from the variation in exposure time across the sample. The limitations of such gradients are outlined in the introduction. Polymerising plasmas offer the advantage of greater control of chemistry and more flexibility in the parameters that are changed as the drawer is closed. In our experiments we have carried out plasma copolymerisation with a fixed discharged power and relatively constant total flow rate. The parameter altered is the feed ratio of the two monomers into the chamber, allowing a continual and opposite change in two chemistries. Gradients have currently been produced across  $\sim 10\text{mm}$ . There is no technological barrier to increasing the size of these gradients, however reducing the size of the gradient is limited by the edge resolution of the mask, which is of the order of  $10\mu\text{m}$  (from our studies of patterned surfaces, and considering that in this application the mask would be raised at least a few  $\mu\text{m}$  above the surface). It would therefore be extremely challenging to create well defined gradients over less than about  $100\mu\text{m}$  using this method.

Gradients have been characterised by XPS, as shown in figure 4, and contact angle measurements. Movement of water droplets on gradients of this scale was not observed, which is almost certainly due to the hysteresis between advancing and receding contact angles being larger than the difference in contact angle

on the two sides of the droplet.<sup>14</sup> It is commonly found that plasma polymers have large hystereses in comparison to the monolayer systems in which movement of droplets has been shown to occur. Cell culture on gradients is still at an early stage, we are employing these surfaces as a combinatorial screen to assist in the rapid selection of surfaces for a particular biological application. As an example, we are culturing melanocytes and keratinocytes on gradients to select two chemistries which will have optimal differential attachment rates for the two cell types. The two selected plasma copolymers will then be patterned, as detailed in the previous section. Other potential applications of the gradients include the migratory control of cells and the separation of proteins in microfluidic devices, through for example, isoelectric resolution over a pH gradient.

### Acknowledgements

This work has been supported by EPSRC grants GR/R28560 and GR/M86996 and BBSRC grant 50/E18528. We would like to thank Prof. R. Bradley (RGU) for access to AFM, Dr. N. Emmison (RGU) and Dr. J. Haycock (Sheffield) for assistance with cell culture and access to equipment.

### References

- [1] R. Singhvi, A. Kumar, G. P. Lopez, G. N. Stephanopoulos, D. I. C. Wang, G. M. Whitesides, D. E. Ingber - *Science* **264**, 696 (1994).
- [2] A. Curtis, C. Wilkinson – *Biomaterials* **18**, 1573 (1997).
- [3] S. Zhang, L. Yan, M. Altman, M. Lasse, H. Nugent, F. Frankel, D. A. Lauffenburger, G. M. Whitesides, A. Rich – *Biomaterials* **20**, 1213 (1999).
- [4] C. A. Scotchford, E. Cooper, G. J. Leggett, S. Downes – *J. Biomed. Mat. Res.* **41**, 431 (1998).
- [5] B. Liedberg, P. Tengvall – *Langmuir* **11**, 3821 (1995).
- [6] N. J. Brewer, R. E. Rawsterne, S. Kothari, G. J. Leggett – *J. Am. Chem. Soc.* **123**, 4089 (2001).
- [7] A. Ohl, K. Schroder – *Surf. Coatings Tech.* **116-119**, 820 (1999).
- [8] C. G. Golander, W. G. Pitt – *Biomaterials* **11**, 32 (1990).
- [9] L. Dai, H. J. Griesser, A. W. H. Mau – *J. Phys. Chem. B* **101**, 9548 (1997).
- [10] N. A. Bullett, R. D. Short, T. O’Leary, A. J. Beck, C. W. I. Douglas, M. Cambray-Deakin, I. W. Fletcher, A. Roberts, C. Blomfield – *Surf. Interface Anal.* **31**, 1074 (2001).
- [11] S. A. Mitchell, N. Emmison, A. G. Shard – *Surf. Interface Anal.* **33**, 742 (2002).
- [12] S. Daniel, M. K. Chaudhury, J. C. Chen - *Science* **291**, 605 (2001).
- [13] A. G. Shard, H. S. Munro, J. P. S. Badyal – *Polym. Comm.* **32**, 152 (1991).
- [14] M. K. Chaudhury, G. M. Whitesides – *Science* **256**, 1539 (1992).

# Propene plasma deposition as an intermediate step in the biochemical modification of implant devices

M. Morra<sup>1</sup>, C. Cassinelli<sup>1</sup>, P. Cahalan<sup>2</sup>, L. Cahalan<sup>2</sup>

<sup>1</sup> *Nobil Bio Ricerche, Villafranca d'Asti,, Italy*

<sup>2</sup> *Percardia, Merrimack, NH, USA*

## Abstract

This communication describes the deposition of hydrocarbon films from propylene plasma as the first step in the building up of interfacial architectures aimed at selected biomedical applications. Deposition is followed by chemical grafting of a hydrogel layer from aqueous solutions and coupling of relevant biomolecules. *In vitro* and *in vivo* results, together with surface characterization data, are presented to show the effectiveness of the interfacial structure built on the plasma deposited layer.

## 1. Introduction & background

The efficacy of implant devices is critically dependent on surface properties. An enormous and ever growing literature on this subject exists. Films deposited from plasma have always been of great interest in the medical devices field, because of their peculiar properties. In particular, in the past it has been suggested that the unique chemistry and the possibility of creating stoichiometries inaccessible to conventional routes were very intriguing features of plasma deposited polymers [1]. Nowadays it is well accepted that the complexity of *in vivo* systems is such that host responses cannot be directed simply by a modification of general surface properties such as wettability or, for instance, of the C/F or C/H ratios. Rather, effective surface modifications are more and more sought by the finely-tuned immobilization of biological molecules that, through their molecular conformation and bioactivity, can affect the local tissue response in a specific way. As a consequence, plasma deposited films as surface layers that can directly affect host responses to implant devices have lost most of their interest. Yet, they continue to play a very important role in the development of new devices, because of some of their other peculiar properties; in particular, they allow the building of tightly adherent, conformal, water and delamination-resistant organic layers, a few tens of nanometer thick, on almost any kind of materials. This way, they open the way to the use of organic chemistry approaches to surface modification even on those materials that are either inorganic or scarcely reactive, such as metals or poly(tetrafluoroethylene) (PTFE).

Deposition of organic films from plasma as an intermediate step in surface modification can be exploited either to introduce surface chemical groups suitable for further coupling, or to deposit surface layer that can then undergo chemical grafting of acrylate monomers [2]. Previous studies have shown that immobilization on a surface-grafted, water-swollen hydrogel layer is an effective way to keep a high activity of immobilized biomolecules [3].

We have used the deposition of polymeric hydrocarbon films from propylene plasma as the first step in the building up of interfacial architectures aimed at different biomedical applications. In particular, our approach relies on the immobilization of biomolecules on an acrylic acid-acrylamide hydrogel layer. The latter provides, in biological aqueous media, a water swollen and relatively unconstrained environment, and it is obtained by Ce(IV)-induced grafting on the plasma deposited hydrocarbon layer [2,4]. This general platform for surface modification has been adopted in the development of two new-generation implant devices, whose performances are critically dependent on the activity of surface-immobilized biomolecules: heparin-coated myocardial PTFE stent-graft; and collagen-coated titanium dental implants [4]. In this communication we present several results related to the just mentioned applications. In particular, the organization of the paper is the following: the next section contains a quick description of the experimental details. Then, specific results involving the characterization of myocardial stents and collagen coated dental implants are discussed. Finally, the implications more directly related to plasma deposition are quickly reviewed.



## 2. Plasma deposition and surface modification

### Plasma deposition

Plasma deposition was performed in a capacitively coupled parallel-plate reactor placed inside a class 10,000 clean room. Samples were located on the water-cooled grounded electrode. Both the reactor and electrodes are made of stainless steel. The reactor volume is about 3 dm<sup>3</sup> and the distance between the electrodes 5 cm. Different treatment conditions were used, as described in the following. To give some guideline, these are typical process parameters: 1 minutes air plasma, 50 W, 20 sccm flow rate (cleaning step), followed by 5 minutes propylene plasma deposition, 50 W, 100 sccm flow rate (flow rate is controlled by a MKS mass flow controller) (deposition step). Treatments were performed either on flat samples, for preliminary trials, or on actual devices as discussed in the relevant section.

**Acrylic acid grafting.** After deposition, treated samples were subjected to acrylic acid grafting. In particular, grafting was performed from a 40% aqueous acrylic acid solution. The solution was gently mixed using a stirrer bar for two minutes. At this point, Argon was gently bubbled in the solution for ten minutes, then 3% of an acidic solution of ammonium cerium nitrate was added, without discontinuing Ar. The solution was mixed while bubbling for two more minutes, then it was gently poured in test tubes, containing the plasma-deposited samples. Grafting was performed for 45 minutes, at room temperature. At the end of the grafting reaction, samples were rinsed overnight in water. In the case of heparin coupling to stent, a certain amount of acrylamide (5-10) was added to the acrylic acid solution.

**Collagen or heparin coupling.** Collagen coupling to grafted Ti surfaces was performed as follows: samples were immersed in a 0.5% collagen, 1% acetic acid aqueous solution. After 2 hours, samples were removed from the solution and rinsed several time in 1% aqueous acetic acid, to remove excess adsorbed collagen. After rinsing, samples were immersed in water containing 0.25% EDC (Ethyl dimethylamminoethylcarbodiimide) and 0.25% NHS (N-hydroxysuccinimide), both from Sigma, and kept overnight in this coupling solution. After coupling, all samples were carefully rinsed with 1% aqueous acetic acid and water, then dried under a hood.

Heparin coupling to grafted stents was performed *via* polyethyleneimine (PEI) coupling to acrylic acid by EDC/NHS, in aqueous solution. Heparin was covalently linked to the aminated surface.

## 3. Results

### 3.1 Heparin coated myocardial stent.

Fig. 1 shows the typical device used in this approach to myocardial implants. It is basically a stainless steel stent bearing a porous PTFE cover. The general principle behind myocardial implant is shown in Fig. 2.

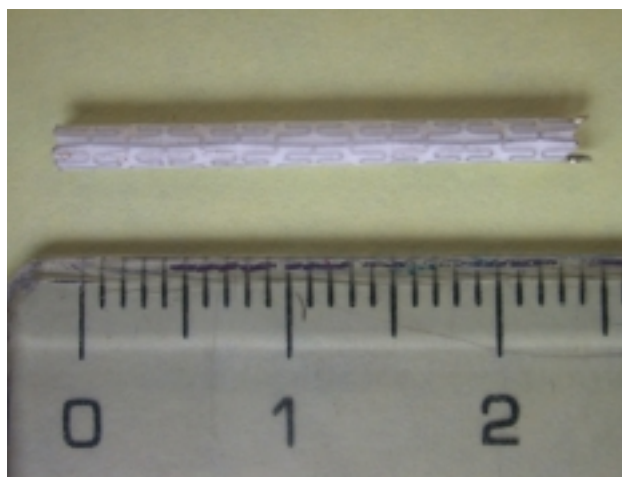


Fig. 1 stainless steel-PTFE graft stent

Myocardial implant establishes a connection between coronary vessel and the left ventricle. It represents a potentially new and novel approach to relieving ischemia by delivering oxygenated blood from the left ventricle of the heart to a targeted coronary vessel. Of course, due to the small diameter and the critical nature of the device, blood compatibility of the device surface is a very important issue. The obvious option to improve blood-compatibility of the stent graft is heparin coupling. Heparin has been used since several

decades as a surface linked anti-coagulant. Despite this long history, and an enormous body of scientific literature on the subject, there are several aspects of heparin functioning that are not yet clear, despite their obvious importance in the development and properties of devices (among them, for instance, the effect of sterilization on heparin activity and shelf-life).

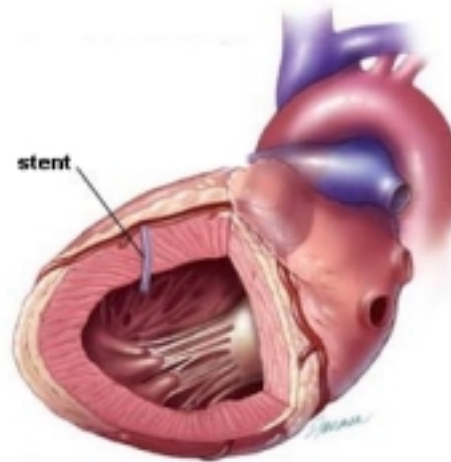


Fig. 2 Myocardial implant establishing a connection between coronary vessel and the left ventricle

Heparin linking through the present process involves first of all the deposition of the film from propene plasma, according to the conditions described in the Experimental section. The following are surface composition data, obtained on flat PTFE coupons by XPS analysis:

Table 1: Surface composition data obtained by XPS analysis on PTFE samples

Sample	C	F	O
Control	32.1	67.7	0.2
Plasma deposited	93.1	3.2	3.7

Previous results show the expect trend in terms of C and F concentration. The Ce(IV) induced chemical grafting reaction of acrylate yields a relatively thick grafted surface hydrogel layer (about 120 nm [4]). Due to the thickness of this layer, the sequential steps that lead to heparin coupling can then be checked by staining (beside, of course, XPS analysis). An anionic layer that thick can be easily stained by cationic dyes such as toluidine blue. After acrylic acid grafting, as reported in the Experimental section, PEI is coupled to the acrylic acid grafted layer, turning the surface layer into a cationic one. The latter can be stained by an anionic dye such a Ponceau S (red). Finally, Heparin is coupled to PEI, making the surface anionic again, with a definite and well known spectral shift when toluidine blue stained as compared to acrylic acid. Typical results are shown in Fig. 3:

VCOAT VC-02-07-002/3





Fig. 3 Results of staining tests showing the effect of the presence of the plasma-deposited layer on the yield of the graft-coupling reaction. The photograph shows test samples after (left to right) acrylic acid grafting, anionic surface, toluidine blue stain; PEI coupling, cationic surface, Ponceau S stain; heparin coupling, anionic surface, toluidine blue stain. (VCOAT is the trademark of the heparin coating). Samples were cut and flattened to show the whole surface.

Fig. 3 shows that some grafting goes on even in the absence of the plasma deposited layer. This is most likely due to mechanical interlocking between homopolymerized acrylic acid and PTFE fibres of the stent graft without plasma deposited layer. This is confirmed by the much higher fastness of the plasma deposited sample in the routine stability test, that is overnight extraction in aqueous SDS. Performances of the heparin coated stents have been evaluated in several *in vitro* tests as well as animal studies. Fig. 4 shows a typical result of thrombin deactivation. This method briefly consists of exposure of a heparinized surface to a solution containing Anti Thrombin III followed by rinsing to leave only the ATIII that is bound to the heparin surface. After this rinsing the surface is exposed to a solution containing a known amount of thrombin. The ability of the heparin/ATIII surface to deactivate thrombin in solution is measured by collecting the solution of thrombin that was exposed to the surface and rinses of the surface. The amount of active thrombin in these collected solutions is determined by using a chromogenic substrate that is cleaved by active thrombin and generates a colour that can be measured spectrophotometrically. The difference in active thrombin left versus the start is the amount deactivated by the heparin/ATIII surface.

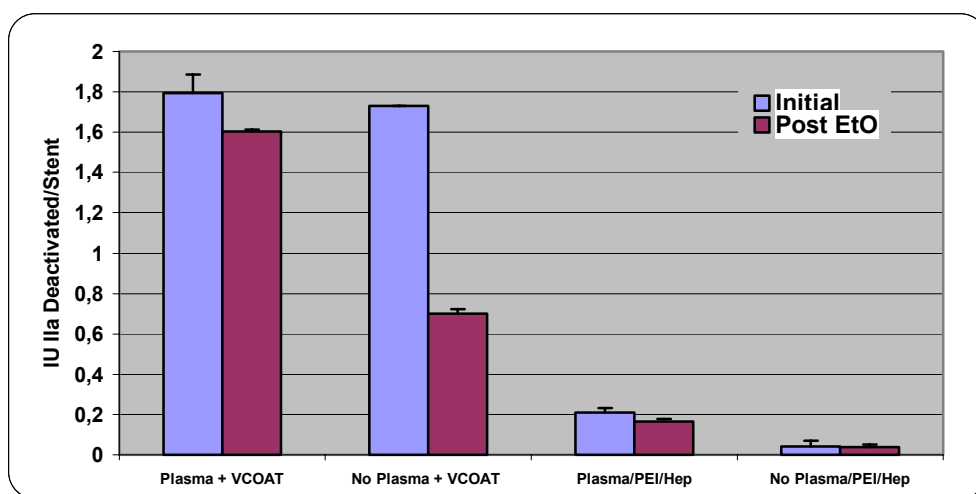


Fig. 4 Thrombin deactivation by selected samples

Note, first of all, that even the residual heparin on the sample obtained without plasma deposition yields a significant activity. Yet, more of 50% of it is lost after EtO sterilisation. As underlined above, these aspects of biomolecules activity at materials surfaces are mostly ignored, critical as they are in devices development.



Note, also, the significant difference between deactivation induced by the heparin coupled to the hydrogel layer as compared to a coupling scheme that lacks the underlying hydrogel [5]. The excellent performance of this coating have been confirmed in animal studies, and human clinical tests are presently going on.

### 3.1 Collagen coated dental implants.

Titanium is the material of choice for load-bearing, bone-contacting devices. The orthopedic and dental implants industry is largely based on the favourable interfacial interaction at the bone-titanium interface, and an extensive literature on osteointegration and related issues exists. Osteointegration is a well established property of titanium implant surfaces and the current success rate is satisfactory. Surface modification of titanium is still a very active area of research, because definite interest exists in surface treatments that can induce acceleration of normal bone healing phenomena. An accelerated stable fixation between bone and implant would allow early or immediate loading of the device, with significant implications in terms of decreased patient morbidity, patient psychology and health care costs [6].

While among currently available dental implants surface modification is obtained mostly through modification of the surface morphology (acid etching, sandblasting), more and more studies are devoted to biochemical methods of surface modification. Biochemical methods are aimed at the control of the tissue-implant interface by the immobilization and/or delivery of proteins, enzymes, or peptides for the purpose of inducing specific cell and tissue responses [6]. Among the molecules of direct relevance to the biochemical modification of bone-contacting surfaces, collagen is commonly used in dental surgery as osteogenic and bone filling material; in the spirit of biochemical modification of implant surfaces [6], implants bearing a surface layer of collagen could be exploited to apply directly to the implant site the properties of this interesting biomolecule.

Deposition from propylene plasma followed by Ce(IV) induced grafting of acrylic acid and collagen coupling has been used in the biochemical modification of titanium implants. XPS analysis shows the modification of the surface chemistry after the different steps [4].

Table 2 Surface composition (% at.) of the different samples, as detected by XPS analysis

Sample	C	O	N	Si	Ti	Other
Untreated Ti	33.9	46.9	1.1	0.7	14.9	N, Na, Mg, Ca
Plasma deposited Ti	97.2	2.5			0.3	
Acrylic acid grafted Ti	61.8	38.2				
Collagen coated Ti	69.2	17.1	12.6	0.9		Cl = 0.3
Collagen, reference#	69.1	17.5	11.7	1.8		

Beside several *in vitro* tests, one month implantation in rabbit femur was performed to check the effect of the coating on the bone healing rate. This animal model and experimental time can give valuable information on bone healing at an early phase which, as previously discussed, is the true goal of surface modification of this kind of implants. Experimental samples are shown below, after toluidine blue staining. The control obviously does not take the dye, while the coated one (on the left) becomes blue colored:



Fig. 5 Experimental samples for implantation in rabbit femur

Percentages of bone-to-implant contact and bone ingrowth in the threaded screw area and mirror area were evaluated by histomorphometry at sacrifice (6 rabbits, each of them bearing two implants per type, the total

number of implants is thus 12 for each type) [4]. The results clearly demonstrate that Collagen coated Ti screws show a higher percent bone contact with the surrounding bone than uncoated Ti. A significant increase of bone to implant contact and bone ingrowth was observed in ColTi versus uncoated Ti (+23.8%,  $p<0.01$ ; +7.6%,  $p<0.01$  respectively). As expected, no significant differences were observed outside the screw threads in the mirror area (MA) of each group thus demonstrating the homogeneity of the implanted bone. The BI/MA rate, on the contrary, showed a significant increase in the collage-coated Ti group in comparison with the uncoated Ti one (+6.7%,  $p<0.005$ ).

#### 4. Discussion on plasma process parameters

In the previous sections we have presented data related to the biological activity, either *in vitro* or *in vivo*, of selected medical devices. From the point of view of plasma processes, it is of interest to remark that the whole interfacial structure is built on the thin ( $\approx 20$  nm) plasma deposited layer. The obtained results show that the thin film deposited from plasma can effectively act as a stable interfacial layer, endowed by excellent durability in aqueous media. The key properties of the propylene plasma-deposited film that make it suitable as the first building block of complex interfacial structures are: reactivity in the grafting reaction; lateral homogeneity; adhesion to the substrate and resistance to delamination in water and in biological fluids. In the case of the stent, it is important to remark that deposition must be obtained even in the inside of the small diameter tubes. In our reactor configuration (diode reactor), the distance between the electrodes is a key parameter to achieve deposition on the inside of a tube: a distance  $L < 5$  cm is required in order to obtain satisfactory results. Film-substrate adhesion and durability is particularly challenging in the case of inorganic materials. The effect of the composite parameter power to flow rate ratio (W/F) on durability of films deposited on Ti samples was evaluated as follows: deposition was performed in different experimental conditions. This was followed by acrylic acid grafting and toluidine blue staining of the grafted layer. The dye taken by the graft was then released by immersion of the samples in high ionic strength solutions, and the adsorbance of the relevant solution was measured. A clear effect of W/F on dye uptake was observed (see. Fig. 6). XPS analysis performed on related samples confirmed that the observed trend was actually due to the delamination of the thin film upon grafting.

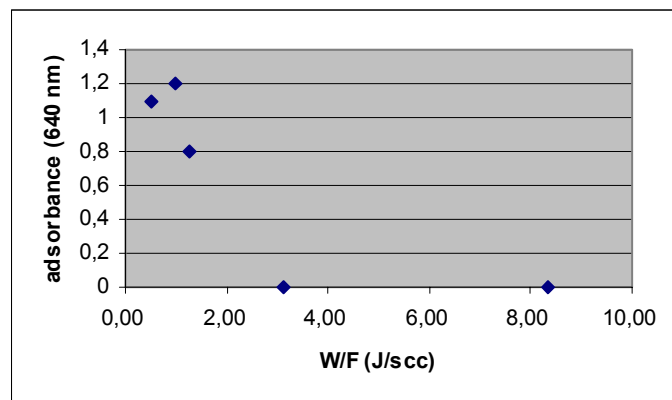


Fig. 6 Effect of the W/F ratio on the stability of the plasma deposited layer

#### References

- [1] B. D. Ratner, A Chilkoti, G. P. Lopez, in "Plasma deposition treatment and etching of polymers", R. D'Agostino, Ed., Academic Press, San Diego, 1990
- [2] M. Morra M, C. Cassinelli, J. Biomed. Mater Res. **37**, 198 (1997)
- [3] J. K Yun, K. DeFife, E. Colton, S. Stack, A. Azeez, L. Cahalan, M. Verhoeven, P. Cahalan, and J. M. Anderson, J. Biomed. Mater. Res. **29**, 257 (1995)
- [4] M. Morra M, C. Cassinelli, P. Cahalan, L. Cahalan, Biomaterials, accepted
- [5] F. W. Jeffrey, S. Keuren, J. H. Wielders, G. M. Willems, M. Morra, L. Cahalan, P. Cahalan, T. Lindhout, Biomaterials, **24**, 1917 (2003)
- [6] D. A. Puleo, A. Nanci, Biomaterials, **20**, 2311 (1999)

# **RF plasma treatment on the inside of small functional devices for biomedical application**

C. Oehr, D. Hegemann, M. Müller

*Fraunhofer Institute for Interfacial Engineering and Biotechnology IGB, Nobelstr. 12, 70569 Stuttgart, Germany;  
<http://www.igb.fraunhofer.de>*

Plasma treatments are very effective in the modification of solid surfaces relating to cleaning, etching, activation, functionalization, and coating. All common materials (polymers, metals, ceramics, glasses etc.) can be treated in the gas discharge. The surface-plasma interaction mainly proceeds via ions, radicals, and VUV. Depending on the gas type and the plasma parameters used, degradation or deposition occurs. Using rather mild plasmas, i.e. low power input, functional groups can be retained and chemically bonded to the surface [1]. The development of these numerous modifications is generally performed on flat surfaces in order to obtain a homogeneous treatment and to simplify the characterization. Much effort is carried out to up-scale these processes for example for large area coatings. However, many functional devices are three-dimensionally formed and possess recesses like cavities (e.g. capillaries), pores (e.g. membranes) or openings (e.g. stencils, textiles or hollow fibers).

Therefore, this work investigates the penetration of active plasma species into small fissures, as well as the inner modification of hollow fibers. For the plasma treatment, RF discharges (13.56 MHz) were used and the reactor geometry and gas flow were adjusted to the sample geometry. To examine the treatment in small fissures with width varying from 6 mm to 15  $\mu\text{m}$  and aspect ratios  $>1$ , a plane parallel electrode configuration was chosen. Due to collisions in the gas phase and surface diffusion, the conformity inside the fissures is better than expected from a pure “sticking” model.

The modification and the film thickness inside the recesses is measured using REM (in cross-section), ESCA and AES (sputtering techniques). The treatment or deposition rate are compared to flat geometries. Plasma activation, functionalization and coating were investigated.

Some applications are presented.

- [1] C. Oehr, D. Hegemann, M. Müller, V. Sciarratta, U. Vohrer, Proc. 14th Int. Symp. Plasma Chem. **Vol. IV**, 1747 (1999).

# Creation of Biochips Employing Microfabrication Technologies

*Y. Horiike<sup>1</sup>, A. Oki<sup>1</sup>, H. Ogawa<sup>1</sup>, M. Takai<sup>2</sup>, S. Momose<sup>3</sup>, A. Yokogawa<sup>3</sup>  
and Y. Takamura<sup>4</sup>*

*<sup>1</sup> National Institute for Materials Science, 1-1 Namiki, Tsukuba, Japan*

*<sup>2</sup> The University of Tokyo, 7-3-1 Hongo, Bunkyo-ku, Tokyo, Japan*

*<sup>3</sup> ROHM Corp., 21 Saiin Mizosaki-cho, Ukyo-ku, Kyoto, Japan*

*<sup>4</sup> Japan Advanced Institute of Science and Technology, 1-1 Asahidai, Tatsunokuchi, Ishikawa, Japan*

## Abstract

We study creation of a variety of biochips enabling us to diagnose multi-items of our health/disease from analyzing a trace of a blood collected by a painless needle. For the goal, we are developing a healthcare chip, a chip examining hepatic functions, and a cell sorter chips and DNA trap/separation chips. The plasma etching contributed currently to fabrication of micro/nano-channels and nano-pillars on a quartz plate.

## 1. Introduction

Much attention is now paid for development of biochips enabling us to check health/disease, read DNA sequence at a high speed, diagnose SNPs, detect cancer cells, treat the affected part by “in vivo” devices, etc. Micro-fluidics lying at the base of fine channels is also studied vigorously. The plasma processes are used currently to etching of micro/nano-structure and treatment of substrate surfaces immobilizing bio-molecules. Especially, the plasma etching technology is indispensable for us to fabricate micro-channels and nano-pillars on a quartz plate. In this paper, we report our recent studies concerning a healthcare chip, a chip examining hepatic functions, and a cell sorter chips and DNA trap/separation chips, which are developed employing microfabrication technologies.

## 2. Healthcare chip

The healthcare chip checks our health condition at home by measuring multi-item markers such as pH, Na<sup>+</sup>, K<sup>+</sup> and Ca<sup>++</sup>, uric acid, lactic acid and glucose using integrated chemical sensors from a trace blood collected by a painless needle [1]. A poly(ethylene terephthalate)(PET) plate (2 x 2 cm<sup>2</sup>) was used because it should be cheap and disposable. The chip equipped with a painless needle of a 100 μm diameter SUS tube with a tip sharpened at an angle of 10 degrees, a U-shaped capillary for centrifugal separation of plasmas from the whole blood, an integrated carbon electrodes coated by ionophore and enzyme films.

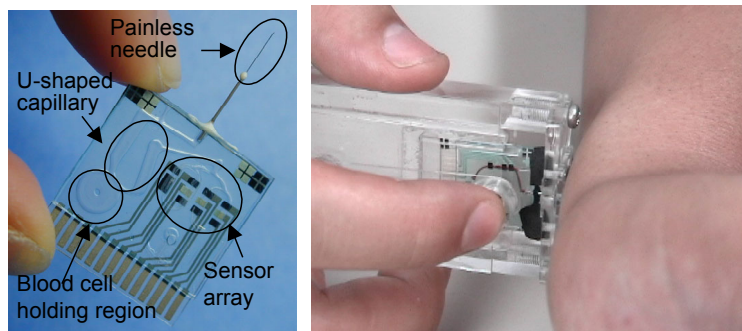


Figure 1. Healthcare chip employing the external pump.

The PET substrate with a channel pattern was pasted with a polyester plate on which carbon electrodes were screen-printed via the photo-polymerized epoxy film. The inner wall coating of the biocompatible MPC (2-methacryloyloxyethyl-phosphorylcholine) polymer whose surface was similar to the bio-membrane [2]. We developed a chip which was inserted a holder and introduces the blood into the channel employing a pump prepared at the outside of the chip as shown in Fig. 1. At present, the chip can measure pH,  $\text{Na}^+$ ,  $\text{K}^+$ , uric acid and glucose. To search the location of the vein, we have developed the blood collection system, which allows us to visualize the vein using near-infrared light (NIR) and then to detect arrival of the needle at the vein surface employing electrical techniques. Since the painless collection of the blood is a key for our goal, we are also developing a new structure (see Fig. 2) in which Si needles and through-holes are separately responsible for piercing into a capillary vessel and extracting the blood, respectively [3]. Anisotropic wet etching and plasma etching with  $\text{SF}_6$  fabricated the former and the latter, respectively.

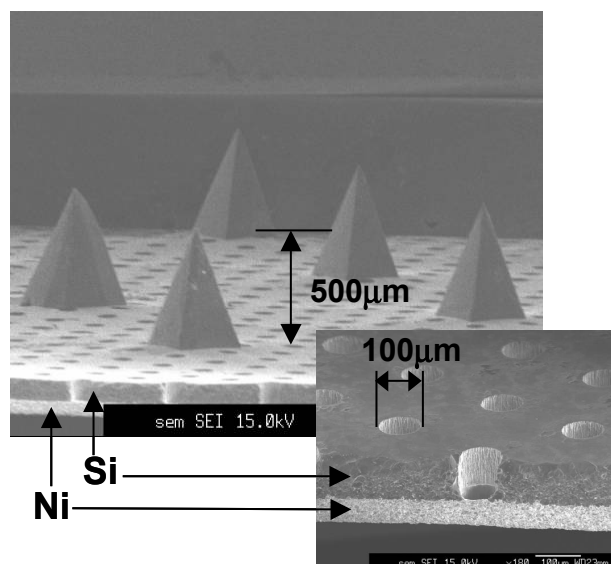


Figure 2. SEM image of Si needle array chip.

### 3. Hepatic function examination chip

We also studied a colorimetric measurement chip checking our hepatic functions by detecting three important markers of GPT, GOT,  $\gamma$ -GTP from small amount of the blood [4]. These measurements were carried out by rate assay method, which measured time-dependent decay of absorption of a light with a wavelength of 340 nm in the plasma and substrate buffers. Therefore, the

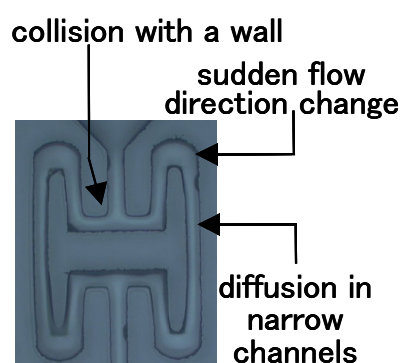


Figure 3. Mixing chamber structure.

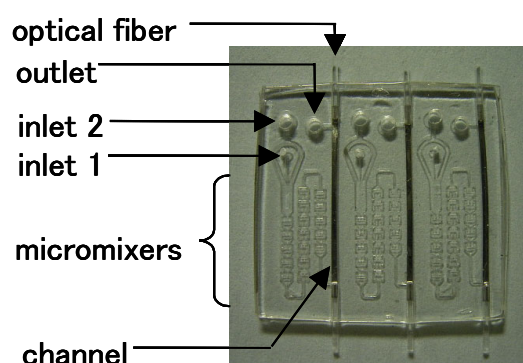


Figure 4. Photograph of chip examining  $\gamma$ -GTP, GOT and GPT activities.

mixing of these solutions is a key technology for the measurements. Figure 3 shows a structure of a mixing chamber [5]. The mixture collides with a wall and then its flow direction is changed suddenly

at a corner. Diffusion of molecules is also promoted in narrow channels. At the present chip, the process was repeated sequentially for 6 stages. The mixing was performed at the wide ranges of drawing velocities. Figure 4 shows a chip examining three markers, which includes three channels with each mixer. Since an incident light should propagate with minimizing loss of the light for the colorimetry, an Al film was coated on the inner walls of the channels. Quartz fibers were equipped with both channels and a 340 nm light, which was produced by a band-pass filter of a W lamp, was introduced to one inlet and the decayed light was detected a photodiode. Correction curves of each enzyme activities after the mixing were measured not only for normal adults but also those for abnormal values.

#### 4. Cell sorter and lymphocyte separation

A cheap and disposable cell-sorting chip conducting individual cell characteristics, are also required because the chip treats the blood and abnormal cells. A cell sorter chip (see Fig. 5) was developed employing a low voltage driven electroosmosis flow (EOF) pump [6], which was set between two branches. Figure 6 shows a detail structure of the EOF pump. Channels with a shallow

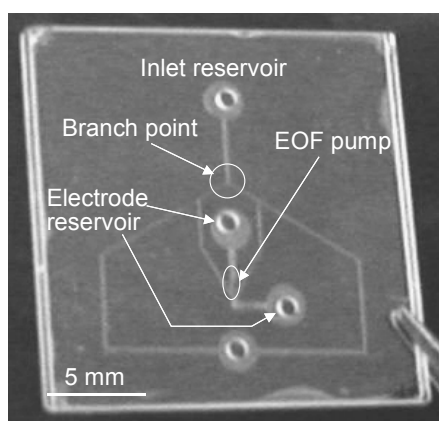


Figure 5. Photograph of a cell sorter chip made by a quartz.

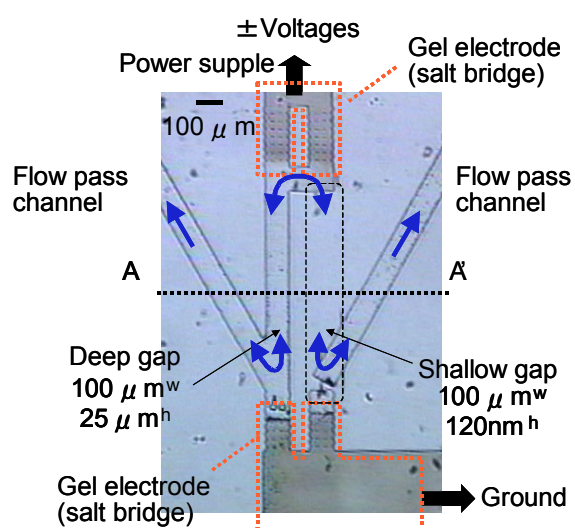


Figure 6. Detail structure of the high pressure EOF pump.

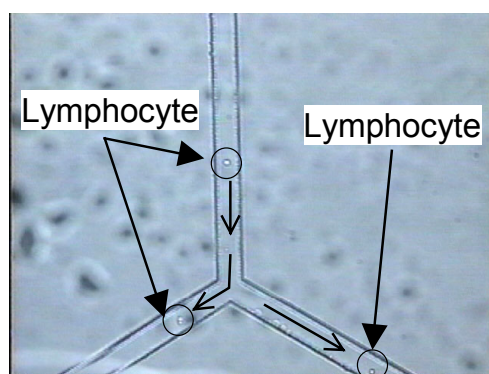


Figure 7. Photograph of an actual cell sorting of lymphocytes.



gap of a 120 nm depth and a deep gap of a 25  $\mu\text{m}$  depth were parallel and sequentially connected through a flow pass channel. Edges of both channels connect with reservoir electrodes supplying a ground potential to a cathode and voltages through conductive gel electrodes. The gel electrode was patterned by a photo-polymerizing technique. Positive and negative voltages added an anode electrode enables us to change the flow direction. Since the flow direction is same, the pump with both channels is operated oppositely. However, the shallow depth channel whose pumping ability dominates the deeper depth one governs one direction pumping. Figure 7 shows a photograph of an actual cell sorting of lymphocytes extracted from a rat.

## 5. Long base pair DNA analysis

### 5-1 Long base pair DNA trapping chip

At present, separation of longer base pair DNA is not studied so much in contrast with that of shorter base pair DNA. For this purpose, we investigated the DNA size separation using a tapered channel as shown in Fig. 8(a). When both the hydro pressure and the electric force were applied at the same time in an opposite direction, we found that larger size DNA was trapped near the narrowest position in the channel as shown in Fig. 8(b). Based on the result, one structure, where the narrowest channel width was 5  $\mu\text{m}$ , was developed as shown in Fig. 9. As first step, a rightward electric force and a leftward stronger hydro force were applied. DNA flowed from the right inlet to be trapped and concentrated at the center as shown in Fig. 9(a), while other substance and buffer solution flowed out to the left side. After 1-minute concentration, by removing the electric force, the concentrated DNA was quickly released to the left side into collecting channel as shown in Fig. 9(b). We now plan that

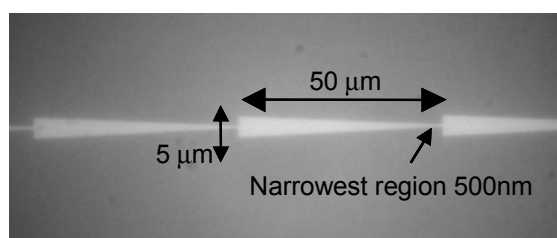


Figure 8(a). Photograph of a tapered channel.

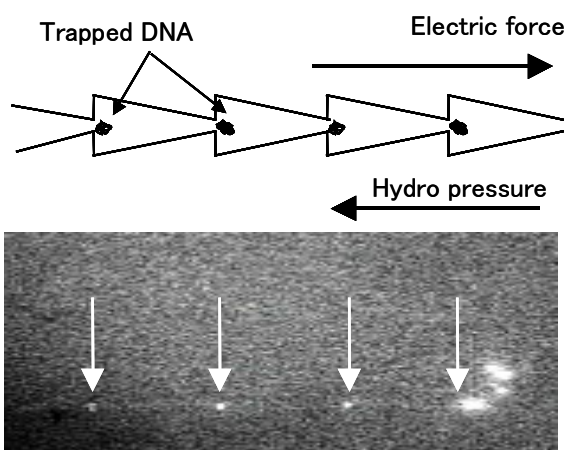


Figure 8(b). Illustration and photograph of the T4 DNA trap.

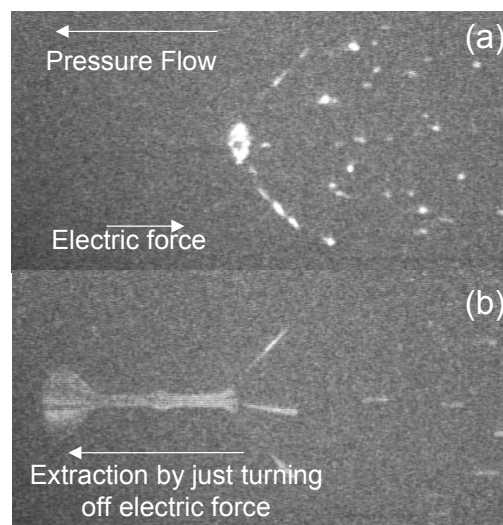
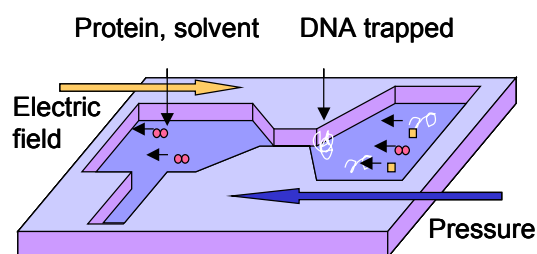


Figure 9. Concentration(a) and release(b) of DNA.

this large DNA selective trapping system is applied to an infection diagnostic chip, where at first then DNA/RNA is trapped and concentrated from the solution after wall lysis of the virus in the plasma, and then they are amplified by the PCR. Finally, DNA resulting from the infection disease is detected.

## 5-2 DNA fast separation chip

Some attempts have been reported to make an artificial gel based on nano-structure fabricated by lithographic techniques for high-performance separation of bio-molecules [7]. A dense pillar structure made of a quartz plate employing fluorocarbon plasma etching with a Ni mask electroplated in a resist

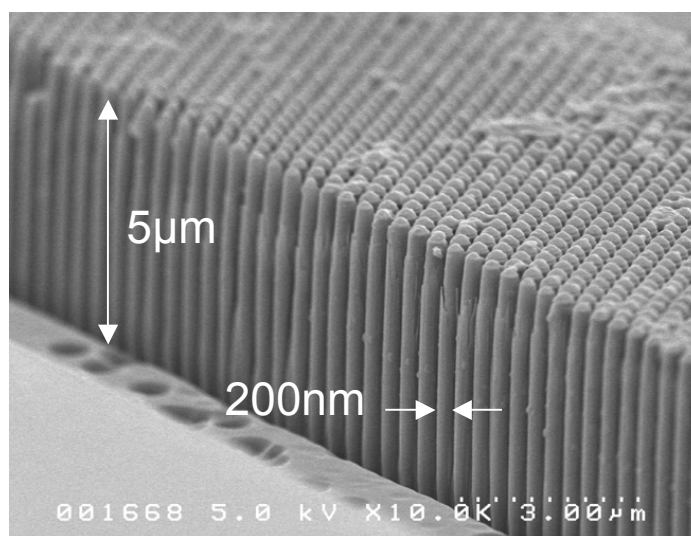


Figure 10. DNA fast separation chip.

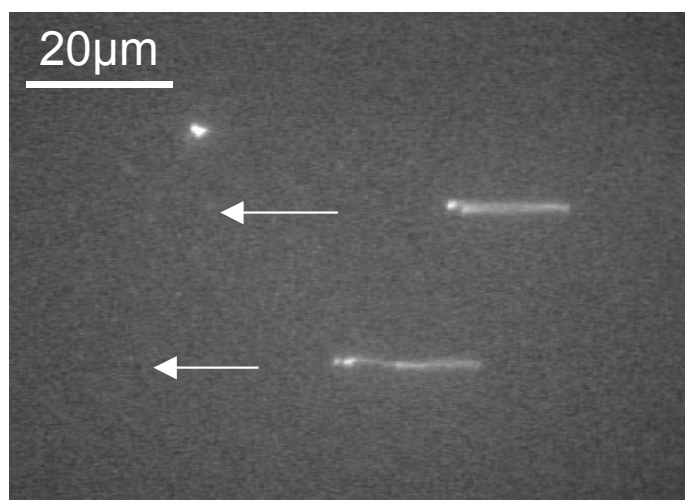


Figure 11. Electrophoresis of T4 DNA in pillar structure.

pattern fabricated by an EB lithography. The diameter, pitch, height of the pillars and the aspect ratio were 200 nm, 400 nm, 5 μm and 25, respectively (see Fig.10). A DNA of T4 of 16Kbp was rounded in the region without pillars, while it stretched and separated by electrophoresis at the pillar region as shown in Fig. 11. As a result, T4 and λDNAs were separated clearly after 20 seconds as shown in Fig.



12. A channel, in which regions with and without pillars were arranged alternately, enhanced the separation.

## 6. Future prospect

Our stance for studies on the biochip is creation of the cheap/disposable biochips, which analyze and measure maximum markers of health and disease from trace amount of a blood collected by a painless needle, thereby contributing to the advanced medical treatment. If the chip enables us to measure many items at the same time, we will be able to check easily and rapidly our health and disease conditions at home by referring a lot of databases stored in the clinic centers through IT network. We wish to make efforts to build up a new science, technology and industry field called by “Healthtronics”.

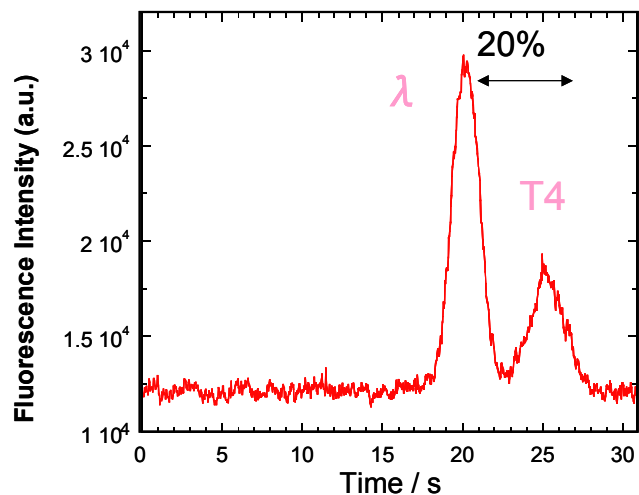


Figure 12. Separation of T4 and  $\lambda$ DNA.

## References

- [1] A. Oki, et al., *2001 Intern. Conf on Solid State Devices and Materials, Tokyo*, (2001) 460.
- [2] K. Ishihara, et al., *J. Biomat. Mat. Res*, **26**, (1992) 1543.
- [3] S. Momose, et al., Submitted to *Micro Total Analysis System ( $\mu$ TAS) 2003*.
- [4] A. Oki, et al., *Jpn. J. Appl. Phys.*, **42**(3B) (2002) L342.
- [5] A. Yokogawa, et al., Submitted to *Micro Total Analysis System ( $\mu$ TAS) 2003*.
- [6] Y. Takamura, et al., *Electrophoresis*, **24** (2003) 185.
- [7] S. W. Tuner, et al., *Monolithic nanofluid sieving structures for DNA manipulation*, *J. Vac. Sci. Technol. B* **16** (1998) 3835.

# Treatment of living cells and tissues using the plasma needle

E. Stoffels, I.E. Kieft, J.L.V. Broers, F.C.S. Ramaekers, D.W. Slaaf

*Department of Biomedical Engineering, Eindhoven University of Technology, Eindhoven, The Netherlands*

## Abstract

We investigate the interactions of a small atmospheric plasma source (plasma needle) with living cells and tissues. The discharge is induced by a radio-frequency voltage applied to a metal pin. This plasma operates at room temperature, in the milliwatt power regime. It causes no thermal or electrical damage to living tissues. Our aim is to introduce plasma treatment as a non-destructive and high-precision technique in fine surgery, to remove cancer cells, scar tissue and to aid wound healing. At present, we use cells in culture as a model system. Several potentially beneficial cell responses have been already identified.

## 1. Introduction

Non-thermal plasma is the only medium that combines exceptional chemical activity with mild, non-destructive character. Such plasmas are capable of virtually any surface treatment, including processing of heat-sensitive materials. Plasma etching, thin layer deposition, cleaning and activation of surfaces are already well-established in material science. Recently, plasmas have started to conquer the world of biomedical technology. Plasma coating of artificial implants to increase their bio-compatibility, surface micro-patterning of scaffolds to control cell adhesion, bacterial decontamination of medical/surgical equipment are just a few examples illustrating the rapidly rising popularity of plasma technology in medicine. The next, logical step in this development is *in vivo* plasma treatment. Plasma interaction with living tissues is a newly launched research line at the Eindhoven University of Technology. In order to achieve beneficial plasma action, the choice of an adequate source is crucial: it must operate under atmospheric pressure, be electrically and chemically safe and it may not cause any thermal damage to the living object. Recently, we have developed a new source (plasma needle) which meets these requirements [1]. Plasma needle is a radio-frequency driven micro-discharge generated at the tip of a sharpened metal pin. The plasma has been characterised in terms of electric and thermal properties, and its non-destructive character during interactions with organic materials has been demonstrated. Plasma can be applied directly to human skin.

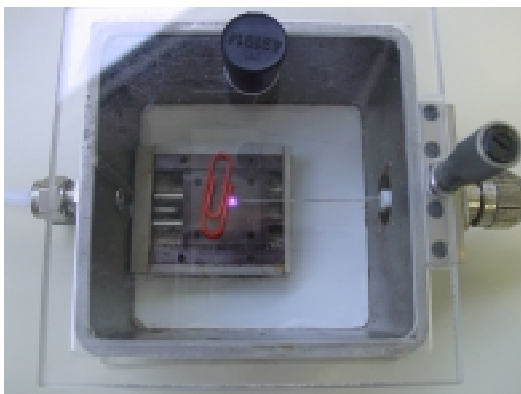


Figure 1: A picture of the plasma chamber (right – rf connection, left – helium inlet).



Figure 2: Plasma torch (right – rf connection, down – helium inlet).

## 2. Plasma appearance and properties

Plasma needle is a radio-frequency (rf – about 13 MHz) driven glow generated at the tip of a sharp tungsten needle (thickness 0.3 mm). We have used two configurations: a metal/plastic plasma chamber, shown in Figure 1 and a hand-held plasma torch (Figure 2). Basically, this is a unipolar configuration, where remote surroundings serve as a grounded electrode. However, when the needle is brought in the vicinity of other objects, the plasma switches to a bipolar mode, where the glow spreads over the object's surface. Some

examples are shown in Figure 3. Similar to other atmospheric glows, the plasma operates most readily in helium. However, this is not a hindrance: for the safety of treated tissues it is favourable to use an inert gas as an ambient atmosphere and allow only small amounts of active species (e.g. air). The helium flow is typically 2 slm. The plasma chamber (Fig. 1) is specially developed to treat cells in culture, placed on flat glass substrates. The chamber is supplied with two external manipulators: one to move the stage on which treated samples are placed, and another one to adjust the distance between the needle and the sample surface. The plasma torch (Fig. 2) is much more flexible – it can serve to treat tissues *in vivo*, perform sterilization of dental cavities, clean and activate various non-regular surfaces. In this configuration the plasma can be also directly observed under a microscope, so that plasma treatment can be visualized real time. In all configurations, typical rf voltages are 200 – 400 V peak to peak, and power consumption in the plasma varies from 50 mW to 1 W.

As shown in Figure 3, plasma can be safely applied to the skin. However, prior to exposing living tissues to the plasma, we have performed rigorous temperature measurements by means of optical emission spectroscopy (rotational temperature from N<sub>2</sub> bands, [1]), thermocouples and a calibrated thermal probe [2]. In all cases it has been established that in the low-power (<0.5 W) operation regime the plasma operates at room temperature and does not pose risk of thermal damage to the tissue. Further in this work we concentrate on refined responses of living cells to plasma treatment.

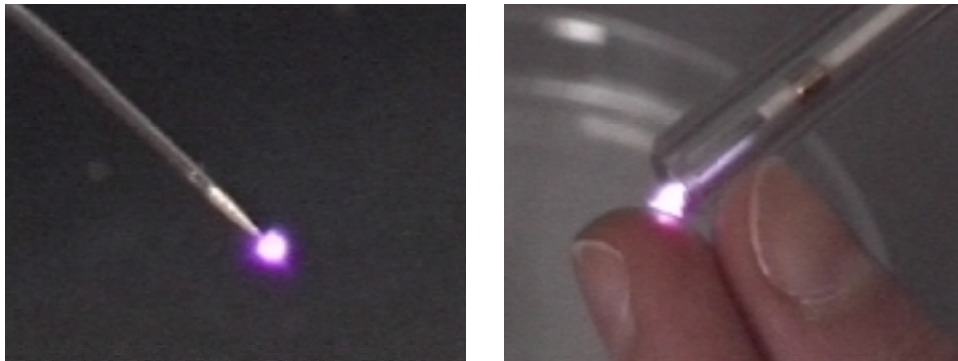


Figure 3: Left: unipolar plasma mode (size of the glow is about 1 mm), right – plasma spreads over the skin.

### 3. Cells in culture

Before plasma techniques are ready for clinical implementation, we must conduct a thorough study of plasma influence on living cells. In this fundamental part of our work we investigate and classify all possible cell responses, and relate them to the applied plasma conditions. We use two model systems: the Chinese hamster ovarian cells (CHO-K1) and the human cells of lung carcinoma MR65. The CHO-K1 cells are basal type, used as a first model to identify general cell responses, while MR65, being human epithelial cells, bring us closer to the intended medical applications (e.g. skin treatment). Cells are cultured on glass substrates, where they spread and form a kind of a two-dimensional tissue (Figure 4). Samples are treated in the plasma chamber for about 30 seconds (1-2 seconds per individual cell).

In contrast to mechanical, thermal or laser methods, plasma treatment should not cause severe injury and cell death (necrosis). In the latter process cell membrane is damaged and the released cytoplasm induces an inflammatory reaction in the tissue. Thus, we concentrate on cell reactions in which the membrane integrity is preserved. One of such refined responses is apoptosis (the programmed cell death). This process is schematically depicted in Figure 5. In the course of programmed cell death, the cytoplasm is contained in membrane-surrounded apoptotic bodies. No damage to the neighbouring cells and no inflammation occurs. Apoptosis can be diagnosed in a late stadium by observation of membrane blebbing, or in an earlier phase when the DNA in the cell nucleus condenses. For the latter diagnostics, fluorescent staining of the cell's DNA in combination with a microscopic study is necessary.

In order to establish the condition of cells after plasma treatment, we apply viability assays standard in cell biology. For observation, a confocal laser scanning microscope (CLSM) is used. The CLSM is equipped with an argon ion laser (488 nm), which excites the fluorescent probes applied to the cells. Confocal microscopy allows for three-dimensional imaging with a spatial resolution of 0.2  $\mu$ m. Typically we use two fluorescent probes: Cell Tracker Green (CTG) and Propidium Iodide (PI). CTG is absorbed by all cells, but only living cells transform it into fluorescent species. This probe is used to verify cell viability: in living cells

the whole cytoplasm displays green fluorescence. PI penetrates only necrotic cells (with damaged membranes) and binds to the DNA and RNA. So-called dual staining (CTG+PI) is applied about 1 hour after plasma treatment, in order to distinguish between dead and living cells.

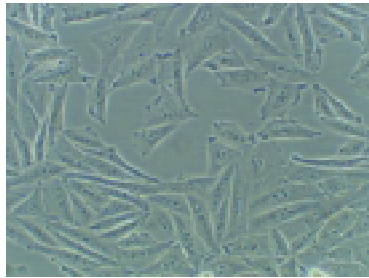


Figure 4: CHO-K1 cells are attached to each other and assume elongated shapes.

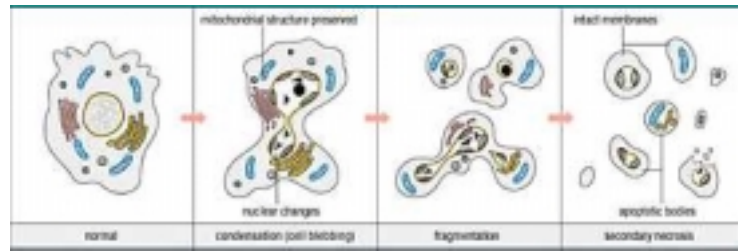


Figure 5: The process of apoptosis: the cell falls apart into small fragments surrounded by the membrane. The cytoplasm is not released.

### 3. Plasma interactions with cells

Of course, it can be expected that a high dose of plasma treatment is lethal to cells. Applying plasma power higher than 0.3 W causes total necrosis in the treated area. A curious fact is that the necrotic cells are not disintegrated (like in case of thermally induced necrosis) but fixed in a way that the cell shape is well preserved. Damage to the membranes has been established using PI staining. At lower doses plasma treatment causes no necrosis, but the desired sophisticated cell responses: apoptosis or (temporary) interruption of cell adhesion.

Apoptosis has been observed at intermediate plasma powers (0.1 – 0.2 W), but so far this process does not seem to be a predominant cell response to plasma treatment. In CHO-K1 about 3% of the cell population became apoptotic 4 hours after treatment (0% in the control sample) and in MR65 the percentage was significantly higher (10%). Possibly, this result can be still improved by better controlling the plasma dose. Some apoptotic cells are shown in Figure 6. Note the characteristic shape of dying cells.

In the same power range, cell deactivation can be obtained. Note that a rather small fraction of the cells in Figure 6 is apoptotic. However, the rest of the cells is also affected. This deactivation process is different from necrosis, because the membrane integrity is preserved (negative results after PI staining). The cells remain unchanged for several days, no activity (movement, proliferation) is observed. The actual condition of the cells is not yet clear. However, this is in principle an interesting process, and it surely deserves to be studied in detail in future. Since the cytoplasm is not released, damage to the tissue should be minimal. This could offer a fast and non-destructive way of deactivating and disposing of unwanted cells (e.g. cells producing scar tissue, or atherosclerotic plaque).

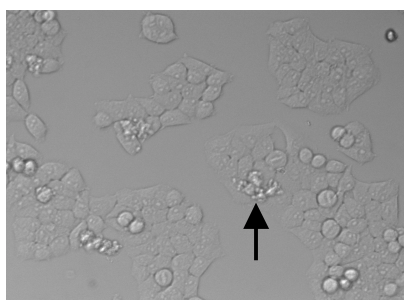


Figure 6: Plasma-treated MR65 cells. Some cells are apoptotic (as indicated), the rest is detached and deactivated.

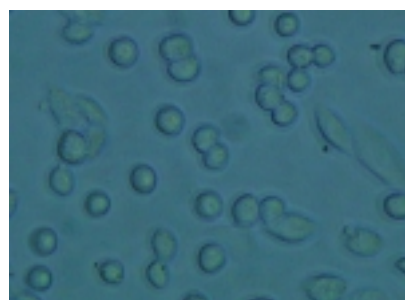


Figure 7: Detached CHO-K1 cells (spherical).

Finally, in the very low-power plasma operation regime, the finest cell response is observed: cell detachment without loss of cell viability. This can be compared to "surface processing" of living cells, where the plasma action is restricted to the membrane. In Figure 7 treated CHO-K1 cells are shown. Since the influenced cells do not form a firmly attached sheet anymore, they assume a spherical shape (minimum surface to volume ratio). Cell detachment seems to be a general feature - similar responses have been observed in MR65 samples. The cells are viable, as confirmed using CTG staining, and they reconstruct a sheet within a few hours. At present we try to elucidate the mechanism of this cell response. Presumably, cell detachment is caused by plasma-induced damage to cell adhesion molecules. These trans-membrane proteins are most

likely attacked by reactive oxygen species (ROS) produced in the plasma. Since the cell remains viable, it repairs the damage on a typical time scale of 4 hours, so that the cell contact is reconstructed. Plasma treatment offers not only a possibility to dispose of the cells, but also to manipulate them. The loose cells can be transferred to another substrate, or rearranged within the tissue. Treatment based on local cell detachment may become a truly minimum-destructive surgical technique.

### **3. Conclusion**

Plasma interactions with living cells do not necessarily cause cell death. Dependent on plasma conditions, several refined cell responses are induced: programmed cell death (apoptosis), cell deactivation and temporary loss of cell-cell interactions. All these plasma interactions open virtually endless possibilities of fine tissue treatment, high-precision cell removal and cell manipulation.

### **References**

- [1] E. Stoffels, A.J. Flikweert, W.W. Stoffels, G.M.W. Kroesen, Plasma Sources Sci. Technol. **11**, 383 (2002).
- [2] E. Stoffels, R.E.J. Sladek, R. Walraven, P.J.A. Tielbeek, Plasma Treatment of Dental Caries, a contribution to this conference.

# Mass-Spectrometric Characterization of Gases and Particles in Reacting Flows

S. Park, F. Liao, D. Lee, S.L. Girshick and M.R. Zachariah

*Department of Mechanical Engineering, University of Minnesota USA*

In this paper we discuss our activities to characterize by mass-spectrometry gases and particles sampled from reacting flows.

First we describe a molecular beam mass spectrometry system for *in situ* measurement of the concentration of gas phase species including radicals impinging on a substrate under thermal plasma chemical vapor deposition (TPCVD). Dynamically controlled substrate temperature has been achieved using a variable thermal contact resistance method via a backside flow of an Argon/Helium mixture. A high quality molecular beam with beam-to-background signal greater than 20 has been achieved under film growth conditions through a small nozzle (75  $\mu\text{m}$ ) within the substrate. Mass discrimination effects have been accounted for in order to quantify the species measurements. We demonstrate that this system has a minimum detection limit of under 100 ppb. Quantitative measurements of hydrocarbon species ( $\text{H}$ ,  $\text{H}_2$ ,  $\text{C}$ ,  $\text{CH}_3$ ,  $\text{CH}_4$ ,  $\text{C}_2\text{H}_2$ ,  $\text{C}_2\text{H}_4$ ) using  $\text{Ar}/\text{H}_2/\text{CH}_4$  mixtures and silicon species ( $\text{Si}$ ,  $\text{SiH}$ ,  $\text{SiH}_2$ ,  $\text{SiCl}$ ,  $\text{SiCl}_2$ ,  $\text{Cl}$ ,  $\text{HCl}$ ) using  $\text{Ar}/\text{H}_2/\text{SiCl}_4$  mixtures have been performed under thermal plasma chemical vapor deposition conditions.

We have also recently developed a single particle mass spectrometer to analyze the elemental composition of individual aerosol particles and apply the technique to study the kinetics of aerosol chemistry. In one example problem metal nitrate aerosols were passed through a tube furnace to induce thermal decomposition and transformation into oxides, and were delivered with high efficiency into the vacuum system of the single particle mass spectrometer using an aerodynamics lens arrangement. The particles were ablated and torn down to atomic ions with a tightly focused, high-power pulsed laser in the extraction field of the time-of-flight mass spectrometer. Mass spectra thus obtained are shown to carry a quantitative signature of the elemental composition of individual particles, and allow for on-line measurement of the stoichiometry transition from nitrate to oxide as the particles passed through a tube furnace. The results were used to calculate the reaction rates and activation energies for the decomposition reaction. In parallel, reaction rates were obtained by conventional thermogravimetric analysis, and a comparison revealed significant differences in measured reaction rates between the aerosol and conventional methods. In particular, it was found that the reaction rates determined in the aerosol phase were significantly higher than those obtained by traditional thermal methods, which we believe is associated with heat and mass transfer limitations associated with bulk methods.

# Plasma deposition of fluorinated micro- / nano- structured coatings

F. Palumbo<sup>1</sup>, R. d'Agostino<sup>2</sup>, P. Favia<sup>2</sup>, G. Cicala<sup>1</sup>, A. Milella<sup>2</sup>

*1 Istituto di Metodologie Inorganiche e dei Plasmi - CNR,  
2 Dipartimento di Chimica – Università degli Studi di Bari  
via Orabona 4, 70126 Bari, (Italy)*

Modulating Radio Frequency Glow Discharges (RFGD) fed with Tetrafluoroethylene (C<sub>2</sub>F<sub>4</sub>), with on time (*t<sub>on</sub>*) and off time (*t<sub>off</sub>*) in the range 1-400 ms, coatings with a unique morphology as shown in figure 1 are obtained. In particular when the Duty Cycle (DC = *t<sub>on</sub>* / *period*) is decreased from 100

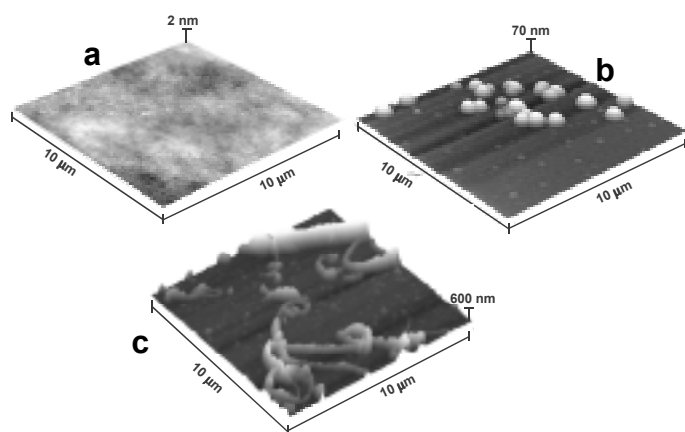


Fig.1 – AFM micrographs of films deposited at 100% (a), 20% (b) and 5% (c) of DC (100 W, 200 mtorr)

% (continuous discharge) to 5 %, the coating passes from a flat morphology, to a ribbons-rich surface. For intermediate DC values the coatings mainly consists of spherulites, whose size distribution changes continuously. The spherulites are more homogeneous in size at higher DC.

For a better understanding of the deposition process, the plasma phase has been investigated by means of Time Resolved Optical Emission Spectroscopy (TROES), and Infrared Absorption Spectroscopy. On the other hand, besides the morphological characterization carried out with AFM, the coatings have

been studied by means of various diagnostic tools: X-ray Photoelectron Spectroscopy, X-ray Diffraction, Imaging-SIMS and FT-IR.

The results show that ribbons regions have an higher Teflon-like character, and crystalline degree. Furthermore it is unlikely that the ribbon- structures can be associated to particulate formation in the gas phase: in fact when the experimental conditions are continuously moved to higher rate recombination regimes (higher pressure and/or power), the ribbons disappear. The following mechanism, based on the AGM one, has been hypothesised to explain the changes in the morphology of the coating. The ribbons growth depends on the competition between the surface migration of small adsorbed radicals towards the nucleation centres, and their reaction with the impinging radicals.

